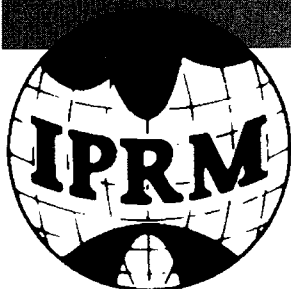


Conference Proceedings



Est. 1989



IEEE



Seventh International Conference on Indium Phosphide and Related Materials

*

May 9-13, 1995
Hokkaido University Conference Hall
Sapporo, Hokkaido, JAPAN

19950626 018

Sponsored by the
Japan Society of Applied Physics
IEEE Lasers and Electro-Optics Society
and the IEEE Electron Devices Society

In cooperation with
the Institute of Electronics, Information and Communication Engineers
Optoelectronic Industry and Technology Development Association
and the
Research and Development Association for Future Electron Devices

REPORT DOCUMENTATION PAGE			Form Approved OMB No. 0704-0188	
Public reporting burden for this collection of information is estimated to average 1 hour per response, including the time for reviewing instructions, searching existing data sources, gathering and maintaining the data needed, and completing and reviewing this collection of information. Send comments regarding this burden estimate or any other aspect of this collection of information, including suggestions for reducing this burden, to Washington Headquarters Services, Directorate for Information Operations and Reports, 1215 Jefferson Davis Highway, Suite 1204, Arlington, VA 22202-4302, and to the Office of Management and Budget, Paperwork Reduction Project (0704-0188), Washington, DC 20503.				
1. AGENCY USE ONLY (Leave blank)		2. REPORT DATE		3. REPORT TYPE AND DATES COVERED FINAL REPORT 1 May 95 - 30 June 1995
4. TITLE AND SUBTITLE Seventh International Conference on Indium Phosphide and Related Materials			5. FUNDING NUMBERS 61102F 2301/AS & BS	
6. AUTHOR(s) Dr Edward L. Labuda			AFOSR-TR 95-0431	
7. PERFORMING ORGANIZATION NAME(S) AND ADDRESS(ES) Inst of Electrical and Electronics Engineering 445 Hoes Lane Piscataway, NJ 08855			8. PERFORMING ORGANIZATION REPORT NUMBER	
9. SPONSORING/MONITORING AGENCY NAME(S) AND ADDRESS(ES) AFOSR/NE 110 Duncan Avenue Suite B115 Bolling AFB DC 20332-0001			10. SPONSORING/MONITORING AGENCY REPORT NUMBER F49620-95-1-0371	
11. SUPPLEMENTARY NOTES				
12a. DISTRIBUTION/AVAILABILITY STATEMENT APPROVED FOR PUBLIC RELEASE: DISTRIBUTION UNLIMITED				
12b. DISTRIBUTION STATEMENT				
13. ABSTRACT (Maximum 200 words) A CONFERENCE WAS HELD				
14. SUBJECT TERMS			15. NUMBER OF PAGES	
			16. PRICE CODE	
17. SECURITY CLASSIFICATION OF REPORT UNCLASSIFIED	18. SECURITY CLASSIFICATION OF THIS PAGE UNCLASSIFIED	19. SECURITY CLASSIFICATION OF ABSTRACT UNCLASSIFIED	20. LIMITATION OF ABSTRACT UNCLASSIFIED	

Conference Proceedings

Seventh International Conference on Indium Phosphide and Related Materials

*

May 9-13, 1995
Hokkaido University Conference Hall
Sapporo, Hokkaido, JAPAN

Sponsored by the
Japan Society of Applied Physics
IEEE Lasers and Electro-Optics Society
and the IEEE Electron Devices Society

In cooperation with
the Institute of Electronics, Information and Communication Engineers
Optoelectronic Industry and Technology Development Association
and the
Research and Development Association for Future Electron Devices

IEEE Catalog #95CH35720

Library of Congress #94-79424

DTIC QUALITY INSPECTED 3

Approved for public release
distribution is unlimited

Joan Bolger
STINFO Program Manager

FOR
OFFICIAL
USE
ONLY
This document is approved and its
release is authorized by AFR 190-12
dated.

EX-100 (AFSC)

The papers in this book comprise the digest of the meeting mentioned on the cover and title page. They reflect the author's opinions and are published as presented and without change in the interest of timely dissemination. Their inclusion in this publication does not necessarily constitute endorsement by the editors, the Institute of Electrical and Electronics Engineers, Inc.

©1995 by the Institute of Electrical and Electronics Engineers, Inc. All rights reserved.

Copyright and Reprint Permissions: Abstracting is permitted with credit to the source. Libraries are permitted to photocopy beyond the limits of U.S. copyright law, for private use of patrons those articles in this volume that carry a code at the bottom of the first page, provided the per-copy fee indicated in the code is paid through the Copyright Clearance Center, 222 Rosewood Drive, Danvers, MA 01923. For other copying, reprint or republication permission, write to IEEE Copyrights Manager, IEEE Service Center, 445 Hoes Lane, P.O. Box 1331, Piscataway, NJ 08855-1331.

IEEE Catalog Number:	95CH35720
ISBN:	0-7803-2147-2 Softbound Edition 0-7803-2148-0 Casebound Edition 0-7803-2149-9 Microfiche Edition
Library of Congress:	94-79424

Accession For	
NTIS GRA&I	<input checked="" type="checkbox"/>
DTIC TAB	<input type="checkbox"/>
Unannounced	<input type="checkbox"/>
Justification	
By	
Distribution /	
Availability Codes	
Dist	Avail and/or Special
A-1	

Indium Phosphide Conference Committee

Conference Chair

Hideki Hasegawa
Hokkaido University
Sapporo, Japan
Tel: +81 11 757 1163
Fax: +81 11 757 1165

Conference Co-Chair

Kenichi Iga
Tokyo Institute of Technology
Yokohama, Japan
Tel: +81 45 924 5064
Fax: +81 45 924 5014

Conference Vice-Chair

Olaf Hildebrand
Alcatel SEL Research Center
Stuttgart, Germany
Tel: +49 711 821 4 5553
Fax: +49 711 821 4 6355

Program Chair

Osamu Wada
Fujitsu Laboratories Ltd.
Atsugi, Japan
Tel: +81 462 48 3111
Fax: +81 462 48 5193

Program Co-Chairs

Derek Lile
Colorado State University
Fort Collins, CO, USA
Tel: +1 303 491 6600
Fax: +1 303 491 2249

Klaus Heime
RWTH Aachen
Aachen, Germany
Tel: +49 241 8077 46
Fax: +49 241 8888 199

Local Arrangements Chair

Takashi Fukui
Hokkaido University
Sapporo, Japan
Tel: +81 11 706 6870
Fax: +81 11 716 6004

Exhibition Chair

Yuichi Matsushima
KDD R&D Laboratories
Kamifukuoka, Japan
Tel: +81 492 66 7823
Fax: +81 492 66 7516

Steering Committee

Co-Chairs

John Bowers
UCSB, USA
Tel: +1 805 893 8447

André Scavennec
CNET, France
Tel: +33 145 295230

Publicity Chair

Joe Lorenzo
RL/EROC, USA
Tel: +1 617 377 2234

Members

Stephen Bland (EPI) Brad Boos (NRL) Timothy Coutts (NREL) Hideki Hasegawa (Hokkaido Univ.)
Avishay Katz (AT&T) Joe Lorenzo (RL/EROC) Rodney H. Moss (BT Res. Lab.) Drew Nelson (EPI)
Richard Nottenburg (USC) Rajendra Singh (Clemson Univ.) Osamu Wada (Fujitsu Labs)

Program Committee

Bulk

Chair
Osamu Oda
Japan Energy Corp.
Toda, Japan

D. F. Bliss
Rome Laboratory
Hanscom AFB
MA, USA

R. Fornari
MASPEC-CNR
Institute
Parma, Italy

C. J. Miner
Bell-Northern
Research
Ottawa, Canada

G. Müller
Universität Erlangen-
Nürnberg
Erlangen, Germany

T. Okumura
Tokyo Metropolitan
University
Hachioji, Japan

M. Tatsumi
Sumitomo Electric
Osaka
Japan

Epitaxy

Chair
Hajime Asahi
Osaka University
Ibaraki, Japan

J. J. Coleman
University of Illinois
Urbana-Champaign
IL, USA

L. Goldstein
Alcatel Alsthom
Recherche
Marcoussis, France

R. H. Moss
British Telecom
Research Labs.
Ipswich, UK

T. Sonoda
Mitsubishi Electric,
Itami
Japan

Y. Takeda
Nagoya University
Nagoya
Japan

W. T. Tsang
AT&T Bell Labs.
Murray Hill, NJ
USA

Processing

Chair
Kiyoshi Asakawa
NEC Corporation
Tsukuba, Japan

S. Arai
Tokyo Inst. of
Technology
Tokyo, Japan

S. Beaumont
University of Glasgow
Glasgow
UK

A. Forchel
Universität Würzburg
Würzburg
Germany

E. Hu
University of California
Santa Barbara, CA
USA

K. Matsuda
Matsushita Electric
Moriguchi
Japan

J. Woodall
Purdue University
West Lafayette, IN
USA

Electron Devices

Chair
Masayuki Abe
Fujitsu Laboratories Ltd.
Atsugi, Japan

Y. Ashizawa
Toshiba Corporation
Kawasaki
Japan

M.-C. F. Chang
Rockwell International
Thousand Oaks, CA
USA

H. Dämbkes
Daimler-Benz
Ulm
Germany

M. Inoue
Osaka Inst. of
Technology
Osaka, Japan

D. Pavlidis
University of Michigan
Ann Arbor, MI
USA

R. H. Wallis
GEC-Marconi Tech. Ltd.
Towcester
UK

Optoelectronics

Chair
Naoki Chinone
Hitachi Ltd.
Kokubunji, Japan

T. Kamijoh
Oki Electric
Hachioji
Japan

T. P. Lee
Bellcore
Red Bank, NJ
USA

O. Mikami
Tokai University
Hiratsuka
Japan

R. Nagarajan
University of California
Santa Barbara, CA,
USA

W. Nijman
Philips Optoelectronics
Centre, Eindhoven
The Netherlands

J. E. A. Whiteaway
BNR Europe Ltd.
Harlow
UK

Table of Contents

Wednesday, May 10

Plenary Session

Plen.1	Optical Networks Towards the 21 Century and the Role of InP-Based Devices	3
Plen.2	Status and Promise of InP Electronics	7
Plen.3	Leading-Edge Optoelectronic Device Production Using Two-Inch Technology	10

WA1: Lasers

WA1.1	High Temperature Operation of AlGaInAs/InP Lasers	14
WA1.2	MOCVD Growth and Characterization of Tensile-Strained $\text{Ga}_{1-x}\text{In}_x\text{As}_y\text{P}_{1-y}$ Quantum Wells for Low Threshold Lasers Emitting at $1.3\mu\text{m}$	18
WA1.3	CW Operation of a $1.3\mu\text{m}$ Strained Quantum Well Laser on a Graded InGaAs Buffer with a GaAs Substrate	22
WA1.4	Four-Wavelength DBR Laser Array with Waveguide-Couplers Fabricated Using Selective MOVPE Growth	26
WA1.5	Effect of $(\text{GaP})_m/(\text{InP})_m$ Short Period Binary Superlattice Period on Quantum Wire Formation by Strain Induced Lateral Layer Ordering in GaInP/AlInP Multi-Quantum-Wire Lasers	29

WB1: Bulk Crystal Growth

WB1.1	Preparation of Homogeneous InP Substrates by VGF-Growth and Wafer Annealing	33
WB1.2	Effect of Annealing Conditions on the Uniformity of Undoped Semi-Insulating InP	37
WB1.3	Iron Segregation in LEC InP Crystals	41
WB1.4	Multicomponent Zone Melting Growth of Ternary InGaAs Bulk Crystal	45
WB1.5	Crystal Anomaly at the Center of S Doped InP Wafers Grown by the LEC Method	49

WA2: Epitaxy for Optical Device Applications

WA2.1	Paper not available	
WA2.2	Muti-Wavelength DFB Laser Arrays Grown by In-Plane Thickness Control	53
WA2.3	InAsP/InGaP All Ternary Strain- Compensated Multiple Quantum Wells and its Application to Long Wavelength Lasers	57
WA2.4	Fabrication of a Polarization Insensitive Electroabsorption Modulator with Strained InGaAs/InAlAs MQW by MOVPE	61
WA2.5	Fabrication of Crystal-Facet Mirrors for Short Cavity Lasers by Selective InP Epitaxy on Etched Sidewalls	65

WB2: HFETs: Performance and Applications

WB2.1	InP-Based HEMTs for Microwave and Millimeter-Wave Applications	68
WB2.2	Low-Noise, High-Speed $\text{Ga}_{0.47}\text{In}_{0.53}\text{As}/\text{Al}_{0.48}\text{In}_{0.52}\text{As}$ 0.1-mm MODFETs and High-Gain/Bandwidth Three-Stage Amplifier Fabricated on GaAs Substrate	73
WB2.3	60 GHz Monolithic LNA Utilizing High-Speed InAlAs/InGaAs/InP HEMT's and Coplanar Waveguides	77

Table of Contents

WB2.4	0.1mm-InAlAs/InGaAs HEMTs with an InP-Recess-Etch Stopper Grown by MOCVD	81
WB2.5	A Technology for Monolithic Integration of High-Indium-Fraction Resonant Tunneling Diodes with Commercial MESFET VLSI Electronics	85
WB2.6	40-Gb/s-Class InP HEMT ICs for Very High-Speed Optical Communications	89

POSTER SESSION I – Bulk and Epitaxy

Bulk Crystal Growth and Characterization

WP1	Study on Microscopic Defects in Fe-doped InP Single Crystals	93
WP2	Reduction of Dislocation Densities in InP Single Crystals by the TB-LEC Method	97
WP3	Photoellipsometry Characterization of Electronic Properties for InP	101
WP4	Evolution of Non-Equilibrium Intrinsic Defects in Indium Phosphide During the Zinc Diffusion from Polymer Spin-on Films	105
WP5	Simulation of Raman Scattering from Nonequilibrium Phonons in InP and InAs	108
WP6	Photoconductivity & Photoluminescence of Cu Diffused p-InP	112
WP7	Raman Scattering Study of the Clustering Phenomena in InGaAsP Grown by LPE on (100) and (111) GaAs	115

MOVPE - Related Growth: New Precursor

WP8	Highly Controlled InGaAs(P)/InP MQW Interfaces Grown by MOVPE Using TBA and TBP Precursors	119
WP9	Metalorganic Vapour Phase Epitaxy of InP Using the Novel P-Source Diteriarybutyl Phosphine (DiTBP)	122
WP10	Highly Efficient Low Temperature Growth of GaInP in a Planetary MOVPE System Using Tertiarybutylphosphine(TBP)	126

MOVPE - Related Growth: surface / Interface

WP11	Effect of Strained Interfacial Layer and Large Misorientation on SQW, 2DEG, and Multisteps in InGaP/(In)GaAs Heterostructures Grown by MOVPE	130
WP12	Unintentional Impurity Incorporation at the Interface between InP Substrate and Buffer Layer Grown by LP-MOVPE	132
WP13	Pyramidal Shaped Pit Formation on InAlAs/Fe-doped InP Structures Grown by MOCVD	136
WP14	Growth Condition Dependence of N-type Carriers at the Interface between InP Substrate and Epitaxial Layers Grown by MOCVD	140

MOVPE - Related Growth: doping

WP15	Heavily Carbon Doped InGaAs Lattice Matched to InP Grown by LP-MOCVD Using TMIn, TMGa and Liquid CCl ₄	144
WP16	Chlorine auto-doping by Chloride Vapor Phase Epitaxial Growth of InP	148
WP17	Step Bunching of InP Caused by Heavy Doping of Se in Metalorganic Chemical Vapor Deposition and Its Application to Device Fabrication	152

MOVPE - Related Growth: novel method and others

WP18	Paper Withdrawn	
WP19	A Novel Technique for Semi-Insulating InP(Fe) by Chloride VPE	155
WP20	Composition Control in the Growth of AlAs _{1-x} Sb _x Alloys	157

MBE-Related Growth: QW /SL

WP21	Optical and Structural Properties of In _{0.53} Ga _{0.47} As/In _{0.52} Al _{0.48} As Multiple Quantum Wells Grown on Vicinal (110) InP Substrates by Molecular Beam Epitaxy	161
WP22	Surface Step Arrangements and Configurations during Molecular Beam Epitaxial Growth on Slightly Misoriented (110) InP Substrates	165

Table of Contents

WP23	Photoluminescence Investigation of InGaAs/InP Quantum Wells Grown by Gas-Source Molecular-Beam Epitaxy with Source-Supply Interruption	169
MBE-Related Growth: doping/composition		
WP24	Pentacarbonyliron Doping for Semi-insulating InP by Chemical Beam Epitaxy	173
WP25	Spinodal-Like Decomposition of InGaAsP/InP Grown by Gas Source Molecular Beam Epitaxy ...	175
WP26	The Incorporation Behavior of As and P in GaInAsP ($\lambda \approx 1.3\mu\text{m}$) on InP Grown by Gas Source Molecular Beam Epitaxy	179
MBE - Related Growth: III-V/II-VI, IV, metal		
WP27	Low Temperature Grown Be-doped InAlP Band Offset Reduction Layer to p-Type ZnSe	183
WP28	Paper Withdrawn	
WP29	Optical and Electrical Properties of InN Grown by the Atomic Layer Epitaxy	187
WP30	Atomic Structures of Au and Ag Films Epitaxially Grown on the InP(001)- p(2x4) Surface	191
MBE - Related Growth: surface cleaning		
WP31	Influence of Arsenic Flux Ratio in the Thermal Cleaning Process on InP (100) Surface Characteristics	195
WP32	Thermal Cleaning and Growth Temperature Effects on Deep Levels of Be-Doped p-InAlAs Grown on InP by Molecular Beam Epitaxy	198
WP33	Investigation of a Molecular Beam Epitaxy Regrowth Procedure Using an In-Situ H_2 Plasma Probed with an InP/InGaAs/InP Quantum Well	202
Characterization: QW/strained structure		
WP34	Island Growth and Phase Separation in Strained InAs _{1-x} P/InP Heterostructures	206
WP35	Lateral Modulation in Strain-Compensated MQW Structures	210
WP36	Influence of Strain on Exciton Lifetime in AlGaInP/GaInP Quantum Wells	213
WP37	Anisotropic Electrical Properties of Modulation-Doped In _{0.52} Al _{0.48} As/ In _x Ga _{1-x} As Pseudomorphic Heterostructures Grown on InP Substrate	217
WP38	Determination of the in-plane Mass in Strained GaInAs/InP Quantum Wells	221
Characterization: surface / interface		
WP39	Chemical Structure of InP Surface in MOVPE Studied by Surface Photo-Absorption	225
WP40	Group-V Atoms Exchange Due to Exposure of InP Surface to AsH ₃ (+PH ₃) Measured by X-ray CTR Scattering	229
WP41	The Determination of Atomic Plane on InP(001) Surface by CAICISS	233
WP42	Distribution of As Atoms in InP/InPAs(1ML)/InP Hetero-Structures Measured by X-ray CTR Scattering	237
Characterization: optical		
WP43	Use of Spectrally Resolved Scanning Photoluminescence for Optimizing the Growth Conditions of InAlAs/InP Heterostructures	241
WP44	The Study of the Optical Properties of In _{0.52} (Al _x Ga _{1-x}) _{0.48} As by Variable Angle Spectroscopic Ellipsometry	245
WP45	Cyclotron Resonance in InP Grown by Organometallic Vapor Phase Epitaxy with TMIn and TBP	249
Characterization: ordering		
WP46	TEM Evaluation of Ordered and Modulated Structures in GaAsSb Crystals Grown on (110)InP Substrates by Molecular Beam Epitaxy	253
WP47	Anisotropic Photocurrent in Long- Range Ordered Ga _{0.5} In _{0.5} P	257
WP48	Raman Spectroscopy Study on Order- Disordered Ga _{0.52} In _{0.48} P on GaAs Grown by MOVPE	261

Table of Contents

Characterization: growth and others

WP49	Donor Passivation in n-AlInAs Layers by Fluorine	265
WP50	Electronic and Structural Properties of Thin SrF_2 Films on InP	269
WP51	Studies on the Influence of Peltier Effect and Electromigration during LPEE Growth of Binary and Ternary Semiconductors	273

Selective Growth

WP52	Selective MOCVD Growth of InP around Dry-Etched Mesas with Various Patterns for Photonic Integrated Circuits	275
WP53	MOCVD Regrowth of InP:Fe, Zn and Si Doped on Patterned Surface by Pulsed Metalorganic Epitaxy(PME)	279
WP54	Regrowth of Semi-Insulating Iron Doped InP Around Crossed Laser Mesas by Hydride Vapor Phase Epitaxy	283
WP55	MOVPE-Overgrowth for Buried InP/ (In,Ga)(As,P) Laser Diode Arrays	287
WP56	Planar InP Burying Growth around a Dry-Etched Mesa by Addition of CH_3Cl during MOVPE	291

Low Dimensional Structures

WP57	Preparation and Optical Characterization of Nanoscale InP-Islands Embedded in $\text{In}_{0.48}\text{Ga}_{0.52}\text{P}$...	295
WP58	$\text{In}_x\text{Ga}_{1-x}\text{As}/\text{InP}$ Multiquantum Well Structures Grown on [111]B InP Substrates	299
WP59	Wavelength Controllability of InGaAs/ GaAs Quantum Dots Emitting at 1.3 μm Region	303
WP60	InP Islands as Self-Assembled Quantum Structures	307
WP61	Optical Properties of Self-Organized InGaAs/InP Dots	311
WP62	Magneto-luminescence Study of Strain and Lateral Confinement Effects in $\text{InAs}_{0.48}\text{P}_{0.52}/\text{InP}$ Quantum Well Wires	315

Thursday, May 11

ThA1: Selective Growth

ThA1.1	MOMBE Growth of InGaAsP Films for Optoelectronic Devices	321
ThA1.2	Selective Area Growth of InP by Plasma Assisted Solid-Source Epitaxy	325
ThA1.3	The Influence of PCl_3 on Planarisation and Selectivity of InP Regrowth by Atmospheric Pressure MOVPE	329
ThA1.4	Improved Selective Growth of InP around Dry-Etched Mesas by LP-MOCVD at Low Growth Temperature	333
ThA1.5	Simultaneous Thickness and Compositional Uniformity in Selective MOVPE Growth	337
ThA1.6	InAlGaAs Selective MOVPE Growth with Bandgap Energy Shift	341
ThA1.7	Temporally Resolved Selective Regrowth of InP around [110] and [-110]Directional Mesas	345

ThB1: Photodetectors

ThB1.1	High-Speed Waveguide Photodetectors	349
ThB1.2	Fabrication of Polarization Diversity Heterodyne Receiver PICs on InP: Status, Challenges and Perspectives	353
ThB1.3	9 GHz Bandwidth InP-Based Integrated PIN-HBT Photoreceiver	357
ThB1.4	A Monolithically Integrated Logic Photoreceiver with Double-Heterojunction Bipolar Transistors	361

Table of Contents

ThB1.5	New Approach for High-speed, High-sensitivity Photodetectors	365
ThB1.6	A Strained InAlAs/InGaAs Superlattice Avalanche Photodiode for Operation at an IC-Power-Supply Voltage	369

POSTER SESSION II - Electron Devices, Optoelectronics and Processing

HEMT Device Physics

ThP1	Reduction of Inelastic Scattering Effect by Introducing Strain-Compensated Superlattice into GaInAs/GaN Multi-Quantum Barrier	373
ThP2	Weak Link Devices Using Lead alloy-InAs/AlGaSb Heterostructures	377
ThP3	Low-Frequency Trapping Phenomena in AlSb/InAs HEMTs	381
ThP4	A Comparative Study of the Low Frequency Noise in InP Based Heterojunction Field Effect Transistors (HFET's)	385
ThP5	Frequency Analysis of the Kink Effect in AlInAs/GaInAs HEMT's	389
ThP6	Paper Withdrawn	
ThP7	Microwave Performance of InP-based HEMTs for Low Voltage Application fabricated by Optical Lithography	393

HEMT Device Design

ThP8	Low Noise Optimization of InP HEMT's	397
ThP9	Monte Carlo Simulation of Diffusion Noise in AlGaAs/InGaAs/GaAs Hetero-structure	401
ThP10	Superior Confinement of Two- Dimensional Electron Gas in an $\text{In}_{0.52}\text{Al}_{0.48}\text{As}/\text{In}_{0.53}\text{Ga}_{0.47}\text{As}$ Modulation- Doped Structure by Inserting a Strained InAs Quantum Well	404
ThP11	Lattice-matched $\text{In}_{0.29}\text{Al}_{0.71}\text{As}/\text{In}_{0.3}\text{Ga}_{0.7}\text{As}$ Doped-channel FETs	408
ThP12	$\text{In}_{0.52}(\text{Al}_{0.9}\text{Ga}_{0.1})_{0.48}\text{As}/\text{In}_{0.53}\text{Ga}_{0.47}\text{As}$ HEMTs on InP Substrates	412
ThP13	InAlAs/InGaAs HEMT Using InGaP Schottky Contact Layer	416
ThP14	Spacer Design to Improve the Breakdown Voltage of InAlAs/InGaAs HEMTs	420
ThP15	The Impact of Pseudomorphic AlAs Spacer Layers on the Gate Leakage Current of InAlAs/InGaAs Heterostructure Field-effect Transistors	424
ThP16	High-Performance Enhancement-Mode InAlAs/InGaAs HEMT's Using Non-Alloyed Ohmic Contact and Pt-Based Buried-Gate	428
ThP17	Characteristics of Iron Doped Pt-InAlAs Schottky Diodes Grown by LP-MOCVD Using Ferrocene	432
ThP18	InGaAs Insulated Gate Field Effect Transistors Using Silicon Interlayer Based Passivation Technique	436
ThP19	AlGaAsSb Buffer/Barrier Layer on GaAs Substrate for InAs Channel with High Electron Properties	440

HBTs

ThP20	High-Speed InP/InGaAs HBT with Reduced Intrinsic Transit Time	444
ThP21	SPICE-Based DC and Microwave Characterization of InAlAs/InGaAs HBT's Used for Large-Bandwidth Integrated Transimpedance Amplifiers	448
ThP22	High Electron Mobility in Heavily-Doped Bases of InP/GaInAs HBTs	452
ThP23	Graded-GaAs _{1-x} P _x Base in Heterojunction Bipolar Transistors with InGaP Emitters	456
ThP24	Paper has been moved to ThB2.2	
ThP25	Reliability Analysis of InP-based HBT's	460

Lasers

ThP26	Photo Pumped Operation of Dry Etched $\lambda=1.55\mu\text{m}$ Vertical Cavity Surface Emitting Lasers	464
ThP27	680nm-Band Self-Sustained Pulsating AlGaInP Visible Laser Diodes	468

Table of Contents

ThP28	Time Dependence of Catastrophic Optical Damage (COD) of 0.98 μ m GaInAs/GaInP Strained Quantum Well Laser	472
ThP29	High-Speed InP-Based Strained MQW Ridge Waveguide Laser	476
ThP30	Increased Lifetime of Aluminum-Free LED's on Si Substrates Grown by MOCVD	480
ThP31	Stable and Low Chirp 1.55 μ m Complex-Coupled DFB Lasers with Absorptive Grating	484
ThP32	1.3 μ m GaInAsP/InP Square Buried Heterostructure Vertical Cavity Surface Emitting Laser Grown by All MOCVD	488
ThP33	1.5 μ m Subpicosecond Pulse Generation from an InGaAsP DFB Diode Laser Synchronized with a Mode Locked Ti:Sapphire Laser	492
ThP34	High Power InGaAsP/InP 1.625 μ m Strained Quantum Well Lasers	496
ThP35	Tensile Strained MQW Semiconductor Optical Amplifier	500
ThP36	InGaAsP Strained MQW-DFB Lasers with High Resonance Frequency and Low Distortion for High Speed Analog Transmission	504
ThP37	High Output Power Operation of 1.3 μ m Strained MQW Lasers with Low Threshold Currents at High Temperature	508
Photodetectors		
ThP38	Fabrication and Performance of a Novel Ultra-Low Capacitance MSM Photodetector for High-Speed OEIC Receiver Applications	512
ThP39	High-Efficiency Monolithic InGaP/GaAs Tandem Solar Cells with Improved Top-Cell Back-Surface Field-Layers	516
ThP40	Waveguide-fed PIN-HFET Receiver at 2.5Gbit/s Integrated on InP	520
ThP41	Optically Controlled S- and N- Shaped Negative Differential Resistances by R-TOPS	524
ThP42	In _x Ga _{1-x} As/InAs _y P _{1-y} Detector for Near Infrared (1-2.6 μ m)	528
ThP43	High-efficiency, Dual-wavelength, Wafer-fused Resonant-cavity Photodetector Operating at Long Wavelengths	532
Optical Modulators		
ThP44	Strain Effects in InAsP/InP MQW Modulators for 1.06 μ m Operation	536
ThP45	Temperature Dependence of InGaAsP Electro-Absorption Modulator Module	540
ThP46	Theoretical Analysis of Enhanced Electroabsorption Change due to Light-hole Subband Transition in Lattice-matched Wide Quantum Wells	544
ThP47	Type 1.5 Coupled Quantum Wells for Electroabsorption Modulation with Low Electric Fields	547
ThP48	InGaAs/InAlAs/InP 1.55 μ m Quantum Wells with Mass-Dependent Width - A Useful Building Block for Polarization- Independent Optical Modulation	551
ThP49	Intersubband Transitions in Conduction Band Quantum Wells: the role of energy band gaps and band off-sets	555
Processing: Etching		
ThP50	GaInAsP/InP Multiple-Reflector Micro-Cavity Structure Fabricated by EB Lithography and Selective Etching	557
ThP51	Controlled Beam Dry Etching of InP by Using Br ₂ -N ₂ Gas	561
ThP52	Dielectric Waveguides Fabricated on InP by Photochemical Processes for OEICs	565
ThP53	First Order Gratings for Gain Coupled GaInAsP DFB-Lasers Made by Maskless Focused Ion Beam Patterning	569
Processing: Passivation		
ThP54	Surface Damage on InP Induced by Photo- and Plasma- Assisted Chemical Vapor Deposition of Passivation Films	573
ThP55	The Effects of Sulfur Concentration on Growth Rate of Selective MOCVD Grown InP	577
ThP56	Characterization of Electron Traps in AlInAs Treated with Plasma	581

Table of Contents

ThP57	Characterization of Surface Recombination Velocity of InP Reduced by Sulfur-treatment and Phosphorous-nitride Film Formation with Raman Spectroscopy	585
ThP58	Ruthenium and Sulfide Passivation of $\text{In}_{0.53}\text{Ga}_{0.47}\text{As}$	589
Processing: Interface		
ThP59	Low Temperature Impurity-Induced Disorder of AlGaInAs/InP Quantum Wells for Long-Wavelength Optoelectronic Applications	593
ThP60	Thermal Stability of $\text{Al}_{0.48}\text{In}_{0.52}\text{As}/\text{Ga}_{0.47}\text{In}_{0.53}\text{As}/\text{InP}$ Heterostructure and Its Improvement by Phosphidization	597
ThP61	Morphological and Electrical Characterization of Al/Ni/n-InP Contacts with Tapered Ni-Layer	601
ThP62	Formation of PN_x/InP Structure by In-Situ Remote Plasma Processes	605
ThP63	The Improvement of Resistivity of Phosphorous Nitride Films Deposited at 100°C on InP Substrates	609
ThP64	Focused Ion Beam Implantation Induced Disorder in InGaAsP Strained Layers MQW Heterostructures	612
ThP65	Characterization of Semiconducting Thin Films on InP for Magneto-Optical Applications	616
ThA2: Novel Etching Techniques		
ThA2.1	Fabrication of InP-Based Quantum-Wires and Its Application to Lasers	620
ThA2.2	Effects of Hydrogen on InP Light-Emitting Devices Etched in a Methane-Hydrogen Environment	624
ThA2.3	Fabrication of 60nm-Pitch Ordered InP Pillars by EB-Lithography and Anodization	628
ThA2.4	Low-Temperature CAIBE Processes for InP-Based Optoelectronics	632
ThA2.5	Chemical Beam Etching of InP in GSMBE	636
ThB2: HBTs: Novel Approaches		
ThB2.1	InP-Based HBTs and Their Perspective for Microwave Applications	640
ThB2.2	Novel Self-Aligned Sub-micron Emitter InP/InGaAs HBT's Using T-Shaped Emitter Electrode	644
ThB2.3	Large-Signal Characteristics of InP-Based Heterojunction Bipolar Transistors and Their Use in Optoelectronic Preamplifier Design	648
ThB2.4	InP/InGaAs Collector-Up Heterojunction Bipolar Transistors Fabricated Using Fe-Ion-Implantation	652
ThB2.5	Integrated AlInAs/InGaAs HEMT/HBT Heterostructure Grown by MBE	656
ThA3: Interfaces and Contacts		
ThA3.1	InP/InGaAs Nanofabrication and Optical Characterization	660
ThA3.2	High-Quality Zn-Diffused InP-Related Materials Fabricated by the Open-Tube Technique	664
ThA3.3	Zn-Implanted Pd-Based Ohmic Contacts to p- $\text{In}_{0.53}\text{Ga}_{0.47}\text{As}$ for the Base Layer of InP/ $\text{In}_{0.53}\text{Ga}_{0.47}\text{As}$ Heterojunction Bipolar Transistors	668
ThA3.4	Non-Au Based Shallow Low Resistance Ohmic Contacts on p-InP	672
ThB3: Bulk Crystal Characterization		
ThB3.1	Paper Not Available	
ThB3.2	High-Spatial-Resolution Characterization of Residual Strain in Commercial LEC-grown InP(100) Wafers	674

Table of Contents

ThB3.3	Electrical Properties of the Hydrogen Defect in InP and the Microscopic Structure of the 2316cm ⁻¹ Hydrogen Related Line	678
ThB3.4	Single-Step Annealing of Be and Si Implants in S.I. InP to Minimize Be Redistribution in the Completed p ⁺ /n Junctions	682

Friday, May 12

FA1: Epitaxy:Characterization

FA1.1	Interface Strain in InGaAs-InP Superlattices	689
FA1.2	Study of As ₄ Beam Induced P-As Exchange Reaction on InP Surface by Photoluminescence and X-ray Diffraction	693
FA1.3	Characterization of InAsP/InGaAsP Strained MQW Crystals for 1.3-μm-Wavelength Laser Diodes Using a Microscopic Photoluminescence Method	697
FA1.4	Atomic Ordering in Strained Layer Multi-Quantum Well Structure	701
FA1.5	GaAs Heteroepitaxy on InP (001) Surfaces Studied by Scanning Tunneling Microscopy	705

FB1: Photonic Integration

FB1.1	DFB Lasers with Integrated Electroabsorption Modulator	709
FB1.2	DFB Lasers Integrated with Mach- Zehnder Optical Modulator and a Power Booster Fabricated by Selective Area Growth MOVPE Technique	713
FB1.3	InGaAsP/InP Strained MQW Laser with Integrated Mode Size Converter Using the Shadow Masked Growth Technique	717
FB1.4	Monolithic Integration of GaInAsP/InP Collimating GRIN Lens with Tapered Waveguide Active Region	721
FB1.5	High Power and Narrow Lateral Far Field Divergence 1.5μm-Eye-Safe Pulse Laser Diodes with Flared Waveguide	725

FA2: HFETs: Physics and Technology

FA2.1	High Speed, High Gain InP Based Heterostructure FETs with High Breakdown Voltage and Low Leakage	729
FA2.2	High Electron Mobility 18,300 cm ² /V•s InAlAs/InGaAs Pseudomorphic Structure Obtained by Channel Indium Composition Modulation	733
FA2.3	Metamorphic in AlGaAs/InGaAs HEMTs on GaAs Substrates with Composite Channels and f _{max} Exceeding 300 GHz	737
FA2.4	High Gm MBE-Grown InP Based HEMTs with a Very Low Contact Resistance Triple Capping Layer	741
FA2.5	Reliability of AlInAs/InGaAs/InP HEMT with WSi Ohmic Contacts	745

Table of Contents

Saturday, May 13

SA1: Epitaxy for Low Dimensional Structures

SA1.1	Growth and Characterization of InGaAs/InAlAs In-Plane Superlattices on (110) InP	751
SA1.2	Selective MBE Growth of InGaAs and InAlAs on High-Index Facets and Its Application to Fabrication of InGaAs Ridge Quantum Wires	755
SA1.3	InAs/InGaAs Self-Assembled Quantum Dots Grown on (311)B GaAs by Molecular Beam Epitaxy	759
SA1.4	Spontaneous Formation of Aligned InGaAs Quantum Dots on GaAs Multi-Atomic Steps by MOCVD Growth	763
SA1.5	Self-Organization Phenomenon of Strained InGaAs Grown on InP(311) Substrates by Metalorganic Vapor Phase Epitaxy	766

SB1: New Lasers and Fabrication Technologies

SB1.1	Quantum Cascade Lasers: Unipolar Intersubband Infrared Laser	770
SB1.2	Transverse Mode and Polarization Characteristics of Double-Fused 1.52- μ m Vertical-Cavity Lasers	773
SB1.3	Novel Current-Blocking Laser Structures Using Directly-Bonded InP-SiO ₂ -InP	777
SB1.4	Direct Bonding of High Quality InP on Si and Its Application to Low Threshold Semiconductor Lasers	781
SB1.5	Free-Orientation Integration by Direct Bonding: Fabrication of (001) InP-Based 1.55 μ m-Wavelength Lasers on (110) GaAs Substrate	785

SA2: MBE Growth and Related Techniques

SA2.1	In-Situ Monolayer Etching and Regrowth of InP/InGaAsP	789
SA2.2	GSMBE Growth of InGaAsP with an "On Site" Arsine Generator	793
SA2.3	MOMBE Growth of Heavily Carbon-doped n-Type InP Using Tertiarybutylphosphine(TBP)	797
SA2.4	Growth Studies on AlPSb, GaPSb New Ternary III-V Compounds for InP-Based Surface Emitting Lasers	801
SA2.5	Molecular Beam Epitaxial Growth of MgZnCdSe on (100) InP Substrates	805

SB2: Reliability and Passivation Techniques

SB2.1	InP-Based Heterojunction FET Processing for High-Reliability Millimeter-Wave Applications	809
SB2.2	Unpinning of Fermi Level at InP Schottky Diode Interfaces Produced by Novel In-Situ Electrochemical Process	813
SB2.3	Cadmium Sulfide Surface Stabilization and Schottky Barrier Enhancement for InP Based Optoelectronic Devices	817
SB2.4	Improvement in Schottky Diode Characteristics of Metal-In _{0.52} Al _{0.48} As Contact Using an In Situ Photochemical Etching and Surface Passivation Process	821
SB2.5	Sulfur-Treated InP Surfaces Studied by Soft X-ray Photoemission Spectroscopy	825

Table of Contents

SA3: MOVPE Growth and Related Techniques

SA3.1	Developing Models of OMVPE Growth from In-Situ X-Ray Measurements	827
SA3.2	Monolayer Growth in InP/GaInAs Quantum Wells Grown by Selective Area MOVPE	831
SA3.3	High-Mobility $\text{Ga}_{0.47}\text{In}_{0.53}\text{As}$ /InP Heterostructure by Atmospheric- Pressure MOVPE Using Cyclopentadienyl Indium	835
SA3.4	Selective MOVPE Growth of InGaAsP and InGaAs Using TBA and TBP	839
SA3.5	Reduced Lattice Distortion in and near Strain-Compensated InGaAs/InGaAsP Multiple-Quantum Well Structures Grown by Metalorganic Vapor Phase Epitaxy on GaAs Substrates	843

SB3: Nanostructure Devices and Characterization

SB3.1	New Quantum Functional Devices	847
SB3.2	Noise Characteristics of InP-Based HBTs	851
SB3.3	Low-Frequency Noise Phenomena in InP-Based HFETs Related to Stress Induced Degeneration and Interface Properties	857
SB3.4	Interface Stability of Metal/InP Based Material Systems	861



Wednesday

May 10, 1995

- | | |
|-------------|---|
| Plen | Plenary Session |
| WA1 | Lasers |
| WB1 | Bulk Crystal Growth |
| WA2 | Epitaxy for Optical Device Applications |
| WB2 | HFETs: Performance and Applications |
| WP | Poster Session I: Bulk and Epitaxy |

Wednesday Papers Not Available

WA2.1 Multistage Epitaxy for Photonic Integration

Wednesday Papers Withdrawn

WP18 On the Use of Remote Plasma Source to Enhance the InP MOCVD Process

WP28 Pulsed Chemical Beam Epitaxy of GaInP/GaP/Si Heterostructures

Optical Networks Towards the 21 Century and the Role of InP-Based Devices

Ichiro Yamashita

Executive Manager

Optical Subscriber Networks Laboratory

NTT Optical Network Systems Laboratories

1-2356 Take Yokosuka-shi, Kanagawa-ken, 238-03 JAPAN

TEL : +81 468 59 8010

FAX : +81 468 55 1283

1. Introduction

Fiber-optic communication systems have been developed from both the decrease in fiber loss and the increase in opto-electronic device speed. To make use of the large bandwidth of optical fibers, high speed systems have already been introduced into the trunk transmission network. In the access network, fiber-optic transmission systems transferring information with wideband have been introduced in the first phase. Now, the introduction of systems which multiplex

narrowband information has started. However, drastic improvements in the cost effectiveness are necessary to serve small businesses and home customers.

This paper presents the overview of fiber-optic systems evolution from both sides technologies of system and opto-electronic device.

2. High Speed Fiber-Optic Systems for Trunk Network

A large number of fiber-optic communication

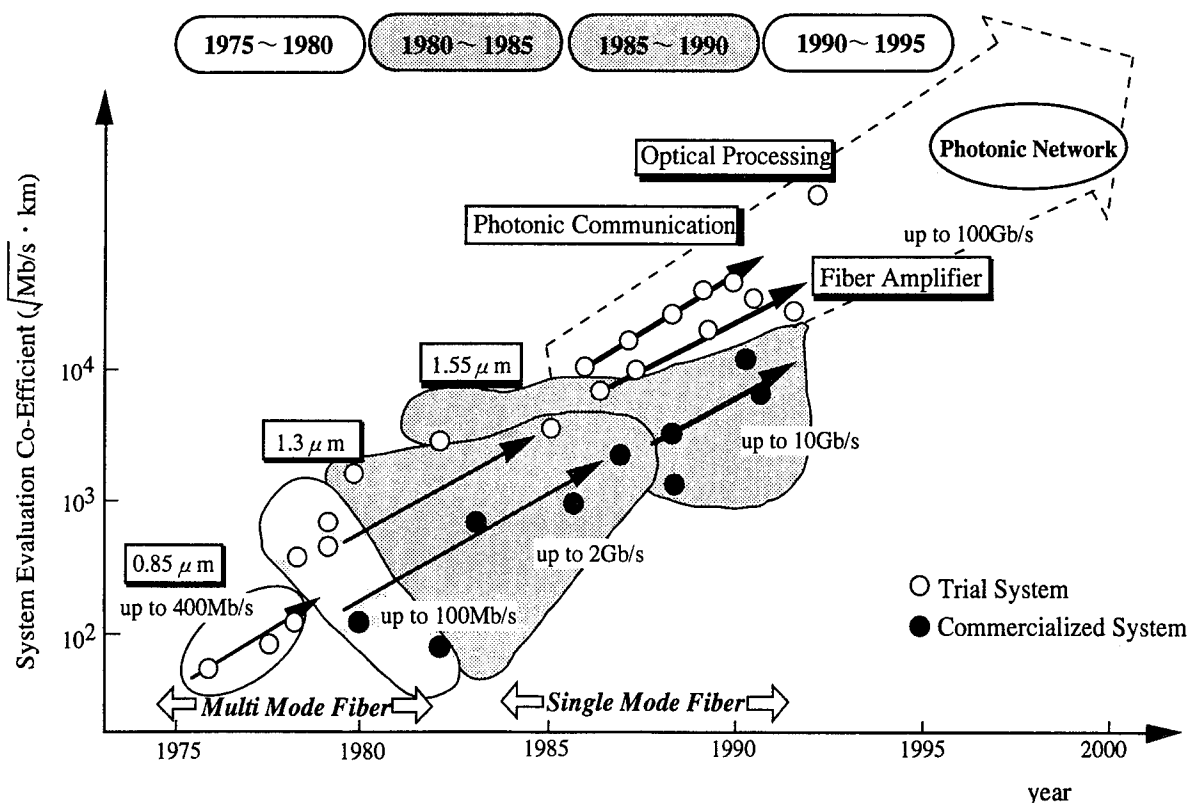


Fig. 1 Evolution of Fiber-Optic Transmission Systems

systems have been introduced into the trunk network as high speed digital systems which are superior to the coaxial cable systems on account of the large bandwidth and low loss in their characteristics. At first, 32 Mb/s system is installed and commercialized in 1975. And then the systems speed-up has been done as 100Mb/s, 400Mb/s, 1.6Gb/s, 2.4Gb/s and now 10Gb/s system is planned to be introduced in the field.

The progress of the systems' speed-up is to be said that it is always the challenge of noise reduction caused by bandwidth enlarge. These are the points to see for fiber-optic systems development, system technologies as single mode optical fiber, long wavelength transmitter and receiver, fiber amplifier and opto-electronic devices.

The introduction of fiber-optic communication systems is contributed to construct nation wide digital trunk network. Super high speed digital transmission lines have made possible to construct logical path network using cross connecting equipments on the physical trunk network. As the result, a number of logical paths are defined such as meshes of net in the fiber-optic physical space. Then cost reduction of long distance lines and high efficiency of communication network operation have been realized. Figure 1 shows the evolution of fiber-optic transmission systems.

3. Cost Effectiveness of Fiber-Optic Systems for Access Network

The introduction of fiber-optic systems in the access network has not yet reached to large scale amount. Because access network is located at the edges of communication network and has some subjects to be solved. One of the important items is cost effectiveness of the system. Generally, access network is constructed by a large number of optical fibers connected between a central office and each customers. It is impossible to apply logical multiplexing technology as used in trunk network, then it is required to use physical multiplexing in access network.

Figure 2 shows the relationship between number of customers meaning capacity of SLT and consumption power and relative cost. The SLT is subscriber line terminal equipment installed in a central office. When number of customers enlarges, cost per customer decreases relatively. However, there exists a limit of total power consumption permitted to a SLT equipment frame, power consumption per customers should be reduced. In a word, cost reduction is really reduction of power consumption itself. For example, power consumption per one customer should be reduced to a few watts to realize an SLT which accommodates 1,000 customers. It is understood that the realization of such SLT is no easy task. The SLT has 1,000 Laser Diodes, 1,000 transmitter and receiver circuits, 1,000 customers information multiplexing circuits, interface circuit be-

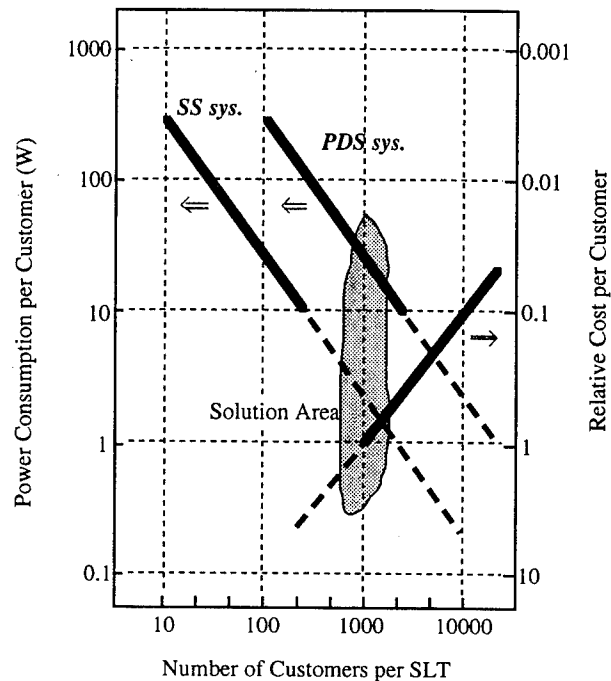
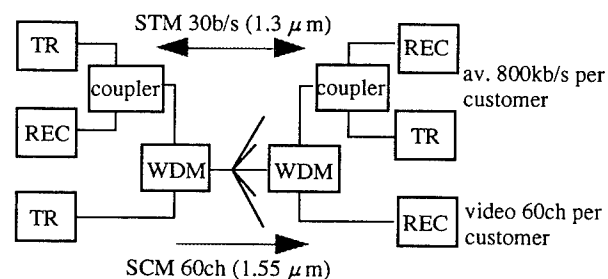
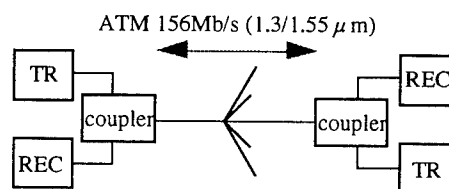


Fig. 2 Relation between Power Consumption Reduction and Cost Effectiveness



(a) Low-Speed Digital Communication and Video Distribution Access System



(b) High-Speed Digital Communication Access System

Fig. 3 PDS Systems Architecture

tween switching machine and etc.

To solve the subject mentioned above, PDS(Passive Double Star) system technology is proposed. The proposal applies multiplexing technology in the central office side, but does not apply in the customers side ONU(Optical Network Unit). It is an realistic idea from the view point of customers capacity and power consumption. The advantage of PDS is to reduce number of circuits in the SLT. For instance, a PDS system which applies an star coupler split to ten, requires 100 Laser Diodes and several tens watts circuit for 10 customers in 1,000 customers SLT .

And the PDS system topology has additional merit for information distribution network. Figure 3 shows PDS systems architectures which have been developed in NTT.

4. Evolution of Opto-Electronic Devices

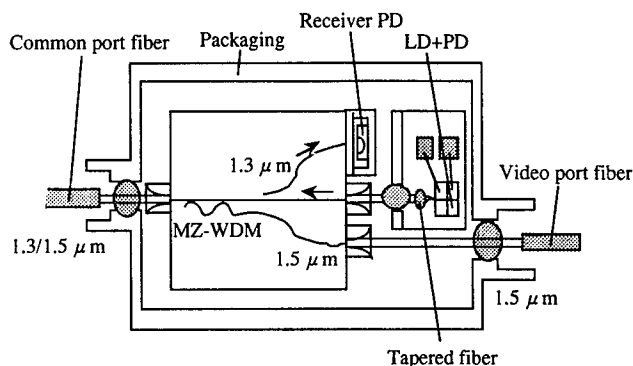
To realize cost effective PDS system, it is obvious that cost reduction of opto-electronic devices in the ONU is indispensable. Small size optical module has been researched and developed to mount LD, PD, 3dB coupler and WDM on a circuit. The optical module does not require super high speed devices but high efficient productivity such as large amount of hundreds thousand or million per year. To meet the requirement, concentric circuit type solid devices and plane type PLC devices have been realized. Figure 4 shows optical module using PLC.

5. Future Development of Fiber-Optic Access Network Systems

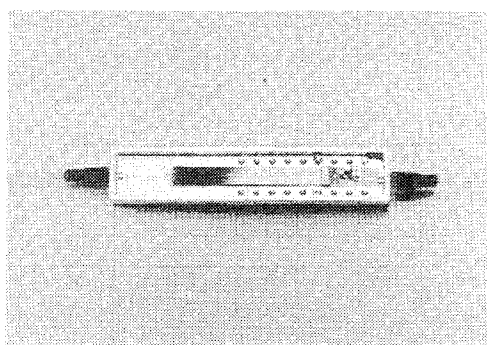
At present, fiber-optic systems is going to be specialized toward several communication types. Figure 5 shows the systems specialization diagram. In the trunk network, SS(Single Star) system is popular which connects point to point and sets LDs both side symmetrically.

In the access network, high speed bulk SS fiber-optic systems were introduced to prepare high speed information leased lines for special large businesses in the first phase. And ADS(Active Double Star) systems which applied SS line architecture were introduced for concentrated customers in buildings and wide spread customers in city re-development areas and rural areas. Introduction of CT/RT(Central Terminal / Remote Terminal) system called in NTT, which is a kind of DLC(Digital Loop Carrier) system, is typical example of ADS. But the CT/RT has limitation of bandwidth toward future coming multimedia communication, for its making use of existing metallic lines at the near part of customers in the system architecture. To break down it, PDS system is proposed and attracted wide attention as in second phase.

Naturally, asymmetric system topology is suitable because of edge location of access network in total



(a) MZ-WDM : Mach-Zehander WDM Circuit



(b) Optical Module Photograph

Fig. 4 Optical Module Configuration and Exterior View

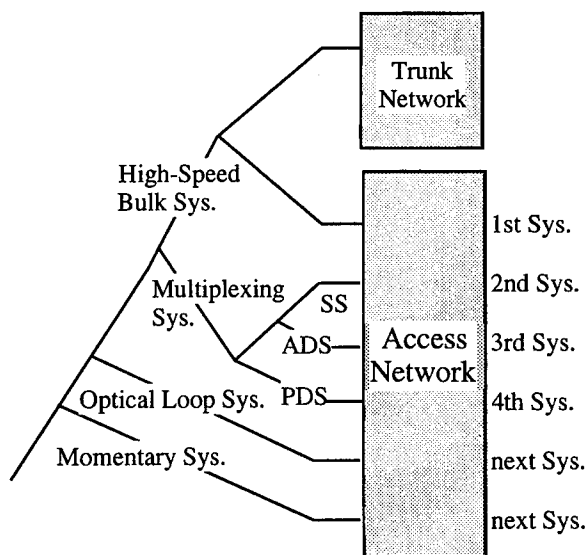


Fig. 5 Fiber-Optic Communication Systems Specialization Diagram

communication network architecture as shown in existing metallic systems. Concentrating functions into SLT installed in a central office and simplifying ONU function is key issue. As an idea, remote sensing type system is proposed as shown in Figure 6. The system has no LD in ONU but optical power is supplied from SLT side and modulated at customer side circuit.

By the way, existing communication systems represented by telephony is real time communication style which transfers speech information in real time. However, non-real time or stored information style is expected to increase such as computer communication. In the non-real time style, communication system has independent parameters on information changing time and information transferring time. Therefore, there is no necessity to transfer two hours movie information in two hours. As shown in Figure 7, a momentary access system is realized, information transferring will be finished in a short time and management capability of stored information will also be improved. Fiber-optic access systems will be added these new functions making use of large bandwidth.

6. Expectation for Opto-Electronic Devices

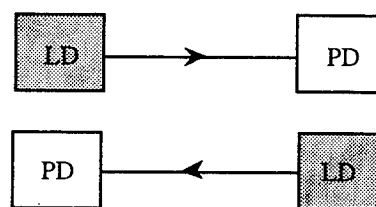
There are some expectation to opto-electronic devices in the fiber-optic access systems development.

- (1) Separation of opto-electronic devices chip bonding and wire bonding with optical fibers.
- (2) Reduction of standard deviation on characteristics of opto-electronic devices
- (3) Reduction of power consumption per transmission processing speed and separation of heat generation sources.

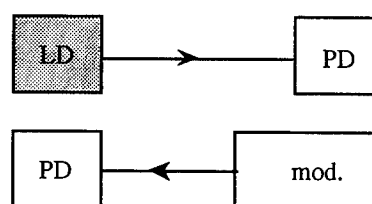
Item (1) is the expectation for productivity increase and cost reduction of opto-electronic devices. Item (2) is come from comparison with metallic system, fiber-optic system has high sensitivity on standard deviation of devices characteristics versus transmission distance capability. Item (3) is expectation that low cost devices have led low cost system realization in the system development history.

7. Conclusion

Evolution on fiber-optic communication system, especially fiber-optic access system toward 21 century, and expectation on opto-electronic devices are considered. Indium phosphide devices are expected to play an important role in the development of fiber-optic systems toward FTTH(Fiber To The Home) to realize new century network construction and to prepare new network services such as multimedia communication.



(a) Symmetrical System



(b) Asymmetrical System

Fig. 6 System Topologies for Access Network

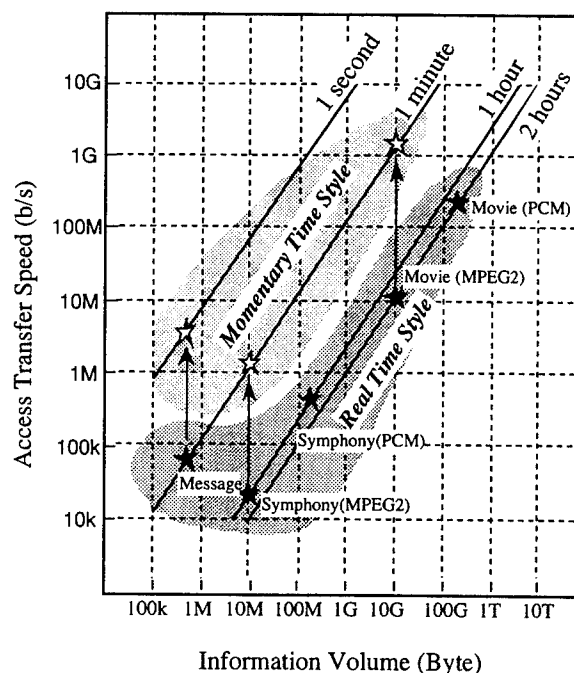


Fig. 7 Access Transferring Speed of Real Time Communication and Momentary Transfer Styles

Status and Promise of InP Electronics

Umesh K. Mishra, ECE Department
University of California, Santa Barbara, CA 93106
e-mail: mishra@xanadu.ece.ucsb.edu

Today it is becoming increasingly clear that the niche markets that compound semiconductor devices will fill rest on

- (i) the traditional advantage of superior electron transport relative to Silicon.
- (ii) the reduced power dissipation due to enhanced mobility (GaAs and InP based materials) and reduced band gap (InGaAs)
- (iii) the need for high speed base band electronics for >40GB/s optical communication.
- (iv) quantum electronic devices.

The list above is by no means complete, though the basis for its limited length is the high cost of epitaxial compound semiconductor technology (especially relative to the rapidly maturing SiGe technology). This paper therefore will address InP based electronics in the context of a cost-viable solution to pressing needs.

Available InP based technologies:

Researchers around the world have made impressive advances in three basic InP based technologies; the AlInAs-GaInAs HEMT, the AlInAs-GaInAs and/or InP-GaInAs HBT, and the AlAs-InGaAs-AlAs Resonant Tunneling Diode (RTD). Each of the technologies have natural applications and a judicious mix of these technologies creates new applications. In this paper each of the technologies will be addressed and their applications emphasized.

InP-based HEMT:

In 1983, Eastman suggested the development of modulation-doped $\text{Al}_{0.48}\text{In}_{0.52}\text{As}/\text{Ga}_{0.47}\text{In}_{0.53}\text{As}$ hetero-structure on InP as a promising candidate for high speed devices¹. The lattice-matched $\text{Ga}_{0.47}\text{In}_{0.53}\text{As}$ alloy on InP maintains three distinct advantages over the lower indium mole-fraction $\text{AlGaAs}/\text{Ga}_{1-x}\text{In}_x\text{As}$ PHEMT. First, the higher ΔE_c (0.5eV)² translates into higher 2-DEG concentration and higher modulation efficiency³. Second, the lower electron effective mass (m_e^*) results in higher electron mobility ($\mu_e > 10,000 \text{ cm}^2/\text{Vs}$). Finally, the higher peak electron velocity in the channel ($2.4 \times 10^7 \text{ cm/s}$) allows shorter transit delays through the device. The combination of high electron mobility and high 2-DEG concentration result in lower channel resistivity.

In 1985, Itoh *et al*⁴ demonstrated the first $\text{Al}_{0.48}\text{In}_{0.52}\text{As}/\text{Ga}_{0.47}\text{In}_{0.53}\text{As}$ HEMT lattice-matched to an InP substrate. Thereafter, several research labs began investigating AlInAs/GaInAs HEMTs on InP substrates (see for example^{5,6,7}). In 1988, Mishra *et al.* at Hughes Research Laboratories reported a unity current cut-off frequency f_T , of 170GHz utilizing a $0.1\mu\text{m}$ gatelength AlInAs/GaInAs HEMT⁸. Later, an f_T of 200GHz⁹ was achieved by increasing the In mole-fraction in the channel, to 62%. Next, a drastic reduction of the parasitic resistance, $R_s + R_d$, was achieved by self-aligning the ohmic contacts to a mushroom-shaped gate *met al*¹⁰. and an f_T of 250GHz was achieved.

Nguyen *et al.* at Hughes Research Laboratories further improved the device performance by i) optimization of $\text{Ga}_{1-x}\text{In}_x\text{As}$ ($X = 0.80$) as the channel material, ii) further reduction in parasitic resistance, and iii) successful reduction in gatelength to 50nm. These improvements advanced the state-of-the-art cut-off frequency to 340GHz (f_T)¹¹. Wojtowicz *et al* and Enoki *et al* have also reported over 300GHz (f_T) Schottky-gate HEMT device performance^{12,13}. It is, therefore, clear that scaling the InP based HEMT by reducing the gatelength, parasitic resistances and increasing the In mole fraction in the channel leads to improved performance.

However, this comes at a price: reduced gate-drain breakdown voltage. To alleviate this problem three approaches have been investigated: the InP channel HEMT, the InGaAs/InP composite channel HEMT and regrown contacts to the channel. The first has the advantage of a higher bandgap channel with high saturated electron velocity, with the disadvantage of a lower electron mobility. The second combines the high electron mobility of GaInAs with the advantages of InP. The electrons reside in the GaInAs in the low field source access region and transfer to the InP sub-channel in the high field region under the gate. The regrown contacts help the on-state breakdown of the device¹⁴ by (i) reducing the electric field in the device induced by the non-uniform electron collection at the drain normally present at ohmic contacts, and (ii) reducing hole injection from the drain.

However, the high performance InP HEMT will only be widely used if the InP based HEMT is made reproducible. The threshold variability of the HEMT can be addressed by using etch-stop layers in the gate region. An alternative is to modulate the 2DEG in the channel with a p^+ gate electrode; the JHEMT. First introduced by Ohata *et al*¹⁵ in the AlGaAs-GaAs system, the concept has been recently developed rapidly in the InP based system by Shealy *et al*¹⁶ with $0.2\mu\text{m}$ gate length devices exhibiting a σV_{th} of 13.7mV , an f_T of 110GHz and an f_{max} of over 220GHz at a drain bias of 1V . The additional advantage of a p^+ gate electrode is the reduced electron injection from the gate into the channel reducing the gate leakage current.

The applications of the InP HEMT are predominantly in high frequency (>Q-band) microwave transmit and receive applications and will be addressed in the talk.

InP- based HBT:

The dominant advantage that the InP based HBT has over the competition is high speed at very low power dissipation. The first MBE grown AlInAs-GaInAs HBT was demonstrated by Malik *et al*¹⁷ and investigated by groups at AT&T¹⁸ and the Hughes Research Laboratories¹⁹. Devices with InP emitters have demonstrated an f_T of over 160GHz at 300K and over 300GHz at 77K ²⁰. This incredible performance is achieved

because of the optimal launch energy ($\Delta E_c = 0.2\text{eV}$) of the electrons into the base region, which has a Γ -L separation of 0.51eV . The reduced electron scattering is evidenced in hot electron transport across the transistor with reduced transit time. The only disadvantage of hot electron transport is the enhancement of impact ionization in the collector due to the higher electron kinetic energy. This is monitored by a reversal of the base current and manifests itself in a further reduced breakdown voltage²¹. The problem may be alleviated by introducing a graded (InGaAs-to-InP) wide-gap collector. An abrupt InGaAs-InP base collector junction is unacceptable because of the collection of electrons in the heterojunction conduction band notch. In addition to introducing collector delay, instability in the I-V curves is observed due to positive feedback introduced by the field dependent tunneling of electrons out of the notch²². Solutions to the problem using an additional dipole-induced hot electron launcher at the base-collector junction, to launch the electrons over the barrier have also been investigated²³.

However, in the opinion of the author, the InP based HBT has two fundamental properties which can be used to great advantage. The first is the low recombination velocity at the InGaAs surface. This enables scaling of the emitter to sub- μm dimensions while retaining a high β for the devices. Though in conventional topologies, scaling the emitter width does not substantially increase the speed of the transistor, the advantage gained in reduced power consumption per function is enormous. This is further aided by the low turn-on voltage of the E-B diode which is based on the low band-gap of the GaInAs base, the second fundamental advantage. The low surface recombination velocity, coupled with the vertical nature of current transport (i.e. no parasitic substrate current) also leads to a low $1/f$ noise corner frequency for the transistor. This can be tailored further by utilizing electron injection at higher energies (abrupt AlInAs-GaInAs versus InP-GaInAs emitter-base junctions) to further reduce surface recombination²⁴. The immediate advantage is in very low phase noise, high frequency VCOs, an essential component of most RF communication systems. Other natural applications utilize the inherent threshold uniformity of the devices in precision circuits such as A/D converters²⁵ and in decision circuits in opto-electronic receivers²⁶. Reliability continues

to be an issue in HBTs though recent results have shown that graded E-B junctions have improved reliability over abrupt junctions²⁷.

Merged Technologies:

The ability to combine HEMTs, HBTs and RTDs on the same wafer leads to circuits with high functionality. Miura *et al*²⁸ have integrated HBTs and RTDs to form hybrid resonant bipolar transistors for use in trigger circuits. Watanabe *et al*²⁹ have integrated InGaAs/AlInAs RTDs with HEMTs to demonstrate single-transistor cell SRAM operation. Yen *et al*³⁰ have integrated RTDs and InGaAs HJFETs to demonstrate Static latches and quaternary to binary converters. Stanchina *et al*³¹ and Walden *et al*³² have formed HEMT/HBT, RTD/HBT and pnp/npn HBTs on the same wafer using growth on pre-patterned substrates and LT AlInAs as an isolation layer. The area of merged technology, though relatively new, has incredible potential for ultra fast and ultra dense circuits.

Conclusions:

In this paper, a review of the development of InP based electronic devices have been presented. The years past have seen a mixture of materials and processing advances and performance improvements through band-gap engineering. The economics of the day however dictate that the deployment of this technology in systems is going to be determined primarily by its cost. It is imperative that a substantial portion of the communities creative potential be directed towards the manufacturability of these materials, devices and circuits so as to improve yield and reduce cost. The past efforts of lattice mis-matched growth on large substrates such as Si need to be revived as the economies of scale have to be leveraged. As the cost is reduced and the reliability enhanced the market is InP's for the taking.

¹ L.F. Eastman, J. Vac. Sci. Technol. B 1 (2), pp. 131-134, Apr.-June 1983.

² R. People, K.W. Wecht, K. Alavi, and A.Y. Cho, Appl.Phys. Lett., Vol. 43, pp. 118-120, 1983.

³ M. C. Foisy, P.J. Tasker, B. Hughes, and L.F. Eastman, " IEEE Trans Electron Dev., Vol ED35, pp. 871-878, July 1988.

⁴ T. Itoh, A.S. Brown, L.H. Camnitz, G.W. Wicks, J.D. Berry, and L.F. Eastman, in Proc.

IEEE/Cornell Conf. on Advanced Concepts in High Speed Semiconductor Devices and Circuits, pp. 92-101, 1985.

⁵ C.K. Peng, M. I. Aksun, A. Ketterson, H. Morkoc, and K. Gleason, IEEE Electron Dev. Lett., Vol EDL-8, pp. 24-26, 1987.

⁶ A.S. Brown, U.K. Mishra, J.A. Henige, and M. Delaney, J. Vac. Sci. Tech., Vol B6, No. 2, Mar./April 1988.

⁷ A. Fatimulla, J. Abrahams, T. Laughran, and H. Heir, IEEE Electron Dev. Lett., Vol EDL-9, pp. 328-330, 1988.

⁸ U.K. Mishra, A.S. Brown, S.E. Rosenbaum, C.E. Hooper, M.W. Pierce, M.J. Delaney, S. Vaughn, and K. White, IEEE Electron Device Lett., Vol. 9, pp. 647-649, Dec. 1988.

⁹ U.K. Mishra, A.S. Brown, and S.E. Rosenbaum, in IEDM's Tech. Dig., pp.180-183, Dec. 1988.

¹⁰ U.K. Mishra, A.S. Brown, L.M. Jelloian, M. Thompson, L.D. Nguyen, and S.E. Rosenbaum, in IEDM's Tech. Dig., pp. 101-104, Dec. 1989.

¹¹ L.D. Nguyen, A.S. Brown, M.A. Thompson, and L.M. Jelloian, "50-nm Self- IEEE Trans on Electron Dev., Vol 39, No. 9, Sept. 1992.

¹² T. Enoki, M. Tomizawa, Y. Umeda, and Y. Ishii, Jpn. J. Appl. Phys. Part 1, Vol. 33, pp.798-803, Jan. 1994 .

¹³ M. Wojtowicz, R. Lai, D.C. Striet, G.I. Ng, T.R. Block, K.L. Tan, P.H. Liu, A.K. Freudenthal, and R.M. Dia, IEEE Electron Dev. Lett., Vol.15, No. 11, November 1994.

¹⁴ Shealy etal, DRC 1994.

¹⁵ Ohata etal ,IEEE MTT-S Microwave Symposium Dig. pp.434-436, 1984.

¹⁶ Shealy etal, Ultrafast Electronics and Optoelectronics Digest, 1995, pp.108-110.

¹⁷ Malik etal, IEEE EDL-4, pp.383-385, 1983

¹⁸ Y.K. Chen etal, IEEE EDL-10, 267-269, June 1989.

¹⁹ Mishra etal, IEEE EDL-10, 467-469, Oct 1989.

²⁰ Laskar etal, DRC 1994.

²¹ Ritter etal, UFEOP Digest, 77-81, 1983.

²² Arnold etal, Appl.Phys.Lett. 53, 373-375, 1988.

²³ Feygenson etal, Electron.Lett., 28, 607-609, 1992.

²⁴ Y.K. Chen etal, UFEOP Digest, 98, 1995.

²⁵ Jensen etal, GaAs IC Symposium Dig., 1994.

²⁶ Walden etal, OFC Tech. Dig. Vol.4, 33, 1994

²⁷ Hafizi etal, Appl.Phys.Lett., Vol.63, 93-95, July 1993

²⁸ Miura etal, IEDM Tech. Dig. 483-486, 1992.

²⁹ Watanabe etal, IEDM Tech.Dig. 475-478, 1992

³⁰ Yen etal, submitted to DRC 1995.

³¹ Stanchina etal, 5th IPRM, 569-571, 1993.

³² Walden etal, GOMAC Tech.Dig., 487-490, 1993.

Leading-Edge Optoelectronic Device Production Using Two-Inch Technology

R. SIMES, R.M. CAPELLA
Alcatel Optronics
91625 Nozay Cedex, France

B. FERNIER, HP MAYER
Alcatel Corporate Research Center

Abstract

InP processing and achieved results on two-inch wafers are reviewed with an emphasis on lasers. High-performance, high-reliability lasers are demonstrated using a "building block" based process.

I. Introduction

Today's optical transport and access networks require high-performance, low-cost optoelectronic devices in high volume to meet increasing market demand for fiber-optic based systems. Most systems applications require lasers with low threshold current and high output power which can operate over a wide temperature range. To respond to these aggressive design objectives in high-volume, a two-inch InP laser process is required.

A number of companies have two-inch InP processes up and running. An informal survey was conducted, and its results will be presented at the conference. For two-inch laser processing, three options have been selected to date: ridge, buried ridge structure (BRS), and buried heterostructure (BH) with blocking layers (planar BH, CMBH, SIBH, etc.). The ridge process [1,2] is the simplest; only a single epitaxy step is required for a Fabry-Perot (FP) laser. The BRS [3,4] process requires an additional non-selective regrowth compared to the ridge process. Fig. 1 presents a cross-section of the BRS laser structure. For the BH structures [5,6], two additional epitaxy steps are necessary, including a selective regrowth over an etched mesa.

In sections II, III and IV of this paper, we review the "building block" based process which has been implemented at Alcatel for the BRS laser and the results obtained to date. In section V, we give a brief review on two-inch OEIC and PIC device work in progress around the world. Work on detectors will be briefly reviewed at the conference.

II. Building Block InP Laser Process

The Alcatel BRS laser process includes the following two-inch building blocks:

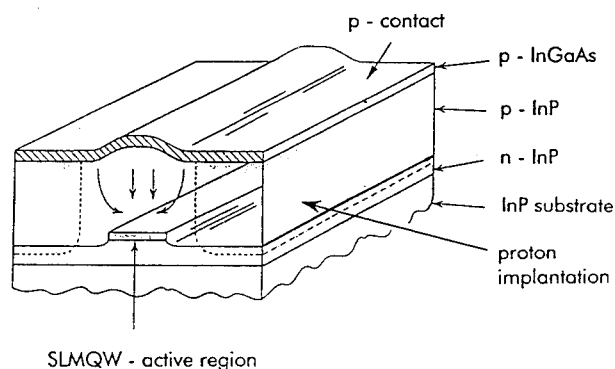


Fig. 1: Diagram of BRS laser.

1. GSMBE first epitaxy
2. grating formation (optional)
3. RIBE mesa formation
4. MOVPE mesa regrowth
5. p/n contact formation
6. implantation

We define a building block to include: a processing step, a characterization step and an accept/reject decision (see Fig. 2). A sequence of building blocks forms the overall process. We have implemented identical building blocks both in R&D and in production. There are many advantages to this approach. Fast, trouble-free transfers from R&D to manufacturing are routinely being achieved. Uniform processing for different products leads to short cycle times (fast customer response), a high "success ratio" of wafers (fewer errors), and optimized (minimized) investments. In addition, the building block approach lends itself to the use of statistical process control, which is essential for a

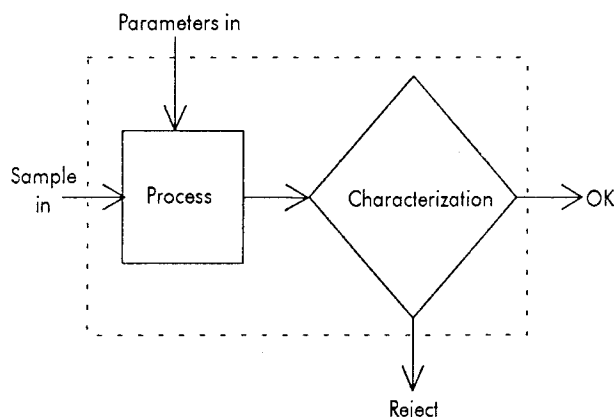


Fig. 2: Building block process definition.

manufacturing environment. Finally, our experience with the building block approach to date is that it allows the customer needs to be fulfilled very efficiently.

The BRS presents several advantages which make its realization relatively simple: the mesa etch depth is $<1 \mu\text{m}$ and is thus easily controllable and the mesa overgrowth is non-selective. The building block process is described in the rest of this section. The first epitaxy is by gas-source molecular beam epitaxy (GSMBE); the source materials are Ga, In, Be, Si, AsH_3 , and PH_3 . Good wavelength control over a wafer and from wafer to wafer are routinely achieved. The strained layer multiple quantum well (SLMQW) active structures are optimized for each application. Fig. 3 presents the threshold current density per QW for 300 μm long,

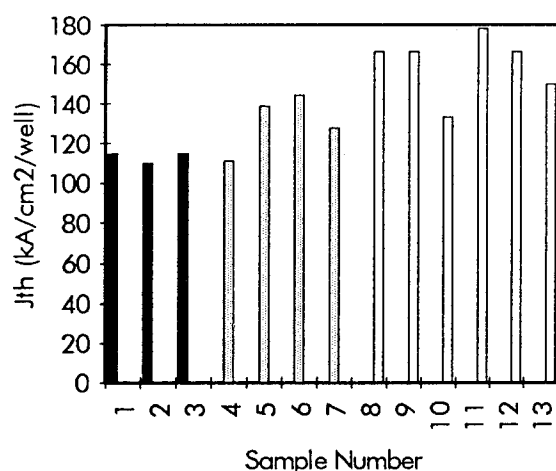


Fig. 3: J_{th} per QW for 300 μm long, broad-area lasers with two different 1.3 μm designs (samples 1 - 7) and one 1.55 μm design (samples 8 - 13).

broad area lasers. These values are low, which is a key factor for low-threshold current lasers, and they are very reproducible. For a distributed feedback (DFB) laser process, a first order grating formation step is included at this point. Reactive ion beam etching (RIBE) is then used to define the laser stripe. The RIBE step permits good control of the active region width. After the dry-etching step, the wafer is overgrown with p-InP and p-InGaAs using a non-selective low-pressure metalorganic vapor phase epitaxy (MOVPE) step. The p-contact is then formed. To minimize the leakage current across the pn InP homojunction, zones that are not in the immediate vicinity of the active region are then implanted with protons. The wafer is then thinned, and the n-contact is deposited. This building block based process makes it possible to produce a wide variety of FP or DFB lasers with only very minor changes in building block parameter inputs.

III. Device Results

Wide temperature range (WTR) lasers:

Fig. 4 presents a typical L-I curve for a 300 μm long, FP 1.3 μm laser with a highly reflecting rear facet coating. The series resistance is $\sim 2.2 \Omega$, and the far-field angles are $\sim 26^\circ$ in the parallel plane and $\sim 30^\circ$ in the vertical plane; this far-field distribution permits simple coupling to an optical fiber. Fig. 5 presents a histogram of the current required for 6 mW, ($I_{6\text{mW}}$) at 85°C for a population of ~ 150 lasers. The lasers were taken from four different wafers made at different times. There is little dispersion in $I_{6\text{mW}}$ around the median value of

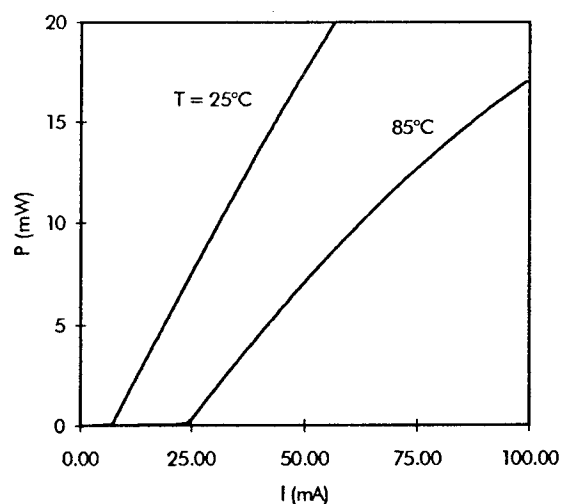


Fig. 4.: L-I curves at 25°C and 85°C for typical FP 1.3 μm laser.

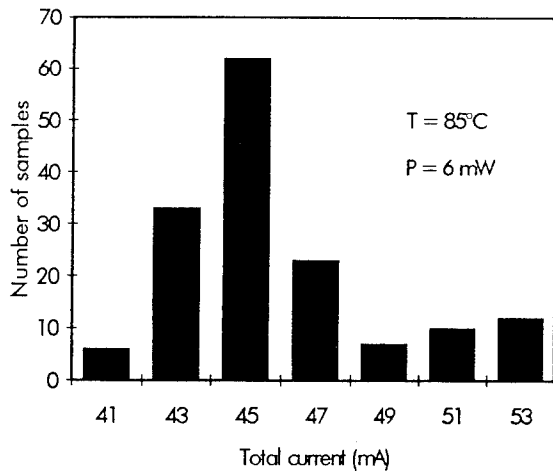


Fig. 5: Total current for 6 mW at 85°C for >150 lasers from four different FP 1.3 μ m wafers..

46 mA. For these same four wafers, the wavelength at 85°C at the 10% and 90% points of the population is 1332 nm and 1340 nm, indicating excellent control. The typical wavelength shift as a function of temperature for these lasers is 0.38 nm/°C; although, 0.31 nm/°C has been demonstrated in a design variant.

WTR DFB lasers have been fabricated and tested between -40 and +85°C. Optimization is in progress, and these results will be presented.

Thermoelectric-cooled DFB devices:

Devices operating at 1.3 and 1.55 μ m have been optimized for data transmission at 2.5 Gb/s. In order to maintain an open eye pattern, the laser structure has been optimized for a high differential gain to obtain a high resonance frequency. For four different 6 QW wafers, median threshold currents after burn-in were 6.5, 6.5, 5.7, and 6 mA with little spread in the data. Threshold currents in the range of 3 - 4 mA have been measured for 300 μ m long, uncoated 4 QW samples. These low values are indicative of high-quality first epitaxy material, low leakage current, and efficient current blocking. The front facet efficiency is ~ 0.15 mW/mA. The wavelength dispersion over a wafer is ~ 4 nm. The typical capacitance of these lasers is 10 - 15 pF, which leads to an RC product compatible with 2.5 Gb/s data transmission. Direct modulation transmission at 2.5 Gb/s over 200 km of standard fiber has been achieved with these lasers with less than 1 dB of dispersion penalty. Fig. 6 presents measured dispersion penalties for 75 fibered lasers over 100 km; the median penalty is 0.5 dB.

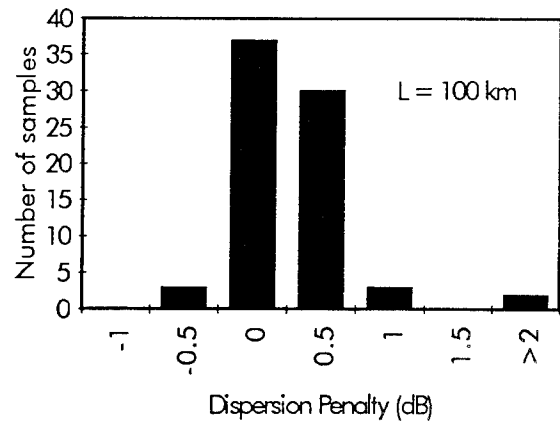


Fig. 6: Dispersion penalty measured for 1.55 μ m lasers after transmission over 100 km of standard fiber. The extinction ratio is 15%, and average power in the fiber is 1.6 mW.

Pump laser structures:

FP 1480 nm laser pumps for use in erbium-doped fiber amplifiers have been realized. There will be a penalty at very high facet powers due to InP homojunction current leakage; however, front facet powers of ~ 125 mW have been measured at 400 mA for 600 μ m long R_{\min}/R_{\max} treated lasers. This performance is acceptable for many standard applications.

IV. Laser Reliability

All lasers are subjected to a 48 hour, 100°C, 200 mA burn-in after mounting on submount. The threshold current changes for four 1.3 μ m FP wafers and four 1.55 μ m DFB wafers are shown in Fig. 7. The median threshold current change is less than 10% (less than 1 mA). The change in external efficiency after burn-in is less than 5% for all lasers. These small changes demonstrate the robustness of the BRS laser structure.

In addition, constant power ageing is in progress on FP and DFB devices. For the FP devices, groups of devices at 20 mW/53°C and at 7 mW/80°C have reached 6500 hours. The change in operating current as a function of time is logarithmic, and we estimate a mean time to failure for these devices greater than 10^6 hours (100 years) at 7 mW/80°C. For reference, the maximum ageing rate calculated using a linear extrapolation of the current required to maintain a constant power is 0.43%/kh at 80°C/7 mW and 0.28 %/kh at 53°C/20 mW. For the 1.55 μ m DFB devices, a group of lasers has reached 3500 hours at 4 mW/80°C, and the maximum

linearly extrapolated ageing rate is 0.9 %/kh. This low ageing rate indicates that the 15 year lifetime requirement for land-line components is easily satisfied. These results demonstrate that all of the building blocks are qualified. As a consequence, new device structures may now be quickly and easily qualified.

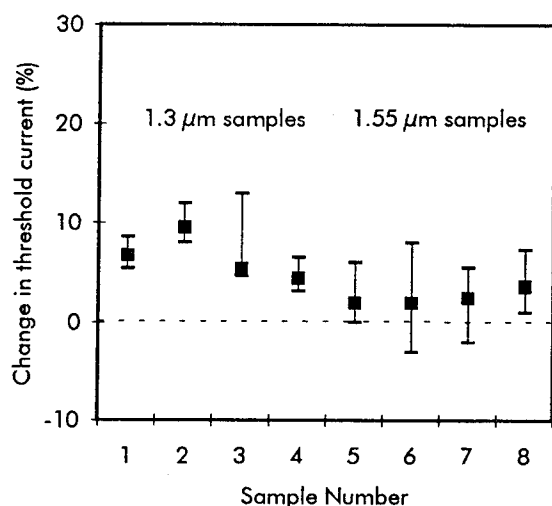


Fig. 7: Percentage change in threshold current after burn-in for lasers (lot size > 40) from four 1.3 μm FP wafers and four 1.55 μm DFB wafers. The squares give the median values and the error bars give the values at 10 and 90% of the population distribution.

V. Opto-electronic integrated circuits/photonic integrated circuits

Work is starting to be reported on full-wafer processing for these advanced device structures. For example, YANO et al. have reported results on three-inch processed OEIC receiver circuits with bandwidths for single circuits of 6 GHz and bandwidths for arrays ranging from 1 to 2 GHz [7]. Digital optical switches are being routinely fabricated by ERMAN et al. [8]; two-inch wafer processing is required because of the large size of the switches ($2 \times 40 \text{ mm}^2$). Several groups have reported two-inch processes for DFB lasers integrated with electro-absorption modulators for long haul transmission at 2.5 Gb/s and/or 10 Gb/s.

VI. Conclusion

InP laser technology has matured to the level where it is possible to produce high volumes of high-performance, high-reliability laser diodes using full wafer processing.

VII. Acknowledgments

The authors acknowledge the important contributions of their Alcatel colleagues to this work. In addition, the authors thank the people from other companies who supplied information for the review of two-inch InP processes. Collaboration with CNET in early phases of this work and funding from France Telecom are gratefully acknowledged.

VIII. References

1. C.E. ZAH et al., IEEE J. Quantum Electron. 30, pp. 511 - 23, 1994.
2. B. STEGMULLER et al., IEEE Photon. Technol. Lett. 5, pp. 597 - 599, 1993.
3. N. BOUADMA et al., Appl. Phys. Lett., 59, pp 22-24, 1991.
4. B. FERNIER et al. European Conference on Optical Communication 1994, Florence, Italy.
5. K. KOJIMA, Optical Fiber Conference 1995, San Diego, CA, USA.
6. O. KJEBON et al. IEEE Semicond. Laser Conf. 1994, Hawaii, USA.
7. H. YANO et al., Trans. Inst. of Electron., Inform. and Comm. Engineers C-I, J77C-I, pp 285 - 292, 1994.
8. M. ERMAN et al., Optical Fiber Conference 1994, San Jose, CA, USA.

High Temperature Operation of AlGaInAs/InP Lasers

WA1.1
(Invited)

(Invite paper)

C. E. Zah, R. Bhat, and T. P. Lee
Bellcore, Red Bank, NJ07701, USA

Introduction

An uncooled laser transmitter is cheaper and more reliable than a thermo-electrically cooled laser transmitter because of its simplicity in packaging. A low-cost, highly-reliable uncooled laser may have a strong influence on pushing fiber deployment closer to the home. For loop applications, the laser transmitter must operate reliably over the temperature range from -40 to 85 °C (1). It is rather difficult to make high performance uncooled lasers in the long wavelength region (1.3-1.55 μm) using the conventional $Ga_xIn_{1-x}As_yP_{1-y}/InP$ material system because the laser temperature performance suffers from Auger recombination in the low bandgap material and poor electron confinement resulting from the small conduction band offset ($\Delta E_c = 0.4\Delta E_g$). We will discuss the design of uncooled lasers which minimizes the change in both threshold current and slope efficiency over the temperature range from -40 to 85 °C (2). To prevent carrier overflow under high-temperature operation, the electron confinement energy is increased by using the $Al_xGa_yIn_{1-x-y}As/InP$ material system (2) instead of the conventional $Ga_xIn_{1-x}As_yP_{1-y}/InP$ material system. Experimentally, the $Al_xGa_yIn_{1-x-y}As/InP$ strained quantum well lasers show superior high temperature performances such as a small drop of 0.3 dB in slope efficiency when the heat sink temperature changes from 25 to 100 °C (3), a maximum CW operation temperature of 185 °C (4), a thermally-limited 3-dB bandwidth of 13.9 GHz at 85 °C (5), and a mean-time-to-failure of 33 years at 100 °C and 10 mW output power (6).

Design Considerations for High Temperature Operation

Several approaches have been investigated to improve the laser temperature characteristics. Strained multiple quantum well active layers are used to reduce the laser threshold current, Auger recombination, and intervalence band absorption through reducing the in-plane hole effective mass by the combination of biaxial strain and quantum confinement.

In quantum well structures, the carrier leakage through the barrier layer is one important factor causing the laser performance degradation at high temperature and high carrier density. Due to the difference in the effective mass, the electron with its lighter effective mass requires a tighter confinement than the hole. Unfortunately, in the conventional $GaInAsP/InP$ quantum well structures, the band offset is not consistent with the above requirement because the conduction band offset ($\Delta E_c = 0.4\Delta E_g$) is smaller than the valence band offset ($\Delta E_v = 0.6\Delta E_g$). To increase the conduction band offset, constant y quaternary quantum wells ($Ga_wIn_{1-w}As_yP_{1-y}/Ga_bIn_{1-b}As_yP_{1-y}$) (7), $InAs_xP_{1-x}$ ternary quantum wells (8), and quantum wells on ternary substrates ($InGaAs$) (9) have been tried by various research groups. We have chosen the $Al_xGa_yIn_{1-x-y}As/InP$ material system instead, for its large conduction band offset ($\Delta E_c = 0.72\Delta E_g$) to provide a strong electron confinement in the well and maintain uniform hole distribution among the wells (2). Moreover, in this material system, it is easier to implement the graded-index separate-confinement heterostructure (GRINSCH) by adjusting the Al to Ga ratio only than by adjusting both x and y nonlinearly in the conventional $Ga_xIn_{1-x}As_yP_{1-y}/InP$ material system because the difference in the covalent radius of Gallium and Aluminum is very small. The GRINSCH provides not only

strong carrier confinement but also efficient carrier injection.

The design of high temperature lasers in terms of the quantum well number and the mirror loss is quite different from that of low-threshold-current lasers. Fig. 1 shows the normalized modal gain as a function of normalized current density for two different operating temperatures (25 and 100 °C, respectively). For room-temperature low-threshold operation, the optimum operating point is designed to be at the intercept A of the 25 °C gain curve and the maximum slope line measured from the origin (10). With this design, the laser will have a poor temperature performance because the operating point A' moves into the gain saturation region at high temperature. To avoid gain saturation at high temperature operation (e.g. 100 °C), the optimum operating point should be designed to be at the intercept B of the 100 °C gain curve and the maximum slope line measured from the origin, at the expense of slightly high threshold current at room temperature (2). We have derived the following simple guidelines for minimizing the temperature sensitivity in threshold current and slope efficiency (2).

$$G_0 > 4 \frac{T_{Jx}}{T_{G_0}} (\alpha_i + \alpha_m) \quad [1]$$

$$\alpha_i + \alpha_m > 4\Gamma\beta N_{th} \frac{T_{th}}{T_{N_{th}}} \quad [2]$$

where G_0 is the modal gain when G/J is maximum, T_x is the characteristic temperature of parameter x, α_i is the internal loss, α_m is the mirror loss, Γ is the optical confinement factor of the multiple quantum well region, and βN_{th} is a carrier density dependent loss due to free carrier and intervalence band absorption. G_0 is proportional to the number of quantum wells. It is easy to satisfy the above relations for AlGaAs lasers since β is relatively small (11). On the other hand, because the intervalence band

absorption is not negligible in 1.3 or 1.55 μm bulk lasers (11), it is important to use strained-quantum wells to reduce β and to maximize the mirror loss, to avoid a decrease in slope efficiency at high temperature. To design uncooled lasers for high temperature operation, we should use strained-layer multiple quantum wells as the active layer with the maximum total well thickness allowed by strain to satisfy Eqs. [1] and [2]. It is contrary to the design for low threshold lasers which requires $G_0 = \alpha_m$ (10) together with a single quantum well and a small mirror loss.

Material Growth and Device Fabrication

The laser material was grown by low-pressure (76 Torr) organometallic chemical-vapor deposition at 625 $^{\circ}\text{C}$ for InP and 700 $^{\circ}\text{C}$ for AlGaInAs (12). The quantum wells are either $\text{Al}_{1.61}\text{Ga}_{1.02}\text{In}_{0.737}\text{As}$ wells (5 nm each, 1.43 % compressive strain) or $\text{Al}_{0.7}\text{Ga}_{0.54}\text{In}_{0.39}\text{As}$ wells (11 nm each, 0.98 % tensile strain). The photoluminescence peak wavelength is around 1.29 μm . The multiple quantum wells are located in the middle of the graded-index separate-confinement heterostructure region. To provide a tight electron confinement in the growth direction, $\text{Al}_x\text{Ga}_y\text{In}_{1-x-y}\text{As}$ quaternary layers (10 nm thick each) with a bandgap large enough to provide an electron confinement energy of 150 meV are used as the barrier layers together with linearly graded waveguide layers (100 nm) on either side of the multiple quantum well region (2). The graded regions

are terminated in $\text{Al}_{0.48}\text{In}_{0.52}\text{As}$ waveguide regions. Carriers and photons are laterally confined by a 3- μm wide ridge waveguide fabricated by a self-aligned process to minimize the series resistance and provide uniform current injection.

High Temperature Static Performances

The light-current characteristics of lasers were measured for several cavity lengths and under various heat sink temperatures to determine the intrinsic material parameters summarized in Table I (2). The intrinsic material parameters per well of both compressive-strained five-quantum-well (CS5QW) and tensile-strained three-quantum-well (TS3QW) lasers are similar in magnitude and in temperature dependence. The tight electron confinement provided by AlGaInAs barriers improves the characteristic temperature of optical modal gain (T_{G_0}) by a factor of two compared with that of the matched seven-quantum-well lasers with GaInAsP barriers reported in Ref. (13). These lasers exhibit excellent temperature characteristics. When the heat sink temperature changes from 25 to 100 $^{\circ}\text{C}$, the differential quantum efficiency reduces by a small amount of 0.3 dB for a CS5QW laser with rear facet high-reflection coated as shown in Fig. 2 (3). A record high CW operating temperature of 185 $^{\circ}\text{C}$ has been obtained for a laser with both facets high-reflection coated as shown in Fig. 3 (4).

Table I Intrinsic material parameters for 1.3 μm AlGaInAs Lasers at three different heat sink temperatures determined from threshold current and slope efficiency as a function of cavity length. The temperature characteristic of the intrinsic material parameter X (such as G_0 or J_{tr}) is quantified by $\frac{1}{X} \frac{dX}{dT} = \frac{d \ln(X)}{dT} = \pm \frac{1}{T_x}$. The optical modal gain as a function of the current density is assumed to be $G = G_0 \ln(\frac{J}{J_{tr}})$.

Wafer	Temperature $T, ^{\circ}\text{C}$	Internal Quantum Efficiency $\eta_i, \%$	Internal Loss α_i, cm^{-1}	Optical Modal Gain G_0 per well, cm^{-1}	Transparency Current Density J_{tr} per well, A/cm^2
CS5QW	25	95	8.6	10.7	169
	65	92.5	10.7	9.62	243
	85	88.8	11.3	8.86	302
	T_x (K)			322	104.8
TS3QW	15	61	5.4	12.1	171
	65	59	8.8	10.6	280
	85	59	10.9	9.63	321
	T_x (K)			313	108.5

High Temperature Dynamical Performances

The intrinsic small-signal modulation responses are measured in the range of 0.1-20 GHz by a parasitic-free optical modulation technique (2). As shown in Fig. 4, the solid lines are the theoretical fittings to the measured data shown in dots for CS5QW lasers. Its maximum intrinsic 3-dB bandwidths are measured to be of 19.5, 15, and 13.9 GHz at 25, 65 and 85 $^{\circ}\text{C}$, respectively. Power roll-off caused by heating prevents further increase of the

modulation bandwidth. The strong carrier confinement also results in small k factors (0.25 ns) which indicate the potential for high speed modulation up to 35 GHz.

High Temperature Reliability

In spite of the aluminum-containing active layer, no catastrophic optical damage was observed at room temperature up to 210 mW for CS5QW lasers and 103 mW

for TS3QW lasers. For aluminum-containing lasers such as AlGaAs lasers under CW operation, the nonradiative region caused by facet oxidation has been reported as a main reason for early stage degradation (14). Thus, it is important to investigate the reliability of $\text{Al}_x\text{Ga}_y\text{In}_{1-x-y}\text{As}/\text{InP}$ lasers under high temperature operation for subscriber loop applications. Thirty 300- μm long CS4QW lasers have been undergoing life test for 8,000 hours. The rear facets of the devices are coated with one-pair high-reflection dielectric coating and the front facets are coated with neutral coating. The aging condition is 10 mW output power into 0.25 numerical aperture at 100 °C. The normalized threshold current change measured at 25 °C versus time is shown in Fig. 5. The changes in threshold current are very small. The lifetime projection is made by the linear extrapolation method. Based on a widely accepted lifetime criterion of a 50 % increase of the original threshold current, the mean-time-to-failure (MTTF) is estimated to be 33 years (2.9×10^5 hours) for operating at 100 °C with more than 10 mW output power.

Conclusions

The favorable band offset of $\text{Al}_x\text{Ga}_y\text{In}_{1-x-y}\text{As}/\text{InP}$ materials system enables us to design lasers with deep quantum wells and at the same time to maintain uniform hole distribution among the wells (2). Following the design guide lines, we have demonstrated that the $\text{Al}_x\text{Ga}_y\text{In}_{1-x-y}\text{As}/\text{InP}$ strained quantum well lasers perform well both statically and dynamically at high temperature. With these newly-designed uncooled lasers, low cost and reliable transmitters are being built for FITL applications.

Acknowledgement

The authors are grateful to Z. Wang, D. Darby, D. Flanders, and J. J. Hsieh of Lasertron for providing experimental data on laser static performances and reliability through research collaboration. We are also thankful to M. A. Koza, F. Favire, N. C. Andreadakis, B. Pathak, M. C. Wang, W. Lin, D. M. Hwang and C. Y. Chen of Bellcore for their help in crystal growth, device fabrication, laser characterization, bandgap calculation and TEM observations.

References

- [1] "Reliability assurance practices for optoelectronic devices in loop applications," Bellcore, TA-TSY-000983, Issue 1, January 1990.
- [2] C. E. Zah, R. Bhat, B. Pathak, F. Favire, W. Lin, M. C. Wang, N. C. Andreadakis, D. M. Hwang, M. A. Koza, T. P. Lee, Z. Wang, D. Darby, D. Flanders, and J. J. Hsieh, "High performance uncooled 1.3 μm $\text{Al}_x\text{Ga}_y\text{In}_{1-x-y}\text{As}/\text{InP}$ strained-layer quantum well lasers for subscriber loop applications," IEEE, J. Quantum Electron., vol. QE-30, pp. 511-523, February 1994.
- [3] C. E. Zah, R. Bhat, B. Pathak, F. Favire, M. C. Wang, W. Lin, N. C. Andreadakis, D. M. Hwang, M. A. Koza, T. P. Lee, Z. Wang, D. Darby, D. Flander and J. J. Hsieh, "High performance uncooled 1.3 μm $\text{Al}_x\text{Ga}_y\text{In}_{1-x-y}\text{As}/\text{InP}$ strained-layer quantum well lasers for fiber-in-the-loop applications," Tech. Dig. of Optical Fiber Comm. ThG1, pp. 204-205, San Jose, CA, February 20-25, 1994.
- [4] Z. Wang, D. B. Darby, G. Pinelli, M. Matsuki, P. S. Whitney, D. C. Flanders, J. J. Hsieh, C. E. Zah, R. Bhat, and T. P. Lee, "High-reliability, high-performance, low-cost coaxial laser module at 1.3 μm for local loop applications," Tech. Dig. of Optical Fiber Comm. W14, pp. 144-145, San Jose, CA, February 20-25, 1994.
- [5] C. E. Zah, M. C. Wang, R. Bhat, T. P. Lee, S. L. Chuang, Z. Wang, D. Darby, D. Flanders, and J. J. Hsieh, "High-temperature modulation dynamics of 1.3 μm $\text{Al}_x\text{Ga}_y\text{In}_{1-x-y}\text{As}/\text{InP}$ compressive-strained multiple-quantum-well lasers," 14th IEEE Int. Semiconductor Laser Conf., Th1.3, pp. 215-216, Maui, Hawaii, September 19-23, 1994.
- [6] C. E. Zah, R. Bhat, T. P. Lee, Z. Wang, D. Darby, D. Flanders, and J. J. Hsieh, "Recent progress on uncooled 1.3- μm lasers for loop applications," Tech. Dig. of Optical Fiber Comm. ThG1, pp. 251-252, San Diego, CA, February 26-March 3, 1995.
- [7] A. Mircea, A. Ougazzaden, G. Primot and C. Kazmierski, "Highly thermally stable, high-performance InGaAsP: InGaAsP multi-quantum-well structures for optical devices by atmospheric pressure MOVPE," J. of Crystal Growth, vol. 124, pp. 737-740, 1992.
- [8] M. Yamamoto, N. Yamamoto and J. Nakano "MOVPE growth of strained InAsP/InGaAsP quantum-well structures for low threshold 1.3 μm lasers," IEEE, J. Quantum Electron., vol. QE-30, pp. 3-9, January 1994.
- [9] H. Shoji, T. Uchida, T. Kusunoki, M. Matsuda, H. Kurakake, S. Yamazaki, K. Nakajima, and H. Ishikawa, "Fabrication of $\text{In}_{0.25}\text{Ga}_{0.75}\text{As}/\text{InGaAsP}$ strained SQW lasers on $\text{In}_{0.05}\text{Ga}_{0.95}\text{As}$ ternary substrate," IEEE, Photon. Technol. Lett., vol. 6, no. 10, pp. 1170-1172, October 1994.
- [10] P. W. McIlroy, A. Kurobe, and Y. Uematsu, "Analysis and application of theoretical gain curves to design of multi-quantum-well lasers" IEEE, J. of Quantum Electron., vol. QE-21, pp. 1958-1963, 1985.
- [11] A. R. Adams, M. Asada, Y. Suematsu and S. Arai, "The temperature dependence of the efficiency and threshold current of $\text{In}_{1-x}\text{Ga}_x\text{As}_y\text{P}_{1-y}$ lasers related to intervalence band absorption," Jap. J. of Appl. Phys., vol. 19, no. 10, pp. L621-624, 1980.
- [12] R. Bhat, C. E. Zah, M. A. Koza, B. Pathak, F. Favire, W. Lin, M. C. Wang, N. C. Andreadakis, D. M. Hwang, T. P. Lee, Z. Wang, D. Darby, D. Flanders, and J. J. Hsieh, "High-performance 1.3 μm AlGaInAs/InP strained quantum well lasers grown by

organometallic chemical vapor deposition," J. of Crystal Growth, vol. 145, pp. 858-865, 1994.

- [13] H. Yamada, T. Terakado, Y. Sasaki, S. Takano, T. Tamura, T. Torikai and T. Uji, "Extremely low operating current 1.3- μ m MQW lasers at high temperature," Proc. of 18th Eur. Conf. on Opt. Comm., vol. 1, paper Mo B3.3, pp. 101-104, Berlin, Germany, 1992.
- [14] W. J. Fritz, L. B. Bauer, and C. S. Miller, "Analysis of aluminum gallium arsenide laser diodes failing due to nonradiative regions behind the facets," 27th Annual Proc. Reliability Phys., pp. 59-64, Phoenix, AZ, 1989.

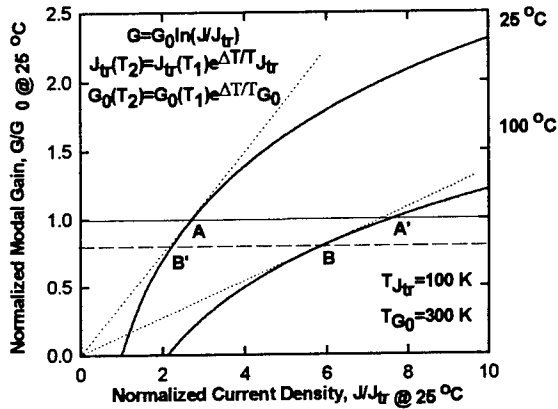


Fig. 1 Normalized modal gain as a function of normalized current density for two different operating temperatures (25 and 100 °C, respectively).

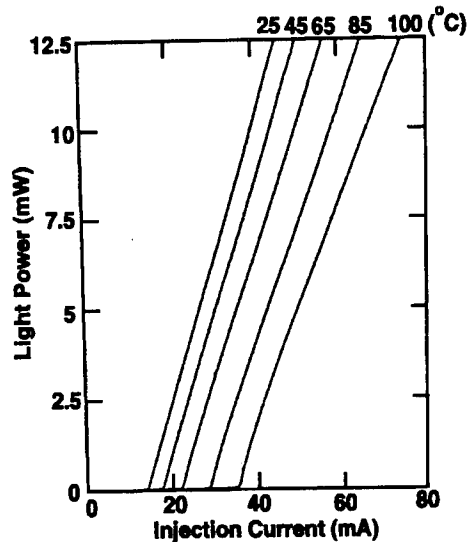


Fig. 2 Light-current characteristics of a 300- μ m long CS5QW laser with a 70 % high reflection coating on the rear facet at various heat sink temperatures.

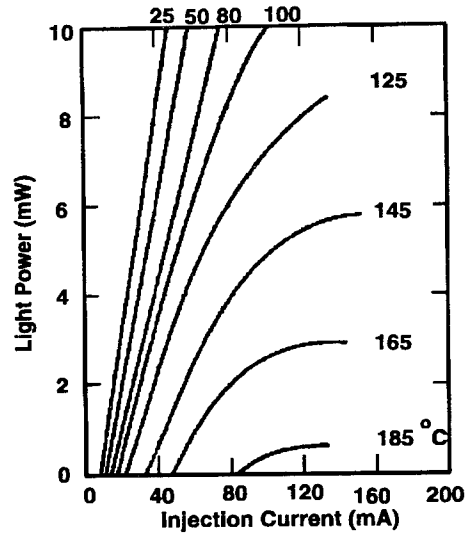


Fig. 3 Light-current characteristics of a 300- μ m long CS5QW laser with a 75 % (85%) high reflection coating on the front (rear) facet at various heat sink temperatures.

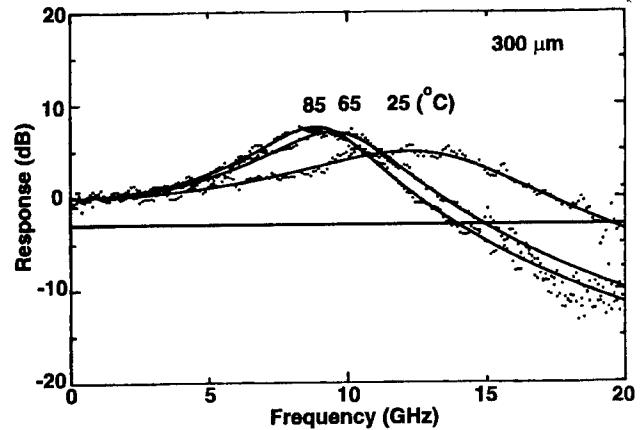


Fig. 4 Small-signal modulation responses of a 300 μ m long CS5QW laser at 25, 65 and 85 °C with bias currents of 153, 137 and 150 mA, respectively.

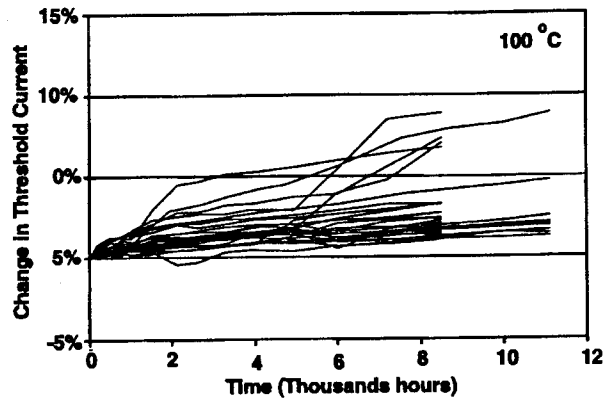


Fig. 5 Normalized threshold current changes of CS4QW lasers measured at 25 °C, as a function of time in life test. The aging condition is 10 mW output power at 100 °C.

MOCVD Growth and Characterization of Tensile-Strained $\text{Ga}_x\text{In}_{1-x}\text{As}_y\text{P}_{1-y}$ Quantum Wells for Low Threshold Lasers Emitting at $1.3\mu\text{m}$

N. Yokouchi, N. Yamanaka, N. Iwai, and A. Kasukawa

Yokohama R&D Laboratories, The Furukawa Electric Co., Ltd.
2-4-3, Okano, Nishi-ku, Yokohama 220, Japan

Abstract - Tensile-strained GaInAsP/InP quantum wells (QWs) grown by low-pressure metalorganic chemical vapor deposition (LP-MOCVD) are investigated for $1.3\mu\text{m}$ laser applications. High resolution x-ray diffraction shows good agreement with theoretical simulation. Photoluminescence spectra have well energy separation due to biaxial tension. The lowest threshold current density for infinite cavity length J_{th}/N_w^∞ of $100\text{A}/\text{cm}^2$ is obtained for the device with -1.15% strain and $N_w=3$. The amount of strain which gives the lowest J_{th}/N_w^∞ is around -1.2% . The tensile strained QW laser emitting at $1.3\mu\text{m}$ is attractive for the light source of fiber in the loop application.

1. Introduction

Semiconductor lasers with low power consumption and stable operation at high temperature without Peltier cooling are important light sources for a fiber in the loop (FITL) application. Strained quantum well (QW) lasers [1, 2] are promised devices for the application since strained materials have superior gain and loss characteristics. Compressive strain reduces the heavy hole effective mass which leads to population inversion at low carrier density. Nonradiative Auger recombination and intervalence band absorption (IVBA) which are serious problems for $1.3\mu\text{m}$ and $1.55\mu\text{m}$ lasers are also suppressed. These effects realize low threshold current density of $98\text{A}/\text{cm}^2$ for $1.55\mu\text{m}$ lasers [3]. In tensile-strained QW lasers, low threshold operation is realized by another effect. An electron to light hole transition is dominant since light hole band moves up to the top of valence band due to the biaxial tension. The transition enhances TM gain compared to TE gain by suppression of spontaneous emission polarized in the growth plane [4]. Auger recombination and IVBA is suppressed by the large separation of light hole and heavy hole subbands. To realize high performance tensile-strained QW lasers, relatively thick well, more than 10nm , is required since the quantum size effect reduces the separation. Low threshold current density of $92\text{A}/\text{cm}^2$ [5] is obtained in $1.55\mu\text{m}$ tensile-strained QW lasers with 12nm -thick single QW. Although high performance $1.55\mu\text{m}$ tensile-strained QW lasers based on $\text{Ga}_x\text{In}_{1-x}\text{As}$ ($x>0.47$) are reported [5, 6], $1.3\mu\text{m}$ devices are not sufficiently investigated [7]. As for tensile strained QW lasers emitting at $1.3\mu\text{m}$, $\text{Ga}_x\text{In}_{1-x}\text{As}_y\text{P}_{1-y}$ is preferable to

$\text{Ga}_x\text{In}_{1-x}\text{As}$ since thicker QW can be applicable. We investigate the potential of $\text{Ga}_x\text{In}_{1-x}\text{As}_y\text{P}_{1-y}$ tensile-strained QWs grown by low-pressure metalorganic chemical vapor deposition (LP-MOCVD) for $1.3\mu\text{m}$ lasers. Very low threshold current density is obtained in graded index separate confinement heterostructure (GRIN-SCH) lasers.

2. Growth and Evaluation of Tensile-Strained GaInAsP/InP QW Structure

LP-MOCVD with a vertical reactor is used for the experiment. Substrate temperature during growth is 600°C . Trimethylindium (TMIn) and triethylgallium (TEGa) are used for group III sources. Phosphine (PH_3 , 30% in H_2) and arsine (AsH_3 , 10% in H_2) are used for group V sources. Figure 1 shows x-ray rocking curve around (400) diffraction and its simulation [8] of a $\text{Ga}_x\text{In}_{1-x}\text{As}_y\text{P}_{1-y}/\text{InP}$ triple QW structure. The best simulation as shown in the figure is obtained by assuming $x=0.49$, $y=0.7$, well thickness $L_w=11.2\text{nm}$ and barrier thickness $L_B=22.3\text{nm}$. The amount of tensile strain is estimated to be -1.15% . Fringes around lower order satellite peaks and good agreement of experimental and simulated curves indicate that abrupt interfaces and good periodicity are obtained. Room temperature photoluminescence (PL) spectra with various strain are shown in Fig. 2. Two clear emission peaks in highly strained materials correspond to an electron - light hole (e-lh) and an electron - heavy hole (e-hh) transitions. The former transition is dominant in the highly strained material. The separations are 30meV and 45meV for materials with tensile strain of -0.73% and -1.15% ,

respectively. These values are close to the theoretical estimation including energy level shifts due to biaxial tension [9] and the quantum size effect.

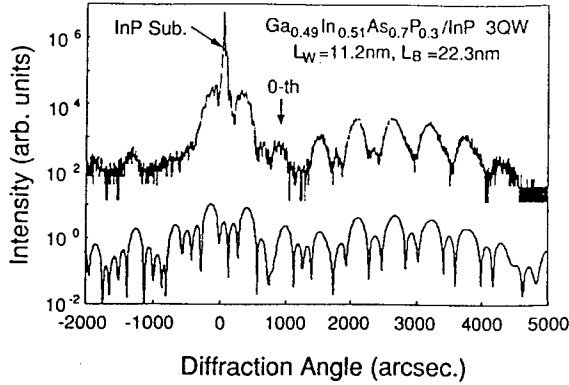


Fig. 1 Measured X-ray diffraction rocking curve and its simulation.

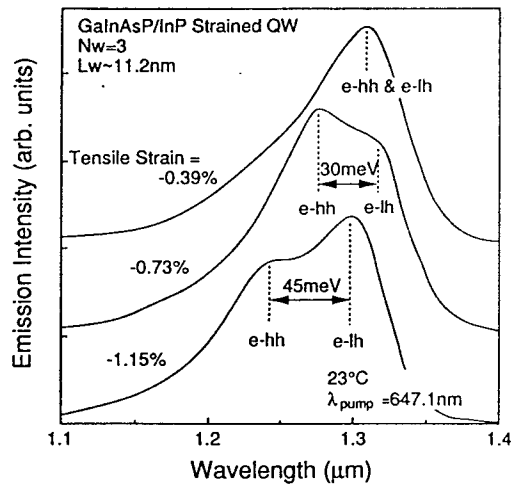


Fig. 2 Photoluminescence spectra of tensile-strained GaInAsP/InP QWs.

3. Threshold Characteristics of GRIN-SCH LDs

GRIN-SCH QW lasers with 20μm-wide ridge waveguide configuration are fabricated. Conduction band diagram of the device is schematically shown in Fig. 3. Tensile strain of -0.8%, -1.15% and -1.42% are investigated. Well number (N_w) of 1, 2, 3 and 4 are prepared for the wafer with -1.15% tensile strain. PL intensity is drastically degraded for the wafer with 4 wells. Surface roughness associated to 3-dimensional growth [10]

is observed in the wafer. In the case of -1.42% tensile strain, same degradation are confirmed in the wafer with $N_w=2$. No lasing operation is obtained in the device from these wafers.

Semi-logarithmic approximation for optical gain g per well is given by [11]

$$g = G_0 \ln \left(\frac{\eta_i J}{N_w J_{tr}} \right) \quad (1)$$

where η_i is internal efficiency, J is injected current density and J_{tr} is transparency current density. G_0 is a gain constant. Threshold current density per well J_{th}/N_w is then given by

$$\frac{J_{th}}{N_w} = \frac{J_{tr}}{\eta_i} \exp \left\{ \frac{1}{N_w \Gamma_w G_0} (\alpha_i + \alpha_m) \right\} \quad (2)$$

where Γ_w is confinement factor of electric field for each well, α_i is internal loss and α_m is mirror loss. Mirror loss is defined by

$$\alpha_m = \frac{1}{L} \ln \left(\frac{1}{R} \right) \quad (3)$$

where L is cavity length and R is averaged facet reflectivity.

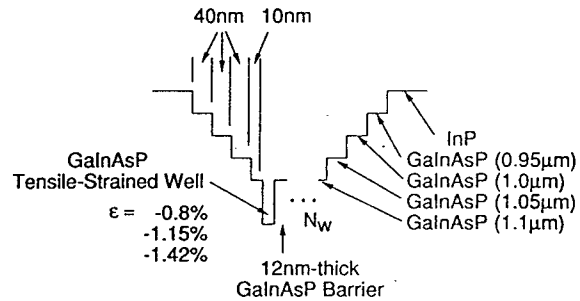


Fig. 3 Conduction band diagram of the investigated device is schematically drawn.

Threshold current density per well J_{th}/N_w for the devices with -1.15% tensile strain are plotted in Fig. 4. The minimum J_{th}/N_w for infinite cavity J_{th}/N_w^∞ (J_{th}/N_w at $\alpha_m = 0\text{cm}^{-1}$) is estimated to be 100A/cm² for the device with $N_w=3$. High reflective (HR) coating is introduced for both facets (for front facet $R_f=0.92$ and rear facet $R_r=0.96$) of the device with $N_w=1$ and $L=200\mu\text{m}$. The light output - current characteristic of the device is shown in Fig. 5.

Threshold current density of 6mA, corresponding current density of 150A/cm², is obtained. This is, to our best knowledge, the lowest threshold current density for 1.3μm tensile-strained QW lasers.

Strain dependence of J_{th}/N_w is shown in Fig. 6. At the -0.8% strain, J_{th}/N_w is higher since the separation of light hole and heavy hole bands is insufficient. At the point of -1.42%, it is difficult to increase well number due to the surface degradation mentioned above. If multiple QW structure can be grown by introducing the strain compensated technique [12], J_{th}/N_w for -1.42% strain can be reduced as predicted in Eq. (2). Tensile strain modifies band structure for both conduction and valence bands. The conduction band moves up and conduction band discontinuity between well and barrier is reduced with tensile strain. This modification results in type-II band lineup if larger strain is applied. From these consideration and experimental results, the amount of strain which gives the lowest J_{th}/N_w is around -1.2%. In the case of 1.55μm emission, the optimized strain is about -1.6% [5, 6], which is slightly larger than that of 1.3μm case. This could be attributed to the small conduction band energy difference between well and barrier layers for 1.3μm lasers.

To reduce the threshold current, narrow stripe of 2.5μm-wide ridge waveguide lasers are fabricated. A very low threshold current of 2mA is obtained under pulsed operation at room temperature in a 160μm-long device ($N_w=3$) with high reflective (HR) coated on both facets as shown in Fig. 7.

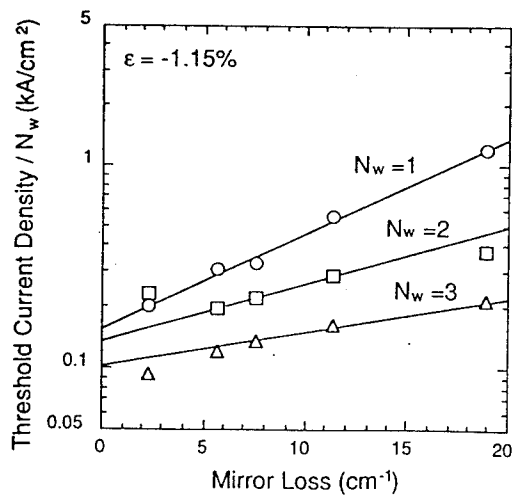


Fig. 4 Mirror loss dependence of threshold current density per well (J_{th}/N_w) for the devices with -1.15% strain.

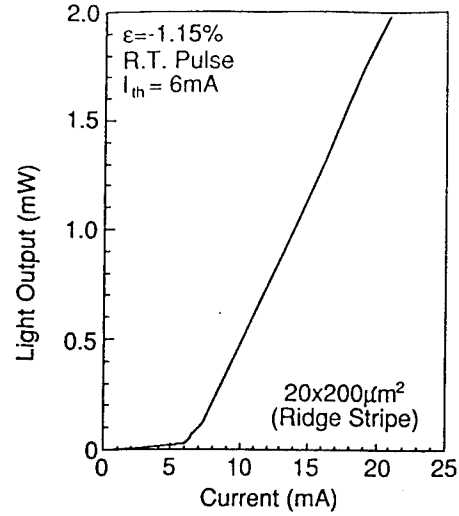


Fig. 5 Light output versus current characteristic of a HR/HR (92%/96%) coated device. A very low threshold current density of 150A/cm² is obtained.

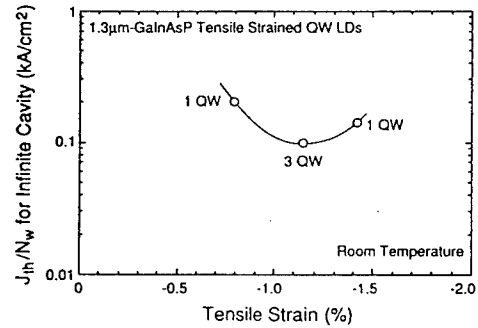


Fig. 6 Tensile strain dependence of J_{th}/N_w for infinite cavity length.

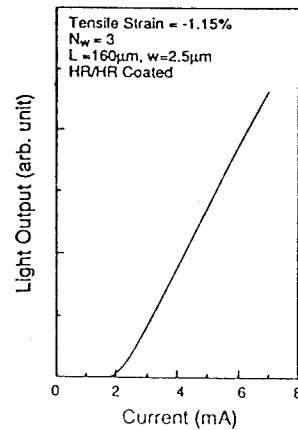


Fig. 7 Light output versus current characteristic of a HR/HR (90%/98%) coated device.

4. Conclusions

Tensile-strained GaInAsP/InP QWs grown by LP-MOCVD are investigated for 1.3 μ m laser applications. X-ray diffraction and PL measurements indicate that high quality MQW structure can be grown routinely. The lowest J_{th}/N_w^∞ of 100A/cm² is obtained for the device with -1.15% strain and $N_w=3$. The amount of strain which gives the lowest J_{th}/N_w^∞ is around -1.2%. Submilliampere operation can be obtained by optimized device structure. The tensile strained QW laser emitting at 1.3 μ m is attractive for the light source of FITL application.

Acknowledgment

The authors would like to thank Mr. S. Kashiwa and Mr. T. Ninomiya for their encouragement through this study.

References

1. A.R. Adams, Electron. Lett., 22, 249, 1986.
2. E. Yablonovitch et al., J. Lightwave Technol., 4, 504, 1986.
3. N. Yamamoto et al., Electron. Lett., 30, 243, 1994.
4. E.P. O'Reilly et al., Electron. Lett., 27, 1417, 1991.
5. P.J.A. Thijs et al., Electron. Lett., 28, 829, 1992.
6. C.E. Zah et al., Electron. Lett., 27, 1414, 1991.
7. P.J.A. Thijs et al., J. Lightwave Technol., 12, 28, 1994.
8. J.M. Vandenberg et al., J. Appl. Phys., 62, 1278, 1987.
9. J. Barrau et al., Electron. Lett., 28, 786, 1992.
10. J.-Y. Emery et al., J. Crystal Growth, 127, 241, 1993.
11. M. Rosenzweig et al., IEEE J. Quantum Electron., 27, 1804, 1991.
12. B.I. Miller et al., Appl. Phys. Lett., 58, 1952, 1991.

CW Operation of a 1.3- μm Strained Quantum Well Laser on a Graded InGaAs Buffer with a GaAs Substrate

WA1.3

T. Uchida, H. Kurakake, H. Soda, and S. Yamazaki

Fujitsu Laboratories Ltd.

10-1 Morinosato-Wakamiya, Atugi 243-01, Japan

Introduction

Strained layer quantum well (SL-QW) structures on a InP substrate have made progress on the threshold current and slope efficiency of a laser, emitting at 1.3 μm [1-2]. Poor characteristic temperature has, however, not been improved. The 1.3 μm strained quantum well laser, grown on a lattice relaxation buffer layer with a lattice constant between that of GaAs and InP, has a high potential to improve the temperature characteristics, because of its carrier overflow suppression from the active region with a large band gap SCH layer[3]. However, the surface roughness and the dislocation caused by the lattice relaxation[4] in the buffer layer hinders the lasing operation of the strained quantum well laser.

We report the first CW operation of a 1.3 μm strained quantum well laser with InGaP cladding layers on the lattice relaxation buffer layer grown by metal organic vapor phase epitaxy (MOVPE). We use a compositionally graded InGaAs/GaAs structure[5] as the lattice relaxation buffer. Significant reduction of the surface roughness of the InGaP cladding layers, due to high Se doping, enables the CW operation of the 1.3 μm SL-QW laser.

Epitaxial growth and sample structure

Figure 1 illustrates the sample structure of the 1.3 μm strained quantum well laser on a graded InGaAs buffer layer with a (100) GaAs substrates. The InGaP cladding layer, the InGaAsP SCH layers and the InGaAs buffer layer are all lattice-matched to the top of the graded layer. The quantum well active layer of In-rich InGaAs is compressively strained ($\Delta a/a \approx 1\%$, where a is the lattice constant of the cladding layer).

Samples were grown by one-step LP-MOVPE (75Torr) at 640-700 $^{\circ}\text{C}$ in the vertical reactor having the radio frequency heating system. The group III sources were trimethylindium (TMI) and triethylgallium (TEG). The group

V sources were AsH_3 and PH_3 . The dopant sources were dimethylzinc (DMZ) for p-type conductivity and H_2Se for n-type conductivity. The growth rate was 1.2-2.4 $\mu\text{m}/\text{h}$. The V/III ratio was 50-250. By controlling the group III flow rate continuously and linearly, we performed the growth of the graded layer.

We characterized the sample by photoluminescence (PL) measurements. The PL peak wavelength was 1.19 μm for the InGaAs buffer layer, 0.79 μm for InGaP cladding layer, 1.11 μm for InGaAsP and 1.31 μm for the InGaAs active layer. They were close to the designed value.

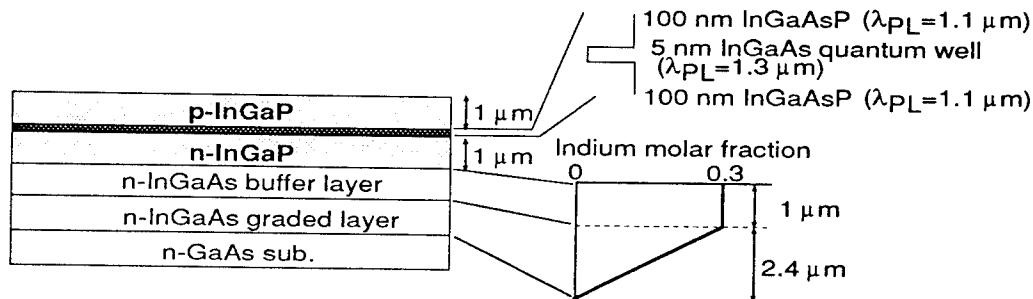


Fig. 1 Sample structure

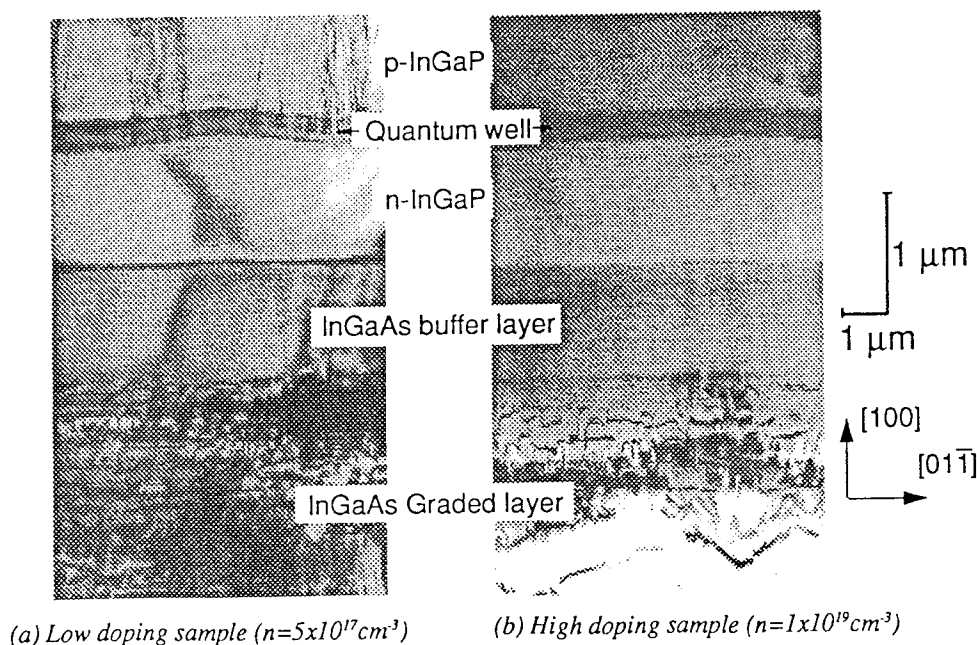


Fig. 2 Cross sectional TEM image of (011) plane

Undulation and generation of dislocations around the SL-QWs

The sample with the Se doped n-cladding layers ($5 \times 10^{17} \text{ cm}^{-3}$) showed very weak PL intensity. Cross-sectional transmission-electron microscopy (XTEM) observation revealed that this PL intensity deterioration is due to dislocations in the vicinity of the InGaAs SL-QW (Figure 2(a)). These defects are not caused by a residual strain of the cladding layer, because the difference between the vertical and lateral lattice spacing is small ($\Delta a/a < 1 \times 10^{-3}$ measured by x-ray reciprocal lattice mapping).

We note that the SL-QW undulates and the dislocations spread out from the slope regions of the undulation. The dislocations are not generated in flat regions. It is not clear what generates the dislocations. Anyway, we assumed that suppressing the undulation of the SL-QWs reduced the defects, and confirmed this by experiment. Taking note of each layer's surface, it is smooth for the buffer layer but very rough for the n-cladding layer. The surface roughness is enhanced by growing the n-cladding layer. This suggests that we should focus on smoothing n-InGaP surface.

Surface smoothing by highly H_2Se supply

We applied the highly H_2Se supply technique to smooth the n-InGaP cladding surface. Y.Kondo et al. found that the highly H_2Se supply enables a flat embedding growth of InP[6]. This technique can be regarded as smoothing the

surface roughness of a ridge waveguide structure. We expected that the highly H_2Se supply has a similar effect on the growth of an InGaP surface and will therefore smooth the InGaP surface.

Figure 2(b) shows XTEM images of a sample with highly doped n-InGaP ($1 \times 10^{19} \text{ cm}^{-3}$). As expected, the InGaP surface roughness was suppressed by the highly H_2Se supply, and no dislocations were formed around the quantum well. Figure 3 shows that Se-doping for optimizing carrier

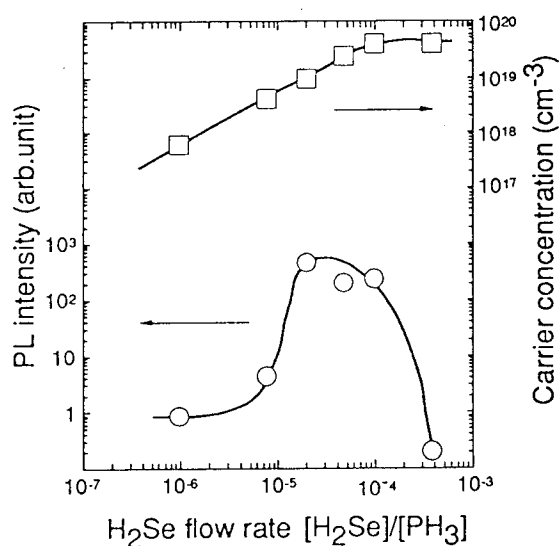


Fig. 3 Dependence of PL intensity on H_2Se supply

concentration ($n=1 \times 10^{19} \text{cm}^{-3}$) greatly improves the PL intensity of the quantum wells. The improvement of the PL intensity is due to the reduction of the dislocation density that operates as a non-radiative center. The carrier concentration is saturated when exceeding the optimum concentration of the H_2Se supply. This excess supply reduces the PL intensity. We think that the excess Se atoms form non-radiative defects.

Laser fabrication

We fabricated a ridge-waveguide laser using the highly Se supply. Figure 4 illustrates the schematic of the ridge-waveguide laser structure which consists of 7 nm twin quantum wells and a 10 nm InGaAsP barrier layer. The n-InGaP had the optimum carrier concentration of $1 \times 10^{19} \text{cm}^{-3}$. We formed a ridge waveguide of 5 μm width. Figure 5 shows

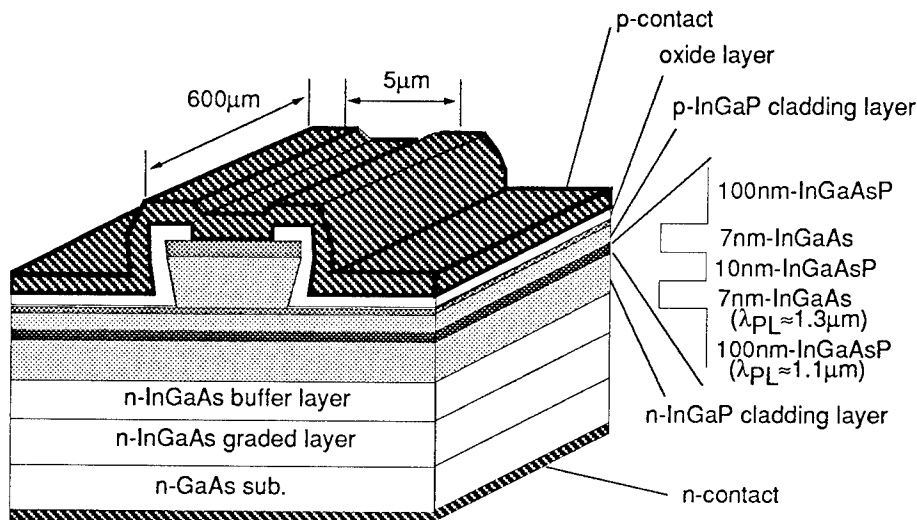


Fig. 4 Schematic of fabricated Ridge waveguide laser

the dependence of light output on current, for a cavity 600 μm long. The laser had a low threshold current of 15 mA and a high output power of more than 15 mW for one facet at room temperature. This is the first CW operation of 1.3 μm SL-QW laser on a lattice relaxed buffer that is largely lattice mismatched with the substrate.

Discussion

We will discuss on the mechanism of InGaP surface undulation and the smoothing effect of highly H_2Se supply. The surface on the compositionally graded InGaAs/GaAs lattice relaxation buffer layers generally has crosshatched in-plane roughness, that is believed to be from gliding of dislocations on the (111) plane[4]. The InGaP surface undulation is not due to gliding of dislocations, because the InGaP was pseudomorphically grown on the InGaAs buffer. The lateral lattice spacing of InGaP was the same as that of InGaAs; it was measured by x-ray reciprocal lattice mapping. As for the other roughening process, the surface roughness is known to be caused by portionally enhanced growth on permanent step, that is given by screw dislocations for instance, or caused by elastic relaxation.

The smoothing process is similar to the method used by Y. Kondo et al.[6]. They suggested that the highly H_2Se supply made the (100) InP surface inactive and the trapping of In atom on the (100) surface difficult. We expected similar effects on both In- and Ga-atoms on (100) surface of InGaP. Then the atoms landing on ridges of InGaP undulation migrate and reach the steps of the slopes, sandwiching the ridges. This effect suppress the growth on the ridges and

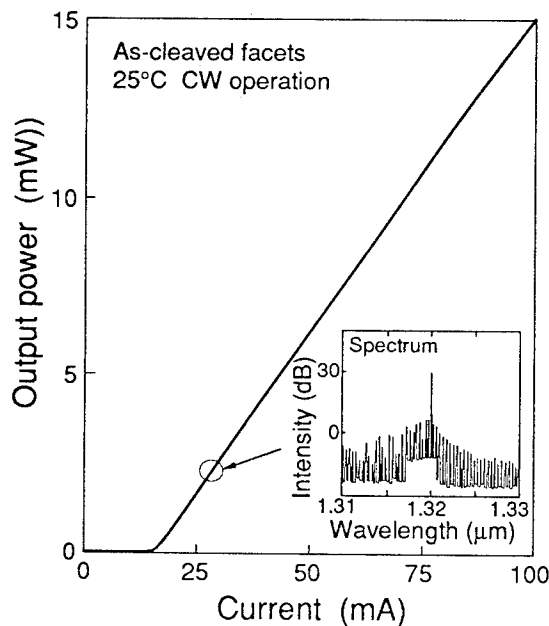


Fig. 5 Light-current characteristic of the ridge waveguide laser

enhance the step flow growth on the slopes. As a result, the valley region is filled up and the n-InGaP surface is smoothed. The experimental results show the highly H₂Se supply reduce the surface roughness, as expected. If there were any permanent steps on the InGaP, the highly H₂Se supply would enhance the portional growth on the sources of the permanent step. We think that the InGaP surface roughness is not caused by the portional enhanced growth due to permanent steps.

It is not completely cleared what enlarges the surface undulation. We found that the growth technique is effective for smoothing the InGaP surface roughness due to lattice relaxation. It is a useful method for fabricating lasers on lattice relaxation buffer layers.

Conclusion

We investigated MOVPE growth of 1.3 μ m lasing SL-QWs with InGaP cladding layers on the compositionally graded InGaAs buffer layers with the GaAs substrate. We found that the surface roughness of the lower InGaP layer causes generation of many dislocations around the SL-QWs. This deteriorated the PL intensity of the active layer. The surface roughness of the InGaP layers was reduced by the highly H₂Se supply. The reduction of the surface roughness significantly suppresses the dislocations around the SL-QWs. This new technique realized the first CW-operation of the 1.3 μ m SL-QW laser with InGaP cladding layers. We achieved a low threshold current of 15 mA and more than 15 mW output power.

Reference

- [1] P.J.A. Thijs, T. Van Dongen, L.F. Tiemeijer, R.W.M. Slootweg, and J.J.M. Binsma, "High output power (380 mW), low threshold current (1.3mA), low linewidth enhancement factor (≤ 2) $\lambda = 1.3 \mu$ m strained quantum well lasers", European Conf. on Optical Communication/Int.Conf. on Integrated Optics and Optical Fiber Communication, Paris, Vol. 3, pp. 48-51, 1991.
- [2] A. Mathur, J. S. Osinski, P. Grodzinski, and P. D. Dapkus, "Comparative study of low-threshold 1.3 μ m strained and lattice-matched quantum-well lasers", IEEE Photonics Technology Letters, Vol. 5, No. 7, July 1993.
- [3] H. Ishikawa, and I. Sucmune, "Analysis of temperature dependent optical gain of strained quantum well taking account of carriers in the SCH layer", IEEE Photonics Technology Letters, Vol. 6, No. 3, March 1994.
- [4] K.H. Chang, R. Gibala, D.J. Srolovitz, P.K. Bhattacharya, and J.F. Mansfield, "Crosshatched surface morphology in strained III-V semiconductor films", J. Appl. Phys. **67** (9), 1 May 1990.
- [5] T.P. Chin, and C.W. Tu, "Heteroepitaxial growth of InP/In_{0.52}Ga_{0.48}As structures on GaAs (100) by gas-source molecular beam epitaxy", Appl. Phys. Lett. **62** (21), 24 May 1993.
- [6] Y. Kondo, K. Sato, and M. Yamamoto, "Self-aligned buried-heterostructure lasers grown entirely by metalorganic vapor phase epitaxy", Appl. Phys. Lett. **62** (11), 15 March 1993.

Four-Wavelength DBR Laser Array with Waveguide-Couplers Fabricated Using Selective MOVPE Growth WA1.4

Y. Katoh, T. Kunii, Y. Matsui, and T. Kamijoh

*Semiconductor Technology Laboratory, Oki Electric Industry Co., Ltd.
550-5 Higashiasakawa, Hachioji, Tokyo 193, Japan*

Abstract

We developed integrated multiwavelength lasers with waveguide couplers using a novel selective metalorganic vapor-phase epitaxy (MOVPE) technique. The lasing wavelength was controlled by modulating the effective refractive index of distributed Bragg reflector (DBR) waveguides. Array lasing wavelengths were distributed from 1548.0 to 1553.5 nm with an average spacing of 1.8 nm. Output power exceeding 100 μ W was obtained for each DBR laser. The propagation loss of the waveguide coupler was about 16 dB for inner ports and 20 dB for outer ports with a 6-dB splitting loss.

Introduction

Wavelength division multiplexing (WDM) technology is expected to be useful in next-generation optical transmission and photonic switching. WDM systems require multiwavelength light sources with highly precise wavelength control. In conventional multiwavelength laser array fabrication, electron-beam lithography or multiple-step of holographic exposure have been used to generate gratings with different spacing [1-3]. These techniques present serious questions in terms of productivity, however. Selective metalorganic vapor-phase epitaxy (MOVPE) growth has been investigated as alternative in this regard [4-6], because the thickness and the composition of InGaAsP layers can both be controlled in-plane in a single growth step. Layer thickness control enables the effective refractive index of waveguide structures to be controlled. Four-wavelength distributed Bragg reflector (DBR) laser arrays were previously fabricated using selective MOVPE growth [7]. In addition, for the application, all channels must be combined with different wavelengths into a single-mode fiber for signal transmission. We developed integrated lasers with waveguide couplers using selective MOVPE technique. This device appears extremely attractive in reducing the risk in packaging with fiber optics and in use with compact multiwavelength light sources.

Device Structure and Fabrication

A four-wavelength DBR laser array was integrated with buried waveguide-couplers based on a Y-branch structure (Fig. 1). The array chip was 4 mm long and 1 mm wide. The device combined a 380- μ m active section, a 500- μ m back DBR section, a 250- μ m front DBR section, and a 200- μ m phase control section. The waveguide had an 800- μ m radius of curvature. The cross section of the waveguide layer structure of the coupler is shown in Figure 2. The lateral spacing between lasers was 250 μ m. A grating with 243.5-nm spacing was holographically formed over only the n-InP wafer of the DBR section. The wavelength was controlled by changing the effective refractive index of the waveguide of the DBR sections. The guide layer (n-InGaAsP : $\lambda_g=1.2$ μ m) thickness was controlled using a selective

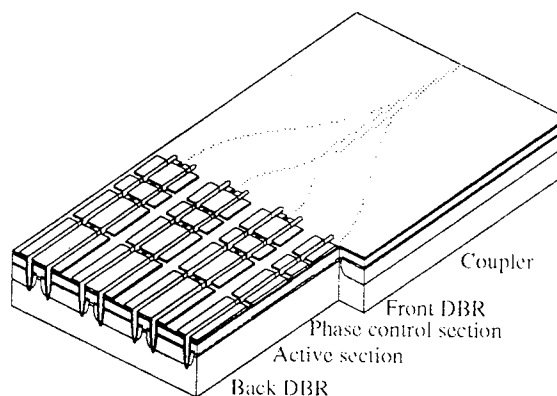


Fig. 1 DBR laser array structure

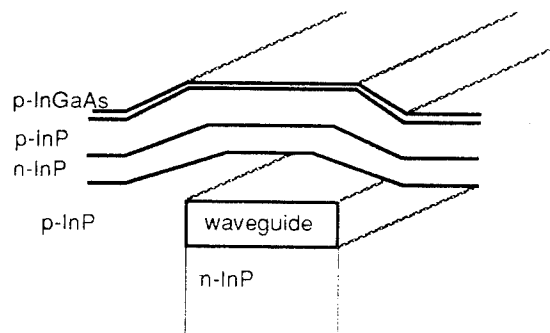


Fig. 2 Cross-section of the waveguide structure of coupler section

MOVPE technique varying the width of selective growth masks. Pairs of SiO₂ mask stripes were patterned 20 μm apart on the substrate only for the DBR sections. The mask stripe widths (W_m) were 0, 6, 12, and 18 μm . In growth, the temperature was 650°C, the pressure was 50 Torr, and TEG, TMI, AsH₃, and PH₃ were used as source materials. The measured thickness of the selectively grown waveguide layers between various mask stripe widths, were 0.192, 0.216, 0.239, and 0.261 μm thick (Fig. 3).

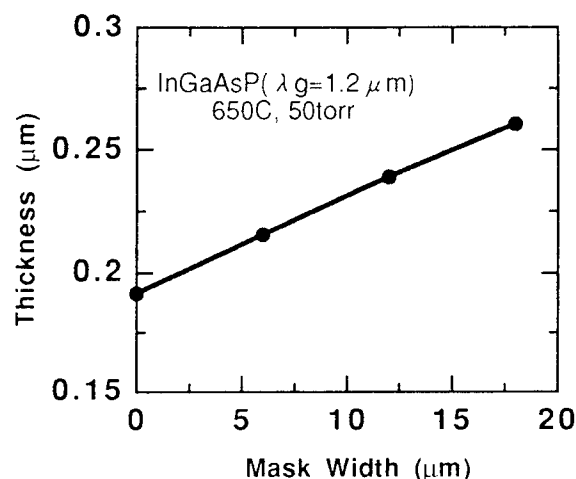


Fig. 3 Thickness of guide layer versus mask width

Thickness increased linearly with the mask width, resulting in different Bragg wavelengths because of the different effective indexes that corresponding to each waveguide. After mask stripes were removed, the MQW active layers, containing seven InGaAs wells each 7 nm thick and 1.3- μm wavelength composition InGaAsP barriers each 14 nm thick, were grown and partially etched to leave an island-like active region. The mesa structure was made by reactive ion beam etching using a Cl₂ + Ar mixture gas. Prior to the regrowth of p-InP and n-InP current blocking layers, the sidewalls of the mesa structure were wet-etched to 1.8 μm in width, and the mesa etching mask of coupler waveguide was removed. Channels were then etched along both sides of the laser stripe to isolate each laser from its neighbor.

Device Characteristics and Discussion

Nearly uniform lasing characteristics were obtained for four-wavelength DBR laser array with waveguide-couplers (Fig. 4). The threshold currents for the typical four-wavelength integrated DBR laser array ranged from 22 to 28 mA, and an output power exceeding 100 μW was obtained for each DBR laser. Fig. 5 shows the output optical spectrum coupled into a single mode fiber. The lasing wavelengths of the array were distributed from 1548.0 to 1553.5 nm with an average spacing of 1.8 nm. This wavelength agreed with calculated values. The side-mode suppression ratio exceeded 30 dB. The propagation loss of the waveguide coupler, separated from the lasers was measured and found to be about 16 dB for inner ports and 20

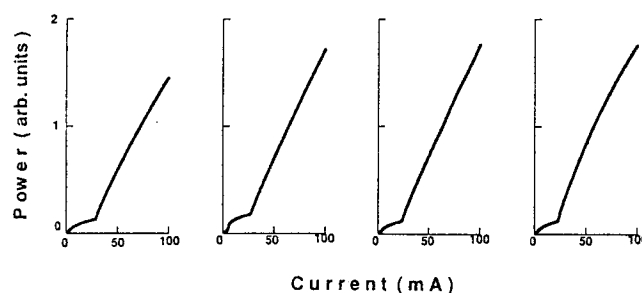


Fig. 4 Driving current versus output power characteristics for DBR laser array

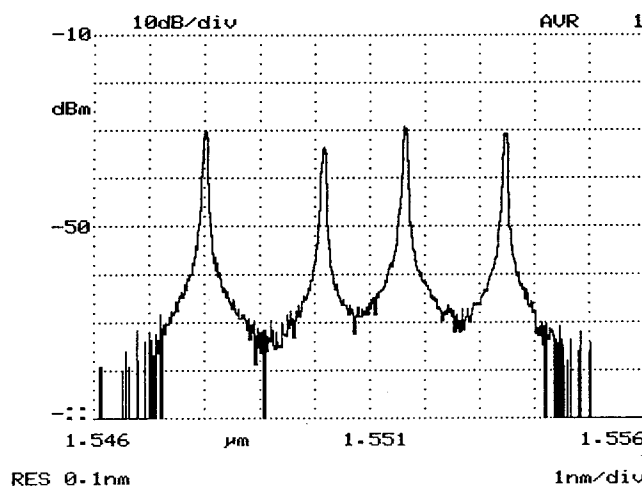


Fig. 5 Output optical spectrum coupled into a single mode fiber

dB for outer ports with a 6-dB splitting loss. This large propagation loss was caused by the optical leakage of blunt Y branch and absorption of p-type doping of buried InP. The sharpness of the vertex of the junction is limited by the quality of the mask, by the photolithography process and by wet-etching of the mesa sidewalls. The doping levels were $2 \times 10^{17} \text{ cm}^{-3}$ (n-type) in the guide layer and $5 \times 10^{17} \text{ cm}^{-3}$ (p-type) in the cladding layer. Estimated κ -value and reflectivity of the front DBR section was 50 cm^{-1} and 70%, respectively. Because of this high reflectivity of front DBR section, the output power from DBR laser section was below 10 mW. By optimizing κ -value ($\sim 25 \text{ cm}^{-1}$), over 10 mW output can be expected. A large part of the propagation loss of the waveguide coupler can be reduced by lowering doping level.

Conclusion

We have developed integrated multiwavelength lasers with waveguide couplers using a selective MOVPE technique. The lasing wavelength was controlled by modulating the effective refractive index of the DBR waveguides. The lasing wavelengths of the array were distributed from 1548.0 to 1553.5 nm with an average spacing of 1.8 nm. The propagation loss of the waveguide coupler was about 16 dB for inner ports and 20 dB for outer ports with a 6-dB splitting loss. Four-wavelength laser outputs were coupled into a single mode fiber. This device appears extremely attractive in reducing the risk in packaging with fiber optics and in use with compact multiwavelength light sources.

References

- 1 NAKAO, M., FUKUDA, M., SATO, K., KONDO, Y., NISHIDA, T., and TAMAMURA, T. : "20-DFB laser arrays fabricated by SOR lithography", IOOC'89, Technical Digest, **4**, pp. 98-99.
- 2 ZAH, C. E., FAVIRE, F. J., PATHAK, B., BHAT, R., CANEAU, C., LIN, P. S. D., GOZDZ, A. S., ANDREADAKIS, N. C., KOZA, M. A., and LEE T. P.: "Monolithic integration of multiwavelength compressive-strained multiquantum-well distributed-feedback Laser array with star coupler and optical amplifiers", Electron.Lett., 1992, **28**, pp. 2361-2362.
- 3 OKUDA, H., HIRAYAMA, Y., FURUYAMA, H., KINOSHITA, J., and NAKAMURA, M. : "Five-Wavelength Integrated DFB Laser Arrays with Quarter-Wave-Shifted Structures", IEEE J. Quantum Electron., 1987, **QE-23**, pp. 843-848.
- 4 GALEUCHET, Y. D., and ROENTGEN, P. : "Selective area MOVPE of GaInAs/InP heterostructures on masked and nonplanar (100) and {111} substrates", J.Cryst.Growth, 1991, **107**, pp. 147-150.
- 5 AOKI, M., SUZUKI, M., SANO, H., KAWANO, T., IDO, T., TANIWATARI, T., UOMI, K., and TAKAI, A. : "InGaAs/InGaAsP MQW Electroabsorption modulator Integrated with a DFB Laser Fabricated by Band-Gap Energy Control Selective Area MOCVD", IEEE J. Quantum Electron., 1993, **QE-29**, pp. 2088-848.
- 6 SASAKI, T., and MITO, I. : "Selective MOVPE growth for photonic integration circuits", IOOC '93 Technical Digest, **4**, pp. 211-212.
- 7 KATOH, Y., KUNII, T., MATSUI, Y., WADA, H., KAMIJOH, T., and KAWAI, Y. : "DBR laser array for WDM system," Electron. Lett., 1993, **29**, 25, pp. 2195-2196.

**Effect of $(\text{GaP})_m/(\text{InP})_m$ Short Period Binary Superlattice Period on
Quantum Wire Formation by Strain Induced Lateral Layer Ordering
in GaInP/AlInP Multi-Quantum-Wire Lasers**

Junji YOSHIDA, Akihiko KIKUCHI,
Ichirou NOMURA, and Katsumi KISHINO
Department of Electrical and Electronics Engineering,
Sophia University
7-1, Kioi-cho, Chiyoda-ku, Tokyo 102, Japan
Tel. +81-3-3238-3323 Fax. +81-3-3238-3321

In this paper, optical anisotropy of the GaInP/AlInP compressively strained multi-quantum wire lasers fabricated by the strain induced lateral layer ordering process in $(\text{GaP})_m/(\text{InP})_m$ short period binary superlattice layers, which is very effective method to fabricate GaInP/AlInP compressively strained quantum wire lasers through a gas source molecular beam epitaxy, was investigated systematically changing $(\text{GaP})_m/(\text{InP})_m$ superlattice period (i.e. monolayer number m). A drastic reduction in threshold current density (J_{th}) was obtained at m of 1.5 and anisotropic lasing characteristics were intensified with increasing m values. Moreover the low J_{th} value of $278\text{A}/\text{cm}^2$ was obtained at m of 1.5 ML with a cavity length of $794\mu\text{m}$.

1. Introduction

AlGaInP red-light emitting semiconductor lasers are crucial devices in realization of high-performance optical information processing systems, and many methods have been studied to improve the lasing characteristics. Among them, quantum wire (QWR) and quantum box/dot (QB/QD) lasers is expected to improve lasing properties drastically compared with bulk and quantum film (QF) lasers. In the QWR and QB structures, the reduction in state density due to two or three dimensional quantum size effects leads to narrower optical gain and to higher differential gain. These effects bring about theoretically improved performances in threshold current density [1], device efficiency, output power, and low temperature dependency of threshold[2]. Moreover, it can be expected that strain QWR lasers can provide further improvement in lasing performances[3].

Very recently, in fabrication of QWR and QD structures, self-crystal-ordering mechanisms during crystal growth have been employed[4][5]. The strain induced lateral layer ordering (SILO) process in $(\text{GaP})_m/(\text{InP})_m$ short period binary superlattice (SPBS) active layers [6] are very effective to fabricate GaInP/AlInP compressively strained multi-quantum wire (CS-MQWR) lasers [4] by a gas source molecular beam epitaxy (GS-MBE).

In this paper, anisotropic lasing characteristics of the GaInP/AlInP CS-MQWR lasers fabricated by the above technology was investigated systematically changing $(\text{GaP})_m/(\text{InP})_m$ superlattice period (i.e., monolayer number m). A drastic reduction in threshold current density was obtained at m of 1.5ML and anisotropic lasing characteristics were intensified with increasing m values. The lowest J_{th} value of $278\text{A}/\text{cm}^2$ was obtained

at m of 1.5 ML with a cavity length of $794\mu\text{m}$. To confirm the formation of quantum wire structures, transmission electron microscopy (TEM) was used and to investigate anisotropic behavior of dipole moment owing to the formation of quantum wires, TM/TE intensity ratios of electroluminescence (EL) were estimated for GaInP/AlInP CS-MQWR lasers structure with $(\text{GaP})_m/(\text{InP})_m$ SPBS active layers.

2. Preparation of GaInP/AlInP MQWR lasers

2.1 Crystal Growth Conditions

In this study, to fabricate GaInP/AlInP CS-MQWR lasers, GS-MBE was employed. In this system, group III beams (Al, Ga, In) were supplied from solid sources, while the group V phosphorus and arsenic beams from cracking gas sources (i.e., 100% PH_3 and AsH_3 gases, respectively).

For n- and p- type dopants, Si and Be were used, respectively. All samples were grown under the standard growth conditions[7]-[9], that is, with the growth rates of $0.86\mu\text{m}/\text{h}$, substrates temperature of $490\text{-}510^\circ\text{C}$, and PH_3 flow rates of 6.8sccm (giving the corresponding V/III ratio of $6.6[9]$).

2.2 Laser Structures

Figure 1 shows a schematic diagram for the investigated lasers, in which 6well MQW active layers consisted of the 18 period $(\text{GaP})_m/(\text{InP})_m$ short period binary superlattice (SPBS) wells and $(\text{GaInP})_3/(\text{AlInP})_2$ superlattice barriers (5nm). The m value was changed from 0.5 ML to 2.0ML (thus, the thickness of well regions was changed). GaInP CS-MQWR active layers were sandwiched between GaInP/AlInP short period superlattice cladding (SLC) layers with 3ML and 2ML thickness combination. In the growth of lasers, first n-

GaAs (70nm) and n-GaInP (10nm) buffer layers were grown on Si-doped (100) GaAs substrates, followed by the sequential growth of CS-MQWR laser layers in the following order: n-AlInP cladding layers (0.7 μ m), undoped SLC layers (80nm), undoped GaInP CS-MQWR active layers, undoped SLC layers (80nm), p-AlInP cladding layers (0.7 μ m), p+-GaInP cap layers (280nm).

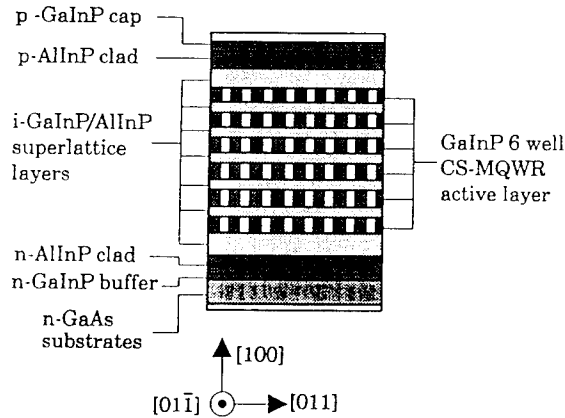


Fig. 1 Device structure of GaInP/AlInP CS-MQWR laser with 18 periods $(\text{GaP})_m/(\text{InP})_m$ SPBS active layers

For estimation of EL polarization and lasing properties, two types of wide-mesa-stripe (50 μ m) lasers were fabricated with different stripe axes, i.e. along [011] and $[01\bar{1}]$ crystal directions, respectively. Note that [011] stripe laser means that the stripe direction was parallel to [011] crystal direction.

3. Dependency of Monolayer Number m of $(\text{GaP})_m/(\text{InP})_m$ SPBS Active Layers on the Formation of GaInP quantum wire structures

3.1 TEM observation

To confirm the formation of quantum wire structures TEM observation was performed for (011) and $(01\bar{1})$ crystal faces of GaInP CS-MQWR lasers with 18 periods $(\text{GaP})_m/(\text{InP})_m$ short period binary superlattice active layers, respectively. When m was below 1ML, quantum film structure was observed for both (011) and $(01\bar{1})$ faces from TEM images. While the m was over 1.2 ML, for the $(01\bar{1})$ crystal face, TEM images showed the compositional modulation, probably which consisted of compressively strained and tensile strain GaInP regions along [011] crystal direction, i.e. indicating the formation of quantum wire structures as shown in Fig. 2, which was the case of the $(\text{GaP})_{1.2}/(\text{InP})_{1.2}$ SPBS active layers. On the other hand, for (011) faces of TEM images, no compositional modulation in $(\text{GaP})_m/(\text{InP})_m$ SPBS active layer was observed even for m over 1.2ML and GaInP film structures were continued along $[01\bar{1}]$ crystal direction. These results showed that the compositional modulation

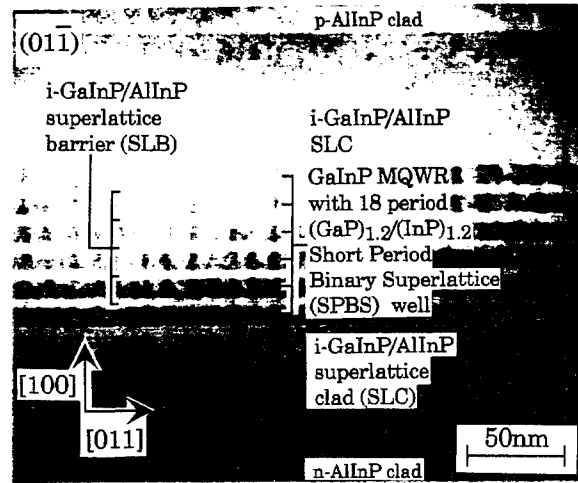


Fig. 2 Cross sectional TEM image on $(01\bar{1})$ crystal face of GaInP/AlInP CS-MQWR laser with 18 periods $(\text{GaP})_{1.2}/(\text{InP})_{1.2}$ SPBS active layers

was occurred for only [011] crystal direction and quantum wires were formed along $[01\bar{1}]$ direction.

3.2 Electroluminescence Polarization

To investigate the anisotropic behavior of dipole moment in the quantum wire structures, the polarized electroluminescence behavior of GaInP CS-MQWR laser structure was investigated for both [011] and $[01\bar{1}]$ crystal directions, respectively.

Figure 3 shows TM/TE EL intensity ratios of GaInP/AlInP CS-MQWR laser structure as a function of monolayer number m of $(\text{GaP})_m/(\text{InP})_m$ SPBS active layers. EL spectra were observed under the low current injection level as current density of 5A/cm² at room temperature direct current drive condition.

For the [011] stripe direction, which data were plotted by closed circles with a solid line, electric field was predominantly TE polarized independently on m values. On the contrary, for the $[01\bar{1}]$ stripe direction, which were plotted by open circles with a dashed line, TM polarized component became larger as increasing m values.

When m was 0.5ML, there were no difference in TM/TE intensity ratio for both [011] and $[01\bar{1}]$ crystal directions indicating that $(\text{GaP})_{0.5}/(\text{InP})_{0.5}$ SPBS active layers was to be quantum film structure. For the case of m of 1ML, TEM images of $(01\bar{1})$ crystal face showed quantum film structure, however, TM/TE intensity ratio was larger for $[01\bar{1}]$ crystal direction than that for [011]. This result indicates that a weak compositional modulation occurred at m of 1ML. Moreover at m over 1.2 ML TM/TE ratios of $[01\bar{1}]$ direction were larger than unity and about 3 times larger than those for [011] direction. This large difference in TM/TE intensity ratios between [011] and

$[01\bar{1}]$ crystal directions indicate an anisotropic behavior of the dipole moment based on the formation of quantum wire structure through compositional modulation along $[011]$ direction in the $(\text{GaP})_m/(\text{InP})_m$ SPBS active layers.

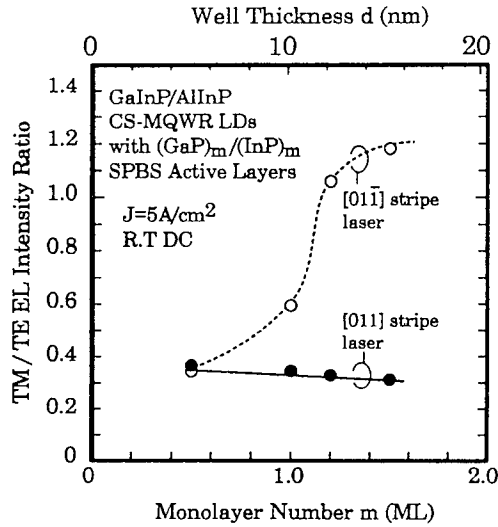


Fig.3 TM/TE EL intensity ratios of GaInP/AlInP CS-MQWR laser structure as a function of monolayer number m of $(\text{GaP})_m/(\text{InP})_m$ SPBS active layers

4. Characterization of GaInP/AlInP CS-MQWR Lasers

4.1 Threshold Current Density

Figure 4 shows threshold current densities of GaInP/AlInP CS-MQWR lasers as a function of monolayer number m of $(\text{GaP})_m/(\text{InP})_m$ short period binary superlattice active layers under the room temperature pulsed condition. The cavity length was around $500\mu\text{m}$. The data plotted by closed circles with a solid line and closed squares with a dashed line correspond to the $[011]$ and $[01\bar{1}]$ stripe lasers, respectively.

When m was 2ML, for $[011]$ stripe lasers, the J_{th} value was larger than that for m of 1.5ML. Furthermore, for $[01\bar{1}]$ stripe lasers, no lasing operation was obtained at 2ML. As the reason of this, it is suspected that the total layer thickness of the MQWR layers had exceeded the critical thickness, increasing the threshold current densities.

Note that for $[011]$ stripe lasers, a remarkable reduction of threshold current density was obtained with increased m value, minimizing at 1.5ML. The difference of threshold current density between $[011]$ and $[01\bar{1}]$ stripes lasers, which was induced by the anisotropic behavior of dipole moment in quantum wires[3], was intensified over 1.0ML maximizing at 1.5ML. Moreover, the lowest J_{th} value of $278\text{A}/\text{cm}^2$,

which was the lowest one of GaInP/AlInP CS-MQWR lasers, was obtained for a $794\mu\text{m}$ cavity length at m of 1.5ML.

The ratios of threshold current density for GaInP/AlInP CS-MQWR lasers of $[011]$ stripe lasers to $[01\bar{1}]$ stripe lasers as a function of m values are shown in Fig.5. Note that for the quantum film lasers' case, the ratio of threshold current density should be unity. Against that, for GaInP/AlInP CS-MQWR lasers the ratio of threshold current density decreased monotonically with increased m value. This tendency may show that as the monolayer number m was increased, the compositional modulation by SILO process in $(\text{GaP})_m/(\text{InP})_m$ SPBS active layers was accelerated to form quantum wires.

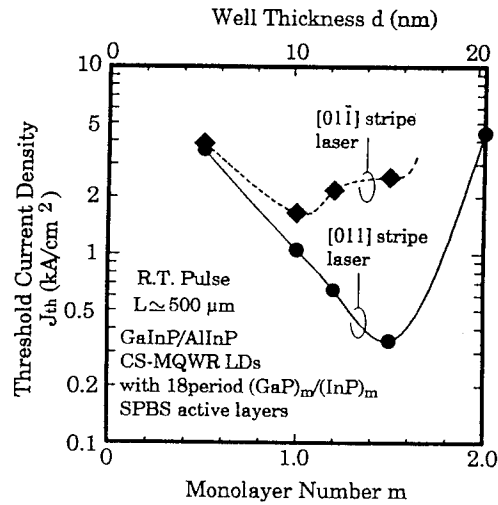


Fig. 4 Threshold current densities of GaInP/AlInP CS-MQWR lasers as a function of monolayer number m of $(\text{GaP})_m/(\text{InP})_m$ SPBS active layers

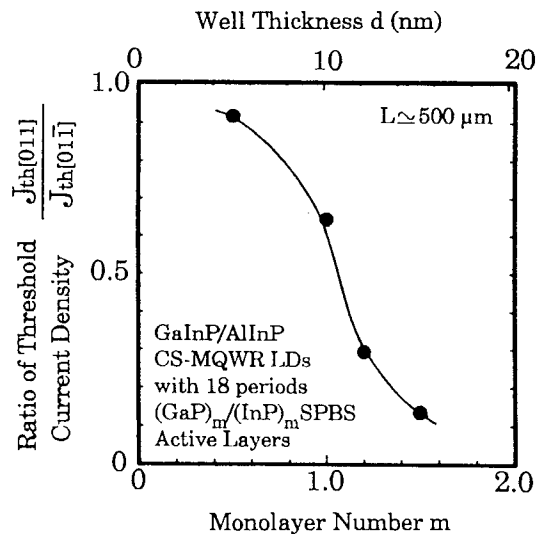


Fig.5 The ratio of threshold current density of GaInP/AlInP CS-MQWR lasers

4.2 Lasing Wavelength

Figure 6 shows lasing wavelength for GaInP/AlInP CS-MQWR lasers as a function of the monolayer number of $(\text{GaP})_m/(\text{InP})_m$ SPBS active layers. The data plotted by closed circles with a solid line and open circles with a dashed line correspond to the $[011]$ and $[0\bar{1}\bar{1}]$ stripe lasers, respectively. The lasing wavelengths of $[011]$ and $[0\bar{1}\bar{1}]$ stripe lasers began to split from each other at m of 1ML. This shows that the compositional modulation by SILO process began to occur at m value of 1ML, which tendency coincided with the above behavior in TM/TE intensity ratio and threshold current densities.

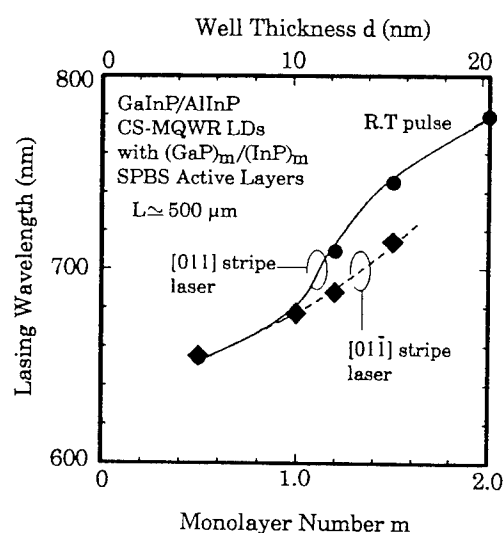


Fig. 6 Lasing wavelength for GaInP/AlInP CS-MQWR lasers as a function of the monolayer number of $(\text{GaP})_m/(\text{InP})_m$ SPBS active layers

5. Conclusion

In conclusion, effect of monolayer number m of $(\text{GaP})_m/(\text{InP})_m$ SPBS periods on quantum wire formation by SILO process in GaInP/AlInP CS-MQWR lasers were investigated systematically. Anisotropic behavior of dipole moment based on formation of quantum wires was reported in terms of TM/TE intensity ratio, threshold current density, and lasing wavelength. It was clarified that the compositional modulation due to SILO process began at m of 1ML and the quantum wire effect due to anisotropic behavior of dipole moment was intensified with increasing m value. The low J_{th} value of $278/\text{cm}^2$ for GaInP/AlInP CS-MQWR lasers was obtained at m of 1.5 ML.

Acknowledgments

The authors would like to thank Prof. K. Shimomura of Sophia University, Profs. S. Arai and M. Asada of Tokyo Institute of Technology for their valuable advises and are also grateful to Drs. D. H. Jang and S. Nahm of

Electronics and Telecommunications Research Institute in Korea for their technical support of TEM observation.

References

- [1] Y. Miyamoto, Y. Miyake, M. Asada, and Y. Suematsu, "Threshold current density of GaInAs/InP quantum box laser," *IEEE J. Quantum Electron.*, vol. QE-25, pp.2001-2006, 1989
- [2] Y. Arakawa and H. Sakaki, "Multidimensional quantum well laser and temperature dependence of its threshold current," *Appl. Phys. Lett.*, vol. 40, pp.939-941, 1982
- [3] S. Ueno, Y. Miyake, and M. Asada, "Advantage of Strained Quantum Wire Lasers," *Jpn. J. Appl. Phys.*, vol. 31, pp.286-287, 1992
- [4] J. Yoshida and K. Kishino, "Room Temperature CW Operation of GaInP/AlGaInP Multiple Quantum Wire Visible Lasers (MQWR-LD)," in *Conf. Dig. 14th IEEE International Semiconductor Laser Conference*, Sept. 1994, paper T3.2, pp. 73-74, Maui, Hawaii, USA.
- [5] N. Kirstaedter, N. N. Ledentsov, M. Grundman, M. Schell, D. Bimberg, V. M. Ustinov, M. V. Maximov, P. S. Kop'ev, Zh. I. Alferov, S. V. Ruvimov, U. Richter, P. Wemer, and J. Heydenreich, "First Observation of Injection Laser Emission from InAs/GaAs quantum dots," in *Conf. Dig. 14th IEEE International Semiconductor Laser Conference*, Sept. 1994, paper W4. PD2, pp. 6-7, Maui, Hawaii, USA.
- [6] P. J. Pearah, A. C. Chen, A. M. Moy, K. C. Hsieh, and K. Y. Cheng, "AlGaInP Multiple Quantum Wire Heterostructure lasers Produced by the Strain-Induced Lateral-layer Ordering Process," *IEEE J. Quantum Electron.*, vol. QE-30, pp.608-618, 1994
- [7] A. Kikuchi, K. Kishino, and Y. Kaneko, "600 nm-range GaInP/AlInP multi-quantum well (MQW) lasers grown on misorientation substrates by gas source molecular beam epitaxy (GS-MBE)," *Jpn. J. Appl. Phys.*, vol. 30 pp. 3865-3872, 1991.
- [8] A. Kikuchi, K. Kishino, and Y. Kaneko, "High-optical-quality GaInP and GaInP/AlInP double heterostructure lasers grown on GaAs substrates by gas-source molecular-beam epitaxy," *J. Appl. Phys.*, vol. 66, pp. 4557-4559, 1989.
- [9] Y. Kaneko, I. Nomura, K. Kishino, and A. Kikuchi, "600-nm wavelength range GaInP/AlInP quasi-quaternary compounds and lasers prepared by gas-source molecular-beam epitaxy," *J. Appl. Phys.*, vol. 74, pp. 819-824, 1993.
- [10] M. Asada, Y. Miyamoto, and Y. Suematsu, "Theoretical Gain of Quantum-Well Lasers," *Jpn. J. Appl. Phys.*, vol. 24, pp. L95-L97, 1985

Preparation of Homogeneous InP Substrates by VGF-Growth and Wafer Annealing

WB1.1
(Invited)

G. Hirt¹, B. Hoffmann², U. Kretzer², A. Woitech¹, D. Zemke¹, G. Müller¹

¹*Institut für Werkstoffwissenschaften (LS 6), Universität Erlangen-Nürnberg,
Martensstr. 7, 91058 Erlangen, Germany*

²*Freiberger Elektronikwerkstoffe, FEW, 09 584 Freiberg/Sachsen, Germany*

Abstract

We have analyzed the microscopic and macroscopic uniformity of as-grown and annealed low Fe-doped InP-wafers grown by different methods (LEC/VGF). Though the annealing is advantageous with respect to the levelling of striations, additional non-uniformity on the microscopic scale is created. The origin of these spots of enhanced photoluminescence might be related to a gettering of Fe at dislocations, which in consequence leaves a vicinity with a reduced Fe-concentration.

1. Introduction

Three major goals have been pursued during the last years in the preparation of semi-insulating InP substrates for optoelectronic applications:

- (i) better uniformity of the Fe-dopant distribution and the electrical and optical properties, respectively;
- (ii) reduction of the defect density (dislocations);
- (iii) reduction of the content of Fe, inevitable for the compensation of residual donors.

The development of the Vertical Gradient-Freeze technique (VGF) has been proven to be an effective means for obtaining better uniformity and reduced dislocation densities. [1,2]. Though a small reduction of the minimum Fe-content can be expected due to a better uniformity on the microscopic scale (absence of growth striations), a significant reduction is possible only by a reduction of the residual donor concentration.

Wafer annealing under Phosphorus atmosphere causes such a reduction of the residual donor concentration, as an annihilation of donor-related intrinsic defects occurs due to the presence of excess Phosphorus [3,4]. Hence, for very pure InP this offers the opportunity to obtain s.i. properties with very low Fe-content ($[Fe] \leq 4 \cdot 10^{15} \text{ cm}^{-3}$) [5].

It is well known from the investigations on annealed GaAs that significant changes occur, depending on the applied temperature regimes and annealing rates [6,7]. For InP, however, only little attention has been attributed up to now to the question, how the annealing affects the microscopic and macroscopic uniformity and the defect distribution in the wafers. Recently, an interesting study on the effects of annealing on defect formation has been published [8], dealing with S-doped and undoped material, with higher residual carrier concentrations.

We now present the results of a comparative study, investigating material, relevant for the processing of semi-insulating InP-substrates by wafer-annealing, including as-grown and annealed LEC- and VGF grown InP-wafers. The applied characterization techniques were high-resolution scanning Photoluminescence, defect sensitive etching and resistivity mapping.

2. Preparation and Characterization of Samples

2" InP-wafers, $\langle 100 \rangle$ -orientated and slightly precompensated with Fe ($[Fe] \leq 4 \cdot 10^{15} \text{ cm}^{-3}$) have been grown by the LEC- or VGF-technique (cf. [2]), having a carrier concentration of $n = 1 \cdot 10^{15} \text{ cm}^{-3}$ and $n = 2.3\text{--}2.8 \cdot 10^{15} \text{ cm}^{-3}$, respectively.

After double faced commercial polishing to a final thickness of 520 μm the wafers subdivided into two parts, one for subsequent annealing and one as a reference sample. Our standard annealing process was applied (900°C for 50 h under a Phosphorus pressure of 1 atm, cooling rate 1.0-1.5 K/min, for details cf. [5]). Approximately 200 μm were removed after the annealing by polishing from both sides, to remove the deteriorated surface layer.

The as-grown and the annealed wafers were first characterized by means of spectrally integrated PL-mappings, using a SCANTEK-system with 5 mW HeNe-excitation (632 nm) and a Si-detector, having a spatial resolution of 20 μm .

Secondly, the density and distribution of defects was investigated by defect sensitive etching, using either BCA-111-etchant [9] for activation with subsequent treatment by AB-solution [10], or Huber-etchant [11] to reveal dislocations, especially in the area related to the high-resolution PL-mappings. Additionally, the electronic properties were determined spatially resolved by Time Dependent Charge Measurement (TDCM) [12] and finally samples were cut from the wafers to perform Hall-effect measurements.

3. Results

Macroscopic PL-Mappings

Fig. 1 and 2 give a comparison of the macroscopic PL-pattern for an as-grown (a) and annealed (b) LEC-wafer as well as for a VGF-wafer. On the as-grown LEC-wafer concentric rings, attributed to a macroscopically inhomogeneous incorporation of Fe across the crystal diameter due to the shape of the growth interface [13], can be detected as well as short-period rings, attributed to so-called rotational striations, i.e. axial fluctuations of the Fe-concentration [13].

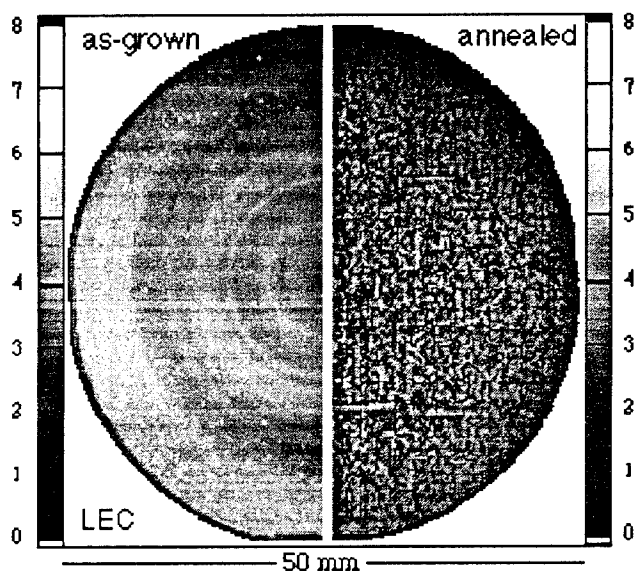


Fig 1: Comparison of overall PL-mappings of the as-grown (a) and the annealed (b) LEC-grown InP-wafer with low Fe-concentration ($[Fe] \leq 4 \cdot 10^{15} \text{ cm}^{-3}$). Gray-scales of PL-intensity are given to visualize mean value and contrast-enhancement.

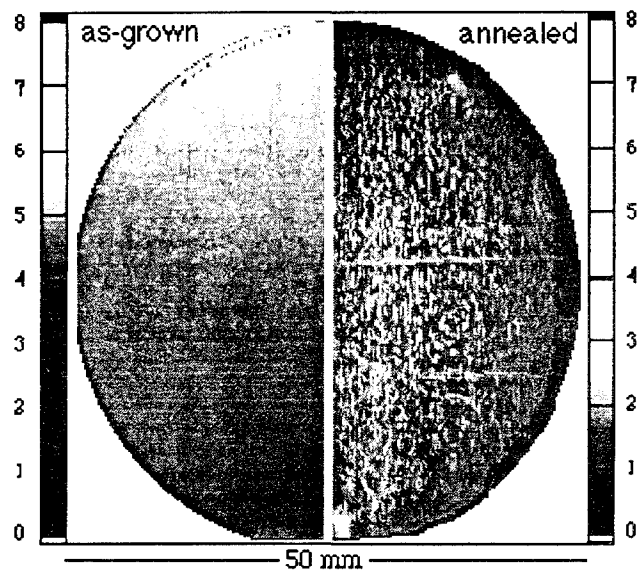


Fig 2: Comparison of PL-mappings of the as-grown (a) and the annealed (b) VGF-grown InP-wafer with low Fe-concentration ($[Fe] \leq 4 \cdot 10^{15} \text{ cm}^{-3}$). Gray-scales of PL-intensity are given to visualize mean value and contrast-enhancement.

These patterns are not present in the as-grown VGF-wafer, due to the more favourable growth conditions (cf. [2]). However, owing to a non axisymmetric thermal field a tilted phase boundary occurred, giving rise to a macroscopic drift of the Fe-content and the PL-intensity across the wafer.

The mappings of the annealed wafers are revealing both on first sight a decrease of the mean luminescence with strong statistical fluctuations on a microscopic scale, having a standard deviation of about 40-50%.

On second sight, the macroscopically radial distribution in the LEC-grown wafer still can be recognized, while the short period (mesoscopic) distribution is not detectable any more. The slight macroscopic drift in the annealed VGF-grown wafer is detectable only after image processing (smoothing).

High resolution PL

Fig.3 gives a comparison of high resolution PL-mappings, obtained on the as-grown LEC- and VGF- wafers (cf. fig. 1) and the annealed LEC-wafer (c). Whereas the presence of striations can be clearly detected in the as-grown LEC-material, causing a standard deviation (S.D.) of 4 %, the microscopic distribution in the VGF-grown wafer is quite uniform (S.D.= 2.5%). In contrast, the high resolution PL-pattern of the annealed wafer reveals, that the microscopic fluctuations are related to distinct points of highly enhanced luminescence, having an intensity up to 3 times the value of the matrix. They show a typical size of $\approx 50\text{-}70 \mu\text{m}$ and indicate some preferential alignment towards $\langle 011 \rangle$ and $\langle 01\bar{1} \rangle$ direction.

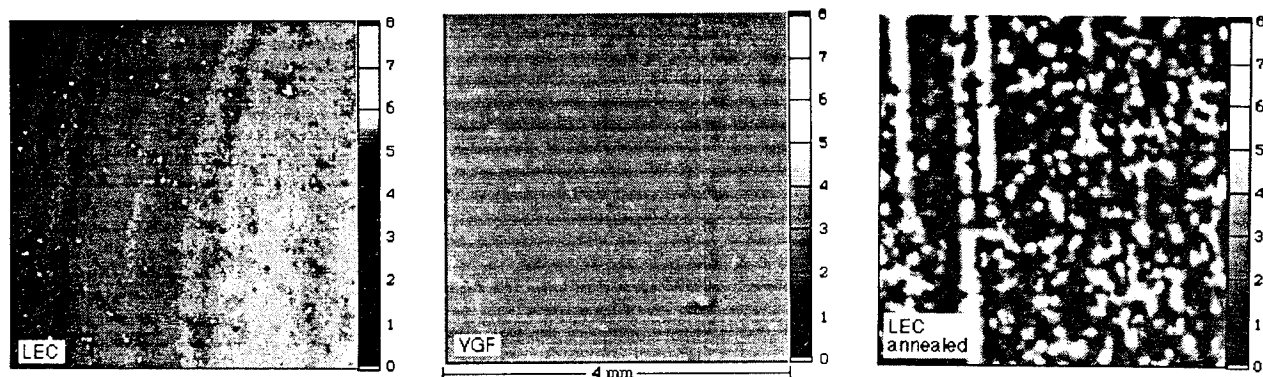


Fig 3: Comparison of high resolution PL-mappings on the as-grown LEC (a) and VGF (b) wafer with the annealed LEC-grown wafer (c).

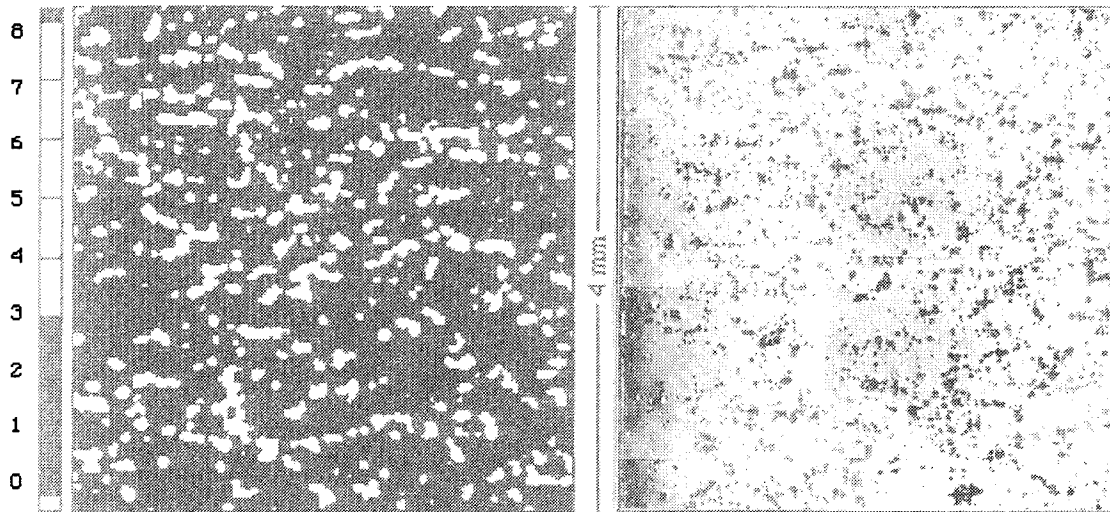


Fig 4.: Correlation of high resolution PL-mapping (a) and the etch-pit distribution, revealed by Huber etchant (b) from the same area of the annealed VGF-grown wafer.

Defect etching

In order to reveal the cause of the local enhancement of the PL-intensity, the distribution of the dislocations, i.e. the etch-pits was determined at the same area by a treatment with the Huber-etchant (fig.4). In order to separate the spots with enhanced luminescence, the image was processed by setting a threshold of 2 times the matrix level, obtaining a binary black and white image (fig.4b). Though a direct correlation is difficult to see, similar patterns can be recognized.

The densities of the bright spots are considerably lower than the etch-pit density (cf. tab. 1), but this could be explained by the fact, that the spatial resolution for the recognition of PL-spots is limited so that single etch-pits in dislocation clusters cannot be distinguished any more.

Analysis of Particular Defects

By a treatment with AB-etchant a type of almond-shaped defects could be revealed (fig. 5). Its density and size is significantly reduced in the annealed material compared to the as-grown material (cf. tab. 1). By IR-microscopy it could be confirmed, that the density and size of these defects were truly revealed by the etchant and not depending on a resistivity-related etching effect.

Subsequent analysis by Energy Dispersive Spectrometry (EDS) on these defects revealed a strongly enhanced In-content (up to 70%In versus 30%P) compared to the practically stoichiometric matrix, suggesting that this defect is related to In-inclusions. Defects with similar phenotype and comparable density, attributed to In-inclusions and so-called S-pits have been observed in LEC-grown crystals before [14].

However, no correlation with dislocations or PL-spots could be found in our samples. Additionally the density of AB-defects is much lower than that of any of the other features.

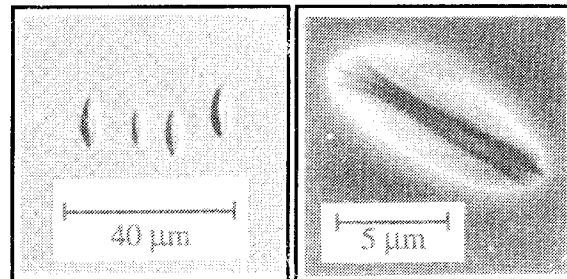


Fig. 5: Defects revealed by treatment with AB-etchant and corresponding SEM-image. EDS-analysis proved an In-surplus.

	as-grown LEC	annealed LEC	as-grown VGF	annealed VGF
Carrier-Concentration n [cm^{-3}]	$1 \cdot 10^{15}$	$3.8 \cdot 10^7$	$2.3 \cdot 10^{15}$	$1.7 \cdot 10^8$
Resistivity ρ [Ωcm]	s.c.	$4.0 \cdot 10^7$	s.c.	$1.4 \cdot 10^7$
PL Standard deviation [%]	4%	40-50 %	2.5 %	45 %
Density of PL-spots [cm^{-2}]	---	7.000	---	5.000
EPD (Huber-etchant) [cm^{-2}]	$1 \cdot 10^5$	$4.6 \cdot 10^4$	$1 \cdot 10^4$	$1.5 \cdot 10^4$
Density of AB-defects [cm^{-2}]	1.800	600	2.000	800

Tab. 1: Comparison of electrical and uniformity data, determined by Hall-effect and high-resolution PL-measurements as well as by defect sensitive etching. The PL-values are representative for the microscopic homogeneity on $4 \times 4 \text{ mm}^2$.

4. Discussion

Effect of annealing on Fe-distribution of as-grown material

The disappearance of striations as well as the remaining presence of macroscopic inhomogeneity in annealed InP-wafers can be explained by the diffusion of Fe during the annealing process. An effective diffusion coefficient of 10^{-9} - 10^{-8} cm² was determined for Fe at low concentrations by our annealing experiments [15]. The diffusion length in this process is in the range of 50-200 μ m - sufficient for a levelling of growth striations with an axial spacing of typically 10-40 μ m, but not sufficient for levelling out macroscopic radial non-uniformities.

Origin of microscopic PL-fluctuations

The creation of microscopically small spots of strongly enhanced photoluminescence seems to be a dominant feature of the annealing process, independent from the preparation and origin of the samples.

Enhanced PL can be either attributed to a reduced density of recombination centers, e.g. Fe [16,17] or due to an enhanced concentration of shallow defects involved in radiative transitions.

In another nominally undoped annealed sample, where no Fe could be detected - neither by means of electrical spectroscopy (deep level transient spectroscopy, DLTS) nor by chemical trace analysis (Glow Discharge Mass Spectrometry, GDMS) - these bright spots do not appear. Hence, it can be concluded that an inhomogeneous Fe-distribution is the cause of the local PL-enhancement.

Because of the qualitative similarity with the etch-pit pattern it might be speculated that Fe is gettering in the stress field around dislocations, leaving a vicinity with a low Fe-content and enhanced luminescence. An inverse, but comparable effect, i.e. a reduced luminescence in the presence of dislocation due to a gettering of donors (S) has been recently observed in annealed, strongly S-doped InP-samples [8].

Having microscopical regions with reduced Fe-content one might suspect a loss of s.i. properties in the vicinity of dislocations. Mappings of the resistivity by means of Time Dependent Charge Measurement (TDCM) with a lateral resolution of 1.25 mm did not reveal such problems (cf. [5]). But test devices (MSM-detectors) with lateral extensions of 60 μ m, produced on annealed wafers, indeed showed variations in the dark current, indicating local fluctuations of the resistivity.

In-related defects

The In-related indicate the presence of excess Indium in both the as-grown and the annealed InP-samples. The reductions in size and density of the defects now have to be discussed in analogy to the kinetics of defect formation in GaAs [6,7].

One explanation is a shift in stoichiometry towards a higher P-content, expectable as the samples were exposed to Phosphorus-pressure which was orders of magnitude higher than the equilibrium pressure. However, the occurrence of In-inclusions even in the annealed material suggests that this material is still In-rich.

The different temperature-time procedures during growth and annealing might also cause a different defect formation due to the thermally activated kinetics and the retrograde solidus line of InP. But then one would eventually expect more differences between the as-grown LEC- and VGF-samples.

5. Conclusions and Outlook

Annealing is advantageous with respect to the levelling of striations. However, additional non-uniformities occur in the annealed wafers, detectable as spots of strongly enhanced luminescence. Their impact on device properties is not fully understood up to now, but it seems to be necessary to prevent their formation in order to achieve homogeneous material for device applications. A better understanding of the kinetics of the defect formation is necessary in order to select the proper temperature-time regimes for the process.

Acknowledgements

The authors gratefully acknowledge the polishing by MCP Wafer Technology (UK) and the helpful discussions and demonstrations of Dr. J.L. Weyher. The work was financially supported by the "Deutsche Forschungsgemeinschaft (DFG)" within the project "Optical Signal Processing" (DFG Mu 632/2).

References

- [1] F. Matsumoto, Y. Okano, I. Yonenaga, K. Hoshikawa, T. Fukuda; *J. Cryst. Growth* **132** (1993) 348
- [2] D. Zemke, I. Grant, G. Wittmann, G. Müller; *Mat. Sci. Eng.* **B28** (1994) 91
- [3] G. Hirt, D. Wolf, G. Müller; *J. Appl. Phys.* **74** (1993) 5538
- [4] K. Kainosho, O. Oda, G. Hirt, G. Müller; *Mat. Res. Soc. Symp. Proc.* **325** (1994) 101
- [5] D. Wolf, G. Hirt, F. Mosel, G. Müller, J. Völkl; *Mat. Sci. Eng.* **B28** (1994) 115
- [6] J.L. Weyher, P. Gall, Le Si Dang, J.P. Fillard, J. Bonnafé, H. Rüfer, M. Baumgartner, K. Löhnert; *Semicond. Sci. Technol.* **7** (1992) A45
- [7] O. Oda, H. Yamamoto, M. seiwa, G. Kano, T. Inoue, M. Mori, H. Shimakura, M. Oyake; *Semicond. Sci. Technol.* **7** (1992) A215
- [8] R. Fornari, J.L. Weyher, S. Krawczyk, F. Nuban, C. Corbel, M. Törnqvist; *Mat. Sci. Technol.* (1995) in print
- [9] J.L. Weyher, R. Fornari, T. Görög, B. Ern  ; *J. Cryst. Growth* **141** (1994) 57
- [10] M.S. Abrahams, C.J. Buiocchi; *J. Appl. Phys. Letters* **54** (1965) 2855
- [11] A. Huber, N.T. Linh; *J. Cryst. Growth* **29** (1975) 80
- [12] R. Stibal, J. Windscheif, W. Jantz; *Semicond. Sci. Technol.* **6** (1991) 995
- [13] A. Seidl, F. Mosel, G. Müller; *Mat. Sci. Eng.* **B28** (1994) 107
- [14] R. Hirano, T. Kanazawa, S. Katsura; *J. Cryst. Growth* **134** (1993) 81
- [15] G. Hirt, D. Wolf, G. Müller; *Proc. of 8th Conf. on S.I. III-V-Materials 1994, Warsaw (Poland)*
- [16] J.Y. Long  re, K. Schohe, S. Krawczyk, R. Coquille, H. L'Haridon, P.N. Favenec; *J. Appl. Phys.* **68** (1990) 755
- [17] Th. Vetter, R. Treichler, A. Winnacker; *Semicond. Sci. Technol.* **7** (1992) 150

Effect of Annealing Conditions on the Uniformity of Undoped Semi-Insulating InP

K. Kainosho, M. Ohta and O. Oda

Electronic Materials and Components Laboratories

JAPAN ENERGY CORPORATION

3-17-35, Niizo-Minami, Toda, Saitama, 335 Japan

Abstract

Undoped semi-insulating InP can be obtained by high-pressure annealing of high purity materials. The reproducibility was however not satisfactory. In the present work, we found that not only Fe concentrations but also Cr and Ni concentrations in annealed wafers were slightly increased. In order to reduce the contamination, conductive InP with a trace amount of Fe was annealed under low phosphorus vapor pressure. The minimum Fe concentration for realizing semi-insulating InP was found to be $1 \times 10^{15} \text{cm}^{-3}$. It was also found that annealing conditions largely affect the resistivity uniformity of undoped semi-insulating InP.

Introduction

The realization of undoped semi-insulating InP is strongly desired because industrially available Fe-doped semi-insulating InP has a large concentration of Fe and shows various disadvantages for its applications, such as the out-diffusion of Fe into epitaxial layers (1), the displacement of Fe by Mg or Zn dopants diffusing into Fe-doped InP substrates during MOCVD process (2) and the slip-like defect formation after epitaxial growth (3).

It was recently found that undoped semi-insulating InP can be realized when undoped conductive InP is annealed under phosphorus vapor pressure (4, 5). The reproducibility of this procedure however was not satisfactory, and the practical use was in delay. In the present paper, we report the effect of annealing conditions on the reproducibility and the resistivity uniformity of undoped semi-insulating InP.

Experiments

Two types of InP wafers with 2 inch diameter were used for high-pressure annealing. One is undoped conductive InP wafers

with the carrier concentration of $(3-5) \times 10^{15} \text{cm}^{-3}$. The other is conductive InP wafers with a trace amount of Fe with the concentration ranging from $1 \times 10^{14} \text{cm}^{-3}$ to $2.5 \times 10^{15} \text{cm}^{-3}$. These wafers have the same conductive properties as undoped wafers. As-cut wafers were etched by a 2% Br_2 -methanol solution, rinsed, dried, and then sealed in evacuated quartz ampoules with high-purity(7N) red phosphorus. The amount of red phosphorus was determined in a way that the pressure of P_4 vapor becomes the desired pressure at annealing temperatures. The phosphorus vapor pressure was controlled to 1 atm and 25 atm.

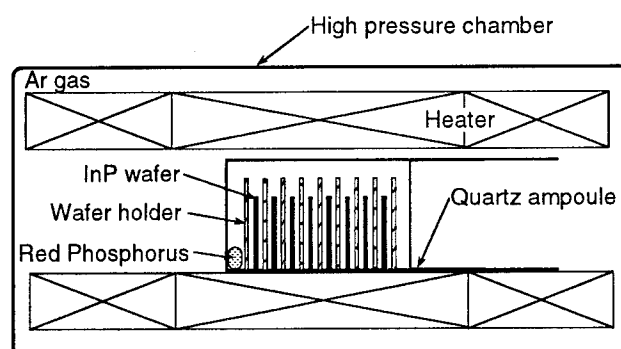


Fig. 1 Schematic Drawing of High-pressure Annealing Configuration.

Fig. 1 is the schematic drawing of high-pressure annealing configuration. The quartz ampoule was set in a high-pressure furnace in which high-pressure Ar gas can be controlled to balance the phosphorus vapor pressure in the quartz ampoule to avoid the rupture of the ampoule. InP wafers were annealed for 40 hours at 910-950°C and then cooled to room temperature. Annealed wafers were removed from the ampoule and they were etched by 50 μm thickness.

Fe concentrations and other impurity concentrations were analyzed by GD-MS (grow discharge mass spectrometry) which is calibrated by samples analyzed by the ICP-MS (inductively coupled plasma mass spectrometry) method. Electrical properties were measured by the van der Pauw method at room temperature using $5 \times 5 \text{ mm}^2$ samples with In electrodes at the four corners. For ohmic contact formation, the samples were annealed at 400°C for 3 minutes in N_2 atmosphere.

Experimental Results and Discussion

Table I shows the analysis data for undoped InP after annealing. In the case of high phosphorus vapor pressure conditions, it is clearly seen that the contamination of Cr and Ni occurred after annealing. On the other hand, in the case of low phosphorus vapor pressure conditions, the contamination did not occur.

Cr and Ni impurities act as deep acceptors in InP and the levels are located at about 0.39eV (6) and 0.48eV (7) below the bottom of the conduction band, respectively. If Cr and/or Ni impurities are major impurities in InP, the resistivity of InP becomes 10^4 - $10^5 \Omega \cdot \text{cm}$. In the case of undoped high-resistive InP after high-pressure annealing, the resistivity was about $10^5 \Omega \cdot \text{cm}$, the similar value which was predicted from Cr, Ni deep levels.

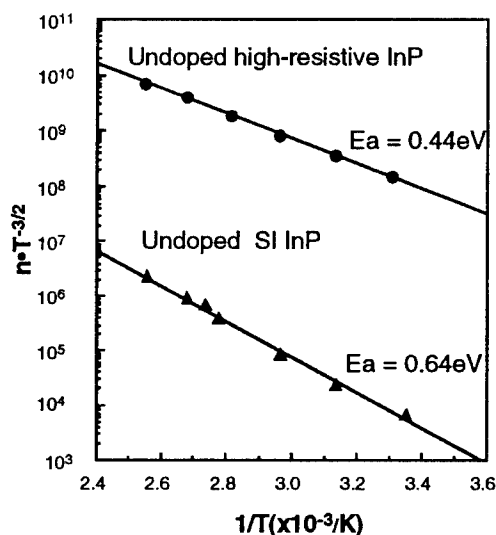


Fig. 2 Activation Energies of Undoped High-resistive and Semi-Insulating InP.

Table I Impurity Analysis of Undoped As-grown and Annealed InP.

Sample No	Si	S	Zn	Cr	Ni	(ppmw)
						Phosphorus vapor pressure
1	<0.005	<0.01	<0.005	0.022	0.02	25 atm
2	<0.005	<0.01	<0.005	0.047	0.017	
3	<0.005	<0.01	<0.005	0.036	0.025	
4	<0.005	<0.01	<0.005	0.03	0.013	
5	<0.005	<0.01	<0.005	0.008	0.013	
6	<0.005	<0.01	<0.005	<0.005	<0.005	1 atm
7	<0.005	<0.01	<0.005	<0.005	<0.005	
8	<0.005	<0.01	<0.005	<0.005	<0.005	
9	<0.005	<0.01	<0.002	<0.005	<0.005	as-grown

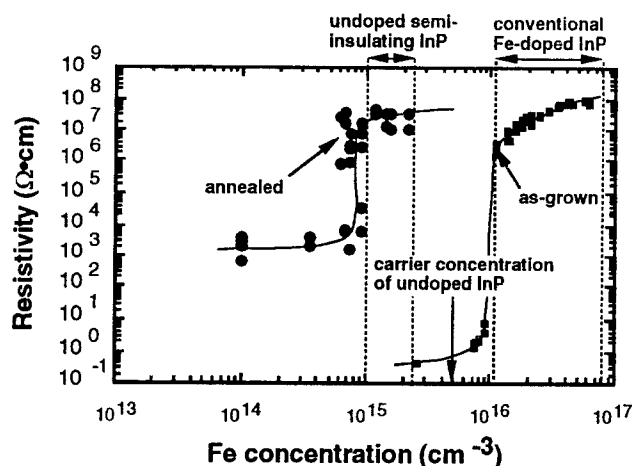


Fig. 3 Relationship between Resistivity and Fe Concentration.

Hirt et al have reported the deep levels measured by DLTS measurement and the compensation mechanism of high-pressure annealed InP (8). It was shown that two deep levels with activation energies of 0.4eV and 0.6eV are incorporated or created in undoped annealed InP. The level of 0.6eV will be due to Fe (9) which acts as the dominating compensation center in high-pressure annealed semi-insulating InP. The origin of the level of 0.4eV was not clearly identified (10).

Fig. 2 shows the activation energies of undoped high-resistive and semi-insulating InP after high-pressure annealing. These activation energies were calculated from the temperature dependence of the carrier concentration. It was found that the activation energy of undoped semi-insulating InP is 0.64eV which can be identified as Fe. It was also found that the activation energy of high-resistive InP is 0.4eV. From the activation energy, this level seems to be due to Cr.

It is therefore speculated that the problem of unreproducibility was caused by Cr and Ni contamination after high phosphorus vapor pressure annealing. We suspected that Cr and Ni atoms are contained as phosphides in red phosphorus, as well as Fe atoms (11). From these results combined with the previously reported results (10, 12), it is suggested that the reproducibility depends on the purity of red phosphorus source.

In order to prevent these contaminations, conductive InP with a trace amount of Fe was annealed under the phosphorus vapor

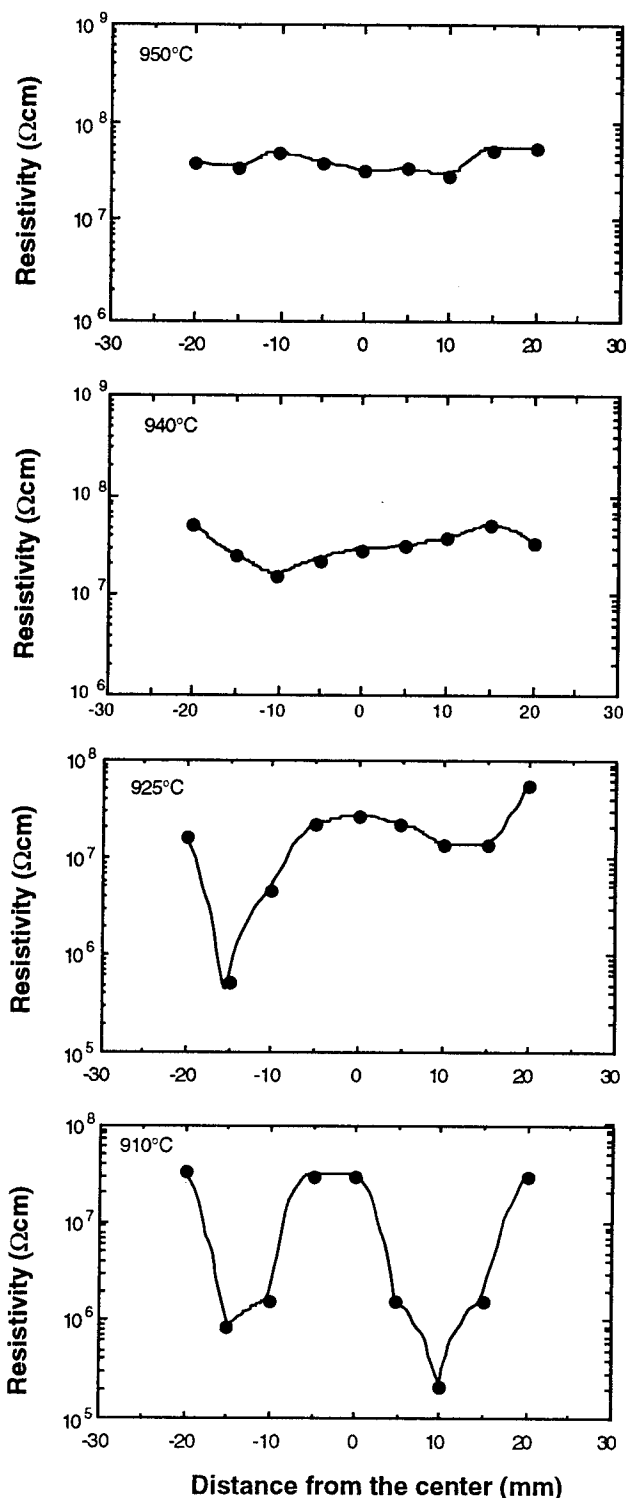


Fig. 4 Effect of Annealing Temperature on the Resistivity Uniformity of 2 inch Diameter Wafers.

pressure of 1 atm. Fig. 3 shows the relationship between the resistivity and the Fe concentration after annealing at 950°C. The resistivity of conventional Fe-doped as-grown crystals is also shown for comparison. It is clearly seen that the minimum Fe concentration for realizing semi-insulating InP by annealing was about $1 \times 10^{15} \text{cm}^{-3}$, which is much lower than that for conventional Fe-doped semi-insulating InP. It was also found that the reproducibility of the semi-insulating behavior becomes satisfactory. Since the Fe concentration level for semi-insulation is extremely very low, these semi-insulating materials can be called as "undoped semi-insulating InP", as in the case of "undoped semi-insulating GaAs" in which carbon is contained with the level of several 10^{16}cm^{-3} (13). In fact, the Fe concentration level in these "undoped semi-insulating InP" is less than the carrier concentration of undoped InP.

Fig. 4 shows the effect of annealing temperature on the resistivity uniformity, examined in the temperature range of 910-950°C under low phosphorus vapor pressure conditions. It is clearly seen that the annealing temperature largely affects the resistivity uniformity. The resistivity uniformity was improved by higher temperature annealing. The mechanism of this uniformity improvement is speculated to be due to the effective activation of residual Fe impurities in InP wafers by higher temperature annealing. The uniformity variation after annealing at 950°C was about 24%. In order to improve further the resistivity uniformity, annealing at higher temperatures with preventing the contamination would be effective.

Summary

It was found that the purity of red phosphorus is a key factor for the reproducible preparation of undoped semi-insulating InP. The Fe concentration for realizing semi-insulating InP with a trace amount of Fe was found to be $1 \times 10^{15} \text{cm}^{-3}$. It was also found that the annealing conditions largely affect the resistivity uniformity of undoped semi-insulating InP.

Acknowledgements

The authors acknowledge Dr. K. Aiki for their encouragement, and Professor Dr. Müller (Universität Erlangen-Nürnberg) for useful discussions. The authors also wish to thank Messrs. N. Kubota, K. Kohiro, M. Uchida and Miss Y. Matsuda for their crystal growth and evaluation of annealed wafers.

References

- (1) D. E. Holms, R. G. Wilson and P. W. Yu, *J. Appl. Phys.* **52**, 3396(1981).
- (2) C. Blaauw, B. Emmerstorfer, R. A. Bruce and M. Benzaquen, *Proc. 6th Conf. on Semi-insulating III-V Materials*, Toronto, 1990 (IOP, 1990) pp137.
- (3) C. Miner, D. G. Knight, J. M. Zorzi, R. W. Streater, N. Puetz and M. Ikisawa, *Inst. Phys. Conf. Ser. No. 135 (Proc. DRIP VI, Santander, 1993)*, 181(1994).
- (4) D. Hofmann, G. Müller and N. Streckfuss, *Appl. Phys.* **A48**, 315(1989).
- (5) K. Kainosho, H. Shimakura, H. Yamamoto and O. Oda, *Appl. Phys. Lett.* **59**, 932(1991).
- (6) G. W. Iseler, *Inst. Phys. Conf. Ser. No. 45*, 144(1979).
- (7) K. Korona, K. Karpinska, A. Babinski and A. M. Hennel, *Acta Phys. Pol.* **A55**, 71(1990).
- (8) G. Hirt, S. Bornhorst, J. Friedrich, N. Schäfer and G. Müller, *Proc. 5th Int. Conf. on InP and Related Materials (Paris, 1993)*, pp313.
- (9) O. Mizuno and H. Watanabe, *Electron. Lett.* **11**, 118(1975).
- (10) K. Kainosho, O. Oda, G. Hirt and G. Müller, *Mat. Res. Soc. Symp. Proc.* **325**, 101(1994).
- (11) K. Kainosho, H. Okazaki and O. Oda, *Post Deadline Papers of the 5th Int. Conf. on InP and Related Materials (Paris, 1993)*, pp33.
- (12) D. Wolf, G. Hirt and G. Müller, *J. Electronic Materials*, to be published.
- (13) T. Kikuta, H. Emori, T. Fukuda and K. Ishida, *J. Crystal Growth* **76**, 517(1986).

IRON SEGREGATION IN LEC InP CRYSTALS

R. Fornari, M. Moriglioni, M. Thirumavalavan(*), A. Zappettini and G. Zuccalli

MASPEC-CNR Institute, Via Chiavari 18/A, 43100 Parma (Italy)

(*) On leave from SSPL, Delhi (India); Scholarship granted by ICTP, Trieste (Italy)

ABSTRACT

Following the recent results about activation of iron diffused in InP [1] we tried to increase the fraction of electrically active Fe atoms in InP crystals grown by the Liquid Encapsulation Czochralski method (LEC) by applying a type of "in-situ" annealing. Actually, by varying the pulling rate and the cooling rate, we observed that the $Fe_{\text{active}}/Fe_{\text{total}}$ ratio can be modified. Though the ratio is normally ranging between 0.60 and 0.70, it is found that the ratio is slightly higher corresponding to low pulling rates and considerably lower for pulling rates > 14 mm/h. The purpose of this paper is that of showing how these growth parameters affect the $Fe_{\text{active}}/Fe_{\text{total}}$ ratio.

INTRODUCTION

Despite the attempts to prepare semi-insulating (SI) InP wafers without intentional doping [1-3], the doping with Fe remains the only practical way to readily obtain high-resistivity InP crystals. In the case of LEC (Liquid Encapsulated Czochralski) growth, the elemental Fe is added to the starting polycrystalline charge in concentrations usually $> 2 \times 10^{19} \text{ cm}^{-3}$. This heavy doping of the charge is made necessary by the very small distribution coefficient of iron $K_{\text{Fe}} = [Fe]_{\text{sol}}/[Fe]_{\text{melt}} \approx 1 \times 10^{-3}$. The starting Fe concentration in the solid is therefore higher than $2 \times 10^{16} \text{ cm}^{-3}$; i.e., sufficient for the compensation of the residual shallow donors which are of the order of $3-5 \times 10^{15} \text{ cm}^{-3}$ in the standard commercial polycrystals. It should be noted that only a fraction of the total incorporated Fe is actually active, which in turn causes the top portion of the ingot to be semiconducting if the initial Fe concentration in the as-grown crystal is below 10^{16} cm^{-3} . Wolf et al. estimated that only about 70 % of the total Fe content contributes to compensation [4]. On the other hand, owing to the axial segregation profile for an impurity with distribution coefficient $= 1 \times 10^{-3}$, there will be a great accumulation of Fe at the tail end of the InP crystal. The Fe density in the host lattice will overcome the solubility threshold and numerous precipitates will form [5]. The last-to-freeze part of the crystal is therefore not usable. The crystal fraction which can be conveniently wafered and exploited is thus defined by the minimum compensation and precipitation limits. A few questions about the Fe doping are still open: for

example, why a Fe concentration $> 1 \times 10^{16} \text{ cm}^{-3}$ is required for compensating $3-5 \times 10^{15} \text{ cm}^{-3}$ residual donors? What is actually the ratio between active Fe (in In sites) and the total Fe atoms and how is this ratio influenced by growth parameters?

It is clear that, if one can totally activate the iron incorporated in the growing InP ingot, the starting Fe concentration can be lowered with a consequent extension of the good SI fraction of the crystal. The purpose of this paper is that of studying the effect of some growth parameters on the $Fe_{\text{active}}/Fe_{\text{total}}$ ratio, in order to maximize this ratio and the yield of SI InP.

EXPERIMENTAL

The leading idea of our experiments is that an annealing in situ, followed by a slow cooling can contribute to enhance the Fe activation. For this reason, seven Fe-doped InP crystals were grown by the Liquid Encapsulated Czochralski (LEC) technique. All of them were $\langle 100 \rangle$ oriented. The starting charge was in any case made of about 600 g of pure pre-pulled InP (residual $n < 5 \times 10^{15} \text{ cm}^{-3}$) and doped with pure iron (99.9999 %) to have an initial concentration in the melt of $5-6 \times 10^{18} \text{ cm}^{-3}$. This corresponds to Fe_{total} concentrations of about $5-6 \times 10^{15} \text{ cm}^{-3}$, taking the generally accepted distribution coefficient $K_{\text{Fe}} = [Fe]_{\text{sol}}/[Fe]_{\text{melt}} = 1 \times 10^{-3}$. The pulling rate of the different crystals was varied between 2 and 15 mm/h, while the cooling rate after completing the growth was in the range 40 - 200 °C/h. The slow-pulled crystals were cooled slowly and the fast-

pulled crystals were cooled more rapidly. It should be noted that in our puller the axial temperature profile outside the boric oxide layer is about 150 °C/cm, therefore a pulling rate of 2 mm/h corresponds to a cooling rate of about 30 °C/h for the emerging crystal whereas at 15 mm/h the crystal is cooled down at a rate of about 225 °C/h. The cooling rate of 30 °C/h is the one which gave the best results in terms of activation of the diffused deep impurities [6]. The list of growth parameters is given in Table I.

Table I

Growth parameters and preset Fe concentration in the starting melt

Crystal #	V_p (mm/h)	Cooling rate (°C/h)	Fe_0 ($\times 10^{18} \text{ cm}^{-3}$)
M 149	2	100	6.0
M 155	2	40	5.08
M 161	3	70	5.8
M 159	8	150	5.40
M 156	10	150	4.93
M 154	15	200	5.67
M 163	15	150	5.68

For the investigation of the physical properties and compensation, the InP crystals were completely wafered and measured by Hall effect at room temperature and as a function of T.

RESULTS AND DISCUSSION

The electrical characteristics of three ingots grown at 15, 8 and 2 mm/h are reported in Table II (see Table I for the corresponding growth parameters). The behaviours are similar but it should be noted that the Hall mobility is higher in the SI wafers from the crystals 155 and 159 (2 and 8 mm/h) with respect to crystal 163 (15 mm/h). This is probably connected with the improved homogeneity of the crystals pulled slowly.

In order to understand how the activation ratio $\gamma = Fe_{\text{active}}/Fe_{\text{total}}$ is actually changing with the pulling rate we adopted the following procedure: we measured the electrical properties of the wafers from the top of the crystals. In particular we considered only the samples having a Fermi level ranging between the conduction band and at least 5 kT ($\approx 125 \text{ meV}$) above the Fe level. In these samples all active Fe levels will be ionized (state Fe^{2+}) and $n \gg p$, therefore the neutrality equation can be written as:

$$(1) \quad n = N_D - N_A - Fe_{\text{active}} \quad \text{or}$$

$$(2) \quad n = N_D - N_A - \gamma Fe_{\text{total}}$$

A plot of the measured Hall concentration vs. the concentration Fe_{total} should thus be linear and provide the value of γ , as slope of the bestfit line, and $(N_D - N_A)$, as intercept. We calculated the axial iron profile using the Pfann law:

$$(3) \quad Fe_{\text{total}} = Fe_0 K_{Fe} (1-g)^{(K_{Fe}-1)},$$

where Fe_0 is the initial concentration of dopant in the melt, K_{Fe} the segregation coefficient and g the solidified fraction. K_{Fe} was assumed to be 0.001 in all growth experiments, which is justified by the fact that the effective distribution coefficient, according to the Burton-Prim-Slichter theory [8], is not significantly affected by a pulling rate varying in our experimental range. The Fe_0 concentrations are those reported in Table I.

Table II

Electrical properties of Fe-doped InP crystals (R_H is the Hall constant)

Sample #	ρ (Ωcm)	μ (cm^2/Vs)	$(qR_H)^{-1}$ (cm^{-3})
M 163-1	0.58	3579	2.9×10^{15}
M 163-40	1.69	2904	1.27×10^{15}
M 163-81	1.4×10^7	1538	2.91×10^8
M 159-2	1.57	3681	1.07×10^{15}
M 159-39	2.5×10^6	1834	1.33×10^9
M 159-75	2.35×10^7	2180	2.94×10^8
M 155-1	0.43	3592	4.03×10^{15}
M 155-36	2.23	3138	8.89×10^{14}
M 155-71	1.48×10^7	2860	1.46×10^8

Some examples of n vs. Fe_{total} plots for crystals grown at different pulling rates are shown in Figure 1. The crystals grown at 2, 8 and 15 mm/h present the highest, intermediate and lowest slope (0.77, 0.59 and 0.49 respectively). These values are in reasonable agreement with the activation factor estimated by DLTS in [4]. A summary of the activation ratios determined by plotting the Hall concentrations against the total Fe concentrations is reported in Figure 2. The data are quite scattered but a well defined trend can be identified: the higher the pulling rate the lower the activation ratio. The minimum value of the activation ratio was found to be 0.20 while the highest was about 0.84.

This variation of γ is very significant in terms of SI wafer yield, as it can be inferred from Figure

3. In order to better understand this point, let us consider an InP ingot initially doped with $6 \times 10^{15} \text{ cm}^{-3}$ Fe atoms and with a constant free electron background of $5 \times 10^{15} \text{ cm}^{-3}$. The assumption of a constant shallow impurity profile is justified by our experience with many undoped crystals where the carrier concentration was seen to increase very slowly, compared with iron profiles.

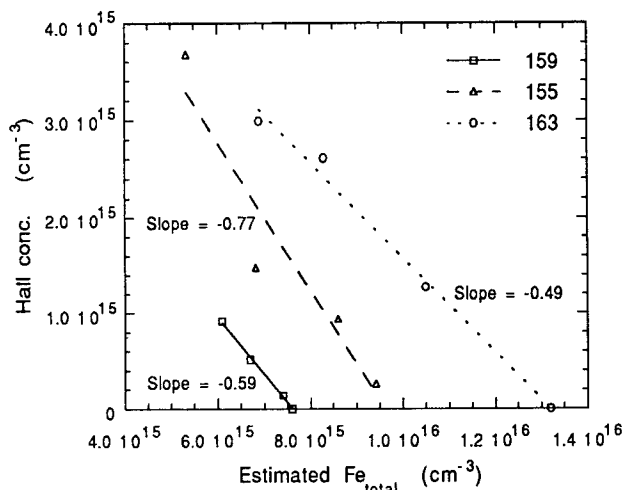


Figure 1: Plots of Hall concentrations vs. estimated total Fe content. The slopes give the values of γ corresponding to different growth conditions.

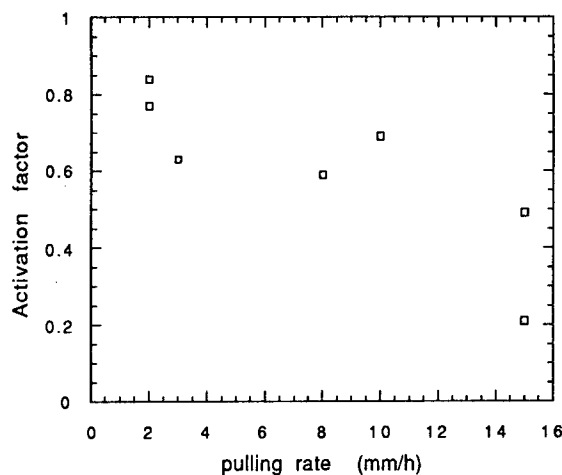


Figure 2: Activation ratio $Fe_{\text{active}}/Fe_{\text{total}}$ in crystals grown at different rates

In Figure 3 we reported the Fe_{total} profile for $K_{Fe} = 0.001$ and the profiles of active Fe, calculated from the equation:

$$(4) \quad Fe_{\text{active}} = \gamma Fe_0 K_{Fe} (1-g) (K_{Fe}^{-1})$$

corresponding to $\gamma = 0.3$ and 0.6 , respectively. It is clear that the compensation will be effective only when $Fe_{\text{active}} > (N_d - N_a)$, that is for $g > 0.25$ in the case of $\gamma = 0.6$ and $g > 0.65$ in the case of $\gamma = 0.3$. Therefore, it is clear that the fraction of SI InP can drastically change even for small variations of γ .

The results of electrical measurements reported above seem to indicate that the iron activation coefficient is sensitive to the pulling speed. This trend cannot be accounted for by considering the link between the effective Fe segregation coefficient and the growth rate. Actually, it is well known that the effective distribution coefficient K_{eff} depends on the pulling rate v , according to the relationship [7]:

$$(5) \quad K_{\text{eff}} = K_0 / (K_0 + (1 + K_0) \exp(-v\delta/D))$$

where δ is the boundary layer thickness and D is the diffusion coefficient of the dopant in the liquid. When the growth rate becomes very high $K_{\text{eff}} \rightarrow 1$. However, if the growth rate is varied within our experimental range, one cannot expect significant changes of the distribution coefficient of iron.

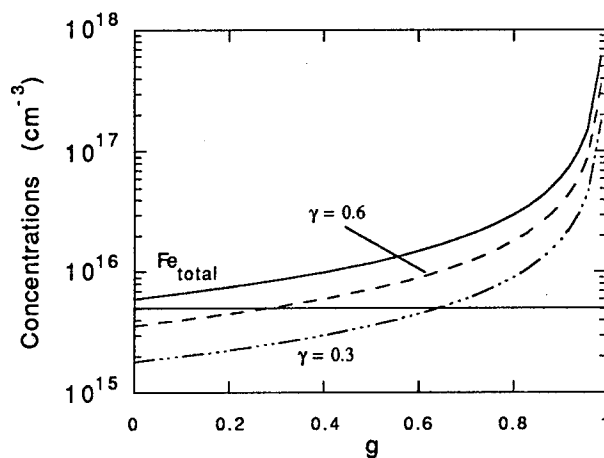


Figure 3: Segregation profile of Fe in InP (corresponding to $K_{Fe} = 0.001$ and $Fe_0 = 6 \times 10^{15} \text{ cm}^{-3}$); profiles of active Fe calculated for $\gamma = 0.3$ and 0.6

In any case it has to be stressed that at higher pulling rates one should have an higher

distribution coefficient, i.e. higher compensation, in the hypothesis of a constant activation ratio. This is very much conflicting with our experimental results. In other words our present data can be explained by considering a change of the iron activation factor due to the different crystal cooling conditions. Such an explanation is also suggested by the results found for annealed undoped SI InP, where the deep impurities incorporated during the high-temperature annealing were giving rise to compensating deep levels only if the post-anneal cooling was sufficiently slow[1]. The present results could be interpreted considering that immediately after solidification, the incorporated Fe atoms can diffuse within the crystal since it remains at high temperature for a relatively long time. Transition element diffusion during growth was indeed observed in the case of GaAs [8], and is likely to be present in InP as well. The diffusion seems to take place via interstitial mechanisms, as suggested by the experimental results of Brozel et al. [9]. They detected a considerable amount of chemical iron in Fe-diffused InP but were unable to locate these Fe atoms by electrical measurements, and concluded that in-diffused Fe atoms had no effect at all on the electron concentrations of the samples. Something similar can happen in LEC InP where, owing to the high temperature in the solid, the incorporated Fe atoms are quite free to move in interstitial sites. When the pulling rate (i.e. the cooling rate, as discussed in the experimental section) is low these atoms have an higher probability to freeze in a substitutional position. Viceversa, high pulling rates will favour the freezing in interstitial sites. However, it must be noted here that some uncertainty exists about this interpretation of the experimental results. Actually, we are considering the Hall concentration along the crystal axis in order to find the γ factor (Figure 1). These concentrations do not exclusively depend on Fe_{active} but also on the residual shallow levels behaviour. In order to remove the residual doubts about the physical mechanisms at the basis of the present experimental observations, we are performing combined IR and chemical spectroscopy. Furthermore, we are testing the doping and electrical uniformity of the crystals grown at different rates.

CONCLUSIONS

From our experimental data it can be argued that the pulling rates can influence the activation ratio Fe_{active}/Fe_{total} of the iron incorporated as dopant during the LEC growth of InP. Pulling rates of 2 mm/h, which in our furnace correspond to

cooling rates of about 30 °C/h, give an activation ratio of about 75-80%, while standard pulling rates of 8-10 mm/h give ratios around 60 %. These results can be useful in order to increase the production yield of SI InP.

Furthermore, we found that the electrical properties of the material grown at low rate are improved with respect to materials pulled in standard conditions.

ACKNOWLEDGEMENTS

The growth activity at MASPEC has been partly supported by the National Project "Materiali Innovativi Avanzati" of MURST (MIA-Tema 18). The authors wish to thank G. Mignoni and M.Locci for technical aid.

REFERENCES

- [1] R. Fornari, A. Brinciotti, E. Gombia, R. Mosca and A. Sentiri, *Mater. Sci. Eng. B28* (1994) 95
- [2] D. Kainosho, H. Shimakura, H. Yamamoto and O. Oda, *Appl. Phys. Lett.* 59 (1991) 932
- [3] D. Hofmann, G. Müller and N. Streckfuss *Appl. Phys. A48* (1989) 3154
- [4] D. Wolf, G. Hirt, F. Mosel, G. Müller and J. Völkl, *Mater. Sci. Eng. B28* (1994) 115
- [5] R. Fornari, C. Frigeri, J.L. Weyher, S.K. Krawczyk, F. Krafft and G. Mignoni, *Proc. of Semi-insulating III-V Materials, Ixtapa 1992*, Ed. W. Ford and C. Miner, IOP, Bristol 1993, p. 39
- [6] R. Fornari, B. Dedavid, A. Sentiri and M. Curti, *Proc. of Semi-insulating III-V Materials, Warsaw 1994*, Ed. M. Godlewski, World Scientific, Singapore 1995, in press
- [7] J.A. Burton, R.C. Prim and W.P. Slichter, *J. Chem. Phys.* 21 (1953) 1987
- [8] M.R. Brozel, B. Tuck, D. Rumsby and R.M. Ware, *J. Cryst. Growth* 60 (1982) 113
- [9] M.R. Brozel, B. Tuck, and E.J. Foulkes, *Phys. Stat. Solidi a* 72 (1982) K159

Multicomponent Zone Melting Growth of Ternary InGaAs Bulk Crystal

T.Suzuki, T.Kusunoki, T.Katoh, and K.Nakajima
Fujitsu Laboratories Ltd.
10-1 Morinosato-Wakamiya, Atsugi 243-01, Japan

A 13 mm thick $\text{In}_x\text{Ga}_{1-x}\text{As}$ crystal with $x=0.14$ has been successfully grown by a method of multicomponent zone melting growth. The alloy composition gradually changes along the growth direction, and this change is well explained by a temperature profile. A good uniformity in the alloy composition along the direction normal to the growth was also achieved.

1. Introduction

Recently, ternary III-V compound substrates are of much interest due to their optical device applications (1-2). Since a ternary compound may change its lattice constant, advances in the growth of ternary compound crystals offer the possibility to fabricate new devices which cannot be made by using binary compound substrates, such as InP or GaAs.

Among these ternary compounds, InGaAs is one of the most important III-V alloys. Excellent characteristics of single quantum well lasers, fabricated on InGaAs ternary substrates were studied experimentally (1) and theoretically (2). Shoji *et al.* (1) recently reported InGaAs/InGaAsP strained single quantum wells (SQWs), which were fabricated on $\text{In}_{0.05}\text{Ga}_{0.95}\text{As}$ showed excellent characteristics. In addition, Ishikawa (2) has theoretically shown that by using an $\text{In}_{0.26}\text{Ga}_{0.74}\text{As}$ substrate, a high performance $1.3\ \mu\text{m}$ laser can be made. Therefore, ternary InGaAs substrates with a high InAs content are a major requirement for developing efficiency lasers (1).

So far, the preparation of an InGaAs single crystal have been tried by some scientists. Bonner *et al.* (3) have grown InGaAs crystals with InAs composition varying from 0.05 to 0.12 using a cooling Liquid Encapsulated Czochralski technique (LEC). Kusunoki *et al.* (4) have developed a double crucible LEC technique supplying a GaAs source material at a constant temperature. By using this technique, a homogeneous $\text{In}_{0.05}\text{Ga}_{0.95}\text{As}$ large bulk crystal could be grown. However, ensuring a continuous supply of source material is so difficult that only small crystals with a high InAs content can be grown (5).

In order to overcome this difficulty, we propose multicomponent zone melting growth, in which the composition of the molten zone is different from that of the crystal. A basic configuration for multicomponent semiconductor growth is applied to the InGaAs alloy bulk. The grown crystals are analyzed by photoluminescence (PL) measurements and chemical etching.

2. Principle of multicomponent zone melting growth

Figure 1 illustrates the principle of multicomponent zone melting growth for a InGaAs bulk. The most important problem in growing the alloy bulk arises from the large separation of the liquidus and the solidus lines in the phase diagram. Therefore, the growth method of normal freezing the melt without any replenishment of the solute gives only a crystal with a non-uniform composition. In multicomponent zone melting growth, the melt zone of $\text{In}_x\text{Ga}_{1-x}\text{As}$ is in equilibrium with the

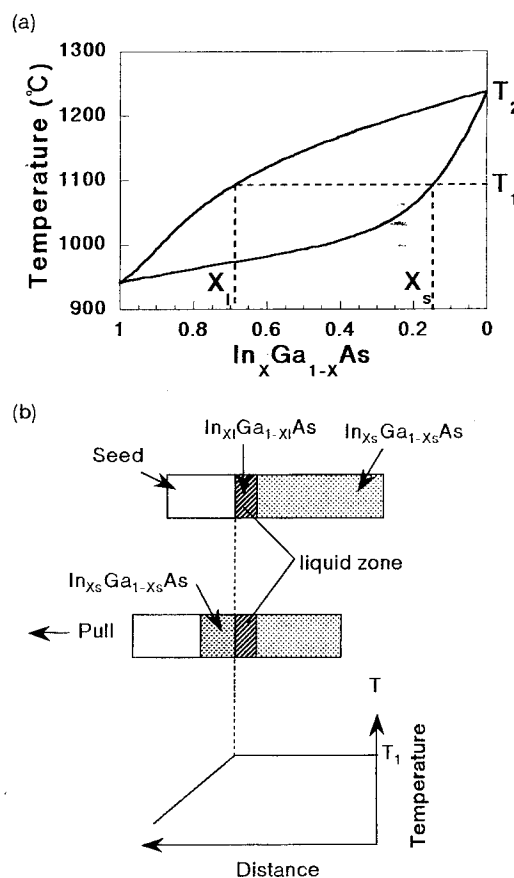


Fig.1 Principle of multicomponent zone melting growth. (a) Pseudo-binary InAs-GaAs phase diagram. (b) Solid and liquid region for the multicomponent zone melting growth.

solid $\text{In}_{x_s}\text{Ga}_{1-x_s}\text{As}$. The temperature at the liquid zone and the source is kept at T_1 . A crystal with the composition x_s is grown on a seed crystal by cooling the seed side. With a movement of the liquid alloy zone, the depletion of a solute element due to the growth is continuously supplied by the dissolution of the source material, which has the same composition as the growing crystal. Therefore, a homogenous $\text{In}_{x_s}\text{Ga}_{1-x_s}\text{As}$ crystal can be grown by this method. This method originally comes from the zone leveling method which was first introduced by Pfann for the growth of uniform doped crystals (6).

In our present work, a basic configuration for the multicomponent zone melting growth is applied to the growth of InGaAs alloy bulk. Namely, InAs is sandwiched by a GaAs seed crystal and a GaAs source. Figure 2 illustrates the growth procedure. The required condition for establishing a zone melt is that the temperature at the InAs position be increased to T_1 and the temperature at the end of the source be below the melting point of GaAs, T_2 . After the InAs is melted, a dissolution of the GaAs source next to the InAs makes the liquid alloy composition equilibrium with the solid x_s solution. Since the depletion of the InAs element in the melt zone is not replenished by the GaAs source in this case, the volume of the liquid zone is gradually decreased during the growth. When constantly increasing the temperature, the GaAs source element is dissolved at the source/zone interface and transported to a growing interface by diffusion and/or convection across the zone due to a temperature gradient (7). Therefore, the solid composition of the grown crystal is determined by the solid-liquid

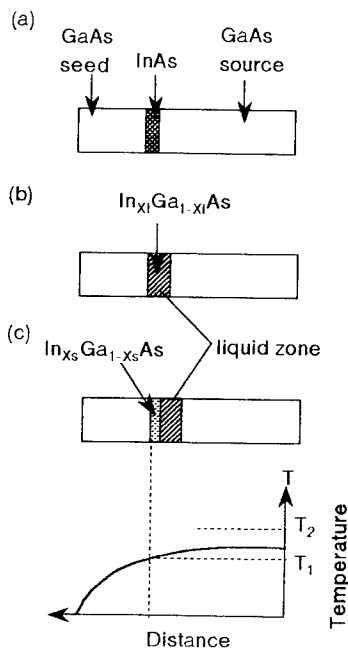


Fig.2 Schematic growth procedure of the present experiment. (a) Initial materials. (b) Melt zone at T_1 . (c) Melt zone migration.

interface temperature. In the present growth procedure, as shown in Fig.2, a homogeneous alloy crystal along the growth direction is not expected to grow. However, the simple setup of a heater and crystals is very useful to examine a validity of this growth method.

3. Experiment

Figure 3(a) is a schematic of the growth apparatus, and (b) is the temperature profile for the center of a hot-zone. An InAs crystal is sandwiched between an upper (111)B orientated seed GaAs crystal and a lower GaAs source crystal. The size of both crystals are $9 \times 9 \text{ mm}^2$ square and 20 mm long, and the InAs has a $9 \times 9 \text{ mm}^2$ square shape for crystal Z-1. A GaAs seed and a source in the growth of crystal Z-11 are cylindrical, both with a diameter of 15 mm. The seed was 7 mm long and the source was 20 mm. The shape of the InAs was an irregular circle with a diameter of about 14 mm. All of these crystals were undoped. They were placed vertically in a 19 mm diameter pyrolytic boron nitride (PBN) crucible. The B_2O_3 is used as an encapsulation with a pressured Ar gas of 10 atoms to suppress the evaporation of dissolved arsenic. The PBN crucible is set in the center of a carbon crucible with a diameter of 120 mm, which stabilized temperature fluctuations. The temperature profile was measured with a PBN crucible filled with only B_2O_3 by using a W/W-Re 5-26 thermocouple. In the growth of crystal Z-1, the growth was carried out by increasing the temperature T_1 to 1133°C at the rate of about 1000°C/h and then keeping the temperature constant. The growth temperature T_1 for crystal Z-11 was raised at 6.6°C/h from 900°C , which is less than the melting point of InAs (942°C), to 1078°C . This results in a slower formation of a liquid alloy zone when compared to crystal Z-1. The temperature at the bottom of the GaAs source is estimated at 1180°C for crystal Z-1 and 1150°C for crystal Z-11. These are lower than the melting point of GaAs (1238°C). Therefore the expected condition shown in Fig.2(c) can be obtained. Other growth parameters are summarized in Table.1.

After the growth, (110) oriented wafers were cut

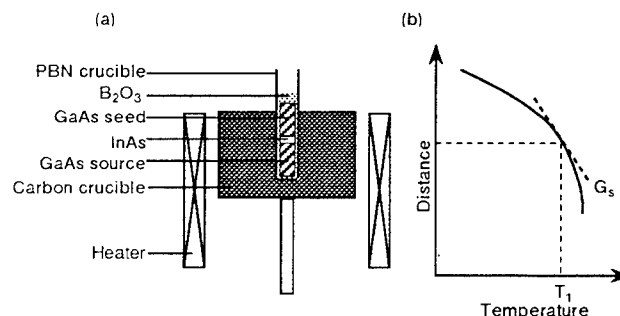


Fig.3 (a) Experimental apparatus for crystal growth and (b) a temperature profile for the center of a hot-zone.

Table 1 Growth parameters of InGaAs crystals.

Sample	T1 (°C)	Growth time (hr)	Thickness of InAs (mm)	Temperature gradient Gs (°C/cm)
Z-1	1133	74	1	25.9
Z-11	1078	24	3	43.7

along the growth direction and mechanically polished. The surface damage was removed by chemical etching with $\text{H}_2\text{SO}_4\text{:H}_2\text{O}_2\text{:H}_2\text{O}=10:1:1$. PL measurements were made at 77K by using a 488 nm Ar^+ ion laser with a spot size of $\sim 0.2 \times 0.2 \text{ mm}^2$. The alloy composition was determined by the wavelength of band-edge emission (8).

4. Results and discussion

Figure 4 shows the outside and cross-sectional views of crystal Z-11. The surface morphology of the GaAs seed and the source is not seen to be much different from the original morphology. In the cross-sectional view, the seeding position can be clearly seen. The seeding position is found to be almost the same as the position of the initial seed-to-InAs interface. This fact means that dissolution of the GaAs seed is negligible, and that the alloy liquid zone was first made from the InAs and the upper part of the GaAs source. Moreover, a 3 mm thick region without a grain structure was observed at the seeding position. While almost the same results were obtained in the crystal Z-1, a grain structure occurs from the seeding position.

A lot of voids were found in Fig.4(b) at the position where the initial InAs is placed. The same result was found in the crystal Z-1. We guess that these voids originated from residual Ar gas left at the seed-to-InAs or InAs-to-source interface.

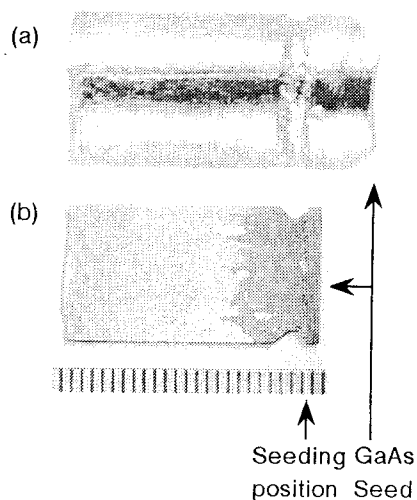


Fig.4 (a) Outside view of grown Z-11 crystal. (b) (110) cross-sectional view of grown Z-11 crystal. 1 div. = 1 mm.

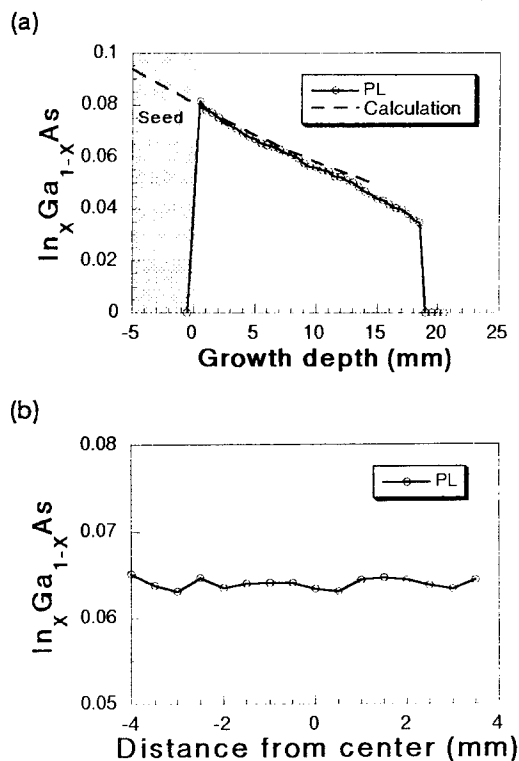


Fig.5 InAs composition profile of InGaAs bulk crystal Z-1 along (a) the direction of crystal growth and (b) the direction normal to crystal growth 8 mm from the seed (near the center of the growth).

Figure 5 shows the alloy composition of the crystal Z-1. A crystal with a solid composition $x=0.08$ has been grown on the GaAs seed as shown in Fig.5(a). This agrees with the observation of the cross-section of the crystal. The InAs composition decreases along the growth direction. At a growth length of 18.5 mm, the stepwise decrease of the alloy composition is observed. From the observation of the etched surface, a residual melt zone can not be observed. Therefore, it is confirmed that the initial liquid InAs is actually consumed during the growth to form the InGaAs crystal.

On the other hand, the InAs composition along the direction normal to the crystal growth shows good uniformity throughout the width of the sample (8 mm), as shown in Fig.5(b), which is better than the InGaAs grown by the LEC technique with a double crucible (5).

The results for crystal Z-11 are similar to that of the crystal Z-1, as shown in Fig.6. Namely, the InAs composition gradually decreases along the growth direction. A good uniformity was also found along the direction normal to the crystal growth.

In the present experiment, the molten zone of InGaAs is moved by the temperature gradient (7). Therefore, InGaAs with the solidus composition equilibrium with the temperature is expected to be grown

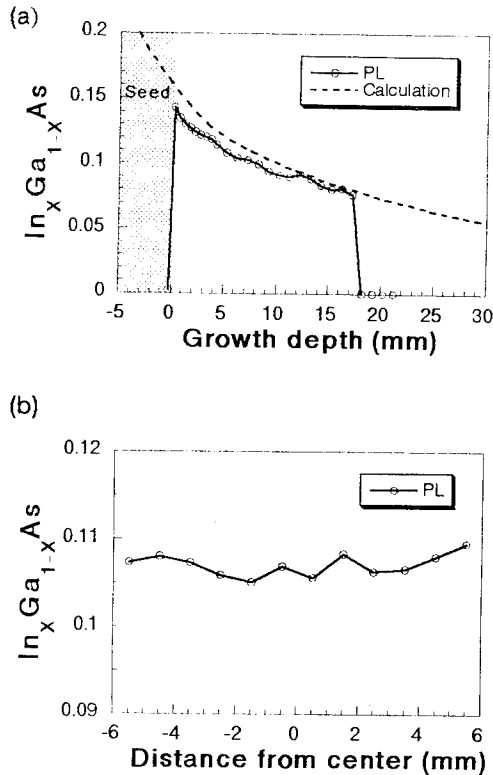


Fig.6 InAs composition profile of InGaAs bulk crystal Z-11 along (a) the direction of crystal growth and (b) the direction normal to crystal growth 7 mm from the seed.

at the upper interface of the melt zone. In the Fig.5(a) and Fig.6(a), the calculated solid composition is also plotted. In the calculation for the phase diagram, the interaction parameter $\Omega_{\text{InAs-GaAs}}=3200\text{cal/mol}$, which shows the best agreement with the growth experiments, is used. The close agreement between the experimental and the calculated profiles indicates that the alloy composition is

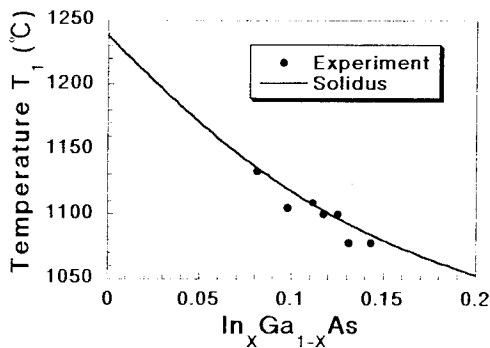


Fig.7 Growth temperature dependence of InAs composition of the InGaAs bulk crystal grown below the seeding position.

determined by the temperature profile. Therefore, the uniformity of the composition in Fig.5(b) shows the uniformity of the temperature normal to the crystal growth.

Figure 7 shows the relationship between the growth temperature T_1 and the InAs composition grown on the GaAs seeds for crystals Z-1, Z-11, and other experiments with the solidus curve. It is clearly shown that the InAs composition at the seeding position is increased by decreasing the growth temperature T_1 . This means that the precise control of alloy composition is accomplished with an accurate establishment of growth temperature and a temperature profile.

5. Conclusions

A multicomponent zone melting method has been proposed for the growth of alloy semiconductors. A basic configuration of the multicomponent zone melting has been applied to the growth of an InGaAs alloy bulk crystal. A 13 mm thick $\text{In}_x\text{Ga}_{1-x}\text{As}$ crystal with $x=0.14-0.08$ was grown on a GaAs seed crystal. A 3 mm thick region without a grain structure was obtained on the seeding position. The alloy composition along the direction normal to the growth shows good uniformity. The gradual change in the composition along the growth direction is well explained by a temperature profile. The alloy composition grown on the GaAs seeds is found to be determined by the growth temperature. As the precise control of a source supply is not necessary in this growth method, it is shown that this method can be very effective for growing InGaAs with a high InAs content.

References

- (1) H. Shoji, T. Uchida, T. Kusunoki, M. Matsuda, H. Kurakake, S. Yamazaki, K. Nakajima, and H. Ishikawa, IEEE Photon. Technol. Lett., Vol. 6, p. 1170 (1994).
- (2) H. Ishikawa, Appl. Phys. Lett., Vol. 63, p. 712 (1993).
- (3) W. A. Bonner, B. J. Skromme, E. Berry, H. L. Gilchrist, and R. E. Nahory, in: Proc. 15th Intern. Symp. on GaAs and Related Compounds, Atlanta, GA, 1988, Inst. Phys. Conf. Ser. 96, Ed. J. S. Harris (Inst. Phys., Bristol, 1989) p. 337.
- (4) T. Kusunoki, K. Nakajima, and K. Kuramata, Proc. Int. Symp. GaAs and Related Compounds, Vol. 129, p. 37 (1992).
- (5) K. Nakajima, T. Kusunoki, and C. Takenaka, J. Crystal Growth, Vol. 113, p. 485 (1991).
- (6) W. G. Pfann, Trans. AIME, Vol. 194, p. 747 (1952).
- (7) D. T. J. Hurle, J. B. Mullin, and E. R. Pike, Phil. Mag., Vol. 9, p. 423 (1964).
- (8) Y. T. Lue, F. A. Thiel, H. Scheiber, Jr., J. J. Robin, B. I. Miller, K. J. Bachmann, J. Electron. Mater., Vol. 8, p. 663 (1979).

Crystal anomaly at the center of S doped InP wafers grown by the LEC method

WB1.5

Y. Iguchi , T. Iwasaki , and N. Yamabayashi

Optoelectronics R&D , Sumitomo Electric Industries , Ltd
1-1-3 , Shimaya , Konohana-ku , Osaka , 554 , Japan

Abstract

Crystal quality of 2" ϕ S doped InP wafers grown by the conventional liquid encapsulated Czochralski(LEC) method was studied by the photoluminescence (PL) mapping technique and the double crystal x-ray diffraction method. Crystal anomaly was found at the center of the wafer. The dark current distribution map of the InGaAs/InP PIN-photo diodes fabricated on the S doped InP substrate revealed that this crystal anomaly at the center increased the dark currents of the photo diodes.

1. Introduction

Sulfur doped indium phosphides are widely used as substrates for the fabrication of optoelectronic devices such as photo diodes(PDs) or light emitting diodes(LEDs). High crystal quality of InP substrates is necessary to the high performance of devices. It is generally considered that 2" ϕ S doped InP wafers grown by the conventional LEC method have some slip dislocations at the periphery but have low dislocation density in the central region, while those grown by vapor controlled Czochralski (VCZ) method have lower dislocation density in the whole region[1]. We have already known that the dark currents of InGaAs/InP PIN-PDs are abnormally high on the slip dislocation of the InP substrate and investigated the mechanism of the increase of the dark currents[2]. Recently, we found out that the dark currents of InGaAs/ InP PIN-PDs are also high at the center of the wafer when they are fabricated on S doped InP substrates grown by the conventional LEC method.

In this study, we describe the crystal anomaly found at the center of 2" ϕ S doped InP wafers grown by the conventional LEC method. In order to investigate this anomaly in detail, we fabricated InGaAs/InP PIN-PDs on those InP substrates. The distribution of dark currents in the wafer was compared with the crystal quality of the S doped InP substrate which had been in advance analyzed non-destructively by the photoluminescence mapping technique and the double crystal x-ray diffraction method.

2. Fabrication and Evaluation of PIN-PDs

Planar type PIN-PDs as shown in Fig. 1 were fabricated. An InP buffer layer , an InGaAs absorption layer, and an InP window layer were sequentially grown by a chloride VPE method on a 2" ϕ conventional LEC-grown S doped InP substrate, oriented (100) 2° off. The p-n junctions were formed in the InGaAs absorption layer by local thermal diffusion of Zn. SiNx film was used for passivation. The p electrode was made of AuZn alloy, and then n electrode was made of AuGeNi alloy. To investigate the distribution of the dark currents in the wafer, the I-V characteristic of each chip was measured by an auto-probing apparatus. Fig.2 shows the distribution map of dark currents at $V_R = 5$ V. Typical value of the dark current at $V_R = 5$ V is 60pA, which shows that the device fabrication is successful. But the dark currents were high not only at the periphery but also at the center of the wafer. The high dark currents at the periphery would be attributed to the effect of

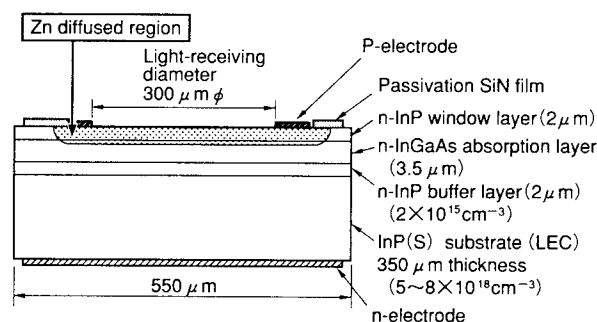


Fig.1 Cross sectional view of InGaAs/InP PIN-PD

slip dislocations of the InP substrate, which has been discussed in Ref.2. On the other hand, the origin of the high dark currents at the center has not been known. Therefore, we evaluated crystal quality at the center of 2" ϕ S doped (100) InP wafer grown by the conventional LEC method in detail.

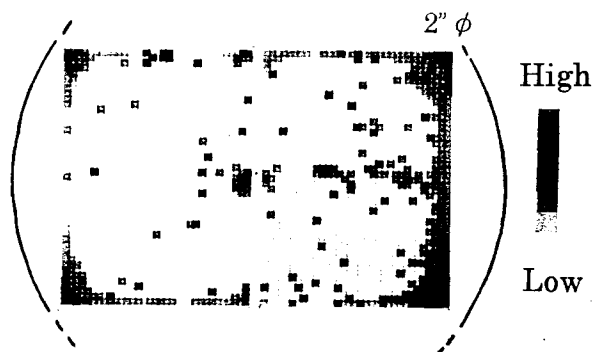


Fig.2 Distribution map of dark currents ($V_R=5V$) of PIN-PDs fabricated on the 2" ϕ S doped InP substrate grown by the conventional LEC method

3. Characterization of S doped InP wafer

Etch pit density (EPD) distribution was evaluated by Huber etching [3] of another (100) wafer which was cut from the neighboring portion of the same crystalline ingot.

Atomic concentration of impurities was measured by secondary ion mass spectrometry (SIMS) and glow discharge mass spectrometry (GDMS) analyses.

PL measurements were mainly carried out at room temperature using a 1 mm sampling grid over the 2" ϕ wafer. The detailed description of the apparatus has been given elsewhere[4]. The 514.5nm line of Ar⁺ laser was used for the excitation and the diameter of the laser spot was about 0.2 mm.

Double crystal x-ray diffraction measurements were performed with a computer controlled topo-goniometer illustrated in Fig.3. The X-stage on which both the first crystal stage and the second (sample) crystal stage are set can be scanned very smoothly. The topograph was recorded on FUJI #80 film or Ilford L4 nuclear plate. Rocking curves were measured by replacing the film with NaI(Tl) scintillation counter. The positions of the rocking curve

measurements were shifted by scanning the X-stage and by changing the height of the pin hole (0.5mm ϕ) slit. The first crystal is a 4" ϕ (100) silicon wafer with low dislocation density and with damage free surface. The Second (sample) crystals were held by sandwiching with thin polyethylene films to achieve the stress free holding. The Cu K α 1 was used for the x-ray source. The topograph was recorded at the pseudo-parallel setting of Si(004)-InP(004) or Si(422)-InP(422). Rocking curves were mainly measured at Si(004)-InP(004) setting.

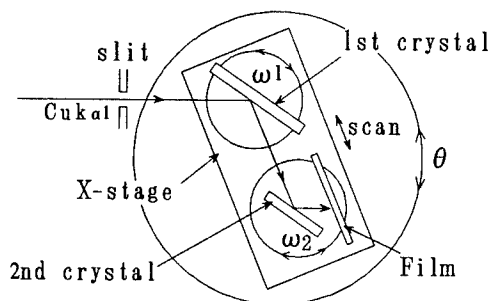


Fig.3 System for double crystal x-ray diffraction measurements

4. Results

In EPD distribution measurements, little dislocation was found at the center of the (100) wafer.

SIMS and GDMS analyses revealed that sulfur concentration at the center was about 1.2 times higher than that at the peripheral region, while the concentration of other impurities was the same.

Figs.4 and 5 show the distribution of PL intensity at the wavelength of 924nm measured at room temperature in the (100) and (011) wafers, respectively. PL intensity was abruptly weakened at the center of the (100) wafer. The low PL intensity region also existed at the central portion of the (011) wafer along the growth axis. The (011) wafer was cut from a crystalline ingot along to the growth axis through the central region. PL measurements were also performed at 4.2K. But the PL spectra remained broad because of heavily doping of sulfur, so that the transition to explain the low PL intensity at room temperature could not be assigned.

Double crystal x-ray topographic image of

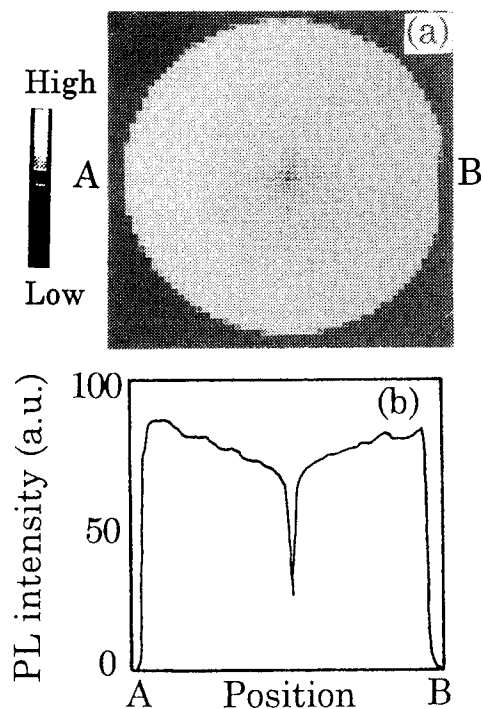


Fig.4 (a) Two dimensional distribution and (b) diametric distribution of PL intensity at the wavelength of 924 nm in the 2" ϕ S doped (100) InP wafer grown by the conventional LEC method

the (100) wafer was shown in Fig. 6, which was recorded at Si(004)-InP(004) setting. In addition to slip dislocations at the periphery and swirl like striation pattern, anomalous contrast was seen at the center. Scanning rocking curve (SXRC) measurements, which was performed by scanning the X-stage at Si(004)-InP(004) setting, made it possible to analyze anomalous contrast at the center quantitatively. The peak angles of the rocking curves were drifted by both the curvature of the wafer and the crystalline anomaly itself. The drift by the curvature was subtracted by assuming that the wafer was curved smoothly, so that we could find that the diffraction angle changed at the center only by a few arc-sec, which was much smaller than the half width of the rocking curve, approximately 15 arc-sec, which is shown in Fig.7(a). Furthermore, SXRC measurements were performed on the back side of the wafer. As shown in Fig.7(b), the anomaly of the diffraction angle at the center was inverted by the

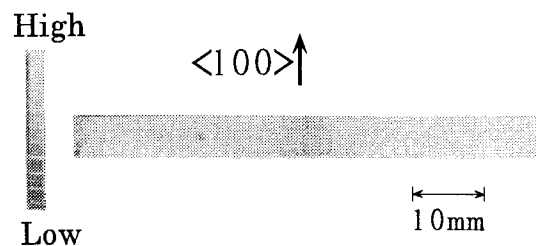


Fig.5 Two dimensional distribution of PL intensity at the wavelength of 924nm in the (011) wafer grown by the conventional LEC method

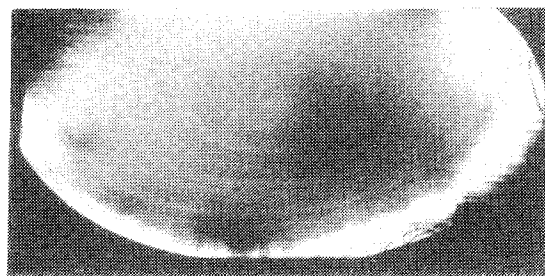


Fig.6 Double crystal x-ray topographic image of the 2" ϕ S doped (100) InP wafer grown by the conventional LEC method

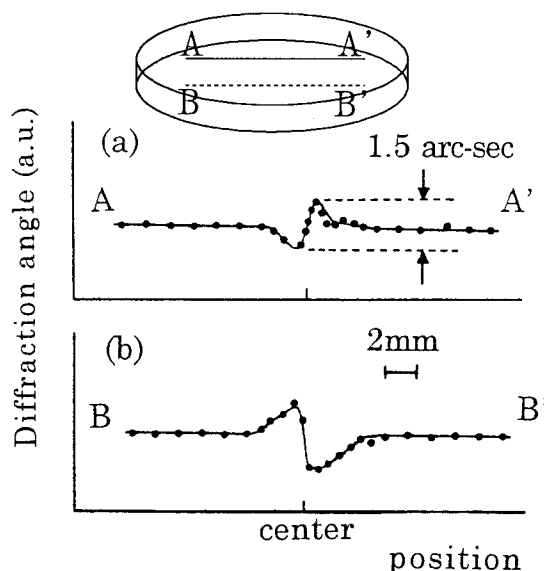


Fig.7 Results of SXRC measurements on (a) front side and (b) back side of the S doped (100) InP wafer grown by the conventional LEC method

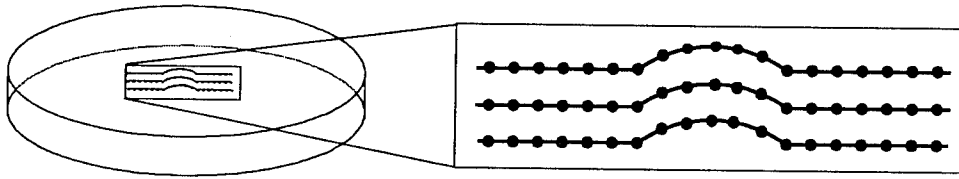


Fig.8 Lattice plane model of the S doped (100) InP wafer grown by the conventional LEC method

measurements on the back side. This results could be explained by the lattice plane model as shown in Fig.8, where the lattice plane was abnormally curved only at the center.

5. Discussion

The origin of the high dark currents of PIN-PDs at the center of the wafer is neither the dislocation of the InP substrate nor the impurities in it. That should be attributed to the crystal anomaly of the InP substrate which was detected by both PL and double crystal x-ray diffraction measurements, because the high dark currents and the crystal anomaly appear at the same position of the 2" ϕ wafer. One probable mechanism to explain that the dark currents become high is the strong stresses or strains in the InGaAs absorption layer. It is well known that the epitaxial growth rate changes due to the facet of the substrate. On the abnormally curved lattice plane as shown in Fig.8, several kinds of facets exist. Therefore, the epitaxial growth proceed at the several growth rates at the center of the substrate, so that strong stresses or strains are generated in the epitaxial layer.

4. Conclusion Remarks

It was suggested that the high dark currents of InGaAs/InP PIN-PDs at the center of the wafer were due to crystal anomaly at the center of the S doped InP substrate grown by the conventional LEC method. This crystal anomaly was detected by both PL and double crystal x-ray diffraction measurements. Furthermore, this crystal anomaly was quantitatively clarified by SXRC measurements which were developed in this study.

On the other hand, in the case of S doped InP substrates grown by VCZ method such increase

of dark currents at the center of the wafer has never been found out. Therefore, VCZ-grown S doped InP wafers are more favorable as substrates for the optoelectronic devices because of the less crystal defects or anomaly both at the periphery and at the center.

References

- [1] M. Tatsumi, T. Kawase, T. Araki, N. Yamabayashi, T. Iwasaki, Y. Miura, S. Murai, K. Tada and S. Akai, Proceedings of the First Int. Conf. on InP and Related Materials for Advanced Electronics and Optical Devices, Okurahoma, 18 (1989)
- [2] T. Iwasaki, Y. Iguchi, Y. Fujimura and N. Yamabayashi, Sumitomo Electric Technical Review, No.38, 26 (June 1994)
- [3] A. Huber and N. T. Linh, J. Cryst. Growth, 29, 80 (1975)
- [4] M. Yokogawa, S. Nishine, K. Matsumoto, S. Akai and H. Okada, Jpn. J. Appl. Phys., 23, 663 (1984)

Multi-Wavelength DFB Laser Arrays Grown by In-plane Thickness Control Epitaxy (invited)

Masahiro Aoki, Makoto Suzuki, and Yae Okuno

Central Research Lab., HITACHI, Ltd.
Kokubunji, Tokyo 185, Japan

Abstract

This paper describes a new method to control the on-wafer lasing wavelength of DFB laser diodes. Oscillation wavelength is controlled on the same epitaxial wafer by using modulated growth thicknesses of selectively grown InGaAs/InGaAsP/InP MQW active waveguides. A five-wavelength MQW-DFB laser array with constant-pitch built-in corrugation demonstrated a controllable lasing wavelength range of 10.1 nm with uniform lasing characteristics. The technique is successfully applied to on-wafer wavelength control of modulator-integrated DFB lasers, which also makes this technique attractive for light sources used in long-haul WDM systems.

Introduction

Wavelength division multiplexing (WDM) is widely recognized as an attractive way to exploit the broad information bandwidth of optical fibers. These systems require multi-wavelength light sources with precise wavelength control, uniform static/dynamic properties, and substantially lower component and assembly costs. For conventional monolithic WDM light sources, the lasing wavelengths of distributed feedback (DFB) or distributed Bragg reflector (DBR) lasers have been controlled by adjusting the pitch of the built-in corrugation transcribed in identical active/passive waveguides [1-3]. However, this requires rather complicated and expensive fabrication techniques such as electron beam lithography. Moreover, the difference between the lasing wavelength and the gain peak wavelengths (the detuning parameter, which is a key factor in DFB laser design) automatically varies for each channel, leading to varying device performance.

This paper describes a new method for simultaneously controlling the lasing wavelength and the gain peak wavelength of MQW-DFB lasers fabricated on identical substrates. This control was attained by using selective area growth (SAG) to enhance layer

thicknesses during metal organic vapor phase epitaxy (MOVPE). The lasing wavelength can be controlled by modulating the thickness of the optical guide layer, thus controlling the effective refractive index of the DFB waveguides [4-6]. At the same time, the gain peak wavelength can be controlled through the modulated thickness of quantum wells, i.e., the quantum energy levels [7,8]. A DFB laser array fabricated using this method has a controllable wavelength range of 10.1 nm with uniform lasing characteristics. This technique is also successfully applied to control the wavelength in a DFB laser monolithically integrated with an external modulator.

Wavelength control of a selectively grown DFB laser array

The device structure and fabrication process are illustrated in Fig. 1. First, parallel stripes of a 0.2- μm -thick SiO_2 mask were formed on a (100) n-type InP substrate in the [011] direction. The gap width between the stripes (W_g) was kept constant at 15 μm and the width of the mask stripes (W_m) was increased in 5- μm increments from 10 to 30 μm [Fig. 1(a)]. These selective masks were arranged with a 400- μm period. Then, a

seven-pair separate confinement heterostructure (SCH) InGaAs MQW structure was selectively grown on this patterned substrate by low-pressure MOVPE. The SCH-MQW on the flat substrate consisted of 4.3-nm-thick InGaAs wells sandwiched by 8-nm-thick InGaAsP (1.15 μm) barriers. The SCH layers were made of 0.11- μm -thick InGaAsP (1.15 μm). Lattice conditions were selected so that all the epitaxial layers were lattice-matched to the InP substrate. Figure 2 shows the W_m dependencies of the enhanced thicknesses for the InGaAsP SCH layers and the InGaAs well layers; these were measured using a CAT-TEM and a high-resolution SEM. We found that increases in the thickness are nearly proportional to W_m and that the increase in the growth rate is almost the same for both InGaAs and InGaAsP. We also measured microscopic photoluminescence ($\mu\text{-PL}$) at a 1- μm focus spot in the center of each gap. A red-shift in the PL spectra is clearly seen as W_m increases, mainly due to the SAG-induced enhancement in the InGaAs well layer thickness. The PL peak intensity and half-width for the selectively grown layers were comparable to those of the reference layer in the flat region, indicating that these selectively grown MQW crystals are of sufficient quality. After SAG, a 240.4-nm-pitch first-order grating was formed on top of the upper InGaAsP guide layer using the interferometric exposure technique. Then, the wafer was further processed into a buried-hetero laser structure with a 1.5- μm -wide active layer.

Figure 3 shows typical I-L curves for an array (a 400- μm cavity with 1%/90% refractive ends) with five different W_m s. The threshold currents range from 14 to 20 mA and slope efficiencies from 0.25 to 0.35 W/A, with no apparent relationship between W_m and these lasing properties. Figure 3 also shows the lasing spectra of this DFB-laser array measured at the 3-mW output level. In this array, all five devices lased at the shorter wavelength mode of the stopband. Stable single mode operation was observed for all the channels with side mode suppression ratios greater than 35 dB. By increasing W_m from 10 to 30 μm , the on-wafer DFB lasing wavelength (λ_{DFB}) was controlled over a 10.1-nm range from 1545.4 to 1555.5 nm with 2.5 ± 0.2 -nm intervals. In Fig. 4, these

λ_{DFB} s are plotted against W_m ; calculated results are also shown that take into account the SAG-enhanced layer thicknesses shown in Fig. 2. Good agreement is clear between the experimental results and the theory based on the effective index method with refractive indices given by the modified single-effective-oscillator (MSEO) method. Figure 4 also shows how the gain peak wavelength (λ_g) depends on W_m . Measured gain spectra below the threshold level peak was between 1529.6 nm ($W_m=10$ μm) and 1574.6 nm ($W_m=30$ μm), which results in levels of detuning ($\Delta\lambda=\lambda_{\text{DFB}} - \lambda_g$) that vary from -19 to +16 nm. Figure 4 also shows good agreement between the measured λ_g values and the theory, taking into account the SAG-induced thickness enhancements and changes in the indium content of InGaAs(P) alloys which were deduced by microscopic Auger electron spectroscopy ($\mu\text{-AES}$). These $\Delta\lambda$ variations can be minimized by enlarging the waveguide layer index, thus widening the controllable range of λ_{DFB} , and/or by widening the well width by introducing tensile strained InGaAs or InGaAsP wells, thus reducing the λ_g shift by using the saturated quantum energy shift for wider well layers.

Application to a modulator-integrated WDM light source

We applied this technique to control the oscillation wavelength of an electro-absorption (EA) modulator integrated DFB laser (Fig. 5). The device structure and fabrication are almost the same as those previously reported [9], except for the selective mask configuration used to control λ_{DFB} . The selective mask patterns formed only in the DFB-laser sections have W_m of 16 to 25 μm in 1.5- μm increments and W_g of 16 μm . Each device was evaluated individually. Figure 6 shows the laser/modulator characteristics of more than 50 devices with seven different W_m s. By increasing W_m from 16 to 25 μm , the on-wafer DFB lasing wavelength (λ_{DFB}) was controlled from around 1550 to 1557 nm, with an averaged channel spacing of about 1 nm.

The figure also plots the uniform laser/modulator performance between the channels, such as 10-15 mA threshold currents, 0.06-0.10 W/A slope efficiencies, on/off ratios of more than 13 dB, and frequency bandwidths of over 11 GHz. These results show the potential of this device as a lightsource used in Gb/s dense WDM systems. This wavelength control is also a key technique to easily prepare a set of discrete devices with different wavelengths.

Conclusion

We have developed a simple method of simultaneously controlling both the lasing wavelength and the gain peak wavelength of DFB lasers by using enhanced layer thicknesses of selectively grown MQW active waveguides. We used this technique for a multi-wavelength InGaAs/InGaAsP MQW DFB-laser array, and a modulator-integrated WDM light source. This technique is attractive for fabricating practical light sources used in WDM applications.

References

- [1] M. Nakao et al., *Electron. Lett.*, vol. 25, pp. 148-149, 1992.
- [2] C. E. Zah et al., in *Proc. 13th. International Semiconductor Laser Conference*, paper K-1, 1992.
- [3] J. M. Verdiell et al., *IEEE Photon. Tech. Lett.*, vol. 5, pp. 619-621
- [4] Y. Kato et al., *Electron. Lett.*, vol. 29, pp. 2195-2197, 1993.
- [5] T. Sasaki et al., *Electron. Lett.*, vol. 30, pp. 785-786, 1994.
- [6] M. Aoki et al., *IEEE Photon. Tech. Lett.*, vol. 6, pp. 789-791
- [7] M. Aoki et al., *J. Quantum Electron.*, vol. 27, pp. 2281-2295, 1993.
- [8] T. Sasaki et al., *J. Crys. Growth*, vol. 132, pp. 435-443, 1993.
- [9] M. Aoki et al., *ECOC'93 ThC12.2*.

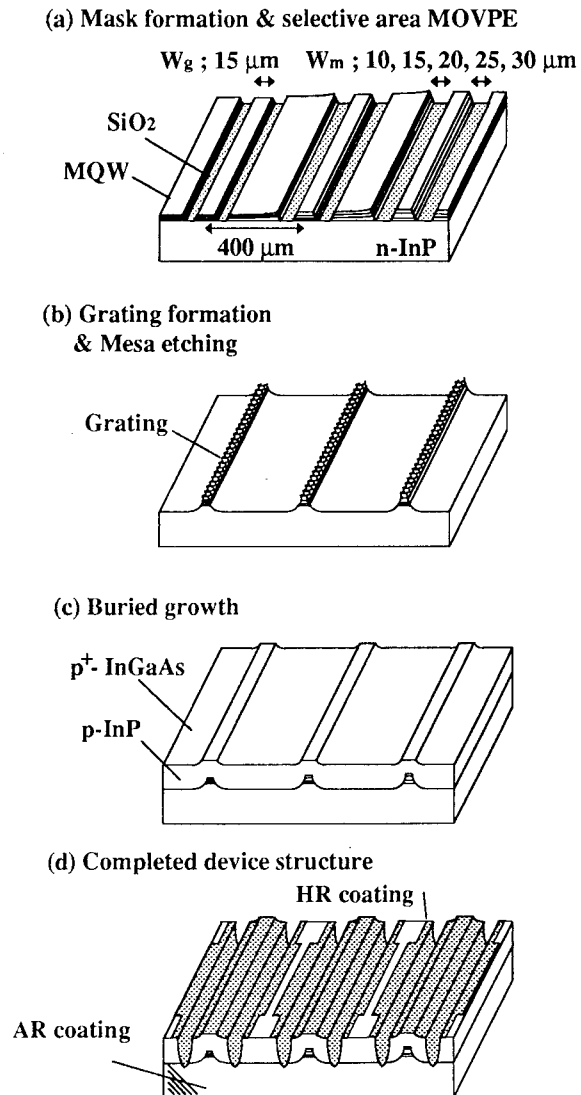


Fig. 1
Device structure and fabrication process of new multi-wavelength DFB-laser array.

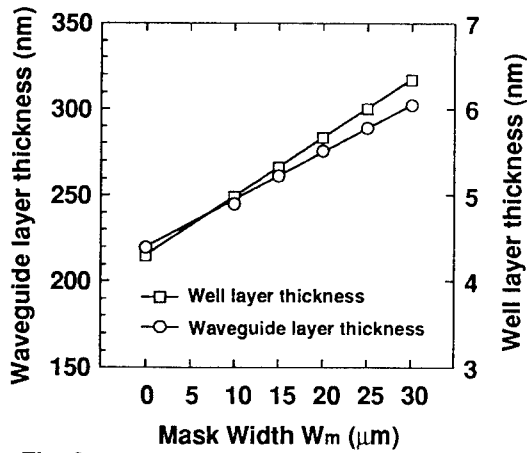


Fig. 2
Growth rate enhancements for InGaAsP waveguide and InGaAs well layers versus selective mask width W_m

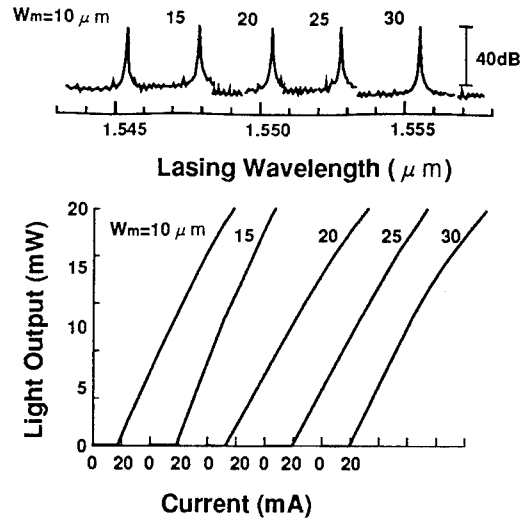


Fig. 3
I-L curves and lasing spectra of the DFB-laser array.

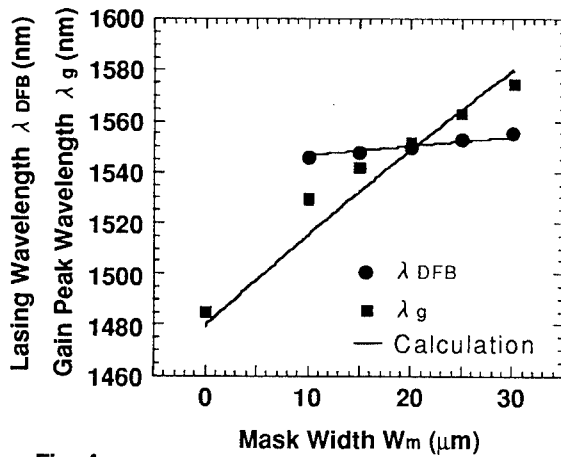


Fig. 4
Lasing wavelength and gain peak wavelength versus selective mask width W_m compared with theoretical results

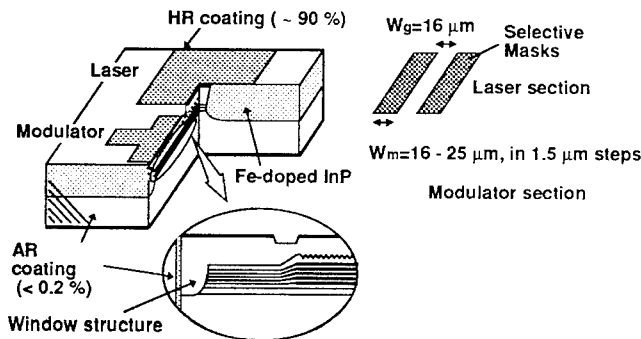


Fig.5
Structure of modulator integrated Multi- λ DFB laser

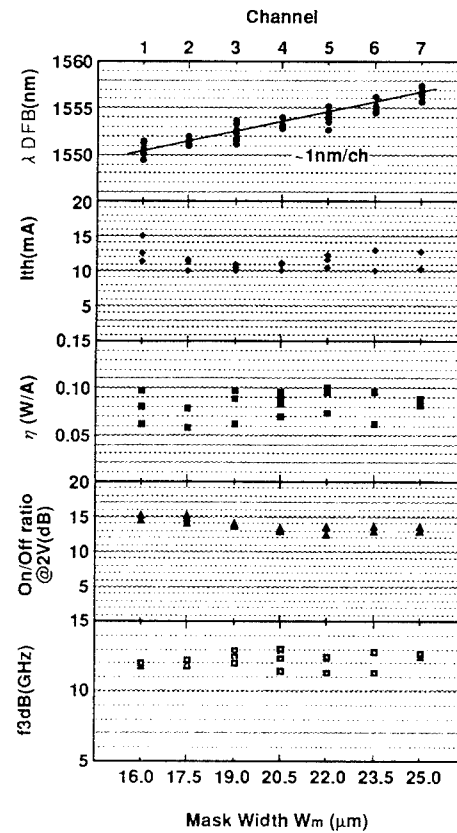


Fig.6
Performance of the 7- λ WDM-integrated laser/modulator

InAsP/InGaP All Ternary Strain-Compensated Multiple Quantum Wells and its Application to Long Wavelength Lasers

N. Yokouchi, N. Yamanaka, N. Iwai, T. Matsuda and A. Kasukawa
Yokohama R&D Laboratories, The Furukawa Electric Co., Ltd.
2-4-3, Okano, Nishi-ku, Yokohama 220, Japan

Abstract

By newly introducing InGaP tensile strained layer as barriers of InAsP compressively strained multiple quantum wells, a high crystalline quality of InAsP/InGaP strain-compensated multiple quantum wells was obtained using metalorganic chemical vapor deposition on (100) InP substrate. Strain compensation was clearly confirmed by the surface morphology, double crystal X-ray measurement and photoluminescence spectrum. First laser consisted of all ternary quantum well active layer was successfully fabricated. The threshold current density of 1kA/cm^2 was obtained, cavity length of $600\mu\text{m}$, without the use of separate confinement heterostructure layer. A very low threshold current density of 300A/cm^2 was achieved in an improved structure emitting at $1.3\mu\text{m}$.

Introduction

The concept of strained-layer enables us to extend the material to be dealt with. The conventional materials for long wavelength lasers are GaInAsP/InP and GaInAlAs/InP. Using a strained-layer, InAsP/InP system can be a candidate for long wavelength lasers. InAsP/GaInAsP compressively strained-layer quantum well layers emitting at $1.3\mu\text{m}$ were reported [1]. This material system has a large conduction band offset as compared to GaInAsP/InP system, resulting in a possibility of improved lasing characteristics at a high temperature due to small electron leakage to an optical confinement layer [2]. However, InAsP has a large compressive strain of about 1.5% with thickness of 8nm to realize an emission wavelength of $1.3\mu\text{m}$. Therefore, the number of wells is limited to only two due to critical thickness [1]. In order to increase the number of wells to improve the temperature characteristics of InAsP/InP strained-layer QW lasers, tensile strained GaInAsP have been incorporated for strain compensation [3]. On the other hand, InGaP layer has a small lattice constant with respect to InP, that is, it works as a tensile-strain. Moreover, InGaP seems to be easy to control the composition since it is a ternary material.

In this paper, we report the growth and characterization of all ternary InAsP/InGaP strain compensated quantum wells for long wavelength laser and the first laser oscillation in this material system.

MOCVD Growth

Low pressure metalorganic chemical vapor deposition (MOCVD) is used for the growth with a growth temperature of 550°C [1]. Double heterostructure clad by InP layer, as shown in Fig. 1, was grown on a (100) InP substrate for sample evaluation. The growth sequence is quite simple as shown in Fig.2. Exact same gas flow rate of trimethylindium (TMIn) and phosphine (PH_3) was used for InAsP and InGaP and arsine (AsH_3) and triethylgallium (TEGa) were introduced into reactor alternatively for the growth of InAsP and InGaP, respectively, with no growth interruption. The thickness and amount of strain are inferred by X-ray diffraction analysis of MQW consisting of InAsP/InP, InGaP/InP and InAsP/InGaP. The amounts of strain for $\text{InAs}_y\text{P}_{1-y}$ and $\text{In}_{1-x}\text{Ga}_x\text{P}$ are derived from Vegard's law as compressive strain of $3.23y$ (%) and tensile strain of $7x$ (%), respectively. Nomarski interference microscope photograph reveals

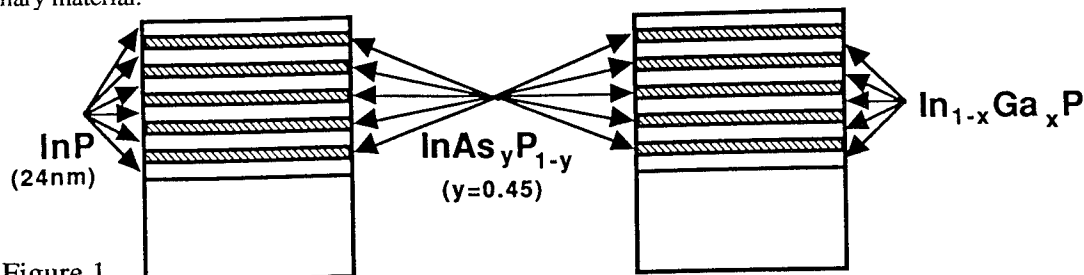


Figure 1
Schematic diagram of InAsP/InP strained-layer quantum wells and InAsP/InGaP strain-compensated quantum wells investigated in this study.

that cross-hatch surface is observed for 5-pair of $\text{InAs}_y\text{P}_{1-y}$ ($y=0.45$, 10nm)/ InP (24nm) strained-layer quantum wells, while mirror-like surface for 5-pair of $\text{InAs}_y\text{P}_{1-y}$ ($y=0.45$; 10nm)/ $\text{In}_{1-x}\text{Ga}_x\text{P}$ ($x=0.08$; 24nm) strain compensated quantum wells. The double crystal X-ray results are shown in Fig.3, together with the simulation results.

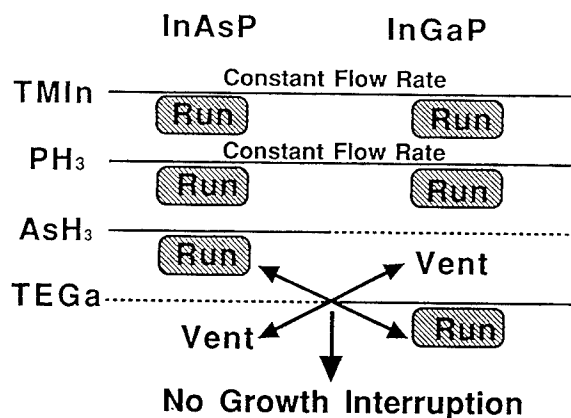
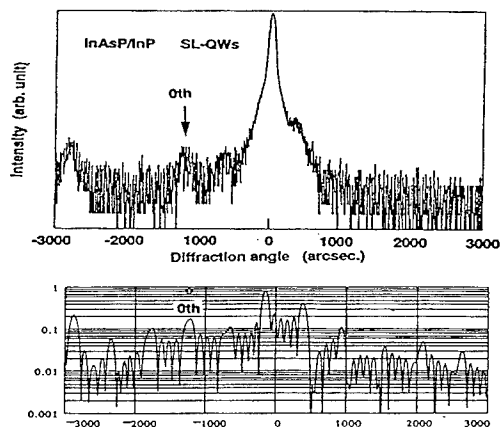


Fig.2 Growth sequence for the growth of InAsP/InGaP SC-QW.

The net strain, ϵ_{NS} is defined as $\epsilon_{NS} = (\epsilon_w L_w N_w + \epsilon_B L_B N_B) / (L_w N_w + L_B N_B)$ is estimated to be 0.42% for sample (a) and 0.12% for sample (b). The full width at half maximums of room temperature photoluminescence spectrum were 50meV and 35meV for InAsP/InP strained-layer quantum wells and InAsP/InGaP strain-compensated quantum wells, respectively. Figure 4 shows the transmission electron microscopy (TEM) photograph of InAsP/InP SL-QW (a) and InAsP/InGaP SC-QW (b). TEM reveals that dislocation occurred for InAsP/InP QWs with 10 wells, while no dislocation for InAsP/InGaP strain-compensated quantum wells with 10 wells.



High crystalline quality strain-compensated InAsP/InGaP quantum wells was obtained.

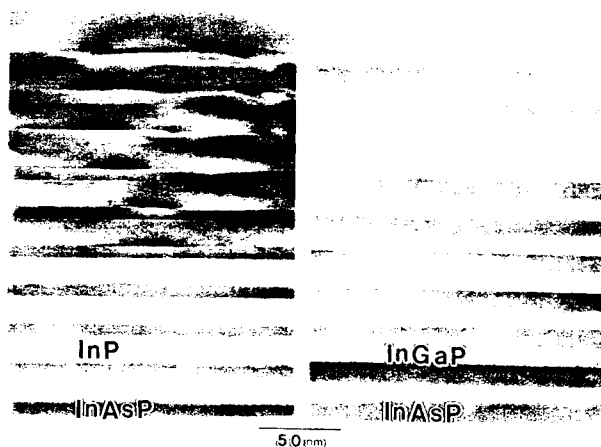


Fig. 4 TEM photograph of InAsP/InP SL-QW (a) and InAsP/InGaP SC-QW (b), together with simulated results.

Application to Long Wavelength Lasers

We have applied InAsP/InGaP strain-compensated quantum wells to the active layer of long wavelength laser. A schematic diagram of InAsP/InGaP strain-compensated quantum well laser is shown in Fig.5. 10-QWs is used to increase the optical confinement factor. Optical confinement layer has not been incorporated in this structure. Threshold current density of 100- μm wide broad area lasers versus cavity length is shown in Fig 6. We have achieved laser oscillation in this material system for the first time. The lasing wavelength was 1.21 μm . It is found to be difficult to grow strain-compensated quantum wells with large amount of strain for 1.3 μm wavelength.

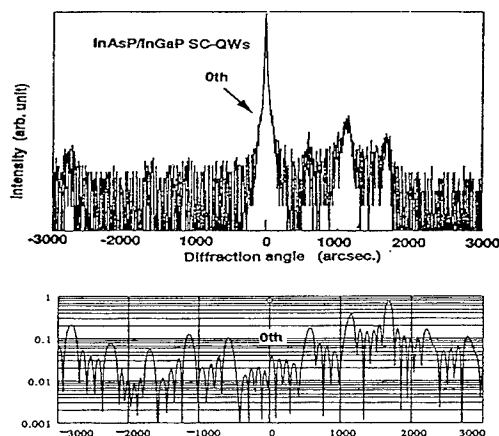


Figure 3 X-ray measurement results of InAsP/InP strained-layer quantum wells and InAsP/InGaP strain-compensated quantum wells, along with simulated results.

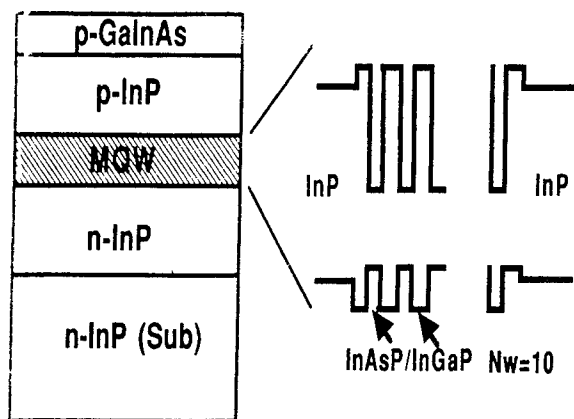


Fig.5 A schematic diagram of InAsP/InGaP SC-QW lasers. No SCH layer is used for this structure.

Threshold current density of 1 kA/cm^2 was measured with a cavity length of $600\text{ }\mu\text{m}$. Lower threshold current density can be expected by optimized layer structure.

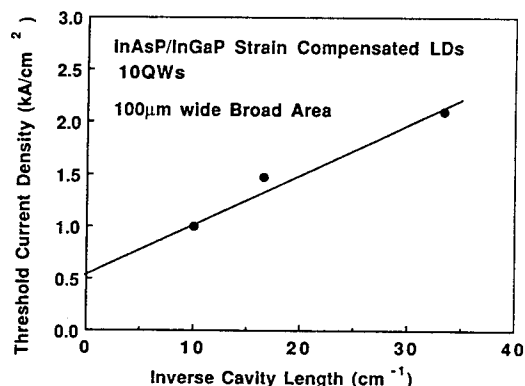


Fig. 6 Threshold current density versus inverse cavity length for InAsP/InGaP SC-QW LDs.

Temperature characteristics of the threshold current under pulsed condition is plotted in Fig.7 for 1mm-long cavity.

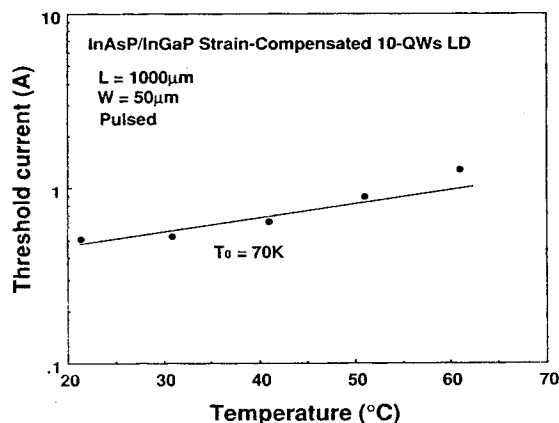


Fig.7 Temperature dependence of threshold current.

The characteristic temperature T_0 is calculated to be 70K in the temperature range of 20-60 $^{\circ}\text{C}$. No improvement in T_0 was observed. This might be attributed non-uniform carrier injection over the 10 QWs.

Improved Layer Structure for 1.3 μm Lasers

As mentioned above, it is difficult to obtain good crystalline quality for 1.3 μm lasers. A thin InP intermediate layer (IML) is inserted between InAsP and InGaP layers [4]. The importance of InP IML has been investigated in terms of crystal quality. Full width at half maximum (FWHM) of room temperature photoluminescence (PL) spectrum, excited by Kr $^{+}$ -laser ($\lambda=647.1\text{ nm}$), is plotted in Fig.8 as a function of InP IML thickness.

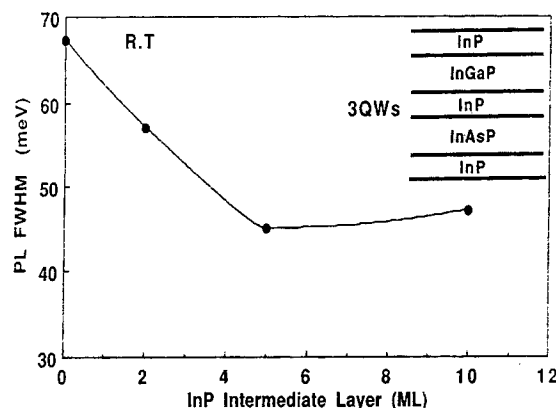


Fig. 8 FWHM of PL spectrum for InAsP/InP/InGaP.

The FWHM of PL spectrum decreases with increase of IML thickness. From this experiment, 5-monolayer (ML) is needed to obtain high crystal quality. The improvement of crystalline quality of InAsP/InGaP SC-QWs with IML is also supported by X-ray measurements, that is higher order satellite peaks are observed, while no satellite peaks for SC-QWs without IML. We think that degradation of crystal quality could be attributed to the "uncontrolled GaInAsP layer" which is formed between InAsP and InGaP layers.

We have applied InAsP/InGaP strain-compensated quantum wells to the active layer of long wavelength laser. Triple quantum wells is used. A 100nm-thick GaInAsP layer with a bandgap wavelength of 1.1 μm is used for separate-confinement-layer in order to increase an optical confinement factor. The effect of strain compensation was confirmed by PL measurement. The FWHM of room temperature PL spectrum was as narrow as

30meV, which is better than that of GaInAsP/InP compressively SL-QW laser wafer with same number of wells. The difference of PL linewidth of laser structure and test structure described above arises from the difference of InP upper cladding layer.

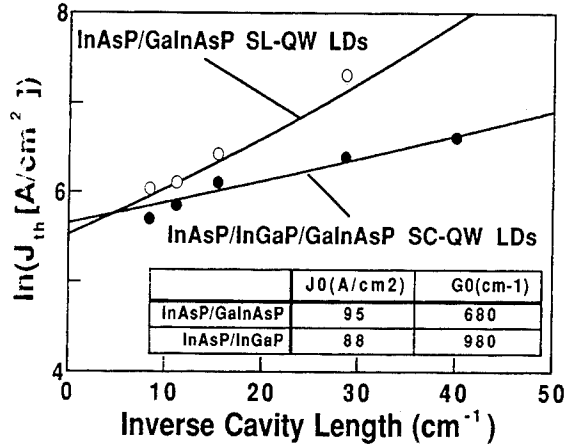


Fig. 9 Threshold current density versus inverse cavity length for InAsP/GaInAsP SL-QW lasers and InAsP/InP/InGaP/InP/GaInAsP SC-QW lasers.

Threshold current density of broad area lasers versus inverse cavity length is shown in Fig 9. We have achieved laser oscillation in this material system for the first time. A very low threshold current density of 300A/cm² was obtained for a cavity length of 1200μm. Assuming the threshold current density as $J_{th} = N_w J_0 \exp\{(\alpha_i + \alpha_m)/N_w \Gamma_w G_0\}$, where N_w is the number of wells, J_0 is the transparent current density, Γ_w is the optical confinement factor, G_0 is the gain coefficient, α_i and α_m are internal loss and mirror loss, respectively, transparent current density of 88A/cm² per well was estimated for infinite cavity length. Lasing wavelength was 1.3μm. The results obtained for InAsP/GaInAsP SL-QW [1] lasers are also shown in Fig.9. Lower threshold current density was obtained in InAsP/InGaP SC-QW lasers. Especially, large difference of threshold current density was observed for short cavity region. This could be attributed to the carrier overflow into the 1.1μm-Q SCH layer in the latter structure. G_0 and J_0 are derived to be 980 cm⁻¹ and 88 A/cm², 680 cm⁻¹ and 100 A/cm² for InAsP/InGaP SC and InAsP/GaInAsP SL-QW lasers, respectively. Lower threshold current

density can be expected for graded-index separate-confinement-heterostructure (GRIN-SCH) for optical confinement layer. Submilliampere threshold current could be attained by narrow stripe lasers such as buried heterostructure.

Conclusion

In conclusion we have investigated the growth of InAsP/InGaP strain-compensated quantum well for long wavelength laser using low-pressure MOCVD, and obtained laser oscillation for the first time. A very low threshold current density of 300A/cm² was obtained for InAsP/InP/InGaP/InP/GaInAsP SC-QW lasers emitting at 1.3μm.

Acknowledgment

The authors would like to thank Mr. S. Kashiwa and Mr. T. Ninomiya for encouragement for this study.

References

- [1] A. Kasukawa, T. Namegaya, T. Fukushima, N. Iwai and T. Kikuta, "1.3μm InAsP1-y-InP Strained-Layer Quantum-Well Laser Diodes Grown by Metalorganic Chemical Vapor Deposition", *IEEE J. Quantum Electron.*, **29**, pp.1528-1535, 1993.
- [2] M. Yamamoto, N. Yamamoto and J. Nakano, "MOVPE growth of strained InAsP /InGaAsP quantum well structures for low threshold 1.3μm lasers", *IEEE J. Quantum Electron.*, **30**, pp.554-561, 1994.
- [3] H. Oohashi, T. Hirano, H. Sigiura, J. Nakano, M. Yamamoto, Y. Tohmori and K. Yokoyama, "High Temperature Operation InAsP-Based MQW Lasers", *IPRM'94*, PDA3
- [4] X.S. JIANG and P.K. L. YU, "Strain compensated InAsP/InP/InGaP multiple quantum well for 1.5 μm wavelength", *Appl. Phys. Lett.*, **65**, pp. 2536-2538, 1994.

Fabrication of a polarization insensitive electroabsorption modulator with strained InGaAs/InAlAs MQW by MOVPE

Susumu Kondo, Kouichi Wakita, Yoshio Noguchi and Naoto Yoshimoto

NTT Optoelectronics laboratories

3-1 Morinosato, Wakamiya, Atsugi, Kanagawa 243-01, JAPAN

Strained InGaAs/InAlAs multi-quantum well (MQW) layers are grown by a low pressure MOVPE technique. Introduction of compressive strain into an InAlAs barrier layer against a tensile strained well layer makes it possible to grow an MQW layer with good quality. By using these layers, we have also demonstrated strained InGaAs/InAlAs MQW electroabsorption modulators with a polarization insensitivity.

Introduction

InAlAs/InGaAs multi-quantum well (MQW) structures are very promising materials for optoelectronics devices such as lasers, modulators and detectors because of their large conduction band offset ($DE_c \sim 0.5$ eV) compared with that of other candidate systems using InP/InGaAs. Especially, MQW electroabsorption modulators have been widely studied for the application of the high frequency modulators in optical communication systems¹⁾. One of the important requirements for electro-optical modulators is low driving voltage and it is attained by using thick well layers which enhance the QCSE (quantum confined stark effect) and optical absorption. There are two solutions in order to obtain a modulator without changing its absorption band edge. One uses quaternary InGaAlAs materials and the other introduces strained layers. Using InGaAlAs makes it possible to optimize the bandgap energy and well thickness independently, and we applied this technique for optical MQW switches. On the other hand, introducing strain into an InGaAs well layer can also control the wavelength and well thickness, independently³⁾. Furthermore, introducing tensile strain can reduce the polarization dependence of an optical modulator because of heavy-light hole degeneracy⁴⁾⁵⁾.

Several attempts have been made using molecular beam epitaxy for these III-V systems

1)3), but few using metal organic vapor phase epitaxy (MOVPE) have been reported.

In this paper, we present the MOVPE growth of an InGaAs/InAlAs strained multi-quantum well structure and its application in a polarization insensitive electroabsorption modulator.

Growth of InGaAs/InAlAs MQW

The low pressure MOVPE apparatus used has a vertical reactor and a leak-tight system. TMI, TEG, TMA, and DEZn are supplied as the In, Ga, Al and Zn sources, respectively. Arsine and phosphine are also used for V-group sources. The growth temperature and V/III ratio in the growth of MQW layer are 665°C and about 100.

Before growing films for the electroabsorption modulator, strain-compensated InGaAs/InAlAs MQW growth was investigated. The following four types of MQW were grown on InP (100) substrates.

- A) lattice-matched InGaAs well and lattice-matched InAlAs barrier,
- B) lattice-matched InGaAs well and 0.4% compressive strained InAlAs barrier,
- C) 0.5% tensile strained InGaAs well and lattice-matched InAlAs barrier,
- D) 0.5% tensile strained well and 0.4% compressive strained barrier.

Sample D is a strain compensated MQW structure. Thickness of the InGaAs well and InAlAs barrier layers are fixed at 120 nm and 70 nm. The as-grown surface of these MQWs with 20

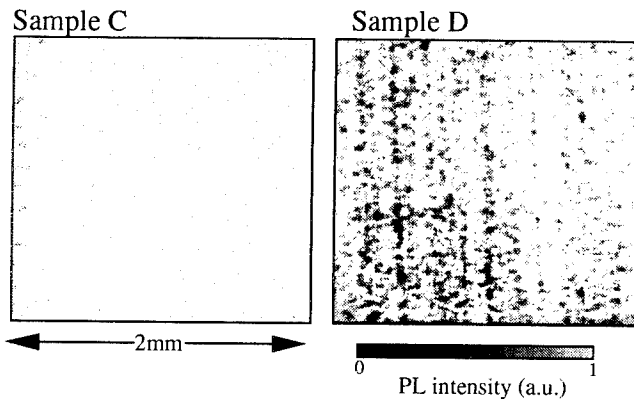


Figure 1 Micro-photoluminescence from samples C and D. C: without compensation D: with compensation. Cross-hatched pattern was observed in the sample C, but no pattern was observed in the sample D.

pairs were smooth in all cases. PL (photoluminescence) peak wavelength from the MQWs with and without strained well are $1.58\mu\text{m}$ and

$1.50\mu\text{m}$, respectively. These values do not depend on stress in the barrier layer. The PL intensity at peak wavelength from C was four times weaker than those from samples A and B. However, PL intensity from sample D was three times stronger than that of sample C. Figure 1 shows the micro photoluminescence⁶⁾ from samples C and D. A cross-hatched pattern was observed in sample C, but no pattern was observed in sample D. Figure 2 shows the X-ray rocking curve of sample D. It is estimated from this curve that the InGaAs well layer has 0.5% tensile strain and the InAlAs barrier has 0.4% compressive strain. In this way, by introducing compressive strain into InAlAs barrier layers, MQWs with good quality can be obtained by introducing tensile strain into InGaAs well layers.

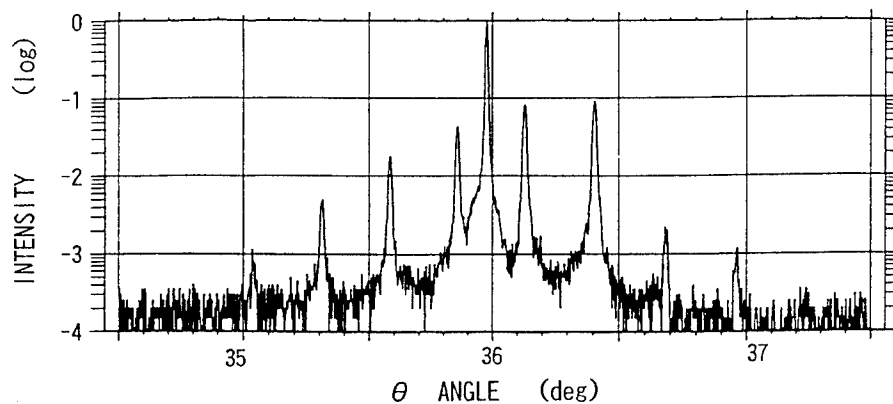


Figure 2 The X-ray rocking curve from sample D. The InGaAs well layer has 0.5% tensile strain and the InAlAs barrier has 0.4% compressive strain.

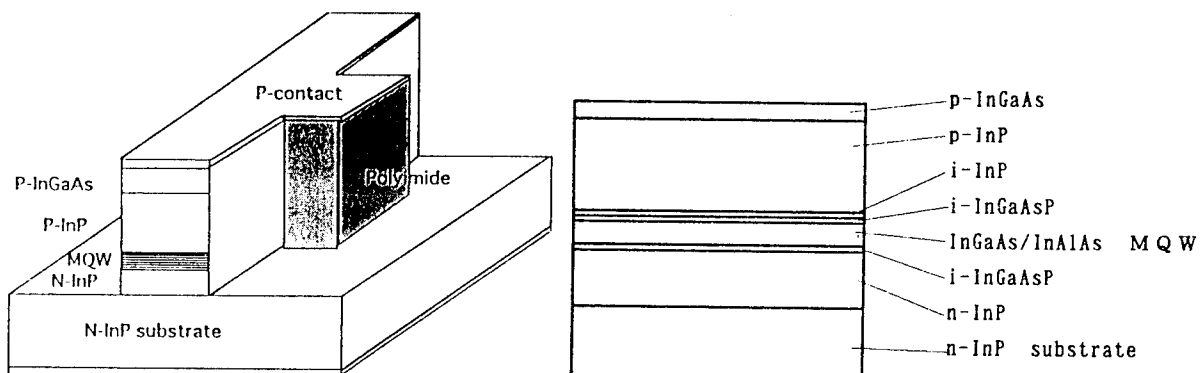


Figure 3 Schematic diagram of the strained InGaAs/InAlAs MQW modulator. The length is $300\mu\text{m}$ and the stripe width is $2\sim 3\mu\text{m}$.

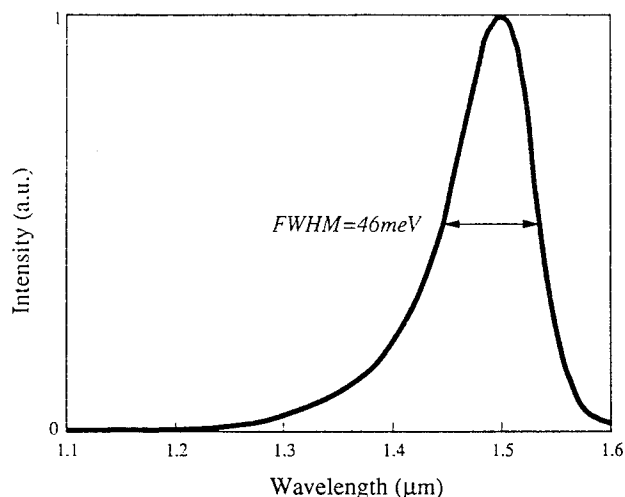


Figure 4 Photoluminescence spectrum from strained MQW layer

Fabrication of modulator

We tried to grow the film for electroabsorption modulators. Figure 3 shows schematic diagrams of the modulator structure and the film structure with a strained InGaAs/InAlAs MQW layer. The MQW structure consists of ten pairs of strained InGaAs well layers and barrier layers. The carrier concentration of the MQW layer is about $1 \times 10^{16} \text{ cm}^{-3}$.

Figure 4 shows the PL spectrum from the MQW layer at room temperature, measured after removing the InGaAs cap layer. The PL peak wavelength is $1.50 \mu\text{m}$, and the full width at half maximum (FWHM) is about 46 meV. A very narrow spectrum can be obtained.

The optical propagation loss through the strained InGaAs/InAlAs MQW waveguide is 1~2 dB/mm.

Figure 5 shows the photocurrent spectra of the strained InGaAs/InAlAs MQW modulator with applied voltages as a parameter. The spectra for the incident light polarization of TM and TE modes are (a) and (b). A similar electroabsorption effects were observed. Introducing tensile strain produces polarization insensitivity as reported for InGaAsP/InGaAsP strained MQWs⁴). Moreover, large shifts in the exciton peak are observed because of the thick quantum well (12 nm).

Figure 6 shows the extinction ratio for several

polarization directions of incident light with wavelength of $1.55 \mu\text{m}$. The absolute transmitted optical power is almost the same for various polarizations. A very small driving voltage of less than 1.6V produces a large extinction ratio of over 30 dB. The frequency response of this modulator is flat from DC up to 19 GHz. And the mean insertion loss between two single mode fibers is 8 dB.

Conclusion

We can obtain a high-quality strained InGaAs/InAlAs MQW structure by MOVPE and develop a polarization insensitive electro absorption modulator.

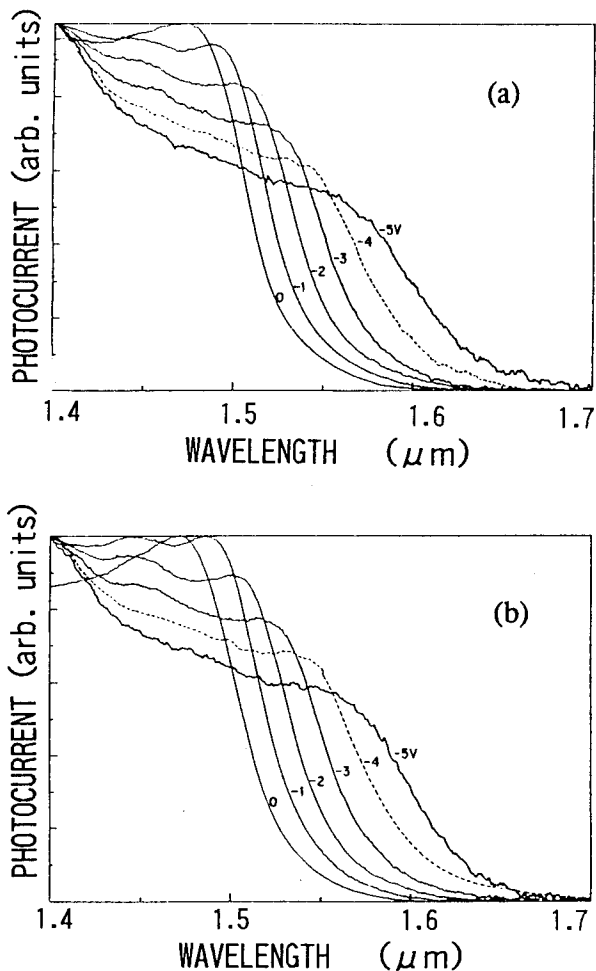


Figure 5 Photoluminescence spectrum from strained InGaAs/InAlAs MQW structure with applied voltage as a parameter. (a): TM (b): TE

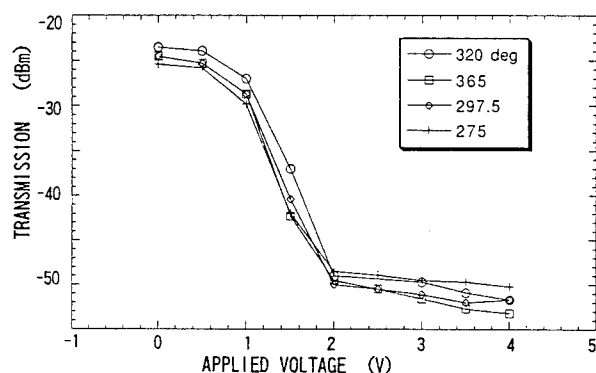


Figure 6 Relationship between applied voltage and transmission power intensity through the strained MQW modulator with several polarized directions as a parameter.

Acknowledgments

The authors thank Drs. J.Yoshida, and M.Yamamoto for their encouragement throughout this work. The authors also thank to Drs. M.Nakao and K.Nakajima for the micro-photoluminescence and X-ray measurements.

References

- 1) K.Wakita, T.Kotaka, O.Mitomi, H.Asai, H.Kawamura and M.Naganuma, J.Lightwave Technol.8, p1027 (1990).
- 2) N.Yoshimoto, K.Kawano, Y.Hasumi, H.Takeuchi, S.Kondo, and Y.Noguchi, "InGaAlAs/InAlAs multiple quantum well phase modulator integrated with spot size conversion structure" IEEE Photonics Technology Lett. 6, p208 (1994).
- 3) T.Ido, H.Sano, D.J.Moss and A.Takai, "Ultra-high-efficiency strained InGaAs/InAlAs MQW electro-absorption modulators" 5th Optoelectronics Confer. (OEC'94) 15B3-1 (1994).
- 4) F.Devaux, "The future of MQW electroabsorption modulators in high bit rate optical communication", 5th Optoelectronics Confer. 14A1-2, (1994).
- 5) J.E.Zucker, K.L.Jones, T.H.Chiu, B.Tell, K.Broun-Goebeler, "Polarization-independent electro-optic wave-guide switch using strained InGaAs/InAlAs quantum wells" Integrated Photon. Research, Pd7 (1992).
- 6) M.Nakao and H.Sugiura, "characterization of InAlAs/InGaAsP strained MQW crystals for 1.3 μm -wavelength laser diodes using a microscopic photoluminescence", in this conference.

Fabrication of crystal-facet mirrors for short cavity lasers by selective InP epitaxy on etched sidewalls

WA2.5

H. Sugimoto, M. Gotoda, T. Isu, and M. Nunoshita

Semiconductor Research Laboratory, Mitsubishi Electric Corporation
Amagasaki, Hyogo 661, Japan

Crystal facets of InP for the reflection mirrors of short cavity laser diodes were successfully fabricated by a novel wafer process without use of cleavage. Selective InP epitaxial growth on sidewalls formed by dry etching realized as vertical and smooth facets as crystal facets formed by cleavage. Grown Facets Short cavity Laser Diode (GFS-LD) with the facet mirrors was proposed and the characteristics were estimated.

Low Threshold Current Laser Diode

Low threshold current is essential for practical applications of laser diodes to optical subscriber networks and inter-board connections in computers. The most simple and realizable way for reducing the threshold current is to minimize the cavity length of conventional lateral Fabry-Perot laser diodes which have been produced commercially. They have excellent and established structures for functions such as carrier-injection path, current blocking, and lateral optical confinement. High reflectivity mirrors fabricated by wafer process without cleavage are indispensable for the short cavity laser diodes. A crystal facet is an ideal mirror of laser diode for reasons of the perfect verticality and the smoothness. We fabricated crystal-facet mirrors for laser diodes without cleavage for the first time.

Grown Facets

Sidewalls with a height of $3\mu\text{m}$ were formed by RIE (Reactive Ion Etching) of (100) InP using a mixture gas of ethane, hydrogen, and oxygen[1]. On the sidewalls and etched bottom surface, InP was grown by a chemical beam epitaxy (CBE) technique using trimethylindium (TMI, 0.8ccm) and phosphine (PH_3 , 8.8ccm) at a substrate temperature of 525°C [2]. An SiO_2 film was used as both an etching mask and a selective mask for the growth. The thickness of the InP growth layer on the (100) bottom surface was about $1\mu\text{m}$. No striation was observed on the sidewall after the growth. Grown facets of the $(01\bar{1})$ just direction were formed on the etched sidewalls, as shown by an SEM photograph in Fig. 1(a). The grown facets were perfectly as vertical and smooth as those formed by cleavage, although the etched sidewalls deviated from the

vertical by 10 degrees and have striations. It was supposed that the growth rate to $[01\bar{1}]$ direction was less than other directions at this growth condition of the high V/III ratio, and $(01\bar{1})$ just facets were obtained.

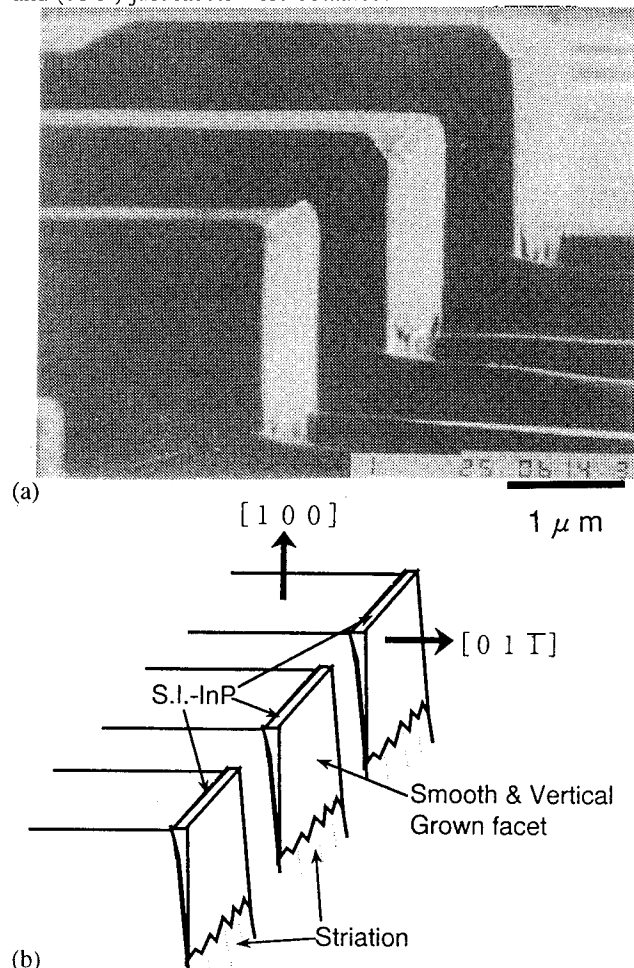
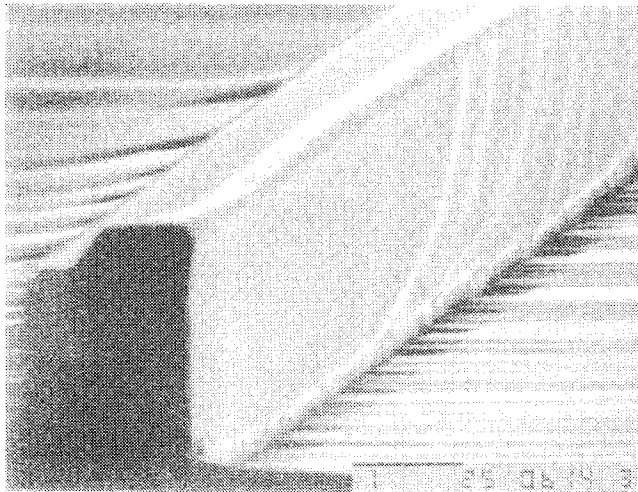


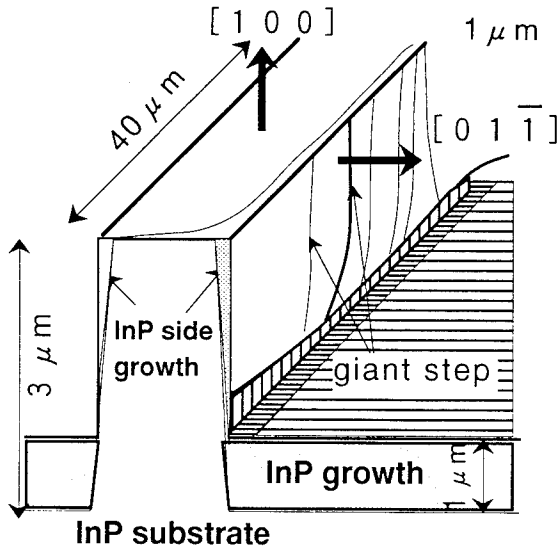
Fig. 1. (a) An SEM photograph of grown crystal facets after CBE growth. The facets were as vertical and smooth as those formed by cleavage. (b) A schematic illustration of the grown crystal facets

Figure 2 also shows an SEM photograph of the sidewall facet with longer length ($>20\mu\text{m}$) along the $[011]$ direction after the CBE growth. White lines observed on the sidewall facet were supposed to be giant crystal steps formed by bunching of atomic steps during the CBE growth. A portion of the facet, however, had no lines of the giant step. It was assumed that so-called step bunching occurred at the portion and crystal growth steps as well as the striations on the sidewall were smoothed out

It was concluded that on the sidewalls with the length of $5\mu\text{m}$ along the $[011]$ direction shown in Fig. 1, the giant step moved to the end of the sidewall as the growth proceeded and the grown facet were atomically smoothed out[3].



(a)



(b)

Fig. 2. (a) An SEM photograph of the $2\mu\text{m}$ wide ridge of which the length along the $[011]$ direction is longer than $20\mu\text{m}$ after CBE growth. (b) A schematic illustration of the grown crystal facets

Proposal of Grown Facets Laser Diodes

Figure 3 shows the proposed structure of a short cavity laser diode with the grown facets used as reflection mirrors, which is named as Grown Facets Short cavity Laser Diode (GFS-LD). The difference between characteristics of the GFS-LD and that without grown facets was estimated. The mirrors of short cavity lasers require a high reflectivity close to 100%, which is realized by high-reflection coats on the mirror surfaces. The scattered loss caused by non-verticality and roughness of etched mirrors is also multiplied by the reflection coats as shown in Fig. 4.

It is estimated that the scattered loss of 3% is induced by even 2 degrees deviation of verticality[4]. The roughness is supposed to also cause the equivalent scattered loss[5]. GFS-LD has ideal mirrors of grown crystal facets with the perfect verticality and the smoothness. There is no scattered loss which effect the characteristics of short cavity laser diode, even if the mirrors are high-reflection coated.

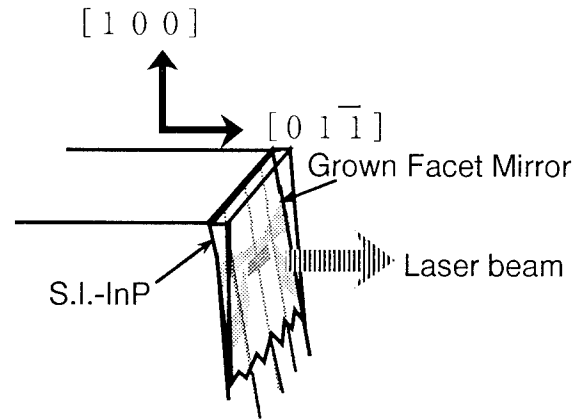


Fig. 3. Proposed structure of Grown Facets Short cavity Laser Diode (GFS-LD). Grown crystal facets are used as reflection mirrors

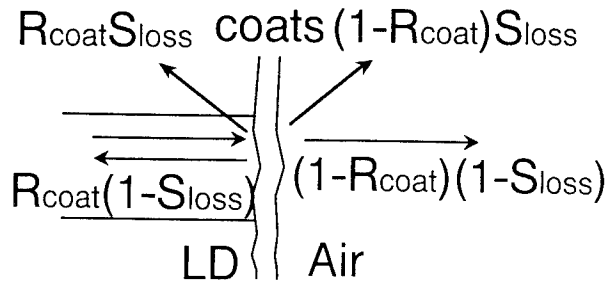


Fig. 4. Scattered loss at a reflection-coated mirror

Characteristics Calculation

The threshold currents of the laser diodes are calculated as a function of the cavity length[6] with a parameter of the reflectivity as shown in Fig. 5. An active layer of the laser is assumed to be normal doublehetero structure. It is supposed that the gain saturates at 1000/cm[7]. The calculation shows that the threshold current for 93% reflectivity is three times larger than that for 99% at a cavity length of 20 μm . This shows that the 6% scattered loss of etched mirrors trebles the threshold current of the short cavity laser diodes.

A calculated external efficiency of light output is also shown in Fig. 5 as a function of the cavity length with a parameter of the reflectivity. The external efficiency for 99% reflectivity increase strikingly with the shortening of the cavity length. The external efficiency for 93% is not improved by the shorting and less than one half of that for 99% in case of 10 μm cavity length.

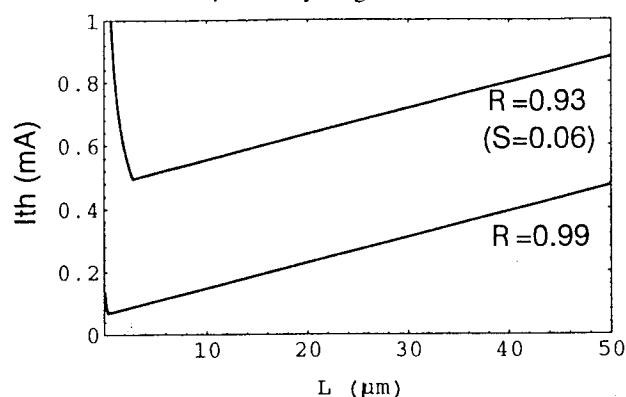


Fig. 5. A calculated characteristic of threshold current as a function of cavity length with the parameter of reflectivity

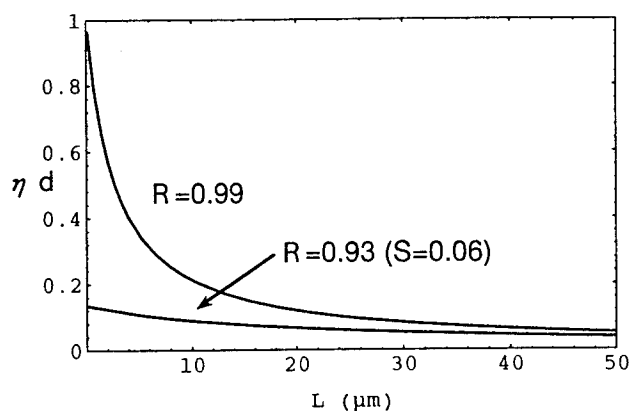


Fig. 6. A calculated characteristic of external efficiency as a function of cavity length with the parameter of reflectivity

The GFS-LD does not have such a scattered loss and the threshold currents of GFS-LDs are able to be reduced to sub-milliamper by shortening cavity length and high-reflection coating.

Device Fabrication

The grown facets were applied to fundamental laser diodes as our preliminary experiment. The grown facets laser diodes with ridge stripe structures were successfully fabricated and oscillated. This revealed that the epitaxy process and the grown facet itself were suited to a laser diode structure.

Conclusion

Crystal facets having no scattering loss are indispensable for the reflection mirrors of short cavity laser diodes. they were successfully fabricated by a novel wafer process of selective epitaxial facet-growth without use of cleavage. Calculation shows that threshold currents of GFS-LDs are reduced to sub-milliamper by shortening the cavity length

Reference

- [1] H. Sugimoto, T. Isu, H. Tada, T. Miura, T. Shiba, T. Kimura, and A. Takemoto, *Journal of Electrochem. Soc.* **140**, pp. 3615-3620 (1993)
- [2] M.Gotoda, H.Sugimoto, S.Maruno, T.Isu, W.Susaki, and M.Nunoshita, *J. Crystal Growth* **145**, pp.675-679 (1994)
- [3] M.Gotoda, H.Sugimoto, S.Maruno, T.Isu, W.Susaki, and M.Nunoshita, *Applied Surface Science* **82/83**, pp.80-84 (1994)
- [4] K.Iga, K.Wakao, and T.Kuniikane, *Applied Optics* **20**, pp. 2367-2371 (1981)
- [5] M.Hagberg, B.Jonsson, and A.Larsson, *J. Vac. Sci. Technol.* **B10**, p.2243-2250 (1992)
- [6] T.Yuasa, T.Yamada, K.Asakawa, M. Ishii, and M.Uchida, *J. Appl. Phys.* **63**, pp.1321-1327 (1988)
- [7] M.Rosenzweig, M.Mohrle, H.Duser, and H.Venghaus, *IEEE J. Quantum Electronics* **QE27**, p.1804 (1991)

InP-Based HEMTs For Microwave And Millimeter-Wave Applications

Phillip M. Smith

Martin Marietta Laboratories
Syracuse, New York 13221

I. Introduction

InP-Based HEMTs have to date demonstrated the best high frequency characteristics of any transistor, including the highest f_t and f_{max} , the lowest noise figures and the highest efficiencies for power amplification. Consequently, much effort is being directed toward the development of these devices for a variety of microwave and millimeter-wave applications where the superior performance of InP HEMT technology is sought despite its relative immaturity at present as compared with GaAs-based devices.

The performance of the InP-based HEMT results directly from the inherent properties of the InAlAs/InGaAs material system, where the high indium content (typically $0.53 \leq x \leq 0.8$) $\text{In}_x\text{Ga}_{1-x}\text{As}$ channel possesses enhanced electron transport properties and the large conduction band discontinuity at the InAlAs/InGaAs hetero-interface permits high two-dimensional electron gas (2 DEG) densities to be obtained.

Previous authors have provided excellent reviews of progress in InP HEMT technology [1], [2]. This paper focuses primarily on the development in our laboratory of InP-based HEMTs for high frequency analog applications, and where possible, our work is placed in the context of the industry at large. Perhaps the single most significant new development reported herein is the increase in device f_{max} to a value of 600 GHz. Our current activity on InP HEMTs is aimed at improving device reliability, developing devices with higher power and efficiency, integrating low noise and power devices into monolithic microwave integrated circuits (MMICs) and improving the producibility of InP HEMT devices and MMICs.

II. Device Structure and Fabrication

In an attempt to optimize the design of the InP HEMT, we have investigated $\text{In}_x\text{Ga}_{1-x}\text{As}$ channels with $x = 0.53$ (lattice-matched) and $0.53 < x \leq 0.75$ (pseudomorphic). Several researchers have reported enhanced DC and high frequency characteristics for pseudomorphic structures [3]-[5]. The highest values of current gain cutoff frequency f_t have been obtained with $\text{In}_{0.80}\text{Ga}_{0.20}\text{As}$ channels [6], [7]. While high f_t is indicative of short transit times and therefore high intrinsic speed, we believe that f_{max} is far more relevant to the performance of microwave transistors because it is defined as the frequency at which power gain, the gain of interest in a high frequency amplifier, goes to unity and

includes important parasitic effects such as gate resistance R_g and feedback capacitance C_{dg} .

In practice, we have observed the highest value of f_{max} , a record 600 GHz as shown in Figure 1, using an $\text{In}_{0.68}\text{Ga}_{0.32}\text{As}$ channel and a double heterojunction epitaxial structure with doped regions both above and below the channel. Not coincidentally, this same device structure has also exhibited the best power-added efficiency and power gain reported to date, as will be described later. In contrast, we find that single-heterojunction lattice-matched InP HEMTs produce the lowest noise figures, consistent with the observations of others who have reported the lowest noise figures for devices with channel indium content ranging from 53 to 60% [5], [8], [9].

Details on our InP HEMT epitaxial layer design, growth and characterization can be found in [10], and the device fabrication process is outlined in [11]. Devices with gate lengths of 0.1 and 0.15 μm and employing the T-shaped gate structure originally reported in [12] have been fabricated.

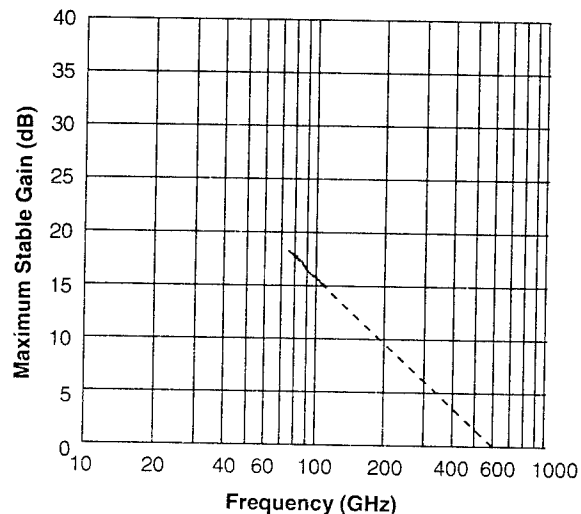


Fig. 1. Maximum stable gain of 0.1 μm x 200 μm InP HEMT, calculated from measured 75-110 GHz S-parameters. An f_{max} of 600 GHz is obtained by extrapolating at -6 dB/octave.

III. Low Noise Performance

Since the superior millimeter-wave noise properties of the InP HEMT first became evident in 1988 [8], the device has attracted considerable attention for high performance receiver applications. We have reported record noise figures of 0.7 dB at 60 GHz [13] and 1.2 dB at 94 GHz [14], and other researchers have achieved comparable results at these frequencies [5], [8]. As shown in Figure 2, InP HEMTs exhibit significantly lower noise figure than GaAs-based InGaAs pseudomorphic HEMTs (PHEMTs). Moreover, their higher associated gain reduces second stage noise contribution, thereby further reducing multistage amplifier noise figure (F_{∞} is a measure of multistage noise figure, and is defined in [14]). Compared with the GaAs-based PHEMT, the InP HEMT allows a reduction of approximately 1 dB in amplifier noise figure at frequencies of 60 and 94 GHz.

Despite reports of further gate length reduction and increased channel indium content [4], [7], the past few years have seen little additional improvement in InP HEMT noise performance. Instead, considerable effort has gone into assessing and improving the reliability of these devices to allow their insertion in practical receiver systems. We have investigated a variety of passivation materials, including polyimide, low temperature (LT) InAlAs [16] and silicon nitride deposited by both PECVD and ECR. We have found that a thin layer of ECR silicon nitride results in the least degradation in InP HEMT DC and high frequency performance [17] and recently reported a passivated 0.1 μm InP HEMT with 0.8 dB noise figure at 60 GHz [18]. Yoshida et al. have reported comparable noise performance with a SiON passivation [9]. As reported in [17], DC life testing of our ECR nitride-passivated InP HEMTs indicates excellent reliability, with median-time-to-failure (MTF) of 10^6 hours at 150°C chip backside temperature and an activation energy of 1.6 eV. Another reliability concern is the apparent sensitivity of InP HEMTs with TiPtAu gate metallization to hydrogen gas which can accumulate in hermetically sealed packages [19], and work is progressing at various laboratories both to modify the device structure to minimize its hydrogen sensitivity and to reduce the hydrogen partial pressure within the package.

Receiver applications employing InP HEMTs include hybrid (MIC) and MMIC amplifiers, operating typically at room temperature but also at cryogenic temperatures for increased sensitivity. We have reported hybrid low noise amplifiers (LNAs) at V- and W-band [14], [20], [21], [22], including a 2-stage amplifier with 1.7 dB noise figure and 17.2 dB gain at 62 GHz and a 3-stage circuit with 3.2 dB noise figure and 17.4 dB gain at 94 GHz. MMIC LNAs have been demonstrated as well. The 3-stage MMIC shown in Figure 3 was designed to cover all of W-band; noise figure is below 5.0 dB with 10.8 ± 1.5 dB gain across the full 75-110 GHz bandwidth, and minimum noise figure is 3.3 dB with 12.6 dB gain at 92.4 GHz [23]. Simulations indicate that MMIC designs with reduced bandwidth centered at 94 GHz should exhibit 2.0 - 2.5 dB noise figure. Cryogenic low noise amplifiers based on InP HEMTs have demonstrated performance competitive with masers and SIS receivers. At 40 GHz and a temperature of 18 K, a 3-stage amplifier containing

Device	18 GHz			60 GHz			94 GHz		
	F_{\min} (dB)	G_a (dB)	F_{∞} (dB)	F_{\min} (dB)	G_a (dB)	F_{∞} (dB)	F_{\min} (dB)	G_a (dB)	F_{∞} (dB)
0.15 μm GaAs PHEMT	0.5	15.1	0.51	1.6	7.6	1.87	1.9	6.1	2.37
0.15 μm InP HEMT	0.3	17.1	0.31	0.9	8.6	1.03	1.4	6.5	1.73
0.1 μm InP HEMT				0.7	8.6	0.80	1.2	7.2	1.44

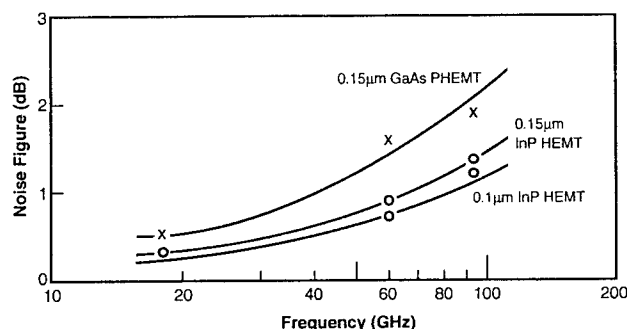


Fig. 2. Best measured room temperature noise performance of InP HEMTs and GaAs PHEMTs produced at Martin Marietta. The fitted curves shown follow the frequency dependence attributed to Fukui [15].

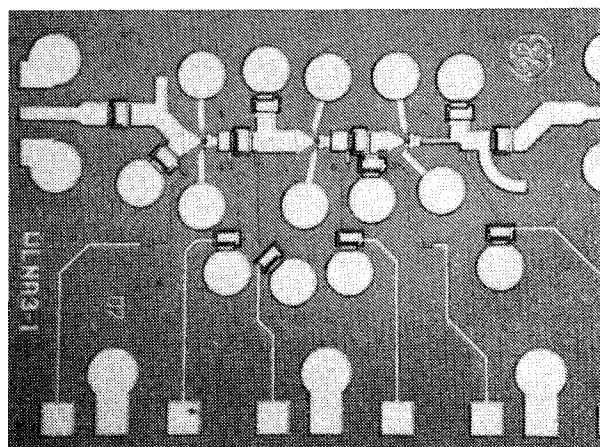


Fig. 3. 3-stage 75-110 GHz low noise MMIC based on 0.1 μm InP HEMT.

one of our InP HEMTs in the first stage has achieved 10.5 K noise temperature [24]. At the same frequency, comparable noise temperatures (10-14 K) have also been reported with devices from other laboratories [25], [26].

IV. Power Performance

Although the superior low noise performance of InP HEMTs is by now widely recognized, the use of InP HEMTs for efficient power amplification has not yet become as widespread. By 1990, InP HEMTs had demonstrated comparable efficiency and higher power gain than GaAs-based PHEMTs, but power density was significantly lower because the breakdown voltage (and hence operating voltage) was limited by the low Schottky barrier height on InAlAs [22]. Primarily through optimization of the epitaxial layer structure, InP HEMTs have progressively improved and present devices exhibit higher power-added efficiencies than GaAs PHEMTs at frequencies of 60 and 94 GHz, as shown in Figure 4 [27]-[30]. A power density of 0.5 W/mm has recently been demonstrated at 60 GHz [29], sufficiently high for applications where the power density must be limited in order to obtain low channel temperatures for high reliability.

InP HEMTs have generated usable levels of output power as well: at 60 GHz, single devices have produced output powers of 192 mW [29] and 155 mW [32]. We have recently developed the multifinger W-band device, shown in Figure 5, which has produced 94 GHz output power comparable to the best reported GaAs PHEMTs with twice the efficiency and 3-4 dB higher power gain, as illustrated in Table 1 [30]. The enhanced power gain is especially significant in that it permits the use of smaller driver stage devices, allowing further increase in multi-stage amplifier efficiency and reduces the number of amplifier stages required, reducing chip size. As InP power HEMTs evolve, their performance will continue to improve. The incorporation of dry-etched via slots under individual source contacts to reduce source inductance, as implemented in the GaAs PHEMTs described in [34], will improve gain and efficiency. MMIC power amplifiers have been reported at 44 GHz [35], [36] and are currently of great interest at 60 and 94 GHz due to the potential for realizing efficient watt-level solid-state transmitters at these frequencies.

Excitement generated by the performance of InP power HEMTs must be tempered by the fact that much work is still needed prior to their insertion into systems. Reliability is largely unknown: there have been no reports of accelerated life testing under RF drive, and DC life testing of low noise InP HEMTs suggests that at a given channel temperature, MTF will be significantly lower (more than an order of magnitude) than that of GaAs PHEMTs [17], [37], probably as a result of the lower MBE growth and ohmic contact alloying temperatures of InP HEMTs. However, the reduced MTF is expected to be offset to some degree by the fact that InP HEMTs will operate at lower channel temperatures than GaAs PHEMTs as a consequence of their higher efficiency and the higher thermal conductivity of the InP substrate as compared with GaAs.

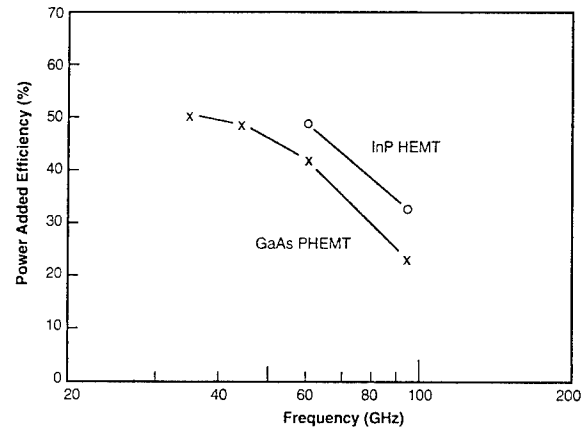


Fig. 4. Highest measured power-added efficiencies of InP HEMTs and GaAs PHEMTs produced at Martin Marietta. InP HEMT data is from [29] and [30], PHEMT data is from [31].

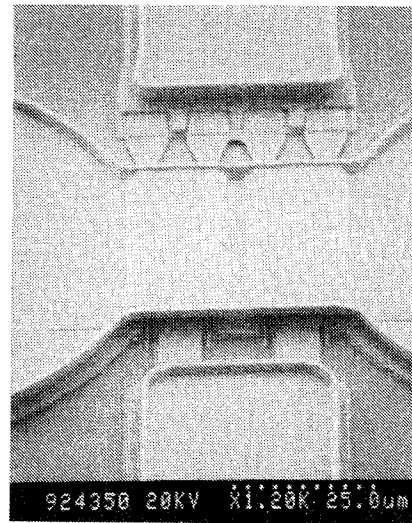


Fig. 5. 0.1 μm gate-length, 200 μm gate-width 94 GHz InP power HEMT. The device is described in detail in [30].

Reference	Device	Gate Width (μm)	94 GHz Performance		
			Output Power (mW)	Power Gain (dB)	Power-Added Efficiency (%)
[29]	0.1 μm InP HEMT	200	54	7.1	31
[30]	0.15 μm GaAs PHEMT	150	45	3.0	16
[32]	0.1 μm GaAs PHEMT	160	63	4.0	13

Table 1. Comparison of 94 GHz performance of the device shown in Figure 5 with previously reported high-power W-band GaAs PHEMTs.

V. Future Trends And Summary

The superior low noise and power performance of InP HEMT technology has been demonstrated. The rate at which this technology can now become mainstream to microwave and millimeter-wave systems will be paced by how rapidly the reliability and manufacturability of InP HEMTs can be advanced. Fabrication techniques such as the selective gate recessing described in [9] will be instrumental in achieving high yield with uniformity, and processes compatible with large wafers (currently 3-inch diameter) must be developed and refined. Although GaAs devices and MMICs will in general be lower in cost than InP devices and MMICs, there are numerous applications for which the enhanced performance of the InP HEMT will make it the technology of choice.

Acknowledgment

The author gratefully acknowledges the many people at Martin Marietta Laboratories in Syracuse, New York who have contributed over the past seven years to the development of InP HEMTs reported in this paper. The support of Drs. Alan Swanson and Walter Butler is also appreciated. Finally, our work has been sponsored in part by NRL under contract N00014-91-C-2063, Rome Laboratory under contract F19628-91-C-0171 and NAWC under contract N60530-92-C-0198.

References

- [1] K. Inoue, "Recent advances in InP-based HEMT/HBT device technology," *4th Int. Conf. On Indium Phosphide And Related Materials*, pp. 10-13, April 1992.
- [2] U.K. Mishra and J.B. Shealy, "InP-based HEMTs: status and potential," *6th Int. Conf. On Indium Phosphide And Related Materials*, pp. 14-17, March 1994.
- [3] U.K. Mishra, A.S. Brown, L.M. Jelloian, M. Thompson, L.D. Nguyen and S.E. Rosenbaum, "DC and RF performance of 0.1 μm gate length $\text{Al}_{0.48}\text{In}_{0.52}\text{As}/\text{Ga}_{0.38}\text{In}_{0.62}\text{As}$ pseudomorphic HEMTs," *IEDM Tech. Dig.*, pp. 180-183, 1988.
- [4] L.D. Nguyen, A.S. Brown, M.A. Thompson, L.M. Jelloian, L.E. Larson and M. Matloubian, "650 Å self-aligned-gate pseudomorphic $\text{Al}_{0.48}\text{In}_{0.52}\text{As}/\text{Ga}_{0.20}\text{In}_{0.80}\text{As}$ high electron mobility transistors," *IEEE Electron Device Lett.*, vol. 13, no. 3, pp. 143-145, March 1992.
- [5] D.C. Streit, K.C. Tan, P.H. Liu, P.D. Chow, J.R. Velebir, R. Lai, T.R. Block, K.S. Stolt and M. Wojtowicz, "MBE growth and characterization of lattice-matched and pseudomorphic InGaAs/InAlAs/InP HEMTs," *4th Int. Conf. on Indium Phosphide and Related Materials*, pp. 682-684, April 1992.
- [6] L.D. Nguyen, A.S. Brown, M.A. Thompson and L.M. Jelloian, "50 μm self-aligned gate pseudomorphic AlInAs/GaInAs high electron mobility transistors," *IEEE Trans. Electron Devices*, vol. 39, pp. 2007-2014, 1992.
- [7] M. Wojtowicz, R. Lai, D.C. Streit, G.I. Ng, T.R. Block, K.L. Tan, P.H. Liu, A.K. Freudenthal and R.M. Dia, "0.10 μm graded InGaAs channel InP HEMT with 305 GHz f_t and 340 GHz f_{max} ," *IEEE Electron Device Lett.*, vol. 15, pp. 477-479, Nov. 1994.
- [8] U.K. Mishra, A.S. Brown, S.E. Rosenbaum, C.E. Hooper, M.W. Pierce, M.J. Delaney, S. Vaughn and K. White, "Microwave performance of AlInAs-GaInAs HEMTs with 0.2 and 0.1 μm gate length," *IEEE Electron Device Lett.*, vol. 9, no. 12, pp. 647-649, Dec. 1988.
- [9] N. Yoshida, T. Kitano, Y. Yamamoto, K. Katoh, H. Minami, H. Takano, T. Sonoda, S. Takamiya and S. Mitsui, "A super low noise V-band AlInAs/InGaAs HEMT processed by selective wet gate recess etching," *IEEE MTT-S Digest*, pp. 645-648, 1994.
- [10] P. Ho, M.Y. Kao, P.C. Chao, K.H.G. Duh, P.M. Smith, P.A. Martin, S.M.J. Liu, K.C. Hwang, J.M. Ballingall, T. Yu and A.W. Swanson, "Materials and device characteristics of InAlAs/InGaAs HEMTs," *Proc. Mat. Res. Soc. Symp.*, vol. 281, pp. 251-267, 1993.
- [11] P.C. Chao, A.J. Tessmer, K.H.G. Duh, P. Ho, M.Y. Kao, P.M. Smith, J.M. Ballingall, S.M.J. Liu and A.A. Jabra, "W-band low-noise InAlAs/InGaAs lattice-matched HEMTs," *IEEE Electron Device Lett.*, vol. 11, no. 1, pp. 59-62, Jan. 1990.
- [12] P.C. Chao, P.M. Smith, S.C. Palmeter and J.C.M. Hwang, "Electron beam fabrication of GaAs low-noise MESFETs using a new tri-layer resist technique," *IEEE Trans. Electron Devices*, vol. ED-32, pp. 1042-1046, June 1985.
- [13] M.Y. Kao, S.M.J. Liu, K.H.G. Duh, P.C. Chao, P. Ho and A.W. Swanson, "A 0.1 μm T-shaped gate InP-based HEMT for low noise application," *4th Int. Conf. on InP and Related Materials*, Paper TUA3, April 1992.
- [14] K.H.G. Duh, P.C. Chao, S.M.J. Liu, P. Ho, M.Y. Kao and J.M. Ballingall, "A super low-noise 0.1 μm T-gate InAlAs-InGaAs-InP HEMT," *IEEE Microwave And Guided Wave Lett.*, vol. 1, no. 5, pp. 114-116, May 1991.
- [15] H. Fukui, "Optimal noise figure of microwave GaAs MESFET's," *IEEE Trans. Elec. Dev.*, pp. 1032-1037, 1979.
- [16] K.C. Hwang, P. Ho, P.C. Chao and K.H.G. Duh, "A novel low-temperature passivation of InAlAs/InGaAs HEMT devices by MBE," *4th Int. Conf. on InP and Related Materials*, pp. 60-62, April 1992.
- [17] K.C. Hwang, A.R. Reisinger, K.H.G. Duh, M.Y. Kao, P.C. Chao, P. Ho and A.W. Swanson, "A reliable ECR passivation technique on the 0.1 μm InAlAs/InGaAs HEMT device," *6th Int. Conf on InP and Related Materials*, pp. 624-627, March 1994.
- [18] M.Y. Kao, K.H.G. Duh, P. Ho and P.C. Chao, "An extremely low-noise InP-based HEMT with silicon nitride passivation," *IEDM Tech. Dig.*, pp. 907-910, 1994.
- [19] P.C. Chao, M.Y. Kao, K. Nordheden and A.W. Swanson, "HEMT degradation in hydrogen gas," *IEEE Electron Device Lett.*, vol. 15, no. 5, pp. 151-153, May 1994.
- [20] K.H.G. Duh, P.C. Chao, P. Ho, M.Y. Kao, P.M. Smith, J.M. Ballingall and A.A. Jabra, "High-performance InP-based HEMT millimeter-wave low-noise amplifiers," *IEEE MTT-S Digest*, pp. 805-808, 1989.
- [21] K.H.G. Duh, P.C. Chao, P. Ho, A. Tessmer, S.M.J. Liu, M.Y. Kao, P.M. Smith and J.M. Ballingall, "W-band InGaAs HEMT low noise amplifiers," *IEEE MTT-S Digest*, pp. 595-598, 1990.

- [22] P.M. Smith, P.C. Chao, P. Ho, K.H.G. Duh, M.Y. Kao, J.M. Ballingall, S.T. Allen and A. Tessmer, "Microwave InAlAs/InGaAs/InP HEMTs: status and applications," *2nd Int. Conf. on InP and Related Materials*, pp. 39-43, April 1990.
- [23] K.H.G. Duh, S.M.J. Liu, M.Y. Kao, S.C. Wang, O.S.A. Tang, P. Ho, P.C. Chao and P.M. Smith, "Advanced millimeter-wave InP HEMT MMICs," *5th Int. Conf. on InP and Related Materials*, pp. 493-496, April 1993.
- [24] M.W. Pospieszalski, NRAO, private communication.
- [25] M.W. Pospieszalski, W.J. Lakatos, R. Lai, K.L. Tan, D.C. Streit, P.H. Liu, R.M. Dia and J. Velebir, "Millimeter-wave, cryogenically coolable amplifiers using AlInAs/GaInAs/InP HEMTs," *IEEE MTT-S Digest*, pp. 515-518, 1993.
- [26] M.W. Pospieszalski, L.D. Nguyen, M. Lui, J. Liu, M.A. Thompson and M.J. Delaney, "Very low noise and low power operation of cryogenic AlInAs/GaInAs/InP HFETs," *IEEE MTT-S Digest*, pp. 1345-1346, 1994.
- [27] M.Y. Kao, P.M. Smith, P.C. Chao and P. Ho, "Millimeter-wave performance of InAlAs/InGaAs/InP HEMTs," *Proc. IEEE/Cornell Conf. on Advanced Concepts in High Speed Semiconductor Devices and Circuits*, pp. 469-477, August 1991.
- [28] K.C. Hwang, P. Ho, M.Y. Kao, S.T. Fu, S.M.J. Liu, P.C. Chao, P.M. Smith and A.W. Swanson, "W-band high power passivated 0.15 μm InAlAs/InGaAs HEMT device," *6th Int. Conf. on InP and Related Materials*, pp. 18-20, 1994.
- [29] P. Ho, P.M. Smith, K.C. Hwang, S.C. Wang, M.Y. Kao, P.C. Chao and S.M.J. Liu, "60 GHz power performance of 0.1 μm gate-length InAlAs/InGaAs HEMTs," *6th Int. Conf. on InP and Related Materials*, pp. 411-414, 1994.
- [30] P.M. Smith, S.M.J. Liu, M.Y. Kao, P. Ho, S.C. Wang, K.H.G. Duh, S.T. Fu and P.C. Chao, "W-band high efficiency InP-based power HEMT with 600 GHz f_{max} ," submitted to *IEEE Microwave And Guided Wave Letters*.
- [31] P.M. Smith, M.Y. Kao, P. Ho, P.C. Chao, A.A. Jabra, K.H.G. Duh and J.M. Ballingall, "A 0.15 μm gate-length pseudomorphic HEMT," *IEEE MTT-S Digest*, pp. 983-986, 1989.
- [32] M. Matloubian, L.M. Jelloian, A.S. Brown, L.D. Ngyuen, L.E. Larson, M.J. Delaney, M. Thompson, R.A. Rhodes and J.E. Pence, "V-band high power AlInAs/GaInAs/InP HEMTs," *IEEE Trans. MTT*, pp. 2206-2210, Dec. 1993.
- [33] D.C. Streit, K.L. Tan, R.M. Dia, J.K. Liu, A.C. Huan, J.R. Velebir, S.K. Wang, T.Q. Trinh, P.D. Chow, P.H. Liu and H.C. Yen, "High-gain W-band pseudomorphic InGaAs power HEMTs," *IEEE Electron Device Lett.*, vol. 12, no. 4, pp. 149-150, April 1991.
- [34] P.M. Smith, D.W. Ferguson, W.F. Kopp, P.C. Chao, W. Hu, P. Ho and J.M. Ballingall, "A high-power, high-efficiency millimeter-wave pseudomorphic HEMT," *IEEE MTT-S Digest*, pp. 717-720, 1991.
- [35] W. Lam, M. Matloubian, A. Kurdoghlian, L. Larson, A. Igawa, C. Chou, L. Jelloian, A. Brown, M. Thompson and C. Ngo, "High-efficiency InP-based HEMT MMIC power amplifier for Q-band application," *IEEE Microwave And Guided Wave Lett.*, pp. 420-422, Nov. 1993.
- [36] W. Lam, M. Matloubian, A. Igawa, C. Chou, A. Kurdoghlian, C. Ngo, L. Jelloian, A. Brown, M. Thompson and L. Larson, "44 GHz high-efficiency InP-HEMT MMIC power amplifier," *IEEE Microwave And Guided Wave Lett.*, vol. 4, no. 8, pp. 277-278, Aug. 1994.
- [37] P.C. Chao, A. Swanson, A. Brown, U. Mishra, F. Ali and C. Yuen, "HEMT devices and circuit applications," in *HEMTs And HBTs*, F. Ali and A. Gupta, Eds., Norwood, MA: Artech House, Inc. 1991.

Low-Noise, High-Speed Ga_{0.47}In_{0.53}As/Al_{0.48}In_{0.52}As 0.1- μ m MODFETs and High-Gain/Bandwidth Three-Stage Amplifier Fabricated on GaAs Substrate

WB2.2

Hans Rohdin, Avelina Nagy, Virginia Robbins, Chung-yi Su,
Chris Madden, Arlene Wakita, Jeff Raggio and Judith Seeger

Hewlett-Packard Co.
P.O. Box 10350
Palo Alto, CA 94303-0867, USA

Abstract

We report on 0.1- μ m-gate Ga_{0.47}In_{0.53}As/Al_{0.48}In_{0.52}As MODFETs fabricated on GaAs substrates by means of the linearly-graded low-temperature buffer-layer (LGLTBL) MBE growth technique. Comparing with control devices on InP substrates we conclude that this is a very promising approach for improved manufacturability with uncompromised performance. GaAs- and InP-substrate MODFETs have a similar combination of maximum current and breakdown voltage. GaAs-substrate MODFETs have lower gate leakage and improved pinchoff. The lower leakage reduces the noise, and on a wafer with low interfacial gate resistance a median minimum noise figure of 0.25 dB at 12 GHz, with 15 dB associated gain, was measured on wafer. High cutoff frequencies are maintained when switching to GaAs substrate, and the g_m -dispersion is reduced. Despite larger dislocation density, mostly contained by the LGLTBL, the FET yield on GaAs appears to be comparable to that on InP. Three-stage amplifiers have been demonstrated with low-frequency gain and bandwidth as high as 33 dB and 20 GHz, respectively.

Introduction

For lattice-matched MODFETs, from a performance standpoint, those on InP are preferable to those on GaAs. InP-based MODFETs have demonstrated lower noise figure, and higher gain and cutoff frequencies [1]. From a manufacturing standpoint, however, GaAs is preferable because of the availability of larger wafers, better robustness, lower cost and established infrastructure. With lattice-mismatched MBE on GaAs, high-performance and lower-cost approaches can be combined. By inserting a linearly-graded low-temperature buffer-layer (LGLTBL) between the GaAs substrate and Ga_{0.47}In_{0.53}As/Al_{0.48}In_{0.52}As MBE device layers, performance comparable to that of lattice-matched control devices on an InP substrate has been demonstrated for both MODFETs and PIN photodetectors [2]. Other buffer-layer approaches (e.g. [3]) have also been successful in achieving basic DC performance comparable to InP-based MODFETs.

In the present paper, we apply the LGLTBL-method to short (0.1 μ m) gate-length MODFETs, and integrate these into an MMIC process. In the following sections we discuss the fabrication, characteristics and performance of the devices and circuit.

Fabrication

The LGLTBL is graded from Al_{0.48}Ga_{0.52}As to Al_{0.48}In_{0.52}As over 1 μ m. While most dislocations are confined to the LGLTBL, the threading dislocation density of the top layers is still large ($<10^7$ cm⁻² in an earlier TEM sample) compared to lattice-matched growth, but we have not seen a significant reduction in device yield.

The layers grown on the LGLTBL are the same as those grown on InP substrates: (1) 0.2- μ m i-Al_{0.48}In_{0.52}As buffer; (2) 125-Å i-Ga_{0.47}In_{0.53}As channel; (3) 20-Å i-Al_{0.48}In_{0.52}As spacer layer; (4) 80-Å n-Al_{0.48}In_{0.52}As supply layer; (5) 100-Å i-Al_{0.48}In_{0.52}As/10-Å i-Ga_{0.47}In_{0.53}As Schottky-barrier layer; (6) 60-Å n-GaAs selective etch layer; and (7) 80-Å n-Ga_{0.47}In_{0.53}As contact layer.

The device fabrication steps are: (1) shallow mesa isolation; (2) non-alloyed ohmic contacts; (3) gate definition in tri-layer resist by electron-beam lithography (EBL) and selective developments [4]; (4) selective dry and/or wet recess; (5) gate deposition/lift; (6) Ta₂N-resistors; (7) first-level interconnect; (8) 1000-Å Si₃N₄ capacitors; and (9) second-level interconnect.

Device Characteristics

In most aspects studied, the GaAs-substrate MODFETs are as good as, or better than, their InP-substrate counterparts. The diode and pinchoff characteristics are improved (Fig. 1). The g_m -dispersion is significantly reduced (Fig. 2), and therefore the somewhat lower DC- g_m does not translate into a lower f_T . In fact, Table I shows larger f_T for the GaAs-substrate MODFETs.

Gate resistance R_g has a large impact on both power gain and noise figure. Typically, extracted values significantly exceed predictions by the classical expression $R_g = r_{ga} W_g / (3N_{gf}^2)$ [5]. r_{ga} is the normalized metallization resistance along the gate finger, W_g the total gate width, and N_{gf} the number of gate fingers. We have found, for our short gate-length devices, that another term, which scales *inversely* with W_g , is significant. This is similar to the case of JFETs where gate *contact* resistance is an

obvious contributor to the total gate resistance. For Schottky-barrier-gate FETs, however, the origin of this term is less obvious. We refer to it as an *interfacial* resistance since a likely origin is a 1-2 monolayer oxide or

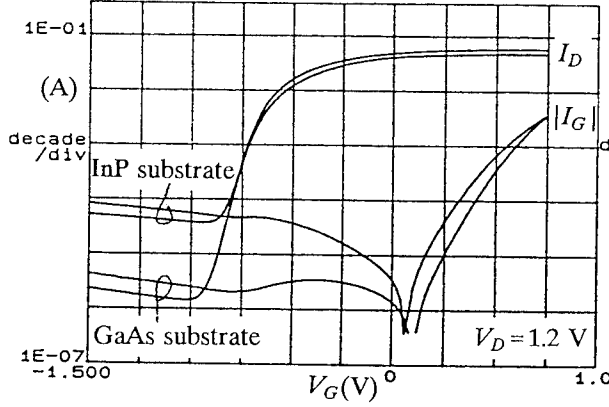


Fig. 1: Gate leakage and drain pinchoff characteristics for 100- μ m MODFETs.

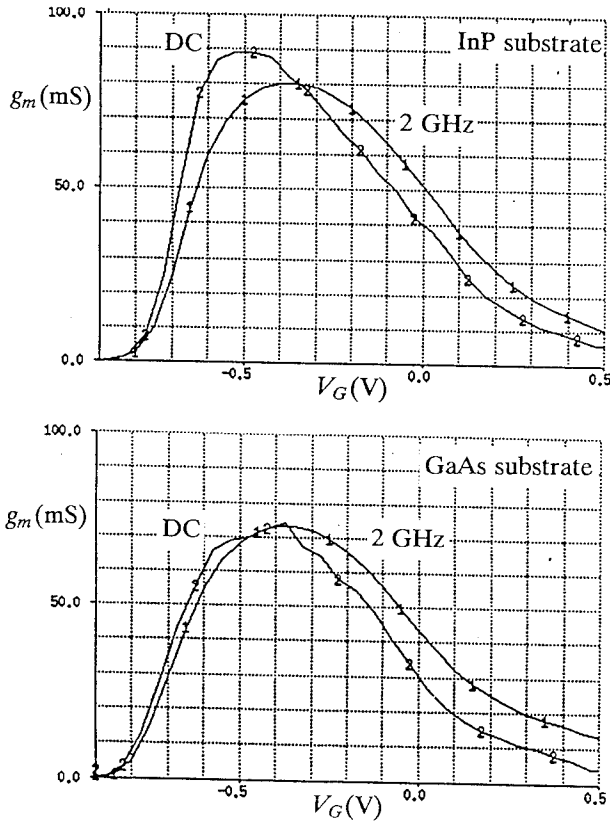


Fig. 2: 0-2GHz $g_m(V_G)$ -dispersion for 100- μ m MODFETs. $V_D = 1.2$ V.

organic residue presenting a tunneling barrier between the metal gate and semiconductor surface states. Such a barrier would result in a mid- $10^{-7} \Omega\text{cm}^2$ interfacial gate resistance* r_{gi} . The new term will then scale inversely also with gate length L_g , for a total gate resistance of

$$R_g = R_{gr} + \frac{r_{ga}W_g}{3N_{gf}^2} + \frac{r_{gi}}{W_gL_g}. \quad (1)$$

R_{gr} represents any residual resistance associated with the gate-feed to the mesa. Another possible origin of the W_g^{-1} term is incomplete metal filling of a small (and relatively deep) gate opening. This would result in a more complicated L_g -dependence.

We estimate R_g for the FET (after converting the measured S-parameters to Y-parameters) from

$$R_g = \frac{\text{Re}[Y_{11}]}{\left(\text{Im}[Y_{11}]\right)^2} - \frac{1}{4\text{Re}[Y_{22}]}, \quad (2)$$

with biases set to zero. The first term represents the total resistance in series with the gate capacitance, and the second term subtracts out the contributions of the source and drain resistances (assumed equal for this zero-bias case). Eqn. (2) is an increasingly accurate direct estimate of R_g as the gated-channel resistance becomes small compared with the ungated access resistances; i.e. for shorter gates, and for gate bias as large as permitted by the requirement of negligible DC gate conductance. We average the right-hand-side of eqn. (2) over ≈ 8 -26 GHz, where the value of $\text{Re}[Y_{11}]$ is large enough to be accurately determined. Fig. 3 shows that the third term on the right hand side of eqn. (1) dominates the second, even for the wider FETs. Overlooking the interfacial gate resistance for short gates like these would lead to an often confusing difference between expected and extracted R_g (e.g. [5]).

In the present comparison, FETs made on GaAs substrates exhibit a lower value of r_{gi} than the control wafer. Together with the lower leakage, this results in better noise performance (Table I), and improved unilateral power gain (Fig. 4). 25% of the improvement in NF_{\min} for the GaAs-substrate MODFETs is due to the lower r_{gi} . The rest is attributed to the much lower leakage. One wafer with circuits (discussed in the next section) had second level interconnect metallization. On this wafer the median minimum noise figure for 200- μ m MODFETs ($N_{gf} = 4$) was 0.25 dB at 12 GHz, with 15 dB

*This would at some frequency (10-100 GHz) be capacitively bypassed.

Table I: 0.1- μ m Ga _{0.47} In _{0.53} As/Al _{0.48} In _{0.52} As Two-Finger MODFETs						
Substrate	FET yield	f_T (GHz) $V_G = -0.4$ V, $V_D = 1.2$ V	r_{ga} (Ω/mm)	r_{gi} (Ωcm^2)	I_G (mA/m) $V_G = -1.0$ V, $V_D = 0$ V	NF_{\min}/G_a (dB) $V_D = 0.75$ V, $I_D = 50$ μ A/m
InP	42/42 = 100%	181 ($\sigma = 8$)	104	$\approx 1 \times 10^{-6}$	≈ 400	0.74/15.1
GaAs	47/48 = 98%	202 ($\sigma = 6$)	82	5×10^{-7}	5.6	0.36/15.2

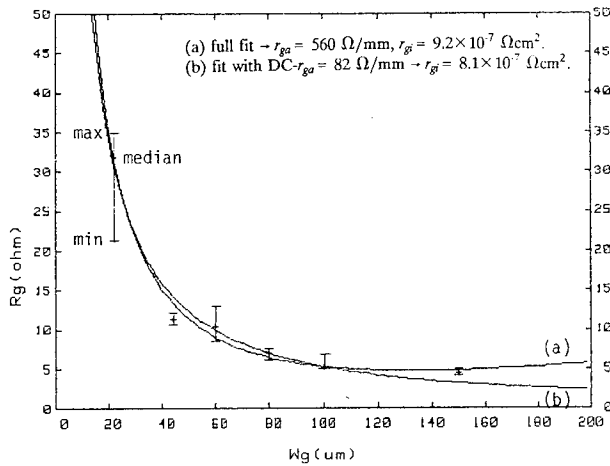


Fig. 3: Gate resistance for two-finger MODFETs on GaAs substrate, versus gate width. The two curves are least-squares fits of eqn. (1) to the median measured values (eqn. (2)). Measurements made on six-finger FETs indicate that fit (b) is more accurate.

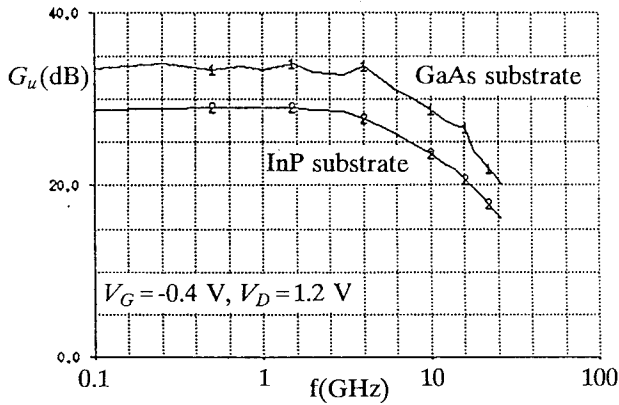


Fig. 4: Mason's unilateral power gain versus frequency for 100-μm MODFETs ($N_{gr}=2$).

associated gain. This noise performance falls on the trend-line for leading-edge low-noise FETs [6].

Fig. 5 shows the maximum drain current $I_D^{(max)}$ versus the breakdown voltage BV_{DS}^G [7] at $I_D=10$ A/m, for 41 wafers (mostly quarters). The 10-A/m definition of BV_{DS}^G was chosen over the typical 1-A/m definition in order to avoid misinterpreting a less-than-ideal pinchoff as a reduction in breakdown voltage. Given the $\approx 10\times$ reduction in L_g (and increase in $I_D^{(max)}$) over the last decades, this appears a prudent redefinition of off-state breakdown, at least for the present analysis. For our typical MODFET, the old definition results in ≈ 4 V lower BV_{DS}^G . Displaying the data as in Fig. 5 reveals an interesting linear correlation between $I_D^{(max)}$ and BV_{DS}^G . This allows fair comparisons between different structures and process approaches, as well as some interesting observations, to be made. First, Fig. 5 shows that the breakdown voltage on GaAs substrate is comparable to

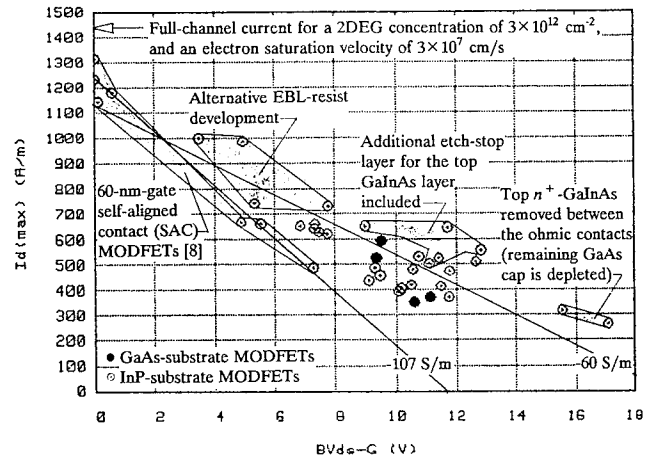


Fig. 5: Drain current $I_D^{(V_G=+0.5V, V_D=V_{DM})}$ versus breakdown voltage $BV_{DS}^G (I_D=10A/m)$, averaged over ≈ 340 mm². FETs are Si_3N_4 -covered. Shaded areas are non-standard as indicated. The -107 S/m straight line is the least-squares fit for the 60-nm-gate SAC MODFETs ($V_{DM}=1V$). The -60 S/m line is the fit to all remaining data; i.e. the 110-nm-gate EBL MODFETs ($V_{DM}=2V$).

that on InP substrate. Second, the y-axis intercepts of the straight-line fits are not far from the expected theoretical maximum full-channel current for these MODFETs. Third, the slope of the fit to the collection of 110-nm-gate EBL-MODFETs is -60 S/m, while for the 60-nm-gate SAC-MODFETs [8], the slope is steeper (-107 S/m). The L_g -dependence, as well as the absolute values, of the slope $dI_D^{(max)}/dBV_{DS}^G$ are similar to those of the output conductance $g_d = \partial I_D / \partial V_D$ [9]. There may be an interesting connection here, since both BV_{DS}^G and g_d are determined by the high-field drain region*. For acceptable BV_{DS}^G , the high fields must be allowed to extend into a surface-depleted ungated drain-side region (e.g. [11]). The surface-depleted region on the source side is the major current limiter, and the equal extent (in our symmetric recess) of this determines where along the $I_D^{(max)} - BV_{DS}^G$ line a data point will fall. This is intentionally demonstrated by the collection of data in Fig. 5 where the top n^+ -GaInAs layer was removed immediately after the ohmic contacts. The spread along the lines in Fig. 5 within each collection of similar devices is due to experiments with etch times, and some irreproducibility due to the lack of a lateral etch stop. Both result in varying extent of the current-limiting surface regions adjacent to the gate.

Three-Stage Feedback Amplifier

Using the GaAs-substrate MODFETs discussed in the previous section we have fabricated 3-stage MMIC

*Zhou *et al.* [10] have proposed that the high g_d in these type of devices is caused by weak impact ionization in the channel, a mechanism that would affect BV_{DS}^G .

amplifiers. The design (Fig. 6) is very similar to that in [12], but the FET widths and feedback resistances are twice as large, resulting in increased low-frequency gain and decreased bandwidth. Neither change was done as a result of a device-specific design optimization. In fact, the layout was made somewhat generically early in the project, before the particular process used here had been developed. Nevertheless, the performance is quite good. The frequency-dependence of S_{21} in Fig. 7 shows a low-frequency gain of 33 dB and a bandwidth of 20 GHz. The peaking at 27-35 GHz is due to the non-optimized interstage transmission-line matching. At 50 GHz the gain is 8 dB. In terms of gain-bandwidth product, the present circuit (890 GHz) compares well with the InP-based amplifier in [12] (500 GHz).

Conclusions

Our results confirm that InP-type MODFETs can be fabricated, without loss of performance, on GaAs substrates, also when gate lengths are pushed to the present practical manufacturing limit of 0.1 μm . This good fortune, made possible by the MBE buffer growth technique, extends to the noise performance as well. Preliminary comparisons indicate that the MODFET reliability is no worse on GaAs substrate. The good yield and uniformity of the devices have allowed us to fabricate what we believe is the first reported MMIC circuit using InP-type devices grown on GaAs. The demonstrated combination of microwave, noise and circuit performance, together with the potential for improved manufacturability, make this technology very promising.

References

- [1] U.K. Mishra and J.B. Shealy, "InP-Based HEMTs: Status and Potential", Proc. 1994 IPRM, p. 14.
- [2] A. Fischer-Colbrie, G.G. Zhou and G. Hasnain, "High Quality $\text{In}_{0.53}\text{Ga}_{0.47}\text{As}/\text{In}_{0.52}\text{Al}_{0.48}\text{As}$ MODFETs and PINs Grown on GaAs Substrates", 1993 EMC, paper A4.
- [3] K. Higuchi, M. Kudo, M. Mori and T. Mishima, "First High Performance InAlAs/InGaAs HEMTs on GaAs Exceeding That on InP", Tech. Dig. 1994 IEDM, p. 891.
- [4] A.S. Wakita, C-Y. Su, H. Rohdin, H-Y. Liu, A. Lee, J. Seeger and V.M. Robbins, "A Novel High Yield Trilayer Resist Process for 0.1 μm T-gate Fabrication", submitted for publication.
- [5] Y. Umeda, T. Enoki, K. Arai and Y. Ishii, "Silicon Nitride Passivated Ultra Low Noise InAlAs/InGaAs HEMT's with n^+ -InGaAs/ n^+ -InAlAs Cap Layer", IEICE Trans. Electron., vol. E75-C, p. 649, 1992.
- [6] L.D. Nguyen, L.E. Larson and U.K. Mishra, "Ultra-High-Speed Modulation-Doped Field-Effect Transistors: A Tutorial Review", Proc. IEEE, vol. 80, p. 494, 1992.

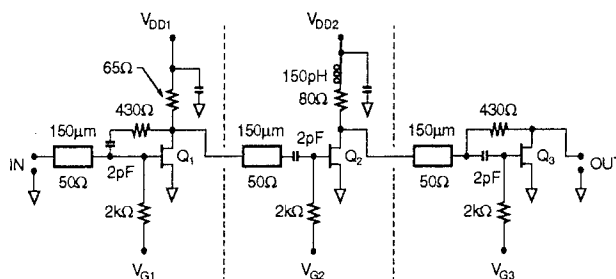


Fig. 6: Three-stage feedback amplifier circuit. The FETs are 200 μm wide ($N_{gf}=4$).

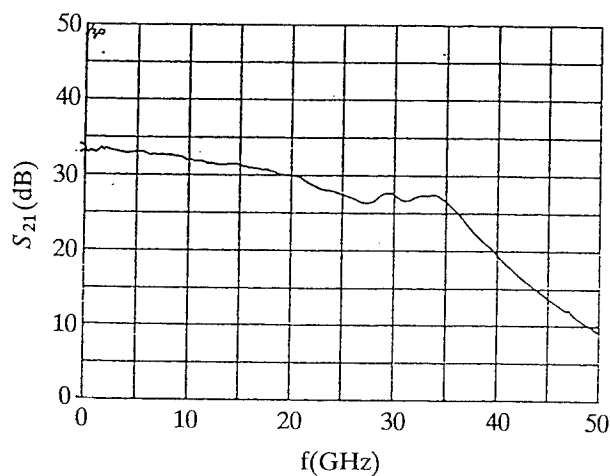


Fig. 7: Gain vs. frequency for the 3-stage amplifier.

- [7] S.R. Bahl and J.A. del Alamo, "A New Drain-Current Injection Technique for the Measurement of Off-State Breakdown Voltage in FET's", IEEE Trans. Electron Devices, vol. 40, p. 1558, 1993.
- [8] H. Rohdin and A. Nagy, "A 150 GHz Sub-0.1- μm E/D MODFET MSI Process", Tech. Dig. 1992 IEDM, p. 327.
- [9] J. Braunstein, P.J. Tasker, A. Hulsmann, K. Kohler, W. Bronner, M. Schlechtweg, " G_{ds} and f_T Analysis of Pseudomorphic MODFETs with Gate Lengths down to 0.1 μm ", GaAs and Rel. Comp., 1993.
- [10] G.-G. Zhou, A. Fischer-Colbrie, J. Miller, Y.-C. Pao, B. Hughes, L. Studebaker and J.S. Harris, Jr., "High Output Conductance of InAlAs/InGaAs/InP MODFET due to Weak Impact Ionization in the InGaAs Channel", Tech. Dig. 1991 IEDM, p. 247.
- [11] H. Daembkes, J. Dickmann, A. Wiersch and H. Kunzel, "Depleted Surface Layer AlInAs/GaInAs/InP HFETs", Proc. 1991 IEEE/Cornell Conf. on Advanced Concepts in High Speed Semiconductor Devices and Circuits, p. 198.
- [12] C.J. Madden, R.L. Van Tuyl, M.V. Le and L.D. Nguyen, "A 17dB Gain, 0.1-70GHz InP HEMT Amplifier IC", Dig. Tech. 1994 ISSCC, p. 178.

60 GHz Monolithic LNA Utilizing High-Speed InAlAs/InGaAs/InP HEMTs and Coplanar Waveguides

WB2.3

M. Berg, J. Dickmann, W. Bischof, S. Koßlowski, and P. Narożny

Abstract— A monolithic two-stage low noise amplifier (LNA) on InP substrate is presented. Coplanar Waveguides and lumped elements are used for the matching and biasing networks. The circuit is fully passivated and contains common ports for the gate and the drain bias. The total chip size is $2\text{ mm} \times 1\text{ mm}$. A gain of 15 dB and an input and output matching better than -8 dB were achieved at 60 GHz.

I. INTRODUCTION

MODERN communication and sensor systems need low noise amplifiers with high gain in the receiver part of front-end circuits. Amplifier circuits presented so far [1], [2], [3] have shown the excellent opportunities of microwave and millimeter-wave monolithic integrated circuits (MMICs) based on InP substrate in combination with coplanar waveguides. Furthermore the best high speed and low noise performance of any type of transistor up into the millimeter-wave range has been demonstrated by unpassivated InAlAs/InGaAs HEMTs [4], [5]. Therefore this type of device is very attractive for such kind of system application.

While mostly microstrip lines (MSLs) are used in MMICs as the transmission media, coplanar waveguides (CPWs) are now becoming an interesting alternative. This is due to the following reasons. Commercial applications need a low cost technology (less time consuming fabrication) which can be provided by using CPWs. CPW circuits are easier to fabricate (no substrate thinning, no back-side metallization) and they show a better electric behaviour (lower grounding parasitics, lower dispersion). There is also no need for via holes,

because the required ground connections are realized by a low inductive airbridge technology. Another advantage is that single device fabrication and CPW-MMIC process sequences are identical, which makes redevelopment or recalculation of discrete devices characterized on wafer for the use in MMICs unnecessary.

II. LAYER STRUCTURE AND CIRCUIT FABRICATION

The active devices are realized in the lattice matched InAlAs/InGaAs/InP material system. The layer structures are grown with MBE and the layer sequence is given in Table I. We use the surface depleted cap layer concept [6] which leads to a very low feedback capacitance C_{GD} and therefore to a low feedback amplification.

The circuit fabrication process is designed in order to meet the requirements for low cost fabrication, i.e. fast throughput, reduced number of mask levels and more relaxed gate dimensions. The circuit fabrication starts with the device isolation which was done by mesa etching using a wet chemical solution. To avoid a conducting path between the gate feed and the InGaAs channel region we

TABLE I
LAYER STRUCTURE USED FOR THE LNA

20 nm	In _{0.53} Ga _{0.47} As	surface depleted
20 nm	In _{0.53} Ga _{0.47} As	$5 \times 10^{17}\text{ cm}^{-3}$ (Si)
20 nm	In _{0.52} Al _{0.48} As	undoped
	δ -Doping Pulse	$5 \times 10^{12}\text{ cm}^{-2}$ (Si)
2 nm	In _{0.52} Al _{0.48} As	undoped
40 nm	In _{0.53} Ga _{0.47} As	undoped
4 nm	In _{0.52} Al _{0.48} As	undoped
4 nm	In _{0.53} Ga _{0.47} As	undoped
250 nm	In _{0.52} Al _{0.48} As	undoped
4 nm	In _{0.53} Ga _{0.47} As	undoped
4 nm	In _{0.52} Al _{0.48} As	undoped
400 μm	InP Substrate	semi-insulating

M. Berg, J. Dickmann, S. Koßlowski, and P. Narożny are with Daimler-Benz AG, Research Center Ulm, Wilhelm-Runge-Straße 11, D-89081 Ulm, Germany

W. Bischof is with ANT Nachrichtentechnik GmbH, Bosch Telecom, Gerberstraße 33, D-71522 Backnang, Germany

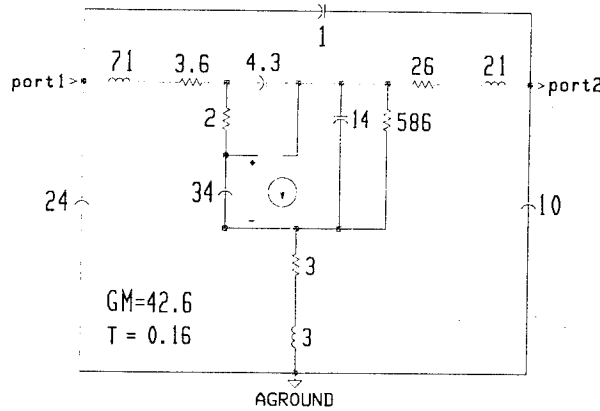


Fig. 1. Small-signal equivalent circuit model for the $0.25 \mu\text{m} \times 60 \mu\text{m}$ InP-HEMT (Resistance unit = Ω , Transconductance unit = mS, Inductance unit = pH, Capacitance unit = fF, Time unit = ps).

use a material selective wet etchant to form an undercut of the InGaAs channel in reference to the InAlAs layers. The ohmic contacts were formed by an AZ image reversal process and the metallization was evaporated Ge/Ni/Au. In order to have an easier and less cost intensive gate process we use quarter micron gates realized with a three layer process consisting of an AZ bottom layer, a germanium intermediate layer and a PMMA top resist. After e-beam exposure of the PMMA layer the gate pattern is transferred into the subsequent layers via an RIE process. The gates have a Ti/Pt/Au metallization and a triangular cross sectional area. For gate recessing we use a material selective etchant.

The ground planes of the MIM-capacitors were defined at the same time as the gate electrodes by e-beam. Therefore we need no extra mask for this process step. For the thin film NiCr resistors we use a sputter process. After that the complete wafer is passivated with a Si_3N_4 layer which is also used as the insulator of the MIM capacitors. After opening of the contact windows through the Si_3N_4 we use a two mask process to form the transmission lines (TMLs), the airbridges for the interconnections and the top electrodes of the MIM-capacitors. $3 \mu\text{m}$ thick sputtered and electroplated gold was used for the metallization.

III. DEVICE AND CIRCUIT MODELING

To provide the design base, single HEMT devices with different gate widths and different layouts were fabricated in separate wafer runs. The

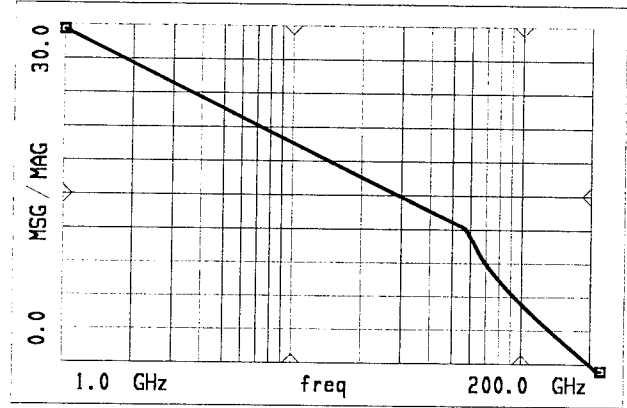


Fig. 2. Small-signal power gain (MSG/MAG) of the $0.25 \mu\text{m} \times 60 \mu\text{m}$ common-source InP-HEMT.

devices are fully passivated and have a coplanar design for on-wafer probing to ensure that the characterization was performed in the CPW environment. Both DC and RF parameters of the different devices were measured and were used in developing device small-signal equivalent circuit models. Typical DC transconductances of the devices are $g_m = 600 \text{ mS/mm}$ and the maximum saturation currents are $I_{DS} = 450 \text{ mA/mm}$.

The RF characterization and the modeling of the devices were based on S-parameter measurements between 0.5 GHz and 26.5 GHz using a network analyzer and an on-wafer probe set. The small-signal modeling was performed with the *Microwave and RF Design System*® software package from Hewlett-Packard.

One difficulty designing an MMIC circuit operating at a frequency far above which has been used to extract the small-signal equivalent circuit (SEC) is the accuracy of the SEC to predict the device performance at higher frequencies. The problems are that at higher frequencies the device behaviour changes from conditional stable to unconditional stable imposing different demands on the matching circuits to be used. Another problem of same importance is, that the gain drops much faster than -20 dB/decade beyond the frequency where $K > 1$ (Fig. 2). Hence it is important to have a precise enough circuit description of the device. According to this requirement we use a SEC with 16 elements as shown in Fig. 1. The parasitic elements of the equivalent circuit have been determined by DC measurements and independent RF measurements on special test structures and passive device layouts. So, for example, the gate resistance

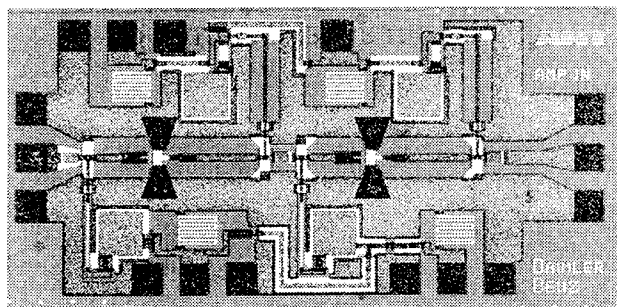


Fig. 3. Photograph of the V-Band LNA chip. The chip dimensions are $2\text{ mm} \times 1\text{ mm}$.

R_G , which has got a strong impact on f_{\max} , has been determined by measurements at microwave frequencies using a special gate end-to-end structure. The given values of the equivalent circuit are related to the active devices used inside the amplifier circuit. These FETs have a two finger U-layout with a gate width of $2 \times 30\text{ }\mu\text{m}$.

Fig. 2 shows the calculated gain (MSG/MAG) as a function of frequency. The current gain cutoff frequency is calculated to be $f_T = 95\text{ GHz}$ and the power gain cutoff frequency is $f_{\max} = 198\text{ GHz}$. The device is stable ($K > 1$) for frequencies above 60 GHz .

The MMIC circuit is a two-stage amplifier design. The two identical single stages are cascaded through a short intermediate line. The simulation of the LNA started with ideal passive elements. After a first optimized result has been achieved, these ideal passive elements (MIM-capacitors, T-junctions, airbridges) were redefined by including additional elements representing parasitics with increasing number of design iterations.

The metal thickness of the plated gold was chosen so that the impact of losses due to the skin effect is at a minimum. The chip was designed using the shortest length of the TMLs possible in order to minimize the total chip size and reduce the loss of each line. For a typical $50\text{ }\Omega$ CPW with a line width of $w = 20\text{ }\mu\text{m}$, a slot width of $w = 17\text{ }\mu\text{m}$ and a metallization thickness of $3\text{ }\mu\text{m}$ we measured an attenuation coefficient of $\alpha \leq 0.4\text{ dB/mm}$ at 60 GHz . The advantage for the designer of such a approach is that the simulation can be done using lossless ideal physical TMLs.

To avoid losses inside the matching subcircuits only reactive LC-networks were used as input and output transformers. The inductances are represented by sections of CPW lines and the

capacitances are realized with MIM-capacitors. Three types of CPWs with different characteristic impedances ($50\text{ }\Omega$, $70\text{ }\Omega$ and $80\text{ }\Omega$) and different geometrical dimensions were used for the amplifier. The $80\text{ }\Omega$ lines have a reduced size and therefore a higher loss and are only used inside the biasing networks. For the stage separation and for the biasing and matching networks we use MIM capacitors and thin film NiCr resistors. Additional capacitors and resistors are used to protect the circuit against electrostatic discharge. Fig. 3 shows a microphotograph of the fabricated InP MMIC.

IV. RESULTS

The circuit was measured on-wafer between $f = 45\text{ GHz}$ to $f = 75\text{ GHz}$. The measured S-parameters as a function of frequency are shown in Fig. 4 and 5. The amplifier chip was biased at $V_{DS} = 2\text{ V}$, $V_{GS} = +0.4\text{ V}$ and $I_{DS} = 44\text{ mA}$. Over the entire measurement frequency range the amplifier was unconditionally stable ($K > 1$). Between $f = 52\text{ GHz}$ and $f = 64\text{ GHz}$ the input and output matching is better than -8 dB . Over the frequency band of $f = 45\text{ GHz}$ to $f = 65\text{ GHz}$ the amplifier shows a gain of $|S_{21}| > 14\text{ dB}$ with a peak value of $|S_{21}| = 15.2\text{ dB}$ at 60 GHz .

The simulated S-parameters are shown in Fig. 4 and 5 as smaller lines for comparison. From Fig. 4 one can see that a large difference between simulated and experimental data occurs for S_{11} . The reason for that has not yet been found. For the other S-parameters there is a good correlation between measured and simulated results especially for S_{21} , which demonstrates that the SEC-description and the circuit design strategy are appropriate.

V. CONCLUSION

We have reported a two stage V-band single chip InP amplifier. We used a very conventional device technology including $L_G = 0.25\text{ }\mu\text{m}$ gates with a triangular cross sectional area and coplanar waveguides as the transmission media. Therefore we needed no substrate thinning, no backside metallization and no via-holes which led to a low cost circuit fabrication.

Good agreement between measured and simulated data verifies both the HEMT and the circuit modeling. The amplifier reaches a gain of 15 dB and an input and output matching better than

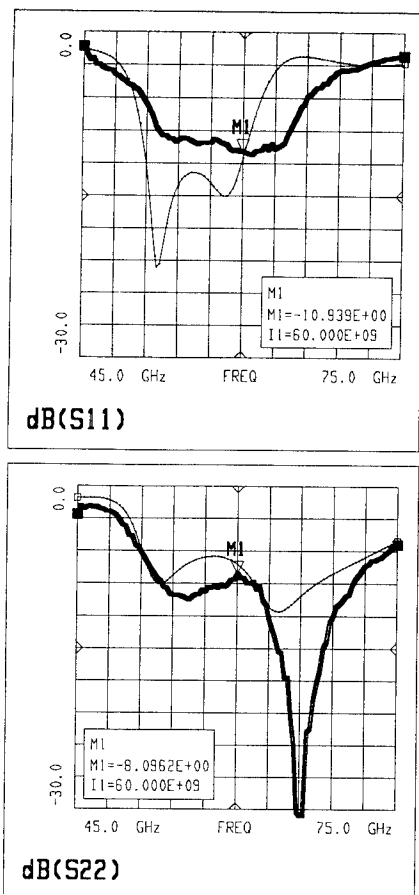


Fig. 4. Measured and simulated input (S_{11}) and output (S_{22}) return loss as a function of frequency.

-8 dB at 60 GHz. To our knowledge this is the first CPW-V-band amplifier realized on this material system and is comparable to the best published values for such a circuit [7].

REFERENCES

- [1] J. Dickmann et. al., "High Gain 28 GHz Coplanar Waveguide Monolithic Amplifier on InP Substrat", *Electronics Letters*, Vol. 29, No. 5, p. 493, 1993
- [2] D.J. Newson et. al., "39 GHz Monolithic Coplanar Waveguide Amplifier Using Doped Channel HFET Technology on InP", *Electronics Letters*, Vol. 29, No. 13, p. 1177, 1993
- [3] Y. Umeda et. al., "Sensitivity Analysis of 50 GHz MMIC-LNA on Gate Recess Depth with InAlAs/InGaAs/InP HEMTs", *IEEE MTT-S Digest*, p. 123, 1994
- [4] P. Ho et. al., "Extremely high gain 0.15 μ m gate-length InAlAs/InGaAs/InP HEMTs", *Electronics Letters*, Vol. 27, No. 4, p. 325, 1992
- [5] L.D. Nguyen et. al., "50-nm Self-Aligned-Gate Pseudomorphic AlInAs/GaInAs High Electron Mobility Transistors", *IEEE Transactions on Electron Devices*, Vol. 39, No. 9, p. 2007, 1992
- [6] J. Dickmann et. al., "Influence of Surface Layers on the RF-Performance of AlInAs-GaInAs HFETs", *IEEE Mi-*

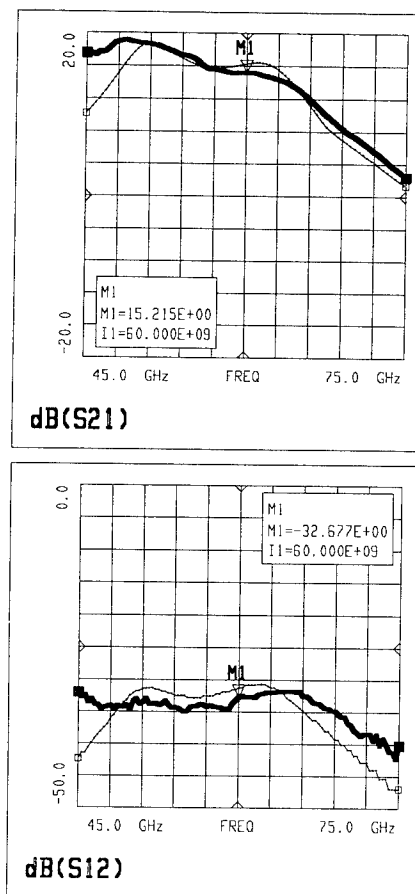


Fig. 5. Measured and simulated forward (S_{21}) and feed-back (S_{12}) transmission as a function of frequency.

crowave and Guided Wave Letters, Vol. 2, No. 11, p. 472, 1992

- [7] R.T. Webster et. al., "Monolithic InP HEMT V-Band Low-Noise Amplifier", *IEEE Microwave and Guided Wave Letters*, Vol. 2, No. 6, p. 236, 1992

0.1- μm InAlAs/InGaAs HEMTs WITH AN InP-RECESS-ETCH STOPPER GROWN BY MOCVD

WB2.4

Takatomo Enoki, Hiroshi Ito, Kenji Ikuta and Yasunobu Ishii
NTT LSI Laboratories

3-1 Morinosato Wakamiya, Atsugi-Shi, Kanagawa Pref., 243-01, Japan

Introduction

Monolithic analog ICs using extremely high-performance InP-based HEMTs that operate up to the millimeter-wave frequency range have been reported recently [1], [2], but the difficulty of controlling the threshold voltage of these HEMTs restricts their applications to analog circuits. To use them in ultra-high-speed digital ICs, the gate-recess depth, doping density, and layer thickness need to be precisely controlled. Recent epitaxial technologies meet the latter two requirements, but controlling gate-recess depth has remained a problem. When the gate length is shortened to improve the device performance, the layer thicknesses become thinner according to the scaling law, and consequently the process margin in the gate recess becomes narrower. The control of the gate-recess depth in GaAs-based HEMTs has been improved by using a selective dry etching of GaAs to AlGaAs or GaInP [3]. For InP-based HEMTs, however, the dry etching selectivity of InGaAs over InAlAs is not high enough to stop the gate recess at the InGaAs/InAlAs interface. Moreover, it is necessary to stop the gate recess in the InAlAs barrier when we use a non-alloyed ohmic cap structure [4]. To overcome this difficulty in manufacturing InP-based HEMTs, InP- and GaInP-recess-etch stoppers have been demonstrated [5], [6], but there have been no reports of devices which is applicable to ultra-high speed ICs. In this paper, we therefore report that high performance and uniform 0.1- μm -gate InAlAs/InGaAs HEMTs suitable for use in ultra-high speed digital ICs can be made by using an InP-recess-etch stopper and a wet etching.

Device Structure and Fabrication Process

Figure 1 shows an HEMT structure grown by MOCVD at 600 °C on a (001) InP substrate. The epitaxial structure consists of a 1700-Å-thick InAlAs buffer, a 120-Å-thick InGaAs channel, a 25-Å-thick InAlAs spacer, a Si- δ -doped plane, a 50-Å-thick InAlAs Schottky barrier, a 40-Å-thick InP-recess-etch stopper, and n^+ -InAlAs/ n^+ -InGaAs cap layers. All materials are lattice-matched to the InP substrate. The doping density of the cap layers is $1 \times 10^{19} \text{ cm}^{-3}$ and the sheet doping density of the δ -doped plane is nominally $4 \times 10^{12} \text{ cm}^{-2}$. The distance between the gate and the channel is 115 Å. Although the undoped InAlAs contains n-type background impurity with a densities on the order of 10^{16} cm^{-3} , the 1700-Å-thick buffer layer is fully depleted and there is no conducting path there.

We also fabricated, by MBE, InAlAs/InGaAs HEMTs without a recess-etch stopper [4] and compared the

characteristics of the MOCVD-based and MBE-based HEMTs.

The fabrication process for the MOCVD-based HEMTs was the same as that for the MBE-based HEMTs [4] except for device isolation. Gate and ohmic electrodes were formed by a liftoff technique and consisted of Ti/Pt/Au metals. SiN was used as a passivation film. The contact resistance of the non-alloyed ohmic electrode was reduced by the n^+ -InAlAs layer under the n^+ -InGaAs cap layer [4]. The sheet resistance of all layers and the ohmic contact resistance were $115 \text{ } \Omega/\text{sq.}$ and $0.07 \text{ } \Omega \cdot \text{mm}$, and there was no indication that the InP-recess-etch stopper degraded the contact resistance.

Mesa isolation for the MOCVD-based HEMTs was achieved by wet etchings using a mixture of citric acid and hydrogen peroxide [7] for the InGaAs and InAlAs layers and a mixture of hydrochloric acid, phosphoric acid, and acetic acid [8] for the InP-recess-etch stopper. The etching selectivity of the citric-acid-based solution between InAlAs and the inserted InP was measured to be over 400. Figure 2 shows the surface of the InP-recess-etch stopper revealed by the citric-acid-based etching. The image was obtained by an atomic force microscopy (AFM). The roughness standard deviation for a $5 \times 5 \text{ } \mu\text{m}^2$ area is only 1.7 Å, and atomic-layer terraces about 3000-Å wide are clearly seen. The surface roughness of the MBE-based HEMTs was measured to be 2.8 Å but no very clear atomic-layer terraces were observed. The image and the roughness value shown in Fig. 2 suggest that the layer thickness under the recessed area is atomically uniform. This atomically flat surface is attributed to the abruptness of the InP/InAlAs interface in the MOCVD growth and to the high selectivity for InAlAs over InP in the gate-recess etching. This is one of the essential advantages of an InP-based material system.

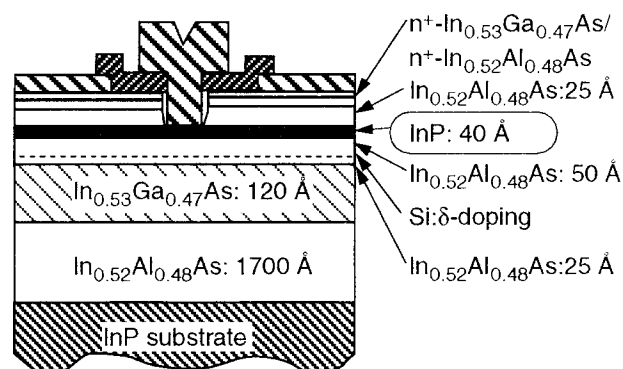


Figure 1. Structure of an InAlAs/InGaAs HEMT with an InP recess-etch stopper

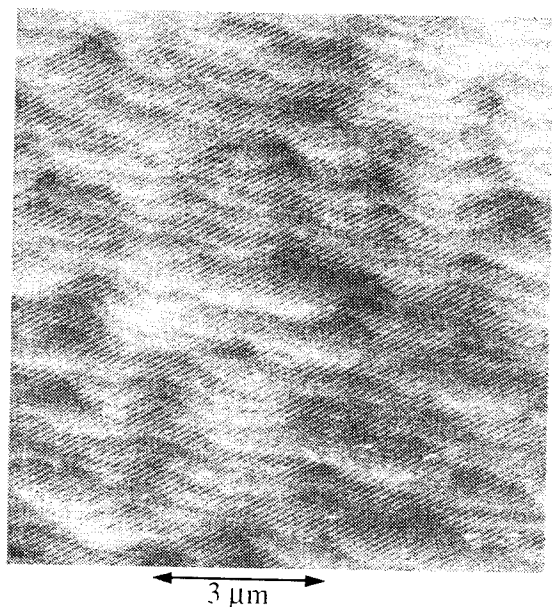


Figure 2. AFM surface image of the InP-recess-etch stopper revealed using a citric-acid based solution. The contrast range is 12.5 Å.

Device Characteristics

Figure 3 compares the typical I-V characteristics for the 0.1-μm-gate MOCVD-based HEMT with the InP-recess-etch stopper with those of a MBE-based HEMT. The transconductance (g_m) of each device is 1000 mS/mm and the devices have similar breakdown voltages; 4.5 V for the off-state and 3 V for the on-state, respectively. Drain conductance (g_d) at drain biases of 1 and 2 V for the MOCVD-based HEMT is respectively 51 and 28 mS/mm, and the g_m/g_d ratio is over 20 throughout the saturation region. For drain biases of 1 and 2 V the g_d 's for the MBE-based HEMT are respectively 71 and 59 mS/mm, or about twice those for the MOCVD-based HEMT. Two

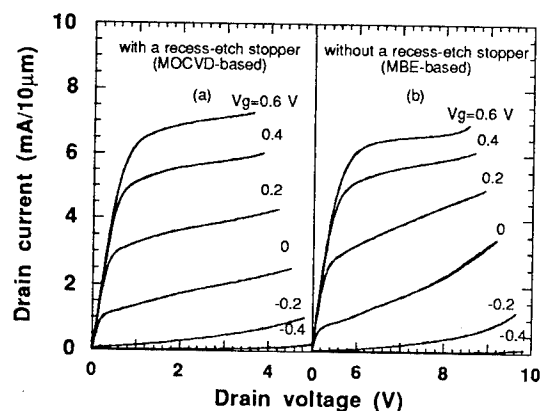
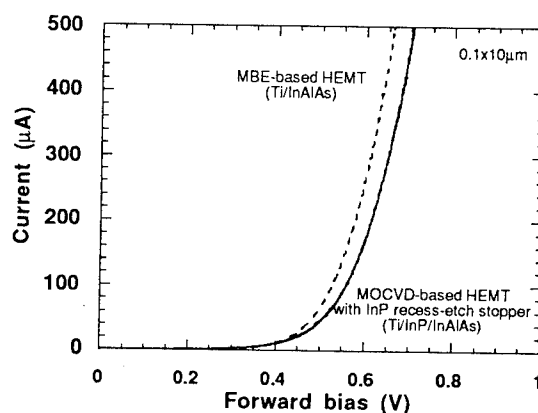


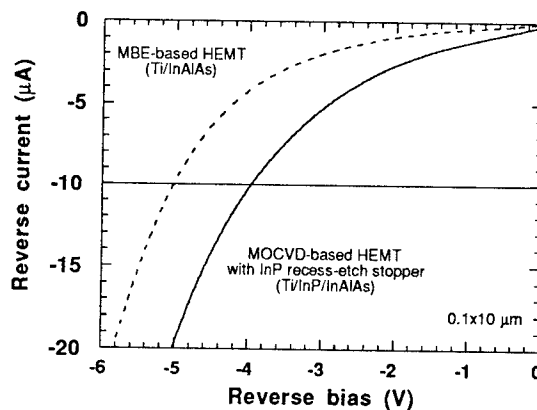
Figure 3. I-V characteristics of InAlAs/InGaAs HEMT with a 0.1 x 10-μm gate: (a) MOCVD-based HEMT with an InP-recess-etch stopper, (b) MBE-based HEMT without a recess-etch stopper

possible reasons for the smaller g_d for a MOCVD-based HEMT were considered. One is the longer effective gate length due to the longer side etching in the gate recess, which results from an over-etching caused by the recess-etch stopper. The other is the relatively higher background impurities in the InAlAs buffer grown by MOCVD, which suppress hole accumulation or the parasitic bipolar effect near the breakdown voltage. Because of the high-frequency performance of the device obtained as shown below, however, the former was discounted as a possibility.

The Schottky characteristics of these gates at forward bias are shown in Fig. 4(a). As can be seen in the figure, the difference in turn-on voltage is quite small between them despite the lower Schottky barrier height of InP. Since the conduction band of the InAlAs barrier is higher than that of the InP-recess-etch stopper by ΔE_c , the gate current is governed by the InAlAs barrier rather than the InP-recess-etch stopper. In contrast to the characteristics at forward biases, as shown in Fig. 4(b), the gate current at reverse bias is higher for the gate with the InP-recess-etch stopper than that for the InAlAs gate. At reverse biases the conduction band of the InAlAs barrier is lower than that of the InP-recess-etch stopper, and the leakage current,



(a)



(b)

Figure 4. Gate current dependence on gate bias of 0.1-μm-gate MOCVD-based and MBE-based HEMTs.

therefore, is dominated by the lower Schottky barrier height of InP. We think, however, that, the leakage current is still low enough for applications in digital ICs.

Although the InP-recess-etch stopper introduces an additional interface under the gate, the thin InP passivates the InAlAs surface at the periphery of the gate. To investigate the impact on the surface, we measured the low-frequency noise of the devices at room temperature. Equivalent input-noise spectra for the devices with and without an recess-etch stopper are plotted in Fig. 5, which shows that there is no significant difference in the low-frequency noise of the devices.

Figure 6 shows distributions of current gain cutoff frequencies (f_T) and maximum oscillation frequencies (f_{max}) of 0.1- μ m-gate MOCVD-based HEMTs with an InP-recess-etch stopper in a two-inch wafer. Total gate width of the devices is 40 μ m which suitable for digital IC applications. The average f_T and f_{max} are respectively 189 and 250 GHz,

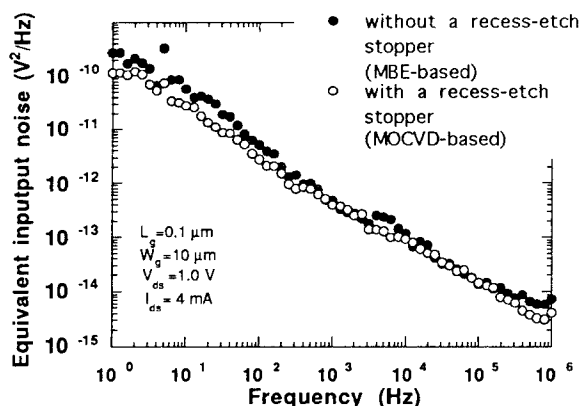


Figure 5. Frequency dependence of equivalent input noise for a 0.1- μ m-gate InAlAs/InGaAs MOCVD-based HEMT with an InP-recess-etch stopper and for an MBE-based HEMT.

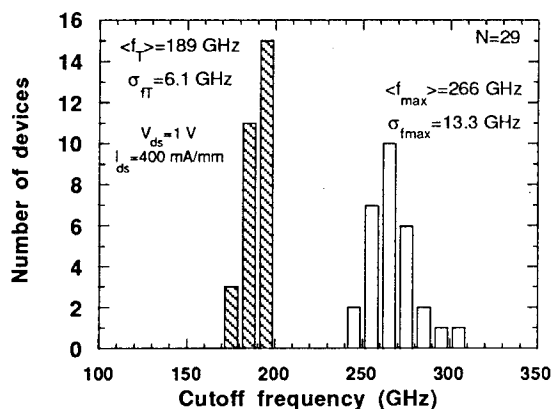


Figure 6. f_T and f_{max} distribution of 0.1- μ m-gate MOCVD-based HEMTs with an InP-recess-etch stopper on a 2-inch wafer. Total gate width is 40 μ m. The bias condition is fixed at $V_{ds}=1.0$ V and $I_{ds}=400$ mA/mm.

and the values are comparable to those of MBE-based devices [4]. The measured device performance thus shows that the additional InP-recess-etch stopper is no disadvantage in terms of high-frequency performance.

Threshold Voltage Uniformity

The key fabrication process parameters that governs threshold voltage for a short-channel device are the barrier thicknesses (or the recess depth) and the short-channel effects. Figure 7 shows the threshold voltage (V_{th}) distribution of 0.1- μ m-gate MOCVD-based HEMTs with an InP-recess-etch stopper and of MBE-based HEMTs without a recess-etch stopper both on 2-inch wafers. The very small standard deviation of 16.2 mV was achieved for 0.1- μ m-gate devices by using the recess-etch stopper. The standard deviation of threshold voltage for 0.7- μ m-gate devices, which are not affected by the short-channel effects, is only 11.2 mV. This variation corresponds to a recess-depth variation of at most 2 Å if we neglect the scatter of the doping density in the wafer. The standard deviation of V_{th} for the MBE-based HEMTs without an recess-etch stopper, on the other hand, is 101 mV and strongly affected by the gate-recess-depth scatter. Atomic order control of the gate-recess depth has thus been achieved by a simple wet etching technique with an incorporation of the recess-etch stopper. The improved V_{th} uniformity is attributed to the abruptness of InAlAs/InP heterointerface grown by MOCVD and the high etching selectivity between the materials obtained by using the citric-acid etchant.

Introducing an additional layer into the barrier layer generally results in a deeper channel and leads to severe short-channel effects. As shown in Fig. 2, however, very thin InP (with a thickness of 40 Å) can act as a recess-etch stopper and the total barrier thickness is still as low as 115 Å. Since the difference between the ΔE_c and Schottky barrier height of InAlAs is at most only 0.2 eV, the barrier thickness can be reduced to less than that of GaAs-based HEMT. The thin barrier and recess-etch stopper enable us to make the channel shallow in order to reduce short-channel effects as well as increase transconductance [9] with

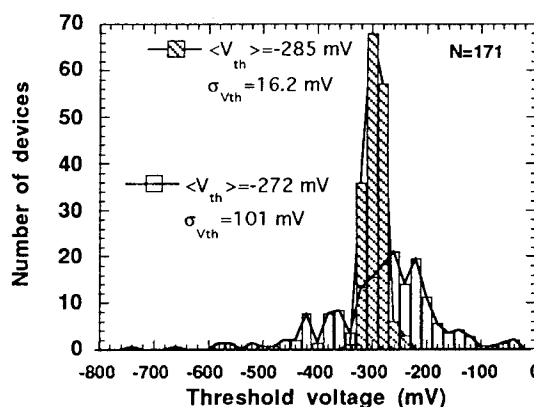


Figure 7. Threshold voltage distribution of 0.1- μ m-gate MOCVD-based HEMTs with an InP-recess-etch stopper and of MBE-based ones without an recess-etch stopper.

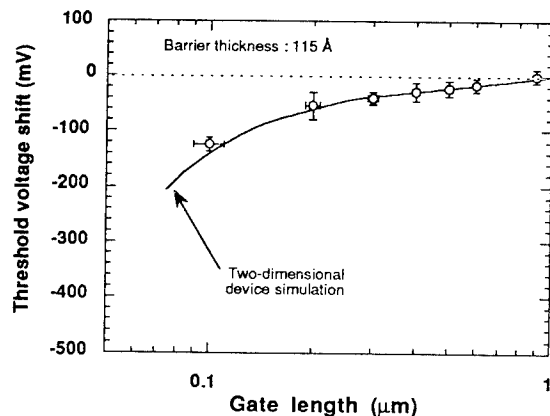


Figure 8. Gate-length dependence of threshold voltage shift.

a large process margin. Figure 8 shows the measured and simulated gate-length dependence of the threshold voltage shift (ΔV_{th}) (from the V_{th} for a 1- μm -gate device). The ΔV_{th} for the 0.1- μm -gate is only 125 mV. This small ΔV_{th} also contributes to the small standard deviation of the threshold for 0.1- μm -gate devices. The ΔV_{th} values produced by a two-dimensional device simulator [10] are also shown by a solid line. The device structure is the same as that of the fabricated device and the simulated ΔV_{th} 's agree well with the measured ones. This means that it is possible to design V_{th} precisely by taking the short-channel effects into account.

Conclusions

A high-performance 0.1- μm -gate InAlAs/InGaAs HEMTs with an InP-recess-etch stopper grown by MOCVD has been developed, and it has been found that the InP-recess-etch stopper does not degrade device performance and does improve the uniformity of the threshold voltage and the designability of device structure. InAlAs/InGaAs HEMT on an InP substrate are thus applicable to ultra-high-speed digital ICs for future communication systems.

Acknowledgments

We thank Takashi Kobayashi, Kenji Kurishima, François Gueissaz, and Toshihiro Ishikawa for their great efforts on MOCVD growth. We are also grateful to Yohtaro Umeda for his support in device characterization and useful discussions, and to Takashi Maruyama for his help in the fabrication process. Special thanks are due to Masafumi Tanimoto for his AFM image analysis and discussions. We also gratefully acknowledge Yoshihiro Imamura for his continuous help and support.

References

- [1] K. W. Chang, H. Wang, R. Lai, D. C. Lo, and J. Berenz, "A V-band monolithic InP HEMT downconverter," Technical Digest of 1993 GaAs IC Symposium, pp. 211-214, 1993.
- [2] S. Kimura, Y. Imai, Y. Umeda, and T. Enoki, "A 16-dB DC-to-50 GHz InAlAs/InGaAs HEMT distributed baseband amplifier using a new loss compensation technique," Technical Digest of 1994 GaAs IC Symposium, pp. 96-99, 1994.
- [3] M. Takikawa, T. Ohmori, M. Takechi, M. Suzuki, and J. Komeno, "Pseudomorphic n-InGaP/InGaAs/GaAs grown by MOVPE for HEMT LSIs," J. Crystal Growth, 107, pp. 942-946, 1991.
- [4] T. Enoki, T. Kobayashi, and Y. Ishii, "Device technologies for InP-based HEMTs and Their Application to ICs," Technical Digest of 1994 GaAs IC Symposium, pp. 337-340, 1994.
- [5] D. R. Greenberg, J. A. del Alamo, and R. Bhat, "A recessed-gate InAlAs/n⁺-InP HFET with an InP etch-stop layer," IEEE Electron Device Letters, Vol. 13, no. 3, pp. 137-139, 1992.
- [6] S. Fujita, T. Noda, C. Nozaki, and Y. Ashizawa, "InGaAs/InAlAs HEMT with a strained InGaP Schottky contact layer," IEEE Electron Device Letters, Vol. 14, pp. 259-261, 1993.
- [7] G. C. DeSalvo, W. F. Tseng, and J. Comas, "Etch rates and selectivities of citric acid/hydrogen peroxide on GaAs, $\text{Al}_{0.3}\text{Ga}_{0.7}\text{As}$, $\text{In}_{0.2}\text{Ga}_{0.8}\text{As}$, $\text{In}_{0.53}\text{Ga}_{0.47}\text{As}$, $\text{In}_{0.52}\text{Al}_{0.48}\text{As}$, and InP," J. Electrochem. Soc., Vol. 139, No. 3, pp. 831-835, 1992.
- [8] Y. He, B. W. Liang, N. C. Tien, and C. W. Tu, "Selective chemical etching of InP over InAlAs," J. Electrochem. Soc., Vol. 139, No. 7, pp. 2046-2048, 1992.
- [9] T. Enoki, M. Tomizawa, Y. Umeda, and Y. Ishii, "0.05- μm -gate InAlAs/InGaAs high electron mobility transistor and reduction of its short-channel effects," Jpn. J. Appl. Phys. Vol. 33, pp. 798-803, 1994.
- [10] M. Tomizawa, A. Yoshii, and S. Seki, "General-purpose device simulation system with an effective graphic interface," IEICE Trans. Electron., E75-C, No. 2, pp. 226-233, 1992.

A TECHNOLOGY FOR MONOLITHIC INTEGRATION OF HIGH-INDIUM-FRACTION RESONANT-TUNNELING DIODES WITH COMMERCIAL MESFET VLSI ELECTRONICS

R.J. Aggarwal, K.V. Shenoy, and C.G. Fonstad, Jr.

Department of Electrical Engineering and Computer Science
Research Laboratory of Electronics
Massachusetts Institute of Technology
Cambridge, MA 02139

ABSTRACT

A novel epitaxy-on-electronics (EoE) technology, developed at MIT, allows the integration of III-V heterostructures and commercial VLSI GaAs circuits. We have designed a monolithic resonant-tunneling diode- (RTD) based static random access memory which uses this technique.

We review both the EoE process and the design and epitaxial growth techniques for high performance $\text{In}_x\text{Ga}_{1-x}\text{As}/\text{AlAs}$ RTDs suitable for memories.

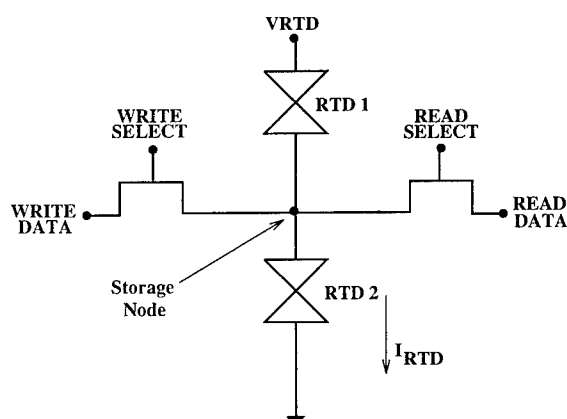


Figure 1: Schematic of an RTD/EFET SRAM cell.

1. INTRODUCTION

GaAs ICs have reached VLSI densities, but there remains a need for a compact GaAs SRAM cell. Demonstrations of SRAM cells built using III-V materials and based on resonant-tunneling diodes (RTDs) have been reported [1, 2]. However, the realization of a robust, VLSI-density integrated circuit technology based on reported integration techniques is uncertain. In work directed at optoelectronic integration, a novel epitaxy-on-electronics (EoE) technology has been recently de-

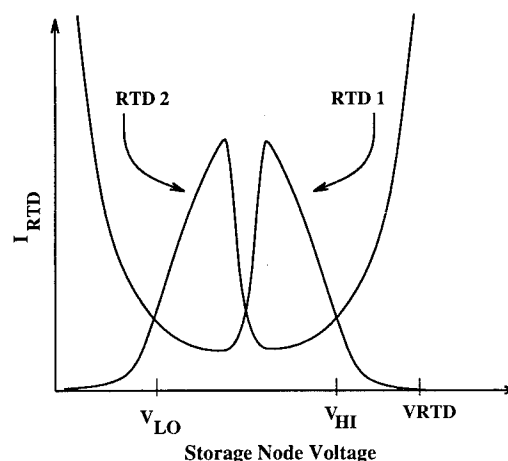


Figure 2: Load-line graph of the diode chain storage element.

veloped at MIT [3, 4]. This technology enables the monolithic integration of III-V heterostructures and commercial VLSI GaAs circuits. This paper reports the design of a monolithic RTD-based SRAM cell employing commercial GaAs VLSI circuits.

2. RTD-BASED SRAM

A RTD-based SRAM cell offers potential area and power savings over traditional 6 transistor GaAs SRAM cells. Figure 1 shows a schematic of our memory cell. For demonstration purposes we have chosen a two transistor implementation. The RTD chain serves as a bistable storage element and the EFETs provide ac-

K.V. Shenoy supported by National Science Foundation and Fannie and John Hertz Foundation Graduate Fellowships.

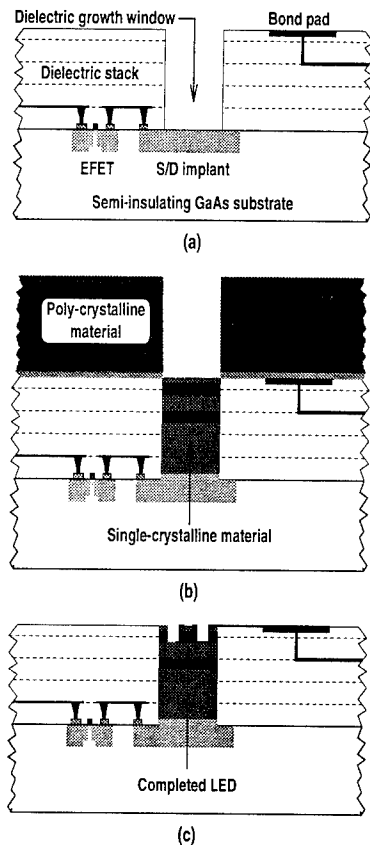


Figure 3: Schematic illustration of the EoE fabrication flow.

cess to the storage element. With additional READ-or-WRITE selection circuitry, the two-EFET architecture can be collapsed to a single-EFET topology. When optimized, this cell could require only the area of a single EFET. Figure 2 shows the electrical characteristics of the storage element. The static power requirements of the cell will be determined by the diode chain bias voltage, V_{RTD} , and the current flowing through the diode chain, I_{RTD} , in the V_{LO} and V_{HI} states. The speed of the READ and WRITE operations will primarily be determined by the diode and EFET abilities to charge the capacitance present at the storage node. Both the static power and speed of the cell are directly related to the RTD peak voltage, valley current, and the character of the diode initial turn-on current. For compatibility with DCFL voltage levels and optimum SRAM performance, we desire an RTD with a resonance voltage under 1 V, a sharp turn-on current, and large peak-to-valley-current ratio (PVCr).

3. EPITAXY-ON-ELECTRONICS TECHNOLOGY

The EoE technology, shown in Figure 3, places time-temperature constraints on our epitaxial process. Targeting VLSI densities of electrical and heterostructure

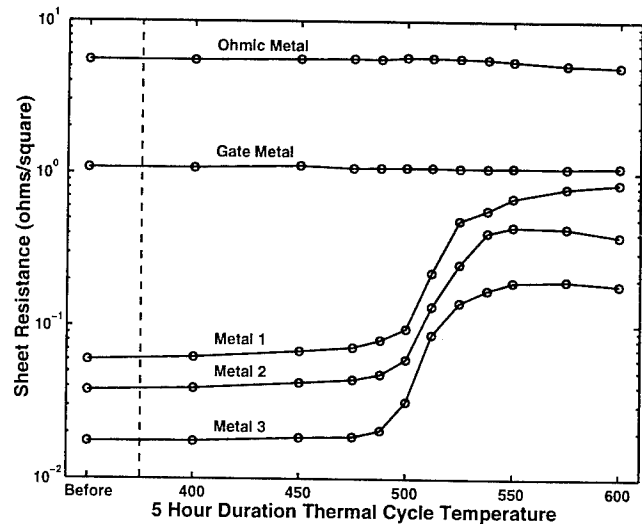


Figure 4: Metal layer sheet resistance after 5 hour thermal cycles. At elevated temperatures a metallurgical reaction, $\text{AlCu}_x + \text{WN}_x \rightarrow \text{Al-Cu-W-N}$, occurs within the interconnect metal layers which increases the sheet resistance.

devices, our starting point is commercial VLSI GaAs metal-semiconductor field-effect transistor (MESFET) circuitry available at foundries such as Vitesse Semiconductor Corp. through the MOSIS/ARPA service. By overlaying existing standard foundry process etches it is possible to specify dielectric growth windows (DGWs) during circuit layout as illustrated in Figure 3(a). The second fabrication step, seen in Figure 3(b), is to epitaxially grow heterostructures on the fully-processed commercial electronics-only GaAs wafer or chip. Single-crystal, device-quality material grows from the GaAs wafer to the top of the interlevel-metal dielectric stack (DGW sidewalls) in the DGWs while poly-crystalline material deposits on the dielectric stack. The poly-crystalline deposits are then removed and heterostructure devices are fabricated with standard processing techniques. The final fabrication step connects the heterostructure devices, an LED in the case of Figure 3(c), and the GaAs circuits.

The heterostructure growth time-temperature upper limit is set by the thermal stability of the underlying electronics. In our studies of the stability of GaAs electronics we have investigated the HGaAs2 [5] and HGaAs3 [6] processes of Vitesse Semiconductor Corp. and the CS-1 process of Motorola. Both lines produce VLSI density, 0.5 μm gate width GaAs E-mode and D-mode MESFETs with refractory metal gates (tungsten-nitride based) and ohmic contacts (nickel based) while interconnect wires are aluminum-copper plated with tungsten-nitride. The ohmic contacts are stable to ap-

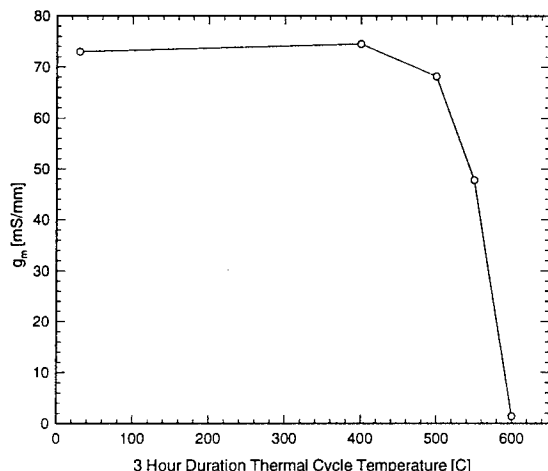


Figure 5: The maximum transconductance, g_m ($V_{DS} = 0.15$ V), of fully processed $50 \mu\text{m} \times 1.2 \mu\text{m}$ gate E-mode MESFETs after 3 hour anneals at temperatures between 400°C and 600°C .

proximately 500°C for three hour thermal cycles. Figure 4 shows the sheet resistance of the various circuit metals as a function of thermal cycle temperature. The GaAs intrinsic transistors are stable to much higher temperatures. Figure 5 shows the transconductance of E-mode MESFETs as a function of thermal cycle temperature. We have shown that the thermally-weak link in the circuits is the multi-layer metal film used in the upper-level interconnect lines, which typically limits epitaxy temperatures to below 475°C growth times to below 5 hours.

4. RELAXED-BUFFER RTDS

The PCVR of GaAs/ $\text{Al}_x\text{Ga}_{1-x}\text{As}$ RTDs grown on GaAs can be improved by replacing GaAs with $\text{In}_x\text{Ga}_{1-x}\text{As}$. $\text{In}_x\text{Ga}_{1-x}\text{As}$ critical thickness limits restrict the indium content of the $\text{In}_x\text{Ga}_{1-x}\text{As}$, and therefore limit the utility of this approach. By using a strain-relieved buffer, the substrate lattice constant can be changed to match that of the diode $\text{In}_x\text{Ga}_{1-x}\text{As}$ layers. We are using this approach to design RTDs suitable for circuit applications.

We use a two-step relaxed buffer to grow high-indium-composition RTDs compatible with the EoE technology. We have recently demonstrated a $\text{In}_{0.22}\text{Ga}_{0.78}\text{As}/\text{AlAs}$ relaxed-buffer RTD with a PVCR of 13:1 [7]. The relaxed buffer consists of $0.55 \mu\text{m}$ of $\text{In}_{0.17}\text{Ga}_{0.83}\text{As}$ and $0.32 \mu\text{m}$ of $\text{In}_{0.22}\text{Ga}_{0.78}\text{As}$ both n-type. The $\text{In}_x\text{Ga}_{1-x}\text{As}$ layers were grown at 480°C and total growth time was 3 hours. Figure 6 shows the electrical characterization of the device. The resonance

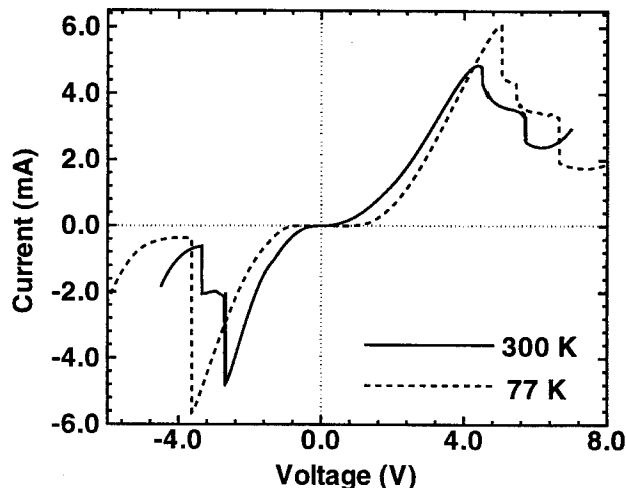


Figure 6: Current-voltage characteristics of a typical $25 \mu\text{m}^2$ $\text{In}_{0.22}\text{Ga}_{0.78}\text{As}/\text{AlAs}$ relaxed-buffer RTD.

voltages in this structure are high due to low buffer and RTD doping concentrations and a narrow RTD well width and are too large to be useful in SRAM cells.

To determine the contribution of the relaxed buffer to the resonance voltage of the RTD, several relaxed-buffer RTDs were grown. Once again, a two-step relaxed buffer grown at 480°C was used. The electrical characteristics were measured using two different four-point probe configurations. For both measurements, the "top" contact of the RTD was the ohmic contact on the RTD mesa. The "bottom" contact was the substrate in one case, and an ohmic contact above the relaxed buffer in the other. The difference in the peak voltage represents the voltage drop across the buffer. Figure 7 shows the I-V characteristics of an $\text{In}_{0.27}\text{Ga}_{0.73}\text{As}/\text{AlAs}$ relaxed-buffer RTD. The relaxed buffer for this RTD consists of $0.2 \mu\text{m}$ $\text{In}_{0.11}\text{Ga}_{0.89}\text{As}$ and $0.2 \mu\text{m}$ $\text{In}_{0.27}\text{Ga}_{0.73}\text{As}$, both doped n^+ . The resonance voltage of this diode is lower than that of Figure 6 because of higher buffer and RTD doping and a wider RTD well. The relaxed buffer voltage drop for this diode, under 30 mV, can be accounted for in future RTD designs. In general, RTDs with heavily doped relaxed buffers are suitable for circuit applications.

5. MONOLITHICALLY INTEGRATED RTD-BASED SRAM DESIGN

Large signal design parameters from relaxed-buffer RTDs were used to design three basic circuits which study the feasibility of integrating RTDs with GaAs ICs: an RTD array, a 1-bit memory cell, and a 4-bit memory array. The RTD array is used to study the quality of the RTD material grown on the GaAs ICs.

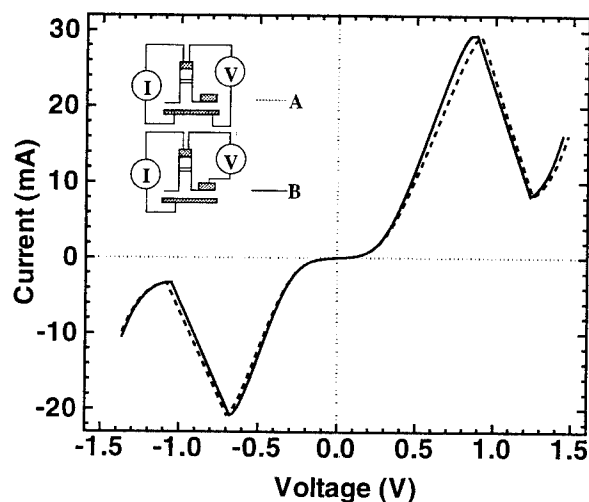


Figure 7: Current-voltage characteristics of a typical $25 \mu\text{m}^2$ $\text{In}_{0.27}\text{Ga}_{0.73}\text{As}/\text{AlAs}$ relaxed-buffer RTD including and excluding the voltage drop contributed by the relaxed buffer.

The 1-bit memory cell characterizes the basic operation of the memory cell. The 4-bit memory array addresses density issues such as the effect of RTD variation on the performance of the memory. Figure 8 shows the simulated operation of a 1-bit memory cell using layout extracted EFET characteristics. The RTDs used in this simulation are those shown in Figure 7. The *Select* signals are applied to gates of the EFETs and the *Data In* signal is applied to the drain of the WRITE EFET shown in Figure 1. The *Data Out* signal is measured at the drain of the READ EFET.

6. CONCLUSION

We have designed a RTD-based SRAM utilizing a novel EoE technology to combine III-V heterostructures with commercial VLSI GaAs circuits. Upper epitaxial time-temperature limits are set by the metal interconnects. Operating within these constraints, we use a relaxed-buffer structure to epitaxially grow high-indium fraction RTDs on GaAs substrates which are compatible for circuit applications. We are presently fabricating the monolithically integrated SRAM circuits.

This work was supported by JSEP through the MIT Research Lab of Electronics and ARPA through the National Center for Integrated Photonics Technology.

7. REFERENCES

- [1] Y. Watanabe, Y. Nakasha, K. Imanishi, and M. Takikawa. Monolithic integration of In-

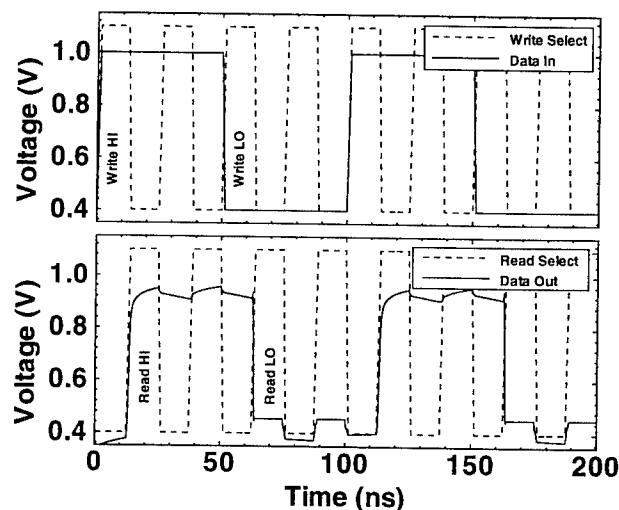


Figure 8: Simulated operation of 1-bit SRAM cell.

GaAs/InAlAs resonant tunneling diode and HEMT for single-transistor SRAM application. In *Proceedings of the 1992 International Electron Devices Meeting*, pages 475-478, 1992.

- [2] S.-J. Wei and H.C. Lin. Multivalued SRAM using resonant tunneling diodes. *IEEE Journal of Solid-State Circuits*, 27:212-216, February 1992.
- [3] A.C. Grot, D. Psaltis, K.V. Shenoy, and C.G. Fonstad, Jr. Integration of LEDs and GaAs circuits by MBE regrowth. *IEEE/LEOS Photonics Technology Letters*, 6(7):819-821, July 1994.
- [4] K.V. Shenoy, C.G. Fonstad, Jr., A.C. Grot, and D. Psaltis. Monolithic optoelectronic circuit design and fabrication by epitaxial growth on commercial VLSI GaAs MESFETs. To be published in *IEEE/LEOS Photonics Technology Letters*, May 1995.
- [5] K.V. Shenoy, C.G. Fonstad, Jr., and J.M. Mikkelsen. High-temperature stability of refractory-metal VLSI-GaAs MESFET's. *IEEE Electron Device Letters*, 15(3):106-108, March 1994.
- [6] E.K. Braun, K.V. Shenoy, C.G. Fonstad, Jr., and J.M. Mikkelsen. Elevated temperature stability of GaAs digital integrated circuits. Submitted to *IEEE Electron Device Letters*, January 1995.
- [7] R.J. Aggarwal and C.G. Fonstad, Jr. High peak-to-valley-current ratio $\text{In}_{0.22}\text{Ga}_{0.78}\text{As}/\text{AlAs}$ RTDs on GaAs using relaxed $\text{In}_x\text{Ga}_{1-x}\text{As}$ buffers. *Electronics Letters*, 31(1):75-77, January 1995.

40-Gb/s-Class InP HEMT ICs for Very-High-Speed Optical Communications

Yuhki Imai, Makoto Nakamura, Shunji Kimura,

Yohtaro Umeda, and Takatomo Enoki

NTT LSI Laboratories

3-1 Morinosato Wakamiya, Atsugi-shi, Kanagawa, 243-01, Japan

INTRODUCTION

Future very-high-volume optical communication systems will require several-dozen-Gb/s ICs. The InP HEMT is one of the best candidates for these ICs due to its inherent millimeter-wave performance. This paper describes 40-Gb/s-class analog InP HEMT ICs that have been used with new design techniques to build high-speed optical receivers. Four kinds of ICs are covered: a preamplifier, a baseband amplifier, a limiting amplifier, and a Gilbert cell. Even in this early development stage, all ICs show promising performances that are superior or compatible to the best-ever reported results.

Design feature

The conventional design for optical-receiver circuits is basically a simple extension of the low-frequency lumped-element design technology used for feedback and differential amplifiers. However, with this approach, its wideband performance is severely limited by transistor performance due to RC cut-off frequency of the lumped-element circuit. Because our target frequency was beyond 40 GHz, we made extensive use of a microwave design with distributed elements to obtain high performance with less transistor-performance sensitivity. The key features of the microwave design applied here are a distributed amplification technique for both linear and non-linear baseband circuits, a microwave feedback technique for the preamplifier and a narrow-band reactive matched amplifier for the limiting amplifier. In particular, the new distributed baseband circuit represents a

breakthrough that promises to boost IC-performance beyond the limit imposed by device performance.

IC fabrication

ICs were fabricated using 0.1-0.15- μm -gate-length InAlAs/InGaAs/InP HEMTs [1]. They use uniplanar MMIC technology with a coplanar waveguide [2]. Microphotograph of distributed Gilbert cell is shown in Fig. 1.

Design and performance

Baseband amplifier

Figure 2 shows a schematic circuit of the new distributed baseband amplifier [3]. A flat gain from DC is achieved using DC matching terminations (R_{d1} and R_{g1}) with dumping resistors (R_{d2} and R_{g2}), which reduce the parasitic effects of the external inductances at the bias terminals. A new loss-compensation circuit using a cascode FET with transmission

lines (Lcg and Lsd) achieves wideband performance because it compensates for the loss of the drain artificial lines with negative resistance. Figure 3 shows the measured S parameters. The amplifier has 16-dB gain with a 3-dB bandwidth of 47 GHz and 1.1-W power dissipation. Chip size is 1.5x4 mm. To our knowledge, this is the widest bandwidth with high gain for state-of-art baseband amplifier ICs.

Gilbert cell

The Gilbert cell is a basic circuit element used in clock extraction circuits, multipliers, and differential detectors. Figure 4 shows a schematic circuit of the new distributed Gilbert cell [4]. It has a distributed structure connecting two unit Gilbert cells with three artificial lines for RF, LO, and IF ports. DC matching terminations (Rgt and Rdt), dumping resistors and resistor-capacitor networks (Rdb, Rgb, Rst and Cst) are also used to insure DC operation. Figure 5 show the measured conversion gain as a function of RF frequency with 1-GHz IF frequency and 10-dBm LO power. The conversion gain was -5 dB with a 3-dB bandwidth of 38 GHz and 2.5-W power dissipation. Chip size is 2x2 mm. This is also believed to be the top wideband performance for reported Gilbert-cell ICs.

Preamplifier

Figure 6 shows a schematic circuit of the preamplifier. Until now, preamplifiers have usually used common-source FETs with parallel feedback from a succeeding level-shift source-follower. However, this one uses a simple one-stage feedback cascode amplifier with controlled feedback[5] and matching circuits to

improve performance. Transmission lines (Tg2, Tf, and Td1) provide optimum positive feedback near the band edge to enhance gain. Tg1 optimizes the input impedance to improve the transimpedance. It has 9-dB gain with a 3-dB bandwidth of 32 GHz and 440-mW power dissipation. Figure 7 shows frequency dependencies of S22 and transimpedance Zt calculated from the measured S parameters. Zt is $43 \pm 2 \text{ dB}\Omega$ and S22 is less than -8 dB with 17 pA/ $\sqrt{\text{Hz}}$ average equivalent input noise current density from 0.05 GHz and 35 GHz. Chip size is 1.5x1.5 mm.

Limiting amplifier

Figure 8 shows a schematic circuit of the limiting amplifier with reactive matchings. For a clock-recovery limiting amplifier, the best way to increase operating frequency is a narrow-band MMIC-type amplifier because it can easily attain millimeter-frequency performance compared with a wideband design [6]. The amplifier had more than 16 dB gain in 34-40-GHz frequency range. Figure 9 shows the measured output power and phase shift deviation (output-signal phase variation) at 38 GHz. It has 17-dB small signal gain and 10-dBm saturation output power with about 10-degree phase shift deviation for input power from -5 dBm to 5 dBm. The power dissipation was 70 mW. Chip size is 1x2 mm.

Conclusion

InP HEMT optical-receiver ICs up to 50 GHz were developed together with new design techniques. Considering their impressive performances, they should have a considerable impact on lightwave applications.

Acknowledgements

The authors wish to thank Y. Akazawa, E. Sano, and Y. Ishii for helpful discussions. They also thank S. Horiguchi and Y. Imamura for their encouragement.

References

- [1] Y. Umeda, T. Enoki, and Y. Ishii, "Sensitivity Analysis of 50-GHz MMIC-LNA on Gate-Recess Depth with InAlAs/InGaAs/InP HEMT's," *IEEE MTT Symp. Dig.*, pp. 123-126, 1994.
- [2] M. Muraguchi, T. Hirota, A. Minakawa, K. Ogawa, and T. Sugeta, "Uniplanar MMIC's and Their Applications," *IEEE Trans. Microwave Theory Tech.*, vol. 36, no. 12, pp. 1896-1901, 1988.
- [3] S. Kimura, Y. Imai, Y. Umeda, and T. Enoki, "A 16-dB DC-50GHz InAlAs/InGaAs HEMT Distributed Baseband Amplifier Using a New Loss Compensation Technique," in *Tech. Dig. IEEE GaAs IC Symp.*, 1994, pp. 96-99.
- [4] Y. Imai, S. Kimura, Y. Umeda, and T. Enoki, "A DC to 38-GHz Distributed Analog Multiplier Using InP HEMT's," *IEEE Microwave and Guided wave Letters*, vol. 4, no. 12, pp. 399-402, 1994.
- [5] K. B. Niclas, W. T. Wilser, R. B. Gold, and W. R. Hichens, "The Matched Feedback Amplifier: Ultrawide-Band Microwave Amplification with GaAs MESFET's," *IEEE Trans. Microwave Theory Tech.*, vol. 28, no. 4 pp. 389-398, 1980.
- [6] Y. Imai, E. Sano, M. Nakamura, N. Ishihara, H. Kikuchi, and T. Ono, "Design and Performance of Clock-Recovery GaAs ICs for High-Speed Optical Communication Systems," *IEEE Trans. Microwave Theory Tech.*, vol. 41, no. 5, pp. 745-751, 1993.

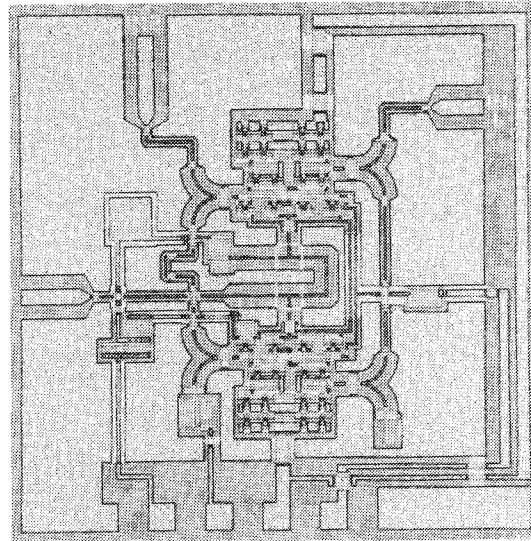


Fig. 1 Microphotograph of Distributed Gilbert cell

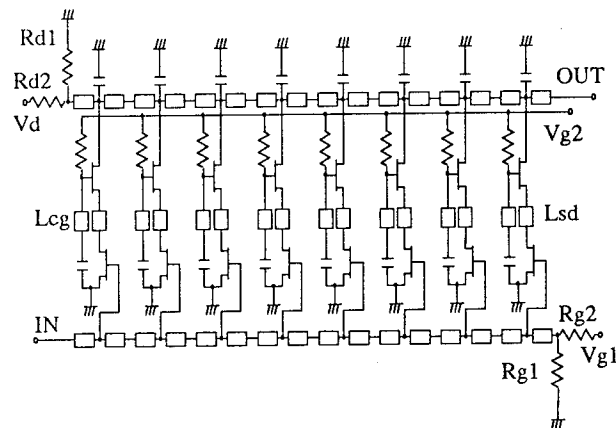


Fig. 2 Distributed baseband amplifier.

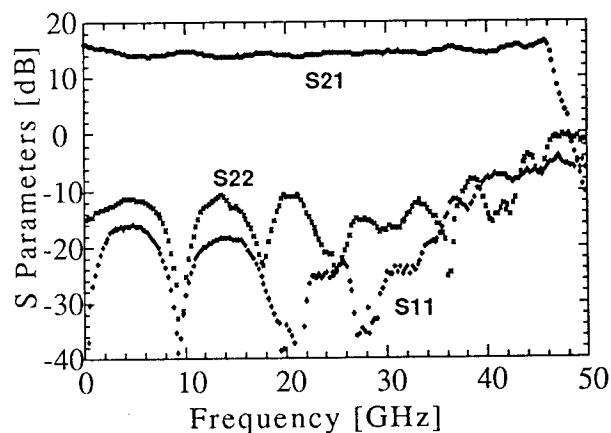


Fig. 3 S parameters for baseband amplifier.

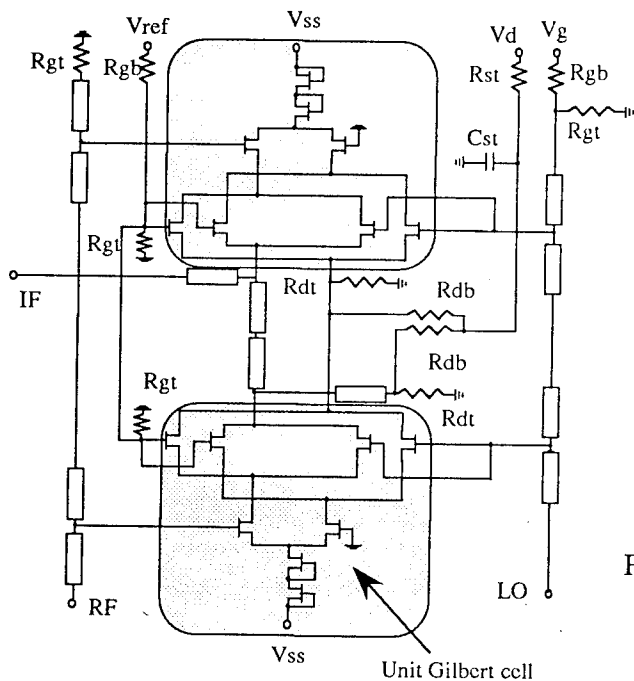


Fig. 4 Distributed Gilbert cell.

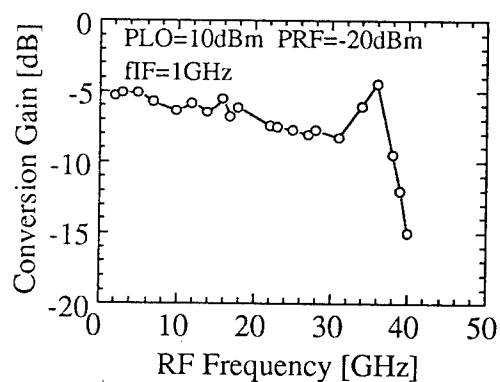


Fig. 5 Conversion gain versus RF frequency for Gilbert cell.

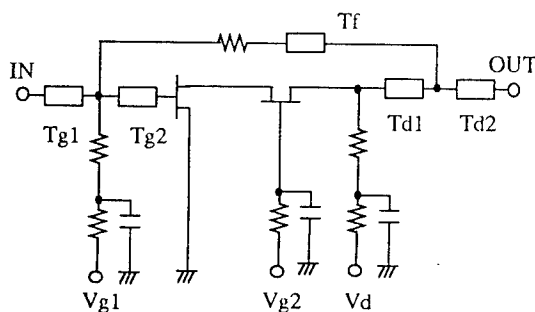


Fig. 6 Preamplifier

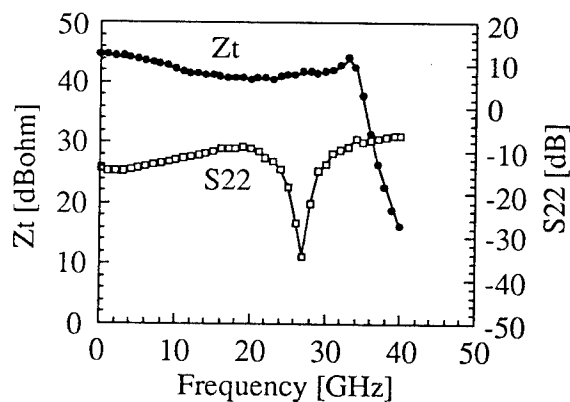


Fig. 7 Zt and S22 for peamplifier.
Zt : Transimpedance.

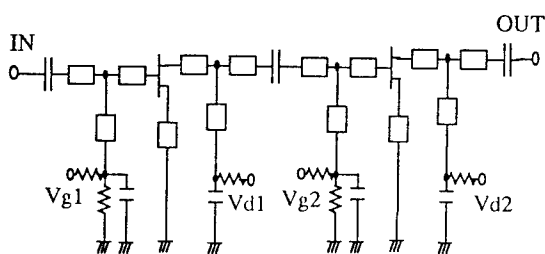


Fig. 8 Limiting amplifier

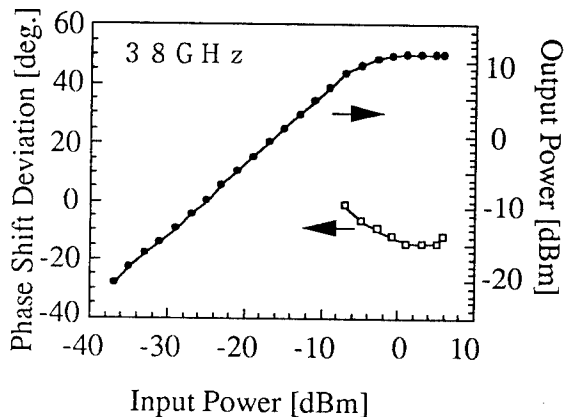


Fig. 9 Phase shift deviation and output power versus input power for limiting amplifier.

Study on Microscopic Defects in Fe-doped InP Single Crystals WP1

K. Kohiro, R. Hirano* and O. Oda

Electronic Materials and Components Laboratories

3-17-35, Niizo-Minami, Toda, Saitama, Japan

*Advanced Materials Research Center

187-4, Usuba, Hanakawa, Kitaibaraki, Ibaraki, Japan

JAPAN ENERGY CORPORATION

Effect of crystal growth conditions on the density of microscopic defects, observed on as-polished Fe-doped InP LEC single crystal wafers, has been investigated by an interference contrast microscope and a laser scattering tomography (LST) system. It was found that crystal rotation speeds affect the density of microscopic defects. In addition, the density depends on the duration for which the InP melt is held in molten state before crystal growth. On the other hand, it was found that the H_2O concentration in B_2O_3 has no correlation with the generation of microscopic defects. The relationship between the microscopic defects and the stoichiometry of grown crystals was investigated by coulometric titration analysis for the indium concentration. The density of microscopic defects is reduced as the indium concentration decreased. From the present results, it is speculated that the origin of microscopic defects is indium or indium oxide.

Introduction

InP is a very optimizing material for long wavelength optoelectronic devices and high frequency electronic devices. It is known that various defects as well as dislocations exist in the crystals grown by the liquid-encapsulated Czochralski (LEC) method. The reduction of these defects may be required from the viewpoint of the device fabrication. The typical defects are grappes (inclusion-like defects) and flat-bottomed saucer-shaped pits (S-pits) which are revealed by Huber etchant (1). Several researchers have studied grappes (2) and S-pits (3), (4), (5), but there are few reports on microscopic defects observed on as-polished InP wafers, about which we will discuss in the present paper.

Even though these microscopic defects are observed on S-, Zn-, Sn- and Fe-doped InP wafers, we have investigated especially the case of Fe-doped InP wafers because of the importance of Fe-doped InP as electronic devices. The relationship between these defects and crystal growth conditions has been investigated by an interference contrast microscope, a laser scattering tomography (LST) system and by coulometric titration analysis.

Experimental

Fe-doped InP single crystals have been grown by the LEC method. The growth was performed by charging B_2O_3 and presynthesized polycrystalline InP with the carrier concentration lower than $3 \times 10^{15} \text{ cm}^{-3}$ in a pyrolytic boron nitride (pBN) crucible. Fe foil was added as the dopant with the concentration of 0.03 wt% in the InP melt. The concentration of Fe in crystals was $(1-8) \times 10^{16} \text{ cm}^{-3}$. The diameter of the grown crystals were 2 inch and 3 inch.

As-cut wafers were polished by using a mechano-chemical method under industrial production. The etchant used to reveal dislocations consisted of H_3PO_4 and HBr , mixed in the volume ratio of 2:1. Microscopic defects and dislocations were observed with an interference contrast microscope on the polished and etched wafers, respectively. The average density of microscopic defects was obtained by counting the defects whole over the wafer.

The LST images were measured by focusing a 300 mV YAG laser beam to cleaved faces of as-polished wafers. Stoichiometry analysis was performed by the coulometric titration method with the accuracy of ± 0.0001 .

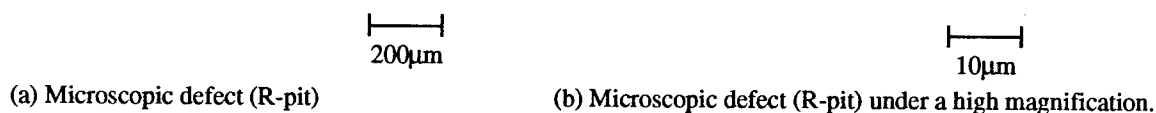


Fig. 1. Microscopic defects (R-pits) on an as-polished Fe-doped InP wafer.

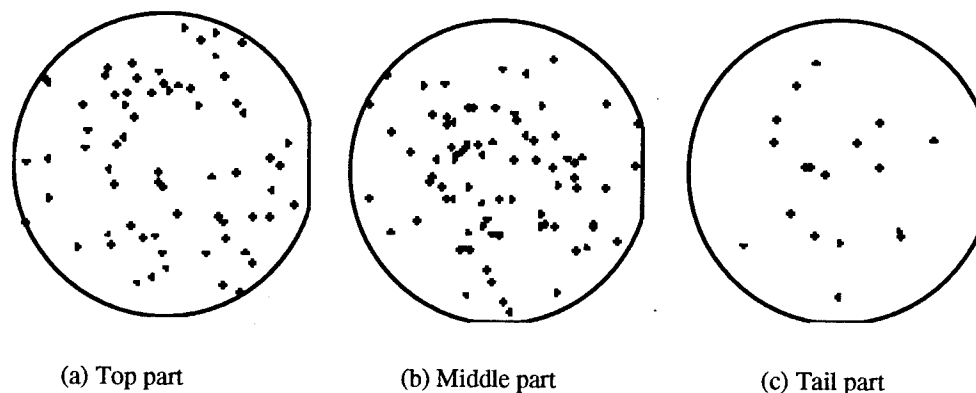


Fig. 2. The distributions of R-pits across the wafers from a 3 inch diameter Fe-doped InP crystal.

Experimental results

Fig. 1 shows typical microscopic defects observed on a polished Fe-doped InP wafer. The defects are shown as pits at low magnifications. By observation at higher magnification, it was found that the defects have rectangular shapes and the size of the defects ranges from 10 to 30 μm . We refer to these defects as R-pits (rectangular shaped pits) from now on. The longer side of the rectangle is always parallel to the (110) plane and this fact suggests that the origin of R-pits is not damages by polishing but defects in crystals.

In the previous paper (6), we studied the relationship between R-pits and dislocations by observing the wafers after Huber etching and found that R-pits may not correspond to dislocation pits. In order to examine the relationship in detail,

we have observed the distribution of R-pits on the wafers. It is well known that InP wafers exhibit a characteristic fourfold symmetry of the dislocation distribution. However, the distribution of R-pits does not correspond to that of dislocations as seen in Fig. 2. The density of R-pits is around $(1 - 10) \text{ cm}^{-2}$, the highest at the middle of the crystal and tends to decrease toward the tail part. Since the average EPDs are about several 10^4 cm^{-2} from top to tail part of the crystal, it is concluded that R-pits have no correlation with dislocations.

In order to examine the parameters which affect the density of R-pits, we have grown single crystals under different growth conditions. Fig. 3 shows the relationship between average densities of R-pits and crystal rotation speeds. It was found that the average densities decrease with increasing the crystal rotation speed.

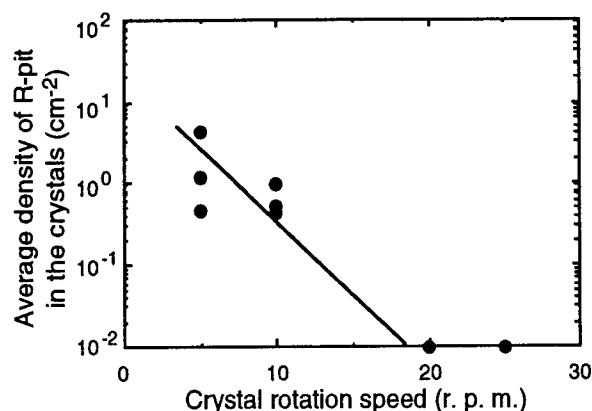


Fig. 3. The relationship between the average density of R-pits and crystal rotation speeds.

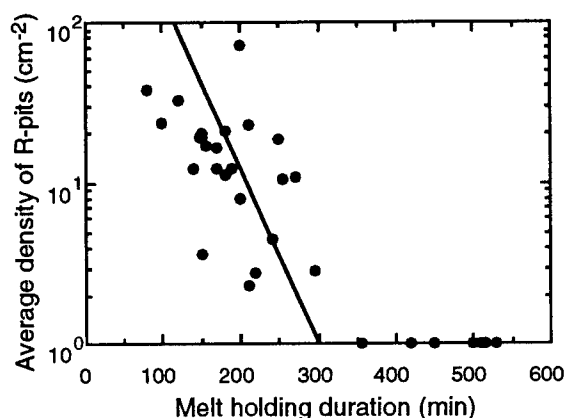


Fig. 4. The density of R-pits as a function of melt holding duration before crystal growth.

Fig. 4 shows the densities of R-pits as a function of melt holding duration before crystal growth. The longer the holding duration is, the fewer the densities. This is probably because the species which are the origin of R-pits are adsorbed into the B_2O_3 encapsulant. It is known that most impurities in GaAs and InP melts react with H_2O in B_2O_3 and are eliminated because of the segregation of the impurity oxides into B_2O_3 (7). In this case, the H_2O concentration in B_2O_3 will affect the density of R-pits. We have grown three crystals using B_2O_3 with different H_2O concentrations of 150, 300, 600 ppmw. Fig. 5 shows LST images for the wafers cut from the crystals grown using B_2O_3 with H_2O concentrations of 150 and 600 ppmw. It is known that IR scattering centers observed by LST correspond to the R-pits (6). As seen in the figure, the density of scattering centers on both samples is the

same within the experimental error. The density of R-pits thus seems to be independent of H_2O concentrations in B_2O_3 .

In order to examine the effect of non-stoichiometry on the density of R-pits, indium compositions in InP wafers have been analyzed by the coulometric titration method (8), (9). Fig. 6 shows the densities of R-pits as a function of the indium concentration. The densities have a tendency to decrease as the indium concentration decreases. When the composition is stoichiometric, most wafers showed no R-pits.

Discussion

As describe above, the formation of R-pits has a strong correlation with the growth conditions. The dependence of the

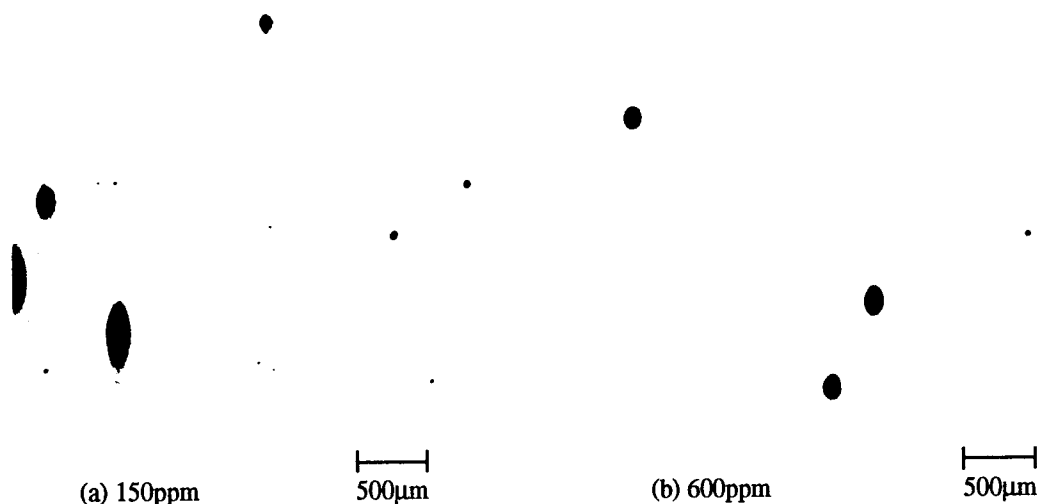


Fig. 5. LST images from the top part of Fe-doped InP crystal with different H_2O concentrations in B_2O_3 .

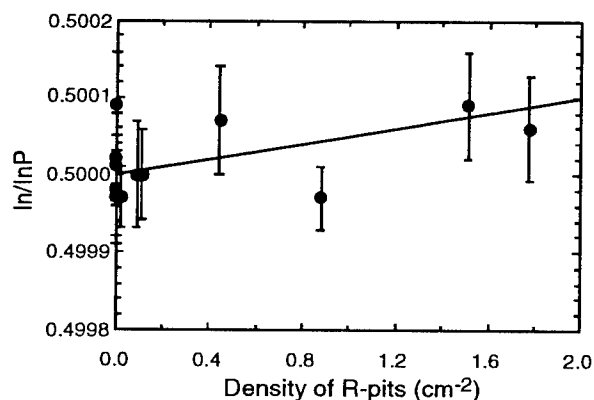


Fig. 6. The relationship between the atomic fraction of indium and the density of R-pits.

densities of R-pits on the crystal rotation speed suggests that the species which is the origin of R-pits have diffusion-controlled characteristics in the melt. When the crystal rotation speed is increased, the thickness of diffusion boundary layer at the solid-liquid interface is decreased. The species which is the origin of R-pits, segregated in the boundary layer, can diffuse out into the melt faster as the crystal rotation speed increases. This will result in the reduction of the densities of R-pits in the grown crystals.

The fact that the densities of R-pits can be reduced by prolonging the melt holding duration before crystal growth helps us largely for considering the origin of R-pits. As mentioned above, it is well known that the encapsulant B_2O_3 has an effect of accumulating various impurity oxide in it. Fig. 4 indicates that the species which is the origin of R-pits can be adsorbed easily in B_2O_3 . We also found that the H_2O concentration in B_2O_3 does not affect strongly the densities of R-pits. It is argued that most impurities in the melt are adsorbed into B_2O_3 by the reaction of them with H_2O in B_2O_3 . It therefore seems that the species which is the origin of R-pits is not impurity which reacts with H_2O . As the species which does not react thermodynamically with H_2O , indium is a possible species. Fig. 6 also supports that the origin of R-pits is related with indium. Indium itself however will not dissolve into B_2O_3 as it is. Therefore, there is also a possibility that indium exists in the melt as the form of indium oxide.

Summary

We have investigated the microscopic defects (R-pits) observed on as-polished Fe-doped InP wafers by an

interference contrast microscope, a LST system and by coulometric titration analysis. There was no correlation between the distribution of R-pits and that of dislocations. The density of R-pits decreases as the crystal rotation speed increases and as the melt holding duration before crystal growth is prolonged. It was found that the H_2O concentration in B_2O_3 has no correlation with the generation of R-pits. Coulometric titration analysis showed that the generation of R-pits is related with the indium concentration. From these results, it is speculated that the origin of R-pits is related with indium or indium oxide.

Acknowledgements

The authors are grateful to Drs. K. Aiki, Messrs. H. Yamamoto, T. Fukui, G. Kanoh and K. Kainosho for useful discussion and for their continuous encouragement. The authors also wish to thank Messrs. M. Ohta, N. Kubota, K. Watatani, K. Nakamoto and Miss Y. Matsuda for their crystal growth, wafer processing and evaluation of grown crystals.

References

- (1) A Huber and N. T. Linh, *J. Cryst. Growth* **29** 80 (1975).
- (2) D. J. Stirling, D. G. Hart and S. Clark, J. C. Regnault and C. R. Elliott, *J. Cryst. Growth* **61** 645 (1983).
- (3) R. C. Clarke, D. S. Roberston and A. W. Vere, *J. Mater. Sci.* **8** 1349 (1973).
- (4) G. T. Brown, B. Cockayne and W. R. Macewan, *J. Mater. Sci.* **15** 2539 (1980).
- (5) B. Sartorius and K. Pfanner, *Appl. Phys. Letters* **54** 2539 (1989).
- (6) R. Hirano, T. Kanazawa and S. Katsura, *J. Cryst. Growth* **134** 81 (1993).
- (7) R. N. Thomas, H. M. Hobgood, G. W. Eldridge, D. L. Barrett, T. T. Braggins, L. B. Ta and S. K. Wang, *Semicon. Semimetals (Academic Press)* **20** 1 (1984).
- (8) O. Oda, H. Yamamoto, M. Seiwa, G. Kano, M. Mori, H. Shimakura and M. Oyake, *Semicond. Sci. Technol.* **7** A215 (1992).
- (9) K. Kainosho, H. Okazaki and O. Oda, *Proc. of the 5th Int. Conf. on InP and Related Mater., Paris*, pp32 (1993).

Reduction of dislocation densities in InP single crystals by the TB-LEC method

R. Hirano and M. Uchida*

Japan Energy Corporation

Compound Semiconductor Materials Department

187-4, Usuba, Hanakawa, Kitaibaraki, Ibaraki 319-15, Japan

*Electrical Materials and Components Research Laboratories

3-17-35, Niizo-Minami, Toda, Saitama, Japan

Abstract

We have developed a modified LEC method with a thermal baffle(TB), by which low dislocation density InP crystals can be grown. In this method, a thermal baffle is set on top of the crucible in order to suppress the gas convection and thus to improve the temperature gradient in the LEC furnace. The dislocation density depends not only on the temperature gradient but also on the other growth conditions, such as crystal/crucible rotational speeds, cooling conditions, and crucible weight. The rotational condition is an important factor for the reduction of the dislocation density since the solid/liquid(SL)interface shape changes with the rotational conditions.

1. Introduction

Reduction of the temperature gradient is effective for reducing the dislocation density. However the lower temperature gradient raises the temperature of the InP single crystal at the surface, which results in a damage because of the high dissociation pressure of InP. To solve this problem, new methods such as VGF[1], VCZ[2] and PC-LEC[3] have been developed. In these methods, even under conditions with lower temperature gradient, the dissociation at the crystal surface can be prevented by introducing the phosphorus vapor into the space.

On the other hand, we have shown that the lower dislocation density crystals can also be grown by the TB-LEC methods[4-6], in spite of the higher temperature gradient compared with the above mentioned methods.

In this paper, we show that the dislocation density depends not only on the temperature gradient but also on the other growth conditions such as crystal/crucible rotational conditions, the cooling conditions in the furnace after the growth and the weight of the crucible.

2. Experimental

A high pressure LEC growth system has been used throughout this investigation. Two inch diameter Sn, S, Fe and Zn doped InP crystals were grown along $\langle 100 \rangle$ with a thermal baffle. Dislocation pits were revealed by Huber etchant[7]. The 13 points average dislocation density was measured for Sn or Fe doped InP and the DF(dislocation-free) area was measured for S and Zn doped InP.

3. Results

Fig. 1 shows the axial temperature gradients in the LEC furnace. The temperature gradient can be reduced using a thermal baffle. The dislocation densities are shown in Table 1. The crystal/crucible rotational speeds were 20 and 15 rpm. The crystals were cooled slowly in the LEC furnace after the growth. As a result, it becomes possible

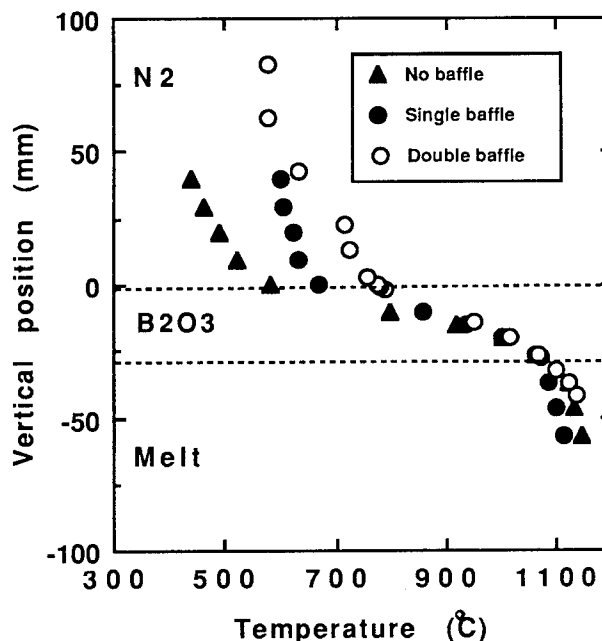


Fig. 1. Axial temperature gradient in the LEC furnace.

Table 1. Dislocation densities of InP crystals (EPD=13 points average dislocation density)
(DF=dislocation free area with dislocation density < 500 cm⁻².)
(Maximum DF area is 69 points x 0.25 cm² = 17.25 cm²)

Dopant	No baffle	Single baffle	Double baffle
Fe, Sn	EPD > 5E4 cm ⁻²	1E4 cm ⁻² < EPD < 5E4 cm ⁻²	2E3 cm ⁻² < EPD < 1E4 cm ⁻²
S	C/C = 3.5E18 cm ⁻³ DF Area < 8 cm ² DF point < (32/69)	C/C = 3.5E18 cm ⁻³ 10 cm ² < DF Area < 12 cm ² (40/69) < DF point < (48/69)	C/C = 3.0E18 cm ⁻³ 15 cm ² < DF Area (60/69) < DF point
Zn	C/C = 3.5E18 cm ⁻³ DF Area < 8 cm ² DF point < (32/69)	C/C = 3.5E18 cm ⁻³ 15 cm ² < DF Area (60/69) < DF point	

to produce 2 inch Sn doped and Fe doped InP single crystals with low dislocation densities less than 5X10³ cm⁻² and large dislocation-free (DF) area crystals doped with S or Zn by the TB-LEC methods.

Figure 2 shows that the dislocation density strongly depends on the crystal/crucible rotational speed conditions. The thermal baffle conditions and the relative

rotational speeds between the crystal and the crucible are shown in Fig. 2. The dislocation densities increase with increasing the relative rotational speeds. The SL interface shape is shown in Fig. 3. The thermal baffle conditions and the relative rotational speeds are shown in Fig. 3. The SL interface can be made flatter by reducing the axial temperature gradient and the relative rotational speeds.

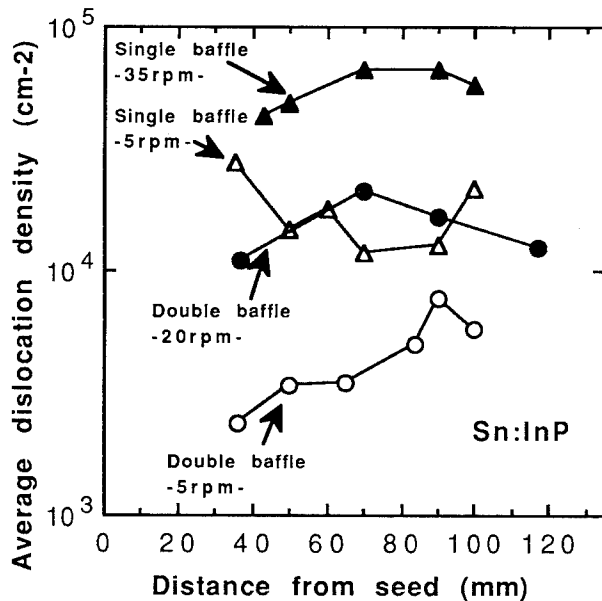


Fig. 2. Average dislocation densities of Sn doped InP crystals as a function of distance from seed. The thermal baffle and the relative rotational speed conditions are also shown.

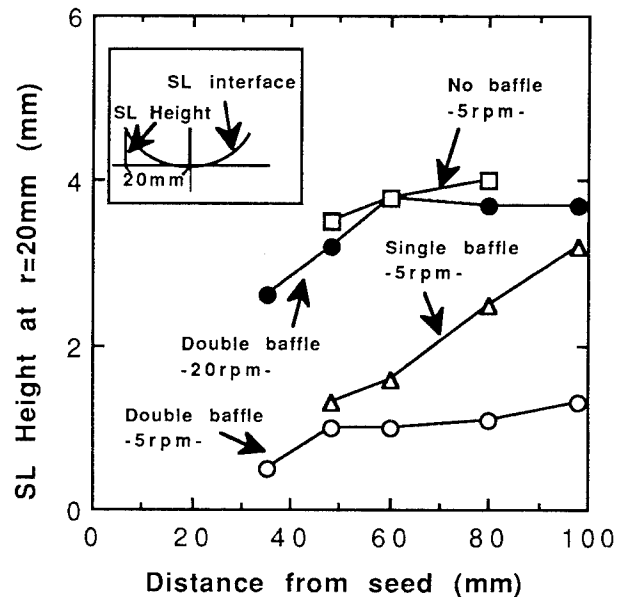


Fig. 3. Solid-liquid interface shape of InP crystals as a function of distance from seed. The thermal baffle and the relative rotational speed conditions are also shown.

Figure 4 shows the dependence of the dislocation densities on the cooling speed after growth. The dislocation densities of the crystal that is cooled slowly is lower than that of the crystal which is cooled fast. Figure 5 shows Huber etched S doped InP wafers. Clear slip lines can be observed in a crystal that is cooled fast.

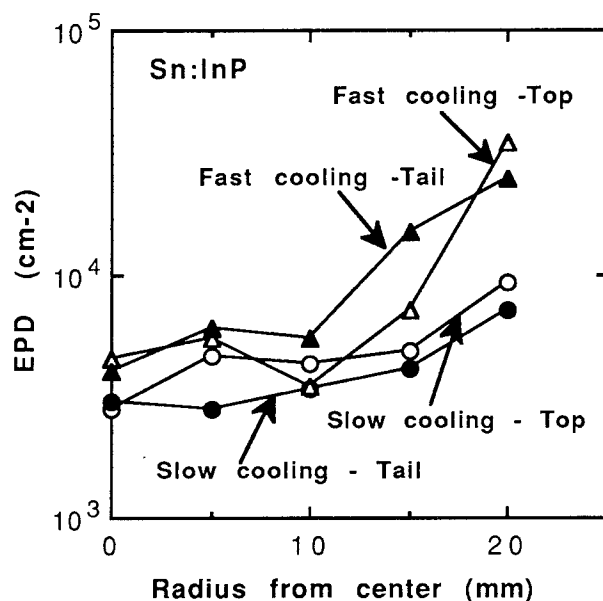


Fig. 4. Dislocation densities of Sn doped InP as a function of radius from center. The cooling speeds after the growth are also shown.

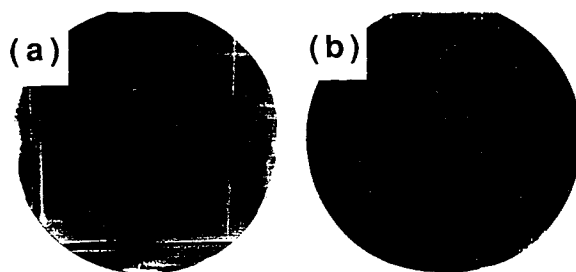


Fig. 5. Huber etched S doped InP wafers. (a) fast cooled sample. (b) slowly cooled sample.

Figure 6 shows the correlation between the weight of the pBN crucibles and DF area of S doped InP crystals. The horizontal axis shows the normalized pBN crucible weight. We define the initial weight of the pBN crucible before using is unity. It is clear that the DF area decreases with decreasing the weight of the crucible.

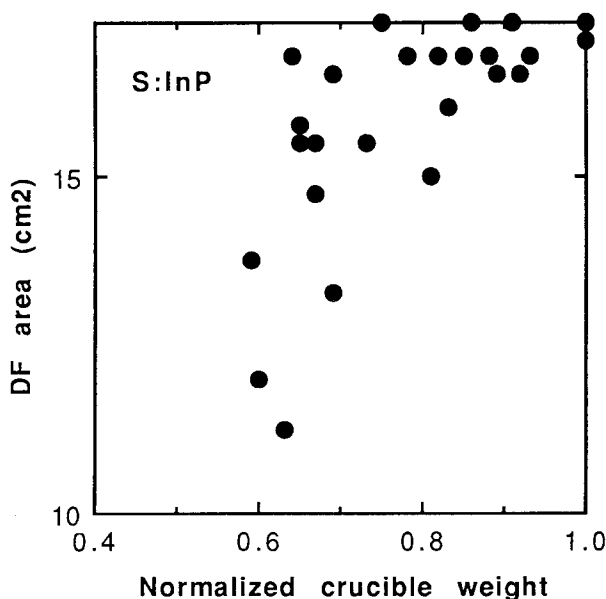


Fig. 6. DF area of S doped InP as a function of normalized weight of pBN crucibles.

3. Discussions

To reduce the dislocation density, reduction of the temperature gradient is effective. As shown in Fig. 1, the axial temperature gradient can be reduced by using a thermal baffle. Table 1 shows that the dislocation densities can be decreased by using the thermal baffle. Figure 3 shows that the SL interface can be made flatter using the thermal baffle. It means that the radial temperature gradient can also be reduced using the thermal baffle. It is well known that the lowering of the temperature gradient raises the temperature of the crystals at the surface, which results in a damage because of the high dissociation pressure of InP. In the TB-LEC method, even if we use the double thermal baffle, dissociation problem was not found. In this case, the temperature of the B_2O_3 at the surface is about 780°C . Though this temperature is not so high compared with other methods, such as VGF[1], VCZ[2] and PC-LEC[3], low dislocation density InP crystals can be grown by the TB-LEC methods by optimizing the other growth conditions.

Figure 2 shows that the dislocation densities strongly depend on the rotational conditions. By controlling the crystal rotation and crucible rotation, the SL interface

shape can be changed. By decreasing the relative rotation number, i.e. the difference between crucible rotation and crystal rotation numbers, the SL interface shape can be made flatter. Even if the temperature gradient is low, the dislocation density could not be decreased under the non-optimized rotational conditions as shown in Fig. 2.

Figure 4 shows that the dislocation densities also depend on the cooling speed in the LEC furnace after the crystal growth. Crystals with low dislocation densities are susceptible to the increase of the dislocation densities by fast cooling since the dislocations are easily generated due to thermal stress during the cooling process. Clear slip lines can be observed in the S doped InP crystal that is cooled fast. We have shown that the dislocation free S doped InP crystals become rectangular in shape[5]. The rectangular shape of the slip lines in Fig. 5 is probably due to the rectangular shape of the crystal.

Figure 6 shows that the dislocation densities depend on the pBN crucible weight. We have shown that the pBN crucible is useful to reduce the dislocation density compared with the SiO₂ crucible[4]. It is probably due to the difference of the thermal conductivity of the materials. In fact, we have found that the SL interface of the crystals grown using the pBN crucible is flatter than that of the crystals grown using the SiO₂ crucible. It is well known that the weight of the pBN crucible decreases with increasing crystal growth number. The decrease of the weight of the pBN crucible means the decrease of the thickness of the pBN crucible wall. Thus the thermal conductivity of the pBN crucible will change with the growth number increase. Then the dislocation densities increase with the decrease of the crucible weight.

4. Conclusions

We have successfully grown low dislocation density InP crystals by the TB-LEC method. For the reduction of dislocation densities, various growth conditions such as axial temperature gradient, crystal/crucible rotational speed, cooling conditions and the weight of the pBN crucible must be optimized.

Acknowledgment

The authors are grateful to Mr. E. Ono, Dr. Y. Taniguchi, Dr. O. Oda and Mr. K. Kohiro for their encouragement.

References

- [1]. T. I. Ejim, F. Simchock and M. Monberg, 1989 Proceedings of the First Int. Conf. on InP and Related Materials for Advanced Electronic and optical Devices, Oklahoma, SPIE Vol. 1144, pp37.
- [2]. M. Tatsumi, T. Kawase, T. Araki, N. Yamabyashi, T. Iwase, Y. Miura, M. Murai, K. Tada and S. Akai, 1989 Proceeding of the First Int. Conf. on InP and Related Materials for advanced Electronic and Optical Devices, Oklahoma, SPIE Vol. 1144, pp18
- [3]. K. Kohiro, K. kainosho, H. Shimakura, T. Fukui and O. Oda, 1990 Proceedings of the Second Int. Conf. on InP and Related Materials for Advanced Electronic and Optical Devices, denver, pp35
- [4]. R. Hirano, T. kanazawa and M. Nakamura, Proc. 4th Int. Conf. on InP and Related Mater., pp546(1992)
- [5]. R. Hirano, I. Itoh, T. Itokawa, H. Onodera and M. Nakamura, Proc. 5th Int. Conf. on InP and Related Mater., pp648 (1993)
- [6]. K. Kohiro, K. Kainosho, R. Hirano, M. Uchida, S. Katsura, H. Kurita, T. Fukui and O. Oda, Proc. 6th Int. Conf. on InP and Related Mater., pp359 (1994)
- [7]. A. Huber and N. T. Linh, J. Crystal Growth 29, 870 (1990)

PHOTOELLIPSONOMETRY CHARACTERIZATION OF ELECTRONIC PROPERTIES FOR InP

WP3

Tadashi Saitoh, Kensaku Nakamura, and Yi-Ming Xiong
Division of Electronic and Information Engineering, Tokyo University of Agriculture and Technology
Koganei, Tokyo 184, Japan

Hideki Hasegawa
Research Center for Interface Quantum Electronics, Hokkaido University
Sapporo 060, Japan

ABSTRACT

Photoellipsometry, a contactless optical method, was used for the characterization of doped InP semiconductor materials. Two types of InP samples were investigated, namely, *p*-InP substrate and undoped InP thin layer (with a thickness of 100 nm) on heavily doped *n*-InP substrate. Our main objective was to determine surface built-in electric field strength, broadening, and critical point energies for each given sample. The measured spectra were analyzed using the Franz-Keldysh theory with the inclusion of broadening effects. Good agreement found between the measured and calculated spectra indicates that theories and models used were appropriate for the samples studied and that the calculated results were reliable.

INTRODUCTION

Since its inception [1-3], photoellipsometry (PE) has proved useful in the characterization of doped semiconductor materials [2-3] and semiconductor microstructures [4-5]. PE incorporates spectroscopic ellipsometry (SE) with the addition of an above-bandgap laser pump beam directed at near-normal incidence onto the sample surface. Shown in Fig. 1 is the schematic diagram of the PE apparatus used, which combines the features of both SE and photoreflectance (PR), thus providing more complete information not available in separate applications. A major advantage of PE is that it allows the direct and simultaneous measurements of the built-in electric field-induced changes in both the real and imaginary parts of the pseudodielectric function $\langle \epsilon \rangle$ of a given semiconductor sample, *i.e.*, $\delta \epsilon_1$ and $\delta \epsilon_2$, on the wavelength-by-wavelength basis without the need for a Kramers-Kronig transformation. This feature allows tighter constraints to be imposed on the models representing more complicated structures, thereby increasing the confidence in the data analysis. The measured PE spectra can be analyzed using the Franz-Keldysh (FK) theory formulated by Aspnes [6] for the determination of the sample's electronic properties such as built-in field strength, depletion width, broadening, critical point (CP) energies, *etc.* It was on the basis of these features that PE was used for the characterization of the given InP samples.

SAMPLES AND MEASUREMENTS

For the two samples measured in this work, one was a *p*-InP substrate with the doping density of about $7.5 \times 10^{17} \text{ cm}^{-3}$ and the other was an InP Van Hoof structure [7], containing an undoped InP layer with a thickness of 100 nm epitaxially grown on top of a heavily doped *n*-InP

substrate with the doping density of about $5.4 \times 10^{18} \text{ cm}^{-3}$. All the PE measurements were taken in room air with the probe beam incidence angle set at 75° , in the spectral region near the InP fundamental bandgap E_0 CP. The power of the laser pump beam was about 10 mW.

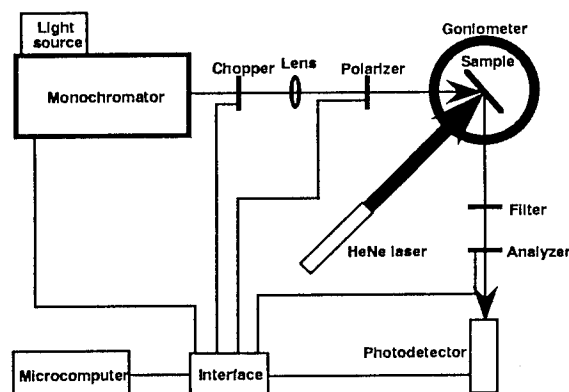


Fig. 1 Schematic diagram of the PE apparatus used in this work.

THEORIES AND MODELING METHODS

For a uniformly doped *p*-InP substrate, its surface Fermi level is pinned, making the energy bands bend downwards and giving rise to a built-in field, which varies linearly from a maximum value at the surface to zero at the edge of the depletion region, in the direction normal to the sample surface [8]. The origin of pinning is not well understood. It could be due to the presence of either surface states, or native surface defects, or both. Similarly, for an InP/*n*-InP Van Hoof structure, its surface Fermi level is pinned. At the interface, the heavily doped *n*-InP substrate pins the Fermi level of the back side of the

undoped layer near the conduction band. As a result, a uniform field is present in the top layer for this type of structure [7]. Under the pump beam illumination, electron-hole pairs (free carriers) are created in the sample. The free carriers generated near the surface region are redistributed via charge separation so as to reduce the band bendings and consequently the original field strength. The changes in the built-in field(s) also alter the dielectric function ϵ of the given material near CPs via the FK effect, which can be measured by SE and analyzed with an appropriate model.

SE measures ψ and Δ as a function of wavelength (or photon energy). These two parameters are related to the sample's optical properties and structure through the following expression [9]

$$\rho \equiv \tan\psi \exp(i\Delta) = R_p/R_s, \quad (1)$$

where R_p and R_s are, respectively, the complex reflection coefficients for light polarized parallel (p) and perpendicular (s) to the plane of incidence.

With each pair of ψ and Δ measured, one can obtain $\langle\epsilon\rangle$, using the two-phase (ambient-substrate) model, from the following expression [9]

$$\begin{aligned} \langle\epsilon\rangle &= \langle\epsilon_1\rangle + i\langle\epsilon_2\rangle \\ &= \epsilon_a \sin^2\phi \{1 + [(1-\rho)/(1+\rho)]^2 \tan^2\phi\}, \end{aligned} \quad (2)$$

where ϵ_a is the dielectric constant of the ambient ($\epsilon_a \approx 1$ in air) and ϕ is the probe beam incidence angle. It should be noted that $\langle\epsilon\rangle$ represents the combined dielectric response from overlayer and substrate and that $\langle\epsilon\rangle$ becomes ϵ only if all the surface effects, *e.g.*, the surface native oxide overlayer, are removed from the substrate. However, $\langle\epsilon\rangle$ is a useful parameter, as it directly relates the measured parameters ψ and Δ to the fundamental properties of interest, such as the true bulk dielectric function of a given material.

PE operates on a similar principle to that of PR, in which an above-bandgap pump beam photogenerates free carriers, which in turn redistribute so as to reduce the built-in field(s) near the sample's surface and/or interface region(s). The field-induced changes in both the real and imaginary parts of $\langle\epsilon\rangle$ can be obtained using [1]

$$\delta\epsilon_1 = \langle\epsilon_1(\text{pump beam off})\rangle - \langle\epsilon_1(\text{pump beam on})\rangle \quad (3a)$$

$$\text{and} \quad \delta\epsilon_2 = \langle\epsilon_2(\text{pump beam off})\rangle - \langle\epsilon_2(\text{pump beam on})\rangle, \quad (3b)$$

where the real and imaginary parts of both $\langle\epsilon(\text{pump beam off})\rangle$ and $\langle\epsilon(\text{pump beam on})\rangle$ can be obtained from Eq. (2). Note that Eqs. (3a) and (3b) were the means by which the measured PE spectra were obtained in this study.

The FK theory formulated by Aspnes [6] describes the electric field-induced effects on semiconductors near CPs.

For a uniform field F , the field-induced change in ϵ due to the FK effect near an M_0 CP, *e.g.*, the E_0 CP, is given by [6]

$$\begin{aligned} \delta\epsilon(F, E) &= \delta\epsilon_1(F, E) + i\delta\epsilon_2(F, E) \\ &\equiv (C\theta^{1/2}/E^2)[G(\eta) + iI'(\eta)], \end{aligned} \quad (4)$$

where E is the photon energy, C contains the interband transition matrix element, and θ and η are given by $(\pi e^2 F^2 / \mu \hbar)^{1/3}$ and $2\pi(E_0 - E)/\hbar\theta$, respectively, where μ is the interband reduced effective mass at the CP. The electro-optical functions G and I' are given by the combinations of Airy functions, their derivatives, and the unit step function.

In the case of a nonuniform field $F(z)$ (*e.g.*, the field in a uniformly doped III-V semiconductor substrate), where its value varies over the depletion width d in the z direction normal to the surface, the field-induced change in ϵ can be obtained from [6]

$$\delta\epsilon(F, E) = -2iK \int_{-d}^0 \delta\epsilon[F(z), E] \exp(-2iKz) dz, \quad (5)$$

where $\delta\epsilon[F(z), E]$, the change due to the local field $F(z)$, can be obtained from Eq. (4) and $K = 2\pi e^{1/2}/\lambda$ is the unperturbed propagation constant of the probe beam in the sample.

In this study, all the effects of broadening were assumed to be Lorentzian type. Accordingly, the field-induced change in ϵ with the inclusion of broadening effects is given by [6]

$$\delta\epsilon(F, E + i\Gamma) = 1/\pi \int_0^\infty \delta\epsilon(F, E') \Gamma dE' / [(E - E')^2 + \Gamma^2], \quad (6)$$

where Γ is the broadening parameter and the unbroadened change $\delta\epsilon(F, E')$ can be obtained from either Eq. (4) or Eq. (5), depending on the sample under investigation.

Batchelor *et al.* [10] recently made electroreflectance studies of GaAs, in which the parameter Γ in an above-bandgap E_g CP region (*e.g.*, in the above- E_0 CP region) was expressed by $\Gamma = \Gamma_0 \exp[\delta(E - E_g)]$, where Γ_0 is the broadening parameter and δ is the proportionality factor. This expression was proposed based on the assumption that, for more highly excited electrons in the conduction band, more rapid relaxation would take place due to the increased chances of being scattered into other states, and therefore Γ would be likely to increase with increasing photon energy. This approach was also adopted in this work.

RESULTS AND DISCUSSION

As an example to illustrate the effects of the pump beam illumination in the samples studied, we show in the Fig. 2 the measured $\langle\epsilon_1\rangle$ and $\langle\epsilon_2\rangle$ spectra from the p -InP

substrate with the doping density of about $7.5 \times 10^{17} \text{ cm}^{-3}$. These spectra were obtained directly using Eq. (2). It can be seen that, as a result of the absorption of the pump beam photons in the sample, visibly large changes occurred near the bandgap region (around 1.34 eV) in both the $\langle \epsilon_1 \rangle$ and $\langle \epsilon_2 \rangle$ spectra. For the same sample, the large FK oscillations can be observed in the above-bandgap region from the measured PE spectra, *i.e.*, $\delta \epsilon_1$ and $\delta \epsilon_2$ spectra, as shown by the circled lines in Fig. 3. These spectra were obtained from Eqs. (3a) and (3b). The exponentially decaying tail seen in the below-bandgap region in the measured $\delta \epsilon_2$ spectrum indicates that photon-assisted tunneling had taken place in the sample during the measurements.

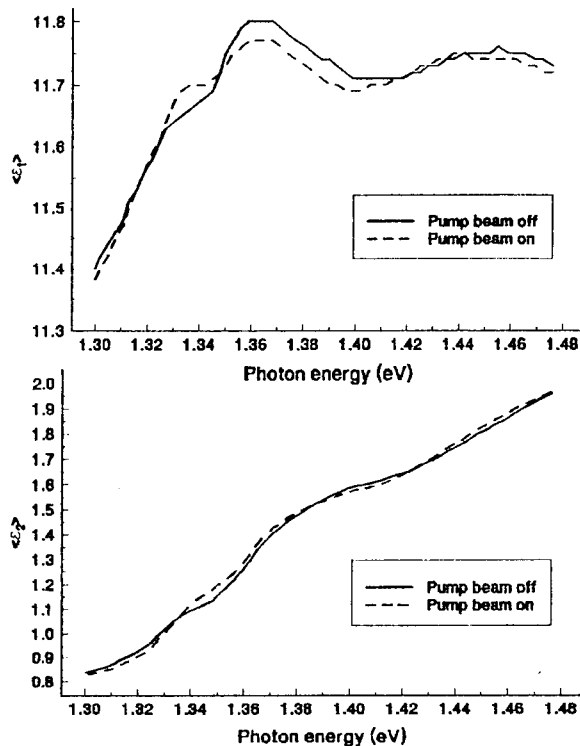


Fig. 2 Measured PE spectra for a *p*-InP substrate with the doping density of about $7.5 \times 10^{17} \text{ cm}^{-3}$.

To quantitatively model the measured spectra for the given sample, Eqs. (5) and (6) were used, in which a linearly decreasing field profile was assumed beneath the sample surface and contributions from the heavy-, light-, and split off-holes were included (note that the interband reduced effective masses of InP at the E_0 and $E_0 + \Delta_0$ CP regions were obtained from Ref. [11]). Shown by the solid lines in Fig. 3 are the calculated spectra based on the theories and model described above. These spectra were obtained using a maximum surface built-in field F_{max} of $1.05 \times 10^5 \text{ V/cm}$, a depletion width d of 70 nm, a broadening parameter Γ_0 of 10 meV with the proportionality factor $\delta = 3 \text{ eV}^{-1}$, and the E_0 and $E_0 + \Delta_0$

CP energies of 1.334 eV and 1.425 eV, respectively. Good agreement between the measured and calculated spectra in the chosen spectral region indicates that the theories and model used were appropriate and that the calculated results were reliable for the given sample under study. The kink in the 1.36 eV region seen in the measured spectra may be due to the interference effect generated by the spectrum from the heavy- and light-holes, respectively, which was something our program was not able to reproduce in the calculated spectra. Note that a similar phenomenon was observed in *p*-GaAs [12].

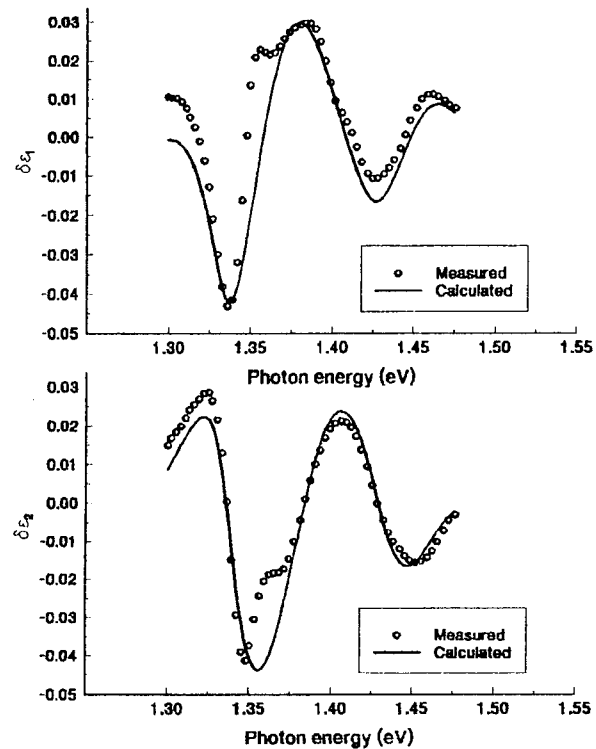


Fig. 3 Measured and calculated PE spectra for a *p*-InP substrate with the doping density of about $7.5 \times 10^{17} \text{ cm}^{-3}$. The calculated spectra were obtained assuming a linearly decreasing field profile near the sample surface region.

The measured PE spectra for the given InP/*n*-InP Van Hooft structure are shown by the circled lines in Fig. 4, from which one can clearly observe the large FK effect, as illustrated, for example, in the $\delta \epsilon_2$ spectrum. The model calculations for this sample was carried out using Eqs. (4) and (6), which means that only a uniform field (*i.e.*, the maximum surface built-in field) was assumed in the top InP layer. This assumption was made based on the analysis described in the previous section of this paper as well as the results of PR spectra obtained elsewhere from the similar structures [7]. The calculated spectra shown by the solid lines in Fig. 4 were obtained using $F_{\text{max}} = 0.35 \times 10^5 \text{ V/cm}$, $\Gamma_0 = 8 \text{ meV}$ with $\delta = 0 \text{ eV}^{-1}$, and $E_0 = 1.339 \text{ eV}$ and $E_0 + \Delta_0 = 1.425 \text{ eV}$. Contributions from the

heavy-, light-, and split off-holes were included in the model calculations. Good agreement between the measured and calculated spectra demonstrates that the theories and model employed were appropriate in the chosen spectral region for the given sample. Note that the broadening parameter obtained for this sample is smaller than that of the doped p -type sample, consistent with the fact that the top InP layer was undoped, therefore causing smaller broadening effect. The discrepancies seen between the measured and calculated spectra may be due to the effect of field inhomogeneity in the top InP layer, which was not considered in the model calculations.

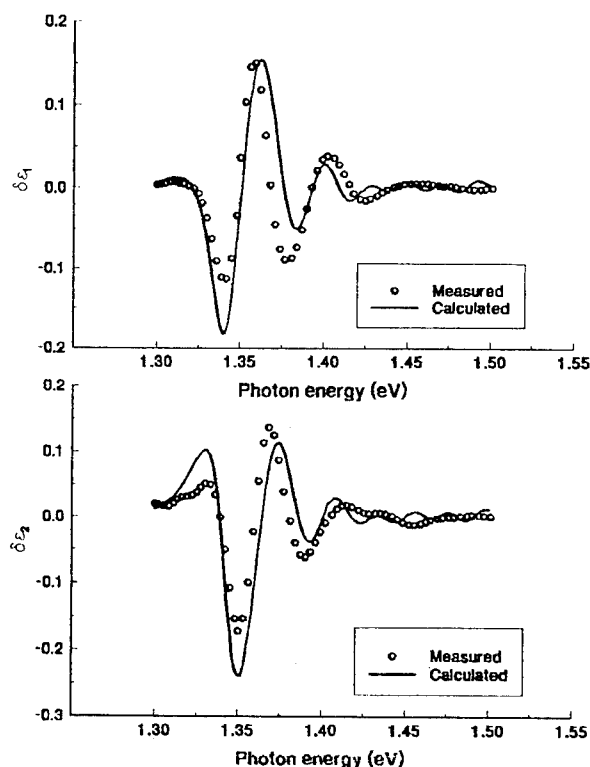


Fig. 4 Measured and calculated PE spectra for an InP Van Hoof structure [7], in which an undoped InP layer with a thickness of 100 nm was epitaxially grown on top of a heavily doped n -InP substrate with the doping density of about $5.4 \times 10^{18} \text{ cm}^{-3}$. The calculated spectra were obtained assuming the presence of a uniform field in the top InP layer.

SUMMARY

In summary, we have shown that PE is a powerful optical method for the characterization of electronic properties of the chosen samples. Detailed analysis of PE spectra allows the determination of sample parameters such as built-in field strength, depletion width, broadening, and CP energies.

ACKNOWLEDGMENTS

We would like to thank Leonix Corp. for letting us use their ellipsometer for the PE measurements. Our sincere thanks are given to Mr. S. Miura of Sumitomo Electrical Industries for providing us with the undoped InP/ n -InP sample.

REFERENCES

- [1] Y.-M. Xiong, Ph.D. dissertation, University of Nebraska, Lincoln (1993).
- [2] Y.-M. Xiong, P. G. Snyder, and J. A. Woollam, *J. Vac. Sci. Technol.* **A11**, 1075 (1993).
- [3] Y.-M. Xiong, P. G. Snyder, and J. A. Woollam, *Thin Solid Films*, **234**, 399 (1993).
- [4] Y.-M. Xiong, C. C. Wong, and T. Saitoh, *Jpn J. Appl. Phys.* (in press).
- [5] Y.-M. Xiong, C. C. Wong, and T. Saitoh, *Jpn J. Appl. Phys.* (submitted).
- [6] D. E. Aspnes, *Handbook on Semiconductors*, ed. T. S. Moss (North Holland, Amsterdam, 1980), Vol. 2, p. 109.
- [7] C. Van Hoof, K. Deneffe, J. De Boeck, D. J. Arent, and G. Borgh, *Appl. Phys. Lett.*, **54**, 608 (1989).
- [8] J. L. Shay, *Phys. Rev.*, **B2**, 803 (1970).
- [9] D. E. Aspnes and A. A. Studna, *Appl. Opt.*, **14**, 220 (1975).
- [10] R. A. Batchelor, A. C. Brown, and A. Hamnett, *Phys. Rev.*, **B41**, 1401 (1990).
- [11] L. Bornstein, *New Series*, ed. O. Madelung (Springer-Verlag, Berlin, 1982), Vol. 17a, p.282.
- [12] Y.-M. Xiong and T. Saitoh, Private Communications.

EVOLUTION OF NON-EQUILIBRIUM INTRINSIC DEFECTS IN INDIUM PHOSPHIDE DURING THE ZINC DIFFUSION FROM POLYMER SPIN-ON FILMS WP4

N. N. Faleev, A. T. Gorelenok, A. V. Kamanin, A. V. Merkulov, I. A. Mokina, E. L. Obukhova and N. M. Schmidt
A. F. Ioffe Physico-Technical Institute, Russian Academy of Sciences
St. Petersburg 194021, Russia

Generation and relaxation of non-equilibrium intrinsic defects (NID) induced by introducing Zn into a lattice of A_3B_5 semiconductors are known to be of first importance in the formation of distribution profiles of both defects and Zn in depth of a diffusion layer (1, 2). These processes are poorly studied experimentally. Most of investigations are generally devoted to an analysis of the final distribution profiles carried an information on a relaxed system. To follow evolution of NID, in the present paper a particular emphasis has been placed on the poorly studied initial diffusion stage (IDS) that corresponds the time interval needed to increase the temperature from room temperature to the diffusion one. The generation and relaxation of NID can manifest themselves in a change of mechanical properties of semiconductors as well as in an accumulation of more stable and extended defects such as dislocations and stacking faults as well as S-pits. The comparison studies of distribution profiles of defects and Zn atoms obtained after both IDS and the final diffusion stage (FDS) were carried out. Moreover, to evaluate the role of NID in the Zn diffusion into InP, the Zn distribution profiles were analyzed in accordance with the calculation for GaAs performed in the context of kick-out mechanism (1).

Experiment

The diffusion from polymer spin-on films doped by Zn was carried out into undoped n -InP (100) ($n = 2 \times 10^{16} \text{ cm}^{-3}$) and semi-insulating InP:Fe (100) in a resistive furnace in an ambient of hydrogen. Heating and cooling rates were 1°C s^{-1} and 2°C s^{-1} , respectively.

The employed technique (3) had no need of any additional protections against surface decomposition. The P and Zn atoms SIMS profiles investigated by IMS4F (CAMECA) were demonstrated that the P evaporation was lacking during the diffusion for a hour at 500°C (Fig. 1).

The X-ray structural technique and chemical exposure of imperfections were applied to monitor the defects. The curvature of structures was measured by High Resolution X-ray Diffractometer TRS-1.

A carrier concentration appropriate to electrically active Zn was measured by Hall effect as well as by Raman scattering excited by Ar-laser (514.5 nm) and detected by spectrometer DFS-24.

The Zn diffusion was carried out for different regimes depended on the relation between the Zn concentration in a

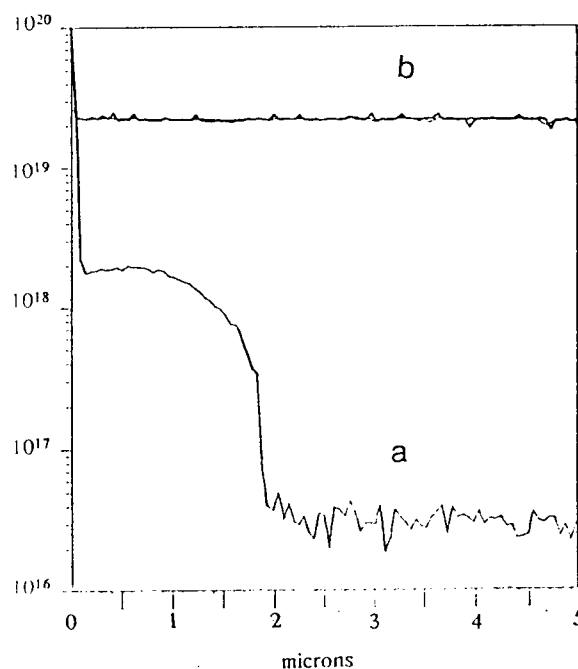


Fig. 1. SIMS distribution profiles of Zn (A) and P (B) after the Zn diffusion at 500°C during a hour.

near-surface region (N_{Zn}) and the Zn solubility limit (L_{Zn}) at the diffusion temperature. Regime I and Regime II corresponded to IDS for $N_{\text{Zn}} < L_{\text{Zn}}$ and $N_{\text{Zn}} > L_{\text{Zn}}$, respectively. Regime III ($N_{\text{Zn}} < L_{\text{Zn}}$) and Regime IV ($N_{\text{Zn}} > L_{\text{Zn}}$) corresponded to the Zn diffusion at the constant temperature during 30–60 min. The diffusion temperature was 450 – 600°C .

Results and discussion

The Zn profiles for Regime III (Fig. 1, curve A) was typical (see, for example, (4)). For Regime II the Zn profiles was observed (Fig. 2, curve A) were known in literature (for example, (5)) as anomalous.

Some authors (6) usually associated the anomalous profile of Zn atoms with supersaturation of NID in the diffusion region (1). The Zn profiles thus conformed to zero and high supersaturation for Regime I and Regime II, respectively. Moreover, in the latter case the NID distribution was irregular over the diffusion region.

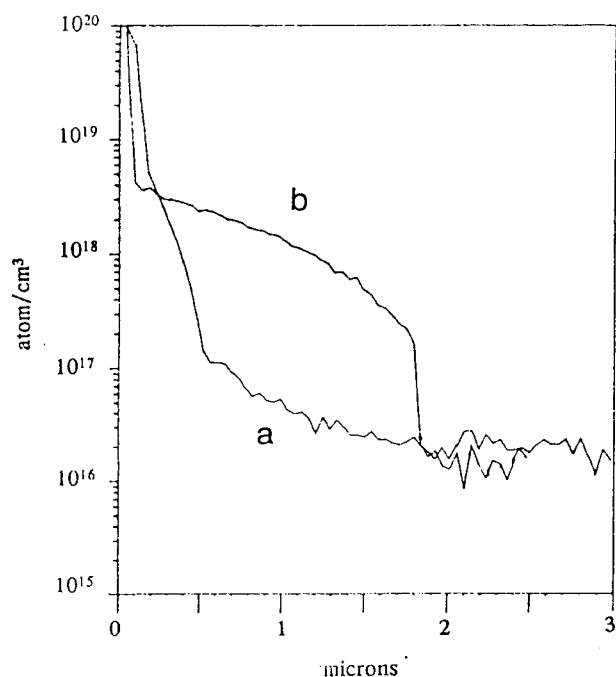


Fig. 2. SIMS distribution profiles of Zn in undoped InP: (A) Regime II after IDS to 450°C; (B) Regime IV at 450°C, 30 min.

Therefore, the distribution profiles of defects with depth of the diffusion layer would be expected to be dissimilar for Regime I and Regime II.

The depth distribution profiles of Zn atoms and defects in InP were investigated. These profiles were compared with those obtained at FDS (Regimes III and IV). The comparison showed that the two-step Zn profile was formed in InP:Fe even at IDS for both Regime I and Regime II (Fig. 3).

The Zn profiles in *n*-InP for Regime I differed from those for Regime II in a depth of Zn penetration only. The shape of the Zn profiles in *n*-InP for Regime II depended on the final temperature.

The Zn profile at the temperature below 500°C is shown in Fig. 2, curve A. For this case the penetration depth of electrically active Zn in the tail of the profile closely coincided with that for Regime IV (Fig. 2, curve B).

The diffusion layers formed at IDS were showed a low concentration of electrically active Zn in the near-surface region. The samples shown in Fig. 2, curve 1 and 2, had the acceptor concentration of $5 \times 10^{17} \text{ cm}^{-3}$ and $4 \times 10^{18} \text{ cm}^{-3}$, respectively.

For Regime II at temperature over 500°C, the Zn profiles liked those shown in Fig. 2, curve A were not usually observed. For this case the Zn profiles for Regime II were closely matched by those for Regime IV. Therefore, time dependence of diffusion was anomalously weak.

Table 1 gives the averaged data, for 5 samples of every types, for the diffusion layer depth distribution of defects obtained at the different Regimes in both InP:Fe and *n*-InP. In all cases the samples were nearly identical in the dislocation density that was 10^4 cm^{-2} .

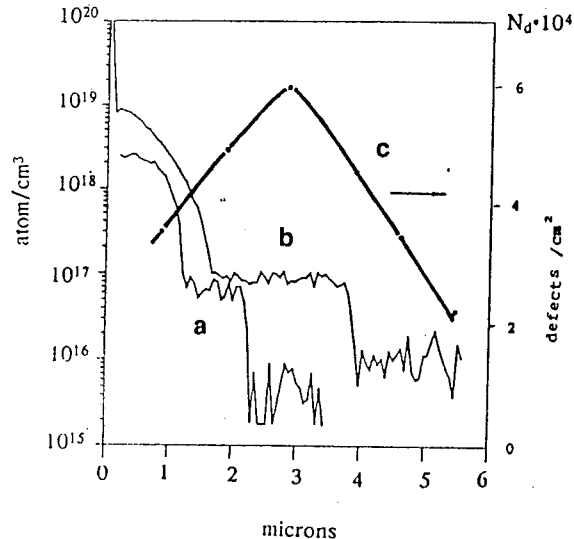


Fig. 3. Distribution profiles of Zn (A, B) and defects (C) in InP:Fe at IDS to 550°C. (A) Regime I, (B) Regime II.

TABLE 1. Density of defect revealed at the various depth of diffusion layers in InP:Fe and undoped *n*-InP.

Regime	Depth (μm)	Defect density ($\times 10^4 \text{ cm}^{-2}$)					
		small-size S		large-size S		D-pits	
		$\langle \text{Fe} \rangle$	n	$\langle \text{Fe} \rangle$	n	$\langle \text{Fe} \rangle$	n
I	0.5-0.8	$\sim 10^2$	$\sim 10^2$	3	2	4	8
	1.5	4	2	5	2	4	5
	2-3	—	2	3	2	3	5
	5	—	2	3	2	3	5
II	0.5-0.8	$\gg 10^2$	$\gg 10^2$	10	1.2	9	2.4
	1.5	10	8	1.5	8	9	7
	2-3	4	4	20	2	10	6
	5	—	4	2	2	5	6
III	0.5-0.8	6	3	3	8	6	6
	1.5	8	3	8	4	6	4
	2-3	6	3	3	4	3	4
	5	—	3	3	4	3	4

IDS occurred with a generation of a great quantity of S-pits (well over 10^5 cm^{-2}). In the case that $N_{\text{Zn}} > L_{\text{Zn}}$ in the near-surface region, the irregular depth distribution of defects as well as their anomalous in-depth penetration into InP were observed (Fig. 3, curve C).

Practically total relaxation of the introduced defects was occurred at FDS for $N_{\text{Zn}} < L_{\text{Zn}}$ during more than 30 min (Regime III). Moreover, in individual cases the dislocation density was observed to decrease from the initial value of $(4-6) \times 10^4 \text{ cm}^{-2}$ to $(1-2) \times 10^4 \text{ cm}^{-2}$, i.e., annealing out defects took place during the Zn diffusion.

The results were supported by X-ray investigations. The curvature of structure decreased to 30 meters after the Zn diffusion for Regimes I and II. FDS (Regime III) caused to increase in the curvature to 300-500 m, i.e., to practically initial curvature of the structure prior to the diffusion.

Conclusions

The investigation showed that the NID relaxation began even at IDS and proceeded very rapidly at 550–600°C. The process developed slower at temperature less more than 500°C as well as in InP:Fe.

Thus, comparison studies of the evolution of S-pits and dislocation at IDS and FDS allowed indirectly to investigate generation and relaxation of NID. It should be noticed that IDS carries more information on these processes than FDS.

References

- (1) T. Y. Tan, S. Yu, and U. Gösele, "Atomistic Mechanisms of Dopant-Induced Multiple Quantum Well Mixing and Related Phenomena", *Opt. Quantum Electron.*, Vol. 23, pp. S863–S881, July 1991.
- (2) M. Uematsu, K. Wada, and U. Gösele, "Non-Equilibrium Point Defect Phenomena Influencing Beryllium and Zinc Diffusion in GaAs and Related Compounds", *Appl. Phys. A, Solid Surf.*, Vol. 55, pp. 301–302, August 1992.
- (3) S. V. Belyakov, L. A. Busygina, A. T. Gorelenok, A. V. Kamanin, V. A. Kukatov, A. V. Merkulov, I. A. Mokina, N. M. Schmidt and T. A. Yure, "Zn Diffusion in InP and InP-Based Solid Solutions from Polymer Film Diffusants", *Sov. Tech. Phys. Lett.*, Vol. 18, pp. 415–416, July 1992.
- (4) B. Tuck and A. Hooper, "Diffusion Profiles of Zinc in Indium Phosphide", *J. Phys. D, Appl. Phys.*, Vol. 8, pp. 1806–1821, October 1975.
- (5) O. Hildebrand, "Anomalous Impurity Diffusion in III–V Compounds: The Consequence of Self-Induced Field Effects", *Phys. Status Solidi A*, Vol. 72, pp. 575–584, August 1982.

SIMULATION OF RAMAN SCATTERING FROM NONEQUILIBRIUM PHONONS IN InP AND InAs

WP5

D. K. Ferry¹, E. D. Grann², and K. T. Tsen²

¹Center for Solid State Electronics Research and Department of Electrical Engineering

²Department of Physics and Astronomy
Arizona State University, Tempe AZ 85287 USA

Introduction

Excitation of semiconductors by intense sub-picosecond laser beams has been a major method of studying the dynamics of far-from-equilibrium electron and hole systems. The thermalization of the initial distributions of these carriers probes the details of the band structure and the dynamics of electron-phonon interactions. We have used 0.6 ps laser pulses at 1.952 eV to study the generation of nonequilibrium LO phonons in both InP and InAs. These two materials provide a contrast in that the thermalization (relaxation) of the Raman signal probes different decay mechanisms. In InP, for example, we find that the decay of the Raman signal is dominated by the lifetime of the LO phonons. To the contrary, in InAs, our studies show that the decay of the Raman signal is dominated by the time required for particles to return to the Γ valley from the L valleys of the conduction band. This time is much larger than the LO phonon lifetime.

Raman Scattering in Semiconductors

Since the original studies of picosecond Raman scattering in semiconductors (1,2), it has become fairly well established that the cooling of the excited electron-hole plasma is dominated by the emission of optical phonons (on the picosecond time scale) and that the deviation of the phonon population from equilibrium is quite important in determining the cooling time of the plasma (3-9). Most of these studies have been carried out in the GaAs and/or GaAlAs system, and the dominant conclusion of these studies is that the decay (or cooling) time of the hot electron-hole plasma is limited by the lifetime of the hot, nonequilibrium polar optical phonons in the system. Typically, this decay time is about 7 ps in bulk GaAs. A buildup of the nonequilibrium phonons creates a "bottleneck" in which the carriers and the phonon population reach a common energy and reabsorption of the phonons slows the overall cooling process of the carriers.

In this paper, we discuss the measurement of nonequilibrium phonon populations in InP and InAs on the picosecond time scale through the use of Raman scattering, which monitors the nonequilibrium phonon population. The two materials used here provide different qualitative behaviors. The decay of the hot plasma in InP corresponds to a decay of the hot phonons, as in GaAs, and the lifetime of this decay is determined primarily by the lifetime of the hot phonons. In the case of InAs, however, the decay is dominated by the long storage times of the carriers in the satellite valleys of InAs, in that the very low effective mass of the Γ valley causes a relatively slow return to this latter valley. As a consequence, the cooling of the hot plasma, and the phonon

population, is governed not by the phonon lifetime, but by the return time of the carriers from the satellite valleys. In the following sections, we discuss the use of Raman scattering in the experiments, and the simulation of the process with an ensemble Monte Carlo technique.

Experimental Techniques

The undoped InAs and InP samples used in this work were grown by molecular beam epitaxy on (001)-oriented undoped InAs and InP substrates, respectively. They were about 2 μm thick.

The time-resolved Raman setup used in our experiment is shown in Fig. 1. The ultrashort pulses were generated by a DCM double-jet dye laser synchronously pumped by the second harmonic of a cw mode-locked Nd:YAG laser. The pulses had an autocorrelation full-width at half-maximum of ≈ 900 fs and an average power of ≈ 50 mW at a repetition rate of 76 MHz. In our pump-probe configuration, the ultrashort pulses were split into two beams of equal intensity but different polarization. An appropriate analyzer was placed in front of the entrance slit of the double monochromator so that the scattered light from the pump pulse was effectively eliminated while scattering from the probe pulse was allowed to be detected. The zero time delay at the sample was determined to within ± 0.3 ps by the observance of the interference effect which occurred when the pump and probe pulses were spatially and temporally overlapped. The dye laser was chosen to operate at $\hbar\omega = 1.952$ eV. The anti-Stokes Raman signal was collected and analyzed by a computer-controlled CCD Raman system. The

experiments were carried out in a backscattering geometry and at room temperature. From the power density of the pump pulse and the absorption coefficients of the samples, the average photoexcited carrier density was estimated to be $\approx 3 \times 10^{15} \text{ cm}^{-3}$ for both InAs and InP.

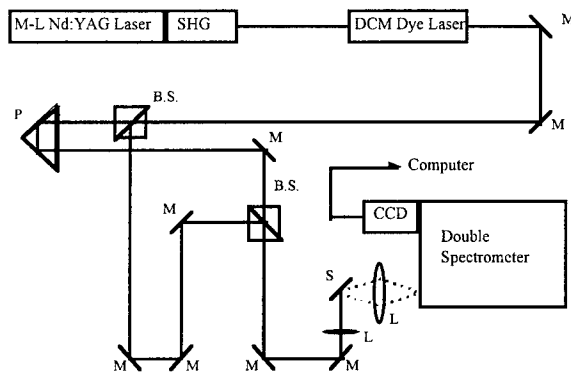


Fig.1 Experimental setup for a time-resolved Raman measurement. The abbreviations are: SHG: second harmonic generation system; M: mirror; B.S.: beam splitter; P: prism; S: sample; L: lens.

Monte Carlo Simulations

Simulations of the laser excited plasma were carried out by the ensemble Monte Carlo technique (10). In this simulation, only the electrons were considered, as the population of the polar modes was of primary interest. Hyperbolic energy bands were assumed for the various conduction bands, and all normal scattering processes were included. Interaction among the electrons was treated by a molecular-dynamics simulation technique, including the role of the exchange energy (11,12).

On the short time scales, which depend upon the system being modeled, the electron distribution undergoes a significant perturbation in the typical time between scattering events. During the first picosecond of relaxation, a finite density of electrons (holes) will lose about 10% of their energy in each 0.1 ps through the emission of a phonon. The phonon scattering is treated in the semi-classical Fermi golden rule model, with the final states of the scattering process being selected by a weighted random selection, as normal in Monte Carlo techniques. During this initial decay, the plasma is modeled by an ensemble of electrons, and this approach has been successfully vectorized. Carrier-carrier scattering, however, is a multi-carrier interaction which requires that these other carriers be available for the interaction. In general, a treatment similar to that for the phonons is possible only if the Coulomb interaction is treated as "instantaneous." For this reason, we treat the Coulomb interaction via a real-space molecular dynamics approach (13).

Modeling of the nonequilibrium phonons is handled within the ensemble Monte Carlo procedure by a secondary self-scattering and rejection process pioneered by Lugli *et al.* (14). The buildup of the phonon population (stored on a grid in momentum space) through emission and absorption processes is monitored throughout the simulation. The difference between the instantaneous value, for a given momentum wave vector, and some prescribed maximum value is used for the rejection technique. The presence of the nonequilibrium phonons slows the energy decay of the hot carriers.

Indium Phosphide

Excitation at 1.952 eV is assumed to create an electron-hole plasma with an approximate density of $3 \times 10^{15} \text{ cm}^{-3}$. This density is taken to be uniform in the excitation volume for the thin samples studied here. With this photon energy, carriers are excited from all three valence bands (the heavy-hole band, the light-hole band, and the spin-orbit split off band). The satellite valleys in InP lie considerably higher than those in the case of GaAs, and here it is assumed that the L valleys are 0.5 eV above the Γ minimum, while the X valleys lie approximately 0.98 eV above the latter minimum (15). At the high energy of the X valleys, there is no excitation into these valleys from the photo-excited electrons. On the other hand, a small but significant number of electrons are scattering into the L valleys. However, by the time at which the peak of the phonon distribution occurs (discussed in the next paragraph), essentially all of the carriers have returned to the central valley of the conduction band. This process is quite fast and a value of the Γ -L coupling constant of $7 \times 10^8 \text{ eV/cm}$ was used. Varying this value, as well as raising the separation energy between these two valleys, had no significant effect on the simulated Raman scattering. This value is comparable to that of GaAs. Once the carriers are in the central valley of the conduction band, cooling is dominated by a cascade of LO phonon emission processes. It is this cascade of emissions that leads to a buildup of the nonequilibrium phonon distribution. The wave vector involved in the emission of the polar LO phonon is quite small, due to the Coulombic nature of the interaction potential, so that the phonons are preferentially emitted into a small volume of phase space. The filling of this small volume is reflected in the buildup of the phonon population, which is treated as a fully momentum dependent quantity. While a small fraction of the carriers do transfer to the satellite L valleys, this number is so small, that it essentially plays no role in the cooling of the hot plasma in InP, as mentioned above. Rather, it is solely the phonon cascade and resultant non-equilibrium LO phonon distribution that governs the overall cooling of the hot plasma.

In Fig. 1, we plot the computed population of the polar LO phonons (with a wave vector appropriate to the range of wave vectors in the Raman scattering experiment) and the Raman signal that is measured for InP. The amplitudes are arbitrary, but the peak in the phonon population corresponds to about a 4-5% increase in the density of phonons. It is noted that the peak in phonon occupation is delayed relative to the start of the laser pulse, and this corresponds to the need for the phonon cascade to occur in order build up the population. The lifetime of the nonequilibrium phonons in the Monte Carlo has been taken to be 2.3 picoseconds and this value leads to a good agreement between the experiment and the simulation.

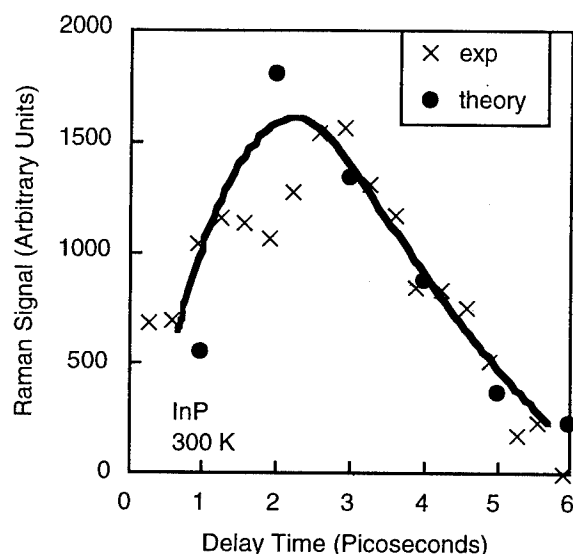


Fig. 1 Response of InP to 0.6 ps laser pulse at 1.952 eV. The solid curve is a guide to the eye for the theoretical fit to the data. The phonon lifetime is 2.0 ps.

Indium Arsenide

The model that we have used for InAs assumes that the L valleys are located approximately 0.72 eV above the Γ minimum, while the X valleys are located approximately 0.98 eV above the latter minimum. Since the band gap of InAs is so small (0.36 eV at 300 K), the electrons are excited well up into the conduction band, and a significant fraction of these are scattered into the X valleys. The latter, however, are scattered to the L valleys quite rapidly, so that the main dynamics after the laser pulse is dominated by the Γ and L valleys. In contrast to the case of InP, however, the coupling between the Γ and L valleys is such that the very low effective mass of the former leads to a quite slow return of the carriers from the L valley to the Γ valley. Indeed, it is this latter factor that is found to dominate the observed cooling of the nonequilibrium phonons.

In Fig. 2, we plot the population of the Γ and L valleys. From the figure, it may be seen that the population of the L valleys decays with a time constant of approximately 6 ps. This may be compared with the simulated and measured population of nonequilibrium phonons in Fig. 3. For the latter, a short phonon lifetime of 0.5 ps has had to be assumed. The storage of the carriers in the L valleys leads to a significant continued generation of nonequilibrium phonons at long times, and the overall decay of the optical phonons replicates the decay of the population of the satellite valleys. Even with an increased coupling constant (a value of the Γ -L coupling constant of 1.4×10^9 eV/cm was used), the return rate is relatively slow and dominates the final distribution of nonequilibrium phonons.

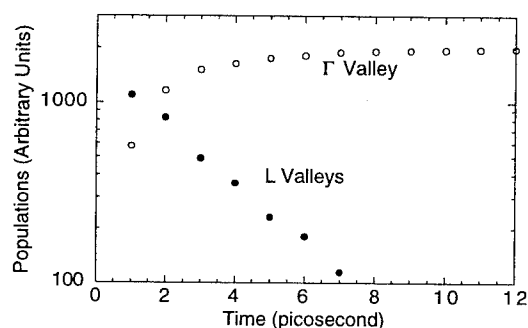


Fig. 2 The populations of the satellite L valleys and the central Γ valley, as a function of time after initiation of the laser pulse. The pulse half-width is 0.6 ps.

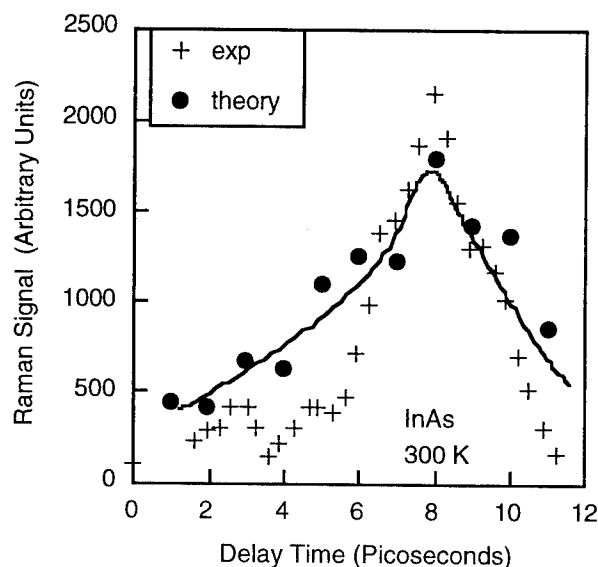


Fig. 3 Response of InAs to 0.6 ps laser pulse at 1.952 eV. The solid curve is a guide to the eye for the theoretical fit to the data. The phonon lifetime is 0.5 ps.

This work was supported by the U.S. Office of Naval Research (DKF) and the U.S. National Science Foundation (KTT).

References

1. D. von der Linde, J. Kuhl, and H. Klingerburg, Phys. Rev. B **37**, 1228 (1980).
2. J. A. Kash, J. C. Tsang, and J. M. Hvam, Phys. Rev. Lett. **54**, 2151 (1985).
3. W. Pötz and P. Kocevar, Phys. Rev. B **28**, 7040 (1980).
4. J. Shah, A. Pinczuk, A. C. Gossard, and W. Wiegmann, Phys. Rev. Lett. **54**, 2045 (1985).
5. P. Lugli and S. M. Goodnick, Phys. Rev. Lett. **59**, 716 (1987).
6. S. Das Sarma, J. K. Jain, and R. Jalabert, Phys. Rev. B **37**, 1228 (1988).
7. K. T. Tseng, R. P. Joshi, D. K. Ferry, and H. Morkoc, Phys. Rev. B **39**, 1446 (1989).
8. R. P. Joshi and D. K. Ferry, Phys. Rev. B **39**, 1180 (1989).
9. R. P. Joshi, K. T. Tseng, and D. K. Ferry, Phys. Rev. B **41**, 9899 (1990).
10. D. K. Ferry, A. M. Krizan, M.-J. Kann, and R. Joshi, in *Monte Carlo Device Simulation: Full Band and Beyond*, Ed. by K. Hess (Kluwer Acad. Pub., Norwall, MA, 1991) pp. 99-121.
11. M. J. Kann, A. M. Krizan, and D. K. Ferry, Phys. Rev. B **41**, 12659 (1990).
12. A. M. Krizan, M. J. Kann, D. K. Ferry, and R. Joshi, Phys. Rev. Lett. **65**, 1619 (1990).
13. D. K. Ferry, A. M. Krizan, M.-J. Kann, and R. P. Joshi, Comp. Phys. Commun. **67**, 119 (1991).
14. P. Lugli, C. Jacoboni, L. Reggiani, and P. Kocevar, Appl. Phys. Lett. **50**, 1251 (1987).
15. D. K. Ferry, *Semiconductors* (Macmillan, New York, 1991).

PHOTOCONDUCTIVITY & PHOTOLUMINESCENCE OF Cu DIFFUSED p-InP

WP6

D.Pal and D.N Bose

Materials Science Center, I.I.T Kharagpur 721302

West Bengal, India

Photoconductivity and photoluminescence measurements carried out on Cu diffused p-InP in the temperature range 70 K -350 K and 10 K - 140 K respectively. With 35 mW/cm² He-Ne laser radiation a high value of $I_{ph}/I_d = 2.6 \times 10^5$ was obtained at 200 K which decreased to 800 at 300 K. The Cu related emission band was obtained at 1.216 eV. From the line-shape and line-width analysis of the emission spectrum the vibrational energy for the ground and excited states were found to be 38 and 14 meV respectively. The configuration co-ordinate diagram of the defect was calculated which showed a small lattice relaxation.

Introduction

It has been observed recently that the electrical and optical properties of Cu diffused InP depend on the diffusion conditions (1). In this work a detailed study of Cu diffused p-InP has been carried out using dark conductivity, photoconductivity and photoluminescence measurements to elucidate the properties. The line-shape, line-width (FWHM) and the variation of intensity with temperature of the PL spectrum have been studied, from which the configuration co-ordinate diagram of the Cu center has been determined.

Experimental

High purity copper films were thermally evaporated on chemically cleaned p-InP (100 , $N_A = 4.6 \times 10^{15} \text{ cm}^{-3}$). Thermal diffusion was carried out in two steps in an open tube under Ar flow. Initially the Cu deposited sample was heated at 300°C for one hour and the temperature was then raised rapidly to 600°C and held for one minute. Surface protection was realized by placing the sample between two undoped InP pieces and covering with polycrystalline InP powder as a phosphorus source. The diffusion depth was found to be 160 μm using cleavage and staining technique, in good agreement with calculations. The Cu film remaining on the surface after the diffusion was removed and the sample polished to obtain mirror finish.

These samples were used for the measurements of SIMS, dark, photoconductivity and photoluminescence measurements. In-Zn pads to form ohmic contacts were fabricated for the photoconductivity measurements.

The temperature variation of dark and photoconductivity were examined between 70 K and 350 K. PL measurements were carried out using a McPherson monochromator and cooled InGaAs detector. An Ar ion laser (488 nm) was used as an excitation source. The samples were mounted on the tip of a closed He refrigerator and PL measurements were carried out between 10 K and 140 K.

Results

SIMS analysis has been carried out showing the penetration of Cu into InP with no loss of surface P. It showed no observable P deficiency on the surface of InP thus confirming that no surface degradation occurred. The resistivities of the control and Cu diffused samples were found to be 10.5 ohm cm and 2.6×10^5 ohm cm respectively.

From the plot of dark current vs temperature, the thermal activation energies of the Cu related deep levels were found to be 0.33 eV and 0.64 eV. The activation energy for the thermal quenching of photocurrent was found to be 75 meV for both above and sub band gap illuminations. At a light intensity of 35 mW/cm² of He-Ne laser, I_{ph} peaks occurred at 100 K and 195 K. The variation of I_{ph}/I_d with temperature is shown in figure 1. The ratio was very large with a maximum value of 2.6×10^5 at 200 K and 800 at 300 K.

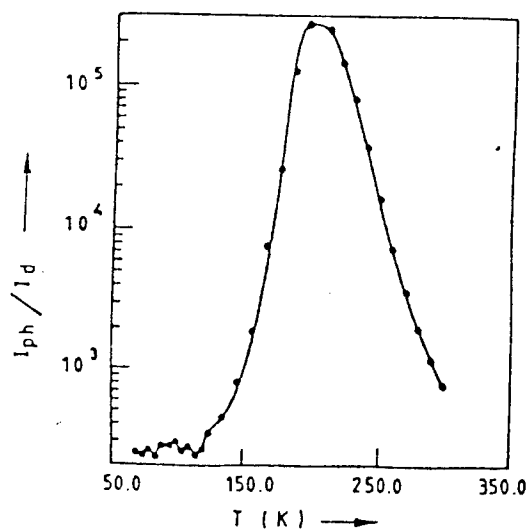


Fig. 1 Variation of I_{ph}/I_d with temperature.

The variation of photocurrent with the applied voltage between the contacts at different light intensities of the tungsten halogen lamp was studied. It was found that the photocurrent starts to saturate after 10 V and this threshold voltage is independent of the light intensity.

The photoluminescence spectrum obtained at 10 K is shown in figure 2. Only one Cu related band was observed. No bands were observed from the control samples. The line-shape of the band was calculated using the equation given below (2).

$$W_p = \sum_p \frac{S^p}{p!} \frac{1}{1 + [E - (E_0 - pE_p)]^2 / \delta^2} \quad \dots\dots\dots 1.$$

where S, p, E_0 , E_p and δ are the Huang-Rhys factor, number of phonons emitted, zero phonon energy & phonon life-time broadening respectively. Figure 2 shows the theoretical and experimental PL spectrum of the Cu band. Excellent agreement with the experimental spectrum was obtained for $S = 2.13$, $E_p = 38$ meV and $\delta = 26$ meV. This shows that the

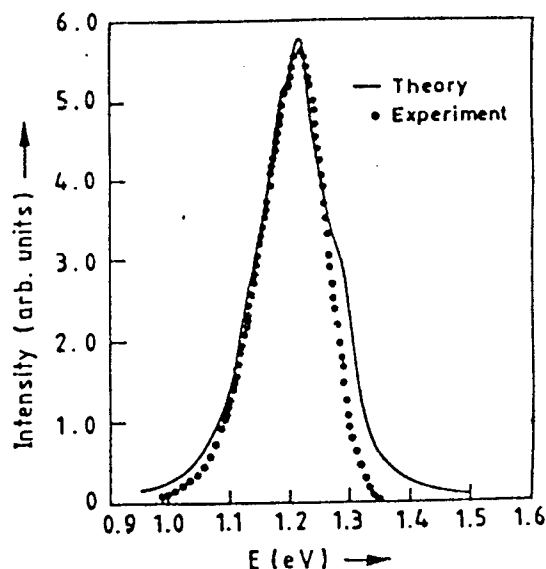


Fig. 2 PL spectrum of the Cu related defect.

coupled phonon energy is exactly the same as that reported for TO phonons (38 meV) at the Γ point.

The half-width of the Cu band was calculated using the CC model equation given below (3)

$$W = A \left(\coth \frac{h\nu_e}{kT} \right)^{\frac{1}{2}} \quad \dots\dots\dots 2.$$

where A is a constant which is equal to W as the temperature (T) approaches 0 K and $h\nu_e$ is the phonon energy of the excited state. Excellent agreement with the experimental

results was found for $h\nu_e = 14$ meV. Figure 3 shows the variation of experimental and calculated half widths with temperature. The FWHM at 10 K was found to be 129 meV. This was constant upto 40 K and increased rapidly thereafter.

Photoluminescence was found to be quenched as the temperature increased from 10 K to 120 K, the peak becoming unobservable at 140 K. The variation of PL intensity with the temperature has been studied. The activation energy for photoluminescence quenching was found to be 77.4 meV.

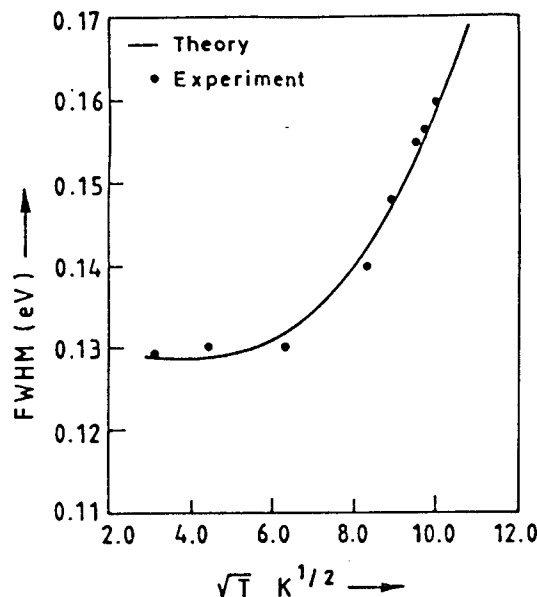


Fig. 3. Variation of line-width with temperature.

Discussion

The defect levels 0.33 and 0.64 eV above the valence band relating to Cu which have been obtained are in good agreement with the reported results(4). These levels may be due to Cu_{In} and $Cu_{In}-V_p$ respectively.

The photocurrent increased with the voltage applied between the two ohmic contacts due to increase of collection efficiency. After a certain voltage the photocurrent saturated because all the photo excited carriers reached the contacts before their recombination.

The configuration co-ordinate diagram has been determined following Hwang et al.(3) and shown in figure 4. The two curves are slightly displaced due to small value of X_0 , which is 0.079 Å.

From figure 2, it is seen that towards the high energy side the experimental curve deviates from the theoretical results and departs from a Gaussian. The CC model predicts a Gaussian emission band only when X_0 is large which is not true in the present case. However a transition from the lowest level of the excited state to the lowest level of the ground state limits the high energy of the emission. There is no such abrupt transition on the low

energy side of the emission band where the line-shape becomes Gaussian. Similar behavior was observed in GaAs (Zn) for the complex defect $V_{As} - Zn_{Ga}$ (3). It has been found that as the temperature increases more levels at higher energies are occupied and the high energy side of the Cu band is less abrupt.

The constant A of equation 2 is just the FWHM at low temperature (10 K) of the Cu band. From the line-width

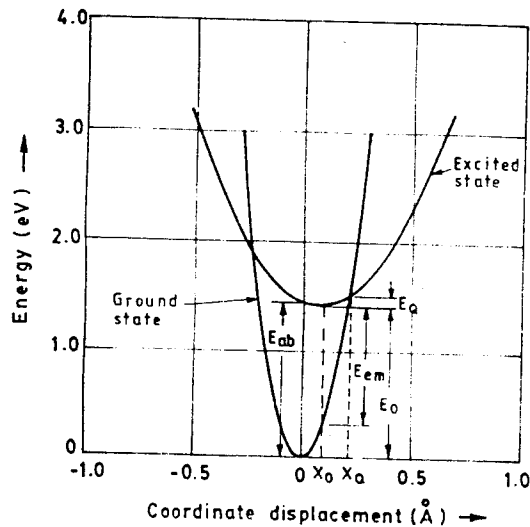


Fig. 4. Configuration co-ordinate diagram of the Cu related defect in InP.

fitting this was found to be 129 meV while experimentally the FWHM of the band at 10 K was 129.5 meV. Thus the experimental value agrees very well with theoretical calculation.

Conclusions

High gain photoconductivity has been observed in Cu diffused InP. Theoretical line-shape analysis of the 1.216 eV band due to Cu in p - InP has been carried out and the configuration co-ordinate diagram has been obtained for the first time.

References

- (1) K. Xie and C.R Wie, Semi-insulating properties and PL quenching in Cu diffused InP", J. Appl. Phys, Vol. 74, pp. 4546-4550, october, 1993.
- (2) H. Temkin, B.V Dutt, W.A Bonner and V.G Keramidas, "Deep radiative levels in InP" J. Appl. Phys. Vol. 53, pp. 7526-7533, November, 1982.
- (3) C. J Hwang, "Evidence for luminescence involving Arsenic vacancy-acceptor centers in p-type GaAs" Physical Rev. Vol. 180, pp. 827-832, April, 1969.
- (4) N. Kullendorff, L. Jansson and L.-Å Ledebø, "Copper related deep level defects in III-V semiconductors" J. Appl. Phys, Vol. 54, pp. 3203-3212, June 1983.

Raman scattering study of the clustering phenomena in InGaAsP grown by LPE on (100) and (111) GaAs

Touko Sugiura, Nobuyasu Hase, Kazumasa Hiramatsu¹ and Nobuhiko Sawaki¹

Department of Electrical Engineering, Toyota College of Technology,
2-1 Eisei-cho, Toyota-shi, Aichi 471, Japan

¹ Department of Electronics, Nagoya University,
Chikusa-ku, Nagoya 464-01, Japan

The quaternary InGaAsP alloys lattice matched to GaAs substrate are one of the most promising materials for the visible opto-electronic devices. The existence of the immiscible region have sometimes made it difficult to get a high performance of the devices. In the immiscible region, the photoluminescence (PL) spectra as well as the X-ray diffraction peak have always shown broadening, which is attributed to the fluctuation of the composition.^{(1),(2)} In the course of the study of the Raman scattering spectra, however, we have found that the phonon energy is well described by the simple theory neglecting the immiscibility.^{(3),(4)}

Since Raman scattering yields valuable information about the nature of the solids on a scale of the order of a few lattice constants, it is able to be used to study the microscopic nature of structural and/or topological disorder.^{(5)~(8)} In this paper, in order to investigate the short range ordering of the crystal, we study the asymmetric broadening of the Raman spectra.

The $\text{In}_x\text{Ga}_{1-x}\text{As}_y\text{P}_{1-y}$ epitaxial layers were grown by LPE on (100) or (111)A GaAs substrates at 785 °C.⁽¹⁾ The thickness of the layers were about 0.8 μm . The surface of the samples grown on (100) GaAs is not smooth in the region of immiscibility, but those grown on (111)A substrate was quite smooth even in the region of immiscibility. The composition was determined by analyzing the PL and X-ray diffraction spectra. Applying Vegard's law for the lattice constants, the requirement for lattice-matching of the quaternary layer to GaAs substrate yields a relationship between the composition parameters x and y as follows:

$$x=1-(0.2155+0.1896y)/(0.4176-0.0125y), \quad (1)$$

According to thermodynamical analysis,⁽¹⁾ the region of immiscibility are to occur in the range of composition $0.1 < y < 0.5$.

The Raman scattering spectra were measured in the backscattering configuration at room temperature using the Argon-ion laser, a double monochromator and a photomultiplier.

Figure 1 display the typical Raman spectra of

$\text{In}_x\text{Ga}_{1-x}\text{As}_y\text{P}_{1-y}$ grown on (100) GaAs substrate. The spectra exhibit several peaks due to GaP, InP, GaAs and InAs modes. The sharp peak found at about 380 cm^{-1} is attributed to the GaP-like longitudinal optical (LO) phonon, and the peak around 270 cm^{-1} is attributed to the GaAs-like LO phonon.

At first sight, both spectra in alloys were not described by a simple Lorentzian but subject to asymmetric broadening. This suggests that the samples include clustering of the composition. We will analyze the asymmetric broadening in terms of two half-widths, i.e., lower half-width Γ_l in the low-energy side and the half-width Γ_u in the high-energy side. The whole spectra could be decomposed to eight modes with

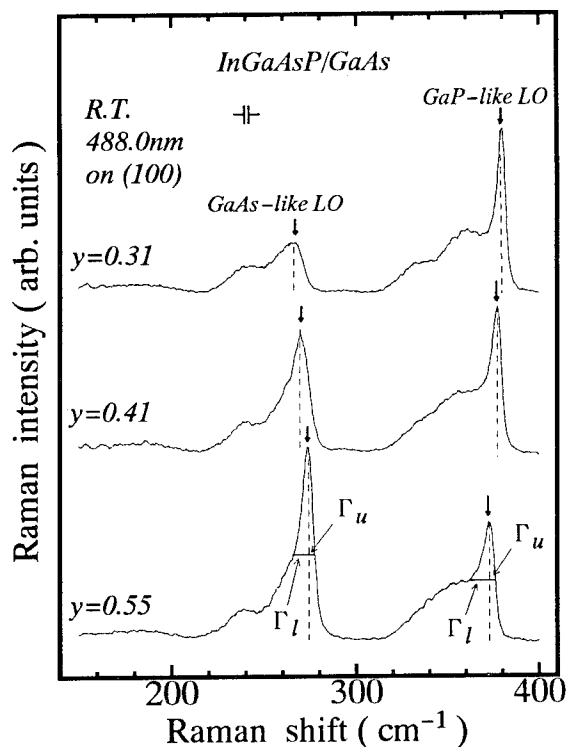


Fig. 1. Raman spectra of InGaAsP/GaAs

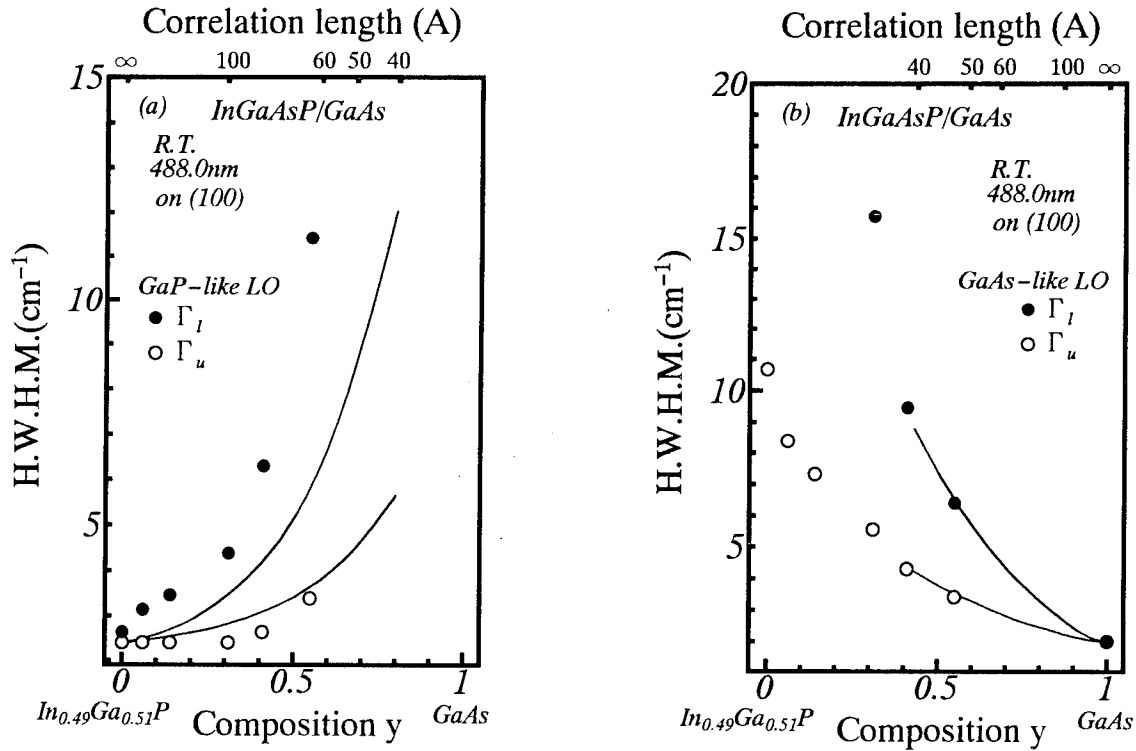


Fig. 2. Upper and lower half width of (a) GaP-like and (b) GaAs-like LO phonon mode as a function of y . The solid lines show the relationship between the correlation length L and the half-width obtained from SC model (see text).

appropriate broadening factor Γ 's. Apparently, the signals due to the GaAs-like LO and GaP-like LO modes are most prominent. So in the following we will concentrate our discussion on these two modes.

The half-width at half-maximum (HWHM) of two LO phonon modes of $\text{In}_x\text{Ga}_{1-x}\text{As}_y\text{P}_{1-y}$ grown on (100) GaAs are shown in Figs. 2(a) and 2(b) as a function of the composition y . As shown in Fig. 2(a), the GaP-like mode is almost symmetric at $y=0$, i.e., $\Gamma_l = \Gamma_u \approx 2.5 \text{ cm}^{-1}$. But asymmetric broadening is enhanced by increasing y . Remarkable enhancement is obtained in the region of immiscibility ($y > 0.14$).

For the GaAs-like LO phonon mode, similar asymmetric broadening can be seen in Fig. 2(b). At $y=1$, i.e., the spectra of LO phonon mode of pure GaAs was of Lorentzian, with $\Gamma_l = \Gamma_u \approx 2 \text{ cm}^{-1}$. The asymmetric broadening is enhanced by decreasing y . It is notable that the broadening is not decreased even in the samples out of the miscibility gap i.e., $y < 0.14$. Obviously, the broadening is enhanced more in the lower half-width, i.e., $\Gamma_l > \Gamma_u$. This is attributed to the clustering effect or the random distribution of the constituent atoms in

the crystal.

For the effect of strain in the growth process, the growth on (111) substrate is greater than that on (100) oriented substrate. Therefore, in the immiscible region, it is considered that to decrease by the effect of the stabilization induced substrate.

We will try to interpret the results in terms of the spatial correlation (SC) model.^{(5)~(8)} Because of the random distribution of atoms in an alloy, the region where we find only GaAs (GaP) bonds forms a GaAs (GaP) cluster. This is not a real cluster (micro-crystal), but for the LO phonon modes it works as a cluster since the mode will be localized within the region. Because the size and distribution of the cluster are not uniform, we will describe it with the correlation function of the Gaussian $\exp(-2r^2/L^2)$, where L is the correlation length that describes the average size of the cluster. The Raman intensity at a frequency ω , is given by

$$I(\omega) \propto \int \exp(-q^2 L^2/4) / \{ [\omega - \omega(q)]^2 + [\Gamma_0/2]^2 \} d^3q, \quad (2)$$

where Γ_0 is the spectral width for $y=0$ (GaP mode), or $y=1$ (GaAs mode).

As the dispersion $\omega(q)$ of the LO phonon, we adopt the analytical model based on a one-dimensional linear-chain model.⁽⁹⁾

$$\omega^2(q) = A + \{A^2 + B[1 - \cos(\pi q)]\}^{1/2}, \quad (3)$$

where $A = 4.26 \times 10^4 \text{ cm}^{-2}$ and $B = 7.11 \times 10^8 \text{ cm}^{-4}$ for GaAs mode and $A = 8.16 \times 10^4 \text{ cm}^{-2}$ and $B = 2.84 \times 10^9 \text{ cm}^{-4}$ for GaP. For simplicity, we assume a spherical Brillouin zone and Wigner Seitz cell.

We can evaluate Γ_l and Γ_u by eqs.(2) and (3) as a function of the correlation length L to fit the experimental results. That is we can estimate the magnitude of the correlation length L as a function of the composition.

The results are shown in Figs. 2(a) and 2(b) by solid lines. Considering the fact that the band width of GaP-like mode is narrower than that of GaAs-like mode, the broadening due to the clustering effect should be more prominent in GaAs-mode in agreement with the experimental shown in Figs. 2(a) and (b). But comparing the analytical results shown in Figs. 2(a) and (b), we know that the correlation length for GaP-like mode is longer than that for GaAs-like mode in the corresponding compositional region. Incidentally, the GaP-like mode in InGaAsP is of the localized mode and GaAs-mode is the gap mode. So the former reflects more the nature of the short range ordering, while the latter reflect the ordering in wider range. Thus the clustering effect will be more prominent is GaAs mode. If this is the case, simple analysis with a single correlation length as given above should be modified to include it. Since the exact dispersion $\omega(q)$ for GaP-mode is not known, we might not give further discussion on this point. Nevertheless it seems reasonable to suppose that the compositional dependence of Γ_l and Γ_u could be explain by the SC model.

Finally let's discuss on the effect of the substrate. Fig. 3 shows the full-width at half-maximum (FWHM) of GaAs-like LO phonon modes in the samples grown on (100) and (111)A substrate. We see that the both FWHM's of samples grown on (100) and (111)A substrates are equal each other. But the FWHM in layers grown on (111)A substrate is narrower than that grown on (100) substrate in the region of immiscibility. It is notable that the broadening of the FWHM of samples grown on (100) GaAs are wider that grown on (111)A substrate even at $y \sim 0$.

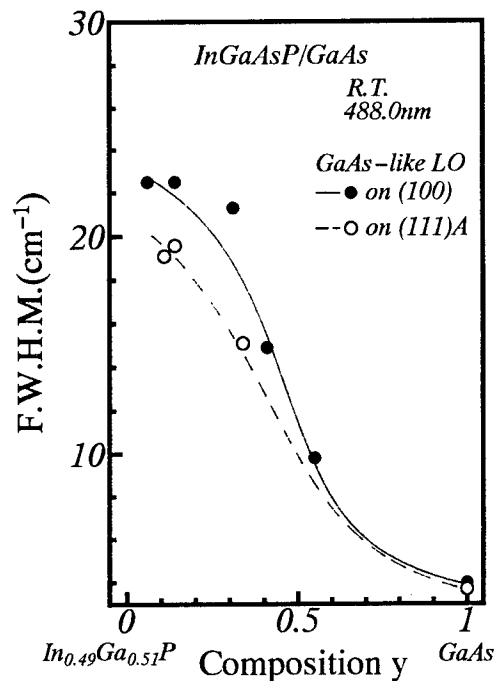


Fig. 3. The FWHM of GaAs-like LO phonon modes in the samples grown on (100) and (111)A substrates. The solid and dashed lines are guides for the eyes.

As for the effect of the substrate on the immiscibility, it is well known that the strain should stabilize the immiscibility in samples grown on (111) surface.⁽²⁾ The results shown in Fig.3 might be attributed to the same origin.

In Summary, the asymmetric broadening of the Raman spectra of $\text{In}_x\text{Ga}_{1-x}\text{As}_y\text{P}_{1-y}$ grown on GaAs substrate has been studied with the spatial correlation model. The broadening phenomena was found to be enhanced in the region of immiscibility, in agreement with the PL observation. But, in Raman measurements, the clustering effect has been found to occur even out of the miscibility gap. The effect is more enhanced in samples grown on (100) substrate than in samples grown on (111)A substrate. This shows that the stabilization of the growth due to the strain has also had a role to restrict the formation of the clustering in the growth process.

The authors would like to thank Dr. Tanaka for preparing some of the samples.

References

- (1) S.Tanaka, K.Hiramatsu, Y.Habu, N.Sawaki, and I.Akasaki, "The Initial Stage of LPE Growth of InGaAsP on GaAs in the Region of Immiscibility", *J. Crystal Growth* Vol. **79** (1986) pp.987-991.
- (2) S.Tanaka, K.Hiramatsu, Y.Habu, and I.Akasaki, "Effect of Lattice Mismatch between Epitaxial Layer and Substrate on Immiscibility of InGaAsP/GaAs LPE Layers", *J. Crystal. Growth* Vol. **87** (1988) pp.446-452.
- (3) T.Sugiura, N.Hase, H.Goto, S.Tanaka, K.Hiramatsu, N.Sawaki, and I.Akasaki, "Raman Scattering of InGaAsP Lattice-Matched to GaAs in the Region of Immiscibility", *Jpn. J. Appl. Phys.* Vol. **32** (1993) pp.2718-2721.
- (4) T.Sugiura, N.Hase, H.Goto, K.Hiramatsu, and N.Sawaki, "Raman scattering study of TO phonon modes in InGaAsP/GaAs", *Semicond. Sci. Technol.* Vol. **9** (1994) pp.1800-1804.
- (5) H.Richter, Z.P.Wang, and L.Ley, "The One Phonon Spectrum in Microcrystalline Silicon", *Solid State Commun.* Vol. **39** (1981) PP.625-629.
- (6) K.K.Tiong, P.M.Amirtharaj, and F.H.Pollak and D.E. Aspnes, "Effects of As⁺ ion implantation on the Raman spectra of GaAs: "Spatial Correlation" interpretation", *Appl. Phys. Lett.*, Vol. **44** (1983) pp.122-124.
- (7) P.Parayanthal and F.H.Pollak, "Raman Scattering in alloy Semiconductors: "Spatial Correlation" Model", *Phys.Rev.Lett.*, Vol. **52** (1984) pp.1822-1825.
- (8) K.Hayashi, N.Sawaki, and I.Akasaki, "Raman Scattering in ZnS_xSe_{1-x} Alloys", *Jpn. J. Appl. Phys.* Vol. **30** (1991) pp.501-505.
- (9) C.Kittel, *Introduction to Solid State Physics* .John Wiley&Sons, 1986, 6th ed., Chap.4 pp. 88-91.

Highly Controlled InGaAs(P)/InP MQW Interfaces Grown

By MOVPE Using TBA and TBP Precursors

T. Nakamura, S. Ae, T. Terakado, T. Torikai and T. Uji
Kansai Electronics Research Laboratory, NEC Corporation
9-1, Seiran 2-chome, Otsu, Shiga 520, Japan

Abstract

This paper reports that abrupt InGaAs/InP MQW interfaces are realized over 2-inch wafer by employing tertiarybutylarsine (TBA) and tertiarybutylphosphine (TBP) in place of AsH_3 and PH_3 , owing to elimination of the arsenic contamination into the InP layer after InGaAs growth and suppression of the As-P exchange reaction at the interfaces.

Introduction

Emerging optical access network systems place a great demand on high performance long wavelength laser-diodes (LDs) to realize low cost, low power consumption and high density integration. MOVPE grown MQW or strained MQW structures with abrupt heterointerfaces provide advantages for improving such LD performance. To obtain abrupt MQW interfaces, it is important to suppress exchange reaction or contamination of group V atoms as causes of roughness at the heterointerfaces, especially at As-P interface [1],[2].

For realizing these MQWs, tertiarybutylarsine (TBA) and tertiarybutylphosphine (TBP) have been recently studied for use as less toxic metalorganic precursors, in place of highly hazardous hydrides AsH_3 and PH_3 in MOVPE [3-7]. Other advantages for the epi-growth as well as less toxic properties have been indicated. For example, the greater cracking efficiency of TBA and TBP results in lower V/III ratio at typical growth temperature [3]. Furthermore, such high cracking efficiency appears to improve group-V compositional controllability [4] and uniformity [5],[6], especially for InGaAsP quaternary alloy growth.

This paper reports that TBA and TBP have the advantage of realizing abrupt heterointerfaces, especially at As-P interfaces.

Experimental

The epilayers were grown at 625°C by low-pressure (75 Torr) MOVPE with a susceptor-rotated horizontal reactor. The group-III sources used were trimethylindium (TMI) and triethylgallium (TEG), and the group-V sources were TBA and TBP. Hydride PH_3 was also used for comparison. 2-inch diameter InP (100) oriented wafers were used as substrates. A

pressure balanced run to vent gas switching scheme was employed to stabilize the growth pressure and thereby the interface composition. Interface analysis was carried out by high resolution X-ray diffraction, photoluminescence (PL) measurements at 4.2 K, and optical transmission measurements.

Results and discussion

Arsenic contamination in InP layer

In order to investigate the dependence of the group-V precursors in the As-P interfaces, two InP (0.08 μm)/InGaAs (0.48 μm)/InP (0.3 μm) DH structures were grown, where InGaAs was grown by TBA at V/III=5, while InP was grown by TBP at V/III=50 and PH_3 at V/III=130, respectively. Figure 1 shows X-ray rocking curves for these DH structures, which have layers consecutively grown without interruption intervals. Besides the InP and InGaAs peaks, a broad peak was observed at the low diffraction angle. From simulated X-ray rocking curves, this peak was attributed to arsenic incorporation into the InP cap layer. Provided that this incorporation's depth-profile is uniform in the thin InP cap layer, the amounts of arsenic composition on the contaminated cap layer were estimated to be 2.2% at the center and 4.5% at the edge of the wafer for PH_3 growth and 1% and 1.5% respectively, for TBP growth. Since the arsenic composition at the edge is twice as high as that at the center, the contamination originates mainly from residual arsenic in the growth chamber rather than from solid phase diffusion. The arsenic contamination was suppressed in the InP cap layer grown by TBP. This is due to higher effective V/III ratio for TBP growth[3], resulting in less arsenic incorporation under InP growth sequence.

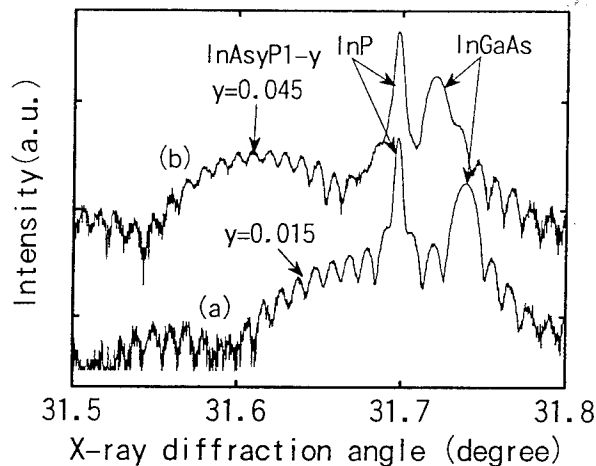


Fig.1: Experimental X-ray rocking curves at the edge of 2-inch wafer for InGaAs/InP DH structures, where InGaAs was grown by TBA, while InP was grown by (a) TBP at V/III=50 and (b) PH_3 at V/III=130, respectively.

As-P exchange at InGaAs/InP MQW interfaces

As mentioned above, TBP is an attractive option due to the arsenic incorporation suppression into successive InP layers. However, it is also important to control the growth interruption interval from InGaAs to InP in order to further suppress the arsenic contamination. InGaAs/InP lattice-matched MQW epilayers ($L_w/L_b=3\text{nm}/10\text{nm}$, $N_w=15$) were grown as a parameter of the interruption flow intervals T , where T is the TBP or PH_3 flow duration during growth interruption prior to InP barrier growth. Figures 2 and 3 show lattice mismatch(ϵ) and PL wavelength at 4.2K, respectively, as a function of the purge time T . In figure 3, ϵ_0 represents the mean lattice mismatch calculated by the following equation, $\epsilon_0=(\epsilon_w L_w + \epsilon_b L_b)/(L_w + L_b)$, where ϵ_w and ϵ_b are bulk lattice mismatches and L_w and L_b are thicknesses. For TBP growth, ϵ gradually reduced from the compressive strain to unstrain(ϵ_0) with increasing T , and accordingly the PL wavelength gradually decreased by 29nm. Since the PL wavelength shift nearly corresponds to monolayer removal from the interfacial region, these results indicate that compressive interfacial InAsP layers were desorbed to form abrupt interfaces. On the other hand, ϵ and the PL wavelength monotonically changed from compressive to tensile strain with increasing T for PH_3 growth. It is suggested that tensile InGaAsP interfacial layers were additionally introduced

as a consequence of As-P exchange reaction at the InGaAs well surfaces. Therefore, higher phosphorous pressure of TBP probably suppress the As-P exchange reaction on the InGaAs surface at optimum purge time. The interface abruptness was evidenced by differential optical transmission spectra at room temperature as shown in Figure 6. Exciton transmission peaks of the ground state electron-heavyhole (e-hh) and electron-light-hole (e-lh) transitions were clearly observed for TBP growth with a $T=45\text{sec}$ interval.

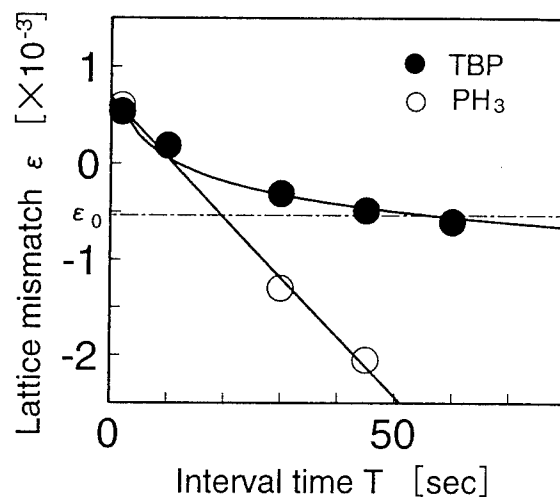


Fig.2: Mean lattice mismatch of InGaAs/InP MQWs as a function of TBP or PH_3 flow interval (T), where T is the TBP or PH_3 flow duration during growth interruption prior to InP barrier growth.

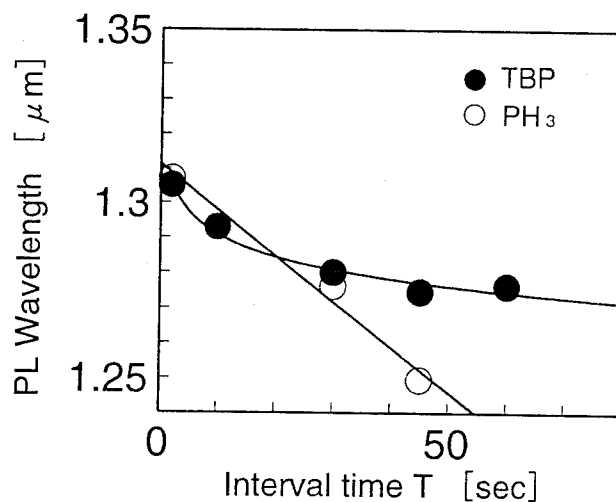


Fig.3: PL wavelength of InGaAs/InP MQWs at 4.2K as a function of interval time T .

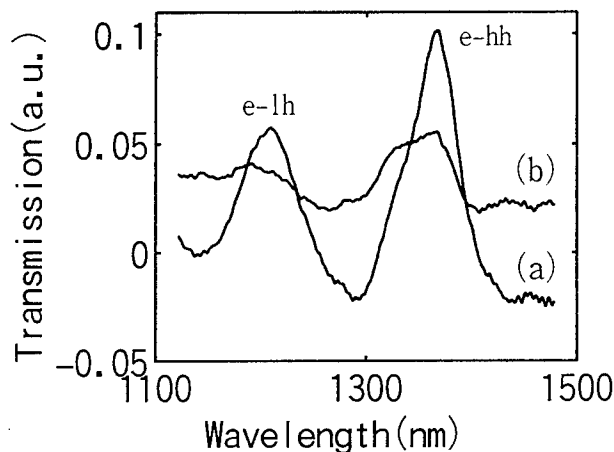


Fig.4: Differential optical transmission spectra of InGaAs/InP MQW at 300K for (a) TBP growth ($T=45$ s) and (b) PH_3 growth ($T=30$ s), respectively.

Summary

In conclusion, we have demonstrated abrupt InGaAs/InP MQW interfaces using TBA and TBP. These precursors are very attractive for suppressing the exchange or contamination of group V atoms at InGaAsP/InGaAsP MQW heterointerfaces. This approach has led to high performance $1.3\mu\text{m}$ MQW-LDs [8],[9].

Acknowledgements

The authors are thankful to Dr.H.Abe for valuable discussion and encouragement.

References

- [1] N. Kobayashi and Y. Kobayashi, "As and P desorption from III-V semiconductor surface in metalorganic chemical vapor deposition studied by surface photo-absorption", *Japan.J.Appl.Phys.*, Vol.30, No.10A, pp.L1699-L1701, October, 1991.
- [2] H. Kamei and H. Hayashi, "MOVPE growth of GaInAs/InP and GaInAs/GaInAsP quantum wells", *J.Cryst.Growth*, Vol.107, pp.567-572, 1991.
- [3] S. H. Li, C. A. Larsen, N. I. Buchan and G. B. Stringfellow, "Pyrolysis of Tertiarybutylphosphine", *J.Electron.Mater.*, Vol18, No.3, pp.457-464, 1989.
- [4] M.Horita, M.Suzuki and Y.Matsushima, "MOVPE growth of InGaAsP using TBA and TBP with extremely low V/III ratio", *J.Cryst.Growth*, Vol.124, pp.123-128, 1992.
- [5] A.Kuramata, S.Yamazaki and K.Nakajima, "Improvement of composition uniformity of InGaAsP crystal grown by MOVPE using AsH_3 and

tBPH_2 ", Extended Abstract of the 22nd Conf. SSDM, pp.501-504, 1990.

- [6] J.L.Zilko, P.S.Davisson, L.Luther and K.D.C.Trapp, "Improved composition uniformity of InGaAsP grown by low pressure metalorganic vapor phase epitaxy using tertiary butyl phosphine as the phosphorus source", *J.Cryst.Growth*, Vol.124, pp.112-117, 1992.
- [7] A.Kuramata, H.Kobayashi, S.Ogita and S.Yamazaki, "MOVPE growth of InGaAsP laser diodes using tertiarybutylarsine and tertiarybutylphosphine", *Int.Symp.GaAs and Related Compounds*, Ser.No 120, Chapter 11, pp.559-562, 1991.
- [8] S. Ae, T. Terakado, T. Nakamura, T. Torikai and T. Uji, "Low threshold $\lambda=1.3\mu\text{m}$ multi-quantum well laser diodes grown by metalorganic vapor phase epitaxy using tertiarybutylarsine and tertiarybutylphosphine precursors", *Proc.7th ICMOVPE*, pp.27-28, 1994 and *J.Cryst.Growth*, Vol.145, pp.852-857, 1994.
- [9] T. Terakado, K. Tsuruoka, T. Ishida, T. Nakamura, K.Fukushima, S. Ae, A. Uda, T. Torikai and T.Uji, "Extremely low thresholds (0.4mA @20°C, 3.0mA @85°C) $1.3\mu\text{m}$ strained MQW lasers with novel P-substrate buried-heterostructure (RIBPBH) grown by MOVPE using TBA and TBP", *Proc.14th IEEE Int. Semicon.Laser Conf.*, PD9, 1994.

Metalorganic Vapour Phase Epitaxy of InP Using the Novel P-Source Ditertiarybutyl Phosphine (DitBuPH)

H. Protzmann, Z. Spika, B. Spill, G. Zimmermann, W. Stolz, E.O.Göbel

Materials Sciences Center and Department of Physics,

Philipps-University, D-35032 Marburg, Germany

P. Gimmnich, J. Lorberth

Department of Chemistry and Materials Science Center,

Philipps-University, D-35032 Marburg, Germany

A variety of monoalkyl, dialkyl as well as trialkyl P-compounds, containing ethyl, isopropyl, and tertiarybutyl rest groups have been synthesized and used for the growth of InP bulk epitaxial layers by low-pressure metalorganic vapour phase epitaxy. Almost uncompensated, n-type InP-layers ($1.0 \cdot 10^{15} \text{ cm}^{-3}$; $59600 \text{ cm}^{-2} \text{ V}^{-1} \text{ s}^{-1}$ at 77K) are realized using the not specifically purified precursor ditertiarybutyl phosphine $((\text{C}_4\text{H}_9)_2\text{-P-H, DitBuPH})$ in combination with commercial TMIn. Layer quality has been investigated by means of optical and scanning electron microscopy (SEM), temperature-dependent van der Pauw-Hall as well as photoluminescence (PL) measurements. All results are compared with those obtained by using PH_3 as P-source.

1 Introduction

The search and development for liquid organic P-compounds as substitutes for the highly toxic and stable Group V hydride PH_3 , which is standardly used in metalorganic vapour phase epitaxy (MOVPE), metalorganic molecular beam epitaxy (MOMBE) or in related growth techniques is attracting increasing attention. This effort is motivated by an enhanced interest in the development of less stable molecules with dramatically reduced toxicity due to security and efficiency enhancement.

In view of the problems associated with the Group V hydride PH_3 , the substitution of the direct P-H-bonds by several rest groups offers some crucial advantages. All the precursors which have been synthesized are liquid at room temperature with reasonable vapour pressures for MOVPE applications so that they can be stored in stainless bubblers in the same way as the Group III substances. This and the decreased toxicity by reduction of direct P-H-functions in the molecules lead to a considerable improvement concerning safety aspects. In this study we confine ourselves to report on results obtained by using ditertiarybutyl phosphine as one of the most promising PH_3 -substitutes among tertiarybutyl phosphine ($\text{C}_4\text{H}_9\text{-P-H}_2$, TBP) and $(\text{H}_2\text{-P-C}_2\text{H}_4\text{-P-H}_2$, BPE) [1, 2].

2 Experimental

MOVPE experiments have been performed in an IR-heated, commercial horizontal reactor (Aix 200, Aixtron Corp.) at a reactor pressure of 100 mbar and a total gas flow of 6.8 slm. Before loading into the reactor substrates (Fe doped InP with exact (100) orientation) have been cleaned and etched in $\text{H}_2\text{SO}_4\text{:H}_2\text{O}_2\text{:H}_2\text{O} = 3\text{:}1\text{:}1$ at room temperature. Inside the reactor they were annealed for 5 min at 680° in PH_3 atmosphere before starting growth. For improved homogeneity the substrate was rotated by using the gas foil rotation principle. The substrate temperature was varied in the range of 530°C to 630°C . The V/III-ratio has been chosen between 3 and 60. The bubbler temperature was kept at 20°C . The vapour pressure of DitBuPH is 8.4 mbar (20°C). A series of InP-bulk layers has been deposited in order to establish the optimized growth parameter range. All layers have comparable thicknesses of about $2.5 \mu\text{m}$.

The surface morphologies of the InP epilayers were observed by optical and scanning electron microscopy (SEM). Hall effect measurements have been carried out by using the standard van der Pauw-Hall

methode. Room- and low temperature photoluminescence measurements have been performed with an Ar^+ -ion laser as excitation source. Excitation energy was 2.41 eV and the excitation power was varied from about 100 mW cm^{-2} to 10 W cm^{-2} . Luminescence signals were selected by a 1 m grating monochromator and detected by an liquid-nitrogen-cooled Ge-detector in lock-in technique.

3 Results and discussion

3.1 Morphology

Apart from the formation of In-droplets when the V/III-ratio is decreased to extremely low values we observe three different morphology features (fig.1:2). In the temperature region below 550°C we observe oval defects (hillocks) with lateral extensions up to $60 \mu\text{m}$ and vertical extensions of about a few μm . The density of defects decreases when the V/III-ratio is reduced and varies from some single defects to about $5 \cdot 10^4 \text{ cm}^{-2}$.

In the mid temperature range 550°C to 570°C excellent featureless morphologies are obtained independent of the V/III-ratio ≥ 3 . Above 590°C however, a strong dependence on DitBuPH partial pressure is observed. According to fig.1 rough surfaces are obtained if the V/III-ratio is too low.

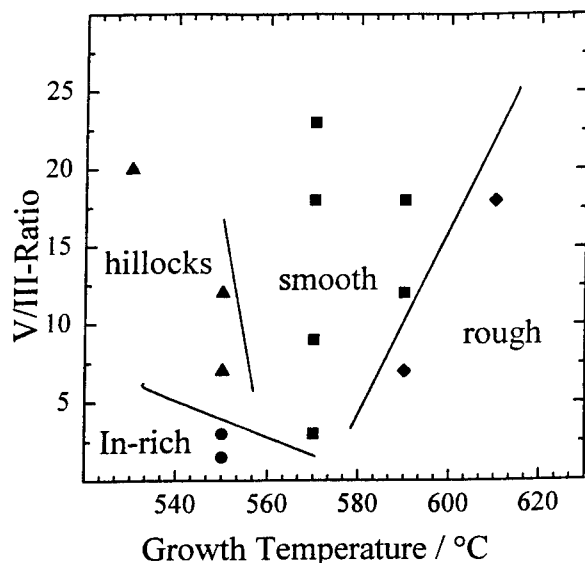


Fig.1. Obtained morphologies as function of temperature and V/III-ratio

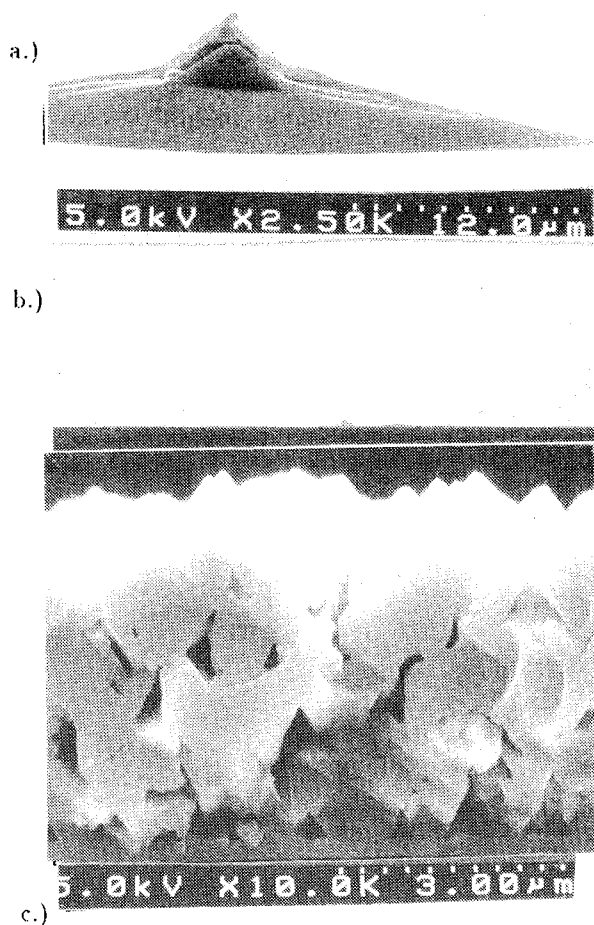


Fig.2. SEM-photographs of the obtained morphologies: a.) obtained surface morphology for temperatures below 570°C ; b.) smooth mirrorlike surface in the mid temperature region, (same scale as in a.); c.) rough morphology in the temperature region above 590°C

This behaviour can be explained by the volatility of phosphorus in this temperature region, so that higher temperatures requires higher DitBuPH partial pressures for surface stabilisation. Another possible explanation for the modified morphology could be a partly surface passivity induced by the existence of rest groups at the layer surface from the DitBuPH molecule. This leads to a partly three-dimensional growth which could explain the observed layer feature.

We have obtained similar surface morphologies by using TBP as P-source, in agreement with literature reports [3].

3.2 Growth investigations

In the investigated growth parameter range the InP growth rate is directly proportional to the TMIn partial pressure in the reactor and almost independent

of substrate temperature and V/III-ratio.

3.3 Electrical properties

The electrical properties of the InP-bulk layers grown by DitBuPH and TMIn as a function of growth temperature for different V/III-ratios are shown in fig.3. The data for standardly grown InP-layers (up triangles) and a theoretical mobility versus carrier concentration curve for zero compensation ($N_A/N_D=0$) (dot line) [4, 5] are included for comparison.

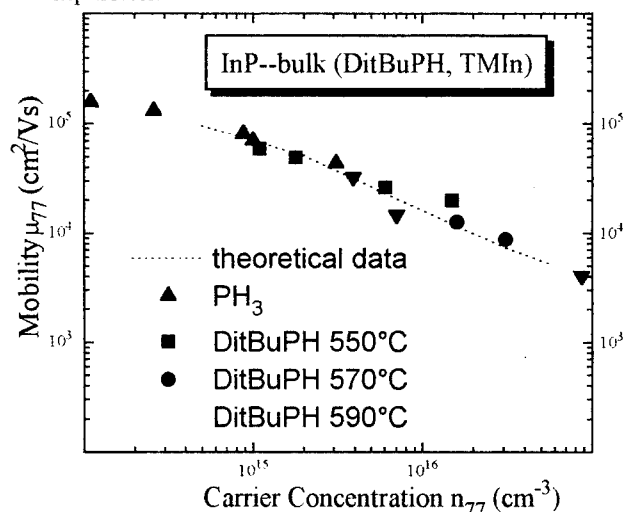


Fig.3. Electron mobility at 77 K of InP epitaxial layers as a function of the net carrier concentration, grown by using PH_3 and DitBuPH

The V/III-ratios varied from 90 to 200 when PH_3 was used as the P-source while they were chosen to be in the range of 3 to 30 in the case of DitBuPH. All layers grown by using DitBuPH exhibit n-type conductivity with carrier concentrations in the range of $n = N_A/N_D = 1 \cdot 10^{15} \text{ cm}^{-3} - 1 \cdot 10^{16} \text{ cm}^{-3}$ for growth temperatures between 550°C and 590°C. For temperatures above 590°C an decrease in mobility is observed caused by the detected deterioration in morphology. With increasing growth temperature an enhancement in carrier concentration is observed suggesting silicon as the residual impurity. As shown in Fig.4 an increase in V/III-ratio leads to an increased donor concentration with a simultaneous decrease in mobility. Below 550°C a residual zinc impurity from the used TMIn batch is responsible for the weak increase in compensation ratio. These electrical characteristics obtained for the used not specifically purified batch of DitBuPH are very promising.

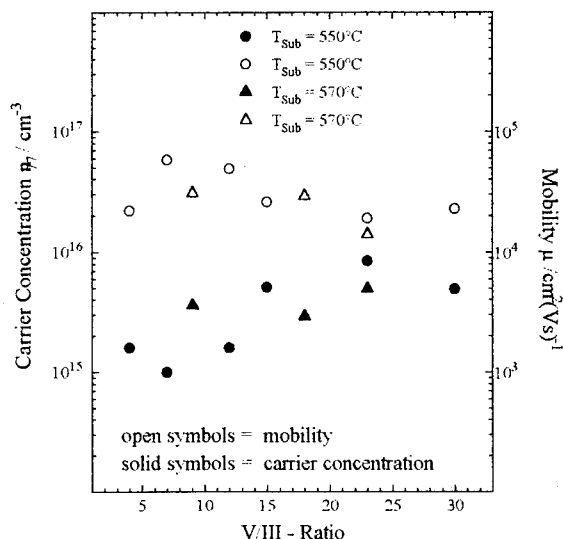


Fig.4. Electron concentration and mobility as function of V/III-ratio

Studies are under way to further reduce the impurity level during chemical synthesis.

3.4 Optical properties

The room-temperature luminescence spectra of the near bandgap spectral region of an InP layer grown by DitBuPH and TMIn at a substrate temperature of 570°C and a V/III-ratio of 9 is depicted in fig.5. The spectrum of a standardly grown InP layer at a substrate temperature of 650°C and V/III-ratio of 270 with comparable thickness is included for comparison.

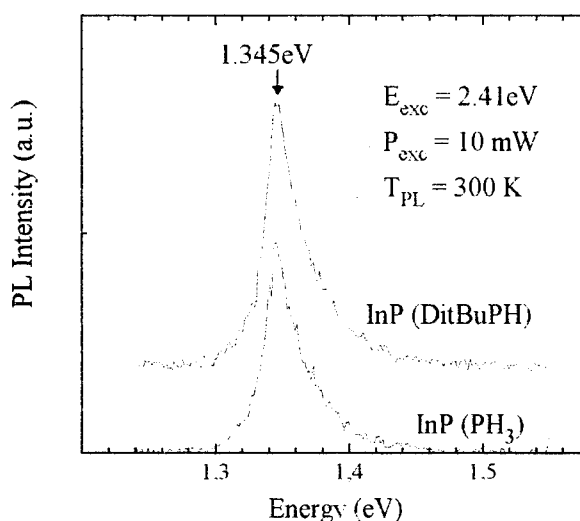


Fig.5. Room-temperature photoluminescence spectra of InP-epitaxial layers grown by PH_3 and DitBuPH respectively

All layers deposited in the range of 550°C to 590°C show comparable luminescence intensities as well as linewidths at 300 K. This indicates the high crystalline quality of the InP-layers deposited by using DitBuPH. Under growth conditions leading to rough surface morphologies, however, luminescence intensities are strongly reduced. Low temperature luminescence is dominated by donor correlated transitions in the near bandgap spectral region. As function of growth parameters two characteristic transitions can be resolved under the measurement conditions (Fig.6).

related transitions in the near bandgap spectral region. As function of growth parameters two characteristic transitions can be resolved under the measurement conditions (Fig.6).

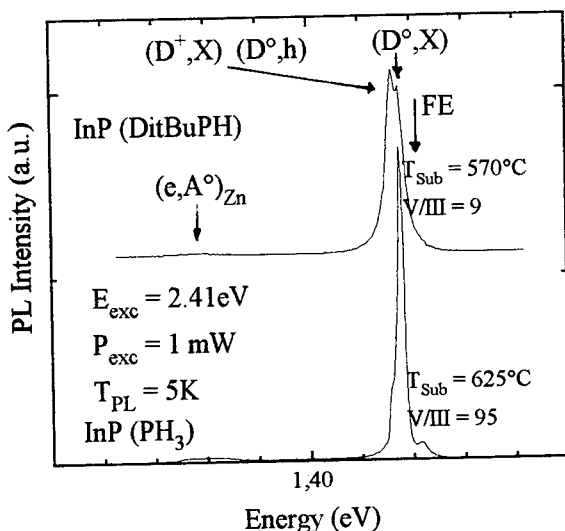


Fig.6. Photoluminescence spectra recorded at 5K of InP epitaxial layers grown by PH₃ and DitBuPH respectively

In the higher energy region we observe a neutral donor bound exciton (1.4167eV–1.4183eV) while the transition observed in the lower energy region is either a ionized donor bound exciton (D⁺,X) or a free hole to neutral donor transition(D⁰,h) (1,4160eV–1.4163eV). The dominant donor is believed to be silicon. Both InP-layers PH₃ and DitBuPH grown exhibit a weak band to neutral acceptor transition (e,A⁰) (1.374eV). This acceptor level is correlated to Zn-impurity presumably in the standard TMIn-source as established by electrical measurements. The discussed transition decreases when growth temperature is increased in accordance with the desorption behavior of zinc.

4 Summary

In summary liquid organic P-compounds with a variety of rest groups have been synthesized and successfully used for MOVPE growth of InP-bulk layers. As the most promising substitute we have

introduced the results of MOVPE growth and characterization of the layers for ditertiarybutyl phosphine (DitBuPH) in comparison with standardly grown layers. We have found a temperature-V/III-ratio area for the growth of featureless smooth epitaxial layers. Nearly uncompensated n-type InP with donor concentrations $N_A-N_D \geq 1 \cdot 10^{15} \text{ cm}^{-3}$ and mobilities $\mu \leq 60000 \text{ cm}^2 \text{ V}^{-1} \text{ s}^{-1}$ have been realized by using this not specifically purified batch of DitBuPH. All measurements concerning electrical and optical properties are comparable with those using PH₃ as P-source.

All off these results demonstrate the great potential of this P-precursor as least toxic substitute for PH₃ in the epitaxial growth of P-containing structures.

5 Acknowledgments

The authors are indebted to Th. Ochs and S. Giebisch for expert technical support during sample preparation. Financial support of this work by the Bundesministerium für Forschung und Technologie is gratefully acknowledged.

References

- [1] C. H. Chen, D. S. Cao, and G. B. Stringfellow, Use of tertiarybutylphosphine for the growth of InP and GaAs_{1-x}P_x. J. of Electronic Materials Vol.17, No.1 (1988)
- [2] V. Soulière, P. Abraham, J. Bouix, M. P. Berthet, Y. Monteil, A. M. Pougnet, R. Mellet, A. Ougazzaden and A. Mircea, Use of high purity trimethylindium-trimethylamine adduct in MOVPE of InP. J. Crystal Growth 124 (1992) 93
- [3] S. P. Watkins et al., J. Appl. Phys. 72 (1992) 2797
- [4] D. A. Anderson, N. Apsley, P. Davies and P. L. Giles Compensation in heavily doped n-type InP and GaAs. J. Appl. Phys. 58 (1985) 3095
- [5] W. Walukiewicz, J. Lagowski, L. Jastrzebski, P. Rava, M. Lichtensteiger, C. H. Gatos and H. C. Gatos Electron mobility and free carrier absorption in InP; determination of the compensation ratio. J. Appl. Phys. 51 (1980) 2659

Highly Efficient Low Temperature Growth of GaInP in a Planetary MOVPE System using Tertiarybutylphosphine (TBP)

*R. Beccard, J. Knauf, G. Lengeling, D. Schmitz and H. Jürgensen
AIXTRON GmbH, Kackertstrasse 15-17, D-52072 Aachen, Germany*

Abstract

In this paper we describe the use of tertiarybutylphosphine (TBP) as a group V precursor for the growth GaInP. Growth has been carried out of in a multiwafer MOVPE Planetary Reactor™. The results demonstrate that very low growth temperatures together with low V/III ratios can be used. The growth efficiency of this gas is very high compared to the standard group V precursor phosphine. Characterization of the GaInP layers by DCXD, photoluminescence and hall measurements reveal their excellent crystalline, electrical and optical properties.

Introduction

One of the most important III-V materials today is (Al)GaInP. From this material several mass products like UHB-LEDs, HBTs or visible lasers are fabricated. Metalorganic Vapour Phase Epitaxy (MOVPE) is the most commonly used technique to grow GaInP-based structures. The tendency to employ MOVPE as a mass production technique increases the demand for cost efficient growth processes. Thus an efficient utilization of the precursors is desirable. Mainly,

this can be achieved by a design of the MOVPE reactors. State-of-the-art MOVPE reactors like the AIXTRON Planetary REACTOR™ already offer a highly efficient utilization of the precursors, e.g. above 40% growth efficiency for group III precursors. The reason for this is the unique design of these reactors that allow a controlled depletion of the gas phase together with an outstanding uniformity of the grown films.

However, the group V compound which is usually phosphine when growing GaInP still has to be used under strong excess conditions. Depending on the application of the GaInP growth, V/III ratios up to 400 are reported in the literature /e.g. 1/. The amount of phosphine cannot be simply reduced since the V/III ratio strongly affects the quality of the films. The only way to reduce the group V consumption is to use alternative precursors. Tertiarybutylphosphine (TBP) is one of these alternative compounds. It has already been used for the growth of different III-V compounds such as InGaAsP /2/. Using TBP has several advantages: Since the decomposition starts at relatively low temperatures, a high concentration of P is available at

the substrate. This should allow low V/III ratios. Additionally, the GaInP might be grown at lower temperatures. Compared to phosphine, the safety hazards are reduced and the handling of the TBP bubbler is much easier.

Experimental

Our growth experiments were performed in an AIX 2400 reactor. This is a multiwafer Planetary ReactorTM allowing the simultaneous growth on 11x2", 15x2" or 5x4" wafers. The reactor is part of the planetary reactor family (AIX 2000, 2400, 3000) which are based on Frijlink's concept [3]. It is fitted with a double Gas Foil RotationTM and a fast run/vent switching manifold.

As precursors trimethylgallium, trimethylindium and TBP were used. The TBP was kept at a temperature of 5°C, the TMGa at -10°C and the TMIIn at 17°C. Substrates used were undoped and n-type GaAs wafers. Both 2" and 4" substrates were used. During heating the substrate, an arsine/hydrogen atmosphere was used in order to prevent the arsenic from evaporating. The reactor pressure was 50 mbar and the total flow rate was 17.2 l/min in all growth runs. The partial pressures for TMGa and TMIIn were $5.3 \cdot 10^{-3}$ mbar and $6.8 \cdot 10^{-3}$ mbar, respectively.

The thickness of the GaInP films was measured optically using a microscope after stain etching. DCXD measurements were made using a Bede QC1 diffractometer. PL measurements were carried out at ISI, KfA Jülich and at Institut für Halbleitertechnik, RWTH Aachen.

Results

1. Growth temperature

The growth temperature was varied between 615 °C and 745 °C. The V/III ratio could be reduced as low as 26. The growth rates as a function of the growth temperatures are shown in fig. 1.

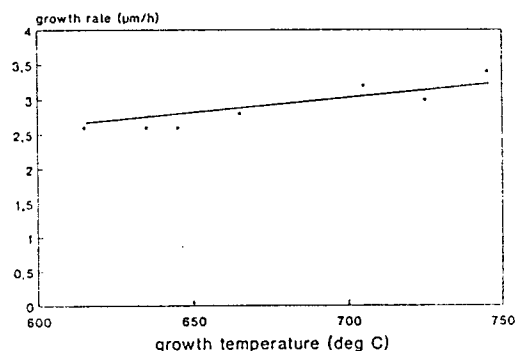


Fig. 1: GaInP growth rate vs. growth temperature

The rate increases slightly towards higher temperatures. Even at 615 °C the growth still seems to be diffusion controlled. Only for temperatures below 650 °C the morphology was insufficient. At 675 °C no difference in the morphology compared to phosphine-grown GaInP layers could be observed. Since typical growth temperatures for the growth of high quality GaInP using phosphine are 700 – 750°C, this means a significant reduction of the growth temperature.

The effect of the growth temperature on the GaInP composition is shown in fig.2. During the variation of the growth temperature the composition of the vapour phase was kept constant. The

lattice mismatch measured by DCXD decreases monotonously indicating that the indium content is reduced. This behaviour, however, is very similar to phosphine-grown GaInP.

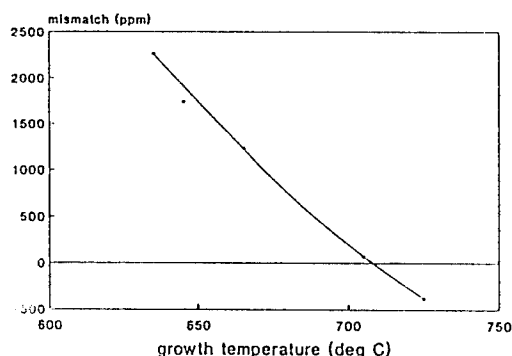


Fig. 2: GaInP mismatch vs. growth temperature

2. Electrical properties

By using Hall measurements the electrical quality of the TBP-grown GaInP was determined. These measurements give some important information about undesired carbon incorporation originating from the TBP. In fig. 3 and 4 the electron concentrations and the Hall mobilities measured at room temperature and 77 K are shown.

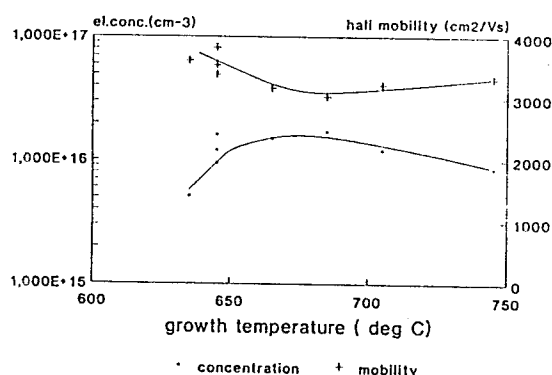


Fig. 3: Carrier concentration and hall mobility vs. growth temperature (300 K)

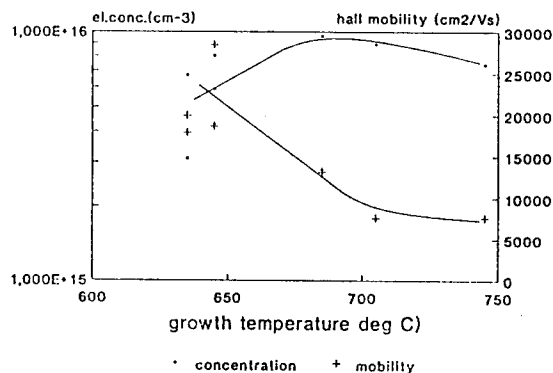


Fig. 4: Carrier concentration and Hall mobility vs. growth temperature (77 K)

These curves indicate that carbon does not play any significant role as a background dopant. Background electron concentrations between 10^{15} and 10^{16} cm⁻³ were obtained. The 77K concentrations are only slightly lower than the 300K values. Mobilities between 3,000 and 4,000 cm²/Vs were achieved at 300K. At 77K the maximum values were around 30,000 cm²/Vs. All these curves indicate that reducing the growth temperature does not have any negative impact on the electrical data. Taking into account both the electrical data and the morphology, an optimum temperature around 650 – 675 °C is found.

3. DCXD and PL

The high quality of the TBP-grown GaInP films is confirmed by DCXD measurements. Half widths as low as 35 arcsec were found (The GaAs substrate line width is 32 arcsec due to the use of an InP reference crystal). PL measurements at room temperature reveal FWHMs of 40 meV. At 2K very sharp peaks with half widths of only 13

meV were found (fig. 5). All these data were obtained from samples grown at a V/III ratio of 26. Typical PL uniformities are below 1 nm across a 2" wafer (fig. 6)

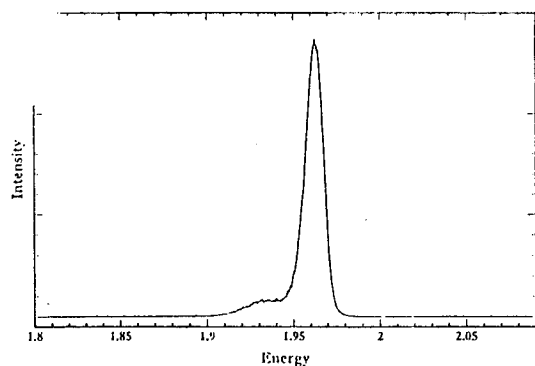


Fig. 5: 2 K PL plot of an GaInP sample

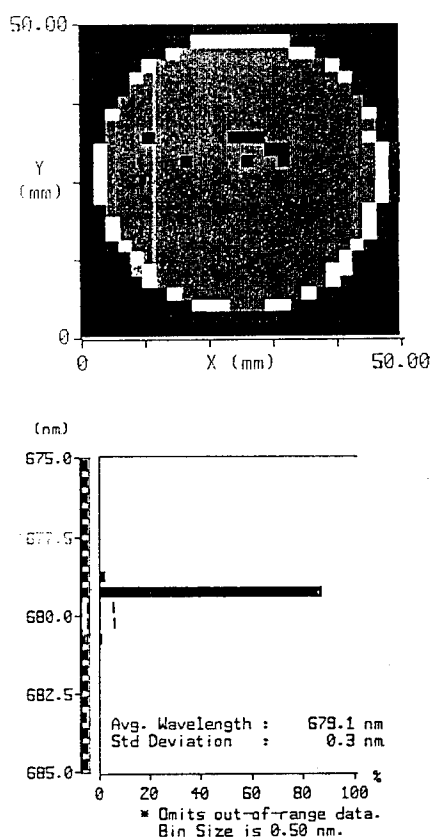


Fig. 6: 300 K PL map of a 2" GaInP

4. Conclusions

The results presented above show that the efficiency in the utilization of group V sources can be significantly increased if TBP is chosen instead of phosphine. Besides the reduced consumption of precursors, further advantages are growth at lower temperatures, the use of less toxic compounds, reduced scrubbing costs etc. Generally, a reduction of the group V consumption by a factor of 4–8 is possible. Together with the high efficiency in using the group III precursors, the AIXTRON Planetary Reactors™ offer a powerful and cost-efficient tool for the mass production of GaInP-based devices.

5. References

- [1] F. Scheffer, F. Buchali, A. Lindner, Q. Liu, A. Wiersch and W. Prost, *J. Crystal Growth* **124** (1992), 475
- [2] J. L. Zilko, P. S. Davisson, L. Luther and K. D. C. Trapp, *J. Crystal Growth* **124** (1992), 112
- [3] F. M. Frijlink, *J. Crystal Growth* **93** (1988), 207

Effect of Strained Interfacial Layer and Large Misorientation on SQW, 2DEG, and Multisteps in InGaP/(In)GaAs Heterostructures Grown by MOVPE

T. Kikkawa, K. Kasai, H. Ochimizu, and H. Tanaka
Fujitsu Laboratories Ltd.,
10-1 Morinosato-wakamiya, Atsugi 243-01, Japan

Recently, $\text{In}_{0.5}\text{Ga}_{0.5}\text{P}/\text{GaAs}$ heterointerface abruptness has received much attentions. Several researchers reported that thin GaP layer insertion into inverted interface (from InGaP to GaAs) improved quantum well (QW) optical quality.¹⁾ However, it is not known what kind of interfaces are required for high electrical performance in InGaP-based HEMT. We studied 2DEG performance in Si-doped (including heavily planar-doping for the first time) InGaP/GaAs heterostructures. We found that Si diffused from InGaP to GaAs, and an $\text{In}_{0.3}\text{Ga}_{0.7}\text{P}$ (not GaP) interfacial layer between Si-doped layer and channel layer is optimum for high 2DEG performance.

Step bunching due to misorientation becomes one of interesting issues in MOVPE. We studied a misorientation effect and found that large misorientation over 10° from (001) improves the SQW quality without inserting a GaP layer at the interface. We also found that InGaP-based HEMT (including inverted-type) performance does not linked with the SQW quality, and that misorientation towards $\langle 111 \rangle \text{A}$ is required for high mobility. We characterized multisteps using atomic force microscope (AFM) and concluded that multistep configuration mainly affects abruptness in device structures.

We used reduced-pressure horizontal reactor. TMGa, TEGa, TMIn, AsH_3 , PH_3 , TBP and Si_2H_6 were used as the precursors. Growth temperatures were 630 to 710°C and growth pressure 76 torr. The 3-inch (001) vicinal GaAs substrates misoriented 0 to 16° ($\{511\}$) towards $\langle 111 \rangle \text{A}$, $\langle 111 \rangle \text{B}$, and $[011]$ were used.

Figure 1 shows the 2DEG performance as a function of Si donor concentration of InGaP electron supplying layer in InGaP/GaAs heterostructures (spacer 2.5 nm). We found that when doping concentration is increased, hall mobility decreases drastically. By observing SdH oscillations, we confirmed that 2DEG mobility was exactly decreased. SIMS measurement suggested that Si diffusion occurred from InGaP to GaAs (Fig. 2). We introduced strained spacer layer to suppress Si-diffusion (Fig. 2) and successfully improved 2DEG performance (Fig. 3). However, we found that GaP spacer reduced mobility due to too much strain and concluded that $\text{In}_{0.3}\text{Ga}_{0.7}\text{P}$ is a sufficient interfacial layer from GaAs to InGaP for HEMT. We then studied planar-doped InGaP/GaAs heterostructures and, using an $\text{In}_{0.3}\text{Ga}_{0.7}\text{P}$ interfacial layer, obtained sharp carrier profile (C-V peak = $8 \times 10^{18} \text{ cm}^{-3}$, FWHM=4 nm) and high mobility of $21000 \text{ cm}^2/\text{Vs}$ for the first time.

We grew InGaP/ $\text{In}_{0.2}\text{Ga}_{0.8}\text{As}$ (14 nm)/GaAs pseudomorphic hetero-structures and confirmed that $\text{In}_{0.3}\text{Ga}_{0.7}\text{P}$ interfacial layer is again effective at the pseudomorphic interface. We calculated the band bending self-consistently and demonstrated that only the Si-diffusion model can explain PL spectra from the strained InGaAs channel (Fig. 4).

We studied the misorientation effect. When the misorientation angles were 10° to 16° from (001), blue shift of PL peak of the InGaP/GaAs SQW was observed without inserting a GaP layer at the interface (Fig. 5). This indicates that As-insertion into InGaP is perfectly suppressed by large misorientation. We tried to grow GaAs/InGaP inverted HEMT structures to compare the SQW characteristics for the first time (Fig. 6). We obtained high mobility reaching $27000 \text{ cm}^2\text{V}^{-1}\text{s}^{-1}$ when misoriented 10° towards $\langle 111 \rangle \text{A}$. When misoriented 16° towards $\langle 111 \rangle \text{A}$, although SQW characteristics are excellent, we could not obtain high mobility. This suggests that, in addition to an abrupt interface characterized by PL, other origins, such as Si diffusion or too small size roughness, controls 2DEG performance.

Using AFM, we observed large step bunching and pit formation close to heterointerface when the misorientation angle is less than 4° except for 0° . However, when over 6° , we observed no step bunching. Therefore, we concluded that multistep configuration mainly affects As/P exchange at the GaAs/InGaP interface which affects the PL characteristics.

We then grew the InGaP/InGaAs pseudomorphic heterostructures using various substrates (Fig. 7,8). PL performance and mobility show different trends compared with the SQW and the inverted HEMT structures. When misoriented towards $\langle 111 \rangle \text{B}$, PL emission intensity from InGaAs channel was decreased dramatically and only low mobilities could be obtained. When towards $\langle 111 \rangle \text{A}$, PL intensity from $[1c-1hh]$ was almost the same but that from $[2e-1hh]$ showed complicated behavior. We found that high mobility was obtained when $[2e-$

1hh] intensity was strong and that the mobility when misoriented towards [111]A was always higher than that towards <111>B. This verifies that A-type step plays a key role for realizing an abrupt pseudomorphic interface from As-containing layer to P-containing layer.

1) Bhat et al., J. Cryst. Growth 124 (1992) 576.

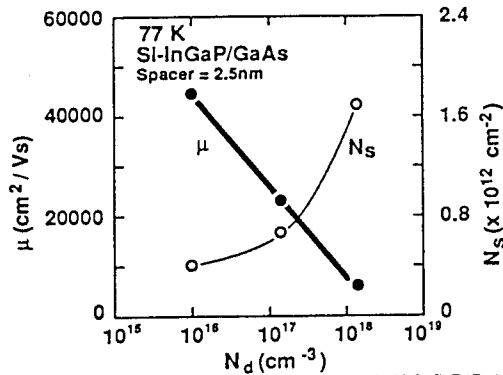


Fig. 1. Dependence of 2DEG characteristics of Si-InGaP/GaAs (spacer = 2.5 nm) heterostructures on donor concentration.

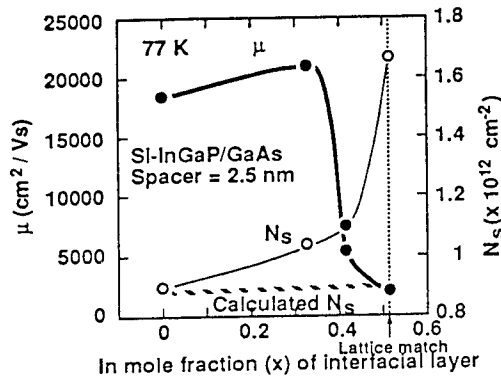


Fig. 3. Dependence of 2DEG characteristics of Si-InGaP/GaAs heterostructures on composition of interfacial layer at 77 K.

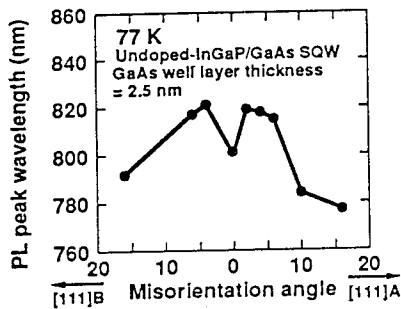


Fig. 5. Dependence of PL emission peak wavelength from InGaP/GaAs (2.5 nm) SQW on misorientation angle.

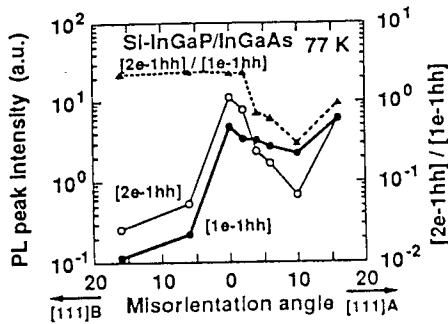


Fig. 7. Dependence of PL spectra from InGaAs channel in InGaP/InGaAs pseudomorphic heterostructures on misorientation angle.

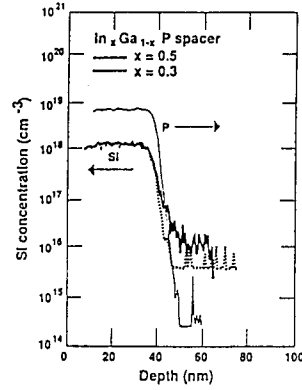


Fig. 2. SIMS profiles of Si-InGaP/GaAs heterostructures. The In composition of interfacial InGaP is (a) 0.5 and (b) 0.3.

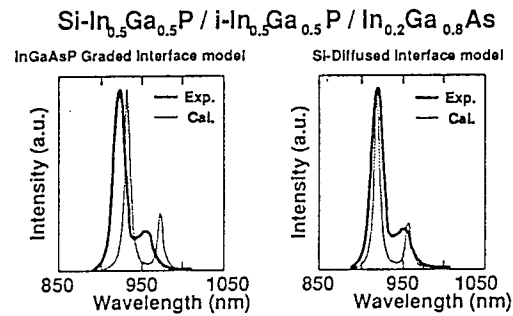


Fig. 4. PL spectra from InGaAs channel in InGaP/InGaAs heterostructures without inserting $\text{In}_{0.3}\text{Ga}_{0.7}\text{P}$. Calculated PL spectra was shown using (a) InGaAsP model and (b) Si-diffusion model.

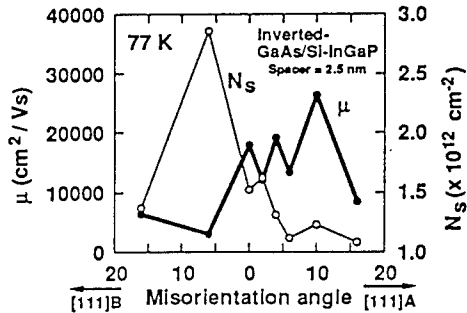


Fig. 6. Dependence of 2DEG characteristics of inverted Si-InGaP/GaAs heterostructures on misorientation angle.

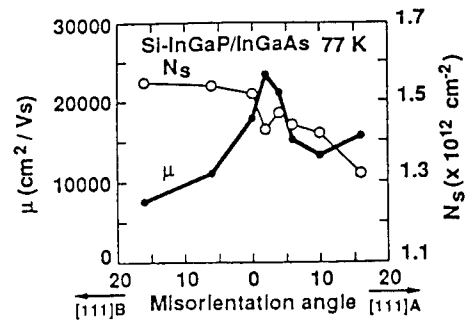


Fig. 8. Dependence of 2DEG characteristics of InGaP/InGaAs pseudomorphic heterostructures on misorientation angle.

Unintentional impurity incorporation at the interface between WP12 InP substrate and buffer layer grown by LP-MOVPE

M. Hollfelder, H. Hardtdegen, [‡]U. Breuer, [‡]H. Holzbrecher, R. Carius and H. Lüth

Institut für Schicht- und Ionentechnik,

[‡]Zentralabteilung für Chemische Analysen

Forschungszentrum Jülich, 52425 Jülich, Germany

Introduction

Multilayer structures for many device applications require a highly resistive and perfect crystalline InP buffer layer. Due to unintentional impurity incorporation at the substrate epitaxial layer interface, this buffer layer is often conductive leading for example to poor pinch off characteristics in diodes. A conductive epitaxial/substrate interface has been reported only for MOVPE growth (1, 2, 3, 4) and was detected to be a Si impurity spike at the interface observed by SIMS measurements. In this study we report on a systematic investigation of the origin of highly conductive epitaxial InP buffer layers and how they can be avoided.

Experimental

All materials in this study were grown in a horizontal low pressure MOVPE reactor (AIXTRON) on a non-rotating graphite susceptor for 2 inch wafer using TMIn and phosphine. Deposition was done on semi-insulating Fe-doped InP substrates, exactly oriented along the $\langle 100 \rangle$ direction. Pd-diffused hydrogen was employed as carrier gas at a reactor pressure of 20 mbar and a growth temperature of 640 °C. InP growth conditions were the same as used for optoelectronic, mesoscopic and high frequency devices in the GaInAs/InP system.

The layers were investigated by SIMS (Secondary Ion Mass Spectrometry), Hall-effect and photoluminescence measurements. SIMS analysis was carried out by a CAMECA IMS 4F using Cs⁺ bombardment for depth profiling. The scanned area was 250 × 250 μm and the analysed area 60 μm in diameter. Ion implantation standards were used for quantification of the respective elements. Electrical characterization was performed by van der Pauw-Hall measurements at 77 and 300 K. High resolution photoluminescence spectroscopy was carried out at 2 K, using the 514.5 nm line of an Ar⁺-ion laser, a Spex 1404 monochromator and a liquid nitrogen cooled Photometrics SDS 9000 CCD camera. The excitation density was lower than 200 mW/cm².

Results and Discussion

A comparison of photoluminescence spectra at 2 K and Hall-effect measurements gave first evidence of inhomogeneous impurity distributions of nominally undoped InP layers. Hall-effect results of two 2 μm thick InP layers in Table 1 show more than one order of magnitude difference in the background carrier concentration, while the corresponding photoluminescence spectra in Fig. 1 indicate only minor differences in the acceptor and donor concentration. The intensity of the donor and ac-

ceptor bound excitons (D⁰X, A⁰X) correlates with the donor and acceptor concentration in the bulk material. Therefore a low compensation ratio can be deduced from the large intensity ratio between the D⁰X transitions of different excited states (n=1..6) and the weak spin split A⁰X recombination for both samples.

Wafer	n _{300 K} cm ⁻³	μ _{300 K} cm ² /Vs	n _{77 K} cm ⁻³	μ _{77 K} cm ² /Vs
a)	5.8 · 10 ¹⁵	2670	2.2 · 10 ¹⁵	25760
b)	3.8 · 10 ¹⁴	4980	3.3 · 10 ¹⁴	112000

Table 1: Hall-effect measurements at 300 K and 77 K of nominally undoped 2 μm thick InP layers with different background carrier concentrations.

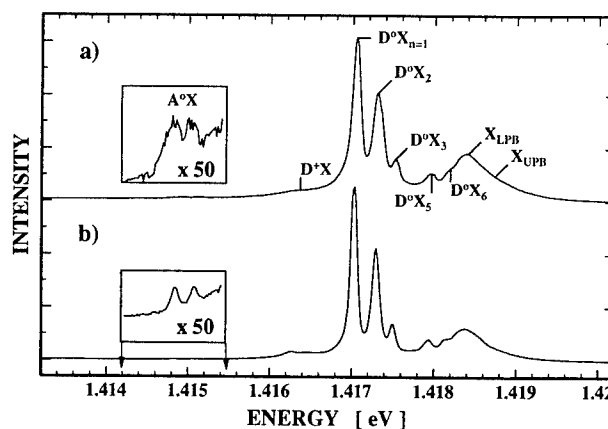


Fig. 1: Excitonic photoluminescence at 2 K of nominally undoped 2 μm thick InP layers recorded at equal conditions. The spectra of layer a) and b) correspond to the Hall-effect measurements in table 1 and show only minor differences in the donor and acceptor concentration.

The narrow FWHMs of 0.10 meV of the D⁰X transitions and the intensity ratio to the free exciton recombina-

tion (X) indicate InP with a donor concentration in the low 10^{14} cm^{-3} (5). This matches to the Hall concentration of sample b). Furthermore a comparison with the theoretical 77 K Hall mobility of Walukiewicz et al. (6) yields a low compensation ratio of 0.05. SIMS depth profiles of samples with similar properties to sample a) exhibit Si accumulations at the substrate-layer interface as reported by different authors (1, 2, 3, 4). Therefore we conclude that the Hall data of sample a) originate mainly from a highly conductive channel at the substrate-layer interface. Since the penetration depth of the 514.5 nm line is approximately 100 nm in InP, the spectra contain no information about the substrate-layer interface.

To determine the origin of the Si contamination we first checked if the epitaxial equipment was the cause for the Si impurity spike by trying to generate a second interfacial layer. Therefore 200 nm undoped InP was deposited on InP substrates which had been previously cleaned in 10% HF for 3 min and rinsed in deionized water (DI-H₂O). This etchant only removes an oxide layer on top of the InP wafer. Before a second 200 nm InP layer was deposited the following procedures were carried out: a) growth interruption, b) growth interruption and leaktest, c) growth interruption, exposure to nitrogen glove box and leaktest, d) growth interruption, exposure to air, a second cleaning process and leaktest. SIMS depth profiles of these four layers are presented in Fig. 2.

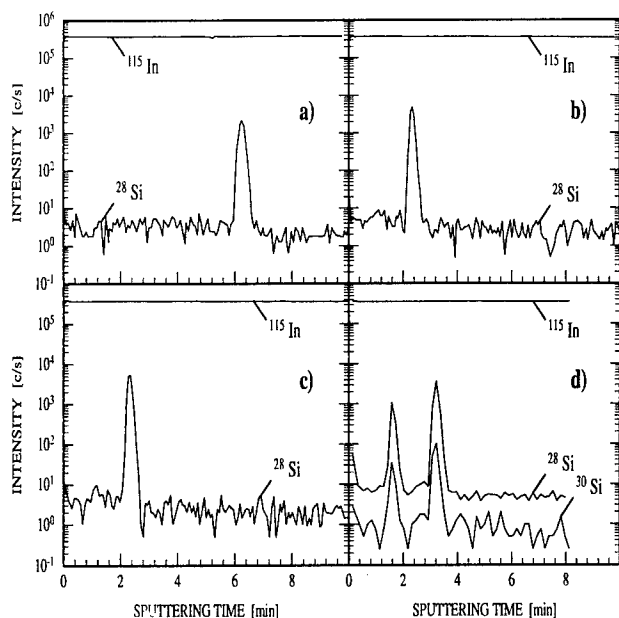


Fig. 2: SIMS depth profiles of two 200 nm thick InP layers grown on an InP substrate with different procedures prior to the second deposition: a) growth interruption, b) growth interruption and leaktest, c) growth interruption, exposure to nitrogen glove box and leaktest, d) growth interruption, exposure to air, a second cleaning process and leaktest. Si is accumulated at the substrate-layer interface.

Although a second interface was generated only one Si accumulation was found for procedures a) to c). The Si peak concentrations are approximately $4 \times 10^{17} \text{ cm}^{-3}$ for a), $8 \times 10^{17} \text{ cm}^{-3}$ for b) and $8 \times 10^{17} \text{ cm}^{-3}$ for procedure c). A second Si spike was detected by SIMS when the cleaning process is repeated as in procedure d). The Si peak concentrations are approximately $6 \times 10^{17} \text{ cm}^{-3}$ and $2 \times 10^{17} \text{ cm}^{-3}$ for the substrate-layer and the second interface, respectively. Since the second Si spike is lower than the first, Si might be partially present in the wafer material. Therefore we conclude that Si is not incorporated by the growth process but it is brought externally into the growth reactor. External Si contamination may have three different causes. First Si is already incorporated in the wafer material, second Si originates from the cleaning process or third Si is adsorbed from exposure to air between cleaning process and loading into the reactor as proposed by Ishikawa et al. (3).

To check on Si contamination in the wafer material, deposition was carried out on substrates from different manufacturers without any pretreatment prior to growth. Additionally we analyzed test wafers with different polishing processes from the same batch. SIMS measurements indicate a Si spike at the substrate-layer interface for all wafers. We found different Si peak concentrations for wafers from different manufacturers as well as for different polishing processes and also for different crystal lots from the same manufacturer. But the measured Si peak concentration is up to one order of magnitude less than for wafer material which had been cleaned prior to deposition with an oxide removal etchant. Fig. 3 shows SIMS depth profiles of wafers of the same crystal lot without pretreatment a) and cleaning with 10% HF prior to growth b).

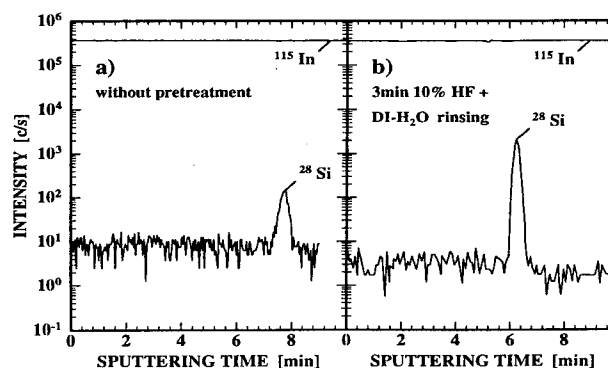


Fig. 3: SIMS depth profiles of InP layers grown on InP substrate with different pretreatments. a) without pretreatment, b) cleaning with 10% HF for 3 min and rinsing in deionized water. The corresponding Si peak concentrations of the interface spikes are approximately $3 \times 10^{16} \text{ cm}^{-3}$ and $4 \times 10^{17} \text{ cm}^{-3}$ for a) and b), respectively. Si is partially incorporated in the wafer material.

We therefore conclude that Si is partially incorporated

in the wafer material and that cleaning with 10% HF for 3 min and rinsing in deionized water increases the Si accumulation at the substrate-layer interface. Si in the wafer material originates probably from the polishing process and its concentration is dependent on the skills of the manufacturer. The depth range of the incorporated Si in the wafer material can not be determined by SIMS, because Si might diffuse out of the substrate during the heating process. SIMS depth profiles of pure wafer material showed Si accumulation at the surface but could not be evaluated, because the sputter equilibrium is not reached close to the surface. From the distance of 200 nm between the two Si spikes in Fig. 2d) we estimate a maximum thickness of the Si accumulation at the substrate-layer interface of 40 nm.

A cleaning process prior to deposition is necessary since the surface morphology of InP layers grown on substrates without pretreatment is not perfectly smooth as determined by a Nomarski interference microscope. Therefore the influence of different cleaning procedures were investigated next. First we checked the influence of rinsing in deionized water after etching. Two wafers from the same lot were etched 3 min in 10% HF. One was rinsed in deionized water and the other just dried with nitrogen. After 200 nm InP deposition the cleaning process was repeated and a second interfacial layer was generated with the growth of further 200 nm. SIMS depth profiles are presented in Fig. 4.

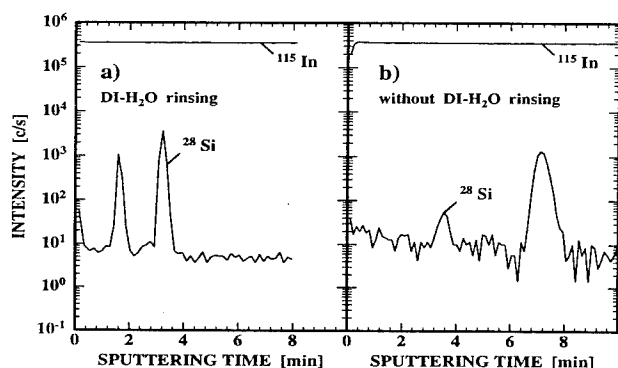


Fig. 4: SIMS depth profiles of two 200 nm thick InP layers grown on an InP substrate from the same lot with different cleaning procedures after etching with 10% HF for 3 min: a) rinsing in deionized water and drying with nitrogen b) only drying with nitrogen. The corresponding Si peak concentrations of the interface spikes are approximately $2 \times 10^{17} \text{ cm}^{-3}$ and $6 \times 10^{17} \text{ cm}^{-3}$ for a) and $9 \times 10^{15} \text{ cm}^{-3}$ and $2 \times 10^{17} \text{ cm}^{-3}$ for b). Rinsing in deionized water increases the Si accumulation.

Since both Si spikes are higher in the case of rinsing in deionized water, part of the Si accumulation originates from the deionized water. Si was detected by mass spectroscopy (ICP-MS) with a concentration of 21 ± 4 ppb. However the Si species should be of a covalent nature because the water is highly resistive as confirmed by con-

ductivity measurements. A possible Si source are the molecular sieves in our deionized water preparation system which consists of Si containing compounds. The difference in Si intensity between the two samples is lower for the substrate-layer interface, i.e. the Si peak concentration is substantially determined by the Si already incorporated in the wafer material. Hall-effect measurements of two 2 μm thick InP layers with the same pretreatment as in Fig. 4 showed a reduction of the 300 K background carrier concentration from $3.0 \times 10^{15} \text{ cm}^{-3}$ to $8.8 \times 10^{14} \text{ cm}^{-3}$ for rinsing with and without deionized water, respectively. A further advantage of the 10% HF etch process without rinsing in deionized water is that remaining F on the surface can bind Si species to form volatile SiF_4 , which desorbs from the substrate during the heating procedure.

In order to reduce the incorporated Si in the wafer material different material removing etchants were analyzed at room temperature. We tested bromine methanol 0.05% and $\text{H}_2\text{SO}_4:\text{H}_2\text{O}_2:\text{H}_2\text{O}$ with volume ratios: 3:1:1, 5:1:1 and 10:1:1. The bromine methanol solution resulted in layers with lower photoluminescence intensity by a factor of 3 and showed additionally a little accumulation of O and C at the substrate-layer interface. The best results as determined by optical and electrical properties were found for the 10:1:1 volume ratio of the $\text{H}_2\text{SO}_4:\text{H}_2\text{O}_2:\text{H}_2\text{O}$ etchant with an etch time of 10 min. This etchant removes approximately 200 nm of InP. Whereas the 3:1:1 and 5:1:1 volume ratios of the $\text{H}_2\text{SO}_4:\text{H}_2\text{O}_2:\text{H}_2\text{O}$ etchant result in layers with not perfect smooth surface morphologies. The electrical properties of the layers can further be improved if a 10% HF etchant for 3 min is used consecutively and the wafer is dried with nitrogen instead of rinsing in deionized water in the last step.

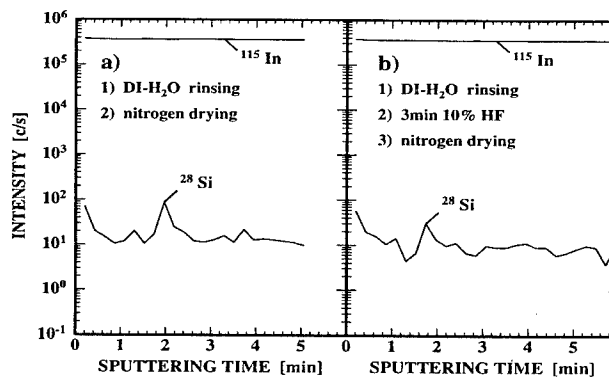


Fig. 5: SIMS depth profiles of 200 nm thick InP layers grown on InP substrate from the same lot with different cleaning procedures after etching with $\text{H}_2\text{SO}_4:\text{H}_2\text{O}_2:\text{H}_2\text{O} = 10:1:1$ for 10 min: a) rinsing in deionized water and drying with nitrogen b) rinsing in deionized water, etching 3 min with 10% HF and drying with nitrogen. The 10% HF etchant without rinsing in deionized water reduces further the Si accumulation.

SIMS depth profiles in Fig. 5 show the effective removal of Si at the substrate-layer interface for the $\text{H}_2\text{SO}_4:\text{H}_2\text{O}_2:\text{H}_2\text{O}$ etchant with and without the additional 10% HF cleaning step. The corresponding Si peak concentrations of the interface spikes do not exceed approximately $2 \times 10^{16} \text{ cm}^{-3}$ and $5 \times 10^{15} \text{ cm}^{-3}$ for a) and b), respectively, whereas the Si detection limit was approximately $2 \times 10^{15} \text{ cm}^{-3}$. The results show that the 10% HF etchant step can additionally reduce the Si accumulation by a factor of 3. This was confirmed by the background carrier concentration of Hall-effect measurements of two $4 \mu\text{m}$ thick InP layers, which were cleaned in the same way as a) and b), respectively. The Hall-effect results are listed in table 2 (f,g). Photoluminescence spectra of these two samples indicate that the real background carrier concentration is even less than found by Hall-effect measurements in comparison with the work of Pen et al. (5). Thus the Hall-effect measurements are still influenced by the low Si accumulation at the substrate-layer interface shown in Fig. 5. Hall-effect measurements of InP layers grown on InP wafers with different pretreatments are summarized in table 2.

Wafer Pre-treatment	$n_{300\text{K}}$ cm^{-3}	$\mu_{300\text{K}}$ cm^2/Vs	$n_{77\text{K}}$ cm^{-3}	$\mu_{77\text{K}}$ cm^2/Vs
a)	$5.7 \cdot 10^{15}$	2660	$1.4 \cdot 10^{15}$	29000
b)	$1.3 \cdot 10^{16}$	1850	$2.8 \cdot 10^{15}$	23700
c)	$3.0 \cdot 10^{15}$	3034	$7.8 \cdot 10^{14}$	54610
d)	$8.8 \cdot 10^{14}$	3540	$6.8 \cdot 10^{14}$	63220
e)	$3.1 \cdot 10^{14}$	4910	$2.8 \cdot 10^{14}$	99350
f)	$6.3 \cdot 10^{14}$	4120	$2.5 \cdot 10^{14}$	108000
g)	$9.6 \cdot 10^{13}$	5020	$8.7 \cdot 10^{13}$	142000

Table 2: Hall-effect measurements at 300 K and 77 K of InP layers deposited on InP wafers with different pretreatments. a) without pretreatment (epi ready wafer), b) 3 min 10% HF + DI- H_2O rinsing (different wafer lot), c) 3 min 10% HF + DI- H_2O rinsing, d) 3 min 10% HF without DI- H_2O rinsing, e) 5 min bromine methanol 0.05% + methanol rinsing, f) 10 min $\text{H}_2\text{SO}_4:\text{H}_2\text{O}_2:\text{H}_2\text{O} = 10:1:1$ + DI- H_2O rinsing, g) 10 min $\text{H}_2\text{SO}_4:\text{H}_2\text{O}_2:\text{H}_2\text{O} = 10:1:1$ + DI- H_2O rinsing + 3 min 10% HF without DI- H_2O rinsing. The best electrical results are obtained for cleaning process g).

Summary and Conclusion

Unintentional impurity incorporation at the substrate epitaxial layer interface results in conductive buffer layers in the LP-MOVPE growth of InP. The impurities were identified by SIMS to be only Si accumulations. Si does not originate from the epitaxial equipment but it is brought externally into the reactor. Two substantial sources of Si contamination were found. First Si is already incorporated in the wafer material, probably by the polishing process and second rinsing in deionized

water as the last cleaning step adds Si to the wafer surface. The Si concentration in the wafer material depends on the skill of the manufacturer while Si contamination in the deionized water is probably due to Si containing molecular sieves. Further possible source of Si are the chemicals used for etching and contamination by exposure to air between the last cleaning step and loading into the reactor as proposed by Ishikawa et al. (3).

To obtain highly resistive buffer layers an etchant has to be used to remove a surface layer first. This reduces the Si already incorporated in the wafer material. The best results were found for the $\text{H}_2\text{SO}_4:\text{H}_2\text{O}_2:\text{H}_2\text{O}$ etchant with a volume ratio of 10:1:1 and an etch time of 10 min. An additional 10% HF etching step for 3 min followed by drying the wafer with nitrogen without rinsing in deionized water further reduces the Si accumulation at the substrate-layer interface. The 10% HF etchant leaves F on the wafer surface which can bind Si contamination to form volatile SiF_4 , which easily desorbs from the substrate during the heating process in the reactor. Whereas rinsing in deionized water desolves F in the water preventing the formation of volatile SiF_4 . This cleaning procedure suppresses the Si contamination at the epitaxial-substrate interface prior to growth and is a good alternative to Si suppression by heating in phosphine atmosphere at very high temperatures during the growth run as proposed by Ishikawa et al. (3).

Acknowledgements

The authors would like to thank K. Wirtz and F. Eggenweiler for technical assistance.

References

- (1) A.M. Huber, M. Razeghi, G. Morilliot, 11th Int. Symp. GaAs and Related Compounds, Biarritz, 1984, Inst. Phys. Conf. Ser. No. 74, Chapter 3, pp. 223-228, (1985)
- (2) A.T.R. Briggs and B.R. Butler, J. Cryst. Growth, Vol. 85, pp. 535-542, (1987)
- (3) H. Ishikawa, S. Miwa, T. Maruyama and M. Kamada, J. Appl. Phys., Vol. 71, pp. 3898-3903, (1992)
- (4) N. Pan, J. Elliot, J. Carter, H. Hendriks and L. Aucoin, 20th Int. Symp. GaAs and Related Compounds, Freiburg, 1993, Inst. Phys. Conf. Ser. No. 136, Chapter 10, pp. 655-660, (1994)
- (5) H.F. Pen, F.A.J.M. Driessen, S.M. Olsthoorn and L.J. Giling, Semicond. Sci. Technol., Vol. 7, pp. 1400-1405, (1992)
- (6) W. Walukiewicz, L. Lagowski, L. Jastrzebski, P. Rava, M. Lichtensteiger, C.H. Gatos and H.C. Gatos, J. Appl. Phys., Vol. 51, pp. 2659-2668, (1980)

Pyramidal shaped pit formation on InAlAs/Fe-doped InP structures grown by MOCVD

T. Noda, A. Sasaki, C. Nozaki and Y. Ashizawa

Toshiba Research and Development Center, 1 Komukai Toshiba-cho, Saiwai-ku, Kawasaki 210, Japan

1. Introduction

Epitaxial growth of semi-insulating Fe-doped InP (InP:Fe) by metal organic chemical vapor deposition (MOCVD) has been studied for electronic and optical device applications. For the growth of InP-based hetero-FETs such as InAlAs/InGaAs high electron mobility transistors (HEMTs), highly resistive InP:Fe buffer layers between InAlAs carrier confinement layers or InGaAs channel layers and InP substrates are particularly important [1,2]. This is because MOCVD grown undoped-InP buffer layers often give leakage currents due to conductive path caused by Si contamination at interfaces between buffer layers and substrates [3]. The use of InP:Fe layers improves the resistivity of the buffer layers. However, the optimum Fe-doping conditions and the influence of doped Fe atoms on upper InAlAs or InGaAs layers have not been made clear. We grew InAlAs/InP:Fe structures, and found that large pyramidal pits were formed on the structures with the Fe-doping concentrations above $2 \times 10^{17} \text{cm}^{-3}$. In a similar case, Knight et al. have reported on the square pits formed on Fe-doped InGaAsP layers [4], but detailed studies on the pit formation have not been made. To clarify the mechanism of the pit formation and the suitable growth conditions of InAlAs/InP:Fe structures for buffer layers of hetero-FETs, we investigated various growth condition dependencies of shape, size and density of the pits.

2. Experiments

Undoped $\text{In}_{0.52}\text{Al}_{0.48}\text{As}$ /InP:Fe structures were grown on Fe-doped (100) InP substrates by low pressure MOCVD. Trimethylindium (TMI), trimethylaluminum (TMA), arsine (AsH_3), phosphine (PH_3) and ferrocene ($(\text{C}_5\text{H}_5)_2\text{Fe}$) were used as source materials. The growth pressure was 9.3kPa. The structures and the growth conditions of layers are shown in Table 1. The thickness of InAlAs layers (d_{InAlAs}), the Fe-doping concentration of InP:Fe layers (N_{Fe}), the growth temperature of InAlAs (T_{gInAlAs}) and the molar ratio of group-V to group-III of InAlAs ($\text{V/III}_{\text{InAlAs}}$) were varied in the range shown in Table 1.

The shapes, sizes and densities of the pits formed on the samples were measured by scanning electron microscopy (SEM) and atomic force microscopy (AFM). An InP:Fe layer was observed by transmission electron microscopy (TEM). The Fe concentrations in the samples were determined by secondary ion mass spectrometry (SIMS). The electrical properties of the samples were investigated by the van der Pauw method.

3. Results and discussions

3-1. Pit shapes and sizes

Figure 1(a) shows a SEM image of an InAlAs/InP:Fe

surface with d_{InAlAs} of 1000nm, N_{Fe} of $6 \times 10^{17} \text{cm}^{-3}$, T_{gInAlAs} of 650°C and $\text{V/III}_{\text{InAlAs}}$ of 600. Many rhombic pits with high uniformity of shapes and sizes were observed. Figure 1(b) shows a cross-sectional image of one of the pits. The pit had pyramidal shape with smooth facets. From the angles between the facets and the surface, the four facets were measured to be close to $(65\bar{1})$, $(6\bar{1}5)$, $(6\bar{5}1)$ and $(6\bar{1}\bar{5})$ planes, which are $\{110\}$ planes tilted 5.2° toward the (100) surface and 7.3° toward the nearest (111)B planes. The samples with d_{InAlAs} of 500nm had also the same facet orientations.

The surface of the samples with thinner d_{InAlAs} of 20nm and 100nm were observed by AFM. Figure 2 shows an AFM image of a sample with d_{InAlAs} of 100nm. The pit shapes and sizes of the samples with d_{InAlAs} below 100nm were not as uniform as those of the samples with d_{InAlAs} above 500nm. The pits had convex slopes rather than flat facets.

Figure 3 shows the pit sizes and the facet angles from the surfaces for the samples with various d_{InAlAs} . It was found from fig. 3 that the pits began to form at the initial stage of InAlAs growth, and that the initial pits had diameters about 100nm. As the InAlAs grew thicker, the pit size increased in proportion to d_{InAlAs} , and the facet angle increased rapidly to 40° , which is approximately the value of the angle between $(65\bar{1})$ and (100).

Table 1 The structures and the growth conditions of InP:Fe layers and InAlAs layers.

Material	Thickness (nm) d	Fe concentration (cm^{-3}) N_{Fe}	Growth temperature ($^\circ\text{C}$) T_{g}	V/III molar ratio V/III
InAlAs	20—1000	undoped	550—700	10—600
InP:Fe	300	undoped, 6×10^{16} — 1.2×10^{18}	650	250

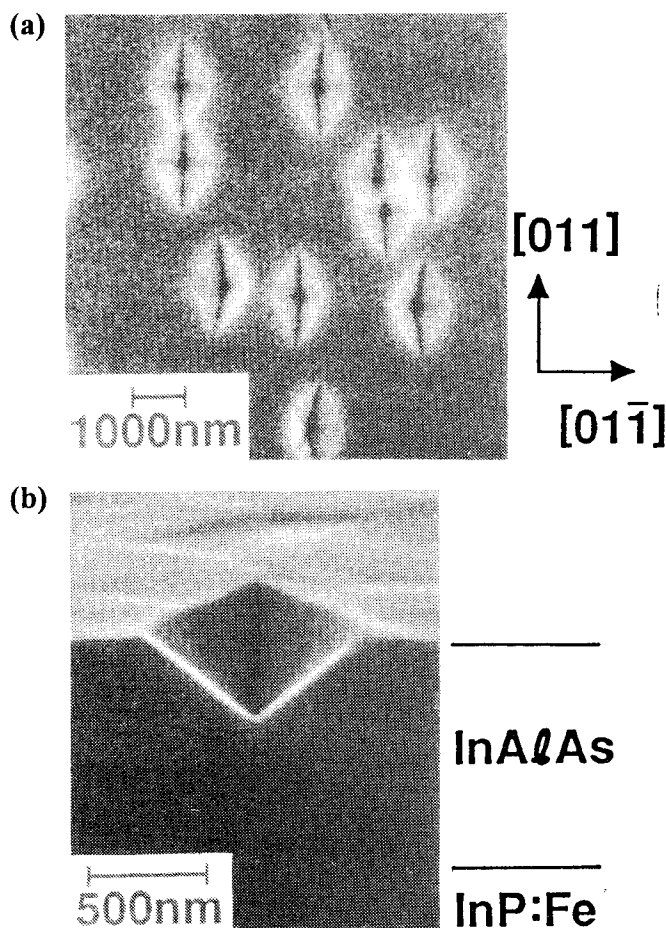


Fig. 1 SEM images of InAlAs/InP:Fe structures. (a) surface, (b) cross-section of (011) plane. ($d_{\text{InAlAs}}=1000\text{nm}$, $N_{\text{Fe}}=6 \times 10^{17}\text{cm}^{-3}$, $T_{\text{gInAlAs}}=650^\circ\text{C}$, $V/\text{III}_{\text{InAlAs}}=600$)

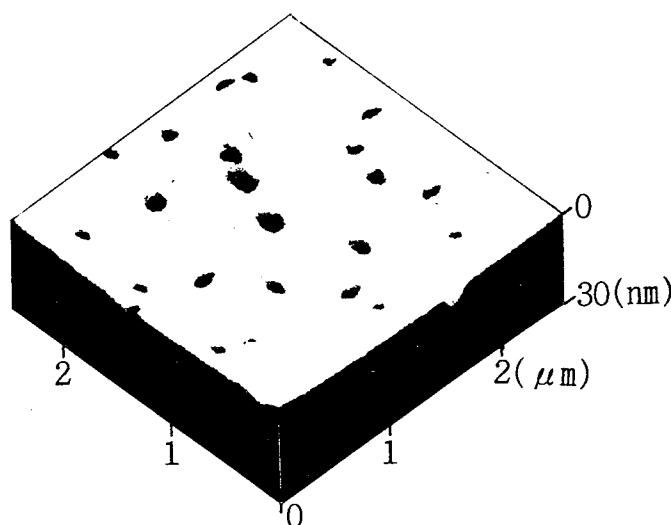


Fig. 2 AFM image of InAlAs/InP:Fe surface. ($d_{\text{InAlAs}}=100\text{nm}$, $N_{\text{Fe}}=1 \times 10^{18}\text{cm}^{-3}$, $T_{\text{gInAlAs}}=650^\circ\text{C}$, $V/\text{III}_{\text{InAlAs}}=600$)

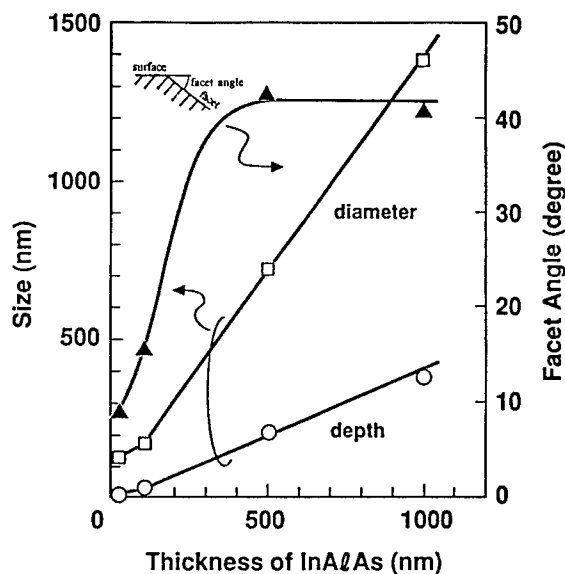


Fig. 3 InAlAs thickness dependence of pit size and facet angle. ○:depth of the pits; □:average value of two diagonals of the surface orifice for the samples with $d_{\text{InAlAs}} \geq 500\text{nm}$, and average diameter for the samples with $d_{\text{InAlAs}} \leq 100\text{nm}$; ▲:facet angle from surface for the samples with $d_{\text{InAlAs}} \geq 500\text{nm}$, and value of depth/(diameter/2) for the samples with $d_{\text{InAlAs}} \leq 100\text{nm}$. ($T_{\text{gInAlAs}}=650^\circ\text{C}$, $V/\text{III}_{\text{InAlAs}}=600$)

The pit shapes and sizes were independent of N_{Fe} . Conversely, T_{gInAlAs} and $V/\text{III}_{\text{InAlAs}}$ both affected the pit size. As the pit density decreased with the variation of T_{gInAlAs} and $V/\text{III}_{\text{InAlAs}}$, (described later), the pit sizes became smaller.

3-2. Pit densities

Figure 4 shows the ferrocene flow rate dependence of pit density. The Fe concentrations in InP:Fe layers were measured by SIMS and were found to be proportional to the ferrocene flow rates. No appreciable diffusions of Fe atoms into the InAlAs layers were observed. While no pits were observed in the range of $N_{\text{Fe}} < 2 \times 10^{17}\text{cm}^{-3}$, the pit density increased linearly with N_{Fe} in the range above $2 \times 10^{17}\text{cm}^{-3}$. Nakai et al. reported that Fe-P precipitates about 10nm in size were formed in InP:Fe layers, when N_{Fe} exceeded the solubility limit of Fe in InP at 650°C about $7 \times 10^{16}\text{cm}^{-3}$ [5]. We also confirmed the presence of precipitates about 15-25nm in size in an InP:Fe layer, by plan-view TEM. From their results of TEM observation, the estimated surface densities of Fe-P precipitates increased from 8×10^6 to $1 \times 10^8\text{cm}^{-2}$, as N_{Fe} increased from 6×10^{17} to $2 \times 10^{18}\text{cm}^{-3}$. These surface densities of Fe-P precipitates almost correspond with the pit densities of our samples for the same value of N_{Fe} . This similarity in N_{Fe} dependence of pit density and Fe-P precipitate

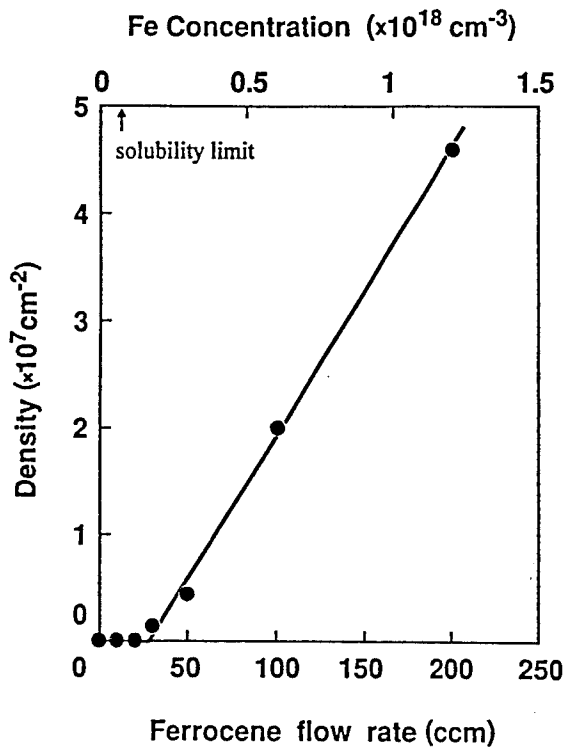


Fig. 4 Ferrocene flow rate dependence of pit density. The value of solubility limit of Fe in InP at 650°C is shown [5]. ($T_{\text{InAlAs}}=650^\circ\text{C}$, $V/\text{III}_{\text{InAlAs}}=600$)

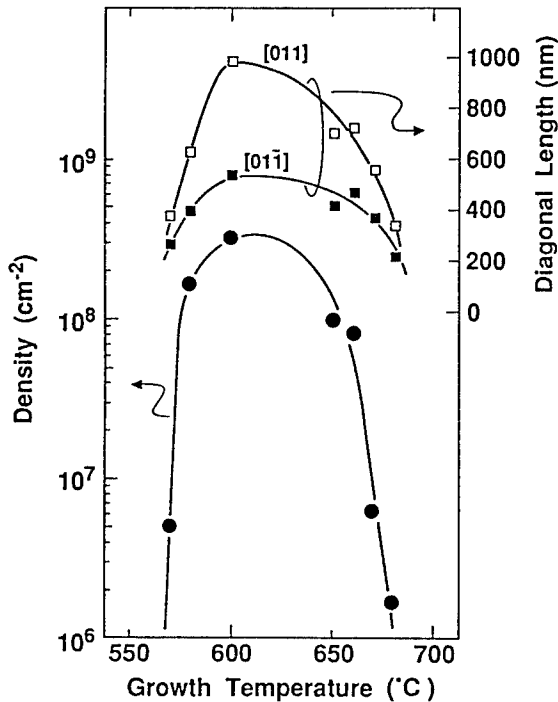


Fig. 5 InAlAs growth temperature dependence of pit density and size. ($N_{\text{Fe}}=1 \times 10^{18}\text{cm}^{-3}$, $V/\text{III}_{\text{InAlAs}}=40$)

density strongly indicates that the Fe-P precipitates are responsible for the pit formation.

Figure 5 shows the T_{InAlAs} dependence of pit density and pit size at $V/\text{III}_{\text{InAlAs}}=40$. The values of both density and size took maximum at 600 °C. In the range of $T_{\text{InAlAs}} < 580^\circ\text{C}$ and $> 660^\circ\text{C}$, the pit density decreased greatly. The $V/\text{III}_{\text{InAlAs}}$ value also affected the density and the size. At $T_{\text{InAlAs}}=650^\circ\text{C}$, as $V/\text{III}_{\text{InAlAs}}$ lowered below 150, the density and the size decreased, and no pits were observed at $V/\text{III}_{\text{InAlAs}}=10$. It is considered that the decrease in size to zero with the variations in T_{InAlAs} and $V/\text{III}_{\text{InAlAs}}$ caused the great decrease of pit density.

3-3. Mechanism of pit formation

From the results of the growth condition dependence of pit shape, size and density, the following mechanism of pit formation is proposed. Figure 6(a) shows a cross-sectional schematic of an initial pit formation. At the initial stage of InAlAs growth on InP:Fe layers ($d_{\text{InAlAs}} \leq 100\text{nm}$), Fe-P precipitates on the InP:Fe surface work as masks, which hinder the growth of InAlAs. Next, lateral growth starts to cover the Fe-P precipitates, and the initial pits are formed on the precipitates. Assuming that the growth rate is smaller as the angle of the pit slope increases, the growth rate of the pit periphery is larger than that of the center. This variation in the growth rate causes an effect such that, as InAlAs grows thicker, the angles of the pit slopes increase, and finally flat slopes form.

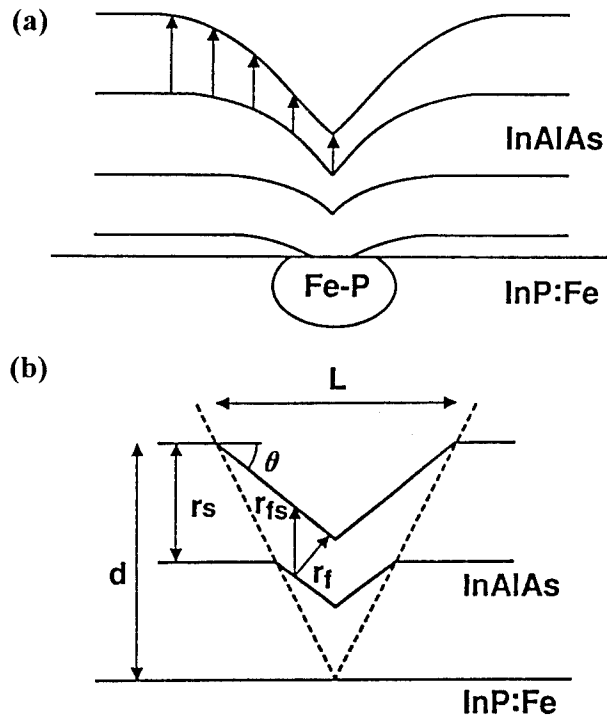


Fig. 6 Cross-sectional schematics of pit formation. (a) $d_{\text{InAlAs}} \leq 100\text{nm}$, (b) $d_{\text{InAlAs}} > 100\text{nm}$.

Figure 6(b) shows a cross-sectional schematic of a pit after the flat slope formation ($d_{\text{InAlAs}} > 100\text{nm}$). The diameter of the cross-section (L) is given by

$$L = (2/\sin \theta) \cdot (\cos \theta - r_f/r_s) \cdot d_{\text{InAlAs}} \\ = (2/\tan \theta) \cdot (1 - r_f/r_s) \cdot d_{\text{InAlAs}} \quad (1)$$

Here, r_s and r_f are the InAlAs growth rate of surface and facet, respectively. The function $r_f (= r_f/\cos \theta)$ is a part of r_f in the direction of the surface, and θ is the angle of the pit slope from the surface. As InAlAs grows, facets whose orientation minimize the value of L appear gradually. Equation (1) indicates that the value of L decreases with the increase of r_f . Therefore planes with high growth rate form flat facets. The growth rate of (110) is probably larger than that of (111)A and (111)B [6]. Therefore the facets of (65 $\bar{1}$), which are a few degrees tilted (110), are obtained. Once a flat facet form, the orientation of the facet is kept constant, because the value of r_f is constant at any point on the facet.

Equation (1) indicates that the pit size decreases as the r_f/r_s of facets increases, and that pits do not form with the condition $r_f/r_s \geq 1$. It is considered that the variation of r_f/r_s being dependent on T_{InAlAs} and $V/\text{III}_{\text{InAlAs}}$ causes the T_{InAlAs} and $V/\text{III}_{\text{InAlAs}}$ dependence of pit size and pit density. As the value of r_f/r_s increases to 1, pit size decreases and finally, pit density greatly decreases.

3-4. Suitable growth conditions for buffer layers of FETs

High sheet resistance and high flatness are required qualities for buffer layers of FETs. We found that the sheet resistance of InP:Fe layers increased with N_{Fe} , even when over the solubility limit, by Hall measurement. Therefore, high Fe-doping over the solubility limit is a way to decrease leakage currents in buffer layers of FETs. When InAlAs carrier confinement layers are grown on the highly Fe-doped InP buffer layers, we should select the InAlAs growth conditions suppressing the pit formation in order to keep flat InAlAs surface. In these conditions, high T_{InAlAs} and high $V/\text{III}_{\text{InAlAs}}$ are expected to be the most suitable, though pits form at too high $V/\text{III}_{\text{InAlAs}}$. This is because the concentration of deep donor in InAlAs, whose origin is residual oxygen, decreases greatly as T_{InAlAs} and/or $V/\text{III}_{\text{InAlAs}}$ are higher [7,8].

4. Summary

In summary, we found that pyramidal pits with high uniformity of shape and size were formed on the InAlAs/InP:Fe heterostructures with the high Fe-doping concentration above the solubility limit of Fe in InP. The pit density depended strongly on Fe-doping concentration and InAlAs growth conditions. The mechanism of the pit formation is well explained by the lateral growth of

InAlAs on the masks of the Fe-P precipitates formed on InP:Fe. The facet orientation of (65 $\bar{1}$) is determined by the orientation dependence of InAlAs growth rate. The pit formation was successfully suppressed by selecting the suitable growth conditions of InAlAs, even with the Fe-doping concentration above the solubility limit. This is very important for the application of InAlAs/InP:Fe heterostructures to high resistive and flat buffer layers of hetero-FETs.

Acknowledgments

The authors would like to thank M. Tomita and C. Takakuwa for SIMS analysis, and M. Azuma, Y. Ikawa and M. Obara for their encouragement.

References

- [1] I. Adesida, K. Nummala, M. Tong, C. Caneau and R. Bhat, "High-performance 0.15 μm -gate-length OMVPE-grown InAlAs/InGaAs MODFETs", Int. Conf. InP and Related Materials, 1993, pp. 405-408.
- [2] S. Fujita, T. Noda, A. Wagai, S. Hosoi and Y. Ashizawa, "Extremely low noise InGaAs/InAlAs HEMT grown by MOCVD", Electron. Lett. Vol. 29, pp. 1557-1558, 1993.
- [3] H. Ishikawa, S. Miwa, T. Maruyama and M. Kamada, "Origin of n-type conduction at the interface between epitaxial-grown layer and InP substrate and its suppression by heating in phosphine atmosphere", J. Appl. Phys. Vol. 71, pp. 3898-3903, 1992.
- [4] D.G. Knight, W.T. Moore and R.A. Bruce, "Growth of semi-insulating InGaAsP alloys using low-pressure MOCVD", J. Crystal Growth, Vol. 1241, pp. 352-357, 1992.
- [5] K. Nakai, O. Ueda, T. Odagawa, T. Takanohashi and S. Yamakoshi, "Epitaxial growth and characteristics of Fe-doped InP by MOCVD", Int. Symp. GaAs and Related Compounds, 1987, pp. 199-202.
- [6] Y. Nagamune, S. Tsukamoto, M. Nishioka and Y. Arakawa, "Growth process and mechanism of nanometer-scale GaAs dot-structures using MOCVD selective growth", Int. Conf. Solid State Devices and Materials, 1991, pp. 689-691.
- [7] S. Naritsuka, T. Noda, A. Wagai, S. Fujita and Y. Ashizawa, "Electrical properties and deep levels of InAlAs layers grown by metalorganic chemical vapor deposition", J. Crystal Growth, Vol. 131, pp. 186-192, 1993.
- [8] S. Naritsuka, T. Noda, A. Wagai, S. Fujita and Y. Ashizawa, "Influence of V/III molar ratio on deep traps in metalorganic chemical vapor deposition grown InAlAs layers", Jpn. J. Appl. Phys. Vol. 32, pp. L925-L927, 1993.

Growth Condition Dependence of N-type Carriers at the Interface between InP Substrates and Epitaxial Layers Grown by MOCVD

M. Nakamura, H. Kurita*, and T. Fukui*

JAPAN ENERGY CORPORATION

Electronic Materials and Component Laboratories

3-17-35, Niizo-Minami, Toda, Saitama, 335 Japan

*Advanced Materials Research Center

187-4, Usuba, Hanakawa, Kita-Ibaraki, Ibaraki, 319-15 Japan

Abstract

We investigated the dependence of n-type carriers at the interface between InP substrates and epitaxial layers grown by MOCVD on the phosphine (PH₃) partial pressure and the growth temperature sequence. The carrier concentration decreases with increasing the PH₃ partial pressure. The carrier concentration also reduces when the temperature during thermal etching is high, and the temperature during the initial growth stage is low. Silicon and oxygen were detected as impurities at the interface by secondary ion mass spectrometry (SIMS) measurement. The silicon concentration is no less than $1 \times 10^{17} \text{ cm}^{-3}$ under all growth conditions. The oxygen concentration varied from $1 \times 10^{17} \text{ cm}^{-3}$ to $8 \times 10^{19} \text{ cm}^{-3}$ and had no relationship with the carrier concentration.

1. Introduction

There is a great deal of interest recently in the epitaxial growth on semi-insulating InP substrates. This occurs largely because of the importance of fabrication of the high frequency devices such as high electron mobility transistors. It is known that there are n-type carriers at the interface between substrates and buffer layers [1-6]. Rakennus et al. and Knauer et al. [3,6] have shown that these carriers reduce the mobility in homo-epitaxial layers on InP substrates. In the case of MBE epitaxial layer on GaAs substrates, Izumi et al. [7] have shown that n-type carriers cause the poor pinch-off characteristics and the current leakage in the MESFET between ohmic metals and epitaxial layers. In this study, we have investigated the dependence of n-type carriers on the PH₃ partial pressure and the growth temperature sequence.

A low pressure MOCVD system was used for growing InP epitaxial layers on Fe-doped InP substrates. These substrates were etched using H₂SO₄:H₂O₂:H₂O (5:1:1, 1 min., at RT.). 0.7 μm thick undoped InP was grown as a buffer layer, followed by 0.3 μm thick S-doped InP with the carrier concentration of about $7 \times 10^{17} \text{ cm}^{-3}$. The pressure was 30 torr and the total flow rate was 15 l/min. Trimethylindium (TMI) and PH₃ were used as source materials. Fig. 1 shows the sequence of epitaxial growth in this study. Two types of PH₃ partial pressure sequence ((a),(b)) and three types of growth temperature sequence ((A),(B) and (C)) were used. Surface morphology was observed by a Normaski microscope. An electrochemical capacitance-voltage (ECV) profiler and a SIMS were applied for the measurement of carrier and impurity concentrations at the interface between substrates and undoped InP layers.

2. Experimental

3. Results

All epitaxial layers grown in this study had mirrorlike surfaces. The carrier concentration at the interface however strongly depended on the growth sequence. Fig. 2 shows an ECV profile under the condition of sequence (B)-(b). N-type carriers exist at the interface and the peak value of the concentration was $5.0 \times 10^{16} \text{cm}^{-3}$. Table 1 summarizes carrier concentrations at the interface under various growth conditions. The carrier concentration decreases with increasing the PH_3 partial pressure. In the case of the temperature sequence B, the carrier concentration decreases from $5.0 \times 10^{16} \text{cm}^{-3}$ to $6.0 \times 10^{15} \text{cm}^{-3}$, as the PH_3 partial pressure increases from 0.8 torr to 1.6 torr. This fact was also observed for other temperature sequences. Under the same PH_3 partial pressure, the carrier concentration decreases when the growth temperature during thermal etching is high, as can be seen by the comparison of the sequence (1) with (3), (2) with (4). It also decreases when the growth temperature at the interface is low (comparison of (3) with (5), (4) with (6)).

We have found by SIMS analysis that silicon and oxygen were detected at the interface. Fig. 3 shows the relationship between the carrier concentration and the silicon concentration at the interface. When the carrier concentration is larger than $1 \times 10^{17} \text{cm}^{-3}$, the carrier concentration increases with the silicon concentration. The silicon concentration is no less than $1 \times 10^{17} \text{cm}^{-3}$ even if the carrier concentration is smaller than $1 \times 10^{17} \text{cm}^{-3}$. The oxygen concentration varied from $1 \times 10^{17} \text{cm}^{-3}$ to $8 \times 10^{19} \text{cm}^{-3}$ and had no relationship with the carrier concentration.

4. Discussion

Ishikawa et al. [5] reported that the origin of n-type carriers was silicon atoms in the ambient air and it could be suppressed by thermal etching for removing silicon atoms absorbed to InP. Our result showed that thermal etching affected the carrier concentration but it could not remove silicon atoms. In the case of the Ishikawas' experiment, silicon planar doped InP layers that had no Si-O bonds were used, therefore, the result might be different from ours. The activation efficiency of silicon is suppressed not only by removing silicon atoms but by making Si-O bonds, as Izumi reported [7]. It indicates

that the activation efficiency of silicon varies under each growth condition and the growth sequence affects it. In our study, under the condition that the carrier concentration decreases, Si-O bonds might exist at the interface. Silicon atoms that have Si-O bonds are more difficult to remove from InP surfaces than those with no Si-O bonds. This is the reason why silicon atoms exist in all samples in our study.

Since InP substrates used in this study are not "epitaxial-ready" ones, there are some surface oxides on these substrates. The structure of these oxides is very complicated. Binary compounds In_2O_3 , $\text{In}(\text{OH})_3$, P_2O_5 , ternary oxides InPO_4 , $\text{In}(\text{PO}_3)_3$, and silicon oxide may coexist [8]. They can not be removed completely only by pretreatment.

If the substrates are well-prepared as "epitaxial-ready" ones that have no silicon and oxygen atoms at the surface, it may be possible to make epitaxial wafers that have no carrier concentration neither impurities at the interface. The present result however shows a possibility to decrease the carrier concentration at the interface by optimizing the MOCVD growth conditions without using special substrates.

5. Conclusions

We have found that the n-type carrier concentration at the interface between InP substrates and epitaxial layers grown by MOCVD strongly depends on the growth conditions. The carrier concentration decreases with increasing the PH_3 partial pressure. The carrier concentration also reduces when the temperature during thermal etching is high, and the temperature during the initial growth stage is low. These growth conditions can depress the activation efficiency of silicon.

Acknowledgments

The authors are grateful to Dr. K. Aiki, Dr. M. Taniguchi and Dr. O. Oda for their encouragement. We also thank Dr. Y. Taniguchi, Mr. Takakusaki and Mr. K. Suzuki for their useful discussions.

References

- [1] A. M. Huber, G. Morillot, S. D. Hkersee, K. Kazmierski, H. Tews, and J. L. Pinland, in: Semi-insulating III-V materials, Eds. D. C. Look and J. S. Blakemore (Shiva, Nanwich, 1984) p. 466.
- [2] M. Benzaquen, D. Walsh, M. Beaudon and K. Mazuruk : J. Cryst Growth 93 (1988) p. 562.
- [3] K. Rakennus, K. Tappura, T. Hakkarainen, H. Asonen : J. Cryst. Growth 110 (1991) p910.
- [4] K. Katsura, T. Fukui, Y. Takahashi, M. Takakusaki, M. Nakamura, O. Oda, Y. Sugiyama, and M. Tacano, in: Proc. 4th IPRM, Newport, USA, 1992, p. 270.
- [5] H. Ishikawa, S. Miwa, T. Maruyama, and M. Kamada : J. Appl. Phys. 71 (1992) p3898.
- [6] A. Knauer, E. Richter, M. Weyers : J. Cryst Growth 146 (1995) p 549-553.
- [7] S. Izumi, N. Yoshida, H. Takano, K. Nishitani and M. Otsubo : J. Cryst. Growth 133 (1993) p123.
- [8] G. Hollinger, J. Joseph, Y. Robach, E. Bergignat, B. Commère, P. Viktorovitch, and M. Froment : J. Vac. Sci, Technol. B5 (1987) p1108.

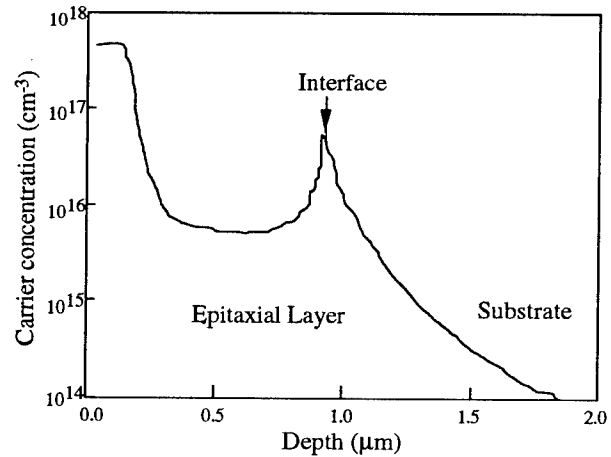


Fig.2 Carrier profile of InP epitaxial layer
(Growth sequence (B)-(b))

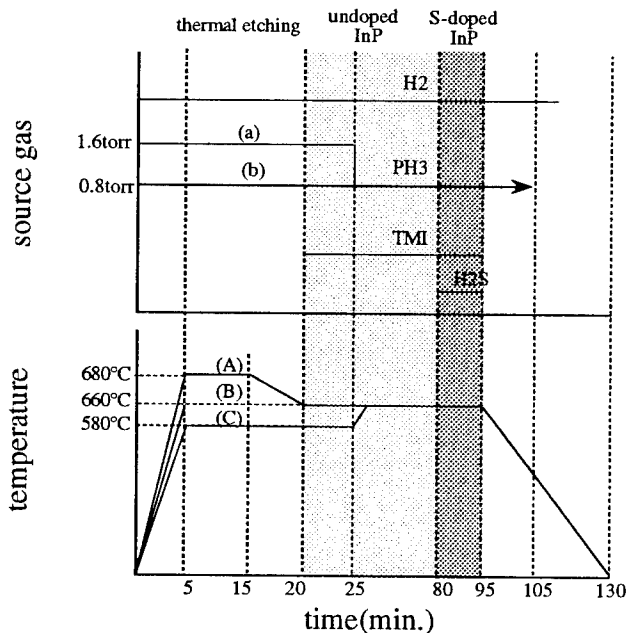


Fig. 1 Epitaxial growth sequence by MOCVD

Table 1 N-type carrier concentration at the interface of various growth conditions

Process	Thermal Etching		Growth* Temperature (°C)	Carrier Concentration (cm ⁻³)
	Temperature	PH ₃		
(1)	A	a	660	2.0x10 ¹⁴
(2)	A	b	660	3.0x10 ¹⁵
(3)	B	a	660	6.0x10 ¹⁵
(4)	B	b	660	5.0x10 ¹⁶
(5)	C	a	580	3.0x10 ¹⁵
(6)	C	b	580	6.0x10 ¹⁵

*at the interface

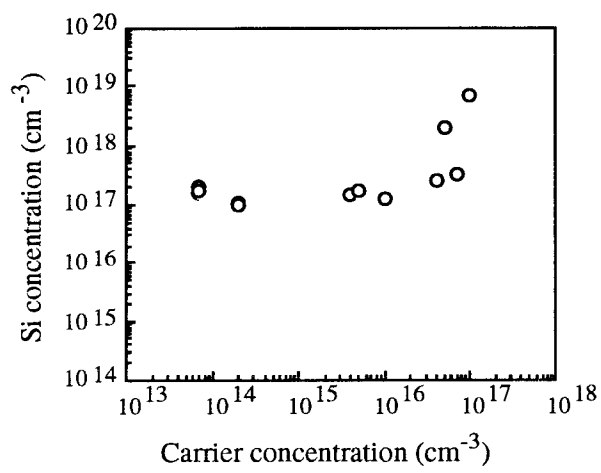


Fig. 3 Relationship between carrier and Si concentrations

Heavily Carbon Doped InGaAs Lattice Matched to InP Grown by LP-MOCVD Using TMIn, TMGa and Liquid CCl₄[†]

K. Hong and D. Pavlidis

Solid-State Electronics Laboratory,
Department of Electrical Engineering and Computer Science,
The University of Michigan, Ann Arbor, Michigan 48109-2122, U.S.A.

Introduction

Heavily carbon doped *p*-InGaAs lattice matched to InP is of great importance for many InP-based microwave and optoelectronic device applications due to its low diffusivity during the growth, device fabrication and operation. However, the growth of C-In_{0.53}Ga_{0.47}As is very difficult compared with that of C-GaAs due to the enhanced amphotericity by the presence of indium. Recently, there have been several reports on the growth of carbon doped *p*-In_{0.53}Ga_{0.47}As. Most of the work to date has been carried out in MBE-like growth environments such as MOMBE(1), GSMBE(2), MBE(3) and CBE(4) and only a small number of reports is available on MOCVD growth(5)(6). Although MOCVD is very attractive due to its simplicity and flexibility, growth of carbon doped materials using this technique is difficult due to the presence of very large amounts of hydrogen at the growth interface, which reduces carbon incorporation and also passivates the incorporated carbon. In addition, it has been reported that the use of metalorganic indium source(TMIn) tends to result in *n*- rather than *p*-type conduction(1). In this paper, we report on the growth of heavily carbon doped *p*-InGaAs($\sim 6.5 \times 10^{19} \text{cm}^{-3}$) lattice-matched to InP by low pressure MOCVD using all methyl metal-organic sources and liquid CCl₄. The impact of annealing conditions on carbon activation and subsequently on the contact resistance is also presented.

Growth of carbon-doped InGaAs

The growth was carried out by a modified EMCORE GS3200 Low-Pressure Metal Organic Chemical Vapor Deposition(LP-MOCVD) system in a vertical mass transport reactor with rotating susceptor. All-methyl metal organic sources(TMIn, TMGa) were used for group III and 100% arsine was used for group V. Liquid, instead of gaseous CCl₄ was used as a carbon source. This was transported from the standard stainless steel bubbler to the reactor through an alkyl delivery line using H₂ as a carrier gas. Although the use of liquid CCl₄ has been reported for growth of carbon doped GaAs by LP-MOCVD(7) and C-In_{0.5}Ga_{0.5}As by GSMBE(2), there is, to our knowledge, no such report for C-In_{0.53}Ga_{0.47}As by LP-MOCVD. Liquid rather than compressed gaseous CCl₄ offers the advantage of easy installation using a standard stainless steel bubbler in a alkyl line. Moreover, the dopant flux can be controlled by the bubbler temperature and pressure which in conjunction with the flow rate of the carrier gas leads to a wider range of dopant flux as imposed by electronic and optoelectronic material requirements.

Since carbon is of amphoteric nature, growth conditions have to be optimized so that carbon is favorably incorporated into As-sites rather than group III sites. Our

studies showed that low growth temperature (<500°C) and V/III ratios (~ 5) are necessary to obtain a *p*-type material. Although this trend is in agreement with previous reports using gaseous CCl₄(5), the trends for the incorporation efficiency of In and Ga are different as explained below.

One of the main advantages of using carbon sources that do not contain major cation or anion materials is that doping level control is independent of growth rate and alloy composition of the material. However, CCl₄ does not follow this rule and tends to affect the growth rate and alloy composition of InGaAs by etching InAs and GaAs at the growth front. Therefore, growth conditions have to be optimized and sometimes even compromised so that growth can take place in a more controllable way. The source incorporation efficiency η is a very useful parameter for investigating the impact of CCl₄ flow rate on the growth rate and alloy composition of InGaAs and has therefore been explored in our study. The source incorporation efficiency of cation A (η_A) can be defined by extending the definition of G. S. Tompa *et al.* for binary materials(8) as shown below:

$$\eta_A = \frac{\text{moles of cation A deposited on 5" susceptor}}{\text{moles of cation A introduced into the reactor}}$$

Fig.1 shows that both the TMGa and TMIn incorporation efficiency (η_{Ga} and η_{In} , respectively) are reduced over the entire temperature range in the presence of CCl₄ ($\sim 4 \text{sccm}$). The reduction of η_{Ga} is in contrast to the

[†]Work supported by ARPA COST(MDA 972-94-1-0004) and URI(DAAL 03-92-G-0109).

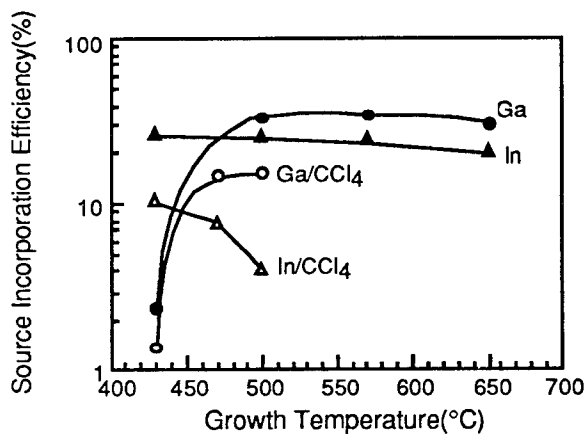


Fig.1 Incorporation efficiency of Ga and In for the case of un-doped and C-doped InGaAs. Both the In and Ga incorporation efficiency is shown to decrease in the presence of CCl_4 (4sccm).

results of earlier reports using gaseous CCl_4 where only the TMIn incorporation at high growth temperature was found to be affected by the presence of CCl_4 (6). The rapid decrease of η_{Ga} below $\sim 450^\circ\text{C}$ is due to the incomplete decomposition of TMGa and is relatively independent of the presence of CCl_4 . However, at temperatures above 450°C η_{Ga} is not sensitive to the growth temperature while this is not the case for η_{In} . The latter is in fact found to decrease in the presence of CCl_4 as the growth temperature increases. As a result, growth rate reduction due to reduced η_{Ga} and η_{In} by the presence of CCl_4 can be minimized by lowering the growth temperature.

The ratio of TMGa and TMIn cation incorporation efficiency $\gamma (= \eta_{TMGa} / \eta_{TMIn})$ is a very important parameter for controlling the alloy composition in ternary materials. This is due to the fact that the solid phase indium composition in an InGaAs layer, x_s , is determined by the gas phase indium composition x_g and γ as below:

$$x_s = \frac{1}{1 + \gamma(1/x_g - 1)}$$

Therefore, in order to achieve a constant solid phase alloy composition i.e. lattice-matched growth, regardless of doping level, γ should be insensitive to the CCl_4 flow rate. Fig.2 shows the cation incorporation ratio γ as a function of CCl_4 flow at various growth temperatures. As can be seen in Fig.2, low growth temperature (430°C) offers a γ which is relatively insensitive to the CCl_4 flow up to a level of $\sim 10\text{sccm}$. As will be seen later on, a high CCl_4 flow level is necessary for maximum carbon incorporation. The results described up to this point lead to the conclusion that the alloy composition of carbon doped InGaAs is

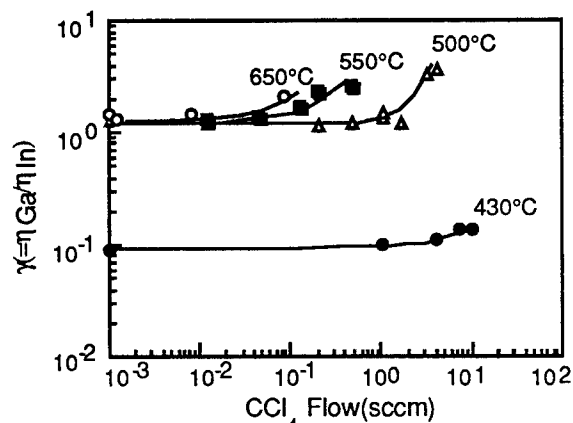


Fig.2 The dependence of cation incorporation ratio (γ) on CCl_4 flow. Low growth temperatures offer alloy compositions which are insensitive to CCl_4 flow up to $\sim 10\text{sccm}$.

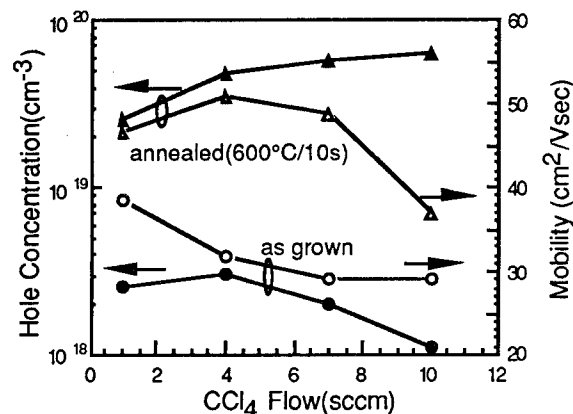


Fig.3 Variation of hole concentration and mobility of C-InGaAs after annealed at 600°C for 10 seconds.

insensitive to the amount of CCl_4 at low growth temperatures. Low growth temperatures of 430°C are therefore recommended for growing C-InGaAs by liquid CCl_4 .

Impact of thermal annealing on carrier activation

The impact of post growth thermal annealing on the electrical properties of C-InGaAs was investigated using samples grown at 430°C . The samples were annealed with RTA in Ar under different annealing conditions. Fig.3 shows the hole concentration and mobility of the as grown and annealed samples doped at various CCl_4 flow rates. The maximum hole concentration achieved was $6.5 \times 10^{19} \text{cm}^{-3}$. The hole concentration of the as grown samples was about the same regardless of the CCl_4 flow rates which ranged from 1 to

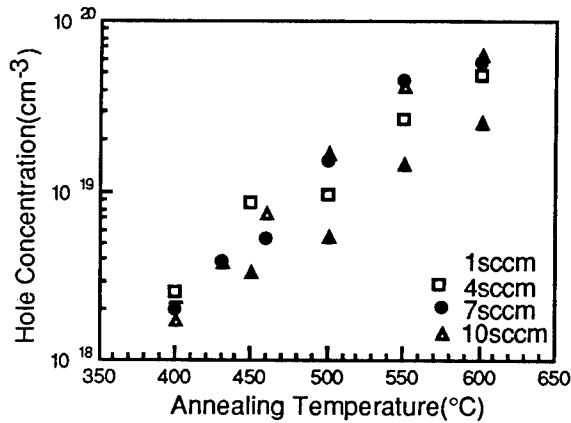


Fig.4 Isochronal annealing of C:InGaAs doped with various CCl_4 flow rates.

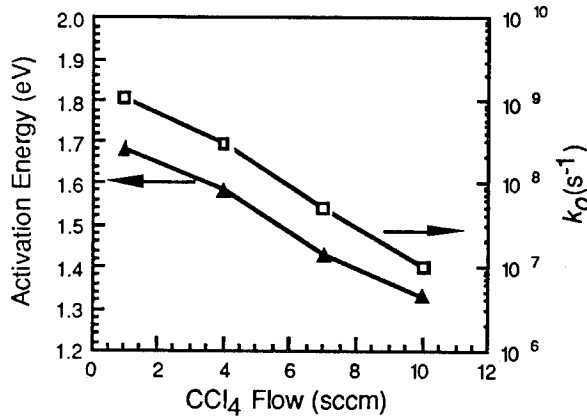


Fig.5 Dependence of activation energy (E_a) and pre-exponential factor of rate constant (k_0) of isochronal annealing on CCl_4 flow.

10 sccm. However, the hole concentration was increased by an order of magnitude by annealing at 600°C for 10 seconds. In addition, in contrast to the case of carbon doped GaAs(9), the hole mobility also increases with annealing. For a better understanding of the impact of annealing on carrier activation, isochronal annealing was performed on these samples. Fig.4 shows the isochronal annealing (10 seconds) of C-InGaAs samples grown with various CCl_4 flow rates. For a better understanding of these characteristics, we represented the hole concentration (p) vs. temperature dependence by the following equation based on first order kinetics(10):

$$\frac{dp}{dt} = -k(p_{\max} - p)$$

$$\text{where } k = k_0 \cdot \exp\left(-\frac{E_a}{RT}\right)$$

Table A. Variation of carbon, hydrogen and hole concentration of C:InGaAs upon annealing at 600°C for 10 seconds. (the sample was doped with 1 sccm of CCl_4)

	as grown	annealed ($600^\circ\text{C}/10\text{s}$)
[C]SIMS	3×10^{19}	3×10^{19}
[H]SIMS	1.5×10^{19}	4×10^{18}
PHall	2.5×10^{18}	2.5×10^{19}
C_V	2.38×10^{19}	2.95×10^{19}
C_{III}	6.25×10^{18}	5×10^{17}
r_V	63.2%	13.6%

Fig.5 provides information on the kinetic processes taking place by permitting evaluation of the pre-exponential factor (k_0) and activation energy (E_a). Both k_0 and E_a were found to decrease with CCl_4 flow in agreement with the hole concentration trends observed in Fig.4. The variation of the kinetic parameters k_0 and E_a with CCl_4 flow suggests that more than a single mechanism is responsible for the carrier activation process.

The increase of hole concentration after post growth anneal has been attributed to hydrogen de-passivation in case of C-GaAs(9) and C-InGaAs(6). SIMS analysis of our samples shows, however, that this increase which exceeds an order of magnitude in the case of our C-InGaAs, could not be correlated quantitatively to hydrogen de-passivation. The carbon and hydrogen atomic concentration evaluated by SIMS and the hole concentration found by Hall measurements can be related to the atomic carbon concentration which occupies group III and V sites (C_{III} and C_V , respectively) and to the interstitial carbon concentration C_i as below:

$$[C]_{\text{SIMS}} = C_V + C_{III} + C_i$$

$$[H]_{\text{SIMS}} = r_V C_V + r_{III} C_{III} + H_i$$

$$PH_{\text{Hall}} = C_V(1 - r_V) - C_{III}(1 - r_{III})$$

Here, r_{III} and r_V are the ratio of hydrogen-passivated carbon atoms which occupy group III and V site, respectively, and H_i is the unionized hydrogen concentration. Since hydrogen is positively charged in p -type materials and subsequently passivates only negatively charged acceptors, r_{III} can be assumed to be zero. By assuming negligible C_i and H_i , we can obtain

$$C_V = ([C]_{\text{SIMS}} + [H]_{\text{SIMS}} + PH_{\text{Hall}}) / 2$$

$$C_{III} = [C]_{\text{SIMS}} - C_V$$

$$r_V = [H]_{\text{SIMS}} / C_V$$

Table A summarizes the above parameters before and after thermal annealing. It shows displacement of carbon atoms from group III site to V site, as well as, reduced hydrogen passivation from 63% to 14% upon thermal annealing. Thus, the combined effect of carbon displacement and

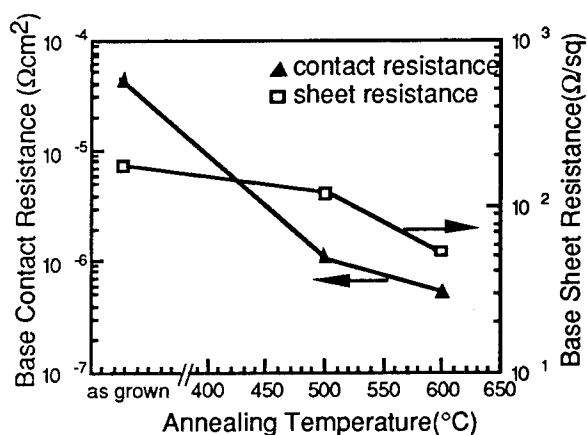


Fig.6 Contact resistivity and sheet resistance of Ti/Pt/Au non-alloyed ohmic contacts made on C:InGaAs annealed at various temperatures. This contact layer is doped with 1sccm of CCl₄.

reduced hydrogen passivation might responsible for the increased hole concentration.

Impact of annealing on contact resistance

Good ohmic contacts to *p*-InGaAs are of great importance since they often impose limiting factor in the performance of devices such as InP/InGaAs HBTs and double heterojunction lasers. Thus, the impact of thermal annealing on the ohmic contact resistance was investigated by depositing Ti/Pt/Au non-alloyed ohmic contacts on a 1000Å carbon doped *p*-InGaAs. This layer acted as external base in an HBT structure which has a 2500Å Zn:InGaAs base ($p \sim 8 \times 10^{18} \text{ cm}^{-3}$), a 4000Å collector ($n \sim 1 \times 10^{17} \text{ cm}^{-3}$) and a 5000Å subcollector ($n \sim 2 \times 10^{19} \text{ cm}^{-3}$). Ohmic contacts on the as-grown base layers showed specific contact resistance values of $4 \times 10^{-5} \Omega \cdot \text{cm}^2$. However, as can be seen in Fig.6 the specific contact resistance decreases rapidly as the post growth annealing temperature increases. Specific contact resistance values as low as $5 \times 10^{-7} \Omega \cdot \text{cm}^2$ could be achieved with contacts formed on a sample annealed at 600°C for 10 seconds.

Summary

In summary, heavily carbon doped InGaAs lattice matched to InP was grown by LP-MOCVD using all-methyl metalorganics and liquid CCl₄ as a carbon source. The impact of growth conditions on conduction type and alloy composition of InGaAs were studied. The effect of thermal annealing conditions on the hole concentration and mobility of C-InGaAs was investigated and carbon displacement from group III site to arsenic site as well as reduced hydrogen passivation is suggested as a possible

mechanism for the significant increase of hole concentration upon annealing. Base specific contact resistances as low as $5 \times 10^{-7} \Omega \cdot \text{cm}^2$ were demonstrated by depositing Ti/Pt/Au non-alloyed ohmic contacts on annealed base layers.

References

- (1) C.R. Abernathy, S.J. Pearton, F. Ren, W.S. Hobson, T.R. Fullowan, A. Katz, A.S. Jordan and J. Kovalchick, "Carbon Doping of III-V Compounds Grown by MOMBE," J. of Crys. Growth, Vol.105, pp.375-382, 1990.
- (2) T.P. Chin, P.D. Kirchner, J.M. Woodal and C.W. Tu, "Highly carbon-doped *p*-type Ga_{0.5}In_{0.5}As and Ga_{0.5}In_{0.5}P by carbon tetrachloride in gas-source molecular beam epitaxy," Appl. Phys. Lett., Vol. 59, No. 22, pp.2865-2867, 1991.
- (3) K. Zhang, W. Hwang, D.L. Miller, L.W. Kapitan, "Carbon doping of GaAs and (In,Ga)As in solid source molecular beam epitaxy using carbon tetrabromide," Appl. Phys. Lett., Vol.63, No.17, pp.2399-2401, 1993.
- (4) C.J. Palmström, B.P. Van der Gaag, J.-I. Song, K.B. Chough, W.P. Hong, S.A. Schwarz and S. Novak, "Growth of Heavy C-doped GaInAs Lattice Matched to InP by Chemical Beam Epitaxy," 21st Int. Symp. on Compound Semiconductors, San Diego, 1994.
- (5) S.A. Stockman, A.W. Hanson and G.E. Stillman, "Growth of carbon-doped *p*-type In_xGa_{1-x}As ($0 < x < 0.53$) by metalorganic chemical vapor deposition," Appl. Phys. Lett., Vol.60, No.23, pp.2903-2905, 1992.
- (6) S.A. Stockman, A.W. Hanson, C.M. Colomb, M.T. Fresina, J.E. Baker and G.E. Stillman, "A Comparison of TMGa and TEGa for Low-Temperature Metalorganic Chemical Vapor Deposition Growth of CCl₄-Doped InGaAs," J. Elec. Mat., Vol. 23, No. 8, pp.791-799, 1994.
- (7) L.W. Yang, P.D. Wright, V. Eu, Z.H. Lu and A. Majerfeld, "Heavily doped *p*-GaAs grown by low-pressure organometallic vapor phase epitaxy using liquid CCl₄," J. Appl. Phys., Vol. 72, No. 5, pp.2063-2065, 1992.
- (8) G.S. Tompa et al., "A Parametric Investigation of GaAs Epitaxial Growth Uniformity in a High Speed, Rotating-Disk MOCVD Reactor," 4th Int. Conf. Metal Organic Vapor Phase Epitaxy (Hakone, Japan), 1988.
- (9) G.E. Höfler, H.J. Höfler, N. Holonyak, Jr and K.C. Hsieh, "Effect of annealing temperature on the hole concentration and lattice relaxation of carbon-doped GaAs and Al_xGa_{1-x}As," J. Appl. Phys., Vol. 72, No. 11, pp.5318-5324, 1992.
- (10) H.H. Lee, Fundamentals of Microelectronics Processing, McGraw Hill, 1990, pp.304-307.

Chlorine auto-doping by Chloride Vapor Phase Epitaxial Growth of InP

T. Iwasaki, Y. Iguchi, N. Yamabayashi, and S. Yoneyama*

Optoelectronics R&D, Sumitomo Electric Industries, LTD

1-1-3, Shimaya 1-chome, Konohana-ku, Osaka, Japan

*Optoelectronic Industry and Technology Development Association

7-5-8, Toyo, Kotoku, Tokyo, Japan

ABSTRACT

Chlorine auto-doping phenomenon is found for the first time in InP epitaxial growth by using $\text{PCl}_3/\text{InP}/\text{H}_2$ system. Chlorine atoms act as donor in the epitaxial layer and the carrier concentration are controlled by the facet of InP substrate. The carrier concentration of the InP layer on (111)B facet is 10^3 times higher than that on the (100) 2° off[110] substrate.

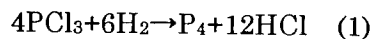
1. Introduction

Carrier confinement technology was described in epitaxial growth method, e.g. MBE.¹⁾ which uses the relation between Si dopant and the substrate facets of GaAs. It is also known that the carrier concentration in the epitaxial layer depends on the substrate orientation, in case of OMVPE.²⁾ In case of GaAs epitaxial layer by Chloride Vapor Phase Epitaxy(C-VPE)³⁾, impurity incorporation on the substrate surfaces have been investigated. And the growth rate and its mechanism in GaAs VPE has been argued with the carrier concentration on the different facets.⁴⁾ For InP epitaxial layer, there were few reports⁵⁾ about that. This paper describes Chlorine auto-doping as donors at first in case of InP epitaxial layer on several facets by C-VPE.

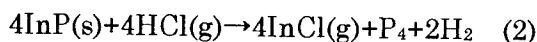
2. Experimental

The C-VPE method for InP was carried out using $\text{PCl}_3/\text{InP}/\text{H}_2$ system.⁶⁾ A schematic diagram of the C-VPE reactor was shown before.⁷⁾ The reactor is made of high pure

quartz. Phosphorus trichloride at first reacts with pure H_2 at high temperature, yielding a gaseous mixture of P_4 and HCl .



Next, the HCl reacts with InP crust formed on In metal source at 800°C , as follows,



And at the growth temperature(600°C), the reaction is reversed on InP substrate. Another independent PCl_3/H_2 supply by-pass the InP source and enter the reaction tube at the growth zone.(eq.(1)) Before epitaxial growth is started, the reactor and the substrate surface are cleaned by "vapour etching".⁸⁾ The intentionally undoped InP epitaxial layer was grown on (111)A, (100) 2° off[110], (011), (211)B, and (111)B InP substrates at the same time.

The Carrier concentration of InP epitaxial layer was evaluated by C-V method and the impurities were analyzed by SIMS analysis. The thickness was measured by stain etching method.

3. Results

The evaluation results of epitaxial layers are summarized in Table 1.

Table.1
Intensity of Cl and carrier concentration and growth rate on various substrate facets

SUBSTRATE FACET	(111)A	(100)2° off [110]	(011)	(211)B	(111)B
Growth rate (nm/min)	6×10^1	6×10^1	1.3×10^2	2.7×10^2	1.6×10^2
Carrier Concentration (cm ⁻³)	$<1 \times 10^{15}$	1×10^{15}	1.5×10^{16}	3×10^{17}	1.5×10^{18}
Intensity of Cl (a.u.)	$<2 \times 10^3$	$<2 \times 10^3$	$<2 \times 10^3$	3×10^4	1×10^5

3-1 Growth Rate

All the substrates with different facets were set within 2 inch diameter in this reactor, where uniform epitaxial thickness was obtained at this growth temperature. Table.1 shows that the growth rate of InP epitaxial layers depend on these substrate facets. The growth rate on the (111)B substrate is about 3 times larger than that on the (100)2° off[110] substrate.

3-2 Carrier Concentration

All of the epitaxial layers were n-type. The carrier concentrations were found to depend on substrate facets and ranged from under 10^{15} cm⁻³ to over 10^{18} cm⁻³. Fig.1 shows the correlation between the carrier concentration and the signal intensity of Chlorine atoms obtained by SIMS analysis. The dot line is detection limit of SIMS for Chlorine atoms. Even the epitaxial layer grown on (211)B Zn doped InP substrate showed n-type with high carrier concentration of 2×10^{17} cm⁻³.

Other impurities as donors besides Chlorine (e.g. Si, S, Sn, C, Se, Te) were not detected as shown in Table.2. These results show that the main donor impurities are Chlorine atoms, not the dopant in the substrate nor impurity from the reactor.

Table.2

Impurities in epitaxial layer on (111)B by SIMS

Carrier Concentration	SIMS analysis			
	Si	S	Sn,C,Se,Te	Cl
1.5×10^{18} cm ⁻³	$<2 \times 10^{15}$ cm ⁻³	$<2 \times 10^{15}$ cm ⁻³	N.D.	1×10^5 a.u. ^(*)

(*) Detection limit; 2×10^3

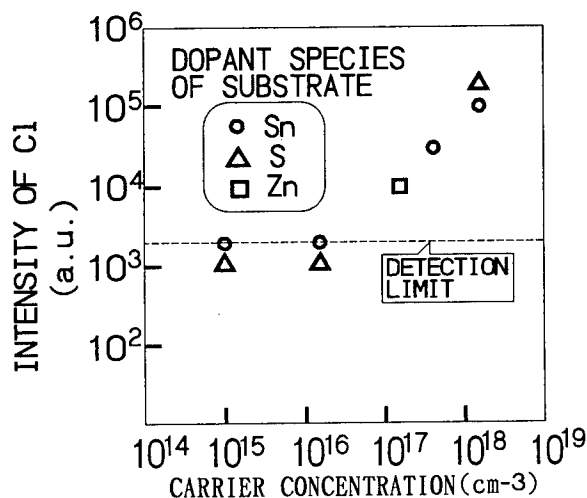


Fig.1 Carrier Concentration vs Intensity of Cl by SIMS

3-3 Surface structure

Optical photographs of the surface morphologies of InP layers are shown in Fig.2. There are three kinds of surface morphologies. Good morphologies were obtained on the $(100)2^\circ$ off[110] and on (011). On the other

hand, that on the (211)B was ruffer than that on $(100)2^\circ$ off[110]. In case of that on (111)B, triangle shape structure was observed. The size of the triangle shape is smaller than that on (111)A. These results implies 3 kinds of growth mechanism in this case.

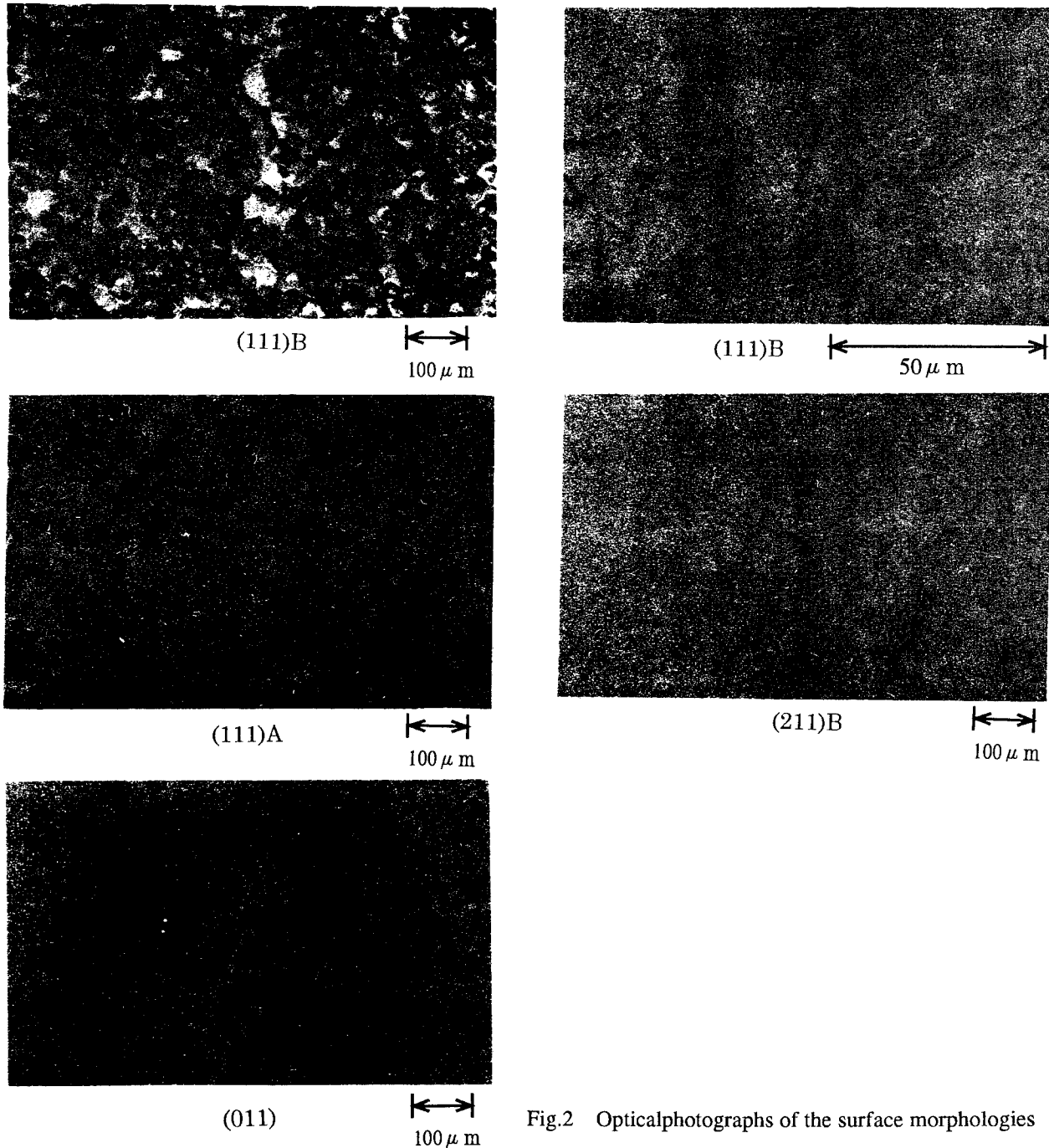


Fig.2 Optical photographs of the surface morphologies

4. Discussion

The carrier concentration is controlled by the substrate facet. In the case of (111)B, covered with phosphorus atoms, the carrier concentration is 10^3 times higher than that on (100)2° off [110]. The difference of facets makes not only the difference of the growth rate but also that of the carrier concentration.

In this experiment for InP by C-VPE, the growth rate and the carrier concentration and the morphologies changed corresponding with the InP substrate facets. In this epitaxial growth system, Chlorine atoms are auto-doped in the epitaxial layers as donors.

The coverage ratio of phosphorus atoms in the substrate surface increases the following order, (111)A, (100), (011), (211)B, (111)B. And the carrier concentration increases according to the same order. The bonding process of InCl with P on surface is important in this growth system. On (111)B facet, covered with phosphorous atoms, InCl adsorb directly to surface phosphorous atom, and InCl molecules should adsorb faster than the desorption of Chlorine atoms. So the Chlorine atoms are contained in the epitaxial layer. On the other hand, on (111)A facet, covered with In atoms, InCl with P₄ or InCl family (e.g. P-InCl) should adsorb slowly, and so almost all of the Chlorine atoms should desorb after InCl adsorbed. So there are few Chlorine atoms and the carrier concentration is low. The carrier concentration is a function of the coverage ratio of phosphorous atoms through the adsorption-desorption process. As for GaAs VPE, it is reported that impurities are incorporated on the B-face than on the A-face and the main

impurity is Si from the reactor.³⁾ According to this result, it is supposed that Chlorine atoms may be one of the important donors in GaAs VPE.

This Chlorine auto-doping process will be developed and become important in the substrate facet design, such as mesa shape, for various device fabrications.

5. Conclusion

Chlorine auto-doping in the epitaxial layer by C-VPE method for InP has been clarified. Chlorine atoms act as donors in the epitaxial layer. The carrier concentration is controlled by the selection of the substrate facet. On (111)B facet, it is over 10^{18}cm^{-3} , which is 10^3 times higher than that on the (110)2° off [110] substrate.

- 1) T. Takebe, J. Crystal Growth 127, 1993, 937
- 2) M. Razeghi, SEMICONDUCTORS AND SEMIMETALS, VOL. 22, PART A, p.307
- 3) J.V. DILORENZO, J. Crystal Growth, 17, 1972, 189-206
- 4) R. CADORET, Curr. Top. Mater. Sci. Vol. 5, 1980, P. 219-277
- 5) G.H. OLSEN, J. Crystal Growth, 59, 1982, 654-658
- 6) L.L. Taylor, J. Crystal Growth 64, 1983, 55
- 7) Y. Miura, and T. Iwasaki, et al, Conf. Proceedings of 2nd Int. Conf. on I.P.R.M., 1990, p. 103
- 8) D.J. ASHEN, J. Crystal Growth, 60, 1982, 225

Step bunching of InP caused by heavy doping of Se in metalorganic chemical vapor deposition and its application to device fabrication

Keiji Takaoka, Mitsuhiro Kushibe, Masahisa Funemizu,
Toshihide Izumiya and Yoshihiro Kokubun

Materials and Devices Research Laboratories
Research and Development Center, Toshiba Corporation
1, Komukai Toshiba-cho, Saiwai-ku, Kawasaki 210, Japan

Abstract

We have found that step bunching occurs in heavily Se doped InP, grown by MOCVD, for both (001) and (111)B planes and that it occurs with a lower Se source gas flow rate for the (111)B plane than for the (001) plane. Using this heavy Se doping, we have successfully fabricated novel planar buried heterostructure lasers on p-InP substrates, in which the Se-doped n-InP current blocking layer does not make contact with the n-InP cladding layer.

Introduction

Novel techniques to control growth rate anisotropy for various different crystal singular planes are required for precise control of three dimensional device structures. A growth rate change caused by Se doping, in InP growth by metalorganic chemical vapor deposition (MOCVD), and its application to maskless selective growth have been reported. [1] We compared the effect of Se heavy doping in InP on the (001) and (111)B planes by MOCVD. By increasing the doping concentration up to a saturation concentration, hillocks appeared on the epitaxial layer surface and macro steps were formed on and around these hillocks for growth on the (001) plane. The formation of hillocks and macro steps indicated a slight decrease in growth rate. Macro steps were also found to be formed on epitaxial layers grown on the (111)B plane under much lower Se source gas flow rate conditions. These phenomena were successfully applied to laser fabrication on p-InP substrates, in which it is necessary to suppress the growth of n-InP on the (111)B and (221)B facets in order to separate the n-InP current blocking layer from the n-InP cladding layer.

Doping Characteristics

N-InP was grown by using trimethylindium, phosphine, and hydrogen selenide (H_2Se) as the source gases. The growth temperature was 670 °C and the pressure was 2.6×10^4 Pa.

As Fig. 1 depicts, the carrier concentration increased in proportion to H_2Se flow rate when the H_2Se flow rate was lower than 1×10^{-7} mol/min but it tended to level off when the H_2Se flow rate was higher than 2×10^{-7} mol/min on the (001) plane. The maximum carrier concentration was $6 \times 10^{19} \text{ cm}^{-3}$. Fig. 2 shows the change of surface morphology, of

(001) InP, with H_2Se flow rate. When the H_2Se flow rate was increased above 1×10^{-7} mol/min, hillocks appeared on the epitaxial layer surface and macro steps were formed on these hillocks. By increasing the H_2Se flow rate still further, these hillocks and macro steps appeared more clearly. Presumably the excess selenium decreased the growth rate on the (001) plane slightly and enhanced growth towards the non-singular plane directions causing step bunching.[1]

The doping efficiency was confirmed to be much higher on the (111)B plane than on the (001) plane as is depicted in Fig. 1. Macro steps appeared for all layers grown on the (111)B plane with Se doping, as

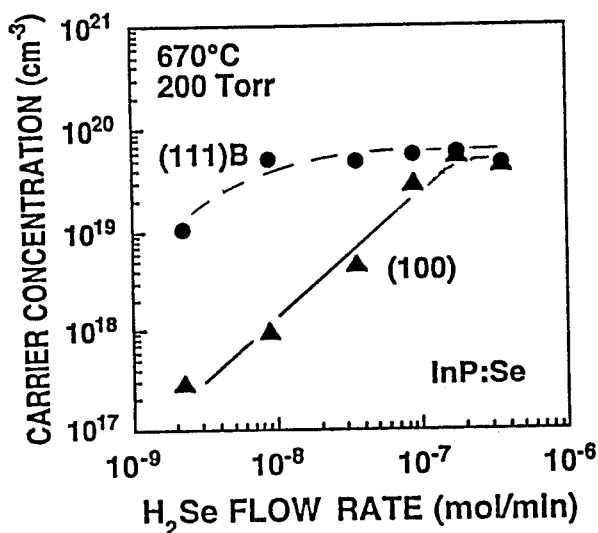


Fig.1 Doping characteristics of H_2Se in InP for (100) and (111)B plane

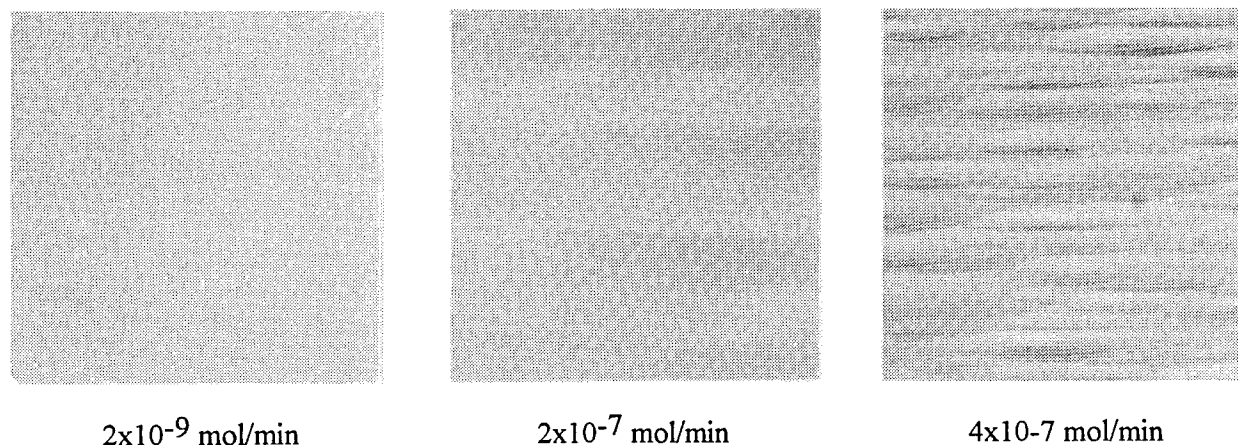


Fig. 2 Surface morphology of (100) InP under various H_2Se flow rate conditions

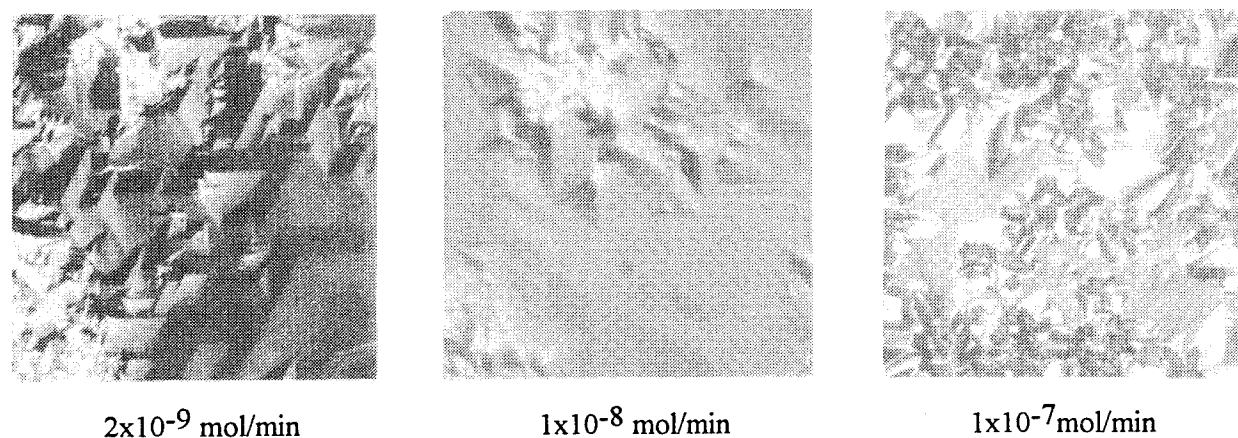


Fig. 3 Surface morphology of (111)B InP under various H_2Se flow rate conditions

can be observed in Fig. 3. These macro steps were caused by the Se doping because they were not observed for InP grown without Se doping. These macro steps also became clearer on increasing the H_2Se flow rate, although polycrystal covered (111)B surface when the H_2Se flow rate was increased above 4×10^{-8} mol/min. It is noticeable that macro steps were formed with much lower Se source gas flow rate for the (111)B plane in comparison to the (001) plane. These results indicate that the Se blocked the InP growth severely on the (111)B plane as compared to (001) plane for the same H_2Se flow rate.

Application to Laser Fabrication

The above substrate orientation dependence of Se doping suggests that an anisotropic growth rate may be obtained by using the proper H_2Se flow rate when relevant facets are nearby on a suitable etched

substrate. We applied Se heavy doping to the fabrication of planar buried heterostructure (PBH) lasers on p-InP substrates.

The schematic cross-sectional diagram of a PBH laser on a p-InP substrate is shown in Fig. 4. This structure is usually fabricated using three-step MOCVD growth as follows. First, a p-InP buffer layer, an active layer (we use a strained InGaAsP MQW structure), an n-InP cladding layer and an n-InGaAs cap layer are successively grown on a p-InP substrate. Next, a mesa stripe structure, in the $\langle 110 \rangle$ direction, is formed with wet etching and a SiO_2 stripe mask. Then a p-InP filling layer, an n-InP current blocking layer, and a p-InP current blocking layer are selectively grown. Finally, an n-InP cladding layer and an n-InGaAs contact layer are grown after the SiO_2 mask and the n-InGaAs cap layer are removed. In these fabrication processes, it is very important that

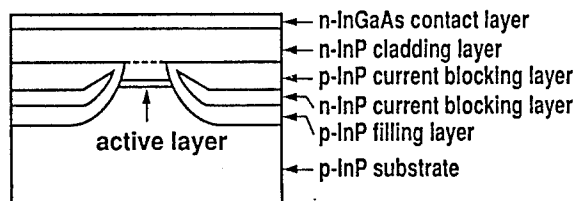


Fig.4 Schematic diagram of a PBH laser on a p-InP substrate

the n-InP current blocking layer does not make contact with the n-InP cladding layer to realize a low threshold current and a high power operation. This is because a large leakage current flows through the n-InP current blocking layer when the n-InP current blocking layer is connected to the n-InP cladding layer.

In the second MOCVD growth, the (111)B and (221)B facets are exposed on the mesa side wall after growing the p-InP filling layer. [2] Then we used Se as an n-type dopant in the n-InP current blocking layer in order to suppress growth on the (111)B and (221)B facets. Though we did not actually investigate the doping characteristics of Se on the (221)B plane, we can expect that it will show an intermediate property between that of (001) plane and (111)B planes.

A cross-sectional SEM image of the typical PBH laser with a heavily Se doped n-InP current blocking layer is shown in Fig. 5. We can separate the n-InP current blocking layer from the n-InP cladding layer

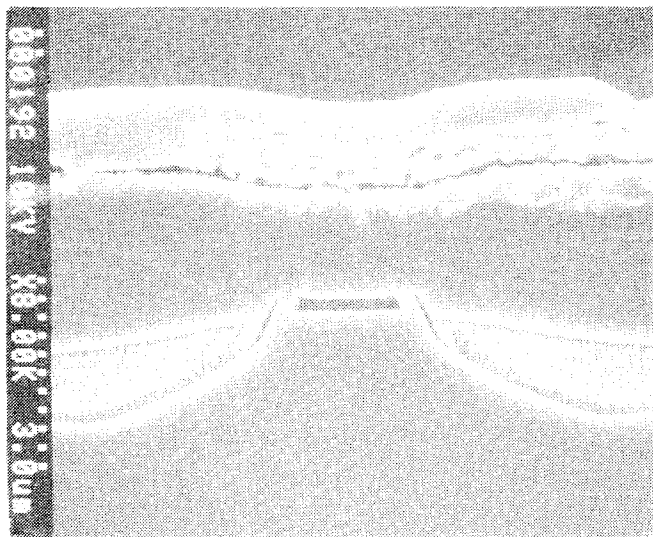


Fig.5 A cross-sectional SEM image of a typical PBH laser with the heavily Se doped n-InP current blocking layer

easily with heavy Se doping, because the growth rate on the (111)B and (221)B facets decreases quickly. Especially, it is noticeable that not only is the growth on the (111)B and (221)B facets suppressed but the growth on the outside area of the mesa side wall is enhanced. This phenomenon is probably related with suppression of the growth on the (001) plane.

Laser Characteristics

We could fabricate PBH lasers whose n-InP current blocking layer did not make contact with the n-InP cladding layer easily by using the above mentioned method, and realized low threshold current operation of 1.3 μm strained InGaAsP MQW lasers. Fig. 6 shows the CW light-current characteristics. The MQW active layer, whose width was about 1.5 μm , consisted of six 0.5 % compressively strained wells, each 7 nm thick. The cavity length was 200 μm and both facets were high-reflection coated ($R_F=70\%$ and $R_R=95\%$). Threshold currents at 20 and 100 $^{\circ}\text{C}$ were 2.0 and 12.0 mA, respectively. The characteristic temperatures of threshold current and slope efficiency were 58 K and 230 K in the temperature range of 20-60 $^{\circ}\text{C}$, respectively.

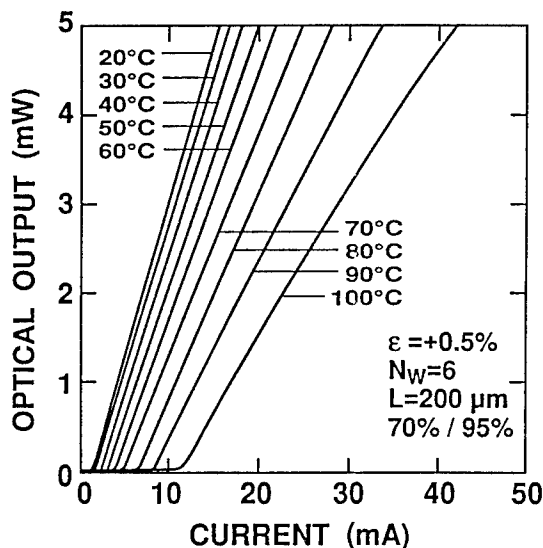


Fig.6 CW light-current characteristics of the laser with the heavily Se doped n-InP current blocking layer

Summary

We investigated the doping characteristics of Se in

A Novel Technique for Semi-insulating InP(Fe) by Chloride VPE

Sun Hongbo Chen Songyan Li Yudong Hu Lizhong Liu Shiyong

The State Key Laboratory on Integrated Optoelectronics

Jilin University Changchun 130023

China

The chloride vapor phase epitaxial (VPE) growth of semi-insulating (SI) InP(Fe) using $N_2 + H_2$ as a carrier gas is reported for the first time. Iron doping is achieved by using $FeCl_2$ generated by reaction of HCl and Fe. The transport of iron as $FeCl_2$ is greatly improved by the use of N_2 . A proper N_2/H_2 ratio for the iron incorporation is discussed and a high value of $5 \times 10^8 \Omega cm$ is obtained. Especially, the technique has been successfully applied to the preparation of multi-quantum-well (MQW) laser diodes, as we haven't found the concerned reports yet.

1. Introduction

The SI-InP epilayer is an important technique for the development of InGaAsP laser diodes and monolithic integrated optoelectronic devices. A large number of studies have been devoted to the VPE. Conventional VPE has recently been extended to include SI InP(Fe) growth capability using $FeCl_2$ by H_2 to form HCl and element Fe. We use $N_2 + H_2$ hybrid gas as carrier, controlling the hydrogen partial pressure to a certain degree. Under a proper N_2/H_2 ratio, SI InP(Fe) film can be obtained. Application of the technique to the MQW structure proved that the quality is of high quality.

2. Experimental

The apparatus is almost the same as conventional In/ PCl_3 / H_2 chloride system except for a Fe-doping line. A multi-layer iron screen mesh (99.99%) is used as the doping source. The Fe doping is carried out as follows! First, high-purity HCl vapor with H_2 carrier is introduced into the Fe source region. Typical HCl flowrate is 10^{-4} mol/min. The HCl is formed by thermal decomposition of PCl_3 . Next the iron source is etched by HCl vapor and $FeCl_2$ is formed by the reaction $Fe + HCl \rightarrow FeCl_2 + H_2$ ($T = 750^\circ C$). The gas with $FeCl_2$ is then mixed with additional N_2 , the resulting gas flow is 400 sccm (96% $N_2 + 4\% H_2$ mole fraction). The gas is transported to the growth region to mix

with the gas from PCl_3 then through In source region. The latter carrier gas consists the same as the former. Other conditions: $T_{sub} = 620^\circ C$ $T_{in} = 780^\circ C$. Total gas flow rate through the growth region is 800 sccm. When growth begin, undoped InP is grown for 5 min first, then "half-doped" layer for 5 min (The carrier gas through Fe source flow rate half of the normally growing valve). Last, the flowrate is adjusted to a normal valve, SI-InP(Fe) is deposited for 10 min.

3. Results and discussion

1. **Resistivity in different N_2/H_2 ratio.** P. L. GILES. et al have examined the In/ PCl_3 / N_2 system and conclude that the growth without hydrogen is impossible for thermodynamic reasons. But with the addition of small amounts of phosphine, InP growth is possible in nitrogen. Instead of phosphine, we use hydrogen directly and corresponding thermodynamic see also our another contribution. In $H_2/PCl_3/In$ system the large hydrogen partial pressure leads to the reaction $H_2 + FeCl_2 \rightarrow HCl + Fe$ and this greatly reduces the amount of $FeCl_2$ which can be transported to compensate residual donors in the grown film. So hydrogen partial must be controlled. Figure 1 shows resistivity versus N_2/H_2 ratio. The line consists of three section, the part I emerges in the situation similar to chloride VPE with only H_2 as carrier. The section II shows the

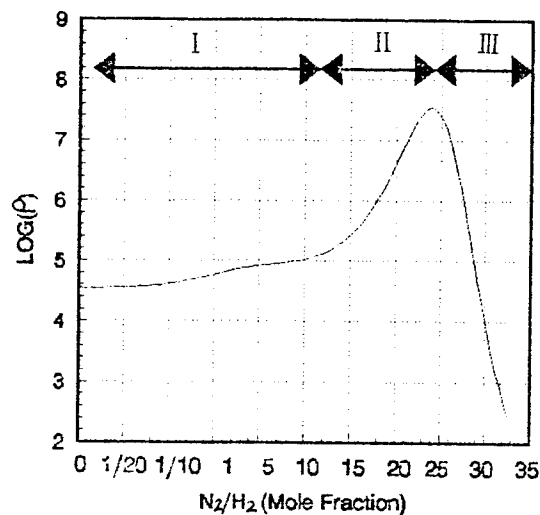


Fig 1 Resistivity versus N_2/H_2

difficult growth condition using almost only N_2 as a carrier as discussed by P. L. GILES. The part I exhibits a ideal result; the resistivity of epilayer in-

creases with the N_2/H_2 ratio. The greater N_2/H_2 ratio, the more $FeCl_2$ is transported. $N_2/H_2 \approx 25$ is critical point in our system.

2. SIMS measurement. The Fe concentration for the film has been measured by SIMS. The iron level is about 10^{17} cm^{-3} and is comparable levels with the best results achieved by VPE.

3. The characteristics of QW laser diode. Successfully we have fabricated the QW-structure-based SI-InP(Fe) epilayer. From the Wafer, the lasers have been prepared by general processure. The threshold current descends from 250mA (with oxide stripe confinement) to 80mA (InP(Fe)-buried). The laser operates stably in the fundamental lateral mode without significant distortion of the far-field patterns, which display high symetry. Far-field full angle at half power $\Theta_{\perp} = 20^\circ$ $\Theta_{\parallel} = 12^\circ$ as Fig2. All above results suggest a successful growth of SI InP(Fe).

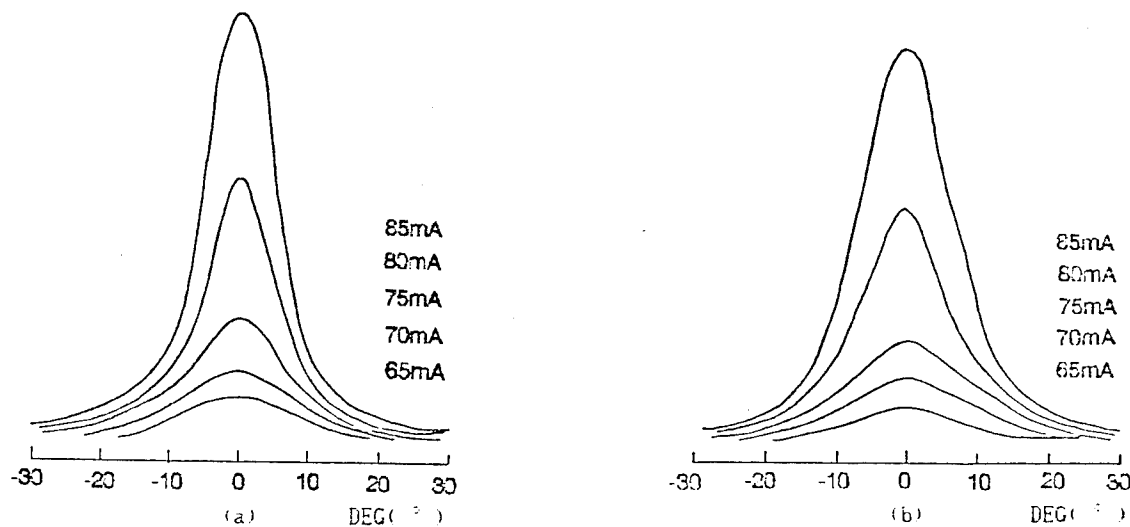


Fig 2 Far-field patterns parellel (a) and perpendiculer (b) to the junction

References

- [1] T. Takanohashi, K. Nakai and K. Nakajima, Japan. J. Appl. Phys. 27(1988)127.
- [2] P. Speier, K. Wunstel and J. J. Tegude, Electron. Letters 23(1987)1365.
- [3] InGaAsP monolithic extended-cavity lasers with integrated saturable absorbers for active, passive, and hybrid mode locking at 8.6GHz APL 62(13), 29 march 1993.

Composition Control in the Growth of $\text{AlAs}_{1-x}\text{Sb}_x$ Alloys

Jehn Ou, and Wei-Kuo Chen

Department of Electrophysics, Chiao-Tung University, Hsin-Chu
Taiwan 30050, Republic of China

Introduction

The deposition of $\text{AlAs}_{1-x}\text{Sb}_x$ films is studied systematically using metalorganic vapor-phase epitaxy technique. The composition of the alloys was found to be dependent strongly on the growth temperature. High concentration of solid Sb can be achieved at an elevated temperature. It is interesting to note that for films grown at 600 °C the AlAs content in AlAsSb becomes simply determined by the input gas ratio of $[\text{TBA}]/[\text{TMAI}]$ as the Sb reactant is supplied sufficiently. Owing to the insensitivity of Sb mole flow rate to solid composition at this particular growth environment, this result could be accounted for by thermodynamic arguments. Following this picture, an improved film controllability can be achieved for the growth of $\text{AlAs}_{1-x}\text{Sb}_x$ compounds.

The novel related III-V ternary compounds, $\text{AlAs}_{1-x}\text{Sb}_x$, lattice-matched to InP or InAs, have made great interesting for a number of optoelectronic devices applications, e.g., 1.3-1.55 μm surface-emitting laser, modulation-doped field-effect transistors and resonant tunneling diodes, owing to their high Γ -bandgap, low refractive index and large heterojunction conduction band offsets (1-4). However, the growth of AlAsSb, where the mixing is occurred on the anion sublattice, appears to be relatively difficult (6-9). Traditionally, the growth of Sb-containing alloys is performed at a low input V/III ratio by adjusting the partial pressure of Sb in group V to obtain the desired composition x . It is generally believed to be related to the high sensitivity of the growth to the growth parameters, such as the input V/III ratio, the Sb partial pressure in group V (X^{V}_{Sb}) and the growth temperature. Samples prepared in the method usually suffers an intolerable amount of composition fluctuation which would ultimately deteriorate the device performances. Therefore, competing in the fabrication of future devices so as to derive an efficient approach capable of accurately and reproducibly controlling the solid distribution has become one of the relevant topics in the study of AlAsSb. In this work, thermodynamic analyses were performed to investigate the dependence of solid composition on various growth parameters. Following a series of experiments, a easier new picture for composition controlling is proposed in the growth of $\text{AlAs}_{1-x}\text{Sb}_x$.

The epitaxial layers were grown on InP (100) substrate in an atmospheric pressure horizontal reactor using a metalorganic vapor-phase epitaxy (MOVPE)

technique. The metalorganic sources trimethylaluminum (TMAI), tertiarybutylarsine (TBAs), and trimethylantimony (TMSb) were used as the sources reactants, and were thermostated at 17 °C, 1 °C, and -17 °C, respectively. The total H_2 carrier flow rate was 1.5 SLM during the growth, which yields a linear gas velocity of 10 cm/s immediately in front of susceptor. Another detailed description is published elsewhere (5). The MOVPE-grown samples were then characterized by x-ray diffraction analysis and energy dispersive analysis of x-ray (EDAX). Scanning electron microscope (SEM) and a Normarski optical microscope were employed for examining the surface morphology of the epilayers. Thickness was measured either by the surface profilometer or the cross-section of SEM. The thermodynamic model employed here has been provided with an indepth description elsewhere (10). In this study, the corresponding equilibrium constants of reaction of AlAs and AlSb were derived from the data of Kubaschewski and co-workers (11,12), and Stull and Sinke (13). Their values are 1.620×10^{22} and 4.824×10^{21} , respectively. The interaction parameter of AlAs-AlSb, 3843 cal/mol, used in the simulation was calculated from the DLP model (14).

Growth temperature, undoubtedly, is one of the important growth parameter for films deposition. In attempt to understand the dependence of solid composition on growth temperature, we grew a series of sample. The input mole flow ratios of TMAI, TBAs, and TMSb were at 36, 15, and 29 $\mu\text{mol}/\text{min}$, yielding a V/III ratio of 1.2. Such a low V/III ratio is generally believed to necessary and favorable of attaining high Sb incorporation and avoiding any Sb droplet formation

(9). Figure 1 shows the dependence of composition x (X_{Sb}^{S}) in $\text{AlAs}_{1-x}\text{Sb}_x$ on reciprocal temperature.

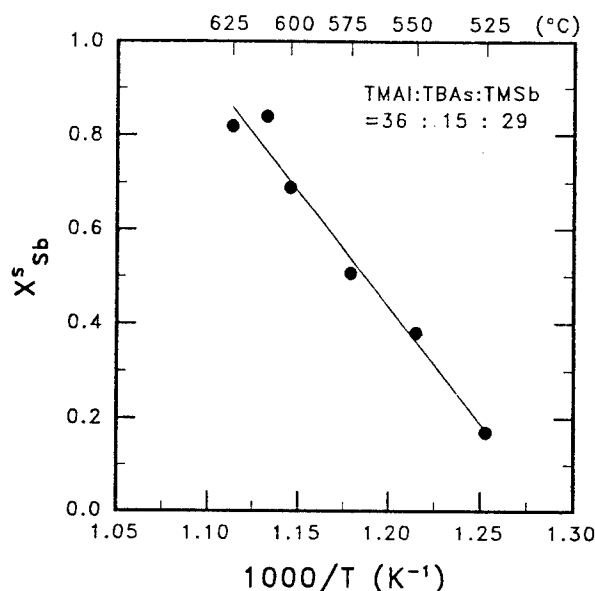


Fig. 1. Composition of AlSb content in AlAsSb as a function of growth temperatures with constant mole flow ratio of $\text{TMAI:TBAs:TMSb}=36:15:29$.

The AlAs content was found to increase continuously as the growth temperature increases from 525°C to 625°C . Among all precursors, the TBAs is presumably to decompose completely in this study, since the pyrolysis of TBAs is nearly completed at a temperature of 500°C (15). On the other hand, the TMSb does not decompose totally until the temperature reaches to 600°C . The increase of Sb concentration at high temperature may at least partially attribute to the cracking efficiency of TMSb. At higher growth temperature, the supply of Sb atoms at the growing interface increase accordingly, and, therefore, higher fraction of Sb can be obtained in the epilayer.

The Sb solid mole fraction (X_{Sb}^{S}) to its gas phase mole fraction (X_{Sb}^{V}) with various V/III ratio is shown in Fig. 2. The decomposition temperature is 600°C at which all reagents are presumed to decompose completely. Therefore, the effect due to the degree of partial decomposition can be minimized. The solid lines in this figure represent the theoretical results calculated according to thermodynamic considerations. As shown in the figure, a linear relationship between X_{Sb}^{S} and X_{Sb}^{V} can be obtained only at $\text{V/III}=1$. As the V/III ratio increases, the AlSb solid content decreases significantly. For $\text{V/III}>5$, almost no Sb concentration can be found in AlAsSb epilayer.

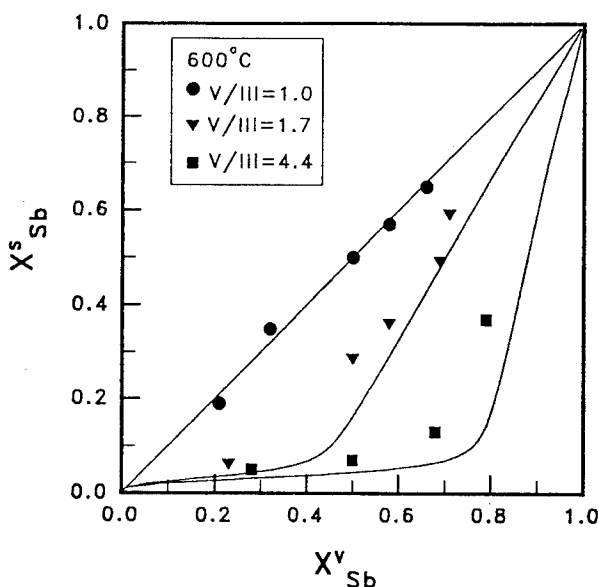


Fig. 2. AlSb mole fraction in $\text{AlAs}_{1-x}\text{Sb}_x$ versus Sb vapor composition in group V at different V/III values. The solid lines represent the theoretical results predicted by thermodynamics.

Experimental data indicate the composition depends strongly on V/III ratio and input gas fraction of Sb in group V. One precaution to be followed during the growth is that the AlAsSb must never be grown at $\text{V/III}<1$. If the true value of V/III ratio is less than unity, excess Al element appears, thereby resulting in poor film quality. These additional constraints cause the growth window for AlAsSb to be even narrower. Therefore, to obtain a specific value of x in $\text{AlAs}_{1-x}\text{Sb}_x$, based on the phase diagram described above, the mole flow rates of all precursors are necessary to be regulated extremely carefully. That makes the preparation of AlAsSb sample difficult.

In Fig. 3(a), we show the X_{Sb}^{S} as function of $[\text{TBAs}]/[\text{TMAI}]$ at growth temperature of 600°C with $[\text{TMSb}]/[\text{TMAI}]=0.5$ and TMAI mole flow rate equal to $9.2 \mu\text{mole/min}$. The fraction of AlSb seems to decrease nearly linearly in the region for values of $[\text{TBAs}]/[\text{TMAI}]$ between 0 and 1. The reduction of solid Sb concentration becomes getting slower for $[\text{TBAs}]/[\text{TMAI}]>1$. To clarify the role of As atom played in the growth, another experiment were performed at different $[\text{TMSb}]/[\text{TMAI}]$ ratios with a fixed $[\text{TBAs}]/[\text{TMAI}]$, ranged from 0.3 to 1.7 as the result in Fig. 3(b).

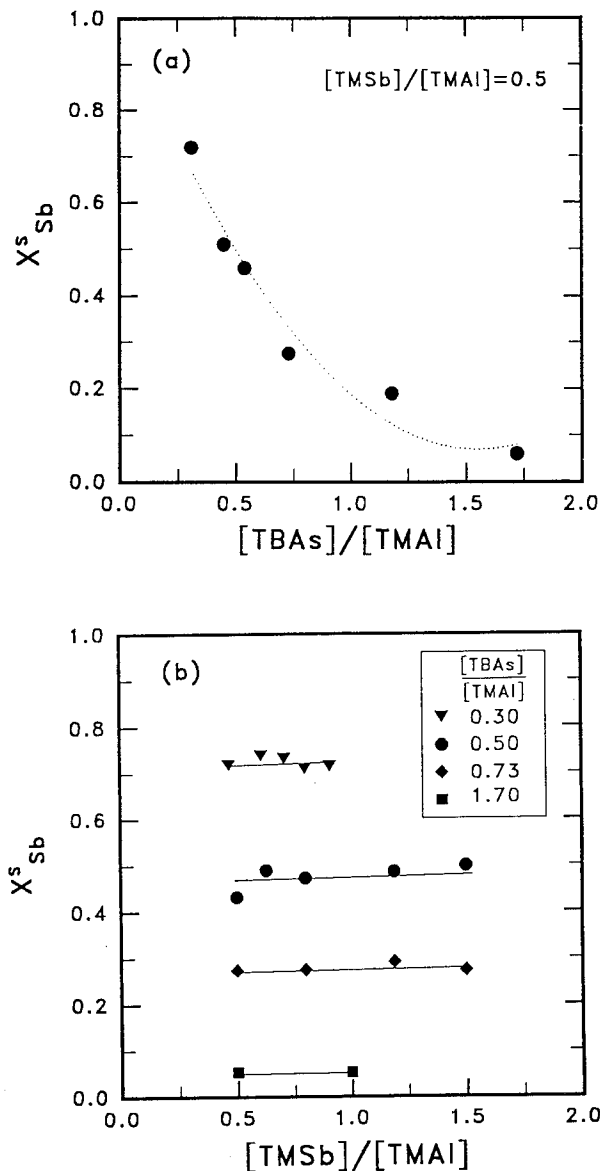


Fig. 3. Dependence of solid Sb concentration on the input partial pressure ratio of (a) $[TBAs]/[TMAI]$ and (b) $[TMSb]/[TMAI]$, respectively.

As shown in fig. 3(b), no matter which value of $[TBAs]/[TMAI]$ is used, the corresponding solid Sb concentration saturates and almost independent of the TMSb mole fraction in the gas phase. The saturated value of solid Sb is inversely proportional to the $[TBAs]/[TMAI]$ ratio. The TBAs together with TMAI quite likely control the overall growth process. This observation coincides with the trend predicted by thermodynamic theory. Since the binary AlAs is more stable than AlSb(8), the As atom has an esteemed

privilege in occupying group V sublattice. Thus, nearly all the As atoms arriving at the growing surface can be incorporated in the solid, provided that its molar flow does not exceed that of TMAI. On the other hand, the Sb atom plays more passive role during the growth, similar to phosphorus atom in the case of GaInP. Therefore, once the Sb is oversupplied, the composition of $AlAs_{1-x}Sb_x$ is simply determined by the partial pressures of arsenic and aluminum reactant. Above discussion indicate that the As/Al input gas ratio, rather than V/III ratio or X_{Sb}^V , is the principal factor for determining the solid distribution. Since only two of the input reactants (Al and As) are required to be accurately controlled, the growth of AlAsSb can apparently be simpler and become comparatively easier.

In conclusion, we have found that the solid composition of $AlAs_{1-x}Sb_x$ is strongly dependent on the growth temperature. A higher temperature seems to be more likely for Sb atoms to incorporate into the films for the growth of $AlAs_{1-x}Sb_x$ alloys. Although the

growth is very sensitive to V/III ratio and X_{Sb}^S , however, in our study we found that the key factor in controlling the composition is the input gas ratio of $[TBAs]/[TMAI]$. Saturation in composition is occurred under a fixed input $[TBAs]/[TMAI]$ gas ratio due to the preferential incorporation of As. Lower value of $[TBAs]/[TMAI]$ ratio yields a higher solid Sb concentration. Therefore, the control of solid composition in AlAsSb appears to be much easier owing to the removal of one of the growth constraint.

Acknowledgments

The authors would like to thank the National Science Council, Republic of China, for financial support of this research under Contract No. NSC84-2215-E-009-028.

References:

- (1) K. Tai, R. J. Fischer and A. Y. Cho, *Electron. Lett.*, Vol. 25, pp. 1159, 1989.
- (2) T. Inata, S. Muto, Y. Nakata and T. Fujii, *Jpn. J. Appl. Phys.*, Vol. 29, pp. L1382, 1990.
- (3) Y. H. Zhang and D. H. Chow, *Appl. Phys. Lett.*, Vol. 65, pp. 3239-3241, 1994.
- (4) S. Tiwari and D. J. Frank, *Appl. Phys. Lett.*, Vol. 60, pp. 630, 1992.
- (5) W. K. Chen and J. Ou, *Jpn. J. Appl. Phys.*, Vol. 33, pp. L402-L404, 1994.
- (6) G. B. Stringfellow, *J. Cryst. Growth*, Vol. 62, pp. 225, 1983.

- (7) T. Fukui and Y. Horikoshi, *Jpn. J. Appl. Phys.*, Vol. 19, pp. L53, 1980.
- (8) H. Seki and Houkitu, *J. Cryst. Growth*, Vol. 74, pp. 172, 1986.
- (9) R. M. Biefeld, *J. Cryst. Growth*, Vol. 75, pp. 255, 1986.
- (10) W. K. Chen and M. T. Chin, *Jpn. J. Appl. Phys.*, Vol. 33, pp. L1370, 1994
- (11) O. Kubaschewski, E. L. Evans and C. B. Aecock, Metallurgical Thermochemistry (Pergamon, Oxford, 1967) 4th ed.
- (12) I. Barin, O. Knacke and O. Kubaschewski, Thermochemical Properties of Inorganic Substances (Springer-Verlag, Berlin, 1977) suppl.
- (13) D. R. Stull and G. C. Sinke, Thermodynamic Properties of Elements (American Chemical Soc., Washington D. C., 1956).
- (14) G. B. Stringfellow, *J. Cryst. Growth*, Vol. 27, pp. 21, 1974.
- (15) M. J. Cherng, H. R. Jen, C. A. Larson, G. B. Stringfellow, H. Lundt and P. C. Taylor, *J. Cryst. Growth*, Vol. 77, pp. 408, 1986.

Optical and Structural Properties of $\text{In}_{0.53}\text{Ga}_{0.47}\text{As}/\text{In}_{0.52}\text{Al}_{0.48}\text{As}$ Multiple Quantum Wells Grown on Vicinal (110) InP Substrates by Molecular Beam Epitaxy

H. Asai, K. Oe, and H. Iwamura

*NTT Opto-electronics Laboratories,
3-1 Morinosato Wakamiya, Atsugi, Kanagawa 243-01, JAPAN*

We investigated the MBE growth and optical characteristics of $\text{In}_{0.53}\text{Ga}_{0.47}\text{As}/\text{In}_{0.52}\text{Al}_{0.48}\text{As}$ MQWs on vicinal (110) InP substrates. The MQWs grown on the (110) substrates tilted towards $[00\bar{1}]$ indicate narrower excitonic linewidth in absorption spectra and stronger PL intensity than those of (001) MQWs. On the other hand, for the MQWs on the (110) tilted towards $[001]$, we observed no excitonic absorption peaks and extremely-weak and broad PL spectra. The TED and TEM observations have clarified that these poor characteristics are due to structural fluctuation and atomic ordering in the MQWs. We also discuss a possible mechanism of the degradation.

I. INTRODUCTION

Over the last two decades, advances in growth techniques, such as molecular beam epitaxy (MBE), have spurred many studies on the optical properties of multiple quantum wells (MQWs) and on their device applications. Almost all the studies, however, have been limited to the (001) MQWs. Recently, there has been increasing interest in the MQWs grown on (110)-oriented substrates from the viewpoints of their novel optical and structural properties, such as in-plane optical anisotropy [1], compositional clustering [2], step bunching [3,4], and CuAu-I type atomic ordering [5-7]. From a practical aspect, it is necessary to use slightly-tilted substrates from the (110) plane to obtain MQWs with a specular surface [8]. However, there are few reports on the relationship between the crystal quality of MQWs and the tilt-directions in misoriented (110) substrates.

In this paper, we clarify the effect of the tilt-direction on the optical and structural properties in $\text{In}_{0.53}\text{Ga}_{0.47}\text{As}/\text{In}_{0.52}\text{Al}_{0.48}\text{As}$ (110) MQWs through the measurement of optical absorption, photoluminescence (PL), transmission electron diffraction (TED), and transmission electron microscopy (TEM). The MQWs grown on the (110) substrate tilted towards $[00\bar{1}]$ indicate narrower excitonic linewidth in absorption spectra and stronger PL intensity than those of (001) MQWs, while the MQWs on the (110) tilted towards $[001]$ are extremely degraded. The TED

and TEM observations show that this degradation is due to structural fluctuation and atomic ordering.

II. EXPERIMENTAL

The 70-period $\text{In}_{0.53}\text{Ga}_{0.47}\text{As}/\text{In}_{0.52}\text{Al}_{0.48}\text{As}$ MQWs were grown on Sn-doped (110) InP substrates by MBE. The substrate orientation was tilted from the (110) plane towards the $[001]$ and $[00\bar{1}]$ directions by 3° . The exact (110) and (001) substrates were also used for comparison. The MQWs were simultaneously grown on the four substrates at $1.3 \mu\text{m/hr}$. The $\text{In}_{0.53}\text{Ga}_{0.47}\text{As}$ well width (L_z) was 8 nm, while the $\text{In}_{0.52}\text{Al}_{0.48}\text{As}$ barrier width (L_b) was 5 nm.

We examined the optical properties of the MQWs by band-to-band absorption and PL measurements. An Ar ion laser (5145 \AA) was used as an excitation light source for PL measurements. We characterized the atomic structure in the (110) MQW by observing the $(1\bar{1}0)$ cross-sections with the TED and TEM under an acceleration voltage of 200 kV.

III. RESULTS

On (110) substrates, in general, it is not easy to grow epitaxial layers with specular surfaces. Figure 1 shows the Nomarski photomicrographs of the surfaces of (110) and (001) MQWs. On the

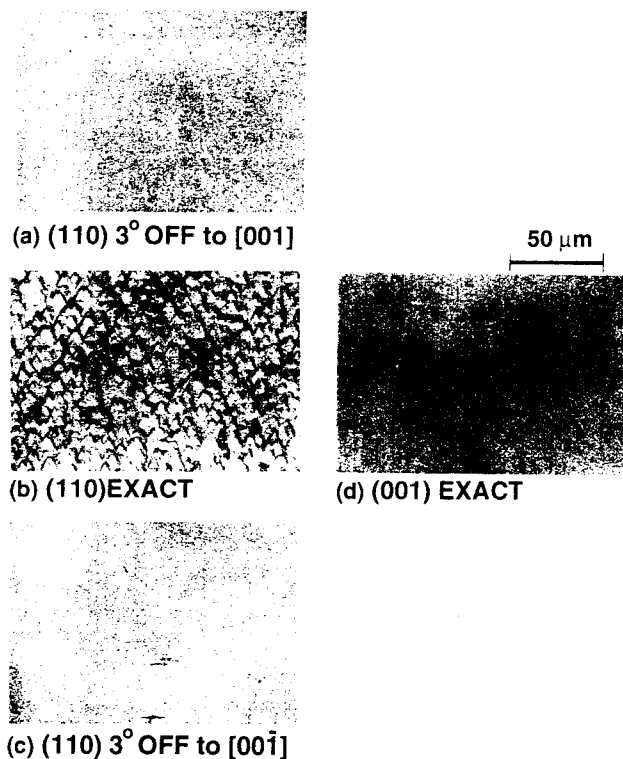


Fig. 1 Photomicrographs of surfaces of InGaAs/InAlAs MQWs grown on a (110) substrate tilted towards [001] (a), on an exact (110) substrate (b), on a (110) substrate tilted towards [00 $\bar{1}$] (c), and on an exact (001) substrate (d).

exact (110) face, one can observe the many hillocks [Fig. 1(b)], in contrast to the specular surface of the exact (001) MQW [Fig. 1(d)]. On the other hand, mirror surfaces were obtained on the slightly-tilted (110) substrates towards the [001] or [00 $\bar{1}$] direction [see Figs. 1(a) and (c)]. Thus, the tilt direction of the vicinal (110) substrates have no influence on the surface morphology.

The optical quality of the (110) MQWs, however, strongly depends on the tilt direction. Figures 2 and 3 show band-to-band absorption and PL spectra at 300 K, respectively. For the MQW on the (110) tilted towards [00 $\bar{1}$], we observed sharper and stronger excitonic peaks [half width at half maximum (HWHM) = 5.9 meV] than that of the (001) MQW (HWHM = 7.1 meV), as shown in Fig. 2. The PL intensity of this (110) MQW was also several times stronger than that of the (001) MQW.

On the other hand, for the tilt towards the [001] direction, we observed no excitonic peaks and only unclear step-like patterns in the absorption spectra, which was similar to that of the exact (110) MQW having the defective surface. Since the step-like patterns in absorption spectra of MQWs reflect the

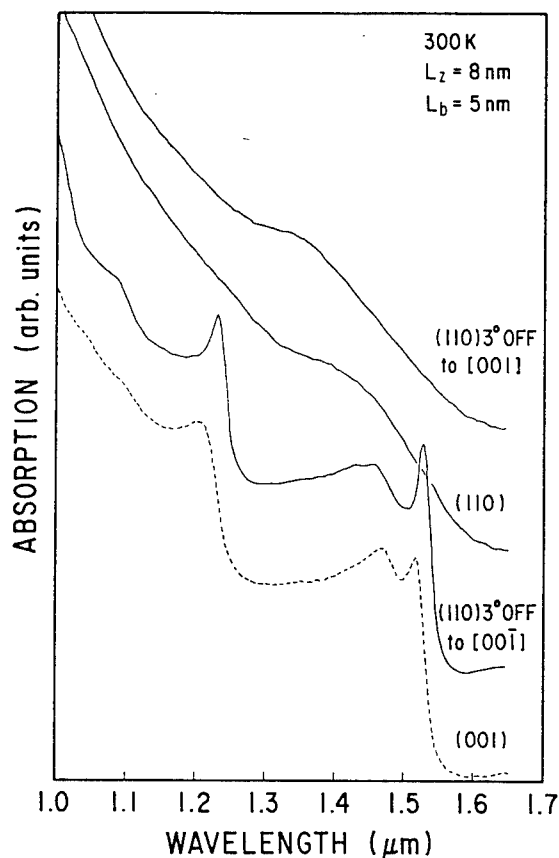


Fig. 2 Optical absorption spectra of InGaAs/InAlAs MQWs ($L_z=8\text{nm}$, $L_b=5\text{nm}$). The solid and dashed curves indicate spectra for (110) and (001) MQWs, respectively.

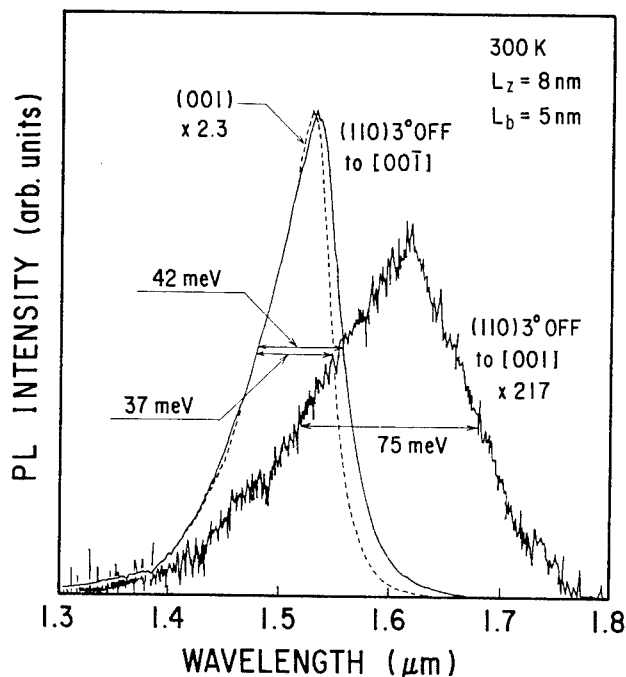
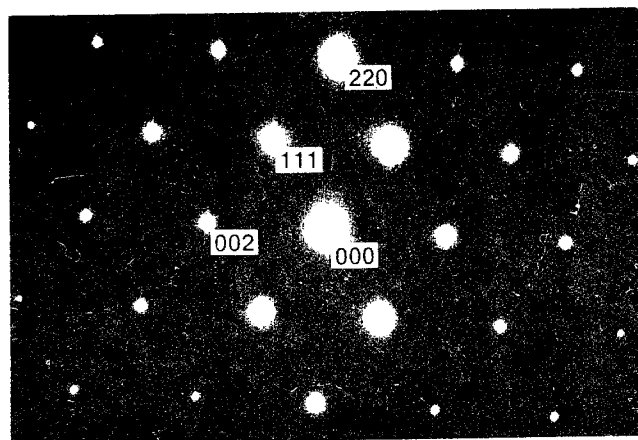
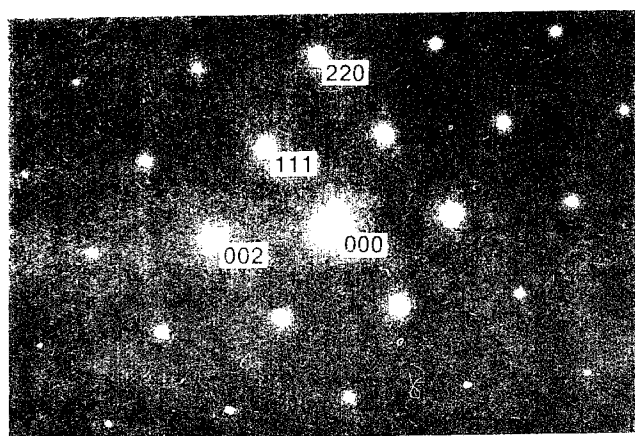


Fig. 3 Photoluminescence spectra of InGaAs/InAlAs MQWs ($L_z=8\text{nm}$, $L_b=5\text{nm}$). The solid and dashed curves indicate spectra for (110) and (001) MQWs, respectively.



(a) (110) 3° OFF to [001]



(b) (110) 3° OFF to [001̄]

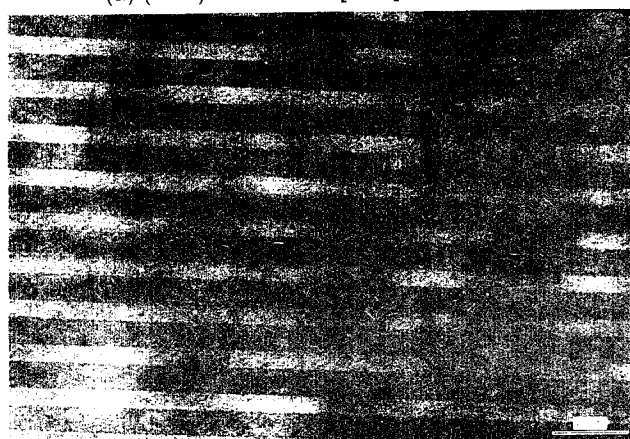
Fig. 4 Transmission electron diffraction patterns of (110) cross-sections in InGaAs/InAlAs MQWs grown on (110) substrates tilted towards [001] (a) and towards [001̄] (b).

two-dimensional density of states, this degradation of the pattern suggests that there are some kinds of structural disorder in the MQWs grown on the (110) tilted to the [001]. The PL intensity of this sample was also one-hundredth as strong as and the linewidth was two times as broad as those of the (001) MQW. These results indicate that the crystal quality of the MQWs grown on the substrates tilted to [001] is extremely degraded.

In order to clarify this degradation, we carried out TED and TEM observations on the (110) cross sections. Figure 4 shows the TED patterns of the misoriented (110) MQWs towards [001] and [001̄]. It is clear from Fig. 4(a) that for the misorientation towards [001], there are forbidden superstructure spots (e. g., 001, 110, ..., etc.), which are elongated to the growth direction, among the allowed Bragg reflections (e.g., 002, 111, 220, ..., etc.). This particular set of reflection spots is associated with



(a) (110) 3° OFF to [001]



(b) (110) 3° OFF to [001̄]

Fig. 5 Transmission electron micrographs of (110) cross-sections in InGaAs/InAlAs MQWs grown on (110) substrates tilted towards [001] (a) and towards [001̄] (b). The dark and bright bands indicate InGaAs and InAlAs, respectively.

the CuAu-I type ordered structure [5-7]. In the perfectly ordered structure, for example, an $\text{In}_{0.53}\text{Ga}_{0.47}\text{As}$ well layer consists of alternating GaAs and InAs monolayers along either the [110] growth direction or the [001] direction normal to the growth axis. The MQWs studied in this work, however, are considered to include a lot of planar defects, such as antiphase boundaries, because the superstructure reflections in Fig. 4(a) are very weak and are elongated along the growth direction. On the other hand, for the sample on the substrate tilted towards [001̄], we observed only the allowed reflections as shown in Fig. 4(b). This indicates that spontaneous ordering of CuAu-I structures occurs only in the (110) MQWs misoriented towards [001]. Figure 5 shows the TEM images on the (110) cross sections of the two samples. It is clear from Fig. 5(a) that the (110) MQW misoriented towards [001] includes a bent-layer

structure and stacking faults. These structures are similar to step bunching or faceting growth observed in AlGaAs/GaAs (110) MQWs [3,4]. On the other hand, the (110) MQW misoriented towards $[00\bar{1}]$ indicates a perfect layered structure, as shown in Fig. 5(b).

From both micro- and macroscopic aspects, we found that the (110) MQWs tilted towards $[001]$ include not only the atomic ordering but also the bent layered structure, while the MQWs tilted to $[00\bar{1}]$ have good crystal quality. Therefore, we can conclude that these structural defects directly cause the degradation of the optical quality in the (110) MQWs tilted towards $[001]$.

Although we can not fully understand the degradation mechanism for the (110) MQWs tilted towards $[001]$, we believe that it strongly relates to the atomic arrangement on the (110) surface.

For the exact (110) surface, both the Group-III and -V atoms are arranged in a zigzag along the $[\bar{1}10]$ direction on the same plane. Each surface atom is bound to the underlying monolayer with one bond and is also bound to neighbor atoms in the same plane with two bonds. The (110) surface, therefore, is relatively stable, because the surface atom has only one dangling bond. This means that it is difficult to grow good crystals on the exact (110) orientation.

On the other hand, there are many atomic steps on the vicinal (110) surface. The impinging atoms, therefore, can be easily incorporated into the atomic steps. Once an atom is bound to a step, growth will proceed along the $[\bar{1}10]$ direction by incorporating successively constituent atoms like a fastener. For the (110) surface tilted towards $[001]$, since the atoms terminating step edges are Group-III elements, step growth must begin by incorporating the Group-V atom into the step. However, the sticking coefficient of Group-V is extremely small or practically zero even at the step edge [9]. Therefore, this hampers the layer-by-layer growth on the (110) surface tilted towards $[001]$, resulting in poor optical and structural quality in the MQWs. On the other hand, for the (110) surface tilted towards $[00\bar{1}]$, the atoms terminating at the steps are Group-V elements. Since the sticking coefficient of the Group-III atom is unity [9], if growth temperature is enough high for the Group-III atoms to migrate easily on the growing surface, step-flow growth occurs. As a result, the MQWs on the (110) surface tilted towards $[00\bar{1}]$ indicate good optical quality and perfect layered structure.

IV. SUMMARY

We investigated the optical and structural properties of $\text{In}_{0.53}\text{Ga}_{0.47}\text{As}/\text{In}_{0.52}\text{Al}_{0.48}\text{As}$ MQWs grown by MBE with regard to the tilt directions in the vicinal (110) substrates. The (110) MQWs tilted towards $[00\bar{1}]$ indicated narrower excitonic linewidth in absorption spectra and stronger PL intensity than those of (001) MQWs, while the MQWs on the (110) tilted towards $[001]$ were extremely degraded. From the TED and TEM observations, we found that this degradation is due to structural fluctuation and atomic ordering. These poor optical and structural properties in the MQWs can be explained by the atomic arrangement on the (110) surface.

ACKNOWLEDGMENTS

The authors would like to thank Yuichi Kawamura for his aid in MBE growth, Hidetoshi Takaoka for his TED and TEM measurement, and Takashi Mizutani and Yoshihiro Imamura for their continuous encouragement.

REFERENCES

- [1] D. Gershoni, I. Brener, G. A. Baraff, S. N. G. Chu, L. N. Pfeiffer, and K. West, *Phys. Rev. B* **44**, 1930 (1991).
- [2] P. M. Petroff, A. Y. Cho, F. K. Reinhart, A. C. Gossard, and W. Wiegmann, *Phys. Rev. Lett.* **48**, 170 (1982).
- [3] S. Hasegawa, M. Sato, K. Maehashi, H. Asahi, and N. Nakashima, *J. Cryst. Growth* **111**, 371 (1991).
- [4] M. Krishnamurthy, A. Lorke, M. Wassermeier, D. R. M. Williams, and P. M. Petroff, *J. Vac. Sci. Technol. B* **11**, 1384 (1993).
- [5] T. S. Kuan, T. F. Kuech, W. I. Wang, and E. L. Wilkie, *Phys. Rev. Lett.* **54**, 201 (1985).
- [6] T. S. Kuan, W. I. Wang, and E. L. Wilkie, *Appl. Phys. Lett.* **51**, 51 (1987).
- [7] O. Ueda, Y. Nakata, T. Nakamura, and T. Fujii, *J. Cryst. Growth* **115**, 375 (1991).
- [8] L. T. P. Allen, E. R. Weber, J. Washburn, Y. C. Pao, *Appl. Phys. Lett.* **31**, 670 (1987).
- [9] C. T. Foxon and B. A. Joyce, in *Current Topics in Materials Science*, edited by E. Kaldis (North-Holland, Amsterdam, 1981), Vol. 7, Chap. 1.

Surface step arrangements and configurations during molecular beam epitaxial growth on slightly misoriented (110) InP substrates

Yoshiaki Nakata, Osamu Ueda, and Shunichi Muto

Fujitsu Laboratories Ltd. 10 - 1 Morinosato-Wakamiya, Atsugi, Kanagawa 243 - 01, Japan

We studied the surface step ordering during molecular beam epitaxial growth on misoriented (110) InP substrates tilting toward the $[00\bar{1}]$ direction using reflection high energy electron diffraction (RHEED) and atomic force microscopy (AFM). During growth of InGaAs, we found that two types of surface steps (single and double monolayer steps) were ordered depending on the growth condition and on the terrace width. The AFM images of both InGaAs and InAlAs surfaces showed that the step edges were little undulated. We also grew InGaAs/InAlAs in-plane superlattices (IPSLs) using single monolayer step ordering. The photoluminescence spectrum had two peaks. The one closed to that of the InGaAs/InAlAs superlattice on the (001) InP substrate, but the other closed to InAlGaAs alloys.

1. Introduction

Growth of laterally modulated structures using step-flow growth on misoriented substrates is a very important technique for directly forming quantum well wire and box array structures without lithographic fabrication process. Petroff et al. [1-3] and Fukui et al. [4-6] have grown fractional layers of GaAs and Al(Ga)As alternately using step-flow growth on misoriented (001) GaAs substrates by molecular beam epitaxy (MBE) and metalorganic chemical vapor deposition (MOCVD). Laterally compositional modulations with the period of the mean terrace width of the substrates have been confirmed by X-ray diffraction [4,5] and transmission electron microscopy (TEM) [1,2,7]. However, the compositional deference between wells and barriers has been far from ideal. Their photoluminescence (PL) spectra have been closed to the homogeneous alloys [8,9].

For the growth of laterally periodic structures (i.e., in-plane superlattices (IPSLs)), it is important to control step edge to be straight as well as the growth to be step-flow mode. These features are, as well known, dependent not only on the growth methods and conditions, but also on the substrate orientations [10] and materials to be grown [11,12]. Recently, we have succeeded in growing the $(\text{InAs})_1/(\text{GaAs})_1$ laterally modulated monolayer superlattices (LM-MSLs) [13,14] and InGaAs/InAlAs IPSLs [15, 16] using single monolayer step ordering on misoriented (110) InP substrates tilting toward the $[00\bar{1}]$ direction. About growth on the misoriented (110) substrates tilting toward the $[00\bar{1}]$ or $[\bar{1}10]$ directions, the phenomena of step bunching [10,17] and giant step formation [18] have been investigated. However, step ordering on misoriented (110) substrates tilting toward the $[00\bar{1}]$ direction have hardly been studied.

This paper describes surface step ordering during MBE growth of InGaAs and InAlAs on misoriented

(110) InP substrates tilting toward the $[00\bar{1}]$ direction, evaluated by reflection high energy electron diffraction (RHEED) and atomic force microscopy (AFM). We also demonstrate the PL spectrum of the InGaAs/InAlAs IPSL grown on these substrates.

2. Experimental

InGaAs and InAlAs were grown by conventional MBE. The substrates were misoriented (110) InP tilting toward the $[00\bar{1}]$ direction. On these substrates, the surface steps of the $(11\bar{1})$ B terminated by group V atoms should be arranged. Prior to growth, the substrates were heated up to about 570°C for 30 seconds under As pressure at about 1×10^{-5} Torr for thermal cleaning. The growth rate was about 0.18 $\mu\text{m/h}$ for both InGaAs and InAlAs. It takes about 4 seconds to grow a single monolayer. Surface steps were evaluated by RHEED with an acceleration voltage of 25 kV and also by AFM operated in air.

3. Results and discussion

3.1. Step arrangements

In growing InGaAs on slightly misoriented (110) InP substrates, we found that the two types of surface steps were ordered. Figures 1(a) and 1(b) are RHEED patterns obtained from the InGaAs surfaces growing on a substrate tilted at 3°. The electron beam incidence was parallel to the step edges ($[\bar{1}10]$ azimuth). Pronounced split spots showing step ordering were clearly observed. The intervals of the split spots were about 1/7 (Fig. 1(a)) and 1/14 (Fig. 1(b)) to those of fundamentals, indicating that single monolayer steps (4 nm wide terraces) and double monolayer steps (8 nm wide terraces) were ordered. These step ordering depended on the growth conditions. Figure 1(c) shows the relationship between the step arrangements and the growth conditions. The

double monolayer steps were ordered either at a lower temperature or at a higher As pressure than those of single monolayer steps, although double monolayer steps with larger terrace widths require a longer migration of atoms than single monolayer

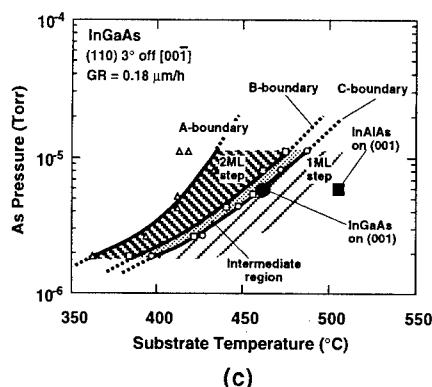
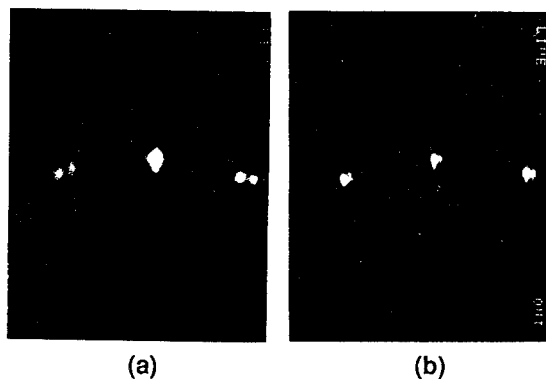


Fig. 1. Typical RHEED patterns obtained from InGaAs surfaces growing on a substrate tilted at 3° toward the [001] direction. (a) Single monolayer step ordering. (b) Double monolayer step ordering. (c) The relationship between the step arrangements and the growth conditions of substrate temperature and As pressure.

steps. The As incorporation, presumably the As related atomic reconstruction at the step edges plays an important role for the ordering of these steps. On the other hand, during the growth of InAlAs, only the RHEED split spots showing single monolayer step ordering were obtained, but split spots of the ordering of double monolayer steps were not observed. This is considered to be because Al migration was insufficient to order periodic 8 nm wide terraces (double monolayer step ordering) at such a low temperature or high As pressure to form double monolayer steps, or because the reconstruction at the step edges was broken by incorporating Al atoms.

When growing on misoriented (001) substrates tilted at 4° toward the [110] direction (mean terrace width of 4.2 nm), transition temperatures from the RHEED oscillation mode (two-dimensional nucleation growth) to the constant response mode

(step-flow growth) [19] were about 460°C for InGaAs and 500°C for InAlAs at the As pressure of 6×10^{-6} Torr, as plotted in Fig. 1(c). On the (110) substrates at the same As pressure of 6×10^{-6} Torr, the lowest temperature for the step-flow growth, in this case, for ordering of double monolayer steps with periodic 8 nm wide terraces, was 420°C for InGaAs, and ordering of single monolayer steps with periodic 4 nm wide terraces was 390°C for InAlAs. That is, the temperatures for step flow growth on the (110) substrates were much lower than those on the (001) substrates. Therefore, the migration length on the (110) substrates is thought to be longer than those on the (001) substrates.

Figure 2(a) shows the critical terrace width of single monolayer step ordering (boundary between the regions of intermediate and single monolayer step ordering

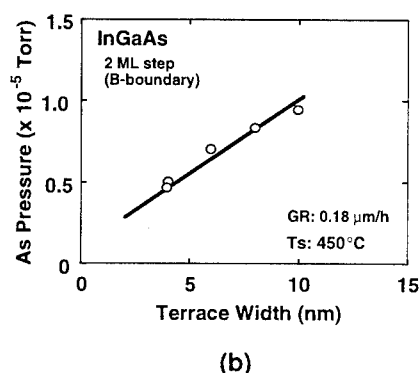
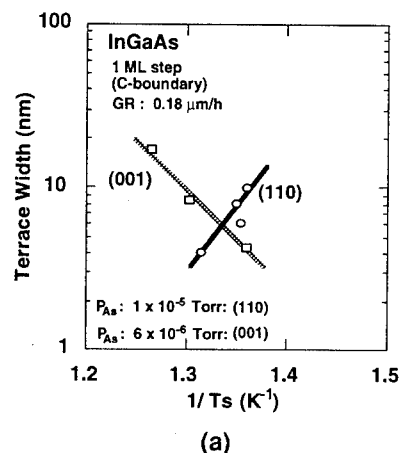


Fig. 2. (a) The critical terrace width of single monolayer step ordering (boundary between the regions of intermediate and single monolayer step ordering: C-boundary in Fig. 1(c)) on misoriented (110) and (001) substrates as a function of growth temperature. (b) The dependence of the minimum As pressure for double monolayer step ordering (boundary between the regions of intermediate and double monolayer step ordering: B-boundary in Fig. 1(c)) on the terrace width growing on misoriented (110) substrates.

step ordering: C-boundary in Fig. 1(c)) on misoriented (110) substrates and also on misoriented (001) substrates as a function of the growth temperature measured by RHEED from InGaAs surfaces growing on substrates with various tilt angles. The substrate tilt directions were $[00\bar{1}]$ on the (110) substrates and $[110]$ on the (001) substrates. As pressures were fixed at 1×10^{-5} Torr for growth on (110) substrates and at 6×10^{-6} Torr for growth on the (001) substrates. On the (001) substrates, wider terraces were formed at higher temperatures. This is because the surface migration length of group III atoms determined the growth mode [19]. On the (110) substrates, the critical terraces became narrower when increasing the temperature. The lower temperature was needed for wider terrace ordering. Figure 2(b) shows the minimum As pressure for double monolayer step ordering (boundary between the regions of intermediate and double monolayer step ordering: B-boundary in Fig. 1(c)) on the (110) substrates as a function of the terrace width. The

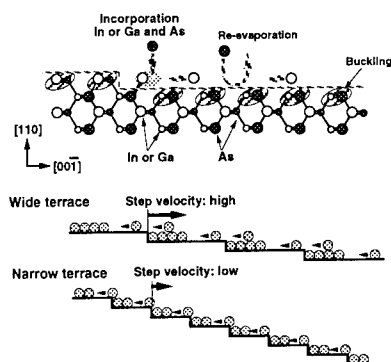


Fig. 3. Schematic diagrams of the step-flow growth on misoriented (110) substrates tilting toward the $[00\bar{1}]$ direction.

As pressure needed for double monolayer step ordering increased linearly with the mean terrace width. On the (110) surfaces, group III and V atoms coexist as shown in Fig. 3. For the step fronts to grow forward, As atoms must be incorporated before group III atoms arrive at the next sites. The arrival rate (step velocity) should become higher with the terrace width. Therefore, a higher As flux should be required for the growth of wider terrace ordering.

3.2. Step edge configurations

Figures 4(a) and 4(b) are AFM images of the InGaAs surfaces ordered in single and double monolayer steps and Fig. 4(c) is an AFM image of the InAlAs surface ordered in single monolayer steps. These were grown on substrates tilted at 1.2° toward the $[00\bar{1}]$ direction. The growth temperatures were 470°C , 455°C and 455°C , respectively and the As pressure was 1×10^{-5} Torr. As shown, periodic terraces were formed aligned to the $[001]$ direction. The periods on average corresponded to the expected terrace widths of 10 nm for single monolayer step ordering and 20 nm for double monolayer step ordering. Step edges were formed almost along the $[\bar{1}10]$ direction and seen to be little undulated. These periodic and straight step formations are quite important for growing laterally periodic structures such as quantum wire array structures.

3.3. IPSL growth

We grew an InGaAs/InAlAs IPSL structure on a substrate tilted at 1.2° toward the $[00\bar{1}]$ direction using single monolayer step ordering. The growth sequences were same as ref.15. Since the X-ray diffraction measurements indicated that lateral interfaces were inclined at about 60° from the growth direction of the $[110]$, the superlattice period

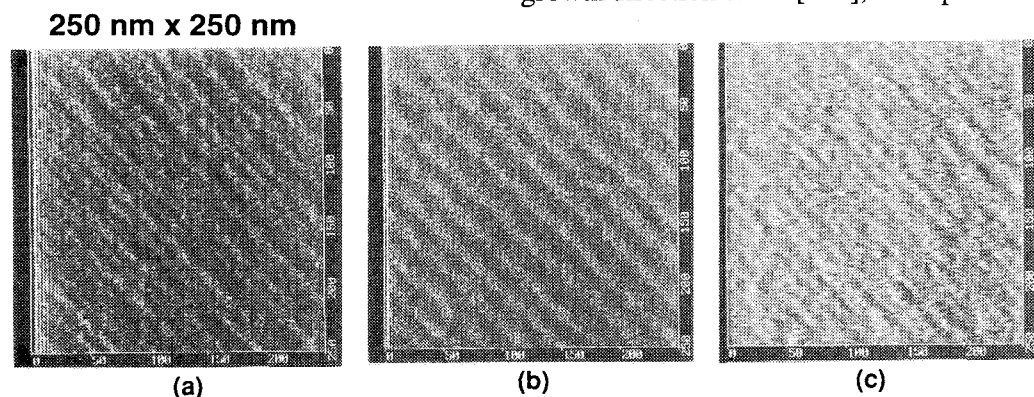


Fig. 4. AFM images of the InGaAs surfaces ordered in (a) single, (b) double monolayer steps, and (c) the InAlAs surface ordered in single monolayer steps. They were grown on the substrates tilted at 1.2° toward the $[00\bar{1}]$ direction. The expected terrace widths are 10 nm for single monolayer step ordering and 20 nm for double monolayer step ordering.

was about 5 nm. The expected schematic structure is shown in Fig. 5(a). Figure 5(b) shows the PL spectrum measured at 77 K. We obtained a peak at the energy of 1.07 eV in addition to a peak at 1.19 eV. The energy of $\text{In}_{0.5}\text{Al}_{0.25}\text{Ga}_{0.25}\text{As}$ alloy on a (001) InP substrate was about 1.15 eV [15]. The higher energy peak is thought to be the

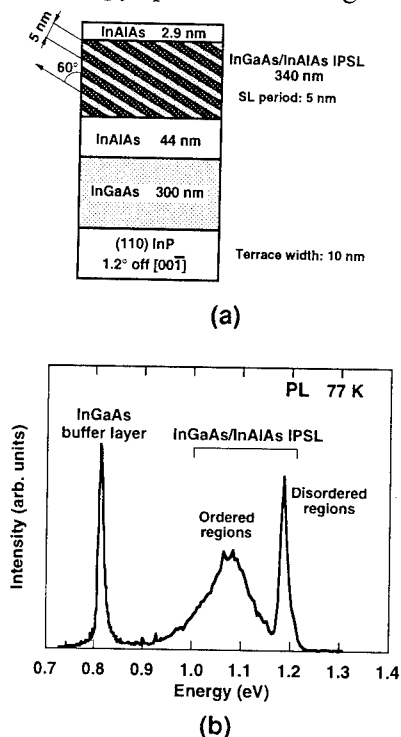


Fig. 5. (a) Schematic diagram of the InGaAs/InAlAs IPSSL structure expected from X-ray diffraction measurements. (b) The PL spectrum of the IPSSL measured at 77 K.

luminescence from the disordered regions with small compositional differences between wells and barriers (the mean Al composition was expected to be slightly higher than that of Ga). The transition energy of the InGaAs (2.5 nm thick)/InAlAs (2.5 nm thick) superlattice on a (001) InP substrate is 1.03 eV [20]. The low energy peak closed to this value, suggesting that InGaAs/InAlAs IPSSL structures with nearly idealized compositional differences were formed partially.

4. Summary

We studied the surface steps during the growth of InGaAs and InAlAs on the misoriented (110) InP substrates tilting toward the $[00\bar{1}]$ direction. During the growth of InGaAs, we found that two types of surface steps (single and double monolayer steps) were ordered. AFM images indicated that step edges of both InGaAs and InAlAs were little undulated. We grew InGaAs/InAlAs IPSSL on the misoriented (110) InP substrate tilted at 1.2° using single monolayer step ordering. We obtained a PL spectrum with a peak closed to a transition

energy of the InGaAs/InAlAs superlattice on the (001) InP substrate in addition to a peak corresponding to the disordered regions.

Acknowledgments

The authors thank Yuji Nishikawa and Atsushi Tackeuchi for PL measurements and for helpful discussions. We also thank Osamu Ohtsuki and Naoki Yokoyama for their encouragement.

References

- [1] P. M. Petroff, A. C. Gossard and W. Wiegmann, *Appl. Phys. Lett.* 45 (1984) 620.
- [2] J. M. Gaines, P. M. Petroff, H. Kroemer, R. J. Simes, R. S. Geels and J. H. English, *J. Vac. Sci. Technol. B* 6 (1988) 1378.
- [3] M. Tsuchiya, J. M. Gaines, R. H. Yan, R. J. Simes, P. O. Holtz, L. A. Coldren and P. M. Petroff, *Phys. Rev. Lett.* 62 (1989) 466.
- [4] T. Fukui and H. Saito, *Appl. Phys. Lett.* 50 (1987) 824.
- [5] T. Fukui and H. Saito, *J. Vac. Sci. Technol. B* 6 (1988) 1373.
- [6] T. Fukui, H. Saito and Y. Tokura, *Appl. Phys. Lett.* 55 (1989) 1958.
- [7] T. Fukui and H. Saito, *J. Crystal Growth* 115 (1991) 61.
- [8] H. Kanbe, A. Chavez-Pirson, H. Ando, H. Saito and T. Fukui, *Appl. Phys. Lett.* 58 (1991) 2969.
- [9] M. Kasu, H. Ando, H. Saito and T. Fukui, *Appl. Phys. Lett.* 59 (1991) 301.
- [10] M. Krishnamurthy, M. Wassermeier, H. Weman, J. L. Merz and P. M. Petroff, *Mat. Res. Soc. Symp. Proc. Vol. 237* (1992) 473.
- [11] P. M. Petroff, M. S. Miller, Y. T. Lu, S. A. Chalmers, H. Metiu, H. Kroemer and A. C. Gossard, *J. Crystal Growth* 111 (1991) 360.
- [12] S. A. Chalmers, H. Weman, J. C. Yi, H. Kroemer, J. L. Merz and N. Dagli, *Appl. Phys. Lett.* 60 (1992) 1676.
- [13] Y. Nakata, O. Ueda, T. Inata, S. Nakamura, M. Yamaguchi, S. Sasa and S. Muto, in: *Proc. 19th Intern. Symp. on GaAs and Related Compounds*, Karuizawa, 1992, Inst. Phys. Conf. Ser. 129, Ed. T. Ikegami, F. Hasegawa and Y. Takeda (Inst. Phys., Bristol, 1993) p.435.
- [14] O. Ueda, Y. Nakata and S. Muto, in: *Proc. 19th Intern. Symp. on GaAs and Related Compounds*, Karuizawa, 1992, Inst. Phys. Conf. Ser. 129, Ed. T. Ikegami, F. Hasegawa and Y. Takeda (Inst. Phys., Bristol, 1993) p.429.
- [15] Y. Nakata, O. Ueda, A. Tackeuchi, S. Nakamura and S. Muto, *J. Crystal Growth*, submitted Proc. 8th Intern. Conf. on Molecular Beam Epitaxy (InGaAs/InAlAs in-plane superlattices grown on slightly misoriented (110) InP substrates by molecular beam epitaxy).
- [16] O. Ueda, Y. Nakata, A. Tackeuchi, S. Nakamura and S. Muto, *J. Crystal Growth*, submitted Proc. 8th Intern. Conf. on Molecular Beam Epitaxy (TEM evaluation of MBE-grown InGaAs/InAlAs in-plane superlattices on slightly misoriented (110) InP substrates).
- [17] M. Krishnamurthy, M. Wassermeier, D. R. M. Williams and P. M. Petroff, *Appl. Phys. Lett.* 62 (1993) 1922.
- [18] S. Hasegawa, M. Sato, K. Maehashi, H. Asahi and H. Nakashima, *J. Crystal Growth* 111 (1991) 371.
- [19] J. H. Neave, P. J. Dobson and B. A. Joyce, *Appl. Phys. Lett.* 47 (1985) 100.
- [20] D. F. Welch, G. W. Wicks and L. F. Eastman, *Appl. Phys. Lett.* 48 (1983) 762.

Photoluminescence investigation of InGaAs/InP quantum wells grown by gas-source molecular-beam epitaxy with source-supply interruption

Kazuhiko Hosomi, Teruo Mozume, Hideo Kashima, Kiyosi Ouchi,
Central Research Lab., Hitachi, Ltd., Kokubunji, Tokyo 185, Japan
Phone: 0423-23-1111 Fax: 0423-27-7679

1. Introduction

Heterostructures made of lattice-matched InGaAs/InP(001) are important for optoelectronic and ultra-high-speed devices. However, high-quality interfaces are more difficult to achieve in InGaAs/InP than in AlGaAs/GaAs. This is due to the additional requirement of lattice matching and the necessity of changing the group V and III species at each interface. Although the growth-interruption technique is commonly used to improve interface abruptness in metalorganic vapor-phase epitaxy (MOVPE) and gas-source molecular-beam epitaxy (GSMBE), there is evidence of compositional intermixing, particularly at the interface of the InP and the InGaAs that it is grown on [1-3]. This is because residual As atoms are easily incorporated into the subsequently grown InP layer due to the high incorporation ratio of As compared to that of P [4].

We have developed a new source-material switching sequence in which source supply-interruption (SSI), meaning that the supply of all sources is stopped at each interface, is introduced during GSMBE of InGaAs/InP heterostructures. This reduces the memory effect of As in the injector as well as the residual As atoms on the InGaAs surface [5]. We have previously reported the high-resolution transmission electron microscopy (HRTEM) and Auger electron spectroscopy (AES) results, which show the formation of perfectly abrupt interfaces.

In this article, we present a detailed study of the effects of SSI on the interface configuration of lattice-matched InGaAs/InP heterostructures. Low-temperature photoluminescence (PL) analysis of InGaAs/InP quantum wells (QWs) with well thickness ranging from 1 to 16 nm was performed and the results were compared with theoretical calculations taking into account transition layer at the heterointerface.

2. Experimental

The layers we studied were all grown in a GSMBE system. Details of this system were reported in Ref. [6]. Elemental Ga and In were used for the group-III growth species which were derived from effusion cells. 100% AsH₃ and PH₃ were decomposed in a low-pressure thermal cracker cell maintained at 900 °C. A cracker-cell shutter and substrate shutter were used, along with run/vent routing, to achieve fast gas switching.

To study the interface structure by PL, InGaAs/InP quantum wells were grown on (001) InP substrates at 460 °C. To form QWs, we first grew a 300-nm InGaAs control layer, followed by six wells of thickness $L_z = 16$ -, 8-, 4-, 3-, 2-, and 1-nm. The quantum-well thickness was determined from the reflection high-energy electron diffraction oscillations assuming a steady-state growth rate, and from transmission electron microscopy (TEM) cross-sectional micrographs. The InP barriers separating the wells were 30-nm thick. The control layer serves as the reference for the PL spectra from which precise energy up-shifts of QW emission can be calculated.

The source switching scheme applied at the interface is shown in Fig. 1. The same switching procedures were followed for each type of interface (InP

to InGaAs and InGaAs to InP). At each interface, a source-supply interruption (SSI) of t_2 seconds was introduced. Details of the growth procedure are reported in Ref. [5]. In this work, we studied the effect of changing the length of the SSI at the InGaAs-to-InP interface, while fixing the SSI at the InP-to-InGaAs interface to 2 seconds.

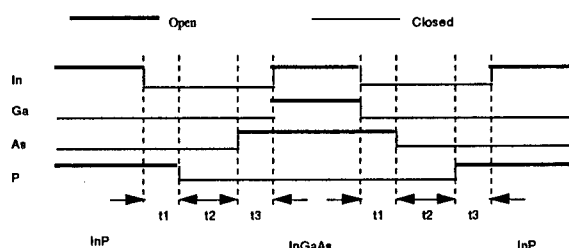


Fig. 1 Switching sequence of source materials using shutters and valves in the growth of InGaAs/InP heterostructures. Every interface of the growing layer is covered by a group-V source, then, after t_1 seconds, all source supply to the substrate is stopped. After t_2 seconds, the group-V species are changed and overlayer growth is started.

PL experiments were performed at 4.2 K using an Ar^+ laser as the excitation source. Luminescence was analyzed with a 3/4-meter grating monochromator and detected with a liquid-nitrogen-cooled Ge p-i-n photo-diode.

3. Results and Discussion

Figure 2 shows the PL spectra of QWs with well thicknesses of 1-, 2-, 3-, 4-, 8-, and 16-nm. The peaks corresponding to each well are clearly resolved. Note that the amplitude of the peaks has been normalized to be the same height of peaks for the InGaAs control layer. The PL peak shifts toward a shorter wavelength are clearly seen as the SSI increases. This movement is most noticeable between the spectra grown with SSI of 0 seconds and that of 12 seconds. The largest shift is observed for the 1-nm well. The results of HRTEM and AES analysis show the optimal SSI for InGaAs-to-InP heterointerface grown with 460 °C lies around 24 seconds [7,8].

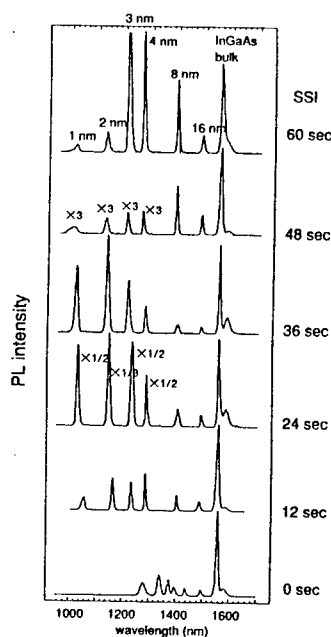


Fig. 2 Source-supply interruption (SSI) dependence in the PL spectrum of InP/InGaAs QWs with well thickness of 1-, 2-, 3-, 4-, 8-, and 16-nm. The amplitude of the peaks has been normalized to be the same height of peaks for the InGaAs control layer. Peaks from the control layer are used as the reference peaks.

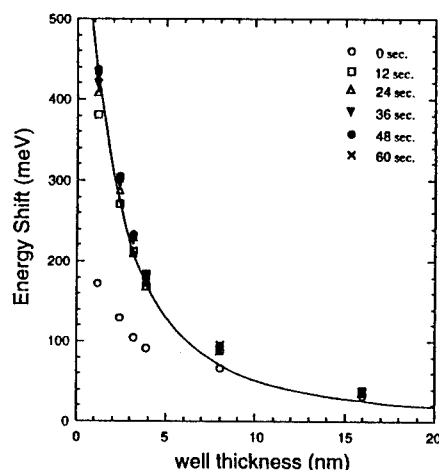


Fig. 3 Source-supply interruption (SSI) dependence of the PL peak energy shifts of InGaAs QWs with well thickness of 1-, 2-, 3-, 4-, 8-, and 16-nm. The solid curve represents calculated results using an envelope function approximation for finite wells, with a conduction band offset of 60%.

Figure 3 is a plot of the PL peak energy shift versus well thickness as a function of the SSI. The solid line in Fig. 3 denotes calculated results using an envelope function approximation [9]. The conduction band offset is set at 60% of the bandgap difference between InGaAs and InP. In the calculation, conduction-band nonparabolisities [10] are not taken into account. In the PL spectra of 1-, 2-, 3-, and 4-nm wells, as the SSI gets longer, there is a clear increase in energy up-shifts. These upward trends in peak energy are attributed to the difference in effective well thickness caused by strained interface layer formation [7,8]. The difference in energy up-shift observed between a 1-nm QW grown with an SSI of 12 seconds and that grown with an SSI of 24 seconds is 26 meV, which corresponds to a 1/2 monolayer fluctuation in well-thickness. Furthermore, the difference in energy up-shift observed between a 1-nm QW grown with an SSI of 12 seconds and that grown with an SSI of 60 seconds, which is 56 meV, corresponds to one-monolayer fluctuation.

To explain these trends toward higher energy, we performed theoretical calculations taking into account interface roughness. In these calculations, the presence of one-monolayer In(Ga)AsP transition layers at the InGaAs-to-InP interface and the changes in the As composition of this layer with changes in the SSI are assumed. Figure 4 shows the modeled SSI dependence in the potential profile. When the SSI is shorter than the optimal time, a transition layer whose potential barrier is lower than that of InP forms at the InGaAs-to-InP interface (Fig. 4(a)). As the SSI gets longer, the potential barrier height increases and an abrupt interface is obtained under the optimal SSI (Fig. 4(b)). When the SSI becomes longer than the optimal time, a transition layer reforms due to the desorption of As atoms from the InGaAs surface (Fig. 4(c)). The calculated results are

shown in Fig. 5 : the qualitative behavior of PL energy up-shifts is fully explained with this model for the QWs grown with SSIs ranging from 12 seconds to 60 seconds.

On the other hand, the difference in energy up-shift observed between a 1-nm QW grown without an SSI and that grown with an SSI of 24 seconds is 208 meV, which is much larger than the difference corresponding to a several-monolayer fluctuation. This is probably due to disorder within the heterostructure caused by intermixing of group V elements. Another possible explanation for this large discrepancy is formation of several InAs layers caused by excess As atoms on the surface.

Figure 6 compares our experimental data to that of other work. Our experimental points are in fairly good agreement with theory and lie higher than the others. For example, energy shift for 1-nm QW from Tsang and Schubert is 260 meV which corresponds to that of a 2.5-nm QW grown with an SSI of 24 seconds. This suggest that the well thicknesses of other work are effectively wider than the designed thicknesses and this discrepancy may be due to the absence of an abrupt interface. One of the origins of discrepancies between experimental energy up-shifts and theory in previous work is such inferior interface quality.

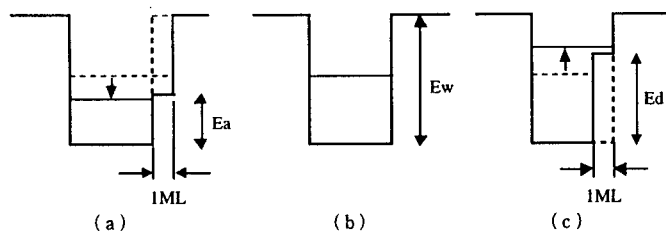


Fig. 4 The modeled potential profile for source-supply interruption (SSI) dependence. When the SSI is shorter than the optimal time, the effective well thickness is wider due to the transition layer, whose potential barrier is lower than that of InP, that forms at the InGaAs-to-InP interface ((a)). As the SSI gets longer, the potential barrier height increases. When the SSI is optimal, an abrupt interface is obtained ((b)). When the SSI becomes longer than the optimal time, the transition layer reforms due to the desorption of As atoms from the InGaAs surface ((c)).

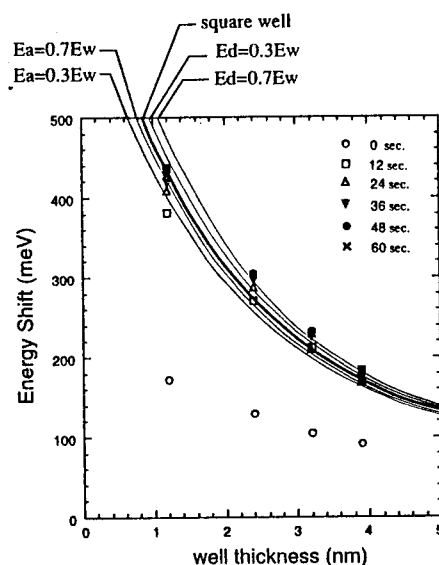


Fig. 5 The results of theoretical calculations taking into account interface roughness. The thick line represent results calculated using an envelope function approximation for finite wells (Fig. 4(b)). The thin lines lying below the thick line represent the calculated results for the case of Fig. 4(a). The thin lines lying above the thick line represent the calculated results for the case of Fig. 4(c)

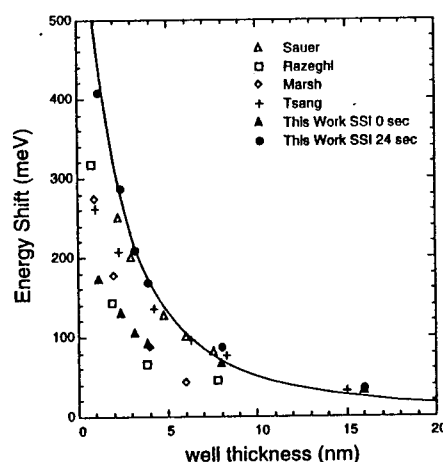


Fig. 6 The comparison of PL peak energy shifts of QWs grown with SSIs of 0 seconds and 24 seconds with other data. Other data are from Sauer *et al.* using MBE [10], Razeghi *et al.* using low pressure MOVPE [12], Marsh *et al.* using MBE [13], and Tsang and Schubert using CBE [11].

The PL full width of half maximum (FWHM) results for our quantum wells are shown in Fig. 7 along with results obtained by Tsang and Schubert [11]. For thin wells, our measured FWHM is wider than that of Tsang and Schubert, who reported the narrowest of the published PL FWHM for InGaAs QWs. However, as discussed above, the energy shift data from Tsang lies lower than ours. We calibrated the QW thickness reported by Tsang and Schubert so as to give the same energy up-shift as our data, and their calibrated data are also plotted in Fig. 7. It is clear that the our data lie below the calibrated data of Tsang and Schubert. To our knowledge, this is the narrowest PL FWHM for InGaAs QWs yet reported.

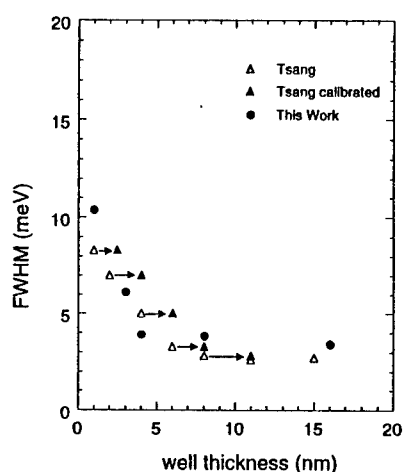


Fig. 7 The PL half-widths for InGaAs QWs grown with SSIs of 0 seconds and 24 seconds as a function of well width. The data from Tsang and Schubert is also shown. Closed triangles represents calibrated data of Tsang and Schubert.

4. SUMMARY

To investigate the effects of source-supply interruption (SSI) on InGaAs-to-InP heterointerface abruptness in GSMBE growth, 4.2 K PL analysis of InGaAs/InP QWs with well thickness ranging from 1 to 16 nm is performed. The results are compared with theoretical calculations in which the existence of In(Ga)AsP transition layers at the InGaAs-to-InP interface are assumed. The observed PL peak energy shifts toward a higher energy as the SSI becomes longer. For the QWs grown with SSIs ranging from 12 seconds to 60 seconds, this tendency can be explained by the simple assumption that a transition layer at the InGaAs-to-InP interface changes with changes in the SSI. However the PL peak energy for the QWs grown without SSI cannot be explained by this model. This is probably due to the disorder of the heterointerface. The calculated peak energy for QWs with no transition layer agrees fairly well with the experimental results for QWs

grown under optimized SSI. Our PL FWHM are narrower than any other yet reported.

References

- [1] D. Grutzmacher, J. Hergeth, F. Reinhardt, K. Wolter, and P. Balk, *J. Electron. Mater.* **19**, 471 (1990).
- [2] G. Landgren, J. Wsallin, and S. Pellegrino, *J. Electron. Mater.* **21**, 105 (1992).
- [3] C. Rigo, A. Antolini, C. Cacciato, C. Coriasco, L. Lazzarini, and G. Salviati, *J. Cryst. Growth* **136** (1994).
- [4] A. M. Moy, A. C. Chen, S. L. Jackson, X. Liu, K. Y. Cheng, G. E. Stillman, and S. G. Bishop, *J. Vac. Sci. Technol.* **B11**, 826 (1993).
- [5] T. Mozume, H. Kashima, K. Hosomito, K. Ouchi, H. Masuda, T. Tanoue, and I. Ohobu, to be published in *J. Vac. Sci. Technol.*
- [6] T. Mozume, H. Kashima, K. Hosomi, K. Ogata, K. Suenaga, and A. Nakano, *Appl. Surf. Sci.* **75**, 233 (1994).
- [7] T. Mozume, H. Kashima, K. Hosomi, K. Ouchi, H. Sato, H. Masuda, and T. Tanoue, *Eighth International Conference on Molecular Beam Epitaxy*, p224
- [8] T. Mozume, H. Kashima, K. Hosomi, K. Ouchi, H. Sato, H. Masuda, and T. Tanoue, to be published in *J. Cryst. Growth*.
- [9] K. Alavi, T. R. Pearsall, S. R. Forrest, and A.Y. Cho, *Electron. Lett.* **19**, 227, (1983).
- [10] R. Sauer, T. D. Harris, and W. T. Tsang, *Phys. Rev. B* **34**, 9023 (1986).
- [11] W. T. Tsang and E. F. Schubert, *Appl. Phys. Lett.* **49**, 220 (1986).
- [12] M. Razeghi, J. P. Hirtz, U. O. Ziemelis, C. Delalande, B. Etienne, and M. Voos, *Appl. Phys. Lett.* **43**, 585 (1983).
- [13] J. H. Marsh, J. S. Roberts, and P. A. Claxton, *Appl. Phys. Lett.* **46**, 1161 (1985).

W. T. Tsang and J. D. Walker
AT&T Bell Laboratories
600 Mountain Ave., Murray Hill, NY 07974

Introduction

We present semi-insulating iron-doped InP grown by chemical beam epitaxy using the gaseous iron $\text{Fe}(\text{CO})_5$. SIMS analysis shows that iron incorporation is proportional to the $\text{Fe}(\text{CO})_5$ flow rate over the $5 \times 10^{17} - 5 \times 10^{19} \text{ cm}^{-3}$ range studied. Use of $\text{Fe}(\text{CO})_5$ as an iron source also leads to high $\sim 10^{18} \text{ cm}^{-3}$ carbon incorporation in the material, but this does not interfere with semi-insulating behavior. The material shows $30 \text{ M}\Omega\text{-cm}$ resistivity for a broad range of $\text{Fe}(\text{CO})_5$ flow rates.

The growth of semi-insulating InP thin films is of interest for current blocking layers in device applications such as high speed laser diodes and field effect transistors. Semi-insulating InP material has been prepared by doping with transition metals such as iron in metal-organic vapor deposition (MOCVD),¹ chemical-beam epitaxy (CBE),² and gas-source molecular beam epitaxy (GSMBE).³ The previous MOCVD work used the gaseous iron sources $\text{Fe}(\text{C}_5\text{H}_5)_2$ and $\text{Fe}(\text{CO})_5$, while previous CBE and GSMBE work used solid iron sources. Here, we report Fe-doped semi-insulating InP prepared by CBE with the gaseous iron source $\text{Fe}(\text{CO})_5$. The Fe-doped InP samples used in this study were grown by CBE. All samples were grown at $2.5 \mu\text{m/hr}$, and at a substrate temperature of 540°C . The $\text{Fe}(\text{CO})_5$ is used in a bubbler at 25°C and H_2 as a carrier gas.

SIMS analysis shows that the incorporation of iron is roughly linear with $\text{Fe}(\text{CO})_5$ flow rate over the $5 \times 10^{17} - 5 \times 10^{19} \text{ cm}^{-3}$ range that was studied. Compared with MOCVD, the solubility limit of iron on CBE is expected to be higher because of the $\sim 100^\circ\text{C}$ lower growth temperatures. Use of $\text{Fe}(\text{CO})_5$ as an iron source also leads to unintentional carbon incorporation in the material, but because of the very low electrical activation of C ($\sim 5 - 15\%$) in InP this does not interfere with semi-insulating behavior. This is shown by the SIMS analysis in Fig. 1. The unintentional oxygen doping was below the background level of the SIMS system ($2 \times 10^{16} \text{ cm}^{-3}$).

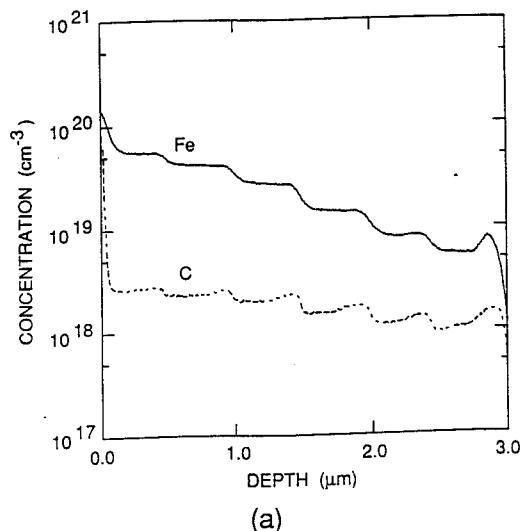
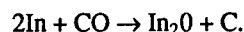


Fig. 1. SIMS depth profile showing Fe and C incorporation in InP, the six steps in concentration correspond to $\text{Fe}(\text{CO})_5$ flow rates of 0.2, 0.4, 0.8, 1.6, 2.4 and 3.2 SCCM .

The incorporation of carbon may result when CO disassociated from the $\text{Fe}(\text{CO})_5$ reacts with indium adatoms by the reaction:



This would produce In_2O molecules that may desorb from the surface of free C atoms that can then be incorporated in the growing crystal. A similar reaction was suggested for carbon incorporation in GaAs from background CO in an MBE chamber. The low unintentional oxygen doping of the material implies that In_2O from the above reaction does desorb and is not incorporated in the material. The implications of high carbon doping in these samples is discussed later.

The resistivity of the Fe-doped InP was determined by making I-V measurements on etched n-i-n posts, where the 'i' layer ($2 \mu\text{m}$) was

doped with iron. The mesa were 240 μm in diameter and were etched through the iron doped layers. A calibration sample without the iron-doped layer had a resistance of 0.6 Ω . The I-V curve for a sample grown with 0.4 sccm estimated concentrated $\text{Fe}(\text{CO})_5$ flow) $\text{Fe}(\text{CO})_5$ (Fe concentration of $5 \times 10^{18} \text{cm}^{-3}$) is shown in Fig 2. This sample has a resistivity of 43 $\text{M}\Omega\text{-cm}$ below 1 V applied bias. A series of these samples with different $\text{Fe}(\text{CO})_5$ flow rates was grown and the results are summarized in Fig. 3. The resistivity is roughly 30 $\text{M}\Omega\text{-cm}$ independent of $\text{Fe}(\text{CO})_5$ flow rate over the 0.05 - 1.6 sccm range used for these measurements. This value of resistivity is near the intrinsic limit of InP at room temperature. The resistance of the 0.05 sccm $\text{Fe}(\text{CO})_5$ sample (Fe concentration of $4 \times 10^{17} \text{cm}^{-3}$) is 15 $\Omega\text{-cm}$, about half that of the other samples. This indicates that 0.05 sccm is approaching the lower limit of semi-insulating behavior for our CBE system.

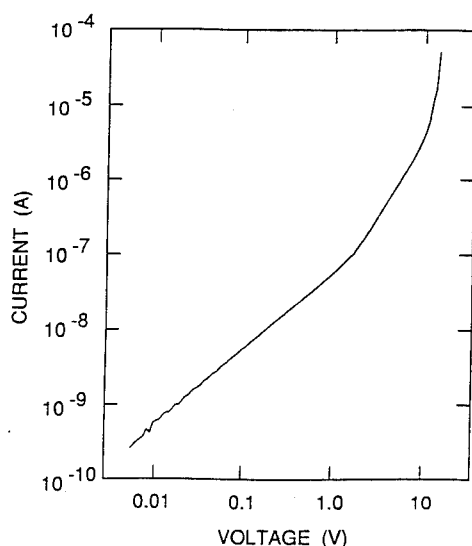


Fig. 2. I-V curve for a 240 μm diameter n-i-n mesa structure with a 2 m 'i' region doped Fe = $5 \times 10^{18} \text{cm}^{-3}$.

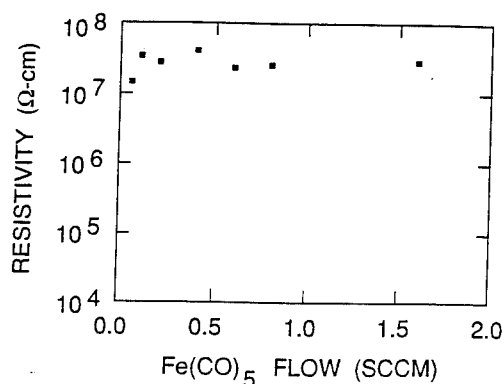


Fig. 3. Measured resistivity of Fe doped InP as a function of $\text{Fe}(\text{CO})_5$ flow rate.

In conclusion, semi-insulating InP has been grown by CBE using the gaseous iron source $\text{Fe}(\text{CO})_5$. The iron incorporation in the InP was found to be proportional to the $\text{Fe}(\text{CO})_5$ flow rate over the $5 \times 10^{17} - 5 \times 10^{19} \text{cm}^{-3}$ range studied. SIMS analysis indicates that the use of $\text{Fe}(\text{CO})_5$ results in significant carbon incorporation, but no oxygen incorporation. Because of the limited electrical activity of carbon in InP, the carbon does not prevent semi-insulating behavior. Resistivities near 30 $\text{M}\Omega\text{-cm}$ were observed for a broad range of $\text{Fe}(\text{CO})_5$ flow rates.

References

1. J. A. Long, V. G. Riggs and W. D. Johnston, Jr., *J. Cryst. Growth* **69**, 10 (1984).
2. W. T. Tsang, A. S. Sudbo, L. Yang, R. Camarda, and R. E. Leibenguth, "*Appl. Phys. Lett.*" **54**, 2236 (1989).
3. M. Lambert, L. Goldstein, A. Perales, F. Gaborit, C. Starck and J. L. Lievin, *J. Cryst. Growth* **111**, 495 (1991).

R. R. LaPierre, T. Okada, B. J. Robinson, D. A. Thompson, and G. C. Weatherly

Centre for Electrophotonic Materials and Devices
McMaster University, Hamilton, Ontario, L8S 4M1

Introduction

A miscibility gap exists in the $\text{In}_{1-x}\text{Ga}_x\text{As}_y\text{P}_{1-y}/\text{InP}$ system resulting in spinodal-like decomposition of the alloy; that is, there exists a range of compositions and temperatures in which the solid solution is energetically unstable and decomposes into regions that are InAs- or GaP-rich. In the case of $\text{In}_{1-x}\text{Ga}_x\text{As}$, the alloy segregates into InAs- and GaAs-rich regions. A spinodal isotherm, that is, a locus of points (x and y) that separate the stable from the unstable regions at a given temperature, may be derived [1]. Fig. 1 shows the spinodal isotherm for InGaAsP at the nominal growth temperature of 450 °C used in these studies. Also shown are various isostrain (-1%, 0%, +1%) and isobandgap (0.75 to 1.35 eV) contours which lie within the spinodal isotherm for many compositions of interest in bandgap engineering. Hence, the decomposition, particularly of tensile strained layers which lie deep in the spinodal isotherm, has been found to impose limitations in various optoelectronic devices such as strain compensated laser structures [2]. The decomposition of InGaAsP layers grown by gas source molecular beam epitaxy on (100) InP substrates has therefore been studied over a wide alloy range with lattice mismatches of -0.5% (compression), 0% (lattice-matched), and +0.5% (tension). The data points labelled (a) to (i) in Fig. 1 indicate samples for which extensive analysis was performed by photoluminescence (PL) and transmission electron microscopy (TEM). In an effort to reduce the decomposition, the kinetics of the growth process were examined by varying the growth temperature, the total group V flux, and the substrate orientation.

Experimental Details

Epitaxial layers of InGaAsP were grown on (100) InP substrates using gas source molecular beam epitaxy (GSMBE) in which the group V constituents are supplied primarily in the form of As_2 and P_2 from the cracking of AsH_3 and PH_3 . The sample structure used in these studies consisted of a 500 Å InP buffer layer, a 1500 Å InGaAsP layer, and a 250 Å InP cap layer, all undoped. The $\text{In}_{1-x}\text{Ga}_x\text{As}_y\text{P}_{1-y}$ compositions, as shown in Fig. 1, were grown over a wide alloy range with lattice mismatches of -0.5% (compression), 0% (lattice-matched), and +0.5% (tension). Nominally, the growth rate was 1 $\mu\text{m/hr}$, the growth temperature was 450 °C, and the total group V flux was 5 sccm. The kinetics of the decomposition were examined by varying the growth temperature, the group V fluxes, and the substrate orientation as described later.

After growth the epitaxial layers were characterized by TEM, PL, and X-ray diffraction (XRD). An XRD spectrum of each sample was measured at room temperature using a symmetric (400) diffraction condition. Front surface PL excitation was provided by the 488 nm line of a 20 mW cw Ar ion laser. The $\text{In}_{1-x}\text{Ga}_x\text{As}_y\text{P}_{1-y}$ compositions were then established by combining XRD measurements of lattice mismatch and PL bandgap determinations [3].

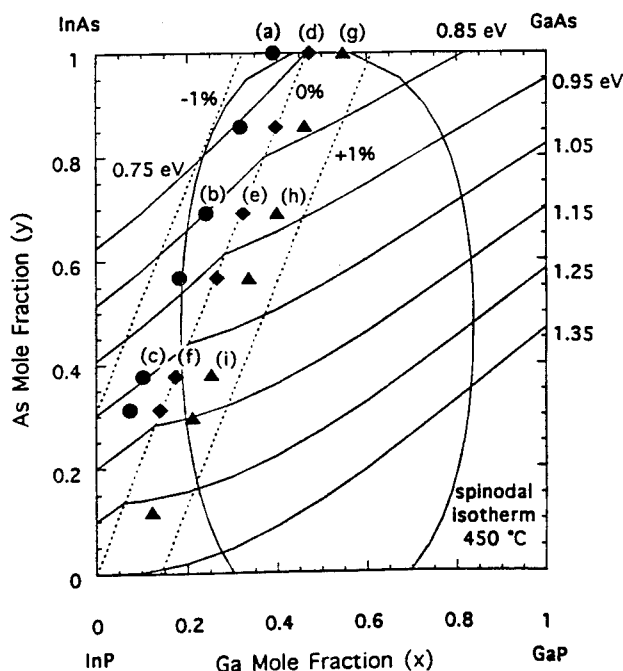


Fig. 1. x - y plane showing isostrain, isobandgap, and spinodal isotherm curves. Data points indicate compositions grown in this work.

Cross-sectional samples for TEM were prepared by mechanical polishing and subsequent thinning by ion beam milling to achieve foil thicknesses of 1000 to 2000 Å for a 120 keV electron beam. Dark-field micrographs were obtained in the $[0\bar{1}1]$ direction using the diffraction vector $g = 022$.

Results and Discussion

Fig. 2 shows a series of dark-field $[0\bar{1}1]$ cross-sectional TEM micrographs with diffraction vector $g = 022$ for the -0.5% compressive (a, b, c) and +0.5% tensile (g, h, i) samples labelled in Fig. 1. The lattice-matched results have been reported elsewhere [4]. The strong contrast modulations are due to elastic relaxation of (022) lattice planes at the free surface of the sample foil such that the electrons do not locally satisfy the Bragg condition. Larger contrast differences between the bright and dark regions are clearly observed for samples grown deeper within the spinodal isotherm of Fig. 1. The size of the compositionally differentiated regions were on average about 100 Å in the $[011]$ direction and 700 Å in the $[100]$ growth direction. From earlier work [4] on lattice-matched samples the size of the compositionally differentiated regions in the $[0\bar{1}1]$ direction were shown to be about 1000 Å.

Fig. 3(a) shows the full width at half maximum (FWHM) of the X-ray layer peaks as a function of nominal composition (As content, y) for the compressive and tensile samples indicated in Fig. 1. Fig. 3(b) shows the X-ray layer peak intensity, normalized with respect to the corresponding substrate peak intensity, as a function of nominal composition. The FWHM of the X-ray layer peaks are significantly broadened, and the normalized layer peak intensities significantly reduced, for tensile layers grown deeper within the spinodal isotherm. The X-ray results can be understood in terms of the variations in lattice constant produced by the InAs- and GaP-rich regions of the decomposed structure.

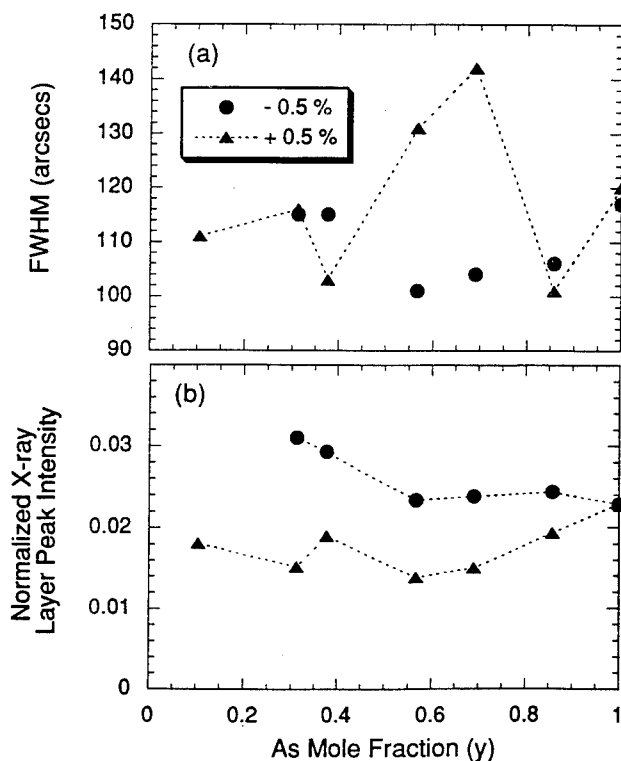


Fig. 3. X-ray FWHM (a) and peak intensity (b) versus composition.

Figs. 4(a) and (b) show the distribution of PL linewidths (FWHM) and integrated PL intensities, respectively, for the low temperature (11 K) and room temperature (300 K) front surface PL spectra of all the samples indicated in Fig. 1. The dashed lines in Fig. 4(a) show the theoretical linewidth for band-to-band transitions in a random InGaAsP alloy, due to thermal and alloy broadening [5].

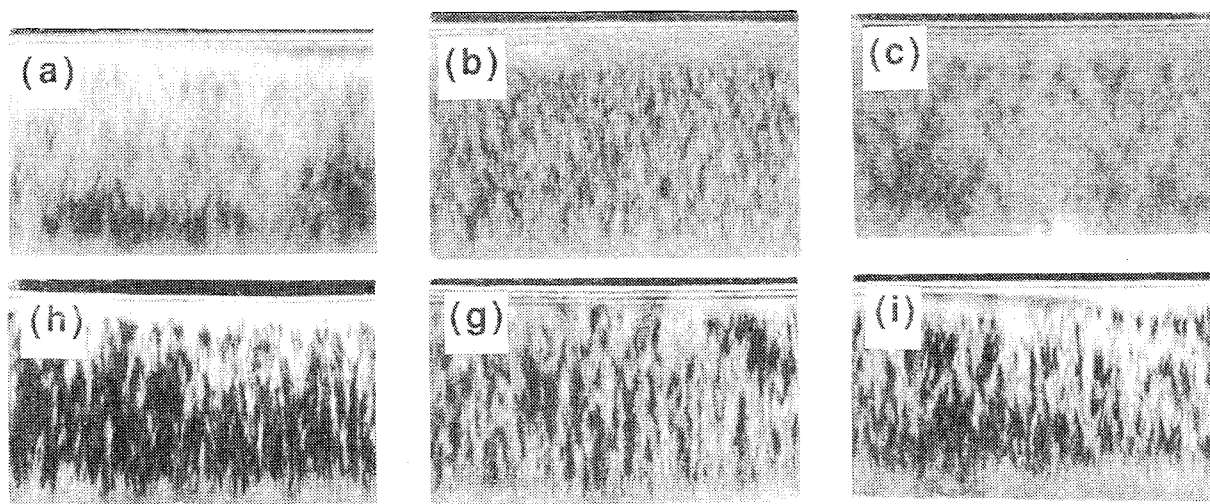


Fig. 2. TEM micrographs along the $[0\bar{1}1]$ direction, using $g = 022$, for the InGaAsP/(100) InP layers as indicated in Fig. 1.

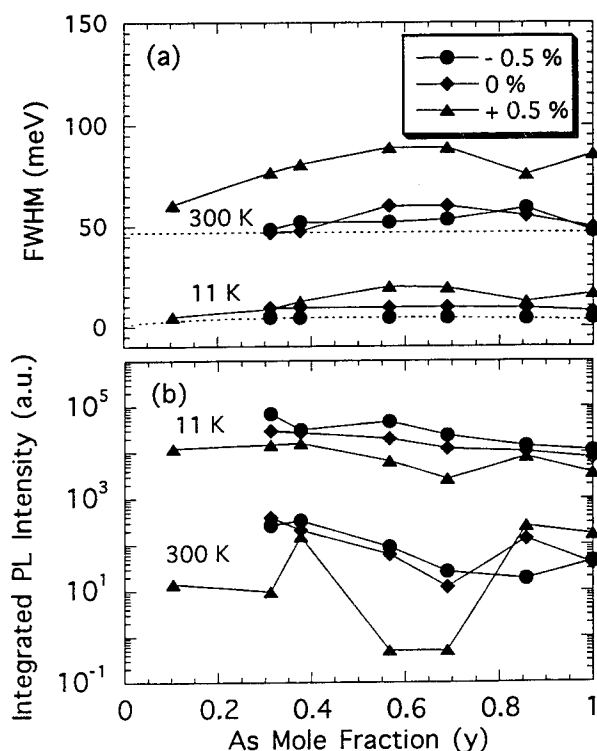


Fig. 4. PL FWHM (a) and integrated intensity (b) versus composition for room temperature (300 K) and low temperature (11 K).

Tensile samples which are grown deeper within the spinodal isotherm have PL linewidths that are much larger than the theoretical broadening and integrated PL peak intensities that are drastically reduced particularly at room temperature. A comparison of the PL results and the TEM analysis shows that increased composition modulation coincides with the PL linewidth broadening and reduction of integrated PL intensity. The decomposition is expected to cause PL linewidth broadening because the composition of the alloy is inhomogeneous over dimensions less than the incident laser beam spot size. The broadening of the PL peaks then suggests a variation in bandgap attributed to a variation in composition caused by the decomposition. Composition modulations also apparently increase non-radiative recombinations, thereby reducing the integrated PL intensity, although the exact nature of the non-radiative mechanisms is unknown at the present time.

PL provides a measure of the compositional variation if the temperature dependence of the peak energy is measured. For example, PL spectra at various temperatures are shown in Fig. 5 for the lattice-matched samples labelled (d), (e), and (f) in Fig. 1. The spectra have been normalized to unity in order to more easily compare differences among the three samples, although one should bear in mind the variations in PL intensity evident in Fig. 4(b). The lattice-

matched samples, (d) and (f), which showed relatively little decomposition in the TEM micrographs [4], exhibit a variation in peak energy and linewidth that is indicative of fairly homogeneous material. The temperature dependence of the bandgap, taken as the PL peak energy, can be described by the Varshni equation with the same parameters as used for InP [6]. Three distinct PL peaks, however, are seen for sample (e) which is grown deeper inside the spinodal isotherm. These peaks have previously been shown to be due to electron-hole recombination in InAs-rich regions (peak 1), regions of nominal composition (peak 2), and GaP-rich regions (peak 3) [4]. Because the composition modulation is much smaller than the carrier diffusion length ($\sim 1 \mu\text{m}$), the carriers become trapped after diffusing into the smaller bandgap InAs-rich regions at low temperatures. This results in a decomposition-induced red-shift of the PL emission compared to that expected for the average composition. As the temperature is increased, the carriers acquire enough energy to diffuse out of the InAs-rich regions, and carrier recombination in the nominal and GaP-rich regions contribute to the PL spectra. Assuming the decomposition occurs toward InAs and GaP, as suggested by theoretical predictions and experimental observations, compositional fluctuations as high as 2.3% in group III and V components have been derived for sample (e) [4].

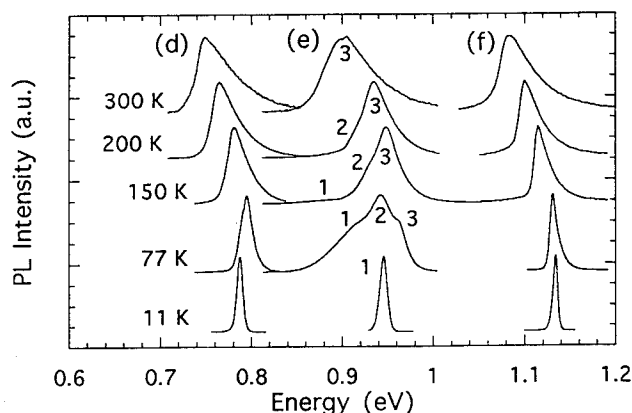


Fig. 5. PL at various temperatures for the lattice-matched samples labelled (d) to (f) in Fig. 1.

To study the effect of growth temperature on the spinodal-like decomposition, lattice-matched 3000 Å thick InGaAsP/(100) InP layers were grown at temperatures of 450, 470, and 490 °C with a total group V flux of 5 sccm to have a composition that would produce a room temperature bandgap wavelength of about 1.5 μm . Similarly, the effect of the total group V flux was examined by growing InGaAsP layers with a room temperature bandgap wavelength near 1.3 μm at a growth temperature of 470 °C but with group V fluxes of 3.75, 5, and 7 sccm. These gas flows correspond to V/III flux ratios of approximately 2, 3, and 4, respectively, at a growth rate of 1 $\mu\text{m/hr}$. As summarized in Table 1, increased growth temperature and

decreased group V flux resulted in: (i) increased PL linewidth broadening and reduction of integrated PL intensity; (ii) significant broadening and reduction in intensity of X-ray layer peaks; (iii) a larger red-shift of the low temperature PL peak energy due to recombination in the smaller bandgap InAs-rich regions, and (iv) a larger blue-shift of the room temperature PL peak energy due to recombination in the larger bandgap GaP-rich regions. The effects of (iii) and (iv) resulted in a smaller bandgap difference, $E_g(11\text{ K}) - E_g(300\text{ K})$, than the value of 67 meV expected from the Varshni equation [6]. These results are consistent with greater decomposition as growth temperature is increased or as group V flux is decreased, as confirmed by TEM analysis [4].

From thermodynamic considerations [1] spinodal decomposition is expected not to occur for sufficiently high growth temperature. InGaAsP layers grown by liquid phase epitaxy, for example, may reveal no spinodal decomposition if the growth temperature is above the critical temperature of $\sim 680^\circ\text{C}$, beyond which no decomposition should occur. However, for GSMBE growth it appears that kinetic limitations, whereby the surface adatom diffusion lengths are reduced via decreased growth temperature or increased group V overpressure, limit the ability of the system to achieve equilibrium resulting in less decomposition.

Other studies [7], involving TEM, PL, and X-ray diffraction measurements, have been used to characterize the decomposition of lattice-matched InGaAsP layers grown on (211)A and B and (311)A and B InP substrates. The decomposition was observed to be inhibited by enhanced group V incorporation on the double dangling group III bonds of B surfaces compared to the single dangling group III bonds of A surfaces. Although not presently understood, the decomposition was also observed to be less on (311)-oriented surfaces compared to (211)-oriented surfaces. Hence, (311)B layers showed the least decomposition compared to the other orientations, including (100).

Table 1. PL and X-ray diffraction results for the temperature- and flux-dependent studies.

Bandgap Wavelength (μm)	≈ 1.5			≈ 1.3		
Growth Temperature ($^\circ\text{C}$)	450	470	490	470	470	470
Total Group V Flux (sccm)	5	5	5	3.75	5	7
PL FWHM (meV)						
11 K	10	14	36	82	32	11
300 K	50	59	82	71	66	56
Integrated PL Intensity (a.u.)						
11 K	10300	8050	1750	1100	2470	7150
300 K	155	65	12	55	77	215
$E_g(11\text{ K}) - E_g(300\text{ K})$ (meV)	43	30	-27	-15	23	46
X-ray FWHM (arcsec)	*	6.7	128	6.2	6.1	5.5
X-ray Intensity (a.u.)	*	0.053	0.025	0.070	0.074	0.105

* overlapping peaks - unreliable value

Conclusions

TEM, PL, and XRD have been used to characterize GSMBE grown $\text{In}_{1-x}\text{Ga}_x\text{As}_y\text{P}_{1-y}/\text{InP}$ layers in terms of a spinodal-like decomposition. Because tensile layers lie deeper within the spinodal isotherm, they were observed to have far more decomposition than lattice-matched or compressively strained layers. Reducing growth temperature, increasing group V overpressure, and the use of (311)B oriented substrates were found to reduce the decomposition in lattice-matched layers indicating the role of surface kinetics in limiting the decomposition. These same efforts are expected to improve the quality of tensile strained layers to facilitate their incorporation in various strained layer structures.

Acknowledgements

This work was funded by the Natural Sciences and Engineering Research Council of Canada and the Ontario Centre for Materials Research. Scott McMaster's assistance with the GSMBE growths is gratefully acknowledged.

References

1. K. Onabe, Jpn. J. Appl. Phys. **21** (1982) 797.
2. A. Ponchet, A. Rocher, J. Y. Emery, C. Starck, L. Goldstein, Indium Phosphide and Related Materials Conference, p. 183 (1994).
3. A. T. Macrander and S. Lau, J. Electrochem. Soc. **138** (1991) 1147.
4. R. R. LaPierre, T. Okada, B. J. Robinson, D. A. Thompson, and G. C. Weatherly, J. Cryst. Growth, submitted (1995).
5. R. Benzaquen, S. Charbonneau, N. Sawadsky, A. P. Roth, L. Hobbs, and G. Knight, J. Appl. Phys. **49**, 5944 (1978).
6. Y. P. Varshni, Physica A **34** (1967) 149.
7. R. R. LaPierre, B. J. Robinson, A. Gupta, D. A. Thompson, and G.C. Weatherly, to be submitted, Surf. Sci.

The Incorporation Behavior of As and P in GaInAsP ($\lambda \approx 1.3 \mu m$) on InP Grown by Gas Source Molecular Beam Epitaxy

Tsuen-Lin Lee, Jin-Shung Liu, and Hao-Hsiung Lin
Room 419, Department of Electrical Engineering,
National Taiwan University,
Taipei, Taiwan, R. O. C.

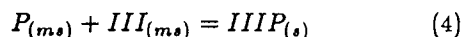
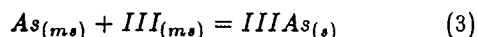
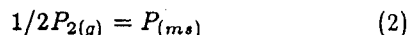
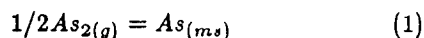
Introduction

$Ga_xIn_{1-x}As_yP_{1-y}$ quaternary alloys on InP are very important for optoelectronic device applications, and have been investigated by molecular beam epitaxy (MBE) techniques (1-7). Because of the complicated sticking behavior of As and P, to understand the incorporation behavior of these two group V elements is a necessary step to precise composition control. Several groups (8-16) have studied this complicated phenomenon. Most of them considered the chemical reactions on the growing surface, and thus introduced many reaction parameters such as the activation energies for chemisorption and desorption, thermo-equilibrium constants etc. These parameters should be determined either by other experiments or by curve fitting to the experimental results, mathematically.

In this report, a series of $Ga_xIn_{1-x}As_yP_{1-y}$ quaternary alloys ($\lambda \approx 1.3 \mu m$) on (100) InP were grown by gas source MBE (GSMBE) with different gas flow rate ratios ($PH_3/(PH_3 + AsH_3)$). A simple growth model, was proposed to describe the group V incorporation behavior quantitatively. Without the complicated chemical reaction parameters, the incorporation probability is controlled by the effective concentrations of the group V atoms on the migration state. Only two parameters, As to P incorporation ratio and the conversion factor between the gas flux rate and the gas flow rate, exist in this model. Furthermore, this model can be expanded to the whole range of alloy compositions by adjusting the incorporation ratio only. It is found that the incorporation ratio strongly depends on the Ga-compositions in $Ga_xIn_{1-x}As_yP_{1-y}$ alloys.

Growth Model

Figure 1 is the schematic representation of the growth model for the interaction of group III atoms and group V atoms on the growing surface. Consider the group V monolayer, the incident group V atoms can adsorb on the growing surface to form a migration state. And then, these group V atoms can either incorporate into the crystal or desorb away from the growing surface. Consider the chemical reactions on the growing surface:



where ms represents the atoms on the migration state; III is group III atom on the migration state, either In or Ga. The reaction rates for the chemical reactions, Eq.(3) and (4), are:

$$e_{As} = k_{As} N_{As} N_3 \quad (5)$$

$$e_P = k_P N_P N_3 \quad (6)$$

where N_3 , N_{As} , and N_P are the concentrations of group III, As, and P atoms on the migration state, respectively, and k_i is the reaction constant of gas source i on the migration state; $i = As$, or P .

Growth Model

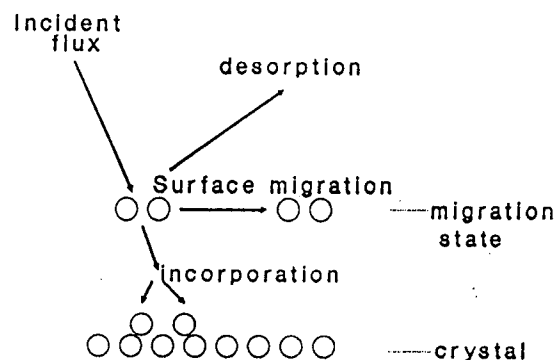


Fig. 1 The schematic representation of the growth model for the interaction of group III atoms and group V atoms on the growing surface.

In addition, mathematically, the rate equations of the atoms on the migration state can be expressed as follows:

$$\frac{\partial N_{As}}{\partial t} = \frac{f_{As}}{m} - e_{As} - d_{As} \quad (7)$$

$$\frac{\partial N_P}{\partial t} = \frac{f_P}{m} - e_P - d_P \quad (8)$$

$$\frac{\partial N_3}{\partial t} = f_3 - e_{As} - e_P \quad (9)$$

where f_i is the flow rate of gas source i , $i = As$ or P ; d_i is the desorption rate of gas source i , $i = As$ or P on the migration state; f_3 is the total flux rate of group III atoms; and m is the flux rate to flow rate conversion factor. The units of the flux rates, desorption rates and the flow rates are ML/sec, ML/sec and SCCM, respectively.

Under steady state conditions, the rate equations are equal to zero. We obtain

$$N_3 = \frac{f_3}{k_{As}N_{As} + k_P N_P} \quad (10)$$

$$e_{As} = \frac{k_{As}N_{As}}{k_{As}N_{As} + k_P N_P} \times f_3 \quad (11)$$

$$e_P = \frac{k_P N_P}{k_{As}N_{As} + k_P N_P} \times f_3 \quad (12)$$

The desorption rate can be written as the migration state density divided by the life time:

$$d_{As} = \frac{N_{As}}{\tau_{As}} \quad (13)$$

$$d_P = \frac{N_P}{\tau_P} \quad (14)$$

where τ_i is the life time of gas source i . Substituting Eqs.(11), (12), (13) and (14) to Eqs.(7) and (8), we obtain

$$\frac{\partial N_{As}}{\partial t} = \frac{f_{As}}{m} - \frac{k_{As}N_{As}}{k_{As}N_{As} + k_P N_P} \times f_3 - \frac{N_{As}}{\tau_{As}} \quad (15)$$

$$\frac{\partial N_P}{\partial t} = \frac{f_P}{m} - \frac{k_P N_P}{k_{As}N_{As} + k_P N_P} \times f_3 - \frac{N_P}{\tau_P} \quad (16)$$

If we assume $k_{As}/k_P = k_1$ and $\tau_{As}/\tau_P = k_2$, and let $k = k_1 \times k_2$, under steady state conditions, Eqs. (15) and (16) can be simplified as:

$$\frac{f_{As}}{m} - \frac{k d_{As}}{k d_{As} + d_P} \times f_3 - d_{As} = 0 \quad (17)$$

$$\frac{f_P}{m} - \frac{d_P}{k d_{As} + d_P} \times f_3 - d_P = 0 \quad (18)$$

Combining Equations (17) and (18), the solid composition ratio of P/As in $Ga_xIn_{1-x}As_yP_{1-y}$ can be solved, analytically:

$$\frac{1-y}{y} = \frac{2f_P}{k f_{As} - f_P - (k-1)f_3 m + \sqrt{4(k f_{As} - f_P - (k-1)f_3 m)^2 + 16k f_{As} f_P}} \quad (19)$$

It should be emphasized that there are only two parameters to be fitted: m and k . Once the m and k factors are determined, the solid compositions of $GaInAsP$ can be accurately controlled by adjusting the gas flow rate. Furthermore, this model can be extended to the whole range of $Ga_xIn_{1-x}As_yP_{1-y}$ quaternary alloys on InP substrate by only changing the

value of k . Remind that k factor describe the influences of the life time and the chemical reaction constant of As to P. So, k can be a good indicator for the incorporation ability of As to P. Moreover, because of the different activation energy for the group V atoms to desorb from $InAs$, $GaAs$, InP , and GaP surfaces (11), it is expected that the value of k will depend on the group III compositions in $Ga_xIn_{1-x}As_yP_{1-y}$.

Experiment

The $Ga_xIn_{1-x}As_yP_{1-y}$ quaternary alloys on (100) InP for the wavelength near $1.3\mu m$ were prepared by VG V80H gas source molecular beam epitaxy (GSMBE) machine equipped with a 400l/s diffusion pump. High purity AsH_3 and PH_3 , controlled by the pressure set-point of a Baratron capacitance manometer, was introduced through a high temperature cracking cell kept at $1000^\circ C$. As for the group III flux, a conventional beam equivalent pressure (BEP) ratio method was used to determine the In and Ga flux ratio. The growth rate was kept at $0.98 ML/sec$, which was measured by cross-section scanning electron microscopy (SEM). After growth, room temperature photoluminescence (PL), electron probe micro-analysis (EPMA) and single crystal x-ray (400) plane diffraction (XRD) were adopted for the determination of the solid compositions of these $Ga_xIn_{1-x}As_yP_{1-y}$ layers.

Results and Discussions

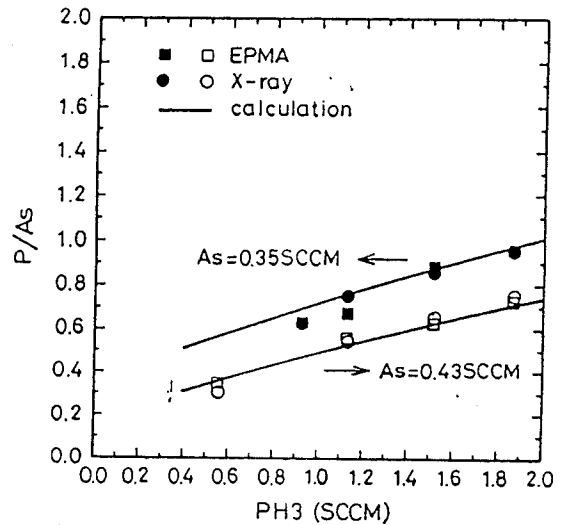


Fig. 2 The solid composition ratio of P/As as a function of the PH_3 flow rate at two different AsH_3 flow rates. Open and closed symbols correspond to AsH_3 flow rate of 0.43 and 0.35 SCCM, respectively. Square and circle symbols represent the results from EPMA and x-ray diffraction measurement, respectively.

Figure 2 shows the solid composition ratio of P/As as a function of the PH_3 flow rate at two different AsH_3 flow rates. Square and circle symbols represent the results obtained by EPMA and x-ray diffraction measurement, respectively. These two methods shows a good agreement with each other. As expected, the solid composition ratio P/As in $Ga_xIn_{1-x}As_yP_{1-y}$ increases as PH_3 flow rate increases, and the larger the AsH_3 flow rate, the smaller the solid composition ratio, P/As . Similar results can be seen in figure 3.

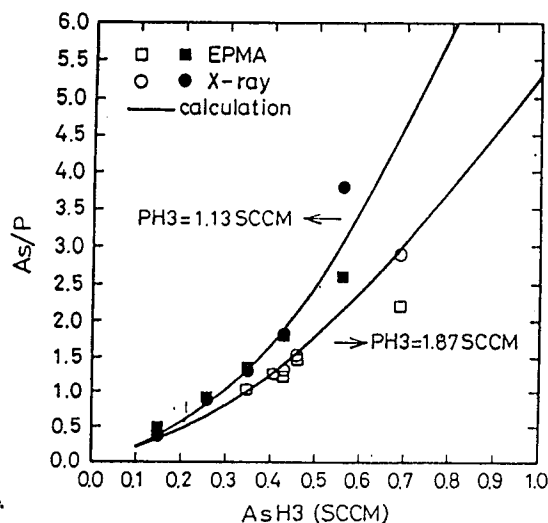


Fig. 3 The solid composition ratio of As/P in $GaInAsP$ as a function of AsH_3 flow rate at two different PH_3 flow rate. The PH_3 flow rates were 1.13 and 1.87 SCCM for closed and open symbols, respectively.

As for the model calculations, the unknown parameters, k and m , in Eq.(19) are determined by fitting the calculation composition ratios to the experimental results. It can be seen, the calculation curves in figure 2 and figure 3 show an excellent agreement with the experimental results. Fitting parameters m and k are 0.496 and 16, respectively. This means that in this GSMBE system, there needs 0.496 SCCM gas flow rate to support 1ML/sec growth rate on (100) InP substrate. Additionally, the k value of 16 implies that the incorporation ability of As atoms on the migration state is 16 times larger than that of P atoms.

Figure 4 shows the mole fraction of P in $Ga_xIn_{1-x}As_yP_{1-y}$ as a function of the gas flow rate ratio ($PH_3/(PH_3 + AsH_3)$). As we can see, it shows a good agreement with the experimental results. The P composition in $Ga_xIn_{1-x}As_yP_{1-y}$ depends on the gas flow rate ratio and V/III flux ratio, especially in the high gas flow rate ratio regions. It should be emphasized that the constraint of lattice matched to InP in ref. (16) is removed in our calculations. This implies that the lattice mismatch has only a little influence on the incorporation behavior of As and P on (100) InP.

Similar results has been reported by chemical beam epitaxy (CBE) technique (13).

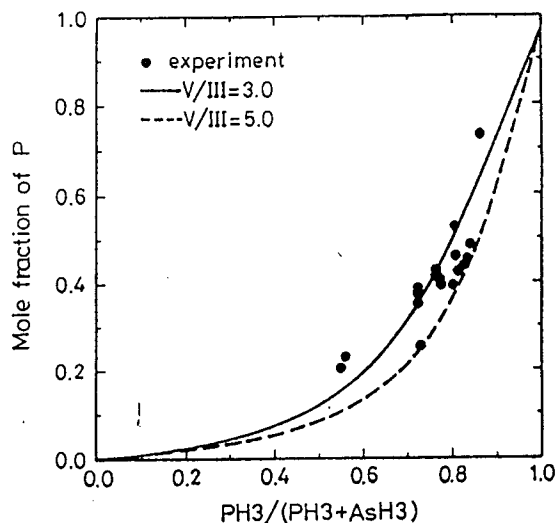


Fig. 4 The mole fraction of P in $Ga_xIn_{1-x}As_yP_{1-y}$ as a function of the gas flow rate ratio ($PH_3/(PH_3 + AsH_3)$). Solid and broken lines represent the calculations with V/III ratios of 3 and 5, respectively, by using the model.

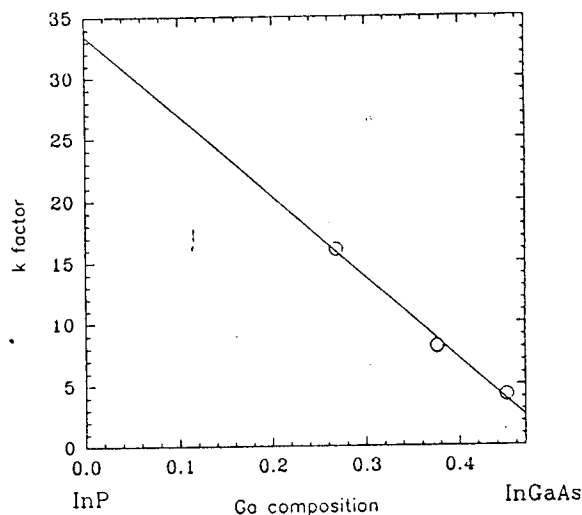


Fig. 5 The k factor as a function of group III compositions in $Ga_xIn_{1-x}As_yP_{1-y}$ at a growth temperature of 490°C.

Because of the different bonding energies of $InAs$, InP , $GaAs$, and GaP , it is expected that the k factor in this growth model will depend on the group III compositions. Figure 5 shows the Ga composition dependence of k factor in $Ga_xIn_{1-x}As_yP_{1-y}$ at a growth temperature of 490°C. As can be seen, the k value strongly depends on the Ga compositions. Using the

linearly approximative line, we can see that the k value can be as large as 33.5 in the near InP regions. This explains why the fast replacement of phosphorus by arsenic occurs at the InP surface when PH_3 is switched off and AsH_3 is switched on, and thus the $InAs_xP_{1-x}$ quantum well can be formed (17). B. W. Liang et al. (11) also observed that for the In -contamination compounds, phosphorus desorption rate constant is always much higher than that of arsenic. In addition, this result also implies that the mixed-group-V composition control in the low Ga composition regions becomes more and more difficult. A small AsH_3 flow rate variation would result in a large As composition change.

Conclusions

A growth model has been proposed to explain the incorporation behavior of As and P in $GaInAsP$ quaternary alloys on (100) InP . According to this model, it is found that the incorporation ability indicator, k , depends on the Ga -compositions in $Ga_xIn_{1-x}As_yP_{1-y}$ alloys. For the $\lambda \approx 1.3 \mu m$ materials the k value is about 16 at the growth temperature of $490^\circ C$. Additionally, the incorporation behavior of As and P on (100) InP mainly depends on the gas flow rate ratio as well as V/III flux ratio, especially in the high gas flow rate ratio regions; the influence of lattice mismatch is negligible at the growth temperature of $490^\circ C$. This model can provide a very useful guide for the epitaxial growth of $Ga_xIn_{1-x}As_yP_{1-y}$ quaternary alloys on InP substrate by GSMBE.

Acknowledgement

This study was supported by the National Science Council of the Republic of China under contract No. NSC-84-2215-E002-008, CSIST under contract No. CS84-0210-D002-028, and the Telecommunication laboratory of the Republic of China under contract No. TL-NSC-83-5104.

References

1. J. N. Baillargeon, A. Y. Cho, F. A. Thiel, R. J. Fischer, P. J. Pearah, and K. Y. Cheng, Appl. Phys. Lett. 65 (1994) 207.
2. M. B. Panish, and S. Sumski, J. Appl. Phys. 55 (1984) 3571.
3. K. Tappura, J. Appl. Phys. 74 (1993) 4565.
4. K. Tappura, and H. Asonen, J. Crystal Growth 127 (1993) 217.
5. H. Q. Hou, and C. W. Tu, J. Crystal Growth 120 (1992) 167.
6. P. Silvestre, M. J. Hafich, T. Vogt, A. Nanda, G. Y. Robinson, J. J. Dudley, J. E. Bowers, K. M. Jones, and M. M. Al-Jassim, J. Vac. Sci. Technol. B10, (1992) 956.
7. M. B. Panish, H. Temkin, and S. Sumski, J. Vac. Sci. Technol. B3 (1985) 657.
8. C. W. Tu, B. W. Liang, and H. Q. Hou, J. Crystal Growth 127 (1993) 251.
9. B. W. Liang, and C. W. Tu, J. Appl. Phys. 74 (1993) 255.
10. T. Nomura, H. Ogasawara, M. Miyao, and M. Hagino, J. Crystal Growth 111 (1991) 61.
11. B. W. Liang, and C. W. Tu, J. Crystal Growth 128 (1993) 538.
12. W. T. Tsang, E. F. Schubert, T. H. Chiu, J. E. Cunningham, E. G. Burkhardt, J. A. Ditzemberger, and E. Agyekum, Appl. Phys. Lett. 51 (1987) 761.
13. J. F. Carlin, A. Rudra, and M. Illegems, J. Crystal Growth 131 (1993) 387.
14. C. T. Foxon, B. A. Joyce, and M. T. Norris, J. Crystal Growth 49 (1980) 132.
15. Y. Matsushima, and S. I. Gonda, Japan. J. Appl. Phys. 15 (1976) 2093.
16. H. Seki, and A. Koukitu, J. Crystal Growth 78 (1986) 342.
17. J. Hergeth, D. Grutzmacher, F. Reinhardt, and P. Balk, J. Crystal Growth 107 (1991) 537.

Low temperature grown Be-doped InAlP band offset reduction layer to p-type ZnSe

K. Iwata, H. Asahi, T. Ogura, J. Sumino, S. Gonda, A. Ohki*, Y. Kawaguchi*, and T. Matsuoka*

The Institute of Scientific and Industrial Research, Osaka University, 8-1, Mihogaoka, Ibaraki, Osaka 567, Japan

*NTT Opto-electronics Labs., Morinosato Wakamiya, Atsugi, Kanagawa 243-01, Japan

To solve the difficulty of achieving low resistance ohmic contact to p-type ZnSe, the use of an intermediate p-type InAlP layer to p-type ZnSe as a valence band offset reduction layer is studied by gas source MBE (molecular beam epitaxy). It is found that the surface morphology of the $\text{In}_{0.5}\text{Al}_{0.5}\text{P}$ layers grown on (001) ZnSe becomes better as growth temperature is decreased. The further use of the group III-flux modulated growth method produces a better surface morphology. It is found that the hole concentrations as high as $2 \times 10^{18} \text{cm}^{-3}$ are easily obtained for p-type InAlP layers grown even at low temperature of 350°C , although a higher Be cell temperature is required than that for a 500°C grown p-type InAlP due to decreased electrical activity of Be in InAlP. Despite the very high Be concentrations, the Be precipitation/segregation is not observed. These results suggest that the Be-doped InAlP layer can be used as an intermediate layer to form the low resistance ohmic contact to p-type ZnSe.

1. Introduction

ZnSe-based II-VI blue-green laser diodes are gathering great interest [1]. However, one of the major problems at present is the difficulty to produce a low resistance ohmic contact to p-type ZnSe. High ohmic contact resistance is a consequence of the deep valence band to the metal electrodes. Au metal produces appreciable energy barriers ($\sim 1.6 \text{ eV}$) when it is deposited onto p-type ZnSe. Until now, attempts to form low resistance p-type ohmic contacts have been conducted by the use of HgSe layers [2] and ZnSeTe graded layers [3] as an intermediate layers between p-ZnSe and metal electrodes, and some improvements were obtained. To solve this problem we have proposed the use of p-type InAlP on p-type ZnSe in order to reduce the valence band offset [4]. Fig.1 shows the band lineup for the II-VI and III-V semiconductors including ZnSe, and the proposed heterostructures using p-InAlP as a valence band offset reduction layer. The valence band offset of the p-type InAlP / p-type ZnSe interface at zero bias is estimated to be as small as 0.43 eV in the case of lattice matched heterojunctions. Moreover, in lattice mismatched conditions, we can expect a decrease of the interfacial energy barrier down to 0.1 eV . Therefore, low resistance ohmic contacts can be expected by using p-type InAlP on p-type ZnSe.

In this paper we report the results on the InAlP growth on ZnSe and low temperature p-type doping in InAlP to form the InAlP band offset reduction layer on p-ZnSe.

2. Experimental procedure

The InAlP layers were grown using a gas source MBE system (ANELVA GBE830). The growth chamber was evacuated by an oil diffusion pump with a liquid nitrogen trap[6].

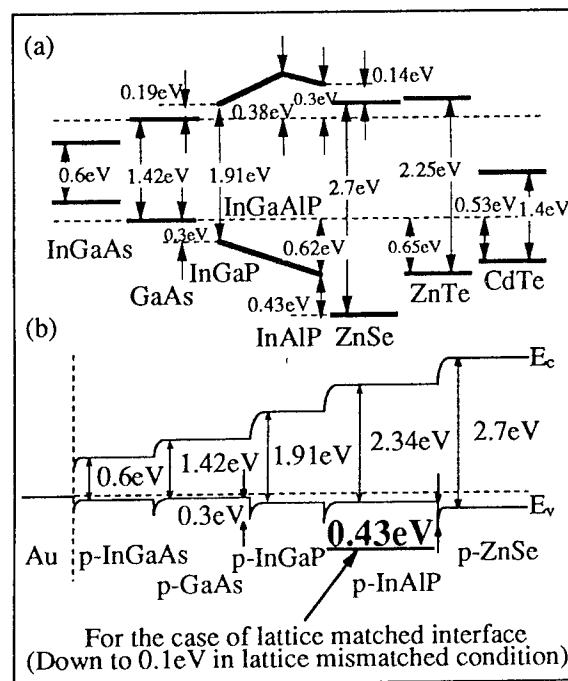


Fig.1. (a) Band lineup for the II-VI and III-V semiconductors, and (b) proposed heterostructures using p-InAlP as a valence band offset reduction layer to produce a low resistance ohmic contact to p-type ZnSe.

Elemental indium(In) and aluminum(Al), and thermally cracked PH_3 were used as group III and group V sources, respectively. The InAlP layers were deposited on the (001) ZnSe epitaxial layers grown on GaAs substrates and the Cr-doped semi-insulating (001) GaAs. The ZnSe layers

were grown by elemental source MBE using elemental Zn and Se as sources [7]. The surface of the ZnSe layer was chemically etched with a solution of saturated Br water : $\text{HBr} : \text{H}_2\text{O} = 1 : 5 : 10$ and was thermally cleaned at 300-350°C for 10min in the gas source MBE growth chamber just before the growth.

The InAlP layers were grown on ZnSe at 350-500°C, which was measured by an infrared optical pyrometer calibrated with the melting point of InSb (525°C). The growth rate was 0.65 $\mu\text{m}/\text{h}$ with a PH_3 flow rate of 1 SCCM. In and Al fluxes were at beam equivalent pressures of 2.2×10^{-8} and 1.4×10^{-7} Torr, respectively. The background pressure during growth was about 3×10^{-6} Torr.

Structural qualities were determined by surface morphology observations using SEM (scanning electron microscopy) and through RHEED (reflection high energy electron diffraction) patterns. $\text{In}_{0.5}\text{Al}_{0.5}\text{P}$ layers on ZnSe were characterized by double crystal X-ray (DCX) diffractometry using $\text{Cu K}\alpha_1$ radiation.

Beryllium was used as the p-type dopant. Be-doped InAlP layers were grown on the Cr-doped (001) GaAs substrates. The electrical properties of the Be-doped $\text{In}_{0.5}\text{Al}_{0.5}\text{P}$ epitaxial layers were determined by Hall measurements.

3. Results and discussions

3.1. $\text{In}_{0.5}\text{Al}_{0.5}\text{P}$ growth on ZnSe epitaxial layer

First of all, we grew undoped $\text{In}_{0.5}\text{Al}_{0.5}\text{P}$ layers on ZnSe layers and studied the RHEED pattern in situ. The RHEED pattern was taken with a $\langle 110 \rangle$ azimuth incidence. RHEED patterns for the ZnSe layer before the InAlP growth shows the clear streaks. However, the growth of InAlP on ZnSe was difficult in the normal growth condition (substrate temperature=500°C) of InAlP growth on GaAs. After the growth of 1-2 ML of InAlP, the streaks pattern failed and a mesh-like pattern appeared. The angle between the two lines of the mesh-like pattern is 109°. This angle is consistent with the angle (109.4°) between the normals of and facets. Therefore, the mesh-like pattern is attributed to the formation of and facets on the InAlP surface.[8]

To improve the surface morphology of InAlP grown on ZnSe, we studied the growth temperature dependence of the InAlP surface morphology. The growth temperature was ranged from 500 to 350°C. From the SEM observations (Fig.2), it was found that the lower the growth temperature at which we grow InAlP layers, the more we obtain good surface morphology. This is an important property in making a p-type electrode structure, because it was recently found that the carrier compensation was induced in the N-doped p-type ZnSe when annealed at above 400°C and consequently the hole concentration decreased. That is, to form the valence band offset reduction layer without deteriorating the electrical properties of the N-doped ZnSe, the growth temperature for the p-type InAlP layer must be lower than 400°C. The result observed in Fig.2 just meets this requirement.

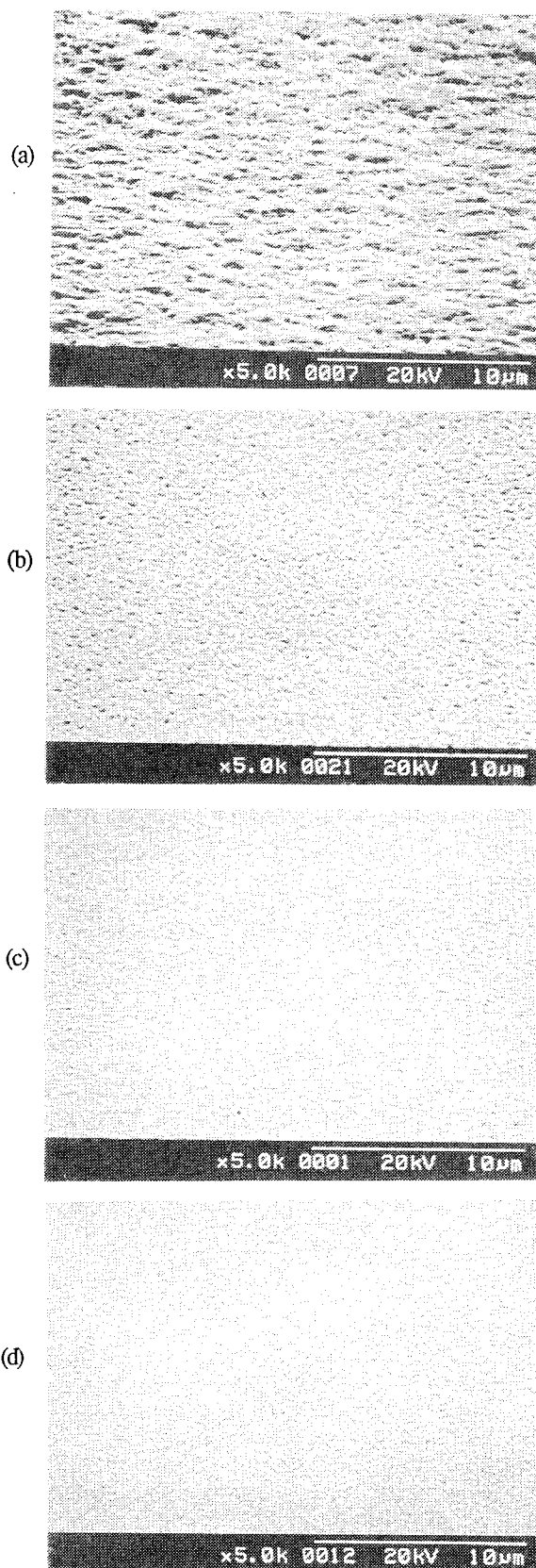


Fig.2 SEM pictures of InAlP layers grown on ZnSe at (a) 500°C, (b) 450°C, (c) 400°C and (d) 350°C.

Furthermore, we also found that the group III-flux modulated growth method applied to the first few MLs (monolayers) of InAlP further improved the surface morphology at 350°C, similar to the growth of GaAs on ZnSe [9]. This improvement is considered to be closely related to the low sticking coefficient of groupV atoms on ZnSe surfaces.

3.2. Be doping of InAlP at low temperatures

To avoid the carrier compensation in the N-doped p-type ZnSe layers during the growth of p-type InAlP band offset reduction layer, the growth temperature must be lower than 400°C. In Section 3.1, we found that the low temperature growth improved the surface morphology of InAlP on ZnSe. In this section, the results on the growth temperature dependence of the Be doping characteristics of InAlP layers is studied. Be doped InAlP layers were grown on the Cr-doped semi-insulating (001) GaAs substrates. The growth temperature was varied as 500, 400, 380 and 350°C.

Fig.3 shows the hole concentration dependence on the Be cell temperature as a function of growth temperature. For the 500°C grown samples, the hole concentration saturates at a value of about $2 \times 10^{18} \text{ cm}^{-3}$ as in other reports [10, 11]. Over the saturated concentrations, Be precipitation was observed in the SEM image. When the growth temperature is decreased, the hole concentration decreases for the same Be cell temperature, and therefore, for the same Be flux. However, by increasing the Be cell temperature, the hole concentration is increased. In the 350°C growth, a hole concentration of as high as $2 \times 10^{18} \text{ cm}^{-3}$ was obtained at the Be cell temperature that is 130°C higher than that in the 500°C growth (Be flux corresponding to $2 \times 10^{20} \text{ cm}^{-3}$ Be concentration in InAlP). Moreover, the surface morphology of these heavily Be-doped InAlP grown at low temperatures shows mirror-like smoothness with no trace of Be precipitates in spite of the very high Be flux.

The heavily Be doped InAlP layers grown on ZnSe layer at 350°C also shows a smooth surface morphology. These results imply that the low temperature grown and heavily Be-doped InAlP layers will be promising as a band offset reduction layer between N-doped p-type ZnSe cladding layers and metal electrodes in laser diode structures.

3.3. SIMS measurement of Be doped InAlP layers grown at low temperatures

It is noteworthy that even the very high Be flux does not produce the Be precipitation in the InAlP layers in the low substrate temperature growth. In order to make sure the reason why the Be cell temperature was required higher than that in the 500°C growth, the relation between hole concentration and Be contents in Be-doped InAlP layers was studied by SIMS (secondary ion mass spectroscopy) measurement. Fig.4 shows the measured relation between hole concentration and Be contents in Be-doped InAlP

layers. The Be concentration in the InAlP layer increases almost linearly with supplied Be flux. However, the hole concentration in the InAlP layer is saturated at the point of $2 \times 10^{18} \text{ cm}^{-3}$ and no increase is observed. These result suggest that the increase in the required Be flux for the low temperature growth is not due to the reduction of Be incorporation but due to the reduction of the electrical activity. The reason for the no observation of the Be precipitation/segregation for the very high Be concentrations in the low temperature growth is not clear at present.

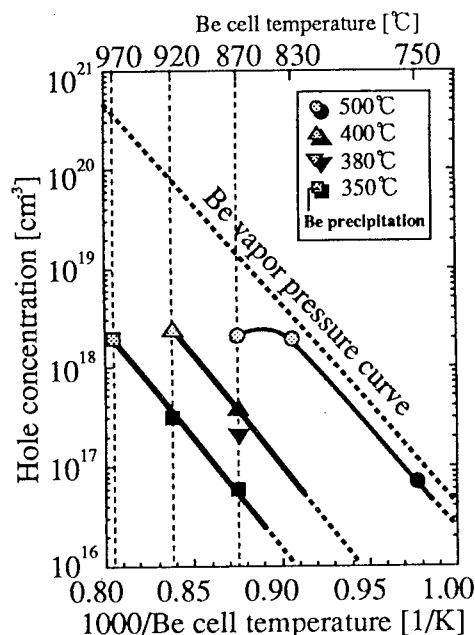


Fig.3. Hole concentration vs. Be cell temperature as a function of growth temperature for the Be-doped InAlP grown on GaAs substrate. Be vapor pressure curve is also shown.

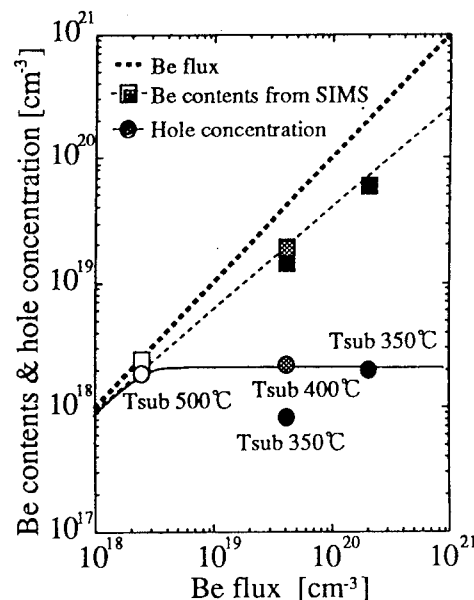


Fig.4 Be concentration and hole concentration vs. Be flux for the Be-doped InAlP.

4. Summary

We have studied the growth of InAlP on ZnSe. The following results were obtained:

- (1) Low temperature growth of InAlP on ZnSe produced a good surface morphology.
- (2) The use of the group III-flux modulated growth method for the growth of the first few layers of InAlP further improved the surface morphology.
- (3) The hole concentration as high as $2 \times 10^{18} \text{ cm}^{-3}$ was obtained in the Be doped InAlP even at low growth temperatures (350°C) at which the thermal-annealing-induced carrier compensation in the p-type ZnSe is avoided.
- (4) The increase in the required Be flux for the low temperature growth is due to the reduction of the electrical activity, but does not produce the Be precipitation /segregation.

It is concluded that Be-doped p-type InAlP layers grown at low temperatures are expected to be useful as a valence band offset reduction layer that produce low resistance ohmic contacts to p-type ZnSe.

Acknowledgments

The authors would like to express their thanks to the Material Analysis Center of ISIR for the X-ray diffraction measurements, T.Yoshinobu and H.Iwasaki of ISIR for the AFM observations and S.Izumi of Mitsubishi Electric Corporation for the SIMS measurement. They are also grateful to Y.Imamura of NTT for his support.

References

- [1] M.A. Haase, J. Qiu, J.M. DePuydt and H. Cheng, *Appl. Phys. Lett.* **59** (1991) 1272.
- [2] Y. Lansari, J. Ren, B. Sneed, K.A. Bowers, J.W. Cook, Jr. and J.F. Schetzina, *Appl. Phys. Lett.* **61** (1992) 2554.
- [3] Y. Fan, J. Han, L. He, J. Saraie and R.L. Gunshor, *Appl. Phys. Lett.* **61** (1992) 3160.
- [4] K. Iwata et al., presented at the 8th Intern. Conf. on MBE, Osaka, Japan, 1994, Workbook pp.285-286.
- [6] H. Asahi, K. Asami, T. Watanabe, S.J. Yu, T. Kaneko, S. Emura and S. Gonda, *Appl.Phys.Lett.* **58** (1991) 1407.
- [7] Y. Kawaguchi, T. Ohno and T. Matsuoka, in: *Extended Abstracts 1992 Int.Conf.on Solid State Devices and Materials*, Tsukuba, 1992 (Business Center for Academic Societies Japan) pp.345-347.
- [8] T. Inoue, T. Ohsuna, Y. Obara, Y. Yamamoto, M. Satoh and Y. Sakurai, *J. Crystal Growth* **131** (1993) 347.
- [9] N. Kobayashi and Y. Horikoshi, *Jap.J.Appl.Phys.* **29** (1990) L236.
- [10] H. Asahi, Y. Kawamura and H. Nagai, *J.Appl.Phys.* **54** (1983) 6958.
- [11] M. Nakajima, A. Takamori, T. Yokotsuka, K. Uchiyama and T. Abe, *J. Crystal Growth* **105** (1990) 116.

Optical and electrical properties of InN grown by the atomic layer epitaxy

T. Inushima, T. Yaguchi, A. Nagase, A. Iso, T. Shiraishi and S. Ooya^{a)}

Department of Communications Engineering, Tokai University

1117 Kitakaname, Hiratsuka, Kanagawa 259-12 Japan

^{a)} Industrial Research Institute of Kanagawa Prefecture

Syowa-machi, Kanazawa-ku, Yokohama 236 Japan

InN single crystal was grown by UV-assisted atomic layer epitaxy under atmosphere pressure. The obtained InN was degenerate n-type semiconductor with the Hall mobility of $64\text{ cm}^2/\text{Vsec}$ and the carrier concentration of $7 \times 10^{20}/\text{cm}^3$. From the plasma oscillation frequency in the reflection spectra, the electron effective mass was determined to be $0.12 m_0$.

Introduction

InN is a III-V compound which forms mixed crystals with GaN and AlN, promising materials for blue-light emitting diode. The physical properties of InN, however, are obscure due to its non-stoichiometry of N concentration and its low dissociation temperature. The first trial for the deposition of InN was made by Hovel et al. by the reactive sputtering method (1). They obtained n-type high mobility InN with the carrier density of $10^{19}/\text{cm}^3$. Tansley et al. reported the high mobility of $5000\text{ cm}^2/\text{Vsec}$ by the use of reactive sputtering method utilizing pre-nitride In as the target (2). The epitaxial InN was grown by Wakahara et al. by the microwave-assisted metal-organic vapor epitaxy (3). They obtained the mobility of $50\text{ cm}^2/\text{Vsec}$ and the carrier density of $7 \times 10^{20}/\text{cm}^3$ (4). The optical and electrical properties of InN were investigated using the polycrystalline samples (5). Here we report on the properties using single-crystalline samples.

Atomic layer epitaxy of InN

To overcome the big difference of the vapor pressures between In and N, we applied the atomic layer epitaxy (ALE) under atmosphere pressure (6). The apparatus used in this experiment is shown in Fig. 1, where InCl_3 and NH_3 are used as source gases, which are blown alternatively on the sapphire surface of (0001) which is kept at 440°C . The whole furnace is kept in a hot-wall condition. The substrate is covered with a monolayer of InCl_3 and excessive InCl_3 is excluded from the surface. Then NH_3 is sent onto the surface to form InN, and Cl ions are extracted from the film as HCl , and excessive NH_3 is evaporated from the surface. During the deposition, we applied UV irradiation by a Deuterium lamp which improved the surface condition to be smooth and increased the crystal morphology. The UV light is applied through the UV-transparent quartz window and it illuminates the substrate from the side. One layer of InN was formed in 40 seconds, and 280 nm-thick InN was grown in 11 hours by the 1000 cycle deposition. The obtained InN shows clear x-ray diffraction from (0002) and its FWHM is 0.18° , which is shown in Fig. 2. From this reflection, the lattice constant of c-axis is 5.69\AA , which is the

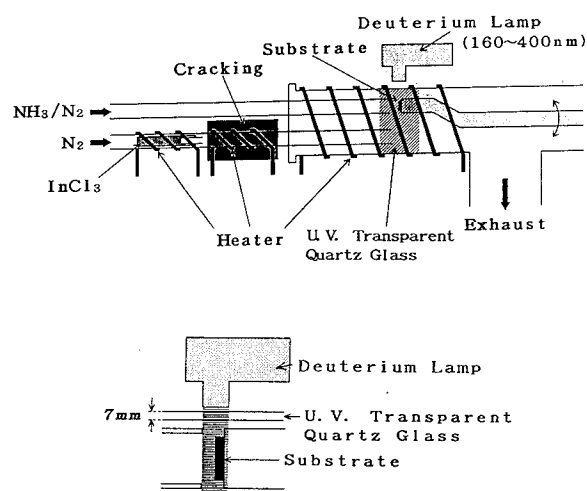


Fig. 1. Schematic view of the ALE furnace used in this experiment.

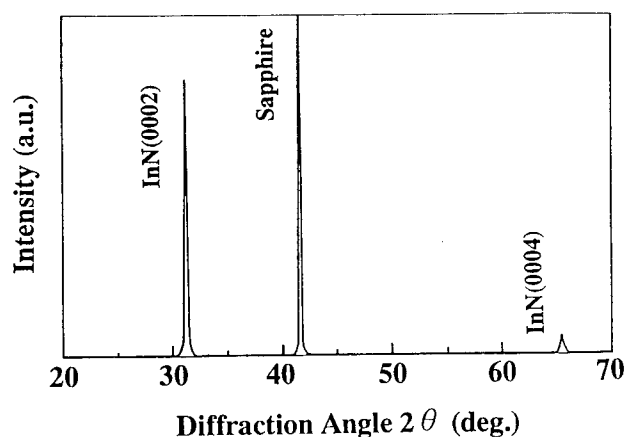


Fig. 2. X-ray diffraction chart of InN grown by UV-assisted ALE.

same as that reported before (7). The improvement of crystal morphology due to UV irradiation is seen in Fig. 2. When the sample is grown without UV irradiation, x-ray diffraction shows some extra (prohibited) reflections, which indicates the existence of big stacking fault in the crystal. The Deuterium lamp has the light intensity from 180 to 360 nm, and NH_3 is dissolved by this light. Therefore the irradiation of the UV light increases the number of active N species in the reaction space, which improves the crystal morphology of InN.

The improvement of the crystal morphology by UV irradiation was investigated using RHEED. The RHEED patterns with and without UV irradiation are compared in Fig. 3. It is seen that the epitaxial layer on the sapphire has hexagonal symmetry with c-axis perpendicular to the



Fig. 3(a). RHEED pattern of InN grown under without-UV irradiation.



Fig. 3(b). RHEED pattern of InN grown under UV-irradiation.

substrate. When the UV-light is not applied during the crystal growth, the RHEED pattern has clear spots with concentric rings. When the UV-light is applied during the growth, the surface becomes smooth and the RHEED pattern shows streaks with the lines perpendicular to the substrate, which indicates that a mirror surface is obtained. From the analysis of the RHEED pattern, it is revealed that the InN grown under UV irradiation still has reflections prohibited by the crystal geometry of $P6mc$, which indicates the systematic insufficiency of nitrogen in InN.

Hall effect measurements

Hall effect measurement was carried out by the use of van der Pauw technique. As for the electrodes, Ag was evaporated onto the sample through a metal mask. The electrodes had a diameter of 200 μm , which were placed at the corners of a square of $2 \times 2 \text{ mm}^2$. Gold-wire leads were bonded to the Ag pads with supersonic solder. The Hall effect and the resistivity were measured from 20 to 300 K in a cryostat equipped with 10 kG electromagnet. The temperature of the sample was controlled by changing the temperature of He gas surrounding the sample. Keithley 7065 matrix card was used to cancel the residual voltage which appeared when the applied current was inverted. From the resistivity (ρ) and the Hall coefficient (R_H), the Hall mobility was obtained by the equation $\mu = R_H / \rho$, which is given in Fig. 4 together with the resistivity as a function of temperature.

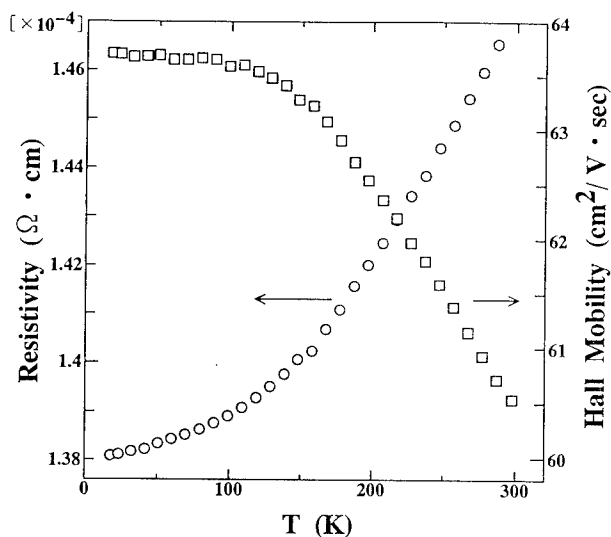


Fig. 4. Temperature dependence of the resistivity and the Hall mobility of InN grown under UV irradiation.

The resistivity shows weak temperature dependence and it is $1.38 \times 10^{-4} \Omega\text{cm}$ at the lowest limit. When the temperature increases, $\rho(T) \propto T^2$ is obtained below 150 K, which changes to $\rho(T) \propto T$ above 200 K. If InN has a metallic conduction, $\rho(T) \propto T^5$ is expected. The carrier density

obtained from the Hall coefficient is $7.1 \times 10^{20}/\text{cm}^3$ at 20 K, which slightly decreases with increasing temperature, and at room temperature it is $7.0 \times 10^{20}/\text{cm}^3$.

The Hall mobility remains constant from 18 to 100 K, and shows a slight decrease above 100 K. It is natural to consider the neutral-impurity scattering to interpret the nearly constant mobility (μ_N) in the low-temperature region. From the neutral impurity scattering formula by Erginsoy (8),

$$\mu_N = \frac{m_e^* e^3}{20 \epsilon_r \hbar^3 N_N}$$

where m_e^* is the electron effective mass and ϵ_r is the dielectric constant of InN, and their values are obtained from the reflection spectra which will be mentioned later. N_N is the number of neutral impurity concentration and is obtained to be $2.5 \times 10^{19}/\text{cm}^3$. This number is smaller than the carrier concentration.

From the results above we conclude that the InN grown by ALE is n-type semiconductor in degenerate condition.

Plasma reflection

The InN films grown by ALE has high carrier concentration. In general the electron gas exhibits both collective and individual particle behaviors. The collective response, called the plasma oscillation, is derived from the collective oscillation of the electron gas. Plasma oscillations are manifest when the carrier life time τ_c is longer than the time defined by the inverse of the plasma frequency ω_p . Figure 5 shows the reflectance spectra of InN film

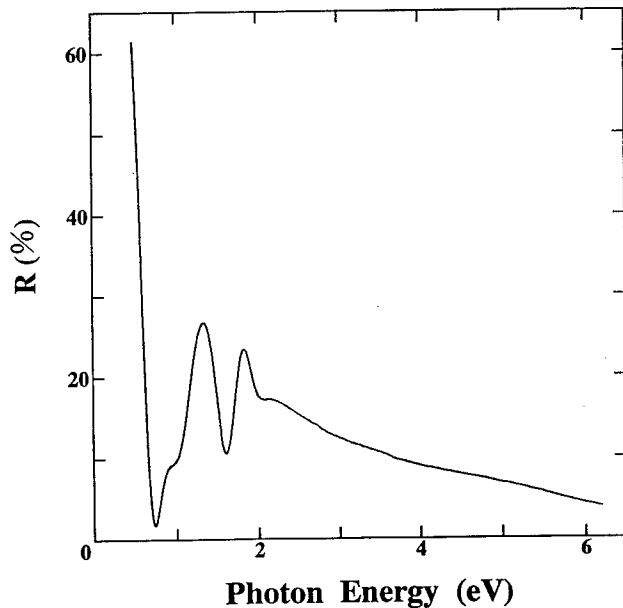


Fig. 5. Reflectance spectra of InN grown under UV irradiation. The minimum of the reflectance corresponds to $\omega_p = 0.735$ eV.

grown on Al_2O_3 substrate. The spectra are taken from 200 to 2500 nm. The spectra have the peak around 2 eV, which is due to the direct band-to-band transition. The peaks below the band gap energy are due to the interference of the transmitted light. The film shows more than 70 % reflectance below 0.735 eV, which is due to the plasma oscillation of the free carriers. From the fringes of the interference and the film thickness (300 nm), the refractive index is determined to be $n=3.91$. This value is larger than 2.85~3.08 which were reported previously (1,2). As the absorption of InN in this energy region can be neglected, the dielectric constant ϵ_r is obtained as $\epsilon_r = n^2 = 15.3$. Then m_e^* is obtained from the following,

$$\omega_p^2 = \frac{Ne^2}{\epsilon_r m_e^*}$$

Using the carrier number of $N=7 \times 10^{22}/\text{cm}^3$, we obtain $m_e^* = 0.12 m_0$. This value is very close to that predicted from the band gap calculation (9).

When we consider the electron effective mass from the k-p perturbation theory, m_e^* is expressed by the band gap energy as follows,

$$\frac{m_0}{m_e^*} = 1 + \frac{2}{m_0} \times \frac{F}{E_g}$$

where E_g is the band gap energy and F is the oscillator strength between the valence and the conduction bands. When we take into account E_g of InN as 1.9 eV (1) and the

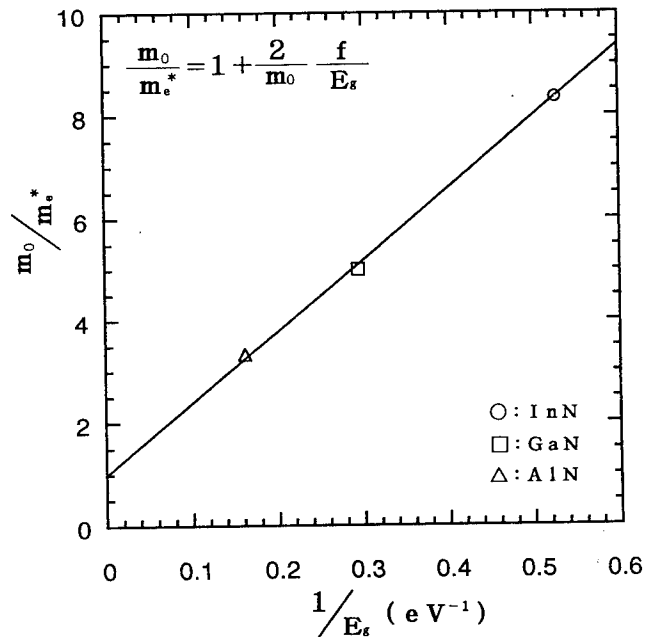


Fig. 6. The relation between the effective mass (m_e^*) and the band gap energy (E_g) for InN together with AlN (10) and GaN (11).

data of AlN ($E_g=6.2$ eV, $m_e^*=0.3m_0$) (10) and GaN ($E_g=3.4$ eV, $m_e^*=0.20 m_c$) (11), the relation is plotted in Fig. 6. We see that these m_e^* s are on a straight line having the coefficient of $2F/m_0=14$ eV, which indicates that these three nitrides have similar band structures and oscillator strengths.

The reflection spectra of high carrier concentration ($7 \times 10^{20}/\text{cm}^3$) was reported by Guo et al., which was measured by SOR-RING (0.38 GeV electron storage ring) from 2 to 20 eV (12). In the reflection spectra there were two major peaks at 2.3 and 5.3 eV, which were weakly observed in Fig. 5. The reflection due to plasma frequency was not observed. The refractive index at 2 eV was around 2.7. When we estimate τ_c of our samples, we obtain $4 \times 10^{15}/\text{sec}$. This value gives $\omega_p \tau_c \sim 6$ and makes the reflectance more than 70 % from Hagen-Rubence relation. This is what we observed in Fig. 5.

In conclusion InN single crystal grown by UV-assisted ALE was degenerate n-type semiconductor with the Hall mobility of $64 \text{cm}^2/\text{Vsec}$ and the carrier concentration of $7 \times 10^{20}/\text{cm}^3$. From the plasma oscillation frequency, the electron effective mass was determined to be $0.12 m_0$.

References

1. H. J. Hovel and J. J. Cuomo, "Electrical and optical properties of rf-sputtered GaN and InN", Appl. Phys. Lett., Vol. 20, pp. 71-73, 1972.
2. T. L. Tansley and C. P. Foley, "Electron mobility in indium nitride", Electron. Lett., Vol 20, pp1066-1068, 1984.
3. A. Wakahara and A. Yoshida, "Heteroepitaxial growth of InN by microwave-excited metalorganic vapor phase epitaxy", Appl. Phys. Lett., Vol. 54, pp709-711, 1989.
4. A. Wakahara, T. Tsuchida and A. Yoshida, J. Crystal Growth, Vol. 99, pp385-387, 1990.
5. T. L. Tansley and C. P. Foley, "Optical band gap of indium nitride", J. Appl. Phys. Vol. 59, pp3241-3244, 1986.
6. K. Higuchi, A. Unno, and T. Shiraishi, "A Possibility of ALE Growth of InN by using InCl_3 ", Mat. Res. Soc. Symp. Proc. Vol. 222, pp169-173, 1991.
7. von R. Juza and H. Hahn, "Über die Kristallstrukturen von Cu_3N , GaN und InN", Z. Allg. Chem. Vol. 239, pp282-287, 1938.
8. C. Erginsoy, Phys. Rev., Vol. 79, pp1013, 1950.
9. C. P. Foley and T. L. Tansley, "Pseudopotential band structure of indium nitride", Phys. Rev. Vol. B33, pp1430-1433, 1986.
10. K. Miwa and A. Fukumoto, Phys. Rev., Vol. B48, pp7897-7902, 1993. The value of m_e^* is obtained from the pseudopotential calculation.
11. S. B. Barker and M. Illegemes, Phys. Rev., Vol. B7, pp743 1973.
12. Q. Guo, O. Kato, M. Fujisawa and A. Yoshida, Solid State Commun., Vol. 83, pp721-723, 1992.

Atomic Structures of Au and Ag Films Epitaxially Grown on the InP(001)-p(2×4) Surface

K. Morita, K. Soda, T. Katoh and M. Hanebuchi

Department of Crystalline Materials Science,
School of Engineering, Nagoya University
Furo-cho, Chikusa-ku, Nagoya 464-01, JAPAN

Introduction

The metal-InP system is of special interest, because of its potential use in high-speed logic, integrated optics and micro wave applications. Nevertheless, there have been a few epitaxial metallization systems of metal and metal compound reported on InP.[1-3] Metal/InP systems are believed to be chemically reactive and the metal reacts with In and/or P to form a mixture of metal-indium and metal-phosphorous compound by high temperature anneals[4,5]. However, we have shown, for the first time, the epitaxial growth of a mono-crystalline AuIn compound on InP(001) by annealing a Au/In(001)-p(2×4) system at temperatures of 250~300°C which has been prepared under an ultra high vacuum condition, [6]. Very recently, we have observed by means of LEED, AES and RBS-channeling techniques that Au films grow epitaxially in the layer-by-layer mode along the [001] direction on the InP(001)-p(2×4) surface by room temperature deposition under a UHV condition[7]. The low temperature epitaxy has been explained in terms of self-annealing due to heat of mixing released in the exothermic interface reaction of Au and In.

Such a low temperature epitaxy is useful for development of the InP devices. Moreover, it has been observed that Ag films grown in the [011] direction in the Stranski-Krastanov (S-K) mode and the islands of Ag(110) crystallites prefer to orient their (001) side surface along the direction of 4 times super lattice, which has been obtained by means of the additional RHEED technique.[8]

In this paper, we compare the atomic structures of Au and Ag films epitaxially grown on the InP(001) -p(2×4), which have been characterized by means of LEED, RHEED, AES and RBS-channeling.

2. Experiments

The InP specimen used was a (001)-oriented, n-type and undoped single-crystalline wafer (Showa Electric Industries Ltd.). The specimen surface was mechanically polished, cleaned in standard solvents, etched in a $\text{H}_2\text{O}:\text{H}_2\text{SO}_4$ solution for 1 min at 60°C and in a $\text{H}_2\text{O}:\text{NH}_4\text{F}$ solution for 1 min at room temperature and finally cleaned in deionized water. The specimen was mounted on a three-axes rotatable goniometer with two-axes linear motion having an angular resolution of 0.025° in a conventional UHV chamber which was connected to a differentially pumped beam line of a 2.0MeV van de Graaff accelerator, and in which a base pressure no more than 4×10^{-10} Torr was regularly achieved. The specimen

surface was cleaned by repeating 0.5 keV Ar^+ sputtering for 20 min at a current density of $0.1 \mu\text{A}/\text{cm}^2$ and subsequent annealing at 300°C for 10 min so that clear LEED spots of p(2×4) could be observed, as shown later. Hereafter, the Au or Ag films with different thickness were deposited on the substrate at room temperature, keeping a pressure less than 4×10^{-9} Torr at a deposition rate of 3Å/min.

At each stage of the surface cleaning and deposition, the specimen surface was observed in-situ by means of the LEED, (or RHEED), AES and RBS-channeling techniques. The RBS-channeling measurement was performed with a 1.5 MeV He^+ ion beam of 1 mm in diameter which was incident along the <001> direction of the InP substrate.

3. Experimental results and discussion

First of all, the results on LEED or RHEED observation are described. A LEED pattern of $p(2 \times 4)$ spots was observed for a cleaned InP(001) surface and a LEED pattern was observed for a Au film, of 20 Å in thickness, deposited onto the cleaned surface. The $p(2 \times 4)$ pattern (a) corresponds to the most commonly observed surface structure of the cleaned InP(001) surface which is modeled by the missing row dimer structure [9]. The $p(1 \times 1)$ pattern for the Au film corresponds to the $c(2 \times 2)$ pattern for the Au (001) face, as explained later. The result indicates that the Au single-crystalline film grows epitaxially along the $\langle 001 \rangle$ direction on the InP(001) surface only by room temperature deposition.

RHEED patterns observed for a Ag film, of 15.8 Å in thickness, deposited onto the InP(001) surface are shown in Fig.1, where the RHEED patterns for a cleaned InP(001) surface are also shown. The RHEED patterns (a) and (c) were observed for the case of the electron beam incident along the $\langle 110 \rangle$ direction of the InP (001) surface and the RHEED patterns (b) and (d) along the $\langle 101 \rangle$. One can see that the RHEED patterns (c) and (d) for the Ag film do not show the reflection diffraction rods, but the transmission diffraction spots, which indicate that the Ag film deposited at room temperature grows in the Stranski-Krastanov (S-K) mode. Since Ag is a face-centered cubic lattice, the

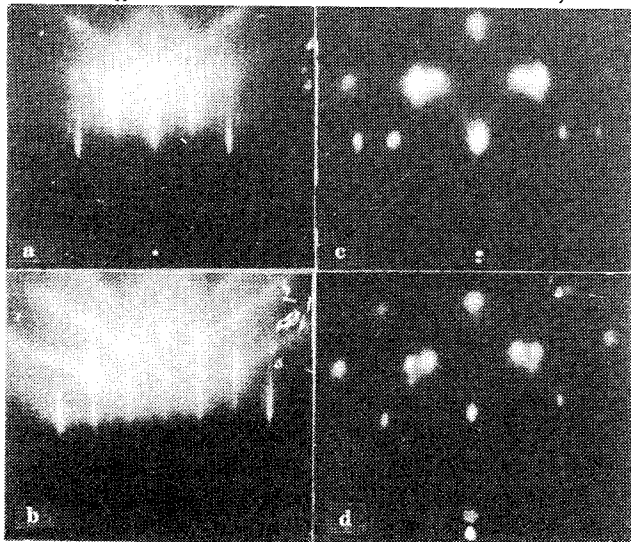


Fig.1 RHEED patterns(a) and (b) from a InP(001)- $p(2 \times 4)$ surface which correspond to the 4 and 2 times superlattice, respectively and (c) and (d) from a Ag film of 15.8 Å in thickness deposited on the InP(001)- $p(2 \times 4)$ surface at room temperature. The directions of the incident electron beam for (c) and (d) correspond to those for (a) and (b), respectively.

RHEED patterns (c) and (d) turn out to be a superposition of transmission diffraction spots for the (110) and (001) faces of the Ag crystal, to which the direction of the electron beam is perpendicular. This result indicates that the Ag film grows along the $\langle 110 \rangle$ direction on the InP(001) surface. The $\langle 110 \rangle$ growth of Ag is quite different from the $\langle 100 \rangle$ growth of Au describe above.

Next, we discuss the orientation of the epitaxially grown film against the InP substrate. The atomic arrangements of the (001) face of fcc Au and of the (001) face of fcc InP are shown in Fig.2 and those of the (011) face of fcc Ag and of (001) face of fcc InP in Fig.3. In Fig.2, the unit cell of Au is rotated azimuthally 45° with respect to the InP unit cell. It is seen from Fig.2 that the Au spacing is 1.7 % smaller than the In spacing. This indicates that the $\langle 001 \rangle$ epitaxial growth of Au is very reasonable. It is also clearly seen from Fig.2 that a LEED pattern of $p(1 \times 1)$ spots for the InP(001) lattice is reduced to $c(2 \times 2)$ spots for the Au (001) lattice by lateral displacement of single atom or pair atoms in the Au unit cell.

It is seen from Fig.3 that the mismatch of 3 times the Ag atomic spacing in the $\langle 110 \rangle$ direction to 2 times the In atomic spacing in the $\langle 110 \rangle$ direction is 4.7 % and the mismatch of the Ag atomic spacing in the $\langle 100 \rangle$ direction to the In atomic spacing in the $\langle 110 \rangle$ direction is 1.1 %. It is also clearly seen from Fig.1 that in (c) the brightness of (1,0) and (-1,0) spots for the (110) face is stronger than that for the (001) face, while in (d) the brightness of (1,0) and (-1,0) spots is weaker. The transposition of the brightness between the two spots in (c) and (d) indicates that the $\langle 100 \rangle$ direction of the Ag (110) crystalline prefers to orient along the $\langle 110 \rangle$ direction of 4 times super lattice of the InP(001)- $p(2 \times 4)$ surface. This preferential orientation of the Ag crystallites may be ascribed to the mismatch between the atomic spacings in Ag and InP lattice. However, the reason why the orientation of the epitaxial growth of Ag is different from that of Au is not understood yet.

The crystalline quality of epitaxially grown films of Au and Ag was investigated by means of the RBS channeling measurement of 1.5 MeV He^+ ion beam along the $\langle 001 \rangle$ direction of the InP(001) substrate. Typical RBS spectra of 1.5 MeV He^+ ion beam from the Au film of 20 Å in thickness deposited on the InP(001) substrate are shown in Fig.4, where open and closed circles represent the random and aligned spectrum in the $\langle 00\bar{1} \rangle$ axial direction of

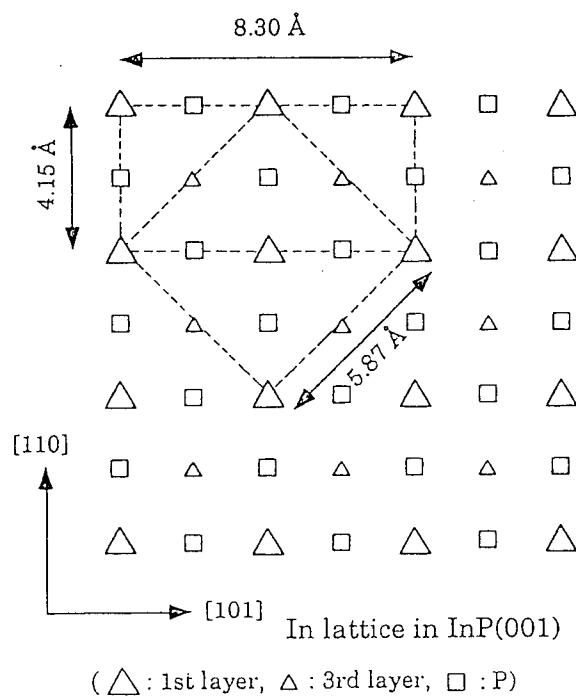
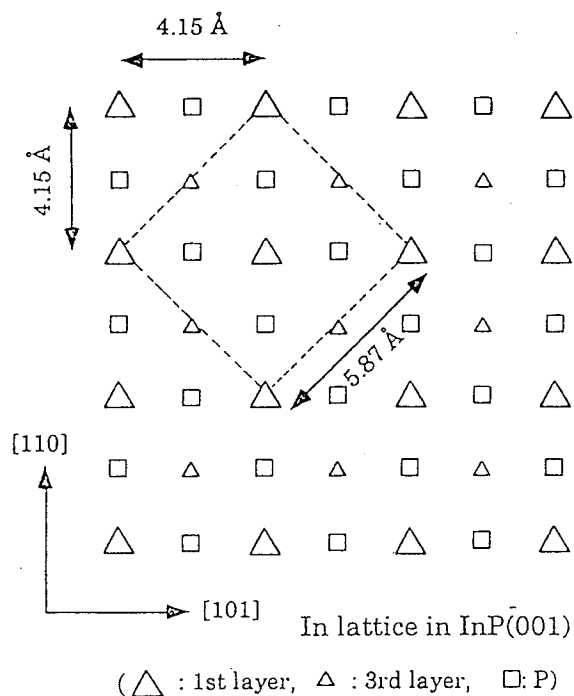
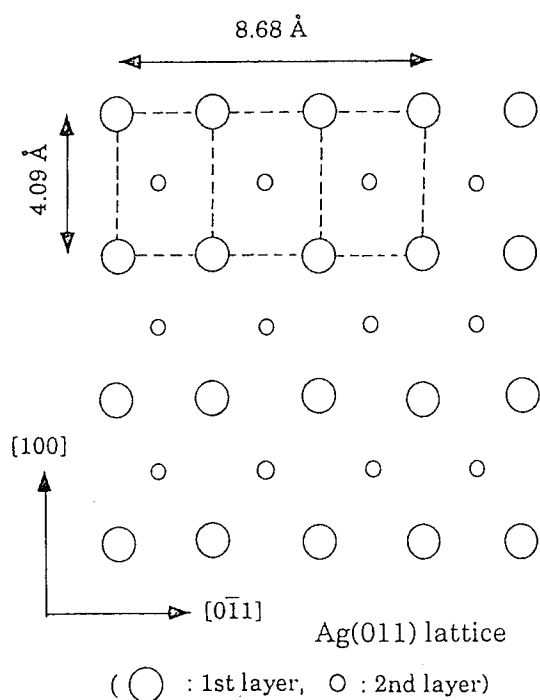
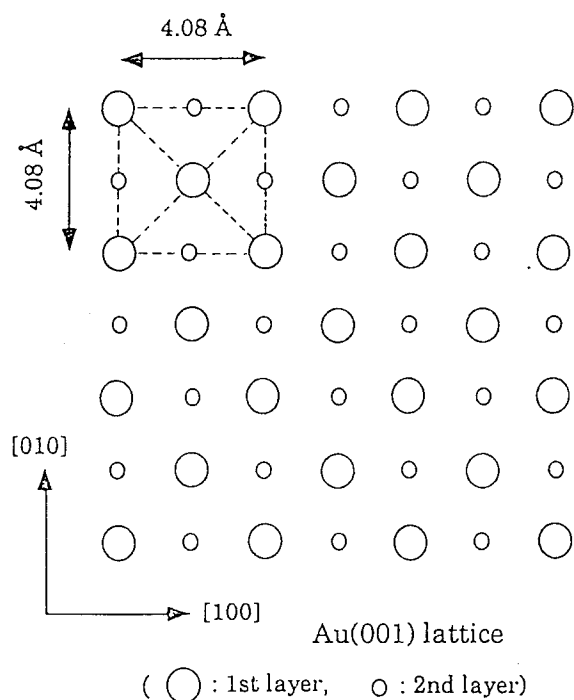


Fig.2 Schematic illustration of atomic arrangements for a Au(001) face and for an InP(001) face. The unit cell of Au is rotated azimuthally 45° with respect to the InP unit cell.

Fig.3 Schematic illustration of atomic arrangements for a Ag(011) face and for an InP(001) face.

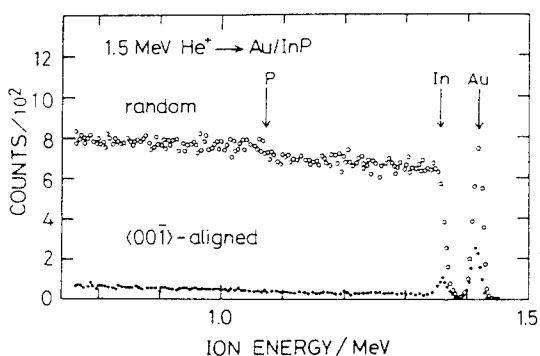


Fig.4 RBS spectra of 1.5 MeV He^+ ions from the Au layer deposited on the InP(001) substrate at room temperature: (○) for random direction and (●) for the $\langle 00\bar{1} \rangle$ channeling direction of the InP substrate.

the InP(001) substrate, respectively. It is clearly seen from Fig.4 that the aligned yield of the Au film is considerably reduced compared with the random yield. From the ratio of the aligned to random yield, it was estimated that the average minimum yield for the Au film was 32.5%. The average minimum yield for the Ag film of 20.7 Å in thickness was found to be 36 %. The large minimum yields are explained quantitatively well in terms of thinness of their films by taking into account the thermal lattice vibration. The result indicates that the crystalline quality of epitaxially grown films of Au and Ag is excellent.

The channeling minimum yield for the Au film of 20 Å thick was numerically calculated by taking into account the displacement of single atom and pair atoms in

the Au unit cell of the (001) face and the thermal lattice vibration. It was determined from comparison between the experimental and calculated minimum yield that the atomic arrangement of Au atoms in the Au(001) unit cell lateral of $c(2 \times 2)$ is a pair atoms displacement and the lateral displacement of Au atoms is 0.18 Å.

Acknowledgements

We are grateful to shown Electric Industrie Ltd. for supplying the specimens of InP crystal used.

References

- 1) H. B. Kim, A. F. Lovas, G. G. Sweeney and T. M. S. Heng. *Inst. Phys. Conf. Ser.* Vol. 33b, 145(1977)
- 2) B. Tuck, K. P. Ip and L. F. Eastman, *Thin Solid Films* Vol. 55, 41(1978)
- 3) N. SSzzylo and J. Oliver, *J. Appl. Phys.* Vol. 50, 1445(1975)
- 4) A. Hiraki, K. Shuto, S. Kim, W. Kammura and M. Iwami, *Appl. Phys. Lett.* Vol. 31, 611(1977)
- 5) P. W. Chye, L. Lindau, P. Pianetta, C. M. Garner, S. Y. Su and W. E. Spicer. *Phys. Rev.* Vol. B18, 5545(1978)
- 6) M. Renda and K. Morita, *Appl. Surf. Sci.* Vol. 41/42, 216(1989)
- 7) T. Katoh and K. Morita, *Appl. Surf. Sci.* Vol. 56-58, 199(1992); Vol. 56-58, 185(1992)
- 8) M. Hanebuchi, T. Katoh and K. Morita, *Appl. Surf. Sci.* (1995) in print.
- 9) X. Hou, G. Dong, X. Ding and X. Wang, *J. Phys.* Vol. C20, L121(1980)

Influence of arsenic flux ratio in the thermal cleaning process on InP (100) surface characteristics

M. Washima, T. Tsuchiya, T. Tani, and H. Sakaguchi

Advanced Research Center, Hitachi Cable, Ltd., 3550 Kidamari-cho, Tsuchiura, Ibaraki 300, Japan

Abstract

Influence of arsenic flux ratio in the thermal cleaning process on InP (100) surface characteristics was investigated using reflected high-energy electron diffraction (RHEED) and atomic force microscopy (AFM). We observed that the reconstruction temperature of an In-stabilized (4×2) structure and an As-stabilized (2×4) structure was dependent on the arsenic pressure. The AFM images showed that the height and number of the InAs islands on the InP surface were determined by the arsenic pressure during the thermal cleaning process.

1. Introduction

The InAlAs/InGaAs system lattice-matched to InP is of considerable interest due to its suitability for high-speed transistors and long-wavelength optoelectronic applications. The molecular beam epitaxy (MBE) of high quality InGaAs and InAlAs epitaxial layers requires a clean and smooth surface of InP (100) substrate. The surface must be thermally cleaned before epitaxial growth in the MBE system. In this substrate thermal cleaning process, arsenic flux is commonly applied in the MBE growth system without phosphorus source.^{1,2)} Desorbed phosphorus is immediately replaced by arsenic at the surface of InP and a thin InAs layer forms on there.³⁻⁸⁾ The inhomogeneous growth of this InAs layer makes surface rough. The growth mode of the InAs layer must be affected by arsenic pressure in the thermal cleaning. Therefore, arsenic pressure is an important parameter in the thermal cleaning of the InP surface.

In this paper, we report the influence of arsenic pressure during this cleaning on the InP surface roughness as measured by atomic force microscopy (AFM) and discuss the island growth of InAs on the surface during this process. We also report the dependence of the surface reconstruction temperature measured by reflected high-energy electron diffraction (RHEED) on arsenic pressure in the thermal cleaning of the InP substrates.

2. Experimental

InP substrates were thermally cleaned under various arsenic pressures in our MBE system. A solid arsenic in a conventional Knudsen cell with a pyrolytic boron nitride (PBN) crucible was used

for an arsenic molecular beam source. The substrates were InP (100) oriented n-type S doped wafers of "ready to use" quality and the substrate was mounted on a 3-inch Si wafer with In solder. The InP substrate temperature (T_s) was measured with a thermocouple and a pyrometer. The InP substrate was then transferred to the main chamber without pre-heating. We measured the arsenic pressure (PAs) with a beam flux monitor (BFM). The BFM was positioned under the InP substrate before heating.

The InP substrate was heated to 590°C at a rate of 20°C/min., held at that temperature for 10 minutes, and cooled to 300°C in the MBE chamber. PAs was kept at the same pressure during this process, as shown in Fig. 1.

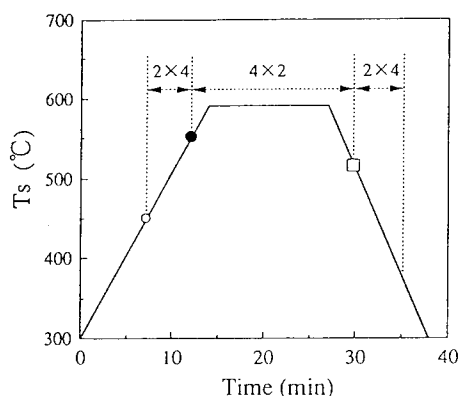


Fig.1. Temperature sequence of thermal cleaning. Arsenic pressure was held constant in the thermal cleaning. Heating of the substrate continued up to 590°C; the (2×4) surface reconstruction changed to (4×2) and cooling changed it to (2×4).

We observed a 30keV RHEED pattern for the incident electron beam of the [110] azimuth. By holding Ts at 590°C for 10 minutes, a fourfold ($4 \times$) RHEED pattern was seen. This showed that the thermal cleaning resulted in a clear InP surface.

We studied the surface roughness of the thermally cleaned wafers using AFM (Park Scientific Instruments SPC-400). Data points were 256×256 in $1 \times 1 \mu\text{m}^2$ scanned area.

3. Results and Discussion

Figure 2 shows dependence of reconstruction temperature on PAs. Changed RHEED patterns were observed under PAs less than 1×10^{-5} Torr, but was not observed over 1.5×10^{-5} Torr, and an In droplet was looked at when the Ts was raised to 630°C.

When Ts was raised to 490°C-540°C, a onefold ($1 \times$) RHEED pattern changed to a twofold ($2 \times$) pattern for an incident electron beam of the [110] azimuth. After Ts was increased to 590°C, a fourfold ($4 \times$) RHEED pattern appeared; this was an In-stabilized (4×2) surface structure. When the substrate temperature was lowered, the In-stabilized (4×2) surface structure formed on the InP substrate changed to As-stabilized (2×4). We therefore realized that the reconstruction temperature of both these structures depended on the arsenic flux.

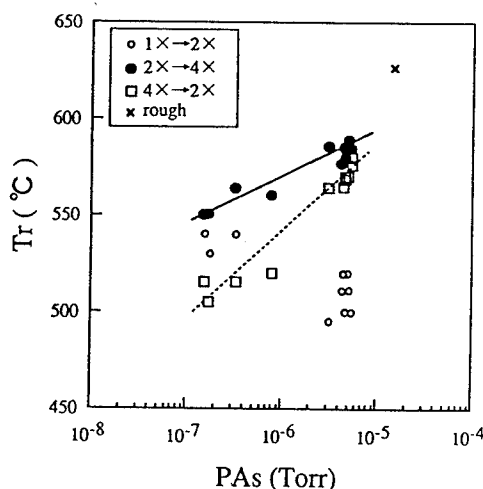


Fig.2. Dependence of reconstruction temperature (T_r) on arsenic pressure (PAs).

Figure 3 shows the AFM images after thermal cleaning of the InP surface. A histogram of the roughness of InAs estimated using AFM images on the InP surface at the $1 \times 1 \mu\text{m}^2$ area is shown in Fig.4: (a) thermally cleaned at an arsenic pressure of 4.5×10^{-6} Torr, (b) at an arsenic pressure of 3.3×10^{-7} Torr, and (c) non thermally cleaned.

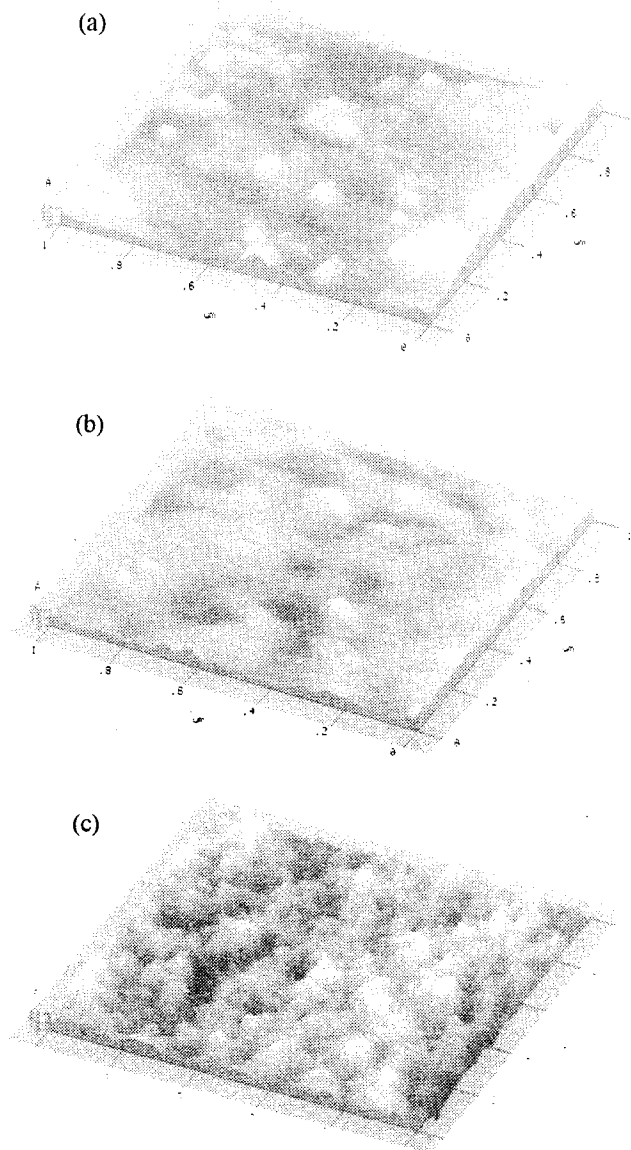


Fig.3. AFM images of InP surfaces which were thermally cleaned at 590°C for 10 minutes under different arsenic pressure (PAs): (a) PAs is 4.5×10^{-6} Torr, (b) PAs is 3.3×10^{-7} Torr, (c) non thermally cleaned InP surface.

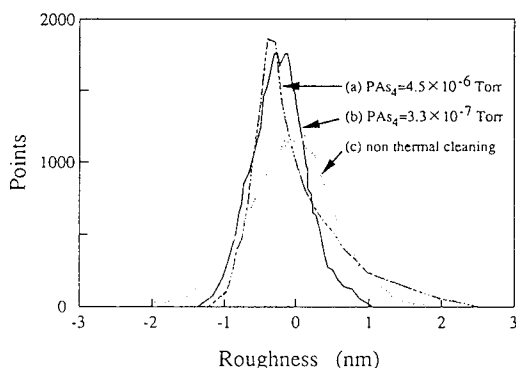


Fig.4. Histogram of roughness of InAs island estimated by AFM images on the thermally cleaned InP surface. Data points were 256×256 in $1 \times 1 \mu\text{m}^2$: (a) PAs is 4.5×10^{-6} Torr, (b) PAs is 3.3×10^{-7} Torr, (c) non thermally cleaned InP surface.

The surface of the thermally cleaned InP under the lower pressure was smoother than that of the non-thermally cleaned InP as shown in Figs. 3 and 4. Under the higher arsenic pressure many large islands of InAs were observed on the surface.

Figure 3 (a), (b) and Fig. 4 (a), (b) suggest that the InP surface morphology and formation of InAs islands were influenced by the arsenic pressure in the thermal cleaning. The amount of InAs must balance with that of the indium which comes from the InP and arsenic on the substrate surface. When there is no arsenic pressure, the excess indium remaining on the surface most likely evaporates because of the high vapor pressure of indium at the temperature of thermal cleaning. Under arsenic pressure, InAs is formed from the indium and arsenic. A thinner InAs layer remains on the surface under the lower arsenic pressure conditions, while a thicker layer remains under higher pressures. Figures 3 (a) and 4 (a) indicate that this thick InAs layer is reconstructed to form large islands under the high arsenic pressure. The mechanism involved in this formation is probably similar to the three dimensional growth of an InAs epitaxy.

4. Conclusion

We successfully prepared a clean, smooth surface on an InP substrate using low arsenic pressure in the thermal cleaning process. The reconstruction temperature of an In-stabilized (4×2) structure and an As-stabilized (2×4) structure were

dependent on the arsenic flux. The height and number of InAs islands were determined by arsenic overpressure during the thermal cleaning process on the InP surface.

5. Acknowledgment

We would like to thank M. Ushiyama of the Central Research Laboratory, Hitachi Ltd. for measurements of the AFM images.

References

- 1) G.J. Davies, R. Heckingbottom, H. Ohno, C.E.C. Wood and A.R. Calawa, "Arsenic stabilization of InP substrates for growth of $\text{Ga}_{1-x}\text{In}_x\text{As}$ layers by molecular beam epitaxy," *Appl. Phys. Lett.* 37(3) (1980) pp. 290-292
- 2) K.Y. Cheng, A.Y. Cho, W.R. Wagner, and W.A. Bonner, "Molecular beam epitaxial growth of uniform $\text{In}_{0.53}\text{Ga}_{0.47}\text{As}$ on InP with a coaxial In-Ga oven," *J. Appl. Phys.* 52 (2) (1981) pp. 1015-1021
- 3) F. Genova, C. Papuzza, C. Rigo, and S. Stano, "Effect of substrate thermal degradation on MBE InGaAs layers," *J. Cryst. Growth* 69 (1984) pp. 635-638
- 4) J.M. Moison, M. Bensoussan, and F. Houzay, "Epitaxial regrowth of an InAs surface on InP: An example of artificial surface," *Physical Review B* 34 (1986) pp. 2018-2021
- 5) G. Hollinger, D. Gallet, M. Gendry, C. Santinelli, and P. Viktorovitch, "Structural and chemical properties of InAs Layers grown on InP (100) surfaces by arsenic stabilization," *J. Vac. Sci. Technol. B* 8 (4) (1990) pp. 832-837
- 6) S. Ohkouchi, and I. Tanaka, "Observation of the InP surface thermally cleaned in an arsenic flux using a scanning tunneling microscope," *Appl. Phys. Lett.* 59 (13) (1991) pp. 1588-1590
- 7) S. Ohkouchi, N. Ikoma, and I. Tanaka, "Surface structure of InP and InAs thermally cleaned in an arsenic flux," *J. Vac. Sci. Technol. B* 12 (3) (1994) pp. 2033-2036
- 8) A. Tanaka, T. Benyattou, and G. Guillot, "Optical properties of InAs/InP surface layers formed during the arsenic stabilization process," *J. Vac. Sci. Technol. B* 12 (4) (1994) pp. 2299-2304

Thermal cleaning and growth temperature effects on deep levels of Be-doped p-InAlAs grown on InP by molecular beam epitaxy

Shigehisa Tanaka, Yasunobu Matsuoka, and Hitoshi Nakamura
Central Research Laboratory, Hitachi, Ltd.
Kokubunji, Tokyo 185, Japan

INTRODUCTION

InAlAs, lattice-matched to InP, is an attractive material for high-speed optical and electrical devices. When it is used with InGaAs, which is also lattice-matched to InP, various high performance devices, such as high electron mobility transistors (HEMTs) or super-lattice avalanche photodiodes (APDs), can be fabricated[1,2]. Molecular beam epitaxy (MBE) is a powerful epitaxial technique to fabricate such kind of heterostructure devices. However, the MBE growth of high quality InAlAs layers has been very difficult because of the high Al concentration and MBE-grown non-doped InAlAs layers tend to easily become highly resistive, indicating the existence of high-density deep levels. To obtain a high quality InAlAs layer, it appears necessary to reduce the density of deep levels. Therefore, deep levels in n-type InAlAs have been investigated by several authors[3,4], but very little work has been done on p-type InAlAs[5]. In this work, we study deep levels in Be-doped p-InAlAs grown by MBE by using the conventional deep level transient spectroscopy (DLTS) method. Based on how the deep levels are affected by growth conditions, optimal MBE growth conditions to obtain a high quality InAlAs layer are determined.

EXPERIMENTAL

To conduct DLTS measurements of p-InAlAs layers, InAlAs pn⁺ diode structures were grown on S-doped n-InP substrates by conventional solid-source MBE with a VARIAN modular GEN II system. Figure 1 shows the device structure and the MBE growth conditions are summarized in Table 1. Prior to MBE growth, degraded surface layers of the InP substrates were removed by chemical etching in 1% Br₂-methanol followed by etching in a H₂SO₄:H₂O₂:H₂O=5:1:1 solution. The thermal cleaning and the epitaxial growth processes were performed under an As₄ pressure. Surface reconstruction during these processes was determined from the reflection high energy electron diffraction (RHEED) patterns.

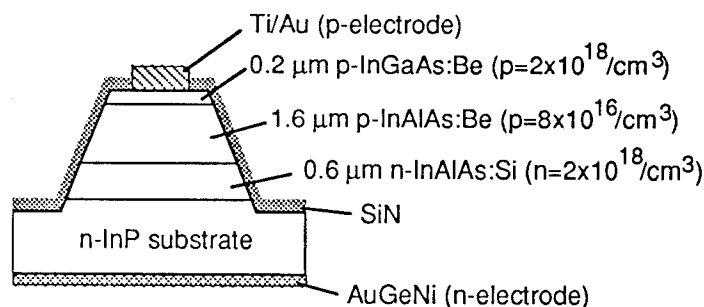


FIG. 1 Schematic structure of the InAlAs pn-junction diode used for DLTS measurement.

TABLE 1 MBE growth conditions

Substrate:	n-InP:S ($n=2 \times 10^{18}/\text{cm}^3$)
Thermal Cleaning Temperature (T_c):	460-560°C
Substrate Temperature (T_{sub}):	400-550°C
As ₄ pressure:	1×10^{-5} Torr
Growth Rate:	1 μm/h

The lattice mismatch between the epitaxial layer and the substrate was evaluated by standard double crystal X-ray diffraction. The estimated values of the lattice mismatch of the samples used in this study was less than 0.1%. Transmission electron microscope (TEM) observation was also performed to evaluate the crystalline quality around the interface between the epitaxial layer and the substrate. As shown in Fig. 1, the devices fabricated for DLTS were circular mesa-type diodes with an area of $1.2 \times 10^{-3} \text{ cm}^2$. DLTS measurements were made with an HP 4064A DLTS analysis system at temperatures ranging from 100 to 500 K.

RESULTS AND DISCUSSION

Figure 2 shows a typical DLTS spectrum of a p-InAlAs layer, which was grown at a substrate temperature (T_{sub}) of 450°C after its InP substrate was thermally cleaned at a substrate temperature of 460°C under an As₄ pressure. Three peaks, named T₁, T₂ and T₃, are clearly observed in Fig. 2 and this indicates

that three different deep levels exist in the p-InAlAs layer. The density of T₁, whose activation energy is estimated to be about 20-30 meV, is thought to be very small compared to that of the other two levels. From the Arrhenius plots of T₂ and T₃, their activation energies were determined as 300 meV for T₂ and 800 meV for T₃. Figure 3 shows the substrate temperature dependence of the densities of T₂ and T₃. As is clearly seen, performing MBE growth at a substrate temperature over 500°C can dramatically reduce the density of T₃. On the other hand, the density of T₂ shows no significant dependence on the substrate temperature.

In the RHEED observation during the thermal cleaning process, four stages of the surface reconstruction on the InP substrate were observed at different temperatures, similar to the case of a GaAs substrate. When the substrate temperature was below 460°C , a weak single crystal-like diffraction pattern was observed. Then around 460°C , a 2×4 reconstruction, i.e., an As-stabilized surface, appeared. This

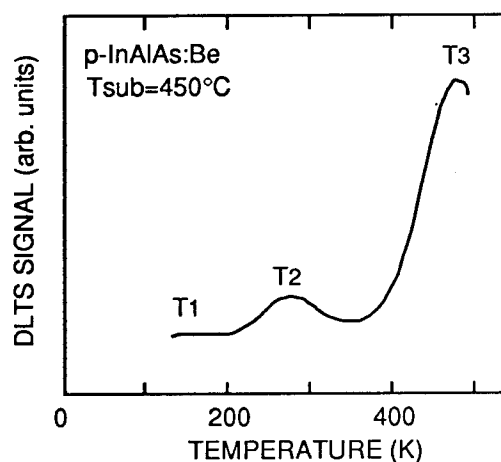


FIG. 2 Typical DLTS spectrum of p-InAlAs:Be. Three peaks, named T₁, T₂, and T₃, are observed, which indicate three different deep levels exist in MBE-grown p-InAlAs:Be.

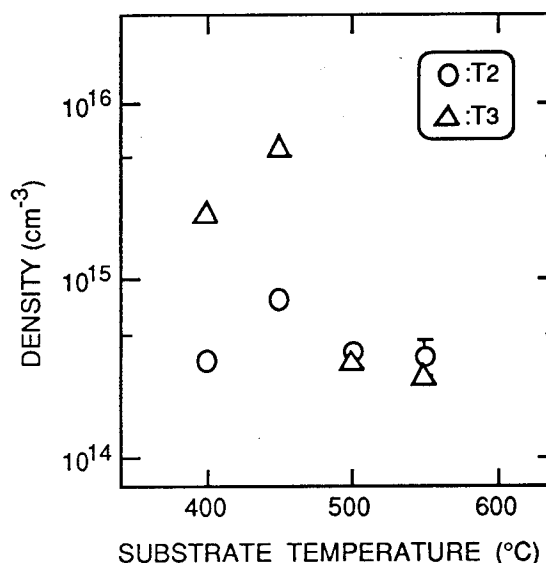


FIG. 3 Substrate temperature dependence of the densities of the T₂ and T₃ levels

indicates that the surface oxides began to desorb at this temperature. The 2x4 pattern gained intensity as the substrate temperature was raised and at around 560°C the RHEED pattern changed from 2x4 to 4x2, which means that the InP surface was stabilized by In atoms. The 4x2 reconstruction could be observed up to 590°C. Above 590°C, the reconstruction disappeared and a weak diffused diffraction pattern with a high scattering background was observed, indicating the substrate had degraded because of excess desorption of P.

Figures 4(a) and (b) show the thermal cleaning temperature dependence of the DLTS spectrum. In Fig. 4(a), both the T2 and T3 peaks can be observed. When the InP substrate was thermally cleaned at 560°C, the T2-peak disappeared completely as shown in Fig. 4(b). Figure 5 shows the cross-sectional TEM photographs of the interface between the InAlAs epitaxial layer and the InP substrate which was thermally cleaned at (a) 460°C and (b) 560°C. When the substrate was cleaned at a substrate temperature of 560°C (the 4x2 condition), no dislocations or defects are observed in the epilayer. On the contrary, in the sample whose substrate was thermally cleaned at a substrate temperature of 460°C (the 2x4 condition), many dislocations and defects are observed around the interface. These dislocations and defects indicate the presence of surface oxides even after the appearance of 2x4 reconstruction. Therefore, the appearance of 2x4 reconstruction cannot be regarded as an indication of complete desorption of the surface oxides. Furthermore, these dislocations and defects are considered to be responsible for the T2 level that appears in Fig. 4(a). This result indicates that when an InP substrate is thermally cleaned under an As₄ pressure, the 4x2 thermal cleaning condition is essential to obtain a high quality epitaxial layer.

By ensuring that the 4x2 thermal cleaning condition is attained and substrate temperature is over 500°C, the density of deep levels can be

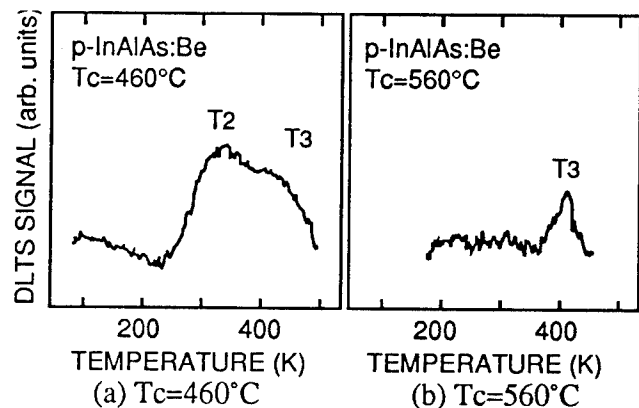


FIG. 4 Thermal cleaning temperature effect on deep levels of p-InAlAs. The T2 level disappeared when the InP substrate was heated to 560°C (b). At this temperature a 4x2 In-stabilized surface reconstruction pattern was observed using RHEED.

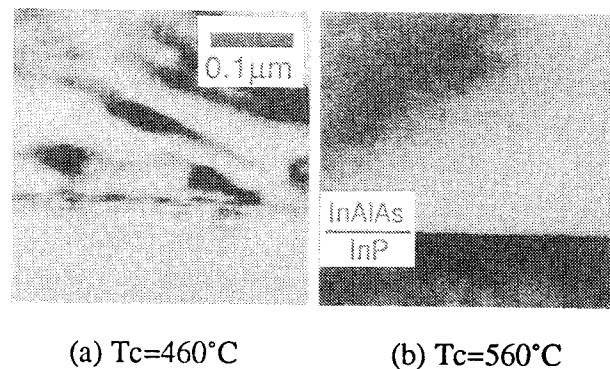


FIG. 5 TEM photographs of the samples of FIG. 4

reduced to about $2 \times 10^{14} \text{ cm}^{-3}$ as shown in Fig. 3, which is low enough for electrical and optical device application. A non-doped InAlAs layer grown under these growth conditions on a semi-insulating InP substrate showed an electron concentration of $7 \times 10^{14} \text{ cm}^{-3}$ and electron mobility of $2000 \text{ cm}^2 \text{ V}^{-1} \text{ s}^{-1}$ at 300 K; this is equal to the highest electron mobility in an

MBE-grown layer yet reported[6].

SUMMARY

In summary, the optimal thermal cleaning condition and substrate temperature needed to obtain a high quality InAlAs epitaxial layer has been established for InP substrates. DLTS measurements revealed that there are two main deep levels in MBE-grown p-InAlAs layers. It was found that for complete desorption of surface oxides, the InP substrates should be heated to the temperature at which the InP substrate surface changes to an In-stabilized surface. Under this thermal cleaning condition, one of the two deep levels was found to disappear. Also, the density of the remaining deep level could be reduced by increasing the substrate temperature. A density as low as about $2 \times 10^{14} \text{ cm}^{-3}$ was reached by applying substrate temperatures above 500°C.

ACKNOWLEDGMENTS

We would like to thank Dr. Fujisaki for his help on the DLTS measurements and valuable discussion concerning the results. We also thank Dr. Koguchi for the TEM observations.

REFERENCES

- [1] L. D. Nguyen et al., IEEE Trans. Electron. Devices, 39(9), p.2007(1992)
- [2] S. Hanatani et al., Proc. of OFC/IOOC '93 ThG3, p.187(1993)
- [3] K. Nakashima et al., phys. stat. sol. (a), 103, p.511(1987)
- [4] W-U. Oh et al., J. Appl. Phys. 74(11), p.7016
- [5] W-P. Hong et al., J. Electron. Mater., 16, p.271(1987)
- [6] L. Aina et al., J. Appl. Phys., 64(10), p.5253(1988)

INVESTIGATION OF A MOLECULAR BEAM EPITAXY REGROWTH PROCEDURE USING AN IN-SITU H_2 PLASMA PROBED WITH AN InP/InGaAs/InP QUANTUM WELL.

V.Drouot, B.J.Robinson, D.A.Thompson

Centre for Electrophotonic Materials and Devices
McMaster University, Hamilton, Ontario L8S 4L7, Canada.

C.Bru, T.Benyattou, G.Guillot

Laboratoire de Physique de la Matière (URA CNRS 358)
INSA, 69621 Villeurbanne Cedex, France.

Introduction:

In the fabrication of advanced optoelectronic devices such as distributed-feedback and distributed Bragg reflector lasers and, especially, monolithically integrated components, epitaxial regrowth steps are generally involved. The conventional thermal cleaning used prior to regrowth by MBE requires high temperature for the desorption of the surface oxide. This high temperature process may induce a roughening of the surface and create defects that are electrically and optically active which degrade device performance. As revealed by Atomic Force Microscopy measurements, desorption of the surface oxide on a GaAs substrate using a Electron Cyclotron Resonance (ECR) hydrogen plasma (H-plasma) has been shown to lead to a smoother surface compared to thermal oxide desorption. A multi-quantum well structure grown on H-plasma cleaned GaAs surfaces has a higher optical quality, than one grown on thermally cleaned surfaces⁽⁶⁾. In the case of InP, thermal desorption involves controlled ramping of the temperature to about $500^\circ\text{C}^{(1-3)}$, considerably higher than the congruent sublimation temperature of 360°C . The use of an ECR H-plasma to remove the oxide on InP has been shown to produce interfaces as good as thermal desorption in an InP(p)/InP(p) regrowth structure, but at a somewhat lower temperature^(4,5). Also, the effects of the PH_3/H_2 flux ratio and the plasma modes have been investigated^(5,7). The activation energy of the oxide etching reaction has been established for two ECR modes and a reaction of the oxide etching has been proposed. In this work, we use a single InGaAs quantum well structure (fig.1) to investigate the effect of a bias potential applied to the substrate during the H-plasma exposure and of annealing performed after the H treatment for growth on InP surfaces. Assessment of the optical quality of the regrowth interface has been achieved by photoluminescence (PL) measurements at 300 and 11 K and photoluminescence excitation spectroscopy (PLE) at 11 K.

Experiments

The experiments have been carried out in a gas source (PH_3 , AsH_3) MBE growth chamber equipped with a shuttered ECR source which allows for a H-plasma exposure of an InP sample surface to be done in a simultaneous phosphorous overpressure. The growth temperature was 460°C for InP and 490°C for InGaAs, measured with a pyrometer. The growth rate was $1 \mu\text{m/h}$.

The structure (figure 1) consists of a $1500\text{-}\text{\AA}$ InP buffer layer, a 36 or $50\text{-}\text{\AA}$ $\text{In}_{0.53}\text{Ga}_{0.47}\text{As}$ quantum well and a $500\text{-}\text{\AA}$ InP capping layer. The regrowth interface is the lower interface of the quantum well. Regrowth interfaces involved removal from vacuum after growth of the buffer layer, a UV-ozone treatment, then return to vacuum. The surface was cleaned, in the growth chamber, with the H-plasma immediately prior to regrowth. Plasma treatments were carried out at growth temperature.

Two types of reference structures were grown for which the sample remained in the growth chamber: the first type of interface, the standard, was generated by only interrupting

growth to permit the change in fluxes and substrate temperature. The second reference type was exposed to a 2-minute H_2 plasma prior to initiating growth of the quantum well. These reference structures enabled the separation of plasma effects from ex-vacuo handling effects.

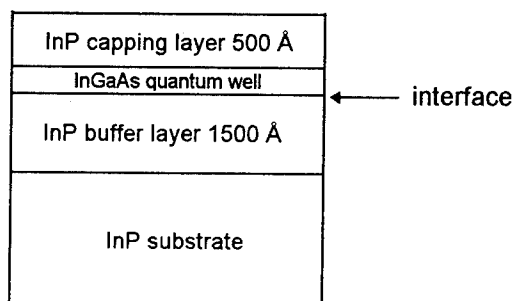


Figure 1. Schematical cross-section of the structure.

Front surface PL excitation was provided by the 488 nm line of a 20 mW cw Ar ion laser. For PLE experiments, the excitation was provided by a 150 W quartz halogen lamp

coupled to a 0.64 m Jobin Yvon monochromator, which allows excitation in the 0.5-1.8 μm wavelength range. The emission was detected by a 0.32 m monochromator and a cooled Ge photodiode.

Results and discussion

1) Effect of H-plasma on InP surface: The reference set of samples consisted of 50-Å InGaAs quantum wells that remained in the growth chamber during the whole growth procedure. The InP buffer layer surface was exposed for two minutes to a H-plasma during the growth interruption. During the plasma exposure the substrate can be either biased, electrically isolated (floating bias) or grounded. When the sample is grounded or isolated, the plasma treatments results in a 10 times lower PL intensity from the InGaAs quantum well, as compared to the standard sample (fig.2.a.b.c). Increasing the plasma exposure time for a grounded substrate results in a further reduction in PL intensity (fig.2.d). Two different ways of minimizing the density of defects created by the plasma were found. Either, biasing the substrate at +30 V during the plasma exposure, or, annealing the sample at growth temperature for 10 minutes in a P_2 overpressure following plasma exposure with grounded substrate, leads to a PL emission which is almost as intense as that from the standard structure (fig.3.a.b.c).

The plasma produces defects at the surface which behave as non-radiative recombination centers. The defects could be structural point defects produced by the impact of the plasma species (H^+ , H^\bullet , H^* , H_2^+ , H_2 , H_2^*) on the surface (typical ion ECR energy ~ 20 eV)^(8,9). They would be removed by the 10' annealing resulting in the observed PL intensity enhancement. When the substrate is biased at +30V, any impinging ions have a lower energy or are repelled. This reduces the production of structural defects and increases the PL intensity.

When the exposure time was increased from 2' to 10' for the grounded bias substrate, the PL intensity decreased by a factor of 4. The full width at half maximum increased from 30 to 36 meV at 300 K and from 9 to 19 meV at 11 K. This may be explained by an increase in the disorder, i.e. surface defects and roughening, caused by the longer exposure to the H-plasma. The higher density of non-radiative defect centers, would account for the decrease in PL intensity. In addition, a roughening of the interface would broaden the PL peak⁽¹⁰⁾.

2) H_2 plasma for oxide desorption: We have investigated the cleaning properties of the H-plasma treatment on an air-exposed InP surface. The optical quality of a 36-Å InGaAs quantum well has been used to study the removal of the oxide by exposure to various plasma conditions. The thinner 36-Å quantum wells have a PL energy removed

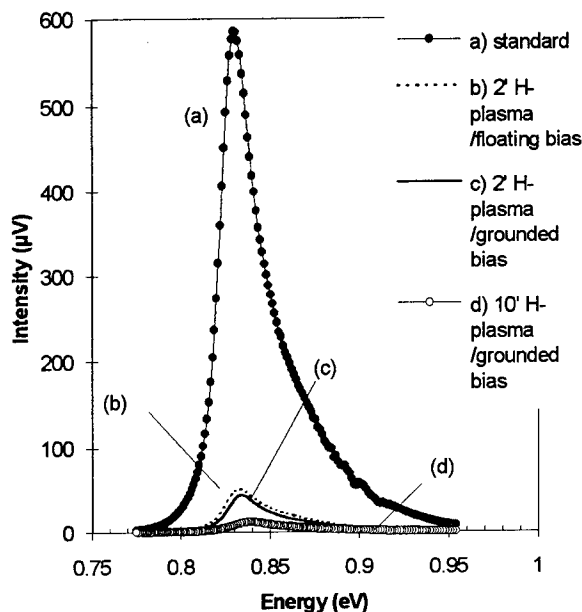


Figure 2. Photoluminescence spectra at 300 K for a reference structure (a), 2' exposure to H-plasma for a grounded substrate (b), a floating substrate (electrically isolated) (c) and 10' exposure to H-plasma for a grounded substrate (d).

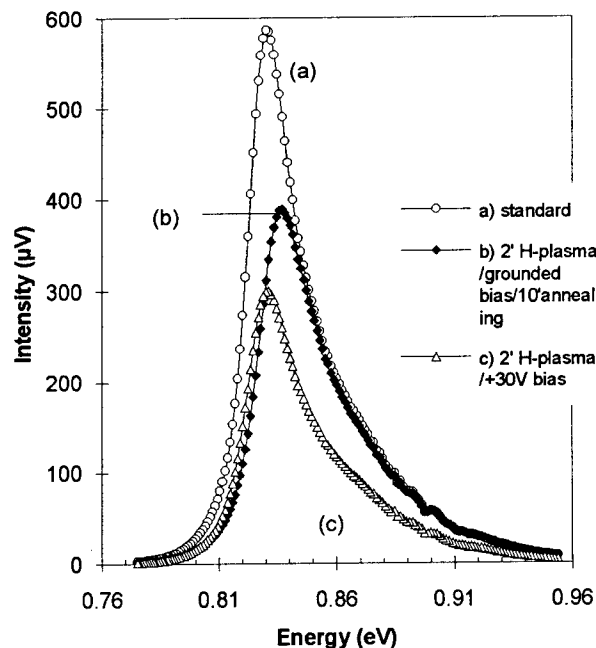


Figure 3. Photoluminescence spectra at 300 K for a reference structure (a), 2' exposure to H-plasma for a +30 V biased substrate (b) and 2' exposure to H-plasma for a grounded substrate followed by 10' annealing (c).

from atmospheric water absorption lines and are more sensitive to the interface quality.

The effect of the plasma exposure time has been investigated with 5' and 10' durations of plasma exposure. On the basis of the results given in figure 3 for the references, a +30 V bias was applied to the substrate and the plasma exposure was followed by a 10' annealing. Another procedure has also been tested, and consists of alternating 30" plasma exposure and 30" annealing by closing the plasma shutter, repeated 20 times. This corresponds to a 10' plasma exposure and a total treatment time of 20'. In all cases (fig.4.a.b.c.d), the RHEED patterns observed after oxide removal revealed a 2×4 surface reconstruction, which indicates an oxide-free InP surface⁽²⁾.

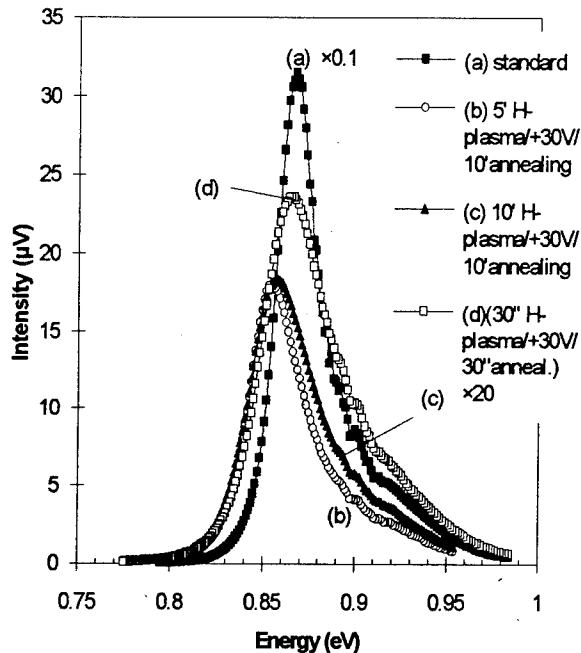


Figure 4. Photoluminescence spectra at 300 K. (a) is a standard structure, (b), (c) and (d) have been processed ex-vacuo (UV-ozone exposure) and exposed to different plasma treatments: (b) biased at +30 V during a 5' exposure to H-plasma, followed by 10' annealing, (c) biased at +30 V during a 10' exposure to H-plasma, followed by 10' annealing and (d) biased at +30 V, 30" exposure to H-plasma followed by 30" annealing, repeated 20 times.

The PL spectra (fig.4) for these samples are broader and more than ten times less intense than for the standard structure that remained under ultrahigh vacuum. From the PL data, all the structures present a comparable intensity at 300 K (fig.4.a,b,c,d), about 15 times lower than the intensity for standard sample, and a similar broadening of the peak

at 11 K (table A) compared to the reference. The regrowth structure cleaned with the alternating plasma exposure sequence exhibits a room temperature PL line broader than any other sample. PLE measurements have been performed on these samples. The PLE spectra (fig.5) display the different excitonic transitions, E_1HH_1 and E_1LH_1 , between the first electron energy level and the heavy and light hole levels. The sharpness of the E_1HH_1 transition resonance decreases when the exposure time is increased from 5' to 10' (fig.5.b.c). The resonance disappears for the sample treated with the alternating procedure (fig.5.d).

Non-radiative centers, introduced at the interface of the well by the air exposure and/or the oxide desorption procedure, reduce the PL intensity. These non-radiative centers could be due to residual impurities incorporated at the bottom interface or intrinsic defects created at the surface during the oxide formation and/or desorption. The PL signal broadening could be due to perturbation at the interface, such as roughness or foreign species. Previous studies based on SIMS measurements have shown that silicon and oxygen are common contaminants present at the interface that the plasma cannot completely remove^(5,11,12).

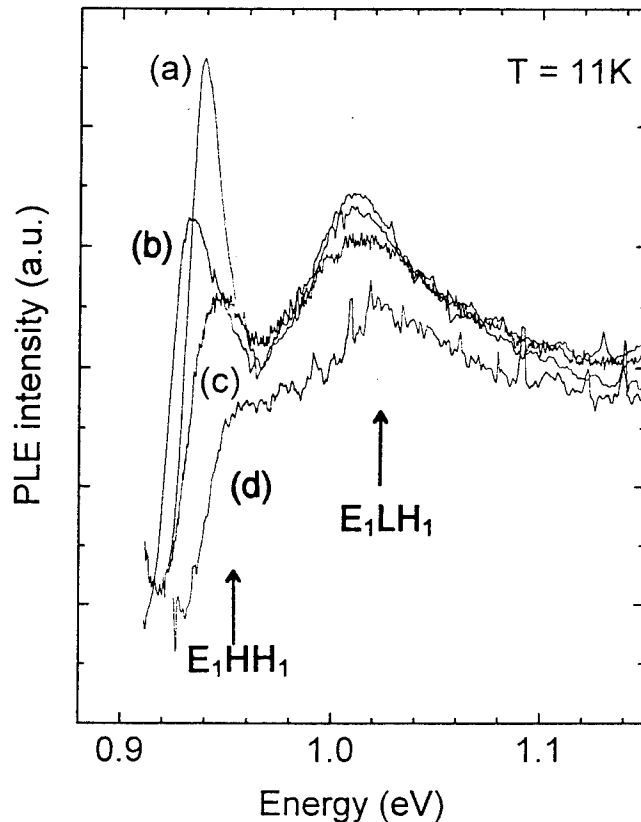


Figure 5. PLE spectra at 11 K for the 36-Å quantum well processed ex-vacuo and their reference. (a), (b), (c) and (d) refer to the same structures as in figure 4.

The PLE spectra give information complementary to the PL about the interface quality. For the 10' plasma exposure (fig.5.c), the excitonic resonance of the different transitions are less sharp than the one for the 5' exposure (fig.5.b). The sharpness of the transitions is a criterion of interface quality as any defect would reduce the exciton lifetime and broaden the transition peak. For the sample treated with the alternating sequence (fig.5.b), the E_1HH_1 excitonic resonance is not detectable. This reveals a much lower quality of the interface for this sample. The Stoke shift (difference between the PL energy and the E_1HH_1 transition energy), reported in table A, is also larger for the 10' exposure than for the 5', which confirm this lower interface quality.

We can conclude from these results that the 5' plasma exposure is enough to remove the bulk of the oxide. A longer exposure time seems to increase the interface perturbation which broadens the E_1HH_1 transition resonance in the PLE spectrum. The longer exposure time does not reduce the non-radiative defect density as the PL intensity is not increased.

For the sample (d) (table A), the rougher interface revealed by the PLE spectra is likely a result of the last short annealing phase (30'') which would not remove the defects created at the surface by the last 30'' plasma exposure.

Conclusion

Various H_2 plasma techniques have been investigated for the purpose of cleaning the surface of InP and minimizing the creation of defects at a regrowth interface. In general, a +30 V bias applied to the substrate and an anneal following the plasma exposure have been found to be beneficial.

The H-plasma exposure effectively removes the bulk of the oxide but does leave some impurities. The regrowth procedure produces non-radiative defects which decrease the PL intensity over a factor of 10 compared to standard continuous growth. The regrowth procedure also broadens

the PL signal by introducing perturbations (roughness and/or impurities) at the interface. The portion of the broadening that may be attributed to roughening at the interface is at least partially overcome by the annealing treatment.

Acknowledgments

Special thanks are deserved by Scott McMaster for his assistance with the GSMBE growths.

References

- (1) D.Gallet, M.Gendry, G.Hollinger, A.Overs, G.Jacob, B.Boudart, M.Gauneau, H.L'Haridon, D.Lecrosnier, J.Electron.Mater. **20**, 963 (1991).
- (2) R.Averbeck, H.Riechert, H.Schlotterer, G.Weinmann, Appl.Phys.Lett. **59**, 1732 (1991).
- (3) D.Comedi, G.Balcitis, B.J.Robinson, D.A.Thompson, Can.J.Phys. **70**, 1043 (1992).
- (4) P.G.Hofstra, D.A.Thompson, B.J.Robinson, G.Hollinger, R.W.Streater, Proc. of 5th Int. Conf. on InP and Related Materials. IEEE Catalog #93CH3276-3, 1993, Paris, pp.95-98.
- (5) P.G.Hofstra, D.A.Thompson, B.J.Robinson, R.W.Streater, J. of Vac. Sci. & Tech.B **11**(3), p.985, 1993.
- (6) N.Kondo, Y.Nanishi and M.Fujimoto, Jpn. J. of Appl.Phys. **33**, L93, 1993.
- (7) P.G.Hofstra, B.J.Robinson, D.A.Thompson and S.A.McMaster, submitted to J.Vac.Sci.Technol.
- (8) L.M.Weegels, T.Saitoh, H.Ooshaki and H.Kambe, Appl.Phys.Lett. **64**, 2661 (1994).
- (9) I.Suemune, Y.Kunitsugu, Y.Kan and M.Yamanishi, Appl.Phys.Lett. **55**, 760 (1989).
- (10) D.Bimberg, D.Mars, J.N.Miller, R.Bauer and D.Øertel, J.Vac.Sci.Technol. B **4** 1014, (1986).
- (11) H.Ishikawa, S.Miwa, T.Maruyama and M.Kamada, J.Appl.Phys. **71**, 3898, 1992.
- (12) S.Izumi, N.Yoshida, H.Takano, K.Nishitani and M.Otsubo, J.Cryst.Growth **133**, 123 (1993).

interface type	PL FWHM (meV)	PL energy (eV)	PLE energy E_1HH_1 (eV)	Stoke Shift (meV)
(a) reference	8	0.930	0.939	9
(b) H-plasma 5'/+30V/ 10' annealing	22	0.913	0.935	22
(c) H-plasma 10'/+30V/ 10' annealing	23	0.916	0.945	29
(d) (H-plasma 30''/ +30V/30'' annealing)×20	21	0.930	A)	A)

Table A. PL and PLE data at 11 K for the 36-Å quantum wells processed ex-vacuo and their reference structure. (a), (b), (c) and (d) refer at the same structures as in figure 4 and 5. For (d), A) denotes no transition observable.

ISLAND GROWTH AND PHASE SEPARATION IN STRAINED $\text{InAs}_{1-x}\text{P}_x/\text{InP}$ HETEROSTRUCTURES

WP34

D.J. Tweet, H. Matsuhata, R. Shioda, H. Oyanagi, and H. Kamei[†]

Electrotechnical Laboratory, 1-1-4 Umezono, Tsukuba, Ibaraki 305 Japan

[†]*Sumitomo Electric Industries, Ltd., 1, Taya-cho, Sakae-ku Yokohama 244 Japan*

Using x-ray diffraction and transmission electron microscopy we have found that $\text{InAs}_{1-x}\text{P}_x$ films deposited on $\text{InP}(001)$ substrates with organometallic vapor phase epitaxy grow in an unusual phase-separated island growth mode related to strain. Initially, pseudomorphic islands of intermediate composition form and grow only until some point in the relaxation process, possibly a critical value of the strain, after which islands of the intended composition begin to appear. Furthermore, both types of islands are found to penetrate deeply into the substrate.

Introduction

$\text{InAs}_{1-x}\text{P}_x/\text{InP}(001)$ quantum wells show excellent promise for long-wavelength optoelectronic device applications, such as $1.3\ \mu\text{m}$ laser diodes (1). Consequently, there have been many growth studies using a variety of techniques such as organometallic vapor phase epitaxy (OMVPE) (1-4), gas source molecular beam epitaxy (GSMBE) (5), atomic layer epitaxy (ALE) (6), chemical beam epitaxy (CBE) (7), and MBE (8). A major theme of this research has been control of the rather large exchange which occurs between P and As atoms at the interfaces (2,4,6-8). Usually, several monolayers of interdiffusion are found, and it has also been reported that the InP on InAs interface is sharper than that of InAs on InP (7).

More generally, there has been much interest in a rich variety of issues associated with the growth of semiconductor heterostructures. These include the critical thickness, t_c , for relaxation of lattice-mismatched systems (3,5,6,9,10), the recent proposition of a critical strain for switching between two different relaxation modes (11), possible strain effects on interdiffusion (12-14), and phase separation (15-18).

Here we report a complex interplay between all of the above mentioned phenomena in a set of $\text{InAs}_{1-x}\text{P}_x$ layers grown on $\text{InP}(001)$ substrates. Specifically, we find that these films grow in an unusual phase-separated island growth mode related to strain. Initially, pseudomorphic islands of intermediate composition form and grow only until some point in the relaxation process, possibly a critical value of the strain, after which islands of the intended composition begin to appear. Furthermore, both types of islands penetrate deeply into the substrate.

Experimental

The $\text{InAs}_{1-x}\text{P}_x$ layers were grown on $\text{InP}(001)$ substrates by low-pressure (OMVPE). The substrate temperature was 620°C and trimethylindium, arsine, and phosphine were used as source gases. A $1000\ \text{\AA}$ InP buffer was grown before the $\text{InAs}_{1-x}\text{P}_x$ layer deposition, and each sample was covered by a $20\ \text{\AA}$ InP cap. Details of the growth conditions have been reported elsewhere (3). Two sets of wafers were examined: Four samples of InAs with intended thicknesses $40\ \text{\AA}$, $100\ \text{\AA}$, $200\ \text{\AA}$, and $1000\ \text{\AA}$, and

five samples of $\text{InAs}_{0.6}\text{P}_{0.4}$ with intended thicknesses $60\ \text{\AA}$, $100\ \text{\AA}$, $200\ \text{\AA}$, $400\ \text{\AA}$, and $1000\ \text{\AA}$. A sample with just the buffer layer was also prepared, to be used as background for the x-ray data.

These thicknesses were chosen to examine the relaxation process. Calculations using Matthews and Blakeslee's model (9) and that of People and Bean (10) yield estimates for t_c of InAs on InP to be $20\ \text{\AA}$ and $40\ \text{\AA}$ respectively, and for $\text{InAs}_{0.6}\text{P}_{0.4}$ on InP to be $40\ \text{\AA}$ and $200\ \text{\AA}$ respectively (3). Previous studies of InAs on InP have reported t_c to be about $20\ \text{\AA}$ (5) or $30\text{--}36\ \text{\AA}$ (6).

The composition, thickness, and morphology of the films were examined using x-ray diffraction (XRD), transmission electron microscopy (TEM), and energy-dispersive x-ray analysis (EDX). The XRD results were obtained with a MAC Science SRA $18\ \text{kW}$ x-ray generator with $\text{CuK}\alpha_1$ radiation selected by a four-crystal $\text{Ge}(220)$ monochromator. A Philips MRD goniometer with Eulerian cradle was used, and a $0.45\ \text{mm}$ slit was set in front of the scintillation counter detector. Cross-sectional TEM observations and EDX microbeam analysis were performed using a Topcon 002B with a Philips 9900.

XRD Results

The measured XRD intensities near the $\text{InP}(004)$ substrate peak are shown in Fig. 1. In the thicker films two peaks are visible, labeled A and B. Thus, there are regions with two different compositions whereas only one was expected, B. In both sets of samples initially there is just region A, which grows only until region B appears.

From the positions of these peaks and those near the $\text{InP}(115)$ reflection (not shown) the lattice constants parallel, a_{\parallel} , and perpendicular, a_{\perp} , to the interface were obtained for the regions corresponding to peaks A and B in each sample. In each case the cubic lattice constant, $a(x)$, of a relaxed layer of the same composition could then be calculated, using bulk elastic constants and continuum elastic theory. Assuming Vegard's Law (a linear dependence of alloy lattice constant on composition) the average P composition, x , of each region was then determined, as shown in Fig. 2(a). Peak B is seen to correspond to the intended compositions in both sets, although there may be a slight decrease in x with increasing thickness in the $\text{InAs}_{0.6}\text{P}_{0.4}$ case. For region A,

x starts out very high, gradually decreasing to a stable value of about 0.75 for the $\text{InAs}_{0.6}\text{P}_{0.4}$ samples and 0.55 for the InAs set. This trend suggests a composition gradient, which is supported by simple simulations of the XRD data. Consistent with this, secondary ion mass spectroscopy (SIMS) measurements of the nominally 60 Å $\text{InAs}_{0.6}\text{P}_{0.4}$ sample show a broad As region extending 200 Å into the sample, well beyond the intended thickness.

The degree of relaxation, defined as,

$$R = \frac{a_{\parallel} - a_s}{a(x) - a_s}$$

where a_s is the InP substrate lattice constant, is shown in Fig. 2(b). From this, t_c of region A is about 40 Å and 200 Å in the InAs and $\text{InAs}_{0.6}\text{P}_{0.4}$ samples, respectively. (Since A may have a composition gradient, interpretation of these numbers is not straightforward.) Note that in the latter set, region A never completely relaxes, probably due to the low As content and the fact that it has stopped growing.

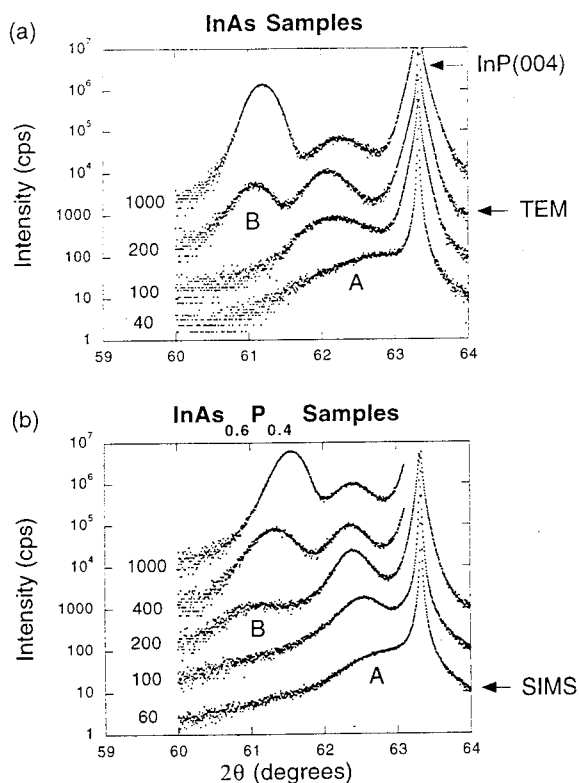


Fig. 1. XRD intensities as a function of scattering angle, 2θ , near the InP(004) substrate peak for specimens with intended composition (a) InAs and (b) $\text{InAs}_{0.6}\text{P}_{0.4}$. The intended layer thickness in Å is indicated for each data scan, which are offset for clarity. The 200 Å InAs sample was examined with TEM and EDX, as shown in Fig. 4. The 60 Å $\text{InAs}_{0.6}\text{P}_{0.4}$ sample with examined with SIMS.

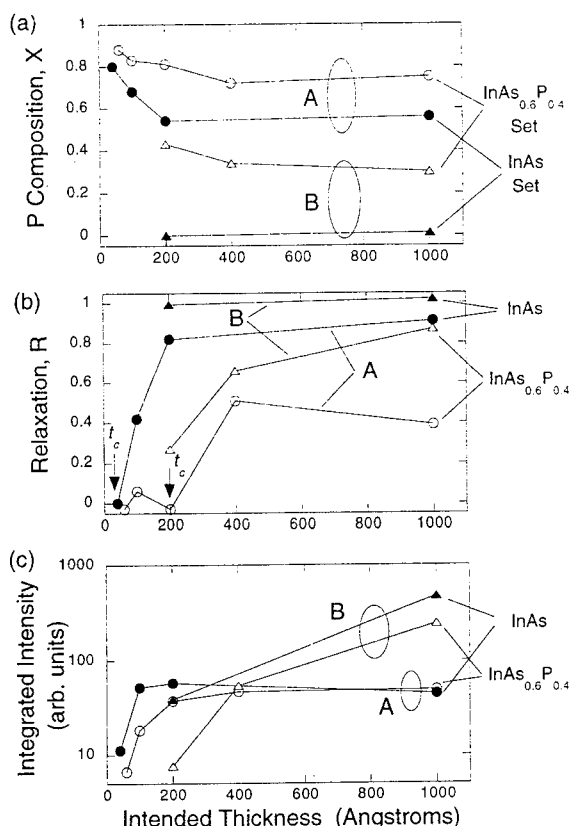


Fig. 2. Plots of (a) x , (b) R and (c) (004) integrated intensities of the A and B peaks vs. intended layer thickness in Å. Note the logarithmic scale in (c). Uncertainties are comparable to the size of the symbols in (a) and (c). In (b), they are ± 0.1 for $R < 0.5$ and ± 0.05 for $R > 0.5$.

Near both InP(004) and InP(115) two-dimensional reciprocal space XRD intensity maps were obtained for all samples. From these, the background-subtracted integrated intensities of the peaks were derived. The results for the A and B peaks near InP(004) are shown in Fig. 2(c); the (115) values exhibit similar trends. As was apparent from Fig. 1, peak A grows only until peak B appears.

To summarize the observations thus far, for the InAs samples initially only A is present, strained to match the InP substrate, and with a high average x . As the thickness increases, A starts to relax, x decreases, and then B (relaxed, $x = 0.0$) appears between 100 Å and 200 Å. From 200 Å, B grows in intensity, but A does not. The $\text{InAs}_{0.6}\text{P}_{0.4}$ set shows similar behavior, just shifted to higher thickness.

At first glance the appearance of B and saturation of A seem correlated with the onset of relaxation in region A, but upon closer inspection this turns out to be not true. For the InAs set, B appears between 100 Å and 200 Å, when region A is already over 40% relaxed, whereas for the $\text{InAs}_{0.6}\text{P}_{0.4}$ samples B first appears at 200 Å, when region A has not yet started to relax. As discussed below, rather than the critical thickness t_c determining this behavior, we find evidence that a critical strain ϵ_c dominates it.

Recently Tersoff and LeGoues (11) reported the existence of a critical strain in SiGe grown on Si. Below ϵ_c , ($\sim 1\%$) the films are smooth, even when thicker than t_c , and relax by a modified Frank-Read mechanism. Above ϵ_c , the films first roughen and then relax via dislocations nucleated at the surface. Here we show that $\text{InAs}_{1-x}\text{P}_x/\text{InP}$ may also exhibit critical strain(s), although the behavior is more complex than that discussed previously.

Using the lattice constants derived from peak A the average strain parallel to the interface experienced by the intermediate layer is

$$\epsilon_A = \frac{a_{\parallel A} - a(x_A)}{a(x_A)}$$

A similar expression is used to calculate ϵ_B , the strain experienced by the intended layer. The magnitudes are shown in Fig. 3(a) and 3(b), respectively. The horizontal scale has been normalized to the thickness at which peak B first appears, estimated as 150 Å and 200 Å for the InAs and $\text{InAs}_{0.6}\text{P}_{0.4}$ sets, respectively. There is a maximum value of $|\epsilon_A| \approx 0.0065$, at which point the mixing stops and peak B appears.

It is also useful to calculate the strain that would be experienced by a layer of the intended composition if it could be deposited pseudomorphically on the mixed layer,

$$\epsilon_{B/A} = \frac{a_{\parallel A} - a(x_B)}{a(x_B)},$$

seen in Fig. 3(c). For the InAs samples, peak B does not appear until $|\epsilon_{B/A}|$ drops to about 0.019. The $\text{InAs}_{0.6}\text{P}_{0.4}$ samples show a nearly constant value of $|\epsilon_{B/A}| = 0.019$. Consequently, it appears that if growth of a layer with strain greater than about 1.9% is attempted, enhanced P-As exchange occurs and a region of intermediate composition forms. Once the strain in this layer reaches about 0.6%, the mixing stops and the layer of intended composition can grow, albeit with a strain of less than 1.9% (Fig. 3(b)). However, more work remains to verify this scenario.

Strain effects on interdiffusion in semiconductor systems have been much debated recently, with some researchers reporting strong changes (12,13) and others not (14). Our XRD results (as well as the TEM and EDX data discussed below) seem to be due to strain-enhanced mixing, but the influence of the surface and other possible factors cannot be ruled out.

TEM and EDX Results

Since XRD can only give information about the average structure, various microscopies were also performed. Nomarski contrast microscopy and atomic force microscopy (AFM) show an initially smooth surface which roughens with increasing layer thickness, indicating an island growth mode. This is confirmed by TEM measurements of the nominally 200 Å InAs sample. Islands 1000 Å tall exist on the surface and also penetrate up to 400 Å into the substrate, Fig. 4. Numerous misfit dislocations are apparent at the island/substrate interface, indicating a sharp change in composition and lattice constant. Other islands exhibit a less distinct interface.

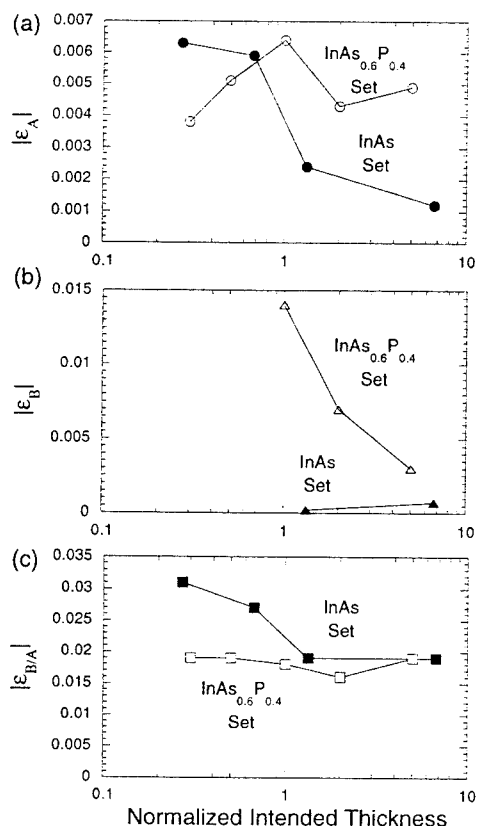


Fig. 3. Plots of (a) $|\epsilon_A|$, (b) $|\epsilon_B|$, and (c) $|\epsilon_{B/A}|$ vs. normalized intended thickness. Note the different vertical scales. Uncertainties are approximately ± 0.001 .

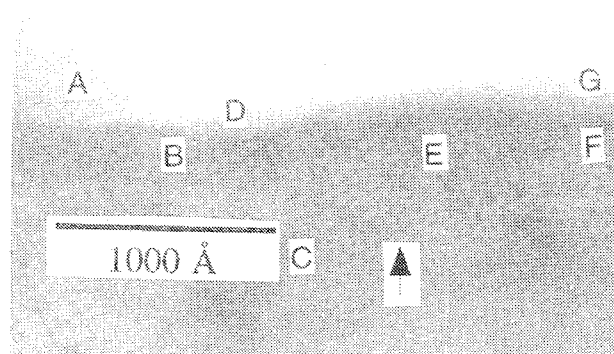


Fig. 4. $\langle 110 \rangle$ cross-sectional TEM micrograph of the nominally 200 Å InAs sample for which EDX data was obtained at the indicated regions. The arrow indicates an area of especially deep penetration.

The composition of various islands has been determined by EDX, showing that some are InAsP and others are InAs. In Fig. 4, region C is the InP substrate, A is InAsP of approximately equal As and P content, B, E, and G are InAsP of high As content, while D and F are InAs. Thus, there is phase separation both parallel and perpendicular to the surface.

This penetration into the substrate is likely due to strain-enhanced diffusion, and apparently causes the appearance of peak A in the XRD data. Although we have not yet proven it with TEM, the penetration should stop when the XRD peak B appears. Note, however, that EDX measurements of other regions of the sample show, surprisingly, that at least some of the islands penetrating into the substrate are pure InAs.

Finally, the observed separation into regions of different compositions does not appear to be related to that commonly observed in III-V ternary and quaternary alloys (15-18). This is usually attributed to phase separation occurring at the growing surface due to the presence of a miscibility gap. To our knowledge, this effect has only been seen in alloys for which a bulk miscibility gap is predicted. In contrast, none is expected for InAsP (15).

Conclusion

In conclusion, we report a complex interplay between relaxation, phase separation, interdiffusion, and strain in $\text{InAs}_{1-x}\text{P}_x/\text{InP}(001)$. Specifically, we find an unusual phase-separated island growth mode associated with strain, which shows deep substrate penetration.

Acknowledgements

The authors gratefully acknowledge useful discussions with Y. Takeda, Y. Kuwahara and P. Fons, and wish to thank the latter for developing Mathematica programs used to analyze the XRD data. We thank Dr. Ikuhara of the Japan Fine Ceramics Center and Dr. Kuroda of Nagoya University for help with the EDX. The assistance of H. Tsuboi with the AFM measurements is also appreciated.

References

- (1) Y. Imajo, A. Kasukawa, T. Namegaya, and T. Kikuta, "1.3 μm $\text{InAs}_y\text{P}_{1-y}/\text{InP}$ strained-layer quantum well laser diodes grown by metalorganic chemical vapor deposition", *Appl. Phys. Lett.* Vol. 61, pp 2506-2508, 23 November 1992.
- (2) R. Shioda, H. Oyanagi, Y. Kuwahara, Y. Takeda, K. Haga, and H. Kamei, "Incorporation Process of the As Atom on the $\text{InP}(001)$ Surface Studied by Extended X-Ray Absorption Fine Structure", *Jpn. J. Appl. Phys.*, Vol 33, pp. 5623-5630, October 1994.
- (3) Y. Kuwahara, H. Oyanagi, R. Shioda, Y. Takeda, H. Yamaguchi, and M. Aono, "Bond Length Relaxation in Ultrathin InAs and $\text{InP}_{0.4}\text{As}_{0.6}$ Layers on $\text{InP}(001)$ ", *Jpn. J. Appl. Phys.*, Vol. 33, pp. 5631-5635, October 1994.
- (4) M. Tabuchi, Y. Takeda, Y. Sakuraba, T. Kumamoto, K. Fujibayashi, I. Takahashi, J. Harada, and H. Kamei, "Atomic-Level Interface Structure of $\text{InP}/\text{InPAs}/\text{InP}$ Measured by X-Ray CTR Scattering", (to be published).
- (5) H. Temkin, D.G. Gershoni, S.N.G. Chu, J.M. Vandenberg, R.A. Hamm, and M.B. Panish, "Critical layer thickness in strained $\text{Ga}_{1-x}\text{In}_x\text{As}/\text{InP}$ quantum wells", *Appl. Phys. Lett.*, Vol. 55, pp. 1668-1670, 16 October 1989.
- (6) Y. Kobayashi and N. Kobayashi, "In Situ Interface Control of Pseudomorphic InAs/InP Quantum Well Structure Growth by Surface Photo-Absorption", *Jpn. J. Appl. Phys.*, Vol. 31, pp. 3988-3994, December 1992.
- (7) P.D. Brown, E.G. Bithell, C.J. Humphreys, P.J. Skevington, P.J. Cannard, and G.J. Davies, "The effect of growth interrupts on CBE grown InP ", *Inst. Phys. Conf. Ser. No. 134*, pp. 373-376, 1993.
- (8) J.M. Moison, M. Bensoussan, and F. Houzay, "Epitaxial regrowth on an InAs surface on InP : An example of artificial surfaces", *Phys. Rev. B*, Vol. 34, pp. 2018-2021, 1 August 1986.
- (9) J.W. Matthews and A.E. Blakeslee, "Defects in Epitaxial Multilayers I. Misfit Dislocations", *J. Cryst. Growth* Vol. 27, pp. 118-125, 1974.
- (10) R. People and J.C. Bean, "Calculation of critical layer thickness versus lattice mismatch for $\text{Ge}_x\text{Si}_{1-x}/\text{Si}$ strained-layer heterostructures", *Appl. Phys. Lett.*, Vol. 47, pp. 322-324, 1 August 1985.
- (11) J. Tersoff and F.K. LeGoues, "Competing Relaxation Mechanisms in Strained Layers", *Phys. Rev. Lett.*, Vol. 72, pp. 3570-3573, 30 May 1994.
- (12) F.H. Baumann, J.-H. Huang, J.A. Rentschler, T.Y. Chang, and A. Ourmazd, "Multilayers as Microlabs for Point Defects: Effect of Strain on Diffusion in Semiconductors", *Phys. Rev. Lett.*, Vol. 73, pp. 448-451, 18 July 1994.
- (13) N.E.B. Cower, P.C. Zalm, P. van der Sluis, D.J. Gravesteijn, and W.B. de Boer, "Diffusion in Strained $\text{Si}(\text{Ge})$ ", *Phys. Rev. Lett.*, Vol. 72, pp. 2585-2588, 18 April 1994.
- (14) W.P. Gillin and D.J. Dunstan, "Strain and interdiffusion in semiconductor heterostructures", *Phys. Rev. B*, Vol. 50, pp. 7495-7498, 15 September 1994.
- (15) K. Onabe, "Unstable Regions in III-V Quaternary Solid Solutions Composition Plane Calculated with Strictly Regular Solution Approximation", *Jpn. J. Appl. Phys.*, Vol. 21, pp. L323-L325, June 1982.
- (16) F. Glas, "Composition variations, clustering and composition fluctuations in III-V alloys", *Inst. Phys. Conf. Ser. No. 134*, pp. 269-278, 1993.
- (17) T.-Y. Seong, A.G. Norman, I.T. Ferguson, and G.R. Booker, "Transmission electron microscopy and transmission electron diffraction structural studies of heteroepitaxial $\text{InAs}_y\text{Sb}_{1-y}$ molecular-beam epitaxial layers", *J. Appl. Phys.*, Vol. 73, pp. 8227-8236, 15 June 1993.
- (18) S.A. Ponchet, A. Rocher, A. Ougazzaden, and A. Mircea, "Self-induced laterally modulated $\text{GaInP}/\text{InAsP}$ structure grown by metal-organic vapor-phase epitaxy", *J. Appl. Phys.*, Vol. 75, pp. 7881-7883, 15 June 1994.

Lateral modulation in strain-compensated MQW structures

Y. Shimose, T. Kikugawa, and H. Nagai

Research Laboratory, Anritsu Corp.

1800 Onna, Atsugi-shi, Kanagawa, 243, Japan

TEL: +81-462-23-1111, FAX: +81-462-23-1600

Abstract

Strain-compensated multiple-quantum-well structures in InGaAsP alloys have been grown by metal-organic vapor-phase epitaxy (MOVPE). Remarkably-periodic lateral-modulated structures have been observed, and their modulation properties are discussed. The modulated structures are enhanced at the InP-rich region and under huge net strain. The modulation period depends on the growth rate.

Introduction

Strain-compensated multiple-quantum-well (MQW) structures have become increasingly important in opto-electronic devices. Although it is possible to grow a large number of MQW without strain relaxation, a laterally-modulated structure, which has remarkable periodicity along the $\langle 110 \rangle$ direction, is often observed^{1),2),3)} and limits the MQW structure total thickness. However, the mechanism of this modulation phenomenon is not clear yet. Furthermore, no systematic study of this phenomenon has been reported with reference to the composition of the MQW structure and growth conditions.

We studied the modulation characteristics of strain-compensated MQW structures in InGaAsP alloys.

Experiment

Strain-compensated MQW structures were grown by low-pressure (150 torr) MOVPE at 600° C on InP (001) substrates. Trimethylindium (TMI) and triethylgallium (TEG) were used as sources for group-III elements, and PH_3 and AsH_3 were used as sources for group-V elements. The MQWs consisted of 10 periods of 6.5 nm thick InGaAsP wells (lattice mismatch of +1.0%), and 9.5 nm thick InGaAsP barriers (lattice mismatch of -0.5%). For growth of the strain-compensated layers, the flows of TMI and PH_3 were kept constant, while the flows of TEG and AsH_3 were changed. The V/III ratio ranged from 300 to 350. The average value of the composition including all wells and barriers in the MQW structure (MQW average composition), ranged from 0.85 to 1.11 eV in bandgap energy. The gas interruption sequence was taken at interfaces between wells and barriers. The MQWs are covered with a 60 nm thick InP cap layer.

Results

A cross-sectional SEM photograph of the MQW structure with the typical lateral modulation is shown in Fig. 1. The lateral-modulated structure in the well and the barrier thickness are seen in the upper half of the MQW stack. The modulation pitch is about 200 nm with 10%-20% deviation.

The photoluminescence (PL) spectrum of this structure with modulation is shown in Fig. 2. The extra peak arising from the thicker well region can be seen on the longer-wavelength side of the PL peak wavelength of the lower half of the MQW stack.

The modulation strongly depends on the composition of the MQW structure. A map of the modulation appearance on the net-strain value vs. MQW average composition plane is shown in Fig. 3. Here, various net strain values were obtained with slight changes in the strain values of barriers or wells. The modulation is more pronounced in InP-rich and large net-strain regions. A InP-rich regions (wide bandgap region), the modulation appears even at almost zero net-strain.

Furthermore, the modulation pitch strongly depends on the growth rate as shown in Fig. 4. The higher the growth rate, the shorter the modulation pitch. The dependence of the well or barrier thickness was also investigated in the 12 to 23 nm range for the MQW period, but the modulation pitch was not dependent at these thicknesses.

It is believed that the modulation structure is caused by unstableness at the stressed interfaces between wells and barriers. Consequently, we

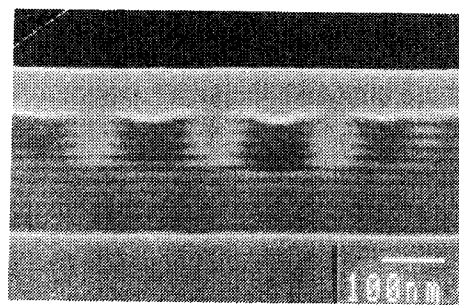


Fig. 1. Cross-sectional SEM photograph of strain-compensated MQW ($\text{In}_{0.90}\text{Ga}_{0.10}\text{As}_{0.53}\text{P}_{0.47}$ / $\text{In}_{0.76}\text{Ga}_{0.24}\text{As}_{0.37}\text{P}_{0.63}$)

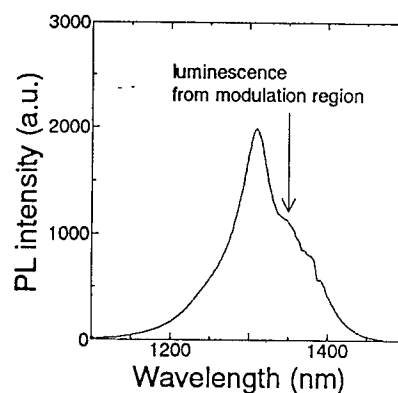


Fig. 2. Photoluminescence spectrum of same MQW structure as Fig. 1 at room temperature. The extra peak at about 1350 nm corresponds to the luminescence from the modulation region

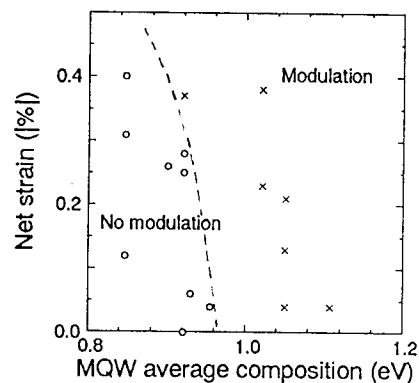


Fig. 3. Map of appearance of modulation as function of net strain and MQW average composition. The well composition ranges from $\text{In}_{0.69}\text{Ga}_{0.31}\text{As}_{0.97}\text{P}_{0.03}$ to $\text{In}_{0.94}\text{Ga}_{0.06}\text{As}_{0.45}\text{P}_{0.55}$, and the barrier composition ranges from $\text{In}_{0.61}\text{Ga}_{0.39}\text{As}_{0.68}\text{P}_{0.32}$ to $\text{In}_{0.81}\text{Ga}_{0.19}\text{As}_{0.27}\text{P}_{0.73}$

grew the MQW structures with a continuously graded composition interface without gas interruption. In this case, the shear stress at the interface is expected to partially relax due to the presence of compositionary grading layers. As shown in Fig. 5, MQW structure with a compositionary grading interface without gas interruption has thin modulated structure.

Discussion and conclusion

We have demonstrated the characteristics of strain-compensated MQW structures in InGaAsP alloys. It is clear that the modulation occurs easily in InP-rich regions and that the modulation pitch depends strongly on the growth rate. Furthermore, elimination of gas interruption at interfaces between wells and barriers suppresses this modulation.

A thinner modulation without gas interruption indicates that the cause of the modulation is related to the shear stress at interfaces between wells and barriers⁴⁾. Furthermore, the growth rate dependence suggests that the modulation probably arises from surface migration of group-III species. At higher growth rates, the atoms cannot migrate for as long as at lower growth rates. Consequently, this modulation seems to be the result of a delicate balance between minimization of elastic energy⁵⁾ and growth kinetics.

The lack of no modulation in the narrow-bandgap region may be attributed to the high arsenic concentration. Since the decomposition yield of arsine is larger than that of phosphine, the actual V/III ratio becomes larger, the

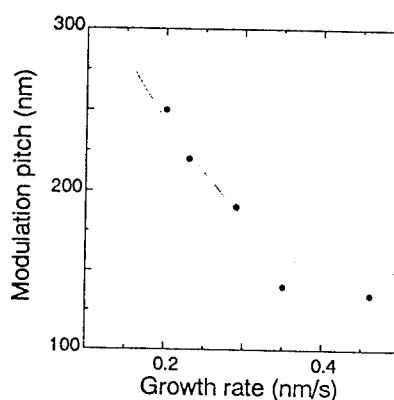


Fig. 4. Modulation pitch as function of growth rate

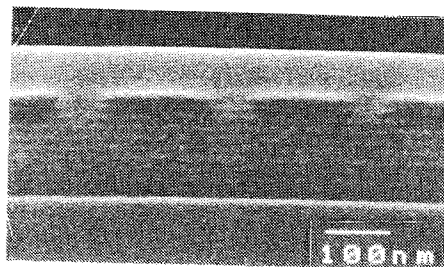


Fig. 5. Cross-sectional SEM photograph of MQW structure with same composition as Fig. 1 but without gas interruption

migration is suppressed by As atoms on the surface.

References

- 1) A. Ponchet, A. Rocher, J.-Y. Emery, C. Starck, and L. Goldstein, *J. Appl. Phys.* **74** (6), 3778 (1993)
- 2) Z. H. Ming, Y. L. Soo, S. Huang, Y. H. Kao, K. Stair, G. Devane, and C. Choi-Feng, *Appl. Phys. Lett.* **66** (2), 165 (1994)
- 3) A. S. Smith, A. T. R. Briggs, K. Scarrott, X. Zhou, U. Bangert, *Appl. Phys. Lett.* **65** (18), 2311 (1994)
- 4) D. C. Houghton, M. Davis and M. Dion, *Appl. Phys. Lett.* **64** (4), 505 (1993)
- 5) F. Glas, *J. Appl. Phys.* **62** (8), 3201 (1987)

Influence of Strain on Exciton Lifetime in AlGaInP/GaInP Quantum Wells

K. Domen, M. Kondo*, and T. Tanahashi

Fujitsu Laboratories Ltd.

10-1 Morinosato-Wakamiya, Atsugi 243-01, Japan

*Fujitsu Limited

1015 Kamikodanaka, Kawasaki 211, Japan

ABSTRACT

We investigated the influence of strain on the exciton lifetime in AlGaInP/GaInP quantum wells grown by metalorganic vapor phase epitaxy. We found that exciton lifetime becomes shorter under compressive strain and longer under tensile strain. We found a strong correlation between the lifetime and the interfacial recombination velocity of the samples. We propose that the degradation in interface quality decreases the area of coherence of the exciton, increasing the lifetime, as the strain moves from compressive to tensile.

INTRODUCTION

Strained quantum well (QW) structures can improve the performance of lasers due to their modified valence band.¹ For GaInP/AlGaInP visible lasers, compressive and tensile strain have been experimentally shown to reduce the threshold current density.^{2,3} Despite these reports on device characteristics, the influence of strain on the crystal nature, such as exciton lifetime, has not been studied. On the other hand, exciton-related lasing is an important issue in wide-energy-gap lasers such as ZnCdSe/ZnSe,⁴ in which excitons remain in a high concentration even at room temperature. To understand the lasing phenomena, study of the exciton radiative process is of great importance. The influence of strain on exciton radiative recombination is an especially important topic, because two candidates for blue or violet lasers, ZnSe in II-VI and GaN in III-V, are based on strained structures.

In this paper, we studied the influence of strain on exciton radiative lifetime in GaInP/

AlGaInP quantum wells. We found that the lifetime grows longer under tensile strain and shorter under compressive strain. We report that the dependence correlates with strain-induced interfacial recombination.

EXPERIMENT

We grew quantum well structures on Si-doped GaAs substrates by metalorganic vapor phase epitaxy at 690°C. We grew the same structures on both (100) and (411)A substrates, to compare the ordered structures of (100) with the disordered structures of (411). When we grew samples on (411), the reactor was somewhat contaminated, so the samples on (411) were lower-quality than those on (100). We did not intentionally dope the samples; their net n type carrier concentration was typically 10^{15} cm^{-3} . Each sample consisted of a 0.2 μm -thick GaAs buffer layer, a 1 μm -thick $(\text{Al}_{0.7}\text{Ga}_{0.3})_{0.5}\text{In}_{0.5}\text{P}$ barrier layer, a 10 nm-thick $\text{Ga}_x\text{In}_{1-x}\text{P}$ well layer, and a 0.2 μm -thick

(Al_{0.7}Ga_{0.3})_{0.5}In_{0.5}P barrier layer. We varied the composition x from 0.41 to 0.58, corresponding to a strain variation from 0.5% tensile to 0.75% compressive.

We examined the lifetimes of these samples by measuring time-resolved photoluminescence (PL) using a NAES700 Time-Resolved Photon Counting System (Horiba). The pump source was a dye laser tuned to 590 nm with a 0.5-ns pulse, a repetition rate of 1 kHz, and an excitation power density of about 40 $\mu\text{J}/\text{cm}^2$. Photoluminescence decay time (τ_{PL}) is equal to the exciton lifetime as long as exciton binding energy is larger than kT

which is true below 180 K,⁵ while it becomes half of band-to-band carrier lifetime at room temperature.⁶

RESULTS AND DISCUSSION

Fig. 1 (a) shows the strain dependence of exciton lifetime (τ_{EX}) for strains from 0.4% compressive to 0.4% tensile at 77 K. Lifetime at 77 K is dominated by exciton recombination, because exciton binding energy is larger than kT .⁵ This exciton recombination is radiative, because PL intensity does not decrease as strain comes from tensile to compressive. On the other hand, the dependence at room temperature for the same samples shown in

Fig. 1 (b) is the reverse of (a). The Lifetime at room temperature is dominated by band-to-band nonradiative interfacial recombination.⁷ We found that the strain dependence for excitons is the reverse of that for free carriers.

We also measured the temperature dependence of τ_{PL} for 0.4 % tensile and 0.4 % compressive samples (Fig. 2). τ_{PL} increases with temperature, peaks, and then be-

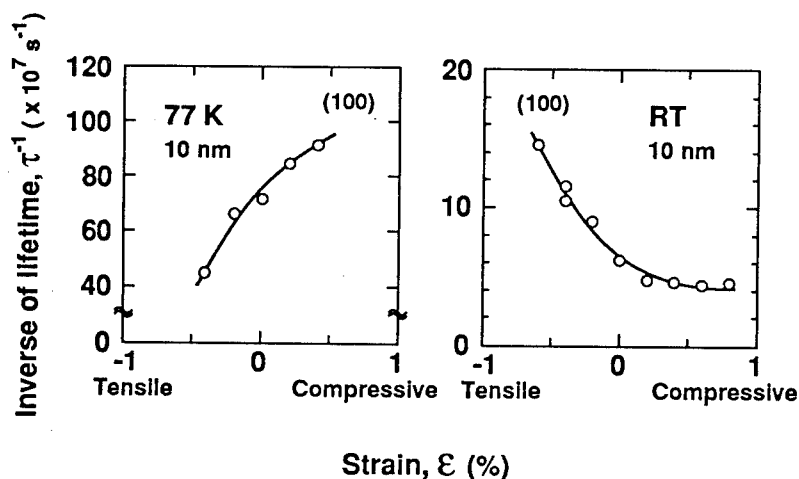


Fig. 1. Inverse of lifetime as a function of strain at 77 K (a) and at room temperature (b).

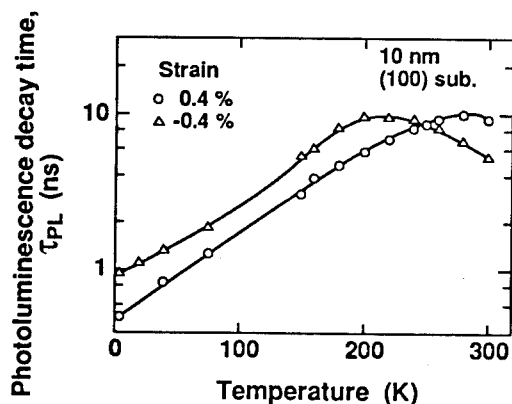


Fig. 2. Photoluminescence decay time versus temperature for samples with strains of 0.4 % and -0.4 % on (100) substrates.

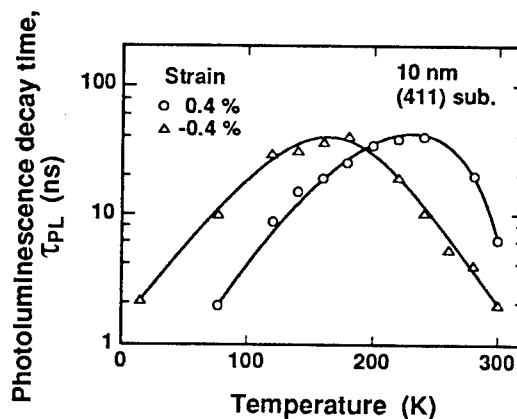


Fig. 3. Photoluminescence decay time versus temperature for samples on (411) substrates.

gins to decrease. The increasing τ_{PL} with temperature is dominated by radiative recombination and decreasing τ_{PL} is by nonradiative. Then the dominant recombination process changes from radiative to nonradiative at the peak lifetime at around 250 K; the peaking temperature depends on strain. Strain dependence at 77 K is thus the reverse of that at 300 K. We also measured the temperature dependence of τ_{PL} on (411) substrates (Fig. 3). It is well known that the ordered structure that appears on (100) substrates for some growth conditions does not appear on (411) substrates. Since τ_{PL} on (411) substrates shows the similar dependencies to that on (100) substrates, the strain dependence is not due to the ordered structure.

According to Feldmann et al.,⁸ τ_{EX} can be expressed as

$$\tau_{EX}^{-1} \propto f^{2D} \cdot A_{coh} \quad (1),$$

where f^{2D} is the oscillator strength and A_{coh} is the area of coherence of the exciton in a QW structure. f^{2D} is a material parameter which can be calculated, while A_{coh} represents crystal quality, a factor which is not yet well understood. We first calculated f^{2D} as

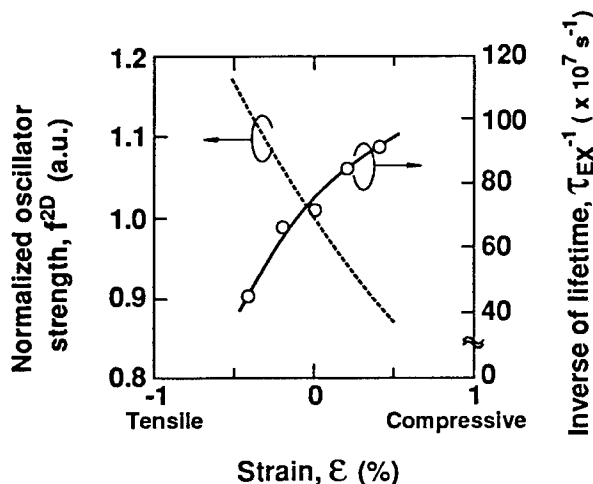


Fig. 4. Strain dependence of calculated oscillator strength is the reverse of that of τ_{EX}^{-1} . 215

shown in Fig. 4 and found that f^{2D} increases under tensile strain due to the large effective mass.⁹ We found that the dependence of f^{2D} on strain is the opposite of that of τ_{EX}^{-1} , indicating that f^{2D} is not the critical factor in these results.

Next we looked at A_{coh} . Feldmann et al. have demonstrated that A_{coh} is inversely proportional to the spectral linewidth and the total mass of the exciton. We plotted the exciton lifetime τ_{EX} versus the linewidth at 4.2 K for all samples in Fig. 5. We found that there is no general relationship between the lifetime τ_{EX} and the linewidth of the exciton among samples on both (100) and (411). If total mass of excitons was ten times larger for (411) than that for (100), the experimental data could be explained by the linewidth and the total mass. However, hole mass on off-angled substrates is reported to be smaller than that on (100) for InGaAs.¹⁰

We suggest that the overall crystal quality influences A_{coh} and therefore the exciton lifetime. For AlGaInP/GaInP double heterostructures, we previously reported that interfacial recombination is the predominant nonradiative process and that interfacial recombination varies with the strain

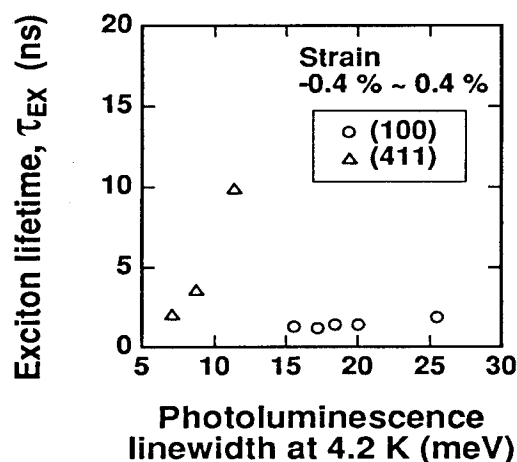


Fig. 5. Exciton lifetime as a function of photoluminescence linewidth at 4.2 K.

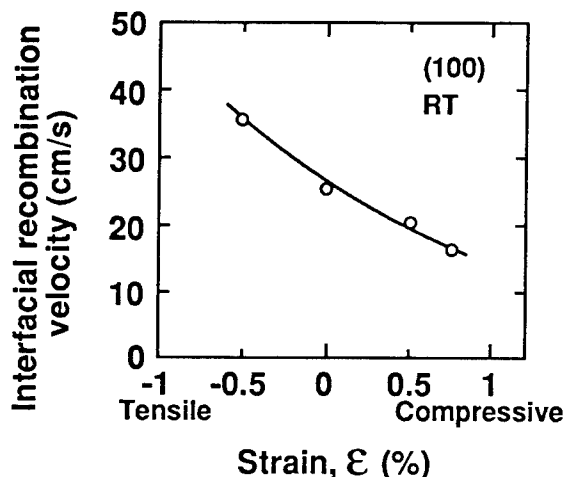


Fig. 6. Dependence of interfacial recombination velocity on strain.

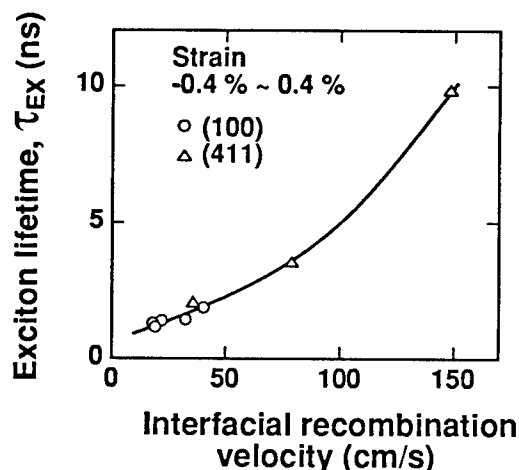


Fig. 7. Exciton lifetime (τ_{EX}) as a function of interfacial recombination velocity.

(Fig. 6).⁷ Figure 7 shows the exciton lifetime τ_{EX} as a function of the interfacial recombination velocity. We found a strong correlation between the two among samples on both (100) and (411). We propose that A_{coh} decreases as the interfacial recombination increases. This is because carriers at interfacial levels may cause exciton scatter, or because interface roughness tends to localize excitons. These factors decrease the area of coherence of the exciton. τ_{EX} thus increases as the interfacial recombination velocity increases. Note that interfacial recombina-

tion on (411) substrates is not always higher than that on (100). As mentioned before, some contamination occurred when we grew samples on (411), which explains the high interfacial recombination. We grew all of samples on (411) in that condition, and strain dependence of interfacial recombination still appeared when contamination occurred.

CONCLUSION

We found that the exciton radiative lifetime becomes shorter under compressive strain and longer under tensile strain. We suggest that the interfacial recombination which varies with strain, influences the area of coherence of the exciton due to scattering and localization of excitons at the interfaces. Thus the exciton lifetime increases because the interfacial recombination increases as strain moves from compressive to tensile.

REFERENCES

- ¹ E. Yablonovitch and E. O. Kane, IEEE J. Lightwave Technol. LT-4, 961 (1986).
- ² T. Katsuyama, I. Yoshida, J. Shinkai, J. Hashimoto, and H. Hayashi, Electron. Lett. 26, 1375 (1990).
- ³ A. Valster, C. J. van der Poel, M. N. Finke and M. J. B. Boermans, Digest of 13th IEEE International Semiconductor Laser Conference, 152 (1992).
- ⁴ A. Nurmikko, and R. L. Gubshor, Physica B 185, 16 (1993).
- ⁵ M. Sugawara, J. Appl. Phys. 71, 277 (1992).
- ⁶ K. Domen, K. Sugiura, C. Anayama, M. Kondo, M. Sugawara, T. Tanahashi, and K. Nakajima, J. Cryst. Growth 115, 529 (1991).
- ⁷ K. Domen, M. Kondo, and T. Tanahashi, Appl. Phys. Lett. 64, 3629 (1994).
- ⁸ J. Feldmann, G. Peter, E. O. Göbel, P. Dawson, K. Moore, C. Foxon, and R. J. Elliott Phys. Rev. Lett. 59, 2337 (1987).
- ⁹ K. Domen, H. Ishikawa, M. Sugawara, M. Kondo, and T. Tanahashi, Appl. Phys. Lett. 66, 466 (1995).
- ¹⁰ T. Ohtoshi, T. Kuroda, A. Niwa, S. Tsuji, and K. Uomi, Digest of 14th IEEE International Semiconductor Laser Conference, 151 (1994).

Anisotropic Electrical Properties of Modulation-Doped $\text{In}_{0.52}\text{Al}_{0.48}\text{As}/\text{In}_x\text{Ga}_{1-x}\text{As}$ Pseudomorphic Heterostructures Grown on InP Substrate

Y. Sugiyama*, K. Sano**, S. Uekusa**, and T. Nakagawa*

* Electrotechnical Laboratory, 1-1-4, Umezono, Tsukuba, Japan

** Meiji University, 1-1-1, Higashimita, Tama, Kawasaki, Japan

Abstract

Anisotropic electrical properties of pseudomorphic $\text{In}_{0.52}\text{Al}_{0.48}\text{As}/\text{In}_x\text{Ga}_{1-x}\text{As}$ heterostructures on the semi-insulating (001) InP substrate grown by molecular beam epitaxy have been investigated. Hall mobility in the direction of (01'1) is larger than that in the direction of (01'1'), and low frequency noise in the former direction is smaller than that of the latter. The maximum Hall mobility and the minimum noise are obtained for the In mole fraction, 0.8, of InGaAs. Allowable channel thickness of pseudomorphic structures is about 10 nm.

Introduction

Modulation-doped InAlAs/InGaAs pseudomorphic heterostructure semiconductors with high electron mobility are most promising for mm-wave low noise transistors[1], optical devices, and highly sensitive magnetic sensors[2]. However, electrical and optical properties of those materials are affected by an anisotropic elastic strain due to an asymmetrical crystallography in zinc-blende structure[3]. We have investigated on an anisotropy of Hall mobility and low frequency noise of pseudomorphic $\text{In}_{0.52}\text{Al}_{0.48}\text{As}/\text{In}_x\text{Ga}_{1-x}\text{As}$ heterostructures on the semi-insulating (001) InP substrate grown by molecular beam epitaxy.

Experiment

The pseudomorphic $\text{In}_{0.52}\text{Al}_{0.48}\text{As}/\text{In}_{0.8}\text{Ga}_{0.2}\text{As}$ heterostructures was grown on the semi-insulating (001)-InP substrate using the flux-stabilized molecular beam epitaxy[4]. The composition of the ternary compound crystal was accurately controlled within an error of less than 0.1 %. The epitaxial growth rate was 1 mm/hr at the substrate temperature of 490 °C. The pseudomorphic $\text{In}_{0.8}\text{Ga}_{0.2}\text{As}$ layers thinner than the critical thickness for the channel and the cap layers were grown. A Greek-cross Hall element with the arms in the direction of (01'1) and (01'1') was used for investigating anisotropical electrical properties of pseudomorphic hetero-structure semiconductors. The ohmic contact was made by alloying the Au/Ni/AuGe film evaporated on the semiconductor. The Hall device was fabricated by

the conventional photolithographic process with the wet chemical etching. All the Hall devices are mounted in the non-magnetic TO-5 package. A cross-sectional view of the heterostructure is schematically shown in Fig. 1.

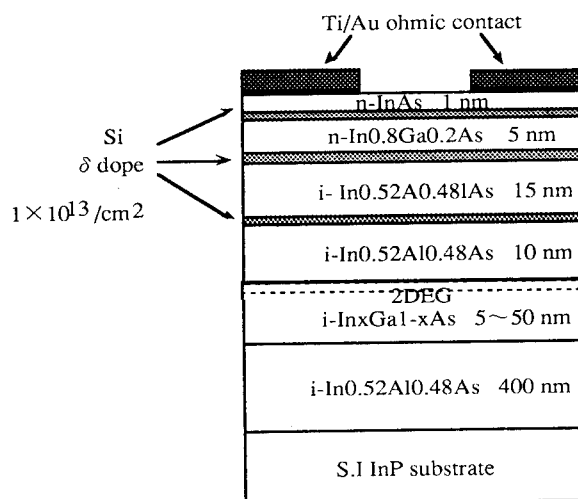


Fig. 1 Cross-sectional view of pseudomorphic $\text{In}_{0.52}\text{Al}_{0.48}\text{As}/\text{In}_x\text{Ga}_{1-x}\text{As}$ heterostructure on the (001) InP substrate.

Anisotropic electrical properties of InAlAs/InGaAs heterostructure have been investigated by the computer-controlled Hall measurement system with a metal-shield cryostat and low frequency noise measurements. In the noise measurement the specimen was placed in the twofold electro-

magnetically shield box made of aluminum and brass plates. A constant current is applied to the specimen from the dry battery cells. The noise voltage was measured by the computer-controlled spectrum analyzer (Advantest TR9404) with a wide range differential amplifier (Ithaco 1201). The 25 measured data were averaged by the computer.

Results and Discussions

The Hall mobility of the specimen with the In mole fraction, 0.7, of InGaAs, and the Hooge's parameter obtained from the $1/f$ noise spectrum are plotted in Figs. 2 and 3 as a function of channel thickness. The Hooge's parameter is given from the noise voltage normalized by the total carrier number, the operating frequency, and the applied bias voltage. The Hall mobility of $(01'1)$ direction is larger than that of $(01'1')$ direction, and the Hooge's parameter of $(01'1)$ direction is smaller than that of $(01'1')$ direction. The Hall mobility decreased drastically with the channel thickness less than 10 nm due to an interface roughness scattering, and also with that more than the critical thickness which is nearly equal to the energy balance model. The Hooge's parameter of $(01'1')$ direction extremely increased with the channel layer thinner than the critical thickness obtained from the relation between the mobility and channel thickness. The allowable channel thickness of pseudomorphic heterostructures are summarized in Table 1. The sheet carrier density was independent of the crystal orientation.

The anisotropy of the Hall mobility of $(01'1)$ to $(01'1')$ directions, and that of the Hooge's parameter of $(01'1)$ to $(01'1')$ directions are shown in Fig. 4. The noise property shows more sensitive to the strain structure rather than the Hall

x of In _x Ga _{1-x} As	Allowable channel thickness (nm)	
	t[mobility]	t[noise]
0.53	10~	10~
0.7	10~50	10~30
0.8	10~20	10
0.9	10~15	5

Table 1 Allowable channel thickness of pseudomorphic heterostructure in the $(01'1)$ direction. t[mobility] shows an allowable channel thickness for the Hall mobility, and t[noise] for the Hooge's noise parameter.

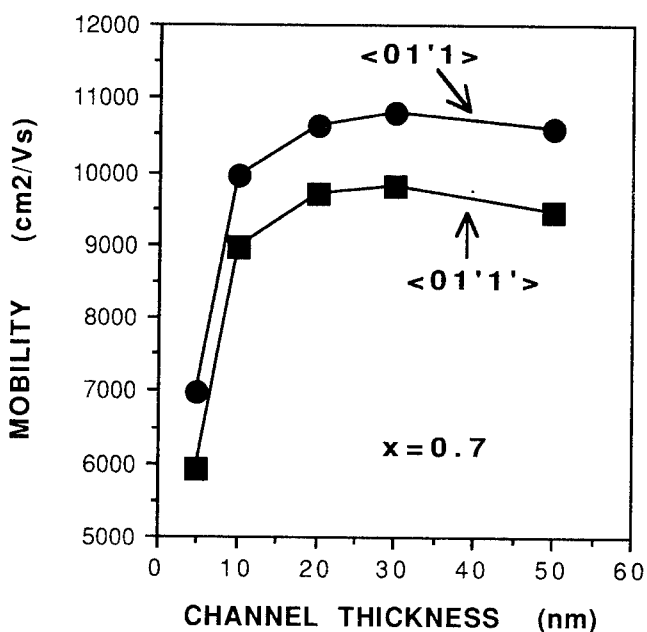


Fig. 2 Channel thickness dependence of Hall mobility of the specimen with the In mole fraction, 0.7, of InGaAs.

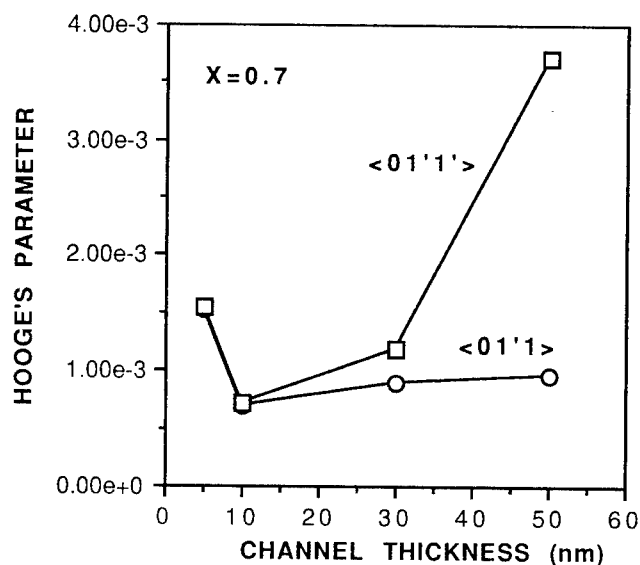


Fig. 3 Channel thickness dependence of Hooge's parameter of the specimen with the In mole fraction, 0.7, of InGaAs.

mobility. The critical thickness of the pseudomorphic heterostructure with the In mole fraction, 0.7, of InGaAs is 10 nm for the mechanical equilibrium model[5] and 100 nm for the energy balance model[6]. We have obtained that the critical thickness for the Hall mobility is suitable for the the energy balance model and that for the noise is suitable for the mechanical equilibrium model.

The critical thickness is dependent of the composition of mixed crystal. We have investigated the anisotropic electrical properties as a function of the In mole fraction of InGaAs within the critical thickness. The Hall mobility and Hooke's parameter are shown as a function of the In mole fraction of InGaAs in Fig. 5 and 6. The Hall mobility of the (01'1) direction increases with increasing the In mole fraction but that of the (01'1') direction drastically decreases over the In mole fraction of 0.8. The noise of both orientations increase over the In mole fraction of 0.8. The noise is minimized for the In mole fraction between 0.7 and 0.8. It has been reported that the anisotropically electronical properties are originated from misfit dislocations formed along the (01'1) direction[7]. Anisotropies of the (01'1') vs (01'1) directions obtained from the previous figures are shown as a function of the composition of InGaAs in Fig. 7. An anisotropy of the Hall mobility is smaller than that of the noise. However, the anisotropy has been observed in the lattice-matched InGaAs system, $x=0.53$.

The eletrical property of the (01'1) direction is superior to the that of the (01'1') direction by a factor of more than 10 %. Thus, the channel of electron devices should be arrayed to the (01'1) direction. It is noted that the optimum In mole fraction with large Hall mobility and small Hooke's parameter can be obtained for about $x=0.8$. Then, the relative degradation of Hall mobility and Hooke's noise parameter due to the asymmetrical scattering properties are about 10 %.

Conclusion

We have investigated anisotropic electrical properties of pseudomorphic $\text{In}_{0.52}\text{Al}_{0.48}\text{As}/\text{In}_x\text{Ga}_{1-x}\text{As}$ heterostructures on the semi-insulating (001) InP substrate grown by molecular beam epitaxy. The Hall mobility in the direction of (01'1) is larger than that in the direction of (01'1'), and 1/f noise in the former direction is smaller than that of the latter. There are an anisotropy of more than 10 % for the Hall mobility and noise of the InAlAs/InGaAs system.

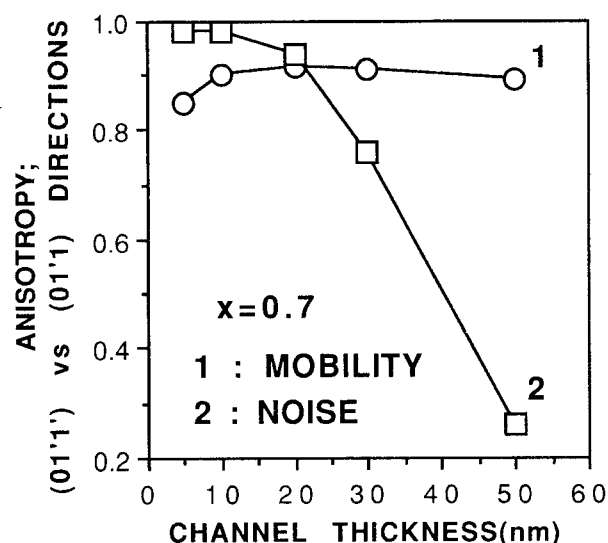


Fig.4 Channel thickness dependence of anisotropies of Hall mobility and noise of the specimen with the In mole fraction, 0.7, of InGaAs.

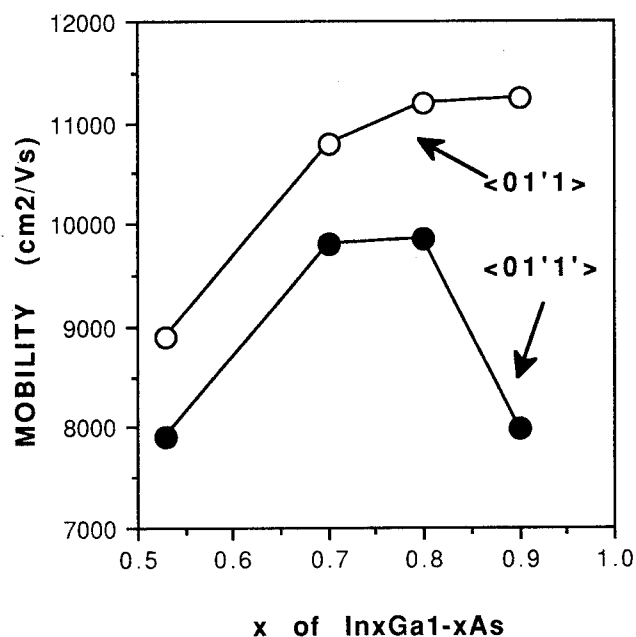


Fig. 5 Hall mobility as a function of In mole fraction of InGaAs.

It should be noted that the channel of electron devices should be arrayed to the (01'1') direction. An optimum composition of InGaAs with a large Hall mobility and a small noise is 0.8. Allowable channel thickness is about 10 nm.

References

- [1] U. K. Mishra and J. B. Shealy: "InP-based HEMTs; Status and Potential," in 1994 Proceedings of Int. Conf. on Indium Phosphide and Related Materials (Santa Barbara), p. 14.
- [2] Y. Sugiyama, Y. Takeuchi, and M. Tacano: "Highly-sensitive InGaAs-2DEG Hall device made of pseudomorphic In_{0.52}Al_{0.48}As/In_{0.8}Ga_{0.2}As heterostructure," Sensors and Actuators, A-34 (1992) 131.
- [3] R.S. Goldman, et al: Appl. Phys. Lett. 65 (1994) 1424, and references therein.
- [4] Y. Sugiyama, Y. Takeuchi, and M. Tacano: "High electron mobility pseudomorphic In_{0.52}Al_{0.48}As/In_{0.8}Ga_{0.2}As heterostructure on InP grown by flux-stabilized MBE", J. Crystal Growth, 115 (1991) 509.
- [5] J. W. Mathews and J. C. Blakeslee: J. Vacuum Sci. Technol., B6 (1976) 1285.
- [6] R. People and J. C. Bean: Appl. Phys. Lett., 47 (1985) 322.
- [7] D. Morris, Q. Sun, C. Lacelle, A. P. Roth, J. L. Brebner, M. Simard-Normandin, and K. Rajan: "Structure property anisotropy in lattice-mismatched single heterostructures," J. Appl. Phys., 71 (1992) 2321.

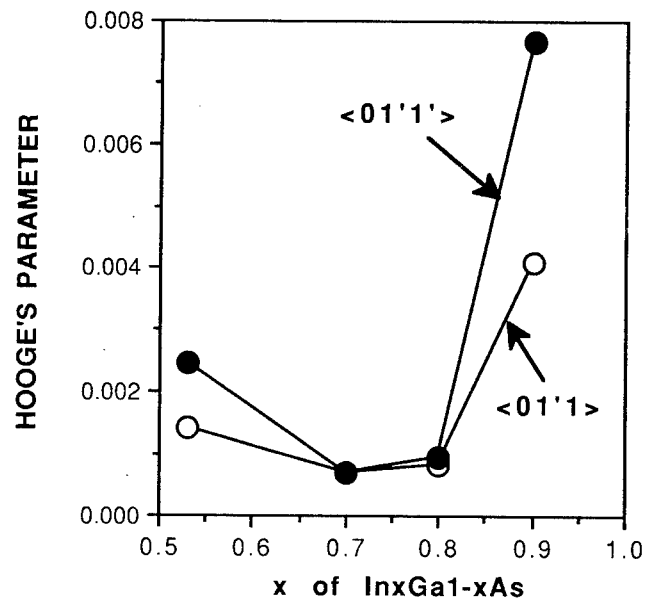


Fig. 6 Hooke's parameter as a function of In mole fraction of InGaAs.

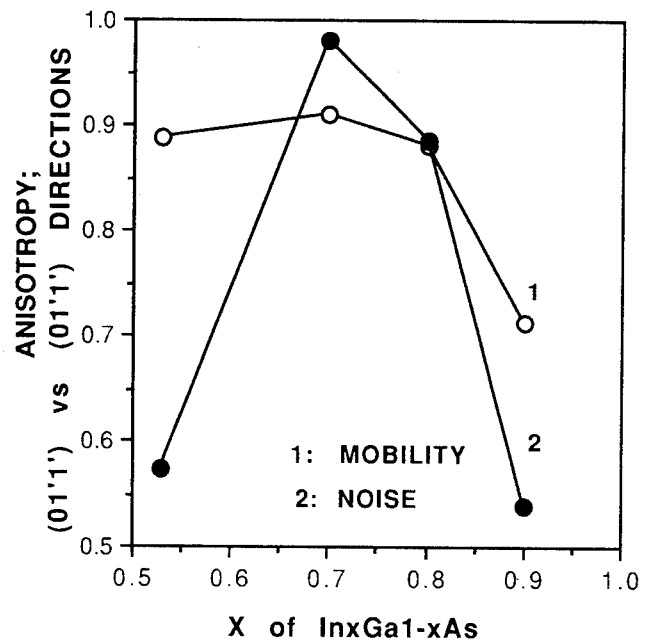


Fig. 7 Anisotropy of Hall mobility and Hooke's noise parameter as a function of In mole fraction of InGaAs.

Determination of the in-plane mass in strained GaInAs/InP quantum wells

V.Härle, S.Rapp, H.Bolay, G.Reyher, A.Dörnen, A.Hangleiter, F.Scholz
4.Physikalisches Institut, Universität Stuttgart Pfaffenwaldring 57, 70550 Stuttgart, Germany
W.Limmer,
Abt. Halbleiterphysik, Universität Ulm, Oberer Eselsberg, 89069 Ulm, Germany
E.Vasiliadou, P.Grambow, D.Weiss,
MPI-FKF, Heisenbergstr.1, 70569 Stuttgart, Germany

Abstract

In this paper we present a determination of the valence band structure of strained GaInAs/InP quantum wells by measuring the effective in-plane hole masses. To determine the masses, we performed low temperature magneto transport measurements (1.5-15 K), magneto luminescence as well as far infrared transmission spectroscopy. Hole carrier mobilities up to 8700 cm²/Vs were obtained for compressively strained samples with a gallium content of $x_{\text{Ga}}=0.3$.

For compressively strained samples all measurements showed a drastical reduction of the valence band masses compared to both, bulk values and the values of unstrained quantum well structures. Tensile strained samples show, according to an indirect band structure at the cross over of light and heavy hole extremely large effective masses. For increasing tensile strain, the band structure becomes again direct, whereas the effective masses show values which are above those of compressively strained samples. Therefore tensile strained samples could only be analysed qualitatively by magneto luminescence. All of our observations are in good agreement with k·p-theory.

A more precise analysis of the Shubnikov-de Haas oscillations showed a spin splitting of the uppermost valence band in compressively strained quantum well structures, leading to two different effective masses.

Introduction

The strain induced optimization of electronic and optoelectronic devices has been established during the last years. Most of the observed improvements are due to changes in the band structure towards a reduction of the effective masses¹. Beside theoretical treatments² almost no experimental investigations of the band structure, leading to a precise understanding, have been carried out. In this paper an experimental determination of the valence band structure near the Γ -point ($k=0$) of pseudomorphic strained Ga_xIn_{1-x}As/InP quantum wells is presented.

To determine the in-plane mass with a reasonable accuracy, three different methods have been performed: i) temperature dependent Shubnikov de-Haas (SdH), ii) magneto luminescence (MPL) and iii) far infrared transmission spectroscopy (FIRTS).

At this point one has to mention, that different experiments lead to different aspects of the band structure. Masses, determined from magneto transport measurements, are related to the first derivative of the dispersion relation with respect to the wave vector

$$\frac{1}{m} = \frac{1}{\hbar^2 k} \frac{\partial E}{\partial k},$$

whereas the density of state mass is given by the second derivative of the energy dispersion³.

For parabolic band structures the different mass definitions are of course identical, describing exactly the same mass. But in the case of nonparabolic band structures one has to distinguish between these different masses.

Experimental

The investigation of strain effects on the band structure requires quantum well structures in order to overcome the problem of critical layer thicknesses. Therefore all samples investigated were grown by low pressure metal organic vapor phase epitaxy (MOVPE) at a growth temperature of 620°C and a reactor pressure of 80 hPa. The precursors used were trimethylindium, triethylgallium, arsine and phosphine. The dopant sources used were hydrogensulfide and diethylzinc. The quantum well composition as well as the well width were adjusted by MOVPE growth parameters and cross-checked by high resolution x-ray diffraction, low temperature photoluminescence and absorption measurements. The quantum wells investigated have a well width of 10nm and vary in composition from $x_{\text{Ga}}=0.2$ to 0.8.

For transport measurements and transmission spectroscopy the quantum wells were p-modulation doped using a symmetrical structure of 50nm zinc doped InP, separated from the well by a spacer layer of 10nm undoped InP. The spacer layer provides a spatial separation of the ionized acceptors in the dopant layer from the 2D-hole gas, leading to a reduction of the Coulomb scattering. The carrier concentration of the 2D-hole gas was varied by different doping levels in the doping layer, so we obtained carrier concentrations from $1 \dots 3 \cdot 10^{12} \text{cm}^{-2}$.

To perform high quality ohmic contacts, a highly zinc doped Ga_{0.47}In_{0.53}As cap layer was grown on top of the structure. After wet etching a Hall-bar structure into the layer structure, ohmic contacts of 10nm Au, 10nm Zn, 5nm Ag, 20nm Au were evaporated and alloyed at 450°C.

n-modulation doped quantum wells were used for MPL. These samples have 10nm wide sulfur doped doping and 5nm wide spacer layers. The wells are also 10nm wide and the carrier concentration of the 2D-electron gas is in the order of $1 \cdot 10^{12} \text{cm}^{-2}$.

MPL and FIR transmission spectroscopy were carried out at low temperatures (2-4.2K), whereas magneto transport measurements were done in the temperature range of 1.6-20K at magnetic fields up to 9T.

Results and Discussion

The observation of SdH-oscillations requires hole mobilities of at least $1000 \text{cm}^2/\text{Vs}$. These mobilities have been observed in compressively strained quantum wells. The highest mobility observed was $8700 \text{cm}^2/\text{Vs}$ and was measured in a sample with $x_{\text{Ga}}=0.3$ and a carrier concentration of $1 \cdot 10^{12} \text{cm}^{-2}$.

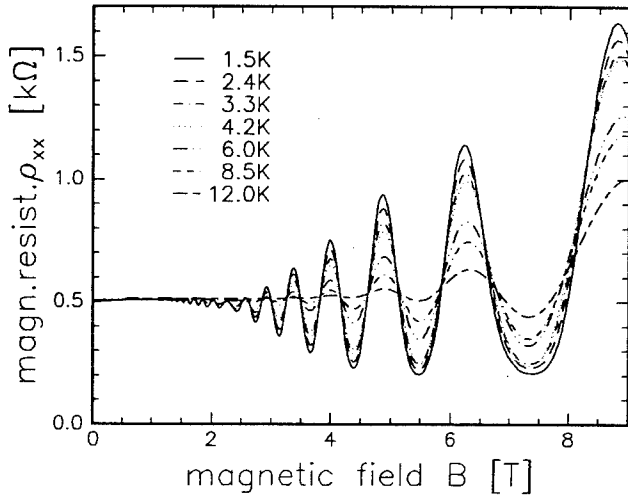


Fig. 1: Temperature dependent Shubnikov de-Haas oscillations of a 10nm wide $\text{Ga}_{30}\text{In}_{70}\text{As}/\text{InP}$ quantum well structure with a carrier concentration of $1 \cdot 10^{12} \text{cm}^{-2}$.

Unstrained as well as tensile strained samples showed mobilities only up to $500 \text{cm}^2/\text{Vs}$, so that in this compositional region no SdH-oscillations have been observed.

In fig.1 we show the SdH-oscillations of the magneto resistance ρ_{xx} measured in a temperature range from 1.5 to 12K. From the temperature dependence of the oscillations, one can extract the effective transport mass utilizing the following equation

$$\rho_{xx} = \rho_0 \cdot \left[1 + 4 \cdot \sum_s \exp\left(-\frac{\pi s}{\omega_c \tau_q}\right) \cdot \frac{\zeta s}{\sinh(\zeta s)} \cdot \cos\left(\frac{2\pi \cdot E_F \cdot s}{\hbar \omega_c} - \pi s\right) \right]$$

with

$$\zeta = \frac{2\pi^2 k_B T}{\hbar \omega_c}$$

Here, ω_c denotes the cyclotron frequency, E_F the Fermi energy, ρ_0 the classical resistance and τ_q the quantum mechanical scattering time related to the broadening of the Landau levels. The effective mass occurs in the cyclotron frequency $\omega_c = eB/m^*$ in the term $\zeta s / \sinh(\zeta s)$. Fitting the temperature dependent oscillation amplitude terms up to $s = 10$ were used, giving the effective mass and the scattering time with a reasonable accuracy.

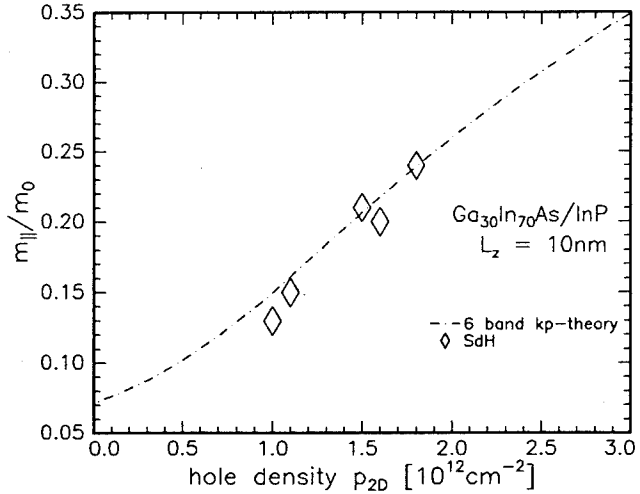


Fig. 2: Carrier dependence of the in-plane effective mass for 10nm wide quantum wells with a gallium content of $x_{\text{Ga}}=0.3$.

In order to probe the band structure in k-space we varied the carrier concentration of the 2D-hole gas as mentioned above. The determined effective transport masses for a gallium content $x_{\text{Ga}} = 0.3$ are plotted in fig.2 as a function of the carrier concentration. With increasing carrier concentration from $1 \cdot 10^{12} \text{cm}^{-2}$ to $1.8 \cdot 10^{12} \text{cm}^{-2}$ we observe an increasing effective mass from 0.13 to $0.24 \cdot m_0$, which is due to the strong nonparabolicity of the band structure. A comparison with 6-band k-p-theory, carried out using Luttinger parameters given by Lawaetz⁴, shows very good agreement with the measured data. The calculated effective mass corresponds to the first derivative of the band structure given above. To evaluate the carrier concentration from the wave vector k , we used the isotropic approximation for the 2D-hole gas. The isotropy for the carrier concentration used was checked by various calculations in different crystal directions.

Furthermore, we measured the effective transport mass as a function of the gallium content from $x_{\text{Ga}} = 0.2$ to $x_{\text{Ga}} = 0.4$ and for a fixed carrier concentration (filled circles in fig.3). We observe an increase of the mass from $0.14 \cdot m_0$ to $0.3 \cdot m_0$ with increasing gallium content.

For gallium contents below $x_{\text{Ga}} = 0.2$, we were not able to observe SdH-oscillations at any temperature. Presumably, the critical layer thickness of the strained quantum wells is exceeded in these samples. A comparison with k-p-theory shows again very good agreement.

Additional calculations (lines in fig.3) of the effective mass as a function of the gallium content for different carrier concentrations were carried out. For increasing gallium

content, these calculations point out the drastic increase of the effective mass, which is due to an increasing band mixing of the uppermost valence bands. The band structure flattens and gets even indirect at a composition where the light and heavy hole bands cross ($x_{Ga} = 0.52$ for 10nm well width). In this region we did not extract any hole masses from our calculations.

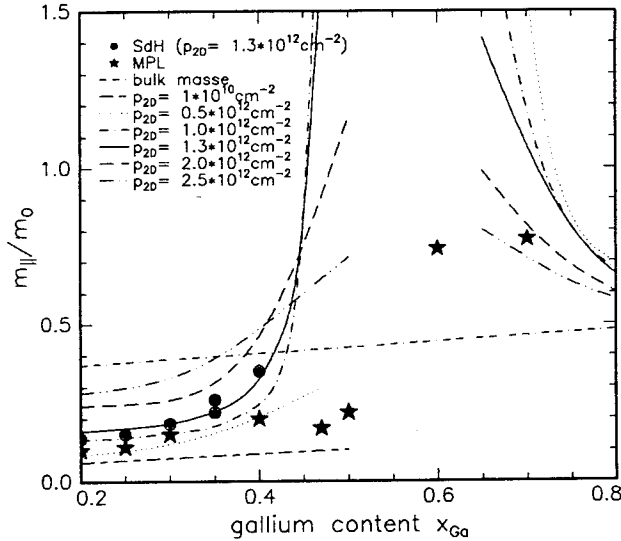


Fig. 3: Effective in-plane mass as a function of the gallium content. Masses calculated from the band structure are compared with measured values from SdH-spectra and magneto luminescence.

According to this increase of the effective mass, it becomes clear why we could not observe any SdH-oscillations for gallium contents above $x_{Ga} = 0.4$. For even larger gallium content ($x_{Ga} > 0.65$), depending on the well width, the band structure becomes direct again but the masses remain rather high. (above $0.6 \cdot m_0$, see fig.3), and SdH-oscillations are still not detectable at temperatures around 1.5K. Furthermore, we show in fig.3 effective masses (filled stars) determined by magneto luminescence (MPL) at 2K. These measurements were carried out on n-modulation doped quantum well structures.

A typical MPL spectra is shown in the inset of fig. 4. It shows the Landau level splitting for a magnetic field of 6T. Fig. 4 shows the behaviour of the Landau levels versus the magnetic field. The Landau levels themselves shift linearly with increasing magnetic field to higher energies and the Landau level splitting is increasing. In agreement with the literature⁵ the Landau level splitting at a fixed magnetic field contains only the electron mass. This is due to k non-conserving transitions from the conduction band into the uppermost valence band. Taking the carrier concentration into account, this mass is in very good agreement with SdH-data, determined from the same n-modulation doped quantum well structures⁶.

On the other hand the observed shift of the magneto luminescence signal versus the magnetic field can only be described by taking reduced masses into account. This is rather evident, since both the conduction band and the

valence band Landau level shift blue with increasing magnetic field.

Knowing now the reduced and the electron mass, one can simply evaluate the effective hole mass at the Γ -point. Even though this method works, one has to take a rather huge error bar into account. One easily gets data which are by a factor of 2 off.

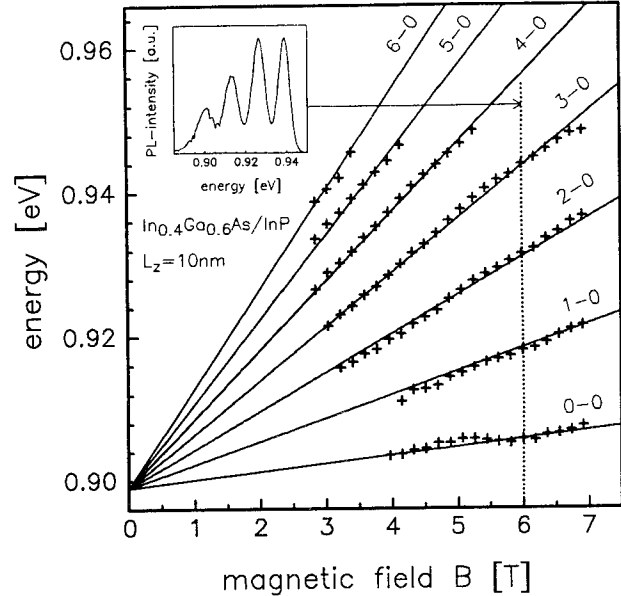


Fig. 4: Landau level shift and splitting versus the magnetic field. The inset shows a magneto luminescence spectra, taken at 2K and at a magnetic field of 6T. From these spectra one can extract the Landau transitions indicated (n^{th} conduction to 0^{th} valence band landau level).

Even though this evaluation method has a limited accuracy, it represents the principle behaviour of the calculated effective hole masses for the lowest carrier concentration of $1 \cdot 10^{10} \text{ cm}^{-2}$ in fig. 3 fairly good. For compressively strained samples, we observe effective masses which are in reasonable agreement with the SdH-data. The obtained values are far below the bulk value, whereas for tensile strained structures the MPL-masses are about twice as high. The step like increase of the effective masses is due to the switching from heavy to light hole type of transitions.

Looking more precisely to the SdH spectra, they show beating patterns (fig. 5), becoming more pronounced with increasing carrier concentration. A Fourier transformation of the SdH-oscillations clearly reveals two sublevels being occupied, with carrier concentrations of $6.3 \cdot 10^{11} \text{ cm}^{-2}$ and $5.7 \cdot 10^{11} \text{ cm}^{-2}$ for a sample with $x = 0.3$. Separating the two levels in the Fourier transform and transforming the spectra back leads to an oscillation patterns of the separated levels, and finally two different effective masses of $m_1 = 0.14m_0$ and $m_2 = 0.19m_0$ ($< 5\text{T}$) could be extracted in this sample.

We also used FIR-transmission spectroscopy to determine the hole masses with a Fourier transform spectrometer at $T = 2.2\text{K}$ at different fixed magnetic fields B. The

transmission spectra $T(\vartheta, B)$ with the dispersion ϑ are normalized to a reference spectrum $T(\vartheta, B_0)$ measured at a magnetic field B_0 where the interesting frequency region is flat. At higher magnetic fields ($B > 3T$) we observe two resonances. At lower magnetic fields ($B < 3T$) only one resonance can be observed. Linear fits of the experimental data (shown in the inset of fig. 6, where the dispersion ϑ versus B is plotted) lead to two effective hole masses $m_1 = 0.19m_0$ and $m_2 = 0.12m_0$ for the lower and the upper branch, respectively.

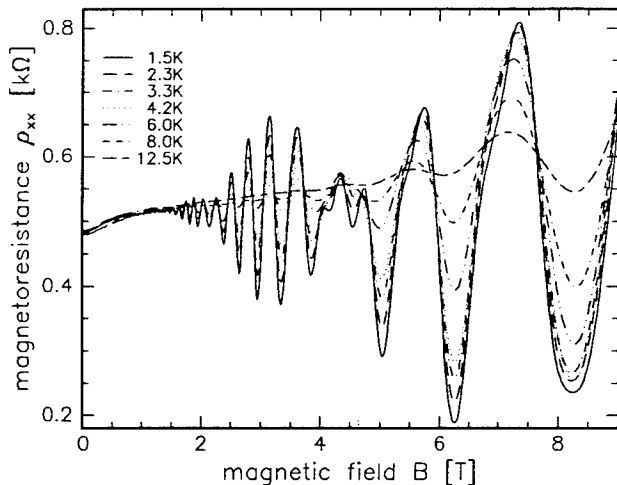


Fig.5: SdH-beating pattern becoming more pronounced with increasing hole concentration.

Since the observed masses are rather large and the carrier concentrations lead to Fermi energies allowing only the first heavy-hole subband to be occupied, any contributions of the uppermost light hole and the second heavy hole subband to these phenomena can be ruled out. We assume to observe two spin-split heavy-hole states. A similar behavior has been observed and discussed in GaAs 2D hole gases, ascribed to the lifting of the spin degeneracy at $k \neq 0$ due to the lack of inversion symmetry⁸.

Possible reasons for the lack in the inversion symmetry are electric field perpendicular to the interface as well as the crystal structure of the III-V bulk compounds which already has a broken inversion symmetry. The electric field may be caused by an asymmetry in the quantum well potential due to doping, layer thickness or surface effects.

Conclusion

In summary, we have determined the valence band structure of pseudomorphic strained $\text{Ga}_x\text{In}_{1-x}\text{As}/\text{InP}$ single quantum well structures by evaluating the effective in-plane hole masses from the SdH-oscillations of the magneto resistance and the Landau level shift/splitting in magneto luminescence. Due to the non-parabolicities of the band structure, we found these masses to be strongly dependent on the carrier concentration. A comparison to values calculated by 6-band $k \cdot p$ -theory showed good agreement. For compressively strained samples, a drastic reduction of the hole mass was observed, leading to hole

mobilities up to $8700\text{cm}^2/\text{Vs}$. In the tensile strained region only low mobilities less than $500\text{cm}^2/\text{Vs}$ were observed. Beating patterns occurring in samples with rather large hole concentrations could be explained by the assumption of zero field spin-split heavy-hole valence band states, due to the broken inversion symmetry.

Acknowledgement

The authors like to thank Prof. M.H. Pilkuhn for his steady interest in this work, A. Weber, P. Burkhard and A. Menschig for discussion and technical support. Parts of this work have been financially supported by the Deutsche Forschungsgemeinschaft (DFG).

¹ C.J. van der Poel, H.P.M.M. Ambrosius, R.W.M. Linders, R.M. Peeters, G.A. Acket, M.P.C.M. Krijn, Appl. Phys. Lett. **63**, 2312 (1993).

P.J.A. Thijs, F. Luuk, P.I. Kuindersma, J.J. Binsma, T. van Dongen, IEEE J. of Quant. Electron. **27** 1426 (1991).

H. Hardtdegen, R. Meyer, M. Hallfelder, T. Schäpers, J. Appenzeller, H. Løken-Larsen, T. Klocke, C. Dieker, B. Lengeler, H. Lüth, W. Jäger, J. Appl. Phys. **73**, 10798 (1993).

² E.P. O'Reilly, Semicond. Sci. Technol. **4**, 121 (1989)
T.C. Chong and C.F. Fonstad, IEEE J. Quantum Electron. **25**, 171 (1989).

E. Yablonovitch and E.O. Kane, J. Lightwave Technol. **LT-6**, 1292 (1988).

³ D.K. Ferry, Semiconductors, Macmillan Publishing Company, N.Y. (1991).

⁴ P. Lawaetz, Phys. Rev. B **4**, 3460 (1971).

⁵ R. Küchler, G. Abstreiter, G. Böhm, G. Weimann, Semicond. Sci. Technol. **8**, 88 (1993).

M.S. Skolnick, K.J. Nash, S.J. Bass, P.E. Simmonds, M.J. Kane, Solid State Comm. **67**, 637 (1988).

⁶ V. Härle, PhD thesis, Stuttgart University (1994).

⁷ S. Rapp, V. Härle, H. Bolay, A. Hangleiter, F. Scholz, W. Limmer, E. Vasiliadou, P. Grambow, D. Weiss, submitted to Appl. Phys. Lett.

⁸ H.L. Störmer, Z. Schlesinger, A. Chang, D.C. Tsui, A.C. Gossard, W. Wiegmann, Phys. Rev. Lett. **51**, 126 (1983).

Chemical Structure of InP Surface in MOVPE Studied by Surface Photo-Absorption

Yasuyuki Kobayashi and Naoki Kobayashi
NTT Basic Research Laboratories

3-1, Morinosato Wakamiya Atsugi-Shi, Kanagawa 243-01 Japan

Abstract

Using surface photo-absorption (SPA) spectra, we established a surface phase diagram of P-stabilized in (001) InP metalorganic vapor phase epitaxy as a function of substrate temperature and PH_3 partial pressure. At 550°C and PH_3 partial pressure of 10 and 30 Pa, the surface is (2x4)-like whose P dimers have a bond axis parallel to $[\bar{1}10]$. As the substrate temperature decreases and the PH_3 partial pressure increases, the surface changes to an excess-P surface due to P excessively adsorbing onto (2x4)-like surface without cleaving the P dimer bond. A c(4x4)-like surface was not observed. Furthermore, we found that a suppression of excessive P adsorption is needed to obtain a high quality InP epitaxial layer by minimizing native defects that might form.

1. Introduction

The chemical structure of a group-V surface during III-V compound semiconductor epitaxial growth affects the epitaxial layer quality and step kinetics. For GaAs metalorganic vapor phase epitaxy (MOVPE), different As structures, i.e., c(4x4)-like [1, 2] and (2x4) γ -like [3] surfaces, have been observed, and these structures have been found to have a significant effect on the step straightening mechanism [3]. Therefore, it is necessary to monitor the chemical structure of the surface during epitaxy to control the epitaxy precisely. For P-stabilized (001) InP, (2x4) and (2x1) surfaces have been observed by reflection high energy electron diffraction (RHEED) during gas-source molecular beam epitaxy (MBE). The (2x1) surface formation was attributed to excess P sticking to the (2x4) surface [4]. The surface structure during InP MOVPE, however, has not yet been clarified. This paper investigates the chemical structure of P-stabilized InP surface during MOVPE using surface photo-absorption (SPA) [5] and compares it with the As structure of GaAs in MOVPE. In order to study the effect of chemical structure on layer quality, InP epitaxial layers were grown

under the conditions of (2x4)-like and excess P surfaces and characterized by Hall measurement.

2. Experimental

We used a vertical MOVPE reactor. The reactor pressure was 10 kPa and the total gas flow rate was 10 l/min. The substrates were semi-insulating (001)-oriented GaAs and InP. The group V sources were arsine (20% in H_2) and phosphine (20% in H_2). The substrate temperature was monitored by a thermoelectric couple and was calibrated with the melting point of InSb (525°C). Linearly p-polarized light from a 150-W Xe-lamp irradiated the substrate surface at an incidence angle of 70° and SPA spectra were measured using an optical multi-channel analyzer. We obtained SPA spectra by supplying AsH_3 and PH_3 onto reference Ga and In surfaces, respectively. These reference Ga and In surfaces were formed by As and P desorption from GaAs and InP, respectively.

3. Results and Discussion

SPA spectra at a fixed azimuth contain both isotropic and anisotropic components due to an

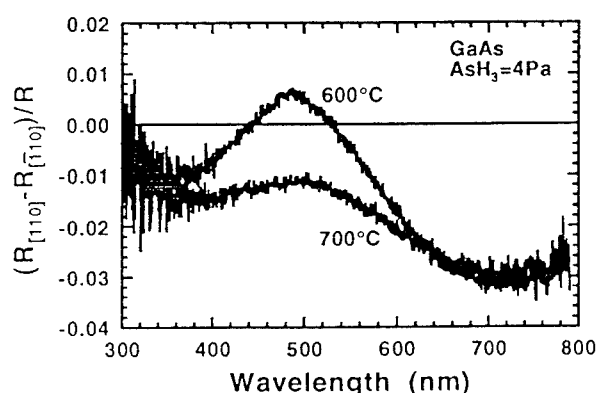


Fig. 1. Subtraction spectra of SPA for (001) GaAs.

electronic transition caused by surface chemical bonds. Taking the difference between the spectra of the $[110]$ and $[\bar{1}10]$ azimuths cancels the isotropic component to produce only an anisotropic spectrum mainly due to the group-V dimers. Figure 1 shows the subtraction spectra for a MOVPE surface of (001) GaAs at substrate temperatures of 600°C and 700°C. The vertical axis is $(R_{[110]} - R_{[\bar{1}10]})/R = \{[(R_{As} - R_{Ga})/R_{Ga}]_{[110]} - [(R_{As} - R_{Ga})/R_{Ga}]_{[\bar{1}10]}\}$. We also measured the subtraction spectra with those for $c(4 \times 4)$ and $(2 \times 4)\gamma$ MBE surfaces to determine the structure in MOVPE by means of comparison. The spectrum at 600°C is for the $c(4 \times 4)$ -like surface. The positive peak at 480 nm is attributed to $c(4 \times 4)$ As dimers that have a bond axis parallel to $[110]$ [6, 7]. The spectrum at 700°C is for the $(2 \times 4)\gamma$ -like surface. The disappearance of $c(4 \times 4)$ As dimers and the appearance of (2×4) As dimers cause an inversion from positive to negative at 480 nm. We describe these MOVPE surfaces using the term "-like", because optical methods respond to the local electronic structure but not to the long-range order of atom arrangements.

Figure 2 shows the subtraction spectrum for the (001) InP MOVPE surface at the substrate temperature of 550°C and PH_3 partial pressure of 30 Pa. The vertical axis is $(R_{[\bar{1}10]} - R_{[110]})/R = \{[(R_p - R_{In})/R_{In}]_{[\bar{1}10]} - [(R_p - R_{In})/R_{In}]_{[110]}\}$. It should be noted that the subtraction is the reverse of the one for

GaAs MOVPE in Fig. 1. A positive peak at 430 nm was observed. We found that P desorption induced by exposing the P surface to flowing hydrogen only makes the intensity of the positive peak at 430 nm decrease due to a decrease of P dimer coverage. In addition, a reflectance difference spectroscopy observation of P-stabilized (2×4) InP surface grown by metalorganic MBE using precracked PH_3 and trimethylindium revealed a peak at around 430 nm [8]. From these results, we can assign the peak at 430 nm to the P dimer bond which is parallel to $[\bar{1}10]$ and can conclude that the surface shown in Fig. 2 is (2×4) -like surface. For InP MOVPE, inversion from positive to negative at 430 nm with the axis $(R_{[\bar{1}10]} - R_{[110]})/R$ in the subtraction spectra could not be observed even by decreasing substrate temperature or increasing PH_3 partial pressure. This result indicates that $c(4 \times 4)$ -like surface was not observed in InP MOVPE. However, by analyzing the isotropic component, there was the phase of excess P adsorbed on the (2×4) -like surface.

Figure 3 shows SPA spectra at the $[\bar{1}10]$ azimuth at 470 and 550°C. For example, SPA reflectivity at 520 nm decreases with decreasing substrate temperature, but the reflectivity at 430 nm remains constant. This decrease in reflectivity was observed for both $[\bar{1}10]$ and $[110]$, indicating its isotropic nature. Therefore, the decrease in reflectivity without a lowering of the contribution of P dimer

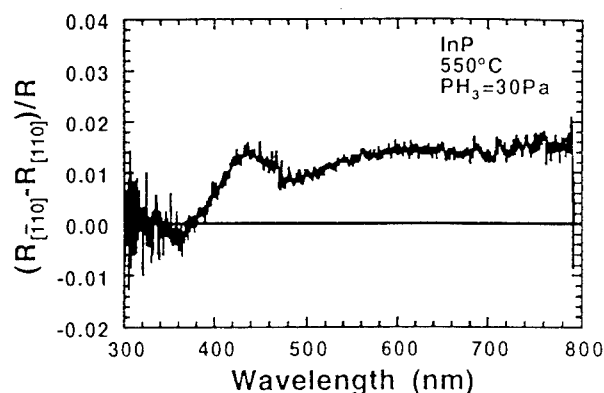


Fig. 2. Subtraction spectra of SPA for (001) InP.

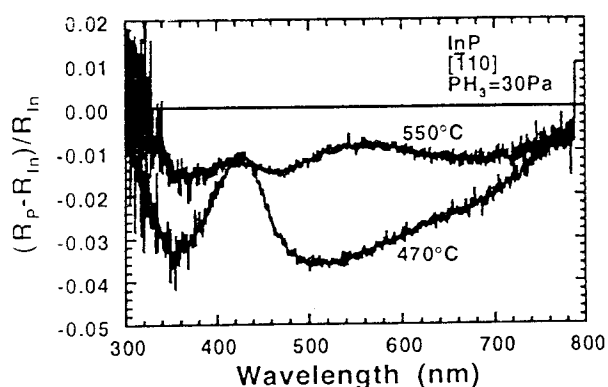


Fig. 3. SPA spectra for InP in the $[110]$ azimuth.

bonds is possibly due to the adsorption of amorphous P atoms on (2x4)-like surface. We found that excess-P surface could be observed by increasing PH_3 partial pressure at temperatures below 530°C .

Figure 4 shows the thus determined phase diagrams of GaAs and InP MOVPE surfaces as a function of the substrate temperature and partial pressure of AsH_3 and PH_3 . For GaAs, the substrate temperature was varied from 550 to 700°C and AsH_3 partial pressure was varied from 1 to 40 Pa. For InP, the substrate temperature was varied from 470 to 550°C and PH_3 partial pressure was varied from 10 to 60 Pa. For GaAs, the (2x4) γ -like surface is stable above 660°C and it evolves to c(4x4)-like as the substrate temperature decreases and the AsH_3

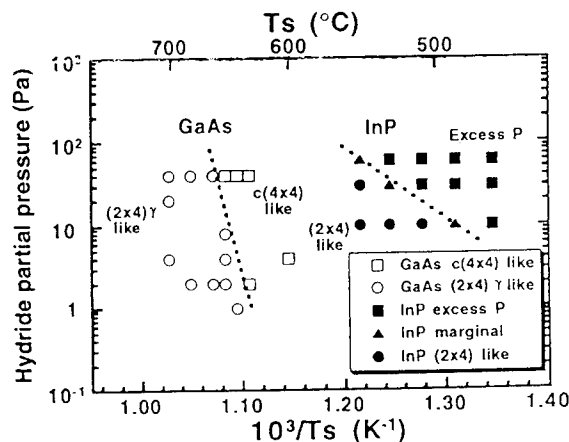


Fig. 4. Phase diagram as a function of substrate temperature and hydride partial pressure.

partial pressure increases. In contrast, the surface is (2x4)-like at 550°C and PH_3 partial pressure of 10 and 30 Pa in InP MOVPE, and it evolves to excess-P surface due to amorphous P excessively adsorbing onto the (2x4)-like surface as the substrate temperature decreases and PH_3 partial pressure increases. It should be noted that a c(4x4)-like surface having two group-V layers structure did not appear in InP MOVPE. These results indicate that the (2x4)-like surface is stable at substrate temperatures around 600°C , which is the temperature level generally used for InP MOVPE, and, in contrast, the c(4x4)-like surface is stable in GaAs MOVPE.

The difference of the P structure during InP MOVPE may influence the epitaxial layer qualities. We grew InP epitaxial layers on (001)-oriented Fe-doped semi-insulating InP substrate under the conditions of different P structures at constant substrate temperature. The samples were characterized by Hall measurement. Figure 5 shows the dependence of 77K carrier concentration and Hall mobility on PH_3 partial pressure. The substrate temperature was fixed at 530°C and the PH_3 partial pressure was varied from 10 to 60 Pa. The growth rate for the InP epitaxial layer was $1\text{ }\mu\text{m/h}$. From Fig. 4, at PH_3 partial pressure of 10 and 20 Pa, the surface structure is (2x4)-like. At around 30 Pa, it is marginal, while, at 40 and 60 Pa, it is

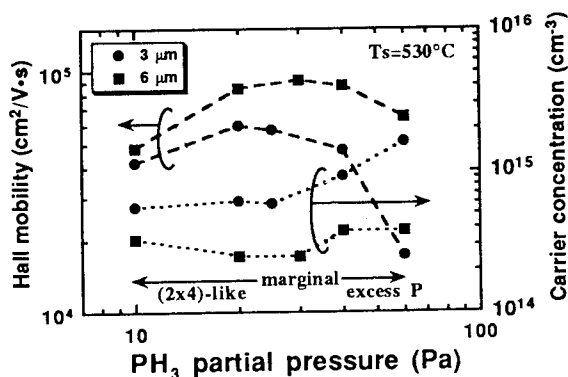


Fig. 5. PH_3 partial pressure vs 77K carrier concentration and Hall mobility.

excess P surface. It has been reported carbon and silicon accumulate at the interface between the InP epitaxial layer and the substrate and the highly conductive interface falsifies the Hall results [9]. Therefore, we grew InP epitaxial layers to thickness of 3 μm and 6 μm . The conduction type was n-type for all samples. A Hall mobility of 92,000 $\text{cm}^2/\text{V}\cdot\text{s}$ and a carrier concentration of $2.5 \times 10^{14} \text{ cm}^{-3}$ at 77K were measured for 6- μm thick sample grown under 30 Pa. The decrease in Hall mobility and the increase in carrier concentration for the samples grown under the condition of excess P surface were observed when compared with those grown under the conditions of (2x4)-like and marginal surfaces.

To identify the donor impurities, we did a secondary ion mass spectrometry (SIMS) analysis of Si and S because it has been reported that these are the predominant donors, which showed n-type conductivity [10]. However, no donor impurities could be detected within our SIMS detection limit ($1 \times 10^{15} \text{ cm}^{-3}$ for Si and $1\text{--}3 \times 10^{15} \text{ cm}^{-3}$ for S). This suggests that n-type conduction might be caused by native defects (for example, phosphorus antisite defects) formed under the condition of excess P surface [11]. Therefore, it is important to suppress the excessively P adsorption to obtain high-quality InP layers. SPA enables us to monitor the surface structure *in situ* and prevents excessive P adsorption.

4. Conclusions

The chemical structure of P-stabilized InP MOVPE was investigated by SPA and a phase diagram was established as a function of substrate temperature and PH_3 partial pressure. We found two phases of (2x4)-like and excess P adsorbed surface on it. A c(4x4)-like surface was not observed. To grow high-quality InP epitaxial layers, it is necessary to suppress excessive P adsorption on (2x4)-like surface.

Acknowledgments

We would thank Dr. Yoshiji Horikoshi and Dr. Kunihiro Uwai for their valuable advice and comments.

References

- [1] I. Kamiya, H. Tanaka, D. E. Aspnes, L.T. Florez, E. Colas, J. P. Harbison and R. Bhat: Appl. Phys. Lett. **60** (1992) 1238.
- [2] Y. Yamauchi, K. Uwai and N. Kobayashi: Jpn. J. Appl. Phys. **32** (1993) 3363.
- [3] Y. Kobayashi and N. Kobayashi: to be published in Jpn. J. Appl. Phys.
- [4] B. X. Yang and H. Hasegawa: Jpn. J. Appl. Phys. **33** (1994) 742.
- [5] N. Kobayashi and Y. Horikoshi: Jpn. J. Appl. Phys. **28** (1989) L1880.
- [6] K. Uwai, Y. Yamauchi and N. Kobayashi: Ext. Abstr. of the Int. Conf. on Solid State Devices and Materials, Chiba, Japan (1993) p.300.
- [7] Y. C. Chang and D. E. Aspnes: Phys. Rev. B **41** (1990) 12002.
- [8] K. Ploska, W. Richter, F. Reinhardt, J. Jonsson, J. Rumberg and M. Zorn: Mater. Res. Soc. Symp. Proc. **334** (1994) 155.
- [9] K. Rakennus, K. Tappura, T. Hakkarainen, H. Asonen, R. Laiho, S. J. Rolfe and J. J. Dubowski: J. Cryst. Growth **110** (1991) 910.
- [10] K. Uwai, S. Yamada and K. Takahei: J. Appl. Phys. **61** (1987) 1059.
- [11] B. W. Liang, P. Z. Lee, D. W. Shih and C. W. Tu: Appl. Phys. Lett. **60** (1992) 2104.

GROUP-V ATOMS EXCHANGE DUE TO EXPOSURE OF InP SURFACE TO $\text{AsH}_3(+\text{PH}_3)$ MEASURED BY X-RAY CTR SCATTERING

N. Yamada, K. Fujibayashi, T. Kumamoto, M. Tabuchi, Y. Takeda, I. Takahashi *, and J. Harada**

Department of Materials Science and Engineering

*Department of Applied Physics

School of Engineering, Nagoya University, Nagoya 464-01, Japan

**The University of Electro-Communications

Chofugaoka, Chofu 182, Japan

Introduction

Heteroepitaxially grown semiconductor layers are used as a base of various functional electronic and optical devices. For example, semiconductor laser diodes consist of a double heterostructure, and HEMTs (high electron mobility transistors) also make use of the heteroepitaxial structures(1,2). In order to realize further high functional devices, a technique to grow heteroepitaxial layers as thin as several Å is strongly required. In such a thin layer structure, the thickness of each layer must be controlled to a thickness as thin as 1ML(monolayer) and the interface layers must be confined to a also 1ML to allow the grown layer to work well as designed.

For III-V semiconductors, OMVPE (organometallic vapor phase epitaxy) and MBE (molecular beam epitaxy) are available to grow such thin layers under control and to make well defined interfaces. However, it is still difficult to obtain the well defined interface of semiconductors which contain different group-V atoms. Because the vapor pressure of group-V atoms is relatively high, the group-V atoms easily diffuse or exchange across the interface. In order to explain the mechanism of group-V atoms exchange at the interface, and to develop a technique to control the interface structure of materials which contain different group-V atoms, we have been investigating the interface of InP/InPAs/InP grown by OMVPE using X-ray CTR(crystal truncation rod) scattering(3,4).

The X-ray CTR is a rod that appears around a Bragg diffraction spot in k-space. It is caused by the abrupt truncation of a crystal at the surface. The shape of the CTR is very sensitive to the atomic scale unperiodic structure of the crystal(5,6). We have demonstrated that it is a very powerful technique to reveal the layer structure of the heteroepitaxially grown samples in the atomic scale(3,4).

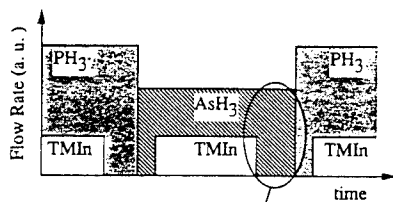
In this work, we investigate the samples of InP exposed to $\text{AsH}_3(+\text{PH}_3)$, in order to study the effect of the purge sequence (Fig. 1) which appears in the growth sequence of InP/InAs/InP structures. The purge sequence is unavoidable to grow heteroepitaxial layers which consist of different group-V atoms, and is considered to affect largely the structure of the interface. The experimental results show that the purge sequence does obstruct the abrupt interface formation.

Experiments

The samples were prepared by exposing the grown InP surface to $\text{AsH}_3(+\text{PH}_3)$ and then capped by 20Å InP layers all in the continuous gas sequence, as shown in Fig. 2. Exposure time of AsH_3 was changed from 0.5 to 30s, and that of $(\text{AsH}_3+\text{PH}_3)$ from 0.5 to 2s. During the growth, the reactor pressure was kept at 76 Torr. Growth temperature was kept at 600°C. AsH_3 and PH_3 were

used for the group-V sources, and TMIn for the group-III source(7). The X-ray CTR measurement was conducted using synchrotron radiation (SR) at the Photon Factory in the National Laboratory for High Energy Physics at Tsukuba. Beam line BL6A₂ was used for the measurement. The wavelength of the X-ray was set at 0.950Å or 1.000Å. X-ray CTR scattering intensity varies widely from 10^2 to 10^7 as for the spectrum of the 0.5s

Gas sequence for InP/InAs/InP growth



Gas sequence for measured samples

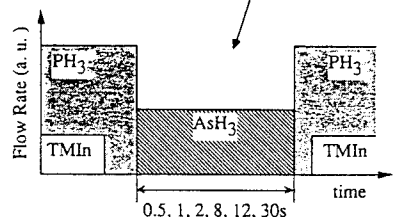


Fig. 1: Gas sequence at top is in the case of InP/InAs/InP growth, and bottom is to study purge effect.

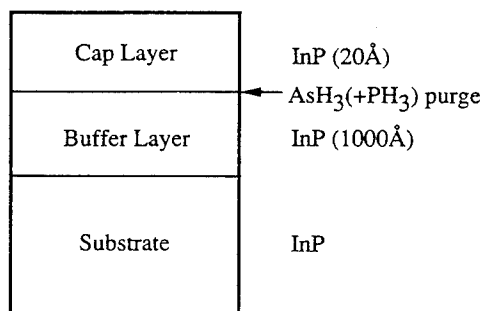


Fig. 2: Structure of measured samples

exposed sample shown in Fig. 3. Therefore, we needed the high intensity of X-ray from the SR. Other spectra are shifted by one order of magnitude each.

The diffraction spots were recorded by a Weissenberg camera with an IP (imaging plate). The diffraction patterns recorded on the IP were read out optically and stored as digital data. The diffraction spot from the (002) plane was used in this work. Subtracting the back ground X-ray diffuse-scattering from the measured X-ray diffraction intensity around the 002 Bragg point, we obtained the CTR spectra. The measured X-ray CTR spectra for the AsH₃-exposed samples are shown in Fig. 3. The spectra of (AsH₃+PH₃)-exposed samples are not shown since the gross shape is similar. Index ℓ which is the abscissa of the figure means the index of k-space.

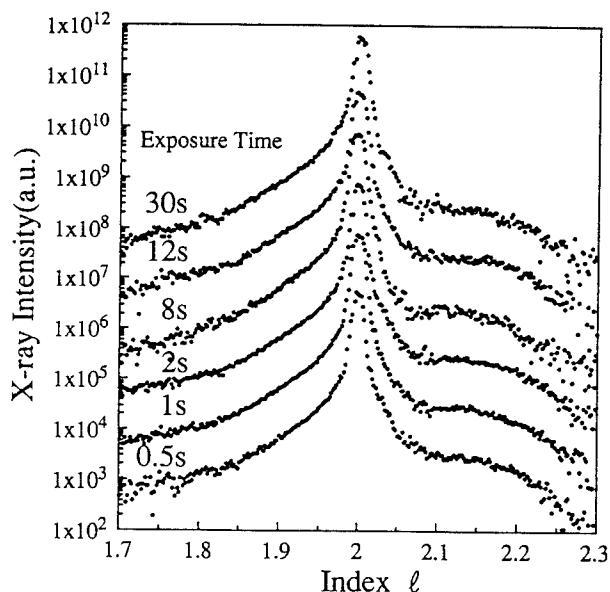


Fig. 3: Measured X-ray CTR spectra. Exposure time is shown at the left end of each spectrum.

In other words, we measured the X-ray CTR along (00- ℓ) direction which is normal to the surface of samples. The shoulders observed in Fig. 3 at ℓ around 2.1~2.2 have information of As atoms contained in InP.

Results and Discussions

In order to analyze the data of the X-ray CTR scattering, we need a model for the samples, and are necessary to calculate the X-ray CTR scattering from the model structure. Comparing the results of calculation and measured data, we decided the best fit values of parameters contained in the model. We assumed the model structure shown in Fig. 4. This model contains parameters such as n_{cap} , n_{het} , x_h , d_{cap} , d_{buf} , $\langle \delta z^2 \rangle$, c/a . n_{cap} and n_{het} are the thickness of the cap layer and of the hetero-layer, respectively. x_h denotes the As composition at the hetero-layer. d_{cap} and d_{buf} denote the extension of As atoms into the InP cap layer and into the InP buffer layer, respectively. The As distribution is assumed to have the formula; $x = x_h \exp(-n/d)$ where n [ML] is a distance from upper or lower interface, and x is the As composition in the layer at the distance n [ML] from the interface. $d=d_{cap}$ or d_{buf} . $\langle \delta z^2 \rangle$ represents the roughness of the surface. c/a indicates the tetragonal distortion of

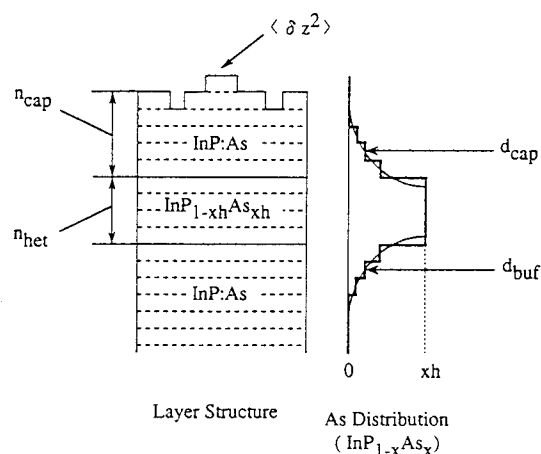


Fig. 4: A model for the calculation. The parameters d_{cap} and d_{buf} are used to determine the As distributions in the cap and bufer layers as $x=x_0 \exp(-n/d)$. $d=d_{cap}$ or d_{buf} .

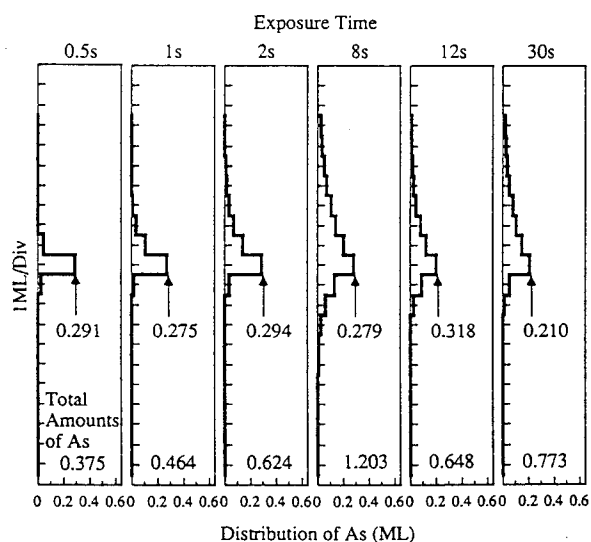


Fig. 5: Profiles of As atom distribution in each AsH_3 -exposed sample.

the InPAs layer, as the ratio of the lattice constants normal(c) and parallel(a) to the surface. By the curve fitting based on this model, parameters were determined at the best fit.

From the results of the curve fitting, the distributions of As atoms can be discussed in the monolayer scale as a function of the exposure time, which are shown in Fig. 5. Considerable amounts of As exist in each sample.

From the distributions it is seen, firstly, that the surface exchanged As/P compositions are almost the same, i.e., 0.3 in all AsH_3 -exposed samples. There must be some mechanism that stops the exchange at that rate. Secondly, the distributions of As atoms in the cap layer and in the buffer layer are very different.

In order to make this difference distinct, As amounts in the cap layer(\circ) and in the buffer layer(\bullet) are separately plotted as a function of the exposure time, which are shown in Fig. 6. In this work, we defined that the layer whose As composition was maximum was the top of the buffer layer. From Fig. 6 it is clear that with increasing exposure time, the amounts of As atoms which were taken in the cap layer increased, and that it saturated after about 10s. The distributions of As atoms in the cap layer is considered due to memory effects of As source gas and/or due to As atoms adsorbed on the InP surface. On the contrary, the amounts of As atoms in the buffer which is about 0.3ML were independent of the exposure time.

The distributions of As atoms for the (AsH_3+PH_3) -exposed samples are shown in Fig. 7. As in the case of the AsH_3 -exposed samples, the amounts of As atoms taken in the cap layers increased with the increasing exposure time. Since the exposure time is not long enough, the amounts of As did not saturate. The distribution of As atoms in the buffer layers also showed similar profiles to the AsH_3 -exposed samples, but the group-V atoms

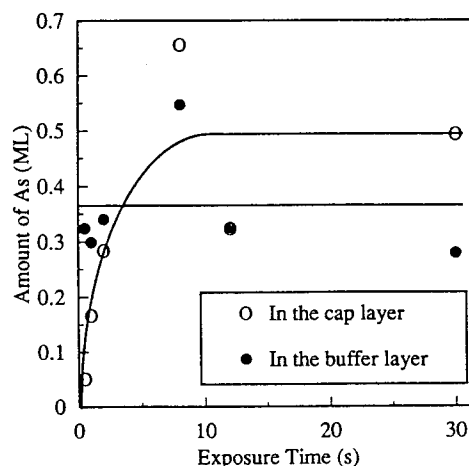


Fig. 6: Amounts of As in the cap layer(\circ) and in the buffer later(\bullet) versus exposure time. Solid line is a guideline of eye.

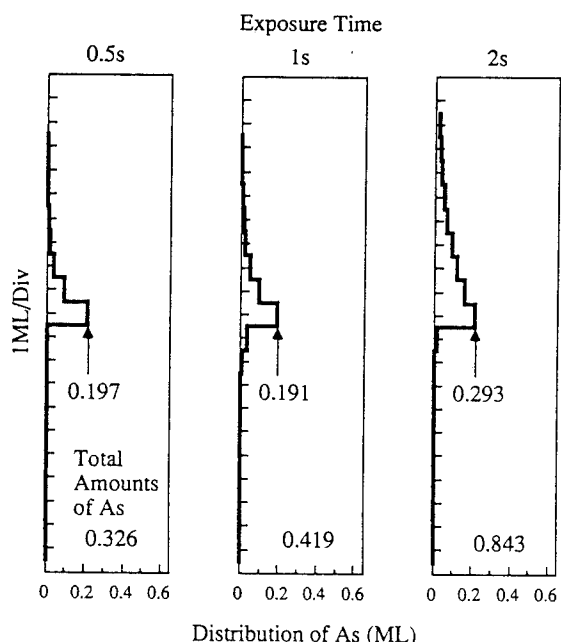


Fig. 7: Profiles of As atom distribution in each $(\text{AsH}_3+\text{PH}_3)$ -exposed sample.

extended toward the buffer layer was much suppressed in the $(\text{AsH}_3+\text{PH}_3)$ -exposed samples.

Conclusions

X-ray CTR scattering measurement was conducted for two types of samples prepared by OMVPE, and the structures of the interfaces were investigated.

It was found that considerable amounts of As atoms exist in all the samples, though the InP surface were only exposed to AsH_3 . The gross shape of the As distribution in the AsH_3 -exposed and $(\text{AsH}_3+\text{PH}_3)$ -exposed samples showed similar profiles. However, in the $(\text{AsH}_3+\text{PH}_3)$ -exposed samples the As distribution into the buffer layer was much suppressed.

Since the long tail of As distribution in the cap layer is a serious obstacle to obtain a sharp heterointerface, a proper gas sequence is needed. Based on the present analysis, even the exposure time of 0.5s is long enough to cause the As distribution into a few ML.

Acknowledgments

This work was performed as a part of the project (Proposal No. 93G195) accepted by the Photon Factory Program Advisory Committee. The authors would like to thank Mr. H. Kamei. All OMVPE-grown samples were prepared by him. This work was supported in part by the Grant-in-Aid for Scientific Research (B) No. 04452174 and the Grant-in-Aid for Encouragement of Young Scientists No. 06750315 from the Ministry of Education, Science and Culture.

References

- (1) I. Hayashi, M. B. Panish, P. W. Foy, and S. Sumski, *Appl. Phys. Lett.*, **17** (1970) 109.
- (2) T. Mimura, S. Hiyamizu, T. Fujii, and K. Nanbu, *Jpn. J. Appl. Phys.*, **19** (1980) L225.
- (3) Y. Takeda, Y. Sakuraba, K. Fujibayashi, M. Tabuchi, T. Kumamoto, I. Takahashi, J. Harada, and H. Kamei, *Appl. Phys. Lett.*, **66** (1995) 332.
- (4) M. Tabuchi, Y. Takeda, Y. Sakuraba, T. Kumamoto, K. Fujibayashi, I. Takahashi, J. Harada, and H. Kamei, *J. Cryst. Growth*, **146** (1995) 148.
- (5) Y. Kashihara, S. Kimura, and J. Harada, *Surf. Sci.*, **214** (1989) 477.
- (6) J. Harada, T. Shimura, M. Tanaka, K. Yakushiji, and K. Hoshi, *J. Cryst. Growth*, **104** (1990) 773.
- (7) H. Kamei and H. Hayashi, *J. Cryst. Growth*, **107** (1991) 567.

THE DETERMINATION OF ATOMIC PLANE ON InP (001) SURFACE BY CAICISS

T. Nishihara, M. Shinohara, O. Ishiyama, and F. Ohtani

Keihanna Research Laboratory, Shimadzu Corporation

Hikaridai 3-9, Seikacho, Sorakugun, Kyoto 619-02, Japan

M. Yoshimoto, T. Maeda, and H. Koinuma

Research Laboratory of Engineering materials, Tokyo Institute of Technology

Nagatsuta 4259, Midoriku, Yokohama 226, Japan

Introduction

InP is an important semiconductor material for GaInAsP/InP heterojunction lasers, GaInAs/InP photo-detectors, AlInAs/GaInAs/InP high electron mobility transistors and heterojunction transistors. In order to achieve the atomically regulated heteroepitaxy of those materials, it is important to control the atomic species and their alignment in the topmost surface of InP substrates.

Although several studies (1-5) have been carried out on the effect of low energy noble gas ion bombardment on the stoichiometry of InP (001) surface for an epitaxial growth, of which is used to remove contaminations of these semiconductor surfaces, the results are almost concluded to be an excess In surface by means of auger electron spectroscopy (AES) and X-ray photoelectron spectroscopy (XPS). There is no determination of topmost atomic species on this surface, because AES and XPS have analysing depths extending over several nanometers. They are impossible to identify the topmost atomic species. Therefore, we have employed coaxial impact collision ion scattering spectroscopy (CAICISS) to determine the species of the topmost atomic plane on InP (001). The characteristic of CAICISS, which is basically low energy ion scattering spectroscopy, is that the experimental scattering angle is taken to 180° (6).

Figure 1 illustrates the situation at the incident angle of 35.3° in $[\bar{1}10]$ azimuth ($[\bar{1}11]$ direction) on InP (001) in the CAICISS condition. In this situation, only the topmost atom can be "seen", because the atom in the second layer is shadowed by a shadow cone formed by the topmost atom. As a result of that, we can directly determine the terminating plane by CAICISS.

In order to remove the contaminations of semiconductor surfaces, sputtering and annealing processes are generally used (7,8). We have observed the sputtered and the annealed InP (001) surfaces to determine the species of the topmost atomic plane on these surfaces by CAICISS.

Experiments

The all experiments were carried out in an ultra high vacuum (UHV) chamber with a base pressure of 1×10^{-7} Pa. The system is equipped with CAICISS (Shimadzu, CAICISS-I), reflection high energy electron diffraction (RHEED), and argon sputter gun. The sample is set up to a manipulator with two-axis rotations, which are correspond to an incident angle and an azimuthal angle, respectively. InP (001) samples used in this study were cut out from wafer to an appropriate size. Before loading in the UHV chamber, they were cleaned in the organic solution.

Several samples of InP (001) were subjected to in-situ CAICISS measurements following as : (a) as-supplied InP (001) at room temperature, (b) InP (001) annealed at from 300 to 550 $^\circ\text{C}$ in UHV, (c) InP (001) sputtered with 1 keV Ar^+ for 20 minutes at 300 $^\circ\text{C}$.

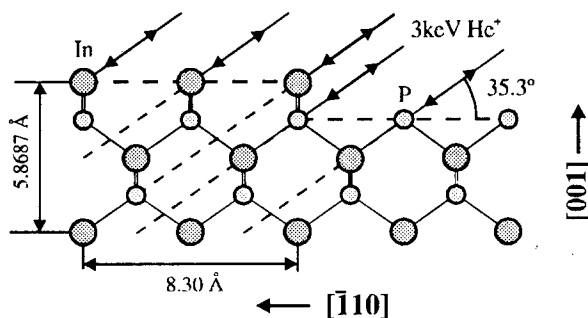


Fig. 1 Schematic cross-section geometry of InP (001) surface along $[\bar{1}10]$ azimuth in CAICISS measurement with incident angle of 35.3°

Prior to the CAICISS measurements, we confirmed a 1×1 RHEED pattern for each sample.

In order to determine the topmost atomic species, we have observed CAICISS spectra at the incident angle of 35.3° in $[\bar{1}10]$ azimuth. He^+ of 3 keV was used in CAICISS as a primary ion, and also observed CAICISS intensity as a function of an azimuthal angle at the incident angle of 35.3° to evaluate surface crystalline quality on sputtered InP (001).

Atomic force microscopy (AFM) was used to observe a surface morphology of as-supplied and sputtered InP (001).

Results and discussion

Figure 2 shows CAICISS spectra which are taken at an incident angle of 35.3° in $[\bar{1}10]$ azimuth. As shown in Fig. 2 (a), (b), and (c), CAICISS spectra exhibit peaks due to He scattering from both In and P at from room temperature to 500°C . If the topmost surface is terminated by In or P, either In or P peak should be observed. This means that both In-terminated and P-

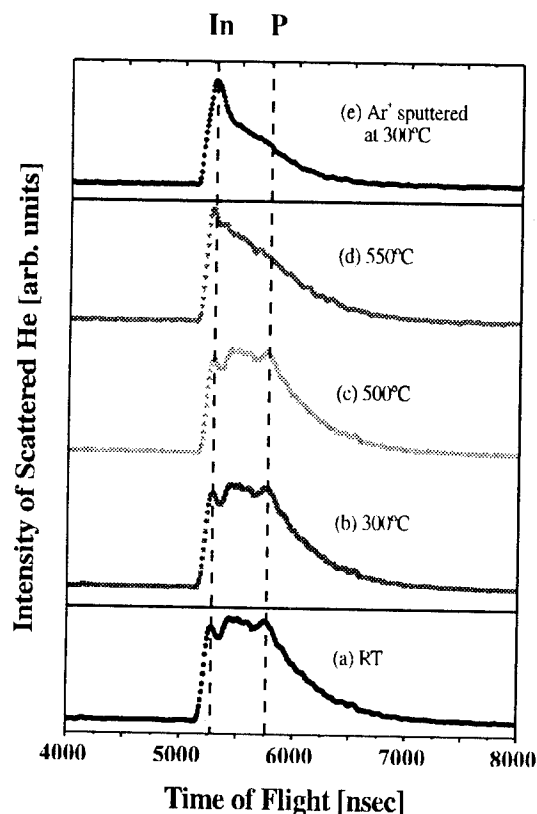


Fig. 2 CAICISS spectra taken at the incident angle of 35.3° in $[\bar{1}10]$ azimuth for InP (001) surfaces of (a) as-supplied, (b)~(d) annealed sample, and (e) Ar^+ sputtered sample at 300°C .

terminated surfaces coexist on this (001) surface. We have also confirmed both In and P peaks in $[110]$ azimuth. It is concluded that the thermally annealing treatment is impossible to form the topmost surface terminated by In or P below 500°C .

On the contrary, when the substrate temperature increased up to 550°C , P peak has disappeared, and only In peak has detected as shown in Fig. 2 (d). According to SEM observation, serious roughness which is attributed to In-island formation was observed on this surface. P desorbs from surface and then the surface is In-rich by annealing at 550°C . In on the surface is easy to diffuse at this temperature, and a nuclei of In is formed (9). As a result of that, coalescing into islands occurs. The annealed surface is not smooth and does not form In-terminated surface.

In order to form the In-terminated surface on InP (001), we have sputtered InP (001) surface with Ar ion of 1 keV for 20 minutes at 300°C instead of annealing treatment. Incident angle of Ar ion was set at 90° (normal incidence). CAICISS spectrum of this sputtered surface is shown in Fig. 2 (e), in which only In peak is observed. It reveals that InP (001) surface is perfectly terminated by In. It is considered that the preferential sputtering of phosphorus contributes to the formation of In-terminated surface. Compared with the case of Fig. 2 (d), The SEM photograph revealed that the surface was smooth and there are not serious damage.

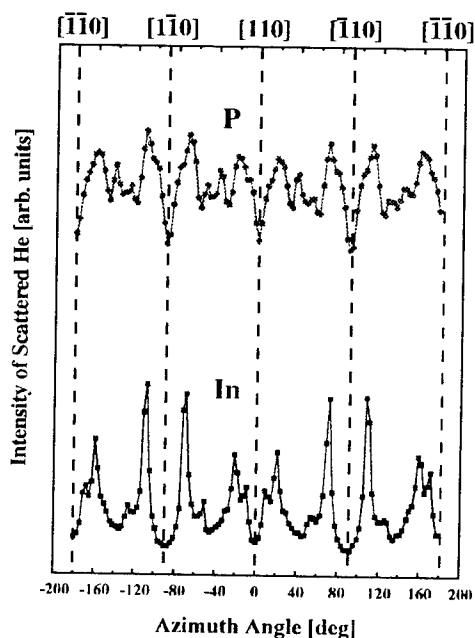


Fig. 3 Azimuth angle dependence of In and P signal intensities at the incident angle of 35.3° for Ar^+ sputtered InP (001) surface.

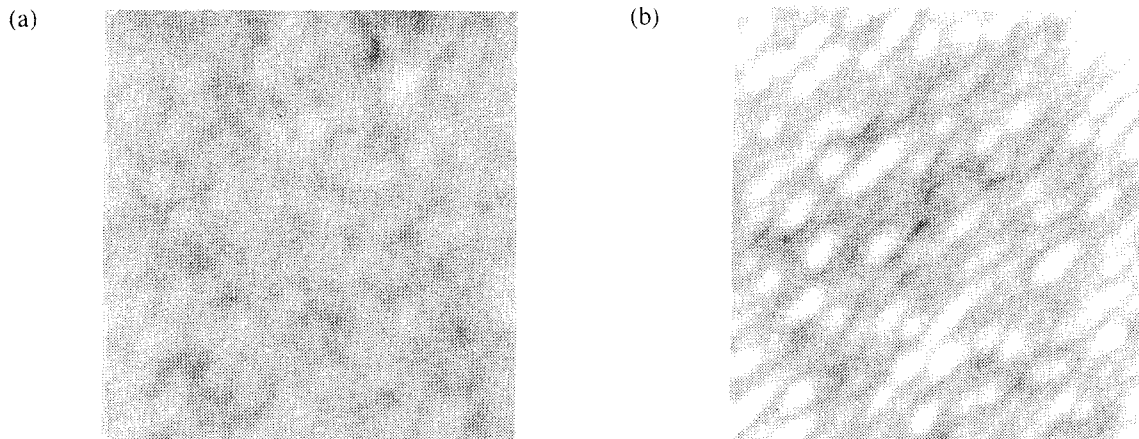


Fig. 4 AFM images of (a) as-supplied InP (001) surface and (b) InP (001) surface after sputtered and annealed at 300 °C. The scanning area is 500 x 500 nm².

The azimuthal dependence of CAICISS spectra has been taken at an incident angle of 35.3° in order to evaluate the surface crystalline quality as shown in Fig. 3. The azimuthal dependence of both He scattering intensity from In and P are exhibited in Fig. 3, of which shapes exhibit 2-fold symmetry with respect to the $\langle 110 \rangle$ axis. This symmetry appears that the atoms underlying the $\langle \bar{1}10 \rangle$ azimuth are arranged differently from those underlying the $\langle 110 \rangle$ azimuth because the ideal bulk truncated surface of InP {001} has only 180° symmetry with respect to the underlying bulk crystal. This means the sputtered surface is zinc-blend structure, and little physical damage exists on sputtered InP (001) surface.

In order to compare the surface morphology between the as-supplied and the sputtered InP (001) surfaces, AFM images above surfaces were taken in air. The scanning area of AFM images is 500 x 500 nm². The as-supplied surface has no regulated structure because of surface contamination, while surface treated by sputtering and annealing at 300 °C was represented a textured structure aligned along $\langle 110 \rangle$ axis. The width of this textured structure was 260 ~ 500 Å and the height was 5 ~ 24 Å corresponding to a few units of InP. According to CAICISS measurements in Fig. 2 (e), this surface is terminated by In. Therefore, it is concluded that this InP (001) surface is composed of double atomic height step.

If the diffusion coefficient has anisotropy on the InP (001) surface, textured structure may be aligned to one direction. It is well known that the surface diffusion coefficient has an anisotropy on Si (001) 2 x 1 surface during the deposition (10-11). We speculate that the diffusion coefficient has the anisotropy on InP (001) surface during the sputtering as well as the case of Si (001) surface.

Conclusion

We have identified that indium top surface without serious roughness can be acquired by Ar⁺ sputtering even if substrate temperature is as low as 300 °C. In AFM observations, this surface exhibits the textured structure, which is composed of double atomic height step. Furthermore, the azimuthal dependence of CAICISS spectra show two-fold symmetry with respect to $\langle 110 \rangle$ axis, which indicates that the crystalline quality of this surface is quite high. Therefore, we consider that this surface is applicable to the substrate for heteroepitaxial growth.

References

- (1) R. S. Williams, "Low Energy Ar Ion Bombardment Damage of Si, GaAs, and InP Surfaces," *Solid State Commun.* Vol. 41, pp. 153-156, No. 2 1982
- (2) O. Wada, "Ar Ion-Beam Etching characteristics and Damage Production in InP," *J. Phys. D*, Vol. 17, pp. 2429-2437, 1984
- (3) C. Jardin, D. Robert, B. Achard, B. Gruzza and C. Pariset, "An AES and ELS Study of InP (001) Surface Subjected to Argon Ion Bombardment," *Surf. Interface Anal.* Vol. 10, pp. 301-305, 1987
- (4) J. B. Malherbe and W. O. Barnard, "Preferential Sputtering of InP : an AES Investigation," *Surf. Sci.* Vol. 255, pp. 309-320, 1991
- (5) J. Zemek, O. A. Baschenko, M. A. Tyzykhov and P. Jiricek, "Altered Layer Composition of Sputtered InP (001) Wafers : Non-destructive Concentration Depth Profiling," *Surf. Sci.* Vol. 318, pp. 421-427, 1994
- (6) M. Katayama, E. Nomura, N. Kanekama, H. Soejima, and M. Aono, "Coaxial impact-collision ion scattering spectroscopy (CAICISS) : A novel method for surface structure analysis," *Nucl. Instr. and Meth.* Vol. B33, pp. 857-861, 1988

- (7) S. Riese, E. Milas, and H. Merz, "k-resolved inverse photoemission of InP (100) surfaces," *Surf. Sci.* Vol. 269/270 pp. 833-837, 1992
- (8) W. Weiss, K. Kasper, K. H. Herrmann, D. Schmeisser, and W. Göpel, "Surface morphology of epitaxial CaF_2 and SrF_2 layers grown onto InP (001) studied by atomic force microscopy and low-energy electron diffraction," *Surf. Sci.* Vol. 268, pp. 319-324, 1992
- (9) D. J. Oostra, R. V. Smilgys, and S. R. Leone, "Initial stages of heteroepitaxial growth of InAs on Si (001) ," *Appl. Phys. Lett.* Vol. 55, No. 13, pp. 1333-1335, 1989
- (10) Y. -Mo. R. Kariotis, B.S. Swartzentruber, M. B. Webb, and M. G. Lagally, "Scanning tunneling microscopy study of diffusion, growth, and coarsening of Si on Si (001)," *J. Vac. Sci. Technol.* Vol. A8, pp. 201-206, 1990
- (11) V. M. Bedanov and D. N. Mukhin, "Anisotropic diffusion and island formation in the MBE growth," *Surf. Sci.* Vol. 297, pp. 127-134, 1993

DISTRIBUTION OF As ATOMS IN InP/InPAs(1ML)/InP HETERO-STRUCTURES MEASURED BY X-RAY CTR SCATTERING

M. Tabuchi, K. Fujibayashi, N. Yamada, Y. Takeda,
I. Takahashi* and J. Harada**

Department of Materials Science and Engineering

*Department of Applied Physics

School of Engineering, Nagoya University, Nagoya 464-01, Japan

**The University of Electro-Communications

Chofugaoka, Chofu 182, Japan

Introduction

For a further development of electronics and optoelectronics, new functions of materials are demanded. Thus, low-dimensional structures such as quantum wells have become to be adopted. Semiconductor lasers with quantum well active layers have a lower threshold current. One- or two-dimensionally confined structures are useful for high speed switching devices because of their high electron mobility[1]. In these cases, the quality of hetero-interfaces comes to play important roles as each layer in the structures becomes thinner. In the quantum structures of a few MLs thickness, the vagueness of the interface in the scale of only a few Å is no longer negligible. Since the interface structure must be controlled or, at least, must be determined in the atomic scale, a technique to characterize the interface in such a scale are strongly required.

X-ray CTR is the diffraction spots extended nominal to the surface for a finite crystal. Its shape is sensitively modified as the structure near the surface is changed[2, 3]. We have successfully applied the X-ray CTR measurement to study the epitaxially grown semiconductor interfaces and have demonstrated that it is a very powerful technique to reveal the atomic scale interface structures embedded in semiconductors [4, 5].

In this work, we investigated InP/InPAs/InP heterostructures. The InP/InPAs/InP system is one of the difficult systems to obtain a well defined interface because of atom exchange between As and P. The distribution of As atoms in InP/InPAs/InP single quantum-well structures with about 1ML InPAs, denoted as InP/InPAs(1ML)/InP hereafter, was clearly obtained by analyzing the experimental data of CTR.

Preparation of Samples

InP/InPAs(1ML)/InP single quantum-well samples were grown by OMVPE[6]. Each InPAs layer was grown on InP (001) substrates followed by a 1000Å InP buffer layer. InPAs layers intended to be 1ML thick were grown on the buffer layers and capped by 20Å InP layers. The growth temperature was 620°C. AsH₃, PH₃, and TMIIn were used as the source gases. The designed As compositions in each sample are 0.18, 0.3, 0.47 and 0.6. Figure 1 shows schematically the source-gas flow sequence during the OMVPE growth. InP surfaces were exposed to AsH₃ during the period t_2 , and InPAs surfaces were exposed to PH₃ during the period t_4 . These periods are important to consider the exchange of As and P atoms at the interfaces and related phenomena.

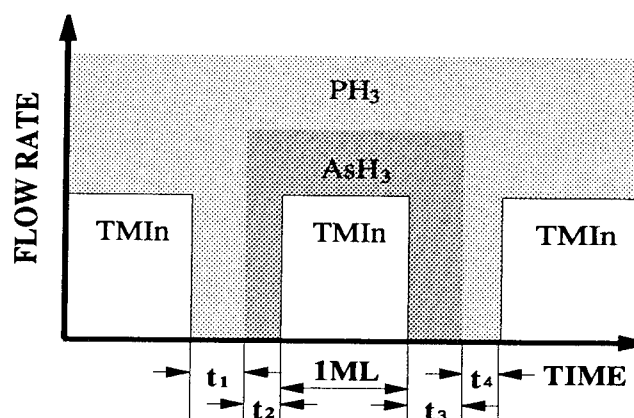


Fig. 1: Source-gas flow sequence during the OMVPE growth.

In this work, t_1 , t_2 , t_3 and t_4 were fixed at 2.0, 0.5, 2.0 and 0.5sec for all samples.

X-ray CTR measurement

X-ray CTR is a rod normal to the surface of the crystal observed in the \mathbf{k} -space around Bragg points. Thus, the X-ray CTR spectra can be measured as the usual X-ray diffraction.

The X-ray CTR measurement was conducted at BL6A2 of the Photon Factory in the National Laboratory for High Energy Physics at Tsukuba. The wavelength of the X-ray was set at 1.000Å or 0.950Å by a bent Si (111) monochromator. The Weissenberg camera was used to record the X-ray diffraction intensity distribution with imaging plates(IP) as a detector.

In this work, the CTR spectra which appear around the 002 Bragg diffraction spot were analyzed. The CTR spectra were obtained by subtracting the background X-ray diffuse-scattering from the measured X-ray diffraction intensity.

Figure 2 shows the measured X-ray CTR spectra. Index ℓ which appears in the figure means the index of the \mathbf{k} -space. The spectra spread widely around the index $\ell = 2$. In the spectra, shoulders are observed at around $\ell = 2.1 \sim 2.2$, which are due to the existence of the InPAs hetero-layers. The information about the distribution of As atoms can be obtained by analyzing the shape.

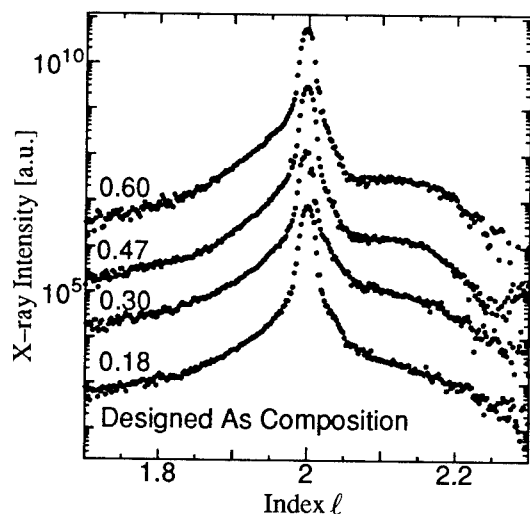


Fig. 2: Measured CTR spectra. Designed As compositions in InPAs layer are shown at left end of each spectrum.

Data Analysis

The X-ray CTR spectra were analyzed by comparing them with theoretically calculated spectra based on a model structure shown in Fig. 3. This model contains eight parameters, n_c , n_h , x_h , $\langle \Delta z^2 \rangle$, d_c , d_b , c/a , and I_0 . n_c and n_h are the thicknesses of the cap layer and the hetero-layer, respectively. x_h is the As composition in the InPAs layer. d_c and d_b represent the distributions of As atoms in the cap and the InP buffer layer, respectively. The As composition x in the layer away from upper or lower interface by nML is assumed to distribute as

$$x = x_h \exp\left(-\frac{n}{d}\right)$$

where d is d_c in the cap layer or is d_b in the buffer layer. $\langle \Delta z^2 \rangle$ indicates the surface roughness. Though c/a and I_0 do not appear in Fig. 3, c/a indicates a tetragonal distortion of the InPAs layer, and is the ratio of the lattice constants normal(c) and parallel(a) to the surface. I_0 is a scaling factor to match the absolute intensity of the measured data to the calculation. We used 'R-factor' to evaluate the curve fitting quality realized by a set of parameters.

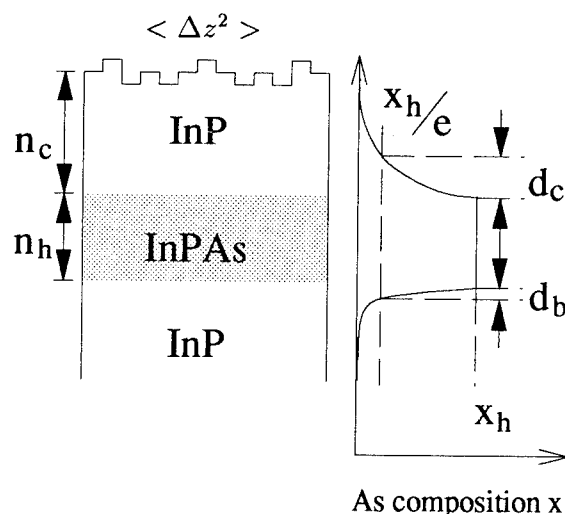


Fig. 3: A model for the CTR spectrum calculation. The parameters d_c and d_b are used to determine the As compositions in cap and buffer layers as $x = x_h \exp(-n/d)$, where $d = d_c$ or d_b .

Table 1: Values of fitting parameters which give the best fit to each measured CTR spectrum.

Designed As Composition	0.18	0.3	0.47	0.6
d_c [ML]	1.39	1.23	1.31	1.44
d_s [ML]	0.00	0.67	0.20	0.31
$\langle \Delta z^2 \rangle$ [ML ²]	0.10	0.12	0.22	0.31
c/a	1.087	1.070	1.068	1.063
Scaling Factor	3.44×10^{-3}	5.37×10^{-3}	3.56×10^{-3}	4.08×10^{-3}
x_H	0.115	0.180	0.391	0.454
n_C [ML]	8	8	9	8
n_H [ML]	1	1	1	1
As Amount [ML]	0.229	0.440	0.734	0.942
R-Factor	1.263×10^{-2}	1.289×10^{-2}	1.250×10^{-2}	1.559×10^{-2}

Results and Discussions

Figure 4 shows the distributions of As atoms represented with the parameters at the best-fit for four samples. The values of parameters which give the best fit curve to the measured data are shown in Table 1. n_H indicates the thickness of the layer with the highest As composition, and x_H indicates its As composition. n_C indicates the thickness of the layer which have the highest As composition. The As amount indicates the total number of As atoms. Figure 5 shows the measured data of the sample whose As composition is designed 0.3 and the curve calculated with the parameters at the best-fit.

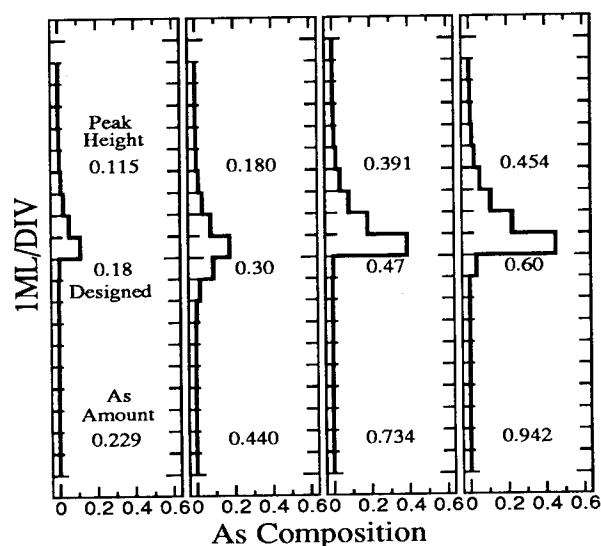


Fig. 4: Profiles of As atom distribution in each sample.

When the R-factor is less than 0.02, we considered that the calculated curve fits well to the measured data as shown in Fig. 5. For all the samples, $\langle \Delta z^2 \rangle$ is less than 0.3. It means that the surfaces are very flat. c/a is nearly equal to the ideal value 1.064 in all samples. n_H s are equal to 1 for all the samples which is just the designed value. n_C are almost constant and closed to the designed value 7ML. These results indicate that the model structure shown in Fig. 3 well represents the real structure of InP/InPAs(1ML)/InP, and the curve fitting goes well.

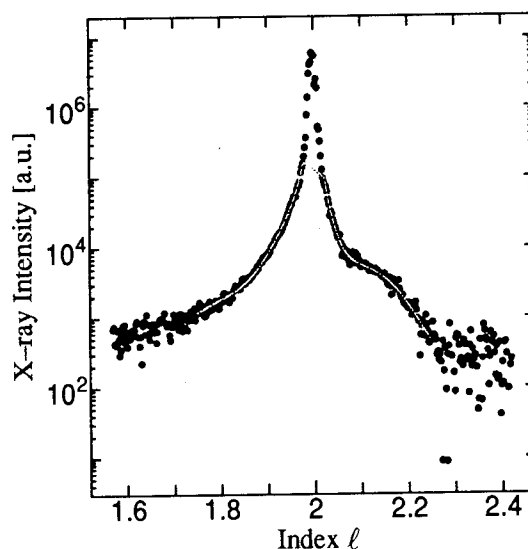


Fig. 5: Example of fitting. Solid dots are measured data, and the dotted line is the result of calculation.

As shown in Fig. 4, it is obvious that the extension of As atoms toward the lower layer is negligible. As atoms extended one-sidedly into upper layers. The peak As composition in the layer is slightly lower than the designed As composition. The value of d_c shows no relation to the designed As composition, and is close to 1ML. The amount of As atoms in all the samples is as much as twice of the As composition (peak height) in the hetero-layer.

Since the extension of As atoms toward the lower layer is very small or stopped after As atoms extended less than 1ML, it is considered that there exists some mechanism to prevent the As atoms on the InP layer from extending into the InP matrix, such as construction of surface recombination structures. The asymmetric distribution of As atoms and the amount of As atoms existing in the grown layer suggest that the origin of the As distribution is not diffusion of the As atoms in the solid phase. It must be caused by the excess As atoms absorbed on the surface or remaining in the gas phase. It indicates that the profile of the distribution of As atoms can be made more abrupt by controlling the source-gas flow sequence properly, i.e., by preventing the absorption of excess As atoms and/or by helping the desorption of them. For example, the AsH₃ purging time t_3 after growing the InPAs layer should be shorter than 2 sec, and the PH₃ purging time t_4 before growing the InP cap layer should be longer than 0.5 sec.

The total amount of As atoms agreed well with the As amount measured by X-ray fluorescence for each sample. It assures correctness of our X-ray CTR measurements and analysis.

Conclusions

The samples of InP/InPAs(1ML)/InP were prepared by OMVPE. The interfaces of these samples were investigated by the X-ray CTR measurement.

The distribution of As atoms around the interfaces were clearly revealed in the atomic scale from the data. It was shown that As atoms extended into only a few MLs under the InPAs. As atoms contained in the InPAs hetero-layer were almost the same as those extended in the InP cap layer. These results suggest that the extension of As atoms in the InP layer occurs due to the absorbed As atoms on the InPAs surface or As atoms remaining in the gas phase. Thus the source-gas flow sequence should be finely controlled to realize abrupt InP/InPAs interfaces.

Acknowledgements

This work was performed as a part of the project (Project No. 93G195) accepted by the Photon Factory Program Advisory Committee. The authors would like to thank Mr. H. Kamei. All OMVPE-grown samples were prepared by him. This work was supported in part by the Grant-in-Aid for Encouragement of Young Scientists No. 06750315 and by the Grant-in-Aid for Scientific Research (B) No. 04452174 from the Ministry of Education, Science and Culture.

References

- [1] T. Mimura, S. Hiyamizu, T. Fujii, and K. Nanbu, *Jpn. J. Appl. Phys.*, **19** (1980) L225.
- [2] Y. Kashihara, S. Kimura, and J. Harada, *Surf. Sci.*, **214** (1989) 477.
- [3] J. Harada, T. Shimura, M. Tanaka, K. Yakushiji, and K. Hoshi, *J. Cryst. Growth*, **104** (1990) 773.
- [4] Y. Takeda, Y. Sakuraba, K. Fujibayashi, M. Tabuchi, T. Kumamoto, I. Takahashi, J. Harada, and H. Kamei, *Appl. Phys. Lett.*, **66** (1995) 332.
- [5] M. Tabuchi, Y. Takeda, Y. Sakuraba, T. Kumamoto, K. Fujibayashi, I. Takahashi, J. Harada, and H. Kamei, *J. Cryst. Growth*, **146** (1995) 148.
- [6] H. Kamei and H. Hayashi, *J. Cryst. Growth*, **107** (1991) 576.

Use of Spectrally Resolved Scanning Photoluminescence for Optimizing the Growth Conditions of InAlAs/InP Heterostructures[†]

K. Hong¹, C. Klingelhöfer², F. Ducroquet³, M. F. Nuban⁴, E. Bearzi³,
D. Pavlidis¹, S. K. Krawczyk⁴ and G. Guillot³

¹) Department of Electrical Engineering and Computer Science, The University of Michigan, Ann Arbor, MI 48109, USA

²) SCANTEK, 17, Chemin du petit bois, 69130 Ecully, France

³) Laboratoire de Physique de la Matière (URA CNRS n°358), INSA de Lyon, 69621 Villeurbanne, France

⁴) Laboratoire d'Electronique (URA CNRS n°848), Ecole Centrale de Lyon, 69131 Ecully, France

Introduction

Metal organic chemical vapor deposition(MOCVD) has been a very attractive technique for the epitaxial growth of III-V compound semiconductors for microwave and optoelectronic device applications due to its simplicity, flexibility and high throughput. As in many other growth techniques, MOCVD requires the optimization of the growth conditions to obtain desirable material properties for specific applications. Among all material properties, spatial uniformity of the electrical and optical properties of the layers are of great concern for any electrical and optical device application. In this work, we demonstrate the use of spectrally resolved scanning photoluminescence(SR-SPL) for determining the uniformity characteristics of MOCVD grown layers and report on growth optimization criteria based on such measurements.

Growth and Characterization Techniques

Experiments were carried out on InAlAs/InP heterostructures. InAlAs is of great importance, since it acts as large bandgap material for InP-based heterostructure devices. Moreover, InAlAs/InP heterostructures are of great interest for high power HEMT applications(1). The samples were grown by a modified EMCORE GS3200 low pressure MOCVD system at the University of Michigan. The growth system consists of a vertical mass transport reactor with rotating susceptor. Trimethylindium (TMIn) and trimethylaluminum (TMAI) were used for In and Al sources, respectively, and 100% arsine and phosphine was used for group V elements.

Spectrally resolved scanning photoluminescence (SPL) measurements were carried out at room temperature using the SCAT-SPEC IMAGEUR of SCANTEK. The photoluminescence signal was excited using a He-Ne laser(632.8nm, 10mW) and measured using calibrated Si or InGaAs photodetectors. For high resolution measurements, the diameter of the laser spot on the sample surface was slightly below 1µm and the scanning step was 0.5µm. Finally, electrical characterization (admittance and deep level transient spectroscopy) of the layers was carried out on Schottky diodes, which were fabricated on the InAlAs layers by depositing Pt/Ti/Pt/Au contacts. The ohmic contacts were formed by depositing Ge/Au/Ni/Ti/Au on the back side of n⁺ InP which was used as substrate.

Impact of growth temperature on InAlAs/InP

The impact of growth temperature on the InAlAs/InP heterostructures was investigated in the range from 550°C to 690°C. Fig.1 shows that the average PL intensity from the InAlAs layer, from the InP buffer and from the InAlAs/InP(type II) interface strongly depend on the growth temperature. Moreover, the PL intensity from InAlAs showed a peak value for heterostructures grown at 650°C.

Capacitance-voltage measurements at room temperature showed that the residual carrier concentration in InAlAs grown at 650°C is more than one order of magnitude lower than in layers grown at 550°C. In addition to offering a low residual concentration, growth at 650°C also offers minimum trap density. This was confirmed by DLTS measurements which have also indicated that InAlAs has three principal traps(E1 = 0.1 - 0.14 eV, E2 = 0.35 - 0.4 eV, E3 = 0.55 - 0.65 eV)(2). To analyze our results, it is worth considering the general PL trends in semiconductors where it is known that the PL intensity is known to increase with doping concentration and decrease with the density of non-radiative recombination centers(3). However, in the case of the InAlAs samples shown in Fig.1, as the growth temperature increases from 550°C to 650°C, the PL intensity increases in spite of the fact that the residual doping level decreases. One can therefore conclude that in the case of the MOCVD grown InAlAs layers reported here, the observed variations of the PL signal are mainly due to strong variation of the concentrations of non-radiative recombination centers. In fact, the maximum PL intensity is observed on layers which contain the lowest density of the three main deep traps(E1, E2 and E3).

[†]Work supported by NSF/CNRS cooperative project (contract No. INT-9217513), ARPA COST(MDA 972-94-1-0004) and URI(DAAL 03-92-G-0109).

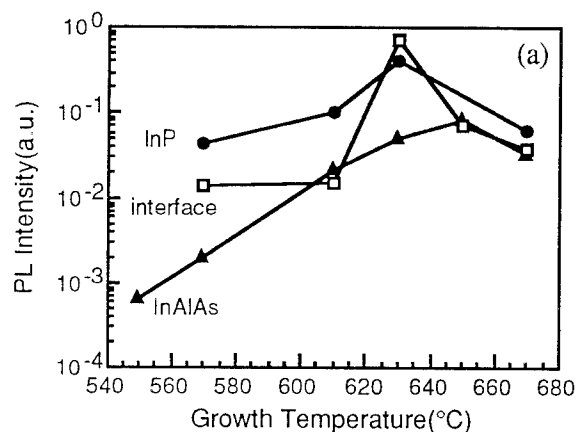


Fig.1 Average PL intensity from the InAlAs layer, InP/InAlAs interface and from the InP substrate measured on InAlAs/InP heterostructures grown at various temperatures.

Although it is not possible to deduce the origin and nature of the traps detected by DLTS and the origin of the non-radiative recombination centers, one can confirm that their density decreases when the growth temperature increases from 550°C to 650°C. A high growth temperature has been also known to help in reducing the reverse leakage current and increasing the breakdown voltage of Pt Schottky diodes fabricated on the InAlAs layers(4) in agreement with the previous work by Luo *et al.* which suggested the presence of As-related defect at lower growth temperatures(5). We can consequently speculate that the crystalline quality of InAlAs is improved when the growth is carried out at 650°C.

Fig.1 shows that the integrated PL intensities from both the InAlAs/InP interface (type II) and from the underlying InP attain a maximum value at a lower temperature, namely 630°C instead of 650°C. The observed increase of PL intensity from the InAlAs/InP interface can also be attributed to the better crystalline quality of InAlAs grown at high temperatures. However, when the growth temperature increases from 630°C to 650°C, the PL intensity from the InAlAs/InP interface and InP decreases in spite of the fact that the PL signal from InAlAs increases. In the light of our previous work(6), this can be associated with thermal degradation of InP which can take place at temperatures higher than 630°C. In particular, phosphorus exodiffusion from InP into InAlAs may take place, which results in the creation of complex defects involving phosphorus vacancies and some residual impurities. In fact, it was observed that the InP layers grown at high temperature showed higher residual carrier concentration, lower mobility and degraded surface morphology. These defects are known to act as efficient non-radiative recombination centers and may be responsible for the decrease of PL intensity from the InAlAs/InP interface and InP at growth temperatures exceeding 630°C.

In short, the optimal growth temperature for the InAlAs itself is about 650°C. The choice of this growth

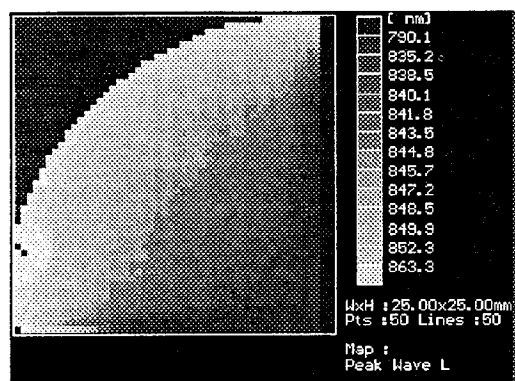
temperature signifies, however, growth above 630°C where the InAlAs/InP interface and the underlying InP material is slightly degraded. A slight compromise needs consequently to be made in terms of InAlAs/InP interface and InP material quality if the growth temperature is set to 650°C for optimum InAlAs growth.

Impact of susceptor rotating speed on spatial uniformity of InAlAs/InP heterostructures / Temperature and growth rate considerations

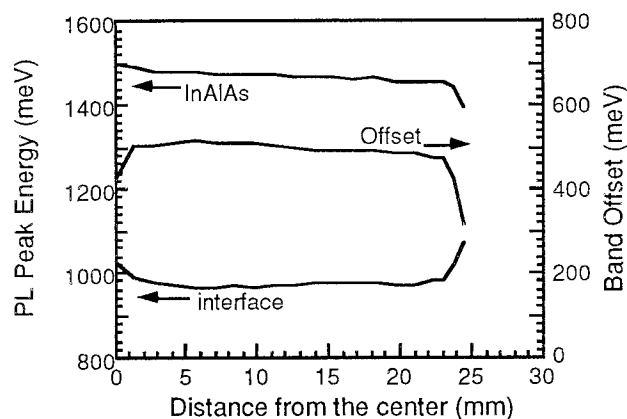
The uniformity of epilayers grown by MOCVD in the mass-transport-limited regime is governed by hydrodynamic factors that determine the flow pattern in the reactor. In the case of the growth system used in this work, the three major hydrodynamic growth parameters are i) reactor pressure, ii) total gas flow through the reactor and iii) rotating speed of the susceptor. Although these parameters can be controlled independently, growth environment optimization requires that they are simultaneously considered. In this study, the reactor pressure and total hydrogen gas flow through the reactor were set to 60 torr and 10 l/m, respectively. The third hydrodynamic parameter, namely rotating speed was then varied in order to examine its impact on spatial uniformity of InAlAs/InP heterostructures. Spatial homogeneity of the InAlAs bandgap and of the conduction band offset were deduced for this purpose from spectrally resolved SPL measurements.

InAlAs/InP heterostructures were grown at 650°C with an AsH₃ flow of 30 sccm. Quarter 2" S.I. InP substrates were loaded in a 2" diameter pocket recessed at the center of the susceptor while the remaining three quarters of the pocket were covered with a dummy silicon wafer. This arrangement allowed rotation of the quarter 2" wafer with respect to the center of the susceptor. SPL patterns obtained in this way correspond to partial(1/4) mapping of 2" wafers rotated with respect to their center.

Figs.2(a) and 3(a) show the cartography of the wavelength of the PL peak from InAlAs grown at 100 rpm and 1000 rpm, respectively. As can be seen from these figures, the sample grown at 100 rpm shows more uniform distribution than the one grown at 1000 rpm. A distinct concentric distribution of the PL peak wavelength is in fact found for the 1000 rpm sample. The variation of PL peak wavelength of InAlAs as a function of distance from the rotating center is plotted in Figs 2(b) and 3(b) along with the variation of energy difference between the conduction band of InP and the valence band of InAlAs at the interface (noted as 'interface') and the conduction band offset between InAlAs and InP. The local apparent conduction band offset was calculated from the measured local bandgap of InAlAs and the type II transition at the InAlAs/InP interface. A more detailed description of this method can be found in a previous report by the authors(7). Figs 2(b) and 3(b) show that in both cases the In mole fraction of InAlAs is increasing towards the edge of the wafer but this variation is more pronounced for the sample grown at 1000 rpm. These figures clearly show that the

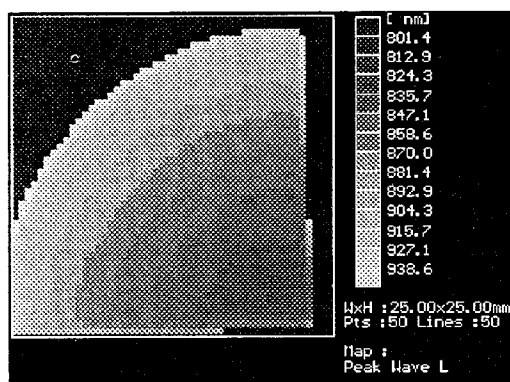


(a)

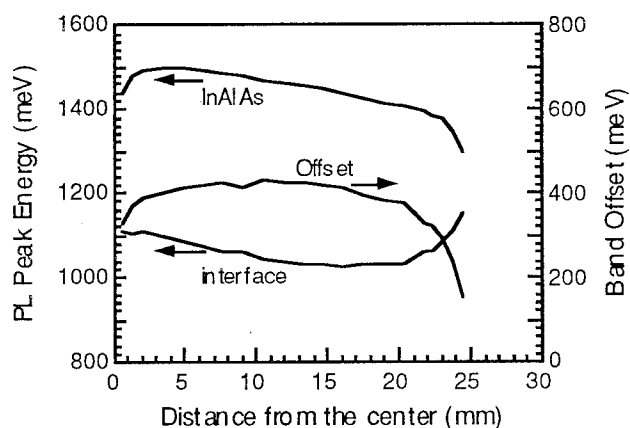


(b)

Fig. 2 (a) Spatial distribution of the wavelength of the PL peak from InAlAs. (b) Distribution of i) InAlAs bandgap energy, ii) energy of the InAlAs/InP interface emission and iii) conduction band offset between InAlAs and InP. The sample was grown at 650 °C and rotated at 100 rpm.



(a)



(b)

Fig. 3 (a) Spatial distribution of the wavelength of the PL peak from InAlAs. (b) Distribution of i) InAlAs bandgap energy, ii) energy of the InAlAs/InP interface emission and iii) conduction band offset between InAlAs and InP. The sample was grown at 650 °C and rotated at 1000 rpm.

spatial compositional uniformity of InAlAs is greatly affected by the choice of rotating speed: for the hydrodynamic growth parameters used in our experiments it appears that a low rotating speed of 100 rpm favors compositional uniformity.

There are several factors that can lead to compositional variation within a wafer. Temperature variation can be one possible source since the In mole fraction of InAlAs is known to be quite sensitive to the growth temperature. Assuming that this is indeed the factor determining uniformity, then the temperature at the center of the susceptor would be expected to be higher than at its periphery since a higher growth temperature is known to result in a lower In mole fraction in InAlAs. However, considering the fact that the heat can be dissipated through the rotating arbor located at the center of the susceptor, the

temperature variation could be exactly opposite. Temperature variations cannot consequently be the factor determining spatial uniformity. This was further confirmed by spectrally-resolved SPL and cartography of the intensity of the PL signal from InAlAs and from the InAlAs/InP interface. As explained by the results of Fig.1, the PL intensity of InAlAs is almost constant near 650°C while the intensity from the interface is monotonically decreasing as the temperature increases. PL intensity cartography of the sample grown at 100 rpm showed that InAlAs intensity remains about the same over the entire wafer, while the interface intensity showed a maximum value near the center which gradually decreases toward the edge of the wafer. These results confirm that growth takes indeed place close to 650°C and that the temperature is slightly lower near the center of the

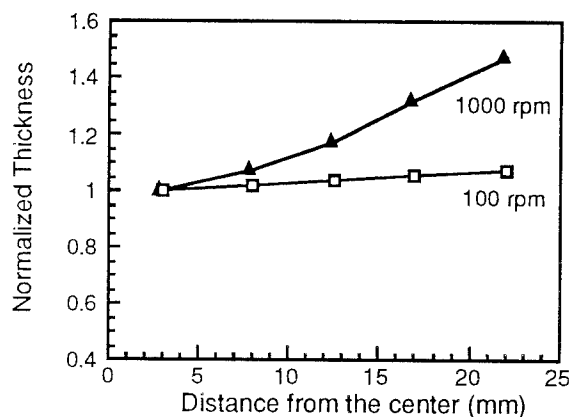


Fig.4 Impact of susceptor rotating speed on the spatial variation of epilayer thickness.

susceptor. In short, temperature cannot be responsible for the compositional variation observed since the temperature characteristics of the susceptor would result in a higher In mole fraction at the center. Such a result would therefore contradict the wavelength cartography data presented in Fig.2a and 3a.

Another possible factor determining the compositional uniformity of the wafers studied in this work is the spatial uniformity of the mass-transport boundary layer. The boundary layer geometry is very closely related to the growth rate and layers grown at higher growth rates usually give rise to higher In incorporation efficiency and thus In mole fraction. In order to investigate the correlation between compositional uniformity and thickness uniformity, the thickness variation of the InAlAs layers shown in Figs.2 and 3 was measured and the results are shown in Fig.4. Fig.4 shows the layer thickness normalized to the thickness value near the center of rotation. The thickness of the layer is found to increase from the center of the wafer to the edge independent of rotation speed. However, as in the case of compositional variation, the thickness variation is much smaller for the sample grown at lower rotating speed. Thus low rotating speed appears to offer a more uniform boundary layer and, as a result of it, a better compositional uniformity as well as thickness uniformity can be obtained. This conclusion, although satisfactory for exploring the better spatial uniformity in terms of composition (Figs.2 and 3) and thickness (Fig.3), it does not agree with the expected boundary layer shape. One would intuitively expect that higher rotating speeds reduce and flatten the mass-transport boundary layer and consequently lead to higher growth rate and better spatial uniformity. This expectation does not obviously apply, probably due to other factors such as reactor geometry which also affect the shape of the boundary layer. Similar deviations have been in fact observed for other parameters such as growth efficiency which is found to increase at low rotating speed as described in a previous report(8).

Conclusion

In summary, optimum growth conditions were determined for InAlAs/InP heterostructure materials based on SPL, structural and electrical characteristics of wafers. The impact of MOCVD growth parameters such as susceptor rotating speed on compositional and thickness uniformity of the layer is also reported using SPL. SPL and complementary thickness measurements showed the correlation between compositional and thickness uniformity and suggest that the spatial uniformity of the boundary layer is responsible for the spatial uniformity of the grown layers. Thus, the use of non-destructive techniques such as SPL is very useful for optimizing growth parameters. Compositional uniformity as determined by SPL could, for example, be a measure for speed, temperature and boundary layer optimization. Our results show that for the MOCVD reactor geometry and growth conditions used, a low rotating speed of 100 rpm appears to be the optimum for better composition and thickness spatial uniformity.

References

- (1) O. Aina, M. Serio, M. Mattingly and E. Hempfling, "Novel AlInAs/InP HEMT," *Electron. Lett.*, Vol.26, pp.651-652, 1990.
- (2) F. Ducroquet, G. Guillot, K. Hong, C. H. Hong, D. Pavlidis and M. Gauneau, "Deep Level Characterization of LP-MOCVD Grown $\text{Al}_{0.48}\text{In}_{0.52}\text{As}$," *Proceedings of the Material Research Society Symposium*, Vol.325, pp.235-239, 1994.
- (3) S.K. Krawczyk and M.F. Nuban, "Room-temperature scanning photoluminescence for mapping the lifetime and the doping density in compound semiconductors," *Materials Science and Eng.*, Vol.B28, pp.452-456, 1994.
- (4) D. Pavlidis, "Material related issues and their characterization with a view to III-V heterojunction device optimization," *Materials Science and Eng.*, Vol.B20, pp. 1-8, 1993.
- (5) J.K. Luo and H. Thomas, "Effect of Growth Condition on Electrical Properties of MBE and MOCVD-AlInAs," *Proc. of the 5th Int. Conf. on InP and Rel. Mat.*, pp.175-178, 1993.
- (6) J.Y. Longer, Ph.D. Thesis, Ecole Centrale de Lyon, Lyon, France, 1993.
- (7) C. Klingelhöfer, S. K. Krawczyk, M. Sacilotti, P. Abraham and Y. Monteil, "Mapping of the band offset at InAlAs/InP interfaces using room temperature spectrally resolved scanning photoluminescence," *Proc. of the 5th Int. Conf. on InP and Rel. Mat.*, pp.195-198, 1993.
- (8) K. Hong, D. Pavlidis, Y. Kwon and C.H. Hong, "MOCVD Growth Parameter Study of InP-based Materials for High-Performance HEMT's," *Proc. of the 6th Int. Conf. on InP and Rel. Mat.*, pp.431-434, 1994.

The Study of the Optical Properties of $\text{In}_{0.52}(\text{Al}_x\text{Ga}_{1-x})_{0.48}\text{As}$ by Variable Angle Spectroscopic Ellipsometry

J.-W. Pan, J.-L. Shieh, J.-H. Gau and J.-I. Chyi
Department of Electrical Engineering, National Central University
Chung-Li, 32054, Taiwan, R.O.C.

The optical properties of $\text{In}_{0.52}(\text{Al}_x\text{Ga}_{1-x})_{0.48}\text{As}$ epilayers with various x values were systematically studied using variable angle spectroscopic ellipsometry in the wavelength range of 310-1700 nm. The refractive indexes were determined. The energies and broadening parameters of the E_1 and $E_1+\Delta_1$ transitions as a function of Al composition were also examined based on the second-derivative spectra of the dielectric function. The comparison between our results and the reported data is presented.

Introduction

The quaternary compound semiconductor InAlGaAs, lattice matched to InP, is an ideal candidate for the implementation of several electronic and optical devices, since its bandgap can be continuously varied from 0.75 eV ($\text{In}_{0.53}\text{Ga}_{0.47}\text{As}$) to 1.47 eV ($\text{In}_{0.52}\text{Al}_{0.48}\text{As}$). Compared to InGaAsP, this quaternary allows better growth control by molecular beam epitaxy (MBE), because only one group V element is involved and the sticking coefficients of the group III elements are close to unity. Recently, the use of InAlGaAs for uncooled laser diodes¹ is gaining attention. Higher conduction band discontinuity to valence band discontinuity ratio of InAlGaAs/InGaAs heterostructure than that of InGaAsP/InGaAs counterpart is thought to be beneficial for laser performance. However, the optical properties of this alloy have not been fully investigated. In this work, the refractive index and the thickness of the InAlGaAs films were measured using variable angle spectroscopic ellipsometry

(VASE) in the wavelength range of 310-1700 nm. Since the dielectric function $\epsilon(E)$ is directly related to the electronic band structure,² the interband critical points (the E_1 and $E_1+\Delta_1$ transitions) as well as the broadening parameters were also determined from the analysis of its second-derivative spectrum,^{2,3} $d^2\epsilon/dE^2$. We have compared these transition energies with those measured by the electrolyte electroreflectance (EER) technique⁴.

Experiment

The InAlGaAs epilayers were grown directly on (100)-oriented InP:Fe substrates by molecular beam epitaxy. The composition and doping level of all the samples are listed in Table I. The lattice mismatch was measured by double-crystal x-ray diffraction to be less than 10^{-3} .

The basic model for the ellipsometry measurements consists of an InP:Fe substrate, an InAlGaAs epilayer and a thin native oxide layer. As

Table I. Properties of the $\text{In}_{0.52}(\text{Al}_x\text{Ga}_{1-x})_{0.48}\text{As}$ epilayers

composition x	doping level (cm^{-3})	nominal thick. (μm)	measured thick. (μm)	oxide thick. (nm)
1	---	0.94	0.952	4.1
0.9	2×10^{17}	1.48	1.413	2.6
0.5	2×10^{17}	1.02	1.032	2
0.38	4×10^{17}	2.26	2.376	3
0.32	5×10^{16}	1.27	1.335	3.7
0	---	1	1.024	1

we didn't know the optical constants of the native oxide of the InAlGaAs layer, we assumed the refractive index of the native oxide varied between 1.8 and 1.7 over the wavelength range of interest.^{2,5,6} The optical constants of InP substrate were measured on an InP substrate. The thicknesses of the thin native oxide and the InAlGaAs layers were variables in the data analysis, and the refractive index of the latter was also a variable. The angle of the incident was varied from 60° to 70° in 5° step to create 3 individual spectroscopic data files.

Results and Discussion

The measured thicknesses of the InAlGaAs layers and the native oxide layer are listed in Table I. The measured thickness of the epilayer agrees within 5.2% of the nominal thickness. The thickness of the surface oxide layer is also in the reasonable range of 1-4 nm. The refractive index of $\text{In}_{0.52}(\text{Al}_x\text{Ga}_{1-x})_{0.48}\text{As}$ with various Al compositions are shown in Fig. 1. The results ($x=1$ and $x=0.5$) obtained by M. J. Mondry et al.⁷ in the long wavelength region (dashed lines) are also shown for comparison. For $\text{In}_{0.52}\text{Al}_{0.48}\text{As}$, the refractive indexes agree very well. However, for the sample with $x=0.5$, the indexes obtained in this work are slightly greater than previous results. This discrepancy may be attributed to the difference of the exact Al compositions of the epilayers. The refractive index as a function of Al composition (x) at the wavelength of 1.55 μm can be expressed as $n(x)=0.12x^2-0.51x+3.6$. In the short wavelength region, there is a maximum value of the refractive index in the range of 4.49 to 4.61 for each layer. This peak is related to the $E_1+\Delta_1$ transition.⁵ In order to determine the critical-point structures, the second-derivative spectra, $d^2\epsilon_2/dE^2$, of the imaginary parts of the dielectric function were performed.^{2,3}

Fig. 2 shows the second-derivative spectra (open circles) of ϵ_2 for the epilayers with various Al compositions. The spectra have two features, corresponding to the E_1 and $E_1+\Delta_1$ transitions, respectively, along the Λ directions of the Brillouin zone (BZ), where the valence and conduction bands are nearly parallel.^{2,4,8} These data can be fitted to the standard two-dimensional (2D) critical point line-shape formula which is defined as^{2,3}

$$\frac{d^2\langle\epsilon\rangle}{dE^2} = A e^{i\phi} (E - E_g + i\Gamma)^{-2}$$

where A is the amplitude, E_g is the energy bandgap, Γ is the broadening parameters, and ϕ is the excitonic phase angle. The solid lines are the fitted results. There is a poorly fitted region in the lower energy

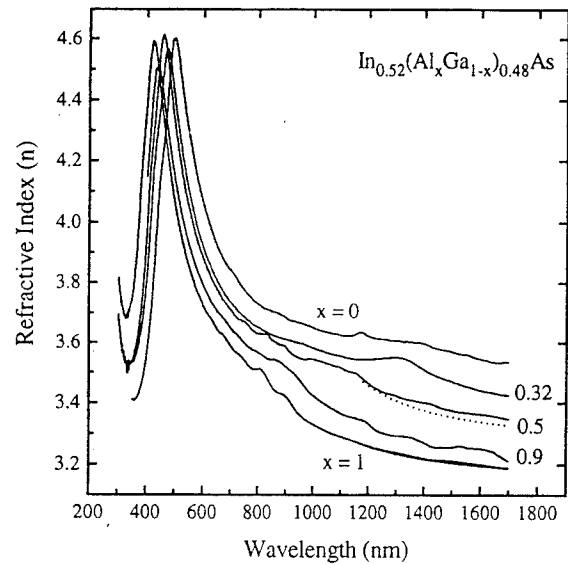


Fig.1. Refractive index of $\text{In}_{0.52}(\text{Al}_x\text{Ga}_{1-x})_{0.48}\text{As}$ with various Al compositions.

side near the E_1 transition. This discrepancy may be attributed to the nonparabolicity effects in the actual density of states,^{8,9} which was not considered in the equation. The energies values of the E_1 and $E_1+\Delta_1$ transitions, the broadening parameters Γ , and the excitonic phase angle ϕ can be evaluated from the fitting process. The excitonic phase angle obtained in this work was about $101^\circ \pm 2^\circ$, which is comparable to the phase angle $\phi=100^\circ \pm 3^\circ$ for InP at room temperature.⁵

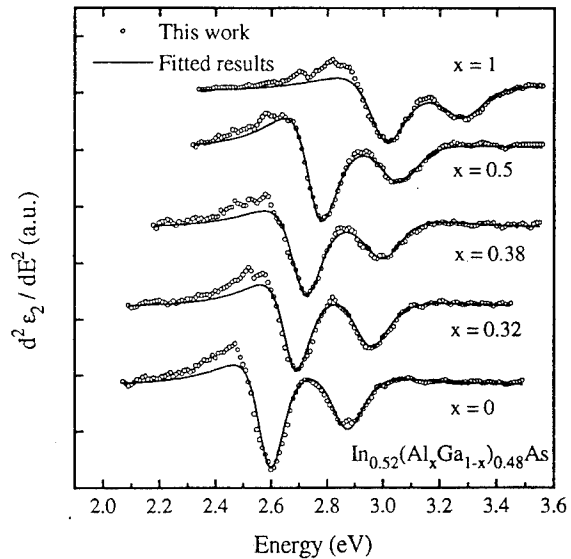


Fig.2. Second-derivative spectra of the complex dielectric function with various x values in the range of the E_1 and $E_1+\Delta_1$ transitions.

The E_i and $E_i+\Delta_i$ energies as a function of Al composition x are shown in Fig.3 by open circles. The resultant spin-orbit splitting Δ_i is plotted in the lower portion of Fig.3. For the purpose of comparison, the results obtained by P. Parayathal et al. using EER technique⁴ are also shown in Fig.3 by the dashed lines. It is evident that these two techniques give very consistent results. For $\text{In}_{0.53}\text{Ga}_{0.47}\text{As}$, the critical-point energies are $E_i=2.59$ eV and $E_i+\Delta_i=2.87$ eV, respectively. These results are also very close to the previous data obtained by spectroscopic ellipsometry¹⁰ as shown by the solid triangles in Fig.3. The solid lines represent the quadratic fit, i.e. $E(x)=A+Bx+Cx^2$, of the experimental values. The parameters A, B, and C are listed in Table II. The bowing parameter C for Δ_i is a negative but very small value, which was also observed in the results obtained by EER techniques⁴ and in other alloy system.¹⁰ The Al composition seems to have no significant effect on the value of Δ_i .

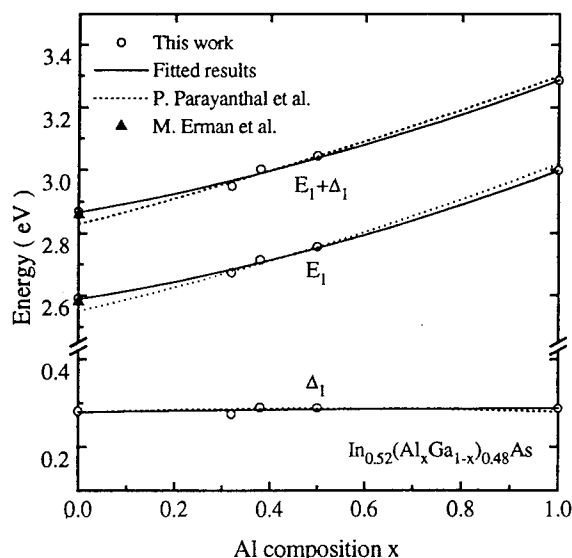


Fig.3. The E_i and $E_i+\Delta_i$ energies as well as the spin-orbit splitting Δ_i as a function of Al composition x .

Table II Values of the quadratic fitting parameters

transition	A(eV)	B(eV)	C(eV)
E_i	2.587	0.252	0.159
$E_i+\Delta_i$	2.867	0.266	0.153
Δ_i	0.279	0.015	-0.007

Fig.4 shows that the broadening parameter Γ of the E_i and $E_i+\Delta_i$ transitions monotonically increases with Al composition. This is thought to be due to the higher electronic density of states^{2,8} for the sample with higher Al content. The slightly scattered data of this work around the dashed line that is a guide for eye is likely due to either composition fluctuation or crystal defects. It can also be seen that the broadening parameter of the $E_i+\Delta_i$ transition is consistently higher than that of the E_i transition, since the lower split-off valence band has larger electronic density of states.^{2,8} Among the samples we studied, $\text{In}_{0.53}\text{Ga}_{0.47}\text{As}$ has the narrowest broadening parameter for the E_i transition, which is 0.094 eV. This result is smaller than 0.107 eV measured on the $\text{In}_{0.53}\text{Ga}_{0.47}\text{As}$ samples grown by gas source MBE.⁸ This again may be due to the composition fluctuation or the defects in the epilayers.

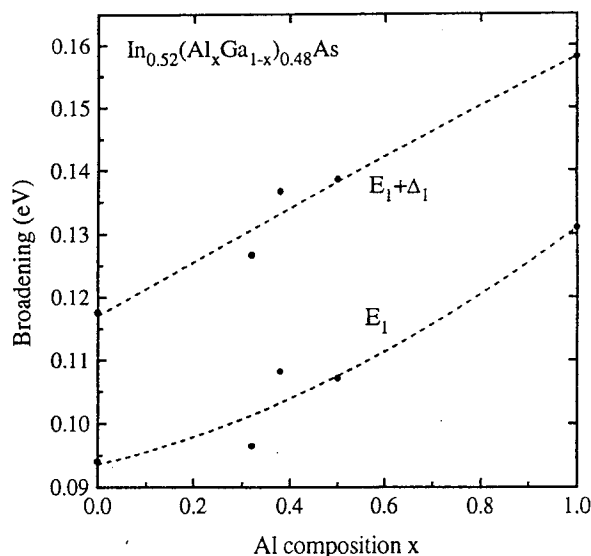


Fig.4. The broadening parameters of the E_i and $E_i+\Delta_i$ transitions as a function of Al composition x .

Conclusion

The refractive indexes of $\text{In}_{0.52}(\text{Al}_x\text{Ga}_{1-x})_{0.48}\text{As}$ with various Al compositions have been measured using variable angle spectroscopic ellipsometry. The refractive index at the wavelength of 1.55 μm can be given as $n(x)=0.12x^2-0.51x+3.6$. The dependence of the energies and the broadening parameters for the E_i and $E_i+\Delta_i$ transitions on the Al composition has been discussed based on the second-derivative spectra of the dielectric function. These transition energies and broadening parameters are all increasing functions of Al composition.

ACKNOWLEDGMENTS

The authors would like to thank Mr. Robert Jann of Saturn Cosmos Co. for his assistance in the ellipsometry measurements and the support of the MBE laboratory of the Center for Optical Science, NCU. This work was supported by the National Science Council of R.O.C. under contract NSC82-047-E-008-179.

REFERENCES

1. C. E. Zah, R. Bhat, B. N. Pathak, F. Favire, W. Lin, M. C. Wang, N. C. Andreadakis, D. M. Hwang, M. A. Koza, T. P. Lee, Z. Wang, D. Darby, D. Flanders, and J. J. Hsieh, "High-Performance Uncooled 1.3- μm $\text{Al}_x\text{Ga}_y\text{In}_{1-x-y}\text{As}/\text{InP}$ Strained-Layer Quantum-Well Lasers for Subscriber Loop Applications," *IEEE J. Quantum Electron.*, Vol. **30**, pp.511-522, 1994.
2. P. Lautenschlager, M. Garriga, and M. Cardona, "Temperature dependence of the interband critical-point parameters of InP," *Phys. Rev. B*, vol. **36**, pp.4813-4820, 1987.
3. H. Lee, D. Biswas, M. V. Klein, H. Morkoc, D. E. Aspnes, B. D. Choe, J. Kim and C. O. Griffiths, "Study of strain and disorder of $\text{In}_x\text{Ga}_{1-x}\text{P}/(\text{GaAs}$ graded GaP) ($0.25 \leq x \leq 0.8$) using spectroscopic ellipsometry and Raman spectroscopy," *J. Appl. Phys.*, Vol. **75**, pp.5040-5051, 1994.
4. P. Parayanthal, C. S. Ro, F. H. Pollak, C. R. Stanley, G. W. Wicks, and L. F. Eastman, "Electroreflectance investigation of $(\text{Ga}_{1-x}\text{Al}_x)_{0.47}\text{In}_{0.53}\text{As}$ lattice matched to InP," *Appl. Phys. Lett.*, vol. **43**, pp.109-111, 1983.
5. H. Burkhard, H. W. Dinges, and E. Kuphal, "Optical properties of $\text{In}_{1-x}\text{Ga}_x\text{P}_{1-y}\text{As}_y$, InP, GaAs, and GaP determined by ellipsometry," *J. Appl. Phys.*, vol. **53**, pp.655-662, 1982.
6. M. Amioti and G. Landgren, "Ellipsometric determination of thickness and refractive index at 1.3, 1.55, and 1.7 μm for $\text{In}_{1-x}\text{Ga}_x\text{As}_{1-y}\text{P}_y$ films on InP," *J. Appl. Phys.*, Vol. **73**, pp. 2965-2971, 1993.
7. M. J. Mondry, D. I. Babic, J. E. Bowers, and L. A. Coldren, "Refractive Indexes of $(\text{Al,Ga,In})\text{As}$ Epilayers on InP for Optoelectronic Applications," *IEEE Photon. Technol. Lett.*, vol. **4**, pp.627-630, 1992.
8. S. M. Kelso, D. E. Aspnes, M. A. Pollack and R. E. Nahory, "Optical Properties of $\text{In}_{1-x}\text{Ga}_x\text{As}_y\text{P}_{1-y}$ from 1.5 to 6 eV determined by Spectroscopic ellipsometry," *Phys. Rev. B*, vol. **26**, pp.6669-6681, 1982.
9. M. Cardona, Modulation Spectroscopy, Suppl. 11 of Solid State Physics, Academic, New York, 1969.
10. M. Erman, J. P. Andre, and J. LeBris, "Spectroscopic ellipsometry study of InP, GaInAs, and GaInAs/InP heterostructures," *J. Appl. Phys.*, Vol. **59**, pp.2019-2025, 1986.

Cyclotron Resonance in InP Grown by Organometallic Vapor Phase Epitaxy with TMI_n and TBP

H. Nakata, K. Satoh, T. Iwao, T. Ohyama, E. Otsuka*,
Y. Fujiwara** and Y. Takeda**

Department of Physics, Faculty of Science,
Osaka University, 1-16 Machikaneyama-cho,
Toyonaka 560, Japan

*Fukui University of Technology, Gakuen 3-6-1,
Fukui 910, Japan

**Department of Materials Science and Engineering,
School of Engineering, Nagoya University, Furocho,
Chikusa-ku, Nagoya 464-01, Japan

Far-infrared magnetoabsorption and optically detected impurity resonance are measured in InP layers grown by organometallic vapor phase epitaxy with trimethylindium and tertiarybutylphosphine. High quality of the layers enables us to observe electron cyclotron resonance as well as the 1s to 2p₊ transition of shallow donors. The mobilities estimated from the linewidth of the cyclotron resonance are in the range 51000- 97000 cm²/Vs at 4.2K.

1. Introduction

Far-infrared (FIR) magnetoabsorption is one of the important techniques to investigate the characteristics of carriers and impurities in semiconductors. The main phenomena observed in the absorption are electron cyclotron resonance and impurity resonance of donors. Cyclotron resonance occurs at the magnetic field B where the frequency of the incident FIR radiation is coincident with the cyclotron frequency $\omega_c = eB/m^*$. The effective mass m^* and the mobility μ are estimated from the resonance magnetic field and the linewidth of the

resonance peak, respectively. Several groups have reported the effective mass m^* of electrons in InP and the values are in the range 0.081 - 0.082 m_0 below 10K (1, 2). On the other hand, impurity resonance is observed when the photon energy of the FIR radiation is equal to the energy separation between the ground and excited states of donors and the selection rule for the transition is satisfied. The most prominent absorption peak in magnetic fields corresponds to the 1s to 2p₊ transition of shallow donors. Such an impurity resonance is observed in InP and the 1s ground state binding energy of shallow donors in zero magnetic field is obtained, which is very close to

Table A Specification of epitaxial InP layers

	#54	#49	#114
Carrier concentration (10 ¹⁵ cm ⁻³)	1.17	1.45	1.62
DC mobility at 77K (cm ² /Vs)	42300	29900	35600
AC mobility at 4.2K (cm ² /Vs)	97400	50600	78600
Compensation ratio	0.35	0.5	0.35
Thickness (μ m)	2	1	1.2

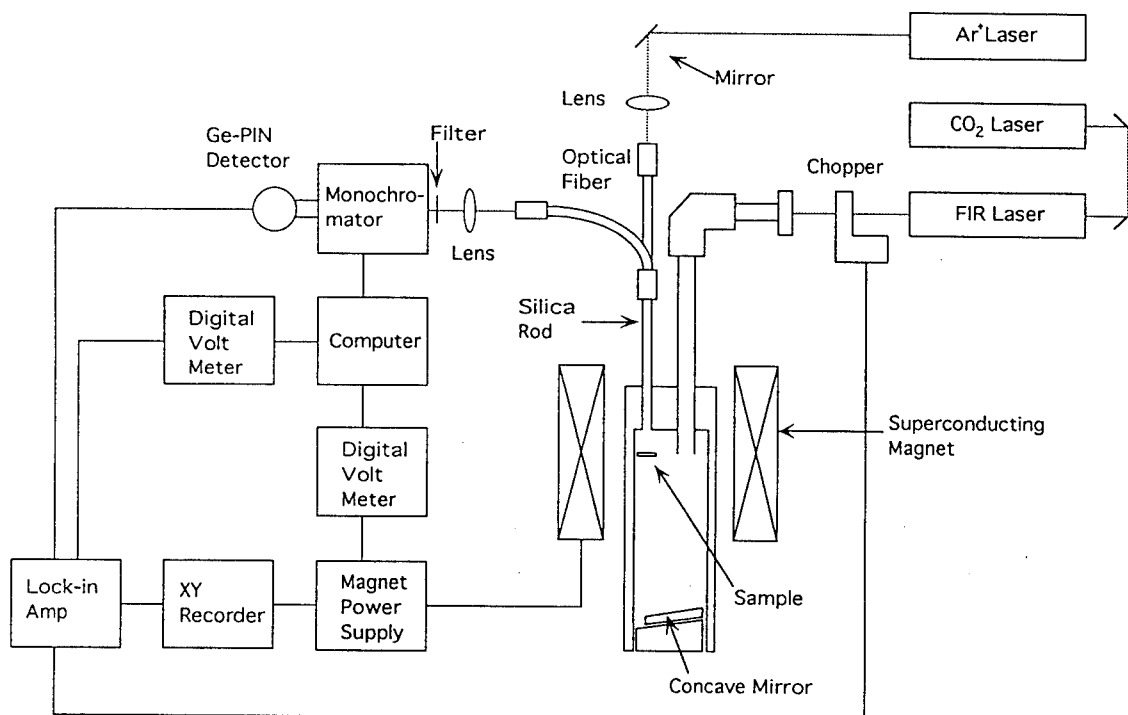


Fig. 1. Schematic diagram of the experimental set-up for optically detected cyclotron resonance (ODCR) and optically detected impurity resonance (ODIR).

7.14 meV based on the effective mass approximation (3, 4). In addition to FIR magnetoabsorption, we investigate the optically detected impurity resonance (ODIR) which is the combination technique of impurity resonance and photoluminescence (PL). It was originally developed as the optically detected cyclotron resonance (ODCR) in microwave region and recently has been extended to FIR region (5, 6). Moll et al. first observed ODCR and ODIR in InP by using FIR lasers (7). We made FIR magnetoabsorption and ODIR measurements of InP epitaxial layers grown by organometallic vapor phase epitaxy (OMVPE) of which source materials are trimethylindium (TMIn) and tertiarybutylphosphine (TBP). TBP was introduced to avoid use of extremely toxic hydride such as phosphine (PH_3). This study reveals that the layers fabricated by the MOVPE method have good qualities enough to observe electron cyclotron resonance. In addition to cyclotron resonance, impurity resonance and ODIR are observed.

2. Experimental

The growth system was previously described in ref. 8. The samples which we study are n-InP layers grown by OMVPE with TMIn and TBP with the growth rate of

$1 \mu\text{m/h}$. The substrate temperature was 580°C and the V/III ratio was kept at 40 during growth. Detailed specification of the layers are listed in Table A.

In FIR magnetoabsorption measurement, the sample was placed in the center of a superconducting magnet applied up to 5.7 T. A xenon flash lamp with the pulse duration of $1 \mu\text{s}$ and the repetition rate of 15 Hz was employed as an excitation source. The light from the lamp was guided through a double core glass rod and shed on the sample immersed in liquid helium. A CO₂ laser pumped FIR laser was used as a probe source. The detector of FIR radiation was an n-InSb set in a magnet driven by persistent current. The signal of the detector was amplified and processed by a boxcar integrator. One of the gates of the boxcar integrator was open at $5 \mu\text{s}$ after the excitation pulse and the other just before the excitation pulse. The logarithmic ratio of the signals at two gates which was proportional to an absorption coefficient, was plotted as a function of magnetic fields.

The detection system of ODIR was newly developed and first applied to a GaAs epitaxial layer. A schematic picture of the system is displayed in Fig. 1. In this case an Ar⁺ laser (20 mW) was employed as an excitation source and the light as well as the luminescence were led to/from the sample through an optical fiber and a silica rod. The radiation from the FIR laser was chopped at the frequency

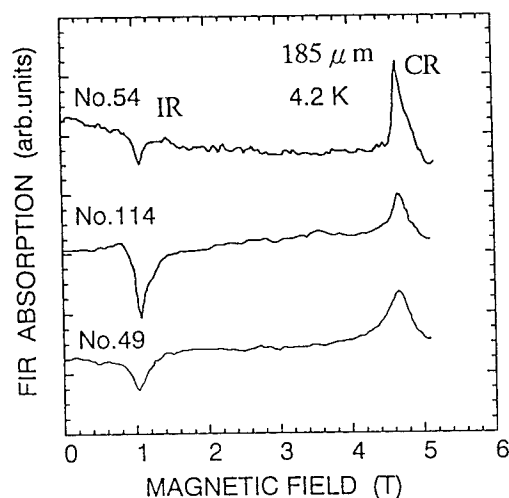


Fig. 2. Far-infrared magnetoabsorption spectra of InP layers. CR and IR indicate electron cyclotron resonance and impurity resonance, respectively.

of 100 Hz, guided through light pipes and focussed to the sample by a concave mirror. The luminescence from the sample was dispersed in a monochromator ($f=250\text{mm}$) after travelling through the silica rod and the optical fiber. A Ge PIN photodiode (North Coast) was used as a detector and the signal was processed in a lock-in amplifier.

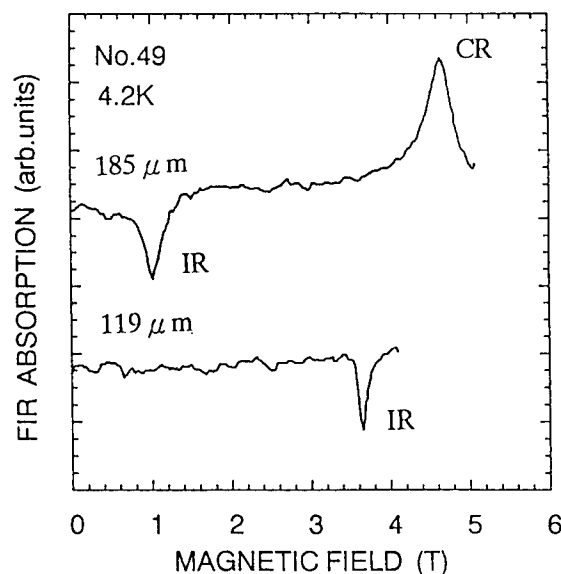


Fig. 3. Far-infrared magnetoabsorption spectra of InP layers for different wavelengths. The peak of impurity resonance shifts to higher magnetic field with increasing photon energy.

3. FIR magnetoabsorption

Typical FIR magnetoabsorption spectra in various samples are shown in Fig.2. The wavelength of the used FIR radiation was $185\text{ }\mu\text{m}$. The peaks indicated as CR and IR signals are electron cyclotron resonance and impurity resonance, respectively. The electron cyclotron resonance appears as increase in absorption and contrary to this, impurity resonance as decrease in absorption caused by the intrinsic photoexcitation. The effective mass of electron is estimated to be $0.081m_0$ from the resonance magnetic field and it is in good agreement with previously reported values (1, 2). The mobility estimated from the linewidths of the resonance peaks are also listed in Table A and ranges from 51000 to $97000\text{ cm}^2/\text{Vs}$. These values are almost twice as high as the DC ones. The mobility becomes higher with increasing layer thickness, coincident with the previously reported results (8). The impurity absorption corresponds to the $1s$ to $2p_{\frac{1}{2}}$ transition of shallow donors which are not identified, since all the shallow donors give the resonance peak at almost the same magnetic field. The absorption intensity is not related to the mobility but to the carrier concentration. It means that mobility does not depend on the impurity concentration. Accordingly, the main mechanism which limits the mobility is other than impurity scattering. Figure 3 shows FIR magnetoabsorption spectra for different FIR wavelengths. The peak observed around 3.7 T for the $119\text{ }\mu\text{m}$ FIR also corresponds to the $1s$ to $2p_{\frac{1}{2}}$ transition. The shift of the resonance peak to higher magnetic field

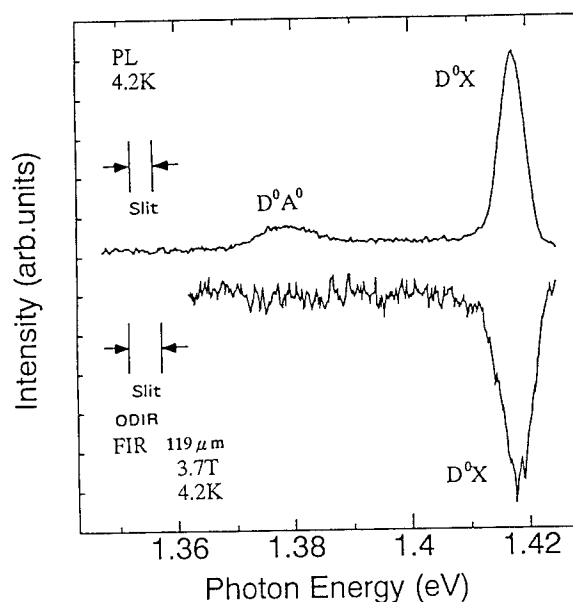


Fig. 4. Spectra of photoluminescence (PL) and optically detected impurity resonance. D^0A^0 is due to donor - acceptor recombination and D^0X to donor bound exciton.

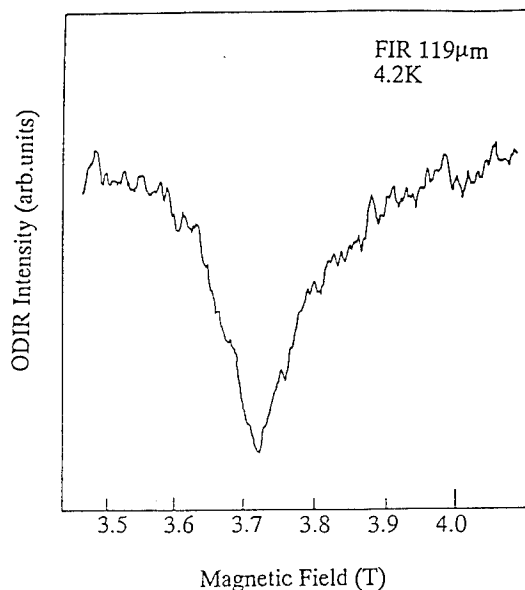


Fig. 5. Intensity of optically detected impurity absorption vs magnetic fields.

ensures that the peak IR is due to the $1s$ to $2p_+$ transition of shallow donors.

Remarkable feature, reduction of the absorption, of the spectra indicates that shallow impurities are ionized by interband excitation, although the impurities are usually neutralized by photoexcitation. The reason is not clear now but one possibility is that neutral impurities are ionized due to screening effect by photoexcited carriers.

4. Optically detected impurity resonance (ODIR)

Typical PL and ODIR spectra are shown in Fig. 4. Donor-acceptor (D^0A^0) and donor bound exciton (D^0X) recombination are observed in PL measurement and only the bound exciton peak is observed in ODIR measurement. ODIR signal is induced by the variation in PL intensity due to FIR absorption of impurity resonance. The mechanism of ODIR is speculated that hot electrons generated by resonant absorption of donor electrons dissociate some kinds of species such as shallow donors and bound excitons. The reason why donor-acceptor recombination peak is not observed in ODIR is that the binding energy of the shallow donor is too large to ionize by impact of hot electrons and the ionization energy of the bound exciton is smaller than the dissociation energy of the donor bound exciton. Figure 5 shows the dependence of ODIR intensity on magnetic fields. The resonance magnetic field and the lineshape are the same as those of impurity resonance.

5. Conclusions

FIR magnetoabsorption and ODIR are measured in the epitaxial layers grown by OMVPE method with TMIIn and TBP. In magnetoabsorption measurement, electron cyclotron resonance and the $1s$ to $2p_+$ transition of shallow donors are observed. Observation of electron cyclotron resonance ensures the high quality of the layers. The electron mobility is estimated to be in the range $51000 - 97000 \text{ cm}^2/\text{Vs}$ from the linewidth of cyclotron resonance. The mobility depends on the thickness of the layer and it is almost twice as high as the DC mobility. The shallow donors are ionized by interband photoexcitation in the present experimental condition and the reason is not clear now. The ODIR signal is observed for donor bound exciton luminescence in addition to FIR magnetoabsorption.

Acknowledgements

The authors would like to thank Y. Ito and Y. Nonogaki of Nagoya University for their technical assistance on InP growth, Showa Denko K. K. for InP wafers and Sumitomo Chemicals Corp. for TMIIn.

Reference

- (1) J. M. Chamberlain, P. E. Simmonds, R. A. Stradling, and C. C. Bradley, *J. Phys. C*, Vol. 4, pp. 138 (1971).
- (2) T. Ohyama, E. Otsuka, S. Yamada, T. Fukui, and N. Kobayashi, *Jpn. J. Appl. Phys.* Vol.22 pp. L742 (1983).
- (3) J. M. Chamberlain, H. B. Ergun, K. A. Gehring, R. A. Stradling, *Solid State Commun.* Vol. 9, pp. 1563 (1972).
- (4) P. E. Simmonds, R. A. Stradling, J. R. Birch, C. C. Bradley, *Phys. Status Solidi (b)* Vol. 64, pp. 195 (1974).
- (5) R. Romenstain and C. Weisbuch, *Phys. Rev. Lett.* Vol. 45, pp. 2067 (1980).
- (6) M. G. Wright, N. Ahmed, A. Koohnian, K. Mitchell, G. R. Johnson, B. C. Cavenett, C. R. Pidgeon, C. R. Stanley, and A. H. Lean, *Semicond. Sci. Technol.* Vol.5, pp. 438 (1990).
- (7) A. Moll, C. Wetzel, B. K. Meyer, P. Omling, and F. Scholz, *Phys. Rev. B*, Vol. 45, pp. 1504 (1992).
- (8) Y. Fujiwara, S. Furuta, K. Makita, Y. Ito, Y. Nonogaki, and Y. Takeda, *J. Crystal Growth*, Vol. 146, pp. 544 (1995).

TEM evaluation of ordered and modulated structures in GaAsSb crystals grown on (110)InP substrates by molecular beam epitaxy

Osamu Ueda, Yoshiaki Nakata and Shunichi Muto

Fujitsu Laboratories Ltd.,
10-1 Morinosato-Wakamiya, Atsugi 243-01, Japan

Abstract

Ordered and modulated structures in GaAsSb grown on (110)InP substrates by molecular beam epitaxy, has been evaluated by transmission electron microscopy. In the electron diffraction pattern from the GaAsSb, superstructure spots associated with CuAu-I type ordered structure are found. When the offset angle of the substrates increases, the ordering becomes stronger. The ordering becomes also stronger with increasing growth temperature in the range 470-530°C. In high resolution images of the crystal, areas with doubling in periodicity of 220 and 200 lattice fringes are observed locally, which is due to CuAu-I type ordering, indicating that the ordering is not perfect and that ordered regions are likely to be microdomains. Modulated structure are also found in both the $\langle 001 \rangle$ and $\langle 1\bar{1}0 \rangle$ directions. Coarse and fine modulated structures are clearly observed, and the periodicity of the coarse structure in the $\langle 001 \rangle$ direction is much longer than that in the $\langle 1\bar{1}0 \rangle$ direction. These findings lead us to conclude that atomic ordering and spinodal decomposition of the crystal are competing on the growth surface via surface diffusion of deposited atoms.

1. Introduction

Atomic ordering and phase separation are major materials issues related to thermal stability of the III-V alloy semiconductors. In our previous reports, we have described a detailed study on the evaluation of CuAu-I type ordered structures in InGaAs crystals grown on (110) InP substrates by molecular beam epitaxy (MBE) (1-6). We have presented microstructure of the ordered structures (1-3), effect of growth temperature and substrate misorientation on the degree of ordering (1-3) and influence of the ordered structure on the two-dimensional electron gas mobility (4). A generation mechanism of the ordered structure has also been proposed and has been experimentally proven (5). On the other hand, generation of ordered and modulated structures in III-V alloy semiconductors where two column V atoms are involved, i.e., $A^{\text{III}}B^{\text{V}}C^{\text{V}}$ has not been clarified yet. In this paper, we describe for the first time a detailed TEM evaluation of both ordered and modulated structures in MBE-grown GaAsSb crystals grown on (110)InP substrates.

1. Experimental

GaAsSb crystals were grown on slightly misoriented (110)InP substrates (3° or 5° off toward the $\langle 001 \rangle$ direction) by MBE. Growth temperatures and V/III gas pressure ratios were kept at 470-530°C and 15 or 20, respectively. The epi-layer was approximately 1.0 μm thick. The lattice-mismatch between the GaAsSb layer and the InP substrate is within 1×10^{-3} . For the structural evaluation of crystals, cross-sectional TEM observation were used. Specimens for TEM were prepared by ion etching. TEM observation was carried out in an ultra-high resolution analytical electron microscope Topcon EM002B operated at 200 keV.

2. Results and discussion

2.1 Ordered structure

Identification of CuAu-I type structures by TED
Figures 1(a) and 1(b) show the TED patterns from a (110) plan-view and a $(\bar{1}10)$ cross-section of an InGaAs crystal grown on a (110) InP substrate tilted by 3° towards the $\langle 001 \rangle$ direction. In both figures, superstructure spots are observed at positions indexed as 001, 110, $1\bar{1}0$, $1\bar{1}2$, $1\bar{1}\bar{2}$, ... This particular set of superstructure spots is associated with a CuAu-I type ordered structure (7,8). In this structure, As atoms preferentially occupy the (000) and $(1/2 \ 1/2 \ 0)$ sites and Sb atoms preferentially occupy the $(1/2 \ 0 \ 1/2)$ and $(0 \ 1/2 \ 1/2)$ sites in each unit cell. A schematic diagram of the atomic arrangement in the CuAu-I type structure viewed along the $[1\bar{1}0]$ direction normal to the growth axis is shown in Fig. 2. From this diagram, one can see that the perfectly ordered material consists of alternating GaAs and GaSb monolayers, i.e., $(\text{GaAs})_1/(\text{GaSb})_1$ monolayer superlattices, when viewed along either the $[110]$ growth direction or the $[001]$ direction.

Substrate orientation dependence of the degree of ordering
Figures 3(a) and 3(b) show TED patterns from $(\bar{1}10)$ cross-sections of GaAsSb crystals grown on (110) InP substrates with tilting angles of 3° and 5° towards the $[001]$ direction. In crystals grown on a (110) pure InP substrate, the intensity of superstructure spots is very weak (not shown), indicating very weak ordering. However, when a substrate tilted by 3° towards the $[001]$ direction is used, the ordering becomes stronger as shown in Fig. 3(a). Also, the ordering becomes stronger in a crystal grown on a substrate tilted 5° toward the $[001]$ direction (Fig. 3(b)). Since tilting of the substrate orientation toward $[001]$ direction introduces periodic arrays of steps on the substrate surface, one can conclude that atomic steps on the growth surface play an important role in the formation of the ordered structures.

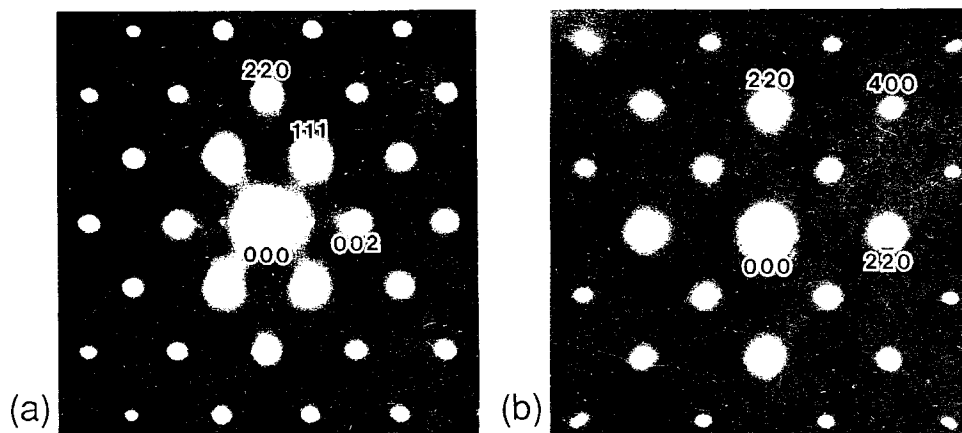


Fig. 1 Electron diffraction patterns from $(\bar{1}10)$ and (001) cross-sections of GaAsSb crystals grown on a (110) InP substrate (3° off toward the $\langle 00\bar{1} \rangle$) at 500°C . (a) $(\bar{1}10)$ cross-section; (b) (001) cross-section.

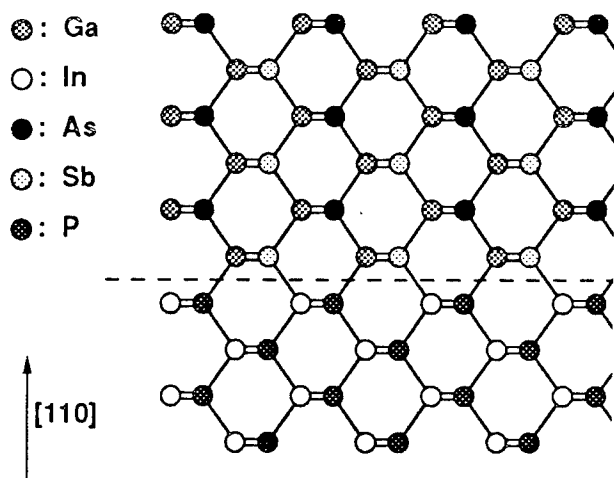


Fig. 2 A schematic diagram of the atomic arrangement of CuAu-I type ordered structure in an GaAsSb crystal viewed along the $[1\bar{1}0]$ direction.

Growth temperature dependence of the degree of ordering In order to clarify the influence of growth temperature on the formation of the ordered structure, we grew GaAsSb crystals on (110) InP substrates tilted toward the $\langle 00\bar{1} \rangle$ direction by 5° , at various temperatures in the range of 470 – 530°C . From TED analysis, it was found that in this temperature range, the degree of ordering increases with growth temperature. These results can be explained by the fact that the mobility of deposited atoms on the growth surface also increases with temperature, and that the formation of ordered structures is thought to be strongly related to the migration and reconstruction of deposited atoms (9,10).

Microstructural characterization of CuAu-I type structure HRTEM analysis was carried out to evaluate the ordered structure on an atomic scale. Figure 4 shows a typical HRTEM image of ordered InGaAs grown on a (110) InP substrate tilted by 3° towards the $[00\bar{1}]$ direction. Doubling of the (002) and the (220) (see arrows) lattice fringes, which is associated with the CuAu-I type structure, is observed locally, suggesting that the crystal consists of both well ordered and non-ordered regions. In the (001) cross-section HRTEM images, doubling of both the (220) and the (220) lattice fringes is observed.

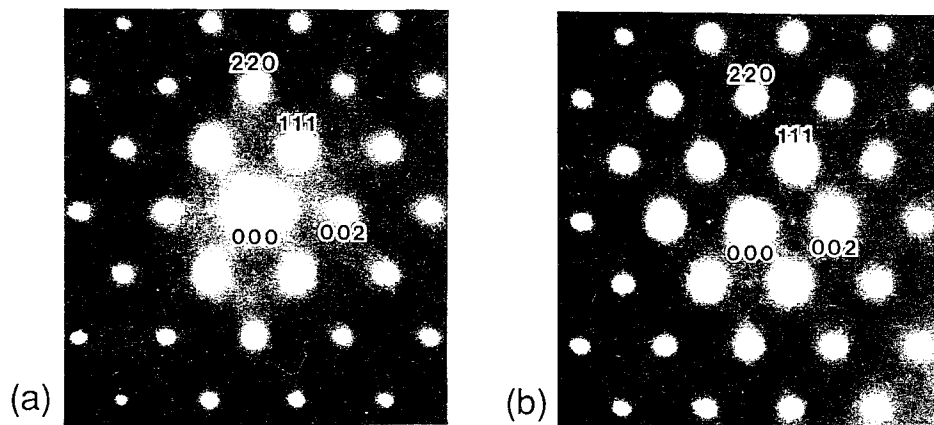


Fig. 3 Electron diffraction patterns from $(\bar{1}10)$ cross-sections of GaAsSb crystal grown on a (110) InP substrate (3° and 5° off toward the $\langle 00\bar{1} \rangle$). (a) 3° off; (b) 5° off.



Fig. 4 A $(\bar{1}10)$ cross-sectional high-resolution TEM image of GaAsSb crystal on a (110)InP substrate (5° off toward the $\langle 00\bar{1} \rangle$) at 500°C .

Key points for the generation mechanism There are three key points for consideration of the generation mechanism of the CuAu-I type ordered structure. First, as shown in Fig. 2, the CuAu-I type ordered structure, for example, in ordered InGaAs, consists of alternating GaAs and GaSb monolayers, i.e., $(\text{GaAs})_1/(\text{GaSb})_1$ monolayer superlattices, when viewed along either the $\langle 110 \rangle$ growth direction or the $\langle 001 \rangle$ direction. Thus, one can conclude that the ordered structures are generated by the periodic formation of GaAs/GaSb double monolayers. Secondly, the results described in Fig. 3 suggest that the steps on the the growth surface play an important role for the ordering, i.e., the steps enhance the generation of ordered structures. Thirdly, in the case of CuPt type ordering, it has been theoretically explained that the ordering is enhanced by surface reconstruction (11), which causes alternative rows of column III or V atoms on the growth surface, e.g., In- and Ga-rows one after another in the $\langle 110 \rangle$ direction on the (001) plane. However, on the (110) plane, since both column III and V atoms occupy sites on the same plane,

surface reconstruction does not occur. Therefore, the atomic ordering on the (110) plane can not be explained by the reconstruction of deposited atoms on the growth surface.

Possible generation mechanism On the basis of these considerations, the following two models are the most probable one (see Fig. 5). These models are basically related to the step flow mode on the growth surface during growth:

Model 1:

Step 1: direct growth of InAs/GaAs monolayer superlattices from the two monolayer step edges;
This step repeats during the growth.

Model 2:

Step 1: growth of two monolayers of alloyed crystal from the two monolayer step edges;
Step 2: immediately following step 1, interchange of column III atoms occurs forming InAs/GaAs monolayer superlattices on each terrace;
These steps repeat during the growth.

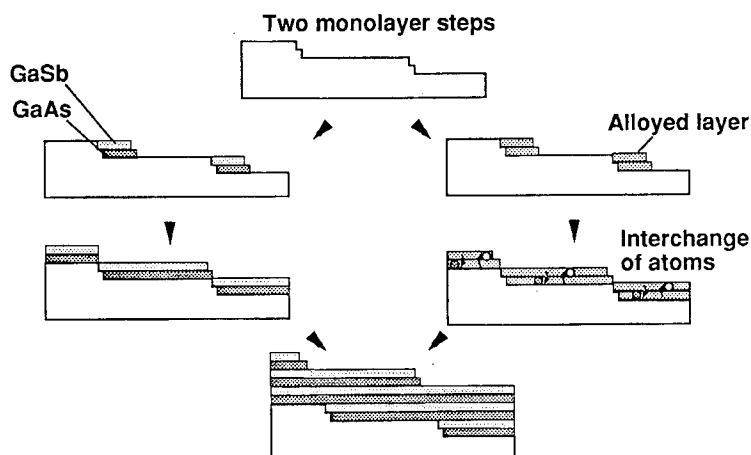


Fig. 5 Possible models for mechanism of CuAu-I type ordering in GaAsSb crystal: ordering from two monolayer steps.

2.2 Modulated structure

Modulated structures were also observed in the crystal. Figures 6(a) and 6(b) are dark-field TEM images from the (110) and the (001) cross-sections of GaAsSb, respectively. In both images, coarse and fine modulated structures (CMSs and FMSs) are clearly seen. The MSs are columnar shaped and the periodicity of the CMSs in the $\langle 001 \rangle$ direction is much longer (25-45 nm) than that in the $\langle 1\bar{1}0 \rangle$ direction

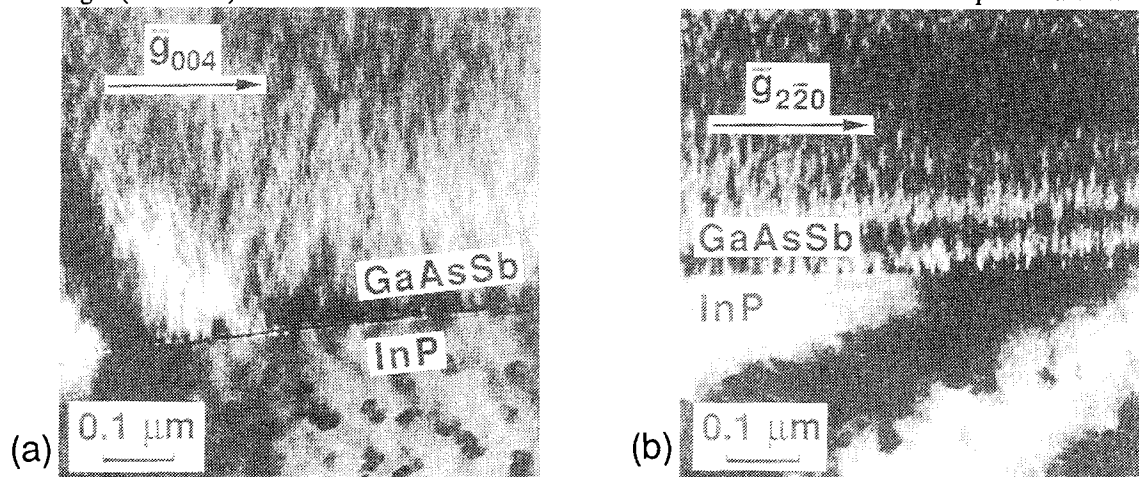


Fig. 6 Cross-sectional dark field images of modulated structure in GaAsSb crystal grown on a (110)InP substrate (5° off toward the $\langle 00\bar{1} \rangle$) at 500°C . (a) (110) cross-section, $\bar{g}=004$; (b) (001) cross-section, $\bar{g}=220$.

3. Conclusions

We have described for the first time a detailed TEM evaluation of ordered and modulated structures in MBE-grown GaAsSb crystals on (110)InP. In the electron diffraction pattern from the GaAsSb, superstructure spots associated with CuAu-I type ordered structure are found. When the offset angle of the substrates increases, the ordering becomes stronger. The ordering becomes also stronger with increasing growth temperature in the range 470 – 530°C . In HRTEM images from the crystal, areas with doubling in periodicity of 220 and 200 lattice fringes are observed locally, which is due to CuAu-I type ordering, indicating that the ordering is not perfect and that ordered regions are likely to be microdomains. Modulated structure are also found in both the $\langle 001 \rangle$ and $\langle 1\bar{1}0 \rangle$ directions. Coarse and fine modulated structures are clearly observed, and the periodicity of the coarse structure in the $\langle 001 \rangle$ direction is much longer than that in the $\langle 1\bar{1}0 \rangle$ direction. From these results, it has been concluded that atomic ordering and spinodal decomposition of the crystal are competing on the growth surface via surface diffusion of deposited atoms.

(12-24 nm). The presence of both structures for growth temperatures placing the composition inside the spinodal region, but only FMSs when the composition is outside this region, suggests that CMSs are generated by spinodal decomposition during crystal growth, while FMSs form during the cooling process after growth (6). From these results, one can conclude that atomic ordering and spinodal decomposition of the crystal are competing on the growth surface via surface diffusion of deposited atoms.

References

- (1) O. Ueda, Y. Nakata and T. Fujii, Appl. Phys. Lett. 58, 705 (1991).
- (2) O. Ueda, Y. Nakata, T. Nakamura and T. Fujii, J. Crystal Growth 115, 375 (1991).
- (3) Y. Nakata, O. Ueda and T. Fujii, Japan. J. Appl. Phys. 30, 2B, L241 (1991).
- (4) Y. Nakata, O. Ueda and T. Fujii, J. Crystal Growth 115, 504 (1991).
- (5) O. Ueda, Y. Nakata and S. Muto, J. Crystal Growth, to be published (MBE-8 conference).
- (6) A. G. Norman and G. R. Booker, Inst. Phys. Conf. Ser. 76, 257 (1985).
- (7) T. S. Kuan, T. F. Kuech, W. I. Wang and E. L. Wilkie, Phys. Rev. Lett. 54, 201 (1985).
- (8) T. S. Kuan, W. I. Wang and E. L. Wilkie, 51, 51 (1985).
- (9) J. E. Bernard, F. Froyen and A. Zunger, Phys. Rev. B 44, 11178 (1991).
- (10) A. Gomyo, T. Suzuki, K. Kobayashi, S. Kawata and I. Hino, Appl. Phys. Lett. 50, 673 (1987).
- (11) O. Ueda, M. Hoshino, M. Kodama, H. Yamada and M. Ozeki, J. Crystal Growth 99, 560 (1990).

Takashi Kita, Akira Fujiwara, Hiroshi Nakayama, and Taneo Nishino

Department of Electrical and Electronics, Faculty of Engineering, Kobe University, Rokkodai 1-1, Kobe 657, Japan

Introduction

Long-range ordering of the column-III sublattice appears spontaneously in $\text{Ga}_{0.5}\text{In}_{0.5}\text{P}$ epitaxial films grown on GaAs (001) by organometallic vapor-phase epitaxy (OMVPE).⁽¹⁾ The ordered $\text{Ga}_{0.5}\text{In}_{0.5}\text{P}$ alternates $\text{Ga}_{0.5+\delta}\text{In}_{0.5-\delta}\text{P}$ and $\text{Ga}_{0.5-\delta}\text{In}_{0.5+\delta}\text{P}$ monolayer planes along two of the four $\langle 111 \rangle$ directions, i.e., $[\bar{1}11]$ and $[1\bar{1}1]$. Electronic structure near the optical band gap in spontaneously ordered $\text{Ga}_{0.5}\text{In}_{0.5}\text{P}$ alloys is a subject which has been extensively studied both experimentally and theoretically.⁽¹⁻¹¹⁾ The monolayer superlattice (MSL) structure originates a band folding from a new Brillouin zone. The level repulsion between the folded state and the Γ state reduces the direct band-gap energy. A periodic crystal field in the MSL splits the four-fold degenerated Γ_{8v} valence-band maximum into two doubly degenerated bands represented by Γ_{4v} and Γ_{6v} degenerated at $k=0$ and Γ_{6v} . These effects are functions of the degree of long-range order. According to the selection rule for electronic-dipole transitions, the split band structure offers anisotropic optical properties.

Recently, optical absorption properties in ordered $\text{Ga}_{0.5}\text{In}_{0.5}\text{P}$ have been studied by photoluminescence-excitation (PLE) spectroscopy.⁽⁸⁻¹⁰⁾ The PLE spectra show anisotropic optical absorptions originated from the valence-band splitting. For applications of such anisotropic properties near the band gap into optoelectronic devices, it is important to investigate properties of photocurrent (PC) responses in ordered $\text{Ga}_{0.5}\text{In}_{0.5}\text{P}$. The PC response is not only a function of absorption coefficient, but also of electronic structure of the junction and transport properties of photo-excited carriers. In this study, we focus our attention on PC responses in the MSL of long-range ordered $\text{Ga}_{0.5}\text{In}_{0.5}\text{P}$ alloys. Based on our analysis of measured PC spectra by theoretical calculations, the properties of the anisotropic PC as well as a statistical distribution of partially ordered domains and the relationship between the oscillator strength and order parameter will be discussed.

Experimental

The samples used in this experiment were ordered $\text{Ga}_{0.5}\text{In}_{0.5}\text{P}$ alloys grown on an exact n^+ -GaAs (001) substrate by OMVPE. The growth temperature and the gas-flow ratio of column-V and -III sources, $f(\text{V})/f(\text{III})$, are key variables in the spontaneous ordering. The growth temperature was in the range of 660-730°C. $f(\text{V})/f(\text{III})$ was 202. The thickness of the undoped epitaxial layer was 1.1 μm . The epitaxial films were horizontally lattice matched to the GaAs substrate within 0.1%. The undoped $\text{Ga}_{0.5}\text{In}_{0.5}\text{P}$ showed n -type conductivity. The residual carrier concentration measured by the capacitance-voltage method was about $5 \times 10^{15} \text{ cm}^{-3}$. A semitransparent-Au/ $\text{Ga}_{0.5}\text{In}_{0.5}\text{P}$ Schottky-barrier diode was used for the PC measurements. The built-in voltage of the Schottky surface was estimated to be 0.8 V by current-voltage characteristics. A monochromatic light was polarized by a polarizer with an extinction coefficient of 10^{-4} . The polarized light irradiated normally the (001) surface of the sample. An incident light was linearly polarized parallel to the $[110]$ and $[1\bar{1}0]$ directions in the (001) plane. The sample temperature was in the range of 15-290 K. Electroreflectance (ER) and transmission-electron diffraction (TED) observation have been performed for the samples used in this experiment. The detailed conditions of the ER measurement are indicated in Ref. 4.

Results and Discussion

Selection Rule for Optical Transition

Figure 1 shows interband transitions in ordered and disordered $\text{Ga}_{0.5}\text{In}_{0.5}\text{P}$. The MSL structure originates a band folding from the new Brillouin zone. The level repulsion between the folded state and the Γ state reduces the direct band-gap energy. A crystal field in the MSL splits the four-fold degenerated Γ_{8v} valence-band maximum into two doubly degenerated bands represented by Γ_{4v} and Γ_{6v} degenerated at $k=0$ and Γ_{6v} . The selection rule for electronic-dipole transitions in the split band structure of ordered $\text{Ga}_{0.5}\text{In}_{0.5}\text{P}$ causes anisotropic optical properties. Two optical transitions of the $\Gamma_{6c}-\Gamma_{4v}$ and $\Gamma_{6c}-\Gamma_{6v}$ have polarization components of x and y and x, y , and z , respectively. Here, x, y , and z are defined by a new symmetry, $R3m$, in the ordered alloy instead of the $F43m$ of the zinc-blende structure of the disordered alloy. Because of rotation of the coordinate system in the MSL, the orthogonal coordinates of x, y , and z are along the $[\bar{1}12]$, $[110]$, and $[\bar{1}11]$ for the $[\bar{1}11]$ MSL, respectively. Similarly, for the $[1\bar{1}1]$ MSL, x, y , and z are along the $[\bar{1}12]$, $[1\bar{1}0]$, and $[1\bar{1}1]$, respectively. Then, if we set polarizations along the $[110]$ and $[1\bar{1}0]$, anisotropic properties will be found in optical processes such as luminescence and absorption in ordered alloys, although the transition in disordered $\text{Ga}_{0.5}\text{In}_{0.5}\text{P}$ is isotropic.

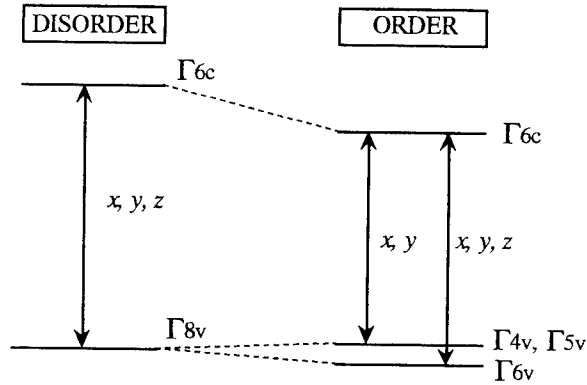


Fig. 1. Schematic depiction of the band diagrams of disordered and ordered states.

PC Spectra

PC spectra of ordered $\text{Ga}_{0.5}\text{In}_{0.5}\text{P}$ with different degree of ordering are shown in Fig. 2. The measurement was performed at 15K. The samples were grown at $f(\text{V})/f(\text{III})$ of 202. The degree of ordering was controlled by the growth temperature. The temperature were 660, 700, and 730 °C. The solid and open circles plot the PC intensities for the incident lights polarized parallel to the $[110]$ and $[1\bar{1}0]$, respectively. At 660°C, the PC spectra show a large band-gap reduction and strong anisotropic properties. The PC-edge energy for the $[110]$ light is lower than one for the $[1\bar{1}0]$ light. With increased the growth temperature, the band edge approaches to that of the random alloy, and the anisotropy becomes small. The observed maximum band-gap reduction is about 100meV. This reduction is caused by the level repulsion between the $\Gamma_{6c}(\Gamma)$ and the folded $\Gamma_{6c}(\text{L})$. The parameter δ of the compositional modulated structures in the ordered $\text{Ga}_{0.5}\text{In}_{0.5}\text{P}$ can be estimated from the magnitude of the reduction.(1,7) The δ of our samples grown at 660, 700, and 730 °C are about 0.07, 0.19, and 0.29, respectively.

The ER measurement reveals signals due to the transitions originated from the valence-band splitting in the ordered alloy, i.e., the $\Gamma_{6c}-\Gamma_{4v}, \Gamma_{5v}$ and $\Gamma_{6c}-\Gamma_{6v}$ transitions. From the ER measurements, the valence-band splitting of the sample grown at 660 °C is ~40 meV. The polarization spectra of this sample show an anisotropic character. The ER signal of the sample grown at 730 °C was observed at 1.98 eV and shows an isotropic character. The transition energy of 1.98 eV is almost same as an energy of the random alloy. The anisotropic character in the PC spectra depends on the selection rule and oscillator strength of the $\Gamma_{6c}-\Gamma_{4v}, \Gamma_{5v}$ and $\Gamma_{6c}-\Gamma_{6v}$ transitions. As shown in Fig. 1, x, y , and z in the ordered alloy are defined by the new symmetry of $R3m$. The PC spectrum is given by a mixture of these transitions for both the $[110]$ and $[1\bar{1}0]$ polarizations. Then, the anisotropy in the PC polarization spectra becomes small rather than the valence-band splitting. On the other hand, the transition in the disordered alloy is isotropic.

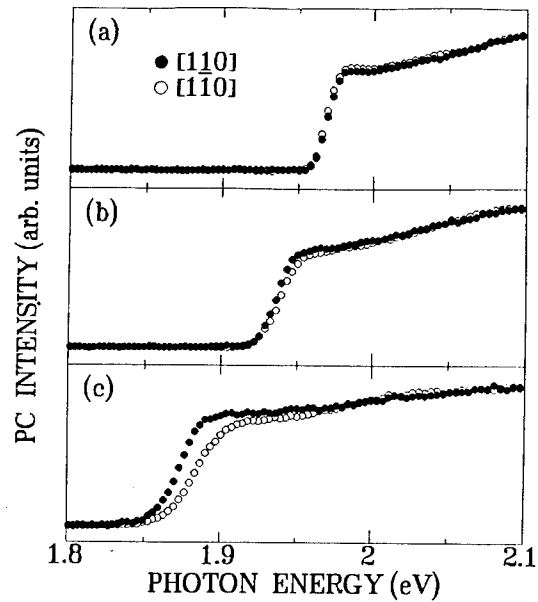


Fig. 2. PC spectra of ordered $\text{Ga}_{0.5}\text{In}_{0.5}\text{P}$ with different degree of ordering.

The PC spectra of the ordered samples don't show clear excitonic lines. ER-line widths of the samples grown at 660, 700, and 730 °C are about 15, 14, and 11 meV, respectively. Then, it is considered that the excitonic features are smeared by the transitions with such wide line width.(1) In fact, the PC-edge structure shows a trend to become steep with lowering the degree of the long-range order.

Theoretical Calculations and Analysis of PC Responses

To investigate a contribution of the split transitions to the PC spectra, we performed theoretical calculations of PC responses in ordered $\text{Ga}_{0.5}\text{In}_{0.5}\text{P}$. Horner et al. qualitatively explained a broad absorption character in the PLE spectra by considering a statistical distribution of partially ordered domains.(10,11) Since it was found that our samples have multi-domain structures, the effect of the distribution, i.e., a distribution of δ , is important to analyze the absorption coefficient. In the case of the analysis of the PC spectra, furthermore, we must treat photo-excited carriers near the junction. Two processes, drift and diffusion, influence the photo response with which light-generated free carriers contribute to the flow of current. The PC in a Schottky-barrier diode is given by

$$I = e\gamma\Phi\alpha\left[\int_0^w \exp(-\alpha x)dx + \int_w^t \exp(-\alpha x - |w-x|/L_p)dx\right] \quad (1)$$

where, α , γ , and Φ are absorption coefficient, quantum efficiency, and photon flux, respectively, L_p the diffusion length of photo-excited holes, w the depletion-layer width, and t the film thickness. This equation indicates that the PC

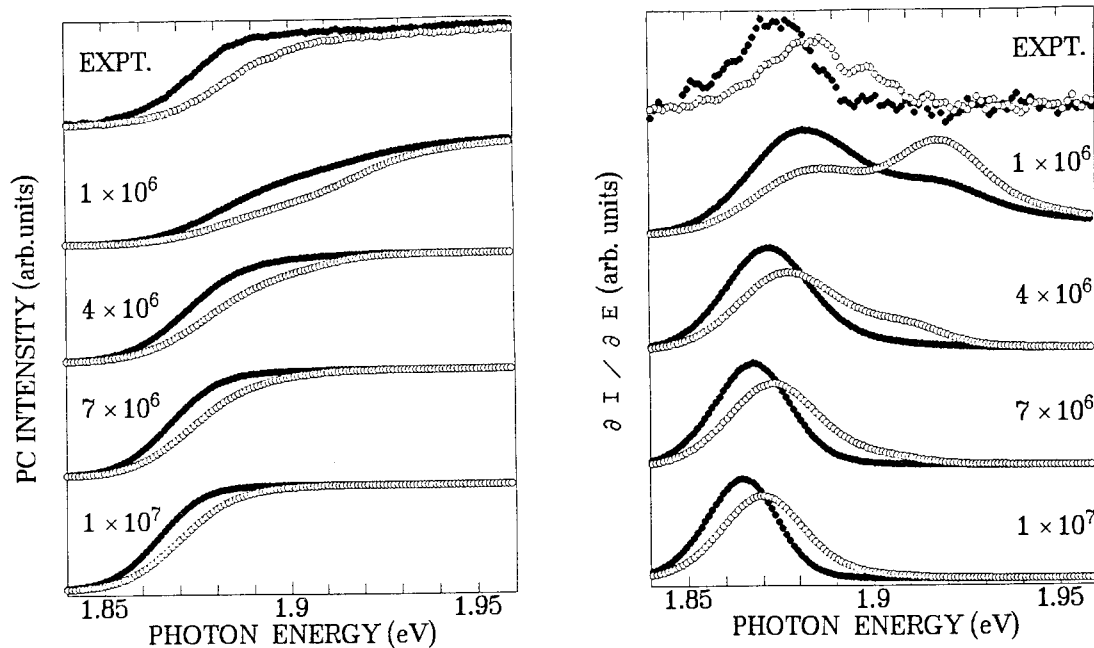


Fig. 3. Theoretical calculations of PC spectra and their differentiated spectra for various $\alpha\hbar\omega / (\hbar\omega - E_g)^{1/2}$.

is not a simple function of the absorption coefficient. In our calculation of PC spectra by using Eq. (1), relative magnitudes of $1/\alpha$ versus L_p , w , and t are parameters to determine the spectral line shape. If a light penetration of $1/\alpha$ is much larger than L_p , w , and t , I is proportional to α . Then, $\partial I / \partial E \propto \partial \alpha / \partial E$. In this case, the PC spectra obey the change of α and its differentiated spectrum will show features corresponding to the transitions. However, when

the relative magnitude of $1/\alpha$ is small, calculated PC spectra shows a steep edge around the lowest $\Gamma_{6c}-\Gamma_{4v}, \Gamma_{5v}$ transition, and the anisotropy becomes small.

In our calculations, we take into account a random alloy fluctuation in GaInP and a Gauss-type distribution of δ in the epitaxial film. Here, δ is 0.29, and a full-width at half maximum of the distribution, $\Delta\delta$, is 0.02. Furthermore, we adopt an influence of the oscillator strength proposed by Wei and Zunger.⁽⁸⁾ In the ordered $\text{Ga}_{0.5}\text{In}_{0.5}\text{P}$, relative oscillator strength of the split two transitions is modified through an interaction by the spin-orbit split band. For the [110] polarization, the relative strength of the $\Gamma_{6c}-\Gamma_{4v}, \Gamma_{5v}$ transition decreases with the atomic ordering. On the other hand, the relative strength becomes decreases for the [1 $\bar{1}$ 0] polarization.

Figure 3 is a calculated result for PC spectra and their differentiated spectra at various $\alpha\hbar\omega / (\hbar\omega - E_g)^{1/2}$, where E_g is a band-gap energy. The measured data of the sample grown at 660°C are shown at the top of the each figure. When $\alpha\hbar\omega / (\hbar\omega - E_g)^{1/2}$ becomes small, i.e., the relative magnitude of $1/\alpha$ becomes large, the PC edge shows gentle edge structure. At this condition, the split transitions tend to reflect on the PC spectra. This feature can be seen in the differentiated spectra in Fig. 3. Figure 4 shows a comparison between the measured and calculated PC and its differentiated spectra for the sample grown at 660°C. The open and closed circles plot the measured data at the [110] and [1 $\bar{1}$ 0] polarizations. The solid and dashed lines are the calculated result. The calculation shows moderate agreements with the measured data at δ of 0.29, $\Delta\delta$ of 0.02, and $\alpha\hbar\omega / (\hbar\omega - E_g)^{1/2}$ of 3×10^6 . Our calculation reveals that the anisotropic character in the PC spectra are

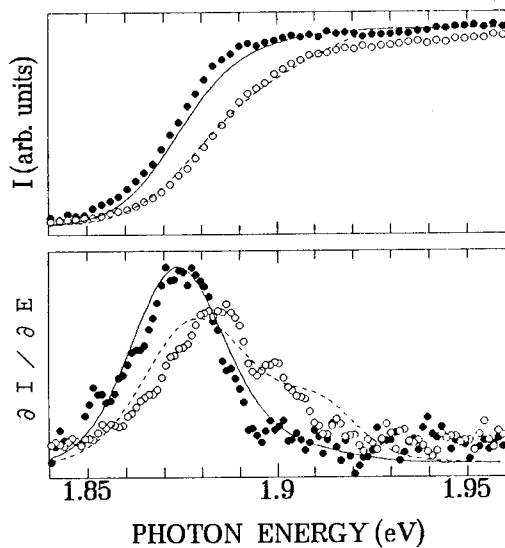


Fig. 4. Comparison between the measured and calculated PC and its differentiated spectra for the sample grown at 660°C. The open and closed circles plot the measured data. The solid lines are the calculated result.

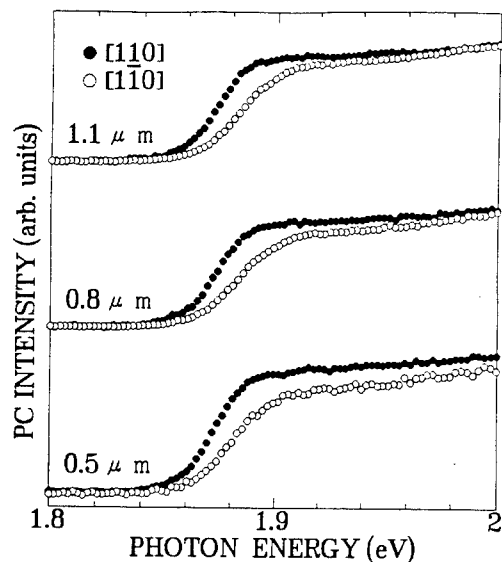


Fig. 5. Epitaxial film-thickness dependence of the PC spectra.

strongly influenced by the film thickness. Figure 5 shows measured film thickness dependence on the PC spectra. With the decrease of the epitaxial film thickness, the polarization spectra show a change especially at the higher energy side. This trend well agree with our calculations. From this result, we can propose a method for control of the polarization in PC spectra by the epitaxial film thickness.

Summary

Anisotropic PC responses of ordered $\text{Ga}_{0.5}\text{In}_{0.5}\text{P}$ alloys have been systematically investigated. The PC edge of the $[110]$ polarization is lower than one of the $[1\bar{1}0]$. The observed anisotropy in the PC spectra is due to a crystal-field splitting at the valence-band maximum in ordered $\text{Ga}_{0.5}\text{In}_{0.5}\text{P}$. From the theoretical analysis of the PC, the electronic structure of the junction and the epitaxial film

thickness have an influence upon the anisotropy of the PC spectra together with the absorption coefficient. Our PC theory well agrees with the measured data. This reveals the following facts: δ has a distribution in the epitaxial film and the oscillator strength for the split transitions are changed by the long-range ordering.

References

1. A. Zunger and S. Mahajan, *Handbook of Semiconductors*, 2nd ed., edited by S. Mahajan, Elsevier, Amsterdam, 1994, Vol. 3, pp. 1139-1514, and references therein.
2. T. Nishino, *J. Cryst. Growth* Vol.98, pp.44-52, 1989.
3. T. Kanata-Kita, M. Nishimoto, H. Nakayama, and T. Nishino, *Phys. Rev. B* Vol.45, pp.6637-6642, March 1992.
4. T. Kanata-Kita, M. Nishimoto, H. Nakayama, and T. Nishino, *Appl. Phys. Lett.* Vol.63, pp.512-514, July 1993.
5. R.G.Alonso, A.Mascarenhas, G.S.Horner, K.A.Bertness, S.R.Kurtze, and J.M.Olson, *Phys. Rev. B* Vol.48, pp.11833-11837, October 1993.
6. K.Sinha, A.Mascarenhas, G.S.Horner, R.G.Alonso, K.A.Bertness, and J.M.Olson, *Phys. Rev. B* Vol.48, pp.17591-17594, December 1993.
7. S. H. Wei and A. Zunger, *Appl. Phys. Lett.* Vol.62, pp.1937-1939, April 1993.
8. S. H. Wei and A. Zunger, *Appl. Phys. Lett.* Vol.64, pp.1676-16798 March 1994.
9. D.J.Mobray, R.A.Hogg, M.S.Skolnik, M.C.DeLong, S.R.Kurtze, and J.M.Olson, *Phys. Rev. B* Vol.46, pp.7232-7235, September 1992.
10. G.S.Horner, A.Mascarenhas, S.Froyen, R.G.Alonso, K.A.Bertness, and J.M.Olson, *Phys. Rev. B* Vol.47, pp.4041-4043, February 1993.
11. G.S.Horner, A.Mascarenhas, R.G.Alonso, S.Froyen, K.A.Bertness, and J.M.Olson, *Phys. Rev. B* Vol.49, pp.1727-1731, January 1994.

Kazuo Uchida

Nippon Sanso Co., Tsukuba Laboratory, 10 Ohkubo Tsukuba, Ibaraki 300-33, Japan

Peter Y. Yu

Department of Physics and Materials Science Division, Lawrence Berkeley Laboratory, University of California, Berkeley, California 94720

Eicke R. Weber

Department of Materials Science and Mineral Engineering, and Materials Science Division, Lawrence Berkeley Laboratory, University of California, Berkeley, California 94720

Nobuhiko Noto

Shin-Etsu Handotai Co., SEH Isobe R&D Center Isobe An-naka, Gunma 370-01, Japan

Abstract

We report the first observation of Single Particle Excitation (SPE) in electronic Raman spectroscopy as well as the plasmon related Raman peak located at 352 cm^{-1} in the ordered $\text{Ga}_{0.52}\text{In}_{0.48}\text{P:Se}$ with a carrier concentration of $>10^{17}\text{ cm}^{-3}$. These observations indicate that there exist the high density thermally excited carriers in the ordered $\text{Ga}_{0.52}\text{In}_{0.48}\text{P:Se}$. However, the disordered $\text{Ga}_{0.52}\text{In}_{0.48}\text{P:Se}$ with almost same amount of carrier concentration does not show either SPE or plasmon related peaks. This implies that the ordering might cause a carrier confinement effect to increase the density of carriers. This confinement effect could be possible if the ordered region with a lower bandgap energy is surrounded by the disordered matrix with a higher bandgap energy in the ordered $\text{Ga}_{0.52}\text{In}_{0.48}\text{P}$.

Introduction

The isovalent ternary semiconductor $\text{Ga}_{0.52}\text{In}_{0.48}\text{P}$ (for brevity this will be referred to as GaInP in the rest of this paper) has been receiving much attention due to the formation of the Cu-Pt type ordering. This ordering has made its properties change and the most apparent one is the red shift of the bandgap energy, that was first recognized in the fabrication of GaInP visible lasers(1) and theoretically explained by Zunger et al.(2). However, the cause of other property changes such as an appearance of long lifetime component in photoluminescence emission, a decrease of Hall mobility and even the details of this order nanostructure including an order parameter are still under investigation. In order to obtain further structural information of the ordering phenomena in GaInP, Raman spectroscopy in ordered GaInP and disordered GaInP has been reported by a number of authors (3~5). Jusserand and Slempek have first described the Raman spectra of disordered GaInP as a modified two-mode behavior(4). Suzuki et al. have performed the Raman spectroscopy for both ordered and disordered undoped GaInP and found a subtle lineshape change in Raman spectra between them(6). Very recently Krost et al. have performed the micro Raman spectroscopy of the (011) plane of GaInP that was grown on patterned GaAs substrates(7). This patterned GaAs enables to grow relatively large ordered GaInP domains. Since disordered GaInP has T_d symmetry while ordered GaInP has C_{3v} , these alloys exhibit the different selection rules. Using these different selection rules as well as a small laser probe of $1\text{ }\mu\text{m}$, they were able to differentiate the Raman signals from ordered and disordered GaInP domains and confirmed that the red shift of the bandgap energy is not due to a composition fluctuation but due to the ordering. In this paper we have measured the Raman spectroscopy of Se doped and undoped ordered and disordered GaInP. It is well known that doping can modify the Raman spectra by introducing free carriers and by producing local vibrational modes(8). Since Se atoms are heavier than P

atoms they replace, they do not give rise to local modes. Free carriers, instead, can scatter light via electronic Raman scattering(9). Such scattering processes can involve single-particle excitations (SPE) and collective excitations (such as plasmons) of the electron gas. Here we report the electronic Raman spectrum in ordered GaInP alloy. According to our knowledge, this is the first report of such spectrum.

Experiment

GaInP samples used in this experiment were grown on GaAs substrates by low pressure Metal Organic Vapor Phase Epitaxy. The (100) surface of GaAs substrates was used for ordered GaInP growth while 15 degree inclined (100) surface along $[111]$ A direction of GaAs substrates was used for disordered GaInP growth. The Cu-Pt type ordering in samples was confirmed by the additional satellite spots observed in the (011) electron diffraction pattern. These satellite spots are consistent with a doubling of the unit cell along the $[111]$ A direction due to the ordering. In nominally undoped samples the electron concentration due to background impurities was found to be less than 10^{15} cm^{-3} from Hall measurements. In doped samples Se was introduced during growth as shallow donors. The donor concentration in the disordered GaInP film was estimated to be $2\times 10^{17}\text{ cm}^{-3}$ from Capacitance Voltage (CV) measurement, while that in the ordered GaInP film was around $3\sim 4\times 10^{17}\text{ cm}^{-3}$. The Raman apparatus used in this study consists of the exciting laser of 488 nm line of an Ar ion laser, Spex 1403 double monochromator and GaAs photomultiplier tube (PMT). The signal from the PMT was analyzed by a single photon counter. We used the cross polarization configuration in which the polarization of the incident laser beam was aligned horizontally, while the polarization of Raman scattered light was vertical. This configuration is preferred because the diffraction efficiency of the gratings inside the monochromator are higher for vertically polarized light with wavelength around 6000 \AA .

Result and Discussion

In Fig. 1 we compared the Raman spectra in our undoped and doped GaInP samples. These Raman spectra have been plotted with the same vertical scale although the zeros of the vertical axis for each Raman spectra have been displaced for clarity.

In general our Raman spectra of the undoped samples agree quite well with those published in the literature(4,5). The sharp peak at 380 cm^{-1} in both spectra has been identified as the longitudinal optical (LO) phonon associated with GaP. For brevity we will refer to this peak as the GaP-LO peak. The lower energy peak at 360 cm^{-1} is attributed to LO phonon associated with InP (InP-LO mode). The much weaker and broader peak centered around 325 cm^{-1} is believed to be the transverse optical (TO) mode in the alloy. We note that the TO phonon mode is forbidden by selection rule in backscattering from a (100) surface of a zincblende-type crystal. The appearance of this TO mode can be attributed to some momentum conservation relaxation due to disorder. Overall the undoped ordered GaInP spectrum has the lowest intensity so its vertical scale has to be enlarged by a factor of 4 in order to be plotted on the same scale as the other spectra. Otherwise there are only very subtle differences between the Raman spectra of the undoped ordered and disordered samples. This is understandable since the LO phonons are not very sensitive to long range ordering of the Ga and In cations in which the relation of each first neighbors is not changed before and after the ordering.

The Raman spectra in Se doped GaInP samples are also shown in Fig. 1. In the disordered GaInP we found no major change in the Raman spectrum upon doping except for a decrease in the intensity and a broadening of the LO phonon peaks. However, the spectrum of the ordered GaInP sample showed significant changes from the undoped sample. First a strong and broad peak centered near the laser line appeared. The region of the Raman spectra near the laser line for both doped ordered GaInP and disordered GaInP are shown in Fig. 2 for comparison. It is clear that this new broad peak is present only in the ordered sample. In addition a rather narrow peak appeared at 352 cm^{-1} in the doped ordered GaInP (see Fig. 1). This peak is absent in the disordered samples and in the undoped ordered sample.

We interpret the broad and strong peak centered near the laser line as due to SPE of the free electron gas introduced by doping. By plotting the Raman spectrum in a semi-log plot in Fig. 2, we see that the Raman spectrum has approximately a Gaussian lineshape. We have fitted this spectrum to the SPE Raman lineshape in the classical high temperature limit(10)

$$\frac{\partial^2 \sigma}{\partial \Omega \partial \omega} = \exp \left[-\frac{(\omega - \omega_c)^2}{(q v_{th})^2} \right] \quad (1)$$

where $\frac{\partial^2 \sigma}{\partial \Omega \partial \omega}$ is the differential cross-section, q is the momentum transferred to the electrons from the photon and v_{th} is the thermal velocity of the electrons. The frequency ω_c is equal to

$$\omega_c = \frac{q^2}{2\hbar m^*} \quad (2)$$

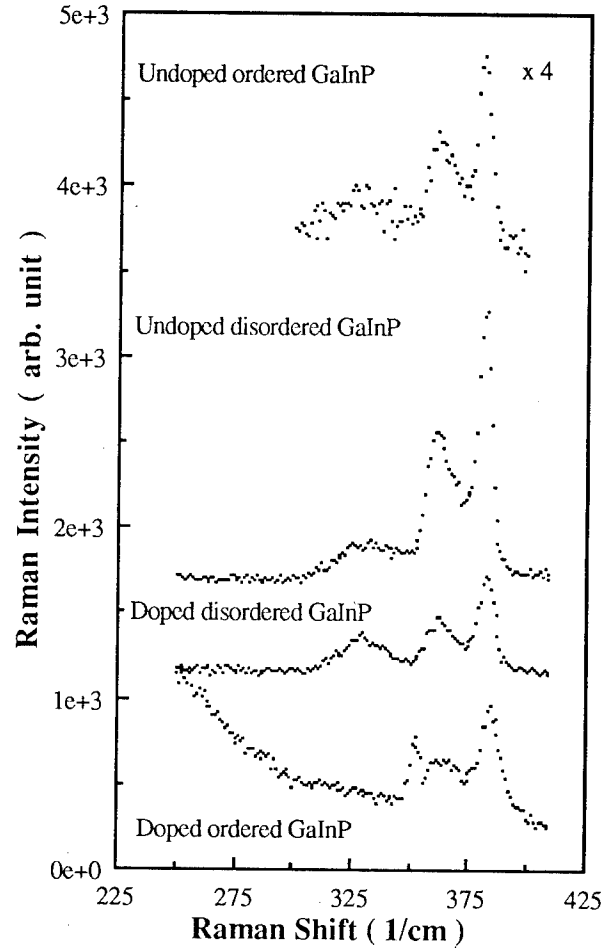


Fig. 1 Raman spectra in undoped and doped ordered GaInP and disordered GaInP obtained at room temperature using the 488 nm line of an Ar ion laser

(m^* is the effective mass of the electron) so that $\hbar\omega_c$ can be regarded as the recoil energy of the electrons. This energy is usually negligible except in Compton scattering involving high energy photons. We estimate that ω_c to be about 32 cm^{-1} in GaInP so it can be neglected in the lowest order of approximation. In principle, we can determine v_{th} and hence the temperature T_e of the electron gas from the SPE lineshape using Eq. 1. To accomplish this we will assume these values for the various material constants of ordered GaInP: n (refractive index at $\lambda=488 \text{ nm}$)=3.4; $q=(4\pi n/\lambda)=8.75 \times 10^5 \text{ cm}^{-1}$; and $m^*=0.075$ times free electron mass. Whenever a parameter is not available for ordered GaInP we have adopted the corresponding value for InP(11). The electron temperature determined from the SPE spectrum in this way is equal to 331 K. This electron temperature is quite reasonable considering that the experiment was performed at room temperature.

There are two possible identifications for the sharper peak at 352 cm^{-1} . One possibility is that this is a LO phonon bound to shallow donors(12). This has been

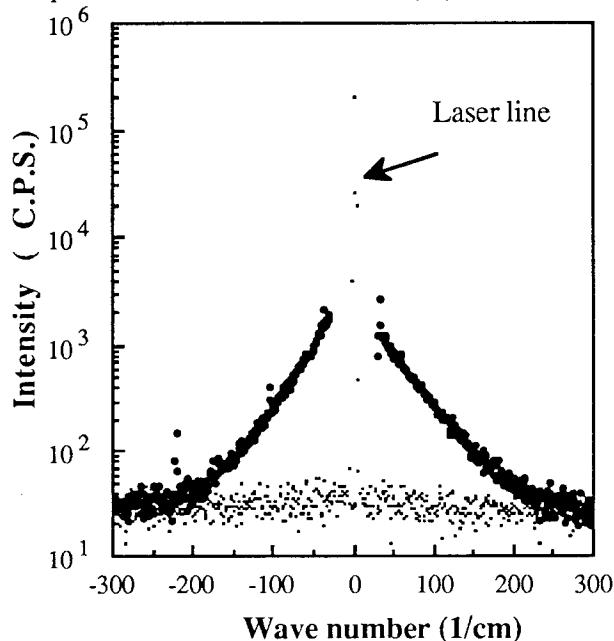


Fig. 2 Raman spectra of doped ordered GaInP (dense points) and doped disordered GaInP close to the laser line to show the electronic Raman peak due to scattering by SPE in the ordered sample

observed mainly in GaP where the conduction band minima occur at X points of the Brillouin zone. These bound LO phonon peaks are usually much weaker than the regular LO phonon peaks. Furthermore they are observable only at low temperatures when the donors are in their neutral charge state. The strong SPE spectrum at room temperature suggests that most of the donors are ionized. This leaves only one other possibility: the 352 cm^{-1} peak is due to light scattering from a plasmon. When the frequency of the plasmon is close to that of an LO phonon, coupled plasmon-LO phonon mode are formed(13). Such coupling will result in an increase in the LO phonon mode frequency. We note that the GaP-LO mode frequency is slightly higher in the doped samples than in the undoped samples. The increase is largest (about 6 cm^{-1}) in the doped ordered sample. Since this shift in the GaP-LO mode is relatively small we can neglect this coupling and interpret the 352 cm^{-1} mode as due to an uncoupled plasmon. The plasmon frequency ω_p in a solid is given by

$$\omega_p = \left[\frac{4\pi N e^2}{\epsilon_\infty m^*} \right]^{1/2} \quad (3)$$

where N is the electron density, e is the electric charge and ϵ_∞ is the high frequency dielectric constant. The dielectric constant ϵ_∞ is equal to 9.0 and 9.6 in GaP and InP respectively(11). Since the value of ϵ_∞ in ordered GaInP is unknown, we will assume ϵ_∞ to be around 9.0 in ordered GaInP. Using these approximation we determine N to be

about $1 \times 10^{18}\text{ cm}^{-3}$ from the measured plasma frequency. One problem with this identification is that the electron density is higher than the concentration of dopants ($3\text{--}4 \times 10^{17}\text{ cm}^{-3}$) introduced by growth. If we assume that the electron density is about $1 \times 10^{18}\text{ cm}^{-3}$ in the doped ordered GaInP sample, we have to conclude that the electron density in the doped disordered GaInP sample must be about 100 times less to account for the absence of any SPE electronic Raman peak. At present it is not clear as to why ordered GaInP and disordered GaInP behave so differently when doped. There are two possible explanations. One is due to a migration of electron from disordered regions to the ordered domains. This would be possible if cylindrical or platelet shaped ordered phases in ordered GaInP exist. This might form a kind of random quantum well structure consisting of ordered GaInP well layers and disordered GaInP barrier layers. In this case electrons would accumulate mostly in these ordered GaInP well layers by the thermalization of carriers since donor electrons from dopants in the disordered matrix will migrate to the ordered regions with a lower bandgap and create a sheet carrier concentration. This sheet carrier concentration is higher than that of the bulk if equal amounts of dopants were incorporated into the epilayer and would be high enough to show SPE. It is understandable why we could not measure the difference in electron concentration between the ordered and disordered GaInP since the CV measurement used to determine the electron concentration is not sensitive to the spatial electron distribution. The other possible explanation is the existence of depletion and accumulation layers near the sample surface. Further work, such as varying the doping concentration and sample temperature, better characterization of the sample surface quality is needed to elucidate the nature of this 352 cm^{-1} peak in the doped ordered GaInP and to understand the difference in behavior between these doped alloys.

Conclusion

The doped ordered GaInP exhibits the SPE as well as a plasmon related Raman peak located at 352 cm^{-1} . These are absent in the doped disordered GaInP sample. This implies that the ordering might cause a carrier confinement effect to increase the density of carriers and this confinement effect could be possible if the ordered region with a lower bandgap energy is surrounded by the disordered matrix with a higher bandgap energy in the ordered GaInP.

Acknowledgment

The authors wish to thank Dr. Zuzanna Liliental-Weber in Lawrence Berkeley Laboratory for the transmission electron microscope analysis of GaInP samples.

References

- (1) A. Gomyo, T. Suzuki, K. Kobayashi, S. Kawata, I. Hino and T. Yuasa, *Appl. Phys. Lett.* **50**, 673(1987)
- (2) S.-H. Wei and A. Zunger, *Phys. Rev. B* **39**, 3279 (1989)
- (3) B. H. Bayramov, V. V. Toporov, Sh. B. Ubaydullaev, L. Hildisch and E. Jahne, *Solid State Commun.* **37**, 963 (1981)

- (4) B. Jusserand and S. Slempek, Solid State Commun. **49**, 95 (1984)
- (5) T. A. Gant, M. Dutta, N. A. El-masry, S. M. Bedair and M. A. Stroscio, Phys. Rev. B **46**, 3834 (1992)
- (6) T. Suzuki, A. Gomyo, S. Iijima, K. Kobayashi, S. Kawata, I. Hino and T. Yuasa, Jpn. J. Appl. Phys. **27**, 2098 (1988)
- (7) A. Krost, N. Esser, H. Selber, J. Christen, W. Richter, D. Bimberg, L. C. Su and G. B. Stringfellow, J. Cryst. Growth **145**, 171 (1994)
- (8) A. S. Barker Jr. and A. J. Siever, Rev. of Mod. Phys. **47**, S1 (1975)
- (9) M. V. Klein, Light Scattering in Solids, ed. by M. Cardona, (Spring-Verlag, Heidelberg, 1975) p. 148
- (10) W. Hayes and R. Loudon, Scattering of light by crystals, (Wiley and Sons, New York, 1978)
- (11) O. Madelung, ed., Landolt-Bornstein New Series, Group III: Crystal and Solid State Physics, Vol. 22, Semiconductors a, Intrinsic Properties of Group IV, Elements, and III-V, II-VI and I-VII Compounds (Springer-Verlag, Heidelberg, 1987)
- (12) P. J. Dean, D. D. Manchon and J. J. Hopfield, Phys. Rev. Lett. **25**, 1027 (1970)
- (13) A. Moradian and G. Wright, Phys. Rev. Lett. **16**, 999 (1966)

Donor Passivation in n-AlInAs Layers by Fluorine

Y. Yamamoto, N. Hayafuji, N. Fujii, K. Kadoiwa, N. Yoshida,
T. Sonoda, S. Takamiya and S. Mitsui

*Optoelectronic & Microwave Devices Laboratory, Mitsubishi Electric Corporation
4-1, Mizuhara, Itami, Hyogo, 664, Japan*

Abstract

Origin and mechanism for the thermal degradation of the n-AlInAs layer are discussed. The thermal degradation of carrier concentration and mobility is found to occur predominantly in the n-AlInAs layer, which is caused by annealing at a temperature less than 450°C. The origin of the deterioration is ascertained to be the thermally diffused fluorine, which passivates donors in the n-AlInAs layer. As the electronegativity of fluorine atom is largest among whole elements, and the atomic radius of fluorine atom is considerably small to pass through the crystal, fluorine atoms are reasonably thought to diffuse into the n-AlInAs layer then react with the free electrons, which results in the F^- scattering centers (F^- : ionized fluorine).

Introduction

$Al_{0.48}In_{0.52}As$ is a very attractive material for both of optical and electronic devices such as laser diode or high electron mobility transistor, because it has a wide band-gap energy while keeping lattice-matching to InP substrate. On the other hand, the thermal degradation of AlInAs /InGaAs system have been recently reported.[1],[2] Reliability for the thermal stress is one of the major problems to be solved, because the fabrication of the devices generally requires some thermal treatments after growth. In this system, several degradation mechanisms such as surface deterioration, defect formation relating to the oxygen impurities and dopant passivation by atomic hydrogen have been suggested.[1]-[5] The origin of the thermal degradation, however, has not been elucidated yet. In this paper, the origin of the thermal instability of this system is ascertained through identifying whole measurable impurities in n-AlInAs layers. Furthermore, the degradation mechanism of this system is also suggested.

Experimental

Si doped $n-Al_{0.48}In_{0.52}As$, Be doped $p-Al_{0.48}In_{0.52}As$ and Si/Be co-doped $n-Al_{0.48}In_{0.52}As$ layers were grown by gas source molecular beam epitaxial (GSMBE) method using the elemental solid sources of group III and AsH_3 gas source. Sn doped $n-Al_{0.48}In_{0.52}As$ and Si doped $n-In_{0.53}Ga_{0.47}As$ were also grown by the conventional molecular beam epitaxial (MBE) method. The substrates used were semi-

insulating (100) InP substrates with 3 inch diameter. Si doped $n-Al_{0.3}Ga_{0.7}As$ layer was also grown as a reference by GSMBE on a semi-insulating (100) GaAs substrate with 3 inch diameter. The growth temperatures for AlInAs, InGaAs and AlGaAs were 480°C, 470°C and 600°C, respectively. The growth rate and the AsH_3 flow rate for the samples grown by GSMBE were 0.8 $\mu m/hr$ and 5 sccm, respectively. The growth rate and the V/III ratio for the samples grown by MBE were 0.5 $\mu m/hr$ and 40, respectively. 1 μm thick Si doped n-AlInAs layers were annealed at 300°C, 350°C, 400°C and 450°C in N_2 and at 400°C in H_2 for 15 min, respectively. The other samples were annealed at 450°C in N_2 for 15 min. Hall measurements were conducted for 1 μm thick Si doped n-AlInAs annealed at 350°C for 15min in N_2 by periodic stripping.[6] The thickness of the removed layer was 50nm per stripping step. In addition, conventional Hall measurements were carried out for whole samples before and after annealing. Secondary ion mass spectroscopy (SIMS) measurements of whole elements detectable as negative ions using Cs^+ primary ion were also conducted for all samples after annealing.

Results and discussion

Figure 1 shows the sheet carrier concentration versus the annealing temperature for Si doped n-AlInAs layers annealed in N_2 and H_2 . The same deterioration of sheet carrier concentration is found as in the AlInAs /InGaAs HEMT structure.[1],[2] The degradation of sheet carrier concentration of the samples annealed in N_2 was larger than that of the samples annealed in H_2 .

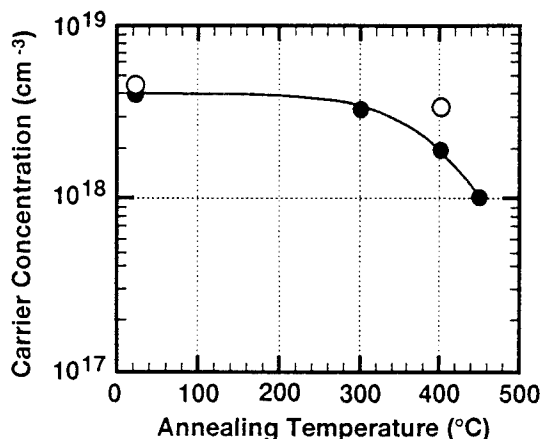


Figure 1 Carrier concentration versus annealing temperature for 1 μ m thick Si doped n-Al_{0.48}In_{0.52}As on InP substrate. Samples were annealed for 15 min in N₂ (●) and H₂ (○).

These data indicate that the degradation of the AlInAs/InGaAs HEMT structure might be caused by the reduction of the carrier concentration in the n-AlInAs electron supplying layer by annealing and that the dopant passivation by atomic hydrogen is not dominant for the degradation of Si doped n-AlInAs layer. The depth profiles of carrier concentration in Si doped n-AlInAs layer, which was obtained by Hall measurements with periodically stripping, is shown in figure 2. The carrier concentration of the removed thin layer $N(x)$ was obtained from equation (1).

$$N(x) = \frac{(\Delta\sigma_s)^2}{e \Delta x \Delta R_s \sigma_s^2}, \quad (1)$$

where e , X , R_s , σ_s are charge of electron, thickness of the layers, sheet Hall coefficient and sheet conductivity, respectively. Δ means the difference of each value between before and after stripping. Carrier concentration decreases in the n-AlInAs layer, and the degree of the reduction is larger near the surface. It is considerable that the degradation is caused by the thermal diffusion of some impurities (impurity) from the surface of the n-AlInAs layer by annealing. Therefore, SIMS measurements were conducted for whole elements. It was found that fluorine was thermally diffused in the n-AlInAs layer by annealing in N₂. The SIMS profile of fluorine in n-AlInAs is also shown in figure 2. Figure 3 shows the relationship between carrier concentration reduction after annealing in N₂ and the fluorine concentration. There is a marked correlation between the carrier concentration and the fluorine concentration. The amount of carrier concentration reduction well coincides with the fluorine concentration. From these data, it is

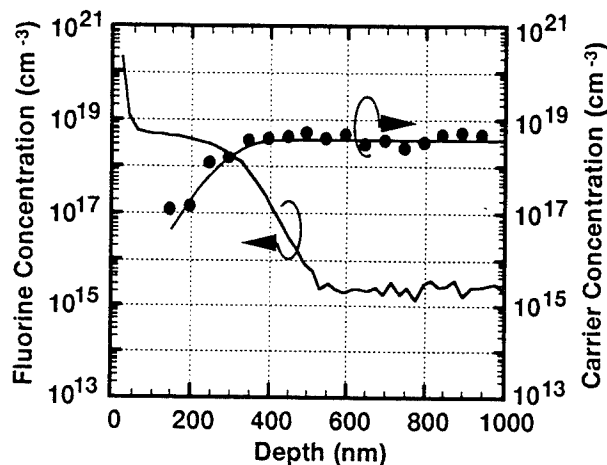


Figure 2 Depth profiles of carrier concentration and fluorine concentration in Si doped n-AlInAs layer annealed at 350°C for 15 min in N₂.

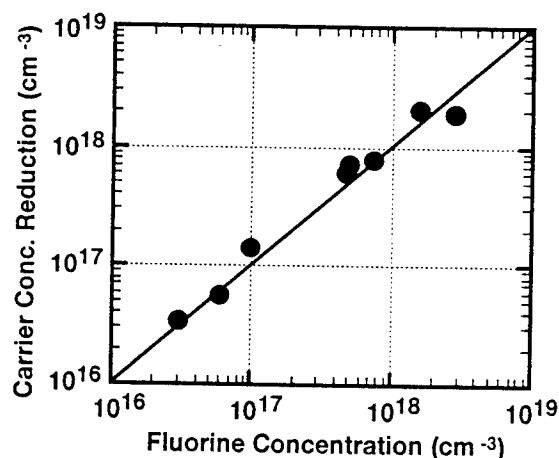


Figure 3 Relationship between carrier concentration reduction and fluorine concentration in n-AlInAs layer.

reasonably thought that fluorine thermally diffuses and inactivates the donors in the n-AlInAs layer.

Next, Hall and SIMS measurements were conducted for two different materials (Si doped n-AlGaAs, Si doped n-InGaAs) before and after annealing. The thermal degradation was not observed for those layers at all. SIMS measurements also show no fluorine detection. These results indicate that the degradation is just peculiar to the AlInAs material.

In order to investigate the influence of the dopant variation on degree of the deterioration, Hall measurements for Sn doped n-AlInAs layer, Be doped p-AlInAs layer and Si/Be co-doped n-AlInAs layer were carried out before and after annealing. Figure 4 shows

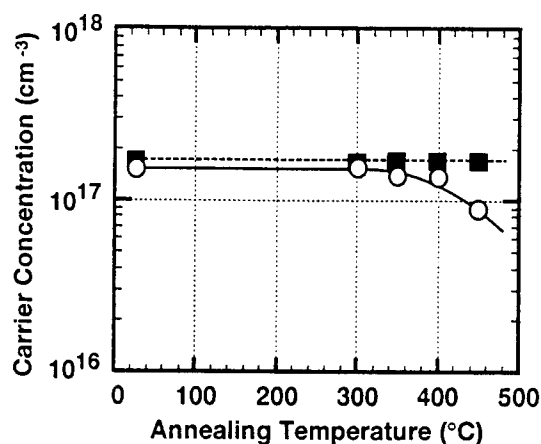


Figure 4 Carrier concentration versus annealing temperature for Si doped n-AlInAs (O) and Be doped p-AlInAs (■). Samples were annealed for 15 min in N₂.

the sheet carrier concentration versus the annealing temperature for Si doped n-AlInAs and Be doped p-AlInAs. Table 1 summarizes the sheet carrier concentration and the mobility of these AlInAs samples before and after annealing at 300K. The similar degradation as in Si doped n-AlInAs layer was found in the Sn doped n-AlInAs by annealing in N₂. Both of the sheet carrier concentration and the mobility decreased in whole n-AlInAs (Si, Sn and Si/Be co-doped) layers while not in the p-AlInAs layer.

Finally, SIMS measurements for all samples were conducted after annealing. The profiles of dopants and fluorine in the AlInAs layers were shown in figures 5(a), 5(b) and 5(c), respectively. These data indicate that fluorine diffuses only into n-AlInAs layers containing a donor impurity (impurities) independent of the dopant variations. In addition, fluorine is thought to become a donor killer only in n-AlInAs layer, that is, a scattering center.

Based on the results above-mentioned, it can be summarized that the electrical deterioration phenomenon occurs as follows: First, fluorine atoms thermally diffuse into the n-AlInAs layer, which is peculiar to the AlInAs material containing a donor impurity (impurities) such as Si and Sn. Then, fluorine

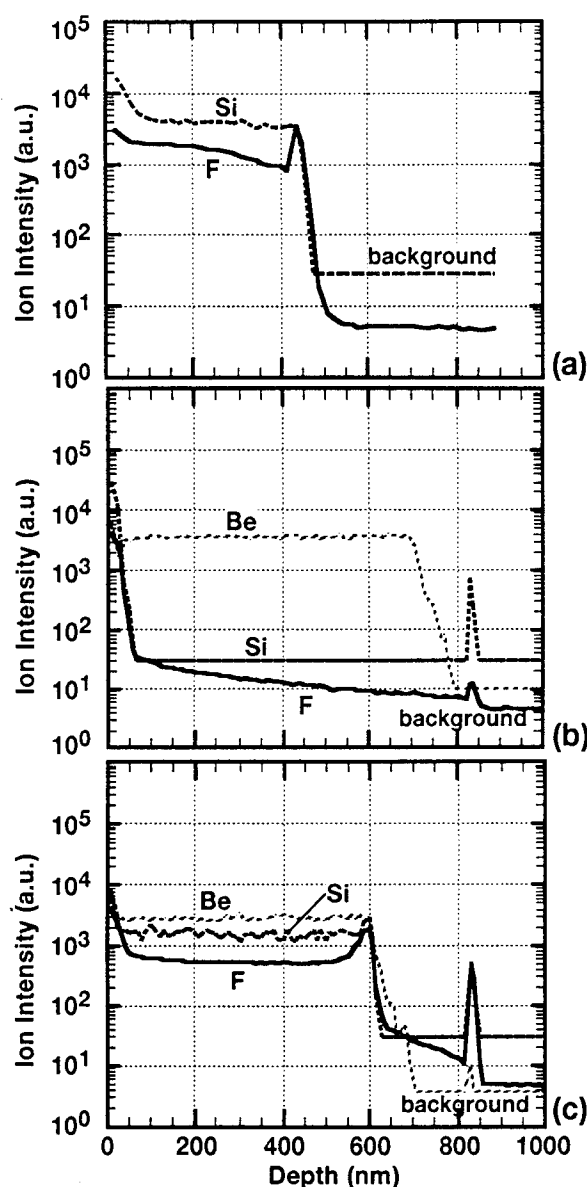


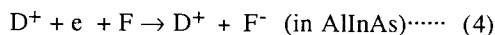
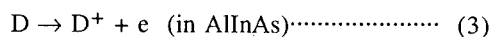
Figure 5 SIMS profiles of silicon, beryllium and fluorine in three different AlInAs layers on InP substrates after annealing at 450°C for 15 min. [(a) Si doped AlInAs layer, (b) Be doped p-AlInAs layer, (c) Si/Be co-doped n-AlInAs layer.]

Table 1 Summary of sheet carrier concentration and Hall mobility at 300K for several kinds of AlInAs layers before and after annealing at 450°C for 15min in N₂.

Material	Sheet carrier concentration (cm ⁻²)		Hall mobility at 300K (cm ² V ⁻¹ s ⁻¹)	
	Before annealing	After annealing	Before annealing	After annealing
n-AlInAs (Si doped)	1.4×10^{14}	3.7×10^{13}	540	509
n-AlInAs (Sn doped)	3.2×10^{13}	1.0×10^{13}	585	550
p-AlInAs (Be doped)	4.2×10^{13}	4.2×10^{13}	17	18
n-AlInAs (Si/Be co-doped)	1.2×10^{14}	1.1×10^{13}	610	447

inactivates the donors in n-AlInAs layers. This attack is not the donor neutralization [7] but the compensation of donors by fluorine atoms, which can be understood from the fact that Hall mobilities decrease by annealing.

Neither thermally diffused fluorine nor degradation of carrier concentration in p-AlInAs layers were observed at all. Those observations lead to a newly proposed thermal degradation mechanism as follows. As the electronegativity of fluorine atom is largest among whole elements, and the atomic radius of fluorine atom is considerably small to pass through the crystal, fluorine atoms are thought to diffuse into the n-AlInAs layer then react with the free electrons supplied from ionized donor (D^+), which results in the F^- scattering centers (F^- : ionized fluorine). The presumed reactions would be written by equation (2), (3), and (4) in order.



This presumed mechanism well explains the phenomenon that sheet carrier concentration and mobility decrease together by annealing. In other words, the degradation is thought to be caused by the donor passivation with fluorine.

Conclusion

Origin and mechanism of the thermal degradation of n-AlInAs layer have been discussed. It has been found that the degradation of the AlInAs/InGaAs HEMT structure is caused by the reduction of the carrier concentration in n-AlInAs layer by annealing. The thermal degradation is peculiar in n-AlInAs layers and is independent of donor dopant variations. It is ascertained that fluorine thermally diffuses and inactivates the donors in the n-AlInAs layer. Fluorine is presumably thought to become a donor killer (scattering center) only

in the n-AlInAs layer, that is, F^- by reacting with a free electron in it, which indicates the donor passivation phenomenon occurs with fluorine.

References

- [1] S. Fujita, T. Noda, A. Wagai, C. Nozaki, and Y. Ashizawa, "Novel HEMT structures using a strained InGaP shottky layer," Extended Abstract of the 5th International Conference on Indium Phosphide and Related Materials, **WC2** (1993) 497.
- [2] N. Hayafuji, Y. Yamamoto, N. Yoshida, T. Sonoda, S. Takamiya and S. Mitsui, "Thermal stability of AlInAs/GaInAs/InP heterostructures," Appl. Phys. Lett. **66** (1995) 863.
- [3] S. J. Pearton, J. M. Kuo, W. S. Hobson, J. Lopata, F. Ren, A. Katz, and M. Geva, "Dopant passivation in AlInAs and InGaP by atomic deuterium," Appl. Phys. Lett., **59** (1991) 2703.
- [4] S. J. Pearton, C. R. Abernathy and J. Lopata, "Thermal stability of dopant-hydrogen pairs in GaAs," Appl. Phys. Lett., **59** (1991) 3571.
- [5] N. Takahashi, H. Ohno, M. Shiota, M. Shimizu, I. Yamamura, Y. Sakamoto, T. Sugini, and J. Shirafuji, "Thermal stability of AlInAs/GaInAs/InP HEMTs," Extended Abstract of the 54th Autumn Meeting of the Japan Society of Applied Physics, **29a-ZP-10** 1242.
- [6] S. R. Blight, R.E. Nicholls, S. P. S. Sangha, P. B. Kirby, L. Teale, S. P. Hiscock, and C. P. Stewart, "Automated Hall profiling system for the characterization of semiconductors at room and liquid nitrogen temperatures," J. Phys. E: Sci. Instrum. **21** (1988) 470.
- [7] J. Chevallier, W. C. Dautremont-Smith, C. W. Tu, and S. J. Pearton, "Donor neutralization in GaAs(Si) by atomic hydrogen," Appl. Phys. Lett. **47** (1985) 108.

Electronic and structural properties of thin SrF_2 films on InP

S. Heun, M. Sugiyama, S. Maeyama, Y. Watanabe, and M. Oshima

NTT Interdisciplinary Research Laboratories, 3-9-11 Musashino-shi, Tokyo 180, Japan

In this paper we present the results of our experiments on the deposition of SrF_2 on InP. Four different substrates were used for these investigations: HF-etched and As-treated InP(100) and (111)B. On these surfaces 35-50Å SrF_2 was deposited at room temperature. We also studied the changes in the films due to annealing. To clarify the morphology of the films, transmission electron microscopy (TEM) and atomic force microscopy (AFM) were employed.

1 Introduction

The alkaline earth fluorides are very promising materials for growing insulating layers on semiconductors. Their crystalline structure (fluorite) is very similar to the diamond or zinc blende structure of commonly used semiconductors [1]. Also the lattice matching for appropriately chosen material combinations is very good, for example -1.2% in the case of SrF_2 on InP [2]. So epitaxial growth can be expected. In addition the alkaline earth fluorides are good insulators with a large band gap (10-12 eV) [3], and they are quite easy to deposit because they sublime as molecules [2]. It has been reported that SrF_2 grows with (111) facets if deposited at 380°C on InP(100) [4]. This is, because the SrF_2 (111) plane is the energetically favoured one [5], and a film with little surface roughness can be expected on a substrate with this orientation. Due to the low non-congruent evaporation temperature of InP [6] the available range of deposition temperatures is limited. Due to this fact and to avoid growth in facets on InP(100), we decided to grow the SrF_2 at RT.

2 Experimental procedure

The experiments were performed in an ultra-high vacuum (UHV) chamber located at the Photon Factory (PF), Tsukuba, Japan. The system consists of an analysis chamber and a chamber for molecular beam epitaxy (MBE) connected by a transfer chamber. Sample preparation and reflection high energy electron diffraction (RHEED) measurements were done in the MBE chamber. Arsenic and SrF_2 were deposited from K-cells. After deposition, synchrotron radiation photoelectron spectroscopy measurements were made at beam-line BL-1A in the PF. These experiments are described in another paper [7]. Samples were mirrorlike polished 350

μm thick n-type InP ($\pm 0.5^\circ$), which were S-doped ($1 \times 10^{19} \text{ cm}^{-3}$). The samples were mounted on a Mo sample holder. The sample preparation is described in detail in another paper [8].

The film thickness calibration was done in two different, independent ways. The attenuation of the XPS In 3d peak before and after deposition of SrF_2 was measured, and from these data the film thickness was calculated. Independent of this, the film thickness was measured with TEM (see fig. 1). Both calibrations agreed within 20%.

After sample preparation the samples were taken out of the UHV chamber and transferred in air for measurements with TEM and AFM.

3 Results and discussion

3.1 Transmission Electron Microscopy

Several cross sectional TEM pictures were taken for the (100) surface. These photographs clarify the crystallinity of thin SrF_2 films on HF-etched and As-treated InP(100). Two of them are shown in fig. 1. Although the amount of SrF_2 deposited on the two surfaces was the same (35Å), the film deposited on the As-treated surface seems to be thicker. The film thicknesses as determined by TEM were 30 to 40Å for SrF_2 on HF-etched InP(100) and 50 to 60Å for SrF_2 on As-treated InP(100). This can be explained by island formation of the film on the As-treated InP surface. If not all of the surface is covered by SrF_2 , the islands are higher than the nominal film thickness. Since TEM sees only a cross section, the film seems to be continuous in the photograph. In a very simple model, assuming rectangular islands, 35% of the surface must be uncovered to explain the observed island height. A more detailed photoelectron spectroscopy study reveals that the SrF_2 grows in Stranski-Krastanov mode. The thickness

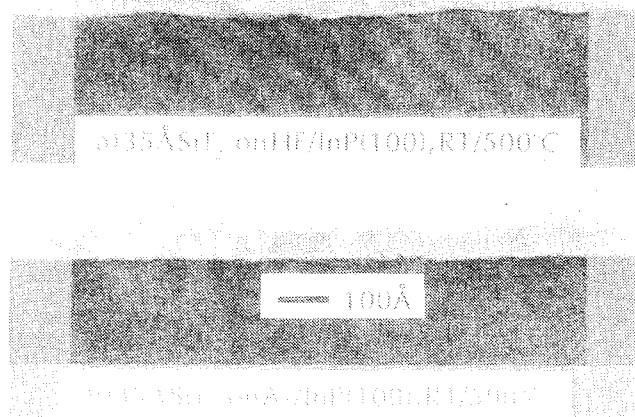


Figure 1: TEM photographs of 35Å SrF_2 , deposited at room temperature on HF-etched InP(100) (a) and on As-treated InP(100) (b). After the deposition and prior to the SEM measurement the samples were annealed at 500°C for 10 minutes.

of the continuous base layer was determined to be 2 monolayers [7].

The interface between SrF_2 and the HF-etched InP(100) surface is very rough, with an amplitude of several monolayers. This is consistent with the spotty RHEED pattern of the uncovered HF-etched InP(100) surface [8]. The lattice fringes of the SrF_2 can be clearly seen, but for most of the crystallites they are not parallel to the fringes of the substrate. So this film is polycrystalline and not epitaxial.

Also the film deposited on the As-treated surface shows a clear lattice image. But the lattice fringes of most of the islands are parallel to the substrate, so the (100) planes of these islands are parallel to the (100) planes of the underlying substrate. No conclusion about the in-plane orientation of these islands can be drawn from the TEM pictures, so the film could be epitaxial or textured. But this question is answered by the RHEED measurements. Since a 1×1 pattern is obtained for this surface, without any indication on a texture, the film is epitaxial [9]. The average size of islands as measured with TEM is 100Å. The tops of the islands are rather flat. The interface between the SrF_2 film and the As-treated InP(100) surface is much flatter than the one between SrF_2 and HF-etched InP(100). This agrees well with the RHEED pattern measured on the un-

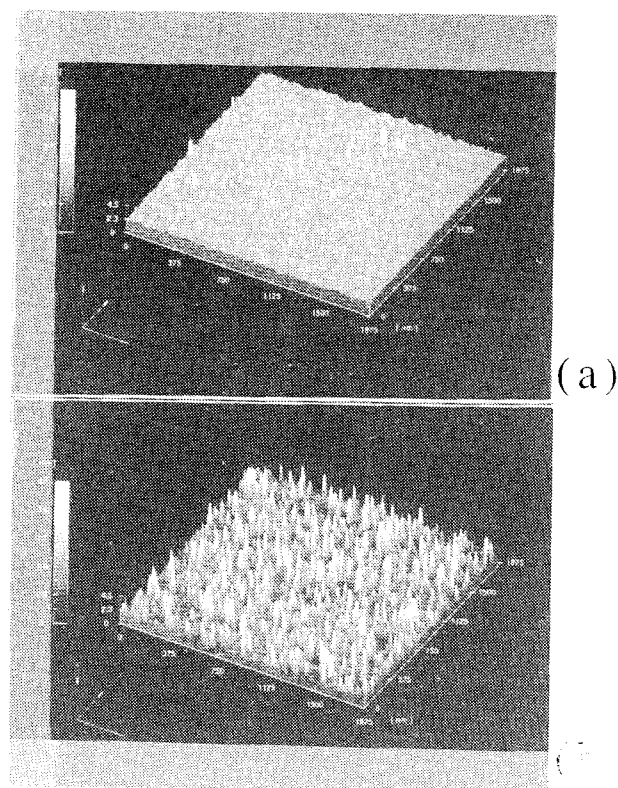


Figure 2: AFM pictures, obtained from two samples: (a) 50Å SrF_2 on HF-etched InP(100), annealed at 500°C, (b) 50Å SrF_2 on As-treated InP(100), annealed at 500°C. For better comparison, both pictures have the same scales in the x, y, and z directions. The surface roughness Δ of (a) is 1.8Å, whereas it is 4.5Å for sample (b).

covered As-treated InP(100) surface [9]. But according to the TEM picture the interface roughness is still several angstroms. Due to the limited resolution of the TEM and due to the roughness of the interface an InAs intra-layer could not be detected.

3.2 Atomic Force Microscopy

All the analytical tools utilizing electrons as a probe have the general disadvantage of strong interaction between the alkaline earth fluoride film and the electrons themselves, which can result in degradation of the film [2]. This is not the case with atomic force microscopy. So we can expect valuable additional information about the surface morphology of the films under study. AFM is also able to measure the quantitative value of the surface rough-

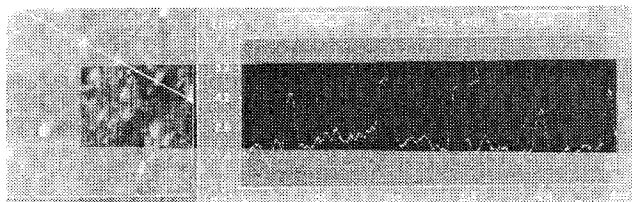
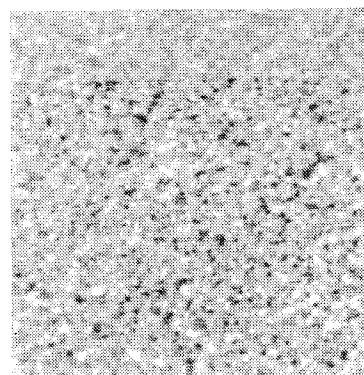


Figure 3: The left photograph shows an AFM picture of 50Å SrF₂, deposited at room temperature on As-treated InP(100) and then annealed at 500°C for 10 minutes. The size is 500nm × 500nm, and the grey scale corresponds to a height difference of 10nm. Along the white line five islands are arranged. The right graph shows the height profile along these islands.

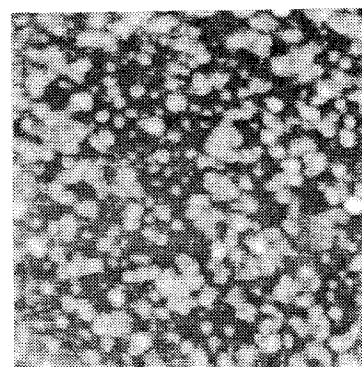
ness Δ , defined as $\Delta^2 = \langle h^2 \rangle - \langle h \rangle^2$ [10], where $\langle \rangle$ denotes an average and h is the height coordinate of each measured point.

AFM measurements were performed on 50Å SrF₂, deposited at room temperature on As-treated as well as on HF-etched InP(100). After deposition and prior to the measurement the films were annealed at 500°C for 10 minutes. In a similar procedure 35Å thick SrF₂ films were prepared on As-treated and HF-etched InP(111). The homogeneity of the films was checked by several measurements at different places on the samples, which always yielded very similar results.

On HF-etched InP(100) the SrF₂ grows as a flat continuous film with small surface roughness. This roughness was measured to be 1.8 ± 0.2 Å. The film consisted of small crystallites with an average diameter of 200Å. The corresponding AFM pictures are shown in fig. 2. In this figure we also show an AFM picture of 50Å SrF₂ on As-treated InP(100). AFM cannot clarify whether the film is continuous or discontinuous, because a tip with a 20nm radius cannot penetrate into voids with a diameter of 20nm. However, on As-treated InP(100) the SrF₂ is found to be in islands with a typical diameter of 250Å. The tops of these islands are quite flat. The surface roughness is 4.5 ± 0.4 Å, which is higher than the roughness of the comparable film on HF-etched InP(100). The picture shown in fig. 3 gives strong evidence for the high mobility of SrF₂ on the As-treated InP surface. It shows five islands arranged in a row, probably



a) 35Å SrF₂ on HF/InP(111), RT/500°C



b) 35Å SrF₂ on As/InP(111), RT/500°C

Figure 4: AFM pictures of 35Å SrF₂, deposited at room temperature on (a) HF-etched and (b) As-treated InP(111). After deposition these films were annealed at 500°C for 10 minutes. Both pictures show an area of 1000nm × 1000nm. The grey scale corresponds to a height difference of 4.2nm for (a) and 14.5nm for (b).

nucleated along a step of the substrate. It is well known that steps are preferred nucleation sites [11], but preferred nucleation of islands along such a step requires the deposited species to have high mobility.

The surface morphology of 35Å SrF₂ on HF-etched InP(111) is shown in fig. 4(a). The film is continuous with a small surface roughness of 2.2 ± 0.2 Å and is composed of small crystallites with a typical diameter of 250Å. Comparing the measurements for SrF₂ on HF-etched InP with different substrate orientations leads to the conclusion that the surface morphologies for the (100) and (111) orientations, as measured with AFM, are very simi-

lar. However, RHEED measurements reveal that the film deposited on HF-etched InP(111) is not polycrystalline but ordered. A detailed study shows that the film crystallites are ordered in a texture [9].

The situation is slightly different for the As-treated InP substrate. Figure 4(b) shows a picture of a 35Å thick SrF₂ film deposited on As-treated InP(111). The film is clearly rough. It consists of separated islands with a typical diameter of 350Å. The surface roughness is $11.7 \pm 1.0\text{\AA}$. Compared to the film deposited on the As-treated InP(100) surface, the main observation, i. e. an island type film, is the same, but the island sizes and the surface roughness are slightly higher on the (111) substrate. Detailed photoelectron spectroscopy measurements clarify the morphology of the film further on. It is shown that the film grows, as on the As-treated InP(100) substrate, in Stranski-Krastanov mode. However, the thickness of the base layer is much larger than on As/InP(100). For As/InP(111) it exceeds 20Å.

4 Conclusions

After deposition of 50Å SrF₂ on HF-etched InP(100) at room temperature a continuous and flat film is obtained. This does not change after annealing at 500°C for 10 minutes. The film is polycrystalline and composed of small, rectangular shaped crystallites with a typical size of 200Å. Its surface roughness is only 1.8Å.

After deposition of 35Å SrF₂ on HF-etched InP(111) a continuous and flat film is also obtained. The SrF₂ grows in layer-by-layer mode. The film remains continuous and flat after annealing at 500°C for 10 minutes. For this film a texture is found. The crystallites have a typical size of 250Å, and the surface roughness is as low as 2.2Å.

On As-treated InP(100) the SrF₂ grows in Stranski-Krastanov mode. After a base layer of 2 monolayers thickness is grown, the film continues to grow in islands. After deposition of 50Å SrF₂ at room temperature and after annealing this film at 500°C for 10 minutes, 35% of the substrate is uncovered by islands. The islands are epitaxial to the substrate. The tops of these islands are flat, but the voids between these islands result in an overall surface roughness of 4.5Å.

In contrast to this, on the As-treated InP(111) substrate SrF₂ grows at room temperature in layer-by-layer mode for the first 20Å. Then islands also begin to form in the film. After annealing at 500°C for 10 minutes the film is epitaxial without any twinning. The islands have flat tops and their typical size is 350Å. The surface roughness of this film is 11.7Å.

References

- [1] A. S. Barriere, A. Elfajri, H. Guegan, B. Mombelli, and S. Raoux: *J. Appl. Phys.* 71 (1992) 709.
- [2] J. M. Phillips, L. C. Feldman, J. M. Gibson, and M. L. Mc Donald: *Thin Solid Films* 107 (1983) 217.
- [3] T. K. Paul and D. N. Bose: *J. Appl. Phys.* 67 (1990) 3744.
- [4] W. Weiss, K. Kasper, K. H. Herrmann, D. Schmeisser, and W. Göpel: *Surf. Sci.* 268 (1992) 319.
- [5] A. Munoz-Yague and C. Fontaine: *SPIE Vol. 944 Growth of Compound Semiconductor Structures* (1988).
- [6] G. J. Davies, R. Heckingbottom, H. Ohno, C. E. C. Wood, and A. R. Calawa: *Appl. Phys. Lett.* 37 (1980) 290.
- [7] S. Heun, M. Sugiyama, S. Maeyama, Y. Watanabe, and M. Oshima: submitted to *Phys. Rev. B*.
- [8] S. Heun, M. Sugiyama, S. Maeyama, Y. Watanabe, and M. Oshima: *Appl. Surf. Sci.* 82/83 (1994) 507.
- [9] S. Heun, M. Sugiyama, S. Maeyama, Y. Watanabe, and M. Oshima: *J. Cryst. Growth*, in press.
- [10] J. Wollschläger, J. Falta, and M. Henzler: *Appl. Phys. A* 50 (1990) 57.
- [11] J. Wollschläger and N. M. Amer: *Surf. Sci.* 277 (1992) 1.

Studies on the influence of Peltier effect and electromigration during LPEE growth of binary and ternary semiconductors

R.S.Qhalid Fareed and R.Dhanasekaran

Crystal Growth Centre, Anna University, Madras - 600 025.

Liquid phase electroepitaxy (LPEE) is one of the novel and recent technique for the growth of compositionally uniform, low dislocation density epitaxial layers of III-V compound semiconductors. In this technique, growth is carried out and sustained by passing an electric current through substrate-solution interface while the temperature of the whole system is kept constant.

In the present communication, a model has been developed to understand the growth kinetics of binary and ternary compound semiconductors during LPEE growth. The two major factors influencing the growth in this technique are Peltier effect and electromigration. In the present model, a transport equation has been solved numerically by incorporating the Peltier effect and electromigration conditions/1,2/. The effect of electromigration due to application of electric field has been incorporated in the diffusion equation as shown in equation 1. Applying the boundary conditions, the new equation has been solved numerically as shown in eqn. 2.

Computer simulation technique has been employed to construct the concentration profiles of the solute atoms in the In rich melt during binary and ternary compound semiconductors of InP and related compounds. In the present communication, the model has been employed to understand the growth kinetics of InP and InAsP semiconductors.

Concentration of Profiles of P in In rich melt during InP growth and As and P in In rich melt during InAsP growth have been constructed under various growth conditions. The influence of Peltier cooling/heating at the interface and electromigration have been incorporated in constructing the concentration profiles. Profiles have been simulated for different change in interface temperature ΔT_p , growth time, different applied electric field ...etc. It is observed that concentration of the solute atoms decreases near the interface as the growth proceeds during Peltier cooling and vice versa (Fig. 1 & 2).

Growth/dissolution rates have been calculated in the absence and the presence of convection. Growth/dissolution rates during Peltier cooling/heating and electromigration have been investigated. In the presence of convection, the effect of thickness of the solute boundary layers has been investigated. Thickness of the epilayers in the absence and presence of the convection has also been calculated. The results are discussed in detail.

1. R.S.Qhalid Fareed, R.Dhanasekaran and P.Ramasamy, J.Appl. Phys. 75 (1994) 3953
2. R.S.Qhalid Fareed, R.Dhanasekaran and P.Ramasamy, J. Cryst. Growth, 140 (1994) 28

The transport diffusion equation

$$D \frac{\partial^2 C}{\partial x^2} - v \frac{\partial C}{\partial x} \pm \mu E \frac{\partial C}{\partial x} = \frac{\partial C}{\partial t} \quad (1)$$

Numerical solution of equation (1)

$$C_{j,n+1} = C_{j,n} + \frac{D\tau}{\epsilon^2} (C_{j-1,n} - 2C_{j,n} + C_{j+1,n}) \pm \frac{\mu E \tau}{2\epsilon} (C_{j+1,n} - C_{j-1,n}) \quad (2)$$

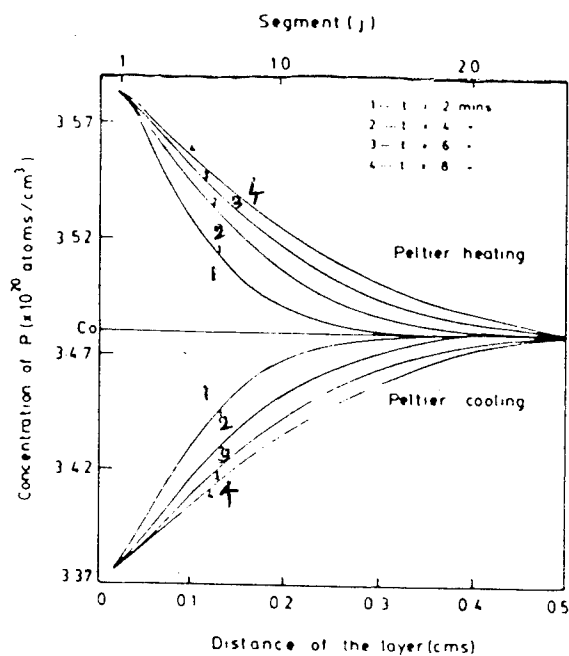


Fig 1

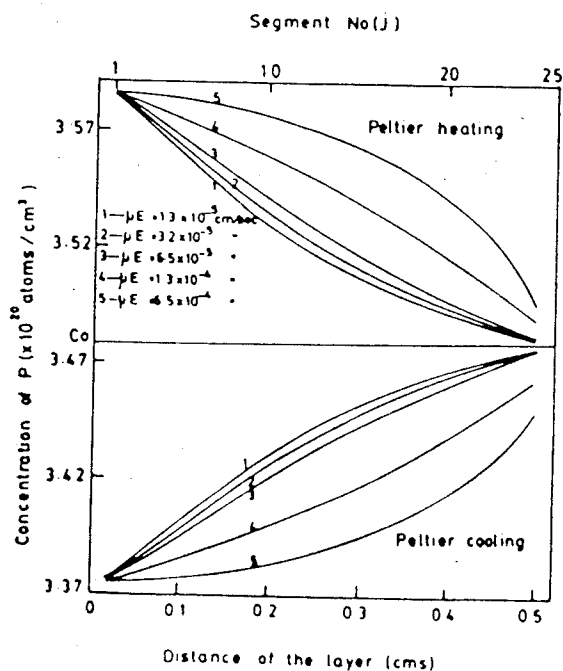


Fig 2

Selective MOCVD Growth of InP around Dry-Etched Mesas with Various Patterns for Photonic Integrated Circuits

K. Goto, M. Takemi, T. Miura, A. Takemoto, Y. Mhashi and S. Takamiya

Optoelectronic & Microwave Devices Laboratory, Mitsubishi Electric Corp.,
4-1 Mizuhara, Itami, Hyogo 664, Japan

Introduction

Selective growth of InP by MOCVD around mesas is an indispensable technique for fabricating photonic integrated circuits (PICs), which include many kinds of waveguide patterns, such as stripes along various crystallographic directions, X-crossings, and Y-shaped bifurcations. Especially, selective growth around *dry*-etched mesa patterns is important for fabricating PICs with highly-reliable buried-heterostructure lasers and waveguides, since dry etching realizes the accurate pattern-transfer as well as the nearly-vertical wall profiles, being independent of crystallographic orientation. Thus, several studies have been published regarding the MOCVD growth of InP around dry-etched mesas(1). All of them are, however, regarding the mesa stripes along [011] or [01 $\bar{1}$] only. MOCVD of InP around the mesa stripes along various crystallographic directions has been investigated only for *wet*-etched mesas which have anisotropic shapes depending on the stripe direction(2). Furthermore, there are only few reports discussing on the embedding growth of various waveguide components for PICs.

In this paper we have investigated the selective growth of a *pn*p-InP layer structure as well as the mass-transport effect around dry-etched mesas with various crystallographic directions of stripes. The behaviors were found to depend remarkably on the stripe direction. The selective embedding growth around waveguide patterns, such as bifurcations or crossings, is also investigated.

1. Experimental procedure

Mesa patterns were formed by the C_2H_6/H_2 reactive ion etching (RIE) process(3) with SiO_2 used as masks on S-doped (100)-oriented InP wafers. The masking patterns contained various components, such as a radial pattern with stripes extending in every 22.5° directions, curved Y bifurcations with a bifurcation angle of 10° , and X-crossings with various crossing angles. A cross section of an etched InP mesa is shown in Fig. 1. The shapes of the mesas were independent of the crystallographic orientation

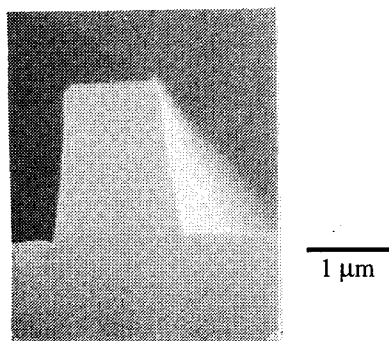


Fig.1. A cross-sectional SEM image of a dry-etched mesa shape.

of the stripes. The mesa width and height were about $1.3\ \mu m$ and $1.8\ \mu m$, respectively. The side walls of the dry-etched mesas were slightly sloping outwards with an angle of about 98° between the substrate plane and the mesa wall.

Growth of InP was performed in a low-pressure (50 Torr) MOCVD reactor with a high-speed rotating susceptor at a rotation speed of 1000 rpm. Growth precursors were trimethyl-indium (TMI) and phosphine (PH_3). H_2S and diethylzinc (DEZ) were used for *n*-type and *p*-type doping, respectively. The PH_3 /TMI ratio (V/III ratio) was about 100, and the growth rate was $1.8\ \mu m/h$ on the (100) flat plane. The substrate was held at $650^\circ C$ in a PH_3/H_2 atmosphere for about 10 min to remove the native oxide on the surface. Then, *p*-InP ($0.2\ \mu m$ -thick), *n*-InP ($0.6\ \mu m$ -thick), and *p*-InP ($0.8\ \mu m$ -thick) were successively grown on the patterned substrates at $625^\circ C$. The carrier concentrations of the *n*- and *p*-InP layer were $7 \times 10^{18}\ cm^{-3}$ and $8 \times 10^{17}\ cm^{-3}$, respectively. The *pn*p layers were designed as the current-blocking layers for the buried-heterostructure lasers on the *p*-InP substrate with the intention of integrating. After the growth, the samples were cleaved in the (011) or (01 $\bar{1}$) plane, and then stain-etched for the SEM observation.

2. Results and discussion

2.1. Dependence of mass-transport and growth behavior on the mesa-stripe direction

Figs. 2 (a)-(e) show the SEM micrographs of the samples having the mesa-stripe patterns along various directions. Here, we denote the direction of the mesa-stripe by the angle from the $[011]$ direction. Thus, 0° , 45° , and 90° correspond to the $[011]$, $[010]$, and $[01\bar{1}]$ direction, respectively. As can be seen in Figs. 2 (a)-(e), the shapes of the dry-etched mesas have been transformed by mass transport before the growth. The way of the transformation as well as the behavior of the embedding growth depends on the mesa-stripe direction.

For the 0° direction, only a slight rounding of the mesa wall was observed near the mesa base, as can be seen in Fig. 2 (a). It can be seen that the growth of the p -InP layer proceeded almost isotropically, being independent of the surface orientation, on variously oriented surfaces, namely, the (100) plane, the nearly-vertical mesa side wall, and other sloped high-index planes. On the other hand, the growth of the n -InP layer proceeded preferentially on the substrate (100) plane and on the sloped high-index planes (indicated by A in the figure) near the mesa base, while it was suppressed on the mesa side wall. As the result, the growth of the n -InP layer planarized the growth surface; growth creeping up the wall, which causes "rabbit ear" growth, was not observed near the mesa edges. This result can be attributed to the low growth rate on the side wall.

For the 22.5° direction, mass transport was observed remarkably, as can be seen in Fig. 2 (b). It seems that the mesa side walls were changed into sloped surfaces due to the mass transport, and then, the growth proceeded on those sloped surfaces. The difference of growth between the p - and n -InP layer was observed also for this direction: The growth of the p -InP layer was isotropic, while the growth rate of the n -InP layer was high on the gently sloped high-index planes (indicated by B) near the mesa base, and was low on the nearly-vertical planes (indicated by C) just below the mesa top. As the result, the surface was planarized by the growth of the n -InP layer, also in this case.

For the 45° direction, mass transport formed flat sloped surfaces on the both sides of the mesa, as can be seen in Fig. 2(c). The growth behavior was rather similar

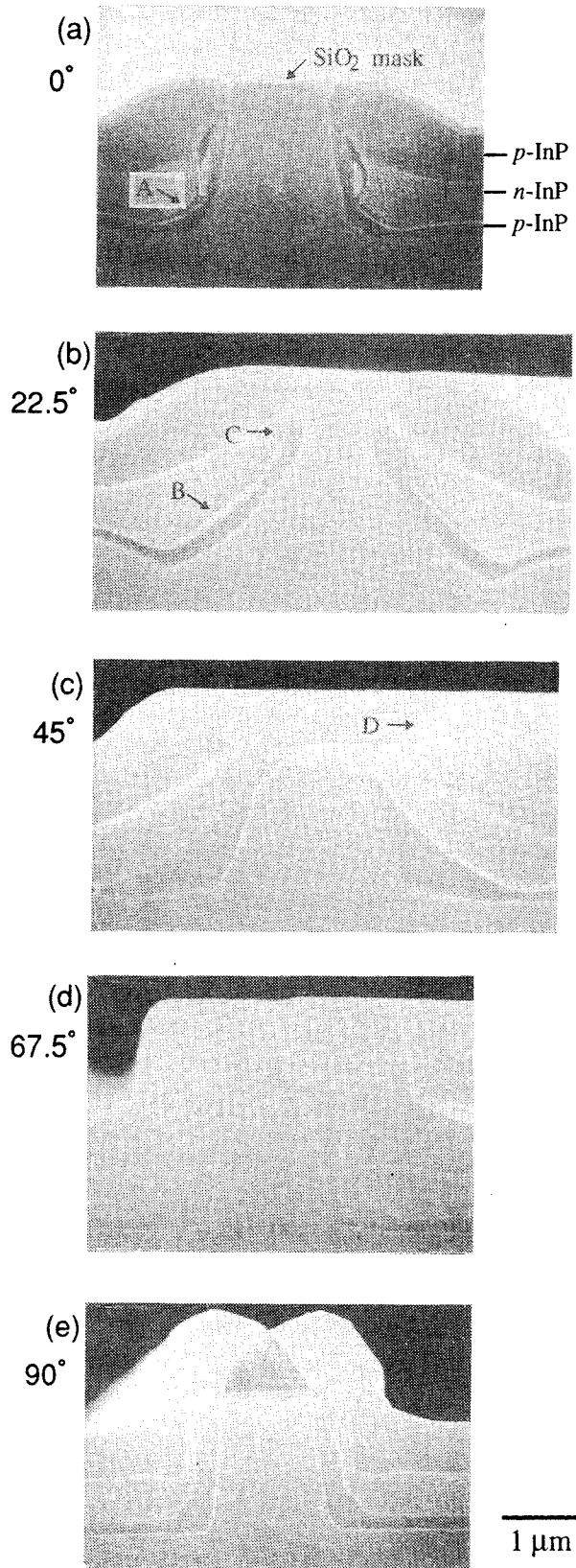


Fig.2. Cross-sectional SEM micrographs of selective growth for the pnp structure around mesas capped with SiO_2 stripe masks which are oriented in different crystallographic directions: (a) 0° ($[011]$ direction); (b) 22.5° ; (c) 45° ($[010]$ direction); (d) 67.5° ; (e) 90° ($[01\bar{1}]$ direction).

to that for the 22.5° direction mesa, but was slightly different in some points. The growth rate of the first p -InP was high at the corner of the mesa base to form sloped planes. Non-growing $\{110\}$ planes were formed from the mesa-top edges to suppress the overgrowth covering the mesa, as indicated by D in the figure.

As the mesa direction approaches the $[01\bar{1}]$ orientation, the extent of the transformation of the mesa shape due to the mass transport was observed to decrease. For the 67.5° and 90° directions, the growth of the n -InP layer as well as the p -InP layer proceeded isotropically, conserving the mesa shape, as can be seen in Figs. 2(d) and 2(e). The growth rate on the mesa side walls was found to be relatively high, and the growth seemed to creep up the wall above the mesa height to cause overhangs that cover the SiO_2 mask.

The observed growth behaviors can be summarized as follows. For the mesa-stripes directed near $[011]$, the growth proceeds preferentially on the sloped high-index planes, while the growth rate on the nearly vertical planes is low. On the other hand, for the mesa-stripe directions near $[01\bar{1}]$, the growth rate on the nearly vertical planes is relatively high to creep up the mesa wall, conserving mesa shapes, while sloped high-index planes is reluctant to be formed.

The most notable mass transport to change the mesa walls into the sloped planes is observed for the stripe direction misoriented from the $[011]$ direction by around 30° . Mass transport is a vapor phase process in which evaporated materials are incorporated again into the solid(4). The observed anisotropy in the observed mass transport is considered to be due to variation in incorporation rates of transported materials into different crystallographic planes. Then, the anisotropic behavior of mass transport as well as that of MOCVD growth can be treated on the same basis.

Anisotropic lateral growth on mesa side walls has been discussed in refs. (1) and (5). It is assumed that the growth rate of InP is proportional to the incorporation rate of In atoms at the step edges on the growing surface. According to the discussion in ref.(5), In atoms are more easily incorporated into the $[011]$ steps than into the $[01\bar{1}]$ steps, because an In atom at the $[01\bar{1}]$ step is bound with two bonds, while an In atom attached at the $[011]$ step is bound with three bonds.

In the case of the mesa at the 0° direction (along $[011]$), the sloped planes formed on the mesa walls comprise the $[01\bar{1}]$ steps, so that the incorporation probability is low.

When the mesa stripe is misoriented from the $[111]$ direction, the sloped walls of the mesa consist of a large number of kink sites. According to ref.(5), the probability

of In incorporation increases with the degree of misorientation, because a kink site has three bonds for binding an In atom. According to the discussion in ref.(1), the preferential growth direction on the sloped walls is perpendicular to the stripe direction for the mesas oriented near the $[011]$ direction. Therefore, the gradient of the sloped walls becomes more gentle as the result of the mass transport as well as the growth.

On the other hand, in the case of the mesa directions near the $[01\bar{1}]$, the preferential direction of the growth on the sloped wall is considered to be the $[100]$ direction (upward in the figures) rather than the direction perpendicular to the stripe direction(1). Therefore, sloped high-index planes is reluctant to be formed in this case.

2.2. Embedding growth around various waveguide patterns for photonic integration

Figure 3 shows the cross-sectional and bird's-eye view of an embedded-grown Y-bifurcation along the $[011]$ direction. A smooth surface was obtained except at the groin of the bifurcation. The X-crossing (at the angle of 30°) mesa waveguide pattern is shown in Fig. 4, (a) as dry etched, and (b) after embedded. A smooth surface without any growth overhanging the mask was obtained also in this pattern. The growths rising above the mesa height were observed only on the $[011]$ sides of the cross point (indicated by arrows in the figure). The dry-etched bifurcation or crossing patterns have a rounded part of the side wall as shown in Fig. 5 (a) at the groin where two stripes meet at a small angle. The rounding is due to the limited resolution of the patterning of the mask, and not due to the dry etching process. The rounded part of the mesa wall on the $[011]$ side contains the planes near (011) . On the (011) plane, the growth creeping up the wall occurs to rise above the mesa height. The rising growth is expected to be suppressed by some extent by improving the resolution of the mask patterning.

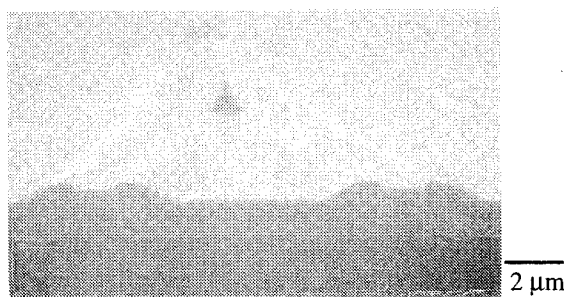


Fig. 3. An SEM micrograph of buried growth around a Y-bifurcation pattern along the $[011]$ direction.

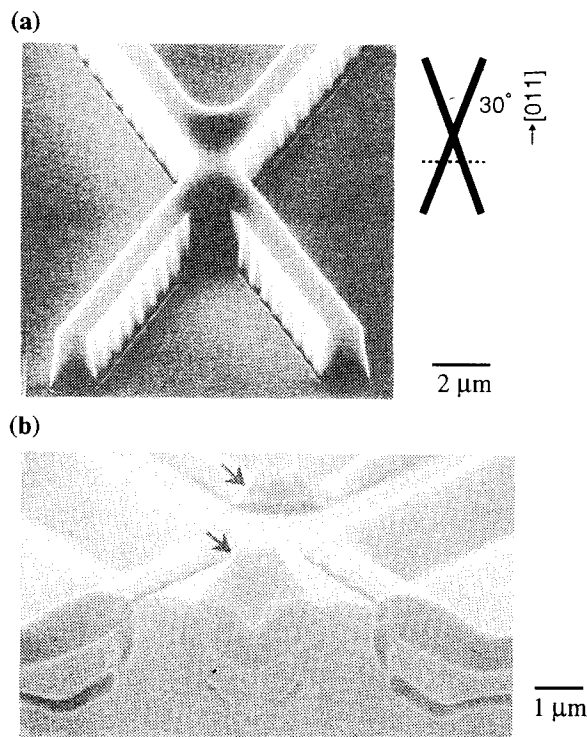


Fig.4. SEM micrographs of an X-crossing (at an angle of 30°) pattern along the [011] direction: (a) as dry-etched; (b) after embedded.

3. Conclusion

We have investigated the behavior of mass-transport, as well as that of MOCVD-growth, around dry etched mesa-stripe patterns along various crystallographic orientations. Those behaviors were found to depend remarkably on the crystallographic orientation of the mesa stripe. The most notable mass transport was observed for the stripe misoriented about 30° from the [011] direction. The growth was observed to proceed preferentially on the sloped high-index planes, planarizing the crystal surface, for the mesa stripes directed near [011]. For the stripe directions near $[0\bar{1}1]$, the growth was observed to creep up the wall, while conserving a mesa shape. Selective growth with sufficient planarity has been obtained for the mesa-waveguide components along the stripe directions near [011]. This planar selective embedding growth for dry-etched mesas is applicable to PICs, and will become an important technique for the fabrication of future PICs.

References

- (1) e.g. N. Nordell, J. Borglind and G. Landgren, "Influence

of MOCVD growth conditions and CCl_4 addition on InP crystal shapes", *J. Crystal Growth*, Vol. 125, 1992, pp. 597-611.

- (2) C. Blaauw, A. Szaplanczay, K. Fox and B. Emmerstorfer, "MOCVD of InP and mass transport on structured InP substrates" *J. Crystal Growth*, Vol. 77, 1986, pp.326-333.
- (3) H. Sugimoto, K. Ohtsuka, T. Isu, H. Tada, T. Miura, T. Shiba, "Reactive ion etching of InP using $\text{C}_2\text{H}_6/\text{H}_2/\text{O}_2$ ", *J. Appl. Phys.*, Vol.72, 1992, pp.3125-3128.
- (4) T. R. Chen, L. C. Chen, A. Hasson, K. L. Yu, U. Koren, S. Margalit, and A. Yariv, "Study and application of the mass transport phenomenon in InP", *J. Appl. Phys.*, Vol. 54, 1983, pp. 2407-2412.
- (5) H. Asai, "Anisotropic lateral growth in GaAs MOCVD layers on (001) substrates", *J. Crystal Growth*, Vol. 80, 1987, pp. 425-433.

D. Bertone, G. Fornuto

CSELT - Centro Studi e Laboratori Telecomunicazioni
via G. Reiss Romoli 274, 10148 TORINO - ITALY

Introduction

Buried heterostructure (BH) devices need the regrowth of InP around mesa stripes containing the active region. A crucial point in embedding the heterostructure laser mesas is the edge overgrowth effect, especially when the stripe height is required to be very high (1). Furthermore, dielectric mask may be present on the semiconductor surface to define the deposition area: e.g. the selective growth of semi-insulating InP around laser mesas for high speed operation devices. After regrowth it is very useful to have a surface as planar as possible for subsequent technological steps and to make good electric contacts. In this work we investigate on the regrowth of InP around mushroom-like cross section stripes, conventional stripes masked with SiN_x and tall mesa stripes with dielectric mask on the top by Pulsed Metalorganic Epitaxy (PME).

Features of the Pulsed Metalorganic Epitaxy (PME)

Pulsed Metalorganic Epitaxy (PME) has been proven to be very effective in the regrowth of InP on mesa stripes having conventional, nearly rectangular shape (2).

The basis of this growth technique is depicted in Fig.1.

PME of InP is different from conventional MOCVD in the introduction of the Trimethylindium (TMIn) flow in the reactor. In the leading case, the Trimethylindium is pulsed into the reactor while maintaining a constant Phosphine (PH_3) flow during the deposition time.

In order to obtain doped material, it is necessary to introduce in the reactor the TMIn and the dopant precursor together. In this way, the growth time became a set of cycles in which the TMIn+dopant are periodically addressed to the vent line and to the reactor line (run line). The actual growth time and by consequence the deposition thickness must be evaluated considering the total time in which the metalorganic precursors have been addressed to the reactor.

If no special growth parameters are required, the reactor pressure, the deposition temperature and the reactants concentration may be the same as in conventional MOCVD; in this way it is possible and very easy to switch from MOCVD to PME and vice-versa, any time only by changing the introduction regime of the metalorganics into the reactor.

Experimental

Stripes formation Mesa stripes were etched in different structures containing the active layer previously deposited by MOCVD or simply on a InP substrate. A Silicon Nitride (SiN_x) film was used as mask for Reactive Ion Etching (RIE) in defining the stripes and for the next selective InP regrowth.

A further selective wet etch was used to obtain the Buried Mushroom Structure (BMS) shown in Fig.2.

In this case the device structure containing the GaInAsP active layer $0.2 \mu\text{m}$ thick and the InP:Zn doped $0.3 \mu\text{m}$ thick was firstly etched by RIE using a SiN_x mask to define the mesa stripe. Secondly, after the SiN_x removal, a selective chemical etch ($\text{H}_3\text{PO}_4\text{-H}_2\text{O}_2$) was used to underetch the active layer, using the upper InP layer as a mask.

Growth conditions A home-made LP-MOCVD system equipped with a patented very fast switch operation manifold was used to perform the deposition runs.

Regrowth experiments were carried out at a temperature ranging from 600°C to 640°C , with a working pressure ranging from 50 mbar to 150 mbar.

Trimethylindium, 100% phosphine, diethylzinc, 100 ppm Si_2H_6 and ferrocene were used for the regrowth of p-type, n-type and semi-insulating InP respectively, using purified

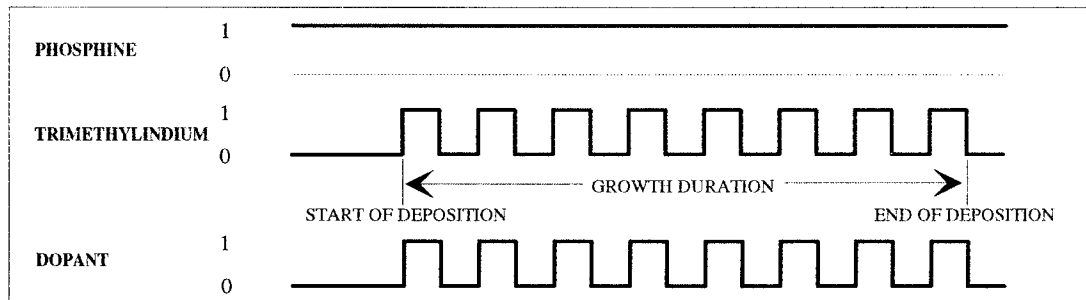


Fig.1- Gas flow pulse mode profiles adopted in this work

argon as carrier gas. As far as concern the growth under PME regime, before starting the deposition, it is necessary not only to fix the number of cycles we intend to use but also to design the shape of the diagram in Fig.1 This means to decide the ratio between the time in which the metalorganics have to be addressed to the reactor (run time) and to the exhaust line (vent time).

Results and discussion

From the regrowth results obtained by PME over different mesa geometries, we can summarise the influence of the growth parameters as follows:

Growth temperature The surface mobility and/or the desorption of metalorganics are strongly influenced by the temperature. This effect, also present in conventional MOCVD, is more evident in pulsed regime deposition. Higher temperature means higher mobility of the chemical species on the surface leading to high selectivity of the regrowth with respect to the dielectric mask if present and make easier to fill narrow and deep channels but making also possible formation of bumps at the edges.

Reactor pressure At lower pressure, higher selectivity of the deposit is observed but the variation over the whole range of pressure (50 mbar to 150 mbar) is not useful so, for practical reasons, we choose to maintain the reactor pressure fixed at 100 mbar.

Metalorganic pulse time This important parameter strongly influences the final shape of the regrowth. At higher run/vent ratio that means 15s of TMIn injection followed by 5s without TMIn in the reactor, the growth is slightly selective. On the contrary, with 5s/15s run/vent ratio, strong and sometimes unwanted selectivity effects are observed. With a run/vent ratio=1 obtained by run time = vent time = 15s, good results were obtained. The absolute value of the run and the vent times are also important. In fact, experiments with a run/vent =1, but run time = 7s = vent time leads to results showing slightly selectivity.

Phosphine flow rate The effect of the phosphine over the regrowth behaviour is the less clear because of its multiple roles during the deposition. A minimum quantity for the protection of the surface may be ensured; over that, at present, is not clear what is the best flow rate because, phosphine itself acts as transporting agent for indium on the growing surface. At lower phosphine concentration, an increase in selectivity was observed with a wide range of final behaviour depending on the quality of the starting surface. In our regrowth experiments we fixed the phosphine flow rate at $4.5 \cdot 10^{-3}$ mol/min.

Metalorganic flow rate For practical reasons, we maintain the flow rate of the trimethylindium at $1.7 \cdot 10^{-5}$ mol/min that is the same value as for conventional MOCVD.

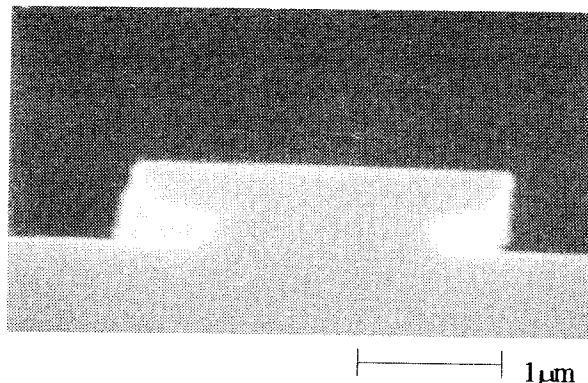


Fig.2- Cross section of a mushroom-like stripe

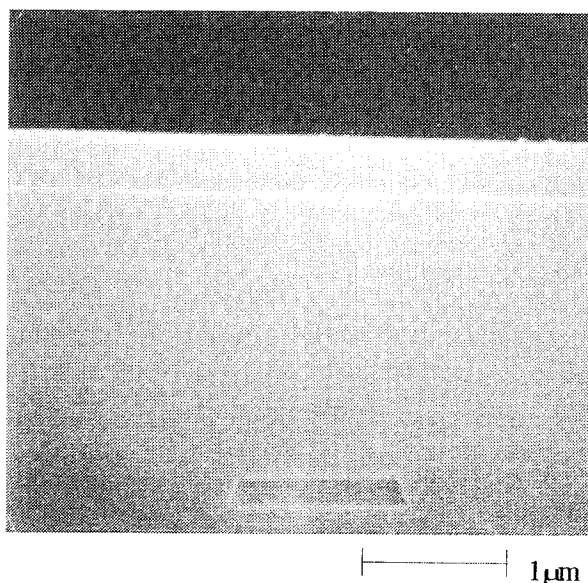


Fig.3- The Buried Mushroom Structure (BMS) after regrowth

As for indium precursor, flow rates of diethylzinc, disilane and ferrocene were set at values for that we already know the respectively carrier concentration of the InP deposited by conventional MOCVD.

From the above considerations, we found a set of growth conditions that allow us to regrowth the mushroom-like structure shown in Fig.2. The regrowth experiment was carried out at 620 °C, by using run time = 15s = vent time pulse mode for both trimethylindium and diethylzinc (flow rate = $2.3 \cdot 10^{-7}$ mol/min). To save deposition time, if the growth conditions are compatible, it is also possible to grow the InP:Zn doped layer under pulsed regime up to the complete filling of the channels, and after to switch to conventional MOCVD up to the end of the regrowth.

In Fig.3 is shown the resulting device structure containing the GaInAs:Zn doped contact layer on the top.

As we can see, a perfect filling of the channels has been obtained, without voids around the embedded active layer.

C-V measurements plot shows that the zinc incorporation is equal in both growth regimes corresponding to $n_a = 1.5 \cdot 10^{18} \text{ cm}^{-3}$. Using this approach, a low threshold current F.P. laser has been realised (3).

Using the same procedure, but doping the InP with Si_2H_6 at a concentration of $3.5 \cdot 10^{-9} \text{ mol/min}$, we obtain the doping level $n_d = 4 \cdot 10^{18} \text{ cm}^{-3}$.

Fig.4 shows a mesa stripe after the first regrowth of InP:Zn doped in presence of the dielectric mask on the top. The growth conditions of the PME growth step were the same as reported above.

Fig.5 shows the perfect selectivity of the deposition; no

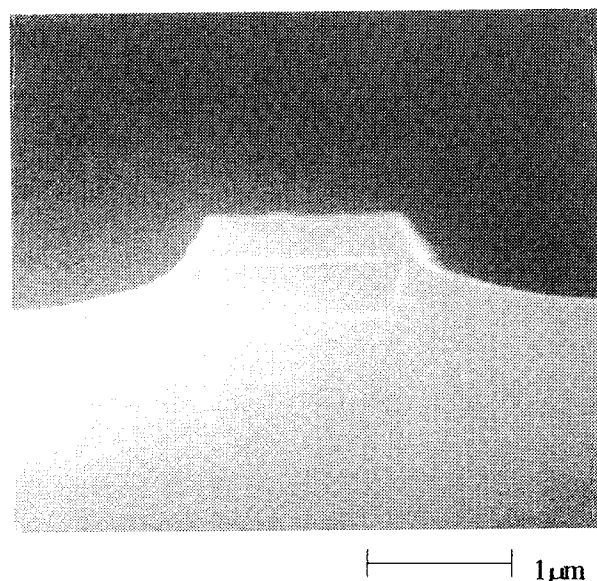


Fig.4- After the InP:Zn regrowth around a masked stripe

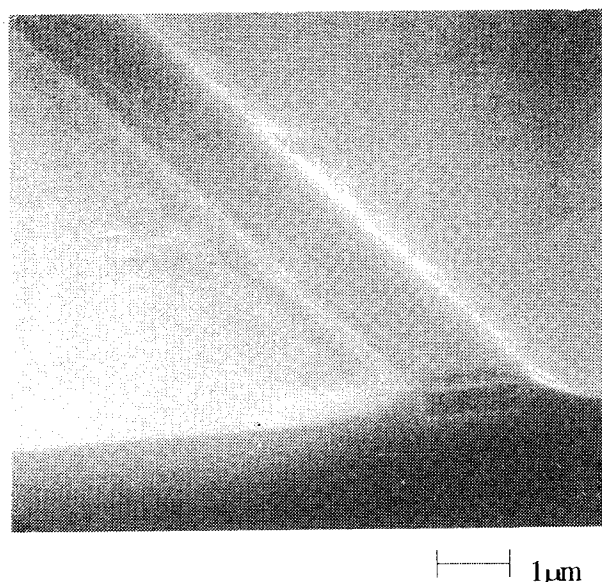


Fig.5- The regrown waveguide showing the perfect selectivity of the deposition

poly InP is present on the SiN_x while a quite flat surface is obtained around the stripe.

After removal of the dielectric mask by HF solution, the second step of regrowth was performed under conventional MOCVD at 620°C , maintaining the same concentration of reactants, to continue the growth of the InP:Zn doped up to the desired thickness ($2 \mu\text{m}$) and finally the GaInAs:Zn doped contact layer on the top. From Fig.6 we can see the perfect planarisation obtained close to the active layer. By this structure, Semiconductor Optical Amplifier (SOA) devices showing good electrical characteristics have been realised.

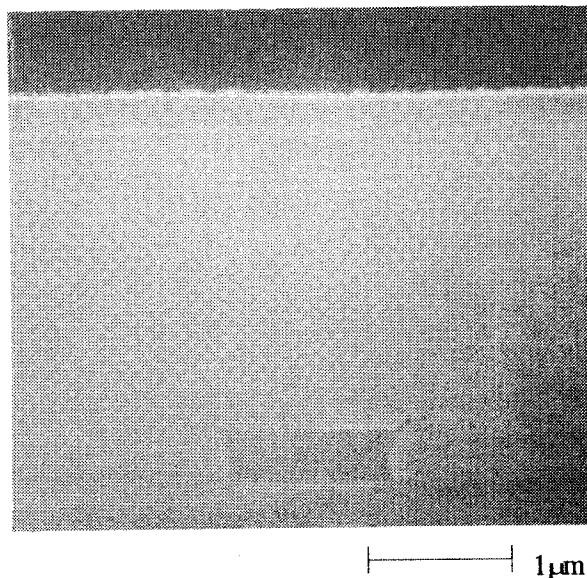


Fig.6- After the second step of InP:Zn regrowth and the final GaInAs:Zn contact layer

For high speed operation devices it is required to grow a semi-insulating current blocking layer laterally the active layer. To be effective, the S.I. layer must be very thick compared to the active layer thickness. These suggestions lead to a very difficult pattern to be regrowth, formed by a tall mesa stripe containing the active layer with a dielectric film on the top to perform the selective epitaxy laterally.

We tried to utilise the above experiences to regrow InP:Fe doped by PME around the mesa stripe $2 \mu\text{m}$ tall by $1.2 \mu\text{m}$ wide with $0.3 \mu\text{m}$ thick SiN_x deposited on the top.

See Fig.7. These stripes have been etched on a InP:S doped substrate by conventional photolithographic process followed by RIE.

As we can see, the resulting lateral surface quality is quite rough after $2 \mu\text{m}$ etch. Preliminary result obtained by using the above mentioned growth conditions is shown in Fig.8. We explored the whole range of temperature from 600°C to 640°C by maintaining a constant run time = 15s = vent time pulse mode; also the reagents concentration was maintained the same as during previous experiences.

We believe that the reduction of the surface migration of indium on the vertical walls of the stripe may reduce bumps formation at the edges.

The first parameter we plan to change is the PH_3/TMI ratio because, as mentioned before, the phosphine plays an important role in transporting the indium species on the surface. The roughness of the wall surface and the InP nearby probably helps the indium migration towards the top of the mesa and hence the bumps formation.

To perform the I-V measurements, on a flat surface of InP:Fe, we regrown a n-type GaInAs layer to make a InP:S/InP:Fe/GaInAs:Sn sandwich.

The measured resistivity was $\rho > 10^8 \Omega\text{cm}$ with the Ferrocene cell at 25 °C bubbled with 95 cc/min of Argon.

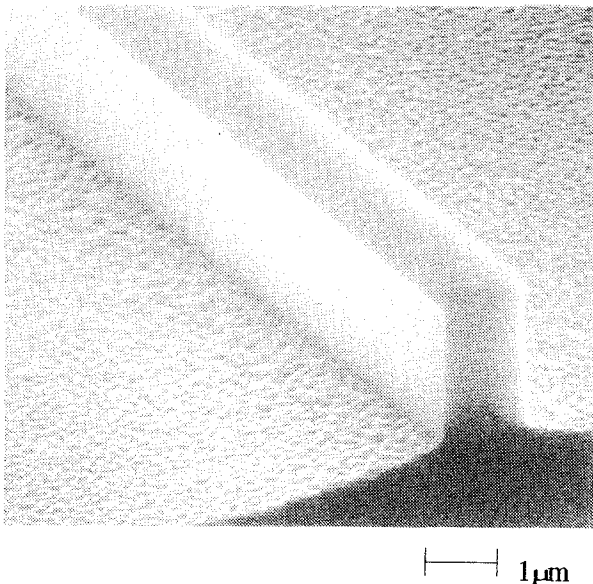


Fig.7- Tall mesa stripe (2 μm high), etched in InP, masked with SiN_x on the top

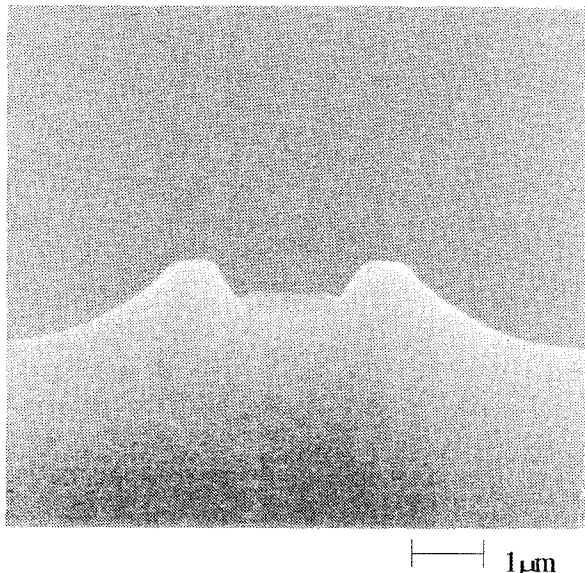


Fig.8- Overgrowth of mesa after InP:Fe regrowth

Conclusions

We have introduced the Pulsed Metalorganic Epitaxy (PME) to solve a number of problems related to the regrowth of InP around mushroom-like cross section stripes and tall mesas masked with a dielectric mask on the top. Semi-insulating InP as well as zinc and silicon doped InP were regrown by pulsing TMI+Ferrocene, TMI+DEZn and TMI+ Si_2H_6 respectively while maintaining a constant PH_3 flow in the reactor.

By the structures we have regrown, both Fabry-Perot lasers and Semiconductor Optical Amplifiers (SOA) have been realised. This fact shows that the material deposited around the active layer by pulsed regime, is good enough for device fabrication. Moreover, PME technique seems a promising tool to regrowth tall mesa stripes.

Acknowledgements

The authors would like to acknowledge the support of G. Morello, R.Y. Fang, G. Magnetti, G. Gastaldi, L. Boschis, R. De Franceschi, F. Gorgellino and A. Stano in obtaining these regrowth results.

References

- (1) J.M. Jovett, D.J. Moule, A.P. Wright and A.T. Briggs - Third Int. Conf. on InP and Related Materials, Cardiff U.K. pp. 208-211, April 1991
- (2) D. Bertone, G.M. Schiavini and A. Stano - Fourth European Workshop on MOVPE, Nijmegen The Netherlands, Poster n. 49, June 1991
- (3) D. Bertone, L. Boschis, G. Fornuto, L. Gastaldi, M. Madella, M. Meliga and A. Stano - 24th European Solid State Device Research Conference, Edinburgh, Scotland, pp. 807- September 1994

REGROWTH OF SEMI-INSULATING IRON DOPED InP AROUND CROSSED LASER MESAS BY HYDRIDE VAPOR PHASE EPITAXY

Takeo Miyazawa, Fumihiko Kobayashi, and Hidefumi Mori

NTT Opto-electronics Laboratories, 3-1, Morinosato Wakamiya, Atsugi-Shi,
Kanagawa Pref., 243-01 Japan

Abstract

It was found that large hollows are left between the crossed laser mesas during the hydride vapor phase epitaxy (HVPE) of semi-insulating InP (SI InP). However, SI InP layers with flat surfaces could be regrown using a channel structure and HVPE. The laser diodes buried in SI InP using this technique had threshold current as low as 22 mA and output power as high as 25 mW. Using this technique, side-injection light-controlled bistable lasers (SILC BLD) were fabricated. The obtained SILC BLDs exhibited good bistable characteristics.

Introduction

A laser diode having a subwaveguide crossed to a main laser together with a saturable absorber is an attractive functional device for future all-optical communication processing (1). This bistable laser diode is called a side-injection light-controlled bistable laser (1). To achieve a low threshold current and high-speed response, the SILC bistable laser diode should be buried in SI InP as usual laser diodes are. Usually, SI InP is regrown around laser mesas in only the $\langle 110 \rangle$ direction. Recently, S. Lourduoss et al. reported that SI InP can also be regrown around laser mesas in the $\langle -110 \rangle$ direction, which cross those in the $\langle 110 \rangle$ direction, using hydride vapor phase epitaxy (HVPE) (2). However, to the best of our knowledge, laser mesas in both $\langle 110 \rangle$ and $\langle -110 \rangle$ directions have not been buried in SI InP simultaneously, *i.e.* there is no report of SI InP regrowth around crossed laser mesas. We have succeeded in burying the crossed laser mesas into SI InP using a channel structure and HVPE for the first time. SILC BLDs were fabricated using this technique and exhibited good bistable characteristics.

SI InP Regrowth

Figure 1 shows crossed laser mesas after regrowth of iron doped SI InP. The InP layer regrew preferentially around the mesas, especially those in the $\langle -110 \rangle$ direction. Large hollows were left between the mesas. Further growth of SI InP resulted in filling up the hollows. However, the SI InP layer grew over the mesas at the same time. This overgrowth of SI InP makes it difficult to fabricate buried mesas for laser diodes.

A flat regrowth surface without overgrowth was obtained using the channel structure shown in Fig. 2. Double channels were dug beside laser mesas. The width of the channels beside $\langle -110 \rangle$ directed mesas was wider than that of the channels beside $\langle 110 \rangle$ directed mesas. This is because the preferential regrowth regions around the $\langle -110 \rangle$ directed mesas are wider than that of $\langle 110 \rangle$ directed mesas. The channel structures were defined by C_2H_6 reactive ion etching using SiO_2 masks, and then buried with SI InP using HVPE. The channels were filled up in as short as 15 minutes by the lateral growth of SI InP from the side walls of the channels and the laser mesas. As a matter of course, no SI InP was grown on the

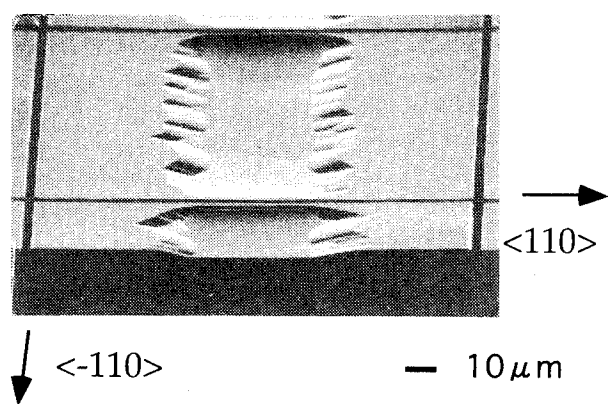


Fig.1 Regrowth surface of crossed laser mesas without channels.

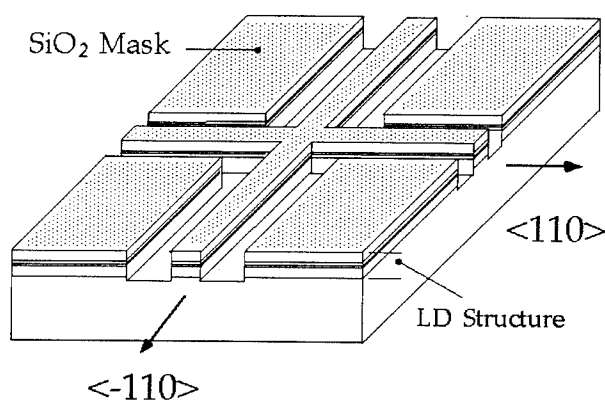


Fig. 2 Channel structure for SI InP regrowth.

SiO₂ masked region other than the channels. Moreover, the regrown surfaces at the channels were flat as shown in Fig. 3.

Laser Performance

The multi-quantum-well (MQW) laser mesas with a 3.0-μm wide active region were buried in SI InP. Subsequently, they were processed into crossed laser diodes and cleaved into both <110> and <-110> directed laser chips with a cavity length of 300 μm. Then, I-V and I-L characteristics of both directions were measured separately.

The I-V characteristics for both directions showed low reverse currents less than 10 μA at reverse voltage of -5V. This results indicates that the regrowth layers are sufficiently resistive and the laser structure was not damaged during the regrowth process.

Figure 4 shows the I-L characteristics for both directions. As shown in the figure, the I-L curves for both directions are almost identical. The threshold currents of the laser diodes in <110> and <-110> directions are 23 mA and 22 mA, respectively. (The minimum threshold current density of our laser wafer was 1.5 kA/cm².) The maximum output power of the laser diodes in <110> and <-110> directions is 25 mW and 23 mW, respectively. These results indicate

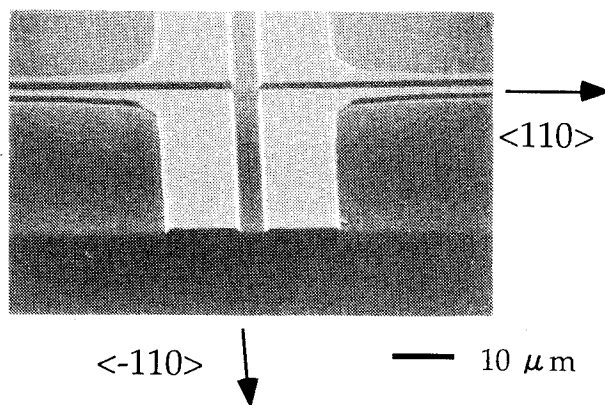


Fig. 3 Regrowth surface of a crossed laser with channels.

that the crossed laser diodes were successfully buried in SI InP.

SILC BLD Device

SILC BLDs as shown in Fig. 5 were fabricated from a MQW laser structure using HVPE and the channel structure technique. The regrowth surface of the SI InP was so flat that the device was processed without difficulty. It consists of the main waveguide laser, a subwaveguide laser, and a saturable absorption region. Bistable laser operation is achieved by nonlinearity of the MQW in the absorption

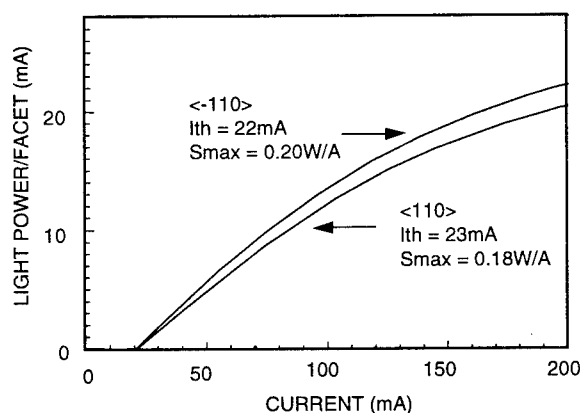


Fig. 4 I-L curves under CW conditions for laser chips in $\langle -110 \rangle$ and $\langle 110 \rangle$ directions.

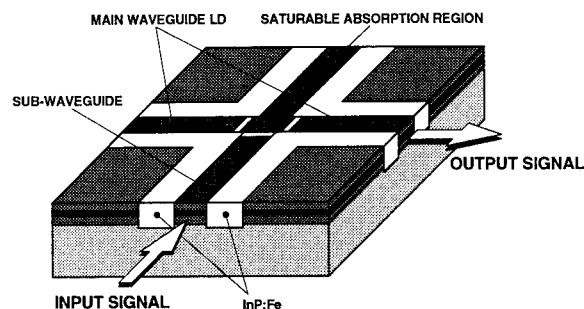


Fig.5 Schematic diagram of SILC BLD buried in SI InP.

region. The subwaveguide amplifies input light and injects it into the absorption region in the main waveguide laser. The injected light lessens the absorption in the absorption region and turns on the main laser.

Figure 6 shows the characteristics of light output as a function of injected current into the main laser. The parameter shown in the figure is control voltage V_c applied to the saturable absorption region. With a decrease in V_c , the hysteresis loop gets larger. This result indicates that the saturable absorption region works even after the regrowth just as well as the main waveguide laser and the subwaveguide laser do.

We also demonstrated turning on SILC BLDs by side-injection of light. The details of the light-control of the SILC BLDs will be submitted elsewhere. These results indicate that our SI InP regrowth technique can be successfully applied to fabricating the SILC BLD.

Conclusion

We have succeeded in burying crossed laser mesas into SI InP with flat regrowth surfaces using a channel structure and HVPE for the first time. The laser diodes buried in SI InP using this technique had threshold current

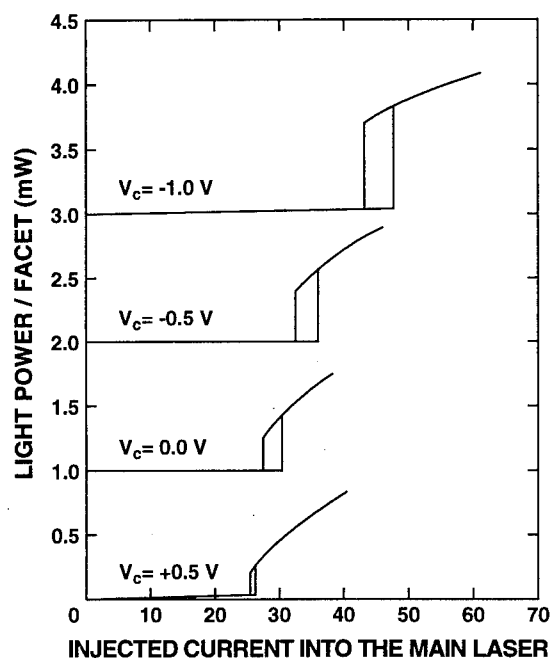


Fig. 6 Light output as a function of injected current into the main laser. The parameter is control voltage V_c applied to the saturable absorber.

as low as 22 mA and output power as high as 25 mW. SILC BLDs fabricated using this technique exhibited good bistable characteristics.

These results indicates that the SI InP regrowth technique using the channel structure and HVPE is promising for fabricating SILC BLDs. This technique is also considered useful for fabricating other integrated opto-electronics devices.

Acknowledgments

The authors wish to express their sincere thanks to K. Nonaka and T. Kurokawa for their useful discussions and help. We would like to thank M. Yamamoto and Y. Kondo for growing the laser structure, K. Kishi for the C_2H_6 reactive ion etching, Y. Itaya and S. Matsumoto for helpful discussions, and H. Asou for assistance in processing the device. They would also like to thank T. Mizutani and Y. Imamura for their continuous encouragement.

References

- (1) N. Nonaka, T. Tsuda, H. Uenohara, H. Iwamura, and T. Kurokawa, "Optical Nonlinear Characteristics of a Side-Injection Light-Controlled Laser Diode with a Multiple-Quantum-Well Saturable Absorption Region", IEEE Photonic Technology Letters., Vol. 5, pp.139-141, February, 1993.
- (2) S. Lourdudoss, O. Kjebon, J. Wallion, and S. Lindgren, "High-Frequency GaInAsP/InP Laser Mesas in $\langle -110 \rangle$ Direction with Thick Semi-insulating InP : Fe", IEEE Photonic Technology Letters., Vol. 5, pp.1119-1121, October, 1993.

MOVPE - overgrowth for buried InP / (In, Ga)(As, P) laser diode arrays

A. Knauer, K. Vogel, U. Zeimer, W. Pittroff, M. Weyers, P. Wolter

Ferdinand - Braun - Institut für Höchstfrequenztechnik Berlin, Rudower Chaussee 5, D - 12489 Berlin, Germany

Introduction

For the realization of Buried Ridge Stripe laser structures (BRS) controlled overgrowth of the active stripe with current blocking and contact layers is necessary. Regrowth with metalorganic vapor phase epitaxy (MOVPE) is an attractive technique for the production of such device. However, it is known that MOVPE overgrowth is very sensitive to the mesa shape (1) and the orientation of the involved surfaces (2-7), the V/III-ratio (2-4), the reactor pressure (2, 4) and the growth temperature (T_g) (2). When mesas are buried by MOVPE growth of "rabbit-ears" at both edges of the mesa (8) as well as the formation of undesired {111} planes (2) makes flat overgrowth difficult. Two - step overgrowth procedures or selective growth with an undercut mask can be used to produce relatively planar structures (9). Good morphology can be obtained also by one step regrowth under specific growth conditions like very high V/III-ratio together with the use of misoriented substrates (2). In this work we studied the growth kinetics of InP and (In,Ga)(As,P) during the regrowth process over rectangular mesas with $\langle 011 \rangle$ oriented sidewalls as a function of the growth temperature, of the mesa orientation and of the mesa size. We demonstrate that small changes in T_g may result in a suppression of growth on the {011} and {111}B planes. Results of overgrown laser structures for laser diode arrays demonstrate the good quality of the developed overgrowth process.

Experimental

Rectangular shaped mesas were formed in the [011] and [0-11] directions on (100) InP:S substrates by RIE. The mesas were passivated by anodic oxide ($d = 250$ nm), which is removed by HF-etching just before MOVPE overgrowth. The mesa height is (1 ± 0.3) μm and the width is varied from 2.5 μm to 5.3 μm . All experiments were carried out in a horizontal MOVPE system at a reactor pressure of 20 hPa with trimethylindium, trimethylgallium, pure arsine and phosphine as precursors in a hydrogen carrier gas flow. To study the development of the InP growth front 80 nm thick (In, Ga)(As, P) ($\lambda = 1.3$ μm) marker layers were deposited after every 170 nm of InP. Growth rates were 1 $\mu\text{m}/\text{h}$ for InP and 0.5 $\mu\text{m}/\text{h}$ for (In, Ga)(As, P). The V/III ratios were 400 and 230, respectively. Growth temperatures of 610°C, 640°C and 660°C were studied.

The surfaces and cleavage planes of the grown structures were examined by scanning electron microscopy in the backscattered secondary electron (BSE)-compo-mode.

The overgrowth of the laser diode arrays consisting of 2 μm wide mesa active stripes oriented in the $\langle 011 \rangle$ direction, which were chemically etched with crescent-like sidewalls by a $\text{Br}_2\text{-HBr-CH}_3\text{COOH}$ etchant, was done at the same conditions. The separately addressable laser arrays were grown on semiinsulating (100) InP:Fe substrates with an n-type (In, Ga)(As, P) ($\lambda = 1.3$ μm) lower contact layer.

Results and discussion

We have studied the effect of growth temperature on the growth behavior over differently sized mesa stripes.

The SEM micrographs in Fig. 1 show the development of the growth front for [011] (Fig. 1a, c) and [0-11] (Fig. 1b, d) oriented stripes of 2 μm width at deposition temperatures of 610°C (Fig. 1a, b) and 660°C (Fig. 1c, d).

For [011] oriented stripes at 660°C the shape of the overgrown layers is determined by kinetically limited growth on the {0-11} faces forming the mesa walls and on the {111}B planes developing at the top edges of the mesas (Fig. 1c). The growth rates in these two directions are similar (about half the value of planar growth in [100] direction). Additionally, {311} planes were developed at the lower mesa edge. The growth rates on the different faces decrease from $r(100) > r\{311\} \gg r\{111\}B \geq r\{0-11\}$. For narrow stripes of a few μm width the triangular shape growing on the mesa top allows for the deposition of quantum wire structures but is not suited for buried laser structures. A decrease of the growth temperature to 610°C (Fig. 1a) results in enhanced growth rates in the $\langle 0-11 \rangle$ directions and in a flat (100) top. Only in the initial stage of overgrowth {0-11} and {111} planes are formed. With increasing growth time the shape is determined by the (100) top and by higher index planes (probably {321}).

For [0-11] oriented stripes {311} planes are developed. Nearly no growth takes place on {111}A planes (Fig. 1b, d), which are only formed at 660°C on the upper mesa edge in the initial phase of growth (Fig. 1d). The growth rates on the (100) top and on the {311} sidewalls are similar and smooth mesas

with some tendency to planarization are obtained. For higher mesas still {011} planes are observed in the initial phase of growth while over low mesas ($\leq 1 \mu\text{m}$) only {311} faces are developed as the sidewalls due to the fast growth on {011} planes.

At 660°C the material transport from the {111}A non-growth planes to the top leads to significant enhancement of the growth rate on the top in the initial phase. For the same reason the growth rate in the lower mesa edge is initially enhanced. These

effects end with the full development of the {311} planes and disappearance of the {111}A planes (Fig.1d). The mesa top is shrinking with increasing thickness of the overgrown layer. This leads to enhanced material transport from the (100) top over the {311} side walls to the bottom. Thus the growth rate on the mesa is reduced in comparison to the one obtained in planar regions. For the {111}B planes this effect is much weaker (Fig.1 c).

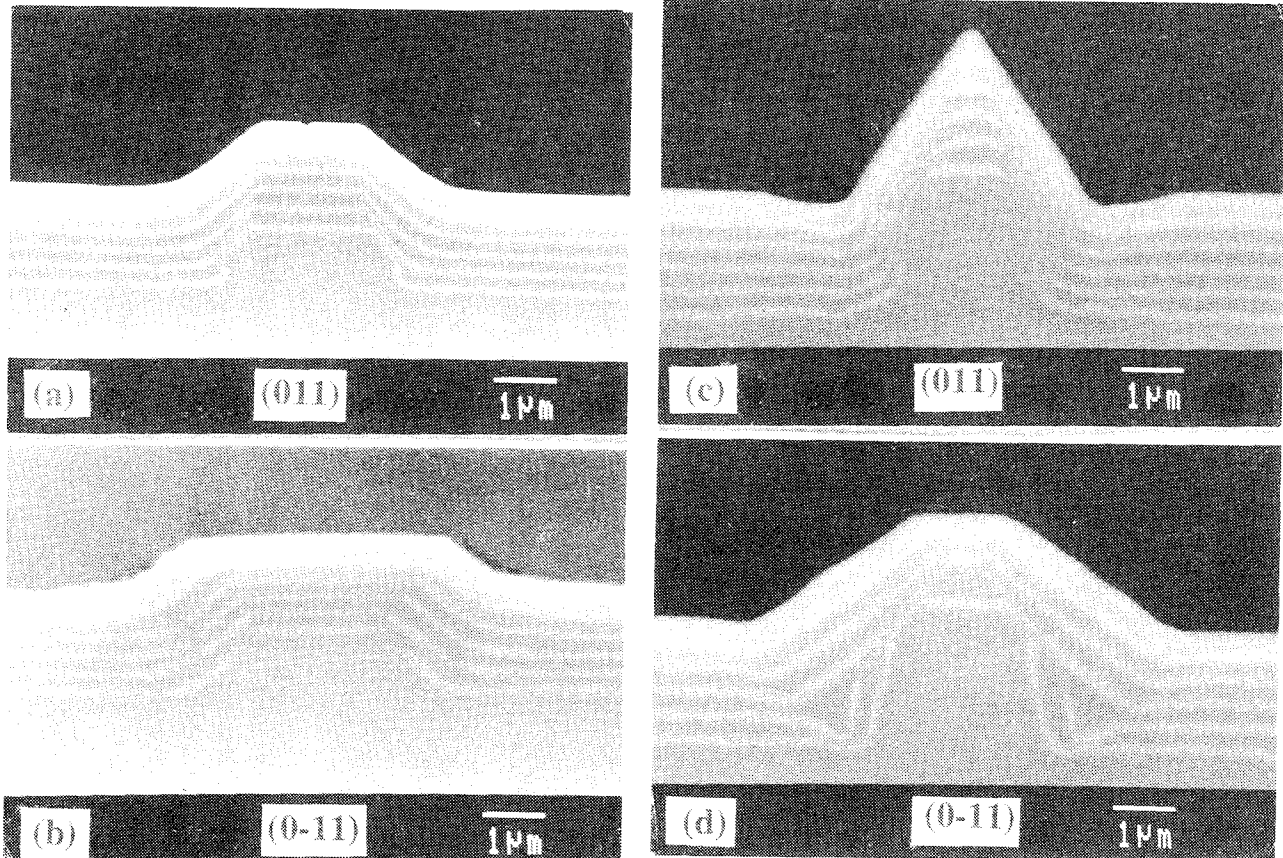


Fig. 1 SEM cross-section micrographs of alternating InP layers (dark contrast) and InGaAsP marker layers (bright contrast) deposited at 610°C (a, b) and 660°C (c, d) over 2 μm wide InP-mesa stripes oriented in $\langle 011 \rangle$ (a, c) and $\langle 0-11 \rangle$ (b, d)

The SEM micrographs in Fig. 2 show the dependence of the obtained shape on mesa width for the [011] (Fig.2a-c) and [0-11] (Fig.2 d-f) oriented stripes $T_g = 660^\circ\text{C}$. Structures deposited at 610°C did not show a significant dependence on the used mesa width neither for the [011] nor the [0-11] orientation due to the reduced diffusion from the slow to the fast growing planes. In this case growth rates on the (100) top are the same as for planar structures. At 660°C mesa widths smaller than 3 μm lead to enhanced growth rate on the top in the beginning of the overgrowth process. For wider mesas ($\geq 4 \mu\text{m}$) the changes in the growth rate on the top caused by material transport are

no longer significant. (For [0-11] oriented mesas it is possible even at $T_g \geq 640^\circ\text{C}$ to increase the growing (100) mesa top width by reducing the mesa high to 0.7 μm .)

Our basic growth studies indicate that under the chosen growth conditions planarization of $\langle 011 \rangle$ oriented mesa structures with vertical {0-11} sidewalls is not achieved. However, this stripe orientation was needed for integration purposes. Thus we have tried to use this orientation but to avoid the vertical {0-11} sidewalls produced by RIE. Mesas (0.7 μm high and 2 μm wide) with crescent-shaped side walls were prepared by chemical etching.

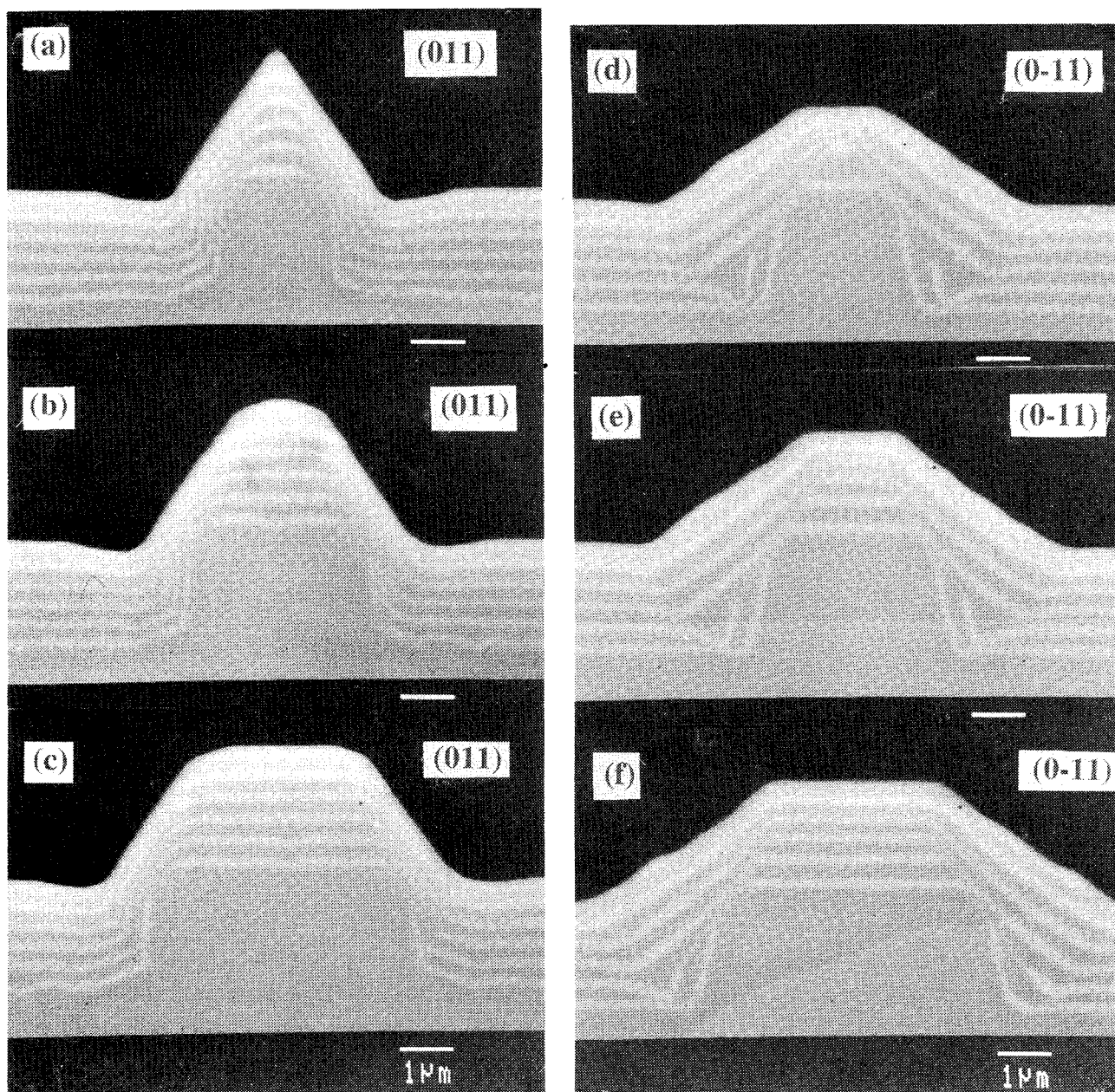


Fig 2 SEM cross-section micrographs of alternating InP layers (dark contrast) and InGaAsP layers (bright contrast) deposited at 660°C over 2.2 μm wide (a, d), 3.2 μm wide (b, e) and 4.7 μm wide InP mesa stripes oriented in $\langle 011 \rangle$ (a-c) and $\langle 0-11 \rangle$ (d-f)

This way the kinetic limitations present on $\{111\}$ A side walls are avoided and planarizing growth in one step is possible even in the $\langle 011 \rangle$ direction (Fig. 3). The buried-ridge stripe (BRS) laser arrays fabricated in this way show low leakage currents and low threshold current I_{th} (8 mA at 400 μm length) indicating that the recombination at the overgrown interfaces is negligible. These properties are combined with a high uniformity of threshold current and output power within the arrays of individually addressable lasers.

Conclusion

The development of the growth front during overgrowth of mesa structures with vertical $\{011\}$ sidewalls has been studied using quaternary marker layers embedded in InP. The shape of the overgrown layer strongly depends on the ridge orientation and the growth temperature. At 660°C growth of InP as well as the quaternary takes place on the vertical sidewalls and on $\{111\}$ B planes developing during growth. Planarizing growth was not possible at 660°C due to the kinetically limited growth on the forming facets.

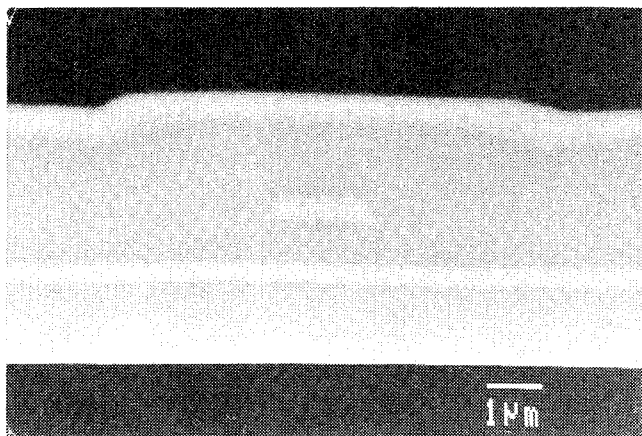


Fig. 3 SEM cross-section micrograph of regrown $\langle 011 \rangle$ oriented laser structures with InP (dark contrast) and upper InGaAsP/InGaAs contact layers. The bright contrast in the center is from the quaternary mesa with crescent-shaped sidewalls.

The formation of these facets can be suppressed by using a small height to width ratio for $\langle 0110 \rangle$ oriented stripes at 640°C . For $\langle 011 \rangle$ oriented stripes the growth temperature has to be lowered further. Here flat (100) top surfaces can be maintained even on $2\text{ }\mu\text{m}$ wide mesas at 610°C . Avoiding $\{011\}$ sidewalls allows a planarization also on $\langle 011 \rangle$ oriented stripes at higher growth temperatures. Using the developed regrowth process, high quality BRS laser array have been fabricated.

References

- [1] R. T. Huang, C. L. Liang, A. Appelbaum, D. Renner, S. W. Zehr, "Selective Growth of InP on patterned, nonplanar InP Substrates by LP-MOVPE", *J. Electron. Mater.* 19, 1313, 1990
- [2] E. Veuhoff, H. Heinecke, J. Rieger, H. Baumeister, R. Schimpe, S. Pröhl, "Improvements in SAE growth of InP by MOVPE", *Proc. of 4. IPRM*, Newport, USA, 210-213, 1992
- [3] G. Zwinge, H. H. Wehmann, A. Schlachetzki, C. C. Hsu, "Orientation-dependent growth of InGaAs / InP for applications in laser-diode arrays", *J. Appl. Phys.* 74, 5516-5519, 1993
- [4] N. Nordell, J. Borglind, "Improved InP regrowth properties in MOVPE by addition of CCl_4 ", *Appl. Phys. Lett.* 61, 22-24, 1992
- [5] E. J. Trush, M. A. Gibbon, J. P. Stagg, C. G. Cureton, C. J. Jones et al, "Selective and non-planar epitaxy of InP, GaInAs and GaInAsP using LP-MOCVD," *J. Cryst. Growth* 124, 249-254, 1992
- [6] R. Westphalen, B. Elsner, M. Maassen, O. Kayser, K. Heime, P. Balk, "Selective embedded growth by LP-MOVPE in the Ga-In-As-P system", *J. Cryst. Growth* 125, 347-362, 1992
- [7] M.-S. Kim, Y. Kim, M.-S. Lee, Y. J. Park, S.-I. Kim, S.-K. Min, "Growth behavior on V-grooved high Miller index substrates by MOCVD", *J. Cryst. Growth* 146, 482-488, 1995
- [8] C. Blaauw, A. Szaplanczay, K. Fox, E. Emmertorfer, "MOCVD of InP and mass transport on structured InP substrates", *J. Cryst. Growth* 77, 326-333, 1986
- [9] Y. Kondo, K. Sato, M. Yamamoto, "Self-aligned BHS lasers grown entirely by MOVPE", *Appl. Phys. Lett.* 62, 1188-1190, 1992

Planar InP Burying Growth Around a Dry-Etched Mesa by Addition of CH₃Cl During MOVPE

T. Takeuchi and S. Yamazaki
Fujitsu Laboratories Ltd.

10-1 Morinosato-Wakamiya, Atsugi 243-01, Japan

Planar burying growth of InP around a dry-etched stripe mesa has been made with metalorganic vapor phase epitaxy (MOVPE) by adding CH₃Cl to the process gases. The planarization effect of CH₃Cl adding is striking especially in relatively-low growth temperature conditions. From the growth behavior around mesas and a study of growth rate modifications, we consider that the migration enhancement of In atom and induced dependence of growth rate on the crystallographic orientation gave the planar burying growth. Using reactive ion etching (RIE) for mesa fabrication and adding CH₃Cl in MOVPE growth, we demonstrated 1.5 μm InGaAsP/InP buried-heterostructure (BH) laser diodes with Fe doped semi-insulating InP layer. We obtained comparable laser characteristics with those of conventional wet-etched mesa laser diodes.

Introduction

Uniform MOVPE growth of an active layer, uniform and precise mesa etching by RIE, and following burying growth by MOVPE are key techniques to improve yield and productivity of long-wave length BH laser diodes. Although the first two techniques have been realized [1, 2], planar InP burying growth by MOVPE around a dry-etched mesa still remains difficult, usually resulting in mask overgrowth and unevenness adjacent to the mask [3]. For planar growth, two kinds of growth methods were attempted. One is raising the growth temperature, for example, up to 680 °C [3]. High temperature growth also have side effects such as fast dopant diffusion to MQW layers. The other method is to add Cl containing materials, such as CCl₄ and 1,1,1 trichloroethane (TCA) to MOVPE process gases [4, 5, 6, 7]. This method was first suggested from the analogy of mesa-shape-independent flat burying growth by Cl containing vapor phase epitaxy (VPE) [8, 9]. Although Cl addition has a remarkable planarization effect, Cl source materials previously used are under control by chloro-fluoro-carbon (CFC) related regulations. Therefore, new Cl sources other than CCl₄ and TCA are desired.

In this work, we present burying growth using monochloromethane (CH₃Cl) as a new Cl source, which is out of the CFC related regulations. We developed a planar growth shape and discuss the effect of CH₃Cl addition. Finally, we fabricated 1.5 μm InGaAsP/InP BH laser diodes with an Fe doped semi-insulating InP current blocking layer, grown using CH₃Cl addition.

Experiment

The striped mesas were formed in the [011] direction on a (100) oriented Sn-doped InP substrate, using RIE with C₂H₆, H₂, and O₂ as the active gases [2]. The mesa shape is a trapezoid whose side-wall is a little tilted towards <111>B from (011). Mesa height is about 2.5 μm . Silicon dioxide

(SiO₂) was used as a mask for both etching and selective growth. Before growth, the mesas were rinsed in H₂SO₄ and water.

Burying growth was performed by low-pressure MOVPE in a vertical reactor. Trimethylindium (TMI) and phosphine (PH₃) are used as source gases. CH₃Cl diluted to 2% in hydrogen (H₂) in a gas cylinder was used as a Cl source. Ferrocene (Cp₂Fe) was used as a dopant for a semi-insulating layer. Growth pressure was 76 torr. The V/III ratio was 120. Growth temperature was varied from 575 to 625 °C. Growth rate without CH₃Cl addition was 3.0 $\mu\text{m/hr}$. As marker layers of growth procedure around the mesas, thin (about 0.015 μm) InGaP layers were inserted periodically. After the regrowth, the samples were cleaved, stained in K₃[Fe(CN)₆]:NaOH:H₂O solution and examined with a scanning electron microscope.

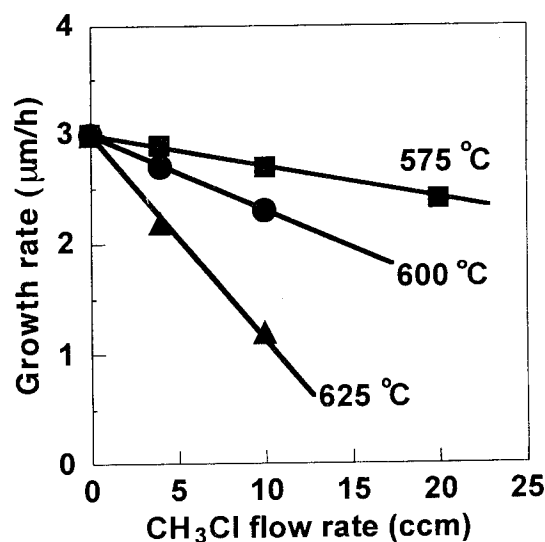


Figure 1. Growth rate reduction on (100) face by CH₃Cl addition at 575 °C, 600 °C, and 625 °C.

Results and discussion

The first change noticed after the addition of CH_3Cl was a reduction of growth rate, as the same for CCl_4 and TCA additions [4, 6]. Figure 1 shows the dependence of growth rate on added CH_3Cl flow rate on a (100) face at various growth temperatures. The reduction rate is proportional to CH_3Cl flow rate and increases with the growth temperature. This reduction was thought to be caused by volatile InCl formation on a surface, through the reaction of In and HCl produced from CH_3Cl decomposition, and successive evaporation of InCl from the surface [4, 6]. So, from the temperature dependence we think that CH_3Cl decomposition proceeds with growth temperature and/or InCl evaporation from the surface is enhanced with the growth temperature.

The clear difference between CH_3Cl and previously reported precursors (CCl_4 and TCA) is the decomposition efficiency estimated from growth rate reduction. Compared with almost the same decomposition ratio of CCl_4 and TCA as that of TMI, the decomposition ratio of CH_3Cl is about 2% that of TMI at 600 °C.

Figure 2 shows the growth behavior around the mesas with and without CH_3Cl addition at various growth temperatures. Without CH_3Cl addition, growth at the mask edge leads to a ridge and an overgrowth above the mask occurring at 575 °C and 600 °C. This feature is extreme at low growth temperatures. At 625 °C the mask overgrowth was not observed; however, the ridge at the mask edge still remained. With CH_3Cl addition, growth shape was significantly

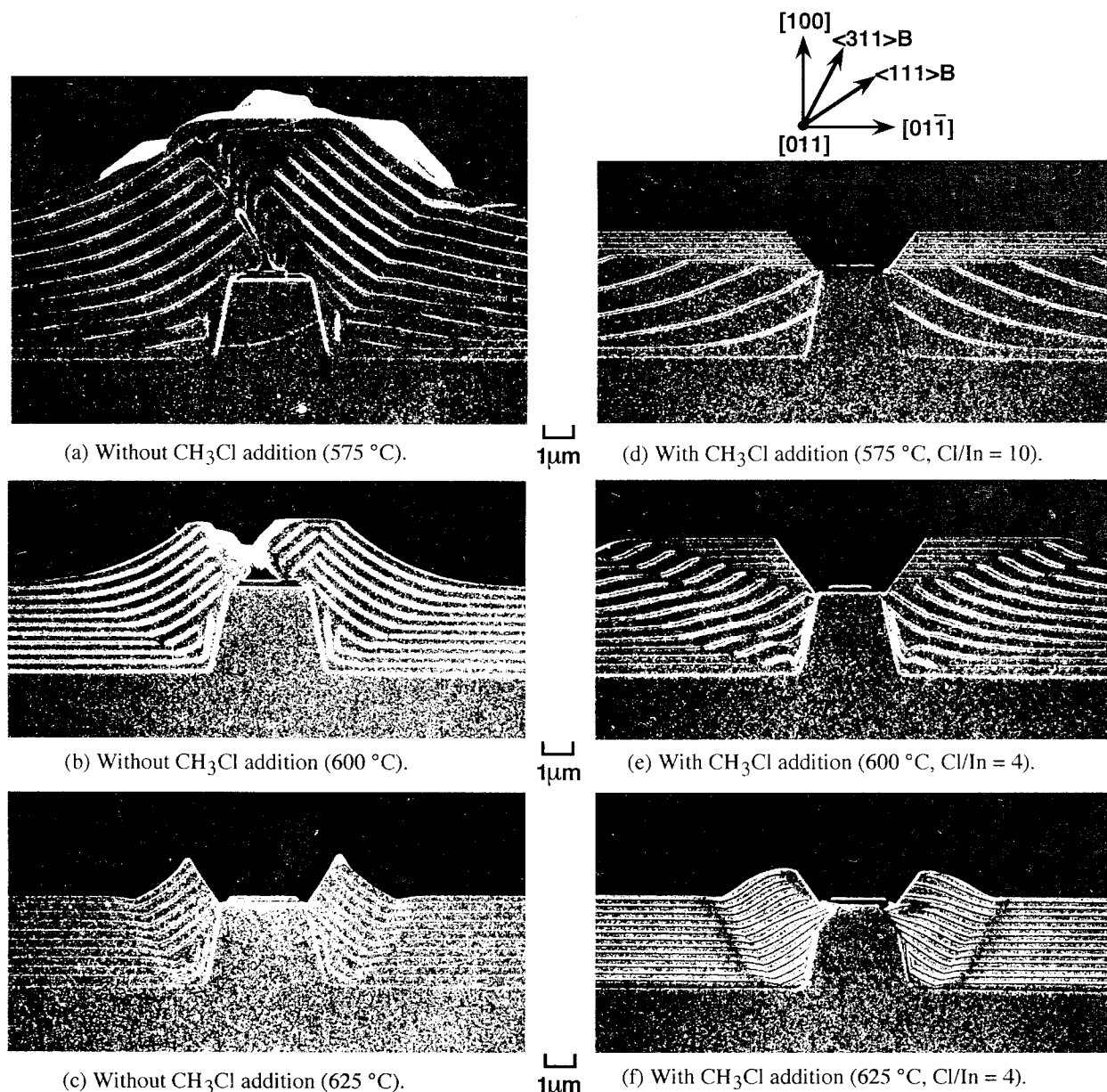


Figure 2. Growth behavior around RIE-etched mesas in $[011]$ direction.

improved. At every growth temperature, a non-growing (111)B facet was formed at the mask edge and the mask overgrowth was completely suppressed. This growth feature is the main effect of CH_3Cl addition and is common to all Cl additions [4, 6]. The most planar regrowth shape was obtained at 575 °C, although regrowth shape without CH_3Cl addition was the worst. At 575 °C growth along the mesa side-wall of the (011) vicinal face was reduced, a rapid-growth face appeared around high index face of (311)B which gradually changes toward (100), and a smooth (100) facet appeared at the mask edge. As the growth temperature got higher, the rapid growth face like (311)B and the smooth (100) facet disappeared and the ridge was formed at the mask edge. The reduction of growth on mesa side-wall was also seen at high temperatures; however, at 625 °C this reduction was excessive and the top of mesa was partially etched away.

Low temperature growth is favorable not only for good planarity but also for low growth rate reduction, as seen in Figure 1. This low growth rate reduction (~10%) with a planar regrowth shape by CH_3Cl addition at 575 °C is noteworthy, compared with TCA addition. In the case of TCA, about 20% of growth rate reduction at 625 °C was reported for the improvement of growth selectivity [6].

From the observation above, the effects of CH_3Cl addition are summarized as follows:

- (1) A complete growth suppression on a (111)B face at the mask edge.
- (2) Growth suppression on a mesa side-wall of a (011) vicinal face.
- (3) Fast growing characteristics on a high-index face, such as (311)B, at a low growth temperature.

For the cause of these effects, Nordell and Karlicek indicated that the growth is limited by the introduced surface kinetics change by the HCl produced from CCl_4 and TCA [5, 6]. However, their discussions were abstract and didn't provide a concrete image of the In atom's behavior on the surface. We considered that induced change of the orientation dependence of the growth rate is a key to study the effects of CH_3Cl addition. Accordingly, we examined the orientation dependence using separate substrates in the same growth run. Substrates used are: (100), (511)A, (511)B, (311)A, (311)B, (211)A, (211)B, (111)A 5° off, (111)B 5° off, (011) 5° off, and (011).

Figure 3 shows the dependence of growth rate on substrate orientation at 575 °C with and without CH_3Cl addition. Without CH_3Cl addition, the growth rate were independent of the substrate orientation. In contrast, with the CH_3Cl addition the growth rate strongly depended on the substrate orientation. This induced dependence is considered to be due to properties of CH_3Cl decomposition to HCl, InCl formation, and InCl desorption, on and from the surface. Generally the growth rate reduction is low on step-less faces

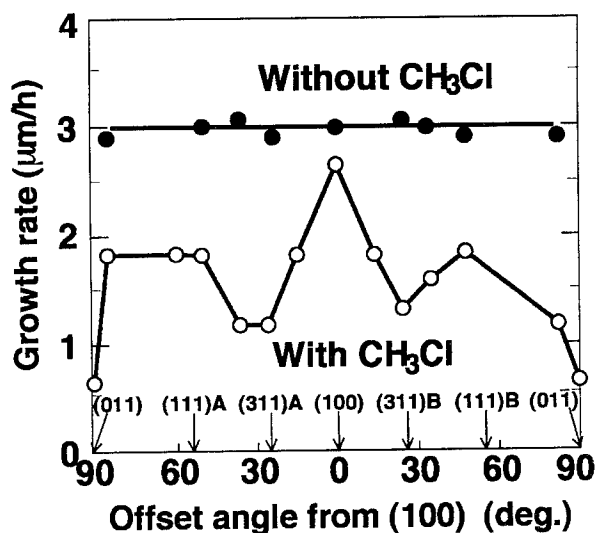


Figure 3. Dependence of growth rate on substrate orientation with and without CH_3Cl addition (575 °C, Cl/In = 10).

of (100), (111)A, and (111)B, and it is increased on high step-density faces of (311)A, (311)B, and (011). This is quite natural, considering that InCl at a step or a kink site may be easily desorbed. The growth rate was lowest on the (011) face. This feature agrees well with growth suppression on a mesa side-wall of a (011) vicinal face (2). However, this dependence of the growth rate doesn't necessarily explain the growth behavior around the mesas. The non-growing (111)B face (1) has a considerable growth rate and the fast-growing (311)B face (3) has a quite low growth rate. We consider that the enhancement of surface migration of In atom from and to adjacent faces with a different orientation plays an important role in determining the growth behavior around the mesas. We think that the non-growing (111)B facet formation at 575 °C and 600 °C is caused by In migration from the (111)B face to an adjacent face, as it occurs naturally without Cl addition at higher growth temperature of 625 °C. From extremely high growth rate on a (311)B face around the mesas, higher than that without Cl addition, we think that the In atoms were supplied from adjacent (100) faces through surface migration.

The mechanism of surface migration enhancement of In atoms on (111)B and (100) faces by Cl addition is not clear at present. However, we will mention two possible explanations. One is that a surface coverage by Cl reduces sticking site or sticking probability for migrating In atoms, like the case of Se high doping [10]. If we assume that a surface coverage rate with volatile Cl is higher at a lower growth temperature, In migration may be greater at the lower growth temperature. This would explain why fast-growing (311)B faces appear at a low growth temperature. The other is that In migrates longer in the form of InCl because the binding strength between InCl and the surface may be loose.

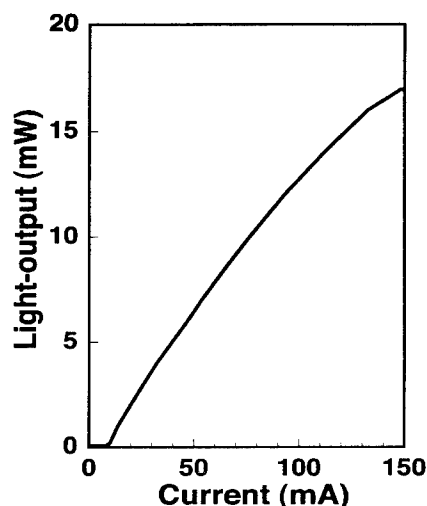
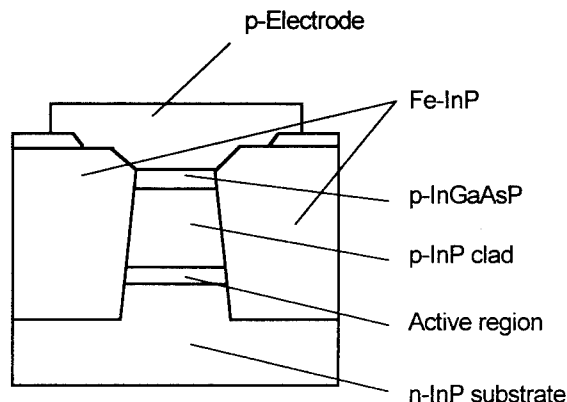


Figure 4. A fabricated laser structure and current vs. light output (I-L) characteristics of an as-cleaved 300 μm long laser diode at room temperature CW operation.

At a high growth temperature the InCl will desorb from the surface rather than migrate on the surface, as a result the fast-growing (311)B face appears at the low growth temperature.

Laser fabrication

We fabricated 1.5 μm semi-insulating buried-heterostructure (SI-BH) laser diodes with InGaAsP/InP strained layer multiple quantum wells. The thickness of the active layer, barrier layer, and separate confinement layer are 5.1 nm, 10.0 nm, and 100 nm, respectively. The active layer consists of 0.8% compressively strained InGaAsP (10 wells). PL wavelengths of the barrier layer and the separate confinement layer are 1.3 μm and 1.15 μm . Burying growth of Fe-doped semi-insulating InP was performed using CH_3Cl addition at the growth temperature of 575 $^\circ\text{C}$. The CH_3Cl /TMI ratio was 20. Estimated Fe concentration was $5 \times 10^{16} \text{ cm}^{-3}$. Undoped n-type impurity concentration measured with electrochemical C-V profiling was increased from about $5.0 \times 10^{14} \text{ cm}^{-3}$ to $1.0 \sim 1.5 \times 10^{15} \text{ cm}^{-3}$ after CH_3Cl addition. This level is low enough to obtain a semi-insulating InP layer.

Figure 4 shows the current vs. light output (I-L) characteristics of an as-cleaved 300 μm long laser diode at room temperature CW operation. The threshold current density of 1.4 kA/cm^2 and the slope efficiency of 0.18 mW/mA were obtained. These values are comparable to those of laser diodes with the conventional wet etched mesas fabricated in our laboratory.

Summary

We investigated burying growth around a dry-etched mesa using CH_3Cl as a new Cl additive during MOVPE. We obtained planar growth shape. We think that migration enhancement of In and induced dependence of growth rate on

the orientation gave the improvement in growth shape. We fabricated 1.5 μm InGaAsP/InP SI-BH lasers applying dry etching and adding CH_3Cl during MOVPE. We obtained comparable laser performances with those of wet etched mesa laser diodes. MOVPE growth with adding CH_3Cl could provide both planar growth shape and a good current blocking layer.

References

- [1] M. Kondo et al., J. Crystal Growth **115**(1991)231.
- [2] M. Matsuda et al., Technical Report of IEICE, OQE91-185, vol. 91, no. 470, 1992, p. 103.
- [3] N. Nordell et al., J. Crystal Growth **114**(1991)92.
- [4] N. Nordell et al., Appl. Phys. Lett. **61**(1992) 22.
- [5] N. Nordell et al., J. Crystal Growth **125**(1992)597.
- [6] R.F. Karlicek et al., J. Crystal Growth **131**(1993)204.
- [7] B.-T. Lee et al., Appl. Phys. Lett. **63**(1993)234.
- [8] B. Hammarlund et al., J. Electron Mater. **20**(1991)523.
- [9] M. Hoshino et al., Appl. Phys. Lett. **48**(1986)186.
- [10] Y. Kondo et al., Appl. Phys. Lett. **62**(1993)1188.

PREPARATION AND OPTICAL CHARACTERIZATION OF NANOSCALE InP ISLANDS EMBEDDED IN $\text{In}_{0.48}\text{Ga}_{0.52}\text{P}$

A. Kurtenbach, K. Eberl, N.Y. Jin-Phillipp*, F. Noll, and F. Phillipp*

Max-Planck-Institut für Festkörperforschung, Heisenbergstr. 1, D-70569 Stuttgart, Germany

*Max-Planck-Institut für Metallforschung, Heisenbergstr. 1, D-70569 Stuttgart, Germany

Introduction

The formation of nanoscale islands due the epitaxial growth of lattice mismatched heterostructures has recently been investigated for many different material combinations [1]. By the three dimensional growth mode the strain energy is reduced at the expense of surface energy. It has been demonstrated that up to a certain thickness the three dimensional island growth occurs dislocation free at least for free standing islands on a surface [2, 3]. Thus it is a promising method to realize quantum dot structures. We report on the preparation of InP islands embedded in $\text{In}_{0.48}\text{Ga}_{0.52}\text{P}$ by solid-source molecular beam epitaxy (MBE). We have investigated the onset of islanding by reflection high energy electron diffraction (RHEED) and atomic force microscopy (AFM). Overgrown InP islands are characterized by cross-sectional transmission electron microscopy (TEM) and photoluminescence (PL) measurements.

Experimental

The samples are grown on semi-insulating (001) GaAs substrates by solid-source molecular beam epitaxy (MBE). The growth was monitored in situ by a RHEED system operated at 20 kV. After oxide desorption, a 200 nm thick GaAs buffer layer is grown at 580 °C with a growth rate of 0.52 ML/s and a beam equivalent pressure (BEP) of 5×10^{-6} Torr. A GaP decomposition source is used to grow layers containing P as group V element [4]. Appropriate growth temperature and BEP for the growth of InP/ $\text{In}_{0.48}\text{Ga}_{0.52}\text{P}$ structures are 470 °C and 5×10^{-6} Torr [4, 5]. A 200 nm thick $\text{In}_{0.48}\text{Ga}_{0.52}\text{P}$ layer which is lattice matched to GaAs is grown on top of the GaAs buffer. Subsequently few monolayers (MLs) of InP are deposited which are overgrown by a 200 nm thick $\text{In}_{0.48}\text{Ga}_{0.52}\text{P}$ cap layer. The growth rates of $\text{In}_{0.48}\text{Ga}_{0.52}\text{P}$ and InP are 1 ML/s and 0.48 ML/s, respectively.

TEM and high resolution TEM (HREM) investigations are carried out in a JEOL 4000FX/EX electron microscope, operated at 400 keV. The normals for the cross-sectional TEM specimens are along [110] and [100], perpendicular to the growth direction.

PL was measured at low temperatures (10 K) using a CW Ar⁺ laser for excitation. The excitation density was about 1 W/cm². The PL was spectrally resolved in a double-monochromator and detected in a photomultiplier tube.

Results and Discussion

The transition from a 2D to a 3D growth mode is illustrated by in situ recorded RHEED patterns. In Fig. 1 RHEED patterns along the [110] direction are shown for an $\text{In}_{0.48}\text{Ga}_{0.52}\text{P}$ surface without any InP (Fig. 1a), with nominally 2.5 MLs InP (Fig. 1b) and 7.5 MLs InP deposition. $\text{In}_{0.48}\text{Ga}_{0.52}\text{P}$ has 2×1 surface reconstruction at a substrate temperature of about 470 °C [4]. The elongated streaks demonstrate the 2D characteristic of the surface. After deposition of more than 2 MLs InP a more and more spotty RHEED pattern develops. This is demonstrated in Fig. 1b and 1c. The spotty pattern starts to appear in the 2.5 MLs sample and is clearly developed in the 7.5 MLs sample. These spots originate from a transmission through 3D islands illustrating a non-2D growth mode [6]. Both diffraction patterns in Fig. 1b and 1c are recorded immediately after deposition of the InP indicating an abrupt start of the island formation without any significant retardation.

A roughening in RHEED is not observed for an InP deposition lower than 2 MLs. This may be due to a limited RHEED sensitivity. Also a growth interruption of 300 s does not result in a more pronounced spotty pattern. In contrast to this, AFM images reveal an island formation of InP on $\text{In}_{0.48}\text{Ga}_{0.52}\text{P}$ already after 1.5 MLs deposition (Fig. 2). The InP growth rate was only 0.25 ML/s in this case in order to find the onset of islanding with better accuracy. The islands in Fig. 2 exhibit a typical height

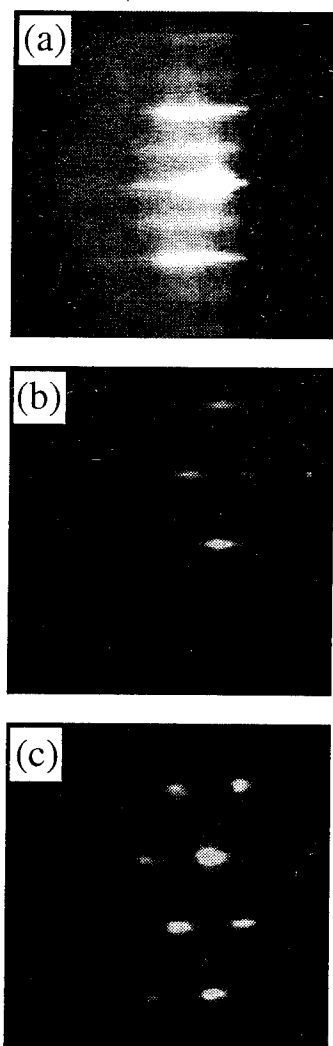


Figure 1: In situ recorded RHEED patterns along the $[110]$ direction at 470°C : (a) $\text{In}_{0.48}\text{Ga}_{0.52}\text{P}$ surface, (b) after deposition of 2.5 MLs InP, (c) after deposition of 7.5 MLs InP

of 8 nm , a lateral size of 30 nm and a density of about $3 \times 10^9/\text{cm}^2$. According to AFM results no islands are detected for 1 ML InP. The first ML InP forms a wetting layer demonstrating the Stranski-Krastanow growth mode of InP on $\text{In}_{0.48}\text{Ga}_{0.52}\text{P}$ for our growth conditions [3].

Samples overgrown with an $\text{In}_{0.48}\text{Ga}_{0.52}\text{P}$ cap layer are investigated by TEM and PL measurements. The RHEED studies illustrated in Fig. 1 suggest that the island formation starts immediately during deposition. To confirm this a $\{002\}$ dark-field (DF) TEM micrograph (Fig. 3a) and a HREM micrograph (Fig. 3b) are taken from $\{100\}$ cross-sections of a overgrown sample containing 2.5 MLs InP. The cap layer is deposited after 1 s growth interruption in this case.

The DF image is mainly sensitive to chemical compo-

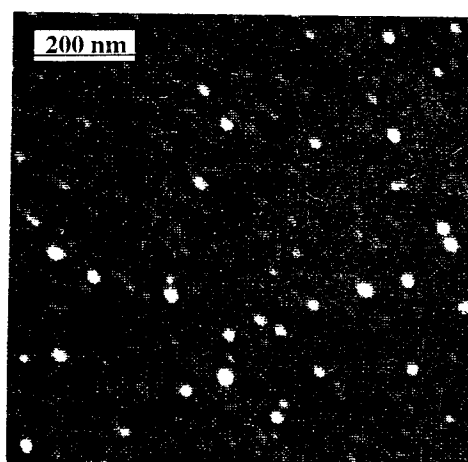


Figure 2: AFM image of sample with 1.5 MLs InP grown on $\text{In}_{0.48}\text{Ga}_{0.52}\text{P}$

sitions, where InP shows a bright and $\text{In}_{0.48}\text{Ga}_{0.52}\text{P}$ a dark contrast. This difference is due to nonequal structure factors which depend on the Indium or Gallium content of the two materials. Fig. 3a reveals clearly the InP region separating the $\text{In}_{0.48}\text{Ga}_{0.52}\text{P}$ cap and buffer layer by such a dark/white contrast. Apparently the InP distribution is inhomogeneous demonstrating that InP islands are evolved in the overgrown sample. A lateral island size of about 20 nm is estimated from Fig. 3a which is in the same order than expected from AFM measurements. The detailed island shape is difficult to extract because the InP content is fluctuating in transmission direction due to the finite thickness of the sample (about 100 nm). In the HREM (Fig. 3b), InP appears darker than $\text{In}_{0.48}\text{Ga}_{0.52}\text{P}$. Strain fields contribute to the long range contrast fluctuations besides differences in the structure factors. According to high resolution micrographs like Fig. 3b we can conclude that the InP island growth is dislocation free for the 2.5 MLs sample demonstrating a high quality growth. In contrast to Fig. 3b misfit dislocations are observed for an InP deposition of nominally 14.5 MLs.

PL measurements on overgrown samples are performed for various InP depositions. We observe a strong InP related PL. As discussed in Ref. [7] the PL energy shifts from 1.85 eV to 1.53 eV when the nominal InP thickness increases from 2 MLs to 10 MLs. The PL linewidths are typically less than 30 meV . The maximum intensity and minimum linewidth of 22 meV is observed for 7.3 MLs InP. Beyond 7.3 MLs the intensity decreases drastically. This indicates the onset of misfit dislocation formation which are observed in TEM for the 14.5 MLs InP sample. The cap layer of these samples was grown after 1 s growth interruption. The PL energy is most sensitive to the height of the islands because the smallest dimension defines the confinement potential. Thus the energy shift indicates a change of the height with

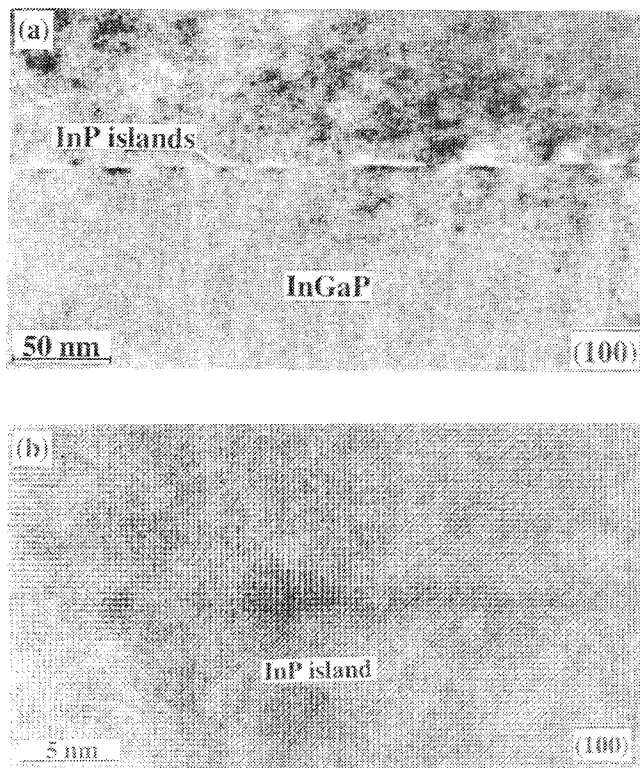


Figure 3: {100} cross-sectional dark field TEM (a) and high resolution TEM (b) for a sample with 2.5 MLs InP embedded in $\text{In}_{0.48}\text{Ga}_{0.52}\text{P}$.

increasing nominal InP thickness.

Fig. 4 shows the dependence of the InP PL on growth interruption times for nominally 3.0 and 7.3 MLs InP. The PL energy position (Fig. 4a) and the PL linewidth (Fig. 4b) are plotted versus the growth interruption. For 3.0 MLs InP the PL energy decreases by about 70 meV when the growth interruption is increased from 1 s to 300 s. At the same time the PL linewidth increases from 27 meV to more than 60 meV for 300 s growth interruption. This influence of the growth interruption on the optical properties is less pronounced for the 7.3 MLs InP samples. In this case the linewidths are almost unchanged. Changes in PL energy and linewidth for different growth interruptions indicate a change of the height or shape of the islands. For short growth interruption the surface diffusion is interrupted and the InP islands are prevented to reach their equilibrium size. Similar results have recently been reported for the growth of InAs/GaAs islands [8].

In summary, we have shown that for the growth of InP on $\text{In}_{0.48}\text{Ga}_{0.52}\text{P}$ by MBE the island formation begins at a critical thickness of about 1.5 MLs due to AFM measurements. RHEED investigations show that the island formation occurs instantaneously (for more than 2 MLs). The sensitivity of RHEED to the islanding starts

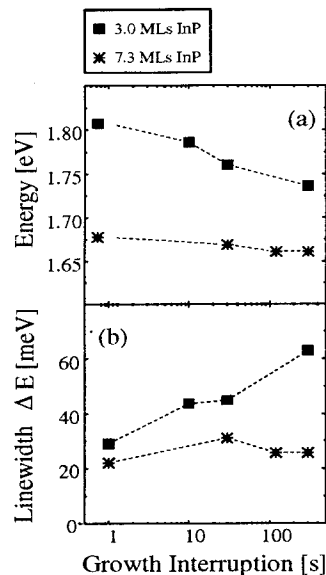


Figure 4: Influence of a growth interruption on InP PL energy (a) and linewidth (b) for samples with nominally 3.0 and 7.3 MLs InP.

not until the deposition of 2 MLs InP. It could be demonstrated by TEM and HREM that islands evolve in presence of an $\text{In}_{0.48}\text{Ga}_{0.52}\text{P}$ cap layer, which is grown after 1 s growth interruption. For low InP deposition the islands are coherently embedded in $\text{In}_{0.48}\text{Ga}_{0.52}\text{P}$ without misfit dislocations. The optical properties are dependent on the amount of deposited InP and growth interruption times. Smallest PL linewidth and thus better island homogeneity is achieved for short growth interruptions.

References

- [1] P.M. Petroff and S.P. Denbaars, "MBE and MOCVD Growth and Properties of Self-Assembling Quantum Dot Arrays in III-V Semiconductor Structures", *Superlattices and Microstructures*, Vol. 15, pp. 15-21, 1994 and references therein
- [2] S. Guha, A. Madhukar, and K.C. Rajkumar, "Onset of incoherency and defect introduction in the initial stages of MBE growth of highly strained InGaAs on GaAs(100)", *Appl. Phys. Lett.*, Vol. 57, pp. 2110-2112, 1990
- [3] D.J. Eaglesham and M. Cerullo, "Dislocation-Free Stranski-Krastanow Growth of Ge on Si(100)", *Phys. Rev. Lett.*, Vol. 64, pp. 1943-1946, 1990
- [4] T. Shitara and K. Eberl, "Electronic properties of InGaP grown by solid-source MBE with a GaP decomposition source", *Appl. Phys. Lett.*, Vol. 65, pp. 356-358, 1994

- [5] A. Kurtenbach, K. Eberl, K. Brunner, and G. Abstreiter, "Self-Assembling InP/In_{0.48}Ga_{0.52}P Quantum Dots Grown by MBE", in *Low Dimensional Structures prepared by Epitaxial Growth or Regrowth on Patterned Substrates*, edited by K. Eberl, P. Petroff, and P. Demeester, NATO ASI Series, Kluwer, Dordrecht, to be published
- [6] M.G. Lagally, D.E. Savage, and M.C. Tringides, "Diffraction From Disordered Surfaces: An Overview", in *Reflection High-Energy Electron Diffraction and Reflecting Electron Imaging of Surfaces*, edited by P.K. Larsen and P.J. Dobson, NATO ASI Series, Plenum, New York 1988, pp. 139-174
- [7] A. Kurtenbach, K. Eberl, and T. Shitara, "Nanoscale InP islands embedded in InGaP", *Appl. Phys. Lett.*, Vol. 66, pp. 361-363, 1995
- [8] J.M. Gerard, J.B. Genin, J. Lefebvre, J.Y. Marzin, D. Barrier, and J.M. Moison, "Nucleation and Growth of InAs Islands on GaAs: An optical Study", in *Low Dimensional Structures prepared by Epitaxial Growth or Regrowth on Patterned Substrates*, edited by K. Eberl, P. Petroff, and P. Demeester, NATO ASI Series, Kluwer, Dordrecht, to be published

$\text{In}_x\text{Ga}_{1-x}\text{As}/\text{InP}$ multiquantum well structures grown on [111]B InP substrates **WP58**

M. Hopkinson, J.P.R. David, E.A. Khoo, A.S. Pabla, J. Woodhead and G.J. Rees

EPSRC Central Facility for III-V Semiconductors, Department of Electronic and Electrical Engineering, University of Sheffield, Mappin Street, Sheffield S1 3JD. United Kingdom.

Abstract

We report the growth and characterisation of $\text{In}_x\text{Ga}_{1-x}\text{As}/\text{InP}$ quantum well (QW) structures grown on [111]B InP substrates. Photoluminescence (PL) from a range of such structures, grown on substrates with optimum misorientation, show PL linewidths and peak positions equivalent to similar [100] structures. Structural studies, using transmission electron microscopy (TEM) and x-ray diffraction (XRD) show that multiquantum well (MQW) specimens exhibit a high degree of uniformity and a low level of defects. With increasing compressive strain ($x > 0.53$) MQW samples eventually show relaxation, observed through an increase of the XRD peak width and through an increase in linear surface morphological features. Room temperature photocurrent measurements on strained p-i(MQW)-n diode structures show a strong excitonic blue shift, demonstrating excellent potential for low voltage, long wavelength, optical modulators.

Introduction

III-V epitaxy on [111]-oriented substrates is currently receiving considerable attention. The unique nature of the [111] surface in III-V semiconductors, with its termination by either group III (A-face) or group V (B-face) atomic planes, results in substantial differences between the growth modes and surface reconstruction with respect to the more conventional [100]. The electronic band structure of [111] QW's is also considerably modified. Anisotropy in the heavy hole sub-band results in a larger effective mass and a lower density of states in the [111] growth direction [1-3], resulting in an increased quantum-confined Stark effect (QCSE) [2,4]. Due to an increased optical matrix element the absorption and PL efficiency should also be enhanced. A further consequence of growth on [111] substrates is that strained QW's exhibit a large internal piezoelectric field [1]. This may be screened by photoexcited carriers or reduced by application of an external field, resulting in an excitonic blue shift.

To realise the potential for [111]-based devices operating at 1.3 or 1.55 μm wavelengths requires the growth of $\text{In}_x\text{Ga}_{1-x}\text{As}$ QW's with InP (or InAlAs) barriers. $\text{In}_x\text{Ga}_{1-x}\text{As}$ on InP offers a further advantage in that compressive and/or tensile strain can be employed, giving increased freedom for device design. Despite some encouraging results on the growth of InP [5], $\text{In}_x\text{As}_{1-x}\text{P}/\text{InP}$ QW's [6] and of InGaAs/AlInAs QW's [4], there have, to our knowledge, been no reports on the growth of lattice matched and strained $\text{In}_x\text{Ga}_{1-x}\text{As}/\text{InP}$ QW's on [111]B InP.

High quality QW structures are difficult to grow on [111]B InP due to the tendency to form pyramidal facets. Promotion of a step-flow growth mode seems to be an

essential pre-requisite for producing smooth films [7]. In principle this can be easily achieved through increasing the mobility of surface group III atoms, e.g. by increasing the growth temperature (T_g) or by using substrates with a high step density. However for indium containing materials the desorption of indium, which is significant about 540°C, imposes an upper limit on T_g . Growth at low T_g , using on-axis substrates results in strong faceting. In InGaAs/GaAs epitaxy, the use of [111]B substrates misoriented a few degrees towards the [2,-1,-1] has been shown to considerably reduce faceting [8]. Recently we have reported that a specularly smooth morphology and excellent optical properties can also be obtained on InP substrates with an equivalent misorientation [9].

Growth and characterisation

$\text{In}_x\text{Ga}_{1-x}\text{As}/\text{InP}$ QW structures have been grown on [111]B InP by molecular beam epitaxy. The solid source growth utilises conventional group III source cells and valved cracker sources for arsenic and phosphorus. Switching between alternate group V species is enhanced by the use of liquid nitrogen-cooled shutters. Details of the growth system have been reported previously [10]. S-doped n^+ InP [111]B substrates, misorientated 2° towards [2,-1,-1] were provided by Crismatec Impact. The substrates were processed 'epi-ready' using a technique previously applied to [100] InP [11]. Using such substrates strong reflection high energy electron diffraction (RHEED) reconstruction was observed at a reproducible oxide desorption temperature of ~525°C. For optimum growth of InGaAs/InP structures T_g was increased to 530-540°C. The V/III ratio was set just above that required for group-V stabilised growth.

We have examined the properties of a number of single and MQW samples. Fig.1. shows 10K PL data from a sample containing 5, 10, 20, 40 and 80Å $\text{In}_{0.53}\text{Ga}_{0.47}\text{As}$ QW's together with a bulk-like layer (1000Å). The sample was nominally lattice-matched ($x=0.53$). Intense, relatively narrow (FWHM=7-15meV), PL is observed from all the quantum wells. The energy upshift due to quantum confinement follows quite closely that of [100] InGaAs/InP QW's, suggesting relative invariance of the band offsets.

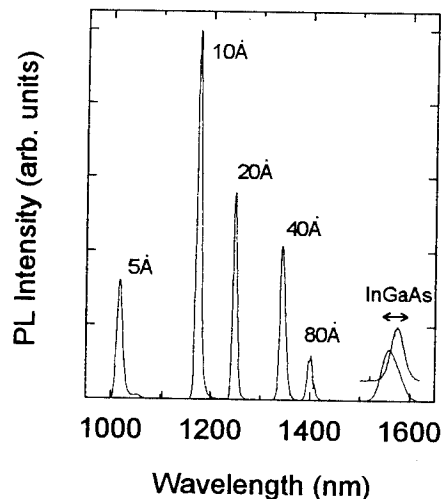


Fig.1 Low temperature (10K) PL spectra of a structure containing $\text{In}_{0.53}\text{Ga}_{0.47}\text{As/InP}$ QW's of different well widths.

In contrast to the QW's the bulk $\text{In}_{0.53}\text{Ga}_{0.47}\text{As}$ layer within this structure exhibits relatively weak, broad PL, which is at a longer wavelength than expected. With increasing excitation power we find this peak shifts to shorter wavelength, eventually reaching 1550nm, the value expected for [100] $\text{In}_{0.53}\text{Ga}_{0.47}\text{As}$. We have observed this behaviour in a number of bulk $\text{In}_{0.53}\text{Ga}_{0.47}\text{As}$ layers. Weak intensity dependent shifts are also observed in 40 and 80Å QW's. The optical power-induced PL shifts are similar to those observed in strained [111] QW's, where they are a consequence of the built-in piezoelectric field. However the InGaAs layers are closely lattice matched, with $\Delta a/a < 1.5 \times 10^{-4}$ by XRD), and have relatively narrow XRD FWHM ($\leq 20\text{meV}$). Strain-sensitive ($g=220$) cross-sectional TEM (x -TEM) shows weak pseudo-periodic contrast in bulk $\text{In}_{0.53}\text{Ga}_{0.47}\text{As}$ layers, suggesting compositional fluctuations on length scales of 100-500Å. This may produce a spatially varying band gap, which may be further enhanced by the piezoelectric effect.

Fig.2. shows a x -TEM micrograph of a nominally

lattice-matched $\text{In}_x\text{Ga}_{1-x}\text{As/InP}$ MQW structure, which consists of 10 periods (80Å QW/200Å barrier). Although well and barrier appear to be slightly thicker than anticipated, the overall structure appears highly regular and uniform. Faint periodic oscillations in the plane of the QW's are observed, which appear related to the compositional fluctuations discussed previously. Fig.3. shows XRD rocking curves for this layer and two compressively strained $\text{In}_x\text{Ga}_{1-x}\text{As/InP}$ MQW's which have 40 periods of (50Å QW/125Å barrier). The lattice matched sample shows a number of narrow satellite peaks, again indicative of a highly uniform periodic structure. The slight shift of the zero order peak (to -180arc.sec) and asymmetry in the satellite peak distribution is indicative of a small amount of residual strain. This is a consequence of residual arsenic grading into the InP barrier layers and is a problem which can be controlled by further optimisation of the growth parameters.

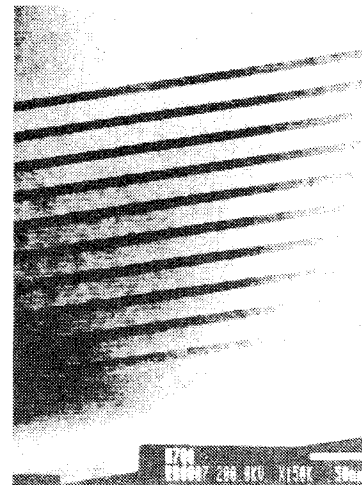


Fig.2 TEM cross section of the $\text{In}_{0.53}\text{Ga}_{0.47}\text{As/InP}$ MQW sample

The high structural quality of the lattice-matched sample is preserved for the $x=0.58$ MQW. However for the $x=0.63$ MQW the XRD satellite peaks are considerably broadened and the background intensity is increased, suggesting a degree of relaxation has occurred. Contrasting sample morphologies reveals the presence of linear defects in the strained samples, with the appearance of twins. These appear always aligned along one of the [110] directions. The defects can be observed only occasionally in the $x=0.58$ sample, but are at a considerably higher linear density ($\sim 200\text{cm}^{-1}$) in the $x=0.63$ MQW.

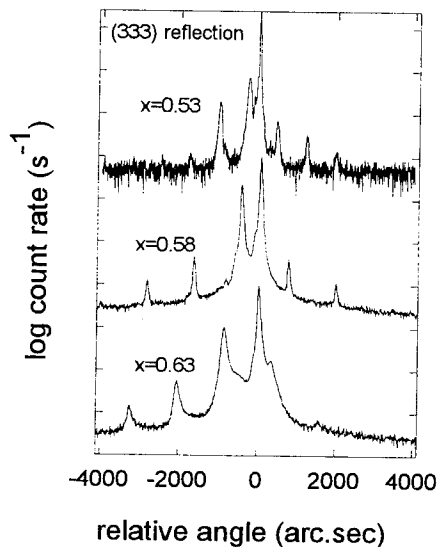


Fig.3 XRD rocking curves, taken in (333) reflection geometry, for a series of $\text{In}_x\text{Ga}_{1-x}\text{As}/\text{InP}$ MQW samples.

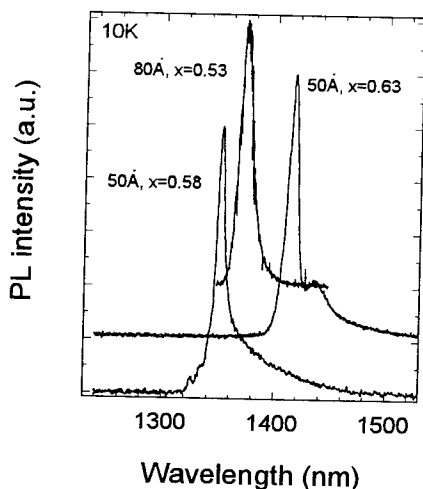


Fig.4 10K PL spectra of the lattice matched and compressive strained $\text{In}_x\text{Ga}_{1-x}\text{As}/\text{InP}$ MQW's of fig.3.

Low temperature PL spectra from the three MQW specimens is shown in fig.4. The PL linewidth is about 9meV for the lattice-matched MQW and this decreases with increased strain down to about 4meV for the $x=0.58$ MQW. The value for the $x=0.63$ sample is slightly higher at 6meV. These values compare very favourably with similar structures grown on [100] InP. The precise

indium composition (x) may vary from the nominal values due to the problems of indium desorption. This may explain why the MQW PL peak positions are not quite as predicted. At room temperature the PL FWHM are in the range 25-35meV. With increasing optical power the strained MQW's show a modest blue shift of up to 20meV, a consequence of the internal piezoelectric field. In contrast the lattice matched sample retains a constant peak position with increasing incident intensity.

Photocurrent measurements

To investigate the effect of external bias the strained MQW structures were grown within the intrinsic region of a p-i-n diode structure. Fabricated 200 μm diameter mesa diodes exhibited reverse leakage currents as low as 2nA at -10V, even for the most highly strained structure ($x=0.63$), although in this case the yield was extremely low (2-3%) due to the high defect density. Under weak monochromatic excitation strong excitonic features are observed in the room temperature photocurrent spectra of these samples. Fig.5. shows the photocurrent spectra of the $x=0.63$ sample. Under the application of a few volts reverse bias the e1-hh1 exciton blue shifts by $\sim 15\text{nm}$. The shift saturates out at about -5V, a voltage consistent with our calculation of the internal piezoelectric field [12]. To our knowledge this is the first observation of a blue shift in the $\text{In}_x\text{Ga}_{1-x}\text{As}/\text{InP}$ material system and as such is an important demonstration of the piezoelectric properties of such QW's.

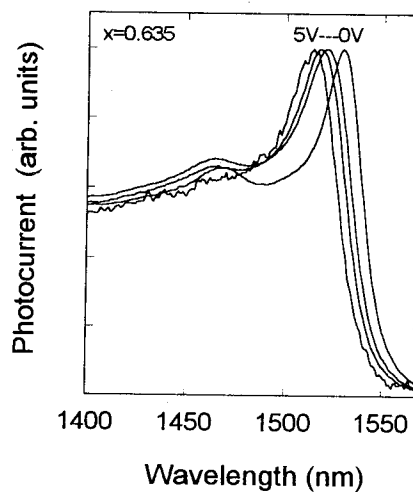


Fig.5 Room temperature photocurrent spectra from an $\text{In}_x\text{Ga}_{1-x}\text{As}/\text{InP}$ ($x=0.63$) MQW pin diode structure at different reverse bias values.

Due to the internal bias of the piezoelectric field, the rate of shift with applied voltage is greater than that expected for equivalent [100] structures. Between 0-1V the shift is $\sim 8\text{nm/V}$, compared to $\sim 3\text{-}4\text{nm/V}$ expected for similar [100] structures. With a zero bias exciton position at 1535nm , close to that required for long wavelength optical communications, we believe these devices offer considerable potential for use as low voltage optical modulators.

Acknowledgements

We thank R.Beanland and R.Murray (Liverpool University) for TEM analysis and discussions. In addition we thank G.Hill, M.Pate and D.M.Carr (Sheffield) for device fabrication/characterisation. The work is supported by EPSRC (UK) under grant no: GR/H45773.

References

- [1] C.Mailhot and D.L.Smith. *J.Vac.Sci.Technol.* A57, 609 (1989)
- [2] T.Hayakawa, T.Suyama, K.Takahashi, M.Kondo, S.Yamamoto and T.Hijikata. *Appl.Phys. Lett.* 52, 339 (1988)
- [3] Y.Kajikawa, N-H Sugiyama, T.Kamijoh and Y.Katayama. *Japan.J.Appl.Phys.* 28, L1022 (1989)
- [4] K.Nishi and T. Anan. *J.Appl.Phys.* 70, 5004 (1991).
- [5] H.Q.Hou and C.W.Tu. *Appl.Phys.Lett.* 62, 261 (1993)
- [6] H.Q.Hou and C.W.Tu. *J.Cryst.Growth.* 127, 199 (1993)
- [7] A.Chin, P.Martin, P.Ho, J.Ballingall, T-H Yu, J.Mazurowski. *Appl.Phys.Lett* 59, 1899, (1991)
- [8] K.Y.Yang, L.J.Schowalter, B.K.Laurich, I.H.Campbell and D.L.Smith *J.Vac.Sci.Technol. B* 11, 779 (1993)
- [9] M.Hopkinson, J.P.R.David, E.A.Khoo, A.S.Pabla, G.Hill, G.J.Rees and G.J.Jacob 6th Int. Conf. of InP and Related Materials, Santa Barbara, pda5 (1994)
- [10] P.A.Claxton, J.S.Roberts, J.P.R.David, C.M.Sottomayor-Torres, M.S.Skolnick, P.R.Tapster and K.J.Nash. *J.Cryst.Growth* 81, 288 (1987)
- [11] D.Gallet, M.Gendry, G.Hollinger, A.Overs, G.Jacob, B.Bodart, M.Gouneau, H.I'Haridon, D.Lecrosnier. *J.Electron.Mats.* 20, 963 (1991)
- [12] A.S.Pabla, M.Hopkinson, J.P.R.David, E.A.Khoo and G.J.Rees. *Electron. Lett.* 30, 1707 (1994)

Wavelength Controllability of InGaAs/GaAs Quantum Dots Emitting at 1.3 μm Region

Nobuyuki Ohtsuka, and Kouki Mukai
Fujitsu Laboratories Ltd.
10-1 Morinosato-Wakamiya, Atsugi 243-01, Japan

Introduction

Quantum dots are predicted to significantly improve the performance of electronic and optoelectronic devices[1]. Recently reported self-organized InGaAs quantum dots grown on GaAs substrates by molecular beam epitaxy (MBE) and metalorganic vapor phase epitaxy (MOVPE) techniques had uniform sizes, high spontaneous emission efficiencies, and quite high densities, not possible with artificially fabricated structures [2-4]. Thus, as a step, we would like to control the quantum size effect, as well as positioning or density of the dots. However, few studies have been done on the controllability of these factors.

In our previous work, we reported the successful growth of 1.3 μm emitting (at 300K) $\text{In}_{0.5}\text{Ga}_{0.5}\text{As}$ quantum dots on GaAs substrates using atomic layer epitaxy (ALE) technique[5]. This wavelength is quite important for optical device application. Further, ALE has the possibility of finely controlling the characteristics of quantum dots, because ALE has more growth parameters than other growth methods.

In this paper, we investigate the photoluminescence (PL) emission characteristics of InGaAs/GaAs quantum dots emitting in the 1.3 μm region under various growth condition using the ALE technique. We demonstrate that the emission wavelength can be controlled by the number of ALE cycles and In composition of the buffer layer. We show the influence on emission characteristics of the supply sequence in ALE.

Experimental

Figure. 1 schematically shows the structure grown in this study. Typically, the quantum dots were grown on a 300-nm thick $\text{In}_x\text{Ga}_{1-x}\text{As}$ ($0 \leq x \leq 0.1$) buffer layer and capped by a 30-nm thick layer having the same composition as the buffer layer. The growth was carried out in a low-pressure MOVPE, RF-heated, chimney reactor. Our growth system was designed for pulse jet epitaxy which can grow self-limited III-V compounds under a wide range of conditions [6]. We used trimethylindium-dimethylethylamine adduct (TMIDMEA), trimethylgallium (TMGa), triethylgallium (TEGa) and 10% arsine (AsH_3) diluted with hydrogen (H_2) as source materials. TMIDMEA, TMGa, and TEGa were kept at 19.2°C, 3.0°C and 17.0°C respectively. Substrates were exactly (001)-oriented GaAs. We grew InGaAs quantum dot structures under 2000 Pa. The source gases for group III and AsH_3 were alternately supplied to the reactor with H_2 carrier gas, separated by H_2 purging pulses. The buffer layer and cap layer were grown by conventional MOVPE at 460°C using TEGa.

We used transmission electron microscopy (TEM) to evaluate the size and the positional distribution of the dots. Plan-view and

cross-sectional TEM were carried out at 300 kV in the standard way after mechanical thinning of samples by Ar ion milling. In the plan-view samples, the ion milling was performed from both surface and substrate side. The optical properties of quantum dots were evaluated by photoluminescence (PL) at 300 K. A 647.1-nm

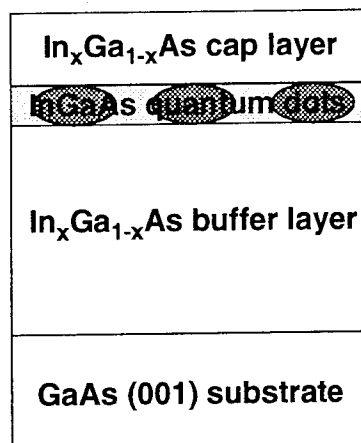


Figure 1 Sample structure used this work.

Kr⁺ laser was used to excite samples. PL emission was dispersed by a 50-cm monochromator and detected by a PbS detector using a conventional lock-in technique

Results and discussion

1. Temperature

A growth temperature of 460°C which we used in our previous work gives distinct self-limiting growth of both GaAs and InAs[7]. However, since we did not know optimum temperature to fabricate high quality InGaAs/GaAs quantum dots, we investigated the relationship between growth temperature and emission characteristics of the dots. Figure 2 shows the PL intensity dependence on growth temperature. In the case of growth temperature below 420°C, the PL intensity from the quantum dots is weak. This may be due to the low surface diffusivity of In atoms in the low temperature region [8]. However, in the case of growth temperature above 480°C, we think that there are two reason for the weak PL intensity. One is the high surface diffusivity of In atoms and the other is arsenic desorption from the growth surface during atomic layer epitaxy [9]. Thus, these results indicate that there is optimum growth temperature to fabricate high quality InGaAs/GaAs quantum dots. We found that optimum growth temperature was 460°C in our case.

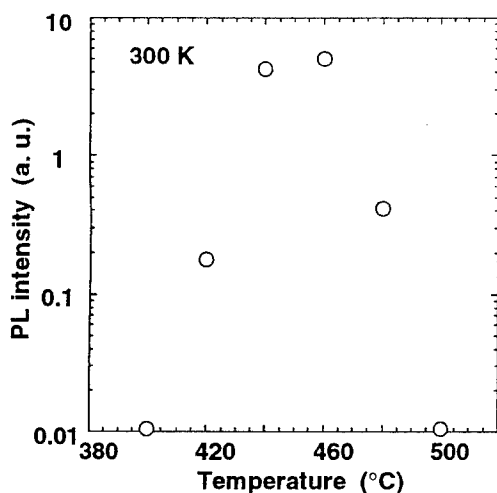


Figure 2 PL intensity dependence on growth temperature for quantum dots

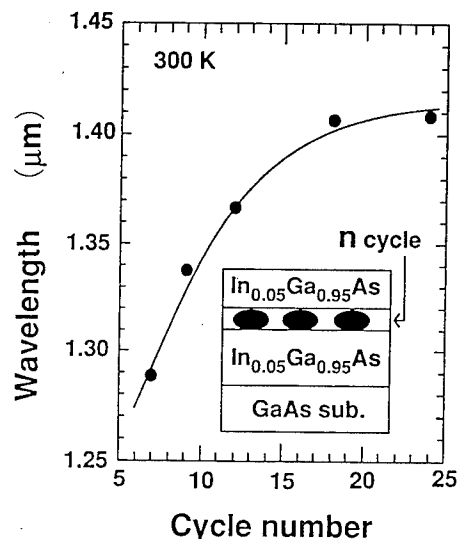


Figure 3 PL wavelength of quantum dots as a function of ALE cycle.

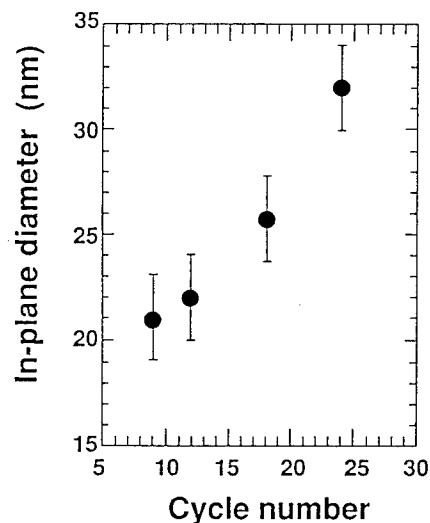


Figure 4 Relationship between the number of ALE cycle and the in-plane dot diameter from TEM images.

2. Number of ALE cycles

Figure 3 shows the PL wavelength of quantum dots as a function of the number of ALE cycles. Reducing the alternate growth cycle number from 24 to 7 decreased the wavelength

from 1.4 to 1.3 μm on a $\text{In}_{0.05}\text{Ga}_{0.95}\text{As}$ buffer layer. Figure 4 shows the relationship between the cycle number of alternate supply and the in-plane dot diameter from TEM images. By changing the cycle from 9 to 24, we can control the in-plane diameter from 20 to more than 30. These results indicate that we can manipulate the dot size by changing the cycle number of alternate supply during growth.

3. Buffer layer

We investigated the influence of In composition of the buffer layer on the formation of InGaAs quantum dots. Figure 5 shows In composition of the buffer layer dependence of the PL wavelength. Increasing the In composition of the buffer layer from 0 (GaAs) to 0.1 ($\text{In}_{0.1}\text{Ga}_{0.9}\text{As}$) increased the wavelength from 1.3 to 1.45 μm with 12 cycles of InAs/GaAs. We used TEM and energy dispersive x-ray analysis (EDX) measurements to evaluate the size and composition of InGaAs quantum dots. It was found that there was no difference in In composition of these InGaAs quantum dots from EDX results. The cause of wavelength variation is dot size variations rather than composition effects. Combining the above results for number of ALE cycles and In composition of the buffer layer, we can control the emission wavelength from 1.1 to 1.5 μm .

4. Supply sequence

We also investigated the influence of emission characteristics on the supply sequence in ALE. Figure 6 shows plan-view TEM images of

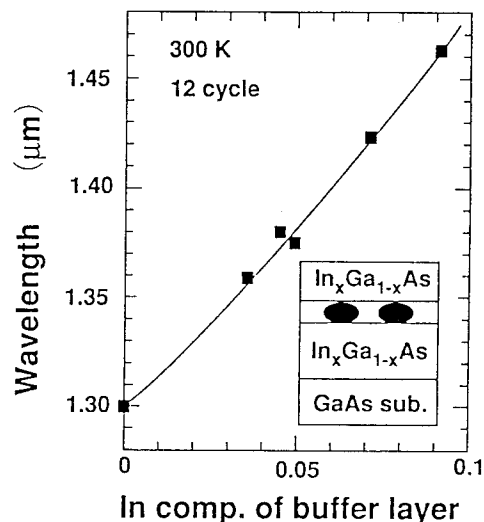
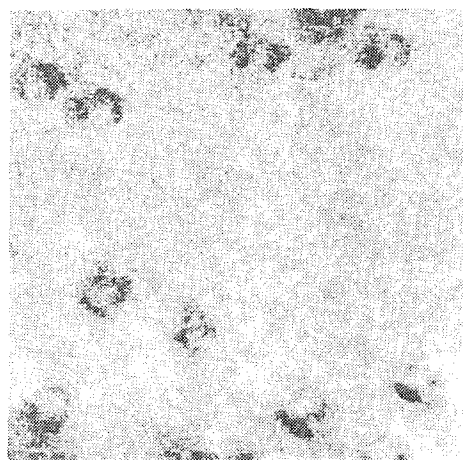
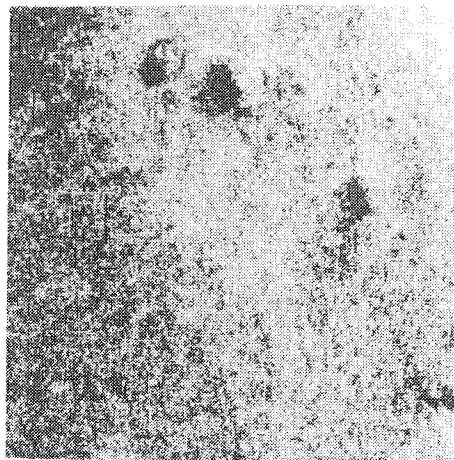


Figure 5 PL wavelength of quantum dots as a function of In composition of buffer layer.

quantum dots using a sequence of "TMIDMEA \rightarrow TMG \rightarrow AsH₃" (A) and a sequence of "TMGa \rightarrow TMIDMEA \rightarrow AsH₃" (B). It was found that the dot density using sequence A is higher than that using sequence B. Thus, the PL intensity of quantum dots using sequence A is stronger than that using sequence B. These results indicate a clear dependence of the formation of InGaAs quantum dots on the supply sequence in ALE.



(A)



(B)

Figure 6 Plan-view transmission electron microscopy image of quantum dots.

Summary

We investigated the PL emission characteristics of InGaAs/GaAs quantum dots emitting in the 1.3 μm region under various ALE growth conditions. We found that there is optimum growth temperature to fabricate high quality InGaAs/GaAs quantum dots. We demonstrated that the emission wavelength can be controlled by the number of ALE cycles and In composition of the buffer layer. Further, we showed the influence of emission characteristics on supply sequence in ALE.

References

- [1] Y. Arakawa and H. Sakaki, "Multidimensional quantum well laser and temperature dependence of its threshold current", *Appl. Phys. Lett.* 40(11), pp. 939-941, June 1982.
- [2] D. Leonard, M. Kishnamurthy, C. M. Reaves, S. P. Denbaars and P. M. Petroff, "Direct formation of quantum-sized dots from uniform coherent islands of InGaAs on GaAs surfaces", *Appl. Phys. Lett.* 63 (23), pp. 3203-3205, December 1993.
- [3] R. Notzel, J. Temmyo, H. Kamada, T. Furuta and T. Tamamura, "Strong photoluminescence emission at room temperature of strained InGaAs quantum disks (200-30 nm diameter) self-organized on GaAs (311)B substrates", *Appl. Phys. Lett.*, 65(4), pp. 457-459, July 1994.
- [4] J. Oshinowo, M. Nishioka, S. Ishida and Y. Arakawa, "Highly uniform InGaAs/GaAs quantum dots (~15 nm) by metalorganic chemical vapor deposition", *Appl. Phys. Lett.* 65 (11), pp. 1421- 1423, September 1994.
- [5] K. Mukai, N. Ohtsuka, M. Sugawara and S. Yamazaki, "Self-formed $\text{In}_{0.5}\text{Ga}_{0.5}\text{As}$ quantum dots on GaAs substrates emitting at 1.3 μm ", *Jpn. J. Appl. Phys.* Vol. 33, No.12A, pp. L1710-L1712, 1994.
- [6] M. Ozeki, N. Ohtsuka, Y. Sakuma and K. Kodama, "Pulsed jet epitaxy of III - V compounds", *J. Cryst. Growth* 107, pp. 102-110, 1991.
- [7] N. Ohtsuka and O. Ueda, "Growth of InAs and $(\text{InAs})_1(\text{GaAs})_1$ superlattice quantum well structures on GaAs by atomic layer epitaxy using trimethylindium-dimethylethylamine adduct", in *Gas-Phase and Surface Chemistry in Electronic Materials Processing*, edited by T. J. Mountziaris, F. T. J. Smith, P. R. Westmoreland, and G. R. Paz-Pujalt, *Mat. Res. Soc. Symp. Proc.* Vol. 334, pp. 225-229, 1994.
- [8] G. S. Solomon, J. A. Trezza and J. S. Harris, Jr., "Substrate temperature and monolayer coverage effects on epitaxial ordering of InAs and InGaAs islands on GaAs", *Appl. Phys. Lett.* 66 (8), pp. 991- 993, February 1995.
- [9] Y. Sakuma, M. Ozeki and K. Nakajima, "Arsenic desorption from the InAs(001) growth surface during atomic layer epitaxy", *J. Cryst. Growth* 130, pp. 147-152, 1993.

InP Islands as Self-Assembled Quantum Structures

C.M. Reaves^a, N.A. Cevallos^b, G.C. Hsueh^c, Y.M. Cheng^a
W.H. Weinberg^a, P.M. Petroff^{a,b}, and S.P. DenBaars^{a,b}

Center for Quantized Electronic Structures, University of California, Santa Barbara CA, 93106

^aMaterials Department, University of California, Santa Barbara CA, 93106

^bElectrical and Computer Engineering Department, University of California, Santa Barbara CA, 93106

^cChemical and Nuclear Engineering Department, University of California, Santa Barbara CA, 93106

Abstract

Self-assembled quantum dots have been grown in the InP/GaInP material system on GaAs substrates. The different types of dots, differentiated by size, exhibit different luminescence features. In particular, peaks at 1.82 eV and 1.57 eV have been observed. Two methods have been utilized to study emission from small regions of the sample: photoluminescence of samples with etched mesas, and cathodoluminescence of samples that have been thinned for electron microscopy. Results from both methods are discussed.

Introduction

Electron confinement in three dimensions (3D) for quantum structures implies novel features for semiconductor device and optoelectronic applications. The motivation to effectively obtain such structures arises from the promise for optical devices due to an inherently sharp density of states (DOS) as well as the switching or capacitance effects resulting from single electron loading for device applications. Previous attempts to process these structures have resulted in non-ideal structures. Recent experiments involving self-assembled quantum dots or islands have been developed via vapor phase epitaxy (VPE) and molecular beam epitaxy (MBE). These islands form as a means of strain energy reduction during the second stage of the the Stranski-Krastanov growth mode. Quantum structures grown by this method that exhibit interesting luminescence have been synthesised with InP on GaInP (1-4), InP on GaAs (5), In(Ga)As on GaAs (6-9), and AlInAs/AlGaAs (10).

In this work, we examine the luminescence properties of InP quantum dots embedded in a GaInP layer. In particular, we will focus on luminescence emission from small regions. To achieve improved spatial resolution, we have utilized photoluminescence of etched samples and cathodoluminescence of thinned samples.

Experimental Details

The samples used in this study were grown by atmospheric pressure metalorganic chemical vapor deposition (MOCVD). Two variations in sample structure were explored; they will be referred to as sample A and sample B. The InP layers were grown with an injected tertiarybutylphosphine partial pressure of 3.2 Torr and an injected trimethylindium partial pressure of 0.014 Torr for sample A and 0.002 Torr for sample B. The substrates were undoped singular GaAs(100). Susceptor temperatures ranged from 640° to 650° C. In all cases, the GaInP composition is lattice matched to GaAs. Additional growth details have been presented in previous reports (1,2).

Sample A was grown as follows: 2000 Å of GaInP was grown on a GaAs substrate, followed by a 2.3 s deposition of InP. The InP layer was capped with a 300 Å layer of GaInP. Sample B was grown as follows: a 1000 Å GaAs buffer layer was grown on a GaAs substrate, followed by a 300 Å layer of GaInP. InP was deposited for 9 s at a lower growth rate. The InP layer was capped with a 300 Å layer of GaInP.

The InP islands have been examined by atomic force microscopy and transmission electron microscopy (1,2). In brief, three types of islands are observed for these growth conditions. Small islands have a height of ~30 Å and a base diameter of ~1200 Å. Medium size islands have a height of ~230 Å and a base diameter of ~1200 Å. These medium islands are

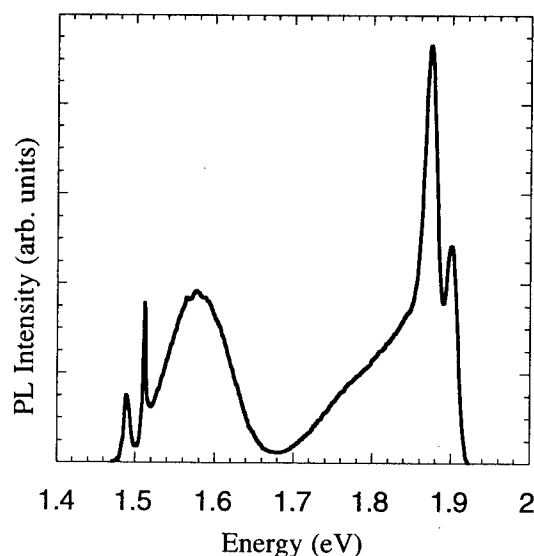


Figure 1. Photoluminescence from sample A at 1.4 K. The features at 1.819 eV (shoulder) and 1.569 eV are attributed to the InP quantum dots.

cap-shaped and coherently strained. Large islands are observed which contain defects and often exhibit facets. The approximate densities are 1 island/ μm^2 for the small islands, 2 islands/ μm^2 for the medium island and < 0.1 islands/ μm^2 for the large islands.

Photoluminescence (PL) was performed on samples submerged in pumped liquid helium. An argon ion laser was used as an excitation source at 4880 Å with a typical power of 10 mW. Luminescence was dispersed by a single grating monochromator and measured by a cooled GaAs photomultiplier. Cathodoluminescence (CL) was performed on samples attached to a cold finger cooled by liquid helium. Samples were placed in a scanning transmission electron microscopy and exposed to an electron beam accelerated with a 120 kV potential. Luminescence was collected by a parabolic mirror, dispersed by a double grating monochromator and measured by a cooled GaAs photomultiplier.

To prepare samples for cathodoluminescence, we use mechanical grinding, dimple grinding, and a final thinning from the backside of the sample, a procedure commonly used to prepare samples for transmission electronic microscopy. For final sample thinning of samples, ion milling and wet chemical etches were used. By removing the substrate, there is less electron backscatter, leading to smaller lateral probe areas. To prepare

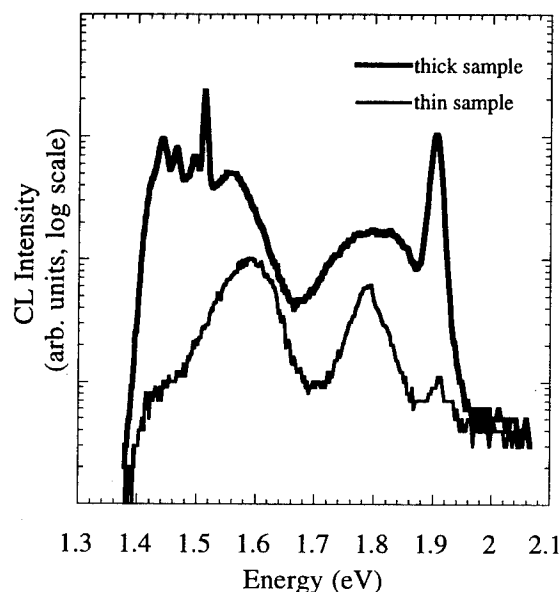


Figure 2. Cathodoluminescence of sample B at 10 K. Note that the intensity axis is logarithmic. Heavy line indicates a spectrum of a thick sample and the light line indicates a spectrum of a sample that has been thinned and probed with a condensed electron beam.

samples for reduced area PL, circular mesas, 3-36 μm diameter were etched into the epilayers. To etch the GaInP and InP layers, $\text{HCl}:\text{CH}_3\text{COOH}:\text{H}_2\text{O}_2$ in a ratio of 1:5:1 was used (10).

Results and Discussion

Broad area photoluminescence was performed to identify the features in the spectrum. As seen in Fig. 1, there are six primary features. The peaks at 1.513 eV and 1.490 eV are the GaAs free exciton transitions and a GaAs acceptor-related transitions. The peak at 1.896 eV is the GaInP in the barrier layers. This corresponds to measurements on bulk samples grown under similar conditions. We attribute the peak at 1.873 eV to the InP quantum well formed during the two-dimensional stage of the Stranski-Krastanov growth mode (1,2). The peak at 1.819 eV is due to the small InP island and the peak at 1.569 eV is due to the medium island. These results are similar to those reported by Carlsson, *et al.* (3)

Although the two samples in this study are slightly different, the broad area luminescence results are similar. The spectrum indicated by

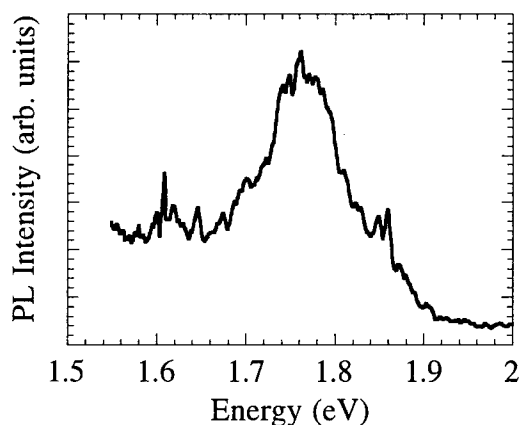


Figure 3. Isolated InP Island Photoluminescence at 3K. Mesa diameter approximately 11-16 μm .

the thick line in Figure 2 is the cathodoluminescence from sample B. The GaAs features are reproduced and the feature at 1.9 eV is due to the GaInP layers. The broad luminescence peaks are present at 1.80 eV for the small island and 1.56 eV for the medium islands. Two additional features are seen in the 1.42 -1.48 eV range which we currently can not explain.

Looking at the CL spectrum for the thinned sample in Fig. 2, the peaks related to the GaAs and the low energy peaks are not present and the peak for the GaInP is much less intense. For the quantum dot peaks, we see that the peaks are narrower. The narrowing can be explained by discrete peaks from an ensembles of dots.

With these self-assembled quantum dots, there is some variation in the size of the dots. This size variation will lead to a variation in the energy levels. A range in energy levels leads to a broad luminescence feature. If a smaller region of the sample is excited, a smaller ensemble of dots will be probed. In the limit of this case, emission from a handful of dots should appear as several narrow peaks.

Isolation of the InP islands in etched mesas have produced luminescence with slightly improved features. Full width at half maximum (FWHM) have been seen to decrease with size of the mesas used. Figure 3 illustrates the the wide emissions obtained due to high excitation powers used on the mesas. Island peaks at 1.61, 1.75, and 1.85 eV.

Figure 4 shows spectra from a thinned region of sample B. Although the signal is weak with respect to the noise, several features can be resolved. The largest feature at 1.825 eV has a FWHM of 8.5 meV. Other features have

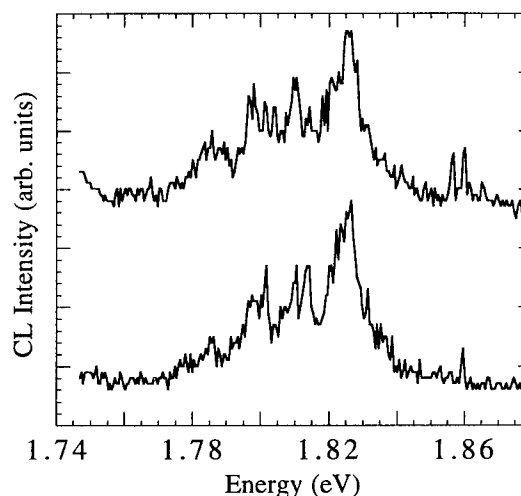


Figure 4. Cathodoluminescence from a thinned region of sample B at 10 K. Due to the weak signal, two spectra from the same spot are shown to help discern luminescence from the noise.

similar widths. In comparison with Marzin, *et al.*, (9) who observed 0.1 meV wide features, we believe we may still be observing emission feature from several dots.

Nishi, *et al.*, (12) calculated the band structure for a spherical InP quantum dot embedded in a GaInP matrix by analytical and finite element methods. For the unstrained case, GaInP/InP/GaInP is a type I heterostructure, with both electrons and holes spatially confined in the InP. Taking into account the strain effects, the conduction band edge increases by 0.19 eV and the valence band edge decreases by 0.11 eV. The net result is that the InP dot will have a calculated bandgap of 1.65 eV (not considering quantum confinement), with a conduction band offset of 0.17 eV and a valence band offset of 0.21 eV (for the lower valence subband). We have observed luminescence from dots at energies not only above the bandgap, as expected for quantum confined structures, but also below the the band gap. Additional studies, both experimental and theoretical, are needed to address these points.

Summary

Self-assembled quantum dots of InP embedded in a GaInP matrix exhibit promising luminescence features. By using etched mesas and thinned samples, improved spatial resolution has been achieved.

Acknowledgements

The authors gratefully acknowledge financial support by QUEST, an NSF Science and Technology Center for Quantized Electronic Structures (grant no. DMR 91-20007), by a NSF Materials Synthesis and Processing Grant (#9202290) (SPD),

References

1. C.M. Reaves, V. Bressler-Hill, M. Krishnamurthy, S. Varma, P.M. Petroff, W.H. Weinberg, and S.P. DenBaars, Sixth Conference on Indium Phosphide and Related Materials, 27-31 March 1994, Santa Barbara, CA, United States, 611-614; C.M. Reaves, V. Bressler-Hill, S. Varma, W.H. Weinberg, and S.P. DenBaars, *Surf. Sci.*, in press.
2. S.P. DenBaars, C.M. Reaves, V. Bressler-Hill, S. Varma, W.H. Weinberg and P.M. Petroff, *J. Crystal Growth*, **145**, 721-727 (1994).
3. N. Carlsson, W. Seifert, A. Petersson, P. Castrillo, M. E. Pistol, and L. Samuelson, *Appl. Phys. Lett.*, **65**, 3093-3095 (1994).
4. A. Kurtenbach, K. Eberl, and T. Shitara, *Appl. Phys. Lett.*, **66**, 361-363 (1995).
5. J. Ahopelto, A. A. Yamaguchi, K. Nishi, A. Usui, H. Sakaki, *Jpn. J. Appl. Phys.*, **32**, L32-L35 (1993).
6. D. Leonard, M. Krishnamurthy, C.M. Reaves, S.P. DenBaars, and P.M. Petroff, *Appl. Phys. Lett.*, **63**, 3203-3205 (1993); D. Leonard, M. Krishnamurthy, S. Fafard, J.L. Merz, and P.M. Petroff, *J. Vac. Sci. Technol.*, **B 12**, 1063-1066 (1994); D. Leonard, S. Fafard, K. Pond, Y.H. Zhang, J.L. Merz, and P.M. Petroff, *J. Vac. Sci. Technol.*, **B 12**, 2516-2520 (1994).
7. P. Chen, Q. Xie, A. Madhukar, L. Chen, and A. Konkar, *J. Vac. Sci. Technol.*, **B 12**, 2568-2573 (1994).
8. J. Oshinowo, M. Nishioka, S. Ishida, and Y. Arakawa, *J. Crystal Growth*, **145**, 986-987 (1994).
9. J.-Y. Marzin, J.-M. Gérard, A. Izaël, D. Barrier, and G. Bastard, *Phys. Rev. Lett.*, **73**, 716-719 (1994).
10. S. Fafard, R. Leon, D. Leonard, J.L. Merz, and P.M. Petroff, *Phys. Rev.*, **B 50**, 8086-8089 (1994).
11. J.R. Flemish and K.A. Jones, *J. Electrochem. Soc.*, **140**, 844-847 (1993).
12. K. Nishi, A.A. Yamaguchi, J. Ahopelto, A. Usui, and H. Sakaki, *J. Appl. Phys.*, **76**, 7437-7445 (1994).

Optical properties of self-organized InGaAs/InP dots ^{WP61}

J. Ahopelto

VTT Electronics, Otakaari 7 B, FIN-02150 Espoo, Finland

H. Lipsanen and M. Sopanen

Optoelectronics Laboratory, Helsinki University of Technology, Otakaari 1, FIN-02150 Espoo, Finland

The possibility to tune the emission wavelength and to reduce the linewidth of self-organized dots is studied. Thin layers of $\text{In}_{0.5}\text{Ga}_{0.5}\text{As}$ was selectively deposited on nanoscale InP islands on (100)GaAs. A tuning range of 100 meV was achieved for the emission from the dots. Also, a minimum FWHM of 8.5 meV was measured from an ensemble of dots, showing that the heteroepitaxial layer on the islands tends to homogenize the active volume of the dots.

Introduction

Utilization of lattice mismatch-induced 3-dimensional growth to form coherent nanoscale islands provides a means to fabricate quantum dot structures with a relative ease. The properties of such dots are determined, besides by the size, by the strain and the composition of the dots. The main difficulty in the utilization of self-organized dots is the inhomogeneous broadening due to a finite size distribution. Although very narrow photoluminescence (PL) peaks have been reported originating from single dots [1], the ensemble line width of such dots is relatively broad, of the order of 50-80 meV [1-3]. Narrower line widths have been reported from InP dots grown by molecular beam epitaxy [4] and from dots grown on (311)B surfaces [5]. The inhomogeneous broadening may limit the use of the self-organized dots in device applications.

The two difficult tasks to be solved concerning the self-organized dots are the minimization of the size inhomogeneity of the dots and the controllability of the emission wavelength. These requirements may be exclusive if the dots are formed from a single material composition. It was recently shown that it is possible to grow selectively heteroepitaxial layers on nanoscale islands to form "heterodots" [6]. In this work we have studied two series of such heterodots with different sizes. By using the structure the inhomogeneous broadening can be reduced and the tunability of the properties of the dots can be achieved. The approach relies on the above mentioned selectivity and to the tendency of the island size to saturate to a certain growth conditions-dependent value.

Experimental

The two structures studied in this work are schematically shown in Fig. 1. The structures were grown by atmospheric pressure metalorganic vapor phase epitaxy (MOVPE) using trimethylgallium (TMGa),

trimethylindium (TMIn), tertiarybutylarsine (TBAs) and tertiarybutylphosphine (TBP) as source materials. As substrates 2°-off (100)GaAs wafers were used.

The structure "A" (Fig. 1(a)) consisted of very shallow InP islands, rather like an undulating wetting layer, and of few larger, partially relaxed islands. To grow such a structure, 2-3 monolayers (ML) of InP was first

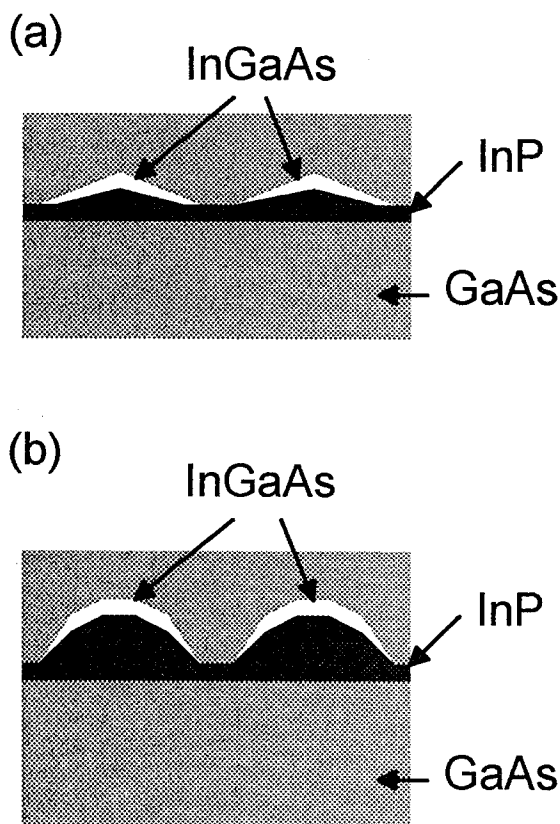


Fig. 1 The two structures studied in this work shown schematically. The structure "A" is shown in (a) and the structure "B" in (b).

deposited at a rate of 0.25 ML/s. Various amounts of $\text{In}_{0.5}\text{Ga}_{0.5}\text{As}$ was then deposited on this surface at a rate of 0.5 ML/s. For optical characterization the islands were capped with a layer of GaAs. Strained quantum wells (QW) without the InP islands but with the same amounts of $\text{In}_{0.5}\text{Ga}_{0.5}\text{As}$ were grown for reference. All the "A" structures were grown at 650 °C.

The structure "B" (Fig. 1(b)) consisted of well developed InP islands with various amounts of $\text{In}_{0.5}\text{Ga}_{0.5}\text{As}$ on top of the islands. The InP islands were first formed by depositing 3-4 ML of InP at 620 °C at a deposition rate of 1.7 ML/s. The temperature was then increased to 650 °C and various amounts of $\text{In}_{0.5}\text{Ga}_{0.5}\text{As}$ was then deposited at rates of 0.5-3.4 ML/s. For optical characterization the islands were capped with a GaAs layer grown at 580 °C.

The size of the islands was obtained from atomic force microscope (AFM) images measured from samples without the GaAs cap layer. The PL measurements were performed at 12 K with a liquid nitrogen-cooled Ge detector using the 488 nm line from Ar⁺-ion laser for excitation.

Results

The deposition of InP on GaAs results in formation of small islands due to lattice mismatch-induced 3-dimensional growth [6,7]. The size and density of the islands can be controlled by the growth parameters. The growth temperature and the deposition rate have a strong effect on the island size and density. At low deposition rate more like an undulating wetting layer is formed instead of distinct islands. By increasing the deposition rate the island formation is enhanced. At higher rates homogeneous islands are formed and the deposition temperature determines the height of these islands. This phenomenon is utilized in this work in forming the heterodots. In addition to the homogeneous islands, larger islands are formed at areal densities two to three orders of magnitude lower than the density of the homogeneous islands. Details of the island formation dependence on the growth parameters will be published elsewhere [8].

Structure "A"

Deposition of InP on (100)GaAs at 650 °C at low deposition rate results in formation of a structure with undulating surface consisting of 2 to 3 ML high and 50 nm wide islands. The areal density of these small islands is close to 10^{10} cm^{-2} . In addition to these shallow islands, larger islands are formed. These are 300-500 nm wide and 100-150 nm high with an areal density of 10^7 cm^{-2} . The large islands are at least partially relaxed [9].

The deposition of $\text{In}_{0.5}\text{Ga}_{0.5}\text{As}$ on this surface results in increase in the height of the undulation. For example, 3 ML of $\text{In}_{0.5}\text{Ga}_{0.5}\text{As}$ increases the height of the shallow islands to 4-5 ML, suggesting that the growth occurs preferentially on top of the islands.

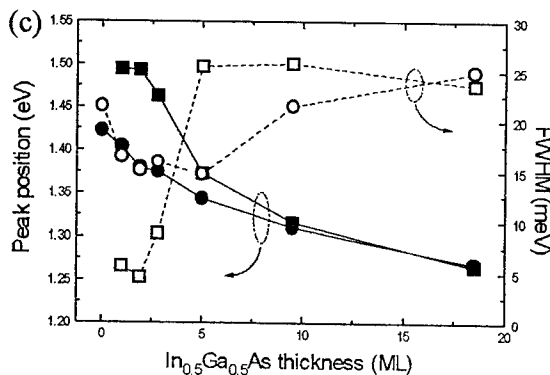
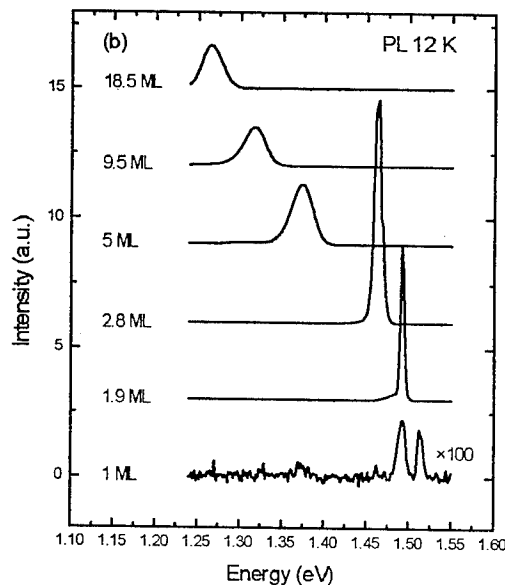
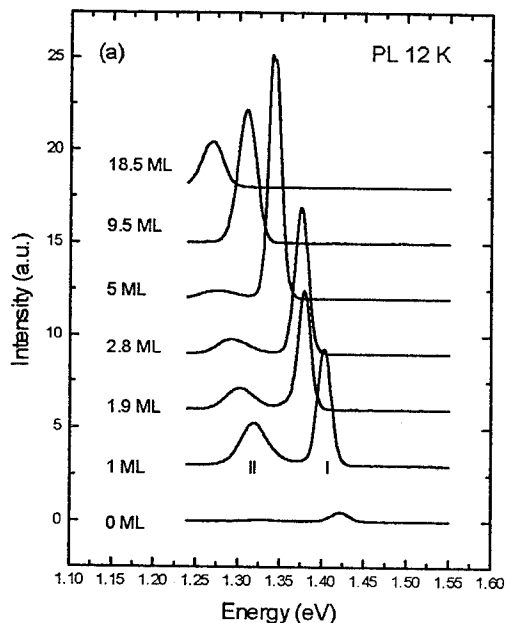


Fig. 2 PL spectra from the structure "A" samples with various amounts of $\text{In}_{0.5}\text{Ga}_{0.5}\text{As}$ (a). PL spectra from the corresponding QW samples (b). Peak position and FWHM as a function of the $\text{In}_{0.5}\text{Ga}_{0.5}\text{As}$ thickness for the "A" samples (circles) and QW samples (squares) (c).

In Fig. 2(a) are shown PL spectra taken at 12 K from samples with various amounts of $\text{In}_{0.5}\text{Ga}_{0.5}\text{As}$. The nominal deposited thickness is shown beside each spectrum. The peak I is assigned to the emission from the shallow islands and the peak II is related to the partially relaxed islands. In Fig. 2(b) are shown the PL spectra from the reference strained QW's with the same amounts of $\text{In}_{0.5}\text{Ga}_{0.5}\text{As}$ as in the samples in 2(a). In Fig. 2(c) are shown the peak position and full width at half maximum (FWHM) values as a function of deposited $\text{In}_{0.5}\text{Ga}_{0.5}\text{As}$ layer thickness for both of the structures. As can be seen, the emission wavelengths of the dot samples (structure "A") are redshifted from the corresponding QW peaks and the wavelength can be tuned in the range of 1.3-1.4 eV. The FWHM varies from 15 to 25 meV, being smaller than the corresponding QW value in the intermediate range of the $\text{In}_{0.5}\text{Ga}_{0.5}\text{As}$ thicknesses.

Structure "B"

At higher InP growth rates distinct islands are formed with the height of the homogeneous islands depending on the deposition temperature. The height of the InP islands grown at 620 °C saturates to 18-20 nm. The areal density is $3 \times 10^9 \text{ cm}^{-2}$. At 650 °C the saturation height is 24-26 nm. In Fig. 3(a) is shown an AFM image of InP islands on (100)GaAs 2°-off substrate grown at 620 °C at the growth rate of 1.7 ML/s. In Fig. 3(b) is shown an AFM image of the structure in Fig. 3(a) after the deposition of 1 ML of $\text{In}_{0.5}\text{Ga}_{0.5}\text{As}$ at 650 °C. The height of the homogeneous islands is increased to 22-26 nm which corresponds roughly to the saturated height of the InP islands grown at 650 °C. In addition to the homogeneous islands, 60-100 nm high islands are formed at a density of 10^7 cm^{-2} . The increase in the height of the islands corresponds roughly to the amount of the deposited $\text{In}_{0.5}\text{Ga}_{0.5}\text{As}$, assuming that the surface coverage of the islands is around 5 %. After the deposition of 2.1 ML of $\text{In}_{0.5}\text{Ga}_{0.5}\text{As}$, the height of the homogeneous islands is 25-28 nm and the height of the larger islands is increased to 100-150 nm. When the amount of the deposited $\text{In}_{0.5}\text{Ga}_{0.5}\text{As}$ is increased to 3.5 ML, the height of the homogeneous islands increases to 27-30 nm. Also the density of the larger islands increases. The results suggests that the size of the homogeneous islands tend to saturate and the extra material is incorporated into the large islands.

PL spectra from these heterodots with various amounts of $\text{In}_{0.5}\text{Ga}_{0.5}\text{As}$ are shown in Fig. 4. The spectra from samples containing the $\text{In}_{0.5}\text{Ga}_{0.5}\text{As}$ layers have four peaks, labeled as I, II, III and IV. The peak I comes from the GaAs cladding layers. The peak II originates from the wetting layer (cf. the emission I from the structures "A", Fig. 2(a)). The peak does not shift with the increasing amount of the deposited $\text{In}_{0.5}\text{Ga}_{0.5}\text{As}$, like in the case of the structure "A", because the extra material is incorporated into the islands. The peak III is assigned to the emission from the $\text{In}_{0.5}\text{Ga}_{0.5}\text{As}$ layer on top of the InP islands. If the $\text{In}_{0.5}\text{Ga}_{0.5}\text{As}$ grew homogeneously over the surface, the wetting layer emission (peak II) would have

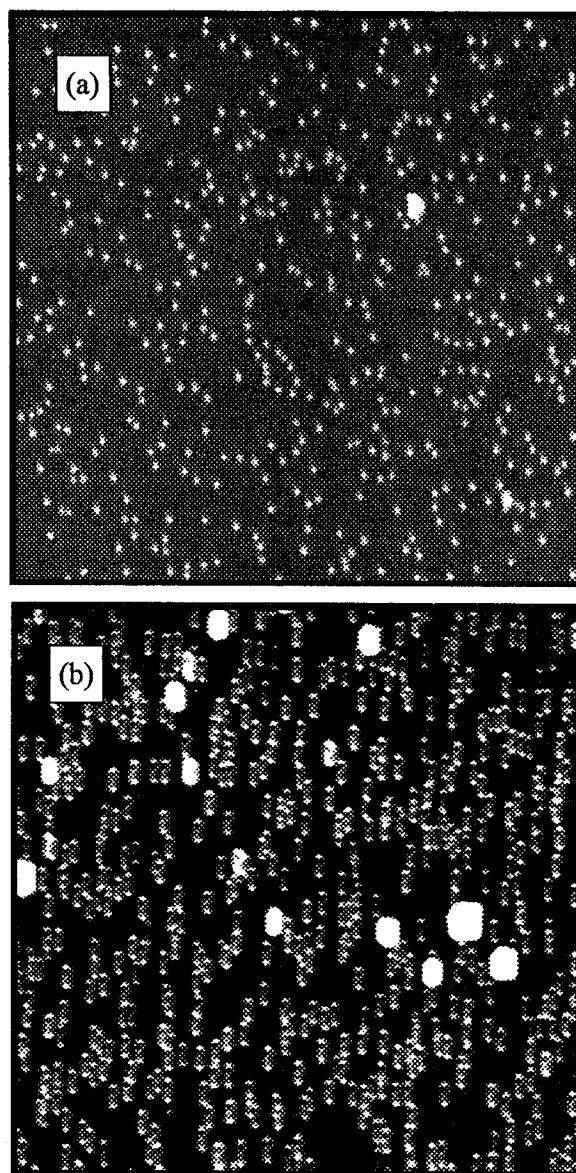


Fig. 3 AFM images ($5 \times 5 \mu\text{m}^2$) of InP islands on (100)GaAs grown at 620 °C (a), and of nominally 1 ML of $\text{In}_{0.5}\text{Ga}_{0.5}\text{As}$ grown at 650 °C on top of InP islands similar as shown in (a), (b). The double images of the islands in (b) are due to the AFM tip.

shifted towards lower energies. Also, the peak III would probably have merged with peak II in that case. The origin of the peak IV is a type II emission from the InP/GaAs interface in the bottom of the islands, as suggested by strain distribution calculations using finite element method (FEM). This means that the sites where the radiative transitions III and IV occur are spatially separated. A weak emission at around 1.3 eV can be observed from the sample with 3.5 ML of $\text{In}_{0.5}\text{Ga}_{0.5}\text{As}$, corresponding the emission from partially relaxed islands in the structure "A" (peak II in Fig. 2(a)).

The FWHM values of the peak III in Fig. 4 are 8.5-9.5 meV. These values are about half of the FWHM values of the structure "A" and only twice as large as the

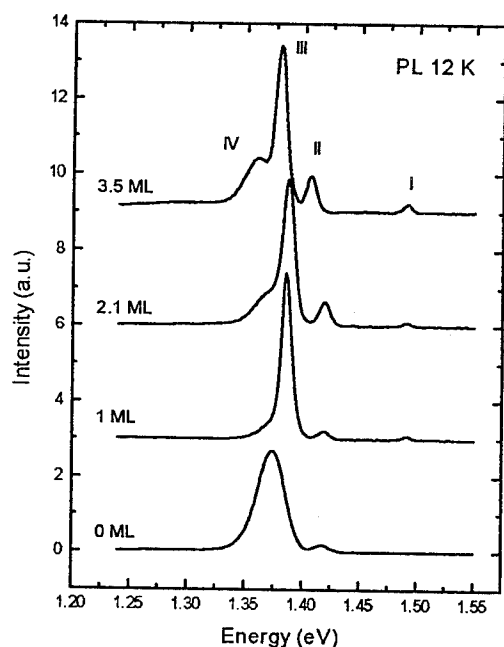


Fig. 4 PL spectra from structure "B" samples with various amounts of $\text{In}_{0.5}\text{Ga}_{0.5}\text{As}$. The numbers on the left hand side of each spectrum corresponds to the nominal, 2-dimensional thickness of the deposited $\text{In}_{0.5}\text{Ga}_{0.5}\text{As}$ layer.

FWHM of the peaks from the reference QW's with similar amounts of $\text{In}_{0.5}\text{Ga}_{0.5}\text{As}$. This narrowing can be partially attributed to the thicker $\text{In}_{0.5}\text{Ga}_{0.5}\text{As}$ layers in the structures "B".

Summary

In this work the possibility to tune the emission wavelength and to reduce the emission linewidth of self-organized dots by selective heteroepitaxy by MOVPE was studied. Various amounts of $\text{In}_{0.5}\text{Ga}_{0.5}\text{As}$ was deposited on two different types of nanoscale InP islands, grown on (100)GaAs. The two types consisted of very shallow islands with the height of the order of 2-3 ML or well developed islands with the height of 18-20 nm. A tuning range from 1.3 to 1.4 eV was achieved for the emission in the case of the shallow islands. The minimum FWHM was 15 meV for these structures. The FWHM was decreased to 8.5 meV when $\text{In}_{0.5}\text{Ga}_{0.5}\text{As}$ was deposited on the 18-20 nm high InP islands. This small value show that it is possible to homogenize the emitting volume in the self-organized dots.

References

1. J.-Y. Marzin, J.-M. Gérard, A. Israël, D. Barrier, and G. Bastard, *Phys. Rev. Lett.* **73**, 716 (1994).
2. D. Leonard, M. Krishnamurty, S. Fafard, J. L. Merz, and P. M. Petroff, *J. Vac. Sci. Technol. B* **12**, 1063 (1994).
3. N. Carlsson, W. Seifert, A. Petersson, P. Castrillo, M. E. Pistol, and L. Samuelson, *Appl. Phys. Lett.* **65**, 3093 (1994).
4. A. Kurtenbach, K. Eberl, and T. Shitara, *Appl. Phys. Lett.* **66**, 361 (1995).
5. H. Kamada, R. Nötzel, J. Temmyo, T. Furuta and T. Tamamura, in *Symposium Record of 13th Symposium on Alloy Semiconductor Physics and Electronics, Izu-Nakaoga, 1994*, pp. 25-26.
6. J. Ahopelto, H. Lipsanen, M. Sopanen, T. Koljonen, and H. E.-M. Niemi, *Appl. Phys. Lett.* **65**, 1662 (1994).
7. J. Ahopelto, A. A. Yamaguchi, K. Nishi, A. Usui, and H. Sakaki, *Jpn. J. Appl. Phys.* **32**, L32 (1993).
8. M. Sopanen, H. Lipsanen and J. Ahopelto, to be published
9. S. P. DenBaars, C. M. Reaves, V. Bressler-Hill, S. Varma, W. H. Weinberg and P. M. Petroff, *J. Crystal Growth* **145**, 721 (1994).

J. Hammersberg¹, M. Notomi², H. Weman¹, M. Potemski³, H. Sugiura², M. Okamoto², and T. Tamamura²

¹ Dep. of Physics and Measurements Technology, Linköping University, S-581 83 Linköping, Sweden

² NTT Opto-electronics Lab., 3-1 Morinosato-Wakamiya, Atsugi, Kanagawa 243-01, Japan

³ Grenoble High Magnetic Field Laboratory, MPI-FKF and CNRS, F-38042 Grenoble, France

Photo luminescence experiments on strained $\text{InAs}_{0.48}\text{P}_{0.52}/\text{InP}$ quantum wires show that the wire-width-dependent blue shift of the transition energy is remarkable larger than the blue shift in lattice matched quantum wires. With magneto-luminescence measurements we are able to prove that lateral confinement effects only partly is the origin of the observed blue shift. The other part comes from the strain energy which is wire width dependent in spite of a constant lattice-mismatch. Our experimental result are quantitatively supported by theoretical calculations.

Introduction

Two-dimensional confinement of carriers in quantum wires (QWW's) is an important phenomenon, both from a fundamental and applied point of view. The confinement in two or three directions is expected to give rise to sharp peaks in the electronic density of states.¹ This should lead to an improved performance of semiconductor lasers due to a narrower gain spectra.² Ideally strained QWW lasers are expected to have the performance enhanced relative to lattice-matched QWW lasers due to a decreased coupling in the valence band and a reduced non-parabolicity.³

Epitaxial growth of semiconductor structures consisting of alternating layers of lattice mismatched (strained) materials makes it possible to modify the original bulk band structure in the semiconductor, i.e. tailor the conduction band and the three valence bands separately. However, in the case of strained QWW's, due to the lattice mismatch between the wire and the lateral barrier, QWW's are not only strained biaxially as the quantum well film (QWF), but also in the growth direction. This has been treated theoretically for compressively strained $\text{InGaAs}/\text{GaAs}$ QWW's.⁴ The problem was treated assuming a three-directional hydrostatic pressure where the wire region is completely compressed by the barrier on all sides. This compression is believed to make the critical thickness of the wire smaller than in the quantum well case, since the strong three-dimensional compression will introduce relaxation through dislocations.⁴ An ideal three-dimensional compressively strained quantum wire would be insensitive to the wire size as the strain is uniform in the wire. However, recent experimental results on compressively strained $\text{In}_{0.2}\text{Ga}_{0.8}\text{As}/\text{GaAs}$ QWW's have shown that the strain distribution can be non uniform in QWW's and that an ideal three-directional compressive strain is not realistic for quantum wires with a large cross-sectional aspect ratio.⁵ By cross sectional transmission electron microscopy it was found that the wire sidewall was under a large compressive strain in the growth direction in comparison to the centre of the wire. This distortion from the additional compressive strain from the barrier had a detected extension in the order of 100 Å into the wire. Due to this the lateral barrier material near the side wall was under a vertical tensile strain by the $\text{In}_{0.2}\text{Ga}_{0.8}\text{As}$ wire.⁵

The quantum wires used in this study are fabricated through e-beam lithography, selective wet-etching of a

strained $\text{InAs}_{0.48}\text{P}_{0.52}/\text{InP}$ QWF. This technique provides the ability to vary the lateral width of the wire without affecting the wire composition. To probe the electronic structure in these strained QWW's we apply a magnetic field perpendicular to the lateral wire potential. The magnetic field generates a lateral harmonic potential where the confinement strength can be varied with the magnetic field strength. In the quantum well case, this potential will generate Landau levels, with a linear energy shift with an increasing magnetic field. However, for QWW's the lateral wire confinement potential is coupled to the magnetic potential, and the magnetic field induced potential has to dominate the lateral potential to be able to generate similar Landau level states as in a QWF. Therefore, a gradual change from wire confinement into magnetic confinement can be observed as the lateral subband states merge into Landau levels states (centred in the middle of the wire) at high fields. We have recently studied this effect in lattice-matched InGaAs/InP quantum wires (fabricated in the same way as the $\text{In}_{0.53}\text{As}_{0.47}\text{P}/\text{InP}$ QWW's) and can therefore make an accurate comparison between lattice-matched and strained QWW's to sort out the strain effects on the electronic structure.^{6,7}

Experimental details

The QWW's fabricated through e-beam lithography, selective wet-etching and overgrowth (similar to the fabrication technique presented in ref. 8). The original structure is a 50 Å thick compressively strained (-1.5 %) single $\text{InAs}_{0.48}\text{P}_{0.52}/\text{InP}$ QWF. The QWF was grown by chemical beam epitaxy on a (001) InP substrate.⁹ The resist pattern on top of the sample was formed by electron beam lithography in the (110) direction.

The high magnetic field measurements (28T) were performed in the Faraday configuration using a 10 MW hybrid magnet at Grenoble High Magnetic Field Laboratory. The sample was excited using the 514.5 nm line from an Ar^+ -ion laser. The laser light was coupled to the sample through an optical fiber with a core diameter of approximately 600 micrometer. The luminescence was collected with the same fiber, dispersed by a Jobin-Yvon single grating spectrometer and detected with a cooled Ge detector using a conventional look-in technique. The excitation power level was approximately 5 W/cm². The experiments were performed at low temperature, 2 K.

Experimental results and discussion

The zero-magnetic field PL spectra of the strained $\text{InAs}_{0.48}\text{P}_{0.52}/\text{InP}$ QWW's show a clear blue shift which is increasing for narrower QWW's as seen in Figure 1 (a). This is well documented in the literature and is due to the increased lateral confinement as the wire width becomes narrower. However, the striking result is that this blue shift still remains at high magnetic field strength, as seen in Figure 1 (b) and (c). This effect can also be seen in Figure 2, which is showing the energy position as function of magnetic field strength. The arrows indicate where the cyclotron orbit diameter $d_c = 2\sqrt{\hbar(2n+1)}/eB$ is the same as the wire width. This field is usually used as an approximate "turning point" from lateral quantum wire confinement to magnetic confinement. However, it is only at magnetic fields higher than this "turning point" where the shift of the transition energies is similar to the shift in the QWF reference, where the magnetic confinement can be considered to completely dominate the lateral confinement. The energy separation between different QWW's and the QWF at high magnetic field strength is in sharp contrast to the results for lattice matched $\text{In}_{0.53}\text{Ga}_{0.47}\text{As}/\text{InP}$ QWW's. There the energy separation between different QWW's is quenched in a high magnetic field. This can be seen in Figure 3 where the energy separation of the lowest subband between a 200 Å and a 350 Å wide InGaAs/InP QWW as a function of magnetic field strength is shown. It can clearly be seen that the energy separation is decreasing towards zero as the magnetic field strength is increased. The absence of any energy separation above 15 T is indicating that the lateral wire confinement is quenched by the

magnetic confinement, and that the electronic states in the wire have merge into Landau states. However, when plotting the energy separation between a 230 Å and a 550 Å wide strained InAsP/InP QWW's (Fig. 3), we observe a similar decrease and flattening at high field strength, but the energy separation saturates at a large finite energy value at high fields. We interpret this large finite energy value to be due to the compressive strain from the lateral barrier. In Figure 4 we plot the energy separation between the luminescence peak of the 230 Å and 550 Å wide strained InAsP/InP QWW's and the reference QWF. From these results we can see that the strain induced shift is larger for narrower wires, indicating that the relative distortion by the additional compressive strain is larger in narrower wires. For QWF's the in-plane strain is determined from the bulk lattice constant of the substrate a_S , and the epitaxial layer a_L , by $\epsilon_{//} = a_S/a_L - 1$ (for $\text{InAs}_{0.48}\text{P}_{0.52}/\text{InP}$ this gives a compressive strain $\epsilon_{//}$ equal to -1.5 %). Since the QWF is not subjected to any additional strain in the growth direction, the strain component in the growth direction, ϵ_{\perp} , for a (001) interface is proportional to $\epsilon_{\perp} = -2(C_{12}/C_{11})\epsilon_{//}$ where C_{11} and C_{12} are the elastic constants.⁹ For the $\text{InAs}_{0.48}\text{P}_{0.52}/\text{InP}$ QWF, ϵ_{\perp} is equal to +1.67 %. For strained quantum wires, an additional compressive strain due to the lateral barrier will decrease ϵ_{\perp} and thereby increase the total hydrostatic compression through the fractional volume change equal to $2\epsilon_{//} + \epsilon_{\perp}$. This increased hydrostatic compression gives via a product with the deformation potentials an increased bandgap. As an arbitrary stress can be treated as superposition of hydrostatic- and shear-strain, one also has to consider the

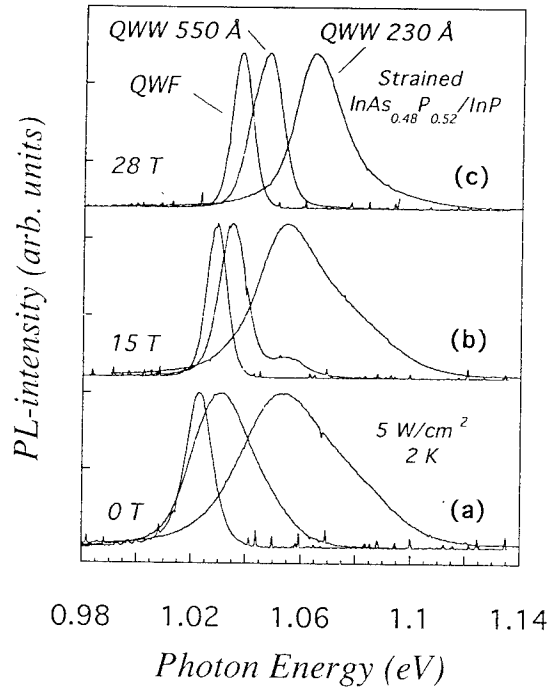


Figure 1. Magneto-luminescence spectra of strained $\text{InAs}_{0.48}\text{P}_{0.52}/\text{InP}$ quantum wires (230 Å and 550 Å wide) and quantum well film reference at zero field (a), at 15 T (b), and at 28 T (c).

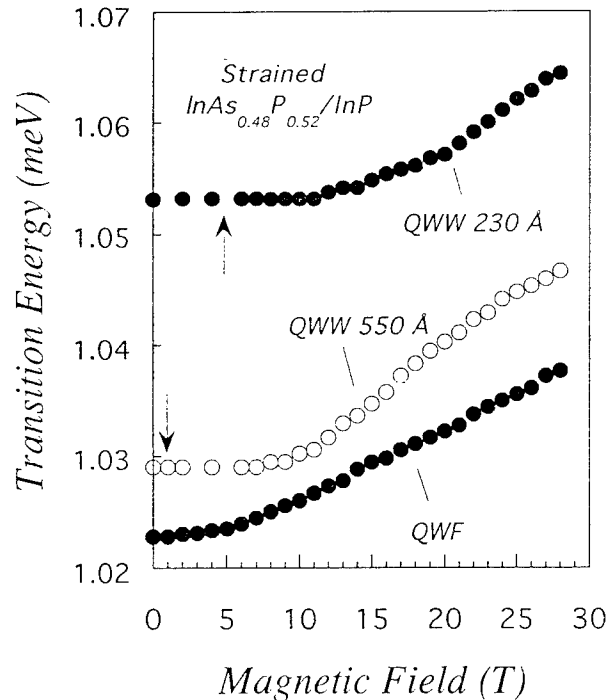


Figure 2. The transition energy position as function of the magnetic field for the strained $\text{InAs}_{0.48}\text{P}_{0.52}/\text{InP}$ quantum wires (230 Å and 550 Å wide) and quantum well film reference.

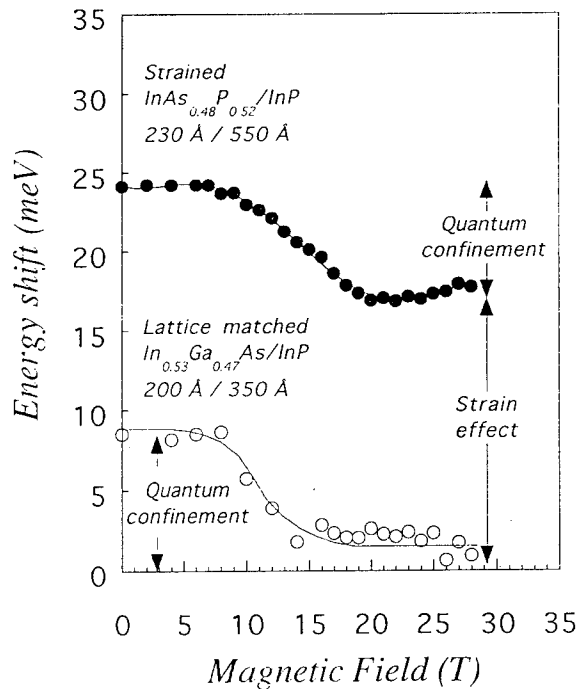


Figure 3. The energy separation between two strained $\text{InAs}_{0.48}\text{P}_{0.52}/\text{InP}$ quantum wires, 230 Å and 550 Å, and two lattice matched $\text{In}_{0.53}\text{Ga}_{0.47}\text{As}/\text{InP}$ quantum wires, 200 Å and 350 Å, as function of magnetic field strength.

effects from the distortion of ϵ_{\perp} in the shear strain to be able to estimate the energy split between the light and heavy hole band and the final band line up.¹⁰ In a first order approximation the split is proportional to $-2(\epsilon_{\perp} - \epsilon_{\parallel})$.¹¹ For a compressively strained $\text{InAs}_{0.48}\text{P}_{0.52}/\text{InP}$ QWF with (001) interfaces the distortion in ϵ_{\perp} will shift the topmost valence band downwards (blue shift of the band gap) and at the same time reduce the energy split between the heavy and the light hole bands. A reduced split between the heavy and the light hole bands will increase the coupling between these bands. However, in quantum wires there is an increased mixing between light and heavy hole character in valence band states as these states are linear combinations of bulk states with both k_x and k_y non-zero.¹² This mixing has a large impact on the reduced hole mass in the valence band in QWW's,¹³ and therefore also for the confinement energy. The shear strain will not affect the conduction band. A non-uniform strain distribution induced by a stressor on top of a QWF-structure has previously been used to create a one-dimensional confinement potential (tensile strain under the mask and compressive at the edge of the mask).¹⁴ The total lateral confinement potential induced by the strain gradient was in that case rather modest (~ 10 meV) and the width was 180 nm. However, it is important to notice that in the case of strained $\text{InAs}_{0.48}\text{P}_{0.52}/\text{InP}$ QWW's, we observe a similar enhancement of the confinement potential due to the compressive strain by the lateral barrier. This means that the lateral wire confinement potential for the QWW's should be considered somewhat harmonically

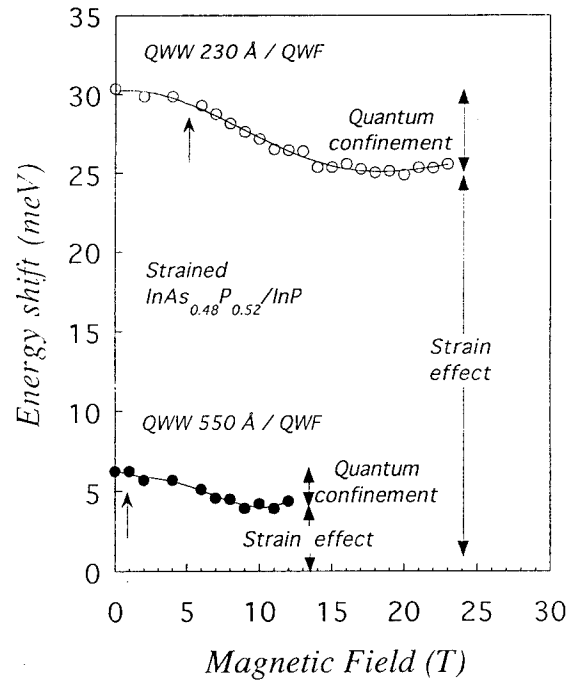


Figure 4. The energy shift for the 230 Å and 550 Å wide quantum wires relative to the $\text{InAs}_{0.48}\text{P}_{0.52}/\text{InP}$ quantum well film reference as function of magnetic field strength.

shaped rather than rectangular shaped, as for lattice matched $\text{In}_{0.53}\text{Ga}_{0.47}\text{As}/\text{InP}$ QWW's. This will, beside a blue shift at zero field, also affect the transition energy shift in the magnetic field. To separate the lateral confinement and the strain effect on the blue shift we have numerically calculated the elastic problem. The energy levels in the wires are evaluated by using the calculated strain in the k-p method, including non-parabolicity for the conduction band and excitonic effects. The details of the calculations will be presented elsewhere.¹⁵ The calculated energy values of the lateral confinement and the strain induced shift are listed in table 1, together with the experimental results. A very good agreement between the calculated and experimental values is obtained.

Wire width (Å)	Confinement (meV)		Strain (meV)	
	exp.	theor.	exp.	theor.
550	2	1	4	8
230	6	9	25	23

Table 1. Experimental and theoretical values of the lateral confinement- and strain-induced energy shift in strained $\text{InAs}_{0.48}\text{P}_{0.52}/\text{InP}$ quantum wires.


Conclusion

By magneto-luminescence measurements we have been able to probe the electronic states in compressively strained $\text{InAs}_{0.48}\text{P}_{0.52}/\text{InP}$ QWW's and separate strain- and confinement-induced blue shifts of the bandgap. The identification of the strain-induced shift is done through a comparison with measurements on lattice-matched $\text{In}_{0.53}\text{Ga}_{0.47}\text{As}/\text{InP}$ QWW's. The results show that the strain distribution is non-uniform and wire-width-dependent. Calculations based on a numerical solution of the elastic problem show a very good agreement with the experimental results. The distortion of the strain distribution is induced by the lateral barrier and therefore has a larger impact on the central region of the wire for narrower wires.

Acknowledgements

Two of the authors (J.H. and H.W.) acknowledges financial support from the Swedish Research Council for Engineering Science (TFR).

- 1 H. Sakaki, Jpn. J. Appl. Phys. **19**, 94 (1980)
- 2 Y. Arakawa and A. Yariv, IEEE J. Quantum Electron. **22**, 1887 (1986)
- 3 T. Yamauchi, T. Takahashi, J.N. Schulman, and Y. Arakawa, IEEE J. Quantum Electron. **29**, 2109 (1993)
- 4 T. Yamauchi, Y. Arakawa, and J.N. Schulman, Surf. Sci., **267**, 291 (1992)
- 5 Y.-P. Chen, J.D. Reed, W.J. Schaff, and L.F. Eastman, Appl. Phys. Lett. **65**, 2202 (1994)
- 6 J. Hammersberg, H. Weman, M. Notomi, T. Tamamura, Superlattice and Microstructures **16**, 143 (1994)
- 7 M. Notomi, S. Nojima, J. Hammersberg, H. Weman, M. Okamoto, H. Iwamura, and T. Tamamura, unpublished
- 8 M. Notomi, M. Naganuma, T. Nishida, T. Tamamura, S. Nojima, H. Iwamura, and T. Tamamura, Appl. Phys. Lett. **58**, 720 (1991)
- 9 H. Sugiura, M. Mitsuhashi, H. Ohashi, T. Hirono, and K. Nakashima, J. Cryst. Growth. in Press
- 10 C.G. Van de Walle, Phys. Rev. B, **39**, 1871 (1989)
- 11 D. Gershoni and H. Temkin, J. Luminescence **44**, 381 (1989)
- 12 J.A. Brum and G. Bastard, Superlattice and Microstructures **4**, 443 (1988)
- 13 Y. Arakawa, T. Yamauchi, and J.N. Schulman, Phys. Rev. B **43**, 4732 (1991)
- 14 K. Kash, B.P. Van der Gaag, D.D. Mahoney, A.S. Gozdz, L.T. Florez, and J.P. Harbison, Phys. Rev. Lett. **67**, 1326 (1991)
- 15 M. Notomi, J. Hammersberg, H. Weman, S. Nojima, H. Sugiura, M. Okamoto, T. Tamamura, and M. Potemski, unpublished



Thursday

May 11, 1995

- ThA1** Selective Growth
- ThB1** Photodetectors
- ThP** Poster Session II: Electron Devices,
Optoelectronics and Processing
- ThA2** Novel Etching Techniques
- ThB2** HBTs: Novel Approaches
- ThA3** Interfaces and Contacts
- ThB3** Bulk Crystal Characterization

Thursday Papers Not Available

ThB3.1 State-of-the-Art Characterization of InP Single
Crystal Wafers

Thursday Papers Withdrawn

ThP6 Lattice matched and Metamorphic InAlAs/InGaAs
HEMTS with 0.13 μ m Gates

MOMBE growth of InGaAsP films for optoelectronic devices

Hideo Sugiura

NTT Opto-electronic Laboratories

3-1 Morinosato-Wakamiya, Atugi-shi, 243-01, Japan

This paper reviews the MOMBE growth features of InGaAsP and their MQWs compared with those of MOCVD, and introduces recent MOMBE topics for optoelectronic devices.

1. Introduction

InP and related compound semiconductors are key materials for both electronic and photonic devices in optical fiber communication. There are three techniques which can produce the high quality compound films and their MQWs: MOCVD, MOMBE, and GSMBE. Although nowadays MOCVD is the primary technique, MOMBE, alternatively called CBE, can produce many kinds of excellent performance devices such as APD, HBT, DBR-LDs, and DFB-LDs for 1.5 μm wavelength [1, 2].

MOMBE growth of InGaAsP and their MQWs have been studied by many researchers. For quaternary compositions, the growth conditions have been established for the films covering the 1.0 to 1.6 μm wavelength range [3]. For MQWs, InGaAs/InGaAsP MQWs have been most extensively studied for 1.5 μm wavelength laser diodes [4]. InGaAsP/InGaAsP and InAsP/InGaAsP MQWs have been recently investigated for 1.3 μm wavelength communication [5].

In MOMBE, metalorganic materials and hydride gases are used as group III and V sources, respectively. The same sources are used in MOCVD. Many growth parameter dependencies of MOMBE films are close to those of MOCVD rather than MBE. One of the typical examples is selective area growth using dielectric masks. In this paper, we describe the MOMBE growth features of InGaAsP and their MQWs compared with those of MOCVD, and introduce recent MOMBE topics for optoelectronic devices.

2. Growth conditions

Figure 1 shows a schematic diagram of the MOMBE apparatus with three chambers. The growth chamber is indirectly connected with the entry lock chamber to avoid water and oxygen.

Source materials are installed in the gas cabinet. Triethylgallium and trimethylindium as group III sources are mixed in a 100C-heated gas cell.

Arsenic and phosphine are mixed and thermally cracked in a 900C-heated cell. Each flux intensity is adjusted using pressure controllers before introducing them in the cells. Some researches use massflow controllers. As for dopants, elemental sources are most often used: Sn and Si for n-type doping and Be for p-type doping. Gaseous dopants such as TESn and DEZn are also successful for devices [6]. A new precursor of Cp2Mg is promising due to its lower diffusive property than Zn [7].

Substrate temperature is monitored using a pyrometer and calibrated using the InSb melting point as 525C. Although small substrates are often glued to a molybdenum holder using indium, two-inch wafers are usually mounted in an indium-free holder.

The flux distribution at the wafer surfaces is determined primarily by the design of the diffuser plate at the outlet of the gas cells. Proper design of the diffuser leads to a highly uniform flux profile. In fact, Ando et al. reported that using their original growth chamber, in which three wafers with 3-inch diameters could be mounted on a holder, the thickness uniformity of AlGaAs and InGaP films was less than 2% for the three wafers [8].

3. Growth characteristics

3.1 InGaAs

Figure 2 shows the growth rate of the InGaAs layer as a function of substrate temperature [9]. The growth rate increases gradually as the temperature increases in the 450-500C range, remains almost constant between 500 and 550C, and drastically falls above 570C. Auger analysis revealed that the InAs growth rate in the InGaAs layer is constant over the entire temperature range and that the GaAs growth rate variation is

responsible for the InGaAs growth rate change. Detailed study of the InGaAs lattice constant revealed that the lattice mismatch $\Delta a/a$ varied with the temperatures by $-0.7 \times 10^{-4}/\text{C}$ in the limited range from 510 to 520C.

3.2 InGaAsP

Figure 3 shows the PL peak wavelength of a single InGaAsP layer (equivalent wavelength = 1.3 μm) as a function of growth temperature [10]. In the range from 490 to 525C, the wavelength gradually decreases with increase in temperature. The wavelength jumps at 535C, which is attributed to the lack of surface group V atoms because of the high temperature. The wavelength and lattice mismatch vary with temperature below 520C by -3 nm/C and $-2.5 \times 10^{-4}/\text{C}$, respectively. That is, the composition of InGaAsP is no less sensitive to growth temperature than that of InGaAs. In spite of the temperature sensitive nature, very uniform composition of 1.3 μm - and 1.5 μm -wavelength InGaAsP has been accomplished by precisely controlling the temperature. Specifically, a 1.4-nm standard deviation of the PL wavelength is achieved across a 2-inch wafer [11]. The run-to-run control of the InGaAsP composition is $\pm 3 \text{ nm}$ in wavelength. It should be noted that quaternary wavelength in MOCVD varies with temperature by -2.7 nm/C due to the phosphine decomposition change. Therefore, temperature control with accuracy of $\pm 1\text{C}$ is needed, irrespective of growth methods that use metalorganics as group III sources.

Recently, InGaAsP growth using TIBGa in MOMBE has been shown to be less sensitive to growth temperature than TEGa. Application to devices, however, has not been reported yet [7].

3.3 InGaAs/InGaAsP MQWs

MOMBE is expected to produce MQWs with sharp interfaces because of its fast flux switching and high vacuum. TEM, X-ray analysis, and PL measurement have revealed that the interfaces are greatly influenced by group V ambient gas during growth interruption rather than switching speed. By optimizing the growth sequence, the interfaces in InGaAs/InGaAsP MQWs are reduced to about two monolayers. Very narrow PL FWHM of 5.3 meV at 4K has been obtained for the InGaAs layer thickness of 45 Å [12].

3.4 InAsP/InGaAsP MQWs

Strained MQWs are of great interest from the point of view of both academic study on critical thickness and better performance of laser characteristics. InAs_{0.5}P_{0.5}-MQWs include compressive strain of 1.5% and have a PL peak at 1.3- μm wavelength.

Figure 4 shows the PL intensity variation of InAsP MQWs with the number of wells grown by MOMBE [5]. The MQWs consisted of 55-Å-thick InAs_{0.5}P_{0.5} wells and 110-Å-thick InGaAsP barriers. The PL intensity gradually increases with the well number from two to ten wells and falls at 14 well. In MOCVD, however, the InAsP MQWs with more than four wells deteriorated in structure due to the highly strained InAsP layers [13]. That is, the critical thickness of MOMBE films is much thicker than MOCVD films. This can be explained in terms of the growth temperature of the two methods: about 520C in MOMBE and 630C in MOCVD. Thus, low-temperature growth is suitable for growing highly strained MQWs.

Low-temperature PL measurement showed very sharp spectra for the MQWs: the FWHM of the MQWs at 4K is 4.1 and 7.8 meV for 80- and 55 Å-thick InAsP, respectively. Laser characteristics of the InAsP MQWs will be described below.

3.5 Others

One of the advantages of MOMBE for doping is low diffusive property of Be atoms. Modulation doped InGaAs/InGaAsP MQWs were grown at 520C, in which Be atoms of $3 \times 10^{18} \text{ cm}^{-3}$ were doped only in the 80-Å thick barrier layers. SIMS study showed that there was no discernible Be diffusion in the doping profile after annealing at 620 C for 30 min. The modulation doped MQW laser served to improve reduction of the lasing linewidth [14].

Selective area growth of (SAG) of InP, InGaAs, and InGaAsP using SiO₂ masks has been demonstrated in many researchers [15]. The growth rate in the window areas are little affected by the mask patterns, which suggests that the metalorganic molecules impinge on the masks do not diffuse to the window area but desorb from the surface. SAG by MOMBE has been applied to fabrication of integrated devices [16, 17].

4. Recent topic devices

4.1 Surface emitting lasers

Surface emitting lasers (SEL) have received attention for potential application in optical information processing. The key element for a low threshold SEL is high-reflective Bragg mirrors. The InGaAsP/InP multilayer reflectors grown by

MOMBE have 98% reflectivity for 24 pairs and nearly 100% for 45 pairs, respectively. These results demonstrate the MOMBE characteristics of long-term stability and precise control of growth rates. The InGaAsP SEL with hybrid mirror consisting of InGaAsP/InP and Si/SiO₂ multistacks operated at a threshold current of 0.3 mA under CW condition at 77K [18].

4.2 Strained MQW LDs for 1.3 μ m wavelength

Optical telecommunication for subscriber systems needs 1.3 μ m wavelength laser diodes that can operate at high temperatures. InAsP/InGaAsP MQW laser is one of the candidates for that purpose because it has a larger ΔE_c than a InGaAsP/InGaAsP MQW. Figure 4 shows the threshold current density dependence of three InAsP MQW lasers on the heat sink temperature. The maximum operating temperature of the lasers, T_{max} , increases with the number of wells: 105C for the 4-well, 136C for the 6-well, and 145C for the 10-well laser. The value, $T_{max}=145C$, is the greatest among reported InAsP MQWs. BH lasers with 10 wells had a threshold current of 7 mA at 30C and power output of more than 15 mW at 110C [19]. Aging tests reveal that BH InAsP laser chips work for more than 5000 h.

4.3 Multiple-wavelength laser diode array

Most of integrated devices, in which different composition layers are formed on a wafer, are fabricated using a number of repetitions of etching and regrowth. Iga et al. greatly simplified the procedure using laser-assisted MOMBE [20]. A laser beam was irradiated on a substrate to locally heats the substrates in order to change the InGaAsP composition utilizing the temperature sensitive composition phenomena mentioned above. Figure 6 shows the laser beam scanned areas and PL spectrum of each area of the InGaAsP MQWs. The peak wavelength ranges from 1.3 to 1.53 μ m corresponding to the irradiation conditions. Iga et al. fabricated a multiple-wavelength laser array in step growth. The lasers operated at wavelengths of 1.31, 1.37, 1.44, and 1.52 μ m. The threshold current with each ridge laser having a 6- μ m width ranged from 30 to 40 mA.

5. Conclusion

MOMBE/CBE allows the growth of film structures almost as designed in terms of composition and thickness. The film quality is good enough for both passive and active

optoelectronic devices, and provides excellent performance. Future efforts will be directed at high-throughput and quaternary film growth including Al.

references

- [1] W.T.Tsang, J.Crystal Growth, **95**(1989)121.
- [2] W.T.Tsang, F.S.Choa, M.C.Wu, Y.K.Chen, R.A.Logan, S.N.G.Chu, C.A.Burrus, Appl.Phys.Lett., **60**(1992)2580.
- [3] W.T.Tsang., E.F.Schubert, T.H.Chiu, J.E.Cunningham, E.G.Burkhardt, Appl.Phys.Lett., **51**(1987)761.
- [4] H.Sugiura, Y.Noguchi., R.Iga, T.Yamada, H.Kamada, Y.Sakai, and H.Yasaka, Appl.Phys.Lett., **59**(1991)958.
- [5] H.Sugiura, M.Mitsuhara, H.Ohashi, T.Hirono, and K.Nakashia, J.Crystal Growth,**147**(1995)1.
- [6] T.Sudersena Rao, C.Lacell, S.J.Rolfe, J.Thompson, P.Marshall, P.Choe-Chong, Appl.Phys.Lett., **65**(1994)1015.
- [7] C.R.Abernathy, J.Vac.Sci.Tehmol. **A11**(1993)869.
- [8] H.Ando, N.Okamoto, S.yamaura, T.Tomioka, T.Takahashi, H.Shigematsu, A.Kawano, S.Shigehiko, and T.Fujii, J. Crystal Growth, (in press)
- [9] R.Iga, H.Sugiura, and T.Yamada, Jpn.J.Appl.Phys., **30**(1991)L4.
- [10] R.Iga, T.Yamada, and H.Sugiura, Jpn.J.Appl.Phys., **32**(1993)L474.
- [11] H.Sugiura, M.Mitsuhara, R.Iga, and N.Yamamoto, J. Crystal Growth, **141**(1994)299
- [12] J.F.Carlin, J.m.Sallese, M.Fays, P.Grunberg, A.Rudra, J.M.Bonard, M.Ilegems and J.D.Ganiere, Optical Engineering (in press)
- [13] Y.Imajo, A.Kasukawa, T.Namegawa, and T.Kikuta, Appl.Phys.Lett., **61**(1992)2506.
- [14] H.Mawatari, R.Iga, H.Sugiura, Y.Tohmori, and Y.Yoshikuni, A.Phys.Lett., **65**(1994)277
- [15] H.Sugiura, T.Nishida, R.Iga, T.Yamada, and T.Tamamura, J.Crystal Growth, **121**(1992)579
- [16] H.Heinecke, J.Crystal Growth, **136**(1994)18
- [17] X.An, H.Temkin, A.Feygusson, R.A.Hamm, M.A.Cotta, R.A. Logan, D.Coblentz, and R.D.Yadvish, Electron.Lett., **29**(1993)645.
- [18] T.Miyamoto, T.Uchida, N.Yokouchi, and K.Iga, J.Crystal Growth, **136**(1994)210
- [19] H.Oohashi, T.Hirono, S.Seki, H.Sugiura, J.Nakano, M.Yamamoto, and Y.Tohmori., J.Appl.Phys., (in press).
- [20] R.Iga, T.Yamada, and H.Sugiura, Appl.Phys.Lett., **64**(1994)983.

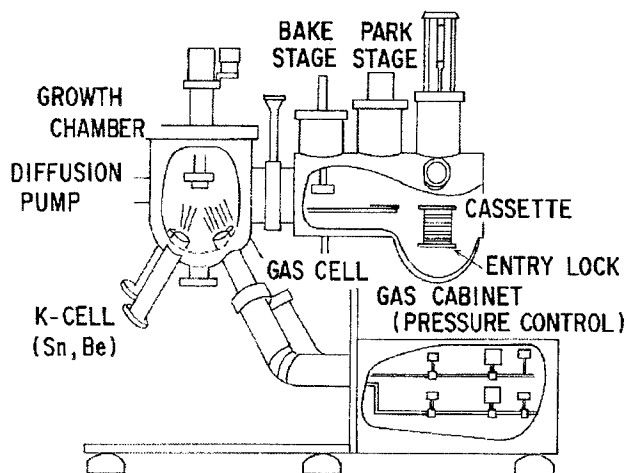


Fig. 1. Schematic diagram of MOMBE apparatus.

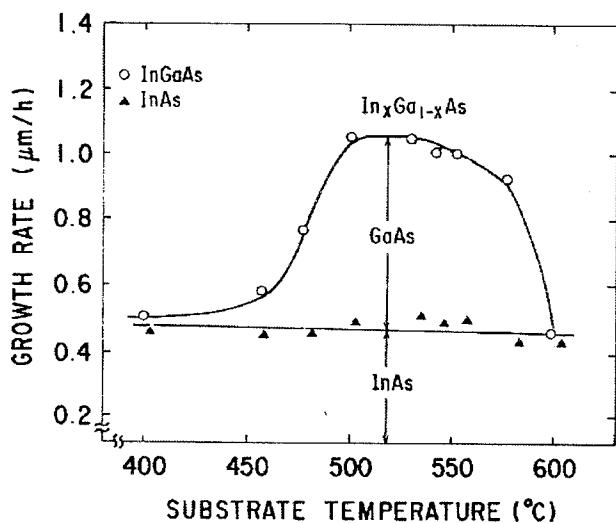


Fig. 2. Temperature dependence of InGaAs growth rate.

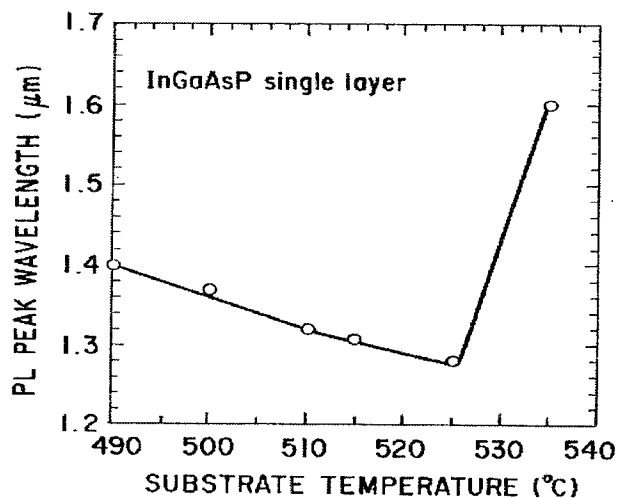


Fig. 3. Temperature dependence of InGaAsP PL peak wavelength.

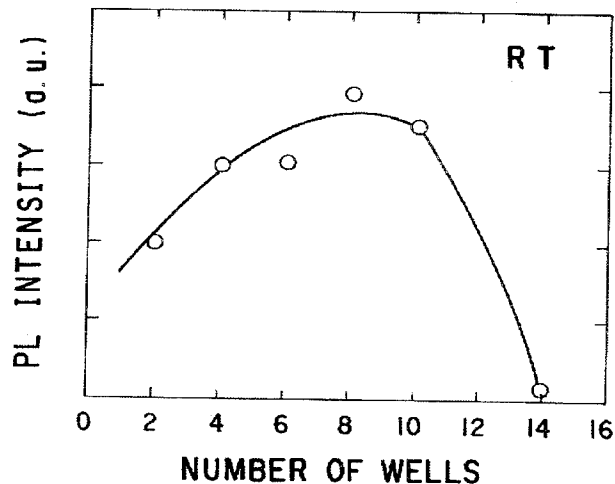


Fig. 4. PL intensity dependence of InAsP MQW on well number.

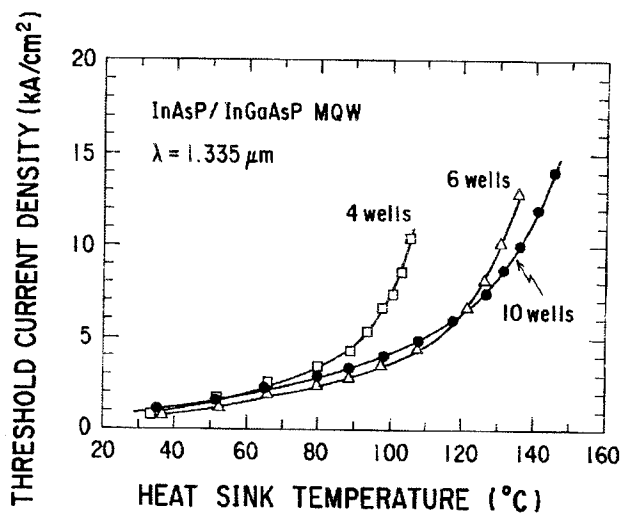


Fig. 5. Threshold current density dependence of three InAsP lasers on heat sink temperature.

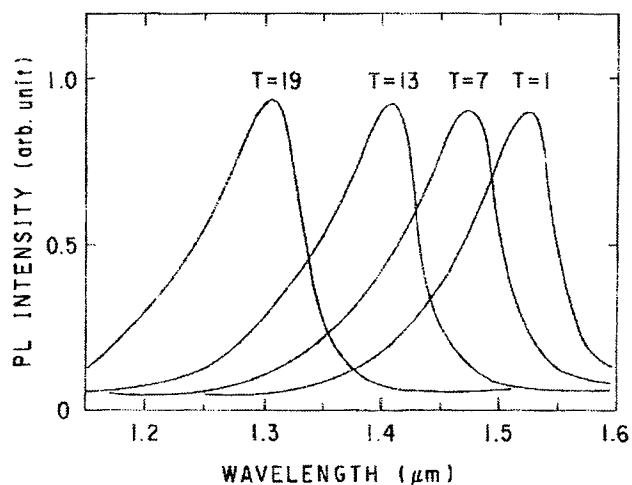


Fig. 6. PL spectra from Ar-laser scanned areas of InGaAsP MQWs.

SELECTIVE AREA GROWTH OF INP BY PLASMA ASSISTED SOLID-SOURCE EPITAXY

ThA1.2

I. Aller and H.L. Hartnagel

Technical University of Darmstadt
Institute for High Frequency Electronics
Merckstr. 25, 64283 Darmstadt, Germany

Abstract

We show that selective growth of InP can be achieved by using solid source epitaxy with an additional hydrogen rf-plasma excited in the reaction chamber. By optimizing the process parameters such as substrate temperature, plasma power and phosphorus overpressure, smooth InP-layers with geometry independent growth rates were grown on SiN-patterned InP substrates without growth on the mask. Further investigations showed that a physical desorption process is the mechanism for selective area growth in this plasma assisted epitaxy method.

Introduction

Selective area growth of III-V compound semiconductors is an important possibility for the development of new integrated device structures (1).

In comparison to other epitaxy methods like Vapour Phase Epitaxy (VPE) (2), Metalorganic Chemical Vapour Deposition (MOCVD) (3) and Metalorganic Molecular Beam Epitaxy (MOMBE) or Chemical Beam Epitaxy (CBE) (4,5) the solid source MBE has certain disadvantages regarding the selective area growth of semiconductors. Though it is possible to grow selectively material on certain crystal planes by MBE for quantum structures (6), selective growth for example of GaAs on the (100)-surface can only be achieved at very high substrate temperatures (700 °C), which is of little technological interest (7). At normal substrate temperatures (550–630 °C) polycrystalline material is also deposited on the mask (8).

Methods to reduce the necessary process temperature for selective area growth of GaAs have been developed using Migration Enhanced Epitaxy (MEE) (9), Electron Cyclotron Resonance Gas Source MBE (ECR-GSMBE) (10) and irradiation of the substrate by atomic hydrogen during MBE (11). Especially the last two processes have the advantage of giving geometry independent growth rates in comparison to VPE and MOCVD, which is important for the realization of selectively grown structures with different dimensions.

In this work we show the possibility of achieving selectivity for the growth of InP by using solid sources and a hydrogen rf-plasma. Complete selective area growth of InP was realized at standard growth

temperatures with growth rates that do not depend on the mask geometry.

Experimental

The epitaxy system being used for our studies has been described in (12). In principal, the reactor is comparable to MBE systems, using red phosphorus and indium as the source materials which are evaporated from effusion cells. In addition to this standard configuration a rf-plasma ($f = 27$ MHz) can be excited in between the cells and the heated substrate, which can be electrically biased.

For all our experiments (100) InP was used as substrate material. Rectangular pieces were cut and patterned with Plasma-CVD deposited Silicon Nitride (SiN) as a mask, which has a thickness of approximately 150 nm. As a pattern rectangular stripes with different widths, ranging from 1 to 150 μm were used with the stripes oriented into [011] and $[0\bar{1}1]$ direction, respectively.

Prior to growth the samples were chemically etched, then loaded into the reactor and finally a low temperature cleaning process in a hydrogen plasma (substrate temperature $T_s = 310$ °C, hydrogen pressure $p(\text{H}_2) = 1 \cdot 10^{-1}$ mbar and plasma power $P_{\text{RF}} = 10$ W) under phosphorus overpressure and with grounded substrate was performed.

Growth was carried out at a hydrogen pressure of $p(\text{H}_2) = 1 \cdot 10^{-2}$ mbar under phosphorus overpressure ($p(\text{P}_4) = 4 \cdot 10^{-3}$ mbar) with different values for the substrate temperature, plasma power and substrate bias voltage. T_s was varied from 560 °C to 630 °C (thermocouple temperature), P_{RF} was in the range from 0 W to 70 W, and the substrate DC-bias ranged from -20 V to 70 V.

Results and discussion

First the substrate temperature and plasma power were optimized for selective growth in this process with the substrate being at floating potential, i.e. electrically isolated.

Fig.1 shows the dependence of selective growth on substrate temperature and plasma power.

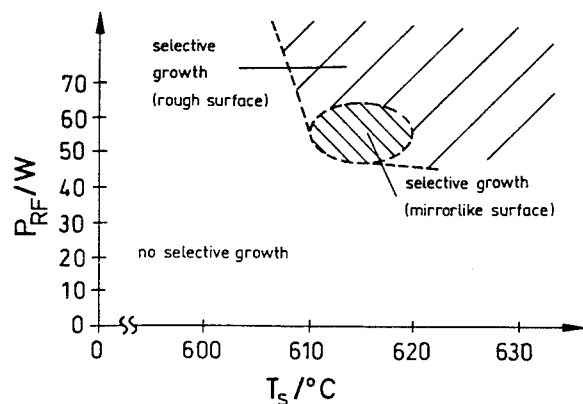


Fig.1: Dependence of selective growth on substrate temperature and plasma power.

As was observed, selectivity can be achieved for T_s higher than 610 °C and P_{RF} higher than 50 W. However, for values exceeding this range the phosphorus overpressure was not sufficient, leading to a rough surface.

In Fig.2 a SEM picture of a selectively grown InP layer after removal of the SiN mask is shown. The surface of the grown layer is smooth and there is no enhanced growth at the stripe edge (The particles on the substrate are due to pin holes in the SiN mask, where material was deposited).

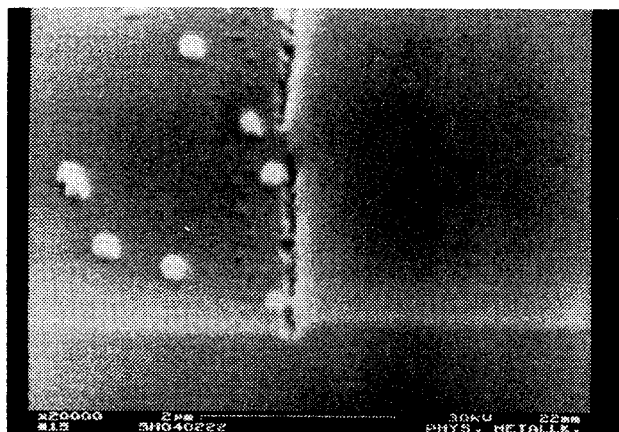


Fig.2: SEM picture of a selectively grown InP layer (right) after removal of the SiN mask

To show that the selectivity is in fact due to the use of a plasma, a layer with the same substrate temperature (610 °C) as for selective growth, but without plasma, i.e. in MBE mode, was grown. Fig.3 shows in comparison two photographs of a selectively grown InP layer (top) and the layer grown by MBE (bottom). As can be seen, there is no deposition of material on the mask in the first case, whereas without plasma poly-

crystalline growth occurs on the mask with a rough surface for the layer in the stripe. This demonstrates that the selectivity is not only due to a temperature effect, but is caused by the plasma.

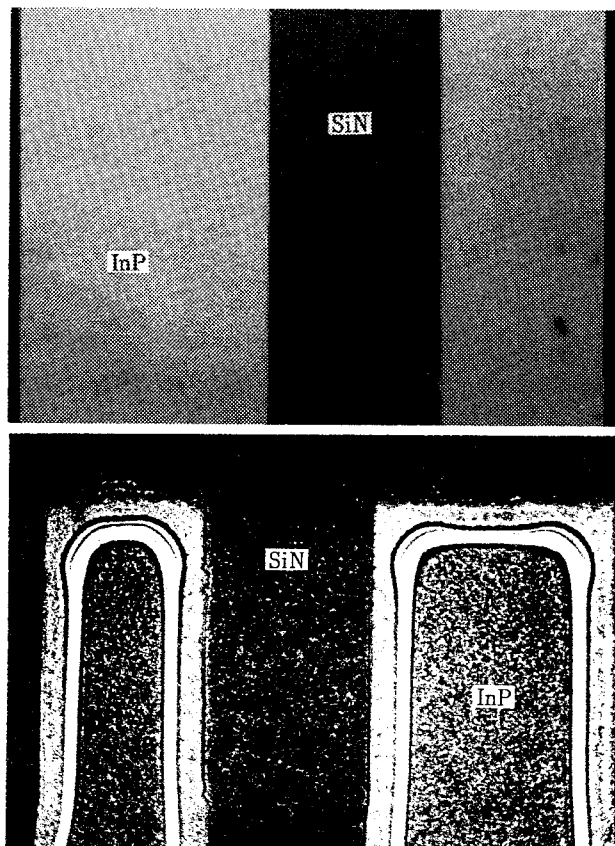


Fig.3: InP layers grown with (top) and without plasma (bottom).

For a selectively grown layer the growth rate in dependence of the stripe width (1 μm to 150 μm) was measured (s. Fig.4). For this sample and for all other selective layers there was no dependence of the growth rate on geometry nor did we observe enhanced growth at the stripe edge.

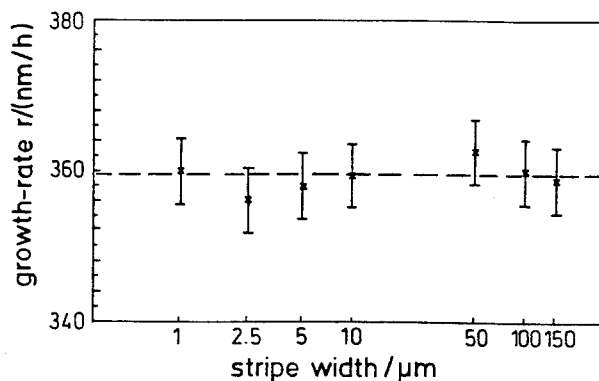


Fig.4: Dependence of growth rate on mask stripe width for selective growth.

This rules out a migration process being responsible for the observed selectivity, since this would lead to enhanced growth rates at the stripe edges and for small stripes due to migrating indium atoms from the SiN mask. Therefore we conclude that the dominating mechanism is a desorption process rather than migration. In Fig.5 the two processes are shown for comparison.

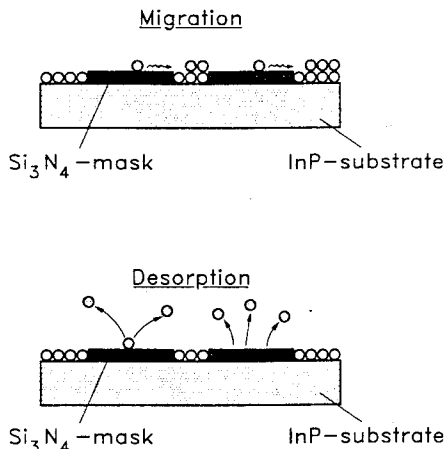


Fig.5: Migration and desorption process

The desorption rate of the indium atoms from the mask and also from the unmasked area does increase with higher substrate temperature and higher plasma power, since the growth rate decreased by increasing the above two parameters.

In order to investigate the desorption process more detailed, the substrate was DC-biased during growth with the previously determined process parameters ($T_s = 620^\circ\text{C}$ and $P_{RF} = 50\text{ W}$) for selective growth at floating substrate. Fig.6 shows that there does exist a certain range for the substrate bias where selective growth occurs. For a DC-bias higher than the floating potential ($V_{\text{Float}} = 55\text{ V}$) no selectivity is achieved,

but the surface of the grown layer remains smooth. For substrate bias being lower than the floating potential first selective growth still occurs, then selectivity stops and for very negative voltages with respect to the floating potential the surface becomes rough.

To explain those effects one has to consider that the mean energy of the impinging ions on the substrate is determined by the voltage difference between the plasma and the substrate. By biasing the substrate more positive than the floating potential the energy of the hydrogen ions decreases, leading to nonselective growth, since the desorption from the mask is not high enough. For more negative bias with respect to the floating potential first selectivity remains, but a further reduction leads to nonselective growth, although the hydrogen ion energy increases even more. To explain this we assume that for large negative substrate bias

the sticking coefficient of indium and phosphorus ions which are also present in the plasma becomes higher and the desorption due to the hydrogen ion bombardment is not sufficient to prevent condensation on the mask. For substrate bias lower than -20 V this effect then leads to a rough surface which is caused by excessive ion bombardment damaging the surface.

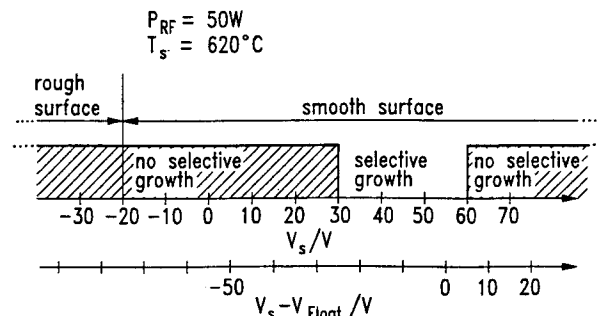


Fig.6: Selectivity dependence on substrate DC-bias.

Finally we carried out the growth with a SiN mask in an argon plasma ($T_s = 620^\circ\text{C}$, $P_{RF} = 50\text{ W}$, $p(\text{Ar}) = 1 \cdot 10^{-2}\text{ mbar}$ and $p(\text{P}_4) = 4 \cdot 10^{-3}\text{ mbar}$) to find out whether the desorption process is based on a physical or chemical reaction.

Using an argon plasma selectivity was also achieved which gives evidence for the conclusion that the plasma assisted selective growth is based on a physical desorption process. Since argon is chemically inactive, we can rule out a chemical desorption process, in which volatile species are formed on the mask which evaporate. Therefore desorption takes place due to an ion bombardment for which the energy has to be optimized. In the case of argon plasma the surface was damaged to a high extent because of the heavy ions striking the sample.

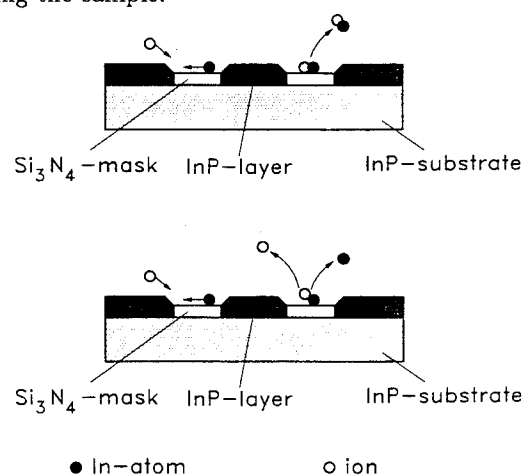


Fig.7: Physical (bottom) and chemical (top) desorption processes.

In Fig.7 the processes for physical (bottom) and chemical (top) desorption are shown for comparison.

Conclusions

We have shown, for the first time, that selective growth of InP can be realized by using solid sources in an MBE-like growth process with an additional hydrogen (argon) plasma. The mechanism for selective growth is based on a physical desorption process of indium ions from the SiN mask due to hydrogen ion bombardment. The growth rate is independent of the mask geometry and selectivity can be influenced by biasing the substrate.

Since the use of solid red phosphorus as a source material in MBE gained interest again due to the development of new sources (valved cracker cell (13)), the possibility of selective area growth with solid sources will be of great interest for future applications.

References

- (1) S. Ando, S.S. Chang and T. Fukui, "Selective epitaxy of GaAs/AlGaAs on (111)B substrates by MOCVD and applications to nanometer structures, *J. Crystal Growth*, Vol. 115, pp. 69-73, 1991
- (2) V.S. Ban, G.C. Erickson, S. Mason and G.H. Olsen, "Selective epitaxy of III-V compounds by low-temperature hydride VPE", *J. Electrochem. Soc.*, Vol. 137, pp. 2904-2908, Sept. 1990
- (3) O. Kayser, R. Westphalen, B. Optiz and P. Balk, "Control of selective area growth of InP", *J. Crystal Growth*, Vol. 112, pp. 111-122, 1991
- (4) N. Furuhashi and A. Okamoto, "Selective growth mechanism of GaAs in metalorganic molecular beam epitaxy", *J. Crystal Growth*, Vol. 112, pp. 1-6, 1991
- (5) W.T. Tsang, L. Yang, M.C. Wu and Y.K. Chen, "Selective area epitaxy and growth over patterned substrates by chemical beam epitaxy", *Electron. Lett.*, Vol. 27, pp. 3-5, Jan. 1991
- (6) T. Sugaya, M. Kaneko, Y. Okada and M. Kawabe, "Fabrication of GaAs quantum wire structures by hydrogen-assisted molecular beam epitaxy", *Jpn. J. Appl. Phys.*, Vol. 32, pp. L1834-L1836, Dec. 1993
- (7) A. Okamoto, "Selective epitaxial growth by molecular beam epitaxy", *Semicond. Sci. Technol.*, Vol. 8, pp. 1011-1015, June 1993
- (8) A.Y. Cho and W.C. Ballamy, "GaAs planar technology by molecular beam epitaxy", *J. Appl. Phys.*, Vol. 46, pp. 783-785, Feb. 1975
- (9) S. Yokoyama, J. Oogi, D. Yui and M. Kawabe, "Low-temperature selective growth of GaAs by alternately supplying molecular beam epitaxy", *J. Crystal Growth*, Vol. 95, pp. 32-34, 1989
- (10) N. Yamamoto, N. Kondo and Y. Nanishi, "Plasma-controlled selective area growth of GaAs by electron-cyclotron-resonance plasma-excited molecular-beam epitaxy", *J. Crystal Growth*, Vol. 99, pp. 302-305, 1990
- (11) T. Sugaya, Y. Okada and M. Kawabe, "Selective growth of GaAs by molecular beam epitaxy", *Jpn. J. Appl. Phys.*, Vol. 31, pp. L713-L716, June 1992
- (12) I. Aller and H.L. Hartnagel, "InP exposure to hydrogen plasma with DC-potential control", *J. Electrochem. Soc.*, Vol. 140, pp. 2715-2720, Sept. 1993
- (13) J.N. Baillargeon, A.Y. Cho, R.J. Fischer, P.J. Pearah and K.Y. Cheng, "Electrical characteristics of InP grown by molecular beam epitaxy using a valved phosphorus cracking cell", *J. Vac. Sci. Technol. B*, Vol. 12, pp. 1106-1109, March/April 1994

The Influence of PCl_3 on Planarisation and Selectivity of InP Regrowth by Atmospheric Pressure MOVPE

M. J. Harlow, P. C. Spurdens and R. H. Moss

Technology Research Unit, BT Laboratories, Martlesham Heath, Ipswich, Suffolk, IP5 7RE, UK.

E-mail: mike.harlow@bt-sys.bt.co.uk

Abstract

The introduction of phosphorus trichloride into the AP-MOVPE growth of InP has been found to dramatically improve the regrowth adjacent to mesa structures. By suppressing growth in the [100] direction and enhancing growth in the [311] directions planar regrowth is achieved. Polycrystalline deposits on dielectric masks can also be completely suppressed.

Introduction

Re-growth of InP onto lithographically defined non-planar structures, selective area epitaxy (SAE), is often a fundamental part of device fabrication. The morphology of this growth step influences both device performance and the ease with which subsequent processing steps can be carried out and in some cases dictates device architectures. In conventional atmospheric pressure MOVPE, growth adjacent to areas of dielectric is enhanced by migration of material from the vicinity of the dielectric to the semiconductor^[1] giving rise to growth rate enhancement and 'ear' formation^[2]. If the dielectric is wider than $\sim 20\mu\text{m}$ then polycrystalline deposition is likely. Both 'ears' and polycrystalline deposits can seriously degrade subsequent lithographic and re-growth steps.

Considerable effort is being made world-wide, using a wide range of techniques, to develop routes to planar regrowth. Growth at reduced pressure can significantly improve selectivity and reduce growth rate enhancement^[3]. Low pressure MOVPE at <10 Torr greatly reduces 'ear' growth. Further improvement is possible by going to still lower pressures and growing by Chemical Beam Epitaxy, CBE. By CBE, when conditions are optimised, growth on the dielectric can be eliminated. By Molecular Beam Epitaxy, MBE, growth occurs equally on semiconductor and dielectric unless impractically high temperatures are used.

An alternative approach to lowering the pressure is to modify growth chemistry at atmospheric pressure. There has been a revival in one of the original epitaxy techniques, Vapour Phase Epitaxy, VPE, and in particular Hydride VPE^[4-7]. In this technique, hydrides are used to transport the group V elements but chlorides are used for the group III's. Selectivity of InP growth by HVPE is excellent with planar overgrowth of $14\mu\text{m}$ high dry etched mesas having

been reported^[8]. A modification of the VPE technique using group III alkyls and group V chlorides has recently been reported^[9].

The potentially more versatile technique is a modification to the MOVPE process by the addition of a chlorine containing compound. Using this method the growth chemistry can be modified to mimic HVPE while retaining the rapid switching, excellent compositional control, range of materials and uniformity of MOVPE in the same system. The simplest chlorine containing compound that could be added to the MOVPE reactor is hydrogen chloride, HCl, but it is known that HCl reacts with trimethylindium, TMIn, to form a low volatility white solid. The use of carbon tetrachloride, CCl_4 , has been reported^[11] as has the use of 1, 1, 1 trichloroethane^[12]. The use of group V chlorides have also been investigated, i.e. AsCl_3 in the growth of GaAs from TMGa and arsine, and PCl_3 in the growth of InP from TMIn and phosphine^[13].

The use of group V chlorides in the MOVPE process has been questioned because of parasitic reactions on mixing with group III alkyls^[14], however in our work, using PCl_3 in the growth of InP has not shown any problems.

Experimental

All growths were carried out in an atmospheric pressure MOVPE kit using TMIn in a stainless steel bubbler held at 40.0°C and 100% PH_3 in a high pressure cylinder. The PCl_3 was held in a borosilicate glass bubbler in a temperature controlled bath between 0°C and -30°C . Growth was in a horizontal, rectangular section, water cooled reactor with IR heating and three zone temperature control. Total gas flow was held near 7 l/min and all growth was on (100) substrates unless otherwise noted. Four batches of reactive ion etched, RIE, vertical walled mesa stripes were prepared on (100) substrate or planar

material for use during the work. The initial batch of mesas were in both $[011]$ and $[0\bar{1}1]$ directions but all subsequent mesas were in the $[011]$ direction only. The test samples each contained four different mesa widths, i.e. $2\mu\text{m}$, $4\mu\text{m}$, $6\mu\text{m}$ and $15\mu\text{m}$ wide and broad areas of dielectric mask $500\mu\text{m}$ wide. The mesas were $5.4\mu\text{m}$ high. One batch of mesas were prepared consisting of $5\mu\text{m}$, $10\mu\text{m}$, $15\mu\text{m}$ and $20\mu\text{m}$ wide square and circular pillars to investigate growth in both directions simultaneously. All mesas had silica dielectric masks on top during growth. Analysis of growth was carried out using optical Nomarski microscopy, to show surface morphology and cleaved cross sections, and by Scanning Electron Microscopy, SEM. Cleaved sections were stained in a solution of potassium ferricyanide and potassium hydroxide, 1:2 by weight, under white light illumination. Atomic Force Microscopy, AFM, was carried out by AEA Technology.

Results

General Features of Growth with PCl_3

The use of PCl_3 in the growth of InP on (100) surfaces has two significant effects. Firstly, the growth rate is reduced in proportion to the concentration of PCl_3 as illustrated in Figure 1.

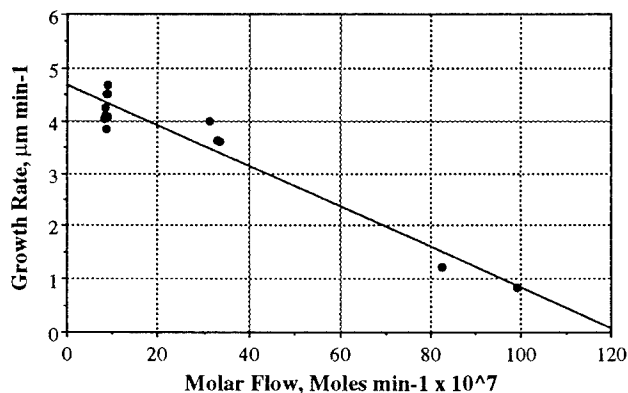


Figure 1. InP growth rate in the (100) direction with the addition of PCl_3 .

The second effect is the degradation of the surface morphology illustrated in Figure 2. Surface relief is approximately 30nm with slope angles of between 2° and 3° with the long axis of the features aligned with the $[011]$ direction. Atomic Force Microscopy (AFM) images show that the features are terraced on the atomic scale with each step being of the order of 3\AA . It was found that the surface morphology could be improved by growing on mis-



Figure 2. (100) surface morphology of InP grown with PCl_3 . White bar is $500\mu\text{m}$ long

oriented substrates. Growth on $(100) \xrightarrow{2^\circ} (110)$ resulted in smooth, specular morphology.

Mesa Regrowth

The improvement of growth adjacent to mesas is illustrated in Figure 3. Growth at 600°C without PCl_3 results in

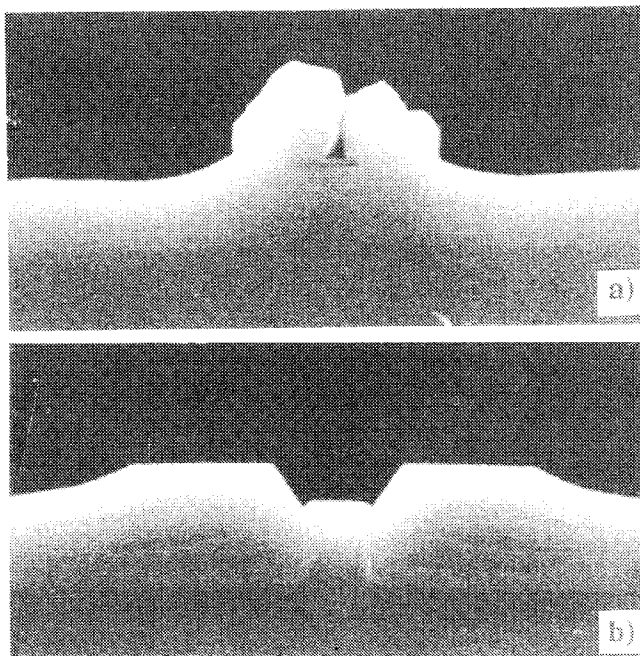


Figure 3. Effect of adding PCl_3 during regrowth of InP adjacent to RIE mesas. a) without PCl_3 , b) with PCl_3

irregular overgrowth of the silica mask whereas with PCl_3 growth is pinned to (111) planes at the mesa edge and terminates at the (100) surface. A range of growth temperatures were investigated and found to significantly affect the shape of the regrowth. At higher growth temperatures (700°C) the region of enhanced growth adjacent to the mesa became narrower but more pointed whereas at lower growth temperature (500°C) depressions

appeared at the mesa edges. In both cases the surface morphology was seen to be smoother than at 600°C. The influence of V/III ratio on growth was studied but found to be less important than growth temperature. As the V/III ratio was increased over the range 15 to 200 the regrowth features were seen to become more angular although the general form of the growth remained the same. The greatest effect of V/III ratio was seen at the lower growth temperature where the depressions at the mesa edge became much more pronounced. Increasing the concentration of PCl_3 during growth further reduces the growth rate enhancement near the mesa as illustrated in Figure 4, where the flow has been increased by a factor of 3.

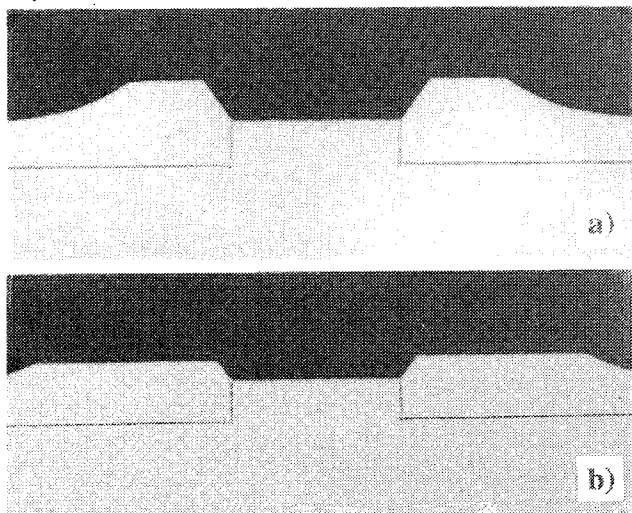


Figure 4. Effect of increasing flow of PCl_3 on mesa regrowth at 600°C. a) $9 \times 10^{-7} \text{ moles min}^{-1} \text{ PCl}_3$, b) $2.5 \times 10^{-6} \text{ mole min}^{-1} \text{ PCl}_3$.

Complete suppression of growth in the [100] direction can be achieved by increasing the PCl_3 concentration to $6 \times 10^{-6} \text{ moles min}^{-1}$. Figure 5 shows one side of a $15 \mu\text{m}$ wide $5.4 \mu\text{m}$ high RIE mesa, regrown with the above PCl_3 concentration, with six alternating layers of p-type and n-type InP.

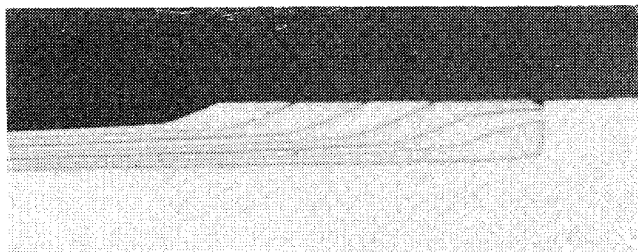


Figure 5. Regrowth of alternating p- and n-type InP around $5.4 \mu\text{m}$ high mesas with $6 \times 10^{-6} \text{ moles min}^{-1} \text{ PCl}_3$.

The growth from the sides of the mesa is seen to proceed on the (311) planes with a growth rate of $11.5 \mu\text{m hour}^{-1}$. This form of growth is very similar to that seen in HVPE^[14] and it is the presence of the fast growing (311) planes which is responsible for the complete suppression of growth in the [100] direction^[15].

Dopant incorporation during PCl_3 assisted regrowth is expected to differ from conventional regrowth as growth proceeds on (311) in preference to (100) surfaces and because of the higher growth rate^[16-17]. As a result dopant precursor flows will have to be modified for regrowth using PCl_3 .

The PCl_3 assisted planarisation seen above has also been observed on mesas formed by wet etching and on in-situ etched mesas formed using PCl_3 etching before regrowth. In both cases growth stopped at the top of the mesa demonstrating that the planarisation is independent of the initial mesa shape.

The planarity of the regrowth is however found to depend on the mesa width and as the mesa width is increased beyond $15 \mu\text{m}$, growth in the [100] direction again becomes significant. Increasing the concentration of PCl_3 does not improve the growth but starts to degrade the surface by introducing etch pits. Improved growth on wide mesas can however be achieved by reducing the growth temperature and growth adjacent to $500 \mu\text{m}$ wide $5.4 \mu\text{m}$ high stripes has been observed with as little as $1.25 \mu\text{m}$ excess growth above the top of the mesa. Thus the technique may also be applicable to butt-coupling in active-passive waveguide devices.

Regrowth of InP around pillars is illustrated in Figure 6.

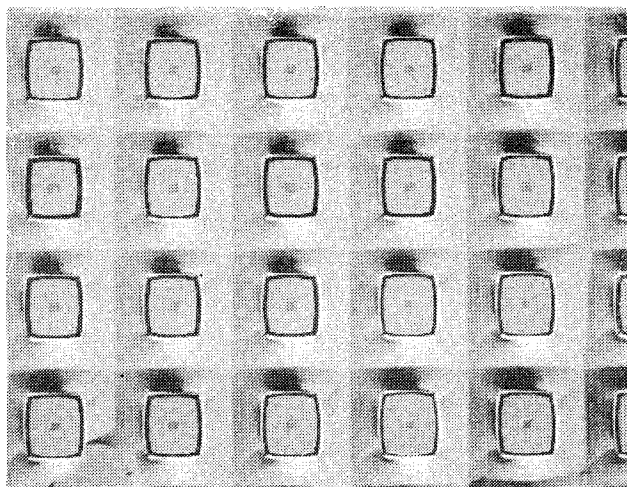


Figure 6. An array of pillars after planarising regrowth with Fe-doped InP. The separation between centres of the devices is $125 \mu\text{m}$.

It can be seen that a square, planar region is formed adjacent to the pillar and that the extent of growth is similar in both $[011]$ and $[0\bar{1}1]$ directions. This behaviour is different to that seen in HVPE in which growth in the $[011]$ direction is significantly faster than in the $[0\bar{1}1]$ direction^[14].

Conclusions

The incorporation of PCl_3 into the AP-MOVPE process has been demonstrated to planarise regrowth adjacent to mesa structures up to $15\mu\text{m}$ wide and completely suppress polycrystalline growth on dielectric masks over $500\mu\text{m}$ wide. The planar regrowth around pillars demonstrates that the vertical extent of the growth is the same in both $[011]$ and $[0\bar{1}1]$ directions. By modifying the growth conditions, near planar regrowth can be achieved adjacent to tall mesa stripes up to $500\mu\text{m}$ wide.

References

- [1] E. J. Thrush, J. P. Stagg, M. A. Gibbon, R. E. Mallard, B. Hamilton, J. M. Jowett and E. M. Allen, "Selective and non-planar epitaxy of InP/GaInAs(P) by MOCVD", *Materials Science and Engineering B21* (1993) 130-146.
- [2] J. L. Zilko, B. P. Segnar, U. K. Chakrabarti, R. A. Logan, J. Lopata, D. L. Van Haren, J. A. Long and V. R. McCrary, "Effect of mesa shape on the planarity of InP regrowths performed by atmospheric pressure and low pressure selective metalorganic vapor phase epitaxy", *J. Crystal Growth* **109** (1991) 264-271.
- [3] N. Nordell and J. Borglind, "MOVPE growth of InP around reactive ion etched mesas", *J. Crystal Growth* **114** (1991) 92-98.
- [4] O. Kjebon, S. Lourdudoss, B. Hammarlund, S. Lindgren, M. Rask, P. Ojala, G. Landgren and B. Broberg, "1.55 μm buried heterostructure laser via regrowth of semi-insulating InP:Fe around vertical mesas fabricated by reactive ion etching using methane and hydrogen", *Appl. Phys. Lett.* **59**(3) 253 (1991).
- [5] B. Hammarlund, S. Lourdudoss and O. Kjebon, "Orientation dependent growth behaviour during hydride VPE regrowth of InP:Fe around reactive ion etched mesas", *J. Elect. Materials* **20**(7) 523 (1991).
- [6] O. Kjebon, S. Lourdudoss and J. Wallin, "Regrowth of semi-insulating iron doped InP around reactive ion etched laser mesas in (110) and $(\bar{1}10)$ directions by hydride vapour phase epitaxy", *Proc. 4th Int. Conf. InP & Related Materials*, Cardiff, 1992. p. 48-50.
- [7] S. Lourdudoss, O. Kjebon, J. Wallin and S. Lindgren, "High-frequency GaInAsP/InP laser mesas in $(\bar{1}10)$ direction with thick semi-insulating InP:Fe", *IEEE Photonics Technology Lett.* **5**(10) 1119 (1993).
- [8] S. Lourdudoss, K. Streubel, J. Wallin, J. André, O. Kjebon and G. Landgren, "Very rapid and selective epitaxy of InP around mesas of height up to $14\mu\text{m}$ by hydride vapour phase epitaxy", *Proc. 6th Int. Conf. InP & Related Materials*, Santa Barbara, 1994. p. 615-618.
- [9] S. Kondo, S. Matsumoto and H. Nagai, "Metalorganic chloride vapor phase epitaxial growth of III-V compounds in a single reactor", *J. Crystal Growth* **132** (1993) 305-314.
- [10] N. Nordell and J. Borglind, "Improved InP regrowth property in MOVPE by addition of CCl_4 ", *Appl. Phys. Lett.* **61**, 21-24 (1992).
- [11] B. -T. Lee, R. A. Logan, R. F. Karliceck, Jr. "Planar regrowth of InP and InGaAs around reactive ion etched mesas using atmospheric pressure metalorganic vapor phase epitaxy", *Appl. Phys. Lett.* **63**(2) 234 (1993).
- [12] R. Azoulay and L. Dugrand, "Selective growth of GaAs by organometallic vapor phase epitaxy at atmospheric pressure", *Appl. Phys. Lett.* **58**(2) 128 (1991).
- [13] D. Robein, B. Rose, M. McKee, R. Mellet, D. Walker, H. Mani, J. Charil and P. Norris, "Selective area epitaxy on InP substrates: A comparison of growth behaviour at low and atmospheric pressure", *European Workshop MOVPE IV*, Poster 47.
- [14] S. Lourdudoss, E. Rodriguez Messmer, O. Kjebon, K. Streubel, J. Andre, G. Landgren, "Morphological modifications during selective growth of InP around cylindrical and parallelopiped mesas", *Materials Science and Engineering B28*(1994) 179
- [15] B. -T. Lee, R. A. Logan, "Growth of InP on etched grooves using atmospheric pressure metalorganic vapor phase epitaxy", *J. Crystal Growth* **140** (1994) 1-8.
- [16] P. R. Berger, S. N. G. Chu, R. A. Logan, E. Byrne, D. Coblenz, J. Lee III, N. T. Ha, N. K. Dutta, "Substrate orientation effects on dopant incorporation in InP grown by metalorganic chemical vapor deposition", *J. Appl. Phys.* **73**(8) 1993, 4095.
- [17] R. Bhat, C. Caneau, C. E. Zah, M. A. Koza, W. A. Bonner, D. M. Hwang, S. A. Schwarz, S. G. Menocal, F. G. Favire, "Orientation dependence of S, Z, Si, Te and Sn doping in OMCVD growth of InP and GaAs: application to DH lasers and lateral p-n junction arrays grown on non-planar substrates", *J. Crystal Growth* **107** (1991) 772-778.

Improved Selective Growth of InP around Dry-Etched Mesas ThA1.4 by LP-MOCVD at Low Growth Temperature

M. Takemi, T. Kimura, T. Miura, Y. Mihashi and S. Takamiya

*Optoelectronic & Microwave Devices Laboratory, Mitsubishi Electric Corporation,
4-1 Mizuhara, Itami, Hyogo 664, Japan*

Introduction

Selective embedding regrowth by metalorganic chemical vapor deposition (MOCVD) is an important technique for fabricating InP-based buried-heterostructure (BH) laser diodes (LD) and photonic integrated circuits (PIC). There have been some reports on the selective growth around chemically wet-etched mesas for forming proper current-blocking layers in BH lasers [1]. In those reports, almost planar regrowth has been achieved by utilizing mask eaves formed by the wet etching. On the other hand, it is difficult to embed dry-etched mesas having no mask eaves under usual growth conditions [2,3]. It has recently been reported that selective regrowth with planar growth surfaces around dry-etched rectangular mesas can be achieved by adopting a rather high growth temperature [4]. There is, however, a fear that the high growth temperature might cause the diffusion of dopants and deteriorate the device characteristics. Another candidate for achieving the almost planar embedding regrowth around dry-etched mesas is to introduce some chlorine compounds into the reactor during MOCVD growth, as has been reported in some reports [5-8].

In this work we applied a high-speed rotating-disk MOCVD reactor to the selective embedding growth around the mesas formed by reactive ion etching (RIE), and investigated the growth conditions which give planar embedding around the mesas. It is shown that almost planar embedding growth can be achieved even at low growth temperature without introducing any chlorine compounds. Moreover, we discuss the effects of dopants on the behaviors in the selective embedding growth. Special attention has been focused on the growth on the side walls of the nearly-rectangular mesas as well as that near the edges of the masks.

Experimental procedure

Mesa stripes were fabricated along the [110] direction on (001) InP substrates by RIE, using sputtered SiO₂ as the mask. The RIE was performed with C₂H₆ and H₂ as active gases. The SiO₂ mask was 2000Å in thickness. Resultant mesa shapes were nearly rectangular without any mask eaves, as shown in Fig. 1. The samples were cleaned in H₂SO₄ prior to the growth.

The selective embedding growth of InP was performed in two types of low-pressure (LP) MOCVD reactors. One is a conventional horizontal-type MOCVD reactor; the other is a vertical-type one having a

high-speed rotating susceptor. The growth precursors were trimethylindium (TMI) and phosphine (PH₃). Hydrogensulphide (H₂S) and diethylzinc (DEZn) were used for n-type and p-type doping, respectively. The selective grown layers consisted of alternating n-InP/p-InP multilayers for the purpose of giving a good contrast for scanning electron microscope (SEM) observation after stain-etching. The growth temperature and the growth pressure were changed in the ranges between 580-660°C and 50-150Torr, respectively. The carrier concentrations of n-type and p-type layers were controlled to be the same for all the samples ($7 \times 10^{18} \text{cm}^{-3}$ for n-InP, $8 \times 10^{17} \text{cm}^{-3}$ for p-InP). After the growth, the samples were cleaved perpendicularly to the mesas, then stain-etched in a FeCN:KOH:H₂O solution, and examined using an SEM.

Results and discussion

Comparison of embedding growth between two types of MOCVD reactors

For the fabrication of BH-LD, it is necessary to embed the masked mesas without overhang growth on the mask in order that further growth after removing the mask can be performed properly. When embedding a mesa stripe along the [110] direction, (111)B facets are usually formed from the edge of the mask. Then, overgrowth on the mask occurs due to the growth on the facets unless the growth on the (111)B plane is suppressed. It is therefore necessary to find out the growth conditions under which the growth on the (111)B facet is suppressed, for the purpose of eliminating the overgrowth on the mask stripe along the [110] direction.

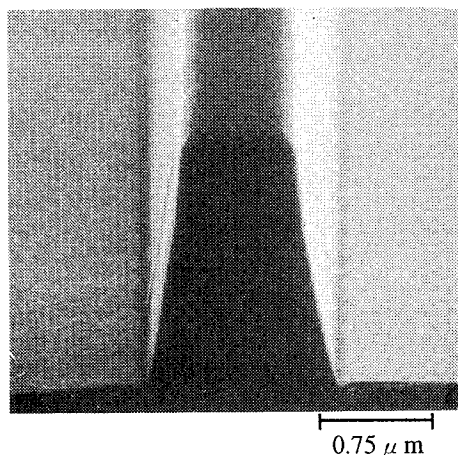


Fig. 1 An SEM micrograph of a dry-etched mesa on an InP substrate used in a growth experiment.

First, we attempted the embedding growth in the conventional MOCVD reactor. Figures 2(a) and 2(b) show SEM micrographs of selective growth around the mesas under high (650°C) and low (600°C) growth-temperature conditions, respectively. As can be seen in Fig. 2(a), (111)B facet planes were completely formed just from the mask edges, and no overgrowth on the mask was observed in the growth at 650°C. It is considered that the growth on the (111)B facet was suppressed owing to the enhancement of the surface diffusion length of the growth species on the (111)B plane under the high growth-temperature conditions. On the other hand, in case of the growth at a lower temperature (600°C) in the same reactor, overgrowth on the mask due to the growth on the (111)B facet was observed, as can be seen in Fig. 2(b). It is considered that the surface diffusion length of the growth species on the (111)B facet is shortened because of the low temperature of the substrate. That is, it is necessary to enhance the migration of the growth species on the (111)B plane by raising the growth temperature in order to suppress the growth on the (111)B facet in the conventional MOCVD reactor.

There is, however, a fear that the high growth temperature might cause the diffusion of dopants and deteriorate the device characteristics, as mentioned in the above. It is therefore necessary to enhance the migration by some other methods than raising the growth temperature.

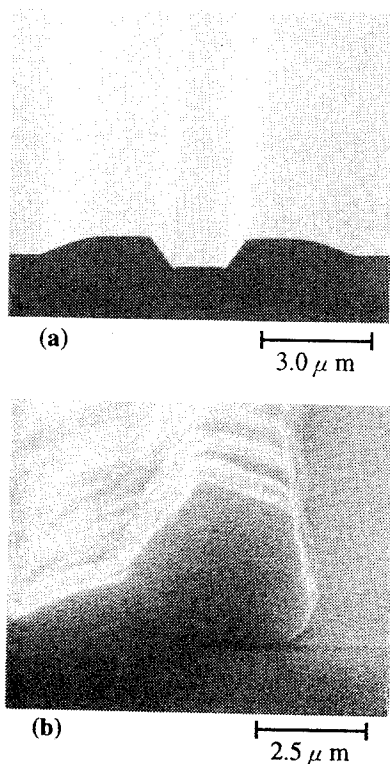


Fig. 2 SEM micrographs of selective growth around dry-etched mesas at (a) 650°C and (b) 600°C. The selective grown layers consist of alternating n-InP (0.2μm) /p-InP (0.05μm) multilayers.

It is well known that the partial pressure ratio of group V to group III source gases (V/III ratio) on the growth surface also affects the diffusion length of the growth species; the lower V/III ratio enhances the surface diffusion length of In atoms [9]. However, the lower limit of the V/III ratio is restricted by the PH₃ partial pressure which is required for the mirror-like growth in the conventional MOCVD reactor. This means that it is difficult to obtain a smooth surface under the low growth-temperature conditions in the conventional MOCVD reactor.

Next, we applied the high-speed rotating-disk MOCVD reactor to the selective embedding growth. When the susceptor rotates at a high speed, the thickness of the stagnant layer becomes thin. Therefore, the time duration during which growth species are heated in the gas phase becomes shorter, and the thermal decomposition of the growth species is suppressed. Thus, the amount of the decomposed PH₃ decreases, resulting in decrease in the effective V/III ratio. In other words, the effective V/III ratio on the growth surface becomes lower by the high-speed rotation of the susceptor in spite of the same value of the input V/III ratio.

Figure 3 shows an SEM micrograph of selective growth around the mesa at a low growth temperature (600°C) in the high-speed rotating-disk MOCVD reactor. As can be seen in Fig. 3, in spite of almost the same condition as the sample shown in Fig. 2(b), the growth on the (111)B facet was suppressed, and no overgrowth on the mask took place at the edges of the mask. This means that the susceptor rotation is advantageous for the embedding growth around a mesa having no mask eaves, when compared to the conventional MOCVD reactor under the same growth condition.

In order to investigate the temperature dependence of the growth, samples were grown at 580, 625 and 660°C in the high-speed rotating-disk MOCVD.

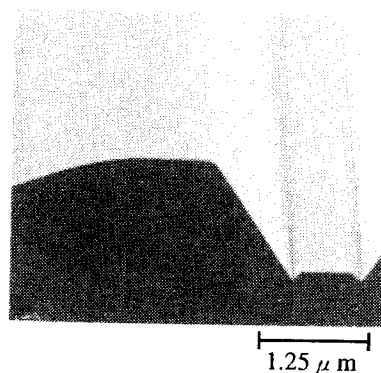
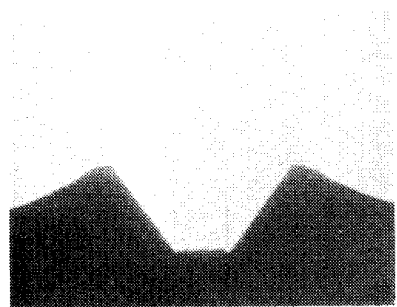
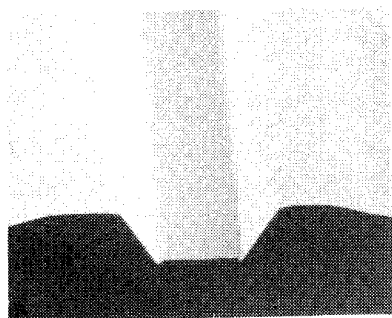


Fig. 3 An SEM micrograph of selective growth around a dry-etched mesa at 600°C and the susceptor rotation speed of 500rpm. The selective grown layers consist of alternating n-InP (0.2μm) /p-InP (0.05μm) multilayers.

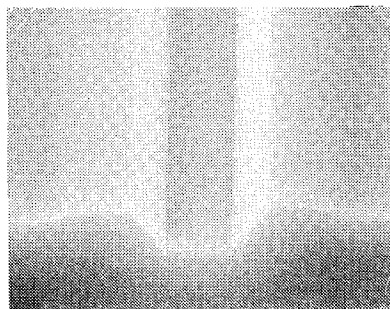
Figures 4 (a)-(c) show SEM micrographs of the samples after the selective growth around dry-etched mesas at these growth temperatures. As can be seen in Figs. 4 (a)-(c), the (111)B plane was formed just from the edge of the mask after the growth at every temperature. Selective embedding growth was thus achieved without any overgrowth on the mask at a growth temperature as low as 580°C. Moreover, no polycrystals were observed on the mask, and the surface morphologies were mirror like. At the lower temperatures than 580°C, surface morphologies were found to become poor.



(a) 580°C



(b) 625°C



(c) 660°C

3.0 μm

Fig. 4 SEM micrographs of selective growth around dry-etched mesas at (a) 580°C, (b) 625°C, and (c) 660°C. The selective grown layers consist of alternating n-InP (0.2μm) /p-InP (0.05μm) multilayers.

The effects of dopants on the growth behavior

For fabricating the BH-LD and PIC, it is very important to know the shapes of embedding growth near the mesa. We investigated the growth behavior of doped InP near the mesas in detail. Figures 5 and 6 show SEM micrographs of the cleaved surfaces of two samples A and B, respectively, after stain-etching. The multilayers of sample A consisted of alternative thick (0.3μm) p-InP and thin (0.05μm) n-InP layers, while those of sample B consisted of alternative thick (0.2μm) n-InP and thin (0.05μm) p-InP layers. The thinner layers were inserted as the marker for the growth patterns. The overall growth behaviors of samples A and B are considered to be dominated by those of p-type and n-type InP, respectively.

As can be seen in Fig. 5, the growth of p-InP occurred in a simple manner. The growth surface on the side walls of the mesa was inclined from the original nearly-vertical orientation to (111)B. After the formation of the (111)B facet downward of the mask, almost isotropic growth occurred, conserving the shape of the growth front.

On the other hand, in case of n-type InP, the growth around the mesa seems to occur in a more complicated manner, as can be seen in Fig. 6. On the nearly-vertical side walls of the mesa, the growth proceeded until the growth surface became parallel to the (110) plane; after the exact (110) plane was formed, the growth of n-InP was entirely suppressed, while that of p-InP proceeded. The growth adjacent to the mesa seems to proceed by the growth on the (113) plane. When the (113) facet reached the top surface of the mesa, a (001) facet was found to be newly formed adjacent to the mask. The growth of n-InP on the (113) plane was enhanced after the emergence of the (001) facet. However, after the

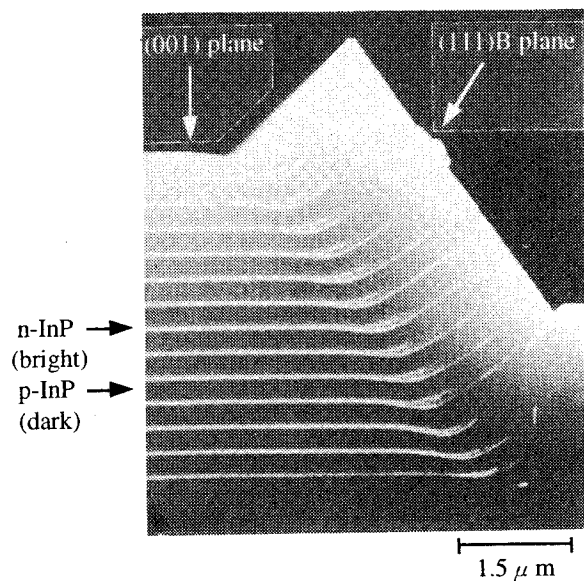
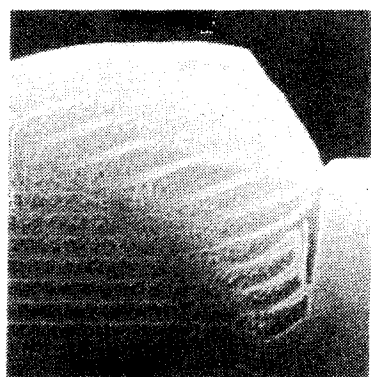
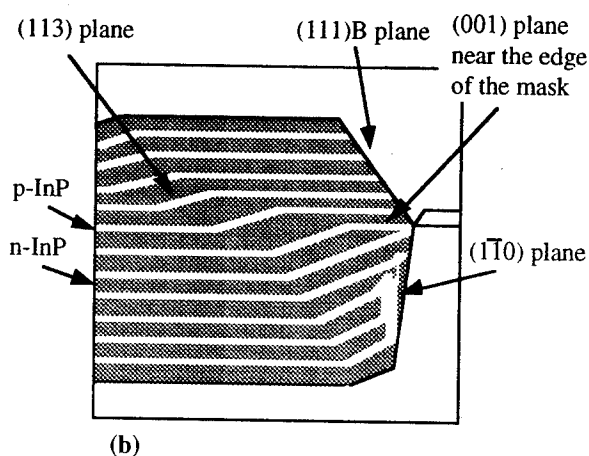


Fig. 5. An SEM micrograph showing the growth behavior of p-type InP at the growth temperature of 625°C. The selective grown layers consist of alternating p-InP (0.3μm) /n-InP (0.05μm) multilayers. n-type InP (bright) layers were inserted as the marker for the growth behavior of p-type InP (dark).



(a)

1.25 μ m



(b)

Fig. 6. (a) An SEM micrograph showing the growth behavior of n-type InP at the growth temperature of 625°C. The selective grown layers consist of alternating n-InP (0.2 μ m) / p-InP (0.05 μ m) multilayers in which p-type InP (bright) layers were inserted as the marker for the growth behavior of n-type InP (dark). A schematic illustration is also shown (b).

plateau of the (001) plane was enlarged, the enhancement of the growth rate on the (113) plane seems to be diminished.

These phenomena observed here for S-doped InP are similar to those reported for Se-doped InP [10]. These results suggest that those strange growth behaviors are the characteristics of group VI dopants. The group VI atoms seems to change the surface energy of InP crystal. Thus, the surface diffusion length of the growth species seems to be affected by the doping of group VI atoms. The surface diffusion of the growth species on the (001) plane is enhanced when the (001) plane is terminated by group VI atoms. On the other hand, the growth on the (113) facet is enhanced until the (001) plateau is enlarged beyond the surface diffusion length on the (001) plane. It is therefore necessary to take into account the effects of the group VI dopants on the growth rates on variously oriented facets, for fabricating the BH-LD and PIC.

Conclusions

We have achieved selective embedding growth of InP around nearly-rectangular mesas formed by RIE, without any overgrowth on the mask even at a low growth temperature of 580°C, using a high-speed rotating-disk MOCVD reactor. This is believed to be due to the reduction in the effective V/III ratio by the high-speed rotation. Moreover, we investigated the effects of dopants on the growth behavior, and found the remarkable difference between n-type and p-type doping in the growth behavior on the side wall of the mesa as well as that near the edge of the mask. These effects of dopants are very useful in optimizing the shapes of the embedding growth for fabricating the BH-LD and PIC.

Acknowledgments

The authors acknowledge Mr. T. Takiguchi and Mr. T. Itagaki for the support of this work.

References

- [1] e.g., Y. Ohkura, T. Kimura, T. Nishimura, K. Mizuguchi and T. Murotani, "Low threshold FS-BH laser on p-InP substrate grown by all-MOCVD," *Electron. Lett.*, vol. 28, pp. 1844-1845, 1992.
- [2] K. Nakai, T. Sanada and S. Yamakoshi, "Planar selective growth of InP by MOVPE," *J. Cryst. Growth*, vol. 93, pp. 248-253, 1988.
- [3] B.-T. Lee, R.A. Logan and S.N.G. Chu, "Observation of growth patterns during atmospheric pressure metalorganic vapor phase epitaxy regrowth of InP around etched mesas," *J. Cryst. Growth*, vol. 130, pp. 287-294, 1993.
- [4] N. Nordell and J. Borglind, "MOVPE growth of InP around reactive ion etched mesas," *J. Cryst. Growth*, vol. 114, pp. 92-98, 1991.
- [5] N. Nordell and J. Borglind, "Improved InP regrowth properties in metalorganic vapor phase epitaxy by addition of CCl₄," *Appl. Phys. Lett.*, vol. 61, pp. 22-24, 1992.
- [6] R.F. Karlicek, Jr., D.L. Coblenz, R.A. Logan, T.R. Hayes, R. Pawelek and E.K. Byrne, "A modified metalorganic chemical vapor deposition chemistry for improved selective area regrowth," *J. Cryst. Growth*, vol. 131, pp. 204-208, 1993.
- [7] B.-T. Lee and R.A. Logan, "Growth of InP on etched grooves using atmospheric pressure metalorganic vapor phase epitaxy," *J. Cryst. Growth*, vol. 140, pp. 1-8, 1994.
- [8] T. Takeuchi and S. Yamazaki, "InP embedding growth over dry-etched mesa by HCl added MOVPE," *Extended Abstract of the 55th Autumn Meeting of the Japan Society of Applied Physics*, 21p-MG-17, p. 284, 1994.
- [9] O. Kayser, "Selective growth of InP/InGaAs in LP-MOVPE and MOMB/CBE," *J. Cryst. Growth*, vol. 107, pp. 989-998, 1991.
- [10] Y. Kondo and Y. Imamura, "The effects of dopant on InP selective growth by MOVPE," *Extended Abstract of the 51st Autumn Meeting of the Japan Society of Applied Physics*, 28a-SX-10, p. 302, 1990.

Simultaneous Thickness and Compositional Uniformity in Selective MOVPE Growth

Mitsuru Ekawa, Takuya Fujii, and Susumu Yamazaki
Fujitsu Laboratories Ltd.
10-1 Morinosato-Wakamiya, Atsugi 243-01, Japan

Introduction

The growth of III-V compounds by selective metalorganic vapor phase epitaxy (MOVPE) is a promising technique for fabricating monolithically integrated devices, such as optical modulator integrated DFB lasers [1] and tapered waveguide lasers [2]. Selective MOVPE modulates in-plane thickness and group III compositional distributions [3-5]. Such integrated devices require good thickness and compositional uniformity in each functional region. Thickness uniformity may be controlled by the mask pattern design. However, it is not clear whether modification of the mask pattern changes thickness distributions of each group III component similarly.

In this work, we controlled InGaAs thickness profiles by a newly-designed mask pattern, and investigated the feasibility of both thickness and compositional uniformity. We found that thickness and compositional uniformity is achieved simultaneously.

Mask pattern design for uniform thickness

Our selective growth theory [6,7] predicts how the thickness distributions of epilayers are affected by the mask pattern design. This enables us to design an optimum mask pattern which achieves good thickness uniformity.

We used two types of selective mask patterns which have striped and open epilayer areas for this work. Figure 1 shows a conventional mask pattern, which is composed of twin rectangular masks. The group III source species supplied over the masked area diffuse laterally in the vapor phase to the adjacent unmasked area, and greatly enhance the growth rate in the narrow striped area. The distribution of the source flux from the masked area to the striped area, as illustrated by arrows in Figure 1, determines the thickness distribution in the striped area. In this conventional mask pattern, the source flux from the masked area to the striped area is reduced near the stripe edge due to the source flux from the masked area to the open area. This results in a monotonic reduction of epilayer thickness in the stripe direction.

We propose a modified mask pattern which improves thickness uniformity in the striped area (Figure 2). An

additional open window inside the rectangular mask area causes a local reduction in the source flux from the masked area to the striped area in the vicinity of the window. Optimizing the window width, W , realizes the thickness uniformity in the striped area.

Experimental

The MOVPE growth was performed on (100) InP substrates at 630 °C and at a growth pressure of 100 Torr. Trimethylindium (TMI), triethylgallium (TEG), arsine (AsH_3), and phosphine (PH_3) were used as source materials. Hydrogen was used as the carrier gas. A 0.2 μm thick SiO_2 film was used as the selective mask. The rectangular mask was 280 μm wide and 600 μm long. The width of the striped area was 20 μm . The stripe direction was aligned to $[01\bar{1}]$. The window width, W , in the modified mask pattern was varied from 40 to 80 μm . The window length was fixed at 360 μm . We grew InGaAs single-hetero (SH) structures for thickness measurements and InP/InGaAs/InP double-hetero (DH) structures for photoluminescence (PL) measurements. The In composition was set to 0.48 at the unperturbed region

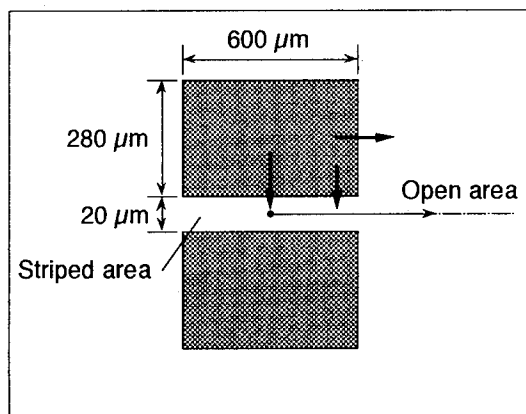


Figure 1. A schematic of a conventional mask pattern composed of twin rectangular masks. Shadowed area shows SiO_2 mask. The arrows represent the group III source flux.

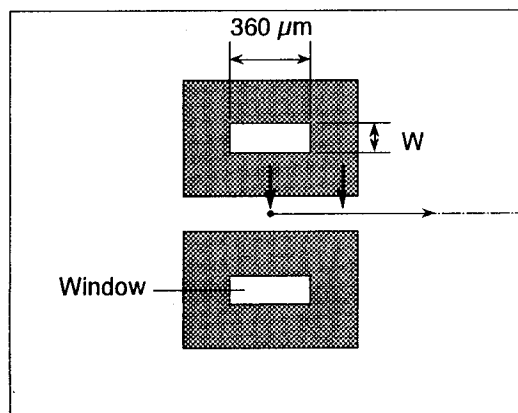


Figure 2. A schematic of a modified mask pattern with open windows inside the rectangular masks.

in all samples. The InGaAs thickness at the unperturbed regions of the DH samples was set to 50 nm in order to avoid inducing the lattice relaxation. We observed no deposition on the mask under these growth conditions.

Thickness and compositional distributions were evaluated in the stripe direction. The epilayer thicknesses were measured by a Dektak profiler after removal of the SiO₂ mask. The compositions of the InGaAs epilayers were evaluated by PL measurements at room temperature. Both measurements were started from the stripe center toward the open area, taking the symmetrical distribution into account.

Results

1. Thickness uniformity

Figure 3 shows how InGaAs thickness distributions in the stripe direction are affected by the open window width. The solid curves are results calculated using our selective growth theory. The theoretical predictions fit well the experimental results. For the conventional mask pattern, the InGaAs epilayer thickness decreased monotonically in the stripe direction. By contrast, for the modified mask pattern, the InGaAs epilayer thickness in the window region was decreased with the window width, and good thickness uniformity was achieved in the window region at $W=80\text{ }\mu\text{m}$. We found that the optimum mask pattern of $W=80\text{ }\mu\text{m}$ also uniformed the thickness of the InP epilayers.

2. Simultaneous compositional uniformity

The difference in thickness distributions between InAs and GaAs components induces the compositional modulation of the InGaAs epilayers. Figure 4 compares the PL peak wavelength distributions in the InGaAs epilayers between the conventional and modified mask patterns. For the

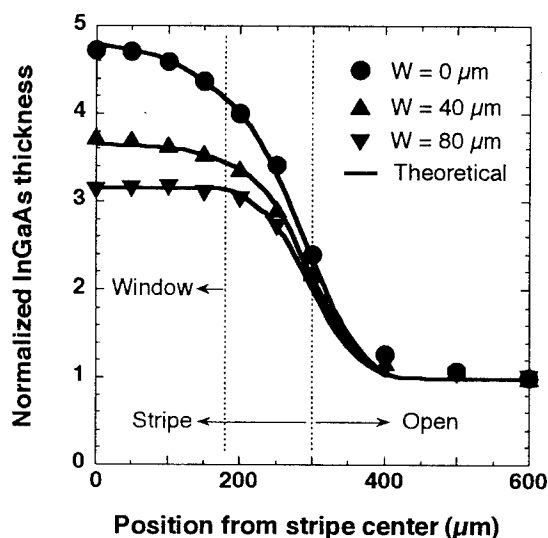


Figure 3. InGaAs thickness distributions for the conventional ($W=0\text{ }\mu\text{m}$) and modified ($W=40, 80\text{ }\mu\text{m}$) mask patterns. The thicknesses are normalized by the thickness at the unperturbed region. The solid curves are theoretically calculated results.

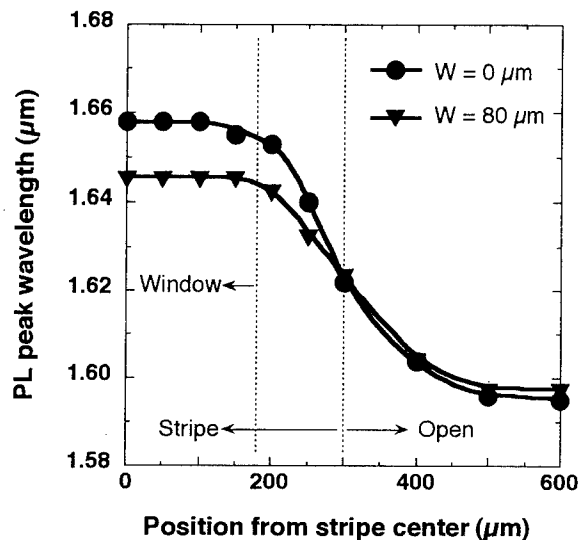


Figure 4. InGaAs PL peak wavelength distributions for the conventional ($W=0\text{ }\mu\text{m}$) and modified ($W=80\text{ }\mu\text{m}$) mask patterns.

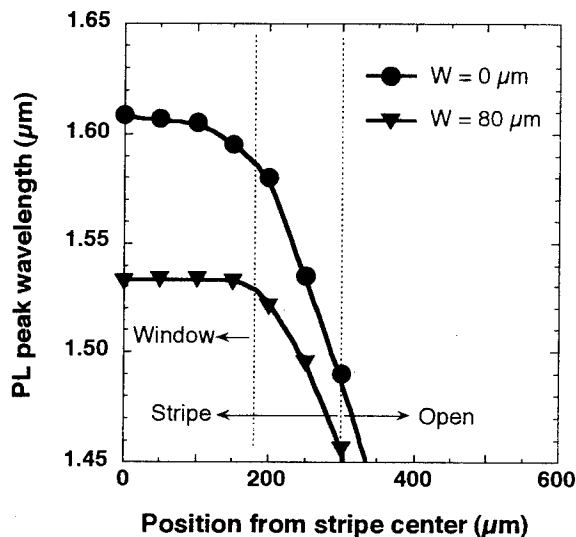


Figure 5. PL peak wavelength distributions of InP/InGaAs MQW for the conventional ($W=0\text{ }\mu\text{m}$) and modified ($W=80\text{ }\mu\text{m}$) mask patterns.

conventional mask pattern, the PL wavelength red-shifted 63 nm at the stripe center, which corresponds to the 5 % enrichment of In composition. This is due to a larger amount of In source flux from the masked area to the striped area. By contrast, the In enrichment is reduced by an additional open window. Both thickness and compositional uniformity was achieved in the striped area simultaneously by the open window of $W=80\text{ }\mu\text{m}$.

We also fabricated InP/InGaAs multiple-quantum-well (MQW) structures (5 periods), where the InP barrier and InGaAs well thicknesses were set to 3.5 nm and 2.3 nm at the

unperturbed region. Figure 5 shows the PL peak wavelength distributions in the MQW structures. For the conventional mask pattern, the PL wavelength shift was no less than 14 nm at a distance of 150 μm from the stripe center. By contrast, for the modified mask pattern where $W = 80 \mu\text{m}$, good uniformity in the PL wavelength was achieved by the thickness and compositional uniformity of the InGaAs well layers in the corresponding striped area.

Discussions

The simultaneous achievement of thickness and compositional uniformity in the striped area indicates the uniform thickness distributions of InAs and GaAs components in the vicinity of the additional open window. In order to discuss this mechanism, we investigated the behavior of In and Ga species in the epilayer region. Figure 6 shows the enhanced thickness distributions of InAs and GaAs components in the open area for the conventional mask pattern. Thickness and PL measurements were performed along the direction illustrated in the insert. The slopes of the semilogarithmic plots show same lateral diffusion lengths in the epilayer area between In and Ga species. We also observed similar lateral diffusion length in the open area in the InP epilayer. These results suggest that the behavior of lateral diffusion in the epilayer area is independent of group III source species and that the amount of group III source flux from the masked area to the epilayer area dominates the compositional modulation of the InGaAs epilayers. Figure 7 shows the enhanced thickness distributions of InAs and GaAs components in the stripe direction, which were obtained from the thickness and PL distributions in Figures 3 and 4. The larger InAs thickness enhancement is ascribed to the larger In source flux from the masked area to the epilayer area. It is worthy of note that thickness enhancements between InAs and GaAs components have an approximately proportional relationship in the striped area. We conclude that modification of the mask pattern changes the source flux distribution in the same proportion between In and Ga species. This mechanism makes the thicknesses of InAs and GaAs components uniform simultaneously.

Summary

We investigated the feasibility of thickness and compositional uniformity in selective MOVPE growth. Using a modified mask pattern with an additional open window in the rectangular mask area, we succeeded in making uniform the thickness distributions of epilayers selectively grown in the striped area. From PL studies, we found that thickness and group III composition were uniform in the same region. Consequently an InP/InGaAs MQW structure exhibited a uniform PL peak wavelength in the striped area. This simultaneous uniformity suggests that the phenomena in the masked area dominate the compositional modulation of InGaAs in selective MOVPE growth.

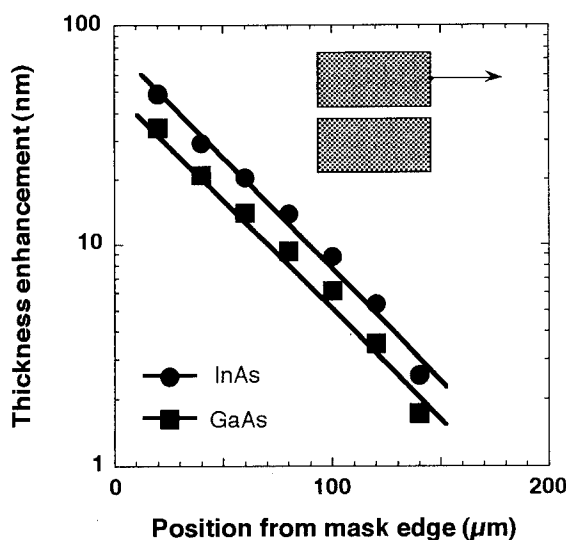


Figure 6. Semilogarithmic plots of enhanced thickness distributions of InAs and GaAs components in the open area. The arrow in the insert represents the measurement direction.

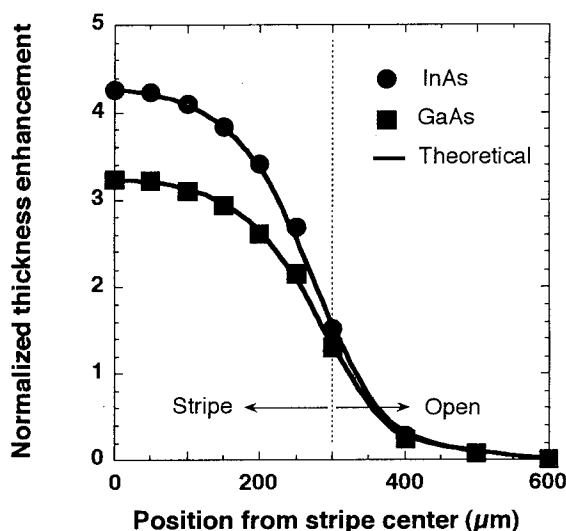


Figure 7. Enhanced thickness distributions of InAs and GaAs components in the stripe direction, which are normalized by each thickness at the unperturbed region. The solid curves are theoretically calculated results.

References

- [1] M.Aoki, H.Sano, M.Suzuki, M.Takahashi, K.Uomi, and A.Takai, "Novel structure MQW electroabsorption modulator/DFB-laser integrated device fabricated by selective area MOCVD growth," *Electronics Letters* Vol.27 No.23, pp. 2138-2140, 1991.
- [2] H.Kobayashi, M.Ekawa, N.Okazaki, O.Aoki, S.Ogita, and H.Soda, "Tapered thickness MQW waveguide BH MQW lasers," *IEEE Photonic Technology Letters* Vol.6 No.9, pp. 1080-1081, 1994.
- [3] M.Gibbon, J.P.Stagg, C.G.Cureton, E.J.Thrush, C.J.Jones, R.E.Mallard, R.E.Pritchard, N.Collis, and A.Chew, "Selective-area low-pressure MOCVD of GaInAsP and related materials on planar InP substrates," *Semicond. Sci. Technol.* 8, pp. 998-1010, 1993.
- [4] T.Sasaki, M.Kitamura, and I.Mito, "Selective metalorganic vapor phase epitaxial growth of InGaAsP/InP layers with bandgap control in InGaAs/InGaAsP multiple-quantum well structures," *Journal of Crystal Growth* 132, pp. 435-443, 1993.
- [5] C.Caneau, R.Bhat, C.C.Chang, K.Kash, and M.A.Koza, "Selective organometallic vapor phase epitaxy of Ga and In compounds; a comparison of TMIn and TEGa versus TMIn and TMGa," *Journal of Crystal Growth* 132, pp. 364-370, 1993.
- [6] T.Fujii, M.Ekawa, and S.Yamazaki, "A theory for metalorganic vapor phase epitaxial selective growth on planar patterned substrates," *Journal of Crystal Growth* 146, pp. 475-481, 1995.
- [7] T.Fujii, M.Ekawa, and S.Yamazaki, "Growth pressure dependence of selective area MOVPE on planar patterned substrates," *Journal of Crystal Growth*, submitted.

InAlGaAs SELECTIVE MOVPE GROWTH WITH BANDGAP ENERGY SHIFT

T. Takeuchi, M. Tsuji, K. Makita and K. Taguchi

Opto-electronics Res. Labs. NEC Corp.

34 Miyukigaoka, Tsukuba-shi, Ibaraki, Japan

Introduction

The selective MOVPE on partially masked substrates is attractive and useful for the fabrication of optoelectronic devices including photonic integrated circuits. The device applications and growth mechanisms of selective MOVPE have so far been extensively investigated mainly in the InGaAsP material system (1),(2). On the other hand, although the InAlGaAs material system with large conduction band discontinuity is also important, few experimental results of the selective growth have been reported (3) because of the difficulty of growing Al-containing materials. Furthermore, there have been no observations on its bandgap energy shift by using different mask width. In this work, the selective MOVPE of InAlGaAs was studied. Almost no polycrystals on the SiO₂ mask were observed, which shows that the selective MOVPE of InAlGaAs is a practical technique for device applications. A large bandgap wavelength shift of 170 nm was achieved with a mesa width of 2 μm and a mask width of 40 μm . This is the first report on the bandgap energy controlling in the InAlGaAs selective growth.

Experimental Procedure

In the experiments, InAlGaAs layers were grown in a low-pressure (70 Torr), vertical type MOVPE reactor. The reagents were trimethylindium (TMIn), trimethylaluminum (TMAI), triethylgallium (TEGa) and arsine (5 % mixture in hydrogen). All epitaxial layers were grown with unintentionally doped condition.

Stripe patterns of SiO₂ film with the thickness of about 100 nm were formed on (100) InP substrates parallel to the [011] direction. Each pattern consists of a pair of the same mask stripes, the width W_m of which was varied from 10 μm to 40 μm . The open area between the mask stripes, whereat a mesa stripe of InAlGaAs was grown, has the width W_o of 2 μm to 15 μm . Before the growth, the wafers were rinsed in organic solvents and cleaned with a H₂SO₄:H₂O₂:H₂O solution. The thickness and the growth rate of InAlGaAs (bandgap wavelength $\lambda \sim 1.3 \mu\text{m}$) on the region without the masks were about 0.3 μm and 1 $\mu\text{m}/\text{h}$, respectively. The growth temperature was 700°C; and the V/III ratio was 200. Beside InAlGaAs, InAlAs were also grown at

almost the same growth conditions for comparison.

In general, selective MOVPE growth of Al-containing materials is difficult. This is due to the high reactivity of Al species with dielectric masks e.g. SiO₂ and/or SiN_x, which results in polycrystalline growth on the masks. Recently, the AlGaAs selective MOVPE with high selectivity was achieved with HCl gas introducing (4). However, when selectively grown layers are directly used as active layers of such as lasers or detectors, the insufficient purification of HCl gas is not reliable. Therefore, in this study, selective MOVPE of InAlGaAs was examined without HCl gas.

Photoluminescence (PL) measurements and auger electron spectroscopy (AES) measurements were used to evaluate the bandgap energies and compositions of the layers. In AES measurements, the focused electron beam diameter was smaller than 1 μm . In PL measurements, the Ar laser beam ($\lambda = 515 \mu\text{m}$) was focused to a diameter of about 1 μm .

Results and Discussion

Figure 1 shows a microphotograph of a wafer surface after the $\text{In}_x\text{Al}_y\text{Ga}_{1-x-y}\text{As}$ selective growth. As can be seen, almost no polycrystals are observed even on the widest $40\text{ }\mu\text{m}$ width mask. High selectivity has been achieved at relatively low growth rate of $1\text{ }\mu\text{m/h}$. At the growth rate higher than $1\text{ }\mu\text{m/h}$, the selectivity was degraded. The low Al content of $y \sim 0.1$ in the experiments has also contributed to the high selectivity.

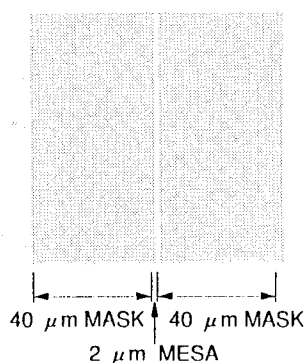


Fig.1 Microphotograph of a wafer surface after the InAlGaAs selective growth.

Figure 2 shows the scanning electron microscopy (SEM) photograph of the mesa structure. Epitaxially grown mesa is surrounded by a (100) top surface and (111)B side facets, and a flat surface was obtained.

These results have proved that selective growth of InAlGaAs is a practical and useful technique for the fabrications of photonic waveguide devices.

Figure 3 shows the PL peak wavelength shifts of InAlGaAs for various W_m and W_o . The data point of $W_m = 0$ represents the PL peak wavelength of the region without the masks. The PL peak wavelength becomes longer with wider W_m and narrower W_o . This tendency is similar to that of the InGaAsP material system (1),(5). A large wavelength shift of about 170 nm was obtained with $40\text{ }\mu\text{m}$ W_m and $2\text{ }\mu\text{m}$ W_o .

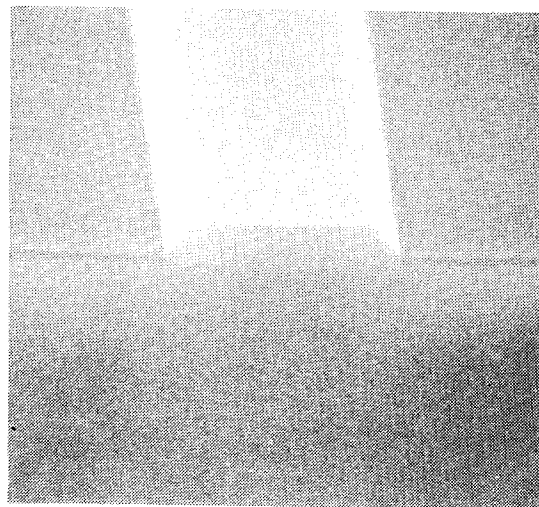


Fig.2 Scanning electron microscopy (SEM) photograph of an $2\text{ }\mu\text{m}$ wide InAlGaAs mesa.

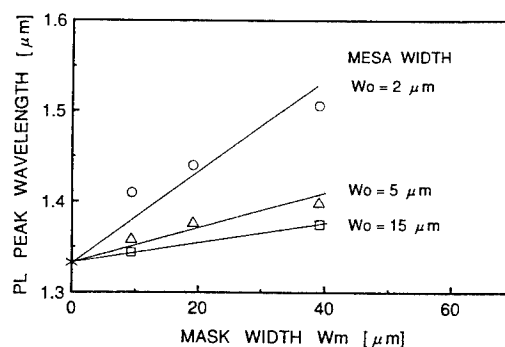


Fig. 3 PL peak wavelength shifts of InAlGaAs for various W_m and W_o . Ar laser was focused onto the center of mesa stripes.

The composition change of InAlGaAs was also examined by AES measurements for the W_o of $2\text{ }\mu\text{m}$. Figure 4 shows the AES signal intensity of In, Al and Ga normalized with that of As. Apparently the signal intensity of In increases with a wider mask width, which means enhancement of the In content. However, the tendency of Al and Ga

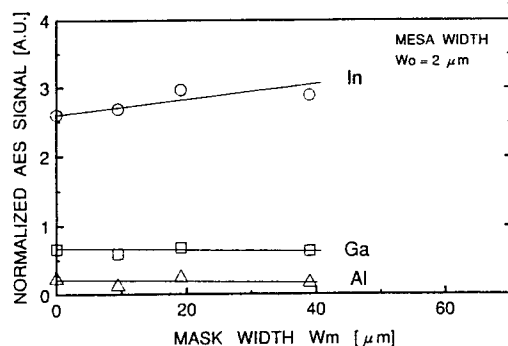


Fig.4 AES signal intensity of In, Al and Ga in InAlGaAs. The intensity was normalized with that of As.

is not clear in these data. From these results, it is revealed that the existence of masks also causes the composition change in selective InAlGaAs growth as well as in InGaAsP growth. The In content is enhanced with a wider mask width, which makes the bandgap energy smaller.

The migration and/or diffusion of group III species is proposed to be the mechanism of the selective MOVPE growth (6)-(9). Especially in the InGaAsP system, the different behavior of In and Ga species during the selective growth is thought to be the origin of the composition change, and it has been well investigated. However, there have been no reports to date about the behavior of group III species during the selective growth of the InAlGaAs material system. Especially to investigate the behavior of Al species, InAlAs selective growth was examined.

The InAlAs growth temperatures were 650°C and 700°C. Other growth conditions were almost the same as those of InAlGaAs. Figure 5 shows the AES signal intensity of In and Al normalized with that of As. The intensity of In increases and that of Al decreases with a wider mask width at both growth temperatures. The intensity change at 650°C is larger than that at 700°C, which suggests larger composition change at lower temperature.

One important factor in explaining the results shown in fig.5 is the decomposition process of

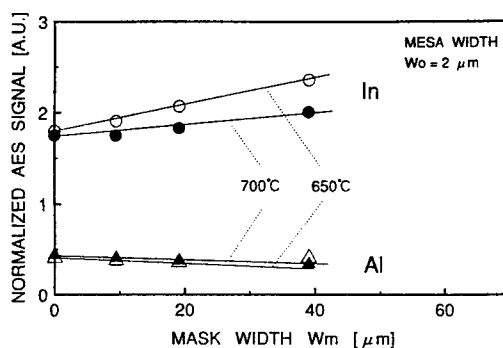


Fig.5 AES signal intensity of In and Al in InAlAs. The intensity was normalized with that of As.

group III species. Although the diffusivity of TMAI is a little larger than that of TMIn, the decomposition temperature of TMAI is higher than that of TMIn (10),(11). This difference of decomposition process leads to lower incorporation enhancement of Al than In. At a high growth temperature of 700°C, the difference in decomposition between In and Al species becomes small, and thus the composition change also becomes small in comparison to that at 650°C. It has been reported that the decomposition process plays an important role in the selective growth of InGaAs (12). In the InAlGaAs material system, the decomposition process also seems to be an important factor in the composition change.

From the viewpoint of device applications, such as photonic integrated circuits, the information about the transition region between two different mask widths is important. Figure 6 shows the PL peak wavelength profile along the mesa stripe of InAlGaAs. The mask pattern, as shown in the inset of fig. 6, consists of two pairs of masks with different widths 10 μm and 20 μm, and they are directly connected. The peak wavelengths gradually shifted at the transition region. The transition length, which was defined as 10 % - 90 % of the total wavelength shift, was about 60 μm. This value is almost comparable to the reported values in InGaAsP (1),(5).

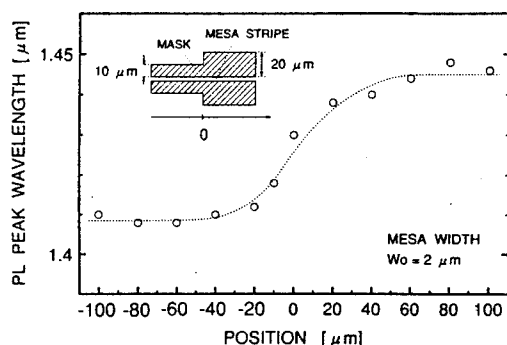


Fig.6 PL peak wavelength profile along a mesa stripe of InAlGaAs.

Conclusion

In conclusion, selective MOVPE of InAlGaAs with almost no polycrystalline growth was achieved. The composition change was also observed in selective InAlGaAs growth. The In content is enhanced with wider mask width, which makes the bandgap energy smaller. A large PL peak wavelength shift of 170 nm with a mesa width of 2 μm and a mask width of 40 μm was achieved. This is the first report on the bandgap energy controlling in the InAlGaAs selective growth.

Acknowledgements

The authors thank K. Kobayashi and I. Mito for their encouragements, and also thank T. Sasaki for his discussions and support.

References

- (1) T. Sasaki, M. Kitamura and I. Mito, *J. Crystal Growth* Vol.132, pp.435-443, 1993.
- (2) T. Kato, T. Sasaki, K. Komatsu and I. Mito, *Electron. Lett.*, Vol.28, pp.153-154, 1992.
- (3) M. Kushibe and K. Takaoka, *ICMOVPE VII Conference Digest*, P1-13, pp.235-236, 1994.
- (4) K. Shimoyama, Y. Inoue, K. Fujii and H. Gotoh, *J. Crystal Growth*, Vol.124, pp.235-242, 1992.
- (5) M. Aoki, H. Sano, M. Suzuki, M. Takahashi, K. Uomi and A. Takai, *Electron. Lett.*, Vol.27, pp.2138-2140, 1991.
- (6) J. S. C. Chang, K. W. Carey, J. E. Turner and L. A. Hodge, *J. Electron. Materials*, Vol.19, pp.345-348, 1990.
- (7) K. Hiruma, T. Haga and M. Miyazaki, *J. Crystal Growth*, Vol.102, pp.717-724, 1990.
- (8) Y. D. Galeuchet and P. Roentgen, *J. Crystal Growth*, Vol.107, pp.147-150, 1991.
- (9) O. Kayser, *J. Crystal Growth*, Vol.107, pp.989-998, 1991.
- (10) M. Suzuki and M. Sato, *J. Electrochem. Soc.*, Vol.132, pp.1684-1688, 1985.
- (11) G. B. String fellow, "Organometallic Vapor Phase Epitaxy," Academic Press, San Diego, CA, 1989.
- (12) C. Caneau, R. Bhat, C. C. Chang, K. Kash and M. A. Koza, *J. Crystal Growth*, Vol.132, pp.364-370, 1993.

TEMPORALLY RESOLVED SELECTIVE REGROWTH OF InP AROUND [110] AND $\bar{1}\bar{1}0$ DIRECTIONAL MESAS

S. Lourdudoss, E. Rodríguez Messmer, O. Kjebon, and G. Landgren
Laboratory of Artificial Semiconductor Materials, Department of Electronics,
Royal Institute of Technology, Electrum 229, S-164 40 Kista, Sweden.

Introduction

The importance of selective regrowth of InP can be recognised from the quantity of publications arising in this field. A majority of the investigations come especially from the MOVPE (Metal Organic Vapour Phase Epitaxy) process, see e.g. [1] and the references therein. A near equilibrium process, HVPE (Hydride Vapour Phase Epitaxy), has been used in the present investigation to study the selective growth of InP around the RIE (Reactive Ion Etching) etched [110] and $\bar{1}\bar{1}0$ directional mesas. The growth was temporally resolved by growing alternating layers of unintentionally doped and n-doped InP. The striking differences in the growth behaviour and immense initial lateral growth rates are presented and discussed.

The implication of an immense lateral growth in device fabrication is exemplified by considering the regrowth of iron doped semi-insulating InP in the fabrication of buried heterostructure lasers.

Experimental

A GaInAsP quaternary layer of thickness $\sim 0.5 \mu\text{m}$ was grown by MOVPE on (001) n-InP substrate. After depositing silicon nitride, conventional lithography cum reactive ion etching using methane and hydrogen were used to create mesas along the [110] and $\bar{1}\bar{1}0$ directions. These were $\sim 2 \mu\text{m}$ broad and $\sim 3 \mu\text{m}$ tall. Selective regrowth of (totally) seven alternating layers of unintentionally doped InP and n-InP was carried out in a HVPE reactor [2] in an ambient of nitrogen. The first five layers were grown in one minute each and the remaining two layers two minutes each. The growth temperatures were 600, 650, 685 and 700°C. The V/III ratio was ~ 6.5 . H_2S of concentration 200 ppm in H_2 was used as the n-dopant gas. The nominal electron concentration in n-InP layers (as found in the n-InP layers grown on planar wafers) was $\sim 1 \times 10^{18} \text{ cm}^{-3}$. After regrowth, the samples were cleaved, stained and analysed by SEM (Scanning Electron Microscopy).

Results and Discussions

The SEM cross-sections of the regrown [110] and $\bar{1}\bar{1}0$ mesas are given in Fig. 1 and Fig. 2, respectively; a, b, c and d in Figs. 1 and 2 correspond to the growth temperatures of 600, 650, 685 and 700 °C, respectively. It is clear that the growth behaviour in the $\bar{1}\bar{1}0$ mesa case is strikingly different from that in the [110] mesa case. Similar features were observed even when regrowth was carried out without nitride mask [3]. Thus these features do not seem to arise from the selective growth but from the difference in the bonding configurations existing on the planes exposed for regrowth [4]. The angle between the wall and the dangling bond on P (or In) on the wall is 125.2° (or 54.8°) in the [110] mesa case and 54.8° (or 125.2°) in the $\bar{1}\bar{1}0$ case. Since the regrowth necessarily has to take place by making use of the dangling bonds both on the (001) and {110} planes, the growth pattern is different in the two considered cases.

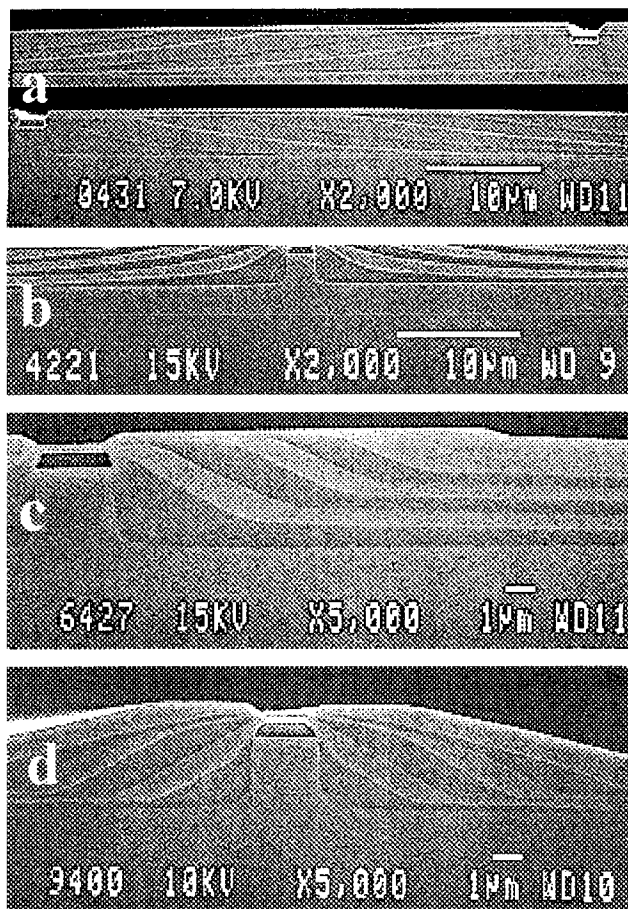


Fig. 1. SEM cross-section of the [110] mesas after regrowth at (a) 600 °C, (b) 650 °C, (c) 685 °C and (d) 700 °C



Fig. 2. SEM cross-section of the $[110]$ mesas after regrowth at (a) 600 °C, (b) 650 °C, (c) 685 °C and (d) 700 °C

Taking into account these differences, the growth already in the very initial stage can be depicted as in Fig. 3 and Fig. 4 for the $[110]$ and $[1\bar{1}0]$ mesa cases, respectively.

How these differences affect further growth can be analysed by considering the net change of dangling bonds when each atom is added to the crystal. However it would be sufficient and proper to consider only the addition of In atom since under the conditions of excess PH_3 with respect to InCl , total adsorption of P atoms takes place readily in analogy to As adsorption in the GaAs growth case [5]. Under such conditions, due to the differences in the orientation of the dangling bonds on P, the net change of dangling bonds at the addition of first In at the kink site is 0 for the $[110]$ mesa case and -2 for the $[1\bar{1}0]$ mesa case. The subsequent addition of In results in a net change of dangling bonds equal to -2 in *all the three principal directions of growth* in the case of the $[1\bar{1}0]$ mesa; but in the case of the $[110]$ mesa, it is -2 only in the mesa direction and zero in the other two directions (upwards and sideways). This explains the abundant growth in the case of the $[1\bar{1}0]$ mesa already in the very first minute, see Fig. 2. This also confirms our previous finding that the (110) walls are "wetted" predominantly with respect to the $(1\bar{1}0)$ walls when very tall mesas are used for regrowth [6-7]. In both cases, it is found that initially the growth takes place in the immedi-

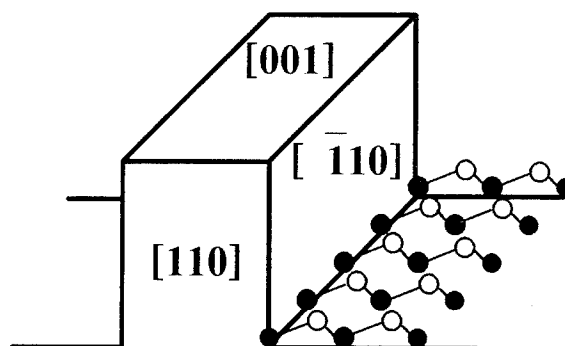


Fig. 3. Schematic view of the very initial regrowth stage in the $[110]$ mesa case. Filled circle is P and open circle is In.

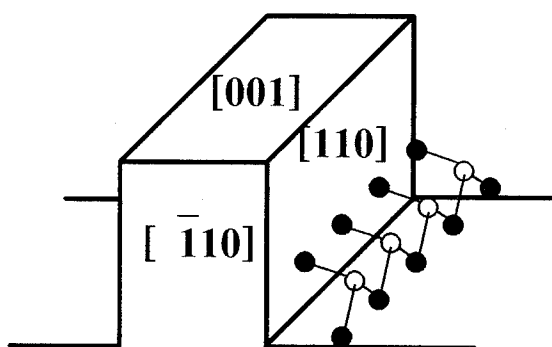


Fig. 4. Schematic view of the very initial regrowth stage in the $[110]$ mesa case. Filled circle is P and open circle is In.

ate vicinity of the mesa wall in big jump or jumps. But when the growth has reached the mesa level, the growth on the (001) plane beside the mesa is not so spectacular. As the growth is in progress, certain other planes emerge, which are identified mostly as $\{hkl\}$ ("l" here is the small case of L and not one). As long as any one of these planes does not act as the stopping plane, a higher density of dangling bonds at the kink sites would favour the growth away from the mesa so as to enable a total planarisation. Hence the growth above the mesa level takes place in smaller jumps at least during the growth time of our experiments.

The dangling bond arguments are general and fundamental to explain the crystal growth behaviour. Cadoret [8] proposed a particular model to explain the anisotropic growth behaviour in the chlorine based growth processes such as Chloride VPE and Hydride VPE. This author postulated the formation of As-Ga-Cl intermediate from the studies on the growth of GaAs on *planar substrates* of different crystallographic orientations and that the growth rate along a particular direction is dependent upon the facility with which the Cl atom can be removed from this intermediate; if Cl atom is not easily removable, e.g. due to steric hindrance, further adsorption of the incoming species becomes difficult and the reaction is considerably slowed down. As a result there can be

certain orientations that are preferable for growth and hence the anisotropic growth. Cl removal is also identified as the rate determining step in GaAs growth by chloride based ALE (atomic layer epitaxy) process [9]. In the HVPE growth of InP, Cl removal from a similar intermediate, P-In-Cl, has been suggested as the rate determining step by Chaput et al. [10]. To the authors' knowledge, this model has not been explicitly employed so far for accounting the growth on *non-planar substrates*. It is indicated here how this model strengthens our dangling bond approach. A scrutiny of the configuration of the adsorbed P-In-Cl intermediate with the help of Fig. 3 and Fig. 4 leads to the identification of one dangling bond on In in the case of the [110] directional mesa and none in the $\bar{1}\bar{1}0$ directional mesa. This is because In in P-In-Cl intermediate is attached to two P atoms in the former case (see Fig. 3) and to three P atoms in the latter case (see Fig. 4). As a result, the intermediate in the [110] mesa case has two resonating structures (since Cl can occupy any one of the two available bonds on indium) unlike that in the $\bar{1}\bar{1}0$ directional mesa which has only one such structure. Hence, Cl removal from the less stable P-In-Cl intermediate of the $\bar{1}\bar{1}0$ mesa is facile which also accounts for an abundant growth in all the directions unlike in the [110] mesa case, as has been mentioned in the previous paragraph.

The initial lateral growth defined as the growth away from the mesa wall at half the height of the mesa in the very first minute is presented in the form of Arrhenius plots in Fig. 5. The decrease in growth rate with the increase of temperature is due to an enhanced pyrolysis of PH_3 to P_2 which is known to reduce the growth rate [11-12]. These curves also

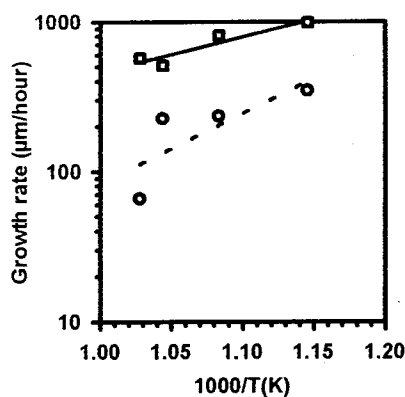


Fig. 5. Initial lateral growth rate as a function of temperature: circle: [110] mesa, square: $\bar{1}\bar{1}0$ mesa.

confirm that the growth is always more abundant in the $\bar{1}\bar{1}0$ mesa at all the investigated temperatures in accordance with the dangling bond arguments and the Cadoret model discussed in the previous paragraphs. A similar trend has also been observed for the case where the regrowth was carried out with-

out mask [3]. However the initial lateral growth rate is always higher when the mask is present for a given mesa orientation. This suggests that when the mask is absent, the availability of the active gases for lateral growth should be less due to the growth on the mesa itself.

We have also analysed various emerging planes and are identified to be {hhl}. Initially the planes with $l/h \leq 3$ are generally formed but progress towards {hhl} with larger values of l/h which are indistinguishable from (001). More detailed results will be published elsewhere.

An immense initial lateral growth rate should be taken into account e.g. to achieve proper amount of iron incorporation during semi-insulating InP:Fe regrowth for buried heterostructure laser fabrication. For example, to achieve $\sim 2 \times 10^{17}$ Fe atoms/cm³ of active iron near the mesa, one should target a value of $\sim 2 \times 10^{18}$ Fe atoms/cm³ (calibrated from growth on planar substrates) if the ratio of initial lateral growth rate to the planar growth rate is 10 as in our case. Thus our regrown lasers exhibit very low leakage currents since the active iron concentration is close to the maximum attainable active iron concentration, 5×10^{17} cm⁻³ [13].

Summary and Conclusions

Temporally resolved regrowth of InP around the [110] and $\bar{1}\bar{1}0$ mesas has been carried out by a near equilibrium process, HVPE. The regrown pattern are strikingly different for the considered two types of mesas. The lateral growth is higher in the case of the $\bar{1}\bar{1}0$ oriented mesas at all the studied temperatures and is understood to be due to a more favourable net change of dangling bonds. This is also supported by a model proposed by Cadoret [8] and Chaput et al. [10]. The initial lateral growth defined as the growth away from the mesa at half the height of the mesa in the very first minute is a decreasing function of temperature and is interpreted to be due to an enhanced pyrolysis of phosphine. An immense lateral growth has to be considered when particular amount of dopant has to be incorporated very near the mesa. This has been exemplified by considering Fe incorporation when InP:Fe is regrown for buried heterostructure laser fabrication.

Acknowledgements

We would like to thank Dr. Nils Nordell for his very valuable suggestions and Prof. Lars Thylén for his support. One of the authors (ERM) would like to acknowledge the partial support from ERASMUS programme and thank Dr. H. Henke and Prof. K. Heime from RWTH, Aachen, Germany, for their support.

References

1. N. Nordell, Metalorganic vapour phase epitaxy for advanced III-V devices, Doctoral dissertation, Faculty of Electrical Engineering, Royal Institute of Technology, Stockholm, Sweden (1993).
2. S. Lourdudoss, B. Hammarlund and O. Kjebon, J. Electron. Mat., 19 (1990) 981.

3. S.Lourdudoss, E.Rodríguez Messmer, O.Kjebon and G.Landgren, to be published in J. Cryst. Growth.
4. N.Nordell, J.Borglind and G.Landgren, J. Cryst. Growth, 125 (1992) 597.
5. H.Asai, J. Cryst. Growth, 80 (1987) 425.
6. S.Lourdudoss, E.Rodríguez Messmer, O.Kjebon, K.Streubel, J.André and G.Landgren, Materials Science and Engineering, B28 (1994) 179.
7. S.Lourdudoss, K.Streubel, J.Wallin, J.André, O.Kjebon and G.Landgren, Sixth international conf. on InP and related materials, Santa Barbara, California, USA, 1994, p. 615.
8. R.Cadoret, in: Current Topics in Materials Science, vol. 5, Ed. E.Kaldis, North-Holland, Amsterdam, 1980, ch. 2.
9. Y.Mochizuki, T.Takada, T.Sakuma, S.Handa, C.Sasaoka and A.Usui, J. Crystal Growth, 135 (1994) 259.
10. L.Chaput, R.Cadoret and M.Mihailovic, J. Crystal Growth, 112 (1991) 691.
11. R.F.Karlicek, Jr., D.Mitcham, J.C.Ginocchio and B.Hammarlund, J. Electrochem. Soc., 134(2) (1987) 470.
12. M.Harrous, J.L.Laporte, M.Cadoret, C.Pariset and R.Cadoret, J. Crystal Growth, 83 (1987), 279.
13. S.Lourdudoss, O.Kjebon, S.Nilsson, N.Nordell and C.Keller, in Semi-Insulating III-V Materials, Ed. M.Godlewski, 1994 (in press)

High-speed Waveguide Photodetectors

ThB1.1
(Invited)

Kazutoshi Kato and Yuji Akatsu

NTT Opto-electronics Laboratories

3-1 Morinosato Wakamiya, Atsugi, Kanagawa, 243-01 Japan

Abstract

Photodetectors offering wide bandwidths and high efficiency are indispensable devices for high-speed optical transmission systems. This paper reviews a proposed multimode waveguide pin-photodiode with a mushroom-mesa structure. This photodiode has a 3-dB bandwidth of 110 GHz and an external quantum efficiency of 50% at a wavelength of 1.55 μm . A high-speed monolithically integrated photoreceiver using the waveguide pin-photodiode is also presented.

Introduction

High-speed optical transmission technology has rapidly developed to the point that 10-Gbit/s transmission is now possible. Experiments on optical transmission speeds faster than 10 Gbit/s are currently being carried out using intensity modulation/direct detection (IM/DD) schemes [1, 2]. These high-speed transmission systems require photodetectors with wide bandwidths and high efficiency.

The photodetector structures are classified as surface-illuminated photodiodes and side-illuminated photodiodes. Surface-illuminated photodiodes have bandwidths inversely proportional to the thickness of the photo-absorption layer. This is because the bandwidth is limited by the carrier-transit time at this layer. On the other hand, the internal quantum efficiency is proportional to the thickness. Thus, there is a trade-off between the bandwidth and the internal quantum efficiency with these photodiodes. The bandwidth-efficiency product is theoretically limited to about 38 GHz at long wavelengths [3].

Side-illuminated photodiodes have optical waveguide structures. In these photodiodes, the light and the photo-generated carriers travel in different directions. This structure permits the bandwidth and the efficiency to be specified almost independently of each other [3].

However, the problem with these side-illuminated waveguide photodiodes (WGPDs) is that it is much more difficult to obtain highly efficient optical coupling to a fiber than it is with surface-illuminated photodiodes. This is because conventional ultra-high-speed WGPDs with InP/InGaAs/InP double heterostructures have poor coupling efficiency due to their thin photo-absorption InGaAs layers.

In this paper, a proposed multimode waveguide pin-photodiode (WGPD) with a mushroom-mesa structure are designed and confirmed experimentally to have both an ultra-wide bandwidth and high efficiency. High-speed monolithically opto-electronic integrated circuits (OEICs) that use the WGPD are also presented.

Ultra-high-speed and high efficiency WGPD design

The trade-off between bandwidth and coupling efficiency in conventional InP/InGaAs/InP WGPDs (Fig. 1(a)) originates from the fact that the InGaAs layer functions as both the photo-absorption/carrier-transit layer of the photodetector and as the core layer of a waveguide. To overcome this problem, we have enlarged the optical field distribution at the WGPD end by adding doped InGaAsP ($\lambda_g = 1.3 \mu\text{m}$) intermediate-bandgap layers between the InGaAs core layer and the InP clad layers [4] as

shown in Fig. 1(b). Since the bandgap energy of the intermediate-bandgap layers is set greater than that corresponding to a 1.55- μm wavelength, photo-carriers are generated and then transit through the depleted InGaAs layer.

We developed two WGPD models to calculate coupling efficiency: one with a symmetric structure and the other with an asymmetric structure (Figs. 1(b) and 1(c)). First, the optical fields of the guided light in the WGPD structures were calculated using the step segment method (SSM) [5]. Our numerical results revealed that, in both the symmetric and asymmetric structures, higher-than-first-order modes appear in the perpendicular direction when the total thickness of the InGaAs and InGaAsP layers is greater than 1.1 μm . We will refer to the WGPDs with higher-than-first-order modes as multimode WGPDs.

	InP	InP
InP	InGaAsP	InGaAs
InGaAs	InGaAs	InGaAsP
InP	InGaAsP	InP
	InP	InP
(a)	(b)	(c)

Fig. 1. WGPD structure model:

- (a) Conventional WGPD structure.
- (b) Symmetric multimode WGPD structure.
- (c) Asymmetric multimode WGPD structure.

Next, we calculated the coupling efficiency by considering the overlap integral between the optical field of the fiber and that of the WGPD. The coupling efficiency between a WGPD and a hemispherically-ended single-mode fiber, which produces a Gaussian beam with a 1.3- μm spot size, is shown in Fig. 2 as a function of the total thickness of the core layer and the intermediate-bandgap layer. For both the symmetric and asymmetric structures, coupling efficiency increases dramatically to as much as 90% when the total thickness slightly exceeds 1.1 μm . This is because the higher-order modes

of the multimode configuration contribute to coupling efficiency.

These results indicate that the electrical and optical properties can be designed almost independently of each other for multimode WGPDs. Multimode WGPDs can simultaneously have ultra-wide bandwidths and high efficiency.

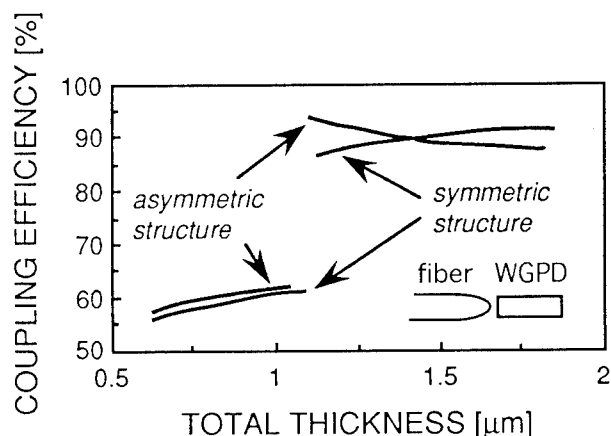


Fig. 2. Calculated coupling efficiency between a WGPD and a hemispherically-ended single-mode fiber as a function of the total thickness of the core layer and the intermediate-bandgap layer. The coupling efficiency increases dramatically when the total thickness slightly exceeds 1.1 μm .

Mushroom-mesa structure

Another problem is that the bandwidth of the WGPDs has been limited not by the carrier-transit time but by the CR-time constant at frequencies above 50 GHz. This is because the contact resistance at the top layer increases when the area of the pn-junction is decreased to reduce capacitance. For a bandwidth of more than 100 GHz, we propose a waveguide structure with cladding layers wider than the core layer, as shown in Fig. 3. We call this structure a mushroom-mesa structure. A mesa with a 1.5- μm -wide InGaAs core layer and 6- μm -wide InP cladding layers is expected to have a resistance less than 10 Ω and to provide 100-GHz operation [6].

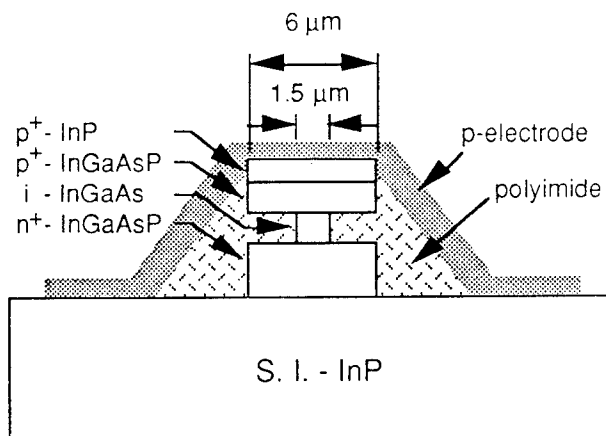


Fig. 3. Schematic viewgraph of a mushroom-mesa structure.

Experimental results

The total thickness of the InGaAs core layer and the intermediate-bandgap layers was designed to be $1.8\text{ }\mu\text{m}$ to provide a multimode configuration. The epitaxial layers were grown by low-pressure metal organic vapor phase epitaxy (MOVPE) on a semi-insulating InP substrate. The mushroom mesa, with $6\text{-}\mu\text{m}$ -wide cladding layers, was formed by $\text{C}_2\text{H}_6/\text{O}_2$ reactive ion etching. Then the InGaAs core layer was selectively etched to $1.5\text{-}\mu\text{m}$ width with a sulfuric acid mixture. The mesa was buried with polyimide and integrated with a $50\text{-}\Omega$ -impedance coplanar transmission line. The fabricated devices were cleaved with automatic cleaving machine into $12\text{-}\mu\text{m}$ lengths. The measured external quantum efficiency using a single-mode fiber with a hemispherical end was 50% (0.63 A/W) for a $1.55\text{-}\mu\text{m}$ wavelength.

Figure 4 shows the frequency response for a $1.55\text{-}\mu\text{m}$ wavelength. The circles indicate measured response at -3 V bias by using an on-wafer probe, a spectrum analyzer with preselected external mixers, and a $1.55\text{-}\mu\text{m}$ wavelength heterodyne optical sweeper. The response is flat and does not decrease even at 75 GHz .

The curve indicates the Fourier transform of the $1.55\text{-}\mu\text{m}$ wavelength short pulse response

measured using an electro-optic sampling [7]. The response has a full-width at half-maximum of 3.4 ps . Considering the sampling system response, we estimate the response of the WGPD to be 3.2 ps , which corresponds to a 3-dB bandwidth of 110 GHz . This is the highest bandwidth yet reported for $1.55\text{-}\mu\text{m}$ photodiodes.

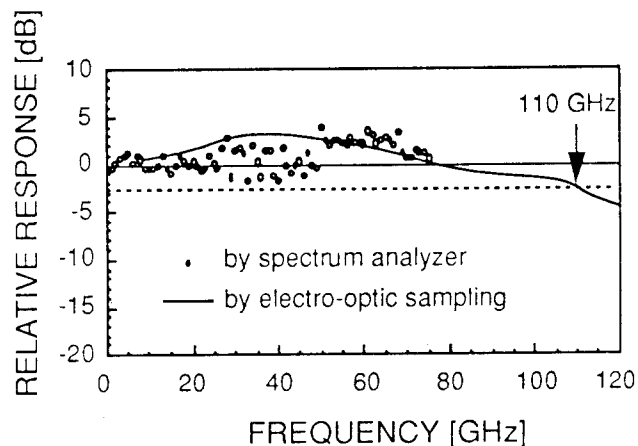


Fig. 4. Frequency response for a $1.55\text{-}\mu\text{m}$ wavelength. Circles indicate measured response at -3 V bias by a spectrum analyzer. A curve indicates the Fourier transform of the short pulse response measured using an electro-optic sampling.

High-speed receiver OEIC using WGPD

The WGPD satisfies the requirements of monolithically integrated ultra-high-speed photoreceivers (receiver OEICs), consisting of photodiodes and high-speed transistors. An OEIC using a WGPD and InGaAs HEMTs was demonstrated.

Figure 5 is a cross-sectional view of the WGPD-HEMT [8]. The WGPD is the top six layers and the InGaAs HEMTs are the bottom seven layers. The InGaAs core layer was designed to be $1.1\text{-}\mu\text{m}$ thick to achieve a 20-GHz bandwidth. The WGPD ($4\text{ }\mu\text{m} \times 25\text{ }\mu\text{m}$) without anti-reflection coating had a responsivity of 0.6 A/W at a wavelength of $1.55\text{ }\mu\text{m}$. The gate length of the HEMTs is $1\text{ }\mu\text{m}$. Figure 6 shows the frequency response. The 3-dB bandwidth of the receiver was 8.3 GHz , that is broad enough to operate at 10 Gbit/s . The speed-limitation factor of this receiver is the response speed of the HEMTs.

We can expect even faster operation with high efficiency from OEICs made using the WGPD and wider-bandwidth amplifiers. The WGPD-HEMT structure is promising to realize ultra-high-speed photoreceivers that operate beyond 20 Gbit/s.

Conclusion

Side-illuminated photodiodes with optical waveguide structures have the advantage of large bandwidth-efficiency products. The proposed multimode waveguide photodiode with the mushroom-mesa structure has a record bandwidth of 110 GHz and an external quantum efficiency of 50% at a 1.55- μm wavelength. A 10 Gbit/s monolithically integrated photoreceiver using the WGPD and HEMTs has also been demonstrated.

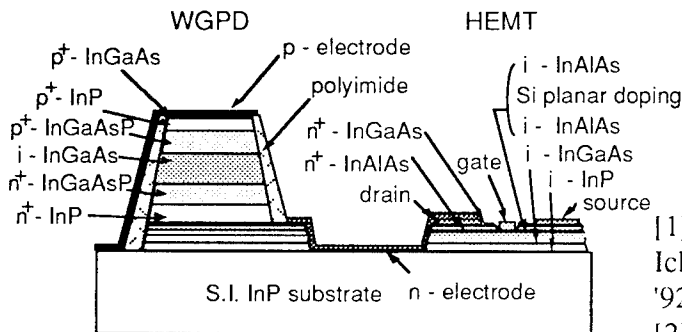


Fig. 5. Cross-sectional view of a receiver OEIC consisting of a WGPD and InGaAs HEMTs. The WGPD is the top six layers and HEMTs are the bottom seven layers.

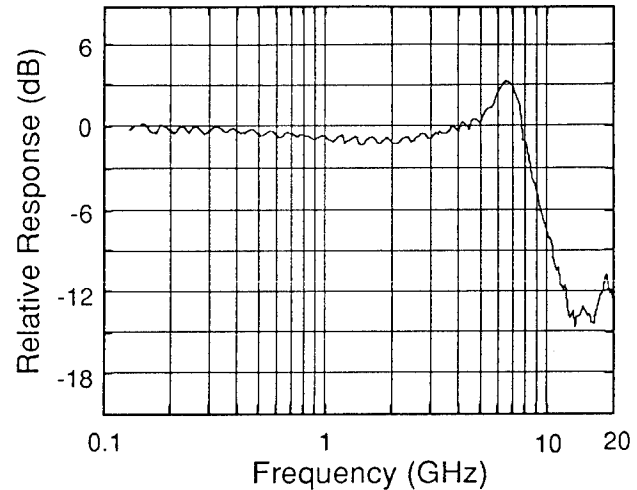


Fig. 6. Frequency response of the WGPD-HEMT. 3-dB bandwidth was 8.3 GHz, which is broad enough to operate at 10 Gbit/s.

References

- [1] K. Hagimoto, Y. Miyamoto, T. Kataoka, H. Ichino, and O. Nakajima, Tech. Digest on OFC '92, San Jose, 1992, paper Tu13.
- [2] Y. Miyamoto, T. Kataoka, K. Hagimoto, and K. Kato, Proc. ECOC '94, pp. 755-758, 1994.
- [3] J. Bowers, and C. Burrus, Electron. Lett., vol. 22, pp. 905-906, 1986.
- [4] K. Kato, S. Hata, K. Kawano, J. Yoshida, and A. Kozen, IEEE J. Quantum Electron., vol. 28, pp. 2728-2735, 1992.
- [5] K. Kawano, K. Wakita, O. Mitomi, I. Kotaka, H. Asai, Y. Kawamura, and M. Naganuma, IEEE J. Quantum Electron., vol. 28, pp. 224-230, 1992.
- [6] K. Kato, A. Kozen, Y. Muramoto, Y. Itaya, T. Nagatsuma, and M. Yaita, IEEE Photon. Technol. Lett., vol. 6, pp. 719-721, 1994.
- [7] T. Nagatsuma, IEICE Trans. Electron., vol. E76-C, pp. 55-63, 1993.
- [8] Y. Akahori, Y. Muramoto, K. Kato, M. Ikeda, A. Kozen, and Y. Itaya, LEOS '94 Summer Topical Meeting, Lake Tahoe, 1994, paper TH2.4.

Fabrication of Polarization Diversity Heterodyne Receiver PICs on InP: Status, Challenges and Perspectives

ThB1.2

Ronald Kaiser

Heinrich-Hertz-Institut (HHI) für Nachrichtentechnik Berlin GmbH
Einsteinufer 37, D-10587 Berlin, Germany, Tel: +49 30 31002 256; Fax: +49 30 31002 558

Abstract: *The results and experiences from the first fabrication of polarization diversity heterodyne receiver photonic integrated circuits (PICs) are reviewed and further improvements towards a possible commercial production in future are outlined. The fabrication process is based on a generic integration concept, which allows the parallel fabrication of not only heterodyne receiver PICs but also different other PIC architectures on the same wafer.*

Introduction

The vision of advanced optical frequency division multiplexing (OFDM) networks with an ultra-high capacity and the potential of maximum management flexibility will only become true, if low cost, high performance, and reliable photonic integrated circuits (PICs) are available. Key components within those intelligent future networks are tunable receiver PICs, which have to meet essential performance specifications like polarization independence, high sensitivity even for high bit rates, high channel selectivity, high and fast wavelength tunability. Basically there are two competing receiver approaches, for direct and heterodyne detection. To date, there is no practical concept for the fabrication of a tunable direct detection receiver PIC, which meets the requirements of polarization independence and fast tunability. Compared to this situation, all specifications described above can be readily performed today in case of a heterodyne receiver PIC, as it was shown by the first presentation of a polarization diversity heterodyne receiver (PDHR) PIC recently (1).

Principle of Polarization Insensitive Heterodyne Receiver PICs

The performance of heterodyne receiver PICs has to be polarization insensitive within real photonic networks, because the optical signals coming out of a standard fibre have random polarizations states. Simple balanced heterodyne receiver PIC architectures (laser diode as local oscillator (LO) + 3 dB coupler for optical signal combining + balanced photodetectors for optoelectronic signal conversion and cancelling out the intensity fluctuations of the laser) are polarization sensitive and therefore not suitable for those applications. An attractive solution is the polarization diversity heterodyne receiver, which combines and detects the light waves of the incoming signal and the local laser separately for their orthogonal polarization states (TE, TM). Hence this architecture requires additional components for polarization handling and a duplication of the elements for signal combining and optoelectronic signal conversion. The addition of the generated currents in the TE and TM channels is at last insensitive to the polarization state at the input port of the receiver.

Trends in Heterodyne Receiver Integration

Since the fabrication of first very simple PICs on InP with the integration of photodetectors and waveguides has been reported in 1985 (2) one of the biggest challenges ever addressed by the research groups in integrated optoelectronics was the integration of a polarization diversity heterodyne receiver. The first somewhat simpler heterodyne receiver PICs, which include a tunable laser diode and a 3dB coupler with integrated balanced photodiodes, have been published by H. Takeuchi et al. (3) and T. Koch et al. (4) in 1989. Further important steps towards the fabrication of a polarization insensitive heterodyne receiver PIC have been done afterwards (5,6). Despite the laser integration the non-availability of an integrable polarization rotator was the biggest challenge for a long time on the way to the PDHR-PIC. This element is necessary because laser diodes emit only in TE-polarization, while the polarization diversity network needs both, TE- and TM-polarized light.

First Integration of a Polarization Diversity Heterodyne Receiver PIC Design and Integration Concept

The designed PIC is subdivided into three main building blocks (c.f. Fig. 1): 1. a local oscillator (4-section DBR laser) with a monitor photodiode, 2. a polarization diversity network for polarization handling and signal combining (one polarization rotator, two mode splitters,

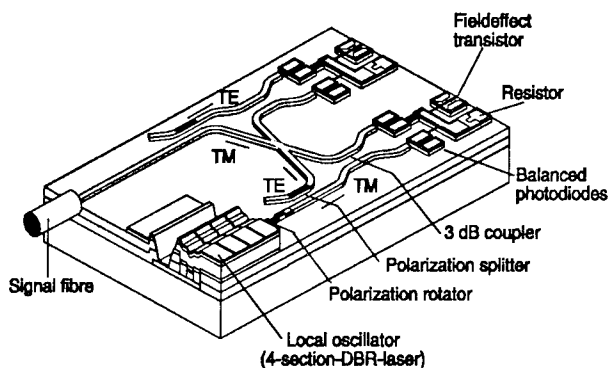


Fig. 1 Schematic view of the of the PDHR-PIC.

two mode filters, two 3dB couplers), and 3. two detector units (altogether two pairs of balanced photodiodes, two junction field effect transistors (JFETs) and four load resistors). The 9 mm long and 0.6 mm wide chip incorporates seven different optical, optoelectronic and electronic devices (altogether 18 devices) and represents, to our knowledge, the most complex integration on InP so far.

The PIC fabrication process is based on a versatile integration concept, relying on a practical technology and the need for good PIC functionality, with the following key issues: 1. capability of satisfying different PIC functions on one wafer from a single, not too complex technological process (not only heterodyning, but also e.g. transceiver and signal generator functions), 2. avoidance of double-functionality of single subelements (e.g. laser diode is not used as both, laser and photodiode), 3. possibility for flexible, widely independent optimization of integrated subelements or building blocks (e.g. use of the butt coupling scheme for laser integration), 4. accomplishment of parallel processing as much as possible (e.g. diffusion, formation of metallic contacts, or deposition of isolation layers for a maximum number of different subelements, etching of p-mesas and contact grooves for the laser diodes in the same process step, combination of the growth steps for laser current blocking layers and network waveguide layers), 5. application of semi-insulating, Fe-doped waveguide layers and substrate material for the electrical isolation between various active elements on the chip, 6. application of different very thin etch stop or etch control layers for accurate dry and wet chemical etching, and 7. application of GaInAs 'angled' absorbing layers for the reduction of internal optical crosstalk.

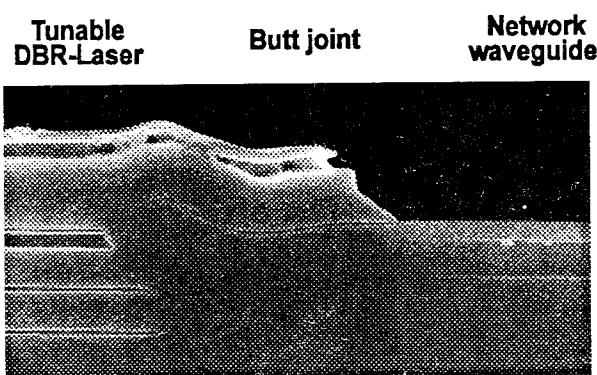


Fig. 2 Cross-sectional view of the butt joint between local laser and waveguide network (SEM-photo).

PIC Fabrication Technology

While the technology for the realization of many subelements in the waveguide network and in the detector unit is based on the experience from previous works (5), different categories of challenges had to be

addressed, e.g.:

A) Laser Integration: Only a few receiver PICs with integrated laser diodes have been fabricated to date, because of its technological challenges (3,4,7). The integration of the tunable DBR laser within the PDHR-PICs was accomplished by butt coupling using selective area MOVPE (Fig. 2). Despite the difficulties correlated with selective area MOVPE the butt coupling scheme was chosen because it permits good coupling efficiency, maximum design flexibility for the waveguide structures, and favourable fabrication tolerances. After an improvement of the selective area regrowth the best coupling efficiencies of several butt joints were measured to be 50 % ... 65 %, which is close to the calculated optimum value of 75...80 % for the chosen structure (8).

B) Integration of a Passive Polarization Rotator: Until 1992, when a passive polarization rotator was demonstrated for the first time by Shani et al. (9), no practical solution for the fabrication of a polarization rotating element was available. At this time, the technology for the complex and rather long architecture of first electrooptically tunable TE/TM mode converters (10) was not suitable for the intended integration. Based on the idea of Shani et al. a more efficient passive device was developed by H. Heidrich et al. (11) for a required 45° polarization rotation within the PDHR-PIC. The performance data of the integrated 550 μm long two-section passive polarization rotators on the first fabricated wafer are given in Table 1.

C) Uniformity of Epitaxial Growth and Vertical Dry Etching: This is a very important task if a high yield production of integrated devices with the designed, vertical geometric device parameters on standard two-inch - or more - diameter wafers is considered, because the layer thicknesses and etch depths from standard epitaxy and dry-etching equipments are commonly varying across the wafer area. The thickness deviations increase towards the perimeter of those wafers and make the performance and yield of different devices or interfaces (e.g. the butt joint between laser and waveguide network) also poorer.

D) Process complexity, wafer yield and handling: The entire fabrication process under laboratory conditions involves at present 23 lithographic exposures, seven growth steps (six MOVPE, one MBE), and - according to our definition - altogether 150-170 single processing and controlling steps. The laser is the most complicated element facing the most technological challenges and encompasses about two thirds of the total effort for the PIC fabrication. About 15 % from all started 2"-wafers at the beginning of the PIC production survived the entire fabrication process, 65 % (!) were broken due to human failures during handling within processing and controlling, and only 20 % were destroyed due to process failures (e.g. during epitaxial growth or dry etching). At last, the most critical "technological step" at present on

4-Sect. DBR Laser	Waveguide Network:	Detector Unit:
Threshold current : 16 ... 24 mA	Polarization ext. ratio: ≥ 19 dB	Photodiodes (PD):
Emission wavelength (*) : 1.55 μm	Deviation of 3 dB balance : ± 0.3 dB	Photodiode quant. eff.: $\geq 90\%$
SMSR (*) : 38 ... 43 dB	Intrinsic network losses: 3 dB	Dark current (-4 V) : ≤ 130 nA
Linewidth (*) : 25 - 40 MHz		Breakdown voltage : 16-20 V
Tuning range : ≤ 5.5 nm	Polarization rotator:	Cut-off frequency (3dB) : ≤ 4 GHz
(*): Lasers not tuned	Rotation angle : 35 ... 43°	JFET:
Coupling efficiency at the	Excess losses : 1.4 ... 2 dB	Transconductance : 120 mS/mm
laser/network butt joint : 50... 65 %		Detector unit (PD+JFET+R):
(calculated values : 75 ... 80 %)		3dB cut-off frequency : 0.9 - 1.0 GHz

Table 1: Compilation of several subelement performance data on the first PDHR-PIC-wafer.

the way to a high yield production of complex PICs is the secure wafer handling by technology people! This situation will be considerably eased by the application of machines for wafer handling in future commercial production lines and of course by a reduction of the entire fabrication effort and the geometric PIC dimensions. From the present point of view a reduction of the fabrication effort for PDHR-PICs is possible down to about 13-17 lithographic exposures, 4-6 growth steps, and altogether 90-120 single processing and controlling steps in laboratory environment by further improvements of PIC design, integration concept and technology (for comparison: a somewhat simpler transceiver PIC for example needs at present about 10-16 exposures, 3-6 epitaxial growth steps and 65-100 single processing & controlling steps under comparable conditions, depending on the PIC design and performance specifications).

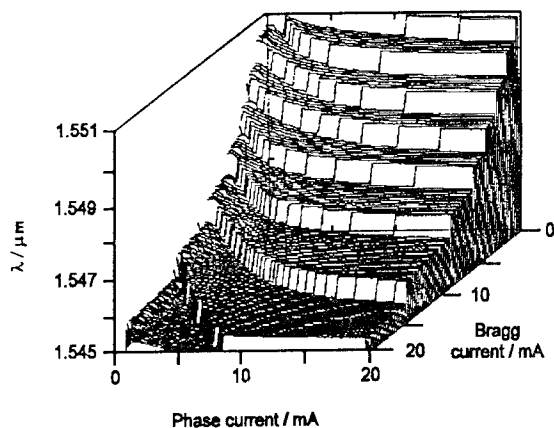


Fig. 3 Wavelength tuning characteristics of the integrated local oscillator.

PIC and Subelements Performances

Different performance data of integrated subelements on the first completed 2"-wafer are listed in Tab. 1 and some of them have been already reported elsewhere (1,12). The tuning characteristics of an integrated DBR laser is shown in Fig. 3. The yield of working

PDHR-PIC subelements on this wafer is for example about 90% for the lasers (threshold currents: 13...40 mA), 90 % for the polarization rotators (rotation angles α : 30°...43°) and more than 90% for the photodiodes (dark currents: ≤ 130 nA at -4V bias). The PDHR-PIC yield on the first wafer for a sufficient operation of all subelements was about 50% (including two JFETs) and about 70% (without the two JFETs). After packaging of some PDHR-PICs, a stable polarization insensitive operation within an experimental OFDM-TV-distribution network was demonstrated (13), without any tendency for a bit error rate (BER) floor (Fig. 4). The measurements confirmed that no extensive linewidth broadening of the LO due to back reflections on the chip is observed!

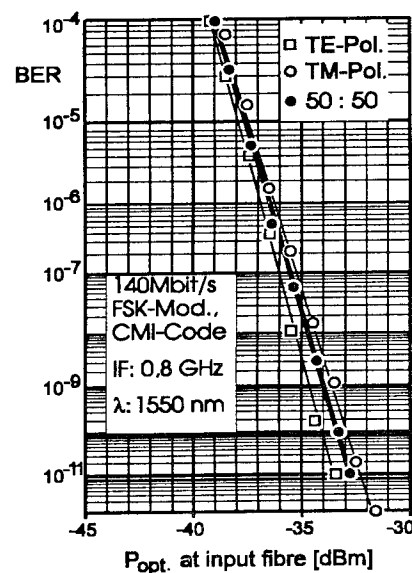


Fig. 4 Bit error rate (BER) vs. received optical power.

Improvements of PIC Technology and Performance

The development of a versatile integration concept, parallel investigations on improved subelements, the PDHR-PIC fabrication itself, the evaluation of the PIC and subelement performance data on the first two completed wafers, and the effort of other groups have

shown a lot of room for further improvements: e.g. 1. reduction of the geometric PIC dimensions for a higher device yield on the wafers [use of vertical coupling schemes (14), multimode interference (MMI) waveguide couplers and waveguide bends with very small radii (15), high quality integrated waveguide mirrors], 2. improvement of the developed PIC integration concept (reduction of the entire fabrication effort, increase of versatility regarding the parallel fabrication of different PIC architectures using DBR and DFB lasers,...), 3. further improvements of the subelements and PIC performance [increase of the local laser tuning range up to the bandwidth of Er-doped fibre amplifiers (16), increase of the laser output power and the coupling efficiency at the butt joint, reduction of laser linewidth and threshold current, increase of the photodetector bandwidth (6,17)], 4. further improvements and standardization of single process steps for high yield production (e.g. uniform epitaxial growth and dry etching on standard wafers, planar and reproducible selective area regrowth by the use of MOMBE, secure wafer handling), and 5. improvement of fibre/chip coupling losses and alignment tolerances by the integration of a spot size transformer (18).

Concluding Remarks

The first fabrication of complex PDHR-PICs and the successful operation of these chips in OFDM-TV-transmission experiments represent an impressive feasibility demonstration featuring today's quality and potential of InP integration technology. The additional parallel fabrication of somewhat simpler balanced heterodyne receiver PICs, transceiver PICs (19), dual wavelength transmitter and optical signal generator PICs (19) on the same 2"-wafer with the same process further demonstrates the versatility of the developed integration concept. The performance of the most subcomponents within the different fabricated PICs is comparable to discrete devices and the yield of working subdevices and PICs on one wafer is very good for this first fabrication run.

Acknowledgments

The author would like to thank all colleagues of the PIC-team and the system group at HHI for their support during development, processing, and characterization of the different PICs and for the OFDM experiments. The work on the heterodyne receiver PIC has been supported by the German Ministry of Research & Technology.

References

- 1) R. Kaiser et al.: "Monolithically Integrated Polarization Diversity Heterodyne Receivers on GaInAsP/InP", *Electron. Lett.*, vol. 30, p. 1446, 1994.
- 2) R. Trommer: "Monolithic InGaAs Photodiode Array

- Illuminated through an Integrated Waveguide", *Electron. Lett.*, vol.21, no. 9, pp. 382-383, 1985.
- 3) H. Takeuchi et al.: "Monolithic Integrated Coherent Receiver on InP Substrate", *IEEE Photon. Technology Letters*, vol. 1, no. 10, pp. 398-400, 1989.
- 4) T. Koch et al.: "GaInAs/GaInAsP Multiple-Quantum-Well Integrated Heterodyne Receiver", *Electron. Lett.*, vol. 25, no. 24, pp. 1621-1623, 1989.
- 5) H. Heidrich: "Progress and Prospects Towards Coherent Receiver Frontend OEICs", *Proc. Europ. Conf. on Integr. Optics (Neuchatel, CH)*, p. 2-17, 1993.
- 6) F. Ghirardi et al.: "10 GHz Bandwidth InP based Polarization Diversity Heterodyne Photoreceiver with High Common Mode Rejection", *Proc. of Opto-electronic Conf. OEC'94 (Chiba, Japan)*, p. 386, 1994.
- 7) P.J. Williams et al.: "Design and fabrication of monolithically integrated DFB laser-wavelength duplexer transceivers for TPON/BPON Access Links", *Electron. Lett.*, vol. 27, pp. 809-810, 1991.
- 8) R. Kaiser et al.: "Integration of Tunable DBR Lasers for Heterodyne Receiver OEIC Applications", *Proc. Conf. of InP & Rel. Mat. '94 (Santa Barbara, Calif., USA)*, p. 476, 1994.
- 9) Y. Shani et al.: "Polarization rotation in asymmetric periodic loaded rib waveguides", *Proc. Integr. Photonic Research Conf. (Monterey, Calif., USA)*, p. 122, 1991.
- 10) M. Schlak et al.: "Tunable TE/TM-Mode Converter on (001)-InP-Substrate", *IEEE Photonics Technol. Lett.*, vol. 3, pp. 15-16, 1991.
- 11) H. Heidrich et al.: "Passive Mode Converter with Periodically Tilted InP/GaInAsP", *IEEE Photonics Technol. Lett.*, vol. 4, no. 1, pp. 34-36, 1992.
- 12) R. Kaiser et al.: "Integration of a Tunable 4-Section DBR Laser within Polarization Diversity Heterodyne Receiver PICs", *Conf. Digest 14th Int. Semicond. Laser Conf. '94 (Maui/Hawaii, USA)*, p. 30, 1994.
- 13) U. Hilbk et al.: "Stable Operation of a Monolithically Integrated InP-Heterodyne Polarization Diversity-Module in an Experimental OFDM System", *Proc. 20th Europ. Conf. on Opt. Commun. '94 (Firenze, Italy)*, vol. 4, p. 75, 1994.
- 14) R.J. Deri et al.: "High-Speed Heterodyne Operation of Monolithically Integrated Balanced Polarisation Diversity Photodetectors", *Electron. Lett.*, vol.28, p. 2332, 1992.
- 15) L.H. Spiekman et al.: "Extremely small fabrication tolerant InP-based power-splitting and combining structures by deep etching", *Proc. Europ. Conf. on Opt. Commun. (Firenze, Italy)*, vol. 2, p. 665, 1994.
- 16) M. Öberg et al.: "Complete Single Mode Wavelength Coverage over 40 nm with a SSG DBR Laser", *Proc. 14th Int. Semicond. Laser Conf. '94 (Maui, USA)*, p. 32, 1994.
- 17) D. Trommer et al.: "Ultrahigh Bandwidth Balanced Mixer Receiver OEIC", *Proc. 6th Conf. of InP & Rel. Mat. (Santa Barbara, Calif., USA)*, p. 476, 1994.
- 18) T. Benner et al.: "Waveguide tapers for efficient coupling of InGaAsP/InP OEIC components to flat-end single mode fibres", *Proc. Europ. Conf. on Opt. Commun. '94 (Firenze, Italy)*, vol. 2, p. 1031, 1994.
- 19) to be published.

9 GHz Bandwidth InP-Based Integrated PIN-HBT Photoreceiver

A.L. Gutierrez-Aitken, K. Yang, X. Zhang, G.I. Haddad, and P. Bhattacharya

Solid State Electronics Laboratory
Department of Electrical Engineering and Computer Science
The University of Michigan
Ann Arbor, MI 48109-2122, U.S.A.

Abstract

An integrated photoreceiver using an InAlAs/InGaAs HBT-based transimpedance amplifier has been fabricated and characterized. The p-i-n photodiode is fabricated using the base, collector and subcollector layers of the HBT. Discrete $5\text{ }\mu\text{m} \times 5\text{ }\mu\text{m}$ emitter area transistors demonstrated f_T and f_{max} of 67 GHz and 123 GHz, at collector currents of 10 mA and 7 mA, respectively. An amplifier with a feedback resistance of $550\text{ }\Omega$ demonstrated an effective transimpedance bandwidth of 14 GHz and a gain of $46\text{ dB}\Omega$, corresponding to a very high transimpedance-bandwidth product of $2.8\text{ THz}\Omega$. The integrated photoreceiver measured -3 dB bandwidth is 9.5 GHz, which to the best of our knowledge is the highest reported till date for a PIN-HBT monolithically integrated photoreceiver.

Introduction

High-speed integrated photoreceivers are expected to have better performance than hybrid designs because of reduced parasitic elements, compactness and high reliability[1]. A scheme of photodiode and transistor integration, first demonstrated by Pedrotti *et al.*[2] in GaAs-based materials, is a p-i-n photodiode and a heterojunction bipolar transistor (HBT) photoreceiver where the p-i-n diode is formed using the HBT base-collector junction. This scheme of integration is extremely interesting due to its simplicity (one-step epitaxy) and the fact that HBT-based photoreceivers are predicted to show better noise performance than FET-based circuits at high bit rates[3]. Using this approach, high speed InP-based photoreceivers with performance similar to the best reported hybrid receivers[4],[5] have been demonstrated.

In this work we report the fabrication and characterization of an InP-based PIN-HBT OEIC photoreceiver using the base, collector and subcollector HBT layers as the p-i-n photodiode. The photoreceiver was implemented using an optimized HBT layer structure and improved fabrication techniques compared to our previous work[6]. A photoreceiver using a transimpedance amplifier with a transimpedance-bandwidth product of $2.8\text{ THz}\Omega$ and a -3 dB bandwidth of 9.5 GHz at $\lambda=1.55\text{ }\mu\text{m}$ was realized. These parameters are, to the best of our knowledge, the highest reported for this material and scheme of integration. The detailed measured and simulated electrical characteristics of the HBT and the transimpedance amplifier are reported elsewhere[7]

p-i-n Photodiode	1000Å	InGaAs	$n=1 \times 10^{19}\text{ cm}^{-3}$	Contact
	700Å	InAlAs	$n=1 \times 10^{19}\text{ cm}^{-3}$	Contact
	1500Å	InAlAs	$n=8 \times 10^{17}\text{ cm}^{-3}$	Emitter
	150Å	InGaAs	$p=2 \times 10^{18}\text{ cm}^{-3}$	Spacer
	850Å	InGaAs	$p=3 \times 10^{19}\text{ cm}^{-3}$	Base
	6000Å	InGaAs	$n=1 \times 10^{16}\text{ cm}^{-3}$	Collector
	5000Å	InGaAs	$n=1 \times 10^{19}\text{ cm}^{-3}$	Subcollector
	100Å	InGaAs	Undoped	Buffer
S.I. InP Substrate				

Figure 1: Profile of the PIN-HBT epitaxial layer.

Device Structure and Fabrication

The HBT heterostructure, shown in Fig. 1, is grown at $500\text{ }^\circ\text{C}$ by solid-source molecular beam epitaxy (MBE) on a Fe-doped semi-insulating InP (001) substrate. The InGaAs collector layer also acts as the absorption i-region of the p-i-n diode, and its thickness, 6000 Å, is optimized taking in consideration the HBT high frequency performance, and the photodiode responsivity and RC time constant. The fabrication of the integrated PIN-HBT with self-aligned base contact and SiO_x side-wall is described elsewhere in more detail[6],[8]. Non-annealed Ti/Pt/Au metalization was used for the emitter and collector ohmic contacts and

Pt/Ti/Pt/Au metalization was used for the base contact. A plasma enhanced chemical vapor deposition (PECVD) SiO_x layer 7600 Å thick is used as antireflecting (AR) coating and isolation for the interconnection metal. The thin-film resistors consist of 320 Å of Ti.

Figure 2 shows the photoreceiver circuit. It consists

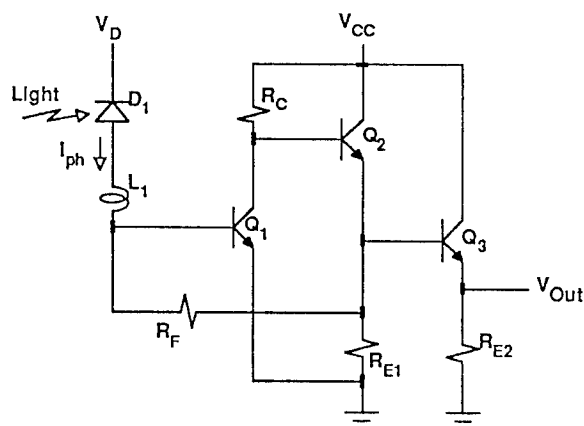


Figure 2: Circuit diagram of the monolithically integrated photoreceiver.

of a $10\text{ }\mu\text{m} \times 10\text{ }\mu\text{m}$ p-i-n photodiode and a $5\text{ }\mu\text{m} \times 5\text{ }\mu\text{m}$ emitter HBT amplifier in a transimpedance configuration with feedback resistor and a buffer stage that provides $50\text{ }\Omega$ matching output impedance. The design requires only two bias voltage supplies, one for the amplifier and the other for the p-i-n photodiode.

Experimental Results

The p-i-n photodiodes demonstrate breakdown voltages as high as -15 V without AR coating and a leakage current of $\leq 10\text{ nA}$ at -10 V . Figure 3 shows the p-i-n dark current before and after the AR coating. The dark current remains below 10 nA for bias voltages less than 4 V for both cases. From the doping profile and electric field calculations a bias voltage of approximately -3 V is sufficient to achieve hole and electron saturated drift velocity. The inset of Fig. 3 shows the reduction of reflectivity due to the AR coating equivalent to a $\sim 20\%$ increase in responsivity. The low dark current value is due to the high quality of the heterostructure and the optimized diode layout designed to provide a more uniform electric field across the diode area. A low photodiode dark current is crucial to enhance the photoreceiver sensitivity and dynamic range. The measured capacitance of a discrete $100\text{ }\mu\text{m}^2$ diode for bias voltages $> 1.5\text{ V}$ is 70 fF which agrees with the value obtained from fitting an equivalent circuit to the measured

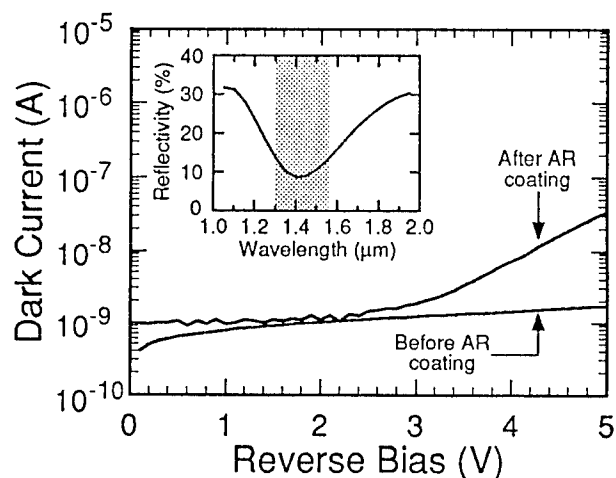


Figure 3: p-i-n photodiode dark current with and without AR coating. The inset shows the reflectivity with AR coating optimized in the range of 1.3 to $1.55\text{ }\mu\text{m}$.

S-parameters in the range of 0.5 to 25.5 GHz . The responsivity of the p-i-n photodiode with AR coating was $\sim 0.47\text{ A/W}$ at $\lambda = 1.55\text{ }\mu\text{m}$.

The HBT demonstrates a DC current gain β of 40 , ideality factors of 1.29 and 1.51 for the collector and base currents, respectively, and a breakdown voltage (V_{ceo}) of 5 V . The common-emitter small signal frequency response of discrete transistors was measured using coplanar probes and a network analyzer. Figure 4 shows the unity current gain cutoff frequency (f_T) and the maximum oscillation frequency (f_{max}) as a function of I_C for a $5\text{ }\mu\text{m} \times 5\text{ }\mu\text{m}$ emitter HBT obtained from current gain (H_{21}) and Mason's unilateral gain (U).

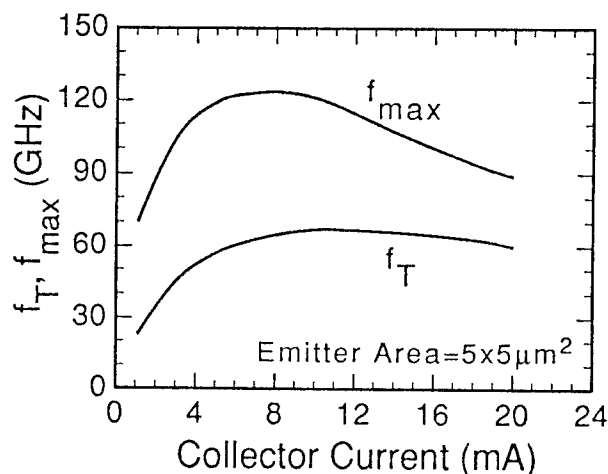


Figure 4: f_T and f_{max} as a function of I_C for a discrete $5\text{ }\mu\text{m} \times 5\text{ }\mu\text{m}$ emitter HBT.

A maximum f_T and f_{max} of 67 GHz and 123 GHz were obtained at collector currents of 10 mA and 7 mA, respectively. The large value of f_{max} is obtained due to the small base resistance (self-aligned base contact and relatively thick base layer) and small base-collector capacitance (thick collector layer). The high-frequency response of the HBT was also measured at a temperature of 80 K in the range of 0.1 to 40 GHz for potential cryogenic applications of the transimpedance amplifier. From these measurements, it is seen that the performance improves marginally at low temperatures.

The transimpedance amplifiers were measured on wafer and the effective electrical transimpedance gain $|Z_{eff}| = |Z_o| \times |S_{21}| / |1 - S_{11}|$, with $|Z_o| = 50 \Omega$ [9], was obtained from S-parameter measurements. Figure 5 shows the transimpedance frequency response for an amplifier with a 550 Ω feedback resistor (R_F). The amplifier demonstrates a flat response with a -3 dB bandwidth of 14 GHz, and a gain of 46 dB Ω . The maximum measured bandwidth was 22 GHz for a gain of 40 dB Ω . The inset of Fig. 5 shows the -3 dB bandwidth of the amplifiers as a function of the transimpedance gain for R_F values of 600, 550, 140, and 127 Ω in order of increasing bandwidth. The maximum transimpedance-bandwidth product $TZBW = Z_T f_{3dB}$ [10] obtained is 2.8 THz Ω .

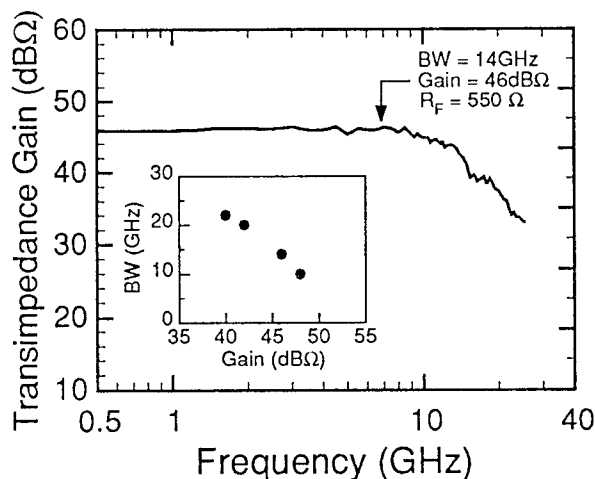


Figure 5: Frequency response of the transimpedance amplifier. The inset shows the -3 dB bandwidth as a function of the gain for different values of R_F .

The optical-to-electrical small-signal frequency response of the p-i-n photodiode and the integrated photoreceiver was measured in the range of 0.13 to 20 GHz using a lightwave component analyzer at a wavelength of 1.55 μm . The circuits were characterized on wafer using coplanar microwave probes and an optical probe to illuminate the photodiode from the top with the modulated laser light through a lensed single mode fiber. Fig-

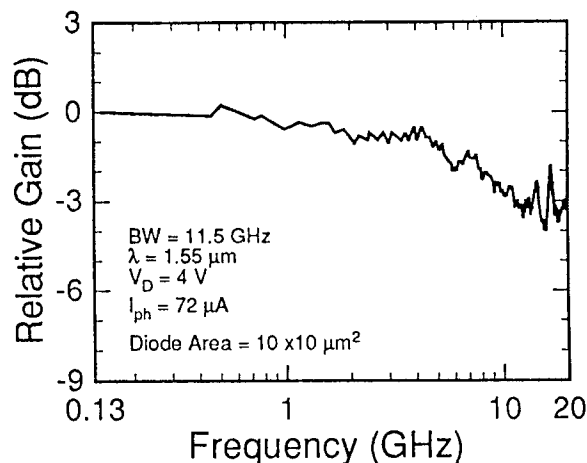


Figure 6: Frequency response of a discrete p-i-n diode.

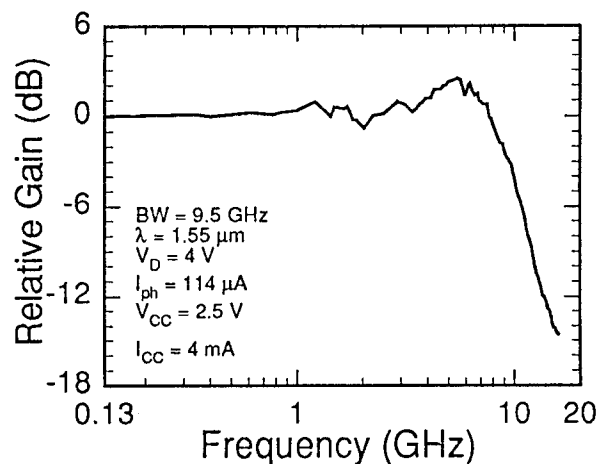


Figure 7: Integrated photoreceiver frequency response.

ure 6 shows the frequency response of the p-i-n diode demonstrating a bandwidth of 11.5 GHz at a bias of 4 V. Figure 7 shows the measured frequency response of the integrated photoreceiver with a 10 $\mu\text{m} \times 10 \mu\text{m}$ p-i-n photodiode, demonstrating a -3 dB bandwidth of 9.5 GHz. This bandwidth is adequate for 14 Gb/s operation. The total power dissipation of the OEIC photoreceiver was only 10.5 mW with a V_{CC} bias of 2.5 V.

Conclusion

In conclusion, we have designed, fabricated and characterized a high-speed InP-based PIN-HBT OEIC photoreceiver using an amplifier with a very high transimpedance-bandwidth product of 2.8 THz Ω , which

to the best of our knowledge is the highest reported till date for a monolithically integrated transimpedance amplifier. The p-i-n photodiode is fabricated using the base, collector and subcollector HBT layers. The $5\text{ }\mu\text{m} \times 5\text{ }\mu\text{m}$ emitter area HBTs demonstrated 67 GHz and 123 GHz for f_T and f_{max} , respectively. The amplifier showed an electrical transimpedance bandwidth of 14 GHz and a gain of 46 dB Ω . The integrated photoreceiver with a $10\text{ }\mu\text{m} \times 10\text{ }\mu\text{m}$ p-i-n photodiode demonstrated an optical-to-electrical small-signal -3 dB bandwidth of 9.5 GHz.

Acknowledgments

The authors would like to thank Drs. L.M. Lunardi and J. Rios of AT&T Bell Laboratories in Crawford Hill, Holmdel, NJ, for the optical characterization of the photoreceivers. This work is supported by the Advanced Research Projects Agency, Grant MDA 972-94-1-0004, and U.S. Army Research Office, Grant DAAL03-92-G-0109.

References

- [1] O. Wada, T. Sakurai, and T. Nakagami, "Recent Progress in Optoelectronic Integrated Circuits (OEIC's)," *IEEE J. Quantum Electron.*, vol. QE-22, p. 805, 1986.
- [2] K.D. Pedrotti, N.H. Sheng, R.L. Pierson, Jr, C.W. Farley, M.J. Rosker, and M.F. Chang, "Monolithic ultrahigh-speed GaAs HBT optical integrated receivers," in *IEEE GaAs IC Symp. Dig.* (Monterrey, CA), pp 205-208, Oct. 1991.
- [3] R.G. Smith, and S.D. Personick: *Semiconductor devices for optical communication*, 2nd ed. New York: Springer-Verlag, 1987.
- [4] S. Chandrasekhar, L.M. Lunardi, A.H. Gnauck, C.A. Burrus, R.A. Hamm, J.W. Sulhoff, and J.L. Zyskind, "A 12-Gb/s High-Performance, High-Sensitivity Monolithic p-i-n/HBT Photoreceiver Module for Long-Wavelength Transmission Systems," *IEEE Photon. Technol. Lett.*, vol. 7, pp. 182-184, 1995.
- [5] L.M. Lunardi, S. Chandrasekhar, A.H. Gnauck, R.A. Hamm, and G.J. Qua, "High-Speed Monolithic p-i-n/HBT and HPT/HBT Photoreceivers Implemented with Simple Phototransistor Structure," *IEEE Photon. Technol. Lett.*, vol. 5, pp. 1316-1318, 1993.
- [6] A.L. Gutierrez-Aitken, J.C. Cowles, P.K. Bhattacharya, and G.I. Haddad, "High Bandwidth InAlAs/InGaAs PIN-HBT Monolithic Integrated Photoreceiver," *Proc. 6th Int. Conf. InP and Rel. Mat.*, pp.247-250, Santa Barbara, CA, 1994.
- [7] K. Yang, A.L. Gutierrez-Aitken, X. Zhang, G.I. Haddad, and P.K. Bhattacharya, "SPICE-Based DC and Microwave Characterization of InAlAs/InGaAs HBT's Used for Large-Bandwidth Integrated Transimpedance Amplifiers," *7th Int. Conf. InP and Rel. Mat.*, Sapporo, Japan, May 1995.
- [8] J.C. Cowles, W.L. Chen, G.O. Munns, and G.I. Haddad, "InAlAs/InGaAs Heterojunction Bipolar Transistors Grown By Chemical Beam Epitaxy (CBE)," *Proc. 5th Int. Conf. InP and Rel. Mat.*, pp. 385-388, Paris, France, 1993.
- [9] R.K. Montgomery, A. Feynson, P.R. Smith, R.D. Yadvish, R.A. Hamm, and H. Temkin, "A 28 GHz Transimpedance Preamplifier with Inductive Bandwidth Enhancement," *IEDM Tech. Digest*, pp 423-425, December 1992.
- [10] M. Blaser and H. Melchior, "High Performance Monolithic Integrated InP Photoreceivers," *Proc. 6th Int. Conf. InP and Rel. Mat.*, pp.239-242, Santa Barbara, CA, 1994.

A Monolithically Integrated Logic Photoreceiver with Double-Heterojunction Bipolar Transistors

Mikio Yoneyama, Eiichi Sano, Shoji Yamahata, and Yutaka Matsuoka

NTT LSI Laboratories
3-1 Morinosato Wakamiya, Atsugi-shi, Kanagawa, 243-01, Japan

Abstract

A simplified logic photoreceiver with a photo detector directly connected to a decision circuit has been monolithically integrated with double-heterojunction bipolar transistors. Neither a preamplifier nor compensation circuits was used in this photoreceiver. A power estimation model was introduced to the simplified photoreceiver. Important device characteristics for error-free operation under practical conditions were quantitatively discussed. A 10-Gbit/s error free operation for a 1.55- μm wavelength was successfully achieved.

I Introduction

As signal processing speeds and complexities are increased, optical transmission techniques have been applied to signal interconnections among all the levels between systems, boards, chips, and LSIs [1-3]. A dense photoreceiver is one of the key components for interchip optical interconnections. A simplified photoreceiver with a pin PD directly connected to a decision circuit (DEC) [4-6] is attractive for such interconnections. Neither a preamplifier nor compensation circuits are used in this photoreceiver. We call this simplified photoreceiver "PD-DEC". To adopt the PD-DEC in actual systems, it must achieve error-free operation under practical conditions such as process-dependent deviation of device characteristics, temperature fluctuation, and noise.

We first introduce a power estimating model [4] to the PD-DEC. By using this model, we derive important device characteristics to achieve error-free operation under practical operating conditions.

Next, as the first step for the simplified configuration, a monolithically integrated PD-DEC is fabricated using the InP/InGaAs Double-Heterojunction Bipolar Transistors (DHBTs) process [7]. The measured eye pattern for a 10-Gb/s NRZ optical input signal has a good eye opening and error-free operation is confirmed.

II. PD-DEC direct connection for optical interconnections

Figure 1 shows the basic photo-transmitter and receiver that are widely used in optical fiber telecommunication systems. Many compensation circuits are required to compensate for temperature fluctuation and signal loss caused by long-haul transmission to achieve error-free operation. Such complex configurations are not practicable because power dissipation and connection density are major concerns in parallel optical interconnections. We remove the compensation circuits and replace the preamplifier with load resistance R_L as shown in Fig. 1(b) because the signal loss including coupling loss is a few dB in optical interconnections. This simplified configuration, PD-DEC, is very attractive in terms of power dissipation and cost, and will be applicable to interconnection systems. In order to achieve error-free operation under practical conditions, we must take into account temperature fluctuation, process-dependent deviations of device characteristics (process deviations), and noise. The threshold current and distinction ratio of the laser diode (LD) are the largest fluctuation factors in these systems. However, as shown in Fig. 2, an excess modulation current for the LD with a range from $I_{th}(T_{max}) + I_{LD0}$ to $I_{th}(T_{max}) + I_{LD1}$ may guarantee successful operation over the full temperature range. In the PD-DEC, the LD driver dominates the total power dissipation of the transmitter and receiver. The power dissipation of the LD driver is estimated by calculating the LD drive current I_{LD1} . We calculate the I_{LD1} to achieve error-free operation. For simplicity, we assume the following:

(1) The bandwidth of each device is much wider than the bit rate.

(2) Process-dependent deviation in each process parameter and total noise energy are approximated by a Gaussian distribution.

(3) Process-dependent standard deviations are simplified to be equal among all the parameters, and we introduce a single parameter σ_{dev} .

The LD drive current I_{LD1} to achieve error-free operation using these assumptions is given by [4]

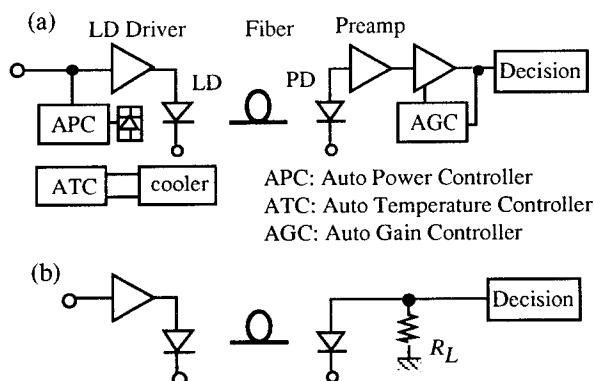


Fig. 1. Schematic diagram of optical-fiber communication systems: (a) basic configuration of telecommunication systems and (b) PD-DEC configuration.

$$(1 - k \sigma_{dev}) \eta I_{LD1} R_L - (1 + k \sigma_{dev}) \eta (I_{LD0} + \Delta I_{th}) R_L = V_{sen} + 2k \sigma_{ref} + 2Q i_n R_L, \quad (1)$$

where η is the product of the slope efficiency of the LD, fiber coupling efficiency, and the sensitivity of the pin PD. The meanings of the other symbols are listed in Table 1. The left-hand side of Eq. (1) is the effective signal amplitude taking into account the decrease in the extinction ratio due to process deviations and ΔI_{th} . The first and second terms on the right-hand side represent decision sensitivity. The third term is for noise. The relation between parameter Q and the bit error rate (BER) is $BER = 1/2 \operatorname{Erfc}[Q/\sqrt{2}]$. Figure 3 shows the R_L and I_{LD1} relationship calculated by Eq. (1) with the parameter values listed in Table 1. The maximum bit rate is defined as $(4 C_{PD} R_L)^{-1}$ where C_{PD} is the capacitance of the

pin PD with parasitic capacitance at the input node of the DEC. I_{LD1} for an η of 0.1 decreases to 20 mA with increasing R_L . This value is less than the drive current required for electrical interconnections with near- and far-end 50 Ω impedance matching. Increasing η to 0.3 effectively contributes to reducing I_{LD1} . The minimum levels of I_{LD1} are determined by ΔI_{th} . Therefore, an LD with extremely low threshold current and high characteristic temperature is very effective in reducing LD drive current. The I_{LD1} can be reduced to 1/3 by reducing I_{th} to 1/5.

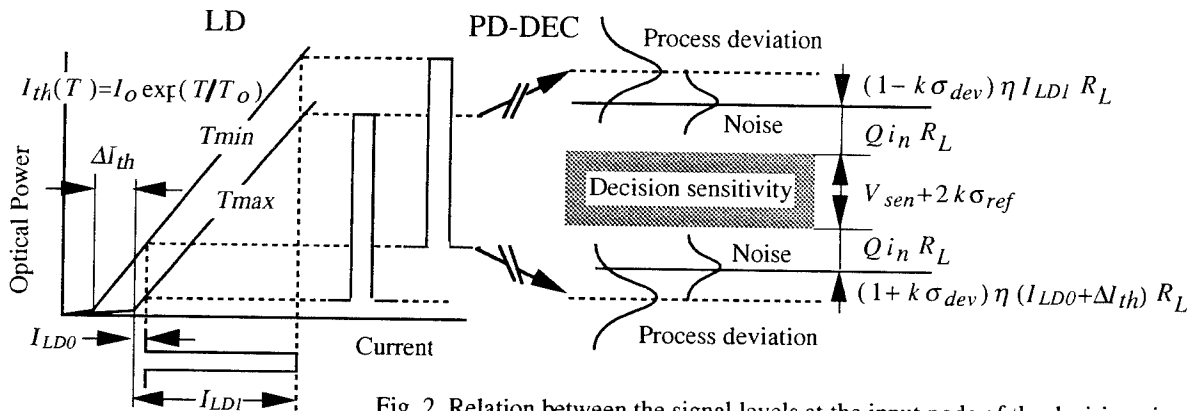


Fig. 2. Relation between the signal levels at the input node of the decision circuit, noise, and decision sensitivity.

Table 1 Parameters used to calculate LD drive current.

parameter		value
Relative Process Std. Deviation	σ_{dev}	0.06
Coefficient 1	k	3
Total Noise Current	i_n	μA 5 [8]
Decision Sensitivity	V_{sen}	mV 40 [9]
Vref Std. Deviation	σ_{ref}	mV 10
LD Drive Current for logic level '0'	I_{LD0}	mA 1.0
LD Threshold Current	I_{th}	mA 5 @30°C
Characteristic Temperature	T_0	K 50 [10]
Temperature	T	°C 0~80
Coefficient 2	Q	- 6 @BER=10 ⁻⁹

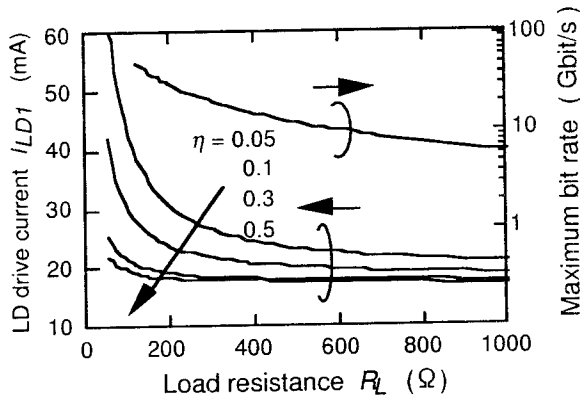


Fig. 3. LD drive current for the PD-DEC versus load resistance. A C_{PD} of 40 fF was assumed.

III. Device Technology

As the first step to the simplified configuration, a monolithically integrated PD-DEC was fabricated using the InP/InGaAs DHBT process.

The layer structure of the DHBT is listed in Table 2. This layer structure offers a number of advantages over conventional DHBTs such as increased break-down voltage, suppression of the electron blocking effect, enhancement of the ballistic transport of electrons, and the simultaneous formation of a high-speed pin PD. These layers were grown by low-pressure metal organic chemical

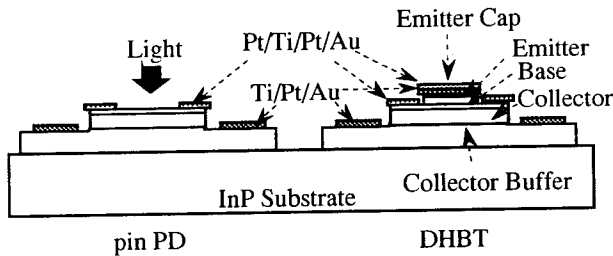


Fig. 4 Schematic cross section of pin PD and DHBT.

Table 2 DHBT Layer Structure

Layer	Material	Thickness (nm)	Doping (cm ⁻³)
Emitter Cap	n^+ - InGaAs	50	3×10^{19}
	N^+ - InP	15	2×10^{19}
Emitter	N - InP	35	3×10^{17}
Spacer	ud - InGaAs	5	—
Base	p^+ - InGaAs	55	2×10^{19}
Collector	ud - InGaAs	400	—
	p^+ - InGaAs	10	2×10^{18}
	ud - InGaAs	10	—
	n^+ - InGaAs	10	2×10^{18}
Collector Buffer	N - InP	170	1×10^{17}
	n^+ - InGaAs	400	5×10^{18}
Buffer	ud - InP	100	—

vapor deposition (MOCVD) on Fe-doped semi-insulating InP substrates.

DHBTs were fabricated by self-aligned HBT processes. Figure 4 shows a schematic cross section of the pin PD and DHBT. The pin PD was formed on the base-to-collector layers of DHBTs as shown in Fig. 4. Measured f_T and f_{max} for $V_{CE} = 1.4$ V were 104 GHz and 156 GHz, respectively. The pin-PD has a diameter of 10 μ m and a sensitivity of 0.27 A/W for a 1.55- μ m wavelength.

IV. Circuit Design

Figure 5 shows a block diagram of the PD-DEC. The input buffer matches the voltage level at the load resistance with the input level of the Master-Slave DFF (MS-DFF). It consists of a differential circuit with a gain of 7 dB. We used DHBTs with a 1.4×4.0 - μ m emitter for the input buffer to reduce parasitic capacitance and power dissipation. The logic swing of the MS-DFF was designed to be 500 mVpp to enhance the speed. The output buffer consists of a differential circuit and can drive 50 Ω with 800 mVpp using open-collector output. DHBTs with a 1.6×6.1 - μ m emitter were used to construct the MS-DFF and the output buffer. The clock reference voltage and the current source voltage are generated on the chip. Figure 6 shows a photograph of the PD-DEC. The chip is 1.0×1.5 mm in size.

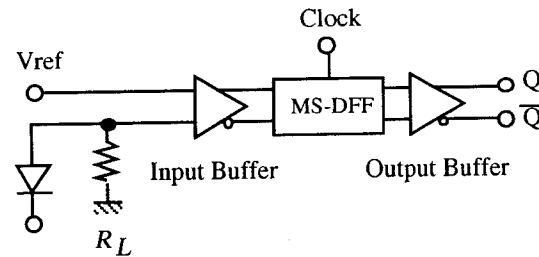


Fig. 5. Block diagram of PD-DEC.

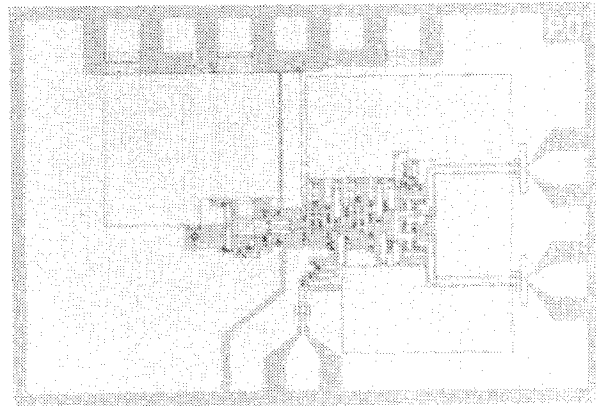


Fig. 6. Microphotograph of the PD-DEC. The chip size is 1.0×1.5 mm.

V. IC Performance

The PD-DEC was tested on a wafer using RF probes. Optical data were 2^7-1 NRZ pseudo-random signals with a wavelength of $1.55\ \mu\text{m}$. The data were introduced to the pin-PD by using a single mode lensed fiber. The measured eye pattern for 10-Gbit/s optical data is shown in Fig. 7. A good eye opening was observed. The rise and fall times (20-80%) of the signal amplitude was about 20 ps. Figure 8 shows the measured sensitivity of the PD-DEC for a bit-error-rate of less than 1×10^{-9} . A decision sensitivity of about 0 dBm at 5 Gbit/s was obtained. The dissipated power was 1.0 W. The output buffer dissipated 25% of the total power. The other 75% can be reduced to 1/5 when DHBTs with a $0.6 \times 1.6\text{-}\mu\text{m}$ emitter [7] are used.

From these results, it is confirmed that the PD-DEC can achieve error-free operation without a preamplifier. The sensitivity can be improved by a factor of ten by using ten times larger R_L while keeping the bit rate, since the time constant of $C_{PD}R_L$ was less than 2.5 ps for the fabricated PD-DEC. Furthermore, optimizing the layer structure of the DHBTs will also improve the sensitivity.

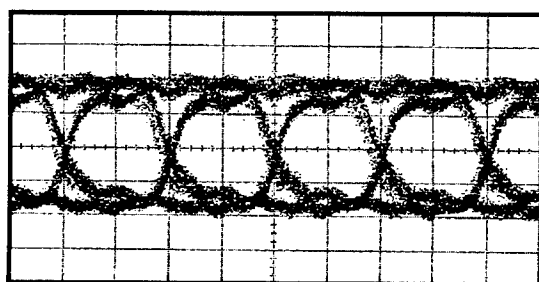


Fig. 7. Measured 10-Gbit/s output eye pattern.

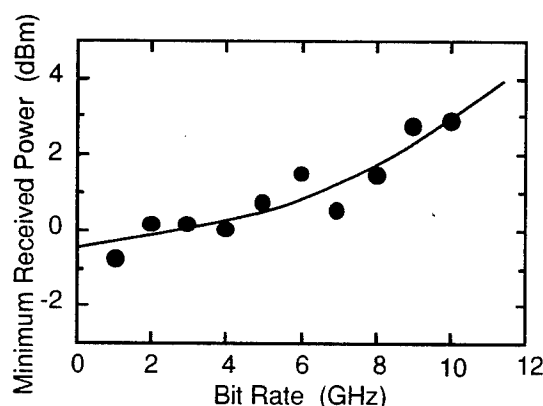


Fig. 8. Input sensitivity of the PD-DEC.

Conclusion

A power estimation model has been introduced to a simplified photoreceiver with a pin PD directly connected to a decision circuit. This configuration is suitable for massively parallel optical interconnections in

terms of power dissipation and cost. The following results are obtained.

- (1) Increasing the total efficiency η to 0.3 effectively contributes to reducing LD drive current.
- (2) Extremely low threshold current and high characteristic temperature of LD.

The simplified photoreceiver has been monolithically integrated with double-heterojunction bipolar transistors.

A 10-Gbit/s error-free operation was successfully achieved. To our knowledge, this is the first successful demonstration of monolithically integrated pin PD/digital circuits for long wavelengths. Studies to confirm error-free operation under the practical conditions are being done and will be reported in the near future.

Acknowledgment

The authors would like to thank S. Horiguchi, and Y. Akazawa for their encouragement and valuable discussions. We also thank T. Otsuji and K. Takahata for their helpful advice.

References

- [1] J. W. Goodman, F. J. Leonberger, S. Kung, and R. A. Athale, "Optical Interconnections for VLSI Systems", *Proc. of the IEEE*, vol. 72, pp. 850-866, July, 1984.
- [2] K. C. Sarawat and F. Mohammadi, "Effect of scaling of interconnections on the time delay of VLSI systems," *IEEE Trans. Electron Devices*, vol. ED-29, pp. 645-650, 1982.
- [3] see the special issue on opto-electronics and LSI, *IEICE Trans. Electron.*, vol. E76-C, no. 1, pp. 90-123, Jan. 1993.
- [4] M. Yoneyama, K. Takahata, T. Otsuji, and Y. Akazawa, "Comparison between optical and electrical interconnections based on transmission error-free condition," *the 7th Karuizawa Workshop on Circuits and Systems*, pp. 163-168, 1994 (in Japanese).
- [5] D. Z. Tsang, "One-gigabit per second free-space optical interconnection," *Appl. Optics*, vol. 29, no. 14, pp. 2034-2037, 1990.
- [6] Y. Uematsu, Y. Yamabayashi, and K. Hohkawa, "A 1.25-Gbit/s four channel GaAs MSI integrated with MSM-PDs for optical interconnection," *LEOS '94*, paper OC/ON1.4, 1994.
- [7] Y. Matsuoka, H. Nakajima, K. Kurishima, M. Yoneyama, and E. Sano, "Novel InP/InGaAs double-heterojunction bipolar transistors suitable for high-speed IC's and OEIC's," *Proc. InP and Rel. Materials Conf.*, pp. 555-558, 1994.
- [8] Y. Akahori, Y. Akatsu, A. Kohzen and J. Yoshida, "10-Gb/s high-speed monolithically integrated photoreceiver using InGaAs p-i-n PD and planar doped InAlAs/InGaAs HEMTs," *IEEE Photon. Technol. Lett.*, vol. 4, No. 7, pp. 754-756, July 1992.
- [9] H. Ichino, N. Ishihara, Y. Yamauchi, K. Nagata, and T. Nittono, "12-Gb/s decision circuit IC using AlGaAs/GaAs HBT technology," *IEEE Solid-State Circuit*, vol. 25, No. 6, pp. 1538-1554, Dec. 1990.
- [10] Y. Itaya, S. Arai, K. Kishino, M. Asada, and Y. Suematsu, "1.6- μm wavelength GaInAsP/InP lasers prepared by two-phase solution technique," *IEEE J. Quantum Electron.*, QE-17, 5, pp. 635-640, 1981.

New Approach For High-speed, High-sensitivity Photodetectors

I-Hsing Tan, John E. Bowers, and Evelyn L. Hu

Electrical and Computer Engineering Department
University of California, Santa Barbara, CA 93106

B. I. Miller and R. J. Capik

AT & T Bell Laboratories, Holmdel, NJ 07733.

The bandwidth-efficiency product of ultra high-speed pin photodetectors has been severely limited by the thickness of the absorbing layer, the diode RC time constant, and the parasitic capacitance from the periphery of device. In this paper, we propose and demonstrate a novel long-wavelength detector structure with a mushroom-like mesa and an air-bridged coplanar metal to significantly cut down both the diode RC constant as well as the parasitic capacitance. The quantum efficiency of this structure can be further enhanced to close to 100% if the long-wavelength detector is fused to a GaAs/AlAs quarter-wave stack (QWS), followed by deposition of a Si/SiO₂ QWS to form a Fabry-Perot cavity.

I. Introduction

High-speed and high-sensitivity photodetectors are required for new high-bit-rate optical communication systems. The photodiode RC time constant and parasitic capacitance from the periphery of the device have put severe limitations to the speed of the detector response for devices with thin absorbing layers. For example, in order to reduce the junction capacitance and gain a 3-dB bandwidth over 100 GHz, the detection area of a long-wavelength pin diode has to be less than 10 μm^2 and the absorbing layer is only 200-nm thick [1]. However, a detector with high-sensitivity would benefit from a larger detector area and thicker absorbing layer. There appear to be intrinsic trade-offs in achieving both high speed and sensitivity. This paper discusses the fabrication of two photodetectors where we have separately optimized the structures for high speed and high efficiency operation, respectively. We believe that the two approaches can be readily combined into a single processing scheme, which would produce, in a single device, both high speed and high sensitivity. The novel ultra-high speed, long-wavelength detector structure involves reduction of the RC time constant of the diode by an undercut, mushroom geometry, and minimization of the parasitic capacitance by using an air-bridged metal waveguide. The active layer of the device is only 180-nm thick, commensurate with ultra high-speed operation. High quantum efficiency can be obtained for devices with thin absorbing layers by employing a resonant-cavity-enhanced (RCE) detector structure: we shall show that a resonant structure with an active layer only 90-nm thick demonstrates greater than 90% quantum efficiency. This is achieved by using *wafer fusion* to bond the In_{0.53}Ga_{0.47}As/InP photodetector into a GaAs/AlAs quarter-wave stack (QWS) on a GaAs substrate. A Si/SiO₂ dielectric mirror was subsequently deposited onto the wafer-fused photodiode to form an asymmetric Fabry-Perot cavity. The external quantum efficiency and absorption bandwidth for the wafer-fused RCE photodiodes were measured to be 94%. To our

knowledge, these wafer-fused RCE photodetectors have the highest external quantum efficiency ever reported for long-wavelength, RCE photodetectors. We believe that greater than 100 GHz of bandwidth-efficiency product will be feasible by combining the wafer-fused detectors with an air-bridged metal waveguide and an undercut, mushroom mesa.

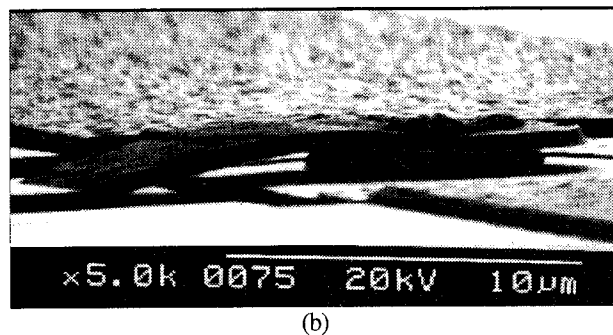
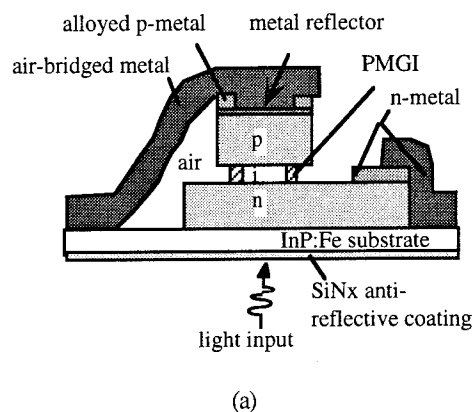


Figure 1 (a) Proposed ultra high-speed detector structure, and (b) the SEM micrograph of the fabricated devices

II. Ultra high-speed detectors

A schematic diagram of the device is shown in Fig. 1(a). Our structure design utilizes an InGaAs/InP double heterostructure to eliminate photon absorption and carrier diffusion in the InP p-doped and n-doped layers. The epitaxial layers were grown on an Fe-doped InP substrate by metal organic vapor phase epitaxy and were composed of a 10-nm intrinsic InGaAs etch-stop layer next to the InP substrate, followed by 508-nm n^+ InP layer, 9-nm graded bandgap layer (GBL), 180-nm intrinsic (i-) InGaAs layer, 9-nm GBL, 100-nm set-back, intrinsic InP layer, 306-nm p^+ InP layer, 9-nm GBL, and 50-nm p^+ InGaAs contact layer. The three GBLs inserted at the hetero-interfaces are to minimize carrier trapping and to reduce the series resistance. The setback InP layer was used to avoid any possible Zn diffusion from p^+ InP layer to the i-InGaAs layer during the growth.

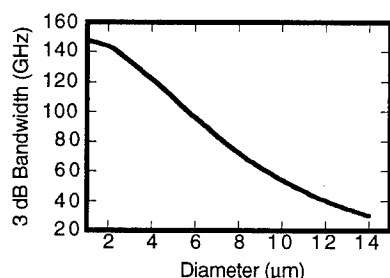


Figure 2 Calculated electrical 3-dB bandwidth for the device structure as shown in Figure 1.

The thickness of the i-InGaAs layer was 180 nm, which can produce a transit-time limited bandwidth as wide as 160 GHz. The bandwidth of the device described here is in fact limited by the diode RC time constant and parasitic capacitance, which can be minimized by undercut etching into the intrinsic InGaAs layer and using an air-bridged metal as shown in Fig. 1. Undercut etching into the InGaAs intrinsic layer can dramatically minimize the effective diode junction capacitance, while not significantly increasing the diode series resistance. We have simulated the device characteristics, and by solving the equation of current continuity, we have found that the total diode RC time constant can therefore be reduced by a factor of 2 to 4 for a device with a p-mesa diameter of less than 10 μm , and with the intrinsic layer diameter 4 μm less than the p-mesa. It has been previously discussed that the parasitic capacitance from the periphery of devices whose side walls have been passivated by polyimide is comparable to the junction capacitance when the device active area is 25 μm^2 or less [1]. The replacement of the polyimide by the air will further reduce the parasitic capacitance by at least a factor of two. As a result, the calculated electrical 3-dB bandwidth versus

the intrinsic layer diameter for our device is shown in Fig. 2, where the bandwidth is greater than 100 GHz for a device diameter $\leq 6 \mu\text{m}$. At the final step of coplanar metal deposition as shown in Fig. 1(a), the non-alloyed metal covering the window of the ring metal will serve as an ohmic contact as well as a metal reflector. Therefore, we expect the quantum efficiency to be enhanced by a factor of ~ 2 with respect to a front-side illuminated detector structure.

To fabricate the mushroom-like mesa structure, we first lift-off evaporate a ring-Ti/Pt/Au/Ni metal on the p^+ InGaAs layer and cover the window of the ring metal by a photoresist mask, followed by Cl_2 dry etching into the i-InGaAs layer with the etch thickness controlled by laser reflectometry. The inner diameter of the ring metal varies from 2 to 10 μm , while the outer diameter is 4 μm greater than the inner one. The dry-etched mesa is then covered by a 200-nm thick SiO_2 mask for the undercut etching. Undercut etching into the intrinsic InGaAs is carried out in a solution of $\text{H}_2\text{SO}_4:\text{H}_2\text{O}_2:\text{H}_2\text{O}$. Next, the n^+ InP mesa is formed by selectively etching in a $\text{HCl}:\text{H}_2\text{O}:\text{H}_3\text{PO}_4$ solution to stop etch on a thin InGaAs layer, followed by AuGe/Ni/Au metal evaporation onto the n^+ InP mesa and metal annealing at 420 $^\circ\text{C}$ for 30 seconds. An example of the undercut etched profile for the mushroom-like mesa without any evaporated metals on the semiconductor surface is shown in the scanning electron microscopic (SEM) image of Fig. 3, where the diameter of the i-InGaAs mesa is 2 μm and the p-mesa is 6 μm .

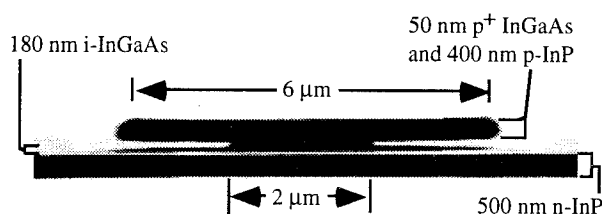


Figure 3 The SEM micrograph of an undercut etched mesa.

Finally, we use a PMGI (SAL 110) re-flow process to both passivate the undercut, etched side walls of the i-InGaAs layer and serve as an initial bridge for the coplanar metal waveguide. The characteristics of the PMGI resist are very similar to the polyimide except that the resist can easily re-flow at a temperature $> 240 \text{ }^\circ\text{C}$ and can be washed away in the SAL 101 developer after being exposed to deep UV illumination. The periphery of the mushroom-like mesa is first covered by the lithographically defined PMGI resist patterns. The PMGI resist is then cured at 250 $^\circ\text{C}$ for 10 minutes to allow the resist to be in tight contact with the side walls of the p-mesa as well as to fill into the undercut etched area. A subsequent 3 μm thick photoresist is spun on the sample and lithography is carried out to pattern a $\sim 1 \mu\text{m}$

thick coplanar metal waveguide. The sample is exposed to deep UV illumination before the metal evaporation and after the metal lift-off. Subsequently, all the unwanted resist is removed in the developer, except for the unexposed resist covering the side walls of the undercut etched InGaAs layer, thus forming an air-bridged metal waveguide. The SEM micrograph of the finished device is shown in Fig. 1(b). Greater than 90% yield of the devices has been obtained by using this process.

I-V measurements carried out on these structures indicate that the diode resistance at forward bias is less than $30\ \Omega$ for a diameter of the undercut etched InGaAs layer less than $5\ \mu\text{m}$, which is at least four times smaller than previous results reported [1] for this device dimension. The reverse breakdown voltage of these detectors is around 10 V and the dark current is $\sim 3\ \text{nA}/\mu\text{m}^2$ at 4 V reverse bias. The low dark current level of our devices indicates our success in passivating the undercut etched detector. High speed measurements using an E-O sampling setup and microwave characterizations of these devices are in progress. While the design bandwidth for these detectors has been much greater than 100 GHz, the corresponding quantum efficiency is calculated to be only $\sim 25\%$ at $1.3\text{-}\mu\text{m}$ wavelength. As a result, the bandwidth-efficiency product for the optimized structure is at most $\sim 35\ \text{GHz}$. In the next section, we will demonstrate the wafer-fused RCE detector which has an extremely high quantum efficiency and is easily integrated with our high-speed demonstrated structure.

III. Wafer-fused RCE detectors

To fabricate a wafer-fused RCE detector centered at $1.3\ \mu\text{m}$ wavelength, the starting materials consist of a *p-i-n* diode plus an InGaAs etch stop layer grown on an InP substrate and a GaAs/AlAs quarter-wave stack on a GaAs substrate. We used a fusing technique, previously described in conjunction with the fabrication of long wavelength vertical cavity lasers [2]. The technique allows accommodation of the large lattice mismatch of 3.7% between the GaAs and InP crystal substrates, resulting in a smooth and uniform interface [3]. The epitaxial side of the InP substrate was brought into contact with the epitaxial side of the GaAs substrate and annealed at $650\ ^\circ\text{C}$ for 10 minutes in the H_2 ambient. Uniaxial stress was applied to the sample to ensure that robust bonding takes place during annealing. The InP substrate was selectively removed after etching the wafer-fused sample in the HCl solution. The etch stop layer was then selectively removed, leaving a *p-i-n* diode structure, $\sim 1\ \mu\text{m}$ in thickness, on the top of the GaAs/AlAs QWS on a S. I. GaAs substrate. The newly exposed surface of the p^+ InGaAs layer, examined under Nomarski contrast, is mirror smooth. The cross sectional image of this wafer-fused sample is shown in the SEM micrograph of Fig. 4. We have also bonded the same *p-i-n* diode structure to a bulk S. I. GaAs substrate, to be used as a reference in the photocurrent measurements. It is also noted that the thickness of the absorbing InGaAs layer is only 90 nm.

To fabricate the mesa-type *p-i-n* diode, Ti/Pt/Au ohmic contacts were lift-off deposited onto the p^+ InGaAs surface to form a $120 \times 80\ \mu\text{m}^2$ mesa, where there is a $50 \times 50\ \mu\text{m}^2$ window in the mesa for the light input. The entire mesa was wet-etched into the n^+ InP layer. AuGe/Ni/Au Ohmic contacts were then formed onto the n^+ InP layer. Both the Ti/Pt/Au and AuGe/Ni/Au metals were annealed in a rapid thermal annealer at $420\ ^\circ\text{C}$ for 30 sec. The p^+ InGaAs layer is then selectively removed from the front window of both wafer-fused samples. The structure with the GaAs/AlAs QWS is already a RCE photodetector having another natural mirror of 30% reflectivity at the p^+ InP/air interface. In Fig. 5, we show the typical photocurrent spectra of the wafer-fused photodiodes. The dash-dotted curve of Fig. 5 is for the wafer-fused photodiode on the bulk GaAs substrate, while the dotted curve is for the wafer-fused photodiodes on the GaAs/AlAs QWS. The photocurrent peak is centered at $1.305\ \mu\text{m}$ and has a full width at half maximum of 35 nm. The external quantum efficiency for the diode on the GaAs/AlAs QWS is 45 %, while that for the reference photodiode on the bulk GaAs substrate is only 6 %. There is already ~ 8 -fold improvement in the quantum efficiency for the photodetector sandwiched by a GaAs/AlAs QWS and a natural, low-reflective mirror formed by the air/semiconductor interface.

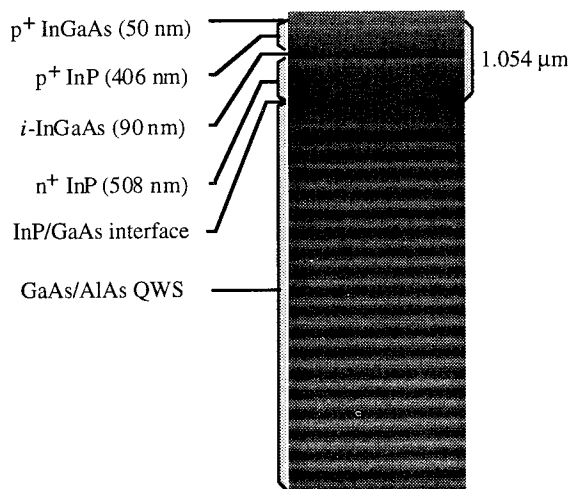


Figure 4 The SEM micrograph of the wafer-fused detectors.

To further improve the quantum efficiency, we have formed a mirror composed of a half λ thick SiO_2 plus one Si/ SiO_2 quarter-wave pair, applied by e-beam evaporation and lift-off, on the front light window of the wafer-fused detectors. While the deposited amorphous Si is slightly lossy and has an absorption coefficient estimated to be $\sim 500\ \text{cm}^{-1}$ at $1.3\ \mu\text{m}$ wavelength, only one quarter-wave thickness

of Si is required for our device. The reflectivity in the wavelength interval between 1.1 and 1.5 μm remains rather flat and has a maximum value of 80 % around the 1.3 μm wavelength. The resulting photocurrent spectrum of the RCE photodetectors sandwiched by both the GaAs/AlAs QWS and dielectric mirror is shown in the solid curve of Fig. 5. The external quantum efficiency of the RCE detectors is measured to be 94 % at the resonant wavelength of 1.3 μm and is ~ 16 times better than that of the reference detectors. To our knowledge, these wafer-fused RCE photodetectors have the highest external quantum efficiency ever reported on the long-wavelength, RCE photodetectors.

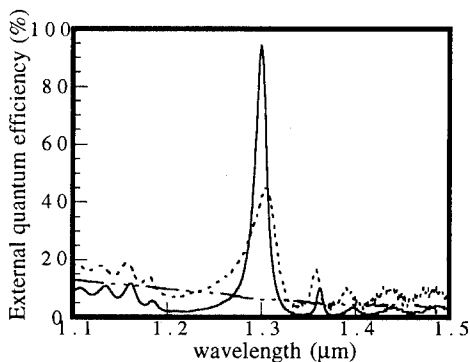


Figure 5 Photocurrent plot of the wafer-fused photodetectors.

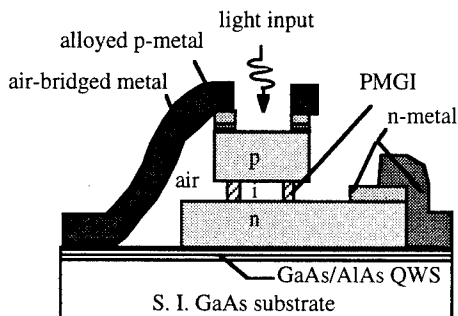


Figure 6 Proposed wafer-fused, high-speed, RCE detectors.

Based upon the promising results of the wafer-fused detectors, we propose a wafer-fused, high-speed, and RCE

detector structure as shown in Fig. 6, where the detector is situated above a non-intentionally doped GaAs/AlAs QWS, in turn overlying a S. I. GaAs substrate. Using the wafer-fused material as the starting substrate, we can apply the air-bridged metal waveguide and undercut etched mesa to fabricate a photodetector that should have both high speed of operation and high quantum efficiency. Our simulations of the device performance indicate that over 100 GHz of bandwidth-efficiency product is very feasible for these detectors. Fabrications of these wafer-fused, high-speed, and RCE detectors are in progress.

IV. Conclusions

High speed photodetectors have been proposed and fabricated where a mushroom-like mesa and an air-bridged metal waveguide reduce the diode RC time constant and the parasitic capacitance, respectively. Greater than 90% yield and low dark current levels for these devices have been achieved by using our developed PMGI re-flow process. Electrical bandwidths greater than 100 GHz are expected for photodiodes having an intrinsic layer area less than 40 μm^2 ; however, the quantum efficiency at 1.3 μm wavelength is only ~ 25 % for these devices. To further improve the sensitivity of the ultra high-speed detectors, we have fabricated wafer-fused, RCE photodiodes that can yield greater than 90% quantum efficiency for absorbing layers as thin as 900 Å. By combining the wafer-fused scheme with the undercut etched mesa and an air-bridged metal waveguide, we predict that over 100 GHz of bandwidth-efficiency is feasible for the long-wavelength photodetectors.

References

- 1 Y. G. Wey, K. Giboney, J. E. Bowers, M. J. Rodwell, P. Silvestre, P. Thiagarajan, 108 GHz GaInAs/InP p-i-n Photodiodes with Integrated Bias Tees and Matched Resistors" *IEEE Photonics Technol. Lett.* vol. 6, no. 11, pp.1310-1312.
- 2 J. J. Dudley, D. I. Babić, R. Mirin, L. Yang, B. I. Miller, R. J. Ram, T. Reynolds, E. L. Hu, and J. E. Bowers, " Low threshold, wafer fused long wavelength vertical cavity lasers" *Appl. Phys. Lett.*, vol. 64, pp. 1-3, 1994.
- 3 R. J. Ram, L. Yang, K. Nauka, Y. M. Houn, M. Ludowise, D. E. Mars, J. J. Dudley, and S. Y. Wang, "Analysis of wafer fusing for 1.3 μm vertical cavity surface emitting lasers" *Appl. Phys. Lett.*, vol. 62, pp. 2474-2476, 1993.

A Strained InAlAs/InGaAs Superlattice Avalanche Photodiode for Operation at an IC-Power-Supply Voltage

S. Hanatani, M. Shishikura*, S. Tanaka*, H. Kitano, T. Miyazaki*, and H. Nakamura*

Telecommunication Division, HITACHI Ltd. Yokohama, Kanagawa, 244 JAPAN

*Central Research Laboratory, HITACHI Ltd. Kokubunji, Tokyo, 185 JAPAN

For operation of an avalanche photodiode (APD) at an IC-power-supply voltage, less than 5 V, a novel edge-coupled waveguide superlattice (SL) APD is proposed. Using a strained InAlAs/InGaAs SL, multiplication factor larger than 10 is experimentally demonstrated at a bias voltage less than 7 V. A wide 3dB-bandwidth of 8 GHz is obtained at a multiplication factor of 3.

Introduction

High sensitive and wide dynamic-range photoreceivers are preferable, not only for large capacity and long haul lightwave communication systems, but for optical links, optical interconnects and other access network systems. Using an APD as a photoreceiver, it is possible to obtain an improvement 5 dB larger a PIN-PD photoreceiver in the sensitivity, and an improvement 10 dB larger than that in the dynamic-range, because it can amplify a received signal within it with its avalanche multiplication. A photoreceiver with an APD has not been introduced into such optical systems so far, because it is complicated and expensive due to its high-voltage operation, which needs a high voltage source, or a DC-DC converter. An operating voltage of conventional Si-APDs is around 200 V, and the one of InP-APDs is larger than 50 V [1]. For use of an APD as a photoreceiver in many optical communication systems, it is important to reduce an operating voltage of an APD up to an IC power supply level, less than 5 V. An APD operating at such a low bias voltage has not ever been obtained.

In this paper, we propose a novel edge-illuminated waveguide (WG) superlattice (SL) - APD for operation at a bias voltage less than 5 V. A multiplication and high-speed characteristics is reported by fabricated the proposed APD with a strained InAlAs/InGaAs SL.

Device Structure

In order to achieve an APD with an operating voltage

less than 5 V, a multiplication layer should have a large ionization rate even at a low electric field. An SL APD is one of the most possible devices, because impact ionization can be enhanced with the SL. Figure 1 shows ionization rates experimentally obtained with an InP [2] and an InAlAs/InGaAs SL [3]. An electron ionization rate of the SL is larger than 10^4 / cm even at an electric field lower than 300 kV/cm, about half an electric field obtained with the InP.

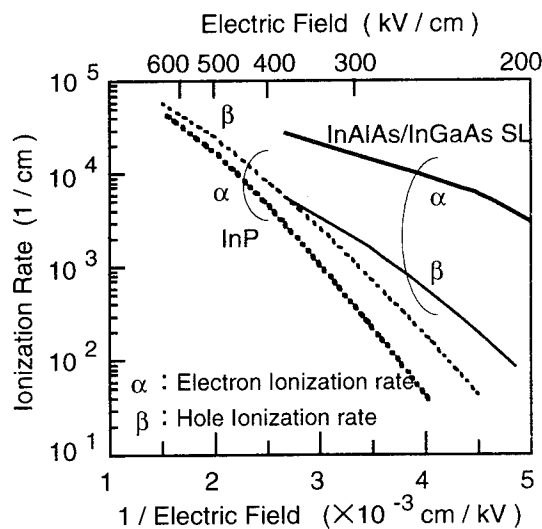


Figure 1 Ionization rates of InP [2] and InAlAs/InGaAs SL [3]

Using the SL, operation at a bias voltage lower than 30 V was obtained with an back-illuminated structure [4]. A total active region thickness of the SL-APD is about 1.4 μm , which consists of a 1.0 μm absorption layer, an 0.2 μm absorption layer and an SL multiplication layer thinner than

0.2 μm . For further lowering the operating voltage, a thinner active region of the APD is necessary. An edge-coupled WG structure is favorable for reducing the active-region thickness, keeping a large quantum efficiency [5].

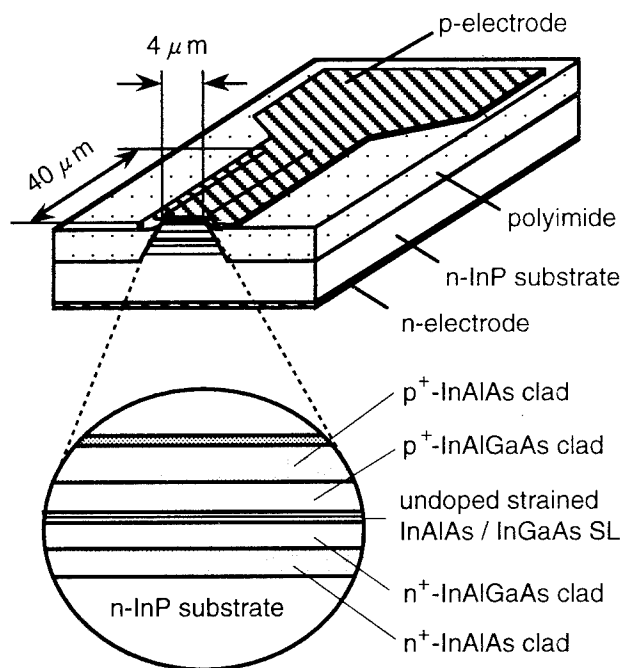


Figure 2 Schematic structure of the edge-coupled WG strained InAlAs/InGaAs SL APD

Figure 2 shows a schematic structure of the edge-coupled WG SL-APD fabricated. The epitaxial layers were prepared on an n-type InP substrate by solid-source molecular beam epitaxy (MBE). An n-type 0.13 μm InGaAlAs second cladding layer, An undoped strained InAlAs /InGaAs SL active layer and a p-type 0.13 μm InGaAlAs second cladding layer were sandwiched by highly doped InAlAs layers. A highly Be-doped InGaAs thin layer was grown for ohmic contact. It is well known that the thinner the active layer, the lower the operating voltage becomes. We, so, designed the SL active layer as an absorption and multiplication one in order to make an active layer thin up to 0.11 μm . Received signal light induces an electron-hole mixed injection, instead of a pure electron injection, into the SL, which may degrade an ionization rate ratio of this SL less than 3. Our calculation shows that with an electron ionization rate larger than $5 \times 10^4 / \text{cm}$, a multiplication factor larger than 3 can be obtained even at an ionization rate ratio less than 3.

Figure 3 shows an energy diagram of the strained $\text{In}_{0.45}\text{Al}_{0.55}\text{As} / \text{In}_{0.63}\text{Ga}_{0.37}\text{As}$ SL active layer.

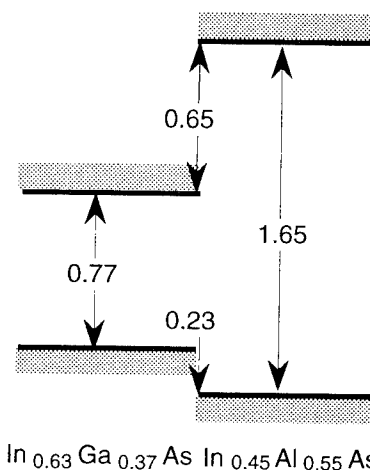


Figure 3 Energy diagram of the strained InAlAs/InGaAs SL

With enlarged conduction-band-edge discontinuity, ΔE_c , and valence-band-edge one, ΔE_v , impact ionization in an SL could be further enhanced and larger ionization rates could be obtained. We can control ΔE_c and ΔE_v by applying strain into a lattice-matched SL. Too much strain accumulation may, however, induce dislocation in an SL. Taking both into account, we introduced tensile strain and compressive one into the InAlAs barrier and the InGaAs well,, respectively, without strain accumulation. The ΔE_c and the ΔE_v of the strained $\text{In}_{0.45}\text{Al}_{0.55}\text{As} / \text{In}_{0.63}\text{Ga}_{0.37}\text{As}$ SL obtained was enlarged up to 0.65 and 0.23 eV, respectively. Compared with the ΔE_c and the ΔE_v of the lattice-matched InAlAs/InGaAs SL, the ΔE_c and the ΔE_v of the strained SL obtained were increased by 0.12 eV, and 0.06 eV, respectively. Well and barrier thicknesses of the SL were 10 and 15 nm, respectively. The InAlAs and InAlGaAs layers are used as clads for confinement of a received signal in the active region. A cut-off wavelength of the InAlGaAs layer was designed to be 1.25 μm for operation at both wavelengths of 1.3 and 1.55 μm . A ridge waveguide fabricated by chemical etching was covered with polyimide for passivation. The waveguide width and the length of the WG SL-APD fabricated were 4 μm and 40 μm , respectively. The p-electrode and the n-electrode were formed by evaporating Ti/Au and AlGeNi, respectively.

Experimental Results

Figure 4 shows the dark current and multiplication factor obtained with the WG SL-APD. A wavelength of 1.3 μm was used for measurement of an photocurrent of the APD. Avalanche multiplication starts at a bias voltage about 5 V and a break-down voltage is about 7 V. An edge break-down was not observed. The maximum multiplication factor attained was larger than 10 at a bias voltage just less than 7 V, which is the lowest to our knowledge. In order to eliminate WG structure dependence of the operating voltage, we measured a photocurrent of a surface-illuminated strained SL-APD fabricated with the same epitaxial layers as the above mentioned WG SL-APD. A multiplication factor obtained with the surface-illuminated SL-APD was larger than 5 at a bias voltage less than 5 V. These results obtained shows that it is possible for the WG SL-APD to operate at a bias voltage less than 5 V by optimizing the WG structure. The dark current was larger than 1 μA at a bias voltage larger than 6 V (multiplication factor about 2). The received power penalty due to the darkcurrent is nor negligible at bit rates lower than 1 Gbit/s. Further research for low darkcurrent SL structure is necessary.

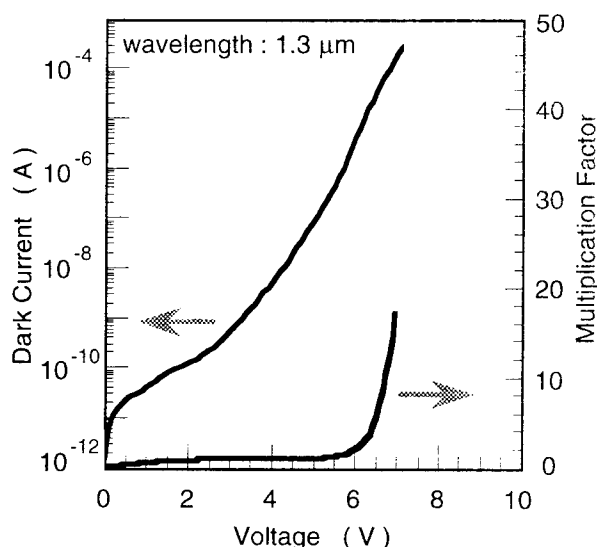


Figure 4 Dark current and multiplication factor of the WG strained SL APD

Figure 5 shows a frequency characteristics of the WG strained SL-APD at a multiplication factor of 3. For measurement, an optical component analyzer (HP8703A) was used at a wavelength of 1.3 μm . Pile-up of

photogenerated carriers in the well is important to high-speed operation [6]. The 3dB-bandwidth attained was 8 GHz without degradation of high-speed characteristics of the WG SL-APD due to carrier pile-up in the SL. The 3dB-bandwidth is considered to be limited by CR-time constant, because it has good agreement with a 3dB-bandwidth calculated using a capacitance of 0.4 pF obtained. Then it is possible to raise the maximum 3dB-bandwidth to 15 GHz by reducing the bonding-pad capacitance through flip-chip bonding.

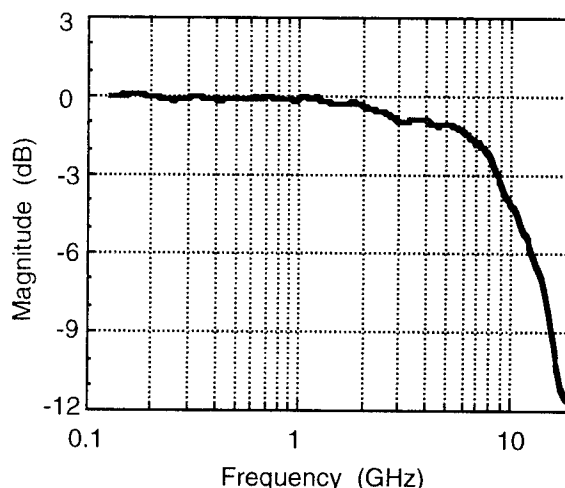


Figure 5 Frequency characteristics of the WG strained SL APD

summary

We propose an edge-coupled WG SL-APD for low bias voltage operation less than 5 V. Introducing strain into an InAlAs/InGaAs SL for ionization rates enhanced, the WG SL-APD was fabricated. Avalanche multiplication factor larger than 10 was achieved at a bias voltage less than 7 V. A wide 3dB-bandwidth of 8 GHz was obtained at a multiplication factor of 3.

Acknowledgments

We would like to thank Dr. Naoki Chinone and Dr. Koji Ishida for encouragement through this work.

REFERENCES

- [1] Y. Matsushima, Y. Noda and Y. Kushiro, IEEE Jour. Quantum Electron. **QE-21**, 1257 (1985)
- [2] L. W. Cook, G.E. Bulman and G.E. Stilman, Appl. Phys. Lett. **40**, 589 (1982)
- [3] T. Kagawa, Y. Kawamura, H. Asai, M. Naganuma and O. Mikami, Appl. Phys. Lett. **55**, 993 (1989)
- [4] S. Hanatani, H. Nakamura, S. Tanaka, C. Notsu, H. Sano and K. Ishida, Tech. Dig. of OFC/IOOC'93, ThG3. 187 (1993)
- [5] M. Shishikura, H. Nakamura, S. Hanatani, S. Tanaka, C. Notsu and S. Tsuji, Tech. Dig. of OEC'94, 13D1-3 68 (1994)
- [6] S. Hanatani, H. Nakamura, S. Tanaka, C. Notsu and K. Ishida, Tech. Dig. of Quantum Optoelectronics, Ser. vol. 7 WB5-1, 243 (1991)

Reduction of Inelastic Scattering Effect by Introducing Strain-Compensated Superlattice into GaInAs/GaInP Multi-Quantum Barriers

Terhoe Loh, Tomoyuki Miyamoto, Youichiro Kurita,
Fumio Koyama and Kenichi Iga

*Precision and Intelligence Laboratory, Tokyo Institute of Technology
4259 Nagatsuta, Midori-ku, Yokohama 226, Japan*

The effect of inelastic scattering on the electron reflection in multi-quantum barriers has been examined for the first time by using the damped resonant tunneling model. The electron reflectivity deteriorates below unity most significantly at discrete energies in the virtual barrier. The largest dip in reflectivity is about 15% for intraband relaxation time of 0.16ps. It is also shown that this deterioration can be reduced by utilizing strain-compensated superlattice in the multi-quantum barriers.

1. Introduction

A sufficiently high heterobarrier for carrier confinement is important for efficient operation of semiconductor lasers. This is especially true for GaInAsP/InP based lasers in which the conduction band offset between active and p-cladding layers is too low for the sufficient confinement of electrons in the active layer. The multi-quantum barriers (MQB) was proposed [1] as an electron wave quantum reflector to enhance the heterobarrier of double heterostructures (DH) for the suppression of carrier leakage for semiconductor lasers. The lattice-matched (LM) GaInAs / InP MQB has been shown to exhibit enhanced electronic heterobarrier by photoluminescence (PL) measurement and n-i-n diode current-voltage characteristics at cryogenic temperature[2]. Recently, 1.55 μ m strained multiple quantum well (MQW) laser loaded with LM AlInAs/GaInAs MQB was reported to show improvement in temperature dependence of laser slope efficiencies[3]. In spite of these improvements, there is no clear quantitative measure of the effectiveness of the MQB as an electron reflector. Recently, the effectiveness of the MQB has also been investigated at room temperature[4]. Although the MQB-loaded n-i-n diode structure has shown a reduction in thermionic current with an applied voltage, the current reduction was less than that theoretically expected. We believe that the additional leakage current component in Ref.4 for room temperature n-i-n diode may be originated from electron scattering while traversing the superlattice (SL) of the MQB.

The proper operation of the MQB relies on the quantum interference of phase coherent electrons. Electron wave loses coherence through inelastic scattering due to many-body interactions with other electrons and phonons. It is necessary to consider the inelastic scattering to design an optimized MQB structure for device applications and to quantify its effectiveness. The effect of the electron scattering in MQB has never been discussed yet. To account

for inelastic scattering using a many-body scattering problem for device analysis would be extremely complicated. In this work, we have accounted for the inelastic scattering in MQB by the damped resonant tunneling model. This approach has been taken recently to model the inelastic electron scattering in double barrier resonant tunneling diodes.[5-7] In this simplified model, electron wave amplitudes attenuate, due to scattering, with a decay coefficient $\gamma=1/l_F$, where l_F is the electron mean free path in analogous to the absorption coefficient for lightwaves in multi-layer optical media.

2. Calculation Method

We have employed the scattering matrix to calculate the electron reflectivities of unstrained InP (barrier)/GaInAs (well) and strain-compensated (SC) GaInP (barrier)/GaInAs(well) MQB's with inelastic scattering taken into consideration. The MQB consists of a first thick layer coupled to a finite length superlattice. We have found that for an MQB, the electron reflectivity at the virtual barrier is reduced below unity due to inelastic scattering at certain discrete resonant modes which originates from the interference between Bragg reflected wave from the minigap of the superlattice and the wave reflected at the first interface of the first thick layer. We identify these modes as Bragg reflected discrete modes in the virtual barrier. These are in close resemblance to Bragg confined modes in a thin slab of semiconductor sandwiched symmetrically between two finite length superlattices[8]. We have also found that for MQB with SC superlattices not only has higher virtual barrier, but also has less reduction in reflectivities at the Bragg modes. This shows that MQB with SC superlattice is less susceptible to the deteriorating effect of scattering.

The electron in MQB obeys the time-independent Schrodinger equation :

$$\frac{d^2\phi}{dz^2} + \frac{2m^*}{\hbar^2}(E - E_c(z))\phi = 0,$$

where ϕ is the electron wavefunction, $E_c(z)$ is the potential of MQB, \hbar is Planck's constant divided by 2π , m^* is the effective mass and E is the energy of the electron. The wave vector of electron in the in-plane direction is taken to be zero. Therefore, consideration is taken only for electron wavefunction in the perpendicular direction (z) of the superlattice. The amplitude reflection and transmission coefficients are derived for well-to-barrier interface (or vice versa) by matching the wavefunctions and its derivatives divided by the respective effective masses at both sides of the interface. The scattering matrix for an interface is built up from the transmission and reflection coefficients for forward and backward incident plane waves. By the scattering matrix cascading rule[10], the amplitude transmission and reflection coefficients for a single barrier are,

$$t_B = t't'e^{jk_B L_B} (1 - r'^2 e^{j2k_B L_B})^{-1},$$

$$r_B = r(1 - e^{j2k_B L_B})(1 - r'^2 e^{j2k_B L_B})^{-1},$$

where t, t', r, r' are the amplitude transmission and reflection coefficients at well to barrier interface and vice versa, respectively. L_B is the barrier width. As the electron wave makes a single traverse across the well of width L_W , the amplitude phase shift is simply $\exp(jk_W L_W)$. Throughout the calculation, the barrier and well wave vectors are $k_B = k_o^B + j\gamma_B$ and $k_W = k_o^W + j\gamma_W$ where $k_o^B = \sqrt{2m_B^*(E - U_o)}/\hbar$, $k_o^W = \sqrt{2m_W^*E}/\hbar$. U_o is the barrier potential height and the potential energy reference is taken at the well bottom. γ_B and γ_W are the scattering attenuation coefficients in barrier and well. In this work, it is assumed $\gamma_B = \gamma_W = \gamma$, such that $\gamma = 1/l_F = 1/(\tau_{in}v)$. τ_{in} is the intraband relaxation time[9] and \hbar/τ_{in} is a measure of spectral broadening. v is the electron velocity given by $v = \sqrt{2E/m_W^*}$, where E and m_W^* are the electron energy and the effective mass of the electron in the well, respectively.

Given the barrier and well amplitude transmission and reflection coefficients and treating each of them as an interface in scattering matrix form and utilizing the cascading rule for scattering matrix, the total coherent probability current transmission ($T_{coh} = |t_{coh}|^2$) and reflection coefficients ($R_{coh} = |r_{coh}|^2$) of the MQB can be calculated. When γ is zero, the unitary relation of $T_{coh} + R_{coh} = 1$ holds. When scattering is present and $\gamma \neq 0$, then $T_{coh}(\gamma \neq 0) + R_{coh}(\gamma \neq 0) < 1$. $1 - T_{coh}(\gamma \neq 0) - R_{coh}(\gamma \neq 0)$ represents the total probability of incoherence. That is, it is the sum of all the individual probability of incoherence in each individual well due to scattering.

The superlattice layers of the MQB are sufficiently thin and it is assumed to be undoped. Therefore, it is correct to assumed that the depletion and space charge effects on

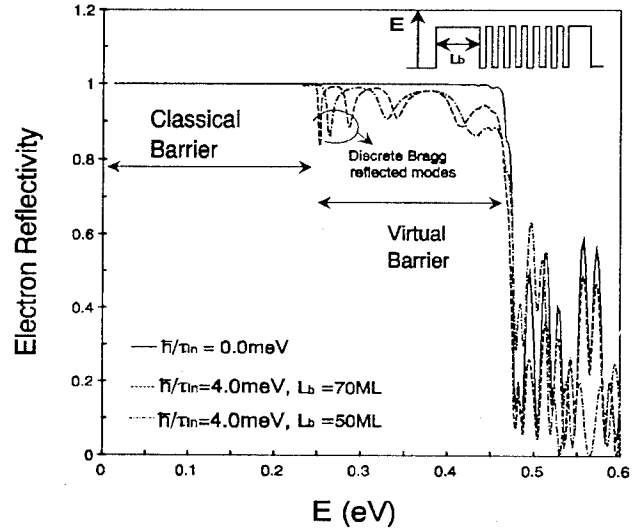


Fig. 1 Electron reflectivities vs E , energy from bottom of well ($\tau_{in}=0.16ps$) for first thick layer of 70ML and 50ML.

the MQB band structure is negligible and self-consistent treatment on MQB band structure is not required. The scattering attenuation parameter above the first thick layer is taken to be zero because scattered carriers are assumed to fall back to the region before the n-i-n structure.

3. Results and Discussions

In figure 1, we show the electron reflectivities for an unstrained MQB (InP barrier and lattice-matched GaInAs well) against E , the energy of electron with zero at the conduction band edge of lattice-matched GaInAs. The solid line is the reflectivity calculated in which scattering is not taken into account. Both the dashed and dashed-dot lines are reflectivities calculated with scattering taken into consideration and scattering broadening factor is taken to be $\hbar/\tau_{in} = 4.0meV$ ($\tau_{in}=0.16ps$). The reflectivity at the virtual barrier is found to reduce below unity significantly at discrete Bragg reflected resonant energies. The lowest dip in reflectivity is about 15% for $L_b=70ML$. It is also observed that the area below the dips increases at the high energy end of the virtual barrier. The reflectivity of probability current at unity means that the electron will be reflected with absolute certainty. However, when the reflectivity is reduced below unity, there exists a certain amount of probability that electron is lost to elsewhere besides being reflected. Since the structure is optimized to have the transmission coefficient to be zero, this deficit, thus, represents the probability of incoherence. As shown by the dashed ($L_b=70ML$) and dashed-dot lines ($L_b=50ML$), the positions of these discrete energies shift when L_b , the thickness of the first InP layer changes from 70ML to 50ML. Therefore, the area under I should be minimized to reduce reflectivity deterioration. The thickness of the first layer should not be too thin to prevent carriers from tunneling into the first miniband of SL.

The virtual barrier is a combination of the continuum above the first thick layer and the minigap of the superlattice. Since there exists semiconductor interfaces at both ends of the first thick InP layer, there arises interference between Bragg reflected wave from the minigap and wave reflected at the first interface of the thick layer. Electron in these Bragg modes penetrate evanescently into the minigap. While the electron exists within the minigap, it experiences inelastic scattering and results in dips in reflectivity within the virtual barrier.

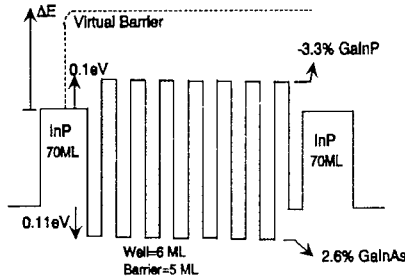


Fig. 2 Schematic diagram of strain-compensated MQB n-i-n structure.

Fig.2 shows the schematic diagram of SC MQB loaded n-i-n structure considered in our study. It consists of 70ML of InP for the first and last barriers, and seven strain-compensated superlattice pairs of 2.6% GaInAs compressive 6ML-wells and 3.3% tensile GaInP 5ML-barriers. The electron masses in well and barrier are linearly approximated. The reflectivities of this SC MQB and the unstrained MQB are calculated for $\tau_{in} = 0.22ps$. Fig.3 shows the reflectivities (left axis) and the probability of incoherence, I (right axis) of both these structures against ΔE , the electron energy above the InP conduction band edge. The reflectivity of unstrained MQB in the virtual barrier dips below unity at the discrete Bragg reflected modes. The

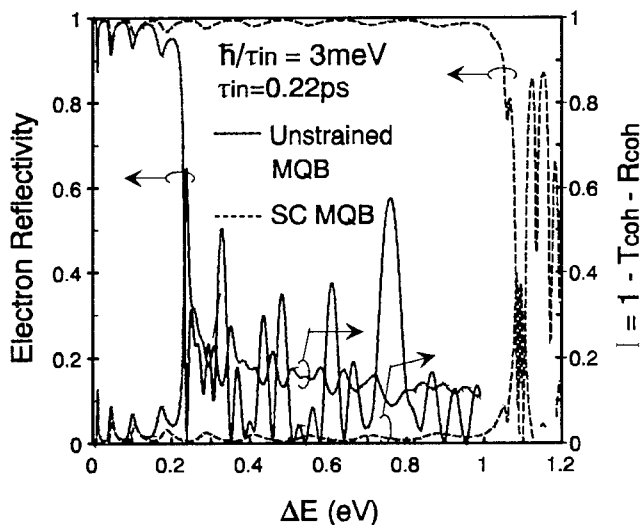


Fig. 3 Electron reflectivities (left) probability of incoherence (right) vs ΔE , electron energy above InP conduction band edge.

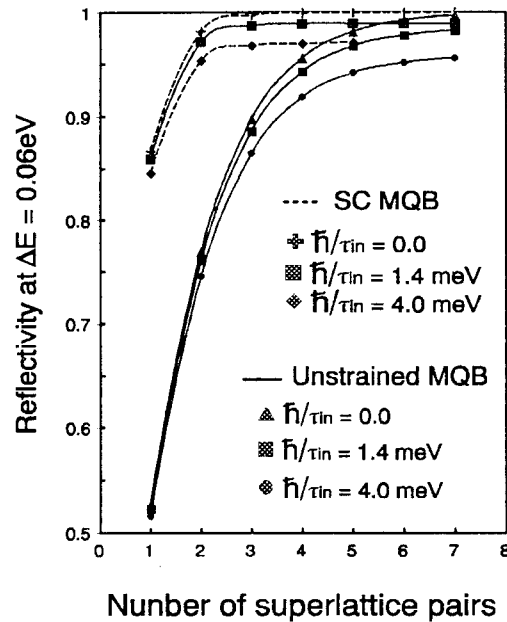


Fig. 4 Reflectivities at $\Delta E=0.06eV$ vs number of superlattice pairs.

dips in reflectivity correspond to peaks in I , the probability of incoherence showing that scattering takes place at these dips. The SC MQB has a wider virtual barrier and reduced I also at many dips in the virtual barrier. This shows that the SC MQB is less susceptible to scattering.

Fig.4 shows the plot of reflectivity at $\Delta E=0.06eV$, which is the location of the second Bragg mode for first barrier thickness of 70ML, against number of SL pairs for both unstrained and SC MQB's, for various scattering broadening factors \hbar/τ_{in} . The reflectivity of the unstrained MQB requires seven SL pairs to saturate, while that of the SC MQB requires only three SL pairs. The SL pair number at which the reflectivity saturates, N_s , tells us the number of SL pairs the electron wavefunction would penetrate into the minigap. Hence, it tells us the unnecessary to have SL pairs larger than N_s in MQB design. At the N_s 'th SL pair, the reduction in reflectivity represents the cumulative probability of incoherence due to scattering. For the same scattering broadening factor, this reduction is less for SC MQB showing that it is less susceptible to scattering.

The smaller N_s for SC MQB is easy to understand when we consider the optical analogy in DBR. A higher barrier and deeper well potential is analogous to greater difference in optical refractive indices of DBR pairs, i.e., higher well to barrier potential steps are more efficient electron wave reflectors and less number of SL pairs are required to completely reflect the electron wave. For reduced N_s and deeper well potential, the electron transit interval between the time when electron first enters the minigap and the time when it reflects out of the minigap is shortened. As a result, the electron on the whole spend less time in the superlattice and, hence, is less susceptible to scattering.

4. Strain-Compensated Superlattice Photoluminescence Characterization

In the effort to realize the SC MQB and to verify the enhanced virtual barrier effect, we have successfully fabricated the strain-compensated 7ML $\text{Ga}_{0.25}\text{In}_{0.75}\text{As}$ (1.7%-compressive) well / 6ML $\text{Ga}_{0.25}\text{In}_{0.75}\text{P}$ (-1.7%-tensile) barrier superlattice structures utilizing the chemical beam epitaxy. Fig.5 shows the room temperature photoluminescence (PL) spectra for two SC superlattices. Namely, 6-well and 10-well SC superlattices, both with the same growth condition. The PL spectra arise from the carrier relaxation from the first miniband of the superlattices. The details of the overall structure are shown at the inset of Fig.5. (The PL spectrum from the InP clad region was also detected at $0.92\mu\text{m}$ peak wavelength but not shown in the figure). The 10-well SC superlattice shows a weaker and broader PL spectrum. This shows that even for strain-compensated structure, crystal quality deteriorates when the superlattice pair number is increased. For the 10-well case, the total thickness of the superlattice may have exceeded the critical thickness for the overall average strain of the structure. It may also be due to interfacial valve sequences not optimized during growth.

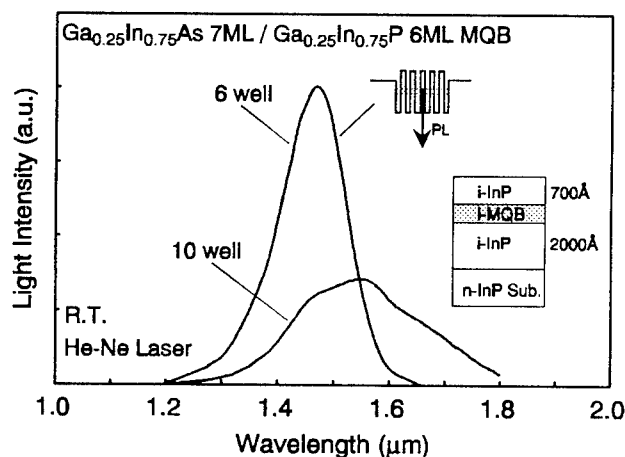


Fig. 5 Photoluminescence spectra for 6 well-SC and 10 well-SC superlattices.

5. Conclusions

In conclusion, we have employed the damped resonant tunneling model in the scattering matrix formalism to study unstrained and SC MQB. Bragg confined modes are found to manifest in the virtual barrier of MQB. It is in these Bragg modes that electron wave penetrates into the minigap of the MQB and experiences inelastic scattering. However, SC MQB has shorter depth of penetration and it is less susceptible to effect of scattering. Experimentally, we have successfully fabricated 6-well SC superlattice with relatively good crystal quality in the effort to realize SC MQB.

The authors wish to thank T. Sakaguchi and T. Hamano of Tokyo of Technology for fruitful and stimulating discussions. This work is supported by a Scientific Grant-In-Aid from the Ministry of Education, Science and Culture, and is partly supported by the grant of the NEDO.

References

- [1] K. Iga, H. Uenohara and K. Koyama "Electron Reflectance of Multi-quantum Barriers". *Electron. Lett.* Vol.22, pp. 1010-1013, July 1986.
- [2] Y. Inaba, T. Uchida, N. Yokouchi, T. Miyamoto, F. Koyama and K. Iga, "GaInAsP/InP MQB Grown by Chemical Beam Epitaxy". *Jpn. J. Appl. Phys.* Vol.32, pp.760-761, Feb 1993.
- [3] H. Shimizu, T. Fukushima, K. Nishikata, Y. Hirayama and M. Irikawa: *14th IEEE International Semiconductor Laser Conference* pp. 26-27, 1994.
- [4] D. Campi, C. Rigo, C. Cacciatori and H. C. Neitzert, "Enhanced Confinement of Electrons at Room Temperature Using a Superlattice Reflector". *Appl. Phys. Lett.* Vol.65, pp. 2148-2150, Oct 1994.
- [5] H. Yuning and S. P. Stapleton, *IEEE J. Quantum Electron.* Vol.29, pp.327-339, Feb 1993.
- [6] M. Jonson and A. Grincwajg, "Effect of Inelastic Scattering on Resonant and Sequential Tunneling in Double Barrier Heterostructures". *Appl. Phys. Lett.* Vol.51, pp.1729-1731, 1987..
- [7] Y. Zohta, "On the Definition of Sequential Tunneling in a Double-Barrier Resonant Tunneling Structure". *Jpn. J. Appl. Phys.* Vol.32, pp. L177-L179, Feb 1993.
- [8] J. Salzman, G. Lenz, E. Baruch and E. Finkman, "Bragg Confinement of Carriers in a Shallow Quantum Well". *Appl. Phys. Lett.* Vol.59, pp.1858-1861, Oct 1991.
- [9] S. H. Park, M. Asada, K. Kudo and S. Arai, "Intraband Relaxation Time in Compressive-Strained Quantum Well Lasers", *Jpn. J. Appl. Phys.* Vol.31 pp.3385-3386, Oct 1992.
- [10] S. Datta, *Quantum Phenomena*, Addison-Wesley, 1989 pp.23-24.

Superconducting Weak Link Devices using Lead alloy-InAs/AlGaSb Heterostructures

Toshihiko Maemoto, Satoshi Izumiya, Hiroyuki Dobashi, Mitsuaki Yano, and Masataka Inoue
Department of Electrical Engineering, Osaka Institute of Technology
5-16-1 Omiya, Asahi-ku, Osaka 535, Japan

Abstract – Fabrication and transport properties of InAs/AlGaSb superconducting weak link devices are reported. Transport property of two terminal devices have been measured between 2.6K and 5.5K, and oscillations of differential resistance due to multiple Andreev reflection have been observed. The three terminal device with a gate showed decent FET performance with transconductance of 314mS/mm at 4.2K although superconducting current has not been modulated on the device for the gate length of 0.74 μ m. The process to reduce contact resistance between the PbIn alloy and InAs is also discussed, which should be crucial to demonstrate superconducting transistor.

I. Introduction

Two-dimensional ballistic electrons in InAs/AlGaSb heterostructures are interesting from a fundamental aspect and also device applications to quantum effect devices. Electrons in InAs/AlGaSb heterostructures are attracting interests for high electron mobility, large conduction band off-set, and strong confinement of electrons in a quantum well. From these properties, it is expected that quantum effects can be observed at relatively high temperatures above the cryogenic liquid temperature. For example, the quantized conductance was observed at temperatures around 77K on InAs/AlGaSb split gate devices [1],[2]. Recently, on lateral surface superlattices with InAs/AlGaSb heterostructure was fabricated by using photolithography and wet chemical etching, Weiss oscillations have been observed by magnetoresistance measurements at 4.2K [3]. These results suggest that a ballistic electrons in InAs/AlGaSb can be applicable to quantum effect devices operating at relatively higher temperatures.

InAs is also one of the candidate to fabricate superconducting weak link devices, because a long coherence length ξ_n can be expected due to the small effective mass of electrons. Superconducting weak links with an InAs heterostructure have been investigated by using several heterostructures [4-6]. In the InAs/AlGaSb superconducting devices, a high superconducting current density and a high $I_c R_n$ product have been demonstrated [4],[6]. In addition, InAs/AlGaSb has the advantage on the stable device processing in comparison with that of InAs/AlSb heterostructures. Therefore, InAs/AlGaSb is one of the key materials for high-speed and low-power devices as well as weak link devices.

In this paper, we report on fabrication and transport properties of InAs/AlGaSb superconducting weak link devices fabricated by using photolithography and wet chemical etching. Transport properties of the devices are presented and the problems to fabricate three-terminal devices are also discussed to demonstrate a superconducting transistor.

II. MBE Growth and Device Fabrication

InAs/AlGaSb heterostructures have been grown by molecular beam epitaxy on semi-insulating GaAs substrate. The used InAs/AlGaSb heterostructure for weak link devices consists of 2000 \AA GaAs buffer layer, 1.5 μ m AlSb buffer layer, 2000 \AA of $\text{Al}_{0.5}\text{Ga}_{0.5}\text{Sb}$ bottom barrier, 150 \AA of InAs channel, 150 \AA of $\text{Al}_{0.5}\text{Ga}_{0.5}\text{Sb}$ upper barrier, and 100 \AA of GaSb cap layer. A GaAs buffer layer was grown on the substrate at 640 $^{\circ}\text{C}$, of which growth rate was 0.5 μ m/h. The AlSb buffer layer was grown at 600 $^{\circ}\text{C}$ to relax lattice strain in the layer. The AlGaSb with 50% aluminum was used for the barrier to confine electrons in the InAs heterostructure. In order to prevent intermixing between As and Sb atoms at the heterostructures, the growth temperatures was decreased from 550 $^{\circ}\text{C}$ to 480 $^{\circ}\text{C}$ just before the growth of InAs channel. An InAs channel was grown at the growth rate of 0.5 μ m/h. A GaSb cap layer was grown to prevent the growth of oxidized layer. InAs/AlGaSb heterostructure has attained to an electron mobility of 102000 cm^2/Vs and a sheet carrier concentration of $9.0 \times 10^{11} \text{ cm}^{-2}$ at 4.2K.

The superconducting weak links with InAs/AlGaSb heterostructure were fabricated by photolithography and wet

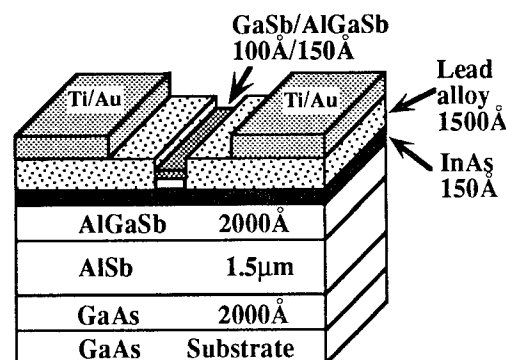


Fig.1 Schematic diagram of an InAs/AlGaSb superconducting weak link.

chemical etching. Although the electron beam lithography has been widely used for making the superconducting weak link, we have successfully fabricated weak link with $0.3\mu\text{m}$ gap by using conventional photolithography [7]. In order to obtain a good ohmic contact between InAs and superconducting electrodes, GaSb/AlGaSb layer was selectively etched by an alkaline solution [8]. Superconducting electrodes of Lead alloy (Pb/In) was made on InAs layer by thermal evaporation [9]. The thickness of Pb/In layer was 1500\AA and the thickness of Lead and Indium were 1230\AA and 270\AA , respectively. Ti/Au bonding metals were deposited on the Lead alloy by electron beam evaporation. The schematic diagram of the fabricated InAs/AlGaSb superconducting weak link is shown in Fig.1. The channel length L_{sd} between Pb/In electrodes changed between $0.3\mu\text{m}$ to $1.0\mu\text{m}$.

III. Transport Properties of the InAs/AlGaSb Weak Links

The current-voltage and differential resistance-voltage characteristics of the superconducting weak links have been measured at around 4.2K . On the weak link device with channel length of $L_{sd}=0.75\mu\text{m}$, superconducting current did not flow. However, nonlinear characteristics was seen as shown in Fig.2, which is expected to be at the critical situation to flow the superconducting current in InAs. Figure 2 shows the differential resistance measured at temperatures between 2.6K and 5.5K on the weak link. In addition to marked dip at zero voltage, the small dips were observed on

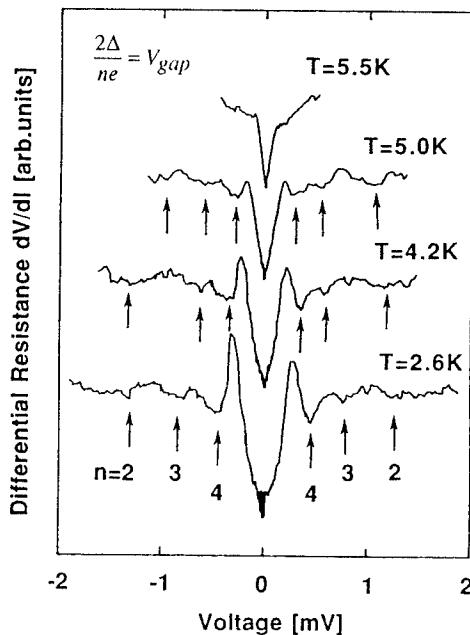


Fig.2 The differential resistance measured at the temperatures between 2.6K and 5.5K on the InAs/AlGaSb weak link with channel length $0.75\mu\text{m}$.

the differential resistance near voltages equal to $V_{gap}=2\Delta/ne$ ($n=2,3,4$). The dips were observed within superconducting energy gap of Lead alloy. The energy gap of the Pb/In alloy 2Δ is about 2.7meV . The differential resistance changed depending on the measured temperatures, and the dips shifted to lower voltage as increasing the temperature. With slightly increasing the temperature, the dip structure became indistinct. From these results, it is understood that this characteristic is an appearance of superconductive effects and a subharmonic gap structure should be due to the multiple Andreev reflection. This effect has been theoretically proposed by M.Octavio et al. [10]. K.Flensberg et al. [11] showed that the dip structures can be explained by multiple Andreev reflections at superconductor/semiconductor interfaces of the weak link. When the coherence length becomes short in comparison with the width of the superconducting electrodes with increasing the temperature, the number of the reciprocating motion of the quasi-particle decreases by increasing the elastic scattering in the channel. The normalized superconducting energy gap is shown in Fig.3 as a function of the T/T_c . The solid curve is the change of $2\Delta(T)$ obtained by BCS theory. The energy gap $2\Delta(T)$ was estimated from the bias voltages where the dips appeared in the characteristic of Fig.2. The experimental results agree well with the theoretical temperature dependence of 2Δ .

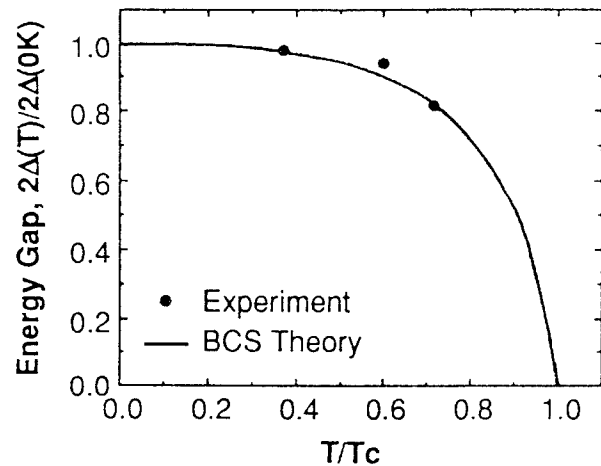


Fig.3 Superconducting energy gap of the sample obtained from the result of Fig.2.

IV. InAs Heterostructure Transistor with a Submicron Gate

We have fabricated InAs heterostructure transistors (FET) with Pb/In alloy electrodes. The transistors have been made by using conventional photolithography and non-alloyed ohmic contacts. Figure 4 shows micrograph of the fabricated InAs channel FET taken by the scanning electron microscope. The channel length L_{sd} and gate length L_g of the sample were found to be approximately $1.1\mu\text{m}$ and

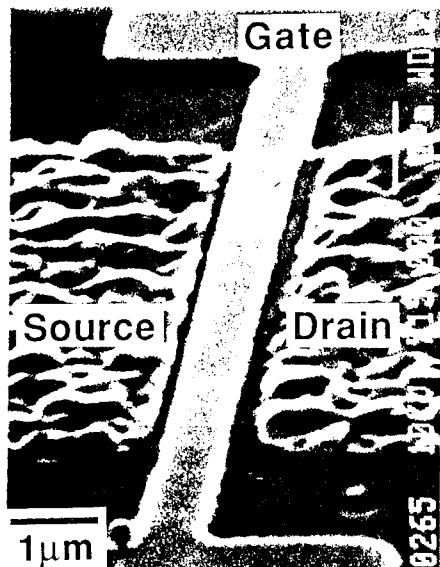


Fig.4 The SEM micrograph of the fabricated InAs/AlGaSb transistor. The gate length was estimated to be $0.74\mu\text{m}$.

$0.74\mu\text{m}$, respectively. Hall-effect measurements by van der Pauw method showed the mobility of 20700 and 40500 cm^2/Vs at 300K and 77K, respectively. The carrier concentration was 1.87×10^{12} and $1.78 \times 10^{12} \text{ cm}^{-2}$ at 300K and 77K, respectively. Figure 5 shows the drain current-voltage characteristics measured at 4.2K. The maximum extrinsic transconductance g_m of the device were 212mS/mm and 314mS/mm at 300K and 4.2K, respectively. The transconductance increased by decreasing of the gate leakage

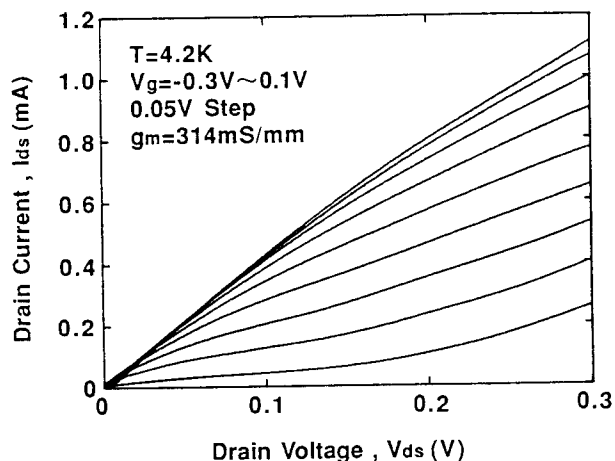


Fig.5 The drain current-voltage characteristics at 4.2K of the transistor shown in Fig.4.

current at 4.2K. The characteristic shown in Fig.5 is not so attractive as the previous results [12],[13]. This transistor has been originally fabricated to modulate the superconducting current by the gate voltage. On the contrary, the superconducting current was not observed. This result should be argued to the shorter coherence length $\xi_n (<1\mu\text{m})$ in comparison with the channel length. In order to flow the superconducting current and modulate it, the electrical properties of InAs should be improved. In addition to the crystal quality, the device structure should be optimized to reduce the contact resistance and a gate leakage current.

InAs/AlGaSb superconducting transistor have fabricated by using electron beam lithography, and photolithography [7]. The channel length and gate length were found to be approximately $0.93\mu\text{m}$ and $0.36\mu\text{m}$, respectively. Slight modulation of the drain current has been observed by an applied gate voltage. Superconducting current, however, was not observed even for the short channel device. This result may be due to the large contact resistance at the superconductor/semiconductor interfaces. The large contact resistance reduces not only superconducting current density but also the transconductance of FET. Therefore, it is crucial to decrease the contact resistance between Pb/In alloy and the InAs layer to demonstrate the superconducting FET. The contact resistance in Pb/In alloy/InAs heterostructure was improved by thermal annealing [7]. We have studied to reduce the contact resistance by using the experiment of transmission line method (TLM). The used sample are shown in the inset of Fig.6. The contacts were made by using the experiment of transmission line method. The used sample are shown in the inset of Fig.6. The contacts were

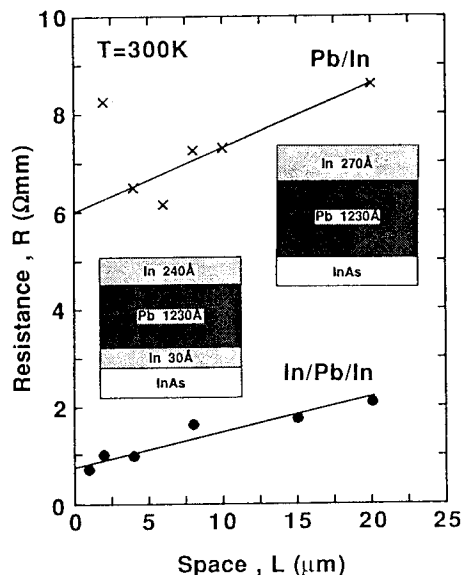


Fig.6 Measurements of the contact resistance. Two different contacts, Pb/In alloy and In/Pb/In alloy on InAs are compared by transmission line method.

made by sequential deposition of Lead and Indium. The contact resistance was decreased from $6\Omega\text{mm}$ to $0.75\Omega\text{mm}$ by inserting 30\AA thick Indium between Lead and InAs. This improvement may be due to the sticky formation of In/Pb/In contact to the InAs. This contact can be used to the InAs/AlGaSb FET by using non-alloyed process. After the further progress on these fabrication process, the InAs/AlGaSb superconducting transistor will be realized in the near future.

Conclusion

We have studied the transport properties of the superconducting weak link devices using Lead alloy-InAs/AlGaSb heterostructures. The multiple Andreev reflection in the InAs/AlGaSb superconducting weak links with channel length $L_{sd}=0.75\mu\text{m}$ have been observed at between 2.6K and 5.0K. The transport properties were attributed to a long electron mean free pass and multiple Andreev reflection in the InAs/AlGaSb weak link. InAs/AlGaSb channel FET with a submicron gate has been fabricated by using photolithography and wet chemical etching. The transconductance showed 212mS/mm and 314mS/mm at 300K and 4.2K, respectively. The contact resistance was decreased from $6\Omega\text{mm}$ to $0.75\Omega\text{mm}$ by inserting thin Indium layer between Lead and InAs interface. The fabrication process to decrease the contact resistance between the In/Pb/In alloy and InAs may be useful for the demonstration of high performance InAs heterostructure FETs and superconducting transistors.

Acknowledgment

We would like to thank A.Kiyose and C.Dohno for technical assistance in device processing. This work was partly supported by the Grant-in-Aid for Science on Priority Area (Quantum Coherent Wave Electronics: Physics and Electronics) from the Ministry of Education, Science and Culture of Japan.

References

- [1] K.Yoh, A.Nishida and M.Inoue, "High Temperature Quantum Effect Devices Using InAs/AlGaSb Heterostructures", Extended Abstracts of the 1993 International Conference on Solid State Device and Materials, pp.327-329, 1993.
- [2] M.Inoue, K.Yoh and A.Nishida, "Quantized conductance observed at high temperatures in InAs/(AlGa)Sb quantum wires", Semicond.Sci.Technol., Vol.9, pp.966-969, 1994.
- [3] S.Osako, K.Tada, Y.Yamamoto, S.Izumiya, M.Yano and M.Inoue, "Fabrication and Characterization of InAs Lateral Surface Superlattices", Abstracts of International Workshop on Metastable and Strained Semiconductor Structures, pp.112-113, 1994.
- [4] C.Nguyen, J.Werking, H.Kroemer, and E.L.Hu, "InAs-AlSb quantum well as superconducting weak link with high critical current density", Appl.Phys.Lett., Vol.57, pp.87-89, 1990.
- [5] J.Nitta, T.Akazaki, and H.Takayanagi, "Transport properties in an InAs-inserted-Channel $\text{In}_{0.52}\text{Al}_{0.48}\text{As}/\text{In}_{0.53}\text{Ga}_{0.47}\text{As}$ heterostructure coupled superconducting junction", Phys.Rev.B, Vol.46, pp.14286-14289, 1992.
- [6] T.Maemoto, K.Yoh and M.Inoue, "Fabrication and Characterization of Superconducting Weak Links with InAs/(AlGa)Sb Heterostructure", Electronics and Communications in Japan, Vol.77, pp.57-64, 1994.
- [7] T.Maemoto, H.Dobashi, S.Izumiya, K.Yoh and M.Inoue, "Fabrication of Superconducting Transistor using InAs/(AlGa)Sb Quantum Wells", Jpn.J.Appl. Phys., Vol.33, pp.7204-7209, 1994.
- [8] K.Yoh, K.Kiyomi, A.Nishida and M.Inoue, "Indium Arsenide Quantum Wires Fabricated by Electron Beam Lithography and Wet-Chemical Etching", Jpn.J.Appl. Phys., Vol.31, pp.4515-4519, 1992.
- [9] M.Murakami, "Thermal stability of Pb-alloy Josephson junction electrode materials: I. Effect of film thickness and grain size of Pb-In-Au base electrodes, J.Appl. Phys., Vol.52, pp.1309-1319, 1981.
- [10] M.Octavio, M.Thinkham, G.E.Blonder, and T.M.Klapwijk, "Subharmonic energy-gap structure in superconducting constrictions", Phys.Rev.B, Vol.27, pp.6739-6746, 1983.
- [11] K.Flensberg and J.Bindslev Hansen, M.Octavio, "Subharmonic energy-gap structure in superconducting weak links", Phys.Rev.B, Vol.38, pp.8707-8711, 1988.
- [12] K.Yoh, T.Moriuchi, and M.Inoue, "An InAs Channel Heterojunction Field-Effect Transistor with High Transconductance", IEEE Electron Device Lett., Vol.11, pp.526-528, 1990.
- [13] C.R.Bolognesi, E.J.Caine, and H.Kroemer, "Improved Charge Control and Frequency Performance in InAs/AlSb-Based Heterostructure Field-Effect Transistors", IEEE Electron Device Lett., Vol.15, pp.16-18, 1994.

W. Kruppa* and J. B. Boos
Naval Research Laboratory
Washington, DC 20375-5320, U.S.A.

* SFA, Inc., Landover, MD 20785, U.S.A.

ABSTRACT

Low-frequency trapping effects in AlSb/InAs/GaAs HEMTs were examined by measuring the transconductance in the frequency range from 1 Hz to 100 KHz. Several device variations with differing cap layers and doping techniques were compared. By varying the bias and temperature, information on the physical location and trap parameters was obtained. A level with an activation energy of 0.12 eV and associated with the AlSb or its interfaces was found. Several other levels associated with different cap layers were also observed.

INTRODUCTION

Recently, AlSb/InAs HEMTs have been investigated for possible application at millimeter-wave frequencies[1-3]. The small electron effective mass in the InAs and the large conduction band offset with AlSb enable high mobilities and large electron densities to be obtained in the resulting 2-DEG. Currently, however, these devices suffer from impact ionization at relatively low electric fields and gate performance anomalies such as large leakage currents and transconductance compression at low gate voltages. These latter effects appear to involve traps at the surface and heterointerfaces as well as other crystal inhomogeneities. The effects of impact ionization on the characteristics of the HEMTs have been described earlier[4]. In this paper, we report on trap-related characteristics particularly the low-frequency dispersion in transconductance.

DEVICE FABRICATION AND CHARACTERISTICS

The AlSb/InAs material was grown by molecular beam epitaxy at 510°C on a semi-insulating, undoped, (100) GaAs substrate. The cross section of the device is given in Fig. 1. In the nominal device, the donors in the AlSb layer

are introduced by an As soak technique. Further details of the material growth are given elsewhere[4]. The sheet carrier density and mobility of the starting material, determined by Hall measurements at 300 K (77 K), were $2.1 \times 10^{12} \text{ cm}^{-2}$ ($1.9 \times 10^{12} \text{ cm}^{-2}$) and $21,000 \text{ cm}^2/\text{V-s}$ ($67,000 \text{ cm}^2/\text{V-s}$), respectively. The devices were fabricated using AuGe/Ni-based source and drain ohmic contacts which were formed by rapid thermal annealing. The Schottky gate contact is Cr/Au formed using a trilevel resist electron-beam lithography process. Device isolation was achieved by wet chemical etching and to reduce gate leakage current, a gate air bridge was formed at the mesa edge.

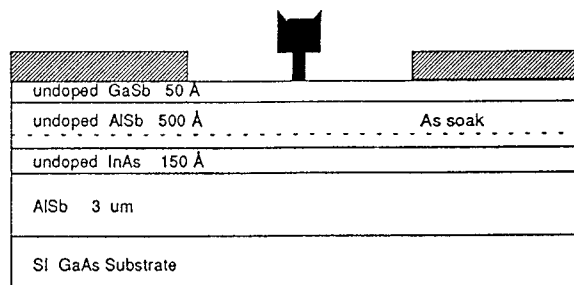


Fig. 1. Device cross section.

The gate length of the HEMTs is 0.35 μm , as determined from SEM measurements, and the total channel width is 50 μm . The source-drain spacing is 3.5 μm . A typical set of drain characteristics is shown in Fig. 2. The devices exhibit the commonly observed transconductance compression at small gate voltages and the high output conductance region at drain voltages above 0.3 V. The maximum dc transconductance observed in the low drain bias region is 90 mS/mm. These HEMTs have maximum f_T and f_{max} values of 50 GHz.

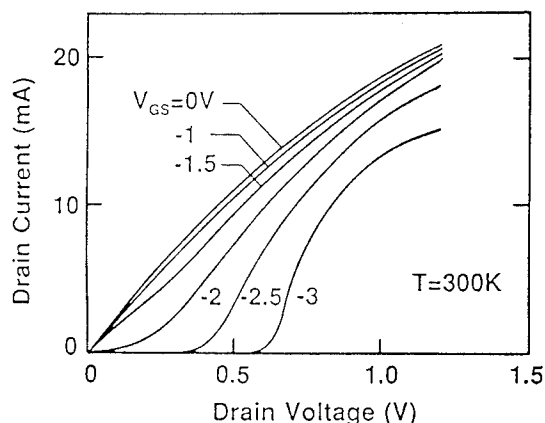


Fig. 2. Drain characteristics.

DISPERSION MEASUREMENTS

To examine trapping phenomena in the gate region, the low-field transconductance was measured at frequencies below 100 KHz. This was done by measuring the voltage gain of the HEMT loaded with a small resistor using an HP-3562A dynamic signal analyzer. The drain voltage was kept small in order to remain below the impact ionization threshold and maintain nearly uniform channel characteristics under the gate. The normalized room-temperature value of g_m for several gate voltages is given in Fig. 3. A significant increase in g_m with frequency is observed at $V_{GS} = 0$. This dispersion diminishes with negative gate voltages and moves to lower frequencies at lower temperatures.

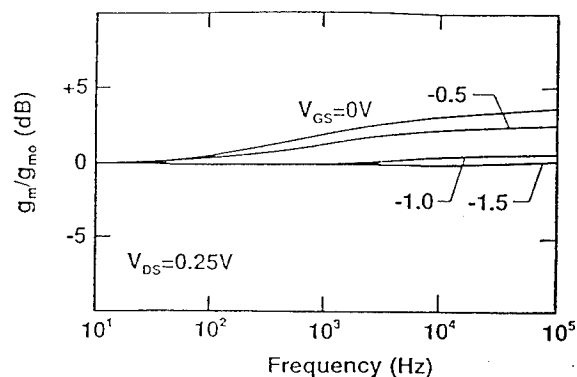


Fig. 3. Room-temperature g_m dispersion as a function of V_{GS} .

At low temperatures, another dispersive mechanism resulting in negative dispersion appears. The effect of temperature on this effect is given in Figs. 4 and 5 which show the transconductance and associated phase response. Since the movement in the transition frequency corresponds to the change of trap emission times with temperature, an activation energy can be obtained. The phase response is convenient for tracking the movement of the transition frequency with temperature because it has a well-defined peak. Arrhenius plots of both mechanisms, obtained by using the movement of the phase extrema, are given in Fig. 6. The activation energies of the high- and low-temperature levels are 0.51 and 0.12 eV, respectively.

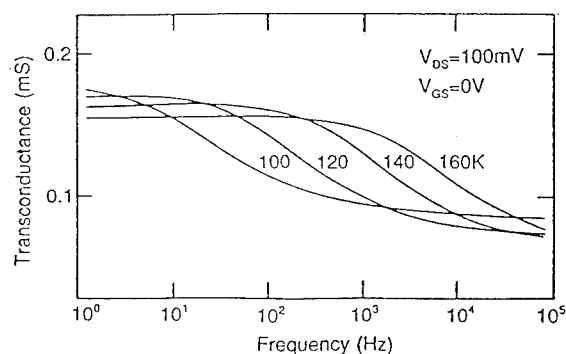


Fig. 4. Low-temperature g_m dispersion as a function of temperature.

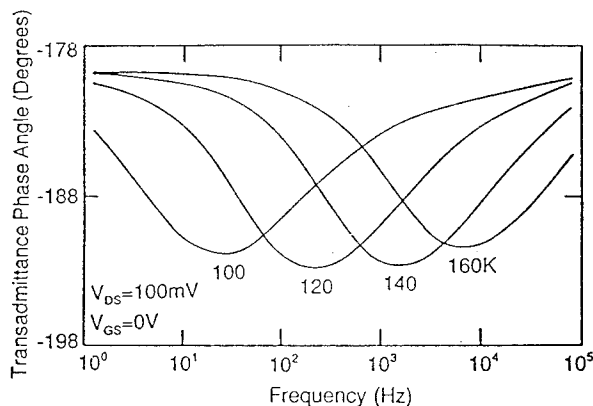


Fig. 5. Low-temperature transadmittance phase angle as a function of temperature.

The amount of low-temperature dispersion diminishes and moves up in frequency with negative gate voltage as shown in Fig. 7. This size reduction is similar to that occurring with the room-temperature effect of Fig. 3. The increase in frequency of the transition could be related to a field-enhanced emission mechanism such as the Poole-Frenkel effect.

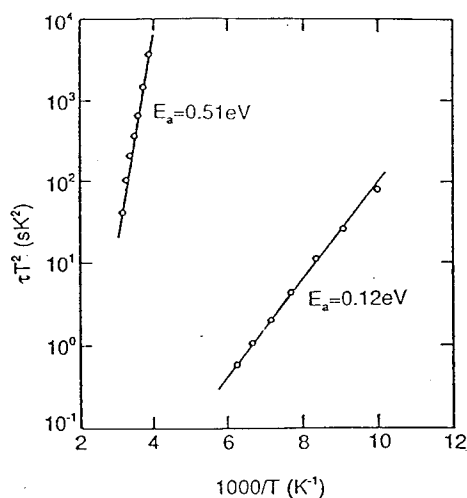


Fig. 6. Arrhenius plot of the two levels causing g_m dispersion.

Since both dispersion effects diminish with more negative gate voltage, the associated traps appear to reside in the layers above the channel. By using several variants in the layer design, additional site allocation can be made. The g_m dispersion as a function of temperature measured on undoped HEMTs with an InAs cap layer is given in Fig. 8. In this case two levels, both causing negative dispersion, can be observed. The corresponding Arrhenius plot is given in Fig. 9. The low-temperature level has the same activation energy as the one seen before, however, the capture cross section is somewhat smaller. The other level is new and has an activation energy of about 0.3 eV. Based on these results, it appears that the 0.51 and 0.12 eV levels of Fig. 6 are associated with the GaSb cap and AlSb layer, respectively. Initial measurements on Te-doped HEMTs showed the same dispersive transconductance behavior as the nominal device discussed earlier. This implies that the traps associated with the AlSb donor layer are not caused by the doping, but rather are intrinsic to the material or its interfaces.

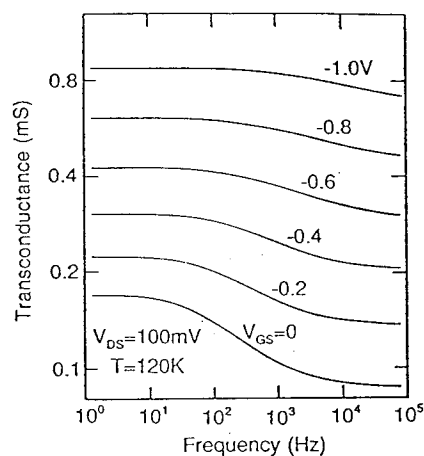


Fig. 7. Low-temperature g_m dispersion as a function of V_{GS} .

Preliminary measurements indicate that some correlation may exist between the transconductance dispersion and gate leakage current. Discrete changes in leakage current have been observed to occur in conjunction with changes in dispersion. It is plausible that

changes in leakage current and dispersion are caused by instability at the interfaces or crystal dislocations.

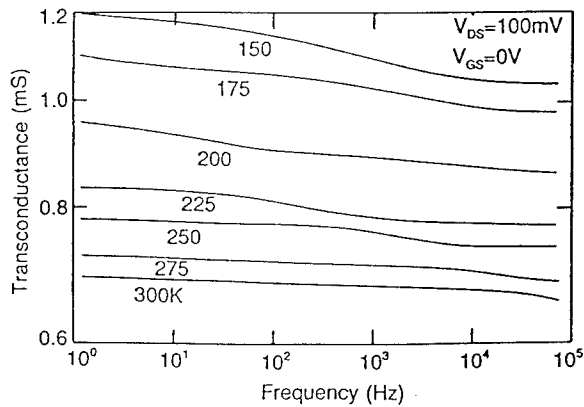


Fig. 8. Transconductance dispersion of undoped HEMT with an InAs cap layer.

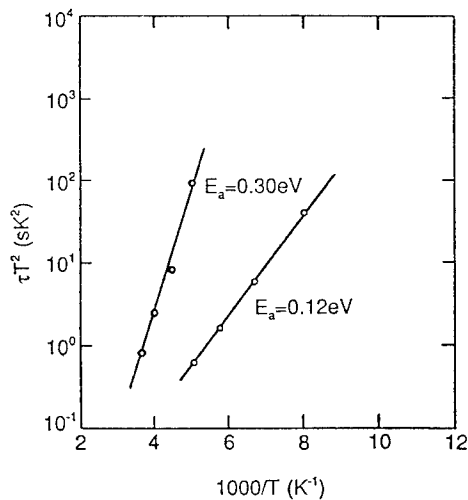


Fig. 9. Arrhenius plot for undoped HEMT with an InAs cap layer.

The low-frequency noise of the devices was also measured as a function of bias and temperature. A nearly perfect $1/f$ characteristic, almost independent of temperature, is observed at zero gate bias and below the impact ionization threshold. The corresponding Hooge parameter is equal to 6×10^{-4} .

Measurements on the output impedance of the transistors discussed here also show the presence of deep-level traps which cause dispersion in the output resistance. It appears that superimposed on the dispersion is impact ionization which starts at a drain voltage of about 0.3 V. The addition of hole current to the gate leakage current also occurs at this voltage. Further studies are being performed to separate more clearly the effects of traps from the impact ionization in these devices.

ACKNOWLEDGEMENTS

This work was supported by the Office of Naval Research. The authors would like to thank B. V. Shanabrook and B. R. Bennett for the material growth, D. Park for the e-beam lithography, and J. Pond for the use of the He refrigerator.

REFERENCES

- [1] K. Yoh, T. Moriuchi, and M. Inoue, "An InAs Channel Heterojunction Field-Effect Transistor with High Transconductance," *IEEE Electron Device Lett.*, Vol. EDL-11, pp. 526-528, 1990.
- [2] X. Li, K. F. Longenbach, Y. Wang, and W. I. Wang, "High-Breakdown-Voltage AlSbAs/InAs n-Channel Field-Effect Transistors," *IEEE Electron Device Lett.*, Vol. EDL-13, pp. 192-194, 1992.
- [3] C. R. Bolognesi, J. D. Werking, E. J. Caine, H. Kroemer, and E. L. Hu, "Microwave Performance of a Digital Alloy Barrier Al(Sb,As)/AlSb/InAs Heterostructure Field-Effect Transistor," *IEEE Electron Device Lett.*, Vol. EDL-14, pp. 13-15, 1993.
- [4] J. B. Boos, W. Kruppa, B. V. Shanabrook, D. Park, J. L. Davis, and H. B. Dietrich, "Impact Ionization in High-Output Conductance Region of $0.5 \mu\text{m}$ AlSb/InAs HEMTs," *Electron. Lett.*, Vol. 29, pp. 1888-1890, 1993.

A Comparative study of the Low Frequency Noise in InP based Heterojunction Field Effect Transistors (HFET's)

P. Rojo-Romeo, P. Viktorovitch, X. Letartre, J. Tardy,

Laboratoire d'Electronique (URA CNRS 848), Ecole Centrale de Lyon, BP 163 - 69131 Ecully Cedex France

D. Thompson and J. G. Simmons

CEMD-Mc Master University, Hamilton, Ontario L8S 4L7 -Canada

1) Introduction

Low-frequency noise (LFN) in III-V Heterojunction Field Effect Transistors (HFET's) is an important limitation of the device performances for applications such as nonlinear circuits that have noise upconversion. The LFN can be converted into the high-frequency range, resulting in undesired phase and frequency modulation. This has motivated investigations of LFN in GaAs/AlGaAs Modulation Doped FET's (MODFET's) [1, 2] and to a lesser extend in InAlAs/InGaAs MODFET's [3, 4]. In this work we present a comparative study of the low frequency noise in different types of HFET's based on InP substrate. Structures with different barrier (AlInAs, InP or a combination of both) and different channel (InGaAs, InGaAsP and InP) materials were investigated. Also, experiments on plain doped AlInAs and AlGaAs resistors were performed for comparison. This study concentrates on LFN sources induced by the distribution of traps within the different layers and interfaces which constitute the structures, resulting in channel carrier number fluctuations. Experiments were made on structures using a TLM configuration, which allows for a normalization procedure of experimental data described in [4].

2) Experimental

Noise power spectra were recorded at room temperature using an Advantest R9211B power spectrum analyser. Measurements were performed on gate free structures of different lengths (ranging from 5 to 160 μm), with a TLM configuration. This structure configuration is helpful to extract easily the noise contribution of the channel from the rough data which include the contribution of the contacts. The channel width is 200 μm for all the structures. DC bias was applied to the sample using voltage sources supplied by low noise batteries. The current noise spectrum S_i was derived from the noise voltage S_v measured across a load resistance R_l , through the relation

$$S_i = S_v [(R_t + R_l) / (R_l R_i)]^2 \quad (1)$$

where R_t is the total resistance of the sample. $R_t = R_{ch} + R_{cont}$, where R_{ch} is the channel resistance, which depends on the length of the measured structure, and R_{cont} is the total contact resistance. Low Frequency Noise (L. F. N) spectra were recorded at room temperature in the frequency range 1Hz-100kHz. All the spectra were 1/f like noise spectra and did not show any significant generation-recombination component (except for one case commented on below).

Figure 1 represents the cross section of the different measured structures, listed below.

MODFET AlInAs/GaInAs structures : they were grown at Ecole Centrale de Lyon using a RIBER 2300 MBE system. Details on the growth conditions are given elsewhere [4,5]. GaInAs channels are lattice matched or compressively strained (fig. 1-a). δ -doped MBE structures were also studied for comparison (fig. 1-b). A MODFET structure, grown at Mc Master University by gas source MBE, with InP buffer and spacer layers was also investigated (fig. 1-c).

HFET AlInAs/InP structures : (fig. 1-d). InP layers were grown at McMaster University. AlInAs layers and GaInAs cap layers were grown at Ecole Centrale de Lyon. A HFET structure with a GaInAsP channel and InP buffer and spacer layers was also grown at McMaster University ; other layers were grown at Ecole Centrale de Lyon (fig. 1-e).

MODFET InP/GaInAs structure : (fig. 1-f) A MODFET structure without any Al containing layer was investigated in order to study the influence of Al on LFN.

MODFET GaAlAs/GaInAs/GaAs structure : (fig. 1-g) In order to compare the influence of the nature of the barrier layers, we have measured a

pseudomorphic structure on GaAs substrate with GaAlAs barrier.

RESISTORS : InP or AlInAs resisors (fig. 1-h) and GaAlAs resistors (fig. 1-i) were also grown for comparison.

All the AlInAs layers are lattice matched to InP. Details on the different structures are given in [5].

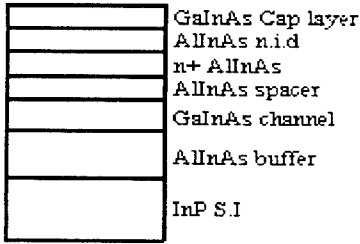


Fig. 1-a

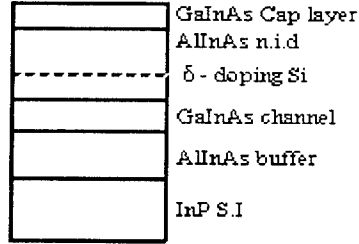


Fig. 1-b

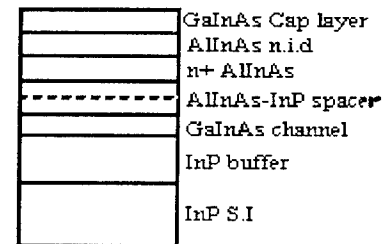


Fig. 1-c

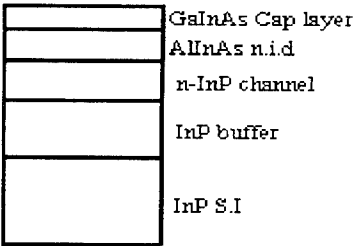


Fig. 1-d

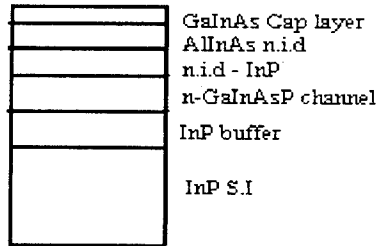


Fig. 1-e

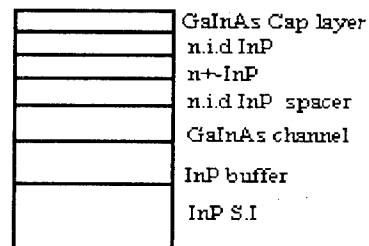


Fig. 1-f

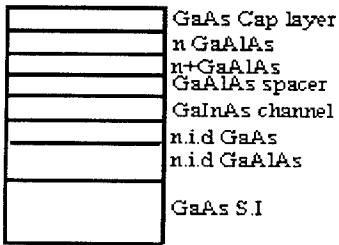


Fig. 1-g

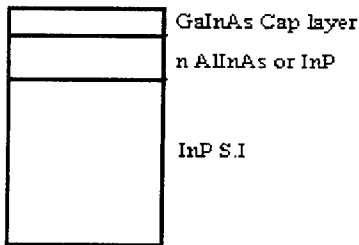


Fig. 1-h

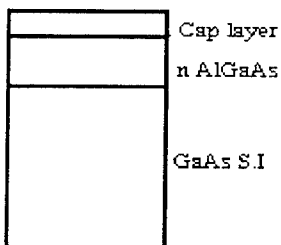


Fig. 1-i

Figure 1. Cross section of the measured structures.

3) Results

The current noise spectrum S_i can be expressed as a function of the channel noise S_{ich} and of the contact noise S_{icont} according to the relation :

$$S_i = (R_{ch}/R_t)^4 S_{ich} + (R_{cont}/R_t)^4 S_{icont} \quad (2)$$

S_{ich} can be expressed as a function of an effective density of traps N_t ($\text{cm}^{-2}\text{eV}^{-1}$) :

$$S_{ich} = qkT(Z/L^3)\mu_n^2 V^2 (N_t/f) \quad (3)$$

where Z and L are the channel width and length, μ_n the mobility, V the voltage across the structure, and f the frequency. Equation (2) can be rewritten as :

$$N_t^* = S_i(R_t/R_{ch})^4 f / [qkT(Z/L^3)\mu_n^2 V^2] \quad (4)$$

$$= N_t + (K/L) S_{gcont}$$

where S_{gcont} is the noise spectrum of the contact conductance, and K a constant if the channel length is the sole variable. N_t^* is a noise index which includes all the contributions to the LFN of the structure. For large L , the measured noise index N_t^* (including the contribution of the channel and the contacts), coincides with N_t which is the noise index of the sole channel. Results of L.F.N measurements on the gate free TLM structures are summarized in figure 2, where the plots of N_t^* versus the channel length L are reported. For L greater than $80\mu\text{m}$, the contribution of the contacts is negligible and $N_t^* = N_t$.

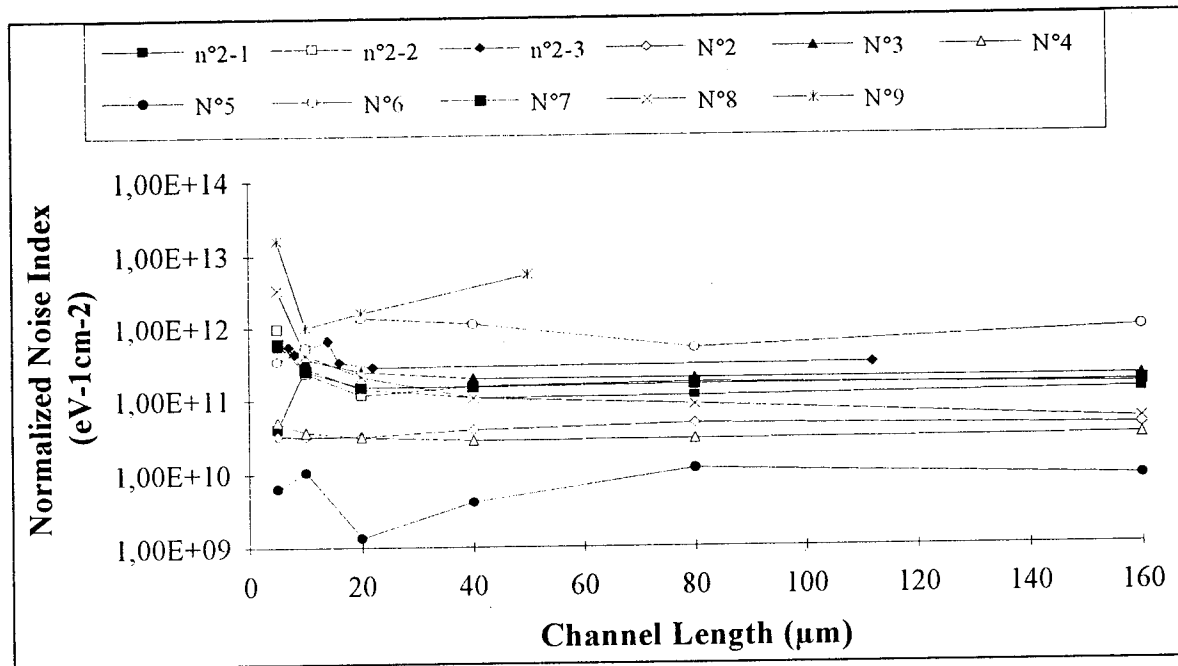


Figure 2 : Noise Index N_t^* of the structures versus the channel length

The values of N_t of the different structures are summarized in the table 1.

Structure n°	1	2	3	4	5	6	7	8	9
Type	MODFET AlInAs /GaInAs	MODFET AlInAs /GaInAs 53% In InP spacer and buffer	HFET AlInAs /InP 53% In	HFET AlInAs/ InGaAsP InP spacer and buffer	MODFET InP /GaInAs 53% In	MODFET GaAlAs /GaAs 20% In	AlInAs doped resistor 52% In	InP doped resistor	GaAlAs doped resistor 30% In
N_t ($\text{cm}^{-2}\text{eV}^{-1}$)	$1-2 \times 10^{11}$	4×10^{10}	2×10^{11}	3×10^{10}	9×10^9	1×10^{12}	1.6×10^{11}	6×10^{10}	5.5×10^{12}

Table 1 : Normalized Noise Index N_t of the structures

These values are the average values measured on the structures with the greatest channel lengths in the TLM configuration.

1) Layers containing Al : Measurements were performed on plain AlInAs resistors, HFET structures with AlInAs layers, and MODFET structures with AlInAs spacer and buffer layers. For all the samples, we obtain a noise index N_t of 1 to $2 \times 10^{11} \text{cm}^{-2}\text{eV}^{-1}$. The strain of the channel has no effect on N_t : Table 2 summarizes the values of N_t of several MODFET structures with different In content. Also is reported, for comparison, the noise index of the structure with δ -doping mode of the barrier. The channel of this structure is lattice matched to InP.

Structure n°	2-1	2-2	2-3
Type	MODFET AlInAs /GaInAs 53% In	MODFET AlInAs /GaInAs 75% In	MODFET AlInAs /GaInAs 53% In δ -doping
N_t ($\text{cm}^{-2}\text{eV}^{-1}$)	1.3×10^{11}	1.5×10^{11}	3×10^{11}

Table 2 : Normalized Noise Index of AlInAs/GaInAs MODFET structures.

Structures 2-1 and 2-2 correspond to fig.1-a, and to structure n°1 in Table 1. Note that there is a

slight increase of the N_t value of the structure with the δ -doping mode of the barrier layer (structure 2-3), compared to structures 2-1 and 2-2, with an uniformly doped barrier. This increase in $1/f$ noise has been observed in δ -doped GaAs-GaAlAs structures.

2) Layers containing InP : The structure n°2 of Table 1 (fig.1-c), which is identical to the structure n°1 (fig.1-a), but with InP spacer and buffer layers, exhibits a significantly weaker value of N_t . If all the AlInAs layers are replaced by InP layers, the value of N_t is divided by more than twenty (structure n°5, Fig.1-f, as compared to structure n°1). From these measurements, it is clear that the influence of the AlInAs spacer and buffer layers is the main contribution to L.F.N in these structures. We obtain the same result with the HFET structure (n°4, fig.1-e), where N_t is much lower than that of a conventional HFET structure (n°3, fig.1-d). The N_t value of a simple plain InP resistor (n°8, fig.1-h), compared to a plain AlInAs resistor (n°7, fig.1-h), confirms that the presence of AlInAs layers increases the noise index of the structures.

3) Layers containing GaAlAs : GaAlAs based structures are known to exhibit important L.F.N. We have performed measurements on two types of structures : a MODFET GaAlAs/GaInAs/GaAs structure (n°6, fig. 1-g) and a plain GaAlAs resistor (n°9, fig. 1-i).

The Al concentration of the GaAlAs layers is 20% in the case of the MODFET structure, and 30% in the case of the resistor structure. The noise index of the two structures are much larger than those of AlInAs and/or InP containing structures. Moreover, the L.F.N spectra of the GaAlAs resistor exhibits generation-recombination features, according to [2]. These features are attributed to the presence of DX centers. For an Al concentration of 20% (structure n°6, fig1-g), the DX center level does not lie within the energy gap, thus no G.R feature is observable in the noise spectra [2]. The values of N_t lie within the range $1-3 \times 10^{11} \text{ cm}^{-2} \text{ eV}^{-1}$ for all the AlInAs based structures ; GaAlAs structures give significantly larger N_t , whereas InP based structures give smaller values of N_t .

4) Conclusion

The main results of this study can be summarized as follows :

- (i) The values of the measured Noise Index N_t span over a wide range : from 10^{10} to a few $10^{12} \text{ cm}^{-2} \text{ eV}^{-1}$, depending on the materials constituting the structures.
- (ii) The lowest noise magnitudes are obtained for structures which are free of Al.
- (iii) In structures with Al, L.F.N sources are induced by traps distributed within Al containing barrier and buffer layers.
- (iv) The noisiest devices are those based on GaAlAs barrier and buffer layers on GaAs substrates.

5) Acknowledgements

The authors wish to thank M. Oustric and M. Gendry from Laboratoire d'Electronique-Ecole Centrale de Lyon, for providing AlInAs based structures, and M. De Murcia, from Centre d'Electronique de Montpellier, for providing the GaAlAs resistor structure.

6) References

- [1] R. Plana, L. Escotte, O. Llopis, H. Amine, T. Parra, M. Gayral and G. Graffeuil, IEEE Trans. Electron Devices, Vol. 40, n°5, May 1993, 852-855.
- [2] F. Pascal, M. De Murcia, G. Lecoy, L. K. J. Vandamme, Solid State Elect. Vol.37, n°8, 1994, 1503-1508.
- [3] G. Ing Ng, D. Pavlidis, M. Tutt, R. M. Weiss and P. Marsh, IEEE Trans. Electron Devices, Vol. 39, n°3, March.1992, 523-532.
- [4] P. Rojo-Romeo, P. Viktorovitch, J. L. Leclercq, X. Letartre, J. Tardy, M. Oustric and M. Gendry, Proceedings of the Sixth Int. Conf. on InP and Rel. Mat. Santa Barbara, Cal. USA, March 27-31, 1994, 423-426.
- [5] P. Viktorovitch, P. Rojo-Romeo, J. L. Leclercq, X. Letartre, J. Tardy, M. Oustric and M. Gendry, submitted to IEEE Trans. on Electron Devices.

Frequency analysis of the kink effect in AlInAs/GaInAs HEMT's

B.-U. H. Klepser, W. Patrick

Laboratory for Electromagnetic Fields and Microwave Electronics, Swiss Federal Institute of Technology Zürich,
Gloriastr. 35, CH-8092 Zürich, Switzerland, Tel. +41-1-632 66 72, Fax. +41-1-632 11 98

A frequency analysis of the transconduction and output conduction of 0.25 μm InP based HEMTs was carried out using S-parameter measurements down to 1 kHz. The advantage of this method is that very low frequency and hf performance is determined using a single measurement sequence. It has been shown that the kink effect in the output characteristics consists of two ranges of a reduced and an increased drain current. Additionally it was found, that while $g_{d,hf}$ increases for more positive gate voltages, $g_{d,dc}$ usually decreases. It is also been shown, that the dc measured transconductance $g_{m,dc}$ is lower than $g_{m,hf}$. This difference is increased for high drain voltages. The frequency analysis shows, that $g_{m,dc}$ is generally decreases at higher drain voltages. Finally, it has been shown that the dispersion output conduction can be up to the GHz range for high drain source voltages.

Introduction

Typical dc output characteristics of InP HEMT's with submicron gate lengths show a kink at voltages around $V_{ds} = 1\text{V}$. These anomalous characteristics have been widely studied and several theories of its physical origin have been presented, for example from trapping effects in the AlInAs buffer layer [1], [2] or impact ionization in the GaInAs channel [3]. Due to their physical origin these effect are influenced by the material design, growth or HEMT processing. At high frequencies this effect can be neglected.

A dispersion is obtained not only in the output conductance but also in the transconductance. Comparing the transconduction g_m derived from dc and hf measurements shows that the dc measured $g_{m,dc}$ is usually smaller than $g_{m,hf}$ [4], [5]. Therefore the dispersion of the transconduction as a function of gate and drain source voltage was investigated.

Although the dispersion of g_d and g_m is primarily at low frequencies, it is one of the major problems when determining a large signal model for the design of high frequency non-linear integrated circuits [6]. Then the output conductance and transconduction are defined as the differentials of the drain current to the drain and gate source voltage respectively. Inserting the dc current into the model only enables the determination of the bias points in a circuit, while the calculation of the hf performance is based on dc g_d and g_m . Calculating a current that fits the high frequency performance, leads to a model that cannot be used to determine dc bias points.

Since the determination of dc and hf characteristics use different measurement techniques (I-V and s-parameter measurements respectively), device characteristics in the frequency range dc up to several MHz have not been widely studied. Pulsed I-V measurements can be

used from dc to several kHz, while s-parameter measurements are used above 100 kHz. Since the dispersion of the output characteristic is primarily in the range of 1 kHz to MHz, a determination based on two different measurement techniques is rather problematic, as device temperature or current drifts could influence the results. Therefore, we have developed a technique to measure the dispersion of the dc characteristics in a single measurement, using s-parameter measurements from 500 Hz to 500 MHz

Experiments

HEMT devices with 0.25 μm long T-gates were fabricated on lattice matched AlInAs/GaInAs HEMT structures. Ohmic contacts were formed using NiGeAu annealed at 340°C [7]. The mesa and gate recesses were wet etched using a mixture of $\text{H}_3\text{PO}_4:\text{H}_2\text{O}_2:\text{H}_2\text{O}$ 1:1:100 and 1:1:150 respectively. Since this wet etch for the gate recess is non-selective, the threshold voltage of the HEMT devices can be varied using different etch times. We found a correlation between gate reces etch depth and kink effect. For shorter etch times, resulting in more negative threshold voltages, the kink in the output characteristics is increased. Finally a Ti-Au metalisation layer was evaporated.

To determine a frequency analysis of the output characteristics, s-parameter measurements were carried out from 500 Hz to 500 MHz using a HP 8751A network analyzer. The dc analysis was carried out by measuring the current voltage characteristics. Additionally, scattering and noise parameters were measured up to 26 GHz. To determine the transconductance g_m and output conductance g_d from s-parameter measurements a very basic transistor model

was used (Fig. 1). The output conductance g_d can be calculated from the measured output reflection S22 towards the load $Z_0 = 50 \Omega$ of the network analyser as follows:

$$g_d = \text{Re} \left\{ \frac{(1 - S_{22})}{(1 + S_{22}) \cdot Z_0} \right\}$$

Then the transconductance g_m can be calculated from the measured S21 and S22 as follows:

$$g_m = \frac{1}{2} \cdot S_{21} \cdot \left(\frac{1}{Z_0} + g_d \right)$$

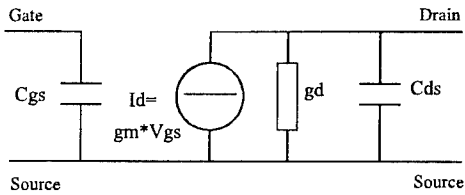


Fig. 1: basic equivalent circuit for the calculation of g_m and g_d from s -parameters

Results and discussion

Fig. 2 shows the output characteristic for a HEMT with a strong kink at $V_{ds} = 0.8 \text{ V}$. The high frequency output characteristics was calculated by integrating the output impedance measured at 4 GHz over the drain voltage U_{ds} : $I_{d,hf} = \int g_{d,hf} dU_{ds}$. To describe the anomaly in the output characteristics, the drain voltage must be divided into two ranges: In range I, the drain voltage is low and the dc measured output conductance $g_{d,dc}$ is lower than $g_{d,hf}$. This leads to a lack of carriers

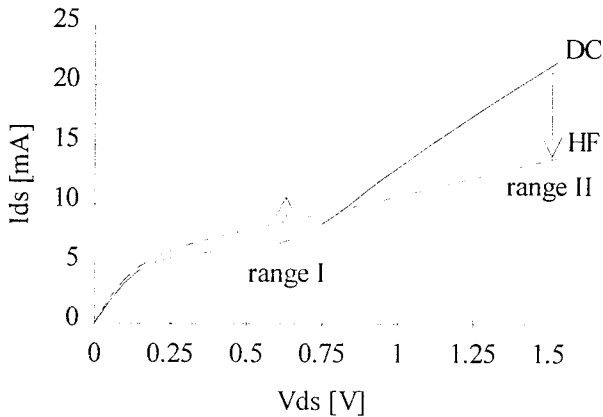


Figure 2: dc measured and hf integrated output characteristics for $V_{gs} = -0.4 \text{ V}$.

and a lower dc current. It is presumed, that carriers are trapped in the AlInAs buffer layer [1], [2]. In range II for high drain voltages, the measured dc output conductance $g_{d,dc}$ is higher than $g_{d,hf}$ due to impact ionization [3]. This results in a higher dc current and a

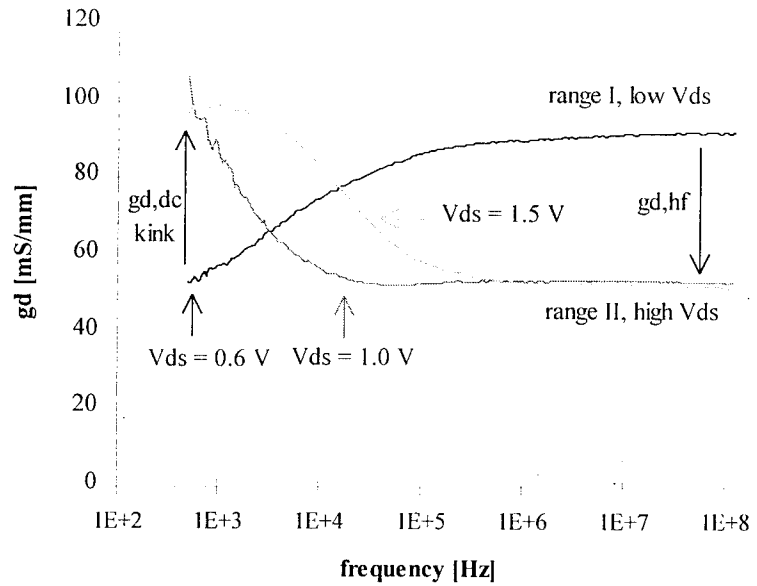


Figure 3: output conductance as a function of frequency. The arrows indicate the change of g_d with the drain voltage V_{ds} at dc and hf.

kink in the output characteristics.

Fig. 3 shows a frequency analysis of g_d , showing a significant dispersion at frequencies below 100 kHz. For low drain voltages, g_d increases with frequency, while for high drain voltages, g_d decreases. The frequency limit is at about 10 kHz. However, it was also found that the frequency limit increases for higher drain source voltages. Further high frequency s -parameter measurements showed, that g_d increases up to 2 GHz for $V_{ds} = 1.5 \text{ V}$. In addition to the increase of $g_{d,dc}$ with higher drain voltages (kink effect), Fig. 3 also shows that $g_{d,hf}$ decreases for higher drain source voltages. This behavior can be described with the two region model for the channel. A larger drain voltage leads to a larger saturation region which is responsible for a lower output conduction.

The measured output conductance for low drain voltages changes significantly when the device is under illumination. This confirms that for low drain voltages the dispersion is due to trapping effects.

Fig. 4 shows the output conductance as a function of

the gate voltage for $V_d = 1V$. It can be seen that $g_{d,hf}$ increases for more positive gate voltages. Similar to the decrease of g_d with higher drain voltages, this can be explained with the two region model. A more positive gate source voltages reduces the gate drain potential and therefore reduces the saturation region under the gate. Therefore g_d increases for more positive gate source voltages.

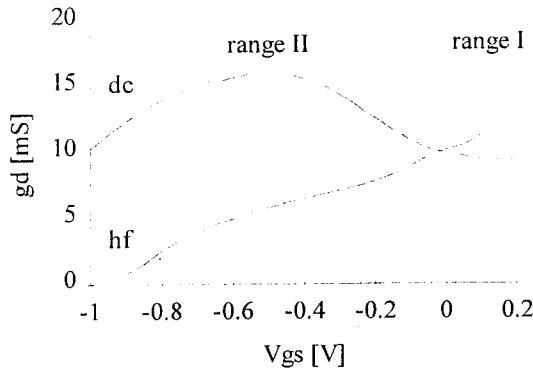


Fig. 4: output conductance as a function of gate voltage at $V_{ds} = 0V$.

Contrary to $g_{d,hf}$, the dc output conductance $g_{d,dc}$ does not increase monotonically with V_{gs} . The reason is, that by increasing V_{gs} , the drain voltage where the kink occurs V_{kink} increases. For a gate source voltage of $V_{gs} = -0.4V$ the kink occurs at $V_{ds} = 0.8V$, as shown in figure 2, while the kink occurs at $V_{ds} = 1V$ for a gate source voltage of $V_{gs} = 0V$. Therefore, range II with $V_d > V_{kink}$ is at negative gate voltages (showing $g_{d,dc} > g_{d,hf}$) and range I with $V_d < V_{kink}$ is at positive

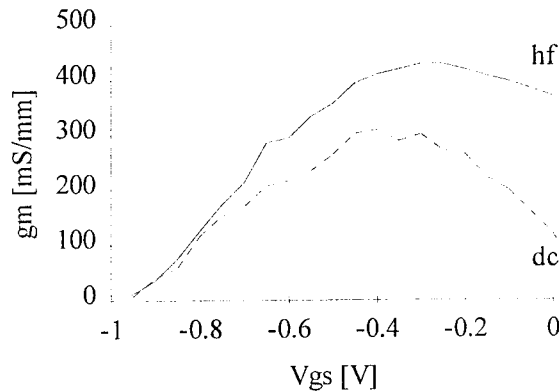


Figure 5: dc and hf measured transconductance for $V_{ds} = 1V$.

gate voltages (showing $g_{d,dc} < g_{d,hf}$). This means, that for more positive gate voltages the bias conditions are shifted from the high field range II towards the low field range I, and therefore the dc output conductance $g_{d,dc}$ decreases therefore for most of the used bias points, (contrary to $g_{d,hf}$).

A dispersion was obtained not only for the output conduction but also for the transconductance. Figure 5 shows the transconductance determined with dc and hf measurements for $V_d = 1V$. It can be seen that $g_{m,dc}$ is lower than $g_{m,hf}$. This behavior is typical for InP HEMT's and it is one of the problems when determining a large signal model. The transconductance $g_{m,dc}$ measured at dc usually decreases with increasing V_d [4], [5]. Therefore dc measurements are mostly carried out at low drain source voltages. However, when determining the transconductance from s-parameter measurements, saturation of $g_{m,hf}$ at about $V_d = 1V$ is obtained [6]. Additionally, figure 5 shows that the difference between $g_{m,dc}$ and $g_{m,hf}$ increases for more positive gate source voltages. Therefore the bias for maximum gain is more positive at high frequencies.

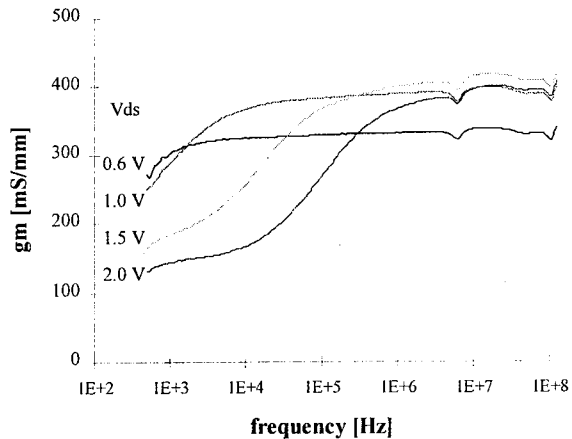


Figure 6: transconductance as a function of frequency

Fig. 6 shows a frequency analysis of the transconductance g_m . It is obtained that g_m increase in general with the frequency. Furthermore, it is shown that $g_{m,dc}$ decreases with higher drain voltages, while $g_{m,hf}$ increases the transconductance $g_{m,hf}$ increases for higher gate drain voltages. The decrease of the transconductance at low frequencies is therefore verified with a single measurement. Again the frequency limit at about 10 kHz. For higher drain voltages, the frequency limit of the transduction increases. Similar to the output conduction, a low

frequency decrease of $g_{m,hf}$ can be obtained up to 2 GHz.

High frequency s and noise parameter measurements on HEMTs have shown no clear correlation between the occurrence of the kink effect and high frequency performance.

Summary

The occurrence of a dispersion of output conductance and transconductance is one of the major problems when determining a large signal model for InP based HEMTs. Therefore we have developed a technique to carry out a frequency analysis of g_m and g_d using a single s -parameter measurement from 500 Hz to 500 MHz. It has been shown, that the kink effect in the output characteristics consists of two ranges of a reduced and an increased drain current. Additionally it was found, that while $g_{d,hf}$ increases for more positive gate voltages, $g_{d,dc}$ usually decreases for higher V_{gs} . Furthermore it was found with a single measurement, that the dc measured transconductance $g_{m,dc}$ is lower than $g_{m,hf}$. This difference is increased for high drain voltages. The measurements show, that the reason is a decrease in $g_{m,dc}$ at higher drain voltages. Furthermore it was found that the frequency limit for the dispersion of both g_m and g_d is 100 kHz for low drain voltages. However, the frequency limit is increased for high drain voltages and a dispersion can be obtained up to 2 GHz.

Acknowledgements

The authors would like to thank Hp. Meier and H. Benedickter for their technical support during the course of this work. The project was supported by the Swiss priority programmes "Optique" (integrated PIN-HEMT photoreceiver), "LESIT" (microwave and gigabit electronics) and by the Swiss PTT.

References:

- [1] A. S. Brown, U. K. Mishra, C. S. Chou, C. E. Hooper, M. A. Melendes, M. Thompson, L. E. Larson, S. E. Rosenbaum, M. J. Delaney, "AlInAs-GaInAs HEMTs utilizing low-temperature AlInAs buffers grown by MBE", *IEEE Electron Device Letters*, vol. 10, pp. 565-567, 1989
- [2] L. F. Palmateer, P. J. Tasker, W. J. Schaff, L. D. Nguyen, L. F. Eastman, "dc and rf measurements of the kink effect in 0.2 μ m gate length AlInAs/GaInAs/InP modulation-doped field-effect transistors", *Appl. Phys. Lett.* 54, pp.2139-2140, 1989.
- [3] G.-G. Zhou, A. Fischer-Colbrie, J. Harris, "I-V kink in InAlAs/InGaAs MODFETs due to weak impact ionisation process in the InGaAs channel", *Proc. InP and rel. mat.*, pp. 435-437, 1994.
- [4] W. Kruppa, J. B. Boos, "Sinusoidal and transient response of traps in double-recessed InAlAs/GaInAs/InP HEMTs", *Proc. of the fifth International Conference on InP and Related Materials*, pp. 251-254, 1993
- [5] Y.-C. Pao, C. K. Nishimoto, R. Majidi-Ahy, J. Archer, N. G. Bechtel, J. Harris, "Characterisation of surface-undoped InAlAs/InGaAs/InP high electron mobility transistors", *IEEE Trans. on Electr. Dev.*, pp.2165-2170, 1990.
- [6] C. G. Diskus, C. Bergamaschi, M. Schefer, W. Patrick, B.-U. H. Klepser, W. Bächtold, "Small and large signal model of a 150 GHz InAlAs/InGaAs HEMT", *ESSDERC 1994*
- [7] B.-U. Klepser, C. Bergamaschi, W. Patrick, M. Beck, "Comparison and optimisation of different ohmic contact metallisations for InP-HEMT structures with doped and undoped cap layers", *Proc. of the Sixth International Conference on InP and Related Materials*, pp. 174-177, 1994

Microwave Performance of InP-based HEMTs for Low Voltage Application fabricated by Optical Lithography

S. Strähle°, B. Henle°, L. Lee° H. Künzel*, E. Kohn°

° Dept. of Electron Devices and Circuits
University of Ulm, Albert-Einstein-Allee 45
D-89069 Ulm, Germany

* Heinrich-Hertz-Institut Berlin GmbH
Einsteinufer 37
D-10587 Berlin, Germany

Introduction

InP-based HEMT structures have demonstrated high $f_t \cdot L_g$ -products, indicative of high overshoot velocities even for moderate gate lengths of $1\mu\text{m}$ [1]. Furthermore, it is possible to tailor the performance of standard HEMT structures on InP for microwave applications at low drain bias. This has been attempted mainly by the use of In-rich strained GaInAs channels of high mobility and overshoot velocity. An $f_t \cdot L_g$ product of $57\text{GHz}\mu\text{m}$ and an f_{max}/f_t -ratio of about 2 have been obtained [2], but the bias condition was not reported. Another approach is a GaInAs/InP composite channel device resulting in a $f_t \cdot L_g$ product of $44\text{GHz}\mu\text{m}$ at 1.5V drain bias [3]. No data on the maximum power gain has been mentioned. In this study, the low voltage high frequency performance of InP-based HEMTs is examined. The device structures used for this study are similar to those mentioned in [2,3]. All the devices are fabricated by simple optical lithography resulting in gate length $\geq 0.5\mu\text{m}$. Although the gate lengths of the devices are greater than half a micron they show remarkable RF properties at low drain bias. Differences are found between the distinctly designed samples concerning their RF properties.

Layer Structures

In this study three different layer structures have been investigated: (A) a standard top-side doped structure, (B) a double-side doped structure and (C) a composite channel structure. The first two samples are grown by Solid-Source-MBE. The third sample contains InP as a sub-channel and is therefore grown by MOCVD*.

Structure (A) is a standard bulk doped AlInAs/GaInAs-HEMT lattice matched to the InP-substrate used as a reference (Fig.1a).

The second device structure (B) is designed for high current, high frequency applications (Fig.1b). It consists of a strained $\text{Ga}_{0.32}\text{In}_{0.68}\text{As}$ channel layer to enlarge the conduction band discontinuity and the electron mobility. The planar doping-spikes are placed in the AlInAs supply and buffer layer above and below the GaInAs-channel respectively. This configuration leads to a high carrier-density in the GaInAs-channel. The transconduction and the modulation efficiency is also improved as it is possible to place the gate very close to the channel. The growth temperature for the buffer was reduced to 300°C which prevents Si movement from the back-side planar doping towards the channel and therefore leads to high electron mobilities in the channel [4].

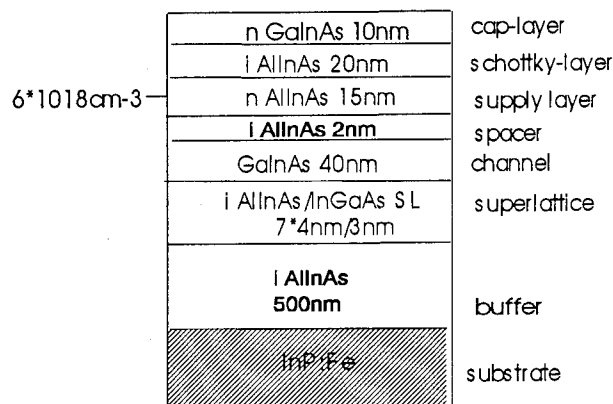


Fig.1a: Structure A is a standard HEMT-Structure used as a reference

Structure (C) consists of a composite QW-channel of GaInAs/InP sandwiched between AlInAs barriers. The GaInAs part of the channel is sub-divided into a strained and a lattice-matched part to increase the electron mobility. The GaInAs-part of the channel will host the entire 2DEG-density at low fields, resulting in a high mobility, a small series resistance and a small intrinsic voltage drop. At higher fields the hot electrons will experience the broad velocity field distribution in the InP sub-channel, which should lead to a high overshoot velocity characteristic. Therefore, a high f_{max} and f_t cut-

off frequency is expected at the same bias point, resulting in a high f_{\max}/f_t ratio.

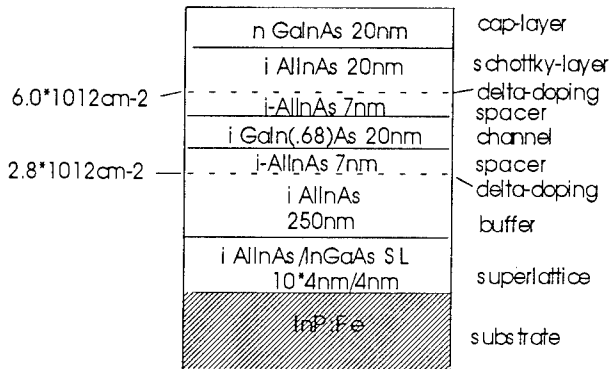


Fig.1b: Structure B designed for high current and high frequency operation. The In-content in the GaInAs channel is 68%.

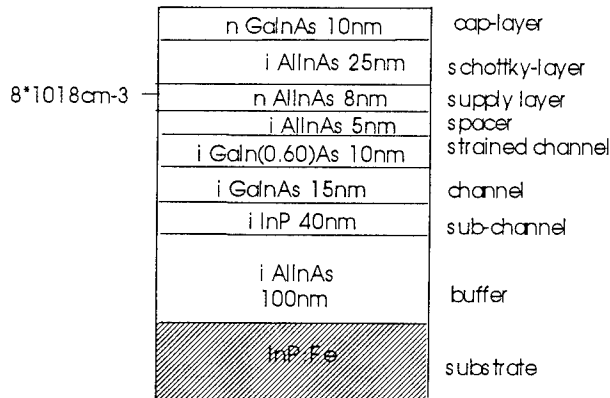


Fig.1c: Structure C with a composite channel of GaInAs/InP designed for high f_r , f_{\max} and f_{\max}/f_t -ratio

Device fabrication

All the devices were mesa isolated by wet chemical etching. In the case of structure (A) and (B) a $H_2SO_4:H_2O_2:H_2O$ etch was used. For structure (C) a $HCL:CH_3COOH:H_2O_2$ -etch has been chosen as InP is not etched by the standard $H_2SO_4:H_2O_2:H_2O$ etch.

For the ohmic contact formation a special two layer resist stack is used to achieve a well defined undercut profile for lift-off. For all the devices e-beam evaporated GeNiAu-contacts are used. The contacts are annealed in a RTA at 360°C for 40s.

The gates are defined by optical contact lithography ($\lambda = 405nm$) using the same two layer resist system as for the ohmic contacts. This process is very reproducible down to a gate length of 0.5 μm . The gate recess is etched selectively. In a first step the GaInAs cap layer is removed

and the width of the recess is defined. In a second step the AlInAs is etched to its final depth. For the selective etch succinid acid (SA) with NH_3 and H_2O_2 is used. The isotropic etch is $H_2SO_4:H_2O_2:H_2O$. The gate metallization is e-beam evaporated and consists of TiPtAu with the following thicknesses 50nm/50nm/300nm.

DC and RF Device performance

With the standard HEMT structure (A) a current density of 460 mA/mm is achieved. The composite channel HEMT (C) having a bulk doped supply layer has current densities of 780mA/mm. The highest current densities of 1000mA/mm are realized with the double-side delta-doped HEMTs structure (B).

	Structure A	Structure B	Structure C
L_g (μm)	0.6	0.6	0.65
V_d (V)	2.0	1.6	1.6
$I_{d,max}$ (mA/mm)	460	1000	780
g_m (mS/mm)	350	680	550
f_t (GHz)@ V_g, V_d	35 -0.1, 2.0	53 -0.4, 1.6	60 -1.3, 1.6
f_{\max} (GHz)@ V_g, V_d	80 -0.1, 2.0	135 -0.4, 1.6	160 -1.3, 1.6
$f_t * L_g$ -product (GHz μm)	21	31.8	39
f_{\max}/f_t	2.3	2.5	2.6

Table 1: DC and RF results obtained for the Devices A, B and C

To reflect a condition representative for high gain and medium power performance, the small signal analysis was performed at the gate bias condition for peak f_t . This condition is depicted for a device of structure (B) in Fig.2. The extrapolation of f_t and f_{\max} is described in [5].

The development of f_{\max} and f_t versus drain bias is shown in Fig.3. All device structures attain their maximum f_t already below $V_d=1.2V$. The lowest bias is needed for structure (B), which also shows the highest open-channel current and thus the lowest series resistances. For sample (A) only a moderate $f_t * L_g$ -product is obtained (see Table1) in combination with a relatively high f_{\max}/f_t -ratio, which is the usual case. Two effects contribute to the limited $f_t * L_g$ -product: (1) the influence of the dynamic series resistances due to the low channel current density, and (2) a hot electron movement with a high field saturation velocity in the collision dominated regime.

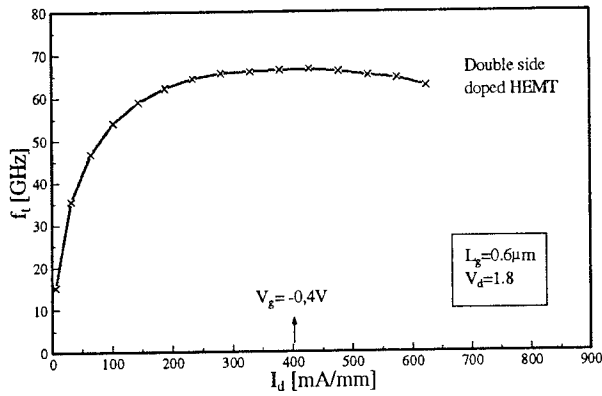


Fig.2 f_t versus I_d . The gate bias for the drain bias scan is $V_g = -0.4V$

For all the devices the f_{\max} profiles develop after the drift-region is established. By extrapolation it can be seen, that this appears at a drain bias of 0.4 to 0.5V (Fig.3).

In the case of the devices (A) and (B) the f_{\max} cut-off frequency curves reach their maximum between $V_d = 1.2V$ and $1.8V$, respectively. In structure (C) f_{\max} is still increasing to beyond 160GHz and only a slight saturation occurs up to this measured drain bias ($V_d = 1.6V$).

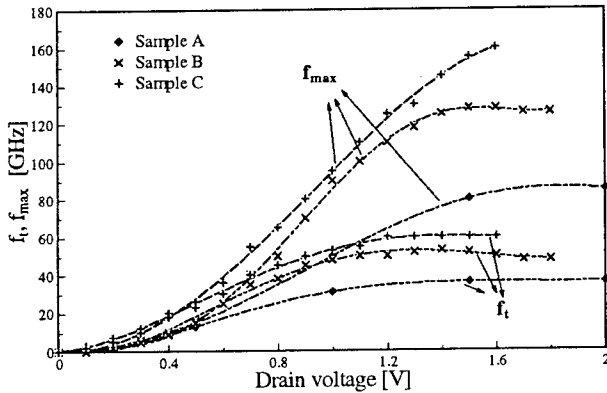


Fig.3: f_{\max} and f_t -curve in dependence of the drain voltage for the three different samples

Discussion

The extrinsic data show that high f_{\max}/f_t -ratios can be obtained at high $f_t \cdot L_g$ products, indicating that the devices operate in the velocity overshoot regime as it is the case for structure (B) and (C).

The highest f_{\max}/f_t -ratio of 2.6 is obtained in the case of the composite channel structure in conjunction with the highest $f_t \cdot L_g$ product of 39GHz μm . This may indeed be attributed to the InP sub-channel, where the electron

dynamics seem to be improved at high fields [5]. The double-side doped device (B) shows optimum performance already in the range of $V_d \approx 1.4V$. At higher bias both f_t and f_{\max} seem to decrease slightly while the f_{\max}/f_t -ratios stay constant. This may indicate that the intrinsic average saturated velocity starts to decrease with further extending the drift-region.

Both cut-off frequencies are influenced by parasitic effects and an attempt needs to be made to reduce the performance of the three structures to the intrinsic device parameters to make them better comparable. The parameter considered here is an effective drift-region length, which is extracted on the basis of an approximate lumped element equivalent-circuit. This has been proved helpful in describing the drift-region characteristics of GaAs- as well as InP-based HFET-devices operating in the saturated velocity regime [6,7]. Here the drift-region is represented by a lateral parallel plate capacitor, which is considered in series with the gate-channel capacitance. The distance of the plates is determined from the intrinsic feed-back capacitance C_{gd} from the standard equivalent-circuit model. The details are described in [6]. This effective length is calculated from eq.1.

$$L_{\text{drift}} = L_g \left(\frac{\epsilon W}{C_{gs,i}} \right)^2 \left(\frac{C_{gs,i}}{C_{gd,i}} - 1 \right) \quad \text{eq.1}$$

The intrinsic capacitances are estimated by subtracting the parasitic capacitances from the extrinsic capacitances. This parasitic capacitances are extracted from s-parameter measurements made on a special designed layout.

In Fig.4 the development of the lateral drift-region represented by the model parameter L_{drift} (eq.1) is plotted in dependence of the intrinsic drain bias (eq. 2). The series resistances (R_s and R_d) are estimated from the DC output characteristic.

$$V_{\text{intr}} = V_D - (R_s + R_D)I_D \quad \text{eq.2}$$

For an intrinsic voltage of about 0.25V the velocity saturation is obtained indicated by the offset. Only for higher intrinsic voltages, where the saturation is still obtained the lateral drift-region starts to develop. For all the three devices a linear relationship is found for the extension of the drift-region. This is in contrast to GaAs-based HEMTs, where a square law relationship is found [7]. This relationship could be explained describing the drift-region as a laterally extended schottky barrier depletion region [8]. The reasons for the faster extension of the drift-region for InP-based devices is not well understood. As a consequence high f_{\max} cut-off frequencies and high f_{\max}/f_t -ratios can be observed at lower drain bias compared to GaAs devices. Good RF

performances for the devices are obtained with an intrinsic voltage of about 0.75V. Reducing the parasitic series resistances further, uncompromised RF performance can be expected for a drain bias of about 1V for 0.5 μ m gate length devices.

The largest lateral extension of the drift-region is found with the composite GaInAs/InP-channel compared at the same intrinsic voltage. The following effects may contribute to the differences in the extension of the drift-region. First, there are differences in the hot electron dynamics due to the different QW-channel configurations especially in the case of the InP sub-channel. Second, different aspect ratios, dependent on the recess configuration, change the effective carrier confinement and the vertical compensation of channel charge due to surface layer states. Third, it has been shown [7] that the buffer layer has also an important influence on the extension of the drift-region.

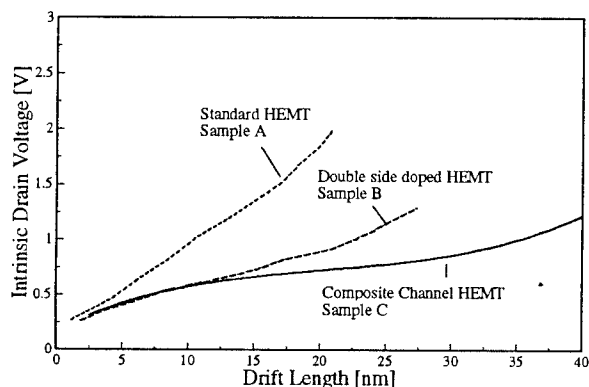


Fig.4 Extension of the drift-region with the intrinsic drain voltage

Conclusion

The RF results of the structures discussed show that uncompromised small RF performance of InP based FETs can be obtained in the low drain bias range below 2V. Even for moderate gate lengths of 0.5 μ m, operation down to $V_d=1$ V seems feasible. The highest cut-off frequencies extrapolated are $f_t=60$ GHz and $f_{max}=160$ GHz at $V_d=1.6$ V. This represents an $f_t L_g$ -product of 39GHz μ m and a f_{max}/f_t of 2.6 at the identical gate and drain bias point. This indicates that high power gain is possible at high overshoot velocity. Three different material structures have been analysed. The drift-region analysis indicate that an optimum design is a structure with high open channel current density realised with high carrier concentration as is the case for sample (B) and (C). The aspect ratio should be high. This has been realized with the double-side planar doped structure, where a deep recess is possible like in structure (B). For improved hot electron dynamics

an InP sub-channel is proposed like in sample (C). A combination of these two structures seems to be the optimum. It is expected that with optimised structures, devices with RF performance up to the millimetre-wave frequency range can be fabricated only by low cost optical lithography.

*The wafers are fabricated by Epitaxial Products, Cardiff (UK);

Acknowledgement

The financial support by the German Research Council DFG is gratefully acknowledged.

References

- [1] E.Kohn; "A Semi-Empirical Comparison of Key Dynamic Properties of GaAs and InP based HFET Structures"
- [2] K.B. Chough, T.Y. Chang, M.D. Feuer, N.J. Sauer, B. Lalevic; "High-Performance Highly Strained Ga_{0.23}In_{0.77}As-/Al_{0.48}In_{0.52}As MODFET's obtained by selective and shallow Etch Gate Recess Techniques"; IEEE Electron Device Letters, Vol. 13, No. 9, 92;
- [3] T. Enoki, K. Arai, A. Kohzen, Y. Ishii; "InGaAs/InP double channel HEMT on InP"; Indium Phosphide and Related Materials, Newport April 21-24 1992, Proceedings pp 14-17
- [4] H.Künzel, H.-G.Bach, J.Böttcher, C.Heedt; "Improved inverted AlInAs/GaInAs two-dimensional electron gas structures for high quality pseudomorphic double heterojunction AlInAs/GaInAs high electron mobility transistor devices" J. Vac. Sci. and Technol. B 12(5), S.2910,1994;
- [5] S.Strähle, B.Henle, E.Kohn; "Low voltage characteristics of InGaAs/InP composite channel HEMT structure fabricated by optical lithography"; Electronics Letters, 1994, Vol.30 No.23;
- [6] S.Strähle, D.Geiger, B.Henle, E.Kohn; "Drift Region Characteristics of InP-based HEMT Devices Evaluated by a Simple Drift Region Model"; 6th International Conf. on Indium Phosphide and Related Materials, March 27-31 1994, Santa Barbara, CA, USA;
- [7] E.Kohn, S.Strähle, D.Geiger, U.Erben; "High Field Drift Domain in GaAs and InP based Heterostructure Field Effect Transistors"; Proc. IEEE Cornell Conference on advanced concepts in High Speed Semiconductor Devices and Circuits; Ithaca New York, Aug., 1993;
- [8] S.H.Wemple, W.C.Niehaus, H.M.Cox, J.V.Dilorenzo, W.O. Schlosser; "Control of Gate-Drain Avalanche in GaAs MESFET's"; IEEE Trans. Elect. Dev., Vol. ED-27, No.6, June 80;

Low noise optimization of InP HEMT's

B.-U. H. Klepser, C. Bergamaschi, M. Schefer, W. Patrick, W. Bächtold

Laboratory for Electromagnetic Fields and Microwave Electronics, Swiss Federal Institute of Technology Zürich,
Gloriastr. 35, CH-8092 Zürich, Switzerland, Tel. +41-1-632 66 72, Fax. +41-1-632 11 98

The influence of the noise figure on both gate and drain source voltage, threshold voltage and transistor size have been investigated for the design of low noise integrated circuits. Therefore, a device model for both high frequency small signal and noise behavior of InP-HEMTs, depending on both gate and drain voltage, has been developed. It was found, that the lowest noise is observed when the drain current for maximum gain is reduced to a third while the drain voltage is reduced to the start of the saturation region $V_{ds} = 0.6$ V. However, it was shown for the first time that the bias for lowest noise is frequency dependent. Modeling scaling effects of the noise behavior shows, that lowest noise is observed for a gate width of 1×40 μm . Multi-finger layouts are preferable for gate widths above 70 μm . Furthermore it is shown, that the optimum width of each finger decreases with the number of fingers.

Introduction

During the past several years significant improvements have been presented for the high frequency and noise performance of High Electron Mobility Transistors (HEMTs). At the present time InP based HEMTs show the highest cut-off frequencies and the lowest noise of all three terminal semiconductor devices. Therefore InP HEMTs are very attractive for integrated microwave and millimeter wave applications [1]. For the design of low noise amplifiers (LNA) or high sensitivity photoreceivers we have focused our attention on the optimization of various circuit design, technology and layout parameters to achieve low noise performance circuits:

- bias voltages for lowest noise
- influence of the gate recess depth, which can vary due to a non-selective gate recess
- scaling effects of the gate width

Usually the noise behavior of the intrinsic HEMT is described by a channel noise source I_{nd} and a correlated gate noise source I_{ng} , with the noise source parameters P , R and the correlation coefficient C , see eqn. 1. Up to now only the influence of the drain current (by variation of the gate voltage) and the transit frequency (by variation of gate width or carrier mobility) on this noise source parameters P , R and C of InP HEMT's have been studied [2], [3]. But since the gate leakage current has a strong influence on the noise figure[4], it has to be taken into account when determining the optimum gate bias for lowest noise. Furthermore, scaling effects of the noise figure are mostly due to the Johnson noise of the gate resistance. Therefore it is necessary to include additional noise sources in a bias dependent noise model, such as gate leakage shot noise, $1/f$ noise and the Johnson noise of

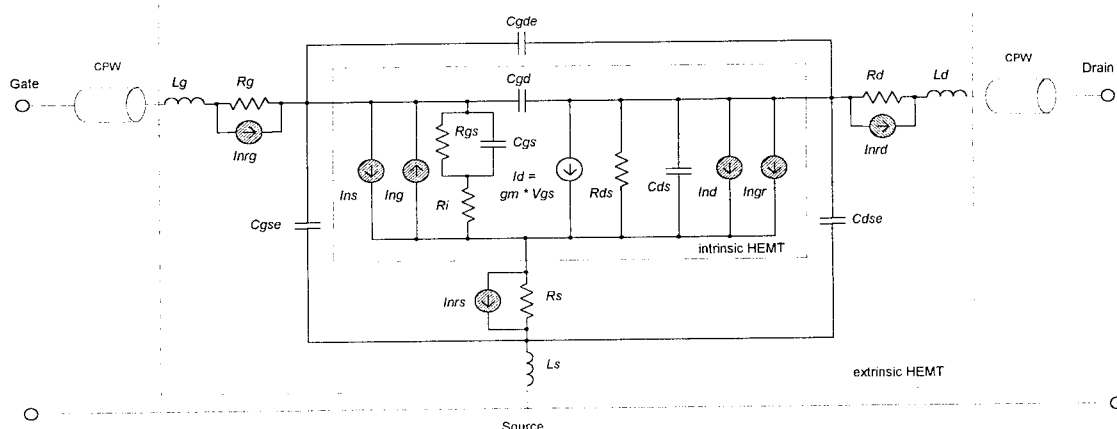


Fig. 1: Equivalent circuit for high frequency and noise behavior

the gate resistance.

Noise model for InP HEMTs

The noise behavior of HEMTs was described using the noise model shown in Fig. 1. As the noise behavior of a HEMT can be described similarly to a MESFET, the present model is based on earlier work [3].

The intrinsic HEMT can be modeled with the channel noise source I_{nd} and an induced gate noise source I_{ng} . The noise source parameters P , R , and the correlation coefficient C are defined as follows [3]:

$$\begin{aligned} |I_{nd}|^2 &= 4 \cdot k \cdot T_0 \cdot \Delta f \cdot g_m \cdot P \\ |I_{ng}|^2 &= 4 \cdot k \cdot T_0 \cdot \Delta f \cdot \frac{\omega^2 \cdot C_{gs}^2}{g_m} \cdot R \\ jC &= \frac{I_{ng}^* \cdot I_{nd}}{\sqrt{|I_{ng}|^2 \cdot |I_{nd}|^2}} \end{aligned} \quad (1)$$

In addition to these intrinsic noise sources, we introduced two more noise sources which are necessary to describe a non-ideal HEMT: gate leakage will lead to a shot noise gate source I_{ns} , and generation-recombination processes introduce a frequency dependent noise source I_{ngr} in the channel. Furthermore the extrinsic parasitic resistances R_g , R_s and R_d contribute as thermal noise sources I_{nrg} , I_{nrs} , I_{nrd} due to Johnson noise.

To improve the accuracy, the extrinsic and parasitic elements are extracted from separate measurements. The extrinsic capacitors and the CPW-parameters were determined from structures fabricated on semi-insulating substrates, the inductors with hot/cold measurements, the resistors from end resistance measurements and the gate leakage current from DC measurements.

Experiments

HEMT devices with 0.25 μm long T-gates were fabricated on lattice matched AlInAs/GaInAs HEMT structures. The gate width was varied from 50 to 150 μm . Ohmic contacts were formed using NiGeAu annealed at 340°C [5]. The mesa and the gate recess was wet etched using a mixture of $\text{H}_3\text{PO}_4:\text{H}_2\text{O}_2:\text{H}_2\text{O}$ 1:1:100 and 1:1:150 respectively. Since this wet etch for the gate recess is non-selective, the threshold voltage of the HEMT devices can be varied using different etch times. To determine the influence of the gate recess depth, the threshold voltage of the HEMT devices was varied between -1V and -0.6V. Finally a Ti-Au metalisation layer was evaporated.

Scattering and noise parameter measurements were carried out up to 50 GHz and 26 GHz respectively. A

typical transition frequency of $f_t = 100$ GHz and a minimum noise figure of 1.8 dB at 26 GHz was achieved. In order to study the bias dependence, two sweeps of the bias voltages around the optimum bias point for high frequency performance ($V_{gs} = 0.3\text{V}$, $V_{ds} = 1\text{V}$) were made. As our setup for noise measurements is only reliable for devices which have gain with respect to the 50 Ω load of the network analyzer, it is difficult to measure HEMTs with small gate widths. Therefore scaling effects and the influence of multifinger gates are determined from simulations.

Results and discussion

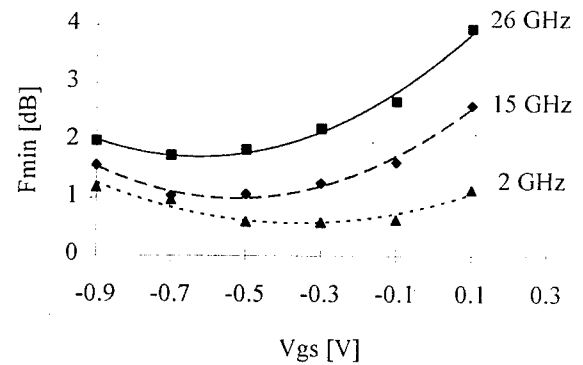


Fig. 2: Bias dependence of the minimum noise figure on the gate source voltage at $V_{ds} = 1\text{V}$.

Fig. 2 shows the minimum noise figure as a function of the gate source voltage. For the same device, the gate bias for maximum gain was determined at $V_{gs} = -0.3\text{V}$. It can be seen, that for frequencies above 10 GHz, the optimum gate voltage is obtained at $V_{gs} = -0.65\text{V}$ and $I_d = 9.0$ mA which is about one third of the drain current for maximum gain. Generally the noise figure decreases for low gate voltages (i.e. low drain currents), since the channel noise is reduced [2], [3]. However, at very low gate voltages, the decrease of the transconductance g_m leads to an increase of the noise figure.

Regarding V_{gs} , we found for the first time, that the bias for lowest noise is frequency dependent. Fig. 3 shows the optimum gate voltage as a function of the frequency. For lower frequencies, the optimum gate voltage is increased. The reason is that for lower frequencies the noise figure is heavily influenced by the gate leakage current, which is reduced for lower gate-drain voltages, i.e. more positive gate voltages. This means that the gate source voltage should be chosen closer to the bias for maximum gain when designing broadband photoreceivers while for the design of high frequency LNAs a more negative gate source voltage is preferable.

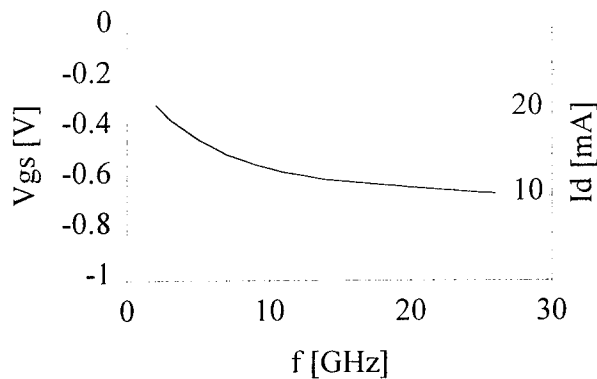


Fig. 3: Gate-voltage for lowest noise as a function of the frequency

Fig. 4 shows the minimum noise figure as a function of drain source voltage. We found, that lowest noise is observed at a fairly low value of 0.6V. Comparing with the output and transfer characteristics, this is the point where the saturation region starts and the gain reaches its maximum value. For higher drain voltages the increase of the gate source capacitance C_{gs} leads to an increase of the noise figure. Our results for the bias dependence of the minimum noise figure for AlInAs/GaInAs HEMT's lattice matched on InP are in good agreement with data obtained for pseudomorphic AlGaAs/InGaAs HEMT's on GaAs [6]. No frequency dependence of the minimum noise with respect to V_{ds} is observed since both gate leakage current (dominating at low frequencies) and channel noise P (dominating at high frequencies) are minimum for low drain voltages.

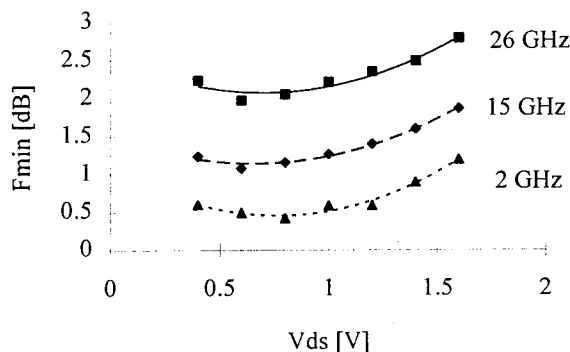


Fig. 4: Bias dependence of the minimum noise figure on the drain source voltage at $V_{gs} = -0.3V$.

When etching the gate recess using a non-selective etch process, the threshold voltage varies with the etch depths. To determine an optimum etch depth for low noise performance and to study the influence of the

variation of the threshold voltage due to process fluctuations, we have determined the minimum noise figure as a function of the threshold voltage, see fig. 5. It is shown that the noise figure decreases for more negative threshold voltages. The same behavior was obtained for the transconductance g_m . However, for threshold voltages below -0.9V, i.e. for very shallow gate recesses, the noise figure is increased. This is due to a higher gate leakage current, which may be attributed to the smaller width of the shallow gate recess (isotropic etching). Therefore an optimum threshold voltage of about -0.8V is obtained, showing both high transconductance and low gate leakage. This means that the gate recess and the correlated threshold voltage depths has only a small direct influence on the noise performance. However, since the drain current depends on the threshold voltage, this can still influence the performance of integrated circuits due to bias shifts.

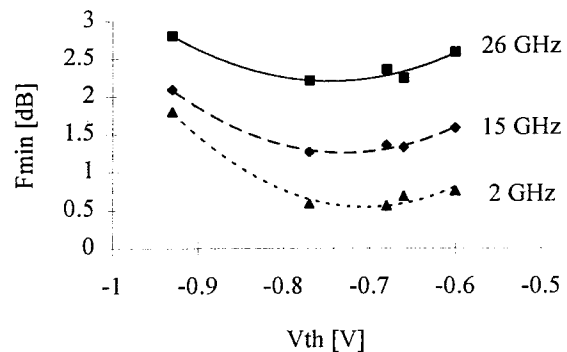


Fig. 5: Minimum noise figure as a function of threshold voltage.

The minimum noise figure for different gate widths is shown in Fig. 6. It can be seen, that the noise figure increases for wider gates. This due to the linear increase of the gate resistance with the gate width. But the simulations also showed, that the noise figure increases for gate widths below 40 μm ; this is an effect attributed to the offsets (for a gate width zero) in the extrinsic gate source and gate drain capacitors C_{gse} and C_{gde} . This offset is due to the geometrical layout of the transistor interconnections.

To reduce the gate resistance, multi-finger gates are generally used when large gate widths are desired. Fig. 7 shows the minimum noise figure as a function of the total gate width for 1, 2 and 4 finger layouts. It can be seen, that the absolute lowest noise is obtained for a single finger layout with a 1x40 μm gate. For total gate widths below 70 μm a single finger layout is preferable. For gate widths between 70 and 120 μm a

two finger layout is desirable. A four finger layout is appropriate for total gate widths greater than 120 μm .

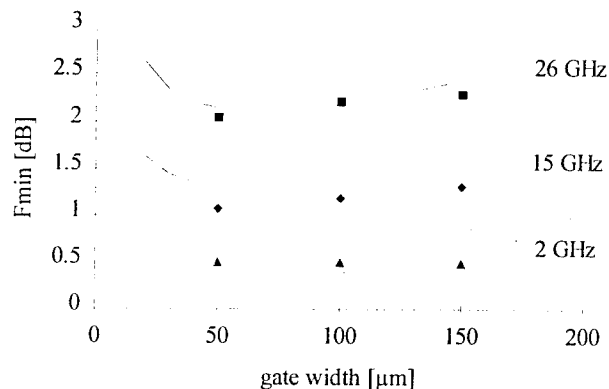


Fig. 6: Measured and simulated minimum noise figure as a function of the gate width at different frequencies at $V_{gs} = -0.3\text{V}$ and $V_{ds} = 1\text{V}$

Furthermore we found, that the optimum gate width for each finger decreases with the number of fingers. However, the influence of the gate width on the minimum noise is rather small, while the influence on the optimum source reflection Γ_{opt} , noise resistance R_n , drain current and input capacitance is large. Therefore the gate width should be determined by these parameters.

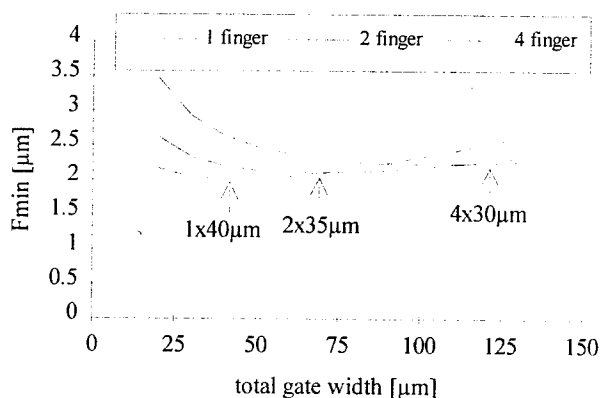


Fig. 7: Simulated minimum noise figure at 26 GHz as a function of gate width for 1, 2 and 4 finger layouts. The arrows indicate the optimum gate width for each layout.

Conclusion

For the design of low noise integrated circuits, an optimum gate voltage was found that reduces the drain current required for maximum gain to about one third. For the drain voltage also a 'U-shape' of the minimum noise figure was obtained. Lowest noise is obtained when the drain voltage is reduced to the start of the saturation region $V_{ds} = 0.6\text{V}$. For higher gate-drain voltages the channel noise is increased, while below

0.6V the transconductance is decreased. To model frequency and scaling effects on the noise behavior, a device model for both high frequency small signal and noise behavior of InP-HEMT's depending on both gate and drain voltage has been developed. The model not only includes the channel and induced gate noise, but also the gate leakage shot noise and the Johnson noise of the gate resistance. It was shown, that these noise sources cause a dispersion of the gate voltage for lowest noise and an increase of the noise figure for wider gates respectively. Modeling scaling effects showed that for gate widths above 70 μm Multi-Finger gates are preferable. Furthermore we found that the optimum width of each finger decreases with the number of fingers.

Acknowledgements

The authors would like to thank Hp. Meier and H. Benedickter for their technical support during the course of this work. The project was supported by the Swiss priority programmes "Optique" (integrated PIN-HEMT photoreceiver), "LESIT" (microwave and gigabit electronics) and by the Swiss PTT.

References

- [1] U. K. Mishra, J. B. Shealy, "InP-based HEMTs: Status and potential", *Proc. of the Sixth Conf. on InP and rel. mat.*, pp. 14-17, 1994
- [2] Y. Ando, T. Itoh, "DC, small-signal and noise modeling for two dimensional electron gas field-effect transistors based on accurate charge-control characteristics", *IEEE Trans. Electron Devices*, vol. 37, pp. 67-78, 1990
- [3] C. Bergamaschi, W. Patrick, W. Bächtold, "Determination of the noise source parameters in InAlAs/GaInAs HEMT Heterostructures based on measured noise temperature dependence on the electric field", *Proc. of the Sixth Conf. on InP and rel. mat.*, pp. 21-24, 1994
- [4] W. A. Striffler, B. T. Pugh, R. D. Remba, "Shot noise in GaAs Metal semiconductor field effect transistors with high gate leakage current", *Solid-State Electronics*, vol. 37, pp. 1763-1764, 1994
- [5] B.-U. Klepser, C. Bergamaschi, W. Patrick, M. Beck, "Comparison and optimisation of different ohmic contact metallisations for InP-HEMT structures with doped and undoped cap layers", *Proc. of the Sixth International Conference on InP and Related Materials*, pp. 174-177, 1994
- [6] J. Wenger, "Quarter-micrometer low-noise pseudomorphic GaAs HEMT's with extremely low dependence of the noise figure on drain-source current", *IEEE Electron Device Letters*, vol. 14, pp. 16-18, 1993

Monte Carlo Simulation of Diffusion Noise In AlGaAs/InGaAs/GaAs Hetero-structure

Y. Wu, G.F. Niu, G. Ruan

Department of Electronic Engineering, Fudan University
Shanghai 200433, CHINA

Abstract

The diffusion noise of 2-D electron gas in AlGaAs/InGaAs/GaAs hetero-structure is studied by Monte Carlo simulation. The dependencies of velocity correlation function on parameters including electric field, charge sheet density, InGaAs thickness are discussed, and comparisons with the AlGaAs/GaAs hetero-structure are made.

Introduction

The AlGaAs/InGaAs/GaAs two-dimensional electron gas FET takes many advantages over its AlGaAs/GaAs counterpart and thus has generated substantial research work. One of the major advantages of two dimensional electron gas FET is its good noise figures, implying a high gain at microwave frequencies. As the main noise source at high frequencies, diffusion noise sets the working limit of electron devices. This paper describes Monte Carlo simulation of diffusion noise in AlGaAs/InGaAs/GaAs hetero-structure.

Simulation

The device under study consists of a 40nm Si doped ($N_d = 10^{18}/\text{cm}^3$) $\text{Al}_{0.15}\text{Ga}_{0.85}\text{As}$, a 10nm undoped $\text{In}_{0.15}\text{Ga}_{0.85}\text{As}$, and a p-type GaAs substrate ($N_a = 10^{15}/\text{cm}^3$). The gate Schottky barrier height is assumed to be 1eV, and ideal AlGaAs/InGaAs and InGaAs/GaAs hetero-interfaces are assumed.

By solving the effective mass Schrodinger and Poisson's equations self-consistently[1], the energy subbands and wave functions are obtained. Then, 2-D scattering rates for both intra-subband and inter-subband transitions are calculated using the Price model[2].

The velocity correlation functions under external electric field are then calculated using Monte Carlo method[3], and the diffusion noise power spectra is obtained by cosine Fourier transform of the correlation functions[4]. Here the low and medium fields are studied, implying that no intervalley or real space transfer occurs and the electron system is completely two-dimensional. The high field case will be presented elsewhere.

Results

Figs. 1 a) and b) show the parallel and transverse velocity correlation functions at 200 and 500 V/cm external electric fields respectively. The charge sheet density n_s is $1 \times 10^{11}/\text{cm}^2$ and the temperature is 77K. With increasing correlation time, the transverse correlation function decays exponentially as in the 3-D case[4], but the parallel correlation function shows clear oscillation whose amplitude decreases with time.

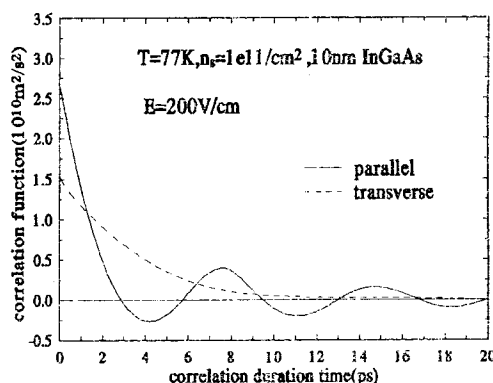


Fig. 1 a) Parallel and transverse velocity correlation functions for 200V/cm electric fields.

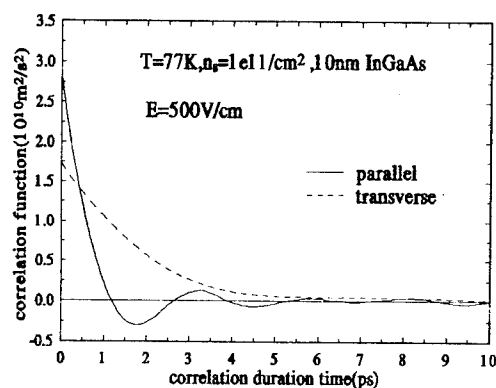


Fig. 1 b) Parallel and transverse velocity correlation functions for 500V/cm electric field.

This oscillation results from the 2-D nature of electron gas. Since the polar-optical phonon (POP) scattering dominates, a electron is accelerated until its energy becomes POP energy when probably it will emit a phonon. Because of the strong anisotropic nature of POP scattering and this periodic phono emission, the parallel velocity correlation function oscillates. Therefore, we can expect that the pseudo period of oscillation T is approximately proportional to the reciprocal of electric field, as shown in Fig. 1. It can also be seen that the amplitude of oscillation decreases with increasing electric field. As a result of the oscillation of correlation function, there is a peak at the resonance frequency $1/T$ in the parallel diffusion noise power spectra, as shown in Figs. 2 a) and b).

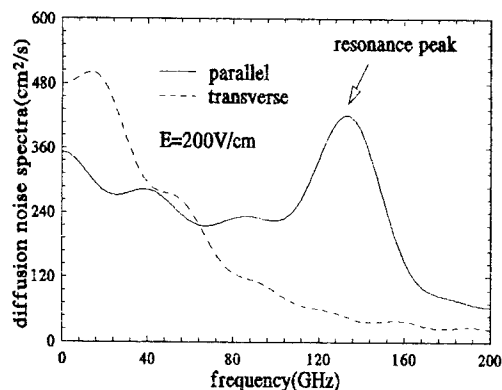


Fig. 2 a) Diffusion noise spectra corresponding to Fig. 1 a).

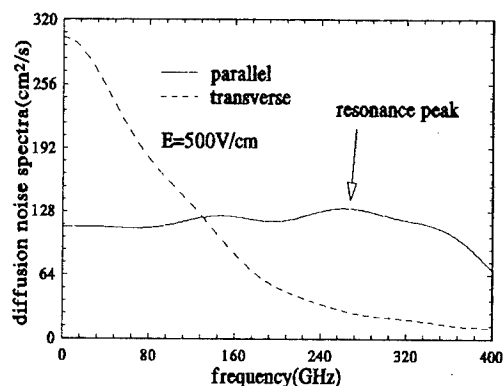


Fig. 2 b) Diffusion noise spectra corresponding to Fig. 1 b).

The above features are similar to those observed in AlGaAs/GaAs hetero-structure[3] because of common 2-D nature of electron gas. However, the parallel correlation function here shows little dependence on the charge sheet density n_s (Fig. 3), as opposed to the situation in AlGaAs/GaAs, where the oscillation amplitude decreases considerably at smaller n_s [3]. We attribute this difference to the stronger quantum confinement in AlGaAs/InGaAs/GaAs, where the separation between the first two subbands changes little with n_s because of double hetero-interfaces[5-6]. In other words, the shape of quantum-well is less sensitive to gate voltage in AlGaAs/InGaAs/GaAs hetero-structure. The subband energy separation is responsible for the magnitude of velocity fluctuations, thus the amplitude of oscillation of the correlation function remains with decreasing n_s from $1e12$ to $1e11/cm^2$. As for AlGaAs/GaAs, decreasing n_s moves closer the subbands considerably[1], thus resulting in much more inter-subband transitions, which in turn reduces the oscillation amplitude of the parallel correlation function.

Increasing the thickness of InGaAs also reduces the amplitude of oscillation of the parallel correlation function, as shown in Fig. 4. The thicker the InGaAs well, the weaker the electron confinement and the smaller the subbands separation, which in turn results in more inter-subband transitions and smaller amplitude of oscillation.

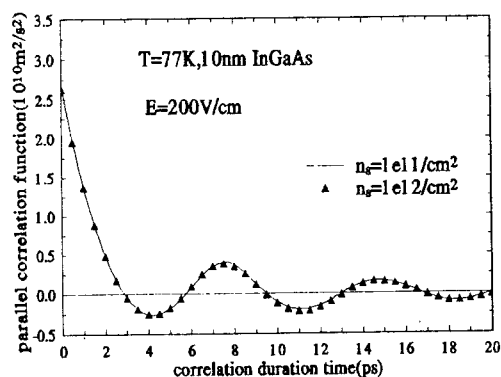


Fig. 3. Parallel correlation functions for different charge sheet density n_s .

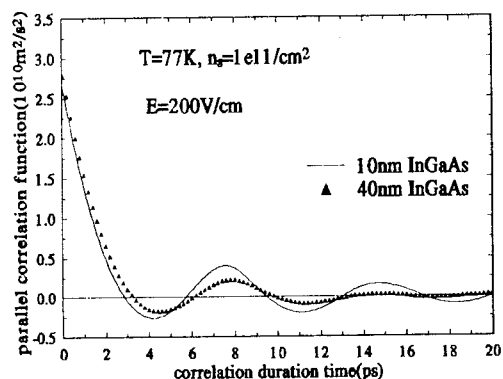


Fig. 4 Parallel correlation functions for different InGaAs thicknesses.

As in AlGaAs/GaAs, the oscillation of velocity correlation function disappears at room temperature and high fields, as shown by our simulation.

Conclusion

The diffusion noise in AlGaAs/InGaAs/GaAs hetero-structure has been studied by Monte Carlo simulation and comparisons with that in AlGaAs/GaAs has been made. The pseudo-period of the oscillating parallel velocity correlation function decreases with increasing electric field. The amplitude of oscillation here is much less sensitive to gate voltage than that in AlGaAs/GaAs. Thicker InGaAs results in smaller oscillation amplitude.

Acknowledgment:

This work was supported by the National Natural Science Foundation of China.

References:

- [1] B. Vinter, "Subbands and Charge Control In a Two-Dimensional Electron Gas Field-Effect Transistor", *Appl. Phys. Lett.*, Vol. 44, pp. 307-309, 1984.
- [2] J. Price, "Two-Dimensional Electron Transport In Semiconductor Layers", *Annal. of Phys.*, Vol. 133, pp. 217-239, 1981.
- [3] J. Zimmermann, Y. Wu, "Diffusion Coefficients of Two-Dimensional Electron Gas In Hetero-Structures", *Solid-State Electron.*, Vol. 31, pp. 367-370, 1988.
- [4] R. Fauquembergue, J. Zimmermann, A. Kaszynski, E. Constant, "Diffusion and the power spectral density and correlation function of velocity fluctuation for electrons in Si and GaAs by Monte Carlo simulation", *J. Appl. Phys.*, Vol. 51, pp. 1065-1071, 1980.
- [5] A. Abou-Elnour, K. Schuenemann, "An Efficient And Accurate Self-Consistent Calculation of Electronic States In Modulation Doped Heterostructures", *Solid-State Electron.*, Vol. 37, pp. 27-30, 1994.
- [6] A. Abou-Elnour, K. Schuenemann, "Closed-Form Calculation of Two-Dimensional Scattering Rates In Semiconductor Heterostructures", *Solid-State Electron.*, Vol. 37, pp. 1817-1824, 1994.

Superior Confinement of Two-Dimensional Electron Gas in an $\text{In}_{0.52}\text{Al}_{0.48}\text{As}/\text{In}_{0.53}\text{Ga}_{0.47}\text{As}$ Modulation-Doped Structure by Inserting a Strained InAs Quantum Well

ThP10

Tatsushi Akazaki, Junsaku Nitta, and Hideaki Takayanagi

NTT Basic Research Laboratories, 3-1 Morinosato-Wakamiya, Atsugi-shi, Kanagawa, 243-01, JAPAN

Takatomo Enoki and Kunihiro Arai

NTT LSI Laboratories, 3-1 Morinosato-Wakamiya, Atsugi-shi, Kanagawa, 243-01, JAPAN

Introduction

$\text{InAlAs}/\text{InGaAs}$ high electron mobility transistors (HEMTs) fabricated from $\text{InAlAs}/\text{InGaAs}$ modulation-doped (MD) structures have demonstrated excellent high-frequency and low-noise performance, compared with $\text{AlGaAs}/\text{GaAs}$ HEMTs⁽¹⁻³⁾. These high performances are explained by the high electron mobility, saturation drift velocity, and sheet-carrier density of the $\text{InAlAs}/\text{InGaAs}$ two-dimensional electron-gas (2DEG) system. Recently, we have demonstrated that electron transport properties and device performance could be further improved by using $\text{In}_{0.52}\text{Al}_{0.48}\text{As}/\text{In}_{0.53}\text{Ga}_{0.47}\text{As}$ normal and inverted HEMTs with an InAs quantum well inserted into the InGaAs channel (InAs-inserted channel)⁽⁴⁻⁷⁾. In addition, we have recently investigated a superconducting device which uses the InAs-inserted-channel inverted modulation-doped structure⁽⁸⁻¹¹⁾. We found that high supercurrent density is obtained through both high electron density and high electron mobility of the 2DEG formed in this structure with no Schottky barrier between the superconducting electrodes and the InAs layer⁽⁸⁾. Therefore, determining the electron transport properties of 2DEG in InAs-inserted-channel modulation-doped structures holds great importance in the development of superconducting devices as well as the application of HEMTs at room temperature. In this kind of structure there is lattice mismatch between the InAs quantum well and $\text{In}_{0.53}\text{Ga}_{0.47}\text{As}$ layer, making it very interesting to study how the strain influences the electron transport properties of the 2DEG formed in the deformed InAs quantum well.

In this letter, we give a detailed analysis based on Shubnikov-de Haas measurement of the effective mass of 2DEG in InAs-inserted-channel $\text{InAlAs}/\text{InGaAs}$ modulation-doped structures. Details about other properties, such as improved 2DEG mobility, are described elsewhere⁽⁴⁻⁷⁾.

Experiment and Discussion

Figure 1 shows the InAs-inserted-channel MD structure. The heterostructure used in this study was grown by molecular beam epitaxy (MBE) on a Fe-doped semi-insulating (100) InP substrate. All InGaAs and InAlAs layers were lattice matched to InP, and the growth temperature for all layers was about 300 °C, since the critical thickness increases at lower growth temperatures⁽¹²⁾. The doping density of the InAlAs carrier-supply layer was $4 \times 10^{18} \text{ cm}^{-3}$. According to some of our previous reports^(4,7), we fixed the InAs layer thickness L_w at 4 nm and the insertion position Z (the distance between the InAlAs spacer layer and the InAs layer) at 2.5 nm. The mobility is highest at a thickness of $L_w = 4 \text{ nm}$, and starts to decrease at $L_w = 5 \text{ nm}$ ⁽⁴⁾. This indicates that 4 nm is under the critical thickness in the $\text{InAs}/\text{In}_{0.53}\text{Ga}_{0.47}\text{As}$ system.

During the Shubnikov-de Haas (SdH) measurements, the sample was kept in the dark. Measurements were taken to determine the sheet-carrier density of 2DEG and to confirm the 2DEG nature of the structures. They were performed using standard Hall-bar geometry in the temperature range from 6 K to 35 K. The applied electric field was carefully suppressed to less than 1 V/m to avoid excess electron heating. A magnetic field of, at most, 8 T was applied normal to the interface.

Figure 2 shows the SdH oscillations of the InAs-inserted-

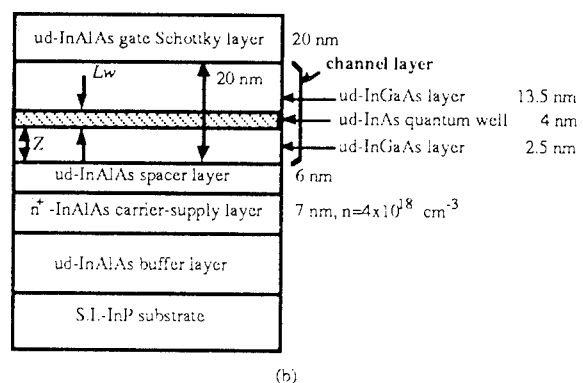
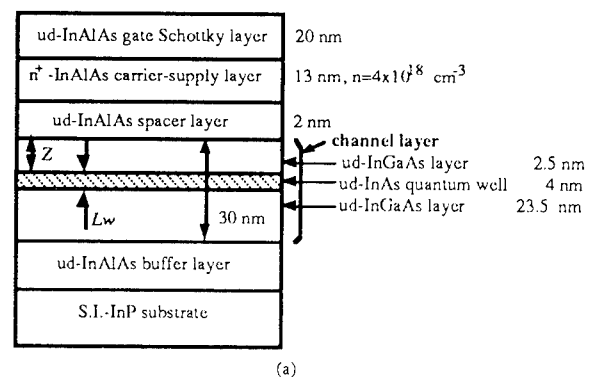


Fig. 1 Layer sequences of the InAs-inserted-channel MD structure: (a) normal configuration and (b) inverted configuration.

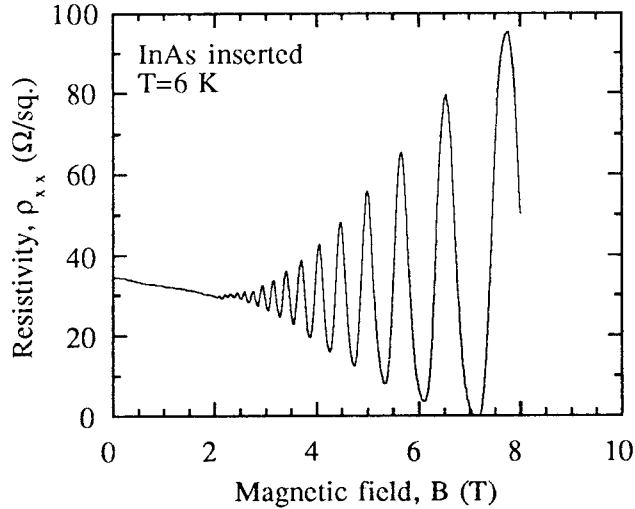


Fig. 2 Shubnikov-de Haas oscillations of the InAs-inserted-channel inverted MD structure.

channel inverted MD structure at 6 K. A single set of oscillations is clearly visible. This indicates that the only ground subband is populated in the InAs quantum well. The sheet-carrier density n_s was estimated to be $2.08 \times 10^{12} \text{ cm}^{-2}$ when $n_s = e \Delta(1/B)/\pi\hbar$, where $\Delta(1/B)$ is the SdH oscillation period. An electron mobility of $87,200 \text{ cm}^2/\text{Vs}$ was obtained when $\mu = 1/(\rho_{xx} n_s e)$. These values are in good agreement with the results of independent Hall measurements taken with the same samples. Figure 3 shows a typical example of the temperature dependence of the SdH oscillation amplitudes from 6-35 K. The effective mass m^* was determined by fitting the experimental data to the theoretical equation expressed by:

$$\Delta\rho/\rho_0 \propto (\beta T/B) [1/\sinh(\beta T/B)], \quad (1)$$

where $\Delta\rho$ is the oscillatory term of ρ_{xx} , $\rho_0 = \rho_{xx}(B=0)$, and $\beta = 2\pi^2 k_B m^*/\hbar e$. The solid line denotes the best fit as determined by the least squares method. Fitting was carried out for the various amplitudes in several different magnetic fields and

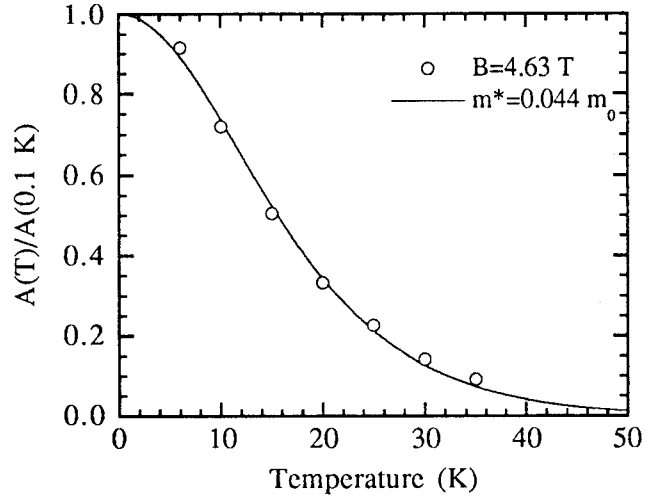


Fig. 3 Temperature dependence of the amplitude of the derivative oscillation in the InAs-inserted-channel inverted MD structure. Open circles denote measured data and the solid line denotes the best fit determined by the least squares method.

the final mass value was derived by averaging them. The results of the determined electron transport properties are summarized in Table I, and compared with the Hall-measurement results.

Recently, Hrivnák has derived semi-empirical relations for the energy gap and electron effective mass in the strained layer as follows⁽¹³⁾:

$$E_{gs} = \frac{m_{sub}}{m} \left(\frac{a_{sub}}{a} \right)^6 E_{g0}, \quad (2)$$

$$m_s = m \frac{E_{gs}}{E_{g0}} \left(\frac{a_{sub}}{a} \right)^2, \quad (3)$$

where m_{sub} is the conduction band-edge mass of the substrate material under the strained layer, m is the conduction band-edge mass of the unstrained bulk material, m_s is the conduction band-edge mass of the strained layer, E_{g0} is the energy gap of the unstrained bulk material, E_{gs} is the energy gap of the

Table I Electron transport properties of the InAs-inserted-channel MD structure studied. Sheet-carrier density (n_s) and mobility (μ) were determined by Hall measurement at 10 K and from Shubnikov-de Haas (SdH) oscillations at 6 K. Notice that the SdH oscillations permit the resolution of two populated subbands with carrier densities n_{s0} and n_{s1} . The effective mass ratio (m^*/m_0) was determined by the temperature dependence of the SdH-oscillation amplitudes.

Type	n_s (SdH, 6 K) ($\times 10^{12} \text{ cm}^{-2}$)		μ (SdH, 6 K) (cm^2/Vs)	n_s (Hall, 10 K) ($\times 10^{12} \text{ cm}^{-2}$)	μ (Hall, 10 K) (cm^2/Vs)	m^*/m_0 (for ground subband)
	n_{s0}	n_{s1}				
inverted	2.08	—	87,200	1.97	84,000	0.044
normal	2.94	0.47	49,800	3.47	55,600	0.051

strained layer, a_{sub} is the lattice constant of the substrate material, and a is the lattice constant of the unstrained bulk material. The energy gap of the strained InAs layer on $\text{In}_{0.53}\text{Ga}_{0.47}\text{As}$ calculated by Eq. (2) is 0.593 eV. The conduction band-edge mass of the strained InAs layer on $\text{In}_{0.53}\text{Ga}_{0.47}\text{As}$ calculated by Eq. (3) is $0.0325 m_0$. The energy gap and conduction band-edge mass of unstrained bulk InAs are 0.411 eV and $0.024 m_0$. The energy gap and conduction band-edge mass of the strained InAs layer are larger than those of the unstrained bulk InAs due to the influence of strain.

In order to further compare the experimental results, we calculated the correction for nonparabolicity in the conduction band as follows⁽¹⁴⁾:

$$p^2 = 2m_0^*E [1 + \alpha E], \quad (4)$$

where p is momentum, $\alpha = (1 - m_0^*/m_0)^2/E_g$, and E is the kinetic energy. The energy dependence of effective mass calculated by Eq. (4) is expressed by:

$$m^* = m_0^* [1 + 2\alpha E], \quad (5)$$

Figure 4 shows the experimental results of the energy dependence of effective mass, compared with the theoretical ones estimated by Eq. (5). The experimentally obtained effective masses of 2DEG in the InAs-inserted-channel MD structure and the conventional one are in good agreement with the theoretically obtained ones of the strained InAs layer on $\text{In}_{0.53}\text{Ga}_{0.47}\text{As}$ and bulk $\text{In}_{0.53}\text{Ga}_{0.47}\text{As}$, respectively. This shows that almost all of the 2DEG in the InAs-inserted-channel MD structure is formed in the strained InAs quantum well. This result also agrees with the result obtained from

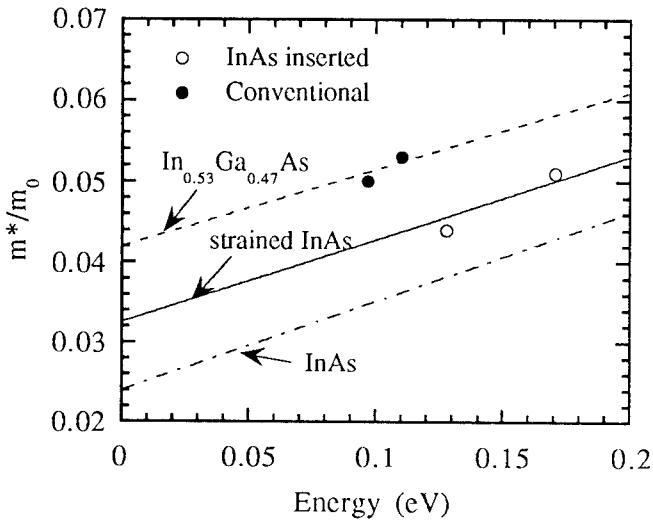


Fig. 4 The energy dependence of the effective mass.

Solid circles represent the experimentally obtained effective mass of the InAs-inserted-channel MD structure while the open circles represent that of the conventional one.

The solid, and two dashed lines represent the expected dependence for the strained InAs, $\text{In}_{0.53}\text{Ga}_{0.47}\text{As}$, and bulk InAs, respectively.

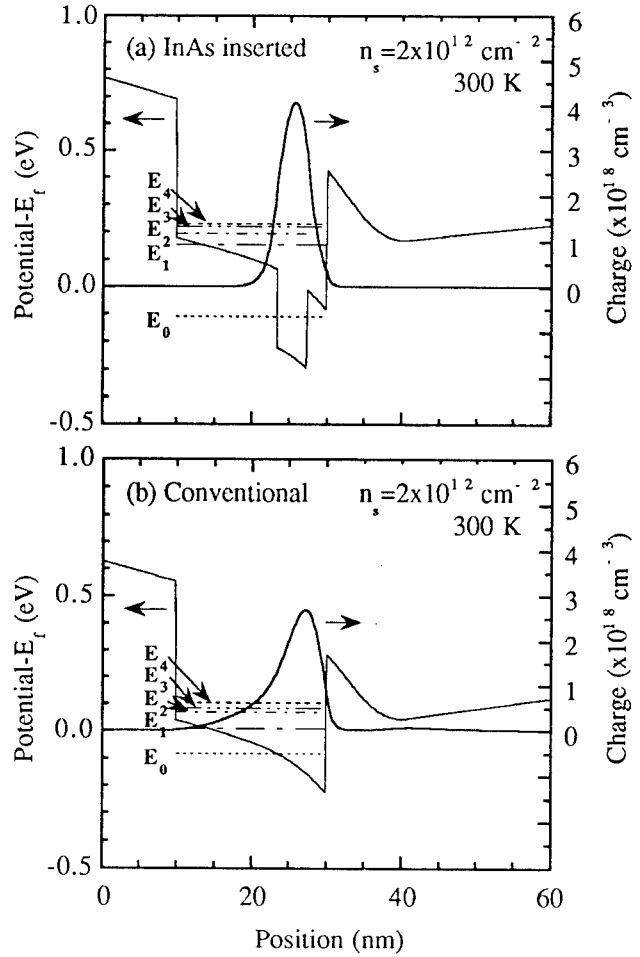


Fig.5 Calculated 2DEG distribution and subband levels in the (a) InAs-inserted-channel structure and (b) conventional inverted modulation-doped structure at 300 K.

the calculated 2DEG distributions, which shows that over 80 % of the 2DEG forms in the InAs quantum well and the thickness of the 2DEG is reduced to 4.8 nm from 6.1 nm (see Fig. 5). The effective masses of 2DEG in the InAs-inserted-channel MD structure are about 30 % smaller than those in the conventional MD structure. This indicates that the effective mass of the strained InAs quantum well is enhanced more than that of bulk InAs due to the influence of strain, but is smaller than that of $\text{In}_{0.53}\text{Ga}_{0.47}\text{As}$.

Conclusions

We have given a detailed analysis based on Shubnikov-de Haas measurement of the effective mass of 2DEG in an InAs-inserted-channel InAlAs/InGaAs modulation-doped structure. The measured effective mass of the InAs-inserted-channel inverted MD structure was found to be $0.044 m_0$ when $n_s = 2.08 \times 10^{12} \text{ cm}^{-2}$. The effective mass of 2DEG in the InAs-inserted-channel MD structure is in good agreement with the calculated one of the strained InAs layers on $\text{In}_{0.53}\text{Ga}_{0.47}\text{As}$. This indicates that almost all of the

2DEG forms in the strained InAs quantum well. These results show that the InAs-inserted-channel MD structure improves the electron confinement, since the 2DEG is confined in the InAs quantum well with the thickness of 4 nm. Therefore it is possible to utilize the excellent transport properties of InAs by the InAs-inserted-channel MD structure.

Acknowledgments

We would like to thank Dr. S. Yamada for his help in Shubnikov-de Haas measurement and Mr. T. Ishikawa for the MBE growth. We also wish to express thanks to Dr. N. Matsumoto, Dr. Y. Imamura, and Dr. Y. Ishii for their encouragement.

References

- (1) U. K. Mishra, A. S. Brown, L. M. Jelloian, M. Thompson, L. D. Nguyen, and S. E. Rosenbaum, "Novel high performance self-aligned 0.15 micron long T-gate AlInAs-GaInAs HEMTs," *IEDM Tech. Dig.*, Washington D.C., 1989, (The IEEE Electron Devices Society, 1989) p.101.
- (2) P.C. Chao, A.J. Tessmer, K.-H.G. Duh, P. Ho, M.-Y. Kao, P.M. Smith, J.M. Ballingall, S.-M. Liu, and A.A. Jabra, "W-band low-noise InAlAs-InGaAs lattice-matched HEMT's," *IEEE Electron Dev. Lett.*, vol. 11, pp. 59, 1990.
- (3) G.I. Ng, D. Pavlidis, M. Quillec, Y.J. Chan, M.D. Jaffe, and J. Singh, "Study of the consequence of excess indium in the active channel of InGaAs/InAlAs high electron mobility transistors on device properties," *Appl. Phys. Lett.* vol. 52, pp. 728, 1988.
- (4) T. Akazaki, K. Arai, T. Enoki and Y. Ishii, "Improved InAlAs/InGaAs HEMT Characteristics by Inserting an InAs layer into the InGaAs Channel," *IEEE Electron Dev. Lett.*, vol. 13, pp.325, 1992.
- (5) T. Akazaki, T. Enoki, K. Arai, Y. Umeda, and Y. Ishii, "High-frequency performance for sub-0.1 μm gate InAs-inserted-channel InAlAs/InGaAs HEMT," *Electron. Lett.*, vol. 28, pp. 1230, 1992.
- (6) T. Akazaki, J. Nitta, H. Takayanagi, T. Enoki, and K. Arai, "Improving the mobility of an $\text{In}_{0.52}\text{Al}_{0.48}\text{As}/\text{In}_{0.53}\text{Ga}_{0.47}\text{As}$ inverted modulation-doped structure by Inserting a strained InAs quantum well," *Appl. Phys. Lett.*, vol. 65, pp. 1263, 1994.
- (7) T. Akazaki, T. Enoki, K. Arai and Y. Ishii, "Improving the Characteristics of an InAlAs/InGaAs Inverted HEMT by Inserting an InAs layer into the InGaAs Channel," to be published in *Solid-State Electron.*, 1995.
- (8) J. Nitta, T. Akazaki, H. Takayanagi and K. Arai, "Transport properties in InAs-inserted-channel $\text{In}_{0.52}\text{Al}_{0.48}\text{As}/\text{In}_{0.53}\text{Ga}_{0.47}\text{As}$ heterostructure coupled superconducting junction," *Phys. Rev. B*, vol. 46, pp. 14286, 1992.
- (9) H. Takayanagi, T. Akazaki, J. Nitta, and T. Enoki, "Superconducting three-terminal devices using an InAs-based two-dimensional electron gas," to be published in *Jpn. J. Appl. Phys.*, 1995.
- (10) T. Akazaki, J. Nitta, H. Takayanagi, and K. Arai, "Superconducting junctions using a 2DEG in a strained InAs quantum well inserted into an InAlAs/InGaAs MD structure," to be published in *IEEE trans. on Applied Superconductivity*, 1995.
- (11) H. Takayanagi, T. Akazaki, and J. Nitta, "Interference effects on the critical current in a clean-limit S-N-S junction," to be published in *Phys. Rev. B*, vol. 51, pp. 1374, 1995.
- (12) G. J. Whaley and P. I. Cohen, "The growth of strained InGaAs on GaAs : Kinetics versus energetics", *J. Vac. Sci. Technol. B*, vol. 6, pp. 625, 1988.
- (13) L. Hrivnák, "The relations for electron effective masses of strained $\text{In}_x\text{Ga}_{1-x}\text{As}$ layers", *Phys. Status Solidi A*, vol. 123, pp. k133, 1991.
- (14) D. F. Welch, G. W. Wicks and L. F. Eastman, "Calculation of the conduction band discontinuity for $\text{Ga}_{0.47}\text{In}_{0.53}\text{As}/\text{Al}_{0.48}\text{In}_{0.52}\text{As}$ heterojunction", *J. Appl. Phys.*, vol. 55, pp. 3176, 1984.

Ming-Ta Yang, Yi-Jen Chan, Jia-Lin Shieh and Jen-Inn Chyi
Department of Electrical Engineering
National Central University, Chungli, Taiwan 32054, ROC

Introduction

High electron mobility transistors (HEMTs) fabricated on InP or GaAs substrates are of great interest for ultra-high-frequency microwave telecommunication applications [1], [2]. An alternative $\text{In}_{0.29}\text{Al}_{0.71}\text{As}/\text{In}_{0.3}\text{Ga}_{0.7}\text{As}$ heterostructure based on GaAs was proposed here, which could provide a larger conduction-band discontinuity (ΔE_c) for a better carrier confinement, resulting in a high carrier density. In addition, by increasing the AlAs mole fraction in the $\text{In}_{0.52}\text{Al}_{0.48}\text{As}$ layer, a higher Schottky barrier height could be obtained due to the increase of bandgap [3]. Therefore, $\text{In}_{0.29}\text{Al}_{0.71}\text{As}/\text{In}_{0.3}\text{Ga}_{0.7}\text{As}$ heterostructure devices grown on unstrained metamorphic buffer have received considerable attention recently, such as HEMTs, HBTs and RTDs. This heterostructure was realized by using compositionally step-graded $\text{In}_x\text{Ga}_{1-x}\text{As}$ buffer up to $x=0.3$ on GaAs substrate [4]. Since the use of this metamorphic buffer, the interfacial dislocations were all confined in it without any penetration into the following active layers. Heterostructure FETs utilized this material system, thus, can achieve a higher In content in the conducting channel without the limitation of critical thickness. Therefore, a lattice-matched, dislocation free layer with a high In content can be successfully obtained on top of this metamorphic buffer. In this study, we utilized a metamorphic buffer to increase the In composition up to 0.3 on GaAs substrates, and grew the doped-channel FET (DCFET) [5] structures based on the $\text{In}_{0.29}\text{Al}_{0.71}\text{As}/\text{In}_{0.3}\text{Ga}_{0.7}\text{As}$ heterostructures.

Material Growth and Characterization

Lattice-matched $\text{In}_{0.29}\text{Al}_{0.71}\text{As}/\text{In}_{0.3}\text{Ga}_{0.7}\text{As}$ metamorphic doped-channel structures were grown in a Riber 32-P molecular beam epitaxy (MBE) system on (100)-oriented semi-insulating GaAs substrates. Fig. 1 shows the device cross-section of metamorphic DCFET (M-DCFET). Layers were grown at 520 °C. The growth rate varied between 0.8 and 1.0 $\mu\text{m/hr}$. depending on the In composition of the epilayers. A metamorphic buffer consisted of step-graded $\text{In}_x\text{Ga}_{1-x}\text{As}$ layers with a compositional increment of $x=0.1/\text{step}$ was first grown. Each step was 200 nm thick. The function of these dislocation filters are to form the potential barriers, and threading dislocations are therefore forced to deflect into the sideways. After the growth of metamorphic $\text{In}_x\text{Ga}_{1-x}\text{As}$ buffer, a lattice-matched doped-channel heterostructure was grown on top of it. As to the M-DCFET active region, it consists a 15 nm thick, Si-doped ($n=3\times 10^{18} \text{ cm}^{-3}$), $\text{In}_{0.3}\text{Ga}_{0.7}\text{As}$ channel sandwiched by the undoped InAlAs layers. The Al mole fraction in the top undoped 20 nm InAlAs was 0.71, which acted as a quasi-insulator to improve the Schottky-gate performance. The final 20 nm $n^+\text{-InGaAs}$ layer was used to reduce the drain and source ohmic contact resistivity.

After the removal of shunt conduction from the InGaAs cap layer, temperature-dependent Hall measurements were made on the samples by using the van der Pauw technique. The temperature-dependent Hall mobility and sheet density for this DCFET heterostructure

were made, and results are shown in Fig. 2. The room-temperature Hall mobility of the 2DEG is 1440 $\text{cm}^2/\text{V}\cdot\text{sec}$ with a sheet charge density of $8.1\times 10^{12} \text{ cm}^{-2}$; while the Hall mobility increased to 1500 $\text{cm}^2/\text{V}\cdot\text{sec}$ with a sheet charge density of $7.4\times 10^{12} \text{ cm}^{-2}$ at 15 K, respectively. These transport characteristics are quite

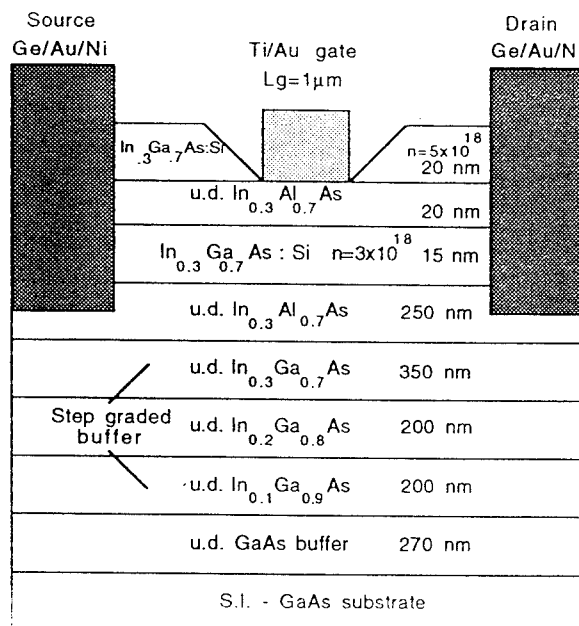


Fig. 1 Device cross-section of $\text{In}_{0.29}\text{Al}_{0.71}\text{As}/\text{In}_{0.3}\text{Ga}_{0.7}\text{As}$ M-DCFETs.

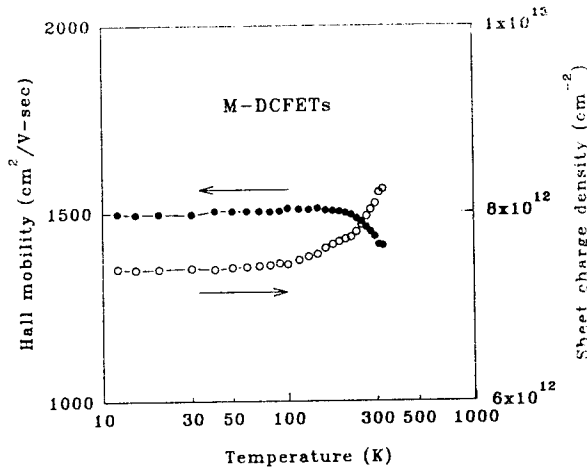


Fig. 2 Temperature dependent Hall-effect results of $\text{In}_{0.29}\text{Al}_{0.71}\text{As}/\text{In}_{0.3}\text{Ga}_{0.7}\text{As}$ M-DCFETs.

comparable to those measured in strained $\text{In}_x\text{Ga}_{1-x}\text{As}$ ($0 \leq x \leq 0.25$) doped-channel layers [6]. This high sheet charge density and low mobility, compared with the HEMTs, is typical for doped-channel scheme, which provides high current density as well as good device performance.

To verify the effectiveness of these metamorphic dislocation filters, we conducted the cross-sectional Transmission Electron Microscope (TEM) analysis. Fig. 3 is a microphotograph taken near a local dislocation cluster from TEM. As can be seen, most of the interfacial dislocations were confined within these metamorphic buffers, and only very small amount of threading dislocations reached the active channel. It suggests that this step-graded buffer is sufficient to filter the dislocation out, and an unstrained $\text{In}_{0.3}\text{Ga}_{0.7}\text{As}$ layer without the dislocation loops can be successfully grown on GaAs substrates.

As to the enhancement of both ΔE_c and Schottky barrier height, we conduct the Arrhenius plots of J/T^2 taken at different forward biases for the $\text{In}_{0.29}\text{Al}_{0.71}\text{As}/\text{In}_{0.3}\text{Ga}_{0.7}\text{As}$ single barrier structure [7]. The barrier height deduced from the evaluation is 0.702 ± 0.05 eV. The conduction band discontinuity determined by this measurement is 0.71 ± 0.05 eV. It is evident that the ΔE_c of $\text{In}_{0.29}\text{Al}_{0.71}\text{As}/\text{In}_{0.3}\text{Ga}_{0.7}\text{As}$ heterojunction is much larger than that of $\text{In}_{0.52}\text{Al}_{0.48}\text{As}/\text{In}_{0.53}\text{Ga}_{0.47}\text{As}$ ($\Delta E_c = 0.52$ eV) and, is certainly beneficial for device applications.

Device Fabrication and Characterization

The $1 \times 50 \mu\text{m}^2$ gate M-DCFETs were realized by the conventional optical lithographical and lift-off techniques. The fabrication of the device started with ohmic contacts, which were carried out by electron-beam evaporation

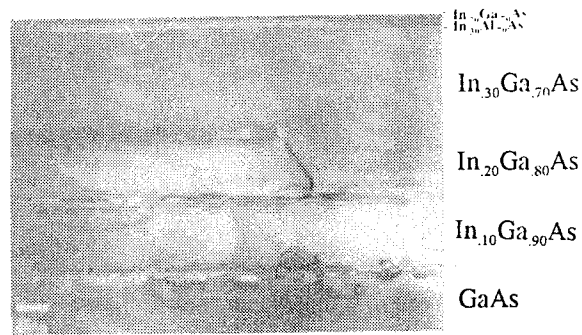


Fig. 3 TEM cross-sectional micrograph of the step-graded $\text{In}_x\text{Ga}_{1-x}\text{As}$ metamorphic buffer.

Ge/Au/Ni/Ti/Au multi-layers metal, followed by a 400°C , 1 min. furnace anneal. The separation between source and drain contacts is $3.5 \mu\text{m}$ for a $1 \mu\text{m}$ -long gate. After gate recess to remove the top $\text{n}^+\text{-InGaAs}$ cap layer, $1 \mu\text{m}$ -long, $50 \mu\text{m}$ -wide Ti/Au gates were evaporated and defined by a lift-off process. Finally, the devices were isolated using a mesa etch, and the gate feeder was separated from the mesa edge with an air-bridge to reduce the gate leakage current [8].

Device I-V characteristics were measured by an HP 4145B semiconductor parameter analyzer. In a convenient way as shown in Fig. 4, we plotted transconductance (g_m) versus drain-to-source current (I_{ds}) of this $\text{In}_{0.29}\text{Al}_{0.71}\text{As}/\text{In}_{0.3}\text{Ga}_{0.7}\text{As}$ M-DCFETs to provide a graphically clean way of comparing current drive. It demonstrated a peak extrinsic g_m of 220 mS/mm at $I_{ds} = 210 \text{ mA/mm}$, and the full width half maximum (FWHM) of this g_m curve is 340 mA/mm . The maximum available channel current ($I_{ds,max}$) as high as 400 mA/mm was obtained from a $1 \mu\text{m}$ -long gate DC test pattern biased at $V_{ds} = 2 \text{ V}$. The source resistance was $1 \Omega\text{-mm}$, corresponding to an intrinsic g_m of 285 mS/mm . From this figure we also observed a good threshold condition, which suggests that the leakage current associated with the impurity effect in metamorphic InGaAs buffer layers is negligible.

Microwave S-parameters were measured in a common-source configuration from 45 MHz to 50 GHz with an HP 8510C network analyzer in conjunction with Cascade direct probes. By calculating the h parameter and power gain, one may determine the current-gain cut-off frequency (f_T) and maximum oscillation frequency (f_{max}). When the device biased at $V_{ds} = 2.5 \text{ V}$ and V_{gs} tuned for maximum transit-frequency f_T , we obtained a bias dependent cutoff frequency as a function of I_{ds} , and results

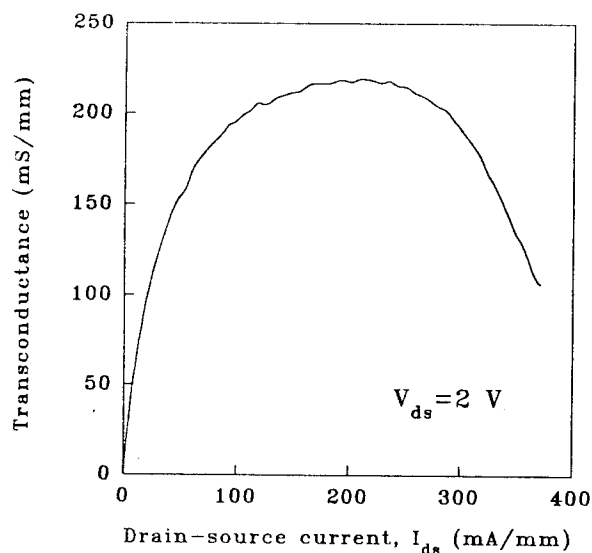


Fig. 4 Transconductance variation of $\text{In}_{0.29}\text{Al}_{0.71}\text{As}/\text{In}_{0.3}\text{Ga}_{0.7}\text{As}$ M-DCFETs as a function of I_{ds} .

As shown in Fig. 5, a peak f_T of 22 GHz and an f_{max} of 51 GHz were achieved from this M-DCFET biased at $I_{ds}=120$ mA/mm with a 1.0 μm -long gate. Based on the help from Microwave Design System (MDS) simulation, a small signal equivalent circuit of this M-DCFET can be obtained by fitting each element value according to the measured S-parameters. The values for each component in the equivalent circuit are shown in Fig. 6. A g_m of 201 mS/mm was obtained from the microwave measurement. R_s , R_g and R_d are 6.67 Ω , 2.51 Ω , and 6.95 Ω , respectively. The C_{gs} was 0.129 pF and R_{ds} was 730 Ω .

Reliability Test

After fully characterizations both DC and RF performance, we conclude that the metamorphic DCFET approach provides a high current capability, and high performance characteristics, without the affection from strain relaxation. Since the reliability of device characteristics is an another critical issue for device application; therefore, the understanding of device aged properties or failure mechanism becomes the key step to prevent the device degradation. For comparison, the reliability testings of pseudomorphic $\text{AlGaAs}/\text{In}_{0.15}\text{Ga}_{0.85}\text{As}$ DCFETs (P-DCFETs), based on the same design of heterostructures, were also included.

The reliability associated with lifetime-testing was conducted under $V_{ds}=5$ V, $V_{gs}=0$ V conditions. Both devices were surface unpassivated. Fig. 7 shows the normalized g_m variations during biased lifetime-testing of both M-DCFETs and P-DCFETs. After 55 hrs. operation the g_m of P-DCFETs dropped 12 % from its original val

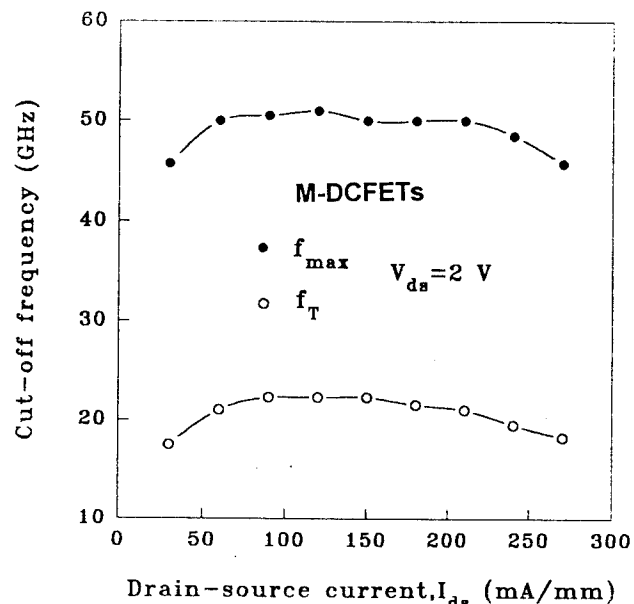


Fig. 5 f_T and f_{max} vs. I_{ds} of $\text{In}_{0.29}\text{Al}_{0.71}\text{As}/\text{In}_{0.3}\text{Ga}_{0.7}\text{As}$ M-DCFETs with a gate-length of 1.0 μm .

while this number was only 7 % for M-DCFETs. Both showed a significant initial deterioration of device performance at very beginning, which is responsible for the so-called infant mortality. After this initial stage, devices become stable before reaching the final wear-out stage. In addition to the g_m , both channel current and channel resistance also presented the same behavior. It translates that M-DCFETs preserved better reliable characteristics than strained DCFETs after bias-stress, and this metamorphic buffer is proven to be reliable.

Conclusions

Lattice-matched and dislocation-free $\text{In}_{0.29}\text{Al}_{0.71}\text{As}/\text{In}_{0.3}\text{Ga}_{0.7}\text{As}$ heterostructures with an improved Schottky barrier height have been realized on GaAs substrates. Through the temperature-dependent Hall effect as well as TEM analysis, we have verified the effectiveness of dislocation filtering from this metamorphic buffer, and it is favorable for device application. Based on the doped-channel approach, we demonstrated a high current capability and high device performance of M-DCFETs. A g_m of 220 mS/mm and an I_{ds} of 400 mA/mm were obtained from a 1 μm -long gate device. An f_T of 22 GHz and an f_{max} of 51 GHz were also achieved from the same gate dimension. In addition, we conducted the reliability testing, and found that a better performance was preserved for M-DCFETs. Metamorphic buffers provide, therefore, a very promising alternative way to achieve high performance of devices without the critical thickness limitation.

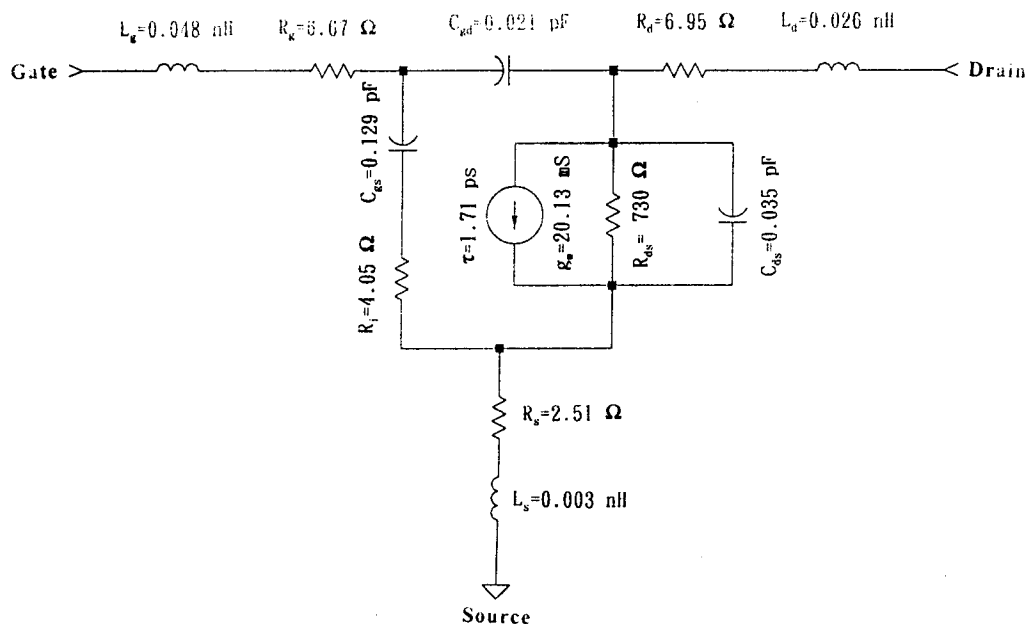


Fig. 6 Microwave small-signal equivalent circuit model of the $\text{In}_{0.29}\text{Al}_{0.71}\text{As}/\text{In}_{0.3}\text{Ga}_{0.7}\text{As}$ M-DCFETs.

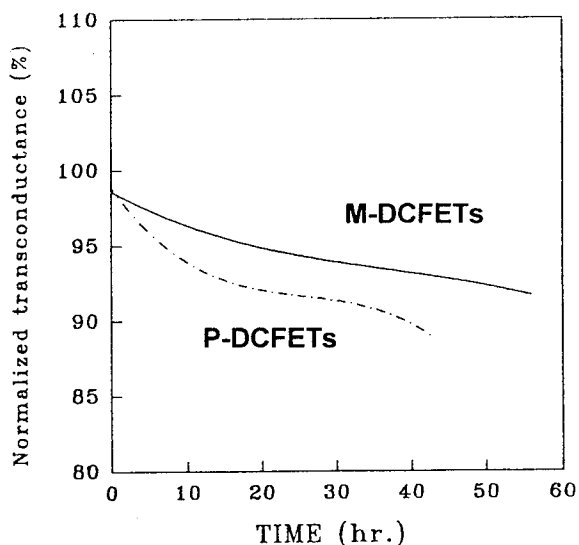


Fig. 7 Normalized g_m variation during biased lifetime-testing of M-DCFET and P-DCFET.

Acknowledgements

The authors would like to thanks for Dr. C. H. Lin (MRL, ITRI) for cross-sectional TEM work. This work is supported by National Science Council (NSC 83-0404-E-008-005), ROC.

References

- [1] M. Wojtowicz, R. Lai, D. C. Streit, G. I. Ng, T. R. Block, K. L. Tan, P. H. Liw, A. K. Freudenthal, and R. M. Dia. IEEE Electron Devices, vol. 15, pp. 477, 1994.
- [2] L. D. Nguyen, P. J. Tasker, D. C. Radulescu, and L. J. Eastman, IEEE Trans. Electron Devices, vol. 36, pp. 2243, 1989.
- [3] K. Imanishi, T. Ishihawa, and K. Kondo, Proc. Intl. Symp. GaAs and Related Compounds, Karuizawa, Japan, pp. 637, 1989.
- [4] J. C. P. Chang, J. Chen, J. M. Fernandez, H. H. Wieder, and K. L. Kavanagh, Appl. Phys. Lett., vol. 60, pp. 1129, 1992.
- [5] H. Hida, A. Okamoto, H. Toyoshima, and K. Ohata, IEEE Electron Devices Lett., vol. 7, pp. 625, 1986.
- [6] M. T. Yang, Y. J. Chan, C. H. Chen, J. I. Chyi, R. M. Lin, and J. L. Shieh, J. Appl. Phys., vol. 76, pp. 2494, 1994.
- [7] J. L. Shieh, J. I. Chyi, R. J. Lin, R. M. Lin, and J. W. Pan, Electronic Letters, vol. 30, pp. 2172, 1994.
- [8] A. Fathimulla, J. Abrahams, T. Loughran, and H. Hier, IEEE Electron Devices, vol. 9, pp. 328, 1988.

In_{0.52}(Al_{0.9}Ga_{0.1})_{0.48}As/In_{0.53}Ga_{0.47}As HEMTs on InP Substrates

ThP12

Chia-Song Wu, Yi-Jen Chan, Tien-Huat Gan, Jia-Lin Shieh and Jen-Inn Chyi

Department of Electrical Engineering
National Central University, Chungli, Taiwan 52054, R.O.C.

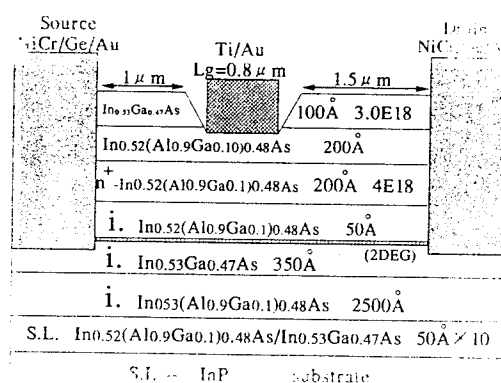
Introduction

InAlAs/InGaAs on InP HEMTs have demonstrated a great potential for the application of microwave and millimeter wave communication [1],[2]. Based on its larger conduction-band discontinuity($\Delta E_c \sim 0.55$ eV), high electron drift velocity, and sheet charge density, a record high f_T of 345 GHz with a 0.065 μm gate-length has been achieved by using this material system[3]. In spite of the high performance of InP-HEMTs, there are several potential limitations for their further applications which are associated with the poor quality of InAlAs epilayer. Owing to the high Al concentration in the In_{0.52}Al_{0.48}As layers, the so-called alloy clustering effect degrades the device performance. A significant "kink" in DC I-V curves, related to the trapping effect, is commonly observed in InP-HEMTs. This is also responsible for a high DC output conductance and a poor channel threshold[4]. Furthermore, a high Al content in the Schottky layer also enhances the formation of surface oxide, resulting in a large gate leakage current, which dramatically deteriorates the device performance.

In this report, we try to improve the quality of In_{0.52}Al_{0.48}As layer, by substituting 10% of Al atoms with Ga atoms, and forming a In_{0.52}(Al_{0.9}Ga_{0.1})_{0.48}As quaternary(Q) layer. This composition of quaternary InAlGaAs layer is used as the Schottky and buffer layers in HEMT structures. With the incorporation of Ga atoms, the alloy scattering can be eliminated due to the higher surface mobility of Ga atoms during the MBE growth. This composition is chosen based on the consideration of maintaining a good Schottky gate performance, where a reasonable high bandgap Schottky layer is necessary. Since it is expected that this InAlGaAs Q-layer can improve the device quality, we particularly focused the reliability and sidegate testings for this InAlGaAs Q-HEMTs. For comparison, the results obtained from the conventional(C) InP-HEMTs are also included.

Q-HEMT Material Growth And Characterization

The epitaxial layers of Q-HEMTs were grown on semi-insulating (100) InP:Fe substrates by a Riber-32P MBE system. Fig. 1 shows the device cross-section of the In_{0.52}(Al_{0.9}Ga_{0.1})_{0.48}As/In_{0.53}Ga_{0.47}As Q-HEMTs. The growth temperature was 530°C, excepting the 500°C for In_{0.53}Ga_{0.47}As layers. We used In_{0.52}(Al_{0.9}Ga_{0.1})_{0.48}As layers as a buffer, a spacer and a Schottky layer to replace the role of In_{0.52}Al_{0.48}As in HEMT designs. The lattice mismatched ratio between InAlGaAs and InP substrates($\Delta a/a_0$) was 2×10^{-3} . A 350Å undoped In_{0.53}Ga_{0.47}As channel was grown on top of a 2500Å thick InAlGaAs buffer layer, and followed by a 50Å Q-spacer and a 200Å Q-Schottky layer ($n=4 \times 10^{18} \text{ cm}^{-3}$). Finally, a 100Å n⁺-InGaAs($n=3 \times 10^{18} \text{ cm}^{-3}$) cap layer was used to improve the ohmic contacts. The



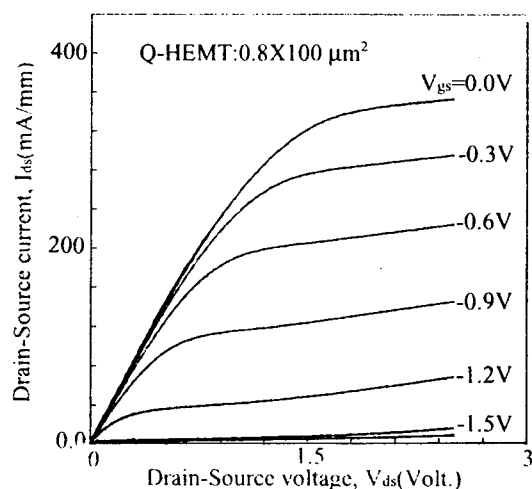


Fig.2. DC I-V characteristics of Q-HEMTs(0.8μm x 100μm) at 300 K.

sample was first characterized by Hall effect measurements. The Q-HEMT had a sheet charge density of $4.0 \times 10^{12} \text{ cm}^{-2}$, corresponding to a mobility of $6230 \text{ cm}^2/\text{V-sec}$ at 300K. The mobility enhanced to $37900 \text{ cm}^2/\text{V-sec}$ with a sheet charge density of $2.6 \times 10^{12} \text{ cm}^{-2}$ at 77K. As to the C-HEMT, a sheet charge density of $3.8 \times 10^{12} \text{ cm}^{-2}$ with a mobility of $6940 \text{ cm}^2/\text{V-sec}$ was obtained at 300K.

Device Fabrication And Characterization

Device fabrication was realized by the conventional optical lithographic techniques, excepting the gate level which was carried out by the Deep-UV light source. The detail of process can be found in Ref. 5. DC I_{DS} - V_{DS} characteristics of this InAlGaAs/InGaAs Q-HEMT with a $0.8\mu\text{m} \times 100\mu\text{m}$ gate dimension, shown in Fig. 2, revealed good channel threshold characteristics. For the Q-HEMTs, the peak extrinsic transconductance (g_m) biased at $V_{DS}=2\text{V}$ was 295 mS/mm and output conductance (g_o) was 10 mS/mm with a $0.8\mu\text{m}$ gate length. The channel threshold voltage was -1.8V . The saturation drain-source current I_{DSS} of 360 mA/mm was obtained at $V_{GS}=0\text{V}$. As to the InAlAs/InGaAs C-HEMT with the same gate-length, it revealed a peak g_m of 262 mS/mm and a g_o of 27 mS/mm. In consequence, Q-HEMTs demonstrate a better DC voltage gain ratio ($g_m/g_o \approx 30$) than that of the conventional-HEMTs($g_m/g_o \approx 10$).

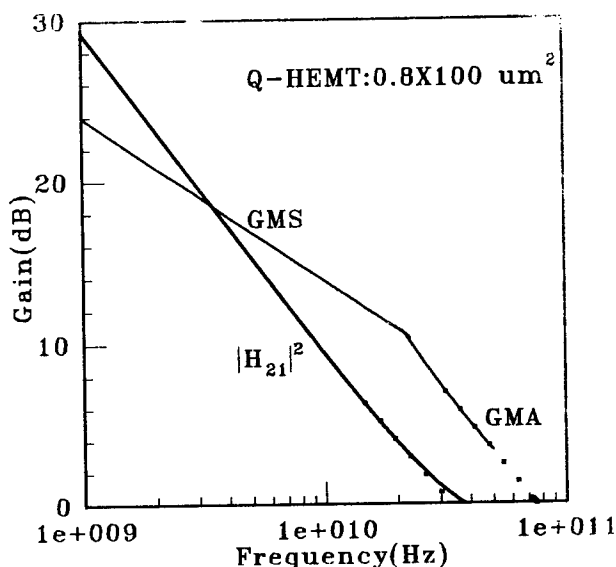


Fig.3. Microwave characteristics of Q-HEMTs at 300K.

Microwave S-parameter measurements from 45 MHz to 50GHz were carried out by a network analyzer in conjunction with a Cascade probe station. Fig. 3 shows the microwave characteristics for Q-HEMTs. The current-gain cut-off frequency (f_T) of 35GHz for Q-HEMTs was determined from H_{21} values by using a -6dB/octave slope extrapolation. The extrapolated maximum oscillation frequency (f_{max}) was 76 GHz. As to the C-HEMTs, an f_T of 22 GHz and an f_{max} of 60 GHz were obtained.

To investigate the impact of InAlGaAs Q-layers acting as a buffer layer, we studied the device sidegating effect, which is related to the trapping effect in the buffer layer [6]. Fig. 4 shows the comparison of sidegating characteristics for both C-HEMTs and Q-HEMTs. Conventional HEMTs revealed a 30% reduction of normalized drain-source current at sidegate voltage of (V_{SG})-20V. However, in the case of Q-HEMTs a slight change of I_{DS} ($\sim 10\%$) was observed. Therefore, by using the InAlGaAs buffer, the sidegating effect which is associated with the deep trap density at the channel/substrates interface, is significantly reduced.

Reliability Evaluations

Based on our previous experiments, the quaternary InAlGaAs HEMTs demonstrated better characteristics of both Schottky diode and buffer layer, which indeed improve the device performance. To evaluate the device reliability of quaternary

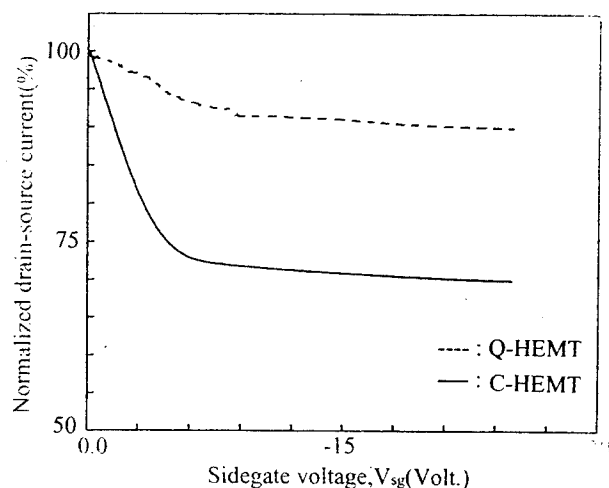


Fig.4. Normalized drain-source current versus side-gate voltage (V_{sg}) in C-HEMTs (solid line) and Q-HEMTs (dash line). Gate dimension: $1\mu\text{m} \times 100\mu\text{m}$.

In AlGaAs HEMTs, we carried out the biasing stress lifetime and thermal stability testings. Both unpassivated C-HEMTs and Q-HEMTs were continuously biased at $V_{ds}=2\text{V}$ and $V_{gs}=-0.5\text{V}$. During the stress-testing, devices were periodically measured by an HP4145B measurement. DC parameters included drain-source current, transconductance, and characteristics of Schottky diode (ideality factor, barrier height) were evaluated. Fig. 5 shows the characteristics of the normalized drain-source current versus stress-time for both Q- and C-HEMTs. Q-HEMTs revealed almost unchange of I_{ds} , and a significant 26% reduction of its original values was obtained for C-HEMTs. Under the same stressed conditions, the g_m of Q-HEMTs remained 97% of its initial value, and this value was 87% for C-HEMTs. In addition, Q-HEMTs presented almost unchanged ideality factor ($n=1.15$) and Schottky barrier height ($\Phi_B=0.54\text{eV}$). However, the n -values increased from 1.16 to 1.26, and the Φ_B decreased from 0.56 eV to 0.4 eV for C-HEMTs. To compare with C-HEMTs, the Q-HEMTs demonstrate a more reliable device performance.

Thermal stability of Schottky performance, testing from 23°C to 170°C , for both Q- and C-HEMTs is summarized in Fig. 6. The gate-leakage current, biased at $V_{gs}=-2\text{V}$, changed slightly (from 0.6 mA/mm to 0.78 mA/mm) for Q-HEMTs, and the ideality factor remained almost a constant (from 1.15 to 1.19). As

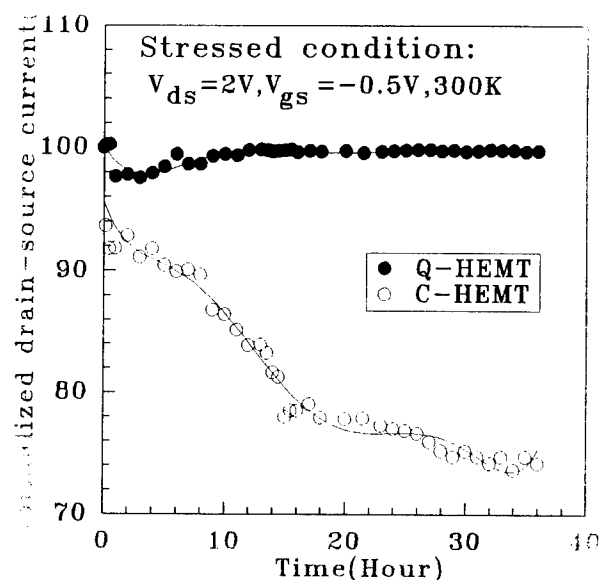


Fig.5. Normalized drain-source current for both quaternary and conventional InP HEMTs as a function of biasing stressed time.

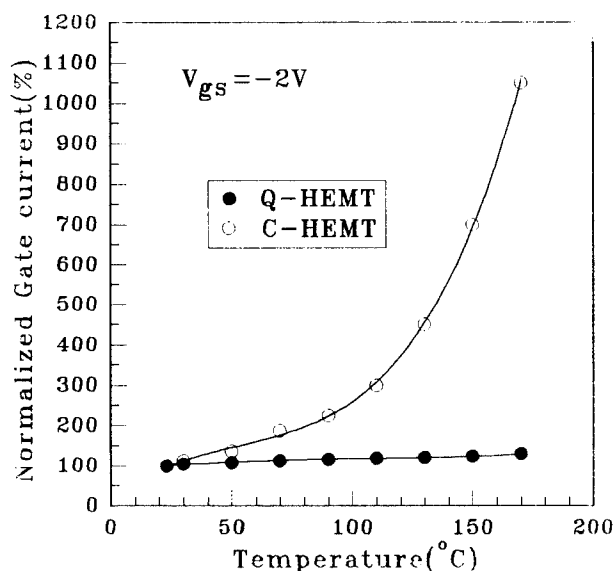


Fig.6. Temperature dependent gate-leakage current for both quaternary and conventional InP HEMTs.

for the C-HEMTs, a dramatical increase of gate-leakage current (from 0.8 mA/mm to 8.4 mA/mm) was observed by increasing the testing temperatures, and n -values behaved the same tendency (from 1.17 to 1.62). Therefore, the thermally-stressed evaluations were consistent with the previous biasing stressed measurements. It concludes that Q-HEMTs are more reliable than C-HEMTs, which is mainly related to the improvement of InAlGaAs layer.

Conclusions

InAlGaAs/InGaAs Q-HEMTs grown on InP substrates were fabricated and evaluated. By adding Ga atoms into the InAlAs layers, it improves the device performance. The DC peak extrinsic g_m increased from 240 mS/mm for C-HEMTs to 295 mS/mm for Q-HEMTs, corresponding to the RF performance of 17 GHz for C-HEMTs and 35 GHz for Q-HEMTs respectively. The sidegating effect is also reduced. Furthermore, the device became more reliable by using this quaternary InAlGaAs as a Schottky and a buffer layer. Therefore, the quaternary InAlGaAs HEMTs can improve device performance, and are more reliable than that of the C-HEMTs, which provide a potential application for microwave communication.

Acknowledgements

This work at NCU was supported by the National Science Council, Republic of China, under contract no. NSC83-0404-E-008-005.

References

- [1] M. Matloubian *et al.*, IEEE MTT-S Int. Microwave Symp. Dig., pp. 721-724, 1991.
- [2] M. Matloubian *et al.*, IEEE Electron Dev. Lett., Vol. 14, No. 4, pp. 188-189, Apr. 1993.
- [3] L. D. Nguyen *et al.*, IEEE Electron Dev. Lett., Vol. 13, No. 3, pp. 143-145, Apr. 1992.
- [4] J. B. Kuang *et al.*, IEEE Electron Dev. Lett., Vol. 9, No. 12, pp. 630-632, Dec. 1988.
- [5] C. S. Wu *et al.*, Journal of The Chinese Institute of Electrical Engineering, Vol. 1, No. 1, pp. 45-50, 1994.
- [6] A. S. Brown, U. K. Mishra, L. E. Larson and S. E. Rosenbaum, Inst. Phys. Conf. Ser. No. 96, pp. 445-448, 1988.

M. Amano, S. Fujita⁺, S. Hosoi⁺⁺, T. Noda, A. Sasaki, Y. Ashizawa

Toshiba Research and Development Center,

1 Komukai Toshiba-cho, Saiwai-ku, Kawasaki 210, Japan

Toshiba Microelectronics Center⁺⁺, 1 Komukai Toshiba-cho, Saiwai-ku, Kawasaki 210, JapanPresent address: Angstrom Technology Partnership⁺, 1-1-4 Higashi, Tsukuba, Ibaraki 305, Japan

1. Introduction

InP-based HEMTs have exhibited excellent DC and RF performances[1,2], and have attracted much attention in millimeter-wave device applications. In InP-based HEMTs, which have an undoped InAlAs Schottky contact (SC) layer, use of an InAlAs SC layer is not necessarily favorable from the viewpoint of attaining precise control of gate recess etch and reliability for thermal stress. In our previous study, we proposed the use of a strained InGaP SC layer as a substitute for the conventional InAlAs SC layer, and showed that HEMTs with an InGaP SC layer (InGaP-SC-HEMTs) enabled selective wet gate recess etching and had better reliability under thermal stress even without a passivation layer[3]. However, the gate characteristics of InGaP-SC-HEMTs behaved poorly compared to those of conventional HEMTs, and exact evaluation of the influence of a strained InGaP layer on RF performance had not succeeded yet. Hence the suitability of the use of an InGaP SC layer remains unclear. In this study, Schottky diode characteristics have been improved by using both annealed Pt for Schottky contact metal and undoped InAlAs for underlayer of the InGaP layer. InGaP-SC-HEMTs with 0.1 μm T-shaped gate have been fabricated using Pt-based metals/InGaP/InAlAs Schottky gate contact in order to clarify the influence of insertion of a strained InGaP layer on DC and RF performances.

2. Schottky contacts on strained InGaP

Electrical characteristics of Schottky contacts formed on layered semiconductor heterostructure, such as Schottky gate contacts in HEMT structures, are determined by not only contact metals but also what materials compose the heterostructure. In order to improve the gate characteristics of InGaP-SC-HEMTs, we investigated Schottky diodes composed of Schottky contact metal, undoped strained thin-InGaP layer, and bulk-semiconductor layer underlying the InGaP layer, which we call underlayer thereafter, about following two points: a) effect of the underlayer on Schottky characteristics, and b) which metal should be adopted for the Schottky contact metal.

First, the effect of the underlayer was investigated. Either InP or InAlAs lattice-matched to InP was applied for the underlayer. The heterostructures were grown on n-InP substrates by MOCVD. Ga content of InGaP was 0.25, and the thickness of the InGaP layer was 10 nm, which was thinner than the critical thickness estimated based on Matthews & Blakeslee's formula[4]. Au was used for the Schottky contact metal, which was deposited by electron beam evaporator. The Schottky current-voltage(I-V) characteristics were measured on these diodes at room temperature. Schottky barrier height (ϕ_B) was calculated based on measured forward I-V characteristics. The obtained ϕ_B of the diodes with the InP underlayer was 0.46 eV. For the diodes with the InAlAs underlayer, ϕ_B was largely dependent on the donor concentration (N_d) of InAlAs. In the case of $N_d=5 \times 10^{17} \text{ cm}^{-3}$, ϕ_B was 0.52 eV, whereas in the case of $N_d=2 \times 10^{15} \text{ cm}^{-3}$, it was 0.65 eV. From these results, the Schottky characteristics of Au/thin-InGaP/bulk-underlayer diodes were improved by

using an underlayer with smaller electron affinity, as discussed in Ref. 5. Therefore we adopted InAlAs with low N_d for the underlayer of a HEMT structure with the InGaP SC layer.

Next, Schottky contact metals on thin-InGaP/InAlAs heterostructure were investigated. In order to obtain a good Schottky contact, use of a metal with a large work function is effective. Pt is one of the typical metals with large work function: the work function of Pt is 5.7 eV whereas that of Ti, which is widely used for Schottky contact metal in HEMT, is 4.3 eV. Moreover, Pt easily diffuses into III-V compound semiconductor materials, and forms stable compound with group-V materials[6,7], which has higher work function than before diffusion[6]. It can be expected that undesirable gate sinking caused by Pt diffusion is minimized by using annealed Au/Pt/Ti/thin-Pt gate contact structures as previously reported on conventional HEMT with an InAlAs SC layer[8]. Schottky diodes with either Pt or Ti contact metal on 10-nm $\text{In}_{0.75}\text{Ga}_{0.25}\text{P}/\text{InAlAs}$ were fabricated to compare Pt contacts with Ti contacts. Pt, Ti/InAlAs diodes were also fabricated for reference. The ϕ_B obtained from the I-V measurements are summarized in Table 1. As shown in Table 1, the ϕ_B of Pt/InGaP/InAlAs diodes was about 0.7 eV, whereas that of Ti/InGaP/InAlAs diodes was 0.59 eV. Thus a relatively high Schottky barrier was obtained by using Pt contacts according to expectation. Moreover, the diodes with Pt contacts were annealed in N_2 ambient at 350 °C for 30 minutes. After annealing, the Schottky characteristics were improved as shown in Fig. 1. The ϕ_B of Pt/InGaP/InAlAs diodes were enhanced to 0.78 eV, comparable to that of annealed Pt/InAlAs diodes. This

enhancement was thought to be caused by Pt diffusion. Two cases are considered in forming Schottky contacts: 1) diffused Pt formed Pt_2/InGaP Schottky contacts, and 2) diffused Pt penetrated through the thin InGaP layer into the underlying InAlAs layer, and a substantial metallurgical junction was formed between PtAs_2 and the InAlAs layer. Since the ϕ_B of the annealed Pt/InGaP/InAlAs was close to that of annealed Pt/InAlAs, the latter case is probable. However it is not possible to conclude which is the actual cause of the Schottky barrier enhancement at the present, only from these results.

Thus good Schottky contacts on strained InGaP were obtained by using annealed Pt/thin-InGaP/InAlAs diode structure, which forms Schottky barrier as high as that of annealed Pt/InAlAs diodes. It should be recalled here that Pt/thin-InGaP/InAlAs structures are better than Pt/InAlAs structures from the viewpoint of reliability of HEMT under thermal stress.

Table 1 Schottky barrier height ϕ_B [eV] of the fabricated diodes

	InGaP/InAlAs	InAlAs
Ti	0.59	0.69
Pt	0.70	0.73
Annealed Pt	0.78	0.78

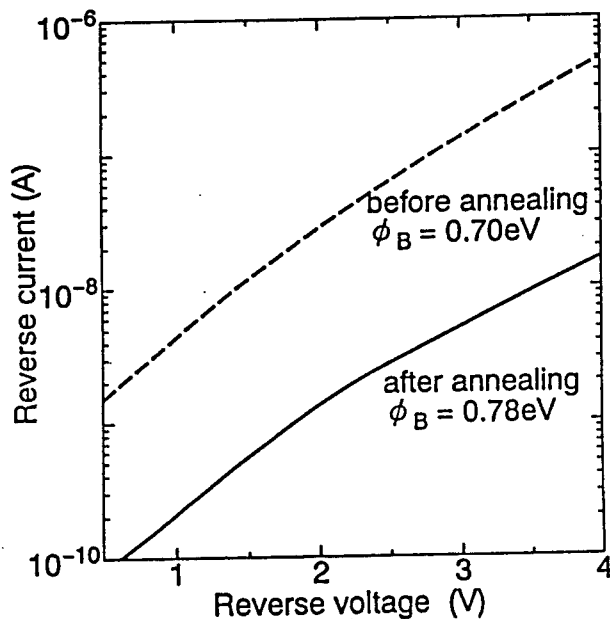


Fig. 1 Reverse current-voltage characteristics of Pt/thin-InGaP/InAlAs Schottky diodes of 200 μm diameter.

3. 0.1 μm T-gate InGaP-SC-HEMTs

InGaP-SC-HEMTs with a 0.1 μm T-shaped gate were fabricated. Fig. 2 shows the schematic cross section of the HEMT structure, which was grown by MOCVD on Fe-doped InP substrates. The SC layer was composed of 5 nm $\text{In}_{0.85}\text{Ga}_{0.15}\text{P}$ and 5 nm undoped InAlAs under-SC-layer. Wet chemical etching was used for mesa isolation. T-shaped gates were fabricated using standard electron-beam lithography and lift-off techniques. Gate recess etching was performed in $\text{H}_3\text{PO}_4/\text{H}_2\text{O}_2/\text{H}_2\text{O}$ solution, which selectively etched the n-InGaAs cap layer. Au/Pt/Ti/thin-Pt metal layers were utilized to form gate contacts. As a reference, conventional InAlAs-SC-HEMTs, which had the same layer structures as those of InGaP-SC-HEMTs except for the SC layer, were also fabricated using the same fabrication process.

Fig. 3 (a) and (b) shows DC characteristics of 140 μm width gate InGaP-SC-HEMTs. As shown in Fig. 3(a), low reverse leakage current was obtained: the leakage current at gate voltage $V_g = -1\text{ V}$ was about 20 $\mu\text{A}/\text{mm}$, whereas that of InGaP-SC-HEMTs fabricated in our previous study[3] was about 500 $\mu\text{A}/\text{mm}$. These good gate characteristics resulted from using both annealed thin-Pt and the undoped InAlAs under-SC-layer. The maximum extrinsic transconductance ($g_{m\text{max}}$) of the InGaP-SC-HEMTs was as high as 1000 mS/mm, whereas that of conventional HEMTs was around 700 mS/mm, as shown in Fig. 4. This result was due to the lower source

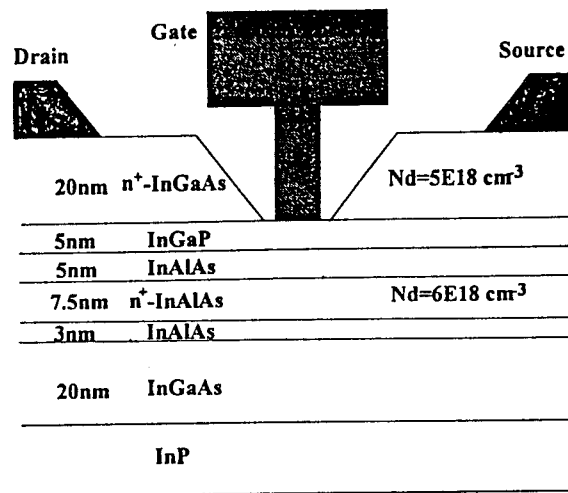


Fig. 2 Schematic cross section of the InGaP-SC-HEMT.

resistance (R_s) of this HEMT structure: R_s of InGaP-SC-HEMTs was about $0.5 \Omega \text{ mm}$, whereas that of conventional HEMTs was $0.7 \Omega \text{ mm}$. This effect was thought to be mainly caused by insertion of InGaP, which has a larger electron affinity than InAlAs. This is an additional advantage of using an InGaP-SC layer.

High frequency characteristics of InGaP-SC-HEMTs were estimated. The current gain (h_{21}) was calculated based on the measured S parameters from 1 to 30 GHz,

and unity current gain frequency (f_T) was estimated by extrapolation of h_{21} . Fig. 5 shows the obtained f_T against drain current of $0.1 \times 200 \mu\text{m}^2$ devices. As shown in Fig. 5, the f_T of the InGaP-SC-HEMTs was more than 140 GHz, which was as high as that of conventional HEMTs. This result means that insertion of strained InGaP layer does not degrade electron transport property of 2DEG in InGaAs channel layer.

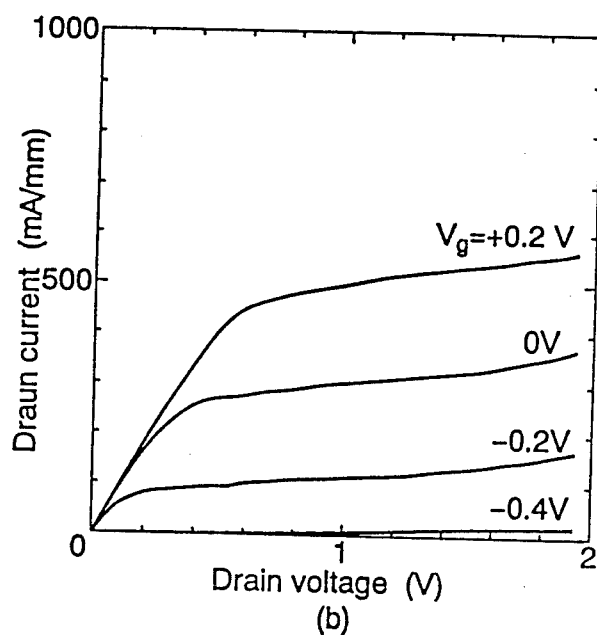
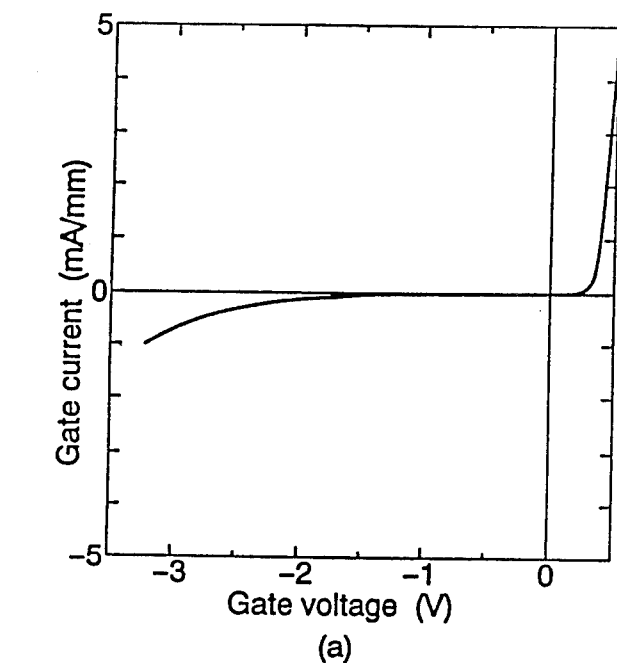


Fig. 3 Schottky gate characteristics (a) and drain current I_d -drain voltage V_d characteristics (b) of a $0.1 \mu\text{m} \times 140 \mu\text{m}$ T-gate InGaP-SC-HEMT.

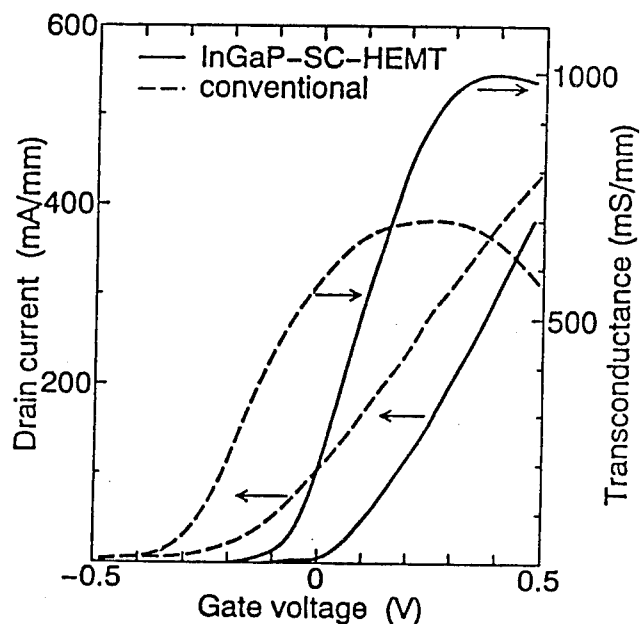


Fig. 4 Extrinsic transconductance g_m and drain current I_d against gate voltage V_g at $V_d = 1.0 \text{ V}$ of an InGaP-SC-HEMT and a conventional HEMT.

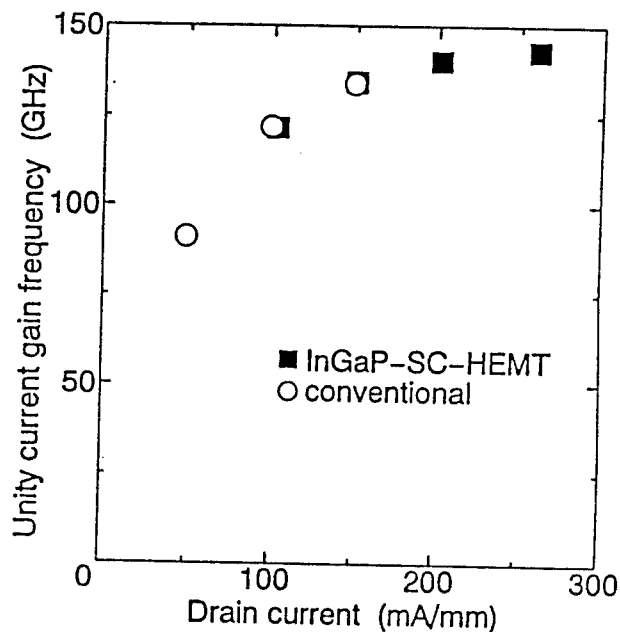


Fig. 5 Unity current gain frequency f_T against I_d at $V_d = 1.0 \text{ V}$ of an InGaP-SC-HEMT and a conventional HEMT.

4. Conclusion

By using both annealed Pt-based gate metals and undoped InAlAs under-SC-layer, gate characteristics of InGaP-SC-HEMTs were improved, and high $g_{m\max}$ and f_T were obtained for 0.1 μm T-gate devices. Moreover, the lower R_s of InGaP-SC-HEMTs is expected to provide better noise characteristic than that of conventional HEMTs.

Acknowledgment

The authors would like to thank M. Azuma, Y. Ikawa and M. Obara of Toshiba Research and Development Center for advice and encouragement.

References

- [1] M. Wojtowicz, R. Lai, D. C. Streit, G. I. Ng, T. R. Block, K. L. Tan, P. H. Liu, A. K. Freudenthal, and R. M. Dia, "0.10 μm graded InGaAs Channel InP HEMT with 305 GHz f_T and 340 GHz f_{\max} ," IEEE Electron Device Lett., vol. 15, pp. 477-479, 1994.
- [2] T. Akazaki, T. Enoki, K. Arai, Y. Umeda, and Y. Ishii, "High-frequency performance for sub-0.10 μm gate InAs-inserted-channel InAlAs/InGaAs HEMT," Electron. Lett., vol. 28, pp. 1230-1231, 1992.
- [3] S. Fujita, T. Noda, C. Nozaki, and Y. Ashizawa, "InGaAs/InAlAs HEMT with a strained InGaP Schottky contact layer," IEEE Electron Device Lett., vol. 14, pp. 259-261, 1993.
- [4] J. W. Matthews and A. Blakeslee, "Defects in epitaxial multilayers," J. Cryst. Growth vol. 27, pp. 118-125, 1974.
- [5] S. Fujita, T. Noda, C. Nozaki, A. Wagai, and Y. Ashizawa, "Schottky characteristics of contacts to complex heterostructures," in Proc. of Mat. Res. Soc. Symp., vol. 326, pp. 469-474, 1993.
- [6] C. Fontaine, T. Okumura, and K. N. Tu, "Interfacial reaction and Schottky barrier between Pt and GaAs," J. Appl. Phys. vol. 54, pp. 1404-1412, 1983.
- [7] S. E. Mohny and Y. A. Chang, "Interfacial reactions in Pt/InP contacts," J. Appl. Phys. vol. 74, pp. 4403-4408, 1993.
- [8] N. Harada, S. Kuroda, and K. Hikosaka, "N-InAlAs/InGaAs HEMT DCFL inverter fabricated using Pt-based gate and photochemical dry etching," IEICE Trans. Electron., vol. E75-C, pp. 1165-1171, 1992.

SPACER DESIGN TO IMPROVE THE BREAKDOWN VOLTAGE OF InAlAs-InGaAs HEMTs

J. TARDY, X. LETARTRE, P. VIKTOROVITCH, M. GENDRY

Laboratoire d'Electronique- LEAME (Unité CNRS #848) - Ecole Centrale de Lyon
BP 163 - 69131 Ecully cedex - FRANCE

D.A. THOMPSON and J.G. SIMMONS

Center for Electrophotonic Materials and Devices - CEMD - Mac Master University
Hamilton, Ontario - CANADA

Introduction

Although outstanding performances for ultra low noise applications at microwave frequencies were achieved on AlInAs/GaInAs HEMTs, a remaining drawback is the low breakdown voltage which impedes further applications requiring high voltage, high drain current (for power devices) or low gate leakage (for optoelectronic devices). In the off state, the gate leakage current is generally attributed to a two step process: first, impact ionization in the channel create electron-hole pairs, secondly, the resulting holes reach the gate where they are collected, thus generating an excess leakage current. Consequently, two parameters are of a prime importance on the high voltage behavior of the HEMT's: the gap (E_g) of the channel material which mainly determines the impact ionization rate and the energy barrier seen by the holes created in the channel (E_B) in their path towards the gate. In order to prevent this leakage, several improvements of the structure design were proposed which all tend to either minimize the ionization mechanism in the small gap InGaAs or to increase the holes barrier:

- i)-The reduction of the channel thickness leads to a larger gap by quantization effects [1].
- ii)-A suitable channel design reduces the electric field in the channel [2,3].
- iii)-An Al-rich InAlAs spacer [4,5] or a InGaP spacer [6,7] increases the hole barrier.

The work presented in this paper shows that the use of a mixed InAlAs/InP spacer rather than a conventional InAlAs spacer considerably improves the breakdown voltage of the devices in taking advantage of the large valence band offset of the InP/InGaAs heterojunction (0.42 eV). Also, this structure is entirely lattice matched thus avoiding the growth problems associated with strained layers. Furthermore the noise associated with this device has been shown to be lower than that of conventional AlInAs/GaInAs HEMTs thanks to the low defect concentration in InP as compared to InAlAs

Theoretical approach

Impact ionization rate in the channel is governed by the threshold energy E_{th} defined as the minimum energy needed to ionize an electron-hole pair. Assuming parabolic bands, the conservation of energy and momentum [8] leads to the two equations:

$$m_n V_i = m_n V_f + m_n V_n + m_p V_p \quad (1a)$$

$$m_n V_i^2 = m_n V_f^2 + m_n V_n^2 + m_p V_p^2 \quad (1b)$$

where m_n and m_p are the in plane effective masses of electrons and holes and V is the velocity. The index refers to the four carriers involved in the process: i for the incident electron, f for the same electron after impact, n and p for the electron and the hole created by impact. Equations (1) have a solution only if the kinetic energy of the incident electron verifies:

$$1/2 m_n V_i^2 \geq E_{th} = E_g \{1 + (1 + m_p/m_n)^{-1}\} \quad (2)$$

Considering an incident electron which has just the threshold energy, the kinetic energy of the generated hole is:

$$E_p = 1/2 m_p V_p^2 = E_g m_n m_p / \{(2m_n + m_p)(m_n + m_p)\} \quad (3)$$

then the barrier seen by the holes is :

$$E_B = \Delta E_v - HH1 - E_p \quad (4)$$

where ΔE_v is the InP/InGaAs valence band offset and HH1 is the first confinement energy of heavy holes (Fig.1). For our two structures we found $E_{th} = 0.79$ eV. However, E_B is 0.19 eV for the conventional structure and 0.32 eV for the structure with a InP/InAlAs spacer.

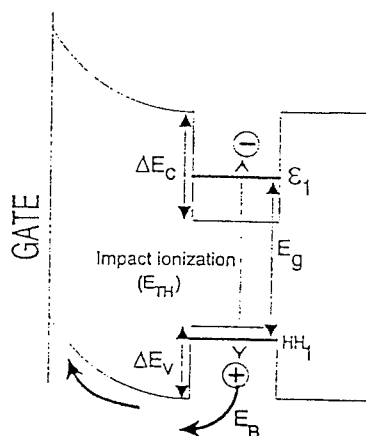


Fig.1: Schematic view of the energy band diagram and of the ionization process in the channel.

Fig.2a and Fig.2b show the cross sections and the actual band structures for the two devices we compared (the band structure is not drawn up to the surface for clarity of the figure). Schrödinger-Poisson calculations were performed to design structures with the same charge transfer in the two channels. A 100Å thick InAlAs spacer for the conventional device and a mixed spacer of 40Å InP/ 60Å InAlAs have been shown to give the same surface charge n_s . The increased barrier for the holes in the structure with the mixed spacer is here clearly evidenced.

InGaAs	cap layer undoped - 7nm
InAlAs	barrier undoped - 25nm
InAlAs	donnor layer 5E18cm ⁻³ - 9nm
InAlAs	spacer layer undoped - 10nm
InGaAs	channel undoped - 50nm
InAlAs	buffer
InP	S.I. substrate

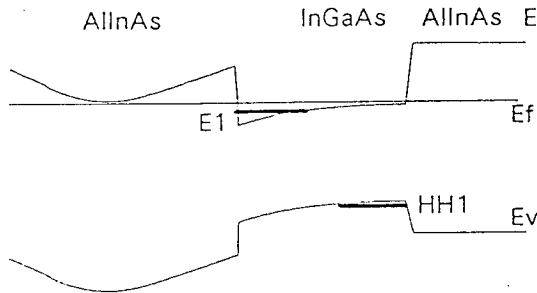


Fig.2a: layer structure and calculated band diagram for the structure with the conventional InAlAs spacer.

InGaAs	cap layer undoped - 7nm
InAlAs	barrier undoped - 25nm
InAlAs	donnor layer 5E18cm ⁻³ - 9nm
InAlAs	spacer layer #1 undoped - 6nm
InP	spacer layer #2 undoped - 4nm
InGaAs	channel undoped - 50nm
InP	buffer
InP	S.I. substrate

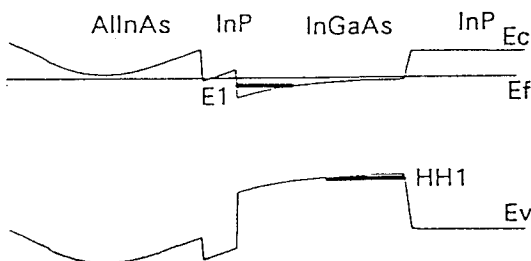


Fig.2b: Layer structure and calculated band diagram for the structure with the mixed InP/InAlAs spacer.

Device fabrication

The structures with conventional InAlAs spacer were grown by MBE at LEAME. The growth temperature was 500°C for all the layers. The structures with the mixed spacer were grown in a two step process: first, the buffer, the channel and the InP spacer were grown at CEMD in a gas source MBE, secondly, the rest of the structure was epitaxially regrown at LEAME. In order to regrow excellent layers after the interruption and transfer of the samples from an MBE system to another one, an optimized surface preparation was applied which has been described in details elsewhere [9]. This procedure is known to lead to a perfectly smoothed and oxide free interface. However, some electrically active traps may remain at this interface which can degrade the electrical characteristics of the device (see below).

Besides the differences in spacer layers, the two structures also differ from each other by the nature of the buffer (InAlAs or InP).

Classical devices processing was then carried out. First mesa isolation was performed and selective etching was used to avoid any contact between the gate and the channel but also between the gate and the InP spacer. Then, Pd-Ge-Ag-Au ohmic contacts were evaporated and annealed at 435°C for 75s onto a hot plate. Pd-Au was used as the gate metal. Devices with gate length from 1 to 4μm and gate width of 150μm were processed.

The breakdown voltage in the off-state was measured in the diode configuration and classically defined as the gate voltage for which the gate current reaches 1mA/mm.

Results

The transfer characteristics $I_D(V_D)$ for a 2μm long FET are shown on fig.3a and 3b.

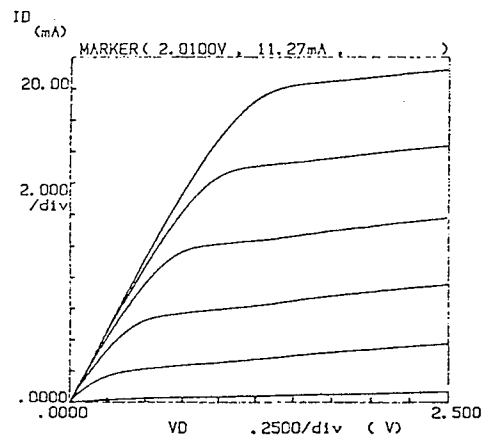


Fig.3a: I_D-V_D characteristics for conventional device. V_g varies from +0.5V to -0.75V with -0.25 steps.

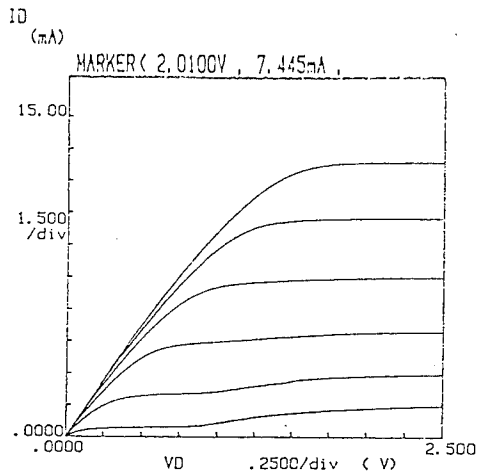


Fig.3b: I_D - V_D characteristics for mixed spacer device. V_G varies from $+0.5V$ to $-0.75V$ with -0.25 steps.

We observe that the saturation current is slightly lower for the device with the mixed spacer. This could be inferred to the presence of states at the InP/InAlAs interface which trap the carriers. The transconductance g_m is also lower. Intrinsic transconductance is only 95 mS/mm instead of 230 mS/mm for the conventional device. Again, the presence of traps can explain this decreasing. The output conductance, g_0 , is seen to be very small for the mixed spacer FET (1.2mS/mm) against 8mS/mm for the conventional device. The voltage gain is then significantly increased when using the new mixed spacer from 29 to 79.

For the mixed spacer device, it is observed a small kink effect when the FET is nearly off whereas the saturation current is very flat in the on-state as we just saw. The release in the channel of charges trapped in the states at the regrowth interface could again explain this behaviour. A refined interface preparation before the regrowth should reduce this excess current and improve the pinch-off.

The breakdown voltage is determined for the device in the off-state biased in a diode configuration with source and drain shorted. Fig.4 reports the reverse characteristics for the two devices.

The breakdown voltage V_{bd} is classically defined as the gate voltage for which a gate current of 1mA/mm is reached. V_{bd} increases from $-8V$ for the conventional device to $-19V$ for the device with the mixed spacer. The gate current at moderate negative gate voltage ($V_g = -2$ to $-5V$) is about two orders of magnitude lower for the device with the mixed spacer. Similar improvement was observed with a pseudomorphic Al-rich InAlAs spacer [4]. The use of highly strained InGaP spacer also led to a similar improvement, the valence band offset with InGaAs being the same as with InP.

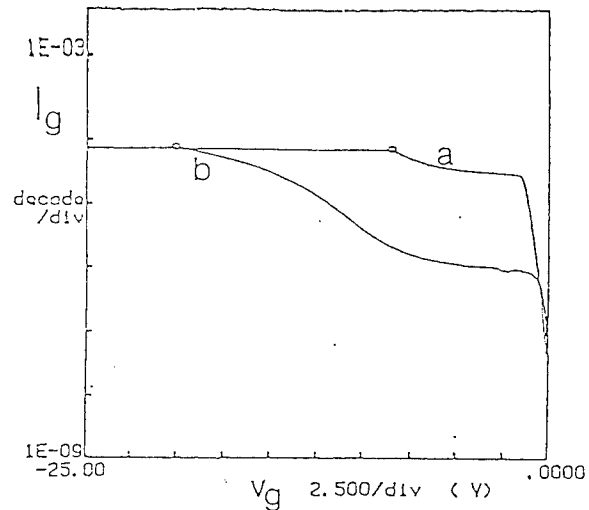


Fig.4: Reverse current voltage characteristics of the gate-to-source diode limited to 1mA/mm.

a) InAlAs spacer: $V_{bd} = -8V$.

b) Mixed InP-InAlAs spacer: $V_{bd} = -19V$.

Conclusion

We demonstrate in this paper a new spacer design for AlInAs/GaInAs HEMTs in view to improve the breakdown voltage. It consists in a mixed InP-InAlAs spacer. A large increase of the breakdown voltage has been obtained as compared to a conventional InAlAs spacer. This is due to the large valence band offset at the InP-InGaAs heterojunction which induce a high barrier for the holes generated by impact ionization. Another point of interest is that structure is entirely lattice matched thus avoiding problems usually encountered with strained layers.

A surface preparation step was included in the process after the transfer from the gas source MBE to the conventional solid source MBE in order to minimize the defects at the interface between InP and InAlAs. Although this surface preparation is well optimized from the growth point of view, a relatively high density of defects remains, resulting in a kink in the I-V characteristics when the device is close to the off-state (due to electron detrapping). All *in situ* growth should avoid this drawback and lead to high grade devices.

At last, it has been observed that when structures without InAlAs or at least without interface between InAlAs and the channel are designed, the noise due to traps in the structures is lowered. Structures with mixed spacer show a Low Frequency Noise Index about one order of magnitude lower than the conventional one [10].

We may conclude that the mixed InP/InAlAs spacer could be a good alternative for low noise devices with high voltage capabilities.

References

- [1] S.R. Bahl and J.A. del Alamo, IEEE-Electron Device Lett. **13** (1992) 123
- [2] K.B. Chough, C. Caneau, W.P. Hong and J.I. Song, IEEE-Electron Device Lett. **15** (1994) 33
- [3] K.B. Chough, W.P. Hong, C. Caneau, J.I. Song, K.I. Jeon, S.C. Song and K. Lee, Electron. Lett. **30** (1994) 453
- [4] C. Heedt, F. Buchali, W. Prost, W. Brockerhoff, D. Fritzsche, H. Nickel, R. Losch, W. Schlapp and F.J. Tegude, IEEE-Trans. Electron. Devices **41** (1994) 1685
- [5] S.R. Bahl, B.R. Bennett and J.A. del Alamo, IEEE-Electron Device Lett. **14** (1993) 22
- [6] F. Scheffer, C. Heedt, R. Reuter, A. Lindner, Q. Liu, W. Prost and F.J. Tegude, Electron. Lett., **30** (1994) 169
- [7] F. Scheffer, A. Lindner, C. Heedt, R. Reuter, Q. Liu, W. Prost and F.J. Tegude, Proceedings of the 6th IPRM Conference, Santa-Barbara, 1994, p.439
- [8] J.P.R. David, M.J. Morley, A.R. Wolstenholme, R. Grey, M.A. Pate, G. Hill, G.J. Rees and P.N. Robson Appl. Phys. Lett. **61** (1992) 2042
- [9] P.G. Hofstra, D.A. Thompson, B.J. Robinson, M.P. Besland, M. Gendry, P. Regreny and G. Hollinger Submitted to J. Appl. Phys.
- [10] P. Rojo-Romeo, P. Viktorovitch, X. Letartre, J. Tardy, D.A. Thompson and J.G. Simmons, These Proceedings

The impact of pseudomorphic AlAs spacer layers on the gate leakage current of InAlAs/InGaAs heterostructure field-effect transistors

ThP15

U. Auer, R. Reuter, P. Ellrodt, C. Heedt, W. Prost, F. J. Tegude

Solid-State Electronics Department, Sonderforschungsbereich SFB 254,
Gerhard-Mercator-University Duisburg, Kommandantenstraße 60, D-47057 Duisburg, Germany

Introduction

The parasitic gate current through the Schottky gate contact of InP based InAlAs/InGaAs heterostructure field-effect transistors (HFETs) may cause a deterioration of the off-state breakdown [1], the unilateral gain and the noise performance [2]. Much effort has been paid to enhance the Schottky barrier height for reducing the (thermionic) field emission electron current by replacing the InAlAs-barrier layer by a high-band-gap material [3-4]. But the main contribution to the gate leakage current at sufficient gate-source and gate-drain breakdown voltages are holes, tunneling to the gate electrode after generation in the InGaAs-channel by impact ionization [5-6]. This hole current can be reduced by increasing the valence band energy barrier in the spacer layer in order to lower the transfer rate [7-8].

In this study the impact of pseudomorphic AlAs containing spacer layers as hole barriers will be systematically investigated. Based on the correlation between the hole leakage current and the gate-drain breakdown voltage, the hole gate current reduction factor is evaluated as a function of the AlAs-spacer thickness.

Experiment

The heterostructures were grown by solid source MBE using a Varian Gen II apparatus. All samples exhibit the following layer sequence (cf. Fig. 1). On top of the buffer, a 20 nm InGaAs channel layer was grown, followed by a d_p thick AlAs- and a d_l thick InAlAs-spacer layer, a 8 nm InAlAs supply layer with a doping level of $5 \times 10^{18} \text{ cm}^{-3}$ and a 20 nm thick InAlAs barrier layer. Finally, a 5 nm undoped and a 5 nm doped ($1 \times 10^{19} \text{ cm}^{-3}$) InGaAs cap layer for ohmic contact formation completes the HFET structure.

cap	5 nm	InGaAs: Si $1 \times 10^{19} / \text{cm}^3$
	5 nm	InGaAs
barrier	20 nm	InAlAs
supply	8 nm	InAlAs: Si $5 \times 10^{18} / \text{cm}^3$
spacer	d_l	InAlAs
	d_p	AlAs (hole barrier)
channel	20 nm	InGaAs
buffer	10 nm	InAlAs
	1 nm	InGaAs
	10 nm	InAlAs
	1 nm	InGaAs
	80 nm	InAlAs
substrate		S.I. InP

Fig.1: HFET layer structures with spacer layers incorporating a strained AlAs layer as a hole barrier.

All layers are lattice-matched to InP except the AlAs spacer layer with the thickness d_p , varying from 0 to 4.3 nm as shown in Tab. 1.

sample	index	d_p (nm)	d_l (nm)
DU338	0 ML	0	2.4
DU321	2 ML	0.5	1.8
DU322	4 ML	1.1	1.2
DU323	8 ML	2.2	0.6
DU367	12 ML	3.2	0
DU368	16 ML	4.3	0

Tab. 1: The AlAs monolayer (ML) number as the sample index, the thickness of the pseudomorphic AlAs (d_p) and of the lattice-matched InAlAs spacer layer (d_l).

In the following, the layer structures are indexed by their AlAs-monolayer number (ML). In samples "0 — 8 ML" the spacer was extended by a lattice-matched InAlAs layer of thickness d_l . The growth was performed at a V/III-beam equivalent pressure (BEP) ratio of 60 and at a growth rate of $0.90 \mu\text{m/h}$ for InGaAs and $0.92 \mu\text{m/h}$ for InAlAs, respectively. After thermally cleaning at wafer temperatures up to 545°C measured by a pyrometer, the growth of the samples started at 420°C in order to increase the InAlAs resistivity. A temperature spike up to 540°C near the buffer/channel interface increases the low field mobilities as shown in [9]. The deposition of the highly strained AlAs-spacer was performed at 440°C for kinetically restricting the migration length of the surface adatoms to inhibit island formation. The temperature changes were performed during growth stops.

No degradation of the Hall mobilities were observed up to eight AlAs monolayers ($d_p \leq 2.2 \text{ nm}$) as shown in Tab. 2, resulting in high transit frequencies of $f_T > 50 \text{ GHz}$ ($L_{\text{gate}} \approx 0.7 \mu\text{m}$) and unilateral gain

cut-off frequencies of $f_{max} > 200$ GHz. The samples indexed by 12 ML and 16 ML show degraded transport properties indicating a relaxation of the strained AlAs layer due to an exceeding the critical thickness.

index	$\mu(300\text{ K})$ (cm ² /Vs)	$\mu(77\text{ K})$ (cm ² /Vs)	$n_s(300\text{ K})$ ($\times 10^{12}$ /cm ²)
0 ML	12400	55400	2.7
2 ML	12400	51500	2.5
4 ML	12100	53800	2.7
8 ML	12800	55100	2.4
12 ML	6310	15400	2.4
16 ML	5380	17700	2.4

Tab. 2: Low-field mobilities and sheet densities at 300 K and 77 K.

Results and Discussion

Our studies reveal a correlation between the hole gate current I_h due to impact ionization and the gate-drain breakdown voltage $V_{B, gd}$ at 1 mA/mm reverse current of the gate-drain diode. In low-band-gap materials like InGaAs, impact ionization can occur even at low drain-source voltages V_{ds} . The generation rate of the electron-hole pairs is proportional to the drain current I_d and the impact ionization coefficient α , depending on the applied drain-gate voltage $V_{gd} = V_{ds} - V_{gs}$. Due to the strong vertical electric field at the drain-end of the gate, a part of the generated holes can tunnel to the gate electrode (cf. Fig. 2), contributing to the gate leakage current in addition to the electron tunneling current I_e through the Schottky-barrier.

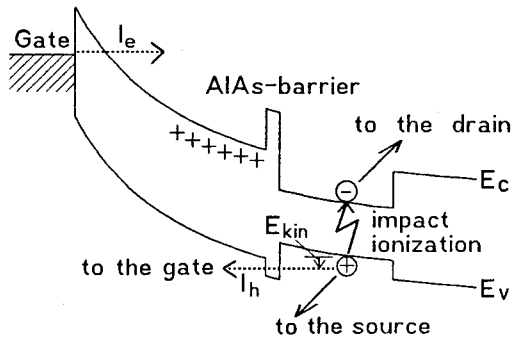


Fig. 2: The estimated band diagram at the drain end of the gate, indicating the origin of the hole gate current.

This hole current deforms the plot of $I_g(V_{gs})$ into a bell-shaped curve as shown in Fig. 3 for a constant $V_{ds} = 3$ V. At gate-source voltages smaller than the

threshold voltage V_T , no holes are generated by impact ionization because $I_d = 0$. Therefore, the gate leakage current at $V_{B, gd} < V_T$ only consists of tunneling electrons.

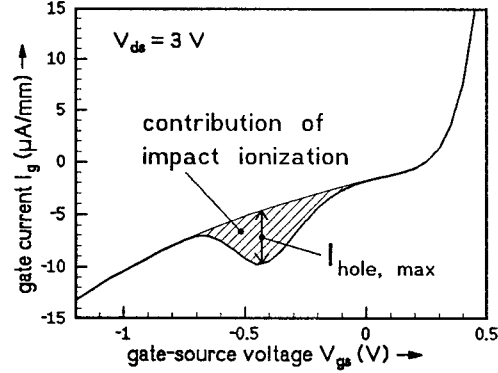


Fig. 3: The gate current of type 16 ML, including the hole gate current I_h at $V_{ds} = 3$ V.

The gate-drain breakdown voltage and the hole gate current are strongly dependent on the gate-recess procedure. The gate-recess was carried out with a succinic acid based etchant, selective on InGaAs to InAlAs, resulting in a lateral etching of the InGaAs-cap layer, and a non-selective phosphoric acid based etchant for defining the threshold voltage. Fig. 4 exemplary demonstrates the dependence of $V_{B, gd}$ and I_h on the etching time in a succinic acid based solution. I_h is represented by the maximum of the hole gate current contribution, $I_{h, max}$, which is extracted according to Fig. 3 at a fixed drain-source voltage $V_{ds} = 3$ V.

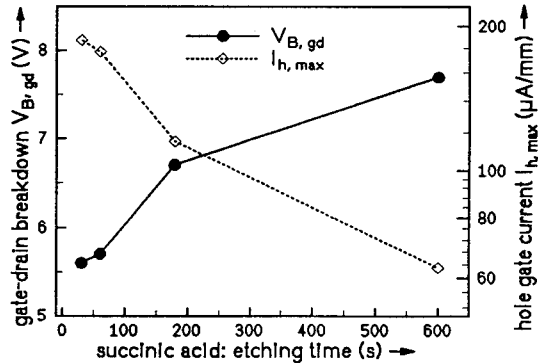


Fig. 4: The gate-drain breakdown voltage at $I_g = -1$ mA/mm and the maximum hole gate current at $V_{ds} = 3$ V of a lattice-matched HFET with a donor concentration in the supply layer of 4×10^{18} cm⁻³. The recess with a succinic acid based solution results in a lateral etching of the InGaAs-cap layer.

The lateral etching of the InGaAs-cap layer by the succinic based solution extends the free InAlAs-surface towards the source and drain contacts. This

corresponds, via surface depletion, with an additional channel resistance, lowering the drain current. Furthermore, the extension of the free surface enhances the length of the high field region at the drain-end of the gate, thereby reducing the lateral and vertical peak electric fields, and increasing the gate-drain breakdown voltage. The increase of V_{gd} is expected to be linear with the additional channel resistance. On the other hand, the channel-gate transfer rate of the holes is exponentially depending on the vertical electrical field, because of the underlying tunnel mechanism. This way, an exponentially decrease of the hole gate leakage with increasing drain-source breakdown voltage is concluded and experimentally demonstrated in Fig. 5 for differently grown and processed samples without an AlAs spacer, represented by a circle. Assuming the same behaviour for the pseudomorphic samples, the parallel shifted lines result, which agree well with the experimental data obtained for the samples of type 12 ML and 16 ML.

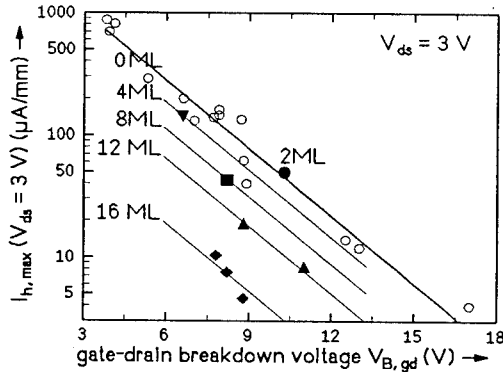


Fig. 5: The maximum hole gate current versus the gate-drain breakdown voltage (the circles represent samples of type 0 ML with different gate recess procedures).

In order to clarify the efficiency of the AlAs-hole barrier, Fig. 6 shows the reciprocal of the normalized maximum hole gate current, $I_{h,l}/I_{h,p}$, in dependence on the AlAs barrier thickness. Here the gate-drain breakdown voltage, reflecting the local electric field, is used as a parameter, kept constant for the comparison. The maximum hole gate current $I_{h,l}$ for the lattice-matched spacer is used as a reference for the maximum hole gate current $I_{h,p}$ for the pseudomorphic spacer. The ratio $I_{h,l}/I_{h,p}$ reflects the reduction factor of the hole transfer rate from the channel to the gate. An example should clarify that procedure. For sample 8 ML, the maximum gate hole leakage current was determined to be $I_{h,p} = 44 \mu\text{A}/\text{mm}$ at $V_{ds} = 3 \text{ V}$. The gate-drain breakdown voltage of that sample is $V_{B,gd} = 8.2 \text{ V}$. The predicted hole gate current of lattice-matched samples, exhibiting

the same gate-drain breakdown voltage, would be $I_{h,l} = 107 \mu\text{A}/\text{mm}$. The reduction factor of the hole gate current by using a 2.2 nm thick AlAs spacer is therefore 2.4.

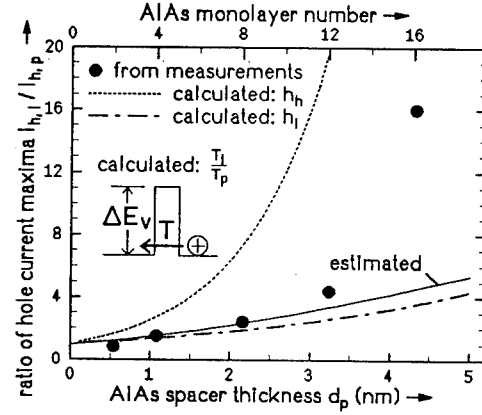


Fig. 6: The reduction factor of the gate hole current for an AlAs spacer of thickness d_p and the calculated ratio of the emission of holes at rest through a potential barrier of the height $\Delta E_{v,l} = 0.23 \text{ eV}$ and $\Delta E_{v,p} = 0.54 \text{ eV}$ for heavy holes h_h and light holes h_l .

Fig. 6 shows that the reduction of the hole gate current, evaluated from measurements on the gate leakage current, is exponentially dependent on the square of the AlAs-spacer thickness. Taking into account the larger spacer thickness of Type 12 ML and 16 ML and the degraded transport properties, resulting in lower electron-hole pair generation rates due to a lower drain current, the estimated curve for non-relaxed layer structures results, demonstrating an exponential hole gate current suppression with an increasing pseudomorphic AlAs spacer layer thickness. The suppression of non-relaxed layer structures is weak and attributed to the reduction in hole tunneling probabilities T through the AlAs spacer layer due to an increase of the valence band discontinuity from $\Delta E_{v,l} = 0.23 \text{ eV}$ (InAlAs/InGaAs) to $\Delta E_{v,p} = 0.54 \text{ eV}$ (AlAs/InGaAs) [10]. The ratio T_l/T_p of the tunneling probabilities T_l and T_p through the lattice-matched and pseudomorphic spacer layer, respectively, is calculated for heavy holes h_h ($m_h^*/m_0 = 0.50$) and for light holes h_l ($m_l^*/m_0 = 0.05$) at rest [11], and plotted in Fig. 6 as a function of the spacer thickness. This model neglects an energy gaining of holes by acceleration in the drain-source-field, resulting in higher tunneling probabilities (cf. Fig. 2). The experimentally determined reduction factors agree with the calculated tunneling probability ratio for light holes at rest, demonstrating the validity of that neglect with the assumption that only light holes are generated by impact ionization.

Conclusion

In summary, pseudomorphic AlAs layers as hole barriers have been inserted in the spacer of InAlAs/InGaAs HFETs. The channel-gate transfer rate of the holes exponentially decreases with the AlAs layer thickness, but the absolute reduction factor is low. The optimum AlAs hole barrier thickness, which is only limited by the critical thickness, can be evaluated as 2.0–2.4 nm (about 8 monolayers). The reduction factor is larger than 2. Despite the large lattice-mismatch of the AlAs layer, no degradation in transport and device performance of type 8 ML could be observed, as demonstrated in Fig. 7 and Fig. 8, showing the drain- and gate-characteristics, respectively. The excellent transport, DC- and RF-data of type 8 ML and the low gate leakage current demonstrate the potential of pseudomorphic AlAs containing spacer layers.

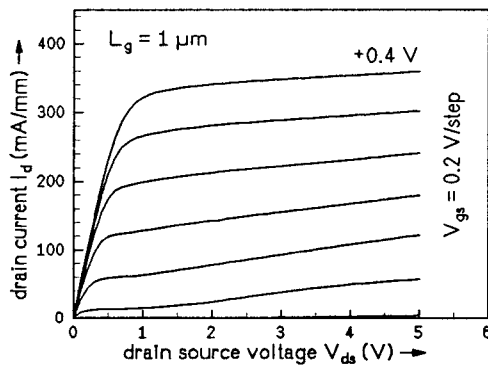


Fig. 7: The output characteristic of type 8 ML.

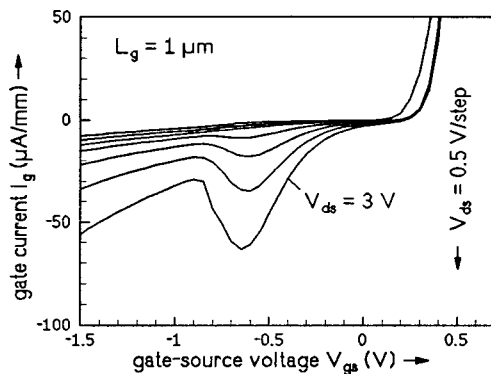


Fig. 8: The input characteristic of type 8 ML.

References

- [1] J. Dickmann, S. Schildberg, H. Dämbkes, S. R. Bahl, and J. A. del Alamo, "Characterization of the breakdown behavior of pseudomorphic InAlAs/InGaAs/InP HEMT's with high breakdown voltages", at *Int. Symp. on GaAs and Related Compounds*, Freiburg, Germany, 1993. *Inst. of Physics Conf. Series*, no. 136, p. 65.
- [2] R. Reuter, S. van Waasen, and F. J. Tegude, "A new noise model of HFET with special emphasis on gate-leakage", *IEEE Electron Device Letters*, vol. 16, no. 2 (1995) p. 169.
- [3] K. Imanishi, T. Ishikawa, and K. Kondo "N-In_xAl_{1-x}As/In_{0.53}Ga_{0.47}As pseudomorphic selectively doped heterostructures with improved Schottky characteristics", at *Int. Symp. on GaAs and Related Compounds*, Karuizawa, Japan, 1989. *Inst. of Physics Conf. Series*, no. 106 (1992) p. 637.
- [4] H. Miyamoto, T. Nakayama, E. Oishi, and N. Samoto, "Low leakage current InAlAs/AlAs/n-InAlAs structures for InAlAs/InGaAs FET applications", at *Int. Symp. on GaAs and Related Compounds*, Freiburg, Germany, 1993. *Inst. of Physics Conf. Series*, no. 136, p. 59.
- [5] F. Buchali, C. Heedt, W. Prost, I. Gyuro, H. Meschede, and F. J. Tegude, "Analysis of gate leakage on MOVPE grown InAlAs/InGaAs-HFET", *Microelectronic Engineering* 19 (1992) p. 401.
- [6] A. A. Moolji, S. R. Bahl, and J. A. del Alamo, "Impact Ionization in InAlAs/InGaAs HFET's", *IEEE Electron Device Letters*, vol. 15, no. 8, (1994) p. 313.
- [7] C. Heedt, F. Buchali, W. Prost, D. Fritzche, H. Nickel, and F. J. Tegude, "Extremely low gate leakage InAlAs/InGaAs HEMT", at *Int. Symp. on GaAs and Related Compounds*, Karuizawa, Japan, 1992. *Inst. of Physics Conf. Series*, no. 129 (1993) p. 941.
- [8] F. Scheffer, C. Heedt, R. Reuter, A. Lindner, Q. Liu, W. Prost, and F. J. Tegude, "High breakdown voltage InGaAs/InAlAs HFET using In_{0.5}Ga_{0.5}P spacer layer," *IEEE Electronics Letters*, vol. 30, no. 2 (1994) p. 169.
- [9] U. Auer, R. Reuter, C. Heedt, H. Künzel, W. Prost, and F. J. Tegude, "InAlAs/InGaAs HFET with extremely high device breakdown using an optimized buffer layer structure", in *Proc. 6th Int. Conf. on InP & Rel. Mat.*, Santa Barbara, CA, 1994.
- [10] S. Tiwari, and D. J. Frank, "Empirical fit to band discontinuities and barrier heights in III-V alloy systems", *Appl. Phys. Lett.*, vol. 60, no. 5 (1992) p. 630.
- [11] H. Beneking, "Halbleitertechnologie", Teubner Verlag, 1991.

High-Performance Enhancement-Mode InAlAs/InGaAs HEMT's Using Non-Alloyed Ohmic Contact and Pt-Based Buried-Gate

Kevin J. Chen, Takatomo Enoki, Koichi Maezawa, Kunihiro Arai, and Masafumi Yamamoto

NTT LSI Laboratories

3-1 Morinosato Wakamiya, Atsugi-shi, Kanagawa Pref., 243-01, Japan

I. Introduction

InAlAs/InGaAs HEMT's lattice matched to InP substrates are emerging as excellent candidates for high-speed computer and communication systems [1,2], owing to the higher low-field electron mobility, the higher peak velocity, and the higher sheet carrier density of these structures. For high-speed digital applications, direct coupled FET logic (DCFL) can be implemented with the simplest circuit configuration [3]. However, the fabrication of high-performance enhancement-mode HEMT's (E-HEMT's) used as drivers in DCFL circuits has to overcome one significant difficulty, namely, the reduction of source resistance (R_S) between source and gate electrodes. The source resistance plays an important role in the ultimate performance of a HEMT [4]. The extrinsic transconductance g_m is related to the intrinsic transconductance g_i and R_S by $g_m = g_i / (1 + g_i R_S)$. Therefore, the source resistance should be kept small compared to the inverse of the intrinsic transconductance in order for the HEMT's to benefit from its high intrinsic transconductance. Since the intrinsic transconductances of InAlAs/InGaAs HEMT's are much higher than that of AlGaAs/GaAs HEMT's, the reduction in source resistance is more critical in pushing the extrinsic transconductance close to intrinsic transconductance in InAlAs/InGaAs HEMT's.

E-HEMT's can be fabricated by carrying out gate recess etching until the channel is fully depleted under zero gate bias [5]. However, due to the side-etching effect, the region around the gate periphery (not covered by the gate electrode) is also depleted and becomes highly resistive. This highly resistive region between source and gate electrodes imposes a large R_S , and a large R_S will degrade the transconductance and cutoff frequencies of HEMT's. Harada *et al* [6] have recently demonstrated an E-HEMT with Pt-based gate by taking advantage of the high schottky barrier (0.83 V) between Pt and InAlAs. This E-HEMT structure shows excellent control and stability of threshold voltage (V_{th}). However, the improvement of R_S has not been reported.

In this paper, we demonstrate greatly improved R_S in an E-HEMT structure using non-alloyed ohmic contact and Pt-based buried gate approaches. First, non-alloyed ohmic contact technique was used to produce very low contact resistance and provides sharply defined ohmic edges. Second, in the fabrication of our E-HEMT's, we first intentionally fabricated depletion-mode HEMT's (D-HEMT's). Subsequently, by annealing the sample at 250°C, these D-HEMT's were changed to E-HEMT's as a result of the Pt-InAlAs reaction taking place under the gate electrode, while the channel region between source and gate remained undepleted. This allowed a small R_S to be maintained. An excellent transconductance (g_m) of 1170 mS/mm was achieved for an E-HEMT with a 0.5- μ m-gate.

II. DEVICE STRUCTURE AND FABRICATION

Figure 1 (a) shows the device structure grown by MBE. The basic device structure used in this study is as follows: a 200-nm InAlAs undoped buffer, a 15-nm undoped InGaAs layer forming the 2DEG channel, a 2-nm undoped InAlAs spacer; a 4-nm (n^+ -doped, $1 \times 10^{19} \text{ cm}^{-3}$) InAlAs carrier supply layer, followed by a 20-nm undoped InAlAs Schottky enhancement layer (SEL), and finally the n^+ -doped ($1 \times 10^{19} \text{ cm}^{-3}$) InAlAs (15 nm)/InGaAs (10 nm) cap layers to facilitate the formation of non-alloyed ohmic contact. The typical electron mobility and maximum sheet electron density of the 2DEG are 9800 $\text{cm}^2/\text{V}\cdot\text{s}$ and $2.7 \times 10^{12} / \text{cm}^2$ at 300 K.

A. Non-alloyed Ohmic Contact Technology

The principle of formation of non-alloyed ohmic contact [7] can be understood from the conduction band profile underneath source and drain contacts, as shown in Fig. 2 (a). The profile is calculated by self-consistently solving Poisson

equation. Unlike the single n^+ -InGaAs cap layer used in conventional alloyed ohmic contact structures, the inserted heavily-doped InAlAs layer between the SEL and the InGaAs cap layer is the critical factor in forming the non-alloyed ohmic contact. As shown in Fig. 2 (a), the undoped InAlAs SEL is sandwiched by its neighboring n^+ -InAlAs layers (the cap and carrier supply layers). As a result, the potential barrier of the SEL is substantially lowered and the tunneling current between the source (or drain) contacts and the InGaAs channel is greatly enhanced.

In our non-alloyed ohmic contact structures, contact resistance (R_C) depends most significantly on two factors: the doping level in all the n^+ -doped layers and the thickness of the carrier supply layer. For structures with a fixed 5-nm carrier supply layer, the measured R_C was 0.16 and 0.067 $\Omega\cdot\text{mm}$ for doping densities of $4 \times 10^{18} \text{ cm}^{-3}$ and $1 \times 10^{19} \text{ cm}^{-3}$, respectively. For a fixed doping density of $1 \times 10^{19} \text{ cm}^{-3}$ in the n^+ -InAlAs layers, R_C was measured at 0.067, 0.08, and 0.25 $\Omega\cdot\text{mm}$ for carrier supply layer thicknesses (L_{CS}) of

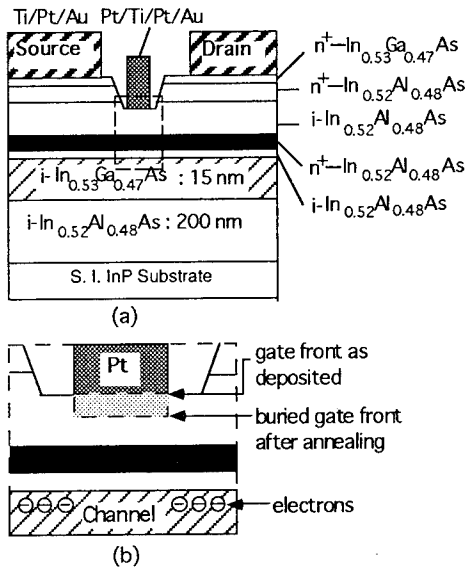


Fig 1: (a) Schematic cross section view of the device structure with non-alloyed ohmic contact layers. (b) Enlarged view of the region under and near the gate electrode.

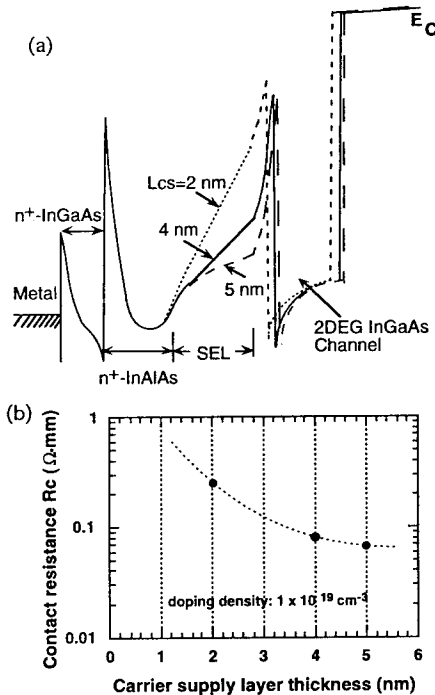


Fig. 2: The non-alloyed ohmic contact. (a) The calculated conduction band profiles for structures with different carrier supply layer thickness. (b) Plot of contact resistance versus the carrier supply layer thickness. The doping density in all of the n^+ -doped layers is $1 \times 10^{19} \text{ cm}^{-3}$.

5-nm, 4-nm, and 2-nm, respectively, as shown in Fig. 2 (b). The physical mechanism for this dependence of R_c on L_{CS} is clearly illustrated in Fig. 2 (a). With a relatively large L_{CS} (5-nm or 4-nm), the effective potential barrier between the SEL and the 2DEG is thin (see the dashed and solid lines in

Fig. 2). When a thin (2-nm) carrier supply layer is used, the effective barrier thickness (dotted line) is dramatically increased and the tunneling current is reduced. The conduction band profile in the cap layers shows negligible dependence on L_{CS} chosen here.

It should be noted that, for more accurate modeling of the conduction band profile, quantized energy levels in the 2DEG channel should be taken into account by performing self-consistent calculations of both the Poisson and Schrödinger equations. The quantum effect in the InGaAs channel will lower the conduction band in both the channel and the InAlAs barrier (mainly the spacer, the carrier supply layer and SEL). Therefore, in reality, the potential of the InAlAs barrier is lower than that shown in Fig. 2 (a).

The attraction of non-alloyed ohmic contact technology lies in the fact that sharply defined ohmic edges can be obtained in the device channel and therefore the gate can be placed very close to the source to minimize the source resistance. This technology also automatically provides very good surface morphology, which is required for good gate-level lithographic definition in integrated circuits. In 2-inch wafers, R_c shows excellent uniformity and wafer-to-wafer reproducibility when the doping level is $1 \times 10^{19} \text{ cm}^{-3}$.

B. Pt-based Buried-Gate Technology

To fabricate enhancement-mode HEMT's in InAlAs/InGaAs material system, a gate metal with a high Schottky barrier is needed. The most commonly used gate metal, Ti/Pt/Au, has a Schottky barrier of 0.65 eV on InAlAs [8], which is only 0.15 eV larger than the conduction band discontinuity (ΔE_C) at the InAlAs/InGaAs heterojunction, and not enough to deplete the channel at zero gate bias. On the other hand, Pt has been shown to provide a 0.83 eV Schottky barrier on InAlAs [6], about 0.3 eV larger than ΔE_C .

In our device fabrication, after defining the device mesa, the mesa-sidewall was selectively recessed using citric-acid-based etchant to reduce the gate leakage current [9,10]. Ti/Pt/Au was deposited by electron beam evaporation as the non-alloyed ohmic contact metals. After a slight wet gate recess etching, Pt(2.8nm)/Ti(30nm)/Pt(20nm)/Au multilayer structures were deposited as the gate electrodes. At this stage, the fabricated HEMT's operated at depletion-mode with $V_{th} = -0.25 \text{ V}$. At $V_{ds} = 2.0 \text{ V}$, the maximum transconductance g_m is about 1030 mS/mm for a device with a $0.5\text{-}\mu\text{m}$ -gate.

Subsequently, the sample was annealed at 250°C in nitrogen forming gas. During the annealing process, Pt-InAlAs reaction took place and Pt sunk into the InAlAs barrier to form metallic PtAs_2 alloy [6]. The sinking of Pt into the barrier shifted the gate metal front closer to the InGaAs channel, as illustrated in Fig. 1 (b). The inserted Ti in the gate metal structure serves as a barrier to prevent the Pt-InAlAs reaction from going to the upper Pt layer and only the bottom Pt reacts. V_{th} shifted from -0.25 V to -0.1 V after 5 minutes' annealing and saturated at 0 V after 10 minutes' annealing. Therefore, by burying Pt gate into InAlAs barrier using annealing, the channel is further recessed and HEMT's can be changed from

depletion-mode to enhancement-mode. The 0.25 V shift in V_{th} corresponds to about 4 nm of shift in the position of the gate metal front. The ratio of the sinking depth to the physical thickness (2.8 nm) of the reacted Pt is about 1.4, consistent with that reported in Ref. [6]. During gate annealing, the source and drain contact resistance remains unchanged.

As illustrated in Fig. 1 (b), the sinking of Pt into the InAlAs barrier does not change the electron density in the channel region between the source and gate electrodes. Therefore, the value of R_S remained unchanged, and was measured at 0.2 Ω -mm measured.

III. DEVICE PERFORMANCE

A. DC Characteristics

The typical dc I - V characteristics for the 0.5- μ m-gate E-HEMT after gate annealing are given in Fig. 3. At $V_{ds} = 2.0$ V, the maximum *extrinsic* transconductance g_m is 1170 mS/mm with an associated I_{ds} of 380 mA/mm. Excellent pinch-off is obtained at $V_{gs} = 0$ V. Using the value 0.2 Ω -mm for R_S , the maximum *intrinsic* transconductance is estimated to be 1520 mS/mm. Drain conductance g_d is 30 mS/mm,

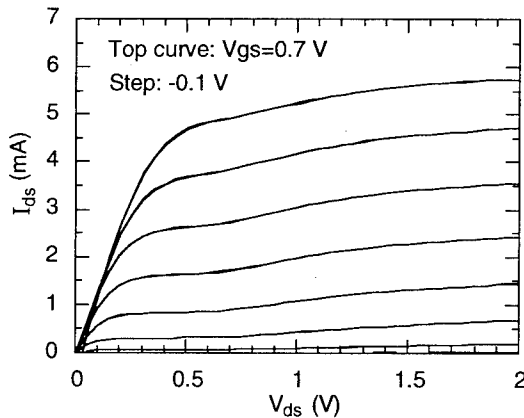


Fig. 3: Source-drain I - V characteristics of an E-HEMT after annealing the gate metal at 250 $^{\circ}$ C for 10 minutes. The gate size is 0.5 μ m \times 10 μ m. Gate voltage ranges from 0 V to 0.7 V in 0.1 V step.

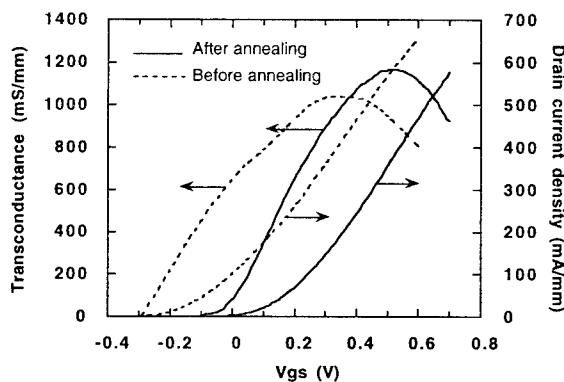


Fig. 4: DC transfer characteristics of a 0.5- μ m-gate HEMT before and after gate annealing.

yielding a voltage gain (g_m/g_d) of 39.

The transfer characteristics for the device both before and after the gate annealing (corresponding to D-HEMT and E-HEMT, respectively) are shown in Fig. 4. As mentioned in Section II, the threshold voltage changes from -0.25 V to 0 V after 10 minutes' annealing at 250 $^{\circ}$ C. Since R_S remained unchanged during the annealing process, the maximum g_m was not degraded but increased further to 1170 mS/mm as a result of the reduced distance between the gate metal and the 2DEG.

To further demonstrate the improvement in R_S gained by the buried-gate approach, we also fabricated E-HEMT's using only wet recess etching. As shown in Fig. 5 (a), in addition to the region under the gate electrode, the channel region around the gate periphery between the source and gate is also depleted due to the side-etching effect during the gate recess etching. The electron density in this side-etched region can not be increased by positive gate bias and so the region

exposed region due to side etching

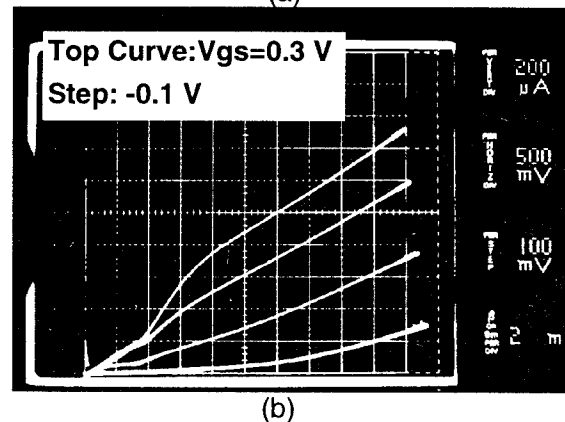
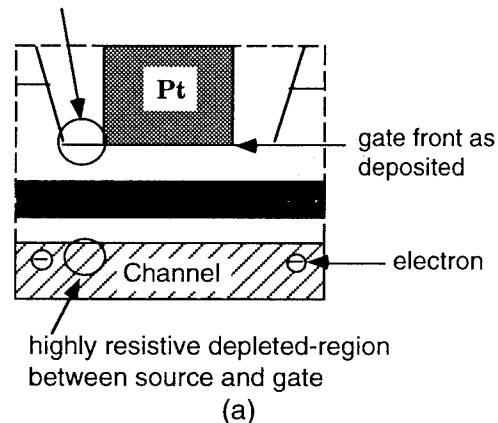


Fig. 5: (a) Schematic cross section of the region around the gate electrode of an E-HEMT obtained using only wet recess etching, showing the highly resistive region exposed region (due to side-etching during the gate recess) around the gate periphery. (b) The source-drain I - V characteristics of such an E-HEMT. Gate voltage ranges from 0 V to 0.3 V in 0.1 V step.

remains highly resistive during the device operation, resulting in a large R_S . The estimated R_S at $V_{ds} = 5.0$ V is $1.5 \Omega\text{-mm}$, about 8 times larger than the value achieved by the buried gate approach. This large R_S results in increased source-drain saturation voltage, and the maximum g_m is degraded to 500 mS/mm, as shown in the I - V characteristics in Fig. 5 (b).

B. RF Characteristics

The on-wafer S-parameters were measured from 0.5 to 25.5 GHz using a Cascade probe station and a HP8510 network analyzer. The results of H_{21} and Mason's unilateral

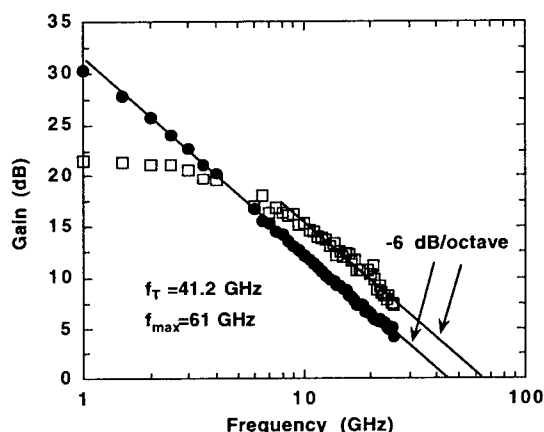


Fig. 6: Current gain and Mason unilateral power gain against frequency for a 0.6- μm -gate E-HEMT with a gate width of 100 μm .

power gain U for a 0.6 $\mu\text{m} \times 100 \mu\text{m}$ device are plotted in Fig. 7. These results were obtained at $V_{ds} = 2.0$ V and $V_{gs} = 0.43$ mA. The current-gain cutoff frequency f_T and the maximum oscillation frequency f_{max} were calculated by extrapolating at -6 dB/octave. As shown in Fig. 6, f_T is 41.2 GHz and f_{max} is 61 GHz.

IV. CONCLUSIONS

High-performance enhancement-mode HEMT's have been demonstrated in InAlAs/InGaAs using non-alloyed ohmic contacts and Pt-based buried-gate technologies. The non-alloyed ohmic contacts technology not only provides very low contact resistance and simplification of device fabrication but also offers clean and sharply defined ohmic edges and good ohmic surface morphology. The Pt-based buried gate approach was used to improve the source resistance. A low R_S of $0.2 \Omega\text{-mm}$ was achieved by using this technique in E-HEMT's. By combining this approach with the non-alloyed ohmic contact technique for the first time, we demonstrated high-performance E-HEMT's with an excellent transconductance of 1170 mS/mm for a 0.5- μm -long gate device. Excellent high-frequency characteristics with an f_T of 41.2 GHz and an f_{max} of 61 GHz were also presented.

ACKNOWLEDGMENT

The authors would like to thank N. Suzuki for MBE growth, Dr. T. Waho for his valuable help in S-parameter measurement, Y. Umeda, Dr. T. Akeyoshi and Dr. T. Mizutani for helpful discussions. They are also grateful to Dr. Y. Ishii and Dr. Y. Imamura for their continuous encouragement.

REFERENCES

- [1] M. Abe, "Ultrahigh-speed InGaAs-based HEMT technology", *Proc. 4rd Int. Conf. InP and Related Materials*, pp. 2-5, 1991.
- [2] U. K. Mishra, and J. B. Shealy, "InP-based HEMTs: status and potential," *Proc. 6rd Int. Conf. InP and Related Materials*, pp. 14-17, 1994.
- [3] M. Abe *et al.* "Ultrahigh-speed HEMT integrated circuits," in *Semiconductors and Semimetals*, R. K. Willardson and A. C. Beer, Eds., vol. 24, R. Dingle, Volume Ed. New York: Academic, 1987, pp. 249-278.
- [4] P. Roblin, L. Rice, S. B. Bibyk, and H. Morkoc, "Nonlinear Parasitic in MODFET's and MODFET I - V characteristics," *IEEE Trans. Electron Devices*, vol. 35, pp. 1207-1214, 1988.
- [5] T. Itoh, A. S. Brown, L. H. Camnitz, G. W. Wicks, J. D. Berry, and L. F. Eastman, "Depletion- and enhancement-mode $\text{Al}_{0.48}\text{In}_{0.52}\text{As}/\text{Ga}_{0.47}\text{In}_{0.53}\text{As}$ modulation-doped field-effect transistors with a recessed gate structure," in *Int. Symp. GaAs and Related Compounds*, Inst. Phys. Conf. Ser. No. 79, (Karuzawa, Japan), 1985, pp. 571-576.
- [6] Naoki Harada, Shigeru Kuroda, Teruhiko Katakami, Kohki Hikosaka, Takashi Mimura, and Masayuki Abe, "Pt-based gate enhancement-mode InAlAs/InGaAs HEMTs for large-scale integration," *Proc. 3rd Int. Conf. InP and Related Materials*, pp. 377-380, 1991.
- [7] T. Enoki, T. Kobayashi, and Y. Ishii, "Device Technologies for InP-based HEMTs and Their application to ICs," *Tech. Dig. IEEE GaAs IC Symposium*, 1994, pp. 337-340.
- [8] L. P. Sadwick, C. W. Kim, K. L. Tan, and D. C. Streit, "Schottky barrier heights of n-type and p-type $\text{Al}_{0.48}\text{In}_{0.52}\text{As}$ " *IEEE Electron Device Lett.*, vol. 12, pp. 626-628, 1991.
- [9] S. R. Bahl, and J  sus A. del Alamo, "Elimination of mesa-sidewall gate-leakage in InAlAs/InGaAs HFET's by selective side-wall etching," *IEEE Electron Device Lett.*, vol. 13, pp. 195-197, 1992.
- [10] M. Tong, K. Nummala, A. Ketterson, I. Adelsida, C. Caneau, and R. Bhat, "InAlAs/InGaAs/InP MODFET's with uniform threshold voltage obtained by selective wet gate recess," *IEEE Electron Device Lett.*, vol. 13, pp. 525-527, 1992.

Characteristics of Iron Doped Pt-InAlAs Schottky Diodes Grown by LP-MOCVD Using Ferrocene[†]

K. Hong, D. Pavlidis and F. Sejalon

Solid-State Electronics Laboratory,
Department of Electrical Engineering and Computer Science,
The University of Michigan, Ann Arbor, Michigan 48109-2122, U.S.A.

Introduction

InAlAs lattice-matched to InP is of great importance as a large bandgap material for various InP-based heterostructures device applications. InAlAs grown by molecular beam epitaxy (MBE) has been very successful for InAlAs/InGaAs high electron mobility transistors (HEMTs) applications and more recently several reports have been also made on the growth of this material using metalorganic chemical vapor deposition (MOCVD)(1). Although MOCVD has been very attractive due to its simplicity and flexibility, growth of aluminum containing materials is relatively difficult since most metalorganic aluminum sources react very easily with oxygen. In this study, we investigate iron doped InAlAs by MOCVD growth and report on the impact of iron doping on the electrical properties of the material using Pt-InAlAs Schottky diodes.

MOCVD Grown InAlAs Considerations

The oxygen incorporation in MOCVD grown InAlAs material leads to defect levels within the bandgap and subsequently degrades electrical and optical properties of the material. In the case of HEMTs, this results, for example, in undesirable characteristics such as poor pinch-off due to leaky buffer and gate-source characteristics. Therefore, it is necessary to render layers of this type less conductive so that leakage from the InAlAs buffers or Schottky layers can be diminished. Iron doping of InAlAs has been explored for this purpose and is reported in this paper. Substituting for group III atoms in the InAlAs, iron is expected to form deep acceptor level by virtue of $\text{Fe}^{+3}/\text{Fe}^{+2}$ transition. Deep acceptors like Fe are more effective than shallow acceptors like carbon in compensating the shallow or deep donors found in MOCVD grown InAlAs and can therefore be used to improve its electrical characteristics. Systematic studies have been reported in the past on Fe doping of InP(2). Although material properties of iron-doped InAlAs grown by MOCVD(3) and by ion implantation(4) have also been explored, there are, to our knowledge, no extensive reports on its electrical properties as used for device applications. A systematic study of material and Schottky diode characteristics using Fe doped InAlAs has been carried out in this work and is reported in the section below.

Growth of Iron-doped InAlAs

The growth was carried out by low pressure MOCVD in a vertical mass transport reactor with rotating susceptor. Trimethylindium (TMIn), trimethylgallium (TMGa) and trimethylaluminum (TMAI) were used for In, Ga and Al sources, respectively, and 100% arsine and phosphine was used for group V elements. The iron source was bis-cyclopentadienyl-iron (ferrocene) which was contained in a stainless steel bubbler in solid form and transported to the reactor by hydrogen carrier gas through standard alkyl delivery lines. The ferrocene bubbler temperature and pressure was kept at 10°C and 500torr, respectively. All structures were grown at 650°C since this offers minimum deep donor levels according to DLTS studies performed on undoped InAlAs(5). Growth reactor pressure was 60torr and total hydrogen flow through the reactor was about 10l/m.

Optical Reflectance Measurements

In order to confirm the introduction of deep traps by iron incorporation in the InAlAs layers, room temperature time-resolved photorefectance studies were performed on iron-doped InAlAs samples. Measurement of carrier lifetime of iron doped materials using time-resolved photorefectance appears to be a better approach than techniques such as time-resolved photoluminescence, in spite of the fact that the latter is a more direct measurement technique. The high density of deep level defects expected in these materials results in recombination

[†]Work supported by ARPA COST(MDA 972-94-1-0004) and URI(DAAL 03-92-G-0109).

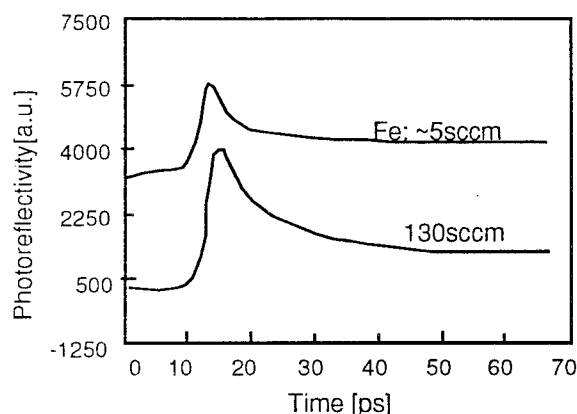


Fig.1 Time-resolved photoreflectance characteristics of Fe-doped InAlAs showing increased levels of deep traps in the presence of iron.

dominated by non-radiative processes and gives rise to poor photoluminescence efficiency. The measurement was based on the conventional pump-probe technique where photo carriers are generated by a short optical pumping pulse (150fs) and the evolution of photo carrier density is deduced by measuring the time-resolved reflectivity signal from the surface(6). Fig.1 shows the evolution of room temperature photo reflectivity from InAlAs samples doped with different ferrocene flow rates. It is clearly seen that the photo-carrier lifetime decreases with the ferrocene flow rate. This indicates enhancement of deep trap presence with ferrocene flow and suggests that better semi-insulating properties should be feasible with higher doping of InAlAs.

Characteristics of Pt-InAlAs Schottky diodes using Fe-Doped InAlAs

In order to investigate the impact of iron doping on the electrical properties of InAlAs, 3000Å of iron-doped InAlAs layers were grown on semi-insulating InP substrates with various ferrocene flow rates. These layers were covered with 60Å of undoped InGaAs layers to facilitate ohmic contacts. To fabricate planar Schottky diodes, Au/Ge/Ni/Ti/Au ohmic metals were deposited on the InGaAs cap layer and annealed by RTA at 375°C for 7 seconds. After this, the InGaAs cap layers were etched using a selective citric acid:H₂O₂ (1:1) solution and Pt/Ti/Pt/Au Schottky metals were deposited on the exposed iron-doped InAlAs layers using an e-beam evaporator.

Fig.2 shows the forward *I-V* characteristics of the fabricated diodes. The measurements were done at room temperature on a circular shaped anode with 100μm diameter. As can be seen from this figure, diodes on undoped InAlAs show sharper turn on characteristics than those on iron-doped InAlAs. Moreover, as the ferrocene flow increases the forward current decreases.

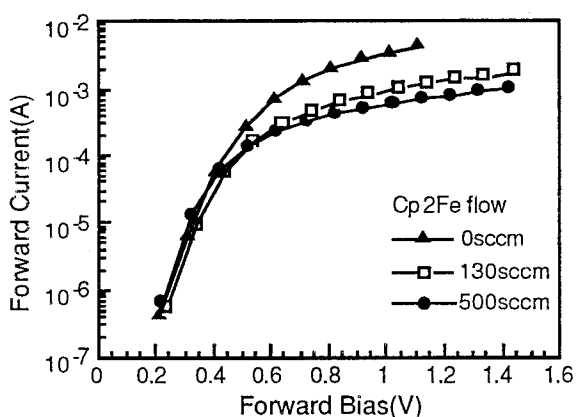


Fig.2 Forward *I-V* characteristics of Pt Schottky diodes indicating sharper turn-on and increased current level in the absence of iron doping.

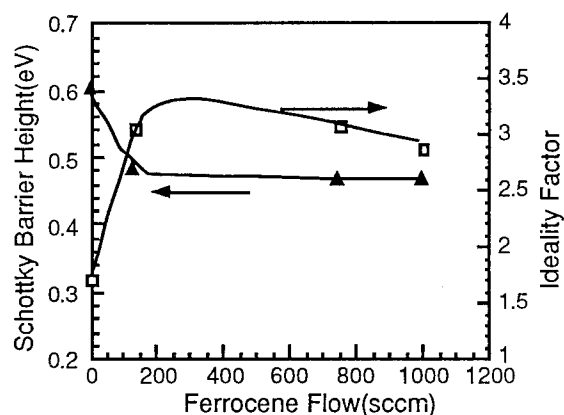


Fig.3 Variation of barrier height and ideality factor as a function of ferrocene flows.

The impact of ferrocene flow rate on diode performance can be more clearly seen by extracting and comparing the diode parameters. Device parameters such as Schottky barrier height, ideality factor and series resistance were extracted from the DC *I-V* characteristics based on thermionic emission theory. To enhance the presence of series resistance, the diodes were biased strongly in the forward region (>1mA). Series resistance and ideality factors were first extracted from the slope and y-intersection of *dV/dlnI* versus *I* curve, respectively. The series resistance and ideality factor values were then used to calculate the Schottky barrier height. Fig.3 shows the variation of Schottky barrier height and ideality factor of the diodes as a function of ferrocene flow rate. As can be seen from the figure, the Schottky barrier height drops from ~0.6eV (undoped InAlAs) to ~0.48eV with the use of small ferrocene flows and tends to saturate regardless of the amount of ferrocene introduced into the reactor. Fig.3 also

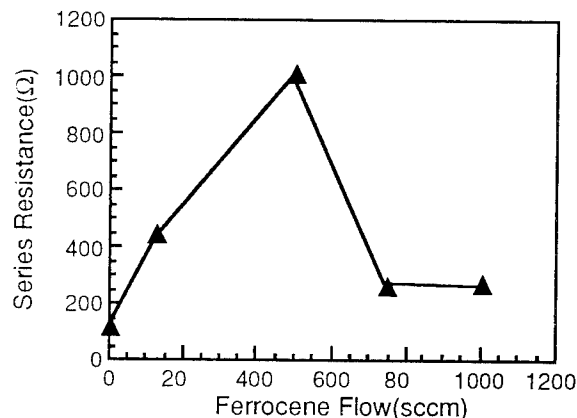


Fig.4 Impact of ferrocene flow on diode series resistance.

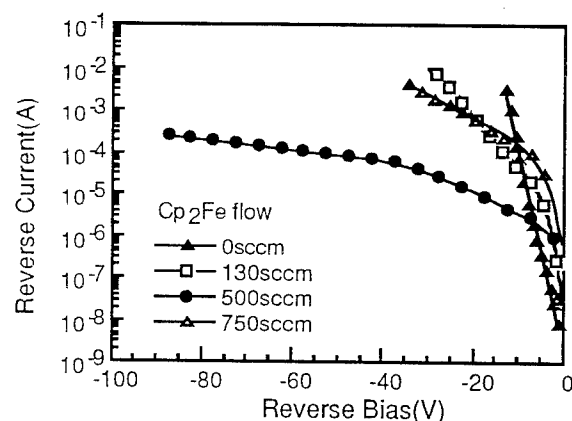


Fig.5 Reverse I-V characteristics showing smaller reverse leakage and increased breakdown up to a critical ferrocene flow rate.

shows that the ideality factor of the diodes increases from 1.7 (undoped InAlAs) to about 3 but is about the same for all iron doped InAlAs diodes regardless of ferrocene flow.

In contrast to the Schottky barrier height and ideality factor, the diode series resistance was relatively sensitive to the ferrocene flow rate as shown in Fig.4. The series resistance was greatly increased with ferrocene flow up to 500 sccm and decreased again for ferrocene flows higher than 500 sccm. The decrease of series resistance with higher iron concentrations is possibly due to iron precipitates which give rise to a conduction path through the epilayer as already reported in the case of iron-doped InP(7). It was also observed that the optimum ferrocene flow that gives highest series resistance shifted to higher flow values when the layer was grown at higher growth rates. This implies that the resistivity of the InAlAs layers can be greatly increased by optimizing the ratio of iron flux to total group III flux which determines the growth rate. The optimum gas phase ferrocene ratio to the total group III flux appears to be ~0.04.

Reverse Schottky characteristics of Fe-doped InAlAs are also of great importance since they indicate the degree of improvement in device performance when this material is employed as Schottky layer for InAlAs/InGaAs HEMTs. Fig.5 shows the room temperature reverse I-V characteristics of the diodes. It can be seen from the figure that the diodes fabricated on undoped InAlAs show almost linear $\log I_r$ vs. V_r relation while the rest of the iron doped diodes showed two distinct slopes with a knee voltage around 7V. Therefore, even though the diode on undoped InAlAs showed lower reverse leakage current in the small reverse bias operation regime ($I_r < 100 \mu A$), the overall reverse leakage and breakdown characteristics were greatly improved with iron-doped InAlAs materials. Extremely high reverse breakdown voltage (~90V) was observed with the sample grown with 500 sccm of ferrocene flow. This sample showed reverse leakage current less than $300 \mu A$ at 90V. However, reverse characteristics showed similar trends as the series resistance, namely a degradation of reverse characteristics when very high ferrocene flows are used. These results indicate that the InAlAs buffer and Schottky cap layers of InAlAs/InGaAs HEMTs can be improved using ferrocene up to certain flow rate beyond which no further improvement can be achieved.

Low frequency noise characteristics

The introduction of iron in InAlAs may give rise to advert effects when this material is employed in device structures. Trap-related abnormalities in device performance and increased noise level could for example, manifest when using Fe-doped InAlAs. The study of low frequency noise in iron doped InAlAs is therefore of great interest since it provides a way of evaluating trap-related device characteristics, as well as, their noise properties. Undoped and iron doped InAlAs were characterized for this purpose and the results are described in this section. The noise current spectra were obtained by characterizing TLM test structures with $75 \mu m$ separation between ohmic terminals and 50 to $100 \mu m$ width. An HP3561 dynamic signal analyzer was used to measure the noise current spectral density from 10Hz to 100KHz. Fig.6a and b show the noise current spectra of undoped and iron doped InAlAs, respectively, measured at room temperature. Both materials showed noise spectra with close to ideal $1/f$ characteristics and no prominent Lorentz-shaped spectra. However, the plot of $(S_i) \cdot (\text{frequency})$ products revealed a very weak Lorentz spectrum near ~40Hz for iron doped InAlAs. The second peak found beyond 10KHz in both materials is not related to material properties and arises from the noise floor characteristics of the measurement system. Since the Lorentzian component is found at a very low frequency in iron-doped InAlAs, we speculate on the basis of expected Arrhenius characteristics that iron

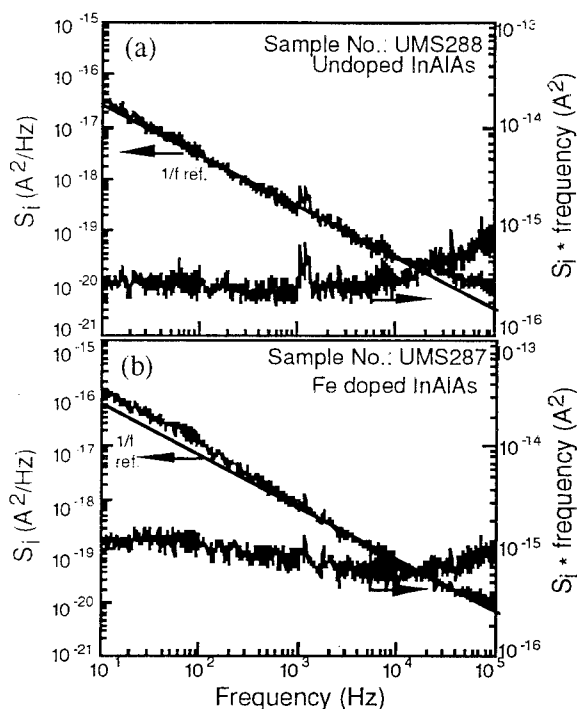


Fig.6 Low frequency noise current spectra S_i and ($S_i \times$ frequency) product of undoped(a) and iron doped InAlAs(b).

introduces generation-recombination traps which have very high activation energy.

Summary

In summary, iron doped InAlAs layers were grown by MOCVD with the purpose of improving the electrical properties of this material. Photoreflectance studies clearly showed the increase of deep traps by introducing iron into the layers. Pt-Schottky diodes were fabricated on undoped and iron doped InAlAs with various iron concentrations and device parameters were extracted to reveal the impact of iron concentration on the electrical characteristics. Although iron doped layers showed lower Schottky barrier height, extremely high reverse breakdown voltage of ~ 90 V could be obtained with properly doped materials. The results showed that the electrical properties of InAlAs can be greatly improved if an appropriate level of iron doping is employed. Beyond certain level of ferrocene flow, the material starts presenting less pronounced semi-insulating characteristics, possibly due to the presence of iron precipitates. Low frequency noise current spectra of iron doped InAlAs showed a Lorentz-shaped spectrum near ~ 40 Hz suggesting an increased

presence of traps with high activation energy in Fe-doped InAlAs.

Acknowledgment

The authors would like to thank J. Kim for time-resolved photoreflectance tests.

References

- (1) L. Aina, M. Mattingly, A. Fathimulla, E.A. Martin, T. Loughran and L. Stecker, "OMVPE Growth of InAlAs and Device Quality AlInAs-based Heterostructures," J. of Cryst. Growth, Vol.93, pp.911-918, 1988.
- (2) J.A. Long, V.G. Riggs and W.D. Johnston, Jr., "Growth of Fe-Doped Semi-Insulating InP by MOCVD," J. of Cryst. Growth, Vol.69, pp.10-14, 1984.
- (3) H. Ishikawa, M. Kamada, H. Kawai and K. Kaneko, "Highly Resistive Iron-Doped AlInAs Layers Grown by Metalorganic Chemical Vapor Deposition," Jpn. J. Appl. Phys., Vol.31, pp.L376-378, 1992.
- (4) J.M. Martin, R.K. Nadella, M.V. Rao, D.S. Simons, P.H. Chi and C. Caneau, "Fe and Ti Implants in $\text{In}_{0.52}\text{Al}_{0.48}\text{As}$," J. Electronic Mat., Vol.22, No.9, pp.1153-1157, 1993.
- (5) F. Ducroquet, G. Guillot, K. Hong, C. H. Hong, D. Pavlidis and M. Gauneau, "Deep Level Characterization of LP-MOCVD Grown $\text{Al}_{0.48}\text{In}_{0.52}\text{As}$," Proceedings of the Material Research Society Symposium, Vol.325, pp.235-239, 1994.
- (6) S. Gupta, G. Mourou, F.W. Smith and A.R. Calawa, "Ultrafast Properties and Applications of GaAs and InP Based Materials Grown by MBE at Low Temperatures," Proceedings of the Material Research Society Symposium, Vol.241, pp.205-215, 1992.
- (7) S. Nakahara, S.N.G. Chu, J.A. Long, V.G. Riggs and W.D. Johnston, Jr., "A Transmission Electron Microscope Study of Iron Phosphide Precipitates in InP Crystals," J. of Cryst. Growth, Vol.72, pp.693-698, 1985.

InGaAs Insulated Gate Field Effect Transistors Using Silicon Interlayer Based Passivation Technique

S. Suzuki, S. Kodama, H. Tomozawa and H. Hasegawa

*Research Center for Interface Quantum Electronics and
Department of Electrical Engineering
Hokkaido University, N-13, W-8, Sapporo 060, Japan*

Introduction

Recently, compound semiconductor high speed devices (HEMT, HJFET etc.) using InP-based materials have demonstrated excellent performance owing to superb electron transport properties of InGaAs. One of the application areas of these devices is the microwave and millimeter wave movable communication which is expected to become more and more important in the so-called "multi-media" era. However, since such an application requires in most cases battery operation, gate leakage currents inherently present in the Schottky gate structure, gives a severe constraint. Lack of low power dynamic memory also limits the functional capability of the system using these devices. These problems can be solved by having insulated gate devices whose realization has, however, been hitherto hindered by the lack of a suitable passivation technology.

Recently, we have shown that the surface state density can be greatly reduced by inserting an MBE grown ultra-thin Si interface control layer (Si ICL) at the interface between InGaAs and the passivation dielectric films (1) on the basis of the disorder induced gap state model (2). Such a technique has been applied to fabrication of planar (3) and recessed gate MISFETs (4), photoconductive detectors (5) and to passivation of near surface quantum wells (6).

The purpose of this paper is to investigate the applicability of the Si ICL-based passivation technique to construction of InGaAs insulated gate field effect transistor (IGFET) devices such as MISFETs and HEMTs. Since most of our previous work has been done in a UHV-based system where the Si ICL was grown on the fresh MBE surface of the compound semiconductor, one of the key problems is how to make the present technique applicable to air-exposed surfaces. Here, HF treatment were applied to InGaAs and InAlAs surfaces. Basic insulator-semiconductor structures were fabricated and characterized by XPS, I-V and MIS C-V techniques. Fat MISFETs and HEMT were also fabricated and feasibility of the present technique is successfully demonstrated.

Experimental

Basic structures and MBE growth

The metal-insulator-semiconductor (MIS) capacitor structures prepared in this study are shown in Fig.1(a) and (b). They are basic capacitor structures for MISFETs and insulated gate HEMTs (IGHEMTs), respectively. For actual fabrication of FET devices, these structures were grown on semi-insulating substrates. The fabrication of the samples were done using the UHV-based system shown in Fig.2 where the MBE, CVD, XPS and other chambers are connected by a UHV transfer chamber. For comparison, Schottky gate and insulated gate AlGaAs/GaAs HEMT capacitors and transistors were also fabricated.

The epitaxial layers of $\text{In}_{0.53}\text{Ga}_{0.47}\text{As}$ and $\text{In}_{0.52}\text{Al}_{0.48}\text{As}$ were grown by molecular beam epitaxy (MBE) at a substrate temperature of 500°C. Carriers for HEMTs were supplied from the Si doped InAlAs layer. Then, epitaxial layers taken out from the MBE growth chamber and either evaluated by Hall effect measurement or subjected to fabrication process of MIS capacitors and IGFETs, exposing the surface to air. In the HEMT structures, the Hall mobilities of 7,500 cm²/V s (300K), 43,000 cm²/V s (77K), and the sheet

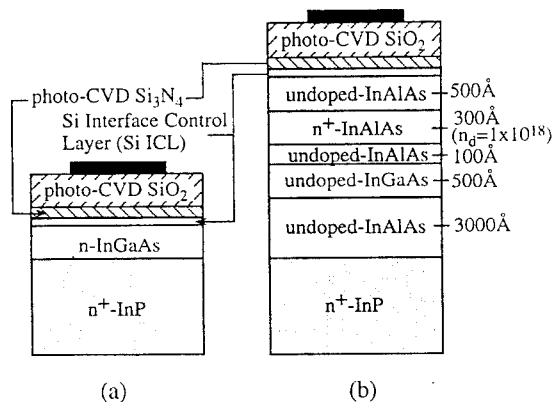


Fig.1 MIS capacitor structures for MISFETs and IGHEMTs.

carrier densities of $4.8 \times 10^{12} \text{ cm}^{-2}$ (300K), $3.3 \times 10^{12} \text{ cm}^{-2}$ (77K) were achieved.

Si ICL-Based Passivation Process

The basic idea of the Si ICL-based passivation is the following. Namely, by inserting an ultrathin Si ICL between

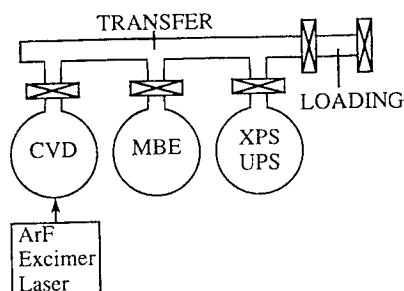


Fig.2 The UHV-based system used for sample fabrication.

the compound semiconductor and the silicon-based insulator film such as SiO_2 combination, chemical bonds of InGaAs are terminated by Si atoms, and then Si atoms are terminated by Si-based dielectrics. The key points of the processing have been found to be maintenance of pseudomorphic nature of the Si ICL with respect to the compound semiconductor and avoidance of direct interface chemical reaction between the compound semiconductor and the excited radicals produced during formation of Si-based insulator films. For the latter purpose, insertion of an ultrathin Si_3N_4 layer has been recently found beneficial(7).

Before application of the Si ICL-based passivation process, the air-exposed surface of the epitaxial layer was first etched chemically and then treated by HF in N_2 ambient. (4) This was to remove the oxide and to adjust the surface stoichiometry to As-rich condition. Then, the sample was introduced through N_2 ambient into the UHV chamber without exposing to air.

The growth of the Si ICL with a thickness of 5-10 Å was done by MBE at a substrate temperature of 250°C, using a Si K-cell as the silicon source. Subsequently, an ultrathin Si_3N_4 and a thick SiO_2 layer were deposited from a gas mixture of SiH_4 and NH_3 and from that of SiH_4 and N_2O , respectively, at 250°C by photo-CVD process using Ar excimer laser (193 nm).

Fabrication of MISFETs and IGHEMTs

To investigate the feasibility of the present technique for practical device fabrication, recessed gate InGaAs MISFETs and IGHEMTs shown in Fig.3 (a) and (b) respectively, were fabricated and electrically characterized. They were fabricated by following procedure. After MBE growth of the basic epitaxial layer structure on the InP

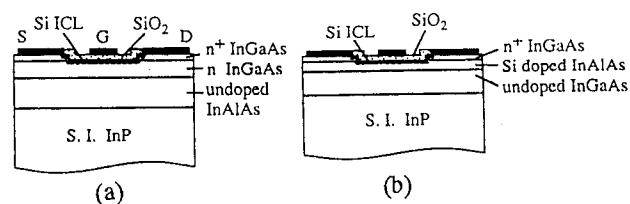


Fig.3 Fabricated recessed gate (a) InGaAs MISFETs and (b) IGHEMTs.

substrate, the standard device processing such as the ohmic electrodes formation, mesa etching and gate recess etching were performed in air. Then, the sample was immersed into HF solution in N_2 atmosphere, and was introduced into UHV-based system without exposing to air. Then, the Si ICL-based passivation structure was formed. Finally, the gate electrode and contact holes were formed.

Results and Discussion

XPS study

In the present experiments, the air exposed InGaAs and InAlAs surfaces were slightly etched and immersed into a concentrated HF solution in nitrogen atmosphere before the sample was introduced into the UHV-based system.

Figure 4 shows the result of the XPS analysis of the InAlAs surface before and after this HF treatment. It is clearly seen that the oxide components on the surface were greatly reduced, leaving the elemental As component. The volatile elemental As component further disappears from the surface during Si ICL formation.

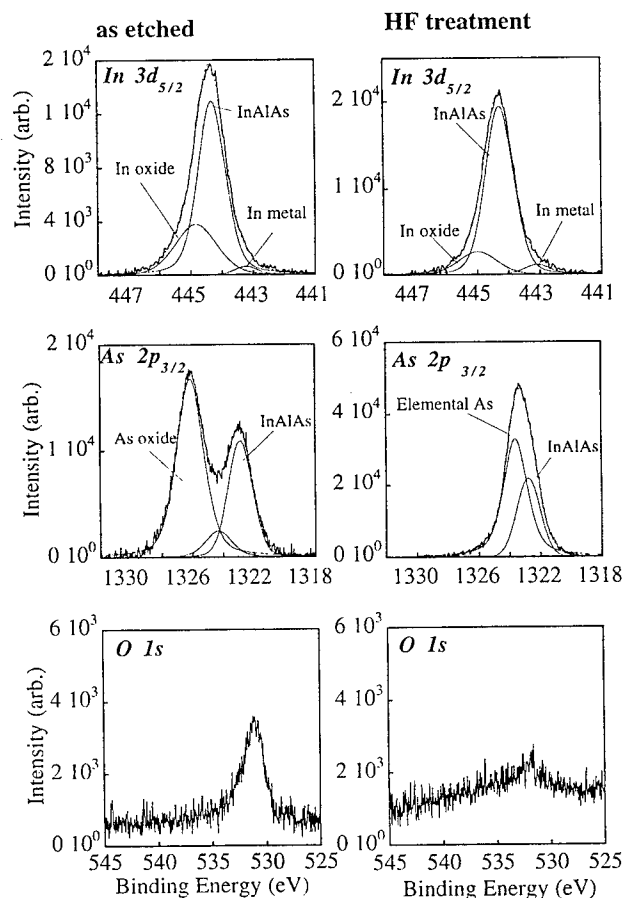


Fig.4 XPS spectra from InAlAs surfaces before and after HF treatment.

I-V study of the passivation structure

The average field dependence of the resistivity of the photo-CVD SiO_2 film deposited on an n^+ -Si film is shown in Fig.5. It is seen that a resistivity of 10^{13} ohm·cm can be obtained up to an average field strength of 5MV/cm.

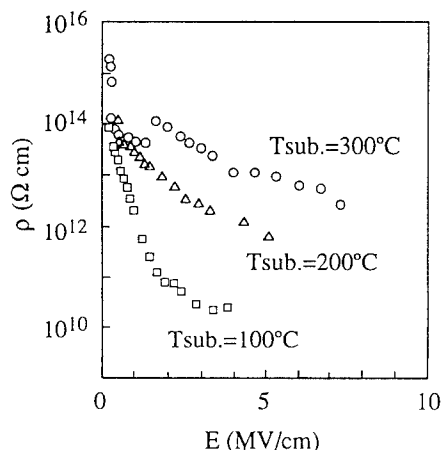


Fig.5 Average field dependence of the resistivity of the photo-CVD SiO_2 film deposited on an n^+ Si film.

MIS C-V curves and their interpretation

The measured C-V curves of the MIS capacitor shown in Fig.1(a) are given in Fig.6. These curves behave similarly with those of the MIS capacitors fabricated in an entirely UHV-based process, showing small hysteresis and small frequency dispersion of the accumulation capacitance. The interface state density distribution calculated from the C-V curves using by Terman method is compared in Fig.7 with that of interface without Si ICL and with the best data obtained by the entirely UHV based process(7). It is clearly seen that the interface state density N_{ss} is reduced by the present Si ICL technique, giving a minimum N_{ss} of $3 \times 10^{11} \text{ cm}^{-2} \text{ eV}^{-1}$, although it is not as good as the best data.

The measured C-V curves of the IGHEMT capacitor shown in Fig.1(b) are given in Fig.8(a) together with its low-frequency ideal curve calculated by a rigorous computer simulation program on the capacitance response of 2DEG in a HEMT structure (8). The C-V curves measured on a Schottky type AlGaAs/GaAs HEMT capacitor are also shown in Fig.8(b) for the purpose of comparison. From the comparison, it can be said that the strong frequency dependence in Fig.8(a) is not necessarily from the interface states at the insulator-semiconductor interface. In fact, a detailed analysis has shown that it is related to rf carrier supply to the InAlAs layer. A relatively good agreement between the ideal curve and the measured curve shows that the interface is basically free of interface states and the carriers in the 2DEG can be well controlled by the gate.

Figure 9 shows the C-V curves of an AlGaAs/GaAs HEMT capacitor with an Al_2O_3 gate insulator obtained by anodic oxidation. This shows the instability problem of an

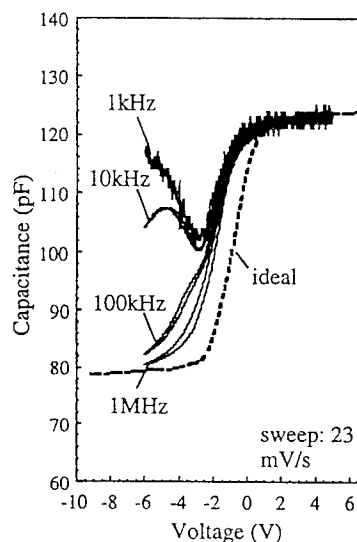


Fig.6 Measured C-V curves of the MIS capacitor.

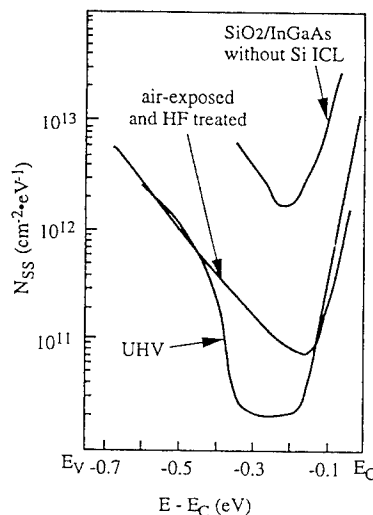


Fig.7 The interface state density distributions calculated from the C-V curves.

IGHEMT device having high density of interface states. Because of capture and emission of carriers at the insulator-semiconductor interface, its threshold voltage moves around according to its past history. It should be noted in Fig.8(a), no such instability problem exists in the IGHEMT capacitor produced by the Si ICL-based passivation technique.

D.C. characteristics of fabricated MISFETs and IGHEMTs

The d.c. I-V characteristics of a fabricated fat MISFETs ($L=6\mu\text{m}$, $W=180\mu\text{m}$) and IGHEMTs ($L=4\mu\text{m}$, $W=180\mu\text{m}$) are shown in Fig.10 (a) and (b), respectively. The both I-V curves show good pinch-off characteristics with small hysteresis and the excellent controllability of drain current by the gate biasing.

The maximum values of g_m value were 61mS/mm for MISFETs and 40mS/mm for IGHEMTs, respectively. The

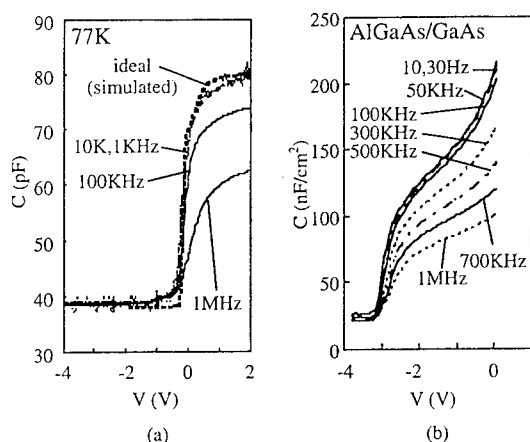


Fig.8 (a) Measured and ideal C-V curves of the IGHEMT capacitor shown in Fig.1(b). (b) Measured C-V curves of a Schottky type AlGaAs/GaAs HEMT capacitor.

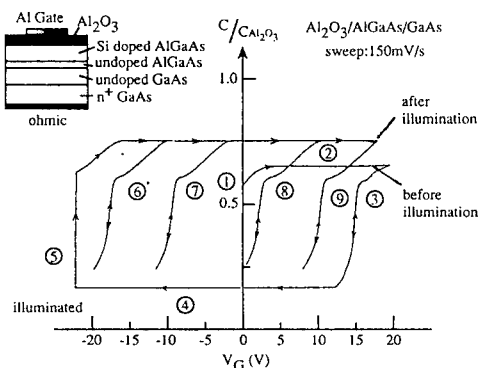


Fig.9 Measured C-V curves of an AlGaAs/GaAs HEMT capacitor with an Al_2O_3 gate.

maximum effective mobility was $3,850\text{cm}^2/\text{V s}$ for MISFETs and $1,800\text{cm}^2/\text{V s}$. The reason for a low mobility for IGHEMTs has been found to be due to unoptimized poor ohmic contact technology. The gate leakage current was well below $1\text{nA}/\text{mm}$ for both device.

Conclusion

The applicability of the Si ICL-based passivation technique combined with the HF treatment to fabrication of InGaAs MISFETs and IGHEMTs was investigated.

XPS, I-V and C-V studies of the basic insulator-semiconductor structures have shown that the present passivation technique controls the interface structure reasonably well and produces interfaces with very low leakage currents and acceptably low interface state densities.

The fabricated depletion mode MISFETs have a good gate control of drain current with good pinch off characteristics. A highest effective channel mobility of $3,850\text{cm}^2/\text{V s}$ was achieved. The gate leakage current was well below $1\text{nA}/\text{mm}$. The fabricated IGHEMTs have also

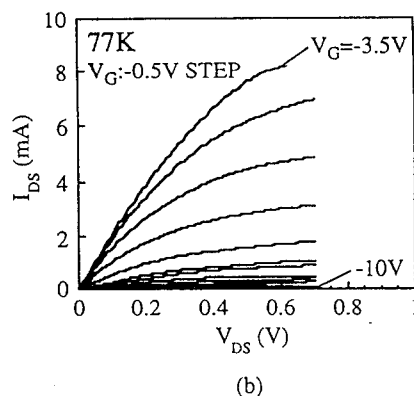
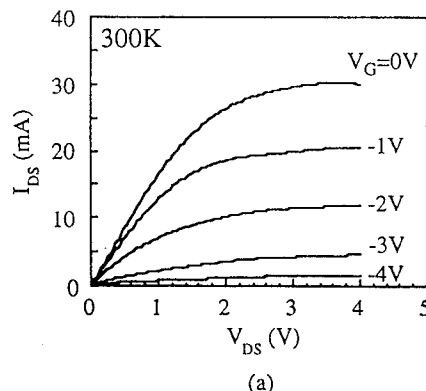


Fig.10 d.c. I-V characteristics of (a) a fabricated fat MISFETs ($L=6\mu\text{m}$, $W=180\mu\text{m}$) and (b) IGHEMTs ($L=4\mu\text{m}$, $W=180\mu\text{m}$).

demonstrated their stability and feasibility.

Reference

- (1) H. Hasegawa, M. Akazawa, H. Ishii and K. Matsuzaki: *J. Vac. Sci. & Technol.*, **B7**, 870 (1989).
- (2) H. Hasegawa and H. Ohno: *J. Vac. Sci. & Technol.*, **B4**, 1130 (1986).
- (3) M. Akazawa, H. Hasegawa and E. Ohue: *Jpn. J. Appl. Phys.*, **28**, L2095 (1989).
- (4) S. Suzuki, Y.G. Xie, T. Sawada and H. Hasegawa: "Control of Semiconductor Interfaces", ELSEVIER, 271 (1994).
- (5) K. Iizuka, J. Akasaka, T. Tsubata and H. Hasegawa: *Int. Phys. Conf. Ser.* **106**, 743 (1990).
- (6) S. Kodama, S. Koyanagi, T. Hashizume and H. Hasegawa: presented at 1995 PCSI, to be published in *J. Vac. Sci. Technol.*
- (7) S. Kodama, S. Koyanagi, T. Hashizume and H. Hasegawa: *Jpn. J. Appl. Phys.* **34**, 1143 (1995).
- (8) H. Tomozawa, K. Numata and H. Hasegawa: *Appl. Surf. Sci.* **60/61**, 721 (1992).

AlGaAsSb Buffer/Barrier layer on GaAs substrate for InAs channel with High Electron Properties

S.Miya, S.Muramatsu, N.Kuze, K.Nagase, T.Iwabuchi, A.Ichii, M.Ozaki and I.Shibasaki

Electronics materials & devices Laboratory, Asahi Chemical Ind. Co., LTD,
2-1, Samejima, Fuji, Shizuoka, 416 Japan
phone: +81 545 62 3403, telefax: +81 545 62 3419

InAs/AlGaAsSb deep quantum well was successfully formed on GaAs substrate and examined for two electron devices; Hall elements (HEs) and field-effect transistors (FETs). With thin buffer layer of 600nm AlGaAsSb on GaAs substrate, we observed high electron mobility more than $20,000\text{cm}^2/\text{Vsec}$ and effective electron velocity of $2.2 \times 10^7\text{ cm/sec}$ at RT for 15nm thick InAs channel. AlGaAsSb, lattice-matched to InAs, was discussed from the view points of insulating property, carrier confinement and oxidation. Reliability data good enough for practical use were also obtained for HEs. We proposed AlGaAsSb as a promising buffer/barrier layers for InAs channel devices on GaAs substrate, and we suggested AlGaAsSb also for InGaAs channel devices.

Introduction

AlGaAsSb is an attractive material for barrier/buffer layers, which lattice constant can be controlled to be matched to InAs. There exists a conduction band offset (ΔE_c) as much as 1.3eV at the InAs/AlGaAsSb interface, so that an AlGaAsSb /InAs/AlGaAsSb structure would be called a deep quantum well (DQW).

In this work, InAs/AlGaAsSb DQW structures were grown on GaAs substrate and examined. To utilize AlGaAsSb for electron devices, besides crystal growth including V-group alloy technique[1], examination of insulating properties of AlGaAsSb, process feasibilities and device reliabilities have to be studied with efforts, for AlGaAsSb or AlSb is well known as an easily oxidized material. For the reason, relatively thin buffer layers of 600nm AlGaAsSb with various Ga content were examined on GaAs substrate and effect of Ga content on oxidation rate was investigated. We found that, with optimal Ga content ($\text{Al/Ga}=0.35/0.65$) InAs/ $\text{Al}_{0.65}\text{Ga}_{0.35}\text{As}_{0.15}\text{Sb}_{0.85}$ DQW was stable and it applied to two kinds of devices. One was Hall elements (HEs) or Hall effect magnetic sensors, with which reliability of the AlGaAsSb layers was confirmed. The other was field-effect transistors (FETs). High electron mobility more than $20,000\text{cm}^2/\text{Vsec}$ and effective electron velocity of $2.2 \times 10^7\text{ cm/sec}$ were obtained in device performances.

Attractive features of InGaAs DQWs with AlGaAsSb buffer/barriers were also suggested, which were deduced from successful results of InAs DQW applications achieved here.

Experiments

1. MBE technique and grown wafers

Using conventional MBE technique, DQW structures, shown in Fig.1, were grown on GaAs substrate with various content of AlGaAsSb.

As buffer layers, we grew GaAsSb, $\text{Al}_x\text{Ga}_{1-x}\text{As}_y\text{Sb}_{1-y}$ ($x=0.2, 0.65, 0.8$) and AlAsSb, all of which were lattice-matched to InAs and 600nm thick, followed by

InAs/AlGaAsSb DQW

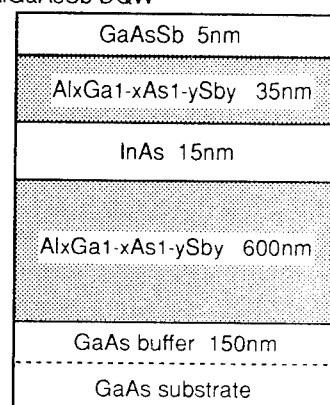


Fig.1 Schematics of InAs/AlGaAsSb deep quantum well structure. For device applications $x=0.65$ and $y=0.85$ were selected.

Buffer/barrier layer	Ts (°C) for InAs	Mobility (cm^2/Vsec)	Ns (10^{12}cm^{-2})	N (10^{17}cm^{-3})	R [□] (Ω)
GaAsSb	450	25400	2.72	9.07	90
$\text{Al}_{0.2}\text{Ga}_{0.8}\text{AsSb}$	455	23700	1.69	11.3	166
$\text{Al}_{0.65}\text{Ga}_{0.35}\text{AsSb}$	465	23500	1.21	8.07	220
$\text{Al}_{0.8}\text{Ga}_{0.2}\text{AsSb}$	490	20000	1.32	8.80	240
AlAsSb	490	13600	2.77	18.5	170

Table 1 Optimized growth temperatures and typical electronic properties of wafers with varied Al content in AlGaAsSb buffer/barriers.

15nm InAs as an active layer and upper barrier of the same content respectively. As/Sb beam-pressure ratio was set, for instance, to be 45 for $\text{Al}_{0.65}\text{Ga}_{0.35}\text{As}_{0.15}\text{Sb}_{0.85}$ and lattice matchings within 1% were confirmed by X-ray diffraction measurements. Without any intentional doping, typical electron densities and mobilities of the samples are listed in Table 1. High electron mobilities of InAs more than $20,000\text{cm}^2/\text{Vsec}$ for all buffers but AlAsSb were achieved. It is found that, among these wafers, only AlAsSb sample was too easily oxidized to be dealt with in ordinal lithography process. At any rate, we successfully made by MBE AlGaAsSb/InAs double heterostructures and especially, $1.2 \times 10^{12}/\text{cm}^2$ and $23,000\text{cm}^2/\text{Vsec}$ were obtained with $\text{Al}_{0.65}\text{Ga}_{0.35}\text{As}_{0.15}\text{Sb}_{0.85}$, which is forming DQW. In practice, high insulating properties of AlGaAsSb buffer layer ($>10\text{M}\Omega$) was confirmed in the following device applications.

It should be noted that in spite of large lattice mismatch over 7% between GaAs substrate and $\text{AlGaAs}_{0.15}\text{Sb}_{0.85}$, electron properties described above are superb, even though the thickness of AlGaAsSb layers is relatively small (600nm) in our growth. We studied, by VCR, images of RHEED pattern during AlGaAsSb growth. Typically in AlGaAsSb growth on GaAs, streaky RHEED pattern changes into spotty after several atomic layer growth of AlGaAsSb and then it changes again to perfectly streaky pattern with growth proceeding. With these data for every sample, we examined growth condition and minimized the thickness of AlGaAsSb, with which the streaky RHEED pattern is recovered from spotty feature, as thin as 35nm.

As detailed growth condition is described in previous paper[2], we will discuss here on two matters concerning the wafers from the view point of device applications.

At first, etch-pit density revealed by citric acid etching was observed in a rage of $10^6/\text{cm}^2$ at the top of upper AlGaAsSb barrier layer (Fig.2). The etch-pits are due to

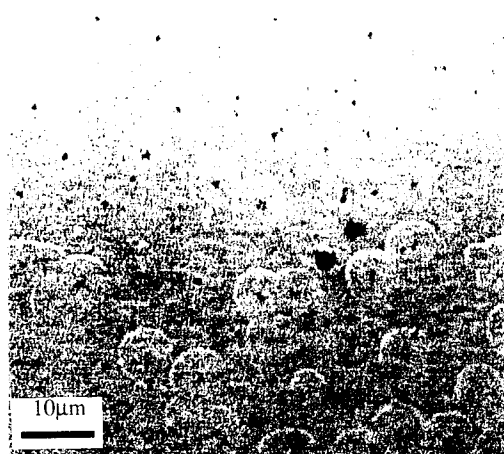


Fig.2 Etch-pits revealed by citric acid. Central dark points in circles are considered directly related to dislocation lines. Dislocation density was in a range of $10^6/\text{cm}^2$.

line-shaped dislocations penetrating upward from the mismatching interface of AlGaAsSb/GaAs, which are also observed in TEM images of grown wafers. As for electron mobilities, these dislocations seem not to decrease the mobilities remarkably. Moreover, in HEs having a rather simple device structure with ohmic electrodes, we found that this dislocation density makes no effect throughout all fabrication processes. In addition, we also grew some samples with AlGaAsSb buffer layers as thick as $2\mu\text{m}$ but no improvements of electronic properties were observed at all. It seems that little disappearance of dislocation lines occurred in the additional growth and the 600nm employed here may be thick enough for an AlGaAsSb buffer layer.

For the second, Ga content of AlGaAsSb was studied. AlAsSb is oxidized immediately when treated with water; it is easily oxidized during ordinal fabrication processes and volume increase of the layer is obviously observed in a treated region. To know the oxidation rate, we measured, for $\text{Al}_{0.8}\text{Ga}_{0.2}\text{AsSb}$ and $\text{Al}_{0.6}\text{Ga}_{0.4}\text{AsSb}$ wafers (600nm thick) partly covered with photoresist mask, heights of the oxidized expansion after long period exposure to humid air. The heights were, in $\text{Al}_{0.8}\text{Ga}_{0.2}\text{AsSb}$, 151nm for 122-day exposure and 240nm for 242-day exposure and, in $\text{Al}_{0.6}\text{Ga}_{0.4}\text{AsSb}$, 14nm and 22nm respectively. It is quite remarkable that, supposing the volume increase is proportional to the amount of oxidization, Al content reduction from 80% to 60% makes the reaction velocity more than 10 times smaller, although precise analysis of the reaction kinetics of oxidization belongs to feature studies. We summarized, in Table 2, comparison of AlGaAsSb with various Ga contents from the view points of oxidization, insulating properties and carrier confinement for DQW applications.

	AlAsSb	$\text{Al}_{0.8}\text{Ga}_{0.2}\text{AsSb}$	$\text{Al}_{0.6}\text{Ga}_{0.4}\text{AsSb}$	GaAsSb
Oxidation velocity (a.u.)	extreamly fast	1	$<1/10$	—
insulation	—	$>10\text{M}\Omega^{\square}$	$>10\text{M}\Omega^{\square}$	—
carrier confinement	best	better	good	broken
ΔEc to InAs		1.3eV	1.2eV	

Table 2 Features of AlGaAsSb with varied Al contents.

Thus we succeeded in preparation of InAs-DQW which has both good electron properties and also feasibility for device applications. From Table 1 and Table 2, Ga content of 60%~80% is favorable. In addition, as a result of temperature-depending Hall measurements of these wafers, we found smooth dependencies on temperature both of mobilities and carrier densities from -50°C to 150°C for buffer/barrier layers of $\text{Al}_{0.8}\text{Ga}_{0.2}\text{AsSb}$ and $\text{Al}_{0.65}\text{Ga}_{0.35}\text{AsSb}$.

2. Device applications

Device fabrications were carried out for HEs and FETs. In both cases, mesa-etching for device isolation was made with 800nm depth revealing GaAs substrate on which probing/wire-bonding pads were formed directly.

(1) Hall elements with practical reliability

Application of DQW to Hall elements with excellent performances was already reported elsewhere[2,3]. Hall element is based on Hall effect and is widely used recently as magnetic sensors in brush-less motors, non-contact switches and so on. For HE is a low-field device. InAs is a quite suited material[4] and InAs/AlGaAsSb DQW is the most favorable for HE; thin layer(15nm) of InAs for high sheet resistance combined with high electron mobility is desirable for high sensitivity, and high carrier density of $8 \times 10^{17}/\text{cm}^3$ also results in a little temperature dependence of input resistance, making driving condition stable in wide range of temperature. Comparison of the device features for InSb HE, GaAs HE, both of which are commercially available, and InAs-DQW HE is summarized in Table 3.

	Output voltage V _H (mV)	Temp. coeff. of V _H	Temp. coeff. of input R	Drive condition
InSb HE*	196 - 274	-	-2%/deg	1V
GaAs HE	60 - 70	-0.17%/deg	0.3%/deg	6V
DQW HE (InAs)	260 - 300	-0.25%/deg	0.2%/deg	6V

* Asahikasei electronics HW 101C ** B = 500G
*** Temperature was ranged from -50°C to 150°C

Table 3 Comparison of device features between InSb (polycrystalline), GaAs and InAs-DQW HEs. InSb HE and GaAs HE are commercially available.

HE chips are fabricated with SiN thin film passivation and assembled in plastic package (standard mini-mold package) using commercial HEs' production line. They showed long life and stability in all items of reliability test, which included high humidity life test, high temperature life test, pressure cooker test, thermal shock test, soldering heat test, etc. These are chosen from the standard test items for commercial HEs[3]. This is the first case, to our knowledge, of a successful reliability report on electron devices constructed with AlGa(As)Sb.

(2) Performances of InAs FETs

InAs/AlGaAsSb FETs [5] were fabricated with non-alloyed ohmic electrodes having contact resistance of $0.1\Omega\text{mm}$. In this study, gate length was ranged from 1 to $2\mu\text{m}$ and device structure was primary; no gate-recess nor gate off-set to source, etc. was employed. DC measurement (Fig.3) showed good pinch off characteristics. Gate leakage current was several tens of μA . RF performance was measured at

$V_{ds}=0.8\text{V}$ and $V_g=-0.4\text{V}$. Correlation between cut-off frequencies and inverse of gate lengths is shown in Fig. 4. Resultant effective electron velocity of $2.2 \times 10^7\text{cm/sec}$ is higher than those of conventional and pseudomorphic HEMTs and approaching that of InGaAs-HEMT on InP substrate.

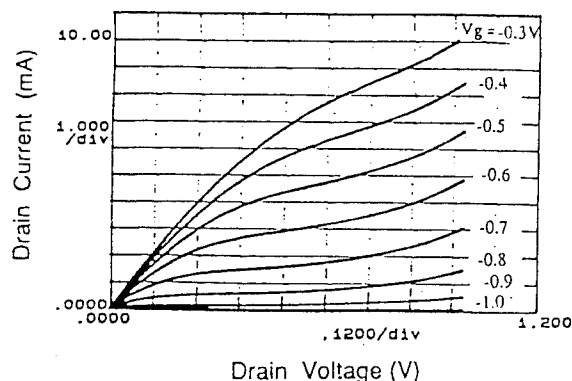


Fig.3 Typical I-V characteristics of InAs FET. Maximum transconductance was 450mS/mm. ($L_g=1.0\mu\text{m}$)

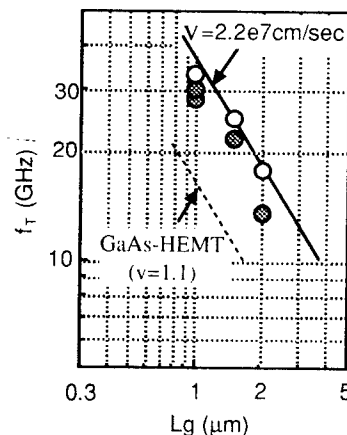


Fig.4 Results of microwave measurements for InAs FETs. Gate length (L_g) was ranged from 1 to $2\mu\text{m}$. Open circles are results for devices with 65% Al content and closed circles are for ones with 80%.

Note that relatively rapid increases of drain-conductance (so called kinks) at near $V_d=1\text{V}$ was observed just similarly to that reported in InAs/AlSb FET[6], which may be due to the onset of avalanche breakdown in InAs. In addition, we have recently got some data with half-micron gates, in which the kinks appeared at lower drain bias such as 0.5V. Also FETs with shorter gate-to-channel distance (15nm) showed smaller kink bias. These are all understood consistently if kinks are due to the narrow band gap of InAs, but careful analysis is needed together with the effort on improving device structure to lower the peak electric field in the channel.

Discussions

As providing a first practical application of InAs-DQW, we developed InAs-DQW HEs with good reliability. As for FETs, more precise studies are necessary. One is related to gate fabrication. Gate leakage current was typically ranged in several tens of μA although some had gate leakage of nA in our devices. From the view point of gate reproducibility and reliability, etch-pit density observed here ($\sim 10^6/\text{cm}^2$) may be too high for the purpose. In order to make the dislocation density lower graded buffer technique would be one of the most favorable.

Here, we describe on growth reproducibility of InAs DQW structure. We are using the MBE machine specially designed by us in which four 2-inch wafers can be grown at a batch. Distribution (3σ) of mobility and carrier density was examined for hundred points in the four wafers to be within 3% and 6%, respectively. As for batch-to-batch reproducibility, residual carriers of InAs/ $\text{Al}_{0.65}\text{Ga}_{0.35}\text{AsSb}$ DQW is rather high and varied. Recently, the reduction of residual carrier density as low as $5.5 \times 10^{11}/\text{cm}^2$ is achieved in our growth. In the current case, after chamber vent for source material charges, higher carrier densities ($< 2 \times 10^{12}/\text{cm}^2$) are obtained for several batches and then we can produce wafers of carrier density ranging within 15% around $5.5 \times 10^{11}/\text{cm}^2$ for more than 50 batches. These results enable us to produce wafers stably for the mass production purpose.

In addition, as a result of this carrier density reduction, we found a new unknown donor level in this system. High mobility more than $27500 \text{ cm}^2/\text{Vsec}$ is also observed in our current growth. Concerning these matters, we will describe detail in the near future.

Possibility of InGaAs DQW InGaAs is a promising material for high speed FETs and it has been studied with InAlAs barriers on InP substrate (InP-HEMT) exclusively. We suggested here that AlGaAsSb could work well as a possible another attractive barrier for InGaAs channel devices on GaAs substrate.

Compared to InAlAs/InGaAs system, AlGaAsSb/InGaAs system has advantages in every aspect of device performances. First of all, an extremely larger conduction band offset (ΔE_c) appears at AlGaAsSb/InGaAs interface than at InAlAs/InGaAs just similar to the case of InAs-DQW. DQW allows much more carriers being confined in thin channel, which is desirable especially for FETs. It has another advantage on indium content; by choosing appropriate antimony content y , lattice constant of $\text{AlGaAs}_{1-y}\text{Sb}_y$ matches to $\text{In}_x\text{Ga}_{1-x}\text{As}$ for all over the range of indium content x , which is restrictedly attained in InAlAs/InGaAs or AlGaAs/InGaAs system within a severe thickness limitation of pseudomorphism. In addition, dielectric constant of AlGaAsSb is larger than InAlAs and effects of strain on channel properties could also be controlled with optimized As/Sb ratio.

AlGaAsSb can be easily grown by MBE on GaAs

substrate instead of InP substrate as described above. In addition, if you need graded buffers to lower the dislocation density, AlGaAsSb is a material also suited for forming graded buffers on GaAs only with the control of Sb content. And finally, AlGaAsSb is stable enough with appropriate Ga content, which is practically demonstrated in this paper.

Conclusion

We discussed advantages of InAs/AlGaAsSb DQW system, by preparing utilizable MBE-grown wafers of good properties and demonstrating two device applications. We developed practical Hall elements of superior performances associated with good reliability for practical use.

Advantages of In(Ga)As DQW FETs were discussed and device characteristics were demonstrated for InAs-DQW. The FET of $1\mu\text{m}$ -gate had f_T value of 33GHz with primary device structure. We proposed AlGaAsSb as promising buffer/barrier layers for InAs channel devices on GaAs substrate, and we suggested AlGaAsSb also for InGaAs channel devices.

Acknowledgement

The authors would like to thank Dr. H. Ai and Dr. K. Mori for their continuous encouragements.

References

- [1] C.A. Chang et al., Appl. Phys. Lett. 31, 759 (1977)
- [2] N. Kuze et al., "InAs deep quantum well structures and their application to Hall elements", Proc. of MBE-VIII, 440 (1994); to be published in J. of Cryst. Growth
- [3] K. Nagase et al., "InAs/AlGaAsSb Quantum Well Hall Elements", Technical Digest of the 12th Sensor Symposium, 209 (1994)
- [4] T. Iwabuchi et al., "High sensitive Hall elements made from Si-doped InAs on GaAs substrate by MBE", Proc. of MBE-VIII, 438 (1994); to be published in J. of Cryst. Growth
- [5] S. Miya et al., "InAs Field-Effect Transistors with a Deep Quantum Well structure", Ext. Abst. of 1994 Int. Conf. on Solid State Devices & Materials, 973 (1994)
- [6] C.R. Bolognesi et al., "Improved Charge control and Frequency Performance in InAs/AlSb-Based HFETs", Elec. Device Lett. 15, 1 (1994)

High-Speed InP/InGaAs HBT with Reduced Intrinsic Transit Time

G.KHRENOV AND E.KULKOVA

Computer Solid State Physics Laboratory, University of Aizu
Aizu-Wakamatsu City, 965-80, Japan

The high-speed characteristics of InP/InGaAs HBTs with two different collector structures have been investigated using an ensemble Monte Carlo particle simulator. A dramatic decrease of the collector delay time has been observed for HBT with non-uniformly doped ($i - p^+ - i - n^+$) collector structure. The collector delay time is reduced due to the extension of the velocity overshoot region in the collector. The parameters of HBT with proposed collector structure ($i - p^+ - i - n^+$) has been optimized in order to obtain the ultimate high-frequency performance under the high collector voltage.

Introduction

Heterostructure bipolar transistors (HBTs) lattice matched to InP have emerged as potential candidates for high-speed digital, microwave and long-wavelength fiber-optic communication systems because of the excellent transport property of InP and its related materials. High-speed InP/InGaAs HBT having a current gain frequency about 175 GHz have been demonstrated in [1]. The analysis of experimental data has shown that the collector charging time and base-collector transit time dominate among the components of the total emitter-collector delay time. Further reduction of the collector charging time was recently realized by reducing the base-collector junction area in HBT with buried subcollector [2]. To minimize the base-collector transit time vertical scaling or high ensemble carrier velocity are required. However, reduction of collector depletion width without decreasing the parasitic resistances is undesirable due to increase of the collector capacitance and hence increase of the collector charging time [3]. Thus, the most attractive way to reduce base-collector transit time is to utilize near-ballistic electron transport in the collector region as long as possible. HBT structure realizing this idea was proposed and investigated in [4]. Unfortunately, the peak current gain frequency in these HBTs can only be obtained over a narrow base-collector bias range. In this report, we propose and study InP/InGaAs HBT with non-uniformly doped collector structure having reduced transit time in comparison with conventional InP/InGaAs HBT structure and lesser sensibility to operation conditions than HBT proposed previously [4].

Device Structures and Model

The schematic band diagrams of the HBTs with con-

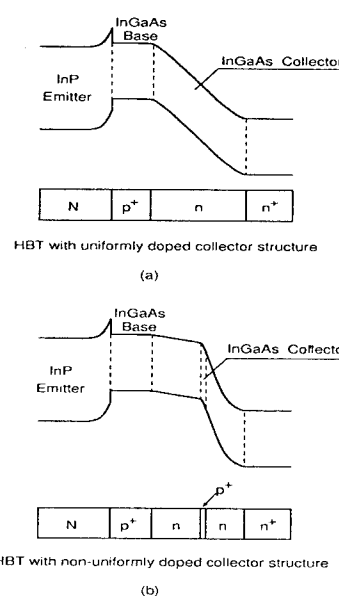


Fig.1 Schematic band diagrams of (a) conventional HBT with uniformly doped collector and (b) proposed HBT with non-uniformly doped collector.

ventional and proposed collector structures are presented in Fig.1. First structure (Fig.1a) is the conventional structure consisting of InP emitter, a 650-Å p^+ ($4 \times 10^{19} \text{ cm}^{-3}$) base, and a 3000-Å n ($2 \times 10^{16} \text{ cm}^{-3}$) collector followed by a heavily doped n^+ ($2 \times 10^{18} \text{ cm}^{-3}$) subcollector layer. Unlike commonly used HBT structure, the proposed HBT has non-uniformly doped collector structure consisting of very thin 20-Å p^+ ($1 \times 10^{18} \text{ cm}^{-3}$) layer inserted between two lightly-doped n ($3 \times 10^{15} \text{ cm}^{-3}$)

layers (Fig.1b). The thicknesses of both lightly-doped layers are the same and equal 1500-Å. This design is proposed to let the electrons stay longer in central valley and hence to keep high electron velocity at least within first lightly-doped n layer. The emitter-base junctions and subcollector layers are the same for both considered HBT designs. The parameters of proposed HBT are chosen to provide high electron velocity under the high current density operation condition (this condition is most important for high-frequency operation). It is necessary to stress here that varying the sheet density of acceptors in p^+ collector layer and its position we have possibility to optimize the HBT structure in order to minimize the collector delay time for any desired operation conditions.

To investigate the operation and to calculate high-frequency characteristics of InP/InGaAs HBTs with conventional and proposed collector structures time-dependent ensemble Monte Carlo particle simulator was developed and implemented. The Monte Carlo particle model takes into account the complex non-parabolic electron spectra and all essential scattering mechanisms. The evolution of the holes in the base region and electrons in the heavily-doped subcollector region is simulated using drift-diffusion approach. First the steady-state simulation of HBT for a given bias condition is performed and the stationary distributions of the potential and carriers concentrations corresponding to this bias are calculated. After obtaining a steady-state solution, an electron bunch consisting of several thousands of electrons is injected from the emitter-base interface for a short time interval. As long as electrons travel across the collector space charge region, they induce non-steady-state collector current. When all injected electrons leave the modeling region, the complex frequency-dependent small-signal base-collector transport factor is calculated directly using the Fourier analysis of the non-steady-state induced collector current [5,6].

Results and Discussion

The operation of HBTs has been investigated at temperature 300 K in the wide range of applied voltages and parameters of transistor structures. The typical average electron velocity profiles for HBTs under consideration are shown in Fig.2 (here the point $x = 0$ corresponds to the emitter-base interface). The operation conditions corresponding to this plot are follows: collector-base voltage $V_{CB} = 1.25$ V and collector current density $J_C = 10^5$ A/cm². It is seen that the peak values of electron velocity are practically the same for both collector structures and approximately equal to 8×10^7 cm/s. In both case the end of velocity overshoot region is associated with rapid population of the satellite valleys. The position of the peak velocity depends on the position of the high electric field domain in the collector region. For conventional uniformly doped collector structure the electric field is

maximum near the base-collector interface. As a result electrons traveling across the collector space charge region rapidly populate the satellite valleys and lose their directional velocity. In contrast, for proposed collector structure the electric field between the base region and collector p^+ -layer is low and electrons remain high velocity over a wide area. Thus, it is possible to expect the substantial reduction of the base-collector transit time in HBT with proposed collector structure.

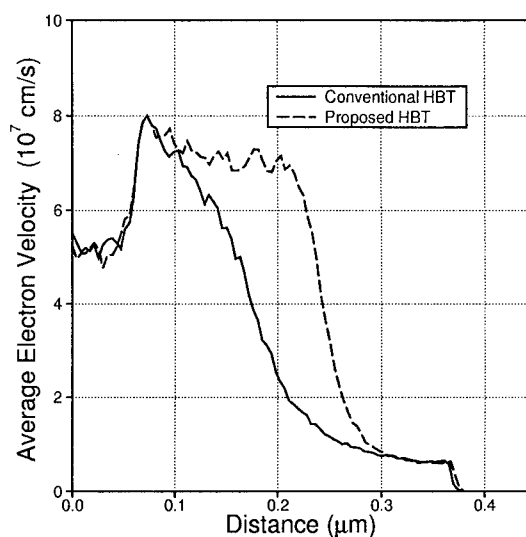


Fig.2 Average electron drift velocity profiles corresponding to HBTs with conventional (solid curve) and proposed (dashed curve) collector structures.

The dependencies of the base-collector delay time on the collector current density for conventional HBT are presented in Fig.3. The base-collector delay time increases with decreasing collector current density for all values of the applied collector-base voltage. This fact is due to change of the electric field distribution at high injection levels. When the collector current density is low, the distribution of the electric field in depletion layer of the collector-base junction is mainly determined by the profiles of impurities and applied voltage. In the case of the conventional HBT the electric field is maximum on the base side of the depletion layer and overshoot effect exists only over a narrow region near the base-collector interface. Increasing the collector current density leads to reduction of the electric field on the base side of the depletion layer and to increase of overshoot region. This is accompanied by an increase of the effective electron velocity in the collector depletion layer, leading to drastic reduction of the base-collector delay time. This effect begins to play important role for $J_C \geq 3 \times 10^4$ A/cm². Increasing the applied collector-base voltage also leads

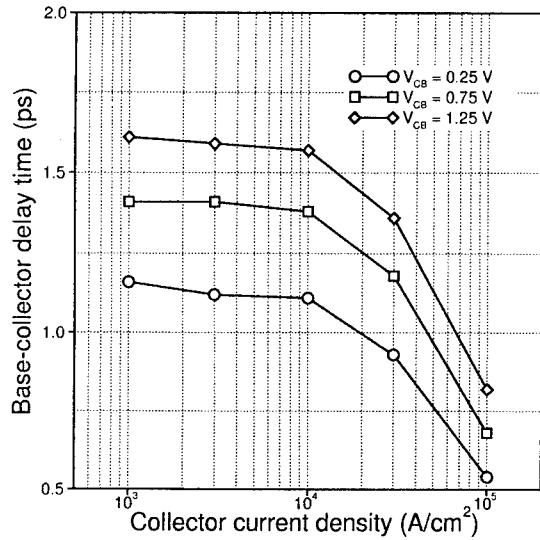


Fig.3 Base-collector delay time versus collector current density for conventional HBT with the collector-base voltage V_{CB} as a parameter.

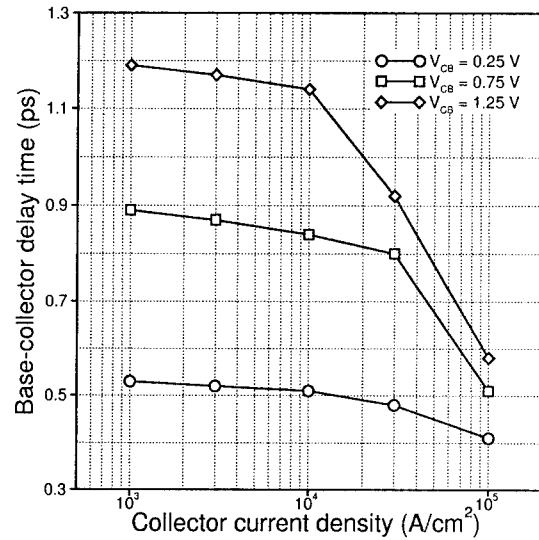


Fig.4 Base-collector delay time versus collector current density for proposed HBT with the collector-base voltage V_{CB} as a parameter.

to increase of the base-collector transit time, resulting from the reduction of the overshoot effect region under the high voltage.

The dependencies of the base-collector delay time on the collector current density for proposed HBT are presented in Fig.4. As for conventional HBT, the base-collector delay time increases with decreasing the collector current density and with increasing the applied collector-base voltage. At the same time, in the wide range of the base-collector voltage and collector current density the proposed HBT has significantly smaller base-collector delay time than HBT with conventional collector structure. In addition, the base-collector transit time of proposed HBT increases more slowly as the collector current density decreases. This fact results from the special distribution of the electric field in the base-collector junction provided by non-uniform doping profile. Even for low injection levels the electric field in the first lightly-doped layer is smaller than the electric field on the subcollector side of the collector depletion layer. This distribution of the electric field is more favorable to exploit overshoot effect as long as possible. Under the small applied voltage ($V_{CB} = 0.25$ V) the base-collector delay time practically does not depend on the collector current density, resulting from the extension of the overshoot region into the second lightly-doped n -layer even under the low collector current density (the satellite valleys are populated only near the subcollector layer).

The dependencies of the base-collector delay time on the applied collector-base voltage for conventional and

proposed HBTs are presented in Fig.5. It is seen that the base-collector delay time of proposed HBT is approximately 40% less than that of conventional HBT in the range of applied voltage V_{CB} from 0.25 V to 1.5 V. This makes essential contribution to reduction of the total delay time for HBT with sub-picosecond delay. For both HBT designs, the base-collector delay time increases with increasing V_{CB} , resulting from the electron scattering into low velocity satellite valleys in the collector.

The presented results show that the low collector-base voltage is the best condition for high-frequency operation of the InP/InGaAs HBTs (this fact for HBT with standard $n - n^+$ collector structure was also observed in [7]). At the same time, the high collector bias is required for many high-frequency applications of HBT. In this connection it should be noted that proposed collector structure has an important side benefit. Varying the sheet density of acceptors in p^+ collector layer and its position it is possible to adjust the HBT structure in order to obtain the ultimate speed of HBT at the desired range of applied voltages. To optimize the structure of proposed HBT to high voltage operation we increase the concentration of acceptors in p^+ layer from $1 \times 10^{18} \text{ cm}^{-3}$ to $1.5 \times 10^{18} \text{ cm}^{-3}$ and shift its position to subcollector (the distance between the base and p^+ layer is equal to $0.2 \mu\text{m}$). The increase of the acceptor concentration leads to increase of the electric field between p^+ layer and subcollector and hence to increase of the collector bias corresponding to near-ballistic transport in the first lightly-doped layer. The base-collector delay time for

conventional and optimized proposed HBTs as functions of the collector bias are presented in Fig.6. As seen, the proposed HBT has very small transit delay time even under the high applied voltage.

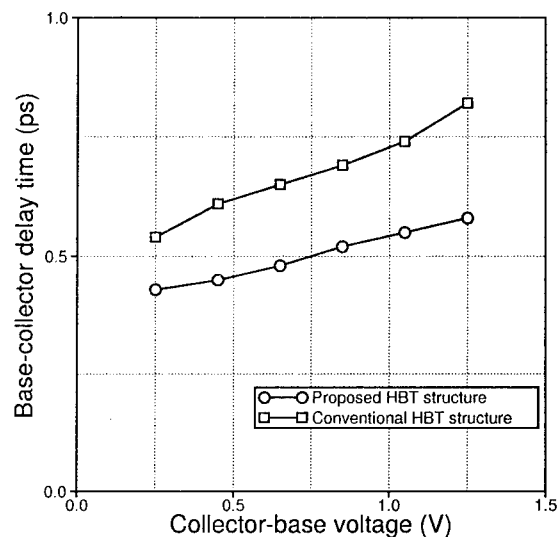


Fig.5 Dependencies of the base-collector delay time on the collector-base voltage for proposed and conventional HBTs.

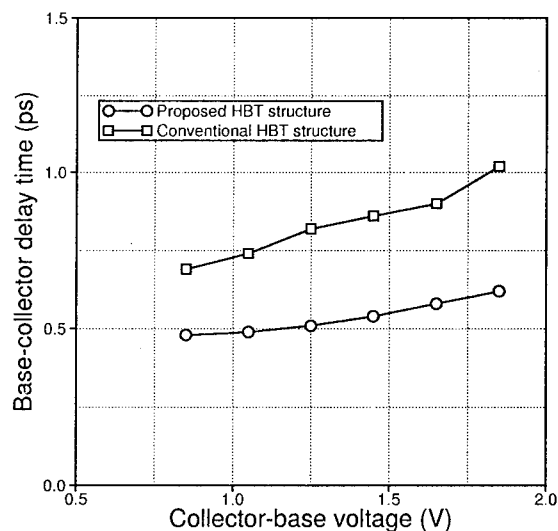


Fig.6 Dependencies of the base-collector delay time on the collector-base voltage for conventional and optimized proposed HBTs.

Conclusions

In conclusion, a new InP/InGaAs HBT structure with an $i-p^+-i-n^+$ doping profile of collector region is presented. Nonequilibrium electron transport phenomena in the base-collector junction is investigated for standard and proposed collector structures by using Monte Carlo particle simulation. It is found that implementation of the proposed $i-p^+-i-n^+$ collector structure essentially reduces the value of the collector transit delay time in comparison with conventional HBT. In addition, the proposed HBT structure is adaptable to operation conditions and can be easily adjusted at desired range of the collector-base voltage and collector current density.

References

1. J.-I.Song, B.W.-P.Hong, C.J.Palmstrom, B.P.Van der Gaag and K.B.Chough, "Ultra-High-Speed InP/InGaAs Heterojunction Bipolar Transistors," IEEE Electron Device Lett., Vol.15, pp.94-96, March 1994.
2. J.-I.Song, M.R.Frei, J.R.Hayes, R.Bhat and H.M.Cox, "Self-Aligned InAlAs/InGaAs Heterojunction Bipolar Transistor with a Buried Subcollector Grown by Selective Epitaxy," IEEE Electron Device Lett., Vol.15, pp.123-125, April 1994.
3. G.Khrenov, V.Ryzhii and S.Kartashov, "AlGaAs/GaAs HBT Collector Optimization for High Frequency Performance," Solid-State Electron., Vol.37, pp.213-214, January 1994.
4. T.Ishibashi and Y.Yamauchi, "A Possible Near-Ballistic Collection in an AlGaAs/GaAs HBT with a Modified Collector Structure," IEEE Trans. Electron Devices, Vol.35, pp.401-404, April 1988.
5. G.Khrenov, V.Ryzhii and S.Kartashov, "Simulation of HBTs and HIGFETs based on AlGaAs/GaAs heterostructure," Technical Digest of 2nd Intern. Conf. on VLSI and CAD, Korea, 1991, pp.215-218.
6. A.Das and M.Lundstrom "Does velocity overshoot reduce collector delay time in AlGaAs/GaAs HBT's," IEEE Electron Device Lett., Vol.12, pp.335-337, 1991
7. A.F.Levi, R.N.Nottenburg, J.K.Chen, P.H.Beton and M.B.Panish, "Nonequilibrium electron Dynamics in Bipolar Transistors," Solid-State Electron., Vol.32, pp.1289-1295, December 1989.

SPICE-Based DC and Microwave Characterization of InAlAs/InGaAs HBT's Used for Large-Bandwidth Integrated Transimpedance Amplifiers

K. Yang, A. L. Gutierrez-Aitken, X. Zhang, G. I. Haddad, and P. Bhattacharya

Center for High Frequency Microelectronics
Department of Electrical Engineering and Computer Science
The University of Michigan
Ann Arbor, MI 48109-2122, USA

Abstract

The DC and small-signal microwave performance of InAlAs/InGaAs single HBT's (SHBT's) used for large-bandwidth monolithically integrated transimpedance amplifiers is characterized based on a new HBT model built in SPICE. Several effects observed from InGaAs SHBT's, which are not accounted for in the conventional Gummel-Poon BJT model, are modeled through a macromodeling approach. The developed HBT model accompanied by a detailed parameter-extraction process predicts accurately measured DC and AC characteristics of the HBT's and transimpedance amplifiers.

Introduction

InP-based HBT's have been widely used in high-speed monolithically integrated optoelectronic circuits due to their ultra-fast performance and compatibility with 1.3-1.55 μm lightwave communication systems [1-3]. For a detailed performance analysis and optimization of these circuits, it is essential to develop a unified HBT model which is valid over a wide range of operating conditions. So far, the efforts of developing such a model based on modern CAD tools such as SPICE and LIBRA have been mainly focused on more widely used GaAs-based HBT's [4-6]. However, such efforts for HBT's based on InP/InGaAs/InAlAs material systems have not been as extensive as GaAs-based HBT's.

In this paper, we present a SPICE-based model and characterization results of InAlAs/InGaAs SHBT's used for high-bandwidth integrated transimpedance amplifiers. The model accounts for typical soft breakdown and forward transit-time delay effects of InGaAs SHBT's by combining relevant equivalent-circuit elements with the Gummel-Poon BJT model available in SPICE. The performance of 2- and 3-stage monolithically integrated transimpedance amplifiers, which demonstrate a transimpedance gain of 42-48 dB Ω and a -3 dB bandwidth of 17-19 GHz, was also analyzed based on the developed model.

Device Performance

Fig.'s 1 and 2 show the DC input and output char-

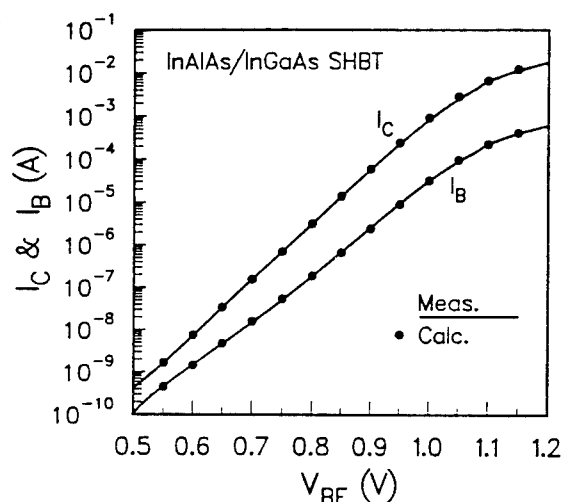


Figure 1: Measured and calculated forward Gummel plot of the InAlAs/InGaAs SHBT.

acteristics of a 5 $\mu\text{m} \times 5 \mu\text{m}$ emitter InAlAs/InGaAs SHBT. The structure was grown by molecular beam epitaxy (MBE) and processed using our self-aligned emitter-base mesa process. The thickness of the undoped InGaAs pre-collector was optimized to be 6000 \AA for use of the InGaAs base-collector junction as a p-i-n photodiode in a shared layer integration scheme of PIN-HBT photoreceivers for 10 to 20 Gbit/s applications [2,3]. The frequency response of the device obtained from measured S-parameters from 1 to 26.5 GHz

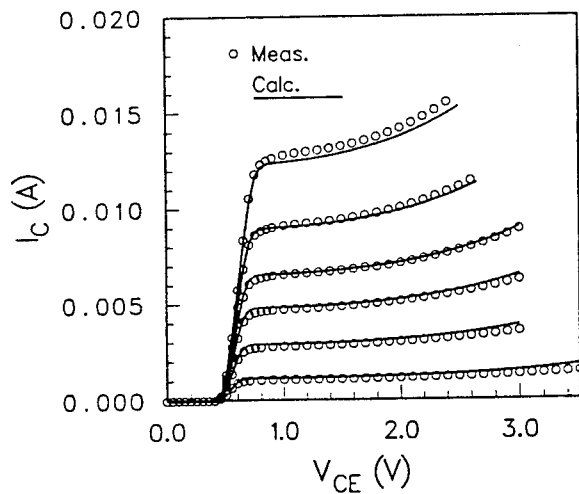


Figure 2: Measured and calculated common-emitter output characteristics of the InAlAs/InGaAs SHBT under constant I_B conditions.

is shown in Fig. 3. The device demonstrates maximum current and power gain cutoff frequencies, f_T and $f_{max}(G_{max})$, of 67 GHz and 90 GHz at $I_C = 10$ mA and $V_{CE} = 2$ V, respectively.

HBT Model and Parameter Extraction

The HBT model was developed based on the Gummel-Poon BJT model available in SPICE (Fig. 4). In order to account for the typical soft-breakdown characteristics of InGaAs-based SHBT's [7,8] shown in Fig. 2, a feedback current source, I_{FB} , is connected externally across the base-collector junction. This current source, which represents the generation and amplification of carriers across the reverse biased InGaAs junction in the forward active mode, is implemented using a polynomial current source available in SPICE as a function of I_C and V_{CB} . The relevant DC parameters of the intrinsic device and extrinsic elements were extracted through fitting to the measured DC characteristics of Fig.'s 1-2.

The AC parameters including the transit time and depletion and diffusion junction capacitances were extracted next. The S-parameters measured over a wide range of DC bias were fitted based on the small-signal equivalent circuit generated by SPICE at a given DC bias from the HBT model shown in Fig. 4. The parasitic capacitance (C_{P1} , C_{P2}) and inductance (L_E , L_B , and L_C) components introduced from the pad and interconnect metals of the test structure were also taken into account. The transit-time delay effect across the collector observed in this study when V_{CB} exceeds ~ 0.9

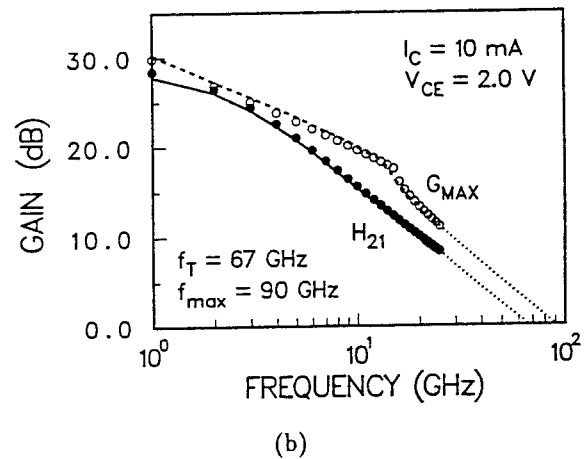
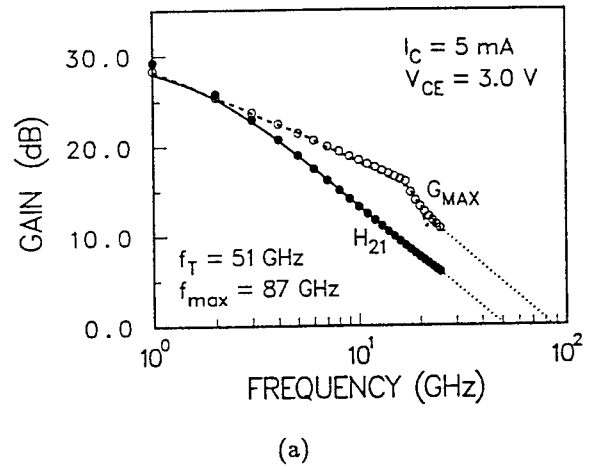


Figure 3: Measured (line) and calculated (symbol) frequency response of the InAlAs/InGaAs SHBT at (a) $I_C = 5$ mA; $V_{CE} = 3$ V and (b) $I_C = 10$ mA; $V_{CE} = 2$ V.

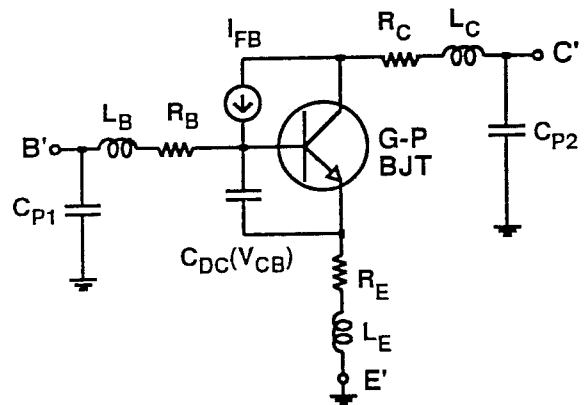


Figure 4: SPICE macro model of the InAlAs/InGaAs SHBT.

Parameter	Value
IS (A)	1.01×10^{-16}
ISE (A)	1.43×10^{-15}
ISC (A)	7.39×10^{-12}
IKF (A)	5.00×10^{-5}
IKR (A)	5.67×10^{-7}
BF	5.70×10^1
BR	1.00×10^{-1}
NF	1.29
NE	1.70
NR	1.06
NC	1.18
NKF	9.61×10^{-2}
RE (Ω)	5.00
RB (Ω)	3.00
RC (Ω)	5.00
CJE (F)	1.20×10^{-13}
CJC (F)	2.70×10^{-14}
MJC	0.25
VJC (V)	0.75
TF (S)	1.85×10^{-12}
I_{FB} (A)	$5.0 \times 10^{-5} I_C V_{CB}$ $+ 3.25 \times 10^{-4} I_C V_{CB}^2$ $+ 5.50 \times 10^{-3} I_C^2 V_{CB}$
C_{DC} (F)	$3.0 \times 10^{-14} (V_{CB} - 0.9)$
$(V_{CB} \geq 0.9 \text{ V})$	

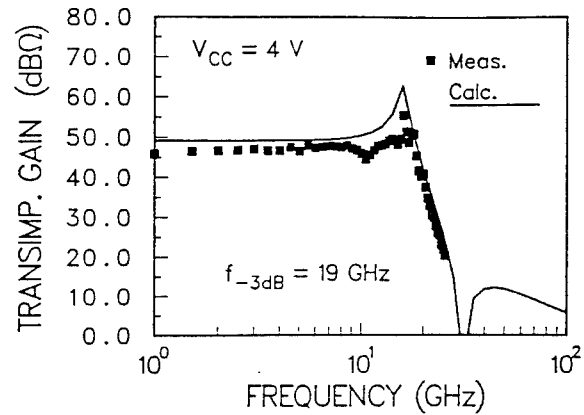
Table 1: Extracted SPICE model parameters of the In-AlAs/InGaAs SHBT.

V was modeled by a voltage-controlled capacitor, C_{DC} , connected across the emitter-base junction. This capacitor contributes to the total diffusion capacitance of the device when the collector transit-time delay becomes significant with an increase of V_{CB} .

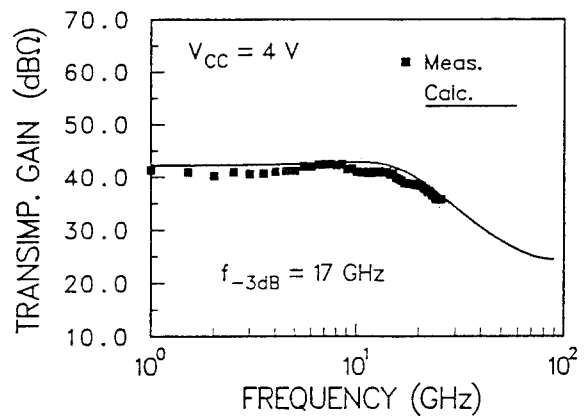
The parameter values extracted through overall fitting and optimization procedures are summarized in Table I. As shown in Fig.'s 1-3, the HBT model with the parameter values listed in Table I predicts accurately the measured large-signal DC and small-signal AC characteristics over a wide bias range.

Circuit Analysis

The performance of fabricated transimpedance amplifiers in two and three gain-stage configurations [3] was measured and analyzed based on the HBT model described previously. The 3-stage amplifier consists of



(a)



(b)

Figure 5: Measured and calculated gain-frequency characteristics of the amplifiers: (a) a 3-stage amplifier and (b) a 2-stage amplifier.

a feedback resistor (R_F) of 610 Ω and a peaking spiral inductor (L_p) of 2.5 nH in the input side, whereas the 2-stage amplifier consists of $R_F = 140 \Omega$ without L_p . The resistance and inductance values of the circuits used in the simulation were extracted from the measured S-parameter data of test structures. The DC operating condition of the circuits is determined by a single supply voltage, V_{CC} . The measured small-signal gain-frequency characteristics of the two amplifiers are compared with the simulation results in Fig. 5. The only input parameter in this simulation was the DC supply bias V_{CC} . The measured total DC currents of transimpedance amplifiers at different supply voltages are shown in Fig. 6 with the SPICE simulation results.

The results show that the simulation accurately predicts the key performance of the circuits. The 3-stage

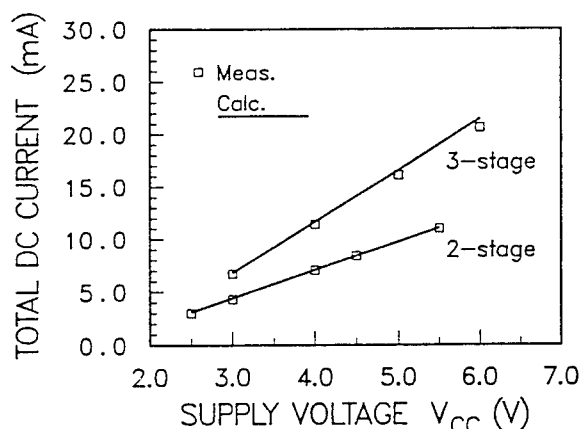


Figure 6: Measured and calculated total DC currents of transimpedance amplifiers.

amplifier exhibits a low-frequency gain of 48 dB Ω . The peaking inductor L_p introduces a gain peak at a frequency of ~ 15 GHz and extends the overall -3 dB bandwidth of this circuit to 19 GHz. The gain peak of the amplifier is smoothened out when this amplifier is used in a full PIN-HBT photoreceiver circuit with inclusion of a photodiode [3]. The 2-stage amplifier, on the other hand, shows flat gain characteristics. The use of a relatively small feedback resistance in this circuit results in a smaller gain of 42 dB Ω and a relatively high bandwidth of 17 GHz, which is comparable to the 3-stage amplifier. The model also predicts accurately total DC currents flowing through the circuits as shown in Fig. 6. The error was found to be less than 5 percent for both amplifiers in a measured bias range.

Conclusion

The DC and microwave characteristics of InAlAs/InGaAs SHBT's and monolithically integrated transimpedance amplifiers were analyzed based on a new HBT macro model implemented in SPICE. The model, which can account for the soft-breakdown characteristics and base-collector transit-time delay effect of the device, was used for full characterization of the DC and small-signal microwave performance of the HBT's and circuits.

It was shown that the implemented model accurately predicts the overall performance of both the device and integrated transimpedance amplifiers.

Acknowledgements

This research was sponsored by the Advanced Research Projects Agency, MDA 972-94-1-0004, and the

U. S. Army Research Office under the URI program, Grant No. DAAL03-92-G-0109.

References

- [1] S. Chandrasekhar, L. M. Lunardi, A. H. Gnauck, R. A. Hamm, and G. J. Qua, "High-speed monolithic p-i-n/HBT and HPT/HBT photoreceivers implemented with simple phototransistor structure," *IEEE Photon. Technol. Lett.*, vol. 5, pp. 1316-1318, 1993.
- [2] J. Cowles, A. L. Gutierrez-Aitken, P. Bhattacharya, and G. I. Haddad, "7.1 GHz bandwidth monolithically integrated $\text{In}_{0.53}\text{Ga}_{0.47}\text{As}/\text{In}_{0.52}\text{Al}_{0.48}\text{As}$ PIN-HBT transimpedance photoreceiver," *IEEE Photon. Technol. Lett.*, vol. 6, pp. 963-965, 1994.
- [3] A. L. Gutierrez-Aitken, K. Yang, X. Zhang, G. I. Haddad, and P. Bhattacharya, "9 GHz bandwidth InP-based integrated PIN-HBT photoreceiver," *Proc. 7th Int. Conf. on InP and Related Materials*, Sapporo, Japan, May 1995.
- [4] M. Hafizi, C. R. Crowell, M. E. Grupen, "The DC characteristics of GaAs/AlGaAs heterojunction bipolar transistors with application to device modeling" *IEEE Trans. Electron Devices*, vol. 37, pp. 2121-2129, 1990.
- [5] P. C. Grossman, J. Choma, Jr., "Large signal modeling of HBT's including self-heating and transit time effects," *IEEE Trans. Micro. Theory Tech.*, vol. 40, pp. 449-464, 1992.
- [6] K. Lu, P. Perry, and T. J. Brazil, "A new SPICE-type heterojunction bipolar transistor model for DC, microwave small-signal and large-signal circuit simulation," *IEEE MTT-S Int. Microwave Symp. Dig.*, pp. 1579-1582, 1994.
- [7] K. Yang, J. C. Cowles, J. R. East, and G. I. Haddad, "Theoretical and Experimental DC characterization of InGaAs-based abrupt emitter HBT's," will appear in *IEEE Trans. Electron Devices*, June 1995.
- [8] D. Ritter, R. A. Hamm, A. Feyngensen, and M. B. Panish, "Anomalous electric field and temperature dependence of collector multiplication in InP/Ga $_{0.47}\text{In}_{0.53}\text{As}$ heterojunction bipolar transistors," *Appl. Phys. Lett.*, vol. 60, pp. 3150-3152, 1992.

High Electron Mobility in Heavily Doped Bases of InP/GaInAs HBTs

Y. Betser and D. Ritter
Department of Electrical Engineering
Technion, Israel Institute of Technology
Haifa, Israel

Abstract

The minority carrier electron mobility in the base of InP/GaInAs HBTs was measured as a function of temperature using a new magneto transport method. At room temperature the mobility was found to be as high as $3400 \text{ cm}^2 \text{ V}^{-1} \text{ sec}^{-1}$ at a base doping level of $3.4 \times 10^{19} \text{ cm}^{-3}$. The measured mobility was compared with calculations carried out using the dielectric function formalism. The dominant scattering mechanisms are ionized impurity scattering and coupled LO phonon-plasmon scattering. The calculations correctly predict the high temperature mobility. At low temperatures a Monte Carlo analysis must be performed to model the experimental results because the electron distribution is non-thermal. The momentum relaxation rate strongly depends on the electron energy due to the elastic nature of the coupled LO phonon-plasmon scattering at low electron energy.

The base transit time is an important component of the emitter to collector delay time in HBTs. It is determined by the electron minority carrier momentum relaxation rate in the base [1]. In heavily doped p-type polar semiconductors, ionized impurity elastic scattering, and inelastic scattering due to the coupled hole gas (plasmon) LO-phonon system are the dominant scattering mechanisms. The complicated dynamic plasmon LO-phonon mode behavior is best described by the mutual valence band and lattice dielectric function $\epsilon(q, \omega)$, and the inelastic scattering rate (in the Born approximation) is then obtained by applying the fluctuation-dissipation theorem [2-3].

Kaneto et al. have calculated the scattering rate and diffusion constant of electrons in p-type GaAs and GaInAs as a function of the base doping level and temperature [4]. However, detailed experimental data was not available for comparison. Here, we present measurements of the electron mobility in p-type GaInAs as a function of temperature for two different doping levels. The results are compared to theory. The most significant result for the purpose of device design is that the value of the electron mobility increases with increasing

doping level, and is as high as $3400 \text{ cm}^2 \text{ V}^{-1} \text{ sec}^{-1}$ at room temperature for a base doping level of $3.4 \times 10^{19} \text{ cm}^{-3}$. The same trend of mobility enhancement with doping level was observed before using the zero-field time of flight technique [5]. An important conclusion is that achieving ultra high doping levels in the base of HBTs is not only important for the purpose of decreasing the base spreading resistance, but also for shortening the base transit time to improve the high frequency performance.

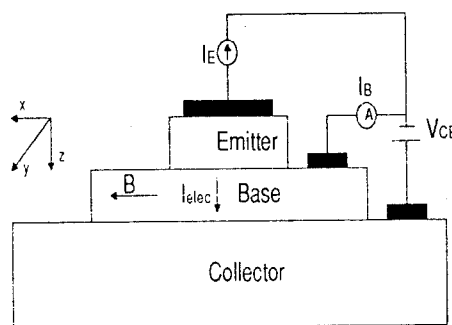


Fig. 1. Schematic diagram of the experimental setup.

The measurements were carried out using a new and simple DC method [6] which consists of measuring the gain of the HBT as a function of a magnetic field applied perpendicular to the direction of the current flow, as shown schematically in Fig.1. In the experiments HBTs with a 4400 Å thick base were used. In such thick base HBTs, the main component of the base current is recombination current in the neutral base. Electron transport in the base is also clearly diffusive. The applied magnetic field decreases the effective diffusion constant of electrons in the base, and the relative change in the base current is proportional to the square of the product of the mobility and the magnetic field [6]. Typical experimental results are shown in Fig.2.

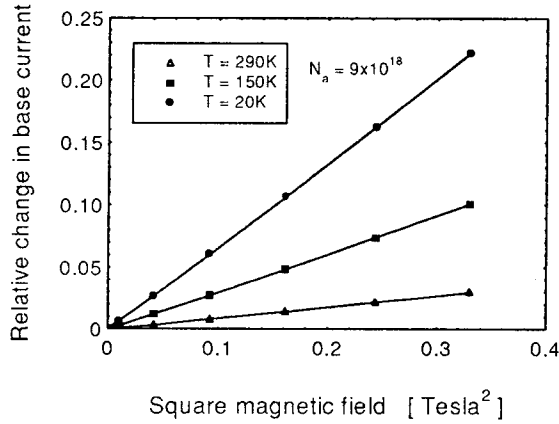


Fig. 2. Relative change in the base current as a function of the square magnetic field.

The mobility obtained from the experiment is related to the drift mobility by [7]:

$$\mu_{\text{drift}} = \sqrt{\frac{\langle \tau_m(E)^3 \rangle}{\langle \tau_m(E) \rangle^3}} \mu_{\text{meas}} = r_\mu \mu_{\text{meas}} \quad (1)$$

where $\tau_m(E)$ is the momentum relaxation time of an electron with a kinetic energy E . For example, for strongly screened ionized impurity scattering the mobility ratio is $r_\mu = 1.33$.

The measured and calculated electron mobility for two doping levels and as a function of temperature is given in Fig.3. Calculations were carried out following Kaneto et al. [8].

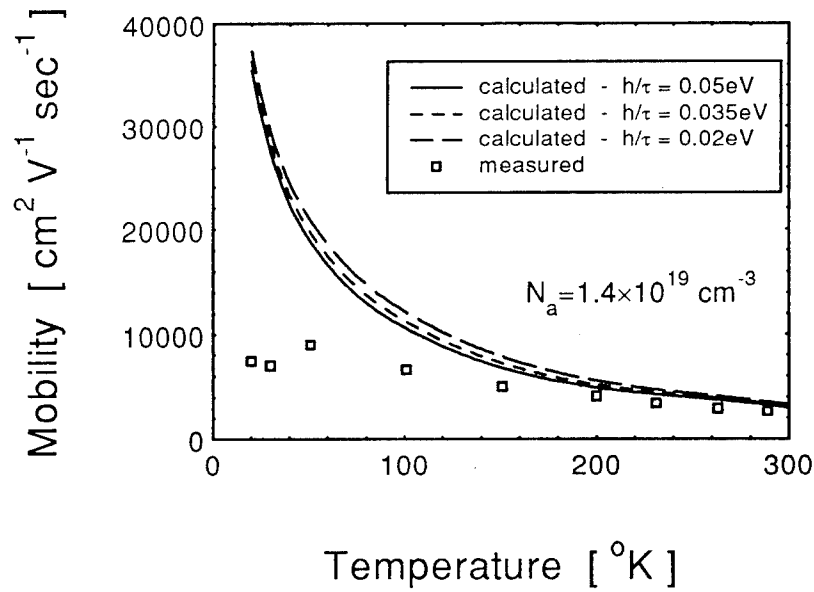
The calculations included obtaining the scattering rate, momentum relaxation rate, and the energy relaxation rate of the electrons due to ionized impurity scattering and coupled LO phonon-plasmon scattering. Alloy scattering [9] was included as well. The lattice dielectric function is given in Ref. [10]. The parameters [11] used in the calculations are listed in Table 1.

Parameter	Value
Electron effective mass ratio	0.041
Light hole effective mass ratio	0.051
Heavy hole effective mass ratio	0.46
Band nonparabolicity (eV ⁻¹)	1.167
Alloy scattering potential (eV)	0.529

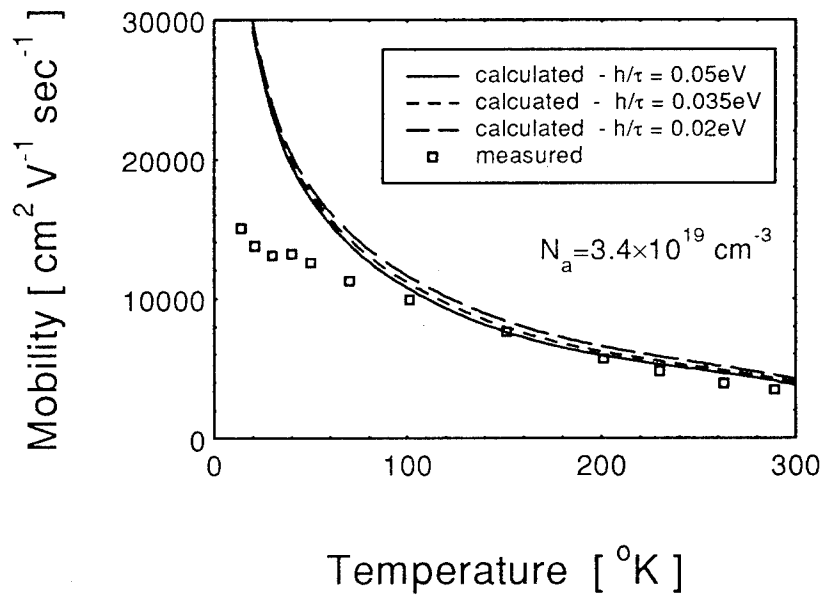
Table 1. Summary of parameters used in the calculations

Kaneto et al introduced a finite time τ between the collisions of holes in the dielectric function, as an additional damping mechanism of the plasma oscillations [8]. This time constant can be estimated using $\mu_h = q\tau/m_h$, where μ_h is the hole mobility, q is the electronic charge and m_h is the valence band effective mass. In our calculations the values of \hbar/τ were assumed to be 0.02, 0.035 and 0.05 eV, corresponding to hole mobility of 120, 70 and 50 cm²V⁻¹sec⁻¹, respectively. As can be seen from Fig. 3, the lifetime parameter τ does not effect the calculation at low temperatures and has a small effect (about 10%) in the high temperature range. This result indicates that at high hole concentrations, the dominant mechanism responsible for the damping of the hole gas collective motion, is the heavy hole to light hole transitions (i. e. the heavy to light hole transition rate is faster than the collision rate).

At high temperatures the calculated mobility corresponds well to the measured mobility. At low temperatures the calculated mobility is higher than the measured one. The discrepancy can be explained if the injected electrons are not in thermal equilibrium with the lattice.



(b)



(a)

Fig. 3 Measured and calculated mobility versus temperature. The doping concentrations are (a) $N_a = 3.4 \times 10^{19} \text{ cm}^{-3}$. (b) $N_a = 1.4 \times 10^{19} \text{ cm}^{-3}$. The values assumed for \hbar/τ are 0.02, 0.035 and 0.05eV.

Fig. 4 shows the energy relaxation rate $E^{-1} \frac{dE}{dt}$ and the momentum relaxation rate $\tau_m(E)^{-1}$ calculated for $N_a = 3.4 \times 10^{19} \text{ cm}^{-3}$ at $T = 20^\circ \text{ K}$. Note that the energy relaxation time is short in comparison with typical base transit times.

Electrons which are injected from the emitter into the base having high kinetic energy do not have sufficient time to thermalize, and therefore experience higher momentum relaxation rate than the thermalized electrons assumed in the calculations.

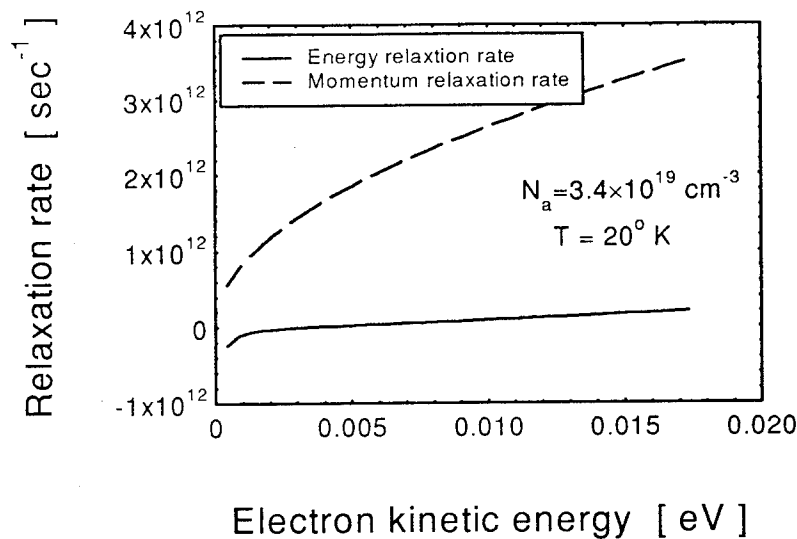


Fig. 4. Energy relaxation rate and momentum relaxation rate calculated at $T = 20^\circ \text{K}$ for $N_a = 3.4 \times 10^{19} \text{cm}^{-3}$.

Finally, we note that for non-elastic scattering mechanisms the relaxation time approximation is not valid. The mobility can be calculated in this case using Rode's iterative method [12]. We have found that the mobility calculated using Rode's method is very close (within 1%) to the value calculated using the relaxation time approximation. This result indicates that the LO phonon-plasmon scattering in heavily doped GaInAs is nearly elastic for thermal electrons, as is also evident from the low energy relaxation rates.

In conclusion, the electron mobility in the base of npn InP/GaInAs HBTs was measured as a function of temperature at two doping levels. It was found that the value of the electron mobility increases with increasing doping level, and is as high as $3400 \text{cm}^2 \text{V}^{-1} \text{sec}^{-1}$ at room temperature for a base doping level of $3.4 \times 10^{19} \text{cm}^{-3}$. The results were compared with a theoretical model based on the dielectric function formalism. The model predicts well the experimental results at high temperatures. At low temperatures the calculated mobility is higher than the measured results. The discrepancy may be a result of non equilibrium transport at low temperatures. A monte carlo analysis is therefore needed to model the low temperature experiments.

References

1. D. Ritter, R.A. Hamm, A. Feyngenson, and P.R. Smith, *Appl. Phys. Lett.*, **64**, p. 2988 (1994).
2. M. E. Kim, A. Das and S. D. Senturia, *Phys. Rev. B*, **18**, p. 6890 (1978).
3. D. Yevick and W. Bardyszewski, *Phys. Rev. B*, **39**, p. 8605 (1989).
4. Kaneto, K.W. Kim, and M.A. Littlejohn, *Appl. Phys. Lett.*, **63**, p. 48 (1993).
5. E. S. Harmon, M. L. Lovejoy, M. R. Melloch, M. S. Lundstrom, D. Ritter and R. A. Hamm, *Appl. Phys. Lett.* **63**, p. 636 (1993).
6. Y. Betser, D. Ritter, G. Bahir, J. Sperling, and G. Bahir, submitted for publication to *Appl. phys. Lett.*
7. Will be published elsewhere.
8. T. Kaneto, K. W. Kim and M. A. Littlejohn, *J. Appl. Phys.*, **72**, p. 4139 (1992).
9. J. W. Harrison and J. R. Hauser, *Phys. Rev. B*, **13**, p. 5347 (1976).
10. K. J. Nash, M. S. Skolnick and S. J. Bass, *Semicond. Sci. Technol.*, **2**, p. 329 (1987).
11. "Properties of lattice-matched and strained Indium Gallium Arsenide", Ed. P. Bhattacharya, (INSPEC, London, 1993).
12. D. L. Rode, in "Semiconductors and Semimetals", vol. 10, Ed. R. K. Willardson and A. C. Beer, ch. 1, (Academic Press, London, 1975).

Graded-GaAs_{1-x}P_x Base in Heterojunction Bipolar Transistors with InGaP Emitters

Michio Ohkubo, Nariaki Ikeda and Takao Ninomiya

*Yokohama R&D Lab., The Furukawa Electric Co., Ltd.
2-4-3 Okano, Nishi-ku, Yokohama 220, Japan*

We have fabricated the graded-GaAsP base HBTs with InGaP emitters for the first time. It was confirmed that heavily carbon-doping into GaAsP, as well as GaAs, could be realized by using MOCVD. The measured current gain was as high as over 100 at a collector current density (J_C) of $3 \times 10^4 \text{ A/cm}^2$. Furthermore, compared with the uniform-GaAs base HBTs, current-gain enhancement due to the built-in field in the base of the graded-base HBTs was also confirmed in a range of $J_C = 1 \times 10^2 \text{ A/cm}^2$ to $3 \times 10^4 \text{ A/cm}^2$.

I. Introduction

State-of-the-art carbon-doped-base AlGaAs/GaAs heterojunction bipolar transistors (HBTs) have exhibited excellent device and circuit performance due to effective hole confinement in the heavily doped base. Recently, there has been increasing interest in the replacement of commonly used AlGaAs emitters with InGaP. Some advantages of the InGaP/GaAs system have been demonstrated, such as high etching selectivity between GaAs and InGaP [1] for high process yield and formation of a sharp p-n junction at the GaAs/InGaP interface [2] for low base leakage current.

In this system, the candidates for the graded-base structure lattice-matched to GaAs are InGaAsP and conventional AlGaAs. However, InGaAsP layers suffer from the immiscible phenomena [3] under the low temperature growth for the carbon-doping. On the other hand, Al incorporation into carbon-doped GaAs is supposed to degrade crystalline quality by the reaction with oxygen. Another feasible candidate is strained system which was successfully demonstrated in InP/In_xGa_{1-x}As ($X=0.53 \Rightarrow 0.46$) HBTs. Therefore, we have selected a tensile strained graded-GaAsP layer for the graded-base structure.

This report describes the first fabrication of graded-GaAsP base HBTs with InGaP emitters grown by MOCVD and characteristics in comparison with uniform-base GaAs HBTs.

II. Carbon-doping into GaAsP

Carbon (C) is the most promising p-type dopant for the practical application of HBTs since its diffusion coefficient is smaller than that of any other dopant. Several carbon sources for the carbon-doped GaAs by MOCVD have been reported, such as carbon tetrachloride (CCl₄) [5] and the methyl group of trimethylgallium (TMGa) [6]. Recently, devices having good characteristics have been reported using CCl₄ as the carbon dopant [7], however, it is now difficult to use this since the production of this source is prohibited until 1995, because of its environmental problems, such as the ozone hole. On the other hand, the method using the methyl group of TMGa as the carbon source under reduced temperature with low V/III supply ratio is the simplest technique. By using this method, carbon-doping into GaAsP could be supposed to be available when P is added to As for the group V source.

Carbon-doped GaAsP layers were grown by low-pressure MOCVD with a vertical reactor. For the growth of the Carbon-doped GaAsP layer, source gases were TMGa for the group III and AsH₃ and PH₃ for the group V. The growth temperature was 600°C, which was measured by the thermocouple in the susceptor.

Figure 1 shows the hole concentration of GaAs and GaAsP as a function of the effective V/III ratio. As the decomposition efficiency of PH₃ is much poorer than that of AsH₃, the effective V/III ratio (V/III) is defined by the next expression;

$$V/III = [AsH_3] / [TMGa] / (1-X), \quad (1)$$

where $[AsH_3]$ and $[TMGa]$ are the supply rate of AsH_3 and $TMGa$ respectively, X is the composition of P in the GaAsP layers, which was measured by X-ray diffractometry and Photoluminescence. As can be seen, C-doping into both materials is possible at hole concentration in excess of $1 \times 10^{19} \text{cm}^{-3}$. Also, hole concentration of both materials was easily controlled by the V/III ratio.

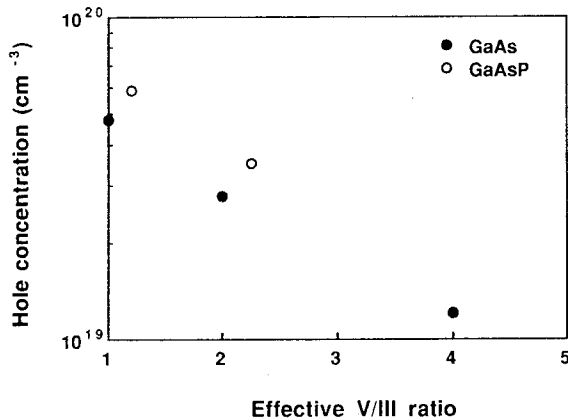


Fig. 1. Hole concentration as a function of the effective V/III ratio.

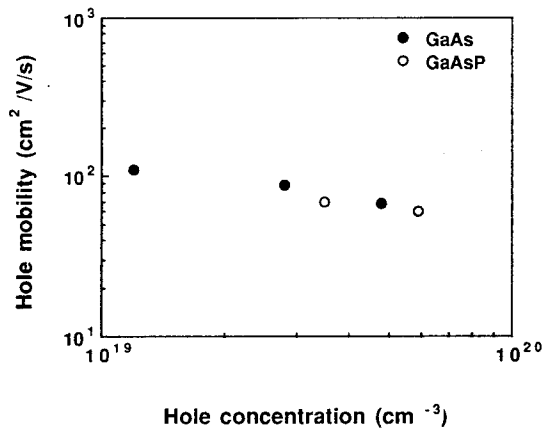


Fig. 2. Hole mobility as a function of the hole concentration.

Figure 2 shows the hole mobility of GaAs and GaAsP as a function of the hole concentration. It is noted that the mobility of both materials was almost equal, which indicates that the base resistance have no difference between both materials at the same hole concentration.

III. Epitaxial Layer Structure And Device Fabrication

The MOCVD grown epitaxial layer structure for the emitter-up HBT is shown in Table 1.

Table 1. Epitaxial layer structure of graded-GaAsP base HBT.

Layer	Material	Thickness(nm)	Doping(cm^{-3})
Cap	n-GaAs	100	$>5 \times 10^{18}$
	n-InGaP	50	3×10^{18}
Emitter	N-InGaP	200	5×10^{17}
Base	p ⁺ -GaAs _{1-x} P _x ($X=0 \Rightarrow 0.09$)	60	3×10^{19}
Collector	n-GaAs	500	$<1 \times 10^{16}$
Subcollector	n-GaAs	500	1×10^{18}

The growth temperature was 600°C for the base layer, and the other layers was under 680°C. The collector layer was 500nm-thick unintentionally doped GaAs ($n < 1 \times 10^{16} \text{cm}^{-3}$). The thickness of compositionally graded-GaAs_{1-x}P_x ($X=0 \Rightarrow 0.09$) base layer (W_B) was 60nm, which is designed as less than the critical thickness predicted by the Matthews and Blakeslee model [8], with C-doped to $p=3 \times 10^{19} \text{cm}^{-3}$ on the GaAs collector. The graded bandgap in the base (ΔE_G) was 0.11eV, means the built-in field ($\Delta E_G/W_B$) for the electrons in the graded-base is as about 18kV/cm. The hole concentration was directly confirmed by the van der Pauw hall measurement. The InGaP emitter layer was 200nm-thick with Si doped to $n=5 \times 10^{17} \text{cm}^{-3}$.

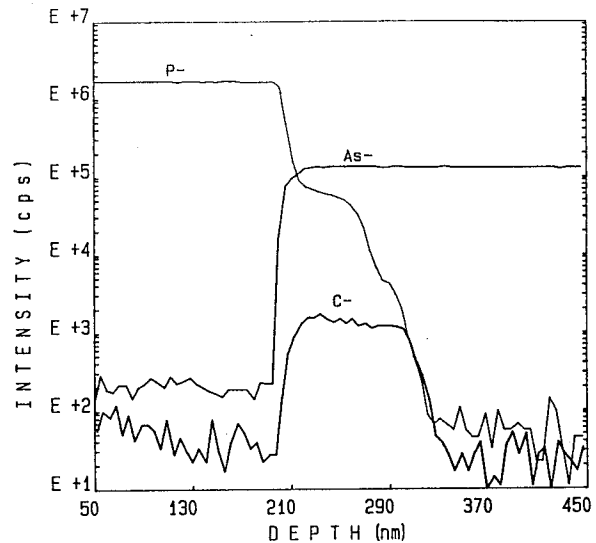


Fig. 3. SIMS profiles of P, As and C in the vicinity of the base layer.

Figure 3 shows the SIMS profiles of P, As and C in the vicinity of the base layer. As can be seen, the C-doped graded-GaAsP base structure was realized. For characteristics comparison, we have also grown the conventional uniform-GaAs base ($p=3 \times 10^{19} \text{cm}^{-3}$) HBT epi-wafer which have the same emitter and collector structure.

After epitaxial growth, both type of HBT devices were fabricated by the same process. Emitter mesas with $110 \times 110 \mu\text{m}^2$ and $12 \times 12 \mu\text{m}^2$ area were formed by wet chemical selective etching process. The devices employed Ti/Au non-alloyed contact to base layers and AuGe/Au alloyed contact to emitter cap and subcollector layers.

IV. Band Discontinuity At Emitter/Base Heterojunction

To investigate the band discontinuity of the InGaP/GaAsP(GaAs)/GaAs system shown in Fig. 4, we have compared the turn-on voltage of the collector current between the graded-GaAsP base HBTs and the uniform-GaAs base HBTs.

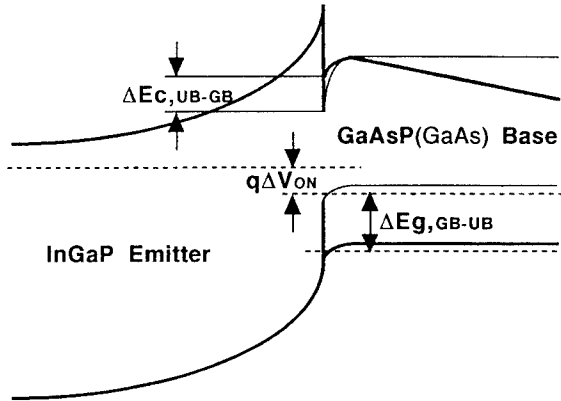


Fig. 4. Schematic band diagram of InGaP/graded-GaAsP and InGaP/uniform-GaAs system.

Figure 5 shows the Gummel plot of the collector current (I_C) of the uniform-base InGaP/GaAs HBT and graded-base InGaP/GaAsP HBT. When defining the turn-on voltage by the emitter-base voltage (V_B) at a collector current of $1 \times 10^{-5} \text{A}$, the turn-on voltage of InGaP/GaAs HBT was smaller than that of InGaP/GaAsP HBT.

Assuming that thermionic electrons from the emitter are injected into the base and diffuse toward the collector [9], the turn-on voltage difference (ΔV_{ON}) measured as 0.06V is roughly attributed to the difference in valence band discontinuity ($\Delta E_{V,UB-GB}$)

between InGaP/GaAs_{0.91}P_{0.09} and InGaP/GaAs, which is given by

$$\begin{aligned} \Delta V_{ON} &= \Delta E_{G,GB-UB} - \Delta E_{C,UB-GB} \\ &= \Delta E_{V,UB-GB} \end{aligned} \quad (2)$$

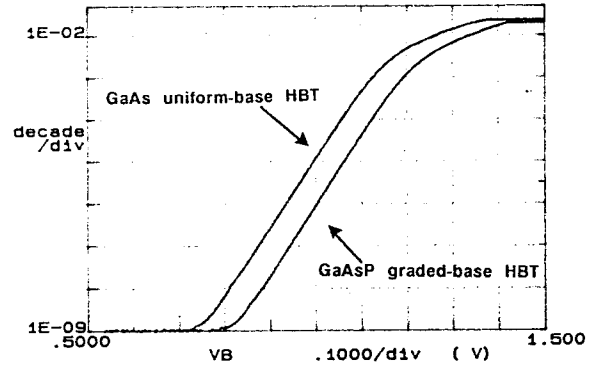


Fig. 5. Gummel plot of the collector current of graded-GaAsP base HBT and uniform-GaAs base HBT.

where $\Delta E_{C,UB-GB}$ is the difference in conduction band discontinuity between InGaP/GaAs and InGaP/GaAs_{0.91}P_{0.09}, $\Delta E_{G,GB-UB}$ is the bandgap difference between GaAs and GaAs_{0.91}P_{0.09}. As $\Delta E_{G,GB-UB}$ is 0.11eV, the $\Delta E_V/\Delta E_C$ ratio of a hypothetical GaAs_{0.91}P_{0.09}/GaAs heterojunction is calculated as about 0.5, which is a little larger than that of the theoretical prediction utilizing the strain dependent band offset model of Anderson and Jones [10].

V. Device Performance

Figure 6 shows the common emitter I-V characteristics of the graded-GaAsP HBT with $110 \times 110 \mu\text{m}^2$ emitter area. The measured current gain was 73 at a collector current density of 700A/cm^2 with a small offset voltage of 0.15V.

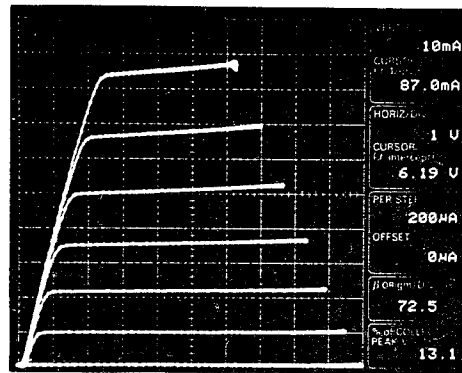


Fig. 6. Common emitter I-V characteristics of the graded-GaAsP HBT.

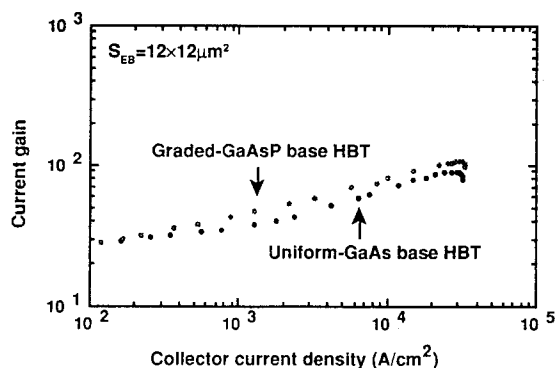


Fig. 7. Collector current dependencies of the current gain of the uniform-GaAs and the graded-GaAsP HBTs.

Figure 7 shows the collector current dependencies of the current gain for the $12 \times 12 \mu\text{m}^2$ emitter area HBTs. The current gain of the graded-base HBT increased as high as over 100 at a collector current density (J_C) of $3 \times 10^4 \text{ A/cm}^2$. Furthermore, current-gain enhancement due to the built-in field compared with the uniform-base HBT was confirmed in a range of $J_C = 1 \times 10^2 \text{ A/cm}^2$ to $3 \times 10^4 \text{ A/cm}^2$. These results show the strained GaAsP-graded base structure is promising for the practical application.

VI. Conclusion

First fabrication of the tensile strained graded-GaAsP base HBTs with InGaP emitters was successfully demonstrated. It was confirmed that heavily carbon-doping into MOCVD grown GaAsP layer, as well as GaAs, was controlled by the V/III ratio. Compared to the uniform-GaAs base HBTs, it was also confirmed that, for the GaAsP/GaAs system, the $\Delta E_V/\Delta E_C$ ratio was about 0.5, which was derived from the Gummel plot of the collector current. Current-gain enhancement due to the built-in field compared with the uniform-base HBTs was also confirmed in a range of $J_C = 1 \times 10^2 \text{ A/cm}^2$ to $3 \times 10^4 \text{ A/cm}^2$.

Acknowledgment

The authors would like to thank Mr. S. Kashiwa for his constant encouragement throughout this work, and Dr. A. Kasukawa and Mr. S. Tanaka for their helpful discussion.

References

- [1] T.Ijichi, M.Ohkubo and T.Kikuta, *IEEE Trans. Electron Devices*, **38** (1991) 21.
- [2] C.R.Abernathy, F.Ren, P.W.Wisk, S.J.Pearton and R.Esagui, *Appl. Phys. Letters*, **61** (1992) 1092.
- [3] S.Tanaka, K.Hiramatsu, Y.Habu, N.Sawaki and I.Akasaki, *J. Crystal Growth*, **79**, (1986) 978.
- [4] K.Kurishima, H.Nakajima, S.Yamahata, T.Kobayashi and Y.Matsuoka, *Int. Conf. SSDM*, Yokohama, 1994, 607.
- [5] B.T.Cunningham, G.E.Stillman and G.S.Jackson, *Appl. Phys. Letters*, **56** (1990) 361.
- [6] G.-W.Wang, R.L.Pierson, P.M.Asbeck, K.-C.Wang, N.-L.Wang, R.Nubling, M.F.Chang, J.Salerno and S.Sastry, *IEEE Electron Device Letters*, **EDL-12** (1991) 347.
- [7] H.Ito, *Electron. Letters*, **23** (1990) 1977.
- [8] J.W.Matthews, and A.E.Blakeslee, *J. Crystal Growth*, **27**, (1974) 118.
- [9] M.Ohkubo, A.Iketani, M.Ikeda and T.Ninomiya, *Jpn. J. Appl. Phys.* **33** (1994) L993.
- [10] N.G.Anderson and S.D.Jones, *J. Appl. Phys.* **70** (1991) 4342.

Reliability Analysis of InP-based HBTs

Kentaro DOGUCHI, Hiroshi YANO, Michio MURATA, and Hideaki NISHIZAWA

Optoelectronics R&D Laboratories, Sumitomo Electric Industries, Ltd.
1, Taya-cho, Sakae-ku, Yokohama, 244 Japan

The reliability of InP-based heterojunction bipolar transistors (HBTs) with AuGe/Ni alloyed ohmic electrodes, which are widely used for n-type ohmic contacts, was investigated. Scanning electron microscopy (SEM) has revealed that the failure mechanism of InP-based HBTs is the diffusion of alloyed electrodes into the GaInAs layer. The activation energy was 0.50 eV. We examined non-alloyed electrodes (Pt/Ti/Pt/Au) for n-type ohmic contacts to improve the reliability of InP-based HBTs. By transmission electron microscopy (TEM) and X-ray diffraction (XRD), the existence of an indium-platinum (In-Pt) layer was observed at the interface between the electrodes and the epitaxial layer. The diffusion was suppressed by this layer and InP-based HBTs with non-alloyed electrodes exhibited stable characteristics under temperature stress.

Introduction

InP-based heterojunction bipolar transistors (HBTs) are advantageous in terms of high-frequency performance and low power consumption, which are related to good properties of GaInAs, compared with GaAs-based HBTs. In the last several years, the reduction of base resistance and base-collector capacitance has been examined to realize the higher performance, and high-speed HBTs for multigigabit-per-second lightwave communication systems have been demonstrated ⁽¹⁾. While attention has been focused on the performance of InP-based HBTs, few data on the reliability of InP-based HBTs have been reported ^{(2), (3)}. The reliability analysis will become one of the major concerns as the development of InP-based HBTs enters the phase of improvement for practical use.

As the development of GaAs-based HBTs advances, it has become clear that the degradation of GaAs-based HBTs is primarily caused by the diffusion of beryllium (Be) as a base dopant. Recently HBTs with a base dopant of carbon, of which the diffusion coefficient is smaller than that of Be, have been actively developed ⁽⁴⁾. In

InP-based HBTs, it is suggested that the degradation of the HBTs is due to the base p-dopant diffusion and the generation of hot electrons at the base-collector junction ⁽⁵⁾. However, details of failure mechanisms have not been fully analyzed yet.

In this paper, we show for the first time the failure mechanism of InP-based HBTs, which is related to alloyed electrodes widely used for n-type ohmic contacts. We also report that Pt/Ti/Pt/Au non-alloyed electrodes for n-type ohmic contacts substantially improve the reliability of InP-based HBTs.

Experiments

The epitaxial layer structure and the schematic view of the transistor are shown in Table 1 and Fig. 1, respectively. The transistor has the conventional mesa structure with non-self-aligned ohmic electrodes. The n-InP emitter layer also acts as a passivation of the extrinsic base surface to reduce the surface recombination current ⁽⁶⁾. HBTs were grown by organometallic vapor

Table 1. Epitaxial structure of GaInAs/InP HBT.

Layer	Material	Doping (cm ⁻³)	Thickness (nm)
Emitter Cap	n-GaInAs	4×10^{18}	400
Emitter	n-InP	4×10^{18}	10
Base	p-GaInAs	8×10^{18}	100
Collector	n-GaInAs	5×10^{16}	500
Subcollector	n-GaInAs	1×10^{19}	300
Substrate	SI-InP	-	-

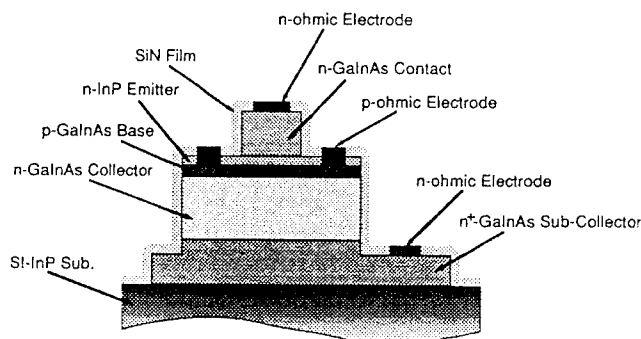


Fig. 1. Schematic cross-section of GaInAs/InP HBT.

phase epitaxy (OMVPE) on a semi-insulating InP substrate. The growth temperature was 650 °C. Triethylgallium (TEG), trimethylindium (TMI), arsine (AsH₃), and phosphine (PH₃) were used as source materials. Diethylzinc (DEZ) and Disilane (Si₂H₆) were used as p-type and n-type dopants, respectively. HBT mesa was formed by wet chemical etching. The emitter mesa dimensions of HBTs were 5 × 5 μm². SiN films for passivation were deposited, and the electrodes were formed by lift-off technique. AuGe (100 nm)/Ni (30 nm) and Pt (20 nm)/Ti (20 nm)/Pt (20 nm)/Au (100 nm) were used for n-type and p-type ohmic electrodes, respectively. Ohmic electrodes were annealed at 400 °C for 1 min.

The lifetest of HBTs has been carried out at 250 °C ambient with a collector current density of 10⁴ A/cm². The measurement of HBTs was performed at room temperature.

Results and Discussions

Gummel plots before and after the lifetest are shown in Fig. 2. The post-stress Gummel plots were measured after a 500-hour lifetest. The result shows that the emitter and collector are electrically shorted under the stress.

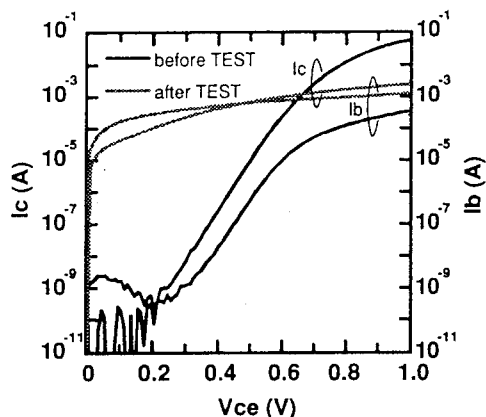


Fig. 2. Gummel plots of GaInAs/InP HBT with AuGe/Ni n-ohmic electrodes before and after 250 °C lifetest.

Fig. 3 shows the cross-sectional view of an SEM micrograph of the emitter region after 250 °C storage for 2700 hours. It is clear that penetration of n-ohmic electrodes (AuGe/Ni) through HBTs layers, which was not observed before the storage, occurred. The occurrence of such wide diffusion on GaAs-based HBTs has not been reported. It causes a short-circuit when the emitter metals reach the collector layer.

In order to obtain an activation energy of the diffusion, lifetest data were taken at 225 and 250 °C. We defined 3

% variation of the turn-on voltage as a failure criterion, and plotted the data as shown in Fig. 4. The activation energy of 0.50 eV was obtained from this plot. It is reported that the activation energy of Au diffusion in InP is 0.48 eV⁽⁷⁾ and the intermixing of Au and In progresses at high temperature for Au/GaInAs contacts^{(8), (9), (10)}. Therefore, this penetration of electrodes is considered the diffusion of Au into the epitaxial layers.

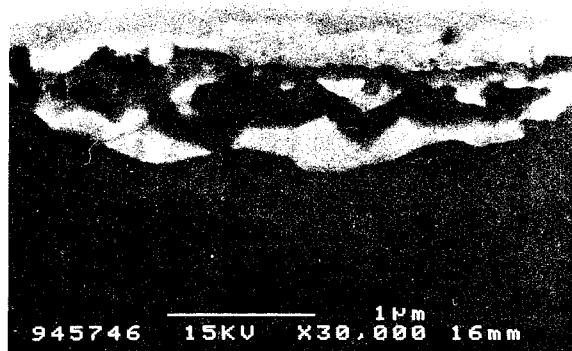


Fig. 3. SEM micrograph of GaInAs/InP HBT with AuGe/Ni n-ohmic electrodes after 250 °C storage.

The key point to improve the reliability is the suppression of such diffusion. We investigated non-alloyed metals for n-type ohmic electrodes to suppress the diffusion. The structure of non-alloyed electrodes was Pt (20 nm)/Ti (20 nm)/Pt (20 nm)/Au (100 nm). The changes in contact resistances of AuGe/Ni and Pt/Ti/Pt/Au with time at 250 °C are shown in Fig. 5. The ohmic contact resistance was obtained by the transmission line method (TLM) and 4 probe current-voltage technique

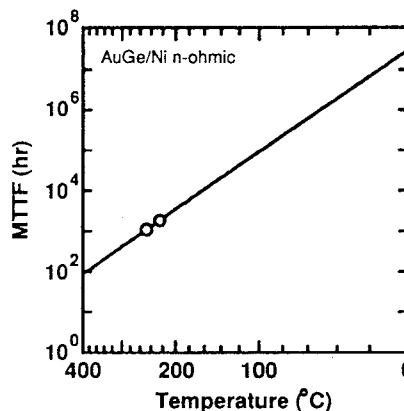


Fig. 4. Arrhenius plot for GaInAs/InP HBT with AuGe/Ni n-ohmic electrodes at $I_c=10^4$ A/cm².

at room temperature. The initial contact resistances of AuGe/Ni and Pt/Ti/Pt/Au are $0.01 \Omega \text{ mm}$ and $0.04 \Omega \text{ mm}$, respectively. It is found that the contact resistances of alloyed electrodes increase drastically at 500 hours. On the other hand, the contact resistances of non-alloyed electrodes show little change for 2700 hours. This result indicates that n-type non-alloyed ohmic contacts are thermally stable.

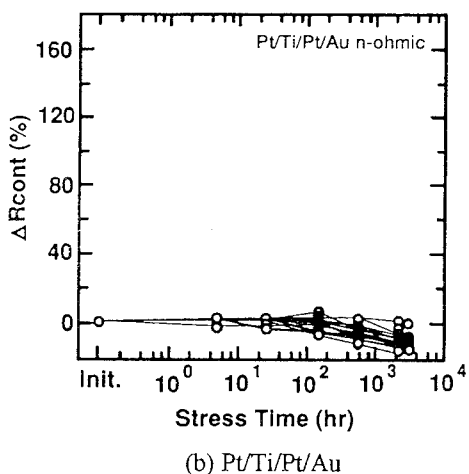
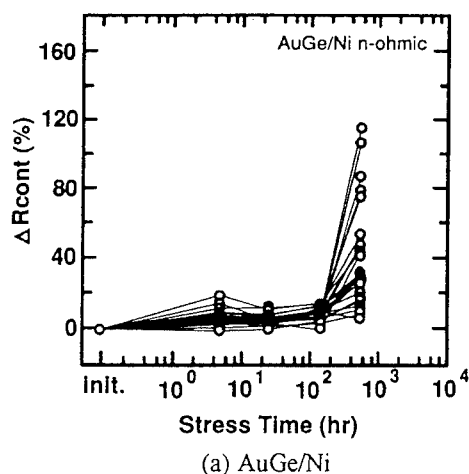


Fig. 5. N-ohmic contact resistance variation with time in 250°C storage.

The microstructure of non-alloyed electrodes was investigated by TEM and XRD. Pt/Ti/Pt/Au evaporated on the HBT structure were used for TEM samples. These samples were stored at 250°C for 168 hours. In this investigation, there was no difference between pre-storage and post-storage samples. The TEM micrograph after the storage is shown in Fig. 6. The existence of an In-Pt layer was observed at the interface. This layer must suppress the diffusion of electrodes into epitaxial layers under high temperature stress.



Fig. 6. TEM micrograph of Pt/Ti/Pt/Au n-ohmic electrode on GaInAs/InP structure after 250°C storage.



Fig. 7. SEM micrograph of GaInAs/InP HBT with Pt/Ti/Pt/Au n-ohmic electrodes after 250°C storage.

HBTs were fabricated using Pt/Ti/Pt/Au for n-type ohmic contacts and were examined under high temperature stress. Fig. 7 shows the cross-sectional view of an SEM micrograph of the emitter region after a 2700-hour storage at 250°C . The wide diffusion of electrodes into epitaxial layers as shown in Fig. 3 was not observed.

Fig. 8 shows Gummel plots of HBTs with non-alloyed electrodes before and after the storage. While Gummel plots of HBTs with alloyed electrodes showed drastic changes as shown in Fig. 2, those of HBTs with non-alloyed electrodes showed little change for 2700 hours. This indicates that non-alloyed ohmic electrodes are very effective for improvement of InP-based HBT reliability.

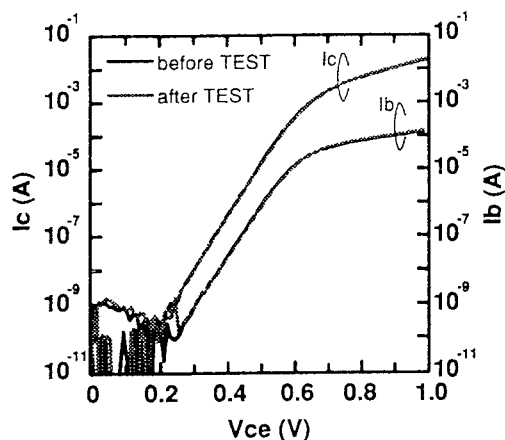


Fig. 8. Gummel plots of GaInAs/InP HBT with Pt/Ti/Pt/Au n-ohmic electrodes before and after 250 °C storage.

Summary

We have reported the reliability analysis of InP-based HBTs. SEM has revealed that the failure mechanism of InP-based HBTs is the wide diffusion of alloyed electrodes into the GaInAs layer. The activation energy of 0.50 eV was obtained by the lifetest. We also investigated Pt/Ti/Pt/Au non-alloyed electrodes for n-type ohmic contacts to improve the reliability of InP-based HBTs. TEM observation has found that the In-Pt layer existed at the interface and suppressed the metal diffusion. As the 250 °C storage test of InP-based HBTs with the non-alloyed ohmic electrodes was carried out, the devices exhibited stable characteristics. This indicates that non-alloyed ohmic electrodes of Pt/Ti/Pt/Au are very effective for improvement of InP-based HBT reliability.

Acknowledgments

The authors would like to thank A. Yamaguchi and T. Yamada for the SEM, TEM and XRD observations. We are also grateful to A. Ishida and M. Kuroda for their encouragement throughout this work.

References

- (1) J.-I. Song, B. W-P. Hong, B.P. Van der Gaag, and K. B. Chough, "Ultra-High-Speed InP/InGaAs Heterojunction Bipolar Transistors," *IEEE Electron Device Lett.*, vol. 15, no. 3, pp. 94-96, 1994.
- (2) M. Hafizi and M. J. Delaney, "Reliability of InP-based HBT's and HEMT's: Experiments, Failure Mechanisms, and Statics," *6th Int. Conf. InP & Related Materials*, pp. 299-302, 1994.
- (3) M. Hafizi, T. Liu, A. E. Schmitz, P. A. Macdonald, M. Lui, and F. Williams, "Power Performance and Reliability of AlInAs/GaInAs/InP Double Heterojunction Bipolar Transistors," *6th Int. Conf. InP & Related Materials*, pp. 527-530, 1994.
- (4) T. Ahmad, A. A. Rezazadeh, and S. S. Gill, "Effect of base dopants on the bias stress stability of AlGaAs/GaAs HBTs," *Electron. Lett.*, vol. 29, No. 19, pp. 1725-1726, 1993.
- (5) M. Hafizi, W. E. Stanchina, R. A. Metzger, J. F. Jensen, and F. Williams, "Reliability of AlInAs/GaInAs Heterojunction Bipolar Transistors," *IEEE Trans. Electron Devices*, vol. 40, No. 12, pp. 2178-2185, 1993.
- (6) E. Tokumitsu, A. G. Dentai, and C. H. Joyner, "Reduction of the Surface Recombination Current in InGaAs/InP Pseudo-Heterojunction Bipolar Transistors Using a Thin InP Passivation Layer," *IEEE Electron Device Lett.*, vol. 10, No. 12, pp. 585-587, 1989.
- (7) S. I. Rembeza, "The Diffusion of Au in InP Single Crystals," *Soviet Physics Semiconductors*, vol. 3, No. 4, pp. 612-613, 1969.
- (8) J. M. Vandenberg, H. Temkin, R. A. Hamm, and M. A. Diguseppe, "Structural Study of Alloyed Gold Metallization Contacts on InGaAsP/InP Layers," *J. Appl. Phys.*, vol. 53, No. 11, pp. 7385-7389, 1982.
- (9) T. Nittono, H. Ito, O. Nakajima, and T. Ishibashi, "Non-alloyed Ohmic Contacts to n-GaAs Using Compositionally Graded In_xGa_{1-x}As Layers," *Jpn. J. Appl. Phys.*, vol. 27, pp. 1718-1722, 1988.
- (10) N. Yoshida, Y. Yamamoto, H. Takano, T. Sonoda, S. Takamiya, and S. Mitsui, "Alloyed and Non-alloyed Ohmic Contacts for AlInAs/InGaAs High Electron Mobility Transistors," *Jpn. J. Appl. Phys.*, vol. 33, pp. 3373-3376, 1994.

Photopumped operation of dry etched $\lambda=1.5\ \mu\text{m}$ vertical cavity surface emitting lasers

K. Streubel, J. André, S. Lourdudoss, A. Karlsson, and T. Heide

Department of Electronics, Royal Institute of Technology, Electrum 229, S-164 40 Kista, Sweden

Introduction

Vertical-cavity surface emitting lasers (VCSEL) exhibit a variety of desirable features including single longitudinal mode operation¹, low threshold², high packing densities and high coupling efficiency to fibers³, which makes them attractive for many applications. For optical fiber transmission, electrically-pumped VCSELs with 1.3-1.55 μm emission are desired, but at present, room temperature CW operation of those devices has not yet been demonstrated. However, many critical fabrication steps such as epitaxial growth of Bragg reflectors, cavity design or mesa

Experimental

The VCSEL top-emitting structure consisted of an epitaxially grown DBR and active region with a dielectric Si/SiO₂ mirror on top. A 45-period stack of nominally undoped quarter wave GaInAsP ($\lambda=1.42\ \mu\text{m}$) and InP layers served as bottom reflector with a close to ideal reflectivity of 99.9%⁶. Bulk active regions consisted of GaInAsP ($\lambda=1.5\ \mu\text{m}$) with a thickness of one optical wavelength. The quantum well sample employed 5 compressively strained (1%) GaInAsP quantum wells and quaternary ($\lambda=1.3\ \mu\text{m}$) barriers. For both samples, the entire structure was grown in a single epitaxial run using metal organic vapor phase epitaxy (MOVPE). 3.5 periods of Si/SiO₂ were deposited into resist openings with varying diameters. A NiCr-metal cap was sputtered on top to protect the dielectric mirror during dry etching. The top mirrors were shaped by a lift-off process⁷ and 12-14 μm high mesas were etched using a CH₄/H₂/Ar reactive ion etching. Finally the mesas were treated in an O₂ plasma and the metal caps were removed using wet chemical etchants. An example of the resulting mesa shape is given in Fig.1. Some samples were selectively regrown with semi-insulating InP using hydride vapor phase epitaxy. The details of the regrowth process are published elsewhere⁸.

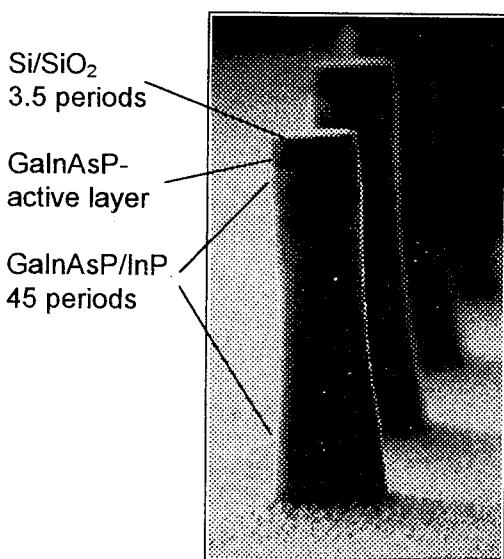


Fig. 1 VCSEL structure and SEM micrograph of an etched mesa. The devices have a diameter of about 4 μm and are 14 μm high. The pillars are separated by 30 μm .

processing can already be investigated on optically pumped devices^{4,5}. We report on the fabrication of VCSEL mesas for 1.5 μm operation. The single lasers were separated by reactive ion etching (RIE) and 12 μm high mesas with diameters ranging from 3 to 100 μm were formed. The performance of the devices was studied as a function of their size.

The devices were optically pumped with the 1064 nm line of either a mode-locked (80 ps, 80 MHz) or a Q-switched Nd:YAG laser (250 ns, 25 kHz). The laser beam was focused to a spot size between 10 and 40 μm , small enough to ensure pumping of a single mesa. The lasers were pumped through the Si/SiO₂ reflector which is transparent at 1 μm wavelength. The emitted light was collected from the same side, coupled into a multimode fiber and detected with an optical spectrum analyzer

Results

Lasing at room temperature was obtained for free standing mesas with diameters ranging from 5 to 100 μm . Emission in a range of 1.48-1.52 μm was detected, depending on the lateral position on the wafer.

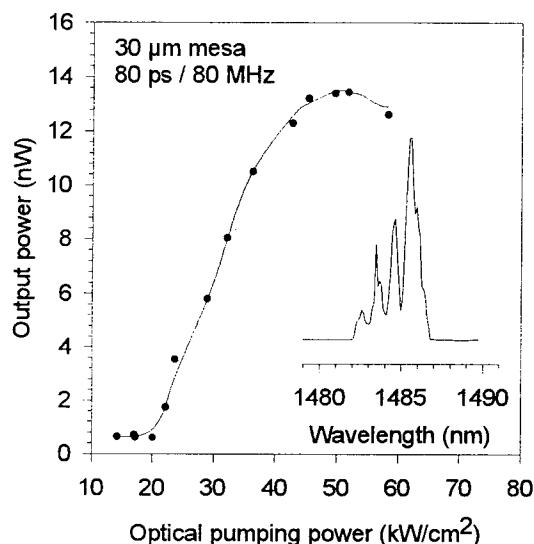


Fig. 2 Equivalent threshold power density for a circular mesa with a diameter of 30 μm . The inset shows the laser spectrum with four transverse modes

Fig. 2 shows the input vs output power curve for a free standing 30 μm diameter mesa at RT. The amount of reflected and absorbed pump light in the top mirror was determined to 40% and $\approx 30\%$ respectively. Using these parameters, the equivalent current density axis with a threshold value J_{th} of 25 kA/cm^2 was calculated. The equivalent threshold current density as a function of the mesa diameter is shown in fig. 3. The samples were excited either with the mode locked laser (filled circles) using a spot size of 30 μm or the Q-switched laser and a spot size of 10 μm (hollow symbols). For the larger mesas, the threshold current density ranges from 25 to 90 kA/cm^2 . In both cases J_{th} increases rapidly, as soon as the mesa diameter becomes smaller than the spot size which is attributed to the more difficult heating of the rather thin pillars.

The properties of the regrown laser mesas were comparable to the free standing laser pillars

except for the fact, that RT-lasing was obtained even with the 3 μm diameter devices using the rather long pump pulses of the Q-switched YAG laser. This demonstrates the improved heat dissipation of the regrown samples which benefits from the low thermal resistance of InP. To our knowledge, these are the smallest 1.5 μm microlasers investigated so far.

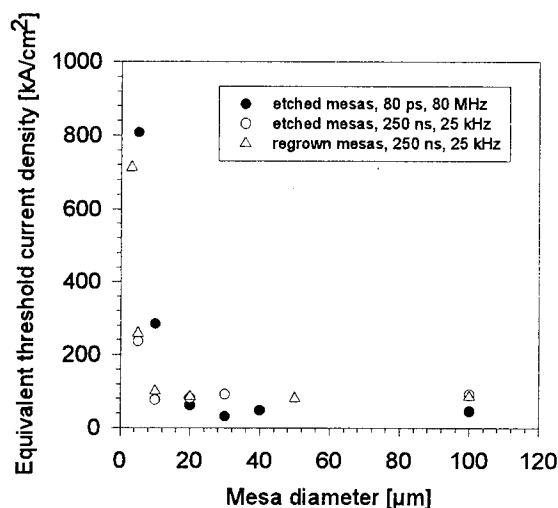


Fig. 3 Equivalent threshold current density as function of the mesa size. The samples were excited with either short (80 ps, 80 MHz) or long pulses (250 ns, 25 kHz) as indicated by the filled and hollow symbols.

Fig. 4 depicts two input-output curves for the 5 quantum well sample, pumped with the long pulses of the Q-switched YAG. The threshold pump power is 360 W/cm^2 corresponding to a current density of 450 A/cm^2 . This very low value compares reasonably well with the results of Lin et. al. who reported a threshold current density of 2 kA/cm^2 for 30 strained quantum wells⁹. However, the lasing operation of this sample was rather unstable with a very low output power which indicates that a sufficient optical gain is difficult to achieve with only five quantum wells.

All devices showed lasing in a single longitudinal mode but a number of higher order transverse modes occurred, when operated above threshold.

Typically 4 transverse modes were found in the spectra of the 100 and 50 μm diameter lasers.

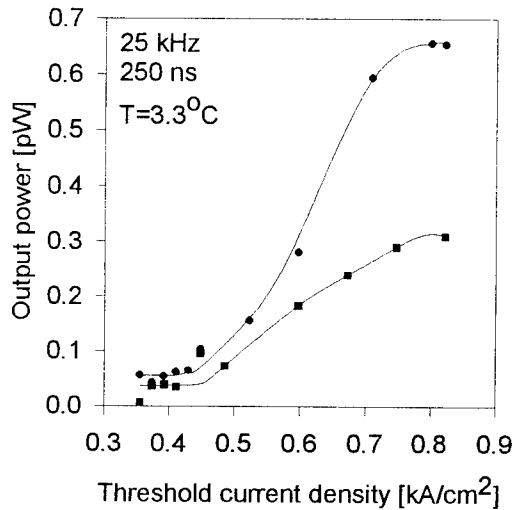


Fig.4 Input-output curves for the 5 QW sample at 3.3°C. The sample was pumped with 250 ns pulses at a repetition rate of 25 kHz.

The transverse modes were also identified in the near field patterns as distinct lobes with polarization dependent intensities (fig.5). The modes appeared equally separated in wavelength by about 0.6-0.8 nm, which complies reasonably well with theoretical predictions¹⁰ as well as with the findings on broad area devices¹¹. The typical width of the laser lines just above threshold was between 0.15 and 0.5 nm (best value 0.11 nm) and increased with pumping to about 0.8 nm. The

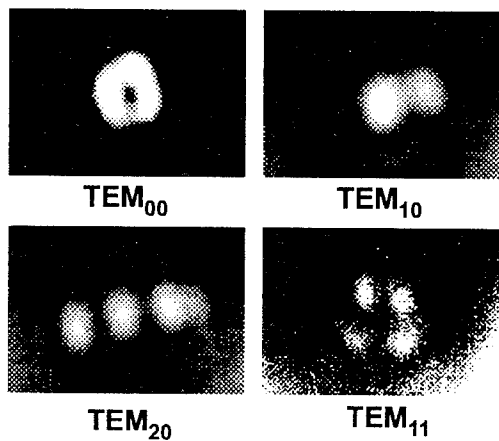


Fig.5 Near field modal pattern images of the discriminated modes

number of modes decreases from 4-5 to 3 or 2 when the mesa size becomes smaller than the spot. An example for a four transverse mode structure is given in the inset of fig.2. Typically the single lines are 0.3-0.8 nm wide with a mode spacing of 0.6-0.8 nm.

The temperature performance of the lasers was examined by mounting the samples on a temperature controlled stage. All devices operated up to at least 60°C, except for the 10 and 5 μm lasers, which were limited to a operation temperature of below 40°C. The difficult heat dissipation in the thin posts in combination with the different temperature shift of the cavity

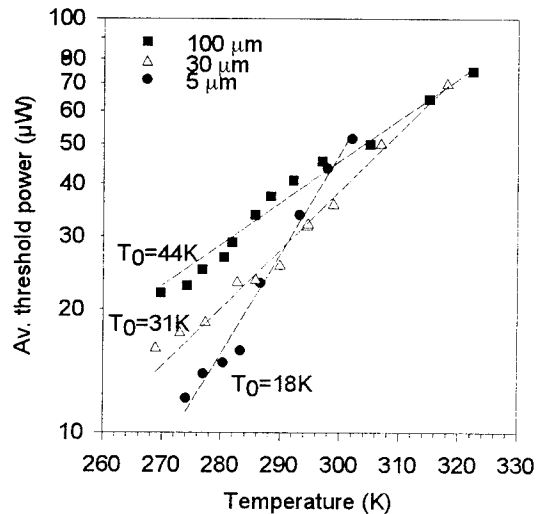


Fig.6 Measured average threshold power vs temperature for mesa diameters of 100, 30 and 5 μm . The characteristic temperatures T_0 are 44, 31 and 18 K respectively.

resonance and the gain peak are responsible for the weak temperature performance of the smallest lasers. The larger devices ($d \geq 50 \mu\text{m}$) operated up to 80°C. The characteristic temperature T_0 was found to decrease systematically from 45 K to 20 K with the laser diameter as depicted in Fig. 6. It shows, that the smallest mesas have the highest temperature dependence due to the more difficult heat dissipation.

The emission shifted towards longer wavelength with temperature at a rate of 0.10-0.13 nm/°C.

This shift is attributed to the thermal expansion of the cavity and the temperature dependency of the refractive index and agrees well with previously reported results^{5,11}.

Summarizing the results, we have demonstrated photopumped RT-lasing operation of free standing micropost VCSELs, even when using the rather long pulses of a Q-switched YAG laser. The equivalent threshold current density increases with the mesa diameter as a consequence of the difficult heat dissipation in the thin posts. RT operation was achieved with 5 μm diameter free standing mesas (80 ps pulses) and 3 μm wide regrown mesas (250 ns pulses). The quantum well laser showed a very low threshold power of 360 W/cm^2 (450 kA/cm^2). The transverse modes structure was discriminated as i.e. TEM_{00} , TEM_{11} , TEM_{20} and TEM_{10} . Typically 4-5 transverse modes were observed on 30-100 μm diameter mesas. The threshold increases in the range between -10 and 60°C with a characteristic temperature around 45 K. Several lasers operated up to 80°C.

Acknowledgement

We would like to thank Prof. John Bowers for the opportunity to perform optical pumping experiments at UCSB and Dubravco Babic for many helpful discussions.

References

- ¹ F. Koyama, S. Kinoshita, and K. Iga, *Room-temperature continuous wave lasing characteristics of a GaAs vertical cavity surface-emitting laser*, Appl. Phys. Lett. 55 (1989) 221
- ² T. Wipiejewski, K. Panzlaff, E. Zeeb, and K.J. Ebeling, *Tunable Extremely Low Threshold Vertical-Cavity Laser Diode*, IEEE Photon. Techn. Lett. 5 (1993) 889
- ³ K. Tai, G. Hasnain, J.D. Wynn, R.J. Fischer, Y.H. Wang, B.E. Weir, J. Gamelin, and A.Y. Cho, *90% Coupling of top Surface emitting GaAs/AlGaAs quantum well laser output into 8 μm diameter core silica fibre*, Electron. Lett. 26 (1990) 1628
- ⁴ J. Dudley, M. Ishikawa, D.I. Babic, B.I. Miller, R. Mirin, W.B. Jiang, J.E. Bowers, and E.L. Hu, *144°C operation of 1.3 μm InGaAsP vertical cavity lasers on GaAs substrates*, Appl. Phys. Lett. 61 (1992) 3095
- ⁵ M.A. Fisher, A.J. Dann, D.A.O. Davies, D.J. Elton, M.J. Harlow, C.B. Hatch, S.D. Perrin, J. Reed, I. Reid, and M.J. Adams, *High temperature photopumping of 1.55 μm vertical cavity surface emitting lasers*, Electr. Lett. 29 (1993) 1548
- ⁶ K. Streubel, J. Wallin and G. Landgren, *High refractive 1.5 μm GaInAsP/InP Bragg reflectors grown by metal organic vapor phase epitaxy*, Mat. Sci. Eng. B28 (1994) 285
- ⁷ K. Streubel, J. André, J. Wallin, and G. Landgren, *Fabrication of 1.5 μm optically pumped GaInAsP/InP vertical-cavity surface-emitting lasers*, Mat. Sci. Eng. B28 (1994) 289
- ⁸ S. Lourdudoss, K. Streubel, J. André, O. Kjebon, and J. Wallin, *Morphological modifications during selective growth of InP around cylindrical and parallelepiped mesas*, Mat. Sci. Eng. B28 (1994) 179
- ⁹ C.H. Lin, C.L. Chua, Z.H. Zhu, F.E. Ejeckam, T.C. Wu and Y.H. Lo, *Photopumped long wavelength vertical-cavity surface-emitting lasers using strain-compensated multiple quantum wells*, Appl. Phys. Lett. 64 (25) 3395
- ¹⁰ K. Tai, Y. Lai, K.F. Huang, T.C. Huang, T.D. Lee, and C.C. Wu, Appl. Phys. Lett., 63 (1993) 2624
- ¹¹ D.I. Babic, J.J. Dudley, K. Streubel, R.P. Mirin, E.L. Hu, and J.E. Bowers, *Optically pumped all-epitaxial wafer fused 1.52 μm vertical-cavity lasers*, Electron. Lett. 30 (1994) 704

680nm-Band Self-Sustained Pulsating AlGaInP Visible Laser Diodes

ThP27

Hideto Adachi, Isao Kidoguchi, Satoshi Kamiyama, and Kiyoshi Ohnaka
Semiconductor Research Center, Matsushita Electric Industrial Co., Ltd.
3-1-1 Yagumo-Nakamachi, Moriguchi, Osaka 570, Japan
Tel: +81-6-906-4921 Fax: +81-6-906-8100

Introduction

We developed 680nm-band AlGaInP visible laser diodes having very low noise characteristics with stable self-sustained pulsation for applications such as optical data storage. AlGaInP visible laser diodes are expected to become the next key device in a field of optical disk system due to its shorter wavelength. Low relative intensity noise (RIN) is required for optical disk systems. Self-sustained pulsation is effective for the reduction of the noise. In the AlGaInP laser diodes, stable pulsating operation in the high temperature range was very difficult due to its low thermal conductivity. We successfully achieved the AlGaInP visible laser diodes with stable self-sustained pulsation and low noise in the temperature ranging from 20 to 50°C.

Background

680nm-band AlGaInP visible laser diodes having very low noise characteristics with stable self-sustained pulsation were developed for applications such as optical data storage. Earlier, self-sustained pulsation phenomena induced by defects were reported in the degraded AlGaAs/GaAs double-heterostructure lasers [1]. Numerous observations or calculation models relevant to the subject have been made, which are thought to be free of defects [2]-[5]. On the other hand, AlGaInP visible laser diodes are expected to become the next key device in a field of optical disk system due to its shorter wavelength [6]. Low RIN is required for optical disk systems. Self-sustained pulsation is effective for the reduction of the noise because of the suppression of mode competition noise in multi-longitudinal mode oscillation. Although the AlGaInP laser diodes with self-

sustained pulsation was reported before [7], [8], stable operation in the high temperature range was very difficult in AlGaInP systems due to its low thermal conductivity. The control of the structure parameters such as stripe width or refractive index step of the ridge stripe is very severe for producing the stably pulsating laser diodes. We successfully achieved the AlGaInP visible laser diodes with stable self-sustained pulsation and low noise in the temperature ranging from 20 to 50°C.

Device Fabrication

We have employed transverse-mode stabilized laser diodes which have a ridge stripe structure. Schematic diagram of the transverse-mode stabilized structure is shown in Fig. 1. The epitaxial growth for the laser structure was carried out on (100) n-GaAs ($n=2 \times 10^{18} \text{cm}^{-3}$) by low pressure MOVPE. A double heterostructure consists of the following layers: an n-GaAs buffer layer ($0.3 \mu\text{m}$, $n=1 \times 10^{18} \text{cm}^{-3}$), an n-(Al_{0.7}Ga_{0.3})_{0.51}In_{0.49}P cladding layer ($1.1 \mu\text{m}$, $n=5 \times 10^{17} \text{cm}^{-3}$), an undoped Ga_{0.51}In_{0.49}P active layer (600\AA), a first p-(Al_{0.7}Ga_{0.3})_{0.51}In_{0.49}P cladding layer ($p=3 \times 10^{17} \text{cm}^{-3}$), a p-Ga_{0.51}In_{0.49}P etch stop layer (90\AA), a second p-(Al_{0.7}Ga_{0.3})_{0.51}In_{0.49}P cladding layer ($0.9 \mu\text{m}$, $p=5 \times 10^{17} \text{cm}^{-3}$), a p-Ga_{0.51}In_{0.49}P layer (500\AA , $p=1 \times 10^{18} \text{cm}^{-3}$), and a p-GaAs capping layer ($0.2 \mu\text{m}$, $p=5 \times 10^{18} \text{cm}^{-3}$). The thickness of first p-cladding layer is defined as $h \mu\text{m}$. In order to stabilize the optical transverse mode, mesa stripe was fabricated in the [0-11] direction. To fabricate the ridge structure, firstly, an acetic acid is applied.

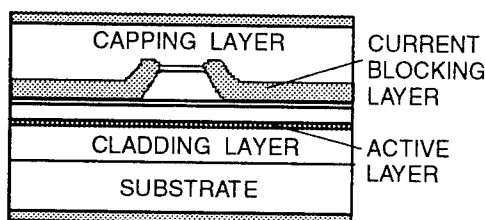
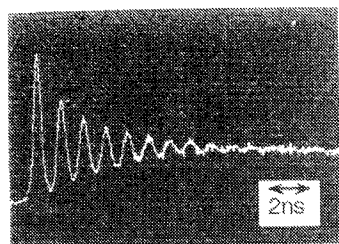
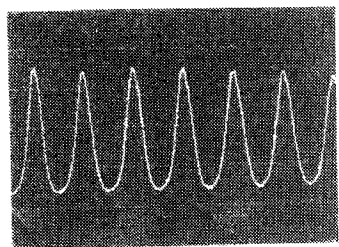


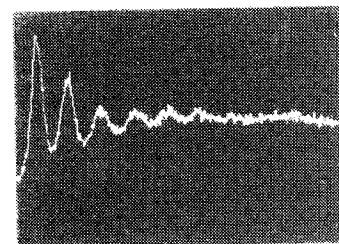
Fig. 1 Schematic cross section of the transverse-mode stabilized AlGaInP visible laser diodes. Ridge structure with current blocking layer control the optical transverse-mode distribution and current injection area at the same time.



A



B



C

Fig. 2 Time evolution of output power of three types of laser diodes. A and C show the relaxation, B shows pulsation.

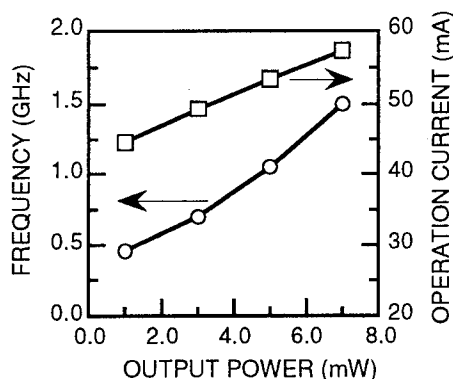


Fig. 3 Pulsation frequency and operation current with various output power.

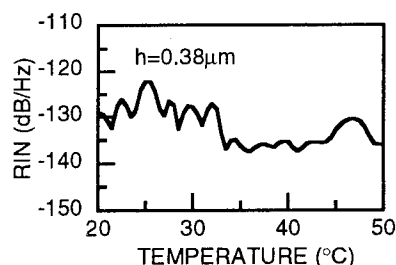
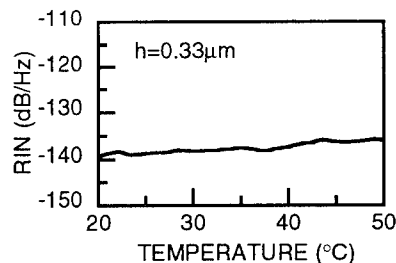
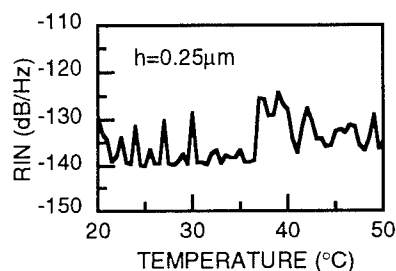


Fig. 4 Relative intensity noise (RIN) with various temperature ranging from 20 to 50 °C. Thickness h are 0.25 μm in sample A, 0.33 μm in sample B, and 0.38 μm in sample C, respectively. The measurement was done at output power of 3.0mW.

Secondly, sulfuric acid is applied to etch preferentially. The acetic acid has the effect to sharpen the form of ridge structure. The mesa was selectively buried by an n-GaAs current blocking layer (0.5 μm , $n=3\times 10^{18}\text{cm}^{-3}$). Finally, a p-GaAs contact layer ($\sim 3.0\mu\text{m}$, $p=5\times 10^{18}\text{cm}^{-3}$) was overgrown. The control of refractive index step between inside and outside of the ridge stripe is important to produce the pulsation because of its great influence on optical transverse mode profile [9]. The refractive index step was controlled by the thickness h of the layer between the current blocking layer and active layer. The refractive index step is reduced as h increases. We fabricated lasers with three different structures. The thickness h of sample A, B and C are 0.25, 0.33 and 0.38 μm , and the built-in refractive index steps are calculated to be 6.6×10^{-3} , 3.4×10^{-3} and 1.2×10^{-3} , respectively. The width of the ridge stripe was 3.8 μm at the bottom, and the cavity length was 350 μm .

Results and Discussions

The threshold currents of samples A, B and C were 36, 40 and 50mA, respectively. The difference of threshold currents is due to the difference in optical confinement. Time evolution of output power is shown in Fig. 2. The relaxation oscillation characteristics were found in sample A and C. Sample B, however, shows the self-sustained pulsation phenomena with a frequency of 0.44GHz. The pulsation frequency and operation current are shown in Fig. 3. The frequency changed in accordance with the injection current. Although the small refractive index step is effective for the self-sustained pulsation [9], the pulsation phenomena could not be observed in the sample C. The RIN was measured under the output power of 3mW and external feedback light of 0.1%. The measurement was done at the frequency of 2.5MHz ($\Delta f=30\text{KHz}$). The results for various thickness h in the temperature ranging from 20 to 50°C are shown in Fig. 4. In the condition that $h=0.25\mu\text{m}$, mode competition noise is obviously found. In $h=0.33\mu\text{m}$, low noise characteristics was realized in the high temperature range. Built-in refractive index step and RIN with various thickness h are shown in Fig. 5. The error bars show the range of RIN in the temperature range. The RIN became minimum at the refractive index step of 3.4×10^{-3} . In the sample B, the RIN was as low as -136dB/Hz in the temperature ranging from 20 to 50°C. Life-testing results for sample B at 50°C under the output power of 5mW are shown in Fig. 6. Good longevity was confirmed. The low RIN value

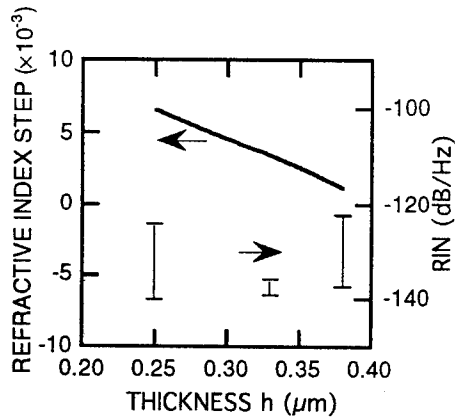


Fig. 5 Built-in refractive index step and relative intensity noise (RIN) with various thickness h of the p-type AlGaInP first cladding layer under the n-GaAs current blocking layer. The RIN was measured in the temperature ranging from 20 to 50°C.

and the low degradation rate indicate that the laser diode, sample B, is suitable for practical use as a light source of the optical disk systems.

In the sample C ($h=0.38\mu\text{m}$), sustained pulsation was not observed. This is attributed to the current spreading toward outside of the ridge stripe. The approximate equation of the injection current density profile in the active layer $J(x)$ is assumed to be

$$J(x) = J_0 \exp \left[\ln \left(\frac{1}{2} \right) \frac{\cosh(bx) - 1}{\cosh(bW) - 1} \right] \quad (1)$$

$$b = \frac{1}{h} \quad (2)$$

where J_0 is the maximum current density, x is the position along the junction plane. The parameter b stands for the current spreading in the layer [10]. The assumed injection current density profile along the

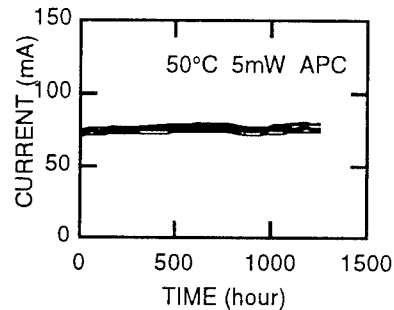


Fig. 6 Life-testing results for sample B ($h=0.33\mu\text{m}$) at 50°C under a constant power of 5mW.

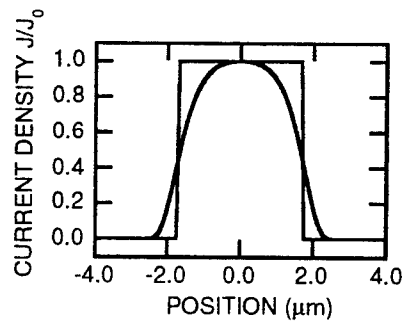


Fig. 7 Current density distribution towards the lateral direction, which was calculated on the equation (1), and (2).

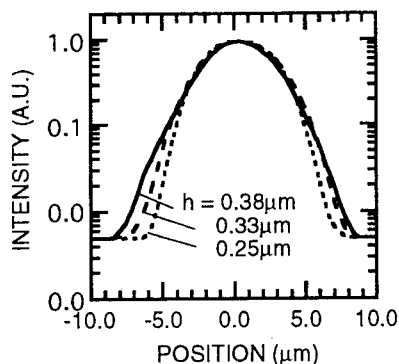


Fig. 8 Near field pattern of output power at the cavity facet of the lasers.

junction plane in case of $h=0.38\mu\text{m}$ is shown in Fig. 7. Straight line shows the profile in $h=0\mu\text{m}$. It is found that the current spreading is occurred in the first p-cladding layer. To confirm that effect, near field patterns of output power at the cavity facet were measured as shown in Fig. 8. In fact, the differences of the near field patterns were found between three types of lasers. The area of saturable absorbing region is reduced by carrier injection outside the ridge stripe. This indicates that the designing of thickness h is very important for pulsating lasers. As a result of the optimum designing, self-sustained pulsation was successfully attained in sample B with thickness h of $0.33\mu\text{m}$ and the ridge stripe width of $3.8\mu\text{m}$ at the bottom.

Conclusion

In conclusion, high reliable 680nm-band AlGaInP visible laser diodes with stable self-sustained pulsation were successfully fabricated by designing the thickness h of $0.33\mu\text{m}$. The lasers achieved RIN of as low as -136dB/Hz in the temperature ranging from 20 to 50°C under the output power of 3mW.

References

- [1] T. L. Paoli, IEEE J. Quantum Electron. **QE-13**, 351 (1977)
- [2] R. L. Hartman, N. E. Schumaker, and R. W. Dixon, Appl. Phys. Lett., **31**, 756 (1977).
- [3] W. B. Joyce and R. W. Dixon, J. Appl. Phys., **46**, 855 (1975).
- [4] R. W. Dixon, and W. B. Joyce, IEEE J. Quantum Electron. **QE-15**, 470 (1979).
- [5] T. L. Paoli, Appl. Phys. Lett., **34**, 652 (1979).
- [6] M. Mannoh, J. Hoshina, S. Kamiyama, H. Ohta, Y. Ban, and K. Ohnaka, Appl. Phys. Lett. **62**, 1173 (1993).
- [7] S. Matsui, H. Takiguchi, H. Hayashi, S. Yamamoto, S. Yano, and T. Hijikata, Appl. Phys. Lett. **43**, 219 (1983).
- [8] T. Ikegami et. al., Proceedings on Conference on Lasers and Electro-optics, 1994 (Anaheim, CA) paper CThB5
- [9] M. Yamada, IEEE J. Quantum Electron. **29**, 1330 (1993).
- [10] N. Chinone, J. Appl. Phys., **48**, 3237 (1977).

Time dependence of catastrophic optical damage (COD) of 0.98 μm GaInAs/GaInP strained quantum well laser

Jun-ichi Hashimoto, Ichiro Yoshida, Michio Murata,
and Tsukuru Katsuyama

*Optoelectronics R&D Laboratories, Sumitomo Electric Industries Ltd.
1, Taya-cho, Sakae-ku, Yokohama 244, Japan*

Introduction

GaInAs/GaInP strained quantum well lasers emitting at 0.98 μm wavelength region are considered to be one of the best candidates for optical pumping sources of Er^{3+} doped optical fiber amplifier because of its low noise amplified characteristics and low power consumption operation. However in this type of laser, a sudden failure by COD took place frequently during the operation [1]-[5], which restricted its practical use seriously. Therefore, it is essential to their practical application to remove in advance the devices in which COD failure would occur during the operation.

The COD occurrence could be explained by the stress-strength model [5]; namely, as shown schematically in Fig.1, due to the crystalline degradation of the output facet during the operation, the critical power level (CPL) at which COD takes place will decrease with the aging time, and finally it will reach the output power level of a laser. At that point, COD will occur instantaneously. Therefore, it is most necessary to clarify this dependence of CPL on aging time in order to be able to predict the time of COD occurrence and remove the inferior devices in which COD would possibly occur during the use.

For this reason, we treated this issue for the first time, and investigated quantitatively the aging time dependence of CPL with a current as a parameter.

Device Structure and Fabrication

Epitaxial layers of the laser were grown by low-pressure (60Torr) metal organic vapor phase epitaxy (MOVPE) on a (100) oriented GaAs substrate. Triethylgallium, trimethylaluminum, and trimethylindium were used as group III sources for GaInP, GaInAsP, and GaInAs. Trimethylgallium was used for GaAs. PH_3 and AsH_3 were used as group V sources. Diethylzinc and Si_2H_6 were used as a p-type and an n-type dopants, respectively.

Fig.2 shows the cross-sectional view of our 0.98

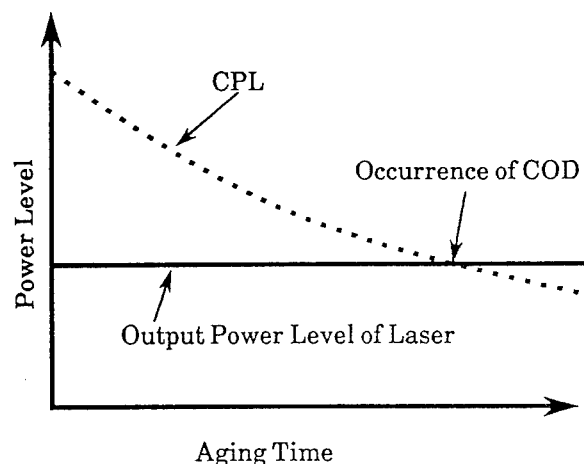


Fig.1 Stress-strength model for COD occurrence

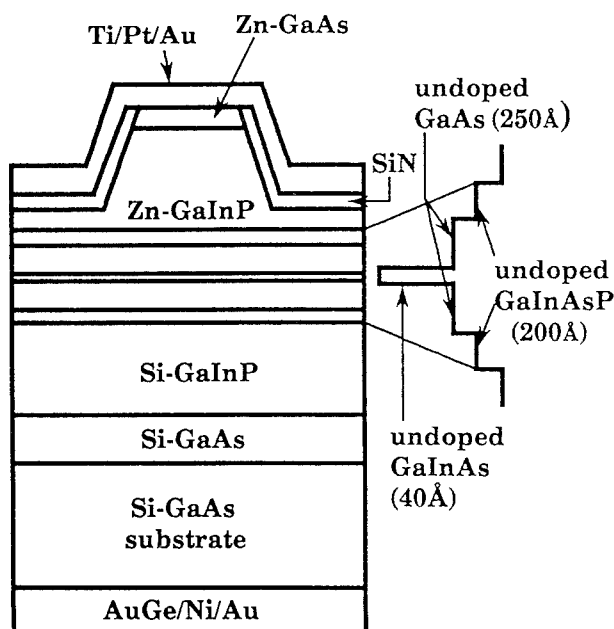


Fig.2 Cross-sectional view of
0.98 μm GaInAs/GaInP
strained quantum well laser

μm GaInAs/GaInP strained quantum well laser used for the aging tests. As illustrated, it consists of a $0.2\ \mu\text{m}$ Si-doped GaAs buffer layer, a $1.5\ \mu\text{m}$ Si-doped GaInP cladding layer, a $40\ \text{\AA}$ undoped GaInAs strained single quantum well active layer sandwiched by $250\ \text{\AA}$ undoped GaAs and $200\ \text{\AA}$ undoped GaInAsP optical confinement layers, a $1.5\ \mu\text{m}$ Zn-doped GaInP cladding layer, and a Zn-doped GaAs contact layer.

A $5\ \mu\text{m}$ -wide ridge waveguide structure was then fabricated by mesa etching and deposition of an SiN thin film. Laser chips were $1000\ \mu\text{m}$ long, and uncoated.

Experimental Procedures

For the experiment, we cleaved 70 laser chips from the same wafer, and mounted them directly on copper heatsinks in the p side up configuration. We then divided them into 10 groups (therefore one group had 7 devices) so that every group would have almost the same distribution of I-L characteristics, and used each of the groups to measure the CPL at each time and current.

Aging tests were performed under automatic current control (ACC) condition in the nitrogen atmosphere at $50\ ^\circ\text{C}$.

As depicted in Fig.3, the CPL after a certain time of aging can be obtained by measuring the I-L

characteristic at $50\ ^\circ\text{C}$, and finding the output power level at which COD occurs.

Results and Discussion

Fig.4 shows one of the results with CPL dependence on time. As shown, the data group of CPL seems to shift towards the lower level with the aging time, which agrees with the stress-strength model mentioned above.

In order to evaluate this shift more quantitatively, we then introduced a statistical treatment in this result; in fact, analyzing the CPL data distribution at each time, we found that in Fig.4, the CPL data at each aging time could be considered to distribute according to the Weibull statistics as one example was shown in Fig.5. In this CPL Weibull distribution which is schematically shown in Fig.6, we defined the characteristic CPL (CCPL) as the power level below which $100 \times (1 - e^{-1})\%$ (63.2%) of the total number of CPL data were existed. The CCPL corresponds to the scale parameter in the normal Weibull analysis, and it can be calculated easily using the Weibull function.

We regarded CCPL as a value which represented the CPL distribution at each time, and plotted its dependence on the aging time in Fig.7 with a current as a parameter. From this result, the

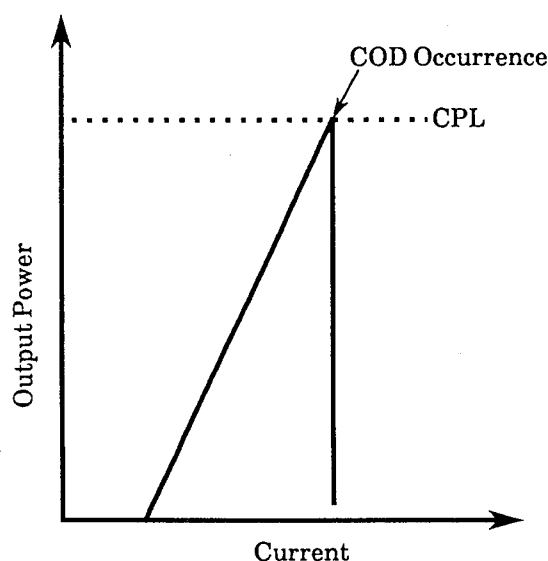


Fig.3 CPL measurement after a certain time of aging

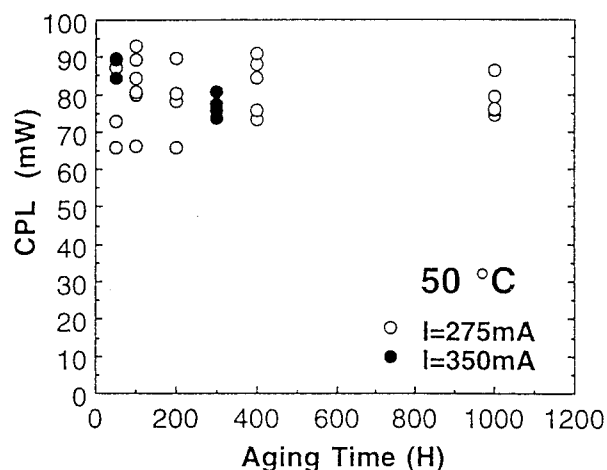


Fig.4 Dependence of CPL on aging time

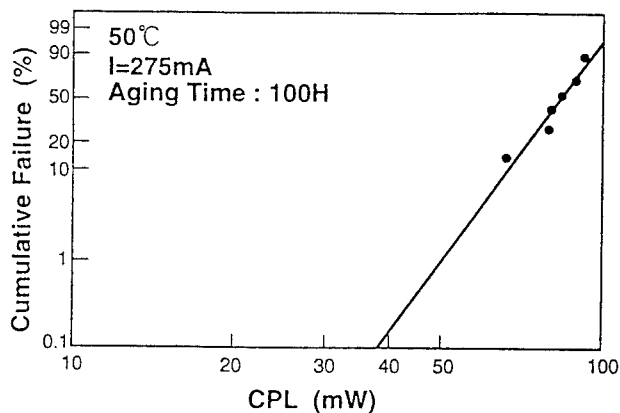


Fig.5 Weibull analysis of CPL distribution

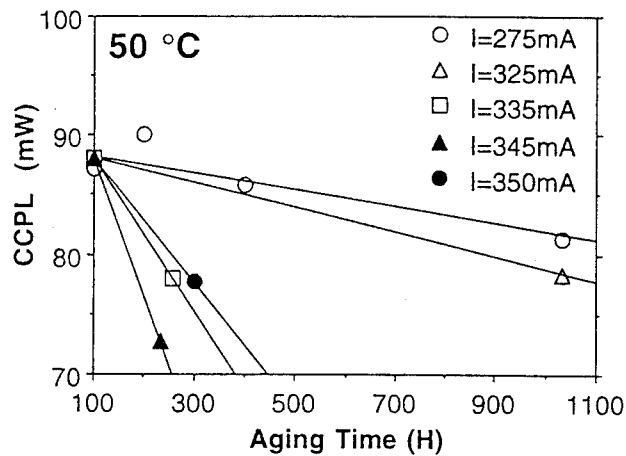


Fig.7 Dependence of CCPL on aging time

following facts were clarified.

- (1) At 100 H, the CCPL is almost the same irrespective of the current.
- (2) After 100 H, the decrease rate of CCPL with time becomes much larger as the current increases.

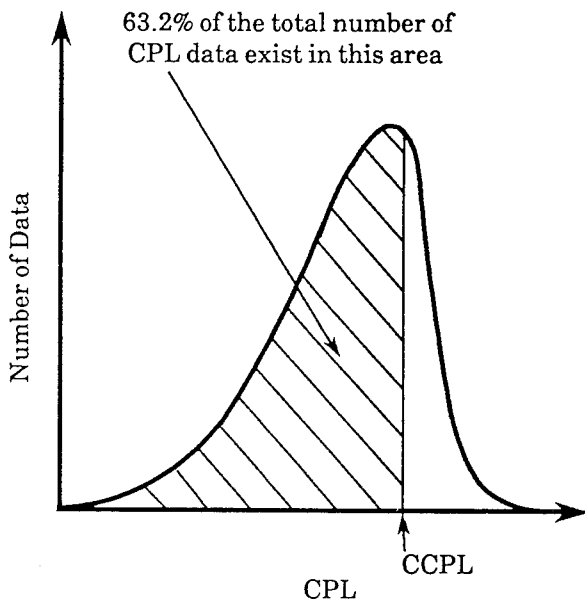


Fig.6 Schematic representation of CPL Weibull distribution

The strong relationship between the decrease rate of the CCPL and the current (I), which could be derived from Fig.7, was represented clearly in Fig.8. In this figure, we find that the decrease rate of CCPL increases by a factor of about 10 when the current increases from 275mA to 350mA.

If we assume the decrease rate of CCPL to be proportional to I^α and calculate α using the least squares method, a large value of about 10 is obtained for it. Consequently, for example, if the operation current is 200mA (which corresponds to about 50mW output per facet), the decrease rate of CCPL is only 0.2mW/kH, so that COD would scarcely occur during the practical use. However, when the operation current increases to 300mA (which corresponds to about 70mW output per facet), the decrease rate of CCPL increases to about 10mW/kH, so that most of the devices are predicted to suffer a COD failure within several thousand hours.

Conclusion

In conclusion, we investigated the aging time dependence of the COD of 0.98 μm GaInAs/GaInP strained quantum well laser based on the stress-strength model. Applying a statistical treatment to

the experimental results, we found for the first time that the CPL data at each aging time were distributed according to the Weibull statistics, and the decrease rate of CPL with time depended strongly upon the current.

Based on these results, it will be possible to design a statistical method by which we can remove in advance the inferior devices which will possibly degrade due to COD within a certain period of operation. This is a next issue to be treated in the future work.

Acknowledgments

The authors would like to thank A. Ishida and K. Murakami for their continuous encouragement.

References

- [1] A. Moser, A. Oosenbrug, E. -E. Latta, T. Forster, and M. Gasser, *Appl. Phys. Lett.*, vol.59, pp.2642-2644, 1991.
- [2] A. Moser, E. -E. Latta, and D. J. Webb, *Appl. Phys. Lett.*, vol.55, pp.1152-1154, 1989.
- [3] A. Moser, *Appl. Phys. Lett.*, vol.59, pp.522-524, 1991.
- [4] A. Moser and E. -E. Latta, *J. Appl. Phys.*, vol.71, pp.4848-4853, 1992.
- [5] M. Fukuda, M. Okayasu, J. Temmyo, and J. Nakano, *IEEE J. Quantum Electron.*, QE-30, pp.471-476, 1994.

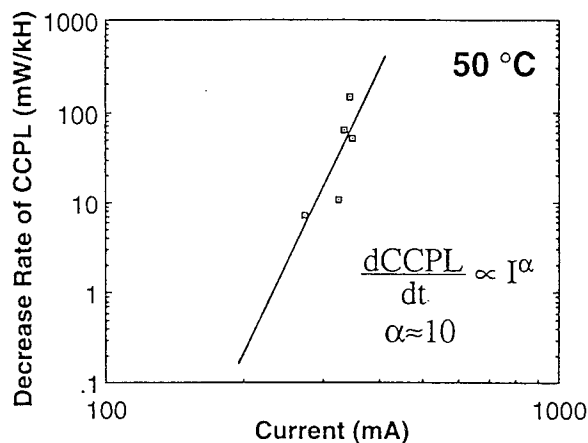


Fig.8 Relationship between decrease rate of CCPL and current

High-Speed InP-Based Strained MQW Ridge Waveguide Laser

A.L. Gutierrez-Aitken, H. Yoon, and P. Bhattacharya

Solid State Electronics Laboratory
Department of Electrical Engineering and Computer Science
The University of Michigan
Ann Arbor, MI 48109-2122, U.S.A.

Abstract

A high-speed ridge waveguide laser with undoped strained MQW active region was fabricated and characterized. The lasers demonstrated typical threshold currents of ~ 20 mA. The electrical impedance of the laser demonstrates -3 dB bandwidths > 34 GHz at high bias currents, indicating that the parasitics in our devices are very small. The best laser demonstrated a -3 dB modulation bandwidth of 20 GHz. This is the highest bandwidth achieved for a ridge waveguide laser operating at $1.55 \mu\text{m}$.

Introduction

A primary requirement of high speed optical fiber communication is a $1.55 \mu\text{m}$ laser diode with a large modulation bandwidth. The heterostructure of choice for this device is an InGaAsP compressively strained multiquantum well (MQW) active region and appropriate lattice matched inner and outer cladding regions and layers for forming ohmic contacts. The compressively strained quantum well active region provides a material with higher gain and differential gain than lattice-matched MQW or double-heterostructure lasers[1, 2]. This offsets the gain saturation to some degree and at the same time allows the realization of a low threshold current, I_{th} , and high modulation bandwidth laser. Although the theoretically predicted modulation bandwidth in these devices, limited by material parameters, carrier dynamics and transport, can be quite high (~ 35 GHz), practical lasers have demonstrated bandwidths of $\sim 20 - 25$ GHz[3, 4]. It is important to note that these bandwidths are obtained in buried heterostructures devices with modulation doping of holes to modify the valence bandstructure in the gain region, or at cryogenic temperatures. The maximum bandwidth has been limited to 17 GHz[5] for a ridge waveguide laser but in GaInAlAs/InP strained material system with benefits of high conduction band discontinuity. The biggest impediment to the realization of higher bandwidths is thought to be the external parasitics, and in particular the resistance of the p-type ohmic contact.

In this work, we have optimized the layout design and fabrication of InP-based single mode ridge waveguide lasers with compressively strained MQW separate confinement heterostructure. This optimization included the formation of reliable low-resistance p-contact on

high-quality p-type InGaAs and the reduction of parasitics. A maximum modulation bandwidth of 20 GHz was measured at 300 K.

Device Structure and Fabrication

The laser diode structure, shown in Fig. 1, has a four period MQW active region with compressively strained (0.38% strain) wells and InGaAsP and InP inner and outer claddings, respectively, and InGaAs contact layers grown by metalorganic chemical vapor deposition (MOCVD). $3 \mu\text{m}$ wide ridge waveguide lasers were fabricated using dry and wet etching. The p- and n-ohmic metalizations are Pt/Ti/Pt/Au and Ni/Ge/Au/Ti/Au, respectively. The specific contact resistance of the p-ohmic is expected to be less than $1 \times 10^{-6} \Omega \cdot \text{cm}^2$ due to Pt-induced Schottky barrier height reduction[6]. A plasma enhanced chemical vapor deposition (PECVD) SiO_2 layer $1.2 \mu\text{m}$ thick is used as isolation for the interconnection metal. Thick Ti/Au ($1.75 \mu\text{m}$) was evaporated to form the interconnection to the n-ohmic and to provide a contact pad on top of the ridge. The device has a ground-signal-ground layout with the p- and n-ohmic contacts in the same plane, allowing the use of a standard coplanar microwave probe to bias and modulate the laser. After thinning the wafer to $\sim 100 \mu\text{m}$, the lasers were cleaved into bars of various lengths. The laser facets were not coated.

Experimental Results

A typical light versus current plot is shown in Fig. 2. The lasers demonstrated threshold currents of ~ 20 mA across the wafer. The electrical impedance of the laser

0.1 μm	$\text{In}_{0.53}\text{Ga}_{0.47}\text{As}$	$\text{p}^+(2 \times 10^{19} \text{cm}^{-3})$	p-contact
1.7 μm	InP	$\text{p} (5 \times 10^{17} \text{cm}^{-3})$	p outer cladding
500 \AA	InGaAsP ($\lambda=1.2 \mu\text{m}$)	i	Inner cladding
	InGaAsP 80 \AA well, $\epsilon_{\parallel}=+0.38\%$, $\lambda=1.55 \mu\text{m}$ 100 \AA barrier, $\lambda=1.2 \mu\text{m}$	i	4 period MQW active region
1000 \AA	InGaAsP ($\lambda=1.2 \mu\text{m}$)	i	inner cladding
1.6 μm	InP	$\text{n} (5 \times 10^{17} \text{cm}^{-3})$	n outer cladding
0.2 μm	$\text{In}_{0.53}\text{Ga}_{0.47}\text{As}$	$\text{n}^+(5 \times 10^{18} \text{cm}^{-3})$	n-Contact
S.i. InP (100) Substrate			

Figure 1: Compressively strained multiple quantum well laser structure.

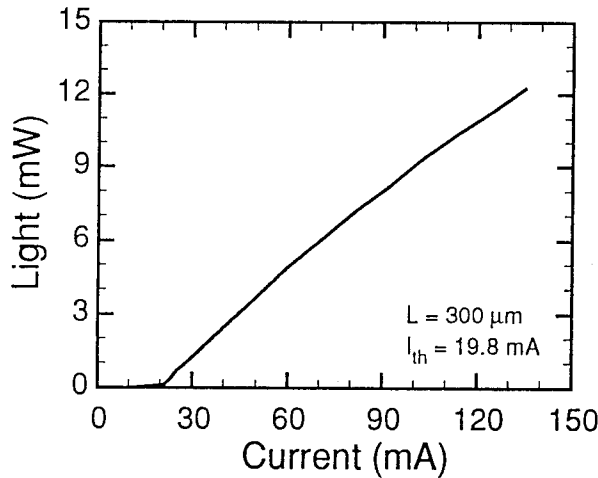


Figure 2: Light versus current of a $3 \times 300 \mu\text{m}^2$ laser without facet coating.

was obtained from S-parameter measurements at different bias currents. The magnitude of the impedance, $\text{Mag}(Z)$, as a function of frequency for bias currents of 10 to 80 mA is shown in Fig. 3 for a laser with $300 \mu\text{m}$ cavity length. At high currents, the -3 dB bandwidth of the laser diode impedance, shown in the inset of Fig. 3 is $>34 \text{ GHz}$, indicating that the parasitics in our devices are very small. We were able to model accurately the laser electrical impedance at currents below and above threshold with the circuit shown in Fig. 4. From the modeled equivalent circuit, values for series resistance, R_s , of 4-5 Ω were obtained independent of bias. The differential diode resistance, R_d , and the diode capacitance, C , showed an inverse relation to the bias current, with values $R_d < 10 \Omega$ and $C < 1 \text{ pF}$ at high bias currents. Also at high bias currents, resonance peaks were observed in the impedance of the laser.

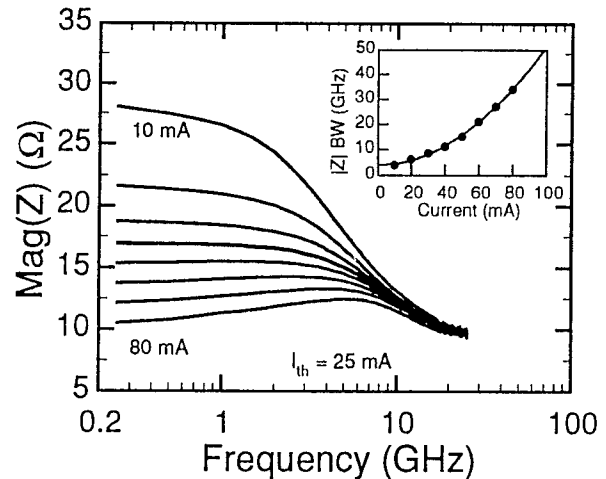


Figure 3: Magnitude of the laser electrical impedance as a function of frequency for different bias currents. The inset shows the -3 dB bandwidth of the impedance as a function of the bias current.

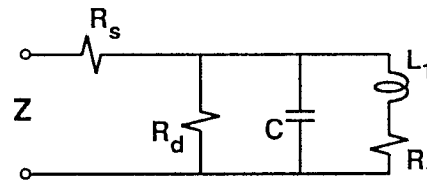


Figure 4: Equivalent circuit of the laser diode below and above threshold current.

The modulation response of lasers was measured with a microwave sweep generator, a high speed InGaAs photodiode and a spectrum analyzer. The measured response was calibrated for the loss due to cables, bias network, and DC blocking capacitor. The microwave probe and the photodetector had bandwidths >40 GHz with deviations of <1dB in this frequency range. A good uniformity of laser frequency response was obtained across the sample with -3 dB bandwidths of ~15-20 GHz. The best laser demonstrated a -3 dB modulation bandwidth of 20 GHz under pulsed conditions as shown in Fig. 5. This is the highest bandwidth achieved for a ridge waveguide laser operating at 1.55 μm . The present experimental setup allowed measurement of accurate modulation response up to 15 GHz, beyond which the -3 dB bandwidth was estimated assuming 40 dB/decade rolloff which was the observed characteristics of our devices at low bias.

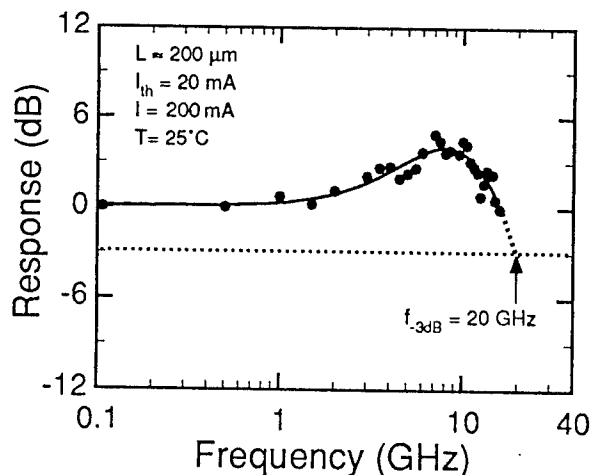


Figure 5: Small signal modulation response of a $3 \times 200 \mu\text{m}^2$ ridge waveguide laser at $I=200\text{mA}$.

The frequency response of the laser was fitted to the standard small signal modulation response

$$|M(f)|^2 = \frac{f_r^4}{(f_r^2 - f^2)^2 + (\gamma/2\pi)^2 f^2} \quad (1)$$

where the resonance frequency f_r and the damping factor γ were used as the fitting parameters. A plot of damping factor as a function of resonance frequency squared is shown in Fig. 6. The extracted K factor of 0.39 ns implies a maximum -3 dB modulation bandwidth of 23 GHz. The present bandwidth limitation may be from damping, transport, and junction heating effect. This demonstrates that ultrahigh modulation bandwidth can be obtained using a low parasitic ridge waveguide laser in more advanced structures employing active regions with compensated strain[7] and

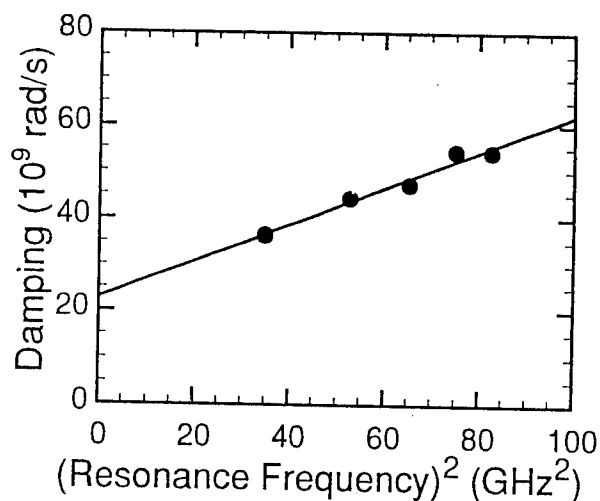


Figure 6: Damping factor as a function of resonance frequency squared as extracted from frequency response measurements.

modulation doping[8] to realize the 40 GHz predicted bandwidth in this material system.

Conclusion

A high-speed ridge waveguide laser with very small parasitics and large electrical impedance bandwidths (>34 GHz) was demonstrated. A maximum -3 dB modulation bandwidth of 20 GHz was obtained for a $3 \times 200 \mu\text{m}^2$ laser at $I=200\text{mA}$. This demonstrates that very high modulation bandwidths can be achieved using a low parasitic ridge waveguide laser in more advanced structures.

Acknowledgments

This work is supported by the Advanced Research Projects Agency Center for Optoelectronics Science and Technology, Grant MDA 972-94-1-0004, and U.S. Army Research Office (URI program), Grant DAAL03-92-G-0109.

References

- [1] M. Nido, K. Naniwae, J. Shimizu, S. Murata, and A. Suzuki, "Analysis of differential gain in InGaAs-InGaAsP compressive and tensile strained quantum-well lasers and its application for estimation of high-speed modulation limit," *IEEE J. Quant. Elec.*, vol. 29, pp 885-895, Mar. 1993.

- [2] P.A. Morton, H. Temkin, D.L. Coblenz, R.A. Logan, and T. Tanbun-Ek, "Enhanced modulation bandwidth of strained multiple quantum well lasers," *Appl. Phys. Lett.*, Vol. 60, pp 1812-1814, Apr. 1992.
- [3] P.A. Morton, R.A. Logan, T. Tanbun-Ek, P.F. Sciortino Jr., A.M. Sergeant, R.K. Montgomery, and B.T. Lee, "25 GHz bandwidth 1.55 μ m GaInAsP p-doped strained multiquantum-well lasers," *Electron. Lett.*, Vol. 28, pp 2156-2157, Nov. 1992.
- [4] R. Yu, R. Nagarajan, T. Reynolds, A. Holmes, J.E Bowers, S.P. DenBaars, and C. Zah, "Ultrahigh speed performance of quantum well laser at cryogenic temperatures," *Appl. Phys. Lett.*, Vol. 65, pp 528-530, Aug. 1994.
- [5] B. Stegmuller, B. Borchert, and R. Gessner, "1.57 μ m strained-layer quantum-well GaInAlAs ridge-waveguide laser diodes with high temperature (130°C) and ultrahigh-speed (17 GHz) performance," *IEEE Photon. Technol. Lett.*, Vol. 5, pp 597-599, Jun. 1993.
- [6] H. Okada, S. Shikata, and H. Hayashi, "Electrical characteristics and reliability of Pt/Ti/Pt/Au ohmic contacts to p-type GaAs," *Jpn. J. Appl. Phys.*, vol 30, pp L558-L560, Apr 1991.
- [7] D. Varga, O. Kjebon, U. Ohlander, K. Streubel, J. Wallin, S. Lourdudoss, T. Klinga, B. Broberg, and G. Landgren, "Low threshold, high quantum efficiency, high speed strain compensated multi quantum well lasers," *Proc. International Conf. Indium Phosphide and Related Materials*, pp 473, 1994.
- [8] J.D. Ralston, S. Weisser, K. Eisele, R.E. Sah, E.C. Larkins, J. Rosenzweig, J. Fleissner, and K. Bender, "Low-bias-current direct modulation up to 33 GHz in InGaAs/GaAs/AlGaAs pseudomorphic MQW ridge-waveguide lasers," *IEEE Photon. Technol. Lett.*, Vol. 6, pp 1076-1079, Sep. 1994.

INCREASED LIFETIME OF ALUMINUM-FREE LED'S ON SI SUBSTRATES GROWN BY MOCVD

T. Egawa¹⁾, A. Tanaka²⁾, J. Dong³⁾, K. Matsumoto³⁾, T. Jimbo¹⁾ and M. Umeno^{1,2)}

¹⁾Research Center for Micro-Structure Devices, Nagoya Institute of Technology,

²⁾Department of Electrical and Computer Engineering, Nagoya Institute of Technology,
Gokiso-cho, Showa-ku, Nagoya 466, Japan

³⁾Nippon Sanso Corporation, Tsukuba Laboratories,
10 Ohkubo, Tsukuba, Ibaraki 305, Japan

Abstract : An InGaP layer on a Si substrate grown by metalorganic chemical vapor deposition exhibits a mirror-like surface morphology, dark spot density of $1 \times 10^7 \text{ cm}^{-2}$ and 77 K photoluminescence peak wavelength of 645.5 nm. In comparison with a conventional Al-contained AlGaAs/GaAs light-emitting diode (LED) on a Si substrate, an Al-free LED on a Si substrate has no a significant growth of dark-line defects. As a result, an increased lifetime has been achieved in an Al-free LED on a Si substrate.

Introduction

Reliable light-emitting diodes (LED's) and laser diodes on Si substrates are key devices in high density applications such as optical interconnections in future optoelectronic integrated circuits (OEIC's) (1-3). GaAs on Si substrate (GaAs/Si) involves a high dislocation density ($>10^6 \text{ cm}^{-2}$) and a large residual thermal stress (10^9 dyn/cm^2), which are introduced by the $\sim 4\%$ lattice mismatch and the $\sim 250\%$ difference in the thermal expansion coefficients between GaAs and Si (4, 5).

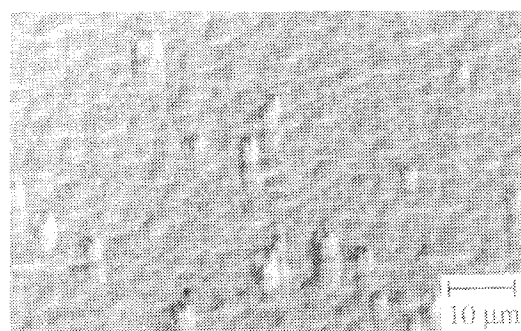
AlGaAs layers are commonly used for cladding and confining layers in conventional structures of LED's and laser diodes on Si as well as GaAs substrates because Al is useful to increase the band-gap energy. Al is well known to cause growth difficulties due to increased incorporation of residual oxygen and carbon for metalorganic chemical vapor deposition (MOCVD) growth. Therefore, the conventional Al-contained LED's and laser diodes on Si substrates, which emit at about 850 nm, suffer from the rapid degradation. We have shown that degradation in the laser diode on the Si substrate is caused by the deteriorations of electrical and optical characteristics, which are related to the defect-accelerated impurity diffusion and the formation of dark-line defects (DLD's) (6, 7). Previous studies on improvement of reliability have been focussed on the reduction of dislocation density and residual stress by uses of post-growth patterning (5), selective-area growth (8) and undercut structure (9). In this study, we report the demonstration of Al-free LED's on Si substrates with increased lifetime. The advantages of the Al-free structure are less surface oxidation, lower surface recombination velocity, reduction of leakage current and improvement of reliability for the LED and laser diode on Si substrates.

Experimental

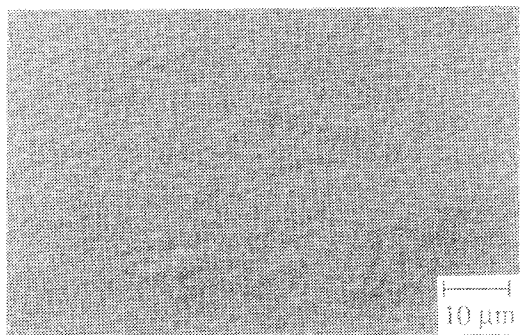
In the first growth step, a 1.7- μm -thick n^+ -GaAs layer was grown by an rf-heated MOCVD at atmospheric pressure on a (100) n^+ -Si substrate tilted 2° toward the [110] direction using the two-step growth technique. During the n^+ -GaAs layer growth at 750°C , the temperature was cycled five times from 350 to 850°C . Thermal cycle annealing is effective in reducing the density of threading dislocations in the active layer (10). In the second growth step, this GaAs/Si was transferred to the low pressure (76 Torr) MOCVD growth system and treated as a substrate for the subsequent growth of a laser diode structure. The structure grown at 700°C consists of a 0.9- μm -thick $n\text{-In}_{0.49}\text{Ga}_{0.51}\text{P}$ lower cladding layer, a 70-nm-thick GaAs lower confining layer, a 7-nm-thick $\text{In}_{0.2}\text{Ga}_{0.8}\text{As}$ active layer, a 70-nm-thick GaAs upper confining layer, a 0.9- μm -thick $p\text{-In}_{0.49}\text{Ga}_{0.51}\text{P}$ upper cladding layer, and a 0.1- μm thick p^+ -GaAs contact layer. The conventional Al-contained AlGaAs/GaAs double-heterostructure LED was also grown on Si substrate. In order to confirm the advantage of the Al-free material, the LED's were fabricated using Ti/Au for the p^+ -GaAs contact layer and Au-Sb/Au for the Si substrate. The characteristics of LED's on Si substrates, in particular, the reliability was measured under automatic current control (ACC) condition at 300 K. Surface morphology was examined under a Nomarski microscope and crystallinity was characterized by photoluminescence (PL) at 77 K and electron-beam-induced current (EBIC) measurements. Cross-sectional structure was also investigated by means of cross-sectional scanning electron microscopy (SEM). Growth of DLD's was studied using an electroluminescence (EL) observation system.

Results and Discussion

Figures 1 (a) and (b) show the as-grown surface morphology for the conventional Al-contained AlGaAs/GaAs and the Al-free LED's on Si substrates, respectively. The surfaces are mirror-like in both samples. However, the Al-contained LED on Si substrate exhibits precipitates, which are probably caused by excess aluminum. Figure 2 shows the cross-sectional SEM micrograph of the Al-free LED on Si substrate. Smooth and sharp InGaP/GaAs heterointerfaces are obtained in the Al-free LED on Si substrate as shown in Fig. 2. The values of dark spot density (DSD) obtained from the EBIC measurement are $9 \times 10^6 \text{ cm}^{-2}$ for the Al-contained LED and $1 \times 10^7 \text{ cm}^{-2}$ for the Al-free LED on Si substrates. The peak wavelength and the full width at half maximum (FWHM) of the PL spectra at 77 K are 642.5 nm and 11.1 nm for the 1.5- μm -thick InGaP layer on GaAs, and 645.5 nm and 17.2 nm for the InGaP layer simultaneously grown on GaAs/Si, respectively. These results indicate that the crystal quality of the InGaP layer on GaAs/Si substrate is good enough for the fabrication of the LED.



(a) Al-contained LED



(b) Al-free LED

Fig. 1. Nomarski micrographs of the Al-contained (a) and Al-free (b) LED's grown on Si substrates by MOCVD.

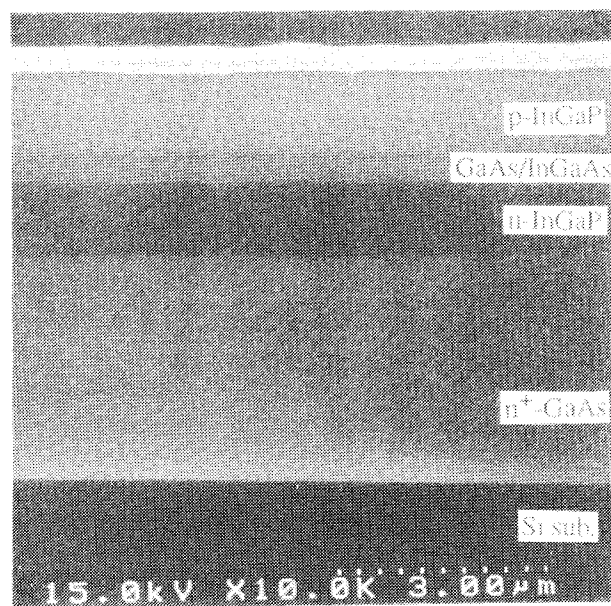


Fig. 2. Cross-sectional SEM micrograph for the structure of the Al-free LED grown on Si substrate by MOCVD.

The current-voltage (I-V) characteristic is shown in Fig. 3. The LED showed the turn-on voltage of 1.5 V and the reverse voltage of 9.3 V at 100 μA , which indicate a good characteristic of p-n junction. The ideality factor calculated from the forward I-V characteristic is approximately 2 in the bias region around 0.5 V. The light output power-dc current (L-I) characteristic at 300 K is shown in Fig. 4. The optical output power was 60 μW at 80 mA, and the efficiency was $1.0 \times 10^{-3} \text{ W/A}$. The peak in the spectrum of emitted light at 985 nm has the FWHM of about 52 nm, and it shifts toward longer wavelength with the increased current due to the thermal effect. Figure 5 shows the comparison of the lifetime for the conventional Al-contained and Al-free LED's on Si substrates. The lifetime at 300 K was examined by measuring the output power at a constant current of 60 mA (480 A/cm^2). The conventional AlGaAs/GaAs LED exhibits the rapid degradation in ten minutes. However, note that the significant improvement was observed in the reliability of the Al-free LED on Si substrate. The output power of the Al-free LED degrades to 50 % of the initial value in the first 13 hours and then maintains stable operation.

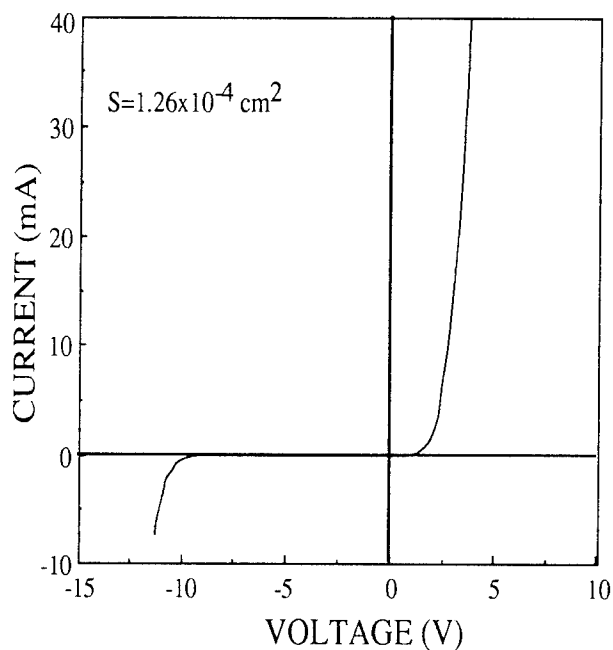


Fig. 3. I-V characteristic of the Al-free LED grown on Si substrate.

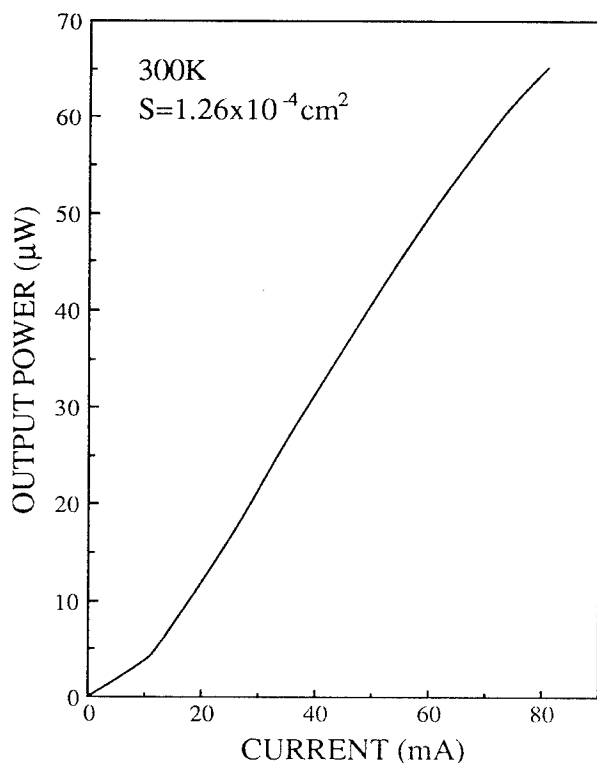


Fig. 4. L-I characteristic at 300 K of the Al-free LED grown on Si substrate.

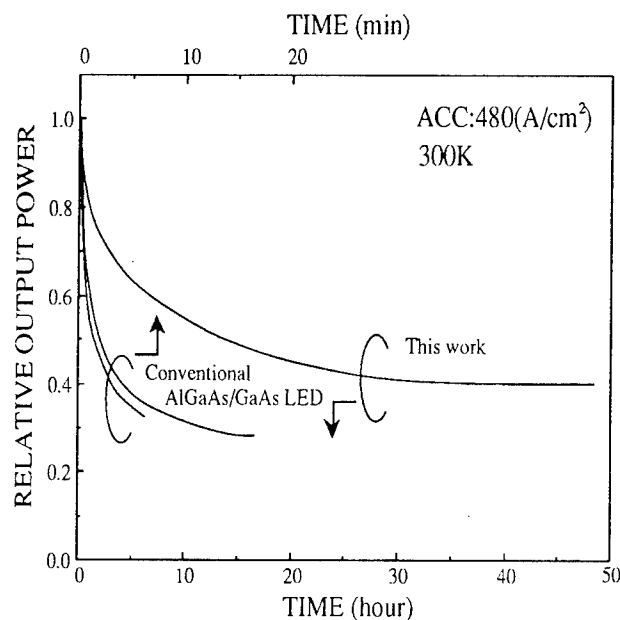
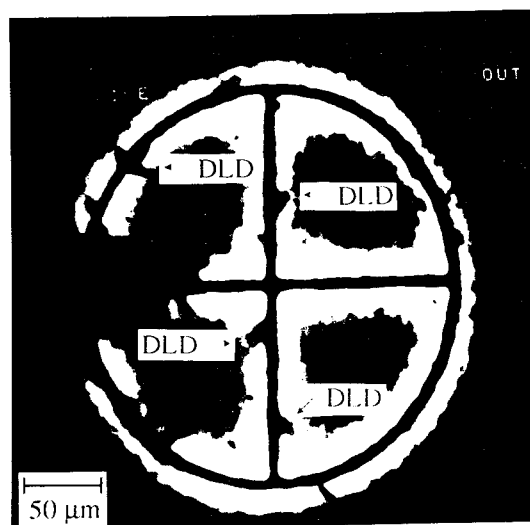
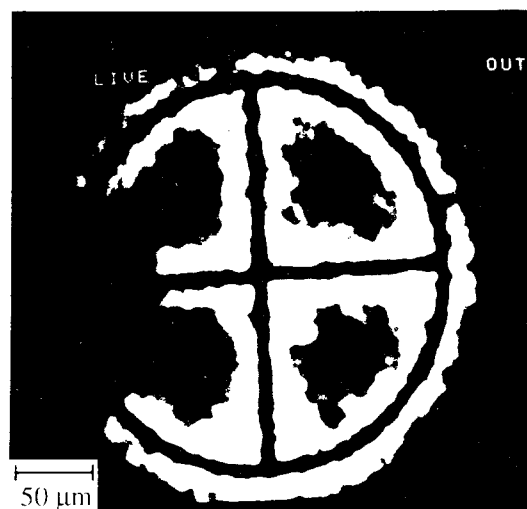


Fig. 5. Comparison of lifetime for the conventional Al-contained and Al-free LED's on Si substrates.

In order to study the optical degradation, the formation of DLD's was compared in the Al-contained and Al-free LED's on Si substrates using the EL observation. Figures 6 (a) and (b) show the EL images of the Al-contained and the Al-free LED's on Si substrate after aging process of 50 hours, respectively. As the aging progresses in the Al-contained LED on Si, the growth of DLD's was clearly observed near the electrodes. The DLD's have a high growth velocity along $\langle 100 \rangle$ direction. The growth velocities of $\langle 100 \rangle$ DLD's were 10 and 50 $\mu\text{m/h}$ at the injected current densities of 0.5 and 1.5 kA/cm^2 , respectively, which depend on the injected current density. These DLD's are three-dimensional dislocation networks where the nonradiative recombination dominates. On the contrary, the Al-free LED on Si showed no significant growth of DLD's as shown in Fig. 6 (b), which indicates the suppression of the optical degradation in this material. We showed that the degradation of laser diode on Si is caused by the deteriorations of electrical and optical characteristics (7). Although the Al-free LED on Si has an increased lifetime in comparison with the Al-contained LED, the Al-free LED on Si still has the decrease of output power in the aging test. This degradation is probably due to the electrical degradation in the p-n junction.



(a) Al-contained LED



(b) Al-free LED

Fig. 6. EL images of the Al-contained (a) and the Al-free (b) LED's on Si substrate after aging process of 50 hours.

Conclusions

We have demonstrated the improvement in the reliability of the LED's on Si substrate using Al-free materials. The growth velocity of the DLD's was decreased in the Al-free LED on Si, which results in the suppression of the optical degradation. This technique is very promising for the fabrication of reliable laser diodes on Si substrates.

References

- (1) H. K. Choi, G. W. Turner, T. H. Windhorn and B. - Y. Tsaur, "Monolithic integration of GaAs/AlGaAs double-heterostructure LED's and Si MOSFET's," *IEEE Electron Device Lett.*, Vol. 7, pp. 500-502, September 1986.
- (2) T. Egawa, T. Jimbo and M. Umeno, "Monolithic integration of AlGaAs/GaAs MQW laser diode and GaAs MESFET grown on Si using selective regrowth," *IEEE Photonics Tech. Lett.*, Vol. 4, pp. 612-614, June 1992.
- (3) T. Egawa, T. Jimbo and M. Umeno, "Optoelectronic integrated circuits grown on Si substrates," *IEICE Trans. Electron.*, Vol. E76-C, pp. 106-111, January 1993.
- (4) H. K. Choi, C. A. Wang and N. H. Karam, "GaAs-based diode lasers on Si with increased lifetime obtained by using strained InGaAs active layer," *Appl. Phys. Lett.*, Vol. 59, pp. 2634-2635, November 1991.
- (5) T. Egawa, Y. Hasegawa, T. Jimbo and M. Umeno, "Effects of dislocation and stress on characteristics of GaAs-based laser grown on Si by metalorganic chemical vapor deposition," *Jpn. J. Appl. Phys.*, Vol. 31, pp. 791-797, March 1992.
- (6) W. E. Plano, D. W. Nam, K. C. Hsieh, L. J. Guido, F. A. Kish, A. R. Sugg and N. Holonyak, Jr., *Appl. Phys. Lett.*, "Dislocation-accelerated impurity-induced layer disordering of $\text{Al}_x\text{Ga}_{1-x}\text{As}$ -GaAs quantum well heterostructures grown on GaAs-on-Si," *Appl. Phys. Lett.*, Vol. 55, pp. 1993-1995, November 1989.
- (7) T. Egawa, T. Jimbo, Y. Hasegawa and M. Umeno, "Optical and electrical degradations of GaAs-based laser diodes grown on Si substrates," *Appl. Phys. Lett.*, Vol. 64, pp. 1401-1403, March 1994.
- (8) Y. Kobayashi, T. Egawa, T. Jimbo and M. Umeno, "Selective-area-grown AlGaAs/GaAs single quantum well lasers on Si substrates by metalorganic chemical vapor deposition," *Jpn. J. Appl. Phys.*, Vol. 30, pp. L1781-L1783, October 1991.
- (9) N. Wada, S. Yoshimi, S. Sakai, C. L. Shao and M. Fukui, "Stable operation of AlGaAs/GaAs light-emitting diodes fabricated on Si substrate," *Jpn. J. Appl. Phys.*, Vol. 31, pp. L78-L81, February 1992.
- (10) T. Egawa, T. Soga, T. Jimbo and M. Umeno, "Room-temperature continuous-wave operation of AlGaAs-GaAs single-quantum-well lasers on Si by metalorganic chemical vapor deposition using AlGaAs-AlGaP intermediate layers," *IEEE J. Quantum Electron.*, Vol. 27, pp. 1798-1803, June 1991.

STABLE AND LOW CHIRP 1.55 μ m COMPLEX-COUPLED DFB LASERS WITH ABSORPTIVE GRATING

Z. M. Chuang, C. Y. Wang, W. Lin, S. C. Ko, M. C. Wang, C. Y. Chang, and Y. K. Tu
Telecommunication Laboratories, Ministry of Transportation and Communications,
Yang-Mei, Taiwan, 32617, ROC.

Abstract

We present our experimental studies in fabricating complex-coupled distributed feedback lasers with a loss grating and a compressively strained InGaAsP multi-quantum well active region. 3 μ m wide ridge waveguide lasers have been successfully fabricated and have demonstrated stable single mode operations. Kink-free light-current characteristics having a relatively low threshold current of around 25mA have been achieved with a 0.18W/A slope efficiency. Stable single mode emission is demonstrated with a 52dB side mode suppression ratio, a low chirp of 0.23nm under 1Gb/s pseudorandom digital modulation, and a spectral linewidth of 15.8MHz with the device operating at 2.5 times the threshold current.

1. Introduction

Distributed feedback (DFB) lasers with single longitudinal mode operation have been the key components in both digital and analog optical fiber communications. Conventional and present commercially available DFB lasers have been fabricated using the $\lambda/4$ -shifted index-coupled structure. Although the $\lambda/4$ -shift approach solved the problem of two mode degeneracy in DFB lasers without phase shift, the device is susceptible to facet reflections and requires very good antireflection facet coatings. Furthermore, because of the concentration of optical intensity near the center of the cavity, the $\lambda/4$ -shifted lasers is subject to spatial hole burning (SHB), which results in degradation of the device includes nonlinearity in light-current characteristics, reduction of side mode suppression ratio(SMSR) and linewidth broadening. Recently, complex-coupled, or partly gain (or loss)-coupled, DFB lasers have been demonstrated to be a promising alternative[1] not only for reducing the SHB effect, but also for several other superior properties. These include a high single mode yield even without facet coatings[2], insensitivity to external optical feedback[3] and reduced chirping utilizing anti-phase grating [4] which has been realized in our device structure.

Figure 1 is a schematic diagram showing the device structure which comprises the strained quaternary multiple quantum well (MQW) active layers and a holographically patterned InGaAs grating. The alternation of materials between InGaAs and InP not only creates a periodic refractive index, but because InGaAs is absorptive

at 1.55 μ m, it also creates a periodic loss distribution. These induce the so-called anti-phase complex-coupling. The InGaAs layer was either n-doped or undoped to avoid self-pulsation instability caused by absorption saturation[5]. In this report, we present a rather simple and well controlled fabrication process, and yet relatively low threshold DFB lasers with stable and low chirp performance have been achieved and demonstrated.

In Section 2, the theoretical aspects and design considerations of fabricating the device are described, followed by the fabrication techniques depicted in Section 3. Finally, the experimental results are presented in Section 4.

2. Design and Theory

A program written based on a transmission matrix method[6] was used to perform the waveguide modal analysis. For simplicity, we only considered the one dimensional case shown in Figure 1, in which the grating is formed by alternating the material between InGaAs and InP, which induces a periodic perturbation to the propagation waveguide mode in both index and loss. This perturbation creates coupling between forward and backward propagation modes. The derivation of the coupled-mode equations has been well established[7], which gives the phase matching condition of the grating coupling and the coupling strength.

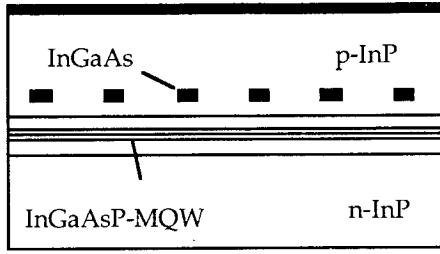


Fig.1 Schematic structure of the complex-coupled DFB lasers with absorptive grating

The phase matching condition determines the Bragg wavelength, which is given by

$$\lambda = 2n_{eff}\Lambda, \quad (1)$$

where n_{eff} is the effective index of the waveguide mode and Λ is the period of the grating. Practically speaking, the possible errors in estimating n_{eff} of the real device include the theoretical modeling of material's refractive index, and the layer thickness and composition control in the growth. In this particular experimental study, we were able to control the Bragg wavelength within ± 10 nm of the designed value. The coupling coefficient considering the first-order grating harmonics can be divided into real and imaginary parts as

$$\kappa_{index} = \Delta n \frac{2\Gamma_g}{\lambda} \sin(\pi D), \quad (2)$$

and

$$\kappa_{loss} = \Delta\alpha \frac{\Gamma_g}{2\pi} \sin(\pi D), \quad (3)$$

where Δn and $\Delta\alpha$ are the index and loss differences between InGaAs and InP, Γ_g is the confinement factor of the waveguide mode in the grating region, and D is the duty factor of the grating defined as the portion of InGaAs in one grating period. One can see that the ratio between the imaginary and real part of the coupling coefficient is a constant in this case and is about 0.32 assuming $\Delta n=0.38$ and $\Delta\alpha=10000\text{cm}^{-1}$. The absorptive InGaAs grating not only induces feedback coupling but also induces loss to the waveguide mode. Assuming in the longitudinal direction, the optical intensity is relatively uniform across one period of the grating, then the optical loss results from the loss grating can be expressed as

$$\alpha_g = \Gamma_g \Delta\alpha D. \quad (4)$$

Although from (2)&(3) the coupling coefficient has its maximum value at $D=0.5$, because it is a Sine function of the duty factor, it decreases only moderately as the duty factor deviates from 50%. However, the grating induced loss α_g changes linearly with the duty factor D . Intuitively, one would expect the optimum duty factor to be less than 50% for a minimum threshold. Indeed, we have found theoretically the minimum threshold gain at a relatively small duty factor of $\sim 25\%$. Since in our case, the InGaAs grating layer is buried in InP, the coupling strength can be controlled precisely by the epi-layer growth. A moderate coupling strength of $\kappa L=1.5$ was designed to achieve a better mode selectivity, higher output efficiency and better linearity. Furthermore, with the anti-phase grating coupling, the designed coupling strength was suggested for reduction of chirping[4].

It was found previously that the photon-generated carriers will saturate the grating absorber and reduce the absorption, which tends to create instability of the device and induces self-pulsation[5,8]. This can be seen in the kinky light-current (L-I) curve and in the broadening of the optical spectrum. An efficient way of eliminating this problem was demonstrated by inversely doping the InGaAs absorber[5]. This creates a built-in electric field and sweeps the photon-generated electron-hole pairs out of the absorption region. In this experimental study, we have fabricated device with n-doped and undoped InGaAs layer, no significant difference has been found between these two cases.

3. Device Fabrication

The epitaxial materials were grown by metal-organic chemical vapor deposition(MOCVD). Starting from the substrate, the first growth grew the bottom InP cladding, the MQW active region, which consists of three 80Å thick, 0.8% compressively strained InGaAsP wells, followed by an InP space layer, the InGaAs grating layer, and stopped after growing an InP grating protection layer. The holographic grating is subsequently formed, followed by the regrowth of the top InP cladding layer and the contact layers consist of InGaAsP and InGaAs. The duty factor was

deliberately reduced to ~25% by overexposure of the thin photoresist grating.

After the regrowth, double-trench 3 μ m ridge waveguides were fabricated on the sample. The ridge etching was done by a combination of reactive ion etching(RIE) and a wet chemical etching using a HCl/H₃PO₄ selective etching solution which stopped on the InGaAs grating layer. Then, the sample was passivated by SiO₂ and a 2 μ m window was then opened on top of the ridge for p-contact using Cr/AuZn/Au. At this point, the sample was thinned down to ~90 μ m and then AuGeNi/Au n-contact metal was evaporated on the back side. Finally, the sample was annealed at 425° C for 15 seconds to alloy the contacts, and the sample was subsequently cleaved into 300 μ m-long-cavity lasers. No facet coatings were applied to the devices.

4. Experimental Results

The device chips were bonded p-side up on a copper heat sink before measurements. Figure 2 are CW L-I curves measured at different temperatures. At 25° C, the threshold current was ~25mA and the maximum slope efficiency was ~0.18W/A. The extents of linearity and maximum power were limited by heating. No kinks were observed in the curve indicating free of self-pulsation.

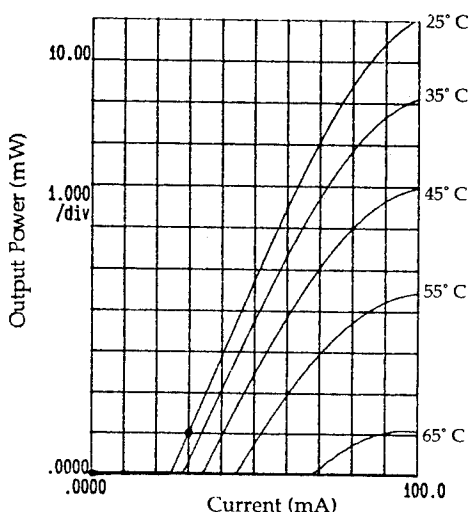


Fig. 2 CW light current characteristics of the complex-coupled DFB lasers

As expected, the single mode yield was quite good even without facet coatings. For most devices,

either with n-doped or undoped InGaAs grating, the emission spectrum stayed in one single mode throughout the measured range up to 10mW with a very high mode selectivity, for example, as illustrated by the spectrum shown in Figure 3 taken at a bias of 2.5I_{th}. In this particular device, the SMSR was as high as 52dB, and the center wavelength was located around 1563nm. The spectral linewidth was measured with a fiber interferometer, the homodyne spectrum is shown in Figure 4, which indicates a 15.8MHz linewidth. This measurement was done by directly coupling the light into the optical fiber without using an isolator.

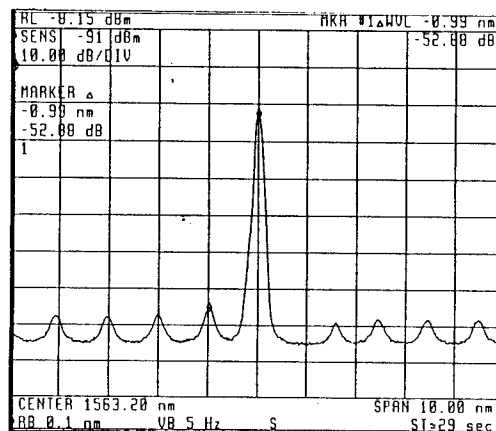


Fig. 3 Lasing spectrum of the DFB laser operating at ~2.5I_{th}, the output power was ~7mW.

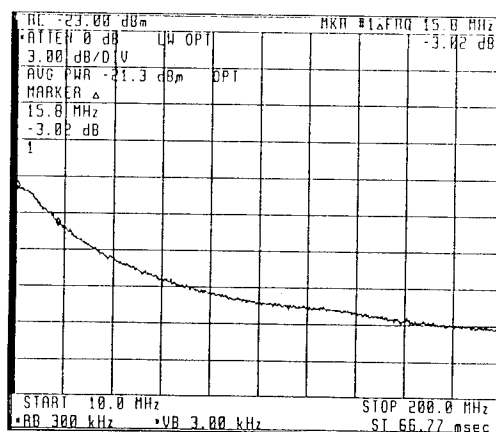


Fig.4 Homodyne spectrum showing a spectral linewidth of 15.8MHz.

Wavelength chirping of the device was measured by modulating the device with a 20mA peak to peak 1Gb/s pseudorandom digital signal. As shown in Figure 5, the spectral width at 20dB down is only 0.23nm. This was measured at a current injection level of ~60mA, which was about two times the threshold current, and at this point the device gave out ~5mW of power.

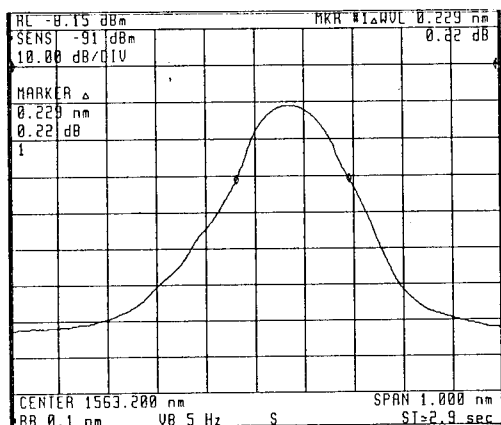


Fig.5 Lasing spectrum under 1Gb/s pseudorandom digital modulation showing a low chirp of 0.23nm.

5. Conclusions

We have successfully fabricated complex-coupled DFB ridge lasers with a relatively simple fabrication process. By utilizing the loss grating coupling, high single mode yield was obtained even without facet coatings. Self-pulsation phenomenon has been completely eliminated by using n-doped or undoped absorptive grating, with a reduced grating duty factor of ~25%. Typical device characteristics having a threshold current of around 25mA, and a slope efficiency of 0.18W/A have been demonstrated with a stable single mode emission indicated by a 52dB SMSR, a low chirp of 0.23nm and a spectral linewidth of 15.8MHz.

Acknowledgements

We would like to express our sincere appreciation to Dr. C. J. Hwang for his helpful comments on semiconductor laser fabrication, and

Dr. C. E. Zah at Bell Communication Research for his discussion on spectral linewidth measurement.

References

- [1] Y. Luo, Y. Nakano, K. Tada, T. Inoue, H. Hosomatsu, and H. Iwaoka, "Fabrication and characteristics of gain-coupled distributed feedback semiconductor lasers with a corrugated active layer," *IEEE J. of Quantum Electron.*, vol. 27, pp1724, June 1991.
- [2] Y. Nakano, Y. Luo, and K. Tada, "Facet reflection independent, single longitudinal mode oscillation in a GaAlAs/GaAs distributed feedback laser equipped with a gain-coupling mechanism," *Appl. Phys. Lett.*, 55 (16) , pp1606, Oct. 1989.
- [3] Y. Nakano, Y. Deguchi, K. Ikeda, Y. Luo, and K. Tada, "Resistance to external optical feedback in a gain-coupled semiconductor DFB laser," *12th IEEE International Semiconductor Laser Conference*, pp72, 1990.
- [4] K. Kudo, J. I. Shim, K. Komori, and S. Arai, "Reduction of effective linewidth enhancement factor α_{eff} of DFB lasers with complex coupling coefficients," *IEEE Photon. Tech. Lett.*, vol. 4, pp531, June 1992.
- [5] Y. Luo, H. -L. Cao, M. Dobashi, H. Hosomatsu, Y. Nakano, and K. Tada, "Gain-coupled distributed feedback semiconductor lasers with an absorptive conduction-type inverted grating," *IEEE Photon. Tech. Lett.*, vol. 4, pp692, July 1992.
- [6] W. X. Zou, Z. M. Chuang, K. K. Law, N. Dagli, L. A. Coldren, and J. L. Merz, "Analysis and optimization of graded-index separate-confinement-heterostructure waveguides for quantum well lasers," *J. Appl. Phys.*, vol. 69 (5), pp2857, March 1991.
- [7] W. Streifer, D. R. Scifres, and R. D. Burnham, "Coupled wave analysis of DFB and DBR lasers," *IEEE J. of Quantum Electron.*, QE-13, pp134, 1977.
- [8] C. Y. Chang, W. Lin, M. C. Wang, T. T. Shi, J. Y. Su, S. C. Ko, Z. M. Chuang, and Y. K. Tu, "1.55 μ m absorptive-grating complex-coupled distributed feedback lasers with high single-longitudinal-mode yield," *International Electron Devices and Material Symposium*, Hsinchu, Taiwan, paper 10-7-22, 1994.

1.3 μ m GaInAsP/InP Square Buried Heterostructure Vertical Cavity Surface Emitting Laser Grown by All MOCVD

S.Uchiyama and S.Kashiwa
RWCP Optoelectronics Furukawa Laboratory***
 Yokohama, Japan

Abstract

In order to improve a buried heterostructure (BH) for GaInAsP/InP vertical cavity surface emitting laser (VCSEL) regrown by MOCVD, we have introduced a square mesa top pattern, of which side was at angle of 45° to <011> direction. A 1.3 μ m GaInAsP/InP square buried heterostructure (SBH) VCSEL with this mesa structure has been demonstrated and low threshold CW oscillation (threshold current $I_{th}=0.45$ mA) at 77K and low threshold room temperature pulsed oscillation ($I_{th}=12$ mA) were obtained.

Introduction


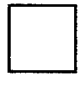




1.3 μ m GaInAsP/InP vertical cavity surface emitting laser (VCSEL) [1]-[6] has many advantages such as low threshold current, dynamic single mode operation, high coupling efficiency to fiber because of narrow circular beam, wafer level testing, two dimensional laser array and a low voltage operation. It is suitable for optical parallel communication and optical inter-connection. To realize its low threshold current and room temperature CW oscillation, buried heterostructure (BH) may be one of the best structure. It was reported that a BH VCSEL with circular mesa by two step liquid phase epitaxial (LPE) growth had the problem of the relatively defective heterointerface that was recognized as pinholes around the circular mesa[4]. This seems to be caused by the (111)-A plane which is likely to appear around the mesa at etching and at meltback in the first regrowth. To overcome this problem, single step maskless planar buried heterostructure (PBH) LPE regrowth was introduced and a near room temperature (14°C) CW oscillation was obtained[5]. On the other hand, It is difficult to apply maskless PBH regrowth to metalorganic chemical vapor deposition (MOCVD), that has some advantages such as a large area epitaxial growth, an excellent uniformity of layer thickness, etc.

In this study, we investigate mesa structure for BH regrown by MOCVD and demonstrate a 1.3 μ m GaInAsP/InP BH VCSEL grown by All MOCVD. We also present low threshold lasing characteristics.

Investigation of mesa structure

In order to get an excellent BH wafer for 1.3 μ m GaInAsP/InP VCSEL, we examined condition of regrowth

Table 1 Mask patterns and photographs of wafer surfaces after regrowth for 3 types of mesas.

Mask Patterns			
Wafer Surfaces after 3rd growth			

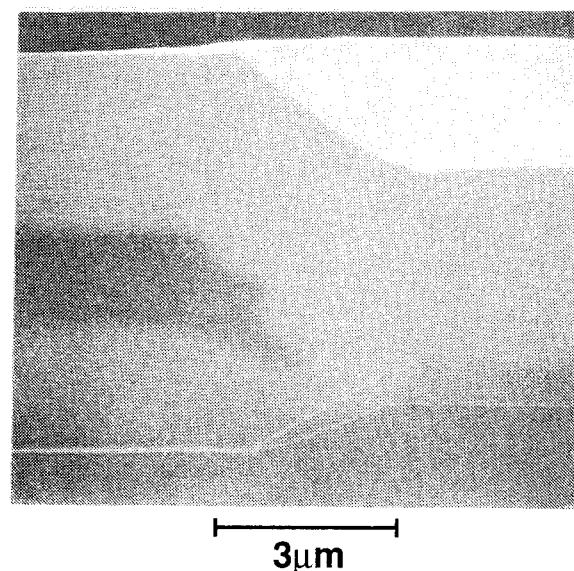


Fig.1 Cross-section of regrown wafer with square mesa.

*RWCP:Real World Computing Partnership

** c/o Yokohama R&D Laboratories,
 The Furukawa Electric Co., Ltd.

around mesas with 3 types of mesa top patterns such as a circular, a square 1 of which side is in $\langle 011 \rangle$ direction, and a square 2 of which side is at angle of 45° to $\langle 011 \rangle$ direction as shown in Table 1. We prepare a wafer for VCSEL grown on (100) n-InP by MOCVD and it is as following layer structure: 0.1 μm n-InGaAs etch-stop layer, 2.0 μm n-InP, 0.65 μm GaInAsP active layer, 0.6 μm p-InP cladding layer and 0.1 μm GaInAsP layer. After SiN_x deposition on the wafer, 3 types of mask patterns stated above are formed. We chemically etch the wafer with KKI-121 etchant ($\text{HCl}:\text{CH}_3\text{COOH}:\text{H}_2\text{O}_2=1:2:1$) to form mesas with 2.5 μm in height. The blocking layers (p-InP and n-InP) are regrown by MOCVD. After removing the SiN_x mask and GaInAsP layer, 1 μm p-InP cladding layer and 0.5 μm $\text{p}^+\text{-InGaAs}$ cap layer are grown by 3rd MOCVD. Photographs of wafer surfaces around mesas are shown in Table 1. It appears that false regrowth in part around circular and square 1 mesas. They are caused by (111) A plane that appears around mesas at etching. On the other hand, regrowing surface around square 2 mesa is smooth and cross-sectional view is also very good as shown in Fig. 1. Because (111) A plane dose not appear around this mesa. Then, we introduce this mesa to VCSEL.

GaInAsP/InP SBH VCSEL

Figure 2 shows our GaInAsP/InP square buried heterostructure (SBH) VCSEL structure. The grown wafer is processed into a short cavity device structure as shown in Fig.2. To get a high reflectivity, we use Si/SiO₂ or Si/Al₂O₃ stacked layer as p-side mirror and Si/SiO₂ as n-side mirror. The sequence of laser processing is as follows. After 3rd MOCVD growth, a AuZn is evaporated

on p^+ -cap layer and to eliminate the large free carrier absorption loss, p-electrode and cap layer just above the active region are removed. A Si/SiO₂ or a Si/Al₂O₃ stacked mirror is deposited by electron beam evaporation method with optical thickness monitor. The refractivity of each mirror is $\sim 99\%$. After a Au are evaporated on the top surface, the substrate is polished down to $\sim 100\mu\text{m}$ and a AuGeNi is evaporated on the back surface. After alloying, a SiN_x is deposited and windows are opened to etch off the substrate. The AuGeNi electrode, InP substrate and InGaAs etch-stop layer are etched off by selective etchant. An Si/SiO₂ stacked mirror is evaporated on the back surface. The laser chips are cleaved and tested without soldering to heat sink.

Characteristics

Figure 3 shows the light output versus current (L-I) characteristics of a VCSEL with Si/SiO₂ mirror for p-side under CW condition at 77K. Low threshold oscillation is obtained. The minimum threshold current is 0.45 mA, which is very close to the best reported value (0.42mA) for 1.3 μm GaInAsP/InP VCSEL at this temperature [5].

The room temperature low threshold pulsed oscillation is also obtained for another VCSEL with Si/Al₂O₃ mirror for p-side. Figure 4 and 5 show its L-I characteristics and lasing spectrum respectively, at room temperature under pulsed conditions (300ns, 2kHz). The minimum threshold is 12mA for a device with 8 μm x 8 μm active region. The threshold current density is about 18kA/cm². Single longitudinal oscillation is also obtained for this device and wavelength is 1.304 μm .

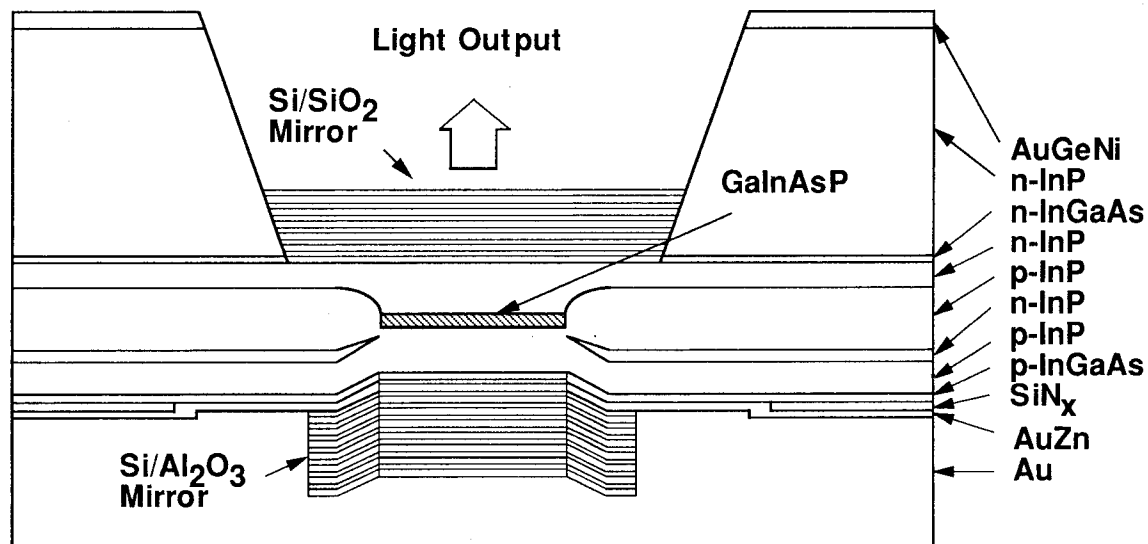


Fig.2 Schematic diagram of 1.3 μm GaInAsP/InP SBH VCSEL

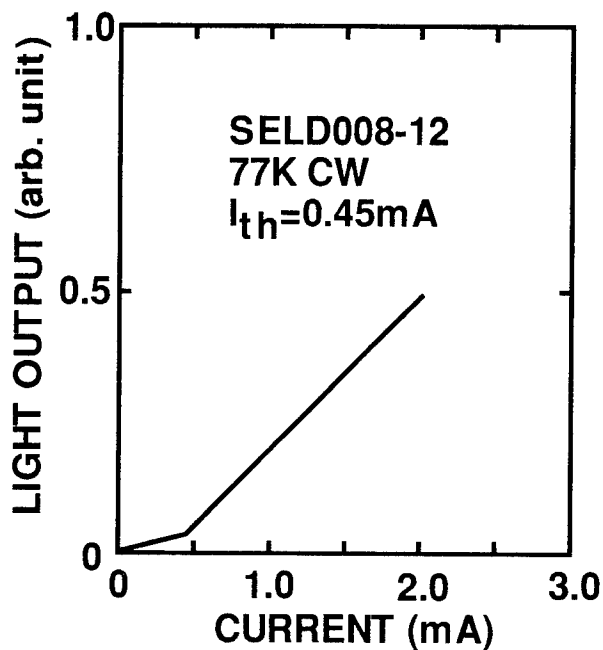


Fig.3 L-I characteristics at 77K.

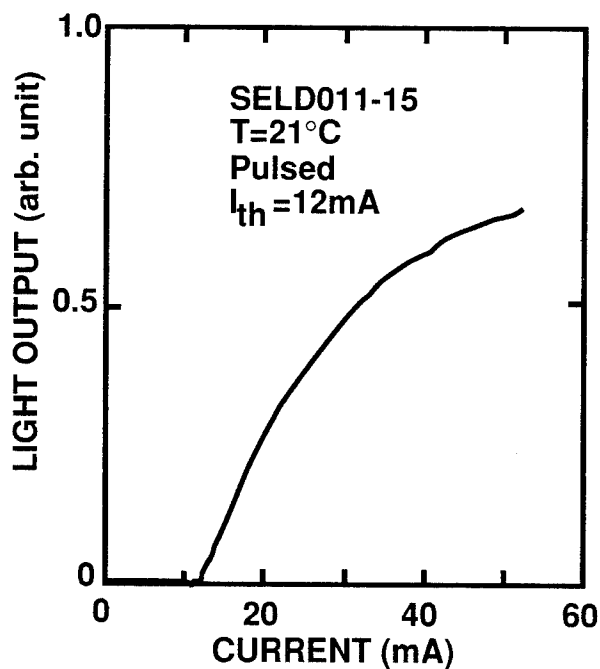


Fig.3 L-I characteristics at 77K.

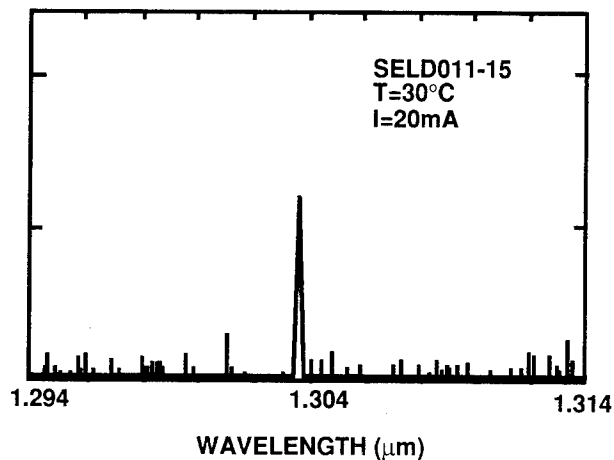


Fig.5 Lasing spectrum at room temperature. The resolution is 0.2nm.

Summary

In summary, we have investigated a mesa structure for 1.3μm GaInAsP/InP BH VCSEL regrown by MOCVD and have found out that a square mesa top pattern, of which side is at angle of 45° to <011> direction, is suitable for BH structure. We have demonstrated a 1.3μm GaInAsP/InP SBH VCSEL with this mesa structure and improved device performances. The low threshold CW oscillation at 77K is obtained. The minimum threshold current is 0.45 mA, which is very close to the best reported value (0.42mA) for 1.3μm GaInAsP/InP VCSEL at this temperature. The low threshold room temperature pulsed oscillation was also obtained and its minimum threshold is 12mA. By optimizing materials and an evaporation condition for high reflectivity mirror and introducing a high gain active layer structure such as multi-quantum well (MQW), room temperature CW oscillation can be expected.

Acknowledgment

The authors would like to thank Prof. K.Iga and T.Sakaguchi of Tokyo Institute of Technology for the measurement of lasing spectra and N.Iwai and N.Yamanaka of the Furukawa Electric Co. Ltd., for their experiment support.

References

- [1] H.Soda, K.Iga, C.Kitahara and Y.Suematsu, "GaInAsP/InP surface emitting injection lasers", Jpn. J. Appl. Phys., 18, p.2329, 1979.
- [2] S.Uchiyama and K.Iga, "Consideration on threshold current density of GaInAsP/InP surface emitting laser with current confining structure", IEEE J. Quantum Electron., QE-22, p.302, 1986.
- [3] H.Wada, D.I.Babic, D.L.Crawford, T.E.Reynolds, J.J.Dudley, J.E. Bowers, E.L.Hu, J.L.Merz, B.I.Miller, U.Koren, U. and M.G.Young, "Low-threshold, high-temperature pulsed operation of InGaAsP/InP vertical cavity surface emitting lasers," IEEE Trans. Photon. Technol. Lett., 3, p.977, 1991.
- [4] T.Baba, K.Matsuoka, F.Koyama and K.Iga "Low threshold 1.3 μ m GaInAsP/InP flat-surface circular buried heterostructure surface emitting laser", in Proc. OEC'92, p.160, 1992.
- [5] T.Baba, Y.Yogo, K.Suzuki, F.Koyama and K.Iga, "Near room temperature continuous wave lasing characteristics of GaInAsP/InP surface emitting laser", Electron. Lett., 29, p.913, 1993.
- [6] J.J.Dudley, D.I.Babic, R.Mirin, L.Yang, B.I.Miller, R.J.Ram, T.reynolds, E.L.Hu and J.E.Bowers, "Low threshold wafer fused long wavelength vertical cavity lasers", Appl. Phys. Lett., 64, p.1463, 1994.

1.5 μm Sub-picosecond Pulse Generation from an InGaAsP DFB Diode Laser Synchronized with a Mode-Locked Ti: Sapphire Laser

H. Takeshita, M. Tsuchiya and T. Kamiya

Department of Electronic Engineering, University of Tokyo
7-3-1 Hongo, Tokyo 113, Japan

Abstract

We report the first successful demonstration of 1.5 μm sub-picosecond pulse generation from a gain-switched InGaAsP distributed feedback laser diode *synchronized* with a mode locked Ti: sapphire laser. Note that the wavelength of 1.5 μm is indispensable in the fiber optic telecommunication system while a mode-locked Ti: sapphire laser can generate sub-picosecond optical pulses at much shorter wavelength. Such *dual wavelength* feature is very attractive and would provide new tools for the pump-and-probe characterization methods, including the electro-optic sampling, of high speed optoelectronic devices.

Introduction

It is quite interesting and attractive to synchronize two sub-picosecond laser pulse sources operating at two different wavelengths if one is set at a wavelength where photo-carriers can be generated in a material and the other at a wavelength where the material is transparent. Such a *dual wavelength* sub-picosecond pulse source is expected to provide a unique tool for the high speed pump-and-probe characterization methods such as electro-optic sampling [1, 2]. Furthermore, a new investigation tool will be brought to very fast optoelectronic devices and materials in the fiber optic telecommunication systems if sub-picosecond pulses are available around 1.3 or 1.5 μm in such a dual wavelength scheme. We report here a successful demonstration of synchronous generation of sub-picosecond optical pulses at 1.55 and 0.74 μm .

In this work, we combined two sub-picosecond lasers, a mode-locked Ti: sapphire laser and a distributed feed back (DFB) diode laser, utilizing the gain-switching operation mode of the latter. The former laser is a well known sub-picosecond pulse source which is tunable in a wide wavelength range from 700 to 1000 nm. The latter is a stable and compact light source, and sub-picosecond optical pulses in the 1.5 μm range are available if one uses InP-based materials like InGaAsP, the gain-switching operation mode, and the fiber optic compression scheme [3].

Note here that the gain-switching mode for a semiconductor laser diode (LD) is advantageous to other pulse generation methods because the timing control of pulse generation is possible through an external supply of electrical pulses. Actually, the synchronization mentioned in this

paper is enabled only with the gain switching technique.

On the other hand, the two wavelengths in this scheme can be independent of each other although the wavelength of a DFB LD is almost fixed. Such feature is quite different from that in the frequency conversion methods, another dual wavelength sub-picosecond optical pulse sources, in which the wavelengths are strictly related to each other.

Connection of Two Lasers

Our method to synchronize a DFB laser to a Ti: sapphire laser is described in the following. Figure 1 shows a schematic illustration of the experimental setup. The mode-locked Ti: sapphire laser is a master pulse source. Hence, the repetition frequency of the system is fixed around 75 MHz. A part of the Ti: sapphire laser pulse is detected by a photo diode (PD). In Fig. 2 (a), electrical wave form measured with a digital oscilloscope at the output of PD is shown. Although the temporal width of the Ti: sapphire laser pulse is as small as 180 femtosecond, the wave form of the electrical pulse is limited by the bandwidth of PD (5 GHz). In addition, the measured wave form was broadened further because of a limited bandwidth of the digital oscilloscope (500 MHz).

Height of the electrical signal thus measured is around 110 mV which corresponds to current of a few mA in a 50 Ω transmission cable. Even though the band width limitation of the digital oscilloscope is taken into account, that value is too small because in order to drive the DFB diode laser in the gain-switching mode one needs current pulses much higher than the threshold current of the laser diode (8 mA) and narrower than a few hundreds picosecond. Therefore,

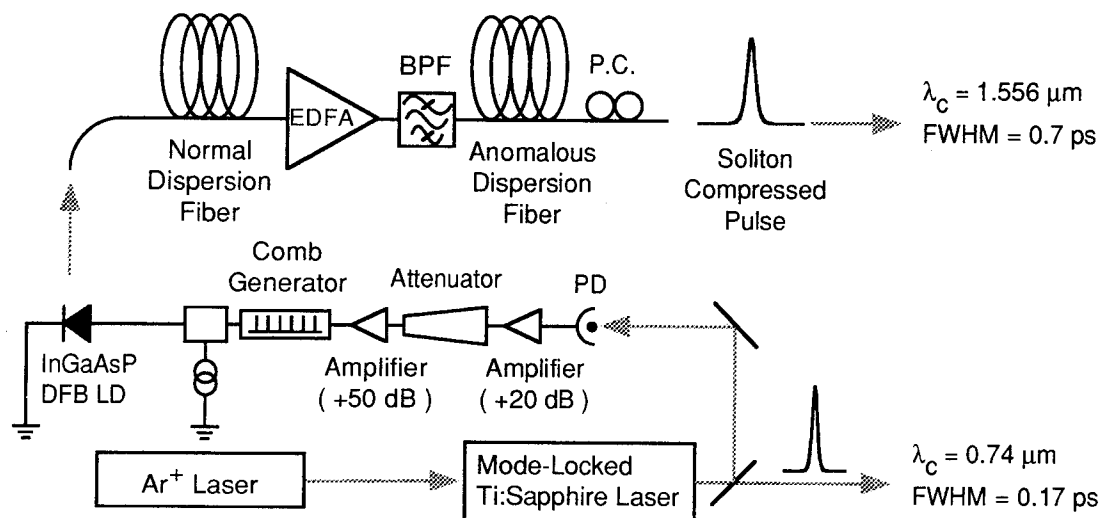


Fig. 1. Setup of dual wavelength sub-picosecond pulse generation system consisting of a mode locked Ti: sapphire, a gain switched InGaAsP DFB laser diode and fiber optics for pulse compression.

electrical amplification and compression of the wave form are required. In addition, a fine adjustment of the current pulse amplitude is necessary so that the chirping characteristics of gain-switched optical pulse are set optimum. Otherwise, the quality of optical pulse shape at the final stage, i.e. after the fiber optic compression, will be degraded drastically [4].

In the experiment, therefore, we inserted two electrical amplifiers, a variable attenuator, and

a comb generator between PD and DFB LD. First, electrical signal generated in PD was boosted up with an electrical amplifier having a gain of 20 dB and a bandwidth of 250 MHz. Its output signal was adjusted using a variable attenuator. Then, the signal was amplified again with another amplifier having a 50 dB gain and a 110 MHz bandwidth. Because of the narrow bandwidth of the second amplifier, the output wave form got similar to a sinusoidal wave as shown in Fig. 2 (b). The electrical wave was then fed to a comb generator, and electrical pulses of around 130 picosecond were supplied to LD, whose output wave form is shown by a solid line

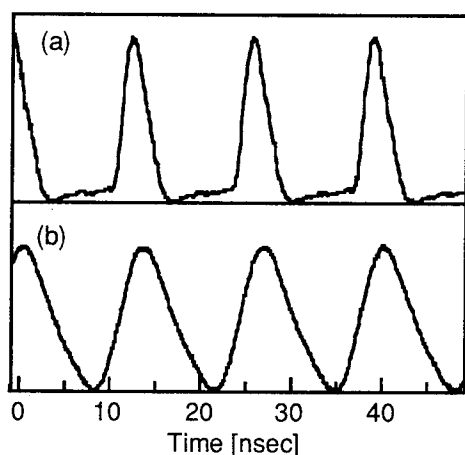


Fig. 2. Electrical wave forms measured with a digital oscilloscope at the output of PD (a), and at the output of the second electric amplifier (b), respectively. Band width of the digital oscilloscope is 500 MHz.

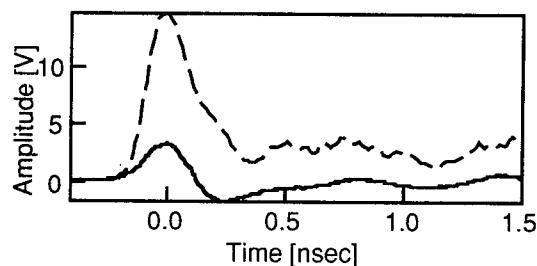


Fig. 3. Wave forms of electrical pulses supplied to the InGaAsP DFB laser diode in the dual wavelength sub-picosecond system (solid line) and in the conventional frequency synthesizer-driver case (dashed line), respectively. In both case, optical pulses are in the sub-picosecond range.

in Fig. 3. Here, the comb generator is a commercially available one which is tuned for an operation at 100 MHz repetition rate.

Optical Pulse Generation & Compression

Such electrical pulse formation enabled the gain-switching operation and resulted in generation of optical pulse with a few tens picosecond width, which is a typical value in a usual frequency synthesizer-driven gain-switching operation.

Such optical pulses were compressed into the sub-picosecond range by a fiber optic compression system, which consists of a normal dispersion fiber (-18.7 picosecond/km/nm) of 1 km, an Erbium doped fiber amplifier (30 dB), an optical band pass filter with full width at half maximum (FWHM) of 3 nm, and an anomalous dispersion fiber (6.96 picosecond/km/nm). A diagram of the compression system is shown in Fig. 1.

By adjusting the attenuator, the bias current of LD, the center wavelength of the band pass filter, and the length of the anomalous dispersion fiber, a fairly good pulse shape in the sub-picosecond range was detected by a autocorrelator. Here, we found out that the bias current should be zero and the length of anomalous dispersion fibers should be 800 m in order to obtain the best result.

For comparison, autocorrelation traces of Ti:sapphire laser pulses (a), DFB diode laser pulses at the end of the normal dispersion fiber (b), and those after the compression by the higher-order-soliton effect in the anomaly dispersion fiber (c), respectively, are plotted in Figs. 4. FWHM of the pulse at the final stage (c) is 0.7 picosecond if one assume a hyperbolic secant as a pulse shape. Note that the wave form in Fig. 4 (c) is practically an impulse response of the whole system including the non-linear optical and electrical elements.

Discussion and Summary

Note that jitters in the system are important issues to be discussed. One can speculate that possible origins of the jitters are (i) the passive mode-locking operation of the Ti:sapphire laser [5], (ii) the electronics used for the connection of two lasers, (iii) the gain-switching operation of DFB LD [6], and (iv) the fiber optics in the compression scheme.

At present stage, we believe that the jitters induced in the electronics between PD and LD are largest since the band widths and the signal-to-noise ratio were not large enough in the

experiment. In Fig. 3, we plotted by a dashed line a wave form generated with a frequency synthesizer set at 75 MHz, an electrical amplifier, and the comb generator. With those electrical pulses fairly good wave form of optical pulse was also achieved in the DFB LD - optical fiber system. However, it is quite different from the wave form of the current pulse measured in the dual wavelength pulse source. Those results indicate that there are large room to be improved in the electronics used here.

In summary, we demonstrated that a gain-switched DFB LD can be synchronized with another pulse laser, and obtained synchronized sub-picosecond optical pulses with temporal widths of 0.7 and 0.2 picosecond at the wavelengths of 1.55 and 0.74 μm , respectively. Although improvements of the system

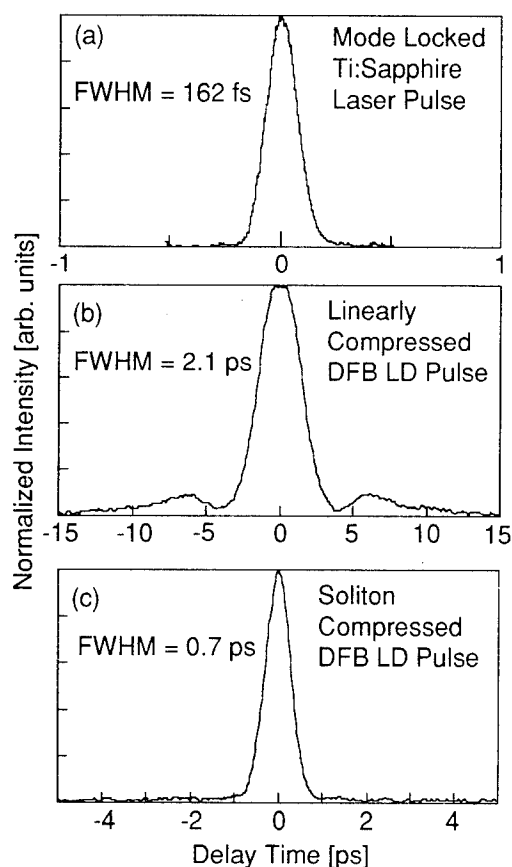


Fig. 4. Autocorrelation trace of mode locked Ti:sapphire laser pulse (a), and those of a pulse from an InGaAsP DFB laser diode at the output of normal dispersion fiber (b) and at the final stage (c).

configuration is necessary, the dual wavelength sub-picosecond pulse source thus obtained is now being applied to an electro-optic sampling system.

Acknowledgments

The authors thank Dr. Y. Ogawa (Oki Electric) for the supply of laser diodes and Mr. H. Takahashi (Hamamatsu Photonics) for his valuable suggestions.

References

- [1] J. A. Valdmanis: *Electron. Lett.* **23**, 1308-1310 (1987).
- [2] R. Sahara, H. Takeshita, K. Miwa, M. Tsuchiya and T. Kamiya: *IEEE J. Quantum Electron.* **31**, 120-125 (1995).
- [3] J. T. Ong, R. Takahashi, M. Tsuchiya, S. H. Wong, R. Sahara, Y. Ogawa and T. Kamiya: *IEEE J. Quantum Electron.* **29**, 1701-1707 (1993).
- [4] H. Takeshita, M. Tsuchiya and T. Kamiya: to be presented in the Sixth Topical Meeting on Ultrafast Electronics and Optoelectronics (Danapoint, Ca, 1995).
- [5] K. S. Giboney, S. T. Allen, J. W. Rodwell and J. E. Bwers: *IEEE Photon. Technol. Lett.* **PTL-6**, 1353-1355 (1994).
- [6] M. Jinno: *IEEE Photon. Technol. Lett.* **PTL-5**, 1141-1143 (1993).

High Power InGaAsP/InP 1.625 μm Strained Quantum Well Lasers

Tsutomu Munakata, Yasumasa Kashima, Shigehiro Kusumoto,
Akio Matoba, and Hiroshi Takano

Optical Device Division, OKI Electric Industry Co., Ltd.

Abstract

A high optical power of over 100 mW has been successfully coupled into a single-mode fiber using 1.625 μm strained multiple quantum well (MQW) lasers. This record coupled power is achieved as a result of the optimization of separated confinement heterostructure (SCH) layer thickness.

Introduction

Development of Er^{3+} -doped fiber amplifiers (EDFAs) has led to the extension of the nonrepeated transmission distance. (1-2) Fiber transfer-and-test systems for the longer distance has become necessary. Recently, high power 1.625 μm laser is required as a light source for new OTDRs (3-4), because its light does not disrupt transmission allowing testing to take place during normal optical fiber usage. The light at the wavelength around 1.625 μm is more sensitive to the bending loss and the loss caused by hydrogen than shorter wavelength. There have been many reports on InGaAs/InGaAsP strained multiple quantum well (MQW) lasers emitting in the infra-red (1.5~2.0 μm) region. (5-8) However, coupled power into a single-mode fiber was too low for application for OTDRs. In designing high power MQW lasers, the optical confinement is an important factor. We optimized thickness of separated confinement heterostructure (SCH) layers and achieved coupled power as high as 100 mW into a single-mode fiber.

Structures and fabrications

A schematic diagram of the strained MQW structure is shown in Fig. 1. The MQW structure consists of five 6-nm-thick $\text{In}_{0.62}\text{Ga}_{0.38}\text{As}$ strained quantum wells separated by 10-nm-thick barrier layers of lattice matched InGaAsP

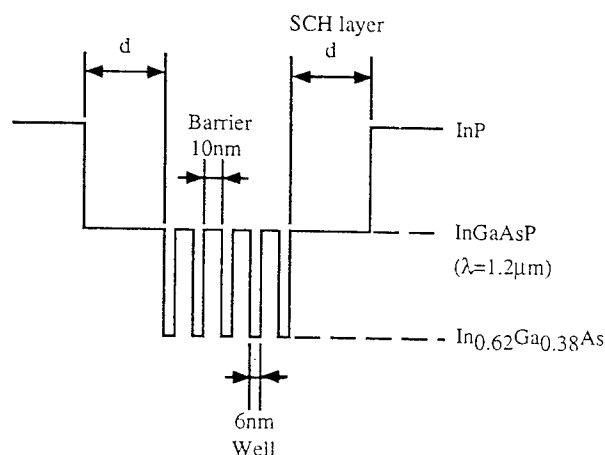


Fig. 1. A schematic diagram of strained MQW structure.

($\lambda=1.2 \mu\text{m}$). In order to investigate the relationship between the SCH layer thickness and the maximum output power, four samples with SCH layer thickness of 15 nm, 30 nm, 45 nm and 60 nm were fabricated. The MQW lasers were fabricated on n-InP substrates using low-pressure metalorganic vapor-phase epitaxy (MOVPE) system. Trimethylindium (TMIn) and triethylgallium (TEGa) were used as sources for group III elements, and phosphine (PH_3) and arsine (AsH_3) were used for group V. The growth temperature and reactor pressure were 610 $^\circ\text{C}$ and 55 torr, respectively. In the first growth step, an n-InP buffer layer ($n=5 \times 10^{17} \text{ cm}^{-3}$), the undoped-MQW layers, a p-InP cladding layer ($p=1 \times 10^{18} \text{ cm}^{-3}$) and a p-InGaAsP cap layer ($p=1 \times 10^{18} \text{ cm}^{-3}$) were successively grown. After formation

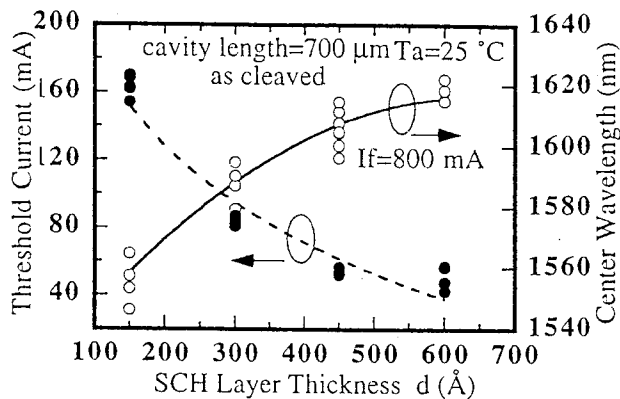


Fig. 2. Dependence of threshold current and center wavelength on the SCH layer thickness.

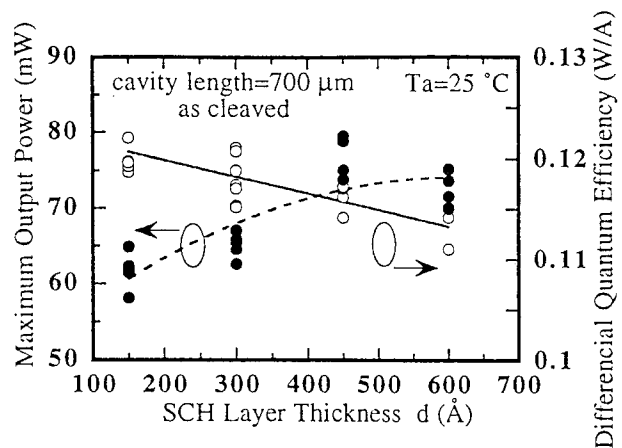


Fig. 3. Dependence of a maximum output power and differential quantum efficiency on the SCH layer thickness.

of oxide stripes along the $\langle 011 \rangle$ direction, 1.7–2.0 μm -wide mesa structures were formed using $\text{HBr-H}_2\text{O}_2\text{-H}_2\text{O}$ solution. In the second MOVPE growth, a buried heterostructure (BH) was fabricated by growing a p-InP ($p=5 \times 10^{17} \text{ cm}^{-3}$) and an n-InP ($n=5 \times 10^{17} \text{ cm}^{-3}$) current blocking layers. The BH is thought to be suitable for achieving a high coupling efficiency into a single-mode fiber because of its small spot size. After the oxide masks and the p-InGaAsP cap layers were etched off, a p-InP cladding layer ($p=1 \times 10^{18} \text{ cm}^{-3}$) and a p-InGaAs contact layer ($p=3 \times 10^{18} \text{ cm}^{-3}$) were grown in the third MOVPE growth. The cavity length of the MQW lasers was 700 μm . A 95 % high-reflective (HR) coating and a 5 % anti-reflective (AR) coating were used on the rear and the front facet, respectively. The laser chips were mounted with junction-down configuration on silicon carbide (SiC) heatsinks.

Results

Optimization of SCH Layer Thickness

Figure 2 shows the dependence of threshold current and the center wavelength on the SCH layer thickness, for the devices with uncoated facets. The increase in the SCH thickness resulted in longer wavelength and lower threshold current. Figure 3 shows the dependence of maximum output power and differential quantum efficiency on the SCH thickness. The differential quantum efficiency decreased as the SCH thickness increased. The maximum output power from the front facet was obtained when the SCH layer thickness was 45 nm. Figure 4 shows dependence of coupling efficiency and the far-field half width perpendicular to the junction on the SCH thickness. The lasers coupled into the fiber using a system of two discrete lenses. The far-field half width perpendicular to the junction increased as the SCH thickness increased. The coupling efficiency remained at about 70 % in spite of changing the SCH thickness (15–60 nm).

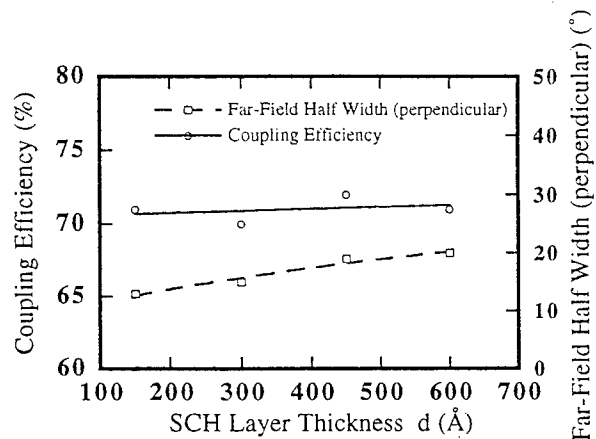


Fig. 4. Dependence of coupling efficiency and far-field half width perpendicular to the junction.

To obtain high coupled power into a single-mode fiber with relatively low driving current, it is necessary for the threshold current to be low, the differential quantum efficiency and coupling efficiency to be high, and gain saturation to be kept at a minimum. The increase in the SCH thickness is believed to result in larger optical confinement factor and absorption loss which in turn result in a decrease in threshold current and differential quantum efficiency. The increase in the SCH thickness results in longer wavelength reducing the band filling effect which in turn minimizes the gain saturation. Coupling efficiency remained constant about 70 % in spite of changing the SCH thickness (15–60 nm). The maximum output power from the front facet is determined by the threshold current, the differential quantum efficiency and the gain saturation. The optimum SCH thickness of 45 nm was determined by this relationship between the SCH thickness and the maximum output power from the front facet.

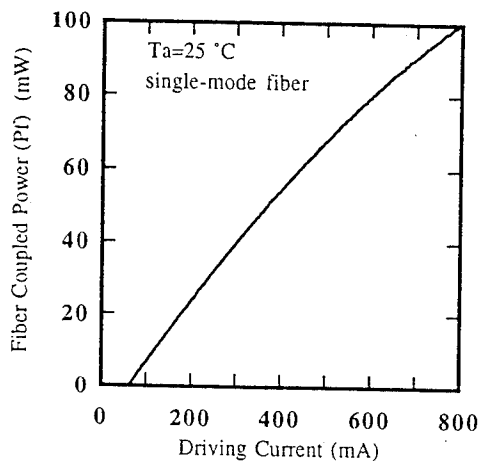


Fig. 5. Coupled power into a single-mode fiber against driving current under pulsed operation.

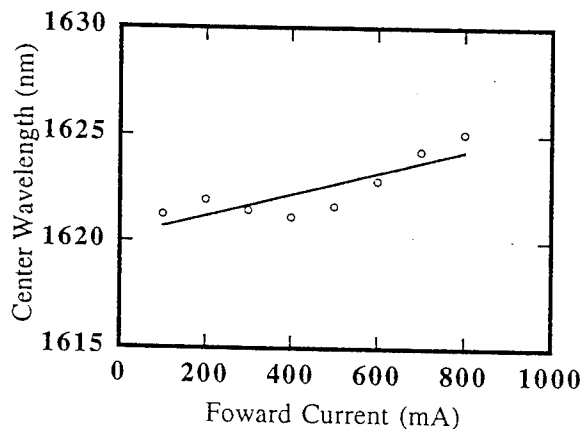


Fig. 6. Center Wavelength vs. Driving Current.

Laser Characteristics

Figure 5 shows the coupled power into a single-mode fiber as a function of driving current under pulsed excitation ($10 \mu\text{s}$ - 1 kHz) at 25°C . The threshold current was 60 mA and the differential quantum efficiency was 0.16 W/A . The coupled power into a single-mode fiber reached 100 mW at a driving current of 800 mA . Figure 6 shows the driving current versus the center wavelength under pulsed operation at 25°C . The center wavelength and spectral half-width were $1.625 \mu\text{m}$ and 7.3 nm at a driving current of 800 mA as shown in Fig. 7. Far-field patterns at the same excitation level are shown in Fig. 8. The full width at half the maximum parallel and perpendicular to the junction were 19° and 27° , respectively. Because of this narrow beam divergence, high coupled power over 100 mW was obtained.

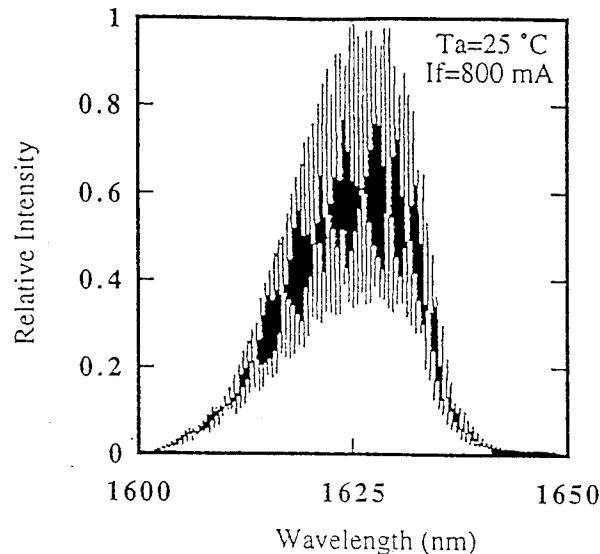


Fig. 7. Emission Spectrum.

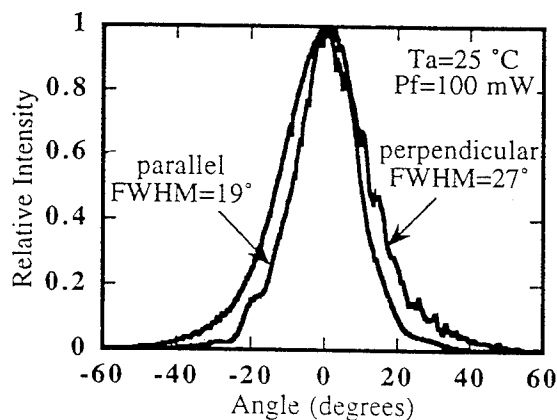


Fig. 8. The far-field patterns at coupled power of 100 mW .

Conclusion

We investigated the relationship between the maximum output power and the separated confinement heterostructure (SCH) layer thickness in $1.625 \mu\text{m}$ strained multiple quantum well (MQW) lasers. The optimum SCH layer thickness of 45 nm was determined by the relationship between the SCH thickness and the maximum output power. When the SCH layers was 45 nm , optical power of 100 mW was coupled into a single-mode fiber at a driving current of 800 mA under pulsed operation at 25°C . To our

knowledge, this is the highest coupled power ever reported in lasing wavelengths longer than 1.6 μm .

References

- 1 K.Aida et al., in Proc. 15th Euro. Conf. Opt. Commun. (Gothenburg), 1989, Paper 7
- 2 N. Edagawa et al., in Proc. 15th Euro. Conf. Opt. Commun. (Gothenburg), 1989, paper 8
- 3 Y. Koyamada, Norihisa Ohta and Nobuo Tomita, "Basic Concept of Fiber Optic Subscriber Loop Operation Systems, " ICC Proceeding (Institute of Electrical and Electronics Engineering, New York), 1540-1544 (1990)
- 4 Shinichi Aoyagi, Eiji Maekawa and Katsuaki Kikuchi, "FITL Upgrading Strategy For B-ISDN, " ICC Proceeding (Institute Electrical and Electronics Engineering), 1290-1294 (1993)
- 5 D. P. Bour, R. U. Martinelli, R. E. Enstrom, T. R. Stewart, N. G. DiGiuseppe, F. Z. Hawrylo and D. B. Cooper, "1.5< λ <1.7 μm strained multiquantum well InGaAs/InGaAsP diode lasers, " Electron. Lett., **28**, 37-39 (1992).
- 6 J. S. Major Jr., J. S. Osinski and D. F. Welch, "8.5 W CW 2.0 μm InGaAsP laser diodes, " Electron. Lett., **29**, 2112-2113 (1993).
- 7 S. Forouhar, A. Larsson, A. Ksendzov, R. J. Lang, N. Tothill and M. D. Scott, "Room-temperature operation of MOCVD-grown GaInAs/InP strained-layer multiquantum well lasers in 1.8 μm range, " Electron. Lett., **28**, 945-947 (1992).
- 8 Mitsuo Yamamoto, Mamoru Oishi, Hiromi Sudo, Junichi Nakano and Nobuyori Tsuzuki, "Strained-layer InGaAs/InGaAsP MQW structures and their application to 1.67 μm lasers grown by metalorganic vapor phase epitaxy, " J. Cryst. Growth, **107**, 796-801 (1991).

Tensile Strained MQW Semiconductor Optical Amplifier

ThP35

Yuko Yamaguchi, Atsushi Yamada, Toshinobu Otsubo, Katsunori Shinone
Koichiro Miyagi and Akira Taniguchi

Reserch Laboratory, Anritsu Corp.
1800 Onna, Atsugi-shi, Kanagawa, 243 Japan
TEL:+81-462-23-1111, FAX:+81-462-23-1600

Introduction

To realize an ultrahigh speed optical transmission system, nonlinear phenomena such as optical DEMUX with four-wave mixing^{(1),(2)} and dispersion compensation⁽³⁾ have recently been investigated. If an optical fiber is employed as a nonlinear device, the fiber needs to be very long for high efficiency because of the very small nonlinear effect of fiber. This causes the system to become unstable. On the other hand, a semiconductor optical amplifier (SOA) is expected to be useful as a nonlinear device, because it is compact and highly efficient as well as being available as a switching device. However, the SOAs so far have been sensitive to polarization and therefore inconvenient in practical use. Under these circumstances we have developed polarization insensitive SOAs using tensile strained quantum wells. In this summary, we report on the characteristics of the nondegenerate four-wave mixing (NDFWM) with these SOAs.

Characteristics of SOA

Structure

The base wafer of the polarization insensitive SOA was grown by LP-MOVPE. The mesa stripe was defined by wet etching and buried by LPE. The active layer of the devices consists of tensile strained $\text{In}_x\text{Ga}_{1-x}\text{As}$ wells ($x=1.65 \mu\text{m}$) and lattice matched InGaAsP barriers ($x=1.3 \mu\text{m}$). The length of the active layer is $600 \mu\text{m}$. Each end has a window facet, and a SiO_x AR coating of single layer was deposited on each. The effective reflectivity is estimated to be less than 2×10^{-4} .

Saturation power and gain

We investigated experimentally the relationship of the gain and saturation power to the strain or the number of wells. In this experiment, the tensile strain of wells were 0, 0.24, 0.45, 0.79%. Input optical wavelength was 1550nm and its power was -25dBm. Figure 1 shows the

dependence of the gain on the tensile strain. The gain of TE mode is 13dB with 0% strain. It decreases with increase of tensile strain to 8dB with 0.79% strain. On the other hand, the gain of TM mode increase with increase of tensile strain. The difference between the gain of TE and TM modes becomes minimum at the strain of -0.45%. Thus, polarization independent SOAs can be obtained.

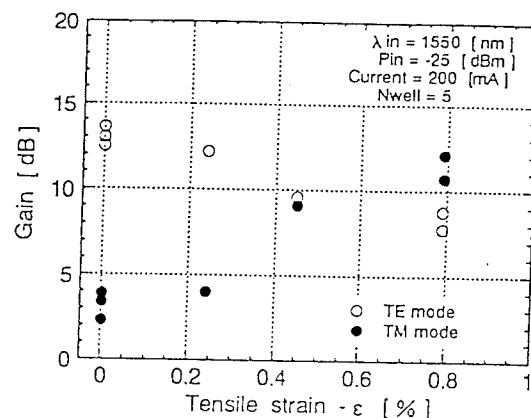


Fig.1 Dependence of fiber to fiber gain on tensile strain

Figure 2 shows the dependence of saturation power on the strain. It is demonstrated that the saturation power decreases with increase of the tensile strain.

Next, the dependence of the gain and the saturation power on the number of wells is shown in Figure 3. It is clear that when the number of wells increases, the gain increases but the saturation power decreases.

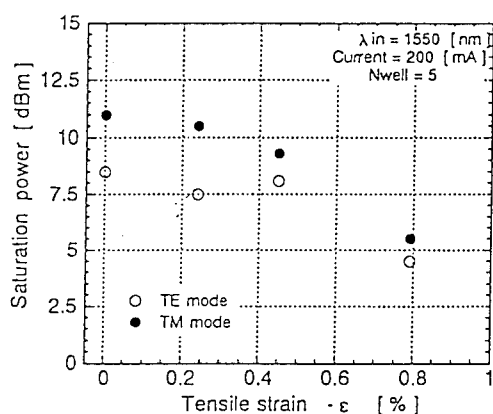


Fig.2 Dependence of saturation output power on tensile strain

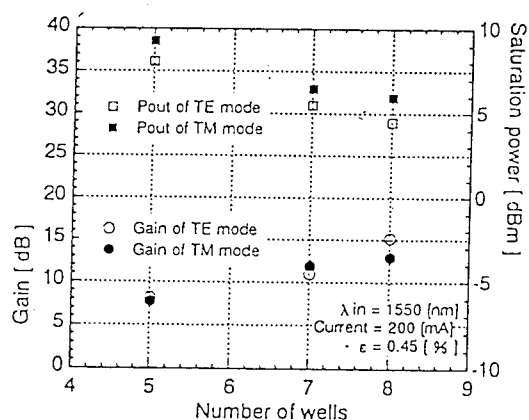


Fig.3 Dependence of fiber to fiber gain and saturation output power on number of wells

Fabrication

We fabricated two SOAs that are polarization-insensitive: one has 5 wells with -0.45% strain and the other has 7 wells with -0.5% strain. The characteristics of each are shown in Table 1. The device of 7 wells has larger gain and smaller saturation power than that of 5wells, because of large number of wells.

Table 1 Characteristics of SOAs at

$\lambda_{sig} = 1550$ [nm] and Current = 200 [mA]

Number of wells		7	5
Gain [dB]	Chip	22.5	18.0
	Fiber out	14.5	10.0
$\Delta G_{TE}/G_{TM}$ [dB]		< 0.2	< 0.5
Saturation output power [dBm]	Chip	10.1	13.0
	Fiber out	6.5	9.0

NDFWM

Experiment

We experimented NDFWM by using the SOAs fabricated. The experimental setup is shown in Figure 4. A DFB-LD light source is used as the pump, and a tunable light source is used as the probe. The wavelengths of the pump and the probe are 1549.8nm and 1551.8nm, respectively. The detuning of 2nm is used so that the signal light can be selected by a filter. After the pump and the probe are amplified by the EDFA, they are coupled with their polarization matched. The output power is measured by an optical spectrum analyzer.

In this experiment, we measured the signal output power as a function of the ratio of the pump input power to the probe input power

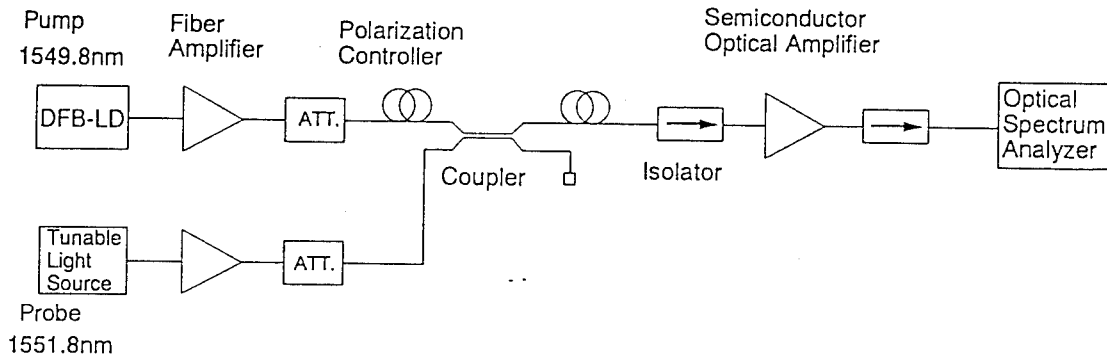


Fig.4 Experimental setup for the measurement of NDFWM

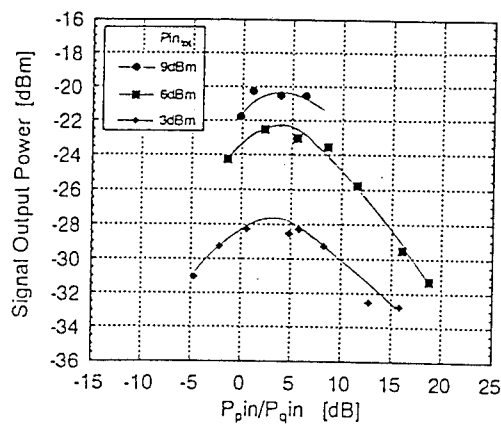


Fig.5 Signal output power as a function of the ratio of pump power to probe power using SOA of 5 wells.

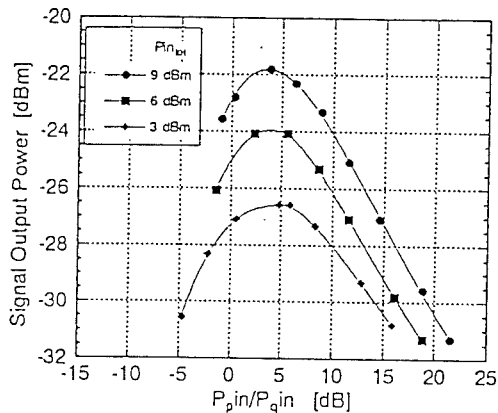


Fig.6 Signal output power as a function of the ratio of pump power to probe power using SOA of 7 wells

$P_{p,in}/P_{q,in}$. Previous results show that when the pump is several dB higher than the probe, the signal becomes maximum.⁽⁴⁾ Figure 5, shows the result for the SOA of 5 wells, and Figure 6 shows the result for that of 7 wells. When the input power is +3dBm, the SOA of 7 wells generated larger signal output power than that of 5 wells. We consider that the result is due to the gain.

However that of 7 wells generated smaller signal power than that of 5 wells when input power is +6dBm. We consider when input power is around the SOA saturation power, the signal power tends to be saturated.

Conclusion

The relationship of the gain and saturation power to the strain or the number of wells is investigated for tensile strained MQW SOAs. It is proven that the saturation power decreases with increase of tensile strain, and that the gain increases with increase of the number of wells but the saturation power decreases. Next we fabricated two SOAs that are polarization-insensitive: one has 5 wells with -0.45% strain and the other has 7 wells with -0.5% strain. The optical gains are 10.0dB and 14.5dB, polarization dependency are <0.5dB and <0.2dB, the

saturation power are 9.0dBm and 6.5dBm, respectively. The characteristics of signal power of NDFWM are investigated using these SOAs. It is suggested that the SOA of larger gain generates larger signal power when the input power is small, while the SOA of larger saturation power generates larger signal power when the input power is around the SOA saturation power.

Reference

- (1)K.Suzuki et al., Electron. Lett., **30**, pp660-661 (1994)
- (2)R.Ludwig et al., ECOC'93, ThP12.2 (1993)
- (3)M.C.Tatham et al., Electron. Lett., **29**, pp1851-1852 (1993)
- (4)A.Yamada et al, NGWA'95, NSaC4 (1995)

InGaAsP Strained MQW-DFB Lasers with High Resonance Frequency and Low Distortion for High Speed Analog Transmission ThP36

H.Watanabe, T.Aoyagi, A.Takemoto, T.Takiguchi, and E.Omura
Optoelectronic&Microwave Devices Laboratory,Mitsubishi Electric Corporation
4-1 Mizuhara,Itami,Hyogo 664,Japan

The resonance frequency have been improved by adopting a strained multiple quantum well (MQW) structure with the strain-compensated layers and optimizing its design. Moreover, it has been demonstrated that our newly developed structure having current blocking layers fabricated by MOCVD is very efficient to suppress the leakage current. As a result, the third-order-intermodulation distortion (IMD3) of -80dBc and relative intensity noise (RIN) of -152dB/Hz have been obtained under a two-tone test at 1.9GHz.

Introduction

High speed DFB lasers have been very attractive for broadband analog applications such as CATV distribution systems with hundreds-channel capacity as well as high-bit-rate digital use. Moreover, recent new application of fiber-optic microcellular radio communication demands for a light source to be low distortion and low noise characteristics up to several GHz with close channel separation. However, nonlinear intrinsic response of laser diodes inevitably causes harmonic or intermodulation distortion, which drastically increases as increasing the modulation frequency. That also enlarges RIN (relative intensity noise) at a high frequency. Furthermore, the leakage current which flows through outside of an active layer causes the degradation of the L-I linearity. The distortion induced by the leakage current becomes remarkable at a high power operation. Therefore, it is necessary to improve the resonance frequency and reduce the leakage current for the solution of the problem.

Laser structure and fabrication technique

1. BH structure

In order to suppress the leakage current which gives rise to the distortion at high bias current, the shape and the position of current blocking layers in the diodes should be optimized. The MOCVD technique has ability to precisely control the growth of those layers. A schematic structure of the DFB laser which is entirely fabricated by MOCVD is shown in fig.1. The fabrication process is briefly described as follows. First, the epitaxial growth of the active layer on a p-type substrate was carried out. Next, the grating layer of InP layer was formed on the active layer so as to be buried in a InGaAsP layer. After the mesa stripe was formed by wet etching, this was successively buried by the p-InP filling layer, n-InP, and p-InP current blocking layers. Finally, the contact layer was grown to complete the structure. We call

this structure Facet Selective- growth Buried Heterostructure (FSBH) [1].

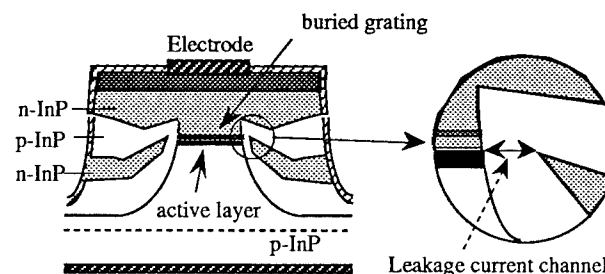


Fig.1 FSBH structure and their leakage current channel.

The leakage current mainly flows through a channel between the active region and the n-InP current blocking layer as shown in fig.1. The leakage current decreases as the width of the channel becomes narrow, resulting in reduction of the distortion. So far, there were problems of a non-uniformity and poor controllability of the leakage current, because LPE technology has difficulty controlling the width of this channel. The FSBH structure utilizing MOCVD technologies makes it possible to precisely control the width of the channel to be $0.1\mu\text{m}$ or less. To confirm the difference of the leakage current, the strength of electroluminescence (EL) emission from InP homojunction near the active layer was measured. Figure 2 shows the dependence of EL emission on the forward injection current. Laser emission was cut off with an optical band pass filter. Nonlinear characteristics of the emission curve corresponding to the leakage current is substantial origin of the distortion. A laser of the conventional BH structure by LPE method is found to show stronger emission compared with the FSBH structure by MOCVD, because that has the wider leakage channel than $0.4\mu\text{m}$. The figure indicates the advantage of FSBH structure in reducing the leakage current. In addition, we have adopted 2-inch diameter wafer

processing. Highly uniform characteristics and excellent controllability are obtained in comparison with the conventional small-size-wafer processing.

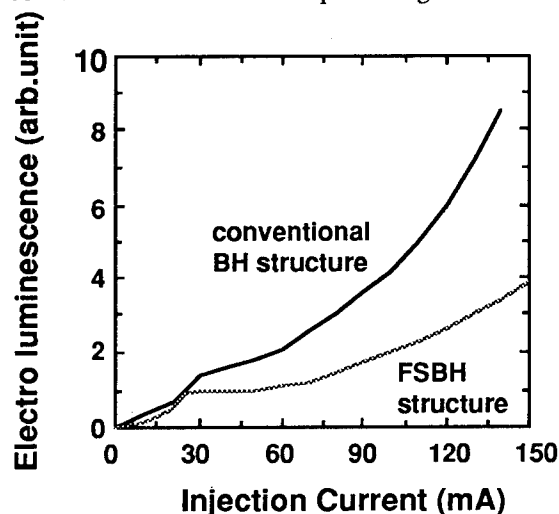


Fig.2 Comparison of electro luminescence intensity between the FSBH structure and a conventional BH structure.

2. Strained MQW structure

High speed analog application requires the high resonance frequency. It is well known that the strained MQW laser exhibits high resonance frequency which is attributed to their high differential gain[2][3]. The strained MQW structure, however, should be optimized to make the resonance frequency still higher. The purpose of this section is to examine the strained MQW structure suitable for the improvement of the resonance frequency experimentally. The most effective way to increase the resonance frequency is considered to improve both of optical confinement and carrier confinement, thereby increasing the differential gain[4].

First, the effect of carrier confinement is examined using FP lasers with the strained MQW structure. In InGaAsP/InP material system, the conduction band offset (ΔE_c) is so small that electrons tend to overflow to barrier layers, resulting in the degradation of the laser performance at high temperature. Overflow of electrons is a serious problem even at room temperature, because the threshold carrier density rises due to the waste of carriers. To examine the influence of carrier overflow, the internal quantum efficiency was estimated. In the experiment, two types of samples whose band gaps energy of barrier layers were $1.10 \mu\text{m}$ and $1.18 \mu\text{m}$ were prepared. Moreover, the optical confinement factor was changed by varying the well width and the well number. Figure 3 shows the relation between the internal quantum efficiency and the optical confinement factor.

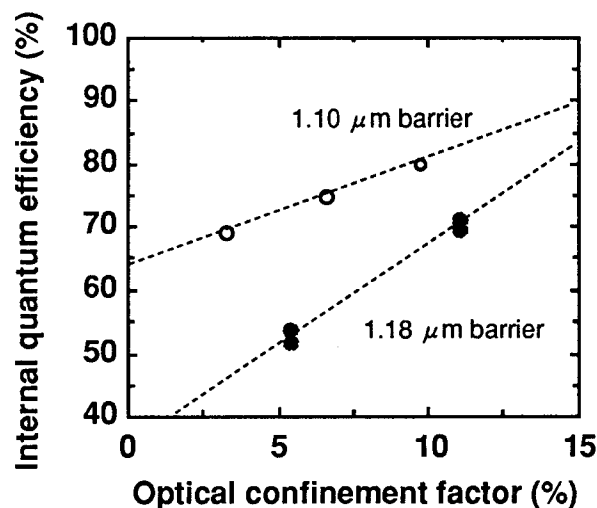


Fig.3 The relation between the internal quantum efficiency and the optical confinement factor in FP lasers.

The internal quantum efficiency was obtained from the extrapolation of the relation between the external quantum efficiency and the cavity length. The difference in the internal quantum efficiency depending on the barrier height is definitely observed. Experimental results exhibit that large barrier height is very effective to suppress the carrier overflow. Furthermore, increase in the internal quantum efficiency as increasing in the optical confinement is also observed, suggesting that the reduction of the threshold carrier density also decreases the carrier overflow. As a result, it is important to increase both of the barrier height and the optical confinement for the complete carrier confinement.

Next, the effect of the carrier confinement on the resonance frequency was examined using the same wafer. Figure 4 shows the relation between the resonance frequency and the optical confinement factor. The cavity length was $300 \mu\text{m}$, and facets were coated to be 30%-60%. The resonance frequency was estimated from RIN spectrum. Devices with $1.10 \mu\text{m}$ barrier have higher resonance frequency due to their high barrier height, being the same as the internal quantum efficiency. The reason is supposed that the differential gain is improved by reduction of the threshold carrier density due to the suppression of the carrier overflow. In addition, the resonance frequency is also improved by expanding the optical confinement. These results are attributed to the effect of the carrier confinement.

The optical confinement effect is further investigated using DFB lasers. The well number (N), the well thickness (L_z) and SCH layer as structural parameters were changed to vary the optical confinement, which implies the control of the carrier density in a well. N were

5,7,10, and 15. L_z were 3nm, 4nm, 6nm, and 8nm. 1.0% compressive strain was introduced into InGaAsP wells in all cases, and InGaAsP barrier layers (1.10 μm band gap) with 5 and 7 wells were 10nm thick and 5nm thick for 10 and 15 wells, respectively. However, there were technical difficulties increasing the well number or the well thickness. That was the degradation of strained layers caused by exceeding the critical thickness in the case of more than 10 wells. In order to solve this problem, strain compensation effect which is obtained by introducing tensile strain to the barrier layers was utilized[5]. 0.5% tensile strain into barrier layers actually allow to successfully grow samples of $L_z=4\text{nm}$, 15wells and $L_z=8\text{nm}$, 10wells. Devices for the experiment were conventional DFB lasers with a uniform grating, whose cavity length was 300 μm , width of the active layer was 1.3 μm , and facets were AR/HR coated. The wavelength was detuned by 10nm shorter than the gain peak.

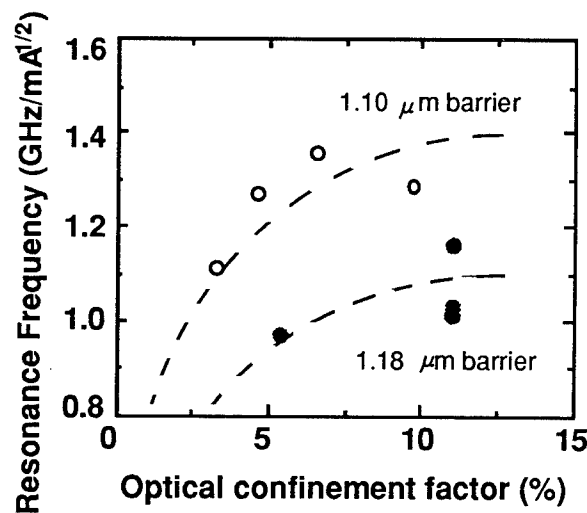


Fig.4 The relation between the resonance frequency and the optical confinement factor in FP lasers.

Figure 5 shows the relation between the resonance frequency and the optical confinement factor Γ , which is calculated with the structural parameters mentioned above. Open circles represent average values of several samples from the same wafer. The resonance frequency is found to increase as enlarging the optical confinement regardless of the well thickness. The carrier overflow is considered to influence on the resonance frequency in lower optical confinement, judging from the case of FP lasers. The average value of $L_z=8\text{nm}$, $N=10$ case attains the resonance frequency of $2.1\text{GHz}/\text{mA}^{1/2}$, which is the maximum value among all kinds of samples. Moreover, a closed rectangular symbol indicates the best value of $2.41\text{GHz}/\text{mA}^{1/2}$

($=5.1\text{GHz}/\text{mW}^{1/2}$) in the $L_z=8\text{nm}$, $N=10$ samples. The differential gain of the best sample is estimated to be $1.1 \times 10^{-16}\text{cm}^2$. Scattering of the measured values depending on the grating phase is unavoidable to some extent. The gain compression factors ϵ of every samples were 1.0 – $3.0 \times 10^{-23}\text{m}^3$, depending on neither the well number nor the well width.

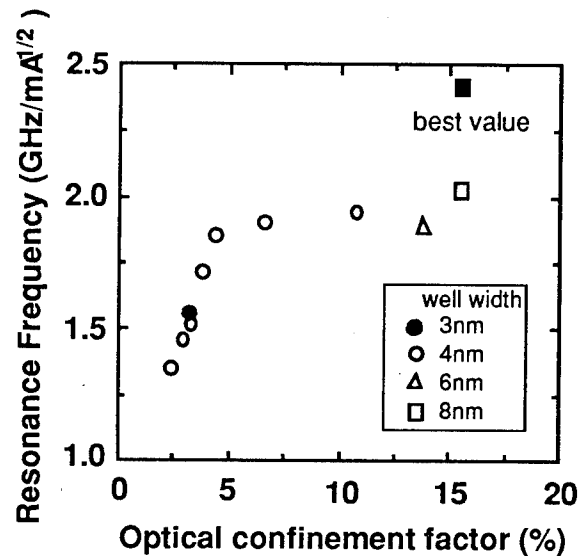


Fig.5 Resonance frequency versus optical confinement factor of strained MQW lasers

Theoretical and experimental results of the distortion

Based on the small signal rate equation, frequency response of the third-order intermodulation distortion (IMD3) at various resonance frequency is calculated as shown in fig.6.

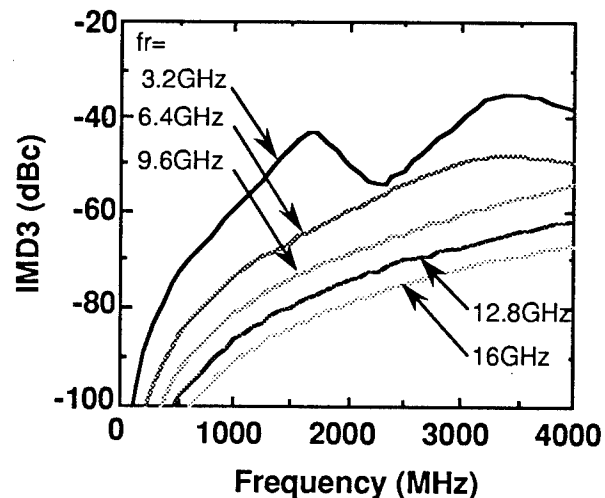


Fig.6 Calculation for frequency response of third order intermodulation distortion (IMD3) with various resonance frequencies

IMD3 is found to be reduced with increase in resonance frequency, because the resonance peak shifts to the higher frequency. Therefore, high normalized resonance frequency is necessary to obtain the low distortion at a given power level. Figure 7 shows a typical behavior of IMD3 with bias current in a sample of 15 wells with 4nm thick. The modulation frequencies were $f_1=1900\text{MHz}$ and $f_2=1900.6\text{MHz}$. The optical modulation depth (OMD) were 20%. Solid line shows the calculation with the same manner of fig.6. Normalized resonance frequency of the sample was $4.1\text{GHz}/\text{mW}^{1/2}$. IMD3 decreased with increase in bias current which is attributed to the increase of resonance frequency. IMD3 decreased down to -80dBc at a bias current 70mA. Excessive distortion due to the leakage current was hardly observed up to high bias current. Such low bias current is also sufficient to realize long-term reliability.

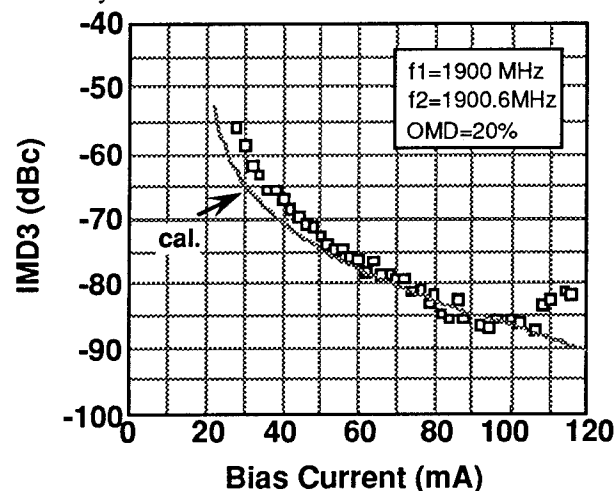


Fig.7 Dependence of IMD3 on bias current for a sample of $L_z=4\text{nm}$, $N=15$.

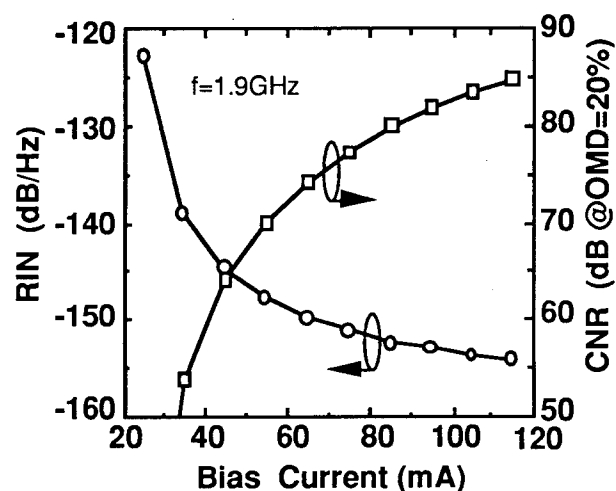


Fig.8 Dependence of RIN and CNR on bias current for a sample of $L_z=4\text{nm}$, $N=10$.

Figure 8 shows RIN and CNR characteristics of 10-well sample at the frequency of 1930MHz depending on bias current. Optical modulation depth (OMD) is 20% and bandwidth is 288kHz in the measurement of CNR. Extremely low RIN of -152dB/Hz is achieved in the range of enough low distortion. These low noise characteristics are attributed to the improvement of the resonance frequency in the same way as the distortion. CNR of 80dB is high enough to be applied to analog transmission systems.

Conclusions

We have investigated the third-order-intermodulation distortion (IMD3) and the noise characteristics in $1.3\mu\text{m}$ strained MQW-DFB lasers under high speed modulation. It was found that improvement of the differential gain was very effective to reduce the distortion and RIN, resulting from a) the introduction of strained MQW with the strain compensated layers, b) increase of the optical confinement and barrier height. As a result, the highest value of resonance frequency of $2.41\text{GHz}/\text{mA}^{1/2}$ was obtained for a sample of ten 8nm-wells. A new buried heterostructure by entirely using MOCVD, named as FSBH structure, was adopted. The FSBH structure enabled us to control the leakage current channel to be $0.1\mu\text{m}$ or less, thereby succeeding in the suppression of the distortion in high bias current. Using these techniques, IMD3 of -80dBc and RIN of -152dB/Hz was obtained under the 2-tone test at 1.9GHz .

References

- [1] Y. Ohkura, T. Kimura, T. Nishimura, K. Mizuguchi, and T. Murotani, "Low threshold FS-BH laser on p-InP substrate grown by all-MOCVD," *Electron. Lett.*, vol. 28, pp. 1844-1845, Sep. 1992.
- [2] H. Lipsanen, D. L. Coblenz, R. A. Logan, R. D. Yadvish, P. A. Morton, and H. Temkin, "High-speed InGaAsP/InP multiple-quantum-well laser," *IEEE Photon. Technol. Lett.*, vol. 4, pp. 673-675, July 1992.
- [3] M. Kito, N. Otsuka, M. Ishino, K. Fujihara, Y. Matsui, "Enhanced relaxation oscillation frequency of $1.3\mu\text{m}$ strained-layer multiquantum well lasers," *IEEE Photon. Technol. Lett.*, vol. 6, pp. 690-693, June 1994.
- [4] M. Nido, K. Naniwae, J. Shimizu, S. Murata, A. Suzuki, "Analysis of differential gain in InGaAs-InGaAsP compressive and tensile strained quantum-well lasers and its application for estimation of high-speed modulation limit," *IEEE J. Quantum Electron.*, vol. 29, pp. 885-895, March 1993.
- [5] B. I. Miller, U. Koren, M. G. Young, and M. D. Chien, "Strain-compensated strain-layer superlattices for $1.5\mu\text{m}$ wavelength lasers," *Appl. Phys. Lett.*, vol. 58, pp. 1952-1954, May 1991.

High output power operation of 1.3 μm strained MQW lasers with low threshold currents at high temperature

ThP37

Masahiro Kito, *Hideyuki Sakai, Nobuyuki Otsuka, Kiyoshi Fujihara, Masato Ishino and Yasushi Matsui

Semiconductor Research Center, Matsushita Electric Industrial Co., Ltd.

*Matsushita Electronics Corporation

3-1-1 Yagumonakamachi, Moriguchi, Osaka 570, Japan

*Nagaokakyo, Kyoto 617, Japan

Introduction

Long-wavelength lasers with low threshold current characteristics over a wide temperature range are required for the optical access networks [1]. High reflection coating and very short cavity have been applied to compressively strained multiquantum well (MQW) lasers to obtain sub-milliampere operation [2],[3]. On the other hand, high output power is also important in order to realized suitable fiber output power even in a simple module that allows non-optimized coupling. Furthermore, small variation in output power at elevated temperature up to 85°C is important for the laser operation without automatic power-control (APC). In this paper, we have investigated the temperature dependencies of the output power and the threshold current for compressively strained MQW lasers on well number.

I. Fabrication of strained MQW structure

Structure: The schematic band diagram of the strained MQW structure is shown in Fig. 1. The multilayer growth was carried out by MOVPE on an n-InP substrate. The MQW layer is composed of 6 nm-thick compressively strained InGaAsP ($\Delta a/a = 0, 0.6, 0.9$, and 1.0 %) well layers and 10 nm-thick InGaAsP ($\lambda_g = 1.15 \mu\text{m}$) barrier layers. The number of quantum wells (N_w) is 5, 7 and 10. The amount of the strain was estimated by measuring X-ray diffraction. The MQW layers are sandwiched by 60 nm-thick separate confinement heterostructure (SCH) layers ($\lambda_g = 1.15 \mu\text{m}$).

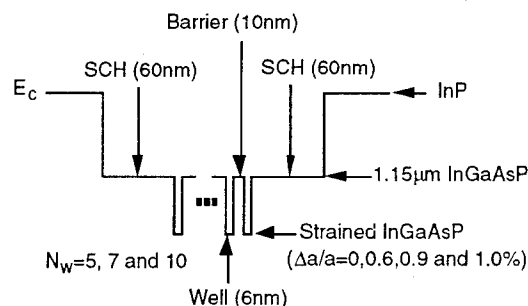


Fig. 1 The schematic band diagram of the strained MQW structure.

Photoluminescence measurement: Figure 2 shows the photoluminescence (PL) linewidth (full width at half maximum) of the samples with 7 wells at room temperature (RT) and 77 K. The X axis represents the amount of the compressive strain in well layers. The PL peak wavelengths of the measured samples range from 1.30 to 1.31 μm at RT. When the amount of the strain is increased from 0 to 1.0 %, the PL linewidth at RT decreases from 38 meV to 24 meV, and that at 77 K is almost constant at about 10 meV. These results indicate that the fabricated strained MQW structures have good crystalline quality and very sharp interfaces. In order to investigate PL characteristics of the strained MQW structure with much larger amount of strain, we fabricated strained MQW structure with InAsP well layers. However, PL intensity was too weak to be detected at RT.

Figure 3 shows the dependencies of PL linewidth and PL peak-shift value from RT to 77 K on the well number, for the 1.0 % strained MQW structures. The large broadening in PL linewidth is observed at the sample with 10 wells. Furthermore, for the samples

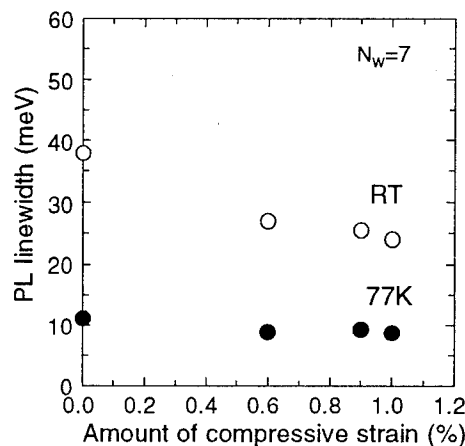


Fig. 2 The dependences of the PL linewidth on the amount of the compressive strain in well layers at RT and 77K.

with 5 and 7 wells, PL peak-shift value is about 60 meV. On the other hand, for the sample with 10 wells, no PL peak-shift is observed. These results indicate that the degradation in crystalline quality

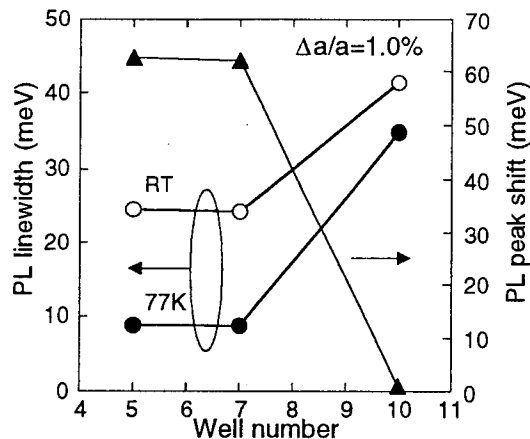


Fig. 3 The dependences of PL linewidth and PL peak shift value from RT to 77 K on the well number for the 1.0% strained samples.

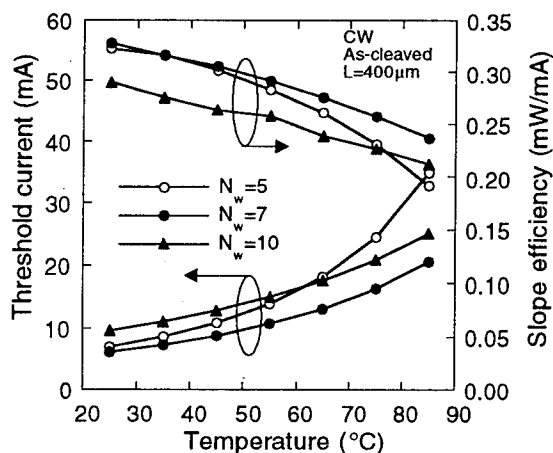


Fig4. The temperature dependences of the slope efficiency and the threshold current for the three types of the strained MQW lasers.

occurs in the sample with 10 wells. We will mention about the reliability of the 1.0 % strained MQW laser with 10 wells in the next section.

II. Device characteristics and Discussions

Three buried heterostructure lasers with strained MQW active layers ($N_w = 5, 7$ and 10 , $\Delta a/a = 1.0\%$) were fabricated by liquid phase epitaxy. The active region width is about $1.2 \mu\text{m}$.

Laser parameter: The internal loss (α_i) and the internal differential quantum efficiency (η_i) were estimated from the relation of the cavity length versus inverse differential quantum efficiency at RT. The values of α_i are 10.7 , 12.3 and 17.4 cm^{-1} for 5 , 7 and 10 wells, respectively. The values of η_i are 93 , 99 and 99% for 5 , 7 and 10 wells, respectively. The values of the optical confinement factor in the well layers are 0.046 , 0.073 and 0.114 for 5 , 7 and 10 wells, respectively.

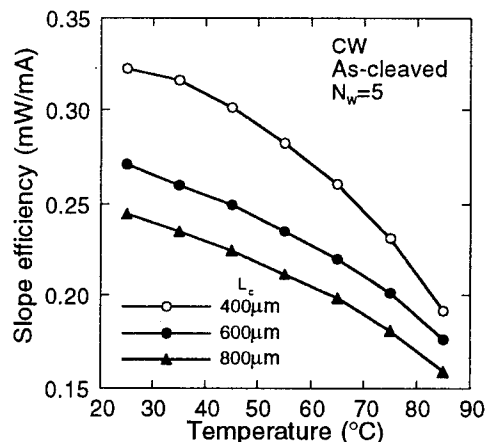


Fig. 5 The temperature dependences of the slope efficiency for the lasers with 5 wells as a parameter of cavity length.

Increase in α_i with well number results from increase in the optical confinement factor [4].

Temperature dependence: In order to realize low threshold current and high output power at high temperature, and to achieve relatively stable output power at elevated temperature up to 85°C , small temperature dependencies of threshold current and slope efficiency are required.

The temperature dependencies of the slope efficiency and the threshold current under CW operation for the three types of the strained MQW lasers are shown in Fig. 4. All lasers have cavity length of $400 \mu\text{m}$ and as-cleave facets. The characteristic temperatures (T_0) estimated from temperature dependencies of threshold current are 37.7 , 50.4 and 62.7 K for 5 , 7 and 10 wells, respectively. The T_0 value is improved with increase in well number. The slope efficiency as well as the threshold current of the laser with 5 wells has larger temperature dependence than that of the laser with 7 or 10 wells. When we define the ratio of the slope efficiency at 85°C (η_{s85}) to that at 25°C (η_{s25}) as η_{s85}/η_{s25} , the values of η_{s85}/η_{s25} are 0.59 , 0.72 and 0.73 for 5 , 7 and 10 wells, respectively.

Figure 5 shows the temperature dependencies of the slope efficiency for the lasers with 5 wells as a parameter of cavity length (L_c). The value of η_{s85}/η_{s25} is improved from 0.59 to 0.65 , with increasing cavity length from $400 \mu\text{m}$ to more than $600 \mu\text{m}$. Furthermore, T_0 value is also improved by about 5 K in the lasers with cavity length of more than $600 \mu\text{m}$. In the laser with 5 wells and relatively short cavity, the carrier density is high and the Fermi level is close to the barrier energy. Therefore, increase in temperature easily induces carrier overflow out of the well layers, which decreases current injection efficiency and increases internal loss in the laser [5]-[7]. As a result, the laser with 5 wells and relatively

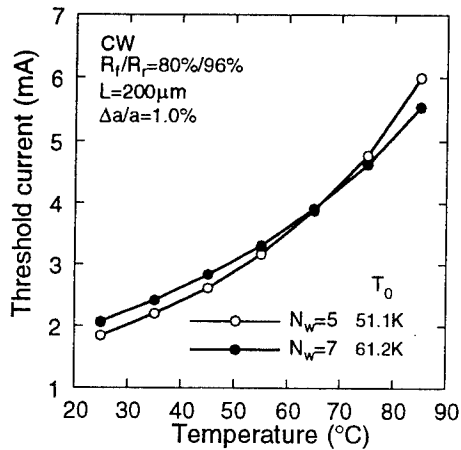


Fig. 6 The temperature dependences of the threshold current for the HR coated lasers with 5 and 7 wells ($\Delta a/a = 1.0\%$).

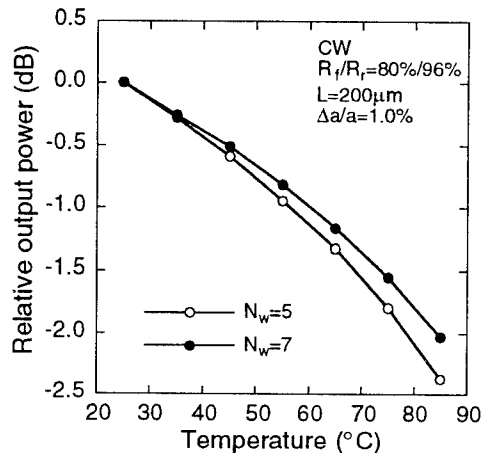


Fig. 7 The temperature dependences of the relative output power for the HR coated lasers with 5 and 7 wells ($\Delta a/a = 1.0\%$).

short cavity shows large temperature dependencies of the slope efficiency and the threshold current. Greater well number can suppress the carrier overflow at high temperature, but increases the internal loss due to larger optical confinement factor. Indeed, in Fig. 4, the laser with 7 wells shows the lowest threshold current and the highest slope efficiency from 25°C to 85°C. Furthermore, the laser with 10 wells shows the deterioration ratio of over 10 % in threshold current at 50°C after the ACC burn-in test under 150 mA at 70°C for 100 hours.

From the results of the PL characteristics in Fig. 3 and the ACC test, it is considered that the degradation of crystalline quality is caused by the large total strain in the laser with 10 wells.

Characteristics of HR coated lasers: In order to decrease the threshold current, high reflection (HR) coating was applied to the lasers with 5 and 7 wells ($\Delta a/a = 1.0\%$). The reflectivity of the front and rear facets are 80 % and 96 %, respectively. The cavity length is

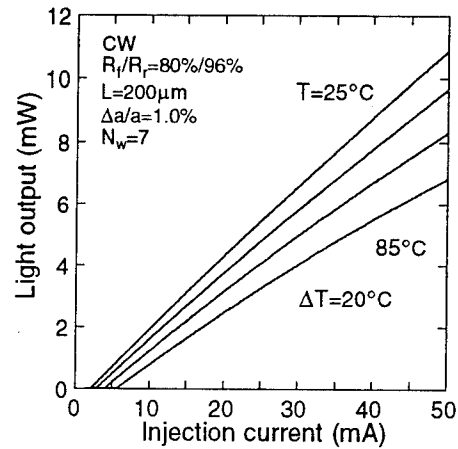


Fig. 8 The light output versus injection current for the HR coated laser with 7 wells ($\Delta a/a = 1.0\%$).

200 μm for each type of the laser. The HR coating is expected to improve the temperature dependencies of the threshold current and slope efficiency due to reduced mirror loss.

Figure 6 shows the temperature dependencies of the threshold current under CW operation for the HR coated lasers with 5 and 7 wells. At 25°C the laser with 5 wells shows lower threshold current of 1.8 mA than the laser with 7 wells due to its smaller internal loss, however, at 85°C the laser with 7 wells shows lower threshold current of 5.5 mA due to its higher T_0 .

Figure 7 shows the temperature dependencies of the relative output power at the injection current of 50 mA for the HR coated lasers with 5 and 7 wells, under CW operation. The light output powers at 25°C are 10.4 and 10.9 mW for 5 and 7 wells, respectively. The variation in output power from 25°C to 85°C for the laser with 7 wells is 2.0 dB, and is smaller by 0.4 dB than that of the laser with 5 wells. The results of Fig. 6 and Fig. 7 show that even with HR coating, the laser with 7 wells shows lower threshold current, higher output power at high temperature, and smaller variation in output power at elevated temperature up to 85°C, as compared with the laser with 5 wells.

Figure 8 shows the CW light output versus injection current for the HR coated laser with 7 wells as a parameter of temperature. The high output powers of 10.9 mW at 25°C and 6.8 mW at 85°C are demonstrated under the injection current of 50 mA. Furthermore, the low threshold currents of 2.1 mA at 25°C and 5.5 mA at 85°C are realized.

III. Conclusions

We have evaluated the temperature dependencies of strained MQW lasers on well number. Smaller well number means larger temperature dependencies of the slope efficiency as well as the threshold current due to enhanced carrier overflow, while greater well number

means degradation in crystalline quality that lowers the reliability of the laser. In this work, the 1.3 μm strained MQW laser with a compressive strain of 1.0 % and 7 wells shows the highest output power of 6.8 mW and the lowest threshold current of 5.5 mA at 85°C, and the lowest variation in output power of 2.0 dB from 25°C to 85°C at the injection current of 50 mA. These characteristics show that the optimized lasers are suitable for light sources of the optical access networks.

Acknowledgment

The authors wish to thank T. Onuma and Dr. M. Ogura for their continued support and encouragement, and S. Kimura for his useful discussion.

References

- [1] E. Kondo, Y. Tanaka, M. Kobayashi and N. Miki, "PDS fiber-optic access systems development and multimedia field trial," 6th International Workshop on Optical Access Networks, pp. 1.3-1-6, 1994.
- [2] K. Uomi, T. Tsuchiya, M. Komori, A. Oka, K. Shinoda and A. Oishi, "Extremely low threshold (0.56 mA) operation in 1.3 μm InGaAsP/InP compressive-strained-MQW lasers," *Electron. Letters*, vol. 30, pp. 2037-2038, 1994.
- [3] T. Terakado, K. Tsuruoka, T. Ishida, T. Nakamura, K. Fukushima, S. Ae, A. Uda, T. Torikai and T. Uji, "Extremely low thresholds (0.4 mA @20°C, 3.0 mA @85°C) 1.3 μm strained MQW lasers with novel p-substrate buried-heterostructure (RIBPBH) grown by MOVPE using TBA and TBP," 14th IEEE Semiconductor Laser Conference '94, PD9, 1994.
- [4] T. Nanegaya, N. Matsumoto, N. Yamanaka, N. Iwai, H. Nakayama and A. Kasukawa, "Effects of well number in 1.3 μm GaInAsP/InP GRIN-SCH strained-layer quantum-well lasers," *IEEE J. Quantum Electron.*, vol. 30, pp. 578-584, 1994.
- [5] H. Hirayama, Y. Miyake and M. Asada, "Analysis of current injection efficiency of separated-confinement-heterostructure quantum-film lasers," *IEEE J. Quantum Electron.*, vol. 28, pp. 68-74, 1992.
- [6] K. Tanaka, K. Wakao, T. Yamamoto, H. Nobuhara and T. Fujii, "Dependence of differential quantum efficiency on the confinement structure in InGaAs/InGaAsP strained-layer multiple quantum well lasers," *IEEE Photonics Technol. Letters*, vol. 5, pp. 602-605, 1993.
- [7] V. Mikhaelashvili, N. Tessler, R. Nagar, G. Eisenstein, A. G. Dentai, S. Chandrasakhar and C. H. Joyner, "Temperature Dependent loss and overflow effects in quantum well lasers," *IEEE Photonics Technol. Letters*, vol. 6, pp. 1293-1296, 1994.

Fabrication and Performance of a Novel Ultra-Low Capacitance MSM Photodetector for High-Speed OEIC Receiver Applications

ThP38

Eugene John, Wen-Yen Hwang, Mukunda B. Das,
Theresa S. Mayer, and David L. Miller

Department of Electrical Engineering, and
Electronic Materials and Processing Research Laboratory
The Pennsylvania State University
University Park, PA 16802

Introduction

The metal-semiconductor-metal (MSM) photodiodes have much lower capacitance compared to the p-i-n diodes with similar surface area. It has been suggested^[1] that the capacitance of MSM photodiodes can be reduced by a factor of four by a serial arrangement of two MSM elements occupying the same total area, and in this arrangement the detected photo-current will be reduced only by a factor of two. For high-speed optoelectronic integrated circuit (OEIC) receivers based on heterostructure HBT's or HFET's the base or gate current of the input transistor often limits the sensitivity of the receiver due to the associated shot noise current generator. For this reason the size of the input transistor is often greatly reduced, and consequently the input capacitance is also reduced to a few ten's of femto-farads. For these OEIC receivers, photodetectors with comparable or much less capacitance are required in order to preserve the bandwidth, and either serially arranged or series/parallel arranged MSM photodiodes can serve as the photodetectors with ultra-low capacitance. In this paper we present experimental results obtained from series and series/parallel arranged MSM photodiodes based on lattice-matched InGaAs/InAlAs heterostructures on InP substrate with 1 μ m thick InGaAs absorption layer and 1.2 μ m interdigitated metallization with 1.2 μ m spacing. We also present results predicting high-speed performance of OEIC receivers based on these ultra-low capacitance MSM photodiodes and compatible state-of-the-art 0.15 μ m gate-length HFET's operated as a cascoded transimpedance amplifier or state-of-the-art HBT's operated in the same fashion. These receivers are shown to yield transimpedance of 72 dB Ω with 3-dB bandwidths of 19.5 GHz, and sensitivity of -28 dBm at the full bandwidth at the standard bit-error-rate of 10⁻⁹.

The MSM Structure

Epitaxial Material: The MBE-grown layer structure used for the fabrication of the interdigitated MSM photodiodes is shown schematically in Figure 1(a). This structure consists of 3000 \AA AlInAs buffer layer, a 270 \AA composition graded InAlAs/InGaAs shot-period superlattice (SPSL) lower layer, a 1.0 μ m InGaAs photo absorption layer, a 270 \AA composition graded InAlAs/InGaAs SPSL upper layer, and a 300 \AA InAlAs Schottky barrier layer. The material was grown by lattice matching on semi-insulating <100> InP substrate at 500 $^{\circ}$ C with a growth rate of 0.8 μ m per hour using the Varian Gen II machine.

Fabrication of MSM Diodes: For the fabrication of MSM diodes a mask set was designed using L-EDIT software package. Mask sets were designed to fabricate both single two-terminal MSM photodiodes, as well as series connected three-terminal novel MSM photodiodes. Figure 1(b) shows the layout of the three-terminal four-element

MSM photodiodes with 1.2 μ m finger width and finger spacing with number of fingers N=11 and length of each finger ℓ =5 μ m. These masks were fabricated at the IBM T.J. Watson Research Center, Yorktown Heights, NY.

The MSM photodiodes were fabricated on the heterostructure material shown in Figure 1(a) using optical lithography and lift-off technique. The processing involved the following steps:

- (a) Spinning of photoresist on the cleaned wafer followed by a bake for 60 mins at 115 $^{\circ}$ C.
- (b) Interdigitated patterns were exposed on the photoresist using UV lithography and the exposed resist was developed.
- (c) After exposure and development two layers of metal (200 \AA Cr, and 1000 \AA Au) were thermally evaporated and lifted off in acetone. Prior to the evaporation of metal native oxide was removed using dilute HF solution.

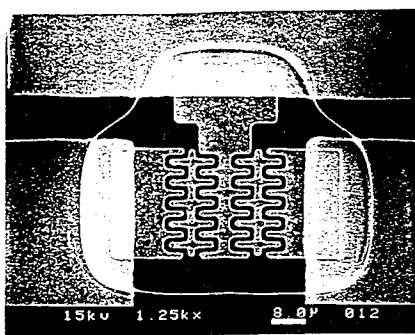
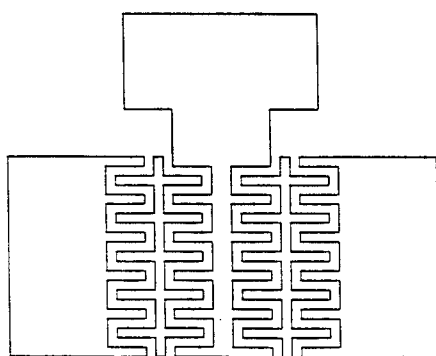
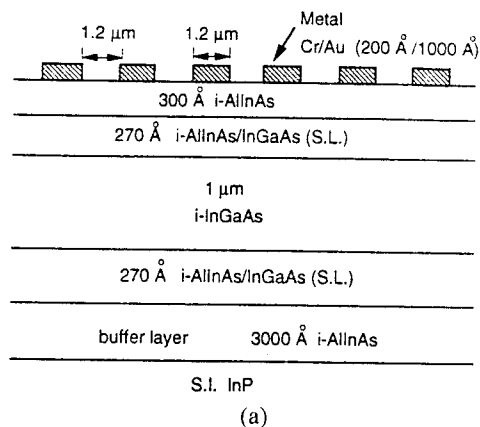


Figure 1 (a) Schematic cross-sectional details of the heterostructure layers used for MSM photodiodes. (b) Layout of a three-terminal four-element interdigitated MSM photodiode metallization pattern. (c) Scanning electron photo-micrograph of a three-terminal four-element MSM photodiodes.

Polyimide was used for protection of areas outside the interdigitated regions and cured for 8 hours at 200°C. Large metal contact pads were formed on polyimide for probing purposes. Figure 1(c) shows the scanning electron photomicrograph of a three-terminal four-element MSM photodiode.

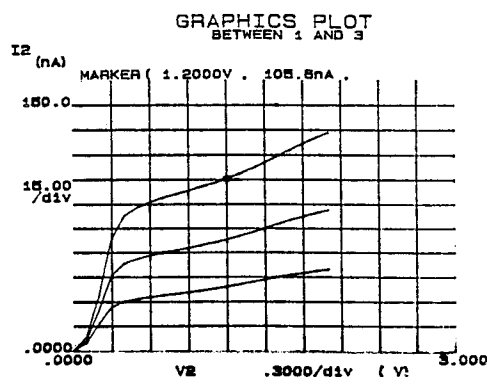


Figure 2. Photo-excited I-V characteristics of the novel three-terminal four-element MSM photodiode between the two outer electrodes.

Characteristics of MSM Photodiodes

The I-V characteristics of the fabricated MSM photodiodes were obtained using the HP 4145B Parameter Analyzer. The typical values of the dark current of a single-element MSM photodiode varied from 3 nA to 10 nA at 1.5 volt. These measurements are comparable to those reported in ref. [3]. With the illumination of the diode active area by the microscope light with increasing intensity the I-V characteristics obtained from a three-terminal four-element MSM photodiode are depicted in Figure 2 when the voltage was applied between the two outer electrodes keeping the third central electrode floating. Almost identical I-V characteristics were obtained between the central and either of the two outer electrodes. These results clearly demonstrated the validity of the original concept that the current generators resulting from optical excitations can relay from one MSM-photodetector element to the next element if they are uniformly illuminated. By shorting the two outer electrodes and performing measurements between these and the central electrode we observed doubling of the detected current for the same illumination. This confirmed the parallel operation of the detected current generators.

Responsivity was measured using a single mode fiber to couple 1500nm laser radiation to the light sensitive area of the MSM photodiodes and the corresponding electrical current was recorded with the help of direct wafer probing. For this purpose a Cascade Microtech probe station (Model summit 9000) with probe head WPH-102-100 was used. Typical values of responsivity for a single-element MSM photodiode was 0.3 A/W at 5 Volts biasing.

Capacitance of the fabricated MSM photodiodes were determined from scattering parameter measurements, with the help of a microwave network analyzer (HP 8510C). The results of measurements of capacitance between the two outer pads of a three-terminal four-element capacitance is depicted in Figure 3. In this case the

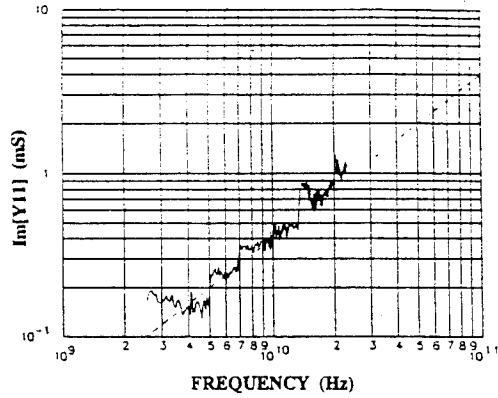


Figure 3. Frequency dependence of $\text{Im}(Y_{11})$ of a three-terminal four-element MSM photodiode between its outer electrodes.

measured value of capacitance was found to be ~ 6 fF whereas theoretically expected value was ~ 1 fF. This result indicate large contributions from the inter-pad fringe capacitances. Measurements on other structures confirmed the presence of this large fring capacitance.

The MSM photodiodes of different finger widths and spacing were tested for their high frequency limitation. For this we used the direct bandwidth measurement setup available at the AT&T Bell Labs, Crawford Hills facilities. This measurement involved up to 20 GHz swept microwave modulated optical signal of 1550nm laser radiations coupled to the test MSM photodiodes. The electrical signal was detected by wafer probing. Figure 4 depicts the results of optical-to-electrical bandwidth measurements for a single-element MSM photodiode with $1.2\mu\text{m}$ finger and spacing. The 3-dB bandwidth is marked at ~ 8.4 GHz when the bias voltage was 6 Volts. Devices with $1.8\mu\text{m}$ and $2.4\mu\text{m}$ finger widths indicated 3-dB bandwidths of ~ 5 GHz and ~ 2.7 GHz, respectively. These reduction of bandwidths were caused by the reduction of electric field as well as by the increase in the electrode spacing in the different MSM diodes tested. However, with appropriately increased applied voltage in serially connected devices should yield the bandwidth comparable to that obtained from individual devices.

MSM Based OEIC Receivers

Design Concepts: Transimpedance OEIC receivers based on ultra-low-capacitance MSM photodiodes described above and compatible high-speed heterostructure bipolar or field-effect transistors (HBT's and HFET's) are potentially capable of providing high 3-dB bandwidth and sensitivity. A design optimization approach to such high-speed OEIC receivers has been suggested recently^[3]. For receivers with highest possible gain \times bandwidth product and maximally flat frequency response it is necessary to configure the input stage of the transimpedance amplifier in the cascoded fashion. In this arrangement the depend-

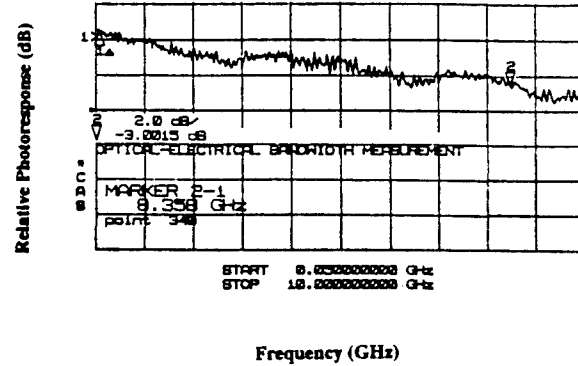


Figure 4. Frequency dependence of optical-to-electrical response of a single-element MSM photodiode with $1.2\mu\text{m}$ metallization finger and $1.2\mu\text{m}$ spacing with 6 volts bias.

ence of the feedback resistance (R_f) on the load conductance (g_L) can be shown to obey the following relationship:

$$R_f = \frac{2(c_L + c_\mu)g_m}{(c_{11} + c_p)g_L^2} \quad (1)$$

In the above equation g_m is the transconductance of the cascoded transistor, c_{11} is its input capacitance, c_p is the MSM photodiode capacitance, c_L is the load capacitance interfacing the unity gain voltage follower, and c_μ is the feedback capacitance of the transistor. The gain \times bandwidth product of this cascoded input stage transimpedance receiver can be expressed in the following manner.

$$R_f \times f_{3\text{-dB}} = \frac{1}{\sqrt{2\pi}} \left(\frac{g_m}{g_L} \right) \frac{1}{(c_{11} + c_p)} \quad (2)$$

For receivers based on HFET's, the load conductance g_L corresponds to the drain output conductance (g_o) of the HFET which is used as a dynamic load resistor.

Bandwidth and Sensitivity Limits: We have calculated the frequency response of MSM-based OEIC transimpedance receivers using both HFET's and HBT's. These calculations are based on the following CE or CS equivalent network parameters of scaled state-of-the-art HBT^[4] and HFET^[5] structures (see Figures 5(a) and 5(b)).

HBT's: The base-to-collector capacitance $c_\pi = 18.5$ fF, the associated conductance $g_\pi = 18.5$ mS, the total collector-base feedback capacitance $c_\mu = 4.5$ fF, the output conductance $g_o = 0.1$ mS, the base resistance $r_{bb'} = 50 \Omega$, and the collector series resistance $r_{cc'} = 20 \Omega$. The effects of the emitter series resistance $r_{ee'} (=13.3\Omega)$ have been included in the values of the parameters c_π , g_π , g_m and g_o given above. The size of the emitter chosen^[3] is $1\mu\text{m} \times 2.5\mu\text{m}$, and the operating collector current $I_C = 0.62$ mA.

HFET's: The gate-to-source capacitance $c_{gs}=18.5$ fF, the associated conductance $g_{gs}\cong 0.2$ mS, the transimpedance $g_m=18.5$ mS, the drain-to-gate feedback capacitance $c_{\mu}=3$ fF, the output conductance $g_o=0.3$ mS, the gate series resistance $r_g=10\ \Omega$, and the drain series resistance $r_d=10\Omega$. The effects of the series source resistance r_s ($=20\Omega$), have been included in the values of the parameters c_{gs} , g_{gs} , g_m , and g_o . The size of the gate chosen^[3] is $0.15\mu\text{m} \times 25\mu\text{m}$, and the operating gate current $I_{DS}=5\text{mA}$.

We present in Table I the key performance characteristics of the high-speed OEIC receivers based on MSM/HBT's and MSM/HFET's, for selected values of feedback resistance and choice of MSM photodiode capacitance (c_p) and load capacitance (c_L). These results were ob-

Table I

[A] HBT				[B] MODFET*			
R_f k Ω	R_L Ω	$f_{3\text{-dB}}$ GHz	$R_f \times f_{3\text{-dB}}$ Ω THz	R_f k Ω	$f_{3\text{-dB}}$ GHz	$R_f \times f_{3\text{-dB}}$ Ω THz	c_L fF
$c_p = 6$ fF							
5	721	19.9	99.5	5.28	19.4	102.5	4.5
3	550	20.6	61.8	7.41	13.9	102.5	7.5
1.5	362	29.1	43.7	9.51	10.8	102.5	10.5
$c_p = 20$ fF							
5	863	13.5	67.5	3.64	19.4	70.7	4.5
3	656	17.4	55.2	5.10	13.9	70.8	7.5
1.5	455	24.6	36.9	6.56	10.8	70.8	10.5

* $R_L = 1/g_o$

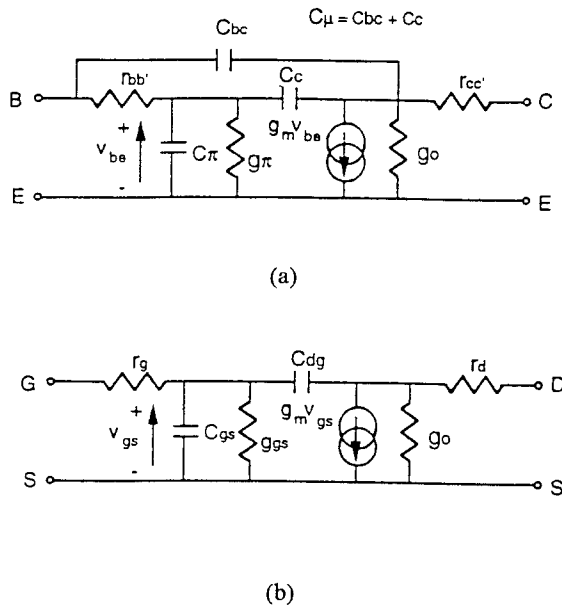


Figure 5. Small-signal equivalent network models: (a)HBT's, and (b) HFET's.

tained by recourse to PSPICE simulations and the results agree with the predicted gain \times bandwidth performance given in eqn (2). It is to be noted that receivers based on HFET's have $R_f \times f_{3\text{-dB}}$ -values independent of R_f , whereas those based on HBT's have values proportional to $\sqrt{R_f}$.

The magnitudes of the minimum detectable optical power (or the sensitivity) to these OEIC receivers based on HBT's and HFET's were calculated^[3] for the standard bit-error-rate of 10^{-9} . These values when $R_f \sim 5$ k Ω and $c_p = 6$ fF were found to be approximately -28 dBm for the full bandwidth of approximately 20 GHz.

Conclusions

We have presented performance of a novel MSM photodetector based on InGaAs/InAlAs lattice-matched

heterostructures on InP substrate. It is demonstrated that four-element series/parallel connected MSM photodiodes offers extremely low capacitance with a modest sacrifice of detected photocurrent. The single-element photodiodes with $1.2\mu\text{m}$ spacing showed low dark current ($\sim 10\text{pA}/\mu\text{m}^2$) when operated with 3 volts, its responsivity was 0.32 A/W at 5 volts bias, and its capacitance was 28 fF including inter-pad fringing capacitance. The $1.2\mu\text{m}$ MSM device indicated a 3 dB optical-to-electrical bandwidth of 8.4 GHz. It is believed that by reducing the finger width and spacing to $\sim 0.5\mu\text{m}$ and increasing the operating voltages for the series connected four-element MSM structures the bandwidth can be extended to 20 GHz. This detector, without large bonding pads, when integrated with the proposed transimpedance OEIC receivers is expected to yield high bandwidth (~ 20 GHz) and high sensitivity -28 dBm at the bit-error-rate of 10^{-9} .

Acknowledgments: This work has been supported by NSF under Grant No. ECS-9202642 and monitored by Dr. Albert Harvey. The authors are indebted to Drs. S. Chandrasekhar, L. Lunardi, and J.M. Rios of AT&T Bell Labs(Crawford Hills), Holmdel, NJ, for their help concerning measurements on MSM devices.

References

1. E. John, and M.B. Das, *IEEE Trans. on Electron Devices*, vol. 41, pp 162-172, 1994
2. C.X. Shi et al., *IEEE Trans. on Electron Devices*, vol. 39, pp 1028-1030, 1992
3. M.B. Das, J.W. Chen and E. John, submitted to *IEEE J. of Lightwave Technol.* (Jan. 1995)
4. Y.K. Chen et al., *IEEE Electron Device Lett.*, vol. 10, pp 267-269, 1989
5. P.C. Chao et al., *IEEE Electron Device Lett.*, vol. 11, pp. 54-62, 1990

High-Efficiency Monolithic InGaP/GaAs Tandem Solar Cells with Improved Top-Cell Back-Surface-Field Layers

ThP39

H. Kurita, T. Takamoto, E. Ikeda, and M. Ohmori
Central Research Laboratories, Japan Energy Corporation
3-17-35 Niizo-minami, Toda-shi, Saitama 335, Japan

Improved back-surface-field (BSF) layers have been adapted for the top cell of a two-terminal, monolithic InGaP/GaAs dual-junction cell in order to recover the top-cell quantum efficiency, which had been reduced significantly by the diffusion of zinc from the p⁺-InGaP BSF into the top-cell base layer. A thick p⁺-InGaP layer and a thin p-AlInP layer have proved to be effective in improving the top-cell quantum efficiency, especially in the long-wavelength region. Although the current-matching between the top- and bottom-cells was not complete, tandem cells with those BSF layers obtained high conversion efficiencies of 27.3% and 26.4%, respectively.

Introduction

InGaP/GaAs tandem solar cells are very attractive for use as super-high-efficiency solar cells, because In_{0.5}Ga_{0.5}P is lattice-matched to GaAs, and the tandem combination of these two materials, the bandgaps of which are 1.9 and 1.42 eV respectively, has a theoretical efficiency of 34%.¹⁾ In developing this tandem cell, the design of the structure of the InGaP cell is the most important consideration. In a previous paper we introduced a p⁺-InGaP back-surface-field (BSF) layer for the single-junction InGaP cell on a GaAs substrate, which enhanced the quantum efficiency of the cell, with the high efficiency of 17.4 % being obtained.

In this paper, it is shown that the structure of the BSF layer of an InGaP cell must be modified when adapted for an InGaP/GaAs tandem cell, because the dopant diffusion from the tunnel diode reduces the effect of the BSF. We report on improved structures of BSF layers, and on the excellent performances of InGaP/GaAs tandem cells using these new BSF layers.

Experiments

Cell Structure and Fabrication Method

Fig. 1 shows a schematic cross section of an InGaP/GaAs tandem cell. The cell was grown in a vertical reactor by a reduced-pressure metalorganic chemical-vapor deposition (MOCVD) epitaxy on a Zn-doped (100) GaAs substrate, which was tilted 5° toward [011]. Triethylgallium (TEG) and trimethylindium (TMI) were used for the Group-III source materials, while phosphine and arsine were used for the Group-V materials. We used silane and diethylzinc (DEZ) for n- and p-type dopants, respectively. Although the growth temperatures of

the top- and bottom-cells were both optimized at 700° C, the top-cell was grown at 650° C in order not to injure the tunnel diode by a higher temperature process.

The GaAs bottom-cell was sandwiched by n⁺ and p⁺-InGaP layers, which acted as the front- and back-surface-field layers for the bottom cell.

Top- and bottom-cells were interconnected by a heavily doped p⁺-n⁺ GaAs tunnel-junction. In order to achieve high doping for n⁺-GaAs in the tunnel diode, the delta-doping method was applied, because it was difficult for Si to be highly doped into GaAs over 3 × 10¹⁸cm⁻³ by the usual steady-doping.

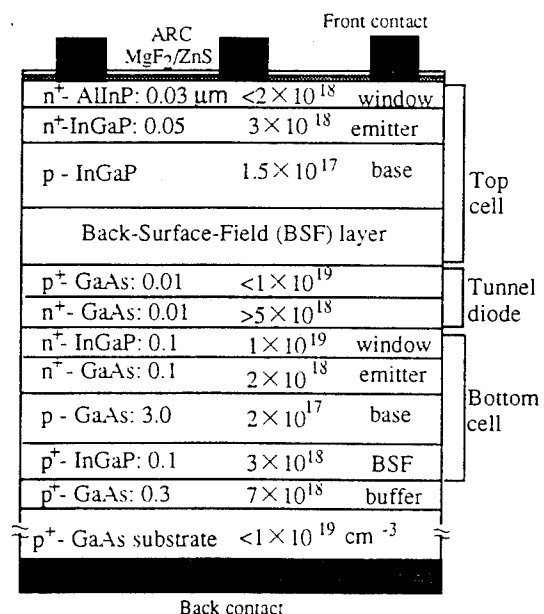


Fig. 1. Schematic cross section of an InGaP/GaAs tandem cell.

The surface of the top-cell was passivated by an $n\text{-Al}_{0.5}\text{In}_{0.5}\text{P}$ layer, with a doping level of about $2 \times 10^{17} \text{ cm}^{-3}$. On the basis of time-resolved photo-luminescence (TRPL) measurement, the effective surface recombination rate was estimated to be about 6,000 cm/s. The minority carrier lifetime in the base layer was estimated by TRPL measurement to be about 5 ns. The backside of the top-cell was passivated by a BSF layer to prevent photo-excited electrons from falling into the tunnel region.

Thin $p^+\text{-InGaP}$ BSF

A $p^+\text{-InGaP}$ layer proved to be a very effective BSF layer for an InGaP single-junction cell.²⁾ Therefore, we first employed it for the InGaP/GaAs tandem cell. Fig. 2(a) shows its structure, which was comprised of a $0.1 \mu\text{m}$ $p^+\text{-InGaP}$ layer with a doping level of $2 \times 10^{18} \text{ cm}^{-3}$ and a $0.025 \mu\text{m}$ $p\text{-InGaP}$ graded-doping layer, where the doping level gradually decreased to the base layer with a carrier density of $1.5 \times 10^{17} \text{ cm}^{-3}$. In the highly-doped BSF layer, the bandgap narrowing is estimated to be about 30 meV, while the shift of the Fermi energy is about 70 meV.³⁾ As a result the barrier height for electrons between the base and $p^+\text{-InGaP}$ is about 40 meV.

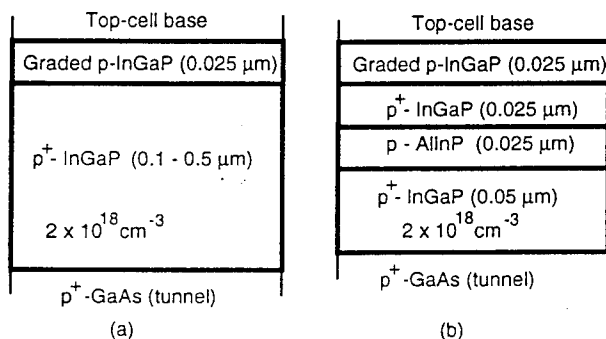


Fig. 2 Schematic cross sections of the top-cell BSF layers. (a): $p^+\text{-InGaP}$ BSF; (b): $p\text{-AlInP}$ BSF.

It was noted that the GaAs tunnel diode was sandwiched by high-doped InGaP layers. This structure, which is called a double-hetero structure tunnel diode, is believed to be effective in increasing the tunnel peak-current I_p .⁴⁾ After annealing the tunnel diode sample at 650°C , the I_p was about 80 mA/cm^2 , while the expected short-circuit current of the solar-cell was about 15 mA/cm^2 .

When this $p^+\text{-InGaP}$ BSF was applied to InGaP/GaAs tandem cells, however, the spectral response of the InGaP top-cell was reduced significantly at the long-wavelength region, as compared to that of an InGaP single-junction cell. It was revealed by Secondary Ion Mass Spectroscopy (SIMS) analysis that zinc diffused strongly from the $p^+\text{-InGaP}$ layer toward the base layer, and significantly reduced the doping level in the BSF layer, as shown in Fig.3.(b). This Zn diffusion made the interface between the base and BSF layers unclear, and reduced the effective base thickness. Fig.4, which is the conduction-band diagram calculated from the SIMS data assuming the full activation of zinc and taking account of the bandgap narrowing due to high-doping, shows that the diffusion of Zn caused the reduction of the BSF barrier height.

Modifications of BSF

In order to overcome the above-mentioned shortcoming of a thin $p^+\text{-InGaP}$ BSF without introducing another material for the p-type dopant, we tried two types of modifications for the BSF structure.

The first BSF modification involved thickening the $p^+\text{-InGaP}$ layer. This was done in order to make the Zn diffusion less effective on the barrier reduction of the BSF layer.

The second type of modification was to replace $p^+\text{-InGaP}$ by $p\text{-Al}_{0.5}\text{In}_{0.5}\text{P}$. $\text{Al}_{0.5}\text{In}_{0.5}\text{P}$ is lattice-matched to GaAs, and has 2.23 eV of band gap, which is much wider than that of $\text{In}_{0.5}\text{Ga}_{0.5}\text{P}$. The structure of this BSF layer is shown in Fig. 2(b). The $0.05 \mu\text{m}$ $p^+\text{-InGaP}$ was inserted between the tunnel diode and the AlInP layer, in order to make a double-hetero-structure tunnel diode. The $0.025 \mu\text{m}$ $p^+\text{-InGaP}$ on the AlInP layer was introduced in order to avoid direct contact between the base and AlInP layers.

While the Zn distribution in the base layer for the cell with a $0.5 \mu\text{m}$ $p^+\text{-InGaP}$ BSF layer is almost the same as that for the cell with a $0.1 \mu\text{m}$ $p^+\text{-InGaP}$ BSF layer as shown in Fig.3, it is shown in Fig.4 that the barrier height of the BSF layer recovered significantly although the recovery was not complete.

In the case of the AlInP BSF layer, the Zn diffusion toward the base layer was significantly reduced, and a very high barrier appeared in the BSF layer, which came from the band discontinuity between InGaP and AlInP .

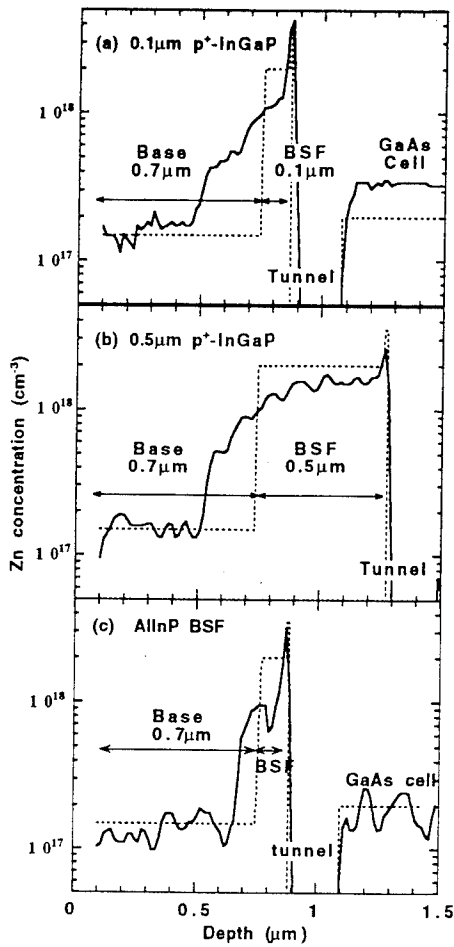


Fig. 3. SIMS data of zinc distribution in tandem cells. (a): with $0.1 \mu\text{m}$ $\text{p}^+\text{-InGaP}$ BSF; (b): with $0.5 \mu\text{m}$ $\text{p}^+\text{-InGaP}$ BSF; and (c): with p-AlInP BSF.

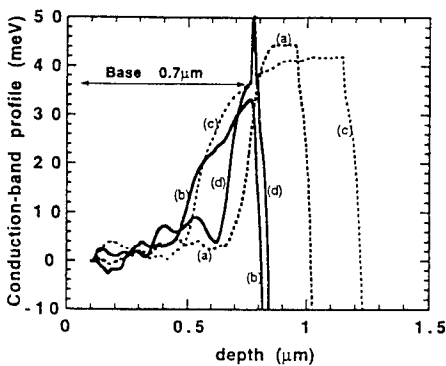


Fig. 4. Conduction-band diagrams in the top-cell base and BSF layers for the various BSF layers. (a): single InGaP cell; (b): tandem with $0.1 \mu\text{m}$ $\text{p}^+\text{-InGaP}$ BSF layer; (c): tandem with $0.5 \mu\text{m}$ $\text{p}^+\text{-InGaP}$ BSF layer; and (d): tandem with p-AlInP BSF layer.

Quantum Efficiency

In Fig. 5, the quantum efficiencies for the top cell are compared among the tandem cells with various BSF structures. The thickness of the base layer of the top-cell was $0.7 \mu\text{m}$, and the grid coverage was 10% for all cells. Thickening the $\text{p}^+\text{-InGaP}$ layer to $0.5 \mu\text{m}$ proved to be very effective for recovering the quantum efficiency. An AlInP BSF layer was also shown to be a good alternative, although the recovery of the quantum efficiency was less than that for the cell with a $0.5 \mu\text{m}$ $\text{p}^+\text{-InGaP}$ BSF layer, which was against expectation from Fig. 3 and Fig. 4.

Fig. 6 shows the bottom cell quantum efficiencies for those two cells. For AlInP BSF, the short wavelength tail was larger than that for the $0.5 \mu\text{m}$ $\text{p}^+\text{-InGaP}$ BSF. This difference comes from the difference in the total InGaP thickness of the top-cell.

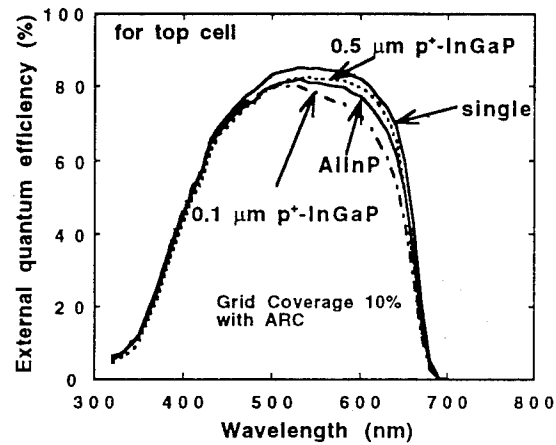


Fig. 5. Spectral responses of the top cells of tandem cells with various BSF layers.

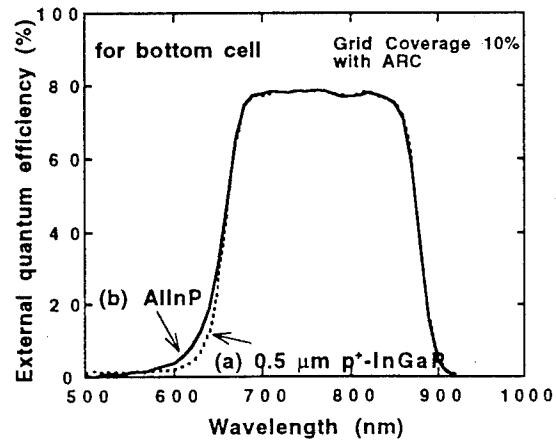


Fig. 6. Spectral responses of the bottom cells of tandem cells. (a): with $0.5 \mu\text{m}$ $\text{p}^+\text{-InGaP}$ BSF; and (b): with p-AlInP BSF layers.

Cell Performance

Fig. 7 shows the AM1.5G cell performances of 1 cm x 1 cm InGaP/GaAs tandem cells with improved top-cell BSF structures. The ARC was a double layer of MgF_2 and ZnS , the thicknesses of which were designed to reduce the reflectivity below 2% in the wavelength region of 400 - 650 nm. The grid coverage was 2%. The base thickness of the top-cell was $0.7 \mu\text{m}$ for the p^+ -InGaP BSF, and $1.0 \mu\text{m}$ for the AlInP BSF; and the total thicknesses of the two InGaP layers in the top-cell were $1.275 \mu\text{m}$ and $1.125 \mu\text{m}$, respectively.

Those two tandem cells achieved high conversion efficiencies of 27.3% and 26.4%, respectively. The 0.9% difference in efficiency comes from the low fill-factor (F.F.) of the tandem cell with the AlInP BSF, which is due to the poor characteristics of the GaAs tunnel-diode in this cell.

It was noted that, when the intensity of light illuminated on the cells was increased intentionally in the long-wavelength region from the normal AM1.5G spectrum, the short circuit current (Isc) was increased for both tandem cells. This indicates that Isc is not determined by the top-cell photo-current, but is determined by the bottom-cell photo-current, which depends upon the total thickness of the InGaP layers in the top-cell. This is consistent with the fact that the Isc for the AlInP BSF is 0.1 mA larger than that for a p^+ -InGaP BSF. In order to achieve the current-matching between the top and bottom cells, thinning of the top-cell base is needed.

Conclusion

BSF structures for the top-cell of the InGaP/GaAs tandem cell have been developed and have proved to be very effective in enhancing top-cell quantum efficiency. The best conversion efficiency achieved so far for 1 cm x 1 cm cells was 27.3 %. Nearly 30 % efficiency is expected achieving current-matching between the top- and bottom-cells by thinning the top-cell base layer and by increasing the peak current of the tunnel diode.

Acknowledgements

The authors wish to thank F. Nagamine and T. Abe of the Japan Quality Assurance Organization for measuring the I-V characteristics of the cells.

This work was supported by the New Energy and Industrial Technology Development

Organization (NEDO) as a part of the New Sunshine Program implemented by the Ministry of International Trade and Industry, Japan.

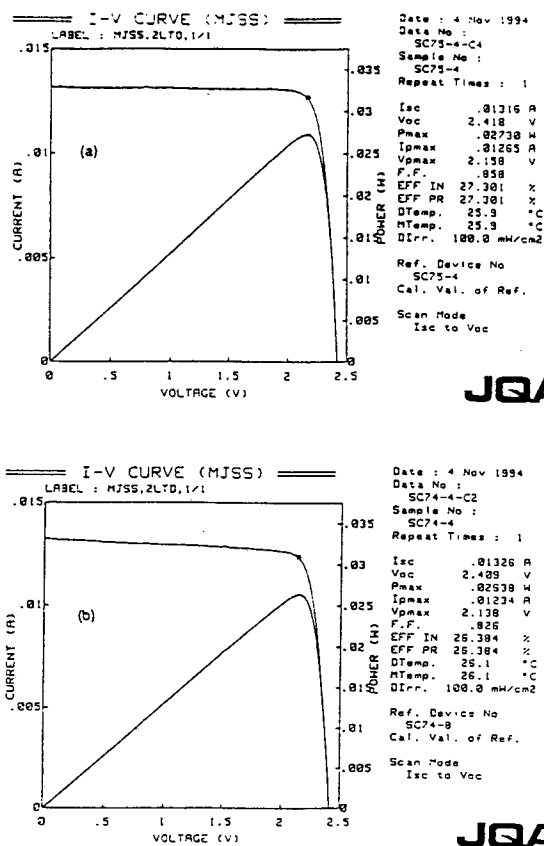


Fig. 7. Current-voltage curves of InGaP/GaAs tandem cells with improved BSF layers. (a) $0.5 \mu\text{m}$ p^+ -InGaP ; and (b): p-AlInP BSF layers.

References

- [1] J. C. C. Fan, et al, "Optimum design of high-efficiency tandem solar cells", 16 th Photovoltaic Specialist Conf. (1982), 692.
- [2] E. Ikeda et al., "17% Efficient InGaP/GaAs Solar Cells by Improved Minority Carrier Lifetime", Proc. 6th International Conf. InP and Related Materials(1994) 500; T. Takamoto et al., "Structural optimization for single junction InGaP solar cells", Solar Energy Materials and Solar Cells, **35**(1994) 25.
- [3] S.M. Sze, *Physics of Semiconductor Devices*, 2nd Edition (John Wiley & sons, Inc. New York, 1981).
- [4] C. Amano, et al., "20.2% efficiency $\text{Al}_{0.4}\text{Ga}_{0.6}\text{As}/\text{GaAs}$ tandem solar cells grown by molecular beam epitaxy", Appl. Phys. Lett. **51**(1987) 1998.

Waveguide-fed PIN-HFET receiver at 2.5Gbit/s integrated on InP ThP40

L.Giraudet, A.Bruno, E.Legros, F.Ghirardi, P.Berthier, A.Scavennec, and A.Carenco

FRANCE TELECOM - CNET/PAB - Laboratoire de Bagneux

196 Avenue Henri Ravera - BP 107 - 92225 Bagneux Cedex - France

S.W.Bland, J.I.Davies

Epitaxial Product International Ltd. Cypress Drive, St.Mellons, Cardiff, CF3 OEG, UK.

Introduction

The development of multi-wavelength optical fibre telecom networks requires the availability of wavelength selective receivers such as heterodyne or WDM photoreceivers. Monolithic integration on a same chip of many devices constituting such receivers appears important to reduce interconnection and assembly difficulty for their practical implementation in future networks. InP, InGaAs, InAlAs and GaInAsP are the materials which will allow this integration and satisfy the 1.3-1.5 μ m wavelength range needed by the fibre. We report the monolithic integration of a building block, a waveguide-fed photoreceiver, comprising a semiconductor waveguide, a PIN photodiode, and a 3 stage low noise preamplifier, based on 0.5 μ m gate length high performance HFETs. Internal sensitivities better than -27dBm at 2.5Gbit/s and -25dBm at 5Gbit/s have been measured.

Integration scheme: substrate patterning

A fabrication scheme has been defined to allow the fabrication of high performance, sub-micron gate length HFETs, together with a full compatibility with further integration of optical devices, such as integrated heterodyne photoreceiver (1). In particular, in order to keep the HFET and waveguide-PIN layers at the same height (fig.1), a substrate patterning technique, widely used for OEIC integration (2,3), has been chosen.

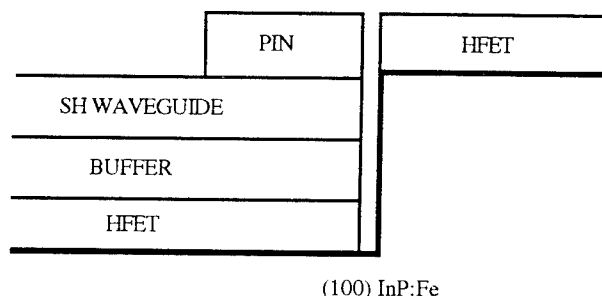


Fig 1: Schematic epilayer stack grown on patterned substrate. The FET layers are kept on top of the device allowing short gate length fabrication.

A CH₄-H₂ RIE and surface preparation process has been developed and optimized to recess 4 μ m-deep trenches in the S.I.-InP substrate, before epitaxial growth of the approximately 4 μ m thick structure. After RIE, a slight chemical wet etch is performed in order to remove damaged material. The process has been characterized using room temperature photoluminescence of n-InP substrates. Fig. 2 represents the recovery of the substrate photoluminescence characteristics (peak intensity and width) after RIE, as a function of the wet etch depth. The initial characteristics of the substrate are recovered after removing only about 200Å of damaged material. Moreover, no difference was observed between the characteristics of waveguide-fed detectors and HFETs fabricated either on planar or recessed substrates, which shows the efficiency of the overall process.

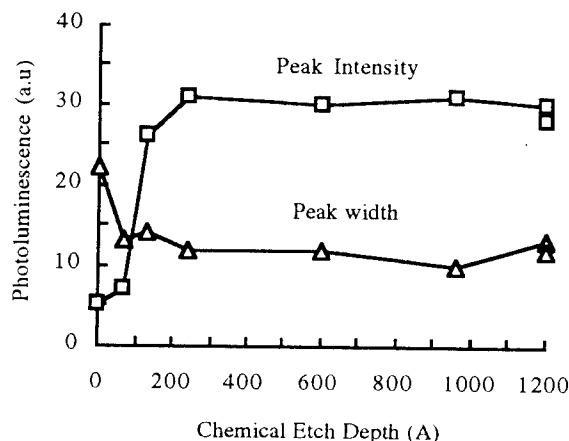


Fig 2: Room temperature photoluminescence characteristics of n-InP substrate after CH₄-H₂ RIE, as a function of the final chemical etch depth.

Material growth and receiver fabrication

A single step low pressure MOCVD growth is used to realize the epilayer stack on the patterned substrates. The growth sequence starts with the AlInAs/GaInAsP based HFET structure (4-5), followed by the InP/GaInAsP single heterostructure waveguide, before the GaInAsP/GaInAs PIN photodiode (6). The photodiode and waveguide layers are then selectively removed from the top of the HFET layers in the electronic part of the receiver, and a 11 step process is realized (5-6). The planarized approach allows the realisation of short gate length (0.5 μ m) low noise HFETs directly on S.I. substrate with deep UV contact lithography. Fig.3 shows a view of the fabricated receivers: 1.5 μ m light is injected in the waveguide (partly shown on the left side) and evanescently coupled in the PIN photodiode. The photocurrent signal is then amplified by the 3 stage amplifier.

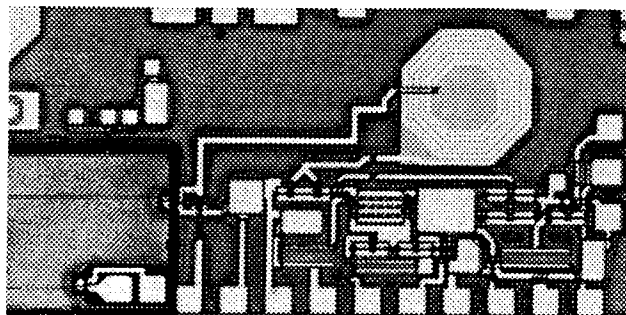


Fig 3: Photograph of the waveguide-fed pin-HFET receiver.

The low noise amplifier circuits, including MIM capacitors, resistors and inductances, have been developed in previous work (7-8).

Waveguide-fed detectors

In order to optimize the detector design, the efficiency of the evanescent coupling between waveguide and photodiode has been studied as a function of the diode length as shown in fig.4.

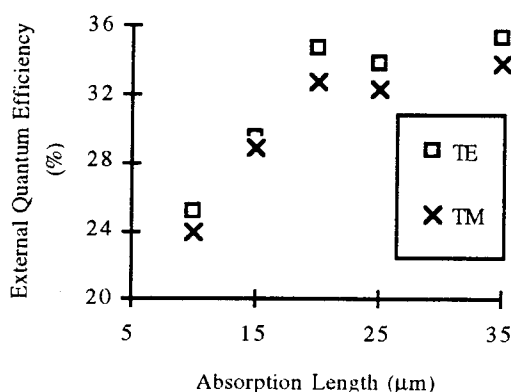


Fig 4: External quantum efficiency of a waveguide-fed photodiode as a function of the diode length.

20 μm long devices, absorbing more than 90% of the guided light, have been retained for the integrated receiver. It is worth noticing that the polarization dependence is very low on this type of device, typically 0.3dB. The waveguide geometry has been optimized for that purpose using a computation of semi-vectorial guided modes in the plane perpendicular to the propagation axis (9). This figure, obtained for 0.9 μm thick and 2 μm width guiding layer, is sensitive to waveguide width, specially for TM polarization.

Fibre to waveguide coupling losses were also experimentally studied. Best devices showed coupling losses better than -4dB with lensed fibres (10), with fibre position tolerances (taken at -1dB from the signal maximum - see fig.5) better than ± 1.2 and $\pm 0.7\mu\text{m}$ in the x and y direction respectively.

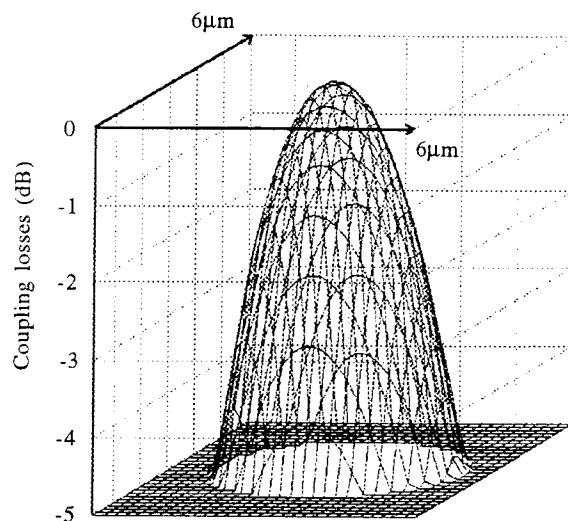


Fig 5: Excess coupling loss of a waveguide-fed photodiode as a function of the fiber misalignment.

A 2dB/cm waveguide propagation loss was measured from waveguide-fed photodiode with various waveguide length. The main contribution to loss is due to the GaInAs HFET contact layer underneath the waveguide (see fig.1). This figure may be reduced to 1dB/cm by increasing the waveguide InP buffer layer thickness from 0.8 μm to 1 μm .

The PIN photodiodes show very low capacitances of about 0.1pF, and leakage currents below 10nA at -5V. Moreover, their bandwidth on a 50 Ω load is in excess of 14GHz.

HFETs characteristics

As shown on fig.6, the integrated 0.5 μm gate length HFETs showed very good high frequency performances with f_t of 30GHz and f_{max} in excess of 50GHz. Moreover, thanks to the GaInAsP channel preventing impact ionization(4), gate leakage current remains lower than 1 $\mu\text{A/mm}$ over the whole bias range. Transconductances are close to 190mS/mm. In all respects, these devices show no degradation compared to the ones fabricated on planar substrates. This validates the efficiency of the planarized fabrication scheme.

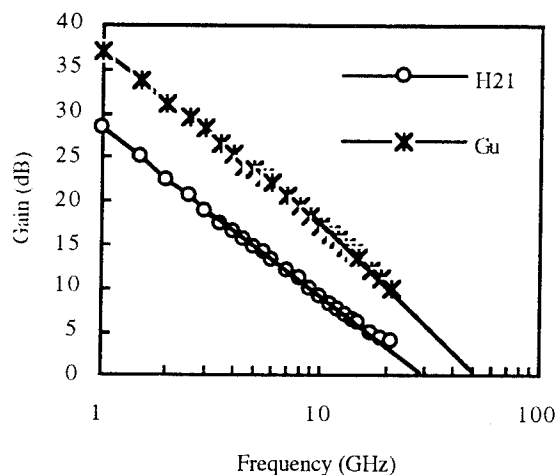


Fig 6: High frequency characteristics of the integrated 0.5 μ m gate length GaInAsP channel HFETs.

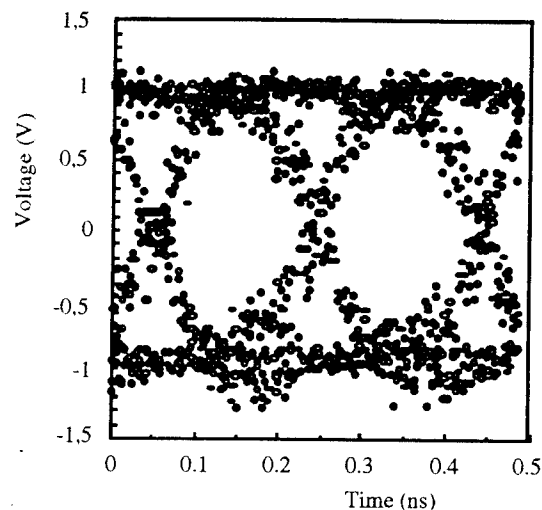


Fig 8: Receiver eye diagram at 5Gbit/s for a BER=10⁻⁹.

Receiver performances

The waveguide-fed receiver response and noise have been measured after cleaving, AR-coating and mounting with biasing circuits and external equalization. As shown on fig.7, an internal gain (referred to diode photocurrent) of 52-55dB Ω was measured on the 3.5GHz bandwidth.

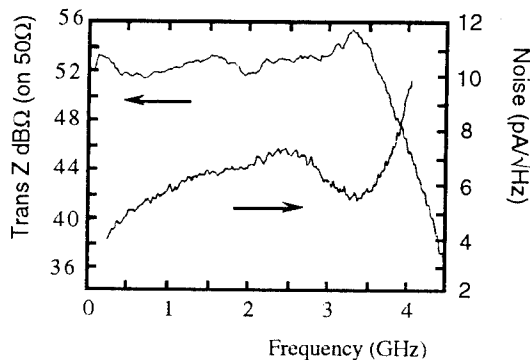


Fig 7: Waveguide-fed receiver gain and noise characteristics.

Very low average input noise densities, close to 6pA/ $\sqrt{\text{Hz}}$, were obtained over both the 1.7GHz and 3.5GHz bandwidths, required for 2.5 and 5Gbit/s operation respectively.

BER measurements were performed both at 2.5Gbit/s and 5Gbit/s. Fig.8 represents the eye diagram at 5Gbit/s for BER=10⁻⁹, and fig.9 shows the BER measurements.

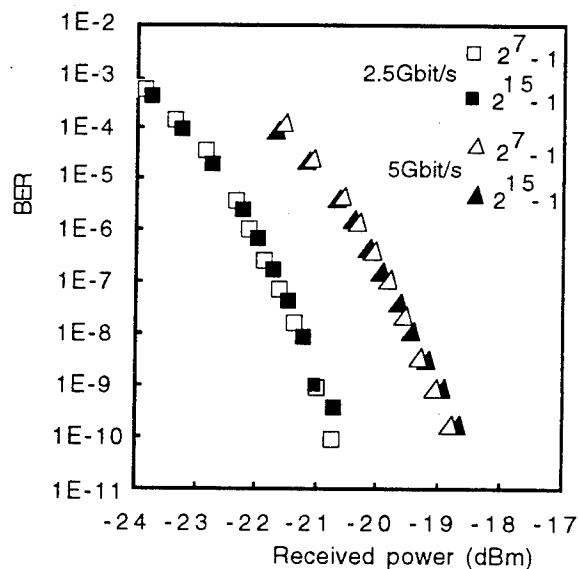


Fig 9: BER characteristics of the waveguide-fed receiver for PBRS length of 2⁷-1 and 2¹⁵-1, at 2.5 and 5 Gbit/s.

PBRS lengths of 2⁷-1 and 2¹⁵-1 were used without noticeable degradation of the receiver sensitivity for the longer one. Moreover, dynamic range in excess of 15dB could be obtained for both bit-rates.

External sensitivities of about -21dBm at 2.5Gbit/s and -19dBm at 5Gbit/s are measured. Unexpected excess coupling losses and polarization dependence were observed on the device: 6.5dB fiber to detector losses and 3.5dB difference between TE and TM modes were measured. As shown above, usual values are about 4dB coupling losses and 0.3dB polarization dependence. The discrepancy could be attributed to a waveguide rib narrowing during receiver fabrication, leading to a more leaky and assymetric mode. However,

internal sensitivities better than -27dBm at 2.5Gbit/s and -25dBm at 5Gbit/s are obtained from these measurements, within a few dBs from state-of-the-art top-illuminated integrated PIN-FET receivers on InP.

Acknowledgements:

We would like to thank M.Vaa and B.Mikkelsen from the Electromagnetics Institute of the Technical University of Denmark for BER measurements and dynamic range evaluation, and also M.Billard, P.Blanconnier, M.Carre, J.P.Chandouineau, M.Foucher, F.Huet, J.Thomas for technical assistance. This work has been supported by the EEC through the ESPRIT-MOSAIC project.

References:

- (1) F.Ghirardi, J.Brandon, F.Huet, M.Carre, J.Thomas, A.Bruno, A.Carenco, "InP based 10GHz bandwidth polarisation diversity heterodyne photoreceiver with electrooptical adjustability" *Photonics Tech. Lett.* Vol6 p814, 1994
- (2) D.Spear, P.Dawe, G.Antell, W.Lee, S.Bland, "New fabrication technology for long-wavelength receiver OEICs", *El. Lett.* Vol25 p156, 1989
- (3) H.Yano, K.Doguchi, M.Murata, N.Nishiyama, G.Sasaki, H.Hayashi, "Fabrication of PIN/HEMT receiver OEICs for Gbit/s lightwave systems on 3-inch diameter InP substrate", *IEICE Journal*, Vol. J77 p285, May 1994.
- (4) P.Berthier, L.Giraudet, A.Scavennec, D.Rigaud, M.Valenza, J.Davies, S.Bland, "InGaAsP channel HFETs on InP for OEIC applications", *J. Light. Tech.*, Vol12, pp2131-2138, 1994.
- (5) P.Berthier, E.Legros, L.Giraudet, A.Scavennec, J.M.Dumas, D.Rigaud, M.Valenza, "High performance InGaAsP channel HFETs on InP for OEIC applications", *Proc. IPRM94*, paper MB4, Santa Barbara, 1994.
- (6) A.Bruno, L.Giraudet, E.Legros, P.Blanconnier, J.Thomas, M.Carre, M.Billard, F.Ghirardi, L.Menigaux, A.Scavennec, A.Carenco "Fabrication and performance of an integrated 3dB coupler-balanced PIN pair-JFET on InP" *Proc. ECIO*, paper 6-8, Neuchâtel, 1993.
- (7) E.Legros, M.Billard, L.Giraudet, A.Scavennec, "Low noise GaAs P-HEMT monolithic integrated circuit for high sensitivity photoreceivers", *Proc. 11th EFOC&N*, the Hague, 1993.
- (8) P.Berthier, E.Legros, L.Giraudet, A.Scavennec, "A 10Gbit/s, -22.4dBm photoreceiver using InP-based HFET preamplifier IC", post deadline paper ThC12.5, ECOC, Montreux 1993.
- (9) G.Hervé-Gruyer and M.Filoché, ALCOR/BPM Software developed and distributed by France Telecom/CNET
- (10) N.Kalonji, J.Semo, "High efficiency, far working distance laser diode-single mode fiber coupling arrangement" *El. Lett.* Vol30 p892, 1994

Optically Controlled S- and N- shaped Negative Differential Resistances by R-TOPS

H. Sakata, K. Utaka and Y. Matsushima

KDD R&D Laboratories

2-1-15 Ohara, Kamifukuoka-shi, Saitama 356, Japan

Introduction

In order to apply to optical signal processing, several kinds of optoelectronic switching devices utilizing negative differential resistance (NDR) characteristics have been studied so far (1-5). We have proposed two types of the devices using NDR. One is a Triangular-barrier Optoelectronic Switch (TOPS), which consists of a triangular-barrier phototransistor (TBP) (6), showing an S-shaped NDR (7). The other is a Resonant-tunneling Triangular-barrier Optoelectronic Switch (R-TOPS), which consists of a double-barrier resonant-tunneling diode (DB-RTD) and a TBP, showing an N-shaped NDR (8). If both S-shaped and N-shaped NDRs are introduced to a single device, we can expect new functions as a result of effective combination of respective features. In this paper we report optically controlled S- and N-shaped NDRs in the structure of an R-TOPS. To our knowledge, this is the first demonstration of an optoelectronic switch which exhibits different types of bistabilities attributed to optically controllable S- and N-shaped NDRs simultaneously.

Device structure

Figure 1 shows a band diagram of the device fabricated, which is the same as the R-TOPS. It consists of a DB-RTD and a TBP, which we used as TOPS in this case. It was composed of InGaAs / (In)AlAs for 1.5 μm wavelength range operation. The TBP had $n^+ - i - \delta p^+ - i - n^+$ structure, and in the DB-RTD a well layer and barrier layers were InGaAs and AlAs, respectively. An S-shaped NDR occurs due to avalanche multiplication in the drain

region of the TBP, and an N-shaped NDR occurs due to resonant tunneling in the DB-RTD. As for the S-shaped NDR, with the bias voltage, avalanche multiplication occurs in the drain region. As a result, electrons and holes are generated in the drain, and the holes move to the gate layer and accumulate in it. Resultant lowering of the potential barrier of the gate increases the majority carrier flow of electrons over the potential barrier from the source to the drain regions. Multiplied holes further lower the potential barrier, so the majority carriers flow moreover. This positive feedback phenomenon between the hole generation and the electron flow through the avalanche multiplication gives rise to optoelectronic switching, when a device structure is optimized and an electric field in the drain is large enough.

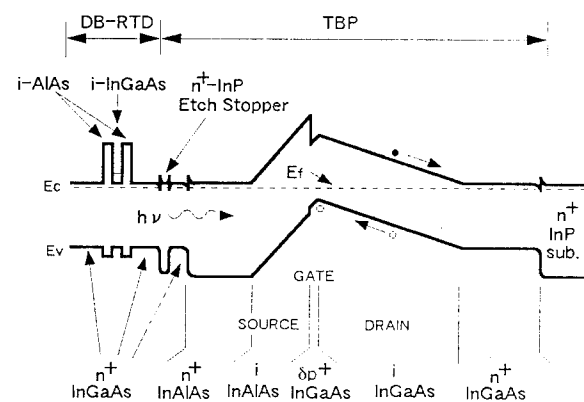


Fig. 1 Band diagram of R-TOPS.

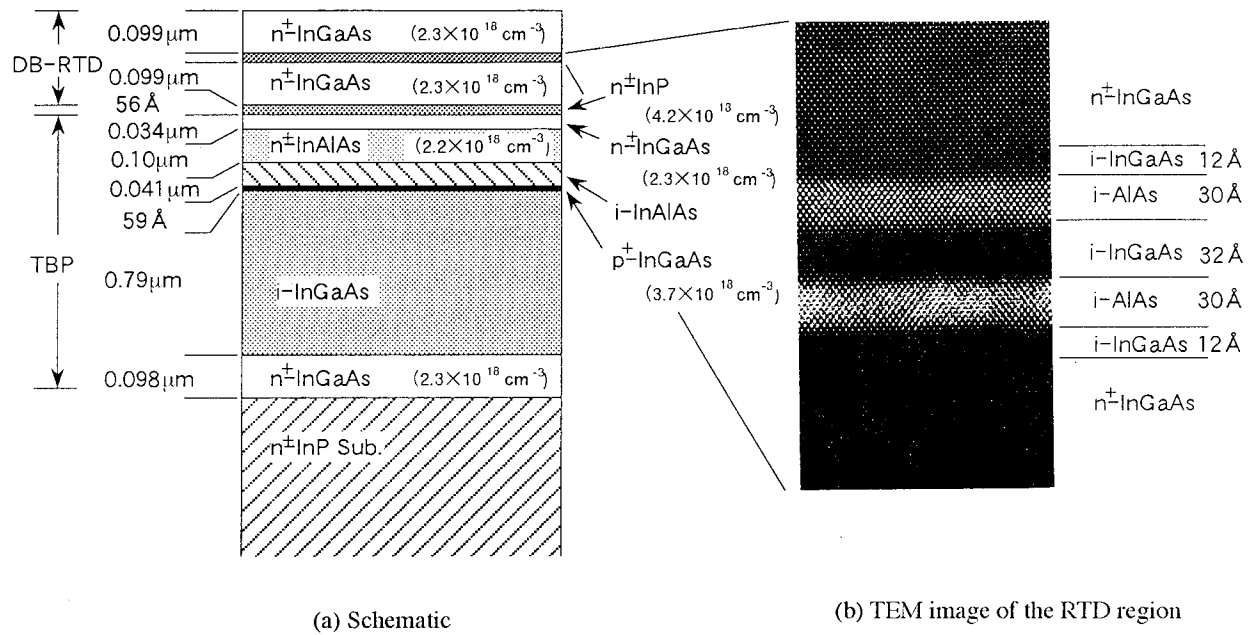


Fig.2 Cross-sections of the device

Figure 2 shows cross-sections of the device in which (a) is a schematic and (b) is a TEM image of the RTD region. The device was grown on an (100) n⁺-InP substrate by gas source MBE, in which 100% AsH₃ and PH₃ were used for group V sources, and silicon and beryllium were used as n-type and p-type dopants, respectively. The growth temperature was 530°C for InGaAs and (In)AlAs. The device structure consisted of n⁺-In_{0.53}Ga_{0.47}As (0.098 μm, 2.3 × 10¹⁸ cm⁻³), i-In_{0.53}Ga_{0.47}As (0.79 μm), δp⁺-In_{0.53}Ga_{0.47}As (59 Å, 3.7 × 10¹⁸ cm⁻³), i-In_{0.52}Al_{0.48}As (0.041 μm), n⁺-In_{0.52}Al_{0.48}As (0.10 μm, 2.2 × 10¹⁸ cm⁻³), n⁺-In_{0.53}Ga_{0.47}As (0.034 μm, 2.3 × 10¹⁸ cm⁻³), n⁺-InP (56 Å, 4.2 × 10¹⁸ cm⁻³), n⁺-In_{0.53}Ga_{0.47}As (0.099 μm, 2.3 × 10¹⁸ cm⁻³), i-In_{0.53}Ga_{0.47}As (12 Å), i-AlAs (30 Å), i-In_{0.53}Ga_{0.47}As (32 Å), i-AlAs (30 Å), i-In_{0.53}Ga_{0.47}As (12 Å) and n⁺-In_{0.53}Ga_{0.47}As (0.099 μm, 2.3 × 10¹⁸ cm⁻³). The device was etched into a mesa with 60 μmφ. Contact to the top layer was formed by evaporating Au / Sn in the

shape of an open ring structure using lift-off technique with SiN_x passivation. Input -light was illuminated to the top of the device with a lensed fiber.

Characteristics

Experimental I-V characteristics at room temperature were drastically changed by different input-light powers as shown in Fig.3(a)~(d). The substrate side was normally positively biased at V_b, and a wavelength of the input-light was 1.55 μm. We measured them using a voltage source without an external resistance. As the bias voltage increased at dark as shown in Fig.3(a), the current was almost 0mA up to 3.9V. However, the current abruptly increased to 37mA at 3.9V due to avalanche multiplication in the TBP. On the contrary, as the bias voltage decreased from 3.9V at dark, it showed the N-shaped NDR due to resonant-tunneling of the DB-RTD, so that the current decreased to 0mA at 2.6V due to the S-shaped NDR. When the input-light power increased to

800nW as shown in Fig.3(b), the turn-on voltage, at which the current changed to the on-state, decreased to 3.3V. However the turn-off voltage, which the current changed to the off-state, changed little by the input-light power. This is due to that the off-state is more sensitive than the on-state. When the input-light power increased to 30 μ W as shown in Fig.3(c), the S-shaped NDR-related characteristics was not observed, but the N-shaped-related one. Here, we can recognize the S-shaped NDR by the turn-on voltage larger than the turn-off one. On the other hand, the relation between these voltages is opposite for the N-shaped NDR. When the input-light power increased to 200 μ W as shown in Fig.3(d), the peak of the N-shaped NDR shifted to lower voltage side due to the voltage drop across the TBP. The N-shaped NDR was always observed regardless of the input-light powers, however, the S-

shaped NDR was only observed at less than 2 μ W in Fig.3(a) and (b). The turn-on voltage as a result of avalanche multiplication decreases with increasing the input-light power. When the input-light power increased, avalanche multiplication did not occur, because the electric field of the drain region became low due to the accumulation of holes in the gate region of the TBP.

Bistabilities in the relation between input-light power and output-current were obtained as shown in Fig.4. The bistability originated from the S-shaped NDR was observed at less than 1.4 μ W, and that from the N-shaped NDR was observed more than 20 μ W. We can recognize that this device exhibits different types of bistabilities attributed to optically controllable S- and N-shaped NDR simultaneously. These bistable characteristics have

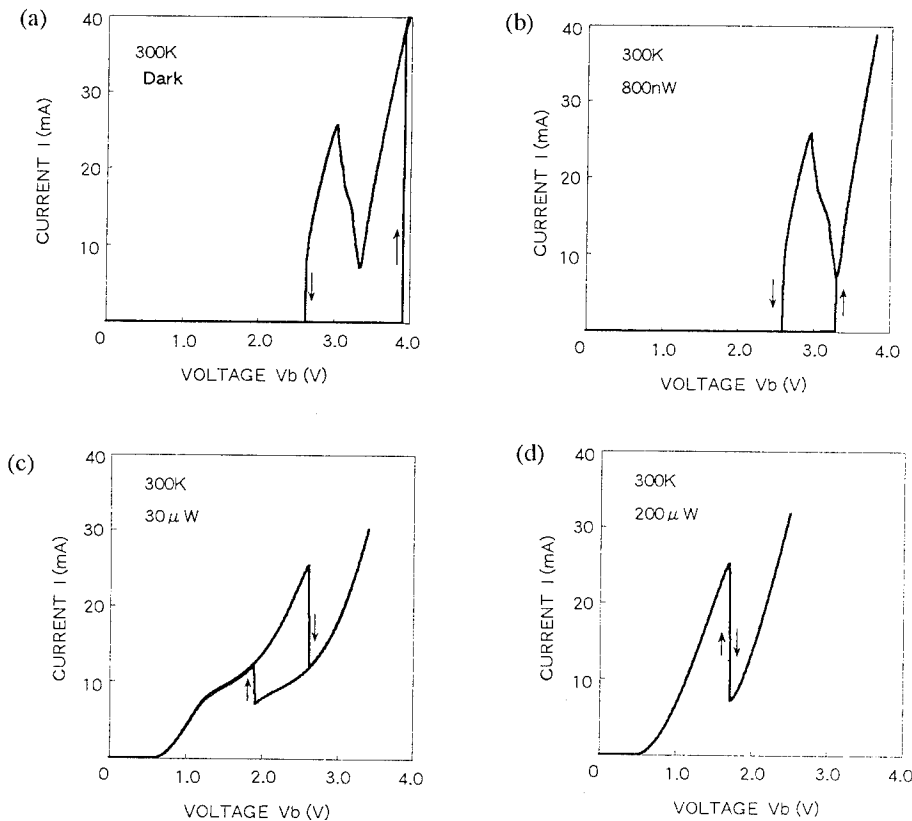


Fig.3 I-V characteristics at different input-light powers of R-TOPS.

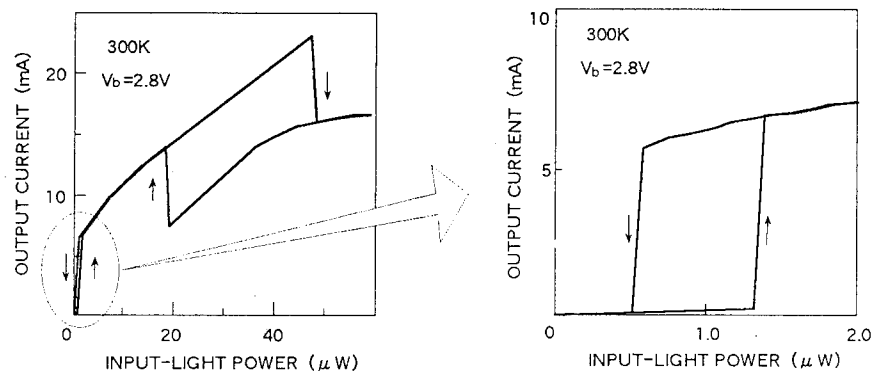


Fig.4 Input-light power vs. output-current characteristic of R-TOPS

different types of behaviors, and it is possible to realize novel operation by combining these characteristics.

Conclusion

In conclusion, we successfully observed S- and N-shaped NDRs by using the R-TOPS simultaneously. Bistabilities originated from S- and N-shaped NDRs were obtained by changing the input-light power. We succeeded to realize bistabilities with opposite behaviors in on- and off-switchings in a single device. So we can apply these functions to a new class of optoelectronic switching device for optical logic circuit.

Acknowledgements

The authors would like to express their thanks to Drs. Y. Urano, K. Sakai and Y. Mimura for encouragement.

References

- (1) G. W. Taylor, J. G. Simmons, A.Y. Cho, and R. S. Mand: 'A new double heterostructure optoelectronic switching device using molecular beam epitaxy', *J. Appl. Phys.* 1986,59 ,pp. 596-600
- (2) G. W. Taylor, R. S. Mand, J. G. Simmons, and A.Y. Cho: 'Optically induced switching in a p-channel double heterostructure optoelectronic switch', *Appl. Phys. Lett.* , 1986,49 ,pp. 1406-1408
- (3) R.S.Mand, Y.Ashizawa and M.Nakamura : 'New double heterostructure optoelectronic triangular barrier switch (OETBS)', *Electron. Lett.* 1986, 22, (18), pp.952-953
- (4) F.Y. Huang and H.Morkoç: 'GaAs/InGaAs/AlGaAs optoelectronic switch in avalanche heterojunction phototransistor vertically integrated with a resonant cavity', *Appl. Phys. Lett.* 1994,64 ,pp. 405-407
- (5) Y.Kawamura, H. Asai, S.Matsuo, and C. Amano: 'InGaAs-InAlAs Multiple Quantum Well Optical Bistable Devices Using the Resonant Tunneling Effect', *IEEE J. Quantum Electron.*, 1992, QE-28 , pp.308-314
- (6) C.Y.Chen, A.Y. Cho, P. A. Garbinski, C. G. Bethea, and B. F. Levine : 'Modulated barrier photodiode: A new majority-carrier photodetector', *Appl. Phys. Lett.* 1981,39 ,pp. 340-342
- (7) H. Sakata, K. Utaka and Y. Matsushima : 'High sensitivity and high gain optical functional device: Triangular-barrier optoelectronic switch (TOPS)', *Electron. Lett.* 1994, 30, pp.1792-1793
- (8) H. Sakata, K. Utaka and Y. Matsushima : 'Novel bistable device;resonant-tunneling triangular-barrier optoelectronic switch (R-TOPS)', *Electron. Lett.* 1994, 30, pp.1714-1716

In_xGa_{1-x}As/InAs_yP_{1-y} detector for near infrared(1-2.6 μ m) ThP42

T.Murakami, H.Takahasi, M.Nakayama, Y.Miura*, K.Takemoto*, D.Hara*.

Hamamatsu Photonics K.K

1126-1, Ichino-cho, Hamamatsu City, Japan

*Sumitomo Electric Industries, Ltd.

1-1-1 Koya-kita, Itami-city, Hyogo 664, Japan

Abstract

This paper describes a high performance In_xGa_{1-x}As/InAs_yP_{1-y} detector with spectral response range from 1 to 2.6 μ m. The detector is fabricated using Chloride Vapor Phase Epitaxy grown wafer. Details of the wafer are presented. The diameter of the detector is 1mm ϕ. Dark current at -1V, Shunt resistance and Responsivity at peak wavelength(2.35 μ m) is 7 μ A, 6kΩ, 1.2A/W, respectively.

Introduction

NIR spectroscopy has been intentionally introduced and developed in the various field such as foods, medical, pharmaceutical science. This causes a necessity of the good detector at NIR wavelength range 1-2.6 μ m. There are some materials for detecting this wavelength. Among them, In_xGa_{1-x}As has a great advantage to others because of low dark current and high responsivity. These are very important for low noise application and detection of low light power. This paper describes the structure of the crystal and the characteristic of the photodiode.

Device material and structure

In_{0.53}Ga_{0.47}As is the excellent material for detecting the light with wavelength range from 0.9 to 1.7 μ m which is widely used in the optical communication. Because the lattice constant of In_{0.53}Ga_{0.47}As is matched to that of the InP substrate. By increasing the content of indium x of In_xGa_{1-x}As, the detectable wavelength range can be extended beyond 1.7 μ m [1]. In_{0.82}Ga_{0.18}As material has a bandgap of 0.47eV and can detect the wavelength range 1-2.6 μ m at room temperature, since $\lambda c = 1.24/E_g$, where E_g is the bandgap. However increasing of x in In_xGa_{1-x}As causes the lattice-mismatch to the InP substrate. This lattice-mismatch introduces the dislocations into the material. That causes generation-recombination centers and reduces the minority carrier lifetime [2]. And also leads to the large dark current and loss of the photocurrent of the detectors [3]. Then the buffer layers with graded composition of InAs_yP_{1-y} are placed between InAs_{0.82}P_{0.18} absorption layer and the InP substrate. The dislocations bend at step interface of each graded layer and are disturbed to enter into next layer. So it is very effective to reduce the dislocation density in the lattice-mismatch materials [4][5]. The quality of wafer for detecting long wavelength beyond 1.7 μ m seriously influences the characteristics of detector. The thickness, carrier concentration and composition of InAs_yP_{1-y} graded layers may be important for reducing the dislocations of each

graded layer and absorption layer which control quality of wafer. Fig.1 shows the fundamental structure of the epitaxial wafer for detecting long wavelength range to 2.6 μ m. The absorption layer is consist of In_{0.82}Ga_{0.18}As. The graded layers and cap layer are consist of InAs_yP_{1-y}. The cap layer has the same composition of the top layer of graded layers. The 4-type wafers were prepared for fabricating the detectors. These wafers were grown using Chloride Vapor Phase Epitaxy (Sumitomo Electric Industries, Ltd). Table.1 shows the difference of 4-type wafers. Type.1 has the 20 InAs_yP_{1-y} graded layers with different composition. These graded layers were grown on the InP substrate keeping the lattice-mismatch about 0.1%. Type.2 has the 12 InAs_yP_{1-y} graded layers with keeping the lattice-mismatch about 0.16% [6]. The each graded layer of Type.1,2 has the thickness of about 1 μ m. Fig.2,3 shows the SEM photograph of Type 1,2 wafers respectively. Both wafers have the sharp and abrupt interfaces each layer.

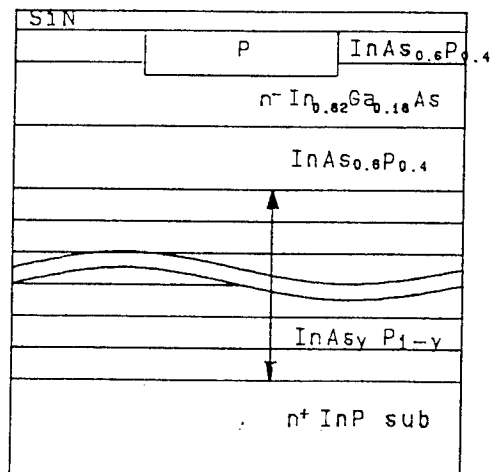


Fig.1 Schematic cross section of In_{0.82}Ga_{0.18}As Photodiode.

Wafer No	Type.1	Type.2	Type.3	Type.4
Amount of graded layers	20	12	12	12
Graded layer thickness (μm)	1	1	0.5	0.5
Graded layer C.C (cm^{-3})	3×10^{15}	3×10^{15}	3×10^{15}	$0.5-1 \times 10^{18}$

Table.1 The difference of 4-type wafers

Type.3 has the 12 $\text{InAs}_y\text{P}_{1-y}$ graded layers with about $0.5 \mu\text{m}$ thickness. Type.4 has the graded layers that was doped with sulfur and the doping concentrations in the range of $0.5-1 \times 10^{18} \text{cm}^{-3}$. The doping to graded layers may reduce the dislocation. And also the cap layer was doped to reduce the surface leakage current. But $\text{In}_{0.82}\text{Ga}_{0.12}\text{As}$ absorption layer was not doped. Because the doping to the absorption layer reduces the depletion width at low voltage and leads to deteriorate the responsivity.

Device characteristics

Regarding to the photodiodes, to reduce the dark current is the important problem. Table.2 shows dark current of 4-type detectors fabricated from Type.1-4 wafers at room temperature. Fig.4 shows dark current characteristic of 4-type photodiodes as a function of reverse voltage at room temperature. These detectors have $1\text{mm} \phi$ active area. The detectors made of wafers of Type.1-3 show the same value of dark current. The detector fabricated from Type.4 wafer shows the smallest dark current.

	Dark current(at-1V, 300k)
Type.1	20-35 (μA)
Type.2	20-30 (μA)
Type.3	25-35 (μA)
Type.4	7-15 (μA)

Table.2 Dark current of 4-type detectors

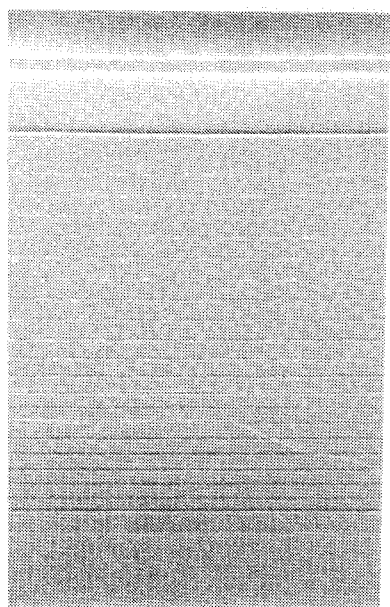


Fig.2 SEM photograph of Type.1 wafer

This shows that the doping is more effective than the amount of graded layers and thickness of each graded layer for reducing dark current of detector. This indicates that the doping decreases the density of dislocations that is active as generation-recombination centers. Fig.5 shows the variation of dark current of Type 4 with reverse voltage at temperature 25,0,-10,-25 $^{\circ}\text{C}$ respectively. The relationship between the temperature and dark current can be given by the expression [7]

$$I_d = I_0 \times \exp(-E_{go}/nkT) \quad (1)$$

where E_{go} is the energy bandgap at 0K and n is a constant between 1 and 2 which depends on the origin of current. n is 1 for pure diffusion current and is 2 for generation-recombination current. From equation (1), n can be expressed as

$$n = [E_{go}(1/T_2 - 1/T_1)] / [k \times \ln(I_{d1}/I_{d2})] \quad (2)$$

where I_{d1}, I_{d2} is dark current at temperature T_1, T_2 respectively. Fig.6 shows n of Type.4 detector that is calculated by equation (2). According to increasing reverse voltage, n change from 1 to 2. Because the generation-recombination current is a function of depletion width which is changed by reverse voltage. As the temperature is lowered, n becomes bigger. This shows that the generation-recombination current dominates dark current at low temperature. At low temperature with high reverse voltage, n exceed 2. This is because tunneling current dominates dark current at high reverse voltage.

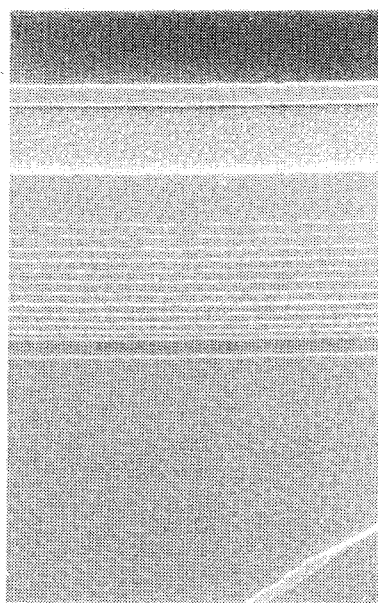


Fig.3 SEM photograph of Type.2 wafer.

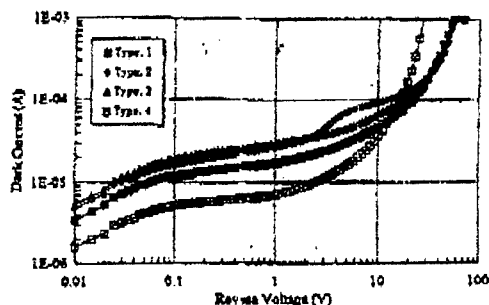


Fig. 4 Dark current characteristic of 4-type $\text{In}_{0.82}\text{Ga}_{0.18}\text{As}$ photodiodes at room temperature.

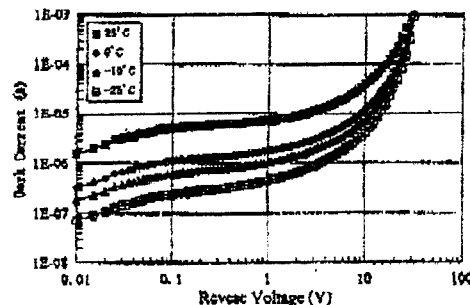


Fig. 5 Dark current characteristic of Type 4 photodiode with different temperature.

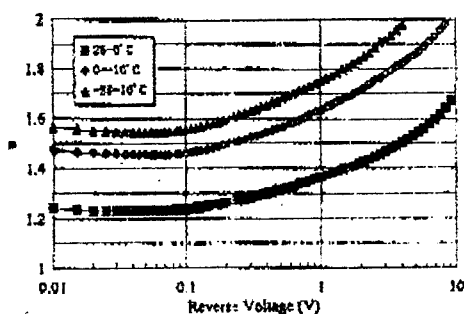


Fig. 6 n of Type 4 $\text{In}_{0.82}\text{Ga}_{0.18}\text{As}$ photodiode with different temperature.

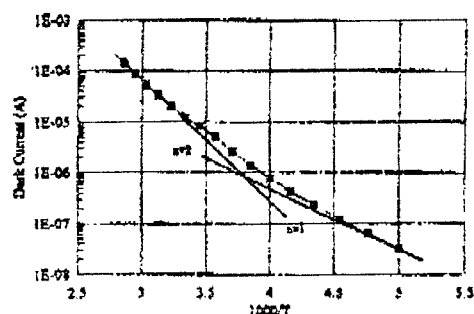


Fig. 7 Variation of dark current with reciprocal temperature at -1V bias.

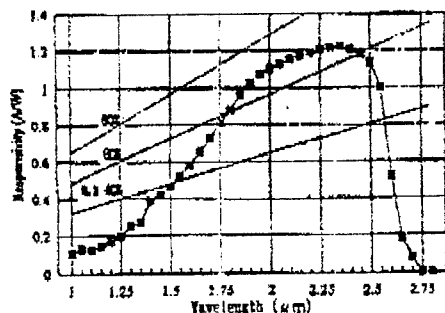


Fig. 8 Spectral responsivity of Type 4 $\text{In}_{0.82}\text{Ga}_{0.18}\text{As}$ photodiodes.

Fig. 7 shows the variation of dark current with reciprocal temperature at -1V bias. Two lines show $n=1, 2$ line respectively. This shows that dark current is dominated by diffusion current at high temperature and by generation-recombination current at low temperature. Fig. 8 shows the spectral responsivity of Type 4 detector. The peak wavelength is about $2.35 \mu\text{m}$. And the long cutoff

Active area diameter	1mm ϕ
Cutoff wavelength	$2.6 \mu\text{m}$
Peak wavelength	$2.35 \mu\text{m}$
Responsivity at λ_p	1.2A/W
Dark current at -1V	7 μA
Shunt resistance at -10mV	6k Ω
NEP	$1.3 \times 10^{-12} \text{ W/Hz}^{1/2}$
D^*	$6 \times 10^{10} \text{ cm} \cdot \text{Hz}^{1/2}/\text{W}$

Table 3 The characteristic of $\text{In}_{0.82}\text{Ga}_{0.18}\text{As}$ photodiode at 25°C

wavelength reaches to about $2.6 \mu\text{m}$. The peak value of responsivity is 1.2A/W. This indicates that quantum efficiency is 63% at the peak wavelength. The responsivity decreases abruptly at about $1.7 \mu\text{m}$. This is the window effect of $\text{InAs}_{0.6}\text{P}_{0.4}$ cap layer that has a bandgap energy $E_g=0.7\text{eV}$. This layer can absorb the light shorter than about $1.77 \mu\text{m}$ and play a part of short wavelength cutoff filter. Then this detector has low quantum efficiency at shorter wavelength region than 1.77

μ m. If the thickness of $\text{InAs}_{0.6}\text{P}_{0.4}$ cap layer can be thinner, the high responsivity can be obtained at shorter wavelength region. The cutoff wavelength is reduced by cooling the detector. The bandgap is influenced by the temperature. The cutoff wavelength is $2.55\text{ }\mu\text{m}$ at -20°C .

Conclusions

The $\text{In}_{0.82}\text{Ga}_{0.18}\text{As}$ photodiodes were fabricated by using 4-type wafers. Type.1 has 20 $\text{InAs}_y\text{P}_{1-y}$ graded layers. Type.2 has 12 $\text{InAs}_y\text{P}_{1-y}$ graded layers. These graded layers were not doped with $1\text{ }\mu\text{m}$ thickness. Type.3 has 12 $\text{InAs}_y\text{P}_{1-y}$ graded layers with $0.5\text{ }\mu\text{m}$ thickness of each layer. Type.4 has 12 doped $\text{InAs}_y\text{P}_{1-y}$ graded layers. All detectors have $\text{In}_{0.82}\text{Ga}_{0.18}\text{As}$ absorption layer for detecting the long wavelength range to $2.6\text{ }\mu\text{m}$. The excellent photodiode for detecting the long wavelength range to $2.6\text{ }\mu\text{m}$ was fabricated from Type.4 wafer. This indicates that the doping is more effective than another parameters for reducing the dislocation in the wafer. Table.3 shows the characteristic of this photodiode. Type.4 wafer has $\text{InAs}_y\text{P}_{1-y}$ graded layers with keeping the lattice-mismatch about 0.16% that is bigger than that of Type.1, and has $0.5\text{ }\mu\text{m}$ thickness less than that of Type.2. These indicate that Type.4 wafer has the thinner epitaxial layer than that of others. This is effective for achieving the good productivity.

Acknowledgments

The authors would like to thank their many colleagues for assistance, advice and discussion.

Reference

- [1] V.S.Ban et al. "Room-temperature detectors for 800-2600nm based on InGaAsP alloys," SPIE Proc. (future Infrared Detector Materials), vol.1106,p.151,1989.
- [2] G.Olsen et al, "Room-temperature properties of indium gallium arsenide detectors optimized for 1.8, 2.1 and $2.5\text{ }\mu\text{m}$," in IEEE LEOS Conf. Proc., Nov.1990.
- [3] A.J. Mosely, M.D. Scott, A.H. moore, and R.H. Wallis, "High efficiency, low leakage MOCVD grown GaInAs/AlInAs heterojunction photodiode for detection to $2.4\text{ }\mu\text{m}$." Electron Lett, vol.22, p.1207, 1986.
- [4] P.Poulain et al. " $\text{In}_x\text{Ga}_{1-x}\text{As}$ photodiodes for the 1.0 to 2.4 micron spectral region prepared by low pressure MOCVD." in Pro. Int. Symp. Gallium Arsenide and Related Compounds(Inst. Phys. Conf. Ser No.74) 1984. ch.6.
- [5] K.Makita, T.Torikai, H.Ishihara, and K.Taguchi, " $\text{Ga}_{1-y}\text{In}_y\text{As/InAs}_x\text{P}_{1-x}(y>0.53, x>0)$ pin photodiodes for long wavelength regions ($\lambda > 2\text{ }\mu\text{m}$) grown by hydride vapor phase epitaxy," Electron. Lett. vol.24, p.379, 1988.
- [6] A.M.Joshi, et al "512 and 1024 Element Linear InGaAs Detector Arrays for Near-Infrared($1\text{-}3\text{ }\mu\text{m}$) Environmental Sensing." SPIE Vol.1735 Infrared Detectors: State of the Art (1992)/287.
- [7] K.R. Linda, et al, "Dark Current Analysis and Characterization of $\text{In}_x\text{Ga}_{1-x}\text{As/InAs}_y\text{P}_{1-y}$ Graded photodiodes with $x>0.53$ for Response to Longer Wavelengths ($>1.7\text{ }\mu\text{m}$). " Jour. of Lightwave Technology, vol.10, no.8, Aug, 1992.

High-efficiency, dual-wavelength, wafer-fused resonant-cavity photodetector operating at long wavelengths ^{ThP43}

S. S. Murtaza, I-H. Tan ^{*}, R. V. Chelakara, M. R. Islam, A. Srinivasan, K. A. Anselm,
J. E. Bowers ^{**}, E. L. Hu ^{**}, R. D. Dupuis, B. G. Streetman, and J. C. Campbell

Microelectronics Research Center
Department of Electrical and Computer Engineering
The University of Texas at Austin, Austin, Texas 78712

^{*}Hewlett-Packard, Optoelectronics Division
370 W. Trimble Rd., San Jose, CA 95131

^{**}Department of Electrical and Computer Engineering
University of California, Santa Barbara, CA 93106

Abstract

Greater than 80% external quantum efficiency has been demonstrated in a dual-wavelength resonant-cavity photodetector. The absorption takes place in an $\text{In}_{0.53}\text{Ga}_{0.47}\text{As}$ absorbing layer which is placed in an InP Fabry-Perot cavity. The top mirror is formed by evaporating one pair of a CaF_2/ZnSe dielectric stack and a GaAs/AlAs dual-wavelength mirror is wafer-bonded to the InP-based cavity to serve as the bottom mirror.

Wide-bandwidth photodetectors are required for high-speed, long-haul optical-fiber communications. Resonant-cavity photodetectors (RECAPs) have been demonstrated [1,2] to be an attractive alternative to waveguiding photodetectors [3,4] in that they can achieve high quantum efficiency with thin absorbing layers for normal incidence. A typical RECAP consists of a thin intrinsic absorbing layer sandwiched between Bragg-mirrors with n-type and p-type spacer layers. This structure forms a Fabry-Perot cavity whose length is typically only a few wavelengths. The optical-field that is built-up inside the cavity because of the multiple

reflections from the top and bottom mirrors gives rise to a high absorption within the thin layer.

The realization of RECAP structures for optical-fiber telecommunications at the low-attenuation wavelength of $1.55\text{ }\mu\text{m}$ or the low-dispersion wavelength of $1.3\text{ }\mu\text{m}$ poses a challenge. The GaAs/AlAs material system can not be used because of the lack of absorption at these long wavelengths. The InP/InGaAsP system, on the other hand, suffers from low refractive-index steps which can lead to poor bottom mirror reflectivities. Tan et. al. [5] have utilized the

advantages of both the material systems by bonding [6,7] an InP/InGaAs p-i-n Fabry-Perot cavity to a GaAs/AlAs mirror. A peak quantum efficiency of 94% at 1.3 μm with a 14 nm linewidth was achieved with a 900 Å-thick absorption layer. This paper is an extension of that approach to a high-efficiency RECAP capable of operating in two separate wavelength bands. The photodiode uses a dual-wavelength mirror and a dual-wavelength resonant-cavity [8,9].

Dual-wavelength mirrors operate on the principle of square wave modulation of the reflected phases from a conventional quarter-wavelength Bragg mirror which consists of alternating layers of high refractive-index and low refractive-index materials. The position of the two high-reflectivity peaks is given by [8,10]

$$\lambda_1 = \frac{\lambda_0 P}{P + 1}$$

$$\text{and } \lambda_2 = \frac{\lambda_0 P}{P - 1},$$

where λ_0 is the central wavelength of the unmodulated Bragg-reflector and P is the periodicity of the modulating term. A mirror with $\lambda_0 = 1.414$ and $P = 11$ was shown to exhibit twin peaks that encompassed 1.3 μm and 1.55 μm [8]. A similar, n-doped, dual-mirror structure was used as the bottom mirror for this work. Figure. 1 shows the reflectivity of this dual mirror. The inset shows a schematic of one unit of the mirror structure. The entire mirror consisted of six repetitions of this unit which was grown in a Varian Gen II MBE system. The growth temperature was calibrated against the oxide desorption temperature which is approximately 580° C for an arsenic over pressure of 1×10^{-5} Torr. A 0.5 μm GaAs buffer was grown prior to the growth of the mirror structure. The growth-rate was 1 monolayer/sec for GaAs and 0.8 monolayer/sec for AlAs. A conventional As₄ cell was used as the arsenic

source. The As/Ga incorporation ratio as measured by reflection high energy electron diffraction was 2.0. This corresponds to a flux ratio measured by the ion gauge (beam equivalent pressure) of 15. The growth rate calibration and the final growth were carried out at a temperature of 600° C.

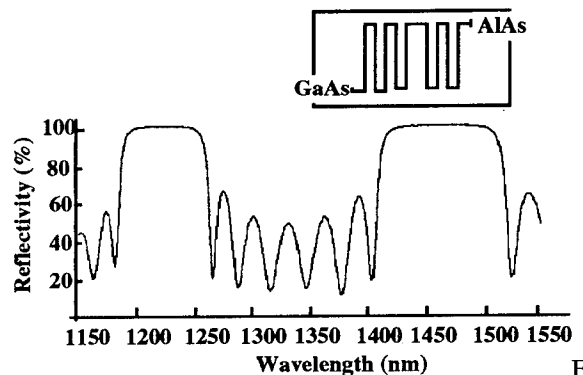


Fig. 1. The measured reflectivity spectrum of the dual-wavelength GaAs/AlAs mirror. The inset shows one period of the mirror structure. The entire epitaxially grown structure consisted of six repetitions of this unit.

The InP p-i-n photodiode structure was grown by low-pressure metal organic chemical vapor deposition (MOCVD) in a modified EMCORE Model GS 3200 UTM reactor at 60 Torr [11]. The alkyl sources employed individual pressure balancing and temperature control and were coupled to a pressure-balanced fast-switching injection manifold. The column III sources were adduct-purified trimethylindium (TMIn) and triethylgallium (TEGa). The column V sources were 100% arsine and phosphine. Purified H₂ was used as a carrier gas. The epitaxial layers were grown at 600° C on a (100) InP substrate. The structure consisted of a 6200 Å p-type InP layer, a 1000 Å undoped InP spacer layer, a 2000 Å undoped In_{0.53}Ga_{0.47}As layer, and a 8300 Å n-type InP layer. The net cavity thickness corresponds approximately to $19\lambda_1/4$ and $15\lambda_2/4$, where λ_1 and λ_2

are the two resonance wavelengths. The entire structure was capped by a 500 Å-thick p⁺-type In_{0.53}Ga_{0.47}As contact layer. Two etch-stop layers consisting of 1000 Å InP and 2000 Å In_{0.53}Ga_{0.47}As were inserted for substrate removal. The composite structure, along with the GaAs/AlAs dual mirror is shown in Fig. 2 .

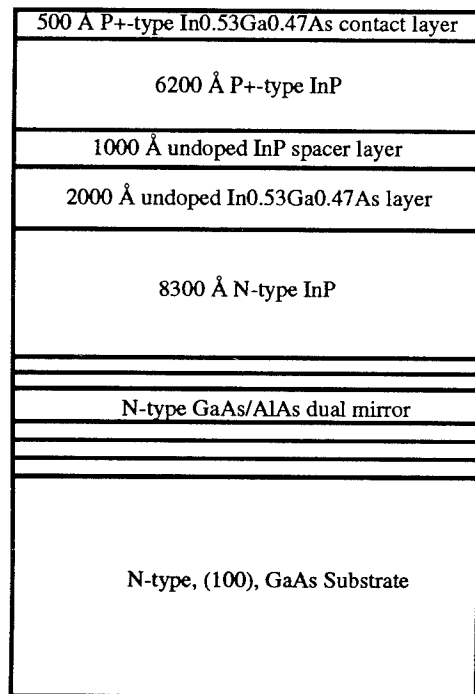


Fig. 2. Schematic cross-section of the wafer-bonded photodiode.

For atomic bonding, the top n-type part of the InP structure was placed in contact with the top surface of the n-type dual GaAs/AlAs mirror. Wafer-bonding was accomplished at 625 °C for 15 minutes in a H₂ ambient. A uniaxial stress was applied to the sample to ensure that robust bonding takes place during annealing. This wafer-bonding technique accommodated the 3.7% lattice-mismatch between the GaAs and InP crystals and produced a smooth and uniform interface [6]. After the bonding process, the InP substrate was selectively removed. This was followed by the removal of the etch-

stop layers. Chrome-gold contacts were then thermally deposited onto the p⁺ In_{0.53}Ga_{0.47}As contact layer followed by the removal of the contact layer everywhere except in the region underneath the metal. Mesa diodes of varying diameters were then etched in a bromine-methanol solution.

The quantum efficiencies of the photodiodes were measured using phase-locked detection and a calibrated Ge reference photodiode. The peak efficiencies were found to be 84% at 1208 nm and 69% at 1468 nm. After evaporation of one period of a CaF₂/ZnSe mirror, the quantum efficiencies increased to 81% at 1215 nm and 86% at 1472 nm. Figure 3 shows the external quantum efficiency spectra of the wafer-bonded photodiode for the two different top mirrors.

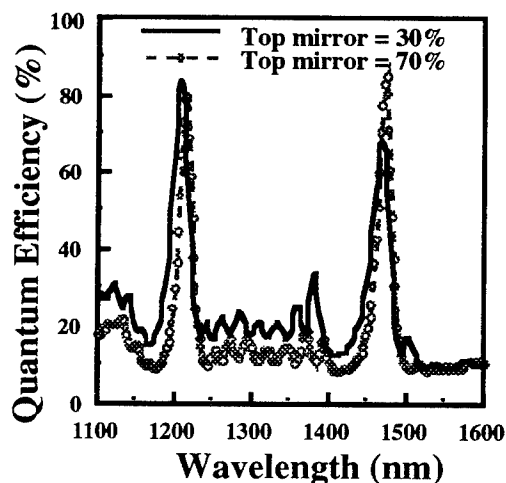


Fig. 3. The external quantum efficiency spectrum of the wafer-bonded dual-wavelength photodetector.

In conclusion, we have demonstrated a novel, high-efficiency, wafer-bonded, resonant-cavity photodetector (RECAP) operating in two distinct wavelength bands close to the technologically important wavelengths of 1.3 μm and 1.55 μm.

The work was supported by grants from the Joint Services Electronics Program (#F49620-92-C-0027), the Texas Advanced Research Program, and the Advanced Research Projects Agency (#MDA972-94-1-0004).

References

1. M. S. Unlu, K. Kishino, J.-I. Chyi, L. Arsenault, J. Reed, N. Mohammad, and H. Markoc, "Resonant cavity enhanced AlGaAs/GaAs heterojunction phototransistors with an intermediate InGaAs layer in the collector," *Appl. Phys. Lett.*, 57, 750-752, 1990.
2. R. Kuchibhotla, A. Srinivasan, J. C. Campbell, C. Lei, D. Deppe, Y. S. He, and B. G. Streetman, "Low voltage high gain resonant cavity avalanche photodiode," *IEEE Photonics Technol. Lett.*, 3, 354-356, 1991.
3. Y.-G. Wey, K. S. Giboney, J. E. Bowers, M. J. W. Rodwell, P. Silvestre, P. Thiagarajan, and G. Y. Robinson, "108-GHz GaInAs/InP p-i-n photodiodes with integrated bias tees and matched resistors," *IEEE Photon. Tech. Lett.*, 5, 11, 1310-1312, 1993.
4. K. Giboney, R. Nagarajan, T. Reynolds, S. Allen, R. Mirin, M. Rodwell, and J. E. Bowers, "172 GHz, 42% quantum efficiency p-i-n travelling-wave photodetector," 52nd Device Research Conference, July 20-22, Boulder, Colorado, 1994.
5. I.-H. Tan, J. J. Dudley, D. I. Babic, D. Cohen, B. Young, E. L. Hu, J. E. Bowers, B. I. Miller, U. Koren, and M. G. Young, "High quantum efficiency and narrow absorption bandwidth of the wafer-fused resonant In_{0.53}Ga_{0.47}As photodetectors," *IEEE Photon. Technol. Lett.*, 6, 811-813, 1994.
6. R. J. Ram, L. Yang, K. Nauka, Y. M. Houn, M. Ludowise, D. E. Mars, J. J. Dudley, and S. Y. Wang, "Analysis of wafer-fusing for 1.3 μ m vertical cavity surface emitting lasers," *Appl. Phys. Lett.*, 62, 2474-2476, 1993.
7. J. J. Dudley, D. I. Babic, R. Mirin, L. Yang, B. I. Miller, R. J. Ram, T. Reynolds, E. L. Hu, and J. E. Bowers, "Low-threshold, wafer-fused long wavelength vertical cavity lasers," *Appl. Phys. Lett.*, 64, 1-3, 1994.
8. S. S. Murtaza, A. Srinivasan, Y. C. Shih, J. C. Campbell, and B. G. Streetman, "Dual mirror and resonant cavity operating at 1.3 and 1.55 μ m," *Elect. Lett.*, 30, 8, 643-645, 1994.
9. A. Srinivasan, S. S. Murtaza, J. C. Campbell, and B. G. Streetman, "High Quantum Efficiency Dual Wavelength Resonant-Cavity Photodetector", to be published.
10. C. P. Lee, C. M. Tsai, and J. S. Tsang, "Dual-wavelength Bragg reflectors using GaAs/AlAs multilayers," *Elect. Lett.*, 29, 22-23, 1993.
11. R. D. Dupuis, J. C. Campbell, and J. R. Velebir, "Planar InGaAs PIN photodetectors grown by metalorganic chemical vapor deposition," *Electron. Lett.*, 22, 1, 48-50, 1986.

P.N. Stavrinou and S.K. Haywood

*University College London, Dept. Electronic & Electrical Engineering, Torrington Place,
London WC1E 7JE, U.K.*

L. Hart

*Interdisciplinary Research Centre for Semiconductors, Imperial College, Prince Consort Road,
London SW7 2BZ, U.K.*

M. Hopkinson, J.P.R. David and G. Hill

*EPSRC Semiconductor Growth Facility, University of Sheffield,
Sheffield S1 3JD, U.K.*

Introduction

The development of high power solid-state lasers such as Nd:YAG and Nd:YLF has stimulated interest in multi-quantum well (MQW) devices operating at 1.04-1.07 μ m [1-3]. Strained MQW structures, such as InGaAs/GaAs (on GaAs) and several InP based systems, are capable of realising structures at these wavelengths. However InP-based systems, in particular InAsP/InP, offer the potential advantage of a much lower level of strain for the same wavelength of operation (for 1.06 μ m ~ 0.6% as compared to ~2% with respect to the substrates). Here we report the electroabsorption response of strained multiple quantum well InAs_xP_{1-x}/InP structures grown by solid source molecular beam epitaxy. In each structure the well width and composition is varied to keep operation around 1.06 μ m. The structures demonstrate excellent electrical properties with room temperature exciton line widths <8meV. Using X-ray diffraction we find that although the strain in these structures is <0.7% some partial relaxation has taken place. Unexpectedly the degree of relaxation does not appear to depend on the total MQW length.

Growth and Structure details

To date most InAsP/InP structures have been grown by chemical beam epitaxy (CBE) (1,2), gas-source molecular beam epitaxy (GS-MBE) (4) and metal-organic vapour deposition (MOCVD) (5). The present structures demonstrate growth of this system by conventional solid source molecular beam epitaxy (SS-MBE). Growth was carried out in a VG V80H MBE system equipped with valved cracker sources, providing stable beams of As₂ and P₂. Conditions were typical of those for high quality InP growth i.e. substrate temperature ~480°C and a P₂/In ratio of ~5. Arsenic incorporation approached unity efficiency for mole fractions below 0.7 and quantum wells are grown by simply opening and closing the arsenic shutter during InP growth.

Further information will be published elsewhere (6).

The devices were grown on n⁺ InP substrates and had 0.2 μ m n⁺ buffer layer (1x10¹⁸cm⁻³), followed by an undoped spacer of 50nm InP. After growth of the active region a 100nm undoped spacer was grown before deposition of the p⁺ InP contact layer (0.5 μ m 5x10¹⁷cm⁻³). The active region for the two structures reported here each contained 30 periods of the following nominal well/barrier composition: M737: 95Å InAs_{0.18}P_{0.82}/100Å InP and M738: 55Å InAs_{0.21}P_{0.79}/100Å InP.

For these compositions and well widths our calculations indicated the zero field heavy-hole exciton transition (n=1hh) should occur at 1.064 μ m. Although by no means specific to strained structures, realising a common operating wavelength with different structures is potentially useful. For example, the well width is known to largely determine the electroabsorption characteristics near the band edge

(namely the quantum confined Stark effect (QCSE) (7)). In selecting the InAsP composition to reach the appropriate operating wavelength, devices utilising the QCSE can be tailored for a particular application.

Structural Characterisation

High resolution X-ray diffraction was used to assess structural properties with measurements taken from various parts of the wafers. Rocking curves from the 004 direction confirmed the well/barrier period to be within a few atomic layers of the nominal values and the observed strong satellite peaks were indicative of good interface quality and periodicity. Reflections from 115 directions suggested the average arsenic in the samples to be slightly different from the nominal values and also indicated some arsenic variation across the wafers. The use of both surface symmetric 004 reflections and high and low incidence asymmetric 115 reflections allowed the degree of strain reflection to be examined. Simulations were carried out based on dynamical diffraction theory. A relaxation factor R , which when zero implies pseudomorphic strain accommodation and when unity indicates complete relaxation, is given as:

$$R = \frac{a_{||} - a_s}{a_c - a_s}$$

where a_s , a_c are the cubic lattice constants for the substrate and active layer respectively and $a_{||}$ is the in-plane lattice constant of the layer. We note that a_c , referring to an active layer of $\text{InAs}_{x_{av}}\text{P}_{1-x_{av}}$ (where x_{av} is the average arsenic throughout the MQW), can be shown to be equivalent to the free standing lattice constant of the $\text{InAs}_x\text{P}_{1-x}/\text{InP}$ MQW (assuming equal elastic constants). Thus relaxation is defined with respect to the free standing MQW structure, i.e. where the strain is distributed between both well and barrier layers.

X-ray analysis indicated some relaxation of the strain is occurring in these and other similar MQW structures (Fig.1). However since the well widths are far below their respective

single layer critical thickness, relaxation is presumably due to the cumulative effect of the strain from successive QWs; a situation also found in $\text{Ge}_x\text{Si}_{1-x}/\text{Si}$ (8) and $\text{InGaAs}/\text{GaAs}$ (9) MQW samples. Misfit dislocations to relieve the strain are introduced at the base (and cap) between the MQW layer. A key point with this 'multilayer' relaxation is that the internal interfaces of the MQW remain coherent, with part of the initial strain in the wells now being redistributed to the barriers (8). A coherent MQW region favours the quality of rocking curves and the good optical properties (next section) observed from all the structures. Furthermore TEM micrographs from similar samples showed no evidence of dislocations in the MQW region.

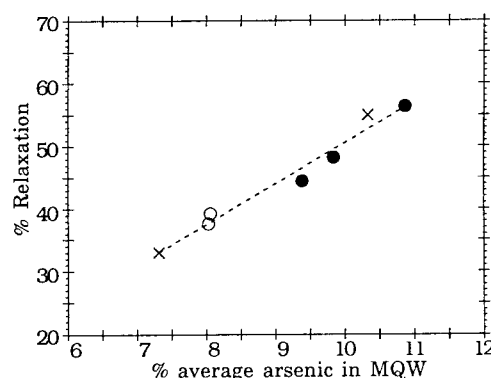


Fig.1. Relaxation versus average arsenic composition in the MQW for a series of InAsP/InP MQWs of 0.6-1.4 μm total thickness. (open circles: M738, closed circles: M737, crosses: other 50 period structures)

In the above figure, relaxation values for several samples are plotted against the average arsenic composition in the structures (found from X-ray), i.e. the misfit between the MQW and the substrate. A linear relationship (dotted line) highlights some unexpected results, e.g. a 50 period sample (MQW length $\sim 1.365\mu\text{m}$) relaxes by a similar amount to M737 (MQW length $\sim 0.63\mu\text{m}$) with both containing $\sim 10\%$ average arsenic. These results are quite different from those found with InGaAs/GaAs MQW samples, comprising 10,15 and 20 periods, which showed increasing relaxation

for an increasing number of periods (i.e. MQW length) (10). At present it is not clear whether the larger number of periods used in our samples (a realistic amount for surface normal devices) causes this apparent insensitivity of absolute MQW length to the relaxation. Further work on this topic is currently underway.

Device properties

Despite the evidence of relaxation, the measured diode characteristics, in these and other structures, are very good (6). For the present set of samples reverse bias dark currents of $<1\text{ nA}$ were obtained for applied fields of up to 200 kV/cm and showed sharp avalanche breakdown fields of typically 380 kV/cm . Intrinsic region doping levels (calculated from C-V measurements) were found to be $2\text{--}3 \times 10^{15}\text{ cm}^{-3}$.

A consistent feature of this material system is the very narrow photoluminescence linewidths often observed (6). Narrow linewidths of $\sim 6\text{ meV}$ (FWHM at 10 K) were recorded for the present samples, suggesting good quality interfaces and growth uniformity.

Photocurrent and absorption spectra were obtained using a tungsten source and 0.3 m monochromator with standard lock-in techniques. Fig.2 shows absorption spectra of M737 and M738 for increasing applied electric fields, demonstrating the quantum confined Stark effect (QCSE) (7) (note: the absorption values refer to $\text{InAs}_x\text{P}_{1-x}$ well material and were extracted using the measured X-ray period and the nominal well/barrier ratio). The half-width at half maximum of both zero field $n=1\text{ hh}$ transitions was $<8\text{ meV}$ and is comparable with InGaAs/GaAs structures operating at similar wavelengths but grown on buffer layers to reduce the effect of dislocations (3). The 13 nm difference between the zero field $n=1\text{ hh}$ transitions is expected considering the measured arsenic compositions (from X-ray), nevertheless their close proximity still warrants a comparison of performance particularly since the QCSE is largely governed by the well width (7).

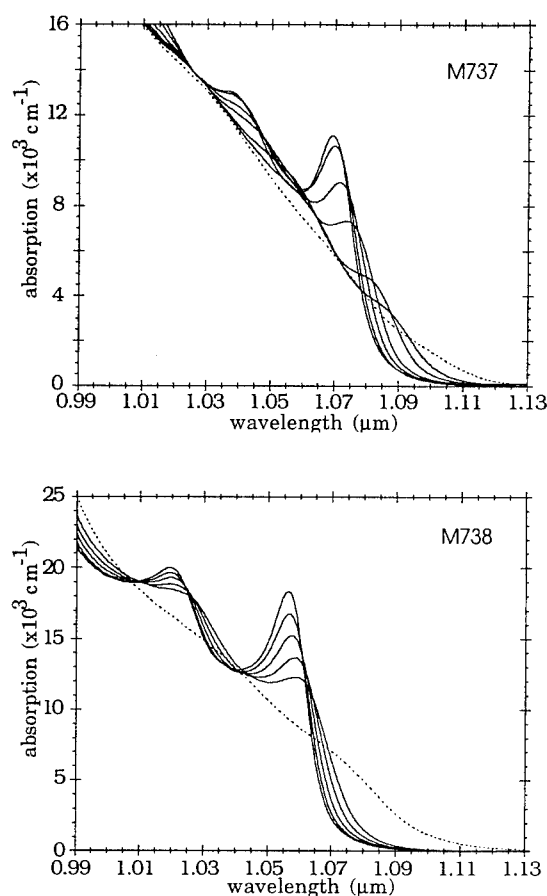


Fig.2. Absorption spectra (for well) under applied fields of 15,35,50,70 and 85 kV/cm (solid lines) and 186 kV/cm (dotted) for M737 (upper), M738 (lower)

As expected, the wider well $n=1\text{ hh}$ peak shows a larger red shift with applied field and results in a more rapid decrease in oscillator strength. While the stronger confinement in the narrow well is responsible for the higher peak absorption and better retention of the exciton with field (Fig.2).

Device performance can be predicted more readily from the total absorption change ($\Delta\alpha$) with applied field shown in Fig.3 (now including the optically inert barrier thickness). Below 85 kV/cm , the wider well sample shows greater $\Delta\alpha$ in both the normally-on and normally-off positions. However for applications requiring a high contrast ratio and which can tolerate greater operating voltage, then the 55 Å

well shows a larger maximum $\Delta\alpha$, especially for normally-on operation (above the band edge).

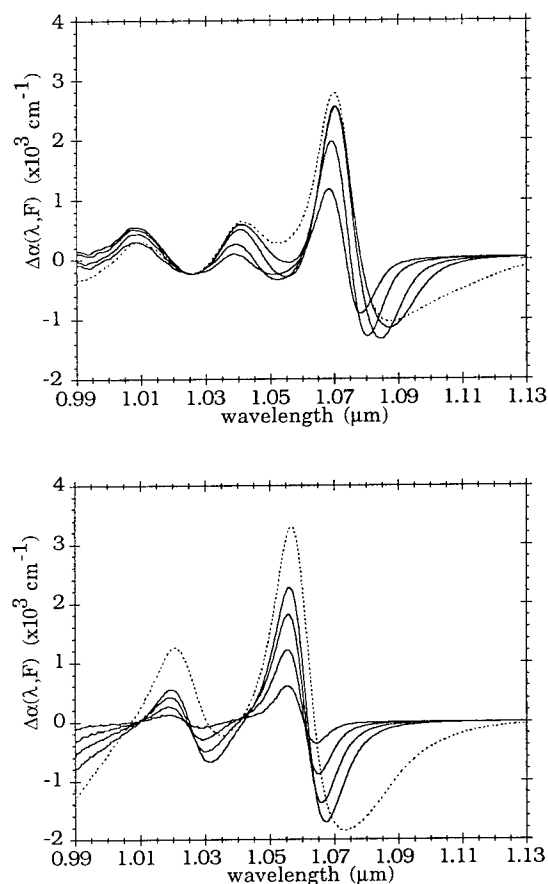


Fig.3. Absorption change (for well+barrier) under applied fields of 15,35,50,70 and 85 kV/cm (solid lines) and 186 kV/cm (dotted) for M737 (upper), M738 (lower)

For the same well parameters, increasing the barrier width has been shown to reduce relaxation (and also the broadening of the exciton resonance). This led to improvements in the effective absorption change and insertion loss for the devices studied (9). This would be consistent with the results found here since increasing the barrier width *reduces* the average arsenic in the MQW region and hence the misfit between the substrate (cf. Fig.1). A series of InAsP MQW samples incorporating these methods are currently being grown and will be reported on at a later date.

In summary we have studied the electroabsorption

response of InAsP/InP MQW p-i-n structures grown for the first time by SS-MBE. Some partial relaxation has taken place due to the cumulative effects of strain in successive QWs. Despite this the electrical properties of the devices were not degraded and demonstrated leakage currents of <1nA for up to 16V reverse bias. In addition while partial relaxation is expected to broaden the exciton line, both structures still displayed line widths of <8meV (HWHM).

Project Support: Engineering and Physical Science Research Council (ESPRC), Defence Research Agency (DRA).

References

- (1) Woodward, T.K., Sizer, II T., and Chiu, T.H. Appl. Phys. Lett., 1991, **58**, pp. 1366-1368
- (2) Woodward, T.K., Chiu, T.H. and Sizer, II T, Appl. Phys. Lett., 1992, **60**, pp. 2846-2848
- (3) Goodwill D.J, Walker, A.C, Stanley, C.R., Holland, M.C., and McElhinney, M., Appl. Phys. Lett., 1994, **64**, pp. 1192-1194
- (4) Hou, H.Q., Cheng, A.N, Wieder, H.H., Chang, W.S.C., and Tu, C.W., Appl. Phys.Lett., 1993, **63**, pp. 1833-1835
- (5) Yamamoto, M., Yamamoto, N., and Nakano, J., IEEE J. Quantum Electron., 1994, QE-30, pp. 554-561
- (6) David, J.P.R, Hopkinson, M, Stavrinou, P.N, and Haywood, S.K, submitted to J. Appl. Phys. (1995).
- (7) Miller, D.A.B, Chemla, D.S., Damen, T.C., Gossard, A.C., Wiegmann, W., Wood, T.H., and Burrus, C.A., Phys. Rev.B, 1985, **32**, pp. 1043-1060
- (8) Houghton, D.C, Perovic, D.D, Baribeau, J.M, and Weatherly, G.C, J. Appl. Phys., 1990, **67**, pp. 1850-1862
- (9) Ghisoni, M., Parry, G., Hart, L., Roberts, C., Marinopoulou, A., and Stavrinou, P.N., Electron. Lett., 1994, **30**, pp. 2067-2068
- (10) Bender, G., Larkins, E.C., Schneider, H., Ralston, J.D., and Koidl, P., Appl. Phys. Lett., 1993, **63**, pp. 2920-292

Temperature Dependence of InGaAsP Electro-Absorption Modulator Module

Hideaki TANAKA, Masayoshi HORITA, and Yuichi MATSUSHIMA

KDD R&D Laboratories

2-1-15 Ohara Kamifukuoka-shi, Saitama, 356, Japan

Introduction

Electro-absorption(EA) modulators are attractive for not only a high speed data-coding modulators (1)-(3), but also an optical pulse generators for soliton transmission systems(4). Among several types of EA modulators, an InGaAsP EA modulator is superior in terms of the small polarization dependence and the wide operation wavelength (1). From the practical point view, hermetically packaged modulator module with pigtail fibers are inevitable in actual optical transmission systems. We have already made the

modulator modules, and demonstrated their high extinction ratio and high frequency operation (5).

Temperature and wavelength dependence of the insertion loss and the driving voltage of the module are also important point in practical use. In this paper, we present detailed temperature and wavelength dependence of the InGaAsP EA modulator module.

Modulator Module

A photograph of an InGaAsP EA modulator module is shown in Fig. 1. As for the modulator itself, the

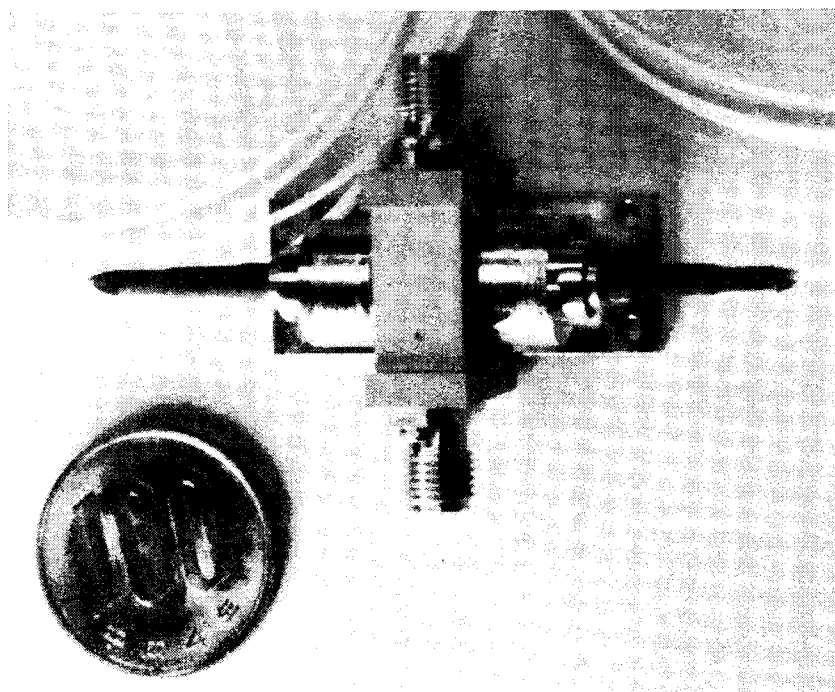


Fig. 1 A photograph of an EA modulator module.

modulator waveguide layers, which were buried with semi-insulating InP, consisted of an InGaAsP modulation layer ($\lambda_g=1.42\mu\text{m}$) and a pile-up prevention layer, as depicted in Fig. 2. The device length was about $170\mu\text{m}$. Both facets were anti-reflection (AR) coated. In the module, electric signal is supplied with a micro-stripline, and two aspherical lenses were used for the optical coupling between fibers and modulator facets. Optical components were fixed by Nd-YAG laser welding to improve the stability as well as the reliability. The packaged modulator had a high frequency response with 3dB-bandwidth of 11.8GHz.

Experiments

The modules were set into a temperature controlled test-box. Tested temperature range was from -20°C to 60°C . A tunable wavelength laser was used as a light source to investigate the wavelength dependence. The input light into the module was TE polarization mode.

Results and Discussion

Fig. 3 shows the insertion loss of the modulator module as a function of the input light wavelength λ_0 for various temperatures with the applied bias voltage of $+0.5\text{V}$. ΔE_g represents the energy difference between the band gap energy of the modulation layer and the photon energy of the input light. For $\Delta E_g < 62\text{meV}$ ($\lambda_0 < 1.528\mu\text{m}$), the insertion loss was increasing as the wavelength being shorter, and strongly dependent on the temperature. These results are caused by a band edge absorption, and a band gap energy dependence on the temperature, respectively. For $\Delta E_g \geq 62\text{meV}$, the insertion loss was slightly dependent on the wavelength and the temperature. The insertion loss was seemed to be limited by both a band edge absorption and the coupling loss between the fibers and the modulator

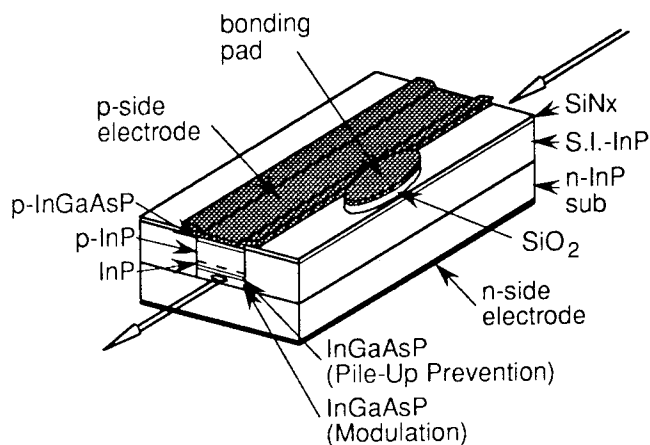


Fig. 2 Schematic structure of the InGaAsP EA modulator.

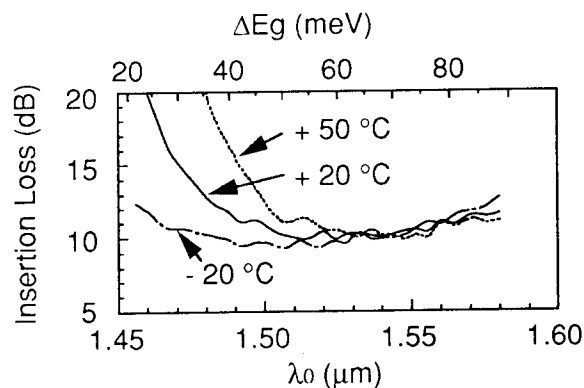


Fig. 3 Wavelength dependence of insertion loss for various temperatures.

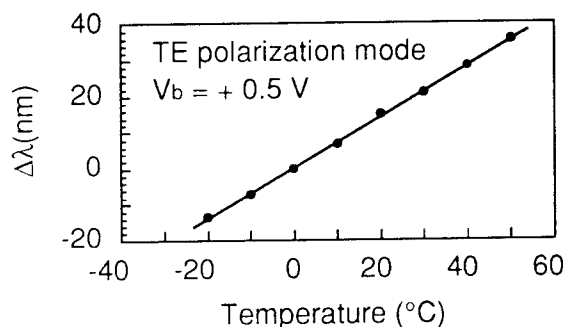


Fig. 4 Band edge shift dependence on the temperature.

facets for $\Delta E_g < 62 \text{ meV}$. On the other hand, the coupling loss was main origin of the insertion loss for $\Delta E_g \geq 62 \text{ meV}$. The dependence of the band edge absorption on the temperature was measured. $\Delta\lambda$ represents the deviation of the wavelength at the insertion loss of -15 dB from that at 0°C . The results are shown in Fig. 4. The wavelength shift per one degree was estimated to be $0.7 \text{ nm}/^\circ\text{C}$. This result almost agrees with that for InGaAsP Fabry-Perot laser diodes. Furthermore, good linearity may indicate the high thermal stability of the module.

To investigate the thermal stability of the optical pass between input and output fibers of the module, temperature dependence of the insertion loss was measured, as shown in Fig. 5. ΔE_g was set to be 62 meV to avoid the effect of band edge absorption. The fluctuation of insertion loss was as small as within 0.5 dB from -20°C to $+50^\circ\text{C}$. Small vibration of the insertion loss was seemed to be due to a residual reflectivity of AR films. High thermal stability of the module was confirmed from these results.

Considering of the low driving voltage, a smaller value of ΔE_g is desirable. On the other hands, it introduces a larger insertion loss. Assuming allowable loss increment from minimum insertion loss is 0.5 dB , the optimum ΔE_g is considered to be $48\text{--}55 \text{ meV}$ at 20°C from Fig. 3. At ΔE_g of 53 meV ($\lambda_0 = 1.512 \mu\text{m}$), temperature dependence of the insertion loss and the driving voltage $V_{20\text{dB}}$ for 20 dB extinction ratio were shown in Fig. 6(a),(b), respectively. In the range of $-20\text{--}+40^\circ\text{C}$, the fluctuation of the insertion loss was less than 0.8 dB . As the temperature being higher from -20°C to $+40^\circ\text{C}$, $V_{20\text{dB}}$ became lower from 5.7 V to 2.9 V . These results suggest the driving voltage can be controlled by changing the temperature, with keeping the insertion loss almost constant.

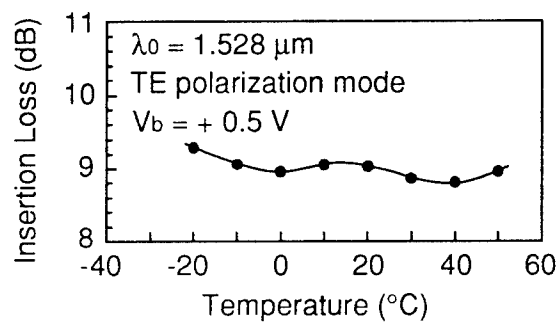
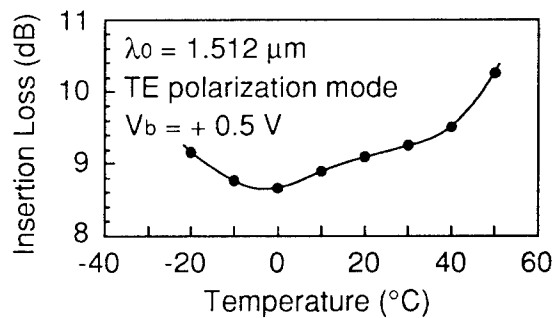
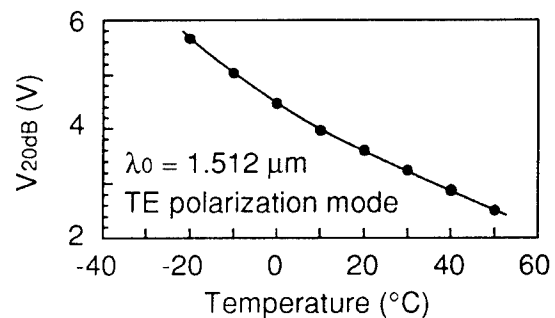


Fig. 5 Temperature dependence of the insertion loss in the case of $\Delta E_g = 62 \text{ meV}$.



(a)



(b)

Fig. 6 Temperature dependence in the case of $\Delta E_g = 53 \text{ meV}$:

(a) insertion loss ; (b) driving voltage.

Conclusion

We have investigated the temperature and wavelength dependence of the EA modulator module. Thermal stability of the module was cleared to be very high. Controllability of the driving voltage has been demonstrated by changing the module temperature. The optimum ΔE_g at 20°C has been estimated to be 48~55meV, in consideration of small insertion loss and low driving voltage.

Acknowledgements

The authors would like to thank Dr. Y. Urano, Dr. K. Sakai, and Dr. Y. Mimura for their encouragement, and Dr. M. Suzuki for his helpful discussion. They would also like to thank Mr. M. Kudo of Nagaoka University of Technology for his experimental support, and the collaborators of Japan Aviation Electronics Industry for packaging the modulators.

References

- (1) M. Suzuki, H. Tanaka and Y. Matsushima, "InGaAsP Electroabsorption Modulator for High-Bit-Rate EDFA System," *Photon. Technol. Lett.*, Vol.4, pp.586-588, June 1992.
- (2) T. Kataoka, Y. Miyamoto, K. Hagimoto, K. Wakita and I. Kotaka, "Ultrahigh-Speed Driverless MQW Intensity Modulator, and 20Gbit/s, 100km Transmission Experiments," *Electron. Lett.*, Vol.28, pp.897-898, May 1992.
- (3) F. Devaux, S. Chelles, A. Ougazzaden, A. Mircea, F. Huet and M. Carré, "10Gbit/s Operation of Polarization Insensitive, Strained InGaAsP/InGaAsP MQW Electroabsorption Modulator," *Electron. Lett.*, Vol.29, pp.586-588, June 1993.
- (4) M. Suzuki, H. Tanaka, N. Edagawa, K. Utaka and Y. Matsushima, "Transform-Limited Optical pulse Generation up to 20-GHz Repetition Rate by a Sinusoidally Driven InGaAsP Electroabsorption Modulator," *J. of Lightwave Tech.*, Vol.11, pp.468-473, March 1993.
- (5) H. Tanaka, S. Takagi, M. Suzuki and Y. Matsushima, "18Gb/s Operation by Lens-Coupled InGaAsP EA Modulator Module," *IEICE Spring National Convention Record*, C-153, March 1993.

Theoretical Analysis of Enhanced Electroabsorption Change due to Light-hole Subband Transition in Lattice-matched Wide Quantum Wells

Takayuki Yamanaka, Koichi Wakita, and Kiyoyuki Yokoyama
NTT Opto-electronics Laboratories
 3-1, Morinosato-Wakamiya, Atsugi, Kanagawa, 243-01 Japan

InP-based multi-quantum-well (MQW) electroabsorption (EA) modulators have attracted much attention for their possibility of low chirping and high frequency modulation [1-3]. It has been conventionally understood that through a large QSCE (the quantum confined Stark effect) shift by enlarging the well width, it is straightforward to achieve large EA change with low applied voltage. However, this is valid only when optical transitions between the lowest subbands can be assumed to be dominant. A sound MQW design for enhancing the EA change can be established only if *all possible* subband transitions are taken into account.

In this work, we have studied theoretically the enhancement of TE-polarized EA change in lattice-matched InGaAsP MQW structures. It is demonstrated that the *light-hole* subband transition plays the dominant role in the enhanced EA change in wide quantum wells.

We have found that the EA change strongly depends on the subband structures through the optical transition strengths. Recently we have also shown that weak electron confinement in InP-based MQW structures is a main cause of spectral broadening under bias [4]. With these in mind, the optical transition strengths are calculated taking into account the field-induced broadening due to the conduction subband structures and the field-dependent valence subband structures [4].

Figure 1(a) shows the calculated $\Gamma_{TE}\Delta\alpha$, i.e., the TE-polarized EA change ($\Delta\alpha$) multiplied by the optical confinement factor (Γ_{TE}), for different well widths. The core layer structure used in this calculation is illustrated in Fig. 1(b). In addition, an applied field strength of 150 kV/cm is assumed. In Fig. 1(a), the total $\Gamma_{TE}\Delta\alpha$ curve

shows a rather smooth well-width dependence due to the field-induced broadening effect. Furthermore, it should be noticed that the total $\Gamma_{TE}\Delta\alpha$ curve have the higher peak value at around $L_w=11.5$ nm due to the transition between the first conduction subband (E1) and the valence *light-hole* subband (LH1). On the other hand, the heavy-hole subband transition (E1-HH1) results in the lower peak value around $L_w=8.5$ nm. In the following, we will clarify why the light-hole subband transition is more dominant.

The calculated absorption spectra for a single QW with $L_w=11.5$ nm and with an applied field of 0 kV/cm and 150 kV/cm, respectively, are summarized in Fig. 2. At 150 kV/cm, it is observed that the transition peaks are broadened and become less intense compared with the zero bias case. Moreover, the E1-HH1 transition is found to be very weak at a wavelength far from the operating wavelength of 1.55 μm . This is due to the large QCSE shift as in the case of large well width. On the other hand, as shown by the dashed line for the 150 kV/cm case in the figure, the peak of the E1-LH1 excitonic transition is found to locate around the operating wavelength, which explains the large enhancement of the EA change there.

Although oscillator strength for all possible transitions in general decreases with increasing well widths, owing to the strong nonparabolicity of the LH1 subband and the larger overlap integral between electrons and light-holes, the oscillator strength for the E1-LH1 transition remains large around the operating wavelength even for large well widths. In the InP-based QW structures, there is no other higher order transition available for enhancing the EA change than the E1-LH1 transition. This is the main reason be-

hind the enhanced peak value that corresponds to the E1-LH1 transition as shown in Fig. 1(a). It should also be noted that the growing Γ_{TE} with increasing well width has a complementary effect to this enhancement.

In conclusion, we have theoretically modeled the QCSE EA change for InGaAsP MQW structures with all possible subband transitions taken into account. We have shown that enhancement of TE-polarized EA change through the E1-LH transition in lattice-matched wide QWs can be exploited to realize highly efficient EA modulators.

References

- [1] K. Sato, I. Kotaka, K. Wakita, Y. Kondo, and M. Yamamoto, "Strained-InGaAsP MQW electroabsorption modulator integrated DFB laser," *Electron. Lett.*, Vol. 29, pp. 1087-1088 (1993)
- [2] F. Devaux, E. Bigan, A. Ougazzaden, B. Pierre, F. Huet, M. Carré, "InGaAsP/InGaAsP multiple-quantum-well modulator with improved saturation intensity and bandwidth over 20GHz," *IEEE Photon. Technol. Lett.*, Vol. 4, pp. 720-721 (1992)
- [3] F. Devaux, F. Dorgeuille, A. Ougazzaden, F. Huet, M. Carré, A. Carencu, M. Henry, Y. Sorei, J.-F. Kerdiles, and E. Jeanny, "20Gbit/s operation of a high-efficiency InGaAsP/InGaAsP MQW electroabsorption modulator with 1.2-V drive voltage," *IEEE Photon. Technol. Lett.*, Vol. 4, pp. 720-721 (1992)
- [4] T. Yamanaka, K. Wakita, and K. Yokoyama, "Field-induced broadening of optical absorption in InP-based quantum wells with strong and weak quantum confinement," *Appl. Phys. Lett.*, Vol. 65, pp. 1540-1542 (1994)

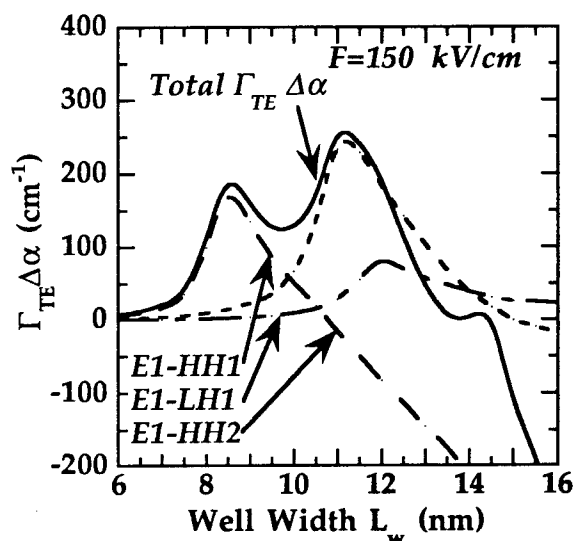


Fig. 1(a) Calculated $\Gamma_{TE}\Delta\alpha$ for InGaAsP/InGaAsP MQW structures with different well widths at the operating wavelength of 1.55 μm . The detailed MQW structure assumed in the calculation is illustrated in Fig. 1(b). The solid line is total $\Gamma_{TE}\Delta\alpha$, and dashed lines are for the decomposed contributions of the E1-HH1, -LH1, and -HH2 transitions, respectively.

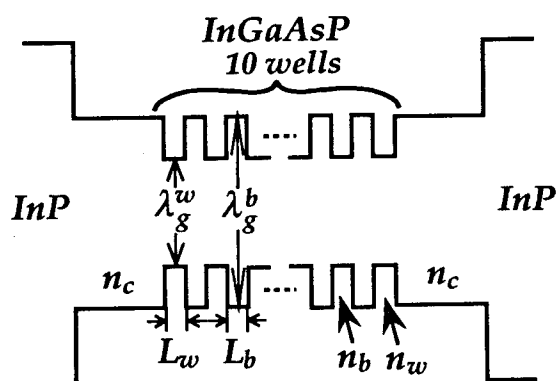


Fig. 1(b) Schematic MQW band structure assumed in the calculation. The bulk band gap wavelength of well and barrier, λ_g^w and λ_g^b , are kept constant at 1.55 and 1.1 μm , respectively. The number of well and barrier width (L_b) are fixed at 10 and 7-nm, respectively. The refractive indices for the well, barrier, and cladding layer, n_w , n_b , and n_c , are assumed to be 3.55, 3.28, and 3.28, respectively.

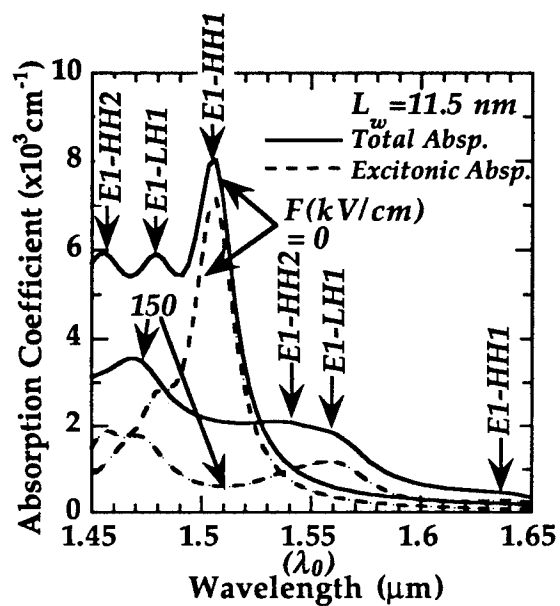


Fig. 2 Calculated absorption spectra for a single QW. The solid lines are for total absorption and dashed lines denote only excitonic transitions. The arrows in the figure indicate the peak positions for the three dominant excitonic transitions, E1-HH1, -LH1, and -HH2.

Type 1.5 Coupled Quantum Wells for Electroabsorption Modulation with Low Electric Fields

Richard T. Sahara, M. Matsuda, K. Morito, H. Soda

Fujitsu Laboratories Ltd.

10-1 Morinosato-Wakamiya, Atsugi 243-01 Japan

Fax: +81-462-48-5193

Introduction

A new quantum structure is proposed, the type 1.5 quantum well, which can be designed to modulate the optical transition oscillator strength with a very low field. The peaking of the oscillator strength and absorption with a low applied field is a practical advantage for modulator applications to reduce the drive voltage and increase the maximum absorption.

Materials and Band Structure

The band structure of the type 1.5 quantum well is shown in figure 2a, while the band structure of a standard type I quantum well is shown in figure 1a for comparison. The proposed type 1.5 quantum well is composed of one main quantum well coupled to a half (valence band only) well on the side. The unusual band structure is possible through the use of strained materials and is suitable for operation at 1.3 micron wavelengths. The material parameters for the two structures are listed in tables 1 and 2 and were calculated¹ for strained InGaAsP on an InP substrate. The type 1.5 quantum well should pose no difficulties in fabrication, since the strain-thickness product of the layers are less than those demonstrated in operating lasers.² Alternately, a similar band structure can be obtained by using InGaAlAs, or InSbAsP materials with or without strain. The narrow band gap of antimonide materials opens the possibility of operation at 1.55 microns.

Transition Wavelength & Wavefunction Overlap

The calculated transition wavelength for the e_0 -

hh_0 , e_0 - hh_1 , and e_0 - lh_0 transitions are plotted as a function of applied field in figures 1b and 2b. Plotted in figures 1c and 2c are the square of the electron and hole wave function overlap which is proportional to the oscillator strength and optical absorption. The transmission wavelength and quantum state wave function were calculated using a model with sine and cosine basis. The type I quantum well undergoes the quantum confined stark effect, red shift with applied field which is accompanied by a decrease in the oscillator strength. Figure 1d shows the electron and hole wave functions plotted against position for various applied external fields. The external field separates the electron and hole wave functions resulting in a reduced wave function overlap. Because of structure's symmetry, the response is identical for both bias polarities. For the type 1.5 quantum well, the wave function overlap is small with no applied field since the hole is located in the slightly deeper, side valence band well. A small negative field drives the hole out of the side well into the main well which increases the wave function overlap for the e_0 - hh_0 transition. This increase in the oscillator strength is similar to the increase in oscillator strength with applied field for type II quantum wells. However, the heavy hole easily shifts position into the main quantum well with the type 1.5 quantum well compared to the relatively high electrical fields needed to drive the heavy hole into the valence band barrier region of a type II quantum wells. The result is the very rapid peak in oscillator strength of the e_0 - hh_0 transition with less than 50 kV/cm of applied field. For stronger negative fields, the electron and hole wave

functions are driven past each other into the right and left side of the main well barriers respectively. Under these conditions, the oscillator strength drops slowly and the transition wavelength increases slowly because of the effective well width is equivalent to the relatively narrow main well. For positive applied fields, the electron is driven towards the left side of the main well while the heavy hole is driven towards the right side of the valence band side well, making the effective width of the well equivalent to the sum of the main well, barrier, plus the side valence band well. The wide effective well results in a very rapid drop in the wave function overlap as well as a large red shift in the transition wavelength.

Barrierless type 1.5 Quantum Well

The type 1.5 quantum well is immune to variations in the barrier layer thickness compared to most quantum tunneling devices and coupled quantum wells. Because the type 1.5 quantum well does not depend strongly on tunneling effects, the behavior of the barrierless type 1.5 quantum well as shown in figure 3a, 3b, and 3c is only slightly different from that with a barrier. This result suggests that the materials should be relatively easy to fabricate.

Modulator Design and Operation

The type 1.5 quantum well can be used as an electroabsorption material with good contrast changes for very low applied fields. An electroabsorption optical modulator with either single or multiple type 1.5 quantum wells in the intrinsic region of the diode should have doping oriented as shown in figures 2a and 3a due to the asymmetry of the structure. For the example used here a signal wavelength of 1.31 microns would be appropriate. Although the signal wavelength is slightly shorter than the optical transition wavelength, the absorption coefficient will be relatively low with no bias due to the low oscillator strength. Operation of optical modulators

with the optical wavelength shorter than the transition wavelength is common for SEED devices. As a negative field is applied, the absorption increases due to the increase in the transition oscillator strength as shown in figure 3c. For standard type I quantum wells, the e_0 -hh₁ transition is not allowed due to the weak transition matrix element. Graphs 2c and 3c show the e_0 -hh₁ transitions which have a significant transition matrix element due to the asymmetry of the well. The signal wavelength should be longer than the e_0 -hh₁ transition wavelength to reduce unnecessary absorption with no applied field. For waveguide modulators, the TE polarization should be used to interact strongly with the heavy hole transitions. The use of tensile strain in the side valence well layer results in a narrow band gap for the light hole. This will introduce some undesired background absorption to the TE polarization when there is no applied field to the material. However, with careful design, the e_0 -lh₀ transition can be kept at a wavelength significantly shorter than the e_0 -hh₀ transition. If narrow band gap, lattice matched materials are used, the deep lh wells should not be a problem. In addition, the small mass of the light hole will shift its transition energy to blue wavelengths.

From figure 2c, with the 4:1 change in the oscillator strength for the lowest transition at -25 kV/cm field, a 12 dB attenuation ratio can be obtained with -3 dB insertion loss making the material attractive for practical optical modulators. Large contrast from wave function overlap modulation is experimentally supported by a >1000 times change in photocurrent with an applied field for type II quantum wells composed of direct band gap materials.³

The type 1.5 quantum well can be designed to enhance specific characteristics. For example, increasing the difference in depth of the main and side valence band wells will produce a greater contrast in the change in the oscillator strength of the e_0 -hh₀ transition. If the difference in well depth is made large, the heavy hole will be

strongly localized in the side well when no field is applied, so the overlap with the electron wave function localized in the main well will be low. When a reverse bias is applied to drive the heavy hole into the main well, nearly the same peak overlap will be obtained. However, because of the deep valence band side well, a larger applied bias will be necessary. If the quantum well becomes wide, the energy difference between the hh_0 state and hh_1 state will be reduced. This will cause more undesired background absorption when no field is applied. However, if the entire well structure is too narrow, there will be a large overlap of the e_0 and hh_0 wave function with no applied field and the range of oscillator strength contrast will be small.

Summary

In summary, a new quantum structure has been proposed and modeled which demonstrates a 4:1 change in the oscillator strength and absorption of the lowest quantized transition with an applied field of only -25 kV/cm. The type 1.5 quantum well is an innovative material for manipulating electron and hole wave functions for improved electroabsorption modulation dynamics.

¹ M. Sugawara, et al, Phys. Rev. B. no. 11, p. 8102, 1993.

² P. J. A. Thijs, et al, IEEE JQE, Vol. 30, no. 2, p. 477, 1994.

³ D. Gershoni, et al, Phys. Rev. Lett. vol 60, no. 5, p. 448, 1988.

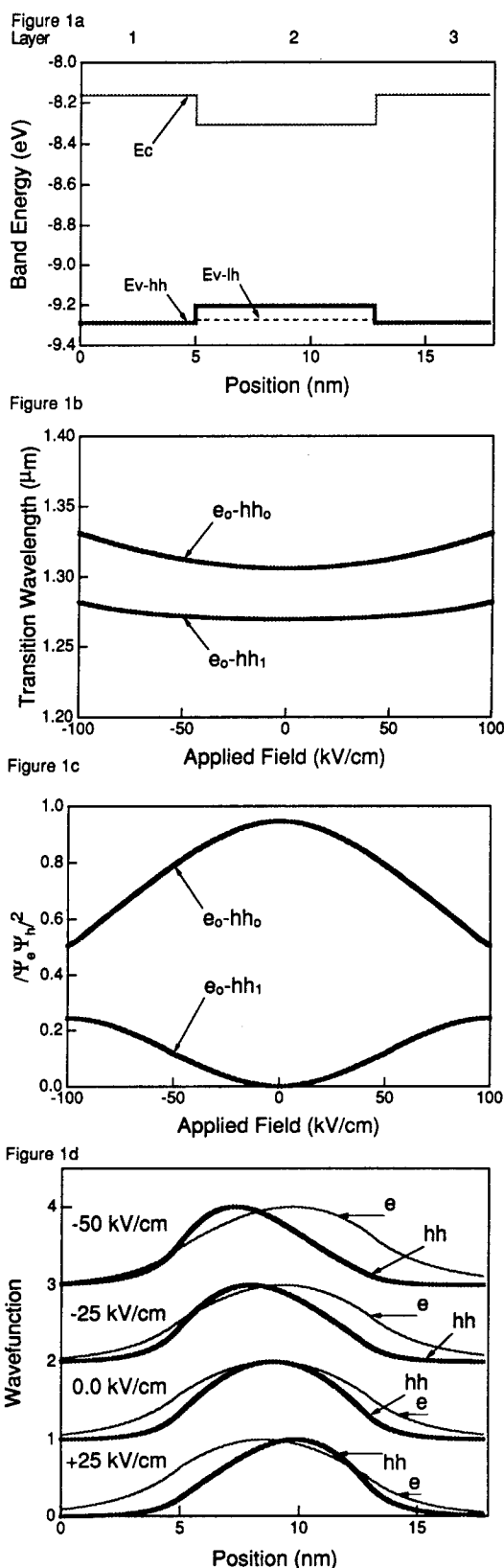


Figure 1 Type I Band Structure vs. Position
 Figure 2 Type I Transition Wavelength vs. Field
 Figure 3 Type I Wave Function Overlap vs. Field
 Figure 4 Type I Carrier Wave Functions vs. Position

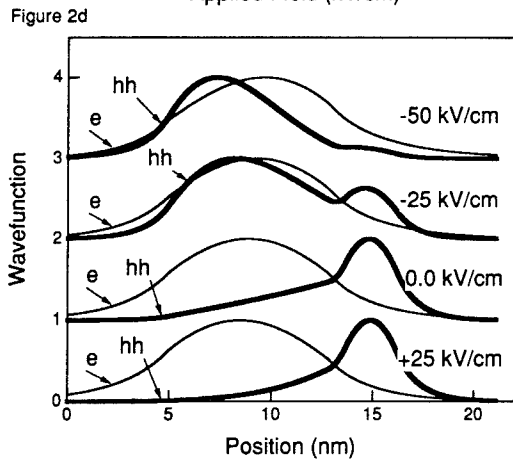
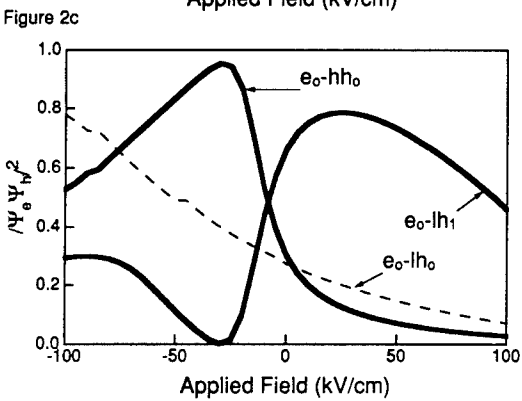
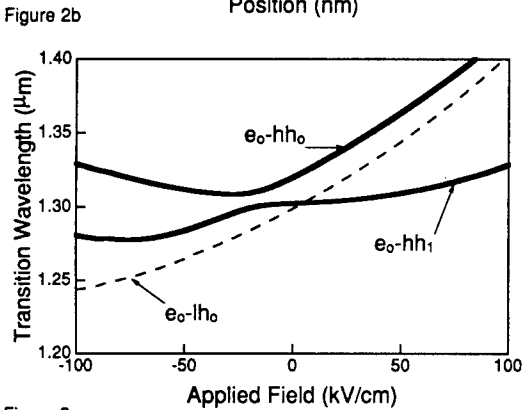
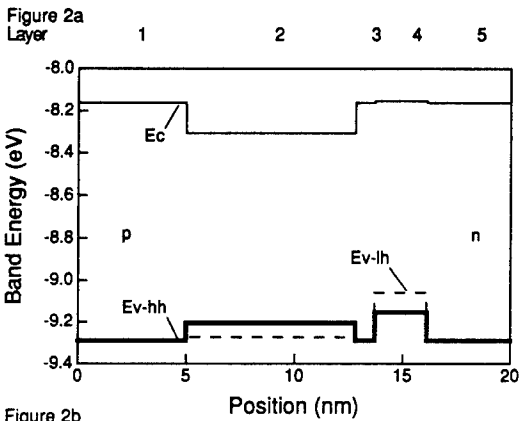


Figure 2a Type 1.5 Band Structure vs. Position
Figure 2b Type 1.5 Transition Wavelength vs. Field
Figure 2c Type 1.5 Wave Function Overlap vs. Field
Figure 2d Type 1.5 Carrier Wave Function vs. Position

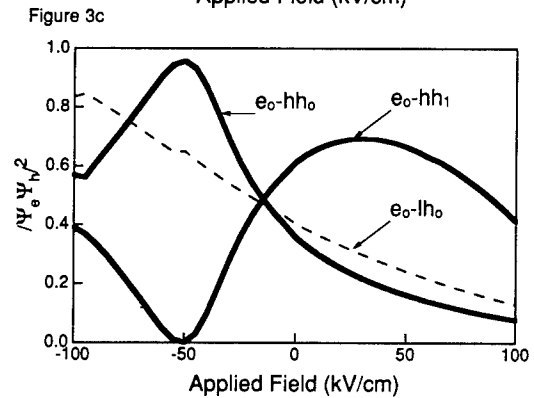
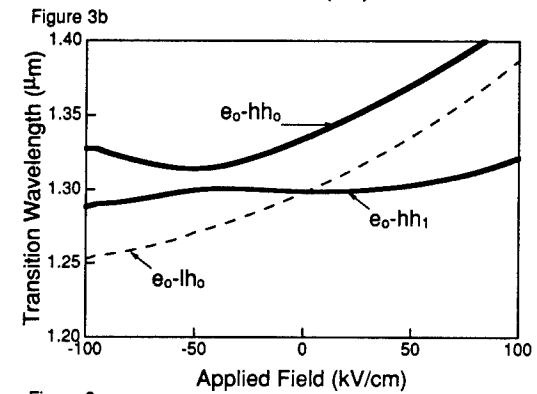
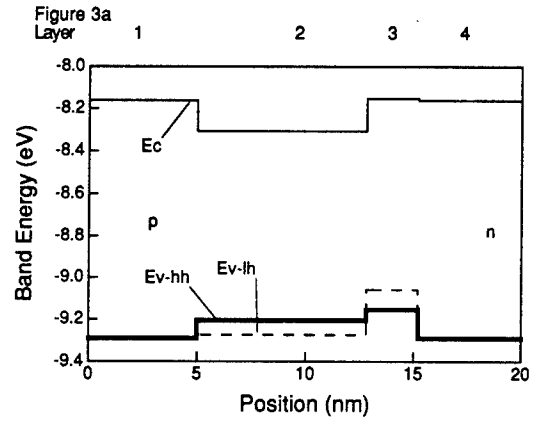


Table 1 Standard Type I Quantum Well

Parameter	Layer 1/3	Layer 2
Thickness (nm)	0.15/0.32	7.8
GaxIn1-xAsyP1-y (x/y)	0.15/0.32	0.06/0.50
Conduction band (eV)	-8.162	-8.307
Valence band heavy hole (eV)	-9.289	-9.205
Valence band light hole (eV)	-9.289	-9.274
Strain InP Substrate(%)	0.0	1.18

Table 2 Type 1.5 Quantum Well

Parameter	Layer 1/5	Layer 2	Layer 3	Layer 4
Thickness (nm)	0.15/0.32	7.8	0.9	2.4
GaxIn1-xAsyP1-y (x/y)	0.15/0.32	0.06/0.50	0.15/0.32	0.54/0.78
Conduction band (eV)	-8.162	-8.307	-8.162	-8.153
Valence band heavy hole (eV)	-9.289	-9.205	-9.289	-9.155
Valence band light hole (eV)	-9.289	-9.274	-9.289	-9.060
Strain InP Substrate(%)	0.0	1.18	0.0	-1.25

Table 3 Barrierless Type 1.5 Quantum Well

Parameter	Layer 1/4	Layer 2	Layer 3
Thickness (nm)	0.15/0.32	7.8	2.4
GaxIn1-xAsyP1-y (x/y)	0.15/0.32	0.06/0.50	0.54/0.78
Conduction band (eV)	-8.162	-8.307	-8.153
Valence band heavy hole (eV)	-9.289	-9.205	-9.155
Valence band light hole (eV)	-9.289	-9.274	-9.060
Strain InP Substrate(%)	0.0	1.18	1.25

ThP48

InGaAs/InAlAs/InP 1.55 μ m Quantum Wells with Mass-Dependent Width

– A Useful Building Block for Polarization-Independent Optical Modulation –

A. Hamakawa, K. Ishihara, T. Yamaguchi, Y. Nakano, and K. Tada

Dept. of Electronic Engineering, University of Tokyo

7-3-1 Hongo, Bunkyo-ku, Tokyo, 113, Japan

Phone (03) 3812-2111 ext. 6777, Fax (03) 5802-3313

Abstract- We describe a new quantum well structure in 1.55 μ m materials where effective width of the well is mass-dependent. This is advantageous for polarization-independent modulation of 1.55 μ m optical waves. An InGaAs/InAlAs multiple quantum well p-i-n diode with such a structure on an InP substrate has been fabricated for the first time, and its photocurrent spectra have been measured. We have observed a larger Stark shift for light-hole-related exciton than that of heavy-hole exciton, which never happened in the conventional quantum wells. Therefore, the same amount of Stark shift for both holes should be possible by adjusting such a quantum well structure with mass-dependent width.

I. Introduction

Quantum well (QW) optical modulators and switches are very promising because of their low driving voltages, small sizes, high speed operation, and monolithic integration capability with other semiconductor optical devices. However, they have a large polarization dependence in their modulation property. Most fiber optical communication systems require polarization-independent devices since the ordinary fiber does not maintain polarization. Therefore, elimination of polarization sensitivity in QW modulators / switches is essential.

In QW waveguides, TE polarization mainly interacts with heavy holes, whereas TM polarization only interacts with light holes. Because heavy holes and light holes have not only different exciton wavelengths but also different Stark shifts, optical modulation efficiency becomes strongly polarization-dependent.

Previously, we have demonstrated a polarization-independent modulator that utilized quasi-parabolic quantum wells (q-PQW's) [1-2], where the Stark shift did not depend on the mass of the holes. Drawback in this case was that the property of the q-PQW structure was too sensitive to variation in epitaxial

layer thickness. This is because there were very thin barriers (one or two atomic layer, typically) inserted near the center of the well that affected the wave functions very much. A small variation in the barrier thickness resulted in a considerable exciton-peak broadening.

Recently, a new approach has been proposed and demonstrated in GaAs based materials [3], where effective width of the QW is larger for light holes than for heavy holes. This would help reducing the polarization dependence since the Stark shift is larger for a wider QW. In other words, the small Stark shift of light holes is enhanced by a larger effective width of the QW, thus giving identical Stark shift for both heavy- and light-hole excitons. We have fabricated GaAs based modulators making use of this novel QW structure (which we call "quantum well with mass-dependent width" or MDW QW), and realized almost polarization-independent modulation [4]. This approach is not sensitive to variation in epitaxial layer thickness, and therefore has better process tolerance.

This paper describes the first demonstration of the MDW QW in a material system for 1.55 μ m optical communication, namely, $\text{In}_{0.53}\text{Ga}_{0.47}\text{As}/\text{In}_{0.52}\text{Al}_{0.48}\text{As}$

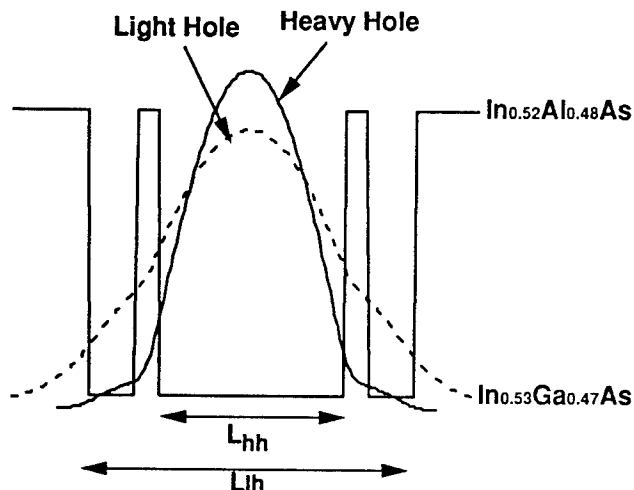


Fig. 1. Wave functions in the InGaAs/InAlAs/InP quantum well with mass-dependent width (MDW QW).

on InP substrates. After a brief description on the operation principle, the epitaxial layer structure grown here is presented. Next, photocurrent spectrum is measured in a InGaAs/InAlAs multiple MDW QW p-i-n diode. Discussion on the Stark shifts of heavy- and light-hole excitons then follows.

II. Operation Principle

The shift of exciton peak energy due to the quantum confined Stark effect (QCSE) in common rectangular potential QW's is expressed as follows [5]:

$$\Delta E = -Cme^2L^4F^2 / \hbar^2, \quad (1)$$

where m is the effective mass of the associated carrier, e the electron charge, L the width of the QW, F the applied electric field, and C is a constant. In this equation, the potential height of the barriers is assumed to be infinite. It can be used as a simple guideline for designing QCSE in QW's. From Eqn. 1, it can be said that the larger the effective mass is, the larger the Stark energy shift would be. Therefore, heavy holes have a larger Stark shift than light holes. This results in polarization dependence of modulation efficiency in QCSE-based modulators (different exciton wavelengths of heavy and light holes are another cause).

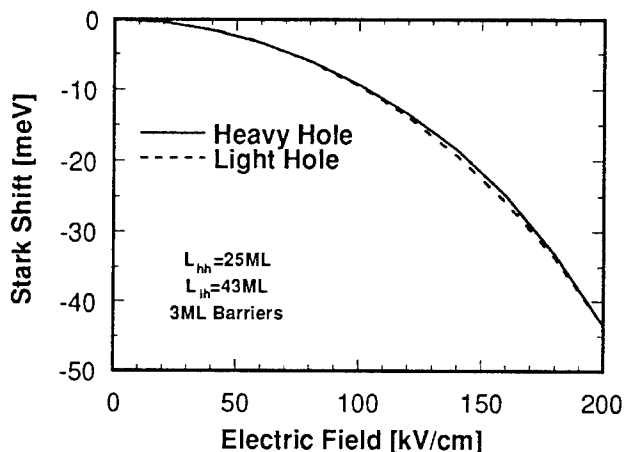


Fig. 2. Exciton peak energy shifts as functions of applied electric field in the InGaAs/InAlAs/InP MDW QW. Heavy- and light-hole excitons are denoted by solid and dashed lines, respectively.

The configuration of our MDW QW is schematically illustrated in Fig. 1. Two thin barriers are inserted in a rectangular QW near the well edges. They are designed in such a way that light holes can go beyond them by tunneling but heavy holes can not. As a result, the heavy hole wave function (solid line) is confined within the "inner" well, whereas that of the light hole (dashed line) extends over to the "outer" well as shown in Fig. 1. Therefore, heavy and light holes have different effective well widths, L_{hh} and L_{lh} . From Eqn. 1, it can also be understood that the Stark shift is larger for wider QW's.

In particular, an identical Stark shift is obtained for heavy and light holes when the following relation is satisfied:

$$m_{hh}L_{hh}^4 = m_{lh}L_{lh}^4. \quad (2)$$

In InGaAs wells, the above equation leads to $L_{lh} / L_{hh} = 1.7$. Therefore, if L_{hh} equals 25 monolayers (ML), L_{lh} should be 43 ML. Figure 2 shows theoretically calculated energy shifts of heavy- and light-hole exciton peaks as functions of applied electric field (where L_{hh} , L_{lh} , and the thickness of the two thin barriers are assumed to be 25, 43, and 3 ML, respectively). The thickness of barriers is determined so as to obtain

p ⁺ InGaAs 0.1μm	Be 4×10 ¹⁹ cm ⁻³
p InAlAs 0.5μm	Be 1×10 ¹⁸ cm ⁻³
i InAlAs 0.1μm	
20 MDW QWs 0.36μm	
i InAlAs 0.1μm	
n InAlAs 0.5μm	Si 1×10 ¹⁸ cm ⁻³
n ⁺ InP substrate	

Fig. 3. Actual epitaxial layer structure grown by MBE.

maximum discrimination between heavy and light holes. Almost perfect matching of the Stark shifts of heavy and light holes is predicted in Fig. 2.

Unlike the q-PQW [1-2], the thin barriers in the MDW QW are placed near the edges of the well where the amplitude of the wave function is not large. As a consequence, it is robust against fluctuation in epitaxial layer thickness caused by process uncertainty.

In order to obtain complete polarization independence, not only the Stark shifts but also absolute peak wavelengths of the heavy- and light-hole excitons should be equal. For this purpose, tensile strain in QW's is useful. It makes exciton transition energies associated with the heavy and light holes closer, and therefore reduces the polarization dependence [6-8]. If the tensile strain is incorporated with this MDW QW, complete polarization-independent modulation would be possible.

III. Experiment

The MDW QW we fabricated here consisted of a In_{0.53}Ga_{0.47}As/In_{0.52}Al_{0.48}As quantum well (44ML-wide) and two thin InAlAs barriers (3ML-thick each)

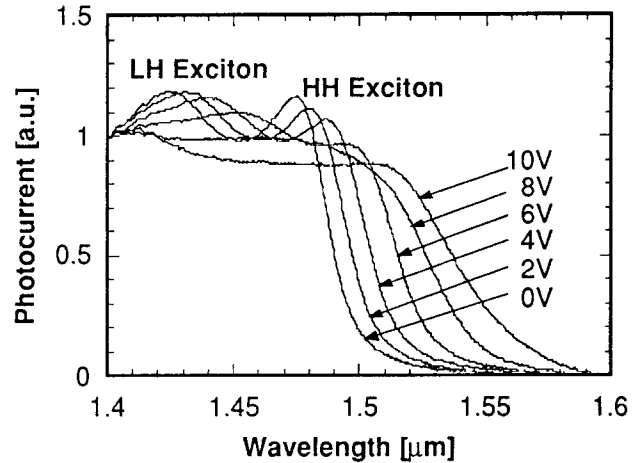


Fig. 4. Photocurrent spectra as functions of applied reverse bias voltage in the InGaAs/InAlAs/InP MDW QW.

at 7ML from the well edges. This corresponds to L_{hh} of 24ML and L_{lh} of 44ML. Actual epitaxial layer structure is illustrated in Fig. 3. The layers were grown on a (100) n⁺-InP substrate by molecular beam epitaxy (MBE).

Twenty sets of the undoped, lattice-matched MDW QW's (separated by 17ML-thick InAlAs barriers) are sandwiched between n-i- and p-i-InAlAs cladding layers (Si- and Be-doped), thus forming a p-i-n diode. The i-InAlAs cladding layers are required to apply a linear electric field to the undoped QW layers. Electrodes are deposited on both sides of the wafer. Areas without the p-side top electrode are reserved to allow illumination of light for photocurrent measurement.

Photocurrent spectra at different reverse-bias voltages for the above sample was measured as shown in Fig. 4. Peaks associated with the heavy-hole and light-hole exciton absorption are clearly observed. They shift toward longer wavelength with the applied reverse voltage (the Stark shift).

The shifts of the exciton peak wavelengths are extracted from Fig. 4, and are plotted in Fig. 5 (in terms of energy) as functions of the applied reverse voltage from 0 through 7V. Above 7V, the light-hole exciton peak becomes too much broadened to determine the peak wavelength (due to reduced confine-

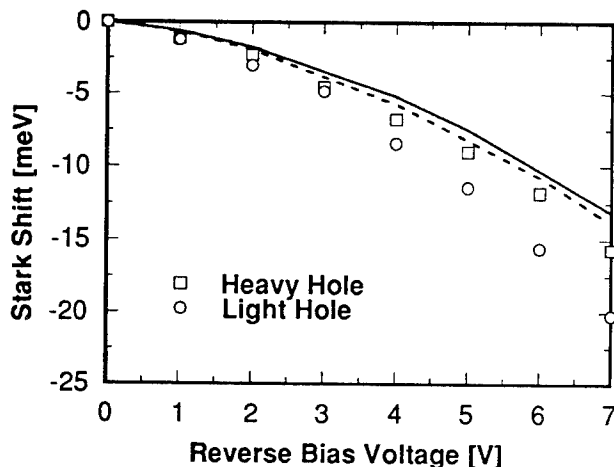


Fig. 5. Experimentally-observed Stark shifts extracted from Fig. 4. Solid and dashed lines are theoretical values for heavy- and light-hole excitons, respectively.

ment). Calculated Stark shifts are also shown in the figure by solid (heavy holes) and dashed (light holes) lines.

Unlike in the conventional QW's, the light-hole exciton peak moves faster than that of the heavy hole in Fig. 4, thus resulting in a larger Stark shift in Fig. 5. This is a strong evidence that the MDW QW structure actually has different effective well widths. In this particular structure, L_{lh} / L_{hh} is calculated to be 1.8, that happens to be larger than the above mentioned value of 1.7. Therefore, we have obtained not the same shifts but a larger shift for the light hole. This is also true for the theoretical curves (the dashed line has a larger shift). The small discrepancy between the experiment and theory in Fig. 5 may be attributed to ambiguity in the material parameters used in the design and theoretical calculation and in converting applied voltage into local electric field. Equal Stark shifts should be available by feeding back this result to the next MDW QW growth.

IV. Conclusions

We have designed and fabricated, for the first time, a new quantum well structure with mass-dependent width (MDW QW) in 1.55 μ m materials for polarization independent Stark shift. We have obtained a larger Stark shift for light-hole-related exci-

ton than that of heavy-hole exciton, which never happened in the conventional quantum wells. Therefore, it should be possible to have the same Stark shifts for both holes by adjusting the MDW QW structure. If the tensile strain, that is able to align heavy- and light-hole peak wavelengths, is incorporated with this MDW QW, a complete polarization insensitivity in 1.55 μ m optical modulation would be possible.

Acknowledgments

The authors would like to thank Dr. K. Nishikata and Mr. M. Irikawa of Furukawa Electric Co., Ltd., for providing epitaxial wafers used in this work.

References

- [1] K. Tada, S. Nishimura, and T. Ishikawa, "Polarization-independent optical waveguide intensity switch with parabolic quantum well," *Appl. Phys. Lett.*, vol. 59, pp. 2778-2780, 1991.
- [2] R. C. Miller, A. C. Gossard, D. A. Kleinman, and O. Munteanu, "Parabolic quantum wells with the GaAs-Al_xGa_{1-x}As system," *Phys. Rev. B*, vol. 29, pp. 3740-3743, 1984.
- [3] T. Yamaguchi, T. Morimoto, K. Tada, and Y. Nakano, "Quantum well with mass-dependent width for polarization-insensitive optical modulation," *Tech. Digest, Topical Meeting on Integrated Photonics Research (IPR'94)*, San Francisco, FF6, 1994.
- [4] T. Yamaguchi, T. Morimoto, K. Akeura, K. Tada, and Y. Nakano, "Polarization-independent waveguide modulator using a novel quantum well with mass-dependent width," *IEEE Photon. Technol. Lett.*, vol. 6, pp. 1442-1444, 1994.
- [5] G. Bastard, E. E. Mendez, L. L. Chang, and L. Esaki, "Variational calculations on a quantum well in an electric field," *Phys. Rev. B*, vol. 28, pp. 3241-3245, 1983.
- [6] J. E. Jucker, K. L. Jones, T. H. Chiu, B. Tell, and K. Brown-Goebeler, "Strained quantum wells for polarization-independent electrooptic waveguide switches," *J. Lightwave Technol.*, vol. 10, pp. 1926-1930, 1992.
- [7] K. G. Ravikumar, T. Aizawa, and R. Yamaguchi, "Polarization-independent field-induced absorption-coefficient variation spectrum in an InGaAs / InP tensile-strained quantum well," *IEEE Photon. Technol. Lett.*, vol. 5, pp. 310-312, 1993.
- [8] Y. C. Chan and K. Tada, "Realization of tensile strain in GaAs substrates for polarization independent optical modulation," *IEEE Photon. Technol. Lett.*, vol. 5, pp. 1380-1383, 1993.

Intersubband Transitions in Conduction Band Quantum Wells: the role of energy band gaps and band off-sets

Lung-Han Peng and Clifton G. Fonstad, Jr.

Department of Electrical Engineering and Computer Science
Massachusetts Institute of Technology, Cambridge, MA 02139

Abstract

A new 14-band $k \cdot p$ analysis of optical intersubband transitions in conduction band quantum wells demonstrates the importance of the energy band gap and the band off-sets in determining the strength of such transitions. In particular it is found (1) that a narrow band gap enhances the TE activity, and is therefore desirable, because of the importance of band mixing, and (2) that carrier confinement in both the valence band (Type I quantum well) and the upper conduction band is necessary for strong TE activity. This paper discusses these observations and supports these conclusions with measurements made on Type-II InP/InAlAs quantum wells

Recent observations of normal incidence intersubband transitions in n type semiconductor quantum wells (QWs) have generated a great deal of interest because of their importance for quantum well, intersubband photo-detector applications. For pseudomorphic n^+ InGaAs /AlAs QWs grown in InP, we have observed¹ intersubband transitions of (i) (x,y) -polarized sensitivity and (ii) strained-induced (x,z) -polarization splittings. Similar (x,z) -polarized activities and splitting effects in strain-relaxed InGaAs QWs were also reported by Li et al.². The use of (x,z) -polarized intersubband transitions has been pursued by Chen et al.³ for obtaining surface-emitted second-harmonic generation and by Akiyama et al.⁴ for controlling electron populations in GaAs/AlGaAs QW waveguides by using x - and z -polarized CO₂ laser radiation with energies resonant to intersubband transitions.

We have recently presented a 14-band $k \cdot p$ analysis⁵ that allows us to compare and classify different compound semiconductors with respect to their suitability and effectiveness for use in devices based on intersubband transitions. In this paper we report infrared (IR) absorption measurements made on Type-II n^+ InP/InAlAs quantum wells and demonstrate that they are consistent with this new theory, and inconsistent with other recent attempts to explain intersubband transitions.

According to the 14 band $k \cdot p$ analysis, the QW conduction subband wave functions at $k_{||} = 0$ can be written as:

$$\begin{aligned} \Psi_c \uparrow = & f_c |S \uparrow\rangle + \frac{P_0 p_z f_c}{E_0 + E} |Z^v \uparrow\rangle - \frac{Q p_z f_{hc}}{E_0 + E} |R_{\downarrow}^v \downarrow\rangle \\ & + O \left\{ \left(\frac{\Delta_0}{E_0 + E} (|Z^v \uparrow\rangle + |R_{\downarrow}^v \downarrow\rangle) \right) - \frac{P_0 p_z f_c}{E_0 + E} |Z^c \uparrow\rangle \right. \\ & \left. - \frac{Q p_z f_{hh}}{E_1 - E} |R_{\downarrow}^c \downarrow\rangle + O \left\{ \frac{\Delta_1}{E_1 - E} (|Z^c \uparrow\rangle + |R_{\downarrow}^c \downarrow\rangle) \right\} \right\} \quad [1] \end{aligned}$$

where E is the subband energy measured from the bottom of Γ_6^c (Γ_1^c) edge, E_0 is bandgap for $\Gamma_6^c - \Gamma_8^v$ ($\Gamma_1^c - \Gamma_{15}^v$)

edges, E_1 for $\Gamma_7^c - \Gamma_6^c$ ($\Gamma_{15}^c - \Gamma_1^c$); and Δ_0 and Δ_1 are the spin-split hole ($\Gamma_8^v - \Gamma_7^v$) and electron gap ($\Gamma_8^c - \Gamma_7^c$), respectively. The momentum matrix element P_0 couples $\Gamma_1^c - \Gamma_{15}^v$, P_1 couples $\Gamma_{15}^c - \Gamma_1^c$, and Q couples $\Gamma_{15}^c - \Gamma_{15}^v$ edges in non-inversion symmetric zinc-blende semiconductors.

For Type-I QWs at $k_{||} = 0$, we note in Eq. (1) that the participation of spatially-confined heavy holes and heavy electrons greatly enhances the ratio of TE- to TM-polarized $\Delta n = 1$ intersubband transitions, the enhancement being on the order of

$$\left[\frac{Q}{P_0} \left(1 + \frac{P_1}{P_0} \frac{E_0 + E}{E_1 - E} \right) \right]^2 \quad [2]$$

This analysis differs from those of 8-band $k \cdot p$ ⁶ or finite-mass difference model⁷ of $\Delta n=2$ intersubband transitions at $k_{||} \neq 0$.

A primary objective of the current study was to use Type II QWs, where the electrons and holes are not simultaneously confined in the same (well) region, to help distinguish between the proposed models. Lattice-matched n^+ InP/InAlAs MQWs samples used in this study were grown on Fe doped semi-insulating [001] InP substrates by gas source molecular beam epitaxy⁸. Samples A and B contained 60 periods of 65Å/70Å and 50Å/70Å n^+ InP/InAlAs MQWs, respectively. Both Samples were silicon doped at 10^{18} cm^{-3} in the InP wells.

The design of the MQW Samples A and B was such that there were three confined states for Sample A ($E_{n=1} = 58 \text{ meV}$, $E_{n=2} = 201 \text{ meV}$, and $E_{n=3} = 344 \text{ meV}$), and two confined states for Sample B ($E_{n=1} = 82 \text{ meV}$, $E_{n=2} = 266 \text{ meV}$). Both samples thus should show $\Delta n = 1$ intersubband transitions, while Sample A can also be used to search for $\Delta n = 2$ intersubband transitions.

Measurements were taken using Fourier transform infrared spectrometer (FTIR). Figure 1 (a) shows the room temperature FTIR transmission data taken at P-polarized 45° oblique angle and it clearly resolves absorption peaks at

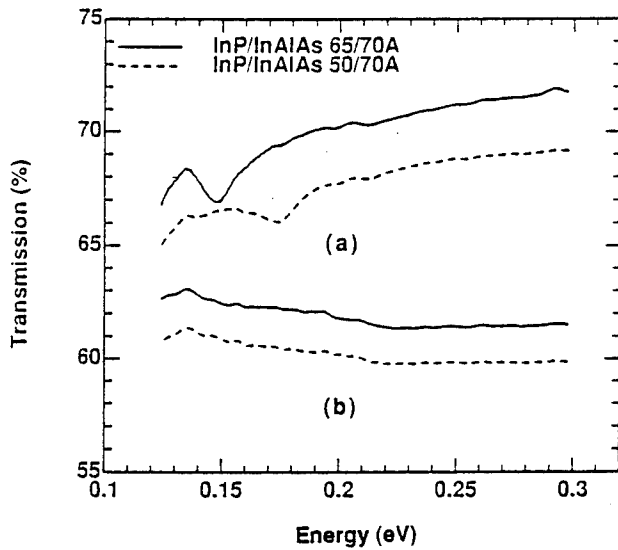


Figure 1: Room temperature FTIR absorption data for Samples A (B) measured in (a): P-polarized 45° oblique angle and (b) normal incidence configurations.

147 meV and 175 meV for Samples A and B, respectively. There are, however, only weak Fabry-Perot interference patterns but no absorption peaks seen in the normal incidence configuration in Figure 1(b). In the edge-waveguide configuration (not shown), the z-polarized 147 meV and 175 meV absorption peaks for Samples A and B were enhanced by a factor of four on thin-polished (60 μm x 4 mm) substrates but no (x,y)-polarized absorption was seen.

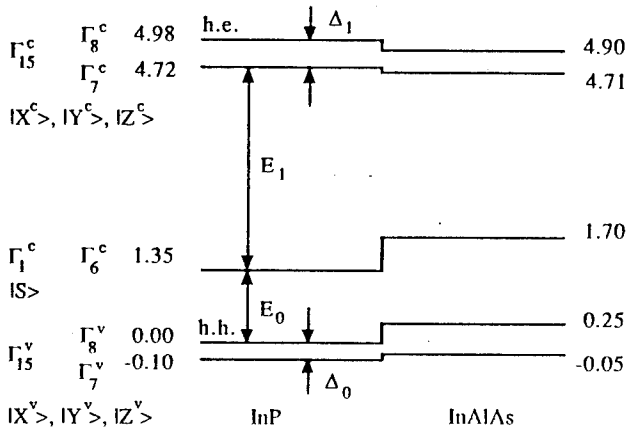


Figure 2: Line-up of the bulk band-edges in type II lattice-matched InP/InAlAs QWs (all numbers are in the units of eV), where $\Gamma_{15}^{c,v}$ is the single group representation of upper conduction (valence) band and $\Gamma_{7,8}^{c,v}$ is the corresponding band edge in the double group representation.

These observations suggest that the z-polarized 147 meV and 175 meV absorption peaks in Samples A and B are associated with the $\Delta n = 1$ intersubband transitions in n^+ InP/InAlAs MQWs. They also agree with (i) the previous investigations made on Brewster angle configurations⁸, and (ii) the use of Eq. (1) in a simple effective mass envelope function calculation which predicts peak energies of 143 meV and 184 meV for Samples A and B, respectively.

The fact that no $\Delta n = 2$ intersubband transitions are observed in Sample A supports the use of the 14-band $k \cdot p$ model to understand QW intersubband activity, and argues against using the 8-band $k \cdot p$ and finite-mass difference models. In type II QWs, the lack of spatial confinement of holes diminishes the observation of (x,y)-polarized $\Delta n = 1$ intersubband transitions. Our experimental data also suggests that heavy electrons are not confined in the InP wells of this InP/InAlAs type II QW (Eq. (1)). This prediction is also consistent with the line-up of the InP/InAlAs band structure constructed by using experimental values of the critical point energies and Γ_1^c band offset shown in Figure 2.

We thank Drs. Y. Kawamura, H. Iwamura, and Y. Imamura of N. T. T. for providing the samples used in this work. This research was supported at M. I. T. by the National Science Foundation, Grant No. ECS-9408155, by the Army Research Office, No. DAAL03-91-G-0051, and by the Joint Services Electronics Program through the M. I. T. Research Laboratory of Electronics, contract No. DAAL 03-92-C-0001.

References

1. J.H. Smet, L.H. Peng, Y. Hirayama, and C. G. Fonstad, Appl. Phys. Lett. **64**, 986 (1994).
2. H. S. Li, R. P. G. Karunasiri, Y. W. Chen, and K. L. Wang, J. Vac. Sci. Technol. B **11**, 922 (1993).
3. Z. Chen, M. Li, D. Cui, H. Lu, and G. Yang, Appl. Phys. Lett. **62**, 1502 (1993).
4. H. Akiyama, H. Sugawara, Y. Kadoya, A. Lorke, S. Tsujino, and H. Sakaki, Appl. Phys. Lett. **65**, 424 (1994).
5. L. H. Peng and C. G. Fonstad, J. Appl. Phys. **77**, 747 (1995).
6. R. Q. Yang, J. M. Xu, and M. Sweeny, Phys. Rev. B **50**, 7474 (1994).
7. Z. Ikonc and V. Milanovic, in Quantum Well Intersubband Transition Physics and Devices, ed. by H. C. Liu, B. F. Levine, and J. Y. Andersson (Kluwer Academic Publishers, Boston, MA, 1994).
8. Y. Kawamura and H. Iwamura, Jpn. J. Appl. Phys. **31**, L 1733 (1992); J. Cryst. Growth (in press).

GaInAsP/InP Multiple-Reflector Micro-Cavity Structure Fabricated by EB Lithography and Selective Etching

Ki-Chul Shin, Munehisa Tamura, Naoki Serizawa, Shinji Kurihashi,
Shigeo Tamura, Masatsugu Hotta, and Shigehisa Arai

Research Center for Quantum Effect Electronic

Tokyo Institute of Technology

2-12-1 O-okayama, Meguro-ku, Tokyo 152, Japan

Phone: +81-3-5734-2512 Fax: +81-3-5734-2907

Abstract: Very uniform multiple-reflector micro-cavity structure was fabricated by electron beam (EB) lithography and selective wet chemical etching. Very small standard deviation of the gap width between micro-cavities, which was only 22nm for the average value of 762nm, enabled us to observe a clear modulation in PL spectrum due to multiple reflection.

1. Introduction

Low threshold current laser is very attractive for optical interconnection and a number of optoelectronics applications[1]. Micro-cavity lasers with very small volume are candidates with great potential to fulfill these requirements. In this work, we present it is possible to attain a sub-mA current operating laser by using a multiple-reflector micro-cavity with high refractive-index difference ($\sim 35\%$), and demonstrate a fabrication process of this structure and lasing property by optical pumping.

2. Design of Multiple-Reflector Micro-Cavity Laser

Figure 1 shows a model of GaInAsP/InP multiple-reflector micro-cavity laser and threshold current dependence on the cavity length (cavity length is a digital) calculated for $1.55\mu\text{m}$ wavelength active medium (compressed strained quantum well 5 layers). In this calculation we assumed that etching of semiconductor being stopped on lower InP buffer layer to obtain high refractive-index difference (about 30%) and polyimide (refractive index $n_L=1.65$) is buried between individual micro-cavities. And also we fixed $l_L (= \lambda/4n_L)$ to $0.27\mu\text{m}$, $l_H (= \lambda/4n_H)$ where n_H is effective refractive index of the active region) to odd times of first order of Bragg condition for lasing wavelength $\lambda=1.55\mu\text{m}$. We used transfer matrix[2] for calculation and neglected diffraction loss. As can be seen in Fig.1, sub-mA threshold current operation can be attained even if the total cavity length less than $100\mu\text{m}$ when the active

region stripe width(W) is assumed to be $1\mu\text{m}$.

3. Fabrication of Multiple-Reflector Micro-Cavity Structure

It is very important to etch a groove with high aspect ratio and vertical shape for obtaining a high refractive index difference. For this purpose, we adopted a two-step wet chemical etching technique

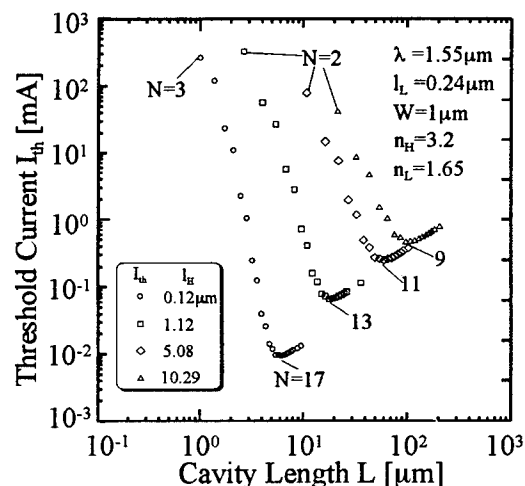
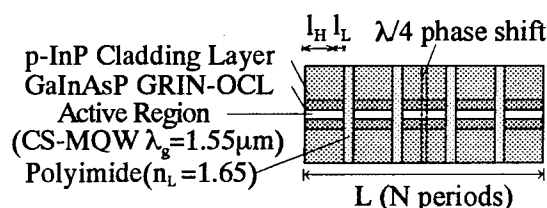


Fig. 1 Schematic view and threshold current of multiple-reflector micro-cavity laser

using HCl-based etchant with GaInAs crystal mask[3,4] since HCl-based etchant has a definite material selectivity for GaInAs/InP system and anisotropic etching rate between (100) plane and (011) plane.

Figure 2 shows the structure of the wafer we used in this experiment and the fabrication process of multiple-reflector micro-cavity structure by using EB-lithography and 2-step wet-chemical etching with GaInAs mask layer as well as contact layer (Zn-doped, 350nm).

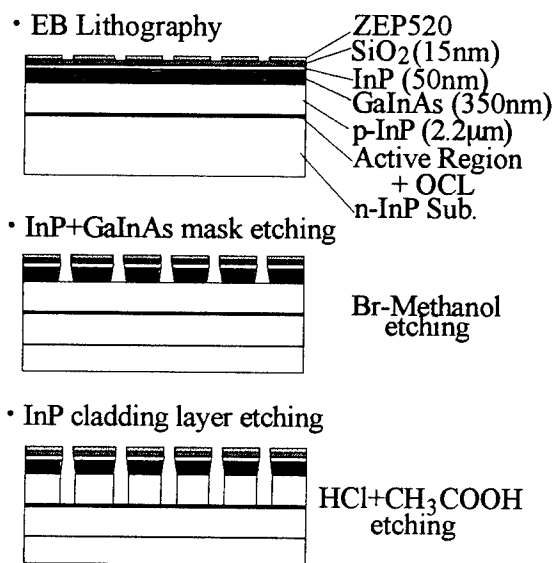


Fig.2 Fabrication process of multiple-reflector micro-cavity

We adopted a PMMA/SiO₂/InP/GaInAs system for making a mask pattern in stead of PMMA/GaInAs[3] system because PMMA is etched by HCl-based etchant during the etching of InP cladding layer (2.2μm depth) which is very long time compared to one referred [3]. InP cap layer was introduced between the SiO₂ and GaInAs because of good adhesion property between them.

At first we formed 15nm SiO₂ on InP cap layer by thermal CVD and then a narrow stripe pattern (0.27μm width) was formed on resist (ZEP520) along [011]direction with the period of 5.2μm by an EB exposure system JEOL JBX-5FE at the maximum acceleration voltage of 50keV with beam current 5nA and area dose 300μC/cm². Samples were developed in MIBK:IPA (=1:1) solution for 1 minute followed by a rinse in IPA for 30 seconds.

And then SiO₂ was etched with a buffered HF (1%, room temperature 20 sec) followed by InP/GaInAs mask layer etching with Br-methanol (0.0125 vol%, 14 sec), and the InP cladding layer was etched with a selective etchant of HCl:CH₃COOH=1:4 (3 min at room temperature).

Figure 3 shows SEM photographs of multiple-reflector micro-cavity structure and histogram of gap width of 100 grooves fabricated by the above mentioned process. InP cladding layer was etched to the depth of 2.2μm vertically, the angle between etched plane and (011) plane was 87 degree. It is very important to adjust a mask pattern to [011] direction exactly for the vertical etching by HCl-based etchant. We could adjust within ±0.5° in EB chamber through the monitor.

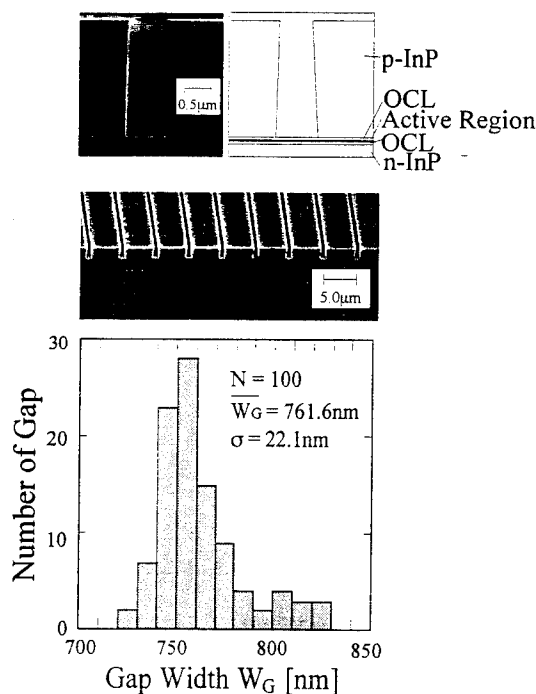


Fig. 3 SEM photograph of multiple-reflector micro-cavity and its histogram of groove size at the bottom

The average groove width between neighboring cavities was measured to be about 762nm at the bottom of the groove. We used a high resolution SEM (Hitachi S5000) and very flat side walls enabled us to do such a measurement. As can be

seen in Fig.3, the standard deviation of the gap width of 100 samples was only about 22nm which is much smaller than the emission wavelength of 1.55 μ m.

However we could not obtain a very small groove size even if the stripe pattern size was 0.27 μ m because it is very difficult to control a stripe width of GaInAs mask by Br-methanol in case of thick GaInAs mask layer. In addition, although undercut was not occurred during Br-methanol etching because of good adhesion between SiO₂ and InP, side etching of GaInAs mask pattern was observed during etching of InP cladding layer. The reason for this side etching of GaInAs mask pattern by HCl-based etchant is due to side etching of InP cap layer when GaInAs mask layer is doped.

We have improved our process to obtain a narrower groove width. The improved process is as follows; we used SiO₂/GaInAs system for making a mask pattern in stead of SiO₂/InP/GaInAs, formed a 0.1 μ m stripe pattern on resist by EB, used thin GaInAs mask layer (50nm), and etched by HBr:HNO₃:H₂O (1:1:8) etchant at 0°C for 2.5 minutes instead of Br-methanol etchant for GaInAs mask layer. Figure 4 shows a SEM view of 405nm groove width of multiple-reflector micro-cavity structure fabricated by this improved process. As can be seen in Fig.4, side etching of GaInAs was not severe compared to one fabricated by the process mentioned before.

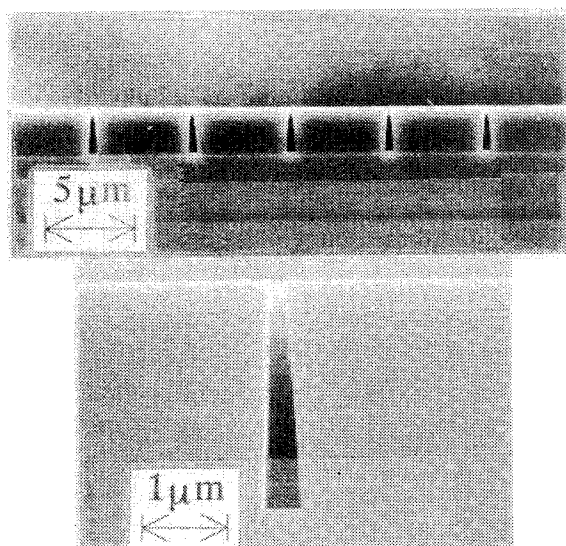
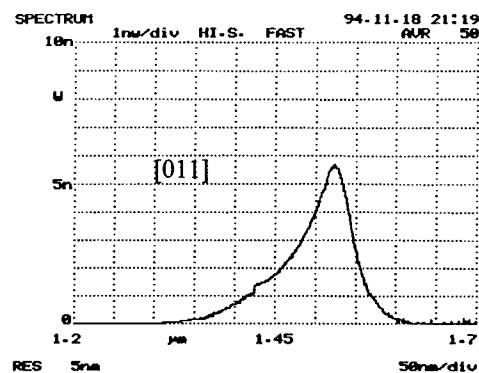


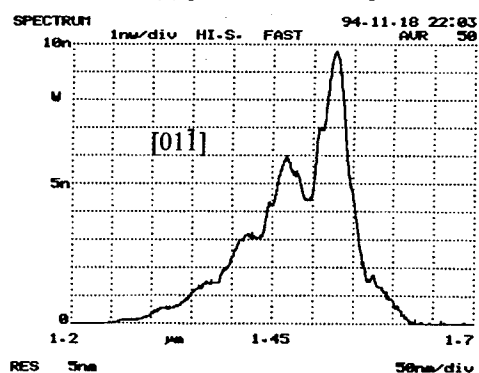
Fig.4 SEM photograph of multiple reflector micro-cavity structure by improved process

4. PL Spectrum and Lasing Property

Figure 5 shows photoluminescence spectra of groove width of 762nm multiple-reflector micro-cavity taken from (a) parallel and (b) perpendicular to the multiple-reflector direction excited with Ar⁺-ion laser (40mW/cm²) at room temperature. PL spectrum to [011] direction (parallel direction to the multiple-reflector) shows normal spectrum of substrate we used. However as can be seen in Fig. 5(b), ripples with an interval of about 60nm was observed. It is in good agreement with the resonant mode spacing of a cavity length of 5 μ m. We can not explain what kinds of resonance modes exist in this multi-reflector micro-cavity theoretically, but we consider resonance modes of 5 μ m cavity is dominant mode in this cavity from Fig. 5(b).



(a) parallel to the stripe



(b) perpendicular to the stripe

Fig.5 Photoluminescence spectra from multiple-reflector micro-cavity.

Figure.6 shows lasing spectrum of multiple-reflector micro-cavity laser under optical pumping at 77K. We used a YAG laser ($\lambda=1.06\mu$ m) as pumping source. The lasing wavelength was

$\lambda=1.49\mu\text{m}$ and interval from a maximum gain peak ($\lambda=1.475\mu\text{m}$) was about 15nm. This result shows that the multiple-reflector micro-cavity structure has a enough strong wavelength selectivity.

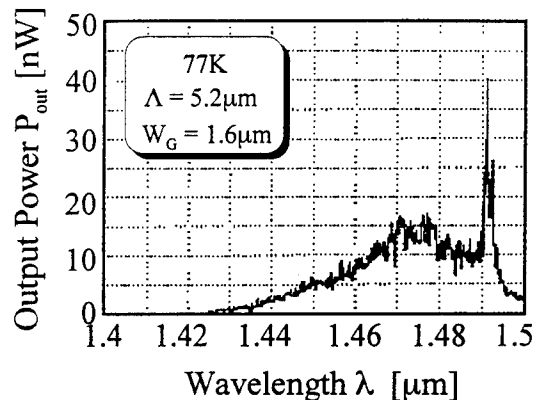


Fig.6 Lasing spectrum of the multiple-reflector micro-cavity laser.

5. Conclusion

We proposed a new type laser having multiple-reflector micro-cavity structure with high refractive index difference and showed this new type laser can be operated at sub-mA current. For the realization of this new type laser, we fabricated the multiple-reflector micro-cavity structure by using EB lithography and 2-step wet chemical etching. The average groove width between neighboring cavities was about 762nm at the bottom of the groove and the standard deviation of the gap width of 100 grooves was only about 22nm. By improving a process, we established a groove width be 405nm and its aspect be about 6. We also succeed in lasing of this laser under optical pumping at 77K . We found out its structure has a strong wavelength selectivity from lasing spectrum.

References

- [1]K.Y.Lau and N. Bar-Chaim, "High Speed Digital modulation of Ultralow Threshold ($<1\text{mA}$) GaAs Single Quantum Laser Without Bias," Appl. Phys. Lett. Vol. 51,pp. 69-71, July, 1987.
- [2]P. Yeh, A.Yariv, and C. Hong, "Electromagnetic propagation Periodic Stratified Media, I. General Theory," J. Opt. Soc. Amer., Vol. 67, pp. 423-438, Apr 1977.
- [3]E. Inamura,Y. Miyamoto, S. Tamura, T.

Takasigi, and K. Furuya, "Wet Chemical Etching for Periodic Structure: Rectangular InP Corrugations of 70nm Pitch and 100nm Depth," Jpn. J. Appl. Phys., Vol. 28, pp. 2193-2196, Oct 1989.

- [4]S. Arai, M. Asada, T. Tanbun-ek, Y. Suematsu, Y. Itaya, and K. Kishino, "1.6 μm Wavelength GaInAsP/InP BH Lasers," IEEE J. Quantum Electron., Vol. QE-17, pp. 640-645, May,1981.

Controlled Beam Dry Etching of InP by using Br₂ - N₂ Gas ThP51

Satoshi Oku, Yasuo Shibata, and Kenichi Ochiai*

NTT Opto-electronics Laboratories, NTT Advanced Technology*

3-1 Morinosato Wakamiya, Atsugi-shi, Kanagawa 243-01, Japan

Abstract

When Indium phosphide dry etching is carried out using a reactive beam extracted from Br₂ - N₂ mixture gas discharge plasma, two distinct types of etching mechanisms come into play as the Br₂ gas pressure is changed. Smooth vertical side walls can be obtained at low Br₂ gas pressure, where the etching rate has no temperature dependence, while undercutting with a temperature dependent etching rate is seen at high Br₂ gas pressure. An analysis of the plasma discharge currents reveals that neutralized Br species generated by the discharge of Br₂ gas itself form the undercut. A waveguide corner mirror with less than 1 dB loss can be made by using an etching beam with no neutralized Br species.

Introduction

Dry etching has been a key technology for the development of integrated photonics devices. The reactive ion etching of InP and related materials has been performed with reactive gases such as Cl₂¹⁾, SiCl₄²⁾, and I₂³⁾, and hydrocarbon gases⁴⁾, ⁵⁾. In these studies, etching process conditions such as gas flow rate, input power for etching plasma generation, and sample temperature were controlled. Although a vertical side wall etching was achieved, no explanation of the etching mechanism was offered. This has recently become an interesting subject because an understanding the etching mechanisms will permit future dry etching process improvements such as damageless etching, loading effect reduction and InP/InGaAsP selective etching. Since the reactions between semiconductor materials and reactive gases are very complex in actual dry etching, an evaluation of a fundamental etching process is necessary under well-controlled etching conditions. This paper describes InP dry etching using a reactive beam extracted from Br₂-N₂ gas discharge plasma. The etching beam characteristics are analyzed on the basis of plasma discharge current.

Experiment

The etching system used in this experiment is shown in Fig. 1. Ion source was electron cyclotron resonance plasma whose impedance matching was automatically controlled. The

etching beam was extracted by applying an voltage V_a between the screen and acceleration grids. The amount and energy of the etching beam could be controlled separately. Br₂ gas and N₂ gas were the etching gases. When only the N₂ gas was used, etching proceeded by physical sputtering. When Br₂ gas was added, chemical reactivity was introduced into the process. The gases were supplied into the plasma chamber through a mass flow controller. The gas pressure was measured with a diaphragm pressure gauge. The N₂ gas partial pressure was kept constant at 0.23 mmHg for all experiments. The Br₂ gas partial pressure was varied from 0 to 0.1 mmHg. Other gases effective for physical sputtering, such as Ar, were not used because of their strong wearing of the molybden grids.

The etching samples were Sn doped n-type InP (001) wafers. After depositing a 0.3- μ m-thick

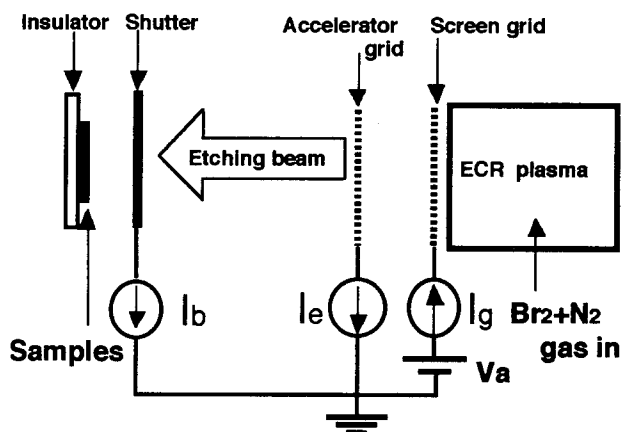


Fig. 1 Schematic diagram of the etching system.

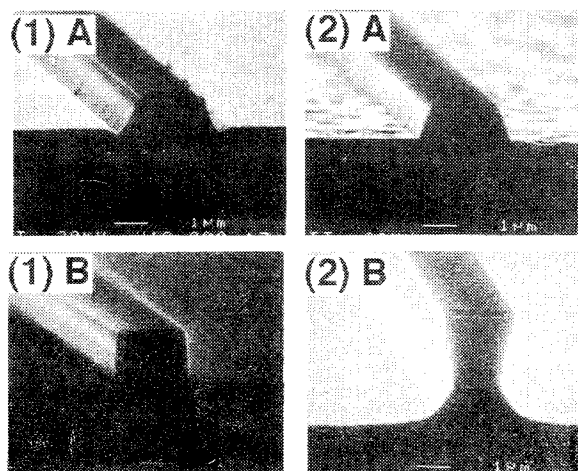


Fig. 2 SEM photographs of the etched stripe pattern. Gas conditions were (1) Br₂ 0.05 mmHg + N₂ 0.23 mmHg and (2) Br₂ 0.1 mmHg + N₂ 0.23 mmHg. Sample temperatures were (A) 40 °C and (B) 140 °C.

SiO₂ layer on the wafer, striped pattern was formed by photolithography. Then, the SiO₂ layer was patterned by C₂F₆ reactive ion etching. The residual photoresist was removed by O₂ plasma. The etching samples were placed on the molybden holder and heated with a buried heater. The sample temperature was measured with a radiation pyrometer from the outside of the etching chamber through a sapphire view port. The temperature ranged from room temperature to 200 °C.

The etching beam characteristics were evaluated by measuring the three currents shown in Fig. 1. *I_g* and *I_e* are the electric currents flowing through the screen and accelerator grids. *I_b* is the beam current monitored by the shutter placed in front of the sample holder. Although charged species were extracted through the two grids, a number of them were changed to non-charged species due to neutralization. There are mainly two neutralizing process: a resonant charge exchange process⁶⁾ and a secondary electron process⁷⁾. Since the mean free path of the gas species was on the order of 30 cm long in these experiments, which is comparable to the distance between the grid and the sample holder, charge exchange collisions would rarely occur. Thus secondary electrons from the sample holder are considered to be the main cause of neutralization. Since the sample were supported by an insulator, only neutralized species could etch the sample. The shapes of the etched stripes were evaluated with a Secondary

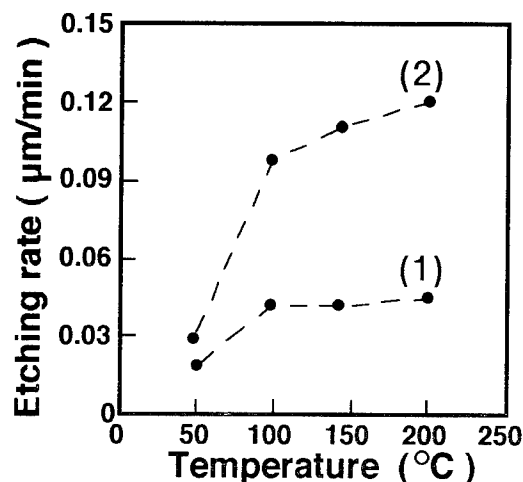


Fig. 3 Temperature dependence of the etch rate. (1) and (2) correspond to gas conditions (1) and (2) in Fig. 2.

Electron Microscope (SEM).

Results

The etching was carried out at different Br₂ gas partial pressures and sample temperatures. The etching shapes were of two typical types, as shown in Fig. 2. Type (1) was obtained at Br₂ gas partial pressure less than about 0.05 mmHg. Trenches formed at the bottom of the mesa when sample temperature was 40 °C, and vertical smooth side walls were formed at temperatures higher than about 100 °C. The etched surface was glossy. On the other hand, type (2) was formed at Br₂ partial pressure higher than about 0.1 mmHg. While the trenches did not form at 40 °C, the etched surface undulated and looked cloudy. The side walls became vertical at 100 °C but they were a little rough. An undercut appeared at higher temperatures, as shown in Fig. 2 (2) B.

The temperature dependence of the etch rate under the two pressure conditions are shown in Fig. 3. The etch rate for the type (1) shape is independent of temperature over 100 °C, whereas that for the type (2) shape continued to increase with increasing temperature. These different temperature dependencies indicate that the etching mechanism differs for two pressures. The currents generated by the plasma discharge were measured to try to discover what that difference is.

The *I_g* and *I_e* for the Br₂-N₂ gas discharge are shown in Fig. 4. While *I_e* and *I_g* for the Br₂ discharge are in the range of 25 ~ 35 mA and 90

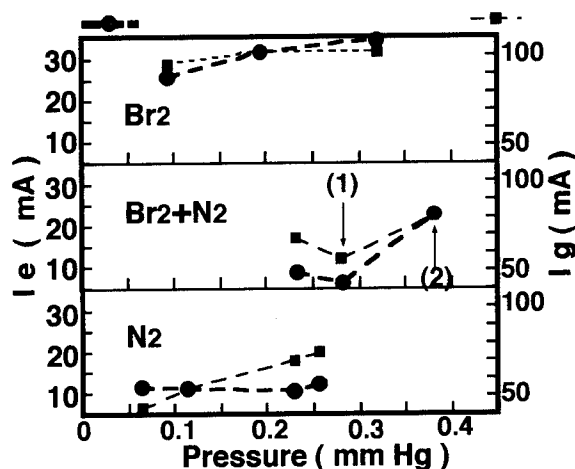


Fig. 4 I_e and I_g as a function of the discharge gas pressure. (1) and (2) correspond to the etching conditions in Figs. 2 and 3.

~ 100 mA (upper graph), those of the N_2 discharge are about 10 mA and $40 \sim 70$ mA (lower graph). In the case of the Br_2 - N_2 mixed gas discharge, I_g and I_e abruptly change at the Br_2 gas pressure higher than 0.1 mmHg (middle graph). This change was also observed in I_b , as shown in Fig. 5. The I_b dropped abruptly from 11 mA to 7 mA when the Br_2 pressure was 0.1 mmHg. Thus, in spite of adding the Br_2 to the N_2 gas, when the Br_2 gas partial pressure was less than 0.05 mmHg, I_g , I_e , and I_b had values similar to those for the 100 % N_2 gas discharge. In the case of Br_2 gas pressure higher than 0.1 mmHg, these currents look like the ones for the 100 % Br_2 gas discharge. The two distinct types of the etching shape ((1) and (2) in Fig. 2) and etch rate temperature dependence ((1) and (2) in Fig. 3) correspond to the different types of discharge ((1) and (2) in Figs. 4 and 5).

Discussion

The etching results can be classified into two types according to the Br_2 gas partial pressure. The etch rate temperature dependence indicates they differ in kind from each other. The difference is associated with the change in beam current I_b .

The electric current I_b of the extracted ion beam is expressed by Langmuir - Child's law as⁸⁾

$$I_b \propto (2e/M)^{1/2} \cdot V_a^{3/2} / L^2, \quad (1)$$

where V_a is the acceleration voltage, L is the distance between two grids, and e/M is the charge-to-mass ratio of the discharge species. M

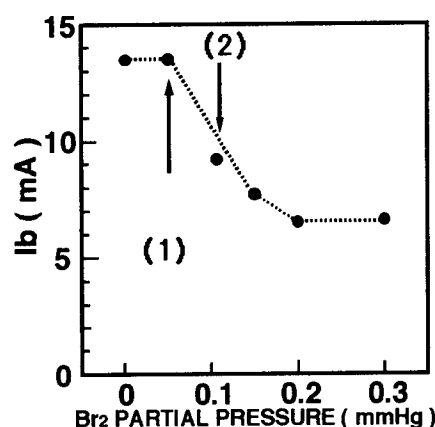


Fig. 5 The beam current I_b as a function of the Br_2 partial gas pressure. (1) and (2) correspond to (1) and (2) in Figs. 2, 3, and 4.

is 28 for N_2 gas discharge. When the partial pressure of the Br_2 gas was increased, I_b abruptly decreased, as shown in Fig. 5. When the Br_2 gas is the discharge species in addition to the N_2 gas discharge, the effective M becomes large due to the large M of Br_2 gas ($M=160$). The I_b reduction can be traced to the change in the effective M in eq. (1).

Although the extracted beam consisted of charged species, only the non-charged neutral species etch the sample on the insulator. Undercut etching was observed with a good relation to the change in plasma discharge currents I_g , I_e , and I_b from N_2 -like discharge currents to the discharge currents associated with added Br_2 , as shown (1) and (2) in Figs. 4 and 5. These results indicate the undercut was formed by non-charged Br_2 species produced by neutralization due to secondary electrons. The etching rate temperature dependence is considered to be due to the temperature dependent chemical reaction between Br_2 species and InP . Vertical side wall etching was obtained when the discharge was sustained by only N_2 gas. In this case, the N_2 beam assisted the reaction between the ambient Br_2 species and InP .

Waveguide reflection mirror

Vertical side wall etching is very effective for forming waveguide reflection mirrors. The size of devices can be reduced by bending the propagated light using these mirrors.

A waveguide with reflection mirrors was made



Fig. 6 SEM photograph of the corner mirror. The slightly contrasting layer 1.5 μm under the waveguide top is the InGaAsP core layer.

on an epi-wafer on which 0.3- μm -thick InGaAsP ($\lambda=1.3 \mu\text{m}$) core layer was sandwiched between n-InP layers. The SiO₂ waveguide mask pattern was made by the same method used to make the samples for etching experiments. The pattern was etched down to 1 μm under the core layer. The obtained mirror shape under the vertical etching condition is shown in Fig. 6. The mirror surface is very smooth. Mirror loss was measured by the attenuation of the 1.55 μm light injected into waveguides containing several such mirrors⁹). Figure 7 shows the measured relative propagation loss of the waveguides as a function of mirror number. The mirror loss is about 1 dB/reflection from the slope of the straight line.

Conclusion

Indium phosphide dry etching was studied by using an etching beam extracted from a Br₂-N₂ gas mixture. The etched shapes and the rate temperature dependence could be classified into two types when the Br₂ gas partial pressure was changed. One was smooth vertical side wall when Br₂ gas pressure was low. The other was an undercut and rough etched surfaces with a temperature dependent etching rate at high Br₂ pressure. The different etching mechanisms between these two types is found to be due to the different etching beam species. Neutralized Br₂ ions generated by the plasma discharge result in the undercut etching. Their generation should be suppressed to form smooth vertical side walls. By

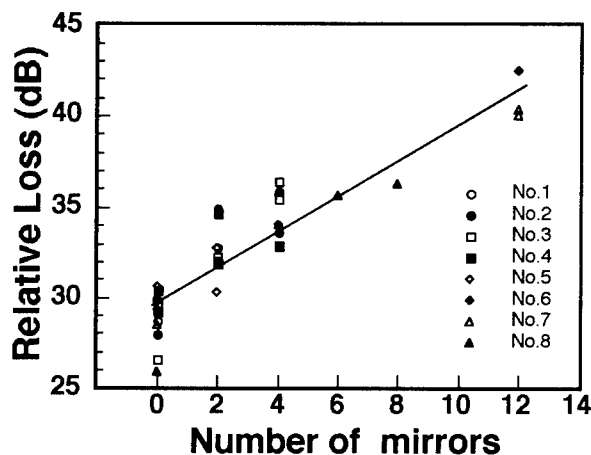


Fig. 7 Measured relative propagation loss as a function of mirror number. The numbers in the figure are for the different samples.

doing so, we were able to form a low-loss waveguide reflection mirror.

Acknowledgements

The authors thank Dr. J. Yoshida for his encouragement. The authors also thank to M. Yamashita for his helpful discussions.

References

- 1) T. Yoshikawa, S. Kohmoto, M. Anan, N. Hamano, M. Baba, T. Takado, Y. Sugimoto, M. Sugimoto, and K. Asakawa, Jpn. J. Appl. Phys., 31, L655 (1992).
- 2) J. Schneider, M. Moser, and K. Affolter, Proc. 5th Inter. Conf. on InP and Related Materials, Paris, 533, 1993.
- 3) S. J. Pearton, F. Ren, and C. R. Abernathy, Plasma Chem. Plasma Process, 14, 131 (1994).
- 4) I. Adesida, K. Nummila, E. Andideh, J. Hughes, C. Caneau, R. Bhat, and R. Holmstrom, J. Vac. Sci. Technol., B8, 1357 (1990).
- 5) F. Ren, S. J. Pearton, B. Tseng, J. R. Lothian, B. P. Sener, and C. C. Constantine, J. Electrochem. Soc., 140, 3284 (1993).
- 6) J. M. E. Harper, J. J. Cuomo, and H. R. Kaufman, J. Vac. Sci. Technol., 21, 737 (1982).
- 7) S. Matsuo, Applied Solid State Science, Supplement 2C, p75, Academic Press (1981).
- 8) H. R. Kaufman, J. Vac. Sci. Technol., 15, 272 (1978).
- 9) Y. Shibata, S. Oku, and M. Kadota, IEEE Photon. Techn. Lett., 35, 586 (1992).

DIELECTRIC WAVEGUIDES FABRICATED ON InP BY PHOTOCHEMICAL PROCESS FOR OEICs

A.Sayah and Y.I.Nissim

FRANCE TELECOM/CNET/PAB, Laboratoire de Bagneux
196, Avenue Henri Ravera BP.107, 92225 BAGNEUX CEDEX (FRANCE)

Introduction

Monolithic integration of optoelectronic devices on InP/InGaAsP based material is a current topic of research for telecommunication applications. The increase of the level of integration requires the increase of the number of optical interconnection between different devices on a single InP chip, as well as the connexion of this chip to others devices. Such optoelectronics integrated circuits (OEIC) require epitaxial layers that are suitable for both the optical waveguides and the devices (photodetector, amplifier) fabrication. Due to the complexity of the epitaxial process the integration of many functions on the same chip is often limited. The use of dielectric waveguides as optical interconnections can ideally leave the interconnection fabrication at the end of the OEIC process. SiO_2 and SiO_xN_y have been often use to fabricate dielectric waveguides on Si substrates with different deposition techniques [1].

The use of Rapid Thermal and UV assisted CVD (RTCVD and UVCVD) is proposed here to fabricate waveguides at $1.5\mu\text{m}$ directly on InP. Three different guide structures are proposed. Very little work has been reported on dielectric waveguides on InP due to two major problems that have been overcome here with these new deposition technics. The first problem is that dielectrics with good structural and optical properties are obtained at temperature higher than the temperature of InP decomposition (P sublimation). Rapid thermal CVD offers the possibility to deposit dielectric materials on InP at temperature as high as 750°C without substrate degradation [2] while UVCVD allow to deposit at temperature close to room temperature. The second problem is caused by the mechanical stresses in the deposited dielectric multilayers due to the mismatch of the thermal expansion of these materials. These mechanical stresses have been studied and compensated in order to fabricate waveguides directly on InP substrate. The attenuation measured on these dielectric waveguides is below 3dB/cm at $1.5\mu\text{m}$.

Rapid Thermal Chemical Vapour Deposition.

Rapid Thermal Chemical Vapour Deposition (RTCVD) is a combination of rapid thermal processing (RTP) and chemical vapour deposition (CVD). It utilizes rapid temperature cycling as a switch to turn on and off thermally driven gas surface reactions. The wafer can be brought to 750°C in less then 5s and can be cooled down to below deposition temperature in less than 2s. The use of highly controllable temperature changes to control the deposition offers with RTCVD the ability to reproducibly grow precisely controlled thin layers with very low defect densities, while minimising thermal exposure. Our RTCVD system is a single horizontal reactor with a quartz chamber, the wafer is supported on a susceptor by four quartz pins and is heated from below with a bank of nitrogen cooled tungsten halogen lamps. The chamber is made of high quality fused quartz and is highly transparent in the spectral range of the lamps, allowing the chamber to remain cool relative to the wafer and thereby recover the advantages of a cold-wall system. A set of UV lamps are mounted above the reactor allowing UV-CVD films to be deposited. A more detailed and complete description of the system can be found in reference [1]. SiO_xN_y films were deposited by RTCVD at 750°C from the reactive gases SiH_4 , NH_3 , N_2O diluted in a carrier gas N_2 with a total pressure of 50T .

Composition control of the SiO_xN_y films was obtained with the N_2O flow rate alone, all the other CVD parameters being constant. The index of refraction of the film was controlled via the N_2O flow rate as can be seen from Figure 1. A continuous variation of the index of refraction from 1.45 (index of refraction of SiO_2) to 2.1 (index of refraction of Si_3N_4) was obtained as measured by ellipsometry at 6328\AA . It has been also verified that the N_2O flow rate is directly connected to the stoichiometry of the SiO_xN_y films; a more detailed description of the deposition parameters and material proprieties can be found in [2].

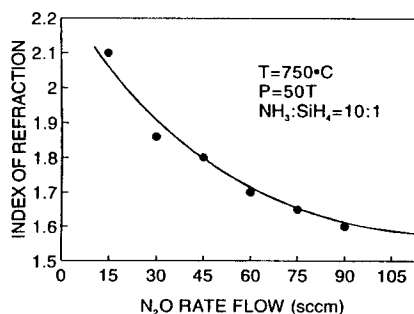


Fig. 1: variation of refractive index of SiO_xN_y as function of N_2O flow rate (i.e. as function of composition).

Conventional optical waveguide.

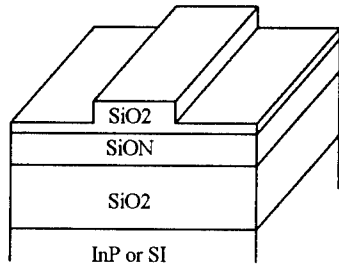


Fig. 2: Schematic diagram of conventional waveguide.

The dielectric waveguide consists of a SiON core sandwiched between two SiO₂ cladding layers as can be seen in figure 2. The thickness and the refractive index of these layers were calculated for monomode propagation at 1.5μm wavelength. The precise calculation was made using BPM code called ALCOR developed at CNET Bagneux [3]. The parameters of the waveguide are:

Structure	Thickness	refractive index
SiO ₂	1μm	1.45
SiON	0.7μm	1.75
SiO ₂	2μm	1.45
Substrate	Si or InP	

The waveguide has been fabricated on Si substrate in order to test the optical quality of dielectric films, the fabrication process of the waveguide consists of, a thermal oxydation of the Si substrate to form 2μm of SiO₂ followed by a SiON film deposited by RTCVD and finally a cover cladding SiO₂ film is deposited also by RTCVD. After lithography, the SiO₂ cover layer is patterned, by reactive ion etching, to permit the lateral confinement of the guided modes. The attenuation measurements of the fabricated waveguide were obtained using the cut-back method where the transmitted intensity of the waveguide with different length is measured. To do so the light from an He-Ne laser operating at 1.5μm was coupled into and out of the waveguide by means of microscope objectives and the output light was measured by a photodiode. To reduce the insertion losses caused mainly by the surface roughness of the entrance and exit facet of the waveguide, an effort has been done to fabricate smooth dielectric waveguide facets. With a trilayer masking technics and a controlled RIE process [4], facets with roughness of about 700Å were obtained. The propagation losses of these dielectric waveguides for the TE₀ mode is then measured to be 2dB/cm at 1.5μm. This result is the

best result obtained with "as-deposited" dielectrics waveguides on Si substrate. In the literature attenuation lower than 1dB/cm can be achieved by annealing the dielectrics waveguides at temperatures higher than 1000°C and for 1h [5] but this process is not suitable for our optoelectronic applications where brittle materials such as InP are used.

Going to InP substrates, the main problem encountered is the mechanical stresses induced by the dielectrics multilayer. Here the thermal SiO₂ is replaced by a 2μm of SiO₂ films deposited by UVCVD at 300°C or by RTCVD at 700°C. SiON is deposited by RTCVD at 750°C. Due to the thermal expansion coefficients mismatch of these materials the thickness of SiON deposited with no cracks is limited to 0.15μm. As the thickness increases cracks begin to appear within the films. For a thickness higher than 0.3μm, the tension increases in the films and induces the peeling off of the multilayers from the substrate. To solve this problem a thin Si₃N₄ film was deposited directly on the InP substrate by RTCVD at 750°C. This thin film compensates the difference of the thermal expansion between SiO₂ and InP, and also present a better adhesion to the InP substrate. Hence it is possible to deposit SiON up to 0.55μm on a 2μm SiO₂ layers. Figure 3 shows the cross-sectional SEM view of the waveguide structure fabricated on InP having the following parameters:

SiO ₂ cover cladding	n = 1.45 d = 1μm	UVCVD (300°C)
SiON core layer	n = 1.75 d = 0.55μm	RTCVD (750°C)
SiO ₂ first cladding	n = 1.45 d = 2μm	UVCVD (300°C)
Si ₃ N ₄ Adhesion film	n = 2.1 d = 0.05μm	RTCVD (750°C)
InP substrate		

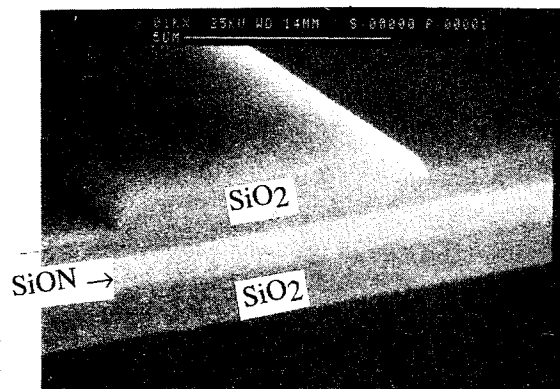


Fig. 3: SEM of conventional waveguide.

The attenuation value of this waveguide on InP substrate is 10dB/cm for the TE₀ mode at 1.5μm. This value is larger than the one obtained by the same dielectric waveguide fabricated on Si substrate. This can be explained by the formation of some slip lines on the InP substrate indicating that the problems of tension are still important in the structure and also by the fact that the cladding layer deposited by UVCVD at low temperature contains a large amount of hydrogen and then contributes to an increase of the attenuation.

In order to balance the mechanical stresses induced by the different dielectric films in the multilayer structure, other types of guiding structure on InP namely ARROW waveguide and Bragg waveguide have been realized.

ARROW waveguide.

Anti-resonant and reflecting optical waveguide (ARROW) have been receiving increasing attention in recent years [6]. In contrast with the conventional waveguide, the optical confinement in the ARROW waveguides is based on the high reflectivity of a Fabry-Perot resonator formed by the cladding layers rather than total reflection. The ARROW waveguide consists of interference cladding layers sandwiched between the core and the substrate. The cladding layers are combinations of films having high refractive index difference like the pair of Si/SiO₂, in order to achieve high reflectivity. To calculate refractive index and thickness of each layer in the ARROW, the powerful matrix method [7] for modelling multilayer structures has been utilized. The ARROW structure calculated is shown in figure 4.

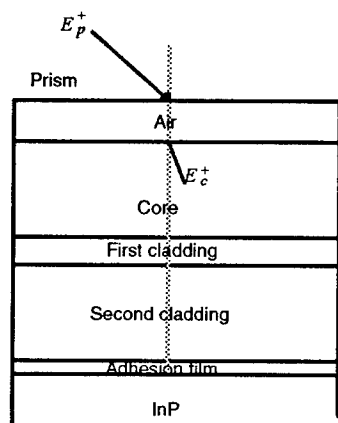


Fig. 4: schematic diagram of ARROW waveguide.

The matrix method consists to introduce a prism medium with refractive index, n_p , greater than the index of the guiding layer at a distance d_p above the structure in the air. The 2x2 transfer matrices are calculated and,

using the boundary conditions, the excitation efficiency $\xi(\beta)$ can be obtained :

$$\xi(\beta) = \frac{|E_p^+|^2}{|E_c^+|^2}$$

where $E_{p,c}^+$ is the field in the above medium and in the core film respectively and β is the propagation constant of the mode. The excitation efficiency is then plotted against β . This plot displays some peaks for given β that are the propagation mode constants. The curve shape around the peak is then fitted to a Lorentzian function whose width corresponds to the attenuation of the guided modes.

The parameters of the fabricated ARROW structure are outlined in the following table and the cross-sectional of the ARROW waveguide is shown in figure 5.

SiO ₂ core layer	n = 1.45 d = 3μm	RTCVD (700°C)
Si first cladding	n = 3.6 d = 0.1190μm	RTCVD (750°C)
SiO ₂ second cladding	n = 1.45 d = 1.5μm	UVCVD (300°C)
Si ₃ N ₄ adhesion film	n = 2.1 d = 0.05μm	RTCVD (750°C)
InP substrate		

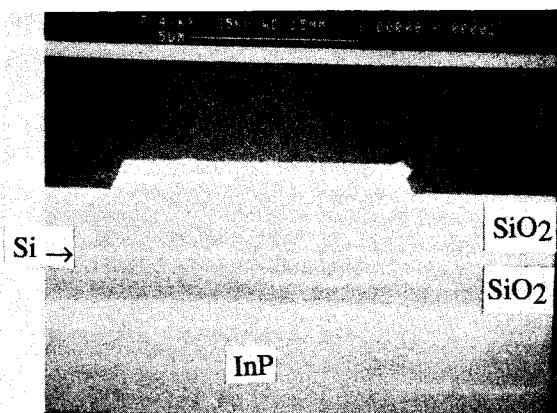


Fig. 5: SEM. of ARROW waveguide.

The propagation losses of the ARROW strip-loaded waveguide with different widths were measured for TE_0 mode at $1.5\mu\text{m}$ wavelength. Attenuation values close to 3dB/cm are obtained when the strip width of the waveguide is $10\mu\text{m}$.

BRAGG reflection waveguide.

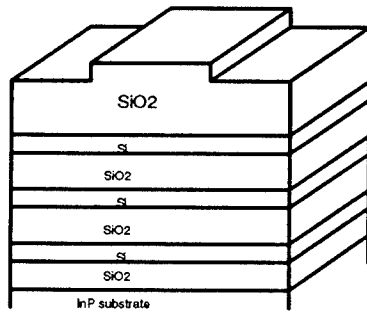


Fig. 6: schematic diagram of BRAGG reflector waveguide

The BRAGG reflector waveguide operates with the same principle as the ARROW waveguides [8]. In the BRAGG waveguide the cladding layers consist of periodic stratified media acting as Bragg reflectors for achieving high reflection at the working wavelength. Figure 6 shows the schematic diagram of a Bragg reflector waveguide. RTCVD has been used to deposit the SiO_2 and Si films. A precise control of the thickness and the refractive index has been obtained with an in situ reflectometry experiment described elsewhere [9]. A Bragg reflector waveguide has been fabricated consisting of 3 periodic quarter-wave Si/ SiO_2 layers as bragg reflector and a $2\mu\text{m}$ SiO_2 guiding layer as can be seen in figure 5. The value of the attenuation measured in this case is 10dB/cm at $1.5\mu\text{m}$ wavelength. This is our first result obtained with this kind of dielectric waveguides on InP substrate. Further experiments are on the way to improve the control of film fabrication. Since only three pairs of Si/ SiO_2 film are used the total thickness of the cladding is reduced to $0.8\mu\text{m}$ (as compared to $2\mu\text{m}$ in the other structures). The reduction of total thickness of the waveguide allows to reduce the mechanical stress. This should be in favour of fabrication directly on InP substrates.

Conclusion.

A complete Si-based dielectric waveguides technology fabricated on InP substrates has been developed. The lowest attenuation measured at $1.5\mu\text{m}$ wavelength is 2 dB/cm without any high temperature annealed of the waveguide structure. This best result is due to the quality of the material obtained by new deposition technics, namely RTCVD and UVCVD. These

deposition technics have proved their compatibility with brittle materials such as InP. They are also compatible with waveguide fabrication at the end of a device or circuit process. The objective is now to integrate this technology into simple OEICs.

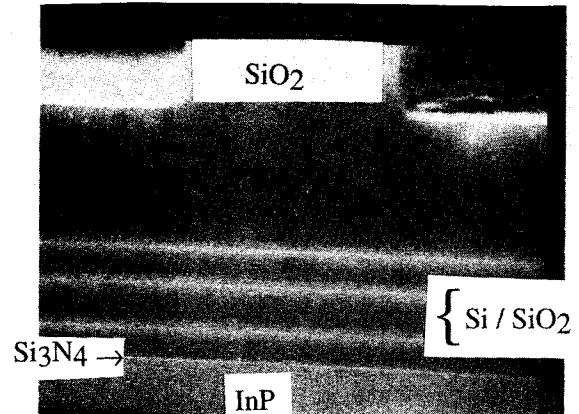


fig. 5: SEM. of BRAGG reflector waveguide.

Acknowledgments.

The authors would like to thank C. Meriadec for technical assistance.

References

- [1] S. Valette, S. Renard, H. Denis, J. P. Jadot, A. Fournier, P. Philippe, P. Gidon, A. M. Grouillet, E. Desgranges, Solid State Technology, Feb., p.69, (1989)
- [2] F. Lebland, doctoral thesis, université de Paris VII, (1992)
- [3] BPM-CNET (ALCOR) software developed and distributed by France Telecom/CNET
- [4] A. Sayah and Y. I. Nissim to be published in J. Non-cryst. Solids
- [5] Massino del Giudice, Franco Bruno, Tito Cicinelli and Marco Valli, App. Opt. vol.29, no.24, p.3489 (1990)
- [6] M. A. Duguy, Y. Kokubun, T. L. Koch, and L. Pfeiffer, Appl. Phys. Lett, vol. 49, p.13, (1986)
- [7] A. K. Ghatak, K. Thyagarajan and M. R. Shenoy, J. Lightwave technol. LT-5, 660, (1987)
- [8] P. Yeh and A. Yariv, Opt. Commun, 19, p.427, (1976)
- [9] Y. I. Nissim CNET internal publication

FIRST ORDER GRATINGS FOR GAIN COUPLED GaInAsP DFB-LASERS MADE BY MASKLESS FOCUSED ION BEAM PATTERNING

J.P. Reithmaier, A. Orth, J. Müller, and A. Forchel
Universität Würzburg, Am Hubland, D-97074 Würzburg, Germany

J. Weber, I. Gyuro, and E. Zielinski
Alcatel SEL AG, Lorenzstr. 10, D-70435 Stuttgart, Germany

ABSTRACT

First order gratings in GaInAsP laser structures were defined by maskless focused ion beam implantation. The optically pumped devices show laser operation at 77 and 300 K. All lasers operate in a single longitudinal mode which is typical for the gain coupled distributed feedback effect. The implanted gratings are thermally stable up to 700 °C and are suitable for an overgrowth process by metal organic vapour phase epitaxy.

INTRODUCTION

Conventional structuring techniques require resist masks and etch processes for the fabrication of distributed feedback (DFB) lasers (1, 2). With a high resolution focused ion beam (FIB) system maskless patterning can be realised, which is contamination free and preserves the planarity of the surface. This technique is therefore very suitable for an overgrowth process, which is necessary for DFB laser structures. With FIB implantation a modulation of the gain is produced. Compared to index coupled DFB lasers, gain coupled structures have a number of advantages. Because of the different coupling mechanism a single mode behaviour even without additional phase shift (3, 4) and a reduced frequency chirp are expected (5). The side mode suppression should be enhanced and problems like mode hopping and spatial hole burning reduced (6, 7).

EXPERIMENT

A high resolution FIB system (Eiko E100) was used to define gratings in GaInAsP/InP separate confinement laser structures. In Fig. 1 the layer structure is schematically shown. The implantation direction and the modified areas in the active region are indicated. The Ga^+ ion beam can be focused to 30 nm in diameter at ion currents of 10 pA between 10 and 150 keV energy (8, 9). For the implantation of the 150 - 250 nm buried active layers of the laser structures an ion energy of 130 keV was used. Because of channeling effects in (100) oriented III/V crystals the energy is high enough for a penetration depth of more than 300 nm. The line dose was varied between $3 \times 10^7 \text{ cm}^{-1}$ and $9 \times 10^8 \text{ cm}^{-1}$, which corresponds to area doses of approximately $5 \times 10^{12} \text{ cm}^{-2}$ and $1 \times 10^{14} \text{ cm}^{-2}$. The periods of the gratings were adjusted to emission wavelengths of the material at 77 K and 300 K. For 77 K grating periods between 220 and 232 nm, for 300 K between 248 and 260 nm were used. For low doses the samples were not annealed while for higher doses a rapid thermal annealing (RTA) step was used (500 - 700 °C, 60 s). To avoid any background signal mesa stripes with 100 μm in width were etched.

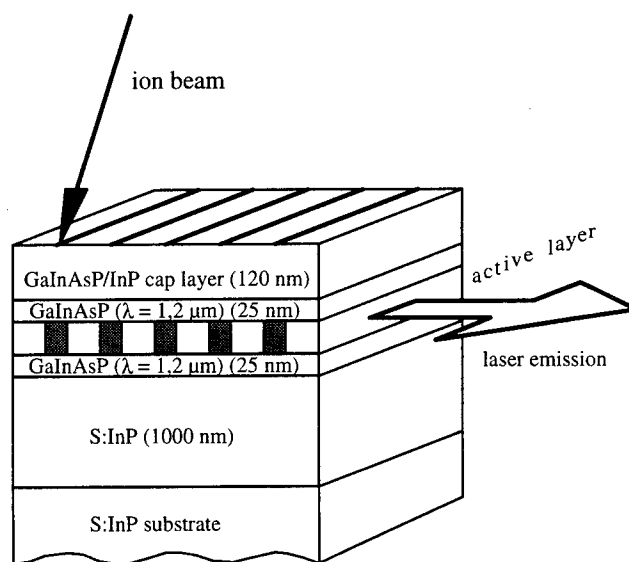


FIG. 1 Schematic layer structure of the DFB-lasers. The active layer consists of 5 GaInAsP QWs with 12 nm thickness (total thickness about 100 nm). The material modification by the ion beam is indicated in the active layer as well as the laser output direction during operation.

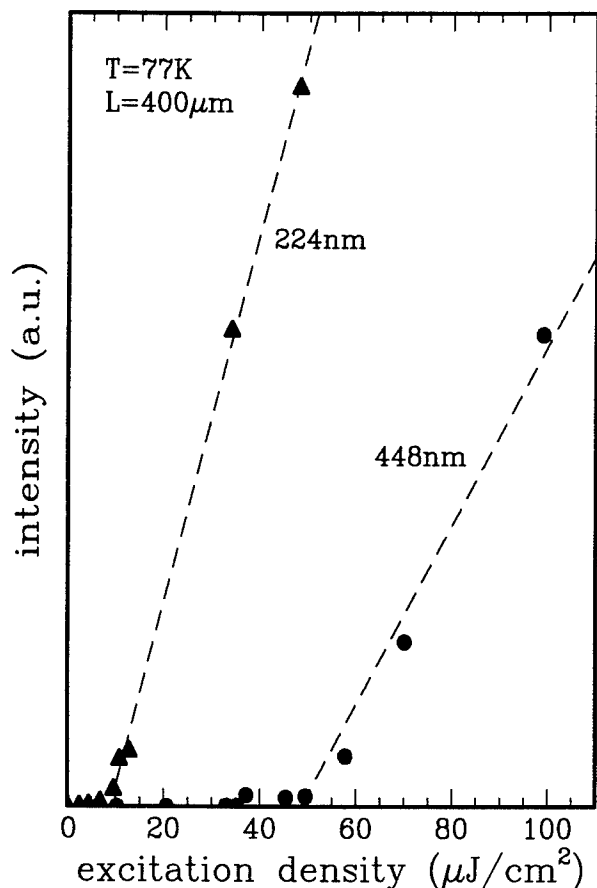


FIG. 2: Light output characteristics of gain coupled DFB-lasers with first (triangles) and second order gratings (dots). The threshold energy densities are $10 \mu\text{J}/\text{cm}^2$ (1. order) and $50 \mu\text{J}/\text{cm}^2$ (2. order).

The laser structures were optically pumped by a pulsed (80 ps) frequency doubled Nd:YAG laser operating at a wavelength of 532 nm. The laser beam was focused through a cylindrical lens to an excitation area of around $200 \mu\text{m}$ in width and a variable length between 0.1 and 2 mm controlled by a slit. The DFB-laser emission was dispersed by a 0.32 m monochromator with a spectral resolution of 0.1 nm and measured by a liquid nitrogen cooled Ge-detector.

LIGHT OUTPUT CHARACTERISTIC

The laser output intensity characteristic at a temperature of 77 K is plotted for first and second order gratings in Fig. 2. Both gratings were defined on the same sample and excited with a stripe length of $400 \mu\text{m}$. They were implanted with the same low dose and not annealed. The output intensity shows a laser typical linear increase with increasing excitation intensity. In comparison to the second order grating the first order grating device shows a reduction of the threshold by a factor of 5. Simultaneously the external quantum efficiency

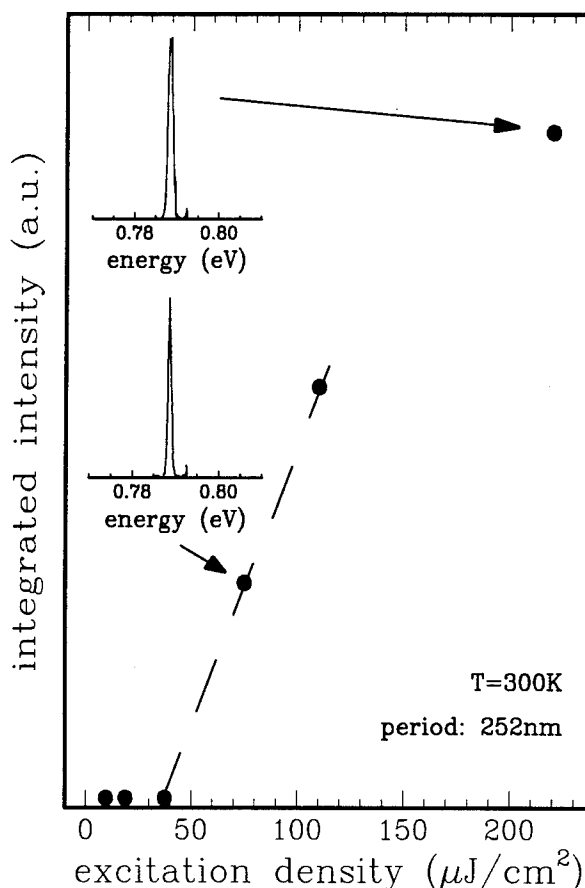


FIG. 3: Room temperature laser output characteristic for a first order FIB implanted DFB grating. The threshold pulse energy density is about $35 \mu\text{J}/\text{cm}^2$. The insets show laser emission spectra at $75 \mu\text{J}/\text{cm}^2$ and $220 \mu\text{J}/\text{cm}^2$.

increases. Although in first order gratings the implanted line density is doubled the improvement to second order gratings is rather high. The main reasons for this significant improvement are the reduction of the radiative loss (10) and a larger feedback effect per unit length which dominates over a possible increased loss due to nonradiative recombination.

For room temperature emission the grating period must be enlarged above 240 nm to get a feedback effect for wavelengths above the band gap energy. In Fig. 3 the light output characteristic for a gain coupled DFB laser is shown operating at room temperature. The first order grating has a periodicity of 252 nm and was implanted with a line dose of $8 \times 10^6/\text{cm}$. No annealing step was used to get an operating device. The threshold pulse energy density is only a factor of 3 higher than for 77 K. The device can be operated up to ten times of the threshold density. But above three times the threshold density the linear response changes due to saturation effects. The emission wavelength is $1.57 \mu\text{m}$.

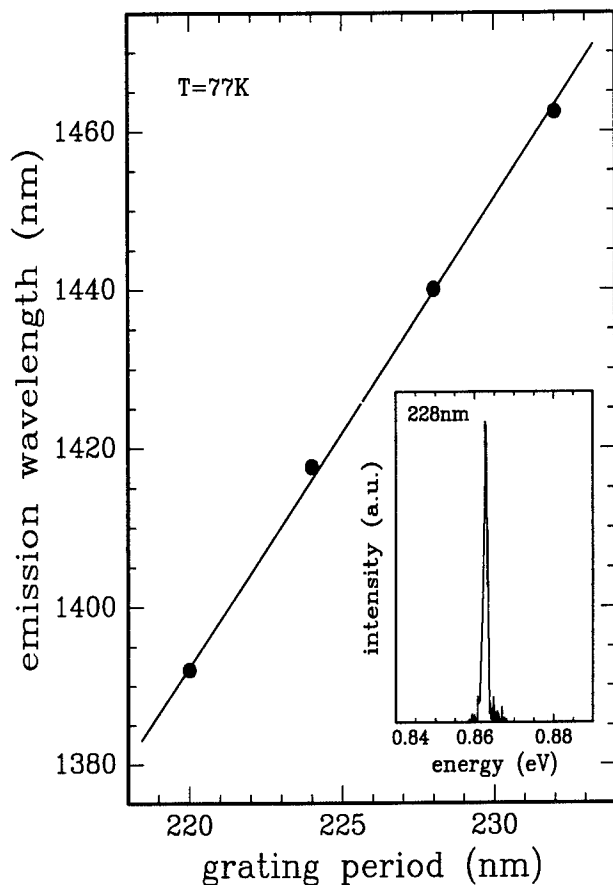


FIG. 4: Emission wavelength of gain coupled DFB lasers versus grating period at 77 K. The straight line corresponds to a linear fit of the data points. The inset shows a laser spectrum for a grating period of 228 nm.

SPECTRAL RESPONSE

The emission wavelength can be controlled very accurately by changing the grating period. In Fig. 4 the emission wavelengths of four devices with different grating periods are plotted. The gratings were defined by FIB implantation on the same sample. The emission wavelength changes linearly with the grating period with a rate of 5.8 (emission wavelength to grating period) within the investigated spectral region. From the statistic deviations of the points from the straight line a reproducibility of the grating period of better than 0.2 nm can be estimated which corresponds to an accuracy of the emission wavelength of about 1 nm.

The inset of Fig. 4 shows a laser emission spectrum for a grating period of 228 nm at an excitation density of $70 \mu\text{J}/\text{cm}^2$. Due to the wide stripe geometry of the mesa etching a large amount of lateral modes are allowed. The spectral width of about 2 meV is therefore mainly caused by amplified higher lateral modes. This effect is more obvious at higher excitation densities, which leads to an asymmetric broadening of the spectra to higher energies as can be seen in insets of Fig. 3.

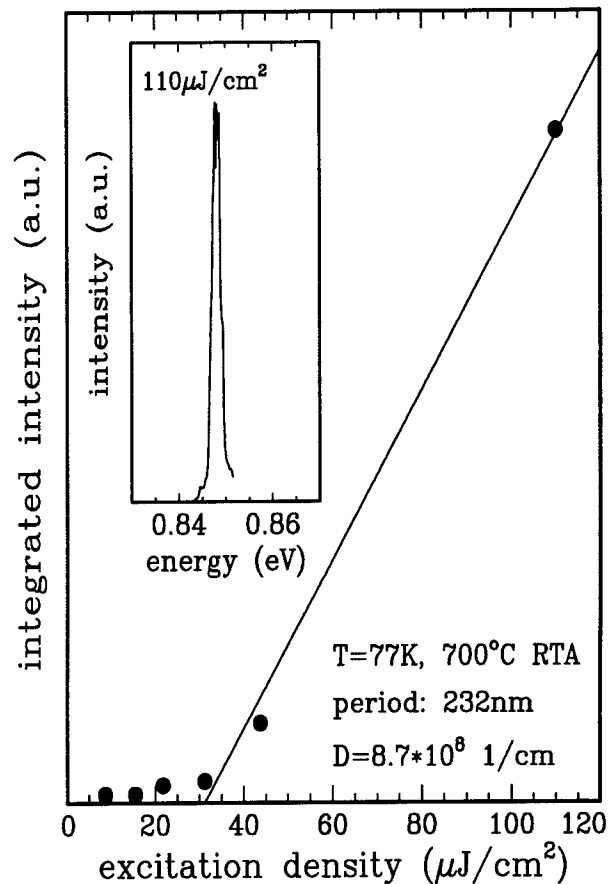


FIG. 5: Laser output characteristic of a grating structure after an annealing step at 700 °C (RTA step). For the implantation a line dose of $9 \times 10^8/\text{cm}$ was used. The inset shows an emission spectrum at high excitation density.

The spectra of Fig. 3 show the laser emission at about 2 and 6 times of the threshold excitation density. Except the above mentioned line broadening effect, the lowest lateral modes show no shift in the emission energy for excitation densities up to 12 times of the threshold condition ($450 \mu\text{J}/\text{cm}^2$). A shift of the emission energy of the lowest lateral mode (low energy side of the peak) could not be observed within the spectral resolution of the measurement set-up of about 0.1 meV. Also no higher longitudinal modes were observed and no mode hopping occurred.

THERMAL STABILITY

For electrically pumped devices an upper cladding layer with a thickness of about $2 \mu\text{m}$ is used to complete the vertical wave guide and to avoid absorption losses in the contacting layers. Therefore an overgrowth process is necessary after the grating definition. In contrast to most of the other techniques, like holography or electron beam based patterning, no resist step is needed for focused ion beam technology and also the planarity of the surface is not

disturbed. These are properties which are favourable for overgrowth processes. But the implanted structure must be stable enough to survive a growth temperature of around 600 to 650 °C during metal organic vapour phase epitaxy.

In order to test the thermal stability of the implanted gratings the samples were annealed by RTA at temperatures between 500 °C and 700 °C for different implantation doses. To get enough feedback from the grating the line dose must be increased with increasing annealing temperature. For a temperature stability of 700 °C a line dose of about 9×10^8 is necessary. In Fig. 5 the laser output characteristic of an annealed grating structure is shown. The threshold excitation density is with 30 $\mu\text{J}/\text{cm}^2$ comparable to the not annealed devices. The inset shows monomode emission at high excitation density.

Two mechanisms can cause the gain modulation in the implanted and annealed grating structures. One is the creation of non radiative recombination centers, which reduce locally the carrier lifetime and therefore modulate the carrier distribution. The second effect is caused by the implantation induced inter diffusion, which leads to a band gap increase for the implanted areas. This band gap modification causes also a modulation of the carrier density. Both effects will reduce periodically the gain in the implanted areas while in the non implanted areas the gain remains or even increases compared to an unimplanted 2D layer.

SUMMARY

Gain coupled DFB laser structures with first order gratings were defined by maskless focused ion beam implantation in GaInAsP heterostructures. The devices were optically pumped and showed laser emission at 77 K and 300 K. First order gratings show in comparison to second order gratings significantly lower thresholds and higher quantum efficiencies. As expected for gain coupled DFB lasers the monomode emission is stable up to the highest excitation intensity and no mode hopping was observed. The implanted gratings are thermally stable up to 700 °C, which is sufficiently high enough for any overgrowth process. Due to the possibility of maskless, contamination free and planar patterning, focused ion beam technology is very suitable for overgrowth processes in combination with high resolution buried patterning.

ACKNOWLEDGEMENT

The support of this work by Alcatel SEL AG and the "Bundesministerium für Forschung und Technologie" is gratefully acknowledged.

REFERENCES

- (1) Y. Nakano, H. Cao, K. Tada, Y. Luo, M. Dobashi, and H. Hosomatsu, "Absorptive-Grating Gain-Coupled Distributed Feedback MQW Lasers with Low Threshold Current and High Single-Longitudinal-Mode Yield", *Jpn. J. of Appl. Phys.*, vol. 32, pp. 825-829, Febr. 1993.
- (2) W.T. Tsang, F.S. Choa, M.C. Wu, K. Chen, A. Logan, S.N.G. Chu, A.M. Sergent, and C.A. Burrus, "Semiconductor distributed feedback lasers with quantum well or superlattice gratings for index or gain-coupled optical feedback", *Appl. Phys. Lett.*, vol. 60, pp. 2580-2582, May 1992.
- (3) H. Kogelnik, and C.V. Shank, "Coupled-wave theory of distributed feedback lasers", *J. of Appl. Phys.*, vol. 43, pp. 2327-2335, May 1972.
- (4) Y. Nakano, Y. Luo, and K. Tada, "Facet reflection independent, single longitudinal mode oscillation in a GaAlAs/GaAs distributed feedback laser equipped with a gain-coupling mechanism", *Appl. Phys. Lett.*, vol. 55, pp. 1606-1608, Oct. 1989.
- (5) Y. Luo, R. Takahashi, Y. Nakano, K. Tada, T. Kamiya, H. Hosomatsu, and H. Iwaoka, "Ultralow chirping short optical pulse (16 ps) generation in gain-coupled distributed feedback semiconductor lasers", *Appl. Phys. Lett.*, vol. 59, pp. 37-39, July 1991.
- (6) T. Sudoh, Y. Nakano, K. Tada, K. Kikuchi, and H. Hosomatsu, "Self-Suppression Effect of Longitudinal Spatial Hole Burning in Absorptive Grating Gain-Coupled DFB Lasers", *IEEE Photon. Technol. Lett.*, vol. 5, pp. 1276-1278, Nov. 1993.
- (7) G. Morthier, P. Vankwikelberge, K. David, and R. Baets, "Improved performance of AR-Coated DFB lasers by the introduction of gain coupling", *IEEE Photon. Technol. Lett.*, vol. 2, pp. 170-172, Mar. 1990.
- (8) J.P. Reithmaier, A. Kieslich, H. Sawaragi, and A. Forchel, "High resolution focussed ion beam implantation with post objective lens retarding and acceleration", *Microelectr. Eng.*, vol. 23, pp. 119-122, 1994.
- (9) A. Kieslich, J.P. Reithmaier, and A. Forchel, "Minimum feature sizes and ion beam profile for a focused ion beam system with post-objective lens retarding and acceleration mode", *J. of Vac. Sci. and Technol. B*, vol. 12, pp. 3518 - 3522, Nov. 1994.
- (10) A strong radiation loss occurs in 2. order gratings due to the light diffraction perpendicular to the sample surface.

Surface damage on InP induced by photo- and plasma-assisted chemical vapor deposition of passivation films

ThP54

Tamotsu Hashizume and Hideki Hasegawa

Research Center for Interface Quantum Electronics and Department of Electrical Engineering, Hokkaido University, Sapporo 060

Introduction

Achievement of low surface damage is a key issue in processing steps for fabrication of advanced InP electronic and optoelectronic devices. Insulating films prepared by various CVD techniques have been used for passivation of device surfaces. However, virtually nothing is known on surface damage.

The purpose of the present paper is to systematically characterize process-induced near-surface defects in InP introduced during photo- and ECR-assisted techniques for insulator deposition compared to conventional PECVD technique. The standard Schottky deep level transient spectroscopy (DLTS) technique, the metal-insulator-semiconductor (MIS) DLTS technique and MIS capacitance-voltage (C-V) techniques were applied to characterize the surface damage in ECR treated, PECVD SiO₂ deposited and photo CVD SiO₂ deposited InP surfaces.

The analysis has shown that photo CVD SiO₂ deposition is superior to PECVD SiO₂ deposition due to absence of process-induced bulk traps and to smaller density of interface states with a narrower spatial distribution.

Characterization methods of surface damage

Schottky DLTS method

Near-surface trap levels induced by various processes can be characterized by standard DLTS technique using Schottky barrier diodes. As for the CVD process, surface damage can be characterized at Schottky interfaces prepared after removal of insulating films. However, for n-InP, because of low Schottky barrier heights (SBHs), it is very difficult to obtain information on deep trap levels and on the depth-profile of the trap concentration.

MIS DLTS and C-V methods

The physical situation when the DLTS technique is applied to a MIS structure is shown in Fig.1. When the emission rate of the deep level and that of the interface states coincide the DLTS setting rate window, the corresponding two peaks appear. The emission rate from the deep level is independent of the bias condition and is determined by $E_C - E_{DL}$, whereas that from the interface states is determined by the energy difference $E_C - E_F$ which changes with the surface potential determined by the bias. Thus, by systematically changing the bias pulse condition, bulk deep levels and interface states can be clearly

distinguished.

In addition, the spatial distribution of the interface states within the insulator can be characterized by combination of the MIS DLTS and C-V methods. This is based on our recent finding⁽¹⁾ that, when interface states possess a spatial distribution, the interface state density (N_{ss}) distribution obtained by C-V method becomes different from that by the DLTS method, as shown in Fig. 2(a). The reason for the difference can be explained in terms of equi-emission rate line for the emission process.⁽²⁾ When interface states are distributed into the insulator with their peak concentration at the interface, the states within the infinitesimal energy difference between E_a and E_b

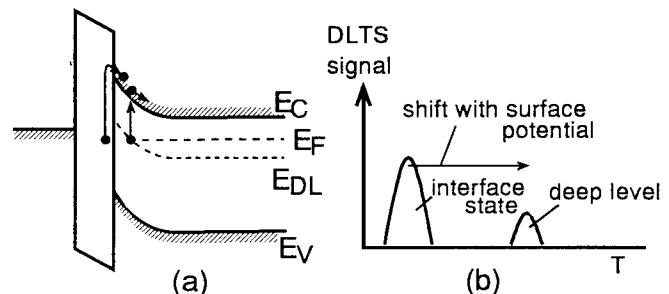


Fig.1 Band diagram and DLTS spectra for MIS DLTS method

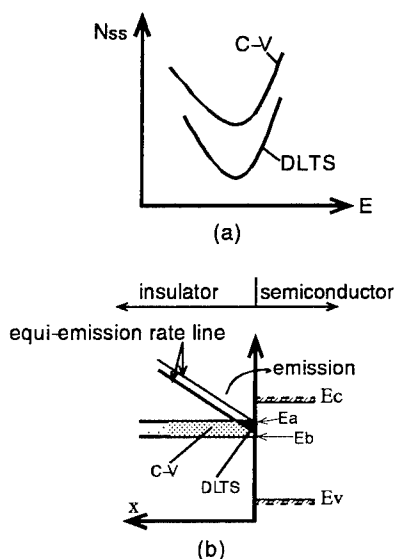


Fig.2 (a) N_{ss} distributions obtained from DLTS and C-V methods and (b) concept of equi-emission rate line

shown in Fig.2(b) have different emission rates depending on their distance x from the interface. This is because the electron emission from the occupied states to the conduction band depends both on the thermal activation energy and the distance from the interface. The emission rate is the same on the equi-emission rate line given by²⁾

$$E_c - E + kT(x/x_{0n}) = \text{const} \quad (1)$$

where x_{0n} is the tunneling decay length. Therefore, the state density calculated from the DLTS peak corresponds to the number of states, as indicated black region in Fig.2(b). On the other hand, the number of the states obtained by the C-V method is basically that of the whole states between E_a and E_b . Thus, comparison of C-V and DLTS results should provide information on the spatial distribution of states. The present argument ignores the effect of the insufficient capture and emission in the real experiments and the effect of the electric field in the insulator. These effects complicate the situation very much. For example, the N_{ss} distribution by C-V method is no longer the true distribution by these effects. The whole analysis should be done using computer fitting as described elsewhere.⁽²⁾

Experimental

As a reference for MIS study, a SiO_2/Si system was prepared by thermal oxidation of a clean n-type Si surface. For InP samples, undoped n-type liquid encapsulated Czochralski (LEC) InP wafers with a

carrier concentration of $5 \times 10^{15} \text{ cm}^{-3}$ were used. The InP surface was treated in HF solution prior to the deposition process for MIS structures. SiO_2 films were deposited by PECVD process using a mixture of SiH_4 and N_2O at 40–300 °C, and a photo CVD process at 250 °C using a mixture of SiH_4 , N_2O and Ar, and ArF excimer laser (193nm). For Schottky DLTS study, Schottky barriers were formed by evaporating Au through a metal mask after removal of insulating films. Au Schottky barriers were also formed on the InP surfaces exposed to the ECR-assisted Ar plasma.

Results and discussion

Schottky DLTS study

Figure 3 shows the DLTS spectra of the Au/n-InP Schottky diodes formed at the surface after the plasma treatment or removal of the insulating films. PECVD deposition of SiO_2 films were found to produce the discrete deep level, lying at 0.35 eV below E_c . Ninomiya et al.⁽³⁾ recently reported that the process-induced defect level was found in the InP surface exposed to H_2 and Ar plasma in the conventional rf-plasma reactor. The "signature plot" of the present level was found to be very close to that of this level. On the other hand, the trap level was absent in the samples processed by photo CVD and exposed to ECR-assisted Ar plasma. Thus, this trap is process-dependent and seems to be due to high-energy plasma damage.

MIS DLTS and C-V study

Typical DLTS spectra obtained for the SiO_2/Si samples under small bias swings are shown in Fig.4. The surface potential change between the injection and emission pulses was controlled so that it becomes constant at each quiescent bias. As shown in Fig.4, DLTS peak moved continuously with the bias, indicating that it is due to interface states which sensitively reflect bias-induced changes in surface potential and emission time constants of responding states. No signal from the bulk deep level was seen.

On the other hand, two peaks, each coming from the bulk deep level and from interface states, were clearly seen in the PECVD SiO_2/InP MIS samples, as shown in Fig.5. The DLTS peak position at around 200K was independent of the bias and remained at the same temperature, corresponding to the emission time constant from the bulk level detected in the Schottky samples.

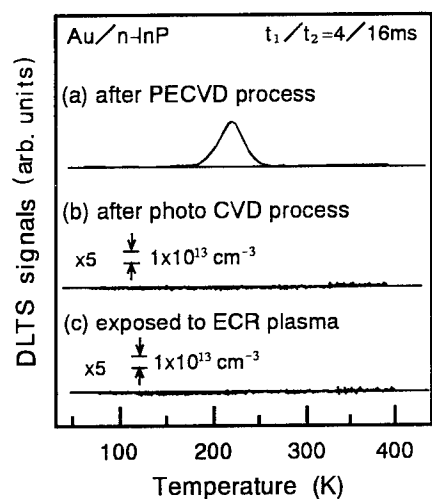


Fig.3 DLTS spectra of Au/n-InP samples

The concentration profile of the observed bulk level is shown in Fig.6. For comparison, previously reported profile of PSG/InP⁽¹⁾ is also plotted in Fig.6. The trap density of the discrete level can be calculated by the DLTS peak height taking into account of small surface potential change.⁽⁴⁾ As can be seen, the bulk level is presented only in the vicinity of the InP surface, within about 2000 Å, and the deposition of PSG film produced less damage than the SiO₂ deposition. Furthermore, the concentration of the observed bulk trap in the PSG/InP system was found to decrease with the increase of the phosphorus content in PSG films.⁽¹⁾

As to the origin of the observed discrete level near the surface, it is noted that preferential etching of phosphorus occurs easily in the InP surface during plasma treatment,⁽³⁾ which can be responsible for vacancy related defects. It has been suggested⁽³⁾ that the formation of a thin phosphorus layer at the InP surface by PH₃ plasma treatment was effective in suppressing the defects related to phosphorus vacancy. The results indicated in Figs. 3 and 6 also seem to support this suggestion. Thus, it seems that the observed bulk level is related to phosphorus vacancies or their complexes created by high-energy plasma damage during PECVD process.

Interface state density distributions

Figure 7 shows the N_{ss} distributions of the thermally-grown SiO₂/Si interface obtained from C-V and DLTS methods. N_{ss} distribution from DLTS is in good agreement with that from C-V. This indicates that the spatial distribution of N_{ss}, if

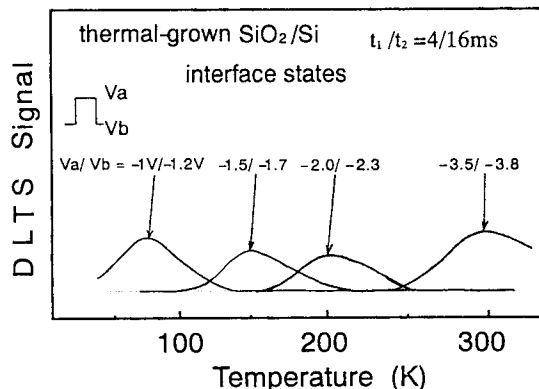


Fig.4. DLTS spectra for the SiO₂/Si MIS sample.

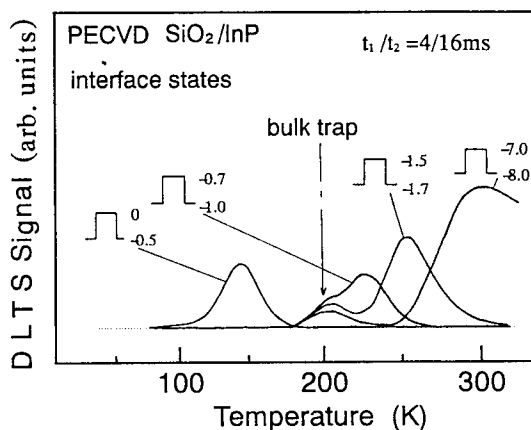


Fig.5. DLTS spectra for the PECVD SiO₂/InP MIS samples.

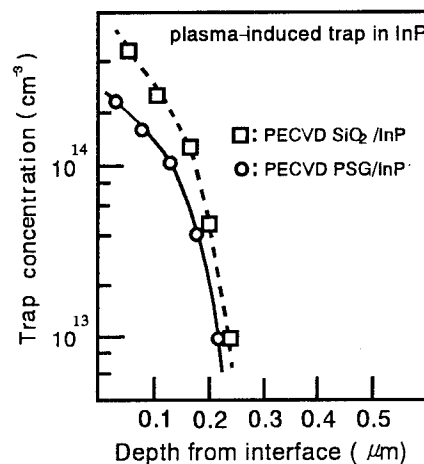


Fig.6 Concentration profiles of the plasma-induced bulk trap in InP

it exists, is very narrow.

On the other hand, the CVD SiO₂/InP systems exhibited large N_{ss} difference in N_{ss} between the two methods, as shown in Fig 8 for PECVD SiO₂ system. As s Both DLTS and C-V results showed similar U-shaped continious distributions with

nearly the same energy position of minimum density, being consistent with the disorder-induced gap-state (DIGS) model.⁽⁵⁾ In addition, the PECVD process gives a higher density of states than the photo CVD process.

By the computer analysis of the results of MIS C-V and DLTS study, true Nss distributions were deduced and the extension of the space distribution was estimated. For calculation, the following functional form of the Nss distribution was used:⁽²⁾

$$N_{\text{DIGS}}(E, x) = N_0 \exp \left[\left(\frac{|E - E_{\text{Ho}}|}{E_0} \right)^n \right] \exp(-x/x_{\text{DIGS}}) \quad (2a)$$

$$N_{\text{ss}}(E) = \int_0^{\infty} N_{\text{DIGS}}(E, x) dx, \quad (2b)$$

where N_0 is the volume density of the DIGS (interface state) continuum and E_{Ho} the charge neutrality point of the DIGS continuum.⁽⁵⁾ The parameters N_0 , n , E_0 and x_{DIGS} characterize the distribution.

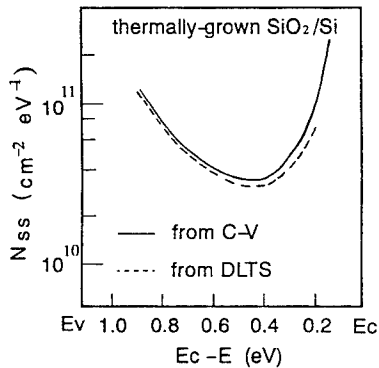


Fig.7. Nss distributions of PECVD SiO₂/Si obtained from DLTS and C-V methods.

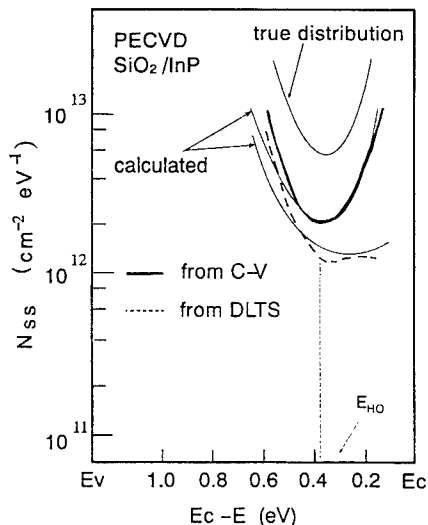


Fig.8. Experimental and calculated Nss distributions of PECVD SiO₂/InP.

Table I. Parameters of the spatial distribution of interface states

	$N_{\text{ss}0}$ (cm ⁻² eV ⁻¹)	x_{DIGS}	n	E_{Ho}
SiO ₂ /Si	3.6×10^{10}	$< 5 \text{ \AA}$	2.0	$E_{\text{c}} - 0.42 \text{ eV}$
PECVD SiO ₂ /InP	6.0×10^{12}	75 Å	1.5	$E_{\text{c}} - 0.38 \text{ eV}$
photo CVD SiO ₂ /InP	1.5×10^{12}	30 Å	2.5	$E_{\text{c}} - 0.38 \text{ eV}$

The true distribution in Fig.8 was determined by varying the parameters in Eq.(2) so that the calculated DLTS and C-V distributions fit the experimental ones.

The values of the parameters thus determined are summarized in Table 1. The obtained value of x_{DIGS} is 75 Å for the PECVD MIS system, which is two or three times larger than that for the photo CVD MIS system. Furthermore, the PECVD MIS structure possesses larger $N_{\text{ss}0}$ with a steeper Nss distribution shape. These results clearly indicate that the damage or disorder induced by PECVD distributes deeper into insulator region because of the high-energy nature. The value of x_{DIGS} of the thermally-grown SiO₂/Si structure is below 5 Å, being consistent with excellent interface properties of this system.

Conclusion

Process-induced near-surface defects in InP introduced during PECVD, photo- and ECR-assisted techniques for insulator deposition were studied using Schottky DLTS, MIS DLTS and MIS C-V techniques.

Interface states and near-surface bulk traps can be clearly distinguished by the MIS DLTS technique. Furthermore, the spatial distribution of the near-surface traps within the deposited insulator can be determined by analyzing MIS DLTS and C-V data. The analysis showed that photo CVD SiO₂ deposition is superior to PECVD SiO₂ deposition due to absence of process-induced bulk traps and to smaller density of interface states with a narrower spatial distribution.

References

- (1) T.Hashizume, H.Hasegawa, R.Riemenchneider, H.L. Hartnagel: Jpn. J. Appl. Phys. **33**(1994) 727.
- (2) L.He, H.Hasegawa, T.Sawada and H.Ohno: J. Appl. Phys. **63**(1988) 2120.
- (3) H.Ninomiya et al.: Jpn.J.Appl.Phys. **32**(1993) L12.
- (4) K.Yamasaki, M.Yoshida and T.Sugano: Jpn. J. Appl. Phys. **18**(1979) 113.
- (5) H.Hasegawa and H.Ohno: J. Vac. Sci. & Technol. **B4**

The Effects of Sulfur Concentration on the Growth Rate of Selective MOCVD Grown InP

D. Veinger, G. Bahir and J. Salzman

Technion - Israel Institute of Technology, Department of Electrical Engineering, Haifa 32000, Israel

Introduction

The ability to grow epitaxial material on predetermined areas of semiconductor substrate has made it possible to fabricate advanced optoelectronic devices. Selective metalorganic vapor phase epitaxial growth of InP/InGaAs structures on a dielectric mask patterned planar InP wafer, has been widely studied for applications of optical devices. In this study, ridge structures with various widths of about $5\mu\text{m}$ were selectively grown on open stripe regions between pairs of mask stripes. In narrow regions, such as the above, both lateral gas phase diffusion and substrate migration contribute to the enhanced growth, and affect the surface flatness. In addition, rabbit-ear growth occurs at both edges of selective grown mesa structure and prevents flat burial of the mesa. In this work we present the results of a study of the effects of sulfur, on the growth rate of InP in selective area growth processes. It was found that the growth rate of the n type InP layer on the open stripes is a sensitive function of the H_2S flow rate. It was also found that the growth rate on (100) planes (mesa top) differ from that on (111)B (side facet), and can be controlled by the H_2S flow rate. A complete growth suppression can be achieved at partial pressure of 2×10^{-3} Torr. Using this novel MOCVD growth technique, a selectively grown buried heterostructure laser diode is successfully fabricated in one step growth.

Experimental

The MOCVD growth was done at 670°C . The pressure was 40 Torr. TMIn , TMGa and PH_3 were used as growth sources. Sulfur was provided by H_2S and p type dopant by diethylzinc. For selective growth, (100) InP substrate were coated with SiO_2 film with thickness of 2000 Å. Mask stripes of $5\mu\text{m}$ width were formed in [011] direction with a $250\mu\text{m}$ period. The TMIn flow rate used for the selective growth process was reduced to 5 ccm (0.1%) in comparison to 85 ccm (0.1%) which is our regular flow rate for unmasked process. This was done in order to achieve the same growth rates of about $2\mu\text{m/h}$ for the selective and non-selective processes. The grown structures were evaluated by SEM. Layer thickness were measured by a stylus profiler. The composition of the layers were evaluated by electron beam microprobe.

the same. The reduction of the growth rate caused by the sulfur doping is clearly seen.

Selectively grown InP

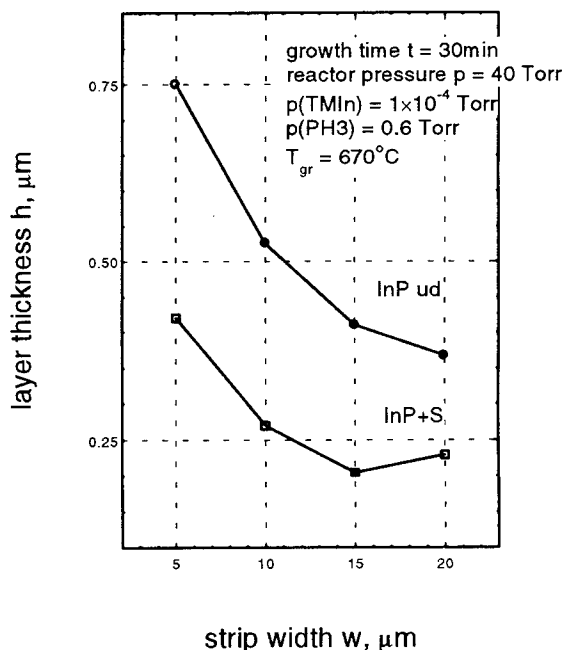


Fig. 1- Growth rate of selectively grown InP layers as a function of strip width.

Results

Fig. 1 shows an example of selective growth rates of S doped InP and undoped InP, versus the strip width. The growth time, the growth temperature and the flow rate of TMIn are kept

The same experiment was carried out again with Zn doped InP and then again with S doped InGaAs. The suppression of the growth rate is achieved only when InP is doped by S. It was also found that the above effect occurs only when the InP layer is grown selectively. Similar effects was recently reported by Kondo[1] which used Se instead of S.

The effects of the H₂S flow rate on the InP growth rate is shown in the SEM cross-sectional views in Fig. 2. Fig. 2a shows the cross section of one of our undoped selectively grown InP layer. The characteristic rabbit-ear growth that occurs on the (111)B mesa facets

is shown. The n type doping is the background doping. Figures 2b to 2d show cross-section views of structures that were grown with different H₂S flow rates from 10^{-3} ccm up to 5×10^{-2} ccm (or partial pressures between 2×10^{-5} Torr to 10^{-3} Torr). All growth processes were done using the same flow rates of the III-V components, and the same growth time 30 minutes. Figures 2b to 2d clearly show that the growth rates of the (001) mesa top and (111)B mesa side facets, can be controlled by changing the H₂S flow rate. In addition, the figures show that the growth rate on the (111)B surface is lower than that of the mesa top surface and some of the species migrate from

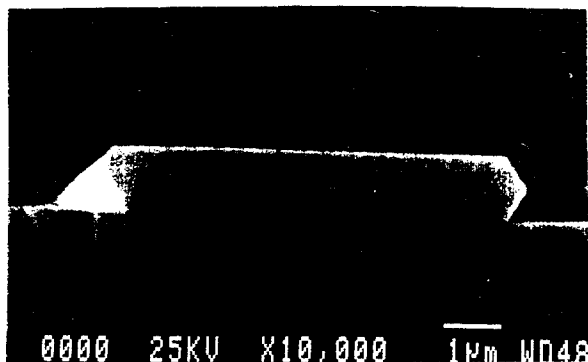


Fig 2a - InP undoped

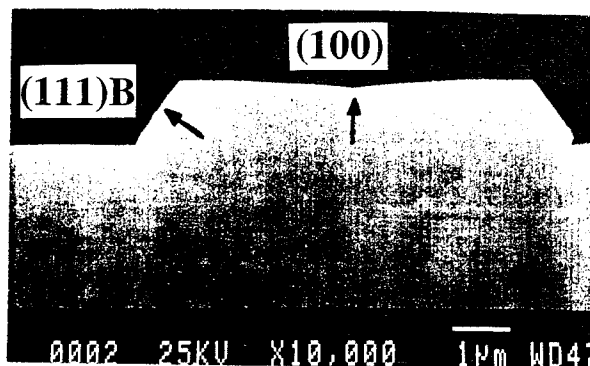


Fig. 2b-InP +S, $n \approx 10^{17} \text{ cm}^{-3}$, $p(\text{H}_2\text{S}) \approx 2 \times 10^{-5} \text{ Torr}$

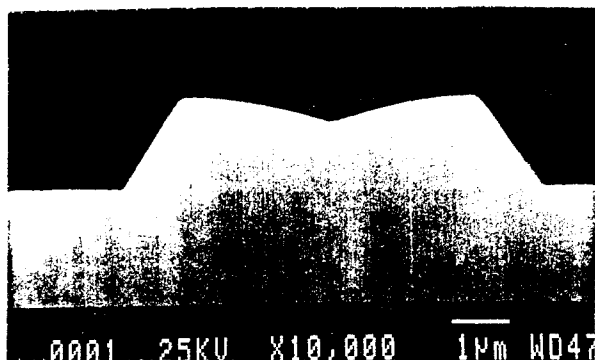


Fig. 2c-InP +S, $n \approx 10^{18} \text{ cm}^{-3}$, $p(\text{H}_2\text{S}) \approx 2 \times 10^{-4} \text{ Torr}$

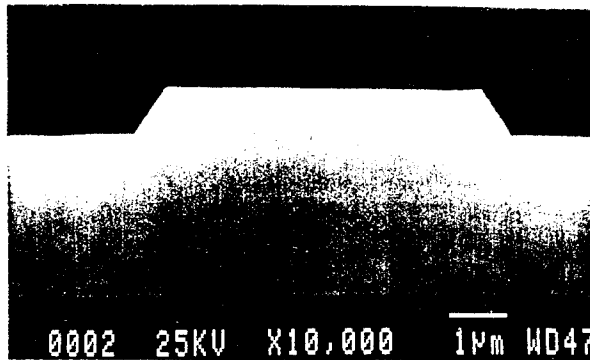


Fig. 2d-InP +S, $n \approx 5 \times 10^{18} \text{ cm}^{-3}$, $p(\text{H}_2\text{S}) \approx 10^{-3} \text{ Torr}$

Fig. 2 SEM cross section of selectively grown n-type InP layers, for different H₂S partial pressure in the reactor.

the (111)B side facet to the (100) surface. These migrating species form significant excess growth at the edges of the (100) surface (see Fig. 2b and 2c). At a certain H₂S flow the growth rate on the (111)B mesa facet is completely suppressed and flat growth on the mesa top is achieved (Fig. 2d).

We employed controlled suppression of the InP growth on the (111)B surface, during the fabrication of selectively grown buried double heterostructure n-InP/InGaAs/p-InP laser, in one growth step. The p type Zn doped layer is grown on the mesa top surface at nearly the same growth rate as it grown on the (111)B facet. Thus, this layer is both the cladding layer and the cover of the InGaAs active layer. The SEM cross section of the laser structure is shown in Fig 3, while the L-I curve is given in Fig. 4.

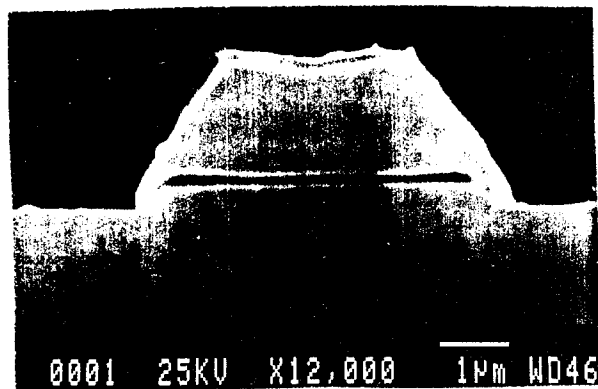


Fig 3- SEM cross section of a selectively grown buried n-InP/InGaAs/p-InP double heterostructure laser diode.

Discussion

The nature of the mechanism that affects the InP growth is not clear yet. The application of various sulfur treatments for stabilization of InP surfaces were reported in number of earlier publications. Surface treatments of H₂S results in the formation of insulating layers, an admixture of InPS₄ and In₂S₃ [2,3]. In our study we assumed that S treatment of InP

InGaAs/InP selectively grown double heterostructure laser diode

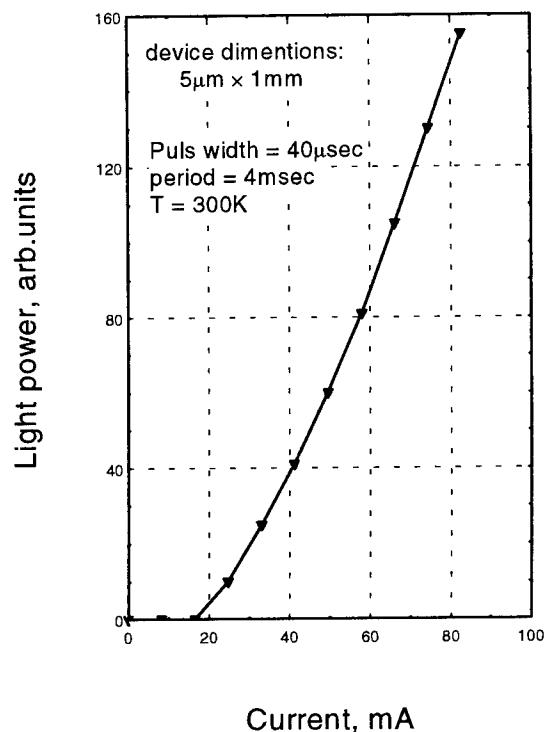


Fig. 4- L-I characteristic of InGaAs/InP selectively grown double heterostructure laser diode.

surfaces results in an inert state of dangling bonds at the surface. This is due to a bonding formation between the S atoms and the In atoms on the surface (similar effect was reported for Se[1]). An excessive supply of H₂S during the InP growth makes the InP surfaces inactive and therefore the trapping rate of the In atoms significantly decreases. This effect is obtained only in the selective process while we reduced the TMIn flow rate by more than an order of magnitude. In addition, growth suppression effect is significantly different at the two planes. In fact, it is more effective at planes with high surface density of P atoms. Therefore, In atoms migrate from the (111)B surface to the (100) surface, as shown in Figs. 2b and 2c. Recent publications [4] show that in case of group VI dopants, the bonding is more favourable on B faces than A

faces. As a result the doping incorporation for sulfur increases monotonically by two orders of magnitude in going from (100) plane to (111)B plane. It seems that the high rate of P atoms replacement by S atoms on the (111)B surface is the main driving force to the differences in growth rate suppression between planes.

Conclusions:

In this work we study the effects of sulfur treatment on the growth rate of InP in selective area growth process. It was found that the growth rate on different planes; mesa top (100) and side facet (111)B could be controlled by the H₂S partial pressure. We used the controlled suppression of InP growth on the (111)B surface, during n-type growth, to fabricate selectively grown buried double Heterostructure n-InP/InGaAs/p-InP laser.

Acknowledgments

This work was performed in the Advanced Optoelectronic Center founded by the American Technion Society. Partial support from the Israel Ministry of Science and Technology (grant # 3685) is acknowledged

References

1. Kondo, K. Sato, and M. Yamamoto; Appl. Phys. Lett. 62, 1188 (1993).
2. R. Iyer, R. R. Chang, and D. Lile; Appl. Phys. Lett. 53, 134 (1988).
3. P. Klopfenstein, G. Baside, M. Rouzeyre, M. Gendry, and J. Durand; J. Appl. Phys. 63, 150 (1988).
4. R. Bhat; Semicond. Sci. Technol. 8, 984 (1993).

CHARACTERIZATION OF ELECTRON TRAPS IN AlInAs TREATED WITH PLASMA

T. Sugino, D. Hirata, I. Yamamura, K. Matsuda* and J. Shirafuji

Department of Electrical Engineering, Faculty of Engineering,
Osaka University, 2-1 Yamadaoka, Suita, Osaka 565, Japan

*Horiba Ltd., Miyanohigashi, Kisshoin, Minami-ku, Kyoto 601, Japan

Abstract

Electron traps have been investigated for MBE grown n-AlInAs by isothermal capacitance transient spectroscopy measurement. Two traps, EO1($E_c - 0.44$ eV) and EO2($E_c - 0.52$ eV), appear for oxygen-plasma treated sample in addition to E1($E_c - 0.47$ eV) and E2($E_c - 0.69$ eV) traps detected for untreated (as-etched) sample. It is found that a reduction in the densities of the four traps occurs due to annealing subsequently after oxygen plasma treatment. The donor concentration, $N_D - N_A$, is reduced by annealing after oxygen plasma treatment. The compensation effect may be attributed to acceptorlike defect centers created by plasma process.

1 INTRODUCTION

AlInAs (Al 48 %) lattice-matched to InP is one of the most promising materials to realize high speed electronic and optoelectronic devices such as InGaAs/AlInAs high electron mobility transistors (HEMT's)⁽¹⁾ and metal-semiconductor-metal (MSM) photodetectors⁽²⁾. There have been several studies on electrical and optical properties of AlInAs grown by MBE and MOCVD and on characteristics of Schottky contacts⁽³⁻⁶⁾. Deep electron traps in AlInAs have been investigated using capacitance transient measurement⁽⁷⁻¹³⁾. Plasma processes such as reactive ion etching and deposition of insulating layer have recently been introduced in device fabrication technology. Oxygen plasma is widely utilized in an ashing process of the device fabrication. Electrical properties in oxygen-implanted AlInAs are also investigated^(14,15). It is important to understand a behavior of traps created by the fabrication processes since the traps give a strong influence on device performance.

This paper describes electron traps in n-AlInAs untreated (as-etched), treated with oxygen (O_2) plasma and annealed subsequently after O_2 plasma treatment detected by isothermal capacitance transient spectroscopy (ICTS) measurement. It is also found that reduction in the trap densities occurs due to annealing after O_2 plasma treatment.

2 EXPERIMENTAL PROCEDURE

N-type AlInAs (Al 48 %) layers grown at 490 °C on (100)-oriented InP substrates by MBE were used in the present experiment. AlInAs was doped with Si to the electron concentration of $1 \times 10^{16} \text{ cm}^{-3}$. The thickness of the epitaxial layer was 1 μm . An ohmic contact on the back side of InP substrates was provided by evaporating AuGe/Ni/Au followed by alloying at 400 °C. AlInAs surface was chemically etched with buffered HF solution for

20 s to remove native oxide just prior to setting specimens into a plasma chamber. O_2 plasma treatment was carried out in an inductively coupled remote plasma reactor operated at 13.56 MHz. O_2 gas was supplied at the flow rate of 15 sccm. The gas pressure and the substrate temperature were regulated at 0.2 Torr and 250 °C, respectively. O_2 plasma was excited by supplying rf power of 20 W to the inductive coil. The treatment time was kept for 5 min. In-situ annealing was also performed at 350 °C for 3 min in the flowing N_2 gas. After finishing the plasma treatment, Schottky contacts were provided in a separate evaporator by evaporating Au through a metal mask for dot definition onto the AlInAs surfaces. The size of the circular electrode was 1 mm in diameter.

In order to evaluate deep electron traps introduced into AlInAs by plasma treatments, ICTS measurement was carried out by using an automated equipment (Horiba DA-1500)⁽¹⁶⁾. The measurement temperature was fixed at 200 and 350 K. The isothermal capacitance measurement was carried out in the time range from 10^{-6} to 1 s. The bias voltage and the filling pulse voltage were determined taking account of the diffusion potential of Schottky contacts evaluated from the true Schottky barrier height. The true barrier height was estimated from the Richardson plot of the saturation current densities measured at various temperatures⁽¹⁷⁾. The trap density was evaluated by integrating the ICTS signal with respect to time.

3 RESULTS AND DISCUSSION

Prior to ICTS measurement, characteristics of Schottky diodes were examined. Figure 1 shows the current-voltage (I - V) characteristics measured at room temperature for Schottky diodes fabricated on AlInAs untreated (as-etched), treated with O_2 plasma and annealed subsequently after O_2 plasma treatment. The effective barrier height and the ideality factors are 0.57 eV and 1.06,

Table 1: Effective and true barrier height, ideality factor and donor concentration of Schottky diodes.

	ϕ_{bn} (eV)	ϕ_{b0} (eV)	Ideality Factor	$N_D - N_A$ (cm ⁻³)
untreated	0.57	0.46	1.06	1.06×10^{16}
annealed	0.58	0.58	1.00	1.30×10^{16}
O ₂ plasma treated	0.67	0.19	1.92	1.07×10^{16}
O ₂ plasma treated + annealed	0.67	0.31	1.73	5.04×10^{15}

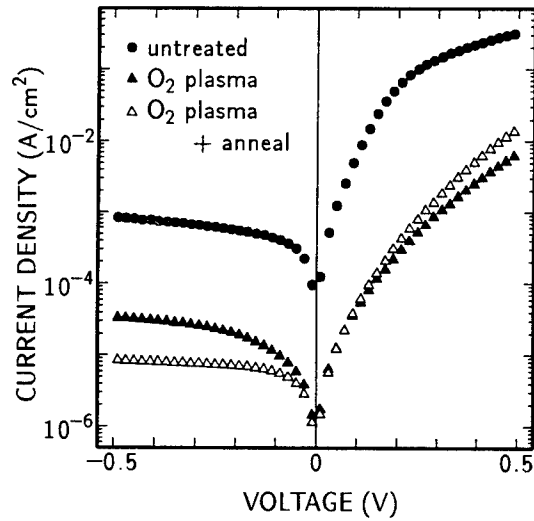


Figure 1: Current-voltage characteristics of Schottky diodes formed on AlInAs untreated, treated with O₂ plasma and annealed after annealed O₂ plasma treatment.

respectively, for the untreated Schottky junction, while they are 0.67 eV and 1.92 for the O₂-plasma treated junction. The ideality factor is found to be degraded by O₂ plasma treatment. No significant difference of the effective barrier height and the ideality factor is observed between the two diodes treated with O₂ plasma and annealed after O₂ plasma treatment. However, a reduction in the reverse leakage current occurs for the sample annealed after O₂ plasma treatment.

The true barrier heights were estimated from Richardson plots. Moreover, capacitance-voltage measurement was performed to evaluate donor concentrations. The effective and true barrier heights, the ideality factors and donor concentrations are summarized in Table 1. Characteristics of annealed Schottky junctions are also shown for comparison. No marked variation in the donor concentration occurs in the O₂-plasma treated diode, while the donor concentration is remarkably reduced for the diode annealed after O₂ plasma treatment in comparison with that of the untreated diode.

Figure 2 indicates ICTS spectra measured at 200 and

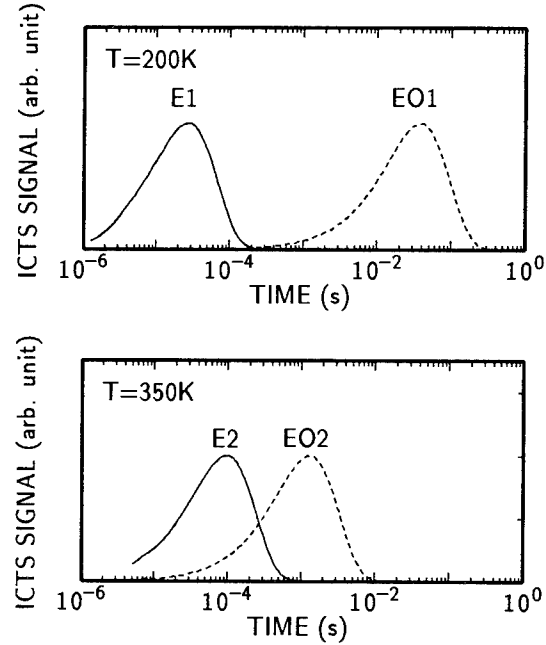


Figure 2: ICTS spectra measured at 200 and 350 K for untreated and O₂-plasma treated samples.

350 K for the untreated and O₂-plasma treated samples. Two peaks, E1 and E2, with time constants of 2.1×10^{-5} and 1.0×10^{-4} s are detected at 200 and 350 K, respectively, for the untreated sample. New peaks, EO1 and EO2, with time constants of 3.6×10^{-2} and 1.3×10^{-3} s appear at 200 and 350 K together with E1 and E2 for the O₂-plasma treated sample.

The activation energies of E1, E2, EO1 and EO2 traps were evaluated to be 0.47, 0.69, 0.44 and 0.52 eV, respectively, from Arrhenius plot of τT^2 . In order to estimate the capture cross section of these four traps, ICTS measurement was carried out with various widths of the filling pulse. The capture cross sections are summarized in Table 2 together with the activation energies.

The densities of the E1 and E2 traps in the region from the surface to 0.2 μm were evaluated to be 4×10^{14} and $1.5 \times 10^{15} \text{ cm}^{-3}$ for the untreated sample and 3×10^{15} and $2 \times 10^{14} \text{ cm}^{-3}$ for the annealed sample, respectively, as shown in Table 3. The increase in the E1 trap density

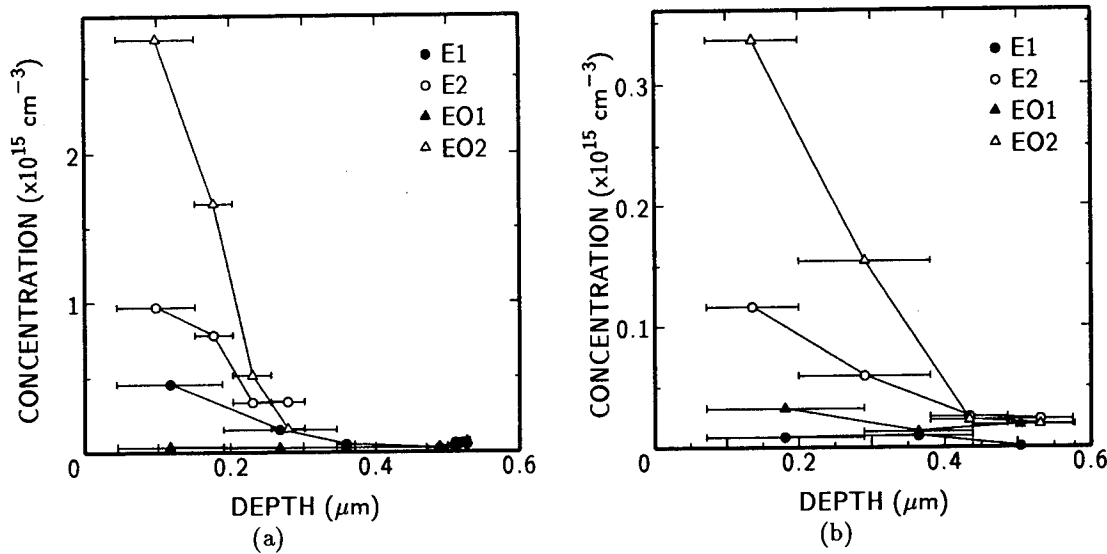


Figure 3: Depth profiles of trap concentration for samples treated with O₂ plasma(a) and annealed subsequently after O₂ plasma treatment(b).

Table 2: Activation energy and capture cross section of electron traps.

	Activation Energy (eV)	Capture Cross Section (cm ⁻²)
E1	0.47	1.16×10^{-13}
E2	0.69	1.52×10^{-14}
EO1	0.44	4.37×10^{-12}
EO2	0.52	1.73×10^{-16}

Table 3: Density of E1 and E2 traps

	E1 (cm ⁻³)	E2 (cm ⁻³)
untreated	4×10^{14}	1.5×10^{15}
annealed	3×10^{15}	2×10^{14}

(Depth region: 0–0.2 μm)

was observed in the surface region of the untreated and annealed samples. The E2 trap density increased in the surface region of the untreated sample.

Figure 3 indicates depth profile of the trap concentration for samples treated with O₂ plasma (a) and annealed subsequently after O₂ plasma treatment (b). The densities of the EO1 and EO2 traps which are detected for the O₂-plasma treated sample are estimated to be 3.8×10^{13} and 2.8×10^{15} cm⁻³, respectively, in the surface region. The concentration of the E1 and E2 traps are 5×10^{14} and 1×10^{15} cm⁻³ in the surface region of

the O₂-plasma treated sample. In the case of the sample annealed after O₂ plasma treatment, a significant reduction in densities of the E1, E2, EO1 and EO2 traps is observed.

The two traps, E1 and E2, detected in the present experiment correspond to E2 ($E_c - 0.48$ eV) and E3 ($E_c - 0.68$ eV) traps observed in MBE grown AlInAs by Luo et al.⁽¹³⁾, respectively. These traps have been suggested to result from an excess of arsenic in AlInAs, since it is observed that an excess arsenic is incorporated into the AlInAs layer during low temperature growth by MBE⁽¹⁸⁾. The E1 trap density increases after annealing, while annealing leads to reduction in the E2 trap density. The arsenic interstitial which is formed in the AlInAs layer by the excess arsenic can migrate during the high temperature anneal and form arsenic small cluster. From the experimental result, the E2 trap may be attributed to arsenic interstitial defects or a complex of an interstitial with other defects. On the other hand, the E1 trap is suggested to be an arsenic related complex defect such as arsenic cluster.

O₂ plasma treatment produces EO1 and EO2 traps,

but it reduces the E2 trap density. Moreover, it is found in the present experiment that the annealing process subsequently after O₂ plasma treatment is effective in reducing the densities of E1, E2, EO1 and EO2 traps. Suppression of the reverse leakage current shown in Fig. 1 is related to a reduction in the trap density due to annealing after O₂ plasma treatment. Further investigations are needed to understand the origin of EO1 and EO2 traps and the annealing effect.

It was reported that an increase of oxygen atoms incorporated into AlInAs during MOCVD growth leads to an increase in donor concentration ($N_D - N_A$), an increase in the reverse current in Schottky junctions and a reduction in the photoluminescence intensity⁽³⁾. In the case of oxygen implantation, on the other hand, the compensated semi-insulating layer is formed in n-AlInAs^(14,15). Although the exact compensation mechanisms are not clear yet, it is considered to account for the observed electrical characteristics of oxygen-implanted AlInAs that the compensation occurs due to acceptorlike lattice defects created by the implantation process. An increase in the electrical resistance of the oxygen-implanted AlInAs is observed by annealing at a temperature of less than 600 °C⁽¹⁵⁾. The experimental result that the donor concentration ($N_D - N_A$) is reduced by annealing after O₂ plasma treatment may be considered to be due to creation of acceptorlike defect centers, although hole traps cannot be detected by the present ICTS measurement.

4 SUMMARY

In order to investigate electron traps by ICTS measurement, Schottky junctions are formed on n-AlInAs untreated, treated with O₂ plasma and annealed subsequently after O₂ plasma treatment. The true barrier height estimated from the Richardson plot decreases for O₂-plasma treated sample in comparison with that of the untreated sample. Degradation of the ideality factor is observed by O₂ plasma treatment. The two electron traps, E1 ($E_c - 0.47$ eV) and E2 ($E_c - 0.69$ eV), are detected in the untreated AlInAs. In addition to these traps, EO1 ($E_c - 0.44$ eV) and EO2 ($E_c - 0.52$ eV) traps appear in the O₂-plasma treated sample. It is found that E1, E2, EO1, and EO2 traps are reduced by annealing subsequently after O₂ plasma treatment. It is considered that a reduction in the donor concentration ($N_D - N_A$) is possibly due to creation of acceptorlike defect centers.

Acknowledgment

The authors are much indebted to Dr. M. Shimizu and Mr. N. Takahashi of Sharp Ltd. for supplying AlInAs crystals.

References

- (1) H. Ohno, J. Barnard, C. E. C. Wood and L. F. East-

man, IEEE Electron Device Lett., EDL-1, 1980, pp. 154-155.

- (2) J. B. D. Soole, H. Schmacher, H. P. LeBlanc, R. Bhat and M. A. Koza, IEEE Photon. Technol. Lett., 1, 1989, pp. 250-252.
- (3) M. Kamada, H. Ishikawa, S. Miwa and G. E. Stillman, J. Appl. Phys., 73, 1993, pp. 4004-4008.
- (4) J. K. Luo, H. Thomas, S. A. Clark and R. H. Williams, J. Appl. Phys., 74, 1993, pp. 6726-6733.
- (5) K. H. Hsieh, G. Wicks, A. R. Calawa and L. F. Eastman, J. Vac. Sci. Technol. B, 3, 1985, pp. 700-702.
- (6) L. P. Sadwick, C. W. Kim, K. L. Tan and D. C. Streit, IEEE Electron Device Lett., EDL-12, 1991, pp. 626-628.
- (7) W-P. Hong, S. Dhar, P. K. Bhattacharya and A. Chin, J. Electronic Materials, 16, 1987, pp. 271-274.
- (8) P. S. Whitney, W. Lee and C. G. Fonstad, J. Vac. Sci. Technol., B5, 1987, pp. 796-798.
- (9) N. Nakashima, S. Nojima, Y. Kawamura and H. Asahi, phys. stat. sol. (a)103, 1987, pp. 511-516.
- (10) H. Hoenow, H. G. Bach, J. Bottcher, F. Gueissaz, H. Kunzel, F. Scheffer and C. Schramm, Proc. 4th International Conference, Rhode Island, 1992, pp. 136-139.
- (11) J. K. Luo, H. Thomas and I. L. Morris, Electron. Lett., 28, 1992, pp. 797-799.
- (12) S. Naritsuka, T. Noda, A. Wagai, S. Fujita and Y. Ashizawa, J. Crystal Growth, 131, 1993, pp. 186-192.
- (13) J. K. Luo, H. Thomas, S. A. Clark and R. H. Williams, Proc. 6th International Conference, California, 1994, pp. 363-366.
- (14) W. Lee and C. G. Fonstad, Appl. Phys. Lett., 50, 1987, pp. 1278-1280.
- (15) S. J. Pearton, W. S. Hobson and U. K. Chakrabarti, Appl. Phys. Lett., 55, 1989, pp. 1786-1788.
- (16) H. Okushi and Y. Tokumaru, Jpn. J. Appl. Phys., 19, 1980, pp. L335-L338.
- (17) S. M. Sze, 'Physics of Semiconductor Devices', Wiley-Interscience Publication, New York, 1981, 2nd ed.
- (18) A. Claverie, K. M. Yu, W. Swider, Z. L. Weber, M. O'Keefe, R. Kilaas, J. Pamulapati and P. K. Bhattacharya, Appl. Phys. Lett., 60, 1992, pp. 989-991.

Characterization of surface recombination velocity of InP reduced by sulfur-treatment and a phosphorous-nitride film formation with Raman spectroscopy

T. Hanajiri, Y. Matsumoto and T. Sugano

Dept. of Electrical and Electronic Eng., Toyo Univ., 2100 Kujirai, Kawagoe, Saitama 350, Japan

T. Katoda

Dept. of Electronic Eng., The Univ. of Tokyo, 7-3-1 Hongo, Bunkyo-ku, Tokyo 113, Japan

Surface recombination velocity of InP was reduced by the process including surface treatment using $(\text{NH}_4)_2\text{S}_x$ solution (sulfur-treatment), annealing in vacuum and formation of a phosphorous-nitride (PN) film by photon-assisted chemical vapor deposition (PA-CVD). The minimum value of surface recombination velocity was $4.1\text{--}4.8 \times 10^3$ (cm/s). Laser Raman spectroscopy was used for characterizing surface recombination velocity.

1. Introduction

InP is an attractive material for enhancement Metal-Insulator-Semiconductor (MIS) Field-Effect-Transistor (FET)s because its electrical properties are favorable for the performance of enhancement n-channel FETs. Surface recombination velocity is one of the most important properties that determine performance and reliability of FETs. In addition, surface recombination velocity of InP is about as much as two orders of magnitude slower than that of GaAs(1). However, it has been impossible to fabricate InP MIS FETs for practical use in spite of many attempts for about twenty years(2),(3). To determine the optimum condition for fabricating FETs of good quality, surface recombination velocity at InP interfaces must be investigated further in detail and it must be much more decreased.

Therefore surface recombination velocity of InP under various conditions of surface treatments and formation of insulator was estimated. In particular, the effect of sulfur-treatment using $(\text{NH}_4)_2\text{S}_x$ solution that is one of the most promising passivation technology of compound semiconductors(4) was studied. Some reports have been published for InP(5)-(7). However, there is not enough quantitative data on sulfur-treatment to discuss physical and chemical mechanism. Furthermore, there is little knowledge on the effect of annealing after sulfur-treatment, although the effect of annealing the sulfur-treated GaAs surfaces has been studied in detail(8).

In consequence, the effects of sulfur-treatment and annealing in vacuum after the treatment were investigated, especially from the following two points. One is the electric properties, that is, the mechanism of reduction of surface recombination. The other is the chemical properties, that is, changes of chemical bonds at the surface. Raman spectroscopy and photoluminescent (PL) spectroscopy were used for characterizing the electric properties, and Auger electron spectroscopy (AES) and X-ray photoelectron spectroscopy (XPS) were used for characterizing the chemical properties.

2. Experimental Procedure

A. Estimation of surface recombination velocity by Raman spectroscopy

It has been demonstrated in a previous paper that Raman spectroscopy provides a quantitative, contactless means for estimating surface recombination velocity at InP surfaces(9). The wavenumber of the plasmon-LO phonon coupled mode ω_+ in Raman spectra shifts to a higher one as the incident laser power density increases because of addition of optically excited carriers to the bulk carrier. Raman spectra from Sn-doped InP (100) surfaces with a carrier concentration of $4.5 \times 10^{17} \text{ cm}^{-3}$ are shown in Fig.1. In Fig.1 the measurement was done with different beam diameters keeping laser power constant. That is, power density is inversely proportional to the square of a beam diameter.

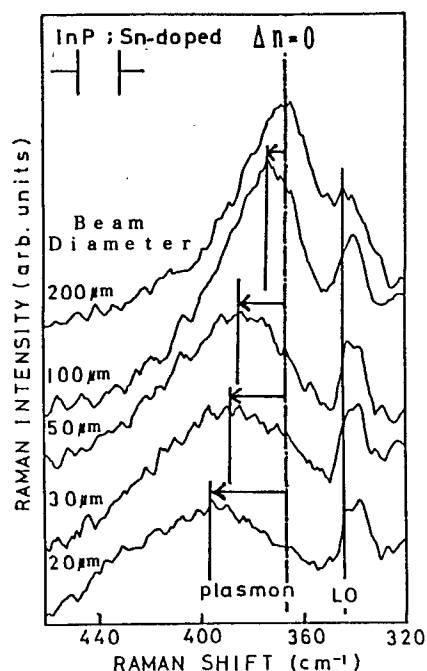


Fig.1 The typical plasmon-LO phonon coupled mode in Raman spectra from n-InP wafers

Photo-excited carriers partially remain without affecting surface recombination. These excess carriers are estimated from an extra shift of the plasmon-LO phonon coupled mode in Raman spectra. Thus surface recombination velocity can be obtained by analyzing the excess photo-excited carriers.

B. Samples preparation

Mirror polished (100) n-InP wafers grown by Liquid Encapsulated Czochralski (LEC) were used. In measurement of Raman spectroscopy, n-InP wafers with a carrier concentration of about 10^{17} cm^{-3} were used to observe more easily an extra shift of the plasmon-LO phonon coupled mode caused by excess carriers. In PL measurement, n-InP wafers with a carrier concentration of about 10^{18} cm^{-3} were used. In AES and XPS measurements, n-InP wafers with a carrier concentration of above 10^{18} cm^{-3} were used to avoid "charge up" phenomena.

The substrate was ultrasonically degreased and then chemically etched with a mixture of $\text{HCl}:\text{H}_2\text{O}_2:\text{H}_2\text{O}$ (4:1:6) for two minutes at room temperature. Sulfur-treatment was done following to this wet-etching. The substrate was dipped in an $(\text{NH}_4)_2\text{S}_x$ solution for 5–10 minutes at 50°C and rinsed in an $(\text{NH}_4)_2\text{S}$ solution and deionized water to remove thin whitish residual amorphous sulfur on the surface and finally it was removed by blowing dry N_2 . Annealing was done in vacuum in less than 1.0×10^{-7} Torr for 30 minutes.

Insulator films used in this study were as follows; [1] SiO_2 films formed by sputtering, [2] Si_3N_4 films formed by sputtering, [3] PN films formed by photon-CVD using PCl_3 carried by pure H_2 and NH_3 as reagent gases. The light from a low pressure Hg lamp (185nm, 254nm) was illuminated.

3. Experimental Results

A. Raman spectroscopy

Raman spectra were measured using Ar^+ laser (514.5 nm) with a power density of $1.2 \text{ (kW/cm}^2\text{)}$ at room temperature with back scattering geometry. A penetration depth of this light into InP is 90 nm. Insulator films used in this experiment have band gaps about 5 eV and are transparent to the light. In consequence, information on surface region including the depletion layer could be obtained, although InP surfaces were covered with insulator films.

A-1. Samples without insulator films As wet-etched and as sulfur-treated wafers were prepared. Both wafers were set in a vacuum chamber and annealed from room temperature to 350°C . Figure 2 shows an extra shift of wavenumber of ω_+ and surface recombination velocity estimated by the shift. From Fig.2 it can be seen that when wafers were not sulfur-treated, surface recombination velocity was $1.3\text{--}2.0 \times 10^4 \text{ (cm/s)}$ at room temperature and it increased gradually with increase in annealing temperature, while when wafers were sulfur-treated,

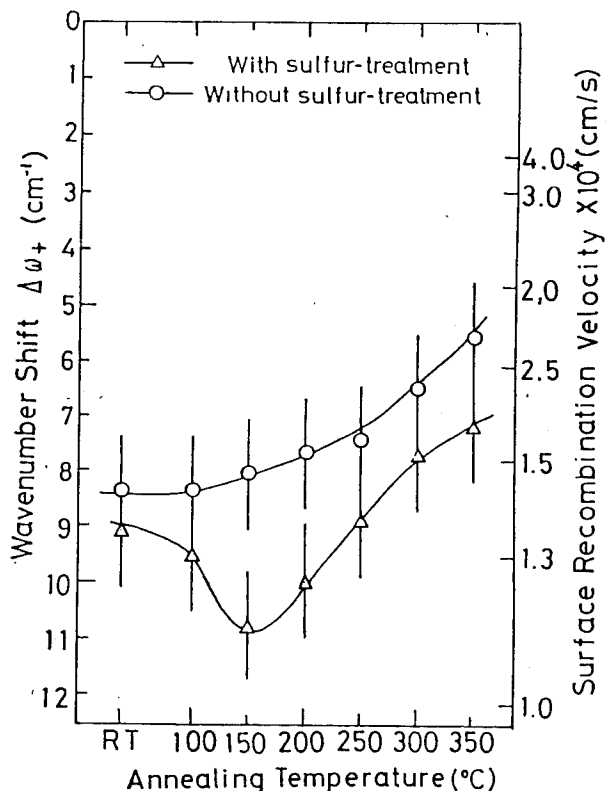


Fig.2 The extra Raman shift of the plasmon-LO phonon coupled mode and the surface recombination velocity at InP surfaces without insulator films

surface recombination velocity was reduced with decrease in temperature, and it was reduced down to $1.0\text{--}1.3 \times 10^4 \text{ (cm/s)}$ when the annealing temperature was 150°C .

A-2. Samples with insulator films All surface treatments (wet-etching, sulfur-treatment and annealing) were done before formation of insulator films. Figure 3 shows typical Raman spectra from samples with various insulator films. Figure 4 shows extra shifts of the plasmon-LO phonon coupled mode and surface recombination velocity obtained from the samples with PN films. When wafers were covered with SiO_2 or Si_3N_4 films, surface recombination velocity was more than 10^5 (cm/s) nevertheless sulfur-treatment and annealing were done. From Fig.4 it is found that surface recombination velocity of samples on which PN films were deposited at a low temperature such as 150°C was lower than that of the samples on which PN films were deposited at a high temperature such as 250°C . Surface recombination velocity was reduced to $4.1\text{--}4.8 \times 10^3 \text{ (cm/s)}$ particularly when wafers were sulfur-treated before deposition.

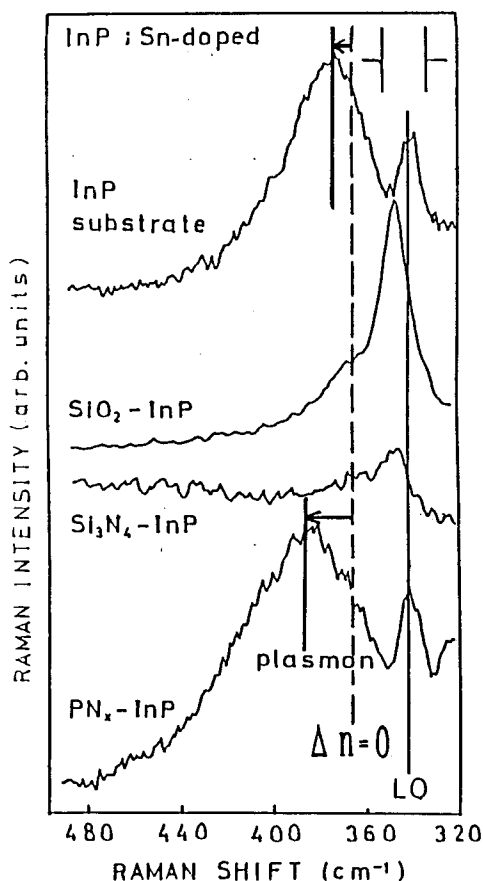


Fig.3 The typical plasmon-LO phonon coupled mode in Raman spectra at InP surfaces covered with insulators

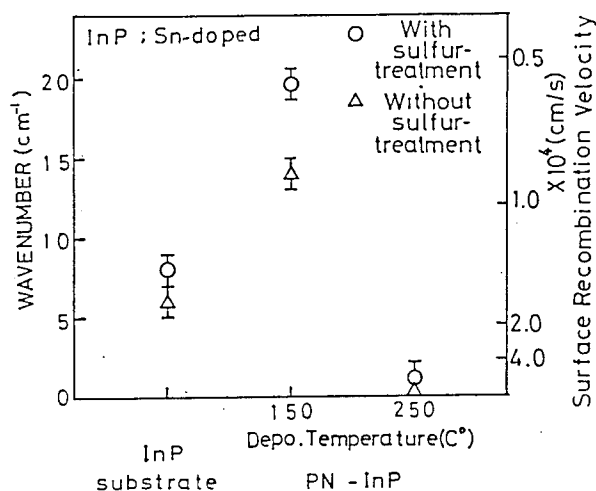


Fig.4 The extra Raman shift of the plasmon-LO phonon coupled mode and the surface recombination velocity at InP surfaces covered with PN films

B. Photoluminescence (PL) spectroscopy

PL measurement has been used to estimate surface recombination velocity of GaAs and InP surfaces(10). PL intensity was enhanced by suppression of surface recombination. PL measurements were done using Ar⁺ laser (all line) at room temperature with a power density on surfaces about 1 (W/cm²). PL spectra of n-InP had a peak at 885 nm corresponding to the band edge emission. Figure 5 shows PL peak intensity of InP. It was measured after it reached constant at about 10 minutes from the irradiation of light. It is seen from Fig.5 that before wafers were annealed, PL intensity increased by several times by sulfur-treatment, and decreased by annealing at over 250 °C.

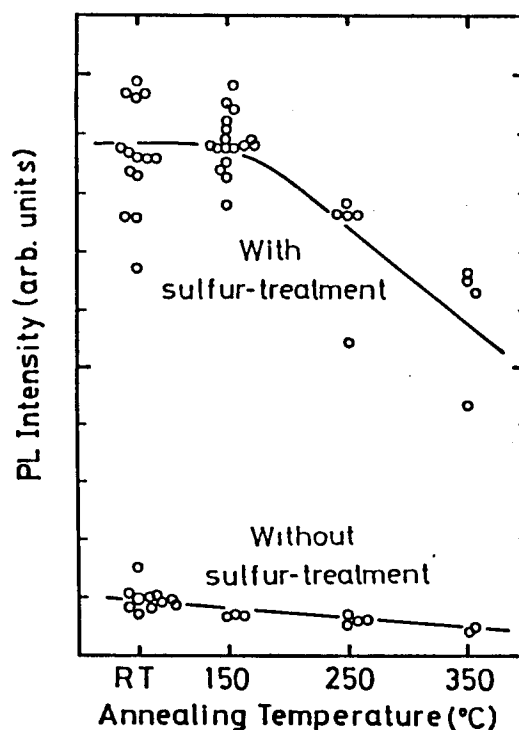


Fig.5 The photoluminescent intensity at the band edge of InP surfaces without insulator films

C. Auger electron spectroscopy and X-ray photoelectron spectroscopy

AES and XPS measurements were performed with ULVAC-PHI model 255 ESCA/AES electron spectrometer. In AES measurement, a primary electron beam of 2 keV was applied. In XPS measurement, a monochromatic Mg Ka X-ray source was used and the adventitious carbon C1s peak at 250.00 eV was chosen as the energy reference. Pure InS and pure In₂S₃ powders were used as standard samples. Annealing was done in the CVD chamber at less than 1×10^{-7} Torr for 30 minutes and

samples were transferred into AES and XPS analysis chamber at less than 2×10^{-7} Torr without exposure to atmosphere. AES and XPS measurements were done within 30 minutes at less than 4×10^{-6} Torr.

Amount of oxygen was dramatically reduced by sulfur-treatment, while the peak of P 2p near 134 eV corresponding to InPO_4 in XPS spectra diminished. From AES and XPS it was also shown that monolayer of sulfur existed at InP surfaces.

Significant change of the atomic concentrations of oxygen and sulfur by annealing in vacuum after sulfur-treatment was not observed. The chemical shifts in $\text{In } 3d_{3/2}$ and $\text{In } 3d_{5/2}$ peaks are shown in Fig.6. At sulfur-treated InP surfaces, In-S bonds were more dominant than P-S bonds before and after annealing in vacuum and the S 2p, $\text{In } 3d_{3/2}$ and $\text{In } 3d_{5/2}$ peaks of InP shifted toward those in In_2S_3 rather than those in InS and these shifts were not changed significantly by annealing in vacuum after sulfur-treatment, although Nannich *et al.*(8) have reported Ga-S bonds, As-S bonds, and S-S bonds coexisted at sulfur-treated GaAs surfaces before annealing and Ga-S bonds were dominant after annealing in vacuum.

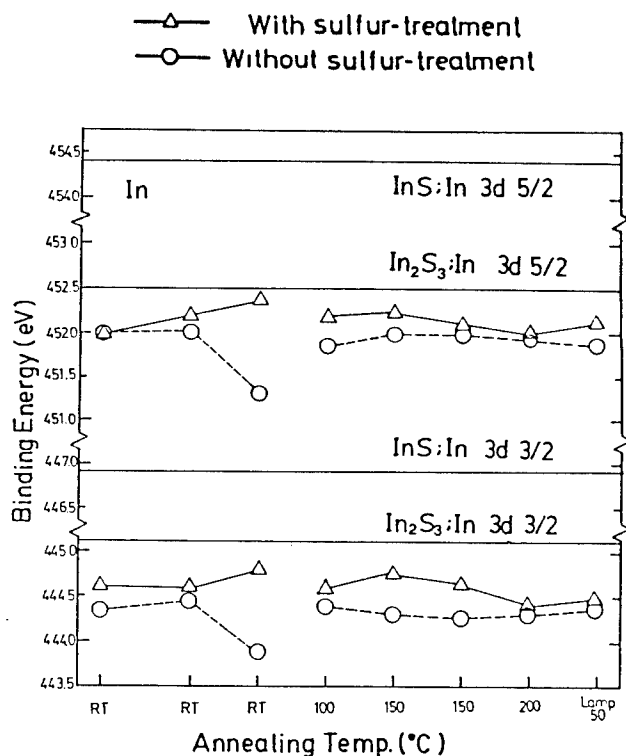


Fig.6 The chemical shift of $\text{In } 3d_{3/2}$ and $\text{In } 3d_{5/2}$ peaks at InP surfaces

4. Discussion

It was shown by Raman and photoluminescence spectroscopies that surface recombination velocity at InP surface was reduced to $1.3\text{--}2.0 \times 10^4$ (cm/s) by sulfur-treatment and following annealing in vacuum at 150 °C. Surface recombination velocity was reduced further by forming PN films using photon-assisted CVD after the sulfur-treatment and annealing in vacuum at 150 °C.

The results obtained with AES and XPS suggested that decrease in oxygen concentration and increase in In-S bonds by the sulfur-treatment induced reduction of surface recombination velocity. In other words, removal of oxide from InP surfaces and termination of dangling bonds, especially phosphorous dangling bonds, are effective to reduce surface recombination velocity.

It is speculated that the optimum annealing temperature such as 150 °C means that such reaction at InP surfaces occurs at a relatively high temperature. In addition, formation of a PN film on a sulfur-treated InP without or with a small damage by photon-assisted CVD passivates the InP surface and reduces surface recombination velocity.

5. Conclusion

Characterization with laser Raman spectroscopy showed that surface recombination velocity of InP decreased by sulfur-treatment followed by annealing in vacuum at 150 °C. Surface recombination velocity decreased furthermore by passivation of the sulfur-treated InP surfaces with PN films formed by photon-assisted CVD.

Acknowledgement

The authors are grateful to H. Okazaki, Japan Energy Co., Ltd. for providing InP wafers and for fruitful discussion.

References

- (1) H.C. Casey, Jr and E. Buehler, *Appl. Phys. Lett.* **30**, 247 (1977)
- (2) Y. Hirakawa, H.M. Park, F. Koshiga and T. Sugano, *Appl. Phys. Lett.* **49**, 351 (1982)
- (3) Y. Hirota, M. Okamura, T. Hisaki and E. Yamaguchi, *J. Appl. Phys.* **67**, 277 (1987)
- (4) H. Oigawa, J. Fan, Y. Nannichi, K. Ando, K. Saiki and A. Koma, *Extended Abstracts of the 20th Conference on Solid State Devices and Materials*, 263 (1988)
- (5) Y. Tao, A. Yelon, E. Sacher, Z.H. Lu and M.J. Graham, *Appl. Phys. Lett.* **60**, 2669 (1992)
- (6) C. Nosaki, S. Yasuami, H. Ishimura and H. Tokuba, *J. Crystal Growth*, **99**, 371 (1990)
- (7) R. Iyer, R.R. Chang, A. Dubey and D.L. Lile, *Appl. Phys. Lett.* **53**, 134 (1988)
- (8) H. Sugawara, M. Oshima, H. Oigawa, H. Shigekawa and Y. Nannichi, *Extended Abstracts of the 21th Conference on Solid State Devices and Materials*, 547 (1989)
- (9) T. Nakamura and T. Katoda, *J. Appl. Phys.* **55**, 3064 (1984)
- (10) H. Nagai and Y. Noguchi, *Appl. Phys. Lett.* **33**, 312 (1978)

RUTHENIUM AND SULFIDE PASSIVATION OF $\text{In}_{0.53}\text{Ga}_{0.47}\text{As}$

S. T. Ali, A. Kumar and D. N. Bose

Semiconductor Division, Materials Science Centre
 Indian Institute of Technology, Kharagpur - 721302, India.
 FAX: +91-03222-2303

ABSTRACT

The effectiveness of chemical surface modification of $\text{In}_{0.53}\text{Ga}_{0.47}\text{As}$ using Na_2S , $(\text{NH}_4)_2\text{S}_x$ and RuCl_3 has been studied through X-ray photoelectron spectroscopy (XPS), spectral response and Schottky barrier height measurements. XPS studies have shown that modification steps caused removal of native oxides and formation of S or Ru bonds with surface atoms. The minority carrier diffusion length L_p thus increased from 1.65 to 1.89 μm due to reduction of surface recombination velocity S_r from 9.5×10^3 to $2.4 \times 10^3 \text{ cm.s}^{-1}$. Increase in Schottky barrier height ϕ_{Bn} from 0.26 to 0.58 eV due to $(\text{NH}_4)_2\text{S}_x$ treatment and reduction in ideality factor also occurred.

Introduction

The ternary compound $\text{In}_{0.53}\text{Ga}_{0.47}\text{As}$, lattice-matched to InP, has numerous applications in optoelectronics because of its high electron mobility and a direct band-gap of 0.75 eV at 300 K. $\text{In}_{0.53}\text{Ga}_{0.47}\text{As}$ is characterised by high surface recombination velocity (S_r) which adversely affects its properties.

In the present study the effectiveness of chemical surface treatments using RuCl_3 , Na_2S and $(\text{NH}_4)_2\text{S}_x$ have been studied and shown to increase minority carrier diffusion length through reduction of S_r . XPS studies showed that passivation was due to removal of native oxides and followed by formation of S or Ru bonds.

Experimental

Liquid Phase Epitaxy grown $\text{In}_{0.53}\text{Ga}_{0.47}\text{As}/\text{InP}$ ($N_d = 10^{15} \text{ cm}^{-3}$) samples were subject to etching in 0.05% Bromo-methanol. The samples were then immersed in 0.01 M RuCl_3 , $(\text{NH}_4)_2\text{S}_x$ or Na_2S in 0.1 N HNO_3 solution for 1 min. In-Au alloy was used as ohmic back contact while evaporated Au formed the Schottky barrier.

XPS was used to elucidate the chemical nature of the surfaces subject to different treatments i.e. air-exposed, etched and passivated.

The spectral response of $\text{In}_{0.53}\text{Ga}_{0.47}\text{As}$ photoanodes were studied in $\text{KOH-Te}^{-2}/\text{Te}_x^{-2}$ redox system. From the $1/\eta_q$ vs $1/\alpha(\lambda)$ plot the minority carrier diffusion lengths (L_p) were determined using the relation:

$$\eta_q = \alpha(\lambda)L_p/[1+\alpha(\lambda)] \quad (1)$$

where η_q is the quantum efficiency and $\alpha(\lambda)$ is the absorption coefficient.

In the presence of surface recombination the minority carrier diffusion length L_{eff} on the surface is reduced from the bulk value L_0 as given by the relation:

$$L_{eff}^2 = [L_0^2/(s+1)]\exp(-Z/L_0) \quad (2)$$

where $s = S_r\tau_p/L_0$, the reduced surface recombination velocity, τ_p is the hole life-time and Z is the distance from the surface.

Results

In Fig.1 are presented the i) In 3d ii) Ga 3p iii) As 3d and iv) Ga

3s / S 2p XPS spectra observed at each step of sample treatment (shown for $(\text{NH}_4)_2\text{S}_x$ treated sample only. The results of XPS studies are given in Table-I.

Curves a) show the spectra from an unetched surface covered with native oxides. This is the classical oxidation behaviour of $\text{In}_{0.53}\text{Ga}_{0.47}\text{As}$ surface, which shows contributions from oxidised In, Ga and As. Curves b) show the spectra of the etched surface, this is the initial surface of $\text{In}_{0.53}\text{Ga}_{0.47}\text{As}$ subject to $(\text{NH}_4)_2\text{S}_x$ treatment. Curves c) describe the spectra obtained after $(\text{NH}_4)_2\text{S}_x$ treatment and a typical air exposure of 10-20 min. before loading into the U.H.V. chamber for XPS.

The As 3d spectra for the unetched sample had a strong peak at 45.0 eV attributable to As_2O_3 .

The peak at 41.0 eV due to As in InGaAs was absent. However a peak at 42.0 eV indicated segregated elemental arsenic (As^0) [3]. The removal of native oxides is confirmed by the absence of the 45.0 eV peak in etched as well as treated samples. The 42.5 eV peak in the sulfide treated samples can be attributed to AsS as given in ref. [3]. The binding energy of arsenic (As^{3+}) in As_2O_3 is 43.5 eV. This peak was absent for treated samples even after two weeks aging.

In 3d and Ga (3s, 3p) spectra showed peaks corresponding to In_2O_3 or Ga_2O_3 for the unetched samples. The treated samples showed the presence of In_2S_3 and Ga_2S_3 [2,1].

The S 2p / Ga 3s spectra were more helpful in studying the incorporation of S. The $(\text{NH}_4)_2\text{S}_x$

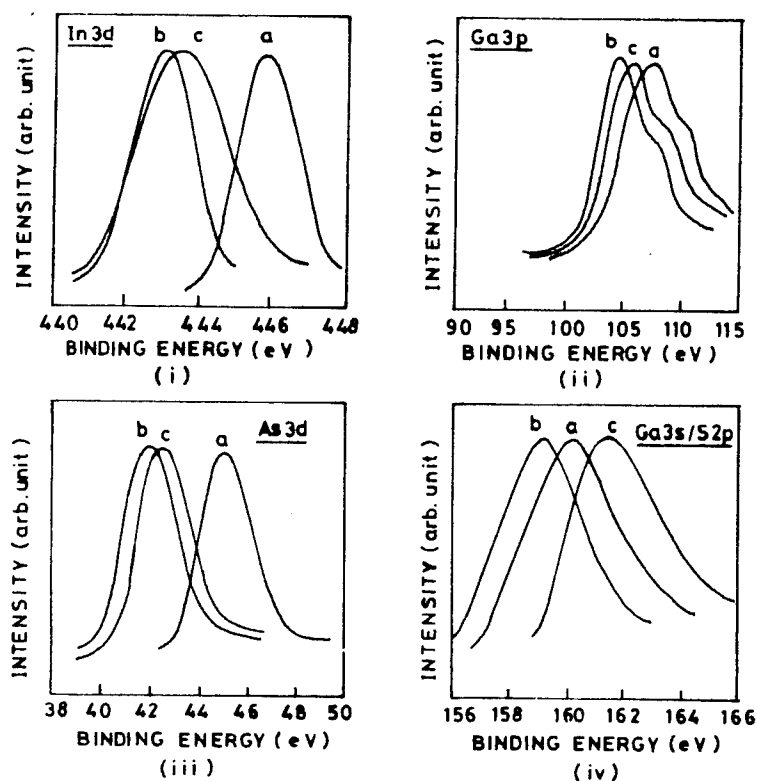


Fig.1 X-ray photoelectron spectra for i) In 3d, ii) Ga 3p, iii) As 3d and iv) Ga 3s / S 2p for (a) unetched, (b) etched and (c) $(\text{NH}_4)_2\text{S}_x$ modified $\text{In}_{0.53}\text{Ga}_{0.47}\text{As}$.

Table-I: XPS data for different surface treated $\text{In}_{0.53}\text{Ga}_{0.47}\text{As}$.

$\text{In}_{0.53}\text{Ga}_{0.47}\text{As}$	BE (eV)	FWHM (eV)	ΔE (eV)	Compounds
<hr/>				
In 3d: Unetched	445.8	2.0	2.8	In_2O_3
Etched	443.0	1.8	0.0	In [1]
$(\text{NH}_4)_2\text{S}_x$	443.5	2.6	0.5	In_2S_3 [2]
Na_2S	443.5	2.5	0.5	In_2S_3
RuCl_3	443.8	2.7	0.8	In-Ru
<hr/>				
Ga 3p: Unetched	106.8	6.0	2.3	Ga_2O_3
Etched	110.0			
$(\text{NH}_4)_2\text{S}_x$	104.5	5.3	0.0	Ga [1]
	109.0	6.0	0.9	Ga_2S_3
Na_2S	105.0	5.8	0.5	Ga_2S_3
	109.2			
RuCl_3	105.5	6.4	1.0	Ga-Ru
	109.0			
<hr/>				
As 3d: Unetched	45.0	2.3	3.0	As_2O_3
Etched	42.0	1.9	0.0	As [3]
$(\text{NH}_4)_2\text{S}_x$	42.5	2.4	0.5	AsS
Na_2S	42.6	2.3	0.6	AsS
RuCl_3	42.6	2.5	0.6	As-Ru
<hr/>				
Ga 3s/ S 2p: Unetched	160.0	3.3	1.0	Ga_2O_3
Etched	159.0	3.0	0.0	Ga [3]
$(\text{NH}_4)_2\text{S}_x$	161.2	3.4	2.2	Ga_2S_3
Na_2S	161.5	3.4	2.5	Ga_2S_3

"-" indicates bond formation

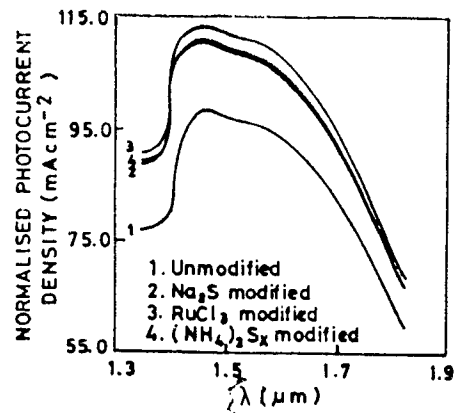


Fig.2a Spectral response of $\text{n-In}_{0.53}\text{Ga}_{0.47}\text{As}$ photoanodes in KOH-Te Tex redox showing increased photoresponse on modification.

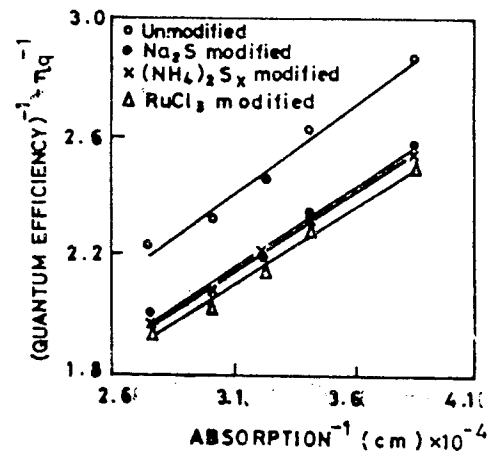


Fig.2b Plot of η_q^{-1} vs $\alpha(\lambda)^{-1}$ showing increased diffusion length (L_p).

Table-II: Summary of J-V and C-V data for $\text{Au/n-In}_{0.53}\text{Ga}_{0.47}\text{As}$ Schottky diode at 300 K. L_p and S_r are also given.

Sample	J_0 (A.cm^{-2})	n	$q\phi_{Bn}^{J-V}$ (eV)	A^{**} ($\text{A.cm}^{-2}\text{K}^{-2}$)	$q\phi_{Bn}^{J-T}$ (eV)	$q\phi_{Bn}^{C-V}$ (eV)	L_p (μm)	S_r (cm/sec)
Untreated	9.4×10^0	2.7	0.28	2.3	0.26	0.34	1.65	9.5×10^3
$(\text{NH}_4)_2\text{S}_x$ treated	3.7×10^{-5}	1.6	0.60	2.0	0.58	0.69	1.85	3.4×10^3
Na_2S "	3.0×10^{-5}	1.5	0.61	2.0	0.57	0.68	1.84	3.6×10^3
RuCl_3 "	4.2×10^5	1.6	0.60	1.9	0.57	0.69	1.89	2.4×10^3

$A^{**} = 4.92 \text{ A.cm}^{-2}\text{K}^{-2}$ was used for $q\phi_{Bn}^{J-V}$

treatment shifted the Ga 3s peak at 159.0 eV to 161.2 eV indicating formation of Ga_2S_3 [1].

The spectral response of $\text{In}_{0.53}\text{Ga}_{0.47}\text{As}$ photoanodes were studied in $\text{KOH-Te}^{2-}/\text{Te}_x^{2-}$ redox system with and without modification [Fig.2a]. Significant increase in long wavelength response was found in all cases of modification. The increase in L_p [Fig.2b] with surface modification is given in Table-II. If the bulk properties are assumed to be unchanged, the increase in L_p can be attributed to a decrease in S_r .

High surface state density also leads to low metal independent Schottky barrier height (ϕ_{Bn}). Removal of Fermi level pinning was directly demonstrated from J-V and C-V measurements of $\text{Au/In}_{0.53}\text{Ga}_{0.47}\text{As}$ Schottky diodes. A Richardson plot showed an increase in ϕ_{Bn} (J-T) from 0.26 eV to 0.58 eV due to $(\text{NH}_4)_2\text{S}_x$ treatment. The reverse saturation current density decreased from 9.4 to $3.0 \times 10^{-5} \text{ mA.cm}^{-2}$ due to Na_2S modification. The values of ϕ_{Bn} can be compared with those of Sugino et al. who obtained 0.70 eV from J-V and 0.55 eV from a Richardson plot of $\text{Au/n-In}_{0.53}\text{Ga}_{0.47}\text{As}$ treated with phosphine plasma. Thus all three methods of chemical modification improved the surface properties of $\text{In}_{0.53}\text{Ga}_{0.47}\text{As}$.

Discussion

Of the elements in InGaAs, Ga is more prone to oxidation than In or As. The presence of O_2 causes oxidation of InGaAs to Ga_2O_3 , In_2O_3 and As_2O_3 . The dangling bonds or the incomplete bonds of As and / or Ga or In atoms in these oxides and elemental As are the cause of the interface states which increase in amount with oxidation. These oxides must be removed from the surface so that modifying ions can react with a clean surface. In the present

studies Br_2 -methanol etching was used to remove native oxides after which the samples were dipped in solution.

The FWHM of XPS peaks for the modified samples increased compared to etched and unetched samples. From the values of chemical shift ΔE for sulfides, it is difficult to determine the dominant phase. However for the compounds In_2S_3 , Ga_2S_3 and AsS it is evident that S atoms are bonded more strongly to In and Ga than As.

Conclusion

XPS examination of InGaAs surface showed that modification involved the removal of native oxides and consequent formation of bonds with Ru and S. S was found to be more strongly bonded to In and Ga than As. Stable modification may thus improve device performance.

REFERENCES:

- [1] M. Procop, "XPS data for sputter cleaned $\text{In}_{0.53}\text{Ga}_{0.47}\text{As}$, GaAs and InAs Surfaces", J. Electron Spectroscopy and Related Phenomena, Vol. 59, pp. R1-R10, 1992.
- [2] D. Gallet and G. Hollinger, "Chemical, structural and electronic properties of sulfur-passivated $\text{InP}(001)(2 \times 1)$ surfaces treated with $(\text{NH}_4)_2\text{S}_x$ ", Appl. Phys. Lett. Vol. 62(9), pp. 982-984, 1993.
- [3] K. Sato, M. Sakata and H. Ikoma, "X-ray Photoelectron Spectroscopy and Electrical Characteristics of Na_2S - passivated GaAs Surfaces: Comparison with $(\text{NH}_4)_2\text{S}_x$ - Passivation", Jpn. J. Appl. Phys. Vol. 32, pp. 3554-3362, 1993.
- [4] T. Sugino, Y. Sakamoto and J. Shirafuji, "Schottky Barrier Height of Phosphidized InGaAs", Jpn. J. Appl. Phys. Vol. 32, pp. L239-L242, 1993.

Low Temperature Impurity-Induced Disordering of AlGaInAs/InP Quantum Wells for Long Wavelength Optoelectronic Applications

Kazuhiko Itaya*, Mark J. Mondry, Philip D. Floyd,
Larry A. Coldren, and James L. Merz**

Department of Electrical and Computer Engineering, University of California, Santa Barbara, Santa Barbara, California 93106, USA

*On leave from Toshiba Co., Kawasaki, Japan, **Permanent address: Department of Electrical Engineering, University of Notre Dame, Notre Dame, Indiana 46556-5637

Abstract

We investigated impurity-induced disordering (IID) in compressively strained AlGaInAs multi quantum wells (MQWs) on InP substrate by Zn diffusion. Complete disordering of AlGaInAs MQW, enhanced by strain, was observed even at the low temperature of 400 °C. On the other hand, unstrained MQW was not completely disordered below 500 °C. The measured hole concentration of the Zn diffused layer at 400 °C was as low as $3 \times 10^{18} \text{cm}^{-3}$. The IID lasers were also fabricated and characterized. No significant optical loss was observed in these lasers.

Introduction

Impurity-induced disordering (IID) of multi-quantum-well (MQW) structures is an attractive process for fabricating low-threshold lasers and integrated-optoelectronic devices, since both carrier and optical confinement in the lateral direction can be realized without regrowth problems (1)-(3). High performance lasers have been realized in the 0.8-0.98 μm wavelengths by using IID process (4)-(7). It has also been desired to apply the IID process to long-wavelength, 1.3-1.5 μm lasers.

Some aspects of the AlGaInAs/InP system have been investigated in terms of the IID process in the long-wavelength range. Several papers describing IID in the AlInAs/GaInAs MQW on InP by Zn diffusion have been reported (8),(9). However, to date, there has been no report on IID in a strained layer AlGaInAs/InP MQW which is considered to be indispensable for the active layer of high performance AlGaInAs/InP lasers (10)(11). A reduction of impurity concentration for the disordering is also desirable especially in the case of p-type impurities, since inter-valence band absorption is extremely sensitive to the hole concentration (9).

In this paper, we describe IID for strained AlGaInAs MQW for the first time. Both Zn diffusion and annealing were done at relatively low temperature below 500 °C to clearly reveal a strain effect in IID. A complete disordering was obtained for strained MQW even at 400 °C. To our knowledge, this is the lowest temperature for IID. The IID lasers were also fabricated and characterized to check the feasibility of the low temperature IID process. No significant optical loss was observed in these lasers.

Experimental

The structure used for the disordering experiments was grown by molecular beam epitaxy (MBE) with elemental solid sources. The growth temperature was 550 °C. Layer compositions were determined by reflection high energy electron diffraction oscillation measurements of fluxes. The Zn diffusion was carried out in an evacuated, closed ampoule using sources of elemental Zn and As. Photoluminescence (PL) measurements at 1.4 K with an Ar-ion laser were carried out in order to investigate the change of the effective bandgap energy with disordering.

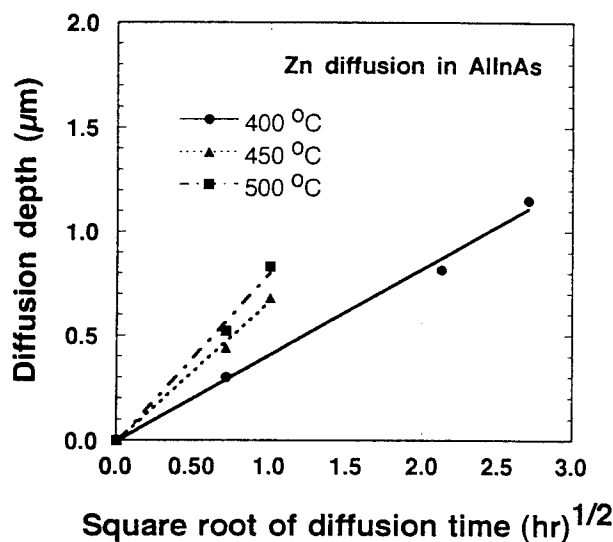


Fig. 1. Temperature dependence of Zn diffusion depth in AlInAs vs. square root of diffusion time.

Results and discussion

Before the disordering experiments, we investigated some of the Zn diffusion characteristics in this alloy system. Figure 1 shows the relation between Zn diffusion depth and diffusion time as a function of annealing temperature. Zn diffusion was performed into lightly n-type doped AlInAs layer, and was measured from a SEM image. The diffusion depth varied as the square root of time, in agreement with the conventional theory. Thus we confirmed that a sufficient diffusion depth for disordering of MQW can be obtained even such a temperature as low as 400 °C.

Figure 2 shows the structure used for the disordering experiments. Two different MQW structures were investigated. One consisted of ten 50Å Ga_{0.48}In_{0.52}As wells, lattice matched to InP, with 70Å Al_{0.28}Ga_{0.20}In_{0.52}As barriers. The other consisted of seven 35Å Ga_{0.3}In_{0.7}As wells, compressively strained 1.1%, with 50Å Al_{0.24}Ga_{0.24}In_{0.52}As barriers. Figure 3 shows PL results for the lattice matched MQW structure. A PL spectra of Zn diffused MQW at 400°C did not change from the as-grown sample. Partial disordering was observed for the sample diffused at 450°C. A blue-shifted PL peak energy for the diffusion at 500°C almost corresponded to that of a completely disordered alloy band-gap, however, it was 19 meV smaller than calculated for an average composition. This discrepancy is

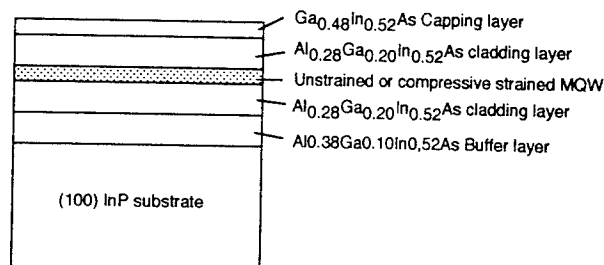


Fig.2. The structure used for the disordering experiments. All of the layers were grown on (100) InP substrate by MBE.

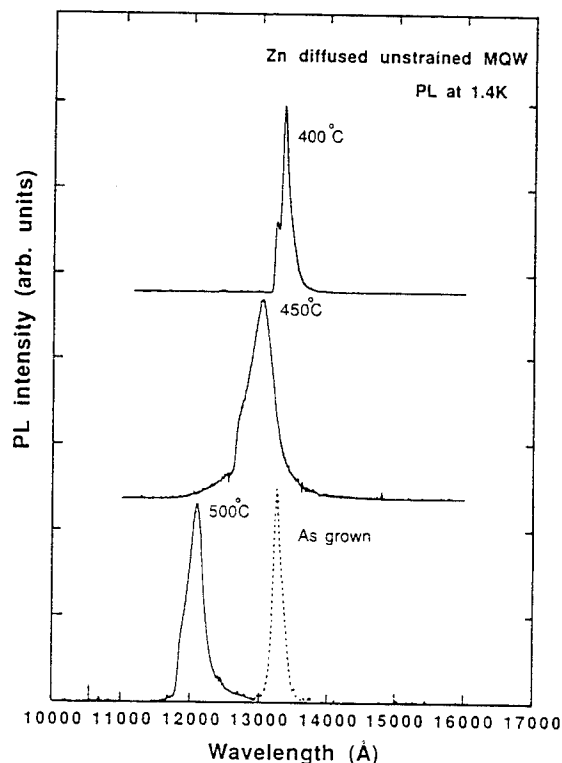


Fig.3. PL results of lattice matched MQW structure diffused with Zn. PL was excited by Ar-ion laser (488nm) and carried out at 1.4K.

considered to be due to a red-shift caused by the p-type Zn impurity. The vapor pressure of Zn is lower with reduced diffusion temperatures. Both low thermal energy and low Zn concentration prevented the unstrained MQW from disordering at low temperature.

Figure 4 shows the PL results of strained MQW structure. Each spectrum showed the

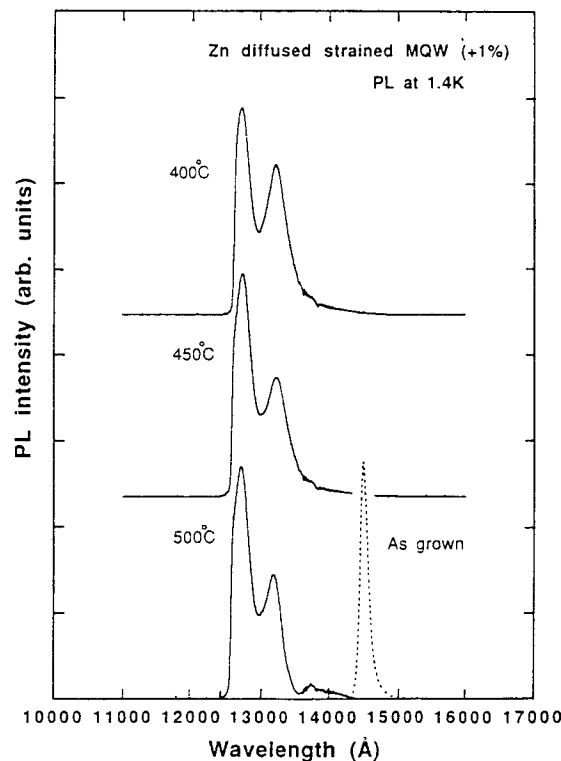


Fig.4. PL results of compressive strained (1%) MQW structure diffused with Zn.

doubled peak spaced by 34meV. The higher peak energy corresponding to the calculated averaged alloy composition of this MQW structure. In the lattice -matched GaInAs/AlGaInAs system, the In concentration is almost uniform in the well and barrier layers, thus intermixing of Ga and Al atoms would be the dominant mechanism for disordering. On the other hand, in the compressively-strained GaInAs/AlGaInAs system, the In concentration in the well is larger than the lattice-matched AlGaInAs barrier layer. These results show that in the case of compressive strained MQW structure, the intermixing of In also contributes to the intermixing of MQW structure. It was clear that the MQW diffused sample was completely disordered even for diffusion at 400°C. The compressive strain effect, combined with Zn diffusion, is considered to be a driving force for this disordering at low temperature. For the Hall measurements showed that the hole concentration of Zn diffused layer was as low as $3 \times 10^{18} \text{cm}^{-3}$.

The IID lasers were also fabricated and characterized to check the feasibility of such a low temperature and low impurity concentration IID process. Figure 5 (a) shows a schematic

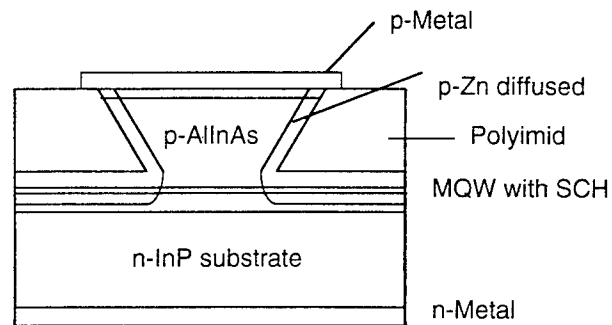


Fig.5 (a). Schematic cross-sectional view of AlGaInAs IID laser by Zn diffusion.

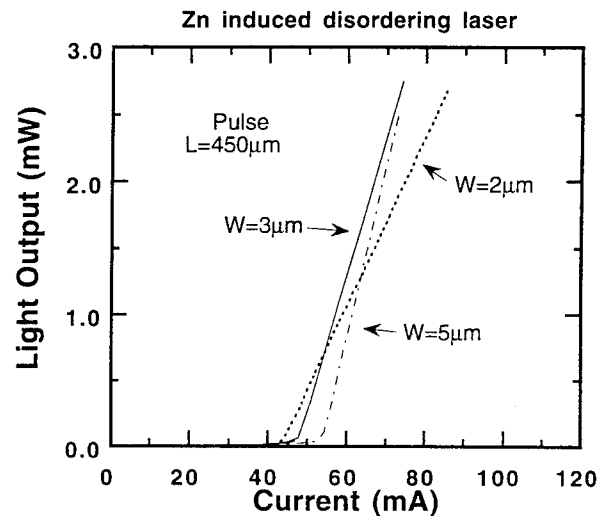


Fig.5 (b). Dependence of light output vs. current (L-I) characteristic on width of IID laser.

cross-sectional view of a ridge laser with IID process. A double heterostructure including 5 periods of compressive strained MQW was grown by MBE on n-type InP substrate. The growth conditions and the layer structure are the same as described in the former section. Si and Be were used for n-type and p-type dopants, respectively. In this laser structure, Zn -diffusion-induced disordering at 400 °C was performed after the formation of an inverse-mesa ridge by a chemical etching. Figure 5 (b) shows dependence of a light output versus current on width of this IID laser at room temperature with pulse operation. The threshold current decreased as the stripe width was reduced, as shown in this figure. The threshold current with a 2 μm -wide active layer was 41 mA. The internal waveguide loss was evaluated to be 25cm^{-1}

from the dependence of the L-I characteristic on the cavity length. The internal waveguide loss for a 50 μm broad area lasers was 10cm^{-1} . The wavelength was 1.56 μm . Laser performance including the internal waveguide loss was much improved compared with the previous report (9). These results show that the low temperature IID of AlGaInAs/InP MQW is a promising process for the realization of low optical loss, integrable optoelectronic device in the long-wavelength region.

Conclusion

In conclusion, strained AlGaInAs MQW was confirmed to show complete disordering even at a temperature as low as 400°C and with a Zn concentration as low as $3 \times 10^{18}\text{cm}^{-3}$, which is considered to be due to the strain enhancement. Lasers were successfully fabricated, and little addition in optical loss was observed in these lasers. These results show that a low temperature IID process in the AlGaInAs system is promising for the realization of low optical-loss, integrable optoelectronic devices in the long-wavelength region.

Acknowledgment

The authors would like to acknowledge the support of the ARPA Optoelectronics Technology Center.

References

- (1) W. D. Laidig, N. Holonyak Jr., M. D. Camras, K. Hess, J. J. Coleman, P. D. Dapkus, and J. Bardeen, *Appl. Phys. Lett.* **38**, 776, (1981).
- (2) N. Holonyak Jr., W. D. Laidig, J. J. Coleman, and P. D. Dapkus, *Appl. Phys. Lett.*, **39**, 102 (1981).
- (3) J. A. van Vechten, *J. appl. Phys.*, **53**, 7082, (1982).
- (4) K. Meehan, J. M. Brown, N. Holonyak Jr., P. D. Burnham, T. L. Paoli, and W. Streifer, *Appl. Phys. Lett.*, **44**, 700, (1984).
- (5) T. Fukuzawa, S. Semura, H. Sato, T. Ohta, Y. Uchida, and H. Nakashima, *Appl. Phys. Lett.*, **45**, 1, (1984).
- (6) A. Kurobe, H. Furuyama, S. Naritsuka, Y. Kokubun, and M. Nakamura, *Electron. Lett.* **22**, 1117, (1986).
- (7) W-X. Zou, K. K. Law, L. C. Wang, J. L. Merz, H. E. Hager, and C. S. Hong, *IEEE J. Quantum Electron.*, **29**, 2097, (1993).
- (8) Y. Kawamura, H. Asahi, A. Kohzen, and K. Wakita, *Electron. Lett.*, **21**, 218, (1985).
- (9) K. Goto, F. Uesugi, S. Takahashi, E. Omura, and Y. Mihashi, *Jpn. J. Appl. Phys.*, **33**, 5774, (1994).
- (10) A. Kasukawa, R. Bhat, C. Caneau, N. C. Andreadakis, B. Pathak, C-E. Zah, M. A. Kaza, and T-P. Lee, *Jpn. J. Appl. Phys.*, 1365, (1992).
- (11) M.J. Mondry, Z. M. Chuang, M. G. Peters, and L. A. Coldren, *Electron. Lett.*, **28**, 137, (1992).

THERMAL STABILITY OF $\text{Al}_{0.48}\text{In}_{0.52}\text{As}/\text{Ga}_{0.47}\text{In}_{0.53}\text{As}/\text{InP}$ HETEROSTRUCTURE AND ITS IMPROVEMENT BY PHOSPHIDIZATION

N. Takahashi, M. Shiota, Y. Zhu, M. Shimizu

Central Research Laboratories, SHARP Corporation, 2613-1 Ichinomoto, Tenri, Nara 632, Japan

D. Hirata*, Y. Sakamoto*, T. Sugino*, J. Shirafuji*

*Department of Electrical Engineering, Faculty of Engineering, Osaka University, 2-1 Yamadaoka, Suita, Osaka 565, Japan

Abstract

A drastic decrease in the sheet carrier concentration of the modulation-doped $\text{Al}_{0.48}\text{In}_{0.52}\text{As}/\text{Ga}_{0.47}\text{In}_{0.53}\text{As}/\text{InP}$ heterostructure has been observed after O_2 plasma treatment followed by thermal treatment up to 350 °C. It has been found that the decrease in sheet carrier concentration is caused by the impurities penetrated from the surface of the epi-layer, and can be suppressed substantially by using PH_3 plasma treatment prior to the O_2 plasma and thermal treatments.

Introduction

There has been considerable interest in the development of $\text{Al}_{0.48}\text{In}_{0.52}\text{As}/\text{Ga}_{0.47}\text{In}_{0.53}\text{As}/\text{InP}$ high electron mobility transistors (HEMTs) for microwave and millimeter wave applications.^{1,2} This alloy system has a number of advantages over the more established AlGaAs-GaAs heterostructure, including the high electron mobility and the larger conduction band discontinuity. These advantages give the promise of the HEMTs with excellent RF and noise performance. However, the degradation of the device characteristics caused by thermal treatment is a serious problem that has to be overcome if excellent performance is to be achieved. Similar to the degradation reported previously^{3,4} the change of the saturation drain current I_{dss} and the pinch-off voltage V_p of the HEMTs during the fabrication process have also been observed in our laboratory. In this work, an investigation has been performed on an $\text{Al}_{0.48}\text{In}_{0.47}\text{As}/\text{Ga}_{0.47}\text{In}_{0.53}\text{As}/\text{InP}$ heterostructure in order to understand and to improve the thermal stability of $\text{Al}_{0.48}\text{In}_{0.52}\text{As}/\text{Ga}_{0.47}\text{In}_{0.53}\text{As}/\text{InP}$ HEMTs.

Experimental

The $\text{Al}_{0.48}\text{In}_{0.52}\text{As}/\text{Ga}_{0.47}\text{In}_{0.53}\text{As}/\text{InP}$ HEMT structure, shown in Fig. 1, was grown on semi-insulating, (100)-oriented Fe-doped InP substrates by molecular beam epitaxy. The epitaxial layer structure consisted of an $\text{Al}_{0.48}\text{In}_{0.52}\text{As}$ buffer layer, a $\text{Ga}_{0.47}\text{In}_{0.53}\text{As}$ channel layer, an $\text{Al}_{0.48}\text{In}_{0.52}\text{As}$ spacer layer, an $\text{Al}_{0.48}\text{In}_{0.52}\text{As}$ donor layer, an $\text{Al}_{0.48}\text{In}_{0.52}\text{As}$ barrier layer and a $\text{Ga}_{0.47}\text{In}_{0.53}\text{As}$ cap layer. After the epitaxial growth, the O_2 plasma and thermal

treatments were performed. The O_2 plasma treatment conditions were as follows, the O_2 gas pressure was 0.5 Torr, the RF power was 50W, the substrate temperature and the treatment time were 150 °C and 15 min, respectively. The thermal treatment was performed in N_2 atmosphere up to 350 °C. Since the change in the I_{dss} and V_p can be monitored by the change in the sheet resistivity and/or the sheet carrier concentration n_s , Hall measurements were carried out on the heterostructure instead of I_{dss} and V_p measurements on fabricated HEMTs. The ohmic contacts for the Hall measurement were formed on the surface of the epi-layer by evaporating $\text{AuGe}/\text{Ni}/\text{Au}$ through a metal mask.

i-GaInAs	2nm
i-AlInAs	25nm
n-AlInAs	5nm
i-AlInAs	3nm
i-GaInAs	20nm
i-AlInAs	250nm
InP Sub. Fe doped	

Fig. 1 Epitaxial layer structure of HEMT investigated in this study.

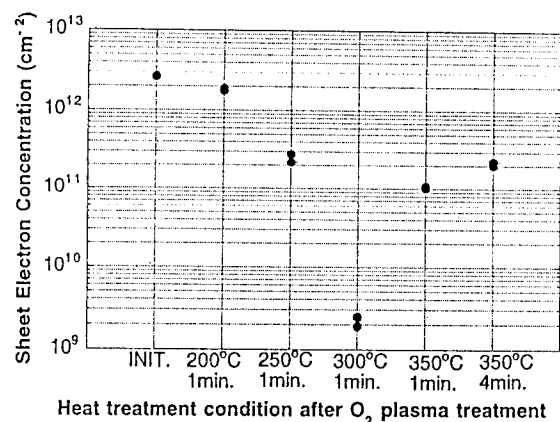


Fig. 2 Change of carrier concentration of HEMT structure due to O₂ plasma and the thermal treatments.

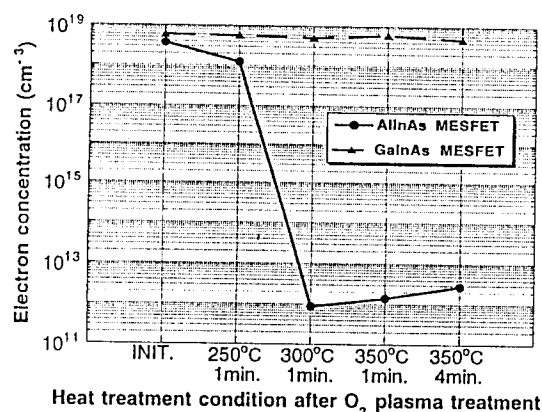


Fig. 3 Change of carrier concentration of MESFET structure due to O₂ plasma and the thermal treatments.

Results and Discussion

The Hall measurement results are shown in Fig. 2. While the n_s of as-grown sample remains almost constant after O₂ plasma treatment or thermal treatment up to 350 °C, respectively, a drastic decrease in n_s has been observed for the samples treated by O₂ plasma followed by thermal treatment. The decrease in n_s observed is believed to correspond to the change in I_{dss} and V_p of the HEMTs during the fabrication process.

The possible reasons for the decrease in n_s include the increase of the surface depletion and the compensation of the donor in the heterostructure.

Since the surface depletion increases with increasing the surface potential, the surface potential was measured using Kelvin probe method. The surface potentials for the as grown, O₂ plasma treated, and the O₂ plasma+thermal treated samples were 0.57, 0.60, and 0.49eV, respectively, no increase in the surface potential corresponding to the decrease in n_s was observed. It is then concluded that the decrease in n_s is caused by the compensation of donor in the heterostructure, which occurs when some complexes are formed in the n-Al_{0.48}In_{0.52}As donor layer, in the Ga_{0.47}In_{0.53}As channel layer or in both. These complexes can trap the conduction electrons and are not thermally ionized at room temperature.

In order to find where the complexes are formed, the measurements were performed on the two kinds of MESFET structures, one with the n-Al_{0.48}In_{0.52}As channel layer and the other with n-Ga_{0.47}In_{0.53}As channel layer, treated under the same conditions as mentioned above. The carrier concentration of the structure with n-Al_{0.48}In_{0.52}As (n-Ga_{0.47}In_{0.53}As) channel layer should keep constant if the complexes are formed only in the Ga_{0.47}In_{0.53}As (Al_{0.48}In_{0.52}As) channel layer. Since the decrease in the carrier concentration has been observed only in the the MESFET structure with the n-Al_{0.48}In_{0.52}As channel layer, as shown in Fig. 3, it is then believed that the complexes are formed only in the Al_{0.48}In_{0.52}As layer.

In the case of O⁺-implanted n-Al_{0.48}In_{0.52}As, the compensation of the donor was believed to be due

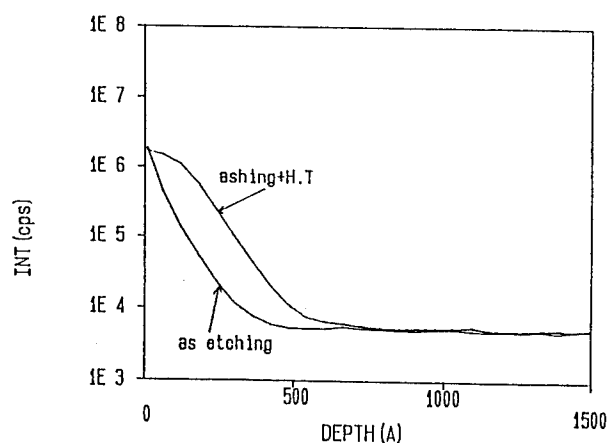


Fig. 4 Oxygen distribution in n-Al_{0.48}In_{0.52}As after O₂ plasma and thermal treatments measured by SIMS.

to both the damage induced and the O_2 -related complexes.^{5,6} In order to identify the generation mechanism of the complexes in this work, the thermal treatment and the measurement were also preformed on the sample exposed to the air without O_2 plasma treatment. Since the similar increase in the sheet resistivity after thermal treatment was also found in the sample exposed to the air for several weeks, the complexes here is believed to be induced by the impurities which penetrate from the surface of the epi-layer.

SIMS measurements were then performed on $n\text{-Al}_{0.48}\text{In}_{0.52}\text{As}$ treated under the same conditions. The distribution of the oxygen in the $n\text{-Al}_{0.48}\text{In}_{0.52}\text{As}$, obtained from the SIMS measurement, is shown in Fig. 4. An increase in the O_2 concentration due to the O_2 plasma treatment can be observed, and the penetration depth of O_2 is about 500Å. It is thus speculated that the complexes are O_2 -related.

For improving the thermal stability of the $\text{Al}_{0.48}\text{In}_{0.52}\text{As}/\text{Ga}_{0.47}\text{In}_{0.53}\text{As}/\text{InP}$ HEMTs, it is important to develop an effective method to suppress the compensation of the donor due to thermal treatment. Since PH_3 plasma treatment of $n\text{-Al}_{0.48}\text{In}_{0.52}\text{As}$ layer has been reported to yield an improvement in the Schottky junction characteristics⁷, a trial has been made here to investigate the effect of phosphidization on the thermal stability of the $\text{Al}_{0.48}\text{In}_{0.52}\text{As}/\text{Ga}_{0.47}\text{In}_{0.53}\text{As}/\text{InP}$ heterostructure. PH_3 plasma treatment was performed prior to O_2 plasma and thermal treatments. The PH_3 plasma treatment conditions are the same as reported elsewhere⁷. As shown in Fig. 5, the change in the

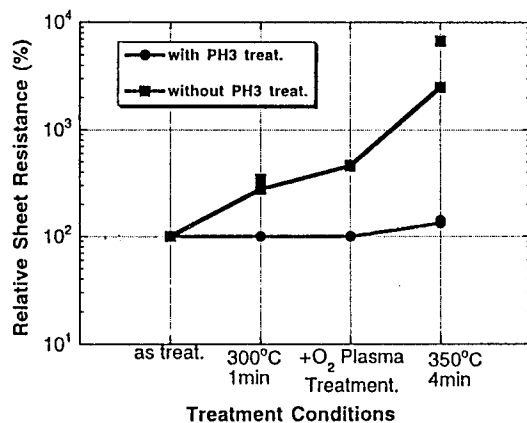


Fig. 5 Change of resistivity of HEMT structure with or without PH_3 plasma treatments.

sheet resistivity of the heterostructure, and thus the compensation of the donor, is suppressed substantially by PH_3 plasma treatment. Phosphidization can thus be expected to be an effective way of improving the thermal stability of the heterostructure.

The oxygen and phosphorus distribution in the $n\text{-Al}_{0.48}\text{In}_{0.52}\text{As}$ after PH_3 plasma, O_2 plasma and the thermal treatments, obtained from SIMS measurement, are shown in Figs. 6a and 6b, respectively. There are two important features about the data in Fig. 6. The concentration of oxygen in $n\text{-Al}_{0.48}\text{In}_{0.52}\text{As}$ shows almost no dependence on PH_3 plasma treatment, and the penetration depth of the phosphorus is the same as

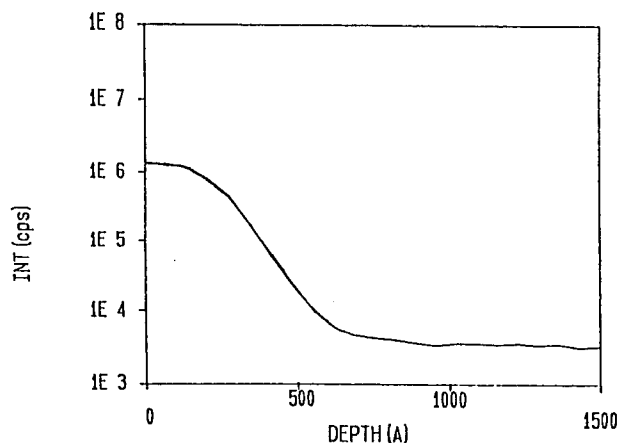


Fig. 6a Oxygen distribution in $n\text{-Al}_{0.48}\text{In}_{0.52}\text{As}$ after PH_3 plasma, O_2 plasma and thermal treatments measured by SIMS.

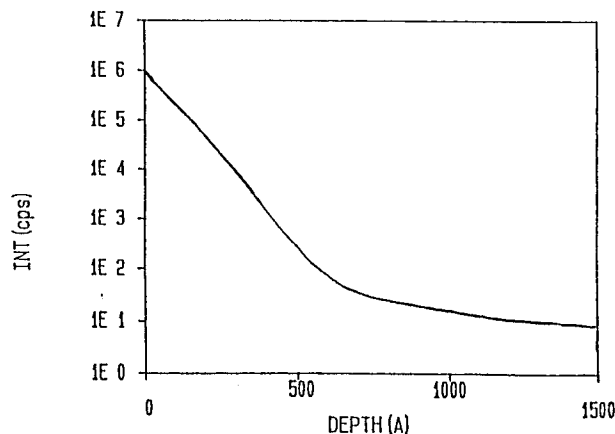


Fig. 6b phosphorus distribution in $n\text{-Al}_{0.48}\text{In}_{0.52}\text{As}$ after PH_3 plasma, O_2 plasma and thermal treatments measured by SIMS.

that of the oxygen. A possible mechanism for the suppression of the compensation of the donor by phosphidization is as follows. In the case of the sample without PH₃ plasma treatment, SiO₂ is formed after O₂ plasma+thermal treatments, which trap the conduction electrons. The heats of formation for P₂O₅ and SiO₂ are listed in Table I⁸. Since the heat of formation of P₂O₅ is smaller than that of SiO₂, as shown in Table I, P₂O₅ is formed instead of SiO₂, and the compensation of the donor is thus suppressed in the case of the sample with PH₃ plasma treatment.

Table I. Heat of Formation of P₂O₅ and SiO₂

	P ₂ O ₅	SiO ₂
Heat of Formation (kcal/mole)	-360.0	-202.6

Summary

A drastic decrease in n_s of the modulation-doped Al_{0.48}In_{0.52}As/Ga_{0.47}In_{0.53}As/InP heterostructure has been observed after O₂ plasma treatment followed by thermal treatment up to 350°C. The decrease in n_s corresponds to the change of the I_{dss} and V_p of the HEMT and is caused by the compensation of the donor in the n-Al_{0.48}In_{0.52}As layer. The compensation is believed to be due to the impurities which penetrate from the surface of the epi-layer. PH₃ plasma treatment has been proved to be an effective way of preventing the compensation. Although the mechanisms are not yet known exactly, it is speculated that SiO₂ is formed after O₂ plasma+thermal treatments, which trap the conduction electrons, and the suppression of the compensation is due to the formation of P₂O₅ instead of SiO₂ in the PH₃ plasma treated samples.

References

- (1) U. K. Mishra, A. S. Brown, S. E. Rosenbaum, C. E. Hooper, M. W. Pierce, M. J. Delaney, S. Vaughn, and K. White "Microwave Performance of AlInAs-GaInAs HEMT's with 0.2- and 0.1- μ m Gate Length," IEEE Electron Device Lett., vol. 9, pp. 647-649, December 1988.
- (2) K. H. Duh, P. C. Chao, S. M. J. Liu, P. Ho, M. Y. Kao, and J. M. Ballingall, "A super low-noise T-gate InAlAs-InGaAs-InP HEMT," IEEE Microwave and Guided Wave Lett., vol. 1, pp. 114-116, 1991.
- (3) M. Tutt, G. I. Ng, D. Pavlidis and J. Mansfield,

Mobility Transistors," Proc. 3rd Int. Conf. InP and Related Materials, Cardiff, 1991, p.101.

(4) S. Fujita, T. Noda, C. Nozaki, and Y. Ashizawa, "InGaAs/InAlAs HEMT with a Strained InGaP Schottky Contact Layer," IEEE Electron Device Lett., vol.14, pp. 259-261, May 1993.

(5) W. Lee and C. G. Fonstad, "O⁺ implantation and annealing in n-type InAlAs," Appl. Phys. Lett., vol. 50, pp. 1278-1280, May 1987.

(6) S. J. Pearton, W. S. Hobson, and U. K. Chakrabarti, "Damage-induced high-resistivity regions in Al_{0.48}In_{0.52}As," Appl. Phys. Lett., vol. 55, pp.1786-1788, Oct. 1989.

(7) T. Sugino, I. Yamamura, A. Furukawa, K. Matsuda, and J. Shirafuji, "Improved Barrier Height of Schottky Junctions formed on Phosphidized AlInAs," Proc. 6th Int. Conf. InP and Related Materials, Santa Barbara, pp. 632-635, 1994.

(8) J. H. Perry, "Chemical Engineers' Handbook", McGraw-Hill Book, 1950, p235, New York, 3rd ed.

Morphological and Electrical Characterization of Al/Ni/n-InP Contacts with Tapered Ni-Layer

S. Miyazaki, T.-C. Lin, C. Nishida, H. T. Kaibe and T. Okumura

Dept. of Electronics and Information Engineering, Tokyo Metropolitan University
1-1, Minami-ohsawa, Hachiohji, Tokyo 192-03, Japan

Introduction

Indium phosphide and related compounds have become a significantly important material for optoelectronic as well as ultrahigh-speed devices. From the practical viewpoint of realization of a metal-Schottky gate field-effect transistor (MESFET), it is a critical issue to find gate contact materials with high Schottky barrier height (SBH). Unfortunately, the experimental values of SBH's for typical metal/InP contacts are relatively independent of the metal work function, and a SBH greater than 0.4 eV is often difficult to obtain on n-InP (1). As a result, several techniques have been reported for increasing the effective SBH on n-InP: surface passivation (2), incorporation of highly doped surface layers (3) and insertion of a thin oxide layer (4)-(5). However, all these techniques require an extra process in order to modify the InP surface prior to the metallization. Therefore, it is still challenging to explore a simple processing technology for fabricating a Schottky contact on n-InP with high SBH.

We have shown that an Al film gives high SBH's for n-InP close to 0.7eV upon rapid thermal annealing (RTA) (6). After annealing at 650°C, the measured current-voltage (*I-V*) characteristic became rectifying as shown in Fig. 1. The formation of AlP upon the exchange reaction between Al and InP plays an important role in the realization of high SBH. However, the reacted films have rough surfaces, usually "balling up," due to irregular alloying as shown in Fig. 2.

In this paper, we show a thin Ni film as the first layer of Al/Ni contacts improved the surface morphology after rapid thermal annealing (RTA). In order to find the optimum fabrication parameters (film thickness, annealing temperature and time, etc.), we have fabricated a unique sample in which the thickness of the inserted Ni layer tapered off in space. The electrical properties were evaluated by using scanning internal-photoemission microscopy (SIPM) (7) which is capable of "mapping" the Schottky diode characteristics.

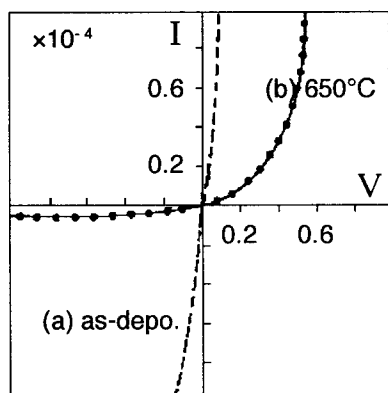


Fig. 1 *I-V* characteristics for the Al/InP before and after RTA at 650°C.

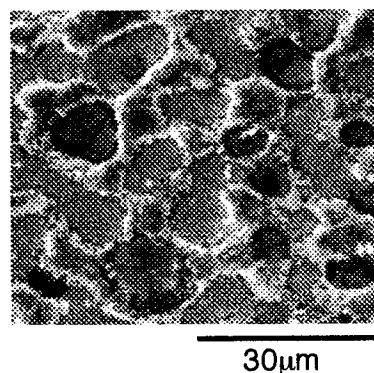


Fig. 2 A typical SEM image for the Al/InP after RTA at 650°C

Experimental

We use lightly-doped n-InP(100) as a substrate, whose carrier concentration was $1.4 \times 10^{16} \text{ cm}^{-3}$. The surface was [100] oriented and chemically etched in a solution of $5\text{H}_2\text{SO}_4 + 1\text{H}_2\text{O}_2 + 1\text{H}_2\text{O}$ for 3 min at 50°C after a standard cleaning process with organic solvents. The front surface of the substrates was covered with a spin-on-glass (SOG) film with rectangle openings of $10 \times 0.1 \text{ mm}^2$ to define the area for the Schottky contact. They were again etched in a solution of $5\text{H}_2\text{SO}_4 + 1\text{H}_2\text{O}_2 + 1\text{H}_2\text{O}$ for 3 min at 50°C , rinsed in deionized water, and dried by flowing nitrogen gas before loading into the vacuum chamber (based pressure $< 5 \times 10^{-7} \text{ Torr}$).

The first layer of Ni was deposited by e-gun evaporation. The tapered structure was realized by sliding a metal shadow mask (blade) placed close to the substrate. The thickness slope of the tapered Ni layer fabricated by this method was about 8 nm/mm . After the top Al layer was deposited by resistance-heated evaporation, the sample was cut into several pieces. A schematic view of the sample is shown in Fig. 3.

The rapid thermal annealing (RTA) was performed under the face-to-face capless condition in an infrared image furnace under hydrogen flow in the temperature range of 450 to 550°C . The heating rate and the holding time at the highest temperature were set to 10°C/sec and 0 – 30 sec , respectively. Then, the sample was cooled down as rapidly as possible.

The surface morphology after RTA was characterized by using the Nomarski-type optical microscope.

The scanning internal-photoemission microscopy (SIPM) is a unique technique, which enables us to map the SBH (7). The outline of the technique is as follows: A light from a $1.3 \mu\text{m}$ laser diode is focused at the metal-semiconductor interface through the semiconductor substrate. Accompanying with the photon absorption, photocurrent due to the so-called internal-photoemission effect is generated, and its magnitude of dependence on the light wavelength reflects the SBH. The spatial distribution of the SBH can be determined by scanning of the laser

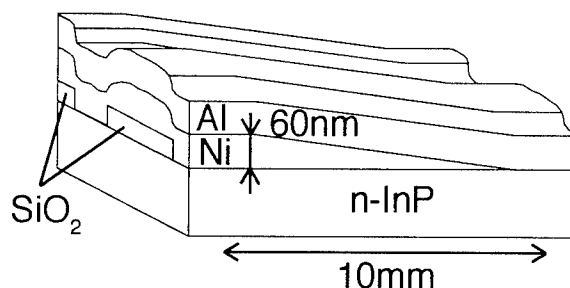


Fig. 3 Schematic view of the sample

beam. Therefore, the inserted-Ni thickness dependence of the SBH as well as the surface morphology can be measured by using a "single sample" as shown in Fig. 3.

The thin film x-ray diffraction (XRD) was measured to identify the reaction products by using samples with an inserted Ni layer with a uniform thickness of 24 nm . An x-ray source of $\text{Cu-K}\alpha$ was used at a grazing angle of 0.9° , which was selected in order not to penetrate the entire thickness of Al or reacted films (8).

Results and Discussion

First of all, we discuss the role of the inserted Ni layer on the reaction between Al and InP. Figure 4 shows the XRD patterns for the Al/InP as well as Al/Ni/InP before and after RTA at various temperatures for 1min. In the previous report (6), we showed that the Al/InP interface was stable upon RTA below 400°C . Significant reaction took place above 650°C resulting in segregating metallic indium (9). The diffraction peak of AIP ($2\theta = 28^\circ$) appeared at 770°C , above the melting point of Al, while no AIP ($2\theta = 28^\circ$) phase was formed upon annealing at 650°C . On the other hand, the XRD measurements revealed the compound formation of AIP and Ni_2P upon RTA even at 450°C . In the AuGe/Ni/GaAs system, the role of a thin Ni layer was thought to lead to formation of more uniform contact phases due to the low-temperature solid-phase reaction between Ni and GaAs (10)-(11). The detection of the Ni_2P phase suggests that the low-temperature reaction between a first layer of Ni and InP plays an important role of the formation of AIP.

No internal-photoemission current was

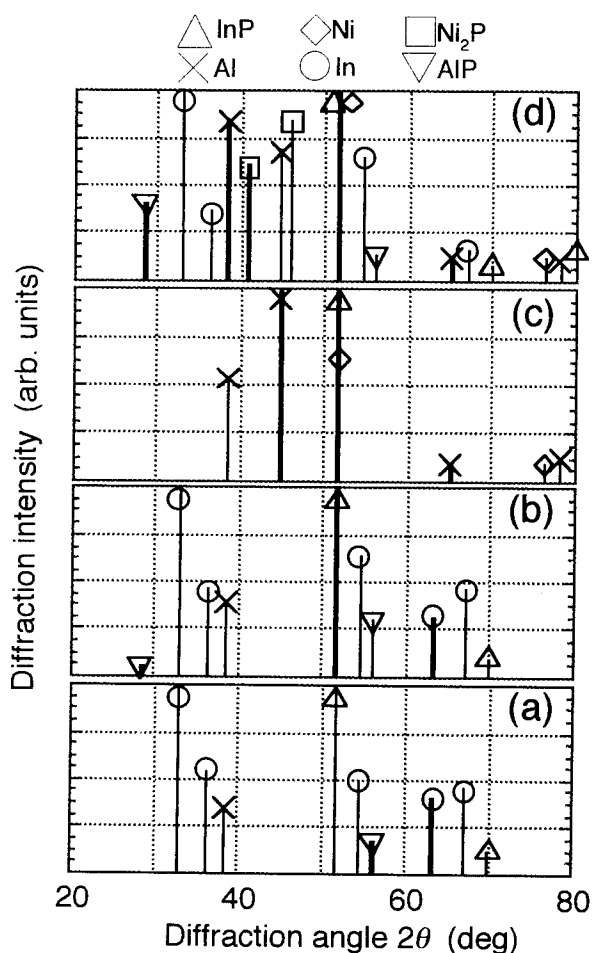


Fig. 4 The XRD patterns for the Al/InP as well as Al/Ni/InP before and after RTA at various temperatures. Four samples are: (a): Al/InP(650°C RTA), (b): Al/InP(770°C RTA), (c): Al/Ni/InP(as-depo.), (d): Al/Ni/InP(460°C RTA)

detected for the as-deposited samples with any thickness of the first layer (Ni). This means that the SBH was too low to form the built-in electric field. The current-voltage measurement revealed that the as-deposited contact showed an ohmic behavior just like the Al/n-InP contact reported in Ref (6).

Figure 5(a) shows the surface morphology and the line profile of the internal photoemission current for the sample annealed at 450°C for 30sec. The internal-photoemission current increased with the thickness of the inserted Ni layer, while no photocurrent flow in the region of no Ni-layer. Since the XRD measurements showed the AlP formation even at this

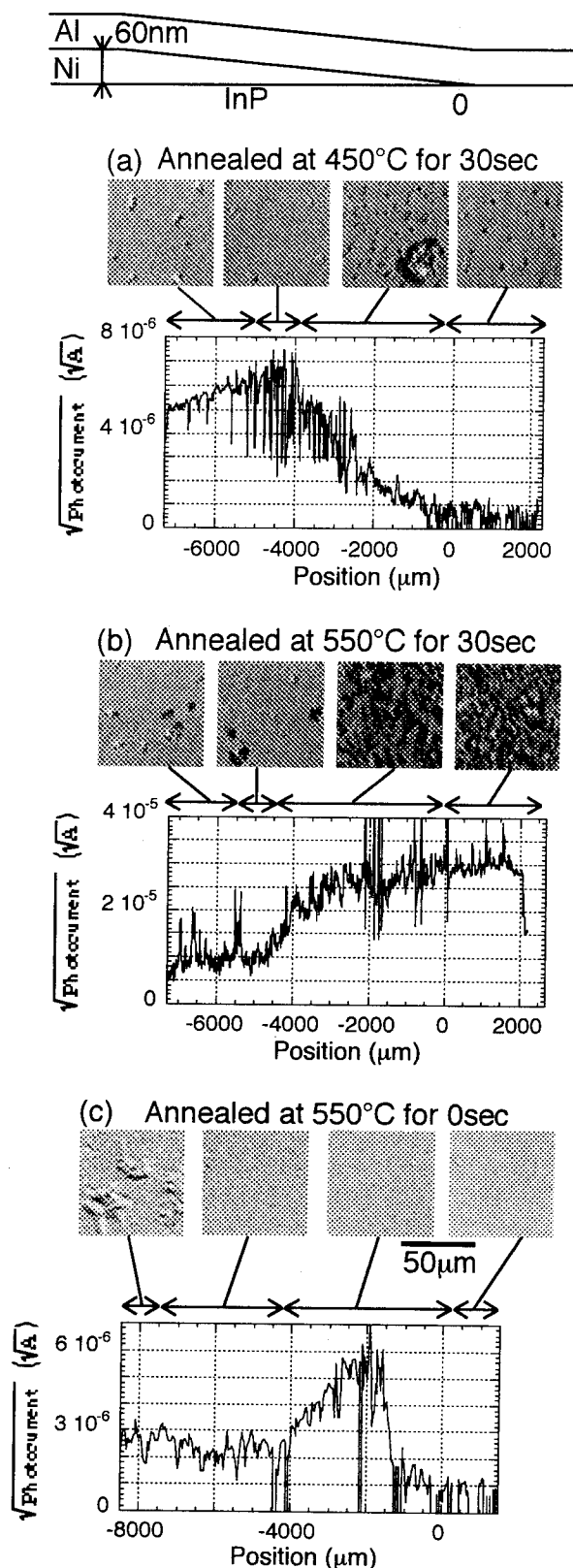


Fig. 5 The surface morphology and the line profile for the Al/Ni/InP after RTA at various temperatures.

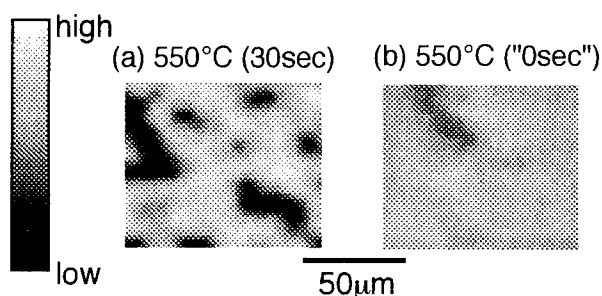


Fig. 6 The typical photocurrent images for the high SBH regions of the Al/Ni/InP annealed at 550°C for 30sec and "0sec".

temperature, the increase of the photocurrent can be attributed to the formation of the metal/AlP (wide-gap)/InP structure which increases the effective SBH.

For the sample annealed at higher temperature of 550°C for 30sec, on the other hand, the high-SBH was realized in the region without the Ni layer as well as that with the Ni thinner than 20nm (Fig. 5(b)). However, in the most part with high SBH's, the surface morphology was poor due to the phase segregated indium. From the morphological point of view, it is clearly seen that the inserted Ni layer with a thickness of around 35 nm improved the uniformity.

Figure 5(c) shows that RTA at 550°C for holding time of 0sec significantly improved the surface morphology in the region with high SBH's. A poor signal-to-noise ratio (S/N) in the photocurrent profile might be due to shunt lossy paths of large area with low SBH's.

Figure 6 shows the photocurrent images for the high SBH regions formed upon RTA at 550°C for holding time of 30 sec and 0 sec, respectively. The "0 sec" annealing improves homogeneity morphologically as well as electrically.

Summary

We have demonstrated that the combination of the scanning internal-photoemission microscopy (SIPM) and the test sample with a tapered inserted layer is an effective way of optimizing the multilayer semiconductor contacts. This

methodology has been applied to the realization of good Schottky contacts n-InP.

Acknowledgments

The authors wish to thank Dr. T. Shirakawa of Sumitomo Electric Co. for providing n-InP wafers.

References

- (1) N. Newman, T. Kendelewicz, L. Bowman and W. E. Spicer, "Electrical study of Schottky barrier heights on atomically clean and air exposed n-InP (110) surfaces", *Appl. Phys. Lett.*, Vol. 46, No. 12, pp. 1176-1178, June 1982.
- (2) T. Sugino, Y. Sakamoto, T. Sumiguchi, K. Nomoto and J. Shirafuji, "Barrier heights of Schottky junctions on n-InP treated with phosphine plasma", *Jpn. J. Appl. Phys.*, Vol. 32, No. 9A, pp. L1196-L1199, September 1993.
- (3) G. P. Schwartz and G. J. Gualtieri, "Metal/p⁺/n enhanced Schottky barrier structures on (100) InP", *J. Electrochem. Soc.*, Vol. 133, No. 5, pp. 1021-1025, May 1986.
- (4) Y. Imai, T. Ishibashi and M. Ida, "Characteristics of InP MIS Schottky diodes prepared by plasma oxidation", *J. Electrochem. Soc.*, Vol. 129, pp. 221-224, January 1982.
- (5) H. Yamagishi, "Schottky contacts on n-InP surface treated by plasma-induced oxygen radicals", *Jpn. J. Appl. Phys.*, Vol. 25, No. 11, pp. 1691-1696, November 1986.
- (6) T.C. Lin, H. T. Kaibe, C. Kaneshiro, S. Miyazaki and T. Okumura, "Microanalysis of Inhomogeneous Reaction and Schottky-Barrier-Change of Al/n-InP Contacts upon Rapid Thermal Annealing", *Proc. IPRM5, Paris*, pp. 691-694, April 1992.
- (7) K. Shiojima and T. Okumura, "Improvement in spatial resolution of infrared scanning internal-photo-emission microscope", *Jpn. J. Appl. Phys.*, Vol. 30, pp. 2127-2128, September 1991.
- (8) M. F. Doerner, S. Brenman, "Strain distribution in thin aluminum films using x-ray depth profiling", *J. Appl. Phys.*, Vol. 63, pp. 126-131, January 1988.
- (9) A. Ismail, A. Brahim, J. M. Palaci and L. Lassabatere, "The interaction of Ag, In and Al overlayer with InP (110): surface and diode studies of the effect of indium interlayers", *Vacuum*, Vol. 36, pp. 217-221, 1986.
- (10) Y.-C. Shih, M. Murakami, E. L. Wilkie and A. C. Callegari, "Effects of microstructure on uniformity and thermal stability of AuNiGe ohmic contact to n-type GaAs", *J. Appl. Phys.*, Vol. 62, No. 2, pp. 582-590, July, 1987.
- (11) C. -P. Chen and Y. A. Chang, "Enhancement of Schottky barrier height to n-GaAs using NiAl, NiAl/Al/Ni, and Ni/Al/Ni layer structures", *J. Vac. Sci. Technol.*, Vol. 12, pp. 1915-1919, Jul/Aug 1994.

FORMATION OF PN_x/InP STRUCTURE BY IN-SITU REMOTE PLASMA PROCESSES

Y. Sakamoto, T. Sugino, T. Miyazaki and J. Shirafuji
Department of Electrical Engineering, Faculty of Engineering, Osaka University,
2-1 Yamadaoka, Suita, Osaka 565, Japan

Abstract

In-situ remote plasma processes consisting of removal of native oxide due to hydrogen (H_2) plasma, surface modification due to phosphine (PH_3) plasma and deposition of PN_x films due to decomposition of PH_3 by nitrogen (N_2) plasma have been developed. The insulating PN_x film with an optical bandgap of 5.3 eV is obtained by remote plasma CVD. $\text{Au}/\text{PN}_x/\text{InP}$ tunneling metal-insulator-semiconductor (MIS) type Schottky junction is formed by the in-situ multi-processes. The effective barrier height is estimated to be as high as 0.83 eV. Enhancement of the effective barrier height is due to both effects of the MIS structure and unpinning of the surface Fermi level.

1 INTRODUCTION

A lot of efforts have been devoted to studies on formation of metal-insulator-semiconductor (MIS) structures in order to achieve not only field effect transistors but also Schottky junctions with a high barrier height.¹⁻³⁾ A mild process at low temperature is necessary to deposit insulating films onto the InP with thermally unstable surface. Phosphorus nitride (PN_x) films is one of the most attractive insulating films for InP and related materials. Deposition of PN_x films are advantageous to suppression of P dissociation from InP surfaces because source material in which P species are contained is used. There have been several reports on deposition of PN_x insulating films by means of thermal, plasma and photo CVD.⁴⁻⁷⁾ Since MIS characteristics depends on interfacial state density, it is important to develop processing technologies to form the interface between semiconductor and insulating layer in addition to deposition process of insulating layers.

In-situ processes consisting of (i) removal of native oxide due to H_2 plasma, (ii) surface modification due to PH_3 plasma, (iii) deposition of PN_x films due to decomposition of PH_3 by N_2 plasma and (iv) evaporation of contact metal have been developed in the present work. Each plasma process is carried out using remote plasma method to avoid plasma damage. In the case when InP surface is treated with H_2 plasma to remove native oxide,

P dissociation may occur at the InP surface exposed to H_2 plasma. On the other hand, PH_3 plasma treatment is effective in modifying InP surfaces with P vacancies.⁸⁾ The present technology is featured by introducing in-situ surface treatment processes due to mild remote plasma prior to insulator deposition process.

This paper describes formation of tunneling MIS type Schottky junctions with PN_x/InP structure by using in-situ remote plasma processes together with characterization of PN_x films deposited by the remote plasma method.

2 EXPERIMENTAL

Figure 1 shows a schematic diagram of the experimental apparatus which was specially designed for plasma treatment with H_2 or PH_3 , PN_x film deposition and in-situ evaporation of Schottky metals. Plasma chamber consists of two remote plasma cells, a sample holder with a heater and a heater for metal evaporation. The remote plasma was excited by supplying RF (13.56 MHz) power to a coil 10 cm away from the specimens. One is used for H_2 plasma treatment and another is for PH_3 and N_2 plasma.

PN_x films were deposited due to decomposition of PH_3 gas by N_2 remote plasma. Si and fused quartz were used as substrates to evaluate optical and electrical properties of deposited PN_x films. The surface of the Si sub-

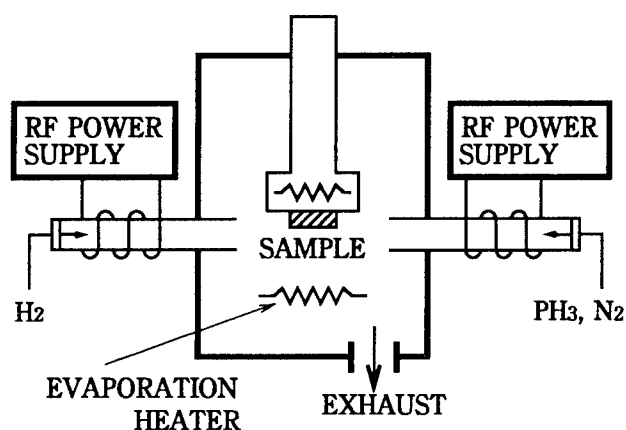


Fig.1 Schematic illustration of experimental apparatus.

strates was chemically etched with a solution consisting of H₂SO₄ and H₂O₂ (20:1) and subsequently with HF solution. Fused quartz was cleaned with acetone. After the substrates were placed on the pedestal, the reactor was evacuated to a base pressure of 3×10^{-6} Torr. The substrate temperature was kept at 250 °C. PH₃ and N₂ gases were introduced into the side arm. PH₃ gas diluted at 10 % with Ar gas was used in the experiment. The gas pressure was regulated at 0.4 Torr. PN_x films were deposited by chemical reaction between PH₃ and radicals fed from N₂-remote plasma. RF power and substrate temperature were 50 W and 250 °C, respectively. Deposition time was 60 min.

Au/PN_x/InP tunneling MIS Schottky junctions were tentatively formed using the in-situ remote plasma processes. N-type LEC InP wafers with (100)-oriented surface was used as a substrate. Prior to formation of PN_x/InP structure, ohmic contacts were formed on the back side of the InP by evaporating AuGeNi, followed by alloying at 370 °C for 3 min. The samples were chemically etched with a solution consisting of H₂SO₄:H₂O₂:H₂O = 5:1:1 for 3 min and a solution of HF:H₂O=1:1 for 1 min. At first H₂ plasma treatment was carried out in order to eliminate the native oxide of InP surface. InP substrates which are treated with H₂ plasma at 95 °C were subsequently treated with PH₃ plasma at 250 °C.

It is expected that the defects introduced by H₂

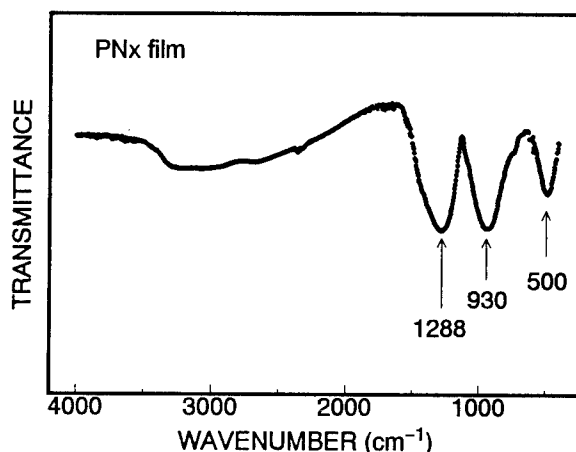


Fig.2 Infrared transmission spectra of PN_x film.

plasma exposure are reduced by PH₃ plasma treatment. After the surface modification by PH₃ plasma treatment, PN_x films were formed by in-situ remote plasma CVD method and metal contacts were provided by in-situ Au evaporation. The size of Schottky contacts was 1 mm in diameter.

3 RESULTS AND DISCUSSION

3.1 Properties of PN_x Films

PN_x films deposited at N₂/PH₃ flow rate ratio of 25 were characterized. The deposited film with 200 nm in thickness was obtained under the present deposition condition. Figure 2 indicates the IR absorption spectrum of PN_x film on Si substrate. Three absorption bands peaked at 1288, 930 and 500 cm⁻¹ are observed significantly. Absorption bands peaked at 1230 and 920 cm⁻¹ are associated with stretching vibrations of amorphous P₃N₅ network.⁹⁾ On the other hand, the band at 500 cm⁻¹ is probably due to bending mode of the P-N network.⁹⁾ These three bands have been found commonly in P₃N₅ samples being independent of the preparation conditions.⁹⁾

The optical absorption was measured with a double-beam (sample / reference) UV-visible spectrometer for PN_x film deposited on fused quartz in order to determine the optical bandgap. The optical bandgap of PN_x

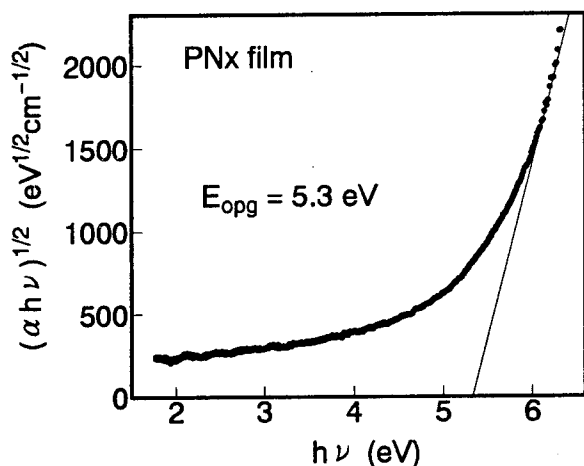


Fig.3 Tauc plot of the deposited PNx film.

film was determined from $(\alpha h\nu)^{1/2}-h\nu$ characteristics, where α is the absorption coefficient and $h\nu$ is the photon energy, as usually used in amorphous semiconductor materials.¹⁰⁾ Figure 3 shows the Tauc plot of the deposited PNx film. The optical bandgap of the PNx film is estimated to be 5.3 eV. It was reported that the optical bandgap of P_3N_5 films is 5.2 ± 0.1 eV.¹¹⁾

3.2 Electrical characteristics of Schottky diodes

In-situ four processes consisting of H_2 plasma treatment for 10 min, PH_3 plasma treatment for 5min, deposition of PNx film for 1 min and Au evaporation were carried out to fabricate an MIS Schottky junction. It was confirmed that native oxide was eliminated by H_2 plasma treatment for 10 min. The thickness of the PNx film was inferred to be 3.3 nm taking account of the deposition rate of 0.055 nm/s.

Figure 4 shows the room-temperature current-voltage (I-V) characteristics of Au/PNx/InP and conventional Au/InP Schottky junctions. On the basis of thermionic emission model,¹²⁾ the effective barrier height is estimated to be 0.45 eV from the saturation current for conventional untreated (as-etched) sample. On the other hand, the effective barrier height as high as 0.83 eV is obtained for Au/PNx/InP MIS Schottky diode. A thin insulating layer with wide bandgap is possibly responsible

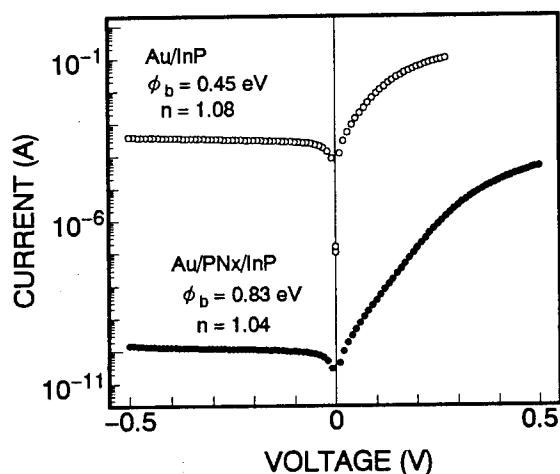


Fig.4 I-V characteristics of conventional Au/InP Schottky diode and Au/PNx/InP MIS Schottky diode.

for enhancement of the Schottky barrier height. Moreover, the ideality factor is estimated to be 1.04.

Figure 5 shows the Richardson plot for the same samples as in Fig.4. The true barrier height is evaluated from the Richardson plot, corresponding to the surface Fermi level position of InP measured from the conduction band edge. The values of the true barrier height for the conventional and the present MIS Schottky junctions are 0.39 and 0.57 eV, respectively. It has already been re-

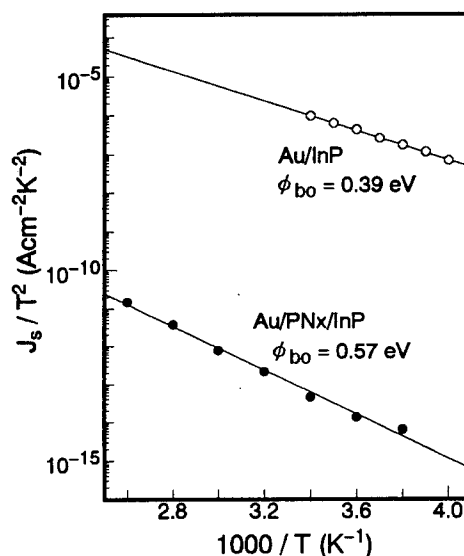


Fig.5 Richardson plot of the same Schottky diodes as in Fig.4.

ported that the surface Fermi level is pinned at about 0.4 eV below the conduction band edge for the conventional n-InP Schottky junction. In contrast to this, the true Schottky barrier height in the present work approaches the Schottky limit (0.7 eV) which is determined by the difference between the work function of Au (5.1 eV)¹³ and the electron affinity of InP (4.4 eV),¹⁴ indicating that the pinning of the surface Fermi level is weakened by reducing the interfacial state density. It is expected that the surface property of InP is further improved by the optimum condition of the PH₃ plasma process.

4 SUMMARY

PNx films with optical bandgap of 5.3 eV is deposited by remote plasma CVD method due to decomposition of PH₃ gas by N₂ plasma. An Au/PNx/InP tunneling MIS Schottky structure is formed by in-situ multi processes such as H₂ plasma treatment, PH₃ plasma treatment, the deposition of PNx film and Au evaporation. The effective barrier height is remarkably enhanced and estimated to be 0.83 eV. The true barrier height is estimated to be 0.57 eV. This means that the true barrier height approaches the Schottky limit, suggesting that the surface Fermi level pinning is weakened. Effectiveness of the present in-situ processes is demonstrated.

Acknowledgment

The authors are much indebted to Dr. T. Shirakawa of Sumitomo Electric Industries Inc. for supplying InP wafers.

References

- [1] S. Loualiche, A. Ginoudi, H. L'Haridon, M. Salvi, A. Le Corre, D. Lecrosnier and P. N. Favennec: *Appl. Phys. Lett.* **54** (1989) 1238.
- [2] Y. S. Lee and W. A. Anderson: *J. Appl. Phys.* **65** (1989) 4051.
- [3] H. Yamagishi: *Jpn. J. Appl. Phys.* **27** (1988) 997.
- [4] Y. Hirota and T. Kobayashi: *J. Appl. Phys.* **53** (1982) 5037.
- [5] Y. Iwase, F. Arai and T. Sugano: *Appl. Phys. Lett.* **52** (1988) 1437.
- [6] J. L. Leclercq, J. Durand, L. Cot, R. Berjoan and C. Dupuy: *Appl. Sur. Sci.* **59** (1992) 289.
- [7] A. Uda, H. Ito, T. Yamada, T. Sugino and J. Shirafuji: *Proc. Symp. on Dry Process* (1990) 63.
- [8] H. Ninomiya, T. Sugino, K. Matsuda and J. Shirafuji: *Jpn. J. Appl. Phys.* **32** (1993) L12.
- [9] S. Veprek, Z. Iqbal, J. Brunner and M. Scharli: *Philos. Mag.* **B43** (1981) 527.
- [10] J. Shirafuji, M. Kuwagaki, T. Sato and Y. Inuishi: *Jpn. J. Appl. Phys.* **23** (1984) 1278.
- [11] Y. Hirota and O. Mikami: *Thin Solid Films* **162** (1988) 41.
- [12] S. M. Sze: *Physics of Semiconductor Devices* (Wiley-Interscience Publication, New York, 1981) 2nd.ed., p. 245.
- [13] H. B. Michaelson: *J. Appl. Phys.* **48** (1977) 4729.
- [14] M. Neuberger: *III-V Semiconducting Compounds* (Plenum, New York, 1971) p. 110.

Improvement of Resistivity of Phosphorous Nitride Films Deposited at 100°C on InP substrate

Y. Matsumoto, T. Suzuki, K. Haga, H. Sasaki, M. Sakuma, T. Hanajiri and T. Sugano

Department of Electrical Electronic Engineering, Toyo University

2100, Kujirai, Kawagoe, Saitama, 350, Japan

T. Katoda

Department of Electronic Engineering, The University of Tokyo

7-3-1, Hongo, Bunkyo, Tokyo, 113, Japan

Phosphorous nitride (PN) films were deposited on InP as gate-insulator films at 100°C by photon-assisted chemical vapor deposition (PACVD) method using PCl_3 and NH_3 as source gasses, and their electrical and optical properties were investigated.

The electrical leakage resistance of PN films was found to depend on the amount of phosphorous within PN films which was changed by the ratio of source gasses (PCl_3/NH_3). As a result, even at 100°C, PN films with resistivity of about 10^9 - $10^{10} \Omega \text{ cm}$ under high electric field (1MV/cm) were obtained without post deposition annealing by optimizing the source gas ratio.

1. Introduction

Phosphorous Nitride (PN) film is one of the most attractive material as gate insulator of InP MIS devices. An advantage of PN films is that the films are deposited under the over pressure of phosphorous, which is effective to suppress the decomposition of InP substrates. Therefore it is possible to fabricate insulator-InP interface with good properties. Several attempts for deposition of PN films on InP using thermal CVD method have been reported (1), (2), (3). In their work, the density of trap states at PN-InP interface of $10^{11} \text{ eV}^{-1} \text{ cm}^{-2}$ was obtained. The effective electron mobility in those InP MISFETs was not so high as expected but it was found to become higher while the deposition temperature is lowered.

Therefore the PN deposition techniques whose deposition temperatures are lower than those of thermal CVD methods and which hardly damage InP surface must be explored.

The deposition of PN films at about 200°C was reported (4), (5). However their MIS diodes showed poor leakage characteristics and large hysteresis in the C-V characteristics caused by charge trapped in the insulator and consequently post deposition annealing was necessary for improvement of electrical properties of such PN films.

Here, improvement of resistivity of PN films by controlling the deposition rate will be reported.

2. Experimentals

Figure 1 shows the schematic sketch of PACVD chamber. A low pressure mercury lamp ($\lambda = 254 \text{ nm}, 185 \text{ nm}$) was used as a light source for excitation of source gasses.

PCl_3 and NH_3 were used as source gasses. PCl_3 was introduced into the PACVD chamber using H_2 as carrier gas. The quantity of PCl_3 gas was controlled by bubbler temperature and H_2 gas flow rate. The NH_3 and H_2 flow rates were controlled by mass flow controllers.

The NH_3 nozzle was placed near the window and PCl_3 nozzle was placed near the substrate because of the window clouding was suppressed effectively in our system.

Typical experimental conditions are shown in table 1.

Undoped n-type InP wafers with carrier concentration of $4.6 \times 10^{15} \text{ cm}^{-3}$ and (100) surface orientation were used as substrates. Substrates were ultrasonically degreased and then chemically etched with $\text{HCl}:\text{H}_2\text{O}_2:\text{H}_2\text{O} = 4:1:6$ mixture

for two minutes. Then substrates were dipped into $(\text{NH}_4)_2\text{S}_x$ solution at 50°C for 10 minutes, rinsed in $(\text{NH}_4)_2\text{S}_x$ and then in deionized water, and dried by blowing dry N_2 onto them before being placed in PACVD chamber.

Al-PN-InP diodes were used for measurement of electrical properties of PN films. Before PN film deposition, ohmic contact was formed by evaporating Au-Ge on the back surface of the substrate and then by heating it at 350°C for 3 minutes in 5% H_2 forming gas. After PN film deposition, Al electrodes with $1.96 \times 10^{-3} \text{ cm}^2$ in area were formed on the PN film.

Substrate temperature (°C)	100~200
Chamber pressure (Pa)	133
Bubbler temperature (°C)	-50~20
NH_3 flow rate (sccm)	50
H_2 flow rate (sccm)	10
Deposition time (min)	60~120

Table.1 Typical experimental conditions of PN film deposition.

3. Results

3.1 Electrical leakage of PN films

Figure 2 shows the current-voltage (I-V) characteristics of Al-PN-InP diodes whose PN films were deposited at 100°C, with various source gas ratios. I-V curves indicate that the conduction mechanism of PN films deposited by PACVD is Frenkel-Poole emission type similar to that of PN films deposited by thermal CVD method. The leakage current of PN films was found to depend strongly on the ratio of source gasses. When the source gas ratio was 1/38, the leakage current at 1MV/cm² was larger than 10 A/cm², but leakage current became smaller as the gas ratio decreased. In consequence when PN films were deposited at 100°C, the reduction of the gas ratio from 1/38 to 1/3800 obviously improved the electrical leakage property of PN films, and the PN film with resis-

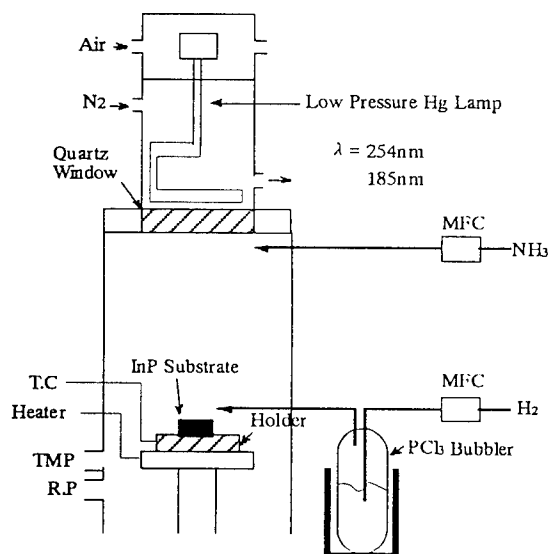


Fig.1 The schematic sketch of PACVD chamber

tivity ranged from 10^9 to $10^{10} \Omega \text{ cm}$ was obtained when the gas ratio was 1/3800.

3.2 Optical properties of PN films

Figure 3 shows XPS spectra of P2p peaks of PN films deposited at 100°C . In order to observe the optical properties of the inside of PN films, all samples were slightly sputter-etched by Ar ions for 2 minutes before XPS analysis.

P2p peaks of PN films can be deconvoluted to two peaks. "P-N" refers to peak at 133.8 eV which is attributed to P-N bonds like those in amorphous PN compounds(6), and "P-N(P-rich)" refers to the peak at 131 eV which is considered to be assigned to P-N bonds in P-rich compounds(6). The height of the P-N(P-rich) peak depended substantially on the source gas ratio. It indicates that the amount of phosphorous which is not nitrized completely is considerably reduced by suppressing the supply of PCl_3 gas when deposition temperature is 100°C .

Figure 4 shows the deposition rate of PN films as function of deposition temperature. When the deposition temperature was 100°C , the deposition rate decreased as the supply of PCl_3 was reduced.

4. Discussion

The close correlation was observed between the electrical properties and the optical properties of PN films deposited at 100°C . It is made clear that the resistivity of PN film changed in accordance with the change of optical properties of PN films. When the source gas ratio of 1/38, the leakage current was significantly large as shown in figure 2, and the P-N(P-rich) peak in XPS spectrum was remarkably stronger as shown in figure 3, than the source gas ratio of 1/3800.

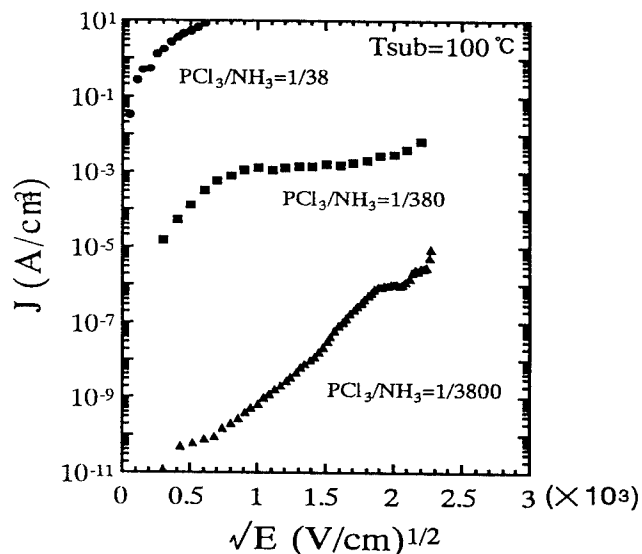


Fig. 2 The current-Voltage (I-V) characteristics of Al-PN-InP diodes whose PN films were deposited at 100°C . E stands for the electric field across PN films. The thickness of PN films was about 1000 \AA for all samples.

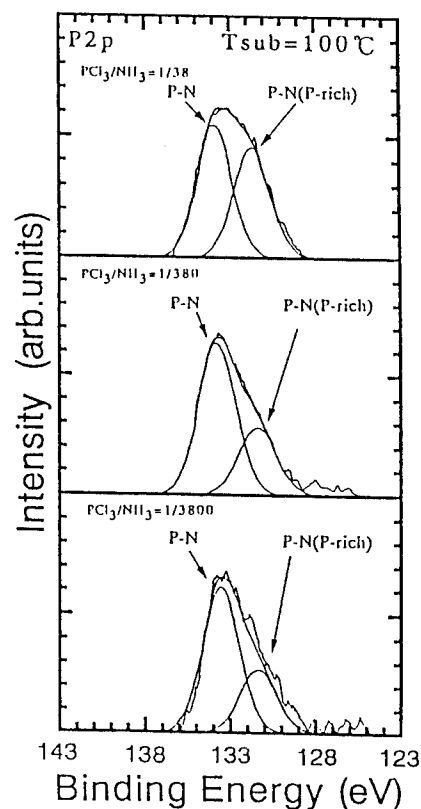


Figure.3 XPS spectra of P2p peaks of PN films deposited at 100°C .

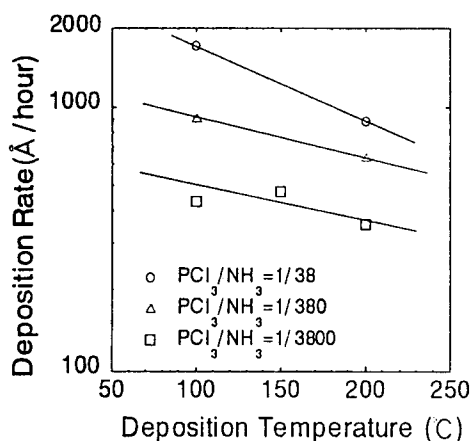


Fig.4 Deposition rate of PN films

We assume that such a change of P-N (P-rich) peak indicates an increase of amount of phosphorous in PN film, and this phosphorous was not nitrized completely.

In our experimental conditions, PCl_3 gas was excited slightly by UV light because the UV light was almost absorbed by NH_3 gas between the UV lamp and InP substrate. Therefore, the deposition process of PN film is thought as follows.

- (1) NH_3 gas is excited by UV light near the window and N-H radicals are generated.
- (2) PCl_3 gas blown onto the InP substrate is heated.
- (3) The heated PCl_3 gas is nitrized by NH_3 radicals.

From the deposition process mentioned above, the synthesis of PN film is considered to be limited by the supply of PCl_3 or adsorbed PCl_3 . In addition, if the deposition temperature is decreasing, the amount of adsorbed PCl_3 is increasing, and consequently, phosphorous rich PN film is formed. The deposition rate shown in figure 4 supports this supposition. Because the deposition rate depends on the source gas ratio at fixed temperature, and this dependence is more remarkable when deposition is 100°C.

Therefore the excess phosphorous which is not nitrized completely must be reduced by suppressing the excess-supply of PCl_3 , particularly when the deposition temperature is relatively low.

5. Conclusion

Electrical and optical properties of PN films deposited at 100°C were investigated. It is found that the electrical resistivity of PN film has a strong correlation with amount of phosphorous within PN films. In addition, the electrical resistivity of PN films becomes higher as the amount of phosphorous within PN films decreases. Even when the deposition temperature is 100°C, PN films with electrical resistivity of about 10^9 to 10^{10} Ω cm under high electric field were obtained

by reducing the source gas ratio from 1/38 to 1/3800 without post deposition annealing.

Acknowledgement

The authors would like to thank Japane Energy Co., LTD for supplying InP wafers and H.Okazaki for helpful discussion.

References

- (1) Y.Hirota and T.Kobayashi, *J.Appl.Phys*, **53**, 5037 (1982)
- (2) Y.Iwase, F.Arai, and T.Sugano, *Appl.Phys.Lett*, **52**, 1437 (1988)
- (3) O.Mikami, MOkamura, E.Yamaguchi, Y.Hirota and Y.Furukawa, *Jpn.J.Appl.Phys*, **23**, 1408 (1984)
- (4) Y.Hirota, and O.mikami, *Electro.Lett*, **21**, 78 (1985)
- (5) Y.H.Jeong, J.H.Lee, Y.H.Bae and Y.T.Hong, *Appl.Phys.Lett*, **57**, 2680, (1990)
- (6) C.D.Wagner, W.M.Rings, L.E.Davis, J.F.Moulder, *Handbook of X-Ray Photoelectron Spectroscopy*, edited by G.E.Muilenberg, (Perkin-Elmer corp, 1979) P.56

Focused Ion Beam Implantation-Induced Disorder in InGaAsP MQW Heterostructures

B.B.Elenkrig, J.Yang, D.T.Cassidy, D.M.Bruce, B.Lakshmi and G.Champion¹

Department of Engineering Physics, McMaster University, Hamilton, Ontario, Canada L8S 4L7
Institute of Microstructural Sciences, National Research Council of Canada, Ottawa, Canada¹

Results of an investigation of the effects of focused ion beam (FIB) implantation - induced intermixing of an InGaAsP-based multiple quantum well (MQW) structure on the room temperature photoluminescence (PL) are presented. The technique of spatially, spectrally and polarization resolved PL was used to study the process of QWs intermixing by Si^+ , Be^+ and B^+ . It was found that implantation in a narrow (about 100 nm) line leads to an enhancement of PL yield. A qualitative explanation for this enhancement is given in terms of spatial bandstructure bending due to a doping effect in a narrow region.

1. Introduction

For the last decade much attention has been paid to optoelectronic devices that utilize in their active regions structures with reduced dimensionality, such as quantum wells (QW), quantum wires (QWR), and even quantum dots (QD). The use of such structures provides the opportunity for bandstructure engineering and thus for control of device properties. Today one can hardly find modern, commercially available high-performance semiconductor lasers that are not based on QW structures. Fabrication of QW structures by using contemporary growing processes such as molecular beam epitaxy (MBE) and metalorganic chemical vapor deposition (MOCVD) has become fairly routine in modern semiconductor technology. Nevertheless, there currently exist just a few options to control the lateral parameters of QWs with a resolution less than 100 nm, which is necessary for providing lateral confinement of carriers. Ion implantation - induced disordering (IIID) is considered one of the promising processes [1]. IIID is a technique for increasing the bandgap of the original QW structure by intermixing the wells with the barriers. In the process, impurities and damage are introduced into the structure by ion implantation. Interdiffusion takes place during a postimplantation thermal annealing step. With the IIID process both the bandgap and the refractive index are modified and this provides one with a route to tailor the electronic and the optical properties of QW structures. Moreover, the composition changes that result from intermixing lead to a lattice mismatch in InP based heterostructures, and hence strain modification [1, 2]. This adds one more positive aspect to the process.

Despite some success achieved in the implementation of the IIID process for modification of the characteristics of lasers [1], the usefulness of this

process for fabrication of lasers is however seriously undermined by the fact that residual defects (after annealing) create centers for nonradiative recombination, and thus substantially reduce optical gain. Usually a dramatic reduction of the PL yield from the implanted part of the QW structure is observed. This is the reason why little success has been achieved in the modification of laser properties by implantation - induced intermixing of QWs directly in the active area of lasers [1]. It has been shown [3,4] that the lateral confinement that is produced by implantation of narrow (less than 100 nm) lines or dots using a narrow mask [3] or FIB [4] instead of a masked solid implantation results in a desirable change of the bandgap and refractive index without a dramatic reduction of the optical gain. A study of the optical properties of FIB implantation induced intermixing in strained layers InGaAsP MQW structures, using a technique of spatially, spectrally and polarization resolved photoluminescence (SPPL) [4,5], showed the possibility to control the efficiency of recombination. It was suggested in [4] that the observed effect of PL enhancement from a Si^+ FIB implanted area could be understood through the creation of a narrow n-type doped region and concomitant spatial bending of bandstructure. This bending causes creation of the well in the conduction band with an enhanced number of electrons in it and a barrier in valence band with holes located outside the implanted region. To observe PL yield enhancement one must pump holes into the barrier region to increase the rate of recombination. Since lateral diffusivity of holes and electrons are substantially different the investigation of this effect for the case of p-type doping becomes an interesting issue.

This work is concerned with the further study of the use of FIB implantation of Si^+ (n-type), Be^+

(p-type) and B^+ (neutral) ions to verify the possibility of effective spatial bandstructure modification without dramatic deterioration of material quality.

2. Experimental

A lattice matched quaternary InGaAsP structure containing three 5.5 nm QWs with 10 nm barriers and etched down to the etch-stop layer [4] was used for Si^+ , Be^+ and B^+ implantation at energies of 100 keV; this energy is sufficient for ions to penetrate into the QW area. The doses for all type of ions varied from 10^{13} to 10^{14} cm $^{-2}$. Implantation was accomplished using the JIBL-104 UHV FIB facility at the Institute for Microstructural Sciences at the National Research Council of Canada. Rapid thermal annealing (RTA) at 750°C for 30 s followed the implantation. A pattern consisting of six areas: one area was created with solid implantation (25 nm step at an ion beam diameter on the order of 100nm), and the other with lines, separated by 0.25 μ m, 0.5 μ m, 1 μ m, 2 μ m and 4 μ m was used for implantation (Fig.1).

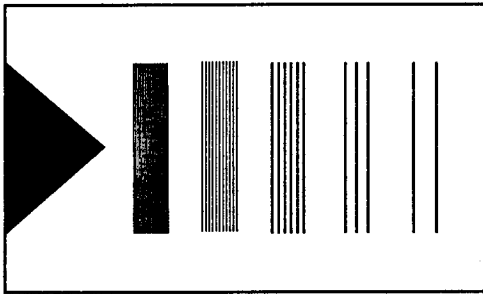


Fig.1 The 2-D pattern of implantation.

This pattern was designed to analyze the effect of lateral ion straggling on the minimum achievable distance between adjacent implantations where the area between them remains unimplanted.

The implantation induced pattern was investigated by measurement of the room temperature PL. The technique for spatially resolved measurements of the PL yield, degree of polarization (DOP), and mean wavelength shift of the PL was proposed, described and used in [4,5]. Light from the QW area (1.31 μ m) was collected by an InGaAs - photodetector. To ensure that there was no influence of luminescence from material adjacent to the MQW with shorter PL wavelength, a 1.1 μ m filter the same as in [4] was used.

3. Results and Discussion

The SPPL technique permits measurement of 2D patterns of DOP, spectrum and PL yield with a spatial resolution of $\sim 1\mu$ m. Since it is difficult to obtain information from the maps of the DOP and spectral shift when reproduced in black and white (color pictures are not available for publication in this Proceedings), attention will be focused on the analysis of PL yield study. The results of the study of DOP and spectral patterns, which give some insight in the process of interdiffusion in InP-based QW heterostructures [4] will be published and discussed elsewhere.

The measured patterns of PL yield from Si^+ , Be^+ and B^+ implanted patterns for doses of 10^{13} cm $^{-2}$ are represented by gray scale in Fig.2. In these images,

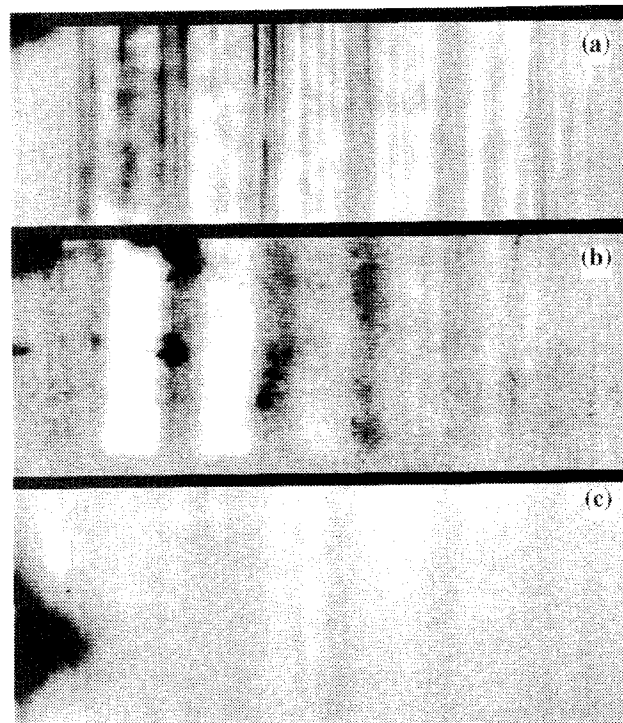


Fig.2. PL yield pattern for Si^+ (a), Be^+ (b) and B^+ (c) implanted regions.

gray represents the background PL yield from the unimplanted region, black regions represent lower PL yield, while lighter colored regions represent higher PL yield as compared to the unimplanted regions. The

reduction of PL intensity in regions with solid implantation is usually observed [1, 2, 4, part of triangle in the maps of Fig.2 in this work] and is explained through the existence of residual centers of nonradiative recombination. The implantation by narrow lines shows an enhancement of PL intensity for patterns with Si⁺ and Be⁺ implantation (Fig.2 a,b). In [4] we have discussed an enhancement of PL yield for Si⁺ - implanted patterns. Since QW intermixing process by FIB leads to a bandgap increase which is confirmed by the blue-shift of the PL spectrum one should expect formation of a lateral quantum barrier, rather than a lateral quantum well, as is necessary for QWR formation. Thus the origin of the observed enhancement is not clear. One possible explanation for this effect, given in [4], is bending of the bandstructure due to n-type doping and the creation of a well for electrons and a barrier for holes. It was pointed out that to observe a PL enhancement one has to pump into the barrier region a certain number of holes to increase the recombination rate. It was also suggested that in this case lateral diffusion length of the holes (i.e. the minority carriers) has to be greater than the width of the barrier. This implies that the conditions for p-type doping should differ from ones for n-type doping because of the different diffusion coefficients for holes and electrons. It means that the effect of PL enhancement with implanted Be⁺, which provides p-type doping must be, generally speaking, more pronounced than for Si⁺, due to greater diffusion length for electrons than that for holes. B⁺, as a neutral ion should not cause any PL enhancement. From Fig.2 (c), one can see that Be⁺-implanted pattern does not result in any substantial enhancement or reduction of PL yield from implanted lines. One can observe reduction of PL intensity with an increase of implanted doses or where solid implantation takes place. If the description of the PL enhancement in terms of a spatial doping effect is correct, it just means that B⁺ is, as it has been expected a neutral ion in InGaAsP.

Implanted Dosage (cm ⁻²)						
10E13		5x10E13		10E14		
	$\Delta\lambda$ (nm)	DOP (%)	$\Delta\lambda$ (nm)	DOP (%)	$\Delta\lambda$ (nm)	DOP (%)
Si	31.5	3.26	-	-	23.6	4.38
Be	6.79	1.348	29.4	3.55	37.6	3.54
B	13.1	3.11	29.2	5.8	-5.1	6.07

Table 1.

The results for spectral shift and DOP (the DOP results display an anisotropy which may be related to strain [4]) for all types of implanted ions are presented in Table 1. It can be seen from these data

that the IID process causes a blue -shift for all types of implanted ions. Just B⁺ implantation with a dose higher than $5 \times 10^{13} \text{ cm}^{-2}$ results in a red shift, which is probably because of a strong nonlinear dependence of the group III and group V diffusion coefficients as a function of B⁺ - doses. The DOP data show a change of the composition of wells toward compression (assuming that anisotropy in DOP is caused by strain) for all types of implanted ions and doses. More detailed analyzes of IID related changes of composition and anisotropy in strained layer MQW structures will be published elsewhere.

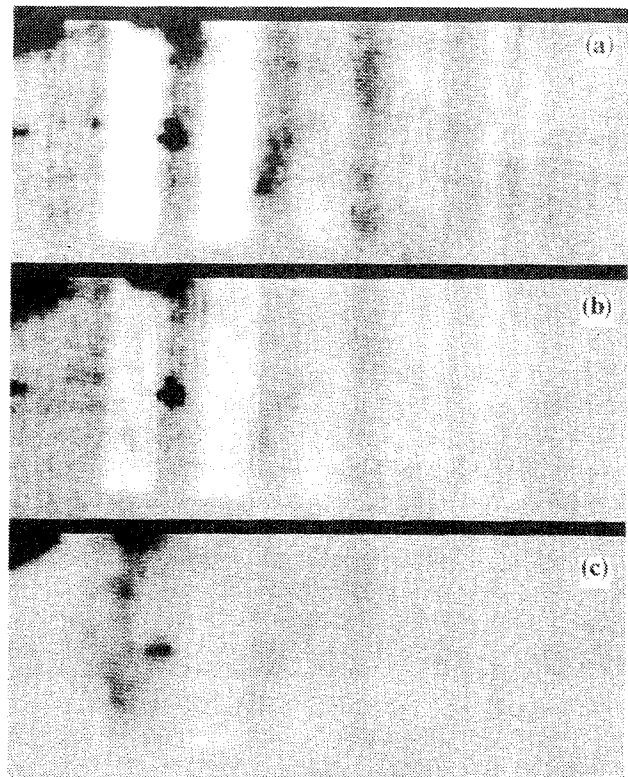


Fig.3 The PL yield pattern for Be⁺ implanted area at different pumping power: P_b = 0.67 Pa; P_c = 0.26 Pa.

Note that a PL enhancement effect can only be observed if it overcomes losses caused by centers of nonradiative recombination, created as a result of implantation. Since a PL intensity enhancement effect is observed in the region with the highest density of implanted lines (spacing between lines 0.25 μm), this could be considered as proof of the existence even at this small spacing of the spatial profile of the bandstructure, necessary for achievement of a PL enhancement effect. To observe enhancement of PL however, one must produce in the implanted area a

number of minority carriers greater than the number of minority carriers in the unimplanted area. This can be realized at certain pumping power. In Fig.3 the results of the measurements of Be^+ - implanted patterns at different pumping powers are presented. From Fig.3 one can see that a reduction of the pumping power leads to a reduction of the contrast between implanted and unimplanted area and even diminishing of the PL enhancement effect in the regions with closely spaced implanted lines. This result supports the proposed explanation of the effect of PL enhancement since it shows that the rate of recombination of carriers and corresponding radiation intensity from implanted area (with the blue-shifted energy) increases faster with pumping power than PL intensity from the unimplanted area.

4. Conclusions

In this work the effect of ion implantation induced intermixing in a narrow area, realized by FIB, has been investigated by using a room temperature PL mapping technique. By implantation of Si^+ , Be^+ and B^+ ions into a InGaAsP MQW heterostructure the effect of PL enhancement from narrow (100 nm) implanted lines was observed and explained through the local bandstructure spatial bending, caused by doping of the material. It was also shown that PL enhancement effect can be observed when the spacing between implanted lines is as small as 0.25 μm . These results suggest opportunities for implementation of

implantation in a narrow regions instead of solid ones for modification of the properties of optoelectronic devices.

5. Acknowledgments

The work of BBE is supported by Bell Northern Research Ltd. He would like to thank Professor J.G. Simmons, Professor D.A. Thompson and Dr. B.J. Robinson for useful discussions.

6. References

1. J.H.Marsh, Semiconductor Science & Technology, **8**, 1993, pp. 1136 -1155
2. B.B. Elenkrig, D.A.Thompson, J.G.Simmons, D.M.Bruce, Y.Si, J.Zhao, J.D.Evans and I.M.Templeton, Appl. Phys. Lett., **65**, 1994, pp. 1239-1241
3. H. Leier, A. Forchel, B.E. Maile, G. Mayer and J. Hommel Appl. Phys. Lett., **56**, (1), 1 January 1990, pp. 48-50
4. J.Yang, B.B. Elenkrig, D.T. Cassidy, D.M. Bruce and I.M. Templeton., Semiconductor Science & Technology, to be published in 1995.
5. J. Yang and D.T. Cassidy, to be published in Appl.Optics, 1995.

Characterization of Semiconducting Thin Films on InP for Magneto-Optical Applications

B.J. Stadler, A. Davis, E.A. Martin, K. Vaccaro, H.M. Dauplaise,

L.O. Bouthillette, S.M. Spaziani, and J.P. Lorenzo

USAF Rome Laboratory, Photonic Components Branch, Hanscom Air Force Base, MA 01731 USA

G. Ramseyer

USAF Rome Laboratory, Reliability Physics Branch, Griffiss Air Force Base, NY 13441 USA

We have investigated the properties of thin film magneto-optical materials grown in the III-V materials system. These materials can be used to expand the functionality of InP opto-electronic integrated circuits (OEIC). Magneto-optical (MO) materials possess unique properties which have already found applicability (in bulk form) in optical systems such as isolators, waveguides, and switches. The materials in this study are epitaxial InGaAs, InGaAsP, and InP films lattice-matched to InP substrates. These films were doped with Mn or Eu with concentrations of 1.3×10^{20} and $1.5 \times 10^{20} \text{ cm}^{-3}$, respectively. The optical and electrical properties of these films agree with expected values, and they show promise for MO applications. In addition, waveguiding has been achieved in InGaAsP films.

Introduction

There are several well known magneto-optical effects, including the Zeeman, Faraday, Kerr, Voigt, and Cotton-Mouton effects. Of these, Faraday rotation has found the most applications in device technology. The Faraday effect involves the rotation of the plane of polarization of light propagating through a material parallel to an applied magnetic field. Along with the applications mentioned above,^[1-3] Faraday rotators have also been used as magnetic and electric field sensors,^[4] optical data storage media,^[5] and spatial light modulators.^[6]

Faraday rotation occurs in a medium when the refractive indices of left- and right-circularly polarized light are unequal. This inequality is due to the splitting of the ground or excited state of a resonant excitation caused by an applied magnetic field. Faraday rotation is therefore strongest near resonant absorption peaks, but it is useful at other wavelengths, as well.

For materials with large absorption coefficients, the Kerr effect can be used to measure rotation upon reflection.^[7] However, in this project, it is our goal to develop materials for use in transmission, as well as reflection.

Other thin film work on MO materials has focused largely on ceramics, such as YIG,^[8] and glasses,^[4] which require substrates and/or growth temperatures that are incompatible with semiconductor processing.^[2] Dilute II-VI semiconductors, like CdMnTe, have also been investigated, both in bulk^[9] and thin film^[10] forms. However, they are not lattice matched to InP. InP substrates are important for eventual integration with other infrared photonic devices, such as laser diodes, operating at the communication wavelengths of 1.3 and 1.5 μm . Magneto-optical properties of III-V materials have been studied for theoretical purposes, and they are sometimes used in the characterization of these materials. However, to our knowledge, this is the first study of thin films of these materials for possible device applications.

In the present study, III-V thin films are doped with transition metals or rare earth elements and characterized. Transition metals, especially Mn, have shown promising MO properties in II-VI semiconductor hosts.^[9] Faraday rotations by rare earth elements, arising from $4f^n \rightarrow 4f^{n-1} 5d$ transitions, also have potential for MO applications. Divalent rare earth ions, such as Eu^{2+} are especially attractive because their $5d$ bands occur at lower energies than those of the trivalent rare earth ions.

Table I- Liquid Phase Epitaxial Growth Conditions

Material*:	IGA	IP	IGAP	MIGA	MIP	EIGA	EIP
Amts in melt: InAs (wt %)	4.20	0	6.24	4.20	0	4.20	0
GaAs (wt %)	2.70	0	1.36	2.70	0	2.70	0
InP (wt %)	0	xs	xs	0	xs	0	xs
Saturation Temperature (°C)	635	645	675	635	645	645	645
Intermediate Temperature (°C)	625	635	645	625	634	635	635
Growth Temperature (°C)	619-625	615-629	635	613-620	615-625	621-625	615-625
Growth Time (min)	0.25-1.5	10.0	5.0	0.25-1.5	10.0	0.5-1.0	10.0

* I- In, G- Ga, A- As, P- P, M- Mn dopant, E- Eu dopant. (xs- excess)

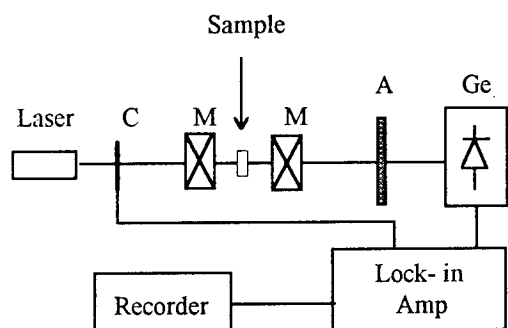


Fig. 1- Schematic of apparatus used to measure Faraday rotation. L=laser, C=chopper, M=magnet, A=analyzer, Ge= photodiode.

Experimental

$\text{In}_{0.53}\text{Ga}_{0.47}\text{As}$, InP or InGaAsP thin films were grown on semi-insulating Fe-doped (100) InP substrates by standard LPE techniques (see Table I). The solvent and main constituent of the melts was indium. Rare earth elements or transition metal dopants (~ 0.1 wt%) were added to the melts; subsequently grown films were characterized.

A small region of each film was preferentially etched away to allow thickness profile to be measured. InGaAs and InGaAsP films were etched with HNO_3 , and InP films were etched electrochemically in a methanol: HCl : HNO_3 (100:3.5:2.4) etch. The lattice parameters were measured via double crystal x-ray diffraction (DCXRD). Carrier concentrations and mobilities were measured by a Hall/van der Pauw technique, both at room temperature (RT) and at 77K. Mn and Eu concentrations were measured by atomic absorption spectroscopy (AAS) and inductively-coupled plasma mass spectroscopy (ICPMS), respectively. Secondary ion mass spectroscopy (SIMS) was used to study the depth profile of the films' chemical composition. Energy dispersive spectroscopy (EDS) was used to estimate the composition of the InGaAsP films.

The optical properties of the films were characterized by standard techniques. Ellipsometry was used to measure the refractive indices. The absorption

spectra were measured by visible/near infrared (VIS/NIR) and Fourier transform infrared (FTIR) spectrometers. The absorption edges of the films were observed with these spectra and confirmed by photoluminescence (PL).

Faraday rotation was measured using the experimental apparatus depicted schematically in Fig. 1. Collimated, polarized light was transmitted normally through the sample, which was mounted in an electromagnet. The output signal was passed through an analyzer (a rotating polarizer) before being focused onto a Ge photodiode. When the analyzer was oriented at 45° , the derivative of the intensity with respect to the modulation angle was at a maximum. This can be expressed by the modulation index,^[8]

$$(1/I)(\delta I / \delta \theta) = 1.15 \% / \text{deg}$$

which is valid for small optical rotations. The magnet was supplied with either direct or alternating current for observation of the maximum field (up to 1450 gauss) and the average change in intensity due to polarization rotation within the sample.

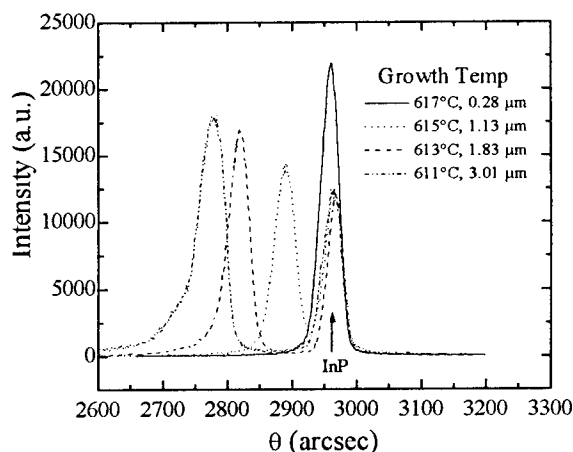


Fig. 2- DCXRD spectra of InGaAs films grown to various thicknesses.

Table II- Properties of Films

Films Type*	IGA	IP	IGAP	MIGA	MIP	EIGA	EIP
Thickness (μm)	0.2-4.28	1.73-4.25	0.52	0.69-3.01	1.70-2.10	2.23-4.84	1.68-2.57
Carrier Type	n	n	n	p	SI	n	n
Ave. RT Carrier Conc. (cm^{-3})	3×10^{17}	2×10^{17}	8×10^{16}	3×10^{18}	SI	5×10^{16}	4×10^{16}
Ave. RT Mobility (cm^2/Vs)	5600	2900	2600	75	SI	7200	3200
Ave. Refractive Index (632.8 nm)	3.725	3.381	3.618	3.728	3.330	3.758	3.448
Absorption Edge (μm)	1.645	0.924	1.298	1.645	0.924	1.645	0.924

* I- In, G- Ga, A- As, P- P, M- Mn dopant, E- Eu dopant.

Results

Measured properties of experimental films are tabulated in Table II. The InGaAs films were found to be lattice matched to the InP substrates, although a lattice mismatch up to + 0.1% was attained by growing at the slightly lower temperatures required to fabricate thicker films (3-5 μ m), see Figure 2. The increase in the lattice constant is probably due to a change in the In:Ga stoichiometry. The composition of the $\text{In}_{1-x}\text{Ga}_x\text{As}_y\text{P}_{1-y}$ films was found by EDS to be $x \sim 0.177$ and $y \sim 0.391$.

The carrier concentrations and mobilities of undoped films indicate that unintentional *n*-type dopants are present. Eu doping led to a decrease in the carrier concentrations, and therefore an increase in mobilities, in both InGaAs and InP films due to gettering effects.^[11] Mn-doped InGaAs films were *p*-type due to the Mn^{2+} state,^[12] and the hole mobilities were low, as expected. Only the Mn-doped InGaAs films had electrical properties that varied with temperature. Mn is a deep-level impurity, as are most transition metals, so the carrier concentration and mobility decrease with decreasing temperature (77K: $p=5 \times 10^{16} \text{ cm}^{-3}$, $\mu_p=40 \text{ cm}^2/\text{Vs}$). The Mn:InP films were semi-insulating which indicates that the Mn levels are deeper in the band gap of InP than that of InGaAs.

Mn concentrations were found by AAS to be ~ 2300 ppm in the InGaAs films when 0.1 wt% Mn was added to the melts. With similar Eu additions to different melts, Eu concentrations in the InGaAs films were found to be ~ 7300 ppm by ICPMS. These values correspond to concentrations of 1.3×10^{20} and $1.5 \times 10^{20} \text{ cm}^{-3}$, respectively. In comparing the Mn concentrations to the hole concentrations in the Mn-doped films, it appears that not all of the Mn ions are electrically active; that is, some Mn^{3+} ions or complexes may be present. The same argument indicates that the Eu must be in the trivalent state. The SIMS data, Fig. 3, shows that the depth profiles were homogeneous, both with respect to the host constituents and the Mn dopants. However, the Eu was somewhat segregated to the surface of the film.

The refractive index of the InGaAs films increased slightly with Eu-doping, but was relatively unaffected by Mn-doping, see Table II. The index of the InP films also increased with Eu-doping, but decreased with Mn-doping. Heavy ions are often used to increase the refractive index of materials, such as in Pb-doped glasses. Mn is fairly close to Ga in atomic mass, but it is lighter than In. Therefore, it will decrease the index of InP and not that of InGaAs. Eu is heavier than any of the host constituents, and therefore it causes an increase in the refractive index of both hosts.

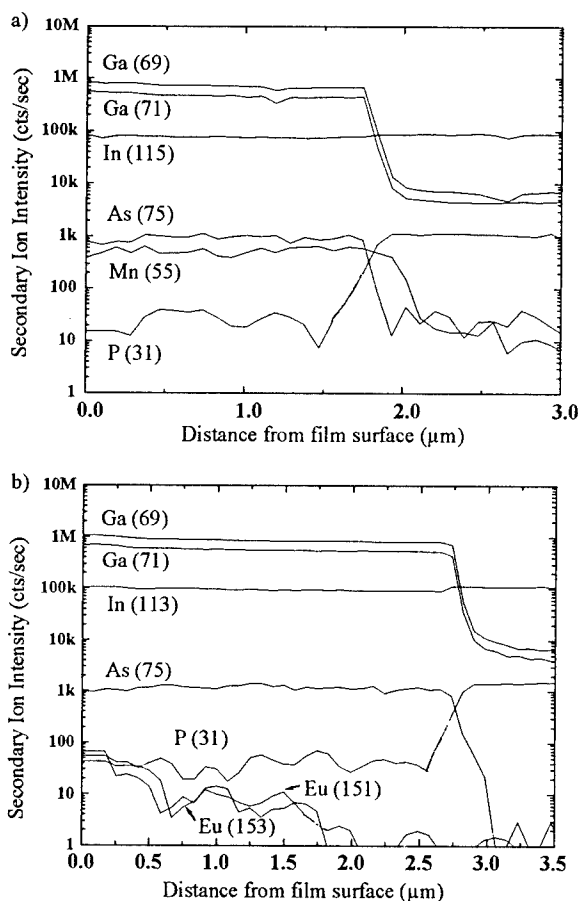


Fig. 3-SIMS spectra of a) Mn:InGaAs film b) Eu:InGaAs film.

The absorption edges of the films were similar to bulk values, and they were not noticeably varied by the addition of dopants. The band edge was seen in the absorption and photoluminescence (PL) spectra as shown in Fig. 4. It should also be noted that no additional absorption peaks were observed with the VIS/NIR or FTIR spectrometers for Mn or Er doped films.

Discussion

It is well known^[13,14] that it is difficult to dope InP with transition metals via liquid phase techniques. This is because transition metal phosphides precipitate out of the melt unless very high temperatures are used. Therefore, our first films were InGaAs films that were prepared undoped as well as with Mn or Eu doping. As reported in the literature, we found that Mn doping lowered the growth temperatures required for film fabrication. However, the absorption edge of these films was located at $1.645 \mu\text{m}$ so that measurements of Faraday rotation in the $1.0\text{-}1.55 \mu\text{m}$ region were not possible. But, measurements of the Kerr effect indicated that these films possessed magneto-optical properties.

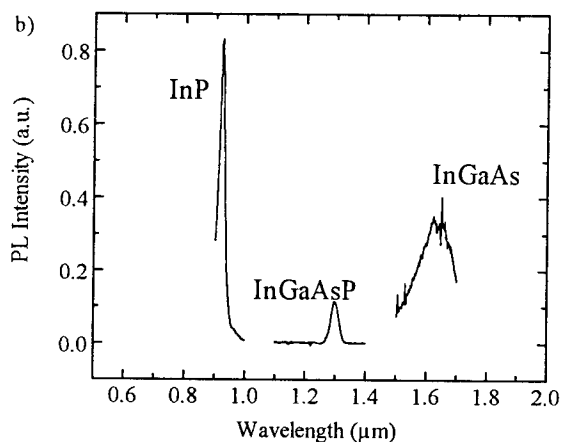
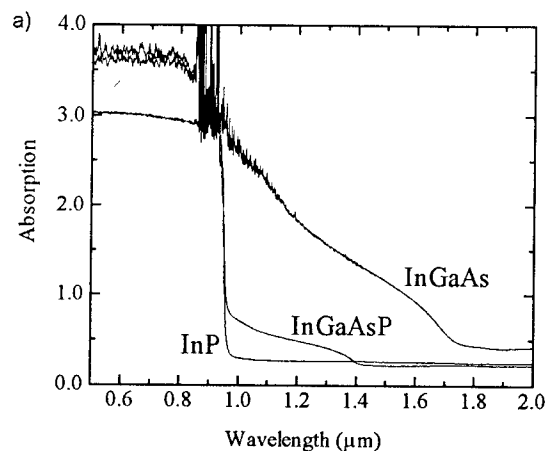


Fig. 4- a) Absorption spectra and b) PL spectra of films.

Next, InP films were prepared, both without dopants and with transition metal or rare earth dopants. The absorption edge of these films was at $0.9238\mu\text{m}$ which allowed measurements at $1.06\mu\text{m}$, $1.3\mu\text{m}$ and $1.55\mu\text{m}$. In our measurements, the Faraday effect was measured with the light transmitted perpendicular to the plane of the film. Therefore, the path length was short, so the Faraday rotation was very small. These effects were obscured by the substrate signal because the substrate had a Faraday effect due to the Fe doping. As mentioned above, Faraday rotation is stronger near a resonant absorption. Therefore, the rotation increases near the absorption edge of the material. This effect was also difficult to see in our samples because the absorption edge of the substrate is the same as that of the film. Therefore, a waveguiding orientation must be adopted. However, the indices of the rare earth-doped films were not substantially higher than those of the substrates, and waveguiding could not be achieved.



Fig. 5- End view of waveguiding at $1.3\mu\text{m}$ in InGaAsP film.

InGaAsP films were fabricated which have refractive indices of 3.618. These films were engineered to have absorption edges at approximately $1.3\mu\text{m}$ so that the absorption edge effects on the Faraday rotation could be exploited. Waveguiding was achieved in these films at $1.3\mu\text{m}$, Fig. 5, and Faraday rotation measurements are in progress.

Conclusion

Both undoped and doped InGaAs, InP and InGaAsP films have been fabricated. Mn concentrations of 1.3×10^{20} and Eu concentrations of $1.5 \times 10^{20} \text{ cm}^{-3}$ were attained. These films have been characterized to better understand their potential to exhibit magneto-optical properties. Initial magneto-optical measurements indicate that these materials will be of interest for magneto-optical applications.

References

- [1] K. Matsuda, H. Minemoto, O. Kamada, S. Ishizuka, *Appl. Opt.* **27** 329 (1989).
- [2] K. Matsuda and S. Ishizuka, *Appl. Opt.* **30** 1963 (1991).
- [3] M. Shirsaki, H. Nakajima, T. Obokata, K. Asama, *Appl. Opt.* **23** 4229 (1982).
- [4] S. Donati, V. Annovazzi-Lodi, T. Tambosso, *IEEE Proc.* **135** [J5] 372 (1988).
- [5] T. Suzuki, C. Lin, A. Bell, *IEEE Trans. Magnet.* **24** 2452 (1988).
- [6] N. Farhat and Z. Shae, *Appl. Opt.* **28** 4792 (1989).
- [7] T. Cheeks, M. Brasil, J. Boeck, J. Harbison, T. Sands, M. Tanaka, A. Scherer, V. Keramidas, *J. Appl. Phys.* **73** 6121 (1993).
- [8] D. Gualtieri, *J. Appl. Phys.* **67** 4793 (1990).
- [9] J. Gaj, R. Gatazka, M. Nawrocki, *Sol. State Commun.* **25** 193 (1978).
- [10] K. Guergouri, M. Ferah, R. Triboulet, Y. Marfaing, *J. Cryst. Growth* **139** 6 (1994).
- [11] A. Davis, H. Dauplaise, J. Lorenzo, G. Ramseyer, J. Horrigan, *Rare Earth Doped Semiconductors*, *MRS Proc.* **301** 151 (1992).
- [12] K. Huang and B. Wessels, *J. Appl. Phys.* **67** 6882 (1990).
- [13] M. Kondo, M. Sugawara, T. Tanahashi, S. Isozumi, K. Nakajima, *Appl. Phys. Lett.* **53** 574 (1988).
- [14] D. Knight and W. Benyon, *J. Cryst Growth* **102** 249 (1990).

Fabrication of InP-Based Quantum-Wires and Its Application to Lasers

Shigehisa ARAI, Munehisa TAMURA, Ki-Chul SHIN, and Shigeo TAMURA

Research Center for Quantum Effect Electronics

Tokyo Institute of Technology

2-12-1 O-okayama, Meguro-ku, Tokyo 152, Japan

Phone: +81-3-5734-2512 Fax: +81-3-5734-2907

Abstract: Fabrication technologies of GaInAs(P)/InP long-wavelength lasers consisting of quantum-wire active region are investigated. A combination of an electron-beam (EB) lithography, a fine-pattern etching, and succeeding OMVPE regrowth became more or less reliable process, that was confirmed through a low threshold current room-temperature CW operation of strained quasi-quantum-wire lasers. Measurements of photoluminescence (PL) intensity dependence on etched wire width revealed a low-damage property of electron-cyclotron-resonance reactive-ion-beam-etching (ECR-RIBE) with Cl_2 gas by applying negative acceleration voltage to the sample. An introduction of a surface cleaning process with H_2 gas just after the Cl_2 ECR-RIBE was found to be effective for further reduction of damage especially for the wire width from 10 to 40nm.

1. Introduction

Low-dimensional quantum-well structures such as quantum-wire and quantum-box structures are very promising for future optical devices because of their superior optical properties[1]–[4], which will be very attractive for realizing lasers with an extremely low threshold current and a narrow linewidth property. Moreover they can provide optical amplifiers with low noise property[5] or compact optical modulators and switches[6]. An adoption of strained quantum-well structures has been demonstrated to be very effective for high performance operation of lasers because hole states unwanted to the laser mode can be eliminated[7],[8]. Then low-dimensional strained quantum-well structures became very attractive and a possibility of an extremely low threshold current operation was predicted[9],[10].

In order to realize such high performance lasers, we have been investigating fabrication process by combining an ultra-fine lithography (patterning and etching) and 2-step OMVPE growth, since the etching and regrowth conditions can be systematically investigated and this procedure can be applied to fabrication of not only quantum-wire structures but also quantum-box structures.

In this paper, we report operation properties of GaInAs/InP quasi-quantum-wire lasers fabricated by adopting a wet-chemical etching, then a low-damage etching property of ECR-RIBE with Cl_2 gas will be presented.

2. GaInAs/InP Quasi-Quantum-Wire Lasers

2.1 Fabrication Process with Wet-Etching

A fabrication process of GaInAs/InP quasi-

quantum-wire lasers employed in our experiments is shown in Fig.1. First, an original DH wafer consisting of multiple-quantum-film (MQF) structure with a thin InP top layer (3–5nm) was grown on (100) p-InP substrate by OMVPE growth. After depositing 20–30nm thick SiO_2 mask, a periodic wire pattern was transferred to a part of the wafer ($20\mu\text{m} \times 3.5\text{mm}$ block, 10blocks with the interval of $600\mu\text{m}$) by an EBX system. A line dose condition was typically 1.3nC/cm for the grating period of 70–100nm for 30nm thick PMMA resist. After etching the SiO_2 mask, wet-chemical etching was done with 40ppm (volume ratio) Br-methanol.

Then the wafer underwent the regrowth process, where a thin (3nm) n-InP cover layer, n-GaInAsP optical confinement layer (OCL), and n-InP cladding layer were successively grown. A BH structure with the active region width of $2\mu\text{m}$ was fabricated by an LPE growth, where the stripe was formed in the direction perpendicular to the wire direction. The period of the BH stripe pattern was set at $300\mu\text{m}$ so as to obtain quantum-film lasers from the same wafer for comparison with quantum-wire lasers.

2.2 Operation Properties

Figure 2 shows a schematic structure of BH quasi-quantum-wire lasers. Three types of quasi-quantum-wire lasers, i.e. lattice-matched multiple-quantum-wire (LM-MQW), compressively-strained (CS)-MQW, and tensile-strained single-quantum-wire (TS-SQW) lasers, were fabricated[11]–[13]. The well thickness W_w , the wire width W_x , the period Λ , the optical confinement factor of the active region ξ , the cavity length L , threshold current and the

density I_{th} and J_{th} are summarized in Table 1.

Room temperature CW operation was obtained with all these samples. The threshold current of the LM-MQW laser was 3–4 times higher than that of quantum-film lasers obtained from the same wafer, while that of CS-MQW and TS-SQW lasers was only 2 times higher. This fact may be due to a poor optical confinement factor and broad gain spectrum of the LM-MQW laser.

Figure 3 shows temperature dependences of threshold current and differential quantum efficiency of the TS-SQW laser and those of quantum-film lasers made on the same wafer [14]. A steep increase in threshold current and a rapid decrease in the differential quantum efficiency may be attributed to inter valence band absorption (IVBA) and Auger recombination. Since these non-radiative processes strongly depend on operation carrier density, poorer characteristics of the quasi-quantum-wire laser is considered to be due to lower optical confinement factor of the active region.

Actually the differential quantum efficiency of the TS-SQF laser was very high and was almost constant at a temperature below 230K. This fact indicates that the waveguide loss of the TS-SQF laser was very low at low temperature and its rapid increase with the temperature may be due to IVBA and free carrier absorption not only in the active layer but also in GaInAsP OCLs. Since there was no observable difference in temperature dependence of the spontaneous emission slope efficiency, there is no severe non-radiative recombination centers in the TS-SQW laser [14]. Similar results were obtained for the CS-MQF and CS-MQW lasers. Hence we can expect much better performance when the threshold carrier density is reduced by increasing the optical confinement factor of the quantum-wire.

3. ECR-RIBE for GaInAs/InP Quantum-Wire

An electron cyclotron resonance reactive ion beam etching (ECR-RIBE) by using Cl_2 gas is one of the most effective method to fabricate uniform MQW and MQB structures. A low-damage and vertical etching was achieved with further reduced ion acceleration energy by applying negative bias voltage $-50V$ to the sample, where a low etching gas pressure (5×10^{-6} Torr) was used. A comparison with wet-chemical etching was done by making a larger size wire structure (200nm–2 μ m) and measuring PL intensity dependence on the wire width, as explained in section 3.1. Then PL intensity dependence of much narrow wire structure (16–40nm) will be given in section 3.2.

3.1 Comparison with Wet-Chemical Etching

First, we measured the PL intensity dependence on the width of GaInAs/GaInAsP/InP wire structures for the wire width between 200nm and 2 μ m and compared with that of wet-chemical etching. As the result, PL intensities of wire structures fabricated by dry etching were almost the same to those by wet chemical etching.

In this experiment, we prepared wafers which consisted of a n-InP buffer layer (3 μ m thick), an i-GaInAsP step-index OCL (200nm thick, $\lambda_g=1.15\mu$ m), lattice-matched i-GaInAs (5nm thick, active layer) / GaInAsP (8nm thick, $\lambda_g=1.15\mu$ m) single-quantum-film (SQF) layer, and an i-InP top layer (10nm thick) by using a low pressure OMVPE. Then a 30nm-thick SiO_2 was deposited by a thermal CVD and stripe mask with various widths were formed on the same wafer by using EB lithography followed by reactive ion etching (RIE) with CF_4 gas. Finally, ECR-RIBE with Cl_2 gas was done. The etched depth was about 50nm.

The PL measurement was done at an extremely low excitation of Ar^+ -ion laser (1W/cm², $\lambda=514.5$ nm) at 77K and 300K after cleaning the sample surface with slow rate wet chemical etchant $H_2SO_4:H_2O_2:H_2O$ in the ratio of 1:1:40 at 0°C for 20sec.

Figure 4 shows the PL intensity of the wire structures normalized by the space filling factor which is the volume ratio of the active region of the wire to that of the quantum-film. The PL data of dry etched samples are indicated by painted circles (●, 77K) and painted squares (■, 300K), and those of wet etched ones using Br-methanol (0.0025 vol. %, 15sec at room temperature) are indicated by open circles (○, 77K) and open squares (□, 300K). As can be seen, normalized PL intensity of the wires fabricated by this dry etching was almost the same to that by wet chemical etching.

From these experimental data, we estimated the sidewall recombination velocity S of the wire structure by using the following eq.(1) [15].

$$\frac{I_{wire}}{I_{film}} = \frac{W/2 - W_d}{S \cdot \tau + W/2 - W_d} \quad (1)$$

where I_{wire} and I_{film} denote the PL intensity of the wire structure and that of the original SQF structure, respectively. W , W_d , and τ are the geometrical wire width, the width of so-called dead layer and the bulk carrier lifetime. Solid and dashed lines in Fig.4 indicate calculated curves where $S \cdot \tau$ product was estimated to be 5.3×10^{-6} cm at 77K and 2.7×10^{-5} cm at 300K. The sidewall recombination velocity S was

estimated to be $2.5 \times 10^3 \text{ cm/s}$ at 77K by assuming that $\tau=2.1\text{ns}$ at 77K under an extremely low excitation level (1W/cm^2 , $\lambda=514.5\text{nm}$)[16].

3.2 ECR-RIBE with H_2 Treatment

Next, we measured the PL intensity of GaInAsP/InP wire structures with the wire width from 10 to 100nm in order to evaluate the dead layer width and to investigate the quantum-wire effect.

In this experiment, we prepared wafers which consisted of a p-InP buffer layer ($2\mu\text{m}$ thick), an p-GaInAsP 3-step-index OCL (30nm thick, $\lambda_g=1.0\mu\text{m}$; 30nm thick, $\lambda_g=1.1\mu\text{m}$; 30nm thick, $\lambda_g=1.2\mu\text{m}$), i-GaInAsP (6.5nm thick, 1%CS)/GaInAsP (12nm thick, $\lambda_g=1.2\mu\text{m}$) 5paired CS-MQF layer and an i-InP top layer (5nm thick) by using a low pressure OMVPE.

Fabrication process of SiO_2 mask was the same as that explained in the section 3.1. Here we tried to examine a surface treatment process with the help of H_2 radicals, and introduced H_2 gas into the ECR-RIBE chamber right after the etching with Cl_2 gas, where the sample bias voltage was changed to 0V. A 24nm wide multiple-quantum-wire pattern with 70nm period and a 39nm wide wire pattern with 100nm period were obtained.

The PL measurement was done by using Ar^+ -ion laser (200W/cm^2 , $\lambda=488\text{nm}$) at 77K and 300K. The normalized PL intensity of dry etched samples with only Cl_2 gas is indicated by open triangles (\triangle , 300K) in Fig.4. The post etching treatment with H_2 gas was found to be effective from PL data indicated by painted triangles (\blacktriangle , 300K; \blacktriangledown , 77K).

After this PL measurement, a wet-chemical etching was done to squeeze the wire width by using solution of $\text{H}_2\text{SO}_4:\text{H}_2\text{O}_2:\text{H}_2\text{O}$ in the ratio of 1:1:40 at 0°C for 21sec. Then a 16nm wide wire pattern with the 70nm period and a 31nm wide wire pattern with 100nm period were obtained. PL intensities of these samples measured at 77K are indicated by painted squares (\blacksquare) in Fig.4. As can be seen, the dead layer thickness of dry etched samples after the H_2 treatment was estimated to be much smaller than 10nm.

4. Conclusion

Fairly low-damage property of ECR-RIBE with Cl_2 gas was obtained with negative acceleration bias voltage of -50V as well as post etching treatment with H_2 . This fabrication process seems to be very attractive for realization of high-density and uniform quantum-wire structures required for lasers with high performance operation.

Acknowledgment

We acknowledge Prof. Y. Suematsu, Prof. K. Furuya, Assoc. Profs. M. Asada and Y. Miyamoto, Prof. K. Iga, and Assoc. Prof. F. Koyama for their fruitful discussions and helpful comments. This work was supported by the Ministry of Education, Science & Culture, Japan, through a Grant-in-Aid for Scientific Research and the Research Center for Quantum Effect Electronics.

References

- [1] Y. Arakawa and H. Sakaki, Appl. Phys. Lett., vol.40, no.11, pp.939-941 (June 1982)
- [2] M. Asada et al., IEEE J. Quantum Electron., vol.QE-22, no.9, pp.1915-1921 (Sept. 1986)
- [3] Y. Miyake and M. Asada, Jpn. J. Appl. Phys., vol.28, no.7, pp.1280-1281 (July 1989)
- [4] Y. Arakawa and A. Yariv, IEEE J. Quantum Electron., vol.25, no.10, pp.1666-1674 (Oct. 1989)
- [5] K. Komori et al., IEEE J. Quantum Electron., vol.28, no.9, pp.1894-1900 (Sept. 1992)
- [6] K. Shimomura et al., IEEE J. Quantum Electron., vol.28, no.2, pp.471-478 (Feb. 1992)
- [7] A. R. Adams, Electron. Lett., vol.22, no.5, pp.249-250 (Feb. 1986)
- [8] E. Yablonovitch and E. O. Kane, IEEE J. Lightwave Technol., vol.LT-4, no.5, pp.504-506 (May 1986)
- [9] S. Ueno et al., Jpn. J. Appl. Phys., vol.31, part 1, no.2, pp.286-287 (Feb. 1992)
- [10] Y. Arakawa, Trans. of IEICE, Fundamental, vol.E75-A, no.1, pp.20-27 (Jan. 1992)
- [11] Y. Miyake et al., IEEE J. Quantum Electron., vol.29, no.6, pp.2123-2133 (June 1993)
- [12] K. Kudo et al., IEEE Photon. Technol. Lett., vol.4, no.10, pp.1089-1092 (Oct. 1992)
- [13] K. Kudo et al., IEEE Photon. Technol. Lett., vol.5, no.8, pp.864-867 (Aug. 1993)
- [14] K. C. Shin et al., to be published in IEEE Photon. Technol. Lett., vol.7, no.4, (Apr. 1995)
- [15] Maile et al., Appl. Phys. Lett., vol.54, no.16, pp.1552-1554 (Apr. 1989)
- [16] M. Tamura et al., SSDM 94, Yokohama, Japan, digest pp.199-201, (Aug. 1994)

Table 1. Summary of $\text{Ga}_{1-x}\text{In}_x\text{As}/\text{InP}$ Quasi-Quantum-Wire Lasers

	x of In	λ (μm)	W_t (nm)	W_b (nm)	Λ (nm)	ξ (%)	L (μm)	I_a (mA)	I_b (A/cm^2)
TS SQW	0.34	1.46	12	30-40	70	0.95	980	16	816
TS SQF	0.34	1.48	12	-	-	1.90	950	8	421
CS SQW	0.70	1.54	3	30-60	100	0.9	910	29	1650
CS SQF	0.70		3	-	-	1.8	920	65	

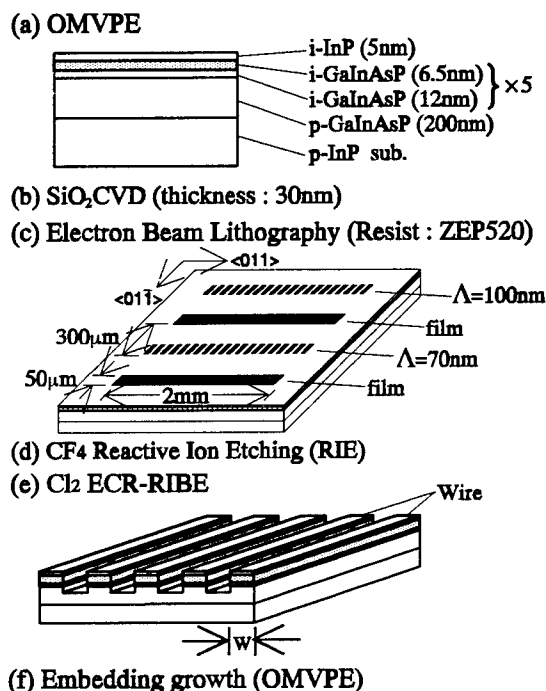


Fig.1 Fabrication process of GaInAs/GaInAsP/InP quantum-wire/quantum-box lasers.

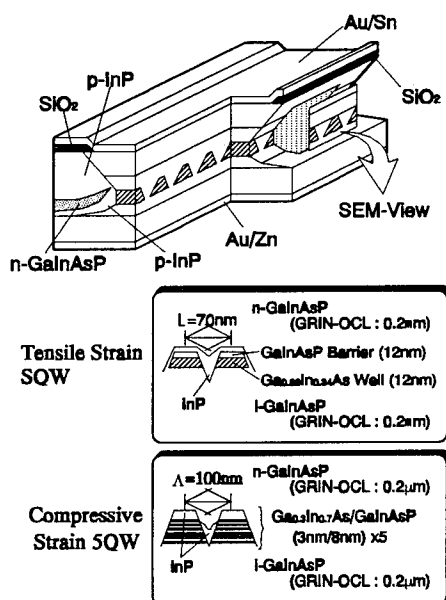


Fig.2 Schematic structure of GaInAs/GaInAsP/InP BH-strained quasi-quantum-wire lasers.

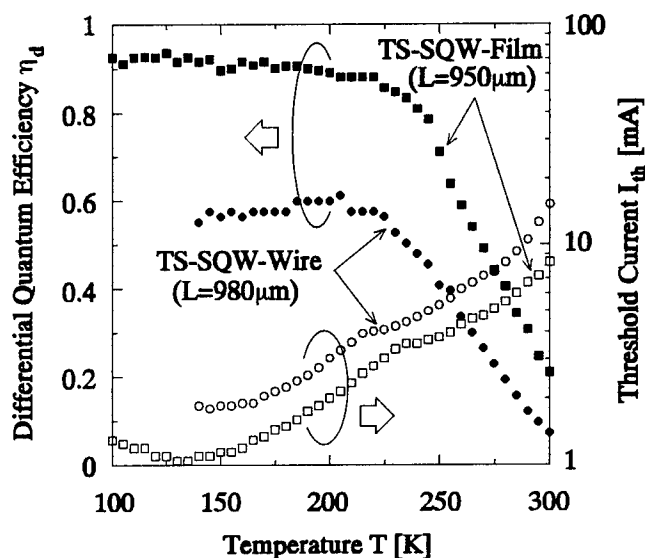


Fig.3 Temperature dependences of threshold current and differential quantum efficiency of TS-quasi-quantum-wire laser and TS-quantum-film laser.

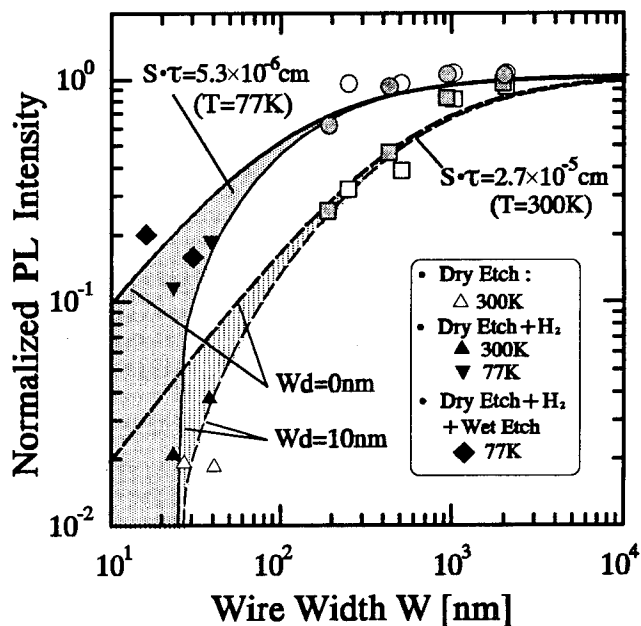


Fig.4 Normalized PL intensity of GaInAsP/InP wire structures fabricated by ECR-RIBE with Cl₂ gas.

Effects of Hydrogen on InP Light-Emitting Devices Etched in a Methane-Hydrogen Environment

Patricia Beck¹, Dennis Derickson², Forrest Kellert² and Tim Bagwell²

¹Hewlett-Packard Laboratories, Palo Alto, CA 94306, USA

²Hewlett-Packard Lightwave Operations, Santa Rosa, CA 95403, USA

Introduction

Research has been conducted on the physical damage and hydrogenation effects during RF plasma exposure (1, 2) and epitaxial growth (3, 4) in the III-V material system. Device consequences of this damage or chemical alteration have received less attention, particularly in active light emitting devices. This paper discusses these effects for lasers and edge emitting light-emitting diodes (EELEDs) which use a ridge waveguide structure. By using analysis techniques such as SIMS we have concluded that methane-hydrogen reactive ion etching (RIE) of InP induces hydrogen levels in an active device which are high enough to significantly alter the device properties. The decrease in light output is substantial, but subsequent annealing times as short as 1 min. at 430 °C can restore power dramatically.

Ridge Waveguide Fabrication

Fig. 1 shows the general device structure analyzed in this work. The substrate is *n*-type InP with a lattice matched $\text{In}_{1-x}\text{Ga}_x\text{As}_y\text{P}_{1-y}$ QW active region for the lasers and bulk InGaAsP active region for the EELEDs. The contact layer is heavily doped and bandgap-graded to InGaAs.

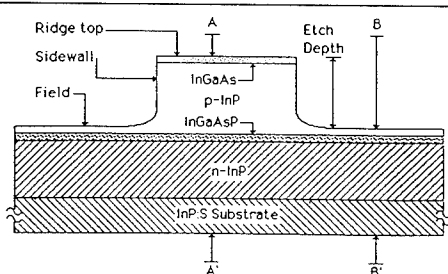
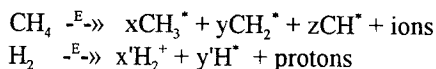


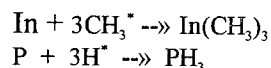
Fig. 1. Material layers. Section A-A' is through the ridge. Section B-B' is through the field.

An EELED has gain and absorber regions while a laser has only a gain region. Each waveguide is fabricated by the same basic process. When current flows between the ridge top contact and the back side of the substrate, light is emitted along the current flowing region. In addition to gain guiding, the light is guided by index differences between InP / $\text{In}_{1-x}\text{Ga}_x\text{As}_y\text{P}_{1-y}$ epitaxial layers in the vertical direction and the index step from the ridge waveguide to the barrier dielectric along the length of the ridge (5).

The ridge confinement structure is produced by first patterning the substrate with an etch resistant material (6, 7) and then RIE etching in an environment consisting of 15% methane in hydrogen at 400 V and 100 W for two to three hours. An increased etch rate may be obtained with the addition of argon to the mix. In the RF excited plasma the methane and hydrogen are thought to split apart to form methyl and hydrogen groups.



When reacted with the InP-based compounds, the end products are methyl-indium or methyl-gallium compounds and hydrides such as phosphine or arsine, reversing the OMVPE process (8).



The side wall etch rate is lower than that of the field. Therefore, side walls are exposed to a hydrogen rich environment (and physical damage) for most of the etch time while the field is removed to a predetermined depth above the active region by active monitoring.

Before removal from the RIE chamber, the sample is exposed to an oxygen plasma to remove the polymer film which has formed during the methane-hydrogen etch. The ridge is coated with a dielectric material. Then the ridge top is etched free of the dielectric and original masking material. Metal is deposited to contact the top of the ridge (*p*-side). After thinning the substrate, metal is applied to the back *n*-side. The wafer is annealed and cleaved into devices. The final device structure is shown in Fig. 2.

Experimental Results

Decreased Light Output

As originally fabricated, both lasers and EELEDs exhibited poor output power. EELEDs with 4- μm -wide ridges and 800- μm -long gain regions produced approximately 100 μW at a drive current of 200 mA. Laser structures of various lengths from the same wafer also showed high threshold current and poor quantum efficiency. Elevated temperature strife testing revealed a slow increase in power over time, for constant drive current. The fabrication anneal was performed at 400 °C for 30 sec. This was found to be insufficient to both anneal the ohmic metals and to relieve damage.

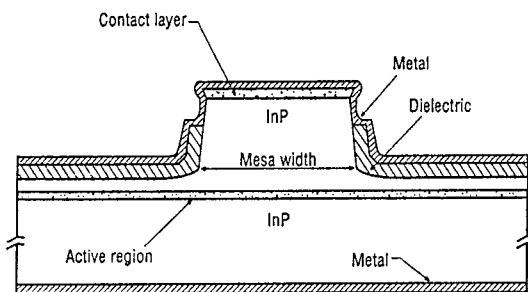


Fig. 2. Cross section of etched ridge structure.

Experimental Heat Treatments

Subsequent higher temperature treatments on a 4- μ m-wide EELED increased device output power four to five times with little change in contact resistance. Below 300 °C noticeable power increases are measured in hours, while above 400 °C the same changes are achieved in minutes. The optimum required heat treatment time varies logarithmically with temperature (Fig. 3), evidence of diffusion processes at work.

Fig. 4 shows the optical output power for a non-heat-treated device compared with the same device annealed at 400 °C, as a function of time. The figure also shows that it is possible to degrade the device with an extended anneal. Wider ridges with similar gain lengths exhibited greater initial output power than narrower ridges and showed less percentage improvement from the temperature treatments. Output from an 8- μ m-wide ridge increased two to three times while that from a 100- μ m-wide ridge showed no quantifiable difference. Although both bulk and QW material were affected, the QW material showed smaller improvements after the heat treatments.

Material Analysis

To study the effects of the methane-hydrogen etching, SIMS analysis for zinc and hydrogen was performed on bulk and QW samples. Referring to Fig. 1, Sample I is

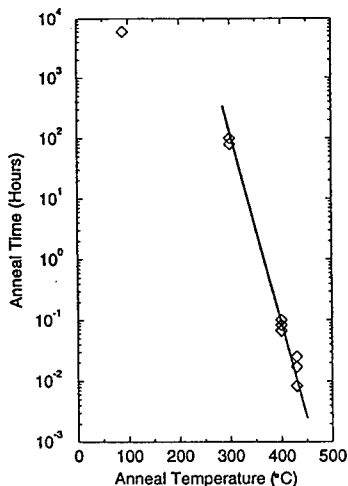


Fig. 3. Anneal time for power recovery vs. temperature.

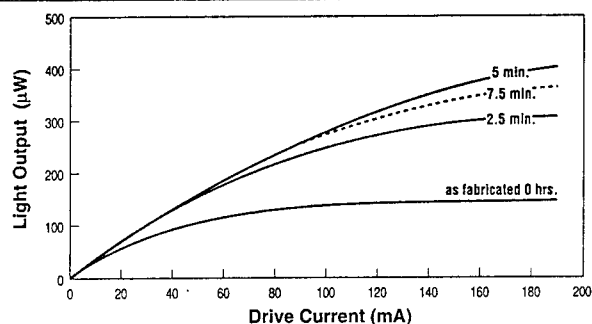


Fig. 4. Output power vs. anneal time at 400 °C for an unheatsunk EELED with a 4- μ m-wide ridge.

taken through Section A-A', samples II-V are through Section B-B'. The following are included:

- (I) Before etching - full structure (bulk material)
- (II) Etched without Argon in the mix (bulk)
- (III) Etched without Ar in the mix (QW)
- (IV) Etched with Ar in the mix (QW),
- (V) Etched without Ar, annealed at 430 °C, 2 min. (bulk).

Profiles show elevated hydrogen levels extending up to 4 μ m into the substrate from the exposed surface (Fig. 5) when compared with the as-grown structure (Fig. 6). After a short high temperature anneal (Fig. 5) the hydrogen returned to as-grown levels except in the active area, which may have a slight affinity for hydrogen, and the interface regions. Particularly obvious is a spike at the undoped epitaxial InP/substrate interface. Since the interface is n -InP/ n -InP, a smooth diffusion profile was expected. The hydrogen appears to be passivating interface defects which anneal out at much higher temperatures. The "after-etch" plots are taken from the field of the sample (refer to Fig. 1) because 4- μ m-wide ridges are too narrow for effective SIMS.

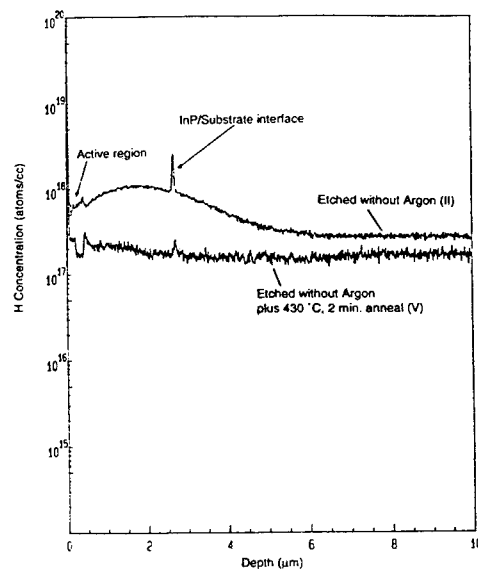


Fig. 5. Hydrogen SIMS data from samples "as etched" (II) and "etched plus annealed" (V).

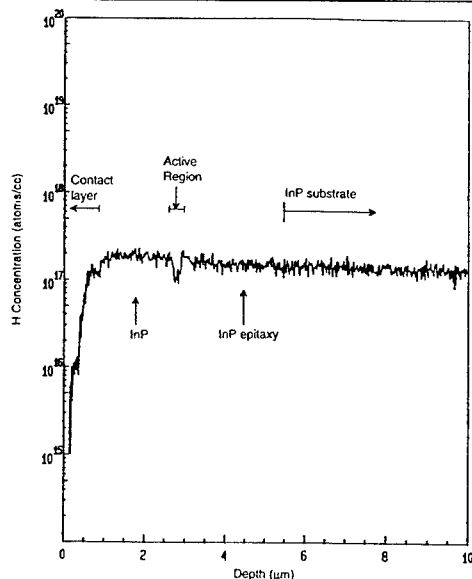


Fig. 6. Hydrogen SIMS data in the "as grown" sample (I).

The amount of hydrogen in InGaAsP relative to InP may not be valid as read directly from the figures because InP was the SIMS reference. The overall changes are valid and values should be compared between regions of similar composition.

These samples were etched in a method identical to the tested light-emitting devices, including the additional oxygen plasma clean before further processing. We believe that the heating which occurs during this step, in the non-hydrogen environment, decreases the surface hydrogen concentration. This "anneal" would explain why the peak concentration is not at the surface in Fig. 5.

The addition of argon to the etch increased the etch rate through physical bombardment and decreased the time that the sample was exposed to the hydrogen plasma. Argon in the etch roughens the surface and there is evidence that plasmas produce substantial damage extending to thousands of angstroms below the surface (9). In identical samples, the reduced exposure time decreased the penetration depth but did not increase the peak concentration, indicating that diffusion played a larger role than damage in the interior hydrogen level (Fig. 7). No difference in zinc level was apparent.

The anneal temperature for which light output is increased within a few minutes fits well with OMVPE growth data (10). After growth of *p*-type InP/InGaAs/InGaAsP, the net acceptor concentrations are depressed. An anneal at 435 °C for 5 min. in a non-hydrogen ambient reactivates the zinc. Fig. 6 shows the background level of this hydrogen after growth and anneal, before device processing.

QW structures were examined as well. They improved less than the bulk devices after annealing. This may be due to their reduced active region thickness (840 Å vs. 1800 Å for bulk), the fact they seemed to be less degraded in the first place and the high probability that the interfaces,

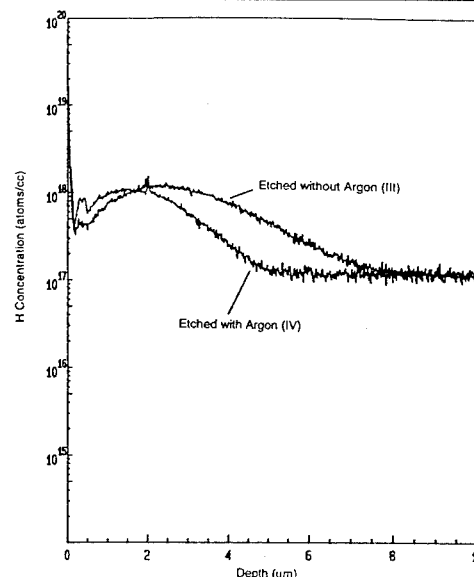


Fig. 7. Hydrogen SIMS data from samples etched without (III) and with Ar (IV).

within the QW structure, are passivated. Hydrogen remaining at the interfaces after the anneal would be difficult to remove.

Reliability Studies

Reliability testing after the high temperature anneals was conducted on EELEDs and lasers at both constant power and constant current. Data from devices operated at 50 °C and 70 °C show that after a short "burn-in" interval of less than 100 hours, the current required to maintain a constant output power slowly decreased. At 7500 hours the required current had decreased by 2% of the initial value, leveled off and showed signs of increasing. Devices operating at 90 °C exhibited a "burn in" followed by a short period of current decrease (to 1000 hours), followed by an increase in current.

Increasing power (decreasing current) is consistent with removal of residual hydrogen. Decreasing power (increasing current) is consistent with normal "wear-out" mechanisms. Although mechanisms compete and the length of each time period varies with temperature, all devices experience a "burn-in", hydrogen anneal and degradation (depicted schematically in Fig. 8). Results are similar for all samples whether capped with silicon dioxide or silicon nitride, annealed on a hot plate or in an RTA.

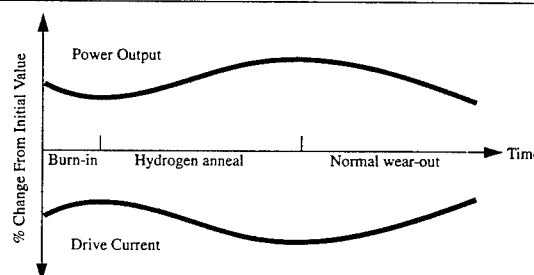


Fig. 8. General trend of reliability data (not to scale).

These devices are normally operated at 20 °C. A typical degradation will therefore not be observed until a time beyond the useful device life, generally 10^4 hours.

Discussion

Hydrogen incorporation seems to become significant as wafers are cooled to 450 °C after growth (10). This may explain why device output is not stable at elevated temperatures. A further anneal at 450 °C or above might rid the wafer of the last few percent, but could change the zinc placement. If zinc moves into the intrinsic active layer the device could be seriously degraded. The zinc profile following etching and after etching plus annealing is shown in Fig. 9. The zinc has moved toward the active region after only two minutes at 430 °C.

We believe that free hydrogen electrically neutralizes the zinc doping (11, 12, 13), degrading the contact and current confining properties of the ridge. Constricted current flow narrows the pumping region. Also, plasma damage can cause non-radiative recombination centers. These combined effects decrease device output power. Wider ridges have less overall change in output power because the hydrogen from the side walls and field area completely washes through a 4- μm device while only a small percentage of a 100- μm device is affected.

Photoluminescence measurements show a decreased peak intensity after the oxygen plasma clean-up which is necessary following methane-hydrogen etching. Polaron measurements of net active donor/acceptor concentration indicate only small changes in the minority carrier dopant in test structures and are inconclusive.

Conclusions

Hydrogen incorporation and an increase in output power after heat treatment has been observed in both bulk and quantum well active region devices emitting light at

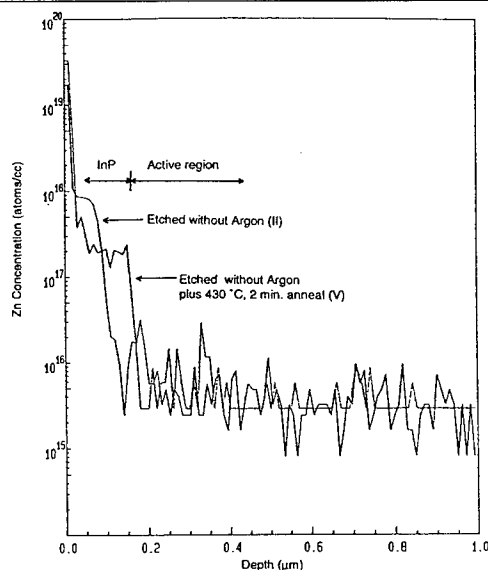


Fig. 9. Zinc SIMS data from samples II and V.

various IR wavelengths. Anneals above 425 °C are effective in driving off hydrogen in a matter of minutes but they must be balanced with the movement of p and n dopants into the active region and degradation of other device layers, particularly metals. Anneals which balance time and temperature have been used to produce EELEDs with 1 mW output power and lasers with 20 mW of output power under normal operating conditions with minimal drift in reliability.

Acknowledgments

We thank Bill Perez for polaron and PL measurements, Dale Lefforge for SIMS and Karen Seaward, Mike Ludowise and N. M. Johnson for helpful discussions.

References

- (1) K. Morit, et al., "Analysis of Damage During InP Hydrocarbon-RIE," Proc. of 4th Int. Conf. on InP and Related Materials, pp. 427-430, 1992.
- (2) T. R. Hayes, et al., "Passivation of acceptors in InP resulting from CH_4/H_2 reactive ion etching," Appl. Phys. Lett., Vol. 55, No. 1, pp. 56-58, 1989.
- (3) S. Cole, et al., "Effect of Cooling Ambient on Electrical Activation of Dopants in MOVPE of InP," Elect. Lett., Vol. 24, No. 15, pp. 929-930, 1988.
- (4) S. Cole, et al., "Anomalous Behavior of Dopants in Atmospheric Pressure MOVPE of InP," J. Crystal Growth, Vol. 93, pp. 607-612, 1988.
- (5) G. P. Agrawal and N. K. Dutta, Long Wavelength Semiconductor Lasers, Van Nostrand Reinhold, N. Y., Sect. 5.4, 1986.
- (6) J. E. Schramm, "Reactive Ion Etching with $\text{CH}_4/\text{H}_2/\text{Ar}$," Dept. of Elect. and Computer Eng. Rpt., U. C. S. B., 1993.
- (7) J. Werking, et al., "Methane/hydrogen-based reactive ion etching of InAs, InP, GaAs and GaSb," Appl. Phys. Lett., Vol. 58, No. 18, pp. 2003-2005, May 1991.
- (8) G. B. Stringfellow, Organometallic Vapor-Phase Epitaxy: Theory and Practice, Chapter 4.2, Academic Press, Boston, 1989.
- (9) P. Viktorovitch, et al., "Passivation of InP for MISFET Applications," Proc. of 4th Int'l. Conf. on InP and Related Materials, pp. 51-55, 1992.
- (10) F. G. Kellert, et al., "Zn-doping in OMVPE Grown InP:Zn/InGaAs/InP $p-i-n$ Double Heterojunctions with InGaAs:Zn Contacting Layers," J. Elect. Mat., Vol. 21, No. 10, pp. 983-987, 1992.
- (11) N. M. Johnson, et al., "Hydrogen passivation of shallow-acceptor impurities in p -type GaAs," Phys. Rev. B., Vol. 33, No. 2, pp. 1102-1105, Jan. 1986.
- (12) W. C. Dautremont-Smith, et al., "Hydrogen Passivation of acceptors in p -InP," J. Appl. Phys. Vol. 66, No. 5, pp. 1993-1996, Sept. 1989.
- (13) V. Swaminathan, "Hydrogen Passivation in III-V Compounds," Proceed. XII State of the Art Prgm. on Compound Semiconductors, Vol. 90-15, p. 20, Electrochem. Soc., 1990.

Fabrication of 60nm-pitch Ordered InP Pillars by EB-lithography and Anodization

T. Takizawa, M. Nakahara, E. Kikuno, and S. Arai

Research Center for Quantum Effect Electronics

Tokyo Institute of Technology

2-12-1 O-okayama, Meguro-ku, Tokyo 152, Japan

Phone: +81-3-5734-2512 Fax: +81-3-5734-2907

Abstract: We obtained 60nm-pitch ordered InP triangle vertical pillars with high density of around 50% by combining electron-beam (EB) lithography and anodization techniques. Furthermore, adopting the dry-etching transfer onto SiO₂, we obtained 40nm-pitch ordered pillars and observed photoluminescence intensity comparable to that from bulk InP substrate that indicates negligible non-radiative recombination.

1. Introduction

Quantum-wire and quantum-box structures are very attractive for their supreme electrical and optical properties[1] applicable to high performance optical devices[2],[3]. However, it is necessary to fabricate low dimensional quantum-well structures with high density and low size-fluctuation[4]. Recently, though a lot of fabrication techniques are attempted to obtain them[5-7], fabrication of high-density low dimensional quantum-well structure available for electro-optical switch and all-optical switching devices, was not realized yet.

We took notice of the vertical etching formation on (111)A surface InP and self-organizing mechanism of anodization[8], and successfully obtained 60nm-pitch ordered InP pillar structure. Furthermore 40nm-pitch ordered InP pillar structure was also obtained.

2. Experiments

2.1 Fabrication Process

In order to fabricate short periodic size-ordered pillars assisted by EB lithography, we used (111)A surface n-InP substrate with high doping density ($1 \times 10^{19} \text{cm}^{-3}$, Sn doped), which is suitable for fabrication of smaller pores by anodization than a low doped substrate.

First, we made a dot patterned SiO₂ mask to fabricate size-ordered structures by anodization. On this substrate an SiO₂ film of 10nm thickness was deposited by a conventional CVD method, and a PMMA resist of 40nm thickness was spin-coated. Next we exposed honeycomb-like dot patterns

perpendicular to three cleaved facets $[\bar{1}\bar{1}0]$ on (111)A surface under the dose condition of $2.3 \times 10^{-6} \text{nC/dot}$ by using EB lithography, as shown in Fig.1(a). Figure 1(b) shows an SEM top view of dot patterns made on PMMA resist. Circular holes of about 30nm diameter were formed on SiO₂ film. The dot pattern was transferred onto the SiO₂ with buffered 1% HF solution, then PMMA resist was removed by organic solvent.

Then we carried out anodization of the InP substrate with the SiO₂ mask in the condition of current density of 40mA/cm^2 , 15% HCl etchant, and etching time of 1min. Figure 2 shows an SEM photograph of the InP substrate after anodization. Bright triangles are InP pillars and dark ones are pores. As can be seen, size-ordered triangular pores, which are independent on the shape of holes on the SiO₂ mask, were formed automatically by anodization etching assisted with EB lithography. It should be noted that high density pillars with the space filling factor of around 50% was obtained. Three sides of triangles correspond to $[\bar{2}11]$ facets perpendicular to cleaved facets.

2.2 Size Uniformity of 60nm-pitch Ordered Pillars

To investigate the dependence between the dose condition and pillar size, we prepared two InP substrates with dot patterned SiO₂ mask provided by different dose conditions of $3.1 \times 10^{-6} \text{nC/dot}$ and $2.3 \times 10^{-6} \text{nC/dot}$. We carried out the anodization for these substrates under the same conditions used in the sample shown in Fig.2. After the anodization, we

measured the side length of triangles and plotted the size-distribution of triangles in Fig.3. Figures 3 (a) and (b) show SEM photographs and histograms of the side length of triangle pillars fabricated with the dose conditions of 3.1×10^{-6} nC/dot and 2.3×10^{-6} nC/dot, respectively. The hatched area in Figs. 3 (a) and (b) indicates the size fluctuation less than 5%, which is considered to be an acceptable limit in application to semiconductor optical devices, especially electro-optical switches[4]. As can be seen, triangle pillars obtained by the lower dose condition have less size-fluctuation than those by the higher dose condition. According to this tendency, it is explained that an etch pit by anodization have a freedom in proportion to the area of the hole on the mask at the initial state of etching to make triangle pores, in other words, the triangle pillar with better uniformity can be formed by smaller mask's holes. The periodicity of mask's holes contributes to the ordered triangle pore formation assisted by the self-organization mechanism of anodization.

2.3 Fabrication of 40nm-pitch Ordered Pillars

We fabricated smaller triangle pillar structures in order to seek for the possibility for quantum-wire structures. The mask fabrication procedure for 40nm-pitch triangle pillars was almost same for 60nm-pitch ones, except for introducing reactive ion etching (RIE) process with CF_4 gas as the dot pattern transferring process into SiO_2 film, so as to suppress over-etching by undercut.

40nm-pitch dot pattern was transcribed onto 40nm thick PMMA resist on (111)A InP substrate with SiO_2 film of 10nm thickness with the dose condition of 1.3×10^{-6} nC/dot. After the development, we transferred the dot pattern into SiO_2 film by the CF_4 RIE process with the condition of CF_4 flow rate of 1sccm, input power of 20W, background pressure of 4.0×10^{-2} atm and etching time of 40sec. After removing the PMMA resist, anodization was done with the same condition used in the fabrication of 60nm-pitch pattern. Figure 4 shows an SEM top view of fabricated 40nm-pitch triangle pillars, where 40nm-pitch ordered triangle pillars are formed even though the size fluctuation seems to be little larger than that in 60nm-pitch ones.

Then, we measured a photoluminescence (PL)

spectrum to reveal the optical properties of 40nm-pitch ordered triangle pillar structure. The pumping light source of an Ar^+ laser with the wavelength of 488nm and the output power of 30mW was used. On the sample used for PL measurement, we made an area blocked against the anodization so as to use it as a reference of bulk InP. Hence PL spectra from the bulk InP and 40nm-pitch ordered InP pillar structure were obtained by only shifting the sample position without varying the alignment condition.

Figures 5 (a) and (b) indicate room temperature PL spectra from InP bulk region and 40nm-pitch triangle pillar region, respectively. The PL peak wavelength was observed at around 0.88 μm , which is little shorter than the intrinsic bandgap wavelength of InP (0.92 μm), and the reason for this can be attributed to a band filling effect in highly n-doped material. The peak at the wavelength of 0.99 μm seen in both figures are attributed to the scattering of Ar^+ laser light from the surface. Especially the 0.99 μm peak in Fig.5(b) was strong due to the scattering from the pillar structure.

The PL intensity from 40nm-pitch pillar structure was comparable to that from InP bulk region. Calculating the absorption ratio in the pillar layer by taking account of the absorption coefficient as the order of 10^4cm^{-1} , the space filling factor of 50%, and the pillar height of 1 μm , approximately 60% of pumping light was assumed to be absorbed in the pillar layer, and the rest of around 40% was absorbed in the bottom InP substrate. Although there is a contribution from the bottom InP substrate, the PL intensity from 40nm-pitch triangle pillars was comparable or little larger than that from InP bulk region. From this fact it is regarded that the anodization process implies very small physical damage.

3. Conclusion

We obtained 60nm-pitch ordered vertical triangle pillar structure on (111)A InP by anodization with HCl assisted by EB lithography. Furthermore, 40nm-pitch triangle pillar structure was also obtained by adopting CF_4 RIE process for fabrication of SiO_2 mask. A low damage property of this anodization process, which was confirmed from PL intensity measurement, is very attractive for

fabrication of high-density and uniform quantum-wire structures.

Acknowledgment

We would like to acknowledge Prof. K. Iga and Prof. K. Furuya, Assoc. Prof. M. Asada and Assoc. Prof. Y. Miyamoto for fruitful discussions. This work was supported by the Ministry of Education, Science and Culture, Japan, through a Grant-in-Aid for Scientific Research and Research Center for Quantum Effect Electronics.

References

- [1] H. Sakaki, "Scattering Suppression and High-Mobility Effect of Size-Quantized Electrons in Ultrafine Semiconductor Wire Structures," *Jpn. J. Appl. Phys.*, Vol. 19, pp. L735-L738, December 1980.
- [2] S. Tiwari and J. M. Woodall, "Experimental comparison of strained quantum-wire and quantum-well laser characteristics," *Appl. Phys. Lett.*, Vol. 64, pp. 2211-2213, April 1994.
- [3] K. Shimomura, S. Arai, and Y. Suematsu, "Operational Wavelength Range of GaInAs(P)-InP Intersectional Optical Switches Using Field-Induced Electrooptic Effect in Low-Dimensional Quantum-Well Structures," *J. Quantum Electron.*, Vol. 28, pp. 471-478, February 1992.
- [4] K. G. Ravikumar, T. Aizawa, K. Matubara, M. Asada, and Y. Suematsu, "Analysis of Electric Field Effect in Quantum Box Structure and Its Application to Low-Loss Intersectional Type Optical Switch," *J. Lightwave Technol.*, Vol. 9, pp. 1376-1385, October 1991.
- [5] E. Kapon, S. Shimony, R. Bhat, and D. M. Hwang, "Single quantum wire semiconductor lasers," *Appl. Phys. Lett.*, Vol. 55, pp. 2715-2717, December 1989.
- [6] P. M. Petroff, A. C. Gossard, and W. Wiegmann, "Structure of AlAs-GaAs interfaces grown on (100) vicinal surfaces by molecular beam epitaxy," *Appl. Phys. Lett.*, Vol. 45, pp. 620-622, September 1984.
- [7] R. Notzel, J. Temmyo, H. Kamada, T. Furuta, and T. Tamamura, "Strong photoluminescence emission at room temperature of strained InGaAs quantum disks (200-30nm diameter) self-organized on GaAs (311)B substrates," *Appl. Phys. Lett.*, Vol. 65, pp. 457-459, July 1994.
- [8] T. Takizawa, S. Arai, and M. Nakahara, "Fabrication of Vertical and Uniform-Size Porous InP Structure by Electrochemical Anodization," *Jpn. J. Appl. Phys.*, Vol. 33, pp. L643-L645, May 1994.

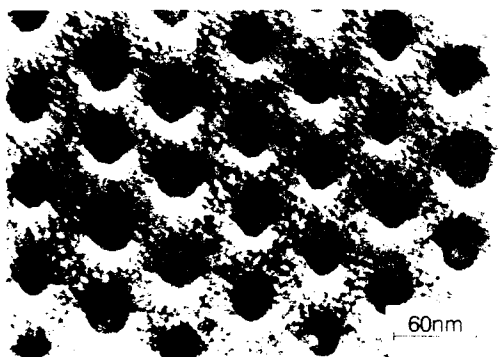
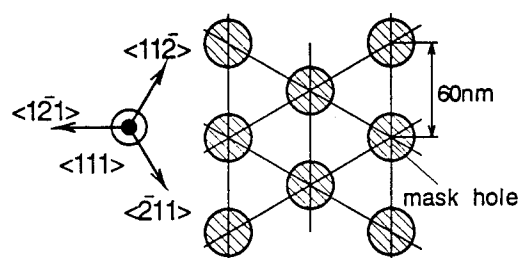


Fig.1. (a) The drawing pattern by EB lithography. (b) The SEM topview of the exposed PMMA resist.

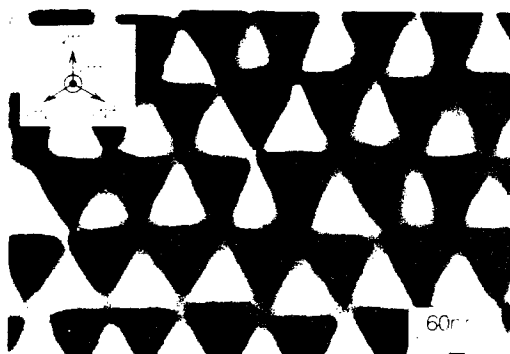


Fig.2. The SEM topview of the anodized (111)A n-InP substrate with a SiO₂ mask.

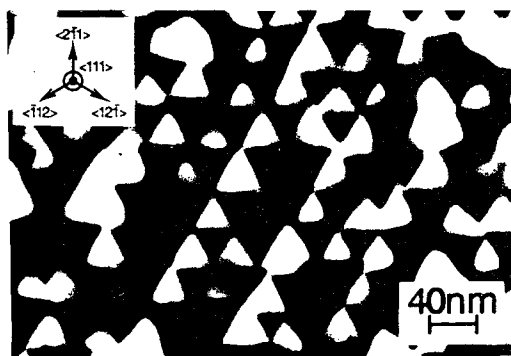


Fig.4. The SEM topview of the 40nm-pitch ordered triangle pillars.

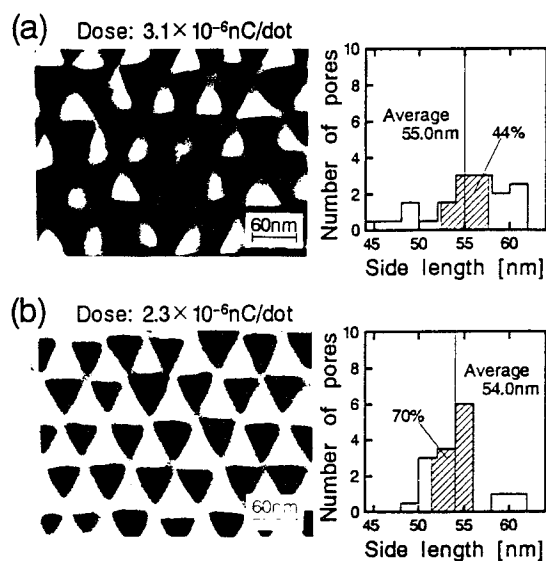


Fig.3. The SEM topview and the histogram of the size fluctuation of triangles in the dose condition of (a) $3.1 \times 10^{-6} \text{ nC/dot}$ and (b) $2.3 \times 10^{-6} \text{ nC/dot}$.

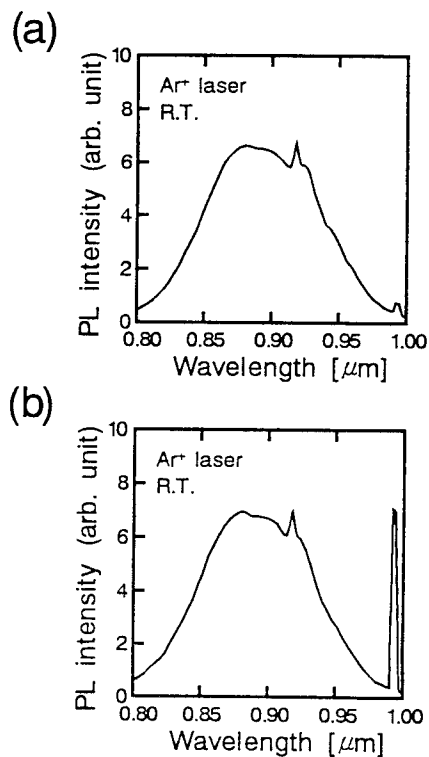


Fig.5. PL spectrum of (a) non-anodized substrate and (b) 40nm-pitch triangle pillars.

Low-temperature CAIBE processes for InP-based optoelectronics

J. Daleiden, K. Eisele, J.D. Ralston
*Fraunhofer-Institut für Angewandte Festkörperphysik,
 Tullastrasse 72, D-79108 Freiburg, Germany*

G. Vollrath, F. Fiedler
*Telekom Forschungs und Technologiezentrum,
 Am Kavalleriesand 3, D-64295 Darmstadt, Germany*

Abstract

We have developed Cl_2/Ar and IBr_3/Ar chemically-assisted ion-beam etching (CAIBE) processes, which allow high-quality etching of InP-based materials such as laser mirrors and gratings at low substrate temperatures ($\approx 0^\circ\text{C}$). Etch rates of 400-750 Å/min and excellent surface morphologies at substrate temperatures between -5°C and $+10^\circ\text{C}$ with both Cl_2/Ar and IBr_3/Ar process (400V Ar ion beam) are achieved. These low temperatures have allowed us to utilize UV-baked photoresists as well as PMMA as etch masks, facilitating very simply process development. Higher substrate temperatures ($+50^\circ\text{C}$ to $+120^\circ\text{C}$) yield still higher etch rates, but at the expense of severely degraded surface morphologies.

An InGaAsP/InP (1.55µm) bulk laser with one facet etched the other cleaved is demonstrated, and compared with a both facets cleaved laser.

Introduction

Chemically-assisted ion-beam etching (CAIBE) is a well-established tool for the fabrication of a variety of integrated optoelectronic components and circuits for both GaAs- and InP-based materials. We have recently developed a UHV CAIBE system, together with a $\text{Cl}_2 + \text{BCl}_3$ etching process, which relaxes many constraints previously reported in the dry-etching of $\text{Al}_x\text{Ga}_{1-x}\text{As}$ -containing optoelectronic device structures [1,2]. In this paper we present Cl_2/Ar and IBr_3/Ar CAIBE processes for the fabrication of optoelectronic devices, such as laser facets, deflecting mirrors, and gratings in the InP/InGaAsP material system.

The material system InP/InGaAsP is of increasing interest for optoelectronic integrated circuits

(OEIC's), and a number of etch techniques and chemistries have been demonstrated in this material.

There have been several studies in etching InP with CH_4/H_2 -processes [3,4,5,6,7]. The limitation of this approaches result from the slow etch rates and the problem of polymer formation.

Previous Cl_2/Ar CAIBE etching studies on InP-based MQW lasers have utilized substrate temperatures $>200^\circ\text{C}$ [8,9] or beam energies $>1\text{keV}$ [10], ruling out the use of standard photoresists as the etch mask.

Experiment

The CAIBE-system was designed and fabricated together with Technics Plasma GmbH and is now commercially available as model RIB ETCH 160 ECR UHV LL.

The compact, metal-sealed UHV etch chamber is fitted out with an electron cyclotron resonance (ECR) ion-beam source (2.45 GHz). In order to achieve low residual water vapor levels, the etch chamber is equipped with a 4000 l/sec (water pumping speed) cryopump and fitted with external bakeout heaters (base pressure 10^{-8} mbar). Automated overnight regeneration of the cryopump with heated N_2 gas is used for regular removal of reactive etch products. A cryo-pumped load-lock chamber and sample transfer system are also integral to the system design. The temperature-controlled sample stage (-5 to $+125^\circ\text{C}$), designed for substrates up to 4-in diameter, can be tilted under computer control ($\pm 90^\circ$). A magnetically activated sample clamping system guarantees precise control of the wafer temperature. This feature has proven to be critical both for the slope of the vertical etch walls of laser mirrors (GaAs and InP) and for the smoothness of the etched surfaces (InP). A pyrometer is used to monitor the temperature of the wafer surface. The reactive gases are introduced through four centro-symmetric tubes pointed towards

the substrate. The process pressure was between $1 \cdot 10^{-4}$ and $6 \cdot 10^{-4}$ mbar. Beam voltages of 300-500V were used with current densities of 0.25 mA/cm^2 , measured with a Faraday cup, which also allows monitoring the beam profile.

The comparatively low temperatures allowed us to use UV-baked photoresists (AZ1518, AZ4521) as etch masks for laser mirror etching as well as e-beam structured PMMA for distributed feedback (DFB)-gratings. The selectivity of photoresist to InP is about 1:4 (Chlorine process) and 1:2 (Iodine process).

Results and Discussion

Surface morphology and etch rates

The problem in etching InP with halogen gases lies in the low volatility of InCl_x and InI_x compared to PCl_x , PI_x at temperatures between $+30^\circ\text{C}$ and $+150^\circ\text{C}$. In this temperature region disproportioning takes place, producing an indium rich surface (Fig.1). One attempt to overcome this difficulties is heating the substrates to temperatures above 150°C , so that InCl_x and InI_x can be removed [8,9]. This rules out, however, the use of standard photoresist as an etch mask.

We found that cooling the substrates to temperatures below $+30^\circ\text{C}$ yields perfectly smooth surfaces (Fig.2).

This phenomenon can be due to a decrease of the volatility of the phosphorus containing etch products at this low temperature, so that the etch rate is lower, and therefore a stoichiometric smooth surface is left. Fig. 3 shows the etch rates of InP as a function of the substrate temperature for the etch gases $\text{Ar}+\text{Cl}_2$, $\text{Ar}+\text{IBr}_3$ and Ar alone.

Ar alone: The ion milling process is almost independent on the temperature, indicating the absence of chemical reactions. This physical process yields almost smooth bottom surfaces, however redeposition problems occur, making this process unpractical.

Ar+IBr₃: The above mentioned phenomena can be clearly seen in this curve. Below a "threshold temperature" of about 30°C , we find very smooth surfaces (Fig.2) with slower etch rates (400 \AA/min). Higher temperatures yield higher etch rates, but at the expense of severely degraded surface morphologies (Fig.1).

Ar+Cl₂: This process yields faster etch rates ($700\text{--}750 \text{ \AA/min}$), better selectivities, and allows us etching DFB-gratings (period 240nm) with PMMA as etch mask (Fig.4).

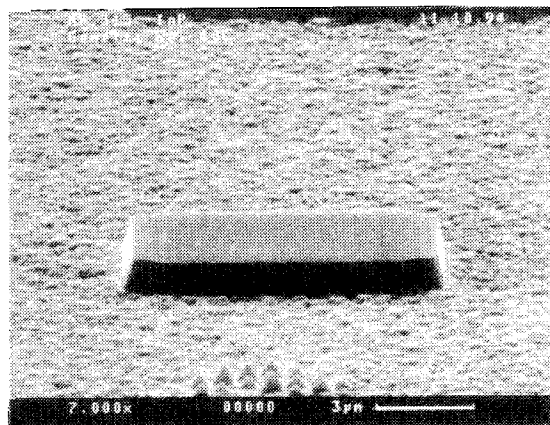


Fig.1: CAIBE-etched InP test structure ($5\text{Ar}+\text{IBr}_3$, $T = 40^\circ\text{C}$, $U_B = 400\text{V}$)

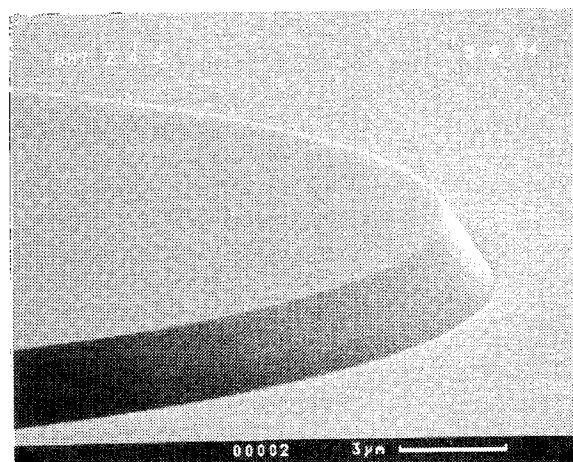


Fig.2: CAIBE-etched InGaAsP/InP disk structure ($5\text{Ar}+\text{IBr}_3$, $T = 0.5^\circ\text{C}$, $U_B = 400\text{V}$)

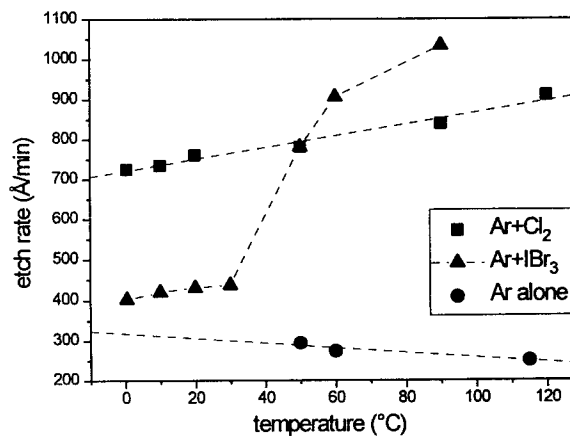


Fig.3: Temperature-dependence of InP etch rate ($U_B = 400\text{V}$)

Etch profile

With all the above described processes the slope of the sidewalls of the structures obtained was negative with respect to the normal (Fig.2) The angle was found to be weakly dependent on the temperature in the range 15-20°C. For laser mirrors this angle should be zero, because for every 10° mirror tilt the reflected intensity is reduced by 50% [11]. To reduce this angle to zero the normal of the substrate has to be tilted relative to the impinging argon beam. With a 45° tilt a mirror surface perpendicular to the substrate plain can be achieved for a fixed low temperature setting (Fig.5). If both mirrors are to be etched in one process the wafer has to be tilt to a positive angle first and a negative angle respectively. This has to be repeated until the desired mirror depth has been achieved. Another way is to perform lithography and etch one mirror side only, and then repeat lithography and etch the other side.

Applications/ Devices

We have recently etched facets in InGaAsP/InP (1.55μm) bulk lasers with the IBr₃/Ar CAIBE process (Fig.5). The lasers were grown by vapor phase epitaxy (VPE). Using a flared wave guide design we etch one facet by CAIBE, the opposite facet was cleaved.

These lasers were compared with reactive ion etched (RIE) waveguides and both sides cleaved. Fig. 6 shows a plot of the threshold current densities as a function of the inverse resonator length.

In this first attempt, we have successfully demonstrated comparable performance for cleaved/etched (ce) lasers to cleaved/cleaved (cc) lasers.

Conclusions

In summary, chemically-assisted ion-beam etching has been used to produce high quality etched facets and DFB gratings in InP-based materials at low substrate temperatures. It was shown that it is possible to use standard photoresists and PMMA as etch masks. The IBr₃/Ar CAIBE process has been considered to be favorable for the etching of laser mirrors, delivering the best surface quality. The surface in the Cl₂/Ar CAIBE process is only slightly inferior but yields faster etch rates and a better

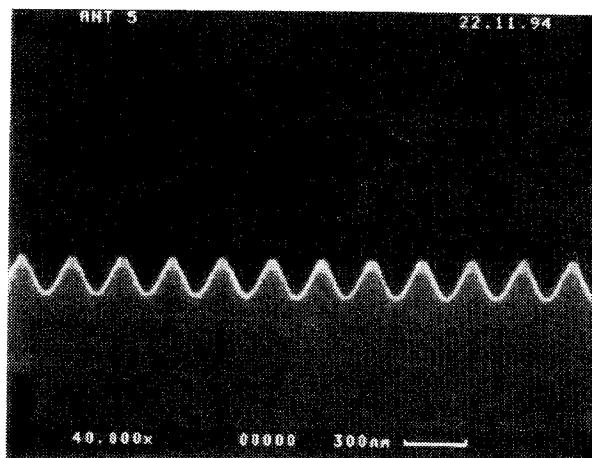


Fig.4: CAIBE etched InP DFB grating (5Ar+4Cl₂, T = -5°C, U_B = 400V)

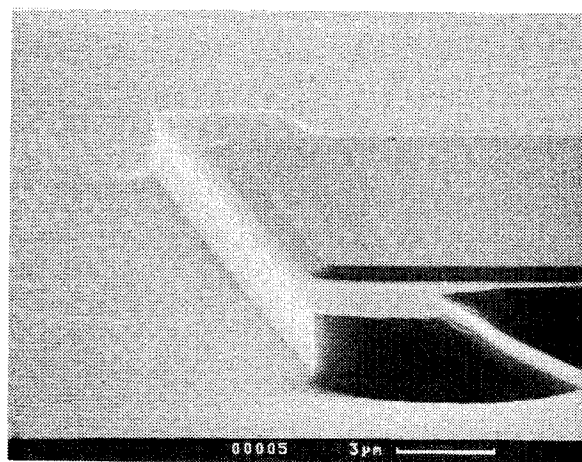


Fig.5: CAIBE etched InGaAsP/InP (1.55μm) flared waveguide laser facet (5Ar+IBr₃, T = 0.5°C, U_B = 400V, tilt 45°)

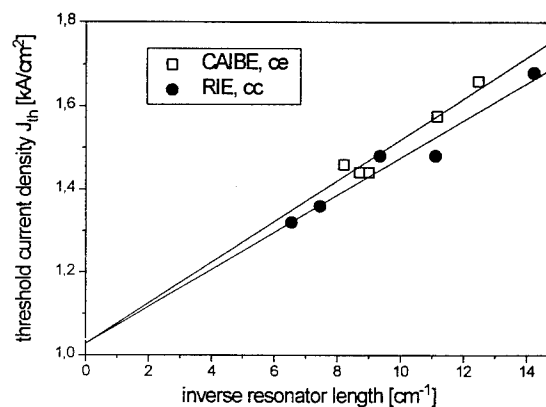


Fig.6: Threshold current density as a function of the inverse resonator length for cc and ce lasers.

selectivity to the mask, so that this process is favorably for nanotechnology, such as DFB gratings masked with PMMA. The comparison between the cleaved facet and the etched facet laser confirms the performance of these CAIBE processes.

Acknowledgments

This work was supported by the German Bundesministerium für Forschung und Technik (BMFT). The authors would like to thank their many colleagues at the Fraunhofer Institut für Angewandte Festkörperphysik who have contributed to CAIBE system and process development. Thanks are due to W. Bronner and G. Kaufel for useful discussions. We also wish to thank H.S. Rupprecht for his continuing support and encouragement.

References

- [1] J.D. Ralston, K. Eisele, R.E. Sah, S. Bürkner, J. Fleissner, K. Bender, E.C. Larkins and S. Weissner, "Enhanced dry-etched mirror process for high-speed and monolithically integrated GaAs-based MQW lasers", Technical Digest: 1994 LEOS Summer Topical Meeting on Optoelectronic Materials Growth and Processing, pp. 24-25
- [2] J. Daleiden, K. Eisele, R.E. Sah, K.H. Schmidt, J.D. Ralston, "Chemical analysis of a $\text{Cl}_2/\text{BCl}_3/\text{IBr}_3$ -chemically-assisted ion-beam etching process for laser-mirrors under cryo-pumped UHV-conditions", submitted for publication.
- [3] G. Meneghini, L. Boschis, C. Coriasso, A. Stano, M. Gentili, L. Grella and M. Figliomeni, " CH_4/H_2 RIE of InGaAsP/InP Materials: An Application to DFB Laser Fabrication", *Microelectron. Engineering*, vol 21, pp. 321-324, 1993.
- [4] J.W. McNabb, H.G. Craighead, H. Temkin and R.A. Logan, "Anisotropic reactive ion etching of InP in methane/hydrogen based plasmas", *J. Vac. Sci. Technol.*, vol. B9, pp. 3535-3537, 1991.
- [5] S.J. Pearton, U.K. Chakrabarti, A. Katz, A.P. Perley, W.S. Hobson, and C. Constantine, "Comparison of CH_4/H_2 reactive ion etching and electron cyclotron resonance plasma etching of In-based III-V alloys", *J.Vac. Sci. Technol.*, vol. B9, pp. 1421-1432, 1991.
- [6] J. Singh, "Magnetron ion etching of InP using mixture of methane and hydrogen and its comparison with reactive ion etching", *J. Vac. Sci. Technol.*, vol B9, pp. 1911-1913, 1991.
- [7] I. Adesida, K. Nummila, E. Andideh, J. Hughes, C.Caneau, R. Bhat, and R. Holmstrom, "Nanostructure fabrication in InP and related compounds", *J. Vac. Sci. Technol.*, vol. B8, pp. 1357-1360, 1990.
- [8] S. Dzioba, S. Jatar, T.V. Herak, J.P.D. Cook, J. Marks, T. Jones and F.R. Shepherd, "High temperature operation of InGaAsP/InP heterostructure lasers and integrated back facet monitors fabricated by chemically assisted ion beam etching", *Appl. Phys. Lett.*, vol. 62, pp. 2486-2488, 1993.
- [9] C. Youtsey, R. Grundbacher, R. Panepucci, I. Adesida, and C. Caneau, "Characterization of chemically assisted ion beam etching of InP", *J.Vac. Sci. Technol.*, vol B12, pp. 3317-3321, 1994.
- [10] Y. Sugimoto, T. Yoshikawa, N. Takado, S. Kohmoto, N. Hamao, M. Ozaki, M. Sugimoto, and K. Asakawa, "Dry Etching Process for GaAs and InP Based Devices", *NEC Res. & Develop.*, vol. 33, pp. 469-480, 1992.
- [11] K. Iga, B.I. Miller, *IEEE J. Quant. Electr.*, vol. QE-18, p.26, 1982.

CHEMICAL BEAM ETCHING OF InP IN GSMBE

J.-L. Gentner, Ph. Jarry and L. Goldstein

Alcatel Alsthom Recherche
Route de Nozay, F 91460 Marcoussis - France

Introduction

The Chemical Beam Etching Technique (CBET) of InP and GaAs based materials using Phosphorus or Arsenic chlorides in a ultra high vacuum growth chamber is an attractive method combined with CBE or GSMBE for complex device fabrication (1). Etching of a few monolayers up to more than one micron on localized area followed by regrowth in the same ultra high vacuum chamber should produce nearly perfect interfaces and find a large application, in particular for the realisation of photonic and optoelectronic IC's.

In this work, we investigated the controlled etching of InP by CBET using diluted PCl_3 in H_2 in a GSMBE growth chamber. We report on the etching rate of InP as function of PCl_3 fluence and substrate temperature, the etched surface morphology and the profile at mask edges. We also demonstrate that *in situ* RHEED can be used during etching as an "atomic layer" precise end point detection.

Experimental set-up

An additional PCl_3 gas injection line has been fitted to a RIBER 2300 Gas Source MBE machine. The Phosphorus Trichloride (PCl_3) is contained in a thermostated glass bubbler included in a conventional pressure/mass flow controlled evaporation circuit. The PCl_3 is evaporated at a constant partial pressure of 0.1 atm. and injected in the MBE chamber through a vent/run manifold and a standard p-BN gas injector cell. Hydrogen or nitrogen have been used as carrier gases in the flow range 1 to 10 sccm. In most of the experiments, the temperature of the injector cell has been fixed at 100°C to avoid either decomposition or condensation of PCl_3 . It has been observed that the decomposition of PCl_3 is noticeable at a temperature higher than about 500°C with H_2 carrier gas and 600°C with N_2 carrier gas.

It is remarkable to note that after more than six months of regular use of PCl_3 in our GSMBE machine, no degradation of the performances of the equipment and the quality of the grown layers have been observed. The only point that has been noticed is a visible etch of the surface of the Ta heater on the substrate holder.

In-situ monitoring by RHEED

All the etching experiments have been systematically monitored by *in situ* RHEED. The typical (2×4) phosphorus dominated reconstruction pattern is always observed. The RHEED pattern is clearly defined and stable during the etching sequences, demonstrating a two dimensional (2D) layer by layer etching mechanism. A degradation to a spotty three dimensional (3D) like pattern has been sometimes

observed, in particular during the early trials when etching was performed under PH_3 stabilisation. This phenomenon is similar to the effect reported by Chiu *et al.* (2,3), who explain the effect by a roughening of the surface due to a limited indium surface diffusion at high phosphorus coverage. In consequence, most of the experiments have been performed without PH_3 addition. The results of all the etching experiments described here demonstrate that the surface of InP is stable under uncracked PCl_3 in a large temperature (420 to 540°C) and pressure (5.10^{-6} to 5.10^{-5} Torr) range.

Static RHEED observation provide also an easy end-point detection technique. Actually, during PCl_3 etching the RHEED pattern changes abruptly from the (2×4) reconstruction pattern typical of phosphorus stabilized InP surface, to a (2×1) pattern when an InP/InGaAsP interface is reached. This end-point detection is in principle "atomic layer" precise and has been proven to be useful in a large experimental domain. This feature is very important for real device application where a precise etch depth control is mandatory. Combining this etching technique, the end-point detection technique described and the capabilities of GSMBE, all in a ultra high vacuum environment, gives also the opportunity to develop new processes with "atomic layer" precise etch and regrowth sequences.

Kinetics of PCl_3 etching

Using the above described end-point detection technique, the etch rate of InP has been measured for different PCl_3 fluences and substrate temperatures. In our procedure, we first grow a thin InGaAsP layer (5 nm thick) followed by a calibrated layer of InP (10 to 100 nm thick). The layers are then

etched using diluted PCl_3 (10%) in H_2 , while the RHEED pattern is observed. The time to etch back the calibrated InP layer grown on top of the InGaAsP layer is monitored. This procedure can be repeated a large number of times without any noticeable degradation of the RHEED diagram, leading to a very simple and practical way of making the study of the etch rate as function of different parameters in one run. On figure 1, the time to etch back the InP layer is plotted as a function of the initial InP thickness for three different runs performed in the same conditions.

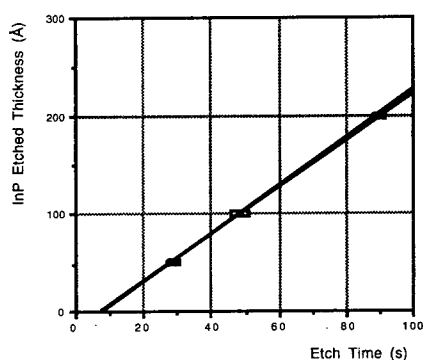


Figure 1: InP etched thickness versus etch time for three different runs with the same parameters ($T_s=480^\circ\text{C}$, $F(\text{PCl}_3) = 0.2 \text{ sccm}$, no PH_3).

As seen on the figure, the experimental results are very reproducible from run to run. This result demonstrates the effectiveness of the experimental procedure and the reproducibility of the etch rate. The dependance of the etch rate on the PCl_3 fluence is shown on figures 2 and 3. On figure 2, the etched depth is plotted as a function of time for different PCl_3 fluences at a substrate temperature of 480°C and with additional PH_3 .

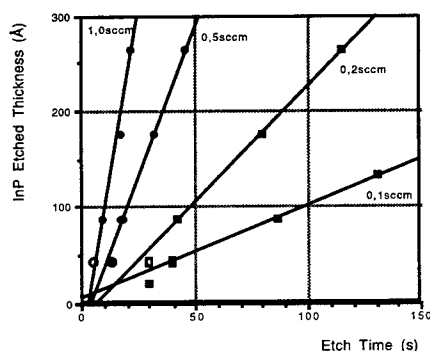


Figure 2: InP etched thickness as a function of time for different PCl_3 fluences ($T_s=480^\circ\text{C}$, with PH_3).

Figure 3 gives directly the measured etch rate for different substrate temperatures as a function of PCl_3 flow rate.

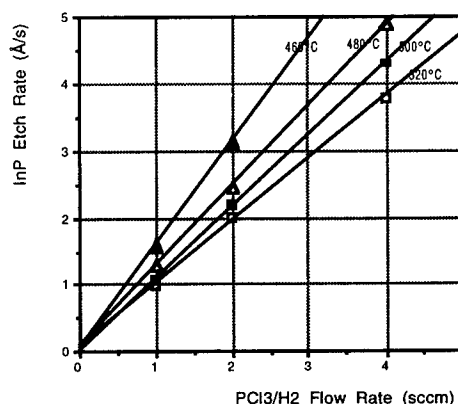


Figure 3: InP etch rate as function of PCl_3/H_2 flow rate for different substrate temperatures ($T_s = 460, 480, 500$ and 520°C).

The etch rate is found linear with PCl_3 flow rate for all temperatures. On figure 4, the etch rate is plotted as a function of the inverse substrate temperature for three different PCl_3 flow rates.

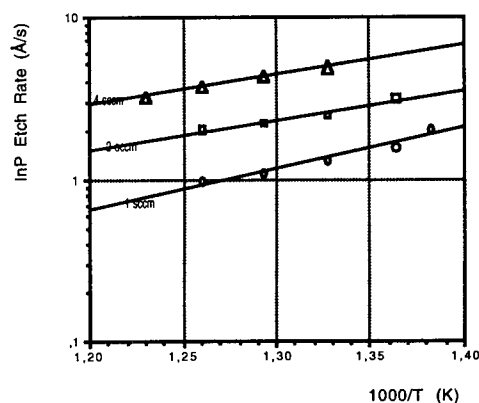


Figure 4: InP etch rate as function of $1/T$ for three different PCl_3/H_2 flow rates ($F(\text{PCl}_3) = 1, 2$ and 4 sccm).

The InP etch rate is found to be a weak function of the substrate temperature, contrary to the first results published by Tsang *et al.* (1).

It has also been noted that changing the carrier gas from H_2 to N_2 does not change the etching rate. This means that H_2 does not play a major role in the surface reaction, as expected at this rather low

substrate temperature. These different observations are consistent with a simple etch mechanism, limited only by the arrival rate of PCl_3 molecules at the surface. The decrease of the etching rate with increasing temperature can be understood as an effect of PCl_3 reevaporation from the sample before reaction.

Etched surface morphology

The surface morphology of 0.2 μm deep etched InP samples is illustrated on figures 5 and 6 for different InP substrates.



Figure 5: surface morphology of an InP:S substrate etched 0.2 μm deep .



Figure 6: surface morphology of an InP:Sn substrate etched 0.2 μm deep.

The etched surfaces are smooth and specular, except for the InP:S doped substrate where a slight roughness is noticed (not clear on this print). The defect density measured on the different substrates is directly related to the substrate dislocation

density. The sulfur doped etched substrates show nearly no defects, while the tin doped etched substrates have a defect density of the order of 3 to $5 \cdot 10^4 \text{ cm}^{-2}$, a value corresponding to the specified etch pit density of the substrate batch which has been used. The purely chemical nature of the etching mechanism, as for standard wet chemical etching, probably explains the preferential etching on surface emerging dislocations. Even if this effect has to be further looked at, the surface morphology of etched samples is compatible with high quality regrowth even for 1 μm deep etched samples.

The roughness of the etched samples have been assessed by AFM (4), the rms roughness value of different samples etched 0.2 μm deep being of the order of 5 Å for the Tin doped substrate, compared to about 1.5 Å on the reference unetched sample. This value is comparable to the value of 8 Å reported by Chiu *et al.* (3) for InP etching by AsCl_3 using a combination of pulse etching sequences with under vacuum recovery periods to enhance the smoothing of the surface microroughness by indium migration.

Uniformity of etch rate

The etch rate uniformity has been evaluated on a 2" InP substrate patterned with SiO_2 . The measured etch depth has a function of the position along a diameter of the sample is given in figure 7.

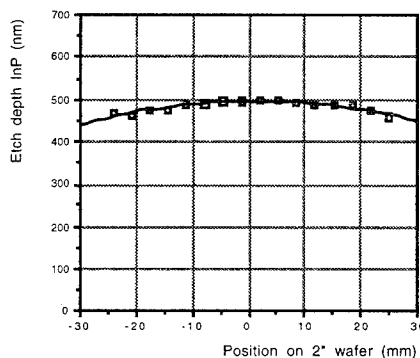


Figure 7: Etch depth uniformity along a diameter.

The etch rate nonuniformity between the center and the edge of the sample is about 5% for a nominal etch depth of about 0.5 μm . This value of nonuniformity and the shape of the etch depth profile matching closely a $1/R^2$ profile are consistent with a "perfect" Knudsen geometry. This means that the measured nonuniformity can be largely improved with a larger cell to substrate distance or an optimised cell to substrate angular geometry. As such, the value of the nonuniformity measured is

already comparable to the etch rate nonuniformities obtained with more standard RIE dry etching techniques.

Etch profile at mask edge

Figures 8 and 9 are SEM views of the mask edge profile after about 0.5 μm deep etching.

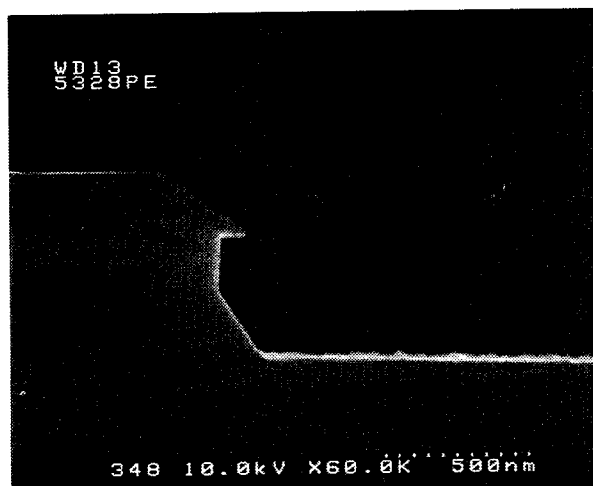


Figure 8: Etch profile along (1-10)

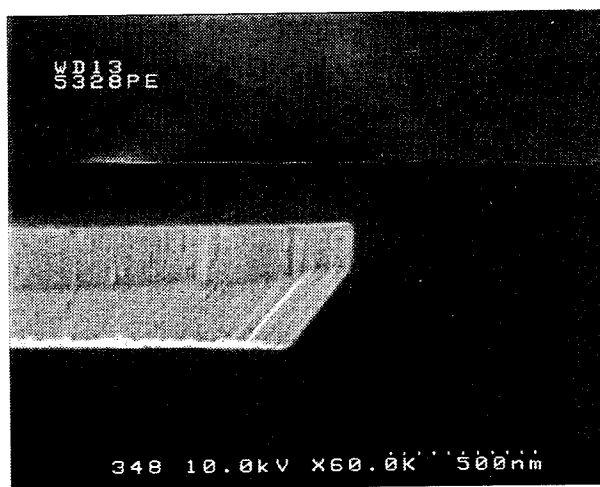


Figure 9: Etch profile along (110)

The profiles are comparable in the two perpendicular (110) orientations and are characterized by a very limited mask undercut (≈ 100 nm) and nearly perfect crystallographic facets. The etched profile is limited

by a vertical side wall below the mask and a (111) slow etching facet at the bottom corner. The SEM views show that the etching is a beam process, as expected, and suggest that the edge profile is limited by the surface diffusion of PCl_3 and by the slow etch rate in the (111) direction.

Conclusion

Molecular Beam Etching of InP using PCl_3 has been demonstrated for the first time compatible with standard GSMBE machines and GSMBE regrowth. The principle of an atomic layer accurate end-point detection technique using in-situ RHEED has been described and used to study the kinetics of PCl_3 etching. The etch rate is found proportional to the PCl_3 fluence and weakly dependent of the substrate temperature. The morphology of etched surfaces and the etch rate uniformity is compatible with high quality regrowth and very precisely controlled etch and regrowth sequences. Etch profile at mask edges are defined by nearly perfect crystallographic facets with a very limited mask undercut. These profiles are very difficult to obtain with other etching techniques and should be very well adapted to Gas Source MBE regrowth.

Acknowledgments

The authors would like to thank C. Graver for SEM observations, J-L. Peyre for wafers processing and D. Keller for the AFM measurements.

References

- (1) W.T. Tsang, R.M. Kapre, and P.F. Sciortino, Jr., "Reactive chemical beam etching of InP inside a chemical beam epitaxial growth chamber using phosphorous trichloride", *Appl. Phys. Lett.*, vol 62 no 17, pp 2084-2086, (1994).
- (2) T.H. Chiu, M.D. Williams, J.F. Ferguson, W.T. Tsang and R.M. Kapre, "Surface roughness during chemical beam etching and its remedy by enhanced cation diffusion", *Appl. Phys. Lett.*, vol 65 no 4, pp 448-450, 25 July 1994.
- (3) T.H. Chiu, M.D. Williams, W.T. Tsang and R.M. Kapre, "Effects of cation diffusion on the monolayer control of chemical beam etching", *J. Vac. Sci. Technol. B*, vol 12, no 6, Nov/Dec 1994.
- (4) measured on a nanoprobe PSI AFM instrument.

InP-Based HBTs and Their Perspective for Microwave Applications

Hin-Fai Chau, William Liu and Edward A. Beam III

Texas Instruments, Inc.
Corporate Research and Development
P.O. Box 655936, M/S 134
Dallas, TX 75265, U.S.A.

Introduction

Significant progress has been made over the past few years in both the technology and microwave performance of InP-based heterojunction bipolar transistors (HBTs). Emphasis has, however, been placed mainly on transistor performance. Other critical issues have largely been ignored, including the influence of InGaAs on device thermal resistance, the role of base-collector leakage current, and the phenomenon of thermal instability. This paper first briefly reviews recent microwave results achieved to date and then investigates the aforementioned critical issues that affect their use in microwave applications.

Recent Microwave Results

Impressive microwave characteristics have been achieved with a current-gain cutoff frequency f_T and maximum oscillation frequency f_{max} as high as 200 GHz [1] and 236 GHz [2], respectively, in single HBTs (SHBTs), and 160 GHz [3] and 267 GHz [4], respectively, in double HBTs (DHBTs). Fig. 1 summarizes recent microwave results of InP-based SHBTs and DHBTs [1-22]. As will be shown later, the poor output conductance and low breakdown voltage of SHBTs due to the base-collector leakage current limit their usefulness to low voltage and low power dissipation applications. Replacing the InGaAs collector with a wide bandgap material such as InP improves the breakdown and output conductance characteristics, but the presence of a base-collector heterojunction in such DHBTs blocks electron transport from the base to the collector, and leads to poor saturation characteristics if the heterojunction is not properly designed. Nevertheless, very impressive f_T and f_{max} comparable to those in SHBTs have been demonstrated.

Design Tradeoffs

1. Junction Temperature

InP is known to have higher thermal conductivity than GaAs (0.68 versus 0.45 W/cm-K at 300 K). It is therefore common to assume that InP-based HBTs run at lower junction temperatures than in GaAs devices having the same power dissipation. This is, however, not necessarily true in the presence of an InGaAs subcollector layer (and also an InGaAs collector layer in SHBTs) because InGaAs has a thermal conductivity of only 0.05 W/cm-K at 300 K. In order to better understand the impact of InGaAs in these devices, the temperature distributions of one-finger and eight-finger GaAs HBTs and InP SHBTs and DHBTs were

calculated using a 3-D thermal simulator developed at TI. InP was taken to be the collector material in the DHBTs. Room temperature thermal conductivity values were used and were assumed to be independent of temperature even though they all decrease with increasing temperature in practice.

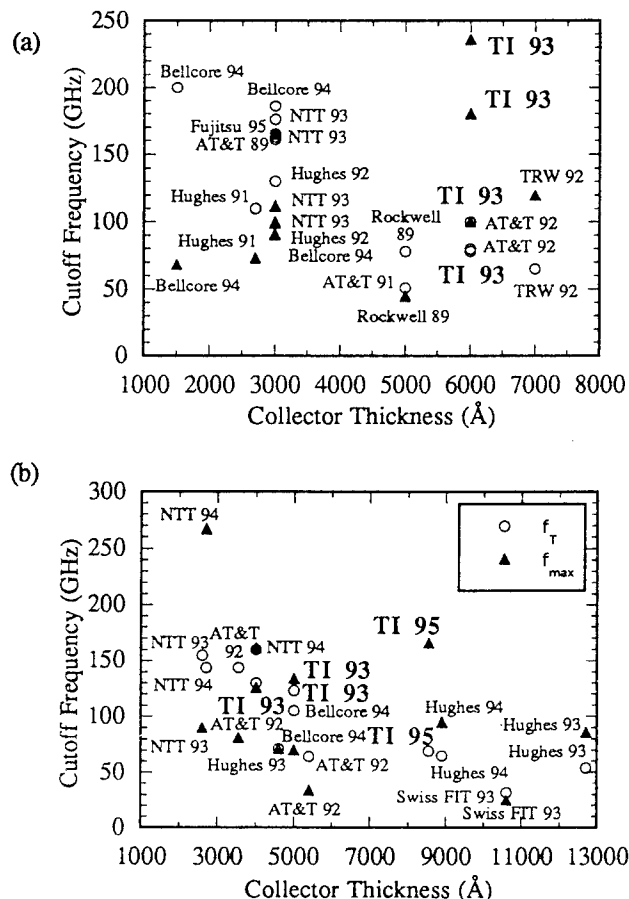


Fig. 1. Recent microwave results of InP (a) SHBTs and (b) DHBTs [1-22].

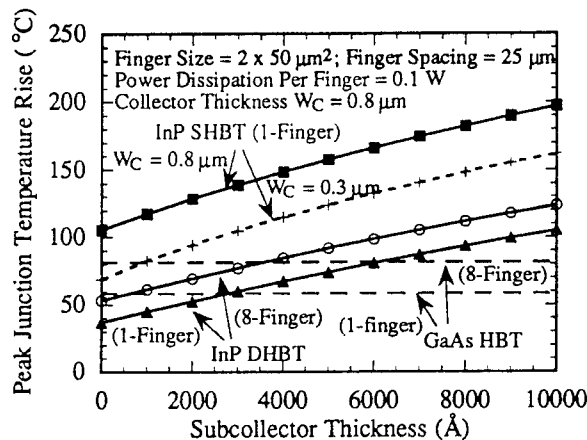


Fig. 2. Dependence of junction temperature rise on subcollector thickness in 1-finger and 8-finger GaAs HBTs and InP DHBTs, and 1-finger InP SHBTs.

Fig. 2 compares the peak junction temperature rises as a function of subcollector layer thickness for 1-finger and 8-finger GaAs HBTs and InP DHBTs, and a one-finger InP SHBT. The junction temperature rises in GaAs HBTs are independent of the subcollector thickness because the GaAs subcollector has a thickness which is negligible compared to the substrate thickness of 100 μm . In contrast, the junction temperatures increase rapidly with increasing InGaAs subcollector thickness in all InP HBTs. The rises in 1-finger InP SHBTs are far more significant than in multi-finger GaAs HBTs and InP DHBTs of the same layer thicknesses. Consider, for example, a subcollector thickness of 3000 \AA , a peak junction temperature rise of 139 $^{\circ}\text{C}$ and an ambient temperature of 25 $^{\circ}\text{C}$ result in a peak junction temperature of 164 $^{\circ}\text{C}$. As will be shown later, such a high junction temperature leads to 2-4 orders of magnitude increase in base-collector leakage current I_{CBO} [23], which goes to the base and gets amplified through the current gain mechanism of the transistor. A similar trend is observed when the subcollector layer thickness is fixed and the collector thickness varies. The increase in I_C is significant, and it leads to the well-known poor output conductance and breakdown-like behavior in the I_C - V_{CE} characteristics of InP SHBTs. Therefore, even though these SHBTs can have large open-base breakdown voltage BV_{CEO} , the breakdown voltage decreases rapidly as the power dissipation increases. Comparison between the thermal distributions in GaAs HBTs and InP DHBTs shows that the latter operates at lower peak junction temperatures only when the InGaAs subcollector layer thickness is less than about 3500 \AA . This is an important consideration especially for power applications in which power performance may be limited by thermal effects.

We have measured the average low-power thermal resistances R_{th} of InP SHBTs and DHBTs of different InGaAs thicknesses in the subcollector and/or collector from different wafer lots. To examine the first order effect of the InGaAs layer on R_{th} , we applied the technique of ref. [24] to the devices and found that R_{th} increases

substantially when more than 3000 \AA of InGaAs is incorporated in the subcollector in DHBTs and is large in SHBTs.

2. Base-Collector Junction Design

In addition to junction temperature considerations, the presence of InGaAs in the collector of an InP HBT has significant influence on the base-collector leakage current. Fig. 3 compares the temperature dependence of base-collector leakage currents in three different types of collector: (a) 7000 \AA n-InGaAs, (b) 8000 \AA n-InP and (c) 50 \AA n-InGaAs setback followed by 288 \AA n-InGaAs/InP grading (of which 50 % is InGaAs) and 8000 \AA n-InP. As shown, by introducing only 194 \AA of InGaAs in the collector, the leakage current increased substantially. Furthermore, an increase in substrate temperature by 100 $^{\circ}\text{C}$ increased the leakage currents in all cases by 2 to 4 orders of magnitude. The impact of this temperature dependence has particularly deleterious effects on InP SHBTs because of their high room-temperature leakage current and poor thermal conductivity. A transistor will blow up when I_{CBO} becomes excessive at elevated junction temperatures [25].

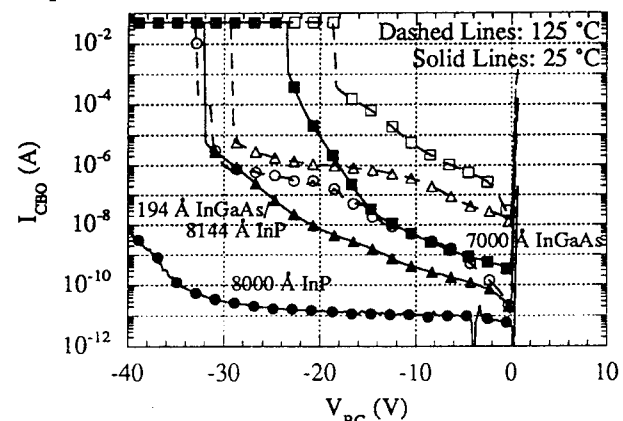


Fig. 3. Measured temperature dependence of base-collector leakage current on the amount of InGaAs in the collector.

In general, an abrupt base-collector heterojunction with an InGaAs setback layer can be used only in thin-collector designs ($< 4000 \text{\AA}$) [17, 21]. Graded heterojunction must be used for thicker collector DHBTs in order to avoid saturation problems or keep small "knee" voltage in the I_C - V_{CE} characteristics. Both step grading and continuous compositional grading using InGaAsP quaternary materials can be used. For example, S. Yamahata *et al.* have recently achieved a f_{max} and f_T of 267 GHz and 144 GHz respectively by applying a step-graded collector to thin collector structures [4]. For power applications in which thick collector and high breakdown voltage are required, a continuous compositionally-graded heterojunction with a proper doping profile needs to be used. Such kind of quaternary layer is, however, difficult to reproduce and maintain lattice matching. Alternatively, a chirped

superlattice consisting of InGaAs and InP layers of variable thicknesses allows an easier control of the grading [26-27]. Our DHBTs designed this way have shown BV_{CBO} of 29 V defined at 1 μ A leakage current (Fig. 3), f_T of 69 GHz, and f_{max} of 166 GHz. Similar type of DHBT power unit cells have demonstrated 1 W output power and 60% power-added-efficiency at 9 GHz [28].

3. Thermal Instabilities

Thermal instability occurs when one finger of a multi-finger transistor (the hot finger) hogs the input base current from the remaining fingers (the cold fingers), causing both I_B , I_C and the junction temperature in the hot finger increase dramatically. Fig. 4 shows the transistor I - V characteristics of a 2-finger $2 \times 10 \mu\text{m}^2$ InP DHBT which was specially designed so that the collector current of each finger can be individually monitored [29]. Fig. 5 illustrates the individual collector currents corresponding to the I - V of Fig. 4. Although it is not clear from Fig. 4 whether thermal instability ever occurs, Fig. 5 clearly demonstrates that the transistor enters thermal instability, that one finger current increases whereas the other decreases to zero. A study on the current gain variation in an InP DHBT is critical to the understanding to the I - V after thermal instability. Our measurements indicated that the current gain β had negligible temperature dependence from 25 °C

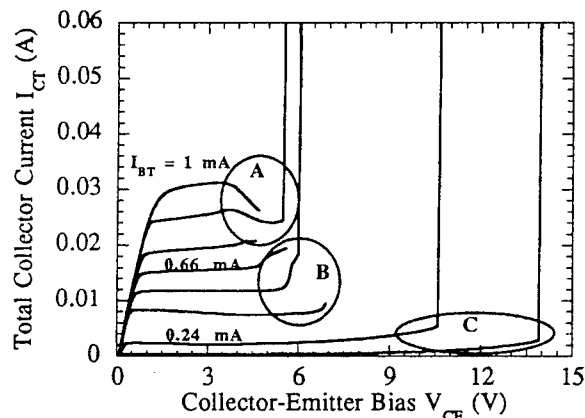


Fig. 4. Measured I_C - V_{CE} characteristics of a 2-finger $2 \times 10 \mu\text{m}^2$ DHBT.

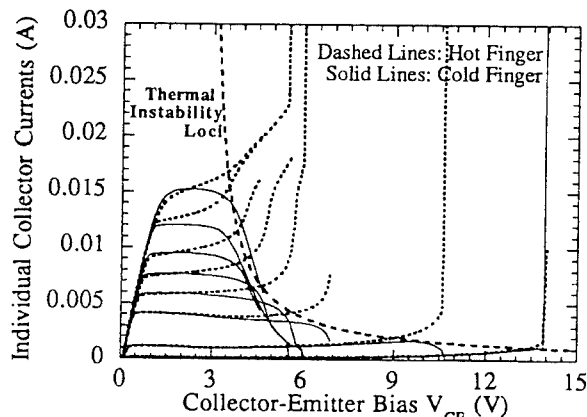


Fig. 5. Measured individual I_C 's corresponding to the I_C - V_{CE} of Fig. 4.

to 200 °C because of the large valence band discontinuity of 0.37 eV at the InP/InGaAs base-emitter heterojunction. As expected, β initially increases with I_C and then drops rapidly as I_C increases above 17 mA for the $2 \times 10 \mu\text{m}^2$ device due to increased electron blocking effect at the base-collector heterojunction.

The familiar collapse of current gain characteristics in GaAs HBTs appears only at high current levels (region A in Fig. 4) [30-31]. While the gain collapses in GaAs HBT due to its current gain decrease with temperature, the collapse in gain in InP DHBT is due to its current gain decrease at high currents. With further increase in V_{CE} in region A, the total I_{CT} suddenly increases toward infinity, irreversibly shorting out the device itself. The failure mechanism is identical to that reported for GaAs HBT, determined to be due to the increasing I_{CBO} at elevated junction temperatures [25]. In region B, the current levels at which the device enters thermal instability is far below 17 mA, β in this region increases as I_C increases. Therefore, when the hot finger current increases during thermal instability, the total I_{CT} increases in contrary to the collapse of current gain in region A. In region C, because the current levels are low, the corresponding V_{CE} at which thermal instability takes place are larger than that in region B. Consequently, the increased current gain in the hot finger after thermal instability leads to a more significant rise of junction temperature, which in turn increases I_{CBO} more substantially. Therefore, soon after the observed increase in the total I_{CT} , the device fails due to excessive I_{CBO} , without displaying a noticeable trend of rapid increase of I_{CT} as in region B. In both regions A and B, the device survives as long as care is exercised and V_{CE} does not increase too much beyond the aforementioned I_{CT} decrease or increase region. However, at low current levels (region C), I_{CT} increases toward infinity without giving a clear indication as to whether a thermal instability condition has occurred. In any case, care must be taken to avoid biasing devices near the thermal instability loci.

Microwave Applications

Microwave circuits typically require low noise and/or high power, as well as high power gain. For microwave power applications, the leakage current needs to be minimized in order for the HBTs to operate at high collector-emitter biases, either by reducing the InGaAs thickness in the collector or other means without increasing the "knee" voltage in the I_C - V_{CE} characteristics. The InGaAs subcollector layer has to be kept thin in order to take full advantage of the good thermal conductivity of InP substrates. InP power DHBTs fabricated at TI typically have a BV_{CBO} of 29 V (Fig. 3), and a gain of at least 19 dB at 10 GHz when they are biased at $V_{CE} = 3$ V. This kind of gain is considerably higher than that in our conventional X-band GaAs power devices which is about 16 dB at the

same frequency. Low current gain is needed for high BV_{CEO} , and high power and high power-added efficiency are expected for these power DHBTs. As for the linearity or intermodulation, InP SHBTs are expected to be worse than GaAs HBTs because of their poor output conductance. However, properly designed InP DHBTs should show comparable linearity as in GaAs HBTs. For low-voltage RF applications, InP SHBTs are still useful because of their simple structures and lower turn-on voltages than GaAs HBTs. Thin collector InP DHBTs with f_T and f_{max} are also very attractive in this category because they are easier to design than thick collector ones. For multipliers, oscillators and broadband communication amplifiers, the $1/f$ noise is quite important. Limited data have shown that InP-based HBTs have indeed lower low-frequency noise than in GaAs-based transistors as expected from their low surface recombination velocity [32-33], but care must be taken when interpreting these results since they depend greatly on the technologies used.

Summary

The technology and microwave performance of InP HBTs will continue to advance rapidly. The InGaAs in the subcollector and/or collector must be minimized in order to maintain good output conductance and linearity, and to avoid thermal instabilities and device failure due to excessive base-collector leakage current at elevated junction temperatures. InP SHBTs have high intrinsic leakage current and will be useful only for low voltage and low power dissipation applications, but properly designed DHBTs will be useful for most microwave applications.

Acknowledgment

The authors would like to thank D. Costa for many useful discussions, and S. Duncan, T. Session and D. Chasse for technical assistance.

References

- [1] J.-I. Song, K.B. Chough, C.J. Palmstrom, B.P. Van der Gaag, and W.-P. Hong, "Carbon-doped based InP/InGaAs HBTs with $f_{max} = 200$ GHz," *IEEE Device Research Conf.*, 1994, paper IVB-5.
- [2] H.-F. Chau and Y.-C. Kao, "High f_{max} InAlAs/InGaAs heterojunction bipolar transistors," *IEEE IEDM Tech. Dig.*, 1993, pp. 783-786.
- [3] Y. Matsuoka *et al.*, "Novel InP/InGaAs double-heterojunction bipolar transistors suitable for high-speed IC's and OEIC's," *IPRM Proc.*, 1994, pp. 555-558.
- [4] S. Yamahata, K. Kurishima, H. Nakajima, T. Kobayashi, and Y. Matsuoka, "Ultra-high f_T and f_{max} InP/InGaAs double-heterojunction bipolar transistors with step-graded InGaAsP collector," *GaAs IC Symp.*, 1994, pp. 345-348.
- [5] H. Shigematsu *et al.*, "Ultrahigh f_T and f_{max} new self-alignment InP/InGaAs HBTs with a highly Be-doped base layer grown by ALE/MOCVD," *IEEE Electron Devices Lett.*, vol. 16, 1995, pp. 55.
- [6] J.-I. Song, B. W.-P. Hong, C. J. Palmstrom, and K.B. Chough, "InP based carbon-doped base HBT technology: its recent advances and circuit applications," *IPRM Proc.*, 1994, pp.523-526.
- [7] H. Nakajima, K. Kurishima, S. Yamahata, T. Koayashi, and Y. Matsuoka, "High-speed InP/InGaAs HBTs operated at submilliampere collector currents," *Electron. Lett.*, vol. 29, no. 21, 1993, pp. 1887.
- [8] H.-F. Chau and E. A. Beam III, "High-speed InP/InGaAs heterojunction bipolar transistors," *IEEE Electron Device Lett.*, vol. 14, pp. 388, 1993.
- [9] L. Tran *et al.*, "InAlAs/InGaAs HBT with exponentially graded base doping and graded InGaAlAs emitter-base junction," *IPRM Proc.*, 1992, pp. 438-441.
- [10] J.F. Jensen, M. Hafizi, W.E. Stanchina, R.A. Metzger, and D.B. Rensch, "39.5-GHz static frequency divider implemented in AlInAs/GaInAs HBT technology," *GaAs IC Symp.*, 1992, pp. 101-104.
- [11] J.F. Jensen *et al.*, "36-GHz static digital frequency dividers in AlInAs-GaInAs HBT technology," *Device Research Conf.*, 1991, paper VIA-5.
- [12] T.R. Fullowan, S.J. Pearton, R.F. Kopf, F. Ren, and J. Lothian, "High yield scalable dry etch process for indium based heterojunction bipolar transistors," *IPRM Proc.*, 1992, pp. 343-346.
- [13] B. Jalali *et al.*, "10 Gbit/s D flipflop using AlInAs/InGaAs HBTs," *Electron. Lett.*, vol. 27, 1991, pp. 1314-1315.
- [14] Y.-K. Chen, R. N. Nottenburg, M. B. Panish, R. A. Hamm, and D. Humphrey, "Subpicosecond InP/InGaAs heterostructure bipolar transistors," *IEEE Electron Device Lett.*, vol. 10, pp. 267-269, 1989.
- [15] C.W. Farley *et al.*, "High-speed ($f_T = 78$ GHz) AlInAs/GaInAs single heterojunction HBT," *Electron. Lett.*, vol. 25, 1989, pp. 846-847.
- [16] W.E. Stanchina *et al.*, "Performance of InAlAs/GaInAs/InP microwave DHBTs," *IPRM Proc.*, 1993, pp. 17-20.
- [17] H.-F. Chau and E. A. Beam III, "High-speed, high-breakdown voltage InP/InGaAs double-heterojunction bipolar transistors grown by MOMB," *IEEE Device Research Conf.*, 1993, paper IVA-1.
- [18] H. Nakajima, "Design and fabrication of high-speed InP-based heterojunction bipolar transistors," *IPRM Proc.*, 1993, pp. 13-16.
- [19] R. Bauknecht, H. Duran, M. Schmatz, and H. Melchior, "InGaAs/InP double heterostructure bipolar transistors for high speed and high voltage driver circuit applications," *IPRM Proc.*, 1993, pp. 565-568.
- [20] A. Feyngenson, R.A. Hamm, P.R. Smith, M.R. Pinto, and R.K. Montgomery, "A 144 GHz InP/InGaAs composite collector heterostructure bipolar transistor," *IEDM Tech. Digest*, 1992, pp. 75.
- [21] A. Feyngenson *et al.*, "InGaAs/InP composite collector heterostructure bipolar transistors," *Electron. Lett.*, vol. 28, 1992, pp. 607-608.
- [22] M. Hafizi *et al.*, "Power performance and reliability of AlInAs/GaInAs/InP double heterojunction bipolar transistors," *IPRM*, 1994, pp. 527.
- [23] R.J. Malik *et al.*, "Temperature dependence of collector breakdown voltage and output conductance in HBT's with AlGaAs, GaAs, InP, and InGaAs collectors," *IEEE IEDM Tech. Digest*, 1991, pp. 805-808.
- [24] R.H. Winkler, "Thermal properties of high-power transistors," *IEEE Trans. Electron Devices*, vol. 14, 1967, pp. 260-263.
- [25] W. Liu, "Failure mechanisms in AlGaAs/GaAs heterojunction bipolar transistors," unpublished.
- [26] P.M. Asbeck, C.W. Farley, M.F. Chang, K.C. Wang, and W.J. Ho, "InP-based heterojunction bipolar transistors: performance status and circuit applications," *IPRM Proc.*, 1990, pp. 2-5.
- [27] M. Hafizi *et al.*, "High-performance microwave power AlInAs/GaInAs/InP double heterojunction bipolar transistors with compositionally graded base-collector junctions," *IEDM Tech. Digest*, 1993, pp. 791.
- [28] M. Hafizi, P.A. Macdonald, T. Liu, D.B. Rensch, and T.C. Cisco, "Microwave power performance of InP-based double heterojunction bipolar transistors for C- and X-band applications," *IEEE MTT-S Digest*, 1994, pp. 671-674.
- [29] W. Liu, "Thermal coupling in 2-finger heterojunction bipolar transistors," *IEEE Trans. Electron Devices*, vol. 42, June 1995.
- [30] W. Liu, S. Nelson, D. Hill, and A. Khatibzadeh, "Current gain collapse in microwave multi-finger heterojunction bipolar transistors operated at very high power density," *IEEE Trans. Electron Devices*, vol. 40, 1993, pp. 1917-1927.
- [31] W. Liu, and A. Khatibzadeh, "The collapse of current gain in multi-finger heterojunction bipolar transistor: its substrate temperature dependence, instability criteria and modeling," *IEEE Trans. Electron Devices*, vol. 41, pp. 1698-1707.
- [32] Y.K. Chen *et al.*, "Reduction of $1/f$ noise current with non-equilibrium electron transport in AlInAs/InGaAs heterojunction bipolar transistors," *IEEE IEDM Tech. Dig.*, 1993, pp. 803-806.
- [33] N. Hayama, S.-I. Tanaka, K. Iionjo, "1/f noise reduction for microwave self-aligned AlGaAs/GaAs HBTs with AlGaAs surface passivation layer," *3rd Asia-Pacific Microwave Conf. Proc.*, 1990, pp. 1039-1042.

Novel Self-Aligned Sub-micron Emitter InP/InGaAs HBT's Using T-Shaped Emitter Electrode

ThB2.2

Hiroshi Masuda, Tomonori Tanoue, Tohru Oka, Akihisa Terano, Michael W. Pierce
Kazuhiko Hosomi, Kiyoshi Ouchi and Teruo Mozume

Central Research Laboratory Hitachi, Ltd., Kokubunji, Tokyo 185, Japan

Abstract

A new self-aligned process for InP/InGaAs heterojunction bipolar transistors (HBTs) using a T-shaped emitter electrode has been developed. In this process, the T-shaped emitter electrode is used to allow the desired spacing between the emitter mesa and the base ohmic contact. The thickness of the emitter cap and emitter can be thinned independently of the base metal thickness. The thin emitter cap and emitter reduces the difference in characteristics due to the two emitter electrode orientations, parallel and perpendicular to orientation flat. A fabricated HBT shows a cutoff frequency (f_T) of 98 GHz with a $0.9 \mu\text{m} \times 4.7 \mu\text{m}$ sub-micron emitter and a maximum f_T of 120 GHz with a $1.4 \mu\text{m} \times 4.7 \mu\text{m}$ emitter after it is embedded.

Introduction

The InP-based heterojunction bipolar transistor (HBT) has great potential due to its high cut-off frequency and circuit performance [1-5]. In conventional self-aligned InP/InGaAs HBTs, the spacing between the emitter mesa and the base ohmic contact is formed by side etching during the emitter etching process [4]. This wet etching process has good selectivity between InP and InGaAs but its ability to shape the etching mesa is limited. The shape of the mesa depends on the crystal plane orientations, and the characteristics of HBTs are affected by whether the emitter electrode orientation is parallel or horizontal to orientation flat. HBTs with an InP emitter have another problem: the wet etching process does not form an undercut in the (111), (111) planes, so side etching has to be controlled by the etching of the InGaAs emitter cap. Recently, a report that this process could be done by ECR dry etching has been published [5]. But, all of these processes have a limit, though in the minimum thickness of the emitter cap and emitter layers, because the total thickness has to be thicker than the base metal thickness to avoid shorting between the emitter and the base electrodes. The new process offers better control when forming the desired spacing around the emitter mesa, because the undercut of the emitter electrode is not affected by isotropic side etching, unlike the conventional emitter etching process. It also avoids the minimum limit on the epitaxial layer thickness by optimizing the thickness of the lower emitter electrode metal.

The proposed structure

An HBT structure using a T-shaped emitter electrode is shown in Fig. 1. This T-shaped emitter electrode is made of two different kinds of metals formed using different etching rates. The bottom metal is WSi, which was selected because of its high etching rate against RIE compared to W, which is the upper metal. These metals were also selected because they are not etched by the semiconductor etchant and are very stable at high

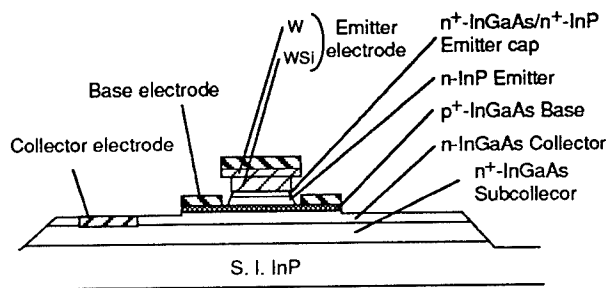


Fig. 1. Cross-sectional view of a HBT structure with a T-shaped emitter electrode.

temperatures. The selectivity of W is more than 10 times that of WSi, so only WSi is etched. The thickness of WSi is designed taking into account the base electrode thickness. The total thickness of the lower metal and the semiconductor layers of the emitter cap and emitter has to be larger than the thickness of the base electrode so the base electrode will not make contact with the emitter electrode. This new structure has an advantage in that the thickness of each metal and semiconductor layer can be designed separately. Then the total thickness of the emitter cap and emitter layers can be reduced and it minimizes the difference of emitter size between different emitter orientations.

Process flow of InP/InGaAs HBTs

The device layer structure for an InP/InGaAs HBT is shown in Table 1. These layers were grown by gas source molecular beam epitaxy (MBE) on a semi-insulating InP substrate of (100) plane. The group III source materials are solid In and Ga, and those of group V are arsine (AsH₃) and phosphine (PH₃). The total thickness of the emitter cap and emitter is 150 nm. This thicknesses is not optimized and it may be possible to reduce total thickness

Table 1. Epitaxial layer structure of the fabricated InP/InGaAs HBT.

Layer	Thickness (nm)	Doping (cm ⁻³)
n ⁺ -InGaAs	50	4E19
n ⁺ -InP	50	2E19
n ⁻ -InP	50	5E17
un-InGaAs	5	-
p ⁺ -InGaAs	50	2-4E19
n ⁻ -InGaAs	300	2E16
n ⁺ -InGaAs	500	2E19

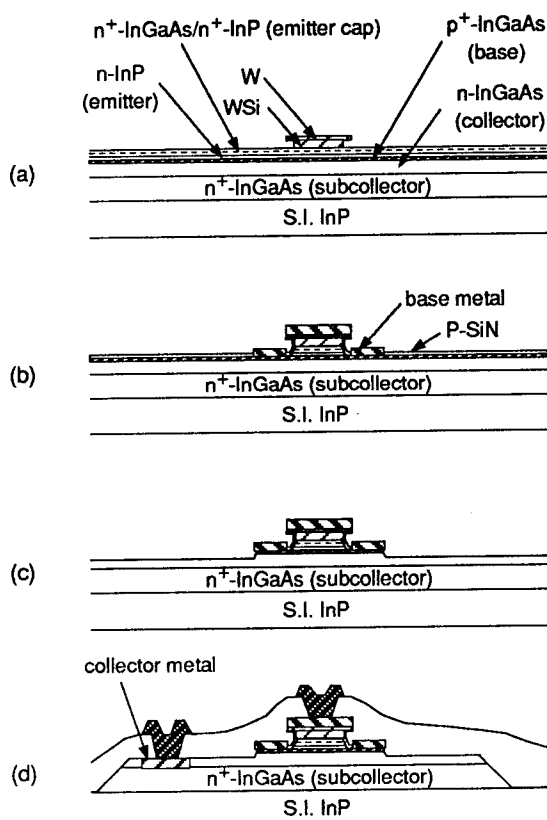


Fig. 2. Fabrication process of a fabricated HBT with a T-shaped emitter electrode.

to less than 100 nm, even if the base electrode metal is much thicker than that.

A schematic of the InP/InGaAs HBT fabrication process is shown in Fig. 2. First, the emitter metals of WSi and W are deposited on the epitaxial layers. The WSi, the lower metal, is 100 nm thick and the W above is 250 nm thick. These are then etched into an emitter electrode by RIE using NF₃ as an etching gas. The etching stop point is determined by monitoring the emission spectrum of the plasma. Next, the emitter cap layer and emitter layer are etched by wet etching using the emitter electrode as a

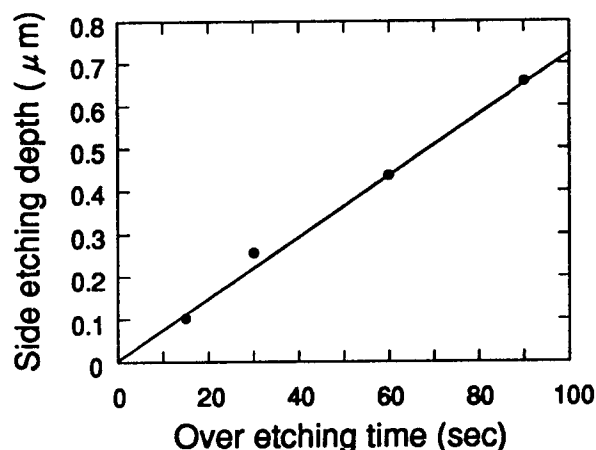


Fig. 3. Dependence of side etching depth on RIE over etching time.

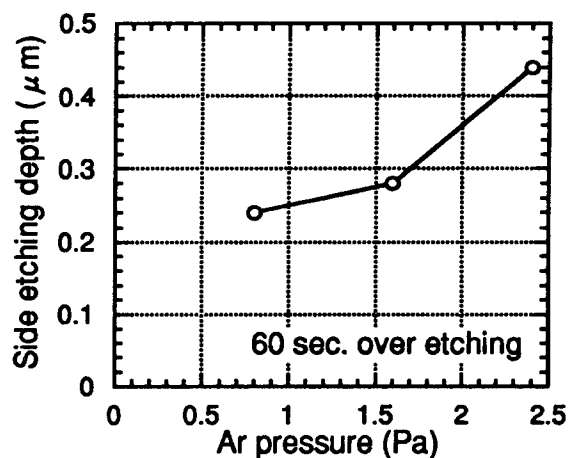


Fig. 4. Dependence of side etching depth on Ar pressure during WSi deposition.

mask. The insulator for emitter base junction passivation is deposited, then the base electrode is formed. The base electrode structure is Pt/Ti/Pt/Au. Then, the base and collector layers are etched by wet etching using the base electrode as a mask. A conventional processes used after base mesa etching: the collector electrode is formed of Ti/Pt/Au, and an isolation mesa, a passivation layer and interconnections are made. We use a PCVD-SiN layer for passivation of the emitter base junction, base collector junction, and for isolation.

Investigations of processes

The dependence of side etching depth on over etching-time is shown in Fig. 3. The side etching depth is linearly proportional to over-etching time. Monitoring the etching stop point and this linearity make the side etching depth very controllable. Figure 4 shows the dependence of side etching depth on Ar pressure during WSi deposition. The Ar pressure varied from 0.8 Pa to 2.4 Pa. The over-etching time is 60 seconds. The WSi target is different from that was used for taking data shown in Fig. 3, so there is a

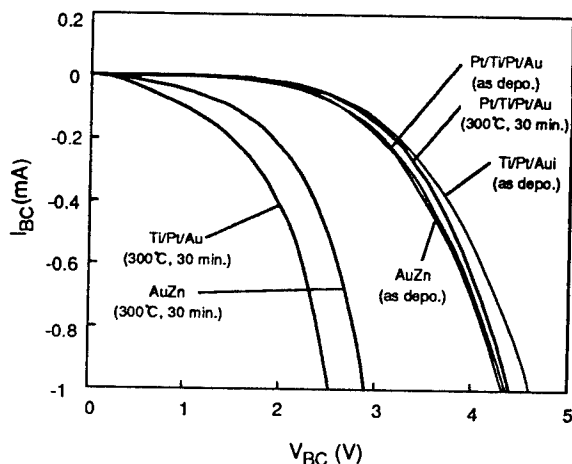


Fig. 5. Comparison of thermal stability of the base ohmic metals.

difference of side etching depth when over etching time is 60 sec. between that is shown in Fig. 3 and 4. The side etching depth increased when Ar pressure increased, because the Si composition increases when Ar pressure increases, thus the etching rate of the WSi also increases. This suggests that controlling Si composition is very important to control the side etching depth.

We also investigated the base metal stability. Although AuZn [6] and Ti/Pt/Au both show good contact resistivity to highly doped p-InGaAs, they are only stable when the maximum temperature during the fabrication process is under 250°C. We found that Au and Ti are easily sintered through the base layer to the collector layer at 300°C after only 30 minutes. This is clearly indicated by the reverse current-voltage characteristics, shown in Fig. 5. While Pt/Ti/Pt/Au shows better thermal stability, it also becomes unstable over 300°C for 30 minutes. The reason for higher stability may be that the Pt reaction layer becomes a barrier to the Ti. But our investigation shows that Ti will sinter through a Pt reaction layer at over 300°C. To overcome this problem, we propose inserting a thin Mo layer between the two Pt layers as a barrier layer to prevent Pt sintering. This new structure shows good stability at temperatures over 400°C.

Cross-sectional scanning electron micrographs of the emitter region parallel and perpendicular to orientation flat (OF), which is formed in the (011) plane, are shown in Figures 6(a) and (b), respectively. The angles of the emitter mesa shape of Figures 6(a) and (b) are about 45 degrees and 90 degrees, respectively. The spacing between the emitter mesa and the base metal is controlled to 0.15 μm , and 0.3 μm , as shown in Figures 6(a) and (b), respectively.

Results and discussion

Figure 7 shows typical current-voltage (I-V) characteristics of two types of fabricated HBTs, shown as Gummel plots. The solid line shows the HBT characteristics when the emitter electrode is perpendicular to OF. The broken line shows the characteristics when the

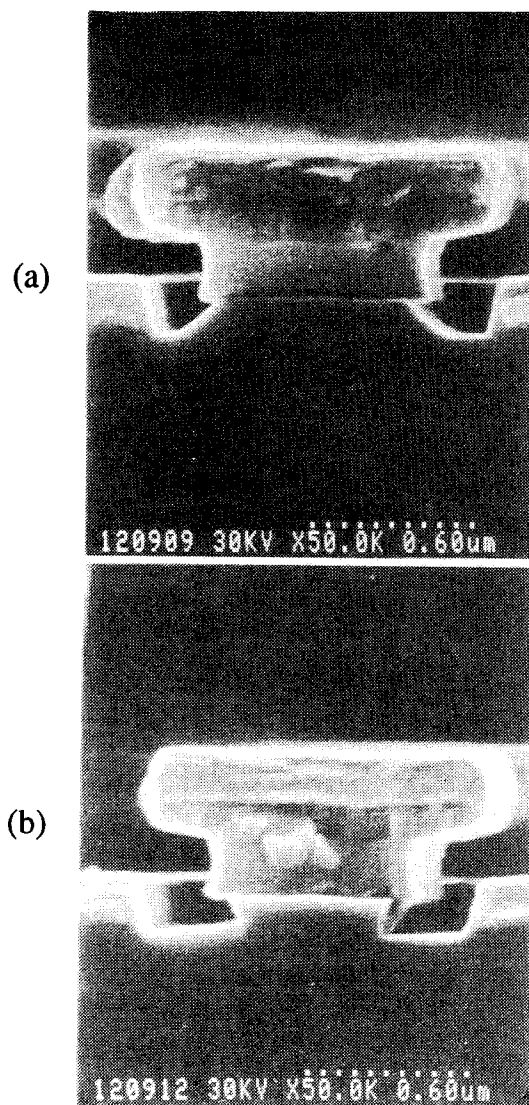


Fig. 6. SEM cross-sectional view of emitter region.

(a) Emitter electrode orientation is parallel to OF.

(b) Emitter electrode orientation is perpendicular to OF.

emitter electrode is parallel to OF. The base-collector bias was 0 V. The emitter electrode size is 2.0 μm x 5 μm (an emitter base junction size equivalent to 1.4 μm x 4.7 μm (perpendicular) and 1.7 μm x 4.4 μm (parallel)). The characteristics of the collector current are almost identically the same and the base current characteristics are also the same when the emitter-base bias is more than 0.8 V. The small difference between the collector current characteristics may be caused by a difference in the mesa shape of the thin emitter layers. The base collector breakdown voltage is over 6 V even if the maximum temperature during processing is 300°C. HBTs with several emitter sizes were fabricated, and Fig. 8 shows the I-V characteristics of three different HBT emitter sizes. Sub-micron emitter HBTs were successfully operated, demonstrating that this new process can be used to fabricate sub-micron emitter HBTs. Figure 9 shows the results of microwave measurement of the fabricated HBT

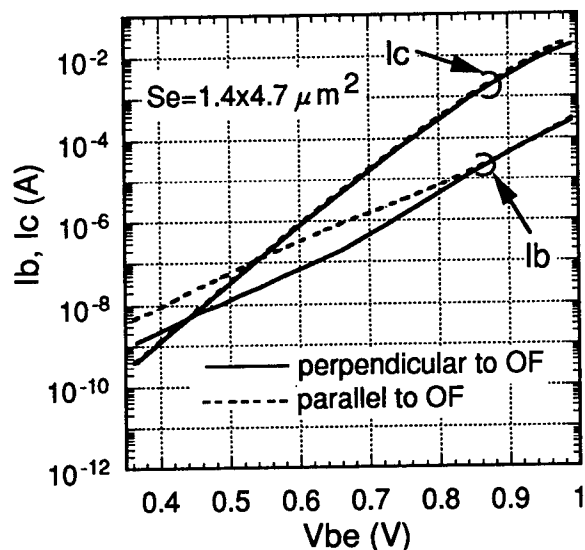


Fig. 7. I-V characteristics of fabricated HBTs with different emitter orientations shown as Gummel plots.

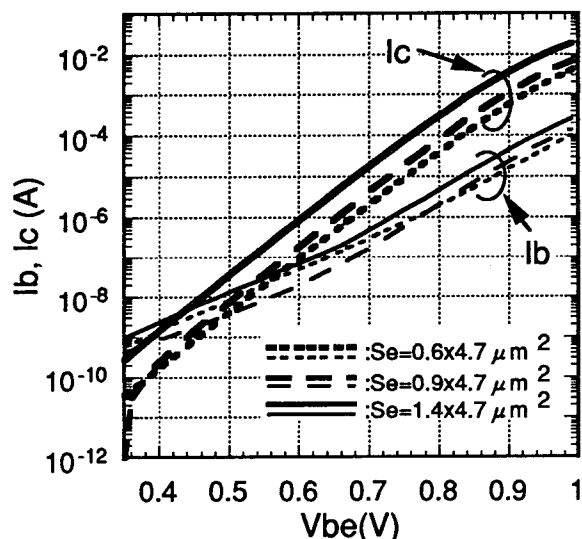


Fig. 8. I-V characteristics of HBTs with different emitter sizes as Gummel plot.

with an emitter size of $1.4 \mu\text{m} \times 4.7 \mu\text{m}$ after it was embedded to remove the effect of the measuring pad. It shows a cutoff frequency (f_T) of 120 GHz was obtained. The sub-micron emitter HBT with an emitter size of $0.9 \mu\text{m} \times 4.7 \mu\text{m}$, shows a f_T of 98 GHz.

Conclusions

In summary, we successfully developed a new process for fabricating HBTs with a T-shaped emitter electrode and fabricated a sub-micron emitter InP/InGaAs HBT using this process. This process makes it possible to reduce the thickness of the emitter cap and emitter independently of the thickness of the base electrode. The process also lets us

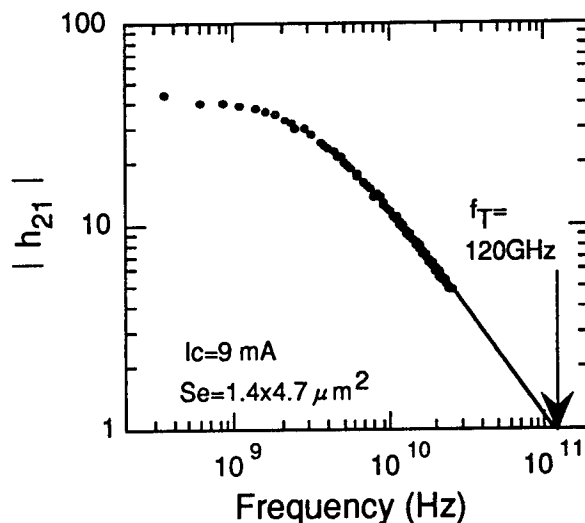


Fig. 8. Microwave measurement result of a fabricated HBT.

minimize the difference in the characteristics of HBTs whose emitters are parallel or perpendicular to the orientation flat. Fabricated HBTs show a high cutoff frequency (f_T) of 98 GHz with a sub-micron emitter of $0.9 \mu\text{m} \times 4.7 \mu\text{m}$ and a maximum f_T of 120 GHz with an emitter size of $1.4 \mu\text{m} \times 4.7 \mu\text{m}$.

References

- [1] R.N. Nottenburg, A. F. J. Levi, Y. K. Chen, B. Jalali, M. B. Panish and A. Y. Cho, "InP-Based Heterojunction Bipolar Transistors," IEEE GaAs IC Symp. Tech. Dig., pp. 135-138 (1989).
- [2] J. -I. Song, Brian W-P. Hong, Chris J. Palmström and K. B. Chough, "InP Based Carbon-Doped Base HBT Technology: Its Recent Advances and Circuit Applications," Proc. InP and Related Materials, 1994, pp. 523-526.
- [3] J. F. Jensen, M. Hafizi, W. E. Stanchina, R. A. Mertzger and D. B. Rensch, "39.5-GHz Static Frequency Divider Implemented in AlInAs/GaInAs HBT Technology," Dig. GaAs IC Symp., pp. 101-104, 1992.
- [4] K. Kurishima, H. Nakajima, T. Kobayashi, Y. Matsuoka and T. Ishibashi, "Fabrication and Characterization of High-Performance InP/InGaAs Double-Heterojunction Bipolar Transistors," IEEE Trans. Electron Devices, vol. 41, pp. 1319-1326, 1994.
- [5] H. Nakajima, "Design and Fabrication of High-speed InP-based Heterojunction Bipolar Transistors," Proc. InP and Related Materials, 1993, pp. 13-16.
- [6] H. Masuda, K. Mochizuki, M. Kawata, K. Mitani, M. Miyazaki and C. Kusano, "The Fabrication Process of AlGaAs/GaAs HBT's with Low Base Resistance and Low Collector Capacitance for 10 Gb/s IC Chip Sets," IEEE GaAs IC Symp. Tech. Dig., pp. 117-120 (1991).

Large-Signal Characteristics of InP-Based Heterojunction Bipolar Transistors and their Use in Optoelectronic Preamplifier Design *

A. Samelis, D. Pavlidis, F. Séjalon
Solid State Electronics Laboratory
The University of Michigan
Ann Arbor, MI 48109-2122

S. Chandrasekhar, L.M. Lunardi
AT&T Bell Laboratories
Crawford Hill Laboratory
Holmdel, NJ 07733

INTRODUCTION

InP/InGaAs-based Heterojunction Bipolar Transistors (HBT's) are attractive for optoelectronic circuits due to their compatibility with 1.3-1.5 μm operation which is combined with high speed but also low noise [1] characteristics. Various photoreceiver circuits have recently been reported where InP-HBT's and PIN diodes are integrated together [2], [3]. The importance of HBT large-signal modeling in the design of OEICs has been addressed recently for the case of AlGaAs/GaAs-based HBTs [4], but not for InP-based HBTs. The design of optoelectronic circuits employing InP-InGaAs single HBTs requires relatively low bias conditions for these devices due to their early breakdown characteristics. The use of large-signal models for InP HBTs could therefore improve the reliability of the design procedures and circuit performance predictions. In this work, a large-signal model incorporating breakdown effects has been developed for InP-InGaAs based HBTs and is validated by comparison of the simulated characteristics with directly measured power characteristics. The impact of the device nonlinear characteristics on the large-signal transimpedance of optical pre-amplifiers is also investigated.

DC AND BREAKDOWN MODELING OF InP/InGaAs-BASED HBT's

The device used in this study had an emitter area of $3 \times 8 \mu m^2$. All DC model parameters were calculated from the device Gummel plots. Forward Gummel-Plots were used to extract the forward saturation current and ideality factor, the base current components and the emitter resistance, R_E . Reverse Gummel-plots were used to determine the reverse saturation current and ideality factor, the reverse base current components and the sum of the base and collector resistances, $R_C + R_B$. Individual R_C , R_B values were evaluated by adjusting their magnitude in order to accomplish good fit between the measured and modeled $I_C - V_{CE}$ characteristics in the saturation region.

A breakdown model was developed by

incorporating to the conventional Gummel-Poon model a current source, I_{BR} , connected in parallel to the base-collector junction. I_{BR} was expressed as $I_{BR} = I_C \times BF \left[\exp\left(\frac{V_{CB} - I_{BR}R_{BR} + M \cdot I_C R_{BR}}{N_{BR} \times V_T}\right) - 1 \right]$, where, I_C is the collector current and BF , R_{BR} , M and N_{BR} are empirical constants selected for optimized fit between the measured and calculated device $I_C - V_{CE}$ characteristics. The multiplication factor of I_C is described by a diode connected in series to a resistor, R_{BR} , and emulates the commonly used expression for the breakdown base current contribution $(M' - 1)I_C$ where $M' = 1/[1 - (V_{CB}/BV_{CBO})^n]$. Models available in circuit simulators such as LIBRA do not account for such breakdown characteristics since employment of a single diode for the base-collector junction of an HBT would lead to unrealistically sharp increase of I_C as V_{CE} approaches the breakdown voltage. Such trends would therefore dis-

*This work has been supported by ARO (DAAL 03-92-G-0109) and ARPA-COST (MDA 972-94-1-0004)

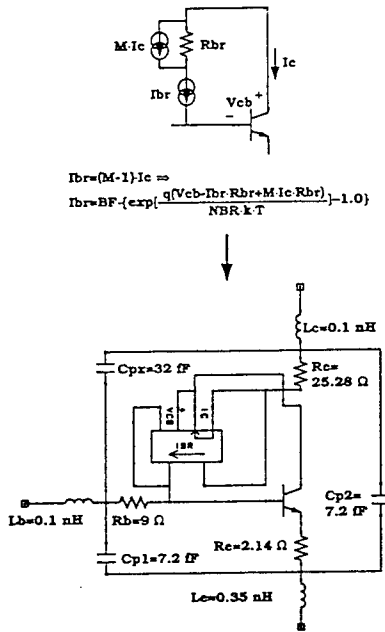


Figure 1: Incorporation of breakdown effects into a Gummel-Poon model schematically (top) and in LIBRA (bottom)

agree with the “soft” breakdown characteristics observed for InP HBT’s and would also be independent of I_c . Figure 1 shows the schematic of the breakdown model and its incorporation into a standard Gummel-Poon model.

An example of simulated HBT characteristics and their comparison to directly measured data is shown in Figure 2 for the HBT under test. Table 1 contains all Gummel-Poon HBT model parameters including the additional parameters related to breakdown.

SMALL-SIGNAL HBT MODEL PARAMETER EXTRACTION

Analytical modeling techniques have been employed for the extraction of HBT equivalent circuit parameters [5]. “Cold” (i.e. $V_{BE} = 0$) S-parameter measurements [6] permitted the exact evaluation of pad-parasitic capacitances and the bias dependence of C_{bc} . An expression, $C_{px} + \frac{C_{bco}}{1 + V_{cb}/V_{jco}}$ was analytically fitted to the low frequency quantity $-\frac{Im[Y_{12}]}{\omega}$, which resulted in $C_{px} = 32 \text{ fF}$, $C_{bco} = 14.14 \text{ fF}$ and $V_{jco} = 1 \text{ V}$. The above parasitics together with series inductors were added to the DC model developed earlier in order to form the complete HBT large-

Parameter	Value
I_S	$2.28386 \cdot 10^{-15} \text{ A}$
β_f	<i>Infinity</i>
β_r	0.00185
η_f	1.35511
η_r	1.08135
I_{SE}	$5.33298 \cdot 10^{-16} \text{ A}$
I_{SC}	$1.47678 \cdot 10^{-9} \text{ A}$
η_e	1.51066
η_c	1.82278
R_C	25.28Ω
R_E	2.14Ω
R_B	9Ω
τ_f	1.7 ps
C_{JE}	35.45 fF
V_{JE}	1.0 V
M_{JE}	0.5
C_{JC}	14.14 fF
X_{CJC}	1
V_{JC}	1.0 V
M_{JC}	0.5
BF	$3.7 \cdot 10^{-4} \text{ A}$
R_{BR}	170Ω
NBR	11.0
M	0.115

Table 1: Parameters of the new Gummel-Poon large-signal model which incorporates breakdown effects

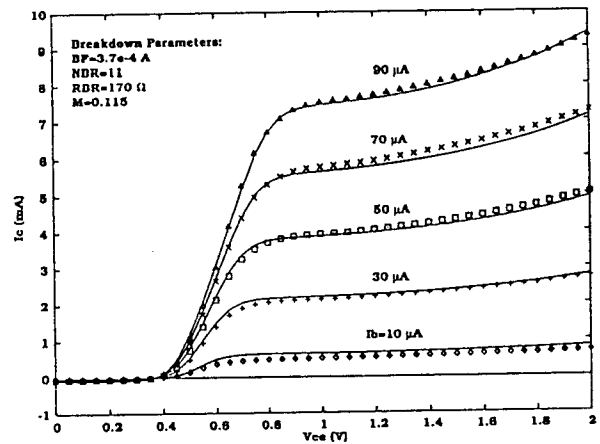


Figure 2: Measured and simulated DC I_C - V_{CE} characteristics of InP/InGaAs single HBT using the new HBT model which incorporates breakdown effects

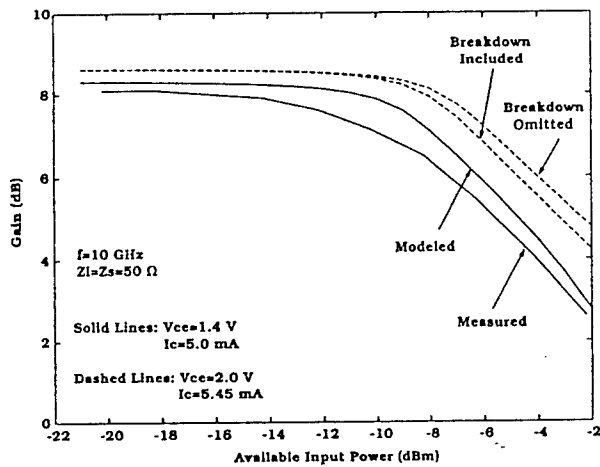


Figure 3: Power characteristics of a $3 \times 8 \mu\text{m}^2$ InP/InGaAs HBT

signal model of this work.

POWER CHARACTERIZATION AND MODELING

The device power characteristics were measured using FOCUS electromechanical tuners and on-wafer probing. The device large-signal characteristics such as output power, gain and transimpedance for various input power levels were calculated using harmonic-balance techniques.

Figure 3 (solid lines) shows the measured and simulated device gain dependence on the available source power at 10 GHz, for $I_C = 5 \text{ mA}$ and $V_{ce} = 1.4 \text{ V}$ bias and loading conditions close to 50Ω . A good agreement is observed between theoretically simulated and directly measured characteristics. One also observes that gain compression takes place at power levels as small as -8 dBm . Depending on design, this may consequently affect the large-signal characteristics of optoelectronic amplifiers employing such transistors.

The impact of breakdown on the small and large-signal gain is also shown in figure 3 (dashed lines) with the help of our model. The bias conditions correspond here to higher I_C and V_{CE} in order to enhance breakdown effects. Breakdown does not affect the device gain under small-signal operation conditions. The large-signal gain degrades, however, faster if breakdown is taken into account in modeling the HBTs.

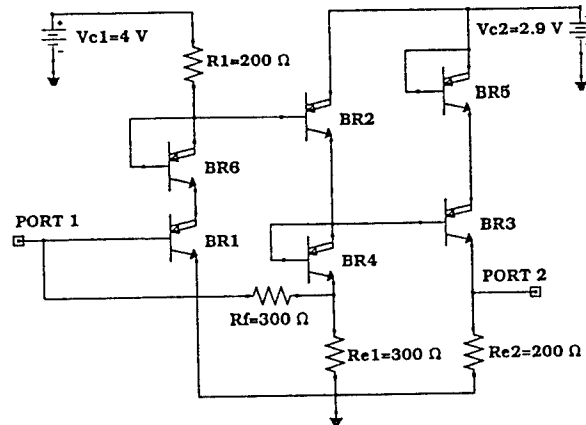


Figure 4: Basic coupled buffer InP/InGaAs preamplifier employing the new HBT model

LARGE-SIGNAL CHARACTERISTICS OF TRANSIMPEDANCE AMPLIFIERS

Two HBT preamplifier designs were studied and their large-signal transimpedance was evaluated. Design A is a basic coupled buffer amplifier while design B is a cascode transimpedance preamplifier with feedback capacitor. The amplifier schematic of design A is shown in figure 4. The new HBT model which accounts for breakdown has been employed in the design of both amplifiers. Using the harmonic balance technique, the large-signal S-parameters of the amplifiers were calculated at different power levels and the effective transimpedance, Z_{eff} , was calculated from $Z_{eff} = 20 \log \left(50 \cdot \frac{|S_{21}^L|}{|1 - S_{11}^L|} \right)$, where Z_{eff} is calculated assuming 50Ω termination and S_{21}^L and S_{11}^L are large-signal S-parameters of the preamplifier. Figures 5 and 6 show the frequency response of Z_{eff} at different power levels for design A and B respectively.

As one observes, Z_{eff} is very sensitive on available input power for design A in the range from -25 to -15 dBm . This behavior is also accompanied by significant variation of the circuit large-signal S-parameters with power as well as strong self-biasing of the individual transistors at even very low power levels. On the other hand, Z_{eff} does not show significant sensitivity with power for design B. Further analysis of this circuit revealed weak dependence on power of the large-signal S-parameters and weak self-

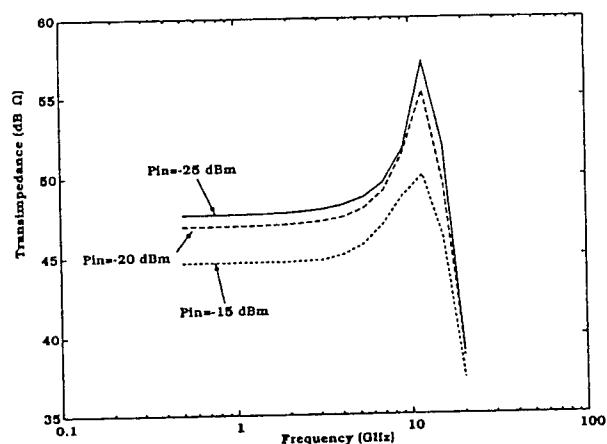


Figure 5: Frequency response of effective transimpedance at different available input power levels for preamplifier design A

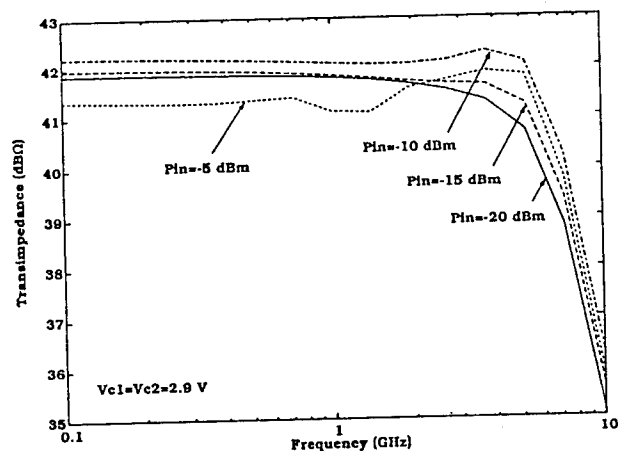


Figure 6: Frequency response of effective transimpedance at different available input power levels for preamplifier design B

bias of the individual transistors. Overall, it appears that, depending on design, the transimpedance Z_{eff} and bandwidth of the optical preamplifier may be sensitive to the input power level. The results also show that performance variations in such cases are observed at relatively small power levels. Furthermore, if self-biasing effects resulting from input power variations become pronounced they may compromise circuit stability and result in poor reliability. OEIC design should consequently account for the large-signal InP HBT characteristics for the accurate prediction of circuit performance.

CONCLUSIONS

In summary, a large-signal model suitable

for InP-InGaAs HBT's was developed. Break-down effects have been incorporated into the Gummel-Poon formulation. The new model was validated by comparisons with on-wafer power measurements. The characteristics of two transimpedance amplifiers of different design were studied using the large-signal models developed for InP/InGaAs HBTs. The analysis showed that circuit characteristics can be modified under large-signal operation. Transimpedance degradation and pronounced self-bias can, for example, take place and these depend on the type of OEIC. Large-signal modeling should therefore be considered for accurate OEIC design.

References

- [1] A.K. Kirtania, M.B. Das, S. Chandrasekhar, L.M. Lunardi, R.A. Hamm and L.W. Yang, "A Comparison of Low-Frequency Noise Characteristics of Silicon Homojunction and III-V Heterojunction Bipolar Transistors", IPRM-94, Dig., pp. 535-538.
- [2] A.L. Gutierrez-Aitken, J. Cowles, P. Bhat-tacharya and G.I. Haddad, "High Bandwidth InAlAs/InGaAs PIN-HBT Monolithically Integrated Photoreceiver", IPRM-94, Dig., pp. 247-250.
- [3] S. Chandrasekhar, L.M. Lunardi, R.A. Hamm and G.J. Qua, "Eight-Channel p-i-n/HBT Monolithic Receiver Array at 25 Gb/s per Channel for WDM Applications", IPRM-94, Dig., pp. 243-246.
- [4] N. Nagano, T. Suzaki, M. Soda, K. Kasahara, T. Takeuchi and K. Honjo, "Monolithic Ultra-Broadband Transimpedance Amplifiers Using Al-GaAs/GaAs Heterojunction Bipolar Transistors", IEEE Transactions on Microwave Theory and Techniques, Vol. 42, No. 1, January 1994, pp. 2-10.
- [5] D.R. Pehlke and D. Pavlidis, "Evaluation of the Factors Determining HBT High-Frequency Performance by Direct Analysis of S-Parameter Data", IEEE Transactions on MTT, Vol. 40, No. 12, December 1992, pp. 2367-2373.
- [6] A. Samelis, D.R. Pehlke and D. Pavlidis, "Volterra Series Based Nonlinear Simulation of HBT's Using Analytically Extracted Models", Electronics Letters, 23rd June 1994, Vol. 30, No.13, pp. 1098-1100.

InP/InGaAs COLLECTOR-UP HETEROJUNCTION BIPOLAR TRANSISTORS FABRICATED USING Fe-ION-IMPLANTATION

Shoji YAMAHATA, Kenji KURISHIMA, Takashi KOBAYASHI, and Yutaka MATSUOKA

NTT LSI Laboratories (TEL: +81 462 40 2891, E-mail: yamahata@aecl.ntt.jp)

3-1 Morinosato-Wakamiya, Atsugi-shi, Kanagawa 243-01, Japan

Introduction

This paper describes the first InP/InGaAs collector-up heterojunction bipolar transistors (C-up HBTs) with base and collector layers regrown onto emitter layer. We used Fe-ion (Fe^+) -implantation to define the intrinsic emitter/base (E/B) junctions and a self-aligned fabrication processing for small-scale C-up HBTs.

The collector-up configuration is attractive for ultra-high-speed and high power gain operation due to its low base/collector capacitance (C_{BC}). For scaling down transistors, the advantage of this configuration over the emitter-up configuration is clear because the parasitic C_{BC} corresponding to the extrinsic area can be neglected. This also makes the C-up HBTs feasible for low power dissipation devices.

Although there are several reports on AlGaAs/GaAs and InAlAs/InGaAs C-up HBTs [1-5], there are few on InP/InGaAs C-up HBTs. The most important process step in the fabrication of C-up HBTs is the formation of a barrier at the extrinsic E/B regions to suppress excess base current under forward bias voltage. In AlGaAs/GaAs and InAlAs/InGaAs heterostructures, highly resistive layers formed by O^+ - or H^+ -implantations in AlGaAs or InAlAs have been used as the barrier layers. In the InP/InGaAs heterostructure, however, it is difficult to form such a barrier layer by conventional ion-implantation-bombardment. We therefore use Fe^+ -implantation to convert an n-type InP layer in the extrinsic emitter into a highly resistive one. This layer is made stabler by the subsequent high-temperature regrowth process, which results in the creation of deep acceptors in the InP layer [6].

1. Diode Characteristics of Fe^+ -implanted InGaAs/InP p-n junctions

It has been reported that the defects created in InP tend to pin the Fermi level in the upper half of the bandgap and that it is therefore difficult to obtain the highly resistivity of n-type material by ion-bombardment. On the other hand, it is well known that many Fe atoms occupying group-III lattice sites act as compensating deep acceptors [7, 8]. A highly resistive InP layer can thus be formed by Fe^+ -implantation and subsequent high-temperature annealing.

To examine a highly resistive barrier layers introduced by Fe^+ -implantation in InP, we fabricated the p^+ -InGaAs/N-InP/ n^+ -InGaAs diode structure corresponding to the extrinsic E/B heterostructure in C-up HBTs. Although there have been many reports on the electrical properties of Fe^+ -implanted InP layers, there have been few reports on the characteristic of Fe^+ -implanted InP/InGaAs heterostructure diode. Table I lists the diode layers, which were grown by low-pressure metalorganic vapor phase epitaxy (MOVPE).

Figure 1 shows cross-sectional schematic views of the fabricated diodes. Fe^+ was first implanted through the N-InP, using a photoresist as a mask. Then the upper p^+ -InGaAs layer was regrown at 650°C onto the entire InP layer. The Pt/Ti/Pt/Au ohmic metal was then formed on the p^+ -InGaAs layer and was sintered at 300°C . The p^+ -InGaAs and the implanted InP layer were then removed by wet-etching, using the Pt/Ti/Pt/Au as a mask, and the Ti/Pt/Au ohmic metal was formed on the unimplanted n^+ -InGaAs layer.

TABLE I. Epitaxial diode structure.

Material	Doping (cm^{-3})	Thickness (nm)
p^+ -InGaAs	2×10^{19}	80
un-InGaAs	undoped	5
N-InP	3×10^{17}	150
n^+ -InGaAs	5×10^{18}	500

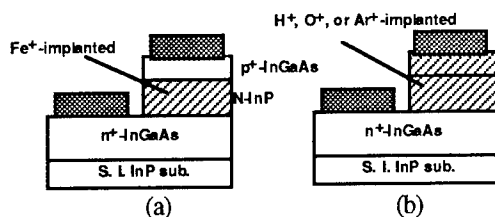


Fig. 1. Cross-sectional schematic views of Fe^+ -implanted and H^+ , O^+ , or Ar^+ -implanted diodes.

For comparison, diodes made by conventional inactive-ion species (H^+ , Ar^+ , and O^+) implantations were also tested, but the implantation of these ions through the $\text{p}^+\text{-InGaAs}$ and N-InP layers differed from that of Fe^+ (See Fig. 1 (b)). In these diodes, the $\text{p}^+\text{-InGaAs}$ layer was not regrown on any of the implanted layers. The subsequent processes, however, were the same as those used to fabricate the Fe^+ -implanted diodes.

The implantation conditions are outlined in Table II. Each implantation energy was chosen to give approximately the same projected range distribution, at least so as to reach the whole InP layer. Ion doses in the range between 1×10^{13} and $5 \times 10^{14} \text{cm}^{-2}$ were optimized to obtain the highest resistivity value.

TABLE II. Implant species, energy, and dose.

Species	Energy (keV)	Dose (10^{14}cm^{-2})
$^{56}\text{Fe}^+$	75	3
$^1\text{H}^+$	40	5
$^{40}\text{Ar}^+$	200	2
$^{16}\text{O}^+$	110	0.1

Figure 2 shows the I-V characteristics of unimplanted (intrinsic) and implanted diodes for which the $\text{p}^+\text{-InGaAs}/\text{N-InP}$ junction was $2 \mu\text{m} \times 10 \mu\text{m}$. The diode made by Fe^+ -implantation has the highest resistivity in the InP layer, and at a forward-bias voltage of 0.9 V its current density is more than six orders of magnitude lower than that of an unimplanted diode.

For Ar^+ - and O^+ -implantations, on the other hand, the current density at a 0.9-V forward-bias voltage is only about three orders of magnitude lower. S. J. Pearton et al. have reported that the high resistivity induced in the InP layer by ion-bombardment easily recovers even after 400°C annealing

[6]. When we use the $\text{p}^+\text{-InGaAs}$ regrowth process accompanied with 650°C annealing after O^+ or Ar^+ -implantation, it is impossible to obtain highly resistive barrier in the InP layer. Therefore, only the highly resistive InP layer formed by Fe^+ -implantation and subsequent regrowth process can provide the barrier suppressing undesirable excess current from an $\text{n}^+\text{-InGaAs}$ layer to a $\text{p}^+\text{-InGaAs}$ layer.

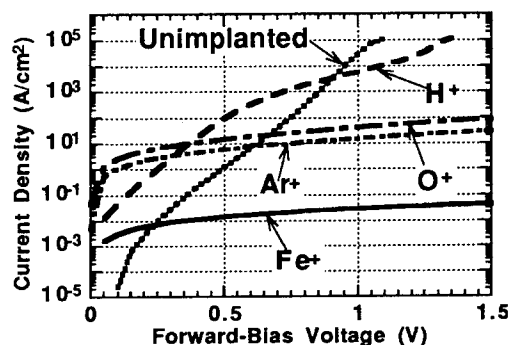


Fig. 2. I-V characteristics of unimplanted and H^+ , Ar^+ , O^+ , and Fe^+ -implanted InP/InGaAs diodes.

2. C-up HBT Fabrication Using Fe^+ -implantation and Regrowth

We used the C-up HBT layer structure indicated in Table III, and Figure 3 is a schematic cross-sectional view of the self-aligned InP/InGaAs C-up HBT. The buffer, subemitter, emitter, and spacer layers were grown by low-pressure MOVPE, and Fe^+ was implanted into the patterned InGaAs spacer and InP emitter layers at a dose of $3 \times 10^{14} \text{cm}^{-2}$ and an acceleration energy of 75 keV. After preheating at 650°C , the base, collector, and cap layers were regrown on the all areas which include Fe^+ -implanted and unimplanted layers.

The Ti/Pt/Au collector electrode was formed and used as a mask when reactive-ion etching performed with Cl_2/Ar mixed gas-plasma excited in an electron-cyclotron-resonance reactor was used to define the collector-mesa. The InGaAs layer was also wet-etched to form an undercut area around the collector-mesa. The total etching depth measured with a stylus-contact-type profiler was approximately 520 nm.

The Pt/Ti/Pt/Au base ohmic metal was evaporated onto

an area including the entire collector-mesa. Owing to the undercut region, the base ohmic contact was self-aligned to the collector with a base-metal overlaid structure [9]. B/E mesa-etching was then performed using a wet-etching system selective for InGaAs and InP layers, and the Ti/Pt/Au emitter electrode was formed. After deep isolation mesa-etching and polyimide film passivation, the processing was completed with Ti/Pt/Au interconnect metallization.

TABLE III. Layer structure for the C-up HBT.

Layer	Material	Doping (cm ⁻³)	Thickness (nm)
C-Cap	n ⁺ -InGaAs	Si:3×10 ¹⁹	120
Collector	un-InGaAs	undoped	400
Base	p ⁺ -InGaAs	Zn:2×10 ¹⁹	80
Spacer	un-InGaAs	undoped	5
Emitter	N-InP	Si:3×10 ¹⁷	50
Sub-E	N ⁺ -InP	Si:2×10 ¹⁹	10
	n ⁺ -InGaAs	Si:5×10 ¹⁸	400
Buffer	un-InP	undoped	100

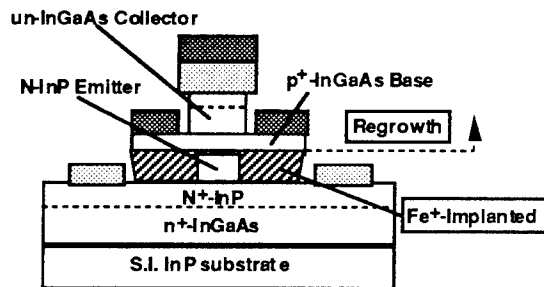


Fig. 3. The C-up HBT fabricated by self-aligned processing.

3. DC and RF Characteristics of C-up HBTs

Figure 4 shows typical common-emitter I-V characteristics for InP/InGaAs C-up HBTs with a 2 $\mu\text{m} \times 5 \mu\text{m}$ collector. The maximum current gain was 8 at a collector current density J_C of about $4.5 \times 10^4 \text{ A/cm}^2$. This figure also shows the small offset voltage due to the area of the E/B junction in a C-up HBT being the same as the area of the B/C junction.

Gummel-plots (J_C and base current density J_B as a function of E/B voltage V_{BE}) are shown in Fig. 5 for a

C-up HBT with a 2 $\mu\text{m} \times 2 \mu\text{m}$ collector. This transistor exhibits a high J_C , more than $1 \times 10^5 \text{ A/cm}^2$, without decrease in current gain. In addition, a high J_C was attained even in transistors with an E/B junction smaller than $1 \mu\text{m} \times 1 \mu\text{m}$. These results confirm that the undesirable excess base current associated with the extrinsic E/B junction is sufficiently suppressed by the combination of the Fe⁺-implantation and subsequent high-temperature annealing (regrowth).

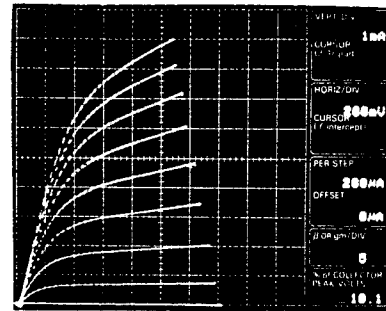


Fig. 4. Common-emitter I-V characteristics for an InP/InGaAs C-up HBT with a 2 $\mu\text{m} \times 5 \mu\text{m}$ collector.

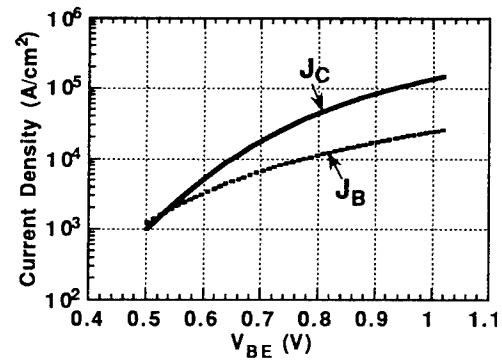


Fig. 5. Gummel-plots for a C-up HBT with a 2 $\mu\text{m} \times 2 \mu\text{m}$ collector.

Microwave C-up HBTs with a 2 $\mu\text{m} \times 10 \mu\text{m}$ collector were characterized by S-parameters measured on a wafer. A cutoff frequency f_T and a maximum oscillation frequency f_{max} were estimated from the frequency dependencies of typical current gain and Mason's unilateral gain. Figures 6 and 7 show f_T and f_{max} as functions of I_C and V_{CE} . We obtained a peak f_T of 21 GHz and a peak f_{max} of 33 GHz. The C_{BC} value at a V_{CE} of 1 V was estimated to be about 4.0 fF from the imaginary part of the Y_{12} parameter in the low-frequency range. This value is very small due to the

C-up configuration.

These are the first high-frequency characteristics reported for InP/InGaAs C-up HBTs. Further improvement of collector-mesa etching and epitaxial regrowth technique will lead to even better high-frequency performance.

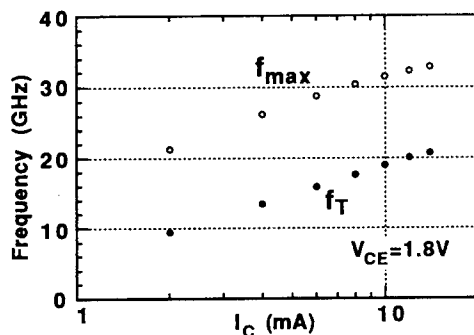


Fig. 6. f_T and f_{max} as a function of I_C for a C-up HBT with a $2\ \mu\text{m} \times 10\ \mu\text{m}$ collector.

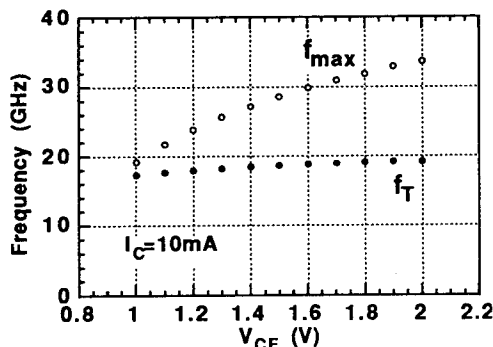


Fig. 7. f_T and f_{max} as a function of V_{CE} for a C-up HBT with a $2\ \mu\text{m} \times 10\ \mu\text{m}$ collector.

4. Summary

We described small InP/InGaAs C-up HBTs with epitaxial base and collector layers regrown onto the emitter layer and with a structure made by using self-aligned fabrication processing. Fe^+ -implantation was used for forming a highly resistive barrier to suppress undesirable excess current from an n^+ -InGaAs emitter contact layer to a p^+ -InGaAs base layer in the extrinsic region. This high resistivity of the Fe^+ -implanted InP layer allows J_C to be greater than $1 \times 10^5\ \text{A}/\text{cm}^2$ even for small-scale C-up HBTs.

For a microwave transistor with a $2\ \mu\text{m} \times 10\ \mu\text{m}$ collector, f_T was 21 GHz and f_{max} was 33 GHz.

Acknowledgments

We are grateful to Y. Ishii and Y. Imamura for their encouragement.

References

- [1] M. F. Chang, N. F. Sheng, P. M. Asbeck, G. J. Sullivan, K. C. Wang, R. J. Anderson, and J. A. Higgins, "Self-aligned AlGaAs/InGaAs/GaAs collector-up heterojunction bipolar transistors for microwave applications," 47th-DRC., IIA-1, 1989.
- [2] S. Yamahata, Y. Matsuoka, and T. Ishibashi, "High-performance small-scale collector-up AlGaAs/GaAs HBT's with a carbon-doped base fabricated using oxygen-ion implantation," IEICE TRANS. ELECTRON., E77-C, p. 1437, 1994.
- [3] S. Yamahata, Y. Matsuoka, and E. Sano, "High-performance collector-up AlGaAs/GaAs HBT's and their application to preamplifier ICs," 7th Asia-Pacific Microwave Conf. Proc., p. 1009, 1994.
- [4] W. Lee and C. G. Fonstad, "Application of O^+ implantation in inverted InGaAs/InAlAs heterojunction bipolar transistors," IEEE Electron Device Lett., vol. 8, p. 217, 1987.
- [5] H. Sato, J. C. Vleck, C. G. Fonstad, B. Meskoob, and S. Prasad, "InGaAs/InAlAs/InP collector-up microwave heterojunction bipolar transistors," IEEE Electron Device Lett., vol. 11, p. 457, 1990.
- [6] S. J. Pearton, C. R. Abernathy, M. B. Panish, R. M. Hamm, and L. M. Lunardi, "Implant-induced high-resistivity regions in InP and InGaAs," J. Appl. Phys., 66, p. 656, 1989.
- [7] J. P. Donnelly and C. E. Hurwitz, "Proton bombardment in InP," Solid-State Electronics, vol. 20, p. 727, 1977.
- [8] M. V. Rao, N. R. Keshavarz-Nia, D. S. Simons, P. M. Amirtharaj, P. E. Thompson, T. Y. Chang, and J. M. Kuo, "Fe implantation in $\text{In}_{0.53}\text{Ga}_{0.47}\text{As}/\text{InP}$," J. Appl. Phys., vol. 15, p. 481, 1989.
- [9] Y. Matsuoka, S. Yamahata, S. Yamaguchi, K. Murata, E. Sano, and T. Ishibashi, "IC-oriented self-aligned high-performance AlGaAs/GaAs ballistic collection transistors and their applications to high-speed ICs," IEICE TRANS. ELECTRON., E76-C, p. 1392, 1993.

Integrated AlInAs/InGaAs HEMT/HBT Heterostructure Grown by MBE

ThB2.5

Y.K. Chen, D. Humphrey, D. Sivco, A.Y. Cho, J. Lothian, J.M. Kuo, F. Ren, J.S. Weiner, A. Tate
AT&T Bell Laboratories, 600 Mountain Ave., Murray Hill, N.J. 07974
M.F. Chang, R. Bernescut
Science Center, Rockwell International Co., Thousand Oaks, CA

Abstract

We report on the integration of AlInAs/InGaAs HEMT and HBT on a single wafer by a single epitaxial growth sequence. The AlInAs/InGaAs emitter-base interface of the HBT is engineered to provide a pulse-doped HEMT structure. Both the HEMT and HBT characteristics are demonstrated successfully. Preliminary microwave measurements indicate both f_T and f_{max} are more than 20 GHz for integrated HEMTs with 1- μ m gatelength. This is the first demonstration of integrated HBT and HEMT operation on the same wafer without multiple regrowth sequences.

Introduction

Both compound semiconductor HEMT and HBT technologies have demonstrated excellent device cutoff frequency and record-setting circuit performance. For many applications, it would be desirable to integrate these two devices on the same wafer to fully utilize the characteristics of both technologies. Similar to the silicon BiCMOS process, it is desirable to use HEMTs for the high impedance, low noise, and low power consumption circuitry and to use HBTs for high speed and current driving circuits. In past, the integration were demonstrated by multiple etch-and-regrowth processes which produced non-planar structures [1]. Because of the fine gate-level lithography of high speed HEMTs, a planar structure is preferred for high yield fabrication process. Previously, modulation-doped emitter or two-dimensional electron gas emitter have been proposed primarily to lower the collector offset voltage of HBTs with an abrupt emitter heterojunction without demonstrating functional HEMT devices[2,3]. In this paper, we further engineer the emitter-base heterojunction to realize the integrated HEMT structure.

Layer Structure and Fabrication Process

The device structure shown in Figure 1 was grown by solid source MBE on semi-insulating InP substrate in the following

sequence: 400 nm n^+ -InGaAs (sub-collector), 500 nm n^- -AlInAs (collector), 20 nm n^- -InGaAs set-back layer, 100 nm p^+ -InGaAs (base), 50 nm n^- -InGaAs (spacer for HBT and 2DEG for HEMT), 30 nm n^- -AlInAs (emitter for HBT and spacer for HEMT), 7 nm n^+ -AlInAs (emitter for HBT and supply layer for HEMT), 30 nm n^- -AlInAs (emitter for HBT and wide-gap barrier layer for HEMT), and 40 nm n^+ -InGaAs (contact layer). The 50 nm-thick InGaAs setback layer between the emitter and base is necessary to generate 2DEG for HEMTs.

	HBT	HEMT
40 nm	n^+ - InGaAs	
30 nm	n^- - AlInAs	emitter
50 nm	n^- - InGaAs	2DEG
100 nm	p^+ - InGaAs	base
20 nm	n^- - InGaAs	
500 nm	n^- - AlInAs	collector
400 nm	n^+ - InGaAs	
Fe-doped semi-insulating InP substrate		

Figure 1. Layer structure grown by MBE

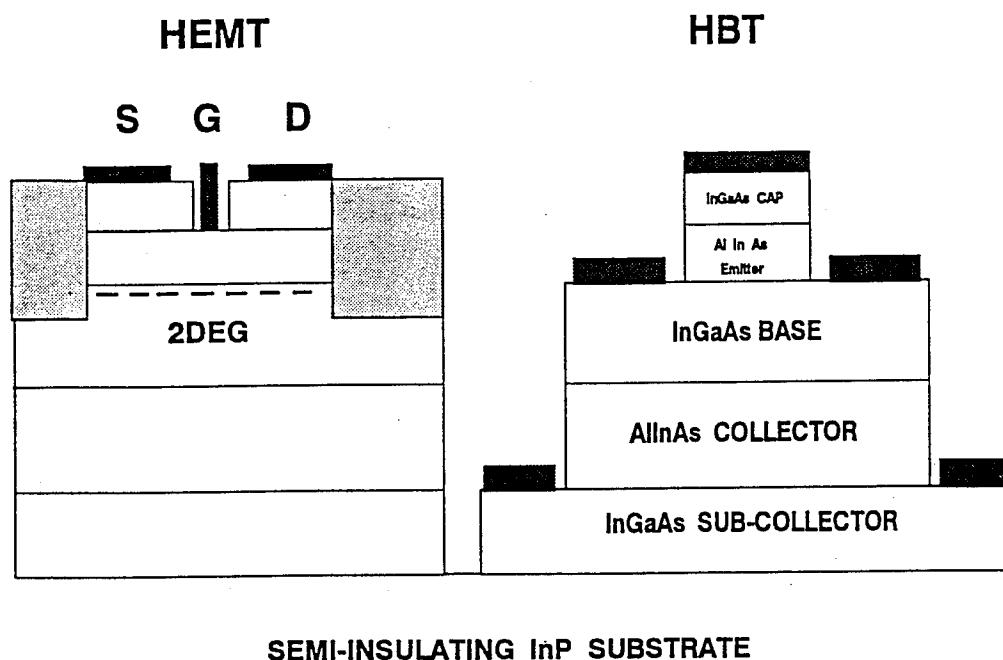


Figure 2. Integrated AlInAs/InGaAs HEMT/HBT heterostructure on InP substrate with a single MBE growth sequence.

The HEMTs and HBTs were then fabricated with contact lithography and wet-etching process as shown in Figure 1. The electrical isolation between devices was achieved by shallow implant to isolate HEMTs and by using deep etched trenches to isolate HBTs.

Device Characteristics

The room-temperature common emitter I-V characteristics of HBT with $40 \times 80 \mu\text{m}^2$ emitter area is depicted in Figure 2. A current gain of 75 is obtained at higher collector current density, while the gain of 9 is obtained at a collector current density as low as 1 A/cm^2 (Figure 3). The drain dc current-voltage characteristics of a $1 \times 50 \mu\text{m}^2$ HEMT is shown in Figure 4. A threshold voltage of -0.25 volts is obtained. Figure 5 shows a peak transconductance of 250 mS/mm is achieved. Because both the gate and the bonding pad for HEMTs are laid on top of the highly doped base layer, the drain breakdown voltage of HEMT is degraded. Nevertheless, the preliminary small signal s-parameter measurement shows a current

gain cut-off frequency (f_T) of 20 GHz as well as a maximum oscillation frequency of 21 GHz.

Summary

In summary, a compact integrated AlInAs/InGaAs HEMT/HBT structure is demonstrated for the first time with a one-step MBE growth. The HEMTs with one-micrometer gate length show excellent microwave performance under low dc bias. This compact structure will simplify the processing steps of low-power mix-mode circuits and OEICs significantly.

Reference

- [1] G. Sasaki, W.P. Hong, G.K. Chang, R. Bhat, and J. R. Hayes, Tech. Dig. IEEE IEDM, 896, (1989)
- [2] A. Sibille, J.F. Palmier, R. Azoulay, and J.C. Esnault, J. Appl. Phys., 66, 442 (1989)
- [3] Q. Wang, Y. Wang, K.F. Longenbach, E.S. Yang, and W.I. Wang, Appl. Phys. Lett., 59, 2582 (1991)

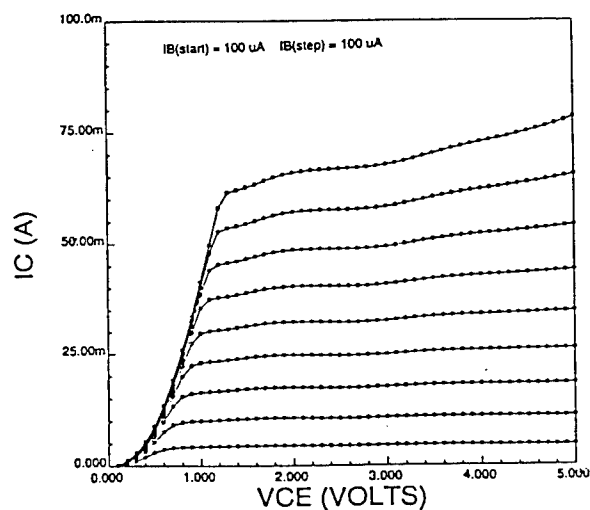


Fig. 3 Common collector I-V characteristics of an integrated HBT with $A_E=40 \times 80 \mu\text{m}^2$.

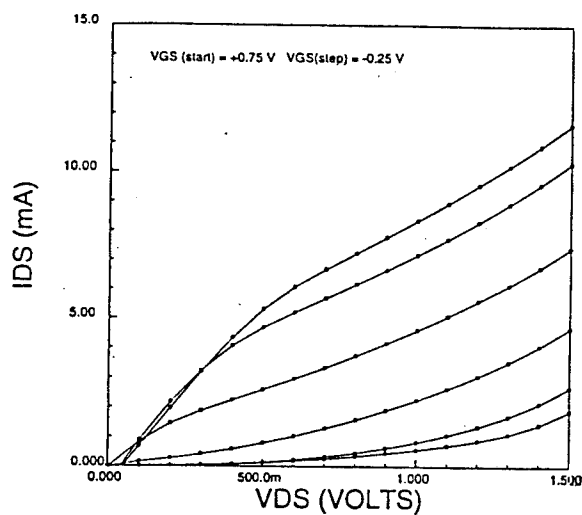


Fig. 5 Common source I-V characteristics of an integrated HEMT with $1 \mu\text{m} \times 50 \mu\text{m}$ gate geometry.

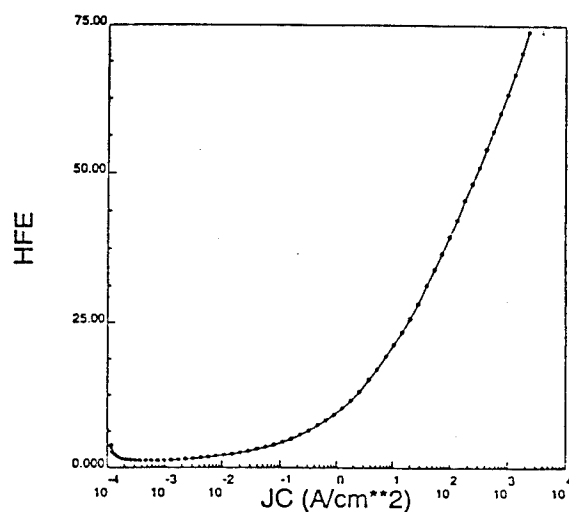


Fig. 4 Large signal current gain of integrated HBT. The current gain is 75 at $J_C = 1 \text{ kA/cm}^2$ and 9 at $J_C = 1 \text{ A/cm}^2$ with $V_{CE} = 2 \text{ V}$.

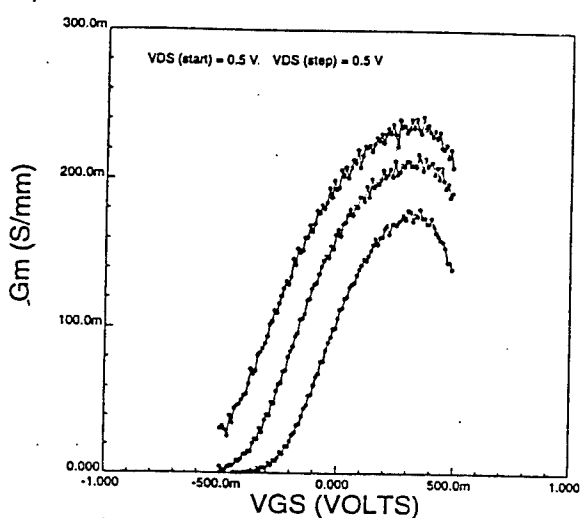


Fig. 6 Common source transconductance of integrated HEMT measured at $V_{DS} = 0.5, 1, \text{ and } 1.5 \text{ V}$, respectively. The peak g_m is 250 mS/mm .

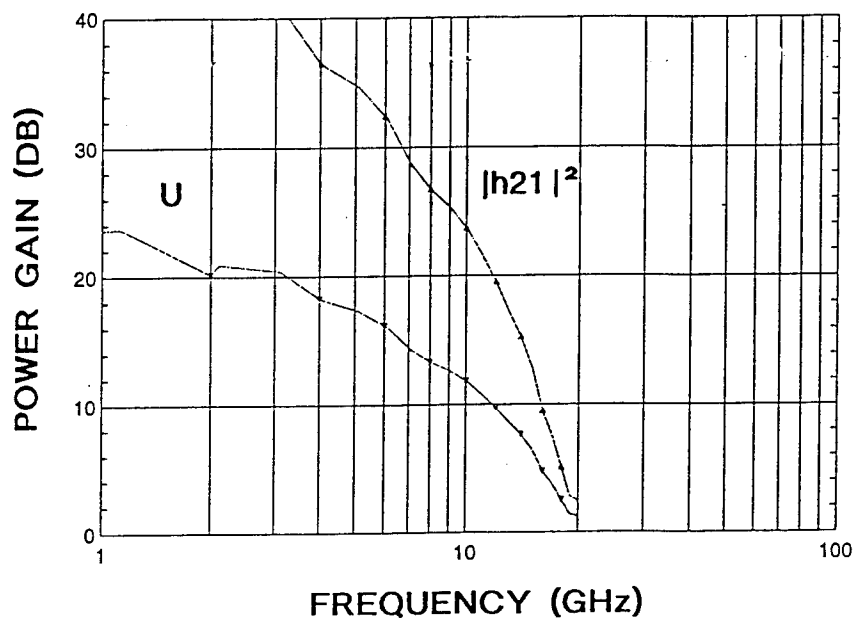


Figure 7 Microwave small signal characteristics of a $1 \times 50 \mu\text{m}^2$ integrated HEMT measured from 1 to 20 GHz. The power gain is degraded somewhat by the heavily doped buried base. Nevertheless, both f_T and f_{MAX} are more than 20 GHz.

InP/InGaAs Nanofabrication and Optical Characterization

A. Forchel, O. Schilling, K.H. Wang, P. Ils, J. Oshinowo, F. Kieseling, W. Braun
Technische Physik, Universität Würzburg, Am Hubland, D 97074 Würzburg

We have developed InGaAs/InP quantum wires and quantum dots with lateral extensions below 20 nm by high resolution electron beam lithography and wet chemical etching. In contrast to dry etched structures the wet etched wires and dots are found to be virtually free of significant optically inactive ("dead") sidewall layers. Time resolved measurements yield rather long lifetimes of about 500 ps for 20 nm wide deep etched wires. The luminescence of the wires and dots shows a strong shift to higher energy as well as features due to transitions between up to four lateral subbands when the characteristic widths is reduced below 50 nm.

Due to the absence of optically inactive sidewall layers the size variation of the emission energy can be modeled quantitatively based on the measured widths of the nanostructures.

Introduction

Quasi-one-dimensional and quasi zero dimensional semiconductor heterostructures are subjects of intense research both because of the opportunities for studying new phenomena in solid state physics and also for possible device applications [1-2]. Due to the reduction of the degrees of freedom for electrons and holes compared to two - dimensional quantum wells, quantum wire and quantum dot structures are expected to show a dimensionality dependence of the density of states versus energy, an increase of the band gap, the formation of a lateral subband structure, an increase of the exciton binding energy, modifications of the energy relaxation and recombination probabilities etc..

In initial studies of the optical properties of wires and dots the lateral nanostructures have been obtained mainly by ion based processes including dry etching and implantation induced intermixing [3,4] Due to the use of ions for the patterning, these wires and dots generally contain a large number of defects. This degrades the quantum efficiencies and results in significant problems for a modelling of the physical properties of the structures. For example, in studies of lateral quantization effects in dry etched InGaAs/InP wires a so called "dead layer" with a widths of about 20 nm had to be assumed in order to correlate the lateral dimensions and the observed quantization effects [5]. More recently, techniques which avoid any process induced damage of the structures have been developed. These include the growth of wires into v - grooves [6], on masked substrates [7] or via self organization phenomena on high index surfaces [8] and the fabrication of dot structures by three dimensional growth in molecular beam epitaxy [9] and metal organic vapour phase epitaxy [10]. The advantages of these approaches include the formation of buried structures with high quantum efficiencies, the lack of process induced

defects etc.. A certain drawback, however, is the limited ability of these techniques to vary the size and shape of the patterns. Furthermore a determination of the geometry and the composition of the structures is often very difficult.

The talk discusses cw and time resolved studies on InGaAs/InP quantum wires with width down to 10 nm and dots with diameters down to 16 nm. The nanostructures have been obtained by high resolution electron beam lithography and wet chemical etching. In the smallest structures the emission energy is increased by about 90 meV due to the lateral confinement. For high optical excitation several lateral subbands are observed which vary consistently with the wire widths.

Wet etching based patterning technology

The quantum wire and dot structures discussed here have been fabricated from high quality InGaAs/InP single quantum wells (thickness 5nm) grown by gas source molecular beam epitaxy. The wafer was cleaved into pieces with typical dimensions of $4 \times 4 \text{ mm}^2$. The pieces were spin coated by a 100 nm thick layer of the positive tone electron beam resist polymethylmetacrylate (PMMA). Wire and dot etch masks with a constant pattern size were defined in arrays with a typical extension of $50 \times 50 \text{ }\mu\text{m}^2$. After the development, Au etch masks with a thickness of about 10 nm were obtained by a lift off step. The change from the resist mask to a metal mask is necessary because the resist mask does not protect the samples from the wet chemical etchant and due to the tone of the resist.

The InGaAs/InP nanostructures were obtained by etching with a $\text{HBr}:\text{CH}_3\text{COOH}:\text{K}_2\text{Cr}_2\text{O}_7$ solution and water. As shown in fig. 1, the etchant removes

InP and InGaAs with similar rates (of about 2 nm/min) for a specific $K_2Cr_2O_7$ - content. Furthermore the etchant provides smooth surfaces in the etched areas. After the etching of the semiconductor the masks were removed by a solution of $KI:I_2:H_2O$. Further details of the fabrication process have been published elsewhere [11,12].

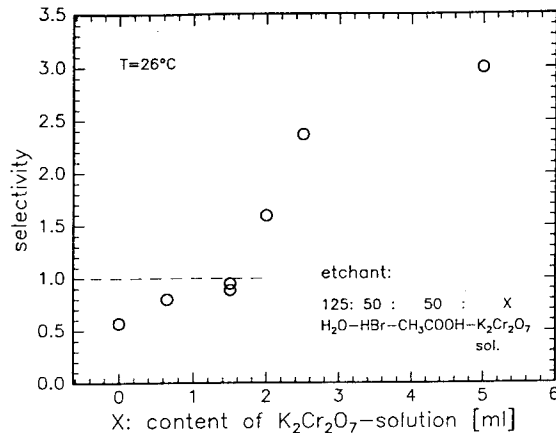


Fig. 1 : Selectivity between InGaAs and InP for an etchant based on $HBr:CH_3COOH:K_2Cr_2O_7$ for varying $K_2Cr_2O_7$ - content.

A variety of samples with about ten arrays with wires and dots of different widths were produced. The arrays are separated by typically 200 μm from each other in order to avoid the simultaneous excitation of several fields by the laser focus (diameter between 40 μm and 100 μm , for Ar and Titanium : Sapphire laser, respectively). For the optical studies the samples were mounted in a variable temperature He dewar. The emission was dispersed by a 25 cm monochromator. For the cw experiments a Ge - detector interfaced with a lock in amplifier was used. The time resolved studies were performed using sub ps excitation pulses from a mode locked $Ti:Al_2O_3$ laser. Sum frequency photons of the laser pulse and the emission were detected by a CCD camera. The overall time resolution of the set up is about 0.3 ps.

In order to analyse the influence of the etched sidewalls on the recombination time constants in the structures we have investigated the dependence of the electron hole pair lifetime as a function of the wire widths. Fig. 2 displays the variation of the lifetime in the wet etched wires at a temperature of 40 K. In going from quasi two dimensional structures to wire widths of about 20 nm the lifetime is reduced from approximately 2 ns to 500 ps.

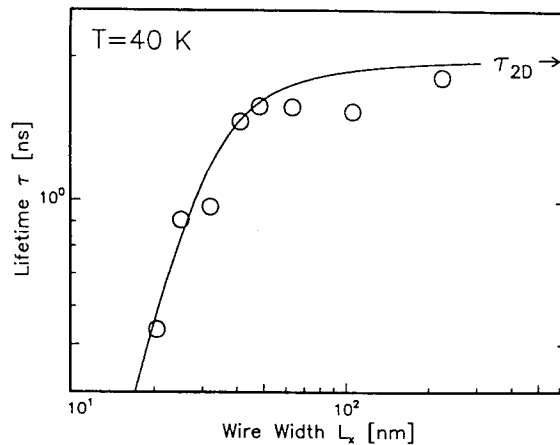


Fig. 2 Wire width dependence of the excitonic lifetime in InGaAs/InP wires defined by wet etching ($T = 40$ K).

The reduction of the lifetime, which is due to nonradiative recombination at the sidewalls, is remarkably small. This is due to the rather small sidewall recombination velocity and due to the absence of dry etch induced defects. The wire widths dependence of the lifetime is particularly strong below 50 nm. This indicates that diffusion of electron - hole (e-h) pairs with a typical diffusion length on the order of 1 μm is not driving the e-h pairs to the surface. As can be shown by calculations of the probability to find e-h pairs within a few nm of the surface, the decrease of the time constant is mainly controlled by the extension of the wave function of the carriers into a thin surface layer [13].

Luminescence study of lateral quantization effects in wet etched InGaAs/InP wires and dots

We have fabricated InGaAs/InP quantum wires with widths down to 8 nm, and quantum dots with diameters down to 16 nm. Luminescence spectra of the wire and dot samples at low and high excitation intensity display clear lateral confinement effects. From the increase of the full width at half maximum (FWHM) of the emission line with decreasing feature size (low excitation power data), we estimate a typical value of the size fluctuations in our structures on the order of $\pm 2-3$ nm.

If the optical excitation intensity is increased the phase space for carriers at the subband edges can be filled completely. This state filling due to the Pauli principle may be used to observe the emission of carriers in higher lateral subbands in the wire and dot structures.

Fig. 3 shows high excitation luminescence spectra recorded at an excitation power of 10 kW/cm^2 on wires with widths between 45 nm and 10 nm. In addition to the shift of the lowest transitions to higher energy, we observe an increase of the energetic positions of all spectral features at high energy when the wire width is decreased.

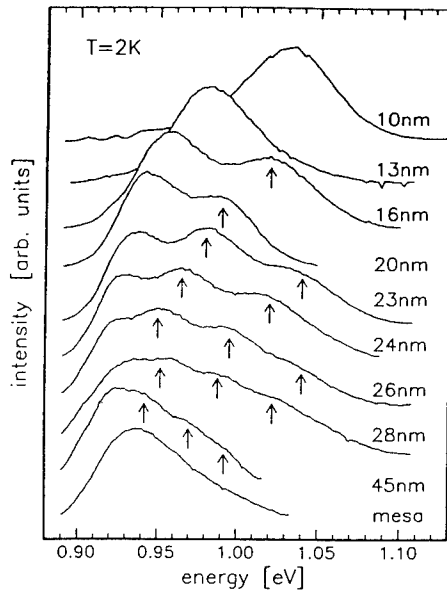


Fig. 3 Luminescence spectra of InGaAs/InP quantum wire arrays with different widths ($T = 2 \text{ K}$). The spectra have been recorded at excitation intensities of 10 kW/cm^2 in order to populate several lateral subbands.

Fig. 4 displays high excitation experiments of quantum dot arrays with dot diameters between 47 nm and 16 nm in comparison with data from a two dimensional mesa structure. With decreasing dot diameter the low energy edge of the emission shifts by up to 90 meV to higher energy. In addition we observe for dot sizes between 47 nm and 25 nm shoulders on the high energy side of the emission bands. With decreasing diameter, these shoulders shift rather fast to higher energy and the energetic distance to the ground state transitions (lowest peaks in Fig. 4) increases. This behaviour is expected for higher state transitions.

We would like to point out that the spectra of the InGaAs/InP dots show no sharp features as expected for optical transitions in fully confined systems. This is in part certainly due to dot size inhomogeneities in the arrays. However, part of the broadening may also be due to temporal fluctuations in the interaction of carrier pairs in the dots with e - h pairs in the lateral barriers.

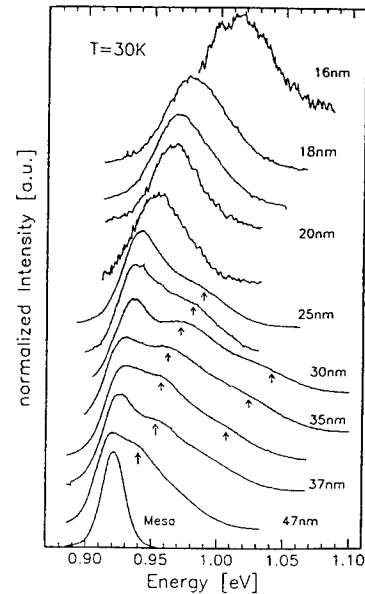


Fig. 4 Luminescence spectra of InGaAs/InP quantum dot arrays with different dot diameters ($T = 30 \text{ K}$).

Furthermore it is noteworthy, that figs 3 and 4 display spectral features only below approximately 1.05 eV. This effect is most likely a consequence of the finite height of the energy discontinuity in the conduction band of the InGaAs/InP quantum well of about 200 meV. Because the vertical and lateral quantization energies in the valence band are small (about 50 meV), an energy of 1.05 eV in figs. 3 and 4 corresponds to the recombination of electrons close to the barrier band gap. Larger lateral quantization energies, which may arise for higher subbands or narrower structures, result therefore in electronic states which are degenerate with the continuum of the conduction band in the InP barrier. Because these states are not confined in the InGaAs wires and dots the transition matrix element with hole states (which are confined to the wires or dots) is small compared to the case when both, electrons and holes are confined.

Fig. 5 shows the wire widths dependence of the transition energies in InGaAs/InP structures with widths between 63 nm and 8 nm. We observe a consistent increase of the different transitions for decreasing wire widths. The solid, dashed, dashed dotted, and dotted lines have been calculated using a very simple model.

In the calculation the vertical and the lateral quantization effects are treated as separable. This is certainly justified for large wire widths, but becomes inaccurate for narrow wires where lateral and vertical quantization effects are comparable. We

assume that a square potential well with an energy discontinuity of the order of the electron affinity (about 5 eV) is formed in the conduction and valence band of the structures. For the electron and holes in the InGaAs effective masses of 0.047 and 0.32 have been used. The different lines describe the wire widths dependence of the different spectral features rather well. By comparison with the model calculation we identify the lowest transition with the e_{11} - h_{11} transition, whereas the second, third and fourth transition are denoted as e_{12} - h_{12} , e_{13} - h_{13} and e_{14} - h_{14} transitions respectively. Here the first quantum number describes the vertical quantization in the InGaAs quantum well. Due to the particular thickness of the InGaAs layer (5 nm) all transitions occur between the lowest conduction and valence band state in the two dimensional structure.

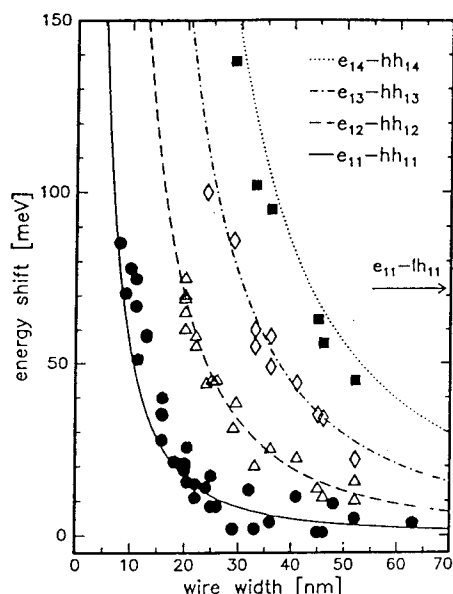


Fig. 5 Wire widths dependence of the transition energies of four subbands in InGaAs/InP wires.

The experimental data agrees well with the calculation taking into account the measured widths of the wires [14]. For the energy dependence of the eigenstates in the etched dots a similarly good agreement can be obtained. This implies that the present wet etched structures contain no significant optically inactive ("dead") layers. This is different to studies of dry etched structures in InGaAs/InP and GaAs/AlGaAs, where dead layers with thicknesses of about 20 nm and 50 nm have been reported [5]. If a dead layer would be present in the wet etched wire, for example, the SEM measured wire widths would have to be reduced by twice the dead layer thickness in order to determine the widths of the optically active part of the structures. Due to the

good agreement of the wire width variation of the transition energies in experiment and calculation based on the SEM measured widths of the structures we conclude that the extension of the dead layers in the wet etched structures is at most comparable to the uncertainties in the wire width determination ($\pm 2-3$ nm).

Acknowledgements

We are grateful for the provision of high quality InGaAs/InP single quantum well wafers by Alcatel SEL, Stuttgart, and Alcatel Alsthom, Marcoussis. The partial financial support of this work by the State of Bavaria, the European Commission and the FTZ German Telekom is gratefully acknowledged.

References

- 1) Y. Arakawa and H. Sakaki, Appl. Phys. Lett. 53, 1033 (1982).
- 2) Y. Arakawa, K. Vahala, and A. Yariv, Appl. Phys. Lett. 45, 950 (1984).
- 3) B.E. Maile, A. Forchel, R. Germann, J. Straka, L. Korte, and C. Tanner, Appl. Phys. Lett. 57, 807 (1990).
- 4) J. Cibert, P.M. Petroff, D.J. Werder, S.J. Pearton, A.C. Gossard, and H.J. English, Appl. Phys. Lett. 49, 223 (1986).
- 5) B.E. Maile, R. Germann, A. Forchel, and D. Grützmacher, Appl. Phys. Lett. 54, 1552 (1989).
- 6) E. Kapon, S. Simhony, R. Bhat, and D.M. Hwang, Appl. Phys. Lett. 55, 2715 (1989).
- 7) Y. Naganume, Y. Arakawa, S. Tsukamoto, M. Nishioka, S. Sasaki, and N. Miura, Phys. Rev. Lett. 69, 2963 (1992).
- 8) R. Nötzel, N. Ledentsov, L. Däweritz, M. Hohenstein, and K. Ploog, Phys. Rev. Lett. 67, 3812 (1991).
- 9) D. Leonhard, M. Krishnamurthy, C.M. Reaves, S.P. Denbaars, and P.M. Petroff, Appl. Phys. Lett. 63, 3203 (1993).
- 10) J. Oshinowo, M. Nishioka, S. Ishida, and Y. Arakawa, Appl. Phys. Lett. 65, 1421 (1994).
- 11) P. Ils, M. Michel, A. Forchel, I. Gyuro, M. Klenk, and E. Zielinski, Appl. Phys. Lett. 64, 496 (1994).
- 12) O. Schilling, A. Forchel, A. Kohl, and S. Brittner, J. Vac. Sci. B 11, 2556 (1993).
- 13) F. Kieseling, W. Braun, P. Ils, M. Michel, A. Forchel, I. Gyuro, M. Klenk, and E. Zielinski, Phys. Rev. B, May 15, 1995 (in press).
- 14) P. Ils, A. Forchel, K.H. Wang, P. Pagnod-Rossiaux, and L. Goldstein, Phys. Rev. B, Oct. 15, 1994.

High-quality Zn-diffused InP-related materials fabricated by the open-tube technique

T. Tsuchiya, *T. Taniwatari, *T. Haga, *T. Kawano

Central Research Laboratory, Hitachi, Ltd., *Fiberoptics Division, Hitachi, Ltd.

1-280, Higashi-koigakubo, Kokubunji-shi, Tokyo 185, Japan

Introduction

The open-tube technique^{1,2)} is expected to provide more precise and reproducible control of Zn diffusion parameters than the sealed-ampule technique. In a recent study,³⁾ high uniformity of hole concentration and diffusion depth in two-inch wafers was obtained by the open-tube Zn-diffusion technique. Moreover, this technique achieved a high hole concentration and low ohmic contact resistance. However, the crystal quality in Zn-diffused materials fabricated by this open-tube technique has not yet been examined.

In this paper, we evaluate, for the first time, the crystal quality of a Zn-diffused thick $\text{In}_{0.76}\text{Ga}_{0.24}\text{As}_{0.55}\text{P}_{0.45}/\text{InP}$ structure created by the open-tube technique. We also investigate the intermixing at the heterointerface of the Zn diffused $\text{In}_{0.47}\text{Ga}_{0.53}\text{As}/\text{InP}$ multiple quantum wells (MQW) structure.

Experiment

Open-tube Zn diffusion was performed at 40 Torr and 400°C using a conventional metalorganic vapor phase epitaxy (MOVPE) machine. The sample was put on a quartz plate (size: 3 inch diameter) in a cold-walled horizontal reactor. Dimethylzinc (DMZn) and phosphine (PH_3) gases were used as diffusion sources in a hydrogen (H_2) atmosphere. The sample surface was continually exposed to the H_2 and PH_3 , and the DMZn was introduced into the

reactor when the diffusion temperature was reached. After diffusion, the DMZn and the heater were turned off simultaneously^{4,5)}. Sealed-ampule Zn diffusion was performed at 550°C in evacuated sealed quartz tubes using zinc-arsenide (Zn_3P_2) powder as the diffusion source. Initially, each sample was chemically etched for 1 min in sulfuric acid. Undoped InP, $\text{In}_{0.76}\text{Ga}_{0.24}\text{As}_{0.55}\text{P}_{0.45}$ (λ_{PL} : 1.3 μm , lattice-matched to the InP substrate), and $\text{In}_{0.47}\text{Ga}_{0.53}\text{As}$ (lattice-matched to the InP substrate) epi-layers with n-type carrier concentrations of 6×10^{14} , 2×10^{15} , and $8 \times 10^{14} \text{ cm}^{-3}$ were used for both Zn-diffusion techniques. Hole and Zn concentration profiles were obtained by C-V etch profiling and secondary ion mass spectroscopy (SIMS)

Results and discussion

Figure 1 shows cross-sectional transmission electron microscopy images of samples obtained by the sealed-ampule technique (a) and the open-tube technique (b). With the sealed ampoule technique, after Zn diffusion, many dislocations arise and $\text{In}_{0.76}\text{Ga}_{0.24}\text{As}_{0.55}\text{P}_{0.45}/\text{InP}$ structure was heavily damaged. Zn and hole concentrations in InP layer were about 10^{19} and 10^{18} cm^{-3} , respectively. Although, a high Zn concentration was obtained, most Zn atoms were unionized and located at the interstitial site⁶⁾. In previous

studies, similar results have been reported^{7,8)}. At high Zn concentration, Zn diffusion induces mixing of the In-Ga, with little diffusion of the As-P between the InGaAsP/InP heterointerface. This interdiffusion causes tensile stress in the Ga-mixed InP layer and compressive stress in the In-mixed InGaAsP layer. Therefore, intermixing-induced stress is accumulated, and generate dislocations⁷⁾. On the other hand, the open-tube technique produces no dislocations or defects. Moreover, with the open-tube technique, the Zn and hole concentrations in InP layer are about $1 \times 10^{18} \text{ cm}^{-3}$, and most Zn atoms are ionized, and located at substitutional sites. These results suggest that In-Ga interdiffusion does not occur in the open-tube Zn diffusion technique.

In order to evaluate In-Ga interdiffusion at the heterointerface, we investigate the photoluminescence spectra of Zn-diffused layers. Figure 2 shows the PL spectra of $\text{In}_{0.76}\text{Ga}_{0.24}\text{As}_{0.55}\text{P}_{0.45}$ layers in Figs. 1(a) and (b). With the sealed-ampoule technique, the PL intensity was drastically decreased after Zn diffusion. Moreover, another PL peak appeared in the long-wavelength region. The drastic decrease in PL intensity is considered to be due to the defects and dislocations in Fig. 1(a). The other peak in the long wavelength is also considered to be due to the In diffusion from the InP to the $\text{In}_{0.76}\text{Ga}_{0.24}\text{As}_{0.55}\text{P}_{0.45}$ layer at the $\text{In}_{0.76}\text{Ga}_{0.24}\text{As}_{0.55}\text{P}_{0.45}$ /InP heterointerface. On the other hand, in the open-tube Zn diffusion, PL intensity was just slightly decreased after Zn diffusion. Moreover, a second PL peak was not observed in the long wavelength region. These results suggest that In-Ga interdiffusion does not occur in the open-tube Zn diffusion technique.

In order to confirm that such interdiffusion does not occur at the

heterointerface, we investigate Zn diffusion into unstrained InGaAs/InP MQW. Figure 3 shows SIMS profiles of Zn, In, and Ga. The thicknesses of the $\text{In}_{0.47}\text{Ga}_{0.53}\text{As}$ and InP layers are 7 and 15 nm, respectively. The number of wells is 15. Quantization of the sample profile was accomplished by analyzing a Zn-doped $\text{In}_{0.47}\text{Ga}_{0.53}\text{As}$ standard sample. Note that in Fig. 3, Zn, In, and Ga concentration are modulated and change drastically, moreover there is no intermixing of In and Ga at the interface between wells and barriers, even for very thin regions. The Zn oscillation observed in the MQWs is due to the difference in solubility of the $\text{In}_{0.47}\text{Ga}_{0.53}\text{As}$ and InP layers^{3,9)}. In a previous study^{7,8)}, the $\text{In}_{0.47}\text{Ga}_{0.53}\text{As}$ well layers and the InP barrier layers are mixed by Zn diffusion in the sealed-ampoule technique⁸⁾, on the other hand, our results indicate that in the open-tube technique $\text{In}_{0.47}\text{Ga}_{0.53}\text{As}$ well layers and the InP barrier layers are not mixed due to Zn diffusion, even for very thin layers.

Conclusion

In summary, we have investigated crystal quality after Zn diffusion by the open-tube technique in MOVPE, for the first time. Unlike the sealed-ampoule technique, crystal quality in $\text{In}_{0.76}\text{Ga}_{0.24}\text{As}_{0.55}\text{P}_{0.45}$ /InP structure is not degraded by Zn diffusion when using the open-tube technique. In the sealed-ampoule technique, many dislocations and defects arise after Zn diffusion, and a second peak of $\text{In}_{0.76}\text{Ga}_{0.24}\text{As}_{0.55}\text{P}_{0.45}$ in the long wavelength region appears. On the other hand, in the open-tube technique, dislocations and defects were not observed, and the second PL peak was not observed, even after Zn diffusion. Moreover, intermixing of In and Ga at the heterointerface between $\text{In}_{0.47}\text{Ga}_{0.53}\text{As}$ well layers and InP

barrier layers did not occur, even for very thin layers.

Acknowledgment

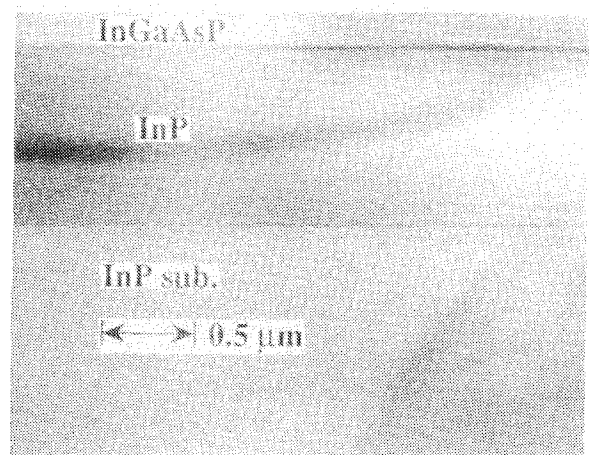
The authors would like to thank Dr. Hiroyasu Shichi and Ms. Yumiko Abe for the SIMS measurements.

References

- 1) M. Wada, M. Seko, K. Sakakibara and Y. Sekiguchi, Jpn. J. Appl. Phys (1989) L1700.
- 2) J. Wisser, M. Glade, H. J. Schmidt and K. Heime, J. Appl. Phys. **71** (1992) 3234.
- 3) T. Tsuchiya, T. Taniwatari, M. Komori, T. Kawano and K. Saitoo, "First International Symposium on Control of Semiconductor Interfaces" Karuizawa, Japan, (1993) 519.
- 4) S. Cole, L. Davis, W. J. Duncan, E. M. Marsh, R. H. Moss, W. J. M. Rothwell, P. J. Skevington and G. D. T. Spiller, J. Crystal. Growth. **107** (1991) 254.
- 5) B. R. Butler, A. T. R. Briggs, S. A. Kitching and A. Chew, J. Crystal **102** (1990) 393.
- 6) G. J. van Gurp, T. van Dongen, G. M. Fontijn, J. M. Jacobs and D. L. A. Tjaden, J. Appl. Phys. **65** (1988) 553.
- 7) H. Park, E. S. Nam, Y. T. Lee and E. Lee, Appl. Phys. Lett. **59** (1991) 2025.
- 8) S. A. Schwarz, et al., Appl. Phys. Lett. **53** (1988) 1051.
- 9) G. J. van Gurp, D. L. A. Tjaden, G. M. Fontijn and P. R. Boudewijn, J. Appl. Phys. **64** (1988) 3468.



(a)



(b)

Figure1. Cross-sectional TEM images taken after Zn diffusion by (a) the sealed-ampule technique and (b) the open-tube technique.

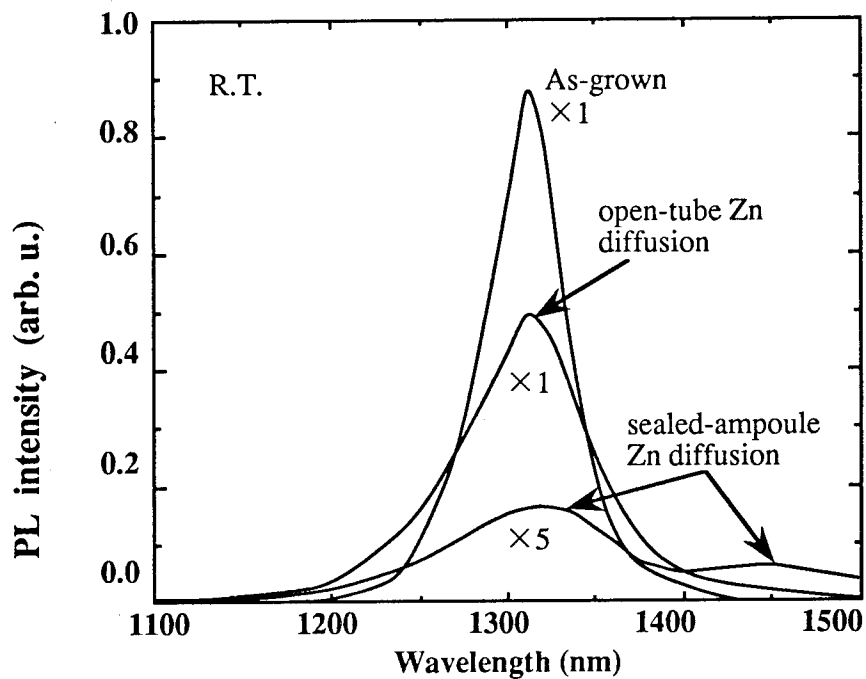


Figure 2. PL spectra of $\text{In}_{0.76}\text{Ga}_{0.24}\text{As}_{0.55}\text{P}_{0.45}$ layers.

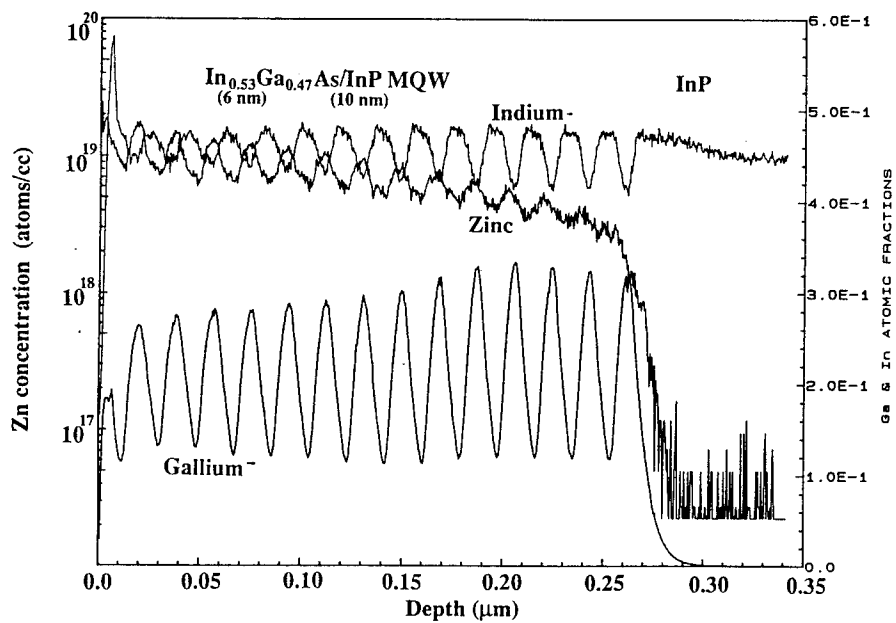


Figure 3. SIMS concentration profiles of an InGaAs/InP MQW after Zn diffusion by the open-tube technique. There are 15 periods.

Zn-IMPLANTED Pd-BASED OHMIC CONTACTS TO p-In_{0.53}Ga_{0.47}As FOR THE BASE LAYER OF InP/In_{0.53}Ga_{0.47}As HETEROJUNCTION BIPOLAR TRANSISTORS

P. Ressel, H. Strusny, K. Vogel, and J. Würfl

Ferdinand-Braun-Institut für Höchstfrequenztechnik, Rudower Chaussee 5, D-12489 Berlin, Germany

W. Wesch and G. Lenk

Friedrich-Schiller-Universität Jena, Institut für Festkörperphysik, Max-Wien-Platz 1, D-07743 Jena, Germany

E. Kuphal, D. Fritzsche, H. Kräutle, and K. Mause

Deutsche Telekom, FTZ, Am Kavalleriesand 3, D-64295 Darmstadt, Germany

Introduction

InP/In_{0.53}Ga_{0.47}As heterojunction bipolar transistors (HBTs) for high-frequency applications impose stringent requirements on the ohmic contact to the thin (≤ 100 nm) p-In_{0.53}Ga_{0.47}As base layer. If high current gain is required, for instance in low-noise front-end applications, it is favorable to limit the base layer doping to values $\leq 1 \cdot 10^{19}$ cm⁻³, while the contact resistivity should be $\leq 1 \cdot 10^{-6}$ Ω cm². Usually, nonalloyed metallizations do not yield sufficiently low contact resistivity in the relevant doping range, whereas alloyed systems suffer from inherent problems with nonplanar interfaces and comparably deep penetration of contact components. Alternatively, low-ohmic contacts on p-In_{0.53}Ga_{0.47}As doped below $1 \cdot 10^{19}$ cm⁻³ can be fabricated by implantation of p-dopant into nonalloyed metallizations. We have recently demonstrated the feasibility of this concept in case of Zn or Cd implanted Pd/Ge contacts on p-In_{0.53}Ga_{0.47}As [1] and show now that Pd/Au-based contacts are even more suitable for this purpose. A comparative study of both systems, e.g. Pd/Ge and Pd/Au/LaB₆/Au, is presented.

Experimental procedure

For the investigation of contact resistivity ρ_c , epitaxial In_{0.53}Ga_{0.47}As layers, Zn-doped to $2\text{--}3 \cdot 10^{18}$ cm⁻³ and 0.5 μ m thick, were grown on semi-insulating InP(001) by metal-organic chemical vapor deposition. For backside secondary ion mass spectroscopy (SIMS) measurements, samples contained quaternary marker layers for depth calibration. These In_{0.6}Ga_{0.4}As_{0.86}P_{0.14} markers, 8 nm thick, are inserted equidistantly into the In_{0.53}Ga_{0.47}As layer, which is Zn-doped to $1 \cdot 10^{18}$ cm⁻³. The marker distance is 50 nm with the first marker located 130 nm below the surface.

The contact resistivity was determined by using the transmission line model (TLM). Test structures were prepared employing a standard lift-off process. Immediately before loading into the vacuum chamber, samples were treated with diluted HF (1%) for 15 s to remove the native oxide, rinsed in deionised water for 45 s and dried in flowing nitrogen. Contact deposition started with the evaporation of 20 nm Pd at a base pressure $\leq 5 \cdot 10^{-8}$ mbar. After this, Zn was implanted with an energy of 5 or 25 keV and a dose of $1 \cdot 10^{15}$ cm⁻². This results in dopant location close to the semiconductor, while radiation damage tailing into the In_{0.53}Ga_{0.47}As layer is kept to a minimum. Theoretical calculations (TRIM [2]) of the concentration of displaced host atoms and implanted ions show that radiation damage drops to a level of $1 \cdot 10^{18}$ cm⁻³ at a depth of approximately 25 nm inside the semiconductor for an implant energy of 25 keV.

However, no radiation damage tailing into the semiconductor is expected for an implantation energy of 5 keV. After the implantation, the deposition process was finished by evaporating 40 nm Pd and 200 nm Ge or 10 nm Au, 100 nm LaB₆, and 100 nm Au. The growth of LaB₆ has been interrupted at a thickness of 50 nm for oxygen flooding to increase its stability against Au diffusion [3]. Contact formation was performed by rapid thermal annealing under flowing nitrogen for 30 s.

Samples for SIMS investigations were prepared analogously to the TLM structures regarding evaporation, implantation, and annealing. After that, they were waxed contact side down on dummy pieces of GaAs, mechanically thinned to a thickness of approximately 150 μ m, and etched selectively down to the In_{0.53}Ga_{0.47}As layer in HCl:H₃PO₄, 1:1. SIMS measurements were performed in a CAMECA *ims* 4f system using a 5.5 keV Cs⁺ ion beam at 42° incidence. MCs⁺ ions (M stands for the analyzed element, for example As, Pd, etc.) were analyzed to minimize the influence of matrix effects, except for Au where the high mass of the metal-Cs cluster exceeds the separation range of the apparatus.

Results and discussion

In Fig. 1, the contact resistivity of implanted Pd/Ge and Pd/Au/LaB₆/Au contacts is displayed in dependence on the

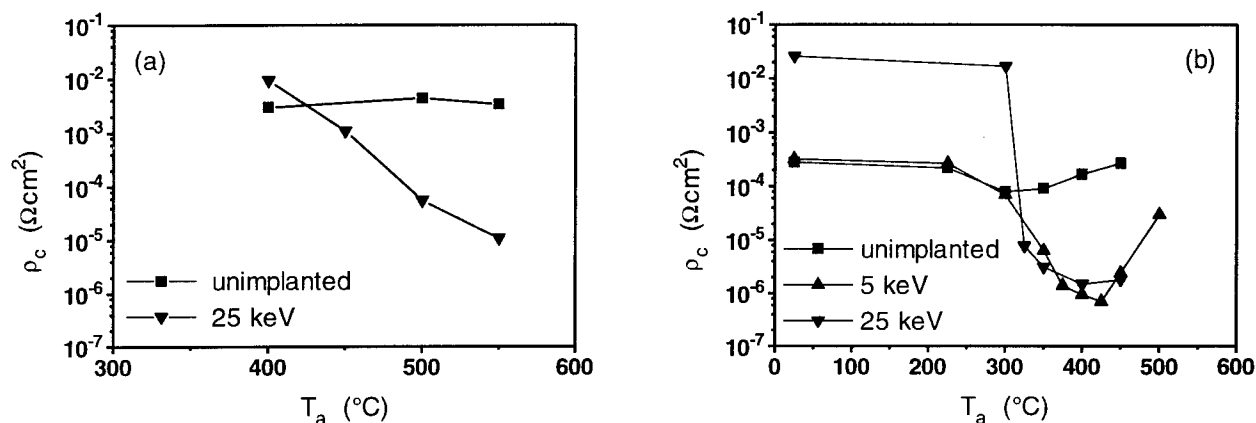


Fig. 1 Contact resistivity ρ_c versus annealing temperature T_a of Zn-implanted Pd/Ge (a) and Pd/Au/LaB₆/Au (b) contacts on In_{0.53}Ga_{0.47}As ($p = 2\text{--}3 \times 10^{18} \text{ cm}^{-3}$) for different implantation conditions.

annealing temperature and for different implantation energies. For comparison, the contact resistivity of analogously treated but unimplanted reference samples is also given. The current-voltage characteristics of unimplanted contacts are nonlinear as expected for doping concentrations $< 1 \times 10^{19} \text{ cm}^{-3}$ in case of p-In_{0.53}Ga_{0.47}As [4,5]. Thus the corresponding ρ_c values were calculated from the differential resistance at zero voltage. The lowest value is $8 \times 10^{-5} \Omega\text{cm}^2$ for Pd/Au/LaB₆/Au contacts annealed at 300 $^\circ\text{C}$. Both implanted and unimplanted Pd/Ge contacts are difficult to evaluate for annealing temperatures $< 400 \text{ }^\circ\text{C}$, probably due to the presence of unreacted Ge. Contact morphology starts to deteriorate at temperatures $> 550 \text{ }^\circ\text{C}$ and $> 500 \text{ }^\circ\text{C}$ for Pd/Ge and Pd/Au/LaB₆/Au contacts, respectively.

Contact implantation with 25 keV results in the occurrence of a thin, highly resistive layer beneath the contact caused by radiation damage tails, which leads to non-

ohmic behavior for low annealing temperatures. This is particularly evident in case of Pd/Au/LaB₆/Au contacts, where ρ_c is approximately two orders of magnitude higher than for the unimplanted reference contacts at annealing temperatures up to 300 $^\circ\text{C}$. Further increase of the annealing temperature results in substantial decrease of ρ_c for both metallizations. Pd/Ge contacts reach a minimal resistivity of $1 \times 10^{-5} \Omega\text{cm}^2$ after annealing at 550 $^\circ\text{C}$. This value is more than two orders of magnitude lower than for the reference contact. Even lower ρ_c is found in case of Pd/Au/LaB₆/Au contacts, where a sharp transition to ohmic behavior occurs between 300 and 325 $^\circ\text{C}$. The minimal resistivity is $1\text{--}2 \times 10^{-6} \Omega\text{cm}^2$ at temperatures of 400–450 $^\circ\text{C}$.

Lowering the implantation energy to 5 keV leads to quite different behavior for both metallizations. Pd/Ge contacts reveal strong lateral nonuniformity of ρ_c with the average value being only slightly lower than for the reference

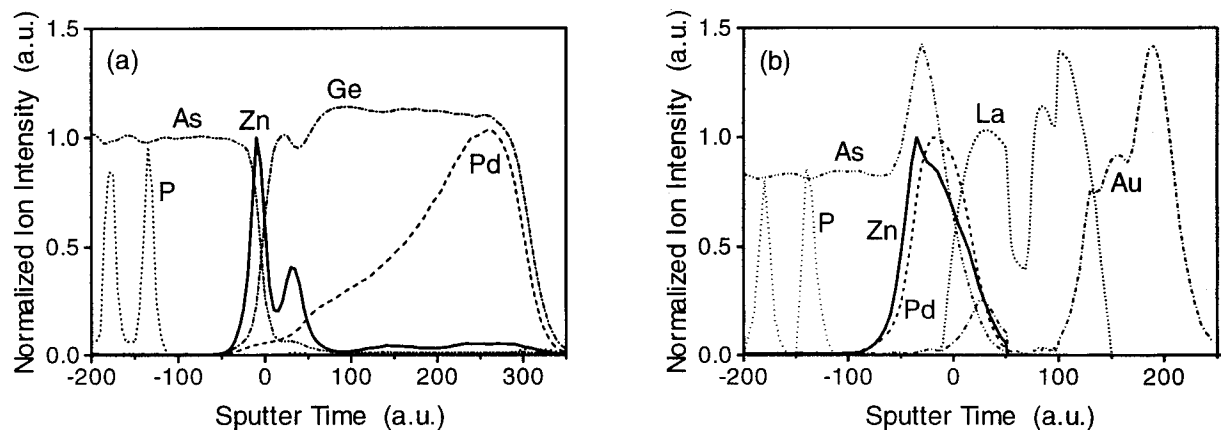


Fig. 2 SIMS spectra of Pd/Ge contacts Zn-implanted with 25 keV and annealed at 550 $^\circ\text{C}$ (a) and Pd/Au/LaB₆/Au contacts Zn-implanted with 5 keV and annealed at 425 $^\circ\text{C}$ (b). Inside the semiconductor region sputter time values correspond to depth in nm.

contacts. On the other hand, for temperatures $>300^\circ\text{C}$ the Pd/Au/LaB₆/Au contact shows only minor dependence on the implantation energy. The resistivity is slightly lower reaching a minimal value of $7 \cdot 10^{-7} \Omega\text{cm}^2$ at 425°C . At temperatures below 325°C , the resistivity is comparable with that of unimplanted contacts indicating the absence of radiation damage tailing into the semiconductor.

The interface of contacts annealed at conditions for minimal ρ_c has been characterized by backside SIMS. In Fig. 2, linear SIMS plots are shown, from which the position of the metallurgical contact interface can be extracted. Its location is related to SIMS signal decay to half of maximum. Inside the semiconductor region, sputter time values correspond to depth in nm as calculated from the known distances of the quaternary marker layers.

The SIMS spectrum of a Pd/Ge contact implanted with 25 keV and annealed at 550°C is shown in Fig. 2(a). The spectrum is representative for annealing temperatures $\geq 400^\circ\text{C}$. The most striking feature is the redistribution of implanted Zn toward the contact interface. The position of the contact interface has not shifted into the semiconductor within the resolution limit of the measurement as inferred from the As and Ge depth distribution.

Pd/Au/LaB₆/Au contacts also exhibit redistribution of implanted Zn into the semiconductor. This is evident from Fig. 2(b), which shows the SIMS plot of a contact implanted with 5 keV and annealed at 425°C . In contrast to Pd/Ge, the contact interface shifts significantly into the semiconductor and appears now at a depth of approximately 45 nm as determined from the Pd depth distribution.

To evaluate the indiffusion of contact species beyond the contact interface into the semiconductor, semi-

logarithmic plots of the SIMS spectra discussed above are given in Fig. 3. Based on implanted calibration samples, ion intensity corresponds to concentration in cm^{-3} inside the semiconductor. In and Ga concentration is normalized to its theoretical value inside $\text{In}_{0.53}\text{Ga}_{0.47}\text{As}$. The diffusion depth is set to concentration decay to the resolution limit of the SIMS measurement.

The diffusion depth of Pd/Ge contacts annealed at 550°C is almost 100 nm as shown in Fig. 3(a). Except for a slight broadening, the shape of the Zn distribution does not vary, when the annealing temperature is raised from 400 to 550°C . In contrast, Pd and Ge indiffusion is much less pronounced at 400°C . Pd/Au/LaB₆/Au contacts implanted with 5 keV and annealed at 425°C exhibit a diffusion depth of nearly 150 nm (Fig. 3(b)). However, this value is as low as 60 nm for a temperature of 375°C , which is already sufficient to yield a low ρ_c of $1\text{--}2 \cdot 10^{-6} \Omega\text{cm}^2$.

The properties of implanted Pd/Au/LaB₆/Au contacts can be understood in terms of consumption of damaged $\text{In}_{0.53}\text{Ga}_{0.47}\text{As}$ during contact formation as well as local doping by indiffused Zn. The transition to ohmic behavior in contacts implanted with 25 keV occurs at temperatures of $300\text{--}325^\circ\text{C}$, when the contact has penetrated 25–30 nm into the semiconductor. This value fits well the extension of the damaged layer estimated by our TRIM calculations. Consequently, ρ_c is only weakly dependent on implantation energy for temperatures $>300^\circ\text{C}$. In this temperature range, implanted Pd/Au/LaB₆/Au contacts apparently behave like conventional Pd/Au/Zn-based metallizations. For the latter it is assumed that Pd and Au dissolve a significant amount of Group-III atoms during annealing by that creating the vacancies necessary for incorporation of indiffused Zn on sites in

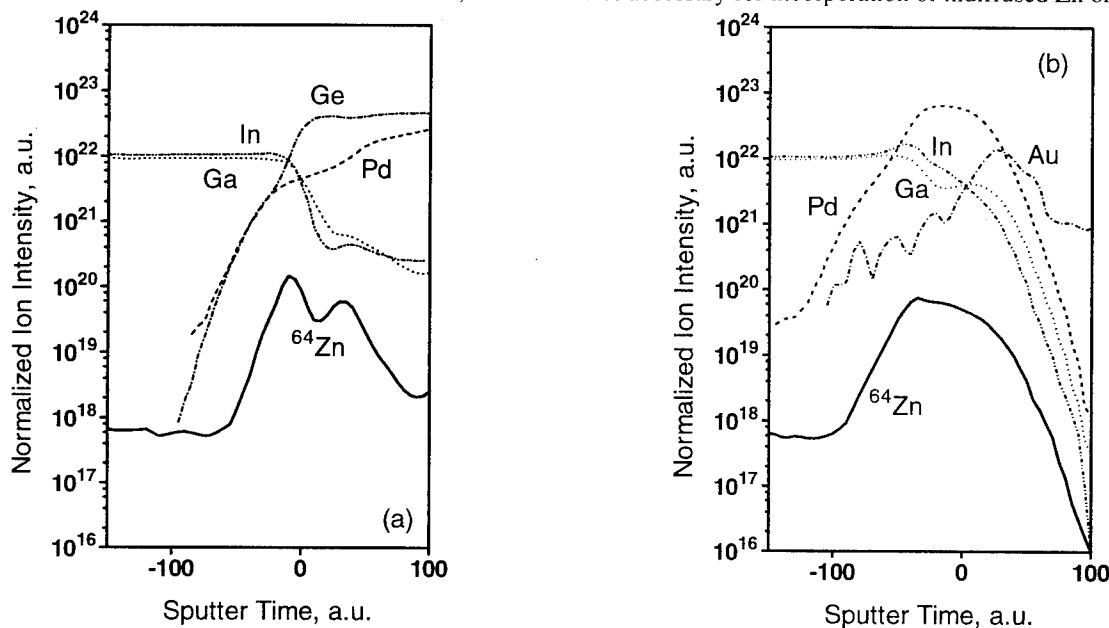


Fig. 3 SIMS spectra from Fig. 2 of Pd/Ge contacts Zn-implanted with 25 keV and annealed at 550°C (a) and Pd/Au/LaB₆/Au contacts implanted with 5 keV and annealed at 425°C (b). Inside the semiconductor region ion intensity values correspond to concentration in cm^{-3} .

the Group-III sublattice [6,7]. Indeed, high uptake of In and Ga by the reacted layer is observed in contrast to Pd/Ge (Fig. 3). Thus, the observed resistivity lowering may be attributed to the creation of a highly doped layer beneath the contact. Since the Zn distribution in Pd/Ge contacts annealed between 400 and 550 °C does not change essentially, the ρ_c decrease in this temperature range may be attributed to increasing Zn incorporation on Group-III sublattice sites combined with progressive annealing of implantation damage. In contrast to Pd/Au/LaB₆/Au, radiation defects providing the required vacancies seem to be the key for ρ_c lowering in this contact scheme since contacts implanted with 5 keV do not show ohmic behavior, although the Zn distribution is almost identical with that of contacts implanted with 25 keV. On the other hand, the compensating effect of residual defects possibly prevents such low resistivities as in case of Pd/Au/LaB₆/Au contacts.

Summary and conclusions

Zn implantation into Pd-based metallizations has been demonstrated to be an effective means for fabricating shallow, low-ohmic contacts on moderately doped p-In_{0.53}Ga_{0.47}As. Implanted Pd/Ge and Pd/Au/LaB₆/Au contacts on In_{0.53}Ga_{0.47}As doped to $2\text{--}3 \times 10^{18} \text{ cm}^{-3}$ exhibit a resistivity decrease by approximately two orders of magnitude compared with the unimplanted reference contacts. The resistivity of implanted Pd/Ge contacts on p-In_{0.53}Ga_{0.47}As is $1 \times 10^{-5} \Omega \text{ cm}^2$, which is comparable to that of conventional alloyed AuZn or Ni/AuZn/Ni contacts in this doping range [8]. Implanted Pd/Au/LaB₆/Au contacts display far lower resistivities. The minimal value found for contacts annealed at 425 °C ($7 \times 10^{-7} \Omega \text{ cm}^2$) is to our knowledge the lowest reported for contacts on p-In_{0.53}Ga_{0.47}As doped below $5 \times 10^{18} \text{ cm}^{-3}$.

During annealing, implanted Zn is redistributed toward the contact interface obviously creating a highly doped layer beneath the contact, which is responsible for the resistivity lowering. The position of the metallurgical interface at conditions for minimal resistivity remains unchanged for Pd/Ge and shifts 45 nm into the semiconductor in case of Pd/Au/LaB₆/Au contacts. The corresponding diffusion depths are 100 nm and 150 nm. However, in case of Pd/Au/LaB₆/Au contacts this value can be kept at approximately 60 nm by using an annealing temperature of 375 °C, which is already sufficient to yield a low resistivity of $1\text{--}2 \times 10^{-6} \Omega \text{ cm}^2$.

Electrical and metallurgical properties of both contact schemes make them attractive candidates for base con-

tacts of InP/In_{0.53}Ga_{0.47}As HBTs. Especially Pd/Au/LaB₆/Au contacts offer very low resistivity with the diffusion depth being well below 100 nm. This metallization is scheme currently integrated in our HBT process combined with further optimization of the contact composition with respect to contact indiffusion and contact resistivity.

Acknowledgments

This work has been performed within the OEIC program of the Deutsche Telekom. The technical assistance of I. Fechner, G. Schöne, W. Seban, H. Tempelhoff, and M. Thiemann is appreciated.

References

- [1] P. Ressel, H. Strusny, D. Fritzsche, H. Kräutle, and K. Mause, "Shallow ohmic contacts to p-InGaAs based on Pd/Ge with implanted Zn or Cd", MRS Symp. Proc. Ser., Vol. 318, pp. 177-182, 1994.
- [2] J. F. Ziegler and J. P. Biersack, The Stopping and Range of Ions in Solids, Pergamon Press, 1985.
- [3] J. Würfl, J. K. Singh, and H.-L. Hartnagel, "Reliability aspects of thermally stable LaB₆-Au Schottky contacts to GaAs", IEEE Reliability Phys. Conf. Proc., Vol. 28, pp. 87-93, 1990.
- [4] L. G. Shantharama, H. Schumacher, H. P. Leblanc, R. Esagui, R. Bhat, and M. Koza, "Evaluation of single ohmic metallisations for contacting both p- and n-type GaInAs", Electron. Lett., Vol. 26, pp. 1127-1129, July 1990.
- [5] P. Ressel, K. Vogel, D. Fritzsche, and K. Mause, "Nonalloyed ohmic contacts for p⁺-type InGaAs base layer in HBTs", Electron. Lett., Vol. 28, pp. 2237-2238, November 1992.
- [6] R. C. Brooks, C. L. Chen, A. Chu, L. J. Mahoney, J. G. Mavroides, M. J. Manfra, and M. C. Finn, "Low-resistance ohmic contacts to p-type GaAs using Zn/Pd/Au metallization", IEEE Electron Dev. Lett., Vol. 6, pp. 525-527, October 1985.
- [7] P. W. Leech, G. K. Reeves, and M. H. Kibel, "Pd/Zn/Pd/Au ohmic contacts to p-type In_{0.53}Ga_{0.47}As/InP", J. Appl. Phys., Vol. 76, pp. 4713-4718, October 1994.
- [8] T. C. Shen, G. B. Gao, and H. Morkoç, "Recent developments in ohmic contacts for III-V compound semiconductors", J. Vac. Sci. & Techn. B, Vol. 10, pp. 2113-2132, Sep/Oct 1992.

Non-Au based shallow low resistance ohmic contacts on p-InP

Moon-Ho Park^{*}, L. C. Wang^{*}, Fei Deng⁺, A. Clawson⁺, S. S. Lau⁺

J. Y. Cheng[⊕], D.M Hwang[◇], C. J. Palmstrom[◇]

^{*} Texas A&M University, College Station, TX 77843-3128

⊕ AT&T Bell Laboratories, Murray Hill, NJ 07974

⁺ University of California, San Diego, La Jolla, CA 92093

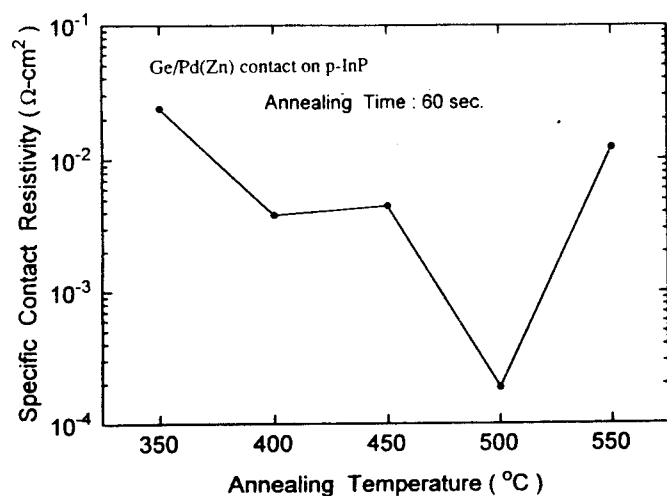
◇ Bellcore, 331 Newman Spring Rd. Red Bank, NJ 07701-7040

We have developed two shallow low resistance Pd-based ohmic contacts on p-InP based on solid-phase reactions. These contact schemes are the Ge/Pd(Zn) and the Sb/Pd(Zn) contacts. Lowest contact resistivity in the order of ~ 2 to $5 \times 10^{-6} \Omega\text{-cm}^2$ has been obtained on p type InP doped to $\sim 2 \times 10^{18} \text{ cm}^{-3}$ grown by chemical beam epitaxy (CBE). The maximum protrusion of the contact into the substrate is $\sim 150 \text{ \AA}$ for samples annealed at 420°C and $\sim 500 \text{ \AA}$ for samples annealed at 500°C , which are shallower than the conventional Au-based ohmic contact on p-InP.

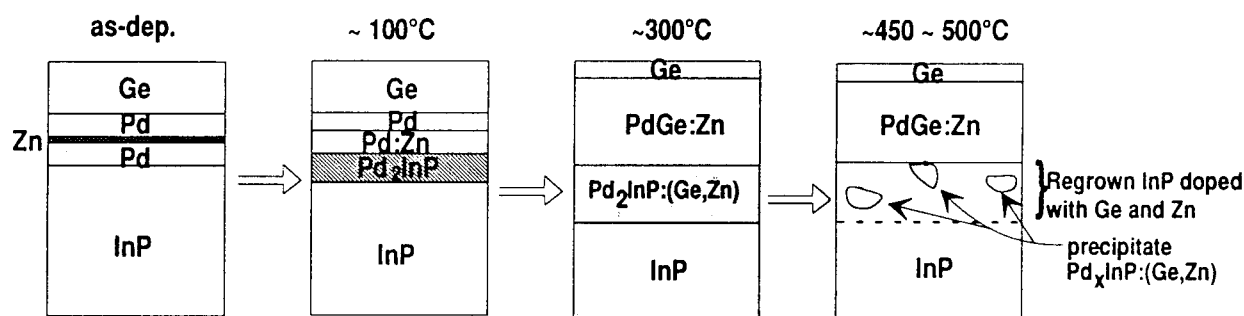
In the Ge/Pd(Zn) contact system, contact resistivities between 5×10^{-5} to $2 \times 10^{-4} \Omega\text{-cm}^2$ can be obtained. Precipitates of trapped materials of $\sim 200 \text{ \AA}$ in dimension during annealing have been observed by cross-sectional transmission electron microscopy (XTEM) technique in the samples annealed at 500°C . A model based on the solid phase regrowth mechanism^[1] is proposed to rationalize the electrical and metallurgical properties. This is the first non-Au based low resistance ohmic contact on p-InP achieved by solid phase regrowth process.

In the Sb/Pd(Zn) contact scheme, we attempt to form $\text{InP}_x\text{Sb}_{1-x} / \text{InP}$ heterostructure to lower the contact resistivity. Rutherford Backscattering Spectrometry (RBS) and XTEM studies showed that the contact/substrate interface is shallow and uniform for samples annealed below 500°C . However, solid-phase regrowth and formation of $\text{InP}_x\text{Sb}_{1-x}$ were not observed. Low contact resistivity of low $10^{-6} \Omega\text{-cm}^2$, however, has been obtained. We will discuss the correlation of the electrical and the metallurgical properties of this contact and possible ohmic contact formation mechanism.

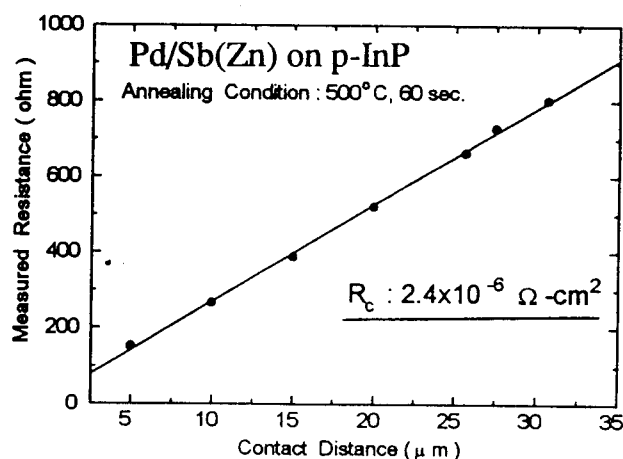
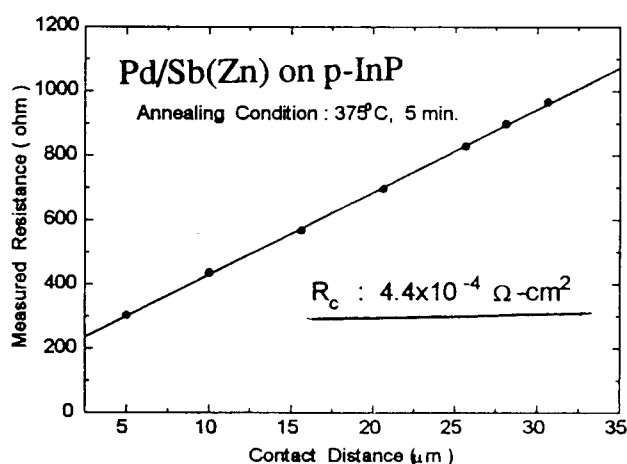
Ref: [1] T. Sands, E.D. Marshall, and L.C. Wang. " Solid-phase regrowth of compound semiconductor by reaction-driven decomposition of intermediate phases ", *J. Mater. Res.*, **3**, 914 (1988).



Contact resistivity vs. annealing temperature for the Ge/Pd(Zn) contact on p-InP ($\sim 2 \times 10^{18} \text{ cm}^{-3}$)



A schematic diagram of the proposed reaction sequence of the Ge/Pd(Zn) contact on InP at elevated temperatures.



Transmission line model measurement for the Sb/Pd(Zn) indicates that low contact resistivity in the order of $10^{-6} \Omega\text{-cm}^2$ has been obtained for samples annealed at 500°C .

*** Metallurgical investigation by cross-sectional TEM will also be presented. **

High-spatial-resolution characterization of residual strain in commercial LEC-grown InP(100) wafers

M. Fukuzawa and M. Yamada

*Department of Electronics and Information Science, Kyoto Institute of Technology,
Matsugasaki, Sakyo-ku, Kyoto 606, JAPAN*

Abstract: By using a high-spatial-resolution scanning infrared polariscope, in-plane components of residual strain have been characterized quantitatively in 2" ϕ LEC-grown Fe-doped InP (100) wafers. Their two-dimensional distribution maps reveal characteristic fine structures such as slip-like patterns originated from crystallographic glides during crystal growth process, highly-strained spots and filaments due to inclusions or voids inside the wafer, or due to scratches on the surface. Solidification factor dependence of residual strain is also examined together with etch pit density and resistivity.

I. Introduction

Residual strain or stress is observed when a part of thermal stress during crystal growth process is frozen into a crystalline ingot while generating dislocation, which is likely to degrade device performances or to cause various problems such as wafer warping and cracking. Therefore, it is very important for wafer makers and users quantitatively to characterize the residual strain as well as the dislocation density.

By using a linear and circular polariscope, Völkl and Müller[1] estimated the residual stress in thick (3mm) InP slices in connection with a numerical analysis of thermal stress in the LEC growth of InP crystals. Müller[2] and Hirano et.al.[3] used an infrared polarization microscopy to see microscopic strain field patterns of precipitates as well as whole-wafer strain patterns, although their measurements were not quantitative but qualitative. By developing a high-sensitive computer-controlled infrared polariscope[4], Yamada et.al.[5] made the first quantitative characterization of residual strain in a LEC-grown InP (100) wafer, and Yabuhara et.al.[6] characterized various commercial InP wafers quantitatively. However, their characterization results were poor in spatial resolution ($\approx 2\text{mm}$) to see fine structures of residual strain distribution. Then, we have recently developed a scanning infrared polariscope[7] as a whole-wafer inspection tool to characterize the residual strain in commercial III-V compound wafers with reasonably high spatial resolution ($\approx 200\mu\text{m}$).

In this paper, we present the high-spatial-resolution characterization results of residual strain distribution measured in various commercial (100) wafers of LEC-grown Fe-doped InP crystal. The three-dimensional distribution map has exhibited characteristic fine structures of residual strain, whose origins are discussed here. Solidification factor dependence of residual strain has also investigated by examining several sets of wafers sliced from the front, middle and back portions of ingots.

II. Quantitative Photoelastic Characterization of Residual Strain

In the present experiment, we used the high-spatial-resolution scanning infrared polariscope [7], which was developed as a whole-wafer inspection tool to characterize the residual strains in commercial III-V compound semiconductor (100) wafers. By using this apparatus, we can measure strain-induced birefringence, and then estimate the following residual strain components [4]:

$$|S_r - S_t| \equiv [(S_{yy} - S_{zz})^2 + (2S_{yz})^2]^{1/2}, \quad (1)$$

$$|S_{yy} - S_{zz}| = k\delta \left| \frac{\cos 2\psi}{p_{11} - p_{12}} \right|, \quad (2)$$

$$2|S_{yz}| = k\delta \left| \frac{\sin 2\psi}{p_{44}} \right|, \quad (3)$$

where δ and ψ are the phase retardation and the principal direction of birefringence plate, d is the plate thickness, $k = (\lambda/\pi d n_0^3)$, p_{ij} 's and n_0 are the photoelastic constants and the refractive index at the probing light wavelength: λ , respectively.

$|S_{yy} - S_{zz}|$ means the difference of the tensile strains along the crystallographic y and z directions while $2|S_{yz}|$ means the shear strain between the y and z directions. $|S_r - S_t|$ means the difference of the tensile strains along the radial and tangential directions in the local cylindrical coordinate system, which may be used as the total figure of in-plane residual strains.

III. Fine Structures in Residual Strain Distributions

Figure 1 shows a series of two-dimensional distribution maps of $|S_r - S_t|$ measured in a commercial 2" ϕ LEC-grown Fe-doped InP(100) wafer by changing the spatial resolution. These maps demonstrate that as increasing

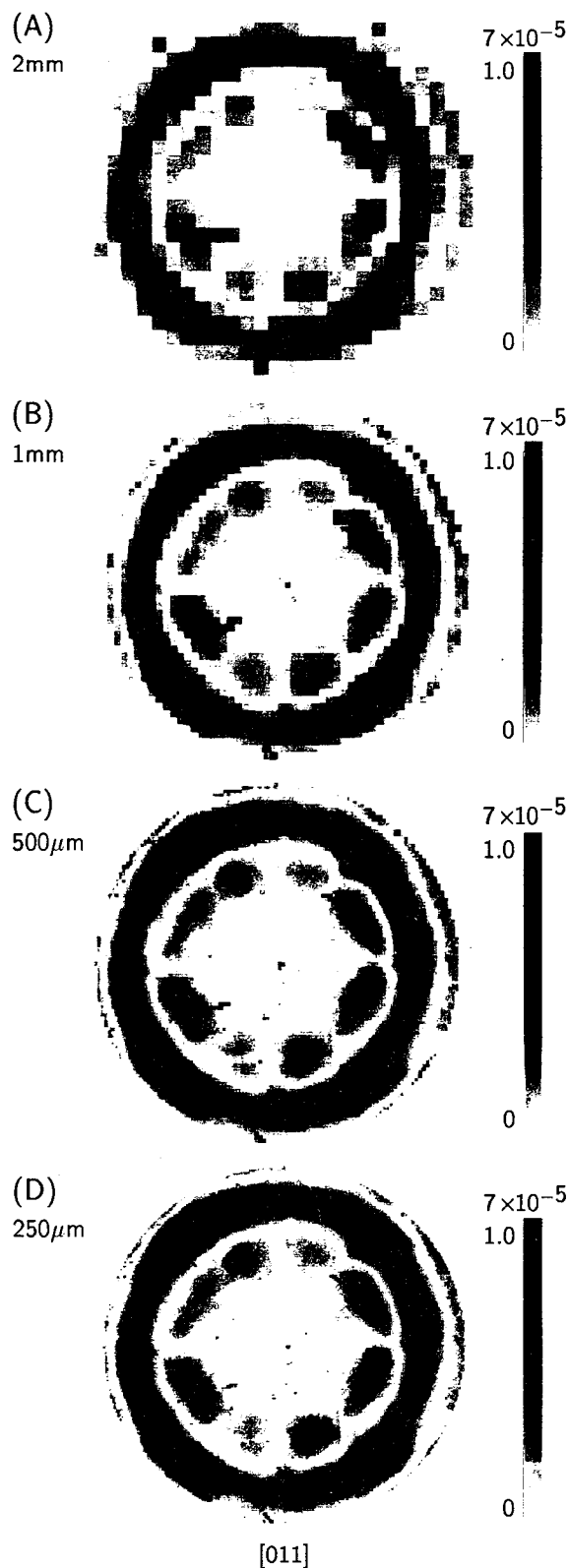


Fig.1 A series of two-dimensional distribution maps of $|S_r - S_t|$ measured with four different spatial resolutions in a commercial 2" ϕ LEC-grown Fe-doped InP(100) wafer. The spatial resolution is noted beside each map.

the spatial resolution, fine structures become clearer and clearer. It is found that there are several characteristic features in fine structures which cannot be observed in the lower-spatial-resolution maps, that is, (A) dark filaments, (B) dark spots, and (C) slip-like patterns which are almost aligned along the $\langle 011 \rangle$ crystallographic directions close to the peripheral region. These are more clearly seen in the three-dimensional display map shown in Fig.2. The dark filaments and spots seen in Fig.1 are corresponding to the sharp peaks in Fig.2. Their peak values attain in maximum about ten times as large as the average value (1.57×10^{-5}) of residual strain in this wafer and their full widths at half maximum are about 250 to 750 μm for the spots, 1500 to 3000 μm for the filaments.

In order to investigate the origin of the dark filaments and spots which are highly strained, we have carefully checked the wafer surface with an optical microscope. We found that there were scratches on the wafer surface corresponding to the three filaments noted by (A1) to (A3) in Fig.2, which were perhaps produced in handling wafer with tweezers. It is well-known that mechanically deformed regions are highly strained. Therefore, we may conclude that the dark filaments observed here are caused by the scratches. It should be noted here that our characterization technique is not affected by the variation in reflectivity due to scratches or surface conditions[4].

On the other hand, we could not find out anything on the surface regions where the spots noted by (B1) to (B3) and the other spots were located. Presumably, there is a possibility that the spots observed here are caused by voids or inclusions inside the wafer, or by birefringent dusts which float down on the wafer surface during the measurement. It was confirmed that the spots noted by (B1) to (B3) were always observed in the repeated measurements. Therefore, we may conclude that there is something inside the wafer which is accompanying strong strain field. It is very interesting that the strong strain field is spreading over the probing light spot size ($\approx 200 \mu\text{m}$). Even if there is a small size of defects such as voids or inclusions, the strain field may spread around the defects, due to strong mismatch between the defect and the crystal structure. By using a infrared polarization microscopy, Muller [2] have found that the strain fields around In and vanadium-rich precipitates with the dimension of tens μm spread over more than hundreds μm .

The slip-like patterns seen in Fig.1 correspond to the ridges indicated by (C1) to (C3) in Fig.2. If we might present here the two-dimensional distribution maps of $|S_{yy} - S_{zz}|$ and $2|S_{yz}|$ instead of $|S_r - S_t|$, then we could clearly see the slip-like patterns in the $2|S_{yz}|$ map rather than in $|S_{yy} - S_{zz}|$ map. This fact indicates that the dominant origin of slip-like patterns is $2|S_{yz}|$, that is, the shear strain between the y and z directions. It

should be also noticed that the slip-like patterns are almost aligned along the $\langle 011 \rangle$ crystallographic directions. Therefore, it may be presumed that the slip-like defects are caused by the $\langle 011 \rangle$ crystallographic glide due to strong thermal stress during crystal growth process[8,9]. This presumption may be supported by the fact that these slip-like patterns are seldom observed in wafers sliced from ingots grown by the vapor pressure controlled Czochralski (VCZ) method, in which the thermal stress is reduced during its crystal growth process. It is noted here that the averaged value of residual strain in VCZ wafers is considerably low compared with that in LEC wafers[6]. The slip-like defects observed here may degrade the epitaxial layer as found by Miner et.al[10].

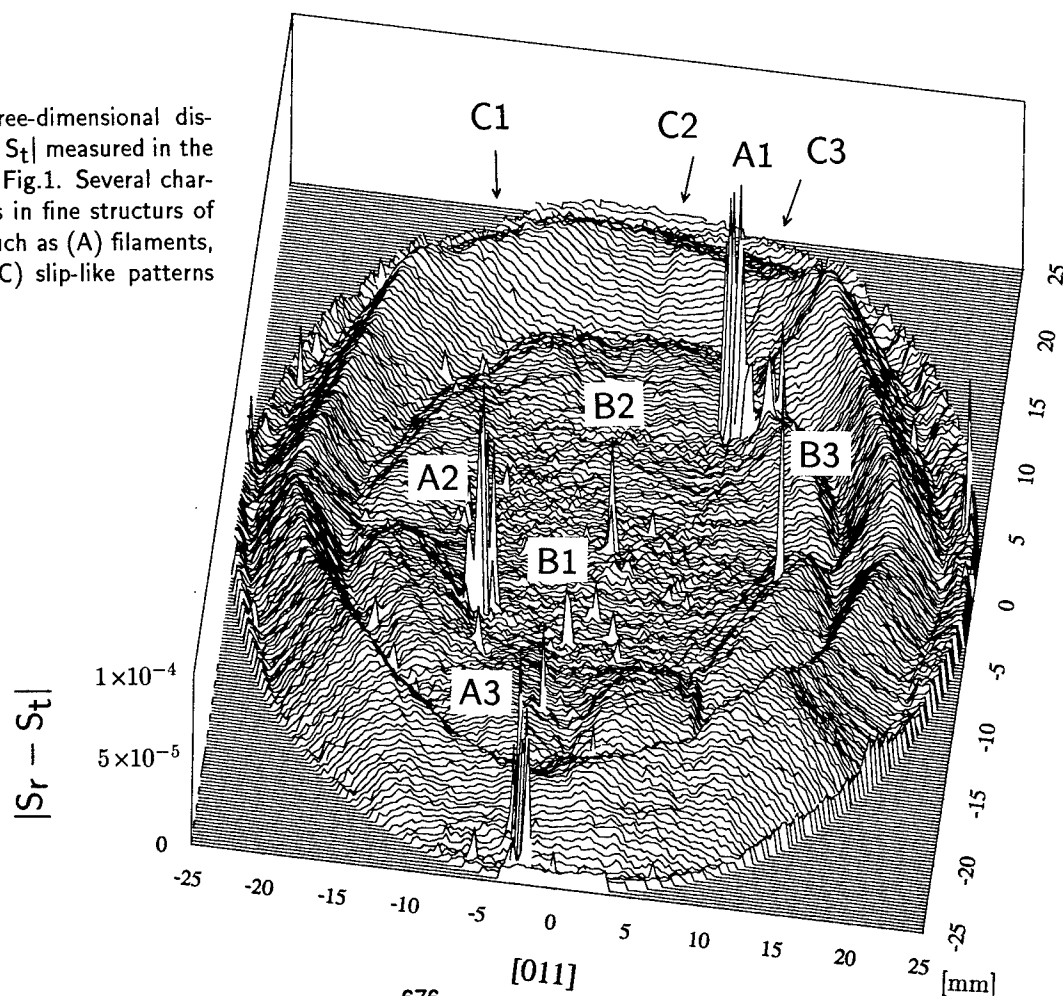
VI. Solidification Factor Dependence of Residual Strain

In order to see the solidification factor dependence on the residual strain distribution, we have systematically examined several sets of wafers sliced from the front, middle, and back portions of Fe-doped InP crystalline ingots. An example is shown in Fig.3. We note here

that the front wafer is intentionally scratched, the middle wafer is the same shown in Fig.1, and the back wafer is cracked in two pieces. We can see many dark filaments due to scratches in the front wafer, confirming the conclusion on scratch-induced strain stated in the previous section. Also, dark spots due to voids or inclusions are found out in all wafers shown here. Furthermore, we can see more clearly a lot of long slip-like patterns in the front wafer than in the middle and back wafers.

On the whole-wafer distribution map of residual strain, it is very difficult for us to find out any characteristic features in the front, middle, back wafers shown in Fig.3. We note here that they varied from wafer to wafer and from ingot to ingot. Then, the value of residual strain averaged over whole wafer was examined together with etch pit density (EPD) and of resistivity as a function of solidification factor. Figure 4 shows the solidification factor dependences of the averaged $|S_r - S_t|$, EPD, and resistivity. Here, we present the results measured in another set of wafers, since the averaged values might be changed by the scratches and crack as shown in Fig.3. It is found that as increasing the solidification

Fig.2. The three-dimensional display map of $|S_r - S_t|$ measured in the same wafer as in Fig.1. Several characteristic features in fine structures of residual strains such as (A) filaments, (B) spots, and (C) slip-like patterns are clearly seen.



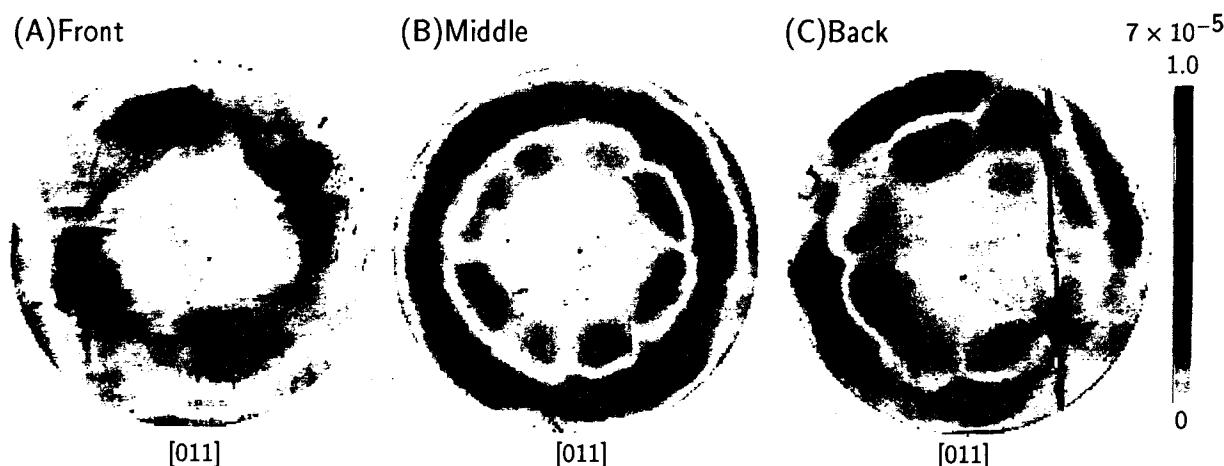


Fig.3. Two-dimensional distribution maps of $|S_r - S_t|$ measured in three wafers sliced from the (A) front, (B) middle, and (C) back portions of a 2" ϕ LEC-grown Fe-doped InP(100) crystalline ingot. The front wafer is intentionally scratched and the back wafer is cracked in two pieces.

factor, the resistivity is increased, because the Fe concentration is also increased and then native shallow donors are compensated with Fe atoms which act as deep acceptors. The Fe concentration of the wafers examined here was in the order of 10^{16} cm^{-3} . It is found in Fig.4 that the averaged values of residual strain and EPD exhibit a tendency that they are increased as increasing the solidification factor, that is, the Fe concentration.

Acknowledgments

The authors wish to thank many wafer and device makers for supplying various sample wafers used in our experiment. The present work was supported by the Grant-in-Aid for Developmental Scientific Research (Subject No.05555004) from the Ministry of Education, Science and Culture of Japan.

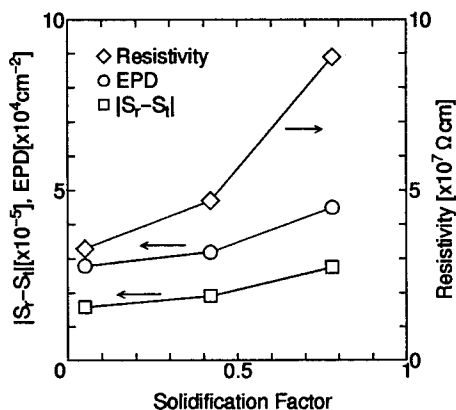


Fig.4 Solidification factor dependences of averaged values of residual strain, EPD, and resistivity measured in a set of 2" ϕ Fe-doped InP wafers.

References

- [1] J. Völkl and G. Müller, "Analysis of thermally induced stress in the LEC growth of InP crystals", *E-MRS Meeting*, (1987), XVI, pp.141-150.
- [2] G. Müller, "Non-uniformity of InP substrate crystals", *E-MRS Meeting*, (1987), XVI, pp.117-130.
- [3] R. Hirano *et.al.*, "Crystal growth of low EPD S-doped (100) InP by facet formation", *Proc. 5th Intr. Conf. on InP and Related Materials*, Paris, (1993), IEEE, pp.648-651.
- [4] M. Yamada, "High-sensitivity computer-controlled infrared polariscope", *Rev. Sci. Instrum.* **64**, (1993), pp.1815-1821.
- [5] M. Yamada *et.al.*, "Quantitative photoelastic characterization of residual strains in LEC-grown indium phosphide (100) wafers", *Proc. 5th Intr. Conf. on InP and Related Materials*, Paris (1993), IEEE, pp.69-72.
- [6] Y. Yabuhara *et.al.*, "Development of low-dislocation-density semi-insulating long 2-inch InP single crystals by the VCZ method", *Proc. 5th Intr. Conf. on InP and Related Materials*, Paris, (1993), IEEE, pp.309-312.
- [7] M. Yamada and M. Fukuzawa, "Scanning infrared polariscope as routine tool for quantitative characterization of residual strains", *Proc. 8th Conf. on Semi-Insulating III-V Materials*, Warsaw, (1994), in press.
- [8] A. S. Jordan *et.al.*, "A thermoelastic analysis of dislocation generation in pulled GaAs crystals", *Bell System Technical J.*, (1980), pp.593-637.
- [9] M. Yamada *et.al.*, "Quantitative photoelastic characterization of residual strain and its correlations with dislocation density profile in semi-insulating LEC-grown GaAs wafers", *Proc. 7th Conf. on Semi-Insulating III-V Materials*, Ixtapa, (1992), IOPP, Bristol, pp.201-210.
- [10] C. J. Miner, *et.al.*, "Characterization of slip-like defects in InGaAs epitaxial layers grown on Fe doped semi-insulating InP", *Proc. 5th Intr. Conf. Defect Recogn. and Image Proc. in Semicond. and Devices*, Santander, (1993), IOPP, Bristol, pp.181-186.

Electrical properties of the Hydrogen Defect in InP and the Microscopic Structure of the 2316 cm^{-1} Hydrogen Related Line

D.F. Bliss, G.G. Bryant, D. Gabbe†, G. Iseler,††, E.E. Haller,††† and F.X. Zach†††

US Air Force Rome Laboratory, Hanscom AFB, MA 01731

†Parke Mathematical Laboratories, Lowell, MA 01854

††MIT Lincoln Laboratories, Lexington, MA 02173

†††Lawrence Berkeley Laboratory, Berkeley, CA 94720

INTRODUCTION

High purity bulk InP crystals have a measured free carrier concentration which is higher than the residual net donor concentration as determined by glow discharge mass spectroscopy (GDMS) and SIMS. Similar discrepancies are found in semi-insulating iron doped InP between measured Fe^{2+} concentrations (equivalent to shallow donors) and the impurity content of the material. The problem of the missing donors is closely related to the achievement of undoped, semi-insulating InP by annealing in P-overpressure^{1,2}, since it has been shown recently that the loss of intrinsic donors is in part responsible for conversion from n-type conductivity to high resistivity $10^7 \Omega\text{-cm}$ material. In this paper we present evidence that a hydrogen-related defect is responsible for the missing donors.

We have studied the microscopic structure of the hydrogen related vibrational mode at 2315.6cm^{-1} by deliberately doping bulk InP crystals with deuterium and resulting in samples codoped with both isotopes. In contrast to the spectrum observed in undoped samples with only hydrogen present, the 2316 cm^{-1} line in hydrogen-deuterium containing samples is split into at least three components approximately 0.5 cm^{-1} apart. This can be explained if the defect contains more than one hydrogen atom; the additional lines are caused by mixed complexes containing hydrogen as well as deuterium. Our results are fully consistent with the defect model proposed by Darwich³ et. al for the defect: a cluster consisting of an indium vacancy and four surrounding hydrogen atoms which contribute four electrons to the trivalent vacancy, leaving one surplus electron available.

Preliminary investigations on samples annealed in P-overpressure at 950°C , show that the 2316 cm^{-1} line disappears from the spectrum and a reduced free carrier concentration is measured.

EXPERIMENTAL

A high pressure crystal growth system was used for crystal growth of bulk InP by the magnetic liquid encapsulated Kyropoulos (MLEK) method. For both the reference crystal and the deuterium doped crystal, 800 grams of high purity (6-9's) indium and 0.4 grams of iron were loaded into a quartz crucible together with the encapsulant. 250 grams of high purity red phosphorus were loaded into a quartz injector ampule and suspended above the crucible. Deuterium doping was accomplished by the addition of 5 grams of heavy water (D_2O) to the B_2O_3 encapsulant. During furnace evacuation an unknown amount of heavy water evaporated, but it was visually apparent that some of the D_2O remained on the hygroscopic encapsulant. The crucible was then heated to 1100°C to melt both indium and encapsulant, after which the injector transfer tube was lowered into the melt for

compounding indium phosphide. The injection process was completed within an hour, the injector was raised, and a (100) seed was lowered into the melt. A two inch diameter Kyropoulos crystal was grown by slowly cooling the melt with the seed in place. Then a flat-topped cylinder was grown as the crystal was slowly pulled from the melt. After several hours of growth, the crystal was removed from the melt and cooled slowly to room temperature.

Annealing experiments were performed in a pressure-balanced quartz ampule to provide a P overpressure of 40 atm. at 995°C . For this experiment a high purity undoped InP crystal was divided and one half was annealed for 19 hours. The free carrier concentration and the hydrogen absorption spectra were measured and compared before and after annealing.

For photoluminescence measurements we used slightly n-type bulk InP samples. Absorption measurements were performed on a Digilab 80E-V vacuum fourier transform spectrometer equipped with a cooled Ge:Cu photoconductor. Spectra were measured with a nominal resolution of 0.125 cm^{-1} , with samples mounted in a continuous flow helium cryostat and cooled to 6.5K.

RESULTS AND DISCUSSION

An interesting feature in the microscopic structure of the 2315.6 cm^{-1} line was observed in the deuterium-doped samples. Figure 1 shows the absorption spectra of semi-insulating iron doped InP samples in the frequency range characteristic for the H-P stretching modes.

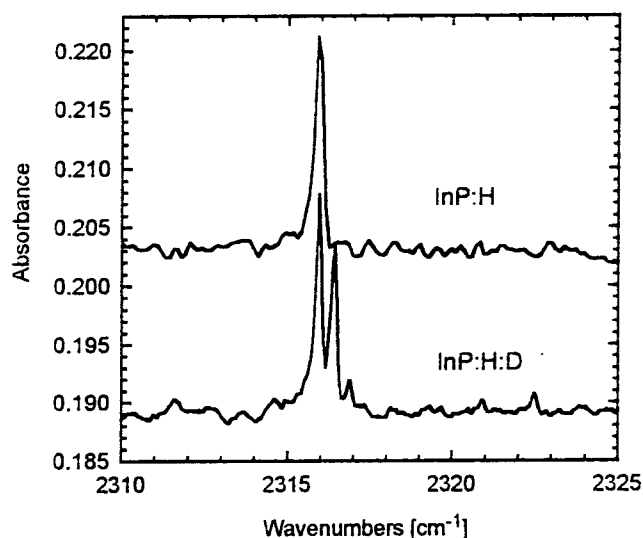


Figure 1 Absorption spectra for InP crystals grown with and without deuterium doping

Comparison of the two spectra obtained on samples grown with and without the addition of heavy water (D_2O), shows a single sharp peak at 2315.6 cm^{-1} which appears as a triplet in the deuterium doped material. A variety of other absorption lines can be seen, prominently located at 2255, 2288, and 2311 cm^{-1} as well as the triplet. A detailed list of all lines observed in our reference sample and the H-D codoped sample is given in table 1. Also provided is a comparison with available literature data and the putative assignments. Except for the line at 2202 cm^{-1} , all lines observed in the reference sample are also found in the H-D codoped sample. But the H-D codoped sample exhibits 5

additional absorption lines, the most obvious ones located in the triplet about the dominant hydrogen absorption peak. In addition three lines are located at 2264.4 cm^{-1} , 2320.5 and 2322.1 cm^{-1} . A comparison with literature values reveals that at least one of them (2322.1) has been associated with hydrogen alone.

Table I Summary of absorption lines between 2000 and 2400 cm^{-1}

this work	other references	reference sample	assignment
2142.7	-	2142.7	
2174.5	-	2174.5	
2178.5	-	2178.5	
-	2202.4	2202.6	$\text{V}_{\text{In}}\text{-H}$
2250.7	2250.78 ⁽³⁾	2250.5	
2254.6	2254.65 ⁽³⁾	2254.6	
2264.4	2262.4 at 77K ⁽⁶⁾	-	
2273.5	2273.4 ⁽³⁾	2273.6	
2287.7	2287.7 ⁽³⁾	2288.2	$\text{Zn}_{\text{In}}\text{-H}$
2311.3	2311.27 ⁽³⁾	2311.4	
2315.6	2315.6 ⁽³⁾	2315.6	
2316.1	-	-	
2316.6	-	-	
2320.5	-	-	
2322.1	2322.12 ⁽³⁾	-	
2333	2332.9 ⁽³⁾	2333	

To verify the presence of deuterium in the sample, we also observed absorption peaks in the spectral region of deuterium related absorption. These peaks were much weaker, indicating that less deuterium than hydrogen was incorporated in the samples. We observed three lines at 1684.5, 1686.3, and 1664.6 cm^{-1} . The latter one is the deuterium analog of the 2287.7 cm^{-1} Zn-H line, while the former two are close to the deuterium equivalent of the 2315.6 cm^{-1} absorption line.

The presence of two different hydrogen isotopes in InP bulk material is helpful in determining the atomic arrangement of hydrogen in the lattice and thus predicting its electronic behavior. Bai⁴ and Nielsen⁵ have studied the absorption spectra of H-D codoped silicon, using both isotopes to separate defects containing only one hydrogen from complexes with more than one hydrogen per defect. In multiple hydrogen complexes partial replacement of hydrogen with deuterium reduces the symmetry of the defect and gives rise to additional absorption lines. In H-D codoped samples it is found that both center lines with

local vibrational modes a 2223 cm^{-1} (hydrogen only) and 1617 cm^{-1} (deuterium only) each split into at least five components. The spectrum is assigned to a fully passivated silicon vacancy ($V_{\text{Si}}\text{H}_4$) which has tetrahedral symmetry consistent with the behavior of the absorption spectrum under uniaxial stress. Upon partial replacement of some of the hydrogen atoms with deuterium a total of 12 lines is expected, five of which could be observed in the region close to the hydrogen line and five more in the region of the deuterium line.

Several studies of the absorption spectra from hydrogen and deuterium ion implanted InP have established that the absorption at 2315.6 cm^{-1} is due to the local vibrational mode of a hydrogen atom bonded to a native defect in InP^{7,8,9}. The frequency of the local vibration suggests that the hydrogen is bonded to a phosphorus atom. In a recent comprehensive study of hydrogen in InP, Darwich³ et al. investigated the uniaxial stress splitting of the 2315.6 cm^{-1} local vibrational mode. Their results indicate the defect has tetrahedral symmetry similar to the case of the 2223 cm^{-1} line in proton implanted silicon. Based on the similarities between the observed stress splittings in the case of the 2223 cm^{-1} line in silicon and the 2315.6 cm^{-1} in InP it has been concluded that the latter is due to a fully passivated indium vacancy ($V_{\text{In}}(\text{PH}_4)$).

Our results provide further evidence for the similarities between the two defects in silicon and InP. They are in agreement with models involving more than one hydrogen atom per defect. In particular the triplet of lines observed in silicon is very similar to the triplet observed here, except that the splitting is smaller (0.5 as opposed to $1\text{--}2\text{ cm}^{-1}$). This is consistent with the shorter bond length (0.142 nm for P-H in PH_4 versus 0.148 nm in SiH_4) and the larger InP lattice constant (0.586 nm versus 0.543 nm in silicon), both reducing the interaction between neighboring hydrogen atoms. Furthermore in the frequency range of the H-P stretching modes we find a total of six lines not observed in the reference sample. This would be in agreement with the expected number of lines based on group theory. However since two of these lines (2264 and 2322.1) have frequencies close to features reported in the literature for samples with hydrogen only, their assignment to H-D complexes is somewhat uncertain.

How does one explain the electrical behavior of this complex? We note that the observation of an electrically active, hydrogen related complex has so far been restricted to partially passivated multivalent defects. More commonly the complexing between

hydrogen and simple defects and impurities leads to passivation, i.e. the removal of an electronic level. In a recent publication¹⁰ we have shown that in semi-insulating InP:Fe there is a discrepancy between the background donor concentration as measured by the Fe^{2+} concentration and the donor concentration obtained from an analysis of the impurity concentrations. In addition, we demonstrated that the difference is caused by the presence of an intrinsic donor related to the absorption at 2315.6 cm^{-1} . Since this line is due to a defect complex, as shown in this work, consisting of an intrinsic defect and several hydrogen atoms, it was not clear if the intrinsic defect alone or the whole complex is responsible for the "missing donors".

We will now propose a simple yet appealing model that may be able to account for all the presently available data. Assuming that the defect consists of an indium vacancy where the four dangling bonds are passivated with hydrogen we note that these four hydrogen atoms contribute four electrons to the bonds. However, the indium atom taken from the crystal contributed only three electrons to the bonds - thus there is one surplus electron in the neutral $V_{\text{In}}\text{H}_4$ defect as shown in Fig. 2.

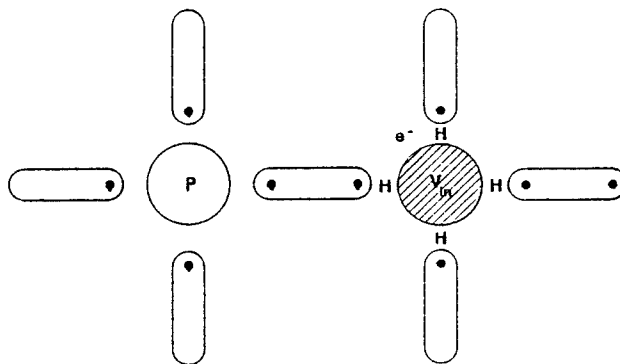


Figure 2 Schematic of $V_{\text{In}}\text{H}_4$ defect

This extra electron is expected to be only loosely bound to the defect, accounting for its donor-like behavior. These are the "missing donors" from the discrepancy between the donor concentration, as

measured by Fe^{2+} , and the impurity concentration of the material (mainly silicon and sulfur). These intrinsic donors can be accounted for by the defect related to the 2315.6 cm^{-1} line.

We have annealed undoped InP samples with free carrier concentrations typically $1\text{--}2 \times 10^{15} \text{ cm}^{-3}$. After annealing at 995°C for 19 hours under high phosphorus overpressure, the samples showed high resistivity similar to what has been observed by Hofmann¹ and by Kainosho². Our absorption spectra measured in the range from 500 to 3500 wavenumbers reveal that the 2315.6 cm^{-1} line has been removed by the annealing process. Other absorption and photoluminescence lines indicate that iron and copper have been introduced during the annealing process. Therefore our observations indicate that the following two mechanisms were involved in achieving the high resistivity: indiffusion of deep iron and copper acceptors and the loss of intrinsic donors which we identify as $\text{V}_{\text{In}}(\text{PH})_4$ complexes. For high purity InP where the shallow donor concentration is dominated by $\text{V}_{\text{In}}(\text{PH})_4$, the combined effect of these two processes is sufficient to explain high resistivities. Our findings are in agreement with the observations by G. Hirt¹¹ et al. They conclude that the conversion to semi-insulating material during the annealing of high purity n-type InP is caused by the loss of intrinsic donors.

CONCLUSION

In summary we have shown that in $\text{H}_2\text{--D}_2$ codoped InP samples a splitting of the 2315.6 cm^{-1} hydrogen related local vibrational mode is observed. This provides further evidence for the assignment of this line to a fully hydrogenated indium vacancy. Based on a simple argument we suggest that this defect shows electrical activity as a donor in agreement with previously reported results. We observe that this defect is lost during annealing under P-overpressure which has been shown to result in semi-insulating material. We suggest that the loss of intrinsic donors is due to the reduction of the VH_4 defect associated with the 2315.6 cm^{-1} line.

REFERENCES

1. D. Hofmann, G. Müller, N. Streckfuss; *Appl. Phys. A* 48 (1989) 315
2. K. Kainosho, H. Shikamura, H. Yamamoto, O. Oda; *Appl. Phys. Lett.* 59 (1991) 932
3. R. Darwich, B. Pajot, B. Rose, D. Robein, B. Theys, C. Rahbi, C. Porte, F. Gendron; *Phys Rev B* 48(1993) 17776
4. G.R. Bai, M.W. Qi, L.M. Xie, T.S. Shi; *Solid State Comm.* 56 (1985) 277
5. B. Bech Nielsen, J. Olajos, H.G. Grimmeis; *Phys Rev B* 39 (1989) 3330
6. D.W. Fischer, M.O. Manasreh, G. Matous; *Semicond. Sci. Technol.* 9 (1994) 1
7. V. Riede, H. Neumann, H. Sobotta, C. Ascheron; *Solid State Comm.* 65 (1988) 1063
8. J. Tatarkiewicz, B. Clerjaud, D. Cote, F. Gendron, A.M. Hennel; *Appl. Phys. Lett.* 53 (1988) 382
9. D.W. Fischer, M.O. Manasreh, D.N. Talwar, G. Matous, J. Appl. Phys. 73 (1993) 78
10. F.X. Zach; *J. Appl. Phys.* 75 (1994) 7894
11. G. Hirt, D. Wolf, G. Müller; *J. Appl. Phys.* 74 (1993) 5538

Single-Step Annealing of Be and Si Implants in S.I InP to Minimize Be Redistribution in the Completed p⁺/n Junctions

B. Molnar
Naval Research Laboratory
Washington, D.C. 20375-5347 USA

Abstract

The electrical characteristics of p⁺/n junctions in semi-insulating InP, formed by using a deep Si implant and a shallow Be implant, are reported. Both the electrical and atomic profiles found by the investigation indicate that the anneal-induced redistribution of Be can be prevented if the Be and Si implants are activated in a single-step anneal. In addition it was found that prolonged anneal time and elevated temperatures have significantly reduced Be compensation near the surface.

Introduction

There is considerable interest in fabricating integrated microwave devices on InP due to its desirable material properties. These devices require selectively-doped p- and n-type regions which are most conveniently formed by localized ion implantation into semi-insulating (S.I) InP substrates. Junction Field Effect Transistors (JFETs) have been investigated for InP microwave amplifiers. For the creation of fully ion implanted JFETs, a low energy Be implant for the p⁺ region and a deep Si implant for the n-channel regions have most often been used (1-6).

In the JFET ion implantation process, there are several significant barriers which need to be overcome for the achievement of optimized p⁺/n structures. These barriers include: a) A double diffusion front which degrades the abruptness of the Be profile is created during the implant activation anneal. b) The hole concentration near the surface is often substantially less than the acceptor concentration.

Several groups have examined aspects of this problem in the past. The results clearly show that more work is necessary to fully understand and optimize the conditions for the InP JFETs.

Experimental Background

The bulk of the material used in this work was liquid-encapsulated-Czochralski (LEC) grown (100) oriented, Fe doped, S.I InP wafers. Undoped wafers were only used to obtain a clear picture of the Be redistribution without the Fe disturbance. All implantations were done at room temperature in a non-channeling direction.

The p-side of the p-n junction was formed by shallow Be implantation in the 25-50 keV energy range. For the n-channel formation the samples received medium dose Si implants. To investigate the influence of the position of the Si implant relative to the Be implant, Si implantation with energy between 90 and 600 keV was chosen. P implantation was also studied. For P/Be co-implantation,

the influence of the position of the P to the Be was examined. The P energy was between 100 and 400 keV.

The implanted layers were activated from 600° C to 850° C using either a furnace anneal (FA) or a rapid thermal anneal (RTA) system. Most often the anneals were performed using a capless close contact technique with a flow of forming gas (7).

The annealed samples were electrically characterized using either C-V profiling or differential Hall measurements. The atomic profiles were derived from secondary ion mass spectrometry (SIMS) measurements using a Cameca IMF-3f ion microprobe.

Results and Discussion

Problems related to the Be implants into the Fe doped InP and their anneals will be illustrated with the help of Figures 1 and 2. Figure 1 shows the SIMS Be profiles

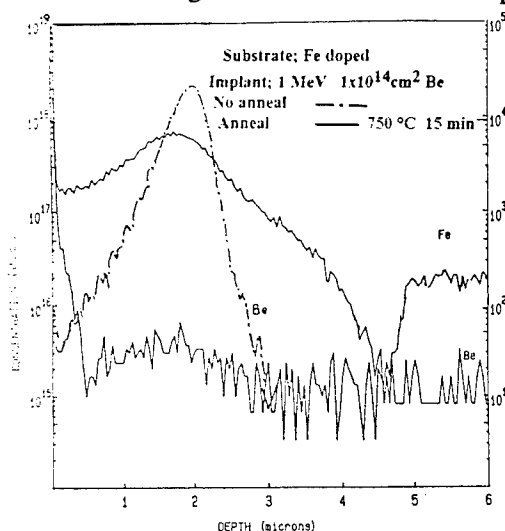


Fig. 1. The SIMS profiles of Be and Fe on a SI InP before and after a 750° C 15 min. anneal.

for a 1 MeV Be implant with a dose of $1 \times 10^{14}/\text{cm}^2$ before and after annealing at 750° C for 15 min. With the use of

high energy the surface influence is minimized. The Fe SIMS profile is only shown after the anneal. The as implanted Be profile approximates a Gaussian distribution with a projected range of 19000 Å and energy straggling of 2100 Å, which is close to the theoretical prediction. The Fe distribution is uniform in the substrate. Significant redistribution of Be and Fe results during annealing. At the surface there is Fe and Be pile up. This is an artifact of SIMS profiling. The annealed Be profile is a slightly diffused version of the as implanted profile, followed by a short concave region with a low concentration tail. As a result of the anneal, significant Fe depletion is created under the annealed Be profile. These results are similar to the observations of Oberstar, et al, (8). In addition, it was found that the Be tail is present in the S.I InP even after an RTA of a few seconds (9).

Figure 2 shows the resulting electrical carrier, Polaron profiles of the same Be implant, as shown in Figure 1 with different activation conditions. The electrochemical

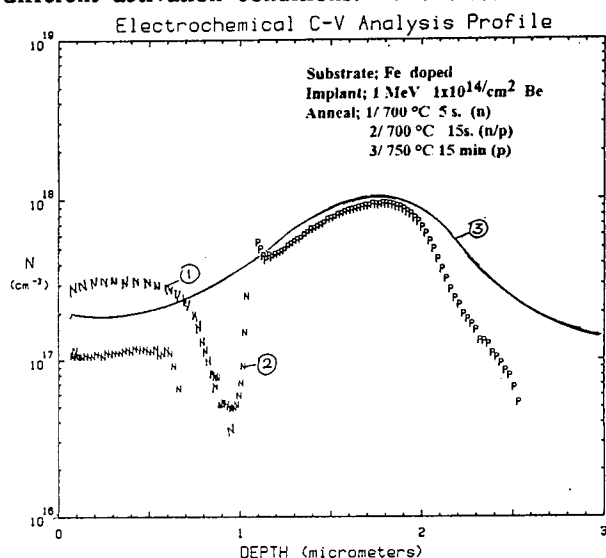


Fig. 2. Electrical carrier profiles of a Be implant with different annealing conditions.

profiling reveals the initial presence of an n-type layer at the surface. With the increase of anneal time, the n-type conductivity decreases as the hole doping from the deep side of the profile advances to the surface. There is some tail in the hole profile after a 15 sec anneal. The tail is substantially increased after a 15 min anneal at 750 C. After 15 min the hole concentration approximates the Be distribution. It is observed that during the short time anneal the implantation damage created n-type conductivity which is not removed (10). The presence of n-type doping after the short anneal added free electrons to the donor implant and compensated the acceptor implant.

Similar n-type conductivity influences the P/Be co-implantation. It was observed that the short time anneal was inadequate since some of the damage of the P implantation was retained which introduced n-type conductivity (10). The hole concentration profiles are compared in Figure 3 after an RTA for the Be and the Be/P co-implanted cases.

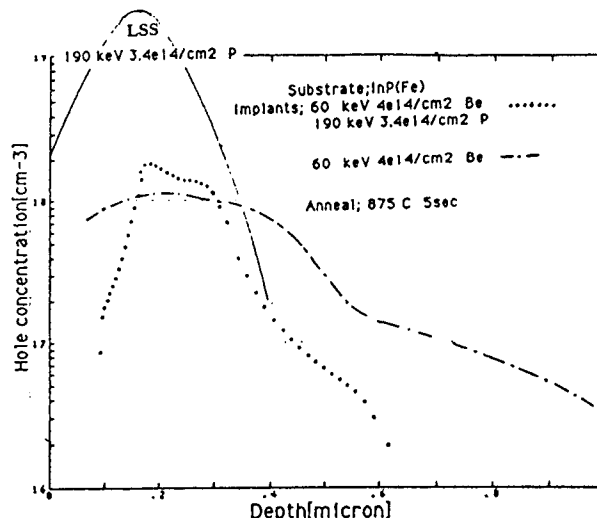


Fig. 3. The activated Be profiles for a 60 keV/4x10¹⁴/cm² Be implants either with (dotted) or without (dashed) a matching P co-implant after RTA.

The LSS profile of a 190 keV/3.4x10¹⁴/cm² P implant is also shown. In the P co-implanted cases the tail is indeed substantially reduced and the activation is increased, as was already shown by Wang (11). However, the n-type doping introduced by the P implantation damage is not eliminated by the short time anneal. The n-type doping leads to a substantially less hole concentration at the surface than the acceptor Be concentration. Thus the P doping limits the achievable gate contact resistance.

The electrical characteristics of p⁺/n junctions using a deep Si implant and a shallow Be implant have been reported by Hausser and Romer (6). They have concluded that it is advantageous to anneal the two implants separately and to use long time anneals. In order to avoid the influence of Fe, they have used undoped, n-type wafers. Isolation between the devices, however, requires a S.I substrate. SIMS studies have been performed on Be implants using unintentionally doped InP. Substantial Be redistribution has been found after either anneals. Such redistribution prevents the formation of an abrupt, shallow p⁺ layer.

Quality JFETs require shallow, highly activated Be layers and a low dose Si implanted n-channel with high Be

mobility. It is found that without an additional P co-implantation, the Be redistribution can be prevented using a single prolonged anneal if the Be and Si implants have an opposing gradient at the junction. The influence of the anneal's sequence for Be and Si implants with an opposing gradient is shown in Figures 4 and 5. In Figure 4 the

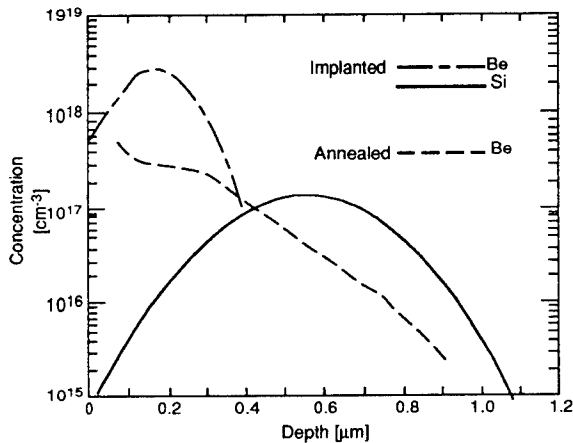


Fig. 4. SIMS atomic profiles of well separated Si and B after two-step implant and anneal cycle.

profiles of Si and Be are shown before and after the anneal cycles. The 600 keV/ $6.1 \times 10^{12}/\text{cm}^2$ Si implant was annealed at 750° C for 15 min, before the 50 keV/ $8.8 \times 10^{13}/\text{cm}^2$ Be is implanted. The Be was activated in a second-step at 750° C for 15 min anneal. The Si and the Be each have an opposing gradient at their junction. There is Be redistribution in this case. This is the same redistribution as the Be redistribution in undoped InP. The annealed Si implant provides an n-type background doping where the Be is located. Without first annealing the Si implant, there is no n-type background during the Be activation.

The case of Si and Be implants' activation with a single 750° C 15 min anneal is shown in Figure 5. The Si implant schedules were: 300 keV/ $4.0 \times 10^{12}/\text{cm}^2$ and 600 keV/ $8.1 \times 10^{12}/\text{cm}^2$. The Be implant was; 50 keV/ $8.8 \times 10^{13}/\text{cm}^2$. The Si level under the Be profile is about $3 \times 10^{16}/\text{cm}^3$.

The implanted Si and Be profiles have an opposing gradient at their intersection. In Figure 5 is shown the depth profiles of the ions and the corresponding holes and electrons. The annealed Be profile at the tail agrees with the as implanted Be profile. At the implanted Be maximum, there is some Be rearrangement. The Be accumulations are in the same regions where some Fe accumulations have been observed after the anneal.

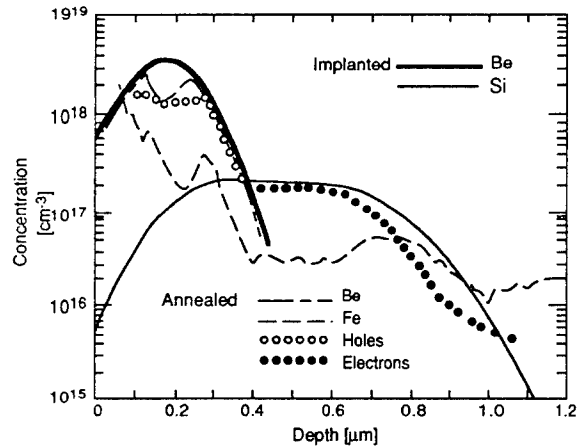


Fig. 5. SIMS atomic profiles and the corresponding electronic profiles of well separated Si and Be implants after a single 750° C, 15 min anneal.

The measured hole profile is in good agreement with the Be atomic profile with an 80% activation. No Si re-distribution has been observed during the annealings. The electron concentration follows the Si profile, but in the end of the Si range it decreases faster than the Si. It can be seen in Figure 5 that the n-type carrier concentration decreased in the same region where the Fe concentration increased. It suggests that the increased concentration of the deep acceptor Fe is compensating the n-type doping of the Si implants.

We have shown, that if the Be and Si implants are well separated, only a single activation anneal is required to prevent Be redistribution. Cases where the Si and Be implants were not separated are shown in Figures 6 and 7. In these examples the Si and Be implants were in the same location. The atomic profiles before and after a two step-implant and anneal cycle are shown in Figure 6. The 90 keV/ $6.0 \times 10^{12}/\text{cm}^2$ and 300 keV/ $6.6 \times 10^{12}/\text{cm}^2$ Si was implanted first and annealed at 750° C for 15 min. Then the 50 keV/ $8.8 \times 10^{13}/\text{cm}^2$ Be was implanted. The Be implant was activated with an additional 850° C 10 sec. anneal. On the annealed Be profile substantial Be redistribution is observable regardless whether RTA or FA is used. The redistribution of the Be is similar to those found in the cases of undoped InP, where there is no Fe interference.

In Figure 7, are shown the SIMS profiles of coinciding Si and Be implants before and after a single anneal at 750° C for 15 min. The Si implants schedules were: 100 keV/ $2.2 \times 10^{12}/\text{cm}^2$ and 240 keV/ $6.4 \times 10^{12}/\text{cm}^2$. The Be implant was: 50 keV/ $8.8 \times 10^{13}/\text{cm}^2$. For the annealed

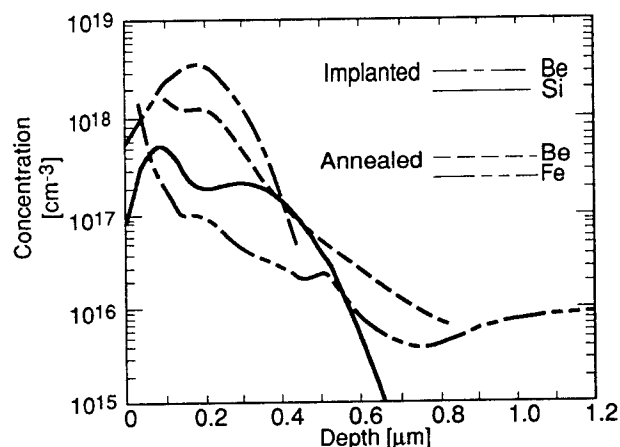


Fig. 6. SIMS atomic profiles of coinciding Si and Be before and after a two-step implant and anneal cycle.

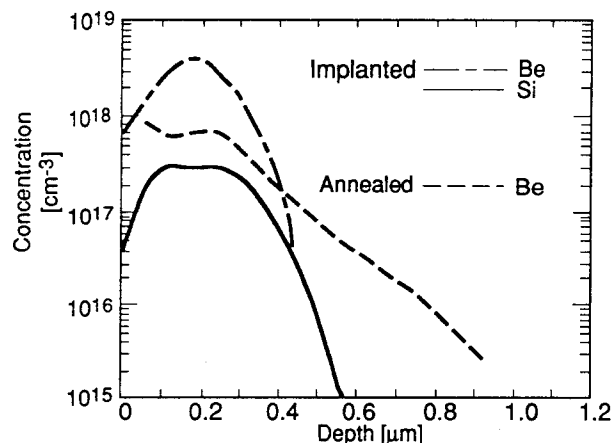


Fig. 7. SIMS atomic profiles of coinciding Si and Be implants before and after a single-step anneal at 750° C for 15 min.

Be profile substantial redistribution is observable regardless whether RTA or FA is used. It was shown, that if the Be and Si implants coincide, the Be redistribution is independent of the anneal cycles.

Conclusions

The influence of two implant annealing sequences and the Si implant's position relative to the Be implant has been studied. In addition, the influence of the co-implanted P was also examined. It has been found that Be redistribution can be prevented without additional P co-implantation by using a single, long time anneal for the well-separated Be and Si implants. Short time anneal of the Be implanted layer revealed the presence of an n-type layer on the surface side of the profile. Long time anneals lead to increased activation of the Be implant without additional Be diffusion.

References

1. K.R. Gleason, H.B. Dietrich, R.L. Henry, E.D. Cohen, and M.L. Bark, "Ion-implanted n-channel InP metal semiconductor field-effect transistor," *Appl. Phys. Lett.*, Vol. 32, pp. 578-581, May 1978.
2. D. Woodhouse and J.P. Donnelly, "Fully ion implanted p-Column InP Field-Effect Transistor," *IEEE Electron Device Lett.* EDL-7, Vol. 6, pp. 387-389, June 1986.
3. C.L. Cheng, K.W. Wang and S.M. Parker, "Fully Implanted InP JFET with an Abrupt p+-n Junction," *IEEE Electronic Device Lett.* EDL-8, Vol. 10, pp. 483-485, October 1987.
4. S.J. Kim, G. Guth and G.P. Vella-Coleiro, "Integrated Amplifiers Using Fully Ion-Implanted InP JFET's with High Transconductance," *IEEE Electronic Device Lett.* EDL-9, Vol. 6, pp. 306-308, June 1988.
5. J.B. Boos, W. Kruppa, and B. Molnar, "Planar, Fully Ion-Implanted InP Junction FET's with a Nitride-Registered Gate Metalization," *IEEE Electronic Device Lett.* EDL-10, Vol. 2, pp. 79-81, February, 1989.
6. W. Haussler and D. Romer, "Fully ion-implanted p-n junctions in InP," *J. Appl. Phys.* 67, Vol. 7, pp. 3400-3408, April 1990.
7. B. Molnar, "Close-contact annealing of ion-implanted GaAs and InP," *Appl. Phys. Lett.* 36, Vol. 11, pp. 927-929, June 1980.
8. J.D. Oberstar, B.G. Streetman, J.E. Baker and P. Williams, "SIMS Studies of Be Implants in Semi-Insulating InP," *J. Electrochem. Soc.* 129, Vol. 6, pp. 1312-1320, June 1981.
9. B. Molnar and H.B. Dietrich, "Comparison of isothermal anneal techniques for Be and Si implanted S.I InP," *Mater. Res. Soc. Symp. Proc.* 52, pp. 423-430, 1986.
10. B. Molnar, T.A. Kennedy, E.R. Glaser and H.B. Dietrich, "Observation of ion-implantation-damage-created n-type conductivity in InP after high-temperature annealing," *J. Appl. Phys.* 74, Vol. 5, pp. 3091-3098, September 1993.
11. K. Wang, "Formation of a shallow p+ layer on InP using a P/Be co-implant," *Appl. Phys. Lett.* 51, Vol. 25, pp. 2127-2129, December 1987.

Friday

May 12, 1995

- FA1** Epitaxy: Characterization
- FB1** Photonic Integration
- FA2** HFETs: Physics and Technology

INTERFACE STRAIN IN InGaAs-InP SUPERLATTICES

FA1.1
(Invited)

A. R. CLAWSON

University of California San Diego, ECE Dept-0407
9500 Gilman Dr., La Jolla, CA 92093-0407

C. M. HANSON

NCCOSC RDTE Div 555
49285 Bennett St., Rm 111, San Diego, CA 92152-5790

1/17/95

Introduction

In a perfectly abrupt heterojunction, an intrinsic crystalline strain is expected due to interface bond lengths that deviate from those of the bulk (1). In reality, heterojunctions also contain additional crystalline strain due to compositional mixing across the interface, *i. e.* some of the atoms on one side of the heterojunction have crossed over to the other side and *vice versa*. It has been the intention of our work to use strain as a measured parameter to better understand the compositional abruptness of the InP/InGaAs heterojunction grown by OMVPE. Our approach has been to intentionally perturb interface compositions by inserting very thin layers of known composition and thickness at interfaces of multilayer superlattice structures and assess the consequences to the measured strain. From this it has been determined what strain is predictable and what strain is an excess due to As/P intermixing. In addition inferences of surface reconstruction behavior and atomic bonding configurations across the heterojunction can be made.

Multiple layer superlattices have been used as the test structure, where for each superlattice period the dimensional change from the inserted layer is a significant fraction of the period thickness. The strain and thickness of the superlattice period can be obtained from x-ray diffraction rocking curves (XRDRC), and a simple analysis can be applied to identify the elastic strain contributions of individual thin mismatched regions.

Initial experiments were performed on InP/InGaAs superlattices in which monolayer equivalents of binaries (InAs, GaAs, AlAs, GaP, AlP) were inserted into one or the other of the InGaAs/InP heterojunctions. We were able to determine which inserted layers would produce the expected strains, and which were exceptions. The next experiments were performed on samples which were primarily either an InP or GaAs matrix in which binary layers or specialized interruptions were introduced periodically to form the superlattice. From this we were able to more clearly determine the behavior of a phosphorus terminated surface exposed to arsine, and the arsenic terminated surface exposed to phosphine.

Interpretation of strain

Strain is attributed to the lattice dimension changes introduced by interface bonds and mismatched regions in an otherwise lattice-matched structure on an InP (001) substrate. It is assumed that the in-plane layer lattice is coherent with the InP substrate and differences in the layer lattice parameters cause elastic distortion of a_{\perp} , the dimension perpendicular to the interface. The strained a_{\perp} dimension is related by known elastic compliance coefficients to the relaxed lattice parameter (2,3). The average $\Delta a_{\perp}/a$ over a single superlattice period and the period thickness are determined directly from XRDRC data, and the measured $(\Delta a_{\perp}/a \times \text{thickness})$ product is equivalent to the sum of the (strain \times thickness) products of all the individual strained regions within the single period.

$$(1) (\Delta a_{\perp}/a)_{SL} \times d_{SL} = (\Delta a_{\perp}/a)_{ML} \times d_{ML} + (\text{unknown})$$

i.e.

$$\left[\frac{\text{strain in } a}{\text{single period}} \right] = \left[\frac{\text{strain due to the}}{\text{inserted layer}} \right] + [\text{excess strain}]$$

Since most of the structure is lattice-matched, the strain is due to the inserted layer and changes in the intermixing across the heterojunction interfaces. In absence of interface intermixing, the strain is due solely to the inserted layer,

thus for a known composition the layer thickness can be determined. For cases where both layer thickness and composition are known the strain can be calculated, and any excess strain can be attributed to intermixing.

Results from the excess strain due to intermixing are limited to a value for the (strain \times thickness) product, thus the actual thickness and alloy compositions cannot be independently known. However, for InP lattice-match, a positive (biaxially compressive) strain can only be due to InAs, thus we can identify an *equivalent* InAs thickness. The InAs-like strain could be from an $\text{InAs}_x\text{P}_{1-x}$ alloy over an arbitrary thickness, as well as from In-As interface atomic bonds.

Although Vegard's law applies independently for substitutions of atoms on both the group III and group V sublattices, strain from intermixing of the constituent elements across the heterojunction interface is only observed for the group V sublattice. Since all the group III elements are incorporated during OMVPE under the high V/III ratio conditions used here, their spatial distribution through the period thickness has no effect on the average lattice parameter and therefore group III intermixing is not measurable by this procedure. This insensitivity to group III intermixing assures the interpretation that any excess strain is due to exchange of group V elements, P and As.

Experimental details

The growth technique used a lamp-heated horizontal reactor at 650°C, 20 Torr pressure with V/III ratios of >200 for InP and >120 for InGaAs. The gas sources were trimethylindium (TMI), trimethylgallium (TMG), arsine (AsH_3), and phosphine (PH_3). Growth rates were $\sim 2 \text{ \AA/sec}$ for each of the constituent III-V binary compounds. Source gas switching was done with careful balance of flows and pressures, and no growth interrupts were used except as noted in the text. All samples were grown on (001) on-orientation substrates.

Results

The initial series of samples consisted of 30 period nominally lattice-matched 90 Å InGaAs - 90 Å InP superlattices in which very thin layers of a mismatched binary III-V (InAs, GaAs, AlAs, GaP, AlP) were introduced locally at one of the interfaces (4). The inserted layers were kept very thin, equivalent to 1 or 2 monolayers, to avoid strain relaxation. In most cases, the strain was proportional to the layer growth time, and inserted layer thicknesses could be calculated using equation 1. The growth rates of very thin layers were found to be identical to thick-layer equilibrium growth rates. The major exceptions were for GaAs or GaP layers introduced at the InP-grown-on-InGaAs interface, which introduced excess strain. The reason for these exceptions is not clear, however, onset of three-dimensional growth mode with the Ga compounds is suspected from the resulting degradation in diffraction patterns and the poor layer morphologies. An important result of this work is confirmation that thin layer growth rates are the same as for thick layers and that strains of inserted layers are predictable.

To study strain from the interactions of As and P at the interfaces, two additional series of superlattices were grown, one based on thin As-compound layers inserted periodically into InP (5) and the other of P-compound layers inserted into GaAs. The same 180 Å period spacing, 30-period superlattice was used.

In figure 1 strain data is shown for InP superlattices with three different inserted strained layers: GaAs, InAs, and InAs-equivalent generated by exposing the InP to AsH_3 (5). One significant feature is the extrapolation of the strain in each case to a nearly identical offset value at zero time. This offset is attributed to In-As interface bonds formed almost spontaneously by a rapid replacement of P by As on the AsH_3 -exposed InP surface. InP overgrowth of As results in the As incorporation as an InAs component. Very slow displacement of As surface atoms by P from PH_3 -exposure allows most of the inserted layer As to remain. The interface layer strain is equivalent to about 2/3 monolayer of InAs. The behavior is similar when an InAs or GaAs layer is deliberately grown. Figure 1 also shows additional time dependent InAs-like strain as As continues to replace P in the InP from the thin layer growth of the As-compounds.

The slow replacement of surface As by P from PH_3 is demonstrated in figure 2. InP was initially exposed to AsH_3 for 1.38 seconds to exchange As for surface P, then a second exposure was made for varying times to either only H_2 or H_2 with 0.02 PH_3 mole fraction (5). Exposure to only H_2 for up to 20 seconds resulted in no change of strain,

thus no loss of As. Exposure to PH_3 slowly reduces the strain for times out to ~ 10 seconds to the strain of the stable

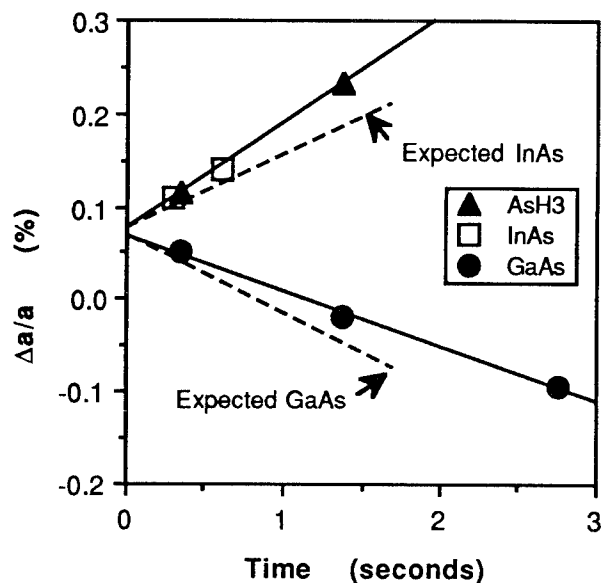


Figure 1. Strain in superlattices (30-periods of 180 Å) formed by inserting thin As-compound layers periodically into InP. The expected strain values are calculated from known layer strains and thicknesses. The zero time offset strain is attributed to InAs interface bonds. An additional excess InAs-like strain component forms as both InAs or GaAs layers grow.

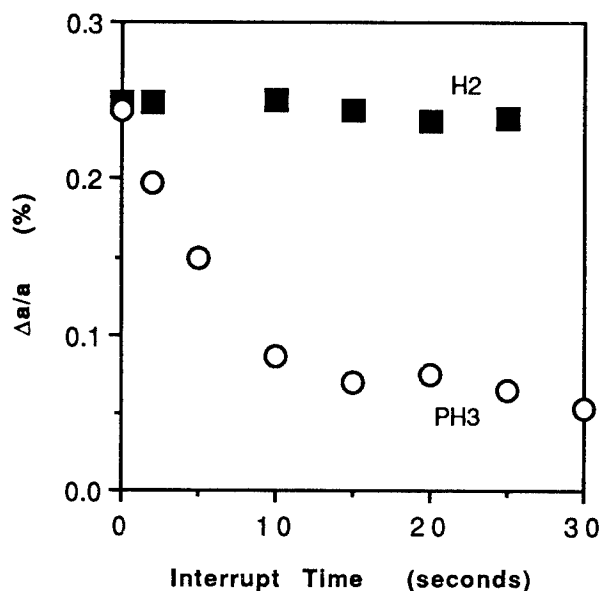


Figure 2: Strain in superlattices (30-periods of 180 Å) formed by two steps: a 1.38 second exposure of InP to AsH_3 followed by growth interruption in either H_2 or PH_3 . This shows slow replacement of surface As by P.

interface ($\sim 2/3$ ML InAs equivalent.) Longer exposure to PH_3 reduces the strain at a much slower rate. This behaves as though weakly-bonded excess surface As atoms are initially removed to expose the more strongly As-bonded interface layer.

In figure 3 is shown GaP-like strain from P replacement of As on a GaAs surface when exposed to phosphine. As with InP superlattices, P replaces As rather slowly, both when forming Ga-P interface bonds and during the longer period P-As exchange. The interface strain is equivalent to 0.5 monolayer GaP and takes about 1 second to form. Rapid replacement of P by As from AsH_3 for these surfaces is confirmed by complete desorption of P during a short pause under only AsH_3 before resuming GaAs growth.

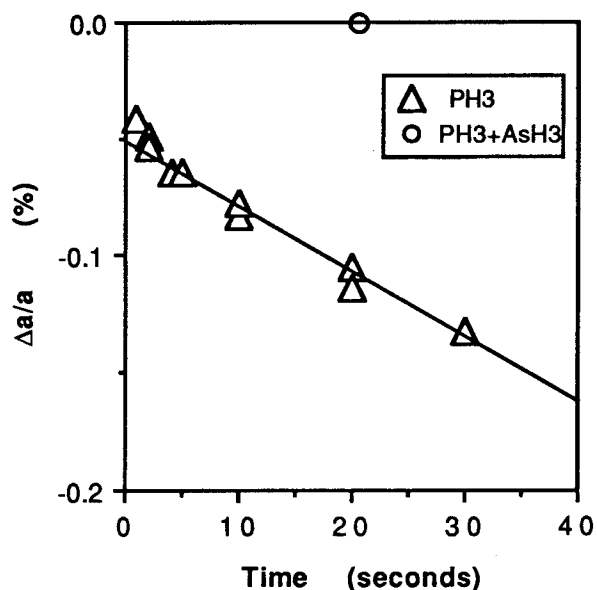


Figure 3. Strain in superlattices (30 periods of 180 Å) formed by PH_3 exposure of the GaAs surface. This shows slow replacement of As by P to form equivalent of a half monolayer GaP interface and shows continuing slow As by P replacement with time. Also shown are superimposed data points for 20 second PH_3 exposed surfaces which were then followed with AsH_3 exposures of 1 and 5 seconds with a resulting complete desorption of the P atoms.

In figure 4 is shown strain for GaAs superlattices formed by introducing different thicknesses of InP or GaP. When InP and GaP layers are introduced (group III alkyls are present), there is no offset strain at the zero time intercept. The tensile strain from GaP inserted thin layers is half that expected from their thickness, while the InP thin layers inserted into GaAs produce compressive strain exactly as expected. These results will be discussed in the next section.

Introduction of P onto the GaAs surface from PH_3 does not affect the growth of subsequent inserted layers. The resultant strain from a two-step inserted layer growth of a PH_3 exposure followed by a GaP or InP layer, shown in

Fig. 4, is exactly the sum of the strain components of the separate steps.

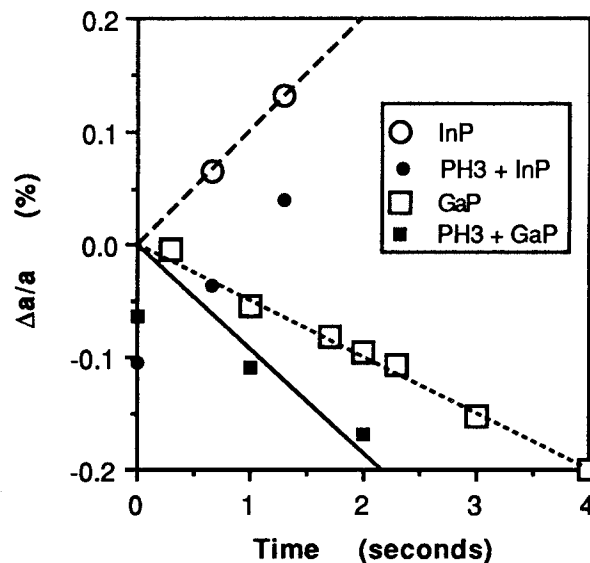


Figure 4. Strain in superlattices (30 periods of 180 Å) formed by inserting thin InP and GaP layers. The expected InP strain (dashed line) is identical to the measured strain. The expected GaP strain (solid line) is double the measured strain which is consistent with the actual layer composition of $\text{GaAs}_{0.5}\text{P}_{0.5}$ (dotted line). A preliminary PH_3 exposure step of 6 sec. for GaP or 10 sec. for InP shows its strain as an added component unaffected by the grown layer.

Discussion

It is generally accepted that As rapidly replaces P on InP surfaces and P more slowly replaces As on GaAs surfaces (6). This behavior has been demonstrated by Reflectance Difference Spectroscopy studies of OMVPE-like exposure of InP and GaAs to the group V hydrides (7). The $2/3$'s monolayer InAs-like interface strain is attributed to the relative rates of the combined fast As-for-P and slow P-for-As exchange processes occurring for our growth conditions. To first order, very rapid arsenic substitution for P on surfaces of InP results in strain from In-As bonds (half a monolayer equivalent InAs for a complete As surface layer), and with InP overgrowth additional In-As bonds are formed to give a full monolayer of InAs. In practice it is expected that during InP overgrowth there is As loss so that some P replaces surface As and the net strain would be somewhat less than a complete monolayer of InAs. It is also possible that the initial As coverage of InP does not occupy all the surface sites so the result is only $\sim 2/3$ monolayer InAs. The designation of this strain as due to an interface layer is supported by reported photoluminescence results for insertion of brief AsH_3 exposure of InP at 600°C . Seifert *et al* (6) conclude that a resulting thin quantum well is due to a 60% As occupied layer. The excess InAs-like time-dependent strain from As-compound growth in InP most likely results from a carryover of As as previously proposed (4,6,8).

On GaAs surfaces the strains from As-P exchange under hydride exposure show similar exchange rate behaviors, except that AsH₃ exposure in the presence of TMG for growth of a GaAs overlayer does not completely desorb surface P, even though in the absence of TMG the phosphorus is readily removed. Also, PH₃ exposure of GaAs shows no interface layer offset strain when growth of InP or GaP takes place. Both the As for P exchange and the P for As exchange are inhibited when group III atoms are added to the surface. This is suggestive of the As-P exchange being highly dependent on rapid surface diffusion for which the Group III atoms introduce a barrier (9).

Some surprising implications in the distribution of atomic substitutions also come from thin layers inserted into GaAs. In the absence of layer growth (with no group III alkyl present) PH₃ exposure results in replacement of surface As within about 1 second, but the total interface strain is only half monolayer GaP-equivalent, rather than a full monolayer expected for complete P coverage of the surface. The strain indicates there is exactly 50% P substitution for As. This implies that the As-P distribution is probably ordered and that this surface is stably configured for AsH₃ exposure at 650°C. We see additional evidence of a preferred 50/50 As/P distribution in growth of nominal GaP on GaAs. The resulting layer strain does not correspond to GaP at the introduced growth rate, but to GaAs_{0.5}P_{0.5}. For the limited number of GaP monolayers investigated here, residual As carryover has combined with P to give this alloy composition. Also, the 50/50 apportioning of captured surface As and P atoms occurs only when Ga atoms are present, and this may be associated with the tensile strain of Ga-P bonds.

The results from growth of InP monolayers inserted into GaAs is anomalous because the perfect correspondence of the measured strain with that of the intended InP thickness shows no evidence of excess As incorporation. This appears contradictory to evidence of As carryover in superlattices on InP substrates. However a difference here is the large compressive strain of the InP. Unlike the superlattices on InP substrates where InP layers have ~0% strain, the InP layers inserted into GaAs has strain of +8% which may provide a mechanism for segregating the available excess As.

The mechanisms for the time-dependent strains due to As-P exchange for P-surfaces exposed to AsH₃ and for As-surfaces exposed to PH₃ look to be very different. Excess InAs-like strain in P-compounds is more consistent with As-carryover at the upper interface than with As diffusion at the lower interface. Confirmation of upper interface carryover has been demonstrated by x-ray scattering measurement of AsH₃-exposed InP surfaces (10). The source of the As excess is still somewhat unclear. Adsorbed surface excess from c(4x4) or d(4x4) GaAs-like surface reconstruction (6) is plausible, but the very large quantity of available As is surprising. No diminishing of the excess As is seen within the few monolayers studied here. For the case of GaAs exposed to PH₃, the excess GaP-like strain behaves more like it is due to diffusion of P into the underlying GaAs. Strain from two-stage growths where InP or GaP are grown over a PH₃-exposed surface show no interaction of

the two steps as one might expect from P-carryover, although P carryover at a low level for long time could look similar. Significant GaAs surface roughening with longer exposures to PH₃ (7) also suggests diffusion of P into the GaAs underlayer.

Conclusions

We have studied the strain in OMVPE grown ultra thin As-compound layers in InP and P-compound layers in GaAs to assess interface behavior relevant to InGaAs/InP heterojunctions. Strain contributions from As-P exchange at the heterojunction interfaces were identified. The very rapid replacement of P by As from AsH₃ and the slower replacement of As by P from PH₃ results in a rapidly formed strain contribution from InAs rich interfaces for superlattices on InP substrates. An additional InAs-like strain in the inserted layers is proportional to the growth time and is attributed to carryover at the upper interface of excess adsorbed surface As into the InP overlayer. P interaction with As-compounds is sufficiently slow that excess negative strain occurs only when deliberate growth interrupts under PH₃ are introduced into superlattices grown on GaAs substrates, and P incorporation behaves more like diffusion into the underlying GaAs rather than as P carryover into the GaAs overlayer. Under our normal growth conditions, growth of thin GaP-compound layers on GaAs incorporates residual As at an exact 50% As-50% P ratio.

Acknowledgements

This work was supported by the Office of Naval Research, Program Element 62234N, Microelectronics Project RS34M40.

- 1 M. S. Hybertsen, J. Vac. Sci. Technol. B 8(4), 773-778 (1990)
- 2 E. A. Caridi and J. B. Stark, Appl. Phys. Lett. 60(12), 1441-1443 (1992)
- 3 J. Hornstra and W. J. Bartels, J. Crystal Growth 44, 513-519 (1978)
- 4 A. R. Clawson and C. M. Hanson, J. Electron. Mater. (to be published)
- 5 A. R. Clawson and C. M. Hanson, Proc. 21st Int'l. Symp. on Compound Semiconductors, Sept. 18-22, 1994, San Diego, CA (Inst. Phys., London, Conf. Ser.) to be published
- 6 W. Seifert, D. Hessman, X. Liu and L. Samuelson, J. Appl. Phys. 75(3), 1501-1510 (1994)
- 7 J. Jönsson, F. Reinhardt, K. Ploska, M. Zorn, W. Richter and J.-Th. Zettler, IPRM 94, Santa Barbara, CA, paper MD2
- 8 X. Jiang, A. R. Clawson and P. K. L. Yu, J. Crystal Growth 147, 8-12(1995)
- 9 M. G. Lagally, Physics Today 46(11), 24-31(1993)
- 10 Y. Takeda, Y. Sakuraba, K. Fujibayashi, M. Tabuchi, T. Kumamoto, I. Takahashi, J. Harada and H. Kamei, Appl. Phys. Lett. 66(3), 332-334(1995)

Study of As₄ Beam Induced P - As Exchange Reaction on InP Surface by Photoluminescence and X-ray Diffraction

FA1.2

B. X. Yang, L. He,⁺ and H. Hasegawa

Research Center for Interface Quantum Electronics and
Department of Electrical Engineering,
Hokkaido University, N13, W8, Sapporo 060, Japan

⁺Present address: Shanghai Institute of Technical Physics, Chinese Academy of Science,
Shanghai, People's Rep. of China.

Introduction

For MBE and MOCVD growth of III-V compound heterostructures containing phosphorus and arsenic compounds, control of the P-As exchange reaction at the growth interface is one of the major factors affecting the interface quality. Although several reports(1-5) have mentioned the presence of this exchange reaction, a detailed investigation has not been made so far.

This paper presents for the first time the result of a detailed investigation on the P - As exchange reaction which takes place on the InP surface when it is exposed to As₄ beam. Characterization was made by growing an additional InP cap layer on the As₄ beam exposed InP surface and analyzing the resultant InP/InAs_xP_{1-x}/InP single quantum well (QW) structure shown in Fig.1 by photoluminescence (PL) and X-ray diffraction (XRD) measurements. The results provide quantitative data on the rate and depth of the exchange reaction as a function of growth parameters which may be useful for MBE growth of P and As containing heterostructures.

Experimental

The growth was performed in an gas source MBE system with a turbo-molecular pump and an ion pump. Solid In (7N) and As (6N), and cracked gas PH₃ were used as the sources. The substrate was (001) InP. The substrate temperature was measured by an infrared pyrometer and controlled by a thermocouple which made a physical contact to the sample holder. Beam fluxes were measured by a quadruple mass spectrometer (QMS) closely located above the substrate holder.

Growth of InP/InAs_xP_{1-x}/InP single QW structures shown in Fig.1 consisted of mainly three steps, including growth of an InP buffer layer, exposure to As₄ beam and growth of an InP cap layer. The buffer and cap InP layers were grown at the same conditions with the growth temperature of 440 °C and the growth rate of 1.5 Å/s. After the growth of the buffer layer, the surface was kept under PH₃ supply for a while in order to smoothen the surface. The substrate temperature was then reduced below 360 °C and PH₃ was switched off. Then, the As₄ exposure process was started by opening the As shutter when the substrate temperature was quickly raised to a target temperature, T_e, i.e. the exposure temperature. The overshooting of the substrate temperature was controlled to be below 10 °C. After the exposure was finished, the As₄ beam was shut off and the substrate temperature was dropped quickly below 300 °C. The exposure time, t_{As}, is defined as the opening period of the As shutter. The cap InP layer was grown after the As cell was completely cooled and the residual As was sufficiently pumped out. For the growth of the InP cap layer, the substrate temperature was again

*In As_xP_{1-x} well produced by
P-As exchange reaction.*

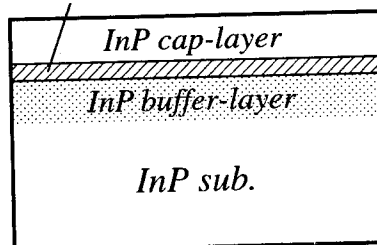


Fig.1 Structure of InP/InAs_xP_{1-x}/InP single QW.

simultaneously rather than opening the P shutter first. This was to prevent the re-evaporation of As and the occurrence of an opposite exchange reaction of As replaced by P.

Growth was monitored by reflection high-energy electron diffraction (RHEED). The RHEED pattern during the growth of both buffer and cap InP layers was a clear streaky (2x4) pattern, and long persistent RHEED oscillations were observed. When the exposure to As₄ started, the streaky (2x4) pattern persisted for about first 2 minutes and then became spotty (at 450 °C). The spotty pattern changed to a streaky one in a few seconds after the start of the growth of the cap layer.

PL measurements of the InP/InAs_xP_{1-x}/InP single QW samples were made by a conventional lock-in detection technique with an Ar⁺ laser (514.5 nm line) as the excitation source (1 W/cm²). The detector was

a liquid nitrogen cooled Ge photodetector (North Coast Scientific Corp.). X-ray rocking curve measurements of the QW samples was made in a high-resolution 3-crystal diffractometer with a Mo target ($\lambda_{K\alpha 1}=0.70926\text{\AA}$) and a Ge (220) monochromator.

Results and Discussion

PL spectra

Figures 2 (a) and (b) show the low temperature (18 K) and room-temperature (300K) PL spectra of several QW samples formed at an exchange temperature of $T_e = 450^\circ\text{C}$ for various values of the exposure time, t_{As} . Intense emissions were observed from all samples. The energy positions of the PL

peaks from the samples with t_{As} of 9 s and 20 s are nearly the same, and those from others shift to lower energy with the increase of t_{As} . When t_{As} increased to more than 40 to 125 s, significant splitting of the peaks occurred. For these peaks, computer deconvolution into Gaussian subpeaks was made as shown by dashed curves. It is noted in Fig.2 (b) that some of the positions of the constituent subpeaks or shoulders of the split spectra agree among different samples, as indicated by arrows in Fig.2 (b).

Some of the samples showed peaks at 1.42 eV in Fig.2 (a) and at 1.35 eV in Fig.2 (b), and these are obviously due to the band edge emissions from InP cap and buffer layers.

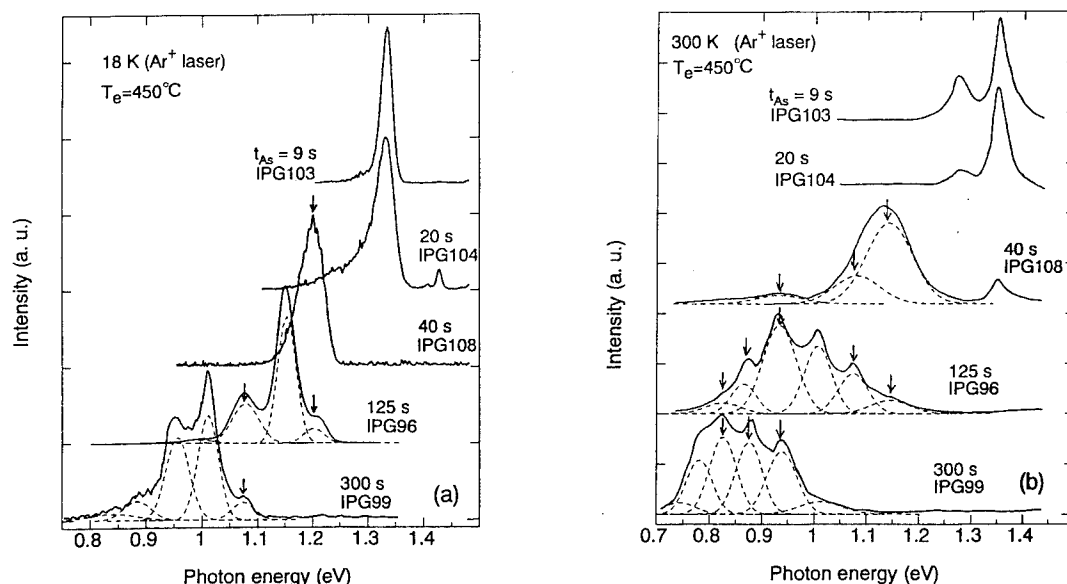


Fig. 2 PL spectra of some InP/InAs_xP_{1-x}/InP QWs at (a) 18 K and (b) 300K. t_{As} denotes the As exposure time.

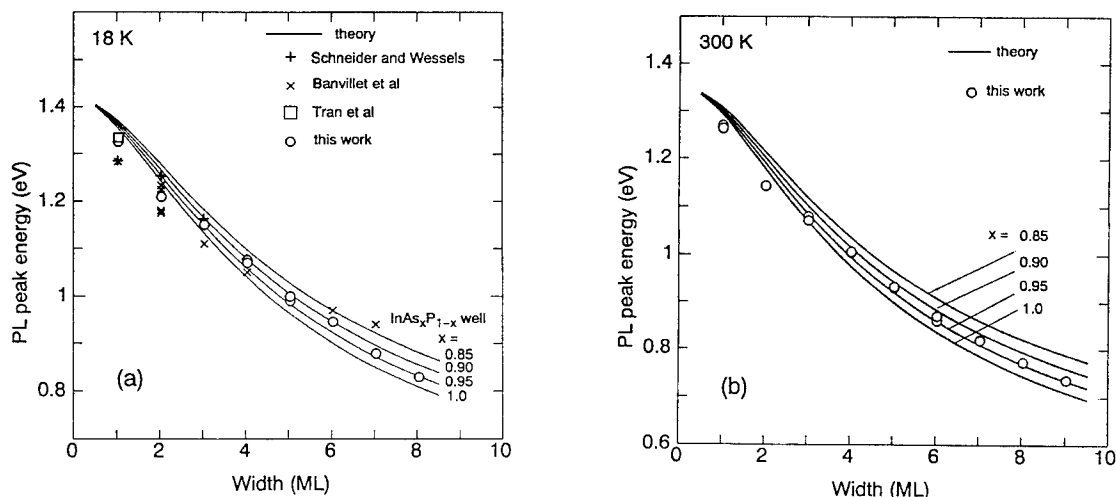


Fig. 3 Dependence of PL energy on the well thickness (in ML) at (a) 18 K and (b) 300 K. The calculations based on envelope function approximation. Some data from the literature are also shown.

Assignment of PL peaks

In order to assign the observed PL peaks, theoretical calculation of the fundamental e1-hh1 transition energy for $\text{InP}/\text{InAs}_x\text{P}_{1-x}/\text{InP}$ QW was performed using the envelope function approximation. The band discontinuity of 310 meV for unstrained InAs/InP , which has been determined by several different methods and widely adopted by many authors (6-8), was used and the effect of strain was also included in the calculation. The material parameters for $\text{InAs}_x\text{P}_{1-x}$ alloy were linearly extrapolated from the widely used values of InAs and InP (10). The results are shown in Fig.3 (a) for 18 K and in Fig.3 (b) for 300 K as a function of the well width in the unit of ML, i.e. the half of lattice constants of strained $\text{InAs}_x\text{P}_{1-x}$ with $x=1.0$ to 0.85.

The assignment of PL peaks in Fig.2 was then done by plotting the experimental energy positions on the theoretical calculations as shown in Fig.3. Here it was assumed that the 1.33 eV peak and the 1.20 eV peak at 18 K (IPG103, IPG104 and IPG108) in Fig.2 (a) correspond to the QWs with the well width of 1 ML and 2 MLs, respectively. The peaks with the next lower energy of 1.15 eV was then assigned to 3 ML QWs, 1.08 eV peak to 4 MLs, and so on. Assignment of PL peaks at 300 K in Fig.3 (b) was done in the same way with the assumption of that the 1.28 eV peak corresponds to 1 ML QW. As seen from Fig.3, the PL energy positions agree well with those for e1-hh1 transitions predicted from the calculations at both 18 K and 300 K. Such assignments seem to be also consistent with the previous reports (11-14). From these results, the As composition of the present QWs should be about 90 - 95%. This is consistent with our X-ray photoelectron spectroscopy (XPS) study of As - P exchange reaction during the thermal cleaning of InP substrate under As_4 pressure.

Thus, PL results in Figs.2 and 3 indicate that the QW width due to the exchange reaction can be more

than 8 MLs in the sample of IPG99. However, observation of a PL peak corresponding to 8 ML QW does not directly mean that the exchange reaction takes place uniformly into the depth of 8 MLs. As mentioned above, RHEED pattern changed to spotty feature when t_{As} exceeded 2 minutes. This indicates that the surface became rough during the exchange reaction. It is thus reasonable to say that 3-dimensional (3D) islands formed on the surface. The island formation mechanism in such non-growth procedure can be well understood in term of the strain relief process where the original 2D layer piles up to form 3D islands (15-16), due to existence of very large strain (3.2%) between InAs and InP . From this viewpoint, the 8 ML QW represents the height of the highest islands, rather than the thickness of a uniform 2D Layer. The splitting of PL peaks in IPG96 and IPG99 samples provides further evidence of this islanding process.

X-ray diffraction

Figure 3 shows the X-ray rocking curves for several samples. The diffraction patterns are different in shape, depending on the growth parameters. However, clear Pendellösung fringes were observed in all samples, indicating that the wells were pseudomorphic (7). In Fig.4, a reference sample of IPG105 with t_{As} of 0 s is also included. Although this sample consisted of only two InP layers for the buffer and cap, there still existed Pendellösung fringes. This implies that the epitaxially grown InP layers have different lattice constants with that of InP substrate. Detailed X-ray diffraction investigations indicated that a very small composition deviation equivalent to $\text{InP}_{0.9955}\text{As}_{0.0045}$ exists in the InP cap layer whereas no such deviation was detected between the buffer layer and the substrate InP . This slight composition deviation in the cap InP layer was attributed to the incorporation of the residual As during the growth.

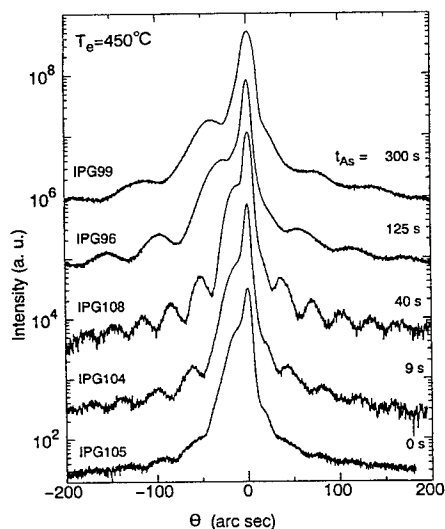


Fig.4 X-ray rocking curves of some samples. IPG105 is a reference sample consisting of only the buffer and cap InP layers.

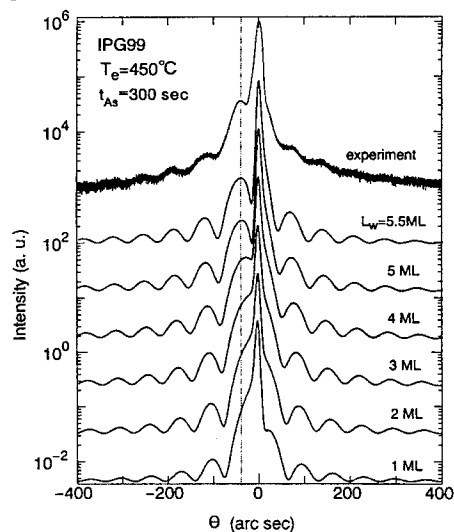


Fig.5 A typical example showing the computer simulation of X-ray rocking curve for determining the average well thickness.

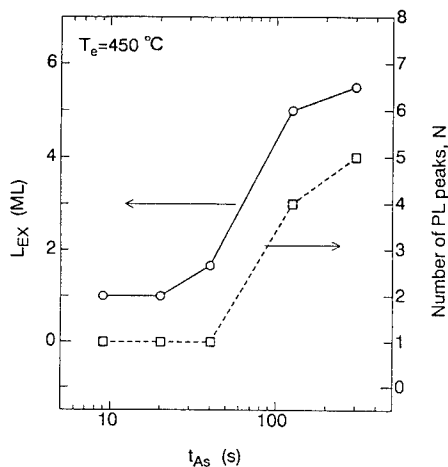


Fig.6 Dependencies of the exchange depth, L_{EX} , and the number of PL peaks, N , on the As exposure time, t_{As} .

Average depth of exchange reaction

Since the compositions of all the layers are known, the average well thickness or the average depth of exchange reaction can be determined by fitting the simulated X-ray rocking curves based on the dynamical diffraction theory to the measured rocking curves. In the simulation, only the thicknesses of QWs and cap layer were adopted as adjustable parameters and the buffer layer was considered as part of the InP substrate. An example (IPG99) of fitting is shown in Fig.5, and here the well thickness was determined to be 5.5 MLs. The cap layer thickness can be precisely determined from the Pendellösung fringe period.

Since the typical X-ray spot size in the diffraction measurements was as large as several millimeters, the thickness obtained here should be an averaged value among various wells having different well thicknesses. Such an averaged well thickness can be interpreted as the average depth of exchange reaction, L_{EX} . Dependence of L_{EX} on t_{As} at the same substrate temperature of 450 °C is shown in Fig.6. As seen in Fig.6, the exchange depth increases with the increase of As_4 exposure time, but trends to saturate when t_{As} is over 2 minutes.

Fluctuation of well thickness

As shown in Fig.2 (a), the PL line-width at 18 K is relatively narrow as 19 meV for 1 ML-thick well formed at $t_{As} = 9$ s (IPG103), but broadens to 40 meV for the same 1 ML-thick well formed at $t_{As} = 20$ s (IPG104). With t_{As} increases further, the line-width becomes wider and then splitting takes place. This indicates that fluctuation of the well thickness increases as t_{As} is increased. As a crude measure of well thickness fluctuation, the number N of PL peaks required for curve fitting is plotted also in Fig.6 vs the exposure time t_{As} . The variation of N seems to follow the variation of the average depth of exchange reaction, indicating the increase of N is mainly due to the formation of 3D islands by strain relief process.

Conclusion

The P - As exchange reaction on InP surface exposed to As_4 beam was studied using PL and x-ray diffraction measurements on $InP/InAs_xP_{1-x}/InP$ single QW structures.

It was found that the XRD technique is useful to determine the average depth of exchange reaction, and the PL technique provides clearer information on the composition change and fluctuation of the reaction depth. XRD technique has shown that the average depth of exchange reaction is not limited to the top monolayer, but penetrates as deep as 5.5 ML for long exposure. The PL results have shown that an exchange efficiency is as high as 90-95%. The splitting in PL peaks was observed when the reaction depth exceeded 2 ML, indicating increase of fluctuation of the reaction depth for strain relief process. Both the reaction depth and the fluctuation of the well thickness increases with the increase of As exposure time but the reaction depth tends to saturate when the average exchange depth reaches 5-6 MLs.

References

- (1) J. Hergeth, D. Grützmacher, F. Reinhardt, and P. Balk, *J. Crystal Growth*, 107, 537 (1992).
- (2) J. Böhrer, A. Krost, and Bimberg, *Appl. Phys. Lett.*, 60, 2258 (1992).
- (3) A. Bensaoula, V. Rossignol, A.H. Bensaoula, and A. Freundlich, *J. Vac. Sci. Technol.*, B11, 851 (1993).
- (4) H. Kamei, and H. Hayashi, *J. Crystal Growth*, 107, 567 (1991).
- (5) J.F. Carlin, A. Rudra, R. Houdré, P. Ruterana, and M. Ilegems, *J. Crystal Growth*, 120, 155 (1992).
- (6) J.R. Waldrop, R.W. Grant, and E.A. Kraut, *Appl. Phys. Lett.*, 54, 1878 (1989).
- (7) K. Huang and B.W. Wessels, *Appl. Phys. Lett.*, 52, 1155 (1988).
- (8) A. Continenza, S. Massidda, and A.J. Freeman, *Phys. Rev. B*, 42, 3469 (1990).
- (9) Y.C. Chen, P.K. Bhattacharya, and J. Singh, *J. Vac. Sci. Technol.*, B10, 769 (1992).
- (10) Ed. O. Madelung, *Landolt-Börnstein Numerical Data and Functional Relationships in Science and Technology*, V22, Springer-Verlag, 1987.
- (11) C.G. Van de Walle, *Phys. Rev. B*, 39, 1871 (1989).
- (12) C.A. Tran, R.A. Masut, J.L. Brebner, R. Leonelli, J.T. Graham, and P. Cova, *J. Crystal Growth*, 124, 596 (1992).
- (13) H. Banvillet, E. Gil, R. Cadoret, P. Disseix, K. Ferdjani, A. Vasson, A.M. Vasson, A. Tabata, T. Benyattou, and G. Guillot, *J. Appl. Phys.*, 70, 1638 (1991).
- (14) R.P. Schneider, Jr., and B.W. Wessels, *Appl. Phys. Lett.*, 57, 1998 (1990).
- (15) C.W. Snyder, B.G. Orr, D. Kessler, L.M. Sander, *Phys. Rev. Lett.*, 66, 3032 (1991).
- (16) J. Tersoff, and R.M. Tromp, *Phys. Rev. Lett.*, 70, 2782 (1993).

Characterization of InAsP/InGaAsP strained MQW crystals for 1.3 μ m-wavelength laser diodes using a microscopic photoluminescence

Masashi Nakao and Hideo Sugiura
*NTT Opto-electronics Laboratories,
 3-1 Morinosato Wakamiya, Atsugi, 243-01 Japan*

A microscopic photoluminescence (μ -PL) method was used to characterize strained InAs_{0.5}P_{0.5}/InGaAsP multi-quantum well crystals with a series of well numbers ($n=2\sim 14$). This method was useful for detecting misfit dislocations in the crystals, especially at the initial stage of their generation. We also measured the μ -PL intensity profile of a laser diode (LD) cavity. The intensity, being mainly influenced by the [011]-directed misfit dislocations, was closely correlated to the LD characteristics such as threshold current.

1. Introduction

Semiconductor laser diodes (LDs) with strained InAsP/InGaAsP multi-quantum wells (MQWs) have attracted much attention for their use in 1.3- μ m wavelength optical subscriber communication systems because of their low threshold current and high temperature operation [1]. Because the lower growth temperature may prevent misfit dislocation generation by a large lattice mismatch of 1.5%, the strained MQW structure has presently been grown by chemical beam epitaxy (CBE) [2] at a growth temperature of around 500°C lower than by metalorganic vapor phase epitaxy (MOVPE) at 650°C [3]. There are many works on strain-induced defects such as misfit dislocations [4-6], which have usually been studied using a transmission electron microscope (TEM) [5] or a cathode luminescence method [6]. Neither of these are suited to testing samples conveniently under processing conditions.

We have reported that the photoluminescence (PL) characteristics show good correlation to the LD characteristics [7]. For example, threshold current of the LD decreased as PL intensity increased. Here we have used a photoluminescence method with microscopic spatial resolution (so-called μ -PL) to analyze highly strained InAsP/InGaAsP MQWs before and after processing of semiconductor laser diodes. We also investigated the relationship between PL and LD characteristics from a smaller area of view such as the cavity area of a LD. The results of the μ -PL method gave us closer correlation between PL intensity and LD threshold current.

2. Experimentals

Crystal growth was carried out by the chemical beam epitaxy (CBE) system [2]. Substrate temperature was 520°C. The samples had separate confinement double heterostructures (SCH): MQWs consisting of 5.5-nm-thick

InAs_{0.5}P_{0.5} and 11-nm-thick InGaAsP ($\lambda_g=1.13\mu$ m) were grown on the pre-etched (100) InP substrates. The number of wells in the MQW was varied from two to fourteen. Samples for PL measurements were covered by a 100-nm-thick p-doped InP layer on the strained MQW layers. For LD samples liquid phase epitaxy (LPE) was used to grow the additional 2- μ m-thick p-InP cladding layer and a 300-nm-thick p-InGaAsP contacting layer.

Two PL systems were used; the first of which is a YAG-laser based photoluminescence (YAG-PL) mapping system reported previously [7]. PL mapping profiles of the epitaxial wafer, such as peak wavelength, intensity, and full-width at half maximum, were examined at room temperature with a high through-put (~ 1 second/point). The high-power YAG-laser (~ 1 W, cw) was used to excite only active layers, i.e. InAsP. The spatial resolution is around 0.1 mm.

The second system is a μ -PL system. A 3-mW He-Ne laser ($\lambda=633$ nm) or a 3- mW YLF laser ($\lambda=1047$ nm) with a beam waste of 5 μ m in diameter is irradiated through a objective lens (25x, NA=0.3) vertically to a sample. The excited carriers are generated in the different depths due to the irradiation of He-Ne and YLF lasers, namely in the vicinity of the wafer surface including the p-InP cladding layer and in the MQW active region, respectively. Photoluminescence from the sample is collected by the same objective lens, and introduced to the detection part consisting of a grating monochromator and an InGaAs detector. Then, μ -PL intensity mapping was carried out at a fixed wavelength around the PL peak position by scanning the sample in the x,y-directions every 2.5 μ m. The sample was set on the x,y-pulse stage with an additional x,y-off-set angle regulation system to keep the distance between the object lens and the sample constant within microns. The μ -PL measurements were carried out at room temperature.

The spatial resolution was estimated to be less than 5 μm .

The wafers with a strained MQW structure were processed into 50- μm -wide stripe lasers, each with a 300- μm -long cavity directed to $[0\bar{1}1]$. This direction was selected for convenience of metallization by electrode patterning. The well numbers investigated here were 4, 6, and 10. The threshold currents of the laser chips without a facet coating were measured at room temperature under pulsed current.

3. Results and Discussion

3.1. Photoluminescence characteristics

Fig. 1 shows results of high power YAG-photoluminescence (YAG-PL) measurements for as-grown InAs_{0.5}Po.5/InGaAsP strained MQW samples represented by open circles. The YAG-PL intensity of wafers varies with their well number (n). That is, the YAG-PL intensity increases gradually with n -value up to $n=8$. At $n=14$ the YAG-PL intensity becomes very low, less than one-tenth of the other values. The samples were annealed at 620°C for 2.5 hours. This annealing condition is same as that for over-growth by LPE in the practice process of LD fabrication. We could not observe any obvious annealing effect on the YAG-PL intensity for samples of $n < 8$, but PL intensity for the sample $n=10$ decreased by a factor of two shown as a closed circle of Fig. 1. Considering the changes in YAG-PL intensity in Fig. 1, it should be noted that the degradation of the strained MQW crystal may start from $n=10$. The YAG-PL method is useful to check the quality of active layers immediately after their growth, however, due to the low spatial resolution (~ 0.1 mm order) it is difficult to identify the origin of quality degradation such as due to misfit dislocations.

To investigate the origin of degradation in the YAG-PL intensity, microscopic photoluminescence ($\mu\text{-PL}$) measurements were performed. Figure 2 shows mapping profiles of the $\mu\text{-PL}$ intensity measured at a fixed wavelength (ca. 1330 nm) under the He-Ne laser excitation for the samples with various well number. Each profile is normalized at its maximum intensity. The observation is carried out in a typical area of 2 mm x 2 mm. No special pattern can be observed in the $\mu\text{-PL}$ intensity mapping results of $n=4$, and intensity variations are as small as 5%. A cross-hatched pattern is observed for the samples of $n > 6$. The contrast of the pattern becomes clearer with increasing well number. At $n=14$ clusters with a very weak $\mu\text{-PL}$ intensity appear. We will show later using a plane view TEM that the lines reflect misfit dislocations.

In order to make clear the generation place of the misfit dislocation, the $\mu\text{-PL}$ intensity mapping was carried out under the YLF laser irradiation, which could be excited

only the MQW region. The observed $\mu\text{-PL}$ intensity profiles were almost same as those of the He-Ne laser irradiation as shown in Fig. 2, except for the difference of absolute $\mu\text{-PL}$ intensity values. These results indicate that misfit dislocations exist in or closed to the MQW layers, and they do not extend to the above InP cladding layer. Because if the misfit dislocation extended to the cladding layer, the recombination process of the excited carriers would be changed and consequently the $\mu\text{-PL}$ intensity profile of He-Ne irradiation would be different from that of YLF. This will be discussed later using TEM cross-sectional view. We have demonstrated the $\mu\text{-PL}$ as a convenient tool for observation of the cross-hatching pattern due to misfit dislocations of the strained InAsP MQW crystals.

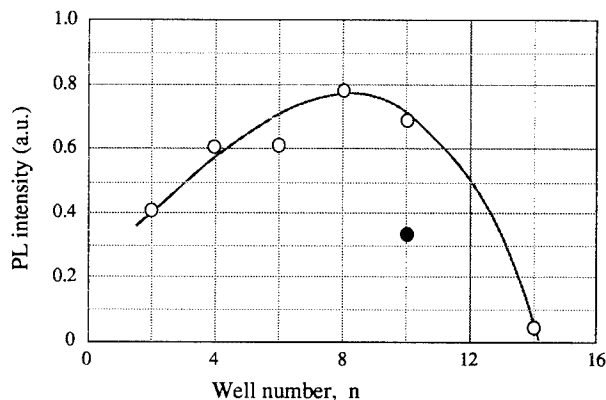


Fig. 1. Well number dependence on YAG-PL intensity. Before (O) and after (●) annealing at 620 °C for 2.5 hrs.

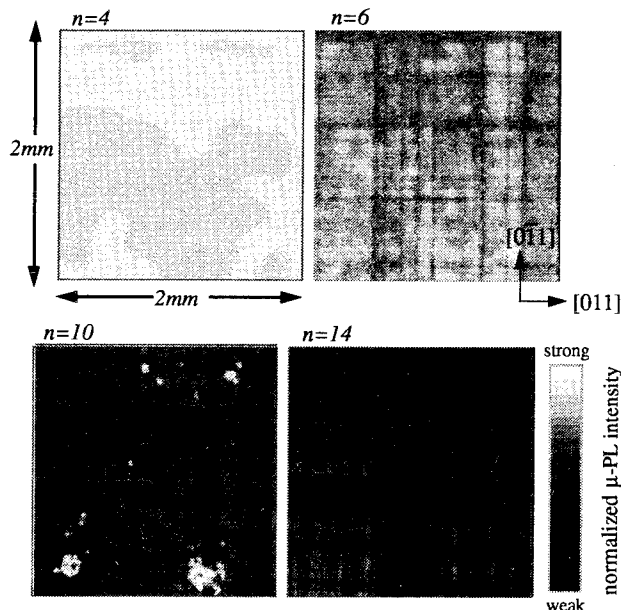


Fig. 2. $\mu\text{-PL}$ intensity profiles for strained InAsP/InGaAsP MQW crystals with $n=4, 6, 10$ and 14 ; measured at 1330 nm.

3.2. TEM observations

Next we observed the samples by using a TEM to clarify the observed cross patterns in the μ -PL images. Fig. 3 shows the plane views of TEM for the samples of $n=8$ and 14. Misfit dislocations directed to $[0\bar{1}1]$ and $[011]$ are observed. A line number of the $[0\bar{1}1]$ -direction is more than that of the $[011]$ -direction. The density of dislocations is in the order of 10^4 cm^{-1} for $n=8$ and in the order of 10^5 cm^{-1} for $n=14$. The line patterns in these TEM-images resembles those of the μ -PL mapping images in Fig. 2. Therefore, we can conclude that the cross patterns observed on the μ -PLs are misfit dislocations. Fig. 4 shows cross-sectional view of TEM for $n=14$ sample. We could observe generation of dislocations at the interface between the strained MQW layer and the buffer layer (shown by white arrows), extending into the buffer layer. It was also found that the misfit dislocations do not extend into the MQW layer. This observation has good agreement with the μ -PL results using the different excitation sources as mentioned above.

3.3. Laser diode characteristics

Figure 5 shows histograms of threshold current density (J_{th}) for wide-stripe type lasers with well number of 4, 6 and 10. There is little difference in J_{th} between $n=4$ and 6 in spite of generating misfit dislocations in the sample of $n=6$ (cf. Fig. 2). The averaged value of threshold current density, as small as 0.7 kA/cm^2 , is fairly low and both dispersion values (σ) are less than $\pm 0.03 \text{ kA/cm}^2$. However, at $n=10$ the value of the threshold current density is distributed in a wide range, i.e. from 0.8 to 2.2 kA/cm^2 , depending on the position in a bar. Here, a large dispersion of threshold current density, i.e., $\sigma=0.44 \text{ kA/cm}^2$, which is one order of magnitude larger than that for $n=6$, could be observed. These results show that misfit dislocation densities of up to 10^4 cm^{-1} (this value was estimated from the TEM plane view of $n=8$ in Fig. 3 and the increasing tendency of dislocation line number which appeared in Fig. 2.) do not seriously influence the LD threshold current and that for the density of more than 10^4 cm^{-1} , i.e. the case of $n=10$, some laser chips deteriorates. In the present LDs the cavity direction was $[011]$. This direction was more generative direction of misfit dislocations, which could be evident from the images of Figs. 2 and 3. The influence of dislocations on the long term LD operation is now under investigation.

The laser chips of $n=10$ were further examined to clarify the threshold current dispersion which appeared in Fig. 5. The results of light output vs. injection current and μ -PL for three neighboring LD chips are shown in Fig. 6a and 6b, respectively. The three chips such as A-C which are $400 \mu\text{m}$ apart are drawn schematically in the same figure. The

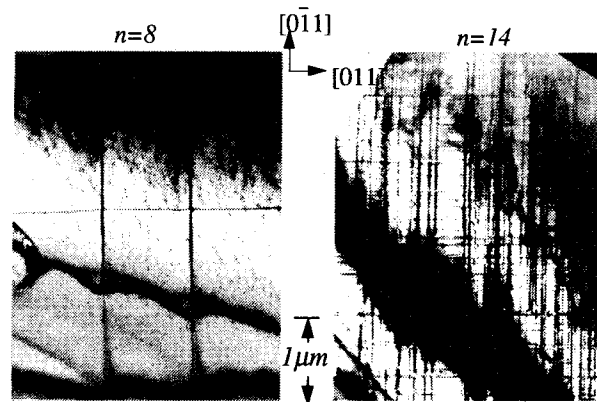


Fig. 3. Plane view TEMs for $n=8$ and 14.

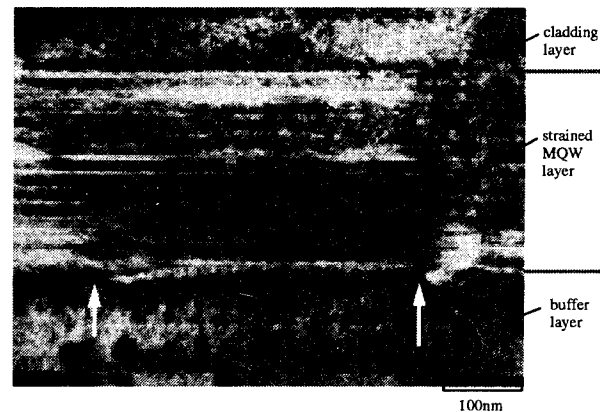


Fig.4. TEM cross-sectional view of $n=14$ sample.

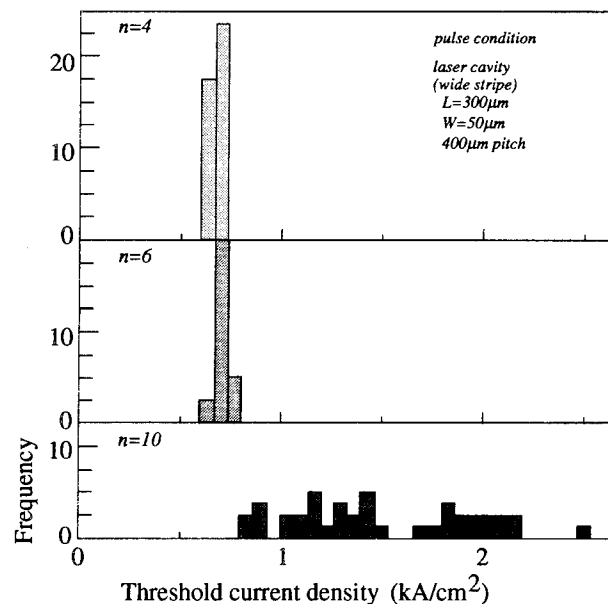


Fig. 5. Histogram of threshold current density for laser diodes with well number of 4, 6, and 10.

threshold current increases in order of B to A to C. To measure μ -PL properties of the chips, the substrate-side of the LD bar was polished chemo-mechanically to remove the metal electrode, and μ -PL spectra were observed from the polished-side. On the Fig. 6b the cavity parts were surrounded by front-side contact metal parts, which appeared strong PL intensity because of highly refractive scattering light. As shown in Fig. 6b, the μ -PL intensity in the region of laser cavities, which strongly depends on the dislocations directed to $[0\bar{1}1]$, decreases in order from B to A to C. It should be noted that the μ -PL results of Fig. 6b do not correspond to the μ -PL mapping of $n=10$ in Fig. 2. This is because samples were annealed during LPE overgrowth. Comparable results to Fig. 6b are those of $n=14$ in Fig. 2. For example, very low μ -PL intensity in the cavity of chip C should correspond to a band region of low intensity in the $n=14$ sample. Comparing the results of Fig. 6a with Fig. 6b, the threshold current value of the three increases as the μ -PL intensity decreases. And the efficiency (dimension is mW/mA), defined as the ratio of light output versus injection current, decreases with the μ -PL intensity. Thus μ -PL observation of a small area such as a cavity gives us useful information about LD characteristics. Thus, we can conclude that the dislocation lines directed to $[0\bar{1}1]$ mainly determine the LD characteristics.

4. Conclusion

We have shown sensitive and convenient observation of misfit dislocations generated in strained InAs_{0.5}P_{0.5}/InGaAsP MQWs crystals by using the μ -PL method. This was assigned by comparing to TEM observation. We have also demonstrated the advantage of the μ -PL method as compared to a traditional YAG-PL method. The μ -PL method is essentially a non-destructive characterization method, therefore we applied it to characterize wafers in the processing of laser diode fabrication. Defects such as misfit dislocations observed by μ -PL measurements were found to significantly influence LD characteristics such as threshold current. This is the first report to show direct correlation between dislocation characteristics and LD properties by μ -PL. We will use this method to examine the quality of grown crystals and try to improve the subsequent LD characteristics by introducing new MQW structures such as stress compenization.

Acknowledgements

We express our thanks to Dr. M. Yamamoto for his continuous encouragement and to Mr. T. Amano and Mr. M. Tomita for the LPE growth and the TEM observation.

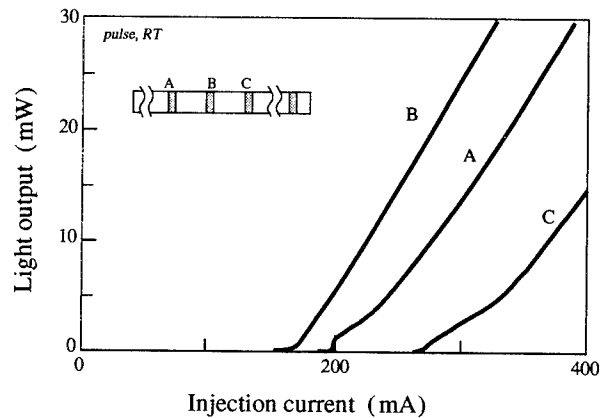


Fig. 6a. The injection current vs. light output curves for 3 neighboring LD chips of A-C shown at the upper left. The well number is 10.

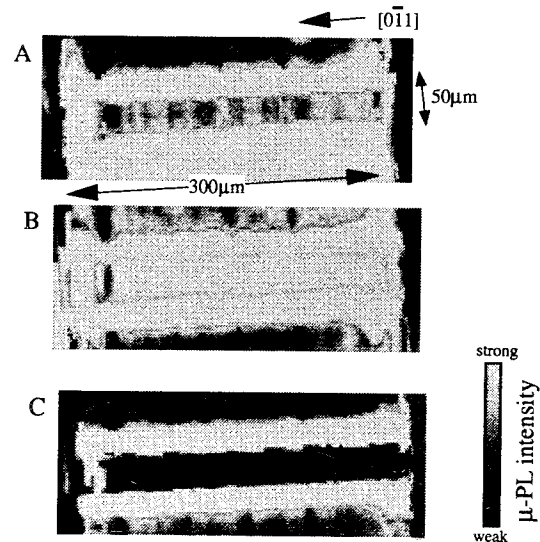


Fig. 6b. μ -PL images for the LD chips shown in Fig. 6a.

References

- [1] M. Yamamoto, N. Yamamoto and J. Nakano, IEEE QE., 30 (1994) 554.
- [2] H. Sugiura, M. Mitsuhashi, R. Iga and N. Yamamoto, J. Crystal Growth, 147 (1995) 1.
- [3] P. J. A. Thijis, L. F. Tiemeiler, P. I. Kuindersma, J. J. M. Binsma and T. van Dongen, IEEE QE-27(1991)1426.
- [4] R. People and J. C. Bean, Appl. Phys. Lett., 47 (1985) 322.
- [5] J. W. Matthews and A. E. Blakeslee, J. Crystal Growth, 27 (1974) 118.
- [6] H. Q. Hou, A. N. Cheng, H. H. Wieder, W. S. C. Chang and C. W. Tuh, Appl. Phys. Lett., 63 (1993) 1833.
- [7] M. Nakao, K. Sato, M. Oishi, Y. Itaya and Y. Imamura, J. Appl. Phys. 63 (1983) 1722.

Nobuyuki Otsuka, Masahiro Kito, *Yasufumi Yabuuchi, Masato Ishino
and Yasushi Matsui

Semiconductor Research Center, Matsushita Electric Industrial Co., Ltd.

* Matsushita Technoresearch, INC.

3-1-1 Yagumonakamachi, Moriguchi, Osaka 570, Japan

Tel: +81-6-906-4921, Fax: +81-6-906-8100

Introduction

Strained layer multi-quantum well (SL-MQW) lasers [1] with large amount of strain are expected to realize high output and high speed operation. However, in such SL-MQW structure, there is a problem that the photoluminescence (PL) intensity is reduced when the total thickness of the well layers exceeds a critical value [2]. Therefore, the clarification of the degradation mechanism of PL characteristics in SL-MQW is very important. In this paper, the dependence of PL characteristics on both SL-MQW structure and epitaxial growth condition is studied. The degradation of PL characteristics in the SL-MQW is confirmed as a broadening of PL linewidth and an unusual temperature-dependence of PL peak wavelength. By using a high-resolution transmission electron microscope (HR-TEM), the structure of atomic ordering [3] is demonstrated over entire barrier layers of the SL-MQW structure with degraded PL characteristics. By increasing growth temperature, elimination of the ordering structure as well as improvement of the PL characteristics have been confirmed even in the SL-MQW structure with large amount of strain.

I. Experiments

Structures: Figure 1 shows the schematic energy-band diagram of studied SL-MQW structure. A lattice-matched InGaAsP buffer layer (PL wavelength $\lambda_g=1.05 \mu\text{m}$, thickness $d_{bu}=150 \text{ nm}$), SL-MQW layers ($\lambda_g=1.3 \mu\text{m}$), and an InP cap layer ($d_c=200 \text{ nm}$) are grown on a (001) just oriented Sn doped n-InP substrate by low pressure metalorganic vapor phase epitaxy (LP-MOVPE). The SL-MQW layers are constructed of strained InGaAsP well layers (compressive strain $\Delta a/a=0, +0.6, \text{ and } +1.0 \%$, $d_w=6 \text{ nm}$) and unintentionally strained InGaAsP barrier layers ($\lambda_g=1.05 \mu\text{m}$, $d_b=10 \text{ nm}$). The number of quantum well (N_w) are 1, 3, 5, 7 and 10. All layers are unintentionally doped.

Growth conditions: The crystal growth is performed

in a vertical LP-MOVPE reactor with resistance heating. Trimethylindium (TMI), triethylgallium (TEG), arsine (AsH_3), and phosphine (PH_3) are used as sources for the growth, and hydrogen as a carrier gas. The epitaxial growths of the SL-MQW structures are carried out at the substrate temperature of 580, 600, and 620 °C. The growth pressure is 60 Torr. TMI and TEG are maintained at 25 °C. TMI is bubbled by hydrogen gas at a rate of 200 SCCM. The flow rate of PH_3 (100 %) is 100 SCCM. The compositions of InGaAsP layers are adjusted by changing the rate of TEG and AsH_3 . The total flow rate is 22 SLM. V/III ratio and growth rate are 240 and 1 $\mu\text{m/h}$ for the growth of InP, respectively. The alloy composition of lattice-matched barrier and buffer layers, which is evaluated by PL peak wavelength at about 293 K (RT), is adjusted to be constant, in each growth at different temperature. The compositions of strained well layer are also adjusted for the PL peak wavelength of SL-MQWs to be 1.3 μm at RT, in each amount of strain and growth temperature.

Measurements: The amount of strain and the thickness of well layers in SL-MQW layers were estimated by the X-ray rocking curve. The optical characteristics were evaluated by the full width at half maximum of PL spectrum (PL linewidth) at the measurement temperature (T_m) of 77 K and the shift of PL peak-energy from RT to 77 K (PL shift). The excitation wavelength in the PL measurements is 514.5 nm. The interfaces of SL-MQW layers and the structure of atomic ordering are observed by using a high-resolution transmission electron microscope (HR-TEM).

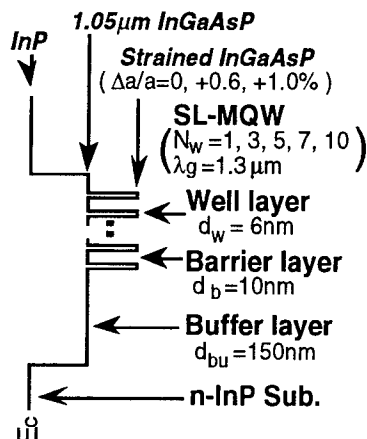


Fig. 1 Schematic energy-band diagram of studied SL-MQW.

II. Results and Discussions

Well number dependence of PL linewidth: Figure 2 shows the dependence of PL linewidth on well number as a parameter of the amount of strain in the well layers. Each sample is grown at the substrate temperature of 580 °C. The PL peak wavelengths of the measured samples range from 1.32 to 1.34 μm at RT. As shown in Fig. 2, the PL linewidth is slightly decreased with increasing well number from 1 to 10, in the case of unstrained MQW structures. However, the PL linewidths largely broaden with increasing well number, in the SL-MQW structures with the strain of 0.6 and 1.0 %. The increase of PL linewidth occurs at 5 wells in the SL-MQW structures with 0.6 % strain, and only at 3 wells in the SL-MQW structures with 1.0 % strain. It is said that, as the amount of strain becomes larger, the degradation of crystal quality in the SL-MQW structures, which is confirmed as the increase of PL linewidth, occurs at smaller well number.

Well number dependence of PL shift: Figure 3 shows

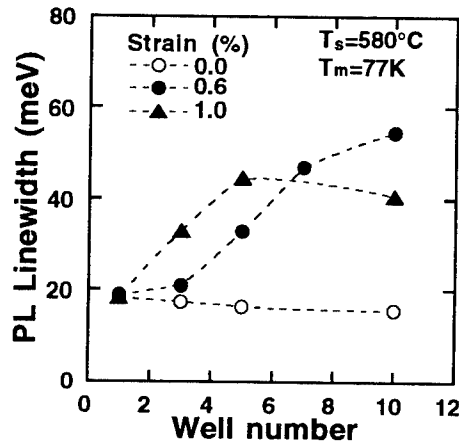


Fig. 2 Dependence of PL linewidth at 77 K on well number for different SL-MQW structures.

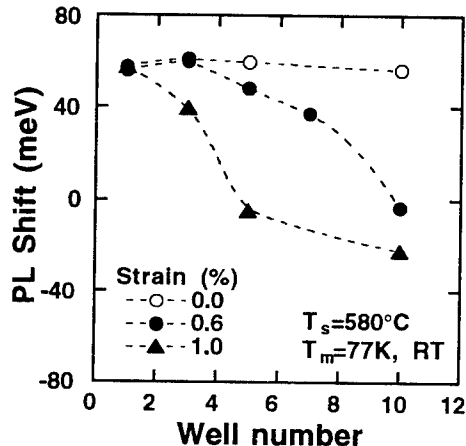


Fig. 3 Dependence of PL shift on well number for different SL-MQW structures.

the dependence of PL shift on well number as a parameter of the amount of strain in the well layers. Each sample with different well number and strain in Fig. 3 corresponds to that in Fig. 2. As shown in Fig. 3, for the unstrained MQW structure, the PL shifts at different well numbers show almost constant values without reduction. However, in the SL-MQW structures with the strain of 0.6 and 1.0 %, the PL shifts decrease with increasing the well number from 1 to 10. Above all, at the SL-MQW with 10 wells and 1.0 % strain, PL peak wavelength shows negative PL shift (opposite to usual temperature-dependence). The reduction of PL shift occurs at 5 wells in the SL-MQW structures with 0.6 % strain, and at 3 wells in the SL-MQW structures with 1.0 % strain. These well-number dependence is very similar to that of PL linewidth. Therefore, the degradation of crystal quality in the SL-MQW, which is also evaluated as the reduction of PL shift, is enlarged with increasing well number and the amount of strain.

WTEM measurement: The clarification of the degradation mechanism in SL-MQW is very important in order to suppress the degradation of crystal quality. The origin of degradation has been predicted to be ascribed to the generation of dislocation or 3 dimensional nucleation. The degraded SL-MQW structure (Type-A : $N_w=10$, $\Delta a/a=0.6$ %, and $T_s=580$ °C), which shows the largest PL linewidth in this study, is investigated. Figure 4 shows a picture of transmission electron microscope for wedge-shape sample (WTEM). As shown in Fig. 4, the WTEM picture reveals sharp interfaces and an excellent periodicity. It is considered that 3 dimensional nucleation is scarcely generated.

TED measurement: TEM samples prepared parallel to both (110) and ($\bar{1}\bar{1}0$) planes are examined by

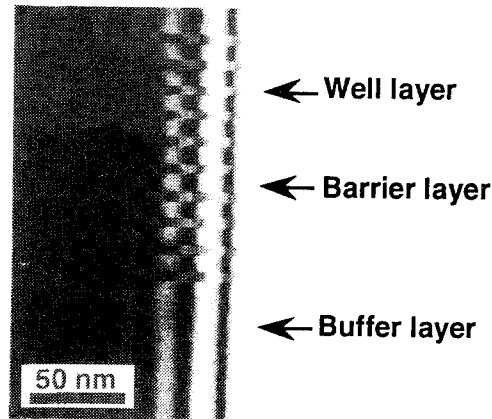


Fig. 4 WTEM picture of degraded SL-MQW structure with 10 wells and 0.6 % strain, grown at 580 °C.

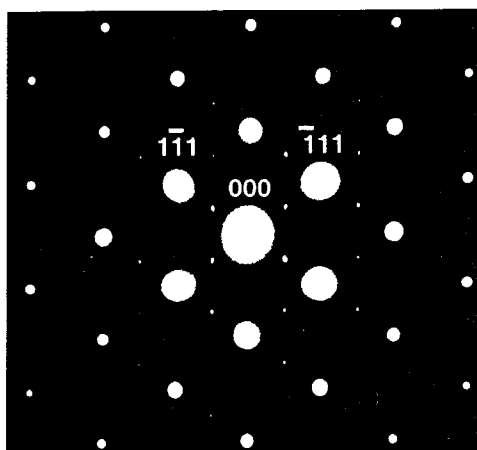


Fig. 5 TED pattern of the degraded SL-MQW, taken in the $\langle 110 \rangle$ direction.

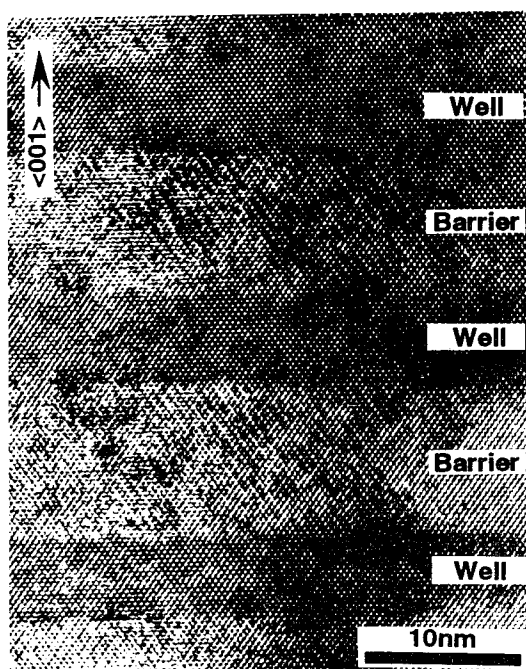


Fig. 6 HR-TEM image of the degraded SL-MQW, taken in the $\langle 110 \rangle$ direction.

a transmission electron diffraction (TED) and a high-resolution transmission electron microscope (HR-TEM). Figure 5 shows TED pattern obtained only from the well and barrier layers of the degraded SL-MQW (Type-A). The picture is taken in the $\langle 110 \rangle$ direction. Superlattice reflection spots, visible as two sets of ordered spots of $1/2(1\bar{1}1)$ and $1/2(\bar{1}11)$, are observed halfway between the fundamental spots of (000) and $(1\bar{1}1)$, and between (000) and $(\bar{1}11)$. These superlattice reflection spots indicate the presence of both variants I and II of CuPt-type atomic ordering due to alternating group III (or V) element atoms on the same set of the two $\{111\}$ planes of their respective

sublattices. The intensity and sharpness of the two sets of spots exhibit that the ordered structure is well developed in both directions. No superlattice reflection spot is seen at the TED pattern taken in the $\langle 1\bar{1}0 \rangle$ direction.

HR-TEM image: A typical HR-TEM image of the degraded SL-MQW (Type-A) is shown in Fig. 6. Doubling in periodicity of $\{111\}$ lattice fringes, i.e., the presence of arrays of bright and dark spots on each second $(1\bar{1}1)$ or $(\bar{1}11)$ fringe, is clearly observed. The structure of atomic ordering is confirmed not in the well layers but in each barrier layer. It is considered that strong ordering occurs in the barrier layers, because the barrier layers are composed of low content of Ga and As atoms. It has been predicted in Ref. 4 that the ordering diminishes with compositions from InP towards lattice matched InGaAs in the case of atmospheric pressure MOVPE growth. No dislocation structure is observed in the TEM image in the SL-MQW (Type-A). So, dislocation is considered to be scarcely generated in the sample. No ordering structure is also seen at the HR-TEM image taken in the $\langle 1\bar{1}0 \rangle$ direction.

Temperature dependence of PL linewidth: It has been also predicted that atomic ordering diminishes as the growth temperature increases, for a fixed composition [4, 5]. So, it is expected that the increase of growth temperature is effective to suppress the degradation of SL-MQW structure. Figure 7 shows the dependence of PL linewidth at 77 K on the amount of strain in the well layers as a parameter of the substrate temperature at epitaxial growth. When the amount of strain is 0.6 and 1.0 %, the PL linewidth shows large values of more than 40 meV for the SL-MQW structures grown at 580 °C. However, when the temperature is increased from 580 to 620 °C, the broadening of PL linewidth is completely suppressed even in the SL-MQW structures with 1.0 % strain.

Temperature dependence of PL shift: Figure 8 shows the dependence of PL shift on the amount of strain in the well layers as a parameter of the substrate temperature. Each sample in Fig. 8 corresponds to that in Fig. 7. As shown in Fig. 8, for the SL-MQW structures grown at 580 °C, the PL shift steeply decreases to negative value, as the strain increases over 0.6 %. However, when the temperature is increased to 620 °C, the reduction of PL shift is also completely suppressed even in the SL-MQW structure with 1.0 % strain. It is said that the degradation of PL characteristics, such as the increase of PL linewidth and the reduction of PL shift, is improved with increasing growth temperature. Also, it is expected that still larger amount of strain and still larger

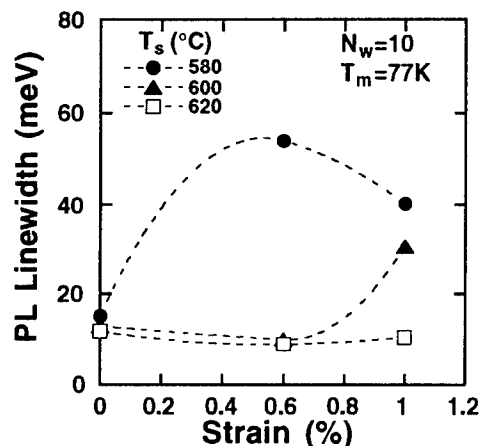


Fig. 7 Dependence of PL linewidth at 77K on the amount of strain for different substrate temperatures at the epitaxial growth.

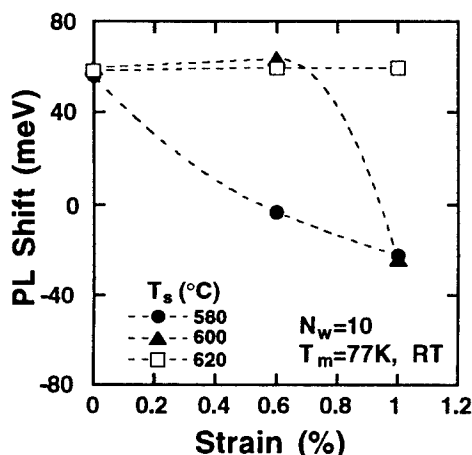


Fig. 8 Dependence of PL shift on the amount of strain for different substrate temperatures at the epitaxial growth.

number of well layers can be introduced with further increasing growth temperature unless the intermixing of P and As becomes dominant at the interfaces of well and barrier layers. Because, the PL linewidth as well as the PL shift shows almost the same values among the unstrained MQW samples grown at different temperature, it is predicted that the ordering in the SL-MQW structure is enhanced by tensile strain unintentionally introduced into the barrier layers.

Temperature dependence of ordering: The nondegraded SL-MQW structure (Type-B : $N_w=10$, $\Delta a/a=0.6\%$, and $T_s=600\text{ }^\circ\text{C}$), which is shown in Fig. 7 and 8, is investigated by using WTEM. The WTEM picture of the SL-MQW (Type-B) reveals sharp interfaces and an excellent periodicity the same as that of SL-MQW

(Type-A). TEM samples of SL-MQW (Type-B) are also prepared parallel to both (110) and $(1\bar{1}0)$ planes, for TED and HR-TEM observation. No superlattice reflection spot observed in TED pattern taken in both $\langle 110 \rangle$ and $\langle 1\bar{1}0 \rangle$ directions. No atomic ordering structure is also observed in the HR-TEM images taken in both $\langle 110 \rangle$ and $\langle 1\bar{1}0 \rangle$ directions. The degradation of PL characteristics in the SL-MQW structure is thought to be explained not only by the generation of dislocation or 3 dimensional nucleation, but also by the generation of atomic ordering.

III. Conclusions

Degraded PL characteristics, such as the increase of PL linewidth and the reduction of the shift of PL peak-energy from RT to 77 K, are observed in the SL-MQW structures with large amount of strain ($\Delta a/a > 0.6\%$) and large number of well layers ($N_w > 5$) grown at low substrate temperature of $580\text{ }^\circ\text{C}$. In TED and HR-TEM pictures taken in $\langle 110 \rangle$ direction, the structure of CuPt-type atomic ordering is clearly observed in each barrier layer of the SL-MQW structure with degraded PL characteristics. By increasing substrate temperature from 580 to $620\text{ }^\circ\text{C}$, the increase of PL linewidth and reduction of PL shift are completely suppressed even in the 10 wells SL-MQW structure with 1.0% strain. Elimination of the ordering structure is confirmed in the SL-MQW structure grown at substrate temperature of $600\text{ }^\circ\text{C}$.

Acknowledgment

The authors wish to thank T. Onuma and Dr. M. Ogura for their continued support and encouragement.

References

- [1] T. Namegaya, N. Matsumoto, N. Yamanaka, N. Iwai, H. Nakayama, and A. Kasukawa, "Effects of Well Number in $1.3\text{-}\mu\text{m}$ GaInAsP/InP GRIN-SCH Strained-Layer Quantum-Well Lasers," IEEE J. Quantum Electron., Vol. 30, pp. 578, 1994.
- [2] T. Takiguchi, K. Goto, M. Takemi, A. Takemoto, T. Aoyagi, H. Watanabe, Y. Mhashi, S. Takamiya, and S. Mitsui, "Improvement of Crystal Quality and Laser Characteristics by Zero Net Strain Structure," J. Crystal Growth, Vol. 145, pp. 892, 1994.
- [3] M.A. Shahid, S. Mahajan, D.E. Laughlin, and H.M. Cox, "Atomic Ordering in $\text{Ga}_{0.47}\text{In}_{0.53}\text{As}$ and $\text{Ga}_x\text{In}_{1-x}\text{As}_y\text{P}_{1-y}$ Alloy Semiconductors," Phys. Rev. Lett. Vol. 58, pp. 2567, 1987.
- [4] S. N. G. Chu, R. A. Logan, and T. Tanbun-Ek, "Atomic Ordering in InGaAsP and InGaAs Grown by Atmospheric Pressure Metalorganic Chemical Vapor Deposition," J. Appl. Phys. Vol. 72, pp. 4118, 1992.
- [5] D. J. Arent, M. Bode, K. A. Bertness, S. R. Kurtz, and J. M. Olson, "Band-gap Narrowing in Ordered $\text{Ga}_{0.47}\text{In}_{0.53}\text{As}$," Appl. Phys. Lett., Vol. 62, pp. 1806, 1993.

GaAs Heteroepitaxy on InP (001) Surfaces Studied by Scanning Tunneling Microscopy

Shunsuke OHKOUCHI, Nobuyuki IKOMA and Masao TAMURA

Optoelectronics Technology Research Laboratory (OTL)

5-5 Tohkodai, Tsukuba, Ibaraki 300-26, Japan

INTRODUCTION

The heteroepitaxy technology of a lattice-mismatched system has been attracting much attention, since it provides an additional freedom for the material design of novel device fabrication. For example, molecular beam epitaxially (MBE) grown GaAs-on-InP optoelectric integrated circuits which combine InP-based long-wavelength optical devices with high-speed GaAs electric devices have been demonstrated[1]. In this heteroepitaxial growth system, however, it is well known that a large number of defects remain in a grown GaAs layer, since the lattice constant of GaAs is 3.7% smaller than that of InP. These defects cause a degradation of the device performance. Therefore, it is necessary to understand the growth mechanism related to defect generation in more detail for further development of the above-mentioned hetero-material device fabrication. In this study, we investigated the growth mode transition process of GaAs heteroepitaxial growth on an InP substrate. The surface structures were observed using an ultra-high vacuum scanning tunneling microscopy (STM) system equipped with an MBE facility.

EXPERIMENTAL

An InP (001) substrate was chemically etched and loaded into the STM multi-chamber system. Details concerning the multi-chamber system have been reported elsewhere[2]. After preheating, the sample was transferred to an MBE chamber and thermally cleaned in an arsenic flux of 3×10^{-3} Pa. The temperature of the sample was gradually raised up to 510 °C in order to remove the surface oxide and to make the surface In-stabilized[3]. After keeping the sample temperature at 510 °C for 3 minutes, a certain amount of GaAs was deposited onto the surface. The amount of GaAs deposition was varied from 1.0 ML to 800 ML. After GaAs deposition, the arsenic flux was shut off and the sample was immediately transferred to the STM chamber for STM measurements. All STM measurements in this study were performed in the constant mode with a tunneling current of 200 pA and a sample bias voltage of -2 V relative to the tungsten tip.

RESULTS AND DISCUSSION

Before GaAs deposition on InP substrates, the surface structures of InP were observed by STM. Figure 1 shows an STM image of an InP

surface thermally cleaned in an arsenic flux at 510 °C for 3 minutes. The STM image showed about 1.6 nm periodic lines of about 0.4 nm width running along the [110] direction. These lines are considered to represent In-In dimer rows of an In-stabilized (4×2) reconstructed structure[3]. Then, a certain amount of GaAs was grown on the InP surfaces, and the surface structures were observed by STM.

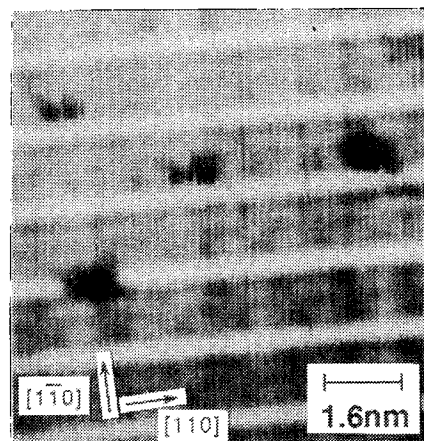


Fig. 1: STM image of an InP surface thermally cleaned in an arsenic flux at 510°C for 3 minutes.

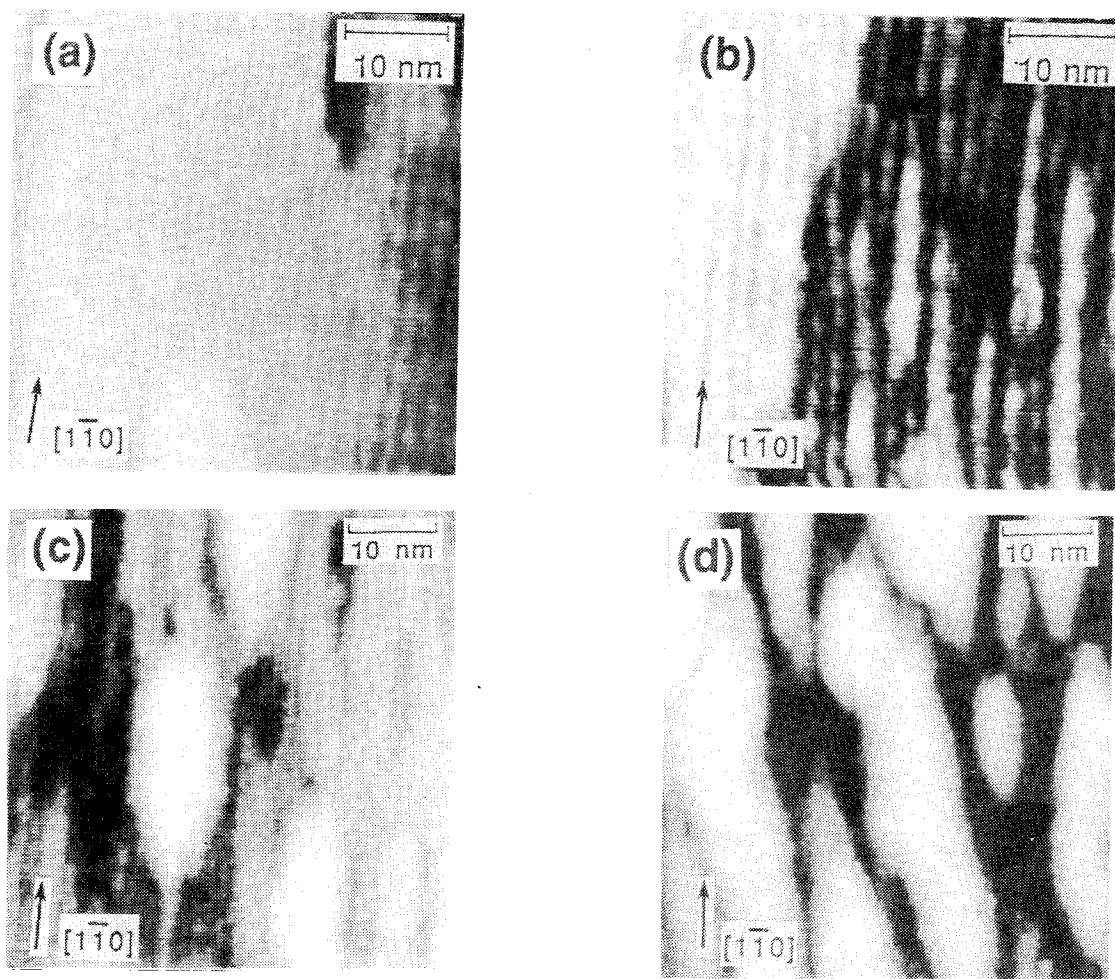


Fig. 2: STM images of GaAs deposited on InP surfaces. The amounts of GaAs deposition are: (a) 1.0 ML, (b) 1.5 ML, (c) 2.5 ML and (d) 4.3 ML. In the initial stage, a growth mode transition from 2D- to 3D-island growth occurred when more than 2.0 ML GaAs was deposited on the surface.

Figure 2 shows STM images of GaAs-deposited InP surfaces in the initial stage for GaAs deposition of less than 5.0 ML. In this stage, a growth mode transition from two-dimensional (2D) to 3D-island growth occurred. Figure 2(a) shows an STM image of a 1.0 ML GaAs-deposited InP surface. In this image, the surface comprises only a (2×4) As-stabilized structure. Although it is not possible to resolve each individual unit cell, dark lines running along the $[1\bar{1}0]$ direction, corresponding to the missing dimer rows, can be seen. An STM image of the 1.5 ML GaAs-deposited InP surface is shown in Fig. 2(b). Although more steps were observed in the image than in that of a 1.0 ML GaAs-deposited surface,

the growth still seems to be 2D on the atomic scale. On the other hand, when 2.5 ML GaAs was deposited on an InP surface, 3D-islands elongated in the $[1\bar{1}0]$ direction were observed (Fig. 2(c)). It is clear that the growth had already changed to 3D. This growth mode transition seems to occur when more than 2.0 ML GaAs is deposited, since the reflection high-energy electron diffraction pattern of this surface changed from streaky to spotty type with this amount of GaAs deposition. Figure 2(d) shows an STM image of a 4.3 ML GaAs-deposited surface. In this image, it is observed that all islands on the surface elongate in the $[1\bar{1}0]$ direction, and that their density increases.

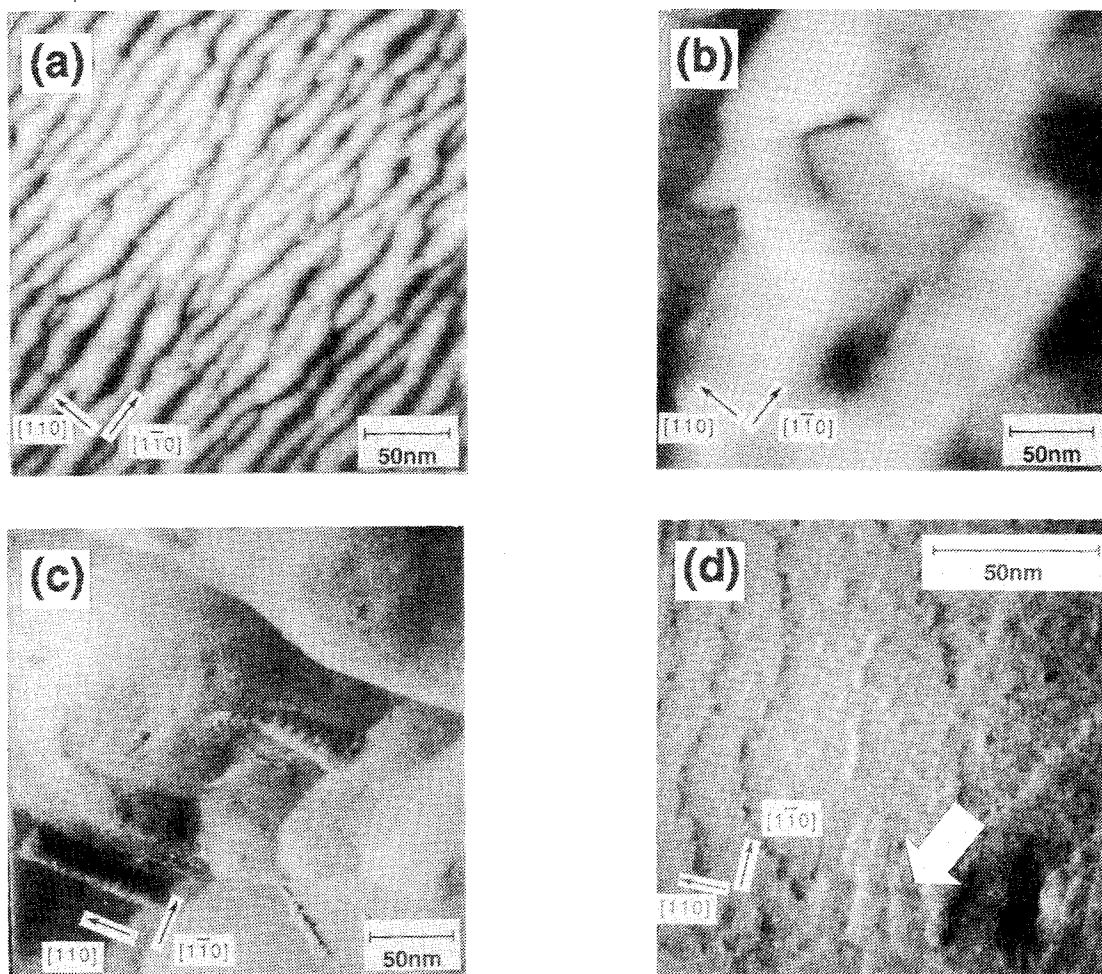


Fig. 3: Larger area STM images of GaAs deposited on InP surfaces. The amounts of GaAs deposition are: (a) 10 ML, (b) 90 ML, (c) 200 ML and (d) 800 ML. The surface structure gradually changed from 3D to 2D with increasing the amount of GaAs deposition.

These islands further elongated along the $[1\bar{1}0]$ direction and coalesced with a greater increase in amount of GaAs deposition. When 10 ML GaAs was deposited on the surface, the islands having a longer shape along the $[1\bar{1}0]$ direction covered the entire surface (Fig. 3(a)). The anisotropy of the island shape disappeared with the following GaAs deposition. In the STM image of a 90 ML GaAs-deposited InP surface, large islands of about $100\text{ nm} \times 100\text{ nm}$ in size were observed (Fig. 3(b)). These large islands then changed to larger domains due to coalescence between the islands, and the surface morphology gradually became flat with further increased GaAs deposition (Fig. 3(c)). Figure 3(d) shows an STM image of an

800 ML GaAs-deposited InP surface. In this case, the surface recovered to a GaAs 2D structure; that is, 1.6 nm periodic dark lines running along the $[1\bar{1}0]$ direction, corresponding to the missing dimer row of a GaAs (2×4) reconstructed structure, can be observed in the STM image. Furthermore, it should be noted that a dark line (indicated by the white arrow) running in the $[110]$ direction between the holes on the surface can be observed. The density of this kind of line was roughly coincident with the dislocation density, which was estimated by a cross-sectional transmission electron microscope observation. This line is therefore considered to correspond to a misfit dislocation line which appeared on the GaAs surface resulting from a

recovery to 2D.

SUMMARY

The growth mode transition processes of GaAs heteroepitaxial growth on an InP substrate were investigated using an STM multi-chamber system equipped with a molecular beam epitaxy facility. During the initial stage, the growth mode transition from 2D- to 3D-island growth occurred with more than 2.0 ML GaAs deposition on the InP surface. This 3D-island structure gradually became flat with increasing the amount of GaAs deposition, and finally recovered to a GaAs 2D structure. Furthermore, an extended dislocation line can be observed in the STM image of the recovered GaAs surface.

ACKNOWLEDGMENTS

The authors would like to thank Dr. I. Tanaka for his cooperation in constructing the STM system. They are also grateful to Dr. Y. Katayama and I. Hayashi for their continuous encouragement.

REFERENCES

- [1] A. Suzuki, T. Itoh, T. Terakado, K. Kasahara, K. Asano, Y. Inomoto, H. Ishihara, T. Torikai and S. Fujita, *Electron. Lett.* 23, 954 (1987).
- [2] I. Tanaka and S. Ohkouchi, *Jpn. J. Appl. Phys.* 32, 2152 (1993).
- [3] S. Ohkouchi, N. Ikoma and I. Tanaka, *J. Vac. Sci. & Technol.* B12, 2033 (1994).

DFB Lasers with Integrated Electroabsorption Modulator

FB1.1
(Invited)

J.J.M. Binsma, P.I. Kuindersma, P. van Gestel, G.P.J.M. Cuypers
R. Peeters, T. van Dongen and P.J.A. Thijs

Philips Optoelectronics Centre, Prof. Holstlaan 4,
5656 AA Eindhoven, The Netherlands

Introduction

Recently, DFB lasers integrated with electroabsorption modulator have attracted wide interest because their low chirp operation makes them highly suitable for high bit rate (STM 64 level of 10 Gbit/s NRZ), long haul 1550 nm transmission over standard - dispersive - single mode fibre (1-4). Also very long distance (> 300 km) systems at 2.5 Gbit/s benefit from the virtually chirp free behaviour of the devices (5-7). In comparison to LiNbO_3 Mach-Zehnder modulators, InP based electroabsorption modulators offer long term stability, compactness, and less vulnerability to self phase modulation (8). In addition, monolithic integration with the DFB laser is possible within the InP materials system. Integration of the electroabsorption modulator to the DFB laser is a very attractive option because of the very low laser to modulator insertion loss and the reduction in packaging effort (and thus cost) compared to external modulators. Moreover, the required matching between modulator bandgap and DFB wavelength is done by the device manufacturer and is of no concern to the user of the device.

In this paper, the design, fabrication and testing of 1550 nm DFB lasers with monolithically integrated electroabsorption modulator are reported. System performance of butterfly-packaged devices in 10 Gbit/s NRZ transmission over standard single mode fibre (SMF) with 17 ps/nm/km dispersion is included. Among the results are 10 Gbit/s transmission without the aid of optical amplifiers up to the theoretical limit of 50 km and up to 150 km using one optical booster amplifier.

Background

Both bulk quaternary layers using the Franz-Keldysh effect and multiple quantum well (MQW) stacks of the Quantum Confined Stark effect type or Wannier Stark effect type have been employed so far in InP based electroabsorption modulators (1-4,9).

Although the MQW modulators offer a higher attenuation efficiency, the Franz-Keldysh type devices show less chirp and are less critical with regard to the exact detuning between modulator bandgap and laser emission. In addition, the Franz-Keldysh modulators are less prone to saturation effects i.e. degradation of attenuation at higher power input from the laser (10). In this work, the attention is focused therefore on integrated modulators of the Franz-Keldysh type.

In principle, DFB lasers integrated with an

electroabsorption modulator should operate entirely chirp free as the laser is biased well above threshold leading to stable single mode emission. Spectral broadening would only be due to the finite pulse duration ΔT from the Fourier limit $\Delta T \cdot \Delta f \sim 1$. Additional chirp, however, is generally introduced by two factors, namely residual facet reflection and phase modulation caused by the variations of the refractive index of the modulator which are accompanied by the changes of the absorption. Both factors determine the temporal distributions of intensity and frequency which are decisive for the obtained system performance. In case of residual facet reflection, light reflected at the modulator front facet is fed back into the DFB laser where it changes the carrier density in the active layer and thus produces chirp (11).

Because the carrier density changes depend on the facet phases, the chirp induced by reflections is depending on laser and modulator bias as well as on temperature. Reflections can be minimized by optimizing the facet coating and the introduction of window structures (4). In addition, the laser can be made less sensitive to reflections by increasing the κL product (11). The reflections affect the chirp over the entire pulse duration proportional to $(1 + \alpha^2)^{1/2}$ (with α being Henry's α parameter for the DFB). The refractive index variations of the modulator, however, mainly play a role during switching giving "transient chirp" (12) due to the phase modulation ($\Delta\phi/\Delta t = \Delta\omega$). The sign of the α parameter of the modulator ($\alpha = dn/dk$ with n and k the real and imaginary parts of the refractive index) determines whether positive chirp during switching on and negative chirp during switching off or vice versa is obtained (10, 12).

Device fabrication

The lateral structure of the DFB lasers with integrated electroabsorption modulator is the Semi-insulating Planar Buried Heterostructure (SIPBH) which is entirely grown by Low-Pressure (LP) OMVPE (13). The growth temperature is 625°C. Laser and modulator active layers are butt-joint coupled by our optimized LP-OMVPE process on 2-inch wafers (14). For comparison, devices with various DFB wavelengths were fabricated by changing the grating pitch while keeping the composition of the modulator layer constant at a luminescence wavelength of 1480 nm. About 2 μm wide mesas are wet-chemically etched with an additional 20 μm wide groove in the p-InP cladding layer at the laser/modulator transition. The SIPBH structure is completed by standard growth procedures (13). The 20 μm wide groove is thereby filled with semi-insulating Fe-doped InP, which leads to an optimal electrical isolation (resistance ~ 100 k Ω) with simultaneous highly efficient optical coupling between laser and modulator. A schematic longitudinal cross-section of the structure is shown in Fig. 1. For improved bandwidth, a second Fe-doped InP regrowth aside 10 μm wide mesas centered around the active layer is carried out in a way similar to ref. (15). The thus obtained structure may be called "Double Semi-insulating Planar Buried Heterostructure" (DSIPBH). The modulator

parasitic capacitance can be reduced in this way to 0.7 pF and bandwidths over 20 GHz are achieved (figures refer to 250 μm long modulators). The modulator front facet is coated with a quarter wave anti-reflective SiO_xN_y coating having $R < 10^{-4}$ at the lasing wavelength. Laser and modulator lengths are 500 and 250 μm , respectively. During fabrication special emphasis is laid on manufacturability by using proven technology (SIPBH, butt-joint coupling, coating, etc.) and as much as possible 2-inch wafer processing.

Results

The room temperature laser threshold current is typically in the range 10 - 15 mA. Fibre coupled powers of 3 - 6 dBm (2 - 4 mW) at 100 mA drive current and zero modulator bias can be obtained ($\lambda = 1555$ nm). The dependence on detuning is shown in Fig. 2 where the output power as a function of modulator bias is plotted for two devices at 1532 nm and 1555 nm lasing wavelength, both having the same ($\lambda = 1480$ nm) modulator layer. The output power strongly decreases with decreasing lasing wavelength, whereas the attenuation amounts to 4 - 5 dB/V in both cases (devices include 50 Ω matching circuit). The α parameter was measured by the Fibre Response Peaks method (16). Small, negative α values are found for $V_{\text{bias}} < -0.5$ V, see Fig. 3. Reliability tests (70°C, 150 mA and -3 V modulator bias) show no extra degradation with respect to commercial DFB lasers.

The devices are packaged in hermetically sealed butterfly packages containing a 30 dB optical isolator, a power monitor, a thermoelectric cooler and a thermistor. The careful matching of the drive circuit leads to an electrical reflection coefficient well below -15 dB up to nearly 20 GHz and a 3 dB bandwidth of 12 GHz (Fig. 4). Modulator sensitivity is 4 dB/V. The spectral width under large signal modulation is independent of laser and modulator bias at a value of 10 GHz, which is determined by the device bandwidth proving that there is no additional chirp.

System experiments at the STM-64 level of 10 Gbit/s showed a small dispersion penalty of ~ 1 dB for transmission over 50 km standard SMF (17 ps/nm/km dispersion), thus attaining the theoretical limit for the first time (3). By using an optical booster amplifier (EDFA) giving 13 dBm output power, the

transmission range is increased to 150 km (17), as is apparent from the BER curves shown in Fig. 5. This is due to both the enhanced power margin and the generation of self phase modulation in the fibre. Finally, at 2.5 Gbit/s, transmission over 460 km standard SMF (limited by fibre availability) was demonstrated (7).

Conclusions

High performance, DFB lasers with integrated electroabsorption modulators with good manufacturability and reliability have been presented. The processing includes proven technology such as laser - modulator butt-joint coupling, SIPBH technology, 2-inch wafer processing and optimized facet coating. Butterfly packaged devices show only 1 dB penalty for 10 Gbit/s NRZ transmission over 50 km standard SMF (theoretical limit) without the use of an optical amplifier. With an optical booster amplifier, self phase modulation in the fibre is exploited and repeaterless 10 Gbit/s transmission is possible over 150 km standard SMF.

Acknowledgements

The assistance with this work by L. Hendrix, A. van Leerdam, J. de Vries and H. Tjassens is gratefully acknowledged.

References

1. H. Soda et al., ECOC'91, Paris, paper WeB7-2, 1991.
2. M. Aoki et al., Electron. Lett., 29, p. 1983, 1993.
3. P.I. Kuindersma et al., Electron. Lett., p. 1876, 1993.
4. P. Ojala et al., Electron. Lett., 29, p. 859, 1993.
5. J.E. Johnson et al., 14th IEEE Semiconductor Laser Conf., paper M4.7, 1994.
6. E.J. Thrush et al., Proceedings 6th IPRM, Santa Barbara, p.72, 1994.
7. P.I. Kuindersma, unpublished results.
8. B. Velschow et al., OFC'95, p.151, 1995.
9. F. Devaux et al., Appl. Phys. Lett., 61, p. 2773, 1992.
10. O. Sahlen, J. Lightwave Technol., 12, p.969, 1994.
11. Y. Kotaki and H. Soda, ECOC'93, Montreux, paper WeP8.6, 1993.
12. J.A.J. Fells et al., Electron. Lett., 30, p. 2066, 1994.
13. P.J.A. Thijs et al., Electron. Lett., 27, p. 791, 1991.
14. A.A.M. Staring et al., IEEE Photon. Technol. Lett., 6, p. 147, 1994.
15. P.A. Morton et al., Electron. Lett., 28, pp.2156-2157, (1992).
16. F. Devaux et al., Electron. Lett., 29 p. 814, 1993.
17. P.I. Kuindersma et al., CLEO'94 Europe, Amsterdam, paper CThH3, 1994.

DFB + Integrated Electroabsorption Modulator

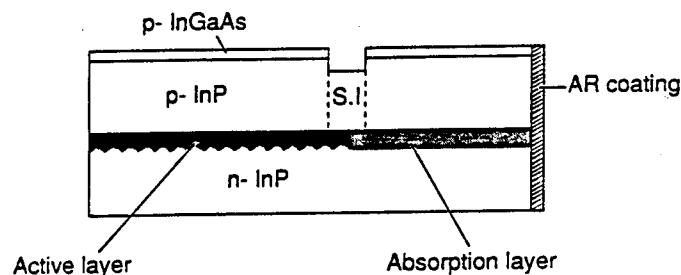
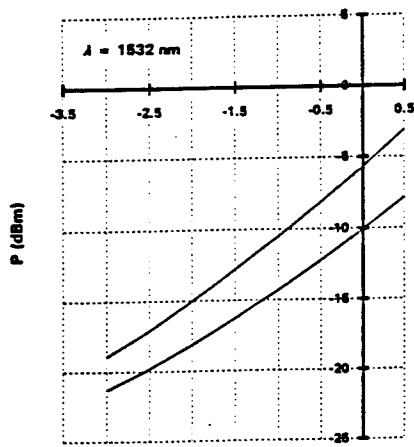
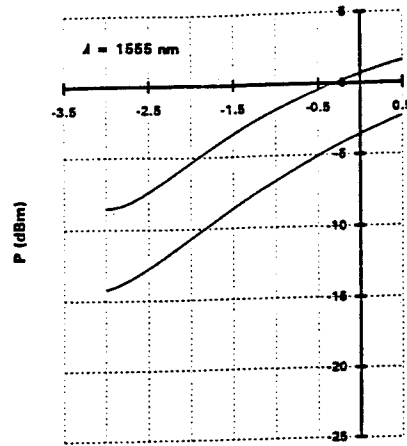


Figure 1: Schematic longitudinal cross-section of DFB laser with integrated electroabsorption modulator.



(a)



(b)

Figure 2: Attenuation curves for 50 Ω DFB-MOD devices with 1532 nm (a) and 1555 nm (b) lasing wavelength. Upper and lower curves at 100 and 50 mA DFB drive current, respectively

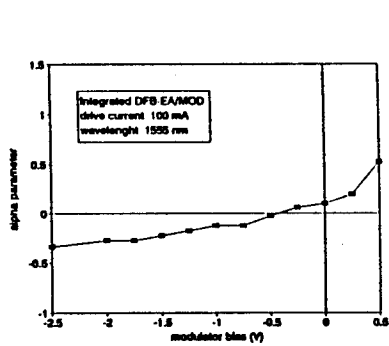
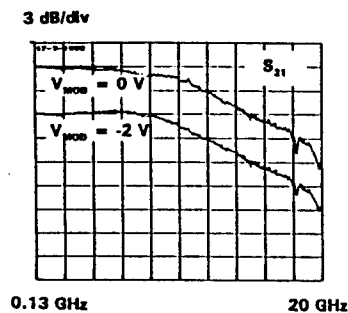
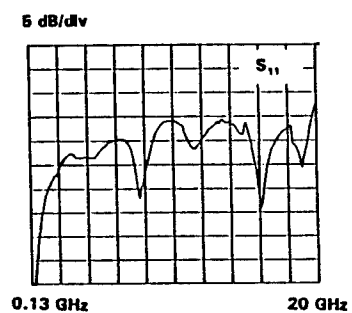


Figure 3: α parameter as a function of modulator bias



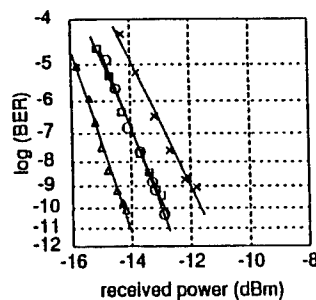
(a)



(b)

Figure 4: (a) S_{21} and (b) S_{11} parameters of butterfly packaged DFB laser with integrated electroabsorption modulator. DFB drive current is 100 mA.

Figure 5: BER curves with optical booster amplifier



Standard SMF
EA-MOD/DFB
CQF195
10 Gbit/s NRZ
 $P = +13$ dBm

○ 0 km
△ 75 km
□ 125 km
× 150 km

DFB lasers integrated with Mach-Zehnder optical modulator and a power booster fabricated by selective area growth MOVPE technique

T. Tanbun-Ek, P.F. Sciortino, Jr., A.M. Sargent, K.W. Wecht, P. Wisk, Y.K. Chen,
C.G. Bethea and S.K. Spitz

AT&T Bell Laboratories
600 Mountain Ave, Murray Hill NJ, 07974

I Introduction

External optical modulators are considered to be the key components for ultra low chirp and high speed modulation(1). Recently considerable progress has been made with DFB lasers integrated with an external electroabsorption modulator that used the selective area growth technique and achieved high performance with low modulation voltage (2V) and low chirp (<0.02 nm) (2-4). The Mach-Zehnder type (MZ) modulator has been proposed as one of the most promising device, since it can achieve virtually zero chirp, thereby maximizing the transmission distance (1). Considerable progress in the design of the semiconductor MZ-type has been accomplished and discrete devices have been demonstrated with satisfactory results (5-9). A successful integration of a Distributed Bragg Reflector (DBR) laser with a MZ modulator has been demonstrated (10). The fabrication processes used in the structure involved etching away the active region and regrowing the passive waveguide. This etch and regrowth technique is in general very complex and special care is needed to avoid the defects generated from the regrowth interface around the Y-branches, thus making it virtually nonmanufacturable. In contrast, selective area growth (SAG) technique (2-3) offers a simple straight forward design and fabrication processes. The SAG not only eliminates the need for etch and regrowth for the in-plane bandgap energy control along the optical axis, but also restricts the crystal growth of the waveguides at the Y-branches into photolithographically defined dielectric film windows formed on the substrate. This yields a better control of the waveguide geometry as well as the crystal quality. Here we report the first monolithically integrated DFB laser with a MZ-type external modulator fabricated by the selective area growth MOVPE technique and operating at the $1.55 \mu\text{m}$ wavelength

II Device structure and fabrication.

The epitaxial growth of all the layers was done at the growth temperature of 670°C and a reactor pressure of 80 mbar. TMIn, TMGa, 100% AsH_3 , and 100% PH_3 were used as the precursors. Tetraethyl Tin and DMZn were used as n and p-type doping, respectively.

The device structure shown in figure 1 consists of a MZ interferometer with two Y-branches, two phase modulator arms and an amplifier section in a Cap Mesa Buried Heterostructure (CMBH) type configuration. The CMBH structure used a $3 \mu\text{m}$ thick Fe-doped InP

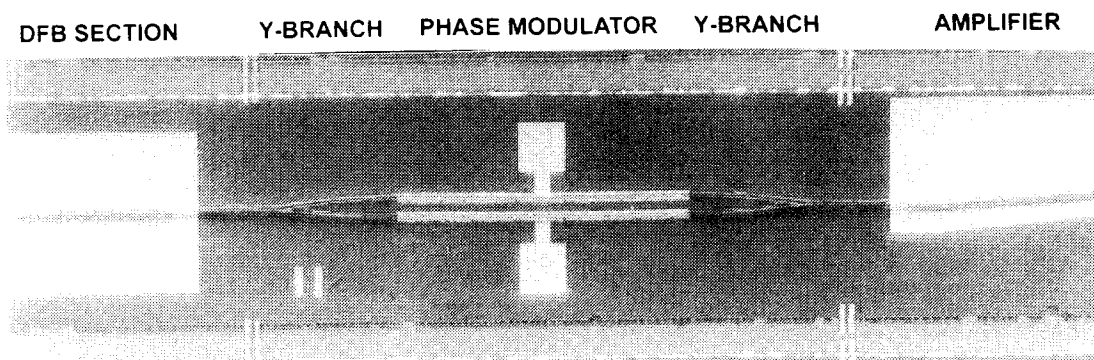


Fig. 1 Microscope picture of the integrated DFB laser with Mach-Zehnder interferometric modulator

($1.5 \times 10^{17} \text{ cm}^{-3}$ of Fe) and a $0.6 \mu\text{m}$ thick n-InP layers as current blocking layers with a subsequent growth of p-InP cladding and p-InGaAs cap layers. The amplifier section consists of an angled waveguide that acts as a traveling wave type optical amplifier. The device was fabricated using 5 steps of low pressure MOVPE growth and the selective area growth technique (2-4). The MQW core waveguides were grown in single continuous MQW layers with the bandgap energy in each part of the devices being adjusted to the designed values by changing the dimension of the dielectric oxide mask. (2-4). The core of the MQW waveguide contains 8 periods of a 0.65% compressively strained InGaAsP quantum well and a nominally lattice matched $1.28 \mu\text{m}$ InGaAsP quaternary barriers and surrounded by 50 nm thick $1.28 \mu\text{m}$ InGaAsP SCH layers on both sides. All the layers are grown directly on a (100) n-InP substrate having a first order grating (pitch= 240.5 nm) partially formed only on the DFB region. The DFB region, the phase modulation region and the amplifier region have a length of $500 \mu\text{m}$, $570 \mu\text{m}$ and $650 \mu\text{m}$, respectively. The angle between the Y-branches was 10 degree. The spacing between the arms were $20 \mu\text{m}$ center to center. Isolation grooves with length of $55 \mu\text{m}$ and depth of $0.7 \mu\text{m}$ deep was formed on both sides of the Y-branches between the DFB laser and the phase modulators thus yielding a typical isolation resistance over $100 \text{ K}\Omega$. The reflectivity of the amplifier side was reduced by the angled waveguide and an antireflection coating. The laser side facet has a high reflectivity coat for high power operation.

III Wavelength control of the selective area growth (SAG)

A spatially resolved micro photoluminescence setup was used to characterize the crystal quality in each of the regions. Figure 2 shows the measured photoluminescence spectra of each region with PL peak wavelengths for the DFB, the phase modulator and the amplifier regions at $1.54 \mu\text{m}$, $1.47 \mu\text{m}$ and $1.52 \mu\text{m}$, respectively. We observed a slightly broader PL halfwidth in the laser and the amplifier region than in the phase modulator regions. This broadening might be due to the inhomogeneity of the selectively grown crystal in those regions. since it has a higher growth rate.

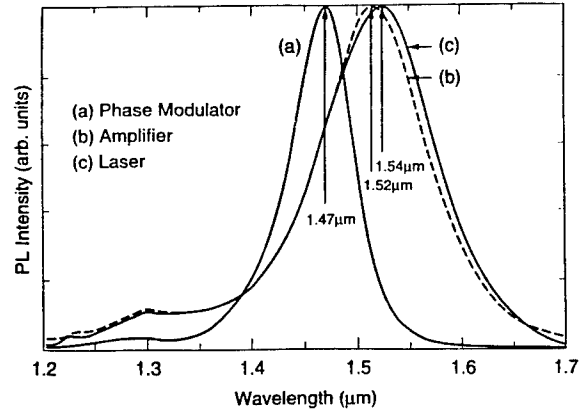


Fig.2 Spatially resolved photoluminescence spectra of each regions in the structure.

IV Loss at the Y-branches.

In order to estimate the loss at the Y-branches, we have fabricated an integrated Fabry-Perot laser with a Y-branch attached to one side. The loss is estimated by comparing the change of the threshold current of the integrated structure as compare to the solitary laser when the Y-branch is cleaved away from the same chip. Using a simple model and neglecting the Interferometric effect at the Y-branch, the loss at the junction can be expressed as

$$\sqrt{\frac{i_c}{i_0}} = 1 + \frac{1}{2\xi L g_0} \ln\left(\frac{1}{C}\right)$$

here i_c , i_0 are threshold currents of the device with and without the branch. ξ is the optical confinement factor in the active region which is estimated to be 10% from the layer structure, g_0 is the threshold gain of the FP with $645 \mu\text{m}$ long which includes the mirror loss (17.7 cm^{-1}) and the absorption loss in the structure (15 cm^{-1}) and is estimated to be 32.7 cm^{-1} . C is the power coupling efficiency of light from the active region to the branch. Also, the recombination of the carrier inside the active region is assumed to be bimolecular so that the quadratic relation between the gain and the current holds. Figure 3 shows the light current characteristics of the devices before and after cleaving away the branch. The output light is observed through the branch side. We observed an increase of roughly 40% in the threshold

current without a significant change in the slope efficiency of the structure. From the above equation, coupling efficiency of 65% was obtained and this corresponds to a loss of approximately 1.75dB. This value is considered low for the branch of this angle.

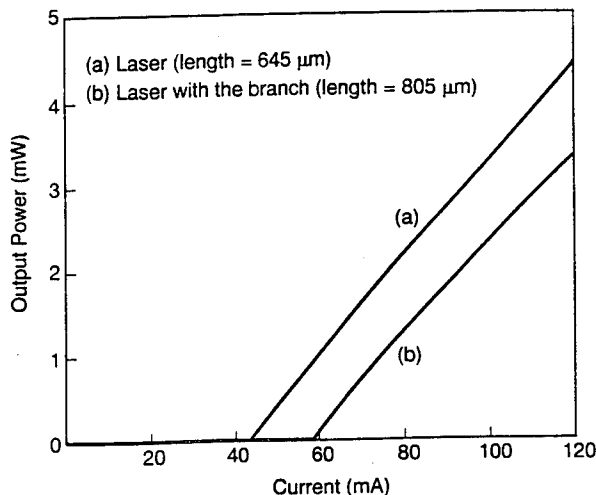


Fig.3 Light current characteristics of the device before and after cleaving away the Y-branch.

V Power divider at the Y-branches.

For efficient modulation, it is important that the Y-branch in the MZ structure acts as a 3 dB power divider. Figure 4 shows the near-field image of the laser light launched from the integrated DFB laser operated above threshold current, into the Y-branches. The image is of the output light observed at the end of the two arms of the phase modulators that were cleaved at the center of the structure.

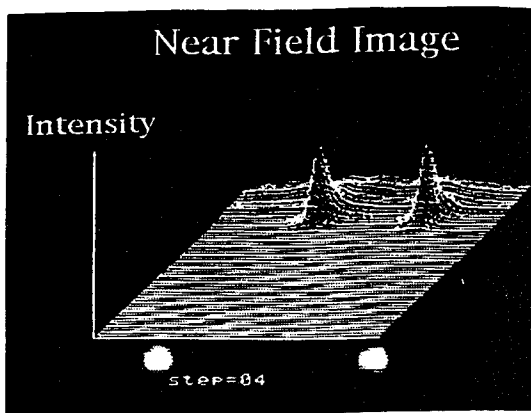


Fig.4 Near Field Image of the light launching from the DFB lasers when observed from the phase modulator arms.

The observed infrared image shows two symmetric beam spots with Gaussian shape profiles both in-plane and perpendicular to the MQW core layer. The splitting ratio was around 100:97 both when the laser was operated above and below the laser threshold current. This near 3 dB splitting ratio of the Y-Branch results from the single continuous growth of the crystal around the dielectric oxide mask used in the selective area growth technique.

V Device Characteristics

Threshold current ranges from 35-55 mA with an output power over 1 mW was observed when the DFB laser section was forward biased and all other parts were left electrically floating. Amplification of 3 dB was observed when the amplifier region was pumped. The relatively low amplification is probably due to the too short a gain peak of the amplifier. The laser wavelength was 1.5473 μm with a side mode suppression ratio of better than 40 dB. Figure 5 shows the attenuation characteristics of the MZ-type modulator as a function of the voltage applied to only one arm of the device. We observed relatively small attenuation when the reverse voltage of one of the phase modulator arm is less than 6 V and the other arm was left floating. The reason for this is not quite clear but it might be due to the fact that the depletion region did not extended throughout the MQW core waveguide or the imperfection of the device fabrication causes an initial phase difference between the two arms of the interferometer. The attenuation of the light increased rapidly as the reverse voltage is increased to 9V. When further reverse voltage is applied, a clear periodic behavior of the attenuation light is observed. The switching voltage between the first maximum attenuation to the next minimum attenuation is as small as 1.5 V with a maximum attenuation of 17.5dB. A similar attenuation characteristic was also confirmed when the reverse voltage was applied to the other arm of the phase modulators, indicating that the light is launched symmetrically into the phase modulator sections. Further improvement of a lower voltage and increased attenuation can be accomplished by both further adjusting the bandgap wavelength of the phase modulators closer to the DFB lasing wavelength thereby increasing the electrorefractive effect near the

bandgap wavelength (11) and optimize the doping profiles in the phase modulator sections.

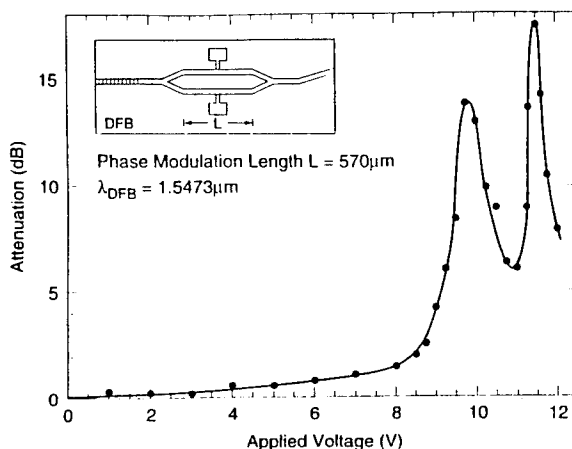


Fig.5 Attenuation characteristics of the integrated DFB laser and a Mach-Zehnder interferometric optical modulator as a function of reverse voltage applied to a single interferometer arm.

In conclusion we have demonstrated the first monolithic integration of a DFB laser with a Mach-Zehnder type modulator fabricated by the selective area MOVPE growth technique. We have achieved a low loss and near 3 dB Y-branch power divider in the structure with the modulator achieving an attenuation up to 17dB and a π phase shift voltage of 2V.

References

- (1) F. Koyama, K.Iga, "Frequency chirping in external modulators," *J. Lightwave Technol.*, Vol. 6, No. 1, pp. 87-92, Jan. 1988.
- (2) M. Aoki, H. Sano, M. Suzuki, M. Takahashi, K. Uomi and A. Takai, "A novel structure MQW electroabsorption modulator/DFB-laser integrated device fabricated by selective area MOCVD growth," *Electron. Lett.*, Vol.27, pp.2138-2140, 1991.
- (3) T. Tanbun-Ek, Y.K. Chen, J.A. Grenko, E.K. Byrne, J.E. Johnson, R.A. Logan, A. Tate, A.M. Sergent, K.W. Wecht, P.F. Sciortino, Jr., and S.N.G. Chu, "Integrated DFB/DBR laser modulator grown by selective area MOVPE growth technique," *J. Of Crystal Growth*, vol.145/1-4, pp.902-906, 1995.
- (4) J.E. Johnson, T. Tanbun-Ek, Y.K. Chen, D.A. Fishman, R.A. Logan, P.A. Morton, S.N.G. Chu, A. Tate, A.M. Sergent, P.F. Sciortino, Jr., and K.W. Wecht, "Low chirp integrated EA-modulator/DFB laser grown by selective area MOVPE," 14th IEEE International Semiconductor Laser Conference, Maui, Hawaii, M4.7, p.41, Sept. 1994.
- (5) J.E. Zucker, T.L. Hendrickson, and C.A. Burrus, "Low-voltage phase modulation in GaAs/AlGaAs quantum well optical waveguide," *Electron. Lett.* Vol. 24, No.2, pp.112-113, 1988.
- (6) H. Takeuchi, K. Kasaya and K. Oe, "Low switching voltage InGaAsP/InP waveguide interferometric modulator for integrated optics," *IEEE Photon. Technol. Lett.*, Vol.1, No.8, pp.227-229, 1989.
- (7) J.E. Zucker, K.L. Jones, B.I. Miller and U. Koren, "Miniature Mach-Zehnder InGaAsP quantum well waveguide interferometers for 1.3 μm ," *IEEE Photon. Technol. Lett.*, Vol.2, No. 1, pp. 32-34, 1990.
- (8) H. Sano, H. Ioue, S. Tsuji, K. Ishida, "InGaAs/InAlAs MQW Mach-Zehnder Optical Modulator for 10 Gbit/s Long-Haul Transmission Systems," *OFC'92 Technical Digest ThG4*, p.223.
- (9) H. Sano, H. Inoue, S. Tanaka, K. Ishida, "High speed InGaAs/InAlAs MQW Mach-Zehnder-type optical modulator," *OFC/IOOC'93 Technical Digest ThK5*, p.215-217.
- (10) J.E. Zucker, K.L. Jones, M.A. Newkirk, R.P. Gnall, B.I. Miller, M.G. Young, U. Koren, C.A. Burrus and B. Tell, "Quantum well interferometric modulator monolithically integrated with 1.55 μm tunable Distributed Bragg Reflector laser," *Electron. Lett.*, Vol. 28, No. 20, pp. 1888-1889, Sept. 1992.
- (11) S. Nojima, "Enhancement of excitonic electrorefraction by optimizing quantum well materials and structures," *Appl. Phys. Lett.*, Vol. 55, No. 18, pp.1868-1870, 1989.

INGAASP/INP STRAINED MQW LASER WITH INTEGRATED MODE SIZE CONVERTER USING THE SHADOW MASKED GROWTH TECHNIQUE

I. Moerman, W. Vanderbauwhede, M. D'Hondt, P. Van Daele, P. Demeester

Department of Information Technology (INTEC), University of Gent - IMEC,

Sint-Pietersnieuwstraat 41, B-9000 Gent, Belgium

W. Hunziker

Swiss Federal Institute of Technology Zürich, Institute of Quantum Electronics,

Micro- and Optoelectronics Lab, Hönggerberg HPT, CH-8093 Zürich, Switzerland

Introduction

In optical communication systems several optical interconnections between semiconductor optoelectronic devices and single mode fibres are required. The very small refractive index difference in a glass fibre results in a weakly guided optical mode with a typical mode size of 8 - 10 μm for 1.55 μm wavelength. Since the mode size in an optoelectronic waveguide device is much smaller ($< 2 \mu\text{m}$) and generally highly asymmetric, there is large mode mismatch between the fibre mode and the device mode, and therefore the fibre-chip coupling efficiency is low.

There are several approaches to improve the fibre-chip coupling efficiency, such as the use of micro-optical imaging elements like micro-lenses or tapered/lensed fibres. Normally, those approaches still suffer from the field symmetry mismatch problem, since only the size and not the shape of the elliptical mode is converted. When using micro-lenses or tapered/lensed fibres, the reduction of the coupling loss is usually at the expense of the alignment tolerances, resulting in high packaging cost.

During the past years, many researchers have therefore focused on the integration of mode size converters with opto-electronic waveguide components, in order to achieve a larger and more symmetric near field pattern at the device facet [1 and references therein]. Such components allow low coupling losses and large alignment tolerances and hence lower packaging costs.

We have previously demonstrated the monolithic integration of a mode size converter with a PBH InGaAsP/InP double heterostructure laser using the SMG technique, which exhibited a coupling loss as low as 4.8 dB to a cleaved single mode fibre [2]. In this paper we present a PBH InGaAsP/InP strained MQW laser with integrated mode size transformer and a coupling loss of 3.3 dB.

Device structure and fabrication

Fig. 1 gives a schematic view of the PBH strained MQW laser. The laser consists of a strained MQW active region, which is buried by p/n-InP current blocking layers. The total cavity length is 650 μm , the width of the active region is 1.5 μm . In the mode size transformer the thickness of the active region is reduced by a factor 3 over a distance of 200 μm . To achieve the vertical tapering of the active layer, we made use of the SMG technique [3,4].

SMG uses a monocrystalline mask, that is held by means of a spacer layer at a certain distance above the substrate. During epitaxial growth the deposition on the substrate takes place through the window in the shadow mask. Thickness changes are fully controlled by the lateral dimensions of the shadow mask and the reactor pressure: the smaller the mask window and the higher the reactor pressure, the larger the growth rate reduction relative to the

nominal growth rate on a non masked substrate. The SMG technique is described in detail elsewhere [4]

The tapered laser requires four growth steps. All growth steps were performed in a low pressure / atmospheric pressure horizontal MOVPE-reactor [5]. In a first growth step, the shadow mask, which consists of a 6 μm InGaAs spacer layer and a 1 μm InP mask layer, is grown on a n-type InP substrate. Then the shadow mask is defined by standard photolithography, non-selective etching through the mask layer and selective etching of the InGaAs spacer layer (see Fig. 2). The shadow mask was designed to achieve adiabatic tapering [6]. The width of the mask window varies exponentially from 150 μm at the start of the taper to 5 μm at the end of the taper over a distance of 200 μm . In this way the thickness decreases more slowly at the end of the taper. The relative growth rate through a 5 μm window is three times lower than that on a non-

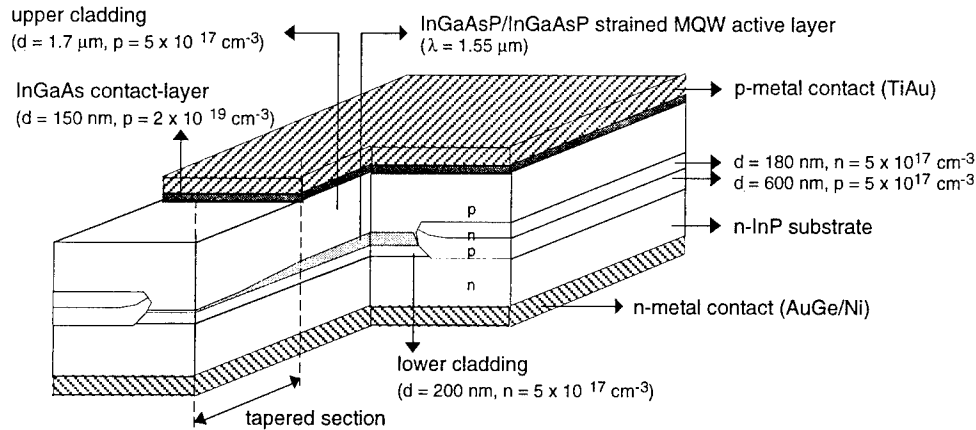


FIG. 1 : Schematic drawing of a PBH strained MQW laser with integrated mode size converter

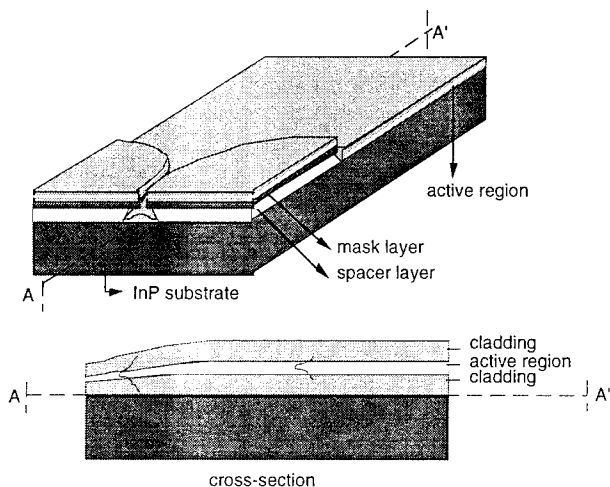


FIG. 2 : Shadow masked growth of the laserstructure

masked substrate. For more details on the growth and the definition of the shadow mask, we refer to [4].

In a second growth step the 200 nm n-InP cladding layer, the active region, and the first part (300 nm) of the p-InP cladding layer are grown using the shadow masked growth technique (see Fig. 2). The active region consists of 4 wells of 7.5 nm 1 % compressively strained $\text{In}_{0.84}\text{Ga}_{0.16}\text{As}_{0.74}\text{P}_{0.26}$ between 15 nm unstrained $\text{In}_{0.75}\text{Ga}_{0.25}\text{As}_{0.54}\text{P}_{0.46}$ ($\lambda = 1.25 \mu\text{m}$) barriers. The MQW is surrounded with 75 nm $\text{In}_{0.75}\text{Ga}_{0.25}\text{As}_{0.54}\text{P}_{0.46}$ separate confinement layers. This growth is performed at atmospheric pressure in order to achieve the highest possible thickness reduction [4].

After this second growth step, the shadow mask is removed. To do so, the deposited layers in the mask window and in the unmasked areas are covered with photoresist. The deposited layers on top of the mask, the

InP mask and the InGaAs spacerlayer are then selectively removed.

After the lift-off of the shadow mask, $3 \mu\text{m}$ wide SiO_2 -stripes are deposited and $1 \mu\text{m}$ high mesas are etched with $\text{HCl}/\text{H}_3\text{PO}_4$ followed by bromine-methanol. In a third growth step the mesas are planarised with p/n current blocking layers.

Then the SiO_2 -stripes are removed and the second part ($1.7 \mu\text{m}$) of the p-InP cladding layer and the 150 nm p^+ -InGaAs contact layer are deposited in the fourth growth step.

Ti/Au p-contacts and AuGe/Ni n-contacts are defined by conventional processing techniques. Current is only injected in the planar section of the laser and not in the taper. Therefore the p^+ -InGaAs contact layer is selectively removed on top of the mode size converter. Since both the reduction of the quantum well thickness and the compositional variations during SMG increase the bandgap in the tapered section [4], the taper behaves as a transparent window.

Experimental results

Lasers were cleaved at different positions in the taper region, which means that taper lengths ranging from $20 \mu\text{m}$ to $200 \mu\text{m}$ were examined. The length of the active section was always $450 \mu\text{m}$.

The non-tapered reference lasers, have a CW threshold current of 7 mA and a differential quantum efficiency of 28.2 % per facet. The laser performance is hardly influenced by the taper integration (see Fig. 2). We observed a slight increase of both threshold current and differential quantum efficiency. A laser with a $200 \mu\text{m}$ tapered section has a threshold current of 8.2 mA and a differential quantum efficiency of 31.5 %.

Due to the taper, the beam divergence, measured at 10 mA above threshold, is decreased from $33.6^\circ \times 32.3^\circ$ to

16.6° x 11.8° (see Fig. 3). The coupling loss, when the laser light is coupled into a cleaved single mode fibre with a core diameter of 8 μm , is reduced from 9.3 dB for a reference laser to 3.3 dB for a tapered laser (see Fig. 3). The measured coupling losses are mean values, since the non AR-coated lasers were very sensitive to Fabry-Perot reflections from the cleaved fibre facet. We observed a Fabry-Perot ripple of 1 dB when the cleaved fibre is moved along its axis close to the laser facet. The alignment tolerances for 1 dB excess loss are $\pm 1.7 \mu\text{m}$ in horizontal and $\pm 1.7 \mu\text{m}$ in vertical direction for a reference laser, and ± 2.1 and $\pm 1.7 \mu\text{m}$ for a tapered laser with a 200 μm taper, respectively.

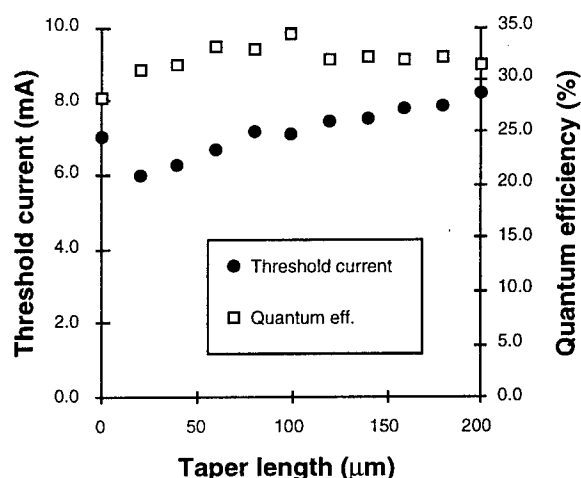


FIG. 3 : Threshold current and external differential quantum efficiency (per facet) as a function of taper length

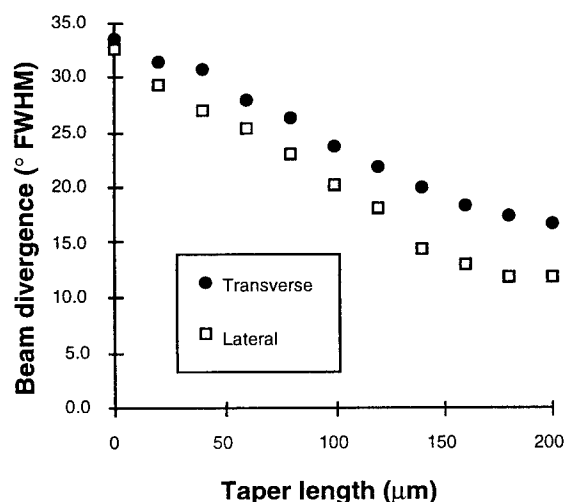


FIG. 4 : Horizontal and vertical beam divergence (FWHM) as a function of taper length.

We also measured coupling losses to lensed fibres producing different Gaussian beam radii between 1.5 and 5.5 μm . The maximum mean value of the coupling loss is 3.3 dB (beam radius of fibre lens : 1.5 μm) for a reference laser and 1.7 dB (beam radius of fibre lens : 2.3 μm) for a laser with a 200 μm taper. Those losses include the Fresnel reflection as well as optical inhomogeneities and aberrations of the fibre lenses. The corresponding 1 dB excess loss alignment tolerances are $\pm 0.85 \mu\text{m}$ in horizontal and $\pm 0.85 \mu\text{m}$ in vertical direction for the reference laser, and ± 1.3 and $\pm 1 \mu\text{m}$ for the tapered laser, respectively.

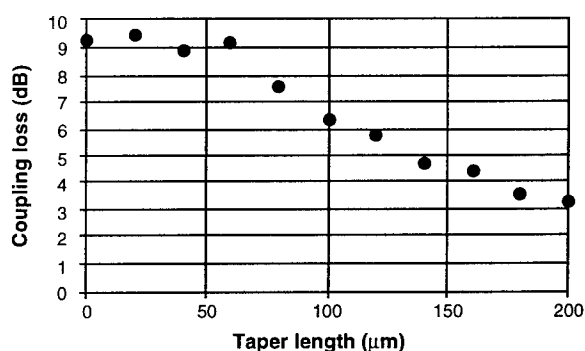


FIG. 5 : Coupling loss to cleaved fibre as a function of taper length.

Conclusion

We have successfully integrated a mode size converter with a PBH strained MQW InGaAsP/InP laser diode using the SMG-technique. The laser performances are hardly affected by the taper integration. Due to the taper, the coupling loss to a cleaved fibre is reduced from 9.3 dB for a non-tapered laser to 3.3 dB for a laser with a 200 μm taper.

Acknowledgements

I. Moerman and W. Vanderbauwhede thanks the IWT (Flemish institute for the promotion of scientific-technological research in the industry) for financial support. This work was supported in part by the European projects UFOS (RACE), MOSAIC (ESPRIT) and the Swiss Federal office for Education and Science. Steven Verstuyft is acknowledged for the skilful processing.

References

- [1] I. Moerman, G. Vermeire, M. D'Hondt, W. Vanderbauwhede, J. Blondelle, G. Coudenys, P. Van Daele, P. Demeester; "III-V semiconductor waveguiding devices using adiabatic tapers";

Microelectronics Journal, Vol. 25, 1994, pp. 675-690.

- [2] I. Moerman, M. D'Hondt, W. Vanderbauwhede, G. Coudenys, J. Haes, P. De Dobbelaere, R. Baets, P. Van Daele, P. Demeester; "Monolithic integration of a spot size transformer with a planar buried heterostructure InGaAsP/InP-laser using the shadow masked growth technique"; IEEE Photonics Technology Letters, Vol. 6, Nr. 8, August 1994, pp. 888-890
- [3] P. Demeester, L. Buydens and P. Van Daele, "Growth velocity variations during metal organic vapor phase epitaxy through an epitaxial shadow mask"; Applied Physics Letters, Vol. 57, Nr. 2, 9 July 1990, pp. 168-170
- [4] G. Coudenys, I. Moerman, G. Vermeire, F. Vermaerke, Y. Zhu, P. Van Daele, P. Demeester, E. Maayan, B. Elsner, J. Salzman, E. Finkman; "Atmospheric and low pressure shadow masked MOVPE growth of InP/InGaAs(P) and InGaAs/(Al)GaAs heterostructures and quantum wells"; Journal of Electronic Materials, Vol. 23, Nr. 2, 1994, pp. 225-232
- [5] I. Moerman, G. Coudenys, P. Demeester, B. Turner, J. Crawley; "Influence of gas mixing on the lateral uniformity in horizontal MOVPE reactors"; Journal of Crystal Growth, Vol. 107, Nr. 1-4., 1991, pp. 175-180
- [6] J.D. Love, W.M. Henri, W.J. Stewart, R.J. Black, S. Lacroix, F. Gonthier, "Tapered single-mode fibres and devices, Part 1: Adiabaticity criteria", IEE Proceedings, Part J, Vol. 138, No. 5, 1990, pp. 343-354

Monolithic Integration of GaInAsP/InP Collimating GRIN Lens with Tapered Waveguide Active Region

S. El Yumin, S. Arai, T. Kimura, H. Kasyou, K. Saito, and A. Ubukata

Research Center for Quantum Effect Electronics,

Tokyo Institute of Technology

2-12-1 O-okayama, Meguro-ku, Tokyo 152, Japan

Phone: +81-3-5734-2512 Fax: +81-3-5734-2907

Abstract: A GaInAsP/InP collimation GRIN lens monolithically integrated with a tapered waveguide laser was realized, and a circular beam divergence ($\theta_{\parallel}=7^{\circ}, \theta_{\perp}=7.5^{\circ}$) was obtained with the output width of $15\mu\text{m}$ and the core thickness of the GRIN lens of about $8\mu\text{m}$.

1. Introduction

In optical fiber communication systems, highly efficient coupling between laser diodes (LDs) or semiconductor laser amplifiers (SLAs) and single mode fibers is very important in order to reduce the driving current and noise figure, respectively. Good coupling is still problematic because the output beam divergence angle of LDs or SLAs is very large, especially perpendicular to junction plane, while the diameter of SMF is very small, so that it is difficult to obtain the lowest coupling loss with butt-joint. There are many approaches and techniques to reduce the coupling loss to SMF, such as by inserting one or more lenses[1][2], by integrating vertically tapered multi quantum well waveguide[3], by fabricating a microlens on the SMF tip[4], and by using integrated optical modeshape adapters[5] with vertically tapered waveguide. However, in order to improve the butt coupling loss, narrow beam divergence of LDs or SLAs in both lateral and vertical directions is essentially required.

To meet this purpose, we proposed a GaInAsP/InP collimating GRIN lens (CGL)[6]

monolithically integrated with a tapered waveguide structure active region. In this work, a circular beam property with narrow beam divergence is presented.

2. Design and Structure

Figure 1 shows the schematic structure of CGL monolithically integrated with a linearly tapered active region. The basic structure of CGL is GaInAsP multi-waveguides with their refractive index $n^2(x)=n^2(0)[1-(gx)^2]$ for $x \leq a$ and $n^2(x)=n_c^2$ for $x > a$, where x is the vertical direction, $n(0)$ and n_c are the refractive indices on the optical axis and the cladding, respectively, a is the distance between the optical axis and the cladding, and g is the focusing constant determined by $\sqrt{\Delta n}/a$, Δn is the relative refractive index difference ($\Delta n = [n^2(0) - n_c^2]/n^2(0)$). The refractive index of $\text{Ga}_x\text{In}_{1-x}\text{As}_y\text{P}_{1-y}$ was calculated using the modified-single-effective-oscillator (MSEO) method. The lattice-matching condition of $y=2.197x$ and the wavelength of $1.5\mu\text{m}$ were used to determine the bandgap wavelength of GaInAsP at a desired refractive index in the fabrication.

To obtain the collimating type CGL, the length has to follow the condition, $L = [(2m+1)/4]L_p$, where the pitch length $L_p = 2\pi/g$, $m=0,1,2,\dots$, and $g = \sqrt{\Delta n}/a$. When the core thickness is $6 \sim 10 \mu\text{m}$ close to that of SMF, $m=0$ and $\Delta n \geq 3\%$, the length of the CGL is calculated to be about $30\mu\text{m} \sim 50\mu\text{m}$, hence an excess loss due to absorption in the CGL is negligibly small even if the absorption loss coefficient is $5 \sim 10 \text{ cm}^{-1}$.

First, we fabricated the CGL by liquid-phase-epitaxy and observed the beam divergence angle of this CGL. The 8-steps GaInAsP waveguide of $1\mu\text{m}$ thickness was grown on n-InP (Sn doped) substrate with $0.05\mu\text{m}$ thick GaInAsP ($l_g=1.50\mu\text{m}$) active layer in the center and 1mm thick p-InP cladding layer on the top. The refractive index difference Δn of waveguides was 5%, and it was to be 9% including the active layer. The upper layers were doped with Zn and the lower layers were doped with Te to form a p-n junction. The soak temperature T_s and the growth temperature T_G were 615°C and 591°C , respectively, and a cooling rate was $0.7^\circ\text{C}/\text{min}$.

The far-field pattern of CGL was observed using the light from a laser diode with the wavelength of $1.50\mu\text{m}$ transmitted through lenses and focused to the CGL. The CGL was biased to monitor the photo current so as to assure best beam coupling condition, at this condition far field patterns of several CGL samples with different device lengths were measured. Figure 2 shows the vertical beam divergence as a function of the CGL length. The collimating length of the GRIN lens was estimated to be around $32\mu\text{m}$ from a best fitting of theoretical curve and the narrowest divergence of

6degree was obtained. This value is better than previously reported result of 12degree[3] in which the number of wells in a multi quantum well structure is changed.

3. A CGL monolithically integrated with tapered active region

To design the CGL monolithically integrated with tapered active region as shown in Fig. 1, it is important to consider the reflectivity at the interface of the tapered active region and the CGL. To minimize the power reflectivity R the equivalent refractive index of CGL was designed closed to that of tapered active region by controlling the thickness and refractive index of each layer, and here R was calculated to be 3.6×10^{-7} . The CGL, designed to have a parabolic index profile with the relative refractive-index difference of 5%, consists of 9 layers of GaInAsP GRIN core region whose thickness is about $8.2\mu\text{m}$. The active region width was $1.5\mu\text{m}$ and $15\mu\text{m}$ at the input end and the output end, respectively, and the length is $800\mu\text{m}$. This device was fabricated by two step LPE growth and selective etching process. The island type SiO_2 mask was used in order to avoid anomalous growth step[8] in the fabrication.

The lasing characteristics of this device was measured with cleaved facets and tested under low duty cycle pulsed operation (200ns, 5kHz) at room temperature. Threshold current I_{th} of samples were achieved about $500 \sim 1000\text{mA}$ for the CGL length of $100\mu\text{m}$ which was approximately 3 times the collimating length. At the output facet the near-field pattern was observed by an IR vidicon camera equipped with a line scan system using $40 \times$

objective lens. Figure 3 shows the near-field intensity profile and beam spot of this device with an injection current of $0.5I_{th}$ ($I_{th}=1.0A$, sample #TA-16). The lateral and vertical width (FWHM) were about $12\mu m$ and $10\mu m$, respectively.

Figure 4 shows the far-field characteristics of this device at $2I_{th}$ ($I_{th}=500mA$, sample #TA-3). FWHM of vertical and lateral beam divergence were obtained to be 7.5degree and 7degree, respectively. Based on above experimental results, coupling loss was estimated using Gaussian approximation method[8]. The core diameter and the refractive index difference of single-mode fiber are assumed to be $10\mu m$ and 0.3%, respectively. Neglecting the lateral and angular misalignment, the coupling loss was estimated to be about -0.1dB. As can be seen here that with improvement of output beam divergence angle in both lateral and vertical direction, lowest coupling loss of SLAs to single mode fiber can be attained.

4. Conclusion

A GaInAsP/InP semiconductor collimating GRIN lens was proposed and fabricated to improve the vertical output beam divergence of LDs or SLAs and simultaneously reducing the coupling loss to single mode fiber. A GaInAsP/InP collimating GRIN lens (CGL) integrated with the tapered active region has been realized. Nearly circular beam spot size of $12 \times 10 \mu m^2$ (lateral \times vertical) was obtained. FWHM of lateral and vertical beam divergence angle has been obtained to be 7 deg. and 7.5deg., and which resulted in the estimation of coupling loss to single mode fiber to be -0.1dB.

Acknowledgment

The authors would like to acknowledge Prof. K. Iga and Prof. K. Furuya, Assoc. Prof. M. Asada Assoc. Prof. Y. Miyamoto for fruitful discussions.

References

- [1] K. Kawano et al., "A new confocal combination lens method for a laser diode module using a single mode fiber," *J. Lightwave Tech.*, LT-3(4), pp.739-735, Aug. 1985.
- [2] H. Ghafoori-shiraz et al., "Microlens for coupling a semiconductor laser to a single mode fiber," *Opt.Lett.*, 11(8), pp.537-539, Aug. 1986.
- [3] T.L. Koch, "Tapered waveguide InGaAs/InGaAsP multi quantum well lasers," *IEEE Photon. Tech. Lett.*, 2(2), pp.88-90, Feb.1990.
- [4] H.M. Presby et al., "Near 100% efficient fibre microlens," *Electron. Lett.*, 28(6), pp.582-584, Mar. 1992.
- [5] T. Brenner et al., "Integrated optical modeshape adapters in InGaAsP/InP for efficient fiber to waveguide coupling," *IEEE Photon. Tech. Lett.*, 5(9), pp.1053-1056, Sept. 1993.
- [6] S.El Yumin et al., "GaInAsP/InP semiconductor vertical GRIN lens for semiconductor optical devices," *IEEE Photon. Tech. Lett.*, 6(5), pp.601-604, May 1994.
- [7] I. H. Choi et al., "A new type 1.5-1.6 μm GaInAsP/InP BIG-DBR laser by an island type mesa process," *Jpn. J. Appl. Phys.*, 26(10), pp. L1593-94, Oct. 1987.
- [8] M. Saruwatari et al., "Semiconductor laser to singlemodefibercoupler," *Appl. Opt.*, 18(11), pp.1847-1856, June 1979.

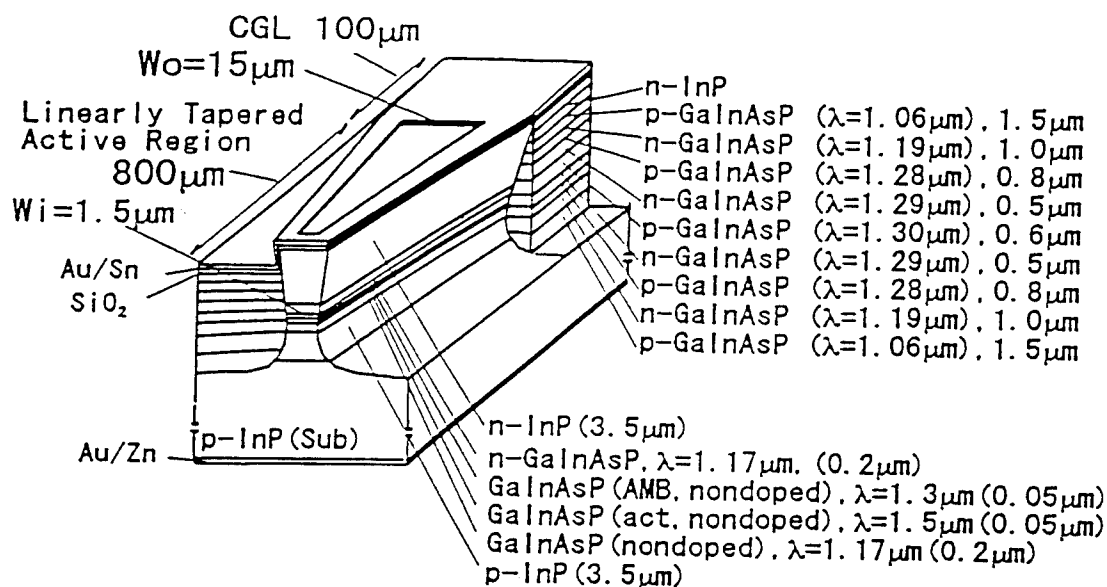


Fig.1 The schematic structure of CGL monolithically integrated with tapered waveguide active region.

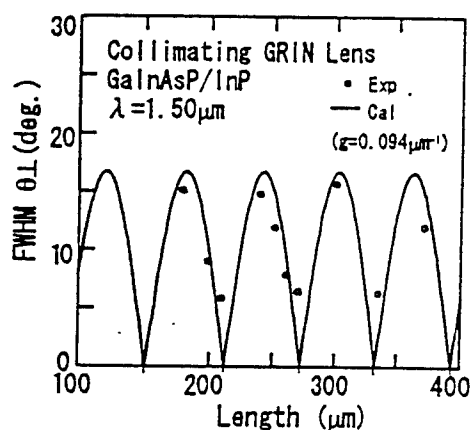


Fig.2 The FWHM of vertical beam divergence as a function of the CGL length. The dashed line indicates the best fitting curve.

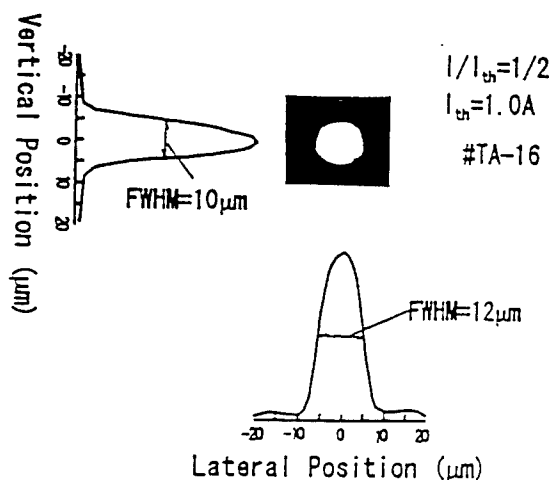


Fig.3 The near-field pattern of a tapered waveguide laser monolithically integrated with a CGL.

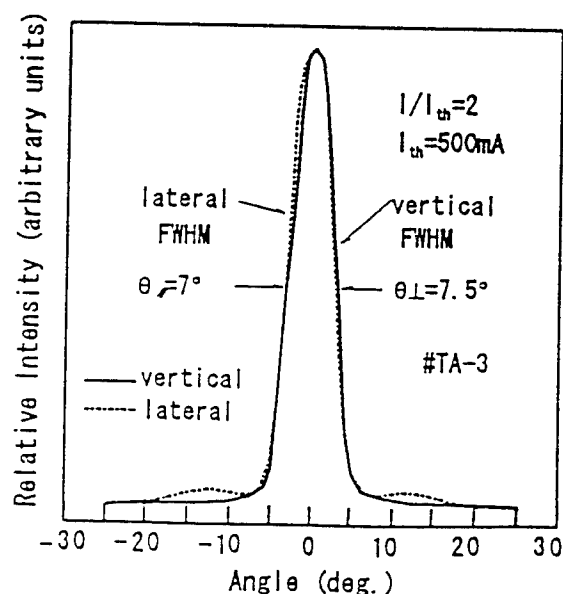


Fig.4 The far-field pattern of a tapered waveguide laser monolithically integrated with a CGL.

High Power and Narrow Lateral Far Field Divergence 1.5 μm -Eye-Safe Pulse Laser Diodes with Flared Waveguide

Takemasa TAMANUKI, Tatsuya SASAKI and Mitsuhiro KITAMURA

Opto-Electronics Research Laboratories, NEC Corporation

34 Miyukigaoka, Tsukuba, Ibaraki 305, Japan

Introduction

The wavelength range around 1.5 μm has been known as less hazardous to human eyes. High power pulse laser diodes (LDs) of this "eye-safe" wavelength range will be attractive for free-space optical measurement systems. For such systems, a narrow beam divergence is effective to decrease the optical component size. In order to obtain the high power and a narrow beam divergence, a variety of devices have been investigated, such as semiconductor amplifiers [1], monolithically integrated master oscillator power amplifiers (MOPA) [2,3], resonant antiguided structure LDs [4], and flared waveguide LDs [5-8]. Flared waveguide LDs can be driven at higher current level than semiconductor amplifier, and several watts output power with nearly diffraction limited beam characteristics were demonstrated in wavelength of 0.98 μm [7]. However high power characteristics under pulsed condition, important for free space measurement systems, at the "eye-safe" wavelength range, have not been clarified yet. In this paper, we report high power and narrow far-field angle, 1.5 μm -eye-safe pulsed lasers with a flared ridge waveguide for the first time. High power (9.6 W) operation, with narrow lateral far field divergence ($3-4^\circ$), has been obtained. These devices will be applicable for free-space optical measurement systems as "eye-safe" light sources.

Structure and Fabrication of Flared LDs

Figure 1 shows a schematic diagram of the fabricated flared LD. In order to maintain fundamental mode in flared waveguide, the buried heterostructure [5] and the self-aligned bent active layer lasers with flared waveguide [6] were reported. In this study, we introduce ridge structure into the flared waveguide to

obtain high output power in terms of decreasing leakage currents outside the active region. The flared LD was fabricated by two-step MOVPE process. First, n-InP cladding, active region and 1 μm -thick p-InP cladding layers were grown on an n-InP substrate. The active region has a separate confinement heterostructure including five quantum wells

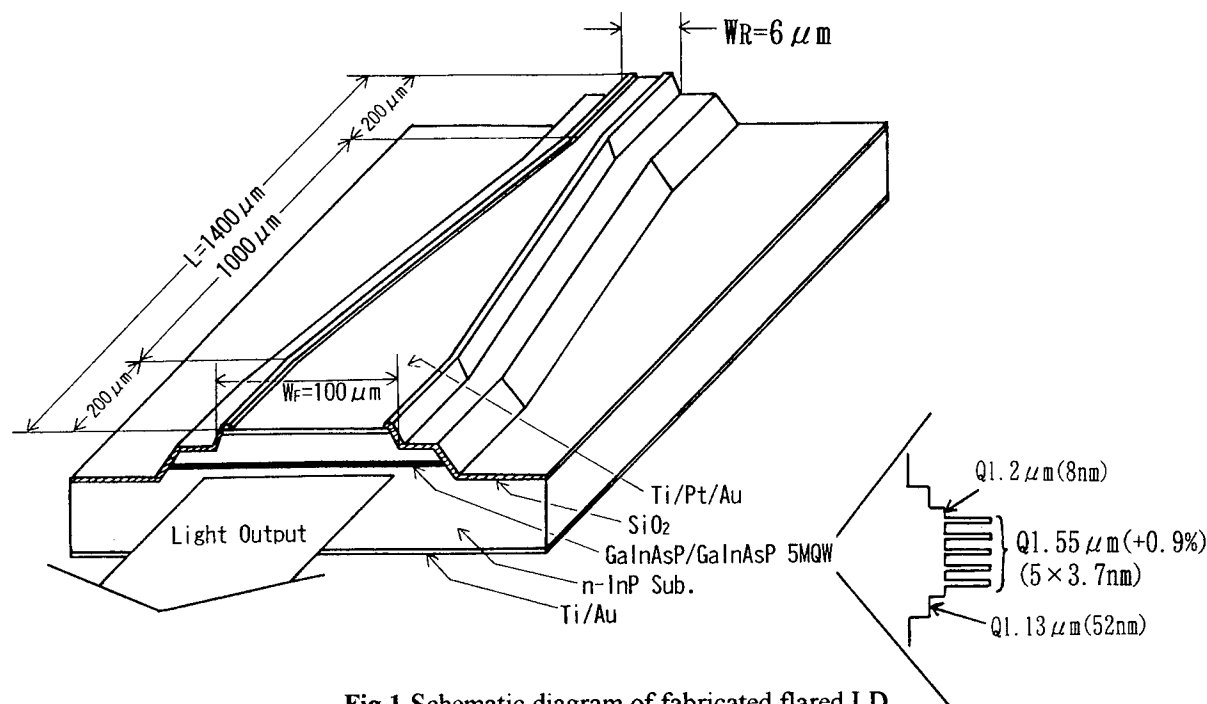


Fig.1 Schematic diagram of fabricated flared LD.

consisting of 3.7 nm-thick 0.9 % compressive strained GaInAsP ($\lambda_g=1.55 \mu\text{m}$) with 8 nm-thick GaInAsP ($\lambda_g=1.2 \mu\text{m}$) barriers. Next, The tapered ridge waveguide, consisting of 0.5 μm -thick p-InP additional cladding and 0.2 μm -thick p-GaInAs contact layers, was selectively regrown between 10 μm -wide SiO₂ mask stripes on the 1 μm -thick p-InP cladding layer. The active region width of the front facet and rear facet are 100 μm and 6 μm , respectively. According to the theoretical estimation with the equivalent index method [9], less than 8 μm stripe width is required for fundamental mode operation. The total cavity length is 1400 μm , consisting of a 1000 μm -long tapered section between

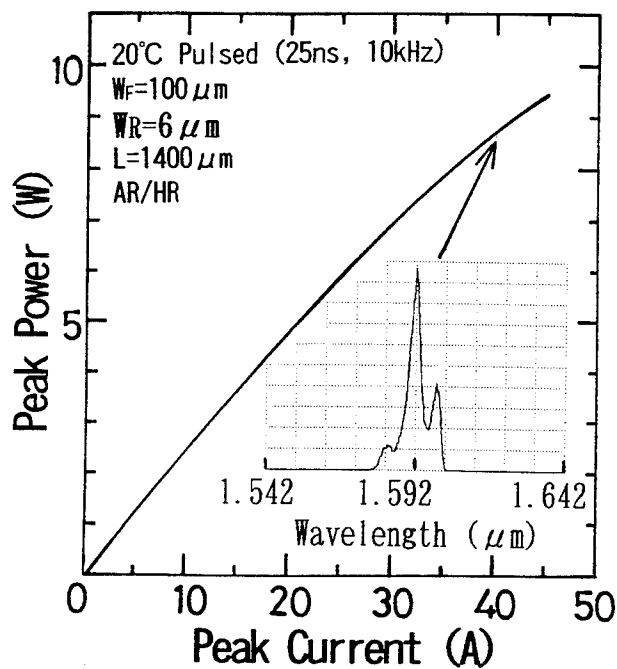


Fig.2 Light output-current characteristics of flared LD.

200 μm -long straight sections. The radiation loss of this linearly tapered waveguide with this angular width is theoretically estimated to be 3 cm^{-1} [10], this value can be neglected in comparison with that of internal absorption loss of semiconductor lasers. The 10 μm outer region from the edge of the ridge mesas were etched to reach the n-InP cladding layer, to prevent reflections and propagation of radiative mode in the tapered waveguide. The reflectivity of the front facet was adjusted to 6 % with a SiN_x low reflective coating, and that of the rear facet was 95 % with a Si/SiO₂ multi-layer high reflective coating. The LD was mounted on a Si heat-sink with junction up

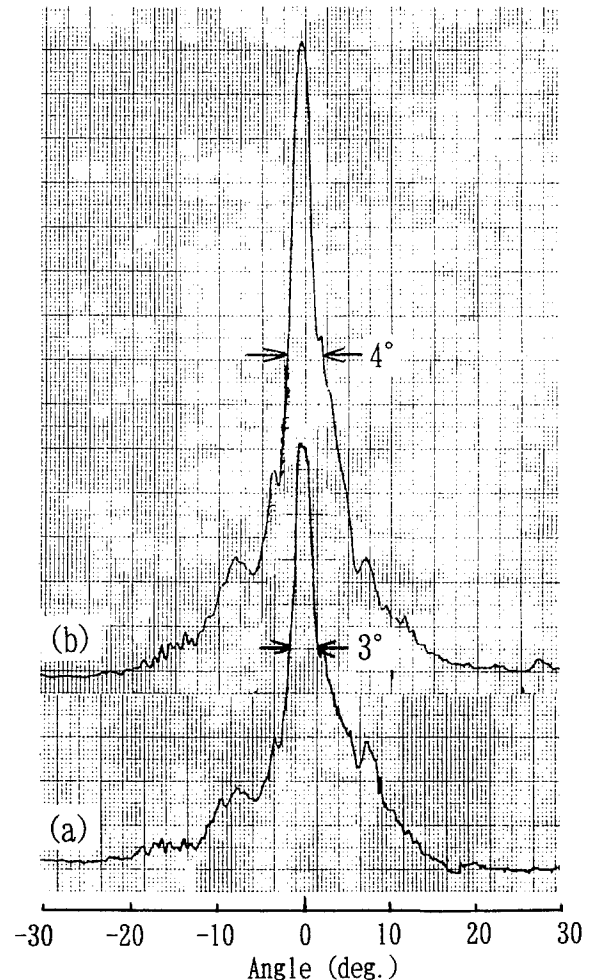


Fig.3 Lateral far-field profiles from a 100 μm wide facet at peak current of 20 A (a) and 40 A (b).

configuration.

Lasing Characteristics

Figure 2 shows light output-current and lasing spectrum of the flared LD at 20°C pulsed condition (25 ns pulse width, 10 kHz period). The measured threshold current and differential slope efficiency were 900 mA and 0.23 W/A · facet, respectively. Maximum output peak power of 9.6 W, with 1.592 μm center wavelength, was obtained at the peak current of 45 A (current density of 61 kA/cm^2). This output power is identical with that of broad area type LDs with 100 μm -wide straight active region. The peak power was limited by the maximum current of the current source and saturation of output power. From independent experiment using the broad LDs, saturation of output power were remarkable above current density of around 50 kA/cm^2 . One origin of this saturation is considered to be temperature rise in

active region. The temperature raise in active region of the flare LD was estimated as 20 K with current of 45 A. This value was estimated from the measured $d\lambda/dT$ value of 54 nm/K, where λ and T represent wavelength and temperature, respectively.

The lateral far-field profiles from the 100 μm wide facet at two different current levels are shown in Fig.3. A narrow and single lobe far field pattern of 3° and 4° are observed at peak current of 20 A and 40 A, respectively. The far field divergence is sufficiently narrow in comparison with that (22°) of the 100 μm -wide broad area LDs. The perpendicular far field divergence is measured to be 45° , which is dependent on QW and SCH structure. The measured lateral far-field is broader than the diffraction limited angle of 1.4° , assuming a 100 μm -wide ridge waveguide aperture. It may be caused by the nonuniform carrier distribution with spacial hole burning as the current is increased. The diffraction limited beam will be obtained by modifying the narrow ridge waveguide section.

Figure 4 shows output power from the front facet against that from the rear facet for the flared LD with both facets as cleaved. The output power ratio, of rear to front facets, is more than 0.9 up to high current levels. In flared LDs that have large different spot widths, a factor of two difference of output power from the different facets has been reported [6]. Our results, however, show that it is possible to reduce this difference by introducing a high mesa structure into the outside the ridge waveguide to prevent unwanted reflections and radiations.

Conclusions

We fabricated high power and narrow far-field angle, 1.5 μm -eye-safe pulsed lasers with a flared ridge waveguide. High power (9.6 W), with narrow lateral far field divergence ($3\text{-}4^\circ$), have been obtained. These devices will be applicable for free-space optical measurement systems as "eye-safe" light sources. Additionally, by decreasing a perpendicular far field divergence, it is easy to collimate the output beam. Such LDs will further attractive for optical range finder, laser radar and so on.

Acknowledgment

The authors would like to acknowledge K. Kobayashi and I. Mito for encouragement, and also

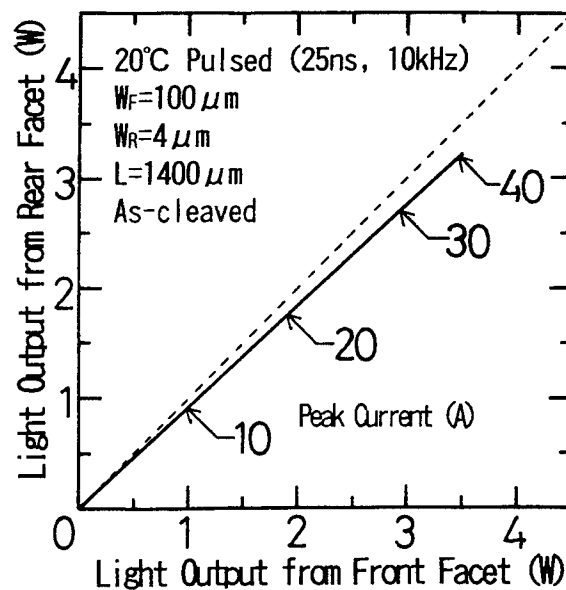


Fig.4 Output power from the front facet against that from the rear facet for flared LD with as cleaved facets.

acknowledge Y. Sasaki for discussions and technical support.

References

- [1] Goldgerg, D. Mehuys, and D. C. Hall, "3.3 W CW diffraction limited broad area semiconductor amplifier," *Electron. Lett.*, vol. 28, pp. 1082-1184, 1992.
- [2] D. F. Welch, R. Parke, D. Mehuys, A. Hardy, R. Lang, S. O'Brien, and S. Scifres, "1.1 W CW, diffraction-limited flared-amplifier master oscillator power amplifier," *Electron. Lett.*, vol. 28, pp. 2011-2013, 1992.
- [3] S. O'Brien, D. Mehuys, D. F. Welch, R. Parke, R. J. Lang, and D. Scifres, "High-power diffraction-limited monolithic broad area master oscillator power amplifier," *IEEE Photon. Technol. Lett.*, vol. 5, pp. 526-528, 1993.
- [4] Botez, M. Jansen, C. Zmudzinski, L. J. Mawst, P. Hayashida, and C. Tu, "Flat-phasefront fanout-type power amplifier employing resonant-optical-waveguide structures," *Appl. Phys. Lett.*, vol. 63, pp. 3113-3115, 1993.
- [5] F. Welch, P. S. Cross, D. R. Scifres, W. Streifer and R. D. Burnham, "High power, AlGaAs buried heterostructure lasers with flared waveguides," *Appl. Phys. Lett.*, vol. 50, pp. 233-235, 1987.
- [6] Shighihara, T. Aoyagi, S. Hinata, Y. Nagai, Y. Mihashi, Y. Seiwa, K. Ikeda and W. Susaki,

- "High-power and fundamental-mode oscillating flared SBA lasers," *Electron. Lett.*, vol. 24, pp. 1182-1183, 1988.
- [7] S. Kintzer, J. N. Walpole, S. R. Chinn, C. A. Wang and L. J. Missaggia, "High-power, strained-layer amplifiers and lasers with tapers gain regions," *IEEE Photon. Technol. Lett.*, vol. 5, pp. 605-608, 1993.
- [8] K. Choi, J. N. Walpole, G. W. Turner, S. J. Eglash, L. J. Missaggia and M. K. Connors, "GaInAsSb-AlGaAsSb tapered lasers emitting at 2 μm ," *IEEE Photon. Technol. Lett.*, vol. 5, pp. 1117-1119, 1993.
- [9] Streifer and E. Kapon, "Application of the equivalent-index method to DH diode lasers," *Appl. Opt.*, vol. 18, pp. 3274-3275, 1979.
- [10] Baets and P. E. Lagasse, "Calculation of radiation loss in integrated-optic tapers and Y-junctions," *Appl. Opt.*, vol. 21, pp. 1972-1978.

High speed, high gain InP-based heterostructure FETs with high breakdown voltage and low leakage

W. Prost, F.J. Tegude

Gerhard-Mercator-University Duisburg, Sonderforschungsbereich SFB 254, Solid-State-Electronics Department
Kommandantenstr. 60, D-47057 Duisburg, Germany, FAX xx49-203-379-3400

Introduction

InAlAs/InGaAs heterostructure field-effect transistors (HFET) on InP-substrates are the best high frequency solid-state three terminal devices available today. Ultra-short gate-length devices [1] exhibit ultra-high speed and low noise but due other performance lacks like high output conductance, gate leakage, and low breakdown voltage they are not suitable for a lot of applications. Moreover, some of these disadvantages are strongly correlated to material properties and quality. Therefore a physical understanding of the underlying mechanism is essential in order to improve device performance by proper design and technology. The knowledge about the reasons of high output conductance [2], high leakage [3-10] and low breakdown voltage [11-13] has been advanced recently, resulting in impressive improvements. In this contribution key issues of this development are addressed and state of the art InAlAs/InGaAs HFET devices are presented. Medium gate-length devices ($L_g = 0.5 \dots 0.8 \mu\text{m}$) combine high gain ($f_{\text{GU}=1} \geq 180 \text{ GHz}$ at $V_{\text{DS}} \geq 5 \text{ V}$), high on-state breakdown voltage and high power driving capability ($V_{\text{DS,max}} \geq 15 \text{ V}$, $I_{\text{D}} \geq 300 \text{ mA/mm}$, $P_{\text{DC}} \cong 4 - 5 \text{ W/mm}$), and low leakage ($I_{\text{G,max}} < 50 \mu\text{A/mm}$ at $V_{\text{DS}} = 3 \text{ V}$) regardless of the chosen growth technique MBE or MOVPE.

1. Leakage and breakdown mechanism

In this section the consequences of InAlAs/InGaAs material drawbacks and HFET design for gate-leakage, output-conductance and breakdown behaviour are discussed. Much attention has been paid to the effect of impact-ionization in the smaller band gap InGaAs channel material [3-6, 8-10]. In fig. 1 the basic layer sequence and contact configuration of an InAlAs/InGaAs HFET is shown. In addition the band diagram of a biased device is sketched both in vertical direction from the gate to the channel and in lateral direction from the source to the drain. Using this diagram the basic contributions to the gate leakage current (cf. fig. 2) can be illustrated. Electrons dominate the gate leakage current in the off-state mode ($V_{\text{GS}} \cong V_{\text{T}}$) due to tunneling through the InAlAs Schottky barrier [13]. As can be seen in fig. 1a the barrier width is extremely small at the drain-end of the gate and becomes even smaller with increasing gate-drain voltage and with higher doping concentration in the InAlAs-carrier supplying layer. Hence both effects result in a higher gate leakage. In the on-state mode ($V_{\text{GS}} > V_{\text{T}}$) three contributions can be separated. Firstly, at negative gate bias holes can be very effectively collected by the gate and result in an excess gate leakage. As shown in fig. 1a these holes are generated in the small band gap InGaAs channel material by impact-ionization at the drain-end of the channel. Photo-current measurements [6] revealed that most of these holes travel to the source and increase the output conductance. Some of them are able to overcome the hole barrier build from the valence band discontinuity at the channel/spacer interface where the barrier is relatively thin (cf. fig. 1a) [5]. The contribution of holes to the gate leakage (cf. fig.2) has opposite dependencies in V_{GS} . At constant drain bias the impact-ionization rate follows I_{D} and hence $+V_{\text{GS}}$ whereas the transfer probability of holes follows $+V_{\text{DG}}$ and hence $-V_{\text{GS}}$ resulting in the typical input

characteristic shown in fig. 2. Secondly, at very high drain bias ($V_{\text{DS}} > 4 \text{ V}$) a second negative excess gate leakage

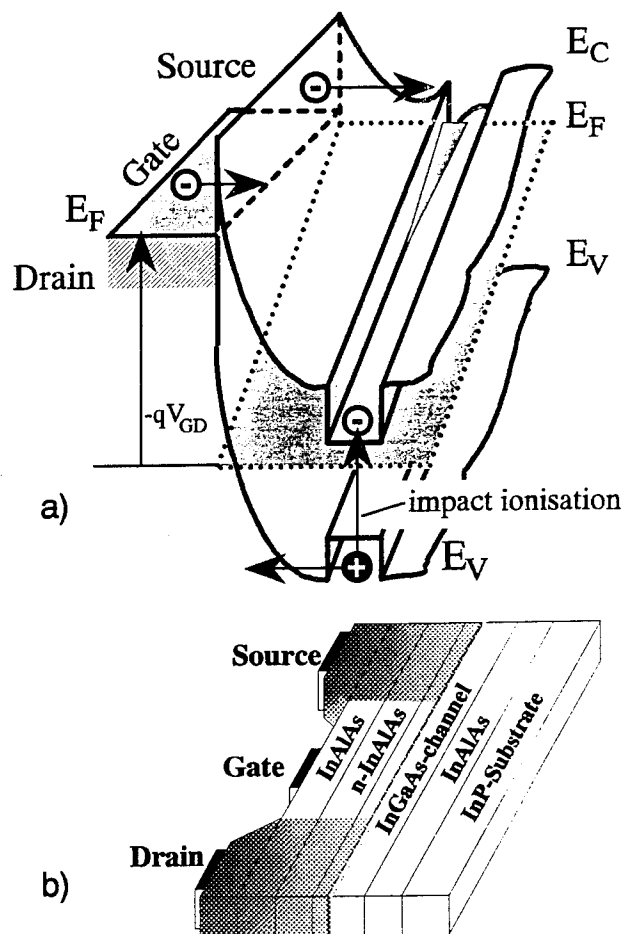


Fig. 1: (a) Schematic band-diagram of a biased InAlAs/InGaAs HFET as a function of lateral and vertical dimensions and (b) basic layer sequence.

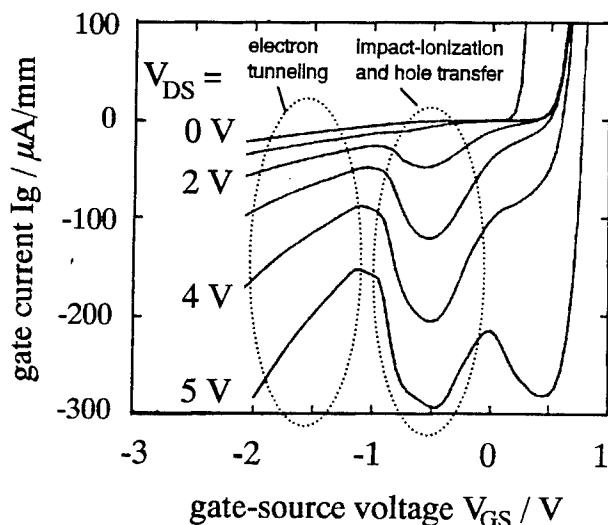


Fig. 2: Gate-leakage current of an InAlAs/InGaAs HFET ($V_T = -1.4$ V) as a function of gate- and drain-bias exhibiting an excess negative gate leakage current.

occurs around $V_{GS} \approx 0.3$ V which origin is not clear yet. Thirdly at very positive gate bias the electron tunneling of the forward biased gate-source diode becomes dominant. The degrading influences on the output conductance of short-channel effects [1] and of high conductivity in the buffer or at the buffer/substrate-interface (cf. 2.1 MBE Approach) can be eliminated by material growth [12,16,17] and device design. Then the influence of impact-ionization is dominant. A further reduction of output conductance requires a lower impact-ionization rate and hence a reduction of the electric field at the drain-end of the device which goes along with a drastical increase of the gate-drain diode breakdown voltage. The reduction of the electric field at the drain-end of the device is mainly provided by a laterally extended gate-recess etch process (cf. 2.3 Device Technology) and is the key step for low leakage, low output conductance and high breakdown. The gate-length itself has a minor influence on the breakdown voltage and a shorter gate-length may improve the speed. However, the design parameters for ultra high speed operation like a very high doping concentration allowing a narrow distance between gate and channel drastically reduce the breakdown voltage to typically less than 3 V.

2. Material Growth and Device Fabrication

The development of the InAlAs/InGaAs HFET was initiated using the molecular beam epitaxy (MBE) [e.g. 3]. But, due to the easier feasibility to perform the growth start on the InP-substrate under phosphorous stabilization the metal-organic vapor phase epitaxy (MOVPE) is very attractive. In the authors group both techniques have been used resulting in a very stimulating discussion and competition. However, two independent approaches are necessary in order to benefit from the individual advantages of both methods.

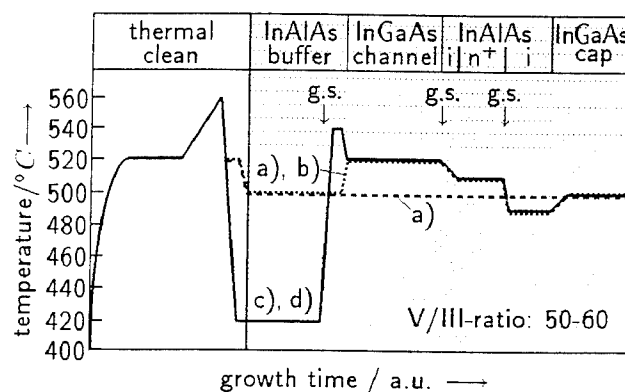


Fig. 3: Wafer temperature T_g during MBE growth of InGaAs/InAlAs HFET with different buffer configurations

2.1 MBE Approach: Among the solid source MBE growth parameters we found that (i) the growth start on InP-substrate and (ii) the buffer optimization has the strongest influences on breakdown. Prior to growth on the "ready for use" s.i. InP:Fe substrates a thermal cleaning cycle is carried out according to fig. 3. We observed that the temperature for oxide desorption varies from batch to batch and has to be adjusted individually. A detailed investigation of the temperature cycle during growth is reported in [12]. We found that the growth of the InAlAs-buffer at reduced temperatures (sample c,d in fig. 4 at $T_g = 420$ °C) resulted in strongly increased on-state breakdown voltage of more than 14 V up to $I_D \approx 300$ mA/mm. After low-temperature growth a growth stop and a temperature spike is necessary to maintain the low field channel mobility above 11.500 cm²/Vs which is a state of the art mobility for lattice matched InGaAs.

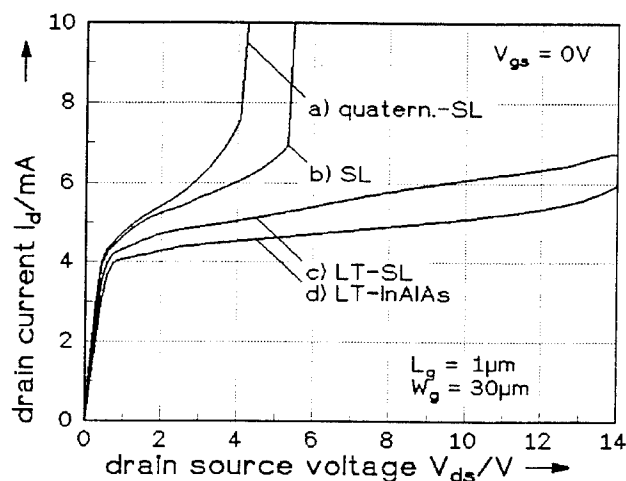


Fig. 4: Output characteristic at $V_{GS} = 0$ V for HFET with different buffer configurations: (a) quaternary InGaAs/InAlAs SL, (b) InGaAs/InAlAs SL, (c) like b but grown at reduced temperature of $T_g = 420$ °C, (d) 114 nm InAlAs grown at reduced temperature of $T_g = 420$ °C.

2.2 MOVPE Approach: Phosphorous containing semiconductors are much easier to grow with a metal-organic vapor phase epitaxy (MOVPE) and are hence a strong motivation for the use of this system for InP-based HFET. MOVPE grown Al-containing semiconductors, however, require additionally efforts in order to avoid drawbacks due to a higher background concentration. InAlAs particularly suffers from a high oxygen load [16]. High quality InAlAs can be provided by means of purification of the hydrides [e.g. 17] and using optimized growth parameters [16]. Recently a novel concept has been developed which totally avoids InAlAs [15]. In order to obtain high voltage and low leakage operation the potential of $\text{Ga}_{0.5}\text{In}_{0.5}\text{P}$ spacer [11] and Schottky barrier [11,18] has been evaluated. The motivation of this work is illustrated in fig. 5. The thin and highly strained $\text{Ga}_{0.5}\text{In}_{0.5}\text{P}$ layers increases the Schottky barrier height and as a spacer the valence band discontinuity. The $\text{Ga}_{0.5}\text{In}_{0.5}\text{P}$ spacer acts successfully on the suppression of hole-tunneling to the gate. Moreover a high etchant selectivity can be used for the

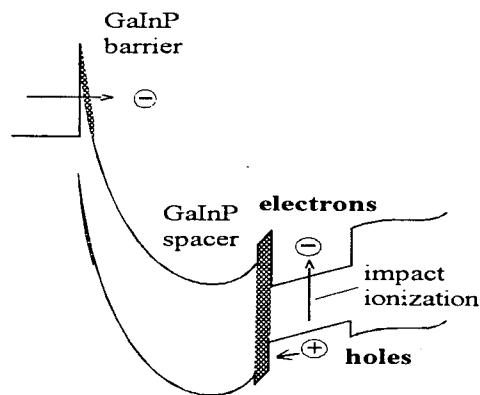


Fig. 5: Schematic band-diagram of an InAlAs/InGaAs HFET with a GaInP spacer and barrier layer, respectively.

lateral extended gate-recess. Experimentally an improved output conductance and breakdown voltage has been demonstrated [11].

2.3 Device technology: High voltage and low leakage HFET require a couple of technological steps which have been elaborated in recent years. The mesa-sidewall leakage has to be reduced after mesa etching using a selective etchant [7]. Ohmic contacts are evaporated using Ge/Pt/Au [11] on MOVPE layers whereas on MBE layers Ge/Ni/Au can also be used. The drain-gate spacing should exceed $L_{DG} \geq 1.5 \mu\text{m}$ if a breakdown voltage in excess of $V_{DG} \geq 10 \text{ V}$ is intended. A lateral etching of the InGaAs cap layer using e.g. a highly selective succinic etchant (selectivity of 70) is necessary to improve the gate-drain breakdown voltage above 10 V. A lateral etch of 350 nm improves the gate-drain breakdown to $V_{DG,Br} (I_{DG} = 10 \text{ mA/mm}) \geq 20 \text{ V}$. A gate length of $L_G = 0.5 - 0.8 \mu\text{m}$ is defined by optical lithography and Ti/Pt/Au is used for the gate-metallization.

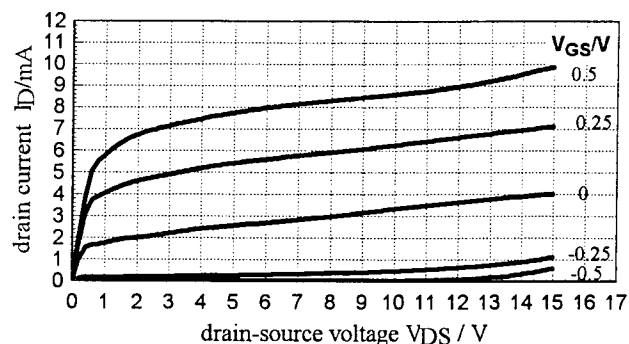


Fig. 6: Output characteristics of an InAlAs/InGaAs MOVPE grown HFET ($L_G = 1 \mu\text{m}$, $L_w = 30 \mu\text{m}$).

3 Device Characteristics and Discussion

The DC output characteristics of a lattice matched InAlAs/InGaAs MOVPE grown HFET ($L_g = 0.7 \mu\text{m}$) with a laterally extended gate-recess are plotted in fig. 6. Typically a 2DEG density of $n_s = 2.5 - 3 \cdot 10^{12} \text{ cm}^{-2}$ is used resulting in a drain-current of $I_{D,max} \geq 300 \text{ mA/mm}$. A broad transconductance profile with $g_{m,max} \geq 400 \text{ mS/mm}$ and a high breakdown voltage of 15 V are provided. Higher current levels up to 1 A/mm are possible but result in a lower breakdown voltage whereas higher breakdown voltages up to 30 V are attainable at lower current levels. Experimentally we observe an upper limit of the current voltage product of $P_{DC} \cong 4.5 \text{ W/mm}$.

RF-measurements were performed on various samples especially at high drain voltages. We generally observe a reduction of the current gain cut-off frequency at higher drain bias due to an extended drain delay time. From $V_{DS} = 2 \text{ V}$ to 8 V typically a reduction from about 40 GHz to 30 GHz ($L_G \cong 0.7 \mu\text{m}$, lattice matched InGaAs-channel) is observed. On the other hand under the same conditions the extended space-charge region at the drain end of the device

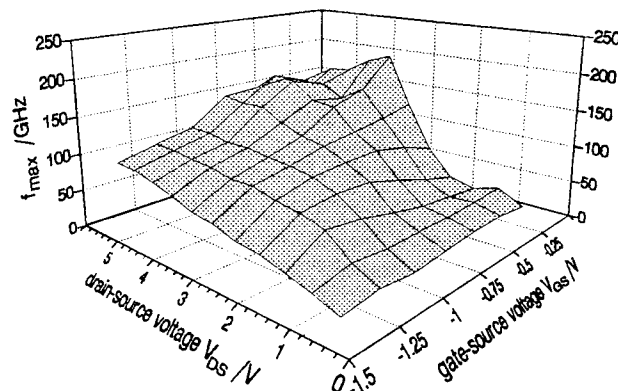


Fig. 7: Evolution of unilateral cut-off frequency $f_{GU=1}$ of a HFET with $L_G = 0.7 \mu\text{m}$ as a function of drain and gate bias

reduces the gate-drain capacitance C_{gd} from 120 fF/mm down to 70 fF/mm and hence increases impressively the gain of the device (cf. fig. 7). We have measured at high drain bias a maximum stable gain ≥ 12 dB at $f = 40$ GHz and a maximum available gain cut-off frequency of typically more than 100 GHz. A low leakage current improves the noise up to about 10 GHz [10]. The influence of the laterally extended gate-recess and the accordingly reduced f_T on the noise behaviour is under investigation. In high power operation the noise of the device is in any case dominated by the high drain current.

4. Conclusions

Most of the physical mechanism determining breakdown, gate leakage, and output conductance of InAlAs/InGaAs HFET have been identified. This understanding led to an impressive improvement with respect to breakdown and power performance of these high frequency devices. MBE as well as MOVPE grown structures have demonstrated that InGaAs FET-channels are suitable for corresponding applications and a replacement by a higher bandgap material is not necessary up to $P_{DC} \cong 4.5$ W/mm. A careful design of layer stacks in terms of buffer, spacer and barrier layers as well as of device layout, i.e. gate-drain distance, gate-recess process makes available the superior transport properties of the InGaAs material for high speed, high gain, and yet high breakdown and power devices.

Acknowledgements: This work was funded by the Deutsche Forschungsgemeinschaft. Cooperation with research groups from Deutsche Telekom, Daimler-Benz, and Alcatel-SEL are gratefully acknowledged. The authors are indebted to U.Auer, W.Brockhoff, F.Buchali, P.Ellrodt, C.Heedt, R.Reuter, F.Scheffer and further colleagues for their excellent contributions to this work.

Literature

[1] L.D.Nguyen, A.S.Brown, M.A.Thompson, L.M.Jelloian, "50-nm Self-Aligned-Gate Pseudomorphic AlInAs/GaInAs High electron Mobility Transistors," IEEE Trans. Electron Devices, vol. 39, no. 9, p. 2007, 1992.
 [2] G.G.Zhou, A.Fischer-Colbrie, J.Miller, Y.C.Pao, B.Hughes, L.Studebaker, J.S.Harris, "High Output conductance of InAlAs/InGaAs/InP MODFET due to Weak Impact-ionization in the InGaAs Channel," Proc. IEDM pp.274, 1991.
 [3] H.Itoh, A.S.Brown, L.H.Camnitz, G.W.Wicks, J.D.Berry, L.F.Eastman, "Depletion- and Enhancement-mode field-effect-transistors with a recessed gate structure," Inst. Phys. Conf. Ser. 79, p.571, 1986.
 [4] D.J.Newson, R.P.Merrett, B.K.Ridley, "Control of gate leakage in InAlAs/InGaAs HEMT's," Electronic Lett., no.27, p.1592, 1991.

[5] F.Buchali, C.Heedt, W.Prost, I.Gyuro, H.Meschede, F.J.Tegude, "Analysis of gate leakage on MOVPE grown InAlAs/InGaAs-HFET," Microelectronic Engineering 19 (1992) 401-404.
 [6] C.Heedt, F.Buchali, W.Prost, F.J.Tegude, D.Fritzsche, H.Nickel, "Characterization of Impact-Ionization in InAlAs/InGaAs/InP HEMT Structures using a novel Photocurrent-Measurement Technique," Proc. 5th InP & Rel. Mat. Conf., pp.243, 1993.
 [7] S.R.Bahl, J.A.delAlamo, "Elimination of Mesa-Sidewall Gate Leakage in InAlAs/InGaAs Heterostructures by Selective Sidewall Recessing," IEEE Electron Device Letters, vol. 13, no. 4, 1992.
 [8] A.A.Moolji, S.R.Bahl, J.A.delAlamo, "Impact-ionization in InAlAs/InGaAs HFET's," IEEE Electron Device Lett., vol. 15, no. 8, p. 313, 1994.
 [9] C.Heedt, F.Buchali, W.Prost, W.Brockhoff, D.Fritzsche, H.Nickel, R.Lösch, W.Schlapp, F.J.Tegude, "Drastical Reduction of Gate Leakage in InAlAs/InGaAs HEMT's using a Pseudomorphic InAlAs Hole Barrier Layer," IEEE Trans. Electron Devices, vol. 41, no.10, pp.1685-1691, 1994.
 [10] R.Reuter, S.vanWaasen, F.J.Tegude, "A New Noise Model of HFET with special emphasis on Gate leakage," IEEE Electron Device Lett., vol. 16, no. 2, 1995.
 [11] F.Scheffer, C.Heedt, R.Reuter, A.Lindner, Q.Liu, W.Prost, F.J.Tegude, "High breakdown voltage InGaAs/InAlAs HFET using $\text{In}_{0.5}\text{Ga}_{0.5}\text{P}$ spacer layer," Electronics Letters, 30(2), 169 (1994).
 [12] U.Auer, R.Reuter, C.Heedt, H.Künzel, W.Prost, F.J.Tegude, "InAlAs/InGaAs HFET with extremely High Device Breakdown Using an Optimized Buffer Layer Structure," Proc. 6th InP & Rel. Mat. Conf., pp.443, 1994.
 [13] S.R.Bahl, W.J.Azzam, J.A.delAlamo, J.Dickmann, S.Schildberg, "Off-State Breakdown in InAlAs/InGaAs MODFET's," IEEE Trans. Electron Devices, vol. 42, no. 1, p. 15, 1995.
 [14] P.Ellrodt, W.Brockhoff, C.Heedt, F.J.Tegude, "Numerical Investigations of Leakage Current of Schottky Contacts on InAlAs/InGaAs/InP heterostructures," Proc. 23rd ESSDERC. Grenoble, Sept. 1993.
 [15] A.MesquidaKüsters, A.Kohl, S.Brittner, Th.Funke, V.Sommer, K.Heime, "A New Al-free HFET-structure: the pseudomorphic p-InP/n-InP/ $\text{In}_{0.75}\text{Ga}_{0.25}\text{As}$ double heterojunction δ -doped HEMT," Proc. 5th IPRM, p. 473, 1993.
 [16] F.Buchali, F.Scheffer, C.Heedt, I.Gyuro, P.Speier, W.Prost, F.J.Tegude, "Evidence of oxygen in undoped InAlAs MOVPE layers," Proc. 4th IPRM, p. 534, 1992.
 [17] N.Pan, J.Elliott, H.Hendricks, L.Aucoin, P.Fay, I.Adesida, "InAlAs/InGaAs high electron mobility transistors on low temperature InAlAs buffer layers by metalorganic chemical vapor deposition," Appl. Phys. Lett., 66(2), 212 (1995).
 [18] S.Loualiche, A.Ginudi, A.LeCorre, D.Lecrosnier, C.Vaudry, L.Henry, C.Guillemot, "Pseudomorphic GaInP Schottky diode and high electron mobility transistor on InP," Appl. Phys. Lett. 55 (20), 2099 (1989).

High Electron Mobility 18,300 $\text{cm}^2/\text{V}\cdot\text{s}$ InAlAs/InGaAs Pseudomorphic Structure by Channel Indium Composition Modulation

T. Nakayama, H. Miyamoto, E. Oishi and N. Samoto
Kansai Electronics Research Laboratories, NEC Corporation
2-9-1 Seiran, Otsu, Shiga 520, Japan

Introduction

InP-based InAlAs/InGaAs heterojunction field effect transistor (HJFET) structures have advantages for use in low noise and high power devices because of their high electron mobility and high sheet carrier density(1). While device performance has been enhanced by increasing the In-content in InGaAs channels(2,3,4,5), increasing In-content above 53% has been reported to decrease the critical thickness of such channel layers(6,7). Decreasing the channel thickness below 10nm leads to degradation of the electron confinement in the channel. Therefore, until now no further enhancement of electron mobility has been obtained with subsequent increases in In-content beyond 80%. In our current study, we have successfully managed to improve electron confinement using a thick, high In-content channel indium composition modulated structure. Using this structure, the highest electron mobility at room temperature yet reported for an InP-based pseudomorphic structure, 18,300 $\text{cm}^2/\text{V}\cdot\text{s}$, has been obtained.

Channel Indium Composition Modulated structure

The Channel Indium Composition Modulated structure contains $\text{In}_{0.53}\text{Ga}_{0.47}\text{As}(1\text{nm})/\text{In}_{0.8}\text{Ga}_{0.2}\text{As}(2\text{nm})/\text{InAs}(4\text{nm})/\text{In}_{0.8}\text{Ga}_{0.2}\text{As}(4\text{nm})/\text{In}_{0.53}\text{Ga}_{0.47}\text{As}(9\text{nm})$ layers as a channel (Fig 1). In this structure, the upper $\text{In}_{0.8}\text{Ga}_{0.2}\text{As}$ (2 nm) layer is inserted to form smooth $\text{In}_{0.53}\text{Ga}_{0.47}\text{As}/\text{In}_{0.8}\text{Ga}_{0.2}\text{As}/\text{InAs}$ heterointerfaces. The lower $\text{In}_{0.8}\text{Ga}_{0.2}\text{As}$ (4 nm) layer is inserted to increase the total high In-content channel thickness up to 10 nm, which is sufficient to obtain high electron confinement. The insertion of these $\text{In}_{0.8}\text{Ga}_{0.2}\text{As}$ layers is based on the experimental results which are described in the "Critical thickness of InAs layer" section. Using this structure, we have successfully increased the thickness of a high In-content channel (including a 4 nm InAs layer) in an FET structure. This thick high In-content channel increases the carrier confinement, which leads to enhancement of electron mobility.

Experiment

Critical thickness of InAs layer

We have based our channel design on a series of growth experiments. In the first experiments, we determined the thickness up to which smooth surfaces can be obtained in InAs growth with molecular beam epitaxy (MBE) under various arsenic (As_4) pressure levels. In subsequent experiments, we determined the maximum thickness of an InAs layer upon which it was possible to form a smooth $\text{In}_{0.53}\text{Ga}_{0.47}\text{As}$ surface with MBE. In both cases, surface morphology was observed during MBE growth by reflection high energy electron diffraction (RHEED).

Growth of Channel Indium Composition Modulated structure

The Channel Indium Composition Modulated structure (Fig.1) was grown on InP(001) semi-insulating substrate by conventional solid source Molecular Beam Epitaxy (MBE). The growth sequence was as follows : (1) a 200 nm $\text{In}_{0.52}\text{Al}_{0.48}\text{As}$ buffer and a 9 nm $\text{In}_{0.53}\text{Ga}_{0.47}\text{As}$ subchannel were grown at 500°C. (2) The substrate temperature was then decreased to 440°C under an As_4 background pressure. (3) 4 nm $\text{In}_{0.8}\text{Ga}_{0.2}\text{As}$, 4 nm InAs, 2 nm $\text{In}_{0.8}\text{Ga}_{0.2}\text{As}$ and 1 nm $\text{In}_{0.53}\text{Ga}_{0.47}\text{As}$ channel layers were grown at 440°C. (4) The substrate temperature was increased to 520°C under As_4 background pressure. (5) A 4 nm $\text{In}_{0.52}\text{Al}_{0.48}\text{As}$

$\text{In}_{0.52}\text{Al}_{0.48}\text{As}$	20nm	Channel layers
$\text{In}_{0.52}\text{Al}_{0.48}\text{As}$ $\text{Si } 3 \times 10^{18} \text{ cm}^{-3}$	20nm	
$\text{In}_{0.52}\text{Al}_{0.48}\text{As}$	4nm	
$\text{In}_{0.53}\text{Ga}_{0.47}\text{As}$	1nm	
$\text{In}_{0.8}\text{Ga}_{0.2}\text{As}$	2nm	
InAs	4nm	
$\text{In}_{0.8}\text{Ga}_{0.2}\text{As}$	4nm	
$\text{In}_{0.53}\text{Ga}_{0.47}\text{As}$	9nm	
$\text{In}_{0.52}\text{Al}_{0.48}\text{As}$	200nm	
InP sub.		

Fig.1 Our new structure including $\text{In}_{0.8}\text{Ga}_{0.2}\text{As}/\text{InAs}/\text{In}_{0.8}\text{Ga}_{0.2}\text{As}$ high In-content layers

The streaks indicate a smooth surface. Although 4 nm had previously been reported to be the critical thickness for a strained InAs layer, RHEED observations of this structure have confirmed a smooth and unrelaxed surface after MBE growth to a 10 nm thickness of high In-content layers including a 4 nm InAs layer.

Carrier confinement and electron mobility

The electron density distribution in the high indium composition layers in each InGaAs channel was calculated by solving Schrödinger's equation self-consistently with Poisson's equation. For our calculation, we chose band gaps of 0.41 eV (InAs), 0.54 eV ($\text{In}_{0.8}\text{Ga}_{0.2}\text{As}$), 0.74 eV ($\text{In}_{0.53}\text{Ga}_{0.47}\text{As}$) and 1.44 eV ($\text{In}_{0.52}\text{Al}_{0.48}\text{As}$), adjusted taking the strain effect into consideration. Conduction band discontinuities were assumed to be 65 % of their corresponding bandgap discontinuities. The electron effective mass in the InGaAs channel was set at $0.041m_{e0}$, where m_{e0} is the free electron mass.

Figure 3 shows profiles of conduction band energy and electron density around the high In-content layers in our structure (a) and two conventional structures (b,c). In our structure, electron density in the InAs layer is above 50 %, and in the high In-content layers in the channel it is above 90 %. By way of contrast, electron confinement in the conventional $\text{In}_{0.53}\text{Ga}_{0.47}\text{As}(4\text{nm})/\text{In}_{0.8}\text{Ga}_{0.2}\text{As}(10\text{nm})/\text{In}_{0.53}\text{Ga}_{0.47}\text{As}(6\text{nm})$ structure was about 70 %, and about 60 % in the conventional $\text{In}_{0.53}\text{Ga}_{0.47}\text{As}(4\text{nm})/\text{InAs}(4\text{nm})/\text{In}_{0.53}\text{Ga}_{0.47}\text{As}(12\text{nm})$ structure. This superior electron confinement in the high In-content channel of our structure contributes to the enhancement of electron mobility.

In our new $\text{In}_{0.8}\text{Ga}_{0.2}\text{As}(2\text{nm})/\text{InAs}(4\text{nm})/\text{In}_{0.8}\text{Ga}_{0.2}\text{As}(4\text{nm})$ structure, room temperature electron mobility was $18,300 \text{ cm}^2/\text{Vs}$ roughly 14 % higher than that in either of the conventional structures (Table 1).

High Indium composition layers	Mobility ($\text{cm}^2/\text{V}\cdot\text{s}$)	Sheet carrier density (cm^{-2})	Carrier confinement
$\text{In}_{0.8}\text{Ga}_{0.2}\text{As}/\text{InAs}/\text{In}_{0.8}\text{Ga}_{0.2}\text{As}$ (our new structure)	18,300	1.9×10^{12}	92%
$\text{In}_{0.8}\text{Ga}_{0.2}\text{As}$ (conventional structure)	16,200	1.6×10^{12}	74%
InAs (conventional structure)	16,000	1.9×10^{12}	61%

Table 1 Electron mobility and sheet carrier density in our new structure and conventional structures

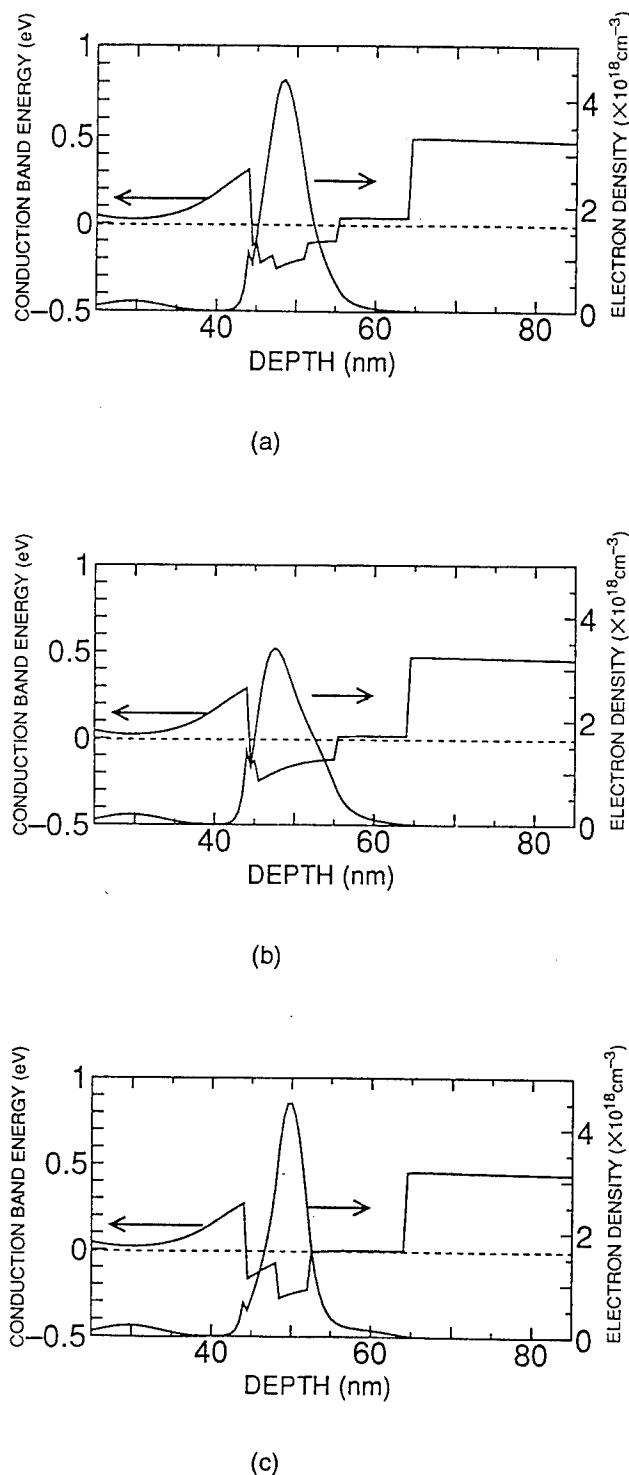


Fig.3 Conduction band structures and electron density profiles around high In-content layers (a) our structure (b) conventional structure with $\text{In}_{0.8}\text{Ga}_{0.2}\text{As}(10\text{nm})$ (c) conventional structure with InAs(4nm)

spacer, a 20 nm $\text{In}_{0.52}\text{Al}_{0.48}\text{As}$ donor containing layer and a 20 nm $\text{In}_{0.52}\text{Al}_{0.48}\text{As}$ undoped layer were grown at 520°C. Steps (2) and (4) are growth interruption steps for changing the substrate temperature.

Carrier confinement and electron mobility

We compared carrier confinement and electron mobility in our new structure with these in two conventional structures. In one, the InGaAs channel included an $\text{In}_{0.8}\text{Ga}_{0.2}\text{As}$ (10 nm) layer. In the other, the InGaAs channel included an InAs (4 nm) layer. The thicknesses of these layers were determined by calculations and electron mobility measurements to be its critical limit (5,8). For our experiments, total InGaAs channel thickness in the two conventional structures was fixed at 20 nm, the same as in our new structure. The carrier confinement was calculated by solving Schrödinger's equation self-consistently with Poisson's equation and the electron mobility was measured by the van der Pauw method.

Results and discussions

Critical thickness of InAs layer

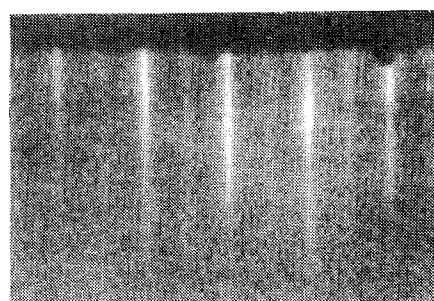
In the first experiments, a streak RHEED pattern was observed on the InAs layer during MBE growth up to a thickness of 8 nm at 440°C substrate temperature under As_4 pressure of 5×10^{-6} Torr (Fig.2(a)). Beyond 8 nm a spotty RHEED pattern appears, indicating that the limit for MBE growth of InAs with smooth surfaces is approximately 8 nm in thickness. This result indicates that an InAs layer accumulates high strain energy corresponding to its thickness of 8 nm, although 8 nm is twice the reported critical InAs layer thickness (4 nm)(5).

In our subsequent experiments, we observed that an $\text{In}_{0.53}\text{Ga}_{0.47}\text{As}$ layer formed on a 6 nm thick InAs layer produced a spotty RHEED pattern (Fig.2 (b)), even though the 6 nm thick InAs layer itself had produced a streak pattern. Our RHEED observations indicate that a rough surface was produced over the 6 nm InAs layer at the instant of heterointerface formation. $\text{In}_{0.53}\text{Ga}_{0.47}\text{As}$ growth on an InAs layer of 4 nm thickness, however, was smooth and produced a streak RHEED pattern. In our experiments, 4 nm was the thickness limit for InAs layers upon which it was possible to obtain smooth $\text{In}_{0.53}\text{Ga}_{0.47}\text{As}/\text{InAs}$ heterointerfaces.

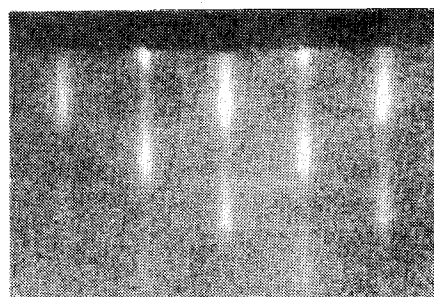
From these results, it appears that, although a smooth surface was formed by InAs growth on a 6 nm InAs layer, a rough surface was formed by $\text{In}_{0.53}\text{Ga}_{0.47}\text{As}$ growth on the layer. This difference indicates that heterointerface roughness may not be caused by high strain energy, but be caused by (1) a large interface free energy at the $\text{In}_{0.53}\text{Ga}_{0.47}\text{As}/\text{InAs}$ heterointerface, and (2) a large difference in surface free energy

between the $\text{In}_{0.53}\text{Ga}_{0.47}\text{As}$ layer and InAs layer(9). In order to counter these, we have inserted a $\text{In}_{0.8}\text{Ga}_{0.2}\text{As}$ layer into the heterointerface. This is because (1) the interface free energy at both the $\text{In}_{0.53}\text{Ga}_{0.47}\text{As}/\text{In}_{0.8}\text{Ga}_{0.2}\text{As}$ and $\text{In}_{0.8}\text{Ga}_{0.2}\text{As}/\text{InAs}$ heterointerfaces is less than that at the $\text{In}_{0.53}\text{Ga}_{0.47}\text{As}/\text{InAs}$ interface, and (2) the difference in surface free energy between the inserted layer and the InAs layer is less than the original difference in surface free energy between the $\text{In}_{0.53}\text{Ga}_{0.47}\text{As}$ layer and the InAs layer.

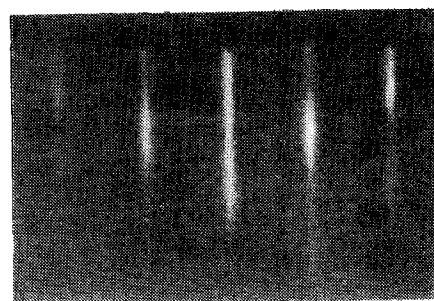
Figure 2(c) shows a RHEED pattern after the growth of $\text{In}_{0.8}\text{Ga}_{0.2}\text{As}(2\text{nm})/\text{InAs}(4\text{nm})/\text{In}_{0.8}\text{Ga}_{0.2}\text{As}(4\text{nm})$ layers.



(a)



(b)



(c)

Fig.2 RHEED pattern

- (a) after 6nm thick InAs layer grown
- (b) immediately formed heterointerface with $\text{In}_{0.53}\text{Ga}_{0.47}\text{As}$ layer on 6nm thick InAs layer
- (c) after $\text{In}_{0.8}\text{Ga}_{0.2}\text{As}/\text{InAs}/\text{In}_{0.8}\text{Ga}_{0.2}\text{As}$ grown

Conclusion

In conclusion, we have successfully obtained the highest electron mobility yet reported for an InAlAs/InGaAs heterostructure using an indium composition modulated channel. With this channel, we have successfully obtained a $\text{In}_{0.8}\text{Ga}_{0.2}\text{As}(2\text{nm})/\text{InAs}(4\text{nm})/\text{In}_{0.8}\text{Ga}_{0.2}\text{As}(4\text{nm})$ channel within InGaAs layers, with smooth $\text{In}_{0.52}\text{Al}_{0.48}\text{As}/\text{In}_{0.53}\text{Ga}_{0.47}\text{As}/\text{In}_{0.8}\text{Ga}_{0.2}\text{As}/\text{InAs}/\text{In}_{0.8}\text{Ga}_{0.2}\text{As}$ heterointerfaces. The thick, high In-content channel in our new structure produced superior electron confinement, contributing to the highest room temperature mobility yet reported for InP-based pseudomorphic InAlAs/InGaAs heterostructures.

Acknowledgements

We would like to thank K. Onda, A. Fujihara, Y. Ando and Dr. M. Kuzuhara for their valuable advice. We are also grateful to Dr. H. Abe for his important encouragement and support.

References

- (1) P.C. Chao, A.J. Tessmer, K.G. Duh, P. Ho, M. Kao, P.M. Smith, J.M. Ballingall, S.-M.J. Liu and A.A. Jabra, IEEE Electron Device Letters **11** 59 (1990)
- (2) L.D. Nguyen, S. Brown, M.A. Thompson, and L.M. Jelloian, IEEE Trans. Electron Devices **39** 2007 (1992)
- (3) R. Lai, P.K. Bhattacharya, D. Yang, T.L. Brock, S.A. Alterovitz, and A.N. Downey, IEEE Trns. Electron Device **39** 2206 (1992)
- (4) Y. Sugiyama, Y. takeuchi and M. tacano, J. Crystal Growth **115** 509 (1991)
- (5) T. Akazaki, K. Arai, T. Enoki and Y. Ishii, IEEE Trans. Electron Device Letters **11** 325 (1992)
- (6) J.W. Matthews and A.E. Blakeslee, J. Crystal Growth **27** 118 (1974)
- (7) R. People and J.C. Bean, Appl. Phys. Letters **47** 35 (1985)
- (8) T. Nakayama, H. Miyamoto, E. Oishi and N. Samoto, Workbook of the Eighth International Conference on Molecular Beam Epitaxy, (1994) pp.424-425
- (9) E. Tournié and K.H. Ploog, J. Crystal Growth **135** 97 (1994)

METAMORPHIC InAlAs/InGaAs HEMTs ON GaAs SUBSTRATES WITH COMPOSITE CHANNELS AND f_{\max} of 350GHz

FA2.3

M. Chertouk, H. HeiB, D. Xu, S. Kraus, W. Klein, G. Böhm, G. Tränkle and G. Weimann

Walter-Schottky-Institut, TU München, D-85748 Garching, Germany

INTRODUCTION

0.13 μ m T-gate metamorphic In_{0.32}Al_{0.68}As/In_{0.32}Ga_{0.68}As HEMTs grown on GaAs substrates were fabricated with composite InGaAs channels, combining the superior transport properties of In_{0.52}Ga_{0.48}As with low impact ionization in In_{0.32}Ga_{0.68}As. The use of composite InGaAs channels leads to excellent DC-characteristics, high drain currents of 750mA/mm, extrinsic transconductances of 600mS/mm combined with still very low output conductance values of 20mS/mm, thus giving g_m/g_o ratios of 30. A maximum frequency of oscillation f_{\max} of 350GHz with current gain cut-off frequency f_T of 150GHz has been obtained at $V_{DS}=1.5V$. These are the best microwave frequency results ever reported for any FET on GaAs substrates. Using theoretical as well as experimental support, we show that excess output conductance in 0.13 μ m lattice matched and metamorphic In_{0.52}Al_{0.48}As/In_{0.52}Ga_{0.48}As HEMTs is based on weak impact ionization in high gate-drain field region.

In_{0.52}Al_{0.48}As/In_{0.52}Ga_{0.48}As HEMTs lattice matched to InP are well suited for high speed and low-noise applications. Unfortunately, the high output conductance and low breakdown voltage remain as obstacles for optimum power performances. In order to overcome such undesirable characteristics, a double-recess gate process or undoped surface cap-layer was introduced to reduce the peak electrical field in the InGaAs channel near the drain. This in turn increases the breakdown voltage and reduces the output conductance [1,2]. 0.15 μ m InAlAs/InGaAs HEMTs have shown excellent high-frequency performance: f_{\max} of 405GHz with f_T of 130GHz have been obtained [1]. The f_{\max} was improved to record values of 455GHz using undoped InGaAs cap-layers [1]. On the other hand a record f_T of 340GHz has been demonstrated with a gate length of 50nm and 80% indium in the channel [3]. However, the associated f_{\max} was only 280GHz. Such results demonstrate the tradeoff between f_{\max}/f_T ratios and f_T values for sub-0.2 μ m lattice matched InAlAs/InGaAs HEMTs. In this paper, we report on novel 0.13 μ m metamorphic InAlAs/InGaAs HEMTs on GaAs substrate with composite InGaAs channels. This leads to a high power gain at higher saturation velocity regime, an f_{\max} of 350GHz and f_T of 150GHz. We demonstrate, with theoretical as well as experimental support, that this performance is due to the wider band gap of the sub-channel, which reduces the impact ionization in high gate-drain field, hence, the output conductance.

I. DEVICE STRUCTURES

Metamorphic InAlAs/InGaAs HEMTs layers (MM) were grown by MBE on GaAs substrates, using low-temperature grown linearly graded InAlAs buffer with an In composition from 0.03 to either 0.32, or 0.52, i.e. the composition corresponding to lattice matched material on InP. The MM-HEMT structure consists of a 250nm thick undoped InAlAs buffer embedded between two ten period superlattices, composite channels consisting of 12nm InGaAs channel layer with an In content of 0.52 on top of 20nm InGaAs with In-content of 0.32, a 2nm InAlAs spacer layer, a 12.5nm InAlAs supply layer doped to $10^{19}cm^{-3}$, a 10nm undoped InAlAs barrier layer and 5nm undoped cap-layers followed by 10nm doped InGaAs ($3 \cdot 10^{18}cm^{-3}$). MM-HEMTs with 32nm thick InGaAs channel and an In-content of 0.32 and 0.52 were also fabricated. Hall mobilities and 2DEG densities, measured at 300K, are

7268 cm²/Vs and $4.75 \cdot 10^{12} cm^{-2}$ for metamorphic composite channel and 6600 cm²/Vs and $4.2 \cdot 10^{12} cm^{-2}$ for MM-structures with an In-content of 0.32.

We have fabricated 0.13 μ m gate length InAlAs/InGaAs HEMTs using e-beam lithography and a selective gate recess etching, giving a lateral gate to recess edge separation of ~ 50nm.

II. DC AND RF CHARACTERISTICS

Metamorphic InGaAs/InAlAs HEMTs with reduced In-content have increased band gaps, leading to drastically lower impact ionization and improved carrier confinement due to higher conduction band discontinuities. 0.13 μ m metamorphic InAlAs/InGaAs HEMTs with an In-content of 0.32 in the channel, corresponding to the wider band gap of 1eV, show extremely low g_o values of 10 mS/mm. This leads

to a g_m/g_o -ratio of ~ 40 , and f_T and f_{max} values of 105 and 310GHz. On the other hand, metamorphic HEMTs with In-contents around 0.52, show high output conductances of 150mS/mm as HEMTs lattice matched to InP. This leads to g_m/g_o -ratio ~ 4.5 and f_T and f_{max} values of 185GHz and 220GHz [8].

Based on these results we have fabricated novel metamorphic HEMTs with composite InGaAs channels, combining the superior transport properties of $In_{0.52}Ga_{0.48}As$ with the low impact ionization in $In_{0.32}Ga_{0.68}As$. The electrons near the source flow in the narrow gap region, thus having high low field mobilities and high carrier densities; hot electrons near the drain flow in the wide band gap sub-channel unaffected by impact ionization.

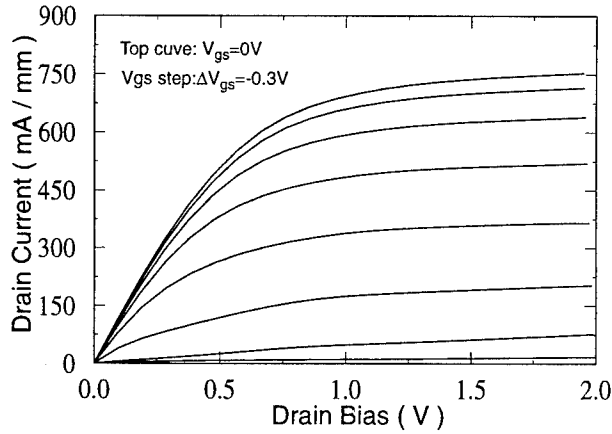


Fig.1: I-V characteristics of 0.13μm metamorphic InAlAs/InGaAs HEMTs with composite InGaAs channel.

The I-V-characteristics of a 0.13μm metamorphic HEMT with composite channel are shown in fig.1. The characteristics show no kink. The DC output conductance confirms the above, showing a value of 20mS/mm at $V_{DS}=2V$ in contrast to with 150mS/mm for lattice matched HEMTs. The composite channel MM-HEMTs have a maximum drain current of 750mA/mm, an extrinsic transconductance of 600mS/mm at $I_{DS}=320mA/mm$. Furthermore, the gate diode characteristics are excellent: a gate breakdown voltage of -7V has been measured at $I_{G-DS}=-1mA/mm$ and forward Schottky junction turn-on voltage of 0.8V. The S-parameters of 150μm-wide MM-HEMTs with composite channel were measured from 2-70GHz using on wafer probing. An f_T of 150GHz and a f_{max} of 350GHz has been obtained for a device with 0.13μm gate length and 150μm gate width, biased at maximum extrinsic transconductance ($V_{DS}=1.5V$, $V_{GS}=-1.25V$ and $I_{DS}=330mA/mm$). The f_{max} was extrapolated with -6dB/octave from the last measurement point of maximum available gain (MAG), where the measured stability factor $k>1$ as indicated in fig.2. Thus an f_{max}/f_T ratio of 2.33 has been obtained in combination with a $f_T I_g$ -product of

19.5GHz.μm, corresponding to an effective carrier velocity of $1.22 \cdot 10^7$ cm/s. Thus we demonstrate novel metamorphic HEMTs, which achieve high f_{max} in the high saturation velocity regime by introducing a wider band gap sub-channel, where the hot electrons can flow in high field drift region unaffected by impact ionization. It is worth noting that the record f_{max} of 350GHz with an f_T of 100GHz has been reported using double gate recess AlGaAs/InGaAs HEMTs [9]. Thus our results advance to the state of the art in terms of high frequency performances ($f_{max}-f_T$) for any FETs on GaAs substrate, furthermore, close to the record f_{max} of 405GHz with an f_T of 130GHz reported for lattice matched InAlAs/InGaAs HEMTs with doped cap-layer [1].

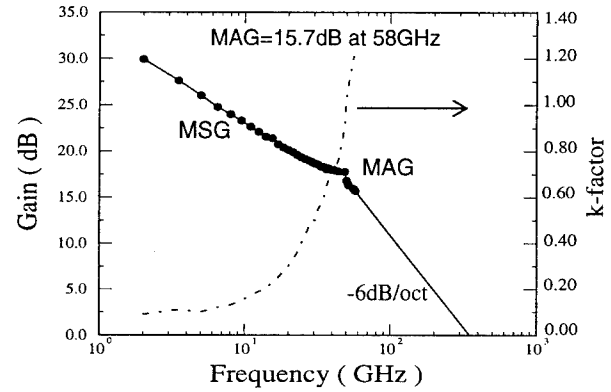


Fig.2: Power gain (MSG and MAG) against frequency for 0.13μm gate length MM-HEMTs with composite channels.

III. PHYSICAL MODEL OF THE OUTPUT CONDUCTANCE IN 0.13 μm InAlAs/InGaAs HEMTs

Here, we present a physical model to explain the excess output conductance in InAlAs/InGaAs HEMTs. Fig.3 shows a cross section of InAlAs/InGaAs HEMTs with the profile of the electrical field in the channel. The electrons are injected from the source side into the high gate-drain electrical field region, namely drift region, with effective length L_{Deff} . In this region impact ionization occurs and starts at $V_{DS}=V_{DS,sat}$. We suggest the following mechanism. Firstly, the electrons generated by the impact ionization flow to the drain and produce an excess drain current ΔI_D . Secondly, holes generated by impact ionization flow either to the gate, if their energy exceeds the valence band offset, or to the source. The output conductance due to weak impact ionization can be expressed as follows :

$$g_o(V_{DS}, V_{GS}) = \Delta I_{DS} / (V_{DS} - V_{DS,sat}) \quad (1)$$

We assume that the high-field region is divided into two parts: one just below the gate, and the other between the gate and drain edges, where the drain and gate biases act laterally. The two subregions are assumed to be completely depleted, and the depletion region can be approximated with a

rectangular shape. The excess drain current ΔI_{DS} due to ionization process can be written as [4]:

$$\Delta I_{DS}(V_{DS}, V_{GS}) = \alpha_n L_{Deff} I_D \quad (2)$$

where α_n is the impact ionization rate in the InGaAs channel. L_{Deff} is the effective length over which ionization occurs and I_D is drain-source saturation current without impact ionization. F. Osaka et al gave an analytical expression of the ionization coefficient α_n for InGaAs materials with Indium content of 0.53 [5]:

$$\alpha_n = 5.3 \cdot 10^7 \exp(-1.95 \cdot 10^8 / E_{max}) \text{ (cm}^{-1}\text{)} \quad (3)$$

The maximum electrical field E_{max} (V/m) in the drift region can also be expressed in a simple manner :

$$E_{max} = (V_{DS} - V_{DS,sat}) / L_{Deff} \quad (4)$$

where $V_{DS} - V_{DS,sat}$ is the voltage drop in the high field drift region. The length of the drift region can be described as a space charge layer; it is therefore proportional to the square root of the drift voltage drop [6]. We can write:

$$L_{Deff} = L_0 (V_{DS} - V_{DS,sat})^{1/2} \quad (5)$$

where L_0 is an adjustable parameter. The saturation drain voltage $V_{DS,sat}$ can be expressed as:

$$V_{DS,sat} = V_{DS} - (V_{GS} - V_{th})$$

where V_{th} is the threshold voltage, and V_{DS} , V_{GS} are intrinsic biases, given by :

$$V_{DS} = V_{DS}' - I_{DS} (R_s + R_d) \text{ and } V_{GS} = V_{GS}' - I_{DS} R_s$$

V_{DS}' and V_{GS}' are the voltage applied at the external G-S and D-S terminals of the device, and R_s , and R_d are the source and drain parasitic series resistances, respectively.

We use the Materka-Kacprzak model for drain current HEMT modelling [7]. The transfer characteristics is expressed by:

$$I_{DS} = I_{DSS} (V_{GS}' - V_{th})^2 \tanh \left[\frac{\beta V_{DS}'}{V_{GS}' - V_{th}} \right] \left[\frac{1}{1 + \theta (V_{GS}' - V_{th})^2} \right]$$

The parameter I_{DSS} is the saturation current, and β , γ , θ are the model parameters. In addition, the threshold voltage V_{th} is expressed as $V_{th0} + \gamma V_{DS}$. The total output conductance in InAlAs/InGaAs HEMTs can be expressed as the sum of the output conductance due to the impact ionization (eq.1) and the output conductance due to the deconfinement of electron from the channel to the buffer:

$$g_o = \alpha_n L_{Deff} I_{DS} / (V_{DS} - V_{DS,sat}) + g_{ob} (1 - V_{GS}/V_{th})^{1/2} \quad (6)$$

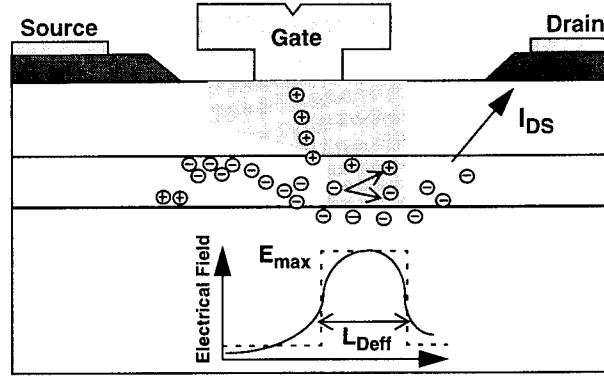


Fig.3: The physical processes of impact ionization and buffer layer conduction responsible of excess output conductance in InAlAs/InGaAs HEMTs.

Note that all parameters I_{DSS} , V_{th0} , β , θ and γ can be extracted from $I_{DS} = f(V_{GS})$ measurements at lower V_{DS} , where the impact ionization is very weak. The presented model uses only two adjustable parameters to calculate $g_o = f(V_{GS})$, namely L_0 and g_{ob} , which affect g_o due to the impact ionization and buffer layer conduction, respectively.

IV. EXPERIMENTAL RESULTS AND DISCUSSIONS

Fig.4 shows a typical bell-shaped characteristic of the output conductance as a function of the gate bias at $V_{DS}=2V$ for $0.13\mu m$ lattice matched InAlAs/InGaAs HEMTs. A good agreement is found between the measurement and our model calculation. The following parameters were used: $I_{DSS}=680mA/mm$, $V_{th0}=-1.39V$, $\gamma=0.075$, $\beta=0.925$, $\theta=0.38$, $L_0=35.5 nm \cdot V^{-1/2}$, $R_s=R_d=0.35\Omega mm$, and $g_{ob}=60 mS/mm$. Note, that the drain current without impact ionization is calculated at $V_{DS}=0.8V$. This bell-shaped characteristic can be explained by the dependance of the ionization process on both I_{DS} and the electrical field E_{max} . These, however, are affected in the opposite direction by gate bias.

This model is supported by several experimental observations on our $0.13\mu m$ lattice matched HEMTs:

- decreasing the band-gap energy of InGaAs channel by increasing the In-contents in pseudomorphic channels from 0.53 to 0.74, strongly raises the output conductance from 140mS/mm to 210mS/mm due to the increasing impact ionization coefficient.
- increasing the lateral gate recess from 50nm to 110nm reduces the g_o about 30% due to the increasing of the drift region length, thus decreasing the channel electrical field.
- by using an undoped InGaAs cap-layer, we reduce the output conductance from 150mS/mm to 40mS/mm at $V_{DS}=2V$, due to the reduction of the potential in the recess edges of drain, i.e. a decreasing the electrical field in the channel.

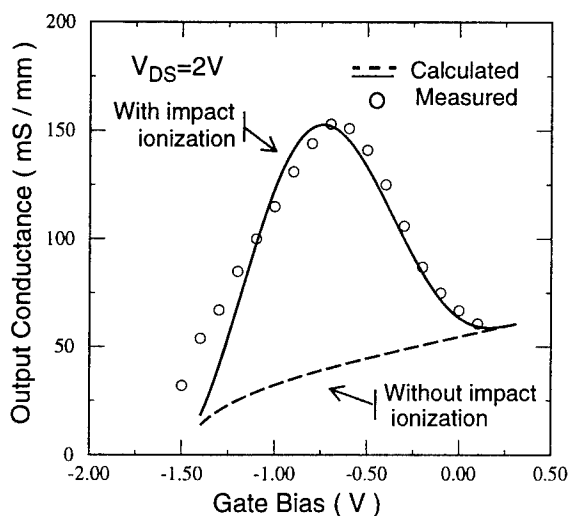


Fig.4 : Calculated and experimental variation of g_o versus gate bias for 0.13 μ m InAlAs/InGaAs HEMTs lattice matched to InP.

d) increasing the gate length from 130nm to 250nm reduces the g_o about 50% due to the increasing of the drift region length, i.e. a decreasing the electrical field in the channel.

We can conclude that, the output conductance in sub- μ m InAlAs/InGaAs HEMTs is due to weak impact ionization in high field gate-drain region of the InGaAs channel and deconfinement of 2DEG from the channel to the buffer.

The model can also be used to calculate the extrinsic transconductance versus gate bias or drain current. The extrinsic transconductance can be expressed by:

$$g_m = \Delta(I_{DS} + \alpha_n L_{Deff} I_D) / \Delta V_{GS}$$

For the calculation of the transfer characteristic, we use the same parameters used for $g_o = f(V_{gs})$. Fig.5 shows that the bell-shape of g_m - I_{DS} changes and the maximum g_m decreases as V_{DS} increases to 2V. The dashed line is the calculated transfer characteristics without impact ionization. It seems that this behaviour is due to the weak impact ionization in high gate-drain electrical field region which reduces the maximum g_m and increases the output conductance. Thus, high power gain can not be achieved at higher drain bias by short gate length InAlAs/InGaAs HEMTs. To overcome these undesirable effects of impact ionization, a wider energy band gap sub-channel is necessary for hot carriers in high field drift region. As shown in Fig.1, the metamorphic InAlAs/InGaAs HEMTs with composite channel show no dependance of g_m and output conductance on drain-source bias. Thus, a higher gain can be reached at high drain bias, where a reduced feed-back capacitance is obtained.

This novel channel concept can be used for lattice matched HEMTs to achieve high f_{max}/f_T ratios with a high f_T .

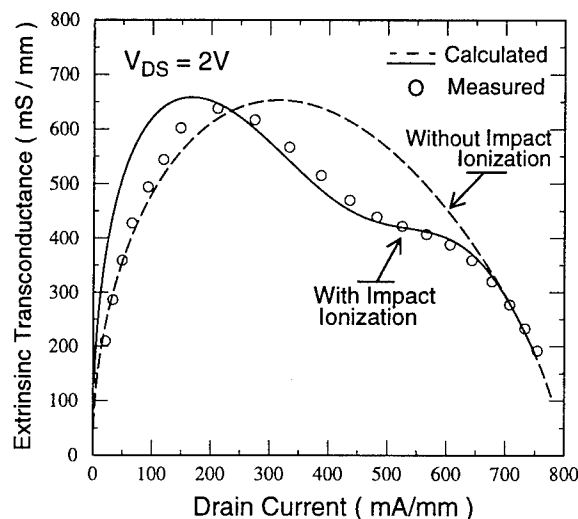


Fig.5: Calculated and measured transfer characteristics of 0.13 μ m lattice matched InAlAs/InGaAs HEMTs.

The wider band gap energy of InP and its higher saturation velocity make this material the best candidate of sub-channel for lattice matched InAlAs/InGaAs HEMTs[6].

In summary, we have designed, fabricated, and demonstrated a novel 0.13 μ m metamorphic InAlAs/InGaAs HEMTs with a composite channel on GaAs substrates with high cut-off frequencies and current drive capability. Such devices exhibit very low g_o of 20mS/mm and state of the art f_{max} values of 350GHz with an f_T of 150GHz. The power gain enhancement is mainly due to the channel design, as confirmed by our theoretical model. Thus, metamorphic growth technology of InAlAs/InGaAs HEMTs with composite channel will become useful if the reliability of the device can be assured.

Acknowledgment: The authors would like to thank the German Federal Ministry of Research and Technology (BMBF) for the financial support and the Microwave group of IAF-Freiburg for high frequency measurements.

REFERENCES:

- [1] P. Ho, M. Kao, P. C. Chao, K. G. Duh, J. Ballingall, S. Allen, A. Tessmer, P. Smith, Electronics Lett., Vol.27, pp.325-326, 1991.
- [2] Y. C. Pao, C. K. Nishimoto, R. M. Ahy, J. Archer, N. Bechtel, J. Haris, IEEE Trans. Elec. Dev. Vol.37, pp.2165-2170, 1990.
- [3] Loi D. Nguyen, A. S. Brown, Mark A. Thompson, Linda M. Jel-loian, IEEE Trans. Elec. Dev. Vol. 39, pp.2007-2014, 1992.
- [4] Ph. Carrer, E. Caqout, J. C. Renaud, L. Nguyen, A. Scavennec, Revue de Phys. App. Vol. 25, pp. 1326-1338, 1990.
- [5] F. Osaka, T. Mikawa, T. Kaneda, IEEE Journal of Quantum Electronics, Vol. QE-21, pp. 1326-1338, 1985.
- [6] S. Strahle, D. Geiger, B. Henle, E. Khon, sixth Inter. Conf. Indium Phosphide and related materials 1994, pp.327-330, 1994.
- [7] J. Michael Golio, "Microwave MESFETs and HEMTs", Artech House, pp. 128-171, 1991.
- [8] H. HeiB, S. Kraus, D. Xu, M. Chertouk, W. Klein, G. Böhm, G. Tränkle, G. Weimann, to be published.
- [9] L. F. Lester, P. M. Smith, P. Ho, P. C. Chao, P. Tiberio, K. G. Duh, E. D. wolf, 1988 IEDM Technical digest, pp.172-175

High Gm MBE-grown InP Based HEMTs with a Very Low Contact Resistance

Triple Capping Layer

Katsuhiko Higuchi, Mitsuhiro Mori, Makoto Kudo and Tomoyoshi Mishima

Central Research Lab., Hitachi, Ltd., 1-280 Higashi-koigakubo,
Kokubunji, Tokyo 185, Japan.

Introduction

InAlAs/InGaAs HEMTs lattice-matched on InP substrates are considered the most promising devices for millimeter-wave and optical communication systems because of their excellent high-frequency and low-noise performance[1]-[6]. However, thermal instability of the alloyed ohmic electrodes is a major drawback of these HEMTs and improvement in this area is a fundamental requirement. The contact resistance of conventional AuGe-alloyed ohmic electrodes is degraded by thermal stress because of the reaction between Au and In[7],[8]. On the other hand, a low potential barrier height between the n-InGaAs and the metal electrodes make it possible to form non-alloyed ohmic electrodes with a low contact resistance on the n-InGaAs[9]. These are more thermally stable than alloyed electrodes. Various non-alloyed ohmic electrodes with contact resistance low enough for device applications have been discussed by several authors[10]-[13]. Non-alloyed ohmic electrodes, however, cause a large parasitic source resistance due to the contact resistance between the n-InGaAs capping layer and the channel layer rather than contact resistance between the n-InGaAs capping layer and the metal electrodes. This high contact resistance is caused by large conduction band discontinuity between a InAlAs layer and a InGaAs layer, which decreases the tunneling current between them[14].

In this paper, we propose a highly-doped triple capping layer consisting of n^+ -InGaAs, n^+ -InAlAs, and n^+ -InGaAs which significantly reduces the contact resistance between the capping layer and the 2DEG channel. It is shown experimentally that the low contact resistance results in a very low parasitic source resistance of the HEMTs with the triple capping layer even though non-alloyed ohmic electrodes are used. The DC characteristics of these InAlAs/InGaAs HEMTs are also reported.

Experiments

A cross-sectional view of an InAlAs/InGaAs HEMT with a triple capping layer is shown schematically in Fig. 1. The epitaxial layers, which were lattice-matched on InP, were grown on InP substrates by molecular beam epitaxy. Growth at a low substrate temperature enabled a very high Si-doping concentration of $3 \times 10^{19} \text{ cm}^{-3}$ in the triple capping layer which consists of a 50-nm-thick n^+ -InGaAs layer, a 20-nm-thick n^+ -InAlAs layer, and a 5-nm-thick n^+ -InGaAs layer. The undoped InAlAs barrier layer was 10 nm thick, the Si-doped ($5 \times 10^{18} \text{ cm}^{-3}$) InAlAs carrier-supplying layer was 12 nm thick, and the undoped InAlAs spacing layer was 2 nm thick. Ti/Au non-alloyed ohmic electrodes were used as the source and drain electrodes. A low contact resistance of $2 \times 10^{-7} \Omega \text{ cm}^2$ was obtained between the electrode and the top n^+ -InGaAs layer, which is a very minor contribution to the total resistance. The gate electrode consisting of Ti/Al metal was formed after recess etching.

The source resistance and the contact resistance between the triple capping layer and the 2DEG channel was evaluated to clarify the advantage of our capping layer. The contact resistance was evaluated by fitting the measured source resistance to the source resistance model proposed by S. J. Lee et al[14] which is illustrated in Fig. 2. Here, ρ_1 and ρ_2 denote the sheet resistance of the capping layer and the channel layer, respectively, and R_1 denotes the resistance of the channel under the spacing near

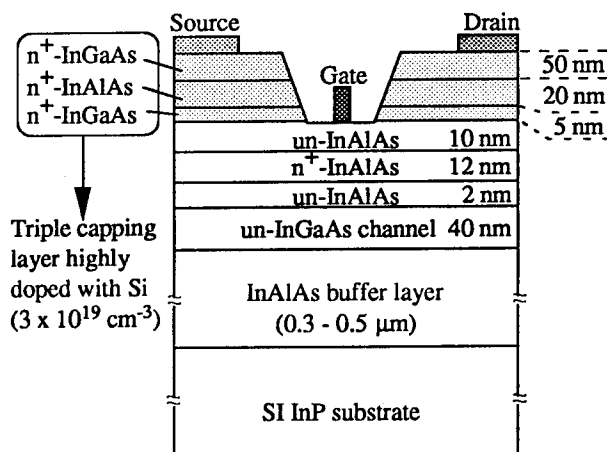


Fig. 1. Schematic cross-sectional view of an InAlAs/InGaAs HEMT with a highly-doped triple capping layer lattice-matched on InP.

the gate and R_{C1} denotes the contact resistance between the source electrode and the capping layer. These four values were determined by Hall measurements and transmission line model measurements. The parameters ρ_{12} and R_{C2} , which are the contact resistance and the effective contact resistance, respectively, between the capping layer and the channel layer were determined by fitting the measured source resistance for various distances L to the expected source resistance for each L based on the model.

Contact resistance for conventional single n^+ -In_{0.53}Ga_{0.47}As capping layers doped at concentrations of $5 \times 10^{18} \text{ cm}^{-3}$, $1 \times 10^{19} \text{ cm}^{-3}$, and $3 \times 10^{19} \text{ cm}^{-3}$ was also evaluated for comparison. The doping concentration of $3 \times 10^{19} \text{ cm}^{-3}$ is almost the limit of Si active doping concentration in InGaAs. For these samples, the thickness of the single capping layers is fixed at 50 nm.

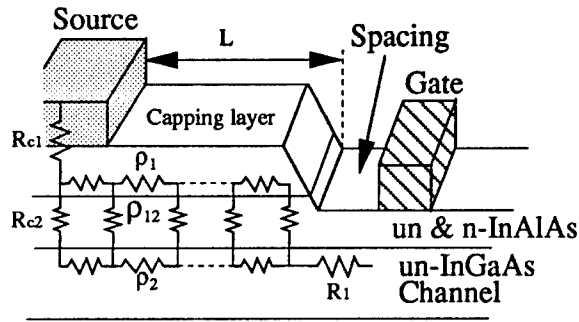


Fig. 2. The equivalent distributed circuit for parasitic source resistance of HEMTs which was proposed by S. J. Lee et al.[15]. The source resistance was analyzed by using this model.

Results and Discussion

The dependence of the contact resistance ρ_{12} and source resistance R_s (at $L=1.6 \mu\text{m}$) on the doping concentration in the capping layer is shown in Fig. 3. In the single capping layers ρ_{12} and R_s were reduced by increasing the doping concentration, however, the values are not low enough for device applications. On the other hand, a contact resistance of $3 \times 10^{-5} \Omega\text{cm}^2$ for the triple capping layer was obtained, which is about one order of magnitude smaller than that of conventional structures with a single capping layer doped to $5 \times 10^{18} \text{ cm}^{-3}$. The contact resistance is also smaller than that of a highly doped ($3 \times 10^{19} \text{ cm}^{-3}$) single capping layer, which means that the large reduction in contact resistance is due not only to the high doping concentration of $3 \times 10^{19} \text{ cm}^{-3}$, but also to the use of three capping structures. We calculated energy band diagrams and electron density profiles for the HEMTs with a conventional single capping layer doped to $5 \times 10^{18} \text{ cm}^{-3}$ and for those with a highly-doped triple capping layer so we could better understand the merits of the triple capping layer. Figure 4 shows the calculated band diagrams and the electron density for the HEMTs with a conventional single capping layer doped to $5 \times 10^{18} \text{ cm}^{-3}$ and for those with a highly-doped triple capping layer. There exist two potential barriers for electrons between the capping layer and the 2DEG channel for the conventional single capping layer. These barriers decrease the tunneling current between the capping layer and the channel and are the cause of the high source resistance. On the other hand, the potential barrier near the capping layer is much lower for the triple capping layer because of the high peak electron density of $4 \times 10^{19} \text{ cm}^{-3}$ in the bottom

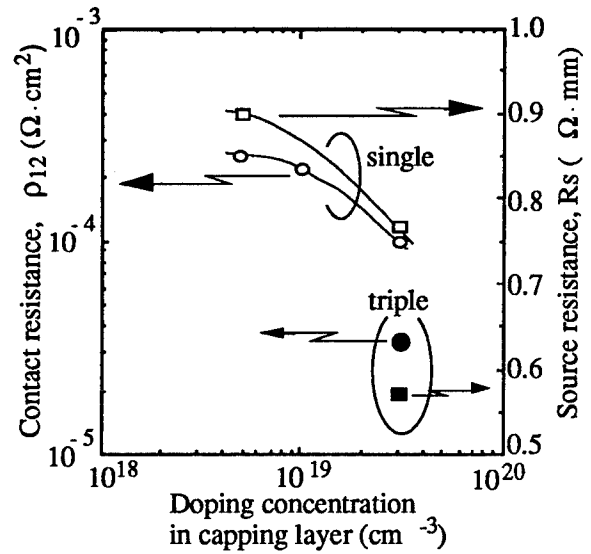


Fig. 3. The source resistance and contact resistance between a single or triple capping layer and the 2DEG channel vs. doping concentration at the capping layer.

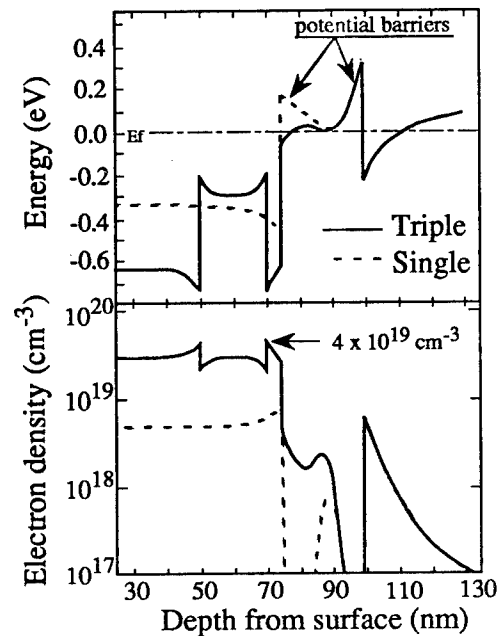


Fig. 4. The energy band profiles and electron density profiles for the triple capping layer and the conventional single capping layer.

n^+ -InGaAs layer of the three capping layers as shown in Fig. 4. This electron density is higher than the doping concentration of the layer. The excessive electrons in the bottom n^+ -InGaAs layer are offered from the n^+ -InAlAs layer as shown in Fig. 4, which lowers the energy barrier to the 2DEG channel more effectively. As a result, the

contact resistance ρ_{12} between the capping layer and the 2DEG channel is significantly reduced.

A low source resistance of $0.57 \Omega\text{mm}$, which is 60% that of a conventional structure with a single capping layer doped to $5 \times 10^{18} \text{ cm}^{-3}$, was obtained from the HEMT with a highly-doped triple capping layer.

The reduction in the source resistance appears to be due to a reduction in the parallel conductive resistance in addition to a reduction in the vertical conductive resistance across the hetero-interfaces which is related to the contact resistance ρ_{12} . To separate these effects, we evaluated the contributions of each element to the source resistance using the parameters obtained from the equivalent distributed circuit for parasitic source resistance shown in Fig. 2. Figure 5 shows the contribution of the vertical conductive resistance for various capping layers. For the conventional single capping layer, the contribution of the vertical conductive resistance across the hetero-interfaces is as large as $0.63 \Omega\text{mm}$. With the reduction of contact resistance ρ_{12} , the resistance element of vertical conduction falls to $0.4 \Omega\text{mm}$. The other components of the source resistance - which include the contact resistance between the capping layer and the source electrode, the resistance element of the two parallel conductive layers, and the resistance of the channel under the spacing near the gate - are reduced by $0.1 \Omega\text{mm}$ to only $0.17 \Omega\text{mm}$. It is clear that the reduction in the source resistance is mainly due to reducing the resistance element of vertical conduction.

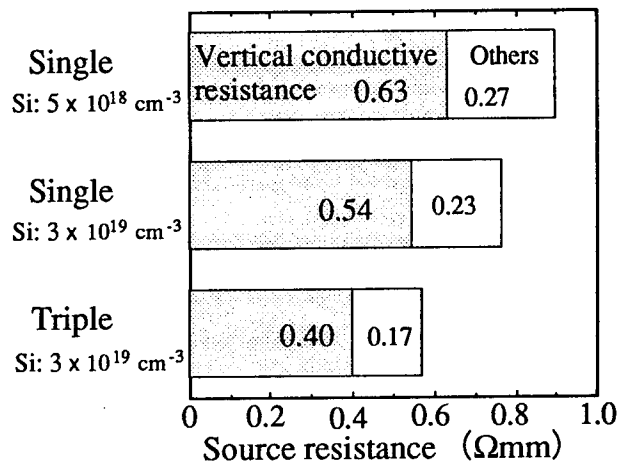


Fig. 5. The contribution of the vertical conductive resistance to the source resistance for the various capping layers. The reduction in source resistance with the triple capping layer is due to the decrease in vertical conductive resistance.

Figure 6 shows the peak extrinsic transconductance (G_m) for HEMTs with a triple capping layer plotted against the gate length together with recently reported data for HEMTs on InP. The calculated peak extrinsic G_m for the HEMTs with single capping layers doped by 5×10^{18}

cm^{-3} and $3 \times 10^{19} \text{ cm}^{-3}$ are also shown in this figure as the solid lines. The values for the single-capping layer HEMTs were estimated using the intrinsic transconductance data from the HEMTs with a triple capping layer. The low source resistance of the HEMTs with a triple capping layer results in very high peak extrinsic G_m for various gate lengths. These values are higher than those for previously reported InP-based HEMTs with the same gate lengths. For the HEMTs with a shorter-gate-length of about $0.4 \mu\text{m}$, the peak extrinsic G_m is especially high compared to previously reported HEMTs because the reduction in source resistance strongly affects the extrinsic transconductance in this region where the intrinsic transconductance is also higher than for longer gate lengths. For a device with a gate dimension of $0.4 \times 20 \mu\text{m}$, a high peak extrinsic G_m of 1 S/mm was obtained, which is 42% higher than recently reported values for HEMTs on InP with the same gate length.

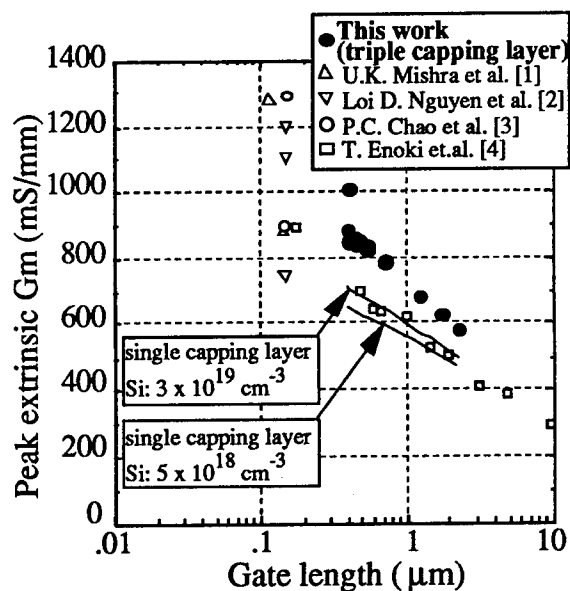


Fig. 6. Peak extrinsic transconductance for HEMTs with a triple capping layer plotted against the gate length together with data recently reported values for HEMTs on InP. Solid lines indicate the estimated peak extrinsic transconductance for HEMTs with single capping layers.

Summary

A highly-doped triple capping layer consisting of n^+ - $\text{In}_{0.53}\text{Ga}_{0.47}\text{As}$, n^+ - $\text{In}_{0.52}\text{Al}_{0.48}\text{As}$, and n^+ - $\text{In}_{0.53}\text{Ga}_{0.47}\text{As}$ was investigated with the goal of reducing parasitic source resistance in $\text{InAlAs}/\text{InGaAs}$ HEMTs. Analysis of the source resistance revealed that the contribution of the resistance element at n^+ - $\text{In}_{0.53}\text{Ga}_{0.47}\text{As}/\text{un-In}_{0.52}\text{Al}_{0.48}\text{As}/\text{un-In}_{0.53}\text{Ga}_{0.47}\text{As}$ channel hetero-interfaces is as large as 70% of the total source resistance when non-alloyed ohmic electrodes are used. The highly-doped triple capping layer reduces the

resistance element of vertical conduction between the capping layer and the 2DEG channel. Thus, source resistance was reduced to 0.57 Ωmm and contact resistance to $3 \times 10^{-5} \Omega\text{cm}^2$ in the HEMTs with a highly-doped triple capping layer. This source resistance is 60% that of HEMTs with a conventional single capping layer, and the contact resistance is one order of magnitude smaller. The low source resistance results in peak extrinsic transconductance as high as 1 S/mm for a device with a 0.4- μm -long gate, which is 42% higher than that of previously reported HEMTs with the same gate length.

References

- [1] U. K. Mishra et al., "Novel High Performance Self-Aligned 0.15 Micron Long T-gate AlInAs-GaInAs HEMTs." IEEE IEDM Tech. Dig. pp. 101-104, 1989.
- [2] L. D. Nguyen et al., "Vertical Scaling of Ultra-high-speed AlInAs-GaInAs HEMTs." IEEE IEDM Tech. Dig. pp. 105-108, 1989.
- [3] P. C. Chao et al., "W-Band Low-Noise InAlAs/InGaAs Lattice-Matched HEMTs." Electron Device Lett. vol. 11, No. 1, pp. 59-62, 1990.
- [4] T. Enoki, K. Arai, T. Akazaki and Y. Ishii, "Novel Channel Structures for High Frequency InP-Based HFETs." IEICE Trans. Electron, E76-C, No. 9, pp. 1402-1411, 1993.
- [5] P. Ho et al., "Extremely High Gain 0.15 μm Gate-Length InAlAs/InGaAs/InP HEMTs." Electron. Lett., vol. 27, No. 4, pp. 325-327, 1991.
- [6] L. D. Nguyen, A. S. Brown, M. A. Thompson and L. M. Jelloian, "50-nm Self-Aligned-Gate Pseudomorphic AlInAs/GaInAs High Electron Mobility Transistors." IEEE Trans. Electron Devices, vol. 39, No. 9, pp. 2007-2014, 1992.
- [7] J. M. Vandenberg, H. Temkin, R. A. Hamm, and M. A. DiGiuseppe, "Structural study of alloyed gold metallization contacts on InGaAsP/InP layers", J. Appl. Phys. 53(11), pp. 7385-7389, 1982.
- [8] P. Zwicknagl et al., "Very low resistance Au/Ge/Ni/Ag based Ohmic contact formation to $\text{Al}_{0.25}\text{Ga}_{0.75}\text{As}/\text{GaAs}$ and $\text{Al}_{0.48}\text{In}_{0.52}\text{As}/\text{Ga}_{0.47}\text{In}_{0.53}\text{As}$ heterostructures: A behavioral comparison," J. Vac. Sci. Technol. B4(2), pp. 476-484, 1986.
- [9] T. C. Shen, G. B. Gao, and H. Morkoc, "Recent developments in ohmic contacts for II-V compound semiconductors," J. Vac. Sci. Technol. B10(5), pp. 2113-2132, 1992.
- [10] L. G. Shantharama, H. Schumacher, H. P. Leblanc, R. Esagui, R. Bhat, and M. Koza, "Evaluation of single ohmic metallizations for contacting both p- and n-type GaInAs," Electron. Lett. 26, pp. 1127-1129, 1990.
- [11] A. Lahav, F. Ren, and R. F. Kopf, "Thermal stability of tungsten ohmic contacts to the graded-gap InGaAs/GaAs/AlGaAs heterostructure," Appl. Phys. Lett. 54, pp. 1693-1695, 1989.
- [12] K. Onda et al., 1994 IEEE MTT-S Digest, TU3F-16, pp. 261, 1994.
- [13] S. Kuroda, N. Harada, T. Katakami, and T. Mimura, "HEMT with Nonalloyed Ohmic Contacts Using $\text{n}^+\text{-InGaAs}$ Cap Layer," IEEE Electron Devices Lett. vol. EDL-8, No. 9, pp. 389-391, 1987.
- [14] Y. Ando and T. Itoh, "Accurate Modeling for Parasitic Source Resistance in Two-Dimensional Electron Gas Field-Effect Transistors," IEEE Trans. on Electron Devices, vol. 36, pp. 1036-1044, 1989.
- [15] S. J. Lee and C. R. Crowell, "Parasitic source and drain resistance in high-electron-mobility transistors," Solid-State Electron. vol. 288, No. 7, pp. 659-668, 1985.

Reliability of AlInAs/InGaAs/InP HEMT with WSi Ohmic Contacts

H.Sasaki, K.Yajima
Kita Itami Works, Mitsubishi Electric Corporation,
 N.Yoshida, O.Ishihara, S.Mitsui
Optoelectronic & Microwave Devices Lab, Mitsubishi Electric Corporation,
 4-1, Mizuhara Itami City, Hyogo 664, Japan

ABSTRACT

We have obtained extremely high reliability on the AlInAs/InGaAs/InP HEMT using WSi ohmic electrodes. The WSi electrode of this device demonstrates high stability under a high temperature ($T_a=170\sim 200^\circ\text{C}$) operating life test. The sample analyzed by a cross-sectional TEM/EDX shows no degradation of WSi/InGaAs interface, on the other hand, titanium (Ti) and fluorine (F) are detected in the AlInAs layer. The estimated degradation mechanism of this device is related with decrease of carrier concentration in the epitaxial layer.

INTRODUCTION

AlInAs/InGaAs/InP based HEMT is to provide superior device performance, because of their higher material properties than the InGaAs/GaAs based HEMT[1]. It is due to the larger conduction band discontinuity between AlInAs and InGaAs which allows for more effective charge transfer into the channel layer and for better carrier confinement. Furthermore, AlInAs has a high doping capability which also allows for a high charge transfer into the InGaAs channel layer.

Recently extremely low noise figure of 0.9dB with an associated gain of 7.0dB at 60GHz was demonstrated for a HEMT with selectively wet-recessed gate [1]. Therefore the InP-based HEMT will likely be a key component, for example, in satellite communication and so on. These devices are required to maintain performance capability for long time operation. However, the reliability of these devices has not received attention that much [2].

The primary degradation mechanism for the InP-based HEMT is an increase in the ohmic contact resistance[3]. Usually AuGe alloyed ohmic contacts have been applied to the InP-based HEMT. These contacts, however, easily migrate to the gate[4], and increase its contact resistance compared to the GaAs-based HEMT [3]. Another mechanisms also demonstrated, a migration of ohmic metal or gate sinking [4], degradation of a passivation [5]. These changes bring about catastrophic failure or serious degradation of its device performance.

On the other hand, InP-based HEMT with non alloyed refractory WSi ohmic contacts are expected to have a excellent thermal stability, because its sufficient thermal stability is recognized under annealing temperature up to 380°C on ohmic contact test patterns [3].

The demonstrated RF performance of AlInAs/InGaAs/InP HEMT with refractory WSi non-alloyed ohmic contacts has an extremely low noise figure of 0.8dB with an associated gain of 8.0dB at 40GHz [6].

In this study, the reliability of AlInAs/InGaAs/InP HEMT with WSi ohmic contacts is examined by high temperature DC accelerated life tests. The degradation mechanisms will be discussed by considering the results of changes of the electrical parameters during life test and the results of the observation of a cross-sectional TEM micrograph and EDX analysis. Finally excellent stability of WSi ohmic electrode for InP-based HEMT will be demonstrated.

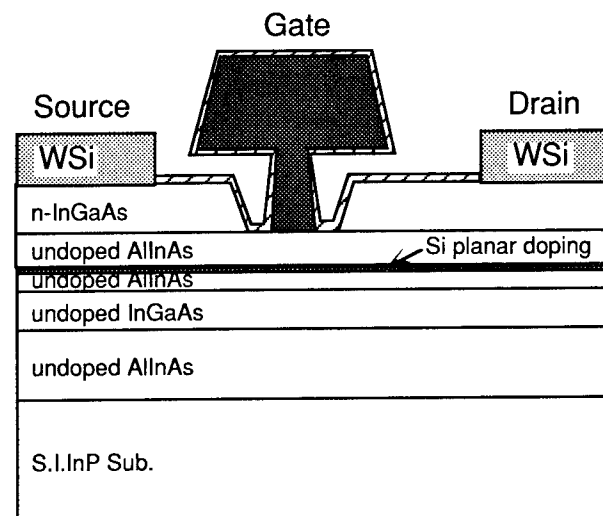


Fig.1 Schematic cross-section of AlInAs/InGaAs HEMT with WSi ohmic contacts.

EXPERIMENTAL

Fig.1 shows a schematic cross-sectional view of the AlInAs/InGaAs/InP HEMT with WSi ohmic contacts which was evaluated in this study. Fig. 2 is a photograph showing a typical AlInAs/ InGaAs/InP HEMT. The gate length and gate width are $0.15\mu\text{m}$ and $120\mu\text{m}$, respectively. The device is planar Si-doped and passivated with a thin silicon oxynitride (SiON) layer. Details of the device fabrication and performance are reported elsewhere [1][6].

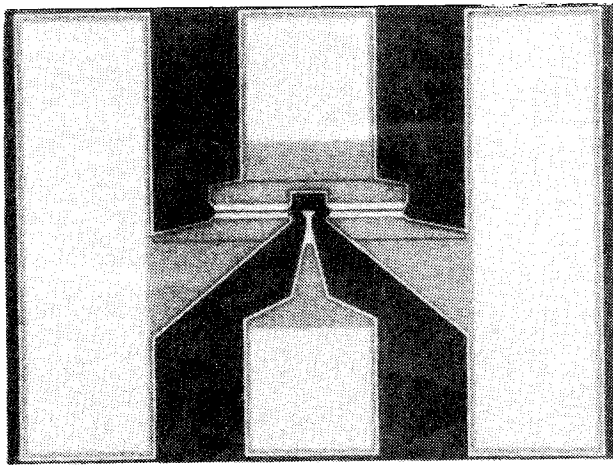


Fig.2 A Photograph of a AlInAs/InGaAs/InP HEMT

DC accelerated life test were performed at temperatures of $T_a=170^\circ\text{C}$ to 200°C and the operating DC parameters were $V_{ds}=0.8\text{V}$, $I_d=12\text{mA}$. In this low temperature regime a thermal accelerated life test is all that is required to demonstrate the intrinsic device reliability and clarify failure mechanisms. The main specific parameters recorded are drain current at zero gate bias (I_{dss}), maximum transconductance (g_m), pinch-off voltage (V_p), and source and drain parasitic resistances (R_s, R_d). After the initial measurement the devices did not receive a burn-in for stabilization. A tested sample was later analyzed in detail by cross-sectional TEM and EDX.

RESULTS AND DISCUSSION

Fig.3 and 4 show the results of changes of I_{dss} and g_m , as a function of time during life test at 170°C for the 10 test devices. I_{dss} shows a gradual decrease, but g_m does not show notable change.

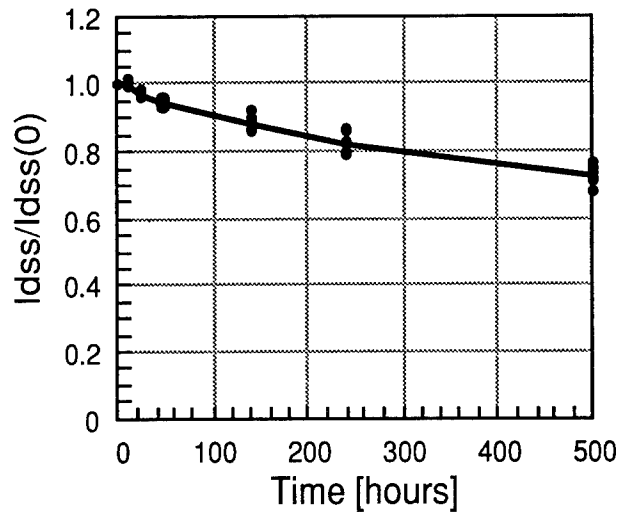


Fig.3 Drain current versus time for the DC bias operational life test at 170°C .

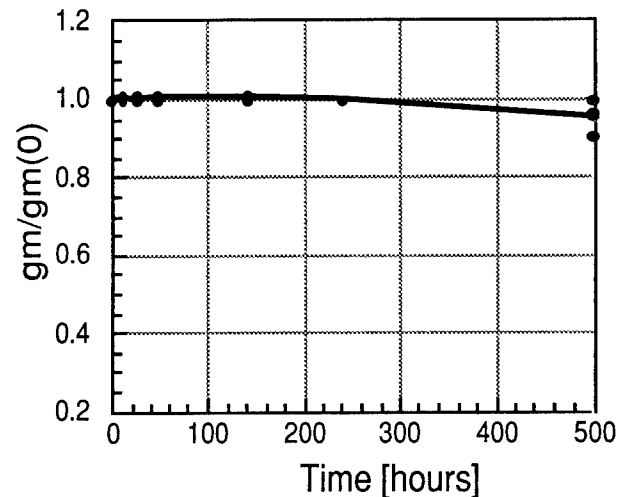


Fig.4 Transconductance versus time for the DC bias operational life test at 170°C .

Fig.5 shows the results of the changes in R_s and R_d as a function of time during life test. A slight increase of parasitic resistances is observed. The R_d varies only less than 40% and the R_s varies 10%. One salient feature is that the degradation of R_d is larger than that of R_s . This larger increase in R_d compared to R_s is probably caused by a stronger electrical field between gate and drain.

Fig.6 shows a change of pinch-off-voltage (V_p) during life test. It shows a slight decrease similarly to the decrease curve of I_{dss} as shown in Fig.3.

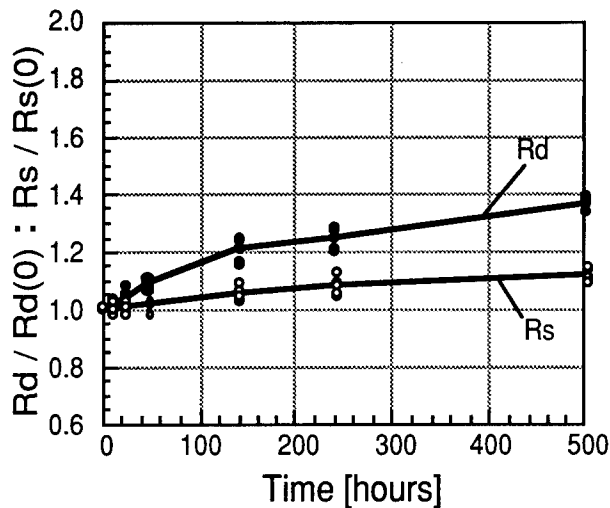


Fig.5 Source and drain parasitic resistances versus time for the DC bias operational life test at 170°C.

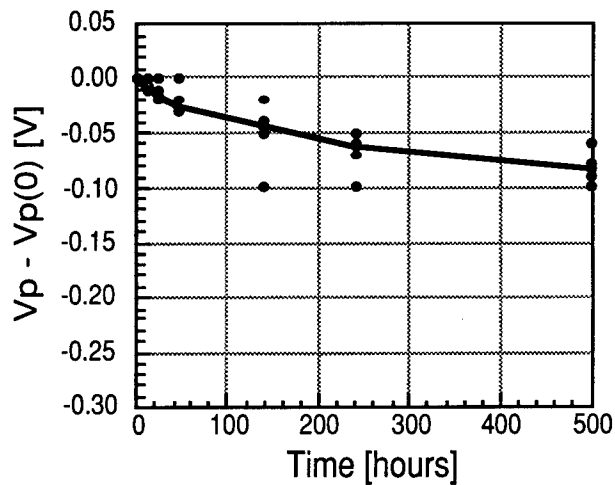


Fig.6 Pinch-off voltage versus time for the DC bias operational life test at 170°C.

Fig.7 shows a micrograph of the cross-sectional TEM after 500 hours aging at 170°C. Fig.8 and Fig.9 are magnifications of parts of Fig.7 in the gate/AlInAs and the WSi(drain)-electrode/InGaAs area, respectively. We cannot observe remarkable degradation around gate (Fig.8) and WSi electrode (Fig.9).

In order to prove the presence of an impurity diffusion, high spatial resolution (10 Å) EDX analysis was performed on the same sample as shown in Fig.7~9. Fig.10 shows an EDX atomic profile of the gate barrier metal (Ti) in the gate/AlInAs interface region. Titanium signal shows a tail inside AlInAs layer, on the other hand, inter-diffusion of WSi and InGaAs can not be observed. We can also observe an impurity (F) in the AlInAs layer

between gate and WSi electrode by EDX.

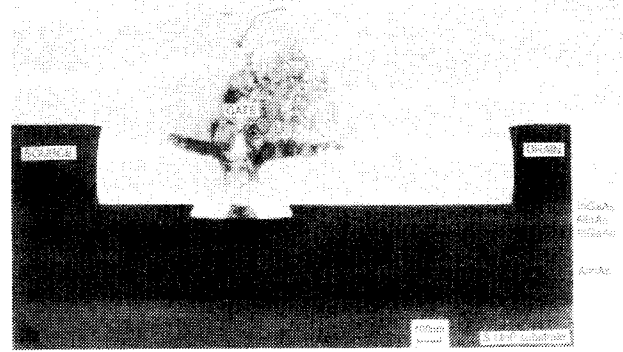


Fig.7 Cross-sectional TEM photograph of AlInAs/InGaAs InP HEMT with ohmic contact.

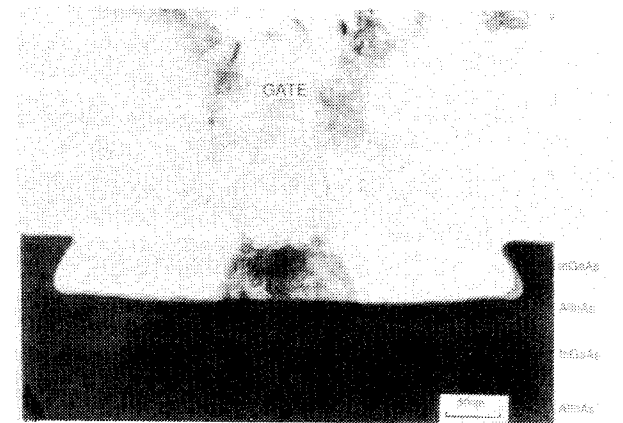


Fig.8 Cross-sectional TEM photograph of AlInAs/InGaAs InP HEMT with WSi ohmic contacts in the gate contact area.

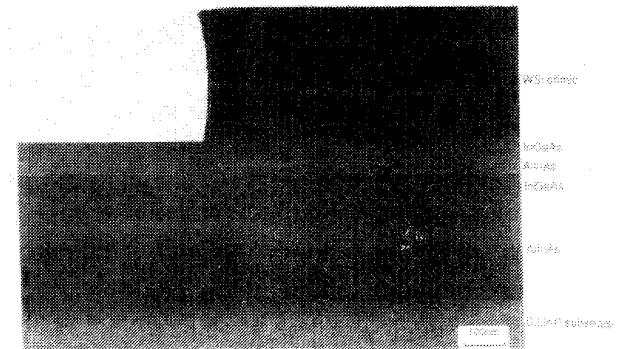


Fig.9 Cross-sectional TEM photograph of AlInAs/InGaAs InP HEMT with WSi ohmic contacts in the ohmic contact area.

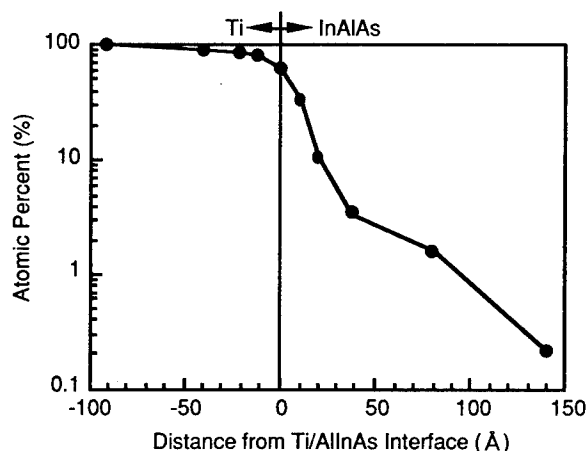


Fig.10 EDX atomic profile of gate metal (Ti) in an AlInAs layer.

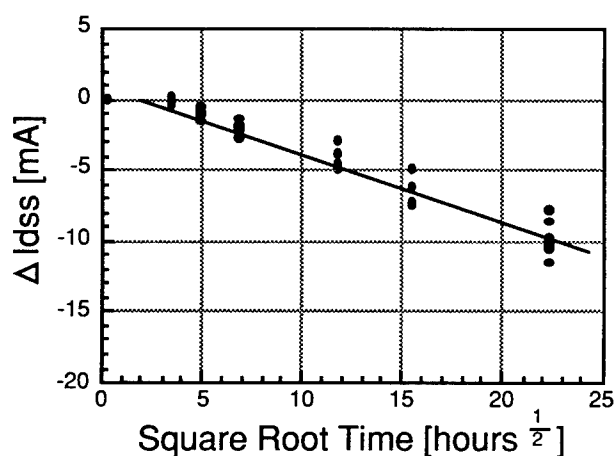


Fig.11 I_{dss} plotted as a function of the square-root of time.

In order to discuss the degradation mechanism, the decrease of I_{dss} is plotted as a function of the square-root of time as shown in Fig.11. It fit quite well to linear dependence on square root of storage time. This type of dependence suggests that the degradation mode is due to diffusion controlled mechanism. EDX analysis shows diffusions of Ti and F into AlInAs layer. We have no information about Ti diffusion into AlInAs, however, N.Hayafuji et.al. demonstrated a decrease of carrier-concentration and electron mobility of Si-doped AlInAs layer by the thermal diffusion of fluorine [7]. Therefore, the changes of I_{dss} and V_p are probably due either to Ti diffusion or to fluorine diffusion into AlInAs resulting in a decrease of carrier concentration in the epitaxial layer.

On the other hand, R_s and R_d reveal little change

during high temperature life test. The analyzed results by cross-sectional TEM and EDX indicate no inter-diffusion of WSi and InGaAs. Therefore it is demonstrated that the WSi ohmic contact has a sufficient stability for AlInAs/InGaAs/InP HEMT.

SUMMARY

High temperature DC accelerated life tests were performed for AlInAs/InGaAs/InP HEMT with WSi ohmic contacts. During life tests, changes of I_{dss} and V_p are observed but R_s , R_d and g_m demonstrate little changes. Cross-sectional TEM and EDX analysis show no WSi contact degradation, however gate electrode (Ti) and fluorine diffusions into AlInAs are observed. It is estimated that the degradation mechanism of this device is the decrease of the carrier concentration in the epitaxial layers by the impurity diffusions. Nevertheless, the WSi ohmic contact for this HEMT has a excellent stability under the high temperature DC operation.

REFERENCES

- [1] N.Yoshida, T.Kitano, Y.Yamamoto, K.Katoh, M.Minami, H.Takano, T.Sonoda, S.Takamiya, and S.Mitsui, "A Super Low Noise V-Band AlInAs/InGaAs HEMT Processed by Selective Wet Gate Recess etching", IEEE MTT-S digest, (1994)645.
- [2] M.Hafizi and M.J.Dlaney; "Reliability of InP-based HBT's and HEMT's: Experiments, Failure Mechanisms,and Statistics"; IPRM(1994)p.299.
- [3] N.Yoshida, Y.Yamamoto, H.Takano, T.Sonoda, S.Takamiya, S.Mitsui; "Alloyed and Non-Alloyed Ohmic Contacts for AlInAs/InGaAs High Electron Mobility Transistor" Jpn.J.Appl.Phys. (1994) p.3373.
- [4] D.J.LaCombe, W.W.Hu and F.R.Bardsley; "Reliability of $0.1 \mu m$ InP HEMT", IEEE/IRPS (1993) p.364.
- [5] K.C.Hwang, A.R.Reisinger, K.H.G.Duh, M.Y.Kao, P.C.Chao, and A.W.Swanson; "A Reliable ECR Passivation Technique on the $0.1 \mu m$ InAlAs/InGaAs HEMT Device"; IPRM(1994)p.624.
- [6] N.Yoshida, Y.Yamamoto, K.Katoh, H.Minami, T.kitano, H.Takano, T.Sonoda, S.Takamiya and S.Mitsui; ; "Low Noise AlInAs/InGaAs HEMT using WSi ohmic contact" Electronics Letters 30(1994) p.1009.
- [7] N.Hayafuji, Y.Yamamoto, N.Yoshida, T.Sonoda, S.Takamiya, and S.Mitsui; "Thermal stability of AlInAs/GaInAs/InP heterostructure"; Appl.Phys.Lett. 66(1995)863.

Saturday

May 13, 1995

- SA1** Epitaxy for Low Dimensional Structures
- SB1** New Lasers and Fabrication Techniques
- SA2** MBE Growth and Related Techniques
- SB2** Reliability and Passivation Techniques
- SA3** MOVPE Growth and Related Techniques
- SB3** Nanostructure Devices and Characterization

Growth and characterization of InGaAs/InAlAs in-plane superlattices on (110) InP

Yoshiaki Nakata

SA1.1
(Invited)

Fujitsu Laboratories Ltd., 10 - 1 Morinosato-Wakamiya, Atsugi 243 - 01, Japan

We studied the surface steps during growth on misoriented (110) InP substrates, and grew InGaAs/InAlAs in-plane superlattices (IPSLs) using molecular beam epitaxy. The surface steps were evaluated by reflection high energy electron diffraction and atomic force microscopy (AFM). We found that two types of surface steps (single and double monolayer steps) were arranged depending on the growth conditions. Step edges of both types were seen to be little undulated in the AFM images. For the IPSL growth, we alternately grew half monolayers of AlAs and GaAs and single monolayers of InAs, keeping the regular arrays of single monolayer steps. The structural studies of IPSLs using transmission electron microscopy and photoluminescence measurements indicated InGaAs/InAlAs IPSLs composed of InAs/GaAs and InAs/AlAs monolayer superlattices were grown with some evidences of disordering. We also grew InAs/GaAs in-plane strained superlattices with the periodicity of about 8 nm on the misoriented (110) InP substrates.

1. Introduction

There is a strong need for a breakthrough in semiconductors, especially in compound semiconductors. Much attention has been paid to quantum wires and quantum boxes as the source of the breakthrough. Growth of laterally modulated structures using step flow growth on misoriented substrates is a very important technique for directly forming quantum well wire and box array structures without lithographic fabrication process. Successful works had been extensively done by Petroff et al. [1-3] and Fukui et al. [4-6]. They had grown alternately fractional layers of GaAs and Al(Ga)As using step flow growth on misoriented (001) GaAs substrates. Most studies, however, focused on the GaAs/Al(Ga)As systems grown on misoriented (001) GaAs substrates. InGaAs or materials including InAs, which are attractive for practical applications, have hardly been investigated.

For the growth of laterally periodic structures (i.e., in-plane superlattices (IPSLs)), controlling the configuration of the surface steps or terraces is crucial, as is controlling the growth mode to be step flow one. These features are, as well known, dependent on not only the growth methods and conditions, but they also should be affected by the substrate orientations to be grown on. Recently, we have succeeded in growing (InAs)₁/(GaAs)₁ laterally modulated monolayer superlattices (LM-MSLs) using regular arrays of single monolayer steps on misoriented (110) InP substrates by molecular beam epitaxy (MBE) [7,8]. This result suggests the potential of these substrates for growing IPSLs.

In this paper, we describe the surface step arrangements and structural features of InGaAs/InAlAs IPSLs grown on misoriented (110) InP substrates by MBE [9, 10]. We also demonstrate growth of the InAs/GaAs in-plane strained superlattices (IPSSLs) on misoriented (110) InP substrates.

2. Experimental

Samples were grown by conventional MBE. The substrates were misoriented (110) InP tilting toward the [00 $\bar{1}$] direction. During growth on these substrates, the surface steps of the (11 $\bar{1}$) B terminated by group V atoms should be arranged. Surface steps were evaluated by reflection high energy electron diffraction (RHEED) with an acceleration voltage of 25 kV and atomic force microscopy (AFM) operated in air. The IPSL structures were evaluated by transmission electron microscopy (TEM) and photoluminescence (PL) measurements.

3. Results and discussion

3.1. Step arrangements

In growing InGaAs on slightly misoriented (110) InP substrates, we found that the two types of surface steps were arranged depending on the growth conditions. Figs. 1a and 1b are typical RHEED patterns obtained from the InGaAs surfaces growing on a substrate tilted at 3°. The electron beam incidence was parallel to the step edge ([$\bar{1}$ 10] azimuth). Pronounced split spots indicated single (Fig.1a, 4 nm wide terraces) and double (Fig.1b, 8 nm wide terraces) monolayer steps were arranged. These step arrangements were controlled by the growth conditions. Fig. 1c shows the relationship between the step arrange-

ments and the growth conditions. The double monolayer steps were arranged at either a lower temperature or a higher As pressure than those of single monolayer steps, although the double monolayer step arrangements with larger terrace widths require longer migration of atoms than single monolayer steps. Presumably, the As incorporation or the As related atomic reconstruction at the step edges plays an important role for these step arrangements.

Fig. 2a and 2b are AFM images of the InGaAs surfaces arranged in single (a) and double (b) monolayer steps grown on the substrates tilted at 1.2° . About 10 and 20 nm wide terraces, comparable to the expected mean terrace widths (single monolayer steps: 10 nm wide, double monolayer steps: 20 nm wide) were formed periodically. Step edges of both types were seen to be little undulated.

In the alternate growth of AlAs, GaAs and InAs for the IPSLs, the RHEED split spots showing single monolayer step arrangements were clearly seen, although the spot profiles changed slightly. On the other hand, the split spots showing the double monolayer step arrangements became unclear. The Al migration is considered to be insufficient to arrange the double monolayer steps, or the reconstruction at the step edges would be broken by incorporating Al atoms. Thus, we used the single monolayer step arrangements for growing the IPSLs.

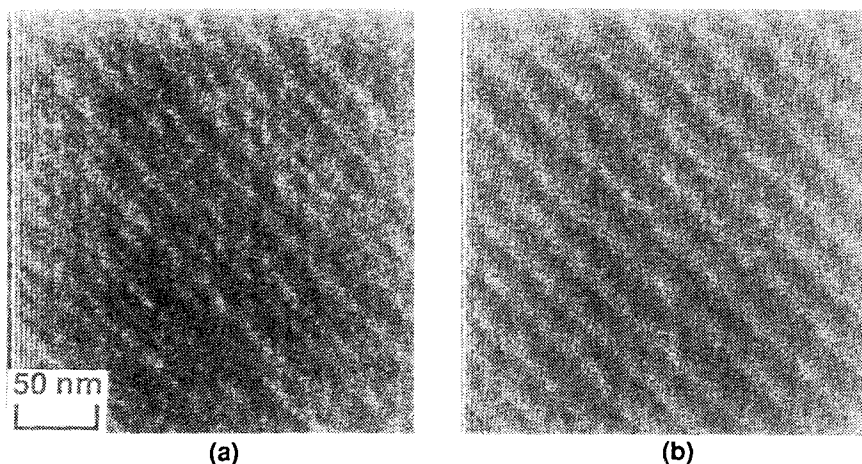


Fig. 2. AFM images of the InGaAs surfaces with (a) single monolayer steps and (b) double monolayer steps.

3.2. IPSL growth and their structures

3.2.1. InGaAs/InAlAs IPSLs

InGaAs/InAlAs IPSLs were grown using alternate growth of half monolayers of AlAs and GaAs and single monolayers of InAs, maintaining the regular arrays of single monolayer steps. The opening and closing shutter sequences for each cell are shown in Fig. 3a. The substrate used was a misoriented (110) InP tilting 3° toward the $[00\bar{1}]$ direction. A schematic diagram of the IPSL structure expected by ideal step flow growth is shown in Fig. 3b. In this case, InGaAs (2 nm wide)/InAlAs (2 nm wide) superlattices composed of InAs/GaAs and InAs/AlAs monolayer superlattices are expected to grow. The growth rates of AlAs, GaAs and InAs were about $0.15 \mu\text{m/h}$. It takes about 5 seconds for single monolayer growth. The substrate temperature was about 440°C . The As pressure for the ternary layers of InGaAs and InAlAs growth was about 3.5×10^{-6} Torr and for the binary layers of IPSL (AlAs, GaAs and InAs) growth was about 1.8×10^{-6} Torr. We changed the As pressure at the interface between the ternary layers and the binary layers without growth interruption by exchanging two As cells.

Fig. 4a is a transmission electron diffraction (TED) pattern from the (110) cross-section. Two types

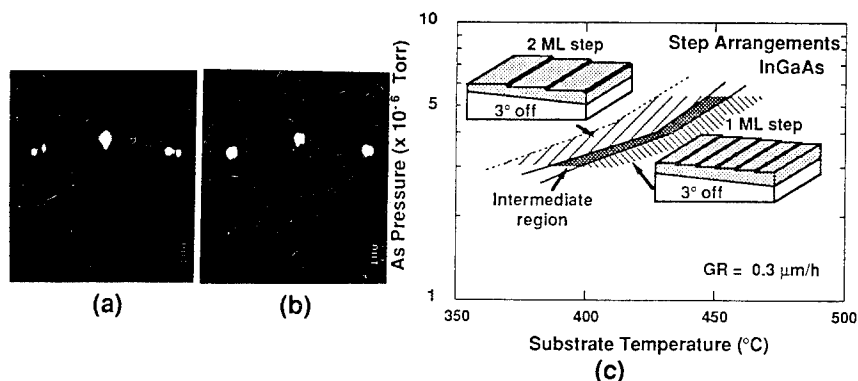


Fig. 1. Typical RHEED patterns showing (a) single monolayer step arrangements and (b) double monolayer step arrangements. (c) The relationship between the step arrangements and the growth conditions.

of superstructure spot pairs double positioned in the $[001]$ direction are clearly observed. One type is observed at about $\{h, k, l \pm 1/6.8\}$ in which h, k, l are all even or all odd, corresponding to such fundamental spots as 002, 220, 111, etc. The other type is observed at about $\{h, k, l \pm 1/13.5\}$ in which h, k, l are either (odd, odd, even) or (even, even, odd), corresponding to such positions of the ordinary monolayer superlattices as 001, 110, 112, etc. These superstructure spot pairs reflected the lateral periodicity in the $[001]$ direction. They are satisfactorily explained by the formation of the structure shown in Fig. 3b.

Fig. 4b and 4c are the $(\bar{1}10)$ cross-sectional view and the (110) plan view of TEM dark field images obtained from an IPSL. In these images, the dark and bright areas correspond to the InGaAs and InAlAs regions, respectively. The InGaAs/InAlAs laterally periodic structures grown just on the InGaAs buffer layer are clearly observed. The periodic direction is almost in the $[001]$ direction. The periodicity is approximately 4 nm on the average, which is comparable to the terrace width expected from the substrate tilt angle (4 nm wide). Although the undulations of periodic contrasts along the growth direction and partial disordering are often observed in the cross-sectional view, a plan view image, which is obtained from a horizontal thin region in the IPSL shows good periodicity and straight contrast along the step edge direction of the $[\bar{1}10]$ direction. This suggests that compositional fluctuations along the step edge direction are smaller than those along the growth direction. This would be fortunate for

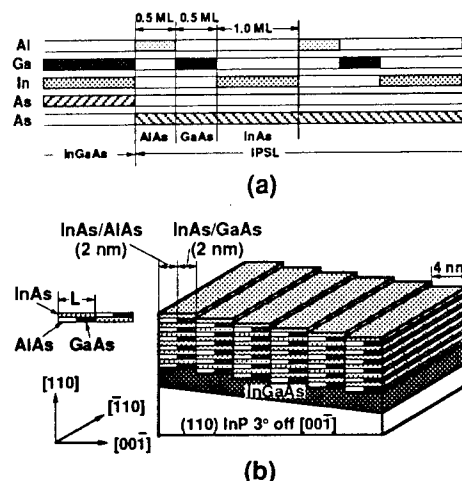


Fig. 3. (a) The opening and closing shutter sequences for the IPSL growth. (b) A schematic diagram of the IPSL structure expected by ideal step flow growth.

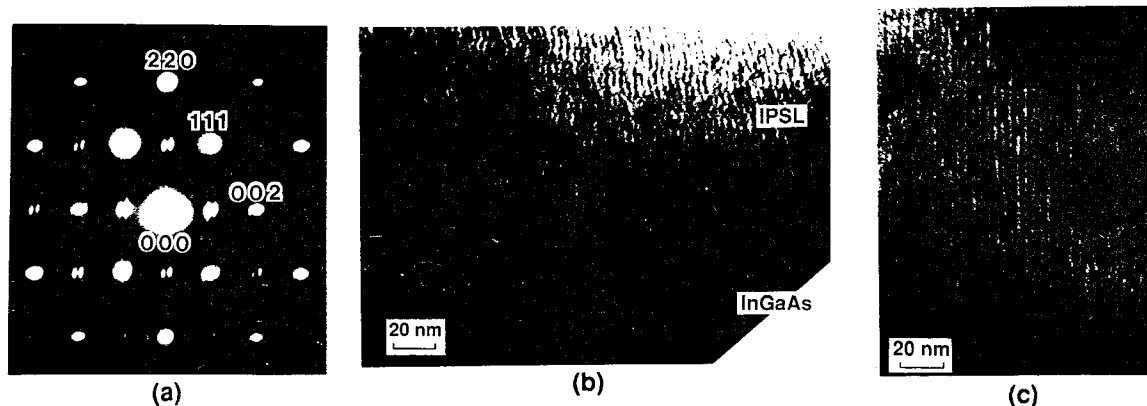


Fig. 4. (a) A $(\bar{1}10)$ cross-sectional TED pattern of the IPSL grown on a substrate tilting 3° . (b) A $(\bar{1}10)$ cross-sectional view of TEM dark field image of the IPSL. (c) A plan-view of TEM dark field image of the IPSL.

growing thinner layers of IPSLs such as quantum well wire array structures.

The PL spectrum of the IPSL measured at 4.2 K is shown in Fig. 5 together with those of the $(\text{InAs})_1/(\text{GaAs})_1$ LM-MSL, the InGaAs (2 nm thick)/InAlAs (2 nm thick) conventional layered superlattice (SL) on a misoriented (110) InP substrate, and the $\text{In}_{0.5}\text{Al}_{0.25}\text{Ga}_{0.25}\text{As}$ alloy on (001) InP substrate. The IPSL spectrum has two peaks. The energy of the main peak is far higher than that of the $(\text{InAs})_1/(\text{GaAs})_1$ LM-MSL and lower than that of the $\text{In}_{0.5}\text{Al}_{0.25}\text{Ga}_{0.25}\text{As}$ alloy. The main peak energy of 1.06 eV is close to that of the InGaAs (2 nm thick)/InAlAs (2 nm thick) conventional layered

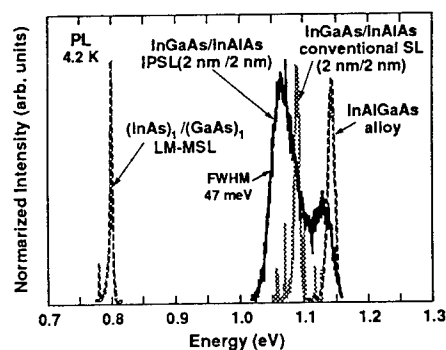


Fig. 5. A PL spectrum of the IPSL measured at 4.2 K.

superlattice, suggesting that InGaAs (2 nm wide)/InAlAs (2 nm wide) superlattices were grown. The other peak (sub-peak) at the energy of 1.13 eV is close to that of $\text{In}_{0.5}\text{Al}_{0.25}\text{Ga}_{0.25}\text{As}$ alloy. This is considered to be the luminescence from the strongly disordered or alloyed regions. The line width of the IPSL spectrum was 47 meV. This is much broader than that of the conventional superlattice of 9 meV. This broadening is presumably due to the compositional fluctuations resulting from undulations of the lateral interfaces along the growth direction and disordering in the IPSL.

3.2.2. InAs/GaAs IPSSLs

We also grew InAs/GaAs IPSSLs together with the InGaAs/InAlAs IPSSLs on a substrate tilted at 1.5° . The InAs/GaAs IPSSLs were grown by alternate growth of half monolayers of GaAs and InAs. During the growth of IPSSLs, the RHEED split spots showing single monolayer step arrangements were kept. The three-dimensional growth with island formation was not observed. A schematic diagram of the cross-sectional sample structure and a (110) cross-sectional TEM image are shown in Fig. 6. Although the lattice-mismatch should exist, laterally periodic structures with the periodicity of about 8 nm were grown.

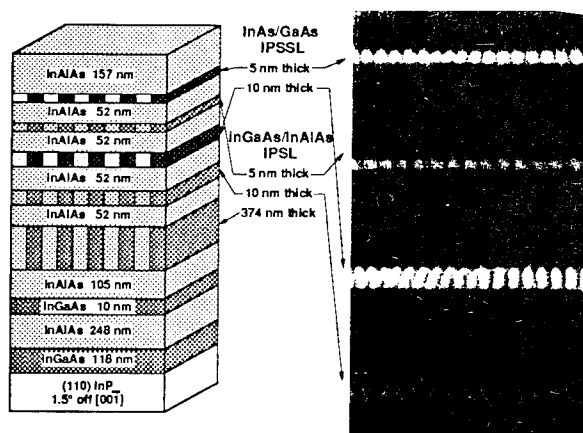


Fig. 6. A schematic diagram of the cross-sectional sample structure and a (110) cross-sectional TEM image.

4. Summary

We studied the surface steps during growth on the misoriented (110) InP substrates, and grew InGaAs/InAlAs IPSSLs by MBE. We found two types of surface steps (single and double monolayer steps) were formed depending on the growth conditions. Step edges of both types were seen to be straight in the AFM images. For the IPSSL growth, we grew alternately half monolayers of AlAs and GaAs and single monolayers of InAs, keeping the regular arrays of single monolayer steps. The TEM observations and PL measurements indicated that InGaAs/InAlAs IPSSLs composed of InAs/GaAs and InAs/AlAs MSLs were grown with some evidences of disordering. We also grew InAs/GaAs IPSSLs with the periodicity of about 8 nm on the misoriented (110) InP substrates.

Acknowledgments

I would like to thank my collaborators in this research. They are Osamu Ueda, Tsuguo Inata, Atsushi Tackeuchi, Yuji Nishikawa, Satoshi Nakamura and Shunichi Muto. I would also thank Osamu Ohtuki and Naoki Yokoyama for their encouragement.

References

- [1] P. M. Petroff, A. C. Gossard and W. Wiegmann, *Appl. Phys. Lett.* 45 (1984) 620.
- [2] J. M. Gaines, P. M. Petroff, H. Kroemer, R. J. Simes, R. S. Geels and J. H. English, *J. Vac. Sci. Technol. B* 6 (1988) 1378.
- [3] M. Tsuchiya, J. M. Gaines, R. H. Yan, R. J. Simes, P. O. Holtz, L. A. Coldren and P. M. Petroff, *Phys. Rev. Lett.* 62 (1989) 466.
- [4] T. Fukui and H. Saito, *Appl. Phys. Lett.* 50 (1987) 824.
- [5] T. Fukui and H. Saito, *J. Vac. Sci. Technol. B* 6 (1988) 1373.
- [6] T. Fukui, H. Saito and Y. Tokura, *Appl. Phys. Lett.* 55 (1989) 1958.
- [7] Y. Nakata, O. Ueda, T. Inata, S. Nakamura, M. Yamaguchi, S. Sasa and S. Muto, in: *Proc. 19th Intern. Symp. on GaAs and Related Compounds, Karuizawa, 1992*, Inst. Phys. Conf. Ser. 129, Ed. T. Ikegami, F. Hasegawa and Y. Takeda (Inst. Phys., Bristol, 1993) p.435.
- [8] O. Ueda, Y. Nakata and S. Muto, in: *Proc. 19th Intern. Symp. on GaAs and Related Compounds, Karuizawa, 1992*, Inst. Phys. Conf. Ser. 129, Ed. T. Ikegami, F. Hasegawa and Y. Takeda (Inst. Phys., Bristol, 1993) p.429.
- [9] Y. Nakata, O. Ueda, A. Tackeuchi, S. Nakamura and S. Muto, *J. Crystal Growth*, submitted Proc. 8th Intern. Conf. on Molecular Beam Epitaxy.
- [10] O. Ueda, Y. Nakata, A. Tackeuchi, S. Nakamura and S. Muto, *J. Crystal Growth*, submitted Proc. 8th Intern. Conf. on Molecular Beam Epitaxy.

Selective MBE growth of InGaAs and InAlAs on high-index facets and its application to fabrication of InGaAs ridge quantum wires

SA1.2

H. Fujikura and H. Hasegawa

Research Center for Interface Quantum Electronics and Department of Electrical Engineering,
Hokkaido University, Sapporo 060, Japan

Introduction

Recently, quantum wires and quantum dots have attracted significant attention because of new quantum mechanical phenomena in solid-state physics and their device applications. For realizing quantum wires and quantum dots, various approaches have been made. Among them, selective and self-organizing growth is promising method because of absence of process-induced damages (1)–(3). To achieve selectivity and self-organizing motion, growth on high index facets is particularly interesting because of possible growth rate modification and related material transfer.

Paying attention to the high mobility and the large conduction band discontinuity of InGaAs/InAlAs system, we have recently studied the growth characteristics of this system on nonplanar substrates and attempted formation of quantum wires by selective molecular beam epitaxy (MBE) (4)–(6). In this paper, we present novel results on MBE characteristics of $\text{In}_{0.53}\text{Ga}_{0.47}\text{As}$ and $\text{In}_{0.52}\text{Al}_{0.48}\text{As}$ layers on pre-fabricated ridge structures with (311)A facets and their successful application to fabrication of InGaAs ridge quantum wires. Sample structures were investigated by scanning electron microscope (SEM). Low temperature photoluminescence (PL) and cathodoluminescence (CL) measurements were made to characterize the fabricated InGaAs ridge quantum wires.

Experimental

As substrates for growth experiments and actual fabrication of ridge quantum wires, mesa-patterned (001) InP substrates with $4\mu\text{m}$ pitch, prepared by photolithography and wet chemical etching, were used. Orientation of the mesas were $\langle\bar{1}10\rangle$ direction and each mesas consists of a terrace with width of $1\mu\text{m}$ and two sidewall (211)A or (111)A facets. Following the substrate preparation, two kinds of the nonplanar starting structures A and B shown in Fig.1 were formed by MBE growth of InGaAs or InAlAs. Structure A and B were grown on the mesa-patterned substrate with (211)A and (111)A sidewalls, respectively.

Growth characteristics was studied by SEM observations for both InGaAs and InAlAs layers with thin marker layers grown on the starting structures under various growth conditions. On the structure A, InGaAs and InAlAs layers were grown within temperature ranges from 400 to 500°C and from 500 to 580°C , respectively. On the other hand, both materials were grown within a temperature range of 500 to 580°C on the structure B. Using the results obtained in the growth experiments, including selectivity of growth, formation of new facets and their developments,

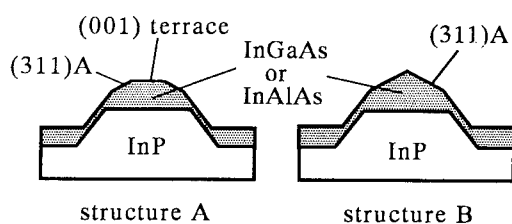


Fig.1 Schematic view of starting structures.

two types of InGaAs ridge quantum wires were successfully fabricated by selective MBE growth. These wires were characterized by PL and CL measurements at low temperatures.

In each MBE growth, substrates were rotated during the growth and the growth rate on the planar substrate was set at $6000\text{\AA}/\text{h}$ throughout this study. As_4 pressure was varied in the range from 1 to 3×10^{-6} Torr, maintaining As stabilized surfaces.

Growth Characteristics

Growth on the starting structure A

Figures 2 shows a cross-sectional SEM image of InAlAs layers with thin marker InGaAs layers grown at 500°C and its schematic drawing. It is seen in Fig.2 that the growth rate is enhanced on the terrace with the terrace width being continuously reduced as the growth proceeds and (311)A facets were formed next to the terrace although the initial sidewalls were (211)A facets. The lines connecting the intersection of the (001) terrace and the

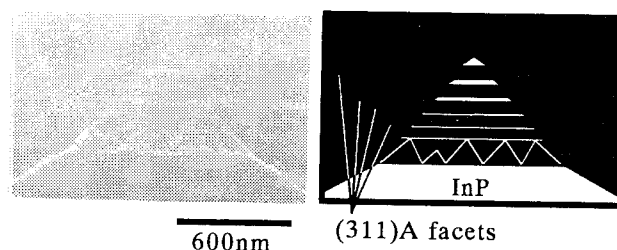


Fig.2 Cross-sectional SEM image of InAlAs layer with InGaAs marker layers grown on the structure A.

(311)A sidewall facets maintains a constant angle, θ , with respect to (001) terrace. It is also seen in Fig.2 that the growth on the terrace tends to be initially irregular. The irregular growth also occurred in other conditions and materials, and particularly InAlAs grown at 580°C show much pronounced irregularity. On the other hand, InGaAs showed less irregularity and an InGaAs layer grown on a narrow terrace ($<1000\text{\AA}$) nor InGaAs layer grown on a wide terrace at a lower temperature of 400°C showed no such phenomenon.

Figure 3 summarizes the ratio of growth rate on the terrace region to that on the planar substrate, r , as a function of the terrace width together with the angle θ for each case. The growth rate of InGaAs grown at 500°C was remarkably enhanced on the terrace while it is less pronounced at 400°C. InAlAs showed much smaller enhancement. The angle, θ , was estimated to be 50° for InAlAs growth at 500°C and 40° for InGaAs growth at 400°C, respectively.

These phenomena seen in Fig.2 and Fig.3, as well as the formation of (311)A sidewalls seen in the growth of starting structures, can be explained in terms of a differences in incorporation rates of group III atoms into each facets. Namely, a slower incorporation rate of group III atoms into (311)A facets than that into (001) terrace leads to migration of group III atoms from (311)A facets to (001) terrace, resulting in the enhancement of growth rate on the terrace and reduction of terrace width. The slower incorporation rate on (311)A facets also leads to development of (311)A facets on the starting structures. The angle θ , between facets is determined by the ratio of the growth rates between the terrace and the (311)A facets as discussed by Jones et al. (7). A larger value of θ for InAlAs than for InGaAs corresponds to a smaller terrace-to-(311)A facet growth rate ratio for InAlAs. The smaller enhancement of growth rate ratio r and a larger value of θ for InAlAs can be explained both in terms of shorter migration length of Al atoms.

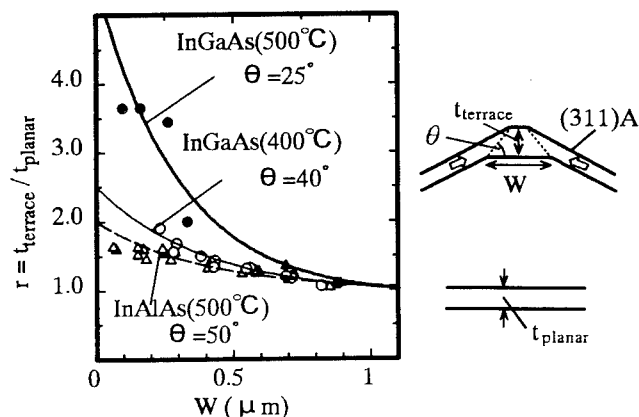


Fig.3 Relation between growth rate ratio (r) and terrace width (W) in the growth on the structure A.

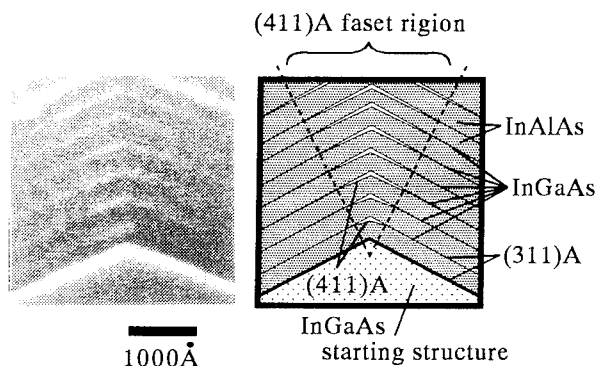


Fig.4 Cross-sectional SEM image of InAlAs layer with InGaAs marker layers grown on the structure B.

Growth on the starting structure B

Figure 4 shows a cross-sectional SEM image of InAlAs layers with InGaAs marker layers grown at 580°C on the structures B and its schematic drawing. In this case, (311)A facet of InAlAs was found to be unstable and (411)A facet gradually expanded at the top as seen in Fig.4. Additionally, InGaAs grew selectively on the (411)A facet region formed at the top of InAlAs ridge and wire like structures were formed. On the other hand, when the growth was made below 550°C, InGaAs and InAlAs grew with uniform thickness and maintained the initial (311)A ridge structures. The above mentioned selectivity can be applied for formation of wire structures on the ridge and the size of such a wire can be controlled by the amount of the InAlAs growth.

The dependence of stable facets on the growth condition can be explained by the change of the incorporation rate of group III atoms at different temperature. For the growth of InGaAs within the whole temperature range studied here and for the growth of InAlAs below 550°C, the incorporation rate of group III atoms into (311)A facet is smaller than that into (411)A facets, so that (311)A facet is maintained. On the other hand, for the growth of InAlAs at 580°C, the group III incorporation rate into (411)A facet becomes smaller than that into (311)A facet, leading to the formation and expansion of (411)A facets as seen in Fig.4.

Fabrication of ridge quantum wires by selective MBE growth

Growth of ridge quantum wires on the structure A

With the knowledge of values of r and θ in Fig.3, the terrace width at a certain point of growth can be accurately determined by the thickness of the layer grown on the planar substrate. Thus, the width of the ridge quantum wire (=width of the terrace) can be also controlled. A cross-sectional SEM photograph of InGaAs wire

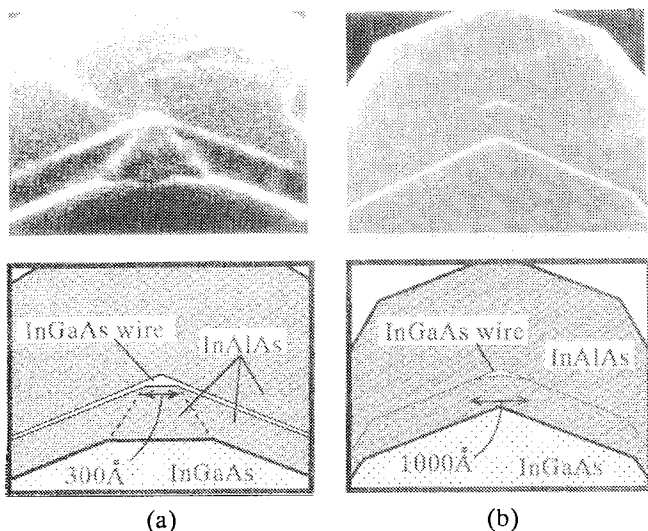


Fig. 5 SEM photograph of InGaAs ridge quantum wires grown on the structure A (a) and structure B (b).

selectively grown on InAlAs terrace is shown in Fig.5(a). The triangular shaped wire with lateral width of 300 Å were successfully formed. In Fig.5(a), the quantum wells are also seen on the (311)A sidewalls.

In this sample in Fig.5(a), the InGaAs wire layer was grown at 500°C to achieve a high selectivity of the growth according to Fig.3. The nominal thickness of the wire layer in this sample was 25 Å. The InAlAs barrier layer and InGaAs starting structure were grown at 500 and 400°C, respectively, to suppress the irregular growth. The advantage of this method is that the width of wires can be reduced far smaller than the lithography-defined terrace width.

Growth of ridge quantum wires on the structure B

Figure 5(b) shows an InGaAs ridge quantum wire grown on the structure B. The wire with a lateral width of 1000 Å was selectively grown on the (411)A facet region on the top of InAlAs ridge. Presence of very thin quantum wells on (311)A sidewall facets can also be recognized in this figure.

In this sample, bottom InAlAs barrier layer was grown at 580°C to form a (411)A facet on the top of the InAlAs ridge. Then, InGaAs wire layer with a nominal thickness of 25 Å and a top InAlAs layer were grown at 550°C. Following the growth of wire layer, growth was interrupted for 1 minute to enhance the gathering of the InGaAs into (411)A facet region (8). Since the width of (411)A facet region (=wire width) can be controlled by the growth itself as seen in Fig.4, uniform wire sizes can be achieved even if the size fluctuation exists in the terrace width of the mesa-pattern defined by lithography.

Optical properties of ridge quantum wires

Ridge quantum wires grown on the structure A

The 4 K PL spectrum of the ridge quantum wire grown on structure A is shown in Fig.6 together with that of reference ridge quantum well. The reference sample had the same structure as the wire except that it had a thick InGaAs well at the top of the terrace. In the spectrum of the ridge quantum wire, an intense and narrow peak is seen at 0.969 eV with a shoulder at high energy side. The ridge quantum well has a broader peak at around 0.8 eV.

The sharp peak in the ridge quantum wire spectrum is believed to originate from the wire itself. In fact, the observed energy shift of 159 meV of the peak of ridge quantum wire from band gap energy of bulk InGaAs agrees excellently with the theoretical value of 156 meV obtained by numerically solving Schrödinger equation by finite difference method using the observed shape and size of the wire. On the other hand, the position of the broad peak in the ridge quantum well was in a good agreement with that of the planar quantum well. The smaller and broad peaks observed above 1.05 eV in the ridge quantum wire and well seems to be originate from InAlAs barrier layers, since these peaks were often seen in the PL spectra of InAlAs layers grown on corrugated substrates without InGaAs wires(5). The shoulders observed at about 1.0 eV in both samples may be due to the thin quantum wells on (311)A facets as seen in Fig.5(a). The strong intensity and narrow width of the peak from InGaAs ridge quantum wire indicates that the wire crystal quality is excellent.

Ridge quantum wires grown on the structure B

The CL spectra of the ridge quantum wires grown on the structure B measured using spot excitation of the sample surface are shown in Fig.7. The solid and broken lines are the CL spectra measured using spot excitation of ridge region, including the quantum wire, and of the bottom groove region, respectively. In the spectrum measured by exciting the ridge region, an intense peak was observed at

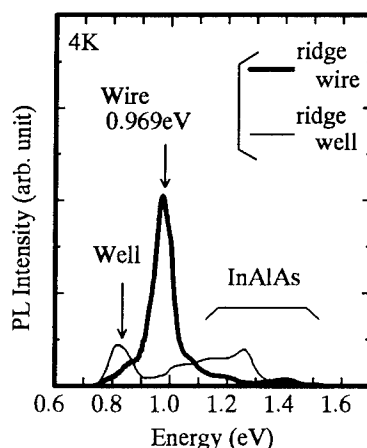


Fig.6 PL spectra of a ridge quantum wire grown on the structure A and these of a ridge quantum well.

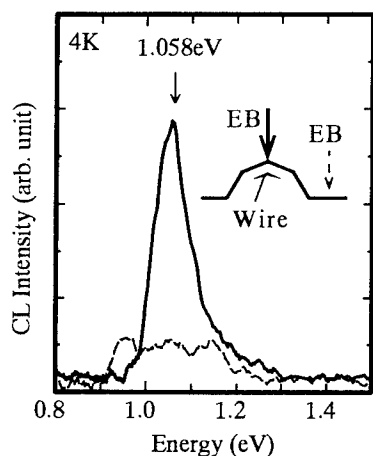
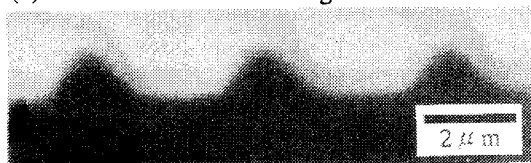


Fig.7 CL spectra of ridge quantum wire grown on the structure B using spot excitation.

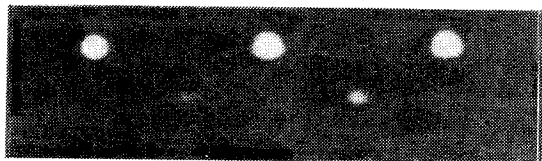
(a) Cross-sectional SE image



(b) Cross-sectional CL image (E=1.058eV)



(c) Cross-sectional CL image (panchromatic image)



(d) Top-view CL image (E=1.058eV)

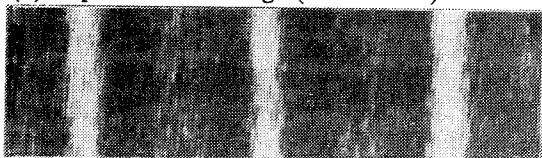


Fig.8 4K CL image of ridge quantum wire grown on the structure B.

1.058eV. On the other hand, the smaller and broader peak is seen in the spectrum of the bottom groove part within a energy range from 0.9 to 1.2eV. The results of observation of CL image to clarify the spatial origins of these peaks are shown in Fig.8. The cross-sectional monochromatic (at 1.058eV) and panchromatic CL images measured at 4K are shown in Fig.8(b) and (c), respectively, together with the corresponding secondary electron (SE) image given in Fig.8(a). A top-view CL image (at 1.058eV) is also shown

in Fig.8(d). In Fig. 8(b) and (d), spots and lines with intense and uniform brightness can be seen at intervals of $4\mu\text{m}$. In the panchromatic image (Fig.8(c)), such bright spots and additional emission spots with a much weaker intensity can be seen.

Since the positions of these bright spots and lines exactly correspond with that of the ridges in SE images, the intense peak at 1.058eV in Fig.7 is found to originate from the InGaAs ridge quantum wire itself. On the other hand, the weak emission seen between the bright spots in Fig.8(c) correspond to wells located at the bottom of the grooves and these were origin of broad peaks in Fig.7. The shoulder observed at the higher energy side of the peak at 1.058eV may be due to thinner wells on (311)A and sidewall facets whose presence was recognized in Fig.5(b). Strong intensity of the emission from the ridge quantum wires in spite of its small volume indicates that the wire crystal quality is excellent. In addition, judging from the uniform brightness of CL image at 1.058eV, uniformity of this wire thought to be very high.

Conclusions

By the growth experiments of $\text{In}_{0.53}\text{Ga}_{0.47}\text{As}$ and $\text{In}_{0.52}\text{Al}_{0.48}\text{As}$ on two types of non-planar starting structures having (311)A facets, detailed growth characteristics were clarified.

Using the results of growth experiments, two types of InGaAs ridge quantum wires were successfully fabricated by selective MBE growth on these starting structures.

The results of low temperature PL and CL measurements indicated that the wires with excellent crystal quality and uniformity can be made by two approaches presented here.

References

- (1) E.Kapon, K.Kash, E.M.Clausen, Jr., D.M.Hwang and E.Colas, Appl. Phys. Lett. 60 (1992) 477.
- (2) R.Bhat, E.Kapon, D.M.Hwang, M.A.Koza and C.P.Yun, J. Crystal Growth 93 (1988) 850.
- (3) T.Demel, D.Heitmann, P.Grambow and K.Ploog, Appl. Phys. Lett. 53 (1988) 2176.
- (4) H.Fujikura, H.Tomozawa, M.Akazawa and H.Hasegawa, Appl. Surf. Sci. 60/61(1992)702.
- (5) H.Fujikura, T.Iwa-ana and H.Hasegawa, Jpn. J. Appl. Phys. 33(1994)919.
- (6) H.Fujikura and H.Hasegawa, accepted for publication in J. Crystal Growth (1995).
- (7) S.H.Jones, L.K.Seidel, K.M.Lau and M.Harold, J. Crystal Growth 108 (1991) 73.
- (8) H.P.Meier, E.Van Gieson, P.W.Epperlein, C.Harder and W.Walter, J. Crystal Growth 95(1989)66.

InAs/InGaAs self-assembled quantum dots grown on (311)B GaAs by molecular beam epitaxy

SA1.3

Kenichi Nishi^{1,2,4}, Richard Mirin^{3,4}, Devin Leonard^{2,4}
Gilberto Medeiros-Ribeiro^{2,4}, Pierre M. Petroff^{2,4} and Arthur C. Gossard^{2,3,4}

¹*Opto-Electronics Research Labs., NEC Corporation*
34 Miyukigaoka, Tsukuba, Ibaraki 305, Japan

²*Materials Dept.,* ³*Electrical and Computer Engineering Dept. and* ⁴*QUEST*
University of California at Santa Barbara, CA 93106, USA

Introduction

Utilization of the 2D-3D growth mode transition during the initial stage of highly strained growth (Stranski-Krastanow (SK) growth) is a novel technique to fabricate dislocation free self-assembled quantum dots (SADs). In(Ga)As SADs on (100) GaAs by molecular beam epitaxy (MBE) showed excellent size uniformity and good optical quality[1,2]. They are also interesting as a strained template for selective growth[3] and a strained dot with localized carrier confinement potentials[4]. Recently, on (311)B GaAs, high quality InGaAs quantum disks were fabricated by growth interruption during metalorganic vapor phase epitaxy (MOVPE) growth[5,6] which resembles the SAD formation method. However, this method is expected to be different from that for SAD by MBE because the disks are not formed on (100) GaAs and the wetting layer that exists under the SAD layer in SK growth was not apparent. In this paper, we report on MBE growth and optical characterization of InAs/InGaAs SADs on (311)B GaAs as well as (100) to study the differences of using (311)B substrates. We also report on a compound SAD structure where the composition of the wetting layer and the SAD layer is changed, which is intended to suppress the luminescence from the wetting layer. The narrowest full widths at half maximum of the PL peak from SADs on (311)B are about 35 meV at 2 K and 40 meV at room temperature, respectively, which are much narrower than those measured from reference (100) SADs. The PL linewidth is not strongly affected by the measurement temperature, which indicates that thermal broadening in PL emission is greatly reduced. These narrow PL spectra demonstrate an advantage of using (311)B substrates in SAD growth by MBE.

Experimental Procedures

Samples were grown by MBE in Varian/Intevac Modular Gen II systems. For all samples, GaAs (311)B and (100) substrates are prepared and bonded side by side on the same Mo block. Before the growth, the substrates are heated up to around 630°C for oxide desorption. After the oxide desorption from both substrates, a GaAs buffer layer was grown at a substrate temperature of 600°C. The arsenic beam equivalent pressure was kept at $8 - 9 \times 10^{-6}$ Torr. Both As₂ and As₄ are used as arsenic species, but no obvious difference was found in critical thickness or in optical quality. After the GaAs buffer layer, an Al_{0.3}Ga_{0.7}As layer, an AlAs/GaAs short period superlattice and a GaAs layer were successively grown in most samples. In some samples, the SAD layer was grown on the first GaAs buffer layer and capped only by GaAs. For SAD growth, the substrate temperature was reduced to 520°C and the InAs/InGaAs SAD structure was formed on the GaAs layer. There, 1 s growth of InAs or GaAs that corresponds to 0.1 or 0.2 monolayer (ML) on (100) was followed by a 2 s arsenic exposure, and this sequence was repeated until the reflection high energy diffraction (RHEED) showed the transformation to a spotty pattern. For compound SAD structures, an InAs or an InGaAs layer was first grown below the critical thickness to form a wetting layer, then a SAD layer whose composition was different from the wetting layer was grown. In the samples for structural characterization, the substrate

temperature was immediately reduced after SAD formation and the samples were kept in vacuum before characterization. Otherwise, the SAD layer was covered by GaAs and the substrate temperature was ramped to 600°C. Then it was covered by an Al_{0.3}Ga_{0.7}As layer and a GaAs layer. In most samples, the wide gap materials are introduced in order to prevent carrier leakage from the GaAs layer adjacent to SAD layer to the substrate or surface. This structure is necessary to yield intense photoluminescence (PL) at room temperature. The conduction band diagram of a typical sample is schematically shown in Fig. 1.

Structural characterization was performed by atomic force microscopy (AFM) to determine the density and shape of SAD structures. PL measurements were performed at 2 K and at room temperature using an Ar⁺ laser as an excitation source. PL was detected by a cooled Ge detector using a

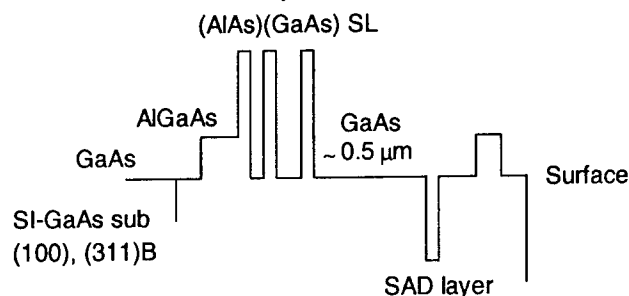


Fig. 1. A schematic conduction band diagram of a typical sample.

phase-locking technique.

Results and Discussion

Structural Characterization

AFM measurements showed that InAs SADs are formed after depositing 1.5 ML on (100) GaAs substrate[7]. However, from RHEED observations, the SAD formation becomes clear only after a growth of 1.7 ML (0.55 nm) of InAs on (100) GaAs. The critical thickness for SAD formation on (311)B GaAs measured by the change in the RHEED pattern is close to that of (100) GaAs (0.55 -0.58 nm: Note that, as the thickness unit of ML is dependent on a crystallographic axis, we will use nm hereafter). Fig. 2 shows the RHEED pattern from a (311)B surface measured along [011] direction. After the SAD formation, chevron patterns between spots are seen in the figure. This indicates that the SAD structure should have certain facets.

In Fig. 3, AFM images of $\text{In}_{0.5}\text{Ga}_{0.5}\text{As}$ SADs on (311)B and (100) GaAs are shown. The SADs are formed after growing nominally 1.45 nm $\text{In}_{0.5}\text{Ga}_{0.5}\text{As}$. Uniform dots with a typical dot diameter of around 30 nm and height of 13 nm are observed on (311)B GaAs although the exact shape can not be resolved. A density of SADs is $2 \times 10^{10} \text{ cm}^{-2}$. Consequently, 14% of the surface is covered by SADs. On the (100) reference sample, the SAD density is lower and the fluctuation in diameter appears greater than that on (311)B. As the uniformity in diameter and height depends on the coverage[7], the grown thickness should be adequate for the SAD formation on (311)B. Although exact calculations were not performed, the dimension of the SAD structure is expected to be small enough to show three-dimensional quantum confinement effect.

It was demonstrated that InGaAs quantum disks on (311)B GaAs fabricated by MOVPE with growth interruption were well aligned[5]. Also in MBE, the SAD structure on (311)B was regular and some of the dots are aligned along certain direction on the surface. From the AFM measurements, the uniformity of the dot size on (311)B substrates seems to be superior to that on the (100) reference samples. Thus, the utilization of (311)B is also expected to be advantageous in fabricating uniform and dense SADs in MBE.

Optical characterization

PL spectra measured from InAs SADs (nominal growth of 0.58 nm InAs) at 2 K are shown in Fig. 4. In these samples, SAD structures are sandwiched by GaAs layers without AlGaAs and superlattice layers. In Fig. 4 (a), PL from SADs on (311)B is observed at 900 nm with a full width at half maximum (FWHM) of 46 meV. An intense and sharp emission is also observed at 866 nm. We believe this peak originates from a wetting layer that exists underneath the SAD layer because a similar intense peak was observed from a control 0.52 nm InAs quantum well sample without SADs. From SADs on (100), PL was observed whose peak position was at 1049 nm with a FWHM of 127 meV. PL from the

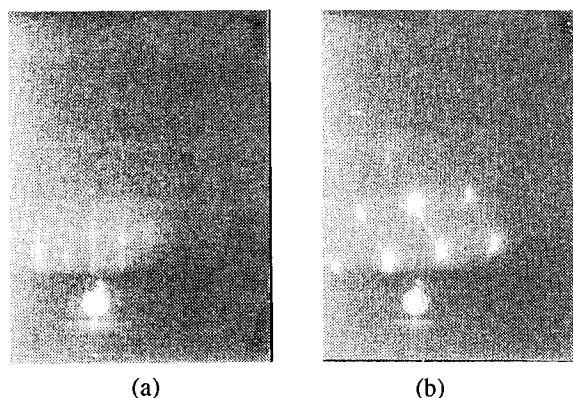


Fig. 2. Reflection high energy electron diffraction (RHEED) patterns measured along [011] direction from (311)B surface (a) before and (b) after SAD formation. Chevron patterns are observed between spots after SAD formation (b).

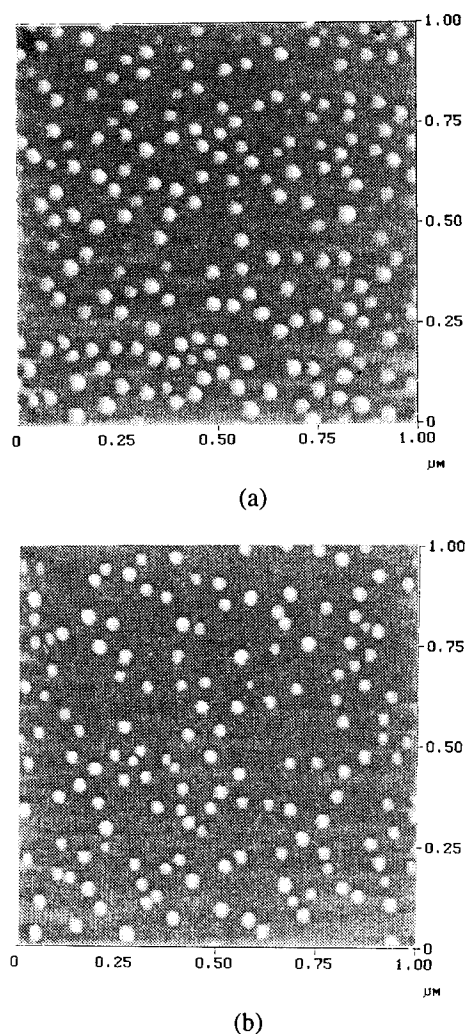


Fig. 3. 1 μm x 1 μm atomic force microscope images of $\text{In}_{0.5}\text{Ga}_{0.5}\text{As}$ SADs on (a) (311)B and (b) (100) GaAs.

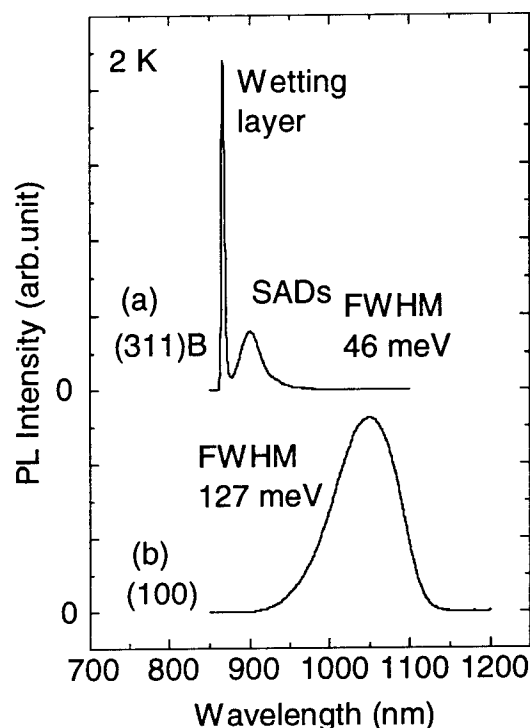


Fig. 4. Photoluminescence spectra from InAs SADs (nominal thickness of 0.58 nm) measured at 2 K. SADs are grown on (a) (311)B and (b) (100) GaAs substrates.

wetting layer was very weak in this sample. Comparing these results, it is found that the PL linewidth from SADs was reduced by a factor of three by using (311)B substrates. Sharp and intense PL from the wetting layer was only observed from the (311)B structures. PL peak intensities from SADs in both samples were almost identical. The same characterization was performed on $\text{In}_{0.5}\text{Ga}_{0.5}\text{As}$ SADs grown on (311)B and (100) GaAs. There, the linewidth from (311)B SADs was 60 meV, while that from (100) SADs was 78 meV. Although the ratio of the linewidths was smaller than InAs SADs, an improvement in the linewidth was observed.

In order to suppress the intense PL from the wetting layer in (311)B, we introduced a compound SAD structure where the composition of the wetting layer and the dot layer is different. The structure consists of InAs SADs on an InGaAs wetting layer as well as InGaAs SADs on an InAs wetting layer. In Fig. 5, PL spectra measured at 2K on the compound SAD structures of InGaAs dots (nominal thickness of 0.85 nm) on InAs (0.42 nm) are shown. The PL from the wetting layer was suppressed and could not be resolved in this scale. The FWHM of the peak from (311)B is 35 meV. A shoulder peak was detected in the PL spectrum from (311)B SADs. An origin for this subpeak is not currently understood. It may be from the dots with different size or from excited states. Further experiments like excitation intensity dependent PL or time-resolved PL measurements should be necessary to identify the origin. At room temperature, this peak is enhanced to show a distinct peak.

In Fig. 6, PL spectra measured at room temperature from

the compound SADs are shown. Intense PL emissions from SADs are observed, indicating that the SAD structures have good optical quality and can be utilized as a light emitting source at room temperature. From the SADs on (311)B, the PL linewidth is observed to be as narrow as 41 meV. This value is almost the same as that from GaAs bulk structure. On the other hand, the PL peak from the SADs on (100) has a width of about 102 meV. As the peak height is not degraded, the reason for this broadening is expected to be the thickness distribution or the different strain effect in different dots.

Thus, it is seen that the SADs on (311)B GaAs had narrower PL peaks than those on (100). As the PL linewidth is not strongly affected by the measurement temperature, this width is governed by the structural distribution rather than the thermal broadening. So the improved size and shape uniformity in (311)B SADs is the probable reason for the reduced PL linewidth.

The growth mechanism for the self-organized quantum disks on (311)B by MOVPE was discussed as a complex interplay of surface energy, strain, and surface diffusion[5]. High surface mobility and surface energy are assumed to be important. It is not straightforward to apply the same discussion to the results in MBE. However, if the high surface adatom mobility on (311)B surface assumed in the previous discussion held as well in the MBE growth, the SAD size uniformity would be expected to be improved because the size can very quickly reach equilibrium during the growth. For the uniformity of the SAD shape that relates

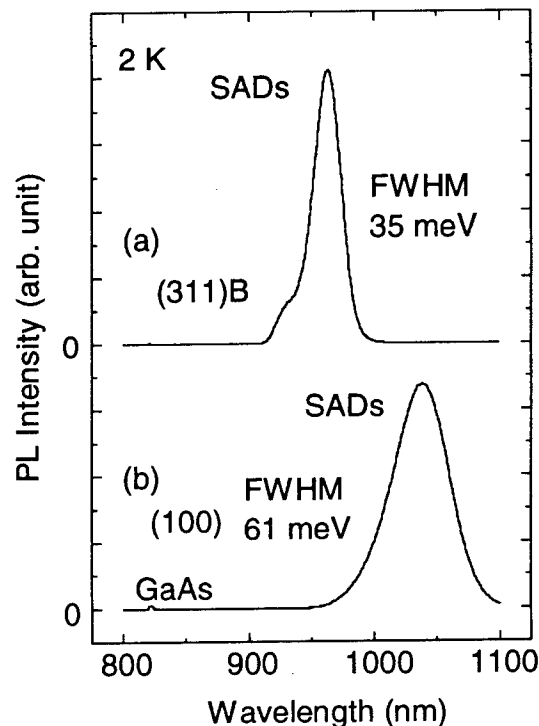


Fig. 5. PL spectra measured from InGaAs/InAs compound SADs on (a) (311)B and (b) (100) GaAs at 2 K. The linewidth of SAD peak from (311)B is as narrow as 35 meV.

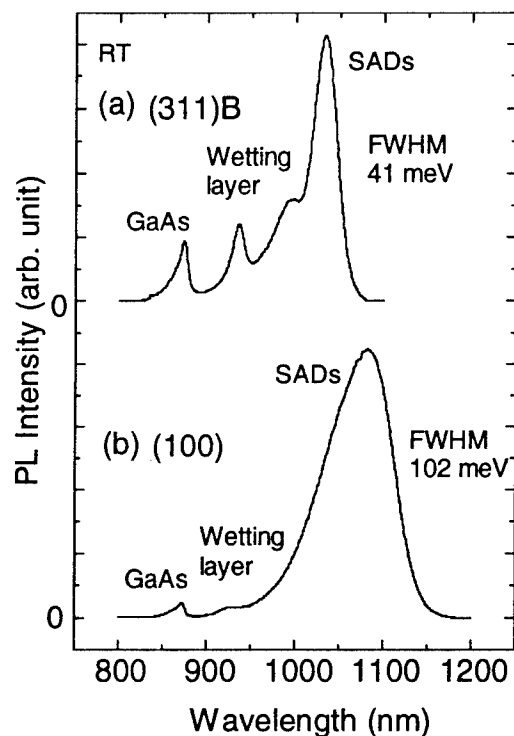


Fig. 6. PL spectra measured from InGaAs/InAs compound SADs on (a) (311)B and (b) (100) GaAs at room temperature. The linewidth of the SAD peak from (311)B is 41 meV.

with the strain magnitude and the strain distribution, the same assumption can apply. In this assumption, when the surface with higher adatom mobility is adopted, more uniform SAD structures can be expected.

When the growth orientation is different, it is expected that some other characteristics are different like In surface segregation or preferable facets in 3D structures. Further growth studies with various growth directions can clarify the origin for improved PL characteristics.

The half width of 41 meV at room temperature from (311)B SADs is comparable to the value observed from the 30 nm isolated disks fabricated by MOVPE[6]. The narrow PL spectra from the SADs demonstrate an advantage of using (311)B substrates in MBE. By optimizing the growth condition, material system and surface orientation, quantum dot structures with high uniformity and good optical quality are expected to be realized in SAD growth.

Conclusions

We have fabricated InAs/InGaAs self-assembled quantum dots on (311)B GaAs substrates. By RHEED observation, the critical thickness for SAD formation on (311)B is measured to be almost the same as that on (100). Uniform SAD structures on (311)B are confirmed by AFM observation. PL measurements on InAs SADs show a reduced linewidth from (311)B SADs compared to (100) SADs. In the measurements, an intense PL peak from the wetting layer that exist under the

SAD layer was observed from the (311)B sample. We introduced compound SAD structures which are intended to suppress the luminescence from the wetting layer. At room temperature as well as at 2 K, narrow PL emissions are observed from the compound SADs of InGaAs dots on an InAs wetting layer. The linewidths are about one half of those from the (100) SADs. The narrowest PL linewidth of 41 meV was obtained at room temperature. One reason for this improvement is expected to be the improved uniformity in (311)B SADs, which may be achieved by the high surface adatom mobility. This improvement demonstrates an advantage of using (311)B substrates in SAD growth by MBE.

Acknowledgments

We would like to thank John English for his help in MBE growths and Kazuhiko Itaya and Song Shi for PL measurements. We acknowledge financial support from NSF Science and Technology Center for Quantized Electronic Structures (QUEST) Grant No. DMR-20007. K.N. would like to thank Kohroh Kobayashi, Kiyoshi Asakawa, Junji Namiki and Sigeo Sugou for encouragement throughout this work.

References

- [1]. D. Leonard, M. Krishnamurthy, C. M. Reaves, S. P. Denbaars and P. M. Petroff, "Direct formation of quantum-sized dots from uniform coherent islands of InGaAs in GaAs surfaces", *Appl. Phys. Lett.* **63**(23), 3203 (1993).
- [2]. J. M. Moison, F. Houzy, F. Barthe, L. Leprince, E. André and O. Vatel, "Self-organized growth of regular nanometer-scale InAs dots on GaAs", *Appl. Phys. Lett.* **64**(2), 196 (1994).
- [3]. J. Ahopelto, H. Lipsanen, M. Sopanen, T. Koljonen, and H. M.-E. Niemi, "Selective growth of InGaAs on nanoscale InP islands", *Appl. Phys. Lett.* **65**(13), 1662 (1994).
- [4]. K. Nishi, A. A. Yamaguchi, J. Ahopelto, A. Usui, and H. Sakaki, "Analyses of localized confinement potential in semiconductor strained wires and dots buried in lattice-mismatched materials", *J. Appl. Phys.* **76**(11), 7437 (1994).
- [5]. R. Nötzel, J. Temmyo and T. Tamamura, "Self-organization of boxlike microstructures on GaAs (311)B surfaces by metalorganic vapor-phase epitaxy", *Jpn. J. Appl. Phys.* **33**(3A), L276 (1994).
- [6]. R. Nötzel, J. Temmyo, H. Kamada, T. Furuta and T. Tamamura, "Strong photoluminescence emission at room temperature of strained InGaAs quantum disks (200-30 nm diameter) self-organized on GaAs (311)B substrates", *Appl. Phys. Lett.* **65**(4), 457 (1994).
- [7]. D. Leonard, K. Pond, and P. M. Petroff, "Critical layer thickness for self-assembled InAs islands on GaAs", *Phys. Rev.* **B50**(16), 11687 (1994).

Spontaneous Formation of Aligned InGaAs Quantum Dots on GaAs Multi-Atomic Steps by Metalorganic Chemical Vapor Deposition Growth

M. Kitamura, M. Nishioka, J. Oshinowo*, and Y. Arakawa

Institute of Industrial Science, University of Tokyo, 7-22-1 Roppongi, Minato-ku, Tokyo 106, Japan

**Department of Physics, Wurzburg University, Am Hubland, D-8700 Wurzburg, Germany*

The InGaAs quantum dots were grown on multi-atomic step structure by MOCVD growth. Then AFM images indicated that these quantum dots are grown not on the terrace but on the multi-atomic step edges. Using this phenomenon, we demonstrate successful alignment of the InGaAs quantum dots by the spontaneous growth without any pre-processing technique. Finally formation of twin InGaAs quantum dots was demonstrated.

Fabrication of quantum dots is important for optoelectronic device application as well as for basic physics.(1) For this purpose, various technological approaches have been performed. Among them, Stranski-Krastanow (SK) growth mode is useful in the formation of quantum dots. This technique has attracted attention because quantum dots are directly formed on substrate without processing such as electron beam lithography, etching process, and ion implantation is required. This growth mode is started with an initial two dimensional layer deposition on the substrate material. After a critical layer deposition thickness is achieved, the surface transforms into three dimensional highly strained dot structures that grow coherently on the surface.

In fact, studies of strained dot structures by SK growth method previously show by molecular beam epitaxy or metal organic chemical vapor deposition (MOCVD).(2-5). Particularly, the diameter of quantum dot as well as 15 nm has achieved by this growth mode in MOCVD.(5) However, the position of the quantum dots were randomly distributed.

In this paper, we demonstrate successful alignment of the InGaAs quantum dots by the spontaneous growth without any pre-processing technique. After a multi-atomic step structure of GaAs epilayer was formed on a GaAs vicinal substrate, InGaAs quantum dots were grown on this structure by MOCVD growth. Then atomic force microscope (AFM) images of indicated that these quantum dots are formed not on the terrace but on the multi-atomic step edges. Further, we show that the InGaAs quantum dots are copulate in a growth condition which is different from that of the dots alignment.

The fabrication method proposed here is that the quantum dots are grown on the multi-atomic step edges

of multistep structure which results from the step bunching through the generation of facets with two different orientations during annealing.(6) By carefully choosing the growth condition, this multi-atomic step edge can be formed on almost straight lines.(6-8) In addition, we have already found that the dot density on GaAs substrate misoriented is higher than that on GaAs (001), which indicates that the quantum dots are easily formed on the step edge than on the terrace.(9) Therefore, by artificially forming the multi-atomic steps during the growth, the position of the quantum dots can be controlled, as illustrated in Fig. 1.

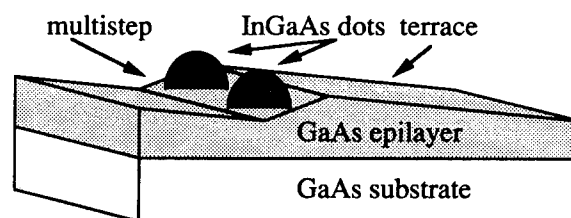


Fig.1: Schematic illustration of InGaAs quantum dots on the multistep edge of GaAs epilayer.

The samples were grown by the MOCVD growth. Trimethylgallium (TMG), trimethylindium (TMI) and arsine (AsH₃) were used as source materials. First, 200nm-thick GaAs layer on a GaAs substrate was grown at 700°C. Then the temperature was decreased to 500°C and the growth was interrupted. Then, In_{0.5}Ga_{0.5}As were grown on GaAs layer at this temperature. During GaAs layer growth, AsH₃ partial pressure was 89 Pa. The V/III pressure ratio was 500. In this condition, multi-atomic step structure appears and step edges of this

structure is formed on almost straight lines. During InGaAs quantum dots growth, AsH_3 partial pressure was 22 Pa. This condition was the same as in previous paper.(9)

To study the difference between with and without misorientation of the substrates, a GaAs (001) substrate and GaAs (001) vicinal substrates were used. The directions of misorientation were [010], [110]A and [110]B directions. The misorientation angle was 2.0° . The surface was studied with an AFM in the air at room temperature.

Figure 2(a) shows an AFM image of the InGaAs-dots grown on GaAs (001) surface. The AFM images of the InGaAs-dots grown on GaAs (001) vicinal surface

toward [010], [110]A, [110]B directions, respectively, are shown in Figs.3(b)-(d). As shown in these figures, there is clear difference among the samples with and without misorientation of the substrates. The multi-steps are clearly formed on the vicinal substrates and the quantum dots are formed on the multi-atomic step edges regardless of the misoriented directions. On the other hand, on the GaAs (001) substrate without misorientation, the quantum dots are no formed anywhere and two-dimensional islands appear between the monolayer steps. The results indicate that the vicinal substrates are useful to form the multi-atomic step structure which lead to localization of the quantum dots at the step edges.

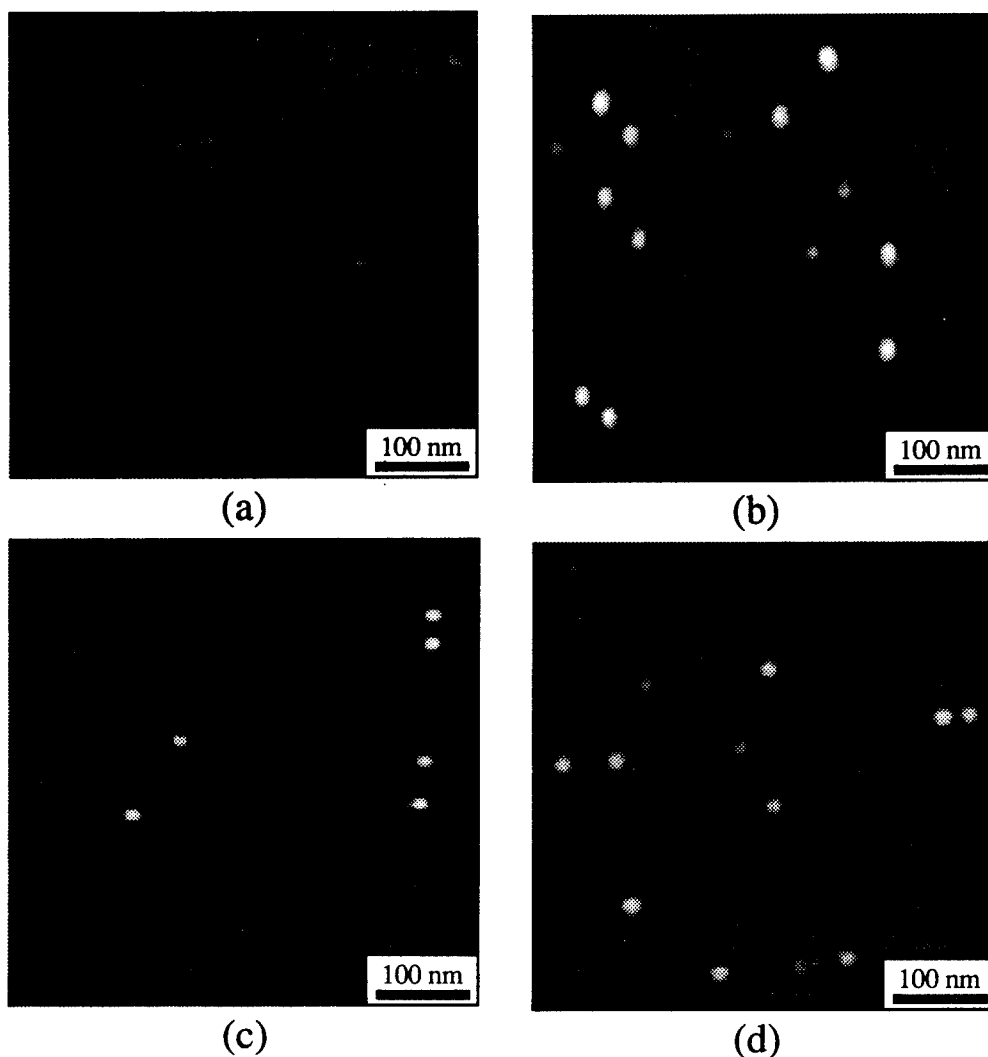


Fig.2: AFM images of InGaAs quantum dots on GaAs surface with various directions of misorientation. (a) no misorientation. The directions of misorientation are (b) [010], (c) [110]A and (d) [110]B. The growth time is 3 sec. The scale is $500 \text{ nm} \times 500 \text{ nm}$.

We found that area dot density increased consistently with the growth time. By choosing growth time, dots density is controlled Figure 4 shows AFM images of the quantum dots grown on the [010]-misoriented surface. The growth time for the InGaAs dots are 3.5 sec. As indicated in the figure, the InGaAs quantum dots are well aligned at the multi-atomic step edges.

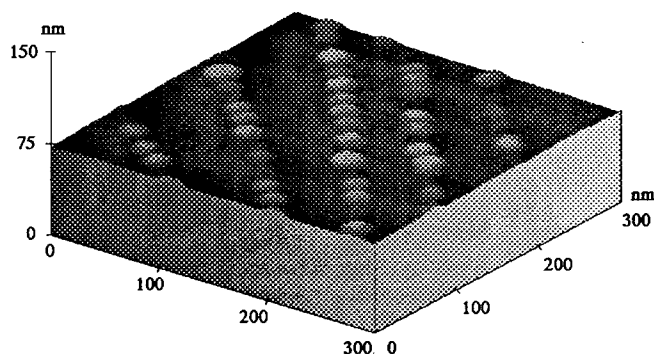


Fig.3: An AFM image of aligned InGaAs quantum dots on [010] misorientated surface. The growth time is 3.5 sec. The scale is 300 nm \times 300 nm.

Finally, successful fabrication of twin quantum dots (TQDs) is demonstrated as shown in fig. 4. The growth condition is as follows. The growth temperature which is higher than that of aligned dots was 600 °C. The partial pressures of TMG and TMI were one fifth as compared with that of aligned dots. The growth time is 25 sec. The GaAs substrate without misorientation was used. The line in which the TQDs stand is parallel or perpendicular to cleaved surface. The distance between

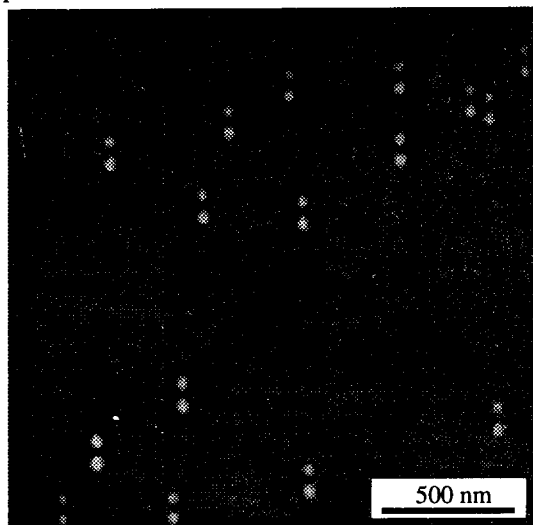


Fig.4: An AFM image of twin quantum dots. The growth time is 25 sec. The scale is 2 μ m \times 2 μ m.

TQDs is close to 100 nm. The size of one dot is large or small than the other. This growth mode is clearly different from the mode of aligned dots. However, the details of mechanism of TQDs formation has yet clarified.

In conclusion, we demonstrated successful alignment of InGaAs quantum dots using spontaneous growth technique through formation of the multi-atomic step in the GaAs epilayer on vicinal substrates. This technique is promising for full *in-situ* formation of the quantum dots with small size. Finally, formation of twin quantum dots was demonstrated.

References

- (1) Y. Arakawa and H. Sakaki, Appl. Phys. Lett., Vol. 40, pp. 939-941, 1982.
- (2) C. W. Snyder, B. G. Orr, D. Kessler and L. M. Sander, Phys. Rev. Lett., Vol. 66, pp. 3032-3035, 1991.
- (3) S. Guha, A. Madhukar and K. C. Rajkumar, Appl. Phys. Lett., Vol. 57, pp. 2110-2112, 1990.
- (4) D. Leonard, M. Krishnamurthy, C. M. Reaves, S. P. Denbaars and P. M. Petroff, Appl. Phys. Lett., Vol. 63, pp. 3203-3205, 1993.
- (5) J. Oshinowo, M. Nishioka, S. Ishida and Y. Arakawa, Appl. Phys. Lett., Vol. 65, pp. 1421-1423, 1994.
- (6) M. Kasu and N. Kobayashi, Appl. Phys. Lett., Vol. 62, pp. 1262-1264, 1993.
- (7) M. Kasu and T. Fukui, Jpn. J. Appl. Phys., Vol. 31, pp. L864-L866, 1992.
- (8) J. Ishizaki, S. Goto, M. Kishida, T. Fukui and H. Hasegawa, Jpn. J. Appl. Phys., Vol. 33, pp. 721-726, 1994.
- (9) J. Oshinowo, M. Nishioka, S. Ishida and Y. Arakawa, Jpn. J. Appl. Phys., Vol. 33, pp. L1634-L1637, 1994.

Self-organization Phenomenon of Strained InGaAs Grown on InP (311) Substrates by Metalorganic Vapor Phase Epitaxy

Jiro Temmyo, Atsuo Kozen, and Toshiaki Tamamura

NTT Opto-electronics Laboratories

3-1 Morinosato Wakamiya, Atsugi-shi, Kanagawa, 243-01 Japan

Richard Nötzel, Takashi Fukui, and Hideki Hasegawa

Research Center of Interface Quantum Electronics, Hokkaido University

W8, N13, Kita, Sapporo, 060 Hokkaido, Japan

Introduction

Precise carrier confinement in reduced dimensional structures such as quantum wires and quantum dots is believed to give a novel density state and improve the performance of optical devices. Since 1984 much work¹⁻³⁾ has been done using a natural formation technique by epitaxial growth and /or a combination of fine lithography, etching and quantum well growth. However, up to now, no superior optical performances has been obtained compared to that of quantum wells. A coherent islanding phenomenon of strained InGaAs films on a GaAs (100) substrate⁴⁾, called the Stranski-Krastanow epitaxial growth mode, has recently been receiving attention again as a useful method for making quantum dot structures⁵⁻⁶⁾ because of its potential for creating damage-free nanostructures. There are some problems, however, such as the inevitable two-dimensional wetting layer residue, poor size-controllability, no ordering, and very narrow optimum growth conditions. Unfortunately, room temperature photoluminescence emission (PL) from buried InGaAs islands have yet been reported.

On the other hand, we have recently found a new phenomenon of the self-organized formation of strained InGaAs microstructures during epitaxial growth by metalorganic vapor phase epitaxy (MOVPE) on a GaAs (311)B surface⁷⁾. This results in nano-scale InGaAs quantum disks surrounded by lower AlGaAs barriers due to mass-transport. On GaAs (311)A surfaces, one-dimensional faceting due to step bunching forms quasi-quantum wire-like morphologies. These phenomena during growth interruption may come from the lower barrier height for adatom migration on high-index planes, compared with that on the (100) surface. The excellent crystal quality and homogeneity in size manifests itself in high PL efficiency and extremely narrow PL spectra at room temperature⁸⁾. Moreover, we have achieved low-threshold operation of a quantum disk laser with a self-organized nanostructure as an active region at room temperature⁹⁻¹⁰⁾. The question arose as to whether the self-organization due to strained systems occurs universally in other III-V compound semiconductor systems. Here, we report that self-organization can occur similarly on InP substrates.

Experimental

The growth apparatus used was a low-pressure metalorganic vapor phase epitaxy (MOVPE) system with substrate temperatures between 600 and 700 °C. Trimethyl alkyls of gallium (TMG), aluminum (TMA), indium (TMI), arsine and phosphine were used as material sources. The growth rate was 1 μm/h for the ternary compounds and 0.6 μm/h for InP. Epitaxial layers with nominal InGaAs

quantum wells and Al_{0.48}In_{0.52}As and/or InP barriers were grown on InP (311)B, (311)A and (100) substrates. Interrupt time after InGaAs epitaxial growth was 2.5 minutes for self-organization. The atmosphere gas during the growth interruption was AsH₃ and/ or PH₃. The epitaxial layers were covered with strained InGaAs cap layers with the same composition and nominal thickness as the inner InGaAs structure. These cap layers exhibit the same morphologies as the inner buried InGaAs structures, which were observed

by high-resolution scanning-electron microscopy (SEM)¹¹ and atomic force microscopy (AFM). For the photoluminescence (PL) measurements the microstructures were overgrown by 50 nm thick layers of InAlAs or InP. All PL measurements were performed at room temperature.

Results and discussion

In the case of compressive In_{0.8}Ga_{0.2}As with In_{0.52}Al_{0.48}As barriers lattice-matched to InP, on the (311)B surfaces, we find well-ordered microcrystal arrays with a base size of 120 nm with buried quantum microstructures as shown Fig.1. The surface morphology of In_{0.8}Ga_{0.2}As grown with the relatively lower substrate temperature of 600°C and a thinner thickness of 3.5 nm shows an inhomogeneous formation of microcrystal including some modulated structures. This indicates the suppression of adatom migration and lateral mass-transport from the AlInAs buffer layer. This suggests a similar formation mechanism with the InGaAs/AlGaAs system⁸) resulting in built-in InGaAs microstructures inside the AlInAs microcrystals. However, the ordering and the homogeneity in size are slightly worse compared with those of the InGaAs/AlGaAs system.

On the InP (311)A surface as shown in Fig.1(b), modulated step-bunching occurs along the [233] direction, which is somewhat different to the InGaAs/AlGaAs system with clear one-dimensional faceting resulting in quasi-periodic wire-like morphology. A slight difference in self-organization phenomena between compressive InGaAs/AlGaAs on GaAs (311) substrates and compressive InGaAs/InAlAs on InP (311) substrates may come from the high vapor pressure of indium compared to gallium.

On the contrary, in the case of 3.5-nm thick In_{0.8}Ga_{0.2}As layer over an InP buffer on a InP (311)B substrate at 650°C, microcrystals are formed with elongated features in the [011] direction, with less pronounced uniformity and ordering as shown in Fig.2(a). Here, the atmosphere gas was PH₃ during the growth interruption to decrease any exchange reaction of the surface group-V atom. It is found that a self-organization phenomenon also occurs in the InGaAs/InP system, similar to the InGaAs/InAlAs system. The pronounced difference in shape of the microcrystals for both strained material systems comes from the difference in the composition elements in buffer layers of InAlAs and/or InP.

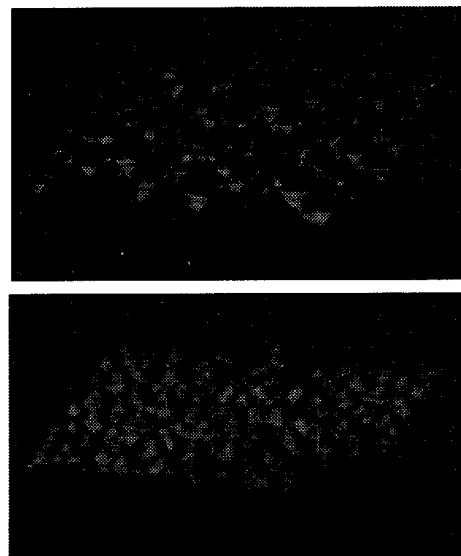


Fig.1 AFM images of the surface morphology developed after the growth of 5-nm-thick In_{0.8}Ga_{0.2}As / Al_{0.48}Ga_{0.52}As (a) on InP (311) B, and (b) on InP (311) A substrates.

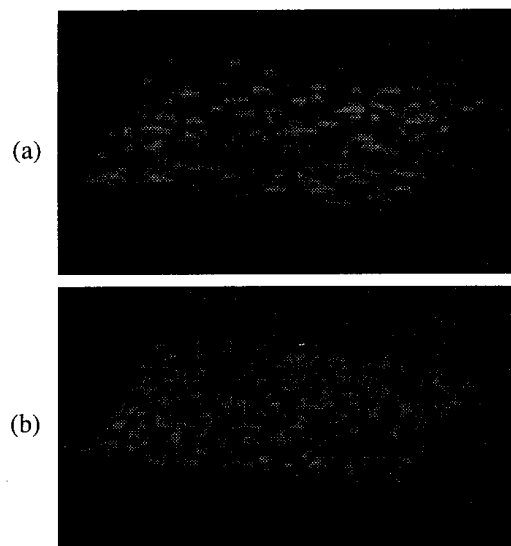


Fig.2 AFM images of the surface morphology developed after the growth of 3.5-nm-thick In_{0.8}Ga_{0.2}As / InP (c) on InP (311) B, and (b) on InP (311) A substrates.

On InP (311)A substrates, both microcrystal and bunching formations can be found as shown in Fig.2 (b), which is also quite different from the InGaAs/AlGaAs system. The poorer adatom migration due to the high vapor pressure of indium and phosphorous may possibly inhibit clear facet formation, a well-defined structure and clear ordering during the self-organization.

Table 1 Surface Morphologies of InGaAs Cap Layers on InP Substrates

Epitaxial Layers					Substrate Temperature (degrees)					0=(100) A=(311)A B=(311)B f=flat b=bunching d=microcrystal m=modulated r=rough l=elongated
Coditions					600	625	650	670	700	
Barrier	Strain	V-gas	InGaAs	d(nm)	*0 A B	0 A B	0 A B	0 A B	0 A B	
In.52Al.48As	Compressive	AsH3	In.8Ga.2As	3.5	f b d/m	f b d/m	f b d	f b/d d	f b/d d	
"	Tensile	AsH3	In.25Ga.75As	3.5			f b d/l		f b r	
InP	Compressive	AsH3	In.8Ga.2As	3.5	f b d/t		f b d			
"	"	PH3	"	3.5	f b f/m	f d/b d	f d/b d			
"	Tensile	AsH3	In.25Ga.75As	3.5			f b d			
"	"	PH3	"	3.5			d d d			

Typical surface morphologies are summarized in Table 1, including the tensile cases of In_{0.25}Ga_{0.75}As with In_{0.52}Al_{0.48}As and/or InP buffer layers. Altogether, for InP (100), (311)A, and (311)B substrates respectively, flat-, microcrystal-like (or modulated step-bunching), and microcrystal-like morphologies can be obtained. One of the features in the InP substrate system is that microcrystal formation possibly occurs on the InP (311)A surface accompanied by a bunching phenomenon. This difference may result from the high vaporizing pressure of indium and phosphorous.

Moreover, in the case of the tensile In_{0.25}Ga_{0.75}As system with an atmosphere gas of AsH₃ during growth interruption the surface morphologies show a similar tendency to the compressive In_{0.85}Ga_{0.15}As system, while the fine structures of the microcrystals for both systems are somewhat different. However, the tensile case with the InP barrier during interruption with PH₃ shows microcrystal images for (100), (311)A, and (311)B surface orientations. It is very difficult to explain the pronounced differences of surface morphologies in the tensile In_{0.25}Ga_{0.75}As/InP system with AsH₃ and/or PH₃. However, even on the InP (100) surface relatively high substrate temperature with phosphine atmosphere may possibly enhance the slight exchange of V-atoms and adatom migration resulting in the inducement of mass-transport.

Finally, we discuss the PL emission from built-in InGaAs microstructures. Concerning the InGaAs/InAlAs system, unfortunately, at the present stage we have no PL emission at room temperature. This is possibly due to the slight intermixing between InGaAs and InAlAs during mass-transport. However, concerning the In_{0.8}Ga_{0.2}As/InP system, we can show the relationship between the peak wavelength of room temperature PL and the growth

temperature for InP (100), (311)A, and (311)B substrates in Fig.3. This result shows that if we use the V-gas of PH₃ during the growth interruption, some exchange of a group-V element of built-in InGaAs microstructures from As to P occurs. This results in large PL shift, and subsequent degradation of interface and crystal quality, which is quite different from the case of InGaAs/AlGaAs system.

Conclusion

We have found that self-organization phenomeon of strained InGaAs on an InP (311) substrate occurs during a growth interruptin in MOVPE growth. These phenomena

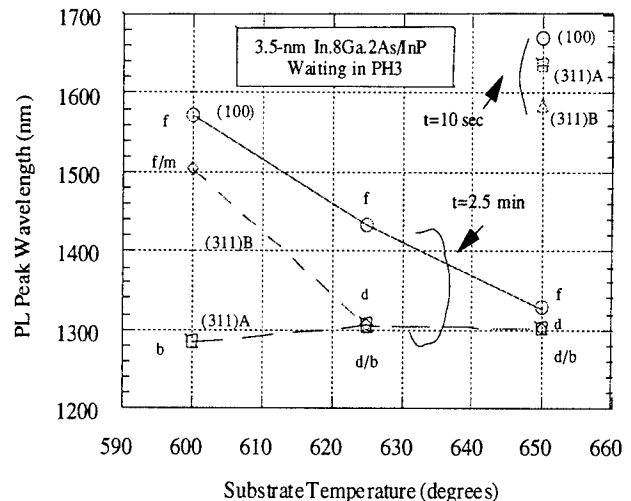


Fig.3 Room temperature photoluminescence peak wavelength versus substrate temperature for InGaAs microstructures on InP (100), (311)A, and (311)B substrates. (t: Interrupt time after InGaAs growth)

are similar to those that occurs in the material system of InGaAs on a GaAs (311) substrate. This suggests that the natural formation of nanostructures due to self-organization phenomena of strained layers on high Miller-index planes of III-V compound semiconductors by vapor phase epitaxy can be a rather common feature.

Acknowledgment: The authors would like to thank Dr. M. Yamamoto and Dr. M. Sugo for their helpful discussions.

References

1. P. M. Petroff, A. C. Gossard, and W. Wiegmann, "Structure of AlAs-GaAs interfaces grown on (100) vicinal surfaces by molecular beam epitaxy," *Appl. Phys. Lett.* **45**, pp. 620-622, 1984.
2. L. Cibert, P. M. Petroff, G. J. Dolan, S. J. Pearton, A. C. Gossard, and J. H. English, "Optically detected carrier confinement to one and zero dimension in GaAs quantum well wires and boxes," *Appl. Phys. Lett.* **49**, pp. 1275-1277, 1986.
3. H. Temkin, G. J. Dolan, M.B. Panish, and S. N. G. Chu, "Low-temperature photoluminescence from InGaAs/InP quantum wires and boxes," *Appl. Phys. Lett.* **50**, pp. 413-415, 1986.
4. S. Guha, A. Mudhukar, and K.C. Rajkumar, "Onset of incoherency and defect introduction in the initial stages of molecular beam epitaxial growth of highly strained $\text{In}_x\text{Ga}_{1-x}\text{As}$ on GaAs (100)," *Appl. Phys. Lett.*, **66**, pp. 2110-2112, 1990,
5. J. M. Moison, F. Houzay, F. Barthe, L. Leprince, E. Andre, and O. Vatel, "Self-organized growth of regular nanometer-scale InAs dots on GaAs," *Appl. Phys. Lett.* **64**, pp. 196-198, 1994,
6. D. Leonard, M. Krisnamurthy, C. M. Reaves, S. P. DenBaas, and P. M. Petroff, "Direct formation of quantum-sized dots from uniform coherent islands of InGaAs on GaAs surfaces," *Appl. Phys. Lett.* **63**, pp. 3203-3205, 1993, .
7. R. Nötzel, J. Temmyo, and T. Tamamura, "Self-organized growth of strained InGaAs quantum disks," *Nature* **369**, pp. 131-133, 1994.
8. J. Temmyo, R. Nötzel, H. Kamada, T. Furuta, and T. Tamamura, "Room temperature photoluminescence emission of strained InGaAs quantum disks self-organized on GaAs (311)B substrates," in *Proceedings of 22nd International Conference on the Physics of Semiconductors*, Vancouver, Aug. 1994 .(to be published)
9. J. Temmyo, E. Kuramochi, T. Nishiya, M. Sugo, H. Kamada, R. Nötzel, and T. Tamamura, "Strained InGaAs quantum disk laser with self-organized box-like nanostructure as active region," in *Conference Digest of the 14th IEEE International Semiconductor Laser Conference*, Hawai, PD-4, Sept. 1994.
10. J. Temmyo, E. Kuramochi, M. Sugo, T. Nishiya, R. Nötzel, and T. Tamamura, "Strained InGaAs quantum disk laser with nano-scale active region fabricated with self-organization on a GaAs (311)B substrate," *IEEE Electron. Lett.* **31**, pp. 209-211, 1995.
11. J. Temmyo, A. Kozen, R. Nötzel, and T. Tamamura, "Self-organization of strained InGaAs microstructures grown by MOVPE on InP (311) substrates," in *Extended Abstracts of the 55th Autumn Meeting, 1994; the Japan Society of Applied Physics*, Nagoya, 20a-T-9, Sept. 1994.

QUANTUM CASCADE LASERS: UNIPOLAR INTERSUBBAND INFRARED LASERS

SB1.1
(Invited)

F. Capasso, J. Faist, C. Sirtori, A. L. Hutchinson,
D. L. Sivco and A. Y. Cho

AT&T Bell Laboratories
Murray Hill, NJ 07974

The recently demonstrated quantum cascade laser is a fundamentally new semiconductor laser (1-3). It relies on only one type of carrier (unipolar laser) and on quantum jumps of electrons between discrete conduction band energy levels of quantum wells. As such the wavelength can be tailored over a very wide range from the mid-ir (a few microns) to the far-ir ($\sim 100 \mu\text{m}$) by simply varying layer thicknesses. Two types of quantum cascade lasers will be discussed. In the original structure the relevant intersubband radiative transition is between states centered in different neighboring wells to facilitate population inversion, i.e. the transition is *diagonal* (Fig. 1). In this design, however, the width of the luminescence transition is relatively broad (FWHM $\sim 22 \text{ meV}$) due to the interface roughness since electrons traverse several heterointerfaces in the photon emission process. As a consequence the peak gain is reduced. To circumvent this problem we designed the structure of Fig. 2 where electrons make a *vertical* radiative transition essentially in the same well (4). This reduces considerably the width of the gain spectrum (FWHM $\approx 10 \text{ meV}$) and therefore the laser threshold current density. To prevent electron escape in the continuum, which is greatly reduced in the case of the diagonal transition, the superlattice of the digitally graded injector is designed to act as a Bragg reflector for electrons in the higher excited state and to simultaneously ensure swift electron escape from the lower states via a miniband facing the latter (Fig. 2). A crucial feature of both structures is that the lower state of the laser transition is separated by an optical phonon ($\approx 30 \text{ meV}$) from the $n = 1$ state. This strongly enhances the scattering of electrons out of the $n = 2$ state. The calculated time is $\tau_{21} \approx 0.6 \text{ ps}$ which is considerably less than the relaxation time between the $n = 3$ and $n = 2$ state (a few ps) thus creating the population inversion condition. Electrons can in turn tunnel out of the $n = 1$ state in a subpicosecond time to prevent electron build-up.

Quantum Cascade Laser with Diagonal Transition

The AlInAs/GaInAs structure grown by MBE comprises 25 stages, each consisting of a graded gap n-type injection layer and a three coupled-well active region, cladded by AlInAs waveguiding layers (1-3). The

undoped active region includes 0.8 nm and 3.5 nm thick GaInAs wells separated by 3.5 nm AlInAs barriers. 3.0 nm thick AlInAs barriers separate the active regions from the digitally graded n-type doped injectors ($\sim 10^{17} \text{ cm}^{-3}$). The samples were processed into mesa etched ridge waveguides and the laser facets were obtained by cleaving. Powers $\approx 30 \text{ mW}$ in pulsed operation and thresholds of 5.8 kA/cm^2 for a 2.8 nm long device have been obtained at $\lambda = 4.3 \mu\text{m}$ and at a heat sink temperature $\sim 100 \text{ K}$ (Fig. 1). The slope efficiency is $\approx 0.1 \text{ W/A}$. An outstanding feature of this laser is that the gain is much less sensitive to temperature than conventional semiconductor lasers. The temperature dependence of the threshold indicates an exponential increase $\sim \exp(T/T_0)$ with a $T_0 = 110 \text{ K}$. Operating temperatures up to 125 K have been achieved with a few mW of power. Well defined longitudinal modes are observed (Fig. 3). The mode spacing is in good agreement with the calculated one ($\frac{1}{2nL_{\text{cav}}} = 0.55 \text{ cm}^{-1}$). The linewidth of the dominant mode ($\sim 0.3 \text{ cm}^{-1}$) is presently limited by heating effects and mode hopping during the pulse. The intrinsic linewidth of these lasers in cw single mode operation is expected to be Schawlow-Townes limited, similar to atomic lasers, without the linewidth enhancement factor typical of diode lasers (1).

Recently we have demonstrated pulsed operation at $\lambda = 8.4 \mu\text{m}$ in a quantum cascade laser with a threshold of 2.8 kA/cm^2 and an optical power of 30 mW at a 100 K heat sink temperature.

Quantum Cascade Laser with Vertical Transition

In this structure (Fig. 3) the 25 active regions consist of a 4.5 nm GaInAs wells coupled to a 3.6 nm well by a 2.8 nm AlInAs barrier. Tunneling injection into the active region is through a 6.5 nm AlInAs barrier and electrons escape out of the $n = 1$ state through a 3.0 nm AlInAs barrier. The superlattice well and barrier thicknesses are respectively $\ell_w = 2.1, 2.1, 1.6, 1.7, 1.3$ and 1.0 nm and $\ell_b = 2.1, 1.9, 2.0, 2.3$ and 2.7 nm in going from left to right in Fig. 2. The waveguiding cladding regions are similar to those of the diagonal transition structure. After processing, the samples were

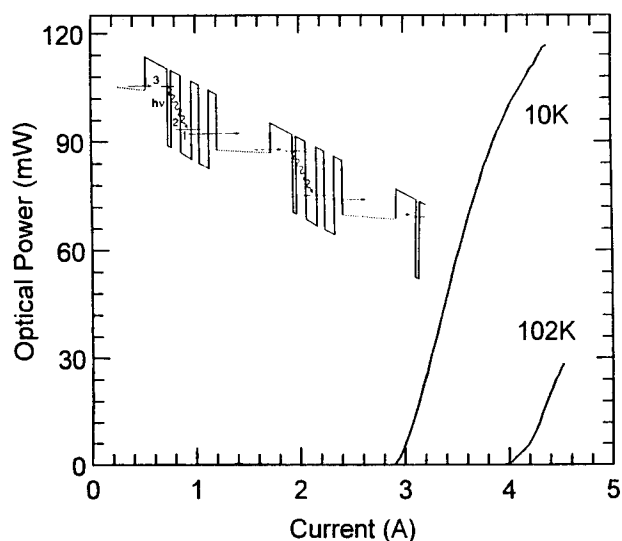


Fig. 1. Peak optical power from a single facet against drive current of quantum cascade laser at two different heat sink temperatures. The collection efficiency is 40%. Inset: Two periods of the 25 stage staircase/coupled well region of the laser under operating conditions. The calculated energy separation between the $n = 3$ and $n = 2$ states of the laser transition (wavy arrow) is 295 meV, and that between the $n = 2$ and $n = 1$ states is ~30 meV.

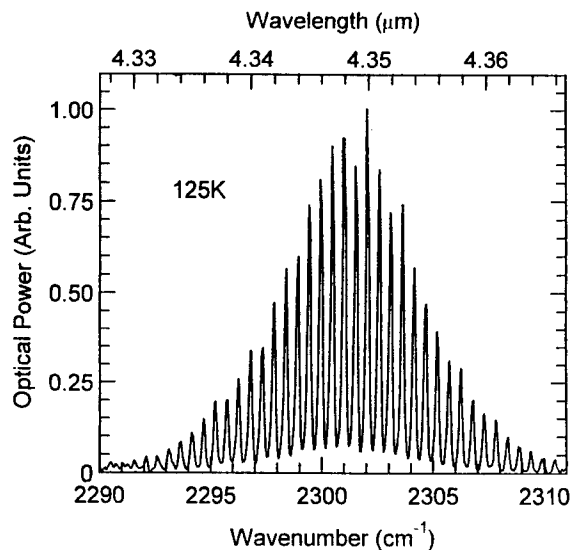


Fig. 3. High resolution emission spectrum showing the longitudinal mode structure for the laser of Fig. 1. The drive current is 6.5 A.

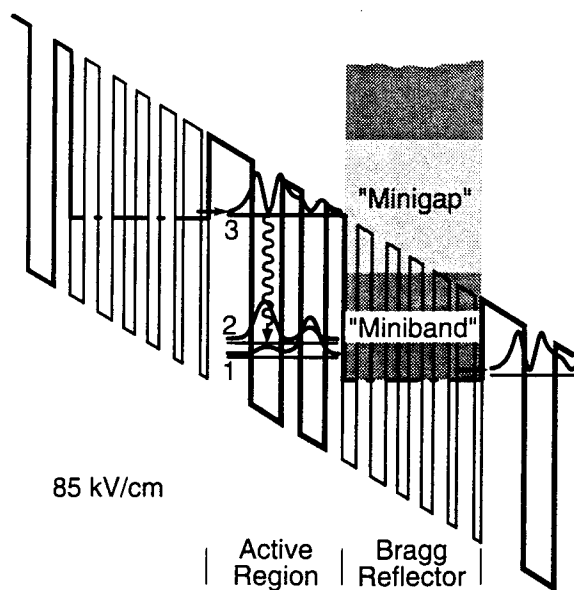


Fig. 2. Schematic conduction band diagram of a portion of the vertical transition quantum cascade $\text{Ga}_{0.47}\text{In}_{0.53}\text{As}/\text{Al}_{0.48}\text{In}_{0.52}\text{As}$ laser structure under positive bias condition and an electric field of $8.5 \times 10^4 \text{ V/cm}$. The dashed lines are the effective conduction band edges of the 20.8 nm thick superlattice graded gap electron injector. As shown, this superlattice is also designed as to create a minigap that blocks the electron escape from level 3. The wavy line indicates the transition responsible for laser action. The moduli squared of the relevant wave functions are shown.

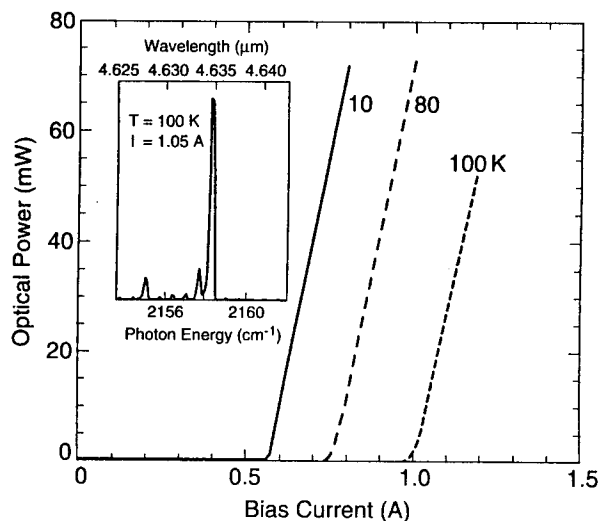


Fig. 4. Peak optical output power from a single facet vs. injection current at various heat sink temperatures for a quantum cascade laser with vertical transition. Inset: High-resolution spectra of the sample above threshold. Near single longitudinal mode operation is observed.

cleaved in $L_{\text{cav}} = 2.4 - 3$ mm length bars. Current pulses of 30 ns were injected in the device with a 20 kHz repetition rate. Fig. 4 displays the L-I curve for a 2.4 mm long device obtained by focusing the light with a $f/0.8$ optics on a fast HgCdTe detector. The peak optical power is ~ 80 mW at 80 K. The measured slope efficiency is 300 mW/A per facet and essentially temperature independent and corresponds to a differential quantum efficiency per period of 4.5×10^{-2} when corrected for the collection efficiency of the apparatus. The threshold density has a value $J_{\text{th}} = 1.7$ kA/cm² at 10 K and 3 kA/cm² at 100 K. Operating temperatures up to 200 K have been demonstrated in an optimized vertical transition laser in pulsed operation. Recently we have shown CW operation with 2 mW of power at 60 K temperature and $\lambda = 4.6$ μm .

References

1. J. Faist, F. Capasso, D. L. Sivco, C. Sirtori, A. L. Hutchinson, and A. Y. Cho, *Science*, **264**, 553 (1994).
2. J. Faist, F. Capasso, D. L. Sivco, C. Sirtori, A. L. Hutchinson, and A. Y. Cho, *Electron. Lett.* **30**, 865 (1994).
3. J. Faist, F. Capasso, D. L. Sivco, A. L. Hutchinson, C. Sirtori, Sung N. G. Chu, and A. Y. Cho, *Appl. Phys. Lett.* **65**, 2901 (1994).
4. J. Faist, F. Capasso, C. Sirtori, D. L. Sivco, A. L. Hutchinson, and A. Y. Cho, *Appl. Phys. Lett.* **66**, 538 (1995).

Transverse-mode and polarization characteristics of double-fused 1.52- μm vertical-cavity lasers

Dubravko I. Babić, James J. Dudley, Klaus Streubel*, Richard P. Mirin, Near M. Margalit,
John E. Bowers, Evelyn L. Hu

Department of Electrical and Computer Engineering, University of California, Santa Barbara, CA 93106, USA

**Department of Electronics, Royal Institute of Technology, Stockholm, S-164 40, Sweden*

Abstract

We report on the transverse mode and polarization characteristics of a novel 1.52- μm vertical-cavity laser that utilizes an InGaAsP strain-compensated quantum-well active layer and two AlAs/GaAs quarter-wave mirrors. The 6 and 8 μm diameter devices exhibit room-temperature pulsed threshold currents as low as 4 mA, and a maximum output power of 14 mW was measured on a 60 μm diameter device.

Long-wavelength vertical-cavity lasers are potentially integrable low-cost sources for optical communication systems. The practical choice for 1.3 μm and 1.55 μm emitting/absorbing material is the quaternary InGaAsP alloy lattice matched to InP. The difficulty in using this material system lies in the relatively small refractive index values that can be achieved by varying the InGaAsP composition. A large refractive index ratio is essential for the realization of high reflection coefficients in practical distributed Bragg reflectors. Furthermore, the thermal conductivity of quaternary alloy is an order of magnitude lower than that of InP. To address these issues we have proposed [1] and demonstrated [2] long-wavelength vertical-cavity lasers (VCLs) using AlAs/GaAs mirrors and InGaAsP active layers bonded by wafer fusion [3]. Using this method, substrates of vastly different lattice constants can be bonded to produce an optically transparent junction that is both electrically and thermally conductive [4]. Wafer fusion opens great possibilities for realization of novel optoelectronic devices that utilize InGaAsP and GaAlAs materials in a single structure. Recently, we reported a new long-wavelength VCL structure that uses two AlAs/GaAs quarter-wave mirrors and an InGaAsP strain-compensated quantum-well active region [5]. These devices were fabricated by two wafer fusion steps and exhibited record values for pulsed threshold current at room temperature. In this paper, we report on devices that have similar mirrors and active layer structure, but were fabricated using improved reactive ion etching. This process improvement has resulted in a threefold reduction in the lowest threshold current value: 4 mA pulsed at room-temperature. Furthermore, we show that, even though these lasers operate in many transverse modes, the light output is highly linearly polarized

with the electric field parallel to the [011] direction. Single mode operation was observed on 6 and 8 μm diameter devices in which the degree of polarization along [011] axis was as high as 97%.

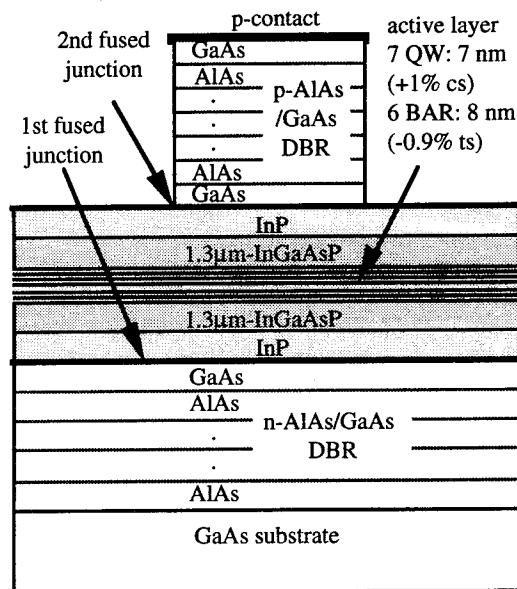


Figure 1. Double-fused vertical-cavity laser structure.

The double-fused vertical-cavity laser structure, shown in Figure 1, uses two MBE-grown AlAs/GaAs quarter-wave mirrors fused to an MOCVD grown InGaAsP active region. The bottom reflector is a Si-doped 25-period GaAs/AlAs mirror designed for 99.8% reflectivity, while the top is a Be-doped 24-period GaAs/AlAs mirror designed for 99.5% reflectivity. In order to reduce the effects of absorption in p-type GaAs and AlAs at long

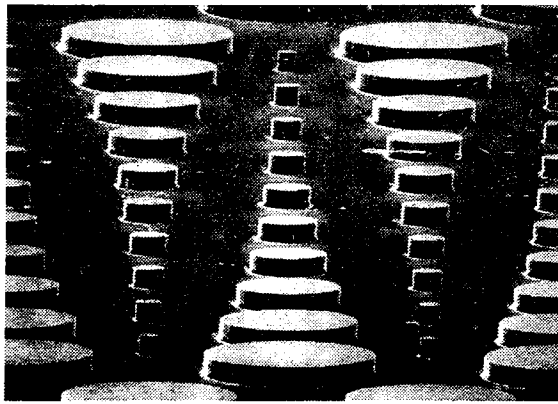


Figure 2. Finished double-fused vertical-cavity lasers. Ten different sizes between 6 and 60 μm inclusive are shown.

wavelengths, the p-mirror features a hybrid doping scheme: The 10 periods closest to the cavity are doped $3 \cdot 10^{17} \text{ cm}^{-3}$, while the rest of the mirror is doped $1 \cdot 10^{18} \text{ cm}^{-3}$. All the interfaces have been linearly graded over 18 nm and doped approximately five times the bulk doping.

Recent studies have shown that strained quantum wells have higher optical gain and lower transparency than unstained quantum wells [6], [7]. In order to achieve the high gain needed in InP-based vertical-cavity lasers the number of wells required exceeds the number of strained wells that can be grown coherently. For this reason, strain-compensated InGaAs / InGaAsP [8] quantum wells have been investigated for long-wavelength vertical-cavity laser applications. In this laser we have used strain-compensated InGaAsP wells and barriers grown under a constant As/P ratio [9]. MOCVD growth under the constant As/P ratio has the advantage of minimizing the group V element interdiffusion during the growth and the subsequent high temperature processing (wafer fusion). The active layer of our double-fused laser consists of seven strained InGaAsP quantum wells (7 nm and 1% compressive strain) with strain-compensating InGaAsP barriers (8 nm and 0.9% tensile strain).

The fabrication process involves two wafer fusion steps: the first step is the fusion of the n-type mirror to the InP active layer, and then after InP substrate removal, the p-type mirror is fused to the other side of the active layer. In order to minimize Be diffusion, the p-type mirror undergoes the high temperature fusion step only once. Both fusion steps are performed at 630°C for 20 minutes in a hydrogen atmosphere [1]-[4]. The InP substrate was selectively removed using a mixture of HCl:H₂O down to an InGaAsP etch-stop layer, while the GaAs substrate was removed using NH₄OH:H₂O₂ spray etching at pH 8.3 [10]. The devices were defined with circular

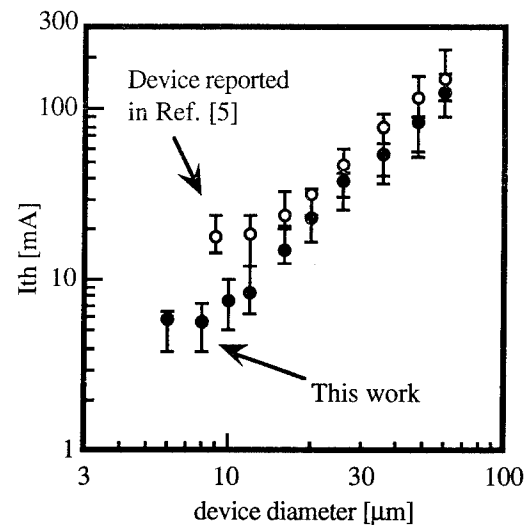


Figure 3: Threshold current as a function of the diameter for devices reported in this work compared to the device reported in Ref. [5]. The error bars indicate the largest and the lowest value measured, while the data point is the median of the measurements.

p-type contacts which were used as a mask in Cl₂ reactive ion etching. An SEM micrograph of finished devices is shown in Figure 2.

All ten laser sizes on the mask (6 to 60 μm inclusive) operate at room-temperature under pulsed conditions (50 ns / 25kHz / 25°C). The lasing wavelength is $1517 \text{ nm} \pm 2 \text{ nm}$, depending on the location on the sample. The lowest threshold current of 4 mA was measured on several 6 and 8 μm devices. The highest pulsed output power of 14 mW was measured on a 60 μm device. The external differential quantum efficiency of devices with diameters larger than 26 μm was approximately 2.5%, while for smaller devices it reduced to below 1%. The temperature dependence of the threshold current shows an exponential behavior around room temperature with a characteristic temperature of $T_0 \approx 28 \text{ K}$. The voltage drop across the devices at threshold ranges from 12 V on the largest to 24V on the smallest devices and is dominated by the p-AlAs/GaAs mirror heterojunction resistance. This high voltage drop can be significantly reduced with an improved mirror design. The uncertainty of our current and voltage measurements is estimated to be $\pm 5\%$.

Figure 3 shows the threshold current of 120 devices (measured in this work) compared to our previous result [5]. The largest and the lowest value of the threshold current measured are shown with the upper and the lower ends of the error bars. The devices reported in Ref. [5] had corrugated sidewalls resulting from selective etching of GaAs over AlAs

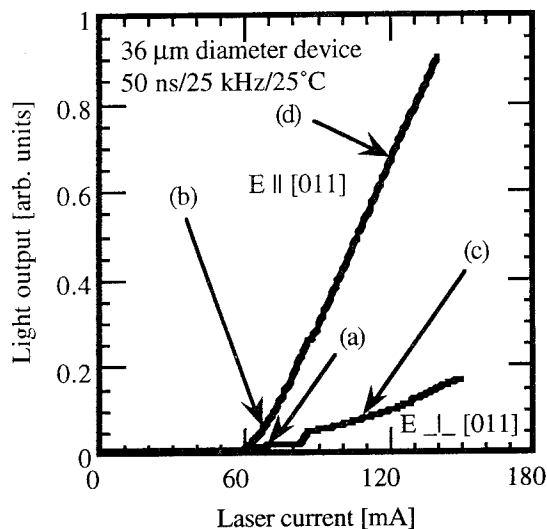


Figure 4: Polarization-resolved light-current characteristics of a 36 μm diameter device. The associated near-field patterns are shown in Figure 5.

and roughness from interruptions during the etch. In this work, the etching was uninterrupted, the GaAs/AlAs selectivity was reduced by reducing the base pressure before the etch three times (down 17 μPa), and the etched devices were kept in N_2 atmosphere to slow down AlAs oxidation. This improved etching scheme resulted in a threefold reduction in the lowest threshold current as well as the operation of smallest devices on the mask (down to 6 μm). The yield on this run was better than 95%: Out of 125 devices of all diameters, 120 were found to lase. The difference between the threshold current data for devices in Ref. [5] and this run clearly indicates that the rough sidewalls have a significant impact on the cavity loss for small diameters, while for large devices both samples show that the best broad-area threshold current density possible with this cavity is in the range 3-4 kA/cm^2 . Further improvement of these values is expected with a better p -type AlAs/GaAs mirror design.

Multiple transverse-mode operation was observed in the near-field patterns and the spectra of devices of all sizes. Most of the 6 and 8 μm diameter devices lased in a single transverse mode up to 3 or 4 times the threshold current. The output from all devices was highly polarized, even when many transverse modes were lasing. In all of the devices tested, the maximum intensity was polarized along the [011] direction (electric field parallel to the [011]).

Figures 4 and 5 show the polarization-resolved light-current characteristics and the associated near-field patterns of a 36 μm diameter device at $I \approx I_{\text{th}}$ and at $I \approx 1.8 I_{\text{th}}$. The existence of a

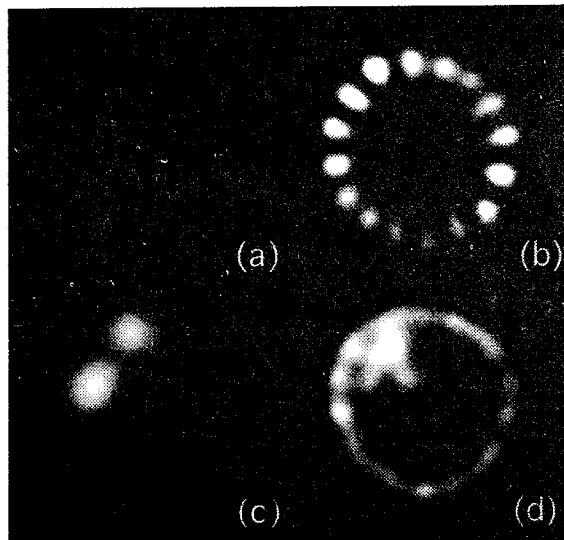


Figure 5: Polarization-resolved near-field pattern for the device with light-current characteristic shown in Figure 4. (a) $I \approx I_{\text{th}}$, E_{\perp} [011], (b) $I \approx I_{\text{th}}$, E_{\parallel} [011], (c) $I \approx 1.8 I_{\text{th}}$, E_{\perp} [011], (d) $I \approx 1.8 I_{\text{th}}$, E_{\parallel} [011].

field pattern with 16-fold radial symmetry at $I \approx I_{\text{th}}$ (Figure 5b) attests the quality of the etched sidewalls and the absence of damage to the active layer from wafer fusion. The absence of emission from the center may be a result of current crowding at the edges and indicates that a large number of transverse modes are already present at threshold. The near-field pattern with the 16-fold radial symmetry clearly exists only with the electric field polarized along the [011] direction. The central region of the laser starts to emit at higher currents (Figure 5d), while the light intensity along the orthogonal direction (Figures 5a and 5c) is much weaker on all device sizes. The cause for this highly polarized behavior is not well understood. We speculate that polarization anisotropy has been introduced by uniaxial strain locally introduced and relaxed by the dislocations at the fused interface. We have performed polarization-resolved measurements of the photoluminescence from the active layer of this device and were not able to observe such anisotropy (note that the InP epilayers are exposed in the completed device to make such measurements possible).

An example of a highly polarized output from a 6 μm device is shown in Figure 6, where at 15 mA the degree of polarization $V = (I_{\text{max}} - I_{\text{min}}) / (I_{\text{max}} + I_{\text{min}})$ was 97%. The threshold current of this laser was below 4 mA, and the linewidth was limited to 0.5 nm by chirping during the pump pulse. The multiple-mode operation of a 10 μm diameter device at two times threshold is illustrated in the polarization-resolved near-field pattern shown in Figure 7.

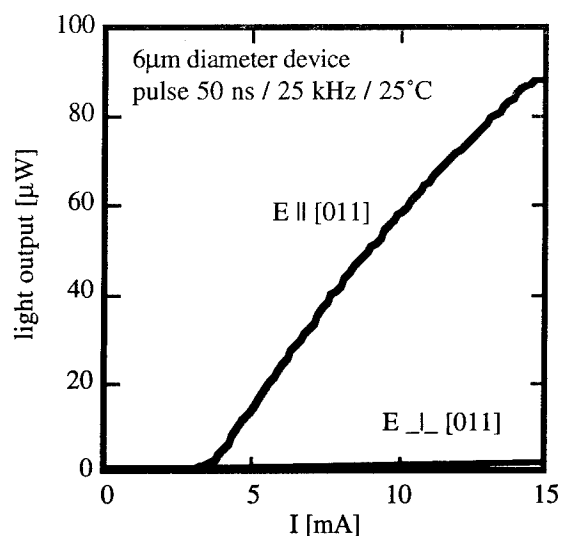


Figure 6: Polarization-resolved light-current characteristic of a 6 μm diameter device. At 15 mA the degree of polarization was 97 %.

Very strong polarization anisotropy has been observed in multi-mode double-fused vertical-cavity lasers. The maximum intensity for all devices occurs with the electric field parallel to the [011] direction. Further investigation of this polarization anisotropy may open possibilities for realization of vertical-cavity lasers with stable and controlled polarization characteristics. Finally, the improved fabrication of double-fused 1.52 μm vertical-cavity lasers resulted in record low values of pulsed threshold current and threshold current densities at room-temperature. With improved p-type Al(Ga)As/GaAs mirrors and a suitable surface passivation continuous-wave room-temperature operating long-wavelength vertical-cavity lasers should be possible.

References

- [1] J. J. Dudley, M. Ishikawa, D. I. Babić, B. I. Miller, R. P. Mirin, W. B. Jiang, J. E. Bowers, E. L. Hu, *Appl. Phys. Lett.* **61**, 3095 (1992).
- [2] J. J. Dudley, D. I. Babić, R. Mirin, L. Yang, B. I. Miller, R. J. Ram, T. E. Reynolds, E. L. Hu, J. E. Bowers, *Appl. Phys. Lett.* **64**, 1463 (1994).
- [3] Z. L. Ziao, D. E. Mull, *Appl. Phys. Lett.* **56**, 737 (1990).
- [4] R. J. Ram, L. Yang, K. Nauka, Y. M. Huong, M. Ludowise, D. E. Mars, J. J. Dudley, S. Y. Wang, *Appl. Phys. Lett.* **62**, 2474 (1993).
- [5] D. I. Babić, J. J. Dudley, K. Streubel, R. P. Mirin, J. E. Bowers, E. L. Hu, *Appl. Phys. Lett.* **66**, 1032 (1995).
- [6] E. Yablonovitch, and E. O. Kane, *J. Lightwave Technol.* **6**, 1292 (1988).

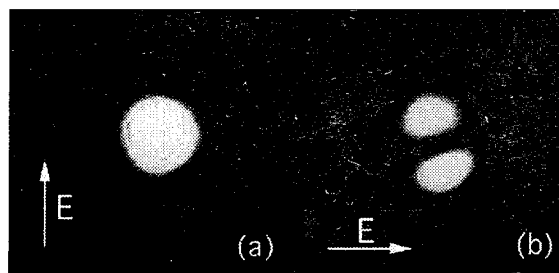


Figure 7: Polarization-resolved near-field patterns of a 10 μm diameter device at two times the threshold current. (a) $E \parallel [011]$ (maximum intensity), and (b) $E \perp [011]$ (minimum intensity).

- [7] S. W. Corzine, R. H. Yan, L. A. Coldren, *Appl. Phys. Lett.* **57**, 2835 (1990).
- [8] C. H. Lin, C. L. Chua, Z. H. Zhu, F. E. Ejeckam, T. C. Wu, Y. H. Lo, *Appl. Phys. Lett.* **64**, 3395 (1994).
- [9] K. Streubel, J. Wallin, G. Landren, U. Ohlander, S. Lourdudoss, O. Kjebon, *J. of Crystal Growth.* **143**, 7 (1994).
- [10] H. Tanobe, T. Tamanuki, T. Uchida, F. Koyama, K. Iga, *Jpn. J. Appl. Phys.* **31** pt. 1, 949 (1992).

NOVEL CURRENT-BLOCKING LASER STRUCTURES USING DIRECTLY-BONDED InP-SiO₂-InP

H. Wada, Y. Ogawa and T. Kamijoh
Semiconductor Technology Laboratory, OKI Electric Industry
550-5, Higashiasakawa, Hachioji, Tokyo 193, Japan

Abstract

We propose a novel laser structure which uses a SiO₂ insulator sandwiched with InP as a current blocking layer. The structure has been successfully fabricated by directly bonding InP to SiO₂. A threshold current density of 1.9 kA/cm² and a maximum output power of 60 mW have been achieved for a 1.3- μ m InGaAsP laser with a bulk active layer and a 300- μ m cavity. This result implies that the leakage current is negligible. The parasitic capacitance has been measured to be 31 pF even for a laser with an area of 300 μ m x 300 μ m.

Introduction

Direct wafer bonding has been shown to be an attractive technology to realize an integration of different materials [1-7]. Various kinds of semiconductors have been successfully integrated onto dissimilar substrates, including InP-on-GaAs [2-4], GaAs-on-Si [5], and InP-on-Si [6,7]. Recently, we have extended this technique to a new material combination of InP-SiO₂. Direct bonding of III-V materials to SiO₂ allows the realization of III-V semiconductor-insulator-semiconductor (SIS) structures which will be useful to realize new III-V devices.

In this paper, we propose a novel laser structure which uses the InP-SiO₂-InP SIS structure as current-blocking (CB) layers. The leakage current and parasitic capacitance are expected to be smaller in this structure than the conventional CB structures such as the p-n-p-n thyristor [8] and the semi-insulating buried heterostructure [9]. A threshold current of 10 mA and a maximum continuous-wave (CW) output power of 60 mW have been successfully achieved for a 1.3- μ m InGaAsP/InP laser with a cavity 300 μ m long. The parasitic capacitance has been measured to be as low as 31 pF even for a laser with a wide area of 300 μ m x 300 μ m.

Device fabrication

The device fabrication process is illustrated in Fig. 1. First, a 0.2- μ m-thick InGaAs etch-stop layer and a 1.5- μ m-thick n-InP layer ($n = 1 \times 10^{18}$ cm⁻³) were grown at 650 °C on an n-InP substrate using low-pressure (50 Torr) metalorganic vapor phase epitaxy (MOVPE). The epitaxial wafer was then directly bonded on a 0.1- μ m-thick SiO₂ CB layer which was deposited on a p-InP substrate using chemical vapor deposition (Fig. 1 (a)). The direct bonding procedure is basically the same as that demonstrated previously [4,7] and can be summarized as follows: The surfaces of the n-InP and SiO₂ were treated with a H₂SO₄:H₂O₂:H₂O solution and rinsed in deionized water. The wafers were then spin-dried and brought into contact just after drying. The wafers adhered to each other, although weakly, even at room temperature. The adhesion is believed to be a result of hydrogen bonding between OH groups absorbed on the wafer surfaces during the

pretreatment. The wafers were then loaded into an annealing furnace and heated at 650°C in a H₂ atmosphere for an hour. The bonds after the heat treatment were strong enough to endure subsequent device processing such as photolithography, etching, regrowth, and cleaving.

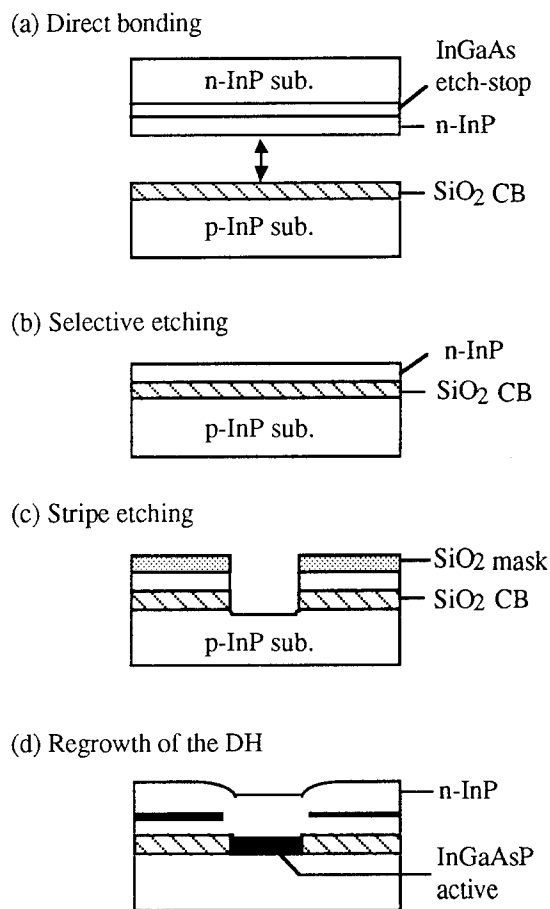


Fig. 1 Laser fabrication process

Fig. 2 shows transmission electron micrographs for the cross section of the bonded InP-SiO₂ interface. It can be confirmed from Fig. 2 (a) that InP and SiO₂ are directly bonded and there are no significant dislocations formed in InP. One of the interesting features at the bonded interface is the formation of crystalline particles in SiO₂, as shown in Fig. 2 (b), observed at some areas of the interface. This suggests that a kind of solid-phase epitaxy takes place at the interface, as reported for deposited SiO₂-InP interface [10], and is believed to be partially responsible for the strong bonding.

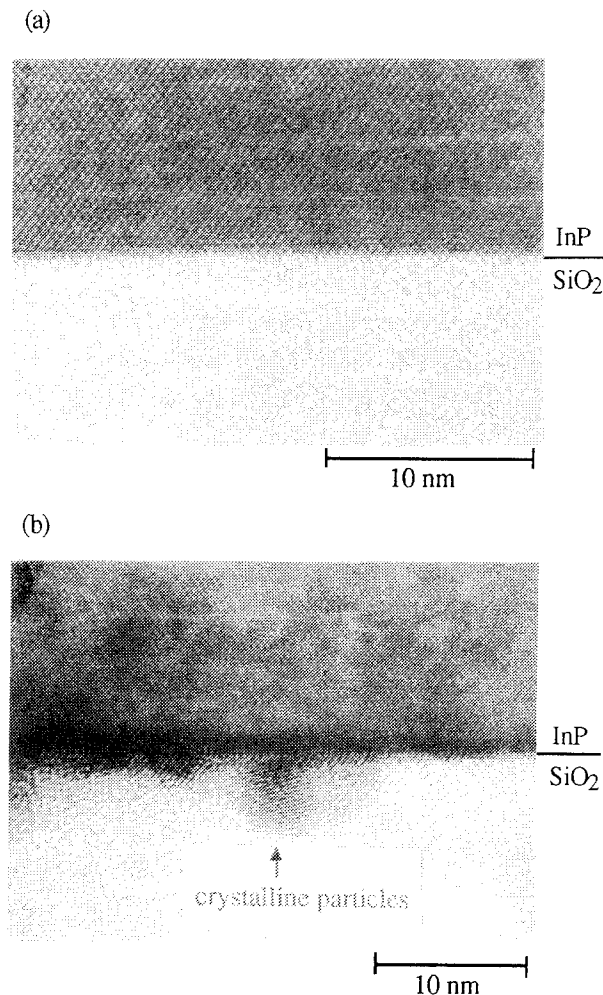


Fig. 2 Cross-sectional transmission electron micrographs of InP-SiO₂ interface bonded at 650 °C. (a) It can be confirmed that the wafers are directly bonded. (b) The formation of crystalline particles are observed.

Next step in the laser fabrication is selective-etching of the substrate. As shown in Fig. 1 (b), the n-InP substrate and the InGaAs etch-stop layer were selectively etched to expose the n-InP layer. A 0.2- μ m-thick SiO₂ etching mask was then deposited and 1.5- μ m-wide stripes were formed along the <011> direction. The n-InP layer was then etched by reactive ion etching (RIE) using Cl₂ and

Ar, and the SiO₂ CB layer was etched with a buffered HF solution. Finally, the surfaces of the exposed p-InP substrate and the sidewall of the etched InP were slightly etched using 3HCl:1H₃PO₄ solution (Fig. 1 (c)).

After the SiO₂ etching mask was removed, a double heterostructure (DH), consisting of a 50-nm-thick p-InP layer ($p = 1 \times 10^{18} \text{ cm}^{-3}$), a 0.12- μ m-thick undoped InGaAsP active layer ($\lambda_g = 1.3 \mu\text{m}$), and a 1.5- μ m-thick n-InP cladding layer ($n = 1 \times 10^{18} \text{ cm}^{-3}$), was regrown on the patterned wafer using liquid phase epitaxy (Fig. 1 (d)). In this regrowth step, the sidewall of the SiO₂ CB layer had to be covered with a thin layer of InP using the mass transport phenomenon [11]. For the mass transport process, the CB layer was slightly side-etched using buffered HF, then the wafer was heated at 660 °C for 45 minutes in a H₂ atmosphere. During the heat treatment, the wafer was covered with an InP wafer [11]. Fig. 3 shows a cross-sectional scanning electron micrograph of the wafer after the regrowth. It can be confirmed the desired DH structure is actually realized.

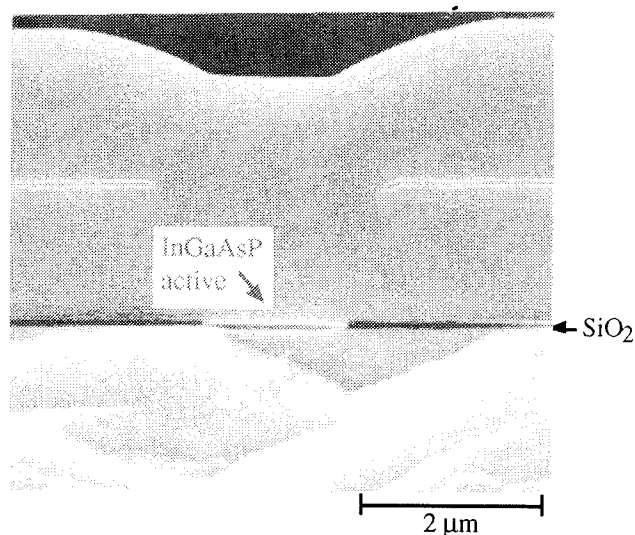


Fig. 3 SEM picture of the wafer after regrown.

Device characteristics

The fabricated lasers were mounted on Si heat sinks with junction-down configuration and tested at room-temperature CW condition. The cavity was 300 μm long and the facets were left uncoated. The lasing wavelength was 1.3 μm . The light-current (L-I) and voltage-current (V-I) characteristics of the SiO₂ CB laser are shown in Fig. 4 (a). The threshold current was 10 mA and the slope efficiency was 0.31 W/A. The width of the active region was measured to be 1.8 μm , with which the threshold current density is estimated to be 1.9 kA/cm². This value is identical to that estimated from the broad area lasers

fabricated with the equivalent active material, which implies that the leakage current is negligible.

The maximum power of 60 mW is comparable to the highest value previously reported for 1.3- μm InGaAsP lasers with 300- μm -long cavity and no coatings [12]. The maximum power is mainly limited by the temperature increase. The laser maintained a single-lobed emission pattern up to the maximum power.

The temperature dependence of the threshold current is shown in Fig. 4 (b). CW operation was achieved up to 110°C. The characteristic temperature T_0 was 72 K between 20 and 70°C, and 42 K between 70 and 110°C.

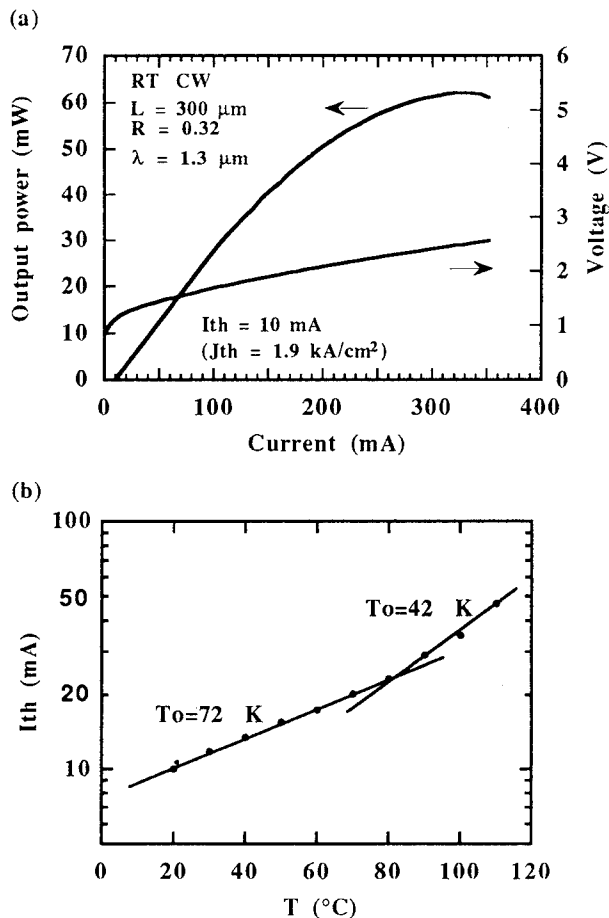


Fig. 4 (a) Light-current and voltage-current characteristics of the SiO₂ CB lasers. (b) Temperature dependence of the threshold current.

The parasitic capacitance was measured at 1 MHz for 11 lasers with the area of 300 μm x 300 μm . The results are shown in Fig. 5. The average capacitance is 31.1 pF. This value is close to the expected capacitance, eS/d , which is estimated to be 36 pF when the dielectric permittivity of the SiO₂ CB layer (ϵ) is 3.98×10^{-11} F/m, the area of the laser chip (S) is 9×10^{-8} m², and the thickness of the CB layer (d) is 0.1 μm . The capacitance can readily be reduced by making the area S smaller, for example, by using a double-channel structure.

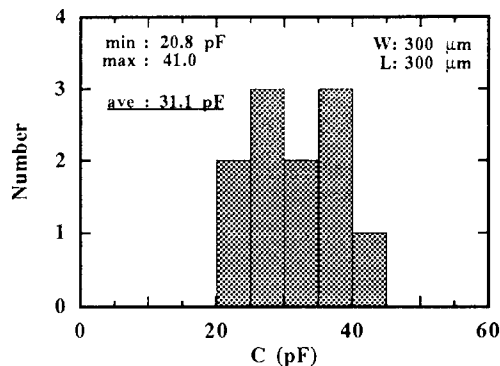


Fig. 5 Measured parasitic capacitance of the lasers with the area of 300 x 300 μm^2 .

Conclusion

In conclusion, we propose a novel laser structure which uses a buried SiO₂ insulator as the current-blocking layer. The structure has been fabricated using direct bonding. A threshold current density of 1.9 kA/cm² and a maximum CW output power of 60 mW have been achieved for a 1.3- μm InGaAsP/InP laser with a cavity 300 μm long. The parasitic capacitance was measured to be 31 pF even for a laser with an area of 300 μm x 300 μm . The capacitance can be reduced by using a double-channel structure.

This proposed fabrication process will be also applicable to other device structures such as three-dimensional integrated circuits and field effect devices with III-V semiconductors.

Acknowledgment

The authors would like to thank Y. Katoh for his contribution to the MOVPE growth, M. Kobayashi for his help in the reactive ion etching.

References

- [1] E. Yablonovitch, D. M. Hwang, T. J. Gmitter, L. T. Florez and J. P. Harbison, "Van der waals bonding of GaAs epitaxial liftoff films onto arbitrary substrates," *Appl. Phys. Lett.*, vol. 56, pp. 2419-2421, 1990.
- [2] Y. H. Lo, R. Bhat, D. M. Hwang, M. A. Koza and T. P. Lee, "Bonding by atomic rearrangement of InP/InGaAsP 1.5 μm wavelength lasers on GaAs substrates," *Appl. Phys. Lett.*, vol. 58, pp. 1961-1963, 1991.
- [3] J. J. Dudley, M. Ishikawa, D. I. Babic, B. I. Miller, R. Mirin, W. B. Jiang, J. E. Bowers and E. L. Hu, "144°C operation of 1.3 μm InGaAsP vertical cavity lasers on GaAs substrates," *Appl. Phys. Lett.*, vol. 61, pp. 3095-3097, 1992.
- [4] H. Wada, Y. Ogawa and T. Kamijoh, "Electrical characteristics of directly-bonded GaAs and InP," *Appl. Phys. Lett.*, vol. 62, pp. 738-740, 1993.
- [5] Y. H. Lo, R. Bhat, D. M. Hwang, C. Chua and C.-H. Lin, "Semiconductor lasers on Si substrates using the

- technology of bonding by atomic rearrangement," Appl. Phys. Lett., vol. 62, pp. 1038-1040, 1993.
- [6] K. Mori, K. Tokutome, K. Nishi and S. Sugou, "High-quality InGaAs/InP multiquantum-well structures on Si fabricated by direct bonding," Electron. Lett., vol. 30, pp.1008-1009, 1994.
- [7] H. Wada and T. Kamijoh, "Effects of heat treatment on bonding properties in InP-to-Si direct wafer bonding," Japan. J. Appl. Phys., vol. 33, p. 4878-4879, 1994.
- [8] G. P. Agrawal and N. K. Dutta, Long-wavelength semiconductor lasers. Van Nostrand Reinhold, 1986, pp.193-211.
- [9] H. Wada, H. Horikawa, Y. Matsui, Y. Ogawa and Y. Kawai, "High-power and high-speed 1.3 μm V-grooved inner-stripe lasers with new semi-insulating current confinement structures on p-InP substrates," Appl. Phys. Lett., vol. 55, pp. 723-725, 1989.
- [10] C. Nozaki, S. Yasuami, H. Ishimura and H. Tokuda, "InP-insulator interface structure studied by high resolution transmission electron microscopy," J. Crystal Growth, vol. 99, pp. 371-374, 1990.
- [11] T. R. Chen, L. C. Chiu, A. Hasson, K. L. Yu, U. Koren, S. Margalit and A. Yariv, "Study and application of the mass transport phenomenon in InP," J. Appl. Phys., vol. 54, pp. 2407-2412, 1983.
- [12] S. Oshiba, A. Matoba, M. Kawahara and Y. Kawai, "High-power output over 200 mW of 1.3 μm GaInAsP VIPS lasers," IEEE J. Quantum Electron., vol. 23, pp.738-743 ,1987.

Direct bonding of high quality InP on Si and its application to low threshold semiconductor lasers

SB1.4

Kazuo MORI, Keiichi TOKUTOME and Shigeo SUGOU
*Optoelectronics Research Laboratories, NEC Corporation,
34, Miyukigaoka, Tsukuba, Ibaraki 305, Japan*

Introduction

A direct bonding has been developed as an approach to fabricating III-V optical devices on Si. An InGaAs/GaAs multiquantum-well (MQW) laser on Si has already been demonstrated.¹ However, no long-wavelength device has yet been fabricated on Si by this technique. We reported the bonding of InGaAs/InP MQW structures on Si.² The etch-pit densities (EPDs) of the InP surfaces were significantly low ($\sim 10^4 \text{ cm}^{-2}$), the lowest values ever reported for the InP/Si system. In conventional heteroepitaxial growth of III-V on Si, it has been reported that high density of threading dislocations are re-introduced from the III-V/Si interface due to thermal stress in the cooling stage.³ In our bonding process, on the other hand, heteroepitaxially grown buffer layers on Si were used intending to relax the thermal stress. In this paper, we report on the dislocation reduction mechanism that we deduced from the transmission electron microscopy (TEM) results and from comparison of three buffer layer structures on Si. We also obtained the first low threshold ($J_{th} \sim 1.7 \text{ kA/cm}^2$) room temperature pulsed operation of InGaAs/InGaAsP MQW lasers on Si.⁶

Experimental

The samples used here were grown with a Varian Modular Gen II MBE system. Gaseous arsine and phosphine cracked at 950°C , as well as In, Ga, and Al metals, were used as sources. Typical sample preparation and bonding processes were as follows.²

An InGaAs layer ($0.3 \mu\text{m}$), which acted as an etch-stop layer during the InP substrate removal after bonding, was first grown on a Fe-doped InP(100) substrate. Then, an InGaAs/InP (5nm/20nm) multiple-quantum-well (MQW) structure, sandwiched between two InP layers ($1.5 \mu\text{m} \times 2$), was grown. In addition, a multiple-layer stacked buffer layer was heteroepitaxially grown on a Si(100) 2° off $\langle 011 \rangle$ substrate. This buffer layer consisted of a GaP layer ($0.3 \mu\text{m}$), a GaAs layer ($1 \mu\text{m}$), an InAlGaAs step-graded layer ($1.3 \mu\text{m}$), and finally, an InP layer ($1.5 \mu\text{m}$).

The InP surfaces of both samples were mirror-polished to reduce surface roughness formed during epitaxial growth, cleaned with $\text{H}_2\text{SO}_4:\text{H}_2\text{O}_2:\text{H}_2\text{O}$ solutions (3:1:1), and rinsed in de-ionized water. The samples were then placed with their mirror-polished sides in contact under a weight of about 300 g/cm^2 and loaded immediately into an annealing furnace for bonding. They were annealed at 700°C for 1 hour in H_2 ambient. After the samples were bonded, the InP substrate as well as the InGaAs etch-stop layer were removed by conventional wet etching.

An etch-pit density (EPD) was measured by etching the InP surface with $\text{HBr}:\text{H}_3\text{PO}_4$ solution (1:2) for 8 seconds. A typical Nomarski contrast photograph of the etched surface is shown in Figure 1, revealing a significantly low EPD of about 10^4 cm^{-2} ; this value is the lowest one ever reported and is comparable to that of Fe-doped InP substrates used for MQW growth.²

Results and discussion

TEM observation

The dislocation propagation characteristics of the bonded structure were studied by transmission electron microscopy (TEM). Figure 2((a)~(c)) shows the cross sectional TEM images of the same sample shown in Figure 1. Figure 2 (a) is a low magnitude bright field image taken with $[01\bar{1}]$ electron beam direction. Because of slight sample rotation of 0.8° about $[100]$ direction in the bonded interface, the upper bonded MQW layer was used for setting the diffraction condition. A higher magnitude bright field image taken by 022 reflection and a high resolution lattice image of the bonded interface are shown in Figure 2 (b) and (c), respectively. These observations confirm that an abrupt interface without any voids is formed in the bonding process.

The InP/InP bonded interface is clearly distinguished in

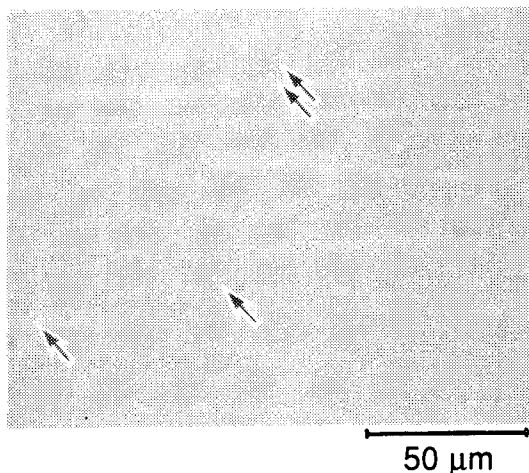


Figure 1 Nomarski contrast photograph of an InP surface etched with $\text{HBr}:\text{H}_3\text{PO}_4$ solution (1:2) for 8 seconds, revealing a significantly low EPD of about 10^4 cm^{-2} .

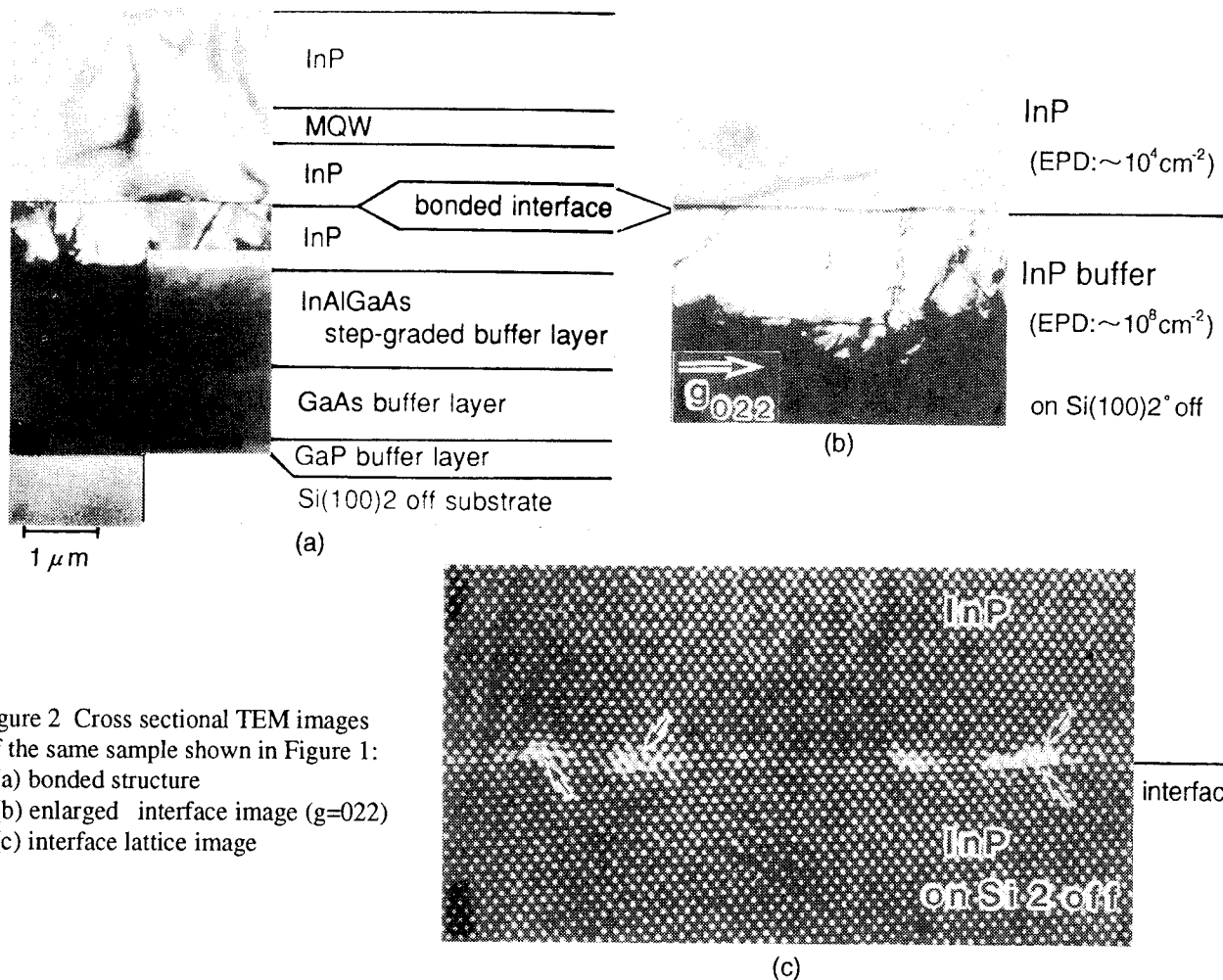


Figure 2 Cross sectional TEM images of the same sample shown in Figure 1: (a) bonded structure (b) enlarged interface image ($g=022$) (c) interface lattice image

Figure 2 (a) and (b), because of the introduction of 60° misfit dislocations with strain field spreading along them in the (100) just/2° off misoriented interface (Figure 2 (c)). In Figure 2 (c), the positions of extra {111} half-planes, which are typical of 60° dislocations, are shown by arrows.

The observed long range waviness of the bonded interface may be due to atomic rearrangement (mass transport) during the high temperature bonding⁴; this long range waviness permits three types of interface structures to exist (schematically drawn in Figure 3 (a)~(c)). Among them, (b) is a theoretical structure when flat substrate surfaces with just and off orientations are bonded. To accommodate the misorientation at the bonded interface, 60° misfit dislocations and "new" (100) lattice-planes with theoretical spacing of $\sim 8.4\text{nm}$ should be introduced in the lower side of the interface. On the other hand, the observed interface structure in Figure 2 (c) corresponds to the structure in Figure 3 (c), where 60° misfit dislocations and "new" (100) lattice-planes are introduced in the both sides of the interface.

No defects were found in the bonded MQW layer over the whole inspected region. Moreover, all of threading dislocations in the buffer layer grown on Si (as high as about 10^8cm^{-2}) were terminated at, or bent along the bonded interface (Figure 2(b)). From these results, we deduced that the

misoriented interface acts as a dislocation blocking layer, probably because of interaction of the threading dislocations with the 60° misfit dislocations in the interface, or with the interface strain field spreading along the 60° misfit dislocations.

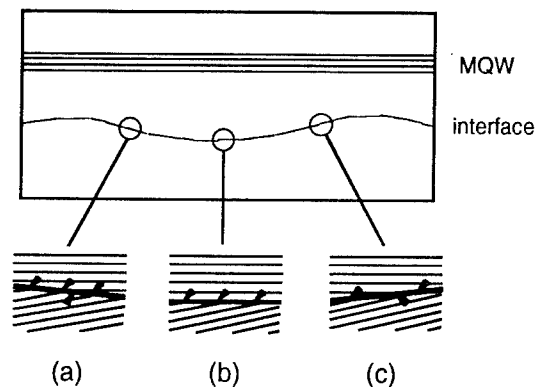
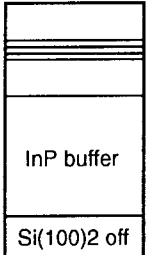
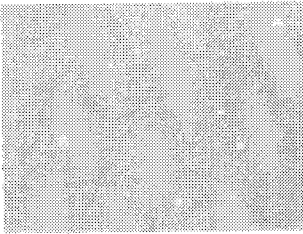
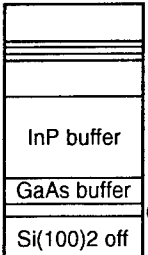
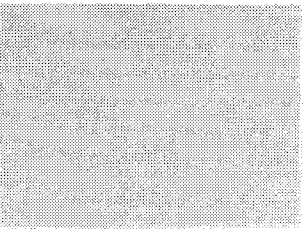
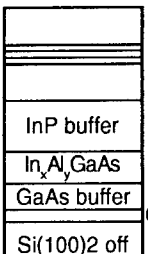
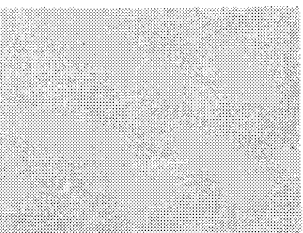


Figure 3 Schematic drawings of three types of interface structures that exist for a bonded interface with long range waviness. Among them, (b) is theoretical one when flat substrate surfaces with just and off orientations are bonded, and (c) is observed one in Figure 2 (c).

Buffer structure dependence

To investigate the dislocation reduction mechanism in detail, three types of buffer layer structures on Si were compared. Figure 4 shows photographs of the InP surfaces etched by $\text{HBr}:\text{H}_3\text{PO}_4=1:2$ solution after bonding. The dislocation density was reduced from $\sim 10^5$ to $\sim 10^4\text{cm}^{-2}$ by using a multiple-layer stacked buffer layer containing GaAs and GaP layers instead of a simple InP layer with the same thickness. The insertion of an InAlGaAs step-graded buffer layer didn't affect the dislocation density. These results indicate that the insertion of GaAs and GaP layers is important to relax the thermal stress and to reduce the propagation of threading dislocations in the buffer layer below the bonded interface (as high as about 10^8cm^{-2}) during the cooling stage.

On the other hand, it has been reported that high density of threading dislocations ($\sim 10^7\text{cm}^{-2}$) were introduced due to thermal stress after high temperature bonding (700°C) when an InP substrate was directly bonded with a Si substrate without any buffer layers.⁵ It is suggested, therefore, that the dislocation density was reduced from $\sim 10^7$ to $\sim 10^5\text{cm}^{-2}$ by the

buffer structure	etched surface (EPD)
	 $1.3 \times 10^5\text{cm}^{-2}$
	 $2.5 \times 10^4\text{cm}^{-2}$
	 $2.0 \times 10^4\text{cm}^{-2}$

$50\ \mu\text{m}$

Figure 4 Photographs of the InP surfaces etched by $\text{HBr}:\text{H}_3\text{PO}_4=1:2$ solution after bonding by using three types of buffer layer structures on Si.

dislocation blocking effect of the (100) just/ 2° off misoriented interface structure.

Application to lasers

InGaAs/InGaAsP MQW lasers ($\lambda \sim 1.55\ \mu\text{m}$) on Si were fabricated by bonding. The structure is shown in Figure 5. Based on the above results, we used the simpler buffer layer structure without the InAlGaAs step-graded buffer layer on Si.

A Be-doped p^+ -InGaAs contact layer (an etch-stop layer : $0.3\ \mu\text{m}$) was first grown on a n-InP(100) substrate, followed by a Be-doped p-InP cladding layer ($1.5\ \mu\text{m}$). Then, a non-doped InGaAs/InGaAsP (5nm/10nm x 4) MQW structure ($\lambda \sim 1.55\ \mu\text{m}$), sandwiched between two InGaAsP ($\lambda_g \sim 1.15\ \mu\text{m}$) optical guide layers ($0.2\ \mu\text{m} \times 2$, Be-doped and Si-doped, respectively), was grown. Finally, a Si-doped n-InP cladding layer ($1.5\ \mu\text{m}$) was grown. In addition, a Si-doped multiple-layer stacked buffer layer was heteroepitaxially grown on a n-Si(100) 2° off<011> substrate. This buffer layer consisted of a n-GaP layer ($0.2\ \mu\text{m}$), a n-GaAs layer ($1\ \mu\text{m}$), a n-InP layer ($1.5\ \mu\text{m}$), a n-InGaAs contact layer ($0.3\ \mu\text{m}$) and finally, a n-InP layer ($1.2\ \mu\text{m}$). Both samples were then bonded and the InP substrate was removed.

The laser structures bonded on Si substrates were processed into $50\ \mu\text{m}$ mesa width stripe lasers with co-planer electrodes. The mesa was formed by wet etching and the surface of the n-InGaAs bottom contact layer, located below the bonded interface, was revealed for the Ti/Au contact. The Si substrate was lapped down to $60\ \mu\text{m}$ and then cleaved into laser-array bars with typically $300\ \mu\text{m}$ cavity length. For comparison, lasers with the same structure were fabricated on InP substrates.

Excellent p-n diode characteristics are retained after the high-temperature annealing at 700°C during bonding. Although the current passes through the n-InP/n-InP bonded interface, the same series resistance as that of lasers on InP substrates was obtained, which means no current barrier exists at the bonded interface.

The lasers on both Si and InP substrates were tested

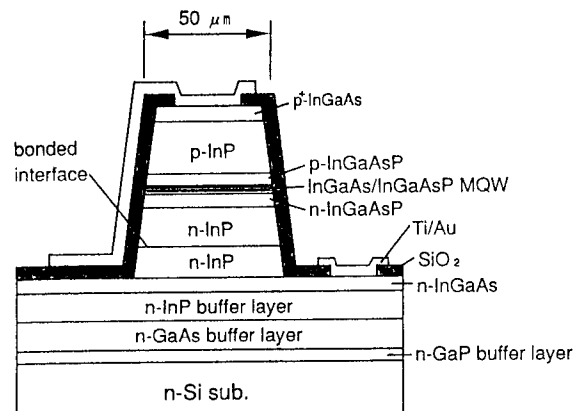


Figure 5 Schematic cross-section of mesa stripe laser with $50\ \mu\text{m}$ mesa width on Si substrate.

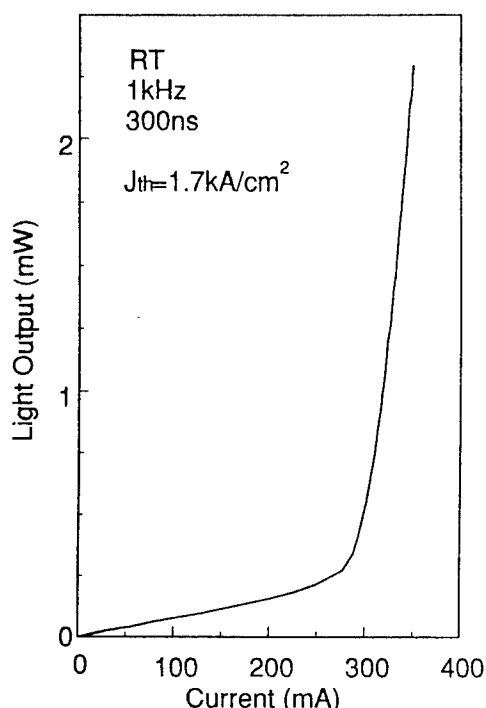


Figure 6 Typical I-L characteristics ($330\ \mu\text{m}$ cavity length) of a laser on Si under RT pulsed operation (300ns-1kHz).

under an RT pulsed condition (300ns-1kHz). Figure 6 shows the typical current-light (I-L) characteristics ($330\ \mu\text{m}$ cavity length) of a laser on Si. The threshold current density is estimated to be as low as 1.7 kA/cm^2 . Furthermore, dependence of the threshold current density (J_{th}) upon the reciprocal of cavity length ($1/L$) was investigated and plotted in Figure 7 for the lasers on Si and InP substrates. Although the data points are somewhat scattered, the lasers on both substrates have essentially similar dependence, demonstrating that the performance of the lasers on Si is comparable to that on InP. This result agrees well with the excellent EPD value of about 10^4 cm^{-2} .

Conclusions

High-quality InP layers were fabricated on Si by direct bonding at 700°C . EPDs of the InP surfaces were significantly low, about 10^4 cm^{-2} , the lowest values ever reported. The dislocation reduction mechanism was investigated by using TEM and by comparing three buffer layer structures on Si. The results indicated that the insertion of GaAs and GaP layers is important to relax the thermal stress and to reduce the propagation of threading dislocations in the buffer layer during the cooling stage (from $\sim 10^5$ to $\sim 10^4\text{ cm}^{-2}$). Furthermore, it was suggested that the dislocation density was reduced from $\sim 10^7$ to $\sim 10^5\text{ cm}^{-2}$ by the dislocation blocking effect of the (100) just/ 2° off misoriented bonded interface.

The first low threshold RT pulsed operation of long-wavelength InGaAs/InGaAsP MQW mesa stripe lasers on Si substrates fabricated by direct bonding was

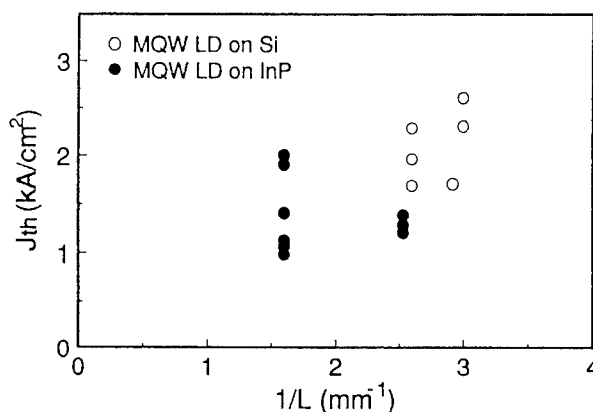


Figure 7 Dependence of the threshold current density (J_{th}) on the reciprocal of cavity length ($1/L$) for lasers on Si and InP substrates: \circ MQW LD on Si, \bullet MQW LD on InP

demonstrated. The mesa stripe broad area lasers had a threshold current density of 1.7 kA/cm^2 , which was comparable to the value for lasers on InP substrates.

Acknowledgements

The authors would like to thank C. Sasaoka, M. Kajita, T. Sasaki, K. Nishi, T. Anan, N. Kuroda, and H. Shimomura for their support and useful discussions. They also thank K. Kobayashi, T. Suzuki, K. Asakawa, and J. Namiki for their continuous encouragement.

References

- [1] Y. H. Lo, R. Bhat, D. M. Hwang, C. Chua, and C.-H. Lin, "Semiconductor lasers on Si substrates using the technology of bonding by atomic rearrangement," *Appl. Phys. Lett.*, **62**, pp.1038-1040 (1993).
- [2] K. Mori, K. Tokutome, K. Nishi, and S. Sugou, "High-quality InGaAs/InP multiple-quantum-well structures on Si fabricated by direct bonding," *Electron. Lett.*, **30**, pp.1008-1009 (1994).
- [3] M. Tachikawa, and H. Mori, "Dislocation generation of GaAs on Si in the cooling stage," *Appl. Phys. Lett.*, **56**, pp.2225-2227 (1990).
- [4] Y. H. Lo, R. Bhat, D. M. Hwang, M. A. Koza, and T. P. Lee, "Bonding by atomic rearrangement of InP/InGaAsP $1.5\ \mu\text{m}$ wavelength lasers on GaAs substrates," *Appl. Phys. Lett.*, **58**, pp.1961-1963 (1991).
- [5] H. Wada, and T. Kamijoh, "Effects of heat treatment on bonding properties in InP-to-Si direct wafer bonding," *Jpn.J.Appl.Phys.*, **33**, pp.4878-4879 (1994).
- [6] K. Mori, K. Tokutome, and S. Sugou, "Low threshold pulsed operation of long wavelength lasers on Si fabricated by direct bonding," *Electron. Lett.*, to be published.

Free-Orientation Integration by Direct Bonding: Fabrication of (001) InP-based 1.55 μ m-Wavelength Lasers on (110) GaAs Substrate

SB1.5

Y. Okuno, M. Aoki, T. Tsuchiya, and K. Uomi,
Central Research Laboratory, Hitachi, Ltd.
Kokubunji, Tokyo, Japan

We propose a new concept "free-orientation integration", which should be implemented by the direct bonding technique. In order to investigate the possibility of such integration, we examine the direct bonding of (001) InP and (110) GaAs. Cross-sectional observation shows that these wafers can be united without generating dislocation. (001) InP-based 1.55- μ m wavelength lasers are fabricated on (110) GaAs. The light-current characteristics of the lasers are almost identical to those of lasers fabricated on (001) GaAs, while the turn-on voltage is higher by about 0.4 V, due to the large band discontinuity at the bonding interface. The results show that device fabrication by direct bonding on different materials with different surface orientations is possible with satisfactory quality.

Introduction

The monolithic integration of various kinds of materials will make new types of integrated devices possible, such as photonic integrated circuits (PICs) and opto-electronic integrated circuits (OEICs). However, integration of different materials has to overcome mismatches in their material properties, such as lattice constants and thermal expansion coefficients. For example, heteroepitaxy such as GaAs-on-Si has been intensely studied as a key technology for developing OEICs [1]. However, the density of threading dislocations is high in the layers grown epitaxially on lattice-mismatched substrates, which makes it hard to create OEICs by heteroepitaxy.

On the other hand, direct bonding has recently received a lot of attention, because this technique can be used to fabricate highly lattice-mismatched hetero-structures without generating any threading dislocations. This technique has been used with good results especially in the case of InP and GaAs [2,3,4,5]. Fabrication of III-V materials on Si has also been reported [6,7,8]. In addition, direct bonding enables us to change the relation of crystallographic axes between wafer pairs, which makes it possible to create novel structures which cannot be obtained

by epitaxial growth [9]. In particular, direct bonding of different materials with variously related crystallographic axes will give us much extended possibilities for device integration [10]. With this as our motivation, we further investigate the possibility of using the direct bonding techniques for free-orientation integration: to freely integrate various kind of material with various crystallographic orientations. In this paper, we examine the direct bonding of (001) InP and (110) GaAs, of which the numbers of dangling bonds are extremely different at the bonding interface, and demonstrate the application of this bonded structure to device fabrication.

Structural properties

Both InP and GaAs substrates used in this study have a range of surface misorientation of 0.3°. Epitaxial growth was performed by conventional low-pressure MOVPE. The direct bonding procedure was carried out as follows: Both InP and GaAs wafers were chemically etched in a mixture of H₂SO₄ and H₂O₂, and cleaned in dilute HF. They were placed face to face, and their horizontal crystallographic axes were adjusted by aligning their (1 $\bar{1}$ 0) cleaved facets to be

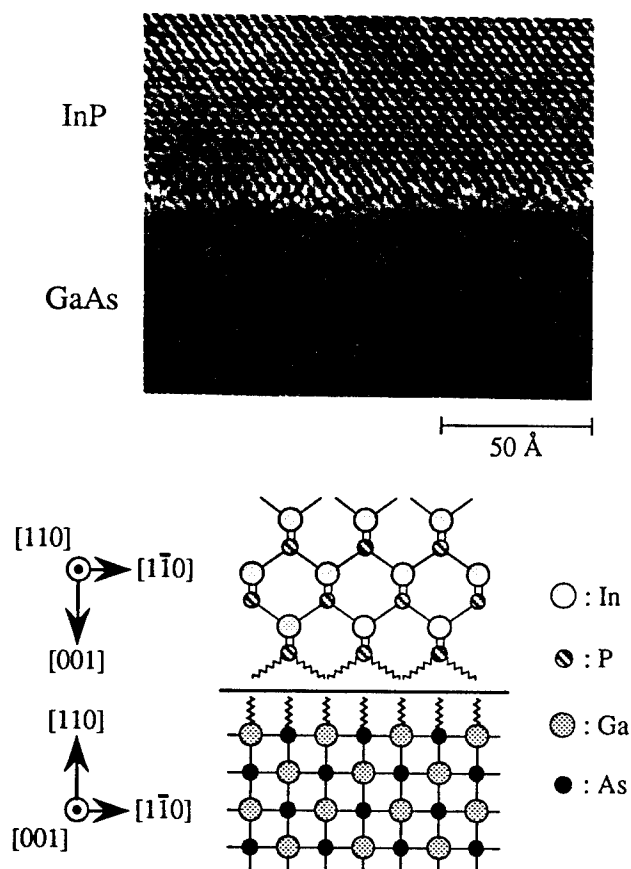
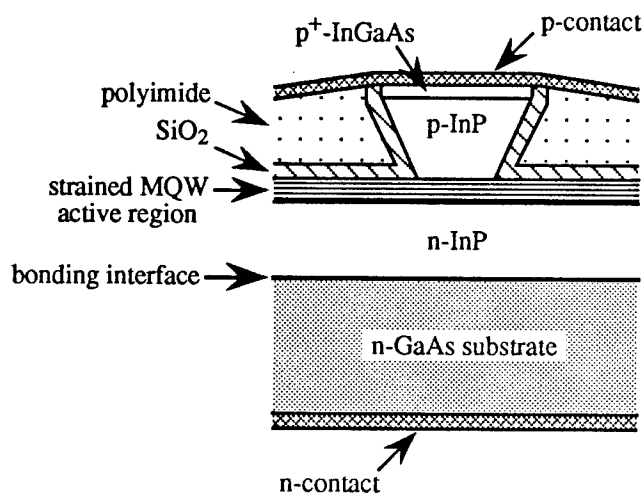


Figure 1 High-resolution cross-sectional TEM image of the bonding interface of (001) InP and (110) GaAs and a schematic lattice model.



parallel. They were then loaded into the MOVPE reactor, and a pressure of 30 g/cm² was applied on them by a tungsten block. They were heated to either 600°C or 700°C for 30 min in H₂ flow.

Figure 1 is a cross-sectional image taken with a high-resolution transmission electron microscope (TEM) of the bonding interface of the (001) InP and (110) GaAs, and a schematic lattice model. It is natural that the manner of bonding between InP and GaAs at the atomic level is very obscure since the number and nature of dangling bonds are largely discrepant at the interface. Even the location of the interface is not clear and the region around the interface seems likely to be somewhat amorphous. Nevertheless, no evidence of either edge-type or 60°-type dislocation is observed. No threading dislocation was observed in low-magnification TEM, which confirms successful elimination of dislocation in the layers.

Device application

(001) InP-based 1.55μm-range long-wavelength laser diodes (LDs) were fabricated on (110) n-GaAs by applying the above method. LDs were also fabricated on (001) GaAs by anti-phase and in-phase direct bonding [10] for

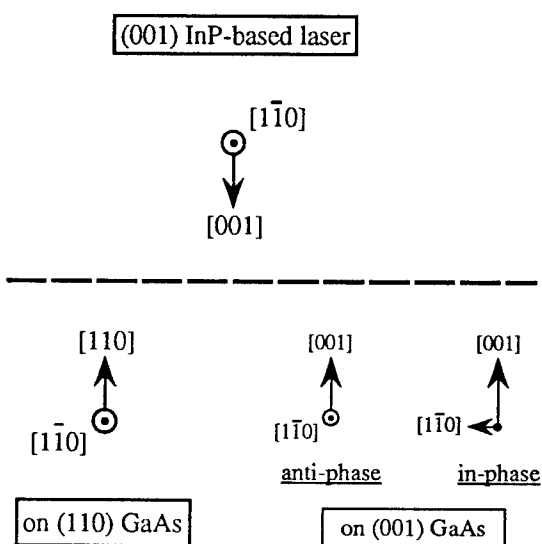


Figure 2 Schematic laser structure and the relation between the crystallographic axes of (001) InP and (110) or (001) GaAs.

comparison. Figure 2 shows the structure of the reversed-mesa ridge-waveguide laser [11] and the relation of the crystallographic axes for each type of direct bonding. The multiple quantum well (MQW) active region, emitting at 1.55 μm , consists of five 6 nm InGaAsP wells with 1% compressive strain separated by 10 nm InGaAsP barriers. The layers for the laser were first grown upside-down on a (001) p-InP substrate and then directly bonded onto three different GaAs substrates. After the p-InP substrate was selectively removed by HCl, a ridge waveguide structure was formed along the $[1\bar{1}0]$ axis of the InP. Figure 3 is a cross-sectional view taken with a scanning electron microscope (SEM) of a LD fabricated on (110) GaAs. The top of the reversed-mesa stripe is about 5.2 μm wide and the waveguide is about 3.0 μm wide. The (001) InP/(110) GaAs interface is very smooth, showing no significant misorientation of cleaved facets between the two wafers.

Figure 4 shows the light-current (I-L) and voltage-current (I-V) characteristics of the LD on (110) GaAs under CW operation at room-temperature, together with those of the LDs on (001) GaAs. The cavity length is 400 μm and the rear facets were coated with highly reflective (HR) film. Note that almost the same I-L characteristics, such as the threshold

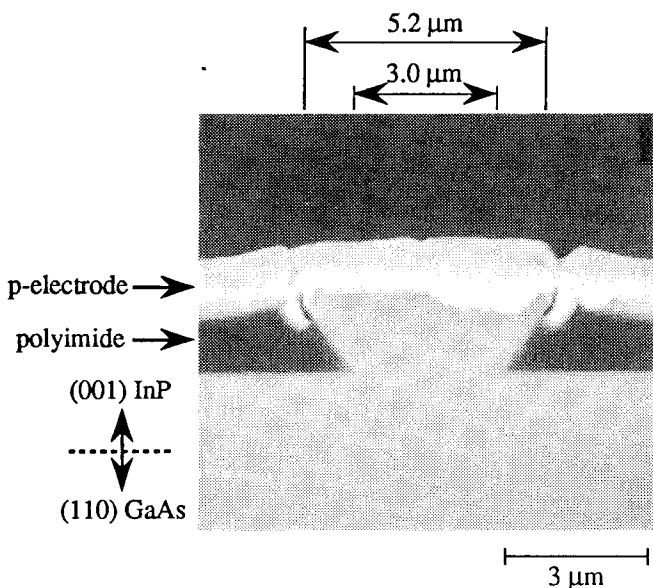


Figure 3 Cross-sectional SEM image of the (001)InP-based 1.55- μm strained MQW LD on (110) GaAs.

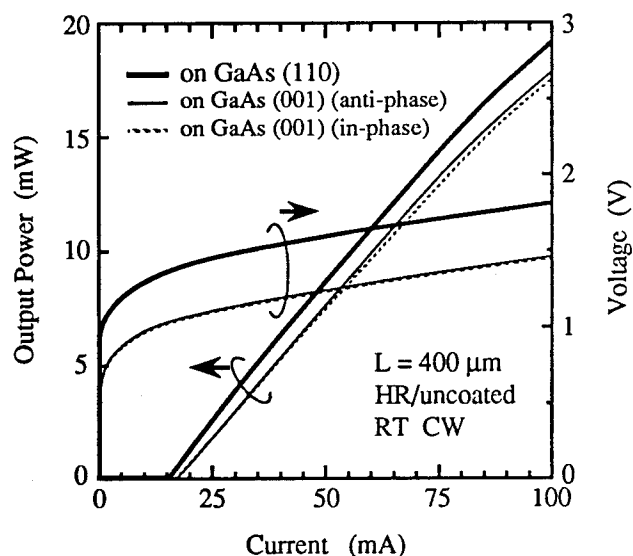


Figure 4 I-L and I-V characteristics of the (001) InP-based LDs on (110) GaAs and (001) GaAs substrates.

current of 15-17 mA and the slope efficiency of about 0.22 W/A, were obtained for all three kinds of LDs. On the other hand, in terms of I-V characteristics, the turn-on voltage of the LD on (110) GaAs is a little bit higher by about 0.4 V than that of both LDs on (001) GaAs. The electrical resistance of the LD on (110) GaAs is equivalent to that of the other two types. These facts mean that there exists a larger barrier height at a bonding interface of different surface orientations, than with a same-surface-orientation interface. Since the I-V properties do not change by rotating the horizontal axes alone, the origin of the higher barrier height is attributed to the large mismatch in the number of dangling bonds: some interface state must be being formed at the (001) InP/(110) GaAs interface due to that mismatch. In this way, we have shown that fabrication of (001) InP-based LD on (110) GaAs substrates is possible with acceptable laser performance. The effect of the bonding interface appears in the higher turn-on voltage, however, the effect is probably not serious, so the LD can achieve high reliability [10].

It is noteworthy that device fabrication on different materials with different surface orientations is possible without degrading device performance. If free-orientation integration is conducted by direct bonding, we will be able to

obtain novel types of integrated devices which cannot be fabricated by epitaxial growth. For example, the (001) InP / (110) GaAs structure of this study can serve as an integrated structure of (001) InP-based LDs and (110) GaAs-based rotating phase-plate as frequency shifter [12]. We think that other types of direct bonding, such as (001) InP and (110) GaP or (111) InP and (110) GaAs should also be possible using the same technique. Direct bonding still doesn't allow bonding of any combination of wafers, however, it should be noted that direct bonding can overcome the differences of both material and crystallographic orientation.

Conclusion

We examined direct bonding of (001) InP and (110) GaAs. We found that this type of direct bonding is possible without generating any dislocation, in spite of the extreme mismatch of dangling bonds. In device application, the LD showed almost identical I-L characteristics as those of LDs fabricated on (001) GaAs. The turn-on voltage increased by about 0.4 V due to the enormous band discontinuity at the (001) InP / (110) GaAs interface, but the resistance was not affected. Therefore, the direct bonding technique has great potential for free-orientation integration, opening up new opportunities for monolithic integration of various devices.

Acknowledgements

We are grateful to Dr. H. Kakibayashi for his expert help in the TEM observation.

References

- [1] S. F. Fang, K. Adomi, S. Iyer, H. Morkoç, H. Zabel, C. Choi, and N. Otsuka, *J. Appl. Phys.* **68**, R31 (1990), and references therein.
- [2] Z. L. Liau and D. E. Mull, *Appl. Phys. Lett.* **56**, 737 (1990).
- [3] Y. H. Lo, R. Bhat, D. M. Hwang, M. A. Koza, and T. P. Lee, *Appl. Phys. Lett.* **58**, 1961 (1991).
- [4] H. Wada, Y. Ogawa, and T. Kamijoh, *Appl. Phys. Lett.* **62**, 738 (1993).
- [5] J. J. Dudley, D. I. Babic, R. Mirin, L. Yang, B. I. Miller, R. J. Ram, T. Reynolds, E.-L. Hu, and J. E. Bowers, *Appl. Phys. Lett.* **64**, 1463 (1994).
- [6] Y. H. Lo, R. Bhat, D. M. Hwang, C. Chua, and C.-H. Lin, *Appl. Phys. Lett.* **62**, 1038 (1993).
- [7] K. Mori, K. Tokutome, K. Nishi, and S. Sugou, *Electron. Lett.* **30**, 1008 (1994).
- [8] H. Wada and T. Kamijoh, *Jpn. J. Appl. Phys.* **33**, 4878 (1994).
- [9] L. Gordon, G. L. Woods, R. C. Eckardt, R. R. Route, R. S. Feigelson, M. M. Fejer and R. L. Byer, *Electron. Lett.* **29**, 1942 (1993).
- [10] Y. Okuno, K. Uomi, M. Aoki, T. Taniwatari, M. Suzuki, and M. Kondow, *Appl. Phys. Lett.* **66**, 451 (1995).
- [11] M. Aoki, T. Tsuchiya, K. Nakahara, M. Komori, and K. Uomi, *IEEE Photon. Tech. Lett.*, **7**, 00 (1995).
- [12] H. Inoue, S. Nishimura, T. Kanetake, H. Takano, Technical Digest of the International Conference on Optical Computing, TuC5, Edinburgh Scotland, Aug. (1994)

W. T. TSANG
AT&T Bell Laboratories
600 Mountain Ave., Murray Hill, NJ 07974

ABSTRACT

We have developed an etching process with real-time counting of each monolayer removed, thus achieving etching with monolayer precision and control. This is an exact reversal of CBE process. The new etching capability which we refer to as monolayer chemical beam etching, CBET, is achieved by employing in-situ RHEED intensity oscillation monitoring during etch. Having both epitaxial growth and etching integrated in the same process and both capable of ultimate control down to the atomic layer precision represents a very powerful combination. This permits instant switching from growth to etching and vice versa, clean regrowth interfaces critical for device applications. The surface morphology is found to be dominated by the surface cation diffusion mechanism. With this understanding, novel methods that takes the advantage of enhanced migration of surface cations have been shown to greatly improve the surface morphology. We also show that CBET can be a very effective means of surface contaminant cleaning prior to regrowth. The effectiveness depends on the strength of chemical reactivity of the contaminant to form volatile chlorides. Using dielectric marks, selective-area etching and etching followed immediately by regrowth having excellent etched and regrown morphologies were obtained.

1. Introduction

Chemical beam epitaxy (CBE) is a versatile semiconductor epitaxial growth technique^{1,2} that utilizes beams of chemicals directly impinging on a heated substrate surface. Under properly controlled conditions, decomposition of metal-alkyls on the surface resulted in the incorporation of the desired elements to produce the epitaxial film in a layer-by-layer fashion. By introducing a chemical that reacts with the substrate materials at growth temperature to form volatile species, the growth is immediately converted into a chemical beam etching (CBET) process^{3,4}. If the etching also proceeds in a layer-by-layer fashion, this process can be viewed as an exact reversal of the chemical beam epitaxy. As in the case of growth, in principle, etching control at monolayer scale is feasible by CBET. For the development of advanced optoelectronic devices where multiple steps of etch and regrowth are needed, such an in situ etching method has the potential of providing an accurate etch depth control, a clean interface without ion damage and fewer processing steps.

In this work we show that etching in a high vacuum growth chamber can be monitored in real-time by means of reflection high energy electron diffraction (RHEED) intensity oscillation. This makes possible etch rate control at monolayer scale. Furthermore, the surface morphology obtained at an etching temperature comparable to the growth temperature of InP or GaAs is shown to be dominated by the surface cation diffusion mechanism.

2. Experimental

The etching experiments were carried out in a CBE system with a gas manifold equipped with a growth-vent switching system, a precision goniometer stage, and 20 KeV RHEED gun^{3,4}. The intensity of the specular beam of the RHEED pattern was measured by using a photodetector with an entrance aperture. AsCl₃ or PCl₃ was used with H₂ carrier gas in a concentration of 5% and a low-temperature (~50°C) injector was used to introduce the gas into the chamber. The (100)-oriented GaAs or InP

substrate was used. Etching of InP was done at substrate temperatures from 450 to 570°C. For the RHEED measurements, etching was done on GaAs at substrate temperatures from 450 to 650°C with cracked AsH₃ flux. The chamber pressure during etching was typically 1×10^{-5} torr. The surface morphology was studied by Nomarski or atomic force microscopy (AFM). The system design is shown in Fig. 1.

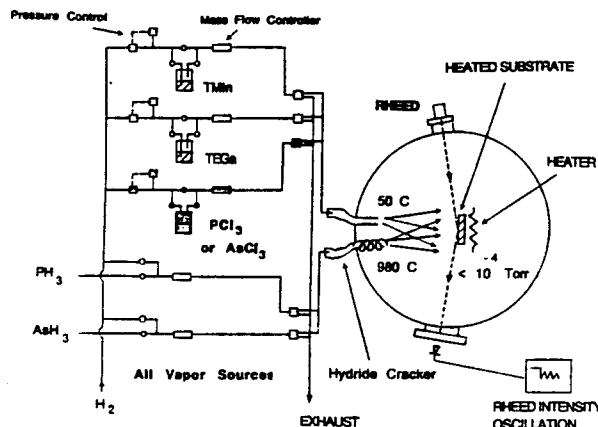


Fig. 1. Schematic diagram showing the CBE/ML-GBET system

3. RHEED Measurements

In the experiment, a clear (2x4) As-rich reconstructed surface RHEED pattern was first established for the incident beam of the [110] azimuth after oxide desorption and annealing at 600°C under cracked AsH₃. Fig. 2 shows the trace of RHEED intensity oscillation from the specular beam immediately after the initiation of GaAs growth by switching in the triethylgallium (TEGa) flow. The period of oscillation corresponds exactly to a single (Ga+As) layer. This provides a real-time growth thickness control with atomic layer precision. On switching out the TEGa flow, the intensity oscillation stops abruptly and is followed by a recovery which is associated with a surface

smoothing effect due to the surface cation diffusion that minimizes the step density.

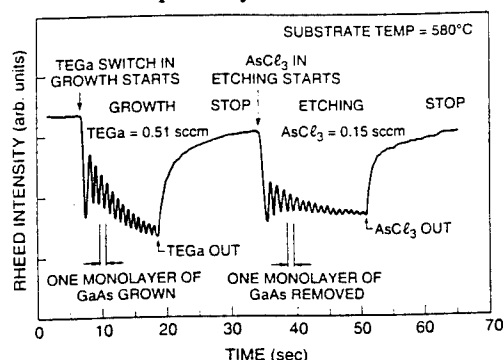


Fig. 2. A trace of the intensity oscillations of the specular beam in the (2x4) RHEED pattern immediately after commencement of GaAs growth by switching in TEGa (left portion) and etching of BaAs by switching in AsCl₃ (right position). Note the abrupt and complete start and termination of growth and etching achieved.

Next, AsCl₃ was switched in from vent. Fig. 2 shows that a damped intensity oscillation starts immediately in a way very similar to the growth situation. The period of oscillation also corresponds to exactly the time required to remove one monolayer of GaAs. The uniform periodicity indicates a constant etching rate. When AsCl₃ is switched out, the oscillation also stops abruptly indicating a clean termination of the etching process. The intensity recovery indicates a smoothing process is taking place. As in the growth case, the oscillatory effect in RHEED suggests that etching occurs via a layer-by-layer process. Thus, we have demonstrated that the chemical beam etching (CBET) process is just the reverse of the chemical beam epitaxy (CBE)⁴. The use of RHEED oscillation is a very powerful method to control the etching with atomic scale precision. This technique should be applicable to other growth-etch chamber, for example, the MOCVD reactor where oscillatory behavior in the optical reflectance spectroscopy has been associated with monolayer growth of GaAs⁵. It should be possible to apply this technique in Si etching because RHEED oscillation is present in Si CBE⁶.

The damping in amplitude of the RHEED oscillations is related to the evolution into a steady-state roughness. The recovery at the end of growth indicates the coalescing of smaller domains to minimize the surface step density. This smoothing process is due to the surface cation diffusion which is faster with higher temperature of lower As flux impinging on the surface. The similarity in the RHEED intensity profiles between etch and growth modes suggests that the etched and the grown surfaces have developed a comparable micro roughness at least in the initial stage. If a steady-state roughness is maintained for etching as in the case of growth, the RHEED measurement provides a powerful means of *in situ* monitoring for control at monolayer scale.

RHEED oscillations also provides a very fast and accurate in-situ measurement of etch rates versus etching parameters which provide very useful insight regarding the

etching mechanisms^{3,4}.

The present technique also allows instant modification of growth rate during growth. An example is shown in Fig. 3. During growth, an AsCl₃ etching beam is switched in at the instant indicated by the arrows. It is seen that the growth rate is abruptly decreased, and in proportion to the amount of AsCl₃ added. The converse can also be done during etching by adding TEGa beam to change the resulting etching rate and morphology as observed previously in the etching of InP using PCl₃.^{3,7}

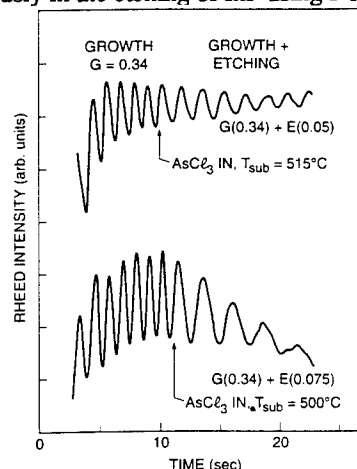


Fig. 3. RHEED intensity oscillations showing the instant modification of GaAs growth rates by switching in a AsCl₃ beam during growth. The modification of etching rate and surface chemistries can also be achieved during etching by adding a TEGa beam.

In Fig. 4, we demonstrate that instant switching between growth and etching and vice versa can be achieved easily. In this experiment the switching-ins and switching-outs were performed manually. In actual applications, they can be performed simultaneously with computer control, if desired.

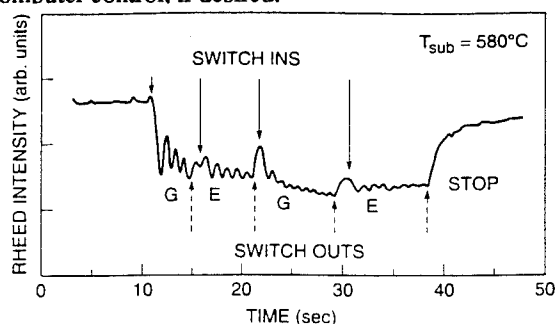


Fig. 4. A RHEED intensity oscillation trace demonstrating instant switching between growth and etching and vice versa. The switchings were performed manually in this experiment. For more precise tuning in switching, computer control can be used.

4. Surface Cleaning by CBET

To investigate the effectiveness of etch cleaning by CBET⁸, the sample is designed to include an intentionally contaminated surface by δ doping of Be which is then etch

cleaned by the AsCl_3 gas. GaAs is regrown on the etched surface and the etched structure is analyzed with secondary ion mass spectroscopy (SIMS). The doping level is about 1/10th of a monolayer which is below the on-set of Be segregation such that the unetched δ -doped layer is well resolved in the SIMS depth profile with a spatial resolution better than 100 Å.

Figure 5 shows the SIMS depth profile of a sample embedded with four Be δ -doped planes each doped to a sheet concentration about one-tenth of a monolayer and separated by about 1000 Å GaAs. The second δ -doped plane below the surface has been etched by about 300 Å using a pulsed etching method which is assumed to have a smoothing effect comparable to the one under continuous etching but without coinjected AsH_3 .⁷ Though some residual Be can still be detected but with an ion count almost two orders of magnitude lower than the unetched peak. For contaminants other than Be, if the formation of volatile chloride is less energetically favorable than BeCl , etch cleaning will be more difficult. Our initial result shown in Fig. 5 on the etch cleaning of Si "contaminated" surface appears to be the case. While the etching of a few hundred Å GaAs nearly removes all the surface Be dopant, AsCl_3 appears much less effective in etching away the Si codoped with Be. In Fig. 5, the Si peak is only reduced by about a factor of 2 after etching.

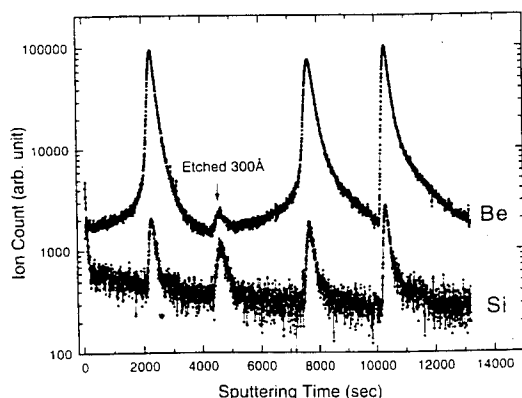


Fig. 5. Log plot of the SIMS depth profile indicating the presence of residual Be at an intensity almost 2 order of magnitude down from the unetched peak. However, the codoped Si peak shows only small reduction in intensity.

5. Selective-Area Etching and Regrowth

The etched profiles of SiO_2 mask patterns obtained under such etching conditions are shown in Fig. 6. The SEM micrograph for the etched cross-section of $\langle 011 \rangle$ oriented SiO_2 stripes have perfectly smooth and featureless sidewalls (Fig. 6a). There is some undercutting of the SiO_2 mask and at the base, $\langle 111 \rangle$ A oriented facets are formed. This anisotropy is characteristic of the chemical nature of etching. The cross-section of $\langle 011 \rangle$ oriented stripes does not show any undercutting of the SiO_2 mask and very smooth $\langle 111 \rangle$ B sidewalls are obtained (Fig. 6b).

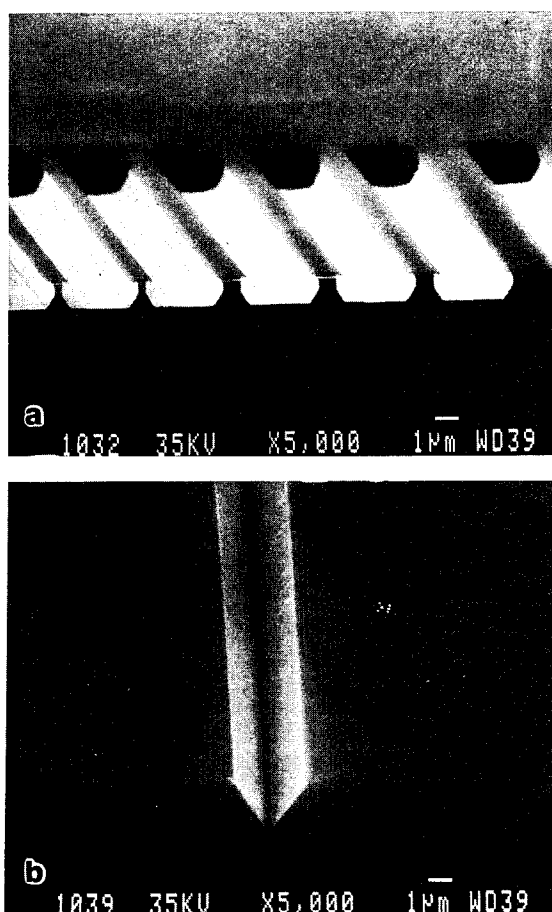


Fig. 6. SEM micrographs of selective-area etching using SiO_2 stripes aligned in (a) the $\langle 011 \rangle$ direction and (b) the $\langle 011 \rangle$ direction. In both micrographs, the SiO_2 masks are still on the surface.

Fig. 7a shows the SEM micrograph of a trial of in-situ etching by CBET followed immediately by a regrowth of InP/InGaAs superlattice (to serve as a time marker) by CBE inside the same chamber. The switch from etching to growth was simply accomplished by gas switchings with a 3 s interruption. The stripes are aligned in the $\langle 011 \rangle$ direction. Etching was conducted at 570°C under an etching rate of ~ 6 angstrom/s. The InP/InGaAs regrowth was carried out at 550°C.

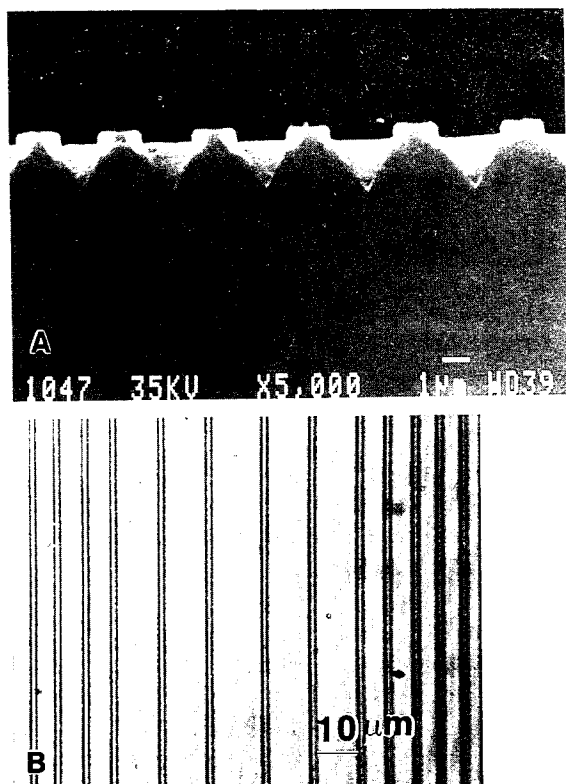


Fig. 7. (A) SEM micrographs of an initial trial of in-situ etching by RCBE followed immediately by a regrowth of InP/In/Ga/As superlattice (to serve as a time marker) by CBE in the same run. The stripes were aligned in the $\langle 0\bar{1}1 \rangle$ direction. The SiO_2 masks are still on the surface. (B) Nomarski optical photograph showing the surface morphology of the regrown structure. (A) $\langle 0\bar{1}1 \rangle$ cross-section; (B) $\langle 0\bar{1}1 \rangle$ top view.

The surface morphology was very smooth as shown by the Nomarski microscope photograph in Fig. 7b.

Because the superlattice was grown in a V-groove consisting of $\langle 111 \rangle_B$ planes, the superlattice is not perfect as revealed by the SEM cross-section.

References

1. W. T. Tsang, in *VLSI Electronics Microstructure Science*, Vol. 21, Eds. N. G. Einspruch, S. S. Cohen and R. N. Singh, Academic Press, New York (1989).
2. W. T. Tsang, *J. Crystal Growth* **120** (1992) 1; 105 (1990) 1.
3. W. T. Tsang, R. Kapre and P. F. Sciortino, Jr., *Appl. Phys. Lett.* **62** (1993) 2084.
4. W. T. Tsang, T. H. Chiu and R. M. Kapre *Appl. Phys. Lett.* **63**, 3500 (1993).
5. D. E. Aspnes, R. Bhat, C. Caneau, E. Colar, L. T. Florez, S. Gregory, J. P. Harbison, I. Kamiya, V. G. Deramidas, M. A. Koza, M. A. A. Pudensi, W. E. Quinn, S. A. Schwarz, M. C. Tamargo and H. Tanaka, *J. Crystal Growth* **120** (1992) 71.
6. S. M. Mokler, W. K. Liu, N. Ohtani and B. A. Joyce, *J. Crystal Growth* **120** (1992) 290.
7. T. H. Chiu, M. D. Williams, J. F. Ferguson, W. T. Tsang and R. M. Kapre, *Appl. Phys. Lett.* **65**, (1994) 448.
8. T. H. Chiu, W. T. Tsang, M. D. Williams, C. A. C. Mendonca, K. Dreyer and F. G. Storz, *Appl. Phys. Lett.* **65** (1994) 3368.

GSMBE GROWTH OF InGaAsP WITH AN "ON SITE" ARSINE GENERATOR

J.-L. Gentner, P. Labrune*, A. Pinquier and J.-C. Parent*
 Alcatel Alsthom Recherche
 Route de Nozay, 91460 Marcoussis - France

* Air Liquide Centre de Recherche Claude-Delorme
 Les Loges-en-Josas, 78350 Jouy-en-Josas - France

Introduction

The safety problem associated with the use of toxic gases is a major concern for the semiconductor industry and for the speciality gas producers. Amongst the different proposed alternatives, the "on site" gas generation is very attractive because the toxic gas is produced at low pressure and in small quantities at demand.

The use of an arsine electrochemical generator has been reported for hydride VPE (1) and MOVPE (2,3).

In this work we report on its first application to Gas Source MBE for the growth of InGaAs and InGaAsP. A prototype arsine generator developed by Air Liquide for MBE applications (4) has been used on a RIBER GSMBE machine. The electrochemical cell has been optimised to produce more than 90% arsine in H₂. To solve the problem of the short/long term stability of the (AsH₃, H₂) mixture, which is critical for InGaAsP growth, the generator is fitted with an Air Liquide proprietary membrane separation stage (5) to further enrich the gas mixture in AsH₃ to a level higher than 99%.

Reported here for the first time is the demonstration of the long term stability of the arsine concentration in the gas mixture produced by the electrochemical generator and the ability to grow InGaAsP quaternary layers and strained multi quantum wells structures with a precise and reproducible As to P composition.

Arsine generator

The principle of the arsine generator is described on the schematic diagram of figure.1.

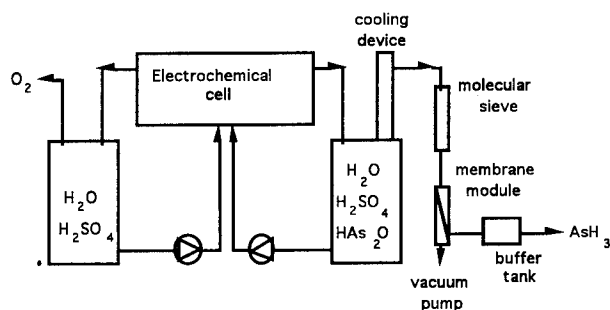


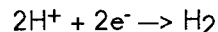
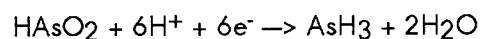
Figure 1: schematic diagram of the arsine generator

The generator is made of three main parts:

- i/ an electrochemical cell for the generation of the AsH₃/H₂ gas mixture,
- ii/ a gas purification stage for the removal of water vapor and hydrogen from the gas stream to end up with the delivery of pure arsine,
- iii/ a control module for the automatic operation of the generator and the safety interlock.

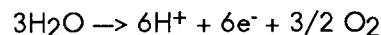
Generation of AsH₃/H₂ mixture

Arsine and hydrogen are generated at the cathode according to the following electrochemical reactions:



To maximize the AsH₃ to H₂ ratio and to reach arsine concentration higher than 90%, the H⁺ to HAsO₂ ratio is kept constant over time. This is made possible through:

i/ the generation of six protons by oxidation of water in the anodic compartment, following the reaction:



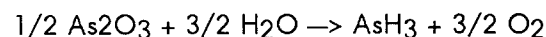
ii/ the adjunction of a saturator containing solid arsenic oxide in the cathodic loop, which leads to the saturation of the solution with HAsO₂ according to the following reaction:



iii/ the use of a cationic membrane to allow for the proton transfer between the anodic and cathodic compartments and, at the same time, to avoid the transfer of arseniate ions to the cathodic compartment.

iv/ the use of a high liquid velocity in the cathodic compartment to keep the HAsO₂ conversion below 10%.

The overall reaction can then be written as follows:

Separation/Purification stage

The water vapor present in the main gas stream is removed in two steps: first on a Peltier cooled condenser held at 3°C, second on a molecular sieve drying column.

The arsine concentration in the AsH₃/H₂ mixture is increased to 99.9% by using a hollow fiber membrane separation stage (5). When the

appropriate membrane is used, the difference in physical properties (dissolution) between AsH_3 and H_2 molecules leads to a much faster diffusion of H_2 through the permeable membrane and to an enrichment of the main gas stream in AsH_3 . The performance of this separation stage can be adjusted by modifying the pressure drop over the membrane with a simple mechanical pump. The arsine concentration in the main gas stream is thus a function of the arsine/hydrogen mixture flow rate at the membrane input and the pressure drop over the membrane.

On figure 2, the performance of this membrane separation stage is demonstrated.

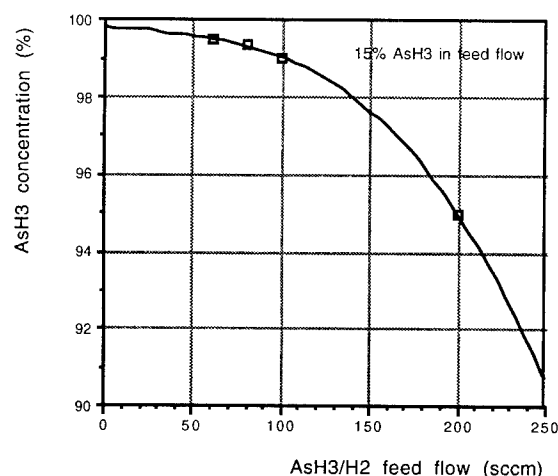


Figure 2: Arsine concentration after the membrane separation stage (arsine concentration in feed flow is 15%).

The arsine concentration in the main gas flow is plotted as a function of the feed flow rate for a feed concentration of 15% AsH_3 in H_2 coming from a gas cylinder. Even starting with this low arsine concentration in the feed gas, the final arsine concentration can be kept over 99.5% for a feed flow of 60 sccm and over 95% up to 200 sccm. This results means that it is possible with this separation principle to stabilize the arsine concentration over 99.5% during the life of the electrochemical cell.

Safety and control module

The electronic control module contains the power supplies for the Peltier cooler, the electrochemical cell and the mass flow controller, a microprocessor unit to control the electrochemical cell parameters, the valves and the different pressure and temperature sensors. Pressure in the cathodic and anodic storage tanks, temperature of the Peltier cooler, signal of the

arsine detector are monitored continuously and if a fault is detected, the generator is immediately stopped and isolated from the rest of the installation.

To have a stable arsine flow in continuous utilisation, arsine is taken from a small capacity which pressure is regulated between a low and a high level. This gives the freedom to use the generator at a higher flow rate than the instantaneous production capacity of the cell for a given period of time. In our case, the production capacity of this prototype electrochemical cell was about 15 sccm at the beginning of the cell life, a value higher than the maximum of 5 sccm needed to run the GSMBE process.

Gas analysis

The gas mixture at the exit of the generator has been monitored over about 40 hours. The evolution of the hydrogen concentration with time is given on figure 3.

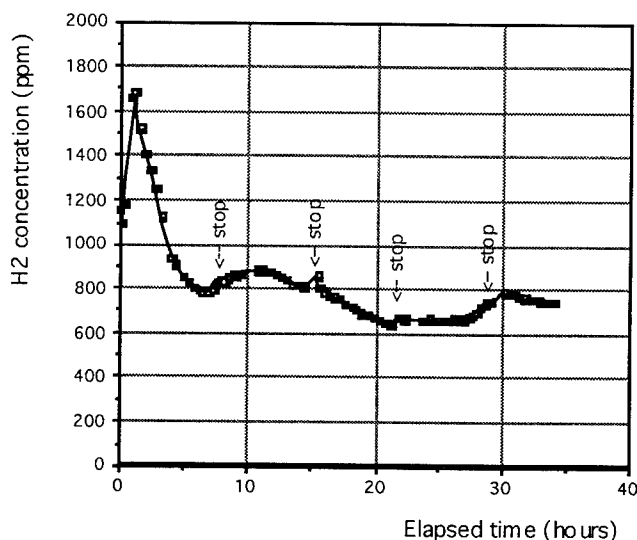


Figure 3: H_2 concentration at the exit of the arsine generator monitored over more than 30 hours. Each stop represents a shut down and restart cycle of the equipment.

It is seen that, once the membrane separation stage is properly adjusted, adjustment which explains the H_2 peak in the first hours, the H_2 content is kept below 1000 ppm over time, even after a number of shut-downs and restarts of the generator. The purity of the arsine produced by the electrochemical generator was analysed by gas chromatography (TBT Discharge Ionization Detector) and compared with ULSI specifications, as given in table A.

Table A

Source/Purity (ppm)	CO	CO ₂	C _n H _m	O ₂	H ₂ O	PH ₃	SiH ₄
ULSI	0,5	0,5	0,5	1	1	0,01	0,01
Generator	0,08	0,5	0,2	1	3	<0,01	<0,01

The overall purity of the arsine produced by the electrochemical generator is very good and satisfies the most severe ULSI specifications. The oxygen level is just at the specification limit and is probably due to a diffusion from the anodic compartment through the cationic membrane. This point can be improved by replacing the water oxidation reaction in the anodic loop by a hydrogen oxidation reaction to produce the necessary protons. In this case, the anodic compartment is simply replaced by a gas diffusion electrode. The high water vapor level can be easily reduced by a modification of the molecular sieve drying column. In any case, these low ppm values for oxygen and water vapor can be reduced to ppb values by using an arsine purifier (ie. Waferpure cartridge from Millipore).

GSMBE experimental results

The prototype arsine generator has been fitted to a RIBER 2300 Gas Source MBE machine. The gas cabinet was modified in order to be able to switch easily from arsine cylinder to arsine generator. The arsine purifier (Waferpure from Millipore) normally used with cylinder arsine was by-passed during the runs with generator arsine to have a direct evaluation of generator performance and gas purity on the layer quality.

The performance of the generator has been tested by growing thick lattice matched InGaAsP layers and compressively strained InGaAsP MQW layers. The results have been compared to reference runs done with cylinder arsine. The results of four series of InGaAsP growth runs with different settings of the separation stage are given in table B.

The photoluminescence wavelength (λ_{PL}) and the lattice mismatch ($\Delta a/a$), deduced from the X-ray rocking curve, are used to calculate the arsenic composition in the grown layer. This value of the arsenic composition can then be compared to the composition of the reference samples grown in the same conditions with cylinder arsine. The same setting of the arsine mass-flow controller has been used for all the runs. As can be seen in table B, the difference in arsenic composition between the test runs and the reference runs is small but measurable for the three first test samples. The adjustment of the separation stage was made step by step, starting with an estimated arsine concentration of about 95% for set 1, and ending with a concentration higher than 99.5% for set 4, conditions in which the test and reference samples cannot be distinguished anymore.

During this adjustment process, we also prepared InGaAsP compressively strained MQW structures of constant X design with lattice matched barriers of the composition given in table B.

Table B

Run number	λ_{PL} (nm)	$\Delta a/a$ (ppm)	Y(As) (%)
set 1/#1	1171	-849	38.9
reference #1	1177	-621	39.7
set 2/#2	1170	-771	38.7
set 3/#3	1173	-204	39.0
set 3/#4	1181	0	40.1
set 3/#5	1180	-142	40.0
reference #2	1181	-118	40.1
set 4/ #6	1184	-240	40.5

On figure 4, the peak photoluminescence of the MQW wafers is plotted and compared to structures grown with cylinder arsine.

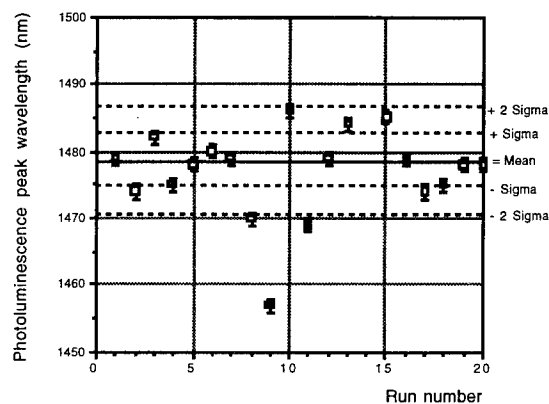


Figure 4: Room temperature photoluminescence peak wavelength as function of run number. (Open symbol: MQW structure grown with arsine cylinder, closed symbol: MQW structure grown with arsine generator).

On the figure are also indicated the mean and sigma values deduced from the statistical analysis of a large number of wafers grown with cylinder arsine. As shown on figure 4, the same trend is seen for the MQW structures as for the lattice matched quaternaries discussed in table B. The first grown wafer has a lower than normal peak photoluminescence wavelength consistent with a deficit in arsine concentration of the order of 5%. After proper adjustment of the separation stage, the photoluminescence peak wavelength of MQW structures is within the standard deviation for the same structure grown with cylinder arsine and with the same mass-flow controller setting.

The adjustment made on the separation stage was to increase the pressure drop over the membrane to increase the diffusion of H_2 . This result is a direct proof of the arsine content of the generated (AsH_3, H_2) gas mixture to be stable above 99.5%.

On figure 5, the room temperature photoluminescence intensity of the same series of MQW wafers demonstrates that the overall quality of the generator and reference wafers is equivalent.

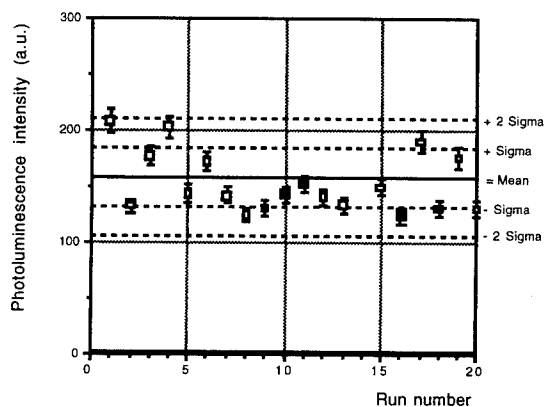


Figure 5: Room temperature photoluminescence peak intensity as function of run number.

(Mean and sigma values are for the normal population)

High quality bulk InGaAs, InGaAsP and MQW structures have been grown with the arsine generator, the quality assessed by all the standard characterization tools being at least equivalent to the test runs with cylinder arsine. The background doping level is about 10^{15} cm^{-3} for thick InGaAsP, as measured by the Hall method.

The evaluation of broad area lasers of $1.48 \mu\text{m}$ MQW structures consisting of six compressively strained wells (0.9%) of 9nm thick, with lattice matched InGaAsP barriers, grown with the arsine generator showed a threshold current density of

0.675 kA/cm^2 and a differential efficiency of 0.236 mW/mA for $600 \mu\text{m}$ long devices, performances comparable to the best results obtained for this structure.

Conclusion

A prototype electrochemical arsine generator fitted with a special hydrogen separation stage has been demonstrated for the first time to solve the medium/long term arsine concentration stability problem experienced before. The ability to stabilize the arsine concentration at a value higher than 99.5% has been proven by the reproducible growth of lattice matched InGaAsP and compressively strained InGaAsP MQW layers. The quality of the InP/InGaAsP layers grown with electrochemically generated arsine has been demonstrated to be comparable to the same layers grown with pure cylinder arsine. Such a hydride generator is particularly well adapted to GSMBE because of the low hydride consumption and because the growth chemistry being unchanged, the generator is directly compatible with existing calibrations and processes.

Acknowledgment

The authors would like to thank M. Darrieus from Air Liquide and P. Jarry from Alcatel Alsthom Recherche for their continuous support during this study.

References

- (1) D.N. Buckley, C.W. Seabury, J.L. Valdes, G. Cadet, J.W. Mitchell, M.A. DiGiuseppe, R.C. Smith, J.R.C. Filipe, R.B. Bylsma, U.K. Chakrabarti, K.W. Wang, "Growth of InGaAs structures using *in situ* electrochemically generated arsine", Appl. Phys. Lett., vol 57 no 16, pp 1684-1686, 15 October 1990
- (2) A.A. Burk, Jr, "Application of an electrochemical arsine generator on a high throughput MOVPE reactor", J. Cryst. Growth, 124, pp 292-299, 1992.
- (3) A. Ougazzaden, A. Mircea, C. Kazmierski and L. Leprince, "High performance strained MQW lasers at $1.3 \mu\text{m}$ by MOVPE using arsine generator system", Electron. Lett., 1994, vol 30 no 20, pp1681-1682, 29 September 1994.
- (4) RIBER/AIR LIQUIDE joint development under French government MRT contract n° 91S 0428.
- (5) Patent pending.

MOMBE Growth of Heavily Carbon-doped n-type InP Using Tertiarybutylphosphine (TBP)

Je-Hwan Oh, Jun-ichi Shirakashi, Fumihiko Fukuchi, and Makoto Konagai
Department of Electrical and Electronic Engineering,

Toshiaki Azuma and Kiyoshi Takahashi
Department of Physical Electronics,

Tokyo Institute of Technology
 2-12-1 O-okayama, Meguro-ku, Tokyo 152, JAPAN

Abstract : Heavily carbon-doped n-type InP was grown by Metalorganic Molecular Beam Epitaxy (MOMBE) using elemental In and tertiarybutylphosphine (TBP). In this study, TBP was employed as both phosphorus and carbon source, and carbon-doping characteristics in MOMBE growth of InP using TBP were discussed for the first time. The electron concentration of carbon-doped InP could be controlled in three orders of magnitude ($n=10^{16}\sim 10^{19}\text{ cm}^{-3}$) by varying the growth temperature and TBP cracking temperature. As the TBP cracking temperature increases, electron concentration was increased and also showed less dependence on growth temperature. This indicates that the overall carbon incorporation in InP may be dominated by the more atomic-like carbon-containing species of the cracked TBP. In addition, the lattice location of carbon impurity atom in InP was estimated for the first time by the observation of a gap mode using Raman scattering spectroscopy. The observed peak at 225 cm^{-1} corresponds to a gap mode due to carbon impurity substituted on In lattice site in InP and shows a good agreement with the theoretical value. This is a direct evidence that carbon from TBP is incorporated on In lattice site and acts as a donor in InP.

1. INTRODUCTION

Recently, carbon (C) has attracted a significant attention as a promising dopant for p-type GaAs and InGaAs materials, because of its low diffusivity and capability of heavy doping [1,2]. Also, carbon has been already successfully used as a base dopant, especially in GaAs- and InP- based heterojunction bipolar transistors (HBTs) [3-5]. In fact, we have successfully fabricated the carbon-doped base InGaP/GaAs HBTs with an ultra-high hole concentration of $1.5\times 10^{21}\text{ cm}^{-3}$ in the base for the first time and the details is described elsewhere [5].

From this point of view, if carbon acts as a well-behaved donor in InP emitter, the improved performance of carbon-doped base InP/InGaAs HBTs would be expected. However, unlike heavily carbon-doped GaAs, the behavior of carbon in InP has not been well understood yet. Therefore, it is very important to investigate carbon-doping characteristics in MOMBE growth of InP. There have been several studies for the effect of growth condition on the carbon residual impurity concentration in MOMBE growth of InP [6-8]. In first

principle calculation, Weyers et al. have reported that carbon is likely to behave as a donor in InP [9]. It is also anticipated that carbon is well-behaved dopant and have advantages for the growth of heavy doped n-type InP as like in case of heavily carbon-doped GaAs.

Besides, tertiarybutylphosphine (TBP) has attracted a considerable interest as a promising replacement of phosphine (PH_3), widely used as a phosphorus source in MOMBE growth of InP, because of its lower pyrolysis temperature and less toxicity [8,10]. In this study, TBP was employed as both phosphorus and carbon source, so-called a carbon auto-doping source, in MOMBE growth of heavy carbon-doped InP. Also, the carbon doping characteristics for MOMBE growth of InP using TBP were discussed in detailed for the first time. Moreover, the lattice location of carbon impurity atom in InP was estimated by the observation of a gap mode due to carbon impurity substituted on In lattice site in InP using Raman scattering spectroscopy.

2. EXPERIMENTAL

The epitaxial growth of InP was performed with a

modified VG V-80H chamber. Elemental Indium (In) and TBP were used as source materials of group III and V, respectively. All carbon-doped InP epilayers were grown on Fe-doped semi-insulating (SI) InP (100) substrates. TBP was introduced into the chamber without a carrier gas and its flow rate was controlled by a mass flow controller (MFC). The newly designed cracking cell which consists of PBN crucible with tantalum (Ta) as a catalyst was employed for the efficient decomposition of TBP in the temperature range of 700 to 1200°C [5]. Carrier concentrations and mobilities of carbon-doped InP epilayers were measured by van der Pauw Hall method. Secondary ion mass spectrometry (SIMS) measurement was used to determine the atomic carbon concentrations in the grown carbon-doped InP epilayers. Also, Raman scattering spectroscopy measurements were performed to investigate the lattice location of carbon impurity atom in the grown carbon-doped InP epilayers.

3. RESULTS and DISCUSSIONS

All carbon-doped InP epilayers grown in this work showed n-type conductivity. Fig.1 shows the dependence of the electron concentration of carbon-doped InP epilayers on growth temperature with various TBP cracking temperature. It is found that electron concentration increases exponentially as the growth temperature decreases and can be controlled in three orders of magnitude ($1.0 \times 10^{16} \sim 1.4 \times 10^{19} \text{ cm}^{-3}$) by changing the growth temperature and TBP cracking temperature. As TBP cracking temperature increases, electron concentration increases. This tendency is more pronounced in high growth temperature region. This result may be explained on the basis of the TBP cracking behavior. In higher cracking temperature, carbon-containing species of TBP should be decomposed into the simpler type ones, although they have been not identified yet. Since these atomic-like carbon-containing species have the lower vapor pressure than that of the more complex type ones, they can be easily adsorbed on the growing surface. Ultimately, this leads to the increase of carbon incorporation. In addition, the growth temperature dependence of the electron concentration becomes weaker and the activation energy for the carbon incorporation becomes lower. That is, under higher TBP cracking

temperature condition, the overall carbon incorporation into InP may be dominated by the carbon-containing species with the simpler type, i.e., atomic-like ones.

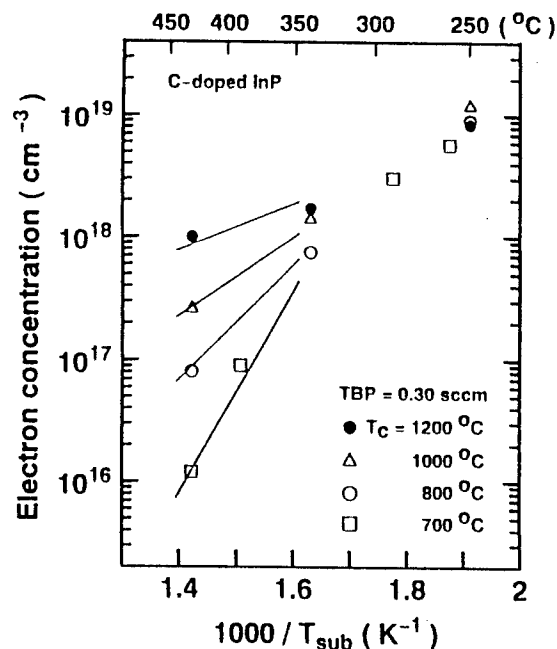


Fig.1. Dependence of the electron concentration of carbon-doped InP epilayers on growth temperature and TBP cracking temperature at constant TBP flow rate of 0.3 sccm.

However, according to Hall and SIMS measurements of InP epilayers grown in low growth temperature (below 350°C), the electrical activity of the incorporated carbon donor was revealed only about 15 percent. This may be explained by the distinct carbon incorporation mechanism as compared with that of the high growth temperature region. Although the complex type carbon-containing species have higher vapor pressure than that of the simpler type ones, they are able to be adsorbed on the growing surface in such low growth temperature. However, it is insufficient to give rise to a favorable surface migration and dissociation of the adsorbed molecules, since the temperature of growing surface is considerably low. Subsequently, this process may lead to the incorporation of carbon-interstitial type. This may be responsible for the reduction in the doping efficiency of carbon dopant and the degradation of electrical properties of InP epilayers grown in low growth temperature.

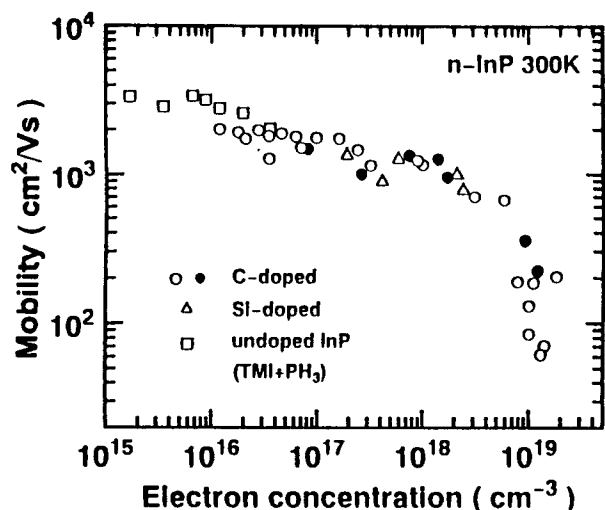


Fig.2. Electron mobilities of n-type InP epilayers measured at 300K plotted as a function of carrier concentrations. The open circle (○) and closed circle (●) indicate the values of carbon-doped InP epilayers grown at TBP cracking temperature of 700°C and 800~1200°C, respectively. The values of silicon-doped(△) InP epilayers doped with Si₂H₆ and undoped(□) InP grown by GSMBE using TMI and PH₃ [ref. 6] are also plotted.

Fig.2 shows the variation of electron mobilities of InP epilayers as a function of electron concentrations measured at 300K. The electron mobility decreases with the increase of electron concentration. These values fall on the extension of those of undoped InP epilayers grown by gas-source molecular beam epitaxy (GSMBE) using TMI and PH₃ (by Morishita et al.) [6]. In the same figure, the electron mobilities of silicon-doped InP doped with disilane (Si₂H₆) in the same growth chamber are also plotted. It is found that the electron mobilities of carbon-doped InP epilayers are comparable to those of silicon-doped InP epilayers. Besides, in the case of carbon-doped InP epilayers with higher electron concentration, it is found that the electron mobilities of carbon-doped InP epilayers grown under higher TBP cracking temperature are somewhat enhanced. This may be attributed to the incorporation of the more atomic-like carbon-containing species in InP.

In general, when a impurity atom is substituted on the heavier atom lattice site of the host crystal, then, local vibrational mode (LVM) in the gap between the optical and acoustic vibration branch, known as a gap

modes, may occur [11]. According to the theoretical investigation for InP by Gaur et al., a carbon impurity substituted on In lattice site (C_{In}) produces a gap mode band at 233 cm⁻¹ [12]. In fact, in the subsequent Raman scattering spectroscopy measurements, we clearly observed the gap modes for C_{In} in InP. Fig.3 shows non-polarized Raman spectra (at 300K) of carbon-doped InP epilayer with electron concentration of $n = 4.3 \times 10^{17} \text{ cm}^{-3}$ and Fe-doped SI-InP substrate. The peak at 225 cm⁻¹ is observed only in the case of carbon-doped sample. This corresponds to a gap mode due to C_{In} and shows a good agreement with the theoretical value. This is a direct evidence that carbon from TBP is incorporated on In lattice site and acts as a donor in InP.

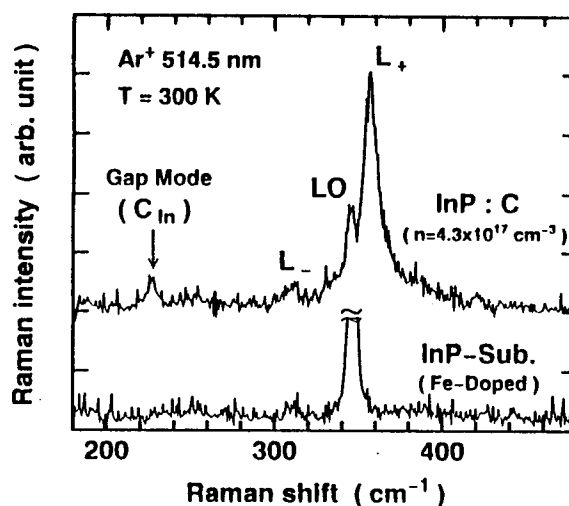


Fig.3. Raman scattering spectra of carbon-doped InP epilayer and Fe-doped SI-InP substrate (excited at 2.41 eV). The peak at 225 cm⁻¹ is assigned to a gap mode due to carbon impurity substituted on In lattice site.

In the subsequent Raman scattering spectroscopy measurements of carbon-doped InP epilayers with various electron concentrations, as shown in Fig.4, the identical peaks at 225 cm⁻¹ are also observed. In addition, this peaks do not shift unlike the plasmon-like coupled plasmon-phonon mode L₊, which is clearly separated from LO phonon peak as electron concentration increase. This result indicates that the peak at 225 cm⁻¹ is a gap mode due to C_{In}, not a plasmon-type excitation of the free electron gas. Therefore, it can be concluded that the observed n-type conductivity of our samples might be due to the carbon donor originated from TBP.

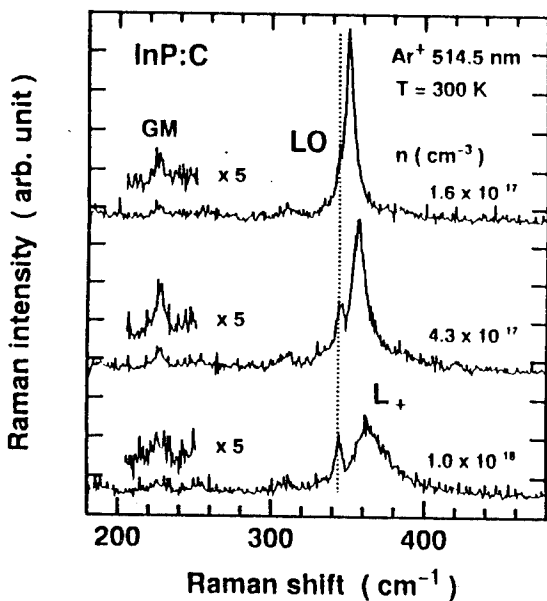


Fig.4. Raman scattering spectra of carbon-doped InP epilayers with various electron concentrations (excited at 2.41 eV).

4. CONCLUSION

Heavily carbon-doped InP epilayers up to electron concentration of $1.4 \times 10^{19} \text{ cm}^{-3}$ were successfully achieved by MOMBE using elemental In and TBP, without the use of external carbon dopant source. In this study, we suggest that TBP can be used as carbon doping source as well as phosphorus source, so-called a carbon auto-doping source. Furthermore, the carbon-doping characteristics in MOMBE growth of InP using TBP were discussed for the first time. It was found that the characteristics of carbon incorporation is affected by the TBP cracking temperature. As the TBP cracking temperature increases, electron concentration was increased and showed less dependence on growth temperature. This indicates that the overall carbon incorporation into InP may be dominated by the more atomic-like carbon-containing species of the cracked TBP. In addition, the lattice location of carbon impurity atom in InP was estimated for the first time by the observation of a gap mode using Raman scattering spectroscopy. The observed peak at 225 cm^{-1} corresponds to a gap mode due to carbon impurity substituted on In lattice site in InP and showed a good agreement with the theoretical value. This is a direct evidence that carbon from TBP is incorporated on In lattice site and acts as a donor in InP.

REFERENCES

- [1] T. Yamada, E. Tokumitsu, K. Saito, T. Akatsuka, M. Miyouchi, M. Konagai, and K. Takahashi, "Heavily Carbon doped p-type GaAs and GaAlAs by MOMBE," *J. Cryst. Growth* **95**, 145 (1989).
- [2] E. Tokumitsu, J. Shirakashi, M. Qi, T. Yamada, S. Nozaki, M. Konagai, and K. Takahashi, "Heavily carbon-doped p-type InGaAs by MOMBE," *J. Cryst. Growth* **120**, 301 (1992).
- [3] W. Liu and S. K. Fan, "Near-Ideal I-V Characteristics of GaInP/GaAs Heterojunction Bipolar Transistors," *IEEE Electron Device Letters* **13**, 510 (1992).
- [4] R. C. Gee, T. P. Chin, C. W. Tu, P. M. Asbeck, and C. L. Lin, "InP/InGaAs HBTs Grown by Gas-Source MBE with Carbon-doped Base," *IEEE Electron Device Letters* **13**, 510 (1992).
- [5] J. Shirakashi, R. T. Yoshioka, T. Azuma, F. Fukuchi, M. Konagai, and K. Takahashi, "MOMBE growth of InP and InGaP with tertiarybutylphosphine for the application of carbon-doped base HBTs," *J. Cryst. Growth* **145**, 935 (1994).
- [6] Y. Morishita, S. Maruno, M. Gotoda, Y. Nomura, and H. Ogata, "Gas Source MBE Growth of InP," *J. Cryst. Growth* **95**, 176 (1989).
- [7] H. Heinecke, B. Baur, R. Höger, and A. Miklis, "Growth of High Purity of InP by MOMBE," *J. Cryst. Growth* **105**, 143 (1990).
- [8] G. Hincelin, M. ZahZouh, R. Mellet, and A. M. Pougnet, "Growth of InP in CBE with high Purity tertiarybutylphosphine," *J. Cryst. Growth* **120**, 119 (1992).
- [9] M. Weyers and K. Shiraishi, "Carbon in III-V Compounds : A Theoretical Approach," *Jpn. J. Appl. Phys.* **31**, 2483 (1992).
- [10] E. A. Beam III, T. S. Henderson, A. C. Seabough, and J. Y. Yang, "The Use of tertiarybutylphosphine and tertiarybutylarsine for the MOMBE of the InGaAs/InP and InGaP/GaAs materials systems," *J. Cryst. Growth* **116**, 436 (1992).
- [11] R. C. Newman, *Growth and Characterization of Semiconductors*, Ed. by R. A. Stradling, Adam Hilger-New York, 1990, pp.105-117.
- [12] S. P. Gaur, J. F. Vetelino, and S. S. Mitra, "Localized Mode Frequency for Substitutional Impurities in Zinc Blende Type Crystals," *J. Phys. Chem. Solids* **32**, 2737 (1971).

Growth studies on AlPSb, GaPSb new ternary III-V compounds ^{SA2.4} for InP-based Surface Emitting Lasers

Hirofumi Shimomura, Takayoshi Anan and Shigeo Sugou

*Opto-electronic NEC Lab. Real World Computing Partnership
clo Opto-Electronics Res. Labs. NEC Corporation
34 Miyukigaoka, Tsukuba, Ibaraki 305, JAPAN*

Introduction

Vertical cavity surface emitting lasers (VCSELs) operating in the long-wavelength region have long been recognized as key devices for optical interconnection systems, but continuous-wave operation at 1.55 μm has not been available because of the lack of a high-reflectance mirror. For 1.55- μm distributed Bragg reflector (DBR), we have proposed an AlPSb/GaPSb material system lattice-matched to InP[1],[2]. This system has a large refractive index at 1.55 μm . A few studies on the epitaxial growth of these materials have been reported in detail[3]. The present paper describes studies of the growth of these materials using gas-source molecular beam epitaxy (GSMBE). The most remarkable feature revealed in this study is that alloy compositions strongly depend on group V supply ratio and growth temperature. We also investigated the optical and electrical properties of GaPSb. 20 pairs of AlPSb/GaPSb DBR reflectivity measurement demonstrates a stop-band width of 206 nm with maximum reflectivity exceeding 99% at approximately 1.66 μm .

Designing a new material system

High-reflectance DBRs require materials with a large refractive index difference between them and small absorption at the operating wavelength. This refractive index difference has great influence on the number of DBR pairs necessary for high-reflectance mirror and on the stopband width. The commonly used InGaAsP/InP material system, however, has a small refractive index difference at 1.55 μm [4].

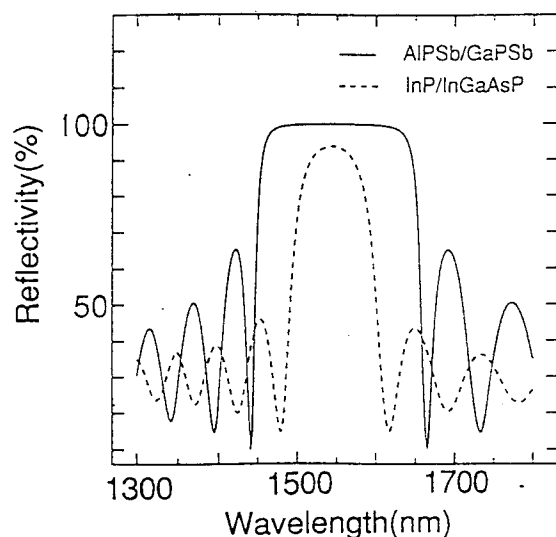


Fig. 1
Theoretically calculated reflectivity for InGaAsP/InP and AlPSb/GaPSb systems. The mirrors consist of 20 pairs of DBR layers.

Figure 1 shows reflectivity spectra of a 20-pair DBR calculated for both an InP/InGaAsP system and an AlPSb/GaPSb system. In the AlPSb/GaPSb system, the number of pairs necessary for achieving high reflectivity is about half of that in the InP/InGaAsP, and is almost the same as that in an AlAs/GaAs system at the 0.98 μm . Several material systems including various antimonide compounds have been proposed recently, such as AlAsSb/GaAsSb DBR[5] and AlAsSb/AlGaAsSb[6]. The former system has a large refractive-index difference similar to that of AlPSb/GaPSb DBR, but would suffer from the absorption in the GaAsSb layer at 1.55 μm . With the latter system, the absorption at 1.55 μm can be reduced when Al composition is increased, but this also reduces the refractive index.

Experimental

Samples were grown by GSMBE. Phosphine gas (PH_3) cracked at 950°C was used as the phosphorus source; the solid sources were Sb, In, Ga, and Al; and the dopants were Be and Si. Sb_4 arrival rate was calibrated by using a nude ion gauge to measure beam equivalent pressure (BEP)[7], and the P_2 arrival rate was calibrated by observing the group V-controlled intensity oscillation of the reflection high-energy electron diffraction (RHEED)[8] of GaP on a GaP substrate. Growth temperatures were measured by a special pyrometer. The exact substrate temperature was obtained by measuring a

reflectivity and a pyrometric emission at 950 nm simultaneously in order to cancel out an apparent oscillation in a pyrometric emission due to interference. A large Sb beam transient is usually observed when using a solid Sb source, so the beam flux decrease was compensated by intentionally increasing cell temperature.

A double crystal X-ray diffraction (XRD) measurement was used to confirm the lattice matching. The surface morphology are observed by using a Nomarski microscope.

Results and Discussion

Growth studies

We used the same Sb beam flux during AlPSb/GaPSb DBR growth because the Sb shutter could then be kept open to eliminate the Sb beam transient. The ternary compositions were controlled by adjusting the PH_3 flow rate, which could be rapidly changed at the heterointerfaces. The growth rates were $0.5 \mu\text{m/h}$.

A 1500 \AA -thick ternary and a 500 \AA -thick InP capping layer were grown in order to examine their lattice constant. A mirror-like morphology was obtained near lattice-matching conditions. The measured difference of the XRD peak of GaPSb and AlPSb from that of the InP substrates is shown in Figs. 2 and 3 as a function of P_2/Sb_4 supply ratio and as a function of growth temperature. Both of the ternary compositions can be controlled by adjusting the P_2/Sb_4 supply ratio. The composition of AlPSb, in particular strongly depends on the group V supply ratio, so the growth of AlPSb requires precise control of the P_2/Sb_4 ratio.

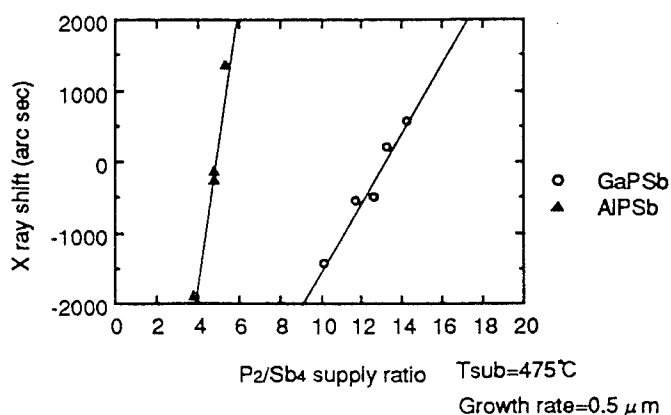


Fig. 2
Experimental lattice mismatch vs P_2/Sb_4 ratio.

Figure 3 shows that the composition of GaPSb is sensitive to growth temperature. Sb desorbs at high growth temperatures, causing surface morphology degradation. The composition of AlPSb, on the other hand, shows only weak

dependence on growth temperature. XRD measurement showed that the rocking curves from GaPSb are wider than those from AlPSb. If this broadening is due to a slight change in growth temperature during GaPSb growth, it would indicate the importance of controlling GaPSb growth temperature precisely.

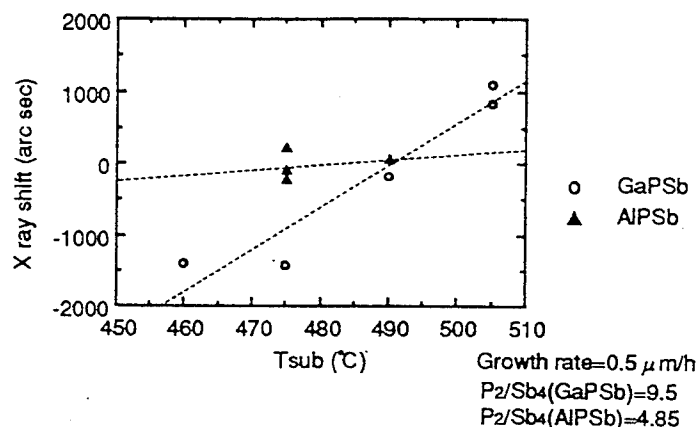


Fig. 3
Experimental lattice mismatch vs growth temperature.

Optical characterization

The refractive indices of GaPSb and AlPSb at $1.55 \mu\text{m}$ were measured with an ellipsometer (marked by closed circles in Fig. 4), and found to be 3.579 and 3.037, respectively, thus confirming the large refractive index difference between them ($\Delta n=0.542$).

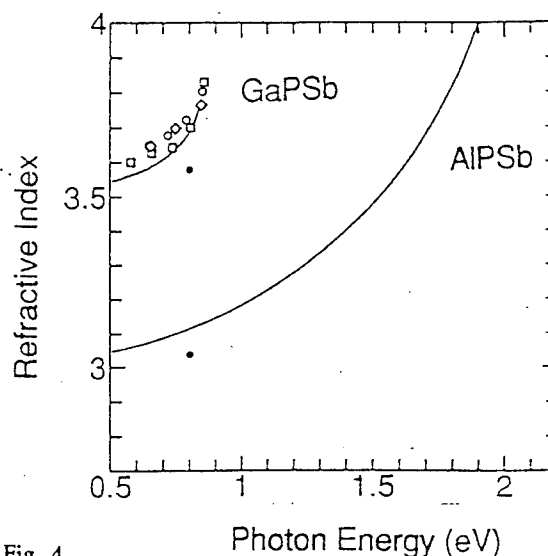


Fig. 4
Photon energy dependence of measured and calculated refractive indices.

The refractive index dispersion relation of GaPSb was obtained using a reflection spectroscopy technique [9]. In Fig. 4 the photon energy dependence of measured refractive indices is plotted together with the calculated refractive index spectra based on simplified models of the interband transitions [10].

A good agreement between measured and calculated spectra was obtained.

The bandgap of GaPSb lattice-matched to InP should be larger than 0.8 eV (1.55 μm) in order to prevent optical absorption in DBR.

Owing to the large bond-length difference between Ga-P and Ga-Sb, a relatively large bowing parameter which reduces the bandgap for GaPSb alloy can be anticipated. The bowing parameter of GaPSb is estimated theoretically to be 2.72 eV [11] and determined experimentally to be 3.6 eV [12] for Γ conduction band minima which gives the bandgap of 0.809 and 0.609 eV for InP lattice matching composition, respectively. Room temperature photoluminescence (PL) and optical transmission were measured to determine the bandgap of the GaPSb layer. A strong PL spectrum with the peak wavelength at 1467 nm (0.845 eV) with a full width at half maximum of 49 meV was observed, yielding the bowing parameter of 2.52 eV, which is close to the value estimated theoretically [2]. The optical transmission spectrum also shows a sharp absorption edge at near 1465 nm, confirming a small absorption at 1.55 μm . It should be noticed, however, that to prevent absorption at 1.55 μm , the antimonide composition should be kept less than 0.6763 (0.6492 when lattice-matched to InP), and that this requires precise composition control.

Doping characterization

The electrical properties of Be-doped and Si-doped GaPSb were characterized by Hall measurements at room temperature. Be and Si concentrations were measured by secondary ion mass spectroscopy (SIMS). We measured a series of 1 μm -thick samples with different dopant concentrations in order to verify the efficiency of doping. The measured hole concentrations in Be-doped GaPSb are plotted in Fig. 5, and are almost the same as Be densities. Thus, Be is effectively incorporated as a p-type dopant.

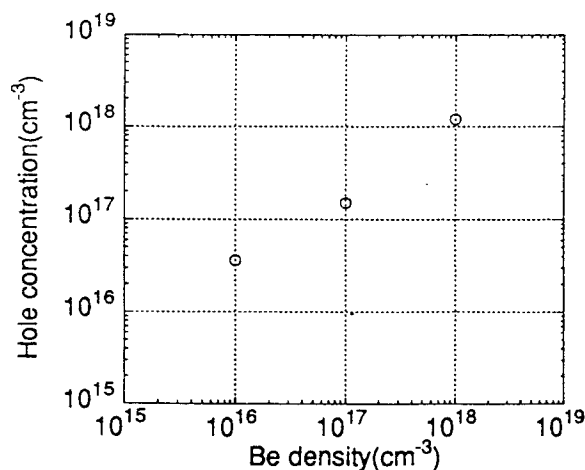


Fig. 5
Hole concentrations as a function of Be density in GaPSb.

The measured carrier concentrations in Si-doped GaPSb (Fig. 6), however do not correspond to Si densities. In the highly doped region, conductivity was n-type and carrier densities (marked by open circles) appear to be nearly half of Si densities. At much higher Si densities, electron concentration seems to saturate at $5 \times 10^{17} \text{ cm}^{-3}$. In the lower-doped region, on the other hand, the data marked by a closed circle showed p-type conductivity. This indicates that the sample contained p-type back-ground impurities.

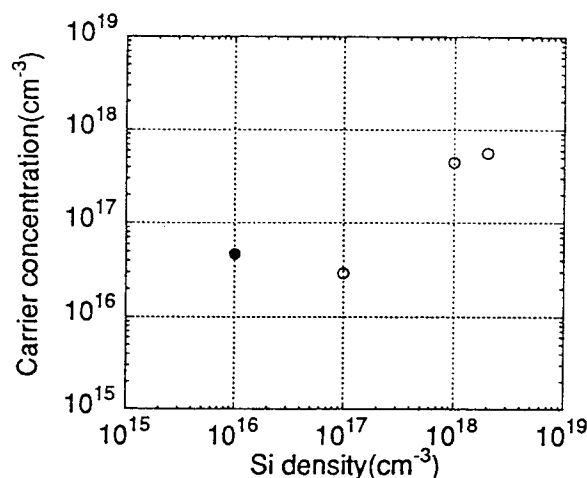


Fig. 6
Carrier concentrations as a function of Si density in GaPSb.

Growth of a highly reflective DBR mirror

Figure 7 shows a cross-sectional scanning electron microscope (SEM) image of an 8-pair of DBR layers. The surface morphology and the layer flatness were excellent. Figure 8 shows the XRD obtained from this sample around the (004) InP reflection. The DBR peak showed close lattice-matching to the InP peak: within 0.1%. The superlattice period estimated from the satellite peak distance is 1% of the design value.

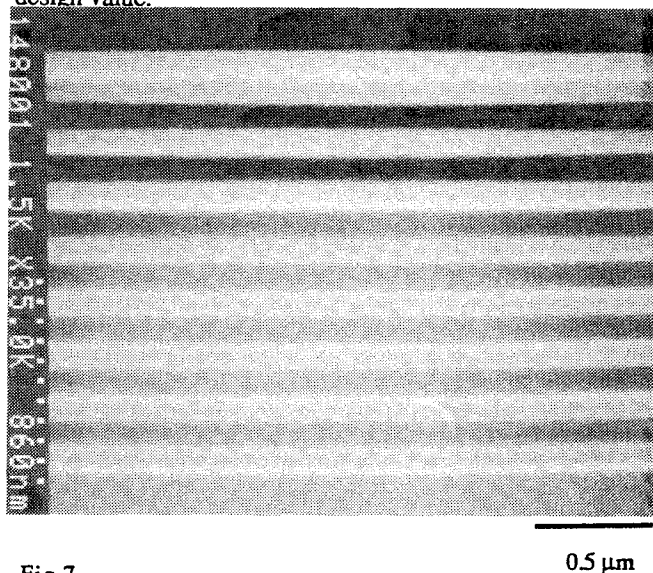


Fig. 7
Cross-sectional SEM image of the 8-pair of DBR layer.

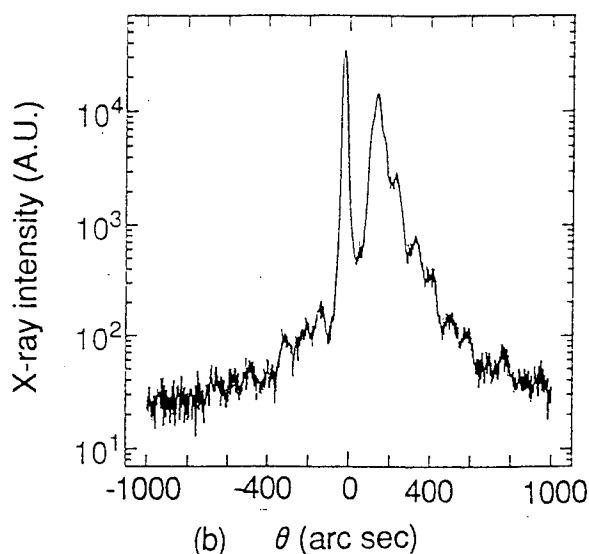


Fig. 8
XRD diagram of the 8-pair DBR.

Figure 9 shows the measured reflection spectrum(a) and the calculated spectrum(b) for a 20-pair DBR mirror. The measured reflectivity spectrum is asymmetrical with a peak reflectivity exceeding 99% near 1628 nm, which is 45 nm off the center wavelength (1583 nm), and with a stop-band width of 206 nm. The high peak reflectivity and wide band-width with only 20 pairs of the DBR layers demonstrate the advantage of using the AlPSb/GaPSb system for the 1.55 μm region. The reduced reflectivity near 1500 nm might be due to absorption in the GaPSb layer. The GaPSb alloy composition was shifted to Sb-rich composition during growth, due to the decrease in growth temperature. We think that this problem can be solved by controlling growth temperature precisely ($\pm 4^\circ\text{C}$).

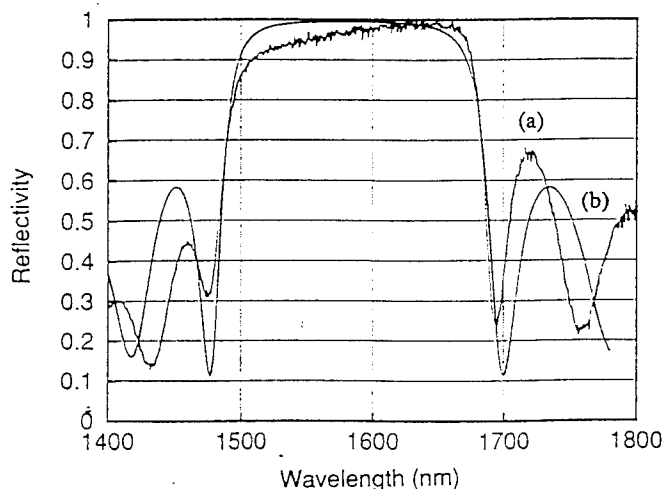


Fig. 9
Measured (a) and calculated (b) optical reflectivity of the DBR mirror with 20 pairs of AlPSb/GaPSb layers.

Conclusions

We demonstrated that an AlPSb/GaPSb system has a large index difference, which is useful for Bragg reflectors in InP-based VCSELs emitting near 1.55 μm . The alloy composition of AlPSb is sensitive to the group V supply ratio, and that of GaPSb is sensitive to growth temperature. Precise control of growth conditions is therefore necessary with this material system. A highly reflective DBR were obtained in this growth study, its reflectivity near 1.6 μm exceeded 99%. The possibility of doping control in GaPSb layers was also demonstrated. This thin DBR structure will be of great help in creating a low-threshold VCSELs for use at long wavelengths.

Acknowledgments

We thank I. Ogura, T. Yoshikawa, K. Mori, and K. Nishi for their invaluable advice and K. Tokutome for his technical assistance, and K. Kobayashi, K. Asakawa and, J. Namiki for encouragement throughout this work.

References

- [1]. H. Shimomura, T. Anan, K. Mori and S. Sugou, *Electron. Lett.* 30(4), 314 (1994).
- [2]. T. Anan, H. Shimomura and S. Sugou, *Electron. Lett.* 30(25), 2138 (1994).
- [3]. S. Loualiche, A. Le Corre, S. Salaun, J. Caulet, B. Lambert, M. Gauneau, D. Lecrosnier and B. Deveaud, *Appl. Phys. Lett.* 59(4), 423 (1991).
- [4]. F.S. Choa, K. Tai, W.T. Tsang and S.N.G. Chu, *Appl. Phys. Lett.* 59(22), 2820 (1991).
- [5]. O. Blum, I. J. Fritz, L. R. Dawson, A.J. Howard, T.J. Headley, J. F. Klem and T. J. Drummond, *Appl. Phys. Lett.* 66(3), 329 (1995).
- [6]. B. Lambert, Y. Toudic, Y. Rouillard, M. Gauneau, M. Baudet, F. Alard, I. Valiente and J.C. Simon, *Appl. Phys. Lett.* 66(4), 442 (1995).
- [7]. G.J. Davis and D. Williams, in *The Technology and Physics of Molecular Beam Epitaxy*, edited by E. H. C. Parker, (Plenum, New York, 1985), p. 38.
- [8]. T. P. Chin, B.W. Liang, H. Q. Hou, M. C. Ho, C. E. Chang and C. W. Tu, *Appl. Phys. Lett.* 58(3), 254 (1991).
- [9]. M.J. Mondry, D.I. Babic, J.E. Bowers and L.A. Coldren, *Photonics Technol. Lett.* Vol. 4, 627-630 (1992).
- [10]. S. Adachi, *J. Appl. Phys.* 53, 5863 (1982).
- [11]. G.B. Stringfellow, *J. Electron. Mater.* 10, 919 (1981).
- [12]. M.J. Jou, Y.T. Cherng, H.R. Jen and G.B. Stringfellow, *Appl. Phys. Lett.*, 52, 549 (1988).

Molecular Beam Epitaxial Growth of MgZnCdSe on (100) InP Substrates

Toshihiro MORITA, Akihiko KIKUCHI, Ichirou NOMURA, and Katsumi KISHINO

Department of Electrical and Electronics Engineering
Sophia University

7-1, Kioi-cho, Chiyoda-ku, Tokyo 102, Japan
Tel. +81-3-3238-3323 Fax. +81-3-3238-3321

We propose sulfur-free wide-gap II-VI quaternary compounds of MgZnCdSe as a material of visible light emitting devices. MgZnCdSe compounds have bandgap energy from 2.1 to 3.6 eV, maintaining lattice-matching to InP substrate. MgZnCdSe lattice-matching quaternary compounds with various Mg composition were grown on (100) InP substrates, for the first time. A wide range of photoluminescence (PL) peak wavelengths from 572 nm (2.17 eV) to 398 nm (3.17 eV) at 15 K was obtained with increasing Mg composition.

1. Introduction

Since Mg chalcogenides (MgS, MgSe, MgTe) were mixed with II-VI wide-gap semiconductors[1], the flexibility of fabricating II-VI semiconductor laser diodes were rapidly spread. That is, combinations of the materials having wide bandgaps and lattice-matching each other can be realized, i.e. as ZnSSe/MgZnSSe/GaAs (which composition range of MgZnSSe corresponds to an area encircled by dashed line in Fig. 1). ZnCdSe/MgZnSSe blue-green separate confinement heterostructure laser diodes (SCH-LDs) with ZnCdSe as an active layer, ZnSSe as guiding layers and MgZnSSe as cladding layers were fabricated. The success of the room temperature continuous wave (RT-CW) operation was obtained[2].

However, there are some problems in using MgZnSSe compounds. That is, sulfur may serve bad influences to GaAs substrates[3], probably being one of origins for producing stacking faults. With increasing bandgap, p-type doping characteristics of the crystal was deteriorated[4]. And it was suggested that the presence of sulfur had some role in the deterioration [5]. On the other hand, by ZnCdSe/MgZnSSe system on GaAs, it is very difficult to fabricate light emitting devices with emission wavelength above 550 nm due to induced high-compressive strain in active layers.

In this paper, novel II-VI quaternary compounds of $\text{Mg}_x(\text{Zn}_y\text{Cd}_{1-y})_{1-x}\text{Se}$, which is lattice-matching to (100) InP substrates, are proposed (see hatched area in Fig. 1). The bandgap energy of MgZnCdSe is estimated (using binary bandgap values) to be from 2.1 eV (i.e. for $\text{Zn}_{0.48}\text{Cd}_{0.52}\text{Se}$, 580 nm) to 3.6 eV (for $\text{Mg}_{0.9}\text{Zn}_{0.1}\text{Se}$, 344 nm) under lattice-matching condition to InP.

The lattice-matching condition of the crystal to InP substrates can be realized by keeping the Zn composition y to be 0.48 because the lattice parameter between MgSe and InP is very close. This property is effective for growing lattice matching multi-layered heterostructures. And due to their wide range bandgap

wavelength, it was also very attractive materials for visible light emitting device. Note that high-performance laser diodes were not realized in the wavelength range from 620 nm to 530 nm, which is a sort of missing wavelength range of semiconductor lasers as long as we use well-known and well-established material systems. From this point of view, MgZnCdSe compounds are very attractive because of high material possibility for realizing the lasers with wavelengths from 580 nm (yellow) to less than 500 nm (blue). Moreover, MgZnCdSe was expected to be free from the problem that II-VI compounds such as MgZnSSe or ZnSSe held, because MgZnCdSe was sulfur-free. Recently, a preliminary stage of experiment for ZnCdSe ternary compounds grown by MBE were reported[6].

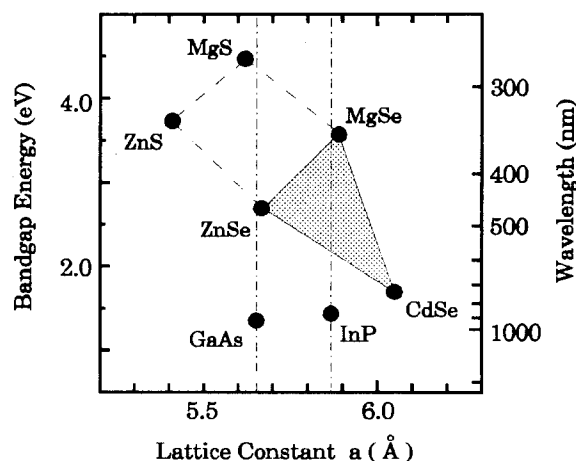
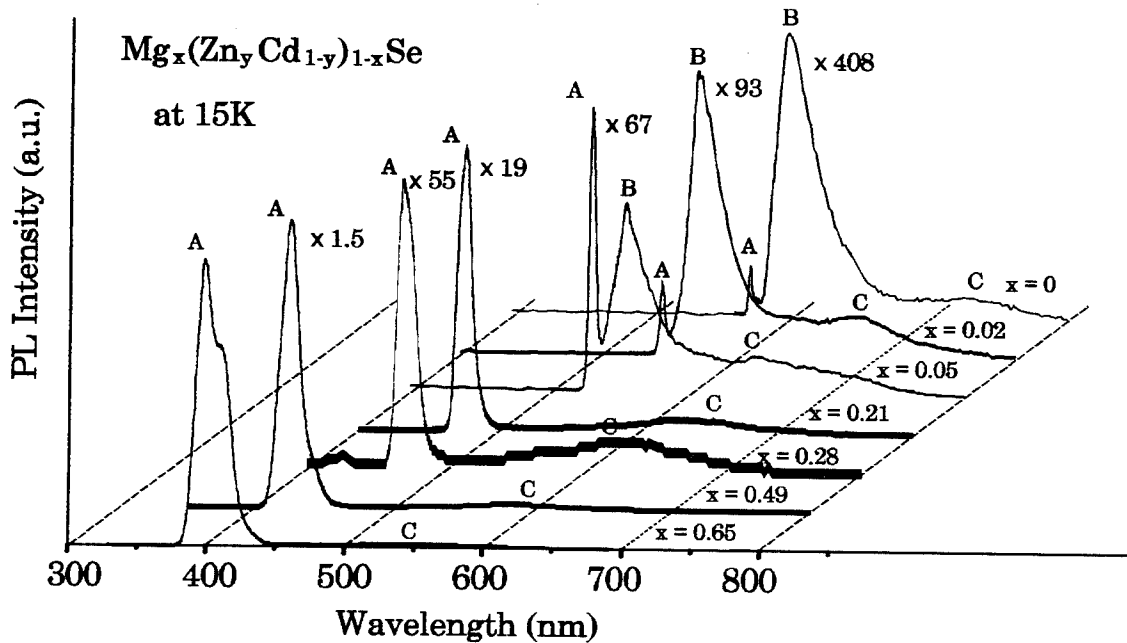


Fig. 1. Relationship between lattice constant and bandgap energy for wide gap II-VI semiconductors including MgZnCdSe.

Table A. Growth conditions of $\text{Mg}_x(\text{Zn}_y\text{Cd}_{1-y})_{1-x}\text{Se}$

Sample	Mg beam pressure ($\times 10^{-8}$ Torr)	Mg composition x	Growth rate ($\mu\text{m/hr}$)	VI/II ratio
a	0	0	0.61	1.64
b	0.6	0.07	0.66	1.52
c	1.1	0.12	0.70	1.43
d	1.7	0.21	0.79	1.27
e	2.3	0.28	0.86	1.16
f	4.2	0.49	0.99	—
g	5.6	0.65	1.04	—
h	0	0	0.66	—
i	0.3	0.02	0.67	—
j	0.5	0.05	0.69	—

Fig. 2. Typical 15K-PL spectra of MgZnCdSe .

2. Experimental

MgZnCdSe layers with various Mg compositions were grown on (100) InP substrates by molecular beam epitaxy (MBE). The source materials were elemental Mg (6N), Zn (7N), Cd (6N-S) and Se (6N-S). After surface thermal cleaning of InP substrates at 480 °C, MgZnCdSe were grown at 280 °C. The equivalent beam fluxes of Zn and Cd were fixed at 1.0×10^{-7} and 2.0×10^{-7} Torr. That of Se was fixed at 1.8×10^{-6} Torr in the sample (a) ~ (g) and 1.2×10^{-6} Torr in the sample (h) ~ (j). While that of Mg was changed from 0 to 5.6×10^{-8} Torr, to change Mg composition. Thus the growth rate was changed from 0.6 to 1.2 $\mu\text{m/hr}$. (the layer thickness from 0.9 to 1.5 μm). The growth parameters of MgZnCdSe are listed on Table A. Lattice mismatching of grown layers ($\Delta a/a$) was in the range

from 0 to +0.37%.

The Mg composition x of $\text{Mg}_x(\text{Zn}_y\text{Cd}_{1-y})_{1-x}\text{Se}$ ($y \cong 0.48$) were roughly estimated from the growth rate increment for MgZnCdSe compared with ZnCdSe . The lattice constant was determined by the θ -2 θ method of X-ray diffraction. The bandgap energy was roughly estimated from the bandedge emission in photoluminescence (PL) spectrum at 15 K under He-Cd laser light (325 nm) excitation. The surface morphology was observed with Nomarski microscope.

3. Results and discussions

Figure 2 shows typical PL spectra of MgZnCdSe with various Mg compositions at 15 K. Each of peak-A is thought to be the bandedge emission. On the other hand, peak-B and -C on the longer wavelength side of

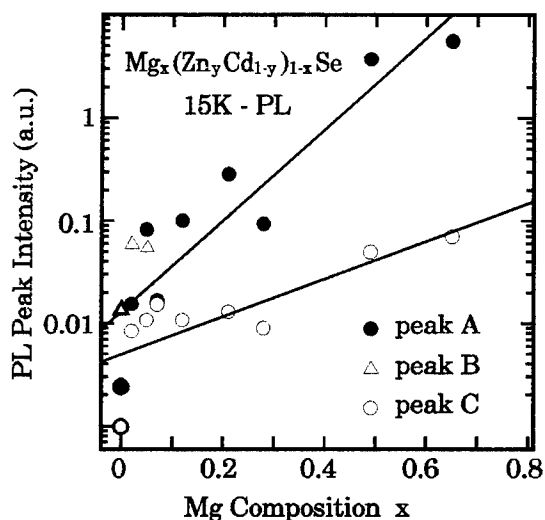


Fig. 3. PL peak intensity of MgZnCdSe as a function of Mg composition.

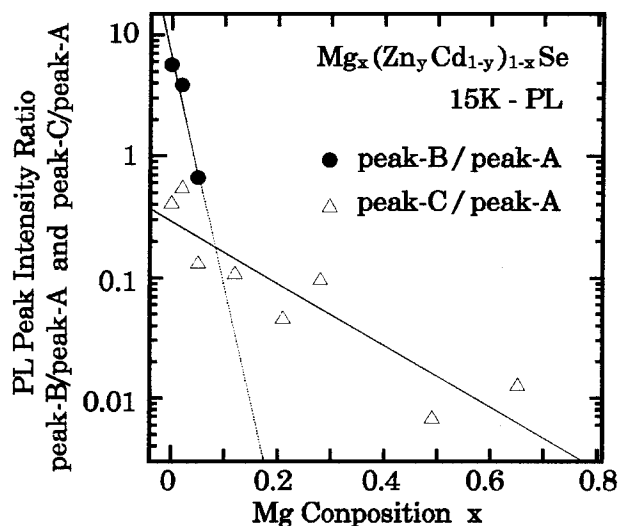


Fig. 4. Ratio of PL peak intensity of MgZnCdSe as a function of Mg composition.

peak-A is thought to be the donor-to-acceptor (DA) emission and the deep level emission caused by native defects etc., respectively, referring to the spectra of other II-VI compounds like MgZnSSe. We notice that peak-B was dominant in a low Mg composition region ($x=0$ and 0.02), while peak-A became dominant in a high Mg composition range ($x=0.05$ to 0.65).

As a function of Mg composition, the intensity of peak-A, -B and -C is shown in Fig.3 and the PL peak intensity ratio of peak-B/peak-A and peak-C/peak-A are shown in Fig. 4. Although an absolute intensity of peak-A, -B and -C got strong with increased Mg composition, the ratio of peak-B/peak-A and peak-C/peak-A decreased. The peak-B and -C should be disappeared at the optimized growth condition.

Figure 5 shows the full width at half maximum

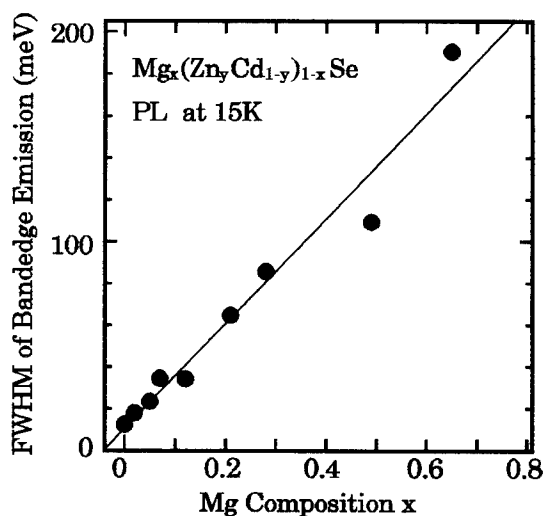


Fig. 5. FWHM of PL peak -A (bandedge emission) as a function of Mg composition.

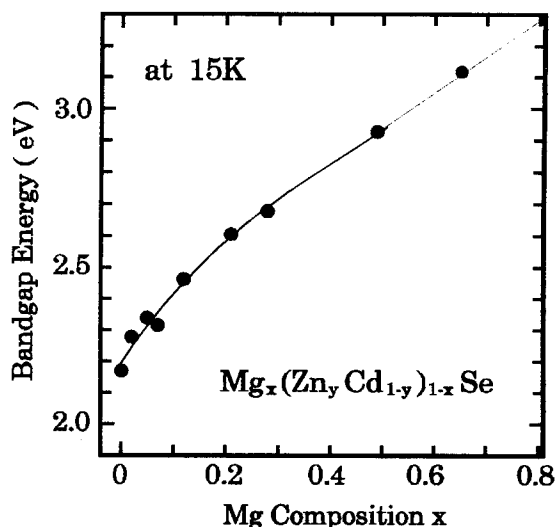


Fig. 6. Bandgap energy of MgZnCdSe at 15K as a function of Mg composition.

(FWHM) of bandedge emission (peak-A) as a function of Mg composition. FWHM of peak-A increased from 12.5 to 190.5 meV with increased Mg composition, which may suggest that crystal compositional uniformity was degraded for such high Mg composition.

Figure 6 shows the bandgap energy as a function of Mg composition, which was estimated from bandedge emission in PL spectrum at 15 K. We can see that with increasing Mg composition the bandgap energy increased monotonically from 2.17 to 3.12 eV. From this figure, the bandgap of MgSe can be extrapolated ($x=1$) to be about 3.6 eV which value is close to a reported bandgap of MgSe at 77 K [1].

In this work, we realized that initial stage of growth was very important to obtain high quality MgZnCdSe crystals. Fig. 7 shows reflection high energy electron

diffraction (RHEED) patterns of ZnCdSe which were grown on (a) perfectly thermal cleaned, (b) imperfectly thermal cleaned InP substrates. The corresponding surface morphologies of ZnCdSe to these RHEED patterns are shown in Fig. 8. A streak (2×4) reconstruction RHEED pattern and an almost mirror-like morphology were observed for the case of (a), while in the case (b), a cross RHEED pattern was observed, which suggested that ZnCdSe may included a twin crystal structure. And the surface morphology was very rough. From this result, we can say that the growth of MgZnCdSe on InP substrate is greatly influenced by the substrate surface conditions before the growth. Thus in order to improve the crystal quality, some initial growth processes, such as introduction of InP buffer layers should be needed.

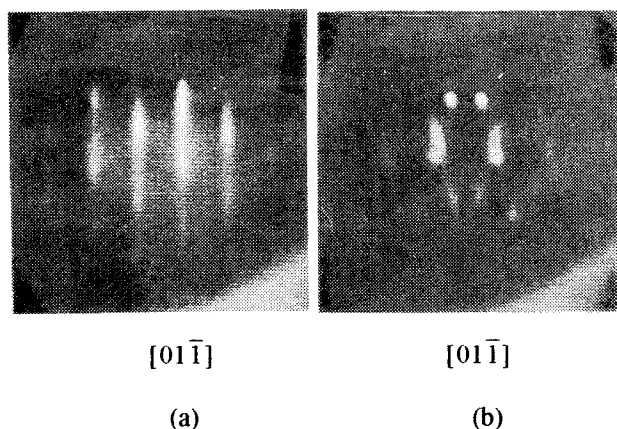


Fig. 7. RHEED patterns of ZnCdSe which were grown on (a) perfectly thermal cleaned, (b) imperfectly thermal cleaned InP substrates.

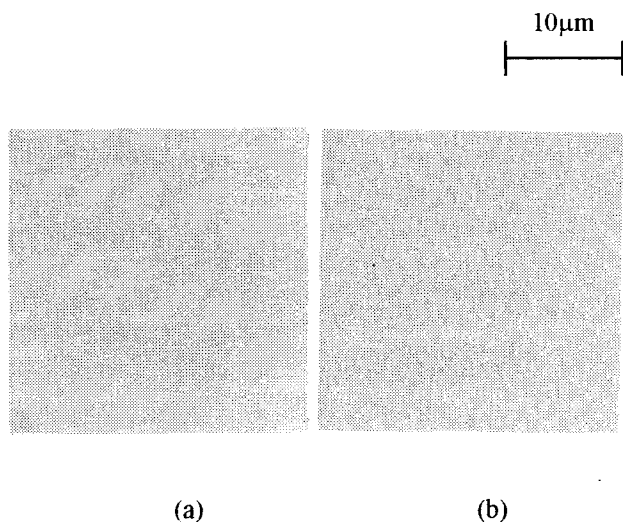


Fig. 8. Surface morphologies of ZnCdSe which were grown on (a) perfectly thermal cleaned, (b) imperfectly thermal cleaned InP substrates.

4. Conclusions

We propose sulfur-free wide-gap II-VI quaternary compounds of MgZnCdSe as a material for visible light emitting devices. MgZnCdSe have bandgap energy from 2.1 to 3.6 eV, maintaining lattice matching to InP substrate. MgZnCdSe lattice-matching compounds with various Mg composition were grown by MBE on (100) InP substrates, for the first time.

With increasing Mg composition, the bandgap energy increased monotonically from 2.17 to 3.17 eV. The PL peak intensity increased dramatically and bandedge emission became dominant for higher Mg compositions. While the FWHM of bandedge emission increased from 12.5 to 190.5 meV with Mg composition, which may suggest that crystal compositional uniformity was degraded for higher Mg composition region.

It was clarified that the growth of MgZnCdSe on InP substrate was greatly influenced by the substrate surface condition before the growth. Thus, some proper processes should be performed in initial growth stage of MgZnCdSe in order to improve the crystal quality.

5. References

- [1] H.Okuyama, K.Nakano, T.Miyajima and K.Akimoto, "Epitaxial Growth of ZnMgSSe on GaAs Substrate by Molecular Beam Epitaxy", Jpn. J. Appl. Phys. Vol. 30, pp. L1620-L1623, September, 1991.
- [2] A.Ishibashi and Y.Mori, "Advances in blue laser diodes", J. Crystal Growth, Vol. 138, pp. 677-685, 1994.
- [3] S.Guha, B.J.Wu, H.Cheng and J.M.DePuydt, "Microstructure and pseudomorphism in molecular beam epitaxially grown ZnCdS on GaAs(001)", Appl. Phys. Lett. Vol. 63, No. 15, pp. 2129-2131, October 1993.
- [4] H.Okuyama, Y.Kishita, T.Miyajima and A.Ishibashi, "Epitaxial growth of p-type ZnMgSSe", Appl. Phys. Lett., Vol. 64, No. 7, pp. 904-906, February, 1994.
- [5] Y.Ichimura, K.Kishino, M.Satake, M.Kuramoto and A.Yoshida, "Characterization of N-doped MgZnSSe Compound System Grown on Intentionally Misoriented GaAs Substrates by MBE.", Workbook, MBE-VIII, B10-4, pp. 278-279, 1994, Osaka, Japan.
- [6] N.Dai, A.Cavus, R.Dzakupasu and M.C.tamargo, "Growth of Lattice-matched ZnCdSe on InP by MBE", Proc., '94EMC, AD9, p. A61, 1994, Colorado, USA.

InP-BASED HETEROJUNCTION FET PROCESSING FOR HIGH-RELIABILITY MILLIMETER-WAVE APPLICATIONS

**SB2.1
(Invited)**

Masaaki Kuzuhara, Kazuhiko Onda, Akira Fujihara,
Emiko Mizuki, Yasuko Hori, and Hironobu Miyamoto

Kansai Electronics Research Laboratories, NEC Corporation
2-9-1 Seiran, Otsu, Shiga 520, Japan

ABSTRACT

This paper describes a novel InP-based FET processing technology for high-reliability microwave applications. High performance InAlAs/InGaAs heterojunction FETs (HJFETs) were fabricated using completely Molybdenum-based electrode technology (COMET). The fabricated 1 μ m gate-length COMET-HJFET exhibited excellent DC and RF performance, including a transconductance of 470mS/mm and a current gain cutoff frequency of 40GHz. High temperature DC bias tests performed on the COMET device demonstrated improved reliability compared to that for the conventional InP-based HJFET. The superior reliability of the developed COMET-HJFET is attributed to the reduced interdiffusion between metals of the electrodes and semiconductors by introducing a refractory metal of Mo as a barrier metal.

INTRODUCTION

InAlAs/InGaAs heterojunction FETs (HJFETs) fabricated on an InP substrate have demonstrated excellent microwave and millimeter-wave performance [1-3]. One important subject to be resolved is a reliability issue. To date, several approaches have been reported to improve reliability by modifying the epitaxial structure of the devices [4,5]. However, there are still concerns about device reliability associated with gate and Ohmic metallizations. This paper describes a novel InP-based HJFET process technology, called completely Molybdenum-based electrode technology (COMET), in which superior reliability is realized without sacrificing excellent DC and RF performances.

DEVICE STRUCTURE AND PROCESS

Figure 1 shows a schematic cross-section of the fabricated COMET-HJFET. The structure was grown by MBE on a 3-inch diameter semi-insulating InP substrate. The layers consist of an undoped InAlAs buffer layer, a 40nm undoped InGaAs channel layer, a 3nm undoped InAlAs spacer layer, a 10nm n-type ($5 \times 10^{18} \text{cm}^{-3}$) InAlAs layer, a 20nm undoped InAlAs Schottky layer, a 20nm n-type ($1 \times 10^{19} \text{cm}^{-3}$) $\text{In}_{0.53}\text{Ga}_{0.47}\text{As}$ cap layer and a 20nm n-type ($1 \times 10^{19} \text{cm}^{-3}$) $\text{In}_{0.7}\text{Ga}_{0.3}\text{As}$ cap layer. Gate electrodes were deposited on the undoped InAlAs Schottky layer to enhance the gate breakdown voltage. The heavily-doped n-type $\text{In}_{0.7}\text{Ga}_{0.3}\text{As}$ cap layer on the top surface was introduced to achieve low contact resistance by nonalloyed Ohmic metallization.

The COMET-HJFET process includes mesa-isolation, conventional photo-lithography, gate metal evaporation, Ohmic metal evaporation and lift-off. Since the COMET process employs Mo/Ti/Pt/Au metal systems for both gate Schottky and Ohmic electrodes, these two electrodes could

be fabricated by a simultaneous electron-beam evaporation of Mo/Ti/Pt/Au (i.e., simplified version of COMET). Such a novel COMET process flow is illustrated in Fig.2. In this work, this simultaneous evaporation technique was employed to fabricate 1 μ m gate-length COMET-HJFETs.

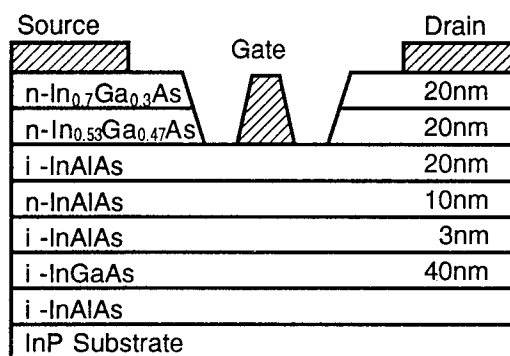


Fig.1 Schematic cross-section of fabricated COMET-HJFET.

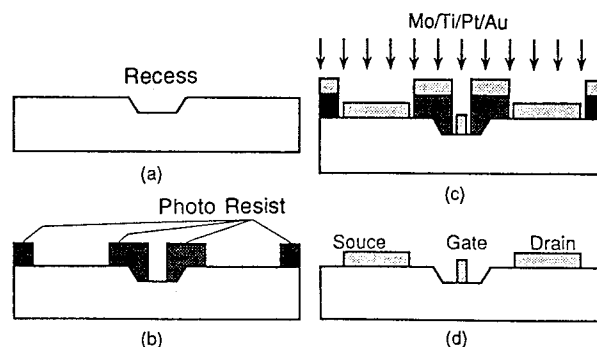


Fig.2 COMET with simultaneous Mo/Ti/Pt/Au evaporation process. (a)recess etching, (b)gate and Ohmic patterning, (c)Mo/Ti/Pt/Au evaporation, and (d)lift-off.

THERMAL STABILITY OF MoTiPtAu SCHOTTKY DIODES

To investigate thermal stability of the gate metal deposited on an InAlAs Schottky layer, two types of Schottky diodes (i.e., Mo/Ti/Pt/Au on n-InAlAs and Ti/Pt/Au on n-InAlAs) were fabricated on semi-insulating InP substrates and heat-treated at various temperatures. The thicknesses of Mo, Ti, Pt and Au were 10nm, 30nm, 30nm and 200nm, respectively. The doping density of the n-InAlAs was $2 \times 10^{17} \text{cm}^{-3}$. Figure 3 shows the measured Schottky characteristics as a function of the stress temperature. The stress time was fixed for 10 minutes. Even after a thermal stress at up to 400°C, the Mo/Ti/Pt/Au diode maintained its initial barrier height of 0.64eV and its initial ideality factor of around 1.15. The Ti/Pt/Au diode, on the other hand, exhibited distinct degradation in the barrier height from 0.65eV to 0.58eV and in the ideality factor from 1.09 to 1.80 after the thermal stress at 400°C. The breakdown voltage, defined at a reverse current density of 20mA/mm², also degraded significantly for the Ti/Pt/Au diode after stress at more than 350°C. Long-term thermal stress tests were also performed. The thermal stress at 300°C for 15 hours for the Ti/Pt/Au diode resulted in degradation in the barrier height from 0.65eV to 0.55eV, the ideality factor from 1.09 to 2.10 and the breakdown voltage from 4.1V to 0.6V, while no significant degradation was observed for the Mo/Ti/Pt/Au diode.

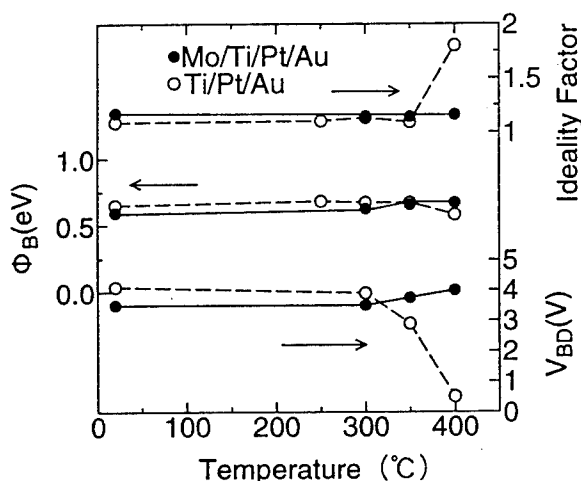


Fig.3 Schottky characteristics as a function of stress temperature. Stress time is 10 minutes.

Auger depth profiling studies, plotted in Fig.4, identified distinct evidence of interdiffusion between Ti and InAlAs for the Ti/Pt/Au diode after the thermal stress (400°C, 30min.), while no significant interdiffusion was observed for the Mo/Ti/Pt/Au diode. The results demonstrate the importance of an introduced thin Mo layer between Ti and InAlAs to prevent interdiffusion and to obtain stable Schottky characteristics against thermal stressing.

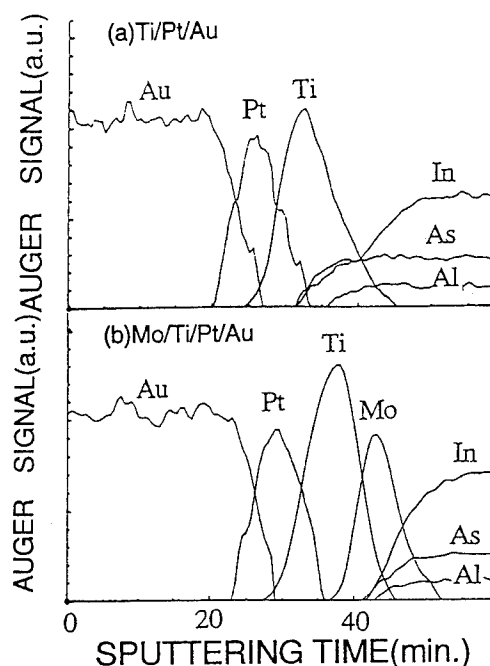


Fig.4 Auger depth profiles after annealed at 400°C for 30min. (a)Au/Pt/Ti/InAlAs, (b)Au/Pt/Ti/Mo/InAlAs.

THERMAL STABILITY OF MoTiPtAu OHMIC CONTACTS

Thermal stability of the nonalloyed Ohmic contacts deposited on n-type ($1 \times 10^{19} \text{cm}^{-3}$) In_{0.7}Ga_{0.3}As were investigated. Figure 5 shows the stress temperature dependence of the contact resistance evaluated for Mo/Ti/Pt/Au and Ti/Pt/Au nonalloyed Ohmic contacts. The stress time was fixed for 5 minutes. The initial value of the contact resistance (R_c) was 0.04 $\Omega \cdot \text{mm}$ for both contacts.

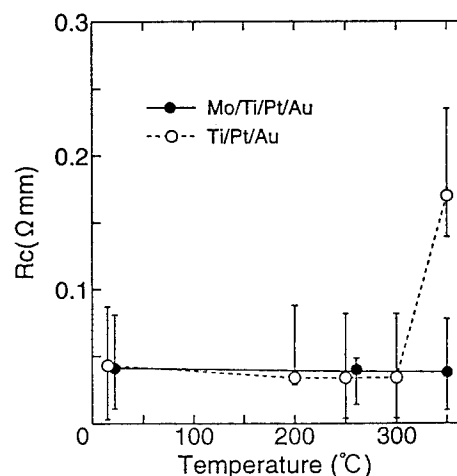


Fig.5 Contact resistance for nonalloyed Ohmics as a function of thermal stress temperature for 5 minutes.

The Mo/Ti/Pt/Au Ohmic contact preserved its excellent initial R_c value after thermal stress up to 350°C, whereas the Ti/Pt/Au contact exhibited significant R_c increase after a 350°C thermal stress by over 400% (i.e., $R_c=0.17 \Omega\cdot\text{mm}$). The results of the long-term thermal stress test at 300°C for 15 hours also demonstrated that the Mo/Ti/Pt/Au contact maintained its low R_c within a 5% change, while the R_c value for the Ti/Pt/Au contact increased to as high as 1.4 $\Omega\cdot\text{mm}$ (i.e., more than 30 times increase).

Auger depth profiles after thermal stress also proved the importance of a thin Mo layer between Ti and InGaAs to prevent interdiffusion and to obtain stable Ohmic characteristics.

DEVICE CHARACTERISTICS

The feasibility of the developed COMET device processing was investigated by fabricating InAlAs/InGaAs HJFETs with a 1 μm gate length using simultaneous evaporation of Mo/Ti/Pt/Au for gate, source and drain electrodes. Typical DC drain characteristics for the fabricated 100 μm gate-width device are shown in Fig.6. The device exhibited good pinch-off characteristics with a threshold voltage of -0.7V. At a drain bias of 1V, a maximum transconductance of 470mS/mm was achieved. The gate-drain breakdown voltage defined at a gate current of -1mA/mm was 3.5V.

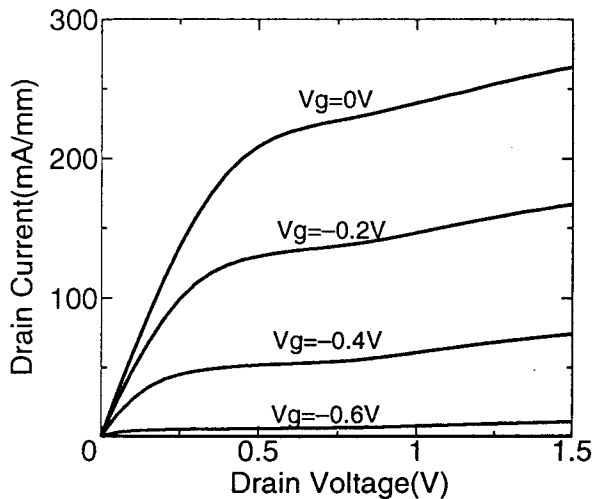


Fig.6 Typical DC drain I-V characteristics of a 1 \times 100 μm^2 COMET-HJFET.

Figure 7 shows the frequency dependence of the current gain calculated from the S-parameters measured up to 40GHz with a drain bias of 1.5V. The current gain cutoff frequency evaluated with a -6dB/oct roll-off was 40GHz. The power gain cutoff frequency evaluated from the frequency dependence of the Mason's unilateral gain at the same bias point was 85GHz.

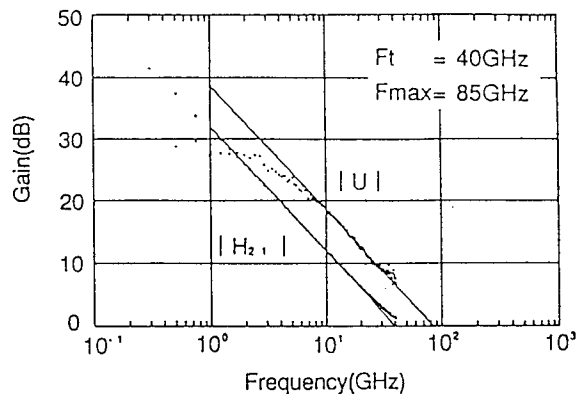


Fig.7 Frequency dependence of current gain and Mason's unilateral gain for 1 μm -gate COMET-HJFET.

RELIABILITY OF COMET-HJFET

High-temperature DC bias tests were performed for the developed COMET-HJFET. Devices were biased at a drain voltage of 1V and at a gate voltage of -0.2V under an ambient temperature of 250°C. Figure 8 shows the g_m degradation ratio as a function of the stress time. For comparison purpose, an HJFET with a Ti/Pt/Au gate and with a Ti/Pt/Au nonalloyed Ohmic source and drain was also tested. Up to 630 hours, the COMET HJFET maintained its high g_m values with only 10% degradation, whereas the Ti/Pt/Au device exhibited considerable degradation in g_m by 60%. Corresponding to the g_m degradation, the source resistance of the Ti/Pt/Au device increased by more than 10 times of its initial value, while the source resistance of the COMET-HJFET was kept relatively unchanged (i.e., about 50% increase). The degradation in the source resistance for the Ti/Pt/Au device is closely related to the increase in the Ohmic contact resistance due to the interdiffusion of Ti and the cap layer of InGaAs.

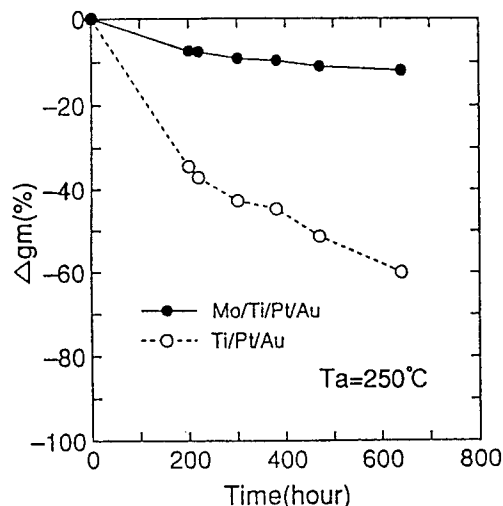


Fig.8 Degradation in g_m for COMET and Ti/Pt/Au HJFETs after DC operation life test at 250°C.

The threshold voltage shift was negligible for the COMET-HJFET, while the Ti/Pt/Au device exhibited a negative threshold voltage shift by $-0.2\sim-0.3\text{V}$ after stressing for 630 hours. The negative threshold voltage shift observed for the Ti/Pt/Au device is principally ascribed to the decrease in the barrier height due to the interdiffusion between the gate metal of Ti and the Schottky layer of InAlAs. These stable characteristics of the COMET-HJFET with respect to the high-temperature DC bias tests indicate that the effective suppression of the interdiffusion both at the gate Schottky diode and at the source and drain Ohmic contacts is of primary importance to achieve superior reliability for InP-based HJFETs.

NOISE PERFORMANCE OF 0.2 μm GATE COMET-HJFET

To confirm the high-performance capability of the COMET-HJFETs for microwave and millimeter-wave applications, COMET-HJFETs with 0.2 μm T-shaped gates were fabricated. The epitaxial structure employed was the same as that shown in Fig.1, except the planar Si-doping used in the InAlAs donor layer. A 0.2 μm T-shaped Mo/Ti/Pt/Au gate was defined using direct-write electron-beam lithography and lift-off technology [6]. The devices were passivated with a plasma-enhanced CVD SiN film prepared at 200°C. The device had a total gate-width of 200 μm with 8 fingers.

The threshold voltage of the fabricated 0.2 μm COMET-HJFET was -0.7V . The maximum extrinsic transconductance was measured to be 500mS/mm with a source resistance of 0.5 $\Omega\cdot\text{mm}$. Figure 9 shows the frequency dependence of the noise performance. The device was biased at a drain voltage of 1.1V with a drain current of 10mA. At 12GHz, the COMET-HJFET exhibited a minimum noise figure of 0.4dB with an associated gain of 15.2dB. Also, the device exhibited a minimum noise figure of 0.79dB with an associated gain of 13.0dB at 22GHz. These noise characteristics are among the

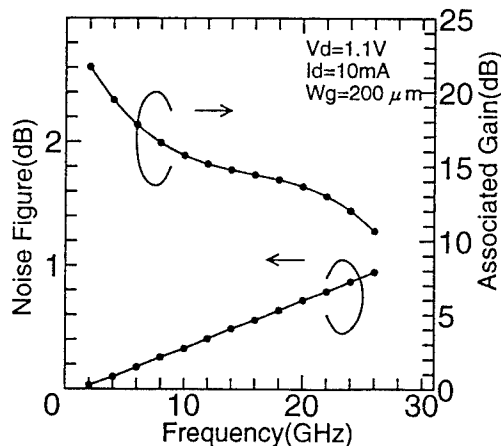


Fig.9 Frequency dependence of noise performance for 0.2 μm COMET-HJFET.

best data reported for the passivated devices with a comparable gate-length, indicating the developed COMET process is promising for highly-reliable and high-performance applications, such as microwave and millimeter-wave low-noise amplifiers and other various ICs.

SUMMARY

We have successfully developed a novel InP-based FET processing technology for high-reliability microwave and millimeter-wave applications. The fabricated 1 μm gate-length COMET-HJFET exhibited excellent DC and RF performance, including a transconductance of 470mS/mm and a current gain cutoff frequency of 40GHz. High temperature DC bias tests performed on the COMET device demonstrated improved reliability compared to that for the conventional InP-based HJFET. The superior reliability of the developed COMET-HJFET was attributed to the reduced interdiffusion between metals of the electrodes and semiconductors by introducing a refractory metal of Mo as a barrier metal.

ACKNOWLEDGEMENT

The authors would like to thank Drs. N. Samoto and M. Funabashi for discussions. The authors also thank Dr. H. Abe for encouragement throughout this work.

REFERENCES

- [1] L.D.Nguyen, A.S.Brown, M.A.Thompson and L.M.Jelloian, "50-nm Self Aligned-Gate Pseudomorphic AlInAs/GaInAs High Electron Mobility Transistors," *IEEE Trans. on Electron Devices*, 39, 2007, 1992.
- [2] P.C.Chao, A.J.Tessmer, K.H.G.Duh, P.Ho, M.Y.Kao, P.M.Smith, J.M.Ballingall, S.N.J.Liu, and A.A.Jabra, "W-Band Low-Noise InAlAs/InGaAs Lattice-Matched HEMT's," *IEEE Electron Device Lett.*, 11, 59, 1990.
- [3] H. Wang, R.Lai, D.C.W.Lo, D.C.Streit, M.W.Pospiezalski and J.Berenz, "A 140-GHz Monolithic Low Noise Amplifier," *Tech. Dig. of IEDM94*, 933, 1994.
- [4] K.C.Hwang, P.Ho, P.C.Chao, and K.H.G.Duh, "A Novel Low-Temperature Passivation of InAlAs/InGaAs HEMT Devices by MBE," *Proc. 4th Int. Conf. InP and Related Mater.*, 60, 1991.
- [5] S.Fujita, T.Noda, C.Nozaiki and Y.Ashizawa, "InAlAs/InGaAs HEMT with A Strained InGaP Schottky Contact Layer," *IEEE Electron Device Lett.*, 14, 259, 1993.
- [6] N.Samoto, Y.Makino, K.Onda, E.Mizuki and T.Itoh, "A Novel Electron-Beam Exposure Technique for 0.1 μm T-shaped Gate Fabrication," *J. Vac. Sci. Technol.*, B8, 1335, 1990.

Unpinning of Fermi Level at InP Schottky Diode Interfaces Produced by Novel *In Situ* Electrochemical Process

SB2.2

N.-J. Wu, T. Hashizume, H. Hasegawa and Y. Amemiya
Department of Electrical Engineering and
Research Center for Interface Quantum Electronics, Hokkaido University
N-13, W-8, Sapporo 060, Japan.

Introduction

Schottky contacts on n-InP have potentially wide applications in high-speed electronic and optoelectronic devices. However, the InP Schottky diodes have produced only low Schottky barrier height (SBH) of about 0.4 eV due to the firm interfacial Fermi-level pinning.¹⁾ Though some approaches by inserting oxide interlayer or applying surface treatments have been used to produce Schottky diodes with high SBHs, but the diodes showed poor reproducibility and poor reverse current-voltage characteristics.^{2,3)} This has been an obstacle to formation of practically useful InP Schottky diodes.

The paper demonstrates that the pinning of Fermi level can be removed at InP metal-semiconductor interfaces produced by the novel *in situ* electrochemical process.^{4,5)} The process consists of anodic etching of InP and subsequent cathodic deposition of metal, both of which are done *in situ* in the same electrolyte. InP Schottky diodes with various metals (Ag, Sn, Cu, Co, Pd, Ni and Pt) have been formed by using different electrolytes based on chloric or sulfuric acid and containing barrier metal ions. The diodes exhibited nearly thermionic emission characteristics. SBH changed over a wide range from 0.35 eV to 0.86 eV. The Pt/InP diodes gave the highest SBH of 0.86 eV which is the highest value ever reported for an intimate metal contact to InP.

Experimental

N-type InP crystals with a donor density of $5 \times 10^{15} \text{ cm}^{-3}$ and (100) orientation were used as substrates. A Ge-Au-Ni contact layer was deposited on the backside of the substrate at room temperature and annealed in H_2 at 350°C for 5 minutes to form an ohmic contact. The front InP surface was masked by a positive-type photoresist film to define circular dots for Schottky contact formation.

Figure 1(a) illustrates schematically the experimental apparatus. The three-electrode electrochemical cell contains an InP substrate electrode, a Pt counter-electrode and a saturated calomel electrode (SCE) as a reference electrode. The InP electrode was fixed with wax to the sample holder. The potential of the InP electrode was controlled by a potentiostat with a pulse generator. Figure 1(b) shows the electric pulse waveforms for avalanche pulse-etching and pulse-plating, respectively. The etching depth was controlled by adjusting amount of holes required for anodic oxidation by application of electric avalanche pulse or photopulse^{4,5)}. After one hundred nanometer thick InP was etched, Schottky barrier was immediately formed by *in situ* pulse-plating of metal on InP. Seven kinds of

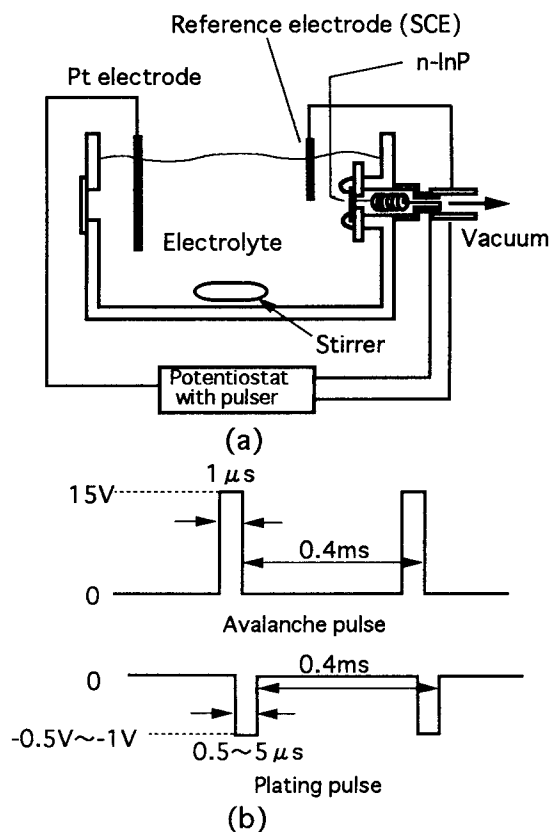


Fig. 1 The electrochemical cell and pulse forms for the etching and plating.

electrolytic solutions, based on chloric or sulfuric acid, i.e., AgCl , SnSO_4 , CuCl_2 , CoSO_4 , PdCl_2 , $\text{NiSO}_4 + \text{NiCl}_2$ and H_2PtCl_6 , were prepared for depositing Ag, Sn, Cu, Co, Pd, Ni and Pt, respectively.

For purpose of comparison, GaAs Schottky diodes were also produced by the novel electrochemical process with the same electrolytes. In addition, InP and GaAs Schottky diodes were formed by conventional vacuum evaporation techniques where metal was deposited on to the substrate surfaces. Prior to vacuum evaporation, surfaces were chemically etched in a solution of $\text{H}_2\text{SO}_4:\text{H}_2\text{O}_2:\text{H}_2\text{O}=3:1:1$.

The structural and electrical properties of the InP and GaAs Schottky diodes produced by the *in situ* electrochemical process were characterized as compared with the diodes formed by the vacuum evaporation, by using atomic force microscopy (AFM), X-ray photoemission spectroscopy (XPS), current-voltage (I-V), capacitance-voltage (C-V) techniques.

Results and Discussion

I-V behavior during plating

Figure 2 shows typical current-potential characteristics as observed during plating of Pt on InP surfaces with direct current (DC) electrolysis and with pulse electrolysis⁽⁶⁾ in the dark. In the DC electrolysis, Pt deposition is predominant in the potential plateau range from -0.3V to -1.1V . For

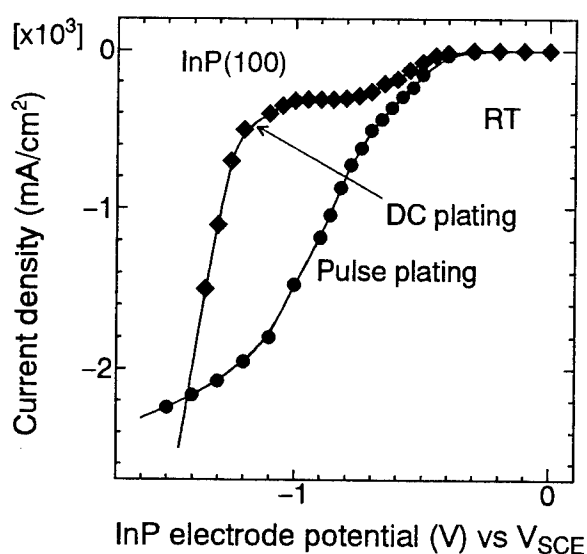


Fig. 2 The current-potential curves of Pt plating on n-InP with DC electrolysis and pulse electrolysis in the dark.

potential lower than -1.1V , strong increase in the cathodic current was observed, and this is due to reduction of H_2 . Although Pt deposition also takes place at the same time, the reduction of H_2 becomes dominant over Pt deposition. In contrast to DC electrolysis, the pulse electrolysis can be carried out under larger overpotential and higher instantaneous current densities. This seems to result in larger densities of Pt nuclei and to decrease the number of defects. In fact, Pt metal films obtained on n-InP were smoother and more uniform. Similar electrochemical behavior was also observed on GaAs electrodes.

XPS and AFM study

Figure 3 shows the observed typical XPS spectra of the surface-sensitive $\text{In}3d_{5/2}$ and $\text{P}2p$ core levels at the Pt/InP interfaces formed by the electrochemical process and the vacuum evaporation. The analysis of the interfaces was done after revealing the interface region by Ar^+ ion sputtering. The interfaces prepared by the novel electrochemical process was almost free of oxide, whereas that by the vacuum evaporation showed the signals of P oxide and In oxide. This indicates that the novel electrochemical process prevents oxide formation as in the case of GaAs⁽⁴⁾. AFM study revealed that the electrochemical etching resulted in smoother surfaces with rms roughness of 0.5nm and 0.7nm for InP and GaAs samples, respectively, as compared with the conventional

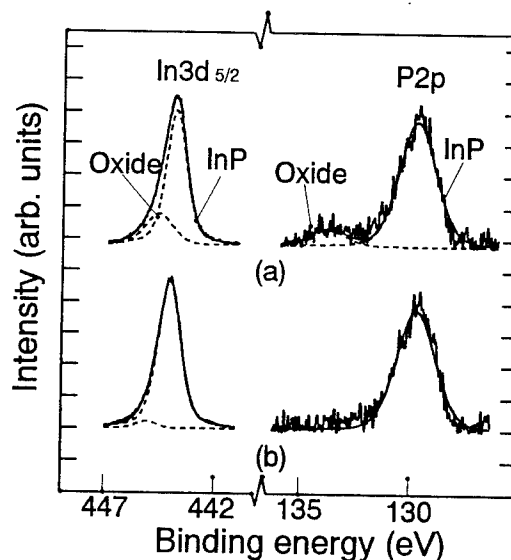


Fig. 3 XPS spectra of $\text{In}3d_{5/2}$ and $\text{P}2p$ core levels from the Pt/InP Schottky interfaces formed by (a) electron beam deposition and (b) novel electrochemical process.

chemical etching. No holes due to local avalanche breakdown were observed on the etched electrochemically surfaces.

I-V characteristic and SBH

The typical I-V characteristics of the InP Schottky diodes formed by the novel electrochemical process are shown in Figure 4. The I-V data were analyzed in term of the thermionic emission model of current⁷⁾. The value of the effective Richardson constant was 9.4 Acm^{-2} . Except for Ni, the Schottky contacts showed nearly ideal

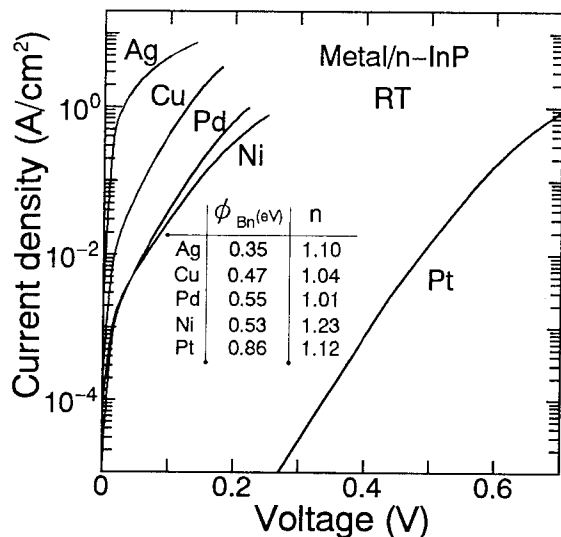


Fig. 4 The forward I-V characteristics of the metal/InP Schottky diodes fabricated by the novel electrochemical process

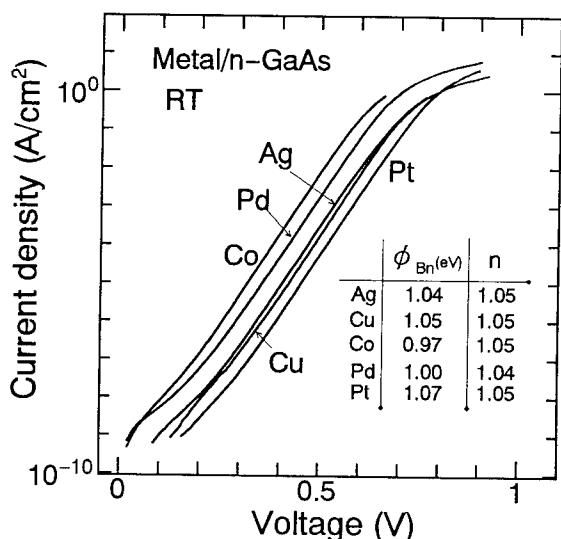


Fig. 5 The forward I-V characteristics of the metal/GaAs Schottky diodes fabricated by the novel electrochemical process

thermionic emission characteristics of ideality factors close to unity. The Pt/InP diode gave the SBH value of 0.86eV. This is the highest SBH ever reported for n-type InP Schottky barrier contact formed by direct intimate contact between metal and semiconductor.

On the other hand, as shown in Figure 5, the GaAs Schottky diodes formed by the same electrochemical process showed large SBHs of about 1eV. Though they showed reasonably good thermionic emission characteristics, SBHs exhibited no clear dependence on the metal workfunction in contrast to the InP diodes.

Table 1 lists the values of the n factor and the barrier heights ϕ_{Bn}^{I-V} and ϕ_{Bn}^{C-V} , obtained from I-V and C-V measurements for the InP and GaAs Schottky diodes, respectively. The ϕ_{Bn}^{I-V} and ϕ_{Bn}^{C-V} values were in good agreement within $\pm 0.02 \text{ eV}$. The ideality factor n were close to unity. The barrier heights of the InP Schottky diodes varied over a wide range from 0.35eV to 0.86eV for Ag, Sn, Cu, Co, Pd, Ni and Pt metals. The barrier heights of the GaAs Schottky diodes are higher than 1eV.

Table. 1 Schottky barrier height and ideality factor of InP and GaAs electrochemical Schottky diodes. ϕ_{Bn}^{I-V} and ϕ_{Bn}^{C-V} were obtained from I-V and C-V measurements, respectively.

Metal	$\phi_m(\text{eV})$	Sample	$\phi_{Bn}^{I-V}(\text{eV})$	$\phi_{Bn}^{C-V}(\text{eV})$	n
Ag	4.26	InP	0.35	0.33	1.07
Sn	4.42	InP	0.43	0.40	1.34
Cu	4.65	InP	0.47	0.47	1.04
Co	5.0	InP	0.48	0.48	1.05
Pd	5.12	InP	0.55	0.56	1.00
Ni	5.15	InP	0.53	0.51	1.23
Pt	5.65	InP	0.86	0.85	1.11
Ag	4.26	GaAs	1.04	1.07	1.05
Cu	4.65	GaAs	1.05	1.06	1.05
Co	5.0	GaAs	0.97	0.96	1.05
Pd	5.12	GaAs	1.00	1.01	1.04
Pt	5.65	GaAs	1.07	1.09	1.05

SBH vs. metal workfunction

The metal workfunction dependence of SBH values of the GaAs electrochemical Schottky diodes is shown in Figure 6 together with the data obtained on vacuum deposited GaAs and InP Schottky diodes. As seen clearly in Fig.6, Fermi

levels are strongly pinned at about 0.4eV and 1eV from the conduction band edge for InP and GaAs Schottky interfaces, respectively.

In contrast to these, it is evident that the SBH values of the InP electrochemical Schottky diodes is strongly dependent on the barrier metal workfunction, as shown in Figure 7. The value of the interface index defined by $S(=d\phi_{Bn}/d\phi_m)$ is found to be as large as 0.4. This indicates that Fermi level pinning at the InP Schottky barrier interfaces is largely removed by use of the novel electrochemical process.

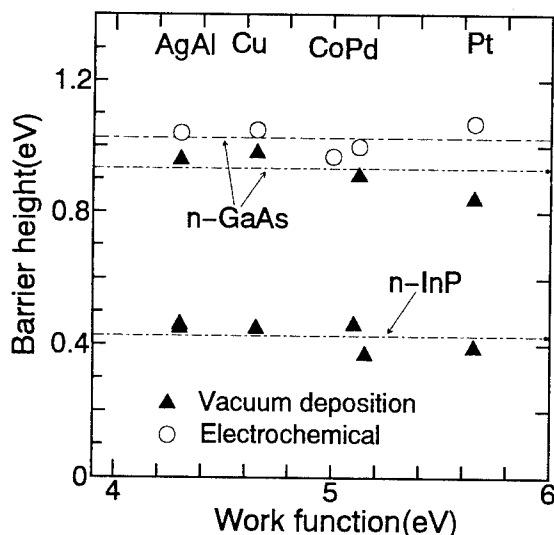


Fig. 6 Metal Work function dependence of SBHs of metal/GaAs diodes formed by the electrochemical process and by the vacuum evaporation and metal/InP by the vacuum evaporation.

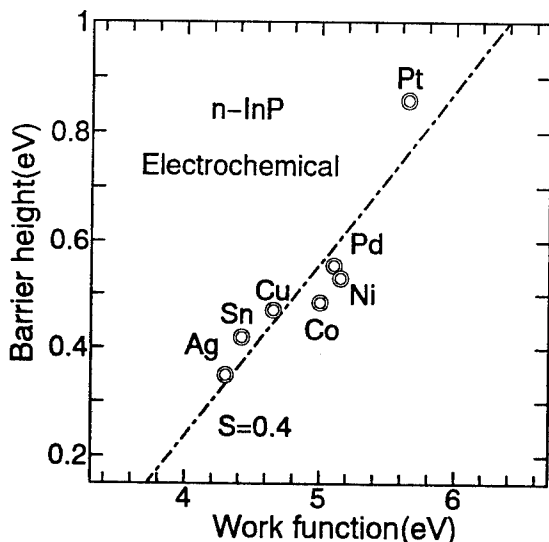


Fig. 7 Metal Work function dependence of SBHs of metal/InP diodes formed by the electrochemical process.

The difference of behavior between the electrochemical and vacuum deposited InP Schottky diodes and that between the electrochemical InP and GaAs Schottky contacts can be explained at least qualitatively in terms of the relationship between the energy involved in the processing and the energy of cohesion at the semiconductor surface.

Conclusion

Schottky diodes with nearly ideal thermionic emission characteristics on n-InP and n-GaAs were formed by a novel *in situ* electrochemical process. The novel electrochemical process produces a smooth and oxide-free Schottky interfaces in contrast the vacuum evaporation process. The SBH values of the InP electrochemical Schottky diodes can be changed over a wide range from 0.35eV to 0.86eV depending on the metal workfunction, removing Fermi level pinning. The Pt/InP diodes gave the highest SBH of 0.86eV.

References

- 1) E. H. Rhoderick and R. H. Williams: *Metal-Semiconductor Contact* (Clarendon, Oxford, 1988) 2nd ed., Chap.2.
- 2) O. Wada and A. Majerfeld: *Electron. Lett.* 14(1978)125
- 3) O. Wada, A. Majerfeld and P.N. Robson: *Solid-State Electron.* 25(1982)381
- 4) N.-J. Wu, T. Hashizume and H. Hasegawa: *Jpn.J.Appl. Phys* 33(1994)936
- 5) T. Hashizume, H. Hasegawa, T. Sawada, A. Grub and H.-L. Hartnagel: *Jpn.J.Appl.Phys* 32(1993) 486
- 6) P. Bingra, H. Gerisher and D. M. Kolb. J. *Electrochem. Soc.* 124(1977)1012
- 7) S. M. Sez: *Physics of Semiconductor Devices* (Wiley, New York, 1981) 2nd ed., Chap.5.

Cadmium Sulfide Surface Stabilization and Schottky Barrier Enhancement for InP Based Optoelectronic Devices SB2.3

K. Vaccaro, S.M. Spaziani, A. Davis, H.M. Dauplaise, E.A. Martin, and J.P. Lorenzo
USAF Rome Laboratory, Photonic Components Branch, Hanscom Air Force Base, MA 01731 USA

Introduction

InP and lattice matched III-V compounds are recognized as desirable materials for high frequency opto-electronic circuits. Lattice-matched and strained ternaries and quaternaries of InGaAlAs or InGaAsP on InP allow the production of high electron mobility transistors (HEMTs), heterojunction bipolar transistors (HBTs), optical detectors, lasers, and other critical opto-electronic devices. Although high quality epitaxial material is commercially available, the ability to form well-behaved interfaces between the epitaxial semiconductor and insulators or Schottky metals remains elusive. A variety of techniques have been used to reduce or eliminate the effects of problematic surface chemistry on device behavior. We have used thin layers of cadmium sulfide to reduce the gate leakage of InAlAs/InGaAs HEMTs ($I_d/I_g=5 \times 10^4$) and the dark current of InAlAs/InGaAs optical detectors ($I_d < 1$ nA). X-ray photoelectron spectroscopy indicates a reduction of surface oxides and the prevention of subsequent group III or V oxide formation.

Background

Thin interfacial layers of elemental silicon have been used to improve the performance of GaAs- and InGaAs-based metal insulator semiconductor field effect transistors (MISFETs).^[1] The silicon interfacial layer terminates the III-V semiconductor surface, reducing the interface state density.^[2] Deposition of an insulator over the silicon results in a superior dielectric/semiconductor interface, allowing modulation of the surface Fermi level throughout the bandgap. The electrical characteristics of GaAs/AlGaAs-based HBTs,^[3] InP-based MISFETs,^[4] and InP/InGaAs metal-semiconductor-metal (MSM) photodetectors^[5] have also been improved by treating samples in sulfur-bearing solutions. In the case of InP, sulfur replaces missing phosphorus at the surface, resulting in a thermodynamically favored and stable In_2S_3 passivating layer.^[6] We are investigating the use of cadmium sulfide (CdS) as an interlayer to improve the electrical characteristics of the InP/insulator interface and the InP-based III-V/Schottky-metal junction.

CdS is a wide-bandgap (2.42 eV) semiconductor. The lattice constant of the zincblende crystal matches to within 0.6% of crystalline InP. Metastable zincblende CdS layers have been grown epitaxially on (110) InP by molecular beam epitaxy and (100) InP by pulsed laser deposition. Recently, hexagonal phase CdS grown on (111) InP by chemical bath deposition (CBD) has been reported.^[7]

Experimental

We used the chemical bath technique to prepare our layers. The CdS is deposited from an aqueous solution of ammonium hydroxide, cadmium sulfate, and thiourea.^[7] The solution is heated (to 30-90°C) in a separate water bath for improved temperature stability, which leads to

improved control of the layer growth rate and crystalline quality. CdS is readily deposited on both (111) and (100) InP substrates, which must be carefully prepared to avoid the formation of native oxides. Low growth rates (20 Å/min) are used to deposit thin layers of approximately 100 Å or less.

An atomic force microscope (AFM) was used to determine the average roughness of deposited films on bare InP substrates. The target thickness of the CdS layer was 50 Å. Scans revealed an increase in average peak-to-peak roughness from 6 Å for HF-etched InP to 15 Å for CdS-covered samples. Auger microprobe measurements showed bulk Cd to S ratios near unity. Auger depth profiles also suggest the deposited material is cadmium rich at the surface and sulfur rich at the CdS/InP interface. X-ray photoelectron spectroscopy (XPS) was used to investigate the effects of CdS treatment on native oxides of InP and InAlAs. An InP sample was oxidized in ozone at 300°C for 10 minutes. The oxides of In and P are clearly visible in the upper XPS curves of Figure 1a and 1b after the ozone-assisted oxidation. After the

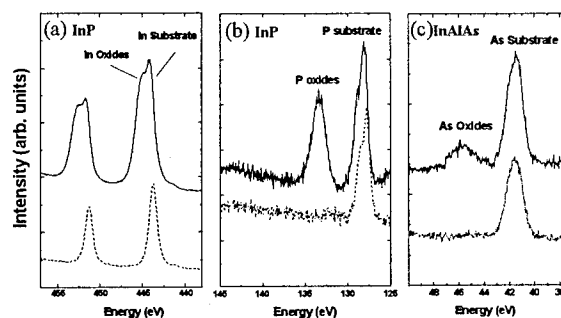


Figure 1. XPS analysis of CdS-treated InP and InAlAs. Upper curves are before CdS treatment, lower curves are after CdS treatment. (a) In3d doublet, (b) P2p, (c) As3d.

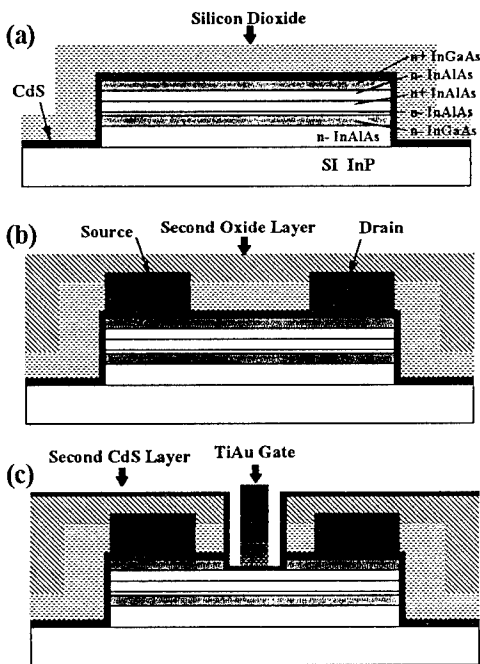


Figure 2. InGaAs/InAlAs HEMT process with CdS passivation.

deposition of a thin layer of CdS, the group III and V oxides are greatly reduced as shown in the lower curves of Figure 1a and 1b. Similar results were obtained for the InAlAs sample of Figure 1c. The InAlAs sample was not intentionally oxidized. Suppression of the InP substrate XPS peaks with CdS films of approximately 150 Å, in addition to the AFM scans, suggests uniform coverage. Photoluminescence (PL) of treated InP samples showed a marked increase in intensity over untreated samples. PL is known to be highly sensitive to surface quality.

HEMT Results and Discussion

The CdS interlayer is used in an InGaAs/InAlAs HEMT process. Mesas are first formed with a phosphoric acid-based etch. After removing the photoresist, the sample is treated in the CdS chemical bath, and SiO₂ is deposited to passivate the entire wafer surface. The SiO₂ layer is deposited at 270°C at 3 Torr using a 5% SiH₄ in He flow of 100 sccm and an oxygen flow of 33 sccm (Figure 2a). AuGeNi contacts are formed with a lift-off process after etching openings in the oxide layer. After contact metalization, a second SiO₂ layer, which protects the ohmic contacts during the second CdS treatment, is deposited (Figure 2b). The channel regions are exposed by etching openings in the double oxide layer, then recessed with a succinic acid-based etch to selectively remove an InGaAs cap layer. The sample is then placed in a CdS bath to passivate the exposed channel region. After treatment, the gate layer is aligned to the recess and TiAu metal is sited with a double layer resist lift-off process (Figure 2c).

Oxide deposition was found to have an adverse effect on device isolation. Samples treated with CdS prior to the first oxide deposition were seen to have less leakage between the InAlAs/InGaAs mesas. Figure 3 compares the surface leakage of CdS-treated and untreated samples after the first oxide deposition and contact metal evaporation. Surface leakage was measured between 1000µm long mesas that are separated by 50µm, before and after a 1 minute, 350°C, forming gas anneal. For untreated samples, an increase in leakage was consistently observed after the ohmic anneal. For CdS-treated samples, leakage current was two orders of magnitude lower than that of untreated samples. There was no significant increase in leakage after the ohmic anneal for the CdS-treated sample.

Figure 4 compares the I-V characteristics of devices with and without channel treatment. Devices with CdS-treated channels had to be annealed 1 minute at 250°C in forming gas before desired I-V characteristics were obtained. The gates are 100µm wide by 1µm long. HEMTs with channel passivation show reduced gate leakage, $I_d/I_g=5 \times 10^4$.

Devices processed without the passivation generally showed higher transconductance. Although there is some non-uniformity in the gate-to-channel spacing, which can be attributed to the recess etch, the lower transconductance may also result from the additional

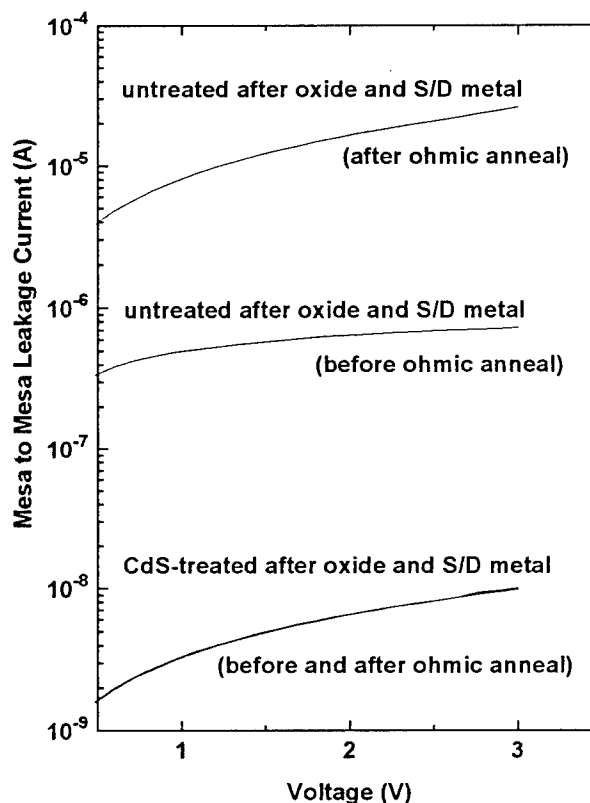


Figure 3. Leakage current between mesa layers with and without CdS passivation.

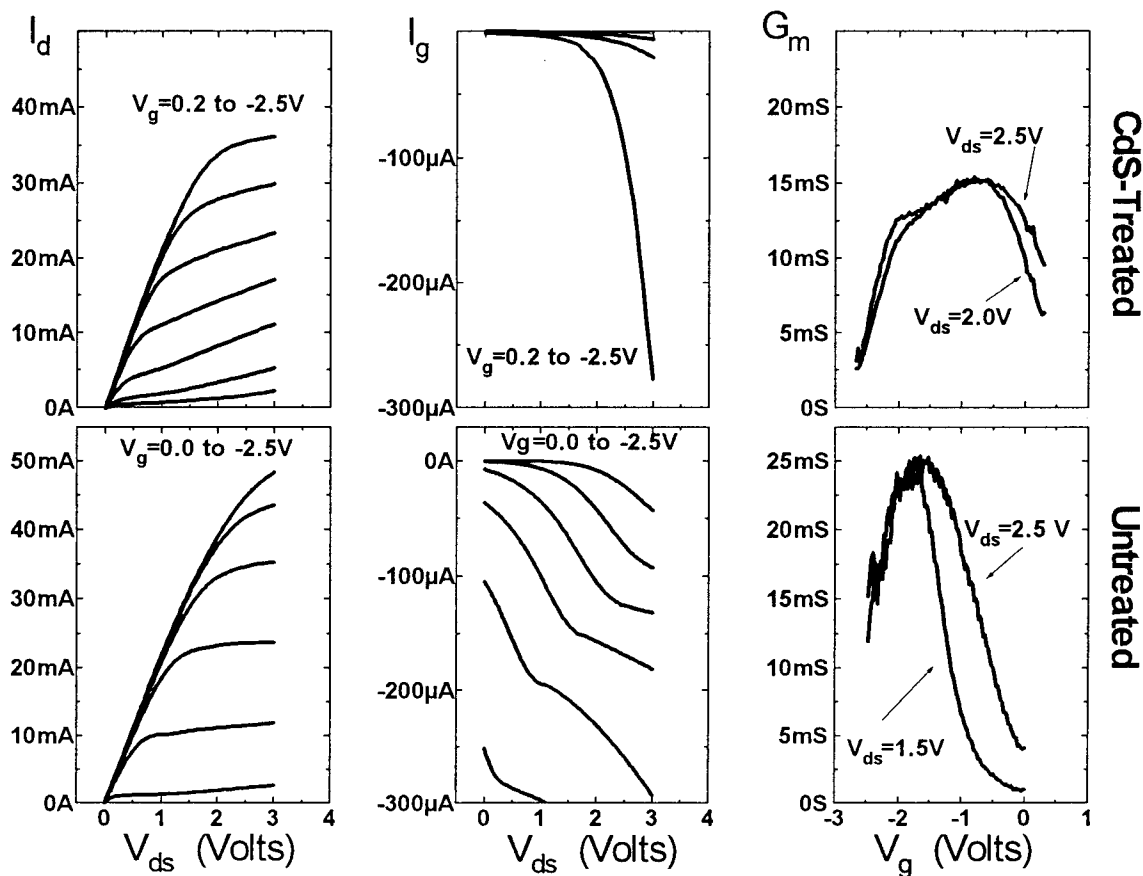


Figure 4. Results of CdS-treated and untreated HEMTs: Drain Current, Gate Current, and Transconductance.

thickness of the CdS passivating layer. Moving the gate further away from the channel would reduce the transconductance. XPS measurements suggest a CdS layer of approximately 50Å. It is also possible that cadmium is doping the InAlAs surface, replacing the Schottky contact with a *pn* junction. If a junction-type gate exists, lower transconductance would be expected since the oxide opening and channel recess are longer than the designed gate length.

MSM Results and Discussion

MSM detectors were fabricated with the four processes illustrated in Figure 5. The detector starting material was nominally undoped InAlAs/InGaAs/InAlAs grown by MBE. MSM-A is our standard process: mesa definition followed by the positioning of TiAu fingers with a double layer resist lift-off. MSM-B is similar to MSM-A, but treated with CdS after the mesa step and before metalization. For MSM-C, the fingers are placed first, the sample is secured to a glass substrate with epoxy, the substrate is removed to expose the epitaxial layers, and the mesas are aligned from the backside of the sample. MSM-D is processed as MSM-C but the surface is CdS treated before the fingers are placed. The mesa is 50μm x 50μm. Finger width to spacing ratios (*w/s*) were 1/1, 2/1,

1/2, and 2/2. A photomicrograph of MSM-D is shown in Figure 6.

Reverse leakage currents for the MSM samples are shown in Figure 7. The CdS treated samples, MSM-B and MSM-D, demonstrate greatly reduced dark currents. The backside mesa processed samples, MSM-C and MSM-D, avoid contacting the low bandgap InGaAs absorbing layer at the mesa sides with the finger metal. Dark currents for MSM-C and MSM-D were measured before and after mesa definition. The dark current of MSM-C is lower than that of the standard sample by an order of magnitude, implying the leakage is not entirely due to side wall coverage. The combination of CdS treatment and backside mesa (MSM-D) produced the most promising results. The dark current of MSM-D is more than three orders of magnitude lower than that of the standard process. The reverse leakage of MSM-D was reduced further by treating the exposed mesa in the CdS chemical bath, thereby completely enclosing the mesa in CdS. Leakage current dropped below 1nA for 50μm x 50μm mesas, as shown in Figure 7.

Responsivity of backside illuminated MSM detectors was approximately 0.5A/W, which was not substantially higher than that of front side illuminated devices. Proper design of the InAlAs buffer layer or an antireflection

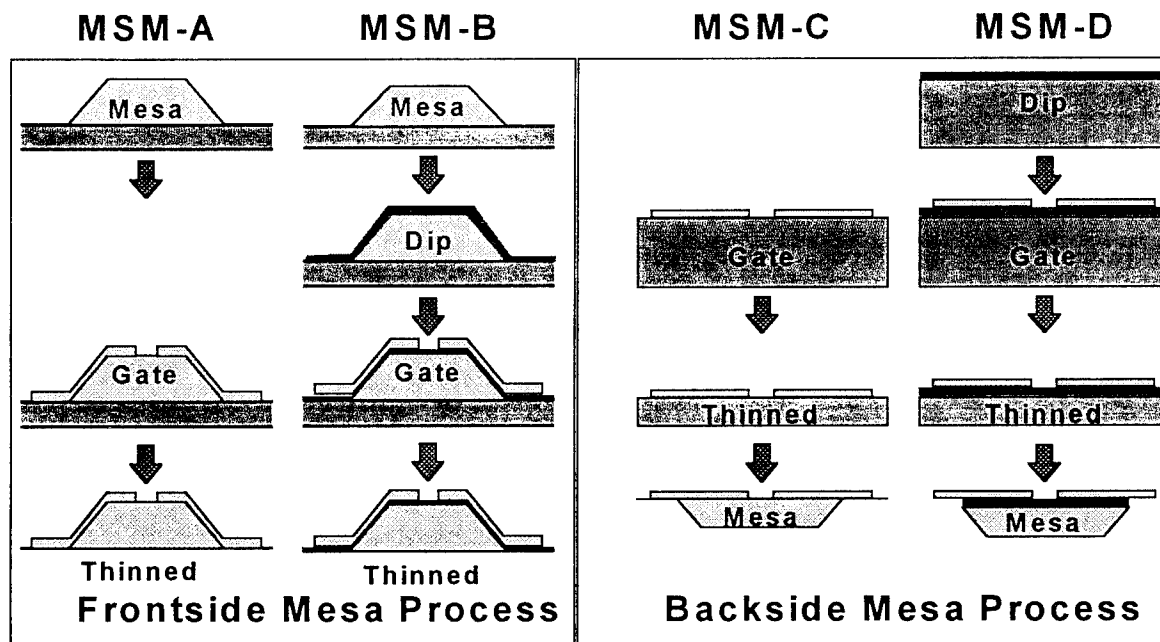


Figure 5. MSM fabrication processes with substrate removal and CdS treatments.

coating would reduce reflection during backside illumination, increasing the responsivity.

Conclusions

We have investigated the use of CdS interlayers grown by CBD. We have deposited CdS on a wide variety of III-V semiconductors. We found that native oxides were reduced by the CdS treatment. CdS-treated and untreated HEMTs and MSMs were compared. Thin, 50Å layers were effective in reducing gate and surface leakage. Backside processing of InGaAs/InAlAs MSMs allows complete coverage of the mesas. The CBD process for

depositing CdS is inherently adaptable to a wide range of optoelectronic device processes.

References

- [1] D.S.L. Mui, Z. Wang, D. Biswas, A.L. Demirel, N. Teraguchi, J. Reed, and H. Morkoc, *Appl. Phys. Lett.* **62**, 3291 (1993).
- [2] H. Hasegawa, M. Akazawa, H. Ishii, and K. Matsuzaki, *J. Vac. Sci. Tech. B* **7**, 870 (1989).
- [3] C.J. Sandroff, R.N. Nottenburg, J.-C. Biscoff, and R. Bhat, *Appl. Phys. Lett.* **51**, 33 (1987).
- [4] R. Iyer, R.R. Chang, and D. Lile, *Appl. Phys. Lett.* **53**, 134 (1988).
- [5] U. Schade, St. Kollakowski, E.H. Bottcher, and D. Bimberg, *Appl. Phys. Lett.* **64**, 1389 (1994).
- [6] D. Gallet and G. Hollinger, *Appl. Phys. Lett.* **62**, 982 (1993).
- [7] D. Lincot and R. Ortega-Borges, *Appl. Phys. Lett.* **64**, 569 (1994).

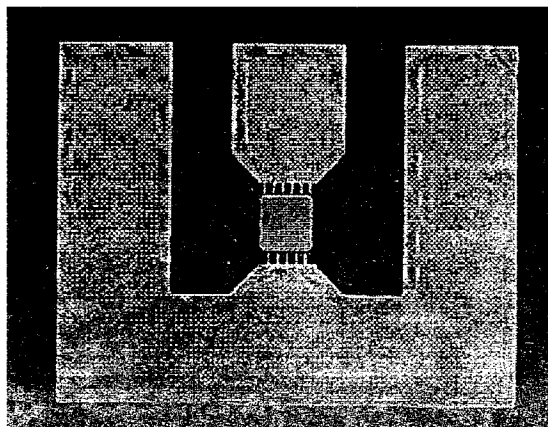


Figure 6. Photomicrograph of completed MSM-D structure after substrate removal. The gate fingers run under the mesa.

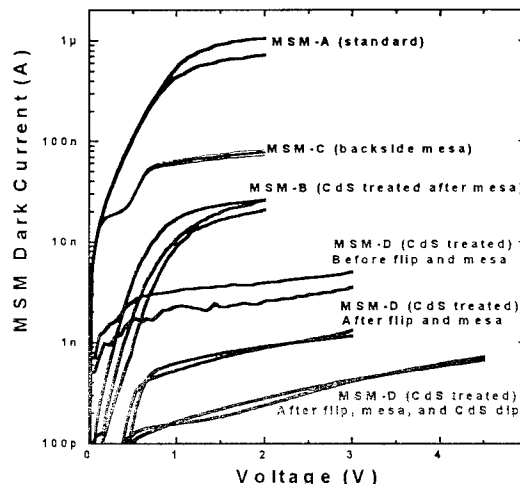


Figure 7. Dark current measurements of MSM structures illustrated in Figure 5.

Improvement in Schottky diode characteristics of metal-In_{0.52}Al_{0.48}As contact using an in situ photochemical etching and surface passivation process

Soheil Habibi, Masahiro Totsuka, Jun Tanaka and Satoru Matsumoto
Faculty of Science and Technology, Keio University, Hiyoshi 3-14-1, Yokohama 223, Japan.

HBr and H₂S gases were used together with a 172 nm Excimer lamp and a deep UV-lamp for photochemical etching and surface passivation of InGaAs/InAlAs material system. Schottky diodes were fabricated on n-In_{0.52}Al_{0.48}As by EB evaporation of Mo/Ti/Pt/Au with the consequent alloying. AES and XPS measurements of the passivated InAlAs surface reveal that the photochemically generated S*-radicals are capable of removing In-O and As-O bonds from the surface and replacing them with In-S and As-S bonds. The reverse bias leakage current of the surface passivated diodes were reduced by 3 orders of magnitude compared to the diodes with unpassivated surface. We obtained an effective barrier height of 0.79 eV and an ideality factor of 1.03, for the fabricated diodes after surface passivation.

1 Introduction

InGaAs/InAlAs heterostructure is an attractive material system for fabrication of high electron mobility transistor (HEMT) devices due to its large conduction band offset and small effective electron mass of InAlAs in barrier layer. However, InAlAs schottky contacts suffer from low schottky barrier height, excessive reverse leakage current and low break down voltage^[1].

The high density of midgap states at unpassivated surfaces of most III-V compound semiconductors results in high surface recombination velocities and Fermi-level pinning that limit the device performance^[2].

To reduce the leakage current of InAlAs based diodes for HEMT application, two ways have been considered. One is the introduction of additional epitaxial layers in HEMT structures^[3] and, the other is the passivation of the surface of the InAlAs layer prior to schottky metal deposition. The Fermi-level unpinning that would result from reduction of surface state density would produce improved Schottky contacts^[2]. Sulfur treatment has been successfully applied for the passivation of GaAs surface^{[4][5]}. But, there are few reports on the passivation of InAlAs. This paper seeks to discuss ways to improve the metal-schottky contact characteristics of In_{0.52}Al_{0.48}As by (1) applying a dry photochemical sulfidation of InAlAs layer based on H₂S gas and a deep Ultra Violet lamp and, (2) depositing a multi-layered Mo/Ti/Pt/Au metal contact to fabricate schottky diode.

We have recently developed a dry photochemical Etching system based on HBr gas and a 172 nm excimer lamp^[6], to selectively etch the InGaAs over InAlAs. Our basic purpose in this experiment is to develop a sulfidation process which is performed in the same chamber as the etching. Thus, the samples are first InGaAs etched using HBr and a 172 nm Excimer lamp then the chamber is thoroughly purged of HBr and without opening it, H₂S gas is introduced into the chamber but this time, it is exposed by a deep UV-lamp. In this way, after the etching

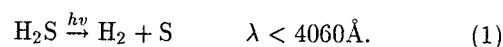
the samples are first passivated by sulfur and then, are brought into contact to the air. Thus, the possibility of the creation of surface states at the InAlAs surface is reduced considerably. After applying this photochemical sulfidation process, the InAlAs surface has been extensively studied by AES and XPS measurements.

Furthermore, the electrical characteristics of the fabricated schottky diodes have been studied by reverse biased I-V measurements, for estimation of the leakage current and break down voltage and, forward bias measured for barrier height ϕ_{Bn} and ideality factor, n determination.

2 Experimental

The epitaxial layer was grown on (100) n⁺-InP substrate by reduced pressure MOVPE. The structure is shown in fig. 1. The top InGaAs layer has two functions. One is the protection of the InAlAs surface and the other is the structural similarity with HEMT device epitaxial structure.

The experimental setup is the same as previously reported^[6]. The system is capable of performing both photochemical etching using HBr gas and sulfur passivation using H₂S gas. For surface passivation, we used H₂S together with a deep ultra violet lamp of Hg+Xe. H₂S starts absorption at about 250 nm with a maximum at about 187 nm^[7]. The absorption spectrum in this region is nearly continuous. The primary process by light absorption at this region appears to be creation of H₂ and S radicals.



After etching of the top InGaAs layer, the chamber is purged of HBr gas and is evacuated again to a base pressure of about 10⁻⁵ Torr by the turbo molecular pump. At this stage, the H₂S gas (H₂S 10% + N₂ 90%) is introduced into the same chamber while the chamber

Sample Structure	
Undoped InGaAs	Thickness, N_d 20 nm
undoped InAlAs	250 nm
n-InAlAs	200 nm, $1E18 \text{ cm}^{-3}$
n-InAlAs	200 nm, $1E18 \text{ cm}^{-3}$
n-InP Substrate	$2-8E18 \text{ cm}^{-3}$

$\text{In}_x\text{Al}_{1-x}\text{As}$; $x=0.52$ (double crystal X-ray Diffraction)
 $\text{In}_y\text{Ga}_{1-y}\text{As}$; $y=0.5$
 Growth Method: Reduced pressure MOVPE

Figure 1: The crystal structure for the samples used in the experiments.

main valve to the vacuum system is kept closed. The passivation was performed at a chamber pressure of 760 Torr, sample temperature of 80°C, and UV-light exposure time of 60 minutes. There was no gas flow during the passivation.

Schottky diodes were fabricated to evaluate the merits of this photochemical process. First ohmic contacts were formed on the $n^+ - \text{InP}$ side (back side) of the samples by evaporating AuNiGe followed by alloying at 350°C for 90 seconds in Nitrogen atmosphere.

We fabricated diodes by adapting (1) an in situ photochemical etching and surface passivation process, (2) only photochemical dry etching and no passivation, (3) wet etching of the cap InGaAs layer in a solution of citric acid: H_2O_2 [1:1]^[8] and no passivation, (4) wet etching and wet passivation by dipping them into $(\text{NH}_4)_2\text{S}_x$ solution at 50°C for 30-60 seconds^[9] and, (5) wet etching and wet passivation. The diode holes were patterned on the samples by usual photo-lithographic techniques using a negative photoresist. After the lithography, samples were loaded into the electron beam evaporator chamber for schottky metal deposition.

The schottky metal was a multilayered deposition of the form Mo/Ti/Pt/Au [2nm/30nm/200nm/200nm] by electron beam evaporation and alloying at 350°C for 10 minutes in Nitrogen atmosphere. The processing techniques and measured results are presented in table A.

3 Results and Discussion

To determine the passivation mechanism, Auger electron spectroscopy AES and x-ray photoelectron spectroscopy XPS measurements of the as-etched surface and photochemically treated in H_2S samples were performed. Furthermore, schottky diodes were I-V measured for determination of reverse leakage current, break down voltage, ideality factor n and schottky barrier height ϕ_{Bn} .

Process	n	ϕ_{Bn} [eV]	Leakage current density [A/cm^2] at -1 V bias
PCE+SSP+Litho+SSP+EB	1.03	0.79	2.66×10^{-8}
PCE+EB	1.57	0.72	3.85×10^{-6}
PCE+Litho+SSP+EB	1.33	0.74	5.41×10^{-7}
WE+Litho+SSP+EB	1.25	0.73	4.85×10^{-6}
WE+Litho+WP+EB	1.34	0.64	2.26×10^{-5}
WE+Litho+EB	1.68	0.61	4.04×10^{-5}

Table A: Processed diodes with their measured data. The following abbreviations have been used: SSP: dry sulfur surface passivation, WP: wet passivation in $(\text{NH}_4)_2\text{S}_x$, WE: wet etching in citric acid, PCE: photochemical etching in HBr gas, Litho: photo lithography, EB: electron beam evaporation (for Schottky metal deposition).

Fig. 2 illustrates the AES spectra of the photochemically surface passivated InAlAs and an as-etched reference sample. In the as-etched surface, a strong oxygen signal appears at 510 eV and the presence of carbon at 272 eV is evident. After the passivation, a signal for sulfur at 152 eV appears. The carbon signal is reduced. So is the oxygen signal. An increase in the intensity of aluminum signal at 1396 eV is also observable. This result suggests that the surface of InAlAs after the photochemical treatment is covered with In-S, As-S and the nonvolatile Al_2O_3 . This Al_2O_3 is formed on the surface after the etching of the cap InGaAs and acts as the etch stop layer for this selective etching system^[6].

Figure 3 is an XPS spectra of the In $3d_{5/2}$, Al 2p and As 3d core levels of the as-etched and dry photochemically treated in H_2S samples taken with a take-off angle of 30° relative to the average surface plane. The small take-off angle measurements will detect the photoelectrons originating near the surface, reflecting the bonds near the surface.

Figure 3(a) is the XPS spectra of the In $3d_{5/2}$ core level. The In $3d_{5/2}$ reference energy values of 444.0 eV for InAs, 444.3 eV for In_2O or In_2O_3 , and 444.7 eV for In_2S_3 are shown by vertical lines. We can see from this figure that the In-O bonds of the as-etched sample have been dissolved by the dry photochemical sulfidation process and in its place In-S bonds have been formed at the near surface of the photochemically treated sample. These In-S bonds represent In_2S_3 .

Figure 3(b) shows the XPS spectra for Al 2p core level. Al 2p reference energy levels of 73.6 eV for AlAs, 74.3 eV for Al_2S_3 and 74.7 eV for Al_2O_3 are illustrated

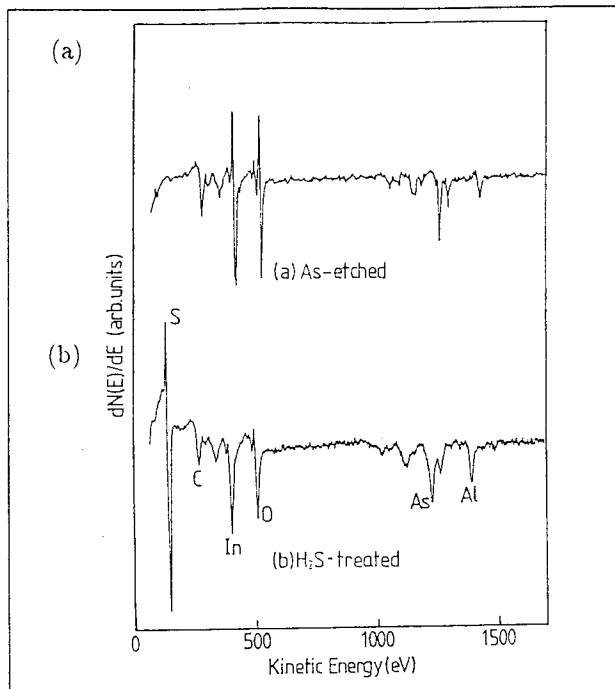


Figure 2: AES spectra from the $\text{In}_{0.52}\text{Al}_{0.48}\text{As}$ surface (a) as-etched surface, (b) dry photochemical sulfidation treatment.

by vertical lines. Here, the Al_2O_3 signal is still dominant, even after H_2S photo-sulfidation process, and the shift towards Al_2S_3 at 74.3 eV is negligible. Thus, one can conclude the nonvolatile Al_2O_3 is not etched away by this photo-sulfidation process.

Figure 3(c) illustrates the As 3d core level of the same sample as in Fig. 3(a) and (b). As 3d reference energies of 40.6 eV for InAs, 41.0 eV for AlAs, 43.5 eV for As_2S_3 and 44.9 eV for As-O are shown by vertical lines. After photochemical sulfidation process the As-In and As-Al bonds have been dissolved and As-S bonds formed at the surface. This As-S bond represents As_2S_3 .

Arsenic oxides are electrically leading materials and are thought to be one of the main causes of the leakage current for schottky diodes fabricated on InAlAs. These XPS analysis suggest that the developed dry photochemical sulfidation process is capable of eliminating the As-O and In-O bonds and replacing them with As-S and In-S bonds, respectively. As for Al_2O_3 , this is a very stable material and as mentioned earlier, is not removed by this photo-sulfidation process. However, Al_2O_3 is an insulating material and does not have any effect on the leakage current of the schottky diodes.

The Fabricated schottky diodes were I-V measured to determine the dependence of the leakage current, break down voltage, schottky barrier height and ideality factor, on the applied passivation process.

The schottky barrier height ϕ_{Bn} and the ideality factor n were determined from a least square fit of the linear

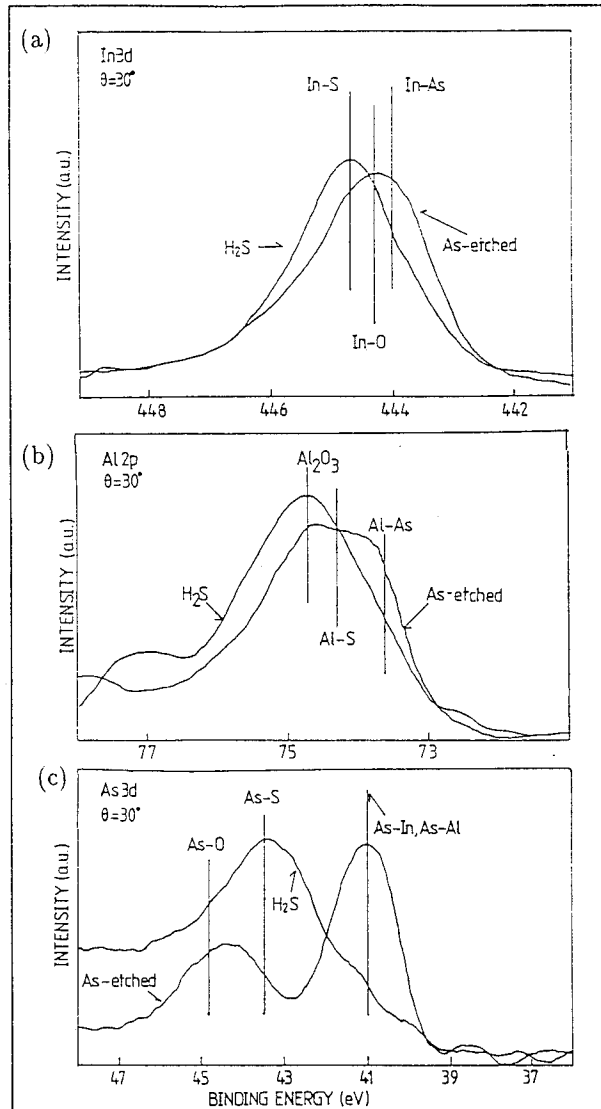


Figure 3: XPS spectra of the (a) $\text{In}3d_{5/2}$, (b) Al 2p, and (c) As 3d core levels from $\text{In}_{0.52}\text{Al}_{0.48}\text{As}$ surface (i) as-etched and (ii) prepared by photochemical sulfidation.

portion of the forward biased I-V curve of Fig. 4, using the expressions:

$$J_F = J_S \exp\left(\frac{qV_F}{nkT}\right), \quad (2)$$

when $qV_F > 3kT$, and

$$\phi_{Bn} = \frac{kT}{q} \ln\left(\frac{A^* T^2}{J_S}\right) \quad (3)$$

where J_F is the forward current density, V_F is the applied voltage, J_S is the saturation current density, and $A^* (= 4\pi q m^* k^2 / h^3)$ is the effective Richardson constant. By taking $m^* = 0.075m_0$ for $n - \text{In}_{0.52}\text{Al}_{0.48}\text{As}$, a theoretical value of $9.00 \text{ A/cm}^2\text{K}^2$ is obtained for A^* .^[8]

The value of the leakage current, at reverse bias, is shown in Fig. 5 and the leakage current density of the

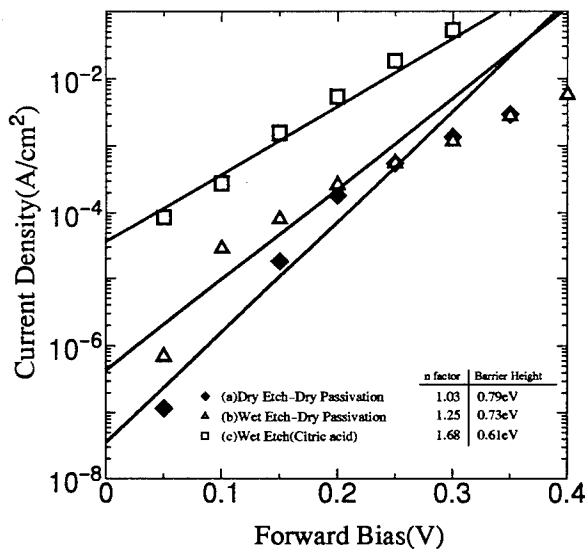


Figure 4: Forward bias I-V characteristics of the fabricated diodes after: (a) dry etch and dry passivation, (b) wet etching and dry passivation, and (c) wet etching of the cap layer.

fabricated diodes, at -1 V bias, is given in table A. It is clear from Fig. 5 that by adapting dry photochemical etching the leakage current of the schottky diode is reduced compared to diodes fabricated by applying wet etching process. Moreover, the combination of dry photochemical etching and *in situ* passivation produces the best diodes, in terms of leakage current reduction. When compared to diodes fabricated only by wet etching, the leakage current reduction is almost 3 order of magnitude. Diodes processed by applying dry etch-dry passivation have a leakage current of about 145 times less than those fabricated by only dry etch and no passivation. This is a remarkable improvement.

4 Conclusion

We have developed an *in situ* process of photochemical etching and surface passivation using HBr and H₂S gases, respectively, for InGaAs/InAlAs material system. AES and XPS spectra of the passivated InAlAs surface showed that In-O and As-O bonds at the surface have been etched away and replaced by In-S and As-S bonds. Thus, reducing the surface states and probability of Fermi-level pinning at the surface. Schottky diodes fabricated by applying this passivation process showed a reduction in reverse bias leakage current of 3 orders of magnitude. Schottky barrier height, ϕ_{Bn} , of 0.79 eV and

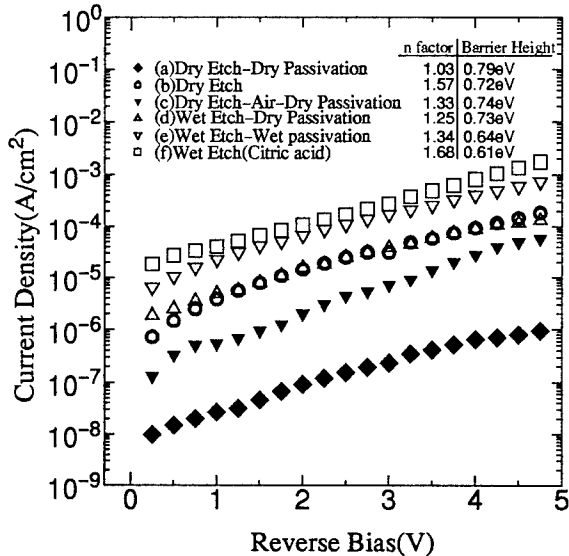


Figure 5: Reverse bias I-V characteristics of the fabricated diodes.

an ideality factor of 1.03 were achieved for the fabricated diodes.

References

- [1] P.D. Hodson, R.H. Wallis, J.I. Davies, J.R. Riffat and A.C. Marshall; Semicond. Sci. Technol. 3 (1988) 1136.
- [2] Carol I.H. Ashby, Kevin R. Zavadil, Arnold J. Howard, B.E. (Gene) Hammons; Appl. Phys. Lett. 64 (18), May (1994) 2388.
- [3] C. Heedt, F. Buchali, W. Prost, W. Brockerhoff, D. Fritzsche, H. Nickel, R. Losch, W. Schlapp, F.J. Tegude; IEEE Trans. elec. device, vol. 41, no. 10, (1994).
- [4] H. Sugahara, H. Oigawa, H. Shigekawa and Y. Nannichi; J. Appl. Phys. 69 (1991) 4349.
- [5] A.M. Green, W. Spicer; J. Vac. Sci. Technol. A 11(4) Jul/Aug (1993) 1061.
- [6] S. Habibi, M. Totsuka, J. Tanaka, T. Kinoshita, S. Matsumoto, S. Iida; J. Vac. Sci. Tech. B, April (1995).
- [7] H. Okabe; "Photochemistry of small Molecules", John Wiley & Sons, (1978).
- [8] N. Tong, K. Nummala, A. Kettensen, I. Adesida, C. Caneau, R. Bhat; IEEE electron device letters, vol. 13, no. 10, Oct. (1992).
- [9] N. Yoshida, M. Totsuka, S. Matsumoto; Appl. Phys. Lett. 39, No. 9, Sept. (1992).
- [10] T. Matsuoka, K. Taniguchi, C. Hamaguchi, and S. Sasa; Jpn. J. Appl. Phys. 29 (1990) 2017.

SULFUR-TREATED InP SURFACES STUDIED BY SOFT X-RAY PHOTOEMISSION SPECTROSCOPY

SB2.5

S. Maeyama, M. Sugiyama, S. Heun and M. Oshim
NTT Interdisciplinary Research Laboratories
3-9-11, Midori-cho, Musashino-shi, Tokyo 180, Japan

Introduction

Sulfur treatment with $(\text{NH}_4)_2\text{S}_x$ is regarded as an efficient surface passivation technique to reduce surface states on both GaAs(1) and InP(2). Although surface chemical bondings of sulfur-treated InP as well as GaAs have been studied by x-ray photoelectron spectroscopy (XPS), the S2p photoelectron spectra obtained by XPS are not necessarily understandable because the S2p peak is split into doublet peaks. In this study, we measured S1s photoelectron spectra by using synchrotron radiation soft x-rays, which have no spin-orbit splitting, to investigate the effect of water rinsing and the change in the sulfur chemical bond by annealing in vacuum after the $(\text{NH}_4)_2\text{S}_x$ -treatment.

Experimental

S-doped n-InP(100) wafers were used as sample substrates. One wafer was dipped into the $(\text{NH}_4)_2\text{S}_x$ solution and then blown with dry nitrogen gas before being loaded into a vacuum chamber. Another wafer was rinsed with deionized water after the $(\text{NH}_4)_2\text{S}_x$ -treatment. The S1s core-level photoelectron measurements were carried out by using 2.7 keV soft x-rays monochromatized by a pair of InSb(111) crystals at the NTT beamline (BL-1A) of the Photon Factory in the National Laboratory for High Energy Physics in Tsukuba, Japan(3). The measurements were done before and after annealing the two $(\text{NH}_4)_2\text{S}_x$ -treated samples with and without a water rinse at 400°C for 10 min in vacuum. Reflection high-energy electron diffraction (RHEED) patterns were recorded to obtain information about the surface structure of the samples before the photoelectron measurements.

Results and Discussion

RHEED patterns of the two samples with and without the water rinse after the $(\text{NH}_4)_2\text{S}_x$ -treatment are shown in Fig. 1. A comparison of them reveals that the rinse made the RHEED pattern clearer. When both samples were annealed in vacuum, the (2x1)

reconstruction reported in ref. (4) was not observed by our RHEED measurements. Although the RHEED patterns after annealing are not shown here, their patterns remained (1x1) structure and there was no difference between with and without the water rinse.

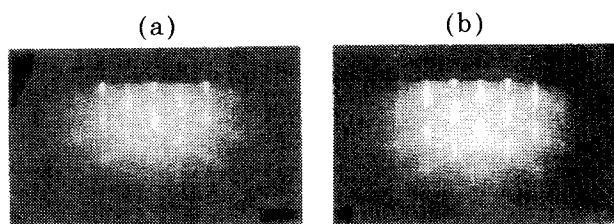


Fig. 1 RHEED patterns of InP(100) (a) without and (b) with rinsing by deionized water after $(\text{NH}_4)_2\text{S}_x$ -treatment.

Figure 2 shows S1s photoelectron spectra for the $(\text{NH}_4)_2\text{S}_x$ -treated InP(100) samples with and without the water rinse and before and after annealing. For comparison, S1s photoelectron spectra before annealing for $(\text{NH}_4)_2\text{S}_x$ -treated GaAs(100) samples with and without the water rinse are also shown in Fig. 3; these were measured in the same manner. The S1s peaks were deconvoluted by assuming four sulfur bonding states: S-In, S-P-In, S-S, and S-O for the $(\text{NH}_4)_2\text{S}_x$ -treated InP surface(4, 5), and S-Ga, S-As, S-S and S-O for the GaAs surface(6).

The S1s spectral change of the InP surface due to the water rinse was found more clearly than that of the GaAs surface. After rinsing the $(\text{NH}_4)_2\text{S}_x$ -treated surfaces with water, the S-O bonds were completely removed for the InP, but not for the GaAs surface, while the S-S bonds drastically decreased for both the InP and GaAs surfaces. This result appears to be consistent with the RHEED pictures of both the InP surfaces with and without the water rinse in Fig. 1. After the samples were annealed, only the S-In bonds were observed for both the annealed InP surfaces in spite of the bonding state being different before annealing. These S1s spectra suggest that annealing the $(\text{NH}_4)_2\text{S}_x$ -treated InP is necessary to complete the surface termination by the S-In bond, although the water rinse is more effective for removing the S-S and S-O bonds from the $(\text{NH}_4)_2\text{S}_x$ -treated InP surface than from the $(\text{NH}_4)_2\text{S}_x$ -treated GaAs surface. The effect of the water rinse on the InP surface is understood by considering the layered structure of the $(\text{NH}_4)_2\text{S}_x$ -treated InP surface indicated by a combined analysis with XPS and surface sensitive synchrotron photoemission spectroscopy: elemental sulfur and sulfur oxides remain on the layer of monosulfides and/or polysulfides(5).

References

- 1) Y. Nannichi, J.F. Fan, H. Oigawa and A. Koma, "Model to Explain the Effective Passivation of the GaAs Surface by $(\text{NH}_4)_2\text{S}_x$ Treatment", Jpn. J. Appl. Phys., Vol. 27, pp. L2367-2369, December 1988.
- 2) R. Iyer, R.R. Chang, A. Dubey and D.L. Lile, "The effect of phosphorous and sulfur treatment on the surface properties of InP", J. Vac. Sci. Technol. B, Vol. 6, pp. 1174-1179, Jul/Aug 1988.
- 3) T. Kawamura, S. Maeyama, M. Oshima, Y. Ishii, and T. Miyahara, "Solid surface analysis beamline BL-1A at the Photon Factory", Rev. Sci. Instrum., Vol. 60, pp. 1928-1931, July 1989.
- 4) D. Gallet and G. Hollinger, "Chemical, structural, and electronic properties of sulfur-passivated InP(001)(2x1) surfaces treated with $(\text{NH}_4)_2\text{S}_x$ ", Appl. Phys. Lett., Vol. 62, pp. 982-984, March 1993.
- 5) F. Maeda, Y. Watanabe and M. Oshima, "Surface chemical bonding of $(\text{NH}_4)_2\text{S}_x$ -treated InP(001)", Appl. Phys. Lett., Vol. 62, pp. 297-299, January 1993.

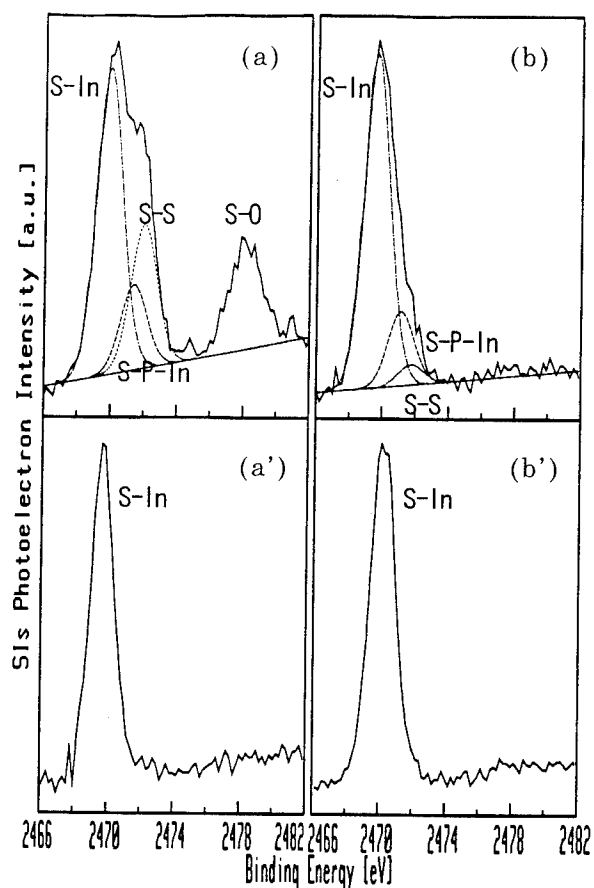


Fig.2 S1s photoelectron spectra for InP(100) (a) without and (b) with rinsing by deionized water after $(\text{NH}_4)_2\text{S}_x$ -treatment, and (a') and (b') then annealed in vacuum.

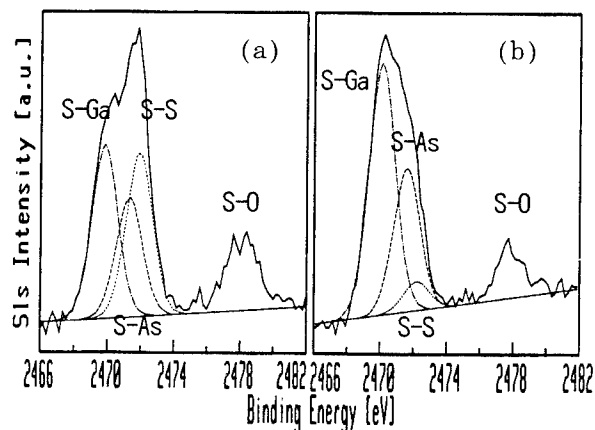


Fig.3 S1s photoelectron spectra for GaAs(100) (a) without and (b) with rinsing by deionized water after $(\text{NH}_4)_2\text{S}_x$ -treatment.

- 6) H. Sugahara, M. Oshima, H. Oigawa, H. Shigekawa, and Y. Nannichi, "Synchrotron radiation photoemission analysis for $(\text{NH}_4)_2\text{S}_x$ -treated GaAs", J. Appl. Phys., Vol. 15, pp.4349-4353, April 1991.

DEVELOPING MODELS OF OMVPE GROWTH FROM *IN SITU* X-RAY MEASUREMENTS

P.H. Fuoss^a, D.W. Kisker^b, G.B. Stephenson^b, S. Brennan^c

SA3.1

^aAT&T Bell Laboratories, Murray Hill, NJ 07974

^bIBM Research Division, Yorktown Heights, NY 10598

^cStanford Synchrotron Radiation Laboratory, Stanford, CA 94309

This paper summarizes our recent x-ray scattering and x-ray spectroscopy experiments looking at the organometallic vapor phase homoepitaxial growth of GaAs. The measured composition profiles and growth rates agree well with predictions by Jensen and coworkers for our reactor. Evidence for the presence of a partially decomposed trimethylgallium layer on the surface during growth at 500°C is presented. A schematic model of growth which includes the presence of this structurally ordered adsorbed layer is presented.

This paper summarizes our recent use of x-ray measurements to determine the atomic mechanisms of organometallic vapor phase epitaxy (OMVPE). Detailed information about OMVPE processes has been difficult to obtain because of the high pressure, chemically reactive environment present during growth. X-ray scattering measurements have been uniquely productive in determining the structure of surfaces during OMVPE growth. For example, we have studied surface smoothness, step ordering, growth modes, growth rates and surface reconstructions. In addition, x-ray spectroscopy measurements have revealed much about the complicated gas phase behavior in the OMVPE reactor. From these scattering and spectroscopy measurements, a more complete model of OMVPE growth is being developed.

The following will discuss some of our new results. First, we will show results profiling the concentration of the arsenic precursor as a function of height above the substrate. Next, growth modes and growth rates are determined by observing ≈ 1 Hz oscillations of the x-ray intensity from the (11 $\bar{1}$) crystal truncation rod near the 110 position. A careful analysis of these growth oscillations suggests that use of trimethylgallium (TMG) as a precursor leads to the adsorption of an organic group on the surface while use of triethylgallium does not. We believe that the desorption of this methyl group is the rate-limiting step in growth of GaAs using TMG.

Experimental Background

The experiments were performed using a purpose-built OMVPE reactors and a diffractometer in which high-quality semiconductor films can be grown while simultaneously allowing the diffraction of x-rays from the surface[1].

The substrates used for these measurements were GaAs(001) wafers 25 mm in diameter and 1 mm thick. For various experiments the wafers were misoriented by 0.25° along the (111)A, 0.25° along the (111)B, or were nominally singular ($<0.05^\circ$ in a random direction). After mounting in the reactor, the sample was annealed at 600°C in flowing

tertiarybutylarsine (TBAs) and H₂ until the surface was smooth as indicated by a sharp and intense 110 CTR. Typical partial pressures were 70 Torr of H₂ and 100 mTorr of TBAs. While under a continuous flow of TBAs, growth was started and stopped by switching either trimethylgallium (TMG) or triethylgallium (TEG) between the reactor and vent line.

X-ray Spectroscopy Measurements

A number of important growth characteristics of an OMVPE reactor are strongly influenced by the gas dynamics of the reactor. For example, growth uniformity is often controlled by flow patterns in the reactor, the temperature distribution controls the pyrolysis of the precursors, and switching of gas flows may limit the production of sharp interfaces and doping levels. Even though these parameters are crucial to the design of a successful reactor, they are difficult to control and even harder to predict. While much effort is being expended on improving modeling of reactor designs and performance, those efforts are limited by the availability of accurate data on existing designs. Data that would be useful include composition and temperature profiles of the gas phase, response of the reactor to transients and accurate measurements of growth rate for a wide range of conditions. X-ray absorption spectroscopy can be used to directly measure compositions in the gas phase.

We have made substantial progress on each of these three issues. As an example, Figure 1 shows the behavior of this signal as the reactor is moved vertically past the stationary synchrotron beam. The fluorescence rate, and hence the number density in the gas phase, is relatively constant at room temperature. At high temperature, the fluorescence rate falls off smoothly as the distance above the substrate is decreased. Since this fluorescence rate is a measure of the number density in the gas phase, it should increase smoothly above the surface simply because the gas density at constant pressure drops with increasing temperature.

Also shown in Figure 1 are computational fluid dynamics (CFD) calculations of the concentration gradients in our re-

actor under these conditions[2]. Clearly there is excellent agreement between the CFD predictions and our data. These calculations confirm that the dominate effect is heating of the gas stream. However, an interesting and unexpected result is the slight downturn in the concentration near the substrate for the room temperature data. This turns out to be due to a pinching effect from the purge flow used to eliminate window deposition.

X-Ray Scattering Measurements

Figure 2 shows the intensity of the 110 and the $\bar{1}10$ reflections as a function of time during two identical pulses of GaAs homoepitaxial growth. Considering the 110 data, the strong oscillations in the scattered x-ray intensity are obvious and correspond to the growth of one GaAs layer. It is possible to use these growth oscillations in much the same fashion as RHEED oscillations in MBE growth. For example, Figure 3 shows the growth rate as a function of TMG partial pressure for two different temperatures. While it was thought that the growth rate was proportional to the TMG partial pressure at these temperatures, these data clearly show that the growth rate is kinetically limited; probably by the decomposition of the TMG species on the surface.

The nature of the growth process using TMG can be further explored by examining the behavior of the CTR's during growth in more detail. In Figure 2, the behavior of the (110) and ($\bar{1}10$) CTR's during growth at 500°C are compared. Several differences between the two azimuths are clear in Figure 2: 1) the oscillations are much stronger at the (110) position, 2) there is a strong initial peak at the (110) and 3)

the weak oscillations at the ($\bar{1}10$) are out of phase with the (110) oscillations. It is interesting to note that none of this behavior is observed during growth using TEG, suggesting that the chemical processes associated with TMG are leading to this behavior.

Our preliminary analysis leads to a model where decomposition of a methylgallium species on the surface is the rate-limiting step. To see this, first consider a simple model in which the surface reconstruction is not a function of island morphology during growth. The intensities of the (110) and ($\bar{1}10$) reflections can be written as:

$$I_{110} \propto \left\{ \left[\frac{1}{2} (f_{As} - f_{Ga}) + f_{surface} \right] [1 - 2\Theta] \right\}^2 \quad (\text{EQ 1})$$

and

$$I_{\bar{1}10} \propto \left\{ \left[\frac{1}{2} (f_{As} + f_{Ga}) - f_{surface} \right] [1 - 2\Theta] \right\}^2 \quad (\text{EQ 2})$$

where $f_{surface}$ is the scattering factor of the atoms occupying the sites at the surface (which are Ga sites in this model), and Θ is the fraction of surface covered by bilayer-height islands (which runs from 0 to 1 as each bilayer is grown). The initial state under a flow of TBAs has a partial second layer of As. The occupancy of this layer is given by $f_{surface} = \sqrt{I_{110}/I_{\bar{1}10}} \approx 0.55$. This result is in qualitative agreement with previous crystallographic studies of this surface.

To understand the behavior of the data in Figure 2 as growth is initiated, we have developed a model shown in Figure 4. The initial starting surface, looking at (1) in Fig-

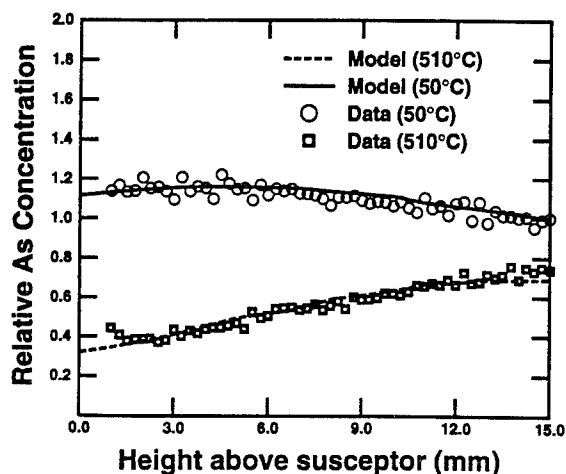


Figure 1: AsK α fluorescence from the gas phase as a function of height above the GaAs substrate. Note that the dependence at high temperature is much stronger than that at room temperature. This can largely be explained by temperature gradients in the gas phase.

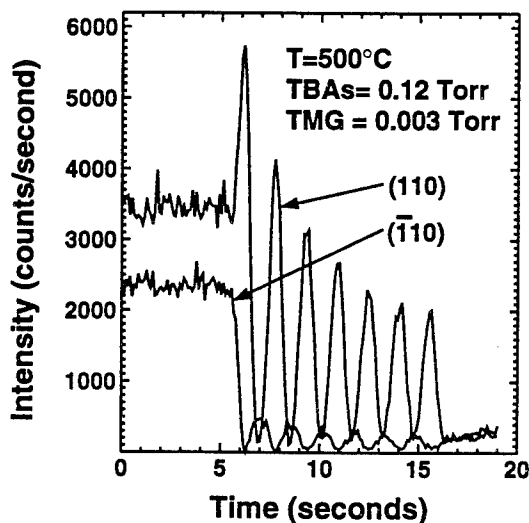


Figure 2: The CTR intensity oscillations for the (110) and ($\bar{1}10$) directions from a GaAs (001) surface during growth at 500°C using TBAs and TMG as the organometallic precursors.

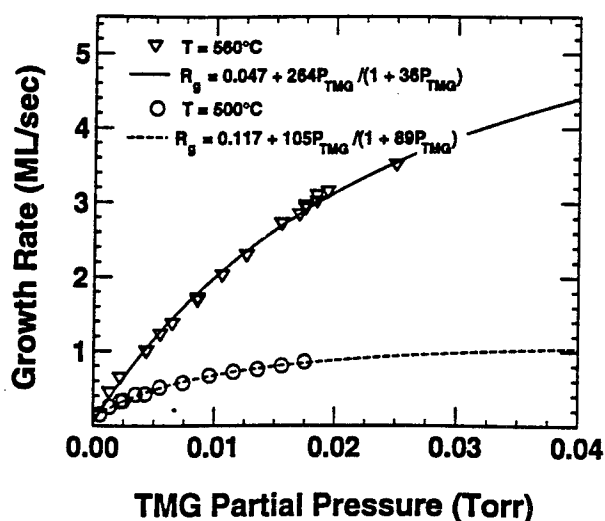


Figure 3: Growth rate as a function of TMG partial pressure for two different growth temperatures. The agreement with the Langmuir-Hinshelwood form (fits) shows that growth is limited by surface chemical reactions.

ure 4, has a partially completed extra layer of arsenic with a coverage of ≈ 0.55 adsorbed on what would normally be gallium sites [4]. We postulate that TMG is only partially decomposed at this temperature and that, at the beginning of growth a methylgallium species either displaces this adsorbed arsenic layer or completes the layer. In either case, looking at (2) in Figure 4, the methylgallium species scatters x-rays more strongly than either arsenic or gallium and enhances the scattering at the (110) position. Similarly, along the $(\bar{1}10)$ direction, the methylgallium species reduces the x-ray scattering by enhancing f_{surface} .

After the surface is saturated with methylgallium, the rate-limiting step for further growth is the desorption of the methyl radicals. As the organic desorbs, sites become available for arsenic and more methylgallium to attach. Such isolated atoms then coalesce into bilayer-height islands. As the island coverage Θ increases, the intensity at the (110) position decreases to zero and then increases, due to the final factor in equations (2-3). Each bilayer produces one oscillation in the intensity.

If the new islands formed on the surface were immediately terminated with the methylgallium species, the intensity of the $(\bar{1}10)$ CTR would oscillate weakly around zero but in-phase with the (110) CTR. There are many possible sources for the weak, out-of-phase $(\bar{1}10)$ scattering shown in Figure 2. For example, the surface of the islands could be saturated with arsenic more rapidly than with the methylgallium species (because of the much higher partial pressure of TBAs), or the edge of the islands might have a

different structure than the center, resulting in an average surface structure that oscillates as the island morphology oscillates. After the TMG source is turned off, the surface gradually returns to its pre-growth state.

This model is consistent with the non-linear growth rate dependence shown in Figure 3 and is supported by the greatly enhanced growth rate, at constant TMG flow, as the TBAs partial pressure is increased. Thus, we believe these results are strong evidence for saturation of the surface with a methylgallium compound during growth with TMG. It should be emphasized that similar effects are not seen under similar conditions using TEG. In that case there is no upward spike at the onset of growth, the growth rate is linear with TEG partial pressure and strong, in-phase oscillations are seen at both the (110) and $(\bar{1}10)$. These differences are consistent with the much different decomposition mechanisms of TMG and TEG.

Summary and Conclusions

In summary, we continue to use x-ray spectroscopy and scattering techniques to study the surface of a film growing in the chemically harsh, high pressure and high temperature environment of organometallic vapor phase epitaxy (OMVPE). The use of x-ray intensity oscillations to study growth rates and growth modes (in much the same way as RHEED analysis has been used in UHV techniques) has been used to study growth processes. In a simple example, we showed that the growth was kinetically limited by the decomposition of the TMG at 500°C and 560°C .

Finally, it is well established that x-ray diffraction techniques can be used to understand the surface structures present during growth[4-8]. In a significant difference from the MBE case where growth occurs on a $p(2 \times 4)$ reconstruction, we typically find either a $p(1 \times 2)$ or a $c(4 \times 4)$ reconstruction at lower growth temperatures and a lattice gas of As dimers terminating the surface at higher temperatures. We find little evidence that the presence of a well-defined reconstruction has any effect on growth kinetics and, in fact, see no change in the growth rate as we cross the well-defined phase transition boundary between the ordered phases and the As dimer lattice gas. However, the nature of these reconstructions is thought to control the shape of islands during growth and to influence the morphology of device structures during epitaxial regrowth[9]; and we are currently exploring the dependency of island size and shape as a function of reconstruction and V/III ratio. While not discussed here, x-ray diffuse scattering associated with these intensity oscillations can be used to probe correlations on the growing surface. Diffusion coefficients and activation energies can be extracted from these correlations and show that OMVPE growth is substantially different than MBE or MOMBE growth [10].

This work was performed in part at the Stanford Synchrotron Radiation Laboratory which is supported by the Department of Energy, Office of Basic Energy Sciences.

References

- ¹S. Brennan, P.H. Fuoss, J.L. Kahn, and D.W. Kisker, Nucl. Instrum. Methods Phys. Res., Sec. A, **291**, 86(1990).
- ²D.W. Kisker, T. Merchant, P.H. Fuoss, T.J. Mountziaris and K.F. Jensen, to be published.
- ³P.H. Fuoss, K.S. Liang and P. Eisenberger, *Synchrotron Radiation Research: Advances in Surface Science*, R.Z. Bachrach, Editor, Plenum Publishing Company, 388(1990)
- ⁴A. Payne, P.H. Fuoss, D.W. Kisker, G.B. Stephenson, S. Brennan, Phys. Rev. B, **49**, 14427(1994).
- ⁵F.J. Lamelas, P.H. Fuoss, D.W. Kisker, G.B. Stephenson, P. Imperatori and S. Brennan, Phys. Rev. B, **49**, 1957(1994).
- ⁶F.J. Lamelas, P.H. Fuoss, P. Imperatori, D.W. Kisker, G.B. Stephenson and S. Brennan, Appl. Phys. Letters, **61**, 1034(1992)
- ⁷D.W. Kisker, P.H. Fuoss, S. Brennan, G. Renaud, K.L. Tokuda and J.L. Kahn, J. of Crystal Growth, **101**, 42(1990)
- ⁸D.W. Kisker, G.B. Stephenson, P.H. Fuoss, F.J. Lamelas, S. Brennan and P. Imperatori, J. of Crystal Growth, **124**, 1(1992).
- ⁹H. Asai, J. of Crystal Growth, **80**, 425(1987).
- ¹⁰D.W. Kisker, G.B. Stephenson, P.H. Fuoss, and S. Brennan, to be published in J. of Crystal Growth, (1994).

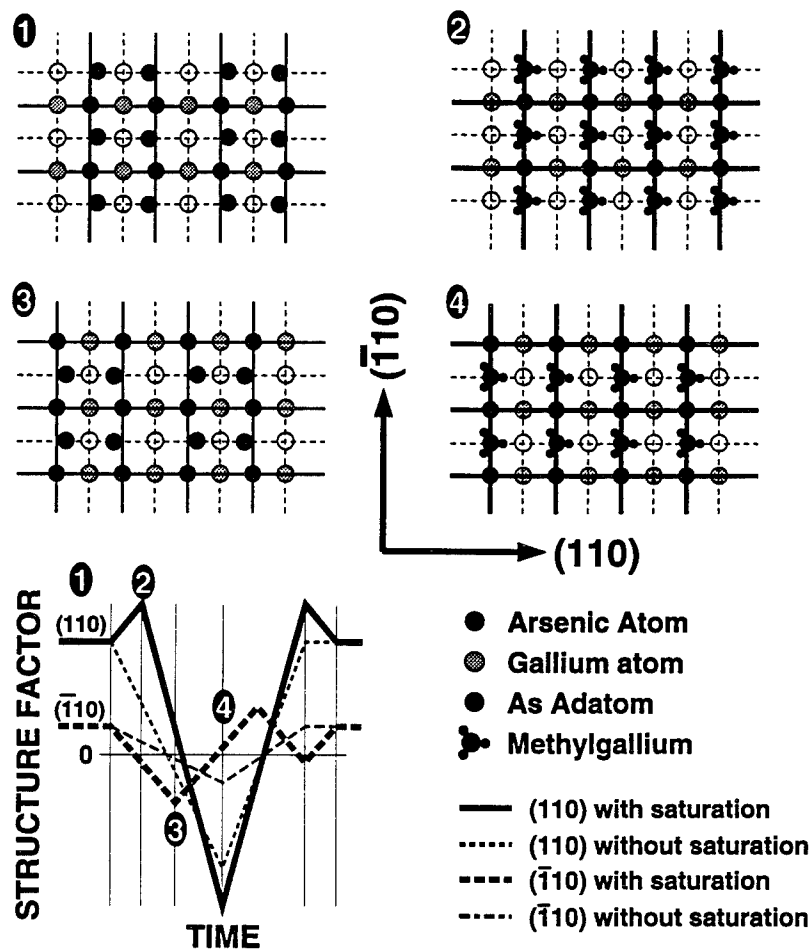


Figure 4: A schematic picture of the postulated growth process. Before the TMG source is turned on (1), the surface has an extra, partially filled layer of arsenic. When growth is started (2), this layer is replaced with a layer of partially-decomposed TMG. This layer then reacts with arsenic and forms islands with a partially filled layer of arsenic (3). These islands are slowly covered with methylgallium and coalesce to form a complete GaAs bilayer (4). At the conclusion of the growth cycle (when the TMG is turned off), the surface slowly recovers to the starting termination. In the real space views, the solid lines represent planes of heavy electron density while the dashed lines represent planes of low electron density.

Monolayer growth in InP/GaInAs quantum wells grown by selective area MOVPE

D. Ottenwälder, G. Frankowsky, M. Wild, O. Gfrörer, A. Hangleiter, F. Scholz

*4. Physikalisches Institut, Universität Stuttgart,
Pfaffenwaldring 57, D-70550 Stuttgart, Germany*

Introduction

Selective area epitaxy on partially masked substrates can be more and more considered as an indispensable tool for monolithic integration of optoelectronic devices [1]. In contrast to planar epitaxy on unmasked substrates, the properties of selectively deposited material depend on the mask pattern. Especially for selective area metalorganic vapor phase epitaxy (MOVPE) the local growth rate and In-content of $\text{Ga}_x\text{In}_{1-x}\text{As}_y\text{P}_{1-y}$ shows an increase towards the mask edges, which has particularly a strong effect on the optical properties of selectively grown quantum wells. Nevertheless, the local variation of the growth rate offers the opportunity to obtain a precise change of effective bandgap using an appropriate mask pattern. Integrated laser-modulator devices without butt coupling have already been successfully realized [1,2].

Furthermore, thickness fluctuations in very thin wells of only a few monolayers give rise to the "monolayer splitting" in luminescence experiments depending on the growth conditions [3-5]. Well known from planar epitaxy, quantum well interfaces seem to be degraded due to an As/P-exchange resulting in a redshift of the PL-spectra compared to atomically smooth interfaces. The local variation of the growth conditions in selective area MOVPE will result in a local change of interface quality over a wide range. Thus, a large variety of interface properties can be seen at a glance. Therefore, we used selectively deposited quantum wells grown under various conditions in order to gain more information about the mechanisms determining the interface quality.

Experimental

All samples were deposited by low-pressure MOVPE at 640°C using TMIn, TEGa, AsH₃ and PH₃ as precursors. A standard reactor pressure of 80mbar was used.

The (100)-oriented InP-substrates were coated with 100nm SiO₂ by electron-beam-evaporation. Periodically arranged stripe openings were defined by conventional photolithography and wet etching (period 600μm, opening width 400μm).

The selectively deposited structures consisted of a 75nm GaInAs reference layer followed by four quantum wells with thicknesses between 0.6 and 5nm separated by 20nm InP as barrier material. In most cases, a 5s H₂-purging step was used when switching between two materials to optimize the interface quality. The nominal thicknesses mentioned here always refer to planar-unmasked growth conditions.

The samples were examined by spatially and spectrally resolved cathodoluminescence (CL) at T=8K using a modified scanning electron microscope at 5-10keV. The measurement procedure consisted of

series of CL-spectra recorded along a linescan perpendicular to the stripe.

Results and discussion

a) Thick quantum wells ($d > 6\text{nm}$)

Fig.1 shows a CL-linescan of a thick quantum well of 5nm nominal thickness and a 75nm GaInAs reference layer. Both linescans show a continuous decrease of their CL-signal towards the edge of the mask. For the mask pattern used in these experiments, the energy shift of GaInAs-bulk layers was about 10meV.

Assuming gas phase diffusion of the growth species from masked substrate areas towards the openings [6], the variation of GaInAs-composition and local growth rate was calculated from planar data and shows a very good correspondence to the experimental data [7].

The comparison between our numerical simulations and experiments enabled us to determine a characteristic transport parameter D/k for different reactor pressures, as illustrated in Fig.2. The compositional

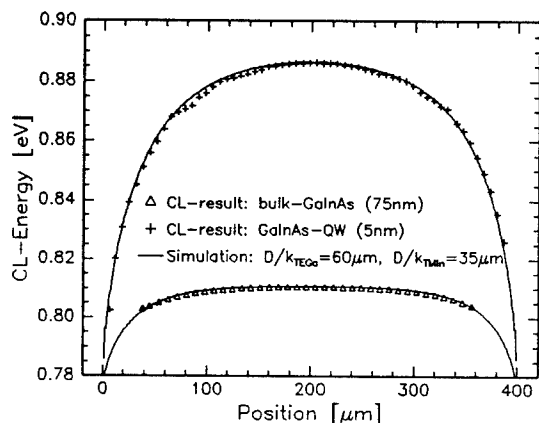


Fig. 1 CL-linescans and corresponding simulation results of selectively grown bulk-GaInAs and a 5nm quantum well. The spectra were recorded perpendicular to the stripe opening.

variation of selectively grown GaInAs seems not to depend on the V/III_{GaInAs}-ratio, chosen between 2 and 35.

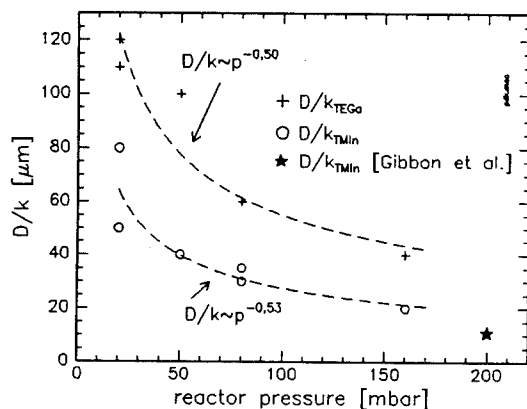


Fig. 2 Transport parameter D/k for TMIn and TEGa for different reactor pressures. The parameter D/k can be considered as some kind of an effective transport length for gas phase diffusion and incorporation.

b) Thin quantum wells ($d < 6\text{nm}$)

Fig.3 shows a survey of all CL-spectra of four quantum wells with nominal thicknesses of 0.6, 1.2, 3, 5nm, recorded along a linescan perpendicular to the stripe. Very thin quantum wells showed a terrace-like variation of their CL-energies with distance from the mask edge. In close vicinity to the edge of each terrace, the CL-intensity decreases, whereas the

luminescence of the next terrace increases. Depending on the growth conditions and mask dimension, each terrace is extended over several $10\mu\text{m}$.

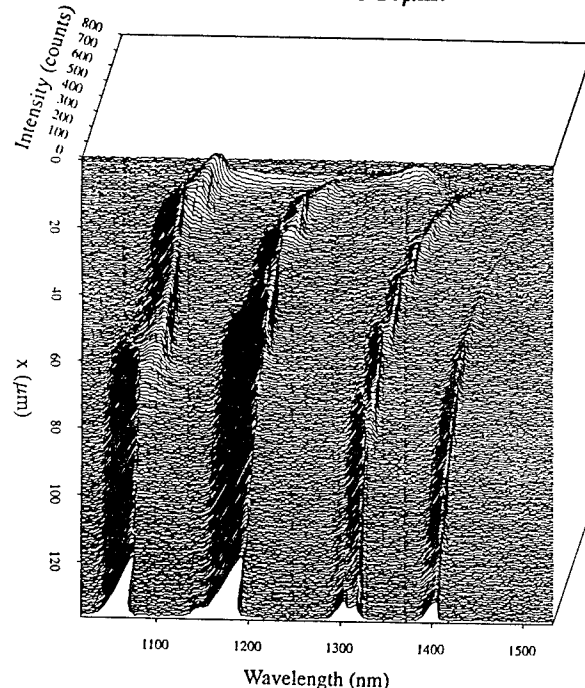


Fig. 3 Monolayer splitting in selectively deposited quantum wells recorded between the edge ($x=0$) and the center of a stripe opening.

We evaluated quantum well thicknesses from the energy of the CL-signals assuming an ideal rectangular potential well with finite barrier height. Taking the measured variation of composition into account, the thickness difference for adjacent CL-terraces is about one monolayer GaInAs, as demonstrated in Fig.4. The absolute value of the thickness in fractional values of monolayers (see Fig.4) must be explained with non-abrupt interfaces defining the quantum wells. An intermediate monolayer at one or both InP/GaInAs-interfaces due to the exchange of As and P can quantitatively explain the deviation from ideally abrupt quantum wells and a thickness of non-integer multiples of monolayers [3].

So we conclude, that the plateaus in CL-spectra can be related to monolayers. Only terrace steps corresponding to a thickness difference of one monolayer have been detected, indicating that the steps are formed at one of the two InP/GaInAs interfaces.

Obviously, surface transport processes responsible for the formation of this interface configuration are of growing importance when decreasing the thickness of quantum wells.

To influence terrace formation during MOVPE

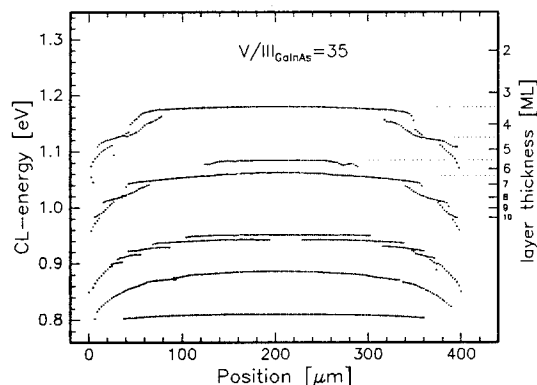


Fig. 4 Terrace-like variation of luminescence for quantum wells (nominal thickness 0.6, 1.2, 3, 5nm) and bulk-GaInAs.

growth, we studied the influence of several epitaxy parameters. A decrease in V/III-ratio and reactor pressure resulted in a disappearance of terrace structure, as illustrated in Fig.5 and 6, respectively.

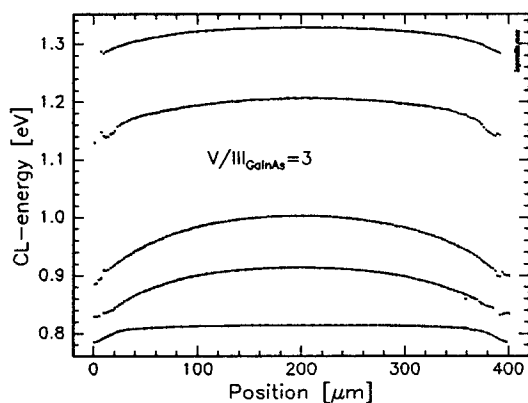


Fig. 5 CL-linescan of 4 quantum wells and bulk-GaInAs grown under identical growth conditions, as compared to Fig.4.

Except: $V/III_{GaInAs} = 3$

The remaining shift in energy, especially of the thinnest quantum well in Fig.5 and 6 is too small to be caused by monolayer fluctuations. The small linewidth for the thin quantum wells in Fig.5 and 6 suggests, that a lateral variation of the interface roughness on a much smaller scale compared to the exciton radius ("microroughness", Ref.[8]) must be responsible for the continuous energy shift. Even for well defined monolayer terraces, the CL-energy within one terraces is not accurately constant, as can

be seen from the outer terraces near the mask edges. Therefore we assume, that a microscopic interface

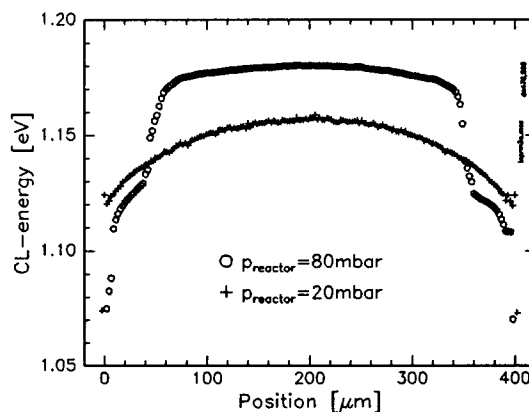


Fig. 6 CL-linescans of 0.6nm quantum wells grown at different reactor pressures

roughness having a length scale significantly below the exciton radius is superimposed on discrete monolayer steps. A slight change in local growth rate results in a variation of the heterojunction roughness. To gain further insight into the mechanisms responsible for the lateral distribution of monolayer steps, we studied the influence of growth interruptions when switching from one material system to the other. Fig.7 demonstrates the effect of an increased H_2 -purging time at both interfaces $InP \rightarrow GaInAs$ and $GaInAs \rightarrow InP$.

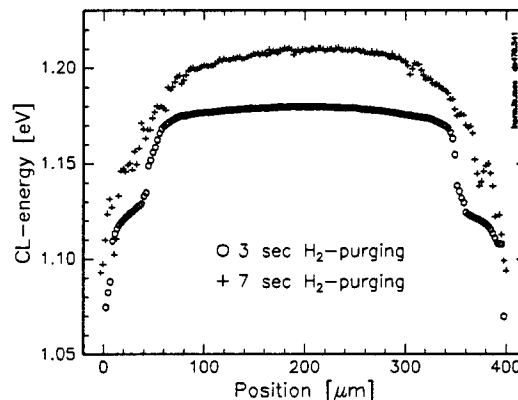


Fig. 7 Influence of H_2 -purging at both interfaces on luminescence. CL-linescan of 0.6nm quantum wells.

Similar to the results in planar epitaxy, an extended H_2 -purging results in a blueshift of quantum well luminescence [3]. Furthermore, monolayer terrace formation is suppressed under these conditions. Asymmetric growth interruptions should clarify,

which interface gives rise to the monolayer steps. We started experiments with AsH₃-purging at the upper (GaInAs→InP) and the lower interface (InP→GaInAs).

Fig. 8 shows CL-scans of three samples, grown without AsH₃-purging as reference, with 5sec AsH₃-purging at the lower and 5s AsH₃-purging at the upper interface. The V/III-ratio of 7 for GaInAs-growth was chosen rather low to inhibit terrace formation.

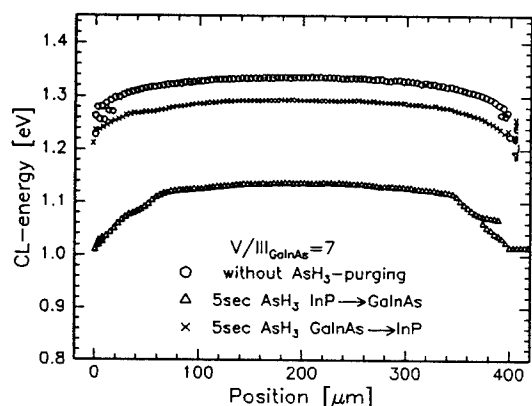


Fig. 8 CL-linescans of 0.6nm quantum wells. Influence of AsH₃-purging at the upper and lower interface (InP→GaInAs). Only scan (Δ) shows a step-like shape.

Additional AsH₃-supply at the lower interface results in a strong redshift and regain of monolayer steps. The equivalent AsH₃-supply at the upper interface doesn't seem to have such a strong influence. We conclude that the lower interface might be crucial for the generation of terrace-steps. Nevertheless, our experiments have so far not been able to prove, whether the monolayer steps are located at the upper or lower interface. Earlier experiments [3] indicated that monolayer steps might be located at the upper interface. Appropriate experiments with growth interrupts will provide more information.

Summary

In summary, we investigated optical properties of selectively deposited quantum wells. As expected for selective MOVPE, composition and growth rate of bulk layers and quantum wells with thicknesses above 6nm are determined by gas phase diffusion. Thin quantum wells ($L_z < 6\text{nm}$) showed a clearly visible thickness variation in monolayer steps. The monolayer steps are extended at least over several 10 μm

depending on the mask pattern. Their formation can be influenced by the growth conditions, especially growth interruptions at the heterointerfaces. Based on our recent experiments, the lower interface (InP→GaInAs) is supposed to be crucial for the generation of monolayer steps.

Acknowledgement

We thank S. Buckner, S. Nagel, P. Burkard and H. Gräbeldinger for valuable assistance. This work has been supported by the Deutsche Forschungsgemeinschaft (DFG).

References

- [1] E. J. Thrush, J. P. Stagg, M. A. Gibbon, R. E. Mallard, B. Hamilton, J. M. Jowett, E. M. Allen; *Mater. Sci. Eng.* **B21** (1993) 130
- [2] T. Kato, T. Sasaki, K. Komatsu, I. Mito; *Electron Lett.* **28** (1992) 153
- [3] K. Streubel, V. Härle, F. Scholz, M. Bode, M. Grundmann, *J. Appl. Phys.* **71** (1992) 3300
- [4] W. Seiffert, D. Hessman, X. Liu, L. Samuelson; *J. Appl. Phys.* **75** (1994) 1501
- [5] D. Grützmacher; *J. Cryst. Growth* **107** (1991) 520
- [6] M. Gibbon, J. P. Stagg, C. G. Cureton, E. J. Thrush, C. J. Jones, R. E. Mallard, R. E. Pritchard, N. Collins, A. Chew; *Semicond. Sci. Technol.* **8** (1993) 998
- [7] F. Scholz, D. Ottenwälder, M. Eckel, M. Wild, G. Frankowsky, T. Wacker, A. Hangleiter; *J. Cryst. Growth* **145** (1994) 242
- [8] C. A. Warwick, R. F. Kopf; *Appl. Phys. Lett.* **60** (1992) 386

High-mobility Ga_{0.47}In_{0.53}As/InP heterostructure by atmospheric-pressure MOVPE using cyclopentadienyl indium

M. Usuda, K. Sato and R. Takeuchi

Showa Denko K.K. Chichibu Works

K. Onuma and T. Udagawa

Showa Denko K.K. Chichibu Research Laboratory

1505 Shimokagomori, Chichibu, Saitama 369-18, JAPAN

Lattice matched Ga_{0.47}In_{0.53}As/InP heterostructure was grown by atmospheric-pressure MOVPE reaction system using monovalent cyclopentadienyl indium (C₅H₅In). The heterointerface characteristics were evaluated using double crystal X-ray diffraction method and wedge TEM technique. The reaction system gave $\Delta a/a = 2.95 \times 10^{-4}$ accompanied with smooth mirror-like surface. The abrupt Ga_{0.47}In_{0.53}As/InP heterointerface was also given. The lattice matched heterostructure showed electron mobilities of $\mu_{300K} = 12700 \text{ cm}^2/\text{Vs}$ at $n_{s,300K} = 4.2 \times 10^{11} \text{ cm}^{-2}$ and $\mu_{77K} = 108000 \text{ cm}^2/\text{Vs}$ at $n_{s,77K} = 3.9 \times 10^{11} \text{ cm}^{-2}$.

1. INTRODUCTION

Lattice matched Ga_{0.47}In_{0.53}As/InP heterostructure has been applied to key materials as millimeter-wave electronic and optical communication devices.

Metalorganic vapor phase epitaxy (MOVPE) method is one of promising techniques to obtain the heterostructure. Metalorganic VPE of indium based layers under atmospheric-pressure has, however, serious polymerization problem between group V hydrides and conventional trialkylindium precursors, such as trimethylindium ((CH₃)₃In) and triethylindium ((C₂H₅)₃In) [1-4].

Previous paper has been reported that monovalent cyclopentadienyl indium (C₅H₅In) is promising indium precursor for atmospheric-pressure growth of InP [5]. Cyclopentadienyl In decomposes readily to metallic indium and cyclopentadiene (C₅H₆) around 250°C [5] and has attractive features as follows:

- 1) Lewis basic nature which allows to prevent polymerization with Lewis base PH₃.
- 2) Rare carbon contaminator for the resultant layers because of thermal stability of C₅H₆.

In this paper, Ga_{0.47}In_{0.53}As/InP heterostructure is grown by atmospheric-pressure MOVPE using monovalent C₅H₅In and characterized.

2. EXPERIMENTAL

GaInAs/InP heterostructure was grown on the (100) mirror surface of Fe-doped InP substrate by atmospheric-pressure MOVPE at 570-640°C. The heterostructure was consisted of 4000 Å GaInAs and 1000 Å InP. Phosphine (10% in H₂) and AsH₃ (10% in H₂) were used as Group V sources. In the growth, C₅H₅In was kept at 50°C and was carried with 120 SCCM of Pd-purified H₂ into quartz reactor equipped with RF heating system. The H₂ transporting gas was kept at 6 SLM. Flow rates of gases were adjusted precisely using He-leak-tight mass-flow controllers. These conditions gave a growth rate of about 25 nm/min.

The lattice match between Ga_{0.47}In_{0.53}As and InP layers was characterized using double crystal X-ray diffraction method and wedge TEM technique. The uniformity in electron mobility of 2" Φ Ga_{0.47}In_{0.53}As/InP heterostructure wafer was measured using array of Hall element possessing Au/Ni/AuGe ohmic contact.

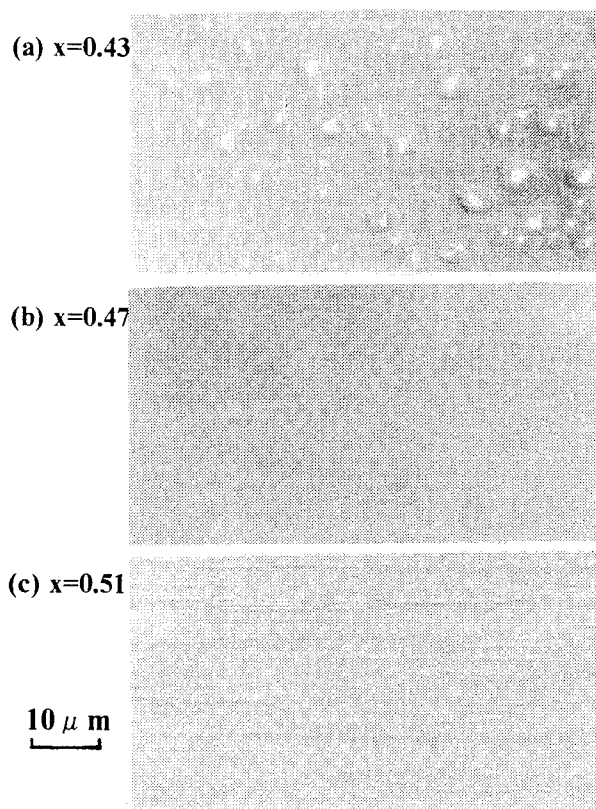


Fig. 1. Nomarski interference photographs of $\text{Ga}_x\text{In}_{1-x}\text{As}/\text{InP}$ heterostructure at various Ga composition (x). (a) $x=0.43$, (b) $x=0.47$ and (c) $x=0.51$.

3. RESULTS AND DISCUSSION

3-1. Crystallographic Characterization of $\text{Ga}_{0.47}\text{In}_{0.53}\text{As}/\text{InP}$ Heterostructure

Figure 1 shows Nomarski interference photographs of $\text{Ga}_x\text{In}_{1-x}\text{As}/\text{InP}$ heterostructure at various Ga composition (x). Gallium composition was evaluated based on the lattice constant by double crystal X-ray diffraction measurement. The surface morphology was drastically changed with Ga composition. Extremely smooth mirror-like surface was obtained at $x=0.47$ (Fig. 1-b). X-ray diffraction pattern at the composition indicated the heterointerface fairly gave lattice matched structure with $\Delta a/a = 2.95 \times 10^{-4}$ as shown in Fig. 2. Contrary to this, mirror-like surface was difficult to obtain

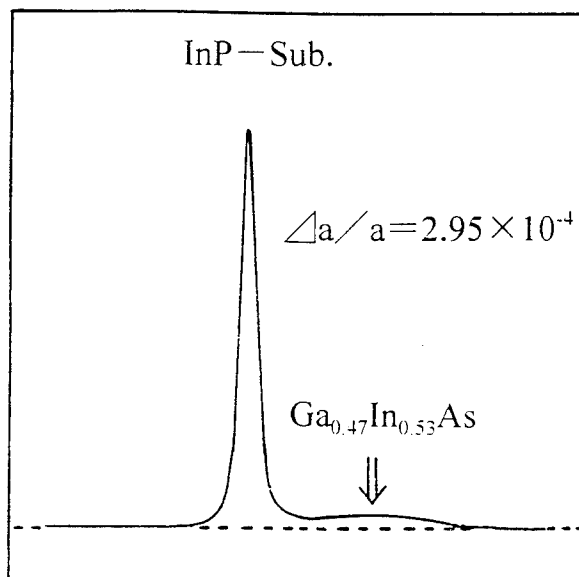


Fig. 2. X-ray diffraction pattern of $\text{Ga}_{0.47}\text{In}_{0.53}\text{As}/\text{InP}$ heterostructure.

at the region far from $x=0.47$. The surface with circular hillocks was obtained at $x=0.43$ (Fig. 1-a). At $x=0.51$, cross-hatched pattern was observed (Fig. 1-c).

Figure 3 shows the $\text{Ga}_{0.47}\text{In}_{0.53}\text{As}/\text{InP}$ heterostructure interface revealed by wedge TEM technique. The heterointerface have superior abruptness without presence of obvious interface strain.

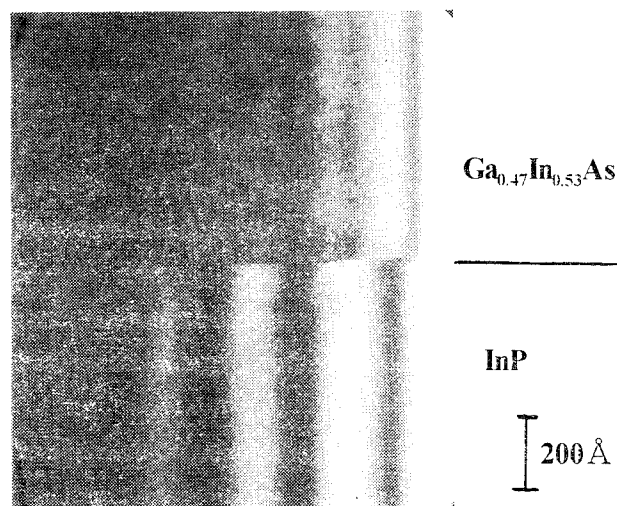


Fig. 3. Wedge TEM photograph for the interface of $\text{Ga}_{0.47}\text{In}_{0.53}\text{As}/\text{InP}$ heterostructure.

Table 1. Electrical properties of $\text{Ga}_{0.47}\text{In}_{0.53}\text{As}/\text{InP}$ heterostructure grown by atmospheric-pressure reaction system using $\text{C}_5\text{H}_5\text{In}$.

Layer No.	Mobility(cm^2/Vs)		Sheet Carrier Concentration(cm^{-2})	
	300K	77K	300K	77K
1	11500	80000	6.4×10^{11}	8.0×10^{11}
2	10500	70000	5.0×10^{11}	6.9×10^{11}
3	10000	76000	9.3×10^{11}	7.0×10^{11}
4	9000	74000	2.4×10^{12}	1.2×10^{12}
5	12700	108000	4.2×10^{11}	3.9×10^{11}

3-2. Electrical Properties of $\text{Ga}_{0.47}\text{In}_{0.53}\text{As}/\text{InP}$ Heterostructure

Electrical properties were evaluated by Hall effect measurements utilizing Van der Pauw geometry and Hall element array.

Table 1 summarizes the electrical properties of $\text{Ga}_{0.47}\text{In}_{0.53}\text{As}/\text{InP}$ heterostructure obtained by Van der Pauw method. The compensation ratio, $K=(N_D+N_A)/(N_D-N_A)$, were calculated based on the theoretical relations between mobility for electrons and free electron concentration in $\text{Ga}_{0.47}\text{In}_{0.53}\text{As}$ at 300K [6]. The compensation ratio of $\text{Ga}_{0.47}\text{In}_{0.53}\text{As}/\text{InP}$ heterostructure ranged between 1 and 2. The relatively lower compensation ratio may probably due to the less carbon contamination in the $\text{Ga}_{0.47}\text{In}_{0.53}\text{As}$ layer.

The maximum mobility was $\mu_{300\text{K}}=12700 \text{ cm}^2/\text{Vs}$ at $n_{s,300\text{K}}=4.2 \times 10^{11} \text{ cm}^{-2}$ and $\mu_{77\text{K}}=108000 \text{ cm}^2/\text{Vs}$ at $n_{s,77\text{K}}=3.9 \times 10^{11} \text{ cm}^{-2}$ as listed in Table 1.

The uniformity in electron mobility of $\text{Ga}_{0.47}\text{In}_{0.53}\text{As}/\text{InP}$ heterostructure was measured utilizing Hall element array with $400 \mu\text{m}$ pitch as shown in Fig. 4. The mobility had homogeneous distribution over 2 inch diameter wafer (Fig. 5). The heterostructure epitaxial wafer gave the average mobility of $9150 \text{ cm}^2/\text{Vs}$ at $n_s=7 \times 10^{11} \text{ cm}^{-2}$. Coefficient of variation in mobility was 0.2%.

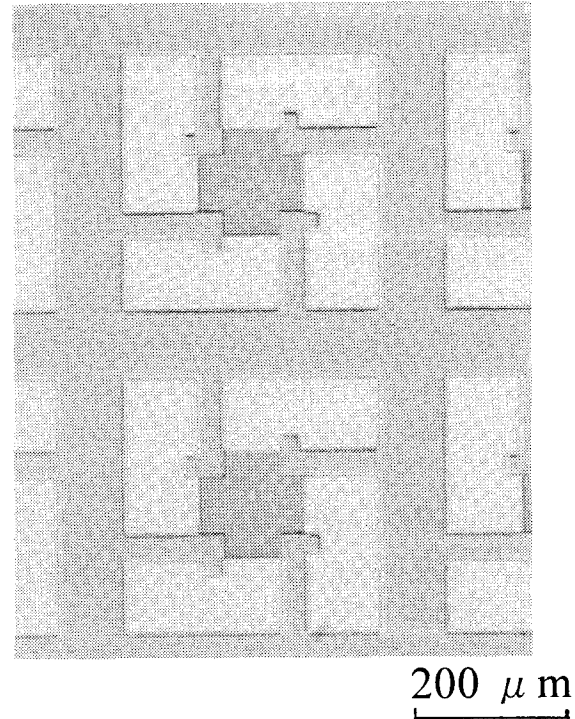


Fig. 4. Microscopic photograph of Hall-element array with $400 \mu\text{m}$ pitch.

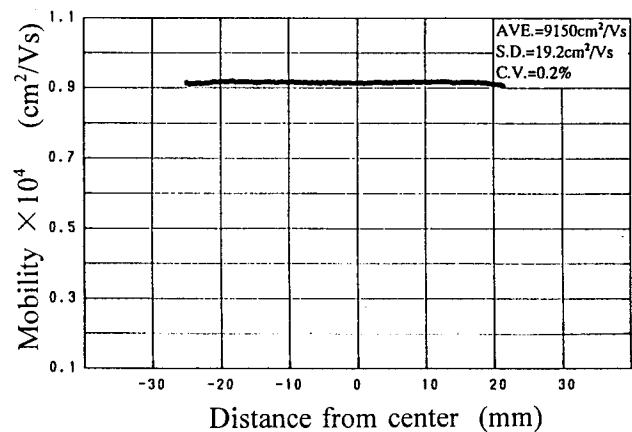


Fig. 5. Uniformity in electron mobility of 2" ϕ $\text{Ga}_{0.47}\text{In}_{0.53}\text{As}/\text{InP}$ heterostructure.

A Hall effect device fabricated utilizing the high mobility characteristics also gave high product-sensitivity of 870 V/AT. The obtained sensitivity is maximum value for $\text{Ga}_{0.47}\text{In}_{0.53}\text{As}/\text{InP}$ heterostructure Hall effect device reported so far [7] .

4. CONCLUSION

The atmospheric pressure MOVPE system using monovalent $\text{C}_3\text{H}_3\text{In}$ has potential advantage for high quality $\text{Ga}_{0.47}\text{In}_{0.53}\text{As}/\text{InP}$ heterostructure with abrupt heterointerface. The reaction system allows to give both high electron mobility over 9000 cm^2/Vs and homogeneous mobility distribution.

5. ACKNOWLEDGEMENT

The authors would like to acknowledge Prof. Dr.Y.Kuniya (Chuo University) for helpful discussions.

6. REFERENCES

1. R.Didchenko, J.E.Alix and R.H.Toeniskoetter, J. Inorg. Nucl. Chem. **Vol. 14**, p. 35, 1960.
2. H.M.Manasevit and W.I.Simpson, J.Electrochem. Soc., **Vol. 120**, p. 135, 1973.
3. B.J.Baliga and S.K.Ghandhi, J.Electrochem. Soc. **Vol. 122**, p. 683, 1975.
4. J.S.Whiteley and S.K.Ghadhi, J.Electrochem. Soc., **Vol. 129**, p. 383, 1982.
5. K.Onuma, A. Kasahara, K. Kato, N. Aihara, and T. Udagawa, J. Cryst. Growth, **Vol.107**, p. 360, 1990.
6. Y.Takeda, GaInAsP alloy Semiconductors Ed. by T.P.Pearsall (J. Wiley & Sons, New York, 1982), p.213.
7. R.Kyburz, J.Schmid, R S.Popovic and H.Melchior, IEEE Trans. Electron Devices, **Vol. ED-41(3)**, p. 315, 1994.

Selective MOVPE growth of InGaAsP and InGaAs using TBA and TBP

Y.Sakata, T.Nakamura, S.Ae, T.Terakado, Y.Inomoto, T.Torikai and H.Hasumi

ULSI Device Development Laboratories, KANSAI Electronics Research Laboratory

NEC Corporation

2-9-1 Seiran, Ohtsu, Shiga, 520, Japan

Introduction

Tertiarybutylarsine (TBA) and Tertiarybutylphosphine (TBP) are promising precursors as the substitute for Arsine (AsH_3) and Phosphine (PH_3), because of their low toxicity and high decomposition efficiency leading to excellent controllability of group-V composition[1]. On the other hand, selective MOVPE growth technology is one of the most attractive method to realize integrated MQW waveguide devices, such as DFB-LD/ EA modulator integrated light source [2][3], because the in-plane bandgap of MQW can be controlled only by changing a dielectric mask geometry [2][3][4]. However, unintentional compositional change is also introduced into barriers and SCH layers in the MQW waveguide, which results in complicated bandgap control and the net strain increase. In this paper, we have demonstrated selective MOVPE growth of InGaAs(P) using TBA / TBP for the first time, and shown the difference from conventional selective growth using AsH_3 / PH_3 . Finally, we proposed the selectively grown MQW structure to overcome the above mentioned problem.

Experimental procedure

MOVPE growth was performed in a horizontal reactor at a temperature of 625°C and a pressure of 75Torr. Trimethylindium(TMIn) and Triethylgallium (TEGa) were used as group- III source materials. (a) TBA, TBP and (b) AsH_3 , PH_3 were used as the group-V source materials. Typically 100nm thick SiO_2 film was deposited on a (100) just oriented Sn-doped InP substrate by atmospheric CVD method. Then a pair of SiO_2 mask stripes was patterned by a conventional photolithography technique and wet etching with buffered HF solutions. The mask stripe width W_m was varied from 4 to $22\mu\text{m}$ and the open stripe width W_o was fixed to $2\mu\text{m}$. These stripes were formed in the [011] directions. This stripe mask pattern was formed on considering direct waveguide formation by epitaxy without etching process [2][5]. A ridge InP /InGaAs(P) /InP DH structures were grown on the open stripe region. Typical growth rates on unmasked area are $0.5\mu\text{m/h}$ for InP, $0.4\mu\text{m/h}$ for InGaAs and InGaAsP.

SEM observations were used for evaluating the selective growth structure and growth rate. Micro-

probe Photoluminescence (PL) measurements at room temperature were used for estimating the bandgap wavelength of selectively grown layers, where Ar laser beam was focused to a $1\mu\text{m}$ in diameter with exciting light power density of 60kW/cm^2 .

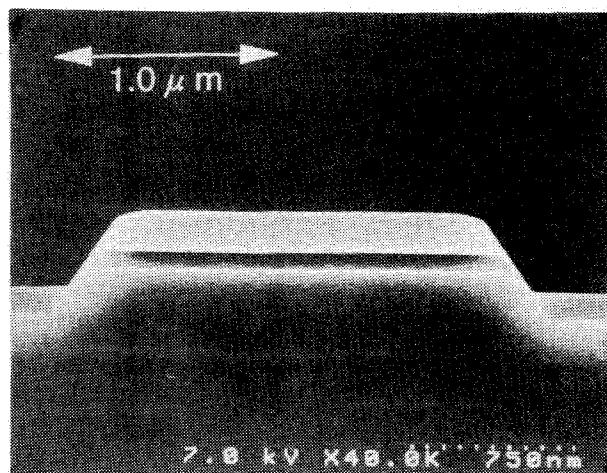


Figure 1. A cross section SEM photograph of selectively grown InP/InGaAs/InP ridge structure using TBA/TBP

Structure of selectively grown layer

The SEM cross section for selectively grown InP/InGaAs/InP layers using TBA and TBP is shown in Fig.1. Smooth interfaces surrounded by (100) top surface and (111)B side facets were realized, and no edge growth was observed. This structure is as excellent as the conventional selective MOVPE growth using AsH_3/PH_3 [4][5]. Furthermore, no polycrystal was appeared on the SiO_2 masks.

Compositional changes of selectively grown layers

The PL wavelength shifts versus W_m , for several composition of InGaAs(P), was shown in Fig.2. In this figure, wavelength shifts were defined as the PL wavelength shift from the minimum mask width ($W_m=4\text{ }\mu\text{m}$) region. Every InGaAs(P) were grown by using TBA/TBP. They show the PL wavelength shift toward longer side with increasing W_m . These wavelength shifts were caused by growing compressive strained (In-rich) InGaAs(P). This feature is explained as long diffusion length and fast incorporation of indium-containing species rather than gallium-containing species [6]. The wavelength shift (composition change) is increasing with longer bandgap-wavelength InGaAs(P). This behavior can be explained by following mechanism. The short bandgap-wavelength InGaAsP has a large indium content at the initial state, therefore, it is hard to increase the indium content, compared with the long bandgap-wavelength InGaAs(P).

Figure 3 shows the PL wavelength of selectively grown InGaAsP as a function of W_m , comparing the selective growth using (a)TBA/TBP and (b) AsH_3/PH_3 . PL wavelength shifted toward longer side with increasing W_m for both (a)TBA/TBP and (b) AsH_3/PH_3 . These wavelength shifts were mainly brought by the indium-increasing mechanism. The PL wavelength shift of the (a)TBA/TBP grown InGaAsP was less than that of the (b) AsH_3/PH_3 grown InGaAsP. This difference was occurred by the high decomposition rate or fast incorporation rate of indium-containing species with the presence of AsH_3/PH_3 .

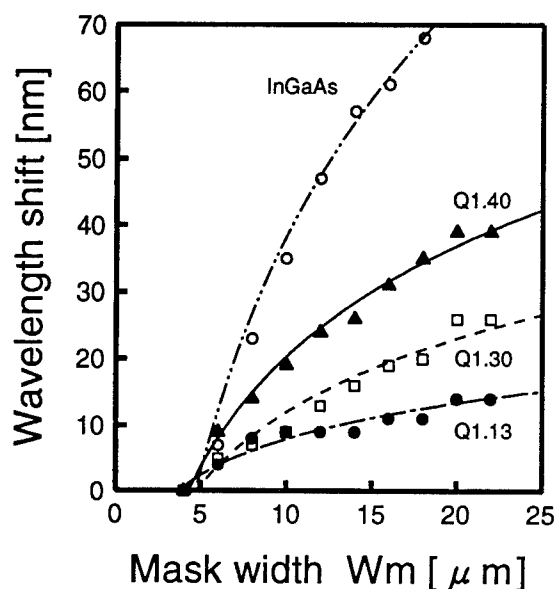


Figure 2. PL wavelength shift of selective grown InGaAs(P) from the minimum mask width ($W_m=4\text{ }\mu\text{m}$) as a function of W_m , for several composition InGaAs(P). Q means InGaAsP (Quaternary), and the numbers show the bandgap wavelength at unmasked region. All InGaAs(P) were grown by using TBA/TBP.

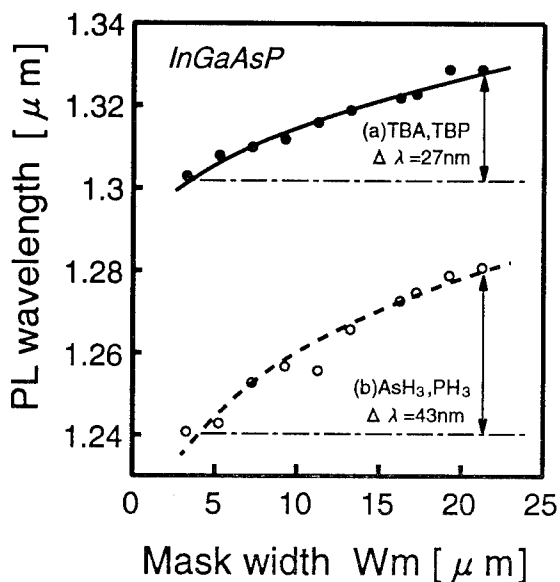


Figure 3. PL peak wavelength of selective grown InGaAsP versus W_m , comparing (a)TBA/TBP and (b) AsH_3/PH_3 . V/III ratio is 90 for both (a) and (b).

In Fig.3, both InGaAsP grown by (a)TBA/TBP and (b)AsH₃/PH₃ were used the same TMIn, TEGa flow rate, however, PL wavelength at unmasked area of (b)AsH₃/PH₃ was about 60nm shorter than that of (a)TBA/TBP. This phenomenon means that, AsH₃/PH₃ caused the high decomposition or fast incorporation of In-containing species, compared with TBA/TBP.

The wavelength shift also strongly depends on the vapor phase lateral diffusion length (L_d) of group-III source materials on the mask region. The growth rate of selectively grown layer is a function of L_d and W_m . We measured the relationship between growth rate and W_m to investigate the L_d .

Growth rate enhancement and vapor phase lateral diffusion length

The normalized growth rate (d/d_0) of selectively grown InGaAsP using both (a)TBA/TBP and (b)AsH₃/PH₃ are shown in Fig4. In this figure, one can see that there are two modes of growth rate enhancement. The former appears in $W_m < 4 \sim 5 \mu\text{m}$ region and indicates the effect of surface migration from SiO₂ masks[7]. The latter appears in $W_m > 4 \sim 5 \mu\text{m}$ region and shows the effect of the vapor phase lateral diffusion. The effect of surface migration is very small, so that, we considered only the vapor phase lateral diffusion effect. In Fig.4, the experimental data were adjusted by the following approximate equation, which is based on a consideration of one dimensional vapor phase lateral diffusion.

$$d/d_0 = 1 + k \cdot (W_m - 4) \cdot \exp\{-(W_m - 4)/2L_d\},$$

where L_d is the vapor phase lateral diffusion length of group-III species, and k is the adjustable parameter related to the incorporation rate, respectively. This calculation is available for the effect of lateral vapor phase diffusion, so that, the starting point was set on $W_m = 4 \mu\text{m}$. From this result, L_d of (a)TBA/TBP growth is smaller than that of (b)AsH₃/PH₃ growth. To make clear the origin of L_d difference, InGaAs(P) was selectively grown using TBA/TBP or AsH₃/PH₃ with several V/III ratios. The dependence of L_d on the V/III ratio is summarized in Fig.5. In this figure, L_d of

(a)TBA/TBP is smaller than that of (b)AsH₃/PH₃ at a given V/III ratio. Because TBA and TBP have higher decomposition efficiency, there are a lot of group-V radicals (such as AsH₂, AsH, PH₂, PH) on the crystal and SiO₂ mask surfaces. These radicals reduce the mean free path of group-III sources, and lead to a parasitic reaction. Therefore, L_d decreased with higher V/III ratio.

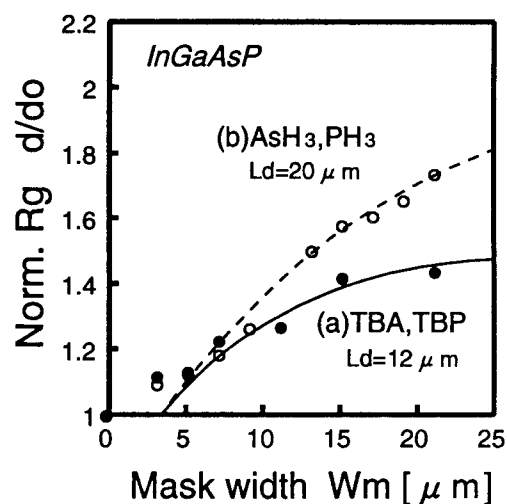
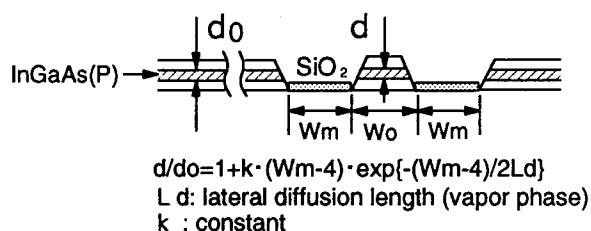


Figure 4. Schematic cross section of selectively grown layer (upper), and Normalized growth rate of InGaAsP against the W_m . V/III ratio is 90 for both (a)TBA/TBP and (b)AsH₃/PH₃. The solid and dashed lines are fitting curves as a parameter of L_d .

Application

Vapor phase lateral diffusion length L_d , using TBA/TBP, can be widely controlled over the wide range of V/III ratio, even in the low V/III ratio. This feature enables to relieve the problem of the selective MOVPE grown MQW waveguide structure, which has unintentional composition and thickness changes in barriers and SCH layers. In

other words, selectively grown MQW waveguide, which consists of the well layers grown by TBA/TBP with lower V/III ratio and the barrier / SCH layers grown by those with higher V/III ratio, has the advantage of improving the bandgap controllability and reducing the net strain of MQW, simultaneously.

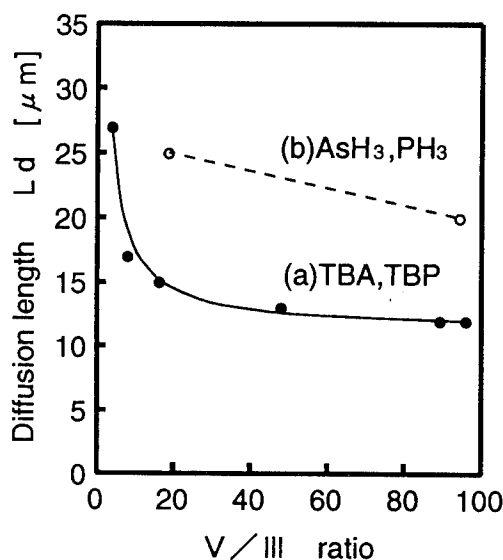


Figure 5. Dependence of lateral diffusion length on V/III ratio for (a) TBA/TBP and (b) AsH₃/PH₃.

Conclusion

Selective MOVPE growth of InGaAs(P) on mask-patterned InP substrate using TBA/TBP was investigated for the first time. Selective growth was achieved with no polycrystal on the SiO₂ masks. Several compositions of InGaAs(P) were selectively grown and the bandgap wavelength shifts were evaluated against the mask width. Larger wavelength shift was observed with longer bandgap wavelength InGaAs(P). From the measurement of growth rate enhancement, vapor phase lateral diffusion length was estimated for several InGaAs(P) with various V/III ratio. It was made clear that lateral diffusion length of group-III species using TBA/TBP can be widely controlled over the wide range of V/III ratio, even in the low V/III ratio. From this feature, the selective MQW growth using TBA/TBP have more

excellent bandgap controllability than that using AsH₃/PH₃, so that it is extensively expected to realize the high performance integrated MQW optical waveguide devices.

Acknowledgments

The authors would like to thank M. Kamoshida, H. Kohzu, H. Abe and T. Uji for their continuous encouragement, and Y. Sasaki, T. Morimoto, T. Mastumoto and T. Sasaki, for helpful discussions.

References

- [1] S. Ae, T. Terakado, T. Nakamura, T. Torikai and T. Uji, "Low threshold $\lambda = 1.3 \mu\text{m}$ multiquantum well laser diodes grown by metalorganic vapor phase epitaxy using tertiarybutylarsine and tertiarybutylphosphine precursors" *J. Cryst. Growth*, **145**, pp.852-857 (1994)
- [2] T. Kato, T. Sasaki, K. Komatsu and I. Mito, "DFB-LD/Modulator integrated light source by band-gap energy controlled selective MOVPE" *Electron. Lett.* **28**, pp.153-154 (1992)
- [3] M. Aoki, M. Suzuki, H. Sano, T. Kawano, T. Ido, T. Taniwatari, K. Uomi and A. Takai, "InGaAs/InGaAsP MQW electroabsorption modulator integrated with a DFB laser fabricated by band-gap energy control selective area MOCVD" *IEEE J-QE*, **29**, pp.2088-2096 (1993)
- [4] T. Sasaki, M. Kitamura and I. Mito, "Selective metalorganic vapor phase epitaxial growth of InGaAsP/InP layers with bandgap energy control in InGaAs/InGaAsP multiple-quantum well structures" *J. Cryst. Growth*, **132**, pp.435-443 (1993)
- [5] T. Sasaki and I. Mito, "Selective MOVPE growth for photonic integration circuits" *Tech. Dig. of OFC/IOOC'93*, ThK1, pp.210-212 (1993)
- [6] Y. D. Galeuchet and P. Roentgen, "Selective area MOVPE of GaInAs/InP heterostructures on masked and nonplanar (100) and {111} substrates" *J. Cryst. Growth*, **107**, pp.147-150 (1991)
- [7] K. Yamaguchi and K. Okamoto, "Lateral supply mechanism in selective metalorganic chemical vapor deposition", *Jpn. J. Appl. Phys.*, **32**, pp.1523-1527 (1993)

Reduced Lattice Distortion in and near Strain-compensated InGaAs/InGaAsP Multiple-quantum Well Structures Grown by Metal-organic Vapor Phase Epitaxy on GaAs Substrates

K. Hiramoto, M. Sagawa, and T. Toyonaka*

Central Research Laboratory, *Fiberoptics Division, Hitachi Ltd.

1-280, Higashi-koigakubo, Kokubunji-shi, Tokyo 185, Japan

Abstract

We have investigated strain-compensated InGaAs/InGaAsP multiple-quantum well (MQW) structures grown by metal-organic vapor phase epitaxy on (001) GaAs substrates, by using photoluminescence (PL) measurements and transmission electron microscopy (TEM). It was found that the lattice distortion in and near the MQW structures caused by compressive strain in InGaAs wells was reduced far below the levels of ordinary InGaAs/GaAs MQW structures when tensile-strain InGaAsP barriers were introduced. Furthermore we have fabricated 0.98- μm laser diodes (LDs) with the strain-compensated QW active layer, and found that the mean time to failure of such LDs is expected to be three to four times longer than that of LDs with ordinary GaAs barriers.

Introduction

Recently, strain-compensated multiple quantum well (MQW) structures have attracted much attention as the active layers of semiconductor laser diodes (LDs) [1-3]. It has been reported that the maximum number of QWs and maximum strain in the QWs that can be attained without causing misfit dislocations can be increased by strain compensation [3], which has improved device properties [1-3]. However, there have been few reports which study the effect of strain compensation on the reliability of semiconductor laser diodes (LDs) [4]. Furthermore, many of these studies dealt with MQWs grown on InP substrates, and there have been few reports on strain-compensated MQWs on GaAs substrates [5]. In this study, we grew strain-compensated QWs consisting of compressive-strain InGaAs wells and tensile-strain InGaAsP barriers (hereafter referred to as strain-compensated InGaAs/InGaAsP QWs) on GaAs substrates, and studied the effect of strain compensation on the reduction of the

lattice distortion in and near the strained MQWs by using photoluminescence (PL) measurements and transmission electron microscopy (TEM). Furthermore, we fabricated 0.98- μm LDs with a strain-compensated InGaAs/InGaAsP QW active layer, and found that the mean time to failure (MTTF) of such LDs is expected to be three to four times longer than that of LDs with conventional GaAs barriers.

Experiments

In_{0.2}Ga_{0.8}As/InGaAsP and In_{0.2}Ga_{0.8}As/GaAs MQW structures were grown on (001) GaAs substrates by metal-organic vapor phase epitaxy (MOVPE). The growth temperature was 650°C and the growth pressure was 40 torr. Triethylgallium (TEGa), trimethylindium (TMIn), arsine (AsH₃), and phosphine (PH₃) were used as source materials. For PL measurements and cross-sectional TEM analysis, 70-nm-thick GaAs buffer layers, 170-nm-thick In_{0.48}Ga_{0.52}P layers lattice-matched to the GaAs substrates, the active layers, and

In_{0.48}Ga_{0.52}P layers were grown successively after the substrates were heated to the growth temperature in an AsH₃ atmosphere. PL measurements were carried out at room temperature using the 514.5-nm line of an argon-ion laser. To evaluate the lattice mismatch ($\Delta a/a$) between the GaAs substrates and the InGaAsP barriers, 70-nm-thick InGaAsP layers were grown on the substrates. The lattice mismatch was measured by X-ray diffraction.

Figure 1 shows the strain-compensated MQW structure. 5-nm-thick InGaAsP layers were inserted between the InGaP layers and the active layers to avoid InGaP/GaAs interfaces. Four types of barriers were studied. The $\Delta a/a$ of these barriers are listed in table 1. The QWs were In_{0.2}Ga_{0.8}As layers which were compressively strained on GaAs substrates with a lattice-mismatch of about 1.4%. The InGaAs layers are 7-nm thick; below the theoretical value of critical-layer thickness (about 15 nm) [6]. The thickness of the InGaAsP and GaAs barriers was 8 nm.

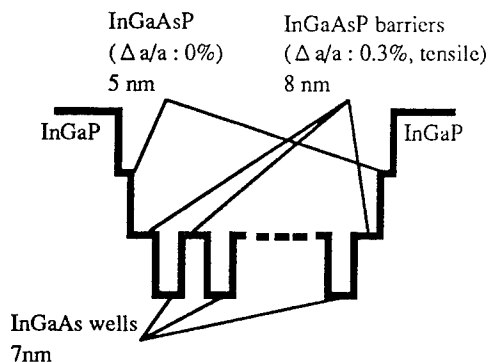


Fig. 1 Schematic figure of the strain-compensated MQW structure. $\Delta a/a$ is lattice mismatch between the barriers and GaAs. The vertical direction shows comparative bandgap energies.

Table 1 Materials of barriers and $\Delta a/a$ between the barriers and GaAs.

	material	$\Delta a/a$
a	GaAs	—
b	InGaAsP	0%
c	InGaAsP	0.3%, tensile
d	InGaAsP	0.6%, tensile

Results and discussion

Photoluminescence properties

Figure 2 shows the dependence of the peak PL intensities of the QW structures with the four types of barriers on the QW number. For each case, when the number of QWs was small, PL intensities strengthened as the number of QWs increased, because of the enlarged light-emitting region. However, in the case of MQWs with GaAs barriers, the PL intensity dropped when the well number exceeded 3, and cross-hatch patterns appeared on the samples when the well number exceeded 2 as indicated by shadow in the figure. On the other hand, when InGaAsP ($\Delta a/a$: 0%) barriers were used, PL intensities increased until the number of QWs exceeded 7, and no cross-hatch pattern was seen on the samples with the well number below 5. As the InGaAsP ($\Delta a/a$: 0%) was almost lattice-matched to GaAs, this result shows that dislocations are more easily created in GaAs than in InGaAsP. Furthermore, no cross-hatch patterns or decreased PL intensities were seen for MQWs with either 0.3 or 0.6% tensile-strain barriers, even in the case of 15 QWs. This shows that, by strain compensation, the maximum number of QWs without cross-hatch patterns on the samples can be increased; by more than 7 and 3 times larger than those in the case of GaAs barriers and InGaAsP ($\Delta a/a$: 0%) barriers, respectively.

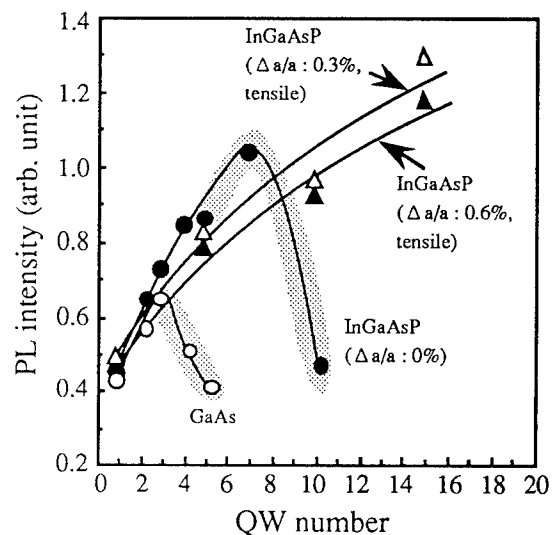


Fig. 2 Dependence of PL intensities of InGaAs/GaAs and InGaAs/InGaAsP QW structures on well number.

Cross-sectional TEM analysis

Figure 3 shows cross-sectional TEM photographs of an InGaAs/GaAs single QW structure. Figures 3 (a) and (b) are the photographs of the same sample at the same position, except that in the case of Fig. 3 (b), the electron beam was applied to the sample at an angle at which thickness fringes are not observed. In Fig. 3 (a), thickness-fringe bending is seen over more than 10-nm-thick region in GaAs layers. On the other hand, the InGaAs/GaAs interface region is about 1-nm thick, as can be seen in Fig. 3 (b). Therefore, this thickness fringe bending is due to lattice distortion in GaAs layers.

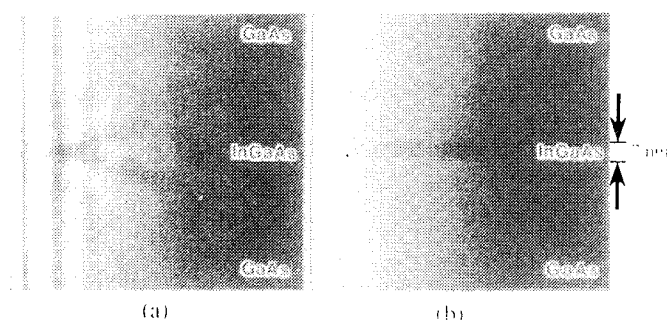


Fig. 3 Cross-sectional TEM photographs of an InGaAs/GaAs strained QW structure.

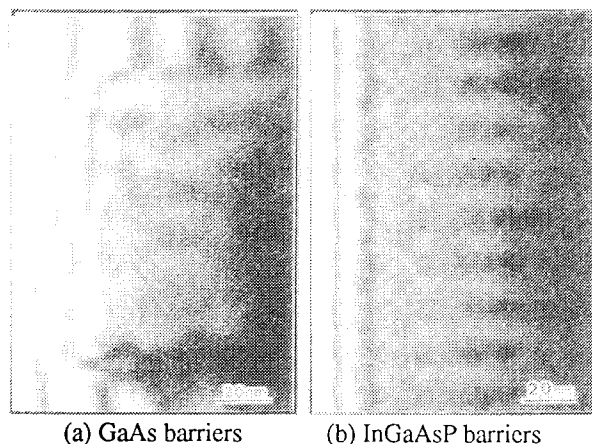


Fig. 4 Cross-sectional TEM photographs of InGaAs strained QW structures with GaAs barriers (a), and InGaAsP ($\Delta a/a$: 0.3%, tensile) barriers (b).

Figure 4 (a) and (b) are cross-sectional TEM photographs of InGaAs strained MQW structures with GaAs barriers and InGaAsP barriers ($\Delta a/a$: 0.3%, tensile), respectively. The number of QWs is 5 for Fig. 4 (a) and 15 for Fig. 4 (b). In Fig. 4 (a), strong thickness-fringe bending in GaAs barriers can be seen as in Fig. 3 (a). On the other hand, in the case of InGaAsP barriers, almost no thickness-fringe bending is seen (Fig. 4 (b)), and the lattice distortion in the MQW structure is thought to be reduced in the case of InGaAsP barriers.

Figures 5 (a) and (b) are the wide view photographs of Fig. 4 (a) and (b), respectively. In Fig. 5 (a), thickness-fringe bending due to lattice distortion is seen in regions more than 100-nm thick in the InGaP layers near the MQW layers. On the other hand, in Fig. 5 (b), no thickness-fringe bending is seen, although the number of QWs is three times larger than that in Fig. 5 (a). This means that the lattice distortion near the MQW structure is reduced by the reduction of average strain in the strain-compensated MQW structure.

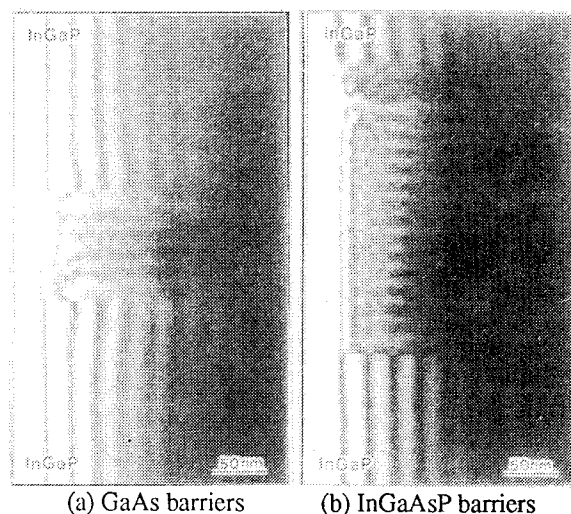


Fig. 5 Cross-sectional TEM photographs of InGaAs strained QW structures with GaAs barriers (a), and InGaAsP ($\Delta a/a$: 0.3%, tensile) barriers (b).

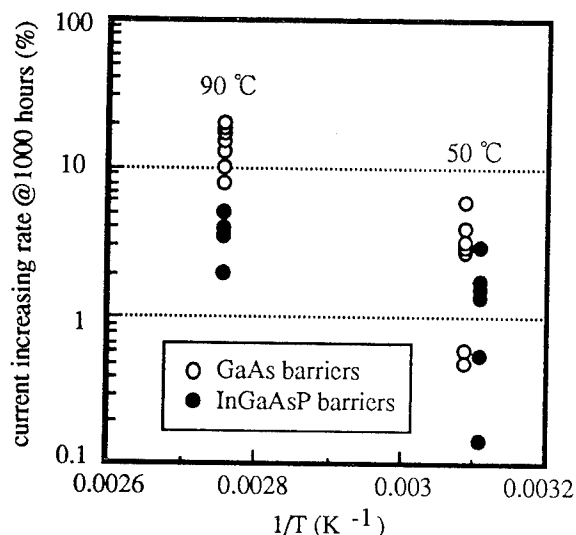


Fig. 6 Increase in percent of 0.98- μm laser drive current at 1000 hours for a constant optical power output of 100 mW at temperatures of 50 and 90°C. The horizontal axis shows the reciprocal of the environmental temperatures.

Reliability of 0.98- μm LDs

To study the effect of strain compensation on the reliability of 0.98- μm LDs, we fabricated two types of LDs: one with tensile-strain InGaAsP barriers ($\Delta a/a$: 0.3%) and the other with GaAs barriers. For both structures, the active layers had a single QW. The LD structures are described elsewhere [7]. Figure 6 shows the increase in percent of these LDs' drive current (ΔI) at 1000 hours for a constant optical power output of 100 mW at temperatures of 50 and 90°C. For both temperatures, the ΔI s of the LDs with InGaAsP barriers are three to four times smaller than with GaAs barriers. This means the mean time to failure (MTTF) of these LDs with tensile-strain InGaAsP barriers is three to four times longer than with ordinary GaAs barriers. This improvement in reliability can be attributed to the reduction of lattice distortion by the strain compensation.

Conclusion

To investigate the effect of strain-compensation on the crystal quality of strained InGaAs MQW structures on GaAs substrates, we grew strain-compensated QWs with compressive-strain InGaAs wells and tensile-strain

InGaAsP barriers on GaAs substrates by MOVPE. By PL measurements and cross-sectional TEM analysis, it was found that lattice distortion in and near the QWs can be reduced by introducing tensile strain InGaAsP barriers.

Furthermore, we have found that the MTTF of 0.98- μm LDs with tensile-strain InGaAsP barriers is expected to be three to four times longer than that of those with ordinary GaAs barriers. This means that the reduction of lattice distortion by strain compensation leads to the improvement of 0.98- μm LDs, and also shows that strain compensation is a good way of achieving high reliability in strained QW LDs.

Acknowledgement

The authors wish to thank R. Tsuneta for TEM analysis, and also thank Dr. H. Kakibayashi for helpful discussions.

References

- [1] C. P. Seltzer, S. D. Perrin, M. C. Tatham and D. M. Cooper, *Electron. Lett.* 28, No. 1 (1992) 63.
- [2] D. Varga, O. Kjebon, U. Ohlander, K. Streubel, J. Wallin, S. Lourdudoss, T. Klinga, B. Broberg and G. Landgren, *Proceedings of 6th Int. Conf. on InP and. Rel. Mat.*, Paper WP22, (1994) 473.
- [3] T. Takiguchi, K. Goto, M. Takemi, A. Takemoto, T. Aoyagi, H. Watanabe, Y. Mihashi, S. Takamiya and S. Mitsui, *Proceedings of 7th Int. Conf. on Metalorganic Vapor Phase Epitaxy*, Paper P3-6 (1994) 276.
- [4] C. P. Seltzer, S. D. Perrin, M. J. Harlow, R. Studd and P. C. Spurdens, *Electron. Lett.* 30 (1994) 227.
- [5] G. Zhang and A. Ovtchinnikov, *Appl. Phys. Lett.* 62 (1993) 1644.
- [6] J. W. Matthews and A. E. Blakeslee, *J. Crystal Growth* 27 (1974) 118.
- [7] M. Sagawa, K. Hiramoto, T. Toyonaka, K. Shinoda and K. Uomi, *Electron. Lett.* 30 (1994) 1410.

NEW QUANTUM FUNCTIONAL DEVICES
--Present Status and Future Prospects of RHET Technology--

SB3.1
(Invited)

N. Yokoyama, S. Muto, K. Imamura, M. Takatsu, T. Mori,
Y. Sugiyama, Y. Sakuma, H. Nakao, and T. Adachihara

Fujitsu Limited, Fujitsu Laboratories Ltd.
Morinosato-Wakamiya, Atsugi 243-01, Japan

Recent research in semiconductor device technology seems to be aimed at reducing costs and decreasing power dissipation, rather than developing new and advanced semiconductor devices. I believe however, that the need to reduce device sizes will continue, even into the next century. When devices enter the nanometer scale, quantum mechanical effects play an important role in the device's function; therefore, it is important to continue basic research in this area to cultivate these new "nanoelectronic" devices.

Recent quantum effect nanometer-scale devices can be divided into three categories.

- 1) Quantum wave devices, which use the electron-wave transport and control the phase of the electron wave.
- 2) Quantum functional devices, which use quantum effects, such as size and tunneling effects in ultrafine structures.
- 3) Atomic or molecular devices, which use the motion of the atom or molecule.

Single electron devices could be included in quantum functional device category. This paper reviews our research activities on quantum functional devices and discusses our future research direction.

RHET Technology

In 1985, we proposed and demonstrated a Resonant-tunneling Hot Electron Transistor, or RHET [1], which uses a resonant-tunneling barrier as an electron injector. When a particular voltage is applied to the base, the resonant-tunneling effect injects electrons from the emitter to the base. Electrons that survive scattering in the base region and reach the collector make up the collector current. When the base voltage increases further, the resonant-tunneling is less and the collector current decreases; therefore, the RHET exhibits a negative transconductance. Using this RHET, we decreased the number of transistors needed in full adders to about one fourth that of conventional bipolar circuits. The RHET could be called the first functional quantum effect device.

Although this RHET circuit used fewer transistors, it used many resistors. To overcome this drawback, we developed a double-emitter RHET [2][3]. The double-emitter RHET shown on the right in Fig. 1 is essentially the same as the RHET on the left, but it has separate emitters and no base electrodes.

Under normal bias conditions in the conventional RHET, electrons in the emitter are injected into the base layer. Electrons scattered in the base region, drain to the base electrode. The

double-emitter RHET turns on when the voltage difference between the emitters exceeds a certain threshold, that is the sum of the emitter barrier's forward and reverse turn-on voltages. The low potential emitter works as an injector of electrons and the high potential emitter works as a sink for scattered electrons, like the base contact of conventional RHETs. Thus, the emitter plays a different role depending on its potential. When the two emitters have the same potential, either both high or both low, the RHET goes off.

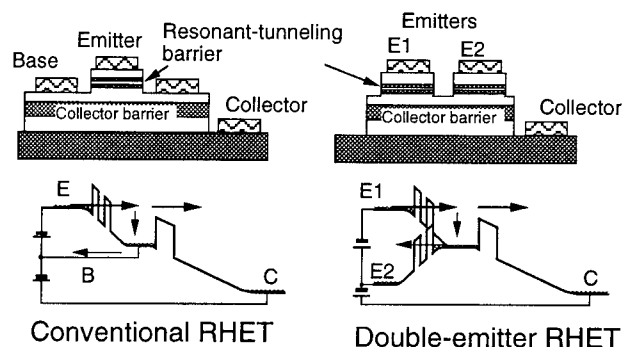


Fig. 1 RHET structures & band diagrams

We plotted the characteristics of a double-emitter RHET with different voltages V_{EE} applied between two emitters (Fig. 2). Bold solid curves indicate the I-V characteristics of the emitter E_1 . The E_1 turns on when a voltage V_{th} is supplied to this emitter. The emitter current peaks at V_p and reaches a minimum at V_v . The lighter solid line is the load line used to determine the operating points with an open collector.

When V_{EE} exceeds the sum of the emitter barrier's V_{th} values (Fig. 2(a)), the emitters turn on and electrons are injected from E_1 into the base layer. With positive collector voltages, the collector current flows. Electrons scattered in the base region pass through E_2 , which acts as a sink for electrons, much like the base electrode in a conventional RHET. Band diagram in this operation is shown on the right bottom in Fig. 1. Hence, the emitter electrode works as both an emitter and a base depending on its potential. Since the transistor does not need a base contact, the fabrication process is easier and the device structure more flexible than that for a single-emitter RHET. The emitter mesa etching tolerance increases and the base layer's range of acceptable thicknesses and doping levels is wider.

As V_{EE} increases, the emitter current increases and peaks at around $2V_p$, see Fig. 2(b). When V_{EE} increases further, both emitters enter nonresonant states, shown in Fig. 2(c), where S_1 and S_2 [2] are in bistable states.

Logic Circuits Using Multi-Emitter RHETs [3]

Figure 3 compares XNOR gates using a conventional RHET and double-emitter RHET. The conventional RHET XNOR gate needed three resistors for an input-voltage adder. In the new circuit, we can feed the input signals directly to the emitters and take the collector voltage as the output. The output is high when the multi-emitter RHET is off. This condition is satisfied only when both inputs are the same logic level. When one input is low and the other high, the potential difference between the two electrodes exceeds the threshold, and the transistor turns on. The output then goes low. This indicates that the circuit acts as an XNOR gate.

We then examined a triple-emitter RHET structure, shown in Fig. 4. We fed three input signals to the three emitters and took the collector voltage as the output. The output is high when the triple-emitter RHET is off. This condition is satisfied only when all the inputs are the same

logic level. When a low level and a high level input occur together, the potential difference between the two electrodes exceeds the threshold and the transistor turns on, bringing the output low. The circuit's logic is described as $ABC + \bar{A}\bar{B}\bar{C}$, and it functions as three input AND/NOR gate. Since the subtraction of input voltages is done in the transistor, no external elements except a load resistor are needed. We can also increase the number of emitters.

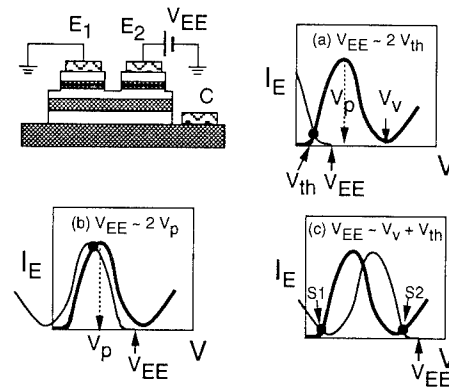


Fig. 2 Operation of double-emitter RHET

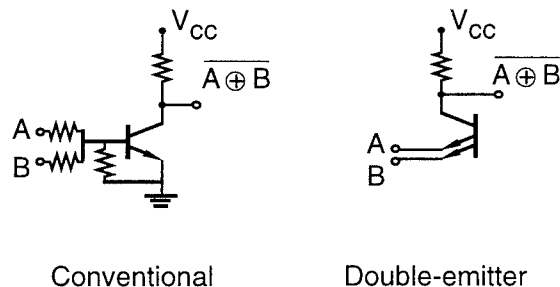


Fig. 3 Comparison of RHET XNOR gates

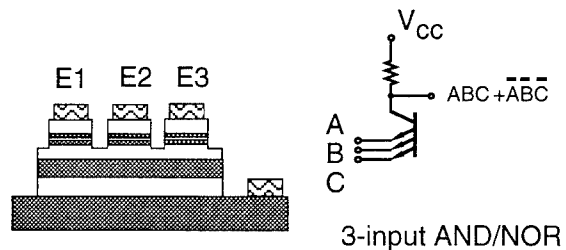


Fig. 4 Triple-emitter RHET structure

Memory Circuits Using Multi-Emitter RHETs [2]

We can also use a double-emitter RHET as a static memory cell (Fig. 5) using the operating mode indicated in Fig. 2(c). We connected word lines WL1 and WL2 to emitters E1 and E2. We also connected the bit line BL to the subcollector. Each emitter has an n-shaped negative differential resistance region, giving two stable states--S1 and S2--when a suitable voltage applied between WL1 and WL2 (Fig. 2 (c)). The electron potential of base region B is higher for S1 than S2.

The main feature of this device is its read and write operations, which use its collector barrier current-voltage characteristics, shown on the right bottom in Fig. 5. No current flows when the base-collector voltage is low. The current increases and decreases quickly with collector-base voltages above and below the bias thresholds. By applying the collector voltages and monitoring the collector current, we can read and change (write) the base potential.

Figure 6 plots the estimated bit density of our new SRAM as a function of the minimum design rule, together with that of conventional Si SRAMs. The bit density of a 1-Gb Si SRAM is expected to reach $10^8/\text{cm}^2$ with a minimum size of $0.1\text{ }\mu\text{m}$. It is believed that further scaling down for higher density is unlikely, due to short-channel effects, problems with making nanometer-scale structures, and increasing chip size.

The bit density of our SRAM chip is higher than that of conventional SRAMs. The chip size of a 1-Gb SRAM is estimated to be about 1.4 cm^2 with a $0.1\text{ }\mu\text{m}$ design rule. If our device could be made using 10 nm rule, a 1-Tb SRAM with a chip size of 14 cm^2 is possible.

Research Directions

Emerging Technologies towards Quantum-Dot-Tunneling Hot Electron Transistor (QHET)

To be able to scale down the SRAM cell with down to a 10 nm design rule, we need a breakthrough in the device process. Recently, we have proposed the use of (111)B substrates to make quantum dots [4]. If we use (111)B substrates and anisotropic etching, we can make inverted tetrahedral-shaped recesses (TSR) having three kinds of (111)A facets, converging to a very sharp bottom. We attempted to make quantum dot structures by growing an AlAs/GaAs heterostructure at the bottom of the TSR. Figure 7 is the SEM cross sectional view of the grown

structure. The bright contrast corresponds to AlAs and the darker contrast corresponds to GaAs. The dot-like structure is 15 nm thick and 30 nm wide. The advantage of this method is that we can position these artificial dots by a mask-window; the sizes of the dots are automatically reduced to less than lithographic limit. Identical dots can be formed based on the uniform shape of TSRs. I think this TSR could be used as an electron injector for QHETs; where valley current will be reduced due to prohibited phonon scattering during tunneling through quantum dots.

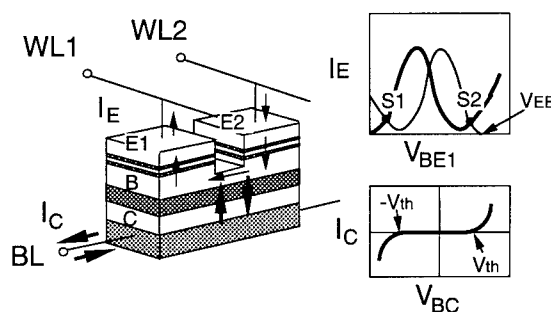


Fig. 5 Double-emitter RHET SRAM cell

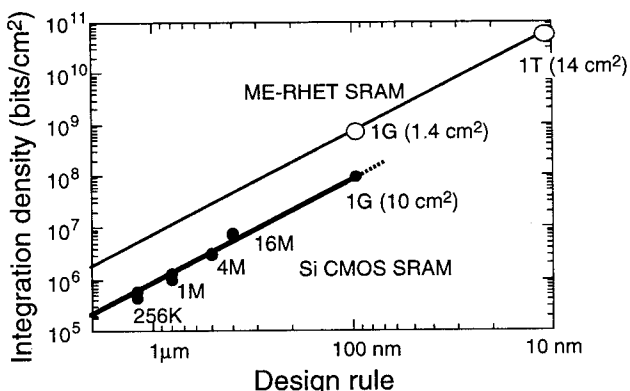


Fig. 6 SRAM integration densities

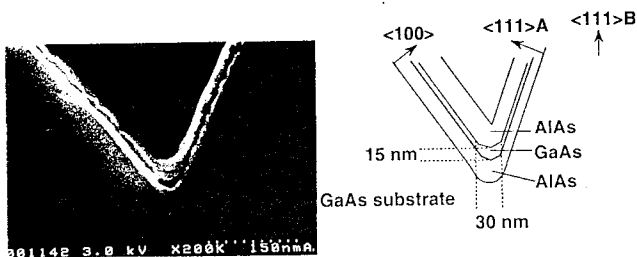


Fig. 7 Quantum dot structure grown at the bottom of the Tetrahedral-Shaped-Recess (TSR)

To make electrical contacts to QHETs, we need a 10-nm wide wiring technique. We think that single crystal metals, that are lattice matched to the semiconductors, could be used for the wiring. The wiring could be embedded in the QHETs. Since NiAl has a negative and InAl has positive mismatch, a combination of NiAl and δ -InAl could be the same lattice constant with InP. We have succeeded in growing 100 monolayer thick InNiAl film of which surface is very smooth, checked by RHEED.

Quantum Functional Bipolar Transistors Operating at Room Temperature

Figure 8 shows a schematic cross section and energy band diagrams of a functional HBT [5]. The HBT has two separate emitters and no base electrodes. The key to this device is the use of heavily doped base and emitters, which allow band-to-band tunneling in reversed bias conditions.

When emitters E1 and E2 are at the same logic level, either low or high, there is no collector current since the base is open. When we apply a positive bias on emitter 2 with respect to emitter 1, the base potential is pulled down due to band-to-band tunneling in this emitter 2. Electrons are then injected from the forward biased emitter 1 to the base region, turning the transistor on. Since emitters 1 and 2 are symmetric, the transistor also goes on when positive bias is applied to emitter 1 with respect to emitter 2.

The device is thus similar to the double emitter RHET and is switched on or off depending on the voltage difference between the two emitters. The important difference between them is that the multi-emitter HBTs operate at room temperature but do not have a negative conductance region.

As with RHETs, by using this device we can reduce the number of transistors, when compared to conventional methods. Also this device can be used as functional phototransistors.

Summary

Using multi-emitter RHETs, logic and memory circuits could be constructed with fewer transistors and resistors. Our research on this quantum functional device will be going in two different direction. One is to scale it down further to make quantum-dot-tunneling transistors, QHETs. I described new process technology to make these quantum dot tunneling structures using a GaAs (111)B substrate, and 10 nm wiring embedded in device structures.

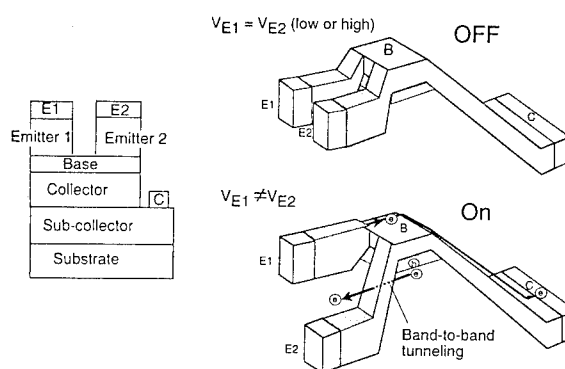


Fig. 8 Quantum functional bipolar transistor

The other direction is to develop more practical quantum functional devices. One example is the development of a multi-emitter bipolar transistor which has highly doped emitter and base regions to allow interband tunneling. This device operates at room temperature and could be potentially used in bipolar circuits. Also this device has a potential to be used as a new functional phototransistor.

Acknowledgments

A part of this work was performed under the management of FED, (the R&D Association for Future Electron Devices) as a part of the R&D of Industrial Science and Technology for Frontier Program supported by NEDO (the New Energy and Industrial Technology Development Organization).

References

- [1] Yokoyama, N. et al., "A New Functional Resonant-Tunneling Hot Electron Transistor (RHET)," *Jpn. J. Appl. Phys.*, **24**, pp. L853-854, Nov. 1985.
- [2] Mori, T., et al., "An SRAM Cell Using a Double-emitter RHET for Gigabit-Plus Memory Applications," *Ext. Abs. 1993 Int. Conf. Solid-State Dev. and Mater.*, pp. 1074-1076, Sep. 1993.
- [3] Takatsu, M. et al., "Logic Circuits Using Multi-Emitter Resonant-Tunneling Hot Electron Transistors (RHETs)," Paper No. TA 7.2 reported at ISSCC, February 1994.
- [4] Sakuma, Y. et al., "New Approach to AlAs/GaAs Quantum Dot Structures using MOVPE on Tetrahedral-Shaped Recesses formed on (111)B GaAs Substrates," 21st Int'l. Symp. on Compound Semiconductors, Sep., San Diego, 1994.
- [5] Imamura, K. et al., "Open-Base Multi-Emitter HBTs with Increased Logic Functions," *Extended Abstracts of the 1994 Int'l. Conf. on Solid State Devices and Materials*, 1994, pp.467-469.

Noise characteristics of InP-based HBTs

(Invited Paper)

Y.K. Chen, D.A. Humphrey, L. Fan^{*}, J. Lin, R.A. Hamm, D. Sivco, A. Y. Cho, and A. Tate
AT&T Bell Laboratories,
600 Mountain Ave., Murray Hill, New Jersey 07974

Abstract

The noise characteristics of InP-based heterostructure bipolar transistors (HBTs) are studied from low frequency to microwave frequency. The non-equilibrium minority carrier transport in the thin base region is very effective in reducing the $1/f$ noise current at low frequency as well as reducing the uncorrelated shot noise current at high frequency. Experimentally, a very low $1/f$ noise corner frequency of 1.55 kHz is obtained in AlInAs/InGaAs HBTs with a 70 nm-thick base. This is the lowest $1/f$ corner frequency amongst any compound semiconductor devices reported to date. Minimum noise figures of 0.46 dB, 2.0 dB and 3.33 dB are also demonstrated at 2 GHz, 10 GHz and 18GHz, respectively, with InP/InGaAs HBTs with a 35 nm-thick base and $3.5\text{ }\mu\text{m} \times 3.5\text{ }\mu\text{m}$ emitter.

I. Introduction

Heterostructure bipolar transistors (HBTs) with high cut-off frequencies and large power density have been demonstrated in the past few years [1-4]. The high cut-off frequency yields larger power gain and better power-added efficiency at the operating bandwidth. These advantages are very desirable for many applications such as portable transmitters in personal wireless communication networks. Many RF and microwave applications, such as front-end amplifiers, mixers, and oscillators, also require low noise over a broad operating bandwidth.

Most microwave low noise applications have been dominated by compound semiconductor FETs such as High Electron Mobility Transistors (HEMTs) and Metal-Semiconductor Field Effect Transistors (MESFETs). To realize this low-noise performance in FETs, very fine gate geometry on the order of hundreds of nanometers has to be used. The minimum noise figure of FETs has a frequency dependence, and the small gate capacitance also makes the broadband matching

network very difficult to realize. On the other hand, HBTs enjoy a more relaxed control of lithography dimensions and a relatively constant minimum noise figure over an extremely large bandwidth up to the current gain cut-off frequency, f_T . The low frequency $1/f$ noise of HBTs is also significantly lower than FETs.

There are many noise sources in an HBT. The dominate noise sources are: generation-recombination noise in the emitter space-charge region, shot noise sources in the emitter junction, and collector junctions, thermal (or Johnson) noise from the base resistance, recombination noise in the extrinsic base region, multiplication noise in the high field collector space charge region, etc. The collective terminal noise characteristics of an HBT is the interplay of these sources with the rest of the device equivalent circuit.

The frequency dependence of the spectral density of the collector noise current can be illustrated in Figure 1. The noise current spectrum shows three regions: (1) $1/f$ roll-off characteristics at low frequency, (2) a flat noise

^{*} L. Fan is now with University of California, Los Angeles, CA.

floor over a very broad bandwidth, and (3) a steep rise ($\sim f^2$) at high frequency. The shot noise, thermal noise, and multiplication noise in the collector depletion region make the broadband noise floor. The g-r noise and recombination noise from the surface and impurities are dominate at low frequency. At very high frequency, those two shot noise sources in the emitter junction and collector junction are no longer correlated by the base and collector transit delays, and total noise current increases substantially.

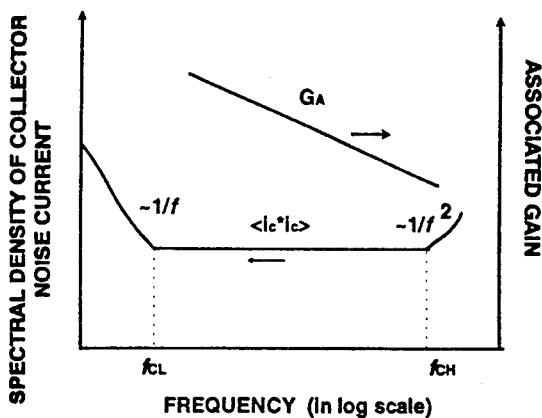


Fig. 1 Illustration of collector noise current power spectrum of a HBT.

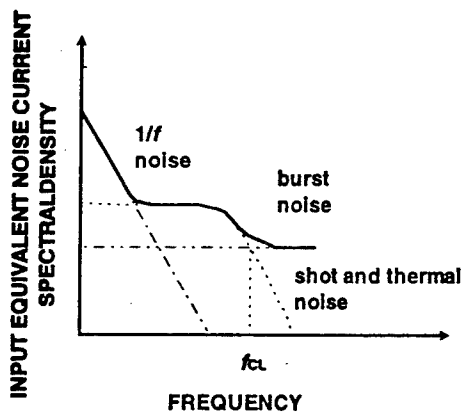


Fig. 2 A typical low frequency noise current power spectrum of an HBT with $1/f$ noise, Lorentzian noise from traps, and broadband noise floor from shot and thermal noise.

II. Low Frequency Noise Characteristics

The low frequency current noise is very important to many applications, such as high precision analog-to-digital converters, ultra-stable microwave oscillators, etc. The low frequency current fluctuations in the oscillating device will be up-converted to the operation bandwidth of the high frequency oscillator, and the stability of the oscillating frequency (or the resultant phase noises) will be significantly deteriorated. In the commonly used GaAs metal-semiconductor field-effect transistors (MESFETs), the generation and recombination currents from the buffer layer as well as the semi-insulating substrate is the major sources of low frequency current noise. Devices based on vertical carrier transport, such as emitter-up bipolar junction transistors (BJTs) or heterojunction bipolar transistors (HBTs), are less sensitive to the electronic defects and imperfections in the buffer layer and substrate material, because the dominant carrier transport mechanism occurs in the emitter and base which are effectively shielded from noise sources in the substrate by the high electrical field in the collector and the highly doped and quasi-neutral n^+ region of the sub-collector contacting layer.

In BJTs or HBTs, the generation-recombination (g-r) current in the emitter-base space charge region, the $1/f$ interface recombination current at the emitter-base heterointerface and the exposed external base region, and the g-r current from deep level traps in the wide-gap emitter of a HBT are major sources of low frequency current fluctuations[5,6]. A typical equivalent input noise current power spectrum at low frequency is illustrated in Figure 2. The low frequency characteristics shows a $1/f$ recombination noise, Lorentzian-shaped g-r burst noise from deep traps, and broadband white noise from junction shot noise and thermal noise. A figure of merit, f_c , low-frequency corner frequency, which is defined as the intercept of the low-frequency $1/f$ noise roll-off and the shot noise floor. Previously, a low frequency noise corner frequency (f_c) of 470 kHz was achieved in an AlGaAs/GaAs HBT[7]. However, the aluminum mole fraction in the emitter has to be limited under 32% to avoid the deep trap effect in AlGaAs. This lowers the emitter-base bandgap

discontinuity in the valence band (ΔE_v) to block the back injection of holes from the heavily doped base, and the maximum base doping concentration is limited. In the InP-based HBT, direct bandgap materials such as InP or AlInAs can be used as emitters. Because of the higher activation energy of the deep traps in these materials, the low frequency random-telegraphic noise produced by these deep traps can be reduced.

The $1/f$ noise current of AlInAs/InGaAs heterojunction bipolar transistors (HBTs) is reduced by utilizing non-equilibrium minority carrier transport through the thin base region. The thin base thickness reduces the scattering of the injected minority carriers toward the extrinsic base region, while the high injection energy from the abrupt AlInAs emitter ($\Delta E_c \sim 0.5$ eV) reduces the effective interaction volume. The burst noise from the deep traps is also suppressed by the use of direct-gap AlInAs emitter with small electron effective mass.

Figure 3 shows the measured input equivalent noise current spectral density of a common-emitter AlInAs/InGaAs HBT with 70 nm-thick base and $3 \times 15 \mu\text{m}^2$ emitter. The $1/f$ noise corner frequency is 1.55 kHz measured at $I_C = 82 \mu\text{A}$. Compared to the transistors of the same size but a thicker (100 nm) base, a 10 dB reduction in the noise current spectral density is observed at the same emitter current density. This low $1/f$ corner frequency is better than most compound semiconductor devices and is comparable to the low noise silicon bipolar junction transistors with a buried base structure.

III. Comparison among various bipolar technologies

To illustrate the low frequency noise characteristics among various bipolar technologies, we measure the noise current spectral density of several bipolar transistors. Table 1 shows the related information of these transistors. Except the carbon-doped AlGaAs HBTs, all the HBTs are fabricated with wet chemical etching and without wide-gap emitter ledges to passivate the extrinsic base region.

Figure 4 shows the equivalent input noise current spectral density at 1 Hz for these transistors measured at various emitter current density. The horizontal axis of the emitter current density is also normalized by the perimeter-to-area ratio to minimize the geometrical variation of these devices.

At low operating current, the high frequency current gain or even power gain is dominated by the dynamic emitter-base junction resistance of low emitter current. In this way, we may think of the horizontal axis as the operating frequency. For a given operating current density, the AlInAs/InGaAs HBTs with a very thin base width have the lowest $1/f$ noise spectral density even without a passivated extrinsic base. The silicon BJT has a diffused base structure and a very good $1/f$ characteristic at low current density. Because of the high recombination velocity of the GaAs surface, GaAs-based HBTs have rather high noise current at low current density. The noise current of InGaP/GaAs HBTs is improved by utilizing the direct-gap InGaP emitter. To improve the low frequency noise, effective surface passivation techniques such as emitter ledges and buried extrinsic base structures will reduce the noise current significantly.

IV. High Frequency Noise Characteristics

It is well known that one of the dominant high frequency noise sources in a bipolar transistor is broad band shot noise from emitter-base junction and base-collector junction, whose spectral density depends on emitter current [8]. These two sources are correlated through the base transport factor and base and collector transit delay for operating frequency below the transit-time cut-off frequency. Therefore, high cut-off frequency at low operating current is needed to reduce shot noise. InP/InGaAs HBTs which exploit the superior transport properties of InGaAs have shown high cut-off frequency at low current because of the low surface recombination velocity of this material system. Nonequilibrium carrier transport in the base and collector of these transistors significantly reduces the forward transit time, τ_F , of the injected electrons [9]. The short intrinsic transit time through the base and collector depletion region increases the

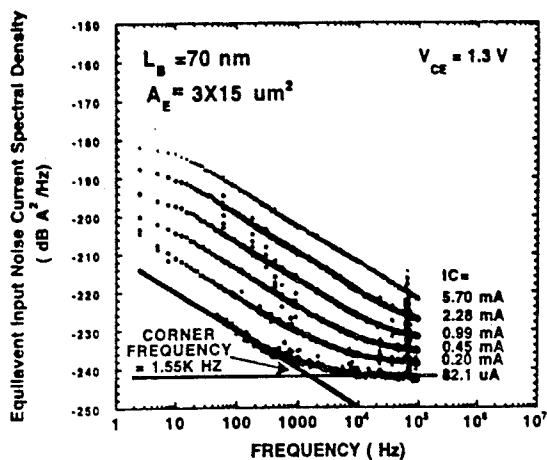


Fig. 3 Measured equivalent input noise current spectral density of an AlInAs/InGaAs HBT with 3 X 15 μm^2 emitter area and 70 nm-thick base. A very low $1/f$ corner frequency of 1.55 kHz is obtained.

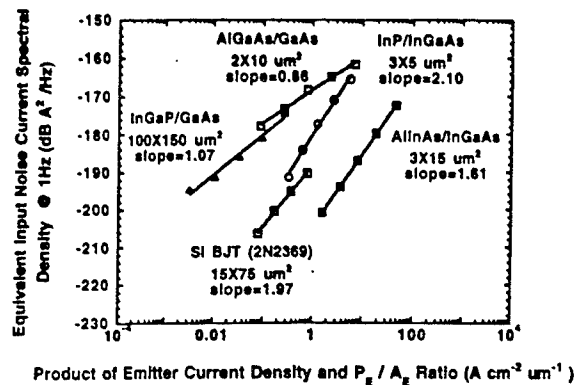


Fig. 4 Comparison of measured equivalent input noise current spectral density at 1 Hz for bipolar transistors made by several technologies as listed in Table 1. The current density of the horizontal axis has been normalized by the perimeter-to-area ratio.

Table 1 Device structure of various HBTs used in the low-frequency current noise measurement.

	Silicon BJT	AlGaAs/GaAs HBT	InGaP/GaAs HBT	InP/InGaAs HBT	AlInAs/InGaAs HBT
Emitter Size (μm^2)	15 x 75	2 x 10	100 x 150	3 x 5	3 x 15
Base passivation	diffusion	ledge	none	SiO_2	SiO_2
Base Dopant	-	carbon	carbon	beryllium	beryllium
Base Doping (cm^{-3})	-	6×10^{19}	1×10^{19}	6×10^{19}	2×10^{19}
Base Thickness (nm)	-	80	85	50	70-100
Maximum Current Gain	250	100	120	50	80-95
f_T (GHz)	0.400	70	-	120	70
f_{max} (GHz)	-	85	-	90	42

transistor cut-off frequency and upper noise corner frequency. Despite the difference in microscopic transport mechanisms between BJT and HBT, the high frequency noise of the InP/InGaAs HBT is dominated by the thermal and shot noises. Therefore, the minimum noise figure can be calculated from the macroscopic equivalent circuit model using the approximation from Hawkins [8].

The room temperature frequency dependence of measured minimum noise figure, F_{min} , and associated gain are plotted in Fig. 5 at collector currents $I_C=0.3\text{mA}$, 0.5mA and 6.7mA . Minimum noise figures of 0.46dB, 1.09dB and 3.33dB with associated gain of 11.6dB, 5.6dB and 1.98dB were obtained at 2GHz, 6GHz and 18 GHz, respectively, with $I_C=0.3\text{mA}$ and $V_{CE}=1.3\text{V}$. As a point of reference, this noise performance is comparable to most published experimental and theoretical noise figures for 1- μm gate GaAs FET's. Very good agreement between the measured F_{min} and the calculated value using Hawkins' approximation.

V. SUMMARY

In summary, we have demonstrated the noise characteristics of InP/InGaAs heterostructure bipolar transistors. In the low frequency regime, because of the reduced interaction volume in the thin base, the injected non-equilibrium minority carriers improve the excess recombination current near the emitter perimeter. Combined with the reduced deep trap density in the direct-gap emitter, the low frequency noise current is reduced significantly in these transistors. In the microwave regime, the measured minimum noise figure agrees well with a modified Hawkins' model and is dominated by the base resistance and operating current (i.e. shot noise). The short transit time for injected nonequilibrium electrons through the base and collector depletion region increase the correlation between the emitter current and collector current, and significantly extends the low noise operation to higher frequency. By reducing both the lateral and vertical dimensions of these HBTs, noise figures less than 1dB may be realized in the millimeter-wave regime.

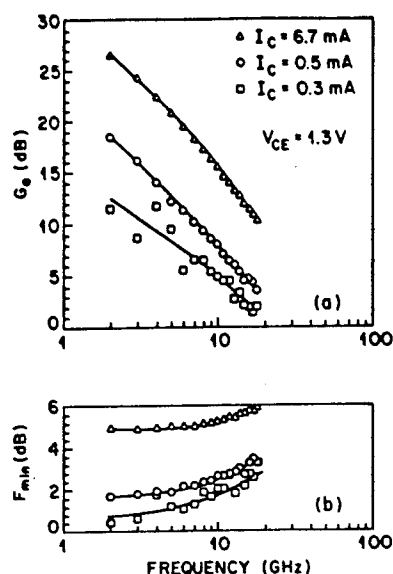


Fig. 5 Measured minimum noise figure (F_{min}) and associated gain (G_A) of an InP/InGaAs HBT with emitter size of $3.5 \times 3.5 \mu\text{m}^2$.

REFERENCES

- [1] H. Kroemer, "Heterostructure bipolar transistors and integrated circuits," *Proc. of IEEE*, vol. 70, pp. 13-25, 1982.
- [2] P.M. Asbeck, et al., "GaAs-based heterojunction bipolar transistors for very high performance electronic circuits," *Proc. of IEEE*, vol. 81, pp. 1709-1726, 1993.
- [3] Y.K. Chen, R.N. Nottenburg, M.B. Panish, D. A. Humphrey and R. Hamm, "Subpicosecond InGaAs/InP heterostructure bipolar transistors," *IEEE Electron Device Lett.*, vol. EDL-10, pp. 267-269, 1989.
- [4] B. Bayraktaroglu, N. Camiliuri, H.D. Shih and H.Q. Tserng, "AlGaAs/GaAs heterojunction bipolar transistors with 4W/mm power density at X band," *Tech. Digest, 1987 IEEE MTT-S Symposium*, pp. 969-972, 1987.

- [5] H. Lin and S.C. Lee, *Appl. Phys. Lett.*, vol. 47, pp. 839-841, 1985; also, D. Costa and J. S. Harris, "Low-frequency noise properties of Npn AlGaAs/GaAs heterojunction bipolar transistors," *IEEE Trans. Electron Dev.*, vol. ED-39, pp. 2382-2394, 1992.
- [6] T.G.M. Kleinpenning and A.J. Holden, "1/f noise in n-p-n GaAs/AlGaAs heterojunction bipolar transistors: impact of intrinsic transistor and parasitic series resistances," *IEEE Trans. Electron Dev.*, vol. 40, pp. 1148-1153, 1993.
- [7] K. Wang, R. Sheng, M.F. Chang, W. Ho, G. Sullivan, Sovero, J. Higgins, P. Asbeck, *IEEE T-MTT*, 38, 1381, (1990).
- [8] R.J. Hawkins, "Limitations of Nielsen's and related noise equations applied to microwave bipolar transistors, and a new expression for the frequency and current dependent noise figure," *Solid-State Electronics*, vol. 20, pp. 191-196, 1977.
- [9] Y.K. Chen, R.N. Nottenburg, M.B. Panish, R. A. Hamm, and D.A. Humphrey, "Microwave noise performance of InP/InGaAs heterostructure bipolar transistors," *IEEE Electron Device Lett.*, vol. 10, pp. 470-472, 1989.

Low-Frequency Noise Phenomena in InP-Based HFETs Related to Stress Induced Degeneration and Interface Properties

V. Sommer, A. Kohl, K. Weigel, A. Mesquida Küsters and K. Heime

Institut für Halbleitertechnik, Lehrstuhl I, RWTH Aachen, Templergraben 55, 52056 Aachen, Germany

Introduction

During the last years, signal and noise characteristics of modern HFET devices have been improved decisively due to the decreasing geometric dimensions as well as due to the application of InGaAs as channel layer with its excellent transport properties. The best values for the frequency limits will be obtained, if InAlAs as doping and barrier layer is used, since in this case both the conduction band offset ΔE_c at the channel interface and the Schottky barrier to the gate are high. However, these devices suffer from degradation effects, mainly shifting the threshold voltage and increasing the $1/f$ -noise level, dependent on electrical and thermal stress, which limits their applicability and which is probably related to the aluminium content of the InAlAs. On the other hand, in HFETs with a carrier supply layer consisting of InP, this sensibility to stress has not been observed. Nevertheless, in this material system ΔE_c is lower and two components have to be exchanged during the epitaxial growth, possibly resulting in a higher concentration of deep traps at the interface, which contribute to the low frequency noise.

Localization of Deep Traps at Interfaces

In the low frequency (LF) range, noise is caused by a change of the conductivity according to the following equation:

$$\Delta \sigma = q \cdot (\mu \cdot \Delta n + n \cdot \Delta \mu) \quad (1)$$

In heterostructures, there are various possibilities how deep traps may affect the channel conductivity.

Figure 1 shows the conduction band of a HFET with traps at different locations (a)-(e) near interfaces. These traps may be created during the epitaxial growth or after the exposure to stress.

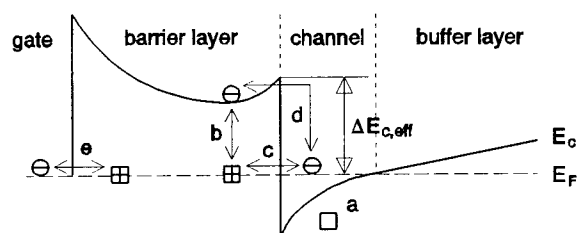


Fig. 1 Possible interactions of deep traps (squares) located at various interfaces in a HFET with free electrons (circles)

The effect of traps located in the substrate can be eliminated by means of a sufficiently thick channel layer or using a pure epitaxial buffer layer below the channel.

First, it can be stated that traps can only contribute to the noise, if their energy level coincide with the Fermi energy. Therefore, although traps probably are located in the channel near the interface (a), these remain neutral and may be neglected concerning their LF-noise contribution.

On the other side of the channel, deep traps in the barrier layer can be activated by changing the temperature or the gate-source voltage. To characterize these traps, their activation energy ΔE_T can be determined by a temperature resolved measurement, while two different generation and recombination processes are possible:

Either, the traps can interact with the conduction band in the barrier according to (b), or the traps exchange their electrons with the channel by tunneling through the barrier (c). In both cases the measured activation energies should coincide approximately with the effective ΔE_c , since the Fermi level is pinned by the high density of states in the 2DEG. Moreover, in case (c) a dependence of the activation energy on the distance between trap and channel will appear, due to the strong electrical field near the interface, which changes the barrier height.

More realistically, the traps are expected to be uniformly distributed at the interface, either locally or with various activation energies. Then a $1/f$ -noise over a certain frequency range can occur according to the models of Mc Whorter [1] and Dutta Horn [2].

Besides the GR-processes discussed so far, a real space transfer of electrons from the channel into the conduction band of the barrier may appear (d), without the assumption of traps [3]. However, since the electrons remain free in both states and can affect the noise merely by means of a small alteration in their mobility according to (1), this effect will not contribute to the noise as long as the equilibrium concentration of electrons in the barrier is small and no parallel conduction appears.

Moreover, traps may be located at the interface to the gate electrode (e). These traps can also affect the LF-noise as shown in the next section.

Effect of the Trap-Induced Electrostatic Field

Up to now the noise contribution of deep traps has been considered exclusively by means of a direct alteration of the conductivity in the channel. However, an additional effect will exist, if the GR-process causes a local separation of charge beneath the gate perpendicular to the channel. In this case, a voltage is induced across the gate-channel capacitance C_G , which modulates the number of free electrons in the channel according to the following equation [4]:

$$\Delta U_{gs} = \frac{N_T \cdot q}{C_G} \cdot \left(\frac{1}{2} - \frac{b}{H} \pm \frac{1}{2} \right) \quad (2)$$

Here, N_T means the number of traps at the distance b below the gate and H the spacing between gate and channel, while the positive and negative signs relate to a charge transfer into the channel and to the gate, respectively. If the gate is biased with a DC voltage, then the trap induced voltage will be compensated by a charge transfer $\Delta Q_{ch} = C_G \cdot \Delta U_{gs}$ via the external line. Therefore, also traps located beneath the gate electrode can modulate the conductivity in the channel.

Additionally, by means of the trap induced voltage, a correlated GR-process may occur, which is illustrated in figure 2.

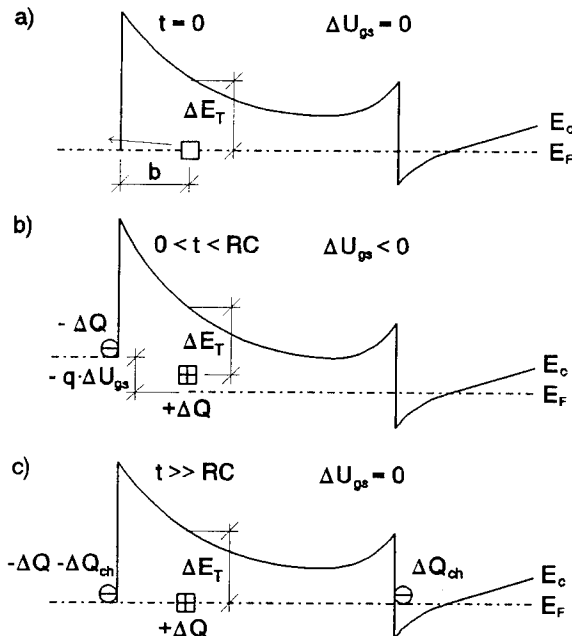


Fig. 2a-c Possible formation of correlated capture and emission events due to a self-induced shift of the energetic equilibrium

If we assume a donor-like trap lying beneath the gate and generating an electron onto the gate, the sign of ΔU_{gs} will be negative. In fig. 2a the conduction band of a HFET

just before a generation event is depicted. The strong band bending causes the trap level to coincide with the Fermi level in a distance b from the gate. If an electron is randomly transferred, then the energy level of the traps will be increased due to the induced electrostatic field, see fig. 2b. Since the occupation probability of traps at the position b is reduced, correlated emission events of all traps in this region may be expected.

After a short period of a few picoseconds, which is determined by the external RC time constant, a new equilibrium has been established (fig. 2c). If a current is impressed, then a noise voltage will appear with an amplitude according to the following equation with the output resistance R_{ds} and the gate length L_g :

$$\Delta U_{ds} = N_T \cdot \frac{q \cdot \mu \cdot I_d \cdot (R_{ds}^{ex})^2}{L_g^2} \cdot \frac{b}{H} \quad (3)$$

Although not shown here, the same correlated process can take place during the capture of electrons or if the charge transfer of acceptor-like traps is considered. However, this mechanism will not be possible, if the traps interact directly with the channel. In this case, the sign of the induced voltage decreases the probability for further emission and capture events, respectively.

Stress Induced Noise in InAlAs/InGaAs/InP HFETs

All noise measurements have been performed in the frequency range from 0.3Hz up to 100kHz for temperatures down to 80K by means of a self-controlled measurement system developed in our institute, exhibiting a very low inherent noise level of $3\text{ nV/Hz}^{-1/2}$ at 1kHz and 100Ω load.

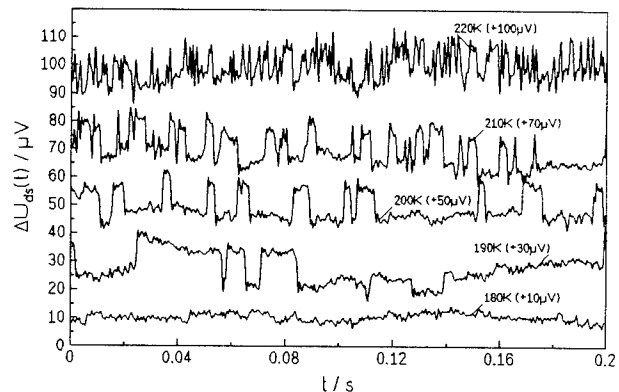


Fig. 3 Measured noise voltage of an InAlAs/InGaAs/InP HFET exhibiting RTS with $I_D = 6\text{ mA}$, $U_{gs} = 0\text{ V}$ and $T = 180\text{ K} - 220\text{ K}$. For separation of the signals, an offset voltage has been added at every temperature, respectively.

As far as no degradation effect is observable, the HFETs with InAlAs as barrier layer show a very low $1/f$ -noise without any superimposed GR-spectra.

However, in some devices also without stress a clear random telegraph signal (RTS) could be measured in the time domain over a certain temperature range as depicted in figure 3.

This RTS corresponds to Lorentz spectra in the frequency domain with an activation energy of 0.34eV, proving the underlying GR-process. The minimum number of traps interacting with the gate can be estimated using (3) to about 300, if a maximum tunneling distance of 5nm is assumed.

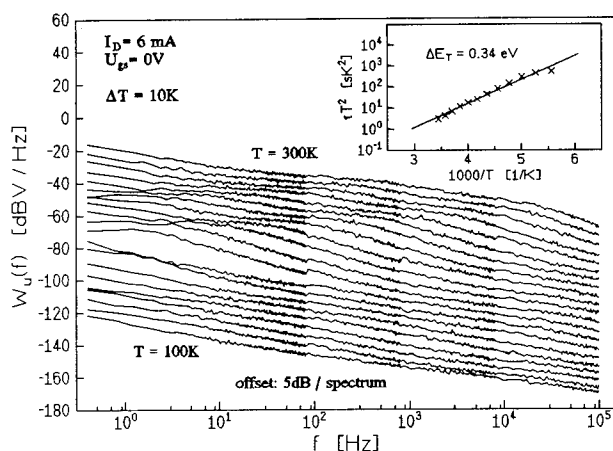


Fig. 4 Spectra of the noise voltages in figure 3. The RTS clearly corresponds to Lorentz spectra in the frequency domain with an activation energy $\Delta E_T = 0.34\text{eV}$

Although the $1/f$ -noise level is not yet increased instantly when RTS occurs for the first time, the onset of RTS seems to indicate the beginning of degradation. If the devices are thermally stressed for 40h at 200°C, the $1/f$ -noise will increase drastically and most of them now show RTS, while at the same time their threshold voltage shifts. However, some devices are not very sensible to stress and neither their noise nor their signal characteristics change significantly.

We suppose that the degeneration is caused by the aluminium content of the InAlAs. Especially at the surface the aluminium atoms may react with the oxygen from the atmosphere dependent on the processing technique, altering the pinning potential at the surface. In [5] it is assumed that an interfacial oxide layer between Ti and InAlAs is formed, possibly creating trap like states.

This assumption is supported by other measurement results: If the temperature is lowered, the channel resistance of the degenerated HFETs will increase, in contrast to the behaviour expected from an increasing mobility. Since the sheet carrier concentration in the channel of ungated

devices does not change, it follows that the threshold voltage depends on temperature.

To examine the physical origin of this shift, in figure 5 the DC characteristic is correlated with the normalized noise power density at 10Hz and 1kHz.

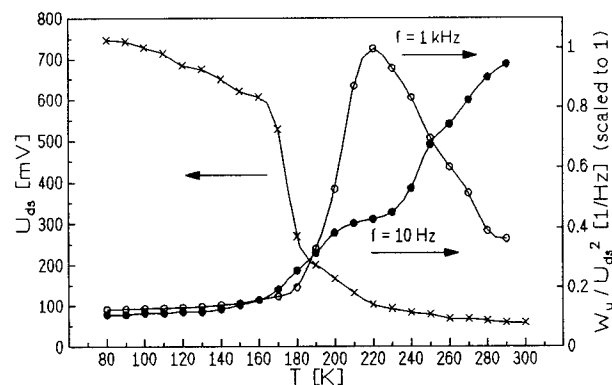


Fig. 5 Correlation between the shifting output voltage and noise power density at degenerated InAlAs/InGaAs/InP HFETs

As can be seen, the noise power at 1kHz exhibits a maximum just at the beginning of the threshold voltage shift. This gives clear evidence for thermally activated traps causing the signal degeneration: At high temperature, all traps remain in their neutral state. If the temperature is lowered and the half of all traps is occupied, then the maximum of the GR-noise can be observed. For still lower temperatures, all traps become ionized and the noise power density therefore decreases again. The same effect appears at 10Hz, while the peak is shifted to higher temperatures.

Interface Related Noise in InP/InGaAs/InP HFETs

In earlier investigations we have proven that the lower interface towards the substrate in InP/InGaAs/InP HFETs causes the main contribution to the LF-noise in these devices [6]. A series of device structures were grown with narrow channels to increase the effect of the interfaces, and different switching sequences at the InP to InGaAs interface. Switching sequences, where the hydrides AsH_3 and PH_3 overlap in time during growth interruption ($t < 0$) are used as well as growth interruptions where the reactor is flushed purely by hydrogen ($t > 0$). The sheet carrier density $n_{s,T}$ of traps located at the interfaces was determined by frequency dependent C-V measurements [7]. These results were compared with LF-noise measurements as depicted in figure 6. The noise power density exhibits the same trend dependent on the overlap time t as the trap density determined from C-V measurements. Since all other technological parameters have been held constant in these structures, this good

conformity shows the dominating effect of the switching frequencies on the LF-noise performance.

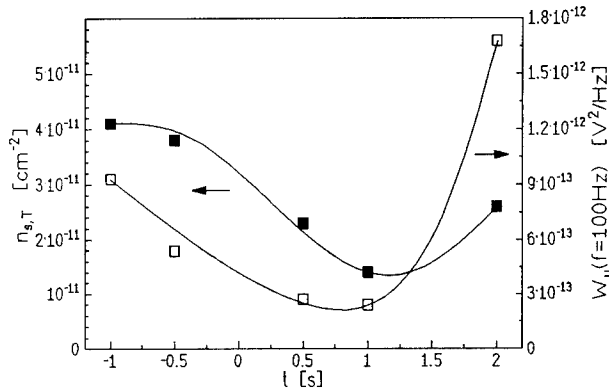


Fig. 6 Correlation between noise power density and trap concentration dependent on the growth interruption time

Additionally to the distinct $1/f$ -noise power density, in HFET structures grown with $t = -1$ s and $t = -0.5$ s a trap with $\Delta E_T \approx 0.3$ eV could be detected, see fig. 7, which possibly indicates phosphorus substituting indium [8]. On the other hand, for $t > -0.5$ s no trap occurred. Therefore, the assumption that indeed deep traps are created at the interface is underlined by these results.

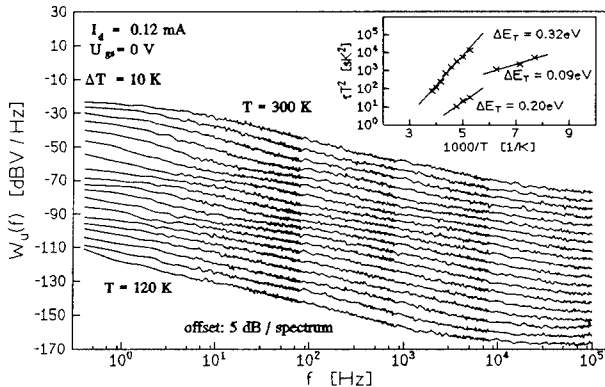


Fig. 7 Measured noise spectra of a structure using a growth interruption time $t = -1$ s revealing a clear trap with $\Delta E_T = 0.32$ eV

Conclusions

Figure 8 shows the normalized noise power density of HFETs with InAlAs as barrier layer and those where InP is used. All transistors were manufactured in our institute using the same geometrical parameters and exhibit almost the same sheet carrier concentration in the channel. The depicted spectrum of the HFET containing InAlAs is a typical result for these devices grown by MBE as long as no degeneration effects occur. On the other side, the HFETs without aluminium were grown by LP-MOVPE and the In mole fraction has been varied from 53% up to 81%, showing excellent device properties [9]. The comparison between both material systems reveals that the

noise of the HFET with InAlAs is slightly lower. This can be understood since during the growth of the interface in this device only one component must be exchanged. Besides, due to the larger conduction band discontinuity the penetration depth of the 2DEG into the barrier is reduced and with it the activation of traps located there. The latter also explains the decreasing noise power with increasing indium portion in the channel of the aluminium-free HFETs. However, at 67% indium, the minimum is reached and further increasing the strain does not improve the noise properties. Concluding, it may be stated that there exist a trade-off dependent on the special application between the slightly better performance of the InAlAs/InGaAs/InP HFETs and those devices with a InP barrier, which are less sensible to stress.

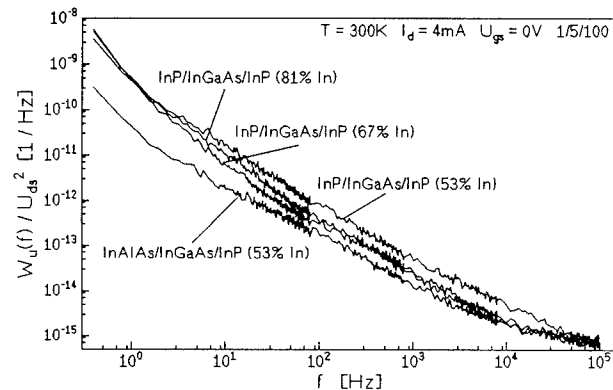


Fig. 8 Normalized noise power of an InAlAs/InGaAs/InP HFET compared to HFETs with InP instead of InAlAs as doping layer and various In mole fractions in the channel

References

- [1] A. L. Whorter; Ed. R. H. Kingston, University of Philadelphia, 1957
- [2] P. Dutta, P. M. Horn; Rev. Mod. Phys., 53, 1981, p. 497
- [3] A. van Die, J. I. Dijkhuis; J. Appl. Phys., 74, 1993, p. 1143
- [4] V. Sommer, J. Hedrich, K. Weigel, O. Perillieux, K. Heime; Solid-State Electronics, accepted for publication
- [5] S. Fujita, S. Naritsuka, T. Noda, A. Wagai; J. Appl. Phys., 73, 1993, p. 1284
- [6] V. Sommer, P.-B. Albert, T. Zerbe, A. Schnell, A. Mesquida Küsters, K. Heime; Proc. 6th Int. Conf. InP and Rel. Mat., St. Barbara (CA), USA, March 1994, p. 415
- [7] A. Kohl, A. Mesquida Küsters, S. Brittner, K. Heime, J. Finders, D. Gnoth, J. Geurts, J. Weitok; Proc. 6th Int. Conf. InP and Rel. Mat., St. Barbara (CA), USA, March 1994, p. 151
- [8] A. P. Seitsonen, R. Virkkunen, M. J. Puska, R. M. Nieminen; Physical Review B, 49, 1994, p. 5253
- [9] A. Mesquida Küsters, A. Kohl, S. Brittner, V. Sommer, K. Heime; Proc. 6th Int. Conf. InP and Rel. Mat., St. Barbara (CA), USA, March 1994, p. 323

Interface stability of metal/ InP based material systems

SB3.4

Y. Ashizawa, C. Nozaki, T. Noda, and A. Sasaki

Toshiba Research and Development Center, 1 Komukai Toshiba-cho, Saiwai-ku, Kawasaki 210, Japan

Abstract

The stability of interfaces between metal (Ni, Pt, Ti, Mo) and III-V compound semiconductors has been investigated by the application of Rutherford backscattering spectrometry (RBS). Metal diffusion and interfacial lattice disorder of the semiconductors were analyzed for various metal/semiconductor samples annealed at temperatures up to 500°C. The interfaces of Ni/GaAs and Ti/GaAs were found to be stable compared to those of Ni/In-based semiconductors and Ti/In-based semiconductors, respectively. Faster diffusion of Pt atoms was observed in In- and As- containing materials than in P-containing materials. Mo/semiconductors were most stable.

Introduction

Degradation of electrical characteristics of InP based HEMTs may take place at low temperature compared to GaAs based HEMTs. The primary failure mechanisms are related to electrodes [1]. The outdiffusion of semiconductor elements and the interdiffusion of metal atoms are observed to account for the increase of the ohmic contact resistances and the deterioration of the Schottky gate contacts. It is, however, not so clear why the differences arise in the reliability of electrodes depending on the material systems of the HEMTs.

There have been many studies on various metal/semiconductor structures and on the interfacial reactions and resulting formation of compounds [2, 3]. The metallurgical interface between the first metal and the compound semiconductor layer plays an important role in determining electrical properties. Although these studies supply enough information on the phases that are in thermal equilibrium, discussion is still lacking on the critical limitations imposed on the compatibility of the device manufacturing processes of InP based HEMTs. Previous research was mostly concerned with binary semiconductors such as GaAs and InP, and not so many studies have been made on metal/ternary compound semiconductors. The increasing demands of miniaturization of devices lead to the idea of the formation of shallow contacts, which require us to use thinner metal layers or refractory metals. It was pointed out that thin metal/compound semiconductor systems cannot be assumed to be closed systems, primarily due to the high volatility of the group V elements and their compounds[4]. Hence the interfaces of thin metal/compound semiconductors would exhibit different stability from those reported in previous literature.

In this paper, the initial stage of interfacial reactions of various thin-metal /semiconductor interfaces was investigated. Practical electrodes used in HEMTs are made up of stratified metal layers, including first metal, barrier metal and Au or Al on top. In this study, the most frequently used first metals and III-V compound semiconductor materials in various types of HEMTs were chosen. Among the possible triggers of the electrode degradation, the interdiffusion of metal atoms was focused

upon. The Rutherford backscattering spectrometry (RBS) was fully used because it supplies information on both compositional variation and structural disorder at the metal /semiconductor interfaces.

Experiment

Metal/semiconductor samples were prepared for combinations of the metals Ni, Ti, Pt, Mo and the semiconductors GaAs, InP, InGaP, InAlAs and InGaAs. InGaP lattice-matched to GaAs and both InGaAs and InAlAs lattice- matched to InP were grown by low-pressure metal-organic chemical vapor deposition (LP-MOCVD). After degreasing and slightly etching the semiconductor substrates, 6 to 7 nm thick metals were deposited by electron beam evaporation. The thinness of the metals was chosen so that the surface peaks of the semiconductor layers in the channeled spectra could be observed without risking dechanneling by the metal layers. After the deposition of metals, the samples were stored in a vacuum dessicator until some treatment was performed in order to minimize the oxidation of the metal surfaces. The samples were annealed under N₂ ambient for 15 minutes at temperatures in the range 150 to 500°C. They were analyzed by RBS using a 2.4 MeV He ion beam. The scattered ions were mostly detected, not at the backscattering position (160°), but at the grazing position (105°) because this angle offers better depth resolution.

Results and Discussion

The recorded channeling spectra of as-deposited metal /InGaAs samples are shown in Fig. 1. The Pt, Ni and Ti signals are clearly observed. The In surface peak is very close to the Mo signal and is observed as a shoulder peak on the higher energy side in the channeling spectra taken at the grazing angle. In Fig. 2, the recorded spectra of Pt/semiconductor samples are shown. It can be seen that ternary compounds semiconductor layers gave higher yield than binary semiconductors.

The interfacial degradation of metal/semiconductor structures was analyzed in two ways: one was the diffusion of metals, and the other was the variation of the surface peaks. The magnitude of the diffusion of metals was estimated by using a parameter, defined as the ratio of the

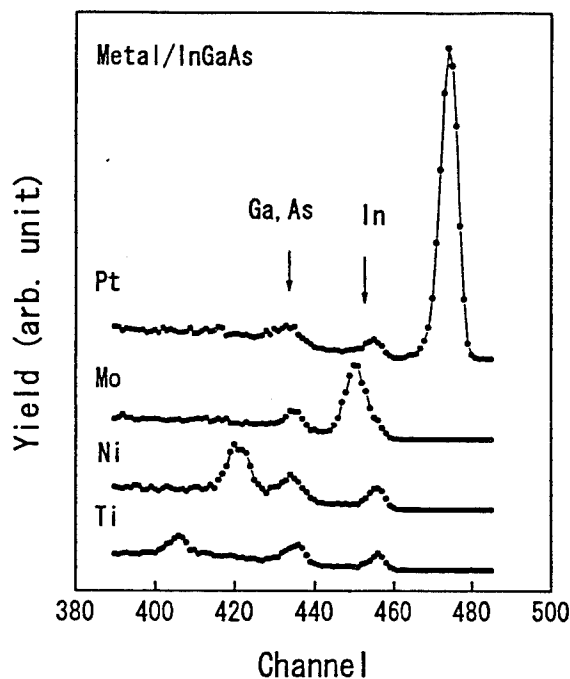


Fig. 1. RBS channeling spectra for as-deposited metal/InGaAs samples.

height to the full width, at half the maximum of the metal signal in the RBS channeling spectra. For the Mo/In-containing semiconductor samples, the In surface peak was taken as part of the Mo signal because the In peak was relatively small.

In the RBS channeling spectra, peaks appear at energy channels that correspond to the surface of the semiconductor layer and these are called surface peaks [5]. The surface peak intensity that corresponds to the number of atoms which the incident He ion beam detects is defined by the area of the surface peak. When the crystal is ideal, the atoms are arranged in order at the lattice sites. When the surface region of the crystal is disordered, the atoms are displaced from the ideal lattice sites. Therefore, when looked upon from the direction of the incident He ions, not only the upper-most atoms, but also the underlying atoms are observed. In this case, the apparent number of atoms at the surface, the surface peak intensity, becomes larger with increasing degree of disorder. The surface peak analysis is useful because it reflects the initial stage of degradation of the metal/semiconductor interface, even when the interfacial degradation is too small to be detected as metal diffusion. Hence the lattice disorder was estimated from the variation of the surface peak intensities related to Ga, As and In. In the analysis of the In surface peak of Mo/In-containing semiconductors, the channeling spectra taken at the backscattering position were used. Because of the limited energy resolution at the grazing position, the Ga and As surface peaks were treated as one broad peak.

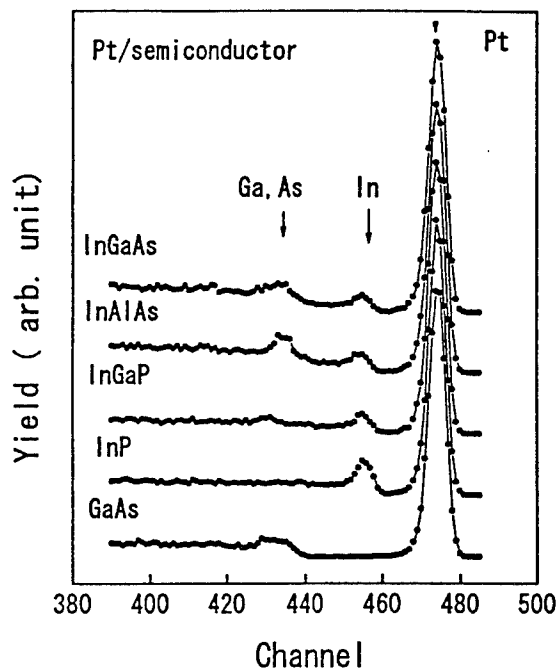


Fig. 2. RBS channeling spectra for as-deposited Pt/semiconductor samples.

Ni/semiconductors

Ni belongs to near-noble transition metals and conventionally used as the first metal in Au, Ge-based ohmic contacts, because of its ability to penetrate thin native oxide at the metal/semiconductor surface, leading to the formation of laterally uniform contacts [2]. Ni atoms were found to diffuse after annealing, even at 150°C as

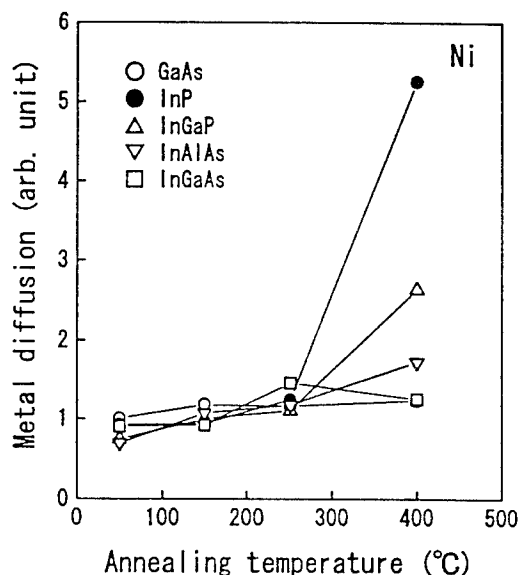


Fig. 3. Diffusion of Ni atoms vs annealing temperature. Magnitude of diffusion was estimated by a parameter defined as the ratio of height to FWHM of metal signal.

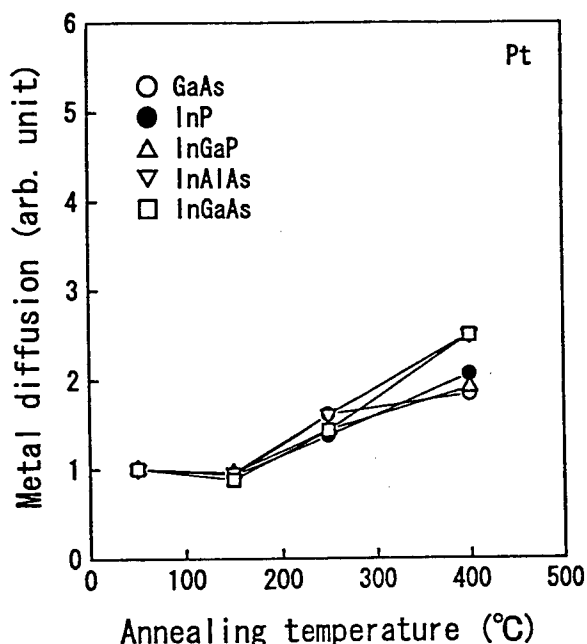


Fig. 4 Diffusion of Pt atoms vs annealing temperature.

shown in Fig. 3. The Ga and As surface peak and the In surface peak also monotonously increased. At higher temperatures, the progress of the Ni diffusion was faster in the order of InP, InGaP, InAlAs, InGaAs, and GaAs. The fast diffusion of Ni atoms in the P-containing materials may be due to the higher vapor pressure of P over In(Ga)P than that of As over In(Al)As. Prominent diffusion of Ni and the segregation of In and P, instead of growth of Ni_xInP ternary phases, was also reported [6]. The interface of Ni/GaAs is considered to be stable compared to those of Ni/In-based materials. This would partially account for the inferior stability of AuGeNi based ohmic electrodes of In-based semiconductor devices.

Pt/semiconductors

The diffusion of Pt atoms was observed in the samples annealed at 250°C as shown in Fig. 4. The initiation of Pt diffusion at higher temperatures than that of Ni diffusion is considered due to Pt-Pt bonds being stronger than Ni-Ni bonds. In the comparison of the magnitude of Pt diffusion in the samples annealed at 400°C, there are differences between the group of InAlAs and InGaAs, and the group of InP, InGaP and GaAs. In thick Pt/GaAs, complete reaction results in the layer sequence of $PtGa/PtAs_2/GaAs$ and leads to self-limiting behavior [7]. In the case of the Pt/InP system [8], the predominant phase was polycrystalline Pt_3InP and Pt_3In at low temperature annealing. The reacted phases proceeded to form In and P richer phases with increasing temperature, resulting in polycrystalline $PtIn_2$, Pt_2In_3 and textured PtP_2/InP . Although the final reaction products at high temperatures

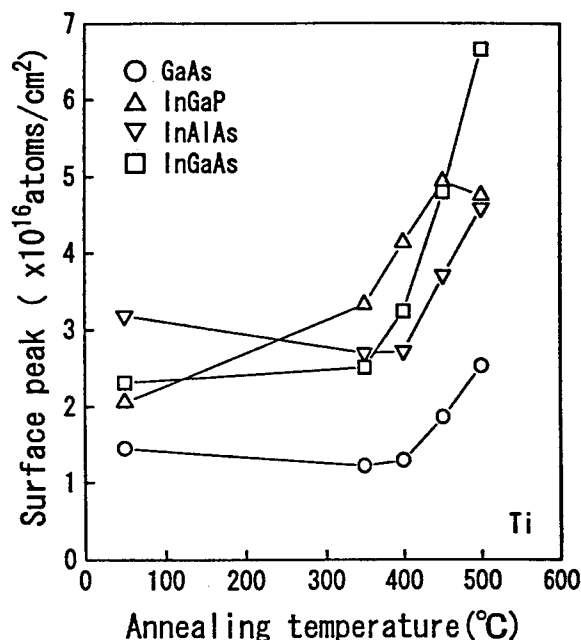


Fig. 5 Variation of surface peak intensity related to Ga and As in Ti/semiconductor samples.

have the same type of phases in both GaAs and InP, the obtained results suggest that the progress of the reaction may be faster in Pt/In- and As-containing semiconductors than in Pt/P-containing semiconductors. These results are important in the application of thin Pt contact layers as the gate contact of HEMTs.

Ti/semiconductors

In Ti/GaAs, TiGa and TiAs are the dominant final products for the solid phase reactions [9]. A limited interfacial reaction between Ti and InP was reported in the Pt/Ti/InP system [10]. Observed diffusion of Ti atoms in this study was small for all semiconductors until the samples were annealed up to 400°C. When annealed at 450°C, Ti diffusion was faster in the order of InP, InGaP, InGaAs, InAlAs and GaAs. Larger differences were observed in the surface peak intensities. The In peak was larger in the order of InGaP, InGaAs, InAlAs and InP. The Ga and As peak was larger in the order of InGaAs, InGaP, InAlAs and GaAs (Fig. 5). Among the observed material interdependence, the only conclusion that can be drawn is that the interface of Ti/GaAs is more stable than those of Ti/In based ternary materials and possibly than Ti/InP. This would account for the inferior stability of the Ti/Pt/Au contacts, including the pad contact, in the InP based HEMTs than in the GaAs based HEMTs.

A comparison of Ti/semiconductor interfaces has been made among GaAs, GaP, InAs, InGaAs and InAlAs which were in contact with Pt/Ti [11]. Ti/semiconductor interfaces were concluded to be more stable when Ga and/or P were present rather than In and As. Their results are not wholly consistent with ours, possibly

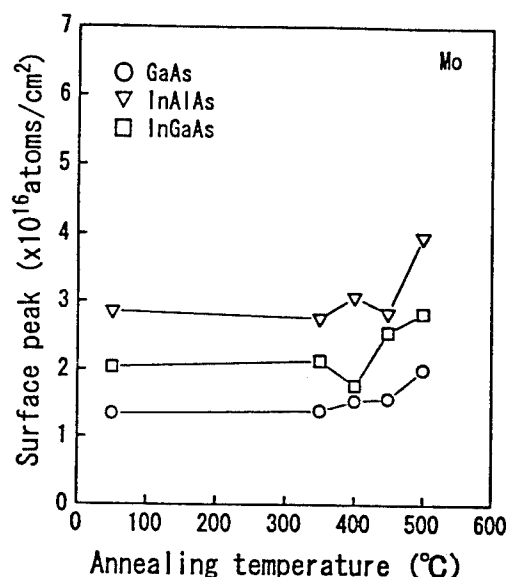


Fig.6 Variation of surface peak intensity related to Ga and As in Mo/semiconductor samples.

because the presence of Pt may affect the Ti/InP interface.

Mo/semiconductors

Mo/semiconductor structures have been found to be the most stable of all semiconductors. The diffusion of Mo atoms was almost negligible in the temperature range under study. The variation of surface peak intensities was also negligibly small for annealing up to 450°C (Fig.6). However an increase of the surface peak intensities was noticed in the samples annealed at 500°C. This result is consistent with the high reliability of Mo based electrodes developed for InP-based HEMTs [12].

Conclusion

In conclusion, the structural degradation of the metal/semiconductor interfaces was successfully observed by RBS. The metal/In based semiconductor interfaces exhibited inferior stability to those of the metal/GaAs interfaces. This explains the fast degradation of InP based HEMTs compared to GaAs based HEMTs.

Acknowledgments

The authors are grateful to M.Azuma, Y.Ikawa and M.Obara for their continuous encouragement.

References

- [1] M.Hafizi and M.J.Delaney, "Reliability of InP-based HBT's and HEMT's: experiments, failure mechanisms, and statistics", Proceedings of 6th Conf. on InP and Related Materials, Santa Barbara, U.S.A., p299 (1994).
- [2] T.Sands, Materials Science and Engineering, "Compound semiconductor contact metallurgy", **B1**, 289 (1989).
- [3] A.Katz, "Indium Phosphide and Related Materials: Processing, Technology, and Devices", chap 9, Artech House, 1992.
- [4] T.Sands, V.G.Keramidas, K.M.Yu, J.Washburn, and K.Krishnan, "A comparative study of phase stability and film morphology in thin-film M/GaAs systems (M=Co, Rh, Ir, Ni, Pd, and Pt), *J.Appl.Phys.* **62**, 2070 (1987).
- [5] L.C.Feldman, J.W.Mayer and S.T.Picraux, *Materials Analysis by Ion Channeling*, Academic Press, Chapter 6, 1982.
- [6] S.E.Mohney and Y.A.Chang, "Interfacial reactions and phase stability in the Ni/InP system", *Mat. Res. Soc. Symp. Proc. Vol.337*, 393, (1994).
- [7] T.Sands, V.G.Keramidas, A.J.Yu, K.M.Yu, R.Gronsky, and J.Washburn, "Ni, Pd, and Pt on GaAs: A comparative study of interfacial structures, compositions, and reacted film morphologies", *J. Mater. Res.* **2**, 262 (1987).
- [8] S.E.Mohney and Y.A.Chang, "Interfacial reactions in Pt/InP contacts", *J.Appl.Phys.* **74**, 4403 (1993).
- [9] K.M.Yu, J.M.Jaklevic and E.E.Haller, "Solid-phase reactions between (100) GaAs and thin-film refractory metals (Ti, Zr, V, Nb, Cr, Mo, W), *Appl. Phys. A44*, 177 (1987).
- [10] A.Katz, B.E.Weir, S.N.G.Chu, P.M.Thomas, M.Soler, T.Boone and W. C. Dautremont-Smith, "Pt/Ti/n-InP nonalloyed ohmic contacts formed by rapid thermal processing", *J.Appl.Phys.* **67**, 3872 (1990).
- [11] W.Savin, B.E.Weir, A.Katz, S.N.G.Chu, S.Nakahara and D.W.Harris, "RBS analysis of intermixing in annealed samples of Pt/Ti/III-V semiconductors", *Mat. Res. Soc. Symp. Proc. vol.181*, p227 1990.
- [12] K.Onda et al., "Highly reliable InAlAs/InGaAs heterojunction FETs fabricated using completely molybdenum-based electrode technology (COMET)", *IEEE MTT-S Digest*, p261, 1994.

Author Index

- Adachi, H. 468
Ae, S. 119, 839
Aggarwal, R.J. 85
Ahopelto, J. 311
Akatsu, Y. 349
Akazaki, T. 404
Ali, S.T. 589
Aller, I. 325
Amano, M. 416
Amemiya, Y. 813
Anan, T. 801
André, J. 464
Anselm, K.A. 532
Aoki, M. 53, 785
Aoyagi, T. 504
Arai, K. 404, 428
Arai, S. 557, 620, 628, 721
Arakawa, Y. 763
Asahi, H. 183
Asai, H. 161
Ashizawa, Y. 136, 416, 861
Auer, U. 424
Azuma, T. 797
- Babić, D.I. 773
Bächtold, W. 397
Bagwell, T. 624
Bahir, G. 577
Beam III, E.A. 640
Bearzi, E. 241
Beccard, R. 126
Beck, P. 624
Benyattou, T. 202
Berg, M. 77
Bergamaschi, C. 397
Bernescut, R. 656
Berthier, P. 520
Bertone, D. 279
Betha, C.G. 713
Betser, Y. 452
Bhat, R. 14
Bhattacharya, P. 357, 448, 476
Binsma, J.J.M. 709
Bischof, W. 77
Bland, S.W. 520
Bliss, D.F. 678
Böhm, G. 737
Bolay, H. 221
Boos, J.B. 381
Bose, D.N. 112, 589
Bouthillette, L.O. 616
Bowers, J.E. 365, 532, 773
Braun, W. 660
Brenan, S. 827
Breuer, U. 132
Bru, C. 202
Bruce, D.M. 612
Bruno, A. 520
Bryant, G.G. 678
- Campbell, J.C. 532
Capasso, F. 770
Capella, R.M. 10
Capik, R.J. 365
Carenco, A. 520
- Carius, R. 132
Cassidy, D.T. 612
Cevallos, N.A. 307
Champion, G. 612
Chan, Y.-J. 408, 412
Chandrasekhar, S. 648
Chang, C.Y. 484
Chang, M.F. 656
Chau, H.-F. 640
Chelakara, R.V. 532
Chen, K.J. 428
Chen, W.-K. 57
Chen, Y.K. 656, 713, 851
Cheng, J.Y. 672
Chenga, Y.M. 307
Chertouk, M. 737
Cho, A.Y. 656, 851
Chuang, Z.M. 484
Chyi, J.-I. 245, 408, 412
Clawson, A. 672, 689
Coldren, L.A. 593
Cuypers, G.P.J.M. 709
- D'Hondt, M. 717
Daleiden, J. 632
Das, M.B. 512
Dauplaise, H.M. 616, 817
David, J.P.R. 299, 536
Davies, J.I. 520
Davis, A. 616, 817
Demeester, P. 717
DenBaars, S.P. 307
Deng, F. 672
Derickson, D. 624
Dhanasekaran, R. 273
Dickmann, J. 77
Dobashi, H. 377
Doguchi, K. 460
Domen, K. 213
Dong, J. 480
Dörnen, A. 221
Drouot, V. 202
Ducroquet, F. 241
Dudley, J.J. 773
Dupuis, R.D. 532
- Ebbinghaus, G. 295
Eberl, K. 480
Egawa, T. 632
Eisele, K. 337
Ekawa, M. 721
El Yumin, S. 612
Elenkrig, B.B. 424
Ellrodt, P. 81, 89, 404, 428
Enoki, T. 770
Faist, J. 105
Faleev, N.N. 851
Fan, L. 10
Ferner, B. 108
Ferry, D.K. 632
Fiedler, F. 593
Floyd, P.D. 85, 555
Fonstad, Jr., C.G. 569, 660
Forchel, A. 41
- Fornari, R. 279
Fornuto, G. 831
Frankowsky, G. 668
Fritzsche, D. 229, 237
Fujibayashi, K. 508
Fujihara, K. 809
Fujihara, A. 337
Fujii, T. 265
Fujii, N. 755
Fujikura, H. 416
Fujita, S. 249
Fujiwara, Y. 257
Fukuchi, F. 797
Fukui, T. 140, 766
Fukuzawa, M. 674
Funemizu, M. 152
Fuoss, P.H. 827
- Gabbe, D. 678
Gan, T.-H. 412
Gau, J.-H. 245
Gendry, M. 420
Gentner, J.-L. 636, 793
Ghirardi, F. 520
Giboney, K.S. 365
Gimmnich, P. 122
Giraudet, L. 520
Göbel, E.O. 122
Goldstein, L. 636
Gonda, S. 183
Gorelenok, A.T. 105
Gossard, A.C. 759
Goto, K. 275
Gotoda, M. 65
Grambow, P. 221
Grann, E.D. 108
Guillot, G. 202, 241
Gutierrez-Aitken, A.L. 357, 448, 476
Gyuro, I. 569
- Habibi, S. 21
Haddad, G.I. 357, 448
Haga, K. 609
Haga, T. 664
Haller, E.E. 678
Hamakawa, A. 551
Hamm, R.A. 851
Hammersberg, J. 315
Hanajiri, T. 585, 609
Hanatani, S. 369
Hanebuchi, M. 191
Hangleiter, A. 221, 831
Hanson, C.M. 689
Hara, D. 528
Harada, J. 229, 237
Hardtdegen, H. 132
Härle, V. 221
Harlow, M.J. 329
Hart, L. 536
Hartnagel, H.L. 325
Hase, N. 115
Hasegawa, H. 101, 436, 573, 693, 755, 766, 813
Hashimoto, J.-I. 472

Author Index

Hashizume, T.	573, 813	Iwao, T.	249	Kohl, A.	857
Hasumi, H.	839	Iwasaki, T.	49, 148	Kohn, E.	393
Hayafuji, N.	265	Iwata, K.	183	Koinuma, H.	233
Haywood, S.K.	536	Izumiya, S.	377	Kokubun, Y.	152
He, L.	693	Izumiya, T.	152	Konagai, M.	797
Heedt, C.	424	Jarry, Ph.	636	Kondo, M.	213
Heide, T.	464	Jimbo, T.	480	Kondo, S.	61
Heime, K.	857	Jin-Phillip, N.Y.	295	Koßlowski, S.	77
Heiß, H.	737	John, E.	512	Kouichi, W.	61
Henle, B.	393	Jürgensen, H.	126	Koyama, F.	373
Heun, S.	269, 825	Kadoiwa, K.	265	Kozen, A.	766
Higuchi, K.	741	Kaibe, H.T.	601	Kraus, S.	737
Hill, G.	536	Kainosho, K.	37	Kräutle, H.	668
Hiramatsu, K.	115	Kaiser, R.	353	Krawczyk, S.K.	241
Hiramoto, K.	843	Kamanin, A.V.	105	Kretzer, U.	33
Hirano, R.	93, 97	Kamei, H.	206	Kruppa, W.	381
Hirata, D.	581, 597	Kamijoh, T.	26, 777	Kudo, M.	741
Hirt, G.	33	Kamiya, T.	492	Kuindersma, P.I.	709
Hoffmann, B.	33	Kamiyama, S.	468	Kulkova, E.	444
Hollfelder, M.	132	Karlsson, A.	464	Kumamoto, T.	229
Holzbrecher, H.	132	Kasai, K.	130	Kumar, A.	589
Hong, K.	144, 241, 432	Kashima, Y.	496	Kunii, T.	26
Hongbo, S.	155	Kashima, H.	169	Künzel, H.	393
Hopkinson, M.	299, 536	Kashiwa, S.	488	Kuo, J.M.	656
Hori, Y.	809	Kasukawa, A.	18, 57	Kuphal, E.	668
Horita, M.	540	Kasyou, H.	721	Kurakake, H.	22
Hosoi, S.	416	Kato, K.	349	Kurihashi, S.	557
Hosomi, K.	169, 644	Katoda, T.	585, 609	Kurishima, K.	652
Hotta, M.	557	Katoh, T.	45, 191	Kurita, Y.	373
Hsueh, G.C.	307	Katoh, Y.	26	Kurita, H.	140, 516
Hu, E.L.	365, 532, 773	Katsuyama, T.	472	Kurtenbach, A.	295
Humphrey, D.A.	851	Kawaguchi, Y.	183	Kushibe, M.	152
Humphrey, D.	656	Kawano, T.	664	Kusumoto, S.	496
Hunziker, W.	717	Kellert, F.	624	Kusunoki, T.	45
Hutchinson, A.L.	770	Khoo, E.A.	299	Kuze, N.	440
Hwang, W.-Y.	512	Khrenov, G.	444	Kuzuhara, M.	809
Hwang, D.M.	672	Kidoguchi, I.	468	Labrune, P.	793
Ichii, A.	440	Kieseling, F.	660	Lakshmi, B.	612
Iga, K.	373	Kikkawa, T.	130	Landgren, G.	345
Iguchi, Y.	49, 148	Kikuchi, A.	29, 805	LaPierre, R.R.	175
Ikeda, N.	456	Kikugawa, T.	210	Lau, S.S.	672
Ikeda, E.	516	Kikuno, E.	628	Lee, T.P.	14
Ikoma, N.	705	Kimura, S.	89	Lee, T.-L.	179
Ikuta, K.	81	Kimura, T.	333, 721	Lee, L.	393
Ils, P.	660	Kishino, K.	29, 805	Legros, E.	520
Imai, Y.	89	Kisker, D.W.	827	Lengeling, G.	126
Imamura, K.	847	Kita, T.	257	Lenk, G.	668
Inomoto, Y.	839	Kitamura, M.	725, 763	Leonard, D.	759
Inoue, M.	377	Kitano, H.	369	Letarte, X.	385, 420
Inushima, T.	187	Kito, M.	508, 701	Letartre, X.	385
Iseler, G.	678	Kjebon, O.	345	Limmer, W.	221
Ishihara, K.	551	Klein, W.	737	Lin, T.-C.	601
Ishihara, O.	745	Klepser, B.-U.H.	389, 397	Lin, H.-H.	179
Ishii, Y.	81	Klingelhöfer, C.	241	Lin, W.	484
Ishino, M.	508, 701	Knauer, A.	287	Lin, J.	851
Ishiyama, O.	233	Knauf, J.	126	Lipsanen, H.	311
Islam, M.R.	532	Ko, S.C.	484	Liu, W.	640
Iso, A.	187	Kobayashi, N.	225	Liu, J.-S.	179
Isu, T.	65	Kobayashi, F.	283	Lizhong, H.	155
Itaya, K.	593	Kobayashi, Y.	225	Loh, T.	373
Ito, H.	81	Kobayashi, T.	652	Lorberth, J.	122
Iwabuchi, T.	440	Kodama, S.	436	Lorenzo, J.P.	616
Iwai, N.	18, 57	Kohiro, K.	93	Lorenzo, J.P.	817
Iwamura, H.	161			Lothian, J.	656

Author Index

Lourdudoss, S.	345, 464	Mozume, T.	169, 644	Ohtsuka, N.	303
Lunardi, L.M.	648	Mukai, K.	303	Ohyama, T.	249
Lüth, H.	132	Müller, G.	33	Oishi, E.	733
Madden, C.	73	Müller, J.	569	Oka, T.	644
Maeda, T.	233	Munakata, T.	496	Okada, T.	175
Maemoto, T.	377	Murakami, T.	528	Okamoto, M.	315
Maeyama, S.	269, 825	Muramatsu, S.	440	Oku, S.	561
Maezawa, K.	428	Murata, M.	460, 472	Okumura, T.	601
Makita, K.	341	Murtaza, S.S.	532	Okuno, Y.	53, 785
Margalit, N.M.	773	Muto, S.	165, 253, 847	Omura, E.	504
Martin, E.A.	616, 817	Nagai, H.	210	Onda, K.	809
Masuda, H.	644	Nagase, A.	187	Onuma, K.	835
Matoba, A.	496	Nagase, K.	440	Ooya, S.	187
Matsuda, M.	547	Nagy, A.	73	Orth, A.	569
Matsuda, T.	57	Nakagawa, T.	217	Oshim, M.	825
Matsuda, K.	581	Nakahara, M.	628	Oshima, M.	269
Matsuhata, H.	206	Nakajima, K.	45, 101	Oshinowo, J.	660, 763
Matsui, Y.	26, 508, 701	Nakamura, H.	198, 369	Otsubo, T.	500
Matsumoto, K.	480	Nakamura, M.	89, 140	Otsuka, N.	508, 701
Matsumoto, Y.	585, 609	Nakamura, T.	119, 839	Otsuka, E.	249
Matsumoto, S.	821	Nakano, Y.	551	Ottenwälder, D.	831
Matsuoka, Y.	198, 361, 652	Nakao, M.	697	Ou, J.	157
Matsuoka, T.	183	Nakata, H.	249	Ouchi, K.	169, 644
Matsushima, Y.	524, 540	Nakata, Y.	165, 253, 751	Oyanagi, H.	206
Mause, K.	668	Nakayama, M.	528	Ozaki, M.	440
Mayer, H.P.	10	Nakayama, H.	257	Pabla, A.S.	299
Mayer, T.S.	512	Nakayama, T.	733	Pal, D.	112
Medeiros-Ribeiro, G.	759	Narozny, P.	77	Palmstrom, C.	672
Merkulov, A.V.	105	Ninomiya, T.	456	Pan, J.-W.	245
Merz, J.L.	593	Nishi, K.	759	Parent, J.-C.	793
Mesquida KÅsters, A.	857	Nishida, C.	601	Park, M.-H.	672
Mihashi, Y.	275, 333	Nishihara, T.	233	Patrick, W.	389, 397
Miller, B.I.	365	Nishino, T.	257	Pavlidis, D.	144, 241, 432, 648
Miller, D.L.	512	Nishioka, M.	763	Peeters, R.	709
Miner, C.J.	773	Nishizawa, H.	460	Peng, L.-H.	555
Mirin, R.P.	759	Nissim, Y.I.	565	Petroff, P.M.	307, 759
Mirin, R.	741	Nitta, J.	404	Phillipp, F.	295
Mishima, T.	7	Niu, G.F.	401	Pierce, M.	644
Mishra, U.K.	265, 745	Noda, T.	136, 416, 861	Pinquier, A.	793
Mitsui, S.	275, 333	Noguchi, Y.	61	Pittroff, W.	287
Miura, T.	528	Noll, F.	295	Potemski, M.	315
Miura, Y.	440	Nomura, I.	29, 805	Prost, W.	424, 729
Miya, S.	500	Noto, N.	261	Protzmann, H.	122
Miyagi, K.	373	Notomi, M.	315	Qhalid Fareed, R.S.	273
Miyamoto, T.	809	Nötzel, R.	766	Raggio, J.	73
Miyamoto, H.	733	Nozaki, C.	136, 861	Ralston, J.D.	632
Miyazaki, S.	601	Nuban, M.F.	241	Ramseyer, G.	616
Miyazaki, T.	369, 605	Nunoshita, M.	65	Rapp, S.	221
Miyazawa, T.	283	Obukhova, E.L.	105	Reaves, C.M.	307
Mizuki, E.	809	Ochiai, K.	561	Rees, G.J.	299
Moerman, I.	717	Ochimizu, H.	130	Reithmajer, J.P.	569
Mokina, I.A.	105	Oda, O.	37, 93	Ren, F.	656
Molnar, B.	682	Oe, K.	161	Ressel, P.	668
Mondry, M.J.	593	Ogawa, Y.	777	Reuter, R.	424
Mori, H.	283	Ogura, T.	183	Reyher, G.	221
Mori, M.	741	Oh, J.-H.	797	Ritter, D.	452
Mori, K.	781	Ohki, A.	183	Robbins, V.	73
Mori, T.	847	Ohkouchi, S.	705	Robinson, B.J.	175, 202
Moriglioni, M.	41	Ohkubo, M.	456	Rodriguez Messmer, E.	345
Morita, K.	191	Ohmori, M.	516	Rohdin, H.	73
Morita, T.	805	Ohnaka, K.	468	Rojo-Romeo, P.	385
Morito, K.	547	Ohta, M.	37	Ruan, G.	401
Moss, R.H.	329	Ohtani, F.	233		

Author Index

- Sagawa, M. 843
Sahara, R.T. 547
Saito, K. 721
Saitoh, T. 101
Sakaguchi, H. 195
Sakai, H. 508
Sakamoto, Y. 597, 605
Sakata, H. 524
Sakata, Y. 839
Sakuma, M. 609
Salzman, J. 577
Samelis, A. 648
Samoto, N. 733
Sano, K. 217
Sano, E. 361
Sasaki, A. 136, 416, 861
Sasaki, H. 609, 745
Sasaki, T. 725
Sato, K. 835
Satoh, K. 249
Sawaki, N. 115
Sayah, A. 565
Scavennec, A. 520
Schefer, M. 397
Schilling, O. 660
Schmitz, D. 126
Scholz, F. 221, 831
Sciortino, Jr., P.F. 713
Seeger, J. 73
Sejalon, F. 432, 648
Sergent, A.M. 713
Serizawa, N. 557
Shenoy, K.V. 85
Shibasaki, I. 440
Shibata, Y. 561
Shieh, J.-L. 245, 408, 412
Shimizu, M. 597
Shimomura, H. 801
Shimose, Y. 210
Shin, K.-C. 557, 620
Shinohara, M. 233
Shinone, K. 500
Shioda, R. 206
Shiota, M. 597
Shirafuji, J. 581, 597, 605
Shiraishi, T. 187
Shirakashi, J.-I. 797
Shishikura, M. 369
Shiyong, L. 155
Shmidt, N.M. 105
Simes, R. 10
Simmons, J.G. 385, 420
Sirtori, C. 770
Sivco, D. 656, 851
Smith, P. 68
Soda, K. 191
Soda, H. 22, 547
Sommer, V. 857
Songyan, C. 155
Sonoda, T. 265
Sopanen, M. 311
Spaziani, S.M. 616, 817
Spika, Z. 122
Spill, B. 122
Spurdens, P.C. 329
Sputz, S.K. 713
Srinivasan, A. 532
Stadler, B.J. 616
Stavrinou, P.N. 536
Stephenson, G.B. 827
Stolz, W. 122
Strähle, S. 393
Streetman, B.G. 532
Streubel, K. 464, 773
Strusny, H. 668
Su, C.-Y. 73
Sugano, T. 585, 609
Sugimoto, H. 65
Sugino, T. 581, 597, 605
Sugiura, T. 115
Sugiura, H. 315, 321, 697
Sugiyama, M. 269, 825
Sugiyama, Y. 217
Sugou, S. 781, 801
Sumino, J. 183
Suzuki, S. 436
Suzuki, M. 53
Suzuki, T. 45, 609
Tabuchi, M. 229
Tabushi, M. 237
Tada, K. 551
Taguchi, K. 341
Takahashi, N. 597
Takahashi, K. 797
Takahasi, I. 229, 237
Takahasi, H. 528
Takamiya, S. 265, 275, 333
Takamoto, T. 516
Takano, H. 496
Takaoka, K. 152
Takatsu, M. 847
Takayanagi, H. 404
Takeda, Y. 237, 249
Takeda, T. 229
Takemi, M. 275, 333
Takemoto, A. 275, 504
Takemoto, K. 528
Takeshita, H. 492
Takeuchi, T. 291, 341
Takeuchi, R. 835
Takiguchi, T. 504
Takizawa, T. 628
Tamamura, T. 315, 766
Tamanuki, T. 725
Tamura, M. 557, 620, 705
Tamura, S. 557, 620
Tan, I.-H. 365, 532
Tanahashi, T. 213
Tanaka, S. 198, 369
Tanaka, H. 130, 540
Tanaka, A. 480
Tanaka, J. 821
Tanbun-Ek, T. 713
Tani, T. 195
Taniguchi, A. 500
Taniwatari, T. 664
Tanoue, T. 644
Tardy, J. 385, 420
Tate, A. 656, 851
Tegude, F.J. 424, 729
Temmyo, J. 766
Terakado, T. 119, 839
Terano, A. 644
Thijs, P.J.A. 709
Thirumavalavan, M. 41
Thompson, D. 385
Thompson, D.A. 175, 202, 420
Tokutome, K. 781
Tomozawa, H. 436
Torikai, T. 119, 839
Totsuka, M. 821
Toyonaka, T. 843
Tränkle, G. 737
Tsang, W.T. 173, 789
Tsen, K.T. 108
Tsuchiya, M. 492
Tsuchiya, T. 195, 664, 785
Tsuji, M. 341
Tu, Y.K. 484
Tweet, D.J. 206
Ubukata, A. 721
Uchida, M. 97
Uchida, T. 22
Uchida, K. 261
Uchiyama, S. 488
Udagawa, T. 835
Ueda, O. 165, 253
Uekusa, S. 217
Uji, T. 119
Umeda, Y. 89
Umeno, M. 480
Uomi, K. 785
Usuda, M. 835
Utaka, K. 524
Vaccaro, K. 616, 817
van Dongen, T. 709
van Gestel, P. 709
Van Daele, P. 717
Vandrerbauwhede, W. 717
Vasiliadou, E. 221
Veinger, D. 577
Viktorovitch, P. 385, 420
Vogel, K. 287, 668
Vollrath, G. 632
Wada, H. 777
Wakita, K. 544
Wakita, A. 73
Walker, J.D. 173
Wang, M.C. 484
Wang, C.Y. 484
Wang, K.H. 660
Wang, L.C. 672
Washima, M. 195
Watanabe, H. 504
Watanabe, Y. 269
Weatherly, G.C. 175
Weber, E.R. 261
Weber, J. 569
Wecht, K.W. 713
Weigel, K. 857
Weimann, G. 737
Weinberg, W.H. 307
Weiner, J.S. 656
Weiss, D. 221

Author Index

Weman, H.	315	Yamaguchi, T.	551	Yoon, H.	476
Wesch, W.	668	Yamaguchi, Y.	500	Yoshida, N.	265, 745
Weyers, M.	287	Yamahata, S.	361, 652	Yoshida, I.	472
Wild, M.	831	Yamamoto, Y.	265	Yoshida, J.	29
Wisk, P.	713	Yamamoto, M.	428	Yoshimoto, M.	233
Woltech, A.	33	Yamamura, I.	581	Yoshimoto, N.	61
Wolter, P.	287	Yamanaka, T.	544	Yu, P.Y.	261
Woodhead, J.	299	Yamanaka, N.	18, 57	Yudong, L.	155
Wu, Y.	401	Yamashita, I.	3		
Wu, C.-S.	412	Yamazaki, S.	22, 291, 337	Zach, F.X.	678
Wu, N.-J.	813	Yang, K.	357	Zah, C.E.	14
Würfl, J.	668	Yang, K.	448	Zappettini, A.	41
		Yang, M.-T. 4	08	Zeimer, U.	287
Xiong, Y.-M.	101	Yang, J.	612	Zemke, D.	33
Xu, D.	737	Yang, B.X.	693	Zhang, X.	357, 448
		Yano, M.	377	Zhu, Y.	597
Yabuuchi, Y.	701	Yano, H.	460	Zielinski, E.	569
Yaguchi, T.	187	Yokouchi, N.	18, 57	Zimmerman, G.	122
Yajima, K.	745	Yokoyama, K.	544	Zuccalli, G.	41
Yamabayashi, N.	49, 148	Yokoyama, N.	847		
Yamada, A.	500	Yoneyama, M.	361		
Yamada, N.	229, 237, 674	Yoneyama, S.	148		